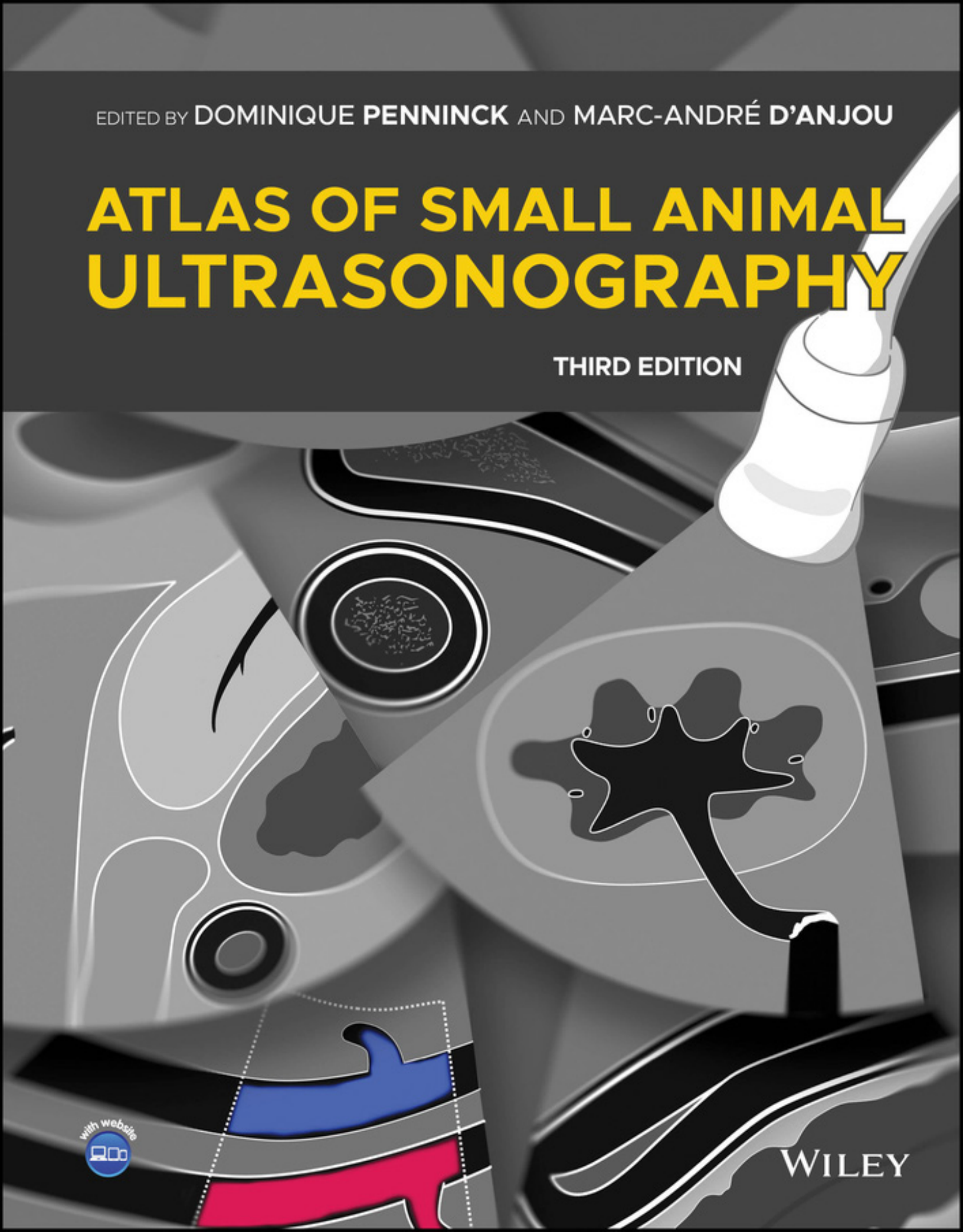
EDITED BY DOMINIQUE **PENNINCK** AND MARC-ANDRÉ **D'ANJOU**

ATLAS OF SMALL ANIMAL ULTRASONOGRAPHY

THIRD EDITION



WILEY

Atlas of Small Animal Ultrasonography

Atlas of Small Animal Ultrasonography

THIRD EDITION

Edited by

Dominique Penninck

Department of Clinical Sciences, Cummings School of Veterinary Medicine
Cummings School of Veterinary Medicine, Tufts University
North Grafton, MA
USA

Marc-André d'Anjou

Animages
Brossard, Québec
Canada

WILEY

Vet-ebooks.com

Copyright © 2025 by John Wiley & Sons, Inc. All rights reserved, including rights for text and data mining and training of artificial technologies or similar technologies.

Published by John Wiley & Sons, Inc., Hoboken, New Jersey.

Published simultaneously in Canada.

No part of this publication may be reproduced, stored in a retrieval system, or transmitted in any form or by any means, electronic, mechanical, photocopying, recording, scanning, or otherwise, except as permitted under Section 107 or 108 of the 1976 United States Copyright Act, without either the prior written permission of the Publisher, or authorization through payment of the appropriate per-copy fee to the Copyright Clearance Center, Inc., 222 Rosewood Drive, Danvers, MA 01923, (978) 750-8400, fax (978) 750-4470, or on the web at www.copyright.com. Requests to the Publisher for permission should be addressed to the Permissions Department, John Wiley & Sons, Inc., 111 River Street, Hoboken, NJ 07030, (201) 748-6011, fax (201) 748-6008, or online at http://www.wiley.com/go/permission.

The manufacturer's authorized representative according to the EU General Product Safety Regulation is Wiley-VCH GmbH, Boschstr. 12, 69469 Weinheim, Germany, e-mail: Product_Safety@wiley.com.

Trademarks: Wiley and the Wiley logo are trademarks or registered trademarks of John Wiley & Sons, Inc. and/or its affiliates in the United States and other countries and may not be used without written permission. All other trademarks are the property of their respective owners. John Wiley & Sons, Inc. is not associated with any product or vendor mentioned in this book.

Limit of Liability/Disclaimer of Warranty: While the publisher and author have used their best efforts in preparing this book, they make no representations or warranties with respect to the accuracy or completeness of the contents of this book and specifically disclaim any implied warranties of merchantability or fitness for a particular purpose. No warranty may be created or extended by sales representatives or written sales materials. The advice and strategies contained herein may not be suitable for your situation. You should consult with a professional where appropriate. Further, readers should be aware that websites listed in this work may have changed or disappeared between when this work was written and when it is read. Neither the publisher nor authors shall be liable for any loss of profit or any other commercial damages, including but not limited to special, incidental, consequential, or other damages.

For general information on our other products and services or for technical support, please contact our Customer Care Department within the United States at (800) 762-2974, outside the United States at (317) 572-3993 or fax (317) 572-4002.

Wiley also publishes its books in a variety of electronic formats. Some content that appears in print may not be available in electronic formats. For more information about Wiley products, visit our web site at www.wiley.com.

Library of Congress Cataloging-in-Publication Data applied for

Hardback ISBN: 9781119863267

Cover Design: Wiley
Cover Image: Courtesy of Marc-André d'Anjou

Set in 10/12.5pt Palatino LT Std by Straive, Pondicherry, India

Vet-ebooks.com

Dedication

To all the pets that kept me sane while glued to the screen during this work.

To my family and friends who stay by my side during difficult times. They rock.

To all the students, residents, and colleagues past, present, and future, for their inspiration.

In memory of my parents, my sisters, and Vincent.

Dominique Penninck

To Annabelle, the roots of my tree.

To Olivier and Héloïse for their inspiring spirit. I am a proud dad.

To all students, interns, residents, and practitioners that show passion for what they do and for whom they want to become.

In memory of Charles and Leo.

Marc-André d'Anjou

Vet-ebooks.com

Vet-ebooks.com

Contents

List of Contributors ix

Preface xi

Accompanying Videos xiii

1. **Practical Physical Concepts and Artifacts** 1
   Marc-André d'Anjou and Dominique Penninck

2. **Point of Care Ultrasound: Abdomen, Pleural Space, Lung and Cardiovascular Applications** 21
   Søren Boysen

3. **Eye and Orbit** 65
   Stefano Pizzirani and Dominique Penninck

4. **Neck** 109
   Julien Fages and Dominique Penninck

5. **Thorax** 139
   Silke Hecht, Gabriela Seiler, and Dominique Penninck

6. **Heart** 173
   Jonathan Lichtenberger, Shari Raheb, and Hugues Gaillot

7. **Hepatobiliary System** 239
   Marc-André d'Anjou, Dominique Penninck, and Heather Spain

8. **Spleen** 287
   Mathieu Harel and Wilfried Mai

9. **Gastrointestinal Tract** 311
   Dominique Penninck, Marc-André d'Anjou, and Heather Spain

10. **Pancreas** 371
    Dominique Penninck, Marc-André d'Anjou, and Mylène Auger

Vet-ebooks.com

11. Urinary Tract 397
Dominique Penninck, Marc-André d'Anjou, James Sutherland-Smith, Emmanuelle Butty, and Marilyn Dunn

12. Adrenal Glands 463
Marc-André d'Anjou, Dominique Penninck, and Pascaline Pey

13. Female Reproductive Tract 481
Delphine Rault and Silke Hecht

14. Male Reproductive Tract 511
Silke Hecht and Julie De Lasalle

15. Abdominal Cavity and Lymph Nodes 547
Marc-André d'Anjou and Éric Norman Carmel

16. Abdominal Vessels 583
Marc-André d'Anjou, Swan Specchi, and Chick Weisse

17. Musculoskeletal System and Peripheral Nerves 611
Marc-André d'Anjou and Laurent Blond

Index 673

Vet-ebooks.com

List of Contributors

Mylène Auger
Animages
Brossard, Québec
Canada

Laurent Blond
Centre Hospitalier Vétérinaire Languedocia
Montpellier
France

Søren Boysen
Department of Veterinary Clinical and Diagnostic Sciences
Faculty of Veterinary Medicine
University of Calgary
Calgary, Alberta
Canada

Emmanuelle Butty
Department of Clinical Sciences
Cummings School of Veterinary Medicine
Tufts University
North Grafton, MA
USA

Éric Norman Carmel
Animages
Brossard, Québec
Canada

Marc-André d'Anjou
Animages
Brossard, Québec
Canada

Marilyn Dunn
Interventional Medicine
Faculté de médecine vétérinaire
Université de Montréal
Saint-Hyacinthe, Québec
Canada

Julien Fages
CENTREDMVET
Montréal, Québec
Canada

Hugues Gaillot
ADVETIA Centre Hospitalier Vétérinaire
Vélizy-Villacoublay
France

Mathieu Harel
SONHAR
Veterinary Diagnostic Imaging
Ecully
France

Silke Hecht
Department of Small Animal Clinical Sciences
College of Veterinary Medicine
University of Tennessee
Knoxville, TN
USA

Julie De Lasalle
Animages
Brossard, Québec
Canada

Jonathan Lichtenberger
Pacific Coast Veterinary Cardiology
Victoria, British Columbia
Canada

Wilfried Mai
School of Veterinary Medicine
Section of Radiology
University of Pennsylvania
Philadelphia, PA
USA

Vet-ebooks.com

Dominique Penninck
Department of Clinical Sciences
Cummings School of Veterinary Medicine
Tufts University
North Grafton, MA
USA

Pascaline Pey
IMPCOM-MEDICAL
Bologna
Italy
and
Antech Imaging Services
Irvine, CA
USA

Stefano Pizzirani
Department of Clinical Sciences
Cummings School of Veterinary Medicine
Tufts University
North Grafton, MA
USA

Shari Raheb
Department of Clinical Studies
Ontario Veterinary College
University of Guelph
Guelph, Ontario
Canada

Delphine Rault
Azurvet Referral Center
Saint Laurent du Var
France

Gabriela Seiler
Department of Molecular Biomedical Sciences
College of Veterinary Medicine
NC State University
Raleigh, NC
USA

Heather Spain
Veritas Veterinary Partners
San Rafael, CA
USA

Swan Specchi
Antech Imaging Services
Fountain Valley, CA
USA
and
AniCura Ospedale Veterinario I Portoni Rossi
Zola Predosa
Italy

James Sutherland-Smith
VetCT
Newton, MA
USA

Chick Weisse
Animal Medical Center
New York City, NY
USA

Vet-ebooks.com

Preface

Advanced imaging modalities keep evolving and diagnostic ultrasound adapts its place in the clinical diagnostic approach. From initial investigation tool addressing specific clinical questions with a point-of-care approach, to complementary tool assisting interventional procedures, ultrasonography has exponentially grown.

For these reasons, we modified the previous Atlas contents to include a chapter on point-of-care ultrasound, a chapter solely dedicated to abdominal vascular studies and added updated information on ultrasound-guided interventional procedures, where it best applies. This edition has a total of 17 chapters and a companion website complements the textbook with numerous annotated video clips. Beyond these changes, new clinical cases with high-quality images were added to reflect what are commonly and less commonly encountered disorders, along with recently cited literature.

Our group of collaborators grew to embrace the larger community of sonographers.

That said, we warmly acknowledge and thank the contributors of the past editions who participated in setting the foundation of this book. As for the past edition, we solicited your comments and suggestions, and incorporated most of them in this third edition.

Supporting annotated video clips referred to in the Atlas can be found on the website *SmallAnimal Ultrasonography.com*. This resourceful website contains supplementary educative material that complements the Atlas and goes beyond.

Cordially on the same wavelength,

Dominique Penninck and Marc-André d'Anjou

Vet-ebooks.com

Vet-ebooks.com

Accompanying Videos

Some concepts are better explained using movies and this is particularly true for ultrasound. We therefore offer a collection of videos for each chapter, each with annotations and some with voice over, covering normal sonographic anatomy and features of common diseases. These video clips can be found in our website www.SmallAnimalUltrasonography.com, under ***The Book/Atlas videos*** section, using the password: **gbh3972pxe**.

To expand your knowledge on common and less common diseases, you can subscribe to a larger collection of videos (260+) under ***Video Memberships*** (sign-up details online).

Chapter 1 – Practical physical concepts and artifacts

- Image formation and other principles
- Propagation of US waves and interaction with tissues
- US beam and spatial resolution
- Gain, TGC and other manual adjustments
- Mirror image artifact
- Shadowing artifact
- Enhancement artifact
- Reverberation artifact
- Refraction artifact
- Speed error and range ambiguity artifacts
- Twinkle artifact

Chapter 2 – Point of care US

- Lung sliding
- B-lines that occur secondary to increased lung density
- Lung point
- Abnormal curtain signs
- Air and fluid bronchograms
- Subxiphoid view of the heart and active cardiac compressions during cardiopulmonary resuscitation in a cat.

Chapter 3 – Eye and orbit

- Normal eye anatomy and scanning
- Asteroid hyalosis
- Cataracts
- Retinal detachment
- Lens luxation
- Lens extrusion
- Intra-ocular neoplasia
- Retrobulbar foreign body

Chapter 4 – Neck

- Normal neck anatomy and scanning
- Thyroid carcinoma
- Parathyroid nodule
- Lymphadenopathy
- Neck abscess and foreign body
- Neck abscess
- Salivary sialocele

Chapter 5 – Thorax

- Normal lung interface
- Thoracic wall mass
- Pleural effusion
- Pulmonary mass
- Mediastinal mass
- Branchial cyst
- Diaphragmatic hernia

Chapter 6 – Heart

- Normal short and long axes of the heart (dog)
- Normal short and long axes of the heart (cat)
- Chronic degenerative valvular disease
- Hypertrophic cardiomyopathy in a cat
- Dilated cardiomyopathy in a dog
- Pulmonary hypertension/cor pulmonale in a dog
- Idiopathic pericardial effusion and tamponade in a dog

Vet-ebooks.com

- Cardiac tumor
- Patent ductus arteriosus in a dog
- Pulmonic stenosis in a dog
- Subaortic stenosis in a dog
- Ventricular septal defect in a cat

Chapter 7 – Hepatobiliary

- Normal liver and biliary system
- Lipidosis
- Steroid-induced and other vacuolar hepatopathies
- Nodular hyperplasia
- Chronic active hepatitis
- Cholangitis /cholangiohepatitis in cats
- Cirrhosis
- Hepatocellular carcinoma
- Hepatic metastases
- Hepatic lymphoma
- Cystadenoma
- Gallbladder mucocele
- Extrahepatic biliary obstruction
- Gallbladder sludge
- Cholelithiasis

Chapter 8 – Spleen

- Normal spleen anatomy and scanning
- Myelolipomas
- Splenic lymphoma
- Nodular hyperplasia and extramedullary hematopoiesis
- Hemangiosarcoma and peritoneal effusion
- Splenic torsion
- Splenic venous thrombus and infarcts

Chapter 9 – Gastrointestinal tract

- Normal GI anatomy and scanning
- Intussusception
- Foreign bodies
- Enteritis
- Lymphangiectasia
- Ulceration
- Lymphoma
- Carcinoma
- Mesenchymal tumor

Chapter 10 – Pancreas

- Normal pancreas
- Pancreatitis in dogs
- Pancreatitis in cats
- Pseudocyst
- Necrotizing pancreatitis in dogs
- Pancreatic carcinoma
- Insulinoma

Chapter 11 – Urinary tract

- Normal kidneys
- Chronic interstitial nephritis
- Acute nephritis
- Pyelonephritis
- Renal lymphoma
- Renal primary neoplasia
- Polycystic renal disease
- Perinephric pseudocyst
- Obstructive nephrolithiasis and hydronephrosis
- Ectopic ureters
- Normal bladder and urethra
- Cystitis
- Polypoid cystitis
- Calculi
- Blood clot
- Ureteral jet
- Bladder tumors

Chapter 12 – Adrenal glands

- Normal adrenal glands in a dog
- Normal adrenal glands in a cat
- Adrenal hyperplasia with PDH in dogs
- Adrenal adenoma and adenocarcinoma in dogs
- Adrenal pheochromocytoma in a dog

Chapter 13 – Repro female

- Normal ovaries and uterus
- Normal pregnancy: different stages
- Pyometra
- Cystic endometrial hyperplasia

Chapter 14 – Repro male

- Scanning of the normal male reproductive tract in a dog
- Benign Prostatic Hyperplasia
- Prostatic tumor
- Prostatic abscess
- Testicular tumor

Chapter 15 – Abdominal cavity and lymph nodes

- Normal abdominal wall, cavity, fat and lymph nodes
- Peritoneal effusions
- Mesenteric mass
- Peritonitis
- Carcinomatosis
- Lymphadenopathy
- Abdominal wall and umbilical hernia

Vet-ebooks.com

Chapter 16 – Abdominal vasculature

- Normal portal system
- Normal abdominal major vasculature
- Portosystemic shunts
- Vascular thrombosis

Chapter 17 – Musculoskeletal system

- Normal shoulder: Scanning technique & Anatomy (dog)
- Normal common calcaneal tendon
- Bicipital tenosynovitis
- Supraspinatus tendinopathy
- Common calcaneal tendinopathy
- Gracilis myopathy in a dog
- Osteomyelitis
- Joint neoplasia
- Supraspinatous/infraspinatous abscess in a dog
- Peripheral nerve sheath tumor
- Vertebral mass invading the spinal canal

Vet-ebooks.com

Vet-ebooks.com

CHAPTER ONE

Practical Physical Concepts and Artifacts

Marc-André d'Anjou[1] and Dominique Penninck[2]

[1]*Animages, Brossard, Québec, Canada*
[2]*Department of Clinical Sciences, Cummings School of Veterinary Medicine, Tufts University, North Grafton, MA, USA*

Fundamentals

Sound is a series of vibrations transmitted through an elastic solid, a liquid, or a gas. Sound waves have variable wavelengths and amplitudes, with a frequency defined as being the number of cycles repeated over a given time interval. A high frequency sound therefore has a shorter wavelength and more cycles per second than a low frequency sound. The human ear can perceive sounds in the range of 20–20,000 cycles per second or up to 20 kHz. Beyond this range, it is called "ultrasound." Ultrasound frequencies used in medical imaging generally vary between 3 and 12 MHz, or 3–12 million cycles per second, which is well beyond what the human ear can perceive.

Electronic linear probes are equipped with a row of **piezoelectric crystals** whose alignment varies from flat (or linear) to convex. The material contained in each one is deformed when it receives an electrical charge and emits a vibration: this is the initial ultrasound pulsation. The ultrasound wave travels through the tissues, generating several returning waves or echoes that upon reaching the probe make the crystals vibrate again, producing a new electric current that travels to the system's computer and provides information on the type of each of the deflected waves. The set of all the deflected waves creates the ultrasound image.

To produce an **image**, the first piezoelectric crystals are stimulated to generate a short ultrasound pulse – consisting of three to four waves – at a precise angle, producing thousands of echoes that are sent back to the probe (Figure 1.1). Shortly after, a new ultrasound pulse leaves the probe at a different angle, generating a new set of echoes that return to the second series of crystals. Assuming a constant wave propagation speed of 1540 m/s in soft tissues, each of these echoes can be located precisely along the trajectory, depending on the time interval between the departing wave and the returning wave. Hundreds of wave lines are produced this way, scanning tissues at high speed to produce over 30 images per second, each one containing thousands of pixels describing the acoustic characteristics of the scanned tissues.

Tissue acoustic characteristics are defined by the **acoustic impedance**, which dictates their level of ultrasound reflection and thus their echogenicity. Impedance is the product of the speed of ultrasound waves through a given tissue multiplied by its density (Table 1.1) (Bushberg et al. 2011). Ultrasound wave reflection is stronger at interfaces of tissues with opposed acoustic impedance, and weaker when traversing an interface of tissues with similar acoustic impedances. Mild variations in acoustic impedance are desirable for tissue examination, resulting in variable echogenicity and echotexture that allow internal architectures to be compared. In fact, not only does the ultrasound system locate the origin of each echo, it also measures its intensity, which is expressed in terms of pixel brightness on the unit monitor (B mode).

Normal **tissue echogenicity** that varies among organs and structures (Figure 1.2) and damaged tissue with altered acoustic characteristics, can be compared. Normal and abnormal structures can be defined in terms of echogenicity as hypoechoic or hyperechoic to their normal state, or to other structures to which they are compared. Fluids without cells or large particles

Atlas of Small Animal Ultrasonography, Third Edition. Edited by Dominique Penninck and Marc-André d'Anjou.
© 2025 John Wiley & Sons, Inc. Published 2025 by John Wiley & Sons, Inc.
Companion website: www.SmallAnimalUltrasonography.com

Vet-ebooks.com

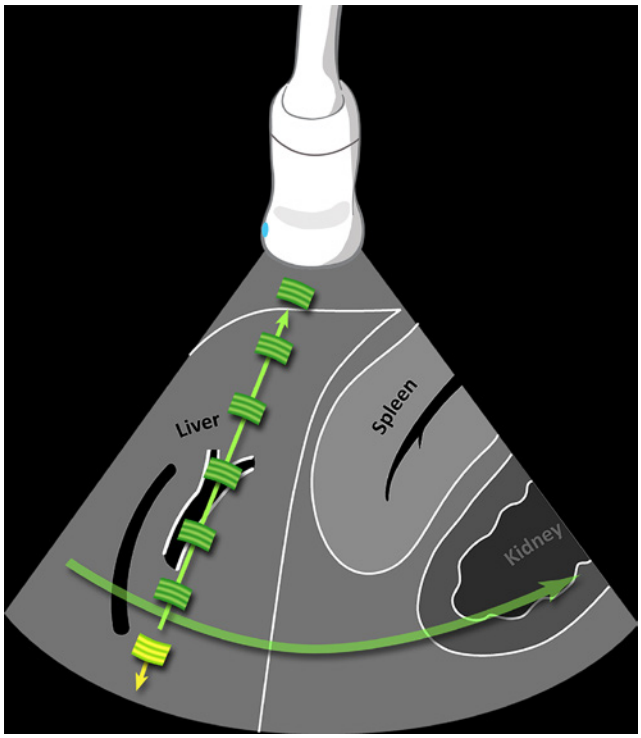


Figure 1.1. Ultrasound propagation and image formation. Each ultrasound image is formed by the addition of hundreds of individual scan lines. Each line is produced after a single ultrasound pulse (in yellow) is emitted by the transducer. As this pulse propagates through soft tissues, many echoes (in green) are generated at interfaces of different acoustic impedance (such as *hepatocytes-connective tissue*), producing an image of variable echogenicity and echotexture. Each echo is anatomically localized based on the time interval between the emitted pulse and its reception. After a specific time, a new pulse is emitted along an adjacent line, producing an additional scan line. Scan lines are generated very rapidly and successively, producing 15–60 images per second, allowing "real-time" ultrasonography.

Table 1.1
Density and speed of sound in materials and biological tissues and resulting acoustic impedance

Material or tissue	Density (kg/m^3)	Speed (m/sec)	Acoustic impedance
Air	1.2	330	0.0004×10^6
Lung	300	600	0.18×10^6
Fat	924	1,450	1.34×10^6
Water	1,000	1,480	1.48×10^6
Soft tissues (in general)	1,050	1,540	1.62×10^6
Liver	1,061	1,555	1.65×10^6
Kidney	1,041	1,565	1.63×10^6
Skull bone	1, 912	4,080	7.8×10^6

Source: Bushberg et al. (2011).

are anechoic, i.e., totally black, because of the absence of reflectors.

Interactions between ultrasound waves and tissues and materials vary, dictating the intensity of echoes generated and the residual intensity of the pulse that pursues its course through tissues (Hangiandreou 2003) (Figure 1.3). For instance, ultrasound waves penetrating fat result in ***acoustic diffusion*** as the primary interaction, reducing the intensity of the initial pulse. This type of interaction also explains the echotexture – i.e., granularity – of the parenchyma that varies among organs. On the other hand, the interaction with a smooth interface that is perpendicular to the beam axis, such as the renal capsule in Figure 1.3, causes ***specular reflection***, which produces intense echoes in the opposite direction of the initial pulse. Some materials like mineral absorb a significant component of the initial pulse energy that becomes too weak to generate echoes from deeper tissues. Ultrasound ***absorption*** can then cause a shadow (see *Artifacts*). Finally, ultrasound waves may change in direction due to ***refraction***. In reality, these types of interactions are often combined, and their presence and relative importance is mainly influenced by the differences in acoustic impedance and by the shape of the tissue (or material) interfaces. These interactions cause the emitted ultrasound pulse energy to eventually become completely dissipated.

Ultrasound Probes and Resolution

Ultrasound probes vary in configurations for specific needs (Figure 1.4). Curved linear probes, also called convex or microconvex, have one or several rows of piezoelectric crystals aligned along a convex surface, with varying beams and paths. These probes produce a triangular image because of the diverging lines of ultrasound waves they generate. The main assets of this type of probe are its smaller curve and its large scanning coverage, making it the ideal probe for assessing

Vet-ebooks.com

the abdomen, particularly the cranial portion along the rig cage. The piezoelectric crystals of the linear probes are distributed along a flat surface, producing a rectangular scan field. The phase interval of the impulsions can also produce a trapezoid-shaped image, allowing it to cover a larger surface. This is especially useful when evaluating superficial organs whose dimension may be greater than the width of the scanned area, such as the kidneys and spleen. The length of the probe's track indicates the width of the area it scans.

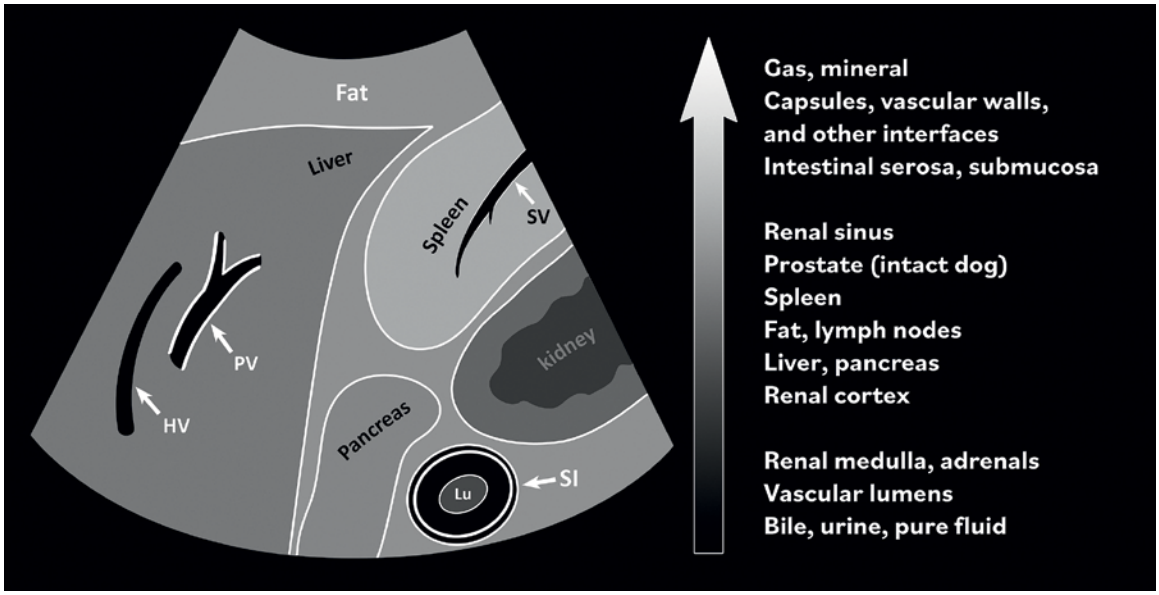


Figure 1.2. **Relative echogenicity of tissues and other materials.** Structures can be recognized and differentiated by their echogenicity. This figure illustrates the relative echogenicity of normal abdominal structures in dogs and cats. Note that the walls of the portal vein (PV) are hyperechoic even when this vein is not perpendicular to the insonation beam, differing from the adjacent hepatic vein (HV). The splenic vein (SV) walls become hyperechoic when perpendicular to the beam. The fluid in the small intestinal (SI) lumen (Lu) is not fully anechoic because of the ingested particles. The renal cortex is often hyperechoic in normal dogs and cats and may become isoechoic to the liver and even to the spleen. The adrenal medulla may be hyperechoic in certain normal animals, sometimes exceeding the echogenicity of the renal cortex. It is important to point out that tissue echogenicity may also be influenced by several equipment-related factors, such as transducer frequency and orientation, focal zone number and position, etc.

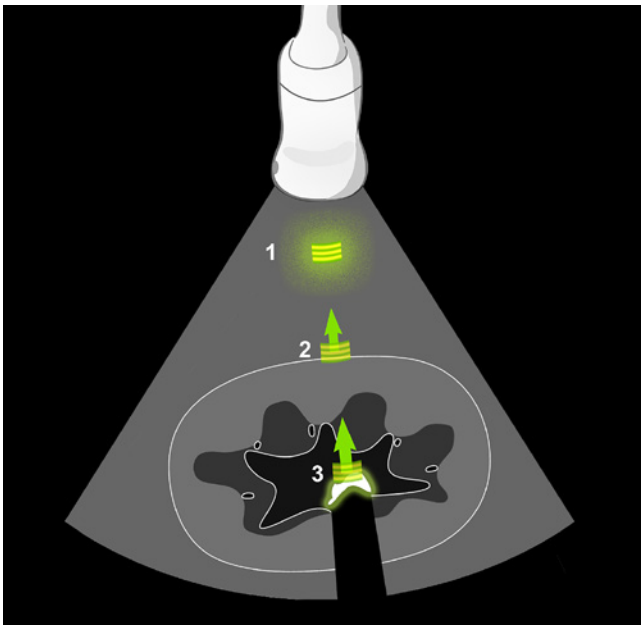


Figure 1.3. **Interactions between ultrasound waves and tissues.** The emitted ultrasound pulse is charged with energy. In this example, the pulse initially interacts with the abdominal fat (1) causing acoustic diffusion and partly losing its energy as it continues its course. When interacting with a smooth, linear interface such as the renal capsule (2), a strong specular reflection occurs that generates a highly intense echo (green arrow). The weaker ultrasound pulse (3) then reaches the renal pelvic calculus that absorbs most of the wave energy, while causing a strong reflection (green arrow). An acoustic shadow is generated, and the initial pulse energy is completely dissipated.

Vet-ebooks.com



Figure 1.4. Practical ultrasound transducers. Most ultrasound units are equipped with convex (A, B) and linear (C) electronic transducers with variable frequencies. A macroconvex probe offering lower frequencies (3–8 MHz) is best suited for the abdomen of large dogs, whereas a microconvex probe (B) of higher frequency and smaller footprint is preferred for the abdomen of small patients and when only a small acoustic window is available (e.g., intercostal approach of a lung lesion). A high-frequency (10–18 MHz) linear probe is most useful for assessing superficial structures on a relatively wide and flat surface (e.g., assessing bowels in a cat, biceps tendon in a dog). A phased array transducer (D) offers a small flat footprint and is ideal for echocardiography.

Spatial resolution is the ability of a system to recognize and distinguish between two small structures located close together. For instance, optimal spatial resolution allows us to distinguish between two small nodules in the liver instead of mistaking them for only one or missing a lesion that is adjacent to a normal structure. The spatial resolution along the path of the ultrasound beam – the *x* axis – is determined by the length of the pulse, which in turns is related to wave frequency (Figure 1.5). As the ultrasound frequency remains constant in depth, so does the axial resolution. Conversely, lateral (*y* axis) and slice-thickness (*z* axis) resolutions vary in depth as the ultrasound beam changes in shape to narrow at the level of the focal zone (Figure 1.6). For a given probe, the axial resolution is generally superior to lateral or slice-thickness resolutions, justifying those measurements be obtained whenever possible along that *x* axis.

Contrast resolution is the same system's ability to differentiate structures that present small differences in acoustic behavior (Figure 1.7). The influence of these two types of resolution is significant and hinges on image quality, the ability to evaluate structures and to detect and describe lesions.

As seen before, ultrasound waves interact with tissues in different ways causing the initial pulse to progressively lose its intensity in depth. This attenuation limits contrast resolution in deeper areas, particularly

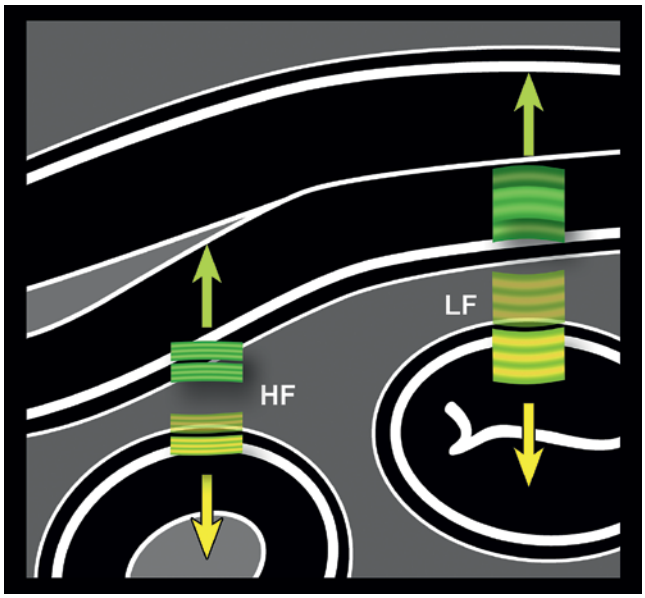


Figure 1.5. Ultrasound frequency versus axial resolution. The higher the frequency, the shorter the pulse. Because the length of the pulse does not change in depth or after interaction with tissues, high-frequency (HF) echoes that come back to the transducer are better discriminated by the system. Closely associated interfaces, such as small intestinal wall layers are then better represented. Conversely, echoes from closely aligned layers generated by a low-frequency (LF) pulse partly overlap and are interpreted by the system as originating from a single interface. This phenomenon is exaggerated in this illustration for better comprehension of this important concept.

Vet-ebooks.com

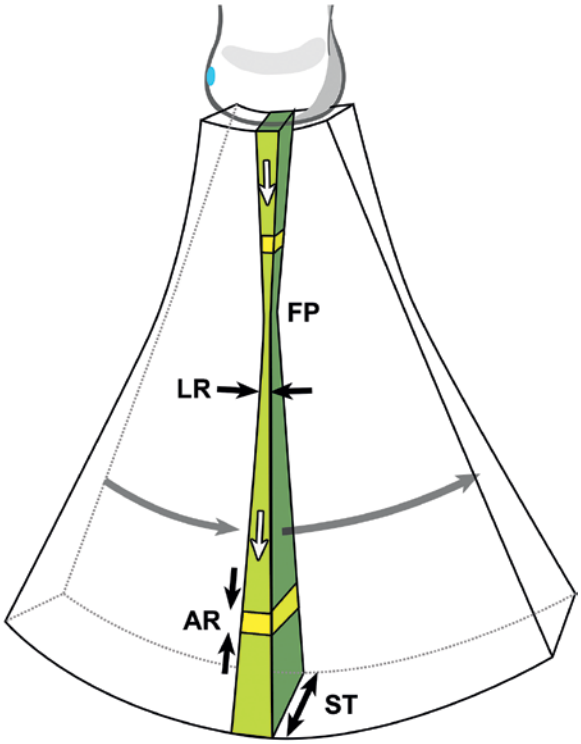


Figure 1.6. Shape of the ultrasound beam in depth. The ultrasound beam is larger at its emission point (piezoelectric elements) before narrowing at the focal point (FP), and becoming larger again further in depth. This change in shape affects the lateral resolution (LR, i.e., beam width) and slice-thickness (ST, elevational resolution), but does not affect the axial resolution (AR), which is dictated by the pulse frequency that remains constant in depth. Generally, the axial resolution is superior to the other resolutions.

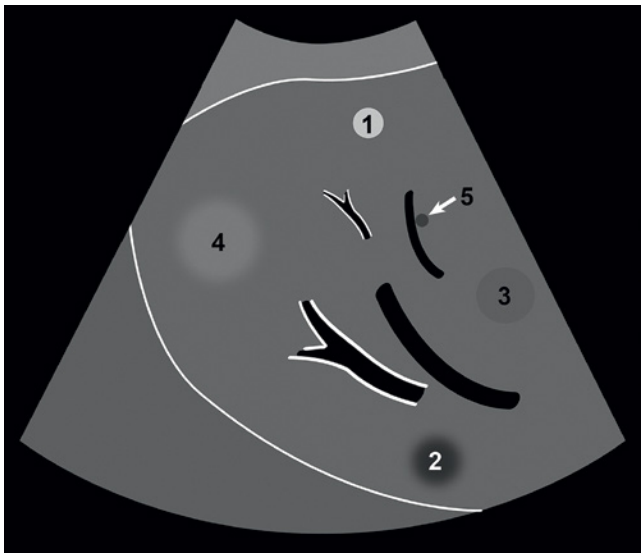


Figure 1.7. Spatial and contrast resolutions. The capacity of an ultrasound system to detect and distinguish structures of small size and similar acoustic characteristics greatly influenced its diagnostic capability. In this illustration, the hyperchoic nodule 1 is clearly depicted. Its characteristics (size, echogenicity, and margin) favor its identification. The hypoechoic nodule 2 is also visualized due to its size and marked hypoechogenicity but has ill-defined contours. Nodules 3 and 4 are larger but less conspicuous because of their echogenicity that is similar to the regional liver parenchyma. Contrast resolution of the system – and certain image adjustments – dictates its capacity to identify structures of characteristics that are similar to the background. The small hypoechoic nodule 5 is differentiated from the adjacent hepatic vein because of sufficient spatial resolution. Lower spatial resolution would cause this nodule to be confused with the vessel.

when using high frequency probes. Indeed, the coefficient of attenuation of ultrasound waves through tissues increases in direct proportion to wave frequency. This can be particularly problematic in certain animals, such as large obese dogs, or with certain disease processes (e.g., lipidosis). The use of lower frequency probes can partially compensate for this loss of signal, but to the cost of reduced detail (lower spatial resolution). Generally, the probe offering the highest frequency but allowing all desired tissues to be imaged with sufficient signal should be selected.

System Adjustments and Image Quality

Images can be frozen to take measurements and add text, prior to recording still or looped images that can be archived or submitted to a colleague for another opinion. But prior to be recorded, images must be optimized. Except for automatic processes, many adjustments can and should be made manually throughout the examination. Changes in tissue depth and acoustic properties require constant adjustments.

The **gain** determines the level of amplification of echoes to compensate for their attenuation in tissues, increasing the brightness of corresponding pixels on the screen. It can be adjusted generally or modulated specifically in depth (Figure 1.8). Time-gain compensation (TGC) is adjusted through sliding knobs, reducing superficial amplification, or increasing depth amplification, for instance. Since ultrasound attenuation will vary from one animal to another and from one abdominal region to another depending on the acoustic characteristics of normal and abnormal tissues, both the general gain and TGC will have to be adjusted during the examination. Recent ultrasound units offer automatic gain adjustment that can serve as a start for further micro adjustment.

Image field **depth** determines the length of the long axis, allowing the same structure to be imaged

Vet-ebooks.com

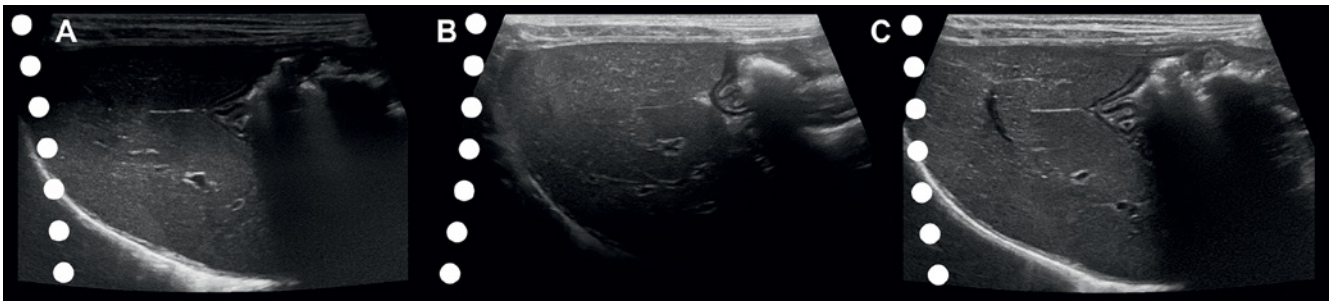


Figure 1.8. **Gain setting.** Because of the attenuation of the ultrasound beam as it travels through soft tissues, the amplification of echoes received must be adjusted according to tissue type and depth. This modulation can be made using time-gain compensation cursors. These three images show the variation in echogenicity of a normal liver with **(A)** insufficient near gain and excessive far gain, **(B)** excessive near gain and insufficient far gain, and **(C)** well-adjusted near and far gains. The lines of dots correspond to the time gain-compensation cursors that were adjusted to obtain each ultrasound image.

completely, or partly. This also needs to be adjusted continually to maximize the visualization of structures in the region of interest.

The ultrasound beam can be electronically **focalized** to reduce its diameter at a specific depth. In the focal zone, the beam's width and thickness are considerably reduced, increasing the capacity of the system to depict small structures along the y (lateral) and *z* (slice-thickness) planes, respectively (see Figure 1.6). Moreover, the intensity of the beam is concentrated over a small area, increasing the signal from tissues in that region, favoring contrast resolution. On recent systems, the focal zone is automatically adjusted during the exam, but, if possible, the focal zone should be manually adjusted during examination at the depth of the region of interest. By using two (or more) focal zones, the beam is narrowed over a greater distance, increasing the spatial and contrast and contrast resolution over a longer depth. The downside however is that using more zones requires more time, thereby reducing frame rate which may limit the examination of moving structure. Multifocal optimization is easier while evaluating structures that are completely immobile.

Noise is an inherent part of all imaging procedures and can become problematic in large patients or when using low-end systems. It results from insufficient signal (i.e., echoes) emanating from tissues and reaching the ultrasound probe, from electric interferences, from artifacts (see *Artifacts*), or from improper signal processing by the unit. The result is a coarse-grained textured and/or greyish image that does not represent normal tissue anatomy, and which limits our ability to view shades of grey (reduced contrast resolution). Noise can be partly reduced by using a higher frequency probe, by switching to the harmonic or compound imaging modes, or by increasing output power.

Spatial compound imaging (which vary in name among brands) refers to the electronic steering of ultrasound beams from an array transducer to image the same tissue multiple times by using parallel beams oriented along different directions (Figure 1.9). Tissues are scanned from different angles, simultaneously, allowing multiple echoes from the same tissue interfaces to be collected and combined, increasing the overall signal and reducing noise. Image contrast is increased, and tissue interfaces become more conspicuous. Tissues boundaries are better outlined and since background noise is reduced, cystic lesions, for instance, are fully anechoic ant thus more easily differentiated from solid lesions. On the other hand, certain useful artifacts such as acoustic shadowing – which helps recognizing mineral for instance – may be less apparent when compound imaging is used. Because multiple ultrasound beams are used to interrogate the same tissue region, more time is required for data collection, reducing the frame rate when compared with that of conventional B-mode imaging. This mode may limit the examination of moving patients.

The **harmonic mode** also increases tissue contrast by selecting echoes at a specific frequency. The term harmonic refers to frequencies that are integral multiples of the frequency of the transmitted pulse (which is also called the fundamental frequency, *f*, or first harmonic). Harmonic frequency echoes (1/2*f*, 2*f*, etc.) develop because of the distortion of the transmitted pulse as it travels through tissues (Ziegler and O'Brien 2002). The initial pulse in fact deforms from a perfect sinusoid to a sharper, sawtooth shape, generating reflected echoes of several different frequencies. The use of higher-order harmonic echoes instead of

Vet-ebooks.com

the fundamental echoes results in improved image contrast and reduced noise, increasing normal and abnormal tissue conspicuity. The reduction of artifacts and clutter is most efficient in the near field (Figure 1.10). This may prove particularly valuable in large patients with thick abdominal walls and subcutaneous fat planes.

Finally, several other aspects can influence the quality of ultrasound images. As for digital radiographs, the quality of the unit monitor (size, dynamic range, brightness, calibration) can influence our ability to accurately assess ultrasound images. Several features can be used and modulated to create scanning presets, for different types of patients or body parts. Sonographers must be aware of the strengths and limitations of their system.

The **extended field of view** (also called **panoramic mode**) imaging allows to obtain panoramic images of several structures/organs or masses that would otherwise not fit in one conventional field of view (Figure 1.11). Measurements can then be performed and were shown to be reliable (Liu et al. 2022). Clinical applications described in humans mostly evolve around the musculoskeletal system (Fitze et al. 2023), obstetric and breast, but it can be applied to any body parts.

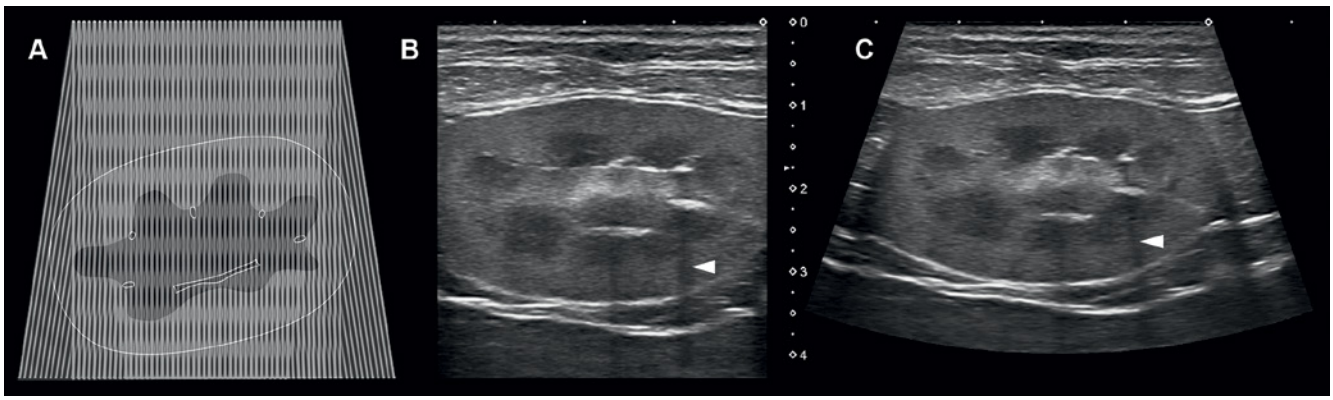


Figure 1.9. **Spatial compound imaging. (A)** With this mode, the same tissue is scanned using different beam angulations (steering) to produce a trapezoidal image that is wider than the footprint of the transducer. **(B, C)** Superficial structures such as this kidney may exceed the size of the image field when the standard linear mode **(B)** is used, whereas spatial compounding expands the width of the image to include the kidney that can be fully assessed and measured **(C)**. Beam angulation also influences the shape of shadowing artifacts (arrowheads).

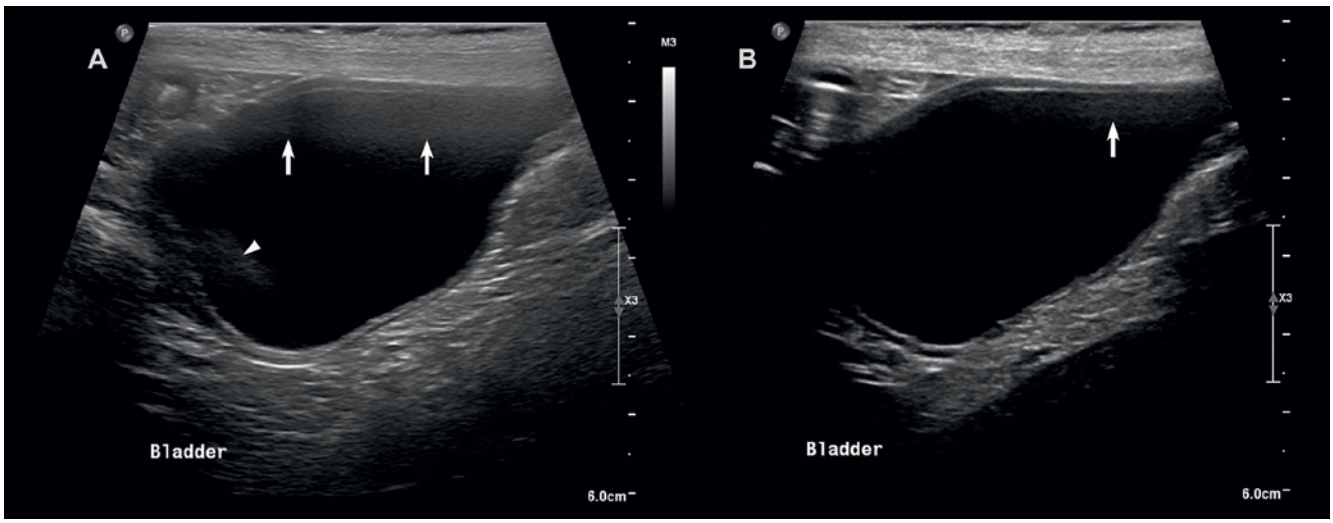


Figure 1.10. **Harmonics mode. (A)** Without this mode, the near field of the image of a bladder is blurred with faintly echogenic artifacts (arrows). Side-lobe artifacts are also more apparent (arrowhead) **(B)** With Harmonics mode, the near field appears crisp, and the outline of the bladder is clear. Near-field artifacts are greatly reduced, and side-lobe artifacts are no longer visible.

Vet-ebooks.com

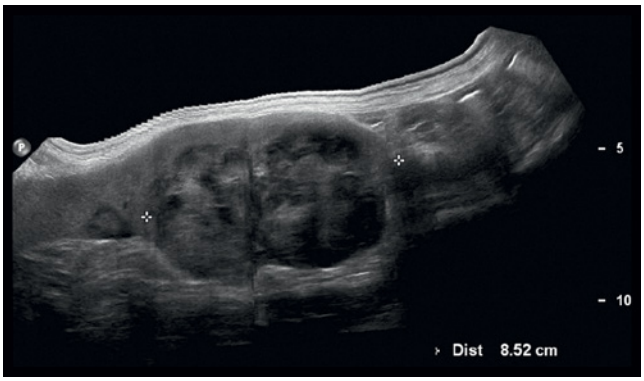


Figure 1.11. Panoramic mode (extended view). 8.5 cm long inhomogeneous abdominal mass is confirmed to originate from the spleen of this dog. The panoramic mode facilitates the measurements of any large mass that exceed the standard field of view. Notice the long and serrated contact line that is the result of manual displacement of the probe.

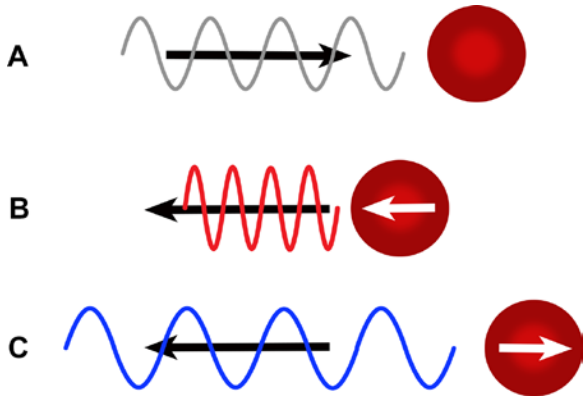


Figure 1.12. Doppler effect. (A) The ultrasound pulse emitted by the probe moves in direction of a red blood cell (RBC) at a specific frequency. **(B)** If the RBC moves toward this pulse, a positive Doppler shift occurs, increasing the frequency of the returning echo. The wavelength is reduced. **(C)** If the RBC moves away from this pulse, the frequency of the returning echo is reduced, and its wavelength is increased. This negative Doppler shift is displayed as a blue signal in the standard Color Doppler mode, whereas blood flow moving in the direction of the probe is displayed in red hue.

Doppler Ultrasound

Introduction

Doppler ultrasound provides information on the presence, direction, and speed of blood flow. A detailed description of Doppler ultrasound is beyond the scope of this Atlas, but the reader is encouraged to consult reference textbooks and articles for further understanding of its concepts (Revzin et al. 2019; Szabo and Kaczkowski 2023).

Doppler ultrasound is based on the interaction of ultrasound with particles in movement leading to a change in the frequency of the echoes received, this phenomenon is known as the ***Doppler effect*** (Figure 1.12) (Boote 2003). This effect is displayed and evaluated with color schemes when using color or power Doppler modes or graphically with spectral Doppler (Figures 1.13, 1.14). The numerous applications of these modes are highlighted in several figures throughout this book, and particularly in Chapter 16.

Flow Imaging Modes

With ***Color Doppler***, a color map is used to display the direction and velocity of the blood flow. The size and location of the interrogation box are adjusted to provide an overall view of the flow in a given region, superimposed on the B-mode image for anatomical localization. Color Doppler is essential for cardiac evaluation (see Chapter 6) but can also serve in the assessment of other body parts. It allows rapid identification of vessels and evaluation of their flow characteristics as well as detecting aberrant vessels such as portosystemic shunts or arteriovenous fistulas and assessing tissue perfusion. Color Doppler mode requires that color maps and B-mode data are acquired simultaneously, limiting temporal resolution, and often reducing the spatial resolution of the underlying B-mode image. Limiting the size of the area of color investigation to the region of interest helps to increase the frame rate, thus improving temporal resolution. Color gain should also be carefully adjusted so that the color signals does not extend beyond vascular walls.

Power Doppler Imaging (PDI) – also known as Energy or Angio Doppler – is more sensitive to flows of low velocity as it displays the summation of all the Doppler shift signals rather than the mean in a given area. This mode is favored for confirming the presence of blood flow, particularly in smaller vessels, or to differentiate blood vessels from other tubular structures such as the common bile duct. When combined with directional PDI maps, this mode can also show flow direction (Figure 1.13) (Kennelly and Moran 2008).

Spectral (or Pulsed wave) Doppler examines blood flow at a specific site and provides detailed graphic analysis of the blood flow. The flow characteristics such as velocity, direction, and uniformity can be precisely assessed over time, i.e., throughout the cardiac cycle (Figure 1.14). Flow velocities and indices can be more accurately measured than with color Doppler.

Vet-ebooks.com

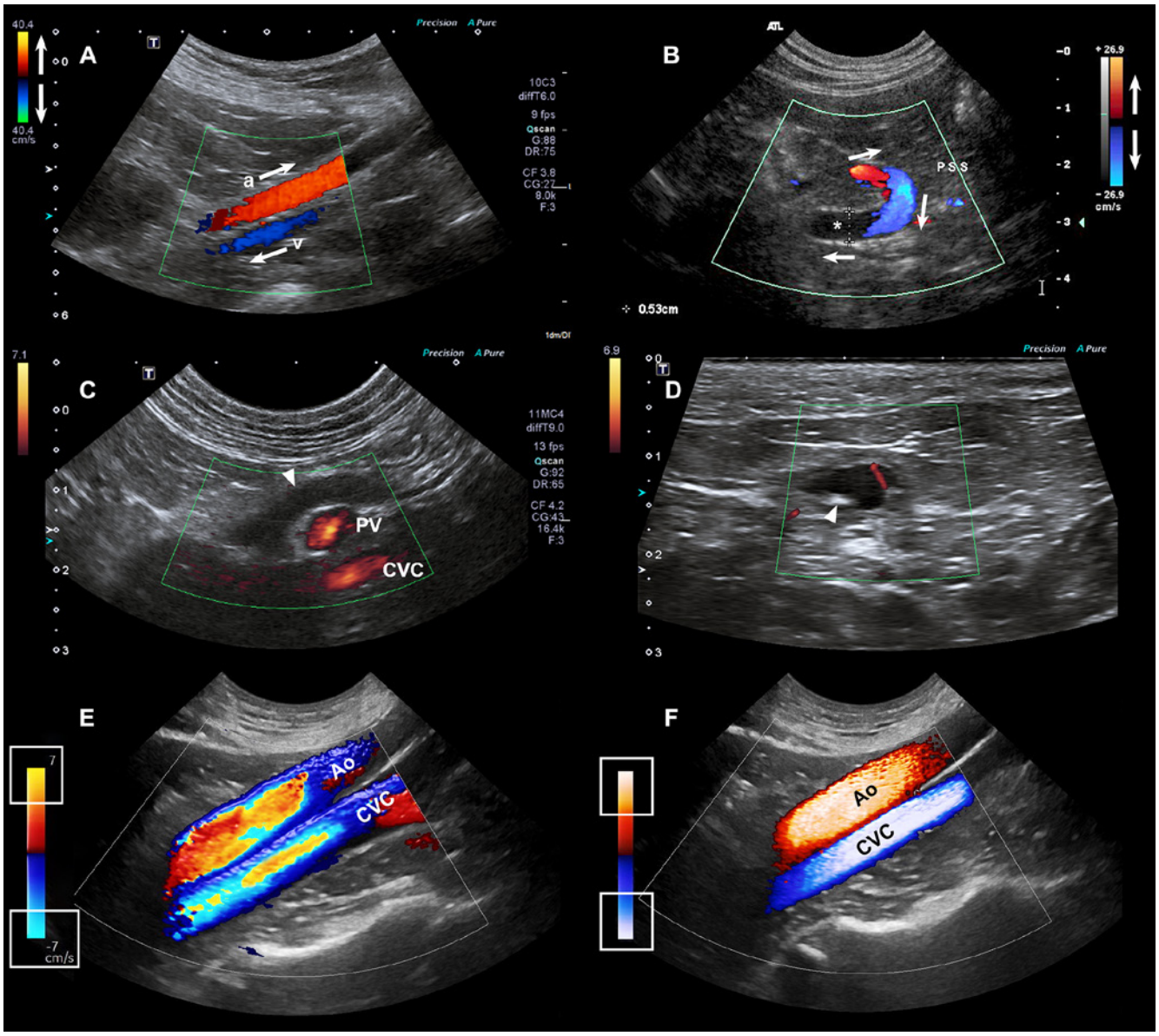


Figure 1.13. **Color and Power Doppler modes. (A)** With color Doppler, the direction of blood flow can be rapidly determined. In this dog, the right external iliac artery (a) and vein (v) show red and blue color hues, indicating flows directed toward and away from the probe, respectively. **(B)** Color hue can change in the same vessel due to a change in direction of the flow, as demonstrated in this tortuous portosystemic shunt (PSS). The arrows indicate the direction of the flow through that shunt. When the flow becomes perpendicular to the probe, a signal void (*) appears because of the lack of Doppler shift. Power Doppler may become useful in such circumstance. **(C)** Power Doppler helps distinguishing this dilated common bile duct (arrowhead) in a cat from the nearby portal vein (PV) and caudal vena cava (CVC). **(D)** Power Doppler may also be used to detect ureteral jet coming from a patent ureter, as opposed to the ipsilateral ureter that is obstructed by a small urolith (arrowhead). **(E, F) Directional Power Doppler imaging**. With conventional color Doppler, the color hues are linked to flow velocity and are affected by scale and pulse repetition frequency (PRF). With the color Doppler settings used in E, flow velocity approaching 7 cm/sec turns from red to yellow when directed toward the transducer and from dark blue to cyan when going away from it (see boxes at the ends of the color scale). When this threshold is exceeded in either direction, flow aliasing occurs, giving a false impression of flow reversal. This is seen in the central part of the aorta (Ao) and CVC that exhibit higher velocities than in the periphery of these vessels. With directional power Doppler, color saturation is rather influenced by the number of moving reflectors; a lighter color indicates more Doppler shift signals perceived, i.e., more moving cells.

Vet-ebooks.com

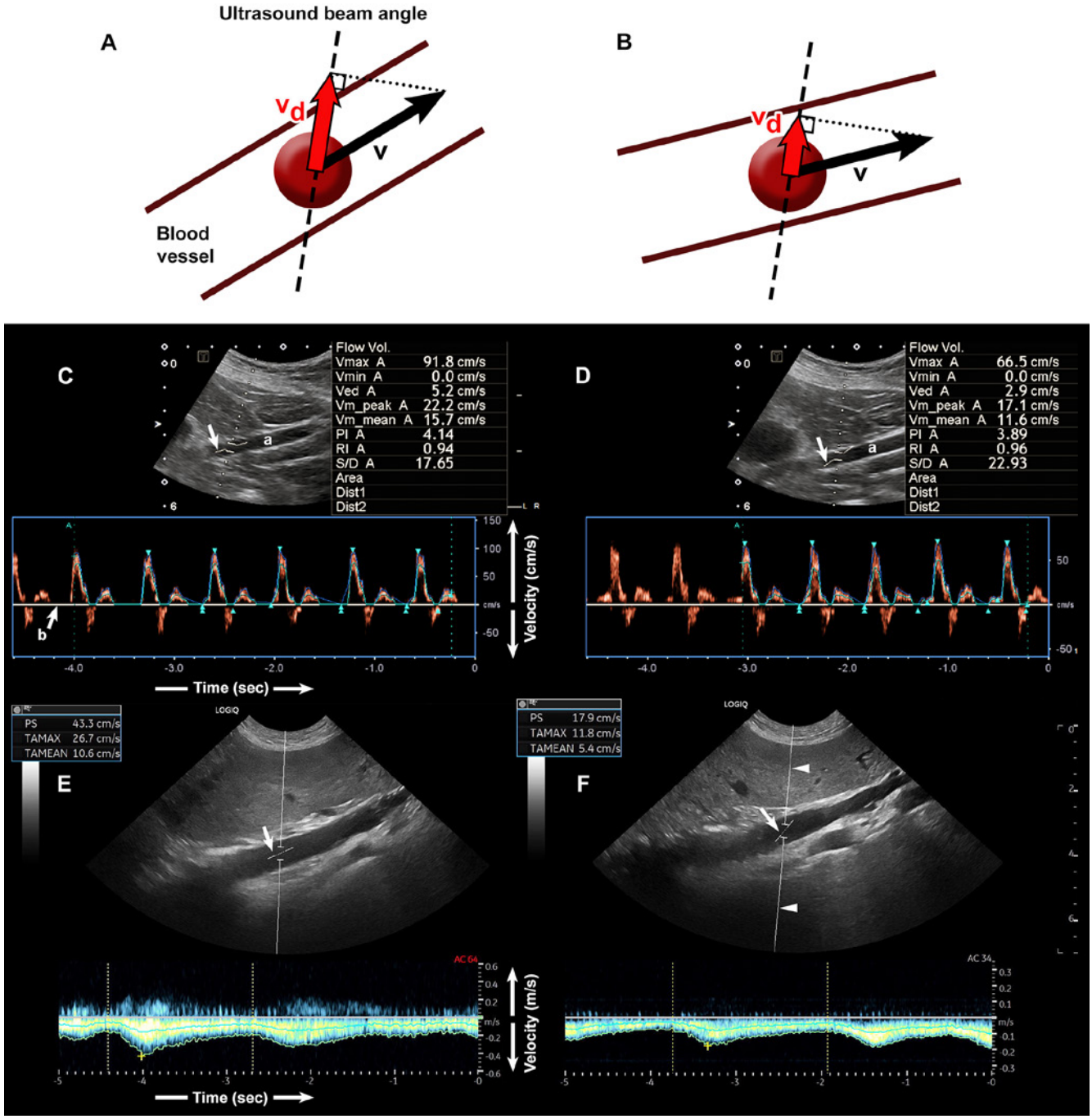


Figure 1.14. Flow velocity measurements using Pulsed (or Spectral) Doppler mode. (A, B) Schematic representation of the impact of flow direction on the estimation of its velocity. Moving blood cells generate a Doppler shift that is used to estimate flow velocity (v_d). When the direction of the flow is more parallel to the axis of the ultrasound beam (such as in A), this Doppler shift is increased, resulting in a higher flow velocity estimation (depicted as the red arrow), whereas, it is lower if the blood flow is more perpendicular (in B). For most accurate estimation of true blood flow velocity (depicted as the black arrows), the angle cursor (in C–F) must be carefully aligned with the direction of the flow. **(C)** The flow in this external iliac artery (a) is mainly directed over the baseline (b), i.e. toward the probe, and pulsates according to the heartbeat. Its changes in direction and velocity are represented over time in this graph. Note that the angle cursor (arrow in B-mode image) was appropriately manually aligned to the long axis of the vessel to measure the velocity vector along that line, which reaches a maximum of 91.8 cm/s and a mean of 15.7 cm/s. **(D)** Changing the angle of this line cursor results in measurement errors. The ultrasound unit estimates the flow velocities based on the measurement of the Doppler shift along that line (66.5 and 11.6 cm/s for maximal and mean velocities, respectively). **(E)** In this dog with hepatitis, the portal venous flow is normally directed toward the liver, smoothly undulating during respiration, with a mean velocity of 10.6 cm/sec. **(F)** Note in this case how flow mean velocity is underestimated (5.4 cm/s) when the angle is not aligned to the long axis of the vein. Manual correction of the velocity vector (arrow) helps the system computer to better estimate true flow velocity along that linear cursor, which must be constantly adjusted since abdominal vessels are examined with variable angles. PS, peak systole velocity; TAMAX, time-averaged maximum velocity; TAMEAN, Time-averaged mean velocity.

Vet-ebooks.com

In fact, the flow patterns of normal and abnormal abdominal vessels have been well described in dogs (d'Anjou et al. 2004; Szatmari et al. 2001) (see Chapter 16). Sonographers should, however, be careful to measure flow using insonation angles – which can be manually adjusted in the sampling window – well aligned to flow movement and not exceeding 60° to limit measurement errors (Figure 1.14).

Artifacts

Introduction

Artifacts are omnipresent in ultrasound, they are often part of the images and may lead to misinterpretations (Hedrick and Peterson 1995; Kirberger 1995; Feldman et al. 2009; Hindi et al. 2013). In medical ultrasound, it is assumed that (i) ultrasound waves always travel in straight lines from their emitting point; (ii) the lateral width and depth of the beam are narrow and constant; (iii) each interface generates a single reflection; (iv) the intensity and location of echoes displayed as pixels on the monitor truly correspond to the reflecting power and anatomical location of structures being scanned; (v) the speed of the ultrasound waves and the coefficient of attenuation are constant within tissues; and that (vi) each echo seen on the screen comes from the most recently transmitted wave. These assumptions are theoretical, and the sound interaction with biological tissues is complex and responsible for many explained and unexplained artifacts. In addition, the understanding of physical properties of artifacts has been studied *in vitro* by several authors (Barthez et al. 1997; Heng and Widmer 2010), but these conditions are not well representing the complexity of numerous factors such as probe frequency, shape, operator settings, nature, and depth of tissues evaluated.

Deleterious artifacts such as gas-induced reverberation can be partly controlled by adequate patient preparation, scanning methods, and system adjustments. Gastrointestinal content is responsible for most artifacts and can partially be reduced by fasting animals before their exam. Poor contact between the probe and the skin, due to hair, debris, or crusts also limits the transmission and reception of ultrasound waves.

Although artifacts are often responsible for image degradation, they can help interpreting images in many instances (Baad et al. 2017). Their recognition is used to detect and confirm the presence of calculi or tissue mineralization, gas, cysts, and foreign bodies.

Acoustic Shadowing

Shadowing is a zone of echoes with reduced amplitude, beyond a highly attenuating or reflective structure. Most of the incident beam is absorbed and/or reflected at the interface. A uniformly anechoic shadow is called clean, while the term dirty shadowing is used when the shadow is inhomogeneous (Hindi et al. 2013; Rubin et al. 1991).

Clean shadowing is encountered when absorption of the incident beam happens at a hyperattenuating interface such as bone, calculi, or compact foreign material that is larger than the ultrasound beam width (Figure 1.15A-B). The shadow may be partial behind calcifications and calculi that measure less than 0.5mm (Hindi et al. 2013), especially when compound imaging is used. Partial shadowing may also appear behind fat or fibrosis (Hindi et al. 2013; Mesurolle et al. 2002), depending on their size, on the attenuation characteristics of the background tissue and on the equipment and settings.

Dirty shadowing is present when the incident beam is mostly reflected, like at a soft tissue-gas interface (Figure 1.15C–E).

Edge shadowing appears as discrete, triangular zones of low amplitude, at the edge of a curved structure (Figure 1.16A, B). When, the curved structure is fluid filled, the edge shadowing artifact borders the enhancement artifact. This type of refractive shadowing can be confusing, especially when it occurs at the cranial aspect of a fluid filled bladder and appears as a "defect" of the wall (Figure 1.16C–D).

Acoustic Enhancement or Increased Through-transmission

Conversely, waves encountering a structure that allows them to pass through more easily (poorly attenuating), such as a liquid-filled cyst, remain of higher intensity when reaching the deeper tissues, allowing echoes of greater strength to come back to the probe. Consequently, these deeper tissues present an artifactual increase in echogenicity (Figure 1.17). **Acoustic enhancement** is typically recognized deep to a fluid-filled structure in a soft tissue background, such as deep to the gallbladder or to a liver cyst, making them easy to identify and distinguish from solid lesions. Tissues deep to the urinary bladder and organs floating in ascites often become hyperechoic.

Vet-ebooks.com

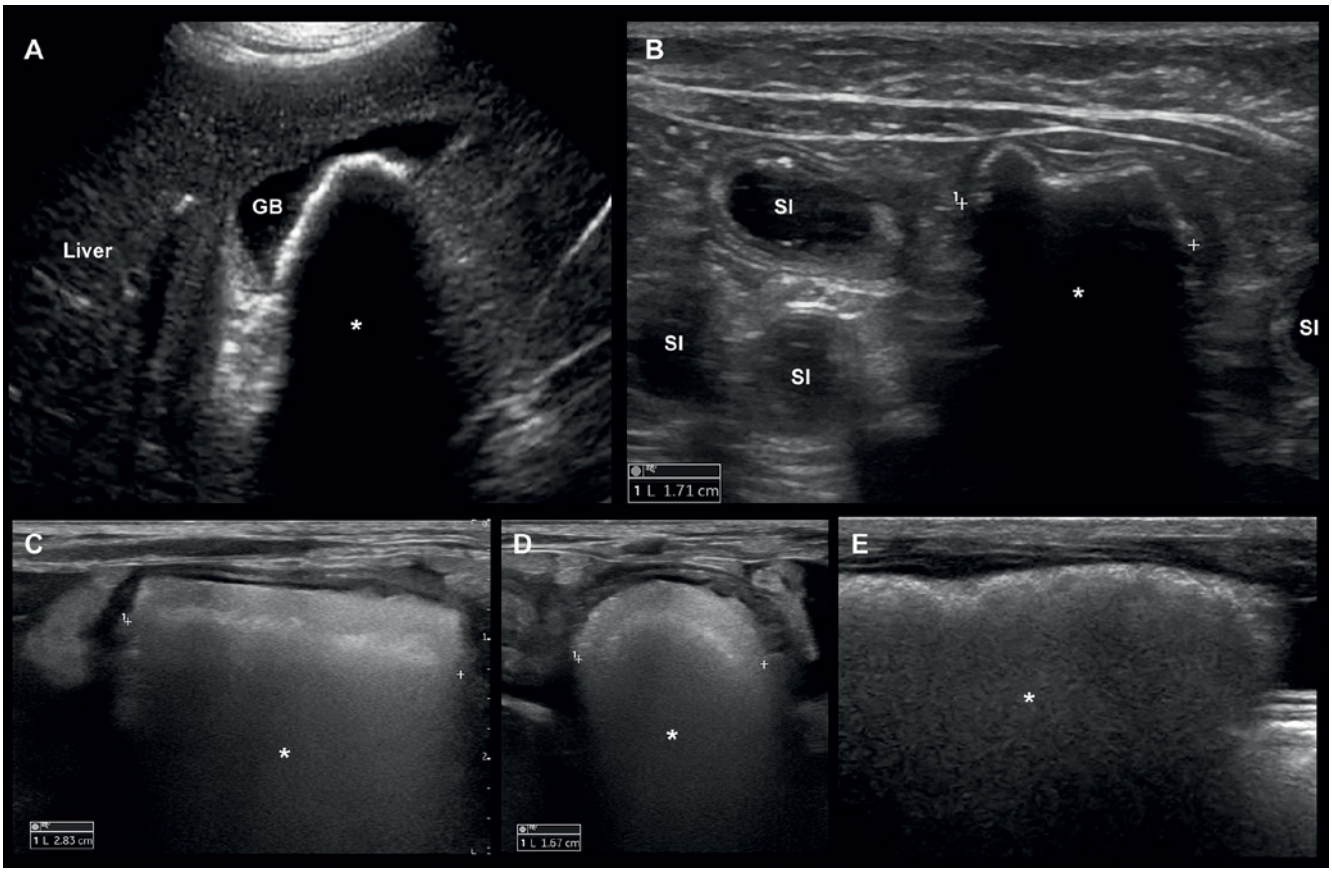


Figure 1.15. **Acoustic shadowing** is a poorly echoic to anechoic zone located below a highly attenuating interface. **(A)** The clean shadow (*) behind this large gallbladder cholelith has the triangular shape of the microconvex probe that was used. **(B)** In this cat, an irregular 1.7-cm-wide foreign body is present in the small intestine, creating a clean shadow (*) that has a more rectangular shape using a linear probe. Nearby small intestinal (SI) loops are filled with fluid. **(C, D)** In this other vomiting cat, there is a cylindrical hyperechoic structure inside the stomach that creates a dirty shadow (*), which was confirmed to represent a foam ear plug. Note the shape of this foreign body in longitudinal **(C)** and transverse **(D)** views as well as the rectangular shape of the artifact using a linear probe. **(E)** Dirty shadowing is also often seen distal to the colon containing gas and stools.

Reverberation

Reverberation artifacts typically appear as a series of multiple equally spaced lines (Figure 1.18A). They occur when the beam hits a highly reflective interface, such as lung, gas in the GI tract or an air pocket, and sends it back as an echo of similar intensity. The high-intensity echo is partly captured by the probe, producing a hyperechoic line at the contact interface, but no echo coming from deeper tissue. The surface of the probe will reflect this high intensity echo and send it back and forth. Since part of the echo is perceived each time it returns, the computer calculates the time passed since the initial launch of the wave pulse and thus records several equidistant hyperechogenic lines. There is decreasing echogenicity of the interface as it goes deeper, due to a gradual loss of wave intensity that rebounds and is attenuated during its trajectory.

Comet tail is a type of reverberation artifact, it appears as a series of short and very closely spaced successive echoes (Figure 1.18B,C,D) that typically decrease in intensity and width in depth. When gas bubbles form thin layers separated by liquid – as in the digestive tract – the waves rebound between the layers, resulting in many echoes that return to the probe at regular intervals, forming a trail of echoes forming a shadow resembling a comet's tail. This artefact is also encountered with metallic pellets and surgical clips (Figure 1.18C). **Ring down artifact** similarly appears as a series of parallel reflective lines that typically extend behind a gas collection. It happens when air bubbles resonate at the ultrasound frequency and then emit reflections. This can be seen associated with gas inside irregular lung surfaces, GI tract, pneumoperitoneum and abscesses. Practically, comet tail and ring down artifacts appear very similar on the screen, even though they result from different physical interactions.

Vet-ebooks.com

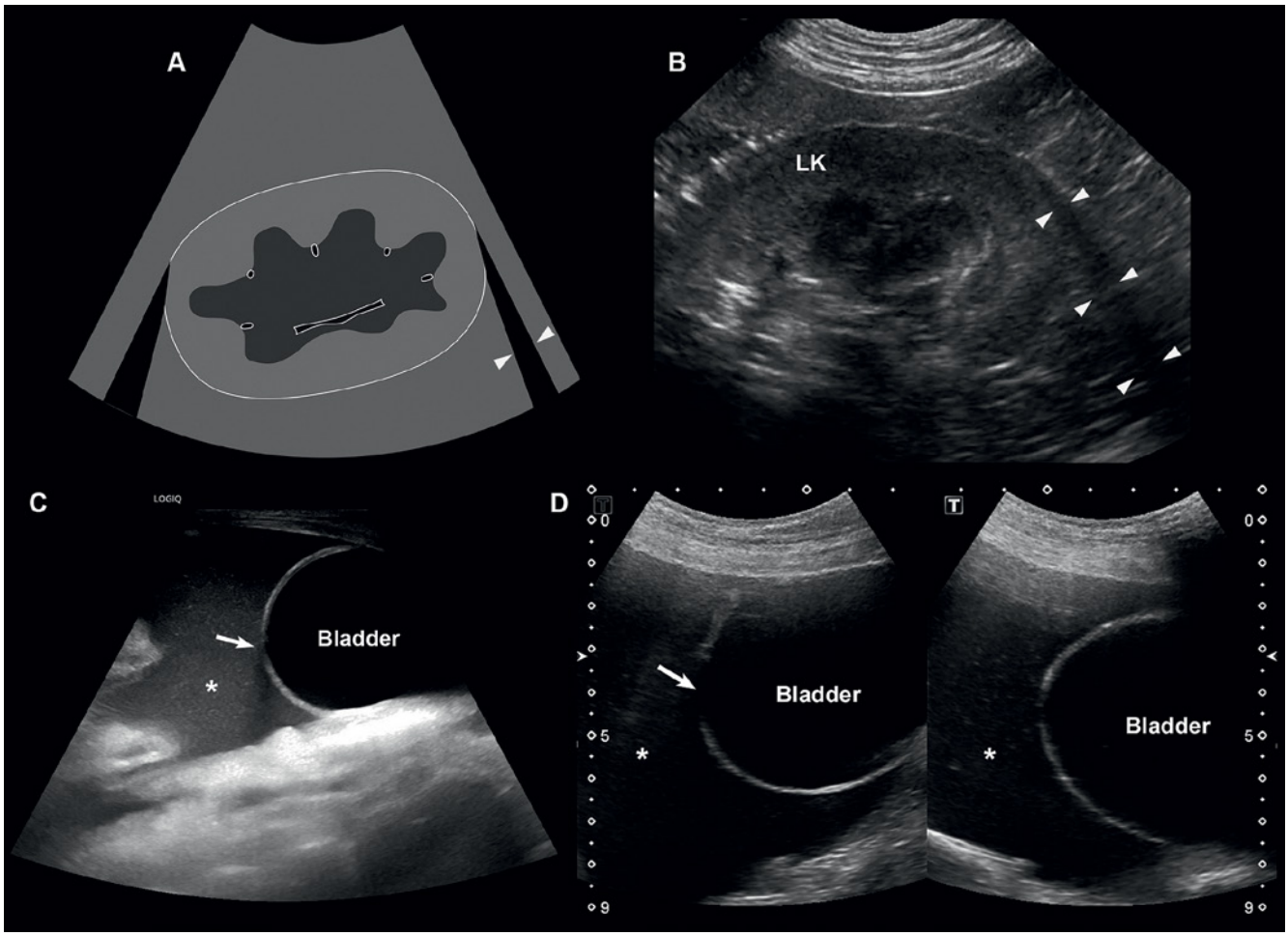


Figure 1.16. **Edge shadowing and refraction. (A, B)** Edge shadowing (arrowheads) is often seen in prolongation of the renal pole. LK, left kidney. **(C)** The curvature of the bladder wall causes beam refraction that results in acoustic shadow (arrowheads) in this cat with echogenic peritoneal effusion (*) due to carcinomatosis. A hole in the bladder wall (arrow) is artifactually created. **(D)** In this dog with cardiac tamponade and marked peritoneal effusion (*), the artifactual hole in the bladder wall (arrow) is attenuated by repositioning the transducer with a different angulation.

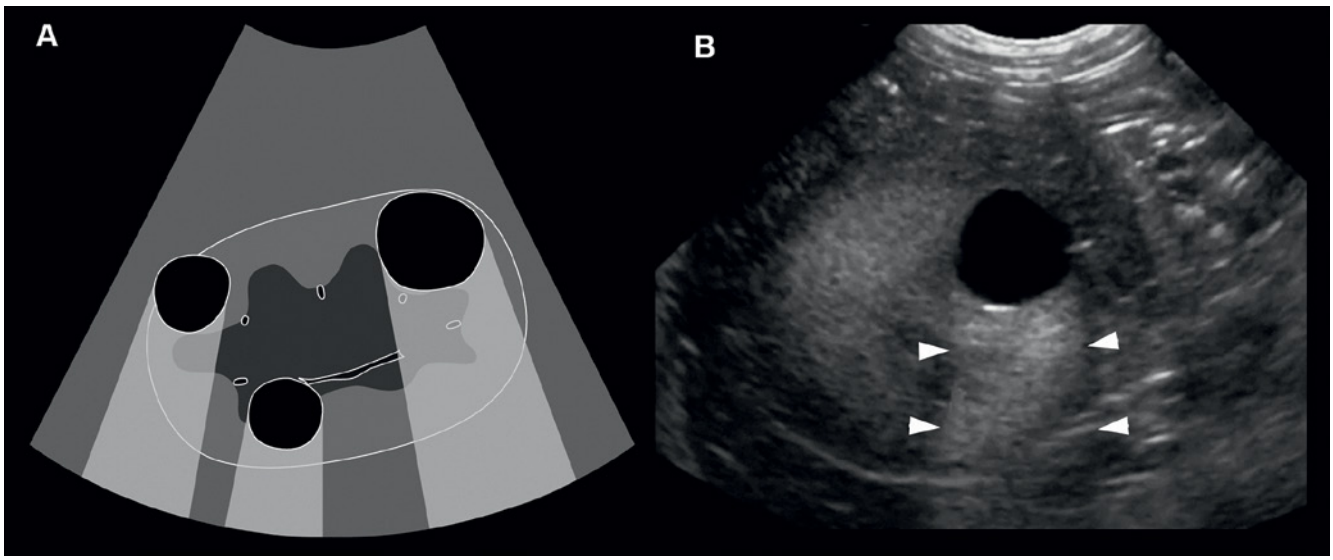


Figure 1.17. **Enhancement. (A)** This artifact is represented by a zone of increased echogenicity, behind a fluid filled structure. On this schematic drawing, several renal cysts are seen associated with distal enhancement **(B)** An example of similar cyst is present in this dog, it is seen as a rounded well-defined anechoic renal cyst associated with clear enhancement (arrowheads).

Vet-ebooks.com

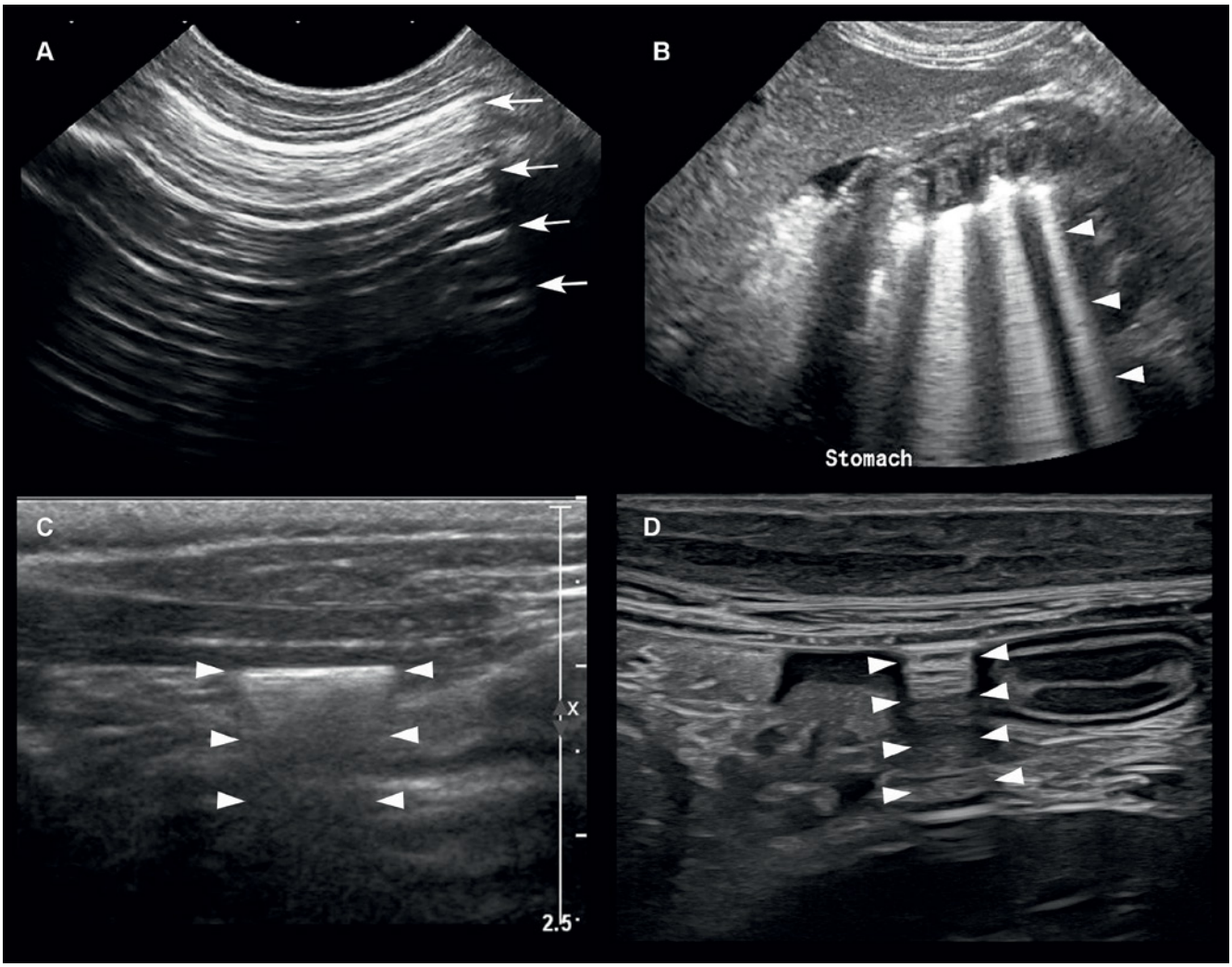


Figure 1.18. **Reverberation and comet tail. Reverberation** appears as series of parallel and equally spaced lines (arrows), when the beam encounters a smooth and highly reflective interface such as large collection of gas inside the colon **(A)**. The colonic wall in the near field is barely visualized. **Comet-tail artifacts** also appear as a series of short and very closely spaced successive echoes (arrowheads) and are often seen between gastric rugal folds **(B)**, with surgical clips **(C)** and with free peritoneal gas **(D)**.

Mirror Image

Mirror image artefact results in the misplacement of a structure, when a large, smooth, curvilinear, and strongly reflective interface is present between tissues. When this reflector is the lung surface, the most encountered artifact of misplaced organ or structure, is the mirror image of the liver and/or the gallbladder on the thoracic side (Figure 1.19A-B), but this artefact can be seen in other anatomical locations and at times be confused with lesions (Figure 1.19C-F).

Volume Averaging

The shape of the main ultrasound beam that serves to generate images changes in depth. Indeed, the exiting ultrasound beam width is similar to the probe width, then narrows at the focal zone, and widens again deeper to the focal point. Practically, this causes more tissue to be included in areas where the beam is largest in thickness and width (Figure 1.20A). Their echogenicities become confounded and averaged to display the brightness of the pixels in those specific regions. This may result in pseudo sludge in fluid-filled anechoic structures such as the gallbladder, cysts or even the bladder, depending on their location and the quality of the probe. Volume averaging – also called **slice thickness** or **beam width** – artifact may then lead to errors in interpreting the content of cystic structures and may limit the conspicuity of small lesions. It may also limit the conspicuity of acoustic shadowing for very small hyperattenuating structures such as stones or linear foreign bodies when the ultrasound beam

Vet-ebooks.com

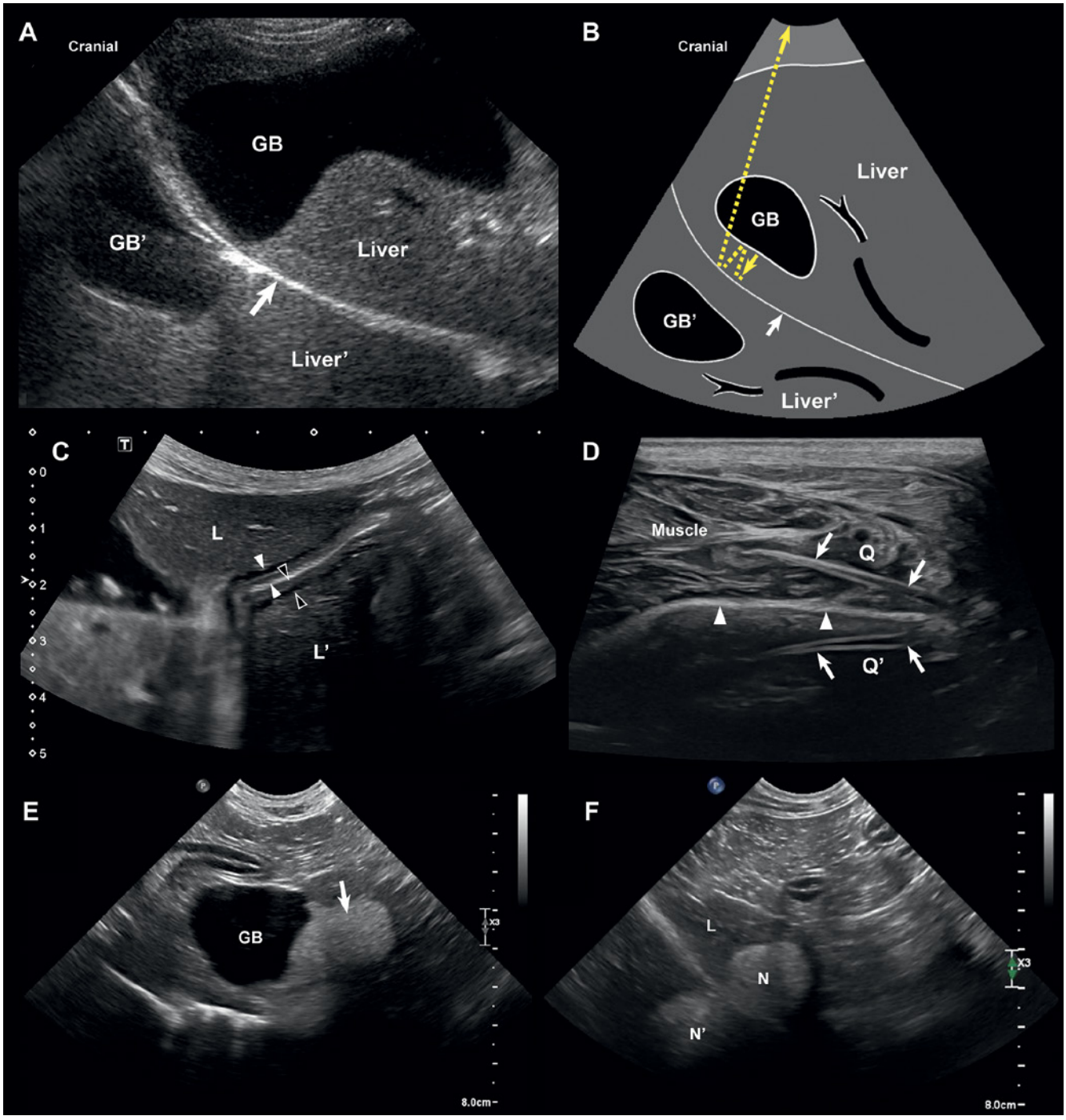


Figure 1.19. **Mirror images. (A, B)** Sonographic (**A**) and schematic (**B**) images of a mirror artifact involving the liver in a dog. The image of the actual liver and gallbladder (GB) is obtained based on the echoes generated during "normal" ultrasound wave propagation. In this case, however, the remaining pulses are not dissipated in deeper tissues, but almost fully reflected at the contact of diaphragm-lung interface (white arrows), which acts as strong reflector. Echoes are thus sent back to the liver and GB, which once more reflect some of the energy back to the diaphragm/lung, before it is redirected back to the transducer (along dashed line). This "second set" of echoes is received long after the first set (producing the true image) and thus interpreted by the machine as originating from the other side of the diaphragm. A mirror image of the liver' and GB' is then added on the monitor underneath the real image. **(B)** In this other dog, the interface of a gas-filled stomach results in a mirror image (black arrowheads) of its superficial wall (white arrowheads). A portion of the liver (L) is also mirrored distally (L'). **(C)** Intraluminal gas in the gastro-intestinal tract can create a double-wall sign (black arrowheads) deep to the superficial wall (white arrowheads), giving the false impression of collapse as in this dog. In this case, the liver (L) is also reflected (L'). **(D)** Bone may also serve as strong reflector, especially when straight and perpendicular to the probe. In this dog with porcupine quills (Q) that migrated inside muscles of the right thoracic limb, there is a false impression of an additional quill (Q') beyond the surface of the humerus (arrowheads). **(E, F)** Two sonograms of the liver of a Border collie cross with organized sludge (arrow) in the gallbladder as seen in **(E)**. On **(F)**, an orthogonal plane of the same region gives the false impression of a hyperechoic hepatic nodule (N) that is also mirrored on the other side (N') of the highly reflective surface of the diaphragm. L, Liver.

Vet-ebooks.com

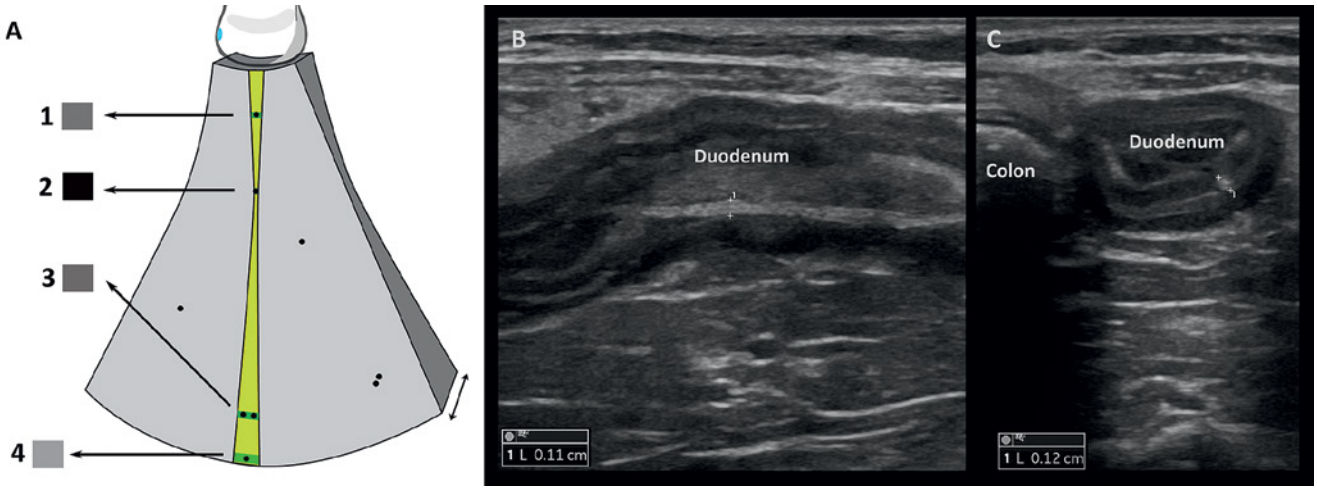


Figure 1.20. Impact of partial averaging on lesion detection. (A) The detection of a lesion is influenced by its size, its echogenicity and its position in regard to the primary ultrasound beam. It is also influenced by the spatial resolution of the system. At a given ultrasound frequency, the lesion will be better depicted at the focal zone. Indeed, the smaller width and thickness of the beam at that level allow the lesion to completely fill the beam, resulting in anechoic pixels on the screen (2). However, if the lesion is in a larger portion of the beam (1 and 3), the resulting image displays pixels of higher echogenicity because of the inclusion of regional liver parenchyma. The displayed pixels in fact reflect the average echogenicity of the sampled tissue. Lesions may even be confounded when multiple in a large portion of the beam (3), or with normal adjacent structures like vessels. Moving the focal zone to the region of interest is essential when assessing small structures, such as when looking for small lesions or when measuring intestinal layers for instance. Using more than one focal zone reduces the beam size over a greater depth. **(B, C)** Very small structures may not generate acoustic shadowing even when dense enough to theoreticality absorb ultrasound waves. Indeed, ultrasound pockets may not be focused enough to be contained in a beam that is narrower than the encountered object. In this cat that ingested a thin string, the foreign object is seen but not the shadow.

width/thickness exceeds the one of these structures (Figure 1.20B) (Goldstein and Madrazo 1981).

Side Lobes and Grating Lobe Artifacts

Side lobes and grating lobes are different types of secondary lobes present on the side of the primary sound beam. Side lobes are present in all transducers and are usually of low intensity; they can create spurious echoes in the near field. Grating lobes are associated with the geometric construction of linear probes (Barthez et al. 1997). The artifacts created by secondary lobes result in misplacement of reflected echoes (Figure 1.21). In clinical situations, secondary lobes artifacts are difficult to differentiate from volume averaging artifacts.

Speed Error and Range Ambiguity Artifacts

When the ultrasound speed is not the assumed 1540 m/s through tissues, error in size or location of structures may happen (O'Brien et al. 2001; Feldman et al. 2009; Hindi et al. 2013). For example, when sound travels through fat (with a velocity of about 1450 m/s), the returning echoes will take longer to come back to the transducer and thus displayed deeper in the image than they really are (Figure 1.22). Speed – or propagation – error artifacts may cause structures to be inaccurately localized or measured.

Ultrasound systems assume that all received echoes are formed from the most recent transmitted pulse. **Range ambiguity** artifact occurs when the system receives echoes from deep structures after the subsequent pulse is emitted, misplacing this structure closer to the transducer than in reality. This happens predominantly when using high pulse repetition frequency and when increasing the number of focal zones (Naganuma et al. 2019).

Anisotropy

This artefact is most described in musculoskeletal ultrasound and consists of a decreased in echogenicity of the structure (such as tendon or ligament), due to an oblique position (rather than perpendicular) of the probe on the body part being evaluated (Figure 1.23). This can be easily corrected by changing the probe angle.

Vet-ebooks.com

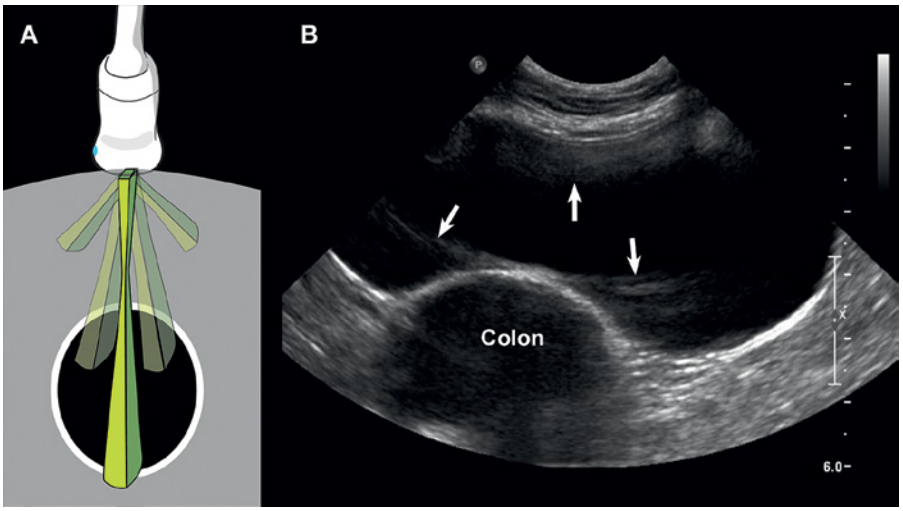


Figure 1.21. **Side Lobes. (A)** Schematic drawing of the main central beam lobe and of the diverging side lobes of lower energy of a probe while imaging a fluid structure such as the bladder. **(B)** Artifactual echoes are projected in the bladder, some in the near field, and some in the far field. Notice, the echoes are curvilinear as they arise from the hyperreflective bladder wall interface that interacts with the side lobe beams. These echoes are erroneously interpreted to originate from the interaction with the main beam.

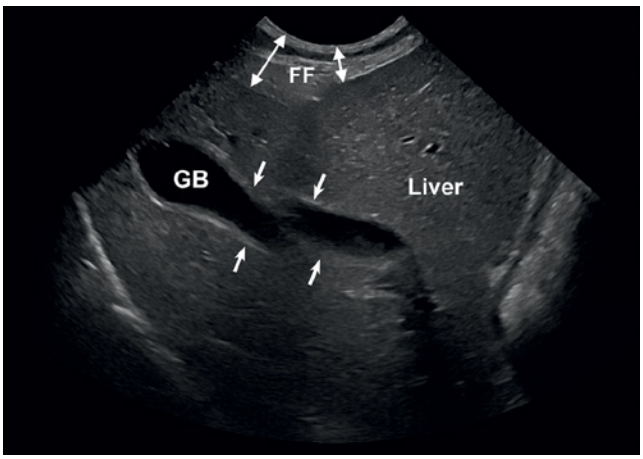


Figure 1.22. **Speed error.** When sound travels through fat (with a velocity of about 1450 m/sec), the returning echoes take longer to come back to the transducer and are thus displayed deeper in the image than they really are. In this dog, the slower velocity of ultrasound waves through fat versus liver (around 1600 m/sec) results in inaccurate displacement of the apex of the gallbladder (GB) further away from the transducer when compared to its neck, with apparent discontinuity between these portions (arrows). Note the different thickness (double arrows) of the falciform fat (FF) that explains this acoustic phenomenon.

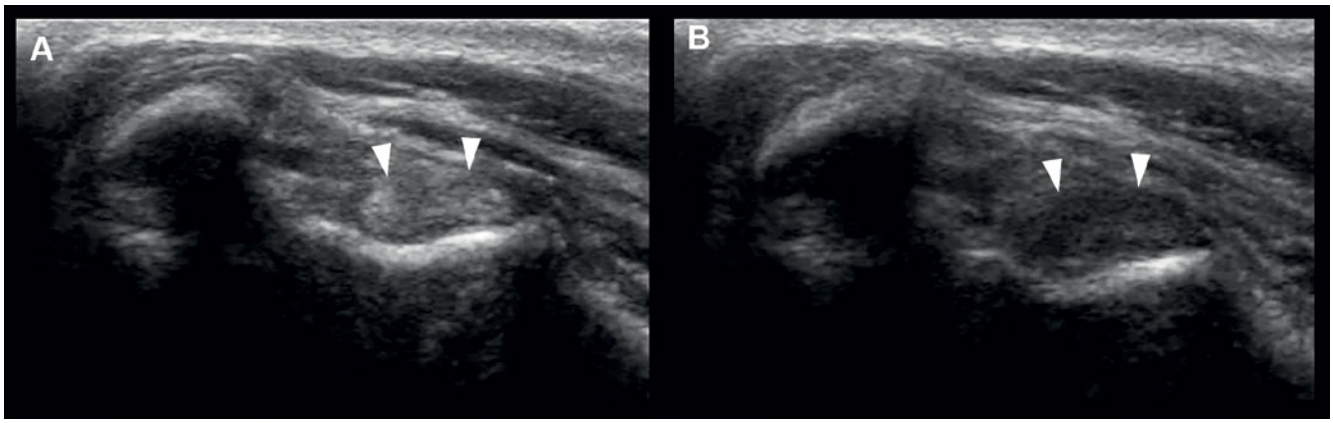


Figure 1.23. **Anisotropy. (A)** Normal cross-sectional appearance of the biceps tendon (arrowheads), with the probe being perpendicular to the structure. **(B)** Decreased in echogenicity of the tendon is due to an oblique position of the probe. This can be easily corrected by changing the probe angle. This artifact can be misinterpreted as core lesion.

Vet-ebooks.com

Electronic Interference

Electronic interferences from devices sharing the same electrical outlet can appear as discrete radiating echogenic spikes (Figure 1.24). This can be easily fixed by having a dedicated power outlet for the ultrasound equipment.

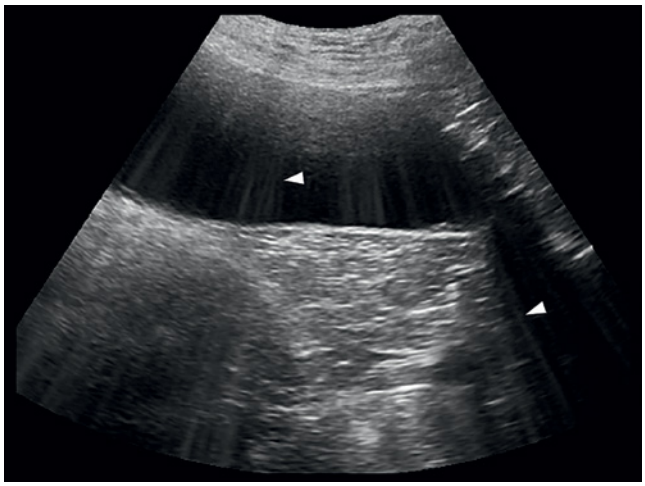


Figure 1.24. Electronic interferences. Discrete highly echogenic spikes (arrowheads) are crossing the entire scan field. They are best seen when they project on poorly echogenic structures. These were due to the use of an electrocutter in the adjacent room.

Twinkling Artifact

When using color flow Doppler, zones of rapidly changing red and blue hues can be seen behind strongly reflective structures such as calculi, or tissue mineralization (Rahmouni et al. 1996) (Figure 1.25). This artifact seems independent to the calculus composition, and it is accentuated by the size and surface of the calcification or calculus (Louvet 2006). It can be encountered with calculi in the bladder, gallbladder, or associated with any tissue mineralization.

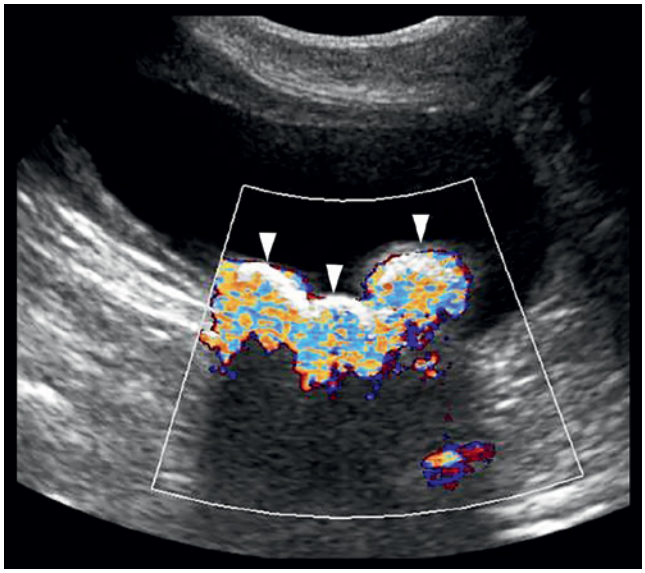


Figure 1.25. Twinkling artifact. Several hyperechoic interfaces associated with shadowing are present in the bladder consistent with calculi. When activating the color flow Doppler mode, zones of rapidly changing red and blue hues (arrowheads) can be seen behind these strongly reflective structures.

Doppler Aliasing

This artifact occurs for a high velocity flow when the Doppler sampling rate – i.e., pulse-repetition frequency (PRF) – is less than twice the Doppler frequency shift of that flow (Hindi et al. 2013). Aliasing causes the high-frequency component of the flow to wrap around the scale, from its positive or negative extremity, depending on its direction (Figure 1.26).

Aliasing can be reduced or eliminated by increasing the velocity scale – which increases the PRF, moving up or down the baseline, increasing the Doppler angle – which increases the Doppler shift, or using a lower ultrasound frequency.

Doppler Flash Artifact

Rapid movement of the patient's body, of a structural component (e.g., heart or arterial pulsation), or of the probe may lead to Doppler shifts interpreted by the system as blood flow. A spurious appearance of blood flow is displayed, limiting the assessment of true vessels. This artifact tends to be more apparent in fluid-filled structures and with ascites (Figure 1.27).



Visit our website at
www.SmallAnimalUltrasonography.com
for complementary video clips with annotations and text on:

- Image formation and other principles
- Propagation of US waves and interaction with tissues
- US beam and spatial resolution
- Gain, TGC, and other manual adjustments
- Mirror image artifact
- Shadowing artifact
- Enhancement artifact
- Reverberation artifact
- Refraction artifact
- Speed error and range ambiguity artifacts
- Twinkle artifact

Vet-ebooks.com

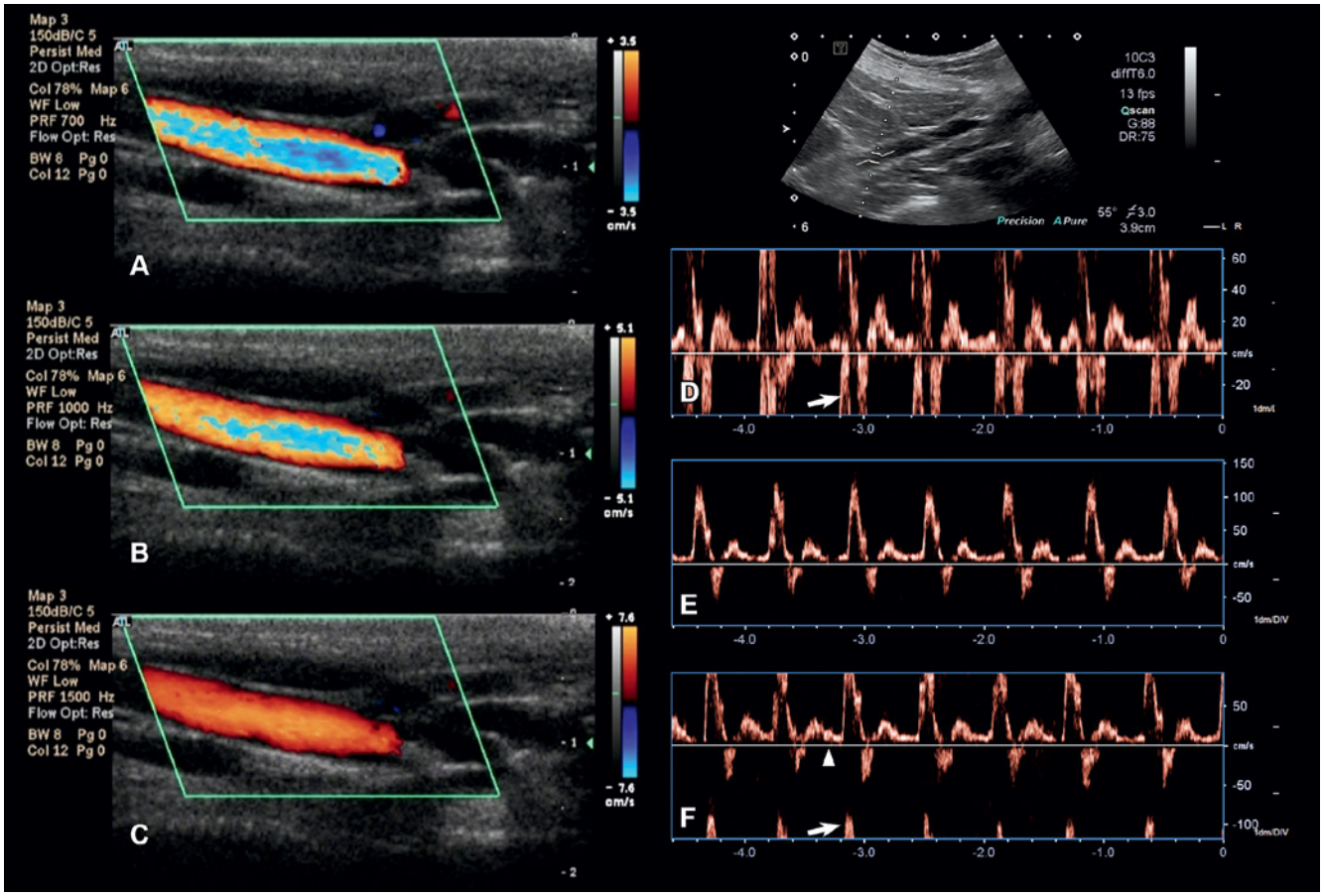


Figure 1.26. **Aliasing artifact. (A)** With **color Doppler**, aliasing appears as a linear or mosaic hue in the center of a high flow velocity vessel and when the measuring scale (on the right, 3.5 cm/sec in this case) is exceeded. **(B)** By increasing the scale to 5.1 cm/sec, the artifact is less pronounced. **(C)** It disappears completely when the scale is increased to 7.6 cm/sec. **(D)** With **Spectral Doppler**, aliasing manifests itself as wrap-around of the flow profile on the opposite extremity of the velocity scale. The measured maximal velocity of this iliac artery (in direction of the transducer) exceeds 60 cm/sec and is interpreted as reversed (arrow). **(E)** Increasing the velocity scale (or pulse repetition frequency) to 150 cm/sec, allows the entire flow spectrum to be included. Note that the calculated maximal velocity of this artery exceeds 100 cm/sec. **(F)** the baseline (arrowhead) position can also be responsible for the onset of aliasing. In this case, it was moved to the positive side, reducing the scale on that side (maximal velocity approximating 75 cm/sec), and resulting in velocity peak wrap-around (arrow).

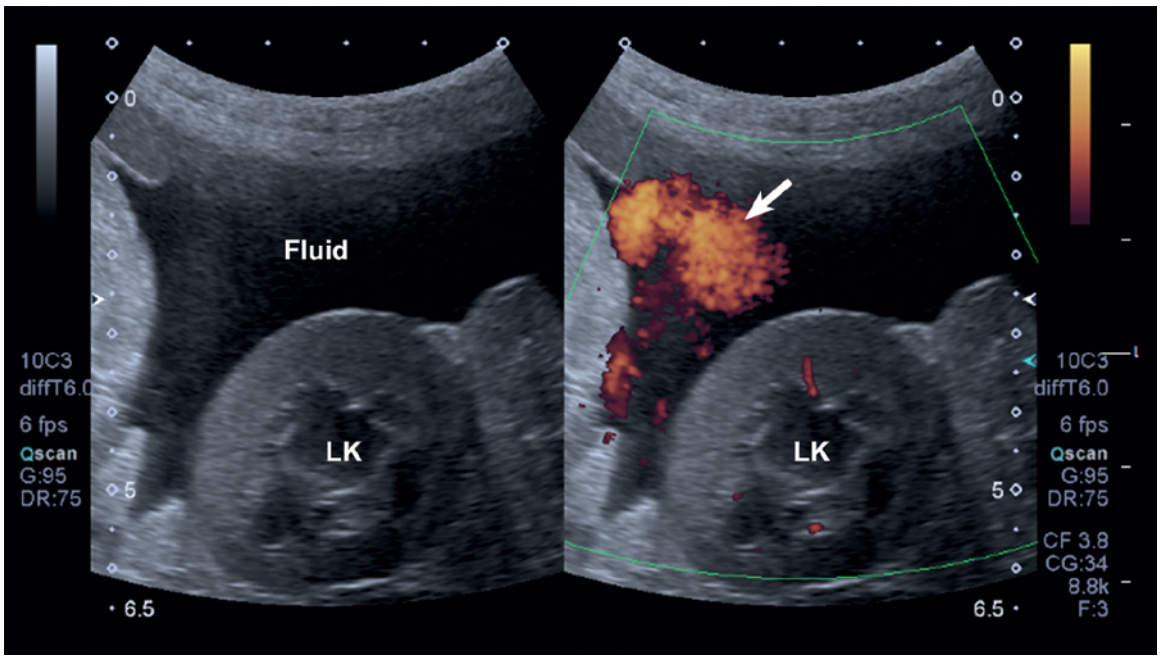


Figure 1.27. **Doppler flash artifact.** Spurious echoes often appear when using Power (or color) Doppler in moving patients or when ascites is present, limiting the assessment of the tissue perfusion in these cases.

Vet-ebooks.com

References

Baad M, Lu ZF, Reiser I, Paushter D (2017) Clinical significance of ultrasound artifacts. Radiographics 37:1408–1423.

Barthez PY, Leveille R, Scrivani PV (1997) Side lobes and grating lobes artifacts in ultrasound imaging. Vet Radiol Ultrasound 38:387–393.

Boote EJ (2003) AAPM/RSNA physics tutorial for residents: topics in US – Doppler US techniques: concepts of blood flow detection and flow dynamics. Radiographics 23: 1315–1327.

Bushberg JT, Seibert JA, Leidholdt EM Jr., Boone JM (2011) Chapter 14 Ultrasound The Essential Physics of Medical Imaging, 3rd edition. Philadelphia, Pa: Lippincott Williams & Wilkins, pp. 500–576.

d'Anjou MA, Penninck D, Cornejo L, Pibarot P (2004) Ultrasonographic diagnosis of portosystemic shunting in dogs and cat. Vet Radiol Ultrasound 45:424–437.

Feldman MK, Katyal S, Blackwood MS (2009) US artifacts. Radiographics 29:1179–1189.

Fitze D, Franchi M, Peterhans L, Frey WO, et al.(2023) Reliability of panoramic ultrasound imaging and agreement with magnetic resonance imaging for the assessment of lumbar multifidus anatomical cross-sectional area. Nature Portfolio-Sci Rep.

Goldstein A, Madrazo BL (1981) Slice thickness artifacts in gray-scale ultrasound. J Clin Ultrasound 9:365–375.

Hangiandreou NJ (2003) B-mode US: basic concept and new technology. Radiographics 23:1019–1033.

Hedrick WR, Peterson CL (1995) Image artifacts in real-time ultrasound. J Diagn Med Sonogr 11:300–308.

Heng HG, Widmer WR (2010) Appearance of common ultrasound artifacts in conventional vs spatial imaging. Vet Radiol Ultrasound 51:621–627.

Hindi A, Paterson C, Barr RG (2013) Artifacts in diagnostic ultrasound. Rep Med Imaging 6:29–48.

Kennelly MM, Moran P (2008). Directional Power Doppler in the midsagittal plane as an aid to the prenatal diagnosis of cleft lip and palate. Prenat Diagn 28:56–58.

Kirberger RM (1995) Imaging artifacts in diagnostic ultrasound-a review. Vet Radiol Ultrasound 36:297–306.

Liu X, Zheng S, Li Y, He W (2022) Use of extended field-of-view ultrasound imaging in giant primary breast angiosarcoma: a case description. Quant Imaging Med Surg 12(1):868–873.

Louvet A (2006) Twinkling artifact in small animal Color-Doppler sonography. Vet Radiol Ultrasound 47:384–390.

Mesurolle B, Ariche-Cohen M, Mignon F, Guinebretière JM, Tardivon A, et al. (2002) Small focal areas of acoustic shadowing in the breast. J Clin Ultrasound 30: 88–97.

Naganuma H, Ishida H, Nagai H, Ogawa M, et al. (2019) Range-ambiguity artifact in abdominal ultrasound. J Med Ultrason 46:317–324.

O'Brien RT, Zagzebski JA, Delaney FA (2001) Ultrasound corner: range ambiguity artifact. Vet Radiol Ultrasound 42:542–545.

Rahmouni A, Bargoin R, Herment A, Bargoin N, Vasille N (1996) Color Doppler kwinkling artifact in hyperechoic regions. Radiology 199(1):269–71.

Revzin MV, Imanzadeh A, Menias C, Pourjabber S, et al. (2019) Optimizing image quality when evaluating blood flow at doppler US: a tutorial. Radiographics 39:1501–1523.

Rubin JM, Adler RS, Bude RO, Fowlkes JB, et al. (1991) Clean and dirty shadowing at US: a reappraisal. Radiology 181: 321–236.

Szabo TL, Kaczkowski P (2023) Chapter 9 Doppler. In Essential of Ultrasound Imaging, 1st edition. Elsevier, pp. 209–241.

Szatmari V, Sotonyi P, Voros K (2001) Normal duplex Doppler waveforms of major abdominal blood vessels in dogs: a review. Vet Radiol Ultrasound 42:93–107.

Ziegler L, O'Brien RT (2002) Harmonic ultrasound: a review. Vet Radiol Ultrasound 43:501–509.

Vet-ebooks.com

CHAPTER TWO

Point of Care Ultrasound: Abdomen, Pleural Space, Lung and Cardiovascular Applications

Søren Boysen

Department of Veterinary Clinical and Diagnostic Sciences, Faculty of Veterinary Medicine, University of Calgary, Calgary, Alberta, Canada

Preparation and Scanning Technique

Abdominal and thoracic focused assessment with sonography for trauma (FAST) exams were developed to rapidly answer a limited number of very focused questions in the emergency setting; does the patient have free abdominal, pleural, or pericardial fluid, or pneumothorax (Boysen et al. 2004; Lisciandro et al. 2008, 2009; McMurray et al. 2016; Mohammad et al. 2014; Montoya et al. 2016; Rice et al. 2021; Robba et al. 2021; Walters et al. 2018). In contrast, POCUS is much broader in scope and is not limited to any specialty, protocol, organ system, or question (Robba et al. 2021). More specifically, POCUS can be defined as the acquisition, interpretation, and immediate clinical integration of ultrasonographic imaging performed patient side by an attending clinician, as opposed to a formal sonographic exam performed by an imaging specialist (Díaz-Gómez et al. 2021). The objective is to answer a specific question or series of questions using a limited number of sonographic windows in patients with well-defined clinical symptoms (Choi et al. 2020; Díaz-Gómez et al. 2021; Rice et al. 2021; Robba et al. 2021). As such, it may comprise single-targeted ultrasound examinations (e.g., urinary volume estimation, renal pelvic dilation, pleural effusion, etc.) or multiple-targeted ultrasound examinations (e.g., underlying cause of shock, respiratory distress, trauma, etc.) depending on the specific question or series of questions to be answered (Choi et al. 2020). With these priorities in mind, the study is often performed in less than 10 minutes, using topical alcohol on unclipped areas of the patient that is placed in an optimal position for comfort. Many common POCUS applications currently used in human medicine are likely translatable to small animals (Table 2.1).

Patient Preparation

POCUS evaluations vary depending on the clinical setting encountered (Figure 2.1). Although standardized protocols are important and recommended in many situations, there is no single POCUS protocol that will work for every patient and the POCUS technique should be adapted to the specific question asked, the clinical situation encountered, and the proficiency of the operator. POCUS is dynamic in nature, often

Atlas of Small Animal Ultrasonography, Third Edition. Edited by Dominique Penninck and Marc-André d'Anjou.
© 2025 John Wiley & Sons, Inc. Published 2025 by John Wiley & Sons, Inc.
Companion website: www.SmallAnimalUltrasonography.com

Vet-ebooks.com

Table 2.1
Main and expanding clinical applications of POCUS in small animals

POCUS	Main clinical applications
Abdomen	• Intraabdominal free fluid • Free abdominal air • Gallbladder (particularly gallbladder wall edema) • Subxiphoid window into the thorax to assess: 1. Pleural effusion 2. Pericardial effusion 3. Pulmonary pathology • Caudal vena cava assessment for vascular volume status • Gastric content and volume • Gastrointestinal motility • Gastrointestinal obstruction • Splenic masses • Retroperitoneal fluid • Renal pelvic dilation • Pyometra, testicular, and pregnancy assessment • Urinary bladder volume estimation
Pleural space and lung ultrasound (PLUS)	• Pleural space pathology 1. Pneumothorax 2. Pleural effusion • Alveolar interstitial syndromes (AIS) • Atelectasis • Bilateral versus unilateral lung ventilation • Endotracheal tube placement • Rib fractures
Cardiovascular	• Pericardial effusion • Left atrial size • Volume assessment • Ventricular ± valvular function • Right heart changes • Cardiac arrest applications 1. Reversible causes of cardiac arrest 2. Presence of intrinsic cardiac activity • Volume status and response to fluid boluses; assesses cardiac and vena cava changes • Vascular 1. Aortic dissection and thromboembolism 2. Carotid artery
Other	• Eye: Intracranial hypertension, optic nerve sheath swelling • Musculoskeletal
US-guided interventions	• Thoracocentesis, abdominocentesis, pericardiocentesis, cystocentesis, fine needle aspiration, nerve blocks

leading to additional focused questions based on the initial sonographic findings, and how those findings integrate into the clinical reasoning for a specific case.

POCUS should be performed in the position in which the patient is most comfortable to minimize patient stress. Patient position may be dictated by underlying injury (e.g., spinal fractures, respiratory distress) and/or interventional procedures (e.g., patients under anesthesia or receiving mechanical ventilation). Localization of some pathology will change with patient positioning, as fluid falls and gas rises (Boysen 2021), therefore the probe position on the animal and its orientation needs to be adapted.

Dorsal recumbency should be avoided unless the patient is stable, tolerates dorsal recumbency well, and there is minimal chance of patient decompensation.

Vet-ebooks.com

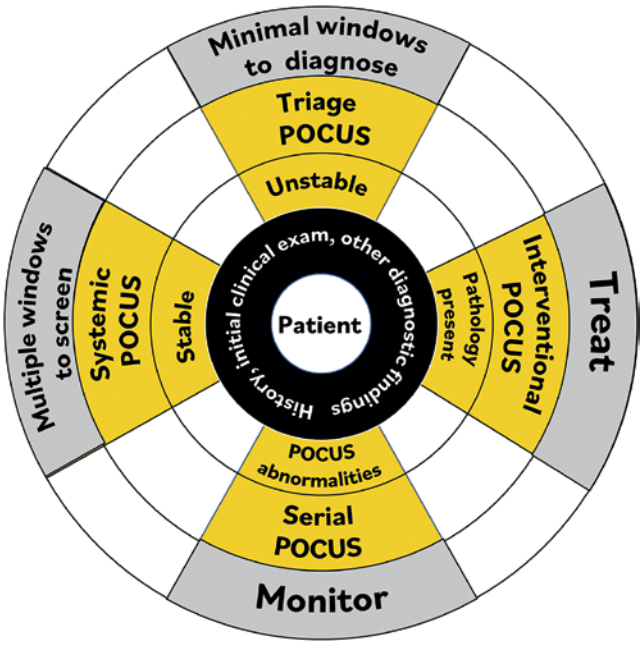


Figure 2.1. POCUS is patient centered and targeted. It is also integrative and has four general applications which vary depending on the targeted-objectives of the scan, history, exam findings, and the clinical setting encountered: **1**.triage POCUS uses the minimum number of windows to identify the most immediate life-threatening and critical conditions; **2**. serial POCUS is applied to monitor progression or resolution of any pathology, and response to therapy; **3**. systemic or multiorgan POCUS uses multiple windows in more stable patients (with or without specialist assistance) to detect asymptomatic conditions, new developments, and/or to ensure sonographically detectable problems have not arisen prior to undertaking procedures, anesthesia, or discharge/service transfer; and **4.** therapeutic POCUS is used to reduce complications of interventions where applicable. POCUS, point-of-care ultrasound. Courtesy of Calgary VPOCUS Academy.

If required, patients can be gently repositioned or encouraged to stand to assess POCUS windows not initially accessible due to patient positioning. However, it is not obligatory to assess all POCUS windows in all patients to arrive at a diagnosis, particularly if the patient is unstable (Loughran 2021). In unstable patients, the objective is to identify immediately life-threatening conditions with the minimum number of sonographic views possible, stabilize the patient, reassess the patient, and then decide if, and what further point-of-care diagnostics, including additional POCUS examinations are required (Figure 2.1). Do not discontinue stabilization efforts or compromise patient safety/comfort; bring the machine to the patient. Only if the patient is sufficiently stable should multiorgan, systemic POCUS be performed.

To maintain efficiency, fur is not clipped but parted to provide access to the skin, and alcohol is used as the coupling agent, with or without gel (Boysen et al. 2004; Lisciandro et al. 2009; McMurray et al. 2016). Alcohol may cause wet hair artifacts on radiographs. It also poses a fire hazard if electrocautery, defibrillators, or laser devices are used following its application. Gel can be added to the probe head in addition to applying alcohol to the patient if image quality is suboptimal. Alternatively, fur can be clipped, and ultrasound gel applied as the sole coupling agent at the probe–skin interface, particularly if image quality remains suboptimal (Boysen et al. 2004). Sedation is rarely required; however, it may decrease anxiety and work of breathing, improving image acquisition in certain settings, particularly for assessment of the lungs and heart.

POCUS Machine and Probe Selection

Almost any ultrasound machine, including handheld units can be used to perform most POCUS evaluations. A designated portable unit is recommended for busy clinics to ensure ultrasound is available and can be transported to the patient as needed. In general, a 5 MHz (larger dogs) to 8 MHz (smaller dogs and cats) microconvex probe and B-mode imaging can be used (Boysen et al. 2004; Lisciandro et al. 2008, 2009; McMurray et al. 2016; Walters et al. 2018). A linear probe is advantageous for vascular access, ultrasound guided nerve blocks, and assessment of the pleura. A phased array is often used for echocardiograms, although a microconvex probe can also be used for all these applications.

With abdominal POCUS (APOCUS), adjust the gain, depth, and focal position as needed to maximize image quality and thoroughly answer each APOCUS question (see Chapter 1 for machine settings). Extending the depth at the subxiphoid location allows evaluation of the heart, caudal lung surface, and the pleural and pericardial spaces (Figure 2.2).

The settings for pleural space and lung ultrasound (PLUS) vary depending on the objective of the scan (e.g., pneumothorax and lung sliding versus B-line identification), which are highlighted in their relative sections. For general PLUS, machine settings are initially optimized to the near field soft tissue structures (Figure 2.3).

For cardiac POCUS (CPOCUS), the depth should be adjusted to include the entire heart, particularly the far wall (Figure 2.4).

Serial POCUS Evaluations

Serial POCUS examinations are recommended to monitor progression/resolution of patients with positive findings (e.g., cavitary fluid volumes, left atrial to

Vet-ebooks.com

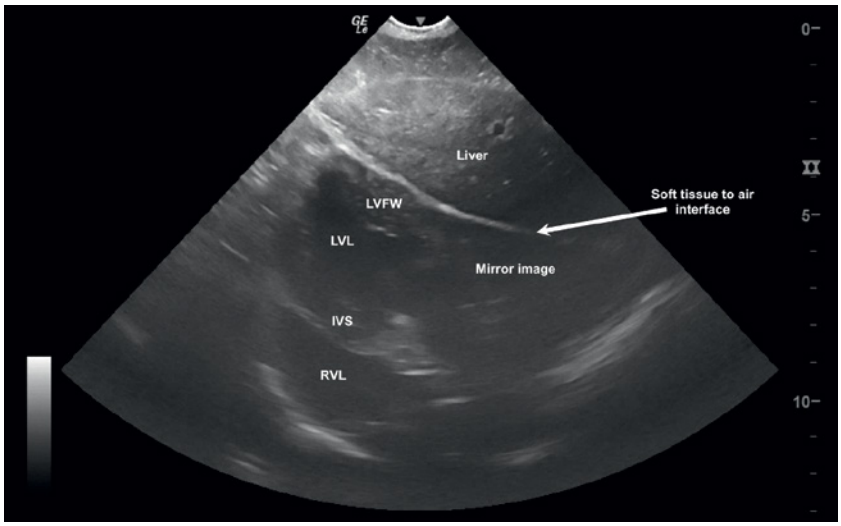


Figure 2.2. Normal image obtained from the subxiphoid (subcostal, or transhepatic) window. Extending the depth at the subxiphoid window allows evaluation of the heart, caudal lung surface, and the pleural and pericardial spaces. The interface of the soft tissues of the abdomen and diaphragm with the caudal visceral pleura of air-filled lung form a hyperechoic interface (the diaphragm). The left ventricular free wall (LVFW) of the heart is visible as a continuous soft tissue structure with the liver and diaphragm (cardiac blend), ruling out significant pericardial effusion, and mirror image artifact can be seen, ruling out pleural effusion within the specific plane of imaging. IVS, interventricular septum; LVL, left ventricular lumen; RVL, right ventricular lumen. Courtesy of Calgary VPOCUS Academy, with permission.

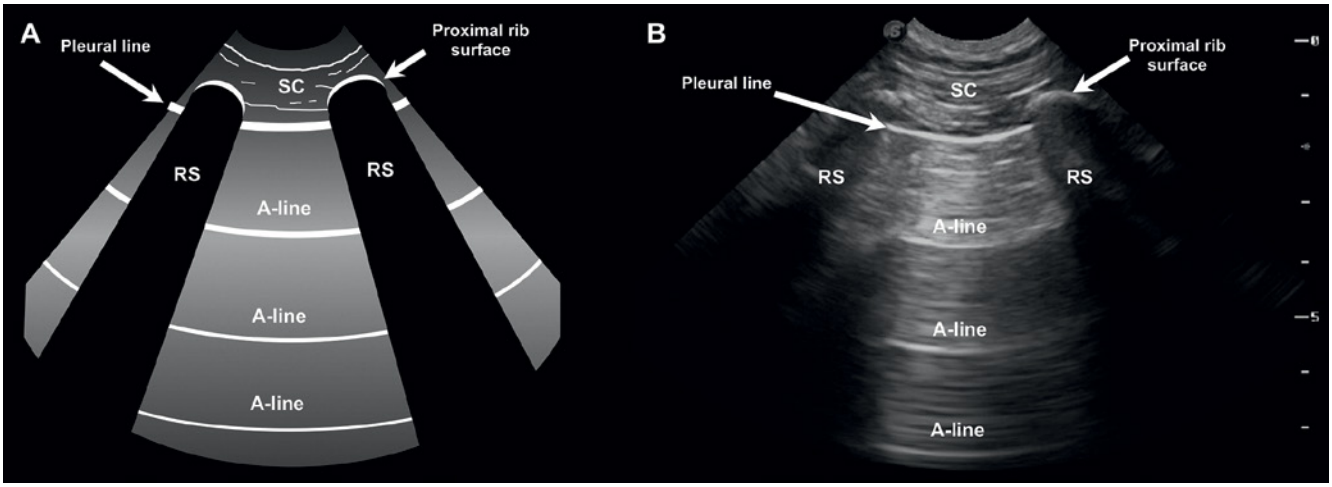


Figure 2.3. Labelled schematic (A) and sonograms (B) showing normal sonoanatomy of pleural space and lung ultrasound (PLUS) when the probe is situated over the ribs in the longitudinal plane (perpendicular to the ribs) with the probe marker directed cranially. Adjust the machine depth setting so the pleural line is visible at the junction between the proximal and middle thirds of the field of view, with the focal position at or just beyond the pleural line. Adjust the gain to maximize appearance of the thoracic wall, while also allowing any far field image artifact to be visualized. RS; rib shadow; SC, subcutaneous tissues. Courtesy of Calgary VPOCUS Academy, with permission.

Vet-ebooks.com

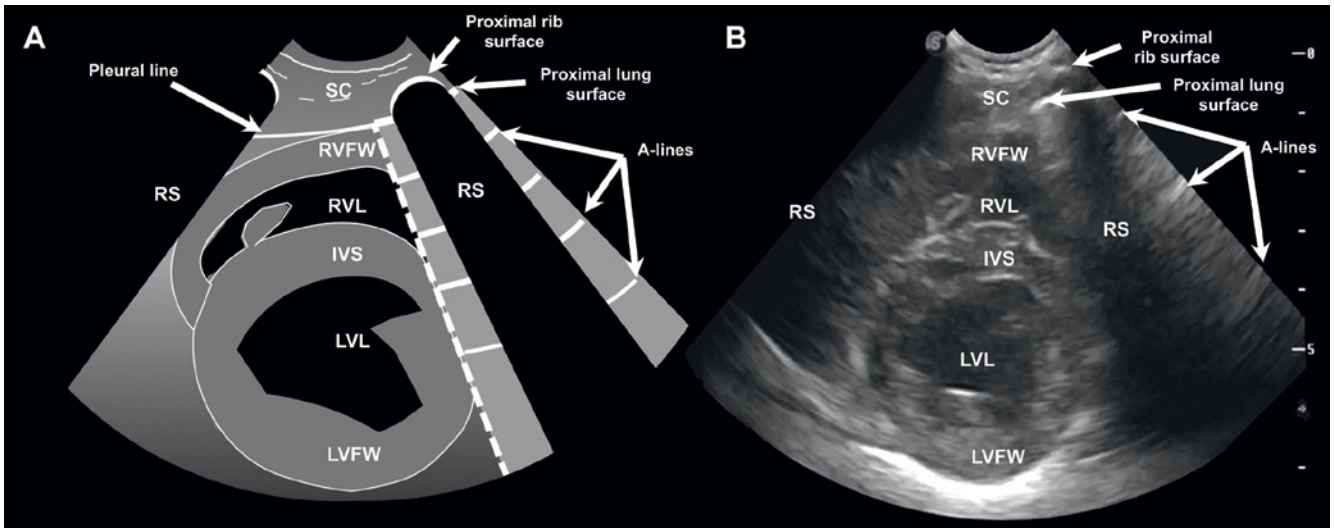


Figure 2.4. Labelled schematic (A) and sonogram (B) showing normal right parasternal short axis sonoanatomy at the level of the left ventricular papillary muscles. Set the depth to ensure the entire heart and pericardium are visible. Set the focal point at the level of the far field wall of the heart. Adjust the gain to easily differentiate the cardiac free wall from the ventricular lumen. Cardiac pre-sets use higher contrasts and lower frequencies making cardiac chamber assessment easier. It is often easier to differentiate cardiac structures if the harmonics filter is turned off. With a microconvex probe, which is often used for point-of-care cardiac assessment in the emergency and critical settings, the rib shadows are often visible, and the lung can often be seen overlying some of the cardiac structures (dotted white line in the schematic). IVS, intraventricular septum; LVFW, left ventricular free wall; LVL, left ventricular lumen; RS, rib shadow; RVFW, right ventricular free wall; RVL, right ventricular lumen; SC, subcutaneous tissues. Courtesy of Calgary VPOCUS Academy, with permission.

aortic ratio size, and/or B-lines in response to therapy, etc.), and to re-assess POCUS negative patients, particularly those that are unstable without an identifiable underlying cause, and/or have received significant quantities of intravascular fluids or other therapeutic interventions. The frequency of serial POCUS exams should be driven by clinical reasoning and assessment and may vary from several minutes to hours.

Sonography of Normal Point-of-Care Ultrasound Organs and Windows

Abdominal Point-of-Care Ultrasound

Most APOCUS exams involve five key abdominal windows to answer binary driven specific APOCUS questions (Boysen et al. 2004; Lisciandro et al. 2009; McMurray et al. 2016; Walters et al. 2018). (Figure 2.5). The key abdominal structures and organs evaluated at each window are listed in Table 2.2. To answer questions rapidly, but thoroughly, at least two sonographic planes (short and long axis), with fanning and rocking movements should be performed at each APOCUS window, ensuring the probe is directed toward abnormalities that may change in location based on patient positioning (fluid falls and gas rises) (Boysen et al. 2004; McMurray et al. 2016).

Transhepatic Imaging of the CVC, Heart, Pleural Space, and Caudal Lung Regions

The subxiphoid window allows transhepatic imaging of the heart, pericardial and pleural spaces, and caudal lung surfaces not accessible trans-thoracically (Figure 2.2). The caudal vena cava (CVC) can also be evaluated at this window (Figure 2.6). This often results in the transducer head being "tucked" under the xiphoid process and orientated almost parallel to the spine (Figure 2.7). In most healthy canine patients, the pericardium contacts the diaphragm, and the heart can be visualized, which is not always true in cats where air filled lung may occupy the space between the diaphragm and the heart, hampering cardiac assessment from the subxiphoid site.

Vet-ebooks.com

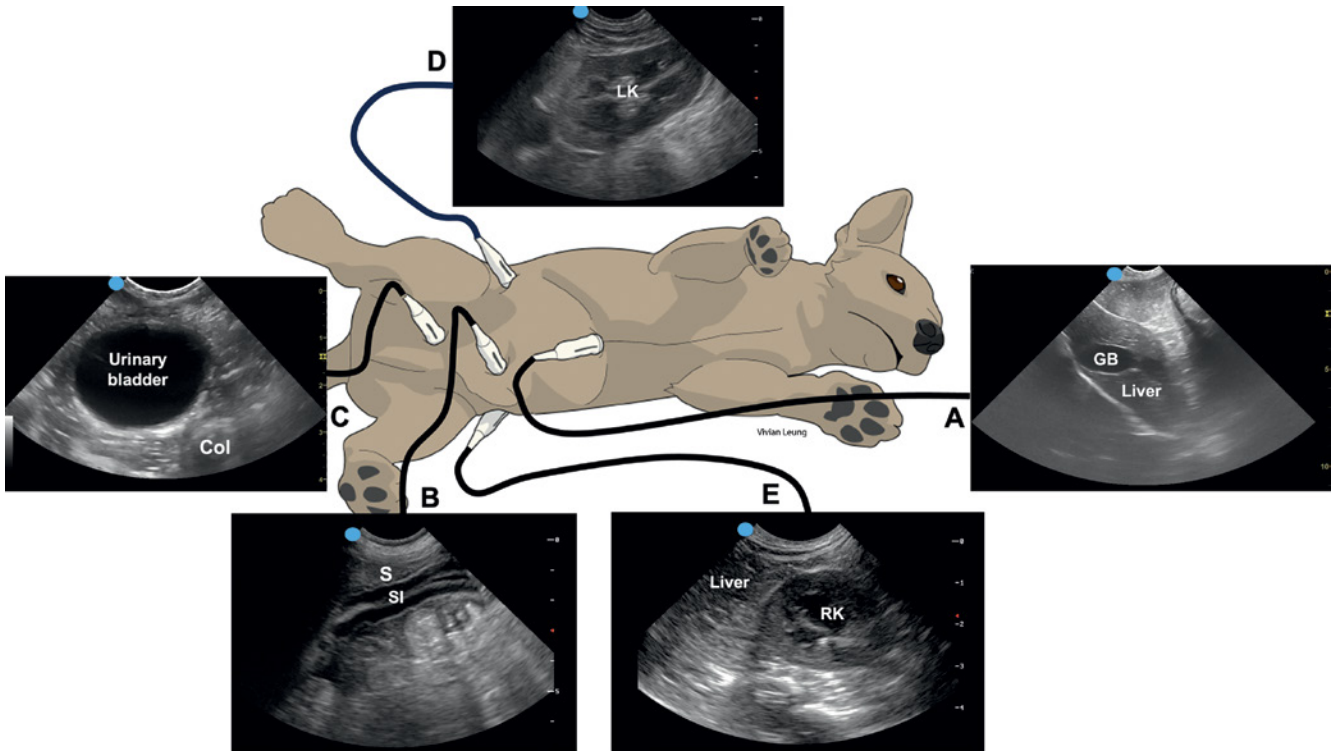


Figure 2.5. **Schematic illustration of the small animal five-point abdominal point-of-care ultrasound (APOCUS) exam and corresponding abdominal windows with images that are classically evaluated**; **(A)** Subxiphoid, **(B)** Umbillical, **(C)** Urinary Bladder, **(D)** Left paralumbar, **(E)** Right paralumbar. Scan the patient in the position the patient is most comfortable (left lateral recumbency is shown in this image). Modify the APOCUS exam to increase the chance of detecting that specific pathology based on how the patient is positioned and where pathology is likely to accumulate (gas rises, fluid falls). GB, Gall bladder; LK, left kidney; RK, right kidney; S, spleen; SI, small intestine; urinary bladder window; Col, colon. Courtesy of Vivian Leung, with permission.

Table 2.2
Key windows and organ identification while performing a 5-point APOCUS exam

APOCUS window	Organs assessed at each window
Subxiphoid	Stomach Liver Gallbladder Caudal vena cava as it crosses the diaphragm Diaphragm–lung interface Pleural space (Transhepatic) Caudal lung lobe regions (Transhepatic) Pericardial space (Transhepatic) Heart (Transhepatic)
Umbilical	Spleen Intestinal loops Gravity dependent regions depending on patient position
Right paralumbar	Right kidney (pelvis and retroperitoneal space) Duodenum
Left paralumbar	Left kidney (pelvis and retroperitoneal space) Spleen
Urinary bladder/pelvic region	Urinary bladder Colon Uterus Trifurcation of the aorta

Vet-ebooks.com

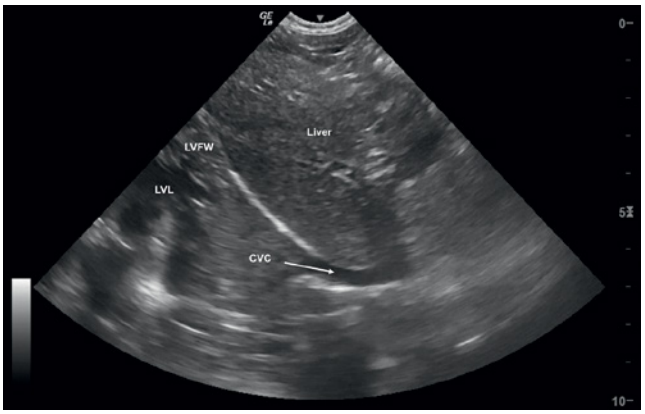


Figure 2.6. Sonogram obtained from the subxiphoid (subcostal) window showing normal sonoanatomy of the liver, caudal vena cava (CVC), heart and caudal lung surface. By fanning across midline, the apex and left ventricular free wall of the heart will be visible in the far field contacting and appearing to "blend" with the diaphragm and liver. The CVC can often be found crossing the diaphragm when the probe is fanned from the heart to the right of the patient, often between planes where the heart and gall bladder (not shown) are visualized. If the CVC is not seen, the depth should be increased as it is often the last structure to be seen in the far field of the image. The CVC may not be visible if gas filled stomach or intestines are overlying it. CVC, caudal vena cava; LVL, left ventricular lumen; LVFW, left ventricular free wall. Courtesy of Calgary VPOCUS Academy, with permission.

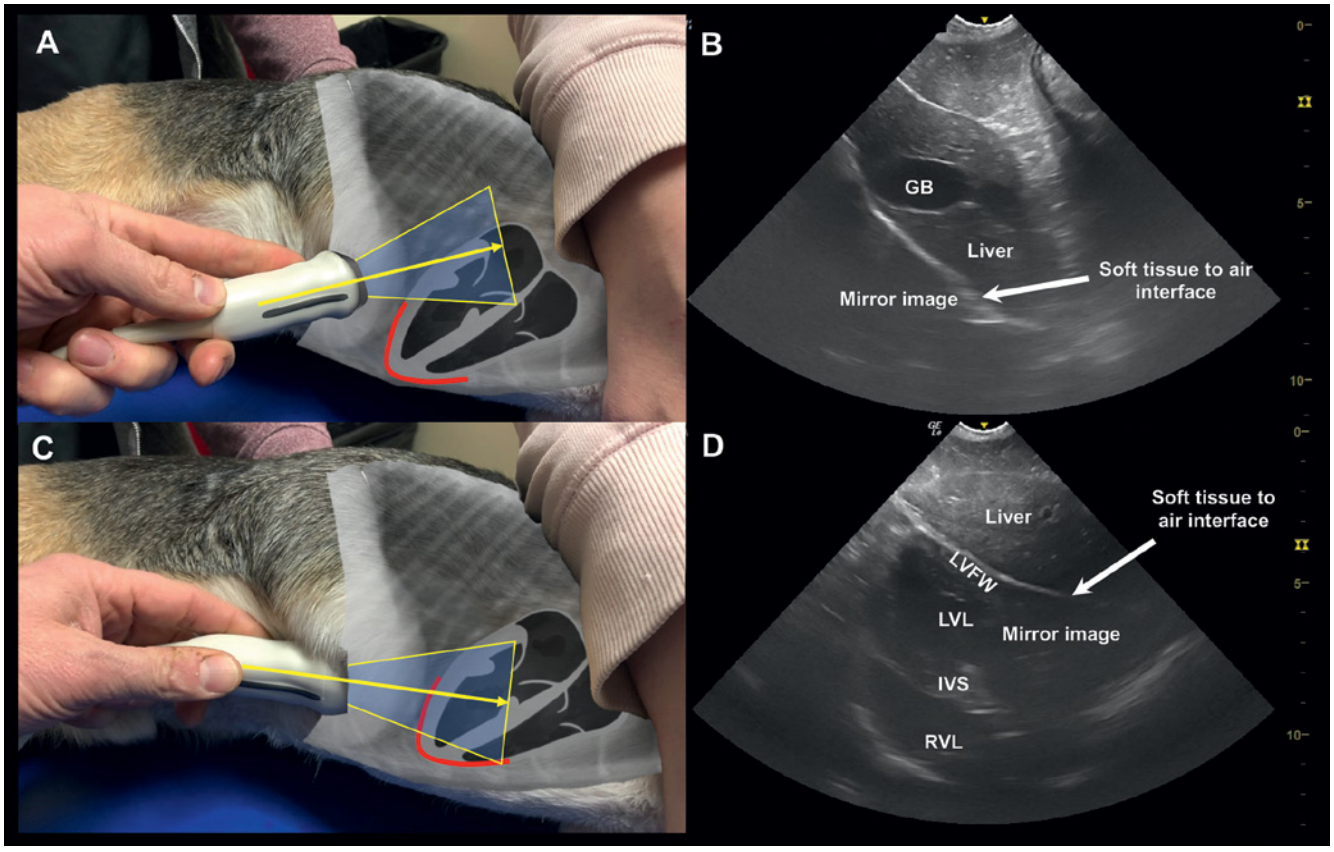


Figure 2.7. Schematic overlay (A, C) and sonograms (B, D) obtained from the subxiphoid (subcostal) window with the probe at a 45° angle to the spine **(A, B)** and rocked more parallel to the spine and tucked under the subxiphoid process **(C, D)**. If the heart is not initially identified **(B)** it may be necessary to rock the probe from the 45° angle **(A)** often used to assess the subxiphoid site, until it is almost parallel to the spine **(C)**. This should allow the apex of the heart (outlined in red) to become visible **(D)**, where it contacts the diaphragm and sternum ventrally. This often results in the probe head being "tucked" under the xiphoid process. The depth setting may also need to be increased if the goal is to assess more of the heart. The heart base region can be difficult to visualize via the subxiphoid window in healthy animals because lung is often interposed between the diaphragm and heart base. GB, gall bladder; IVS, intraventricular septum; LVFW, left ventricular free wall; LVL, left ventricular lumen; RVL, right ventricular lumen. Courtesy of Calgary VPOCUS Academy, with permission.

Vet-ebooks.com

Pleural Space and Lung Ultrasound (PLUS)

Protocols

They are multiple lung POCUS protocols published in veterinary medicine, all of which scan different lung regions and a different percentage of lung surface area (Armenise et al. 2019; Boysen et al. 2019; Lisciandro et al. 2008, 2014; Rademacher et al. 2014; Rigot et al. 2024; Vezzosi et al. 2017). In human medicine, the recommendation is to use lung ultrasound protocols that evaluate more surface area as they have a higher sensitivity and specificity for detecting pathology (Demi et al. 2023). However, they take longer to perform, and the clinician must therefore balance the risk of missing pathology against the time required to perform sonographic examination. Including the subxiphoid window and evaluating the abdominal curtain sign may allow identification of pathology otherwise missed with traditional transthoracic ultrasound protocols (Lee 2016, 2017). The author prefers the Calgary PLUS technique (Figure 2.8) which includes knowledge of sonographically definable lung and pleural space borders, long and short axis probe orientations, and the sites pleural space pathology is most likely to localize (Figure 2.9).

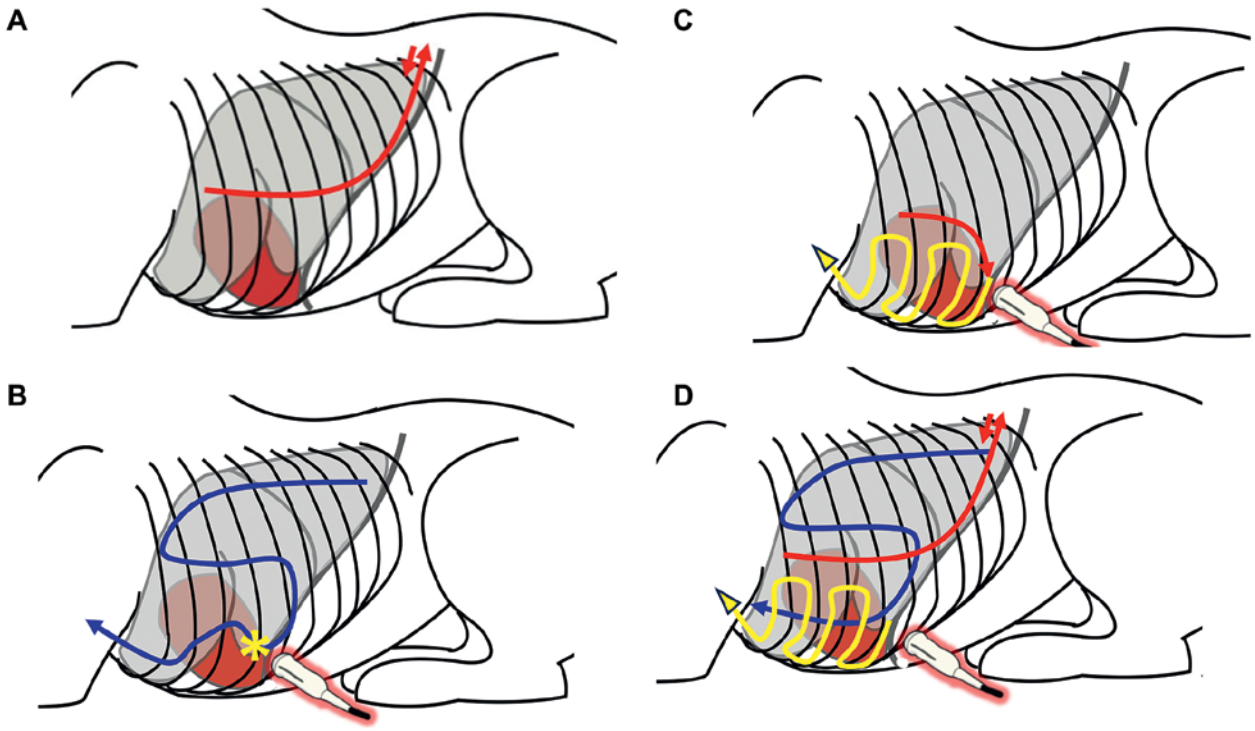


Figure 2.8. Schematic images of the PLUS approach to assess for pneumothorax, lung surface pathology, and pleural effusion. (A) Identification of the abdominal curtain sign (ACS) and caudal dorsal site for pneumothorax (red curved arrow). Start midway up the thorax with the probe perpendicular to the ribs (probe marker directed cranially) just caudal to the front limb (cranial lung border). Keeping the probe perpendicular to the ribs, slide caudally from the starting point until the ACS is identified. Next sweep dorsally along the ACS until the hypaxial muscles are encountered and the pleural line disappears. The probe is then swept ventrally off the hypaxial muscles until the pleural line just reappears (the most gravity-independent site; short red arrow). **(B)** Assessment of lung surface regions between the defined cranial and caudal lung borders (blue curved arrow). Start at the caudo-dorsal site. At the pericardio-diaphragmatic (PD) window (yellow asterisk), the probe can be turned parallel to the ribs **(C)**. Time permitting, the subxiphoid site can also be assessed (red outlined probe). **(C)** Assessment of pleural effusion and ventral lung pathology. Identifying the PD window (red arrow) with the probe situated perpendicular to the ribs helps differentiate pleural and pericardial effusion. In the sternal or standing patient, turn the probe parallel to the ribs at the PD window (with the probe indicator marker directed dorsally) and slide ventrally until the sternal muscles fill 1/3 to 1/2 of the ultrasound image. This identifies smaller volume pleural effusion. Keeping the probe parallel to the ribs slide dorsally or ventrally within each intercostal space (yellow arrows) from the ACS caudally to the thoracic inlet cranially. Time permitting the subxiphoid site can also be included (red highlighted probe). **(D)** All three components of the PLUS approach overlaid. Adapted from Boysen et al. (2019)/Frontiers Media S.A./CC BY 4.0.

Vet-ebooks.com

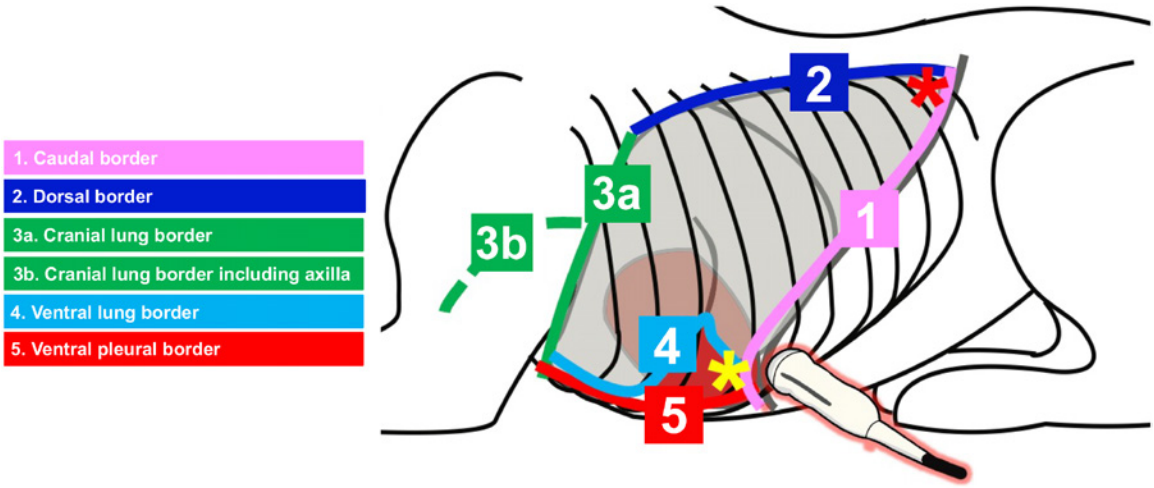


Figure 2.9. Schematic image highlighting the five sonographically-defined pleura and lung borders of healthy patients. **1**. The **caudal border** is the abdominal curtain sign (pink outline).**2.** The dorsal border is comprised of the hypaxial/sublumbar muscles (dark blue outline). **3a**. The **cranial border** is defined by what is sonographically visible due to the musculature and presence of the thoracic limb (green outline). **3b.** The lung surface area can be expanded by sliding the probe under the limb into the **axilla** regions (green dotted line).**4.** The **ventral lung border** (light blue outline) **5.** The **ventral pleural border** is shown in red and includes the sternal/pectoral muscles. The red asterisk identifies the most caudal dorsal site where free pleural gas will accumulate at the caudo-dorsal border with animals in a sternal or standing position. Small volume pleural effusion will accumulate between the lung and sternal muscles ventrally (red outline). The yellow asterisk indicates the pericardio-diaphragmatic window, a good site to identify and differentiate pleural and pericardial effusion. The probe indicates the subxiphoid window which allows the caudal lung, pleura, heart, and pericardial space to be assessed through the transhepatic view via the abdomen. Identifying sonographically defined PLUS borders helps prevent confusion of normal sonographic findings for pleural space or lung pathology, orientates operators to where the probe is situated over the thorax, and ensures the most sensitive sites pleural space and lung pathology localize are properly evaluated. Courtesy of Calgary VPOCUS Academy.

Lines and Signs of PLUS

Bat Sign

The BAT sign refers to the characteristic appearance of the pleural line and two adjacent ribs and forms the mnemonic – "**B**one or **A**ir with the probe **T**ransverse to the ribs." It is identified when the probe is positioned within an intercostal space, over lung, perpendicular to the ribs, with the marker directed cranially (Figure 2.10A, B). If placed between and parallel to the ribs, only the pleural line is seen, which is not interrupted by the ribs (Figure 2.10C).

In healthy animals, the pleural line is comprised of the parietal (inside lining of the thoracic wall) and the visceral linings (lung surface). It is the difference in acoustic impedance occurring between the thoracic wall and air-filled lung that causes the pleural line to appear hyperechoic. The pleural line is key to identify as lung ultrasound involves interpretation of artifacts arising from this line. These artifacts change depending on the underlying status of the lung and pleural space.

Lung Sliding

Using real-time B-mode ultrasound, lung sliding (aka the glide sign) is usually identified along the pleural line (more specifically the parietal lining) as a horizontal to-and-fro shimmer. The shimmer results from the visceral pleura sliding along the parietal pleura during lung inflation and deflation that occurs with the respiratory cycle. When visible, the presence of lung sliding in the absence of a lung point rules out space-occupying pleural pathology directly below the probe location it is visualized. Lung sliding is lost when the pleurae are separated or adhered to one another, when the lung is overinflated, and when the soft tissue to air-filled lung interface is lost. (Table 2.3).

Lung sliding can be more challenging to appreciate when a large percentage of ultrasound beams bounce back and forth between the ultrasound probe and the pleural line (e.g., ultrasound beams that strike the pleural at a 90° angle), making the pleural line appear more hyperechoic. Thus, making the pleural line appear "grainier" (less hyperechoic) helps visualize lung sliding. Tricks to enhance lung sliding include

Vet-ebooks.com

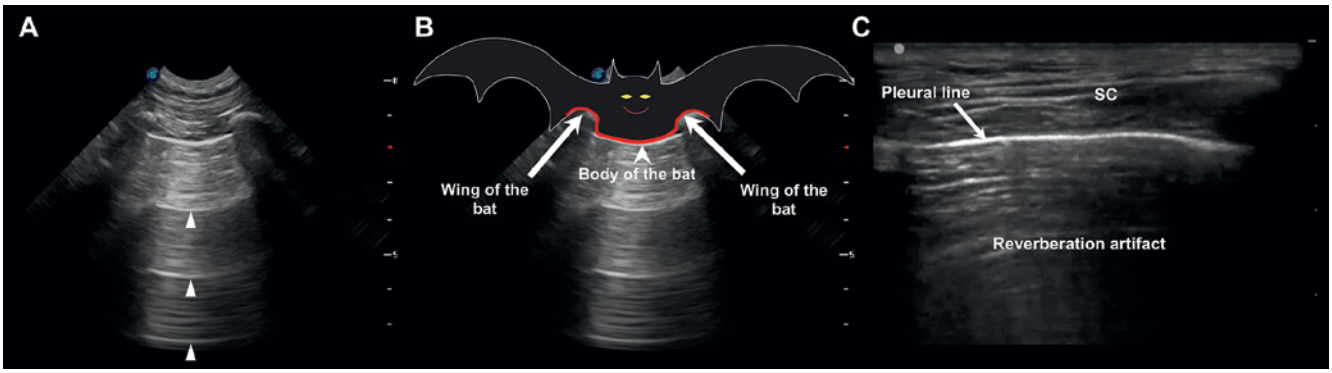


Figure 2.10. Unlabelled and labelled sonograms depicting normal sonoanatomy with the probe perpendicular (A, B) and parallel (C) to the ribs. (A) Unlabelled sonogram depicting the normal sonoanatomy of the "**bat sign**." The pleural line is the first white line below the ribs that joins the rib shadows. A-lines (arrow heads) are created by the reflection of the ultrasound beam between two highly reflective surfaces: the ultrasound probe and a soft tissue-air interface, which occurs when healthy lung or pneumothorax interfaces with the parietal pleura. Changing the angle of insonation of the probe from 90° relative to the pleura decreases the percentage of returning ultrasound beam, causing A-lines to be less visible or to even disappear. **(B)** Labelled sonogram with overlaid schematic of a bat depicting the sonoanatomy that comprises the "bat sign." The proximal rib surface of two adjacent ribs form the wings of the bat (short convex downward red lines, white arrows), while the pleural line forms the body of the bat (concave upward long curved red line, arrow head) when the probe is situated perpendicular to the ribs. The depth is at 7 cm to allow far field A-lines to be identified. **(C)** Sonogram obtained with a linear probe orientated parallel to the ribs and the depth set at 5 cm. A linear probe may provide better detail and assessment of pleural abnormalities. Turning the probe parallel to the ribs allows a larger area of the pleura to be assessed without interference from the ribs and their shadows. The classic bat sign is, however, lost, which can sometimes make it challenging to identify the pleural line with confidence. SC, subcutaneous tissues. Courtesy of Calgary VPOCUS Academy, with permission.

Table 2.3
Conditions that result in a loss of lung sliding along the parietal lining

Pathology for affected lung sliding	Examples

Separation of the pleura	• Pleural effusion
	• Pneumothorax
	• Other space occupying pathology
	  • Diaphragmatic hernia
	  • Pleural space masses
	  • Pleural foreign bodies

Adhesions	Fibrosing pleuritis, prior pleurodesis
Decreased lung sliding	Feline asthma
Loss of a soft tissue air interface between the parietal lining and lung surface	Consolidation/atelectasis

turning off the artifact reduction settings (e.g., harmonics mode), fanning the probe or centering the probe over a rib to change the angle of the ultrasound beam striking the pleural surface, setting the depth at a minimum, moving the focal zone to the location of the pleural surface, and decreasing the gain to decrease the echogenicity of the pleural line.

Lung sliding can also be difficult to identify in patients with rapid shallow breathing patterns that result in minimal movement of the lung across the thoracic wall (e.g., tachypnea/hyperpnea, feline asthma, panting). To assist with proper interpretation of lung sliding, the probe should be held steady and lung sliding should ideally be interpreted when the patient is not moving.

Lung Pulse

The lung pulse refers to rhythmic movement of the visceral pleura along the thoracic wall because of cardiac vibrations transmitted through motionless lung. It is equivalent to a "mini lung slide" and confirms the parietal and visceral pleura are in apposition to one another. The lung pulse is typically lost when lung sliding is present (lung sliding dominates the lung pulse) or when the visceral pleura is separated from the parietal pleura. The lung pulse becomes more difficult to visualize in well aerated lung and in lung regions located distal to the heart. In healthy dogs and cats, it is possible to identify the lung pulse during the respiratory pause between respirations, particularly over lung regions in proximity to the heart.

Vet-ebooks.com

A-lines

A-lines are a type of reverberation artifact appearing as hyperechoic (white) horizontal lines running parallel and equidistant from the skin to the pleural line (Figure 2.10A).

B-lines

B-lines (Figure 2.11), also referred to as **lung rockets**, **comet tails,** and **ring down artifacts** in the literature, are a hyperechoic vertical sonographic lung surface reverberation artifact that occurs with increased lung density (i.e., decreased lung aeration) at the lung periphery. Depending on the quantity identified, they may be a normal finding or may be representative of pulmonary pathology or atelectasis. Up to three B-lines can be identified in a single sonographic window of healthy cats and dogs (Armenise et al. 2019; Boysen et al. 2019; Lisciandro et al. 2014; Rademacher et al. 2014; Rigot et al. 2024; Vezzosi et al. 2017). In healthy animals, they are believed to result from normal interlobar septa and/or regions with microatelectasis at the lung periphery (Goffi et al. 2018). Although 10–50% of healthy cats and dogs have B-lines (more B-lines are identified with protocols that scan more lung surface area), the majority of sonographically accessible lung surface will not contain B-lines (Armenise et al. 2019; Boysen et al. 2019; Lisciandro et al. 2014; Rademacher et al. 2014; Rigot et al. 2024; Vezzosi et al. 2017). A recent publication in cats with no clinical signs and normal 3-view thoracic radiographs identified 2/67 cats with a single region of coalescing B-lines over a single hemithorax (Rigot et al. 2024). Due to the variation in number of B-lines reported with different lung protocols in healthy animals, and the small number of studies in healthy dogs and cats reported to date, the clinical context must be considered when deciding if identified B-lines represent a normal finding or if lung pathology is likely.

Abdominal Curtain Sign

The abdominal curtain sign (ACS) is a normal sonographic artifact of healthy animals (Figure 2.12). It orientates the operator to the area of the thorax being viewed (caudolateral lung margin) and can be used to identify pleural space (pneumothorax, pleural effusion) and lung pathology (Boysen et al. 2019).

The ACS is visible along the entire caudal lung margin of healthy animals except at the pericardiodiaphragmatic (PD) window located caudo-ventrally. At this location, the lungs do not cover the heart and diaphragm, allowing the diaphragm to be seen curving away from the thoracic wall (Figure 2.13).

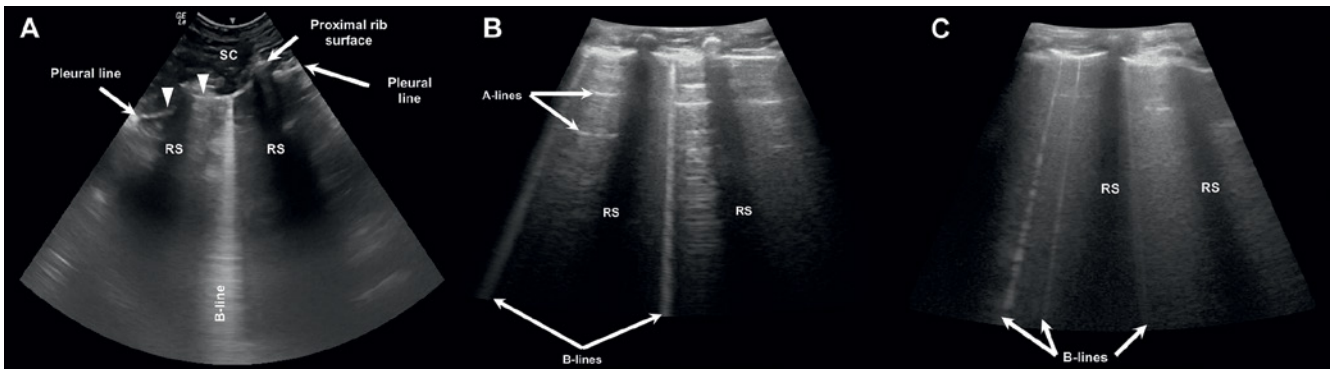


Figure 2.11. Sonograms depicting variation in the normal number of B-lines that can be identified within a single sonographic window during pleural space and lung ultrasound (PLUS). B-lines are defined by the following five criteria: (1) vertical white/hyperechoic projections; (2) originating from the lung surface of the pleural line; (3) extending through the far field without fading; (4) swinging to-and-fro with lung sliding; and (5) often obliterating A-lines if present. If present, it is more common to find a single B-line **(A)** at one to two locations on either hemithorax or two B-lines **(B)** at a single location when scanning the lung surfaces. Although rare, three B-lines **(C)** have been reported at a single sonographic window of healthy cats and dogs; however, the presence of three B-lines is rare and should not occur at multiple lung locations. Finding more than two positive sites on either hemithorax, regardless of the number of B-lines at each site, should raise concern for underlying lung pathology. It is therefore always necessary to interpret B-lines considering the entire clinical picture and integrate the PLUS findings with other clinical findings. The appearance of B-lines will vary depending on the transducer used and machine settings, particularly the gain, depth, frequency, and focal position, which can change B-lines from conical **(A)** to laser like **(B, C).** NOTE the step in the pleural line (arrow heads), which is often referred to a "step sign," can be a result of artifact and does not represent pathology. RS, rib shadows; SC, subcutaneous tissues. Courtesy of Calgary VPOCUS Academy, with permission.

Vet-ebooks.com

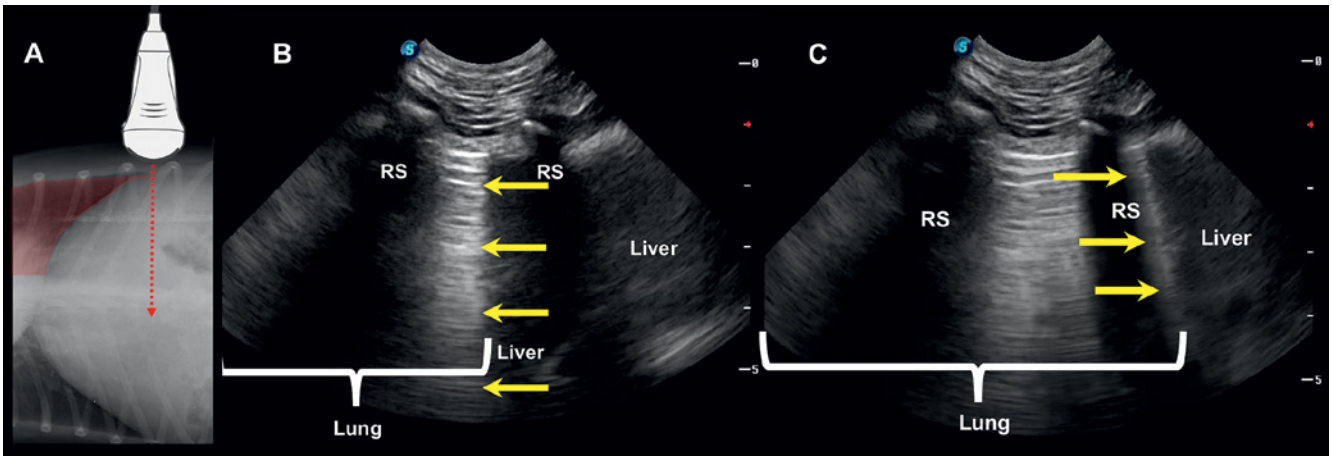


Figure 2.12. Overlaid caudal thoracic radiograph (A) and sonograms (B, C) depicting the abdominal curtain sign. (A) The abdominal curtain sign is defined as the sharply demarcated vertical edge artifact (red dotted arrow) that occurs along the caudolateral lung margins where air filled lung overlies the diaphragm and soft tissues of the abdomen along the costophrenic recess. The region caudal to the curtain sign are visible, while the region cranial to the curtain sign create reverberation artifact, rendering the underlying tissues nonvisible. **(B)** On expiration, the curtain sign and abdominal contents both move cranially (yellow arrows). **(C)** As the thoracic wall and diaphragm contract during inspiration the abdominal contents will move caudally, and the lung will expand and slide into the costophrenic recess, causing the curtain sign to also move caudally (yellow arrows). Although the curtain sign may move more than the abdominal contents, both normally move in the same direction during the same phases of respiration. RS, rib shadow. Courtesy of Calgary VPOCUS Academy, with permission.

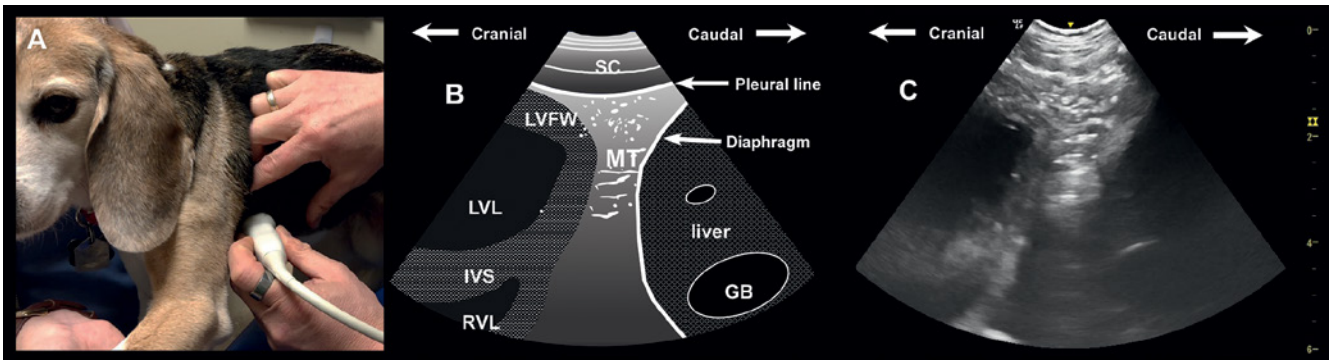


Figure 2.13. Photograph (A), schematic (B), and sonogram (C) of the PLUS technique used to identify the pericardiodiaphragmatic (PD) window, which is a good site to differentiate pericardial and pleural effusions. **(A)** The PD window is identified transthoracically and bilaterally (left shown) in the lower third of the thorax when the probe is positioned perpendicular to the ribs, marker directed cranially. **(B, C)** The PD window is sonographically confirmed when the heart and the diaphragm become visible within the same sonographic window. It should be the only site on the hemithorax where the diaphragm is visible curving away from the thoracic wall when the probe is orientated perpendicular to the ribs. There is no lung covering the cardiac notch, and the presence of mediastinal tissue and fat forming the mediastinal triangle (MT) allow the ultrasound beam to reach the diaphragm; at all other locations, air-filled lung fills the costophrenic recess creating the vertical edge artifact of the abdominal curtain sign. In cats and some dogs that have a small cardiac notch, there may be a small segment of air-filled lung overlying the mediastinal tissues, in which case the diaphragm is not visible curving away from the thoracic wall. GB, gall bladder; IVS, intraventricular septum; LVFW, left ventricular free wall; LVL, left ventricular lumen; RVL, right ventricular lumen; SC, subcutaneous tissues. Courtesy of Calgary VPOCUS Academy, with permission.

Defining a Normal Lung Surface

The lung surface can be considered normal at a particular probe location when the following two criteria are met: (i) **lung sliding is visible**. This indicates the lung is in contact with the thoracic wall and it is therefore possible to assess if the lung surface is normal or abnormal. (ii) **There are ≤3 B-lines and no visible echogenic lung tissue** (Figure 2.11). The lungs should not be assessed when lung sliding/lung pulses and/or B-lines/echogenic lung tissue are not visible,

Vet-ebooks.com

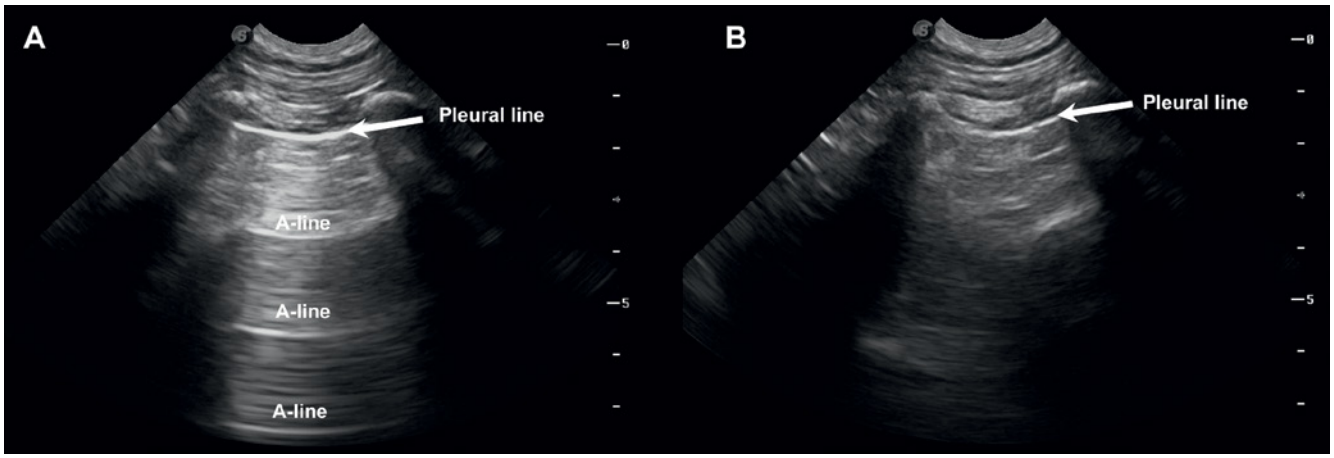


Figure 2.14. Sonograms showing variation of A-lines based on the angle of insonation and the percentage of ultrasound beam that is bounced between the probe and the pleural line. (A) The greater the proportion of ultrasound beam that returns to the probe from the pleural line, the brighter the pleural line appears, and the more evident A-lines become. This occurs when more ultrasound beams strike the pleural line at a 90°-angle. **(B)** The less ultrasound beam there is returning to the probe the "grainier" the pleural line appears, the less visible A-lines become, and the easier it is to see lung sliding. This occurs when the probe is fanned so less ultrasound waves strike the pleural line at 90° and bounce back to the probe. These images are obtained from the same healthy dog, suggesting A-lines are not an obligatory criterion to determine if the lung surface is normal or not. Courtesy of Calgary VPOCUS Academy, with permission.

as it is not possible to tell if the lung is separated from the thoracic wall due to interposed air (pneumothorax). **NOTE**: The presence of only A-lines is often used to define normal lung surfaces; however, A-lines are not always visible depending on the angle at which the ultrasound beam strikes the pleural line (Figure 2.14).

Ventral Pleural Border

When the probe is orientated parallel to the ribs in the ventral thoracic regions, the sternal/pectoral muscles can be visualized interfacing with either lung or cardiac muscle, depending where along the thorax the probe is situated (Figure 2.15). Scanning the ventral pleural border with the probe parallel to the ribs in a standing/sternal animal is more sensitive at identifying small volume pleural effusion than protocols that use a perpendicular probe orientation and fail to scan the most ventral regions of the pleural space (Boysen et al. 2019, 2022a, 2022b).

Z-lines and Other Vertical Line Artifacts

There are numerous (>20) incidental hyperechoic vertical line artifacts associated with lung ultrasound, which if differentiated from B-lines, have little to no clinical significance. The most common is the Z-line, which is a normal finding in healthy dogs and cats. Z-lines can be differentiated from B-lines by the fact they do not move with lung sliding, do not extend to the far field, and do not erase A-lines (Figure 2.16). They are ill-defined and disappear after 2–10 cm. Their significance is unknown (not associated with known pathology) and they are commonly identified in >80% of healthy animals (Martins et al. 2019). They can also be identified in patients with pneumothorax as they originate at or above the parietal pleura. I-lines meet all the criteria of a B-line, except they are very short and do not extend to the far field of the image. They may be seen in healthy animals, arise from the pleural line and move in synch with respirations. Their significance is unknown.

Cardiac Point-of-Care Ultrasound

In general, the aim of cardiac point-of-care ultrasound (CPOCUS) is not to identify a specific etiology, but rather to identify functional cardiac derangements, particularly in patients presenting with signs of shock, cardiac arrest, and/or acute cardiopulmonary failure. Although CPOCUS may incorporate multiple right and left parasternal and subcostal (subxiphoid) windows, in its most basic form, it incorporates subjective and/or objective interpretation of only three key echocardiography views: right parasternal long axis, right parasternal short axis, and subcostal (subxiphoid) views (Figure 2.17A–C). Some key features and applications of basic CPOCUS are summarized in Table 2.4.

Vet-ebooks.com

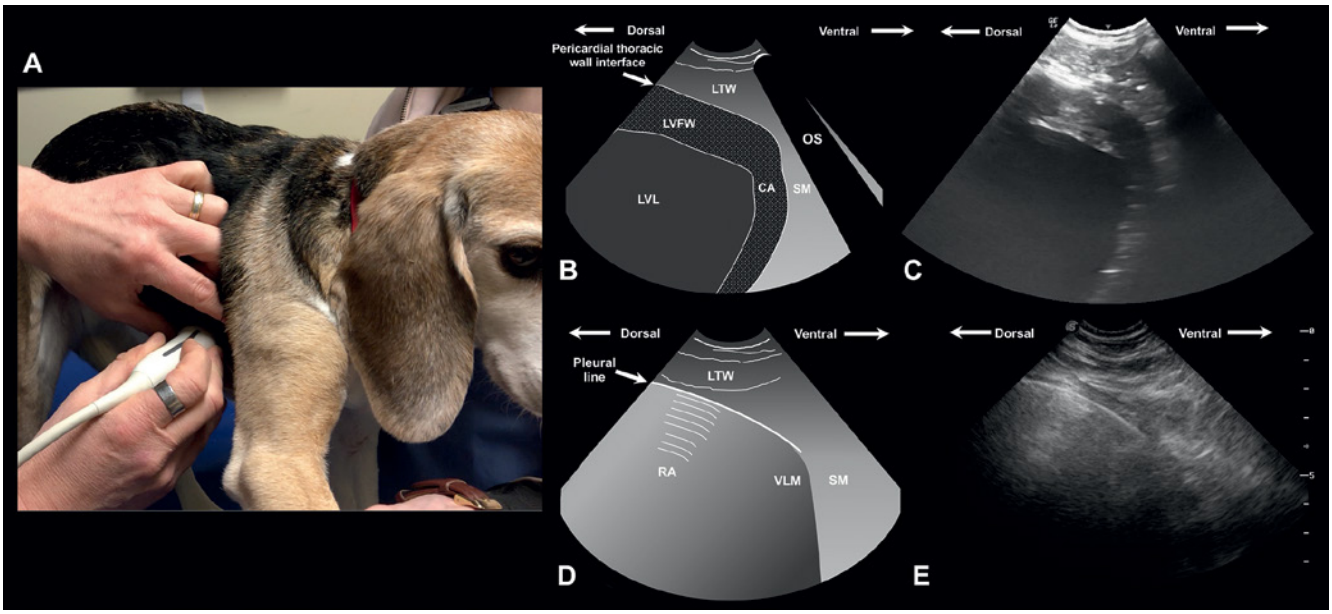


Figure 2.15. Photograph (A), schematic (B, D), and sonograms (C, E) of the PLUS technique used to identify smaller quantities of pleural effusion with the probe orientated parallel to the ribs when the animal is in a standing (shown) or sternal position. (A) Turning the probe parallel to the ribs, marker directed dorsally, and scanning between the sternal muscles and ventral lung/cardiac surfaces increases the chances of detecting small volumes of pleural effusion. Sliding the transducer ventrally until the sternal muscles fill 1/3 to 1/2 of the ultrasound image will identify the cardiac apex **(B, C**) and/or the ventral lung margin **(D, E**). If patients are in lateral recumbency, the widest gravity dependent site should be assessed. CA, cardiac apex; LTW, lateral thoracic wall; LVFW, left ventricular free wall; LVL, left ventricular lumen; OS, osseous shadowing; RA, reverberation artifact; SM, sternal muscles; VLM, ventral lung margin. Courtesy of Calgary VPOCUS Academy, with permission.

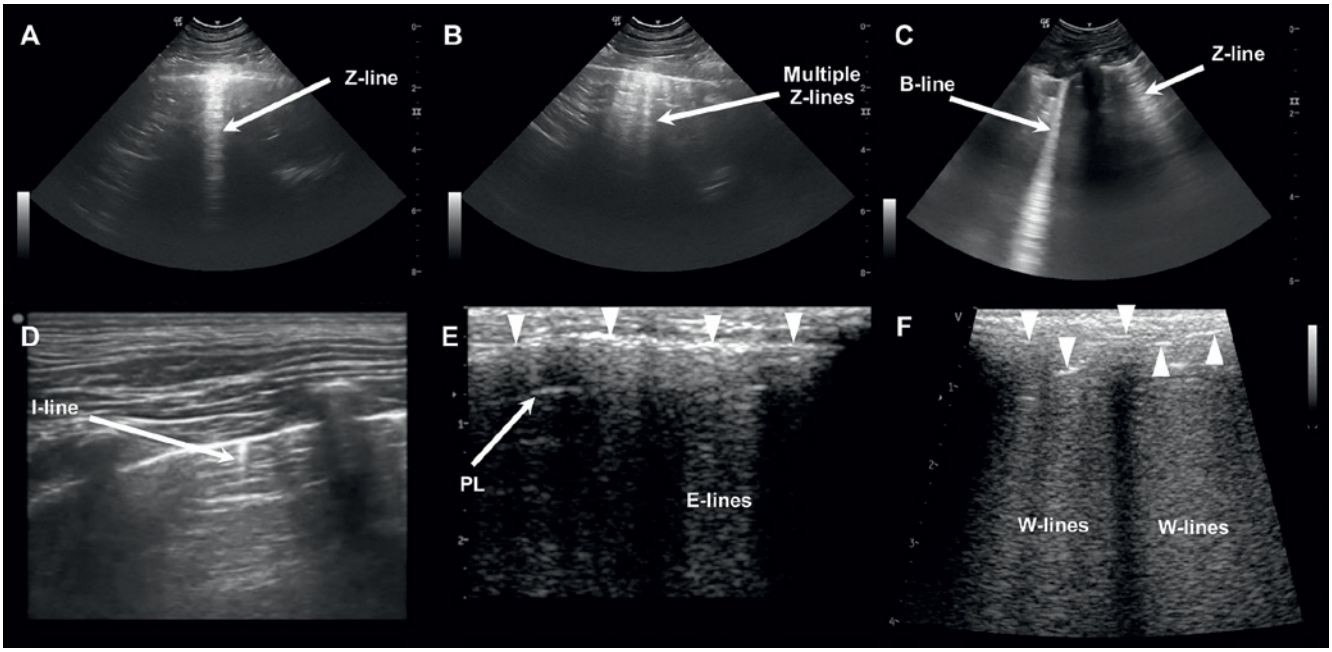


Figure 2.16. Sonograms identifying several hyperechoic vertical artifacts that can be confused for B-lines. (for full caption, see facing page)

Vet-ebooks.com

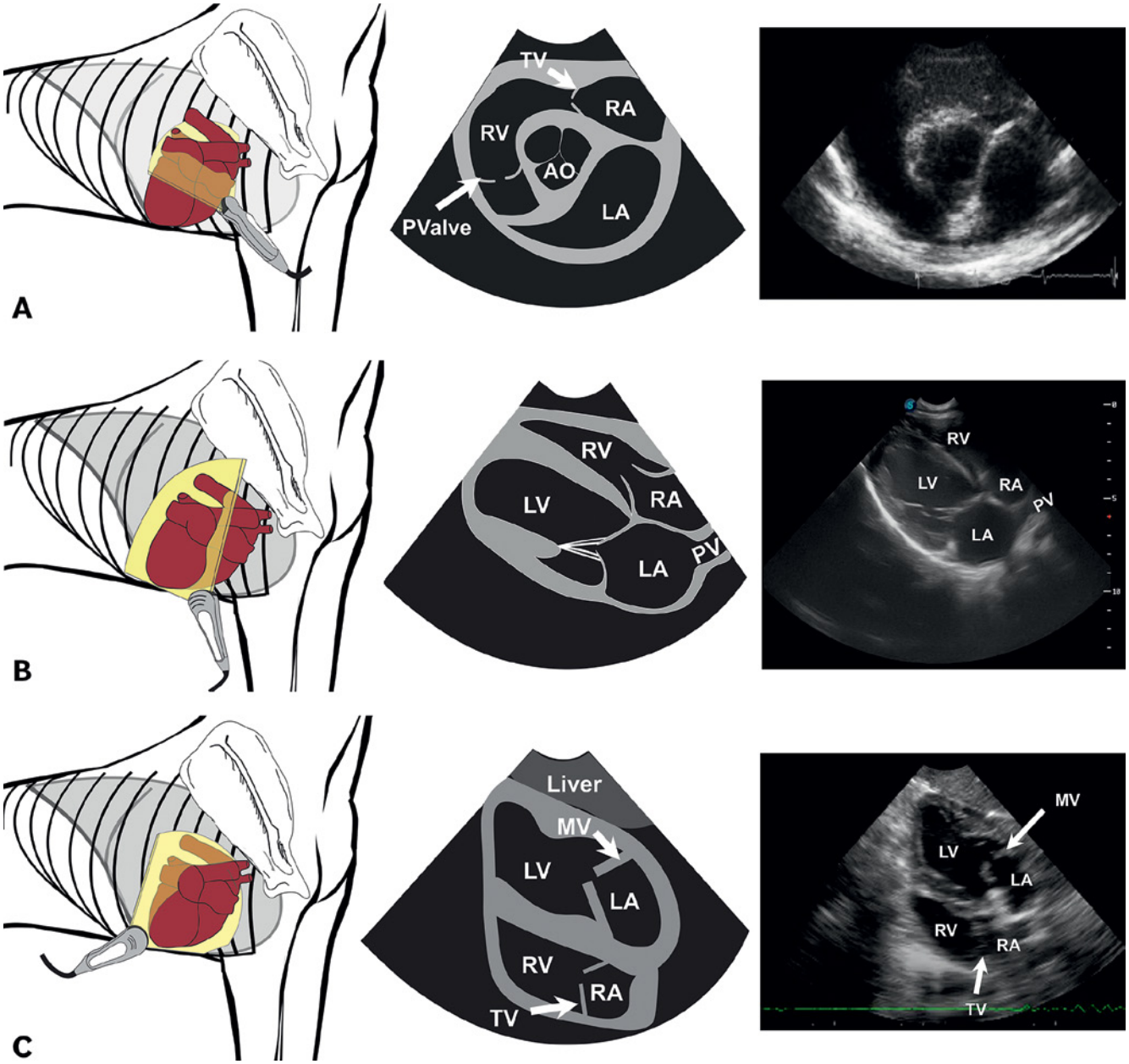


Figure 2.17. Schematic and sonograms of the three key echocardiography views which include **(A)** the right parasternal short axis view, **(B)** right parasternal long axis view, and **(C)** the subxiphoid (subcostal) view. LA, left atrium; LV, left ventricle; MV, mitral valve; PV, pulmonary vein; PValve, pulmonary valve; RA, right atrium; RV, right ventricle; TV, tricuspid valve; AO, aorta. Courtesy of Calgary VPOCUS Academy.

Figure 2.16. Sonograms identifying several hyperechoic vertical artifacts that can be confused for B-lines. Vertical hyperechoic artifact should be carefully assessed to ensure they meet the criteria required to call them a B-line. **(A)** A single Z-line is visible. Z-lines do not extend to the far field of the image, fading with depth. A-lines are often accentuated and visible within the Z-line artifact, and most importantly, they do not move with lung sliding. **(B)** Several Z-lines can be seen in the same image. Ensure the transducer is held stationary and the patient remains as still as possible when trying to differentiate B-lines from Z-lines as motion of either the transducer and/or patient can give Z-lines the appearance they are moving, which makes it even harder to differentiate them from B-lines. **(C)** Comparison of a single B-line and a Z-line. Note the B-line is more clearly defined, consistently hyperechoic throughout the entire image and that the Z-line fades becoming less distinct within the far field of the image. **(D)** A single I-line. I-lines may be more easily detected with a linear probe, as shown. **(E)** E-lines seen in a cat with subcutaneous emphysema. They can be easily confused for B-lines. E-lines however originate within the subcutaneous tissues above the pleural line, often obscuring it and preventing the lung surface and true lung artifact from being visualized. **(F)** W-lines are a variation of E-lines, they originate from subcutaneous air bubbles located at different levels within the subcutaneous tissues. PL, pleural line. Images E & F Courtesy of Katarzyna Kraszewska, PhD, Vetcardia Veterinary Clinic Warsaw, with permission. Remaining images courtesy of Calgary VPOCUS Academy, with permission.

Vet-ebooks.com

Table 2.4
Key windows and cardiac features assessed while performing a cardiac POCUS exam

CPOCUS windows	Cardiac structures assessment
Right parasternal long-axis four-chamber view	• **Shape of Left Atrium**: A rounded left atrium may indicate enlargement • **Left Atrial Size**: A left atrium wider than 16 mm in a normal sized cat (18 mm in large cats, e.g., *Maine Coon*) is considered diagnostic for left atrial enlargement. • **Left and Right Ventricular Chamber Size**: The left ventricle should be larger than the right, and the apex of the left ventricle should extend further than the right ventricle. • **Left Ventricular Lumen**: Subjective assessment. A small lumen can be the consequence of hypovolemia, obstructive disease or increased wall thickness. • **Wall Thickness**: Wall thickness is relative to the size of the left ventricular lumen. Underfilling of the left ventricle creates pseudo-hypertrophy, it is frequent in hypovolemic patients and should be suspected if other volume parameters indicate hypovolemia (small left atrium or flat caudal vena cava). • **Contractility**: Subjective assessment.
Right parasternal short axis views: short axis trans-ventricular view ("Mushroom view")	• **Left Ventricular Lumen**: Subjective assessment. A small lumen can be seen in hypovolemia, obstructive disease or increased wall thickness. • **Left Ventricular Wall Thickness**: Wall thickness should be considered in relation to the dimension of the left ventricular lumen. Thin ventricular walls support cardiac enlargement due to volume overload (i.e., dilated cardiomyopathy, iatrogenic fluid overload) or regional lesions (myocardial infarction). Thick ventricular walls can be indicative of hypovolemia, or of ventricular hypertrophy. Assessing the left atrium (LA) helps differentiate the latter two conditions as the LA tends to be small with hypovolemia and enlarged with ventricular hypertrophy associated with cardiomyopathies. • **Contractility**: Subjective assessment focuses solely on the movement of the ventricular wall and the changes in the luminal area. • **Ventricular Septum**: The ventricular septum in the short axis view is assessed for any signs of deviation. A normal septum should create a round contour of the left ventricle, and thus bulge toward the right ventricular lumen. Flattening of the septum is often associated with increased right ventricular pressures. • **Right Ventricular Lumen**: The right ventricular lumen should appear as a smaller and semilunar structure located around the larger, round left ventricle.
Right parasternal short axis valvular view ("Fishmouth view")	• Assess the transition of the trans-ventricular view (toward the apex) and the trans-aortic view (toward the base).

Right parasternal short axis trans-aortic view or "Mercedes and whale view"	• **Left Atrial Size**: *s*ubjective assessment that can be complemented by one of two techniques.
	  • **Left Atrial to Aortic Ratio**: Normal values are between 1 and up to 1.5
	  • **Drawing Aortic Circumferences Within the Left Atrium**: In a healthy animal, this should be less than 2.5 circumferences.
	• **Left Atrial "Smoke Sign"**: is caused by turbid flow and is suggestive of hypercoagulable states, particularly in cats.

Acquiring all windows and views within a window is often unnecessary. For example, the LA:Ao ratio can still have diagnostic value, even if it is the only view obtained (Loughran 2021).

Right Parasternal Short-axis Views

At the right parasternal window, there are three short-axis views that are often identified to help answer key CPOCUS questions (Figure 2.18A–C):

"**Mushroom view**" (Figure 2.18A): A common view for estimating volume status and contractility at the left midventricular/papillary muscle region just below the mitral valve.

"**Fish mouth view**" (Figure 2.18B): Obtained at the level of the mitral valve and serves as a landmark to obtain other views: the Mercedes and whale as well as the mushroom view.

"**Mercedes and the whale view**" (Figure 2.18C): Allows assessment of the LA:Ao ratio and is usually

Vet-ebooks.com

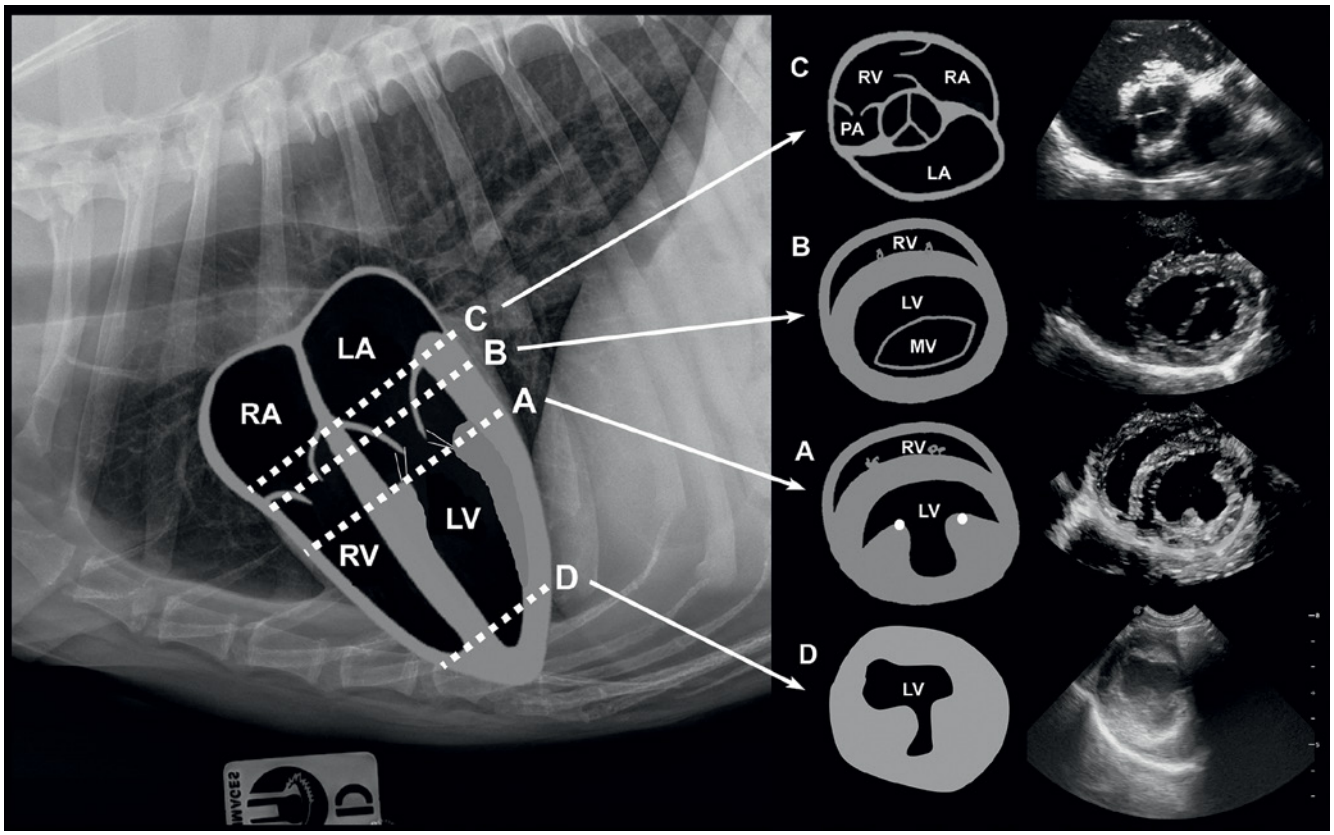


Figure 2.18. Schematic heart overlaid over a canine lateral thoracic radiograph with corresponding schematic and sonograms of the right parasternal short axis windows of the heart from the apex to the heart base. (A) Right parasternal view at the level of the papillary muscles ("mushroom" view) is initially obtained, just below the mitral valve. **(B)** Right parasternal view at the level of mitral valve ("fish mouth view). Just below the mitral valve is where volume status and contractility are assessed while the window just above the mitral valve is where the left atrial to aortic ratio is identified. **(C)** Aortic root where the left atrial to aortic ratio is obtained ("Mercedes and whale" view). **(D)** When the probe is near the apex of the heart, only the left ventricle and an absence of the right ventricle is seen. At this level, the left lumen appears small and the walls thick, which should not be confused for cardiac hypertrophy or pseudohypertrophy. LA, left atrium; LV, left ventricle; MV, mitral valve; PA, pulmonary artery; RA, right atrium; RV, right ventricle. Courtesy of Calgary VPOCUS Academy, with permission.

obtained by fanning the probe from the fish mouth view toward the heart base.

Reference intervals vary slightly depending on where measurements are made, if the pulmonary vein is included, and the ultrasound beam angle of insonation (angle at which the ultrasound beam strikes the target organ or structure of interest), which may vary with patient position, and with the operator's skill level. In general, a normal LA:Ao ratio should be between 1 and 1.5 in cats and dogs, with no statistically significant difference noted between standing and right lateral measurements (Burnotte et al. 2023; Chetboul et al. 2005; Fox et al. 1985; Häggström et al. 2016; Marchesotti et al. 2019; Rishniw et al. 2019; Visser et al. 2019).

Right Parasternal Long-axis Views

The **four-chamber view** at the right parasternal long-axis window allows the sonographer to subjectively evaluate the size of all cardiac chambers (Figure 2.19); left atrium (LA), left ventricle (LV), right atrium (RA), and right ventricle (RV) (DeFrancesco and Ward 2021). The RA and the LA should be of similar size (1 : 1 ratio). The interatrial septum should lie in a relatively neutral position and not bulge into either atrium. The RV internal chamber diameter is approximately one-third that of the LV internal diameter. The free wall of the RV is equal to one-third to one-half the thickness of the LV free wall. The interventricular septum and the LV free wall are normally similar in thickness. Interpretation of

Vet-ebooks.com

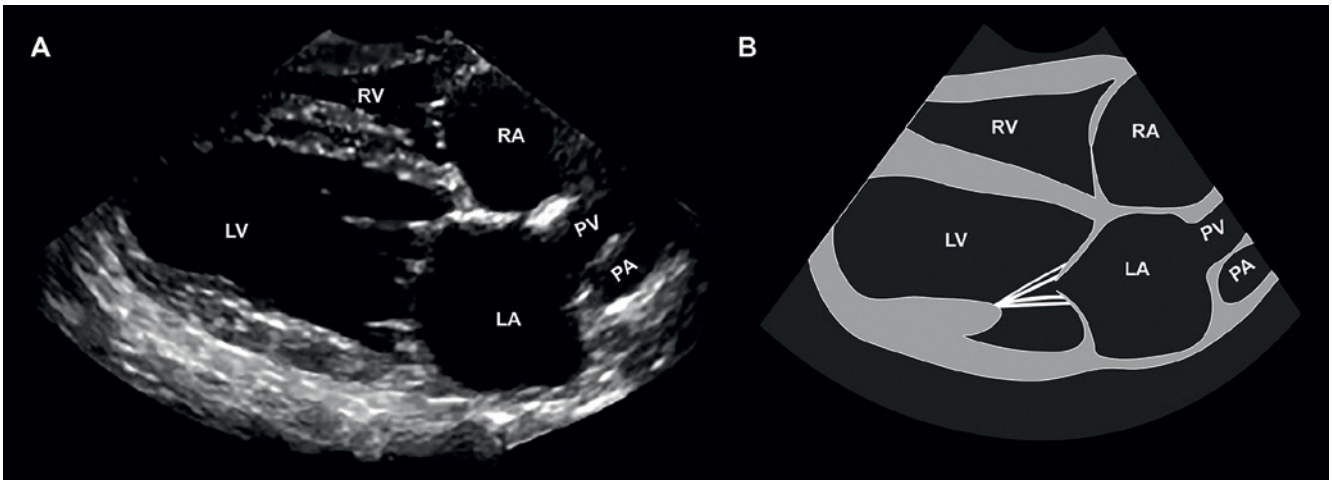


Figure 2.19. Sonogram (A) and schematic (B) of the right parasternal long axis four-chamber view of the heart. The four-chamber view at the right parasternal long-axis window allows the sonographer to subjectively evaluate the size of all cardiac chambers. The RA and the LA should be of similar size (1 : 1 ratio). The intra-atrial septum should lie in a relatively neutral position and not bulge into either atrium. The RV internal chamber diameter is approximately one-third that of the LV internal diameter. The interventricular septum and the LV free wall are normally similar in thickness. If visible the pulmonary vein (in long axis) and pulmonary artery in short axis can be compared to each other. They should roughly be 1 : 1 in healthy animals. LA, left atrium; LV, left ventricle; PA, Pulmonary artery; PV, pulmonary vein; RA, right atrium; RV, right ventricle. Courtesy of Calgary VPOCUS Academy, with permission.

changes in chamber size, wall thickness, and contractility in the right parasternal long-axis views are similar to changes in the right parasternal short-axis views.

Sonographic Features of Common Pocus Disorders

Abdominal POCUS Disorders

Abdominal POCUS is a useful clinical tool for the diagnosis and management of numerous underlying abdominal pathologies. The specific goal-directed questions and key organs to assess at each window of the APOCUS exam are listed in Table 2.5 and illustrated in Figure 2.20.

Peritoneal Effusion

Abdominal POCUS is often used to look for peritoneal effusion, particularly in patients with sudden clinical deterioration, such as hypotension, and in trauma settings. Free fluid usually appears as anechoic to hypoechoic triangular collections between organs and structures, although it may also appear hyperechoic in some instances (e.g., highly proteinaceous or cellular fluid) (see Chapter 15 for more information).

Free peritoneal fluid tends to accumulate at gravity dependent regions, although it can also be focal or localized in some instances (e.g., pancreatitis, gastrointestinal dehiscence). Therefore, APOCUS should thoroughly evaluate each site using multiple sonographic planes, in both long and short axes, considering patient position and where fluid will accumulate, ensuring gravity dependent regions and suspected sites of pathology are assessed. Although the context may provide important clues regarding the nature of the fluid (e.g., blunt trauma is often associated with hemorrhage) abdominocentesis, ideally ultrasound guided, and fluid analysis should always be considered. Repeating APOCUS serially may be particularly relevant in penetrating trauma where fluid accumulation in the abdomen is often delayed and may be easier to detect following fluid resuscitation.

Pneumoperitoneum

Free intraperitoneal gas can be challenging to differentiate from gas within the lumen of the intestinal tract. Free gas often localizes below the parietal peritoneum and is less affected by respirations (Coppolino et al. 2013). By contrast, hyperechoic gas within the GI system is intraluminal (located below proximal intestinal walls) and often moves with respirations. Both linear and convex transducers can be used to detect free gas, although linear transducers (10–12 MHz) may

Vet-ebooks.com

Table 2.5
Key POCUS pathology identified at each abdominal POCUS exam window

APOCUS window	Clinically driven question(s) to answer
Pathology that may be seen at any of the 5 "classic" windows of the APOCUS exam	Pneumoperitoneum which varies with patient positioning (Figure 2.21) Free abdominal fluid which varies with patient positioning
Subxiphoid	Caudal vena cava (CVC) size and index (Figure 2.22) Pericardial effusion (Figure 2.23) Pleural effusion (Figure 2.24) Caudal lung pathology (Figure 2.25) Gallbladder halo sign (Figure 2.26) Gastric motility Cardiac activity during cardiopulmonary resuscitation (CPR) (Figure 2.52)
Umbilical	Splenic lesions/masses
Right paralumbar	Retroperitoneal injury Renal pelvic dilation Duodenal motility
Left paralumbar	Retroperitoneal injury Renal pelvic dilation
Caudal abdomen/pelvic inlet	Urinary bladder volume (Figure 2.27) Pyometra Aortic thromboembolism in cats

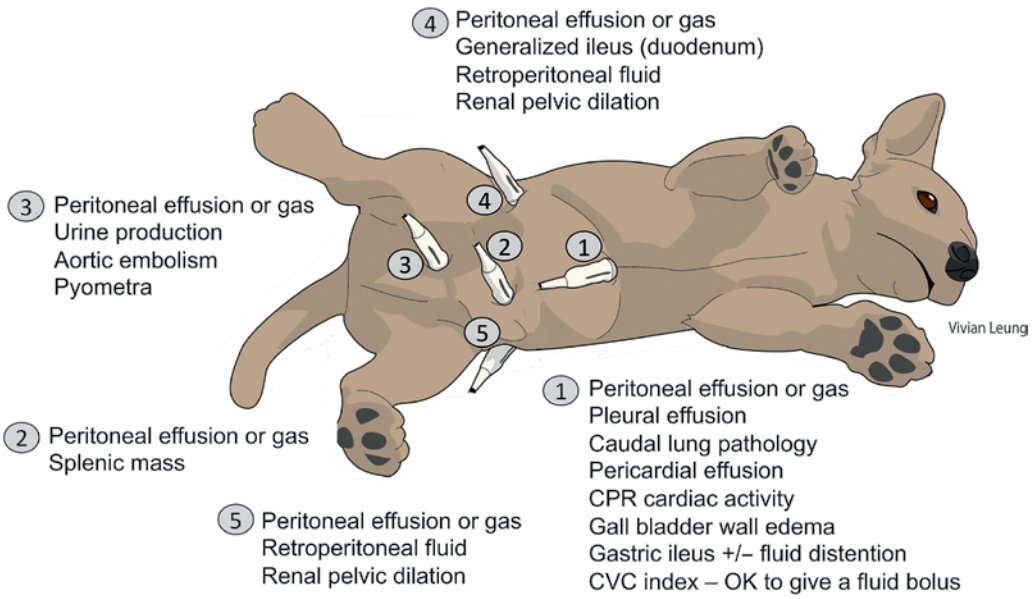


Figure 2.20. The five-point abdominal point-of-care ultrasound (APOCUS) exam and binary driven questions that are addressed. Some questions expand all five windows, while others are specific to each of the five sites scanned. CPR, cardiopulmonary resuscitation; CVC, caudal vena cava. Courtesy of Vivian Leung.

Vet-ebooks.com

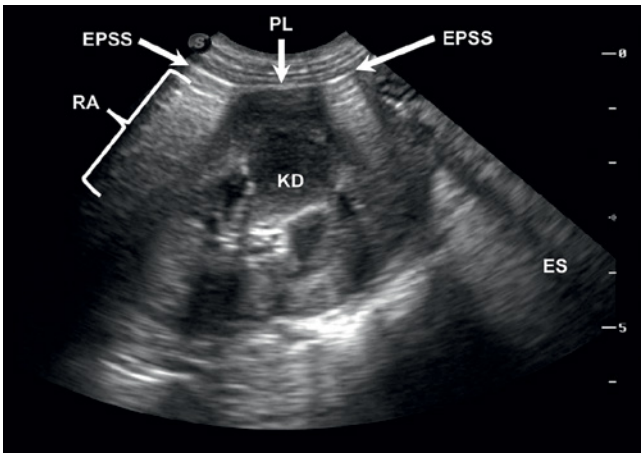


Figure 2.21. Sonogram of free gas in the abdomen. Reverberation artifact created where free air contacts the parietal (shown) and visceral (not shown) peritoneum, creating artifact which obscures the structures below it. Air is a strong reflector creating increased echogenicity where free gas contacts soft tissue structures situated below the ultrasound probe. In this example the enhanced peritoneal stripe sign (EPSS) occurs along the parietal (PL) peritoneum. ES, edge shadow; KD, kidney; RA, reverberation artifact. Courtesy of Calgary VPOCUS Academy, with permission.

be more accurate at detecting its presence (Coppolino et al. 2013).

Three classic findings help identify free gas: **reverberation** artefact (see Chapter 1), the **enhanced peritoneal stripe sign** (EPSS), and the **shifting phenomenon** (Coppolino et al. 2013; Kim et al. 2014) (Figure 2.21). The EPSS is a strongly hyperechoic line formed by gas contacting a reflective surface such as the parietal (e.g., peritoneal lining of the abdominal wall) or visceral (e.g., splenic capsule) peritoneum. The EPSS can change locations with altered patient positions, which is less likely with intraluminal GI gas (Coppolino et al. 2013). A compressive scissor maneuver can also be applied to demonstrate air movement supporting the presence of free gas. With compression, air will move away from the probe, making free gas less obvious, while releasing compression may favor its detection (Coppolino et al. 2013). Free gas may accumulate over time as gas leaks from hollow viscus organs, and serial APOCUS examinations should be used in highly suspected cases.

Caudal Vena Cava (CVC) Size and Index

Although controversial, the caudal vena cava (CVC) diameter (CVCd) and collapsibility index (CVCCI) are often used in the clinical setting as a means of assessing volume status and fluid responsiveness, respectively (Corl et al. 2017; Darnis et al. 2018; Preau et al. 2017) (Figure 2.22). A common site to assess the CVCd and CVCCI in dogs and cats is the subxiphoid site (Darnis et al. 2018; Hultman et al. 2022). An enlarged or distended CVC with a CVCCI change less than 20% (cats) to 25% (dogs) suggests increased RA pressure, which is often secondary to hypervolemia, congestive heart disease, or cardiac tamponade (Darnis et al. 2018; Hultman et al. 2022) (Figure 2.22). If CVC assessment suggests increased RA pressure, other clinical parameters including additional POCUS examinations should be considered, particularly PLUS to assess for B-lines and pleural effusion, and CPOCUS to assess volume states and pericardial effusion. If the CVC is "flat" and collapsed, (Figure 2.22) hypovolemia should be suspected (Gui et al. 2015; Pereira et al. 2020). There is considerable overlap in the CVCCI between euvolemic and hypovolemic patients. It is therefore common to group euvolemic and hypovolemia patients together when assessing the CVC as "likely" acceptable to receive a fluid bolus, provided there are no contra-indications to fluid bolus therapy.

Pericardial Effusion at the Subxiphoid Site

At the subxiphoid site, pericardial effusion appears sonographically as an anechoic space adjacent to and surrounding cardiac structures, curving away from the diaphragm. It is easiest to appreciate when the apex of the heart can be identified (Figure 2.23).

Pleural Effusion at the Subxiphoid Site

At the subxiphoid site, pleural effusion appears as an anechoic to hypoechoic accumulation distal to and outlining the diaphragm (Figure 2.24).

Caudal Lung Pathology at the Subxiphoid Site

The identification of more than three B-lines radiating from the diaphragm/visceral lung interface, or presence of echogenic lung tissue, should prompt consideration of decreased caudal lung aeration (Figure 2.25).

Vet-ebooks.com

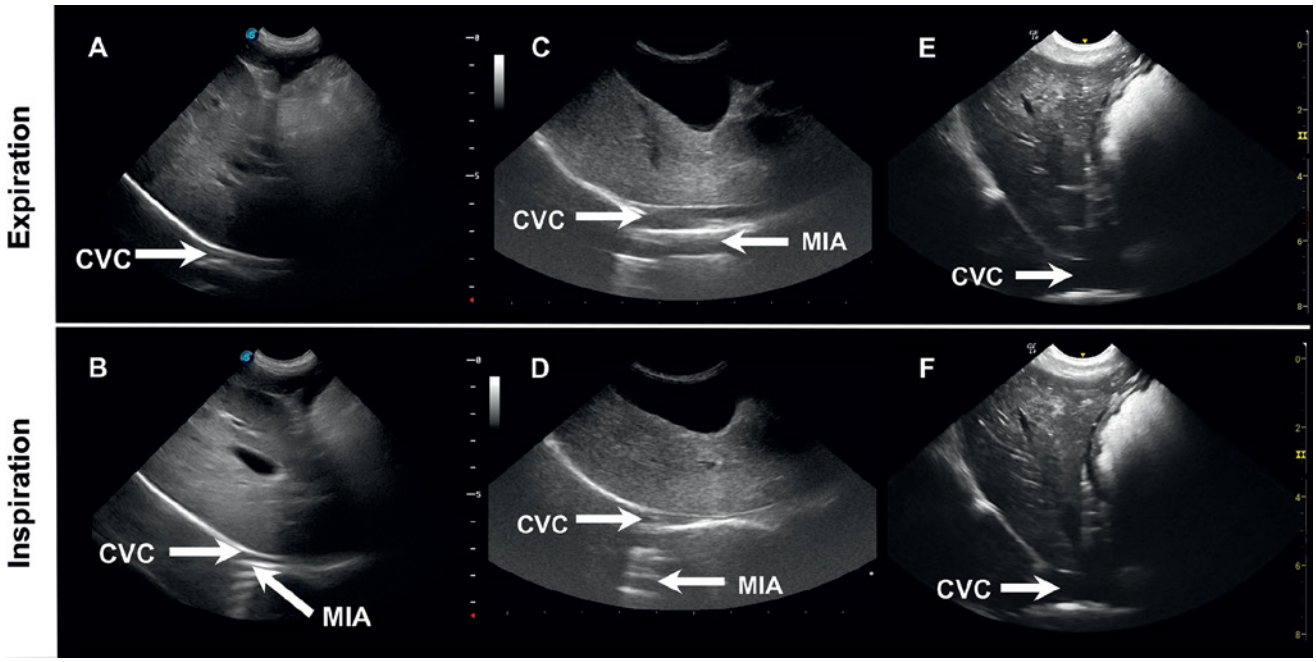


Figure 2.22. **Sonograms of the caudal vena cava (CVC) diameter in expiration and inspiration** where the CVC crosses the diaphragm at the subxiphoid site. **(A, B)** Hypovolemic patient where the CVC is "flat" and collapsed during all phases of respiration. In these situations, it can be difficult to appreciate the degree of change between inspiration and expiration. **(C, D)** Euvolemic patient where the CVC is easily visible on expiration and collapses by more than 25% on inspiration. **(E, F)** Volume overload where the change in the diameter of the CVC between expiration and inspiration are minimal, and the CVC appears "distended" throughout the respiratory cycle. Note: do not confuse mirror image reverberation artifact (MIA) of the CVC for vessels or the aorta. Courtesy of Calgary VPOCUS Academy, with permission.

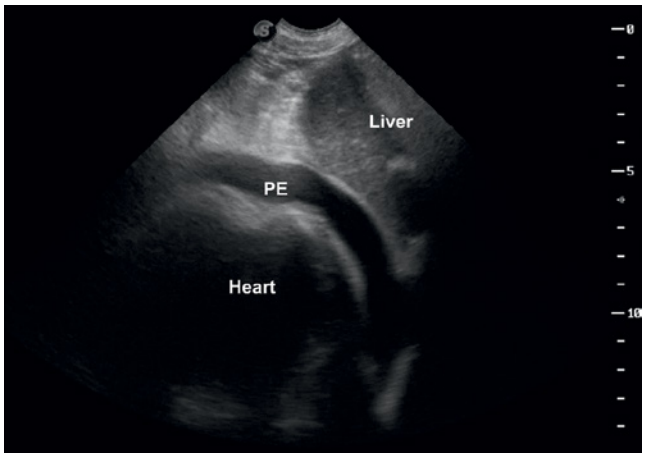


Figure 2.23. **Sonogram of pericardial effusion identified in a dog at the subxiphoid (subcostal) window.** At the subxiphoid window, the liver provides a nice acoustic window into the thorax. If the probe is rocked more parallel to the spine with the ultrasound beams directed more cranially and ventrally, the heart and pericardial sac are often visible. With pericardial effusion (PE) fluid can be seen curving away from the diaphragm, following the contours of the heart. Courtesy of Calgary VPOCUS Academy, with permission.

Gallbladder Wall Edema (Halo Sign)

The gallbladder can be visualized to the right of midline at the subxiphoid window and should be assessed for wall thickening with striation (halo sign, Figure 2.26), which is suggestive of edema. Although the halo sign is not specific for any disease, in unstable patients, it is often associated with anaphylaxis, right-sided cardiac congestion (right-sided heart failure or pericardial effusion), sepsis, or volume overload following aggressive fluid loading.

Urinary Bladder Volume Estimation

Urinary bladder volume calculation, and estimation of urine production with serial calculations, can help diagnose oliguria or anuria, urinary retention, and reduce urinary catheterization in some patients

Vet-ebooks.com

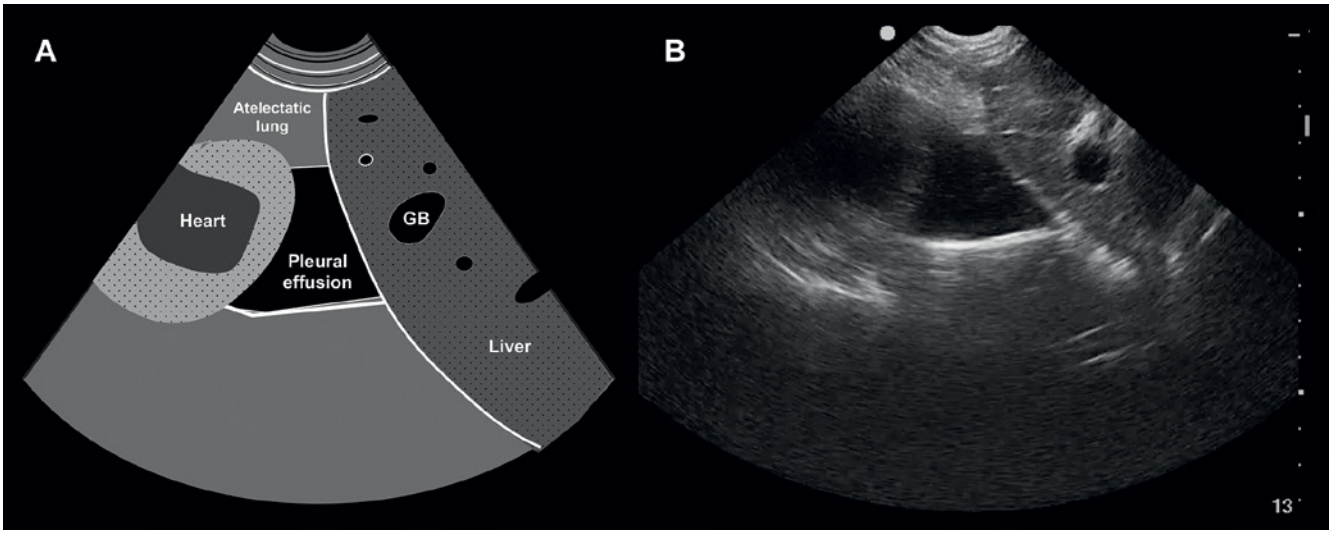


Figure 2.24. Schematic (A) and sonogram (B) of pleural effusion identified via the subxiphoid window in a dog. Extending the depth setting at the subxiphoid site allows the region beyond the diaphragm and into the thorax to be visualized. With pleural effusion, mirror image artifact is lost and effusion can easily be detected curving along the diaphragm. If the patient is in a standing position the probe may need to be rocked cranially to assess the more ventral regions of the pleural space where fluid will fall due to gravity. GB, gall bladder. Courtesy of Calgary VPOCUS Academy, with permission.

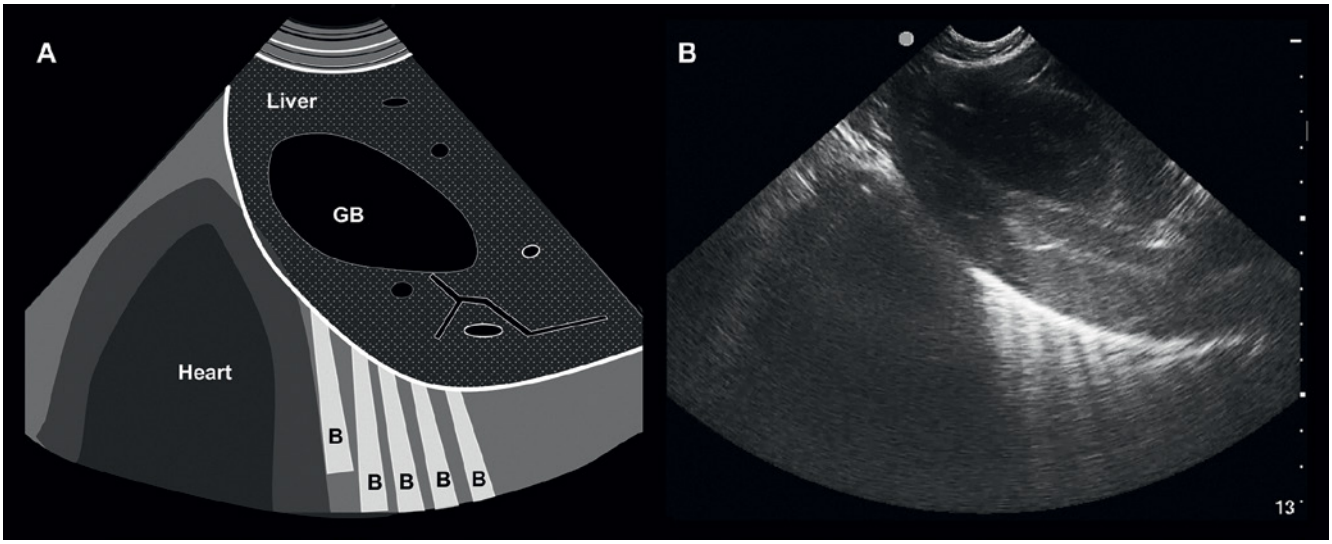


Figure 2.25. Schematic (A) and sonogram (B) of the caudal lung surface obtained via the subxiphoid view. The caudal lung surface, which is not visible transthoracically, can be assessed along the soft tissue-to-air interface represented by air filled lung in contact with the diaphragm. In this example there are increased B-lines radiating away from the soft tissue-to-air interface into the far field of the image. There should not be more than 2–3 B-lines visible when assessing the caudal lung fields of dogs and cats at the subxiphoid window. B, B-line; GB, gallbladder. Courtesy of Calgary VPOCUS Academy, with permission.

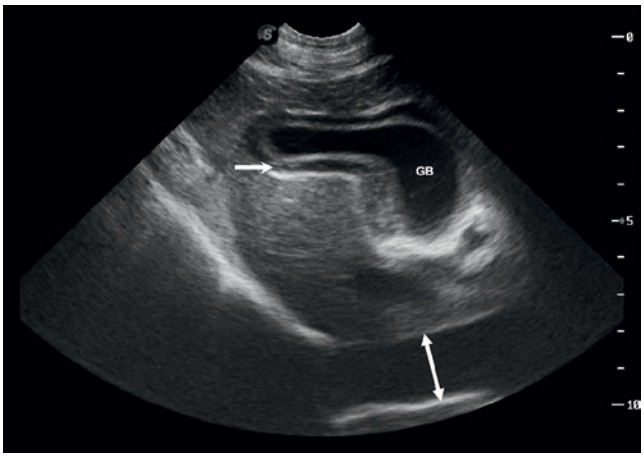


Figure 2.26. Sonogram obtained from the subxiphoid (subcostal) window in a dog that presented with a suspicion of **pericardial effusion** based on triage examination findings. Gallbladder (GB) wall thickening with subtle striations referred to as a "halo sign" (arrow), represents GB wall edema. Note also the distended caudal vena cava (double headed arrow), which supports increased right atrial pressure as a cause of the halo sign, which was confirmed to be secondary to pericardial effusion. Courtesy of Calgary VPOCUS Academy, with permission.

Vet-ebooks.com

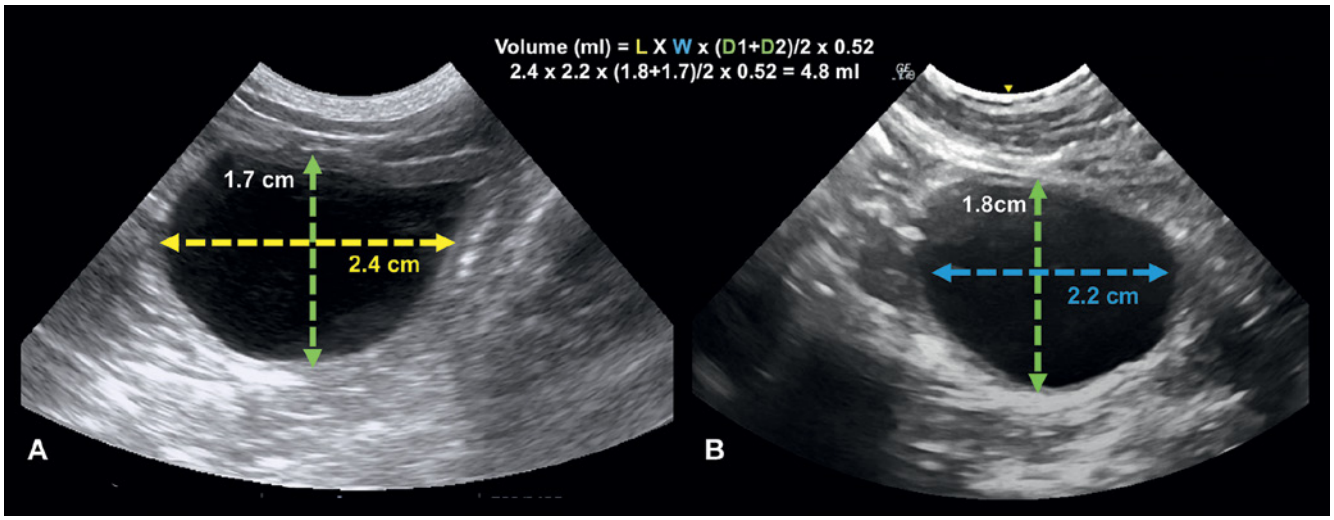


Figure 2.27. Sonograms in longitudinal (A) and transverse (B) views of the urinary bladder for volume estimation in an oliguric dog. Many ultrasound machines can calculate urinary volume via calculations derived from tracing the circumference of the urinary bladder in longitudinal and transverse axis. Alternatively, it can be calculated by measuring the length, width, and depth of the urinary bladder, multiplied by 0.52 (correction coefficient can vary based on the shape of the bladder). **(A)** In the long axis view, the length (L, yellow dashed double -arrow) and depth (D1, green dashed double-arrow) are recorded. **(B)** The width (W, blue dashed double-arrow) is recorded in the short axis view as is the depth (D2, green dashed double-arrow). Measuring depth in both long and short axis planes and dividing by two to get an average provides an easy way to verify the widest diameter was correctly obtained in both planes; if the two depth measurements vary greatly (e.g., more than 15%), consider repeating the measurements as the probe may be orientated obliquely to the urinary bladder, to either side of the widest diameter of the urinary bladder, have more pressure applied in one plane versus the other, or the patient may have urinated during measurement. Courtesy of Calgary VPOCUS Academy, with permission.

(Figure 2.27). The formula: $L \times W \times D \times 0.52$ may be the most accurate of the urinary volume formulas studied in dogs and cats (Kendall et al. 2020).

Common Pocus Disorders of the Pleural Space and Lungs

PLUS is broadly used to search for pleural effusion, pneumothorax, and pulmonary pathology through identification of increased B-lines and echogenic lung tissue. Sonographically detectable lung pathology is only visible at the lung surface (visceral pleura). Pathology that does not involve the lung surface is not sonographically visible. Fortunately, evidence in human medicine suggests most pulmonary pathology results in B-lines and/or echogenic lung tissue that are sonographically detectable at the lung surface, which is likely similar in veterinary medicine (Nazerian et al. 2015; Marini et al. 2021). The lung surface is not visible with pneumothorax as air inhibits the transmission of ultrasound beams.

Pneumothorax

Four key criteria should be assessed in deciding if a patient has pneumothorax (Figure 2.28) or not; (i) **lung sliding/lung pulse**, (ii) **B-lines/echogenic lung tissue**, (iii) **lung point,** and (iv) **abnormal curtain signs** (Boysen 2021). If history and clinical findings support a diagnosis of pneumothorax, thoracocentesis is indicated when lung sliding, lung pulse, and lung pathology are not visible at the most sensitive sites where free pleural gas accumulates. If the patient is sufficiently stable, the operator may increase the likelihood of diagnosing pneumothorax by finding the lung point and/or an abnormal ACS. Although not reported in veterinary medicine, M-mode ultrasound has been used to assess lung sliding that is difficult to visualize with B-mode ultrasound (Avila et al. 2018) (Figure 2.29).

The **lung point** is defined as the site within the thorax where the visceral pleura of the lung recontacts the parietal pleura of the thoracic wall in patients with pneumothorax (Figure 2.30). It is sonographically identified as a clear demarcation or "sudden appearance" of lung sliding that is seen at the transition from pneumothorax to lung along the lateral thoracic wall.

Vet-ebooks.com

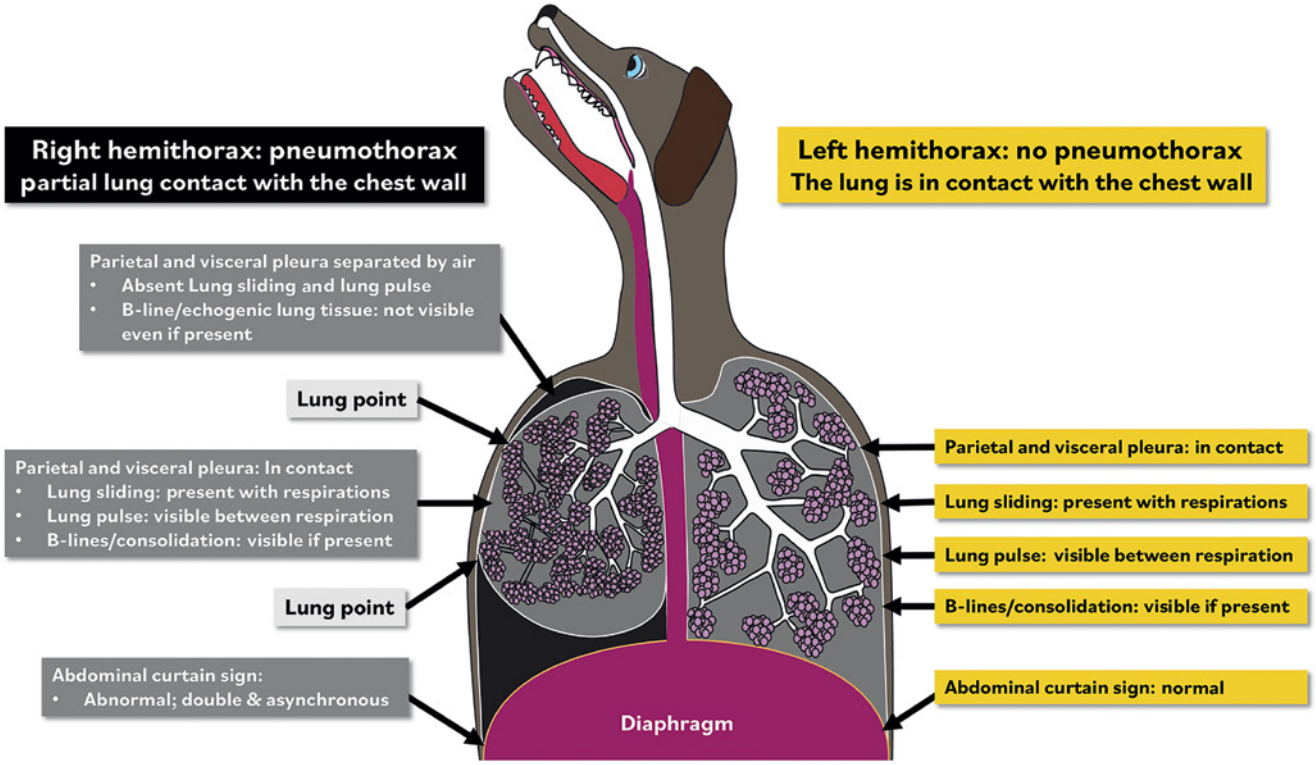


Figure 2.28. **Schematic image comparing the sonographic findings when a moderate unilateral pneumothorax is present** (pneumothorax shown in black, right hemithorax). Each arrow represents different sonographic findings when the probe is placed over the pneumothorax, and where there is lung in contact with the thoracic wall. The location of the abdominal curtain sign (ACS) is also shown. A pneumothorax will often result in an abnormal ACS due to free pleural gas interacting with the costophrenic recess when it displaces the lung lobe cranially. With massive pneumothorax where lung fails to recontact the thoracic wall, there will not be a lung point and there will be an absence of B-lines/consolidation, lung pulse, and lung sliding over the entire hemithorax. Courtesy of Calgary VPOCUS Academy.

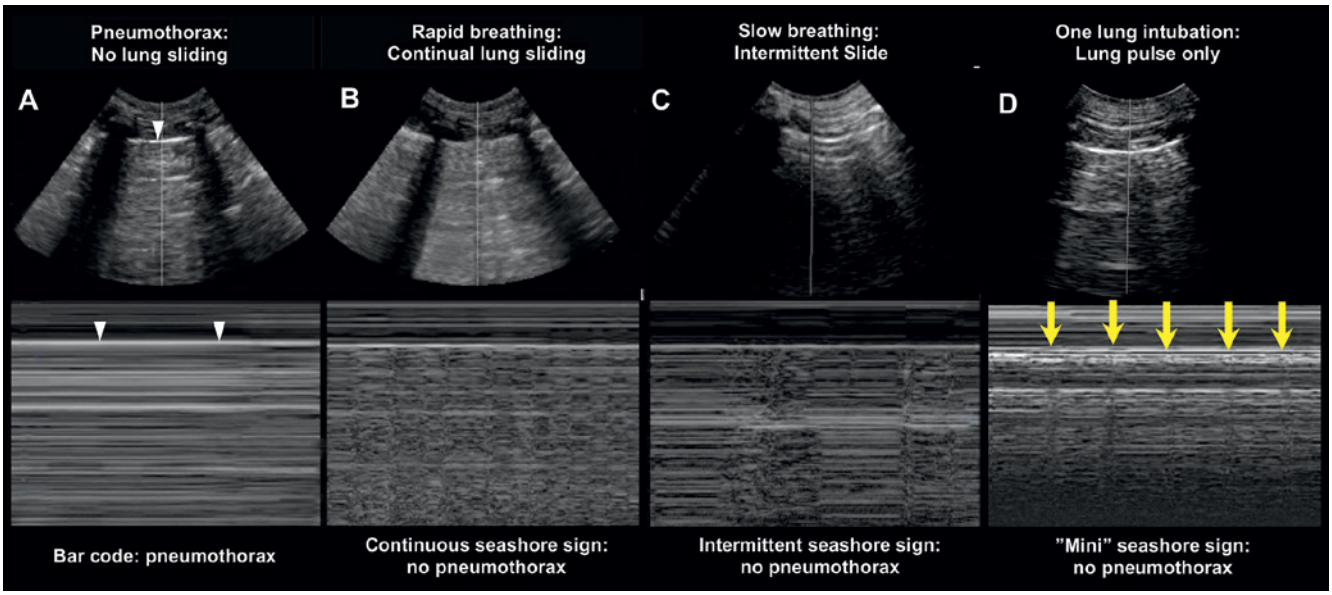


Figure 2.29. **Use of M-mode to assist with the diagnosis of pneumothorax.** Note that the patient and probe movement will create artifact originating from the skin surface, which makes M-mode more challenging to interpret. **(A)** When pneumothorax is present, M-mode will not detect any motion above or below the pleural line (arrowheads), creating what is referred to as a "bar code" or "stratosphere" sign. **(B)** When the lung is in contact with the thoracic wall and the patient breathes, M-mode will detect motion at the pleural line, creating a "seashore" pattern, similar to the pattern left by waves rolling onto a sandy shore that originate at the pleural line and extend to the far field of the M-mode image. **(C)** With apnea or long pauses between breaths an alternating "seashore" and "bar code" pattern is seen. **(D)** The presence of a lung pulse on M-mode creates a very regularly spaced "mini seashore sign" (yellow arrow) because of cardiac oscillations radiating to the lung surface. This can be seen during periods of apnea or with single lung lobe intubation. Courtesy of Calgary VPOCUS Academy, with permission.

Vet-ebooks.com

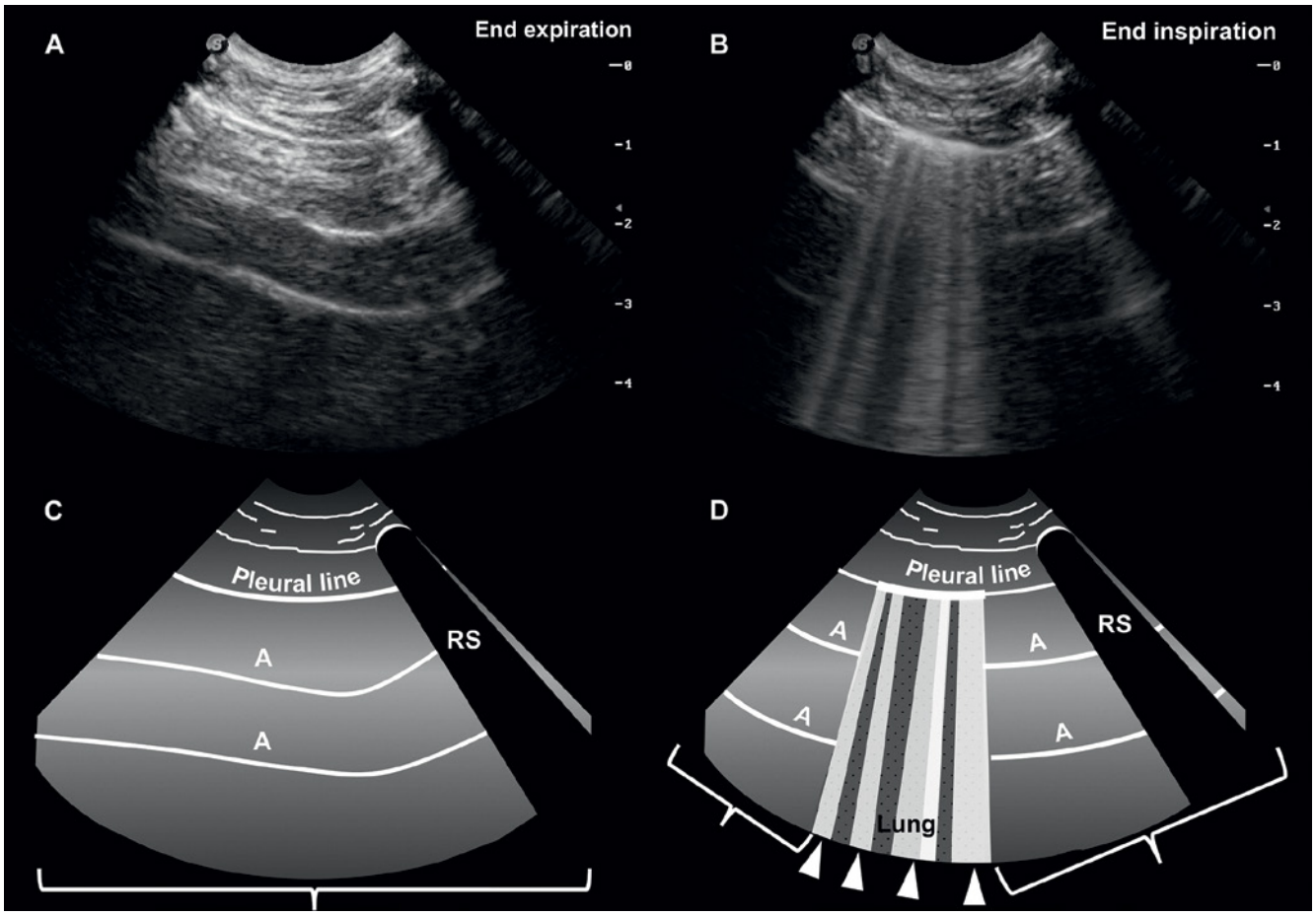


Figure 2.30. Sonograms (A, B) and schematic (C, D) images of a patient with pneumothorax during expiration and inspiration. (A, C) At expiration, there is no lung sliding (not visible in a still image) or B-lines visible. Only the mirror image artifact of a pneumothorax is appreciated (region within white bracket). **(B, D)** During inspiration lung suddenly becomes visible within the region of pneumothorax. Underlying B-lines (arrowheads) "break into" the region of pneumothorax as well, due to the underlying presence of contusions and compression atelectasis. To either side of the lung, pneumothorax is still present (white brackets). The appearance of the lung point varies depending on how the lung recontacts the thoracic wall and can suddenly appear within the image as shown in **(B, D)** or may slide into the image from one side (not shown). Moving the transducer from a region of lung where lung sliding is absent, to the lung point or a region of lung where lung sliding suddenly becomes visible strongly supports the diagnosis of pneumothorax. A, A-lines; RS, rib shadow. Courtesy of Calgary VPOCUS Academy, with permission.

The lung point will not be seen if the lung fails to recontact the thoracic wall (massive/complete pneumothorax). With underlying loss of lung aeration (e.g., pulmonary contusions, atelectasis), B-lines and/or echogenic lung tissue will be seen in association with the lung point.

Identification of an **asynchronous or double curtain sign** in patients with supporting history and clinical findings indicates pneumothorax on that side of the thorax. All three ACS classifications (normal (Figure 2.31), asynchronous (Figure 2.32) and double (Figure 2.33)) have been identified in dogs with pneumothorax, with a normal ACS visible in regions below (standing/sternal patient) or to either side (lateral patient) of the pneumothorax, and abnormal ACS visible within the regions of pneumothorax (Boysen et al. 2019).

Exclusion Criteria

The identification of lung sliding and/or a lung pulse, in the absence of a lung point, excludes pneumothorax at that probe location, as both are only created when the lung is in contact with and moves along the thoracic wall. A lack of a lung sliding should prompt consideration of pneumothorax; however, lung sliding is not always easy to identify, even in healthy patients (Husain et al. 2012). Furthermore, the lung pulse is difficult to

Vet-ebooks.com

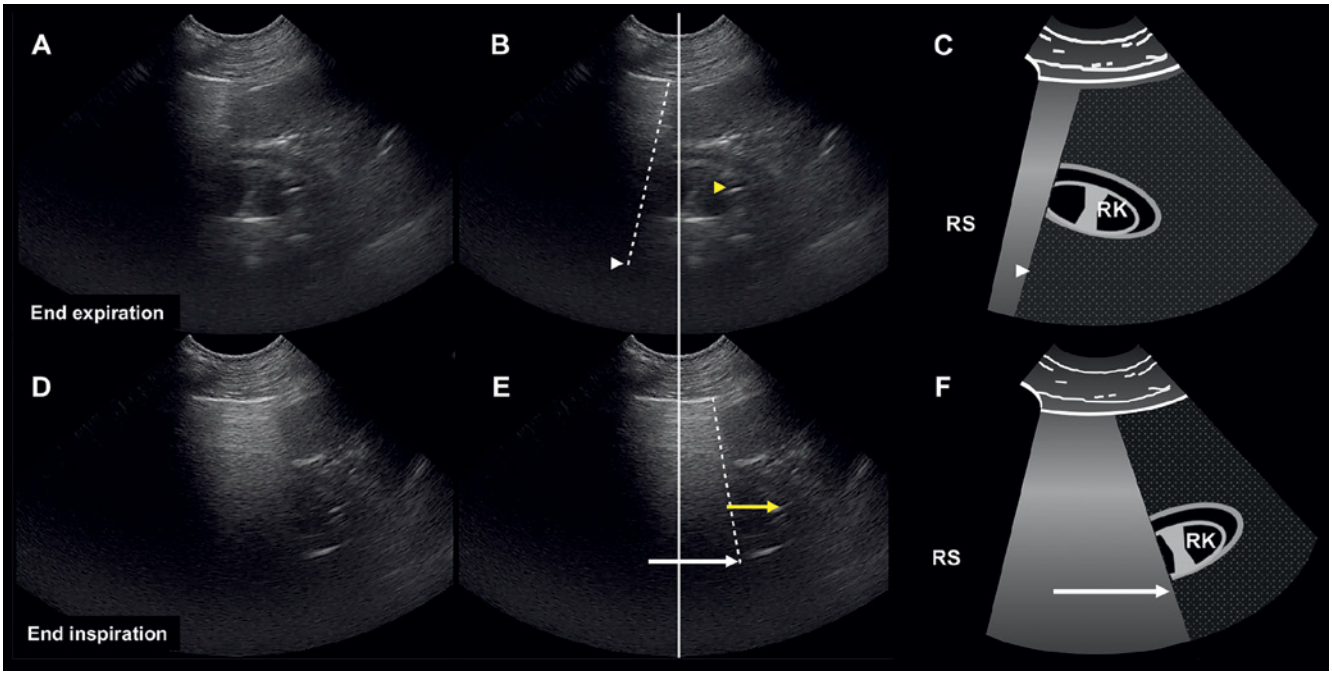


Figure 2.31. Sonograms and schematic images of a normal abdominal curtain sign at end expiration (A–C) and end inspiration (D–F). The ultrasound probe, marker cranially (left of the image) was positioned over the right paralumbar region at the level of the right kidney between the 11th and 12th intercostal spaces, and incorporates the air/soft tissue interface between the abdomen and the thorax which appears as a vertical edge artifact (curtain sign). The solid gray line provides reference to direction and degree of movement of abdominal contents and the abdominal curtain sign (ACS) between end inspiration and end expiration. **(A–C)** At the end of expiration the ACS (white dashed line, white arrowhead) and part of the right kidney/abdominal contents are on the left side of the sonogram. **(D–F)** During inspiration the ACS (white dashed line, white arrow) and abdominal contents (yellow arrow) both move caudally. The extent of movement is depicted by the length of the arrow. Although the two may not move at the same rate (white arrow is longer than the yellow arrow), both are synchronized in that they both move in the same direction as each other during the phases of respiration. A, A-line; RK; right kidney; RS, rib shadow. Arrow shows direction of movement of the vertical edge during inspiration. Boysen et al. (2019)/Frontiers Media S.A./CC BY 4.0.

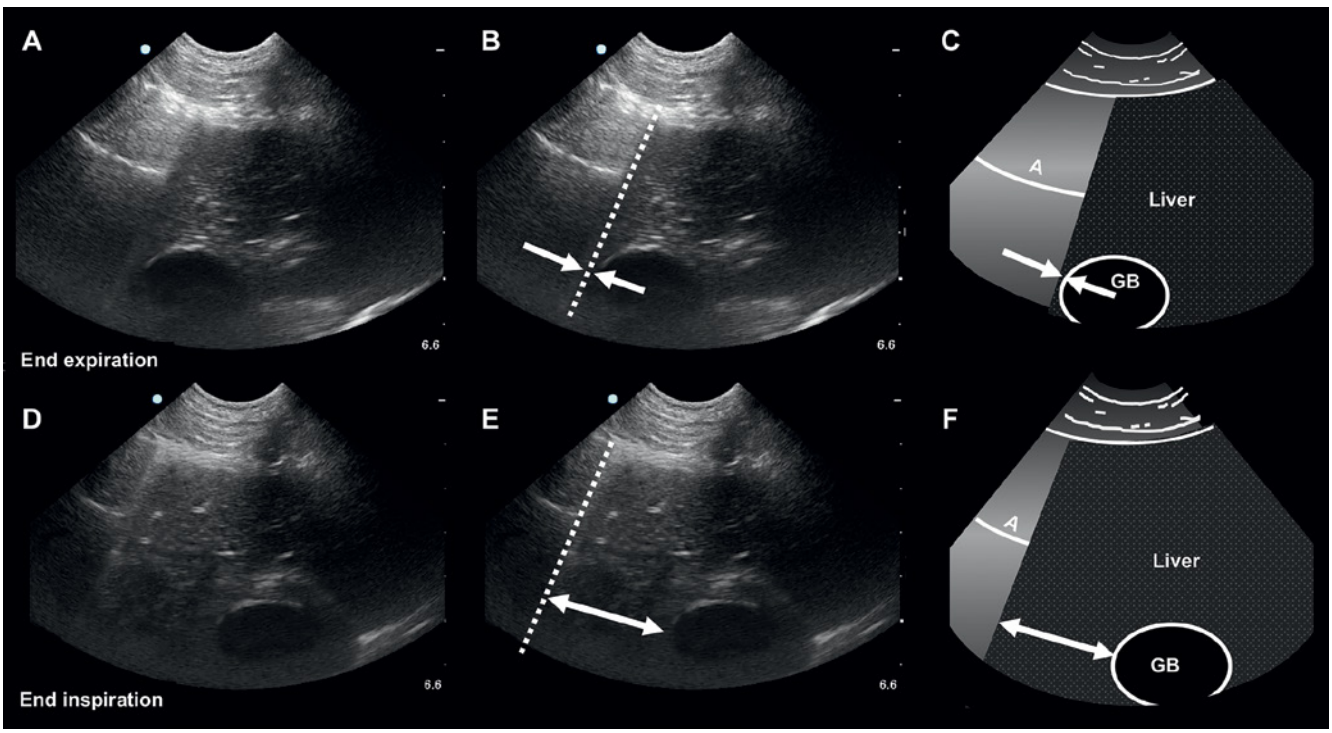


Figure 2.32. Sonograms and schematic images of an asynchronous curtain sign at end expiration (A–C) and end inspiration (D–F). (for full caption, see facing page)

Vet-ebooks.com

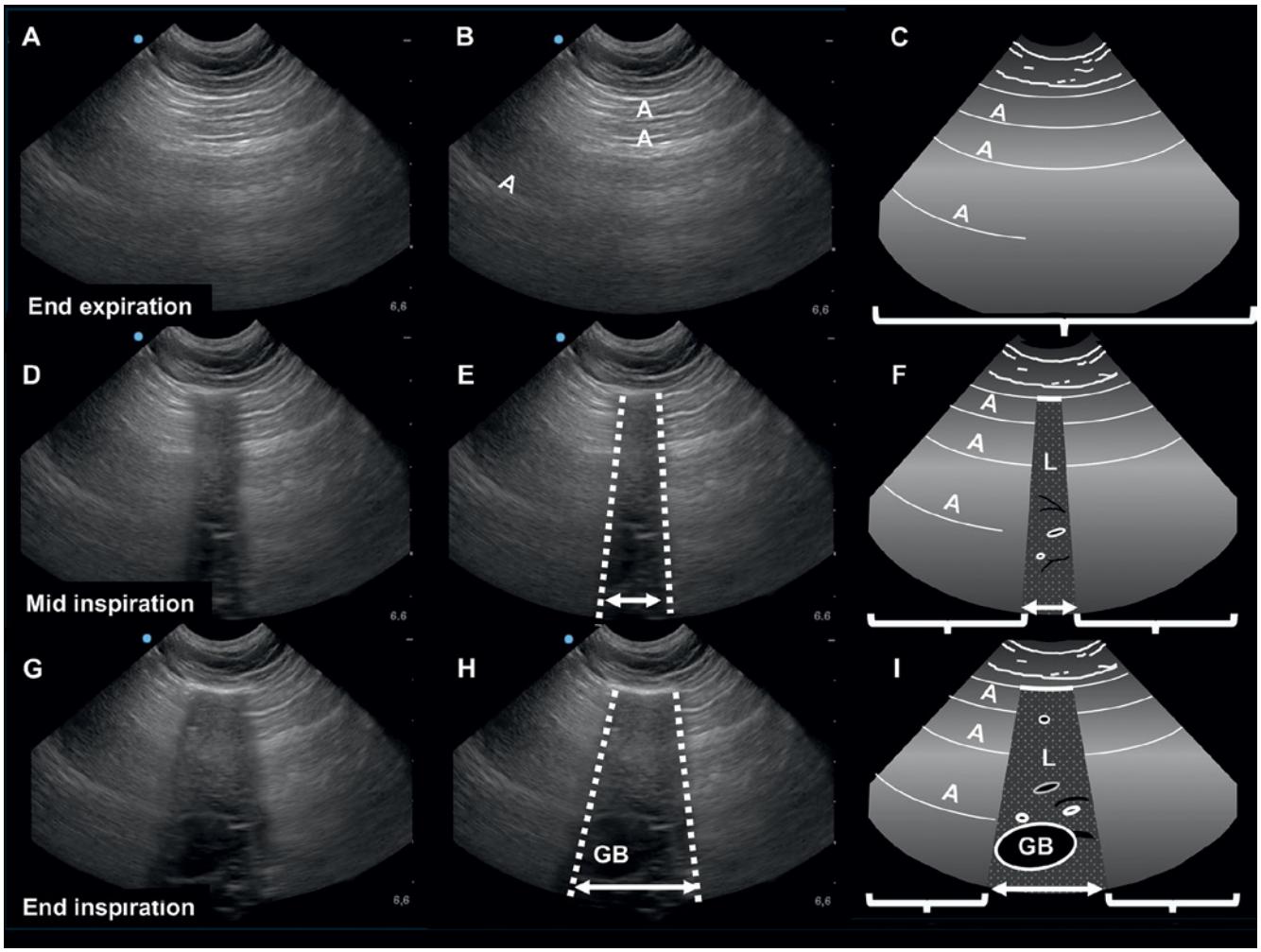


Figure 2.33. Sonograms and schematic images of a double curtain sign at end expiration (A–C), mid inspiration (D–F), and end inspiration (G–I). The ultrasound probe marker is directed cranially and positioned over the right paralumbar region between the 9th and 10th intercostal spaces. **(A–C)** At end expiration only a pneumothorax is present, so there is no visible curtain sign and no visible abdominal content. **(D–F)** At mid inspiration, the abdominal contents suddenly appear within the region of pneumothorax (double white arrow heads), creating two vertical edge curtain signs (white dotted lines). **(G–I)** At end inspiration the visible soft tissues within the region of pneumothorax have enlarged (double white arrow heads) and the vertical edge artifacts have moved further away from each other. The white brackets represent regions of pneumothorax, which the soft tissues "break into." GB, gallbladder; A, A-line; L, liver. Boysen et al. (2019)/Frontiers Media S.A./CC BY 4.0.

Figure 2.32. Sonograms and schematic images of an asynchronous curtain sign at end expiration (A–C) and end inspiration (D–F). The ultrasound probe marker is directed cranially and positioned over the right paralumbar region between the 9th and 10th intercostal spaces, and incorporates the air/soft tissue interface between the abdomen and the thorax which appears as vertical edge artifact known as a curtain sign. **(A–C)** At the end of expiration the ACS (dotted white line) and the gall bladder (GB) are to the left of center on the sonogram. **(D–F)** During inspiration, the vertical edge of the curtain sign moves further cranially and opposite to the direction to the abdominal contents. The asynchronous curtain sign occurs when the vertical edge artifact moves in the opposite direction to the abdominal contents during the respiratory cycle. Toward each other on expiration (white arrows) and away from each other on inspiration (double headed white arrow). Courtesy of Calgary VPOCUS Academy, with permission.

Vet-ebooks.com

identify at lung regions more distal from the heart, which is where uncontained pleural air tends to accumulate.

Unless associated with the lung point (see below), the sonographic identification of B-lines and/or echogenic lung tissue exclude pneumothorax at the location the probe is situated over the thorax. This is because visible B-lines and echogenic lung tissue always indicates the lung surface is also visible, excluding interposed air.

Pleural Effusion

Pleural effusion appears as anechoic to hypoechoic accumulations between the thoracic wall, diaphragm, and lung surfaces (Figure 2.34). Its appearance varies with the cellularity and quantity of the effusion, probe location, patient positioning, and the presence of adhesions. It often occupies the costophrenic angle/recess when assessed transthoracically in standing/sternal patients, allowing the diaphragm to be seen curving away from the thoracic wall (Figure 2.35). As the quantity of effusion increases, the lungs may become atelectatic, appearing as floating echogenic structures (termed the "jellyfish" sign in the human literature) (Montero-Yéboles et al. 2022, Figure 2.36). The sensitivity and specificity of detecting pleural effusion may be increased by including the subxiphoid window (Figure 2.24), locating the PD window (Figures 2.13, 2.35), and by turning the probe parallel to the ribs and assessing the ventral pleural regions between the lung/heart and sternal muscles (Boysen et al. 2020, 2022) (Figures 2.15, 2.37).

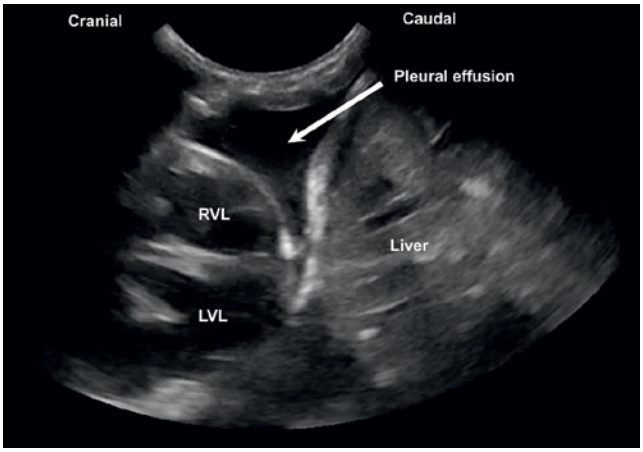


Figure 2.35. Sonogram of pleural effusion in a dog with the probe perpendicular to the ribs at the level of the pericardio-diaphragmatic (PD) window. When pleural effusion accumulates at this site it fills the costophrenic recess, separating the diaphragm from the thoracic wall and allowing the diaphragm to be visualized curving away from the thoracic wall. The PD window is a good site to differentiate pleural from pericardial effusion. LVL, left ventricular lumen; RVL, right ventricular lumen. Courtesy of Calgary VPOCUS Academy, with permission.

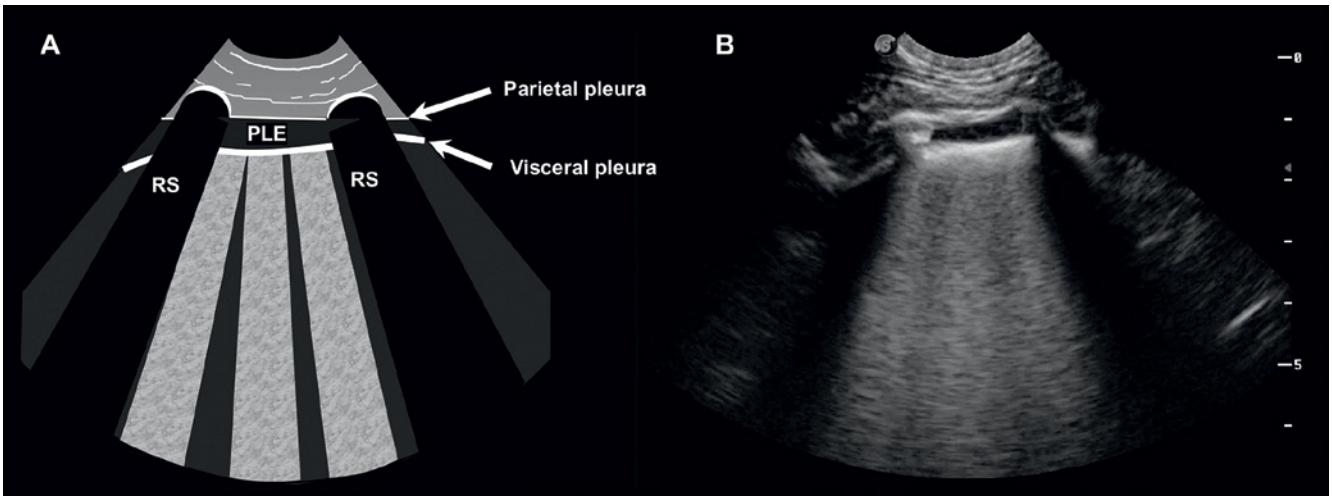


Figure 2.34. Schematic image (A) and sonogram (B) of pleural effusion in a dog. The probe is perpendicular to the ribs just above the level of the costophrenic recess. As fluid separates the parietal and visceral pleura lung sliding is lost. When pleural effusion (PLE) is present with the probe perpendicular to the ribs the two pleurae tend to remain parallel to each other, with interposed fluid forming an anechoic "strip." Note the presence of ring down artifact originating from the visceral pleura deep to the effusion. This should not be interpreted as lung pathology, as decreased lung aeration due to compressive atelectasis secondary to the pleural effusion (or other pleural space occupying lesions) will increase lung density and cause the appearance of hyperechoic vertical artifact similar to B-lines or even lung consolidation. RS, rib shadow. Courtesy of Calgary VPOCUS Academy, with permission.

Vet-ebooks.com

Increased B-Lines

As lung density increases B-line numbers will increase in number, eventually coalescing and forming a white "sheet" called "white lung" (Figure 2.38). Increased extravascular lung water (EVLW) is the most common cause of increased B-lines, but any process that increases lung density, including atelectasis, fibrosis, collagen, neoplastic cells, and inflammatory cells can result in increased B-lines (Demi et al. 2023) (Figure 2.39). History, concurrent diagnostic testing, and mapping the PLUS profile by scanning multiple lung regions and lung surface area bilaterally, and assessing the pleural space helps determine the underlying cause. Monitoring B-lines serially for progression or resolution may also help determine if B-lines are a normal variation or if true pulmonary pathology is present.

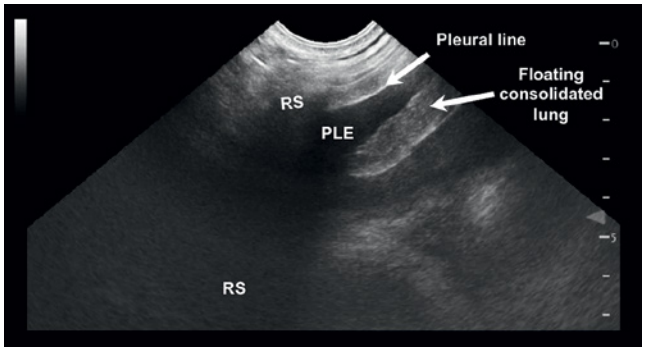


Figure 2.36. Sonogram of pleural effusion and lung atelectasis forming an echogenic band in a dog with pleural effusion. With moderate pleural effusion, compressive atelectasis of the lung can occur resulting in echogenic structures, representing the lung floating in the effusion. PLE, pleural effusion; RS, rib shadow. Courtesy of Calgary VPOCUS Academy, with permission.

Lung Consolidation

When the ratio of peripherally aerated to nonaerated lung tissue falls below 5–10% (Bhoil et al. 2021; Miller 2016), the acoustic impedance between the thoracic wall and lung is decreased to a point the ultrasound beam is transmitted through the underlying lung tissue, appearing as echogenic tissue of variable shape. Similar to causes of increased B-lines, these areas of decreased or absent aerated lung have different causes (Figure 2.39). Unlike B-lines, which can occasionally be normal and will increase with even mild increases in lung density, echogenic tissue is always abnormal. Broadly, echogenic tissue can be classified as partial, where the echogenic tissue region within the pulmonary lobe encounters air-filled lung

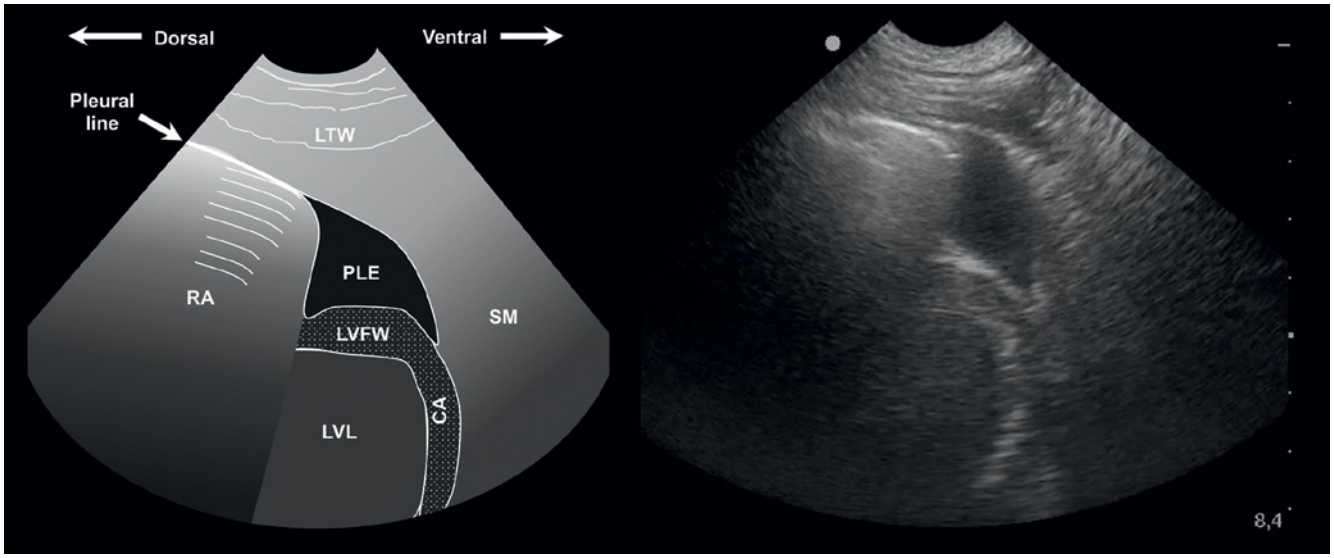


Figure 2.37. Schematic image (A) and sonogram (B) of pleural effusion with the probe orientated parallel to the ribs and the probe marker directed dorsally. Turning the probe parallel to the ribs and sliding the probe ventrally so that 1/3 of the image is filled with ventral sternal muscle (SM) will often allow smaller quantities of pleural effusion (PLE) not visible with the probe situated perpendicular to the ribs to be identified. The shape of the fluid at this location is often triangular, similar to a spinnaker sail, and is therefore often referred to as the "sail sign". In this image the probe is located over the heart, where the cardiac apex sits against the sternal muscles. CA, cardiac apex; LTW, lateral thoracic wall; LVFW, left ventricular free wall; LVL, left ventricular lumen; RA, reverberation artifact from air filled lung. Courtesy of Calgary VPOCUS Academy, with permission.

Vet-ebooks.com

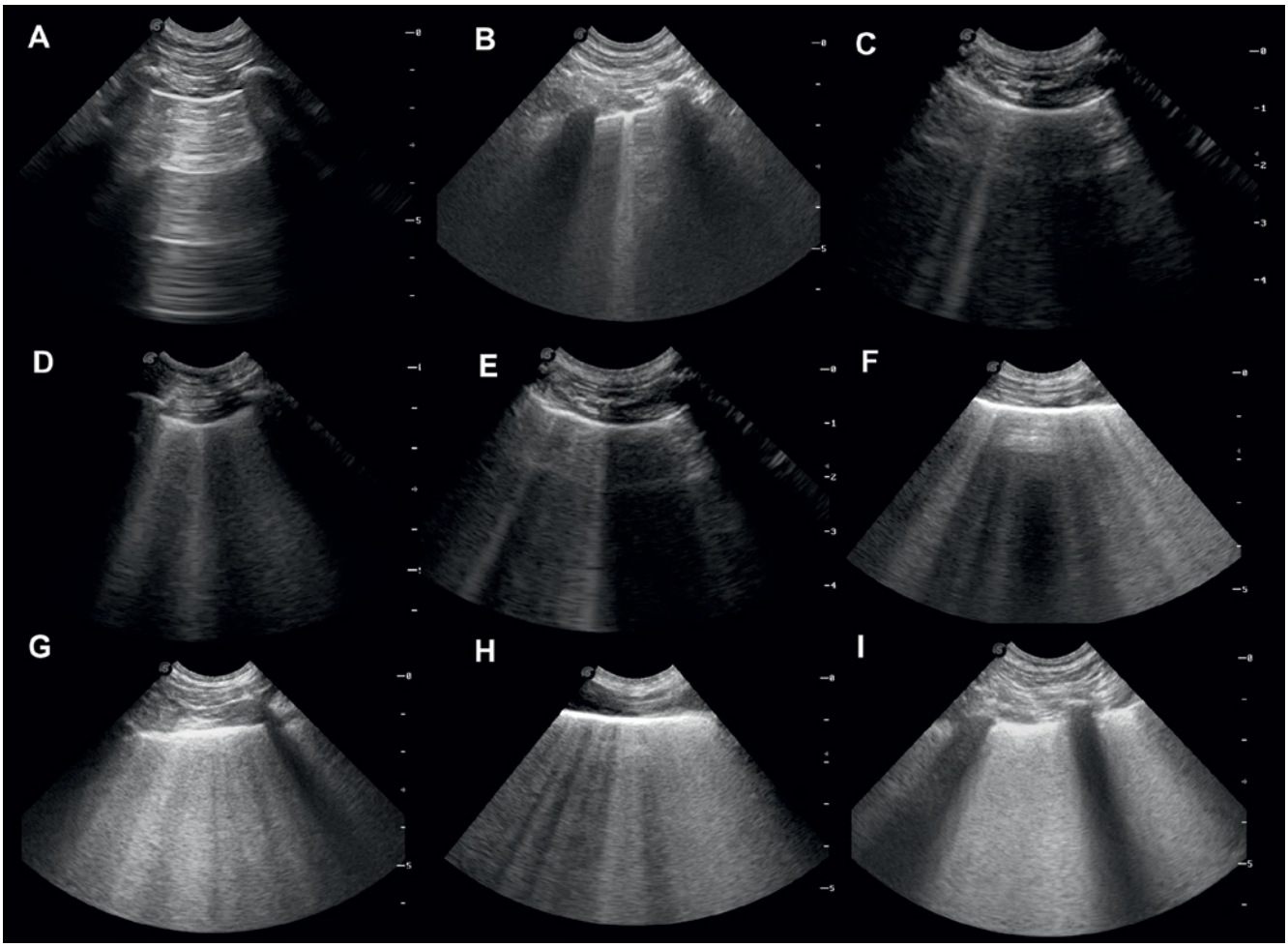


Figure 2.38. Sonograms demonstrating progressive loss of aerated lung and subsequently increased B-line formation from (A) (healthy lung, only A-lines are visible) to (I) (white lung). Provided sufficient air is present at the periphery of the lung (>5–10%) the ultrasound beam is reflected from the lung surface resulting in the vertical hyperechoic artifact of B-lines (lung tissue not visualized, only artifact seen). With more severe loss of aerated lung B-lines start to coalesce and form solid sheets, referred to as "white lung" **(H, I)**. Courtesy of Calgary VPOCUS Academy, with permission.

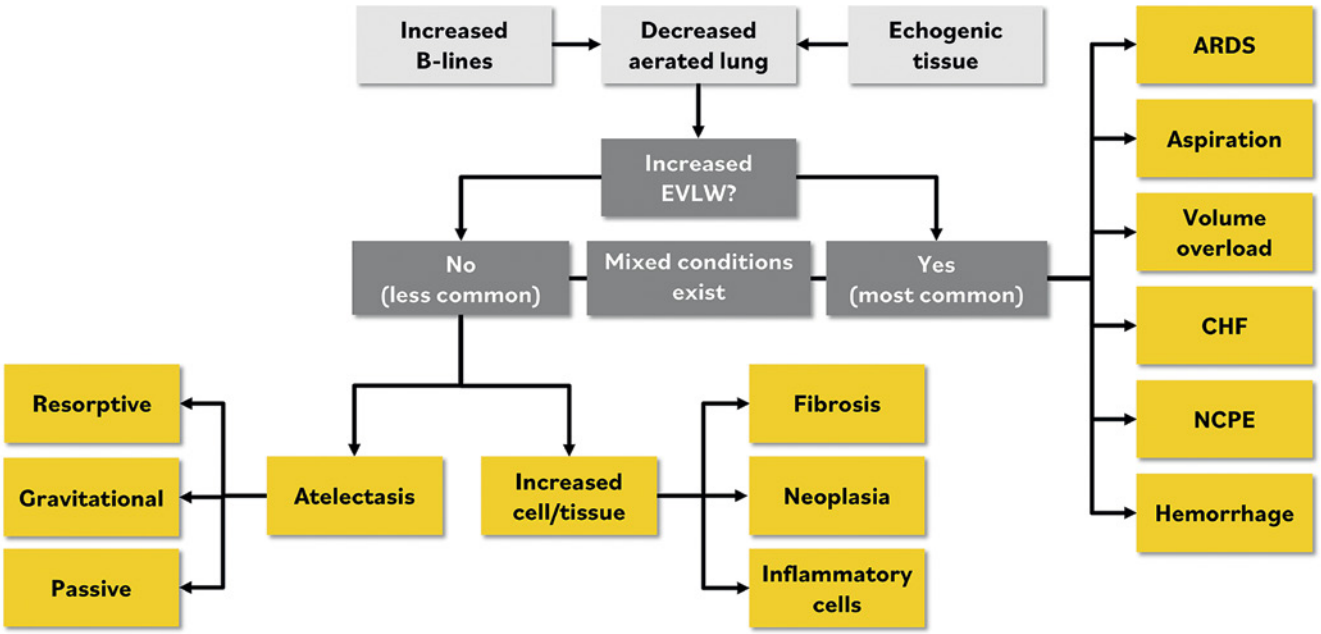


Figure 2.39. Diagnostic algorithm for increased B-lines and lung consolidation. (for full caption, see facing page)

Vet-ebooks.com

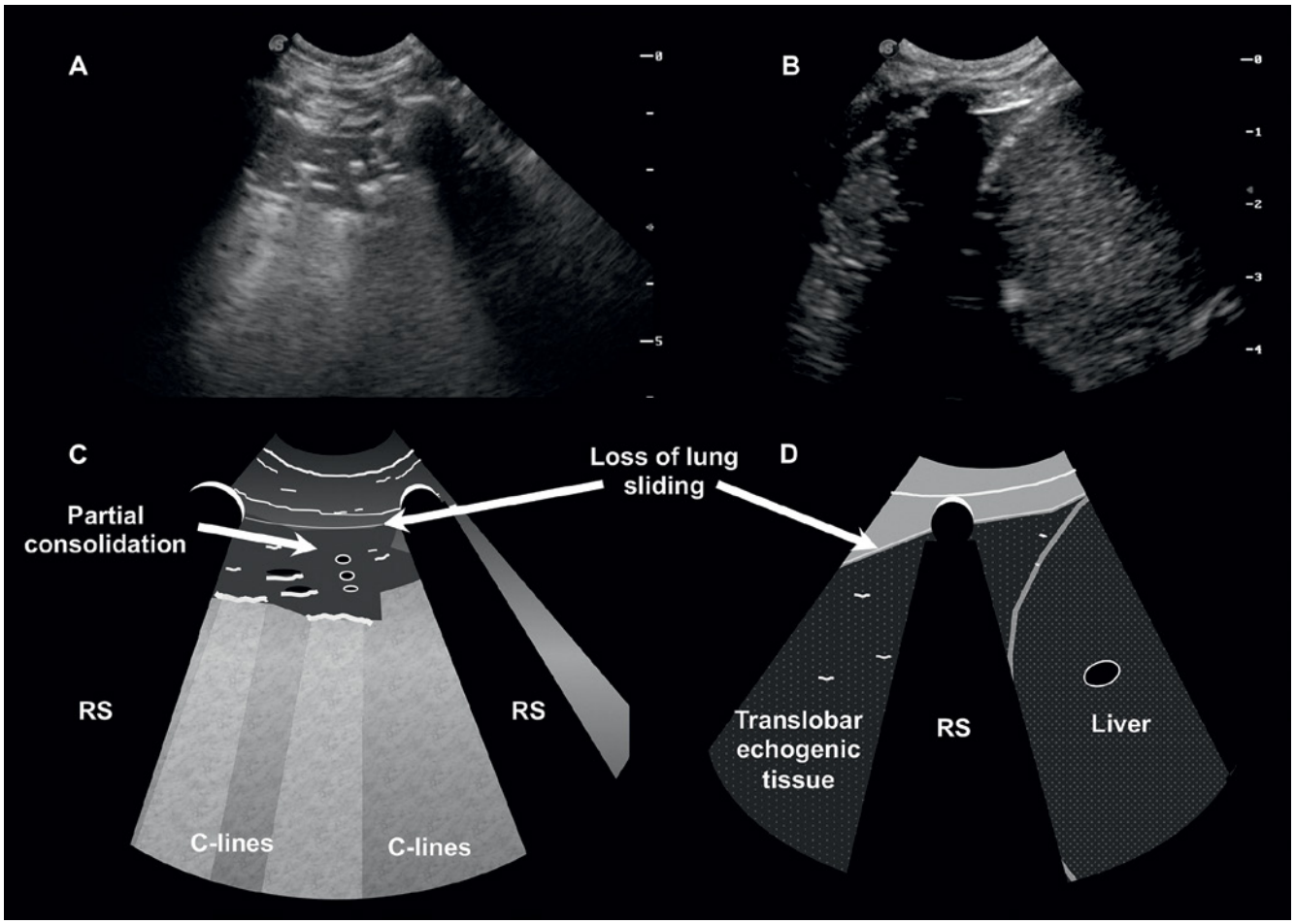


Figure 2.40. Sonogram (A, B) and schematic (C, D) images with visible echogenic lung tissue. They can be classified as partial **(A, C)** or complete **(B, D). (A, C)** With partial, the acoustic window created by the echogenic lung tissue encounters a higher percentage (>5–10%) of air-filled lung deep to the tissue which reflects the ultrasound beam. At the site where the ultrasound beam is reflected (echogenic tissue to air filled lung interface), ring down artifact (lighter shaded areas) can often be seen (referred to as a C-lines in human medicine). Although these ring down artifacts may move in sync with the respiratory cycle, unlike B-lines, they do not arise from the lung surface; they arise from the deep border of echogenic lung tissue. **(B, D)** By contrast, with translobar echogenic lung tissue, the entire lung lobe from one surface of the other can be seen. Because the soft tissue air interface is lost between the lung and thoracic wall when echogenic lung tissue is present the pleural line is less hyperechoic and lung sliding is lost (not appreciated in a still image). RS, rib shadow. Courtesy of Calgary VPOCUS Academy, with permission.

distal to this region, or translobar, where the entire lung lobe from one surface to the other is involved (Figure 2.40). A partial consolidation can be further classified as a shred, nodule, or wedge sign (Figure 2.41, Table 2.6). Parenchymal characteristics of echogenic tissue can be further classified based on the presence or absence air and fluid bronchograms, the former further classified as static or dynamic.

Figure 2.39. Diagnostic algorithm for increased B-lines and lung consolidation. Although not well understood, B-lines are believed to arise when there is decreased aerated lung at the lung periphery, regardless of the cause. It is therefore possible to have increased B-lines arise from extra-vascular lung water (EVLW) causes (e.g., left-sided congestive heart failure), and non-EVLW causes (e.g., infiltrative disease, fibrosis, atelectasis). ARDS, acute respiratory distress syndrome; CHF, congestive heart failure; NCPE, non-cardiogenic pulmonary edema. Courtesy of Calgary VPOCUS Academy.

Vet-ebooks.com

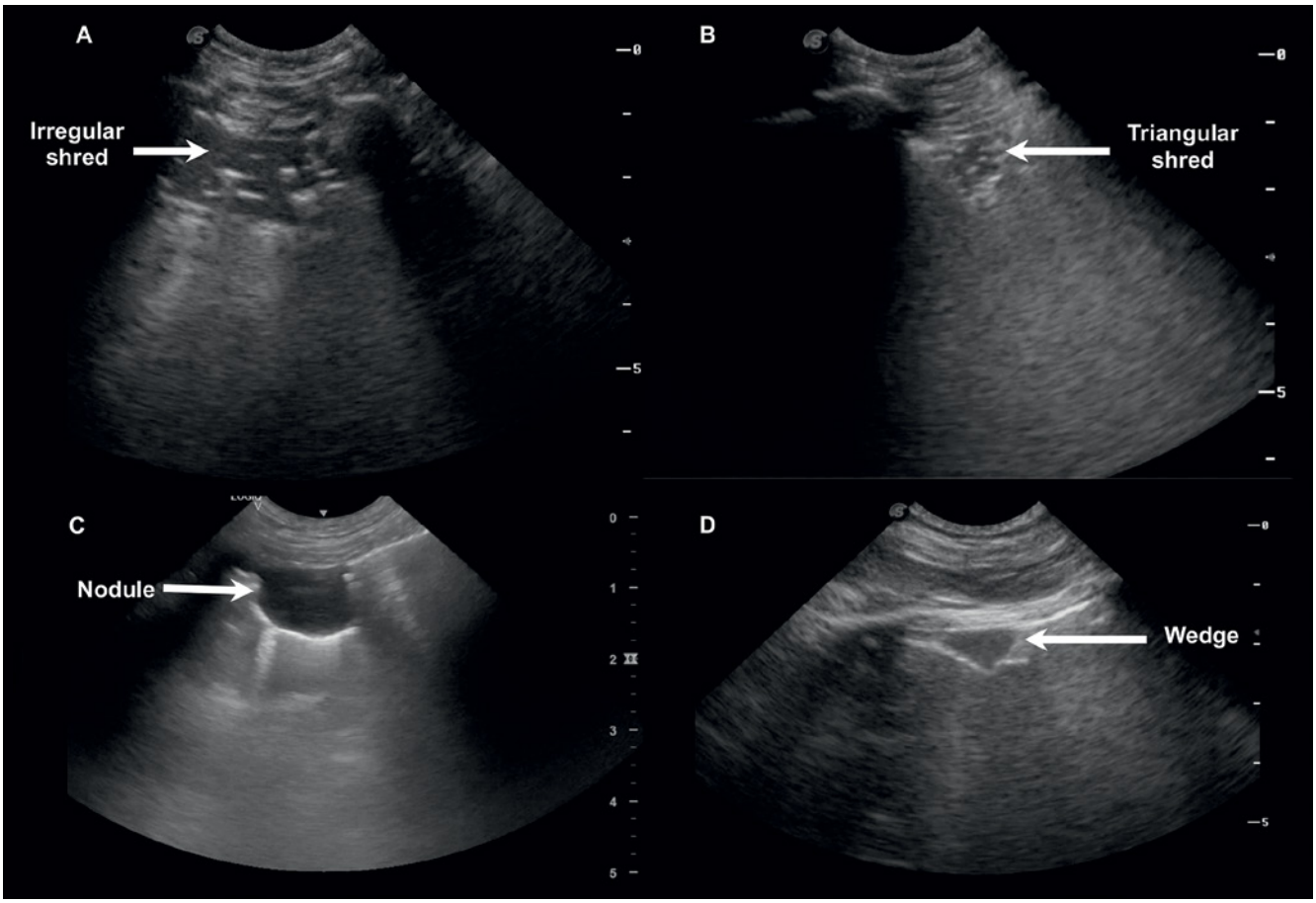


Figure 2.41. Sonograms of different types of partial echogenic lung tissue. (A, B) "Shred" signs occur when there is a focal tissue-like pattern in apposition to underlying (deeper) air-filled lung. The boundary between the echogenic lung tissue and aerated lung appears "shredded" (fractal/shredded border). The parenchyma associated with shred signs often contain air bronchograms (white punctate to linear dots and lines) and fluid bronchograms (anechoic circles and lines). Often seen with inflammatory lung pathology (e.g., acute lung injury and aspiration pneumonia). **(C)** "Nodule" signs differ from the shred sign in that the distal border between the tissue-like pattern and aerated lung is often well defined, smooth, and circular. The differential diagnoses for nodule signs are similar to radiographs, with neoplasia and fungal disease being the more common causes **(D)** "Wedge signs" result in well demarcated wedge or triangular lesions, often devoid of parenchymal characteristics. They are classically associated with pulmonary thromboembolism (PTE). Note that triangular lesions are not specific to "Wedge" signs and PTE and can also be seen with shred signs **(B).** Note that lung sliding will be lost between the partial echogenic lung tissue and the thoracic wall. Courtesy of Calgary VPOCUS Academy, with permission.

Air/Fluid Bronchograms

The sonographic appearance of **echogenic lung tissue**, particularly with shred and trans-lobar distribution, vary depending on whether the smaller airways contain air (air bronchogram, Figure 2.42) or fluid (fluid bronchogram, Figure 2.43) (Lee 2016, Lee 2017; Liu et al. 2023; Montero Baladía et al. 2018; Shah et al. 2022).

Mixed fluid and air bronchograms may co-exist in the same echogenic lung tissue or in different regions of the same lung lobe. When bronchioles within consolidation remain patent, communicating with the large airways, changes in air movement (>1 mm) with tidal volume can create visible movement of air (Lee 2016, Lee 2017). This air movement within small airways creates a "shimmering" referred to as a dynamic air bronchogram. In people, dynamic air bronchograms are most often seen with pneumonia and inflammatory induced echogenic lung tissue. In contrast, static air bronchograms may occur with atelectasis or inflammatory induced echogenic lung tissue. A complete lack of air bronchograms is suggestive of complete atelectasis although severe pneumonia or lobar hemorrhage cannot be excluded.

Vet-ebooks.com

Table 2.6
Lung ultrasound pathologies

Increased B-lines
Increased extravascular lung water (EVLW; i.e., "wet" lung causes)
- Cardiogenic edema
- Fluid overload
- Noncardiogenic pulmonary edema
- Acute respiratory distress syndrome (ARDS)
- Aspiration pneumonia
- Contusions/hemorrhage

Non-EVLW causes of increased B-lines (i.e., "dry" lung causes)
- Fibrosis/amyloidosis
- Inflammatory cell infiltrate
- Neoplastic cell infiltrates
- Atelectasis

Nontranslobar echogenic lung tissue
- Shred sign (Figure 2.41A, B)
  - Pneumonia
  - Hemorrhage
  - Inflammatory-associated increases in extravascular lung water (e.g., ARDS)
  - Thromboembolic disease
  - Neoplasia
  - Atelectasis
- Nodule sign (Figure 2.41C)
  - Fungal
  - Primary or metastatic neoplasia
  - Abscesses
- Wedge sign (Figure 2.41D)
  - Pulmonary thromboembolism
  - Not specific and may result from other pathologies causing shred signs

Translobar echogenic lung tissue (Figures 2.40B, D, 2.42A, B)
- Pneumonia
- Hemorrhage
- Inflammatory-associated increases in extravascular lung water (e.g., ARDS)
- Atelectasis

E-Lines

E-lines (and W-lines) are a type of comet tail artifact that results from subcutaneous emphysema. They originate within the subcutaneous tissues and therefore obliterate the pleural line, making its identification and interpretation challenging (Figure 2.16E, F). Applying continual gentle pressure to the ultrasound probe (provided the patient can tolerate it) may displace E-lines allowing the pleura to be interpreted.

Cardiac Pocus Abnormalities

The CPOCUS questions addressed are usually focused to myocardial contractility, left ventricular filling, right ventricular dilatation, or the presence of other obvious abnormalities (e.g., pericardial effusion). Extensive quantitative calculations are not the goal of CPOCUS. When time and training allow, simple calculations can be performed, but are not necessary as a good correlation between visually estimated (qualitative) and formally measured (quantitative) cardiac parameters has been reported in small animals. CPOCUS compliments PLUS in the evaluation of patients with respiratory distress (i.e., the finding of diffuse bilaterally increased B-lines should prompt CPOCUS evaluation to assess the left atrium for congestive heart failure). In contrast, the absence of B-lines in a patient with respiratory distress essentially rules out cardiac causes, and other respiratory pathologies should be considered. Applications of veterinary CPOCUS are presented in Table 2.4.

Pericardial Effusion

Pericardial effusion appears as a circular accumulation of fluid adjacent to and surrounding the cardiac chambers, separating the pericardial sac from the heart. Both right parasternal short- and long-axis views demonstrate the extent of pericardial fluid accumulation (Figure 2.44). Be sure to extend the depth to visualize the entire heart. In the short-axis view fan from the cardiac apex to the base through all planes to ensure all cardiac anatomy is correctly identified and pericardial effusion is not confused for cardiac chambers. If it is unclear anechoic fluid accumulation is pericardial or pleural in origin assess the subxiphoid window (Figure 2.45) and/or PD windows (Figure 2.46).

Pericardial Tamponade

Cardiac tamponade (intrapericardial pressure >right ventricular diastolic pressure) due to pericardial effusion is relatively common in dogs but is rare in cats. The right parasternal four-chamber long-axis view may be more sensitive for diagnosing cardiac tamponade compared to the short-axis views (Figure 2.47). With cardiac tamponade, there is diminished contraction of the heart, paradoxical compression or collapse (cyclic) of cardiac chambers, and paradoxical septal motion. Arguably one of the earliest signs occurs

Vet-ebooks.com

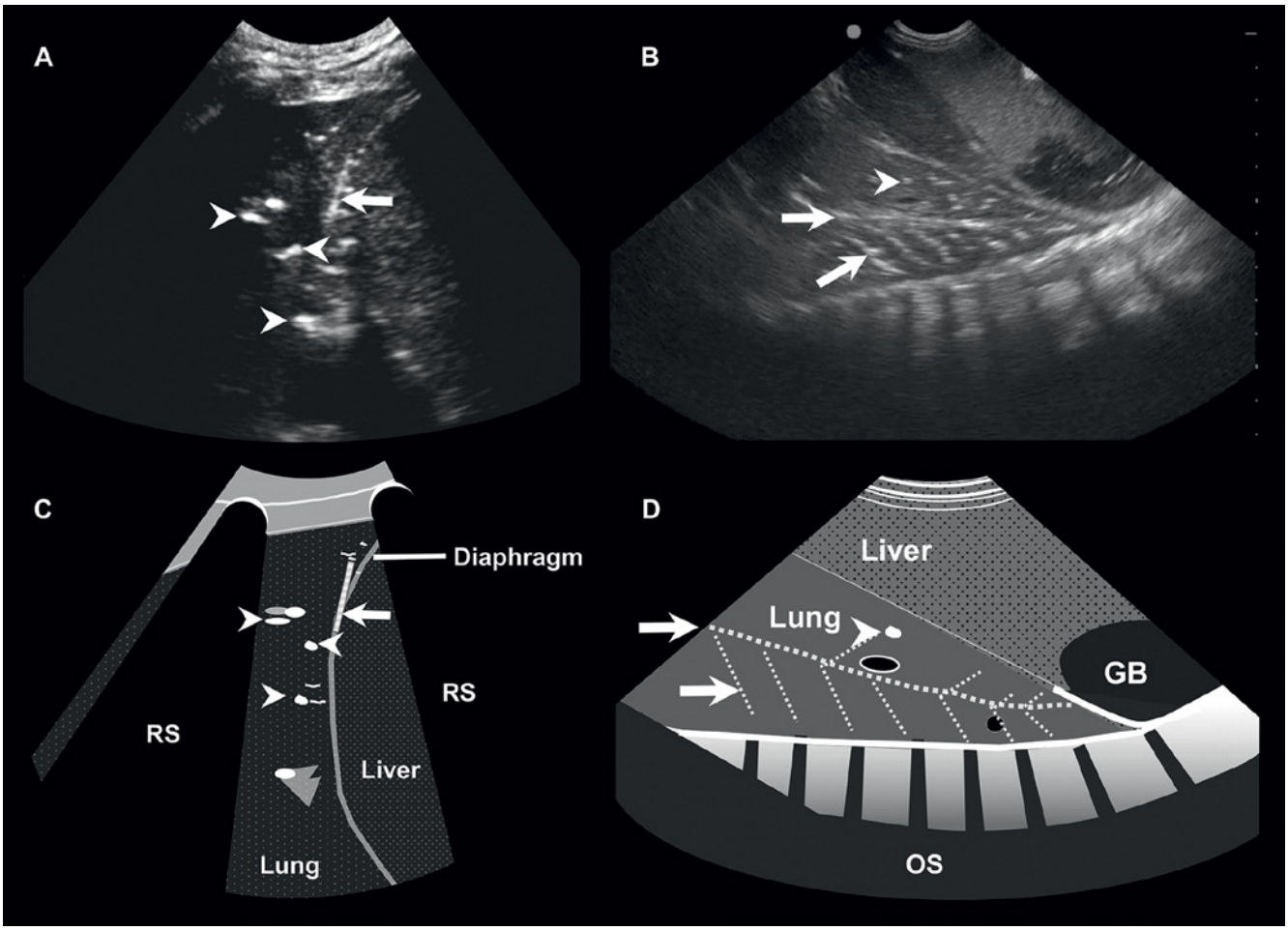


Figure 2.42. Sonogram (A, B) and schematic (C, D) transthoracic lateral lung surface (A, C) and subxiphoid caudal lung surface (B, D) images of air bronchograms. Air bronchograms appear as punctate (arrow heads) or linear (arrows) hyperechoic foci visible between the hyperechoic walls of bronchi on a transthoracic view of the lateral lung surface **(A, C)** and the subxiphoid view **(B, D)** of the caudal lung regions. They may be seen in partial or translobar ehogenic lung tissue. With pathology the branching airway architecture is often preserved **(B, D),** while they may be more parallel with atelectasis (not shown). Note the presence of osseous shadowing (OS) distal to the translobar echogenic lung **(B, D)**. RS, rib shadow; GB, gall bladder. Courtesy of Celine Pouzot-Nevoret, with permission.

when the RA free wall collapses into the atrium, intermittently reducing atrial chamber size, which is easily assessed on the right parasternal four-chamber long-axis view (Figure 2.47). Note that tamponade is a clinical diagnosis and the finding of shock in a patient with identifiable pericardial effusion should prompt an increased index of suspicion for tamponade.

Left-Atrial-Aortic Ratio (LA:AO)

Most patients presenting with respiratory distress secondary to congestive heart failure have LA:Ao ratios ≥2, well above upper reference limits (Ward et al. 2018). If the LA is enlarged, it suggests increased LA volume and/or pressure which is often associated with left-sided congestive heart failure or iatrogenic fluid overload. Alternatively, in cats (not yet studied in dogs), if >3 times, the area of the aorta can subjectively fit within the LA, the LA should be considered enlarged (Loughran et al. 2019) (Figure 2.48 and refer to Chapter 6 on Heart). Using both methods in cats is a good way to help confirm if the LA is truly enlarged. A small LA:Ao (≤1 : 1) suggests pseudohypertrophy (Figure 2.49). **Pseudohypertrophy** results from hypovolemia and decreased ventricular filling which causes decreased LA and LV chamber size, and the appearance of a thickened interventricular septum and ventricular free wall (Figure 2.50). This tends to resolve with restoration of effective circulating volume.

Vet-ebooks.com

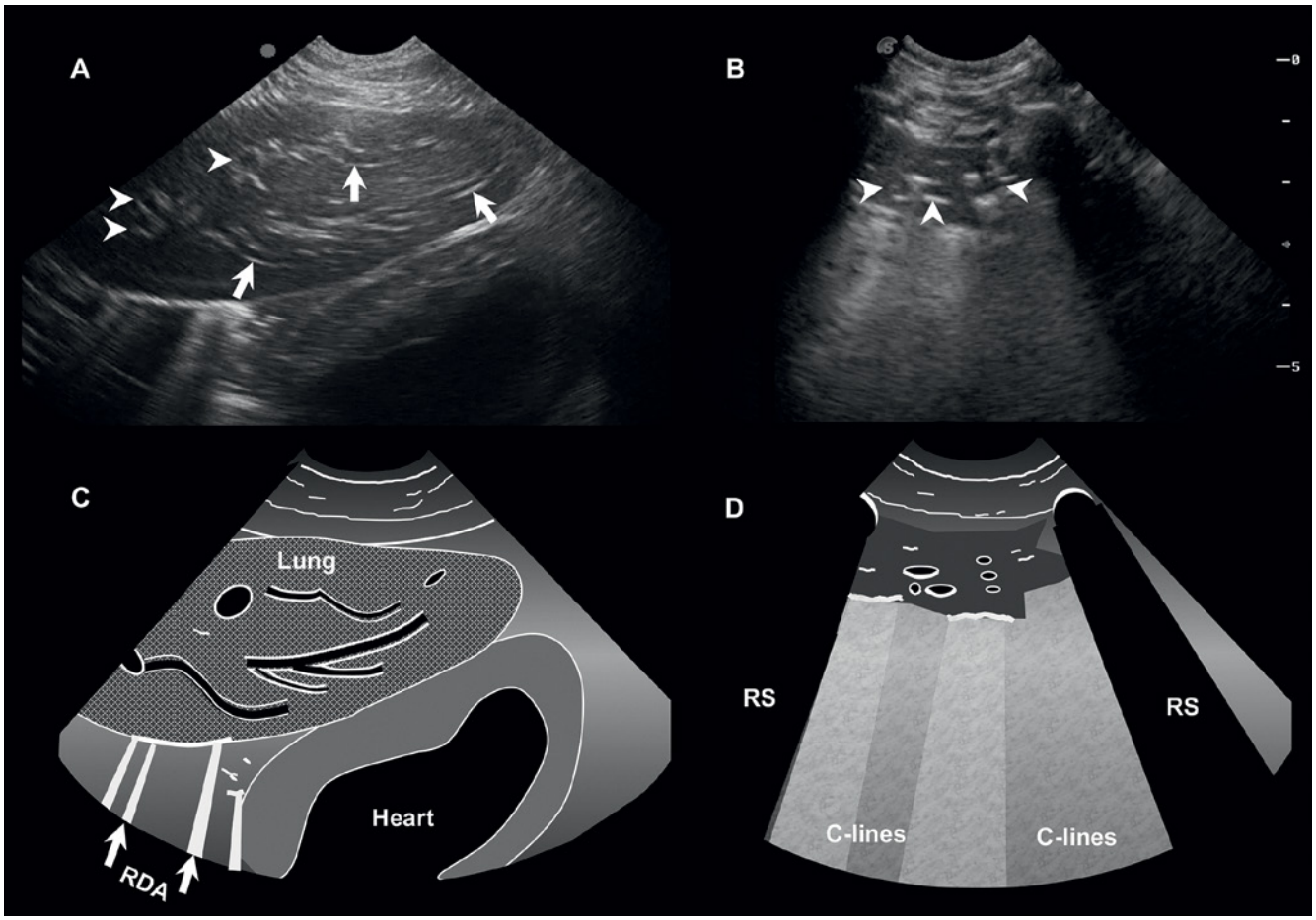


Figure 2.43. **Sonogram (A, B) and schematic (C, D) images of fluid bronchograms**, which appear as anechoic circular (arrow heads) or linear (arrows) fluid filled structures visible between the hyperechoic walls of bronchi. Similar to air bronchograms, they may be seen with translobar **(A, C)** and partial **(B, D)** echogenic lung patterns. Fluid bronchograms can be difficult to differentiate from pulmonary vessels, although some may have air visible in addition to fluid. Doppler pulmonary imaging, although challenging in small animals, may help differentiate vessels and fluid bronchograms. RDA, ring down artifact; RS, rib shadow. Schematic images courtesy Calgary VPOCUS Academy, with permission.

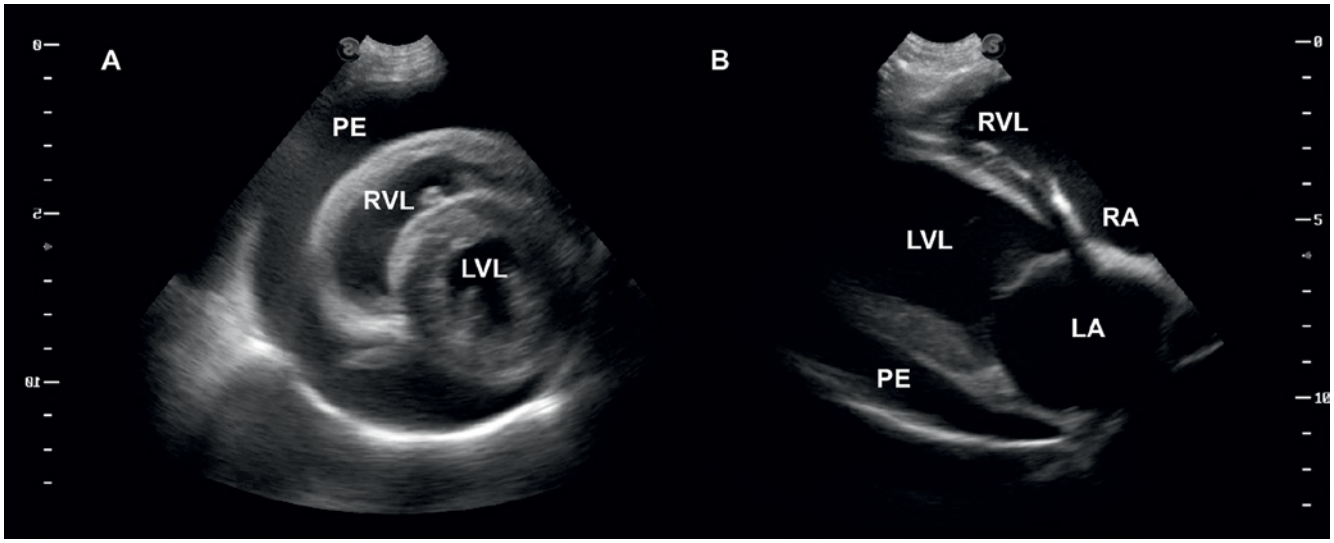


Figure 2.44. **Sonograms of pericardial effusion using the right parasternal window with the probe situated directly over the heart. (A)** In the short axis view at the level of the papillary muscles (mushroom view). **(B)** In the long axis four-chamber view. LA, left atrium; LVL, left ventricular lumen; PE, pericardial effusion; RA, right atrium; RVL, right ventricular lumen. Courtesy of Calgary VPOCUS Academy, with permission.

Vet-ebooks.com

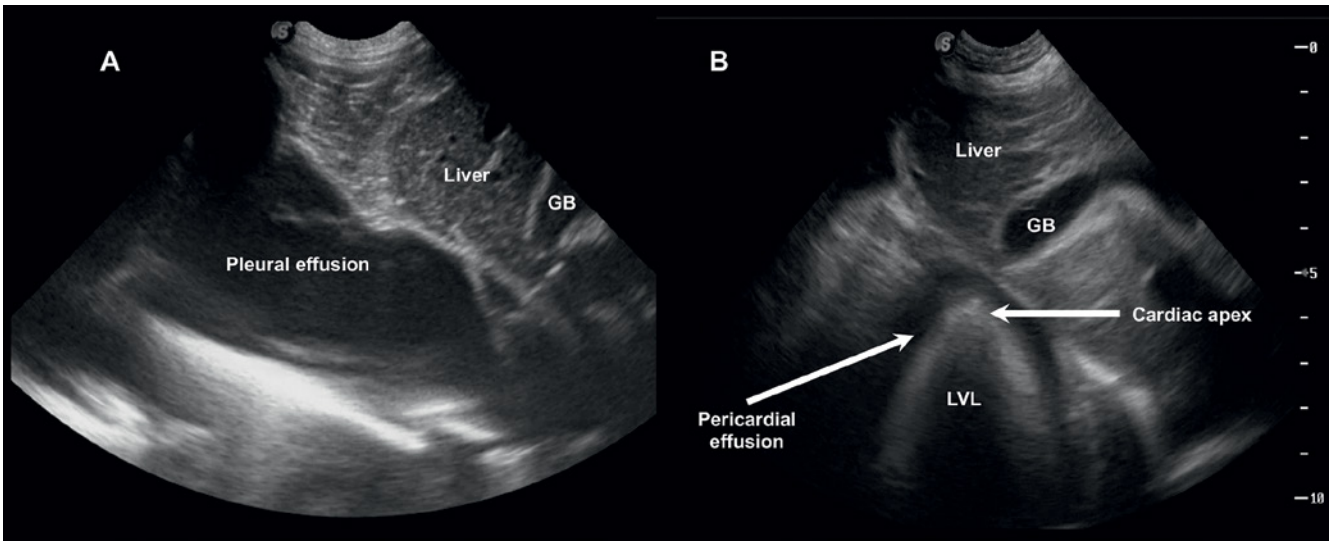


Figure 2.45. Sonograms of pleural (A) and pericardial (B) effusion obtained via subxiphoid window. (A) When pleural effusion accumulates at this site, it is uncontained and tracks along the diaphragm. **(B)** With pericardial effusion, the fluid is contained by the pericardial sac and tracks around the apex of heart and away from the diaphragm. GB, gall bladder; LVL, left ventricular lumen. Courtesy of Calgary VPOCUS Academy, with permission.

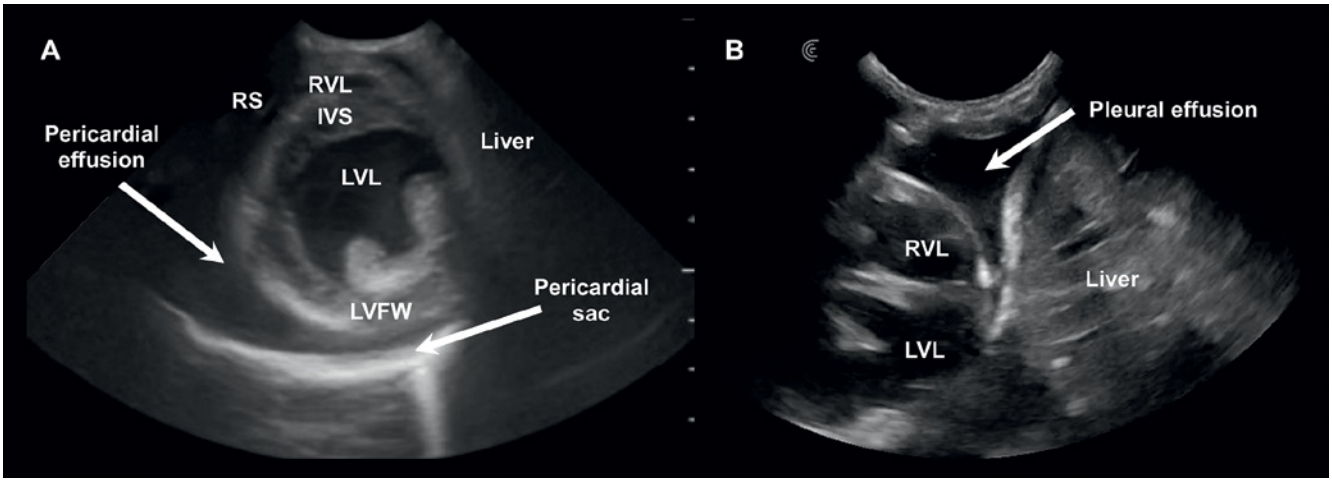


Figure 2.46. Sonograms of pericardial (A) and pleural (B) effusion at the pericardio-diaphragmatic window. (A) With pericardial effusion, the fluid tracks around the heart and away from the diaphragm and does not fill the costophrenic recess. **(B)** When pleural effusion accumulates at this site, it will fill the costophrenic recess, separating the diaphragm from the thoracic wall and allowing the diaphragm to be visualized curving away from the thoracic wall. IVS, intraventricular septum; LVFW, left ventricular free wall; LVL, left ventricular lumen; RS, rib shadow; RVL, right ventricular lumen. Courtesy of Calgary VPOCUS Academy, with permission.

Left Ventricular Lumen Size and Function

The subjective identification of an enlarged LV lumen may suggest volume overload or conditions causing myocardial dysfunction (e.g., dilated cardiomyopathy). Both can be associated with increased B-lines on lung ultrasound. Assessing LV contractility is important to help differentiate the two conditions (increased with volume overload, decreased with dilated cardiomyopathy).

With practice, ventricular contractility can be subjectively assessed by estimating the relative change in size of the LV lumen during diastole and systole, which should be roughly 30–50% in dogs and 40–60% in cats (Fox et al. 1985; Häggström et al. 2016; Marchesotti

Vet-ebooks.com

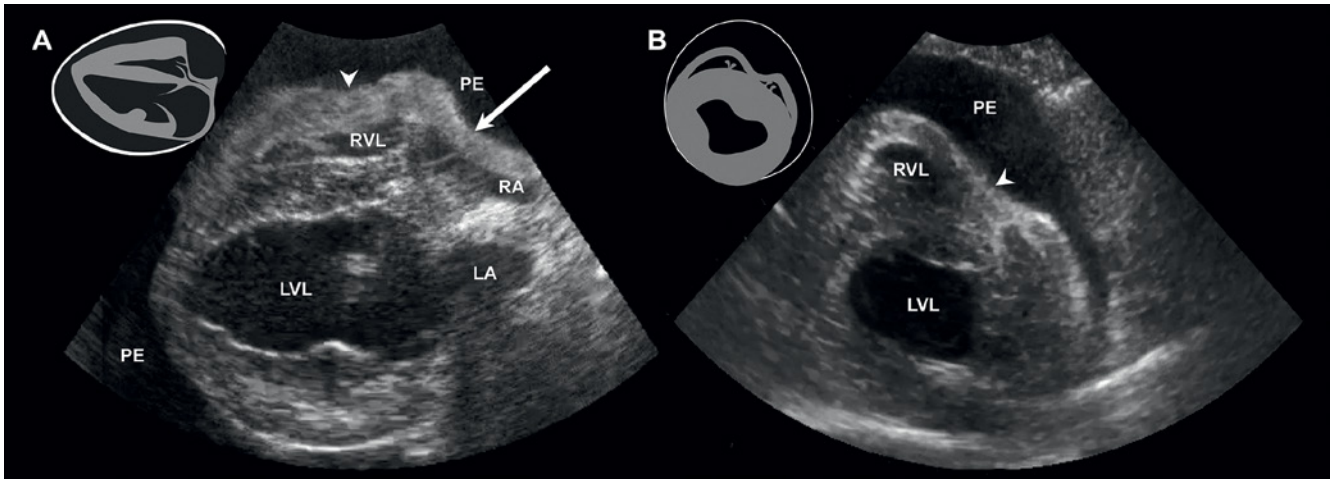


Figure 2.47. Schematic images and sonograms of tamponade secondary to pericardial effusion obtained from the right parasternal long (A) and right parasternal short (B) axis views. Note that the right atrium (white arrow) and right ventricle (arrowhead) are collapsed. LA, left atrium; LVL, left ventricular lumen; PE, pericardial effusion; RA, right atrium; RVL, right ventricular lumen. Courtesy of Calgary VPOCUS Academy, with permission.

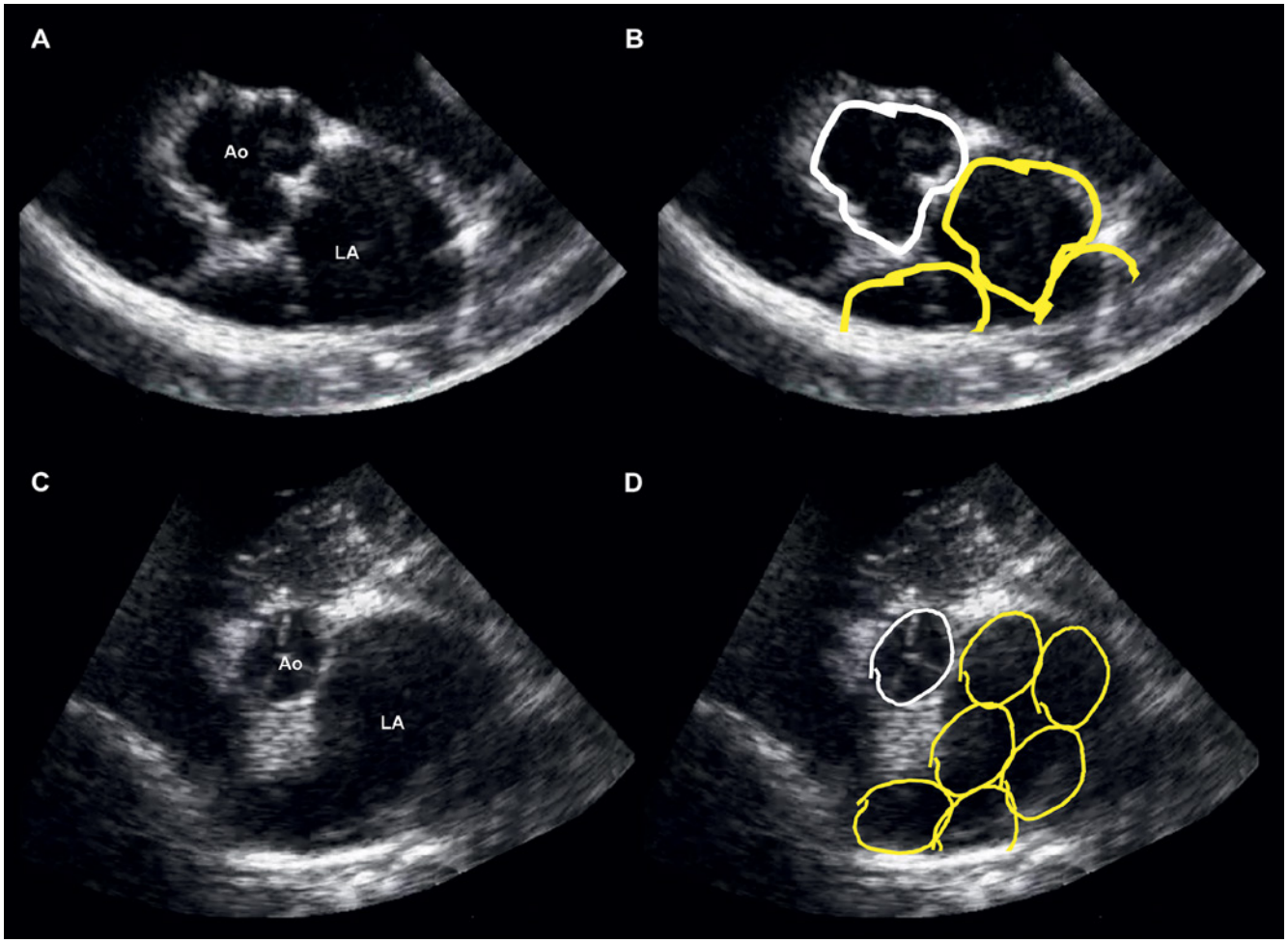


Figure 2.48. Sonograms of the left atrium demonstrating how many times the area of the aorta can subjectively fit within the left atrium. (A, B) Normal left atrial size compared to the aorta. **(B)** The number of times the area of the aorta can fit within the left atrium is normally less than 2.5. **(C–D)** An enlarged left atrium. **(D)** Note that more than 4.5 areas of the aorta can fit within the left atrium. This patient had left sided congestive heart failure and was started on furosemide following a cardiac point-of-care ultrasound evaluation. Ao, aorta; LA, left atrium. Courtesy of Calgary VPOCUS Academy, with permission.

Vet-ebooks.com

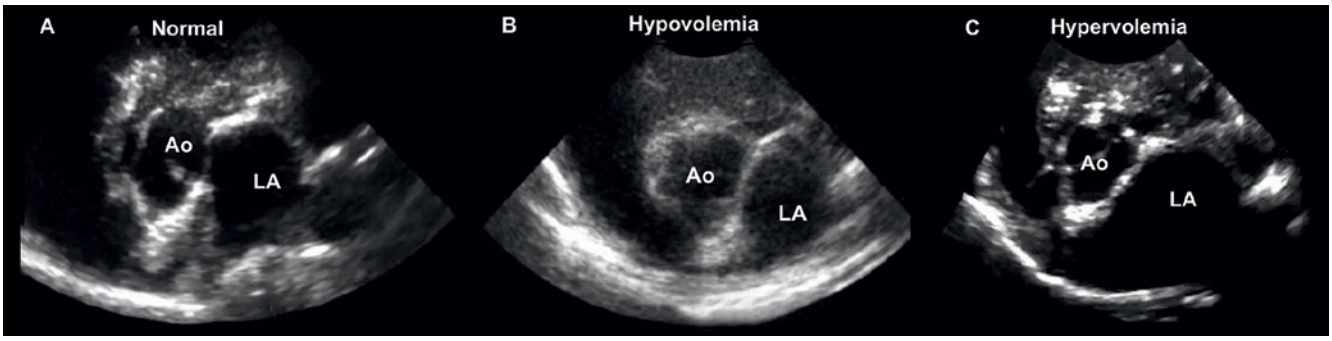


Figure 2.49. Right parasternal short axis views of the heart at the level of the left atrial to aortic ratio (Mercedes and whale sign) and their relative change in size with changes in patient intravascular volume status. (A) Left atrial:aortic ratio view from a euvolemic dog during diastole. **(B)** Left atrial:aortic ratio view obtained from a hypovolemic dog. **(C)** Left atrial:aortic ratio view obtained from a volume overloaded dog (hypervolemia) that received too much intravascular fluids. Ao, aorta; LA, left atrium. Courtesy of Calgary VPOCUS Academy, with permission.

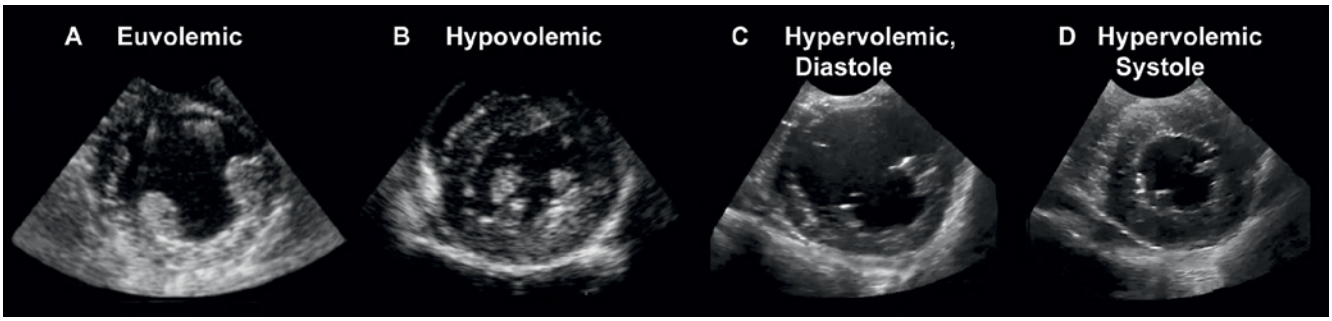


Figure 2.50. Right parasternal short axis views of the heart at the level of the papillary muscles (mushroom view), and the change in cardiac walls and chamber sizes with changes in patient intravascular volume status. (A) Mushroom view obtained from a euvolemic dog during diastole. **(B)** Mushroom view obtained from a hypovolemic dog during diastole. **(C)** Mushroom view obtained from a hypervolemic dog during diastole. **(D)** Mushroom view obtained from a hypervolemic dog during systole, demonstrating the hyperdynamic state of the heart which is often seen with hypervolemia, and helps differentiate the large lumen and thin ventricular walls seen during hypervolemia during diastole from dilated cardiomyopathy. Courtesy of Calgary VPOCUS Academy, with permission.

et al. 2019; Rishniw et al. 2019; Visser et al 2020). Hyperdynamic/increased contractile states can occur in hypervolemic patients (Figure 2.50) provided there is no concurrent myocardial dysfunction, in high sympathetic drive states (e.g., stress), and in patients that have decreased afterload (e.g., arterial vasodilation) without myocardial dysfunction. Decreased contractility can be seen with conditions associated with poor myocardial contractility (e.g., dilated cardiomyopathy or sepsis), and cases with increased afterload (e.g., severe arterial vasoconstriction).

The subjective finding of a decreased LV lumen size with thickened ventricular walls may suggest pseudohypertrophy secondary to volume depletion or true myocardial hypertrophy. To help differentiate the two, LA size should be evaluated: LA size is normal to small in patients with pseudohypertrophy and often enlarged in patients with cardiomyopathy.

Right Sided Heart Changes

Flattening of the interventricular septum combined with an enlarged RV chamber, and/or increased RV wall thickness suggests increased RV pressures or volume (Gelé et al. 2024; Lyssens et al. 2022; Reinero et al. 2020) (Figure 2.51). These presentations arguably take more skill to identify and interpret. If this triad of

Vet-ebooks.com

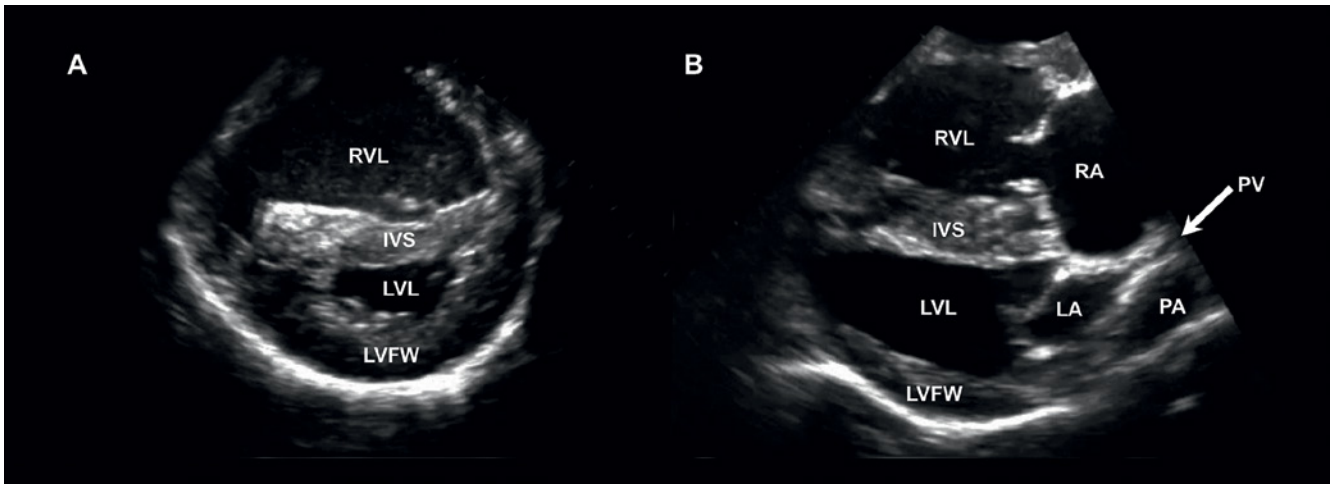


Figure 2.51. Sonograms of right sided cardiac enlargement obtained from the right parasternal short (A) and long (B) axis views. (A) Short axis view demonstrating intraventricular septal flattening and an enlarged right ventricular lumen. **(B)** Long axis view demonstrating significant enlargement of the right atrium and right ventricle when compared to the left atrium and left ventricle. Also note that the pulmonary artery (PA) and pulmonary vein (PV) can be compared in the long axis view. They should normally be roughly equal in size. In this image the PV is collapsed and much narrower than the PA. Also note the intra-atrial septum is bulging into the left atrium, versus having a flat or neutral appearance. These findings should prompt consideration of pulmonary hypertension, which was confirmed and found to be a result of pulmonary thromboembolism in this case. IVS, intraventricular septum; LA, left atrium; LVFW, left ventricular free wall; LVL, left ventricular lumen; RA, right atrium; RVL, right ventricular lumen. Courtesy of Calgary VPOCUS Academy, with permission.

right heart findings is present, causes of pulmonary arterial hypertension (e.g., heartworm disease), chronic bronchopulmonary disease (e.g., dynamic airway disease/obstruction, chronic bronchitis, or pulmonary fibrosis), and pulmonary thromboembolism (PTE), should be considered.

POCUS IN THE CPR SETTING

CPOCUS may be helpful during cardiopulmonary resuscitation (CPR) to identify reversible causes of arrest and determine if mechanical cardiac activity is present, provided it does not interfere with CPR efforts (Ávila-Reyes et al. 2021; Kedan et al. 2020). The subxiphoid window can been used to detect cardiac activity during CPR and can predict survivability to hospital admission in patients presenting without a pulse (Figure 2.52). During human cardiopulmonary resuscitation, CPOCUS has also been used to evaluate for cardiac standstill when deciding to stop CPR. CPOCUS can also help guide early post-arrest management by allowing rapid assessment of reversible causes of arrest, including pericardial tamponade, hypovolemia, cardiogenic shock, RV failure (air emboli), and pneumothorax (Ávila-Reyes et al. 2021; Hussein et al. 2019; Kedan et al. 2020).

POCUS AND MONITORING FLUID THERAPY

A combination of POCUS findings can be used to assess a patient's volume status and monitor response to fluid therapy (Argaiz et al. 2021; Kaiser et al. 2023; Pourmand et al. 2019) (Figure 2.53). Patients with a history of aggressive fluid therapy and combined cardiac POCUS findings of a hyperkinetic heart (increased fractional shortening), an enlarged LA, distended CVC, and increased B-lines on PLUS should prompt consideration of fluid overload. Because PLUS provides dynamic information, the change in B-line count can be used to monitor for development of pulmonary edema secondary to fluid therapy, and the effectiveness of decongestive therapy in patients with congestive heart failure or fluid overload (Kaiser et al. 2023; Murphy et al. 2021).



Visit our website at **www.SmallAnimalUltrasonography.com** for complementary video clips with annotations and text on:

- Lung sliding
- B-lines that occur secondary to increased lung density
- Lung point

Vet-ebooks.com

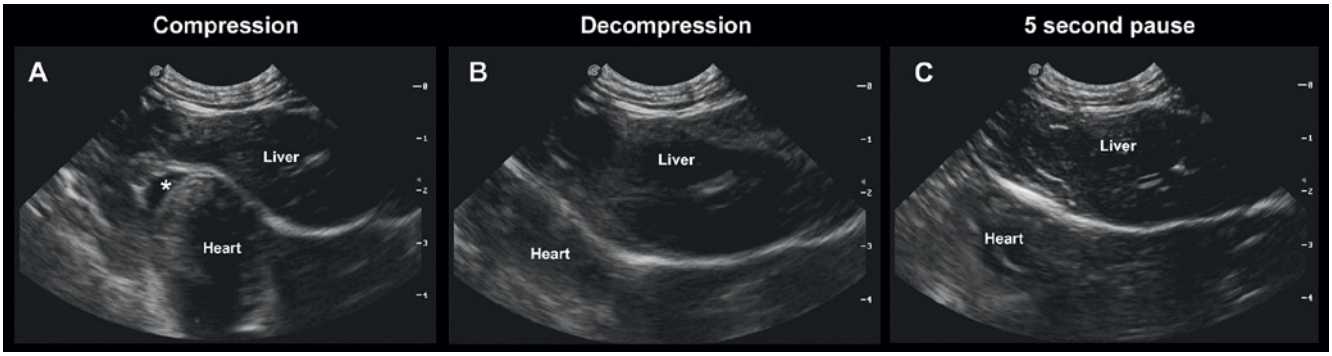


Figure 2.52. Sonograms of the heart obtained from the subxiphoid window in a cat undergoing cardiac compressions during cardiopulmonary resuscitation (CPR). (A) The heart can be seen blending with and compressing the liver during active cardiac compression phase of CPR. Note: a small quantity of pericardial effusion is present (asterisk) **(B)** The same cat during the decompression phase of active CPR. **(C)** The heart is visible during the 5–10 second pause when compressors are swapped. It is possible to assess the presence or absence of cardiac activity while swapping compressors, which is strongly associated with survival in people. Courtesy of Calgary VPOCUS Academy, with permission.

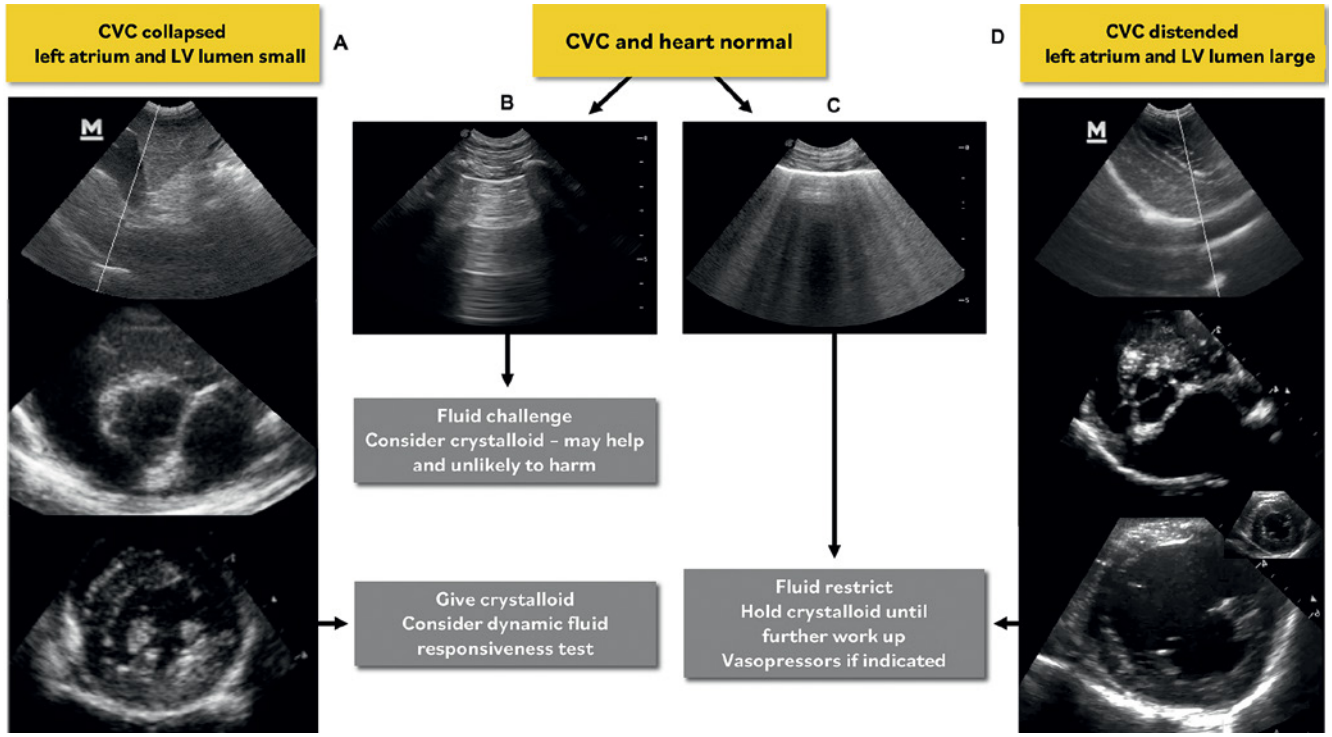


Figure 2.53. Algorithm for of point-of-care ultrasound (POCUS) to guide fluid resuscitation. Column (A) shows POCUS findings of a flat collapsed caudal vena cava (CVC), small left atrial lumen (decreased left atrial:aortic ratio), and a small left ventricular lumen and thickened left ventricular septum and free wall thickness, which combined with absent B-lines and echogenic lung patterns on pleural space and lung ultrasound (PLUS) supports a fluid bolus/challenge. **Column (B)** If the CVC and cardiac POCUS are unremarkable and there is an absence of finding on PLUS, and clinical findings support fluid resuscitation; a fluid challenge may help and is unlikely to cause harm. **Column (C)** If the CVC and cardiac POCUS are unremarkable, but there are B-lines and/or echogenic lung tissue visible on PLUS, further work up is recommended to determine the cause of lung changes prior to initiating fluid therapy. **Column (D)** The combined POCUS findings of increased B-lines and/or echogenic lung patterns on PLUS, large left atrium, large distended ventricular lumen in diastole with hyperkinetic contractions (insert shows systole) and gallbladder wall edema suggests caution, and fluid therapy should be restricted until the patient is assessed further to identify the underlying cause. Adapted to veterinary medicine by the author based on human point-of-care ultrasound fluid resuscitation guidelines. Lee CW, Kory PD, Arntfield RT (2016) Development of a fluid resuscitation protocol using inferior vena cava and lung ultrasound. J Crit Care 31(1):96–100 [175]. Courtesy of Calgary VPOCUS Academy, with permission.

Vet-ebooks.com

- Abnormal curtain signs
- Air and fluid bronchograms
- Subxiphoid view of the heart and active cardiac compressions during cardiopulmonary resuscitation in a cat

References

Argaiz ER, Koratala A, Reisinger N (2021) Comprehensive assessment of fluid status by point-of-care ultrasonography. Kidney360 2(8):1326–1338.

Armenise A, Boysen RS, Rudloff E, Neri L, et al. (2019) Veterinary-focused assessment with sonography for trauma-airway, breathing, circulation, disability and exposure: a prospective observational study in 64 canine trauma patients. J Small Anim Pract 60(3):173–182.

Avila J, Smith B, Mead T, Jurma D, et al. (2018) Does the addition of m-mode to b-mode ultrasound increase the accuracy of identification of lung sliding in traumatic pneumothoraces? J Ultrasound Med 37(11):2681–2687.

Ávila-Reyes D, Acevedo-Cardona AO, Gómez-González JF, Echeverry-Piedrahita DR, et al. (2021) Point-of-care ultrasound in cardiorespiratory arrest (POCUS-CA): narrative review article. Ultrasound J 13(1):46.

Bhoil R, Ahluwalia A, Chopra R, Surya M, et al. (2021) Signs and lines in lung ultrasound. J Ultrason 21(86):e225–e233.

Boysen SR (2021) Lung ultrasonography for pneumothorax in dogs and cats. Vet Clin North Am Small Anim Pract 51(6):1153–1167.

Boysen SR, Rozanski EA, Tidwell AS, Holm JL, et al. (2004) Evaluation of a focused assessment with sonography for trauma protocol to detect free abdominal fluid in dogs involved in motor vehicle accidents. J Am Vet Med Assoc 225(8):1198–204.

Boysen S, McMurray J, Gommeren K (2019) Abnormal curtain signs identified with a novel lung ultrasound protocol in six dogs with pneumothorax. Front Vet Sci 6:291.

Boysen S, Chalhoub S, Gommeren K (2022a) Clinical application of PLUS: Is there pleural effusion, yes/no? In Boysen S, Chalhoub C, Gommeren K, eds. The Essentials of Veterinary Point-of-Care Ultrasound: Pleural Space and Lung. Groupo Asis Biomedia: Zaragoza Spain, pp. 91–109.

Boysen S, Chalhoub S, Romero A (2022b) Veterinary point of care ultrasound probe orientation for detection of pleural effusion in dog cadavers by novice sonographers: a pilot study. VECCUS online 2020. Ultrasound J 12:45.

Burnotte P, Gommeren K, Kennedy CR, Boysen SR, et al. (2023) Left atrial measurement in lateral versus sternal recumbency in cats undergoing focused cardiac ultrasound examination. Can Vet J 64(10):951–956.

Chetboul V, Tidholm A, Nicolle A, Sampedrano CC, et al. (2005) Effects of animal position and number of repeated measurements on selected two-dimensional and M-mode echocardiographic variables in healthy dogs. J Am Vet Med Assoc 227(5):743–747.

Choi WJ, Ha YR, Oh JH, Cho YS, et al. (2020) Clinical guidance for point-of-care ultrasound in the emergency and critical care areas after implementing insurance coverage in Korea. J Korean Med Sci 35(7):e54.

Coppolino F, Gatta G, Di Grezia G, Reginelli A, et al. (2013) Gastrointestinal perforation: ultrasonographic diagnosis. Crit Ultrasound J 5(Suppl 1):S4.

Corl KA, George NR, Romanoff J, Levinson AT, et al. (2017) Inferior vena cava collapsibility detects fluid responsiveness among spontaneously breathing critically-ill patients. J Crit Care 41:130–137.

Darnis E, Boysen S, Merveille AC, Desquilbet L, et al. (2018) Establishment of reference values of the caudal vena cava by fast-ultrasonography through different views in healthy dogs. J Vet Intern Med 32(4):1308–1318.

DeFrancesco TC, Ward JL (2021) Focused canine cardiac ultrasound. Vet Clin North Am Small Anim Pract 51(6):1203–1216.

Demi L, Wolfram F, Klersy C, De Silvestri A, et al. (2023) New international guidelines and consensus on the use of lung ultrasound. J Ultrasound Med 42(2):309–344.

Díaz-Gómez JL, Mayo PH, Koenig SJ (2021) Point-of-care ultrasonography. N Engl J Med 385(17):1593–1602.

Fox PR, Bond BR, Peterson ME (1985) Echocardiographic reference values in healthy cats sedated with ketamine hydrochloride. Am J Vet Res 46(7):1479–1484.

Gelé RR, Burnotte P, Valcke A, Walker TG, et al. (2024) Retrospective evaluation of a right heart parameter score in the assessment of precapillary pulmonary hypertension in dogs (2017-2021): 135 cases. J Vet Emerg Crit Care 34(3):277–284.

Goffi A, Kruisselbrink R, Volpicelli G (2018) The sound of air: point-of-care lung ultrasound in perioperative medicine. Can J Anaesth 65(4):399–416.

Gui J, Guo J, Nong F, Jiang D, et al. (2015) Impact of individual characteristics on sonographic IVC diameter and the IVC diameter/aorta diameter index. Am J Emerg Med 33(11):1602–1605.

Häggström J, Andersson ÅO, Falk T, Nilsfors L, et al. (2016) Effect of body weight on echocardiographic measurements in 19,866 pure-bred cats with or without heart disease. J Vet Intern Med 30(5):1601–1611.

Hultman TM, Boysen SR, Owen R, Yozova ID (2022) Ultrasonographically derived caudal vena cava parameters acquired in a standing position and lateral recumbency in healthy, lightly sedated cats: a pilot study. J Feline Med Surg 24(10):1039–1045.

Husain LF, Hagopian L, Wayman D, Baker WE, et al. (2012) Sonographic diagnosis of pneumothorax. J Emerg Trauma Shock 5(1):76–81.

Hussein L, Rehman MA, Sajid R, Annajjar F, et al. (2019) Bedside ultrasound in cardiac standstill: a clinical review. Ultrasound J 11(1):35.

Kaiser RS, Sarkar M, Raut SK, Mahapatra MK, et al. (2023) A study to compare ultrasound-guided and clinically guided fluid management in children with septic shock. Indian J Crit Care Med 27(2):139–146.

Vet-ebooks.com

Kedan I, Ciozda W, Palatinus JA, Palatinus HN, et al. (2020) Prognostic value of point-of-care ultrasound during cardiac arrest: a systematic review. Cardiovasc Ultrasound 18(1):1.

Kendall A, Keenihan E, Kern ZT, Lindaberry C, et al. (2020) Three-dimensional bladder ultrasound for estimation of urine volume in dogs compared with traditional 2-dimensional ultrasound methods. J Vet Intern Med 34(6):2460–2467.

Kim SY, Park KT, Yeon SC, Lee HC (2014) Accuracy of sonographic diagnosis of pneumoperitoneum using the enhanced peritoneal stripe sign in Beagle dogs. J Vet Sci 15(2):195–198.

Lee FC (2016) Lung ultrasound-a primary survey of the acutely dyspneic patient. J Intensive Care 4(1):57.

Lee FCY (2017) The curtain sign in lung ultrasound. J Med Ultrasound 25(2):101–104.

Lisciandro GR, Lagutchik MS, Mann T, Voges AK, et al. (2008) Evaluation of a thoracic focused assessment with sonography for trauma (TFAST) protocol to detect pneumothorax and concurrent thoracic injury in 145 traumatized dogs. J Vet Emerg Crit Care 18(3):258–269.

Lisciandro GR, Lagutchik MS, Mann KA, Fosgate GT, et al. (2009) Evaluation of an abdominal fluid scoring system determined using abdominal focused assessment with sonography for trauma in 101 dogs with motor vehicle trauma. J Vet Emerg Crit Care 19(5):426–437.

Lisciandro GR, Fosgate GT, Fulton RM (2014) Frequency and number of ultrasound lung rockets (B-lines) using a regionally based lung ultrasound examination named vet BLUE (veterinary bedside lung ultrasound exam) in dogs with radiographically normal lung findings. Vet Radiol Ultrasound 55(3):315–322.

Liu J, Chi JH, Lu ZL, Fu W (2023) The specific signs of lung ultrasound to diagnose pulmonary hemorrhage of the newborns: evidence from a multicenter retrospective case-control study. Front Pediatr 18(11):1090332.

Loughran K (2021) Focused cardiac ultrasonography in cats. Vet Clin North Am Small Anim Pract 51(6):1183–1202.

Loughran KA, Rush JE, Rozanski EA, Oyama MA, et al. (2019) The use of focused cardiac ultrasound to screen for occult heart disease in asymptomatic cats. J Vet Intern Med 33(5):1892–1901.

Lyssens A, Lekane M, Gommeren K, Merveille AC (2022) Focused cardiac ultrasound to detect pre-capillary pulmonary hypertension. Front Vet Sci 1(9):830275.

Marchesotti F, Vezzosi T, Tognetti R, Marchetti F, et al. (2019) Left atrial anteroposterior diameter in dogs: reference interval, allometric scaling, and agreement with the left atrial-to-aortic root ratio. J Vet Med Sci 81(11):1655–1662.

Marini TJ, Rubens DJ, Zhao YT, Weis J, et al. (2021) Lung ultrasound: the essentials. Radiol Cardiothorac Imaging 3(2):e200564.

Martins A, Gouveia D, Cardoso A, Gommeren K, et al. (2019) The detection of Z-lines, C-lines, I-lines in dogs using veterinary point of care ultrasound. Incidence of Z, I and B lines detected with point of care ultrasound in healthy shelter dogs. J Vet Emerg Crit Care 29:S17–S39.

McMurray J, Boysen SR, Chalhoub S (2016) Focused assessment with sonography for triage in non-trauma dogs and cats in the emergency and critical care setting. J Vet Emerg Crit Care 26(1):64–73.

Miller A (2016) Practical approach to lung ultrasound. BJA Educ 16:39–45.

Mohammad A, Hefny AF, Abu-Zidan FM (2014) Focused assessment sonography for trauma (FAST) training: a systematic review. World J Surg 38(5):1009–1018.

Montero Baladía M, Arroyo Diez M, Badallo Areválo O (2018) Basic sign in lung echography. Liquid and air bronchogram: differentiation. Med Intensiva (Engl Ed) 42(8):e19.

Montero-Yéboles R, Arroyo-Marin MJ, Jaraba-Caballero S, Gómez-Guzman E, et al. (2022) A pleural ultrasound image of a collapsed lung surrounded by pleural fluid ("jellyfish sign") may correspond to an intrapericardial mass. J Ultrasound 25(2):387–390.

Montoya J, Stawicki SP, Evans DC, Bahner DP, et al. (2016) From FAST to E-FAST: an overview of the evolution of ultrasound-based traumatic injury assessment. Eur J Trauma Emerg Surg 42(2):119–126.

Murphy SD, Ward JL, Viall AK, Tropf MA, et al. (2021) Utility of point-of-care lung ultrasound for monitoring cardiogenic pulmonary edema in dogs. J Vet Intern Med 35(1):68–77.

Nazerian P, Volpicelli G, Vanni S, Gigli C, et al. (2015) Accuracy of lung ultrasound for the diagnosis of consolidations when compared to chest computed tomography. Am J Emerg Med33(5):620–625.

Pereira RM, Silva AJLCD, Faller J, Gomes BC, et al. (2020) Comparative analysis of the collapsibility index and distensibility index of the inferior vena cava through echocardiography with pulse pressure variation that predicts fluid responsiveness in surgical patients: an observational controlled trial. J Cardiothorac Vasc Anesth 34(8):2162–2168.

Pourmand A, Pyle M, Yamane D, Sumon K, et al. (2019) The utility of point-of-care ultrasound in the assessment of volume status in acute and critically ill patients. World J Emerg Med 10(4):232–238.

Preau S, Bortolotti P, Colling D, Dewavrin F, et al. (2017) Diagnostic accuracy of the inferior vena cava collapsibility to predict fluid responsiveness in spontaneously breathing patients with sepsis and acute circulatory failure. Crit Care Med 45(3):e290–e297.

Rademacher N, Pariaut R, Pate J, Saelinger C, et al. (2014) Transthoracic lung ultrasound in normal dogs and dogs with cardiogenic pulmonary edema: a pilot study. Vet Radiol Ultrasound 55(4):447–452.

Reinero C, Visser LC, Kellihan HB, Masseau I, et al. (2020) ACVIM consensus statement guidelines for the diagnosis, classification, treatment, and monitoring of pulmonary hypertension in dogs. J Vet Intern Med 34(2):549–573.

Rice JA, Brewer J, Speaks T, Choi C, et al. (2021) The POCUS consult: how point of care ultrasound helps guide medical decision making. Int J Gen Med14:9789–9806.

Rigot M, Boysen SR, Masseau I, Letendre JA (2024) Evaluation of B-lines with 2 point-of-care lung ultrasound protocols in cats with radiographically normal lungs. J Vet Emerg Crit Care 34(2):143–152.

Vet-ebooks.com

Rishniw M, Caivano D, Dickson D, Vatne L, et al. (2019) Two-dimensional echocardiographic left- atrial-to-aortic ratio in healthy adult dogs: a reexamination of reference intervals. J Vet Cardiol 26:29–38.

Robba C, Wong A, Poole D, Al Tayar A, et al. (2021) Basic ultrasound head-to-toe skills for intensivists in the general and neuro intensive care unit population: consensus and expert recommendations of the European society of intensive care medicine. Intensive Care Med 47(12):1347–1367.

Shah A, Oliva C, Stem C, Cummings EQ (2022) Application of dynamic air bronchograms on lung ultrasound to diagnose pneumonia in undifferentiated respiratory distress. Respir Med Case Rep 30(39):101706.

Vezzosi T, Mannucci T, Pistoresi A, Toma F, et al. (2017) Assessment of lung ultrasound b-lines in dogs with different stages of chronic valvular heart disease. J Vet Intern Med 31(3):700–704.

Visser LC, Ciccozzi MM, Sintov DJ, Sharpe AN (2019) Echocardiographic quantitation of left heart size and function in 122 healthy dogs: a prospective study proposing reference intervals and assessing repeatability. J Vet Intern Med 33(5):1909–1920.

Walters AM, O'Brien MA, Selmic LE, Hartman S, et al. (2018) Evaluation of the agreement between focused assessment with sonography for trauma (AFAST/TFAST) and computed tomography in dogs and cats with recent trauma. J Vet Emerg Crit Care 28(5):429–435.

Ward JL, Lisciandro GR, Ware WA, Viall AK, et al. (2018) Evaluation of point-of-care thoracic ultrasound and NT-proBNP for the diagnosis of congestive heart failure in cats with respiratory distress. J Vet Intern Med 32(5):1530–1540.

Vet-ebooks.com

Vet-ebooks.com

CHAPTER THREE

Eye and Orbit

Stefano Pizzirani and Dominique Penninck

Department of Clinical Sciences, Cummings School of Veterinary Medicine, Tufts University, North Grafton, MA, USA

Preparation and Scanning Technique

The ocular structures present anatomical complexities, topographic depths, and challenges that require different probes and window choices to achieve the best diagnostic results among the various breeds.

A range of transducer frequencies that span from 8 to 50 MHz, linear and microconvex probes can be used for different ocular parts in different clinical conditions, keeping into consideration the anatomical variances among different species and breeds. More information on equipment, ocular physics, resolution of different probes, and clinical indications for ocular ultrasound has been detailed in Bentley et al. (2021).

There are few standard methods for imaging the globe and the orbit. For **globe** evaluation, high-frequency (12 MHz and above) transducers can be applied directly on the cornea (Figure 3.1) or at the limbus. The globe can be geometrically compared to a sphere. The planes of the sections can be changed according to the needs. Visual axis defines axial (central corneal) sections. Paraxial meridional (sagittal) sections are obtained when the plane of the section does not follow the visual axis, but still involves the center of the lens (Figure 3.2A, C). If the probe is maintained on the corneal surface, using a fanning motion, the globe is scanned from one side to the other with sagittal sections that may follow the meridians (usually keeping the center of the lens in the section) or without toggling and obtaining sections that are paraxial and parallel to the visual axis plane (obtaining parallel sections) (Figure 3.2D, F). When obtaining sagittal sections of the whole globe, only sections from 10 to 3 o'clock in the right eye (OD) and from 9 to 2 o'clock in the left eye (OS) are necessary. Sections parallel to the visual axis can be achieved moving the probe without changing the scanning direction (Figure 3.2D, F). If the position of the probe is at the limbus or in perilimbal areas, meridional (radial) or transverse (perpendicular to the visual axis and parallel to the iris plane) sections can be obtained; the probe can then be moved laterally or rostrally to caudally (Figures 3.3, 3.4). Once the standard approach is performed, ad hoc selected oblique planes can help to delineate a lesion more accurately.

For **orbital** evaluation in dogs, probe frequencies and shapes may change depending on the breed (brachycephalic versus dolichocephalic versus mesocephalic), and the available equipment. In mesocephalic and dolichocephalic dogs, it is best obtained with lower-frequency microconvex probes using the transcorneal positions and/or the temporal fossa window given the increased depth to examine. Images obtained with the transducer applied directly on the cornea are usually of higher quality.

In some instances, the globe can also be scanned through the eyelid. Artifacts and image degradation may occur when imaging through this window, although in breeds with thinner eyelids and eyelids that are poorly haired, using abundant coupling gel may obviate this inconvenience.

The technique of imaging through the closed lid in brachycephalic dogs (or the temporal fossa approach in dolichocephalic dogs) is recommended if there is a defect in the corneal surface, recent globe trauma, recent ocular surgery, the patient is severely blepharoplastic, or when the swelling of the periocular tissues prevents manual opening of the eyelids.

The examination is generally performed with the patients awake. A topical anesthetic (proparacaine 0.5% eye drops) is applied at a dose of one to two drops

Atlas of Small Animal Ultrasonography, Third Edition. Edited by Dominique Penninck and Marc-André d'Anjou.
© 2025 John Wiley & Sons, Inc. Published 2025 by John Wiley & Sons, Inc.
Companion website: www.SmallAnimalUltrasonography.com

Vet-ebooks.com



Figure 3.1. Probe placement on the eye of a dog using the corneal surface. The probe is oriented to obtain horizontal ocular meridians.

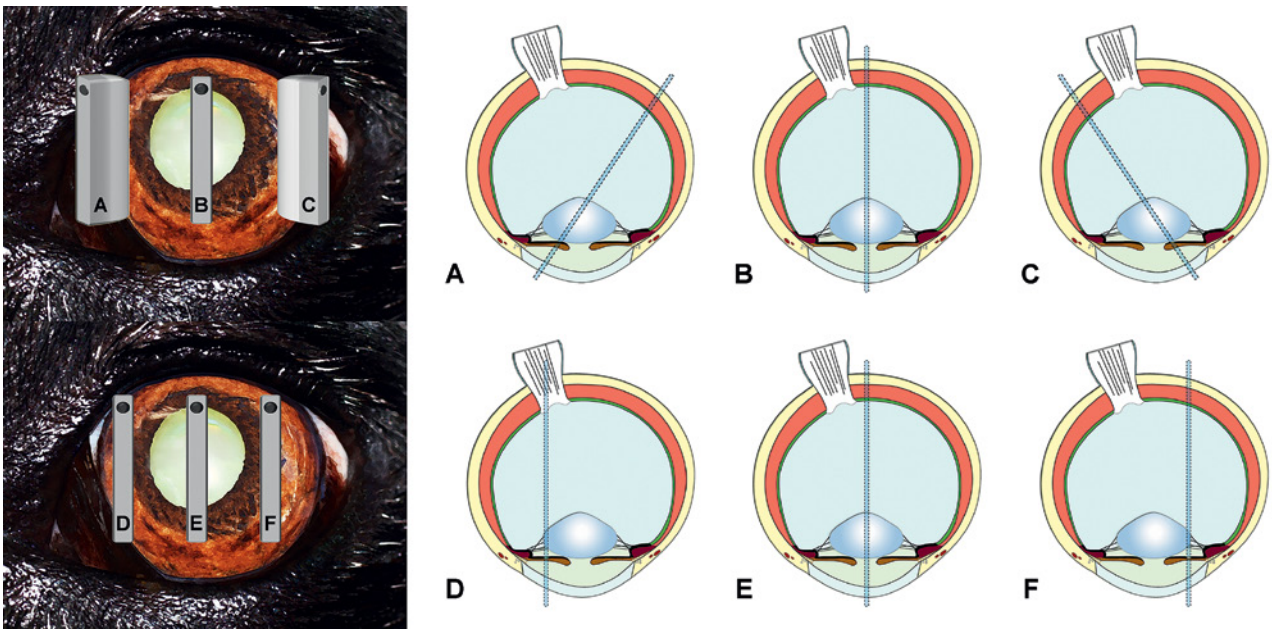


Figure 3.2. Probe position and orientation of the beam using the corneal surface. Schematic sections show the section through the lens center. The probe is placed on the cornea and moved laterally to produce sagittal (meridional) vertical sections **(A–C)** with the lens included in the view. Parallel paraxial sections **(D–F)** are obtained moving the probe laterally without toggling. These sections are helpful in evaluating the anterior chamber and iris, besides the posterior segment. For both orientations, vertical, horizontal, and oblique sections are obtained.

to the cornea 1 minute before the examination. With painful eyes, the application can be repeated a few times every 30–60 seconds. A sterile, water-soluble lubricating acoustic gel is recommended. It is important that the gel does not contain preservatives or scents. At the end of the examination, the gel should be abundantly flushed from the eye with approved sterile eyewash. For the safety of the imager and the patient, mild sedation of a noncollaborative patient may be advised if manual restraint is inadequate to securely position it. Depending on the sedation/anesthetic agent(s) used, the globe may tend to rotate ventrally. Ventral rotation of the globe may render transducer positioning more difficult; in this case, a conjunctival forceps or a stay suture applied to the limbus in a strategic position may be necessary to move the globe in an axial alignment.

Transducers with a range from 7.5 to 50 MHz are commonly used to image the orbit and the globe. Probes with frequencies between 75 and 100 MHz have been developed (Aubin et al. 2003; Bentley et al. 2003; Sherar et al. 1989; Silverman et al. 2006; Pavlin et al.

Vet-ebooks.com

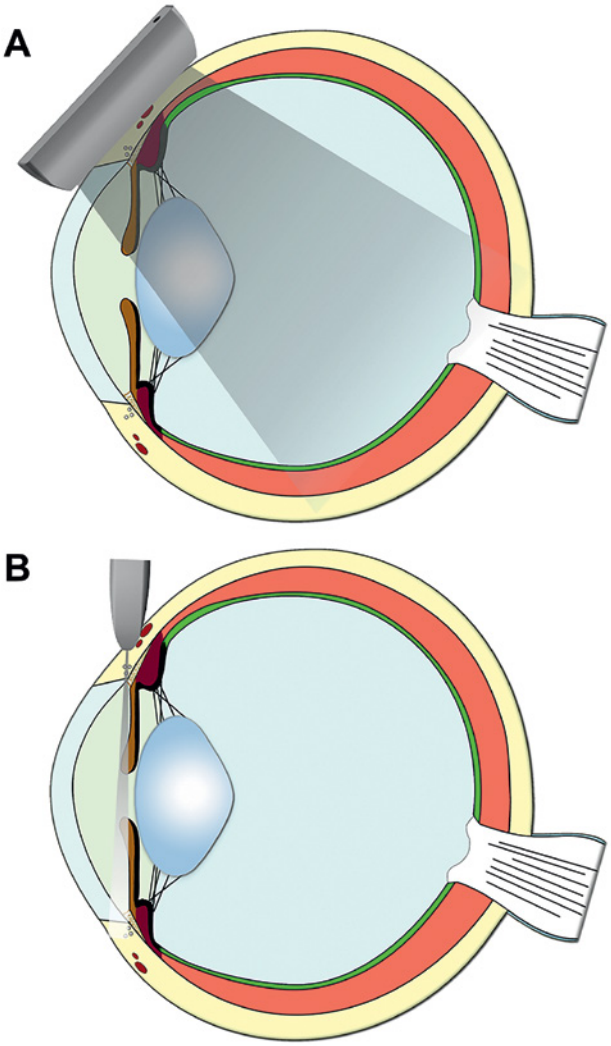


Figure 3.3. Probe placement and direction of the beam through the eye using the limbal and perilimbal approach. Radial **(A)** or transverse **(B)** basic sections can be obtained; the probe can be then moved rostrally to caudally with parallel or oblique directions according to the case. Both these sections can be oriented around the clock to produce the best images.

1995) but their clinical use in veterinary ocular ultrasonography has not yet been reported.

Ultrabiomicroscopy (UBM) uses very high-resolution probes in the 35–50 MHz range (Kumar et al. 2016) to evaluate cornea, anterior chamber, iris, ciliary body, and anterior lens. High-frequency probes can provide axial and lateral resolutions of up to 30 and 60 µm, respectively (Silverman 2009). The posterior segment of the globe and the retrobulbar area are often best imaged with the 7.5–18 MHz transducers. A linear transducer provides optimum imaging of the near-field structures, and in our experience, a linear 18 MHz probe is excellent for the globe, although the ergonomics with a sector or convex probe with a small footprint may be easier. The patient's eyelids are manually held open by the restrainer while the head is secured (Dziezyc and Hager 1988; Hager et al. 1987). The dimension and shape of high-frequency probes (35–50 MHz) make the dorsolateral quadrant easier to image in awake patients (Figure 3.5).

Large-breed dogs, especially dolichocephalic patients, are often more difficult to image because they are naturally enophthalmic and may squint or retract the globe further into the orbit and thus limit access to the eye. This may be particularly challenging when using a linear probe. The globes of mesocephalic and brachiocephalic breeds are generally more naturally protruding and therefore more accessible.

For both globe and orbital evaluations, the probe position marker is usually placed on the nasal side of the globe for a horizontal plane and dorsal (12 o'clock) for a vertical plane (Figure 3.6).

The directional terms used with reference to the globe can be anterior and posterior, rostral to caudal, dorsal to ventral, and medial and lateral (nasal to temporal).

The zygomatic salivary gland, located ventrally to the globe, can be imaged with the probe placed ventrolaterally to the zygomatic arch (Figure 3.7). Doppler imaging or standardized A-mode scanning may provide additional vascular and biometric information.

Ultrasonographic Anatomy of the Normal Eye

Ocular ultrasonography evaluates the globe and orbital structures within and outside of the myofascial cone, including lacrimal and salivary (zygomatic) glands.

The **globe wall** is made by three different layers: the outer fibrous coat (anteriorly represented by a transparent cornea and laterally and more posteriorly by the white sclera), the middle vascular coat (the uveal tissue, which consists anteriorly of the iris and ciliary body and posteriorly of the choroid), and the retina (the innermost layer) that covers only the posterior segment. The spaces inside the globe are represented by the anterior and the posterior chambers and the vitreous cavity (Figure 3.8).

In the normal eye, the anterior chamber, posterior chamber, and vitreous body are anechoic, with few reflectors occasionally present (Figures 3.8, 3.9). The thickness of the cornea and various parts of the eye has

Vet-ebooks.com

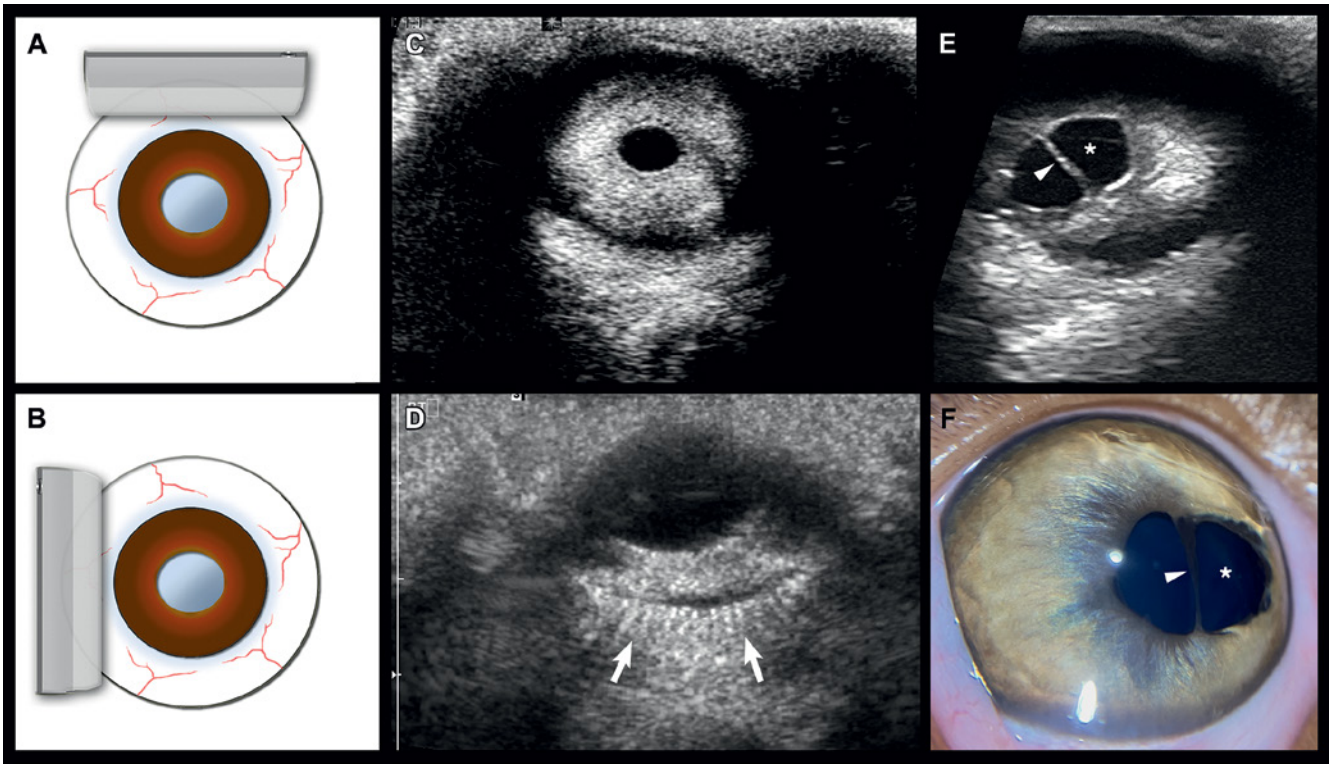


Figure 3.4. Limbal and perilimbal approach. (**A, B**) Horizontal and vertical transverse planes through the limbus. These positions allow the visualization of the iris and ciliary body with ciliary processes. **(C)** The iris encircles the pupil (central anechoic space, of variable size). **(D)** The iris is seen in close apposition to the peripheral striated ciliary processes (arrows). The marker should be placed nasal (medial) in the horizontal position and dorsal in the vertical position. **(E, F)** Transverse UBM sonographic image and clinical picture, respectively, showing a case of pseudopolycoria due to iris hypoplasia (Rieger's anomaly) in an 11-month-old Australian Shepherd. The arrowhead indicates the edge of the normal pupil while the asterisk points to the missing iris tissue. Courtesy of Dr Laurent Bouhanna, Ophtavet clinic, France.



Figure 3.5. Ultrabiomicroscopy (UBM) probe. Photograph of the fluid-filled covering cup used with some of the 35–50 MHz UBM probes. Notice the size and shape of the transducer, which allow an easier evaluation of the dorsolateral quadrant of the eye. The reference scale is in mm.

Vet-ebooks.com

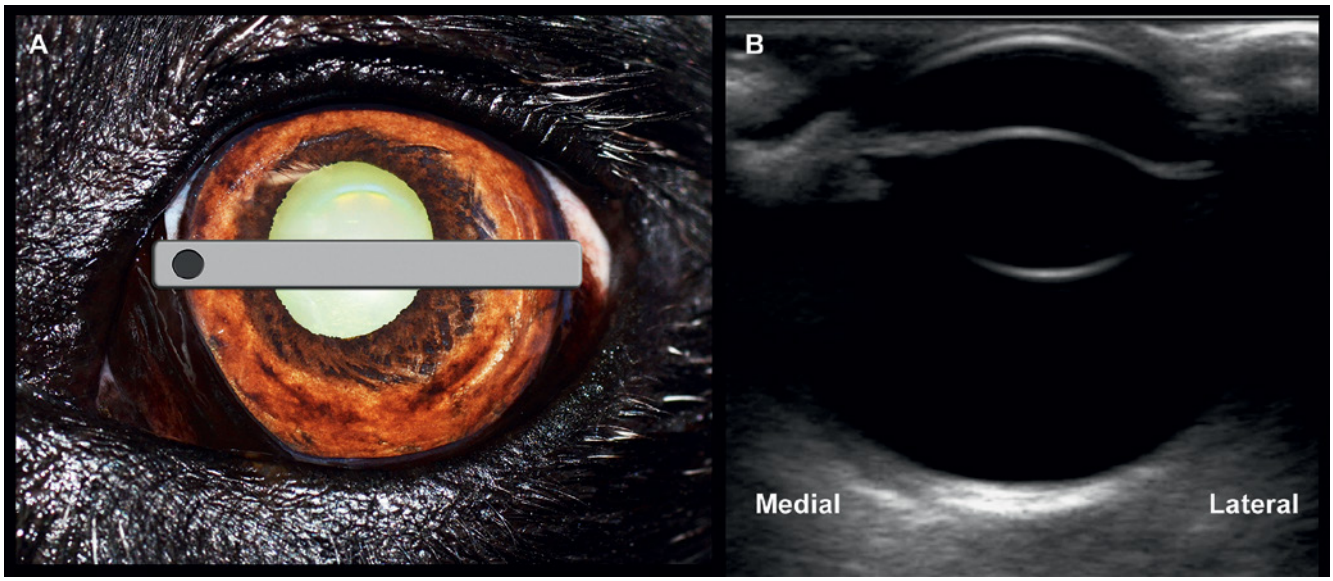


Figure 3.6. **Horizontal plane. (A)** The probe is seen oriented horizontally on the cornea. The position of the marker is nasal (medial). (**B)** The corresponding sonogram, displaying the medial side of the eye on the left side of the image.

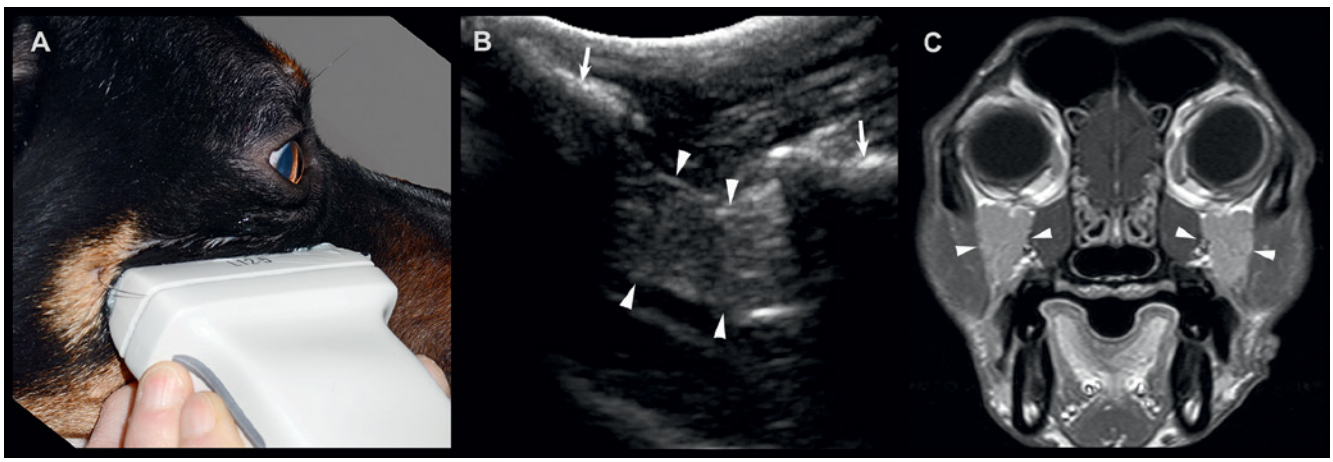


Figure 3.7. **Zygomatic gland scanning. (A)** Images of the zygomatic salivary gland are obtained by firmly placing the transducer ventral to the zygomatic arch and caudoventral to the globe, using toggling to obtain ranges of images. The probe marker should be kept rostral. **(B)** The zygomatic salivary gland is identified as a well-defined echogenic tissue (between arrowheads) located deep to the zygomatic arch depicted by the hyperechoic shadowing bone (arrows). **(C)** Transverse T1-weighted contrast-enhanced magnetic resonance image. The zygomatic gland is identified by the arrowheads ventral to the eye.

been recorded in different species (Boroffka et al. 2006; Cottrill et al. 1989; Schiffer et al. 1982), with small animals having a thickness of about 0.5–0.6 mm.

The **lens** is positioned axially and slightly anteriorly within the globe. It is suspended by zonular ligaments attaching peripherally to the ciliary body and divides the anterior and posterior chambers from the vitreous cavity. The lens physically supports the iris anteriorly and their close contact is responsible for the anterior bowing of the iris (Figure 3.9).

With high-frequency and UBM probes (18–50 MHz), the cornea presents as a double parallel echogenic line with a nearly anechoic center (Figure 3.9). The outer line represents the change of impedance between the coupling gel and the corneal epithelium/basal membrane. The stroma has lower acoustic impedance and appears hypo- to anechoic (Tang 2012; Tang and Liu 2011). The inner discrete hyperechoic line represents the distal change in impedance between the Descemet's membrane/corneal endothelium with the aqueous (Pavlin and Foster 1995). The corneoscleral junction (limbus) is defined by the transition between the poorly reflective corneal stroma and the highly reflective scleral tissue (Figure 3.9) and can only be

Vet-ebooks.com

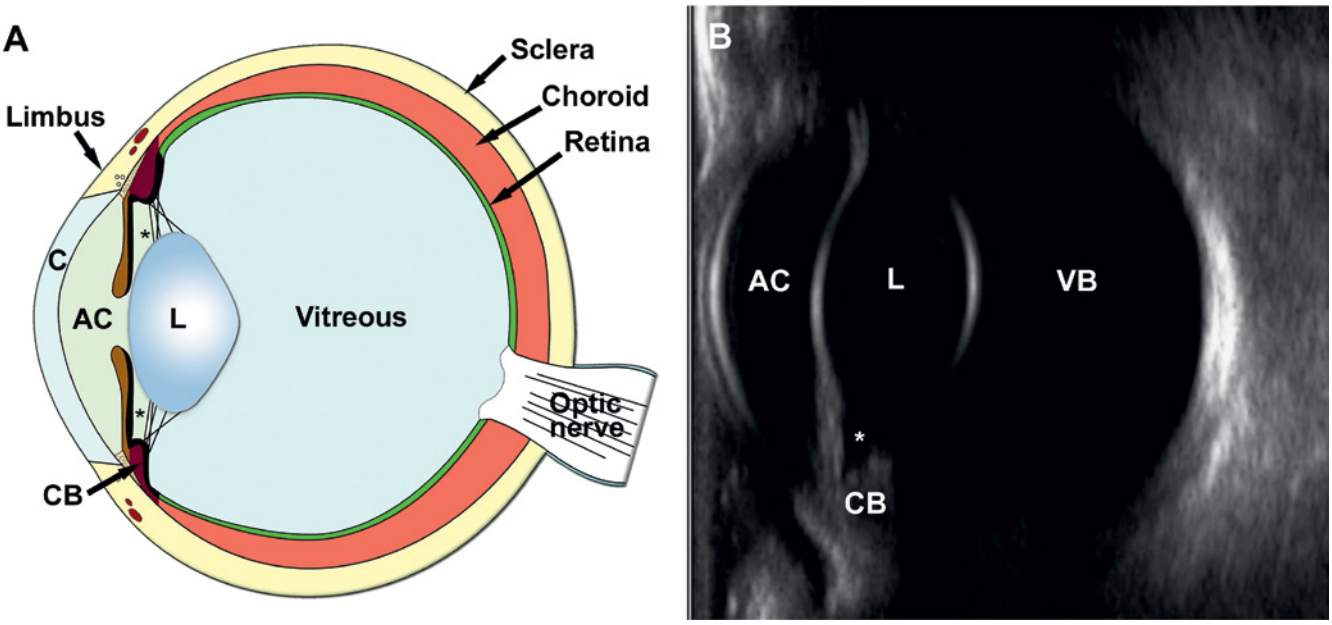


Figure 3.8. **Normal ocular globe. (A)** Schematic drawing of ocular structures. **(B)** Corresponding sonogram of a normal eye. The globe has a three-layered outer shell and contains the fluid-filled anterior and posterior chambers, and the vitreal chamber (filled with vitreous body); these chambers all have an anechoic appearance. The posterior chamber is marked by an asterisk (*). AC, anterior chamber; C, cornea; CB, ciliary body; L, lens; VB, vitreal body.

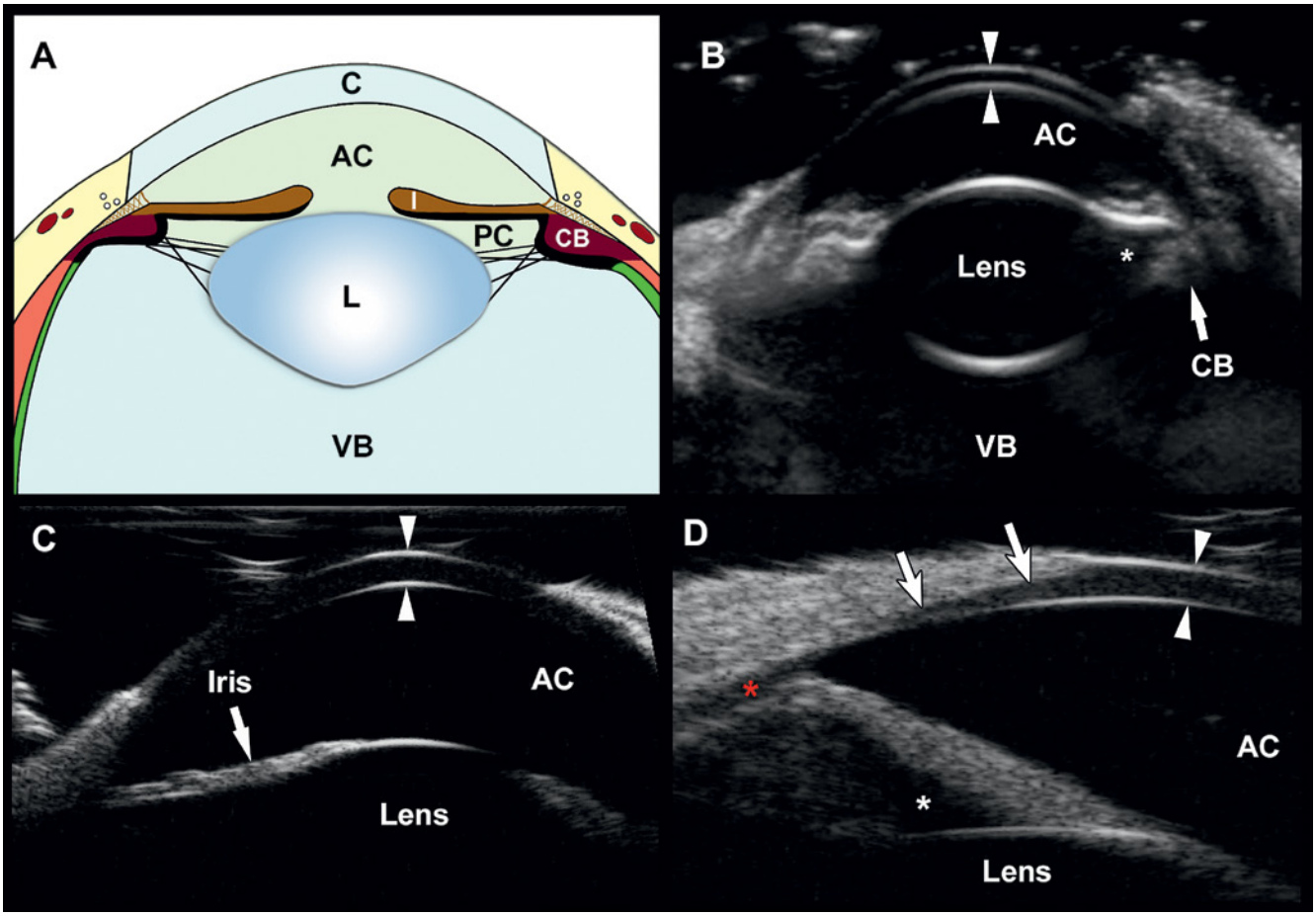


Figure 3.9. **Normal anterior segment of the eye.** (for full caption, see next page)

Vet-ebooks.com

accurately evaluated using UBM technology. The sclera is imaged as a highly reflective structure compared with the cornea. The sclera can usually be roughly differentiated from the overlying episclera and the underlying ciliary body using higher frequencies.

The **anterior chamber** can be difficult to image because of its compressibility, size, and location in the near field. Better evaluation of the anterior chamber is achieved with UBM. The depth of the anterior chamber varies with breed and age. Normal depth is usually in a range of about 3–4 mm in the dog. The cornea, the iris, and the central anterior lens capsule delineate the anterior chamber, which is filled and distended with anechoic aqueous humor (Figure 3.9).

Perilimbal radial (meridional) or transverse sections perpendicular to the ciliary processes are used with UBM to investigate the opening of the cleft and the ciliary processes. With a standard sagittal section, perpendicular to the limbus, the ciliary processes are hypoechoic and have a triangular shape, but they cannot be evaluated individually (Figure 3.10A, B). With a transverse section perpendicular to the globe curvature, a wider evaluation of the cleft is possible and allows multiple ciliary processes to be seen on the same image (Figure 3.10C, D).

The normally shallow **posterior chamber** is located between the iris and the lens; it contains aqueous humor produced by the ciliary body, which flows from the posterior chamber to the anterior chamber through the pupil. The uvea represents the middle vascular layer of the globe and is made of the ciliary body and the iris anteriorly and the choroid posteriorly (Figure 3.8).

The **iris** is a dynamic, stromal and muscular, contractile diaphragm with a central opening (the pupil). Depending on the amount of light exposure, the size of the pupil can vary rapidly in diameter. The sphincter and dilator muscles in the iris control the pupil size. The pupil appears as an anechoic void in the central iris (Figure 3.4C). When the pupil is constricted or when the beam is off axis, the iris may be mistaken for the anterior surface of the lens at a lower ultrasound frequency. However, the iris leaflets are thicker and ill-defined, while the anterior lens capsule is a discrete, linear hyperechoic interface. The ciliary body is highly vascular and its posterior junction with the choroid (and overlying retina) is named *ora ciliaris retinae*. This transition cannot be seen with ultrasonography. The aqueous humor is produced by the nonpigmented ciliary epithelium, which lies on the inner surface of the ciliary processes. The ciliary body contains muscle fibers that regulate the position of the lens. The lens is supported by the suspensory ligaments (zonulae). The zonulae may occasionally be seen as ill-defined striations that attach to the lens contour. The iris, ciliary body, and zonulae are often best imaged from a transverse or oblique view.

Anterior to central, the lens is composed of an outer capsule, anterior epithelium, lens cortical (perinuclear) fibers, and nucleus. Posterior lens is inversely similar but lacks a posterior subcapsular epithelium. The capsule is like an envelope that encases the highly soluble lens' proteins and fibers. The lens fibers that make up the majority of the lens are positioned in layers, with the cortex forming the outer layer of the lens and the nucleus located in the center. The gel-like density of the vitreous body contributes to support the lens position posteriorly.

The internal appearance of the normal lens is anechoic. Curvilinear hyperechoic interfaces appear at the anterior and posterior margins of the lens, as a result of specular reflections, when scanned perpendicularly (Figure 3.9B). The surface of the lens is smooth and slightly convex. The size of the lens varies with the species and age. The anterior surface of the lens can be difficult to separate from the iris with standard probes unless the pupil is dilated. The normal nucleus in a young animal has the same appearance as the cortex of the lens. With age (in dogs usually starting around 5- to 6-year-old), the nuclear density increases (nuclear sclerosis) and the nucleus becomes more visible (because of the changed impedance between the cortex and the nucleus) (Figure 3.11).

With UBM, the anterior lens shows a bilinear, sharply defined structure. This is due to the change in acoustic impedance between the aqueous and the capsule and between the capsule/epithelium and the lens cortex (Figure 3.12).

Figure 3.9. Normal anterior segment of the eye. (A) Schematic drawing of the anterior segment of the eye. **(B)** High-resolution (12 MHz) sonogram of the cornea, anterior and posterior chambers, ciliary bodies (CBs). The cornea appears as two discrete hyperechoic curvilinear interfaces (arrowheads). The asterisk (*) indicates the posterior chamber. **(C)** Normal cornea (between arrowheads) and anterior chamber imaged (AC) with a 35-MHz probe in the axial section. The iris and the anterior lens capsule are in mutual contact. **(D)** Perilimbal radial section with a 35-MHz probe. The ciliary cleft is visible and normally open (red asterisk). The cornea (arrowheads), corneal–scleral junction (arrows), anterior chamber (AC), anterior lens capsule, part of the iris and the posterior chamber (white asterisk) can be seen. AC, anterior chamber; C, cornea; CB, ciliary body; I, iris; L, lens; PC, posterior chamber; VB, vitreous body.

Vet-ebooks.com

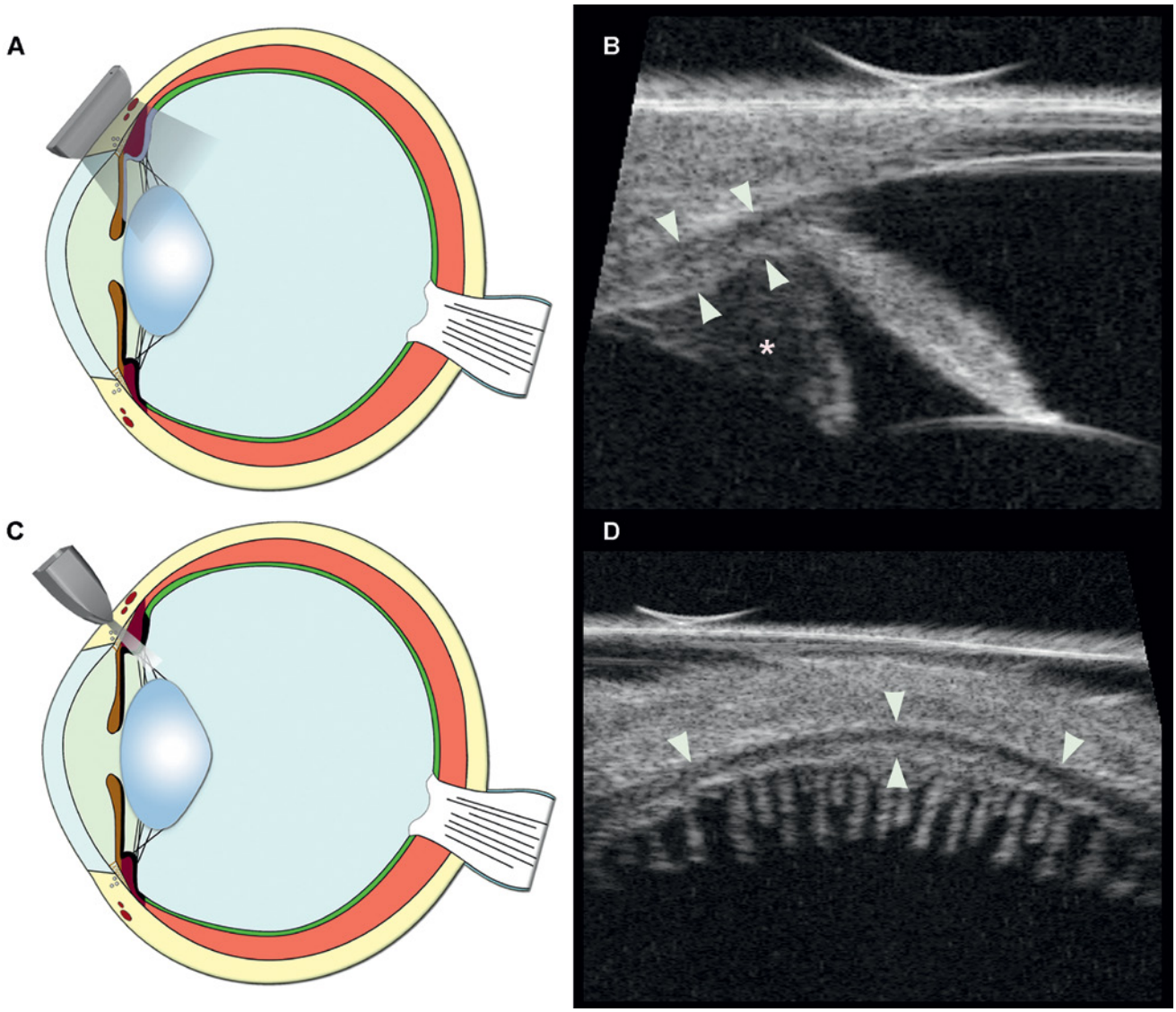


Figure 3.10. A 35-MHz UBM probe is used to evaluate the iridocorneal angle, the ciliary cleft, and the ciliary body. **(A)** Schematic illustration of a limbal radial (meridional) section. **(B)** Note the triangular shape of the ciliary process indicating the correct position of the probe (*). The ciliary cleft appears as a hypoechoic space between the sclera and the ciliary body (arrowheads). In this case, it is normally open. It is important not to press the probe on the ocular wall, to avoid indentation and possible change in the morphology of the angle. **(C)** Transverse section, perpendicular to the ciliary body. **(D)** Ultrasonographic image corresponding to probe position illustrated in C. The cleft appears as a linear hypoechoic space when normally open (arrowheads). The ciliary processes in this section appear as slender, finger-like hyperechoic structures directed to the center of the eye.

Posterior to the lens and extending to the posterior aspect of the globe is the **vitreous body**, which fills the vitreal cavity. The vitreous body is a thick, mostly acellular, gelatinous structure composed of 98% water, mucopolysaccharides, and hyaluronic acid. The vitreous cavity is bounded anteriorly by the lens zonules peripherally and posterior capsule axially and posteriorly by the retina (Figure 3.11). The vitreous body attaches primarily at the region of the optic disc (vitreous base) and at the ora ciliaris retinae and forms the hyaloid fossa, a fibrillar dense indentation, to adapt the posterior surface of the lens. The vitreous body is densely packed at the posterior surface of the lens except at the attachment of the hyaloid canal (Cloquet's or central canal). This canal extends from the posterior surface of the lens through the vitreous body to the optic disc on the posterior surface of the globe. This virtual space in the vitreous body contains the hyaloid artery in an embryonic eye (Figure 3.13). Remnants of this vessel may be present in adults.

Vet-ebooks.com

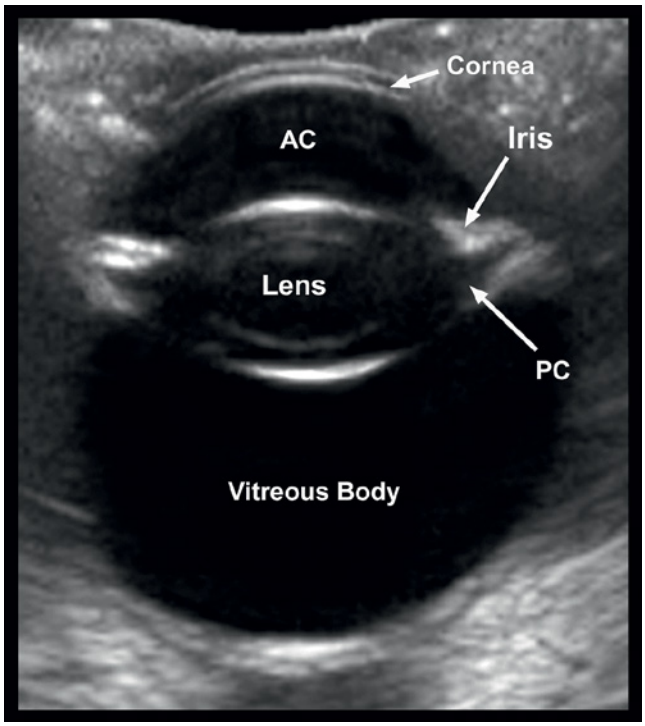


Figure 3.11. Transcorneal axial plane of a normal globe in a 7-year-old patient. The anterior chamber (AC) and vitreous body are anechoic. The lens in this older dog shows evidence of nuclear sclerosis. PC, posterior chamber.

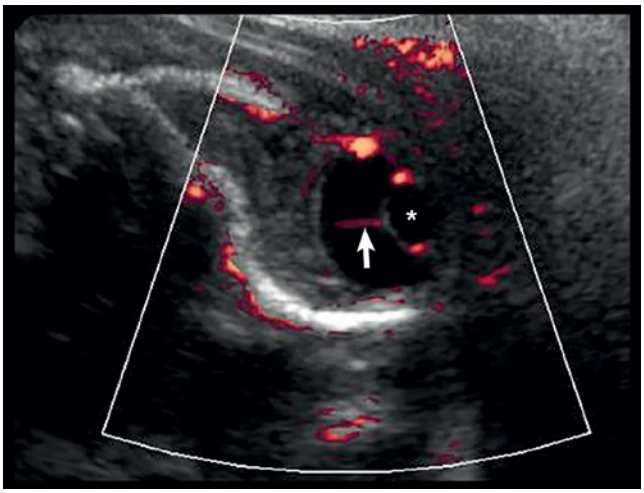


Figure 3.13. Fetal eye. This is the globe of late-term fetus. Note the straight line from the posterior surface of the lens to the posterior surface of the globe (arrow). This is a patent (color flow Doppler) hyaloid vessel supplying nutrition to the lens. This vessel typically is not present after birth. The asterisk indicated the lens.

The posterior surface of the vitreal body, located near the retina, does not have a true membrane but is referred to as the posterior hyaloid membrane.

The **posterior wall of the globe** is formed by a thin, ill-defined hyperechoic, smooth layer that represents the combined layers (from inner to outer) of the retina, choroid, and sclera. With ocular ultrasound, there is no clear demarcation between the three layers in the normal globe, and the echogenic line is referred to as the RCS complex (De La Hoz Polo et al. 2016). The retina extends from the optic nerve to the ora ciliaris retinae located just posteriorly to the ciliary body. Located slightly ventrally and medially in the posterior wall of the globe in dogs and cats is the optic disc. The optic nerve courses in a straight or undulating course from the posterior surface of the globe at the optic disc into the periorbita of the retrobulbar region, to the optic canal in the sphenoid bone (Figure 3.14A).

The **retrobulbar space** (periorbital cone), which includes the extraocular muscles, optic nerve, arteries and veins, and periorbital fat, can also be sonographically evaluated (Figure 3.14B).

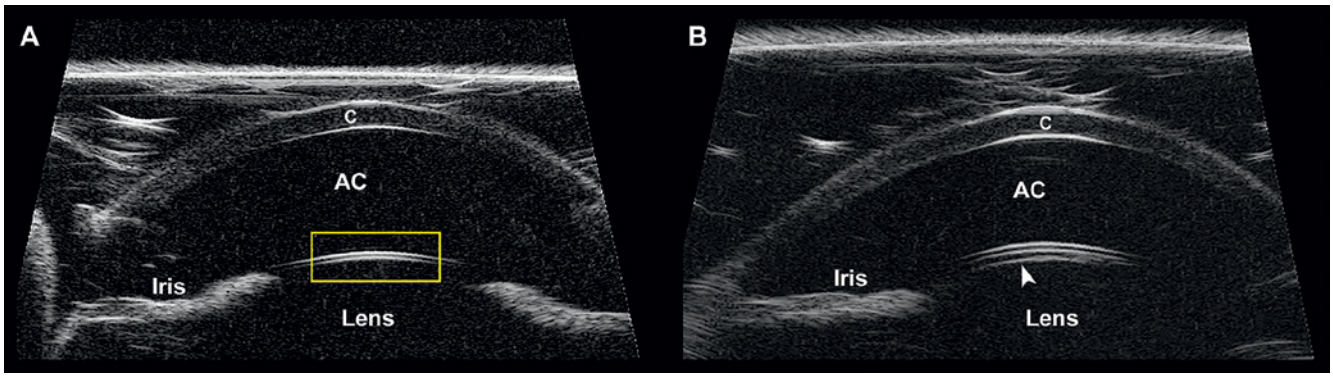


Figure 3.12. Transpupillary sagittal axial views of the anterior segment with 35 MHz contact probe. (A) Normal globe showing a double parallel hyperechoic line defining two different zones of acoustic impedance between aqueous, lens capsule, epithelium, and anterior cortex (square box). **(B)** Similar section in another patient showing a third, hyperechoic line corresponding to an incipient anterior subcapsular cataract (arrowhead).

Vet-ebooks.com

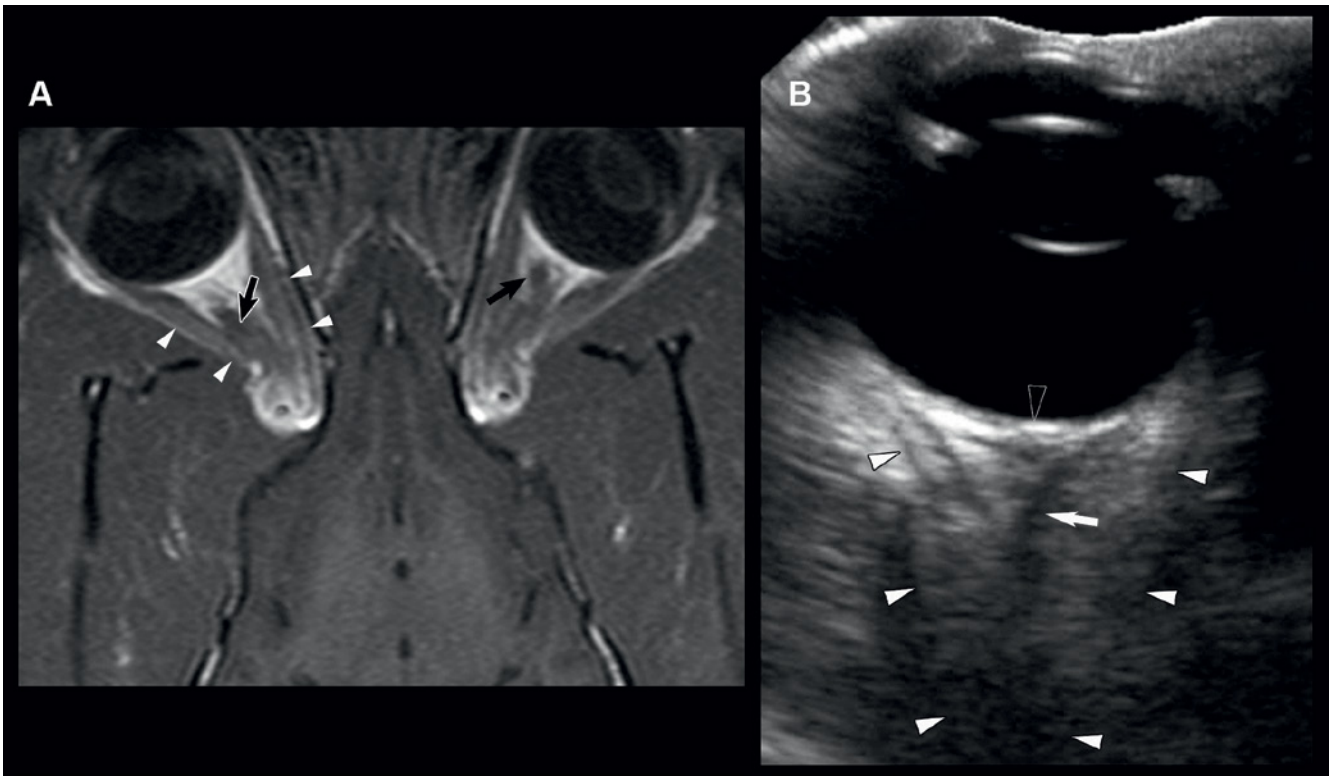


Figure 3.14. Normal optic nerve and retrobulbar space. The optic disc and nerve in dogs and cats are located slightly ventrally and medially on the posterior wall of the globe. **(A)** This dorsal magnetic resonance (MR) image displays the extraocular muscles (arrowheads), and the optic nerve (arrows) is difficult to identify because of its wavy course. **(B)** Sonogram of the retrobulbar space. The optic disc is a short discrete hyperechoic interface (black arrowhead). Posterior to it, the hypoechoic optic nerve (arrow) is partially visualized, encircled by extraocular muscles (white arrowheads) and fat present in this conical retrobulbar space.

The frontal bone, which forms the medial wall of the orbit, appears as a hyperechoic interface associated with shadowing. The extraocular muscles are hypoechoic linear structures that attach to the equatorial and postequatorial zones of the globe. The **optic nerve** is a thin, linear, hypoechoic structure outlined by adjacent hyperechoic fat. Measurements of the optic nerve sheath diameter (ONSD) with 6–15 MHz linear probes and a focal distance at 3–5 mm posteriorly to the globe have been reported in normal dogs and cats; ONSD varies between 0.91 and 3.82 mm, with a positive linear correlation with body weight (Dupanloup and Osinchuk 2021; Lee et al. 2002; Smith et al. 2018). However, the wide lateral resolution of these frequencies (Ng and Swanevelder 2011; Silverman 2009) must be considered when fine clinical information is sought (Vitiello et al. 2022). The lobular lacrimal gland, which is on the lateral (temporal) side of the orbit, and the zygomatic salivary gland, which is ventral and caudal to the globe and ventral to the orbital cone, can also be imaged (Figure 3.7).

Sonography of Ocular and Orbital Abnormalities

Cornea and Anterior Segment

The anterior segment of the eye is best evaluated using a high-resolution linear transducer (18–24 MHz) or UBM (up to 60 MHz). The thickness, echogenicity, and appearance of the layers of the cornea may be altered or disrupted with developmental defects, inflammation, degeneration, neoplasia, trauma, or specific corneal disorders, such as bullous keratopathy and corneal sequestra (Figure 3.15).

Most of the posterior stroma of the cornea and the endothelium with its Descemet's membrane develop from the neuroscrest, which also contributes to the fetal formation and perinatal cleavage of the anterior chamber. Developmental defects like persistent pupillary membrane (PPM) and Peters' anomaly will be congenitally present and can cause various grades of corneal and lens opacities and anterior chamber abnormalities (Figure 3.16).

Vet-ebooks.com

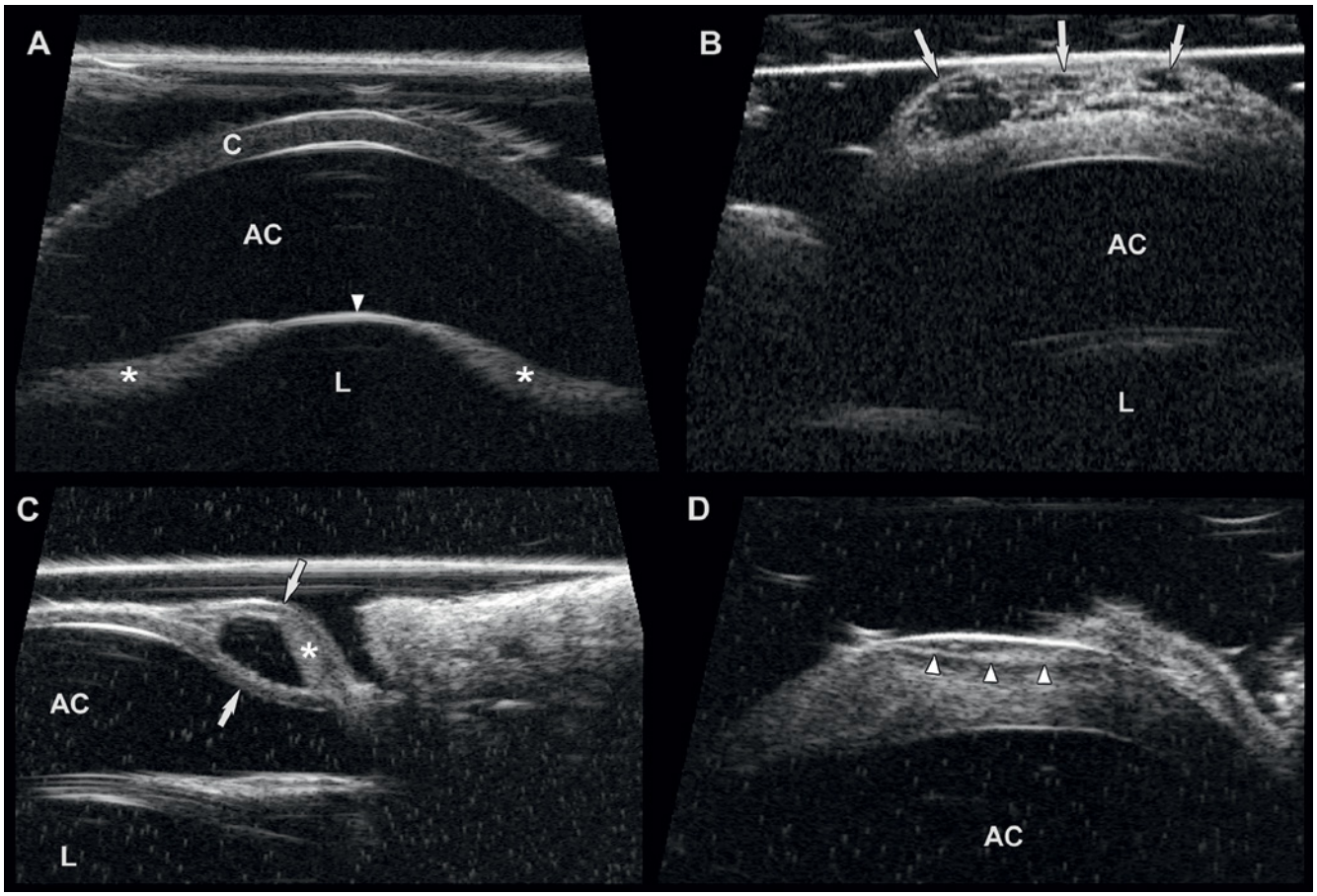


Figure 3.15. **Corneal changes in dogs and cats. (A) Normal cornea**. The axial transpupillary section also shows the ultrasonographic anatomy of the anterior chamber (AC). The iris leaflets (*) and the anterior lens capsule (arrowhead) are in contact, and the anterior bowing of the iris reflects the anterior lens curvature. **(B) Feline bullous keratopathy**. The anterior stroma shows multiple fluid-filled areas (arrows). The entire cornea thickness is severely increased. **(C)** Vertical section of a **corneal inclusion cyst** in a dog. The anechoic cavity involves the midstroma. The echoic cellular component of the fluid (*) is deposited at the bottom of the cavity (the left side is dorsal). **(D) Intrastromal corneal sequestrum** in a cat. The cornea is thickened, and the hyperechoic linear interface indicated by the arrowheads represents the sequestrum.

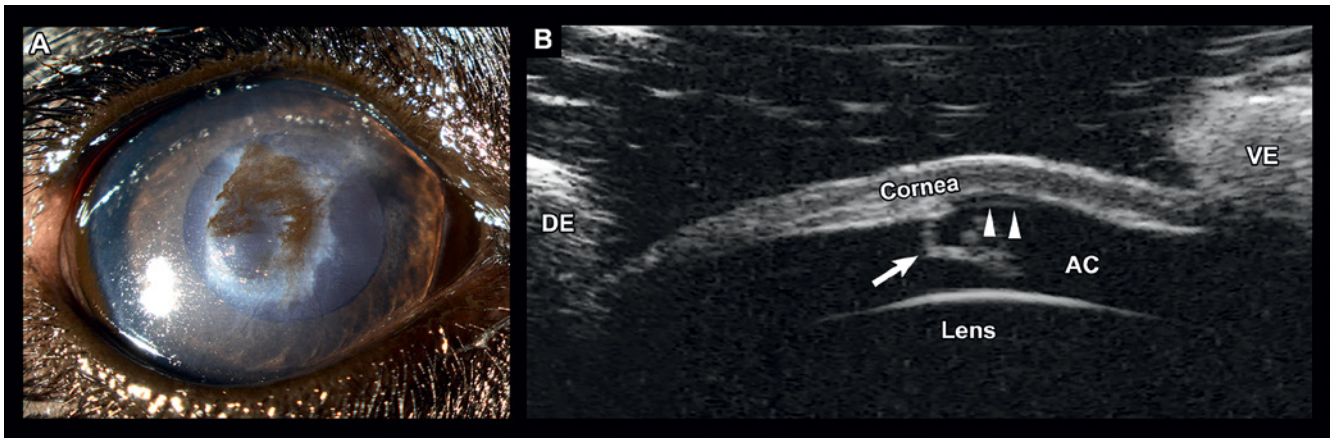


Figure 3.16. **Peters' anomaly in a 4-month-old Dachshund. (A)** Clinical picture of the right eye showing axial corneal pigmentation and fibrosis. Opacities of the anterior axial capsule are also present. **(B)** 35 MHz UBM of the anterior chamber in the same eye showing posterior keratoconus (arrowheads) and echoic strands of likely mesenchymal tissue spanning from the lens to the cornea (arrow). The dorsal (DE) and ventral (VE) eyelids, the anterior chamber (AC), and lens are labeled.

Vet-ebooks.com

Corneal or limbal infiltration caused by neoplasia or granulation tissue may be identified as focal thickening of the cornea and/or sclera. Determining the depth and involvement of the lesion is helpful for surgical planning because the prognosis is more guarded for full-thickness corneal involvement or if a limbal lesion extends beyond the sclera to or from the ciliary body (Figures 3.17, 3.18). Scleral thickening can also be seen with scleritis or episcleritis (Figure 3.18A); in these cases, although the ocular examination would be sufficient, ultrasound can be used to evaluate the amount of thinning and staphylomas, especially in chronic cases.

The cornea and the sclera merge at the limbus or corneoscleral junction and internally form the iridocorneal angle (ICA) with the iris. In small animals, this angle represents the entry site for aqueous humor outflow that happens posteriorly to the ICA, into the cleft (Pizzirani and Gong 2015). Any primary or secondary change in the angle and cleft may interfere with normal flow of the aqueous humor and cause an increased intraocular pressure. Perilimbal radial (meridional) and transverse sections with UBM are useful for investigating the width of the ciliary cleft and estimating the risk of glaucoma (Figure 3.19) or for the presence of other pathologies (Figure 3.20).

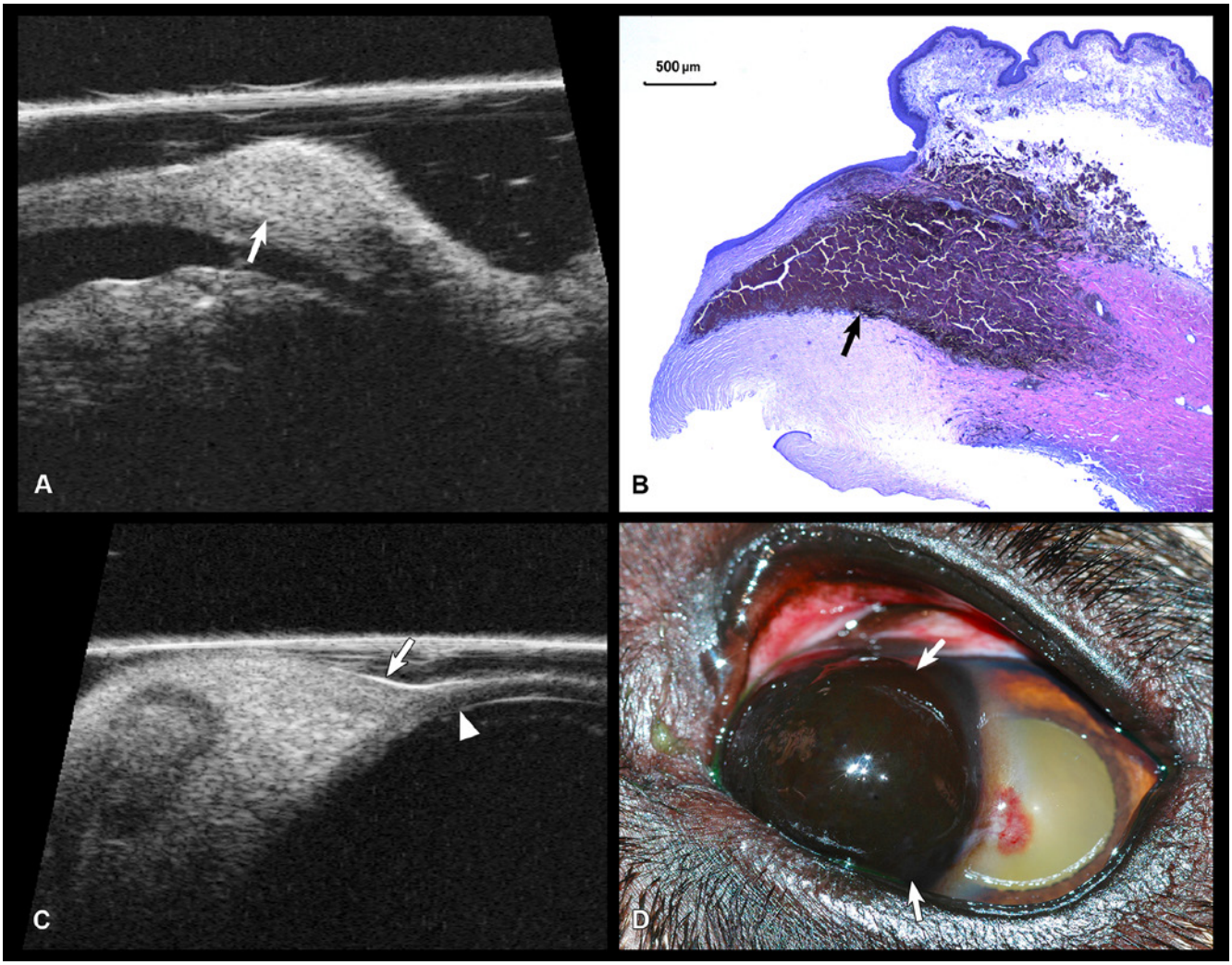


Figure 3.17. Limbal neoplasia in two dogs. The images illustrate two limbal melanocytomas with different levels of extension. **(A)** Limbal radial section with a 35-MHz probe. The hyperechoic mass is extending to a partial depth into the corneal and scleral tissues. The arrows indicate the inner mass margin at ultrasonography and in the corresponding histologic section **(B)**. **(C)** Invasive, full thickness limbal melanocytoma. Radial section in perilimbal/corneal position using a 35-MHz probe. The mass is extending to invade the inner portion of the cornea. The hyperechoic corneal epithelium is lifted (arrow) to follow the outer contour of the mass while the inner corneal hyperechoic Descemet membrane and endothelium disappear inner to the mass (arrowhead). **(D)** Clinical photograph of the melanocytoma (arrows) illustrated in C.

Vet-ebooks.com

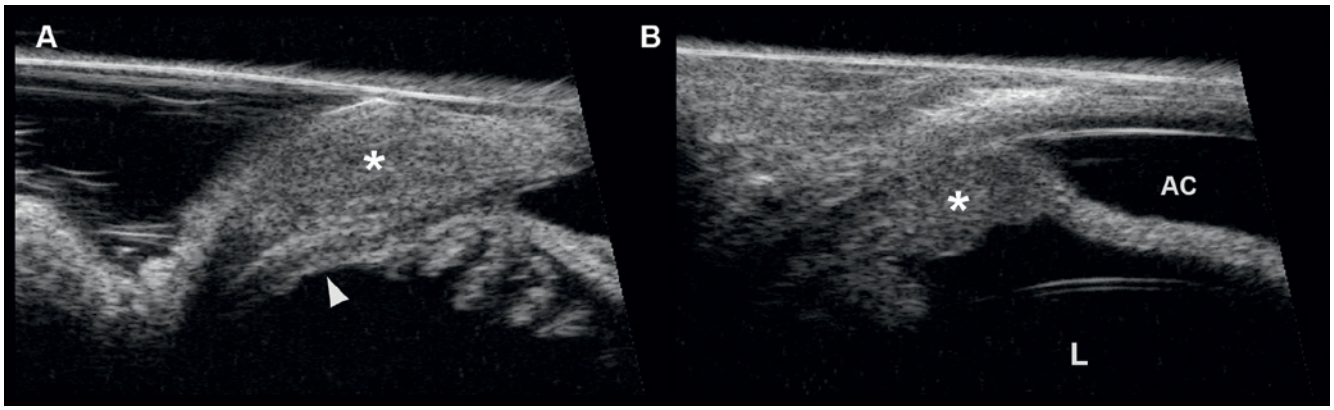


Figure 3.18. **Evaluation of lesion extension. (A) Granulomatous scleritis in a dog**. The sclera appears thickened and uniformly echoic (asterisk). The ciliary cleft is respected (arrowheads) and ciliary processes (arrow) are not involved. **(B) Melanocytoma of the anterior uvea**. The base of the iris and the ciliary body are enlarged and uniformly echoic (*). The ciliary cleft is obstructed/invaded anteriorly. Although the sclera shows an overall normal consistency and thickness, the cleft invasion and the intimate apposition of the uveal mass raise concerns for an extension into the uveal-scleral outflow. AC, anterior chamber; L, lens.

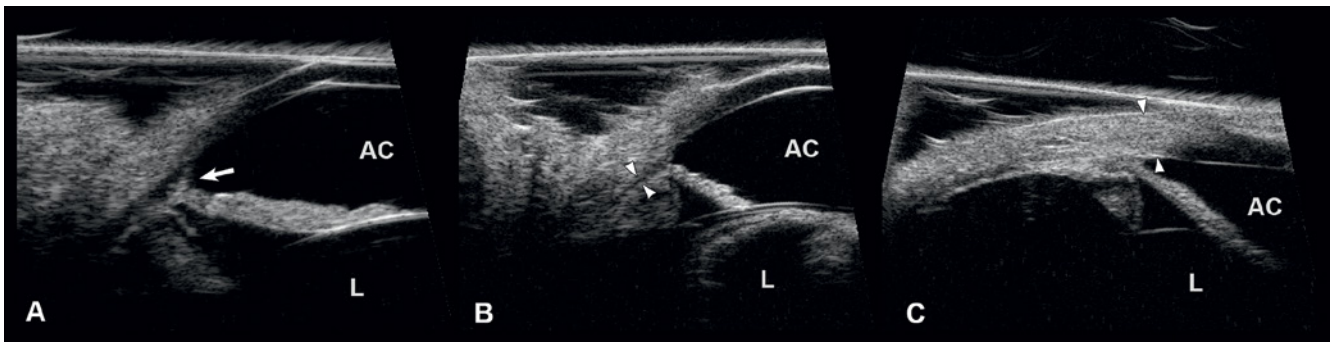


Figure 3.19. **UBM evaluation of the iridocorneal angle. (A)** Basset Hound, 2-year-old with pectinate ligament dysplasia (arrow) but with open cleft and normal intraocular pressure. **(B)** American Cocker Spaniel, 10-year-old with mature cataract and reduced opening of the cleft (arrowheads). The patient developed glaucoma 3 months after cataract surgery. **(C)** American Cocker Spaniel, 8-year-old with acute glaucoma. The cleft is closed, and the cornea (arrowheads) is mildly edematous.

An enlarged anterior chamber may be associated with glaucoma, aphakia, or posterior lens dislocation. A shallow anterior chamber may be associated with an intumescent cataract in diabetic patients (Figure 3.21), an anteriorly subluxated lens (Figure 3.34B), vitreal expansion (brachycephalic dogs and aqueous misdirection in cats), or intraocular neoplasia (Figures 3.22, 3.23). Caution should be used by the operator not to exert excessive pressure with the transducer and herein causing flattening of the corneal curvature and shallow anterior chamber, posterior displacement of the iris leaflet, and consequent modification of the ICA (Figure 3.24). Cells and fibrin debris within the aqueous humor often present as echogenic foci that usually move around by ocular motion (Figure 3.25).

The main abnormalities associated with the uvea include neoplasia, inflammation, and cysts. Tumors of the iris and ciliary body may present as focal echogenic nodules (Figure 3.26) or as diffuse infiltrative processes. Masses are usually arising from the uveal tissues, less commonly from the lens and they appear attached to or expanding the iris, ciliary body, lens, or pressing on the cornea (Figure 3.22). The most frequent intraocular tumor in dogs and cats is melanocytic neoplasia (often benign in dogs, usually malignant in cats) (Figure 3.27), and it is more commonly associated with the anterior uvea (Dubielzig et al. 1998). Ciliary bodies can also be affected by other tumors, such as lymphoma, adenoma, adenocarcinoma, and medulloepithelioma or metastatic disease (Dubielzig 2002; Dubielzig et al. 2002, 2010; see Figure 3.23). Imaging will provide information about the density, topographic characteristics, and vascularization patterns, but not about the histologic nature of masses.

Vet-ebooks.com

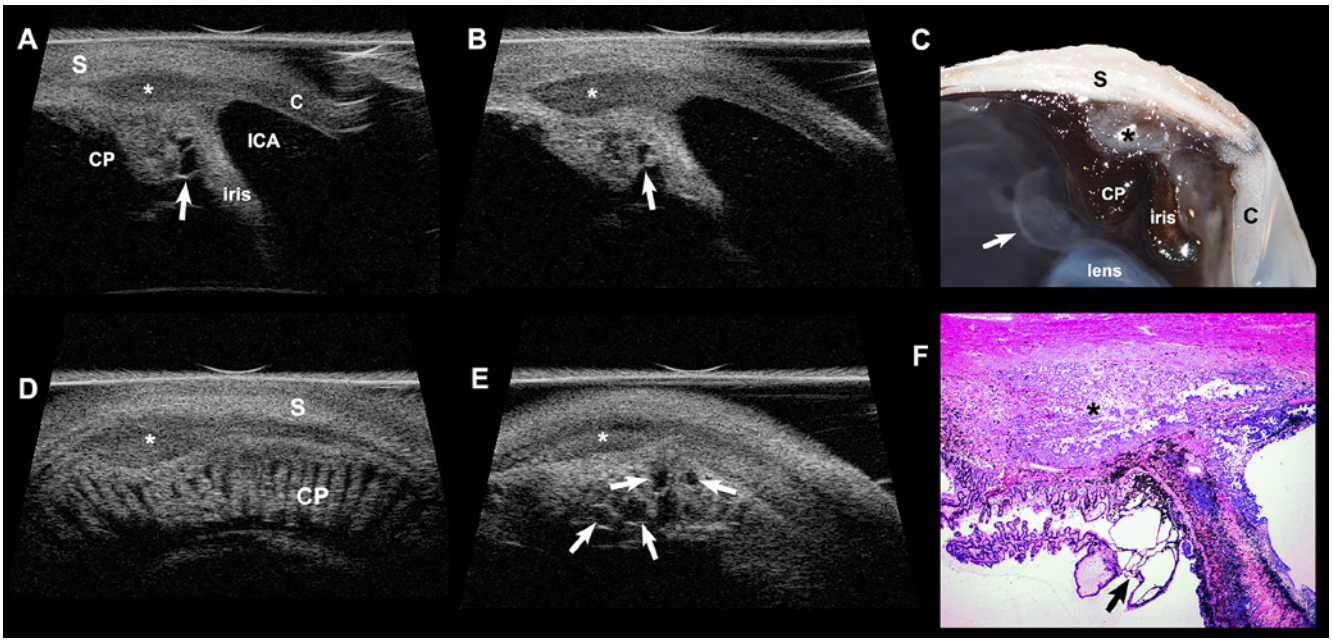


Figure 3.20. **Diffuse corneal edema and buphthalmos OD** of a 9-year-old German shepherd. **(A, B)** are 35 MHz UBM radial sections at 6 and 8 o'clock positions, respectively. The iridocorneal angle (ICA) is expanded by a soft homogenous hypoechoic tissue that extends mostly into the cleft (*). **(C)** is the gross pathological section of the globe after fixation. The whitish tissue is equivalent to the hypoechoic image of the cleft at UBM. **(D, E)** represent transverse perpendicular sections at the posterior limbus at 6 and 8 o'clock positions, respectively. The cleft is invaded and expanded by hypoechoic tissue. **(F)** is a microscopic picture at lower magnification of the tissue invading and expanding the ICA and cleft. The neoplasia was characterized by highly undifferentiated neoplastic cells originating from the endothelium lining the trabecular beams. Cornea (C), ciliary processes (CP), irido-corneal angle (ICA), iris, lens (L), and sclera (S) are labeled in the pictures. Multiple iridociliary cysts (arrows) are present in the peripheral sulcus, posteriorly to the iris and within the ciliary processes.

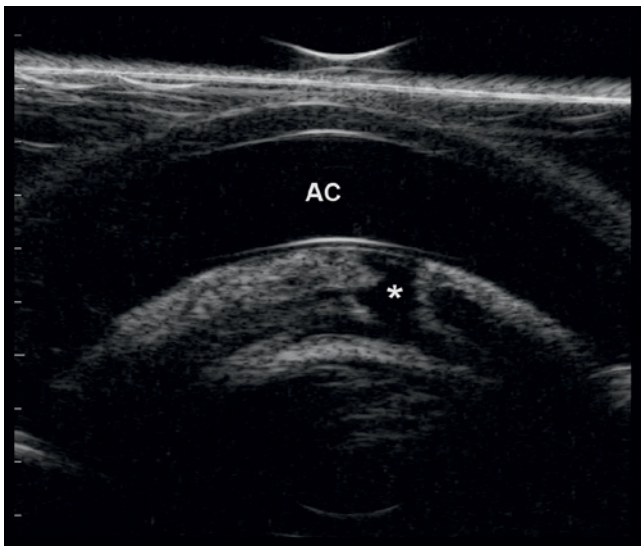


Figure 3.21. **Intumescent cataract in a diabetic dog.** The anterior chamber (AC) is shallower, and an anechoic fracture of the anterior cortex is visible (*). This is a common finding in intumescent cataracts.

Tumors may be difficult to distinguish from blood clots or granulomas (Gallhoefer et al. 2013). The presence of vascular flow within a mass is often helpful in determining whether the mass is a blood clot or a tumor and may assist in determining the tissue of origin. Lymphoma may have very echogenic thickening of the iris and ciliary body (Figure 3.22A), echoes in the anterior and posterior chambers, and thickening of the choroid, with possible retinal detachment. When an ocular mass is first detected, screening for metastatic disease is highly recommended. Feline primary intraocular lymphoma is possible and considered part

Vet-ebooks.com

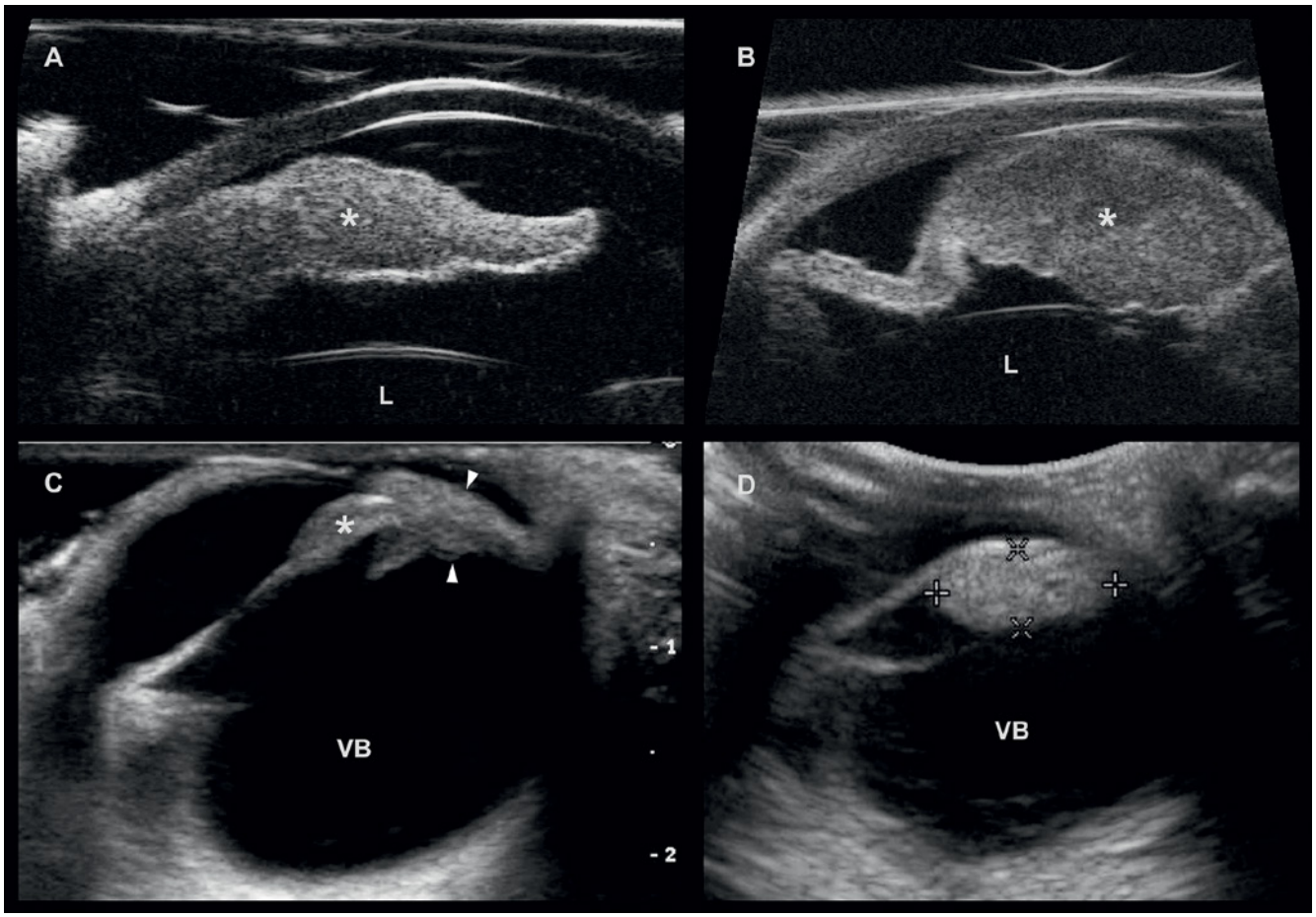


Figure 3.22. **Anterior uveal masses. (A) Iridal lymphoma in a cat**. The iris is diffusely thickened by neoplastic infiltrate (*). **(B) Melanocytic neoplasia of part of the iris in a dog** (*). **(C) Melanocytic neoplasia of the anterior uvea in a dog**. Parasagittal section of the globe showing peripheral iris thickening (*) and extension of the neoplastic process to the ciliary body (arrowheads). **(D)** Another case of **uveal melanocytic neoplasia in a dog** shows posterior iridal invasion (between cursors). VB, vitreous body.

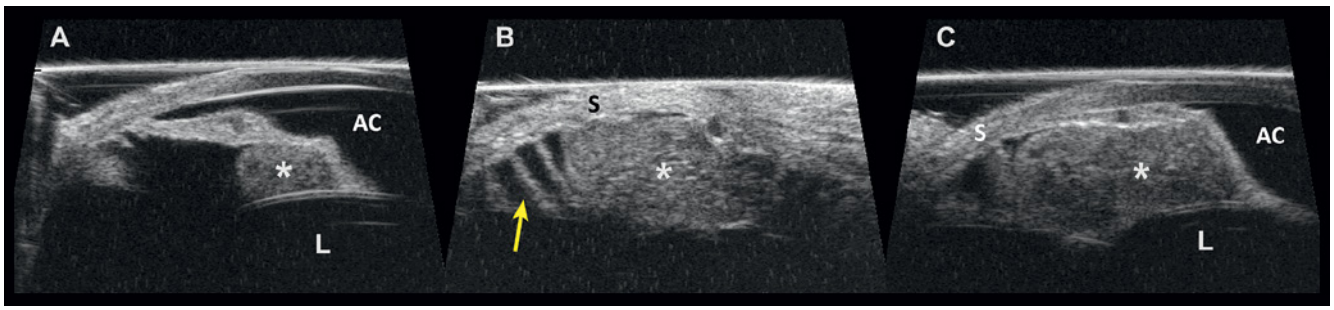


Figure 3.23. **Ciliary body adenoma in a dog. (A)** Sagittal perilimbal 35 MHz section showing a mass (*) separating the iris and the lens (L) and displacing the iris leaflet forward. **(B)** Transverse limbal section showing the mass (*) originates in the ciliary processes region (arrow) and appears in this section not to invade the sclera (S). **(C)** Peripheral oblique section showing the mass (*) occupying the posterior chamber and sparing the sclera. The different sections help to characterize the echogenicity, shape, and extension of the mass. AC, anterior chamber.

Vet-ebooks.com

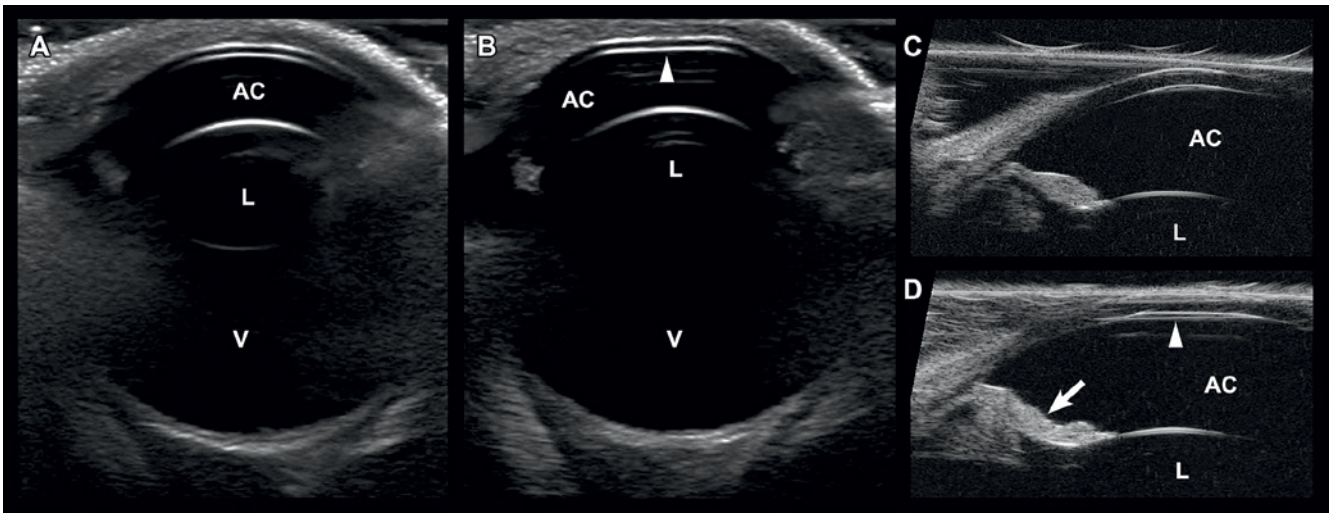


Figure 3.24. **Technical artifacts.** (for full caption, see facing page)

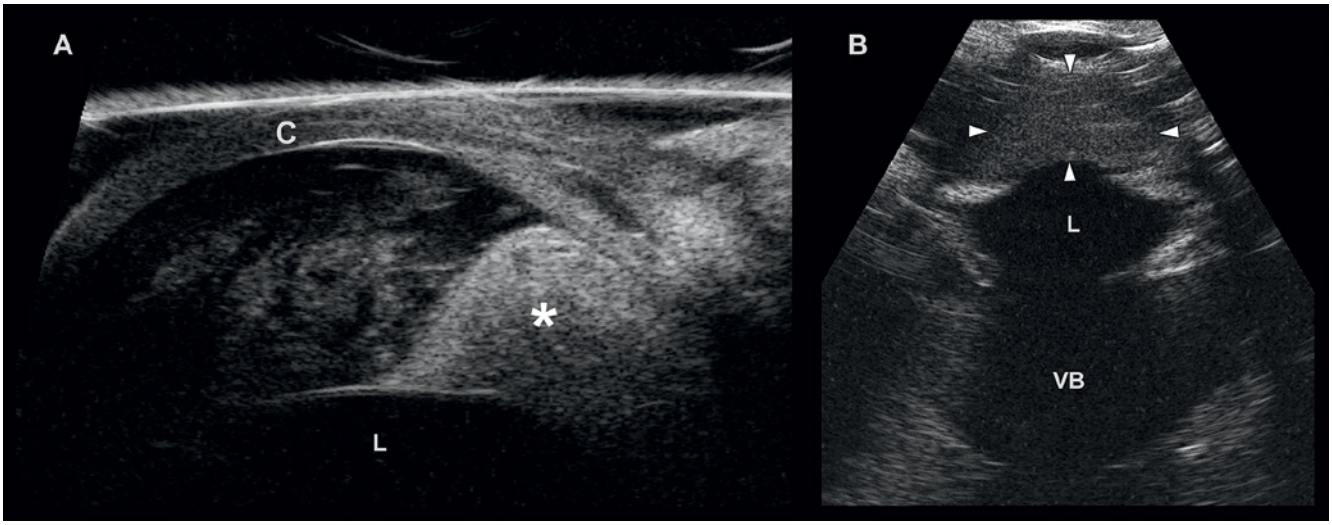


Figure 3.25. **Anterior chamber abnormalities. (A)** Cellular debris/fibrin in anterior chamber associated with an iris mass (*). **(B)** Anterior chamber hyphema. The hypoechoic homogeneous collection of frank blood is outlined by arrowheads. C, cornea; L, lens; VB, vitreal body.

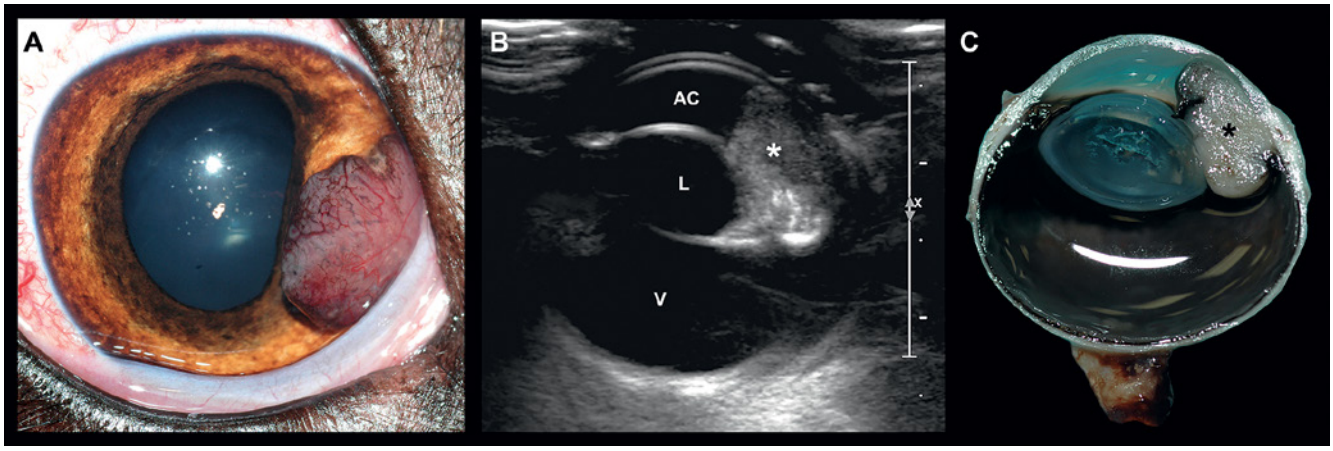


Figure 3.26. **Ciliary adenoma in a dog with an iridal mass**. (for full caption, see facing page)

Vet-ebooks.com

Figure 3.24. **Technical artifacts. (A)** Transpalpebral sagittal section of a normal globe with an 8–18 MHz probe. **(B)** Similar section but with slight pressure causes corneal flattening (arrowhead). The anterior chamber shape is artifactually changed. **(C)** Transcorneal paraxial section of a normal globe with an UBM 35 MHz rigid probe. **(D)** Similar section in the same globe using an excessive pressure causing corneal flattening (arrowhead) and artifactual posterior bowing of the iris leaflet (arrow). AC, anterior chamber; L, lens; V, vitreous.

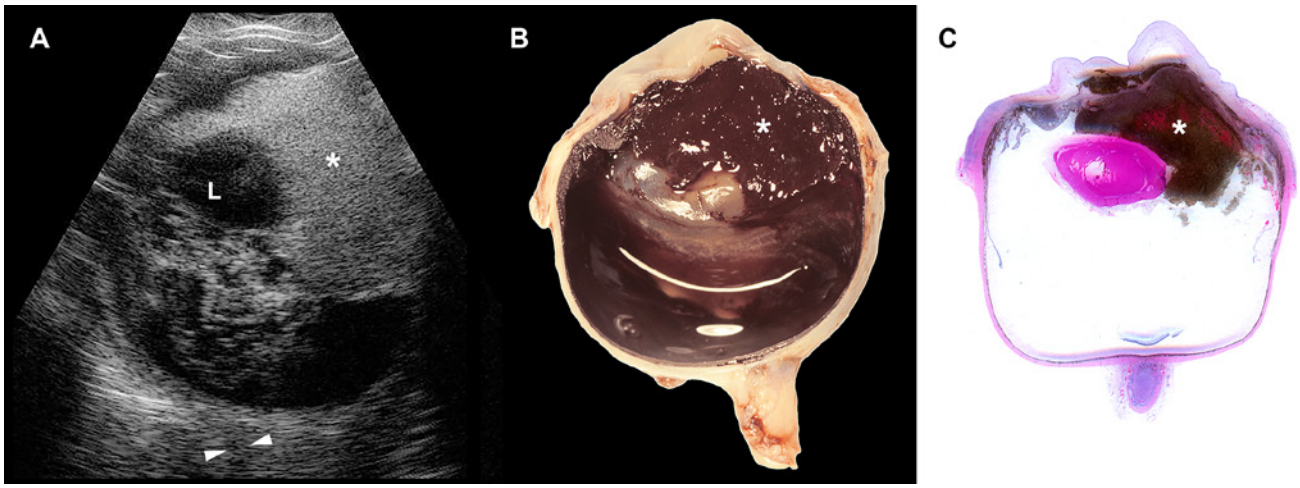


Figure 3.27. **Uveal melanocytic neoplasia in a dog. (A)** Sonogram showing a homogenous hyperechoic mass (*) invading the anterior and posterior chambers, enwrapping a normal lens (L), and associated with vitreal reflectors and membranes some of which connecting to the optic nerve (arrowheads). **(B, C)** Gross pathologic and histologic sections, respectively, of the same globe, showing the extension of a heavily pigmented mass (*).

of central nervous system lymphoma as reported in humans (Rissi et al. 2022; Sagoo et al. 2014) and it occurs in the absence of other organs involvement.

Uveitis is the generic term to indicate a rupture of the ocular barriers (inflammation) and ultrasonography is not primarily used for its diagnosis but can assess some of its complications such as retinal detachment, the presence of synechiae and iris bombe (Figures 3.28, 3.29), or to rule out primary causes of the disruption of the ocular barriers, like trauma, neoplasia, or lens rupture.

Iridociliary cysts are common, often incidental, findings affecting the posterior surface of the iris or/and the pars plicata of ciliary body. They present as singular or multiple thin-walled anechoic structures. UBM has a better axial resolution and represents the best modality for cyst visualization (Liu et al. 2022). Cysts usually form from the uveal neuroepithelium lining the posterior chamber and, if detached, may float into either the anterior chamber or, rarely, the vitreous body. They may occur in any breed, but Golden Retrievers, Labrador Retrievers, Great Danes, Boston Terriers, and American Bulldogs are predisposed (Corcoran and Koch 1993; Deehr and Dubielzig 1998; Pumphrey et al. 2013; Sapienza et al. 2000; Spiess et al. 1998). Albeit cysts may represent an incidental finding, and they have also been associated with pigmentary uveitis or glaucoma. Their direct or indirect role has yet to be established (Figure 3.30); they must be interpreted as a likely sign for chronic friction, inflammation, and pigment dispersion associated with epithelial mesenchymal transition (EMT) of the ciliary body neuroepithelium.

Lens

Echogenic abnormalities associated with the lens include congenital anomalies such as congenital primary aphakia (CPA), PPM, remnants of the tunica vasculosa lentis (TVL) or persistent hypertrophic primary vitreous (PHPV), cataracts (cortical or nuclear, at different stages), resorbed cortical material with

Figure 3.26. **Ciliary adenoma in a dog with an iridal mass**. Photograph **(A)**, horizontal sonogram using an 18 MHz linear probe **(B)**, and the corresponding gross specimen **(C)** of the globe. **(B)** There is a large echogenic mass extending into the anterior chamber and in the ciliary body posteriorly (*). **(C)** Gross section shows the ciliary adenoma (*) spreading from the ciliary body through the iris stroma into the anterior chamber. AC, anterior chamber; L, lens; V, vitreous.

Vet-ebooks.com

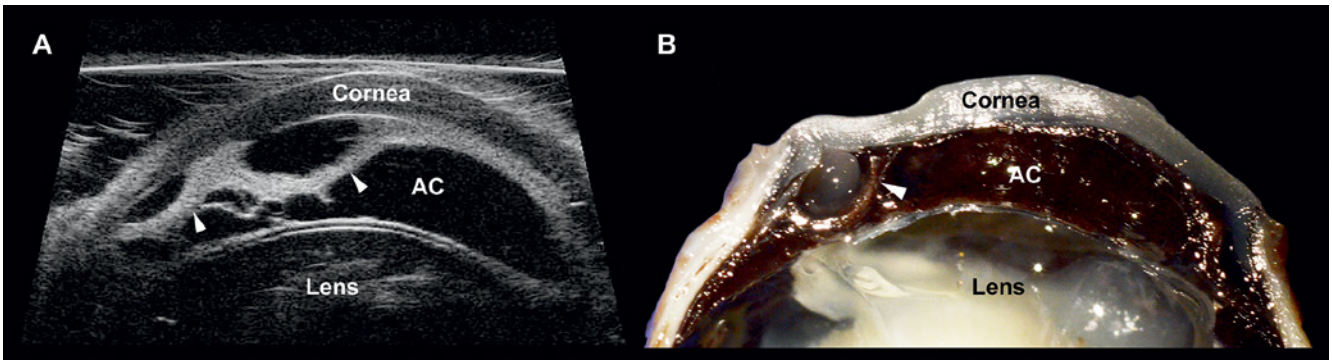


Figure 3.28. **Anterior synechiae.** Axial sagittal views of the anterior segment of a dog presented with patchy darkening and diffuse corneal edema in both eyes. **(A)** UBM image with a 35-MHz probe. The anterior chamber shows thick echoic membranes spanning between the lens and cornea (arrowheads) **(B)** Gross pathologic section of the same eye in a slightly different orientation showing pigmented anterior synechiae (arrowhead). The anterior chamber (AC) is filled with pigmented inflammatory tissue.

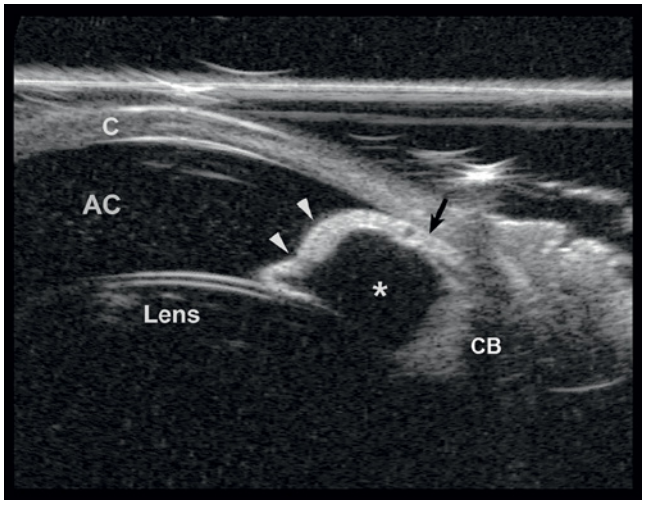


Figure 3.29. **Posterior synechia and iris bombe in a dog with chronic uveitis and secondary glaucoma.** Axial section with a 35-MHz UBM probe. The iris edge is attached to the anterior lens capsule because of chronic uveitis and posterior synechia formation. The posterior chamber (*) is distended, and the iris is pushed forwards (arrowheads). The iridocorneal angle is obstructed by apposition of the peripheral iris and cornea (arrow) and no ciliary cleft is visible. AC, anterior chamber; C, cornea; CB, ciliary body.

modification of the capsular profile, intumescence (swelling) of the lens, rupture of the anterior or posterior capsule with herniated cortical material, posterior ectasia or lenticonus, subluxation, or dislocation.

Congenital anomalies, when the cornea preserves transparency, can also be diagnosed or suspected during clinical examination, while in more severe cases, the corneal or the lens opacity may require an ultrasound to achieve the correct diagnosis (Figures 3.31, 3.32).

Cataracts are degenerative changes in the solubility of lens proteins (Gelatt and MacKay 2005). A cataract produces increased echoes in various locations within what should appear as a normally anechoic lens. The echogenicity, shape, and size of the lens may differ according to the type and stage of cataract and its duration.

The most used classifications for cataracts are based on the topography of the degenerations and stage of maturation, which translate into echoic abnormalities of different locations and intensities. According to their location within the lens, cataracts will be addressed as capsular, cortical (anterior, posterior, or equatorial), perinuclear, or nuclear (the core of the lens) (Figure 3.33).

The classification based on the stage of progression of the cataract is clinically more useful and includes incipient, immature, and mature cataracts with <10% of the volume, 10–100% of the volume with partial opacity, and 100% complete opacity, respectively. These stages usually maintain the lens volume, which instead may be increased in diabetic mature hyperosmotic cataracts (intumescent). The latter may consistently reduce the depth of the anterior chamber

Vet-ebooks.com

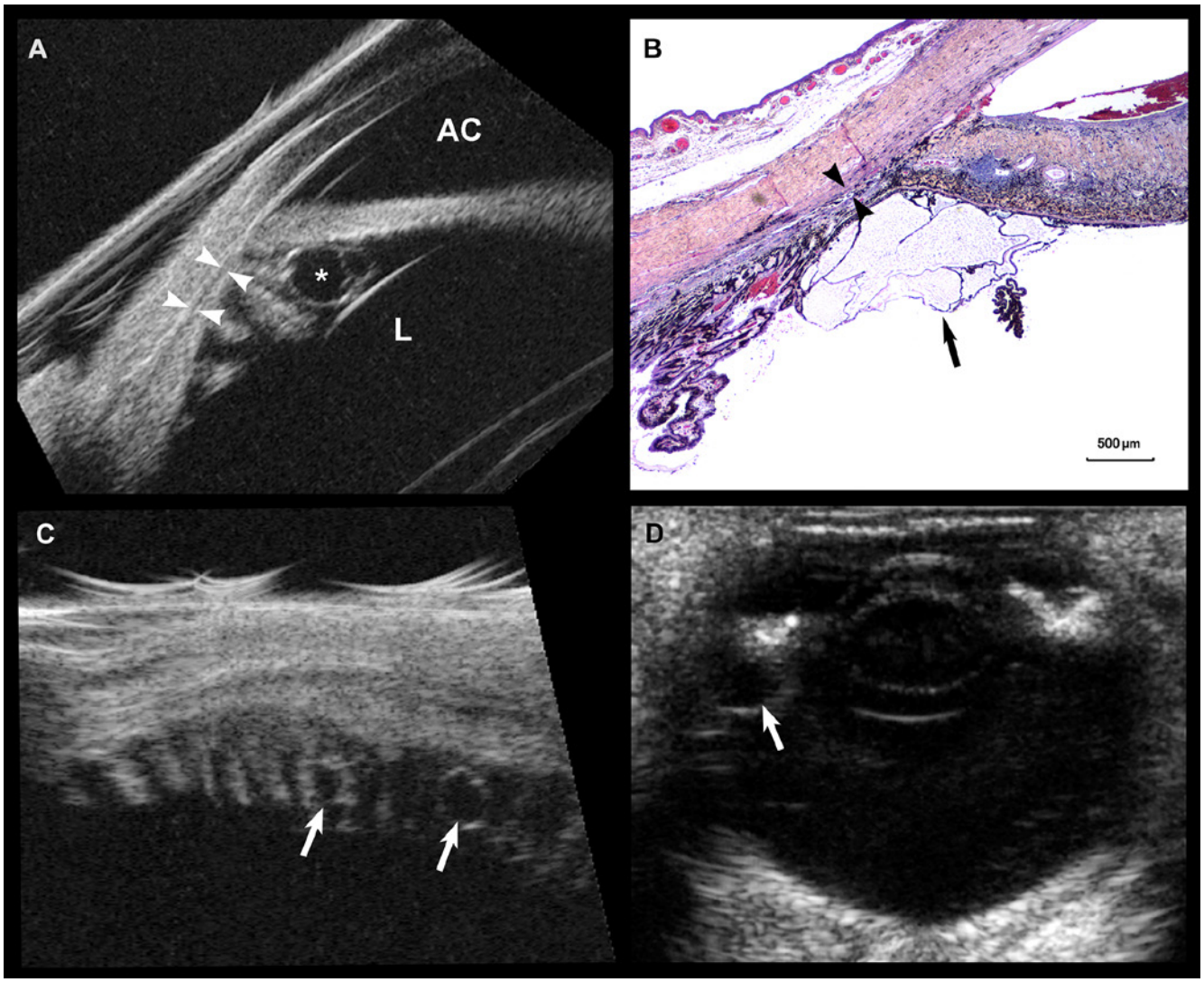


Figure 3.30. **Iridociliary cysts.** These are characterized by a round structure that has a hyperechoic membrane and an anechoic center (*). **(A)** Radial limbal section with a 35-MHz ultrabiomicroscopy (UBM) probe showing multiple iridociliary cysts and a collapsed cleft (arrowheads) in an American Bulldog with glaucoma. **(B)** Histologic section of the ultrasonographic image shown in **(A)**. **(C)** Transverse perilimbal section with a 35-MHz UBM probe that shows the presence of two hypoechoic ciliary cysts between ciliary processes (arrows). **(D)** Axial section of a canine globe showing a large iridociliary cyst (arrow).

(Figure 3.21) and increase the risk of capsular stretching and rupture. In one clinical study comparing lens morphometry in normal and cataractous lenses, diabetic cataracts had an increased axial thickness of 8.4 ± 0.9 mm while nondiabetic mature cataracts had a thickness of 7.4 ± 0.9; immature and normal lenses were about 1 mm less (Williams 2004). When capsular tears occur, they usually involve the equator, which makes them more difficult to see at initial ocular examination (Figure 3.34).

More rarely, when the capsular tear is small, limited portions of cortical material can herniate in the virtual space of Berger or fall in the posterior segment (Figure 3.35).

When during clinical evaluation a moderate to severe uveitis is present or the anterior lens curvature and thickness are not homogeneous, an equatorial tear needs to be ruled out with ultrasonography using higher frequency linear probes (ideally >14 MHz). Hypermature and Morgagnian cataracts are late stages with cortical liquification and resorption (Figure 3.33E). In these stages, the lens thickness is reduced, and the capsules appear wrinkled; these changes can be assessed ultrasonographically. Resorption can be detected as a decrease in the anteroposterior width of the lens and an increased depth of the anterior chamber. In a cortical cataract, the anterior and/or posterior and/or equatorial cortices

Vet-ebooks.com

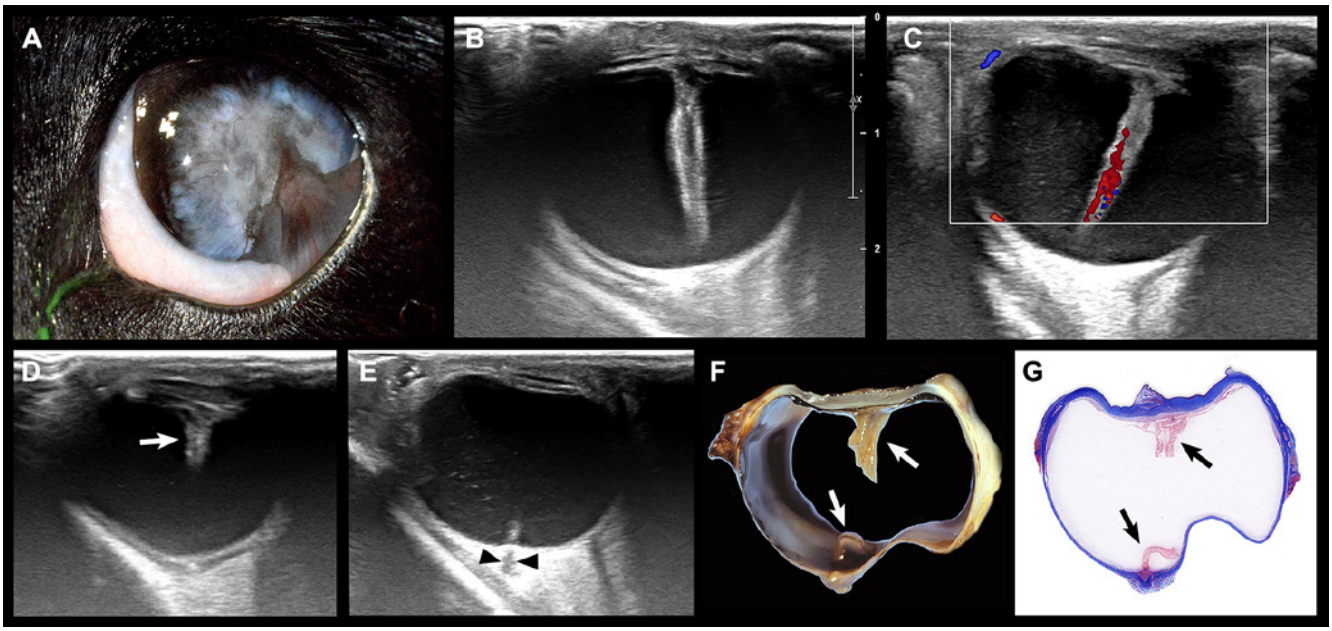


Figure 3.31. **Congenital aphakia and retinal detachment in a 3-month-old male Siberian Husky presented for a congenital blindness and anterior surface changes in both eyes**. **(A)** Clinical picture of the left eye showing corneal fibrosis and sclerocornea. **(B–E)** Sagittal sections obtained with a linear 18 MHz probe. Missing anterior chamber and no lenticular tissue can be seen. A hyperechoic vascularized structure, histologically identified with the retina (arrows), can be seen extending from the anterior surface of the globe to the optic nerve (**E**, arrowheads). **(F)** Gross pathological picture of the same eye depicting the aberrant vascular structures (arrows). **(G)** Micropicture of a PAS stain showing no lenticular material present. The midvitreal retina has been sectioned during preparation. These severe congenital multiple malformations (the retina was also dysplastic) have been associated in humans with mutations of the FOXE3 gene.

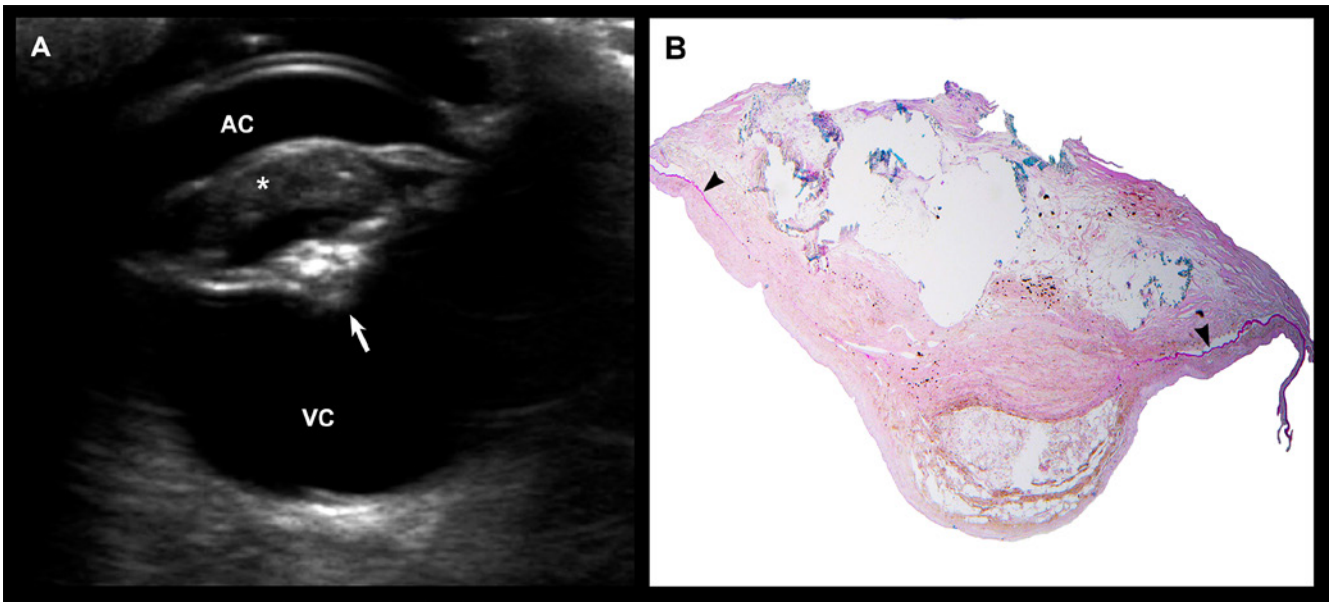


Figure 3.32. **Posterior lenticonus. (A)** Axial section of a canine globe with an intralenticular organized hemorrhage and cataract. The lens opacity was preventing the clinical assessment of the posterior segment of the eye. An ultrasound showed an echoic lens (*) with a protruding posterior hyperechoic pole (arrow). **(B)** Histologic section (periodic acid-Schiff stain) of the posterior lenticular plaque seen at ultrasound after cataract surgery. The specimen shows fibrotic and mineralized tissue representing a congenital malformation (PHPV). The posterior capsule is visible as a thin purple line (arrowheads) fading into the center of the plaque. AC, anterior chamber; VC, vitreal cavity.

Vet-ebooks.com

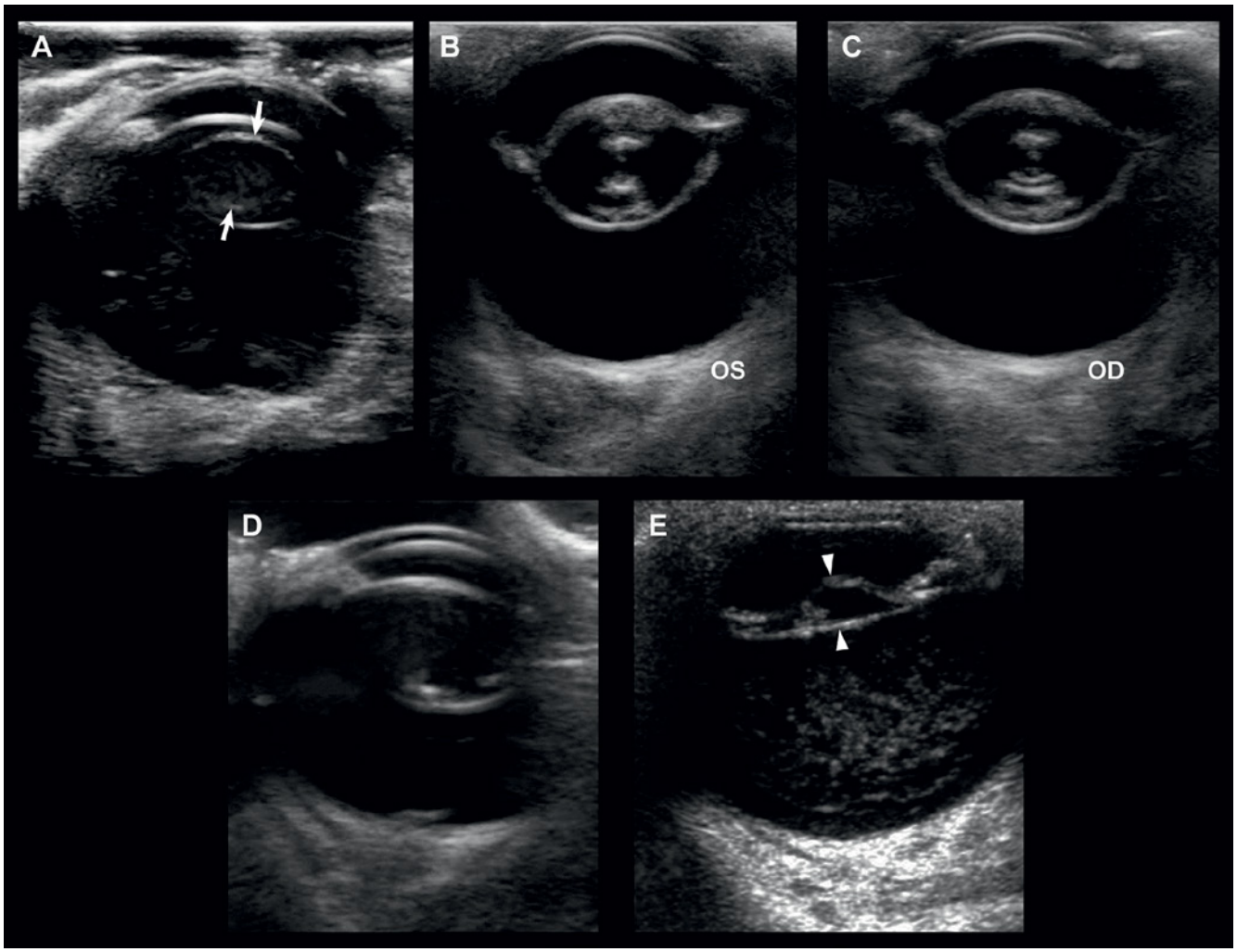


Figure 3.33. **Lens changes. (A) Dense nuclear sclerosis** is noted in the eye of this 11-year-old Shih Tzu. Notice the faint curvilinear echogenic lines (arrows) bordering the nucleus. This is a common finding in the aging eye. **(B) Posterior axial cortical cataract** in a 1-year-old miniature Poodle. Irregular echogenic change is noted in the posterior cortical region of the eye. **(C) Perinuclear and early cortical changes** are noted in this canine eye. **(D) Mature cataract** with dense opacities affecting the cortex © and the perinucleus (P), anteriorly and posteriorly as well, while the nucleus of the lens (N) is still mostly anechoic. Anterior chamber (AC) and vitreal cavity (VC) are labeled. **(E) Hypermature/Morgagnian cataract**. Note that the lens (arrowheads) volume is greatly reduced due to lens material resorption and liquefaction. The echoes in the vitreous are consistent with degenerative changes often associated with advanced cataracts (asteroid hyalosis).

become echogenic. When the cortical suture lines are affected, they may become echogenic and be identified especially from a transverse plane, while in intumescent cataracts they become hypoechoic when compared with the rest of the cortex (Figure 3.21) due to increased lenticular water content and separation (fracture) of the cortex along the suture lines. A nucleus that becomes uniformly echogenic can be associated with aging changes (nuclear sclerosis) (Figure 3.33A) or with early onset/congenital cataracts. Incipient or immature cataracts usually and eventually progress to involve the entire lens.

Changes in lens stiffness, volume, or degenerative changes may stress the zonules, resulting in partial or complete rupture of the ligaments. Lens subluxation or complete dislocation may then occur. Primary lens luxation, deriving from abnormal zonular formation due to genetic mutations, has also been reported in specific canine breeds (Farias et al. 2010; Lazarus et al. 1998; Sargan et al. 2007; Oliver et al. 2018). Subluxated lenses, partially or completely displaced, are still located in front of the vitreous body and behind the iris. Flattening or posterior direction of the iris leaflets may be seen, or loss of connection between lens and iris may be visible

Vet-ebooks.com

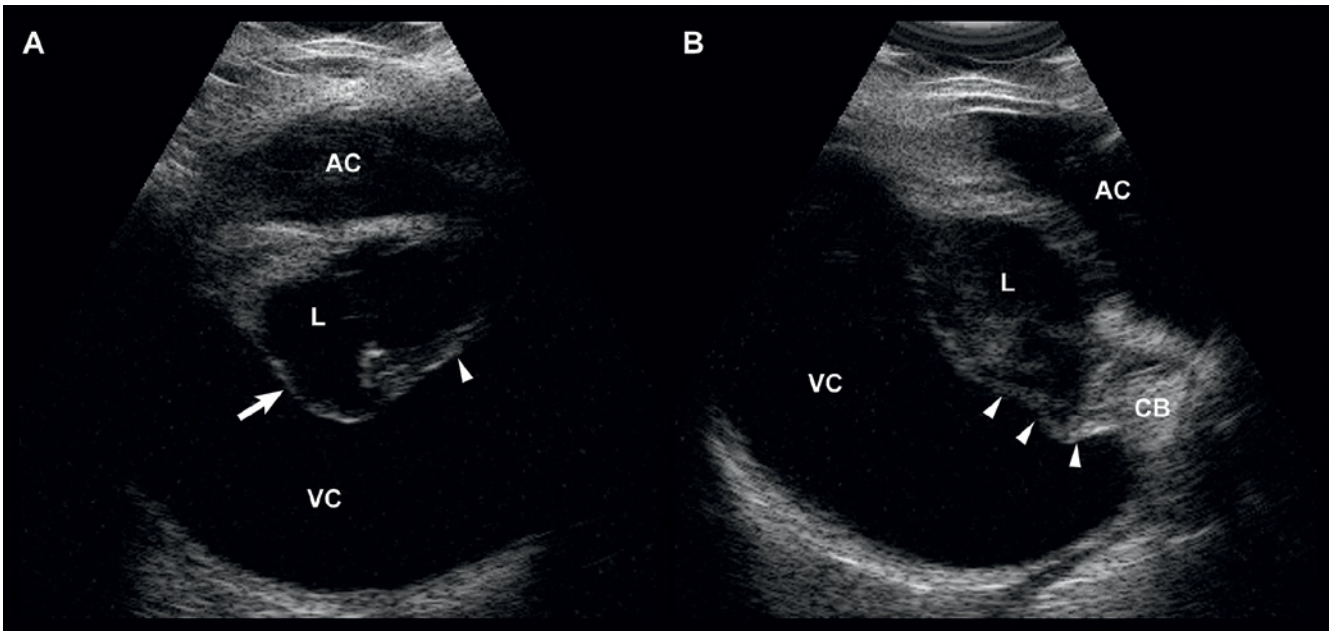


Figure 3.34. Capsular rupture in a 3-year-old Labrador. (A) Paraxial vertical section showing mild echogenicity of the lens content (L). The lens shape is abnormal, showing volumetric discrepancy between the dorsal (arrow) and ventral (arrowhead) portions. Variation in lens volume and thickness in the same eye, associated with moderate uveitis as in this case, indicate possible peripheral rupture of the capsule. **(B)** Oblique paraxial section showing irregular morphology of the posterior lens capsule (arrowheads) and abnormal lens adhesion and increased echogenicity of the ciliary body (CB), supporting the clinical diagnosis of phacoclastic uveitis because of equatorial lens capsule rupture. In this case, clinical examination also revealed a deeper anterior chamber corresponding to flattening of the anterior lens surface. AC, anterior chamber; VC, vitreal cavity.

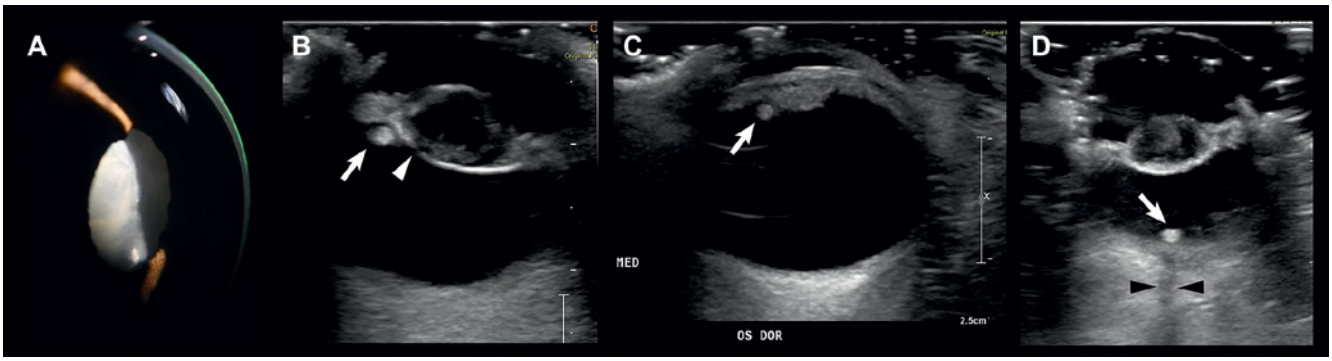


Figure 3.35. Cataract and cortical material extrusion/herniation. (A) Clinical slit lamp picture showing a decreased lens volume with irregular flattening of the anterior surface of the lens. **(B)** Ultrasonographic sagittal section suggesting a discontinuation on the posterior lens capsule (arrowhead) and a hyperechoic nodular material collecting peripherally at the posterior equator (arrow). **(C)** Transverse paraxial peripheral section showing the nodular material (cortical lens material) posterior to the equatorial lens. Reverberation artifacts are present. **(D)** Sagittal oblique (note the width of anterior chamber and reduced posterior vitreal cavity volume) paraxial view showing another cortical fragment herniated and fallen in the posterior segment, causing a shadowing (arrowheads) over the retrobulbar tissues.

(Figure 3.36A). Lens luxation may cause the lens to migrate into the anterior chamber or fall within the vitreal space. In anterior luxation, the anterior lens capsule is immediately posterior to the cornea (Figure 3.36B), while in posterior lens luxation, the lens may be visualized near the retina or within the vitreal space (Figure 3.36C).

In focal zonular ruptures, **vitreal herniation** in the anterior chamber may be seen first. Luxation of an artificial intraocular lens can also be recognized (Figure 3.37).

Vet-ebooks.com

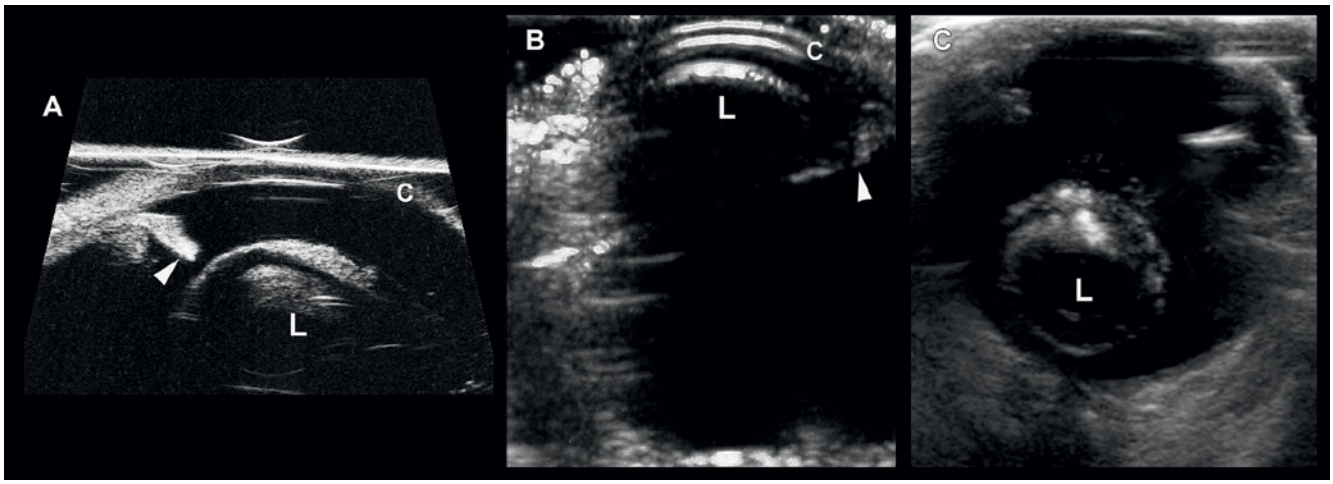


Figure 3.36. **Lens displacement. (A) Lens subluxation** in a 13-year-old Lhasa Apso. The lens outer cortex and the nucleus are hyperechoic (cataract) and the lens is displaced ventrally, showing a lack of contact with the iris leaflet (arrowhead). **(B) Anterior lens luxation**. The hyperechoic anterior lens capsule is just posterior to the cornea, indicating that the lens (L) is clearly displaced within the anterior chamber, anteriorly to the iris and ciliary bodies (arrowhead). The two superficial hyperechoic curved lines represent the cornea (C). **(C) Posterior lens luxation**. The echogenic lens (cataract) has completely dislocated into the vitreal cavity, near the optic disc. Irregular curvilinear structures are seen near the posterior lens capsule.

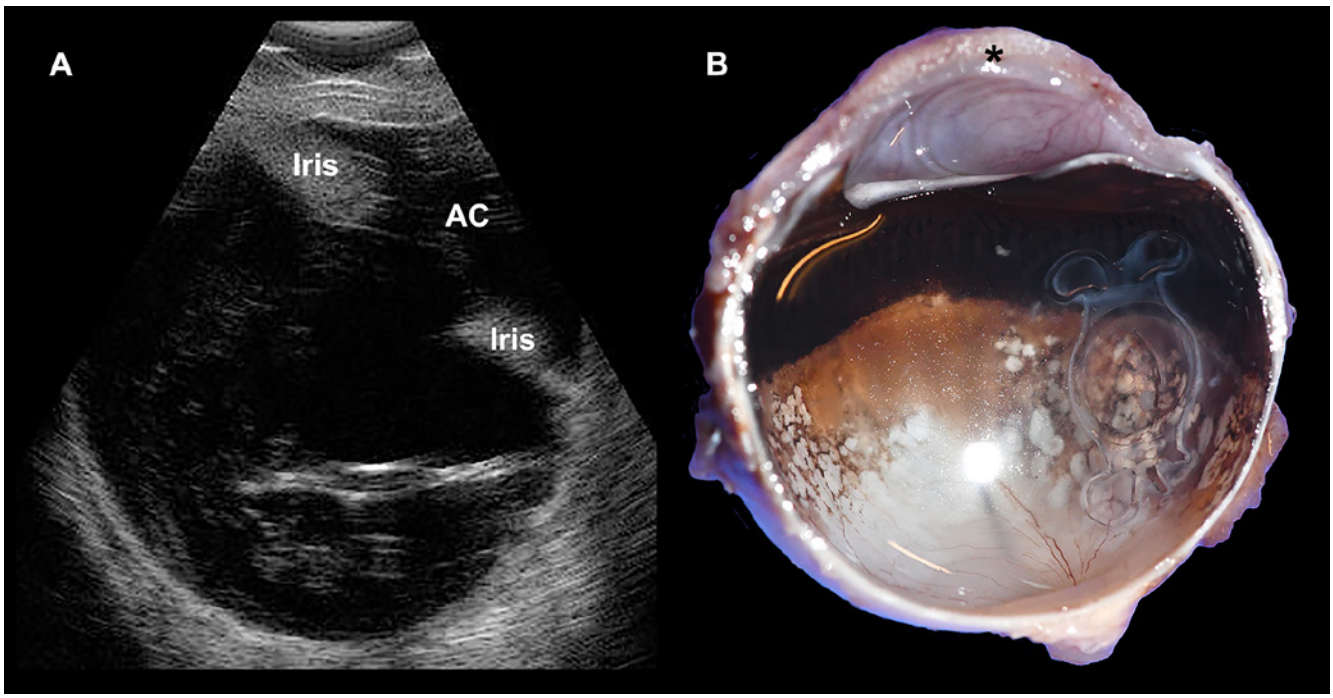


Figure 3.37. **Luxation of an intraocular lens (IOL).** Siberian Husky, 8-year-old, SF who had cataract surgery OU 5 years prior was presented for corneal redness, thickening, and buphthalmia of the left eye. **(A)** Transpupillary sagittal oblique section showing the IOL floating within vitreal syneresis (liquefaction). Ill-defined multiple vitreal echoes are present, indicating vitreal degeneration. **(B)** Gross pathological section of the same globe, showing the luxated IOL. The corneal thickening (*) resulted from corneal squamous cell carcinoma.

Posterior lenticonus is a developmental anomaly of the lens with localized cone-shaped protrusion of the axial portion of its posterior surface (Figure 3.32), in association with a retrolenticular fibrous or fibrovascular membrane. It represents one of the multiple possible anomalies present within the PHPV complex (Figures 3.38, 3.39). Posterior focal paraxial capsular ectasias may seldom occur, likely

Vet-ebooks.com

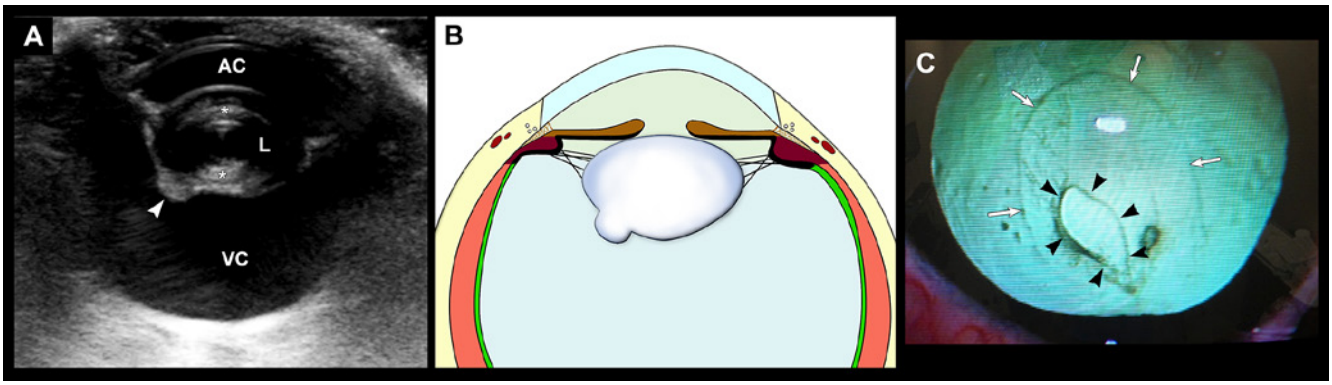


Figure 3.38. **Cataract and capsular ectasia. (A)** Vertical axial section of a canine globe presented for cataract evaluation. The lens (L) is normally sized and presents anterior and posterior cortical cataracts (*). In addition, a discrete rounded echoic mass is seen protruding from the posterior capsule dorsally (arrowhead). A hyperechoic line can be seen lining the mass. **(B)** Schematic illustration of the ultrasonographic findings of posterior capsular ectasia. **(C)** Intrasurgical photograph of the case described in A and B. Posterior capsular ectasia was identified at surgery. The anterior capsulorexis is indicated by the arrows, while the arrowheads indicate the dorsal, paraxial area of capsular ectasia after fragmentation and aspiration of the lens material. AC, anterior chamber; VC, vitreal cavity.

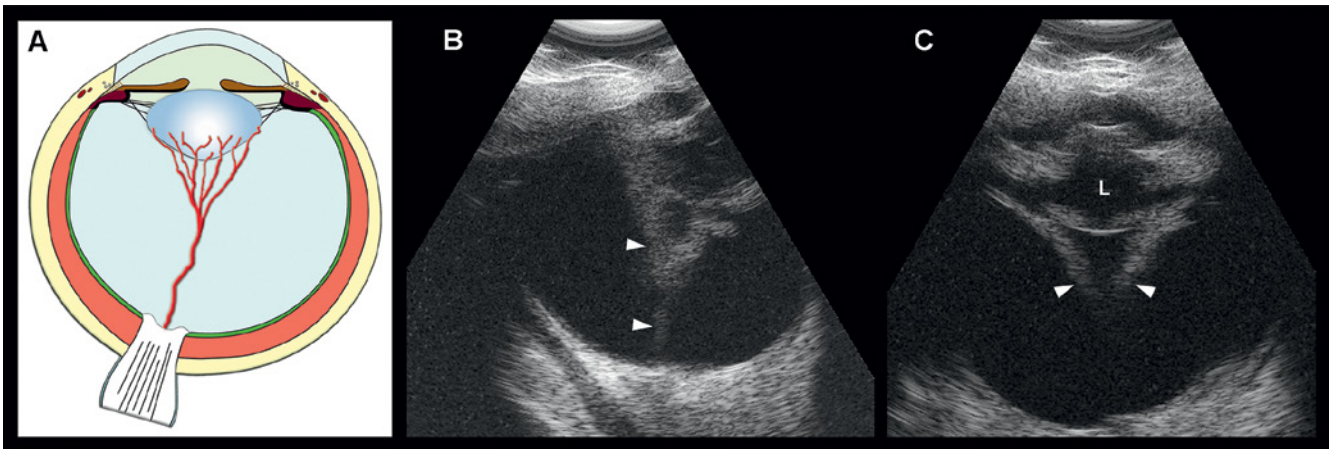


Figure 3.39. **Persistent hypertrophic primary vitreous in a 3-month-old Boxer with bilateral cataract. (A)** Schematic drawing showing the vascular distribution of the primary vitreous in the posterior segment. **(B)** Slightly oblique paraxial section showing abnormal echoic tissue (arrowheads) expanding from the posterior lens (L) to the optic nerve area in a triangular shape consistent with persistency of the fetal fibrovascular tissue **(C)** Axial section showing echoic structures projecting into the posterior vitreous body posteriorly to the lens.

as an early stage of focal capsular stretching before the rupture, and manifest as an isolated protrusion of the posterior thin capsule without cortical herniation (Figure 3.38). Posterior or peripheral capsular irregularities are important to recognize prior to surgery because they can lead to surgical complications when removal of the lens is attempted.

Vitreous and Retina

Posterior segment changes include congenital and acquired vitreous echogenic modifications as well as alterations in the shape of the globe.

Persistent and hyperplastic primary vitreous is a congenital condition (Bayon et al. 2001; Gemensky-Metzler and Wilkie 2004; Grahn et al. 2004), in which the primary vitreous (hyaloid artery and posterior TVL) incompletely regresses after birth. A step ladder classification of different grades has been published (Stades 1980), which includes various combinations of capsular plaques and cataracts, posterior lenticonus, and connective-tissue strands (retrolenticular fibrovascular tissue) between the posterior surface of lens and the area of the optic nerve. A funnel-shaped echogenic retrolenticular structure emerging from the lens and coursing to the optic disc may be seen in these cases (Figure 3.39). The strand

Vet-ebooks.com

between the surface of the lens and the area of the optic nerve may contain patent hyaloid vessels. Color Doppler may be helpful in assessing the presence of vascular flow (Boroffka et al. 1998) (Figure 3.40). However, ultrasonographic diagnosis can be only presumptive since other conditions, like a gliotic detached retina collecting at the axial center of the posterior segment, can provide similar images.

Other congenital malformations like CPA may present similar vitreal findings, with a detached, dysplastic, and gliotic retina that may assume the same ultrasonographic appearance (Figure 3.31).

Acquired vitreal opacities include asteroid hyalosis, synchysis scintillans, degenerating vitreous strands and hemorrhage, the presence of fibrovascular membranes, posterior vitreous detachment, retinal detachment, subretinal transudates/exudates, increased volume of the optic papilla, or the presence of a foreign body or a mass.

Echogenic foci or degenerated vitreal fibers within the vitreous are common findings in older patients and can be associated with several conditions. Asteroid bodies appear as dot-like reflectors within the normally anechoic vitreous body (Stringer et al. 2017). Degenerated vitreal membranes (floaters) appear as mildly echoic lines within the vitreous. They usually smoothly move with the globe movements. These reflectors are more common in eyes that have sustained trauma or are affected by some chronic inflammatory or degenerative changes.

Asteroid hyalosis is the most common vitreal degeneration in older patients and in specific breeds (brachycephalic and Italian Greyhounds). These small foci of 0.03–0.1 mm calcium–lipid complexes are discrete pinpoint reflectors suspended in the vitreous framework (Figure 3.41). Their number may widely vary from a few to a large number and may cause blurry vision (fly biting in small animals) and carry a higher risk for retinal detachment.

In **synchysis scintillans**, the bodies are not suspended. Because of the vitreal body liquefaction, these bodies sink to the bottom of the globe. With ocular movements, they float inside the less dense vitreous following inertia and gravity. This is often seen in eyes with end-stage disease and vitreal syneresis (liquefaction). Vitreal degeneration is often identified in dogs with cataracts. In one study, vitreal degeneration was seen in 55, 89, and 100% of dogs with immature, mature, and hypermature cataracts, respectively (Dietrich et al. 1995).

A **detached vitreous** may appear as one or several thin, curved lines with varying reflectivity. Anechoic fluid may accumulate between the retracted vitreal body and the retina (Figure 3.42). Detached vitreous can be an incidental finding in older patients. However, it could be a sentinel sign for focal retinal detachments and careful assessment of the posterior wall is needed when vitreal detachment is found. Lines are sometimes difficult to differentiate from retinal detachments, although vitreal membranes are usually less echoic than retinal tissue.

Echoes floating within the vitreous may be caused by inflammation, infection, or hemorrhage. Hemorrhage into the vitreous may produce a multitude of echoes within the anechoic vitreous cavity; it varies in appearance and often depends on the duration, severity, and location of the bleed (Figure 3.43).

Hemorrhage may be seen as diffuse point-like multiple echoes and when limited in extension they may appear as focal reflectors, which may be difficult to

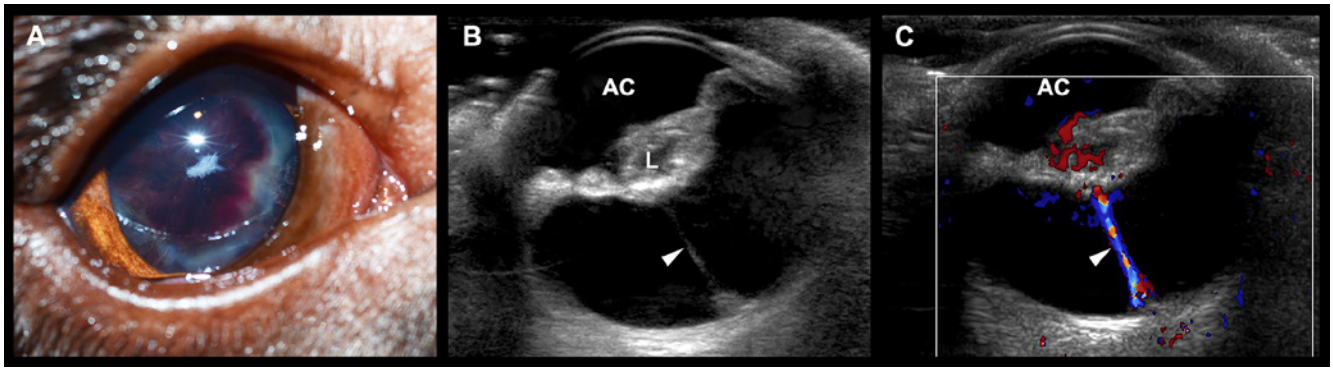


Figure 3.40. Congenital cataract and persistent hypertrophic primary vitreous in a 2.3-year-old German Shorthair Pointer. **(A)** Clinical image of the right eye affected with a partial hypermature reabsorbing cataract and presence of a lenticular hemorrhage. **(B)** Ultrasound image of the same eye showing increased depth of the anterior chamber (AC) due to lens (L) reabsorption and flattening of the anterior lens curvature. The lens body is inhomogenously hyperechoic. The vitreal cavity has a linear echoic discrete strand (arrowhead) connecting the posterior lens to the optic papilla, which appears increased in shape. **(C)** Continuous wave Doppler showing blood flow in the lens and within the linear strand (arrowhead).

Vet-ebooks.com

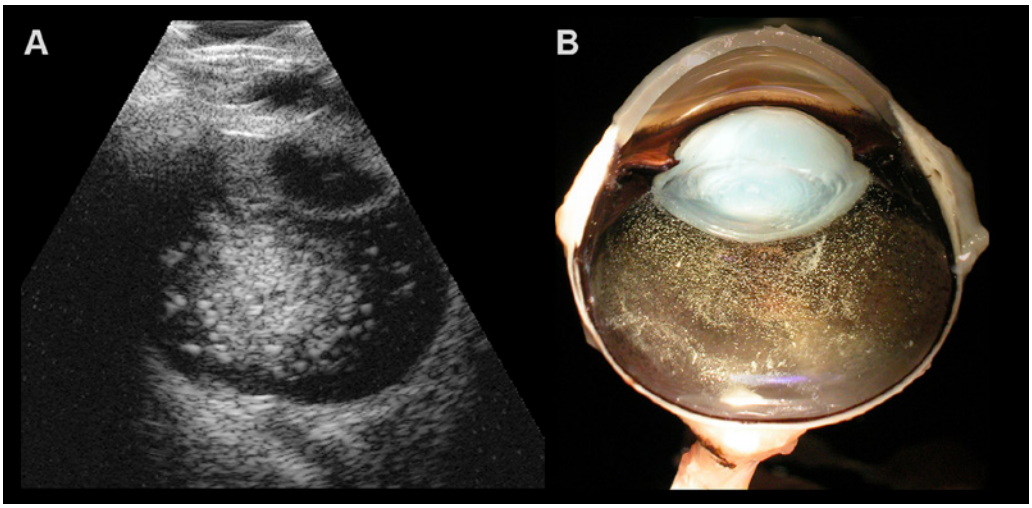


Figure 3.41. **Asteroid hyalosis. (A)** The vitreal cavity contains multiple hyperechoic granular structures consistent with accumulation of vitreal degenerative bodies made of calcium and phospholipids (asteroid hyalosis). **(B)** Gross section of a globe showing the corresponding disease in another dog. Multiple white bodies are visible posteriorly to the lens. Courtesy of Dr R. Dubielzig, University of Wisconsin, USA.

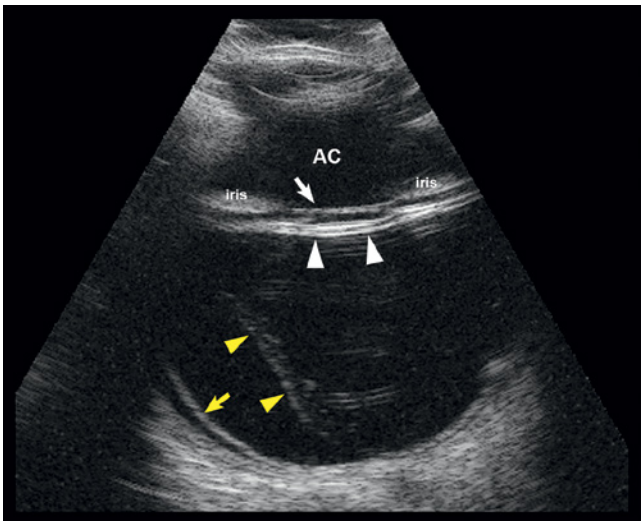


Figure 3.42. **Vitreal and retinal detachment.** Vertical axial sonogram showing vitreal detachment (yellow arrowheads) and corresponding retinal separation (yellow arrow) after cataract surgery. Note the different echogenicity of the two structures, with retinal tissue usually being more echoic than the vitreous cortex. The anterior lens capsule is indicated by the white arrow and the prosthetic intraocular lens by the white arrowheads. Multiple reverberations can be seen as linear echoic parallel lines in the vitreal body. AC, anterior chamber; I, iris.

differentiate from asteroid bodies (Stringer et al. 2017). Erythrocytes often precipitate onto a pre-existing vitreous strand, acquired membrane, or the posterior hyaloid membrane. Fibrous (vascularized) strands may develop secondary to clot formation or from inflammatory disease and vitreal fibers. These strands may cause tractional retinal detachment when they contract, and often they are present simultaneously making the differentiation between fibrous membranes, clots, and retinal tissue difficult (Treadwell et al. 2015; Zeiss and Dubielzig 2004) (Figure 3.44).

Blood within the vitreous framework typically is absorbed more slowly (Zeiss and Dubielzig 2004). Blood clots into the vitreous may mimic a mass (Gallhoefer et al. 2013). In these cases, color flow Doppler may be useful in their differentiation.

Ocular ultrasound is the preferred imaging modality to detect retinal detachment. However, false positives and false negatives are possible. Its sensitivity and specificity in humans have been reported to be 88 and 87%, respectively (Chu et al. 2017). In veterinary medicine, retinal separation/detachment can be missed up to 30–40% of the cases confirmed at histopathology (Gallhoefer et al. 2013).

The retina normally adheres firmly to the optic disc posteriorly and to the ora ciliaris retinae anteriorly. In exudative retinal detachment, the retinal layers remain attached at these two sites but may be separated from the adjacent choroid by fluid or exudate. A detached retina commonly appears as a discrete, thin echogenic interface with an underlying anechoic space. The echogenicity can vary from mild to moderate. Increased echogenicity might be a sign of fibrosis (gliosis). The detachment may occur focally or along the entire surface between the optic nerve head and the ora ciliaris retinae. Such a complete retinal detachment appears as a V-shaped structure (Figure 3.45).

Vet-ebooks.com

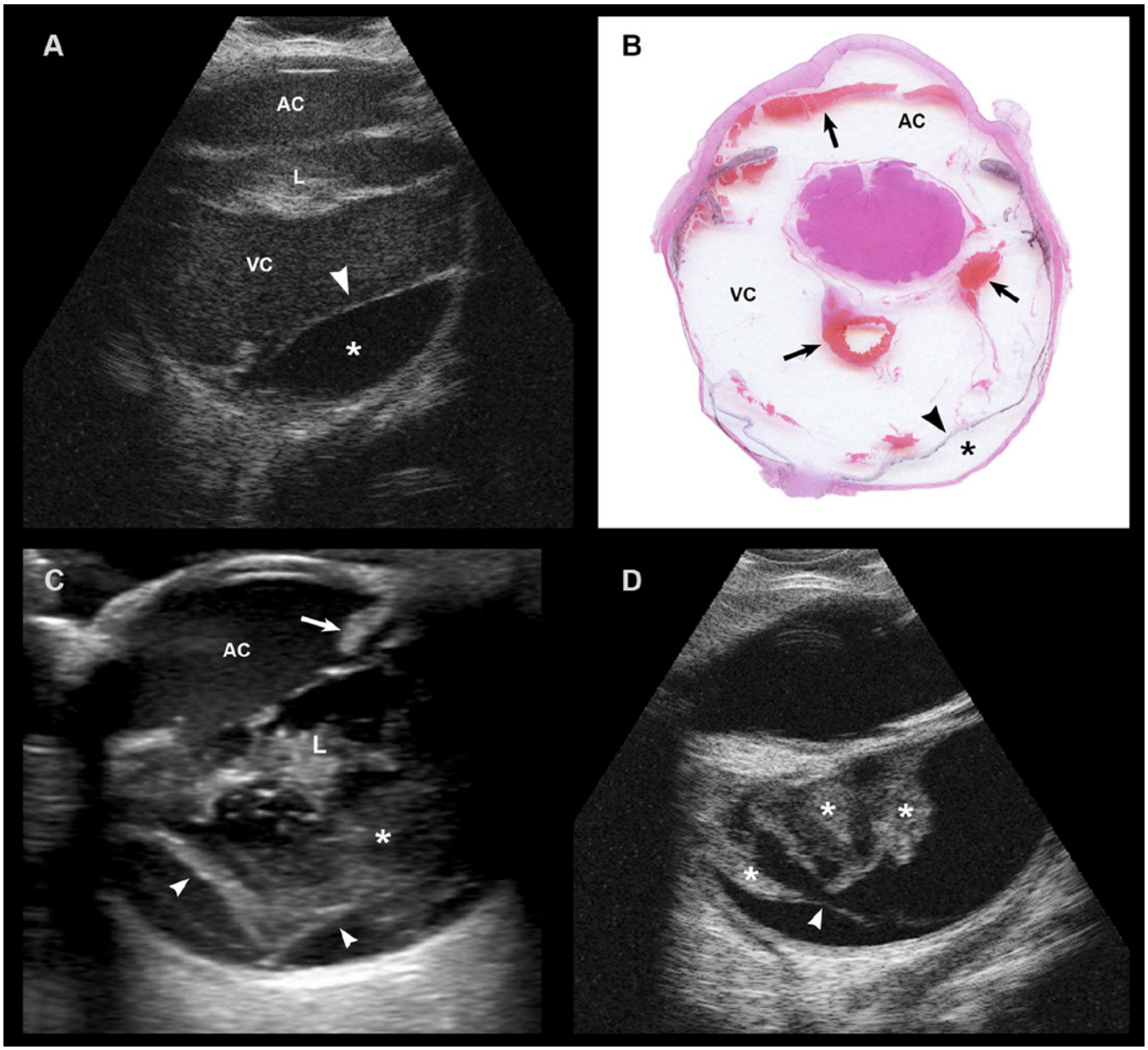


Figure 3.43. **Vitreal hemorrhage. (A, B)** Sonogram and histologic section of a canine globe after severe blunt trauma and hyphema. The sonogram in **(A)** shows hypoechoic homogenous material filling the anterior chamber (AC) and the vitreal cavity (VC). A retinal separation is present (arrowhead) and the subretinal space is anechoic (*). The histologic section in B confirms the sonographic findings. Most of the fresh blood present in the ocular cavities has been lost during specimen preparation. Remnants of a frank hemorrhage are still visible (arrows). **(C)** Severe ocular trauma. The anterior chamber (AC) is filled with hypoechoic material. The iris is directed posteriorly (arrow) and the lens is ruptured. The vitreal cavity contains echoic material consistent with blood (*). The retina is detached (arrowheads). **(D)** Organized vitreal hemorrhage in a cat several weeks after lens removal due to lens luxation. The echoic masses indicated by asterisks are fibrin and blood clots. One of them is adhering to the retina and separates it from the choroid (arrowhead).

A **retinal detachment** is diagnosed when the detached leaflets can be followed to their attachment at the optic papilla, anteriorly to the hypoechoic retrobulbar optic nerve, otherwise possible vitreal membranes may have similar imaging features (Vrablik et al. 2015). If a giant tear occurs at the level of the ora ciliaris retinae, the retinal layers fold to the center of the posterior segment or ventrally because of gravity (Figure 3.46).

Different mechanisms of retinal detachment include a retinal tear with vitreous material migrating into the subretinal space (rhegmatogenous detachment), traction from vitreal strands, and

Vet-ebooks.com

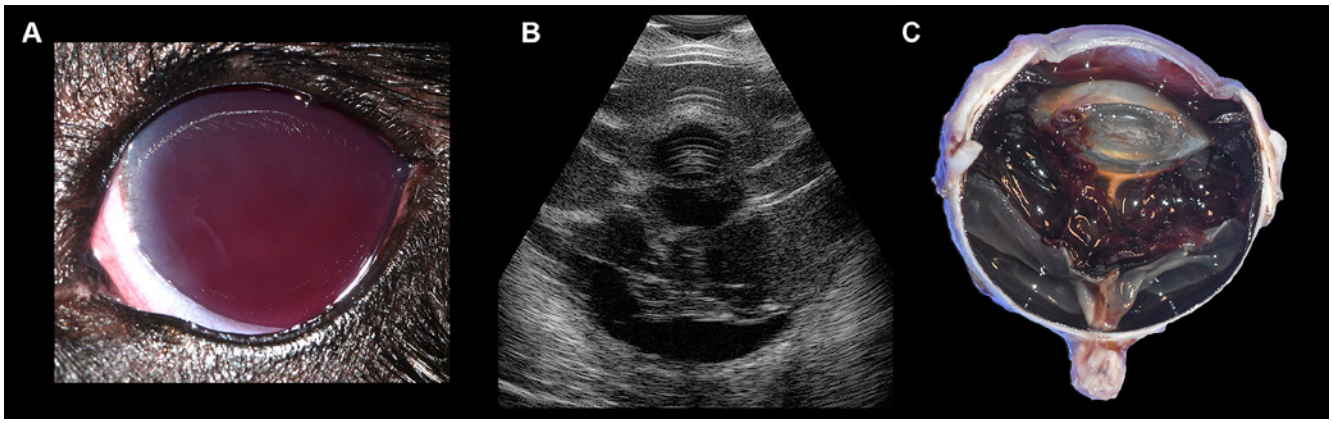


Figure 3.44. **Canine ocular gliovascular syndrome (COGS) in a Labrador.** (for full caption, see facing page)

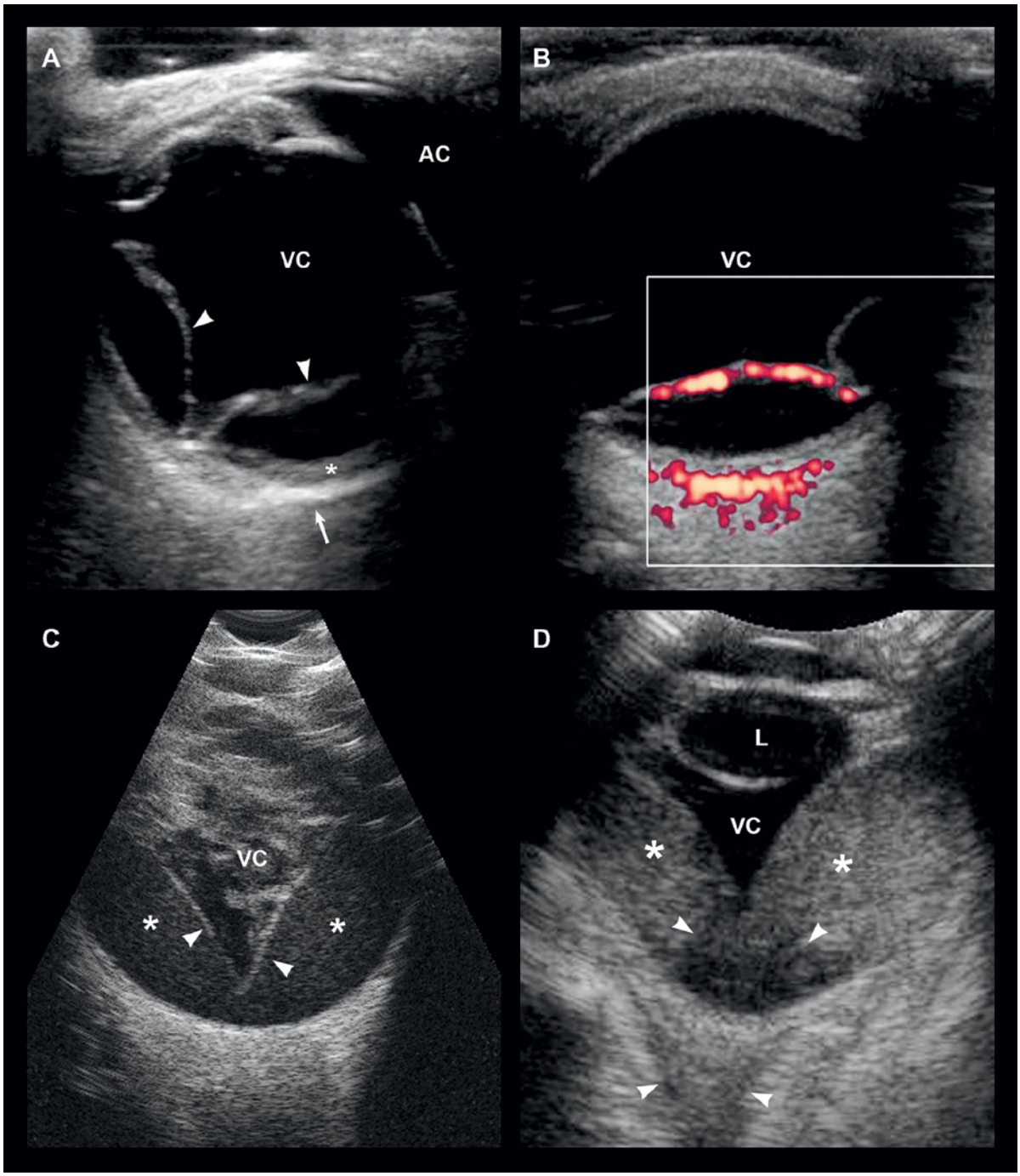


Figure 3.45. **Retinal detachment.** (for full caption, see facing page)

Vet-ebooks.com

Figure 3.44. Canine ocular gliovascular syndrome (COGS) in a Labrador. (A) Hyphema and increased intraocular pressure were the presenting signs. **(B)** Ocular ultrasound showed the posterior segment randomly filled with echoes of different intensities. **(C)** Intraocular hemorrhages and clots were present associated with fibrovascular membranes and retinal detachment.

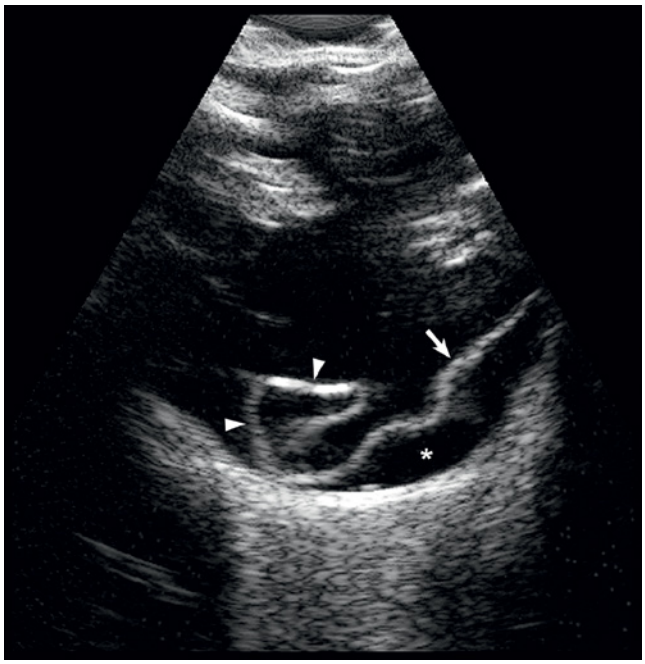


Figure 3.46. Giant retinal tear. Vertical paraxial section. The hyperechoic linear structure indicated by the arrowheads represents a torn dorsal retinal tissue folding ventrally because of gravity. The detachment has occurred peripherally at the level of the ora ciliaris retina. The ventral retina is also separated from the underlying choroid (arrow). The ventral subretinal space is visible (*).

subretinal accumulation of fluid (transudate) or inflammatory exudate/hemorrhage.

Doppler imaging and contrast-enhanced ultrasonography have been used to assess ocular vascular flow in canine eyes (Hong et al. 2018; Lee et al. 2002) and to differentiate retinal detachment from vitreous membrane (Labruyere et al. 2011). Finding a blood flow in a vitreal membrane does not reliably confirm retinal tissue. Indeed, a PHPV or fibrovascular membranes can have blood vessels. Presence of fibrovascular membranes in the canine ocular gliovascular syndrome (COGS) may show similar ultrasonographic images with vascular flow, but is not necessarily associated with retinal tissue (Figure 3.44).

Hypermature cataracts have a higher incidence of retinal detachments because of the common association with vitreal degeneration and fibrosis. Trauma, inflammation, tumors, or systemic hypertension may also cause a detachment.

The choroid is difficult to evaluate. However, when it is affected by severe inflammation and it is edematous or congested, it can be visualized as a hypoechoic layer between the outer sclera and the retina. Retinal detachment is often a result of severe choroiditis (Figure 3.47). A **choroiditis** may cause fluid or an exudate to accumulate between the retina and the choroid. When exudate or hemorrhage results from choroiditis, the retina is separated from the choroid and echogenic material is identified in the subretinal space (Figure 3.45).

Tumors involving the posterior segment are rare but should always be suspected when the clinical examination of the posterior segment is difficult or impossible, and there is clinical presence of intraocular hemorrhage, retinal detachment, variation in the anterior chamber depth, and/or increased intraocular pressure (Figures 3.48, 3.49).

Most common **primary tumors** extending and invading the vitreal cavity include melanocytic neoplasia and ciliary adenoma/adenocarcinomas of the ciliary epithelium, while among metastatic neoplasms hemangiosarcomas are more common (Krieger et al. 2022). Medulloepitheliomas are rare, while posttraumatic fibrosarcomas are common in cats (Dubielzig et al. 2010). Astrocytomas and meningiomas arising from the optic nerve papilla are rare but should be considered when the mass seems to involve the optic nerve area. Lymphomas are the most common multicentric tumors, followed by histiocytic sarcomas (Krieger et al. 2022). Morphological changes in the shape of the globe affecting the posterior segment are also recognizable.

Figure 3.45. Retinal detachment. (A) The retina is detached (arrowheads) and the choroid is thickened (*). The scleral wall is indicated by the arrow. **(B)** Color Doppler used in the same patient shown in A. Intense blood flow is detected in the retina and in the choroid and sclera. **(C)** "Seagull wings" sign (arrowheads) in a dog with retinal detachment and subretinal hemorrhage (*). Echoic material consisting of vitreal hemorrhage is also present in the VC. **(D)** Axial plane. Exudative retinal detachment in a dog affected with blastomycosis. Note the retina has lost some of its echoic signal due to inflammation. The subretinal space is filled with uniform echoic material (*). The less echoic areas in the posterior portion of the globe and in the retrobulbar space (arrowheads) might represent a swollen optic nerve. AC, anterior chamber; L, lens; VC, vitreal cavity.

Vet-ebooks.com

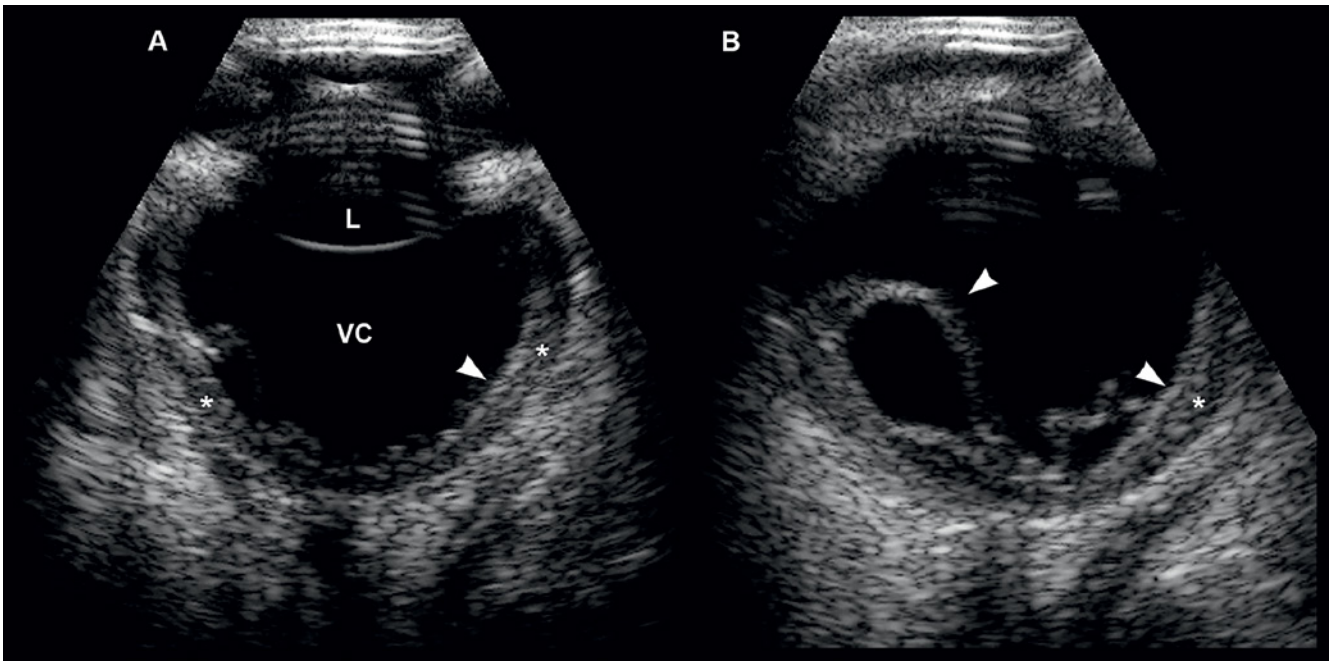


Figure 3.47. Choroiditis and retinal detachment. (A, B) Axial and paraxial sections of a canine eye affected with immune-mediated choroiditis. The thickened edematous choroid (*) is hypoechoic to the retinal layer (arrowheads). Retinal detachment is present in B. L, lens; VC, vitreal cavity.

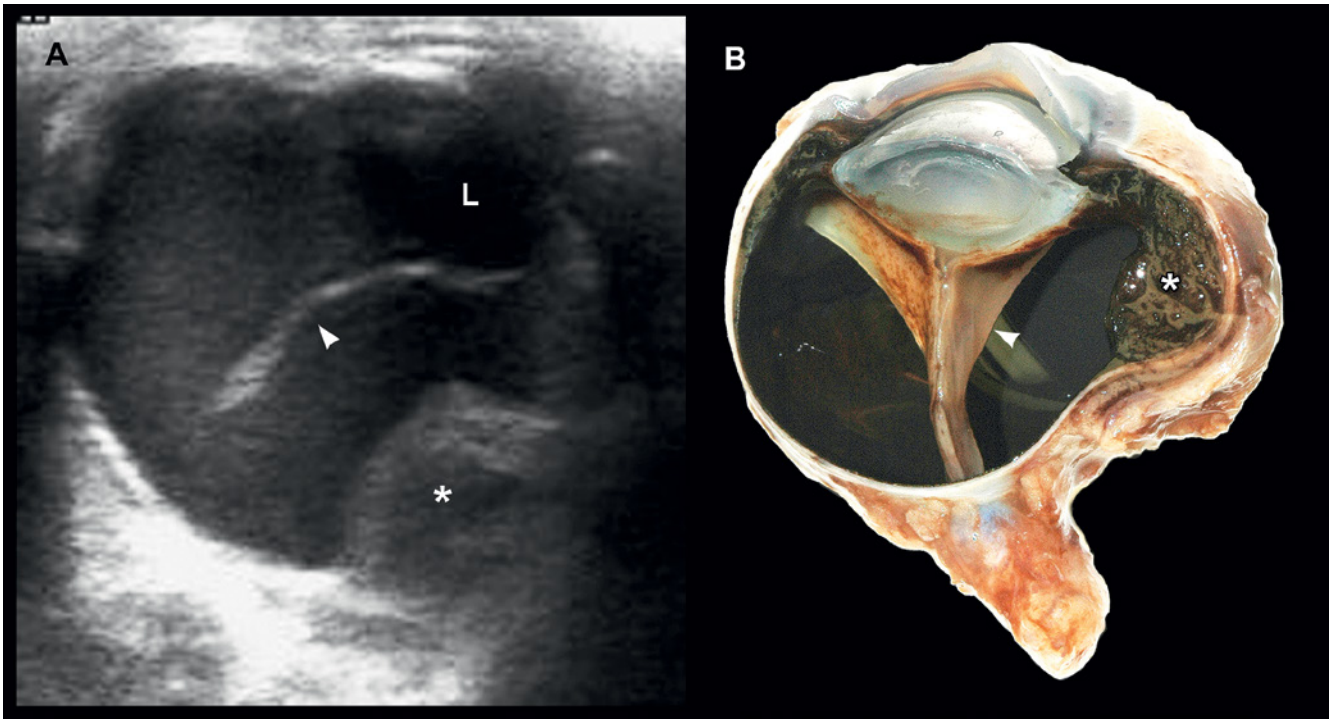


Figure 3.48. Choroidal hemangiosarcoma in a dog. (A) Paraxial horizontal sonogram at presentation. The patient was admitted for acute-onset unilateral blindness in the right eye. Clinical examination revealed "morning glory" retinal detachment in the left eye. The right eye was normal. The sonogram of the left eye shows a mass affecting the lateral wall of the posterior segment (*) and complete retinal detachment (arrowhead). **(B)** Corresponding findings at gross section. L, lens.

Vet-ebooks.com

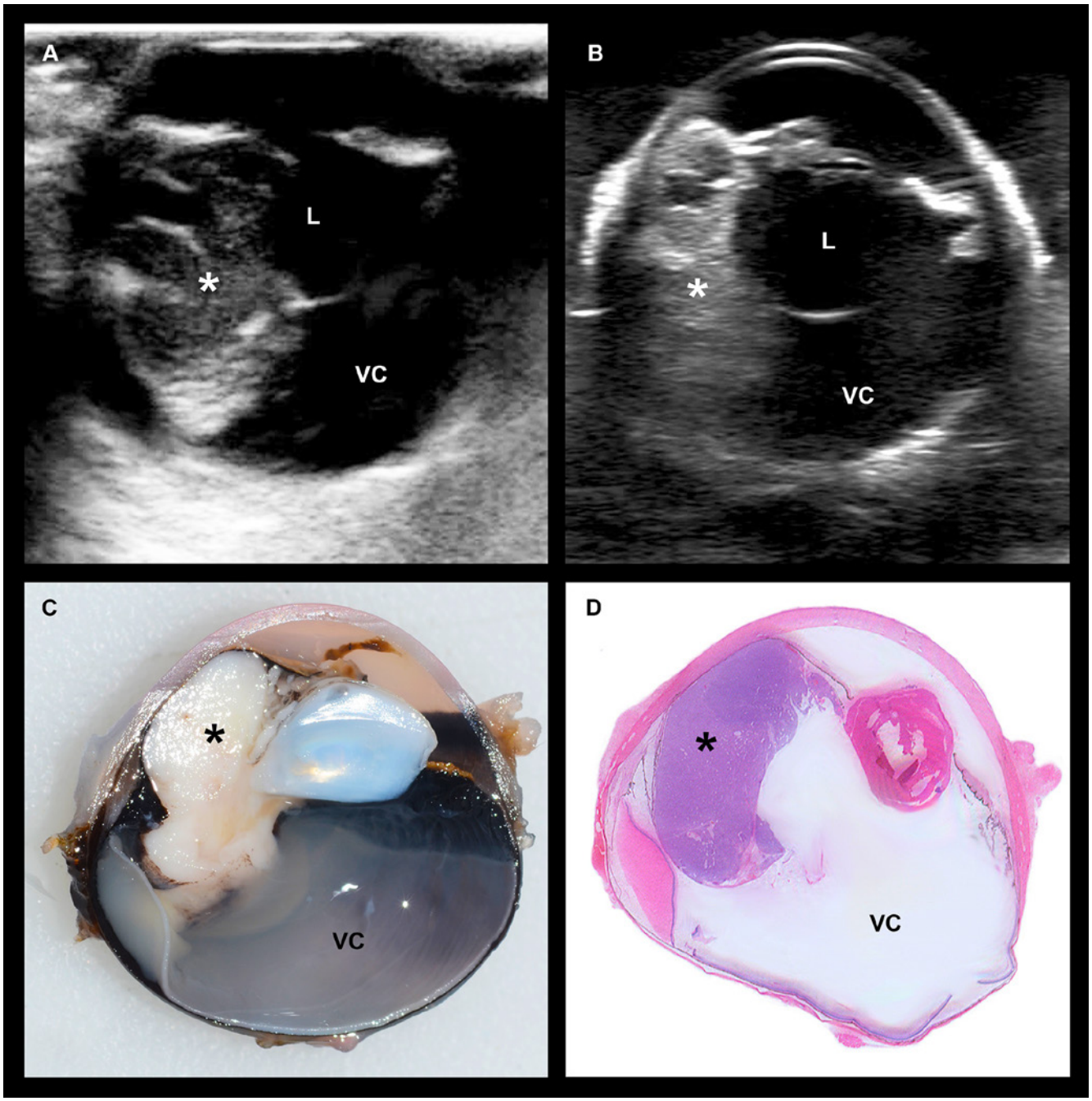


Figure 3.49. **Intraocular tumor invading the posterior segment. (A–D)** Horizontal axial sections of a globe affected with a large ciliary adenoma showing as an echogenic mass on the nasal aspect of the globe (*). The tumor develops from the ciliary body, enwraps the lens (L), invades the posterior chamber, and diffusely extends posteriorly into the vitreal cavity (VC).

Microphthalmos (reduction in eye volume) may be caused by developmental defects or may be acquired (phthisis bulbi) secondary to chronic diseases (uveitis or end-stage glaucoma) or trauma (Figures 3.50, 3.51).

Buphthalmos (an enlarged globe) may instead be associated with large intraocular masses or chronic glaucoma. Pressure from scleral thickening or extraocular diseases has also the capacity to indent or modify the shape of the globe (Figure 3.52).

Intraocular and Retrobulbar Foreign Bodies

The appearance of intraocular foreign bodies varies depending on their nature, size, shape, and location. Wooden material is commonly associated with shadowing. A typical comet-tail artifact is instead seen distal to a metallic foreign body such as a pellet gun (Figures 3.53, 3.54).

Vet-ebooks.com

Figure 3.51. **Traumatic globe rupture in a cat. (A)** Paraxial meridional sonogram. The vitreal cavity (VC) appears severely decreased when compared with the anterior chamber (AC) and lens (L). Echogenic structures of different intensity are visible in the posterior segment and were interpreted as vitreal (*) and choroidal hemorrhages (#). A lens dense area in the posterior wall was identified and suspected to correspond to a globe rupture (R). **(B)** Sonogram performed on the globe after enucleation. A linear hyperechoic interface (arrowhead) confirmed retinal detachment and subretinal hemorrhage (#). Globe rupture along the posterior wall was suspected (R). **(C, D)** Gross and histologic sections confirming vitreal hemorrhage (*), retinal separation (arrowhead), subretinal hemorrhage (#), and posterior globe rupture. The scleral rupture had occurred several weeks before admission of the cat and fibrous tissue is bridging the defect.

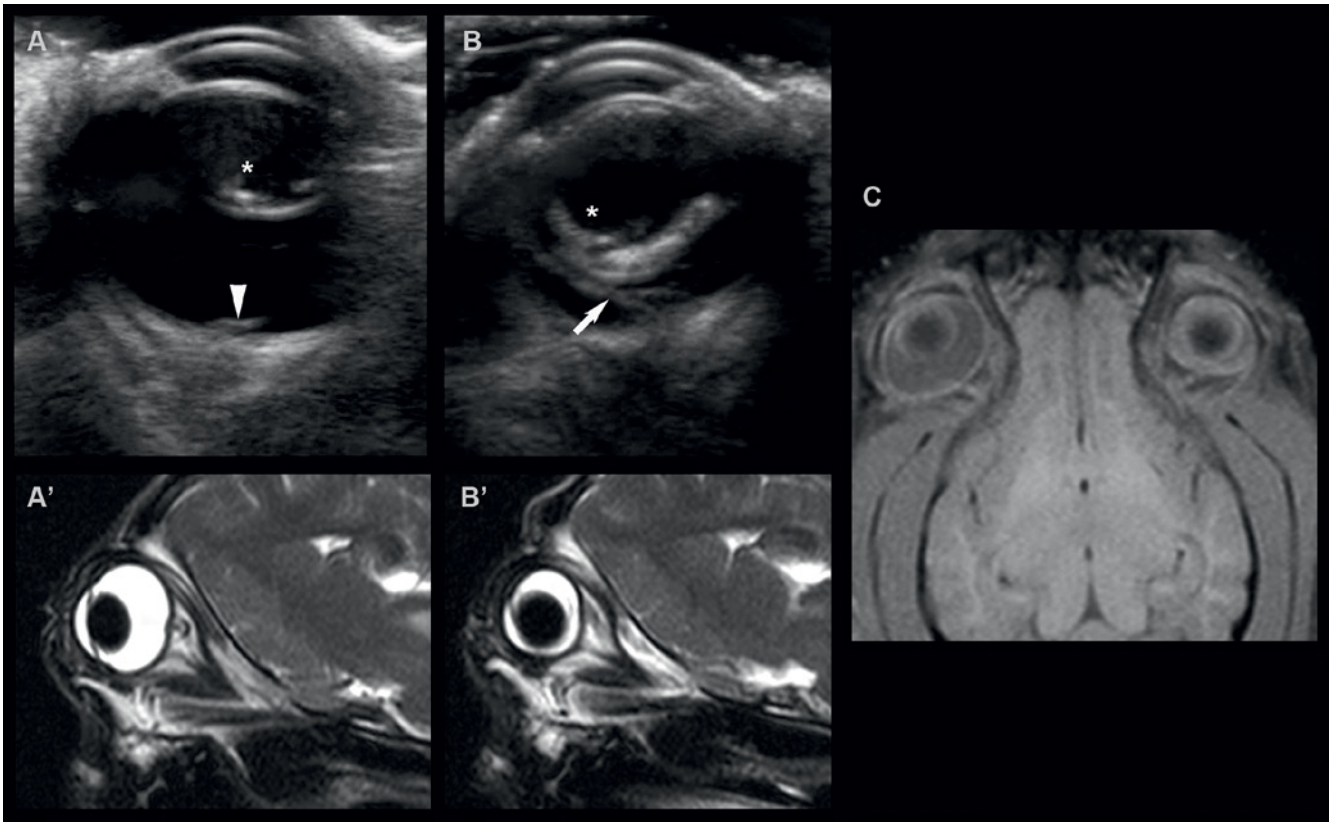


Figure 3.50. **Congenital microphthalmia in a 1-year-old miniature Poodle presented for acute blindness.** Sonographic (**A**) and sagittal T2 magnetic resonance image (MRI) (**A′**) of the right eye. Notice the immature cataract evidenced by echoes within the lens (*). A small bulge is noted at the level of the optic disc (arrowhead), which may represent a swollen optic nerve. Sonographic (**B**) and T2 MRI image (**B′**) of the left eye. This eye is smaller than the right. Echoes are also present in the lens (*). In addition, a curvilinear structure (arrow) is seen obliquely crossing the vitreous body, representing the detached retina. **(C)** Dorsal T1 postcontrast image of both eyes, illustrating the size asymmetry of the eyes.

Porcupine quills often appear as double paralleling hyperechoic lines, and few of them may be present (Figure 3.54). When present, a hypoechoic tract or cavity around the foreign body may assist in locating it.

Plants parts, like grass awns are difficult to identify with ultrasound (Figure 3.55). They often appear as linear or fusiform hyperechoic interfaces casting an acoustic shadow. With time, purulent material might collect and appear poorly echogenic. Fistulous tracts are also possible and suggestive of foreign body migration.

Specular reflections from the bones forming the orbit should not be mistaken for foreign bodies. Retrobulbar

Figure 3.52. **Diffuse scleritis in a dog. (A)** Paraxial section showing a severely thickened scleral wall (S). Arrowheads indicate the outer wall of the globe. A retinal detachment is present as hyperechoic linear images in the posterior cavity of the globe (arrows). **(B)** Axial section. L, lens. Power angio-Doppler mode showed moderate vascular flow within severely inflamed scleral tissue and partially in the retina. **(C)** Histopathologic section of the same globe after enucleation. The scleral wall (S) is thickened and the posterior vitreal cavity deformed. Retinal detachment is present (arrows).

Vet-ebooks.com

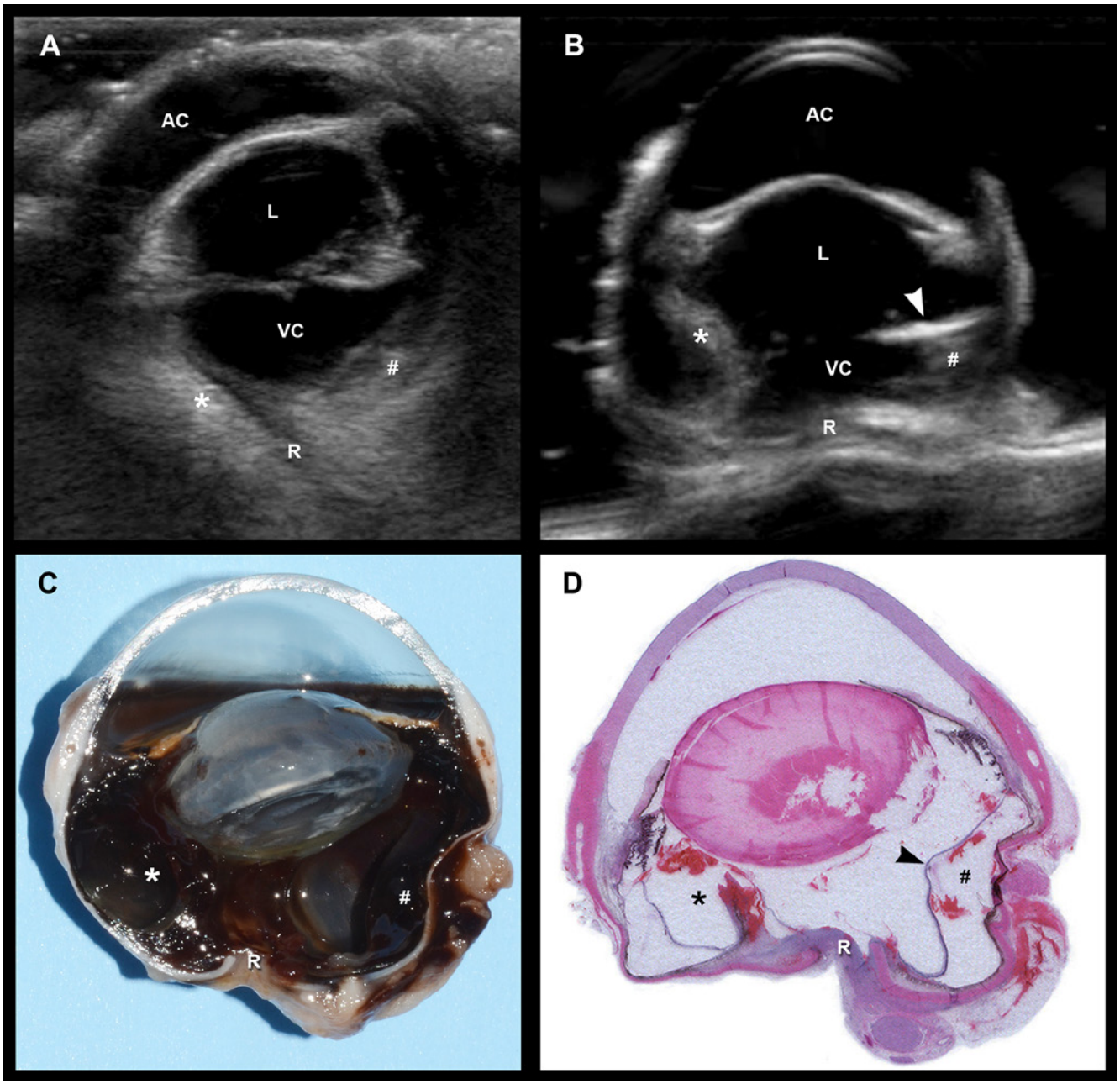


Figure 3.51. **Traumatic globe rupture in a cat.** (for full caption, see facing page)

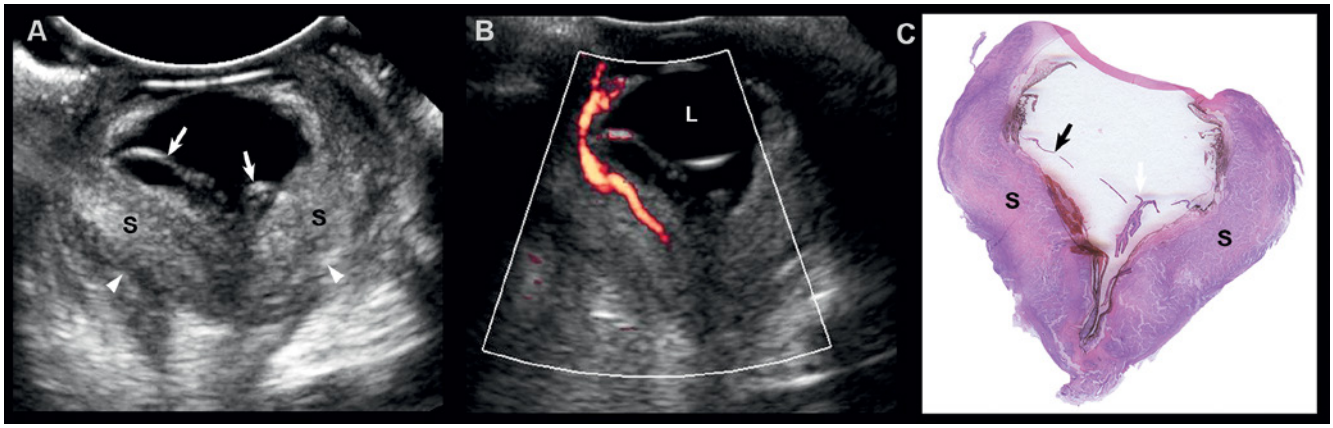


Figure 3.52. **Diffuse scleritis in a dog.** (for full caption, see facing page)

Vet-ebooks.com

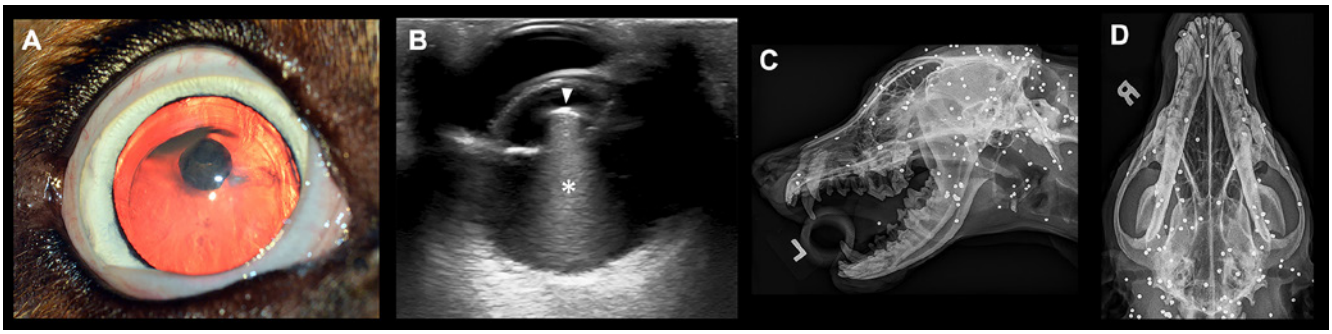


Figure 3.53. **Gun pellet in lens. (A)** Clinical presentation of the right eye of a dog rescued 3 months before ocular examination. The clinical picture shows an immature cataract and a round dark body within the lens. **(B)** Ocular ultrasound showing a metallic foreign body located into the posterior cortex (arrowhead) and causing a comet-tail artifact (*). A pellet gun bullet was surgically extracted. **(C, D)** Radiographs of the head of the same patient showing numerous radiopaque pellets. AC, anterior chamber; L, lens. Courtesy of Dr. Federica Maggio, TuftsVETS, Walpole, MA, USA.

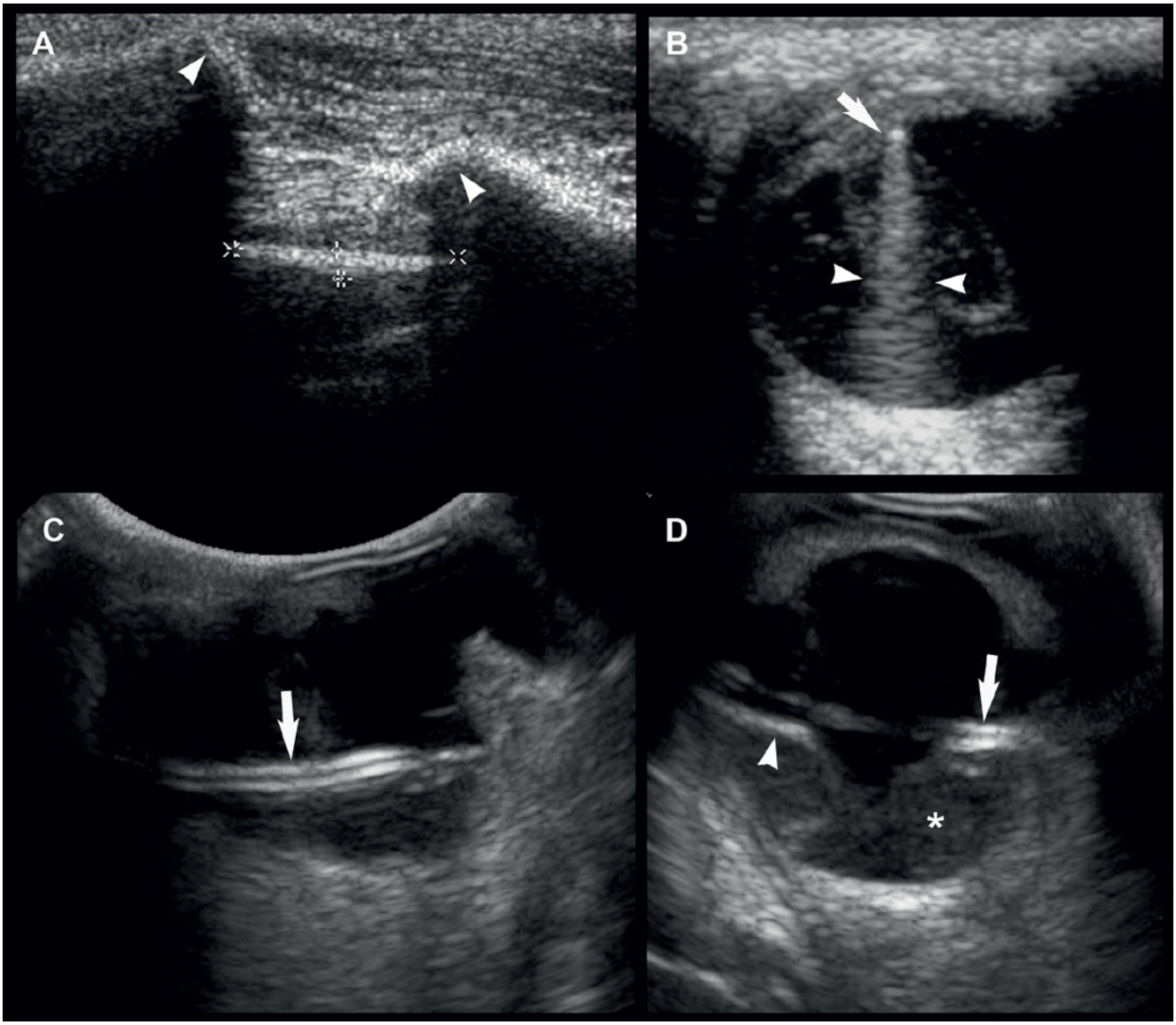


Figure 3.54. **Foreign bodies. (A) Wooden stick**. A hyperechoic line associated with shadowing is present between the margins of the zygomatic bone (arrowheads). The globe is to the left of the image. The wooden foreign body is between the cursors. **(B) Pellet-gun metallic foreign body (BBs)** (arrow) with associated comet-tail artifact (arrowheads). **(C, D) Porcupine quill** in a dog. Two discrete hyperechoic parallel lines (arrow) representing a porcupine quill are crossing the vitreous body and causing the retinal detachment (arrowhead) and subretinal hemorrhage/exudate (*).

Vet-ebooks.com

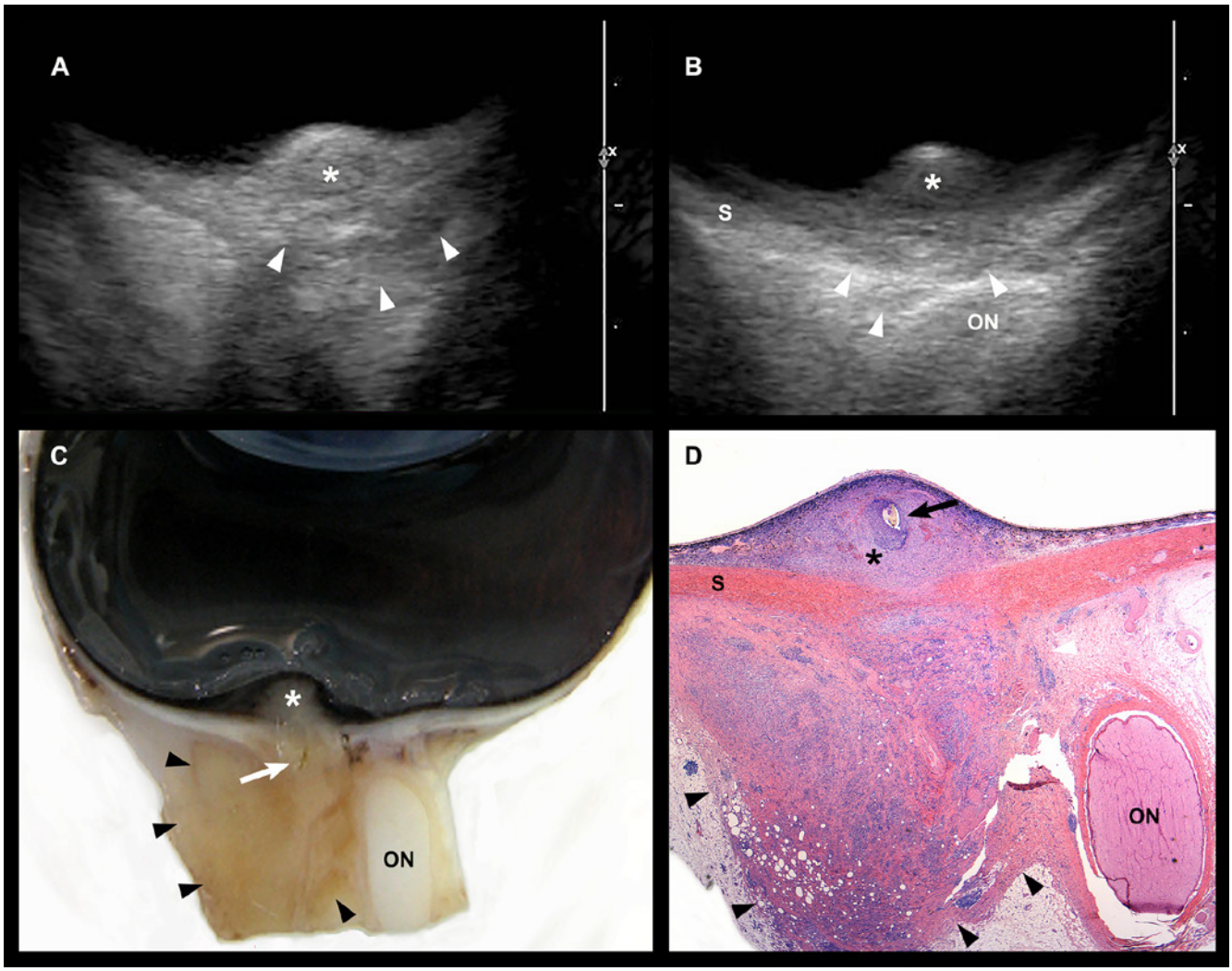


Figure 3.55. **Posterior wall foreign body (vegetal). (A, B)** Two sagittal images with a linear 17 MHz probe, with focal distance (*x* on the right bar) set on the posterior wall of the globe. In the sonograms, the retinal and choroidal layers appear distinct (arrows) and separated from the more echoic sclera (S). A hypoechoic nodular lesion (*) expands the posterior globe wall in proximity of the optic nerve (ON). The area affected with inflammation within the posterior pole is indicated by arrowheads. **(C, D)** Gross pathologic (C) and histologic section (D) images of the same area after globe enucleation. The asterisk and the arrowheads correspond to the ultrasonographic images, while the arrow indicates a small foreign body. The inhomogeneous hypoechoic area on A and B was caused by a pyogranulomatous inflammatory reaction to a small plant material (arrow). Note the ultrasonographic similarities with the optic nerve meningioma illustrated in Figure 3.62.

foreign bodies are difficult to diagnose at ultrasonography. A combination of different modalities is often required; computed tomography (CT) and magnetic resonance imaging (MRI) offer useful information for their detection (Figure 3.56).

Orbital Disease

The bone surrounding the ocular cone limits the sonographic evaluation of orbital lesions. CT or MRI provides better topographic information for orbital diseases, but a combination of modalities is often necessary (Penninck et al. 2001).

Sonographic abnormalities reported with orbital neoplasia include blunting of the posterior aspect of the globe; discrete, hypoechoic mass in the retrobulbar space; or discrete, highly echogenic mass/interface deforming the posterior aspect of the globe (Attali-Soussay et al. 2001; Morgan 1989). Retrobulbar malignancies present as variable echogenicity and size masses, with various degrees of deformity of the posterior aspect of the globe (Figure 3.57).

Vet-ebooks.com

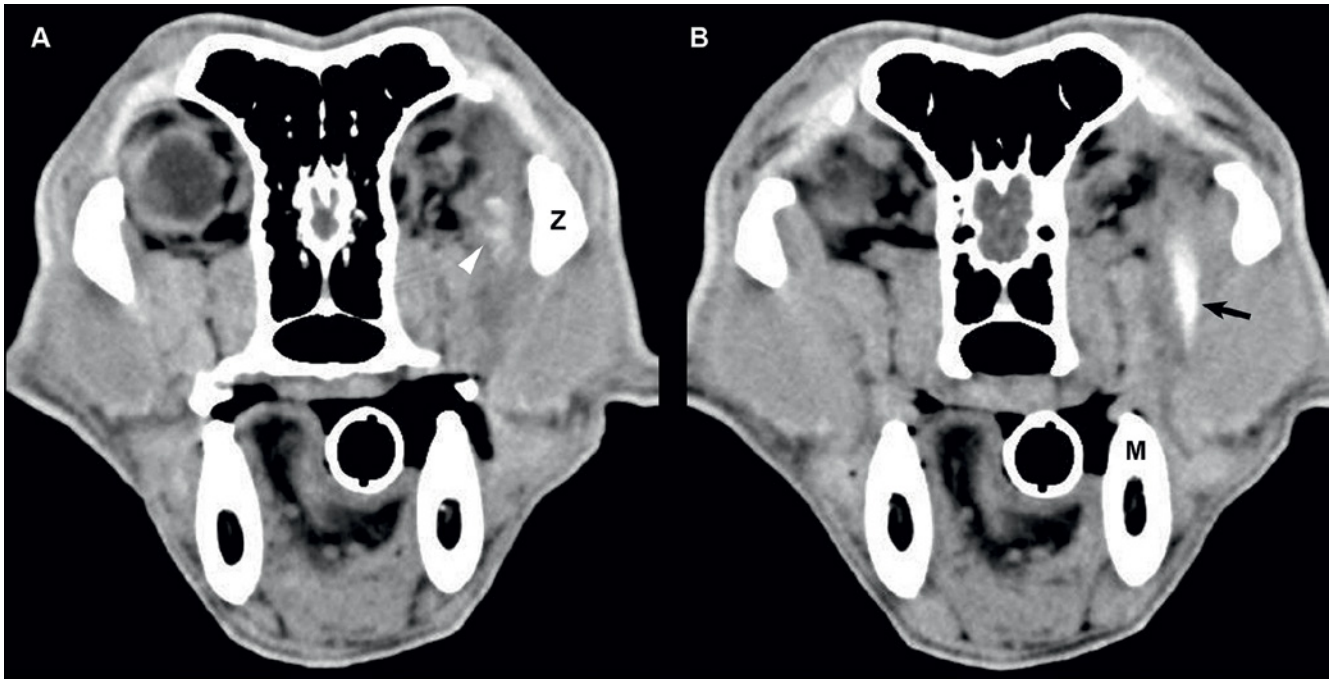


Figure 3.56. **Computed tomography (CT) of retrobulbar wooden foreign body in a 7-year-old Labrador with long-standing jaw pain.** (for full caption, see facing page)

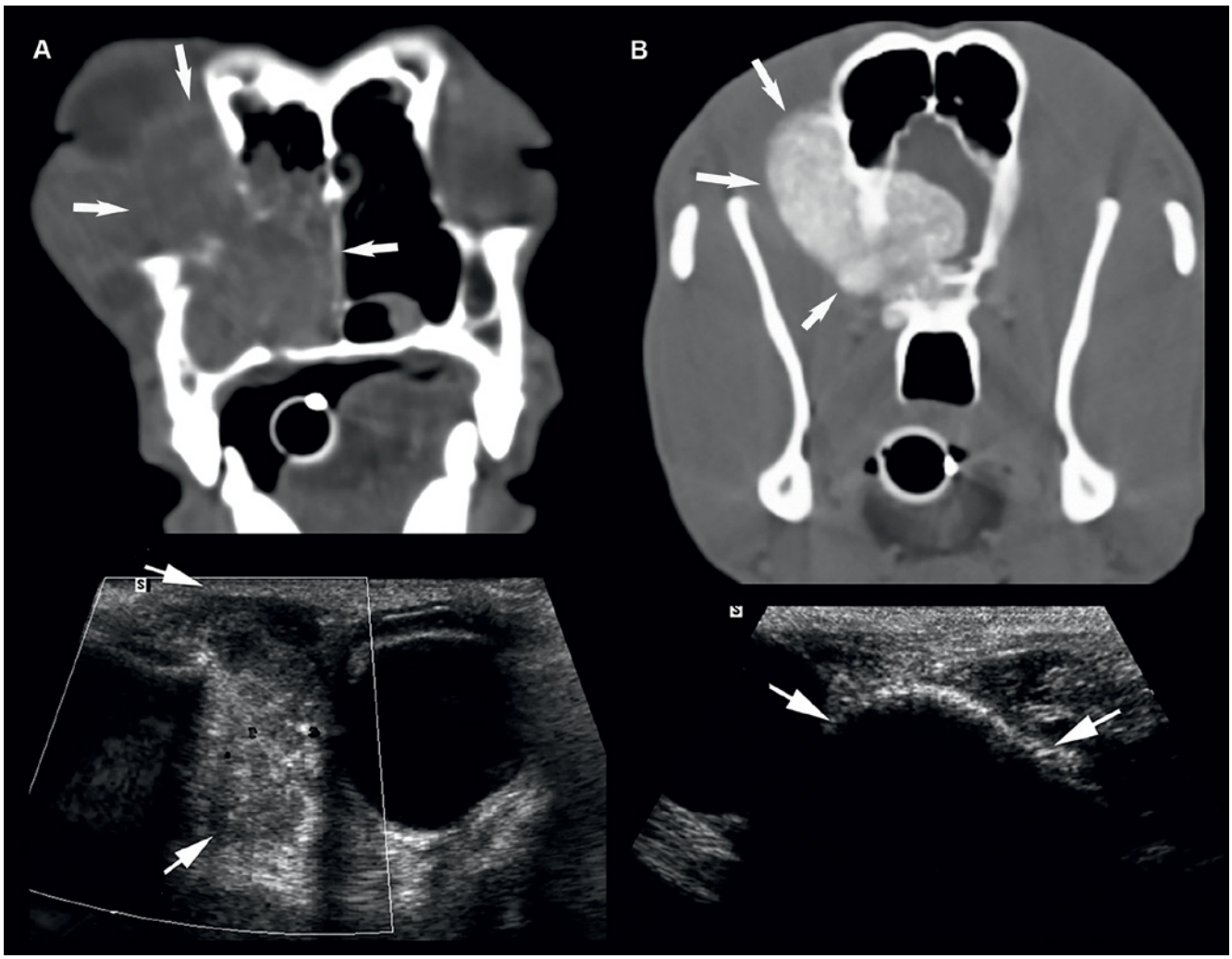


Figure 3.57. **Periocular tumors and secondary displacement of the globe.** (for full caption, see facing page)

Vet-ebooks.com

Figure 3.56 **Computed tomography (CT) of retrobulbar wooden foreign body in a 7-year-old Labrador with long-standing jaw pain. (A)** The tip of a hyperdense structure (arrowhead) is noted in the retrobulbar space (enucleation was performed a few months earlier), medial to the zygomatic arch (Z). **(B)** This structure is about 4 cm long (arrow) and lies medial to the mandibular ramus (M). CT is useful in detecting deep-seated foreign bodies depending on their nature.

Tumors involving the tissues, organs, and sinuses around the eye include nasal tumors, primary benign or malignant bone tumors, oral melanomas, squamous cell carcinomas, and hemangiosarcomas. Although, as mentioned above, ultrasound is not a specific or sensitive modality for bone evaluation, in case of masses eroding or compressing adjacent osseous structures, an irregular appearance of the affected bone tissue can be observed (Figure 3.55).

The appearance of inflammatory changes varies depending on the orbital tissues affected. Sonographic findings vary from a diffuse hyperechoic to a discrete hypoechoic region (abscess) with possible blunting of the posterior aspect of the globe (Figure 3.58).

Acute retrobulbar cellulitis can result in hypoechoic streaks of fluid dissecting the orbital tissues without a discrete hypoechoic lesion (Lewis et al. 2014). Retrobulbar cellulitis may or may not deform the globe (Figure 3.59). Retrobulbar abscesses appear as hypoechoic cavitary lesions and ultrasound-guided aspiration may be useful in confirming the diagnosis.

Additional periorbital tissues that may affect the globe include the lacrimal gland and the zygomatic gland (Giudice et al. 2005). Either inflammation or neoplasia may affect the size, shape, and echogenicity of the different periorbital glands. Enlargement or a mass from the affected glands can displace the globe (Figure 3.60).

The optic nerve is a curvilinear, hypoechoic structure coursing from the posterior surface of the globe into the orbital cone. Abnormalities of the nerve include **neuritis** (Figure 3.61) with diffuse enlargement of the optic nerve and optic papilla, or neoplasia with either focal or diffuse enlargement (Figure 3.62). Tumors of

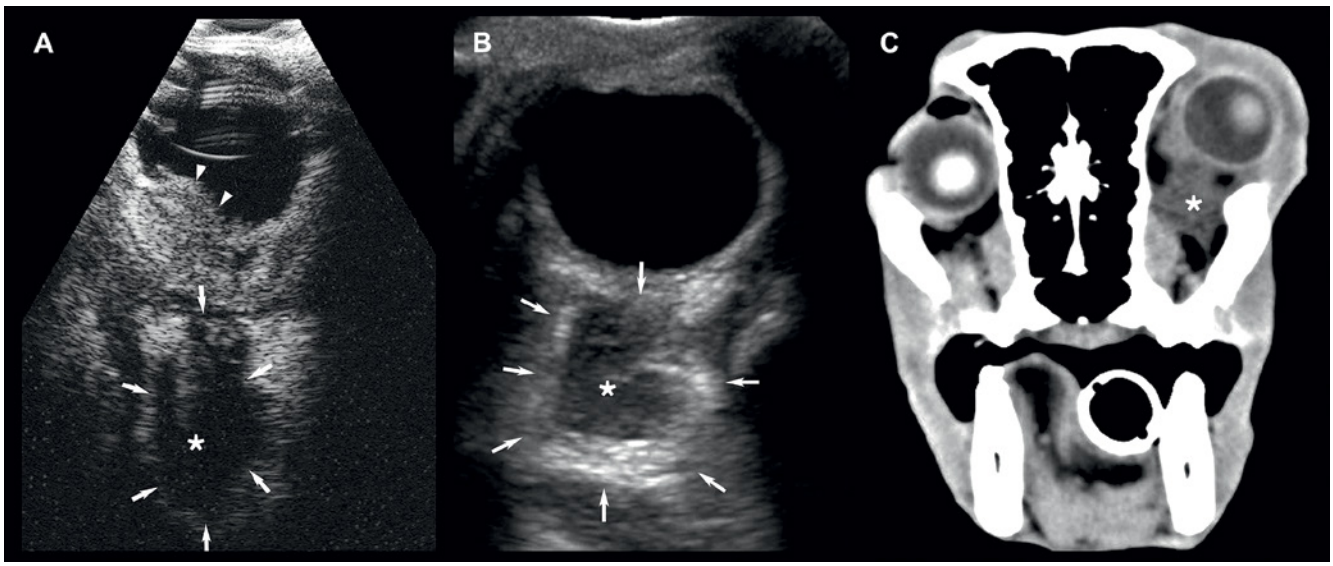


Figure 3.58. **Orbital abscesses in two dogs. (A)** In this dog, an irregular poorly echogenic cavitary lesion (arrows and asterisk) is noted in the orbital space. Adjacent to the lesion, the posterior ocular wall is thickened and creates an abnormal bulge (arrowheads) into the posterior vitreous body. **(B)** Sonogram of a 2-year-old mix dog presented for right-sided exophthalmos. Sonogram of the retrobulbar region showed an irregularly shaped hypoechoic cavity (asterisk) measuring about 1.4 cm by 1.2 cm, corresponding to the inhomogeneously hypoattenuating lesion displacing the eye dorsolaterally, as seen in **(C)** on this transverse CT image of the head (soft tissue window).

Figure 3.57. **Periocular tumors and secondary displacement of the globe.** The corresponding computed tomographic image is displayed at the top of each case. **(A) Nasal adenocarcinoma** with extensive lysis of the bony orbit and extension into the periorbital tissues. The globe is displaced laterally and dorsally (arrows) in this oblique horizontal. **(B) Osteosarcoma** involving the skull, with secondary ocular involvement. Note the hyperechoic and shadowing mass (arrows) displacing the globe dorsally.

Vet-ebooks.com

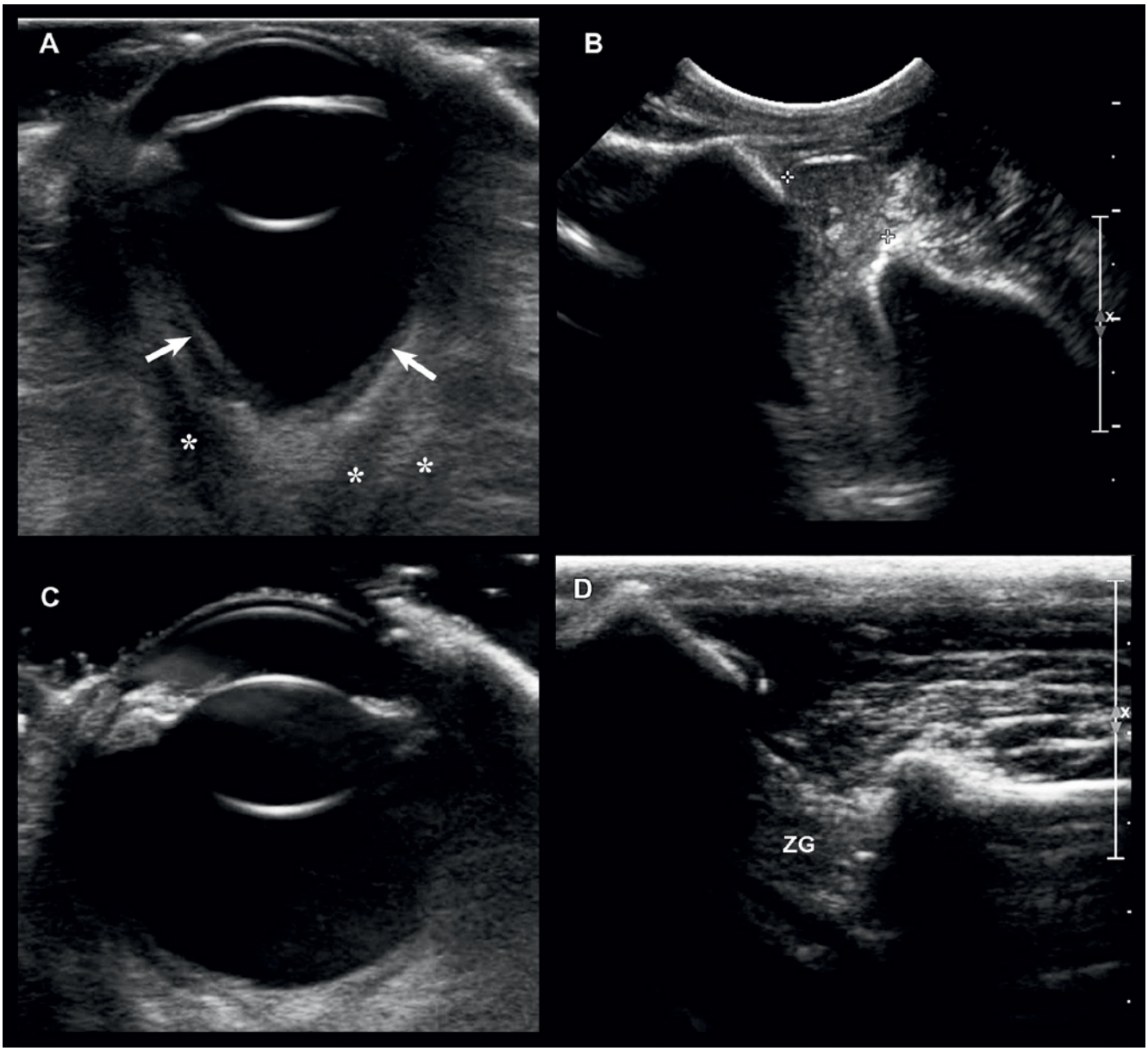


Figure 3.59. **Orbital cellulitis in a Jack Russell Terrier. (A)** The globe has a conical shape (arrows) secondary to compression from the inflammation affecting the surrounding orbital tissues. There are hypoechoic streaks along the extraocular muscle bundles likely representing inflammation (*). The immediate retrobulbar fat appears mildly hyperechoic, likely representing steatitis. **(B)** The zygomatic gland (between cursors) is thickened, possibly as an extension of the inflammation. **(C)** A few days after treatment with a combination of oral antibiotics, the globe shape returned to its normal shape. **(D)** The zygomatic gland (Z) has a normal size.

the optic nerve include meningioma, neurofibroma, gliomas, and lymphoma (Cho 2021).

The group of extraocular muscles includes the four rectus muscles (dorsal, medial, ventral, and lateral), the retractor bulbi muscle, and the dorsal and ventral oblique muscles. Normally, the muscles attach in the equatorial zone of the globe or more posteriorly (retractor bulbi) and form a cone whose tendinous annulus of Zinn is located at the posterior apex of the orbital bony wall. The muscles run around the optic nerve and present as hypoechoic, being surrounded by hyperechoic fat. Extraocular muscle **myositis** is an immune-mediated condition in which ultrasonography may be helpful in diagnosis and results in finding enlarged and hypoechoic muscles (Allgoewer et al. 2000). Young Golden Retrievers seem to be predisposed (Carpenter et al.1989) (Figure 3.63).

Vet-ebooks.com

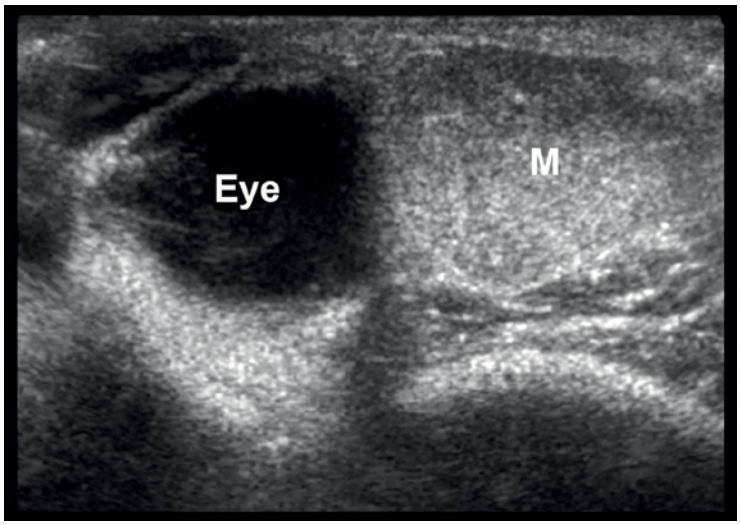


Figure 3.60. **Lacrimal gland adenoma.** A homogeneous echogenic mass (M) is lateral to and displacing the globe in this horizontal section.

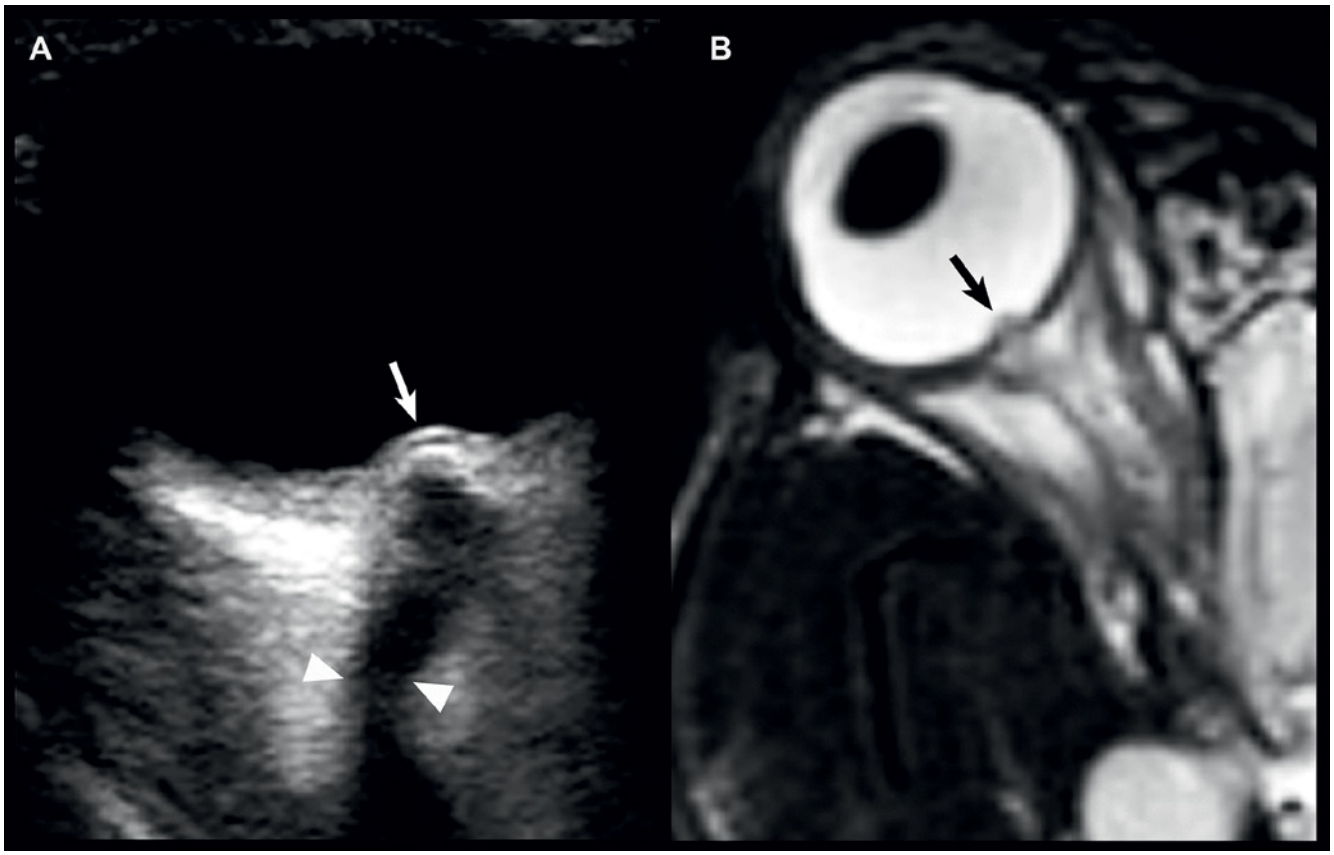


Figure 3.61. **Optic neuritis.** An indentation (arrows) into the globe at the optic disc is seen in both the ultrasound **(A)** and the magnetic resonance **(B)** images. The optic nerve, appearing as a less echoic linear area extending posteriorly to the globe (arrowheads), is thickened.

Vet-ebooks.com

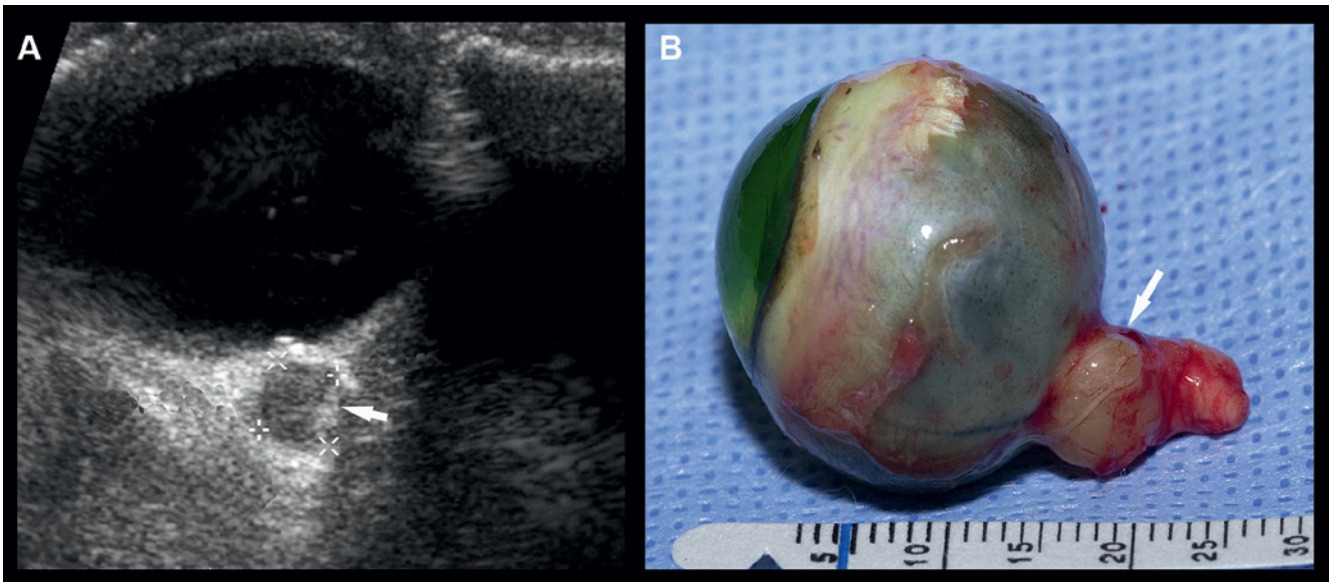


Figure 3.62. **Optic nerve meningioma. (A)** Sonogram showing a poorly echogenic mass/thickening of the optic nerve (arrow, and between cursors). **(B)** Enucleated globe corresponding to the sonographic image in A. The mass involves the optic nerve (arrow).

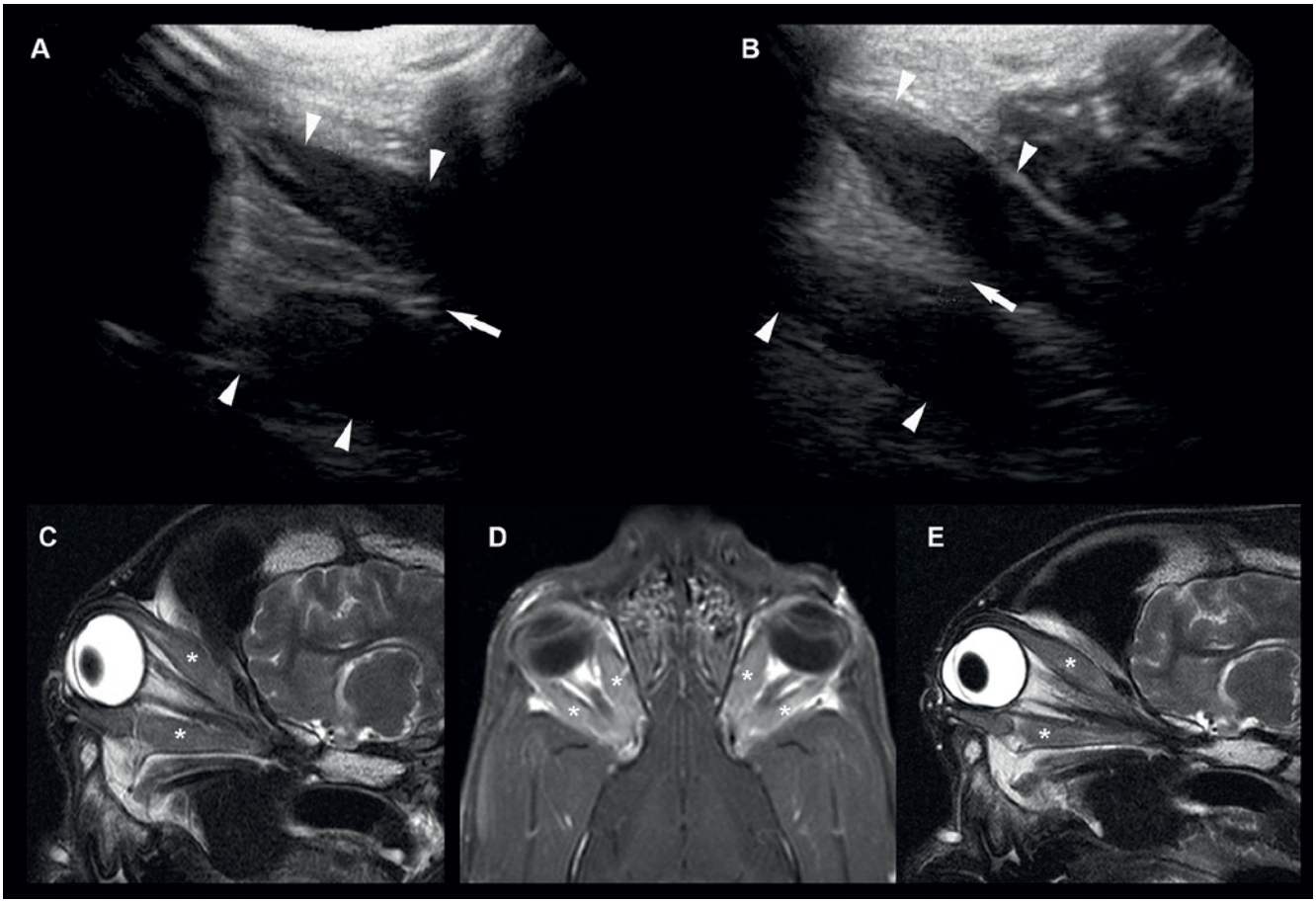


Figure 3.63. **Polymyositis of extraocular muscles associated with bilateral exophthalmia.** Longitudinal sonograms through the orbital fossa of the right **(A)** and left **(B)** retrobulbar region of a 2-year-old mixed-breed dog. Thickened extraocular muscles (arrowheads) are seen around the fat (arrow) encircling the optic nerve. **(C–E)** T2 sagittal magnetic resonance (MR) image of the right orbital region, outlining the right **(C)** and the left **(E)** thickened extraocular muscles (*). In **(D)**, the dorsal T1-weighted MR image shows the symmetrical bilateral myositis, considered likely immune-mediated in this 9-month-old Labrador.

Vet-ebooks.com

Interventional Procedures

Ultrasound-guided fine-needle aspiration and/or core biopsies of lesions in the periorbital or retro-orbital region can safely be performed. This technique enables visualization of the lesion and assists the safe needle placement into the lesion; this can be done with assistance from a guide attached to the probe or by using a freehand technique. Aspiration or biopsy in the retro- or peri-orbital region with ultrasound guidance is helpful in avoiding structures such as the optic nerve, the globe, and main vessels. Ultrasonographic assistance is also helpful in placing the needle within the mass or infiltrate to sample for cytology or to drain an abscess cavity (Figure 3.64).

Additionally, ultrasound can be useful in assisting the surgeon in locating retrobulbar foreign objects and minimizing regional trauma to the globe and surrounding tissues (Figure 3.65).



Visit our website at **www.SmallAnimalUltrasonography.com** for complementary video clips with annotations and text on:

- Normal eye anatomy and scanning
- Asteroid hyalosis
- Cataracts
- Retinal detachment
- Lens luxation
- Lens extrusion
- Intraocular neoplasia
- Retrobulbar foreign body

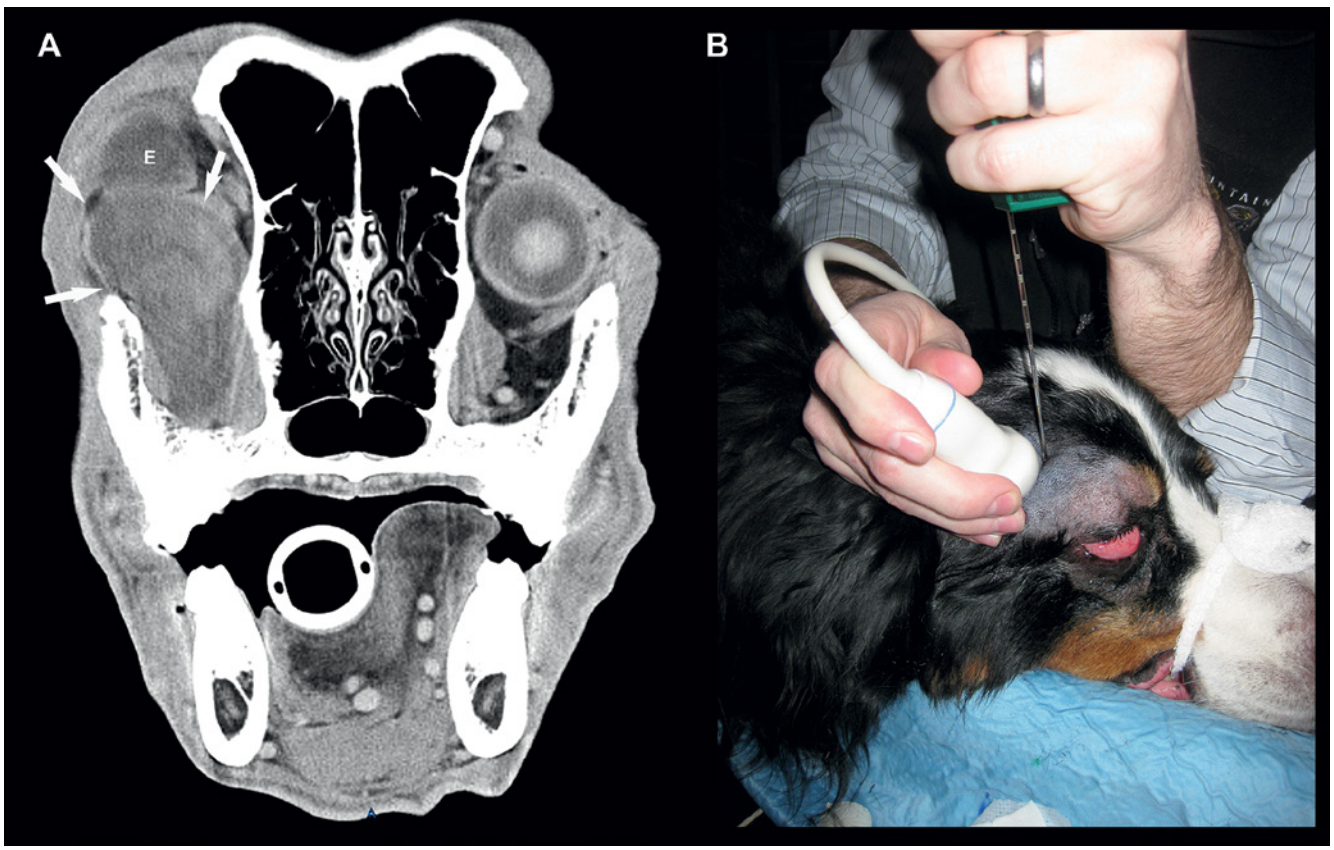


Figure 3.64. **Ultrasound-guided freehand biopsy of a retro-orbital mass. (A)** Computed tomography (CT) image of the large and poorly enhancing retrobulbar mass (arrows). The eye (E) is markedly displaced dorsally. **(B)** The 18-gauge core needle placed in an automated biopsy gun is engaged into the retrobulbar lesion that was diagnosed as an **orbital schwannoma** on histopathological evaluation.

Vet-ebooks.com

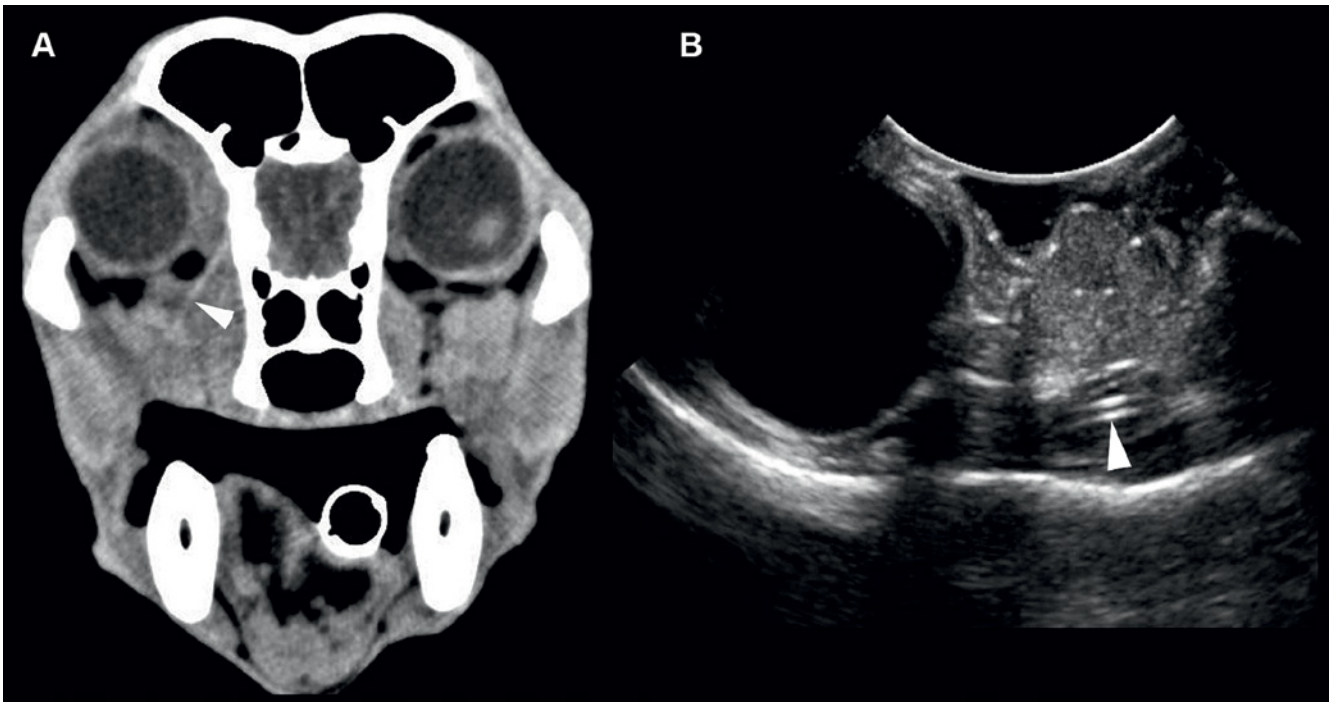


Figure 3.65. Intraoperative assistance for quill removal in a 10-year-old Jack Russell Terrier with prior porcupine quilling. (A) On computed tomography (CT), two quills (only one is displayed in this image-arrowhead) were identified in the retrobulbar space. **(B)** Careful intraoperative ultrasound evaluation allowed the quills to be identified with minimal trauma and the eye to be saved.

References

Allgoewer I, Blair M, Basher T, Davidson M, et al. (2000) Extraocular muscle myositis and restrictive strabismus in 10 dogs. Vet Ophthalmol 3:21–26.

Attali-Soussay K, Jegou J, Clerc B (2001) Retrobulbar tumors in dogs and cats: 25 cases. Vet Ophthalmol 4:19–27.

Aubin ML, Powell CC, Gionfriddo JR, Fails AD (2003) Ultrasound biomicroscopy of the feline anterior segment. Vet Ophthalmol 6:15–17.

Bayon A, Tovar MC, Fernandez del Palacio MJ, et al. (2001) Ocular complications of persistent hyperplastic primary vitreous in three dogs. Vet Ophthalmol 4:35–40.

Bentley E, Miller PE, Diehl KA (2003) Use of high-resolution ultrasound as a diagnostic tool in veterinary ophthalmology. J Am Vet Med Assoc 223:1617–1622.

Bentley E, Pizzirani S, Waller K (2021) Ophthalmic examination and diagnostics. Part 3: diagnostic ophthalmic ultrasound. In Gelatt K, ed. Vet Ophthalmol, 6th edition. Wiley: Hoboken, NJ, pp. 733–756.

Boroffka SA, Verbruggen AM, Boevé MH, Stades FC (1998) Ultrasonographic diagnosis of persistent hyperplastic tunica vasculosa lentis/persistent hyperplastic primary vitreous in two dogs. Vet Radiol Ultrasound 39:440–4.

Boroffka SA, Voorhour G, Verbruggen AM, Teske E (2006) Intraobserver and interobserver repeatability of ocular biometric measurements obtained by means of B-mode ultrasonography in dogs. Am J Vet Res 67:1743–1749.

Carpenter JL, Schmidt GM, Moore FM, Albert DM, et al. (1989) Canine bilateral extraocular polymyositis. Vet Pathol 26:510–512.

Cho J (2021) Ocular ultrasound abnormalities and optic nerve sheath diameter in dogs and cats. Vet Clin Small Anim 51 1295–1314.

Chu HC, Chan MY, Jeffrey Chau CW, Wong CP, et al. (2017) The use of ocular ultrasound for the diagnosis of retinal detachment in a local accident and emergency department. Hong Kong J Emerg Med 24(6):263–267.

Corcoran KA, Koch SA. (1993) Uveal cysts in dogs: 28 cases (1989–1991). J Am Vet Med Assoc 15:545–546.

Cottrill N, Banks WJ, Pechman RD (1989) Ultrasonographic and biometric evaluation of the eye and orbit of dogs. Am J Vet Res 50:898–903.

De La Hoz Polo M, Torramilans Lluís A, Pozuelo Segura O, Anguera Bosque A, et al. (2016) Ocular ultrasonography focused on the posterior eye segment: what radiologists should know. Insights Imaging 7(3): 351–364.

Deehr AJ, Dubielzig RR (1998) A histopathological study of iridociliary cysts and glaucoma in golden retrievers. Vet Ophthalmol 1:153–158.

Dietrich U, Kostlin R, Tassani M (1995) Ultrasonographic examination of the eyes of dogs with cataracts [abstract]. Vet Radiol Ultrasound 36:436.

Dubielzig RR (2002) Tumors of the eye. In: Meuten D, ed. Tumors in Domestic Animals, 4th edition. Blackwell: Ames, IA, pp. 739–754.

Vet-ebooks.com

Dubielzig RR, Ketring KL, McLellan GJ, Albert DM (2010) Veterinary Ocular Pathology: A Comparative Review. Elsevier, Edinburgh

Dubielzig RR, Steinberg H, Garvin H, Deehr AJ, et al. (1998) Iridociliary epithelial tumors in 100 dogs and 17 cats: a morphological study. Vet Ophthalmol 1:223–231.

Dupanloup A, Osinchuk S (2021) Relationship between the ratio of optic nerve sheath diameter to eyeball transverse diameter and morphological characteristics of dogs. Am J Vet Res 82(8):667–675.

Dziezyc J, Hager DA (1988) Ocular ultrasonography in veterinary medicine. Semin Vet Med Surg 3:1–9.

Farias FH, Johnson GS, Taylor JF, Giuliano E, et al. (2010) An ADAMTS17 splice donor site mutation in dogs with primary lens luxation. Invest Ophthalmol Vis Sci;51(9):4716–21.

Gallhoefer NS, Bentley E, Ruetten M, Grest P, et al.(2013) Comparison of ultrasonography and histologic examination for identification of ocular diseases of animals:113 cases (2000–2010). J Am Vet Med Assoc 243:376–388.

Gelatt K, MacKay E (2005) Prevalence of primary breed-related cataracts in the dog in North America. Vet Ophthalmol 8:101–111.

Gemensky-Metzler A, Wilkie DA (2004) Surgical management and histologic and immunohistochemical features of a cataract and retrolental plaque secondary to persistent hyperplastic tunica vasculosa lentis/persistent hyperplastic primary vitreous (PHTVL/PHPV) in a bloodhound puppy. Vet Ophthalmol 7:369–375.

Giudice C, Marco R, Mirko R, Luca M, et al. (2005) Zygomatic gland adenoma in a dog: histochemical and immunohistochemical evaluation. Vet Ophthalmol 8:13–16.

Grahn BH, Storey ES, McMillan C (2004) Inherited retinal dysplasia and persistent hyperplastic primary vitreous in miniature schnauzer dogs. Vet Ophthalmol 7:151–158.

Hager DA, Dziezyc J, Millchamp NJ (1987) Two-dimensional real-time ocular ultrasonography in the dog: technique and normal anatomy. Vet Radiol 28:60–65.

Hong S, Park S, Lee D, Cha A, et al. (2018) Contrast-enhanced ultrasonography for evaluation of blood perfusion in normal canine eyes. Vet Ophthalmol 22(1):31–38.

Krieger EM, Pumphrey SA, Wood CA, Mouser PJ, et al. (2022) Retrospective evaluation of canine primary, multicentric, and metastatic intraocular neoplasia. Vet Ophthalmol 25(5):343–349.

Kumar RS, Sudhakaran S, Aung T, (2016) Angle-closure glaucoma: imaging. In: Giaconi JA, Law SK, Nouri-Mahdavi K et al., eds. Pearls of Glaucoma Management, 2nd edition. Berlin, Germany: Springer-Verlag, pp. 517–530.

Labruyere JJ, Hartley C, Holloway A (2011) Contrast-enhanced ultrasonography in the differentiation of retinal detachment and vitreous membrane in dogs and cats. J Small Anim Pract 52:522–530.

Lazarus JA, Pickett JP, Champagne ES (1998) Primary lens luxation in the Chinese shar pei: clinical and hereditary characteristics. Vet Ophthalmol 1(2–3):101–107.

Lee H, Chang D, Lee Y, Eom K, et al. (2002) Use of color Doppler imaging for determining the resistive index of the medial long posterior ciliary artery in clinically normal conscious dogs. Am J Vet Res 63(2):211–4.

Lewis DL, Butts CJ, Moreno-Walton L. (2014) Facing the danger zone: the use of ultrasound to distinguish cellulitis from abscess in facial infections. Case Rep Emerg Med ;2014:935283. doi: 10.1155/2014/935283.

Liu D, Lutchman CR, Persad K, Simpson ER (2022) Evaluation of the characteristics of primary iridociliary cysts using ultrasound biomicroscopy at a tertiary care centre. Can J Ophthalmol 58(3):224–228. doi: 10.1016/j.jcjo.2022.01.018.

Morgan RV (1989) Ultrasonography of retrobulbar diseases of the dog and cat. J Am Anim Hosp Assoc 25:393–399.

Ng, A. and J. Swanevelder (2011) Resolution in ultrasound imaging. Contin Educ Anaesth Crit Care Pain 11(5): 186–192.

Oliver JAC, Rustidge S, Pettitt L, Jenkins CA, et al. (2018) Evaluation of ADAMTS17 in Chinese shar-pei with primary open-angle glaucoma, primary lens luxation, or both Am J Vet Res79(1):98–106.

Pavlin CJ, Foster FS (1995) Ultrasound biomicroscopic anatomy of the normal eye and andexa. In Pavlin CJ, Foster FS, eds. Ultrasound Biomicroscopy of the Eye. New York: Springer-Verlag, pp. 47–60.

Penninck DG, Daniel GB, Brawer R, Tidwell AS (2001) Cross-sectional imaging techniques in veterinary ophthalmology. Clin Tech Small Anim Pract 16:22–39.

Pizzirani S, Gong H (2015) Functional anatomy of the outflow facilities. Vet Clin North Am Small Anim Pract 45(6):1101–26.

Pumphrey SA, Pizzirani S, Pirie CG, Needle DB (2013) Glaucoma associated with uveal cysts and goniodysgenesis in American bulldogs: a case series. Vet Ophthalmol 16:377–385.

Rissi DR, McHale BJ, Miller AD. (2022)Primary nervous system lymphoma in cats. Vet Diagn Invest 34(4):712–717

Sagoo MS, Mehta H, Swampillai AJ, Cohen VM, et al. (2014) Primary intraocular lymphoma. Surv Ophthalmol 59(5):503–516.

Sapienza JS, Simo FJ, Prades-Sapienza A (2000) Golden retriever uveitis: 75 cases (1994–1999). Vet Ophthalmol 3:214–246.

Sargan DR, Withers D, Pettitt L, Squire M Gould DJ, et al. (2007) Mapping the mutation causing lens luxation in several terrier breeds. J Hered 98(5):534–8.

Schiffer SP, Rantanen NW, Leary GA, Bryan GM (1982) Biometric study of the canine eye, using A-mode ultrasonography. Am J Vet Res 43:826–830.

Sherar MD, Starkoski WB, Taylor WB, Foster FS (1989) A 100 MHz B-scan ultrasound backscatter microscope. Ultrason Imaging 11:95–105.

Silverman RH (2009) High-resolution ultrasound imaging of the eye – a review. Clin Experiment Ophthalmol 37(1):54–67.

Silverman RH, Cannata J, Shung KK, Gal O, et al. (2006) 75 MHz ultrasound biomicroscopy of anterior segment of eye. Ultrason. Imaging 28:179–188.

Smith JJ, Fletcher DJ, Cooley SD, Thompson MS (2018) Transpalpebral ultrasonographic measurement of the

Vet-ebooks.com

optic nerve sheath diameter in healthy dogs. J Vet Emerg Crit Care (San Antonio) 28(1):31–38.

Spiess BM, Bolliger JO, Guscetti F, Haessig M, et al. (1998) Multiple ciliary body cysts and secondary glaucoma in the Great Dane: a report of nine cases. Vet Ophthalmol 1:41–45.

Stades FC (1980) Persistent hyperplastic tunica vasculosa lentis and persistent hyperplastic primary vitreous PHTVL/PHPV in 90 closely related Doberman Pinschers: clinical aspects. J Am Anim Hosp Assoc 16:739–751.

Stringer CEA, Ahn JS, Kim DJ (2017) Asteroid Hyalosis: a mimic of vitreous Hemorrhage on point of care ultrasound. Can J Emerg Med 19(4):317–320

Tang J (2012) Ultrasonic Characterization of Corneal and Scleral Biomechanics. Dissertation Thesis, The Ohio State University

Tang J, Liu J (2011) Variance of speed of sound and correlation with acoustic impedance in canine corneas. Ultrasound Med Biol 37(10):1714–1721

Treadwell A, Naranjo C, Blocker T, Zarfoss M, et al. (2015) Clinical and histological characteristics of canine ocular gliovascular syndrome. Vet Ophthalmol. 18(5):371–80

Vitiello L, De Bernardo M, Capasso L, Cornetta P, et al. (2022) Optic nerve ultrasound evaluation in animals and normal subjects. front med (Lausanne) 8: 797018. doi: 10.3389/fmed.2021.797018.

Vrablik ME, Snead GR, Minnigan HJ, Kirschner JM, et al. (2015) The diagnostic accuracy of bedside ocular ultrasonography for the diagnosis of retinal detachment: a systematic review and meta-analysis. Ann Emerg Med 65(2):199–203.

Williams DL (2004) Lens morphometry determined by B-mode ultrasonography of the normal and cataractous canine lens. Vet Ophthalmol 7:91–95.

Zeiss CJ, Dubielzig RR (2004) A morphologic study of intravitreal membranes associated with intraocular hemorrhage in the dog. Vet Ophthalmol 7:239–243.

Vet-ebooks.com

CHAPTER FOUR

Neck

Julien Fages[1] and Dominique Penninck[2]

[1]*Centredmvet, Montréal, Québec, Canada*
[2]*Department of Clinical Sciences, Cummings School of Veterinary Medicine, Tufts University, North Grafton, MA, USA*

Scanning Technique

Because the ventral cervical region is anatomically complex, ultrasound is uniquely suited to evaluating cervical organs and tissues that are not readily characterized on survey or contrast radiographs. In addition to defining gross anatomy of the neck, high-resolution ultrasound can also be used to examine very small structures such as the thyroid and parathyroid glands. High-frequency (8- to 24-MHz) linear transducers, combined with tissue harmonic imaging and/or compound imaging techniques, provide the best images of small structures and those with complex internal architecture.

For ultrasonography of most structures, the animal is positioned in dorsal recumbency with the area of interest clipped (Figure 4.1A). Because many of the structures in the neck are symmetrically paired, it is useful to compare them. Positioning the patient so that the neck is as straight as possible is important to locate anatomical landmarks reliably and to compare both sides of the neck. Any structure can also be investigated while the animal is in lateral recumbency (Figure 4.1B) according to operator preference or for dyspneic animals, with the caveat that anatomy may appear somewhat distorted and comparisons to the contralateral neck will be impaired. For imaging the tympanic bullae, positioning the patient in sternal recumbency (Figure 4.1C) or seated with the head held straight and extended is preferred.

Although the ultrasound beam cannot penetrate air within hollow structures such as the tympanic bullae, trachea, and larynx, the interface between air and adjacent soft tissues can still be evaluated for regularity of contours and physiological motion as exemplified by examination of the vocal folds. Sonographic assessment of the cavities of these structures becomes possible in case of fluid accumulation or soft-tissue proliferation.

In addition to two-dimensional B-mode imaging, color flow Doppler, power Doppler, and pulsed-wave Doppler imaging can be used to evaluate vascularity of organs, vessels, and tissues. Flow characteristics of large vessels such as the common carotid artery and external jugular vein can be determined with color and pulsed-wave Doppler.

Normal Sonographic Anatomy

There are a few anatomical landmarks that are useful for locating cervical structures of clinical interest (Figure 4.1D). Normal size values for these landmarks are reported in Table 4.1.

Thyroid and Parathyroid Glands

The left and right thyroid lobes lie between the common carotid artery and the trachea and are often positioned at slightly different levels craniocaudally. The sternohyoid and sternothyroid muscles border the gland ventrally, and the esophagus usually borders the left lobe dorsally. To locate the thyroids, place the transducer in a transverse plane centered on the trachea just caudal to the larynx and move it caudally until

Atlas of Small Animal Ultrasonography, Third Edition. Edited by Dominique Penninck and Marc-André d'Anjou.
© 2025 John Wiley & Sons, Inc. Published 2025 by John Wiley & Sons, Inc.
Companion website: www.SmallAnimalUltrasonography.com

Vet-ebooks.com

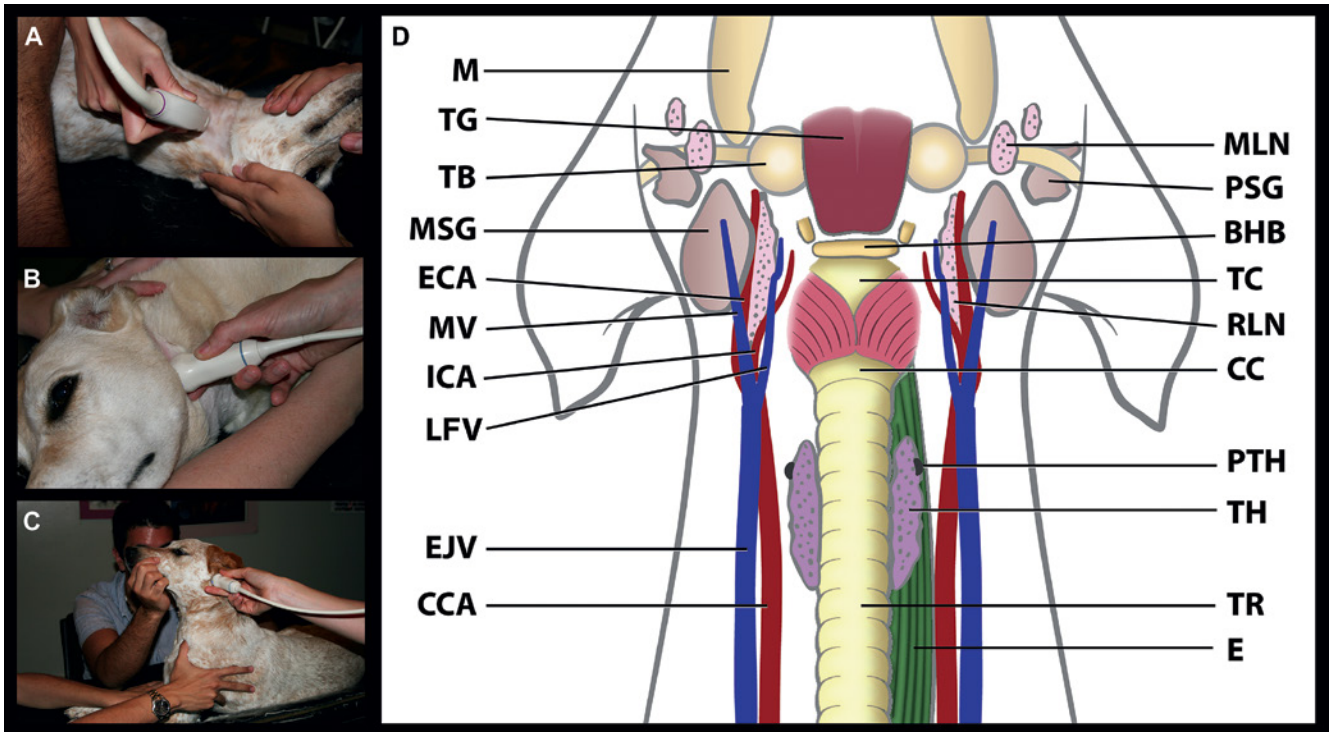


Figure 4.1. Ultrasound approach to the neck of a dog and normal regional anatomy. (for full caption, see facing page)

Table 4.1
Measurements of normal structures in the neck

Structure	Width/diameter (mm)	Height (mm)	Length (mm)	Volume (mm^3)
Thyroid, dog				
Mixed breed	16 (8–28)	8 (4–21)	22 (10–55)	
Beagles	5.3 (3.3–7.3)	5.3 (3.3–7.3)	24.5 (20.4–28.5)	380
Akitas				63–1,912
Golden Retrievers				
Left	4.3 (3.3–6.4)		24.8 (18.9–32.4)	447 (178–805)
Right	4.9 (3.1–8.5)		24.4 (18.3–33.1)	501 (132–1,061)
Toy and Miniature Poodles				128–713
Parathyroid, dog				
Mixed breed	2.3 (1.3–3.3)	1.7 (0.9–3.1)	3.4 (2.1–7.6)	
Thyroid, cat				66–103
Left		3.3 (2.5–4.1)	20.5 (18.9–22.1)	89 (66–112)
Right		3.0 (2.4–3.6)	20.3 (18.7–21.9)	80 (61–99)
Lymph nodes, dog				
Mandibular				
Left	10.0 (6.3–13.6)	4.1 (2.4–5.3)	13.5 (8.3–19.3)	310 (90–700)
Right	8.6 (2.0–13.8)	3.9 (1.9–5.1)	12.7 (4.7–19.6)	260 (10–710)
Medial retropharyngeal				
Left	9.8 (4.4–19.2)	5.5 (3.2–8.5)	19.0 (11.4–25.4)	580 (150–1,440)
Right	9.4 (4.0–16.0)	5.3 (3.0–8.2)	18.8 (13.7–26.7)	520 (110–1,440)
Superficial cervical				
Left	8.5 (4.2–14.8)	4.1 (2.5–6.7)	14.8 (5.9–22.4)	320 (50–790)
Right	8.3 (4.1–13.9)	4.1 (2.2–6.9)	14.5 (6.1–21.3)	290 (50–810)
Lymph nodes, cat				
Medial retropharyngeal	3.3 (2.0–6.0)	11 (6–18)	20.7 (13.0–32.0)	
Vagosympathetic trunk	1.2 ± 0.4			

Combined data from Wisner et al. (1991, 1994), Reese and Ruppert (2001), Taeymans et al. (2005), Bromel et al. (2005), Liles et al. (2010), Nemanic and Nelson (2012), and Ruppel et al. (2019).

Vet-ebooks.com

Figure 4.1. Ultrasound approach to the neck of a dog and normal regional anatomy. (A) Dorsal recumbency is convenient for imaging most of the structures of the neck. It enables comparison of bilaterally symmetrical structures, and to easily maintain the sagittal and transverse orientation. **(B)** Lateral recumbency is an alternate position for investigating the structures of the neck. **(C)** Sternal positioning for ultrasonography of the tympanic bulla. **(D)** Illustration of main anatomical structures of the neck that are evaluated with ultrasound or serve as landmarks. BHB, basihyoid bone; CC, cricoid cartilage; CCA, common carotid artery; E, esophagus; ECA, external carotid artery; EJV, external jugular vein; ICA, internal carotid artery; LFV, linguofacial vein; M, mandible; MLN, mandibular lymph node; MV, maxillary vein; PSG, parotid salivary gland; PTH, parathyroid; RLN, retropharyngeal lymph node; TB, tympanic bulla; TC, thyroid cartilage; TH, thyroid gland; TG, tongue; TR, trachea.

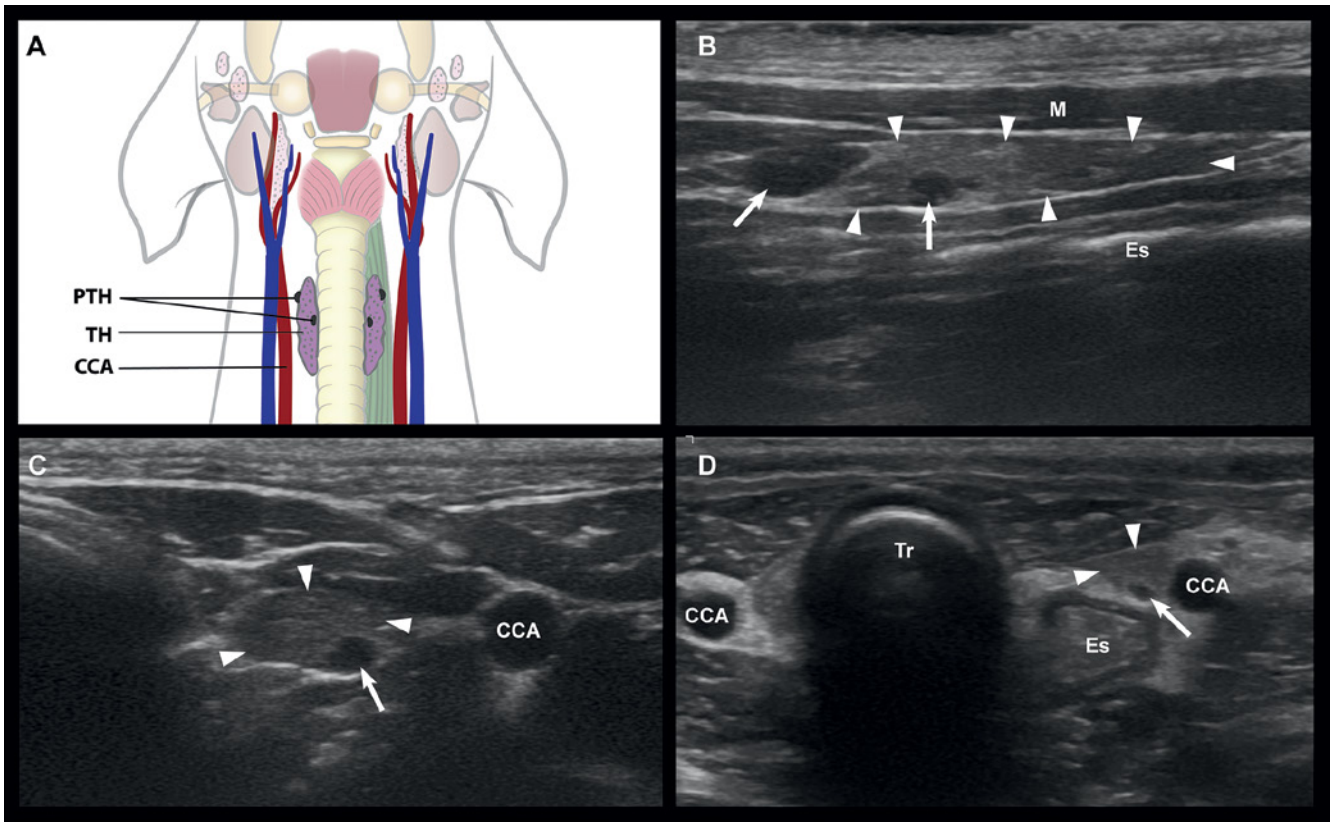


Figure 4.2. Normal thyroid and parathyroid glands in dogs. (A) Illustration of the anatomical location of the thyroid and parathyroid glands in the canine neck. **(B)** In this sagittal sonographic image, the normal thyroid (arrowheads) is fusiform to elliptical and hyperechoic to the surrounding musculature (M) and esophageal (Es) wall. Two parathyroid glands (arrows) are visible. **(C, D)** The normal right thyroid (place a marker) in transverse section between the trachea (Tr) and common carotid artery (CCA), and adjacent to the esophagus (Es). Note the hypoechoic parathyroid glands (PTH, arrows).

triangular structures are seen between the trachea and the carotid (Figure 4.2A). Each thyroid lobe may also be located separately by sliding the probe lateral to the trachea and by following the correspondent common carotid artery on cross section, which serves as a useful landmark. Once a thyroid is located, rotate the transducer 90° to a sagittal plane. This motion can be challenging because the thyroid gland is thin. Alternatively, the transducer may need to be angled medially from a parasagittal plane within the jugular furrow.

The thyroid is fusiform in sagittal section with a thicker and more rounded cranial pole, and oval or triangular in transverse section (Figures 4.2D–F, 4.3). Thyroid glands in dogs and cats are normally hyperechoic to the adjacent musculature. The glands are surrounded by a thin hyperechoic capsule, are uniformly echogenic, and have a fine echotexture. Small vessels may sometimes be seen as anechoic structures coursing through the thyroid tissue, which can be confirmed with Doppler mode. Both canine and feline thyroids can be imaged by using a 10- to 24-MHz linear transducer for best resolution. Cats may also occasionally have ectopic thyroid tissue located in the caudal cervical region or cranial mediastinum.

Vet-ebooks.com

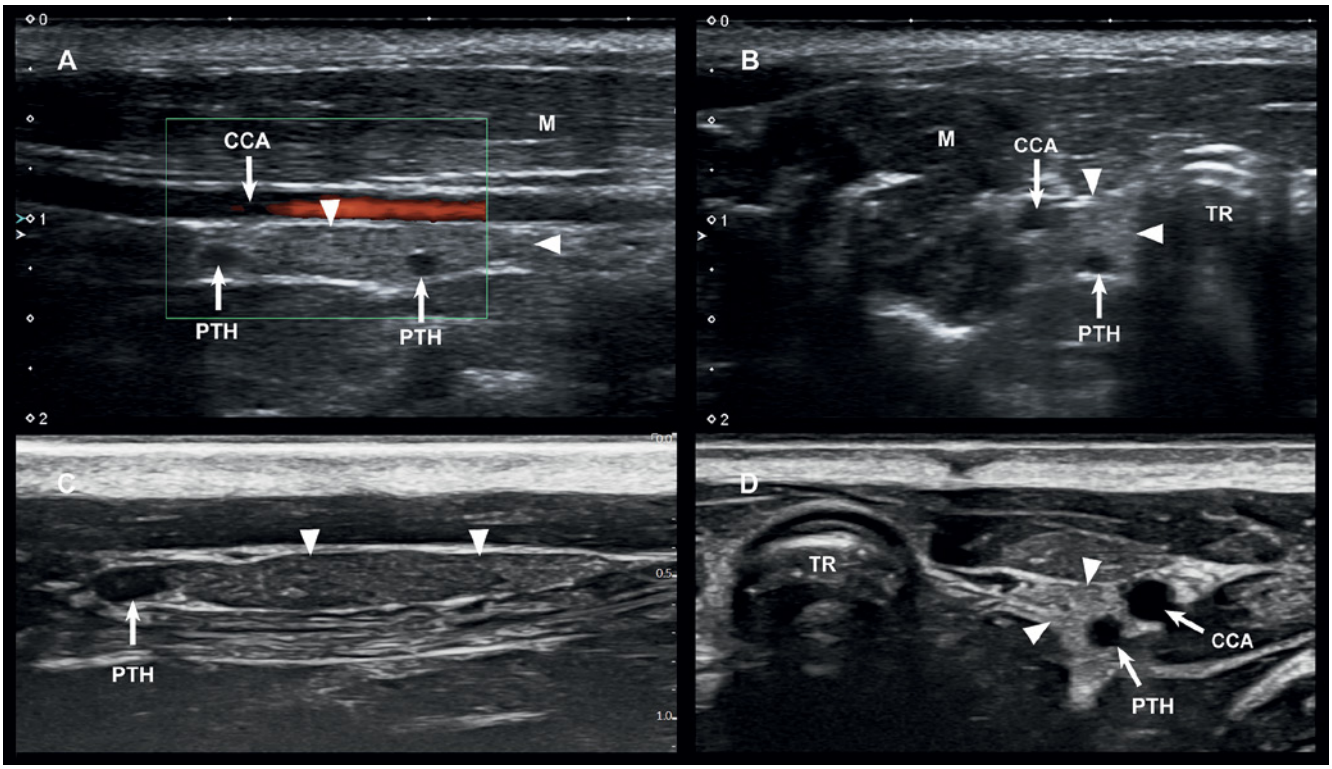


Figure 4.3. Normal thyroid and parathyroid glands in two cats. The right thyroid gland (arrowheads) is fusiform in the longitudinal plane **(A, C)** and triangular to oval in the transverse plane **(B, D)**. The common carotid artery (CCA) is nearby and serves as a useful landmark for localization. Two parathyroid (PTH) glands appear as well-defined spherical to oval structures that measure 1 mm in this cat **(A)**, located cranially and caudodorsally, respectively, while only one is noted cranially on the sagittal image of the other gland **(C)**. On this transverse image **(D)**, a smaller parathyroid gland is noted in a more central location (arrowheads). M, muscles; TR, trachea.

Thyroid volume can be estimated by measuring the length, width, and height of the gland, and using the formula $V = \pi/6$ (length × width × height) to calculate volume (V). The thyroid gland volume is correlated with body weight and body surface area more than with breed. There is more intraobserver variability in measuring the length of the glands because they taper caudally, and the distal limit may be difficult to define (Table 4.1) (Taeymans et al. 2005).

On average, there are two parathyroid glands associated with each thyroid lobe for a total of four. One is located at the cranial aspect of each thyroid lobe (external glands) and one is within the thyroid gland parenchyma (internal glands). However, there is wide normal individual variation in both parathyroid numbers and distribution. Normal parathyroid glands are usually well margined, hypoechoic to anechoic, and less than 2 mm in diameter and 3.3 mm long (Reusch et al. 2000; Wisner et al. 2002) (Figures 4.2C, D, 4.3). While the size of the normal canine parathyroid gland is around 2–3 mm, it has also been found to vary widely. All parathyroid glands are not always visible in normal dogs and are frequently not seen in cats (Woods et al. 2018). Thyroid lobules surrounded by connective tissue can appear similar in position and appearance to parathyroid glands (Liles et al. 2010) and may be mistaken for parathyroid tissue, especially in older cats as their prevalence is higher (Woods et al. 2018).

Salivary Glands and Lymph Nodes

The **mandibular salivary gland** is easily visible caudal to the ramus of the mandible, and between the maxillary and linguofacial veins as they join to form the jugular vein (Figure 4.4A). The monostomatic portion of the sublingual salivary gland shares the same fibrous capsule with the mandibular salivary gland and it may not be distinguished as a separate entity.

In the parasagittal imaging plane, the mandibular salivary gland is caudal to the more hypoechoic digastricus muscle, with the medial retropharyngeal lymph node (LN) medial to it (Figure 4.4A–C). To image the mandibular salivary gland in a sagittal orientation, the transducer can be rotated slightly from

Vet-ebooks.com

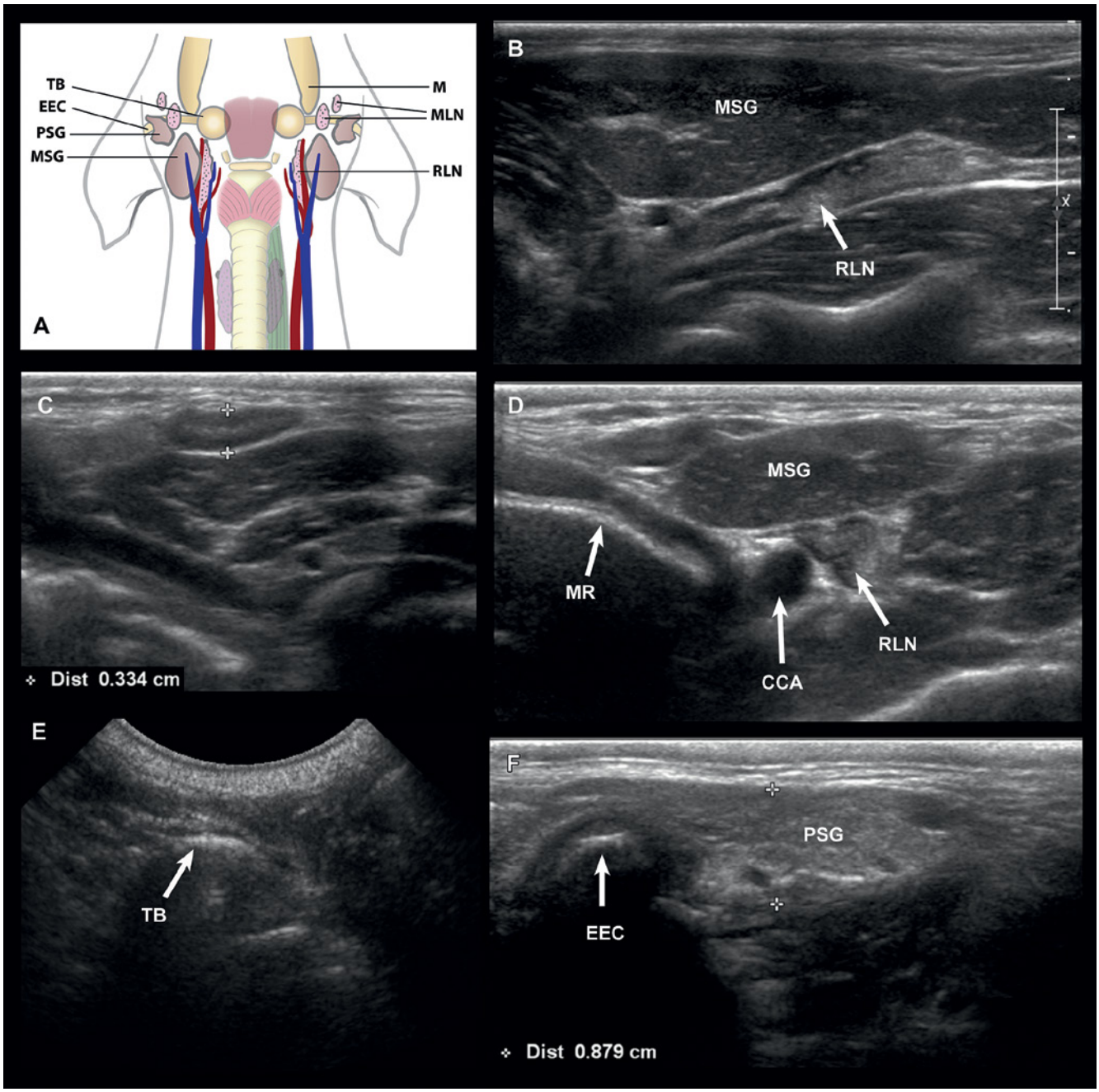


Figure 4.4. **Normal lymph nodes and salivary glands. (A)** Illustration of the anatomical location of these structures in the canine neck. EEC, external ear canal; M, mandible; MLN, mandibular lymph node; MSG, mandibular salivary gland; PSG, parotid salivary gland; RLN, retropharyngeal lymph node; TB, tympanic bulla. Sagittal **(B)** sonographic image of the MSG and medial retropharyngeal (RLN) lymph node. **(C)** Sagittal sonographic image of one of the MLNs. This node shows a hypoechoic halo in this asymptomatic dog and is considered normal. Cranial is to the left of the image. The MSG has a striated echotexture with a central linear echo. It is adjacent to the more hypoechoic digastric muscle overlying the hyperechoic interface of the mandibular ramus (MR). The RLN lymph node is more echogenic and located obliquely dorsomedial to the salivary gland. The lymph node is located lateral to the common carotid artery (CCA) in the transverse plane **(D)**. **(E)** Sagittal sonogram of the tympanic bulla. Note the hyperconvex interface with deep acoustic reverberation. **(F)** Sagittal image of the normal PSG, which is located caudal to the EEC. Note that the gland partly encircles the canal ventrally.

Vet-ebooks.com

the parasagittal plane relative to the head and neck. It is well defined, large and ovoid in shape, with a hyperechoic capsule and linear echogenic streaks within finely textured hypoechoic parenchyma (Figure 4.4B, C). A large centrally located hilum is characteristic of this gland.

Moving dorsally from the mandibular salivary gland by using a dorsal plane, the parotid salivary gland appears as a less-distinct, heterogeneous, mildly hyperechoic, and poorly marginated structure lateral or caudal to the curvilinear external ear canal and tympanic bulla (Figure 4.4E, F). When normal, minor salivary glands are usually not seen on ultrasound.

The **medial retropharyngeal LNs** are caudomedial to the mandibular salivary gland. The medial retropharyngeal LN is larger than most other cervical LNs and measures around 0.5 cm in height and 2 cm in length (Ruppel et al. 2019), although its size varies among dogs. They are mostly isoechoic to hyperechoic compared to salivary glands and have smooth margins. The cranial portion of these nodes is typically wider than the caudal part, which is more fusiform. In cats, reference measurements are $20.7 \times 12.4 \times 3.7$ mm (Nemanic and Nelson 2012). The LNs decrease in size with increasing age.

Mandibular LNs are very superficially located, oval structures located lateral and cranial to the mandibular salivary glands and clustered around the linguofacial vein. They are typically less than 0.5 cm thick and 1–1.5 cm long in dogs and are usually mildly hypoechoic to surrounding fat, although they can be nearly isoechoic to the fat (Figure 4.4D). There are usually 2–3 LNs on each side. Mandibular and medial retropharyngeal LNs are easily seen in normal dogs. The deep cervical LNs are generally poorly developed and usually not seen when normal and are located along the trachea. The superficial cervical LNs (commonly referred to as prescapular nodes), located superficially in the lateroventral aspect of the caudal neck, cranial to the supraspinatus muscle, are often paired and significantly larger than those in the cranial cervical region. Their size is positively correlated to body weight, with a mean length of 1.5–2.3 cm, a mean width of 0.8–0.9 cm, and a mean height of 0.4–0.5 cm (Silver et al. 2012; Ruppel et al. 2019).

Body weight positively correlates with LN size. Dogs younger than 2 years old and dogs older than 7 years old tend to, respectively, have larger and smaller LNs.

Tongue and Esophagus

The tongue is attached to the paired mylohyoid and geniohyoid muscles that are attached to the ramus of the mandible and the hyoid apparatus. The mylohyoid originates from the medial side of the mandible, and the geniohyoid from the ramus of the mandible. Both muscles attach to the basihyoid bone caudally. The tongue is hyperechoic to the supporting musculature and is best approached ventrally, between the rami of the mandible with the dog positioned in dorsal recumbency (Figure 4.5B, C) (Solano and Penninck 1996).

Caudal to the larynx, the esophagus lies along the trachea, and usually runs to the left of the trachea at the thoracic inlet but can at times be seen on the right. The lumen of the esophagus may contain a small amount of gas and mucus or fluid (Figure 4.5D–E) and may have a star shape in transverse orientation. In a sagittal orientation, the muscularis layer is visible as a hypoechoic band, and gas or fluid may be seen in the lumen. The esophagus can be seen dorsal to the left common carotid artery and left thyroid gland (Figure 4.2F) and is often located along the left side of the trachea.

Larynx and Trachea

Just caudal to the tongue, the thyroid and cricoid cartilages have echogenic surfaces and produce acoustic shadowing in the far field. In a sagittal orientation, the epiglottis is a short echogenic line parallel to the transducer surface and dorsal to the cranial portion of the thyroid cartilage. Its motion during swallowing assists in its identification.

In transverse section (Figure 4.6B), the thyroid cartilage is superficial and V-shaped. Between the arytenoid cartilages and the vocal folds are hypoechoic bands medial to the wall of the thyroid cartilage (Figure 4.6B).

Orienting the transducer transversely ventral to the thyroid cartilage shows the moving vocal folds (Bray et al. 1998). The transducer is then moved caudally to the junction of the thyroid and cricoid cartilages and directed cranially toward the vocal folds, which are attached to the vocal process of the arytenoid cartilage dorsally and the thyroid cartilage ventrally. The vocal folds consist of the vocal ligaments located craniomedially, and the vocal muscle continues laterally and caudally from it to join with the larynx. The vocal ligaments appear as vertical hyperechoic bands in the center of the larynx (Figure 4.6B). The air-filled space between the vocal folds is the rima glottis (Figure 4.6B). Mineralization of the laryngeal cartilages may hinder viewing of the vocal folds through the thyroid cartilages.

The trachea contains air that causes reverberation artifacts and acoustic shadowing. Consequently, only

Vet-ebooks.com

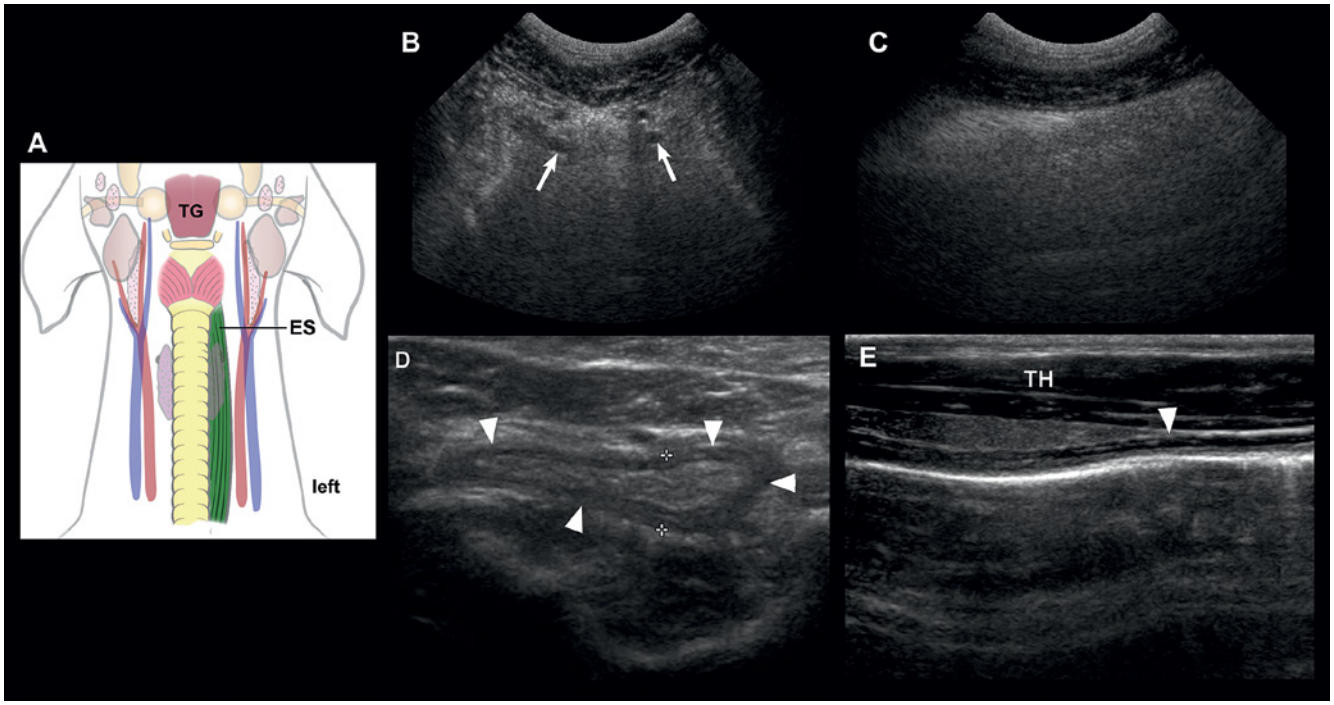


Figure 4.5. **Normal tongue and esophagus of a dog. (A)** Illustration of the anatomical location of the base of the tongue (TG) and esophagus (ES) in the canine neck. **(B)** The muscle of the tongue is hyperechoic to the more ventral geniohyoid and mylohyoid muscles. In a parasagittal orientation **(C)**, the fibers have a diagonal pattern. **(B)** In a transverse orientation, the round hypoechoic structures (arrows) represent the lingual and sublingual veins. The lingual muscles have a butterfly shape. **(D, E)** Transverse **(D)** and longitudinal **(E)** sonographic images of the esophagus (arrowheads). The muscularis, submucosa, and mucosa are hypoechoic, hyperechoic, and hypoechoic, respectively. In the longitudinal plane **(E)**, there is gas in the lumen causing a hyperechoic linear interface deep to the external wall (arrowhead).

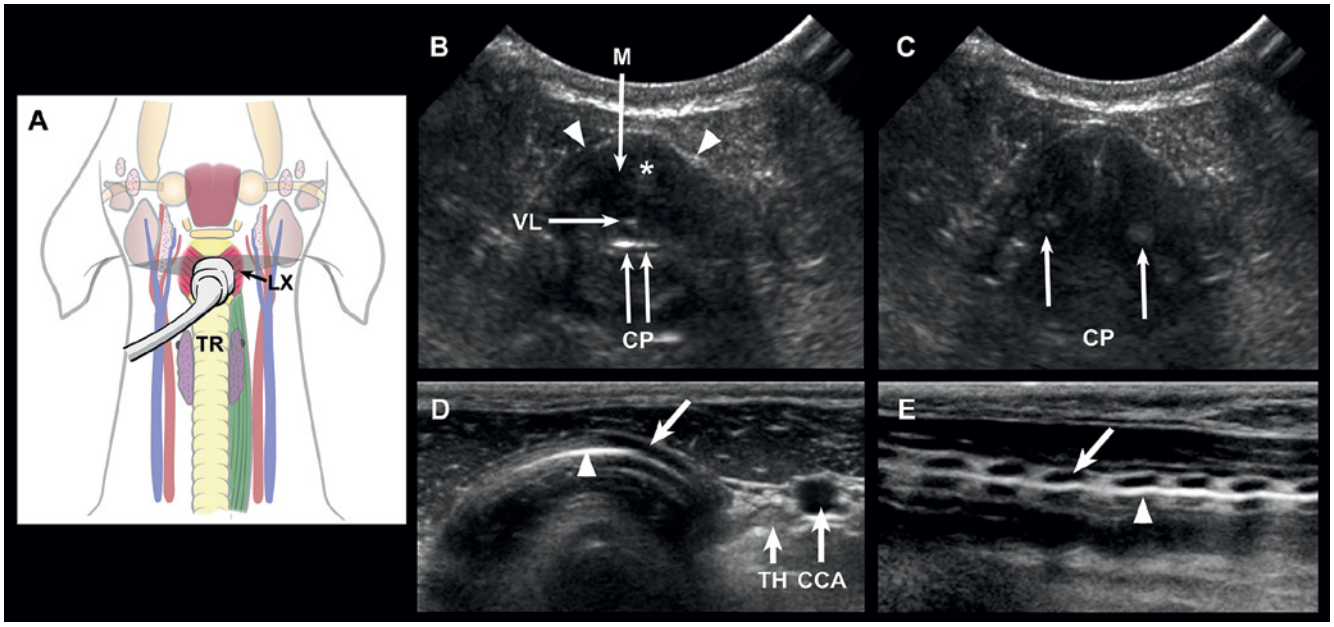


Figure 4.6. **Normal larynx and trachea of a dog. (A)** Illustration of the anatomical location of the larynx (LX) and trachea (TR) in the canine neck. **(B)** Transverse sonogram of the larynx taken through the thyroid cartilage at expiration. Ventral is at the top of the image, and the right side is on the left. The thyroid cartilage is visible as a hyperechoic V-shaped line (arrowheads). The rima glottis is the air-filled space (asterisk) between the hyperechoic vocal ligaments (VLs). Dorsal to the VL, the cuneiform processes of the arytenoid cartilages appear as hyperechoic dots. The vocal muscles (M) are hypoechoic and fill the space between the ligaments and the thyroid cartilage on either side. **(C)** Transverse image of the canine larynx taken during inspiration. The cuneiform processes move in abduction in inspiration (arrows) and in adduction in expiration (compare with **B**). Transverse **(D)** and longitudinal **(E)** sonographic images of the trachea. The rings (arrows) are hypoechoic and delineated axially by the hyperreflective gas interface (arrowheads). CCA, left common carotid artery; TH, left thyroid gland; CP, cuneiform processes.

Vet-ebooks.com

its near walls (ventral and lateral) can be examined using ultrasound. In a transverse plane, the trachea appears as a hyperechoic, convex interface with distal acoustic shadowing obscuring the lumen (Figure 4.5D). In a longitudinal view, the tracheal rings are visible as small, regularly spaced hypoechoic structures with central hyperechoic dots when partly mineralized (Figure 4.5E).

Vessels and Nerves

The major neck vessels that can be seen with ultrasound are the external jugular veins and their primary tributaries and the common carotid arteries and their major branches (Wisner et al. 1991). Other vessels, such as thyroid arteries and internal jugular veins, are smaller and seen inconsistently. All these structures should be imaged in a transverse or sagittal plane. Some may be seen from ventral midline, whereas others may be seen well with the transducer positioned lateral to midline.

The **external jugular vein** (Figure 4.7A) lies superficially within the jugular furrow. Cranially, the maxillary and linguofacial veins join to form the external jugular vein at the caudal aspect of the mandibular salivary gland (Figure 4.7A, B). The jugular vein is easily compressed, so very little transducer pressure should be used to image it. The transducer should be placed in the jugular furrow in a sagittal orientation and angled 45° toward midline. The wall of the jugular vein is thin, and the lumen is anechoic. With color Doppler or pulsed-wave Doppler ultrasound, a smooth, laminar flow is seen (Figure 4.7E). This is sometimes difficult to demonstrate because the Doppler signal is weakest when the vessel lies at nearly 90° to the beam. Slight angulation of the transducer in a caudal direction, as well as beam steering, will increase the Doppler signal and help confirm the direction of the flow. Weak pulsatile flow referred from the carotid artery will be seen occasionally.

The **common carotid artery** is in close association and parallel to the trachea. The artery has a thick, hyperechoic wall and anechoic lumen (Figure 4.7B–D), with a pulsatile Doppler waveform (Figure 4.7F). Each artery is located at the dorsolateral margin of the trachea, and the sternohyoid and sternothyroid muscles are located ventromedially to them. The sternocephalicus muscle lies between the common carotid artery and the more superficial jugular vein. The common carotid artery branches into the internal and external carotid arteries medial to the mandibular salivary gland. The external carotid artery continues in a straight line from the common carotid artery, whereas the internal carotid artery is slightly smaller in diameter and travels medially and dorsally at a 30° angle (Figure 4.7B–D). The carotid bulb, a focal dilatation of the arterial lumen at the origin of the internal carotid artery, can be seen occasionally.

In a transverse orientation, the carotid sheath appears hyperechoic and encompasses the common carotid artery, vagosympathetic trunk, and internal jugular vein. The vagosympathetic trunk is dorsal to the common carotid artery and appears hypoechoic. It can be seen from the laryngeal region to the thoracic inlet, and no visible vascular structures are within it. The vagosympathetic trunk is approximately 1.2 ± 0.4 mm in diameter, which varies with the weight of the animal (Reese and Ruppert 2001).

External Ear Canal and Tympanic Bullae

The external ear canal and tympanic bulla are best imaged with a curvilinear transducer of medium to high frequency or a high-frequency linear transducer with a short footprint as the contact area for imaging these structures is small (Dickie et al. 2003).

The external ear canal and bulla are imaged from both a lateral approach and a ventral approach (Figure 4.1B, C) with the patient in sternal, seated, or lateral recumbency. The tympanic bulla and cross section of the external ear canal are visible as curvilinear hyperechoic lines filled with air-producing reverberation artifacts (Figure 4.4E, F). In a transverse plane with respect to the head, the external ear canal appears in a longitudinal orientation. The ear canal lies just caudal to the zygomatic arch, with the masseter muscle lateral to the arch and the sternocephalicus muscle and parotid salivary gland caudal to it (Figure 4.4F). The horizontal portion of the ear canal is imaged from a ventral position in either a longitudinal or transverse orientation. From the longitudinal position, the transducer can be rotated slightly to view the tympanic bulla and external ear canal in the same image.

The tympanic bulla itself is composed of thin bone and is filled with air. The normal bulla wall appears as an echogenic convex line, and the air within it causes reverberation artifacts and shadow deep to the bone margin. The bone is thin enough that the ultrasound beam penetrates it, and therefore within the bulla cavity the presence of soft tissue or fluid caused by a middle ear disorder can be identified.

The maxillary artery can be identified with color Doppler caudally and laterally to the tympanic bulla at the junction of the external ear canal and the bulla.

Vet-ebooks.com

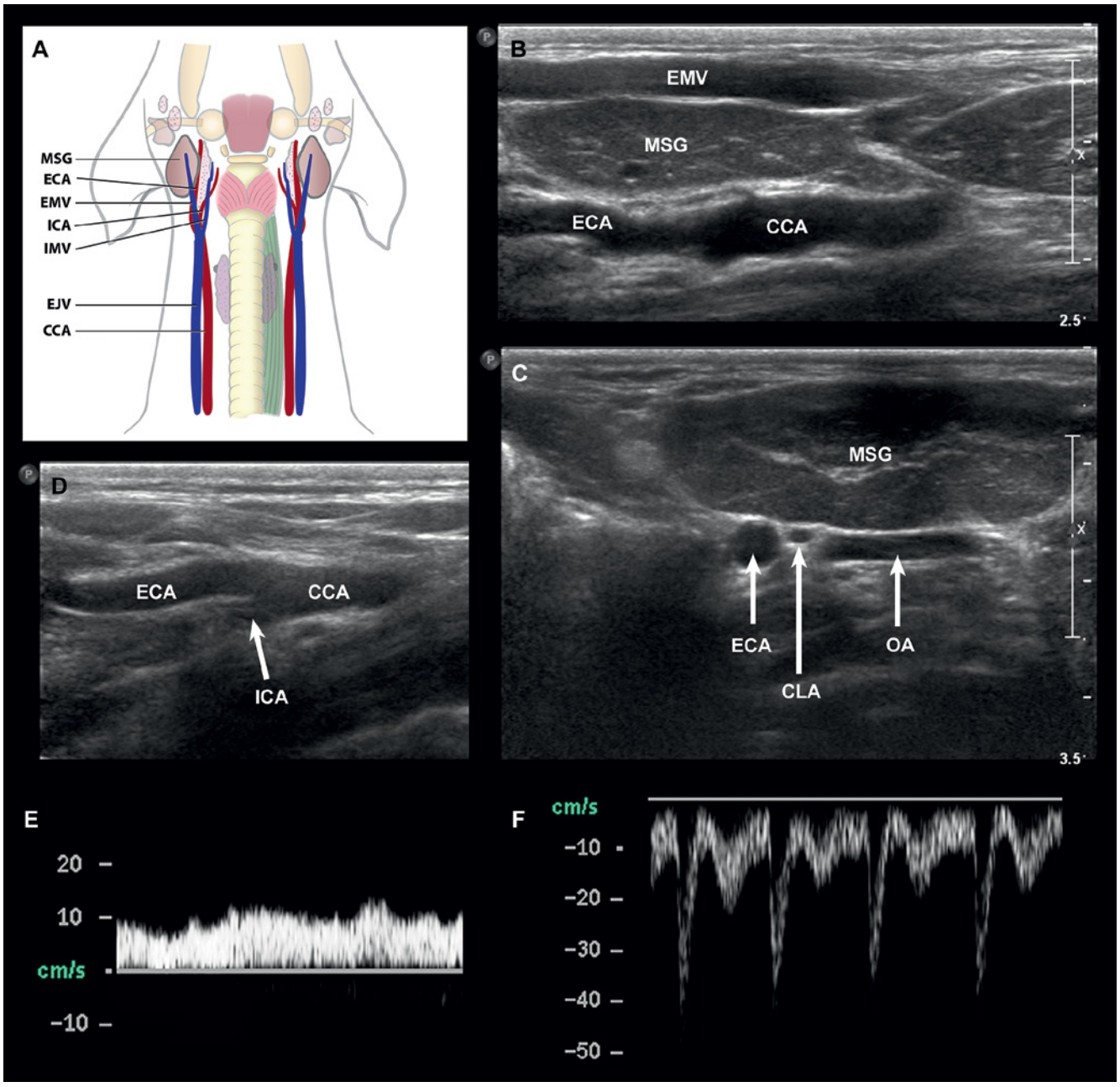


Figure 4.7. Images of the carotid arteries, jugular veins, and mandibular salivary glands of a normal dog. (A) Illustration of the anatomical location of these structures in the canine neck. The common carotid artery (CCA) subdivides into the external carotid artery (ECA), ventrally, and the internal carotid artery (ICA), which extends dorsally. The external jugular vein (EJV) subdivides into the external maxillary vein (EMV), ventrally, and the internal maxillary vein (IMV), which extends dorsally. The mandibular salivary gland (MSG) lies cranial to these bifurcations. **(B, C)** Sagittal **(B)** and transverse **(C)** images of the CCA, EMV, and MSG. Note the low echogenicity and coarse echotexture of the gland. CLA, cranial laryngeal artery; OA, occipital artery. **(D)** Sagittal images of the common carotid artery at its site of bifurcation into the ECA and the ICA. **(E, F)** Pulsed-wave Doppler signature of the external jugular vein **(E)** and common carotid artery **(F)**. The venous flow is directed toward the transducer, has lower velocity, and is laminar and therefore more constant **(E)**. The arterial flow is directed away from the transducer with pulsatile flow of higher velocity **(F)**.

Vet-ebooks.com

Sonographic Features of Neck Disorders

Thyroid Glands

Hyperthyroidism caused by functional thyroid adenoma or adenomatous hyperplasia is very common in older cats (Mooney 2002). This can manifest as a discrete nodule within the thyroid gland or as diffuse thyroid enlargement with or without areas of cavitation. Ultrasound can be used to measure the volume of the thyroid glands to detect enlargement. Although this is not a functional test as is nuclear scintigraphy, enlarged glands are indicative of thyroid diseases. Both thyroid lobes are affected in 63% of cats and both ectopic thyroid disease and thyroid carcinoma are relatively uncommon in hyperthyroid cats (Peterson and Broome 2015). **Hyperplastic thyroid glands** are hypoechoic or isoechoic to surrounding tissue and hypoechoic to normal thyroid. In **thyroid adenomas**, the glands can be focally or diffusely affected, often with a lobular margin and tubular shape (Figure 4.8). However, a distinction between the two can often not be made.

Thyroid glands occasionally contain incidental **cysts** showing distal acoustic enhancement. These cysts can be confused with normal parathyroid glands, which can also appear hypoechoic or anechoic but without distal acoustic enhancement. The cyst may be irregular in shape, but its margin should be visible in both planes. Large thyroid cysts can cause clinical signs in cats, such as dysphagia or dyspnea. Thyroid cysts appear to develop most often in cats with long-standing hyperthyroidism but can also occur rarely in cats with nonfunctional thyroid tumors. Regardless of thyroid status, cysts are equally likely to be benign as malignant (Miller et al. 2017). Thyroid and parathyroid neoplasia, such as thyroid cystadenoma and parathyroid adenocarcinoma, can also appear cystic (Phillips et al. 2003) (Figures 4.8, 4.9). In a retrospective study of hypercalcemic dogs without cervical mass, 15% of dogs had at least an incidental thyroid nodule (Pollard et al. 2015), including cysts, adenomas, adenocarcinomas, and nodular hyperplasia.

Thyroid carcinoma is a rare but aggressive neoplasia that affects dogs more often than cats. It often presents at an advanced stage, with the mass involving a large area of the ventral cervical region and distorting local anatomy. This may make localizing the origin of the mass to the thyroid difficult. On ultrasound examination, the mass appears heterogeneous and hypoechoic to

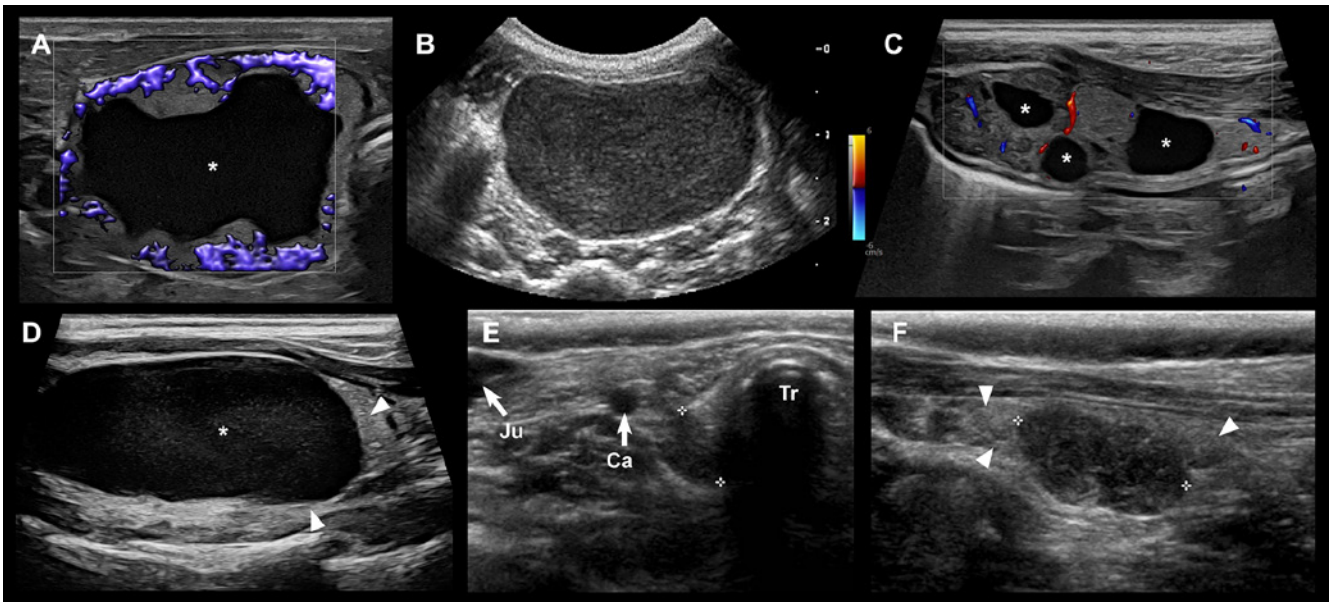


Figure 4.8. **Thyroid adenoma and adenomatous hyperplasia in cats and a dog. (A)** Sagittal image of the right thyroid lobe of a 6-year-old domestic short-hair cat with adenomatous hyperplasia. The gland is markedly enlarged by a central fluid cavity (*), whereas the peripheral tissue is hypervascular. **(B)** Sagittal image of a thyroid cystic adenoma in a 16-year-old Burmese cat. The lesion is primarily cystic but filled with echogenic fluid mimicking a solid mass. **(C, D)** Presumed multicystic bilateral thyroid adenoma in a cat. The cystic component (*) is particularly large in **(D)**, with a thin parenchymatous remaining portion (arrowheads). **(E, F)** Transverse **(E)** and sagittal **(F)** images of a microfollicular adenoma in a 10-year-old Beagle dog. An irregular, hypoechoic nodule (8 mm wide and 1.7 cm long, between calipers) extends beyond the margins of the normal thyroid tissue (arrowheads). Ca, carotid artery; Ju, jugular vein; Tr, trachea.

Vet-ebooks.com

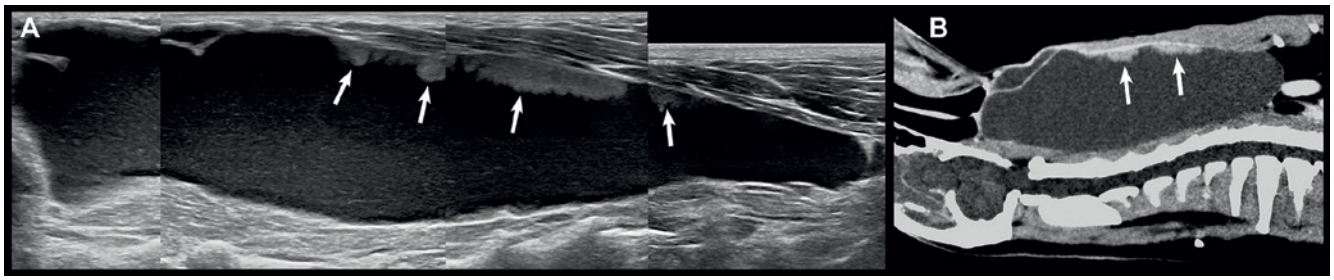


Figure 4.9. Thyroid cystadenocarcinoma in an 11-year-old cat. Composite ultrasonographic **(A)** and CT **(B)** sagittal images with multifocal proliferative irregular bands of tissue present along the inner wall of the cystic mass, mostly ventrally (arrows).

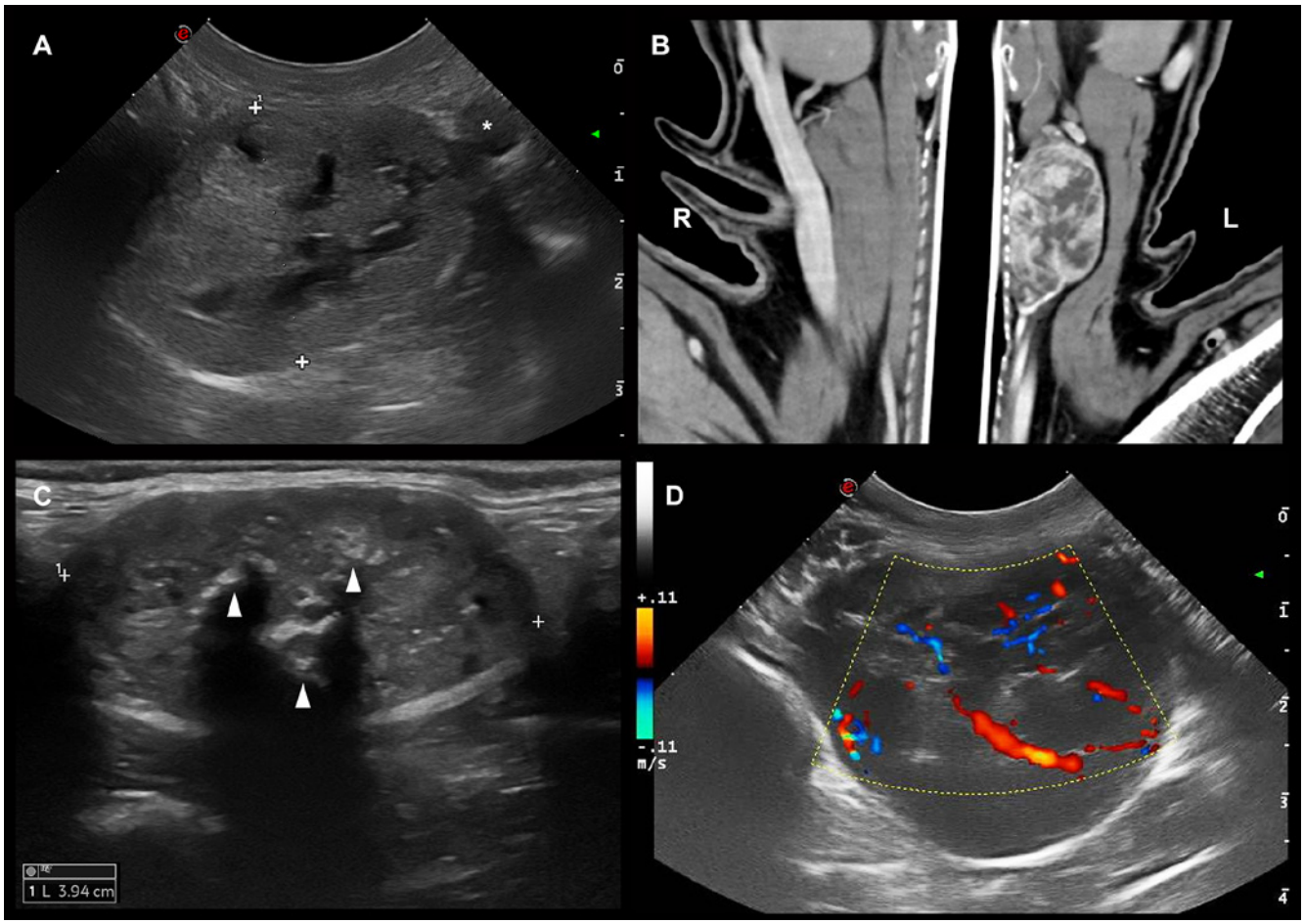


Figure 4.10. Thyroid carcinoma in three dogs. (A) Transverse sonographic image of the left thyroid gland of a 9-year-old Newfoundland dog. The large heterogeneous thyroid carcinoma is displacing the common carotid artery (*) laterally. Ill-defined internal hypoechoic areas are present and exhibit a fluid-attenuating signal on CT (**B**; dorsal plane) L, left; R, right. **(C)** In this 12-year-old Chow-Chow, foci of mineralization are within the mass, causing acoustic shadowing (arrowhead). **(D)** Power Doppler of a thyroid carcinoma in a 10-year-old Australian Sheepdog, which is highly vascularized.

normal thyroid tissue, with good to poor margination (Figures 4.10, 4.11). The trachea and esophagus may be displaced ventrally and laterally, and the enlarging mass can cause upper-airway obstruction. The local vasculature, trachea, esophagus, and fascial planes can be compressed or invaded by thyroid carcinoma. Because of their higher sensitivity and specificity, computed tomography (CT) or MR may, however, be the preferred modality to diagnose these features (Figures 4.10B, 4.11C, D, and 4.12) (Taeymans 2012). They are moderately to strongly vascularized with often high internal signals on Doppler evaluation (Figure 4.10 D). Mineralization of

Vet-ebooks.com

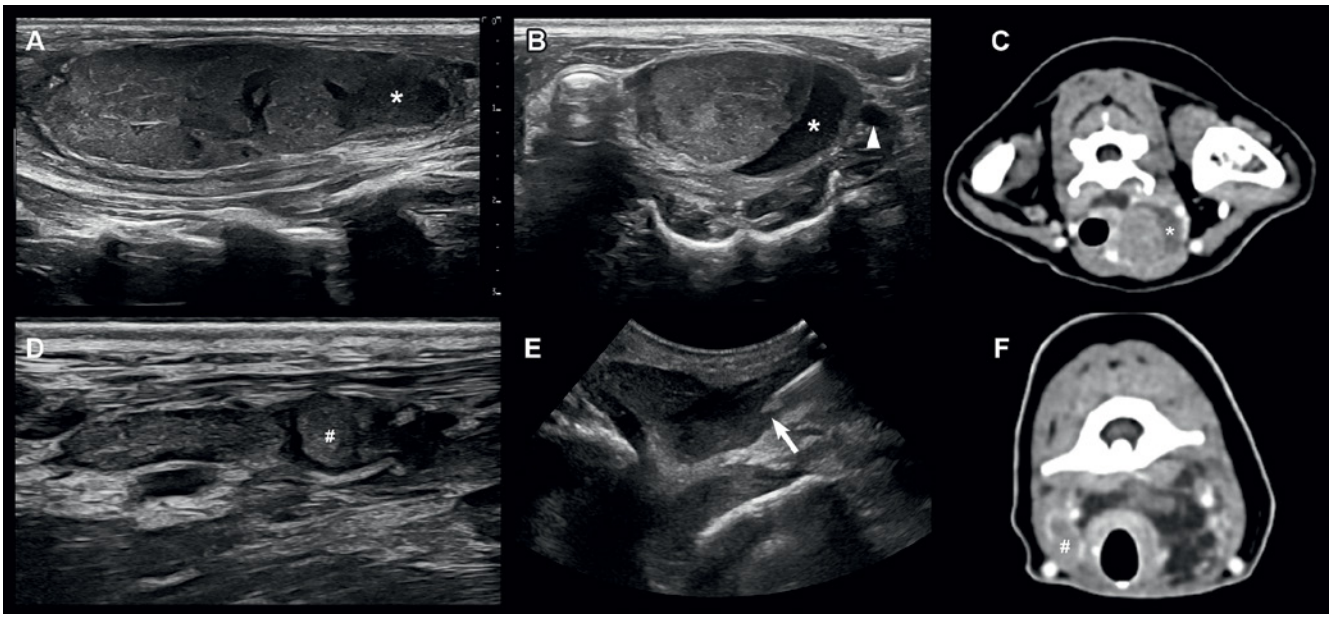


Figure 4.11. Thyroid carcinoma in a cat. Sagittal **(A)** and transverse **(B)** images of a left thyroid carcinoma and corresponding CT image **(C)**. The large thyroid carcinoma is displacing the common carotid artery (arrowhead) laterally. Internal echogenic fluid accumulation (asterisk) is present at its caudomedial aspect with a crescent shape in the transverse plane **(B, C)** and corresponding fluid-attenuating signal (asterisk) on contrast-enhanced computed tomography (CT) image (**C**; transverse plane). **(D–F)** Contralateral medial retropharyngeal lymph node, with nodular thickening of its caudal pole (#). **(D)** On the sagittal ultrasonographic image, the caudal pole is rounded with an internal hyperechoic signal. This rounded thickening was noted on contrast-enhanced CT image (**F**; transverse plane) and ultrasound-guided FNA of the LN was performed **(E)**. The arrow points at the tip of the 21G needle located in the LN.

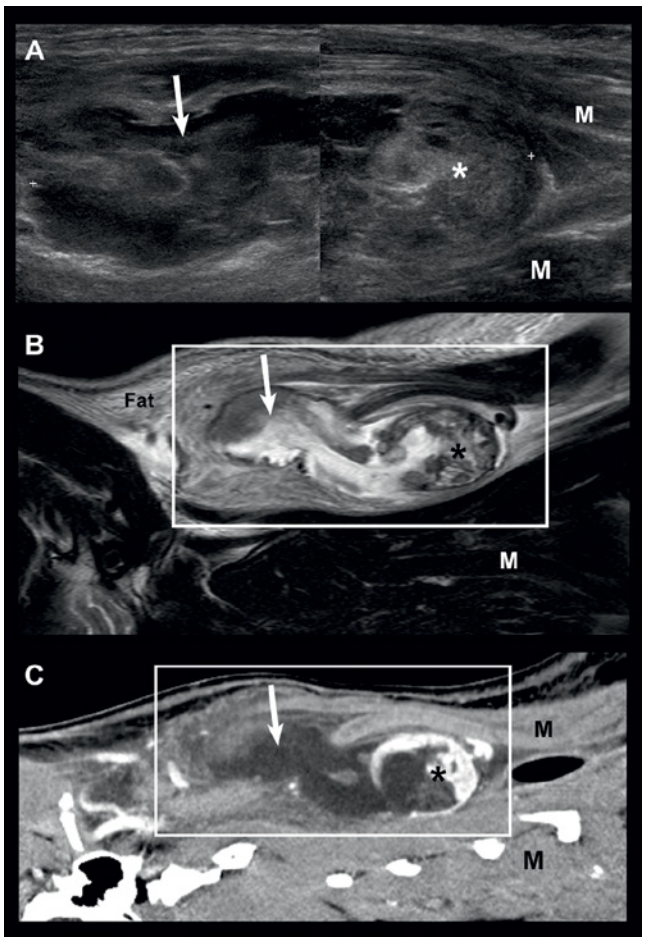


Figure 4.12. Comparative imaging for thyroid carcinoma in a dog. Sonographic images **(A)** of the hemorrhagic mass (arrows) with corresponding sagittal T2-weighted MR **(B)** and CT **(C)** images. In ultrasound **(A)**, the carcinoma (*) is mixed in echogenicity, with a hemorrhagic component cranially that is mixed in echogenicity **(A)**, MR signal intensity **(B)**, and CT attenuation characteristics **(C)**. M, muscles.

Vet-ebooks.com

the mass can be observed in about 50% of cases as hyperechoic foci with distal acoustic shadowing (Figure 4.10C), and metastasis to the medial retropharyngeal LNs is not uncommon (Figure 4.11E, F). In the absence of local tissue invasion and areas of mineralization or metastatic disease, differentiation of thyroid adenoma from other masses cannot be made with ultrasound. Malignant transformation of ectopic thyroid tissue can occur separately or concurrently with thyroid gland carcinoma (Figure 4.13). In contrast to carotid body tumors, which are laterally located, malignant transformation of ectopic thyroid tissue is typically found midline, often ventral to the larynx (Taeymans et al. 2012).

Contrary to cats, dogs are more often affected by primary **hypothyroidism**. In one study, hypothyroid glands were more rounded on transverse imaging rather than their normal triangular shape (Reese et al. 2005). However, a later study of normal dogs revealed many with a similar transverse shape, making the earlier observation nonspecific. Hypothyroid glands are also hypoechoic and smaller than normal lobes (Figure 4.14). They may be heterogeneous in echotexture and have an irregularly shaped capsule (Bromel et al. 2005; Taeymans et al. 2007).

Parathyroid Glands

Dogs with hypercalcemia may have primary or secondary parathyroid disease, and ultrasonography often helps to differentiate between them (Reusch et al. 2000). **Primary hyperparathyroidism** is caused

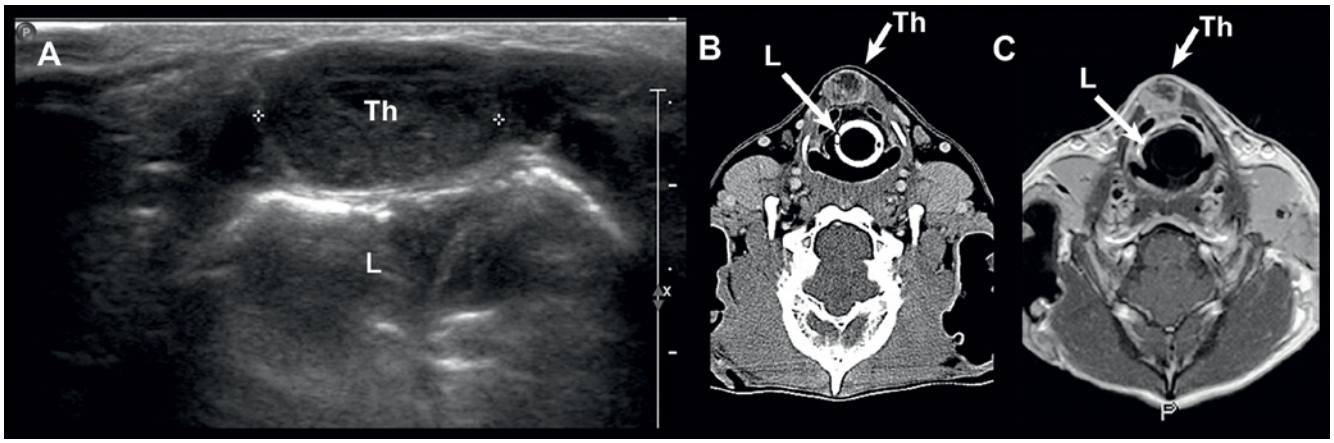


Figure 4.13. Comparative imaging of an ectopic thyroid carcinoma in a dog. Ventral is on top of these transverse ultrasound **(A)**, postcontrast CT **(B)**, and T1w MRI **(C)** images. A soft-tissue mass consistent with ectopic thyroid (Th) proliferation showing peripheral contrast enhancement is noted along midline, ventral to the larynx (L). Local invasion of the ventral laryngeal musculature is noted on MRI.

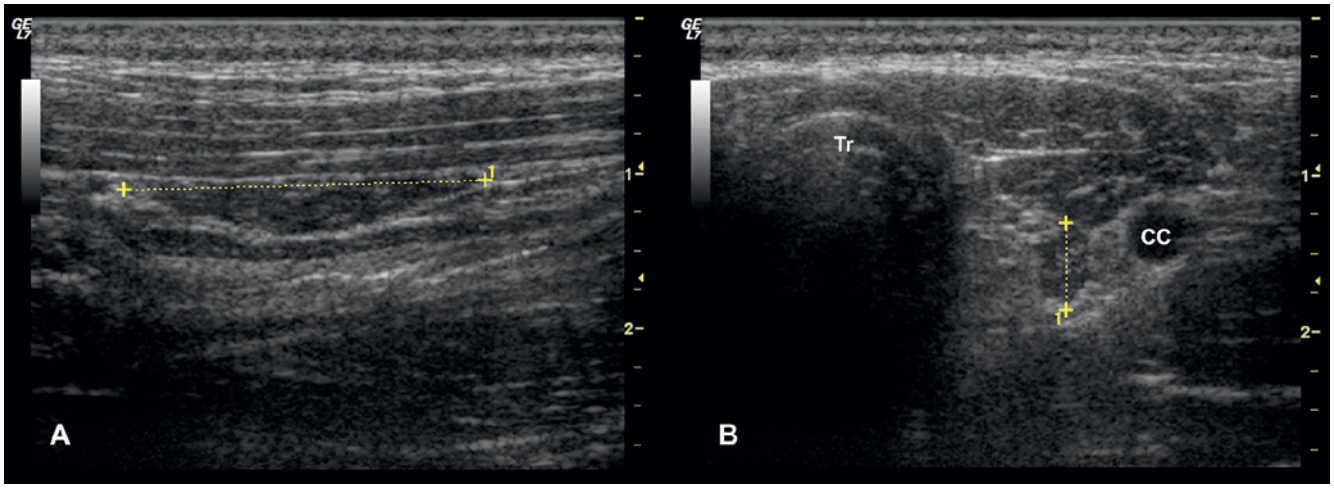


Figure 4.14. Left thyroid lobe of a dog with hypothyroidism. Sagittal **(A)** and transverse **(B)** images of the small thyroid lobe are outlined by cursors. It is irregular and hypoechoic to the surrounding tissues (arrows). CCA, common carotid artery; Tr, trachea.

Vet-ebooks.com

by hyperplasia, adenoma, or less commonly, adenocarcinoma and presents as a single parathyroid nodule. Rarely, two to three concurrent parathyroid nodules occur with primary hyperparathyroidism. **Secondary hyperparathyroidism** is caused by parathyroid hyperplasia secondary to renal disease or nutritional deficiencies, typically with all parathyroid glands being mildly enlarged.

Parathyroid nodules are hypoechoic and may be heterogeneous and may have distal acoustic enhancement. They tend to be well circumscribed and are round or oval (Figure 4.15). Parathyroid nodules that are greater than 3–4 mm in diameter are more likely to be parathyroid adenomas or carcinomas, whereas those less than 3–4 mm in diameter are more often primary hyperplastic, or secondary to chronic renal disease or hypercalcemia of malignancy (Secrest and Grimes 2019; Wisner et al. 1997). Although neoplastic parathyroid glands tend to be larger than hyperplastic glands, there is an important overlap between their sizes. Therefore, caution should be taken for using size as a sole criterion to differentiate hyperplasia from neoplasia and normal versus abnormal parathyroid glands (Secrest and Grimes 2019). Measuring the parathyroid glands to differentiate acute from chronic renal failure was reported. In acute renal failure, parathyroid length overlapped with the measurements of normal parathyroid glands, while in dogs with chronic renal failure, the parathyroid glands were longer (Reusch et al. 2000).

There is little information on feline parathyroid glands; however, normal feline parathyroid glands are often not visible on ultrasound examination and are generally less than 2 mm in width (Woods et al. 2018).

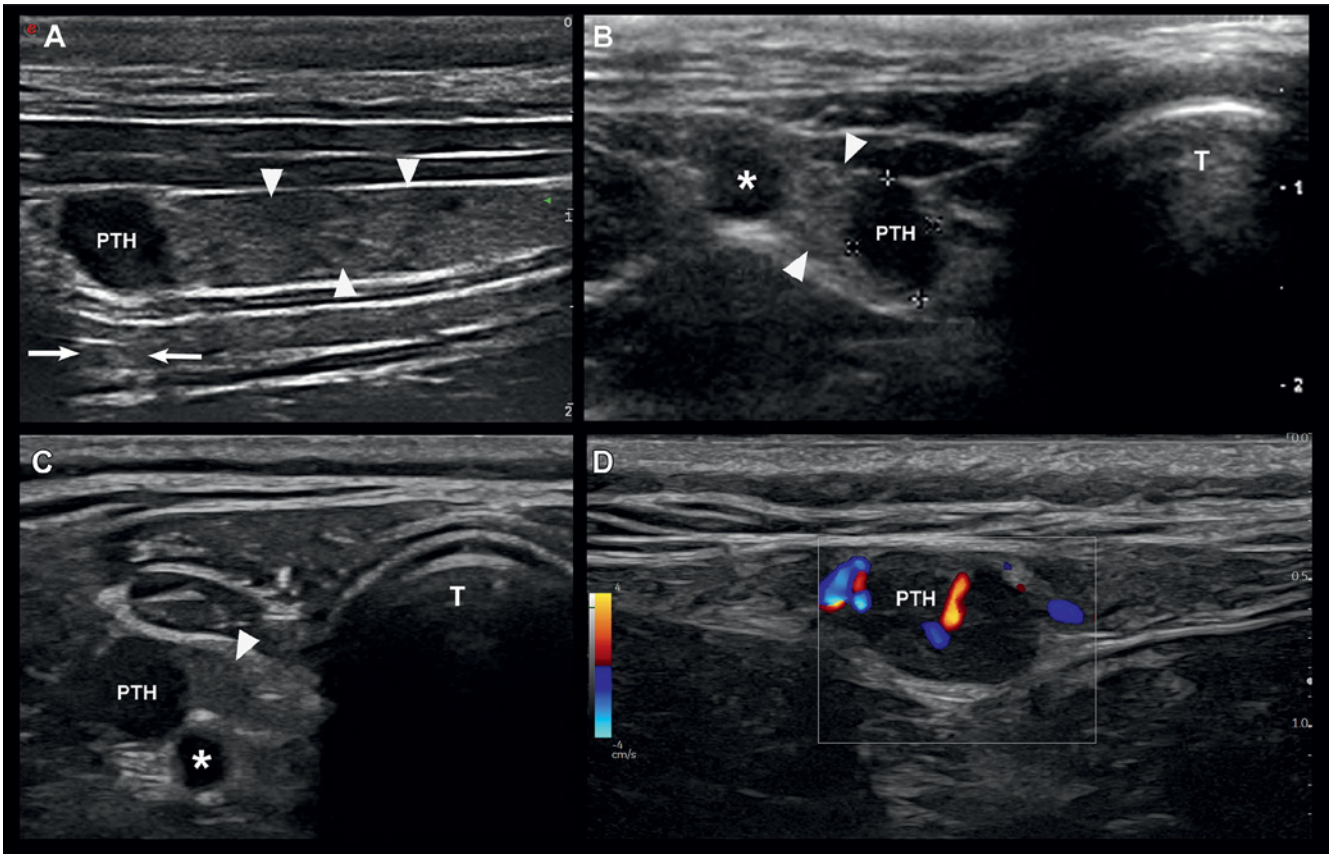


Figure 4.15. Parathyroid adenoma in three dogs. (A) Sagittal image of the right thyroid (arrowheads) and parathyroid (PTH) gland of a 10-year-old English Setter. A discrete hypoechoic nodule measuring 7 mm in diameter is present cranially. **(B)** Transverse image of the right thyroid (arrowheads) and parathyroid (PTH) gland of a 10-year-old Siberian Husky. A discrete hypoechoic nodule (between the cursors) measuring 8 × 4 mm is deforming the medial contour of the thyroid gland (arrowheads). The diagnosis is parathyroid chief cell adenoma. The adjacent common carotid artery (asterisk) seen on cross section should not be confused with a parathyroid nodule. T, trachea. **(C, D)** Transverse and sagittal images of the right PTH of a 12-year-old Dachshund with parathyroid adenoma, at the craniomedial aspect of the thyroid gland (arrowheads) and ventrolateral to the carotid artery (*). Although such nodules can sometimes exhibit distal enhancement (**A**, arrows), Doppler evaluation can confirm the vascularized tissular nature of the nodule **(D)**. T, trachea.

Vet-ebooks.com

Lymph Nodes and Soft Tissues

The mandibular LNs in dogs are considered enlarged with length > 2 cm, width > 1.5 cm, and height > 0.5 cm. The medial retropharyngeal LN can be considered enlarged with length > 3 cm, width > 2 cm, and height > 1 cm. The superficial cervical LN can be considered enlarged with length > 2.5 cm, width > 1.5 cm, and height > 1 cm (Ruppel et al. 2019).

Enlarged mandibular, retropharyngeal, or cervical LN may be caused by local inflammation, tumoral infiltration, or regional metastatic disease. Tumors of the mouth often metastasize to the mandibular LNs. LNs affected by **inflammatory** or **neoplastic diseases** are enlarged, rounded, and hypoechoic (Figures 4.16, 4.17), often surrounded with hyperechoic fat. The margins of the LNs can be indistinct if there is local inflammation.

Cavitation can also occur in reactive nodes because of **abscessation** and in metastatic nodes because of hemorrhage and necrosis. Metastatic LNs can be hypoechoic or heterogeneous without enlargement. They tend to become rounder and thicker from their normal oval or elongated shape. Most sonographic features overlap between reactive and metastatic LNs, and fine-needle aspiration or biopsy is generally needed for a diagnosis. Measurement of short and long axes (as well as their ratio), evaluation of flow distribution on Doppler, resistivity and pulsatility indexes, and sonoelastography can however help in differentiating benign from malignant LNs (Belotta et al. 2019; Seiler and Griffith 2018).

Lymphoma causes generalized peripheral lymphadenopathy in dogs, but rarely in cats. Affected LNs of the head and neck are enlarged and hypoechoic to nearly anechoic. The nodes may have indistinct margins and disrupted internal architecture. In dogs with lymphoma, the cervical and mandibular LNs tend to enlarge to a lesser degree than the retropharyngeal LNs (Figure 4.16C, D). These hypoechoic LNs may also

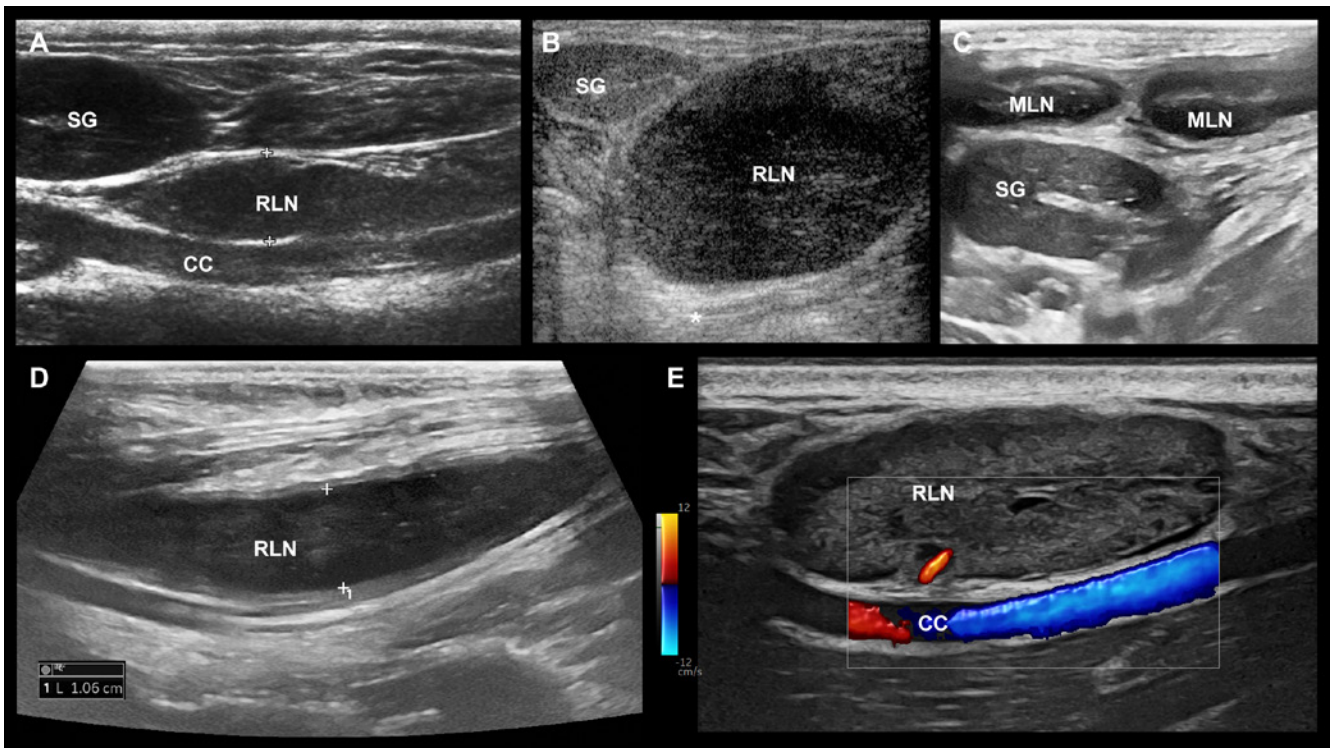


Figure 4.16. **Mandibular and medial retropharyngeal lymphadenopathy in three dogs (A–D) and a cat (E). (A)** Sagittal image of a reactive retropharyngeal lymph node (calipers) in a dog. It is hypoechoic and oval shaped, with a margin that is homogeneous in echotexture and slightly irregular. CC, common carotid artery, SG, mandibular salivary gland. **(B)** Sagittal image of markedly enlarged, ovoid, and hypoechoic medial RLN surrounded by hyperechoic fat (asterisk); a fine-needle aspirate was performed and suppurative lymphadenitis was diagnosed. The normal SG is just cranial to the enlarged medial RLN. **(C, D)** Transverse image of right MLN **(C)** and sagittal image of an RLN **(D)** in another dog with multicentric lymphoma. Although these lymph nodes are also abnormally thickened and hypoechoic, they remain fusiform. **(E)** Sagittal image of a retropharyngeal reactive lymphadenomegaly in a young cat of unknown etiology. The ipsilateral common carotid (CC) is seen immediately dorsal to the lymph node.

Vet-ebooks.com

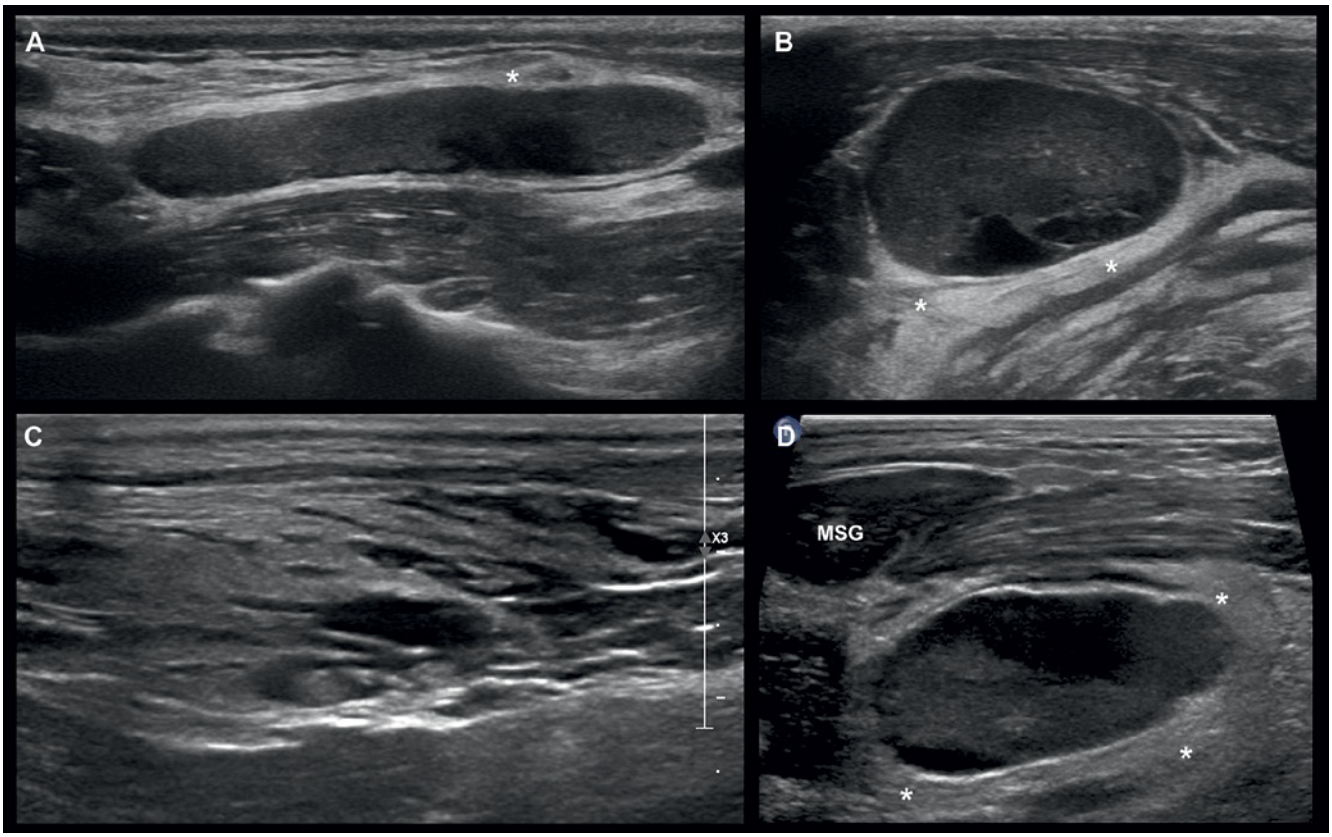


Figure 4.17. Lymphadenitis in two dogs. (A) Sagittal image of a retropharyngeal lymph node and (**B**) transverse image of ipsilateral cervical superficial lymph nodes in a 10-year-old dog. The LN is enlarged, rounded, and inhomogeneous with internal hypoechoic areas. Surrounding steatitis is present (*). Sampling of the LN indicated pyogranulomatous lymphadenitis. **(C)** Sagittal image of the left side of the neck of a 7-year-old Labrador cross presented for 2 days of neck swelling. Numerous anechoic striations are crossing the superficial planes of the neck, representing edema. **(D)** The left retropharyngeal lymph node was enlarged (1.9 cm thick by 4.2 cm long) and inhomogeneous, surrounded by steatitis (*). Sampling of the lymph node led to the diagnosis of suppurative lymphadenitis. MSG, mandibular salivary gland.

have distal acoustic enhancement and be surrounded by hyperechoic tissue. The distal enhancement can cause the nodes to be confused with anechoic cysts.

Other cervical masses that are nonlymphoid, thyroid, or parathyroid in origin, such as lipomas, hemangiosarcomas, fibrosarcomas, hematomas, and abscesses can be found in the neck and may appear solid, cystic, or complex (Gooding et al. 1977). Neoplastic masses are usually solid or complex, and hematomas are complex or cystic. Acutely, hematomas appear as hypoechoic masses with a hypoechoic center. With time, septations can develop, echogenicity increases, and a capsule may form (Wisner et al. 2002). Hematomas should become smaller with time. Lipomas are usually well marginated, are elliptical, and are striated and hyperechoic to surrounding musculature. However, lipomas can be infiltrative and poorly defined. Interfascial planes or muscles can be infiltrated. CT and MRI can be quite valuable in discriminating these processes and better assessing their extent, especially if surgery is an option.

Penetrating wounds from the skin or esophagus, with or without foreign bodies, may cause diffuse or localized cellulitis of the soft tissues of the neck (Figures 4.17–4.19). Edema can be seen dissecting between fascial planes or within the subcutaneous fat as anechoic or hypoechoic areas separated by thin hyperechoic septa. Inflamed fatty tissues are often thickened, hyperechoic, and hyperattenuating, and echogenic fluid may accumulate between fat planes (Figures 4.17–4.19). **Abscesses** are often septated, with echogenic fluid surrounded by a variably thick wall (Figures 4.18C, D, 4.19C, D). Foreign bodies can be challenging to identify. Their detection is greatly influenced by their acoustic characteristics and by their size, location, and shape (Figure 4.19). Among them, wooden splinters and porcupine quills in endemic areas are common. These latter are characterized by two

Vet-ebooks.com

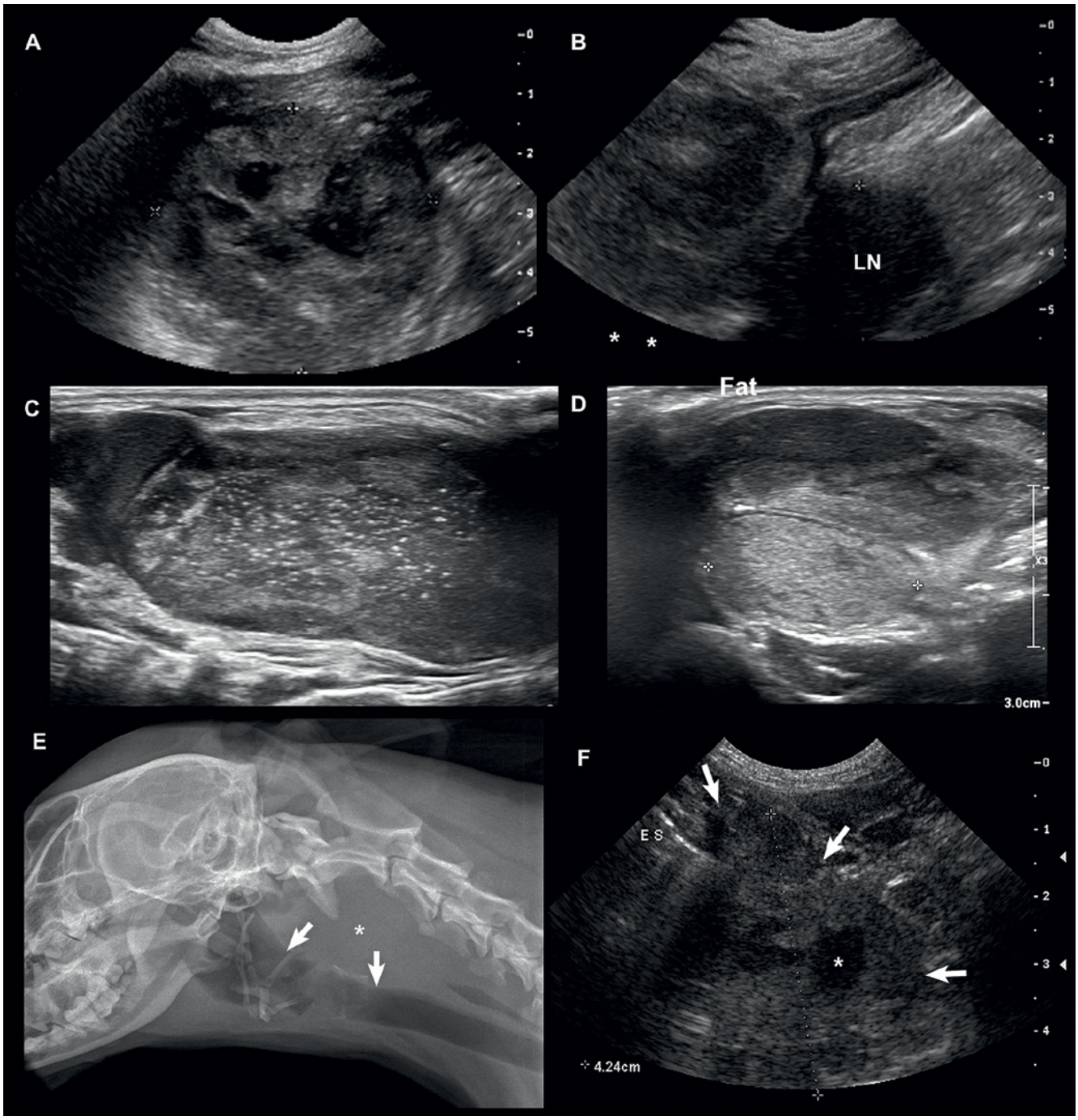


Figure 4.18. **Septic suppurative cellulitis and abscess formation in two dogs and a cat. (A, B)** Sagittal images of the cranioventral neck in an 11-year-old Irish Setter, on which a multicavitated mass measuring about 4.5 × 6 cm is caudoventral to the larynx. A local lymph node is enlarged and hypoechoic (LN). **(C, D)** A large abscess was seen in this 4-year-old diabetic Maine Coon cat. **(C)** Numerous echogenic speckles are noted throughout the cavity. **(D)** The medial retropharyngeal lymph node deep to the abscess was enlarged (between calipers) and hyperechoic. The adjacent tissues are hyperechoic (steatitis), and no foreign body was found. The abscess was successfully drained. **(E, F)** Retropharyngeal abscess in a dog. **(E)** Lateral oblique radiograph of the head and neck of a dog with a history of difficulties in swallowing and of neck pain. A soft-tissue mass effect (asterisk) is in the retropharyngeal region, causing ventral displacement of the nasopharynx, larynx, and trachea (arrows). **(F)** Transverse sonogram in the region of the mass. A large, irregular, moderately echogenic mass (arrows) is lateral and caudal to the esophagus (ES). This mass has a thick wall encircling an irregular cavity filled with echogenic fluid. Fine-needle aspirations and surgical biopsies confirmed the presence of a sterile, pyogranulomatous abscess of uncertain origin.

Vet-ebooks.com



Figure 4.19. **Examples of foreign bodies in dogs. (A)** Migrating grass awn in a 2-year-old Australian shepherd dog. The foreign body has a characteristic shape and is embedded in a fluid-filled abscess (between calipers). **(B)** Sewing needle and associated cellulitis in a dog. The needle tip (arrow) is close to the thickened esophagus (E) and the carotid artery (arrowhead). TR, trachea. **(C, D)** Wooden splinter in the ventral neck of a 4-month-old Italian Greyhound puppy. **(C)** There is a linear strongly hyperechoic line casting strong distal shadowing, corresponding to the wooden foreign body. It is surrounded by an oblong tract delineated by echogenic thick wall with internal echogenic fluid. Abscess formation is present at its ventromedial aspect (*) as well as regional steatitis. **(D)** On transverse image, the wooden splinter exhibits a short thick curvilinear hyperechoic interface with distal shadowing (arrowheads). The abscess (between calipers) cavity is well seen (*). **(E, F)** In the other dog, sagittal (E) and transverse images (F) of a wooden foreign body showed a similar hyperechoic interface associated with strong acoustic shadowing (arrowheads). It was detected shortly after the dog ran in the woods. Interestingly, there is minimal reaction around this large foreign object.

Vet-ebooks.com

well-defined mural parallel hyperechoic lines. Although they often tend to break, a tapering extremity can be visualized. Depending on porcupine subspecies, multiple additional less-conspicuous hyperechoic lines between and parallel with the walls can be observed (Le Roux et al. 2017). Cystic lesions are rare and usually thyroid or branchial in origin (Wisner et al. 2002).

Salivary Glands

Disorders that affect the salivary glands include true cyst, sialolith, sialoadenitis (Figure 4.20), sialocele/mucocele (Figure 4.21A, C, and D), salivary duct cyst (Figure 4.21B), and neoplasia.

Most of these conditions are rare in dogs and cats. Localization of the lesion is based on the anatomical site and surrounding landmarks. Common findings in inflammatory or obstructive disease include enlargement and decreased echogenicity of the gland. The salivary ducts may be enlarged, and fluid filled when obstructed, and occasionally a focal shadowing **sialolith** is visible within the duct lumen. **Zygomatic sialadenitis** causes enlargement and the appearance of a retrobulbar mass of variable echogenicity (Cannon et al. 2011). **Sialoceles** are thin-walled fluid-filled structures with anechoic to echogenic contents. These can be difficult to trace to the origin of the salivary gland. Sialoceles may be associated with sialadenitis. Edema or steatitis may appear as alternating hypoechoic and hyperechoic regions in the surrounding tissues. Ultrasonographic characteristics of mucoceles are reported to vary with the chronological stage of the disease. Compared to acute cases, the volume of anechoic material may decrease in subacute to chronic presentations, combined with an overall increasing heterogeneity of the lesion (Torad and Hassan 2013). Neoplasms of the salivary gland may disrupt the normal capsule and normally uniform echogenicity.

Various morphological diagnoses of primary neoplasia of the salivary gland have been reported in dogs and cats including adenocarcinoma, carcinoma, malignant mixed, adenoma/cystadenoma, anaplastic adenocarcinoma, and malignant melanoma, with adenocarcinoma being the most common tumor type in both species (Cray et al. 2020; Lenoci and Ricciardi 2015). Cystic lesions, nodular lesions, and enlarged salivary glands can be aspirated to determine their origin.

Tongue and Esophagus

Ultrasonography can be used to identify mass lesions at the base of the tongue, such as foreign body, abscess (Figure 4.22), or tumor. It can also be used to monitor correct placement of an endotracheal tube in the cervical esophagus or to confirm megaesophagus (Wisner et al. 2002). Other lesions, such as paraesophageal abscess or esophageal wall thickening, can also be detected (Figures 4.23, 4.24).

Larynx and Trachea

Neoplasia (Figure 4.25), trauma, inflammation (Figure 4.26), and cysts can affect the larynx and paralaryngeal structures (Rudolf and Brown 1998). The most common neoplasia of the larynx in cats is lymphoma and in dogs is malignant epithelial neoplasia (Carlisle et al. 1991). These tumors can appear as masses

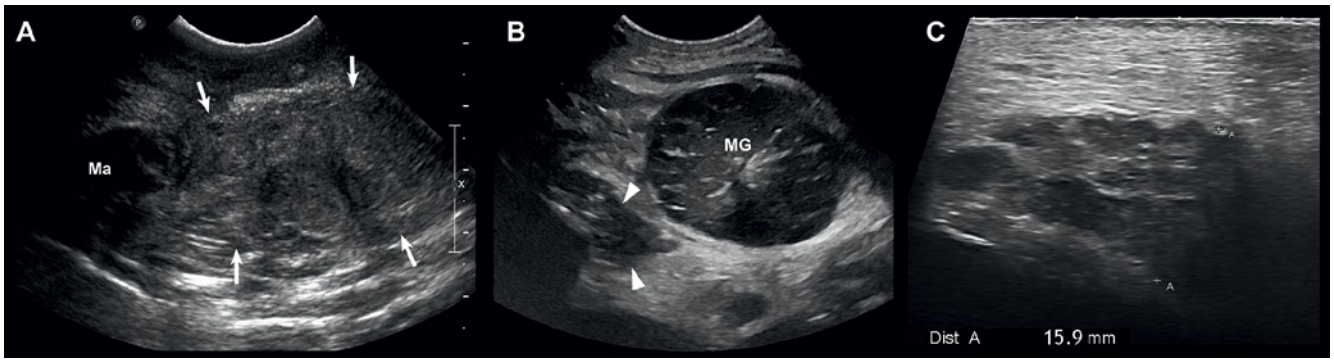


Figure 4.20. **Sialadenopathy in dogs. (A)** Sialadenitis in a dog. On this sagittal image, the right mandibular salivary gland is ovoid, hypoechoic, mildly heterogeneous, and enlarged (arrowheads), just caudal to the mandible (Ma). **(B)** Presumed phenobarbital-responsive sialadenosis in an 8-year-old mix breed dog. On this sagittal image, the left mandibular gland (MG) is rounded, markedly hypoechoic with an increased volume and regular margins. At its rostral aspect, the monostotic part of the sublingual salivary gland is partially seen as a heterogeneous echogenic triangle (arrowheads). **(C)** Unilateral parotid sialadenitis in an 8-year-old French bulldog. The right gland is enlarged, hypoechoic, and heterogeneous, surrounded with hyperechoic fat.

Vet-ebooks.com

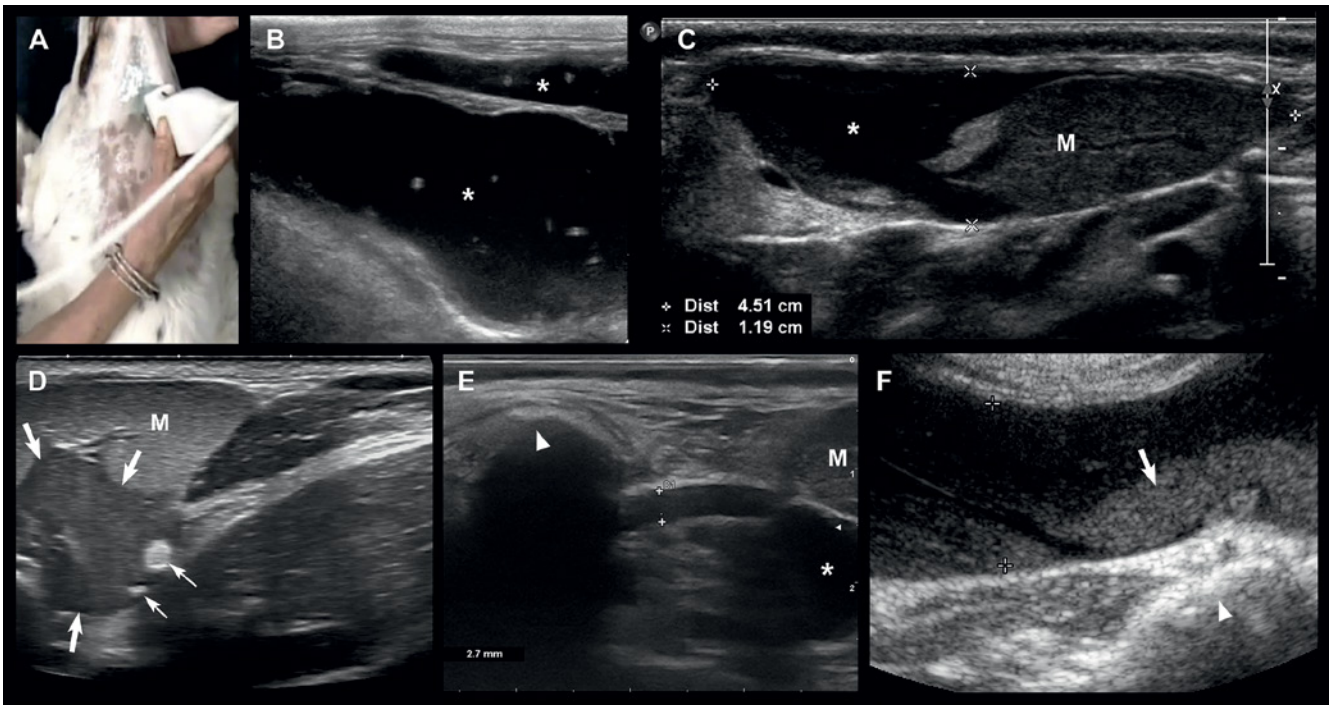


Figure 4.21. Sialocele in four dogs and a salivary duct cyst in a cat. (A, B) Sublingual sialocele in a 6-year-old Labrador cross with a swelling ventral to the cranial neck that started about 2 years but got bigger recently. **(A)** The probe is placed on the side of the swelling, ventral to the mandible; this location supports a sublingual origin. **(B)** Corresponding sagittal sonogram displaying a bilobed cystic structure (*) containing several small pebble-like structures. Surgery confirmed the sublingual origin of the sialocele and the concretions found in the fluid were proteinaceous, cellular debris. **(C)** In another dog, a large cyst (*) expands the cranial margin of the mandibular salivary gland (M, cursors). **(D)** Four-year-old Dachshund dog with a mandibular gland (M) sialocele (arrows) containing echogenic fluid and several well-defined hyperechoic sialoliths (thin arrows) casting shadows. **(E)** In the other dog with mandibular (M) sialocele (*), a dilated salivary duct is seen deep to the mandible (arrowhead), presumably obstructed. **(F)** Salivary duct cyst in a cat. On this sagittal image, a well-demarcated, fluid-filled structure is ventral and lateral to the mandibular bone (arrowhead). The cyst (between cursors) contains hyperechoic sedimenting debris (arrow).

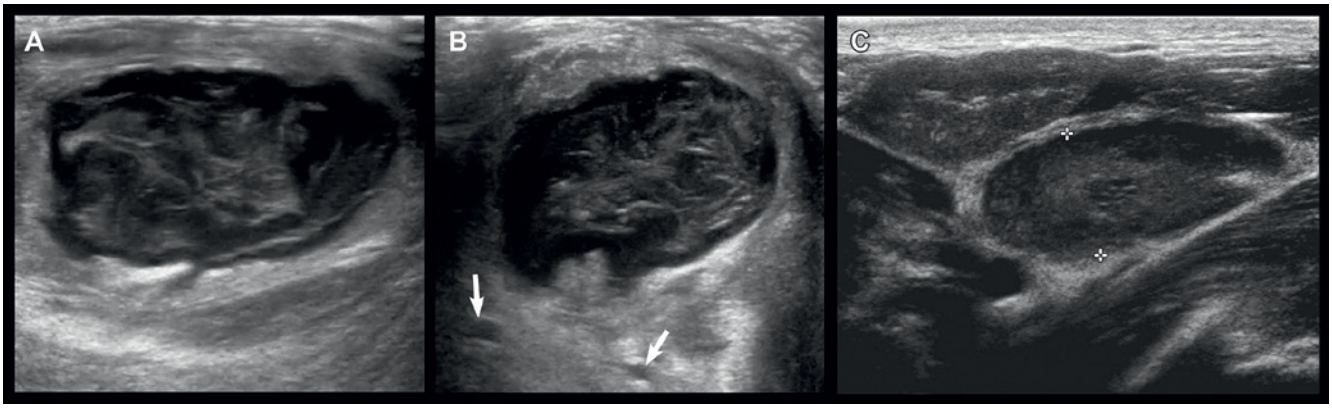


Figure 4.22. Tongue Abscess in a 6-month-old Golden Retriever with ventral mandibular swelling, poor appetite, and fever. Transverse **(A)** and sagittal **(B)** sonograms were performed along the ventral intermandibular space and a large cavitary lesion with inhomogeneous and partially mobile material was present at the base of the tongue. Small arrows point to lingual vessels. Both retropharyngeal lymph nodes **(C)** were about 1.3 cm thick and inhomogeneous. Pus was sampled from the lesion and the abscess was confirmed and debrided at surgery. No foreign body was identified.

Vet-ebooks.com

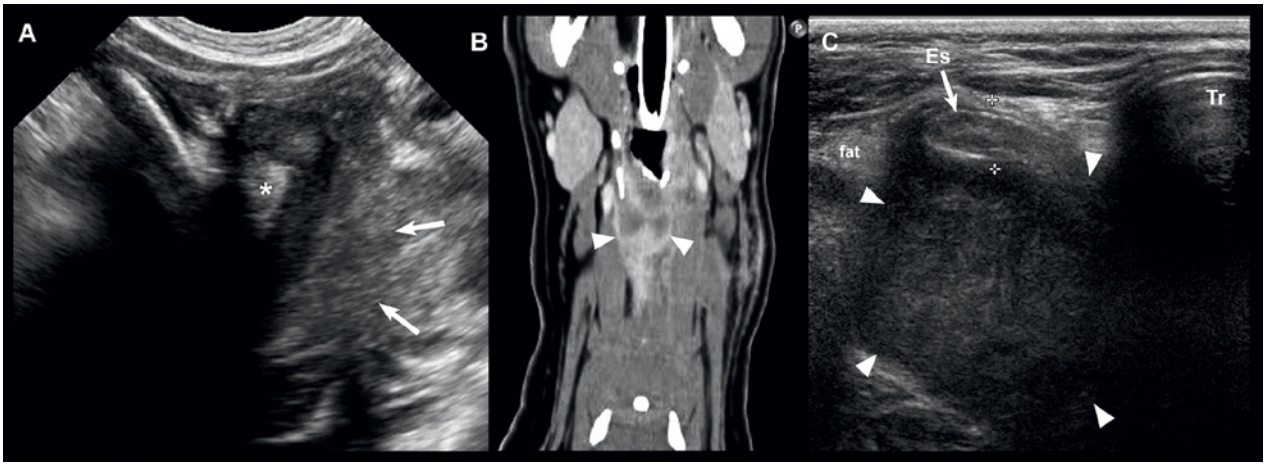


Figure 4.23. **Paraesophageal abscess in two dogs. (A)** A hypoechoic ill-defined region (arrows) is present in the paraesophageal region, caudal to the thyroid cartilage. The esophageal wall is thickened, and a small amount of echogenic fluid is in the lumen (*). The dog was present with dysphagia, decreased appetite, facial nerve paralysis, and voice change. Cytological interpretation of the sampled mass showed neutrophilic to pyogranulomatous septic inflammation, which was likely the result of a penetrating foreign body. **(B)** Corresponding contrast-enhanced computed tomography image in the dorsal plane. The mass (arrowheads) is hyperattenuating with internal hypoattenuating areas corresponding to fluid accumulations. **(C)** In this other dog, the abscess appears as a large, poorly echogenic mass (arrowheads) dorsal to the esophagus (Es, between calipers), associated with regional hyperechoic fat. The cellular fluid mimics a solid soft-tissue mass. Tr, trachea.

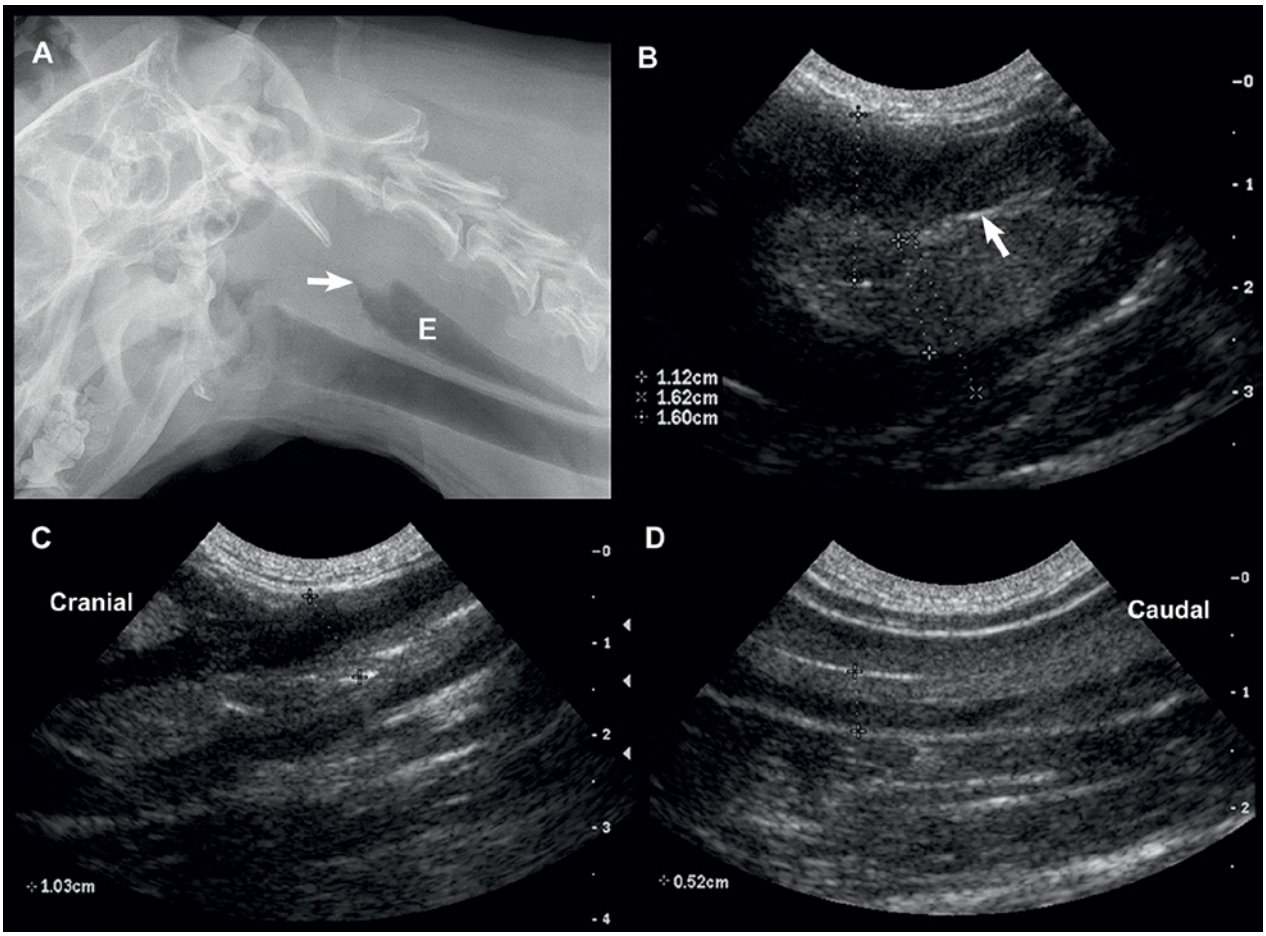


Figure 4.24. **Idiopathic esophageal hypertrophy in a dog. (A)** Lateral radiograph of the cranial neck in a dog with chronic swallowing disorder. The esophagus (E) is abnormally dilated with air, and a soft-tissue mass-like projection is noted within its cranial lumen (arrow), in the region of the cricopharyngeal muscle. **(B–D)** Transverse **(B)** and sagittal **(C, D)** sonograms of the diffusely and markedly thickened esophagus, involving in particular the muscular layer. The mucosa is hyperechoic and confluent with the submucosa. Cranial and caudal portions of the esophagus are represented in **(C)** and **(D)**, respectively. The arrow points to the collapsed lumen. Mucosal and muscular hyperplasia and hypertrophy, as well as nonspecific inflammation, were diagnosed by means of ultrasound-guided biopsies. There was no evidence of neoplasia.

Vet-ebooks.com

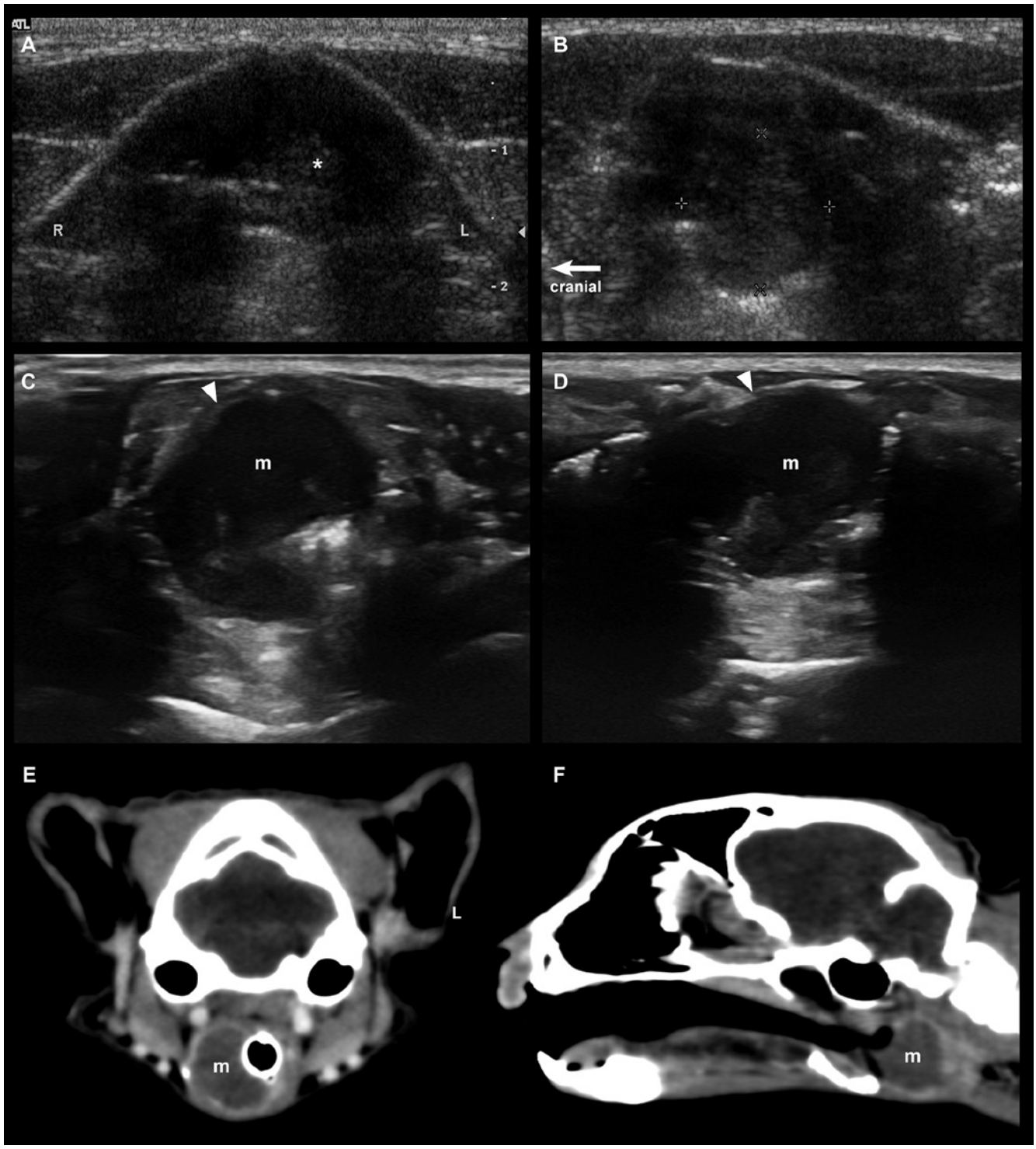


Figure 4.25. **Laryngeal neoplasia in a dog and in a cat. (A)** Transverse image of the larynx through the thyroid cartilage. An ill-defined soft-tissue mass (asterisk) is within the left (L) side of the lumen of the larynx, corresponding to a melanoma in a dog. R, right. **(B)** In the left sagittal orientation, the mass is better delineated (calipers) originating from the left laryngeal wall. Cranial is to the left side of the image. **(C, D)** Transverse and sagittal sonographic images of a laryngeal lymphoma in the cat. The hypoechoic mass (m) invades the right vocal fold, filling most of the laryngeal lumen at that level. The outside wall (arrowheads) of the larynx remains distinct. **(E, F)** Corresponding transverse and sagittal contrast-enhanced computed tomography (CT) images showing a well-defined hypoattenuating right-sided laryngeal mass (m).

Vet-ebooks.com

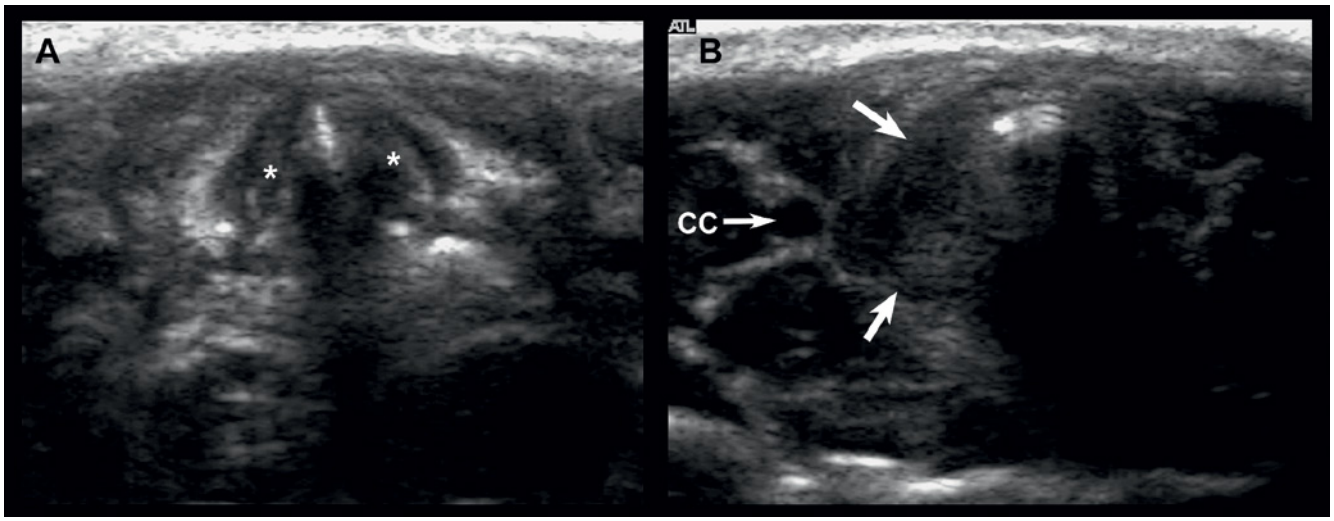


Figure 4.26. **Lymphofollicular laryngitis in a cat. (A)** Transverse image of the larynx with the right side on the left of the image. The vocal folds (*) appear normal at this level. **(B)** Just caudal to the vocal folds is a lobulated, hypoechoic mass (arrows) involving the right side of the larynx and trachea, in contact with the right common carotid artery (CC).

in the laryngeal wall and may also distort or obliterate the normal laryngeal structures. **Lymphoma** in cats appears as a well-circumscribed, hypoechoic, or mixed echogenic mass arising from the ventral or lateral larynx (Figure 4.25). The mass may narrow the lumen of the larynx or displace the larynx to the side. **Squamous cell carcinoma** may appear more destructive and occurs in the ventral larynx as well as on the vocal cords. **Laryngeal cysts** have been reported infrequently in dogs and cats and may originate from the epiglottis, laryngeal wall, or paralaryngeal tissues. They are seen as anechoic masses distorting the rima glottis.

Laryngeal paralysis, which is a neuropathy of the recurrent laryngeal nerve, causes unilateral or bilateral paralysis of the vocal folds. Ultrasound can be used to evaluate the motion of the vocal folds and cuneiform cartilages to diagnose the condition. The criterion for diagnosing laryngeal paralysis is reduced or asymmetrical motion of the vocal folds. This appears as a lack of abduction of the cuneiform cartilages and vocal folds during inspiration on one or both sides (Figure 4.27). Approximately 50% of dogs with laryngeal paralysis have abnormal dorsal and ventral movement of the arytenoid cartilages that is caused by the unaffected contraction of the cricothyroid muscle (Rudorf et al. 2001). Signs of severe upper-airway obstruction include collapse of the pharynx during inspiration, paradoxical movement of the vocal folds (blowing laterally during expiration), and caudal displacement of the whole larynx.

Laryngeal paralysis and vocal cord thickening have been reported in cats (Taylor et al. 2009). Vocal cord thickening can be caused by inflammation, edema, or neoplasia. The anatomy and motion of the cuneiform cartilage are like those of dogs, but the smaller size of the feline larynx may cause incomplete visibility of the vocal folds.

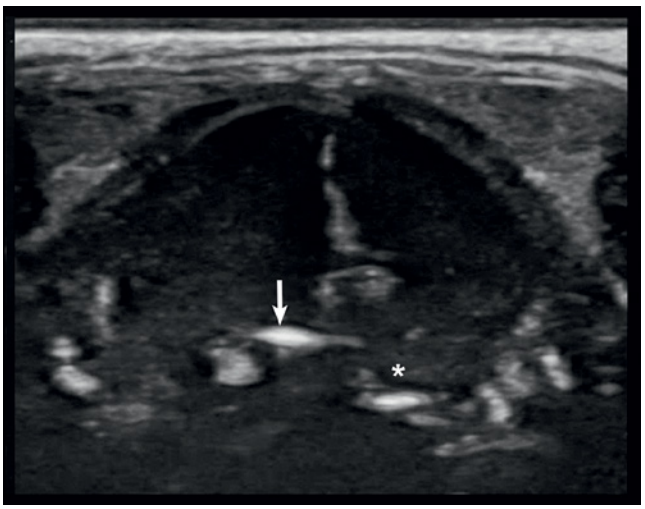


Figure 4.27. **Laryngeal paralysis in a cat.** In this cat with unilateral laryngeal paralysis, the right cuneiform process of the arytenoid cartilage (*) fails to abduct during inspiration, compared to the left (arrows).

In dogs with **tracheal collapse**, the hyperechoic air column appears oval to flat depending on the severity of the collapse (Rudorf et al. 1997). The dorsal tracheal membrane is not visible directly, but this alteration in the shape of the air column is indicative of annular ring collapse. The flattening of the air column may

Vet-ebooks.com

worsen slightly with the head in an extended position. Other tracheal lesions such as masses, trauma, or tracheitis and edema may occasionally be seen (see Chapter 5, Figure 5.36).

Vessels

Abnormalities involving the carotid artery and jugular veins include **thrombosis** in hypercoagulable animals (e.g., hyperadrenocorticism and protein-losing nephropathy) and may be a complication of catheter placement. The acute thrombus may be anechoic and is recognized only by a flow void in the color Doppler signal, although such void can also be attributed to perpendicular imaging. More chronically, the thrombus becomes more echogenic and visible in B-mode imaging. Stenosis of these vessels can occur as a complication of surgery, trauma, or invasive neoplasia. Stenosis appears as a narrowing of the vessel lumen, typically with increased velocity in the center of the stenosis and turbulent flow beyond the stenosis.

Carotid-body tumors, also known as **chemodectomas,** are rare neuroendocrine tumors that arise from the pressure sensors in the carotid artery and more commonly seen in brachycephalic breeds. Chronic hypoxia and overstimulation of the carotid bodies caused by brachycephalic syndrome may contribute to the increased prevalence of disease in these breeds. On ultrasound examination, these tumors are located at the bifurcation of the common carotid artery into the internal and external carotid arteries, dorsolateral to the larynx (Figure 4.28). Tumors may surround the common carotid artery and its branches and are generally highly vascular. They are typically hypoechoic to surrounding tissues, lobulated, and well marginated and can easily be confused with (ectopic) thyroid masses (Fife et al. 2003; Taeymans et al. 2012; Wisner et al. 1994). Fine-needle aspirates should be performed with caution, considering the vascularity and proximity of major vessels.

Any invasive tumor, such as thyroid carcinoma, can cause local distortion of vasculature. Invasion of the common carotid artery can cause erosion of the wall and massive hemorrhage (Slensky et al. 2003). Local vessels may be infiltrated by the neoplasia (Figure 4.29), recruited into the tumor, compressed, or thrombosed. Other small vessels may also distend to supply the mass. Tumors of the caudal neck and thoracic inlet may also invade local vessels or cause thrombosis. Thrombosis may be visible as an intraluminal heterogeneous structure either partially or fully filling the lumen, or in the acute phase may not be visible. If the cranial vena cava is thrombosed, distended, or occluded, veins may be seen more cranially. Obstruction of venous flow may also cause subcutaneous edema of the head and neck, which will appear as hyperechoic bands interlaced with anechoic fluid layers.

Arteriovenous fistula in association with a recurrent thyroid carcinoma has been reported in the neck (Wisner et al. 1994). These abnormal connections between the arterial system and the venous system often have multiple tortuous vessels with arterial flow characteristics. The local veins may be distended, and subcutaneous edema may develop.

Cervical masses such as lymphoma and thyroid carcinoma may also involve the vagosympathetic trunk, causing Horner's syndrome (Melian et al. 1996) and

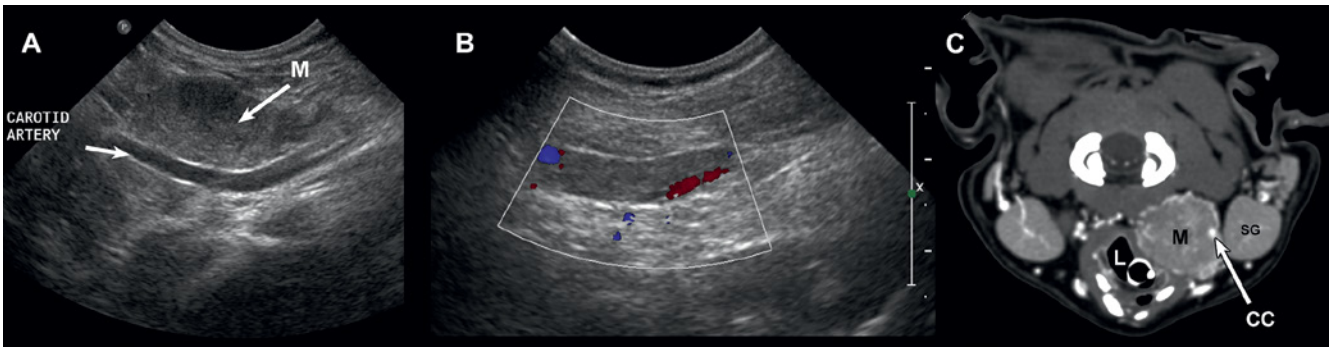


Figure 4.28. Chemodectoma in a 10-year-old dog. Sagittal B-mode **(A)** image of a neck mass and sagittal color Doppler **(B)** of the neighboring external jugular vein. A smooth, well-circumscribed mass (M) of low echogenicity is noted ventral to the common carotid artery. A moderately echogenic thrombus (arrow) fills most of the external jugular vein. **(C)** Transverse contrast-enhanced computed tomography (CT) image of the mass (M) demonstrating the characteristic position surrounding the carotid artery (CC) of a mass arising from the carotid body, and the marked vascularity of the mass. The adjacent larynx (L) is compressed. SG, mandibular salivary gland.

Vet-ebooks.com

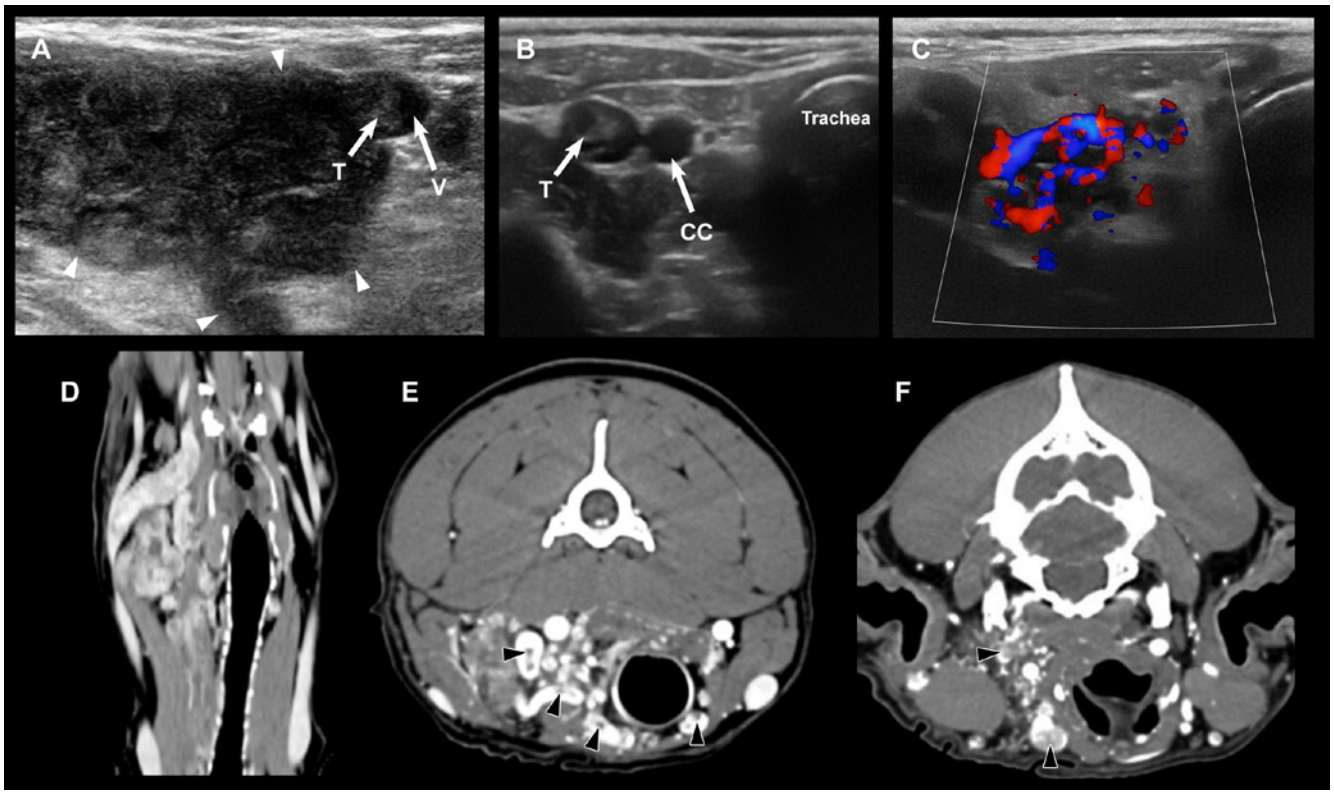


Figure 4.29. **Venous invasion and thrombosis in two dogs. (A)** Transverse image of a thyroid carcinoma. A large, ill-defined, hypoechoic mass (white arrowheads) has replaced the thyroid gland. The tumor thrombus (T) continued into the thyroid vein (V). **(B, C)** In another dog with suspected right thyroid carcinoma (not shown), heterogeneous echogenic thrombus (T) is noted in the lumen of the dilated right thyroid vein **(B)** and regional collateral venous circulation is particularly detected on Doppler evaluation (**C**). CC, common carotid artery. **(D–F)** Corresponding contrast-enhanced computed tomography (CT) images (**D)** dorsal plane; (**E, F)** transverse plane) acquired during the venous phase. Numerous small collateral vessels are present in the right submandibular region. Some of them exhibit internal filling defects, corresponding to thrombi (black arrowheads).

laryngeal paralysis (Schaer et al. 1979). There is also a single report of a neoplastic mass originating from the vagus nerve (Ruppert et al. 2000).

External Ear Canals and Tympanic Bullae

Middle-ear disease is often characterized by the presence of fluid in the tympanic bulla. Fluid in the bulla appears hypoechoic, replacing the normal gas shadows. The transmission of the ultrasound beam through the fluid also renders the far wall of the bulla visible (Figure 4.30). If air and gas are present in the bulla, a dependent scanning position may be the most sensitive. Fluid in the bulla can also be found incidentally as a transient effusion rather than because of inflammatory or obstructive disease, so its presence should be correlated with clinical signs of middle-ear disease.

Tumors and inflammatory polyps may fill the bulla and external ear canal and extend into the peripheral soft tissues in case of severe infection or malignant processes (Figures 4.31, 4.32). Variable echogenic tissue and fluid collections may then be observed at the periphery of the bulla and ear canal. The tympanic wall may also become irregular or interrupted due to new bone formation or lysis, respectively. In such cases, severe bacterial otitis media, neoplasia, osteomyelitis, craniomandibular osteopathy, or cholesteatoma should be considered.

Special Procedures

Tissue sampling of neck lesions is most often performed using a fine-needle aspirate, though tissue-core biopsies of larger lesions can safely be performed with ultrasound guidance (Figures 4.11F, 4.31C, and 4.33). However, because of the high vascularity of some organs and masses such as those of thyroid origin, and the presence of large arteries and veins often adjacent to cervical lesions, particular care should be taken when either fine-needle aspiration or tissue-core biopsy is attempted.

Vet-ebooks.com

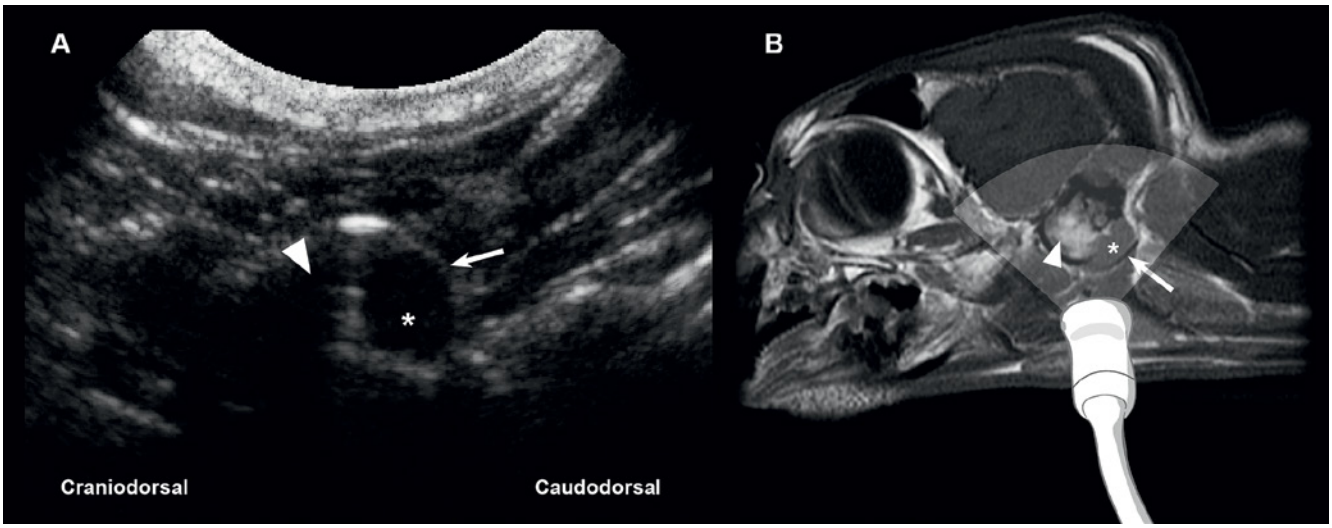


Figure 4.30. **Otitis media in a cat. (A)** Sagittal image of the tympanic bulla. The sonogram is taken from the ventral position. The ventromedial compartment of the bulla is filled with anechoic fluid (*) and the near wall is seen more clearly (arrow). The far wall is also visible because the fluid has transmitted the ultrasound. The dorsolateral compartment (arrowhead) appears hypoechoic, and there is no reverberation artifact, suggesting soft-tissue content. **(B)** Magnetic resonance (MR) T1-weighted postcontrast sagittal image of the tympanic bulla. The MR image confirms the presence of fluid in the ventromedial compartment (*) and contrast-enhancing soft tissue in the dorsolateral compartment (arrowhead). The arrowhead points to the caudoventral wall, as in **(A)**.

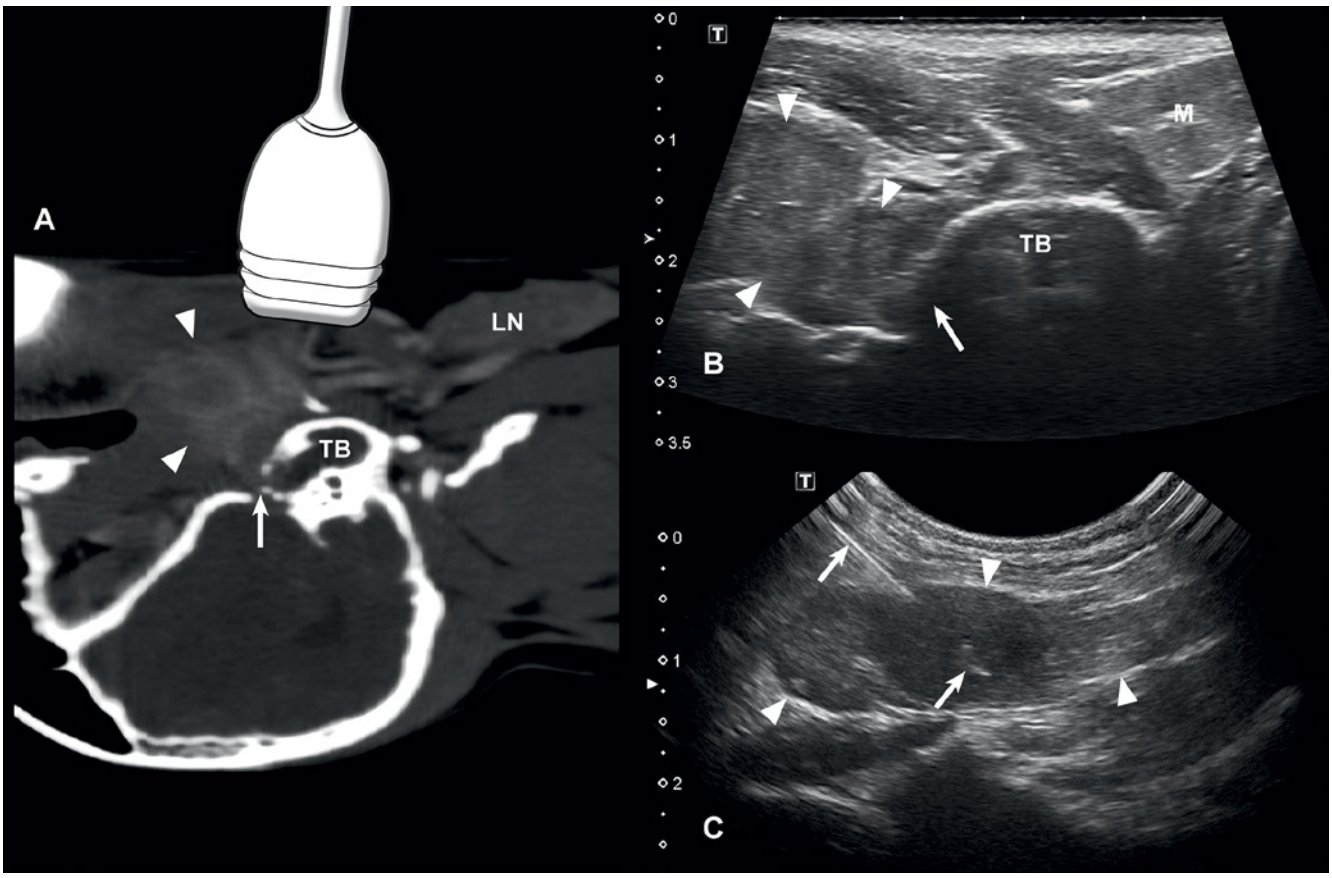


Figure 4.31. **Infiltration of the tympanic bulla by a carcinoma in a dog. (A)** Computed tomography (CT) image reformatted in the sagittal plane with an overlying linear probe placed to obtain image **(B)**. An ill-defined hyperattenuating mass (arrowheads) is present at the rostroventral aspect of the tympanic bulla (TB). The mass is seen to invade the rostral wall of the bulla (arrow). The bulla was otherwise filled with fluid. The nearby retropharyngeal lymph node (LN) is enlarged. **(B)** Corresponding sonographic image, with the dog placed in dorsal recumbency, showing a moderately echogenic mass (arrowheads) with focal lysis of the rostral wall (arrow) of the TB. **(C)** The adjacent retropharyngeal lymph node (arrowheads) was fine-needle-aspirated, revealing metastasis. The arrows point to the proximal third and distal extremity of the inserted 38-mm-long, 22-gauge needle. M, mandibular salivary gland.

Vet-ebooks.com

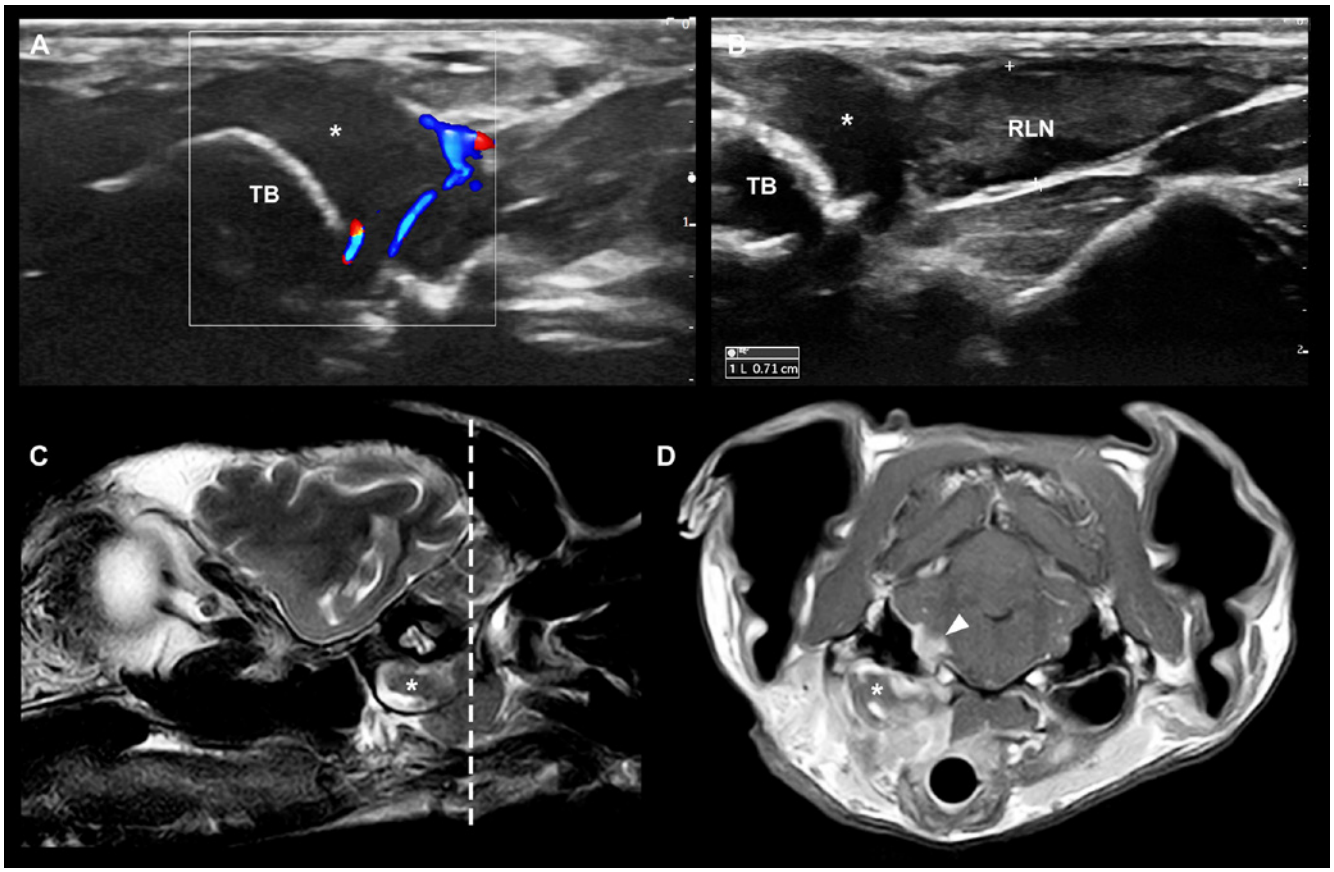


Figure 4.32. Neoplastic infiltration of the right tympanic bulla in a cat. (A, B) Sagittal **(A)** and oblique **(B)** sonographic images with the probe placed ventrolateral to the right tympanic bulla (TB). Hypoechoic vascularized relatively well-defined tissue (asterisk) is lining the external margins of the tympanic wall, thicker at its caudal aspect. Discontinuity of the wall was not detected on ultrasound evaluation. On corresponding magnetic resonance (MR) images (**C** T2-weighted sagittal image and **(D)** T1-weighted post-contrast transverse image), similar tissue is also noted into the tympanic bulla (asterisk), with ill-defined enhancement, mostly peripheral, also involving the inner ear and right ventrolateral aspect of the posterior fossa (white arrowhead). Ultrasound-guided sampling of tissue ventral to the right tympanic bulla and ipsilateral retropharyngeal medial LN (RLN) both yielded a diagnosis of lymphoma.

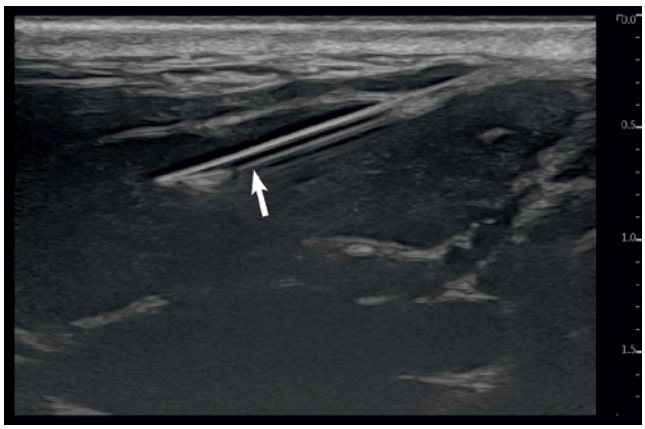


Figure 4.33. Ultrasound-guided fine needle aspiration of a retropharyngeal lymph node. Sagittal image of an enlarged RLN in a 2-year-old cat during FNA with a 21G needle (arrow).

Vessels of masses and tissues can be identified with color and power Doppler imaging to gauge vascularity, to map vessels prior to fine-needle aspiration or biopsy, and to determine the operability of a mass lesion.

Parathyroid ablation has also been implemented using both chemical (ethanol) (Figure 4.34) and radiofrequency methods (heat) (Long et al. 1999; Pollard et al. 2001) as an alternative to surgery. Both methods were safe and successful in the few clinical trials reported. In a retrospective study of 32 dogs with primary hyperparathyroidism, heat ablation treatment was followed by hypercalcemia resolution in 69% of cases. Larger parathyroid nodule size and concurrent hypothyroidism were associated with treatment failure (Bucy et al. 2017). In a retrospective study of 24 dogs, ethanol ablation treatment was followed by hypercalcemia resolution in 85% of cases (Gutin et al. 2015).

Vet-ebooks.com

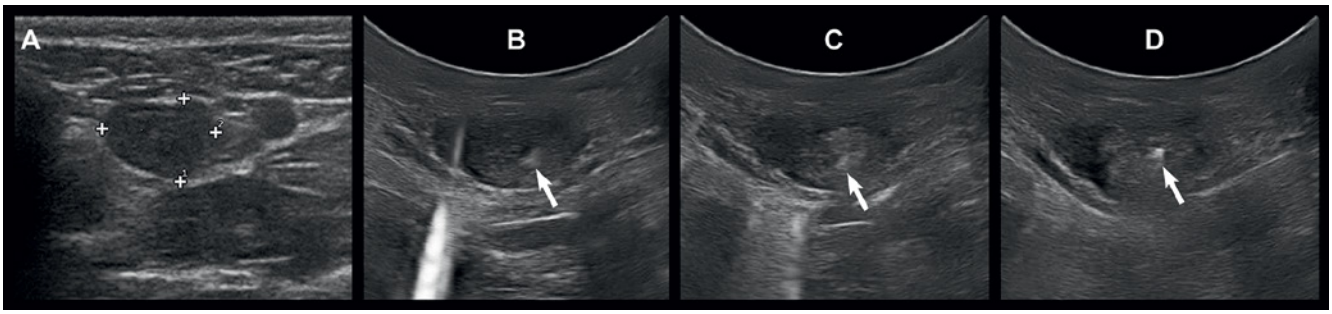


Figure 4.34. Ethanol ablation of a parathyroid nodule in a 15-year-old dog. (A) Sagittal image of the thyroid gland with the hypoechoic parathyroid nodule at its cranial aspect. It measures up to 7.7 mm in length and 5.6 mm in height. The width was also measured on the transverse image (not shown) to evaluate the nodule's volume. An equivalent volume of 95% alcohol was then injected into the nodule. **(B)** Needle placement in the center of the nodule (arrow). **(C, D)** Progressive injection of alcohol, which led to a progressive hyperechoic and slightly hyperattenuating signal diffusing into the nodule, from the tip of the needle (arrows) toward the periphery of the nodule. Slight needle repositioning can be attempted to optimize alcohol diffusion into the nodule, if needed.

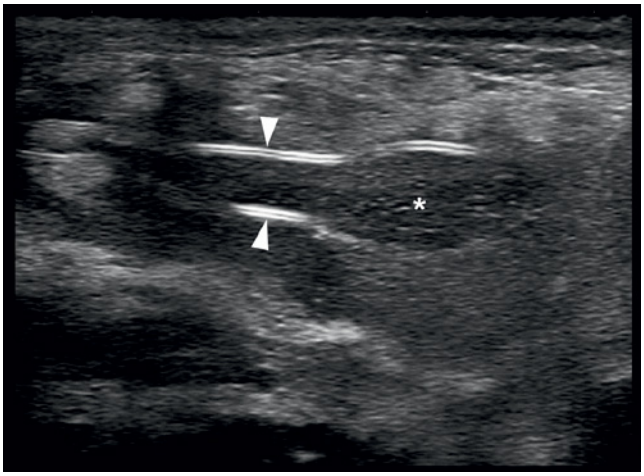


Figure 4.35. Penrose in a dog following surgical excision of a salivary gland tumor. The walls of the Penrose drain appear as thin double-line structures, floating in an echogenic collection (*) that was confirmed to be an abscess at surgery.

Postsurgical monitoring when swelling is present may also be useful. Detection of seroma, abscess, or left surgical material such as gauze, penrose, and catheter can guide the next therapeutic step (Figure 4.35).



Visit our website at **www.SmallAnimalUltrasonography.com** for complementary video clips with annotations and text on:

- Normal neck anatomy and scanning
- Thyroid carcinoma
- Parathyroid nodule
- Lymphadenopathy
- Neck abscess and foreign body
- Neck abscess
- Salivary sialocele

References

Belotta AF, Gomes MC, Rocha NS, Melchert A, et al. (2019) Sonography and sonoelastography in the detection of malignancy in superficial lymph nodes of dogs. J Vet Intern Med 33(3):1403–1413.

Bray JP, Lipscombe VJ, White RA, Rudorf H (1998) Ultrasonographic examination of the pharynx and larynx of the normal dog. Vet Radiol Ultrasound 39(6):566–71.

Bromel C, Pollard RE, Kass PH, Samii VF, et al. (2005) Ultrasonographic evaluation of the thyroid gland in healthy, hypothyroid, and euthyroid golden retrievers with nonthyroidal illness. J Vet Intern Med 19:499–506.

Bucy D, Pollard R, Nelson R (2017) Analysis of factors affecting outcome of ultrasound-guided radiofrequency heat ablation for treatment of primary hyperparathyroidism in dogs. Vet Radiol Ultrasound 58(1):83–89.

Cannon MS, Paglia D, Zwingenberger AL, Boroffka SA et al. (2011) Clinical and diagnostic imaging findings in dogs with zygomatic sialadenitis: 11 cases (1990-2009). J Am Vet Med Assoc 239(9):1211–1218.

Carlisle CH, Biery DN, Thrall DE (1991) Tracheal and laryngeal tumors in the dog and cat: literature review and 13 additional patients. Vet Radiol 32:229–235.

Cray M, Selmic LE, Ruple A (2020) Salivary neoplasia in dogs and cats: 1996-2017. Vet Med Sci 6(3):259–264.

Dickie AM, Doust R, Cromarty L, Johnson VS, et al. (2003) Ultrasound imaging of the canine tympanic bulla. Res Vet Sci 75:121–126.

Fife W, Mattoon J, Drost WT, Groppe D, et al. (2003) Imaging features of a presumed carotid body tumor in a dog. Vet Radiol Ultrasound 44:322–325.

Gooding GA, Herzog KA, Laing FC, McDonald EJ Jr (1977) Ultrasonographic assessment of neck masses. J Clin Ultrasound 5:248–252.

Guttin T, Knox VW 4th, Diroff JS (2015) Outcomes for dogs with primary hyperparathyroidism following treatment

Vet-ebooks.com

with percutaneous ultrasound-guided ethanol ablation of presumed functional parathyroid nodules: 27 cases (2008-2011). J Am Vet Med Assoc 247(7):771–7.

Le Roux C, Venter FJ, Kirberger RM 2017 Cervical porcupine quill foreign body involving the spinal cord of a dog: a description of various imaging modality findings. J S Afr Vet Assoc 88:e1–e7.

Lenoci D, Ricciardi M (2015) Ultrasound and multidetector computed tomography of mandibular salivary gland adenocarcinoma in two dogs. Open Vet J 5(2):173–8.

Liles, S.R., Linder, K.E., Cain, B., Pease, A.P. (2010) Ultrasonography of histologically normal parathyroid glands and thyroid lobules in normocalcemic dogs. Vet Radiol Ultrasound 51:447–452.

Long, C.D., Goldstein, R.E., Hornof, W.J., Feldman, E.C., et al. (1999) Percutaneous ultrasound-guided chemical parathyroid ablation for treatment of primary hyperparathyroidism in dogs. J Am Vet Med Assoc 215:217–221.

Melian C, Morales M, Espinosa de los Monteros A, Peterson ME (1996) Horner's syndrome associated with a functional thyroid carcinoma in a dog. J Small Anim Pract 37: 591–593.

Miller ML, Peterson ME, Randolph JF, Broome MR, et al. (2017) Thyroid cysts in cats: a retrospective study of 40 cases. J Vet Intern Med 31(3):723–729.

Mooney CT (2002) Pathogenesis of feline hyperthyroidism. J Feline Med Surg 4:167–169.

Nemanic S, Nelson NC (2012) Ultrasonography and noncontrast computed tomography of medial retropharyngeal lymph nodes in healthy cats. Am J Vet Res 73(9):1377–85

Peterson ME, Broome MR (2015) Thyroid scintigraphy findings in 2096 cats with hyperthyroidism. Vet Radiol Ultrasound 56(1):84–95.

Phillips DE, Radlinsky MG, Fischer JR, Biller DS (2003) Cystic thyroid and parathyroid lesions in cats. J Am Anim Hosp Assoc 39:349–54.

Pollard, R.E., Long, C.D., Nelson, R.W., Hornof, W.J. et al. (2001) Percutaneous ultrasonographically guided radiofrequency heat ablation for treatment of primary hyperparathyroidism in dogs. J Am Vet Med Assoc 218:1106–1110.

Pollard RE, Bohannon LK, Feldman EC. (2015) Prevalence of incidental thyroid nodules in ultrasound studies of dogs with hypercalcemia (2008-2013). Vet Radiol Ultrasound 56(1):63–7.

Reese S, Ruppert C (2001) Ultrasonographic imaging of the vagosympathetic trunk in the dog. Vet Radiol Ultrasound 42:272–275.

Reese S, Breyer U, Deeg C, Kraft W, et al. (2005) Thyroid sonography as an effective tool to discriminate between euthyroid sick and hypothyroid dogs. J Vet Intern Med 19:491–498.

Reusch CE, Tomsa K, Zimmer C, Hoerauf A et al. (2000) Ultrasonography of the parathyroid glands as an aid in differentiation of acute and chronic renal failure in dogs. J Am Vet Med Assoc 217:1849–1852.

Rudolf H, Brown P (1998) Ultrasonography evaluation of laryngeal masses in six cats and one dog. Vet Radiol Ultrasound 38:430–434.

Rudorf H, Herrtage ME, White RA (1997) Use of ultrasonography in the diagnosis of tracheal collapse. J Small Anim Pract 38:513–518.

Rudorf H, Barr FJ, Lane JG (2001) The role of ultrasound in the assessment of laryngeal paralysis in the dog. Vet Radiol Ultrasound 42:338–343.

Ruppel MJ, Pollard RE, Willcox JL (2019) Ultrasonographic characterization of cervical lymph nodes in healthy dogs. Vet Radiol Ultrasound 60(5):560–566.

Ruppert C, Hartmann K, Fischer A, Hirschberger J, et al. (2000) Cervical neoplasia originating from the vagus nerve in a dog. J Small Anim Pract 41:119–122.

Schaer M, Zaki FA, Harvey HJ, O'Reilly WH (1979) Laryngeal hemiplegia due to neoplasia of the vagus nerve in a cat. J Am Vet Med Assoc 174:513–515.

Secrest S, Grimes J (2019) Ultrasonographic size of the canine parathyroid gland may not correlate with histopathology. Vet Radiol Ultrasound 60(6):729–733.

Seiler GS, Griffith E (2018) Comparisons between elastographic stiffness scores for benign versus malignant lymph nodes in dogs and cats. Vet Radiol Ultrasound 59(1):79–88.

Silver, T.I., Lawson, J.A., Mayer, M.N. (2012) Sonographic characteristics of presumptively normal main axillary and superficial cervical lymph nodes in dogs. Am J Vet Res 73:1200–1206.

Slensky KA, Volk SW, Schwarz T, Duda L, et al. (2003) Acute severe hemorrhage secondary to arterial invasion in a dog with thyroid carcinoma. J Am Vet Med Assoc 223:649–653.

Solano M, Penninck D. (1996) Ultrasonography of the canine, feline and equine tongue: normal findings and case history reports. Vet Radiol Ultrasound 37(3):206–213.

Taeymans O, Duchateau L, Schreurs E, Kramer M, et al. (2005) Intra- and interobserver variability of ultrasonographic measurements of the thyroid gland in healthy beagles. Vet Radiol Ultrasound 46:139–142.

Taeymans O, Daminet S, Duchateau L, Saunders JH (2007). Pre- and post-treatment ultrasonography in hypothyroid dogs. Vet Radiol Ultrasound 48:262–269.

Taeymans O, Penninck D.G, Peters R.M (2012) Comparison between clinical, ultrasound, CT, MRI, and pathology findings in dogs presented for suspected thyroid carcinoma. Vet Radiol Ultrasound 54(1):61–70.

Taylor S.S, Harvey A.M, Barr F.J, Moore A.H, Day M.J. (2009) Laryngeal disease in cats: a retrospective study of 35 cases. J Feline Med Surg 11:954–962.

Torad FA, Hassan EA (2013) Clinical and ultrasonographic characteristics of salivary mucoceles in 13 dogs. Vet Radiol Ultrasound 54(3):293–8.

Wisner ER, Mattoon JS, Nyland TG, Baker TW (1991) Normal ultrasonographic anatomy of the canine neck. Vet Radiol Ultrasound 32:185–190.

Wisner ER, Nyland TG, Mattoon JS (1994) Ultrasonographic examination of cervical masses in the dog and cat. Vet Radiol Ultrasound 35:310–315.

Wisner ER, Penninck D, Biller DS, Feldman EC, et al. (1997) High-resolution parathyroid sonography. Vet Radiol Ultrasound 38:462–466.

Wisner ER, Mattoon JS, Nyland TG (2002) Neck. In Nyland TG, ed. Small Animal Diagnostic Ultrasound. Philadelphia: WB Saunders, pp. 285–304.

Woods SJ, Palm C, Sheley M, Feldman EC, et al. (2018) Ultrasonography does not consistently detect parathyroid glands in healthy cats. Vet Radiol Ultrasound 59(6):737–743.

Vet-ebooks.com

Vet-ebooks.com

CHAPTER FIVE

Thorax

Silke Hecht[1], Gabriela Seiler[2], and Dominique Penninck[3]

[1]*Department of Small Animal Clinical Sciences, College of Veterinary Medicine, University of Tennessee, Knoxville, TN, USA*
[2]*Department of Molecular Biomedical Sciences, College of Veterinary Medicine, NC State University, Raleigh, NC, USA*
[3]*Department of Clinical Sciences, Cummings School of Veterinary Medicine, Tufts University, North Grafton, MA, USA*

Preparation and Scanning Technique

Focused thoracic ultrasonography has gained popularity in recent years as a fast and noninvasive screening test in small animal emergency cases ("TFAST"; Boysen and Lisciandro 2013). This technique differs from standard thoracic ultrasonography, which is typically preceded by thoracic radiography or thoracic computed tomography (CT) to confirm the presence of a lesion amenable for ultrasonographic investigation, identify a suitable acoustic window, and rule out entities, such as pneumothorax, which may preclude or limit a meaningful ultrasonographic examination (Tidwell 1998). This chapter covers the regular ultrasonographic examination of the thorax in dogs and cats. TFAST is discussed in Chapter 2.

In normal animals, evaluation of intrathoracic structures is hampered by the interposition of aerated lung tissue. Collapsed or consolidated lung, thoracic masses, or pleural effusion can provide a suitable acoustic window. As pleural effusion may facilitate the examination of intrathoracic structures, thoracocentesis should be postponed (especially in mild cases) until the ultrasonographic examination has been performed, unless the patient has respiratory compromise (Larson 2009).

To optimize image quality, hair should be clipped in the region to be scanned, and acoustic gel should be applied. An intercostal approach is mostly used and involves examination of the thoracic structures by positioning the transducer on the chest wall between ribs (Figure 5.1). Animals are generally positioned in lateral recumbency, although scanning in sternal recumbency or while a patient is standing may be considered in compromised patients or for an initial screening. A thoracic inlet approach aids in visualizing cranial thoracic lesions (Figure 5.1). A subxiphoid or subcostal (transhepatic) approach may be used to assess caudal mediastinal or pulmonary lesions. With the animal in dorsal or lateral recumbency, the transducer is aimed cranially under the rib cage (Figure 5.1).

Some examiners prefer imaging the dependent portion of the thorax by using a cardiac table. This approach optimizes the acoustic window, because pleural effusion accumulates in the dependent portion of the thorax, and the pulmonary structures in the near field contain less air because of positional atelectasis. However, ultrasound-guided interventional procedures are difficult to perform using this approach, and the field of view is limited to the size of the table window and the ability to position the area of interest over the opening.

Usually, a curvilinear or microconvex sonographic probe with a small footprint should be selected when using an intercostal window, although a linear probe may also be used. The optimal frequency depends on the size of the animal and the location of the lesion. For the examination of the cranial mediastinum in large dogs, a 5-MHz transducer may be used, whereas examination of small superficial pulmonary lesions necessitates the use of a higher-frequency transducer (10 MHz or higher). Curvilinear transducers are best suited for transhepatic or thoracic inlet approaches.

The examination is performed in at least two planes, depending on the nature, size, and location of the lesion(s).

Atlas of Small Animal Ultrasonography, Third Edition. Edited by Dominique Penninck and Marc-André d'Anjou.
© 2025 John Wiley & Sons, Inc. Published 2025 by John Wiley & Sons, Inc.
Companion website: www.SmallAnimalUltrasonography.com

Vet-ebooks.com

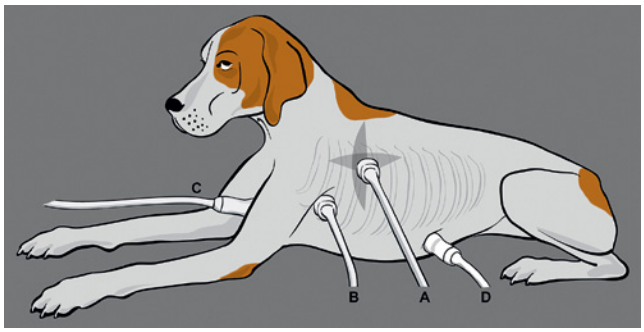


Figure 5.1. Ultrasonographic examination of the thorax. The patient can be examined while standing or in sternal, lateral, or dorsal recumbency. **A)** With the intercostal approach, the transducer is placed on the thoracic wall in the area of interest, previously detected on radiographs or computed tomography (CT). **B)** To better evaluate the cranial mediastinum, the thoracic limbs are pulled forward. The transducer is placed on the thoracic wall caudal to the elbows and dorsolateral to the sternum. **C)** The thoracic inlet approach can be used to evaluate the most cranial aspect of the thoracic cavity. The transducer is placed on midline on the caudal neck and aimed caudally into the thorax. An initial dorsal plane view is useful to identify the trachea, esophagus, and great vessels. **D)** A subxiphoid or subcostal (transhepatic) approach may be used to assess caudal mediastinal or pulmonary lesions, with the transducer aimed cranially under the rib cage. For this approach, access to the caudal thoracic cavity is easier when the animal is in dorsal or lateral recumbency.

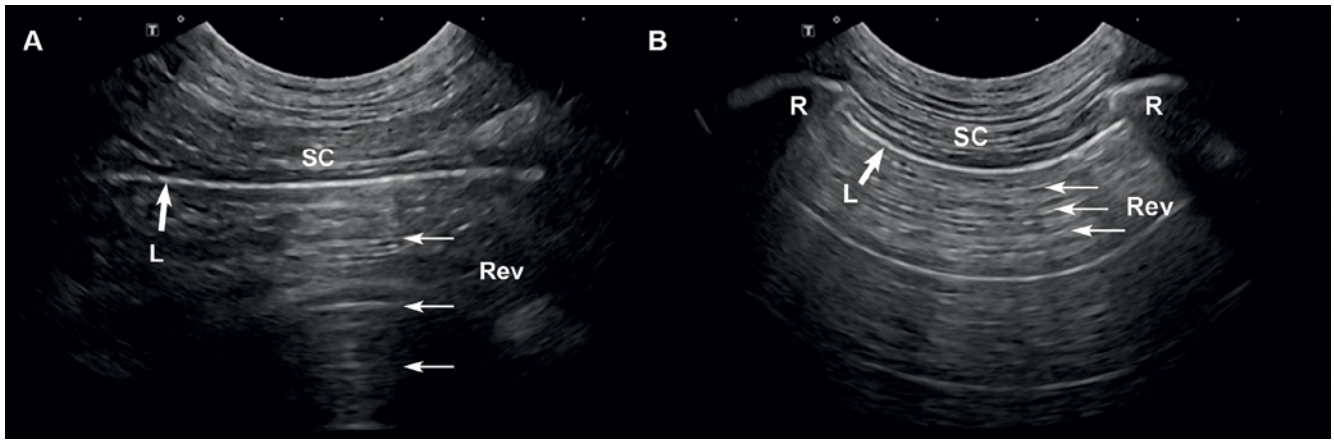


Figure 5.2. Normal thoracic wall imaged with an intercostal approach. Longitudinal (**A**) and transverse (**B**) ultrasonographic images. The subcutaneous tissues (SC), which include muscle, fat, and fascial planes, are recognized as multiple alternating hypoechoic and hyperechoic layers in the near field. The lung surface (L, arrow) appears as a smooth, strongly hyperechoic line. Distal to the lung surface are dirty shadowing and reverberation artifacts (Rev) that prevent evaluation of the normal air-filled lung. The ribs are visible as strongly hyperechoic curvilinear structures (R), with clean distal shadowing in the far field.

Color, Power, or Spectral Doppler imaging is often limited in the thorax due to artifacts created by respiratory motion. Doppler imaging, when used with an appropriate velocity scale for the vessel or structure interrogated, may provide useful information about vascular patency and vascularity of thoracic mass lesions.

Contrast-enhanced ultrasound utilizes the highly reflective qualities of gas-filled microspheres or microbubbles injected intravenously. These microbubbles stay strictly intravascular and are small enough to circulate through the lungs and allow evaluation and quantification of microvascular perfusion. Since the method highlights even small microvessels, it can be used to establish necrotic or cystic regions within a mass lesion or to detect a lack of blood flow after vascular thrombosis or compression as with lung lobe torsion (Caivano 2016, Linta et al. 2017). Contrast-enhanced ultrasound has proved useful to characterize pulmonary and mediastinal mass lesions but lacks the specificity to differentiate benign from neoplastic mass lesions (Rick 2019).

Normal Sonographic Anatomy

Intercostal Approach

The soft tissues of the **thoracic wall** (skin, subcutaneous fat, and muscle) appear as layered tissues of alternating echogenicity in the near field (Figure 5.2A–D). The parietal pleura is rarely recognized as a discrete

Vet-ebooks.com

structure but may be differentiated from the visceral pleura in real time by the sliding motion of the lung during respiration. The ribs appear as smooth, curvilinear, hyperechoic structures with distal acoustic shadowing (Figure 5.2C, D). The **lung** interface is seen as an echogenic linear band with distal reverberation artifacts also called dirty shadowing. The repetitive echogenic horizontal lines of the reverberation artifact are often referred to as A-lines. The pulmonary parenchyma deep to the lung surface cannot be evaluated in normal animals because of these artifacts.

Evaluation of the normal cranial and caudal mediastinum by means of an intercostal approach is often hampered by the interposition of aerated lungs. However, **cranial mediastinal vessels** may be visualized as tubular anechoic structures that show flow on Doppler examination if the angle of insonation is not perpendicular (Figure 5.3).

The **thymus** may be visible in young animals and appears as echogenic, coarse, well-vascularized tissue in the ventral mediastinum cranial to the heart (Seiler 2011). Care must be taken not to confuse abundant mediastinal fat with intrathoracic lesions. The sternal lymph nodes may occasionally be identified in normal animals.

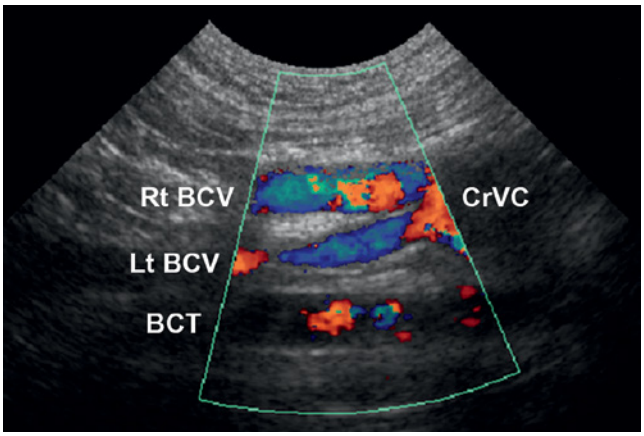


Figure 5.3. Normal cranial mediastinum in a dog when using right intercostal approach (dorsal plane) and color Doppler. The cranial mediastinal vessels are clearly visible. The confluence of the brachiocephalic veins to form the cranial vena cava is observed. BCT, brachiocephalic trunk; CrVC, cranial vena cava; Lt BCV, left brachiocephalic vein; Rt BCV, right brachiocephalic vein.

Transhepatic (Subcostal) Approach

The diaphragm–lung interface appears as a curvilinear, strongly hyperechoic structure in the far field cranial to the liver (Figure 5.4). The diaphragm cannot be readily distinguished from the adjacent hyperechoic lung interface, except in cases of pleural effusion or consolidation of the caudal lung lobes, or if thickened. The caudal vena cava passes through the diaphragm to the right of midline. The **caudal thoracic esophagus** is occasionally seen traversing the diaphragm (Figure 9.3). Using this approach, the examiner must be aware of the commonly observed mirror artifact (Figure 5.4; see also Figure 1.19).

Thoracic Inlet Approach

Mediastinal fat, the cranial thoracic trachea, and the esophagus are typically visualized when using a thoracic inlet approach. Cranial mediastinal vessels and occasionally sternal or cranial mediastinal lymph nodes are also visible.

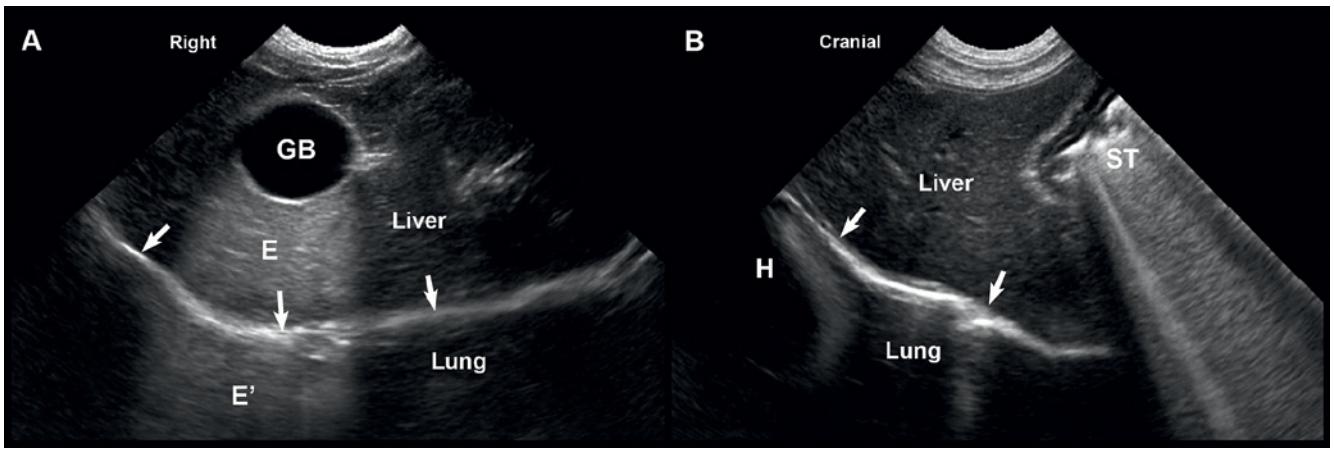


Figure 5.4. Normal caudal thorax in a dog when using a transhepatic (subcostal) approach. Transverse **(A)** and sagittal **(B)** images. The diaphragm–lung interface (arrows) appears as a curvilinear hyperechoic line cranial to the liver. A mirror image of the hyperechoic acoustic enhancement (E) deep to the gall bladder (GB) is in the lung region (E'). H, heart; ST, stomach.

Vet-ebooks.com

Sonographic Features of Thoracic Disorders

Lesions of the Thoracic Wall

Thoracic wall lesions include neoplasms, inflammatory lesions, and traumatic changes. Ultrasound allows assessment of the extent and margination of a lesion, bone involvement (such as in rib neoplasms, traumatic, or pathological fractures), echogenicity and echotexture (solid and/or fluid-filled), invasion of adjacent structures, and the presence of foreign material or gas (e.g., in abscesses). Inflammatory lesions affecting the thoracic wall include cellulitis, abscesses, and granulomas. Ultrasound enables the identification of fluid pockets indicative of abscessation (Figure 5.5), necrosis, or seroma. Ultrasonography has been proven to be more accurate than fistulography in the detection of foreign material in soft tissues in animals with chronic draining tracts or abscesses (Armbrust et al. 2003). Depending on their size and composition, **foreign bodies** are usually hyperechoic to the surrounding soft tissues and often cast an acoustic shadow (Schultz and Zwingenberger 2008; Figures 5.6, 5.7).

In cases of thoracic **trauma**, ultrasonography can be used as an alternative to radiography in the diagnosis of rib fractures, especially for unstable patients. Findings include discontinuity of cortical alignment (Figure 5.8A–C) as well as edge shadowing and reverberation artifacts arising from the margin of the displaced rib segment (Hurley et al. 2004). However, based on the literature on human patients, ultrasonography does not significantly increase the detection rate of rib fractures, may be uncomfortable for a patient, and is more time-consuming than radiography. During the healing process, the rib fracture fragments become rounded and are surrounded by hypoechoic tissue, presumably representing organizing hematoma and fibrous callus formation (Figure 5.8D–F).

A thoracic wall mass is convex, in broad-based contact with the chest wall, and displaces the normal lung interface (**extrapleural sign**). In contrast to most mass lesions originating from the pulmonary parenchyma, the angle between the extrapleural mass and the adjacent thoracic wall is obtuse (Figure 5.9). Additionally, the dynamic visualization of lung motion underneath thoracic wall lesions confirms their extrapulmonary origin.

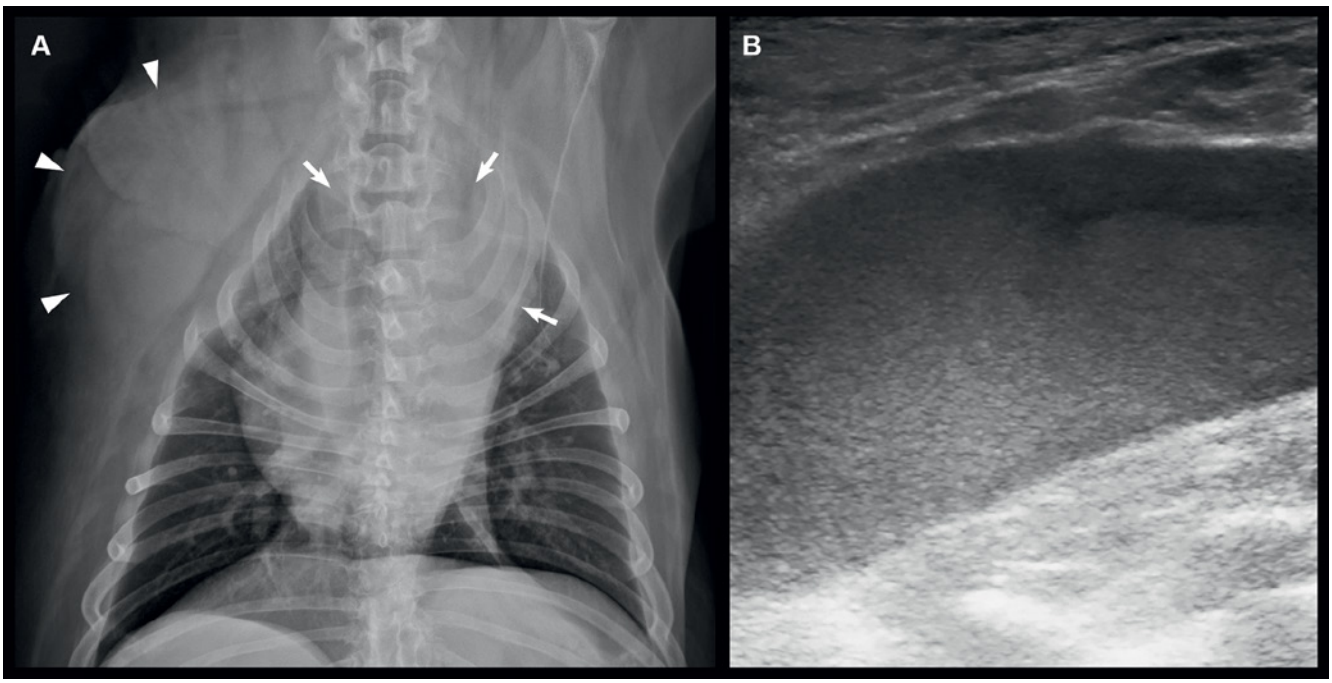


Figure 5.5. Thoracic wall abscess in an 8-year-old English bulldog that had recently undergone amputation of the right front limb due to an osteosarcoma. (A) On the ventrodorsal thoracic radiograph, there is marked focal soft-tissue swelling associated with the right cranial thoracic wall, extending from the caudal neck to approximately the sixth right rib (arrowheads). Note also an increased opacity in the left cranial mediastinum and mild rightward displacement of the trachea due to the concurrent presence of a heart base mass (arrows). **(B)** On ultrasound, there is a focal large cavitary lesion associated with the subcutaneous tissues of the right thoracic wall containing highly echogenic fluid (pus).

Vet-ebooks.com

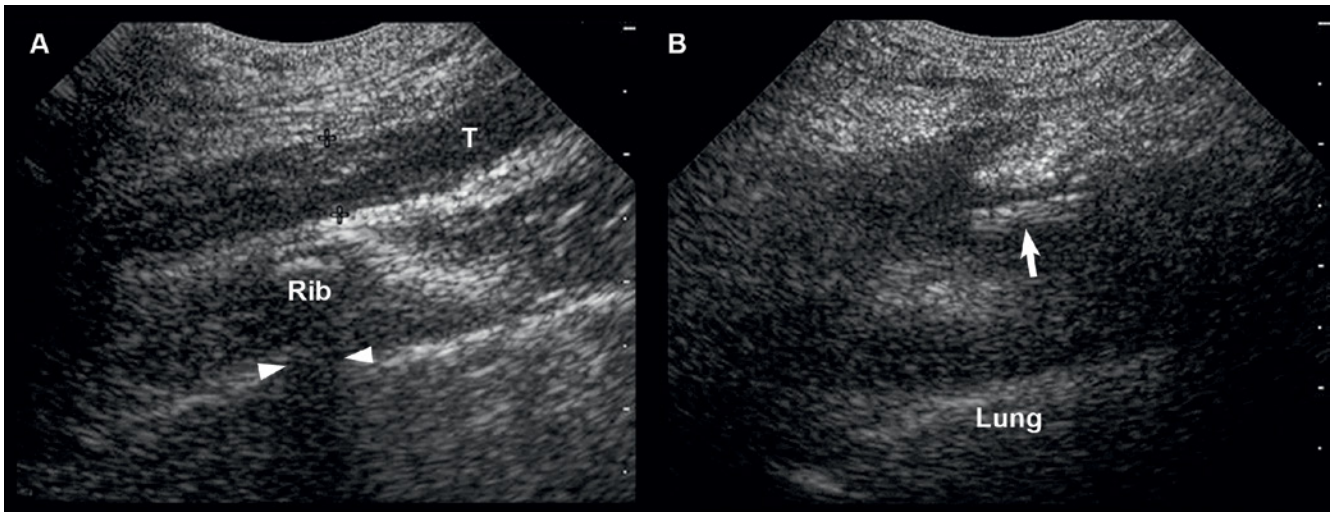


Figure 5.6. **Thoracic wall foreign body. (A, B)** In a 7-year-old German Shorthaired Pointer with a chronic draining wound, sonograms of the draining tract **(A)** and foreign body **(B)** are shown. The draining tract (T) appears as a 6-mm-wide tubular space within the subcutaneous tissues of the thoracic wall immediately superficial to the ribs. Notice the shadowing associated with the visible rib (arrowheads). At the termination of the tract, a hyperechoic, sharp-edged structure of 9 × 2 mm is noted, consistent with a foreign body (arrow). The foreign body is surrounded by hypoechoic material, consistent with an abscess. A wooden splinter was identified at surgery.

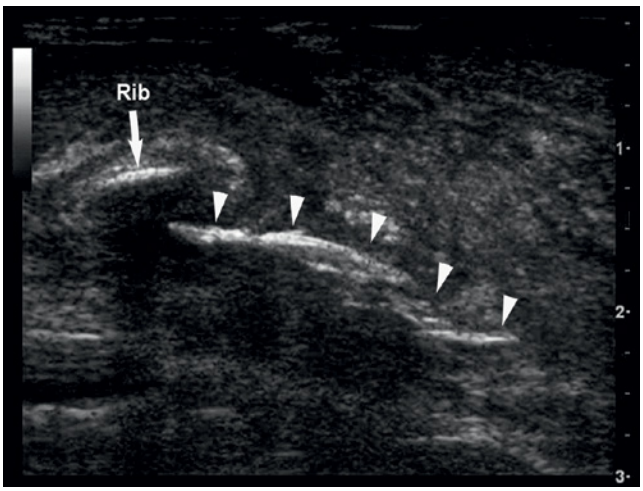


Figure 5.7. **Thoracic wall foreign body.** An irregular-shaped hyperechoic and hyperattenuating foreign body (arrowheads) is present near a rib of this English Setter with a draining tract and was suspected to represent plant foreign material. Note the hypoechoic inflammatory tissue located superficially along the thoracic wall. A grass awn was removed under ultrasound guidance. Courtesy of Dr Ulrich Zeyen, Centro Veterinario Specialisito, Rome, Italy.

Benign or malignant neoplastic processes, such as infiltrative lipomas or soft-tissue sarcomas, may invade the thoracic wall and appear as masses or swelling of variable size and echogenicity (Figures 5.10, 5.11).

Bony masses originating from ribs or sternum are most commonly neoplastic in etiology (e.g., chondrosarcoma or osteosarcoma). These masses cause irregular disruption of the smooth contour of the affected bone and are accompanied by an intrathoracic and/or extrathoracic mass lesion of variable size and echogenicity (Figures 5.12, 5.13). Metastatic disease may involve one or several bones of the thoracic wall and cause variable alteration in their normal hyperechoic, shadowing surface. The osseous proliferative and/or lytic changes encountered in aggressive bone lesions are typically irregular and poorly defined when compared with benign processes such as rib fractures. In cases where there is doubt, thoracic radiographs or CT may help to further characterize these changes.

Abnormalities of the Pleura and the Pleural Space

Pleural Effusion

Ultrasonography is useful in detecting and characterizing **pleural effusion**; identifying or ruling out an underlying problem, such as a cranial mediastinal mass; and guiding

Vet-ebooks.com

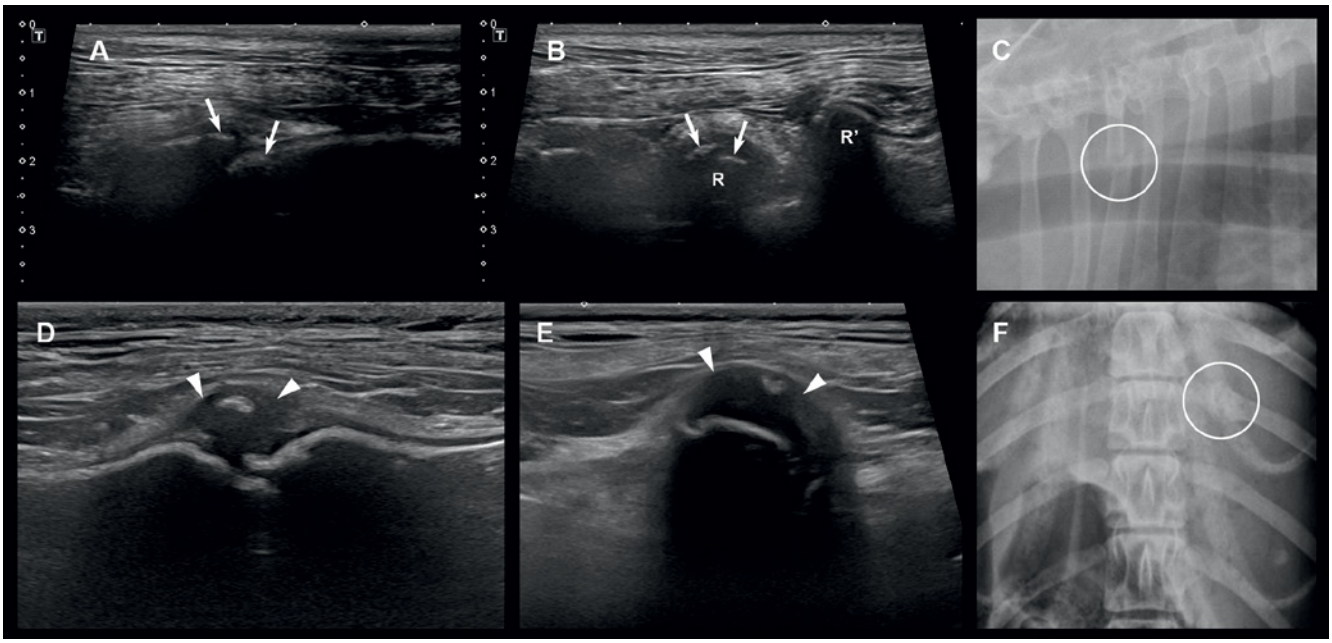


Figure 5.8. **Acute and chronic rib fractures in two different dogs. (A–C)** Acute fracture of the second rib in an 11-year-old mixed-breed dog. Ultrasound images obtained in the long **(A)** and transverse-axis **(B)** plane of the affected rib (R) show a disruption of the rib contour (compared to the adjacent normal rib, R'), with displacement and partial overlapping of sharply marginated bone fragments (arrows), and mild, heterogeneous adjacent soft-tissue swelling. The fracture is indicated by the circle on the corresponding radiograph **(C)**. **(D–F)** Chronic (healing) rib fracture in a German Shepherd dog. Long-axis **(D)** and transverse plane (in relation to the rib, **E**) ultrasound images show rounded edges of the hyperechoic fracture fragments and surrounding hypoechoic tissue (arrowheads), presumably representing organizing hematoma and fibrous callus formation. The fracture is indicated by the circle on the corresponding radiograph **(F)**.

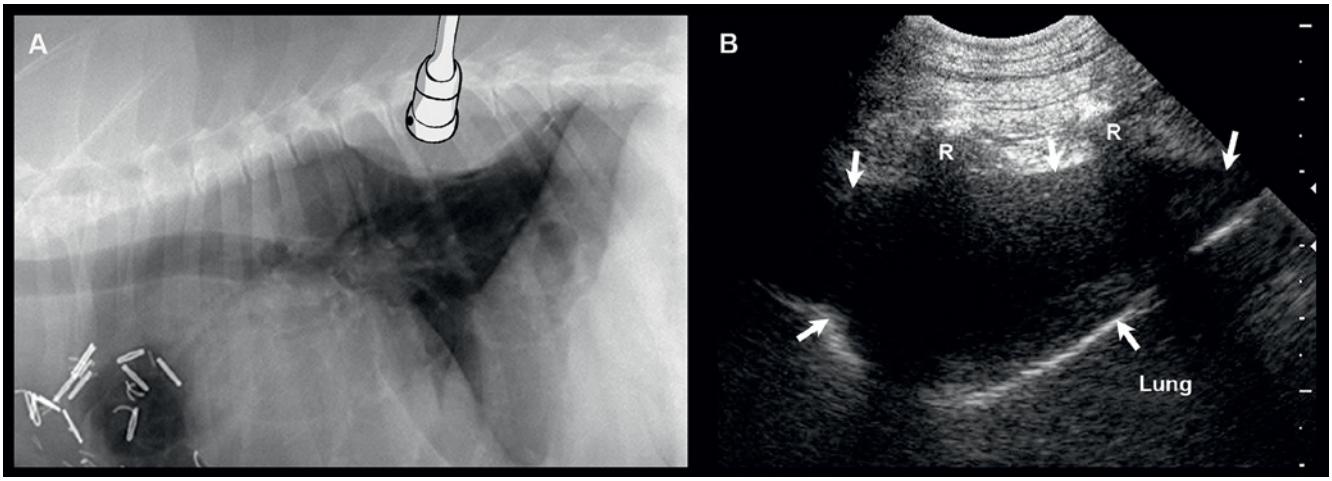


Figure 5.9. **Extrapleural mass (metastatic thymoma) in a 7-year-old elkhound. (A)** On this right lateral radiograph, there is a fusiform mass lesion associated with the caudal dorsal thorax (under the sonographic probe). This mass is in broad-based contact with the dorsal thoracic wall (extrapleural sign). Surgical hemoclips from previous removal of a cranial mediastinal mass (thymoma) are noted in the cranial ventral thorax. **(B)** The tumor, which is visualized by using a left dorsal intercostal approach, appears as a homogeneously hypoechoic mass lesion (arrows) forming an obtuse angle with the adjacent thoracic wall. The hyperechoic interface of the normal lung and acoustic shadows associated with ribs (R) are visible in the far field.

Vet-ebooks.com

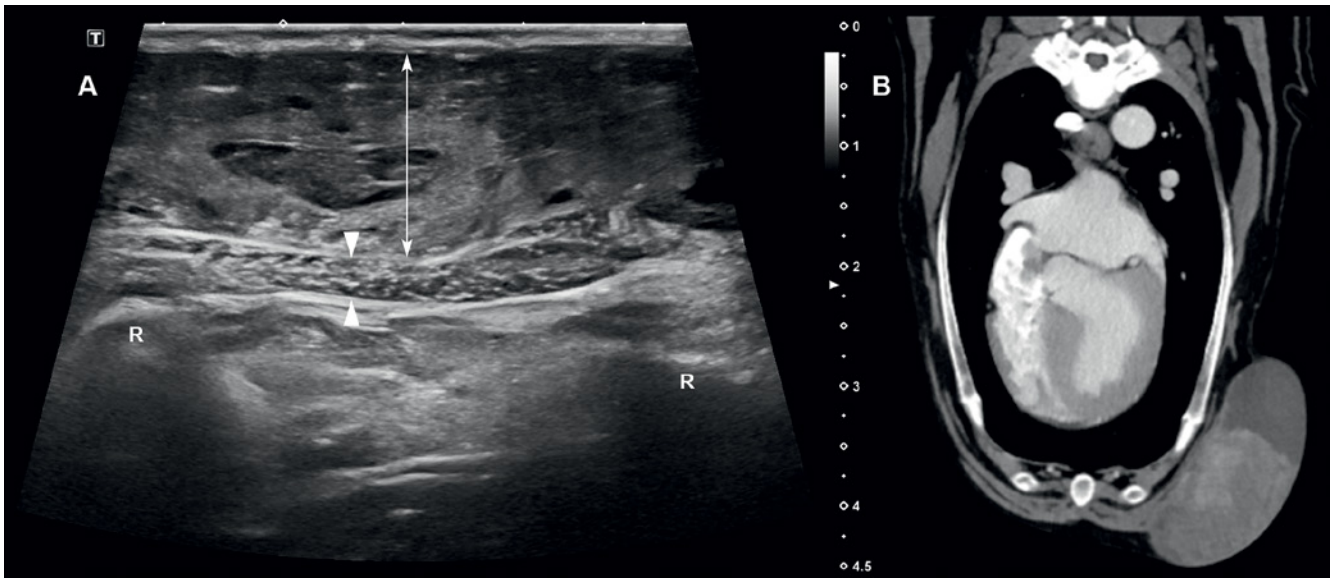


Figure 5.10. Grade I/low-grade soft-tissue sarcoma of the thoracic wall in a 10-year-old Great Dane dog. Long-axis ultrasound image **(A)** and transverse CT image **(B)** of the left thoracic wall. **(A)** A heterogeneous, cystic soft-tissue mass (double-arrow) is visible within the thoracic wall. The subjacent deep pectoral musculature (arrowheads) is not involved and moved separately to the mass lesion when examined in real time. Ribs are indicated with R. **(B)** The mass is visible in the left ventral thoracic wall and has a similar heterogeneous attenuation with variable contrast enhancement. In this case, the pectoral musculature and lack of involvement are better depicted with ultrasound over CT imaging.

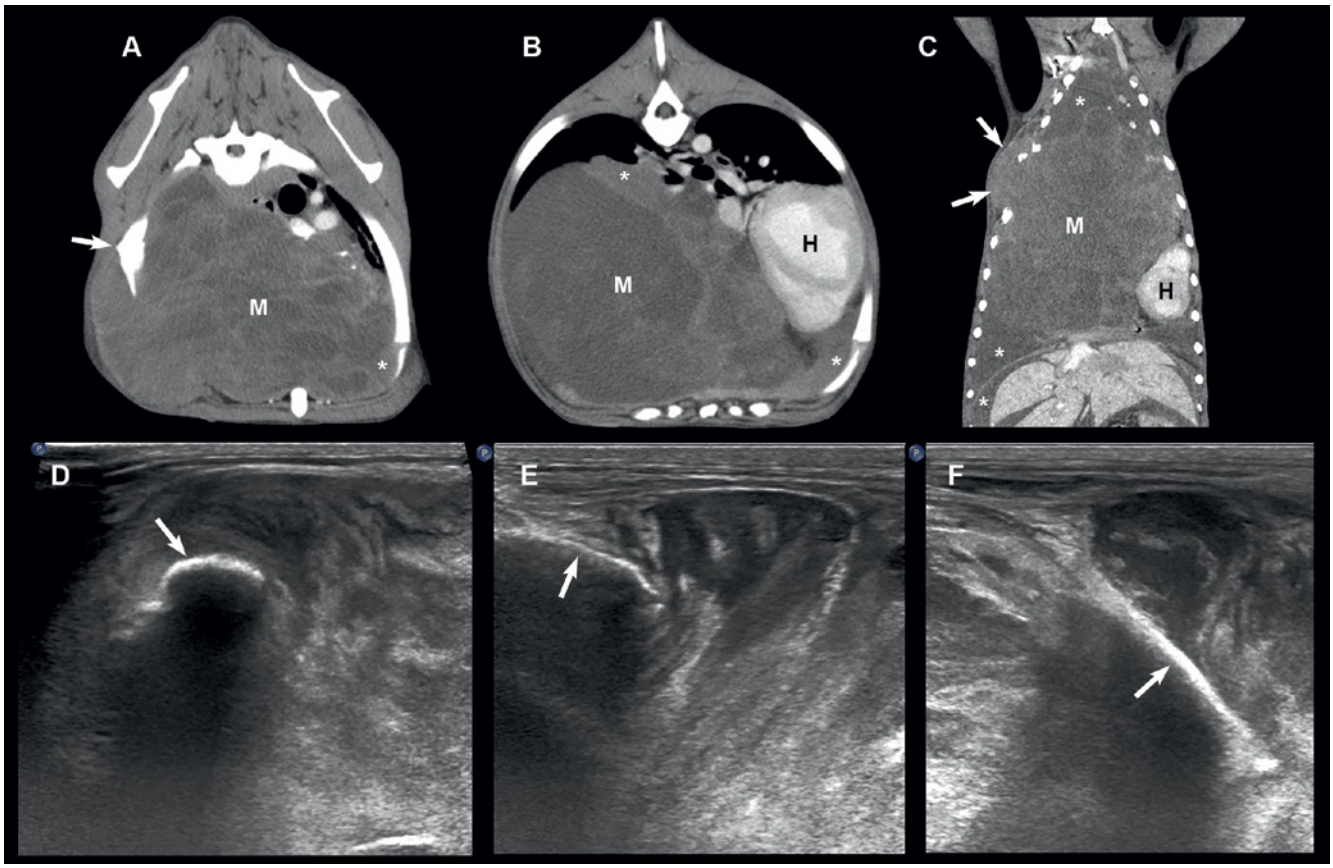


Figure 5.11. Anaplastic sarcoma involving the thoracic wall in a 1-year-old German Shepherd dog. Transverse **(A, B)** and dorsal reformated **(C)** CT images show a large heterogeneous soft-tissue attenuating mass (M) occupying most of the thorax and peripherally infiltrating the thoracic wall (arrows), resulting in displacement and heterogeneous thickening/remodeling (arrowhead) of the right fourth through sixth ribs. The heart (H) is displaced toward the left and abuts the left thoracic wall. There is evidence of both pleural and abdominal effusion (*). Ultrasound images **(D–F)** demonstrate the heterogeneous and extensive nature of the mass that infiltrates around and in between ribs (strongly hyperechoic interfaces indicated by arrows with distal shadowing (S)).

Vet-ebooks.com

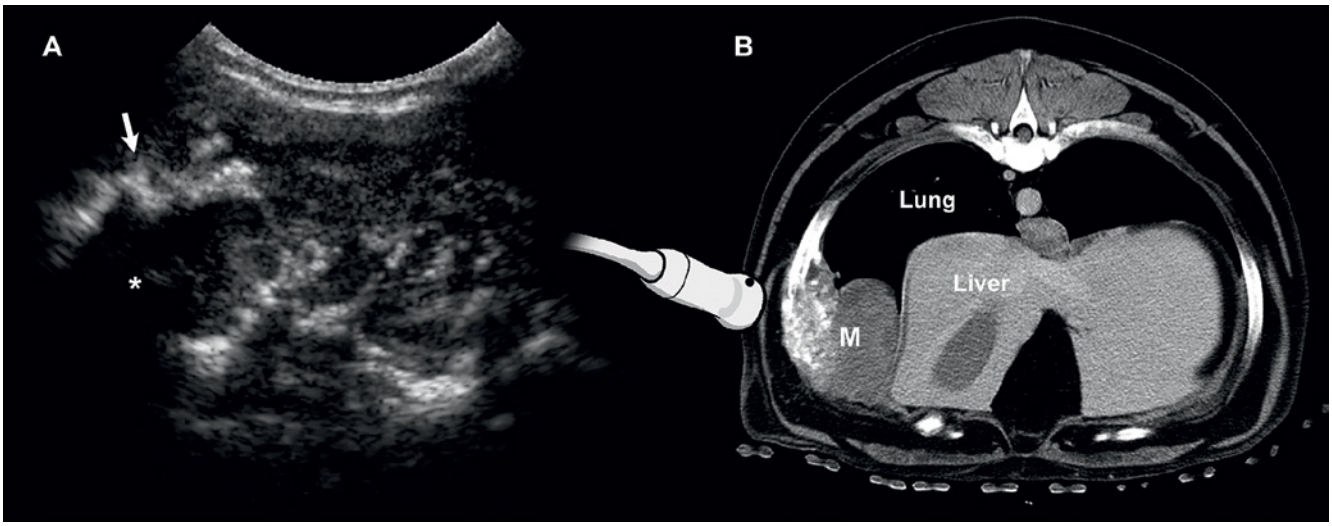


Figure 5.12. Rib osteosarcoma in a 10-year-old Rottweiler. Transverse sonographic **(A)** and CT **(B)** images of the 11th right rib **(B)**. There is an aggressive osteolytic and osteoproliferative rib mass (M) that extends into the right caudoventral thorax. Ultrasonographically, the mass is mixed in echogenicity, and hyperechoic foci (arrow) are associated with acoustic shadowing (*), consistent with mineralization.

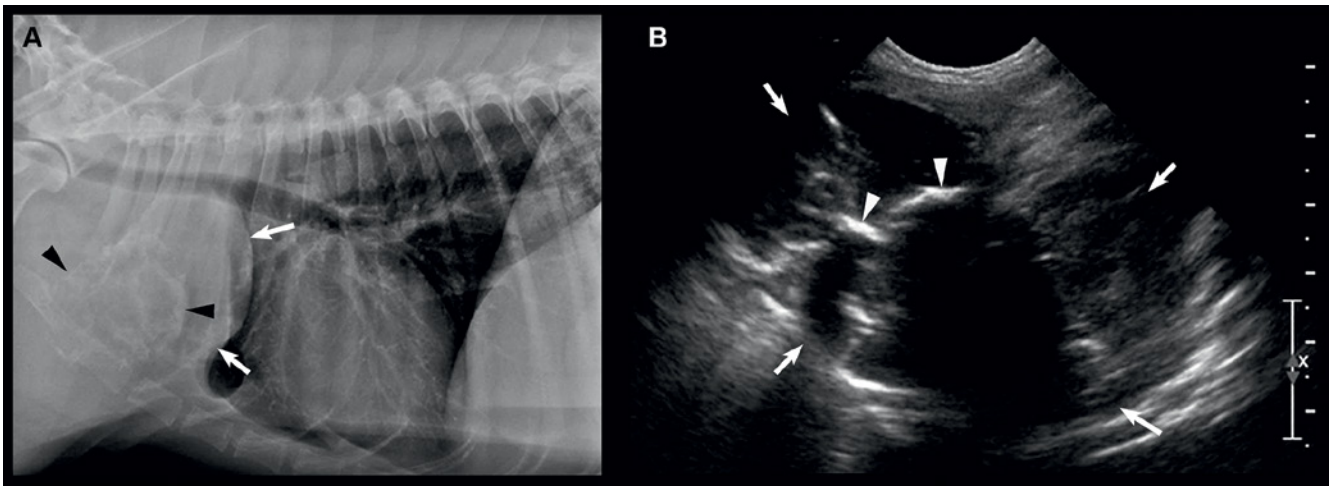


Figure 5.13. Primary rib tumor in an 11-year-old Labrador. (A) On the lateral thoracic radiograph, there is a large soft-tissue mass (white arrows) associated with the cranial ventral thorax at the level of the costal cartilages of the second pair of ribs that shows irregular amorphous mineralization (black arrowheads). **(B)** Transverse plane ultrasonographic image of the rib mass (white arrows). The mass is of mixed echogenicity, with multiple hyperechoic areas (white arrowheads) corresponding to the mineralization seen radiographically. Strong acoustic shadowing is seen distal to these mineralized regions.

sampling or therapeutic thoracocentesis. Pleural effusion appears as variably echogenic fluid separating the lung surface from the thoracic wall and diaphragm. The fluid echogenicity is mainly influenced by the concentration of free cells. Transudates, modified transudates, and chylous effusions are typically slightly echogenic or anechoic (Figure 5.14A–C). Exudates (e.g., pyothorax), malignant pleural effusions, or actively hemorrhagic effusions are usually moderately echogenic (Figure 5.14D) (Lin et al. 2020).

Free fluid may be differentiated from trapped fluid pockets by scanning the patient in different positions. Although free fluid accumulates in the dependent portion of the thorax, trapped fluid is not influenced by gravity and remains in the same region of the pleural space.

Chronic pleural effusion causes echogenic strands to develop within the pleural space, consistent with pleural adhesions or fibrinous bands (Figure 5.15).

Vet-ebooks.com

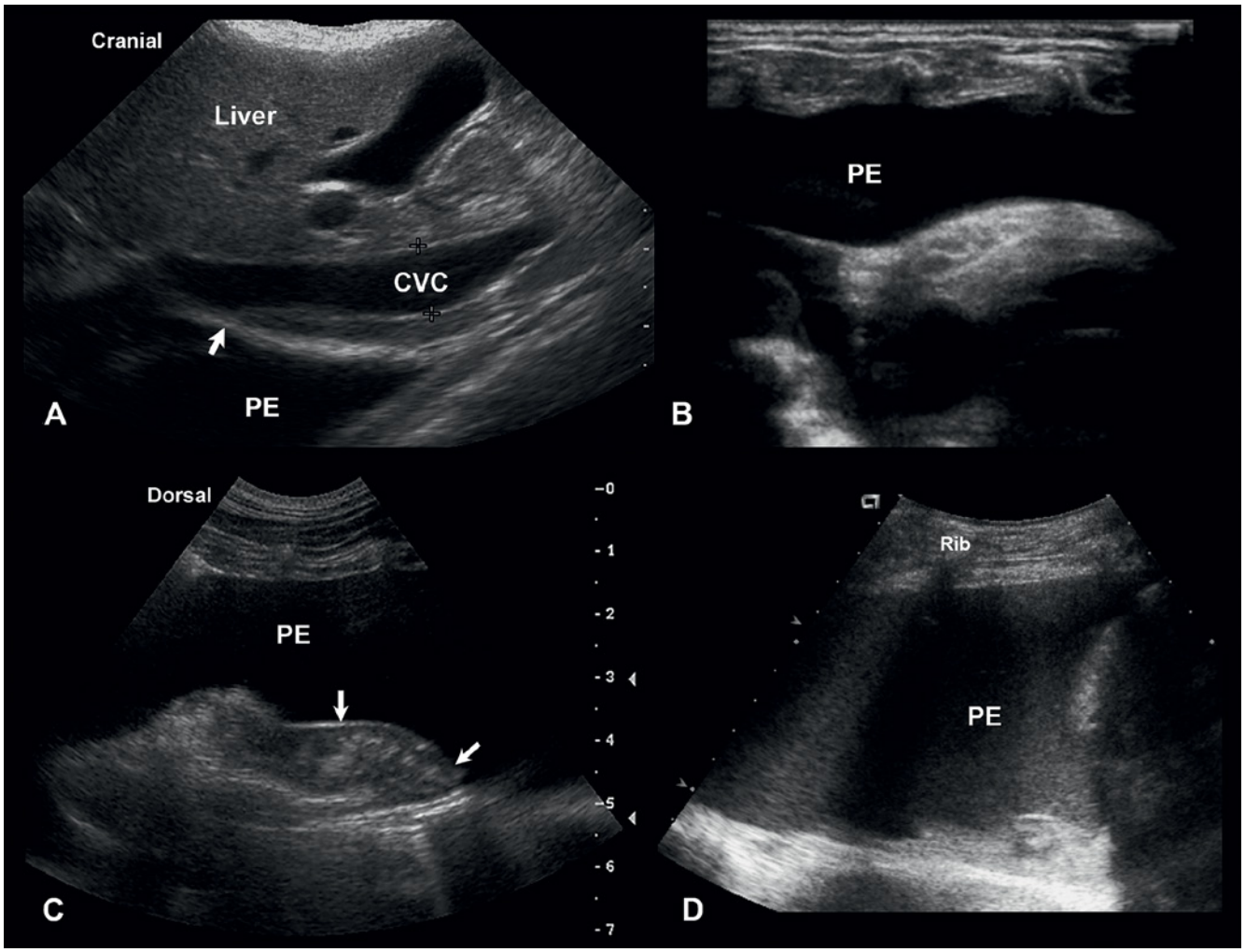


Figure 5.14. Pleural effusion (PE) in four patients. A subcostal/transhepatic **(A)** or intercostal approach **(B–D)** is used in these examples. **(A)** Anechoic PE in a cat with **congestive heart failure**. The effusion is seen cranial to the hyperechoic interface of the diaphragm (arrow). The caudal vena cava (CVC) is distended. **(B, C)** Anechoic PE is also noted in a 16-year-old cat with a modified transudate **(B)**, and in another cat with severe **chylothorax (C)**. Notice the concurrent lung lobe collapse (arrows). **(D)** Markedly echogenic PE is present in a 9-year-old Labrador Retriever with generalized **lymphoma**.

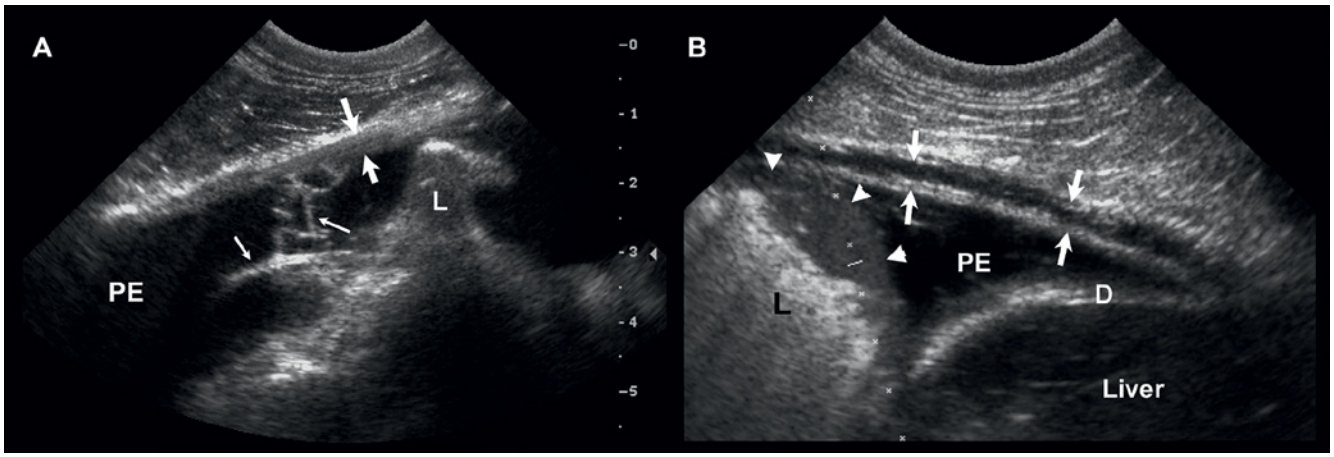


Figure 5.15. Chronic pleuritis in a 2-year-old cat. Ultrasonographic transverse images **(A, B)** of anechoic pleural fluid (PE) associated with lung atelectasis (L). Hyperechoic lines (thin arrows) are visible within the fluid, consistent with pleural fibrin strands and indicative of chronicity. The superficial parietal pleura (arrows) is irregularly thickened and hypoechoic. The visceral pleura of the left caudal lung lobe is also markedly thickened (arrowheads). Pleural effusion (PE) separates the lung lobe from the diaphragm **(B)**.

Vet-ebooks.com

Pleural Lesions

The pleural cavity can be affected by inflammation (**pleuritis**), in which case parietal and/or visceral thickening can be observed in association with pleural effusion (Figure 5.15).

Pleural neoplasia (such as carcinomatosis, mesothelioma, and metastatic disease) can also occur. The detection of small pleural nodules and masses on radiographs is commonly hampered by the presence of pleural effusion. On ultrasonographic examination, pleural neoplasia manifests as irregular thickening, nodules, or masses of variable echogenicity associated with the pleura. Lesions arising from the parietal pleura are readily recognized, especially in the presence of pleural effusion (Figures 5.16–5.18). Even in the absence of pleural effusion, differentiation between pulmonary and parietal pleural lesions is usually possible based on real-time ultrasonography. Whereas a pulmonary lesion moves with respiration, a nodule or mass arising from the parietal pleura remains stationary in comparison with the sliding lung (Figure 5.19; Mattoon and Nyland 1995). However, large masses of pulmonary origin that encompass most of a lung lobe may not exhibit a normal sliding pattern. Nodules or masses arising from the visceral pleura cannot be easily distinguished from lesions originating from the pulmonary parenchyma.

Pneumothorax

Ultrasonography is increasingly used in emergency care as a screening procedure to diagnose or rule out pneumothorax in patients with acute respiratory compromise, especially after a reported trauma (see Chapter 2 POCUS). Ultrasonographic screening of the pleural space for complications including pneumothorax is recommended after interventional procedures, and the examiner should be aware of the ultrasonographic appearance of this abnormality. Free air within the pleural space creates similar reverberation artifacts as normal lungs. However, the classic **gliding sign** of the lung against the parietal pleura is not observed. In cases of concurrent pleural effusion, a gas–fluid interface may be visualized. Ultrasound can detect even small amounts of free air within the pleural space (Hwang 2018). Care should be taken not to mistake stationary gas within gastrointestinal structures such as dilated stomach or megaesophagus with pneumothorax. Correlation with radiographs prior to thoracocentesis is ideal if the patient is clinically stable.

Abnormalities of the Mediastinum

In animals with a wide mediastinum on radiographs, ultrasound facilitates the differentiation of fat accumulation from fluid or mediastinal masses. Additionally,

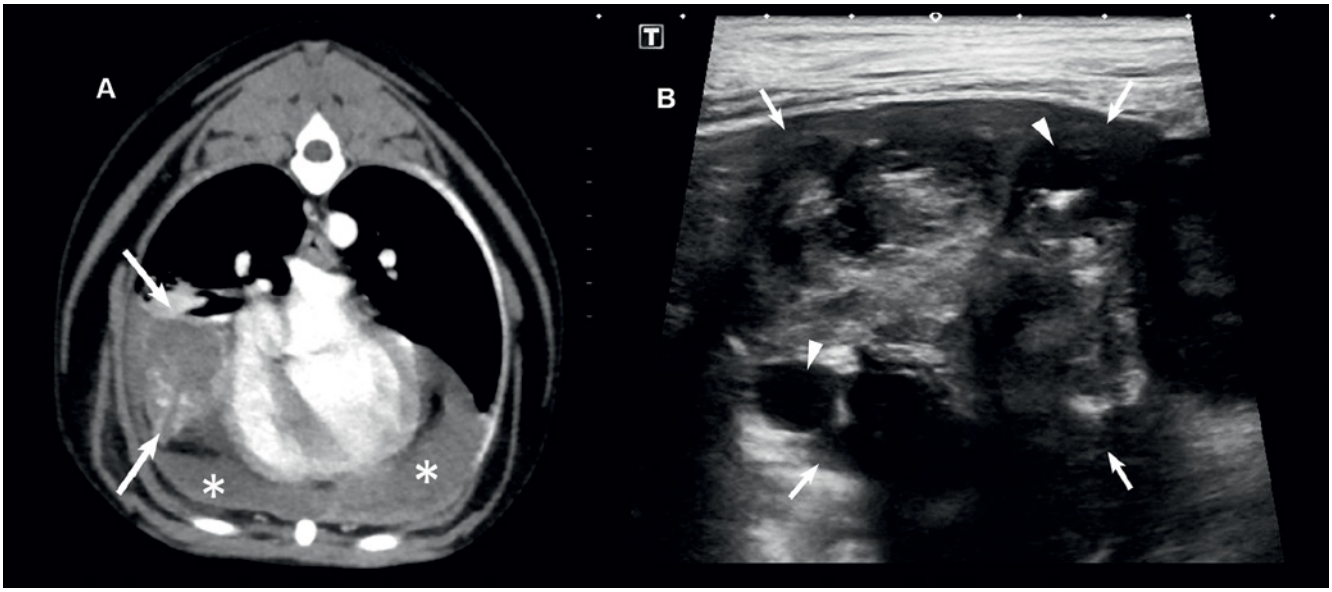


Figure 5.16. Pleural mass (hemangiosarcoma) in a 13-year-old Fox Terrier. Transverse CT image **(A)** and transverse intercostal ultrasonographic image **(B)** show a markedly heterogeneous mass within the right pleural cavity (arrows). There are multiple fluid-filled cavitary regions within the mass (arrowheads). Note concurrent pleural effusion on CT (*) not seen on this ultrasound image.

Vet-ebooks.com

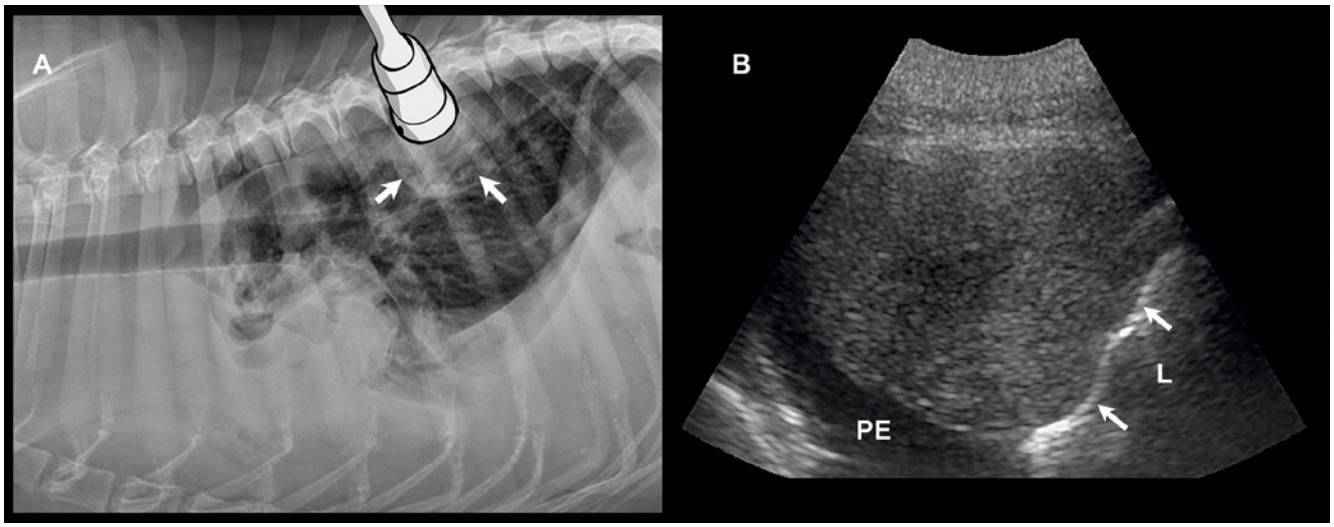


Figure 5.17. Pleural carcinomatosis and cranial mediastinal mass in a 9-year-old dog. (A) Left lateral radiograph of the thorax. Moderate pleural effusion (PE) as well as a cranial mediastinal mass cause dorsal displacement of the trachea and lungs. A round soft-tissue opacity is associated with the dorsal thorax bordering the thoracic spine (arrows; under ultrasound transducer). **(B)** Intercostal ultrasonographic image of the dorsal thoracic mass. The mass is seen arising from the pleura, is of moderate echogenicity, and is separate from the hyperechoic lung interface (L, arrows) in the far field. PE is also present. Fine-needle aspirates of the cranial mediastinal and pleural lesions were consistent with carcinoma.

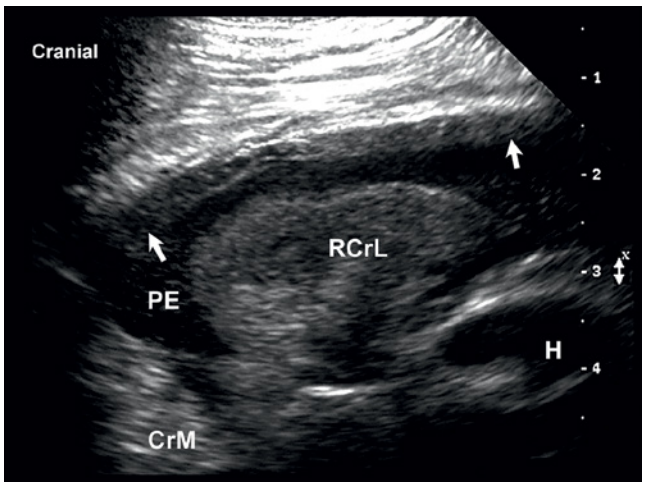


Figure 5.18. Pleural carcinomatosis and pulmonary carcinoma in a 10-year-old cat. On this dorsal ultrasonographic image obtained using an intercostal approach, the right cranial lung lobe (RCrL) is rounded, irregular, and has soft-tissue echogenicity because of replacement of normally air-filled parenchyma by neoplastic cells. Echogenic fluid (PE) separates the lung lobe from the parietal pleura. The parietal pleura (arrows) is thickened, slightly irregular, and unusually hypoechoic. CrM, cranial mediastinum; H, heart.

it enables the identification of a cranial mediastinal mass in the presence of pleural effusion, allows characterization of cranial mediastinal mass lesions (cystic in contrast to solid), may aid in the assessment of middle or caudal mediastinal lesions, and is helpful

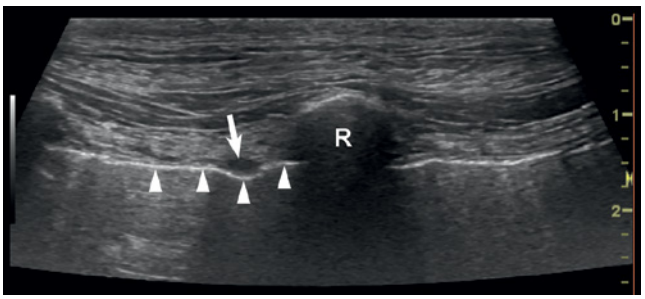


Figure 5.19. Parietal pleural nodule in an 8-year-old Labrador Retriever with bicavitary effusion. The ultrasound image acquired using an intercostal approach shows a small, ovoid, hypoechoic nodule (arrow) associated with the parietal pleural surface, which focally indents the adjacent lung surface (arrowheads). The lung was seen sliding deep to the nodule on live examination while the nodule remained stationary. R, Rib.

in identifying a window suitable for interventional procedures.

Cranial Mediastinal Masses

These are mostly found in the cranioventral mediastinum and may be accompanied by pleural effusion (Reichle and Wisner 2000). Their visualization depends on their location, size, and the presence of a suitable acoustic window. Differential diagnoses for cranial mediastinal masses include branchial cysts,

Vet-ebooks.com

lymphadenomegaly, neoplasms (e.g., lymphoma or thymoma and rarely ectopic thyroid carcinoma), inflammatory lesions (abscesses or granulomas), and hematomas. Fat accumulation may be confused with an infiltrative tumor; however, it usually does not distort the mediastinal vessels or lymph nodes.

Cranial mediastinal cysts are occasional incidental findings in cats (Zekas and Adams 2002). They are often well circumscribed, thin-walled with or without septations, and filled with anechoic fluid (Figures 5.20, 5.21).

Enlarged sternal lymph nodes are recognized as rounded nodules or masses of variable size, margination, echotexture, and echogenicity immediately dorsal to the sternum (Figures 5.22–5.24). As the peritoneal cavity is partly drained by these nodes, diagnostic imaging of the abdomen for underlying disease processes may be warranted in affected patients. Although reactive lymph nodes tend to be smaller than neoplastic or granulomatous lesions, ultrasonographic differentiation of these entities and differentiation of an enlarged lymph node from a cranial mediastinal mass lesion of other etiology may not be possible without sampling.

Masses of inflammatory or neoplastic etiology may appear similarly rounded or lobulated, solid or cystic, and homogeneous or inhomogeneous (Figures 5.25–5.32). Large lesions may infiltrate the surrounding structures, hampering determination of their origin. Cranial mediastinal **lymphomas** tend to appear as solid masses (Figure 5.25), while **thymomas** more commonly have a cystic component (Figure 5.26) (Tidwell 1998). However, cranial mediastinal masses cannot be differentiated based solely on their ultrasonographic appearance, and histopathology or cytology is needed to assess the nature of the lesion.

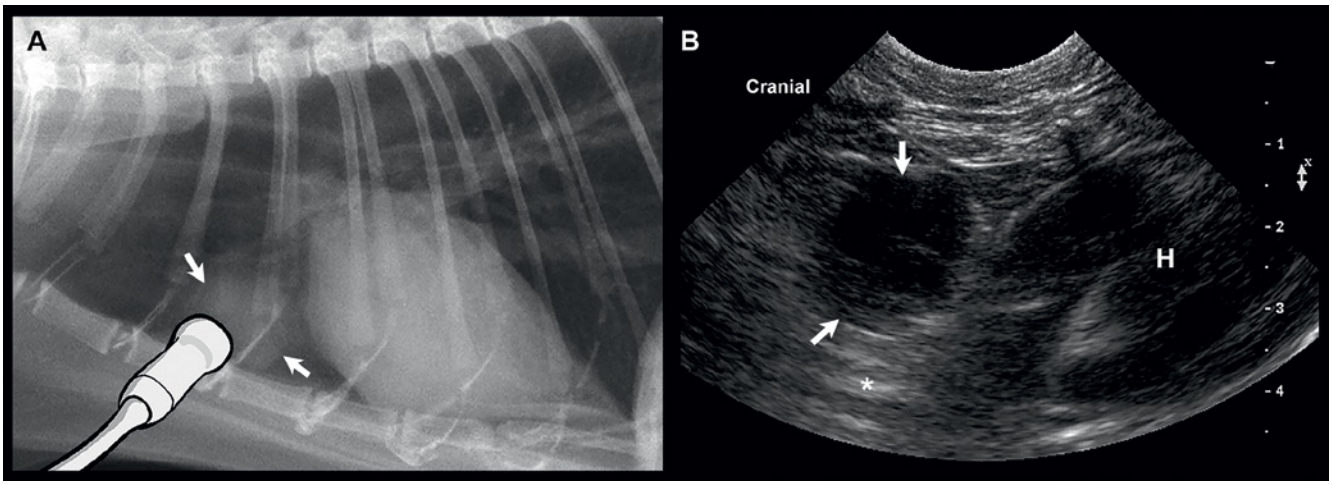


Figure 5.20. **Cranial mediastinal cyst in a 9-year-old cat. (A)** Lateral thoracic radiograph demonstrating an ovoid soft tissue opacity cranial to the cardiac silhouette (arrows, under ultrasound transducer). **(B)** Ultrasonographic image obtained by using an intercostal approach immediately dorsal to the sternum at the level of the fourth intercostal space. Cranial to the heart (H) is a round anechoic structure with distal enhancement (*), consistent with a cranial mediastinal cyst.

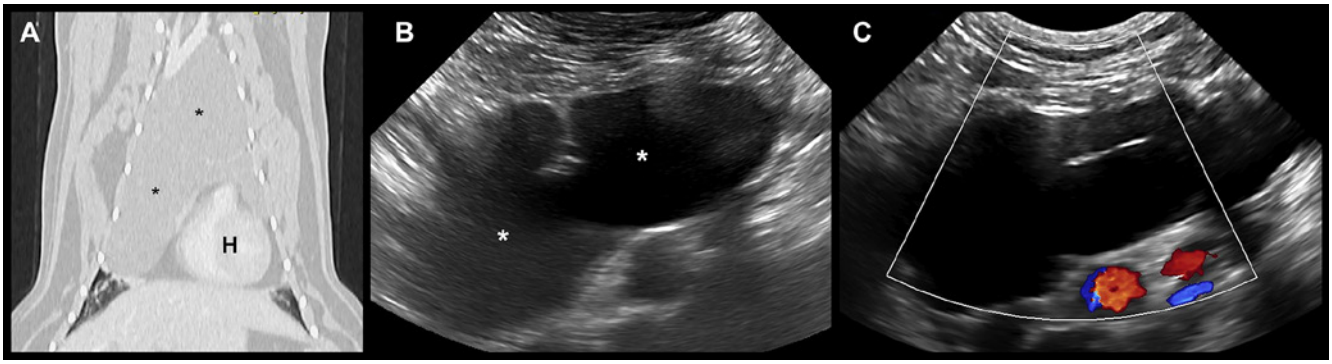


Figure 5.21. **Large cranial mediastinal (branchial) cyst in a 15-year-old cat with mildly decreased appetite. (A)** Dorsal reconstructed CT image shows a large, hypoattenuating cystic structure (*) displacing the heart (H). **(B, C)** Ultrasound images display similarly the large, lobulated fluid-filled (*) mass supportive of a branchial cyst. Color flow Doppler assessment **(C)** allowed to locate the main mediastinal vessels to be avoided during the drainage of 40 mL of clear fluid.

Vet-ebooks.com

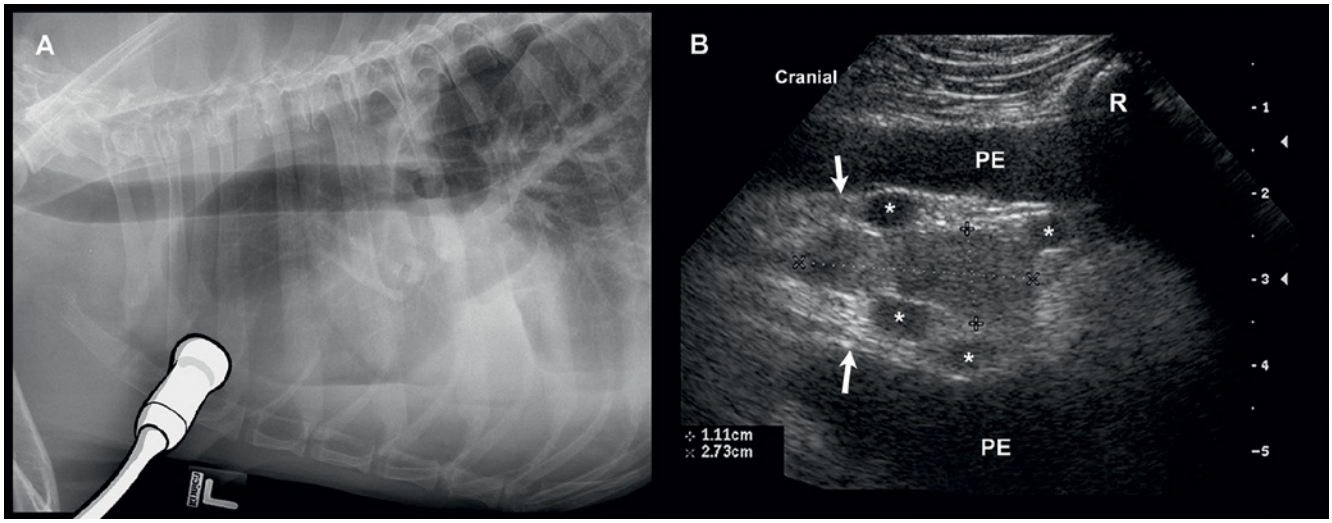


Figure 5.22. **Reactive sternal lymph node in a dog with chylothorax. (A)** Lateral thoracic radiograph showing pleural effusion that masks thoracic structures including the cardiac silhouette. The lung lobes are retracted from the body wall and appear rounded, consistent with chronic effusion. **(B)** Ultrasonographic image obtained at the right second intercostal space immediately dorsal to the sternum. Mildly echogenic effusion (PE) is present on both sides of the cranial mediastinum (arrows). A mildly enlarged sternal lymph node (cursors) is surrounded by hyperechoic fat and vessels (*). R, Rib.

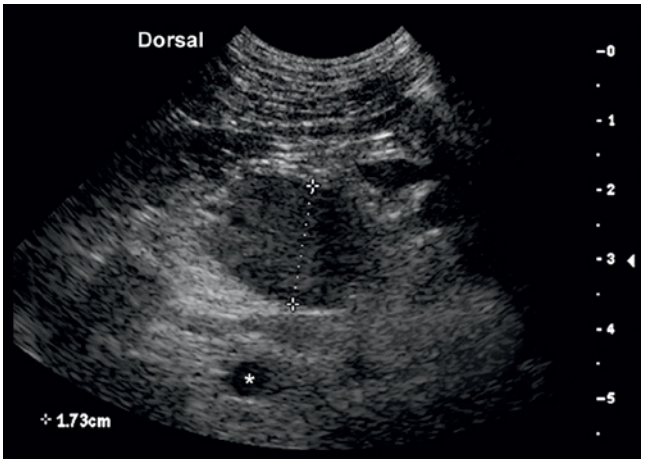


Figure 5.23. **Metastatic sternal lymph node in a dog with splenic hemangiosarcoma and hemoabdomen.** Transverse ultrasonographic image of an enlarged sternal lymph node (cursors) via an intercostal approach dorsal to the sternum at the level of the second intercostal space. The enlarged lymph node appears as a round hypoechoic nodule surrounded by echogenic fat and adjacent to anechoic vessels (*). The final histopathologic diagnosis was metastatic hemangiosarcoma.

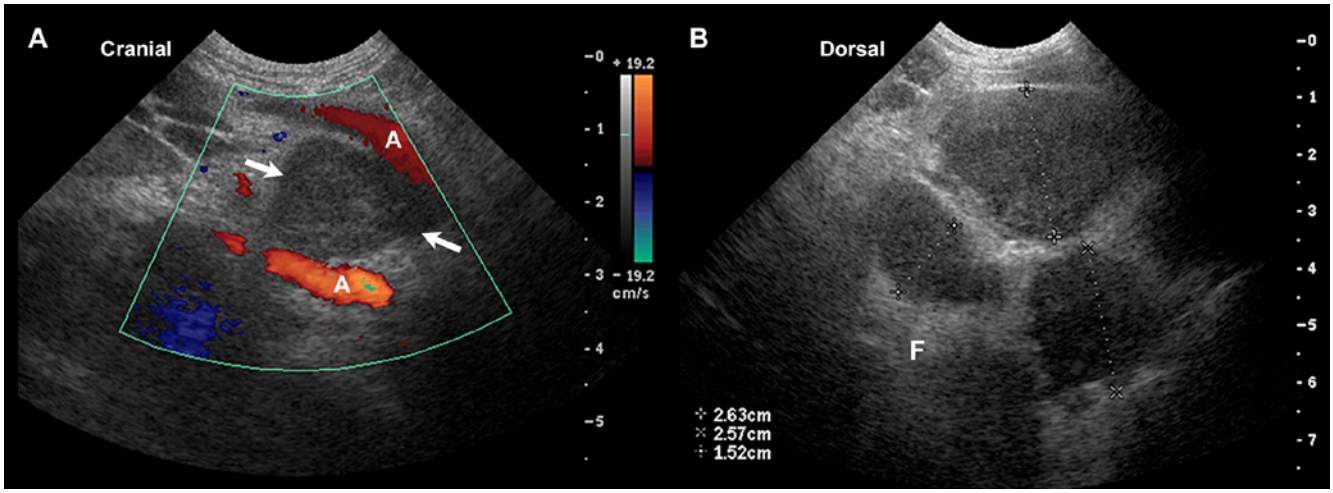


Figure 5.24. **Mediastinal lymphadenopathy in a 5-year-old Bernese mountain dog with disseminated histiocytic sarcoma.** Sagittal color Doppler **(A)** and transverse B-mode **(B)** intercostal sonographic images of the cranioventral thorax. A cranial mediastinal mass was suspected on radiographs. Multiple well-defined, hypoechoic nodules and masses (arrows and cursors) are surrounded by mediastinal hyperechoic fat (F) and arteries (A).

Vet-ebooks.com

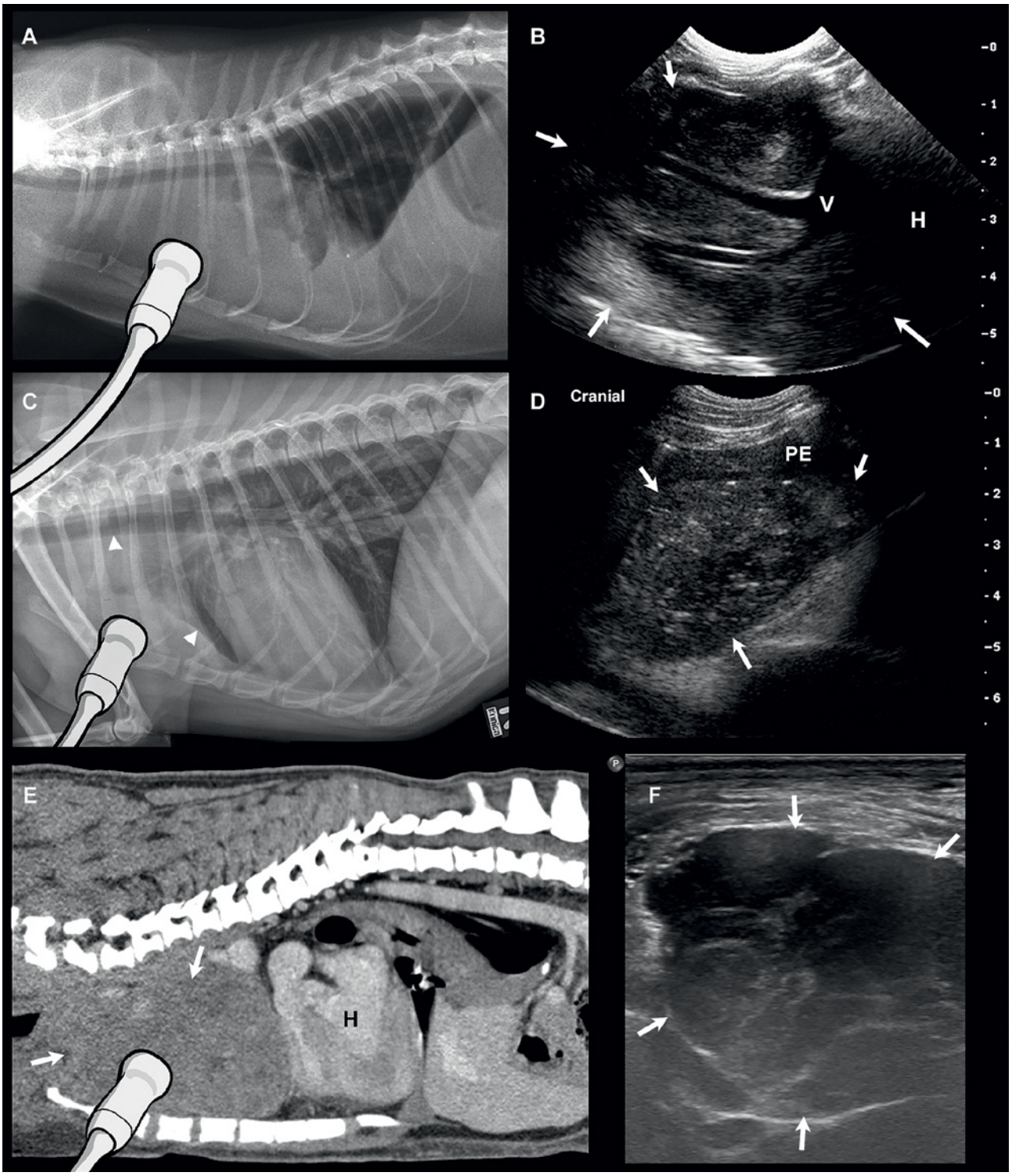


Figure 5.25. **Cranial mediastinal lymphomas in 1 cat and 2 dogs. (A)** On the lateral thoracic radiograph of a 4-year-old cat there is a large cranial mediastinal mass silhouetting with the heart and displacing the trachea dorsally. Pleural effusion is also present, as indicated by scalloped fluid opacity associated with the ventral thorax, pleural fissure lines, and retraction of the caudodorsal lung lobes from the thoracic wall and diaphragm. **(B)** Longitudinal sonogram via an intercostal approach. A large homogeneous mass (arrows) is associated with the cranial mediastinum and in contact with the heart (H). Large vessels are visible within this mass as anechoic tubular structures with strongly hyperechoic vessel walls (V). Lymphoma was diagnosed based on histopathology. **(C)** Lateral thoracic radiograph showing a large soft-tissue opacity in the cranial mediastinum of a 7-year-old Labrador Retriever. The opacity is displacing the trachea and cranioventral lung margin dorsally (arrowheads). **(D)** Corresponding ultrasonographic image obtained using a dorsal oblique plane through a right intercostal window. A well-defined hypoechoic mass with hyperechoic speckles is identified in the cranial mediastinum (arrows). A small amount of anechoic pleural effusion (PE) is also observed around the mass. **(E)** Sagittal reconstructed CT image of the thorax in a 3-year-old English Bulldog. There is a large cranial mediastinal mass that displaces the heart caudally. **(F)** Corresponding ultrasonographic image obtained using a transverse right intercostal approach shows that the mass is mostly hypoechoic, with heterogeneous linear to ill-defined central hyperechoic regions.

Vet-ebooks.com

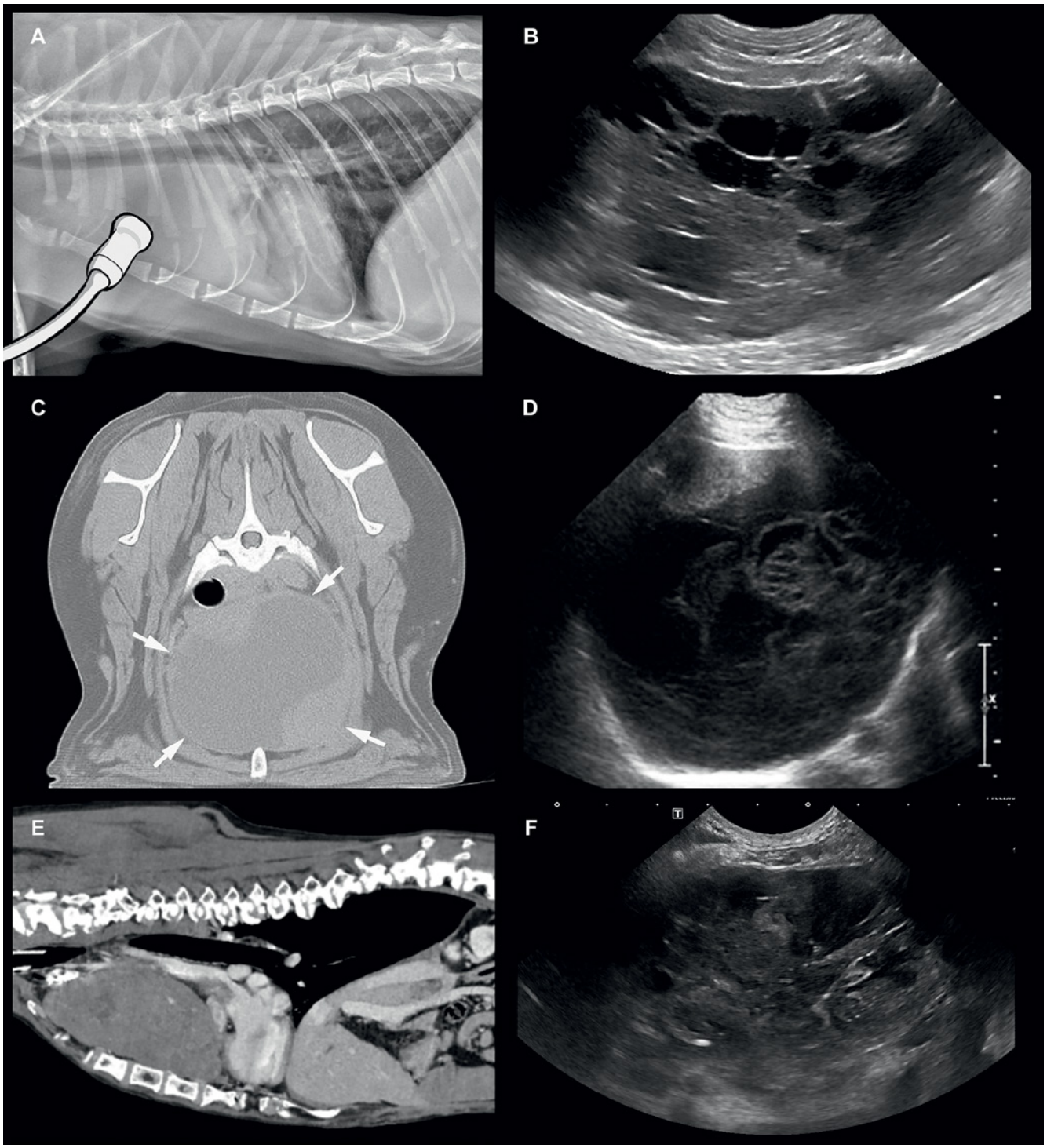


Figure 5.26. **Thymomas in 1 cat and 2 dogs. (A)** Lateral thoracic radiograph of an 8-year-old cat with a large cranial mediastinal mass causing dorsal displacement of the trachea and silhouetting with the cardiac silhouette. **(B)** Ultrasonographic image obtained through a cranial intercostal approach shows a large cranial mediastinal mass lesion of mixed echogenicity, with several anechoic cavities. **(C)** Transverse CT image of the cranial thorax in an 11-year-old mixed breed dog with a large cystic cranial mediastinal mass (arrows). **(D)** Ultrasonographic image of the same mass showing a large cystic component. **(E)** Sagittal reconstructed CT image of the thorax in an 11-year-old German Shepherd dog. There is a large heterogeneously contrast-enhancing cranial mediastinal mass that displaces the heart caudally and the trachea dorsally. **(F)** The corresponding ultrasound image demonstrates the heterogeneous and cavitary nature of the mass.

Vet-ebooks.com

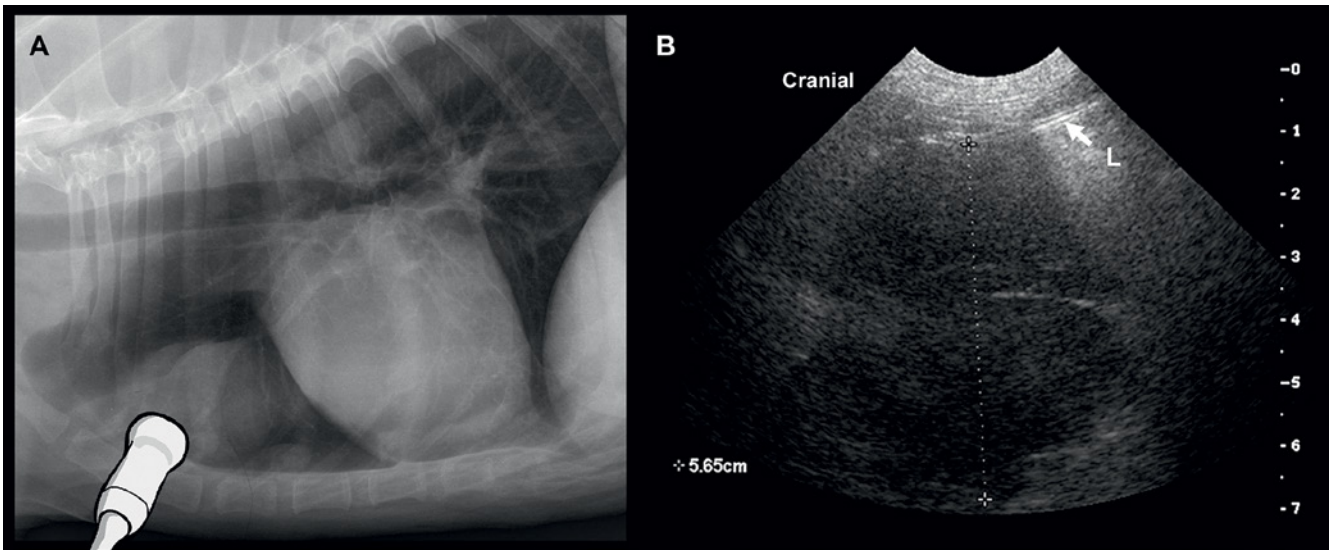


Figure 5.27. **Cranial mediastinal mass in an 11-year-old mixed-breed dog. (A)** On this lateral thoracic radiograph, a well-circumscribed round soft-tissue opacity in the cranial thorax is suspected to originate from the mediastinum, supported by the ventrodorsal radiograph (not shown). **(B)** Using right parasternal intercostal approach, a lobulated hypoechoic mass is noted (between cursors). Fine-needle aspiration yielded a cytologic diagnosis of **mast cell tumor**. L, lung interface.

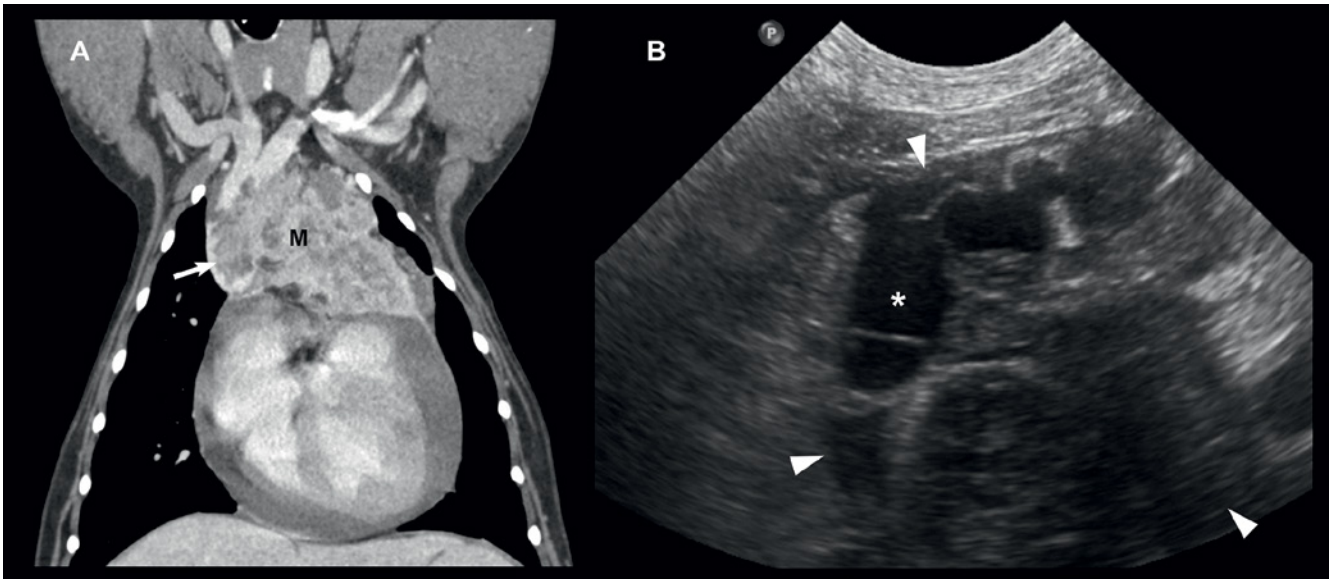


Figure 5.28. **Cranial mediastinal mass with vascular invasion in an 11-year-old Beagle. (A)** On the dorsal reconstructed CT image, a large heterogeneously contrast-enhancing mass (M) is present cranial to the cardiac silhouette and invades into the cranial vena cava (arrow). **(B)** The ultrasonographic image acquired through a left cranial intercostal approach shows a large heterogeneous mass (arrowheads) with multifocal cavitary regions (*). Fine-needle aspiration cytology was consistent with a **neuroendocrine tumor**, most likely **thyroid carcinoma**.

Other Mediastinal Lesions

Radiography (including contrast procedures) and thoracic CT remain the imaging modalities of choice for the diagnosis of lesions associated with the dorsal mediastinum, trachea, esophagus, and heart base. Transesophageal ultrasonography may also be of great value when available. Large heart base tumors may be visualized using a trans-cardiac or an intercostal approach (Figure 5.33). Esophageal dilatation, foreign bodies, and masses (neoplasms or granulomas) may occasionally be visualized via a thoracic inlet or transhepatic approach, depending on their location and size (Figures 5.34, 5.35).

Ultrasonography has been described as an alternative to fluoroscopy in the diagnosis of tracheal collapse

Vet-ebooks.com

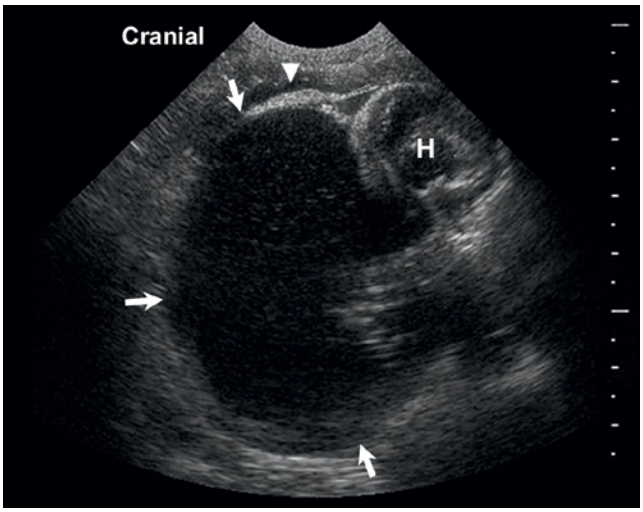


Figure 5.29. Cranial mediastinal mass in a domestic long-haired cat. The examination is performed by using a right intercostal approach. A large mass, mixed in echogenicity, with a large, hypoechoic cavitary component (arrows) is cranial to the heart (H). A small amount of pleural effusion is present in the near field (arrowhead). The histopathologic diagnosis was **adenocarcinoma**.

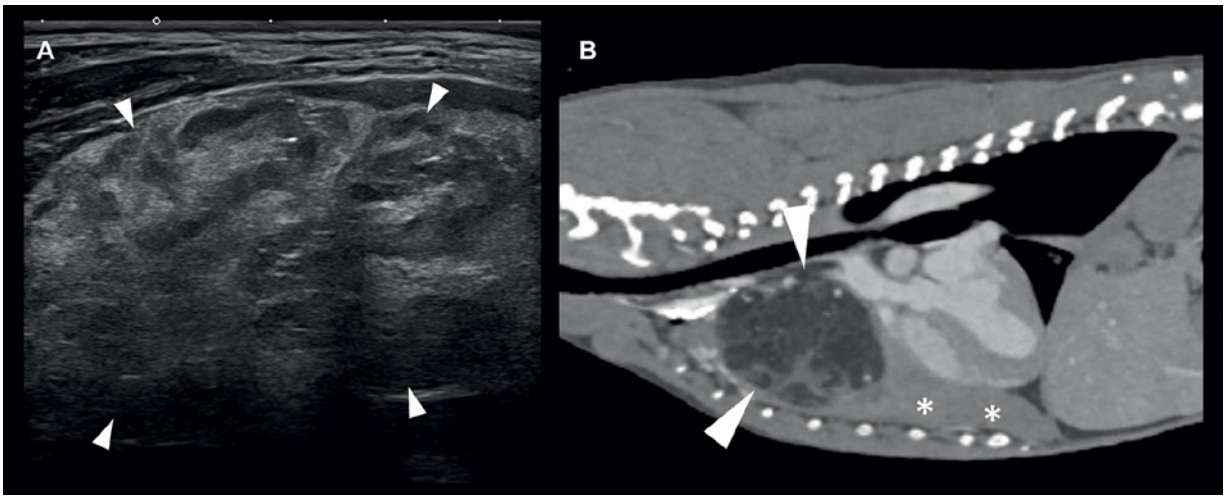


Figure 5.30. Unusual cranial mediastinal mass in a 10-year-old Maltese. **(A)** On the ultrasound image acquired using an intercostal approach, there is a large, heterogeneous mass (arrowheads) associated with the cranial mediastinum. This mass has a coarse hyperechoic appearance with interspersed hypoechoic areas. **(B)** On the sagittal reformatted CT image, rounded fat attenuating tissue is present in the cranial aspect of the mass (arrowheads), while the caudal aspect (*) is homogeneously soft-tissue attenuating. The heart is displaced caudodorsally. Based on the attenuation of the lesion on CT, a presumptive diagnosis of a **lipoma or liposarcoma** was made.

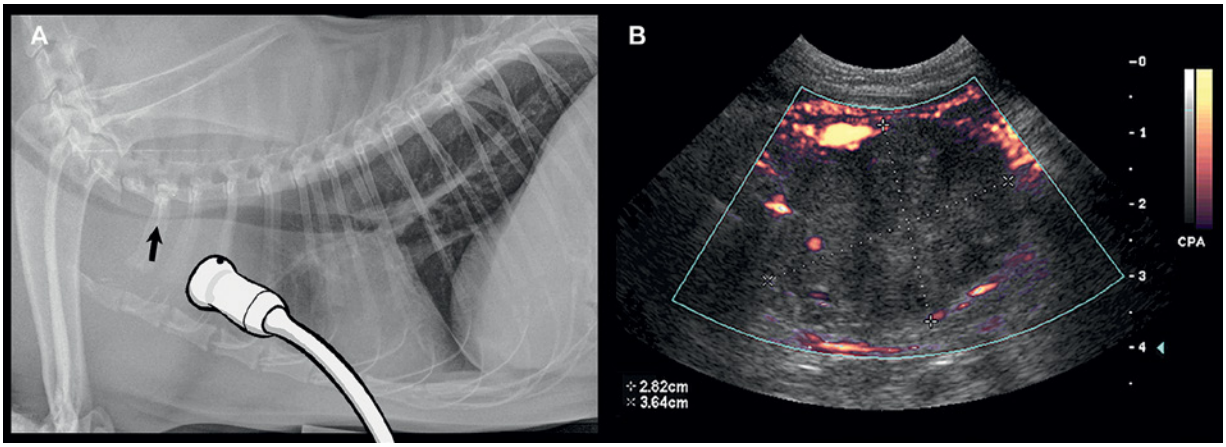


Figure 5.31. Cranial mediastinal granulomatous mass in a cat. (A) On this lateral thoracic radiograph, there is a large, ill-defined, cranial mediastinal mass displacing and compressing the trachea (black arrow). Severe swelling also extends throughout the neck. **(B)** This transverse sonogram via an intercostal approach shows a large heterogeneous mass (cursors) associated with the cranial mediastinum. Increased vascularity is noted at the periphery of the mass using power Doppler. **Cryptococcosis** was diagnosed based on ultrasound-guided fine-needle aspiration.

Vet-ebooks.com

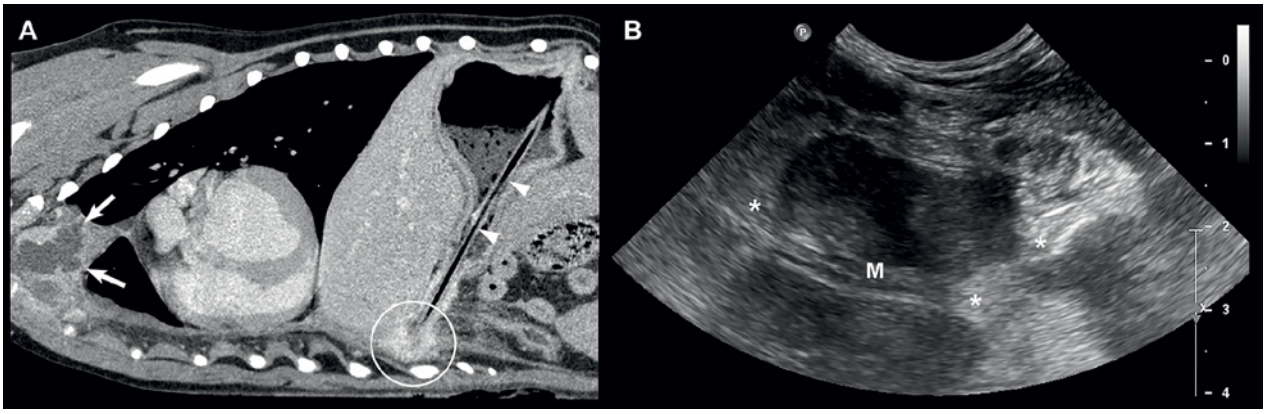


Figure 5.32. **Cranial mediastinal abscess in a 1-year-old mixed breed dog with a perforating gastric foreign body (wooden skewer). (A)** On the reconstructed oblique sagittal CT image, there is a linear hollow structure associated with the gastric lumen (arrowheads). The ventral tip of this foreign body extends into the peritoneal cavity, resulting in focal fluid modeling consistent with peritonitis (circle). Associated with the cranial mediastinum at the level of the thoracic inlet, there is a heterogeneous, cavitary, moderately contrast-enhancing mass lesion with several nonenhancing regions (arrows). **(B)** On the ultrasound image acquired using an intercostal approach, the cranial mediastinal mass (M) is markedly heterogeneous and bordered by hyperechoic fat (*). Ultrasound-guided fine-needle aspiration of the mass yielded suppurative fluid. The cranial mediastinal abscess was believed to represent an abscessed sternal lymph node secondary to peritonitis. Courtesy of Dr. Mylène Auger.

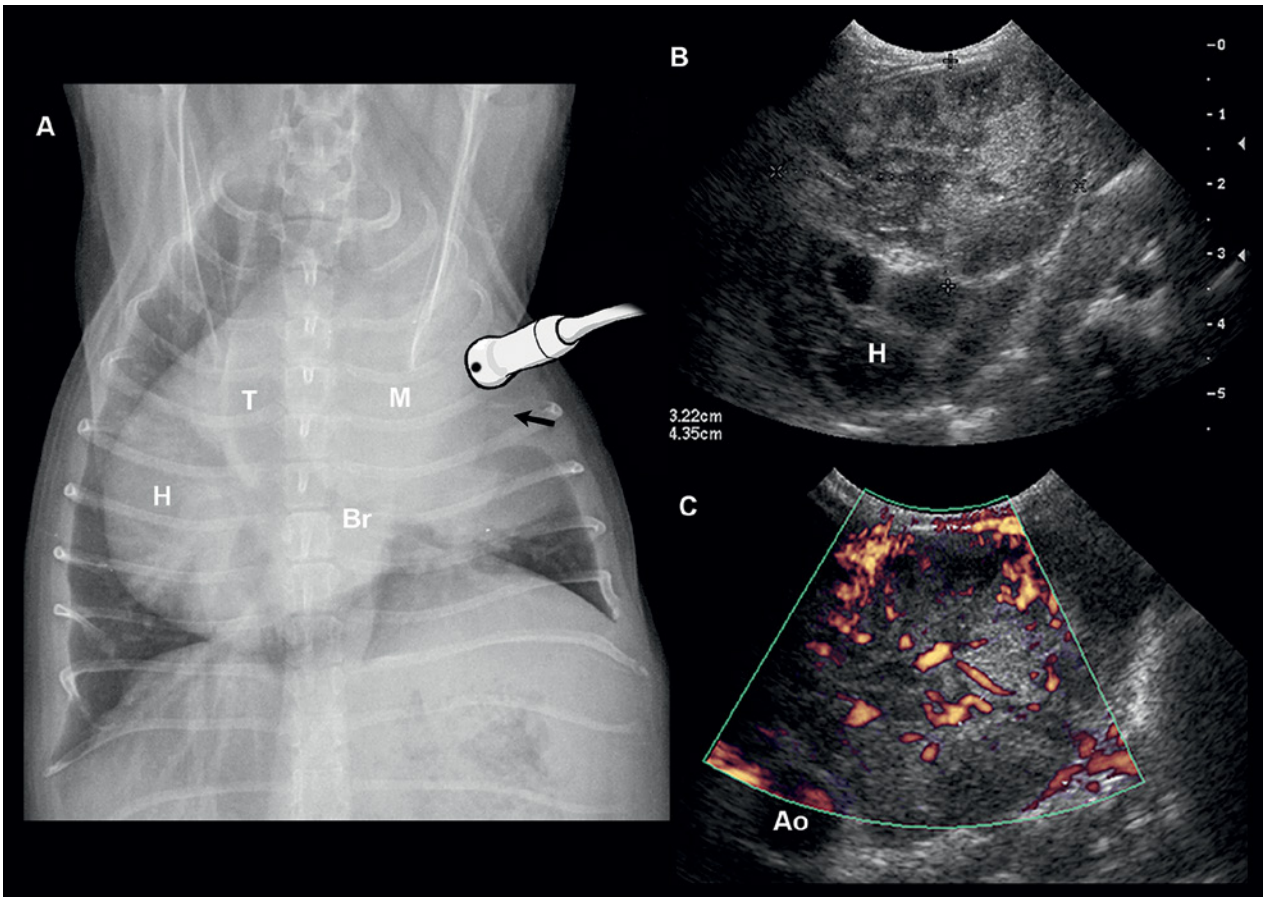


Figure 5.33. **Heart base tumor in a small-breed dog. (A)** The ventrodorsal thoracic radiograph shows a large soft-tissue mass (M) in the left cranial thorax. The trachea (T) and cardiac silhouette (H) are displaced to the right, and the left mainstem bronchus (Br) is partially compressed. The increased opacity identified in the left mid-thorax adjacent to the mass (arrow) is thought to represent a focal alveolar pattern or a small-volume pleural effusion. **(B)** B-mode sonogram obtained using a transverse intercostal approach (as shown in **A**) demonstrates a well-defined mixed echogenic solid mass (cursors) displacing the heart (H). **(C)** When power Doppler is used, this mass appears strongly vascularized. The aorta (Ao) is in the far field, adjacent to the mass. A **neuroendocrine tumor** was highly suspected on cytological specimens obtained with fine-needle aspiration.

Vet-ebooks.com

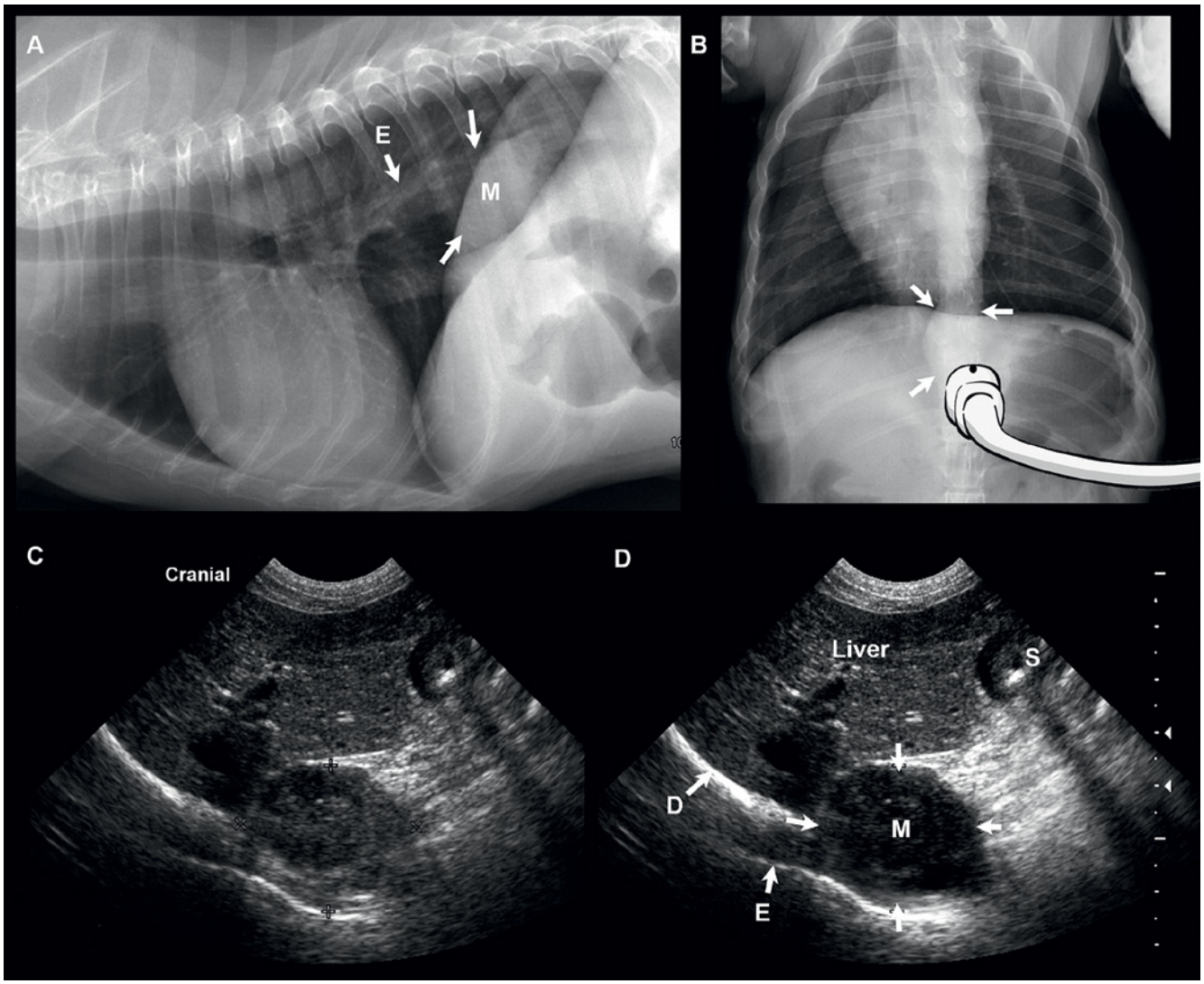


Figure 5.34. **Esophageal mass in a 14-year-old Welsh Corgi. (A, B)** Orthogonal thoracic radiographs reveal a homogeneous soft-tissue opacity mass (M, arrows) associated with the caudal mediastinum, in the region of the esophagus (E), summating with the diaphragm. **(C, D)** Ultrasonographic and enhanced labeled images obtained with a ventral transhepatic approach (sagittal plane, at the location of the transducer in (B)). At the level of the esophageal hiatus, the mass (M, arrows) is associated with the esophagus (E). Liver and stomach (S) are visible in the near field, and the lung–diaphragm interface (D) manifests as a curvilinear, strongly hyperechoic structure bordering the esophageal mass.

(Rudorf et al. 1997). Additionally, it may prove useful in distinguishing between tracheal collapse and other causes of tracheal narrowing, such as tracheal wall thickening or compressive mass lesions (Figure 5.36). The ultrasonographic examination is performed using a thoracic inlet approach and is therefore limited to the cervical and cranial thoracic trachea.

Pulmonary Disorders

The ability to assess pulmonary lesions depends on their location and size as well as the presence of a suitable acoustic window. Normally aerated lungs, and lesions surrounded by normally aerated lungs, cannot be evaluated ultrasonographically. However, when fluid or cells replace the air within alveoli and/or airways, or if a lung lobe collapses, evaluation of the affected lung becomes possible. Pulmonary abnormalities commonly detected and investigated by means of ultrasonography are atelectasis, consolidation, torsion, and pulmonary nodule/mass. When present, pleural effusion facilitates the evaluation of lobar size, shape, and contour. A composite of the main ultrasonographic features of different pulmonary disorders is shown in Figure 5.37. Although these sonographic findings are helpful in establishing a preliminary diagnosis, fine-needle aspirations or biopsies are required in many instances to confirm.

Vet-ebooks.com

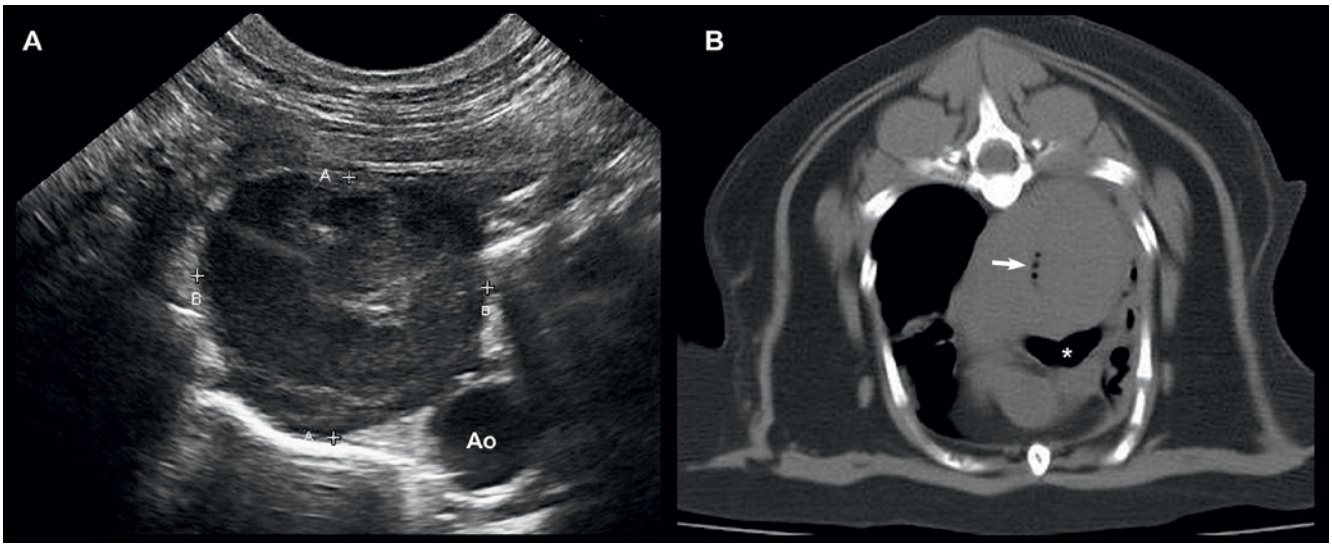


Figure 5.35. Esophageal mass in a 16-year-old cat presented for a 6-month history of regurgitation. The sonographic image **(A)** via a transhepatic approach shows a large mass, ventral and to the left of the aorta (Ao). At this location, the collapsed lumen is not visible. The corresponding transverse CT image **(B)** shows the mass with a small amount of gas in the lumen (arrow). The trachea (*) is partially compressed. Ultrasound-guided fine-needle aspirates were performed. The cytological diagnosis was **round-cell tumor** (either histiocytic sarcoma or lymphoma).

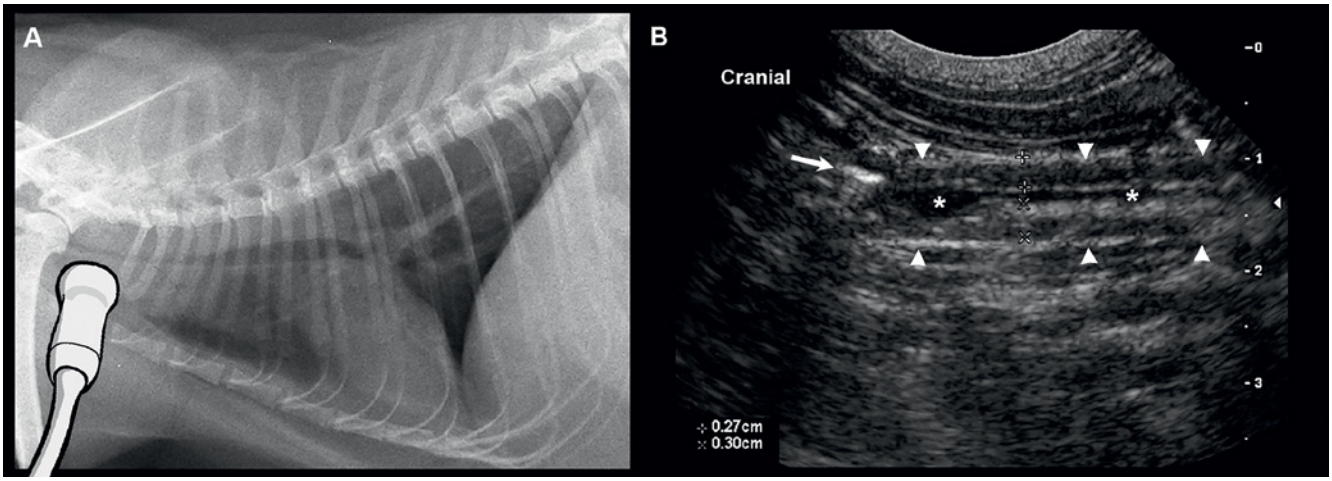


Figure 5.36. Tracheal wall thickening caused by eosinophilic airway disease in a 4-year-old cat. (A) The lateral thoracic radiograph shows extensive narrowing of the cranial thoracic trachea. **(B)** An ultrasonographic examination of the trachea (arrowheads) is performed by using a thoracic inlet approach. The tracheal wall (cursors) is thickened (0.3 cm) and hypoechoic. Anechoic material (*), consistent with mucus, is present within the severely narrowed tracheal lumen. A gas bubble is present more cranially, appearing as a reverberating hyperechoic focus (arrow).

Atelectasis

Atelectasis (pulmonary collapse) may occur secondary to increased pressure within the pleural space (pneumothorax or pleural effusion), may be a sequela to bronchial obstruction, or may result from decreased pulmonary compliance and inability of the lung to inflate properly. Ultrasonographic assessment of the atelectatic lung is possible in cases of concurrent pleural effusion or adjacent compressive mass but can be difficult if atelectasis is caused by other factors such as pneumothorax. Atelectatic lung lobes appear as small, smoothly marginated, triangular structures, outlined by pleural fluid, when present (Figure 5.32A). The echogenicity of atelectatic lungs depends on the amount of residual air within the air spaces. Linear and speckled hyperechoic foci,

Vet-ebooks.com

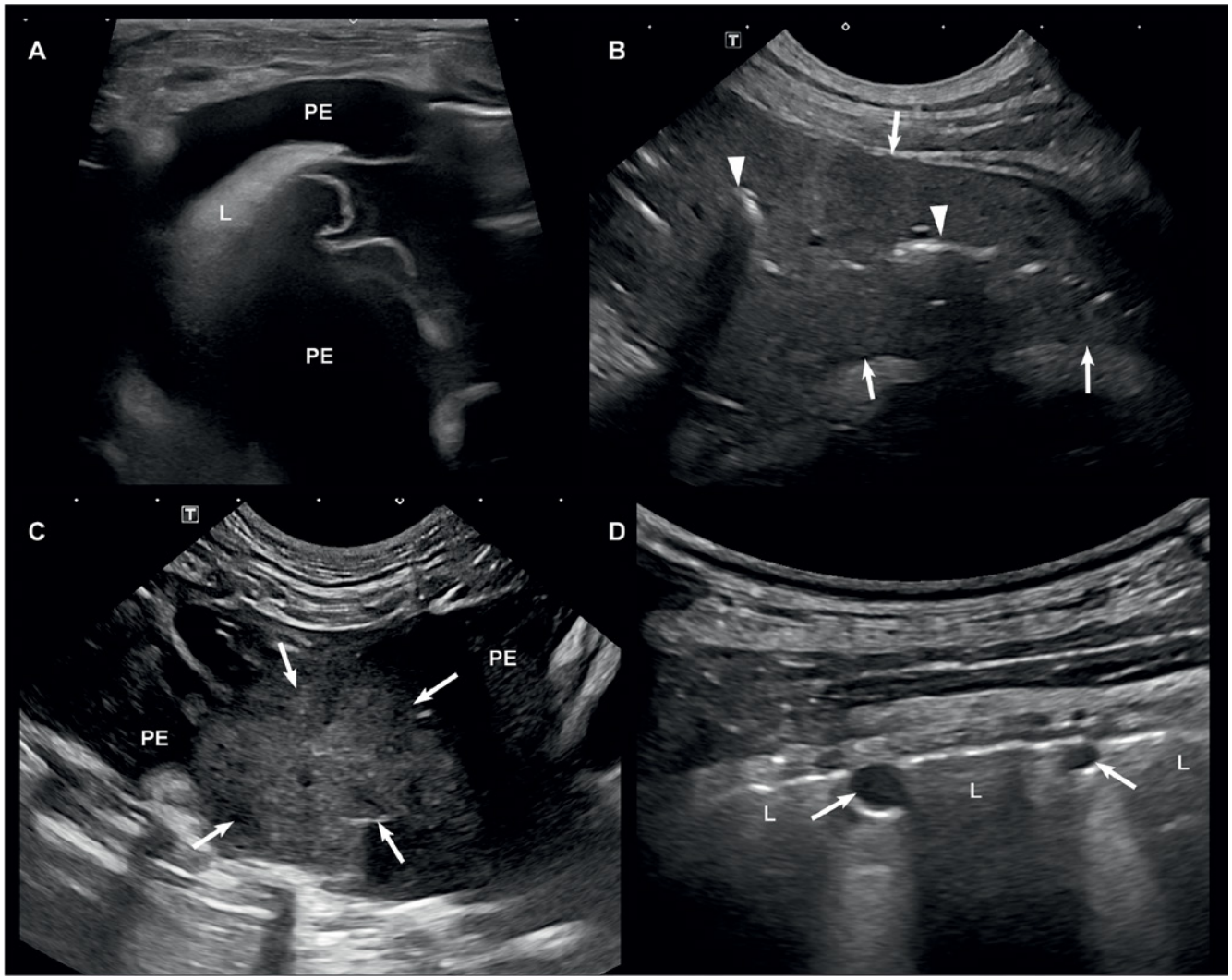


Figure 5.37. Sonographic images of common pulmonary abnormalities. (A) Atelectasis. The lung is collapsed because of pleural effusion (PE). The affected lung lobe (L) is reduced in volume but retains its normal shape and appears hyperechoic. **(B) Consolidation**. Pulmonary parenchyma is filled with fluid or replaced with inflammatory or possibly neoplastic infiltrates. The affected lung lobe (arrows) is hypoechoic, with few hyperechoic foci representing trapped air (arrowheads) but retains its normal size, shape, and contour. **(C) Pulmonary mass**. With increasing size, pulmonary mass lesions cause loss of the normal shape and margination of a lung lobe, with distortion of the pulmonary border and loss of the normal triangular form of a lung lobe (arrows). The echogenicity of pulmonary mass lesions is variable. Adjacent PE is present in this case. **(D) Pulmonary nodules**. Lung nodules are typically rounded, hypoechoic, and well demarcated from the peripheral aerated lung (arrows). These nodules can only be detected if they are in contact with the thoracic wall. L, aerated lung.

indicating residual air within bronchi and alveoli, as well as bronchial walls, are often seen. Observing the lung lobe during the respiratory cycle may show an intermittent increase in linear and speckled foci if some air still cycles through the bronchial tree. Additionally, vessels can be visualized, particularly by means of color or power Doppler, although respiratory motion may affect the quality of the Doppler signal. Completely collapsed lung lobes tend to be similar in echogenicity and echotexture to liver. In cases of obstructive atelectasis, ultrasonography may prove useful in the identification of the obstructive lesion (e.g., mass).

Consolidation

Early or mild pulmonary infiltrative diseases result in multifocal interruption of the normal lung surface by small hyperechoic foci with distal shadowing called "comet-tail" or "ring-down" artifacts (Louvet and

Vet-ebooks.com

Bourgeois 2008). In more advanced cases, when fluid or cells uniformly infiltrate the pulmonary air spaces, the lung often has an echogenicity and echotexture similar to liver (**hepatized lung**) (Schwarz and Tidwell 1999). The affected lung lobe typically retains its normal shape and volume (Figures 5.37A, 5.38, and 5.39). Air-filled bronchi appear as hyperechoic **air bronchograms** radiating from the hilus and are commonly associated with reverberation artifacts or dirty shadowing. Residual air within alveoli also remains hyperechoic (Figure 5.39). If the bronchial lumen is filled with secretions or cellular debris, **fluid bronchograms** develop, which resemble vessels but can be distinguished by means of color or power Doppler by their lack of blood flow (Figure 5.40). Although pulmonary consolidation is most commonly associated with pneumonia, it may also be encountered in lung contusion, lung lobe torsion, and infiltrative pulmonary neoplasia (Figures 5.40–5.42). Imaging features that allow a prioritization of lung lobe torsion over other differential diagnoses include concurrent pleural effusion; dispersed, hyperechoic, and reverberating

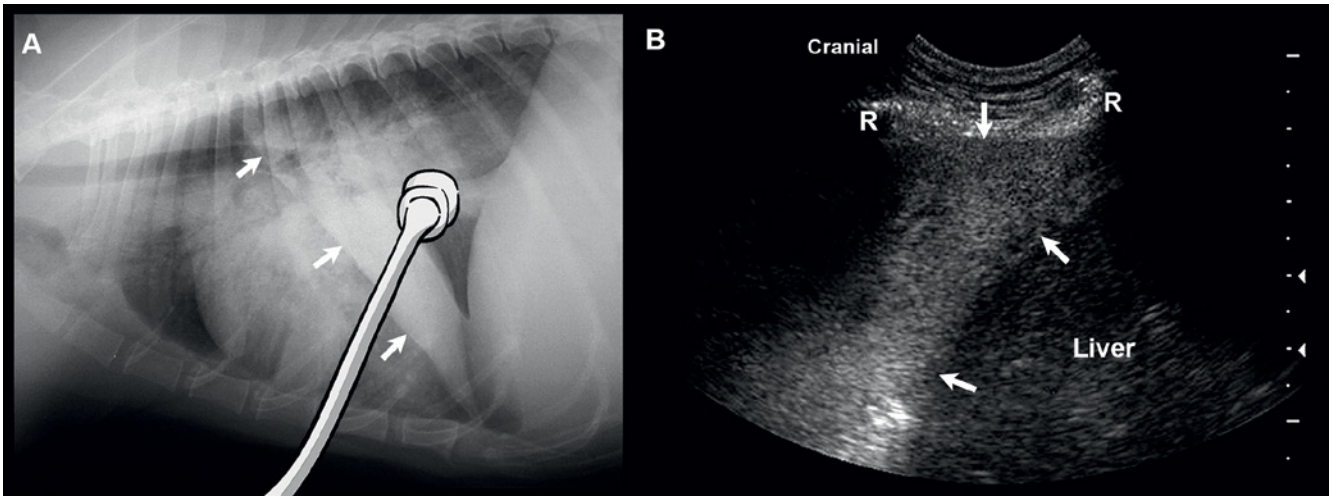


Figure 5.38. Acute suppurative pneumonia with hemorrhage in a 10-year-old Labrador Retriever. (A) The right lateral radiograph of the thorax shows an alveolar pattern in the left caudal lung lobe and a clear border between the left cranial and caudal lung lobes (lobar sign [arrows]). There is also a mixed unstructured interstitial to alveolar pattern in the left cranial lung lobe. **(B)** The ultrasonographic examination is performed in a dorsal plane using a left caudal dorsal intercostal approach. The left caudal lung lobe is homogeneously echogenic (arrows) and is hyperechoic to the hepatic parenchyma seen caudal to the diaphragm. Acoustic shadows related to superficial ribs (R) are present.

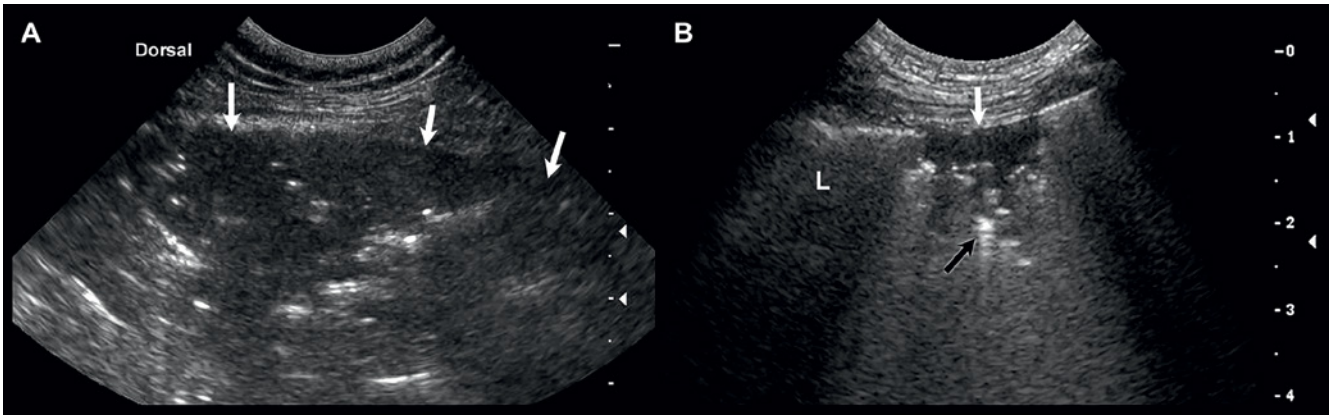


Figure 5.39. Aspiration pneumonia in two dogs. Both examinations are performed with a right intercostal approach. **(A)** The right middle lung lobe (arrows) is homogeneous and mostly hypoechoic, with a few hyperechoic foci representing gas inclusions. The lung lobe retains its normal triangular shape and size. There is no evidence of pleural effusion. **(B)** Focal pneumonia (white arrow) involving the right middle lung lobe appears as an irregular, hypoechoic region with gas speckles associated with comet-tail artifacts (black arrow). Deeper foci of pneumonia cannot be visualized because of overlying aerated lung (L).

Vet-ebooks.com

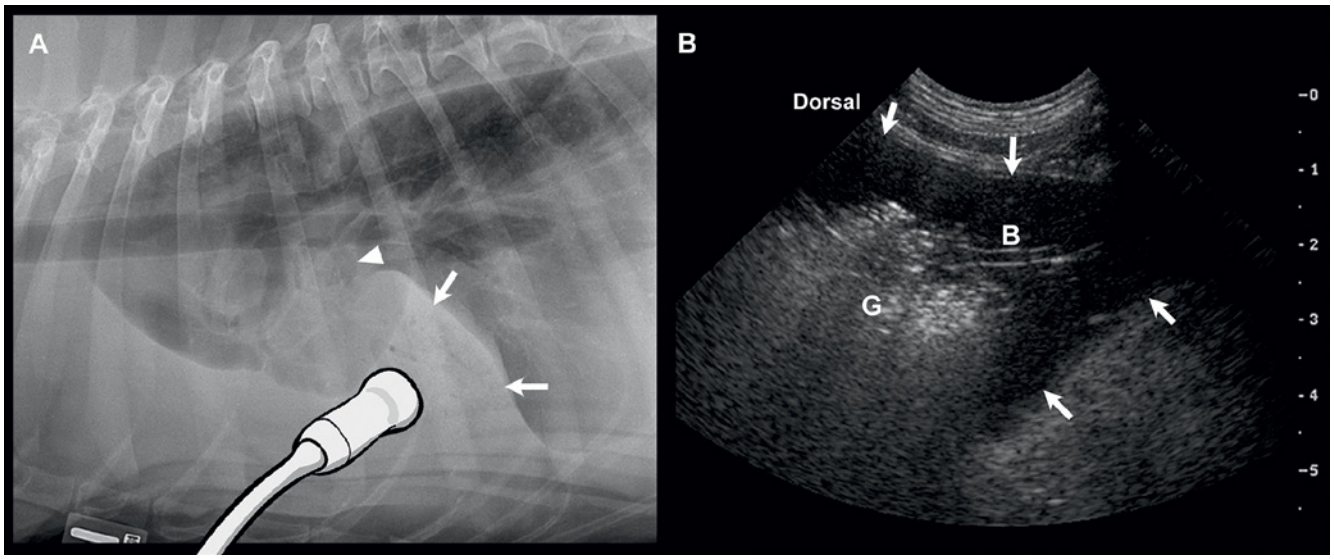


Figure 5.40. Torsion of the right middle lung lobe in a 5-year-old mixed, large-breed dog. (A) On the lateral thoracic radiograph, marked pleural effusion is noted as well as right middle lung lobe opacification and enlargement (arrows). The lobar bronchus is interrupted (arrowhead), and punctate and linear gas foci are observed in the consolidated lobe. **(B)** The ultrasound examination is performed by using a right intercostal approach at the level of the sixth intercostal space. The peripheral portion of the lung lobe is hypoechoic ("peripheral band sign"), and dispersed hyperechoic foci in the central portion are associated with reverberation artifacts, consistent with gas (G). This pattern is commonly encountered with lung-lobe torsion. A fluid-filled bronchus (fluid bronchogram) appears in the apex of this lobe (B).

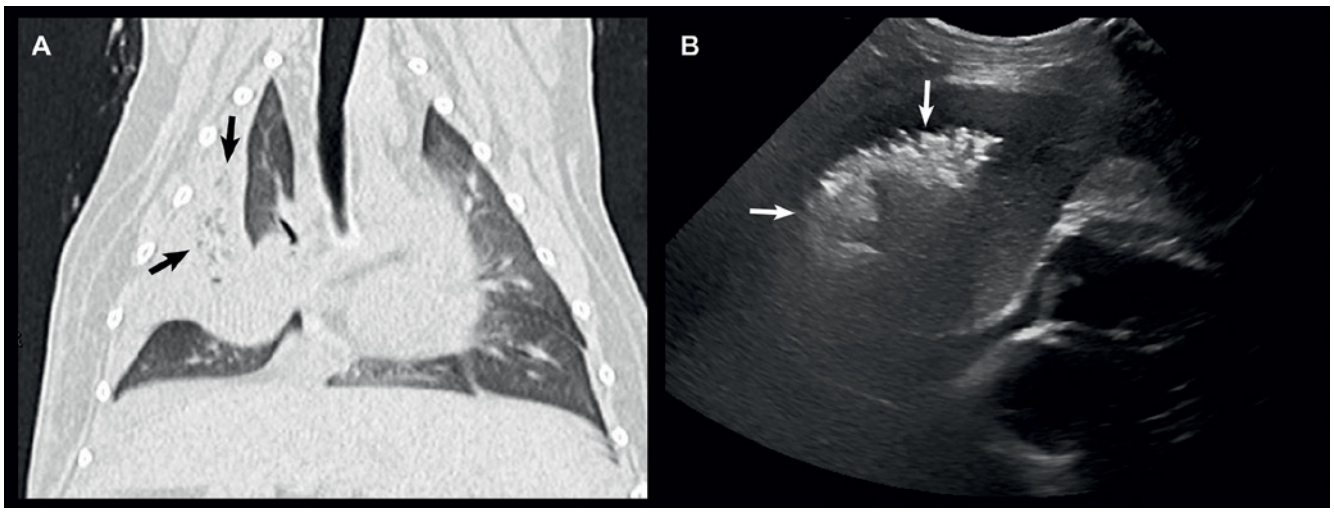


Figure 5.41. Lung-lobe torsion in a 6-year-old Chihuahua presented for increased respiratory rate and lethargy. (A) On the dorsal reconstructed CT image, the right middle lung lobe is consolidated and there is evidence of central vesicular emphysema (arrows) as well as a small amount of pleural effusion. **(B)** The sonogram displays a similar central accumulation of gas foci compatible with an emphysematous pattern (arrows), surrounded with hypoechoic lung tissue ("peripheral band sign"). A torsion was confirmed surgically.

foci indicating **vesicular emphysema** (d'Anjou et al. 2005); and a peripheral hypoechoic region of the affected lobe ("**peripheral band sign**"; Belmudes et al. 2021) (Figures 5.40, 5.41). Color or power Doppler can prove useful in confirming the lack of flow in a twisted lobe. However, ultrasonographic differentiation of infiltrative lung pathologies, which may even coexist in the same lobe, may not be possible and requires further examination with CT (angiography), laboratory tests, and/or tissue sampling.

Vet-ebooks.com

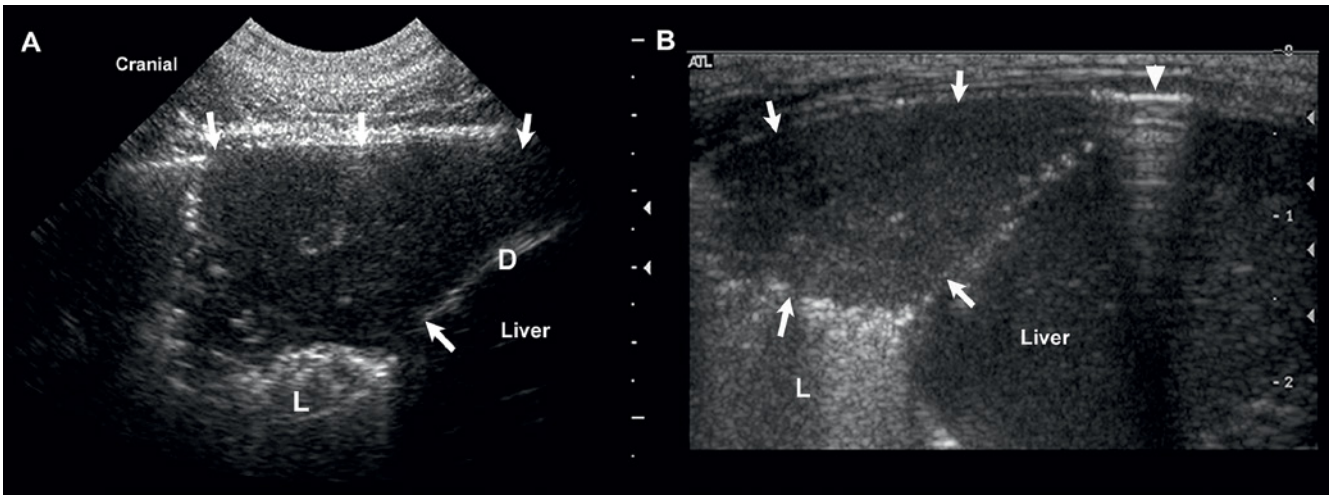


Figure 5.42. **Uniform lung consolidation in two dogs. (A) Bronchoalveolar carcinoma** in a 15-year-old mixed-breed dog. Dorsal sonogram using a right intercostal approach. The tip of the right caudal lung lobe (arrows) is uniformly hypoechoic and has retained its normal triangular shape. The abnormal portion of this lobe is in contact with the diaphragm (D). The normal lung portion, which remains aerated, is seen in the far field (L). **(B) Traumatic lung contusion** in another dog in which the affected portion of the right caudal lobe (arrows) is uniformly moderately echogenic. Additionally, a short linear hyperechogenicity is in the caudolateral portion of the pleural space (arrowhead), in association with a comet-tail artifact, consistent with mild pneumothorax. L, normal aerated lung.

Pulmonary Masses and Nodules

Although pulmonary masses in small animals are most commonly neoplastic or possibly granulomatous in etiology, abscesses, cysts, or hematomas may be encountered on occasion. In the absence of pleural effusion, pulmonary masses can be evaluated ultrasonographically only if located at the periphery of the lung field.

Pulmonary neoplasms and granulomas are usually hypoechoic or of mixed echogenicity. They cause focal disruption of the reflective lung surface and commonly form an acute angle with the thoracic wall (Figures 5.43–5.52). Lung masses or nodules are easily identified as pulmonary in origin when they move with the rest of the lung during respiration. This feature may not be observed in cases of pleural adhesions. In contrast to atelectasis or consolidation, pulmonary mass lesions frequently cause distortion of the normal contour of the affected lung lobe. Central tumor necrosis can vary in appearance and may resemble a pulmonary abscess, particularly when it is hypoechoic or anechoic. Air cavities and dystrophic mineralization, appearing as hyperechoic foci with or without reverberating and shadowing artifacts, are often seen in primary lung tumors.

Pulmonary metastases may be recognized as peripherally distributed, round, hypoechoic nodules moving with the aerated lung (Figure 5.49). Larger metastases may show similar ultrasonographic features as primary pulmonary neoplasms.

Primary and metastatic neoplasms are ultrasonographically indistinguishable from granulomas and other inflammatory nodules and masses, necessitating cytological or histological analysis for a definitive diagnosis (Figures 5.50–5.52). The signalment and clinical history are helpful in prioritizing the differential list.

Pulmonary cysts, acute hematomas, pneumatoceles, abscesses, and occasionally tumors can be fluid-filled. Cysts are usually thin-walled and contain anechoic fluid. Abscesses, hematomas, and cavitary neoplasms have variable wall thickness and margination, and the echogenicity of their contents may range from anechoic to echogenic (Figures 5.47, 5.53, and 5.54). Abscessing pneumonia may also cause lobar enlargement and marked heterogeneity, mimicking neoplasia and necrosis. Furthermore, these processes can coexist.

Diaphragmatic Disorders

Hernia

Although challenging, ultrasonography can be a useful imaging tool in diagnosing traumatic diaphragmatic hernias, true (congenital) diaphragmatic hernias, and congenital peritoneo-pericardial diaphragmatic hernias (PPDHs) (Lin et al. 2020; Spattini et al. 2003).

Vet-ebooks.com

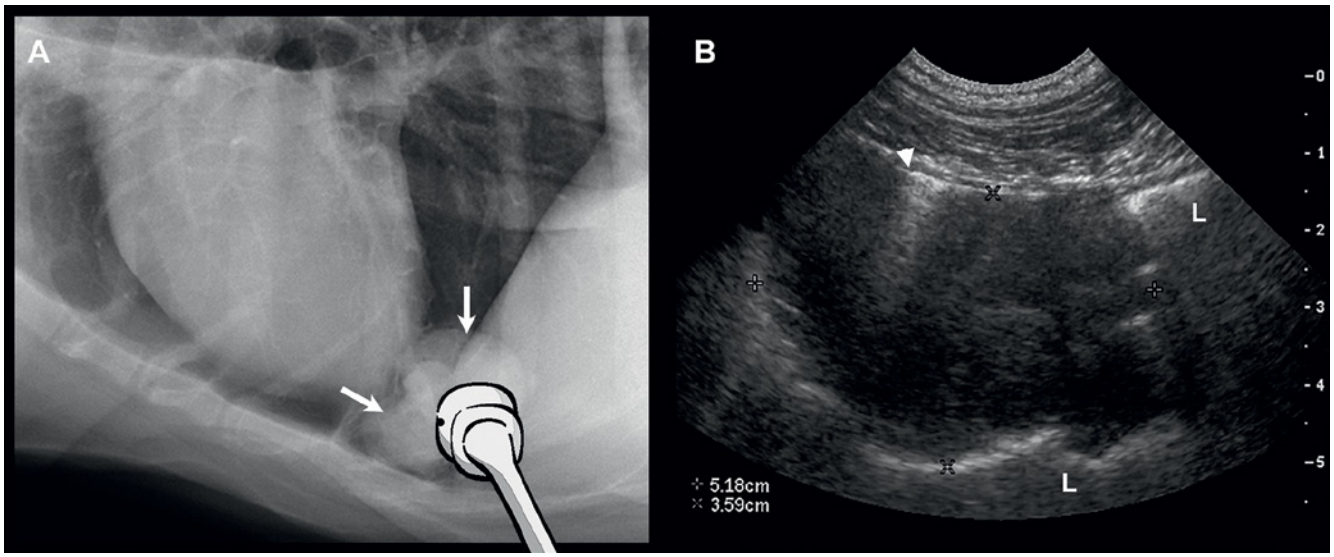


Figure 5.43. Disseminated histiocytic sarcoma in a 6-year-old Bernese Mountain dog. (A) On the left lateral radiograph, there is an approximately 5-cm soft-tissue mass in the caudal ventral thorax, summating with the diaphragm (arrows). **(B)** The ultrasonographic examination of the right caudal ventral thorax was performed using an intercostal approach immediately dorsal to the sternum. The mass (cursors) is irregular, homogeneous, hypoechoic, and associated with the ventral aspect of the right caudal lung lobe. The peripheral border is strongly hyperechoic and associated with reverberation artifacts, consistent with an aerated portion of the lung lobe (L). On real-time examination, it was seen to be sliding with respiration. A reverberating artifact originating from the pleural space and consistent with free air is also observed in the near field (arrowhead).

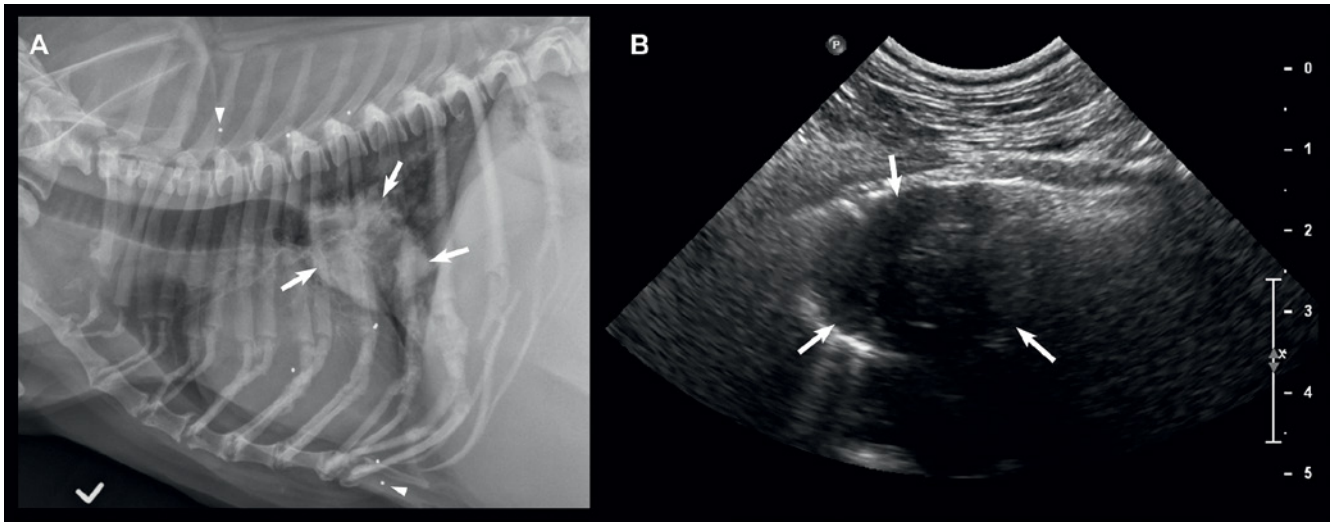


Figure 5.44. Pulmonary carcinoma in a 15-year-old Dachshund. (A) On this left lateral view of the thorax, there is a focal irregularly marginated soft-tissue opaque mass associated with the right caudal lung lobe (arrows). Multifocal pinpoint metal opacity foci associated with the thoracic wall (two indicated by arrowheads) are consistent with previous ballistic injury. **(B)** Transverse ultrasonographic image using a transverse right dorsal intercostal approach. The pulmonary mass (arrows) is hypoechoic, with pinpoint interspersed hyperechoic foci. The adjacent normal aerated lung (L) was seen intermittently sliding over the mass during real-time investigation.

The ultrasonographic characteristics of a diaphragmatic hernia or rupture are an irregular or asymmetrical cranial aspect of the liver and the presence of abdominal viscera in the thorax (Figures 5.55–5.57). Visible disruption of the diaphragm may be seen on occasion.

If an ultrasonographic examination is performed to confirm or exclude a diaphragmatic hernia, the examiner

Vet-ebooks.com

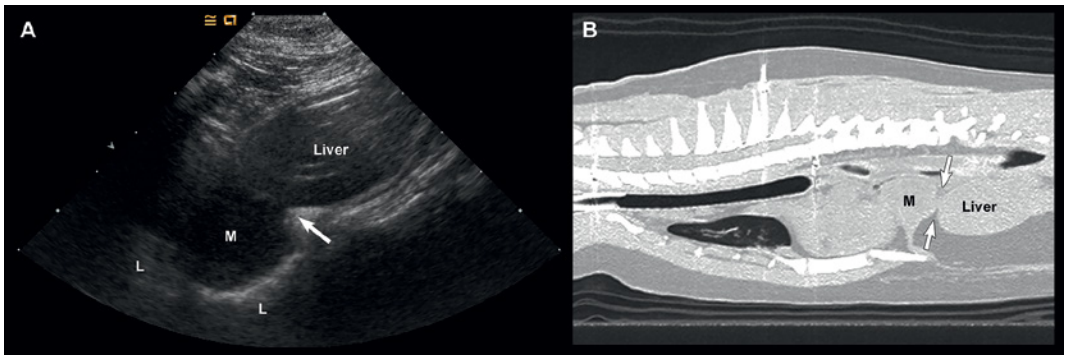


Figure 5.45. Accessory lung lobe mass in an 11-year-old cat. On the ultrasound image acquired using a transhepatic approach **(A)** and on the sagittal reconstructed CT image **(B)**, the mass (M) is well-circumscribed and forms an acute angle with the diaphragm (arrows). Normally aerated lung (L) borders the mass. The diagnosis of carcinoma was based on thoracocentesis and fluid analysis of a small-volume pleural effusion not visible on these images.

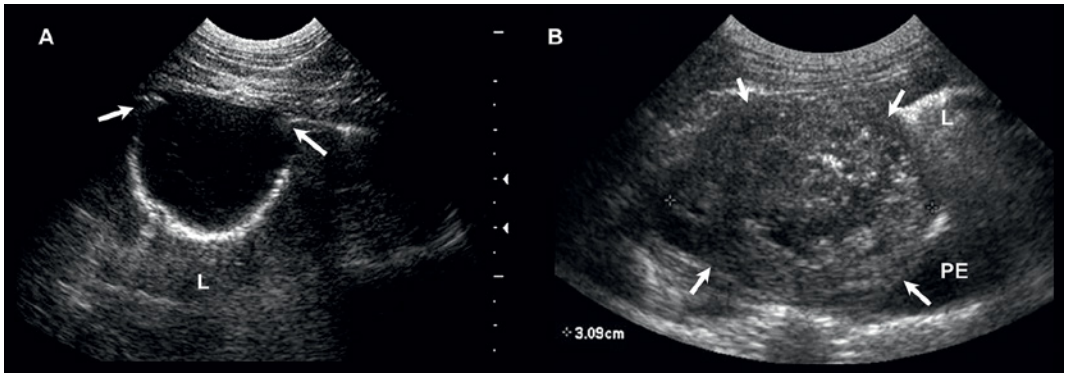


Figure 5.46. Pulmonary carcinoma in a dog and a cat. (A) This examination in an 8-year-old Labrador Retriever was performed using an intercostal approach. The pulmonary mass is well circumscribed, almost anechoic, forms an acute angle with the thoracic wall (arrows), and is surrounded by normally aerated lung parenchyma (L). **(B)** This examination was performed using an intercostal approach in a 12-year-old cat. A 3-cm mixed echogenic mass (arrows) associated with the pulmonary parenchyma distorts the normal lung margins. The adjacent normal lung is characterized by a hyperreflective interface (L). A small amount of pleural effusion (PE) is present.

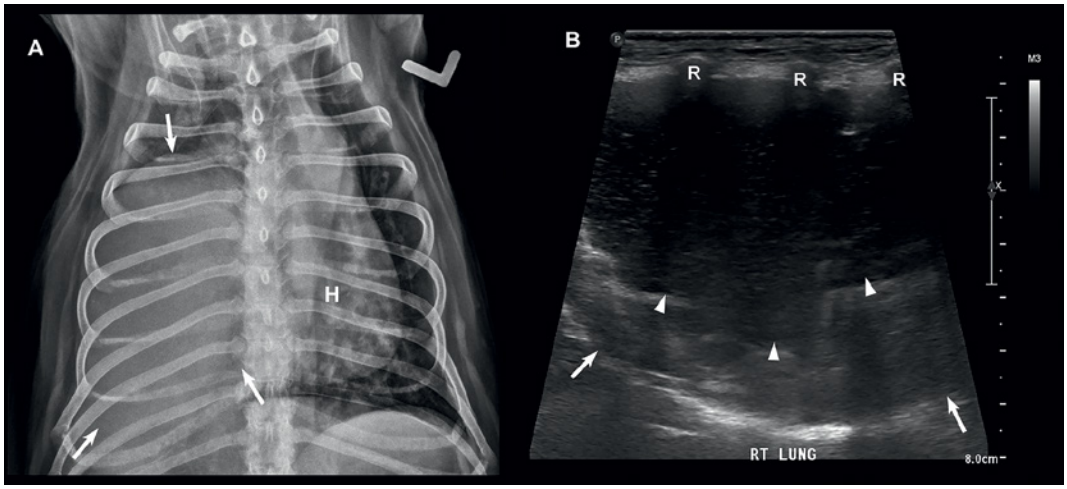


Figure 5.47. Unusual primary lung tumor in a 15-year-old Jack Russell Terrier. (A) On the ventrodorsal view of the thorax, there is a very large, homogeneously soft-tissue opaque right caudal pulmonary mass (arrows), believed to involve at least the right caudal and possibly the right middle lung lobe, displacing the cardiac silhouette (H) to the left. **(B)** The ultrasonographic image obtained using a dorsal plane right intercostal approach shows part of the large mass. The periphery of the lesion consists of hypoechoic solid parenchyma, most evident in the far field (arrows). The center of the lesion (arrowheads) contains a large amount of echogenic fluid. Part of the lesion is obscured by distal shadowing from hyperechoic ribs (R) in the near field. A diagnosis of **mucinous adenocarcinoma** was made based on the analysis of the fluid aspirated from the lesion.

Vet-ebooks.com

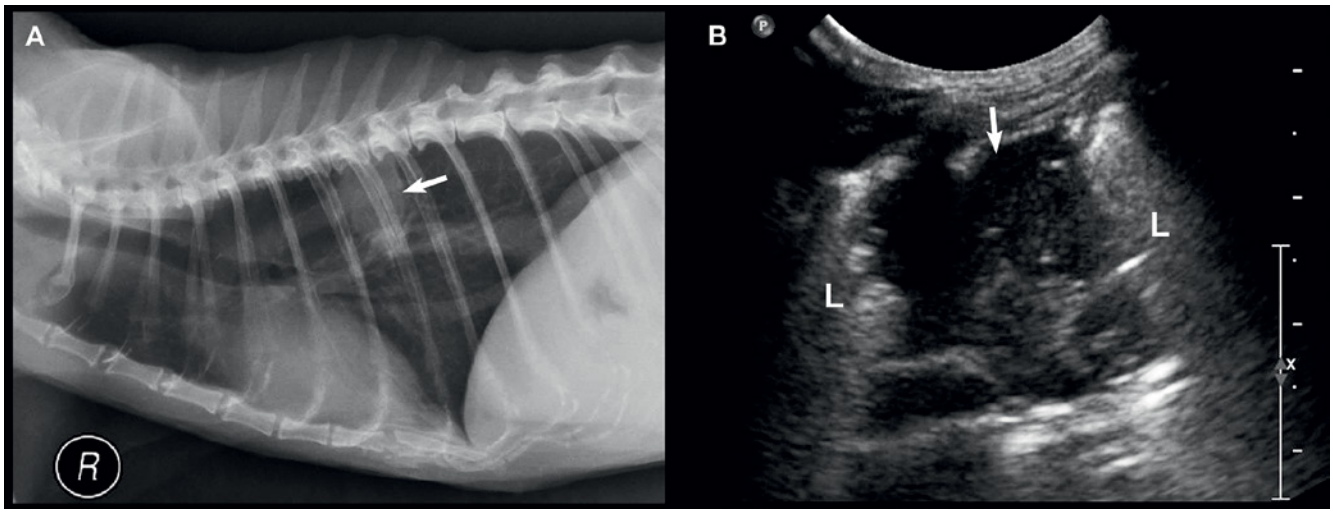


Figure 5.48. **Pulmonary lymphoma in an 18-year-old cat. (A)** The right lateral thoracic radiograph shows a discrete soft-tissue mass (arrow) located in the left caudal lung lobe. **(B)** The sonogram performed using a left intercostal approach shows a poorly echogenic pulmonary mass (arrow), surrounded by aerated lung (L).

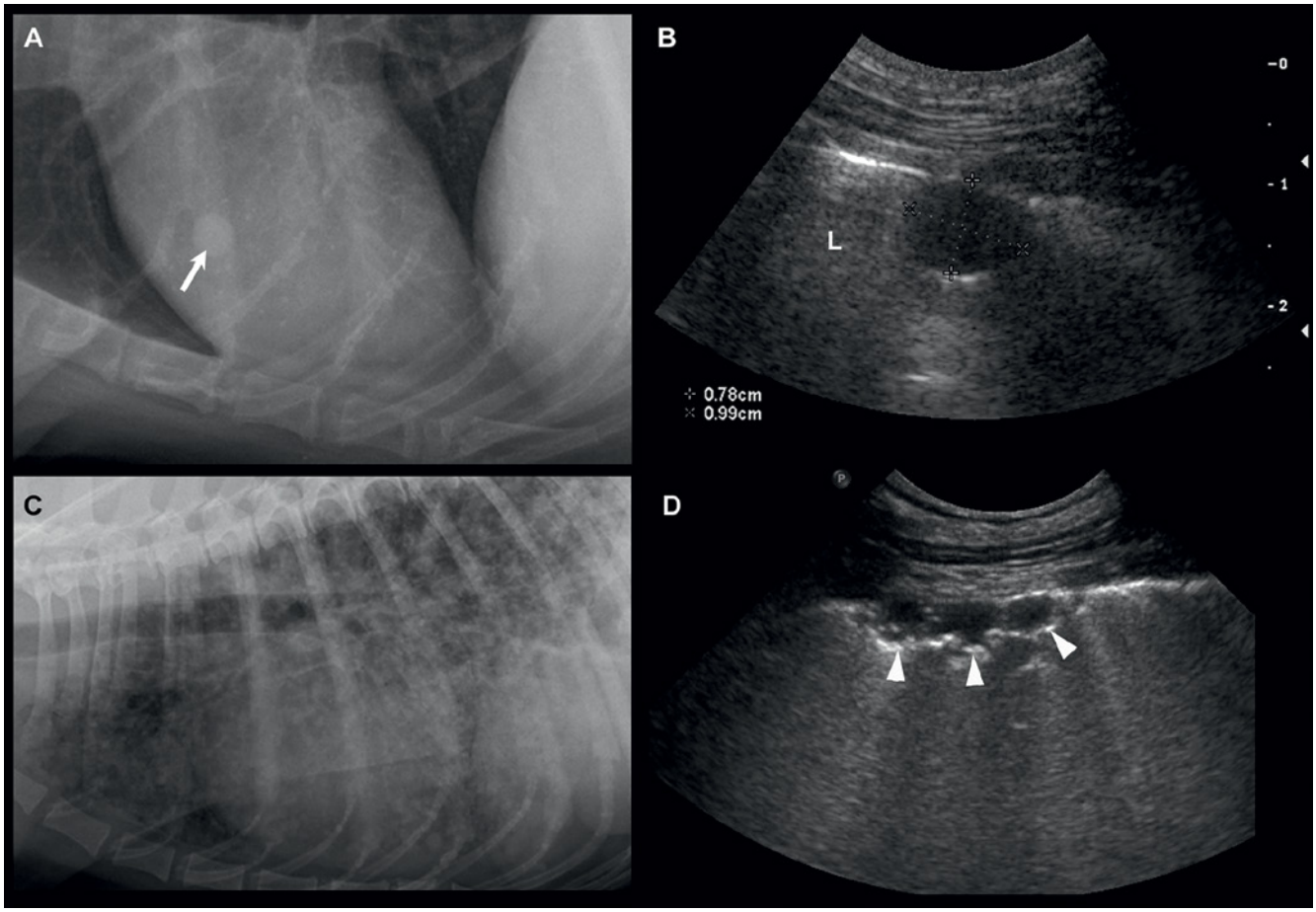


Figure 5.49. **Pulmonary metastases in two dogs. (A)** A small, round, soft-tissue opacity is noted on this left lateral thoracic radiograph (arrow) of a Dalmatian with a history of weight loss. **(B)** Using a left intercostal approach, a spherical hypoechoic nodule is seen at the superficial aspect of the lung (L). Ultrasound-guided fine-needle aspirate revealed a **metastatic sarcoma**. An abdominal fibrosarcoma was also detected. **(C)** This lateral thoracic radiograph in an 8-year-old Golden Retriever with a 2-week history of cough shows numerous small ill-defined soft-tissue nodules affecting all lung lobes. **(D)** Using both left and right intercostal approaches, numerous small, hypoechoic nodules (arrowheads) are observed at the superficial aspect of the lung. Fine-needle aspiration using ultrasound guidance revealed a **histiocytic sarcoma**.

Vet-ebooks.com

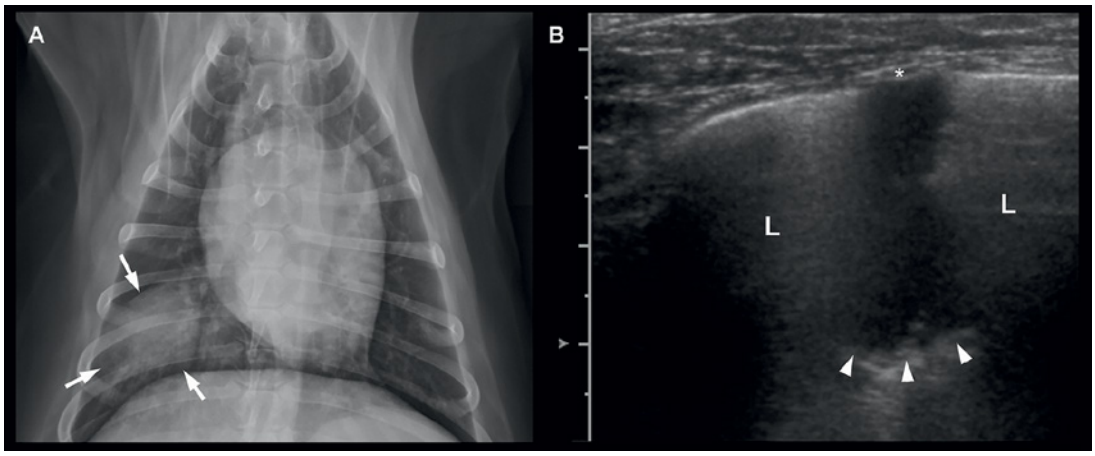


Figure 5.50. **Fungal granuloma (blastomycosis) in an 11-year-old Cocker Spaniel. (A)** This slightly oblique ventrodorsal radiograph of the thorax reveals a soft-tissue mass associated with the right caudal lung lobe (arrows). **(B)** Ultrasonographic image obtained using a right dorsal intercostal approach. A small portion of the pulmonary infiltrate (arrowheads) can be seen, despite the surrounding aerated lung (L). A rib (*) is limiting full visualization of the lesion.

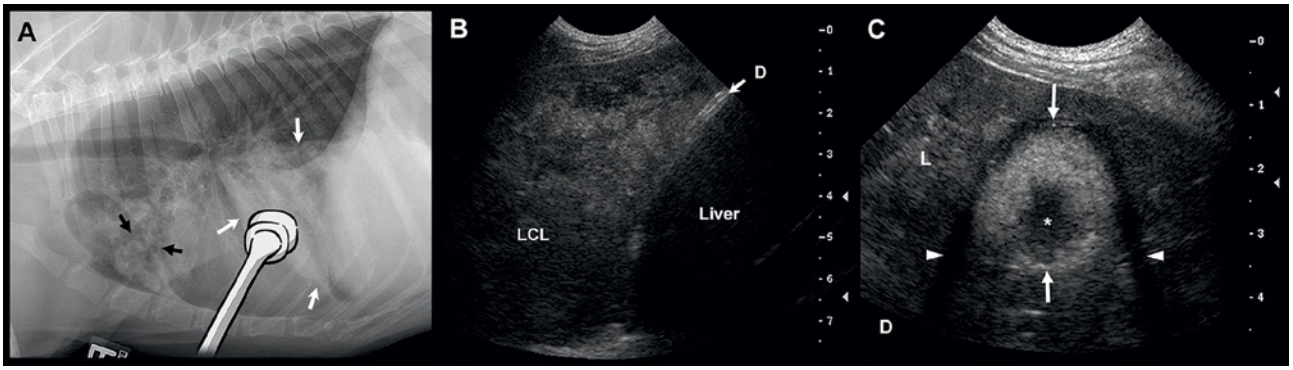


Figure 5.51. **Chronic pyogranulomatous pneumonia in a large-breed dog. (A)** A soft-tissue opacity mass lesion is noted in the caudoventral lung field on the right lateral radiograph (white arrows). An alveolar pattern is also apparent in the cranioventral lung field as well as irregular, air-filled, dilated bronchi consistent with bronchiectasis (black arrows). **(B)** On this ultrasonographic image obtained through the left sixth intercostal space, a large portion of the left caudal lung lobe (LCL) in contact with the diaphragm (D) is heterogeneous, moderately echogenic, and enlarged. **(C)** Sonogram of a portion of this lung lobe (L). There is a spherical hyperechoic mass (arrows) with an irregular hypoechoic center (*) and a thin hypoechoic rim. Edge-shadowing artifacts are seen at the margins of the lesion (arrowheads). Fine-needle aspiration confirmed the presence of a pyogranuloma.

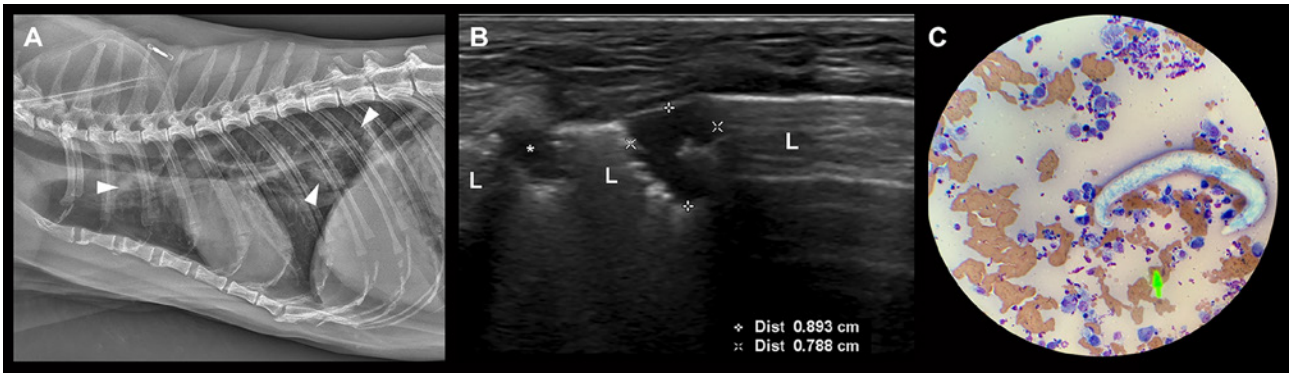


Figure 5.52. **Parasitic granulomas in a 13-year-old cat.** This patient had completed chemotherapy treatment for splenic lymphoma 3 months prior and had normal thoracic radiographs 2 months before these images were obtained. **(A)** On thoracic radiographs, there are multifocal poorly defined soft-tissue opacity nodules throughout the lung fields (arrowheads). **(B)** Ultrasound image obtained using a right caudal dorsal intercostal approach shows a roughly C-shaped hypoechoic nodule of 0.9 × 0.8 cm (between cursors) and an additional approximately 0.5 cm diameter nodule (*) associated with the right caudal lung lobe. These nodules are bordered by a normally aerated lung parenchyma (L). Fine-needle aspiration cytology was consistent with mixed inflammation with parasites compatible with ***Aelurostrongylus abstrusus***. **(C)** Image of a cytology slide of the lung aspirate of this patient including a parasite.

Vet-ebooks.com

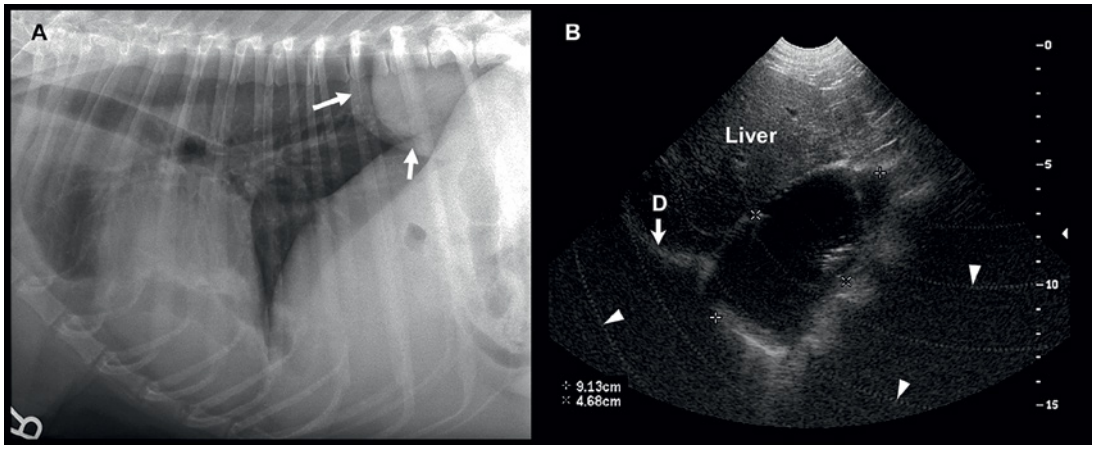


Figure 5.53. **Pulmonary abscess in a 5-year-old collie. (A)** On the lateral thoracic radiograph, there is a large, well-circumscribed, homogeneous soft-tissue opaque mass lesion associated with the caudal dorsal lung fields immediately cranial to the diaphragm (arrows). **(B)** Ultrasonographic examination performed by using a transhepatic approach (oblique transverse to dorsal plane). The abscess (cursors) is seen immediately cranial to the diaphragm (D). It is anechoic and surrounded by a thin, hyperechoic rim. The concentric dotted lines (arrowheads) represent an artifact likely caused by electrical interference.

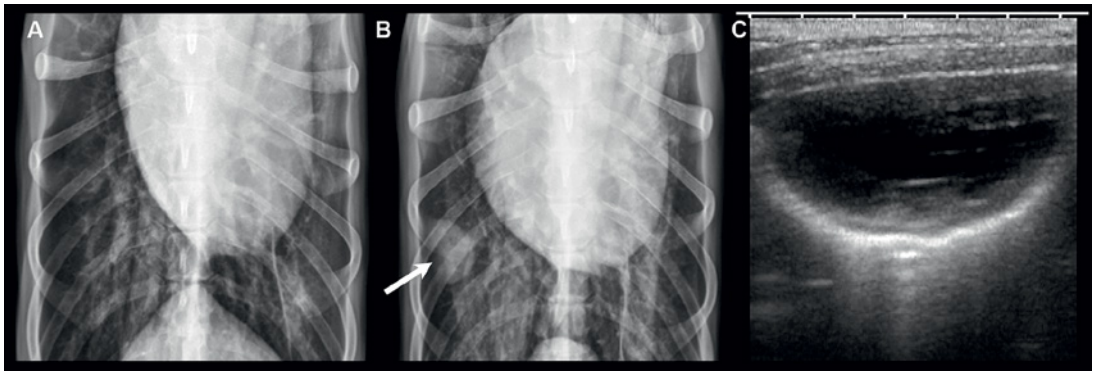


Figure 5.54. **Traumatic pulmonary hematoma in a 9-year-old Scottish Deerhound.** Radiographs and sonogram of the lung after bronchoalveolar lavage. **(A)** The ventrodorsal radiograph, at the time of presentation, reveals a generalized unstructured interstitial pattern. No other abnormality is detected at this time. A bronchoalveolar lavage was then performed. **(B)** Recheck radiographs 6 days later show a homogeneous 3-cm mass lesion associated with the right lung at the level of the sixth rib (arrow). **(C)** Ultrasonographic examination performed using a linear probe with a transverse intercostal approach. An anechoic, well-circumscribed lesion of 3 cm diameter is associated with the lung. Aspiration yielded blood, consistent with a hematoma.

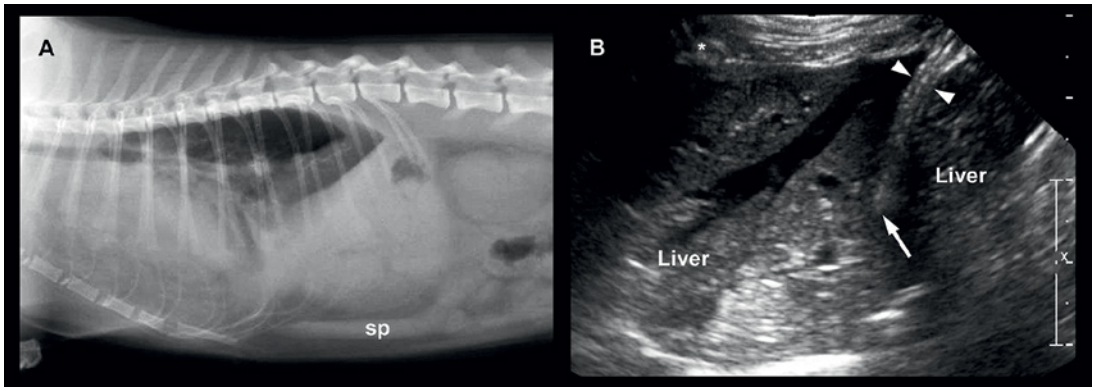


Figure 5.55. **Traumatic diaphragmatic rupture in a 1-year-old cat. (A)** On this lateral radiograph including the caudal thorax and cranial abdomen, there is increased opacity to the caudal thorax, the diaphragm is indistinct, and the spleen (sp) is displaced into the cranioventral abdomen, leading to the diagnosis of traumatic hernia. **(B)** Longitudinal sonogram via a left caudal intercostal approach. The liver is displaced into the thoracic cavity. Part of the diaphragm remains visible (outlined by arrowheads). The diaphragmatic contour becomes indistinct in the far field (arrow). A small amount of anechoic pleural effusion is present between the herniated liver lobes. Part of the liver is still present in the cranial abdomen. A rib (*) in the near field is creating a strong acoustic shadow.

Vet-ebooks.com

must be aware of common artifacts occurring at the level of the diaphragm. If the animal has ascites, refraction of the beam at the liver surface may cause the diaphragm to appear discontinuous. The commonly seen mirror-image artifact might be mistaken for a herniation of liver into the thorax (see Figure 1.17). Adhesions between herniated organs and the pleural cavity and/or diaphragm may exist and appear as echogenic strands floating or adhering to the walls and organs. The ultrasonographic diagnosis of a PPDH is usually straightforward if abdominal organs (e.g., liver or intestine) are present within the pericardial sac (Figures 5.58, 5.59).

Other Diaphragmatic Disorders

Other disorders of the diaphragm are rare. Benign or malignant mass lesions are occasionally encountered (Figures 5.60, 5.61).

Ultrasound-Assisted Procedures

Ultrasound is useful to aid diagnostic or therapeutic **thoracocentesis**, especially if only a small volume of pleural effusion is present (Figure 5.62A), or when

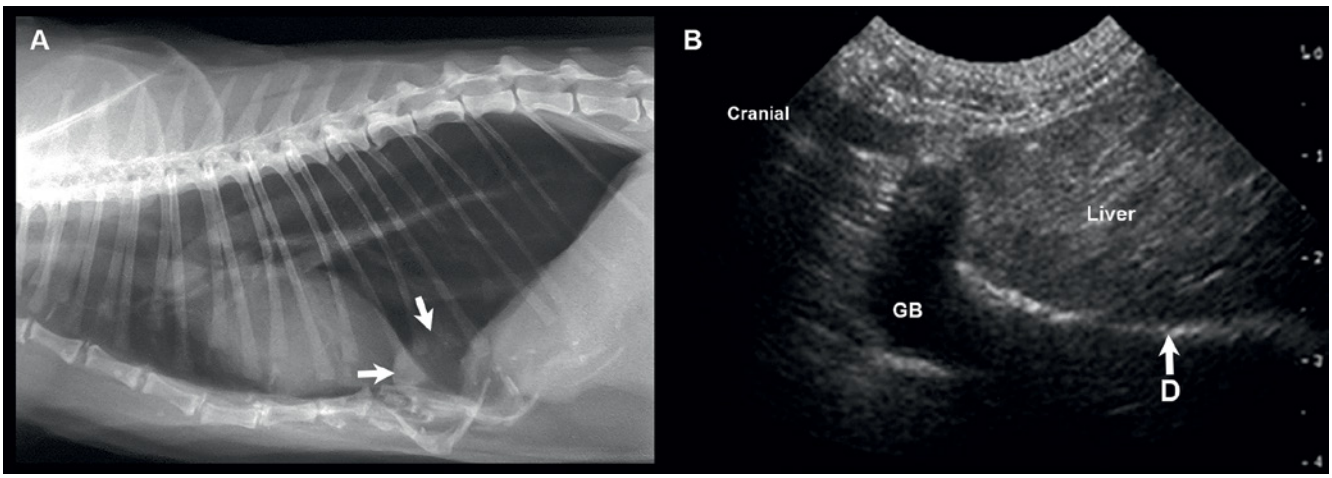


Figure 5.56. True (congenital) diaphragmatic hernia with herniation of the gall bladder in a cat. (A) On the lateral thoracic radiograph, a well-circumscribed, round soft-tissue opacity (arrows) is present between the diaphragm and cardiac silhouette. **(B)** The ultrasonographic examination is performed by using a right ventral intercostal approach. The diaphragm (D) is the strongly hyperechoic curvilinear structure in the far field. The diaphragm is discontinuous in the near field, with herniation of the gall bladder (GB) into the thoracic cavity.

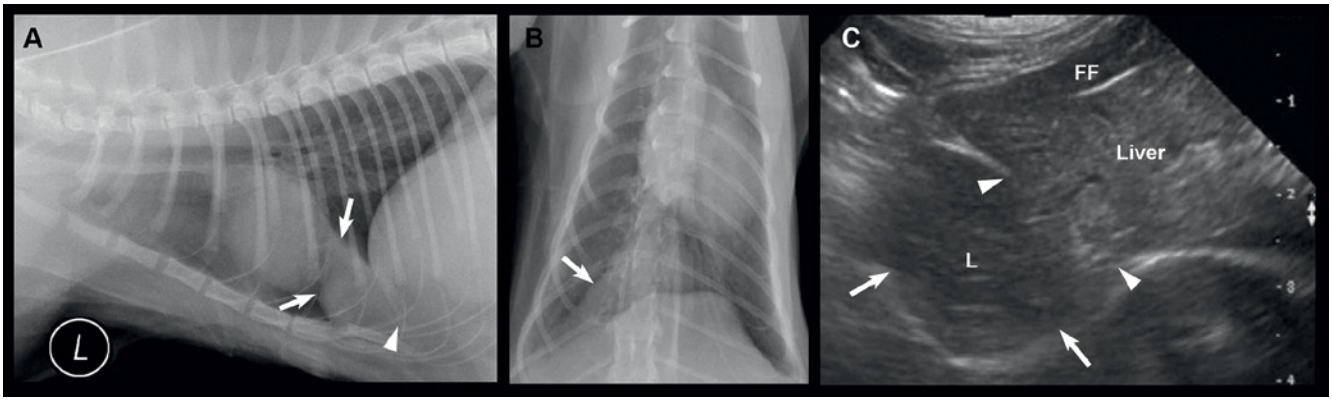


Figure 5.57. True (congenital) diaphragmatic hernia in a 14-year-old cat. (A, B) On the lateral **(A)** and mildly oblique ventrodorsal **(B)** views, there is a focal smoothly marginated fat to soft-tissue opaque structure associated with the right caudal ventral thorax (arrows). The ventral aspect of the diaphragm separating this structure from abdominal falciform fat appears unusually thin (arrowhead). **(C)** The sonographic examination reveals a focal defect associated with the diaphragmatic contour (diaphragm indicated by arrowheads), with part of the liver (L) being herniated into the caudal ventral thorax (arrows). This was an incidental finding during work-up of this patient for hyperthyroidism and planning of radioiodine therapy. FF, falciform fat.

Vet-ebooks.com

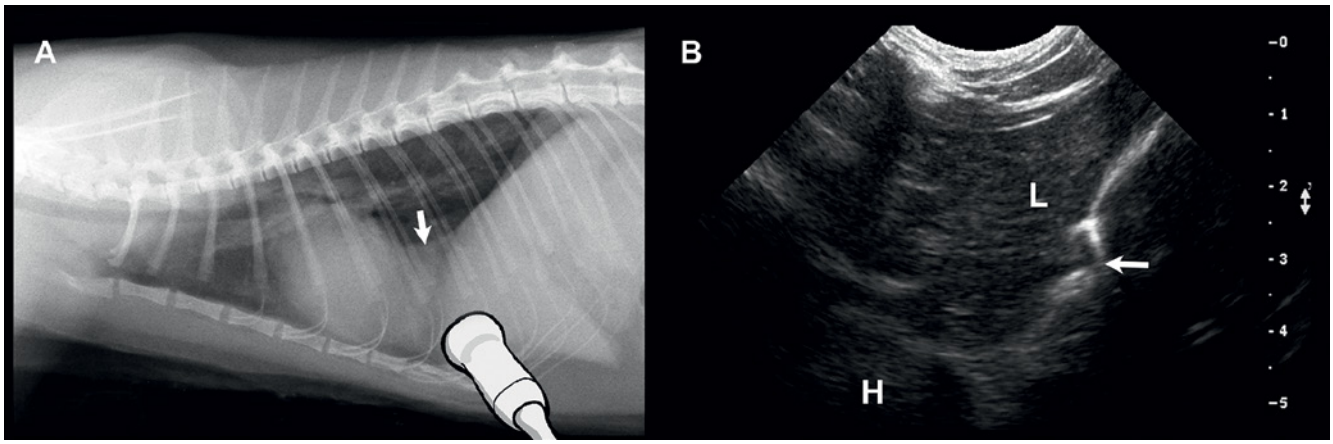


Figure 5.58. Peritoneo-pericardial diaphragmatic hernia in a 2-year-old cat. (A) The lateral thoracic radiograph reveals loss of the ventral part of the diaphragmatic silhouette and silhouetting of abdominal and peritoneal contents. A "mesothelial remnant" sign is noted ventral to the caudal vena cava (arrow). The cardiac silhouette is enlarged. **(B)** Ultrasonographic examination performed using an intercostal approach. There is discontinuity of the diaphragm (arrow), and hepatic parenchyma (L) is visible in the near field, cranial to the diaphragm, and close to – and displacing – the heart (H).

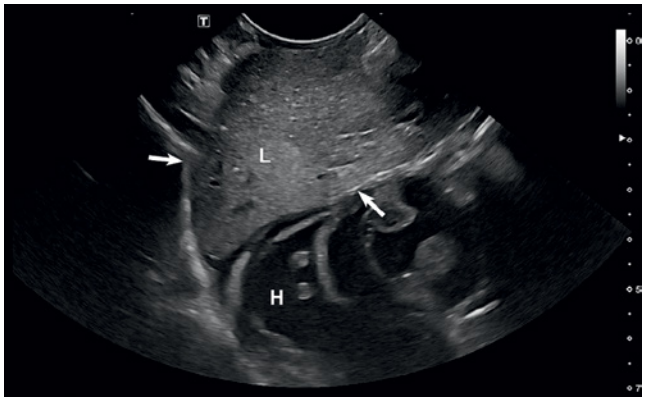


Figure 5.59. Congenital peritoneo-pericardial diaphragmatic hernia in a 3-month-old Golden Retriever. Ultrasound image of the diaphragm in a transverse plane. There is a large defect in the diaphragm (arrows) and portions of the liver (L) extend into the pericardial sac and are located directly next to the heart (H).

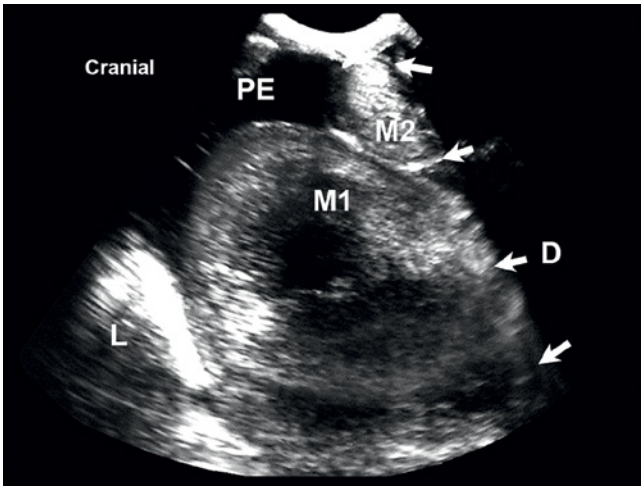


Figure 5.60. Diaphragmatic rhabdomyosarcoma in a 4-month-old cat. Sonogram was obtained with an intercostal approach. Two mixed echogenic mass lesions (M1, M2) are arising from the diaphragm (D, arrows). The larger mass measures more than 6 cm in maximum diameter, and the smaller mass measures 2.5 cm. The lung is displaced cranially (L) and there is anechoic pleural (PE) and peritoneal effusion.

septations between fluid pockets interfere with blinded centesis. Additionally, **fine-needle aspiration or biopsy** of thoracic mass lesions is commonly performed. These procedures are safe and have a high diagnostic yield (Grimes et al. 2019; Wood et al. 1998; Figure 5.62B, C). An intercostal approach is used most commonly. Patient preparation (sedation with or without anesthesia, sterile preparation) is performed in a routine manner. Depending on the size and location of the lesion, 20- to 25-gauge injection or spinal needles are used for fine-needle aspiration and 16- to 18-gauge biopsy needles are used to obtain core biopsy samples. Fine-needle aspiration can be performed freehand, with an extension tube or directly attached to a syringe of 5–10 mL, enabling, with practice, faster and safer interventions. Biopsy samples can also be obtained freehand or by using a biopsy guide. To facilitate fine-needle aspiration or biopsy of pulmonary lesions, it might be necessary to induce respiratory standstill for the duration of the procedure, warranting endotracheal intubation of the patient. Tissue sampling of intrathoracic structures is generally considered a safe procedure. Potential complications include pneumothorax and hemorrhage, which are usually mild and

Vet-ebooks.com

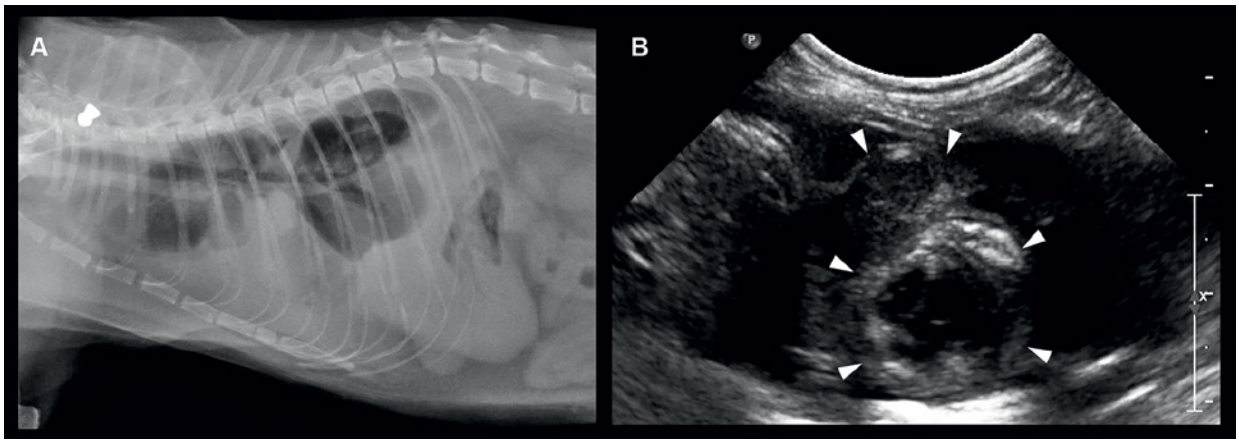


Figure 5.61. **Sarcoma with diaphragmatic involvement in a 6-year-old domestic shorthair cat. (A)** On this right lateral radiograph, there is a marked increased opacity in the thorax, which was confirmed on ultrasound as a combination of pleural effusion and thoracic masses. A gun pellet is superimposed on the cranial thoracic spine. **(B)** The ultrasonographic image was obtained via a subcostal approach. A complex, cavitated nodule (arrowheads) is floating in the caudal thorax and is attached to the diaphragm. An inhomogeneously echogenic mass was noted in the left caudal lung lobe (not shown). Fine-needle aspirates of these lesions were diagnostic for sarcoma, probably metastatic from a recently removed soft-tissue sarcoma.

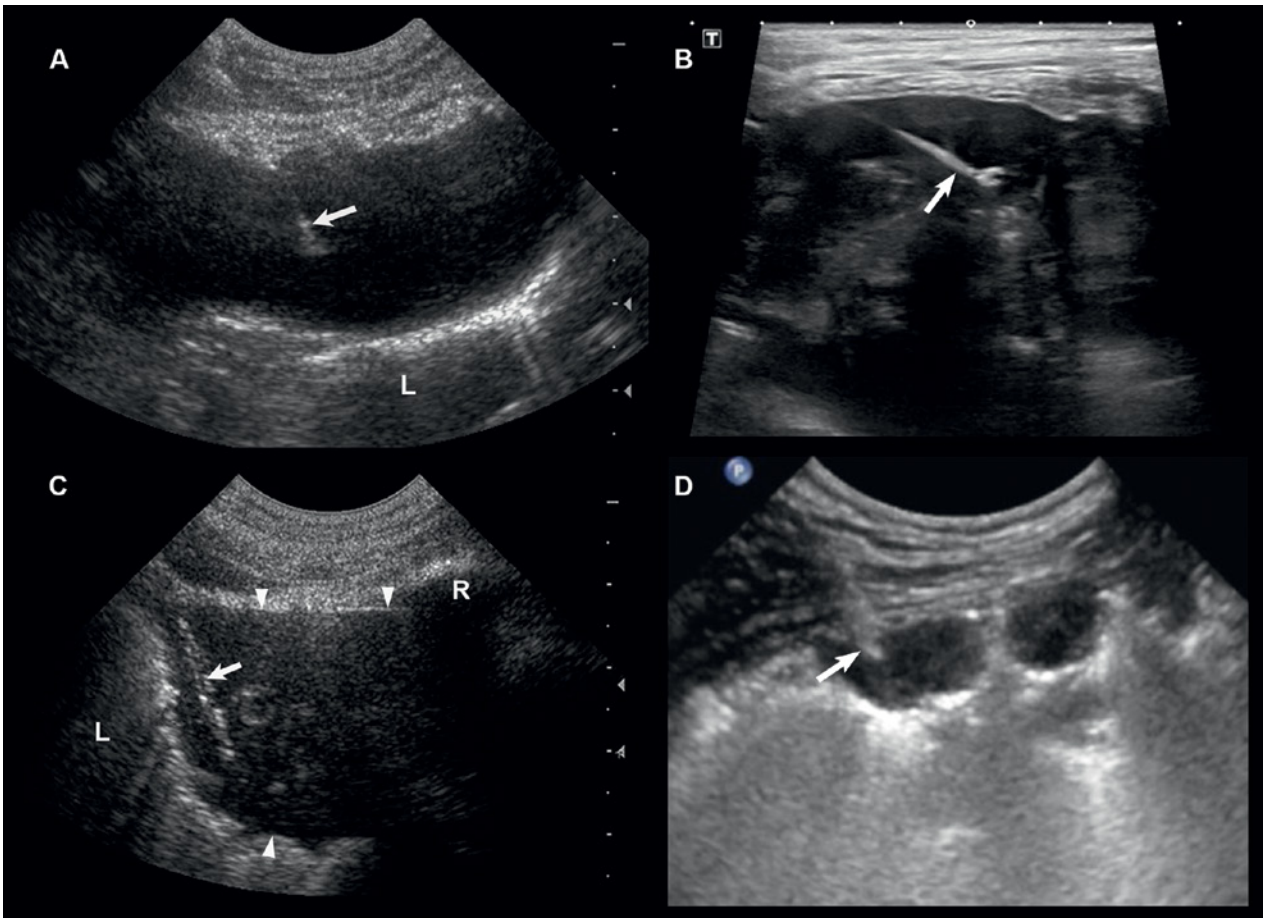


Figure 5.62. **Ultrasound-assisted procedures. (A) Thoracocentesis** in a cat with pleural effusion. The needle (arrow) appears as a hyperechoic line within the pleural space. **(B) Fine-needle aspiration** (FNA) of a thoracic mass. The needle (arrows) is visible as a hyperechoic line that traverses the thoracic wall at an oblique angle before entering the mass. **(C) Biopsy** of a pulmonary mass (bronchoalveolar carcinoma) in a dog. Two closely aligned needle tracts stay visible as hyperechoic lines (arrow) right after the truCut biopsy was performed on the periphery of the mass (arrowheads) adjacent to the aerated portion of the lung (L). There is no evidence of pneumothorax. There is a hyperechoic superficial margin of a rib (R) with associated acoustic shadowing in the near field. **(D) FNA** of one of several superficial, small, hypoechoic pulmonary nodules in an 8-year-old Golden Retriever. Sampling was performed using a 22-gauge needle. The arrow points to the tip of the needle. The diagnosis was histiocytic sarcoma.

Vet-ebooks.com

self-limiting. Needle-tract implantation during fine-needle aspiration of thoracic lesions is extremely rare but has been reported in a dog with a pulmonary carcinoma (Vignoli et al. 2007). Intraoperative assistance for tracing draining tracts and foreign material dissecting the thoracic wall and possibly entering the thoracic cavity can be useful to the surgeon, as it will reduce the length of the procedure and minimize soft-tissue trauma.



Visit our website at **www.SmallAnimalUltrasonography.com** for complementary video clips with annotations and text on:

- Normal lung interface
- Thoracic wall mass
- Pleural effusion
- Pulmonary mass
- Mediastinal mass
- Branchial cyst
- Diaphragmatic hernia

References

Armbrust LJ, Biller DS, Radlinsky MG, Hoskinson JJ (2003) Ultrasonographic diagnosis of foreign bodies associated with chronic draining tracts and abscesses in dogs. Vet Radiol Ultrasound 44:66–70.

Belmudes A, Gory G, Cauvin E, Combes A, et al. (2021) Lung lobe torsion in 15 dogs: peripheral band sign on ultrasound. Vet Radiol Ultrasound 62:116–125.

Boysen SR, Lisciandro GR (2013) The use of ultrasound for dogs and cats in the emergency room: AFAST and TFAST. Vet Clin North Am Small Anim Pract 43:773–797.

Caivano D, Birettoni F, Bufalari A, De Monte V, et al. (2016) Contrast-enhanced ultrasonographic findings in three dogs with lung lobe torsion. J Vet Med Sci 78:427–430.

d'Anjou MA, Tidwell AS, Hecht S (2005) Radiographic diagnosis of lung lobe torsion. Vet Radiol Ultrasound 46: 478–485.

Grimes CN, Fry MM, LeBlanc CJ, Hecht S (2019) The lung and intrathoracic structures. In Cowell R, Valenciano A, eds. Cowell and Tyler's Diagnostic Cytology and Hematology of the Dog and Cat, 5th edition. St. Louis: Elsevier, pp. 269–288.

Hurley ME, Keye GD, Hamilton S (2004) Is ultrasound really helpful in the detection of rib fractures? Injury 35:562–566.

Hwang TS, Yoon YM, Jung DI, Yeon SC, et al. (2018) Usefulness of transthoracic lung ultrasound for the diagnosis of mild pneumothorax. J Vet Sci 19:660–666.

Larson M (2009) Ultrasound of the thorax (noncardiac). Vet Clin North Am Small Anim Pract 39:733–745.

Lin CH, Lo PY, Lam MC, Wu HD (2020) Usefulness of chest ultrasonography in predicting diagnosis in non-emergency small animal patients with lung parenchymal and pleural disease. Front Vet Sci 18, doi: 10.3389/fvets.2020.616882.

Linta N, Baron Toaldo M, Bettini G, Cordella A et al. (2017) The feasibility of contrast enhanced ultrasonography (CEUS) in the diagnosis of non-cardiac thoracic disorders of dogs and cats. BMC Vet Res 13:141.

Louvet A, Bourgeois JM (2008). Lung ring-down artifact as a sign of pulmonary alveolar-interstitial disease. Vet Radiol Ultrasound 49:374–377.

Mattoon JS, Nyland TG (1995) Thorax. In Nyland TG, Mattoon JS, eds. Small Animal Diagnostic Ultrasound. Philadelphia: WB Saunders, pp. 325–353.

Reichle JK, Wisner ER (2000) Non-cardiac thoracic ultrasound in 75 feline and canine patients. Vet Radiol Ultrasound 41:154–162.

Rick T, Kleiter M, Schwendenwein I, Ludewig E, et al. (2019) Contrast-enhanced ultrasonography characteristics of intrathoracic mass lesions in 36 dogs and 24 cats. Vet Radiol Ultrasound 60:56–64.

Rudorf H, Herrtage ME, White RA (1997) Use of ultrasonography in the diagnosis of tracheal collapse. J Small Anim Pract 38:513–518.

Schultz RM, Zwingenberger A (2008) Radiographic, computer tomographic and ultrasonographic findings with migrating intrathoracic grass awns in dogs and cats. Vet Radiol Ultrasound 49:249–255.

Schwarz LA, Tidwell AS (1999) Alternative imaging of the lung. Clin Tech Small Anim Pract 14:187–206.

Seiler G (2011) Thorax. In Barr F, Gaschen L, eds. BSAVA Manual of Canine and Feline Ultrasonography. BSAVA: Gloucester, pp. 29–36.

Spattini G, Rossi F, Vignoli M, Lamb CR (2003) Use of ultrasound to diagnose diaphragmatic rupture in dogs and cats. Vet Radiol Ultrasound 44:226–230.

Tidwell AS (1998) Ultrasonography of the thorax (excluding the heart). Vet Clin North Am Small Anim Pract 28: 993–1015.

Vignoli M, Rossi F, Chierici C, Terragni, R, et al (2007) Needle tract implantation after fine needle aspiration biopsy (FNAB) of transitional cell carcinoma of the urinary bladder and adenocarcinoma of the lung. Schweiz Arch Tierheilkd 149:314–318.

Wood EF, O'Brien RT, Young KM (1998) Ultrasound-guided fine-needle aspiration of focal parenchymal lesions of the lung in dogs and cats. J Vet Intern Med 12:338–342.

Zekas LJ, Adams WM (2002) Cranial mediastinal cysts in nine cats. Vet Radiol Ultrasound 43:413–418.

Vet-ebooks.com

Vet-ebooks.com

CHAPTER SIX

HEART

Jonathan Lichtenberger[1], Shari Raheb[2], and Hugues Gaillot[3]

[1]*Pacific Coast Veterinary Cardiology, Victoria, British Columbia, Canada*
[2]*Department of Clinical Studies, Ontario Veterinary College, University of Guelph, Guelph, Ontario, Canada*
[3]*ADVETIA Centre Hospitalier Vétérinaire, Vélizy-Villacoublay, France*

ECHOCARDIOGRAPHIC TECHNIQUE

Instrumentation

To perform a thorough cardiac study, ultrasound instruments should include hardware and software with the ability to perform motion mode (M-mode), two-dimensional (2D) imaging, color Doppler imaging (CDI), and spectral Doppler imaging, including pulsed wave and continuous wave Doppler (PWD and CWD).

Echocardiography differs from abdominal ultrasonography in that transducer placement is confined to limited windows of access between the ribs and aerated lung. This limitation imposes the need for a small transducer footprint. Echocardiographic examinations are therefore best performed using sector (phased-array) transducers. The transducers used for veterinary studies should provide adequate imaging across a wide range of depths considering the variation in patient size and conformation. Suggested guidelines for transducer frequencies include 7–12 MHz for cats and similarly sized dogs, 4–7 MHz for dogs in the 5–40 kg range, and 2–4 MHz for large dogs (>40 kg). Modern transducers are multifrequency and allow the echocardiographer to change frequency during the exam without having to constantly switch transducers. The authors currently use three different phased-array transducers for cardiac studies in small animals with the following bandwidths: a 4–12 MHz transducer for cats and small-breed dogs, a 2.4–8 MHz transducer for medium to large-breed dogs, and a 1.4–4.6 MHz transducer for large and giant-breed dogs. The animal conformation and body condition also play a role in transducer selection. For example, barrel-chested breeds (e.g., English Bulldogs) often require lower frequencies than deep-chested breeds (e.g., Greyhounds).

When performing an echocardiogram, a concurrent electrocardiogram may be valuable or essential, depending on the goals of the study.

Patient Preparation and Positioning

An echocardiogram is best performed in a darkened room and calm environment. Most patients can be examined without sedation under gentle manual restraint. If sedation is required, the authors' preference is to use mild sedatives that can be administered at home prior to the examination such as gabapentin (especially useful in cats) and/or trazodone. Injectable butorphanol is also often used in hospital and has minimal hemodynamic effects. If deeper sedation is necessary, it is important to consider the hemodynamic effects of the drugs used when interpreting images. For example, dexmedetomidine is known to cause bradycardia, valvular regurgitation, and a reduction in systolic function (Kellihan et al. 2015).

Most echocardiographers perform echocardiograms with the animal in lateral recumbency starting on the right side (Figure 6.1). A table with a cutout located at the edge of the table is usually used. One to two assistants are usually holding the animal, and the front limbs are being pulled forward slightly. Anecdotally, cats seem to resist having their forelimbs pulled forward; instead, the author(s) suggest the handler hook a finger behind the elbow of the cat to push the limb forward, which seems to be better tolerated. Alternatively, echocardiograms can be performed in a

Atlas of Small Animal Ultrasonography, Third Edition. Edited by Dominique Penninck and Marc-André d'Anjou.
© 2025 John Wiley & Sons, Inc. Published 2025 by John Wiley & Sons, Inc.
Companion website: www.SmallAnimalUltrasonography.com

Vet-ebooks.com



Figure 6.1. Patient positioning for transthoracic echocardiography in lateral recumbency. Examination of a dog using a table with two cutouts. This dog is gently restrained by two assistants. The echocardiographer is holding the transducer with the right hand while operating the control console with the left hand. **(A, B)** The dog is positioned in right lateral recumbency to obtain right-parasternal views. **(C, D)** The dog is positioned in left lateral recumbency to obtain left apical views and left cranial views.

standing position, with the animal held against the assistant with the head gently turned away from the echocardiographer to widen the intercostal spaces (Chetboul et al. 2005). The acoustic window is identified by palpating the apical impulse. A small square of hair is then clipped, or the hair can be parted using isopropyl alcohol, and a generous amount of ultrasound gel is used for acoustic transmission.

Abbreviations and conventions used throughout this chapter are displayed in Table 6.1.

Image Optimization

While a specific cardiac preset is usually selected at the beginning of the exam, it is important for echocardiographers to be familiar with the most common instrumentation settings to obtain optimal quality images. Some basic recommendations are provided below for 2D imaging, CDI, and spectral Doppler imaging (Tables 6.2–6.4) (Anderson 2016; Bonagura and Luis Fuentes 2015; Chetboul and Taton 2018; Lai et al. 2006; Mitchell et al. 2019).

CDI is a pulsed-wave modality in which velocity characteristics are encoded to a color display and overlaid onto the real-time 2D echocardiographic image. The following blood flow characteristics can be determined using this modality: timing, direction, surface area, relative velocity, and presence of turbulence. Optimal CDI settings are important to ensure adequate visualization of normal and abnormal blood flow patterns and to appropriately describe valvular regurgitant jets (Table 6.3). For example, settings such as the velocity scale (Nyquist limit) influence the appearance of the regurgitant volume. Consistent settings should be used when performing longitudinal studies for patients with chronic degenerative valvular disease for example. Some degree of aliasing can be seen even with normal blood flow velocities and spectral Doppler should always be used to confirm the presence of abnormal blood flow velocities.

Spectral Doppler consists of **PWD and CWD** (Table 6.4). Optimal alignment between blood flow and the ultrasound beam is crucial to obtain accurate spectral Doppler signals and peak velocity measurements. Therefore, it is important to obtain echocardiographic views, which allow the ultrasound beam to be aligned as parallel to blood flow as possible. CWD is mainly used to measure elevated blood flow velocities, which is impossible with PWD due to signal aliasing.

Conventional Two-Dimensional, M-Mode And Doppler Echocardiography: The Normal Heart

This section presents the sequence of images obtained for a complete cardiac examination as well as some additional images that can be acquired in specific situations. While most textbooks cover different imaging modalities (i.e., 2D, M-Mode, and Doppler imaging) separately, the section below integrates all modalities

Vet-ebooks.com

Table 6.1
Abbreviations and conventions used throughout this chapter

Anatomical designations	
AML	Anterior mitral valve leaflet
Ao	Aorta or aortic
AV	Aortic valve
CaVC	Caudal vena cava
CrVC	Cranial vena cava
CT	Chordae tendineae
IAS	Interatrial septum
IVS	Intraventricular septum
LA	Left atrium or left atrial
LAA	Left atrial appendage
LC	Left coronary cusp of the aortic valve
LPA	Left pulmonary artery
LV	Left ventricle or left ventricular
LVOT	Left ventricular outflow tract
LVW	Left ventricular wall
MV	Mitral valve
NC	Noncoronary cusp of the aortic valve
P	Pericardium
PM	Papillary muscle
PML	Posterior mitral valve leaflet
PT/PA	Pulmonary trunk/artery
PV	Pulmonic valve
RA	Right atrium or right atrial
RAA	Right atrial appendage
RC	Right coronary cusp of the aortic valve
RPA	Right pulmonary artery
RV	Right ventricle or right ventricular
RVOT	Right ventricular outflow tract
RVW	Right ventricular wall
TV	Tricuspid valve
Echocardiographic modality	
CDI	Color Doppler Imaging
CWD	Continuous-wave Doppler
M-mode	Motion mode
PWD	Pulsed-wave Doppler
TDI	Tissue Doppler imaging

Table 6.1
(Continued)

2D	Two-dimensional (imaging/ echocardiography)
Transducer position and orientation	
Ap	Apex
Bs	Base
Ca	Caudal
Cr	Cranial
LAp	Left apical
LPS	Left parasternal
LAx	Long axis (orientation)
RPS	Right parasternal (position)
SAx	Short axis (orientation)
Diseases and conditions	
AI	Aortic insufficiency
AS	Aortic stenosis
ASD	Atrial septal defect
CHF	Congestive heart failure
LCHF	Left-sided congestive heart failure
DMVD	Degenerative mitral valve disease
DCM	Dilated cardiomyopathy
HBT	Heart base tumor
HCM	Hypertrophic cardiomyopathy
HOCM	Hypertrophic obstructive cardiomyopathy
MR	Mitral regurgitation
PDA	Patent ductus arteriosus
PE	Pericardial effusion
PHT	Pulmonary hypertension
PI	Pulmonic insufficiency
PS	Pulmonic stenosis
RCM	Restrictive cardiomyopathy
SAM	Systolic anterior motion of the mitral valve
SAS	Subaortic stenosis
TOF	Tetralogy of Fallot
TR	Tricuspid regurgitation
TRV	Tricuspid regurgitation maximal velocity
VSD	Ventricular septal defect

Table 6.2
Key 2D imaging settings used to optimize spatial, contrast, and temporal resolution

	2D imaging
Grayscale maps and colorization	With most systems, the grayscale map can be chosen based on the preference of the echocardiographer. Colorization of the image is also possible (e.g., blue, sepia, and light pink). It is recommended to use a consistent grayscale map to allow comparisons between studies.
Harmonic imaging	Harmonic imaging is usually preferred over fundamental imaging, especially in medium to large dogs. This reduces background noise and improves endocardial border definition. Note that some tissues such as cardiac valves may appear thicker.
Transducer frequency	The echocardiographer should select the highest possible frequency that provides sufficient depth penetration.
Depth	The lowest possible depth should be used in order to display the entire region of interest (i.e., heart and great vessels) without including peripheral structures such as the lungs.
Sector size	The smallest possible sector size should be used in order to display the entire region of interest (i.e., heart and great vessels) without including peripheral structures such as the lungs.
Frame rate	High frame rates (50–150 image frames per second) are recommended in echocardiography due to the dynamic nature of the heart and rapid heart rates encountered in veterinary patients. The frame rate can be increased by reducing the image depth and narrowing the sector width.

Vet-ebooks.com

Table 6.2
(Continued)

2D imaging	
Overall gain	The gain should be set high enough to visualize tissues with a low reflector intensity while maintaining blood-filled areas relatively anechoic (black).
Time gain compensation (TGC)	The TGC is used to compensate for attenuation (loss of ultrasound signal intensity and amplitude for deeper structures). The goal is to maintain a similar echogenicity for tissues of similar acoustic properties. The distal gain (deeper) is usually set higher than the proximal gain. For some cases, the mid-section gain is set lower to maintain the left ventricular cavity relatively anechoic.
Dynamic range/ compression	A low dynamic range produces an image that is very black and white (high contrast), whereas a high dynamic range produces an image that has more shades of grey (softer image). For cardiac images, adequate contrast is desirable while still allowing the visualization of low-amplitude structures such as thrombus or thin-walled segments.
Focus	The focus should be set at the depth of the region of interest.

Table 6.3
Key color Doppler imaging settings

Color Doppler imaging	
Color map	A blue away and red toward (BART) map is standardly used. Variance in flow velocity can be highlighted using shades of green and yellow.
Sector size	The size and location of the color box should be adjusted to cover the region of interest. A more narrow color box will improve the frame rate and a shorter (i.e., not too deep) color box will increase the velocity scale.
Color gain	The color gain should be set as high as possible while avoiding background speckling or noise.
Color Doppler velocity scale or pulse repetition frequency (PRF)	The velocity scale or pulse repetition frequency (PRF) is adjusted to set the Nyquist (aliasing) limit. The goal is to obtain minimal aliasing when visualizing laminar blood flow. A good starting Nyquist limit is around 70 cm/s in each direction. The Nyquist limit should be reduced when interrogating low-velocity blood flow such as through an atrial septal defect.

Table 6.4
Key spectral Doppler settings

Spectral Doppler	
Velocity scale	The velocity scale should be set to display the spectral Doppler tracing as large as possible without aliasing.
Baseline	The baseline should be set to ensure that the spectral Doppler tracing fills the display.
Sweep speed	The sweep speed should be adjusted based on heart rate. At least three spectral Doppler beats should be visualized simultaneously on the screen.
Sample volume	The sample volume size (1–5 mm) should be adjusted to minimize spectral broadening and to obtain the clearest Doppler signal.
Gain	The gain should be set high enough to properly visualize the Doppler signal, but excessive gain should be avoided to accurately interpret the peak velocity.
Wall filter	Filters are set to eliminate low-velocity signals near the zero baseline.

and presents images in the order of acquisition. While some variations exist between echocardiographers, it is recommended to always follow the same sequence of acquisition to avoid omissions.

Cardiac image orientation and transducer placement are referenced with respect to the heart itself. The central left ventricular (LV) axis can be conceptualized as an imaginary line that extends between the cardiac apex and base in the center of the LV lumen. When the transducer is oriented such that the scan plane includes or is parallel to this axis, a long-axis image (LAx) is obtained. If the scan plane is perpendicular to this axis, a short-axis image (SAx) is obtained (Figure 6.2). Most images are obtained from two relatively small access windows that surround the heart on both the right and left sides of the ventral

Vet-ebooks.com

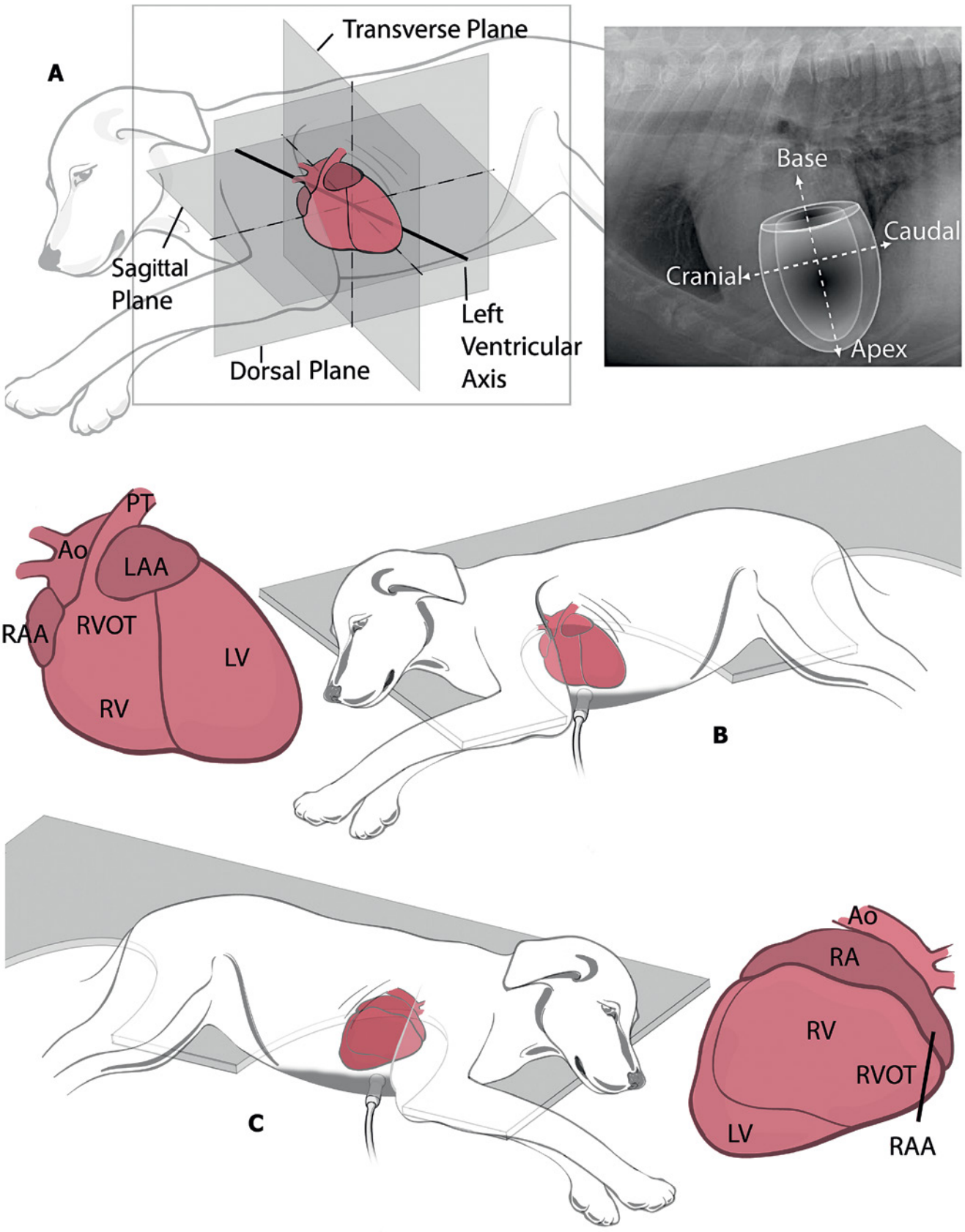


Figure 6.2. **Echocardiographic orientation and anatomy. (A)** A prevailing coordinate system is defined in terms of the LV axis for the individual's heart. The terms *base* and *apex* are specific to the heart and do not usually correspond precisely with *dorsal* and *ventral* directions referenced with respect to the animal. Similarly, the *cranial-caudal* axis of the heart is perpendicular to the *base-apex* axis and does not coincide precisely with the anatomical definitions. **(B, C)** The transducer is most commonly applied to recumbent patients from below with the aid of a specially designed table. See Table 6.4 for abbreviation definitions.

Vet-ebooks.com

thorax, i.e., next to the sternum (parasternal). Additional access can be gained from the subcostal (subxiphoid) position when imaging the heart through the liver.

Right-parasternal Views

Right-parasternal Long-axis Views

The exam usually starts with the right-parasternal (RPS) LAx views (Figure 6.3). The transducer is positioned at the 4th or 5th intercostal space to the right of the sternum, with the index marker oriented cranially toward the animal's shoulder. By convention, the index marker corresponds to the right side of the screen. The LAx four-chamber view is obtained by fanning so that the LV central axis lies within the scan plane. From this view, slight cranial angulation and twisting bring the left ventricular outflow tract (LVOT) and aorta into view.

- **Long-axis Four-chamber View (Figure 6.4)**
  The LAx four-chamber view provides an overall idea of cardiac morphology and function. Structures demonstrated by this view include the four chambers of the heart as well as both atrioventricular valves. The heart should be oriented as horizontal as possible on the screen. Ideally, this view should include the entire LV without apical foreshortening. CDI is used to assess blood flow through the mitral valve and tricuspid valve and to identify valvular regurgitations. CDI is also used to identify interventricular or interatrial septal defects.
- **Long-axis Left Ventricular Outflow Tract View (Figure 6.5)**
  This view is predominantly used to visualize the LVOT, aortic valve, sinuses of Valsalva and ascending aorta. CDI is used to identify the presence of aortic/subaortic stenosis (AS/SAS) as well as aortic insufficiency. Depending on the beam angle, the right coronary and noncoronary cusps or the right coronary and left coronary cusps are seen. It can be quite useful to use the zoom function to visualize the cusps thoroughly (especially if endocarditis is suspected) or to evaluate the coronary anatomy. The LAx LVOT view is also a good view to inspect the membranous septum for the presence of a ventricular septal defect (VSD). If the probe is moved more cranially, a larger portion of the ascending aorta can be seen, which is important when looking for a heart base mass. Depending on the animal and the beam angle, a portion of the left atrium and the mitral valve may or may not be present with this view. In cats, the mitral valve is often seen and this view is used to identify systolic anterior motion (SAM) of the septal leaflet.

Right-parasternal Short-axis Views

A SAx image is obtained from the LAx position by applying a 90° clockwise transducer rotation so that the LV cross-section is as close to circular as possible. Angulation in the apex-base direction yields a series of RPS SAx views, depending on the transection level (Figure 6.6).

- **Short-axis – Apex Level (Figure 6.7)**
  The apical RPS SAx view is not systematically obtained but is useful to inspect the apical portion of the LV. Abnormalities such as an apical aneurysm, a myocardial infarct, or focal hypertrophy that can cause intracavitary blood flow obstruction can be seen using this view.

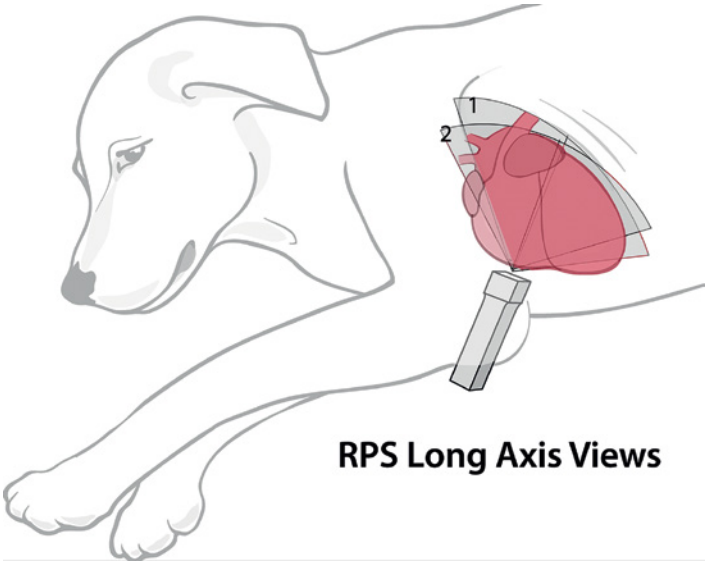


Figure 6.3. Right-parasternal long-axis scanning technique. For RPS LAx views, the transducer is positioned so that the scan plane contains, or is parallel to, the LV central axis. The index marker is oriented cranially. **1:** Four-chamber view. **2:** LVOT view.

Vet-ebooks.com

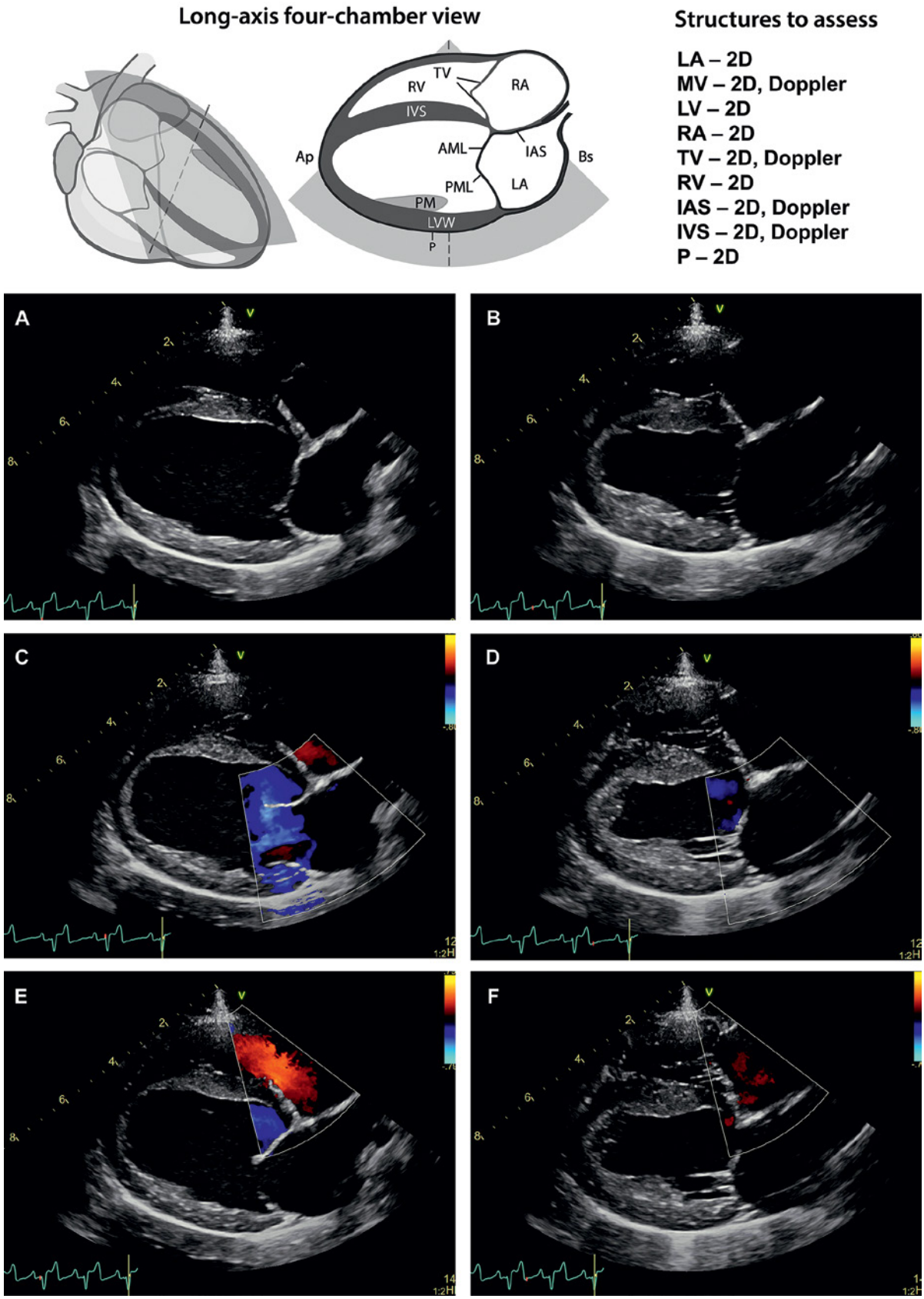


Figure 6.4. **Long-axis four-chamber view. (A, B)** 2D image in diastole **(A)** and systole **(B)**. **(C, D)** CDI of the mitral valve in diastole **(C)** and systole **(D)**. There is laminar transmitral flow in diastole. No mitral regurgitation is noted in systole. **(E, F)** CDI of the tricuspid valve in diastole **(E)** and systole **(F)**. There is laminar transtricuspid flow in diastole. No tricuspid regurgitation is noted in systole.

Vet-ebooks.com

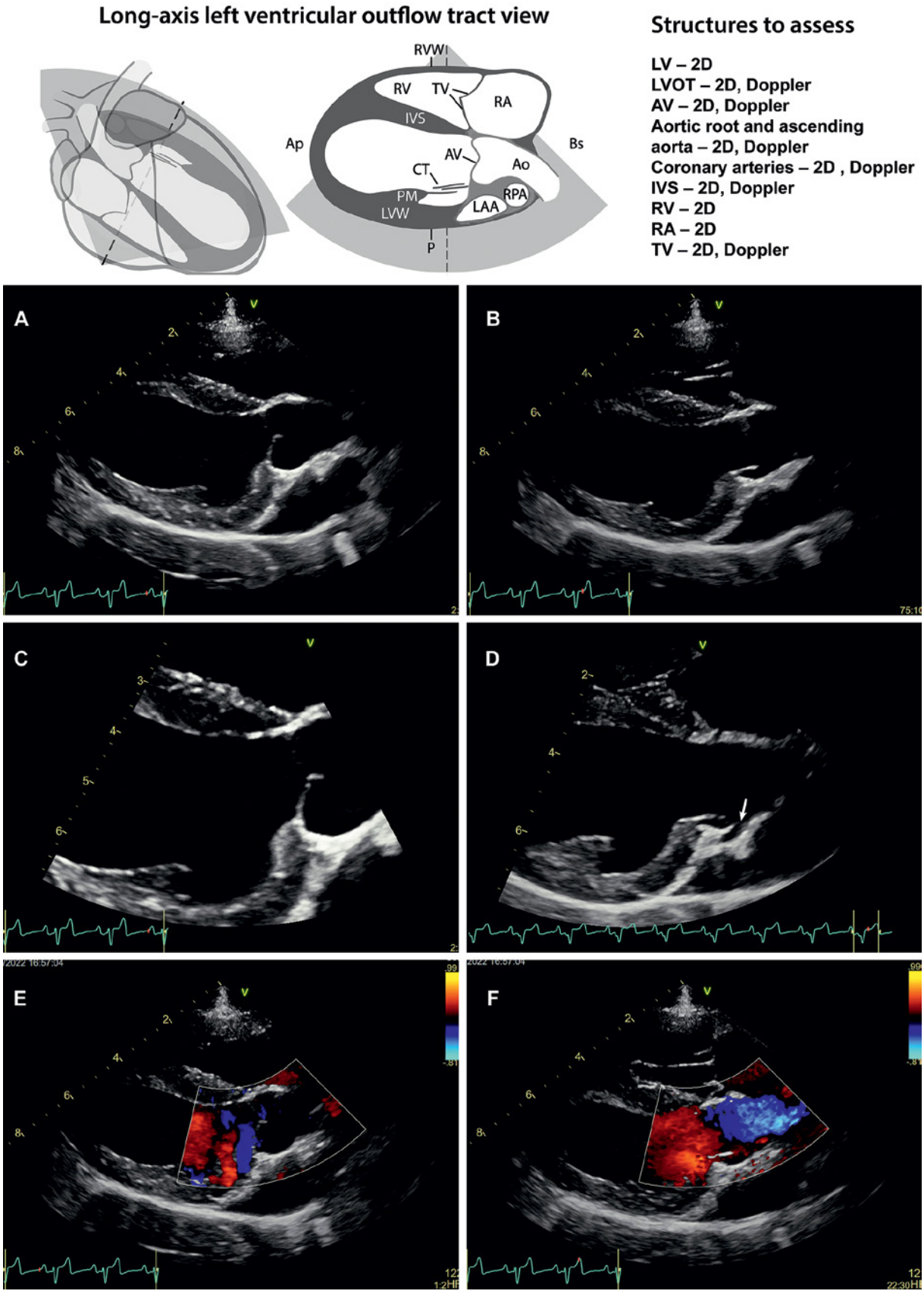


Figure 6.5. **Long-axis left ventricular outflow tract view. (A, B)** 2D image in diastole (A) and systole (B). **(C, D)** Zoom of the LVOT and aortic valve, the arrow shows the left coronary artery. **(E, F)** CDI of the LVOT and aortic valve in diastole (E) and systole (F). There is laminar transaortic flow in systole. No aortic insufficiency is noted in diastole.

Vet-ebooks.com

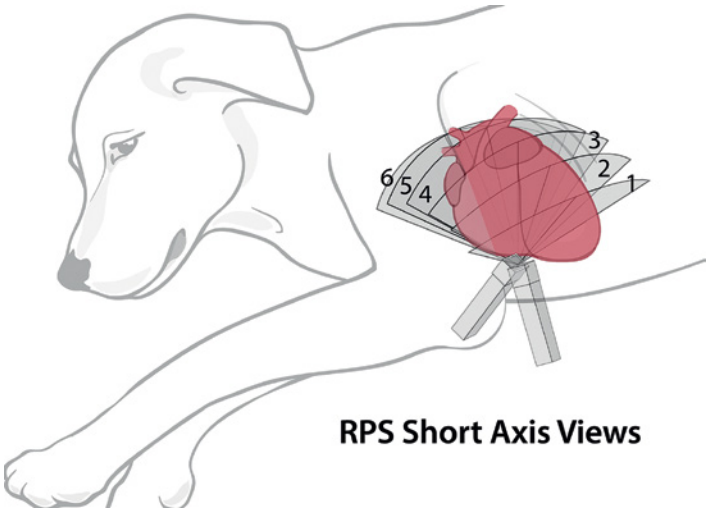


Figure 6.6. **Right-parasternal short-axis scanning technique.** For RPS SAx views, the transducer is positioned so that the scan plane slices perpendicularly to the LV central axis at the level of the papillary muscles. Numbers 1–6 refer to the scan plane orientation and image obtained. **1:** Slice 1 at the apex level. **2:** Slice 2 at the papillary muscle level. **3:** Slice 3 at the chordal level. **4:** Slice 4 at the mitral valve level. **5:** Slice 5 at the aortic valve level. **6:** Slice 6 at the pulmonic valve level.

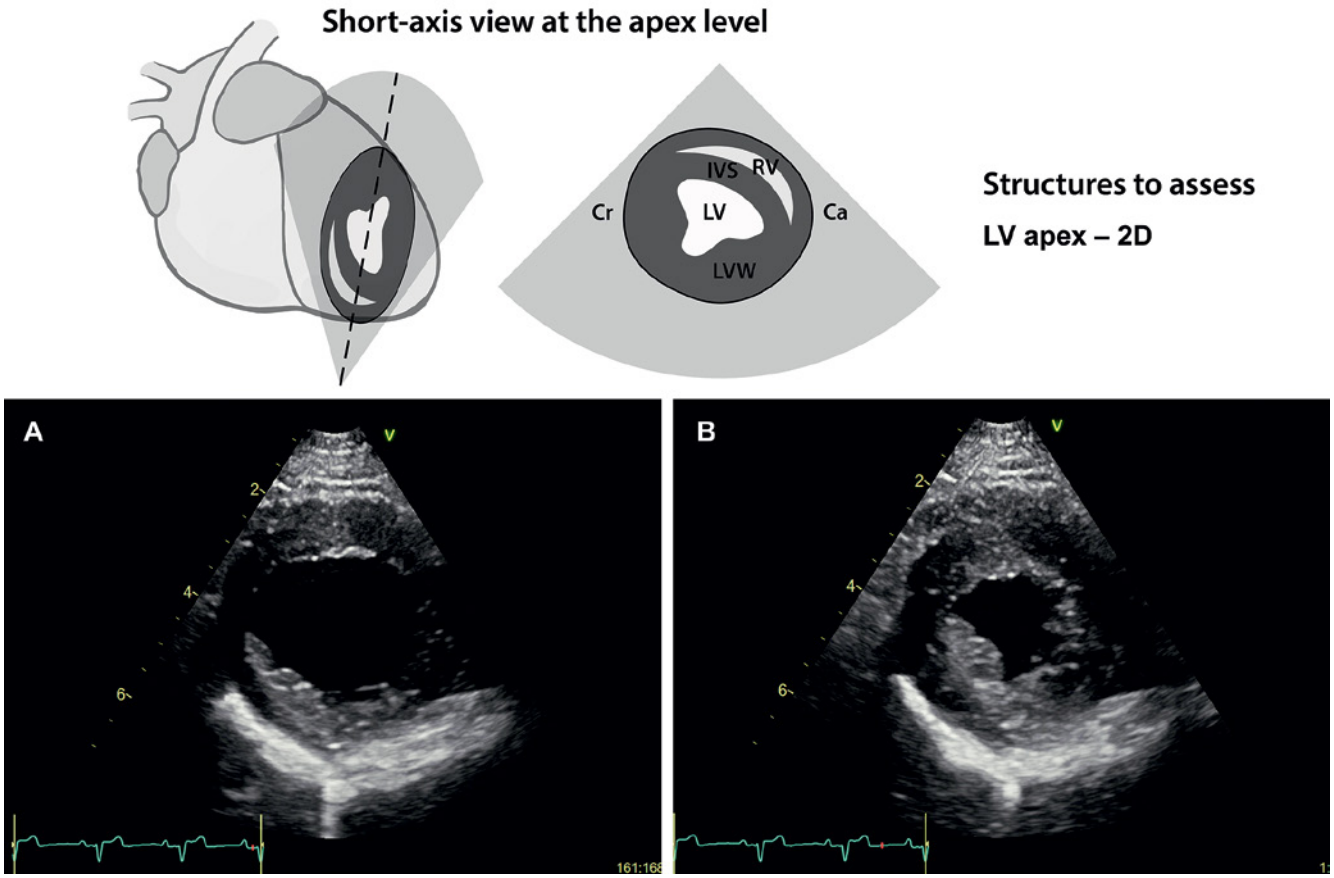


Figure 6.7. **Short-axis view at the apical level. (A, B)** 2D image in diastole (A) and systole (B). The LV apex is seen predominantly. The right ventricle cannot be clearly visualized at this level.

- **Short-axis – Papillary Muscle Level (Figure 6.8)**
  This is one of the most important views, used to identify LV eccentric or concentric hypertrophy and to evaluate systolic function. This view is obtained at the level of the papillary muscles, just below the mitral valve. The LV cavity is seen as a "mushroom"

Vet-ebooks.com

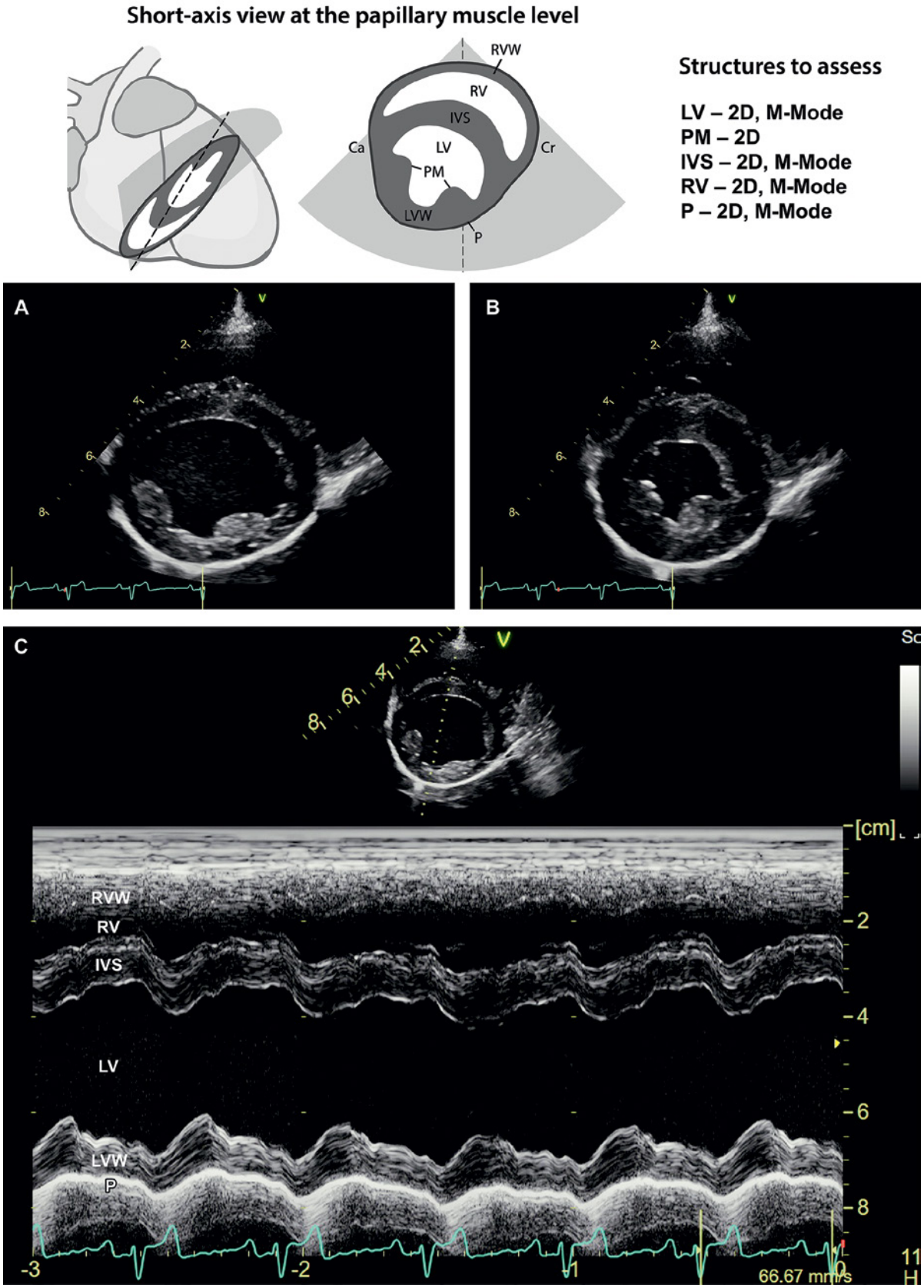


Figure 6.8. **Short-axis view at the papillary muscle level. (A, B)** 2D image in diastole **(A)** and systole **(B)**. **(C)** M-mode image obtained from the same view. The M-line is positioned in the middle of the LV cavity, in between the two papillary muscles, and should be perpendicular to the interventricular septum and LV free wall.

Vet-ebooks.com

shape due to the presence of two papillary muscles. The posterior (caudal) papillary muscle is seen on the left of the screen and the anterior (cranial) papillary muscle is seen on the right of the screen. The echocardiographer should aim to obtain a relatively circular LV with symmetrical papillary muscles. The right ventricle is visualized in the near field with a crescent shape. A right ventricular (RV) papillary muscle is often seen in the RV lumen and should not be mistaken for a thrombus, a cardiac tumor, or an abnormally thickened interventricular septum (IVS). This view is also useful to visualize the pericardium and identify pericardial effusion if present.

The **M-mode** is generated from this view to measure LV dimensions and fractional shortening (FS). To obtain an M-mode study, the echocardiographer places the M-line in the middle of the LV cavity, in between the two papillary muscles. The M-line should be perpendicular to the IVS and LV free wall. The structures crossed by this line are then being displayed over time. Time is shown along the horizontal axis (in seconds) and depth from the transducer is shown along the vertical axis (in cm).

- **Short-axis – Chordal Level (Figure 6.9)**
  This cross section at the level of the chordae tendineae is of limited use and is not often recorded during routine examinations.
- **Short-axis – Mitral Valve Level (Figure 6.10)**
  This view is used to assess the mitral valve in cross section. At this level, the papillary muscles are not visible anymore. The anterior (= septal) mitral leaflet (AML) is adjacent to the IVS and the posterior (= parietal) leaflet (PML) is adjacent to the free wall of the left ventricle. The mitral valve closes during systole and opens in two phases during diastole (fully during early diastole and partially during late diastole). This can be visualized easily using M-mode. The M-mode at the mitral valve level is used to measure the E-point to septal separation (EPSS) for example.
- **Short-axis – Aortic Valve Level (Figure 6.11)**
  This view, obtained at the level of the aortic valve, is also one of the most important short-axis views. It is especially useful to assess left atrial (LA) size by measuring the left atrial-to-aortic ratio. The aorta should be as circular as possible and, ideally, the three aortic cusps should be visible. Coronary anatomy may also be assessed using this view.
- **Short-axis – Pulmonic Valve Level (Figure 6.12)**
  The last RPS SAx view shows the pulmonary trunk (also called main pulmonary artery) as well as its bifurcation into the right and left pulmonary arteries. Only a small portion of the left atrium is now visible between the right atrium and the right pulmonary artery. CDI along with spectral Doppler should then be used to evaluate blood flow through the right ventricular outflow tract (RVOT), pulmonic valve, pulmonary trunk, and proximal portions of the pulmonary left and right arteries. This view is also used to identify the presence of a patent ductus arteriosus (PDA).

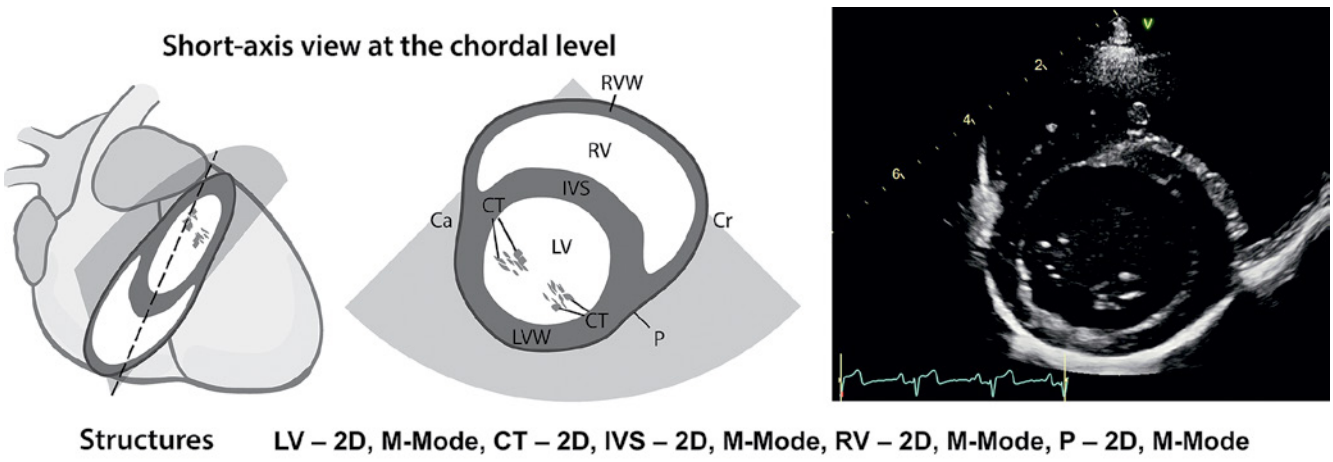


Figure 6.9. Short-axis view at the chordal level. 2D image showing multiple bright dots within the LV cavity. These are the chordae tendineae in cross section.

Vet-ebooks.com

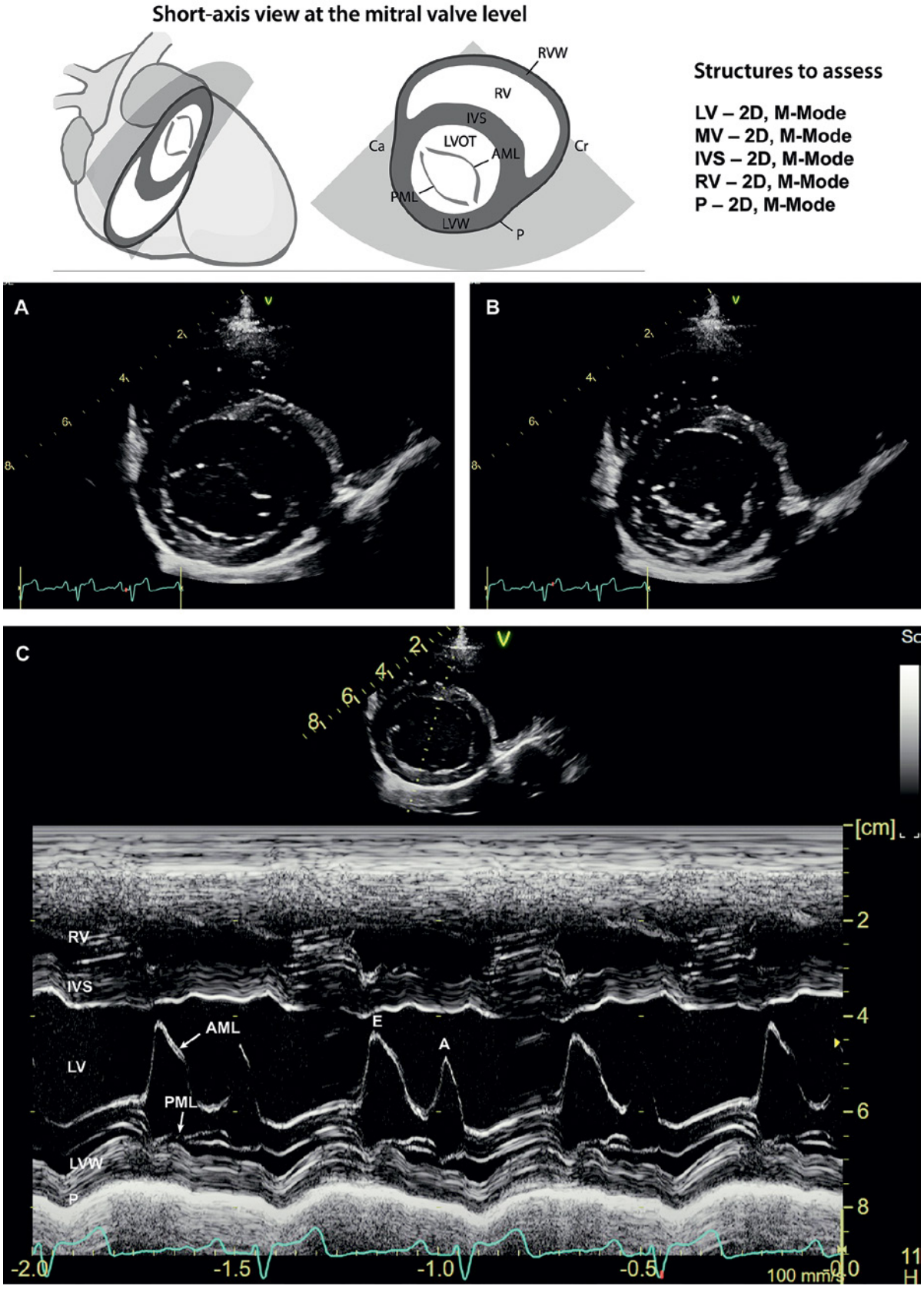


Figure 6.10. Short-axis view at the mitral valve level. (A, B) 2D image in diastole when the mitral valve leaflets are separated from each other **(A)** and in systole when the mitral valve leaflets are apposed **(B)**. **(C)** M-Mode recording showing the motion of the mitral valve leaflets (AML and PML). During diastole, the mitral valve opens in two phases: fully during early diastole (E) and partially during late diastole and atrial contraction (A).

Vet-ebooks.com

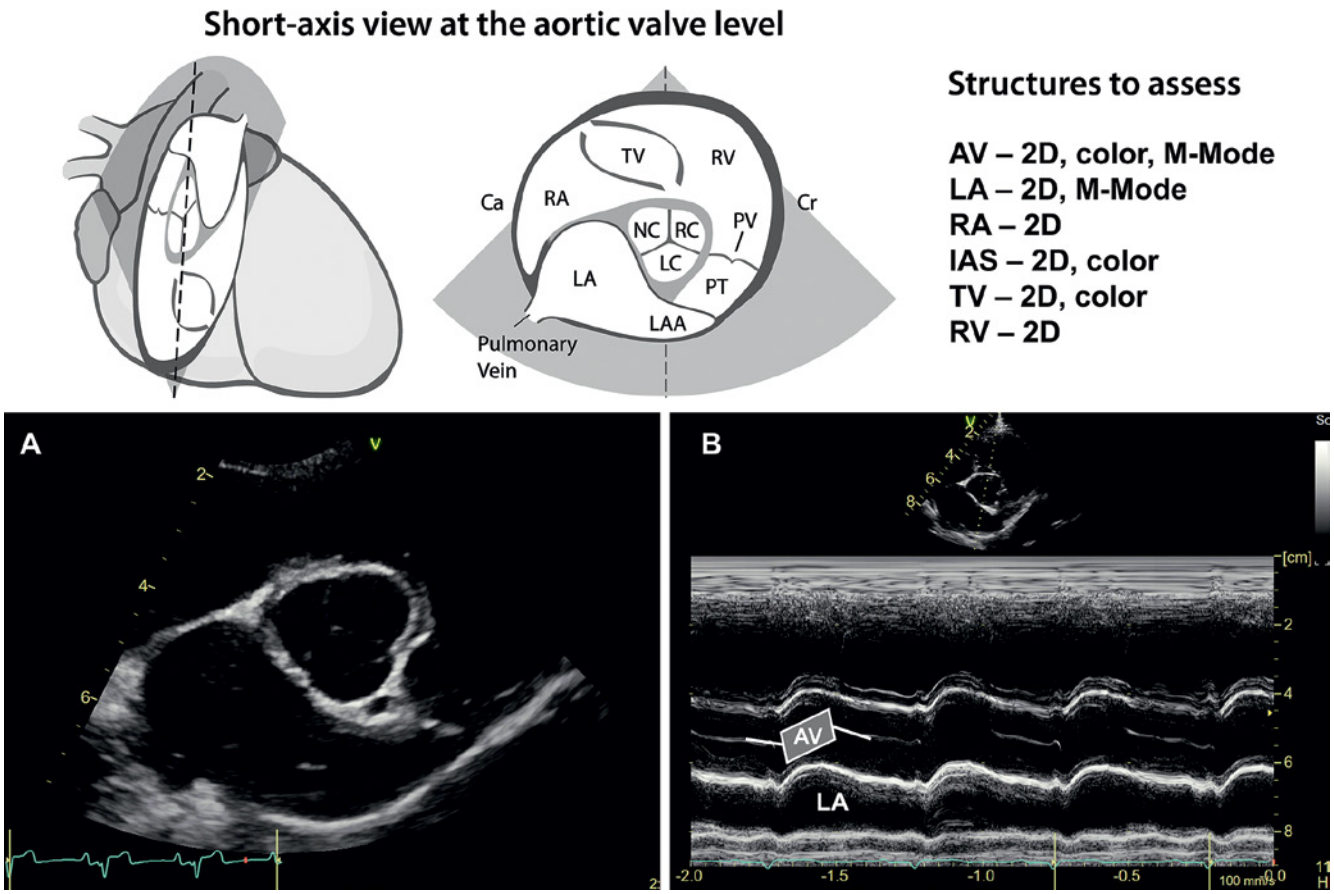


Figure 6.11. **Short-axis view at the aortic valve level. (A)** 2D image obtained in early diastole when the aortic cusps are closed. **(B)** M-Mode recording showing the motion of the aortic cusps. The M-line crosses the right ventricle, the aortic valve, and the junction between the left atrium and left auricular appendage. The aortic valve is open during diastole and closed during systole. The aortic cusps can be somewhat difficult to visualize in healthy individuals for which the aortic cusps are not thickened.

Left-parasternal Views

Apical Views

Apical images are best obtained with the patient in left lateral recumbency, with the transducer applied to the left ventral thorax from below (Figure 6.13). A true apical view results when the transducer is placed at an extreme ventral and caudal location, approaching a subxiphoid position. The transducer is angled cranially so that the central ultrasound beam is pointed toward the heart base along the LV central axis. The true apical view may be technically challenging, so a slightly more cranial transducer position may be suitable but results in a foreshortened LV view that is unsuitable for ventricular quantification.

- **Apical Four-chamber View (Figure 6.14)**
  Structures demonstrated by this view include the four chambers of the heart as well as both atrioventricular valves, this time in a vertical base-apex orientation. This is ideal to evaluate blood flow through the mitral valve using PWD. The transmitral flow pattern is used to assess LV diastolic function and filling pressures. If present, mitral valve regurgitation velocity can be measured using CWD. Tissue Doppler imaging (TDI) is employed to quantify the velocity of motion of cardiac tissue directly. TDI may provide valuable information about both systolic and diastolic function and ventricular filling pressures, especially when used in conjunction with mitral inflow recordings. The most common use of TDI in veterinary cardiology is to record the longitudinal (base-apex) velocity of the mitral annulus from the left apical four-chamber position. Velocity recordings may be obtained from either the septal or lateral side of the mitral annulus, adjusting transducer position so that annular motion of the chosen site is directed along the Doppler scan line to the extent possible.

Vet-ebooks.com

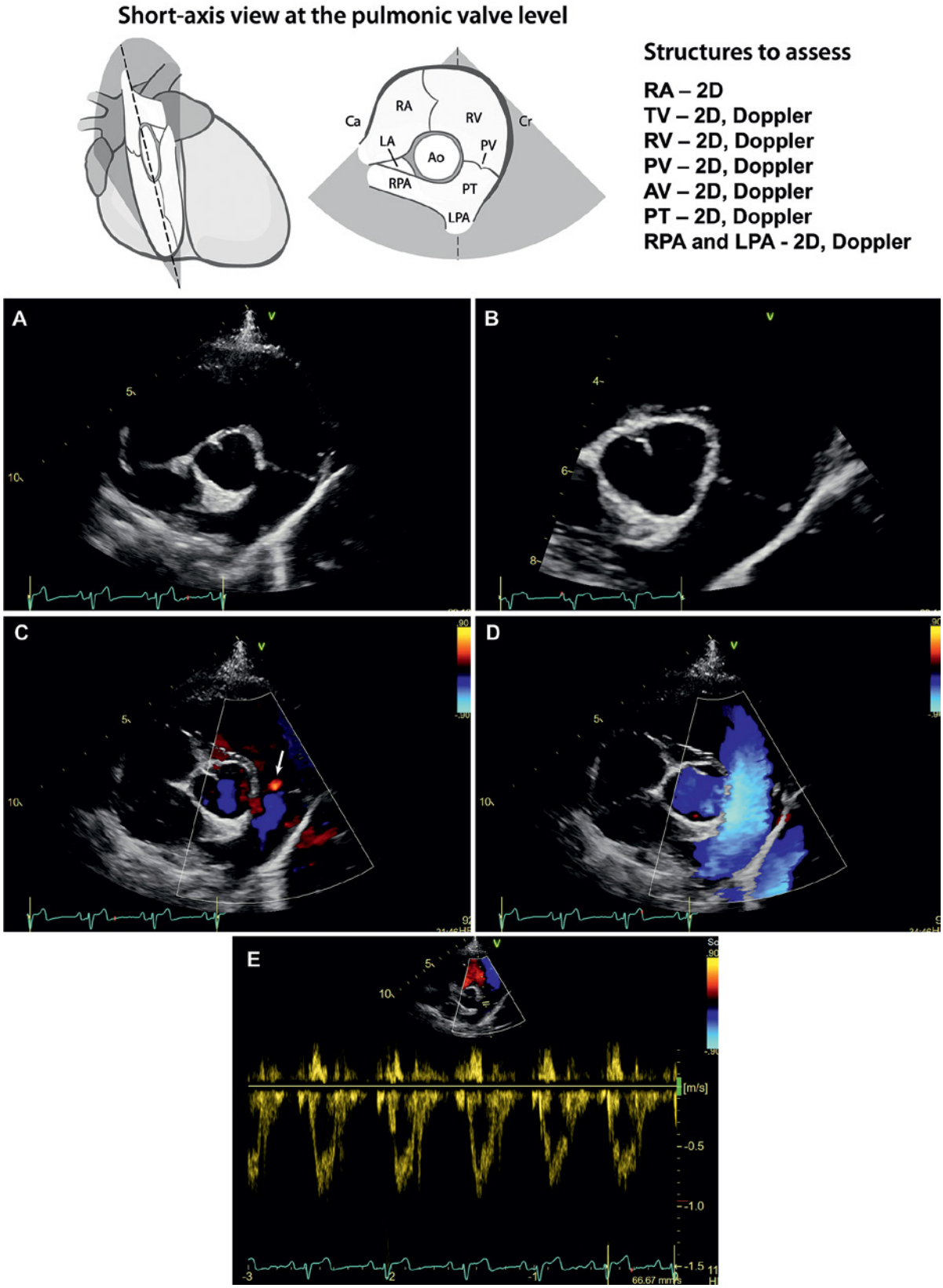


Figure 6.12. **Short-axis view at the pulmonic valve level. (A, B)** 2D images in diastole during pulmonic valve closure. **(B)** is a zoomed image showing the pulmonic valve and aortic valve simultaneously. **(C, D)** CDI of the RVOT, pulmonic valve, and pulmonary trunk in diastole **(C)** and systole **(D)**. Trace pulmonic insufficiency is seen during diastole. This is considered physiological. There is laminar transpulmonic flow in systole. **(E)** PWD shows laminar blood flow across the pulmonic valve in systole. Note that the sample volume is placed at the tips or slightly distal to the opened valve cusps.

Vet-ebooks.com

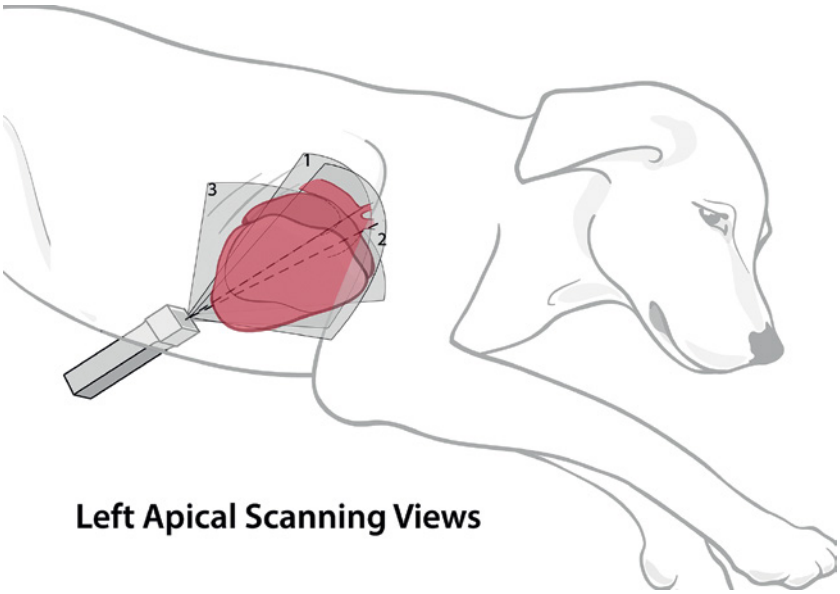


Figure 6.13. Apical scanning technique. The transducer is positioned at the left apex of the heart. Cranial angulation brings the long axis of the heart into the scan plane. **1:** Apical four-chamber view. **2:** Apical LVOT tract view. **3:** Apical two- or three-chamber view.

- **Apical Left Ventricular Outflow Tract View (Figure 6.15)**
  Cranial angulation of the transducer from the apical four-chamber position brings the aortic root into the scan plane and enables visualization of the aortic valve. This scan plane constitutes the apical LVOT image and often is suitable for aortic flow-velocity quantification.
- **Apical Two-chamber or Three-chamber View (Figure 6.16)**
  From the apical four-chamber view, an 85–90° clockwise twist yields the apical three- and two-chamber views. A better alignment with aortic blood flow may be achieved using the three-chamber view. The apical two-chamber view is challenging to obtain and only useful when performing advanced LV function assessment using speckle tracking imaging or 3D volume quantification.
- **Modified Four-chamber View Optimized for the Right Cardiac Chambers (Figure 6.17)**
  Over the recent years, assessment of RV function has been receiving increasing attention (Visser 2017). Most RV function indices are acquired from a modified apical four-chamber view optimized for the right heart. To obtain this view, the transducer is placed slightly more cranially compared with the usual apical four-chamber view with varying degrees of caudal angulation.

Left Cranial Views

Left cranial views are obtained preferably with the patient in left lateral recumbency. The transducer is positioned so that it is cranial to the heart, at the fourth to fifth intercostal space, and approximately at the level of the costochondral junction in the dorsal-ventral direction.

Baseline left cranial long-axis images are first obtained with the scan plane oriented parallel to the ascending aorta, twisting so as to include a longitudinal view of this structure (Figure 6.18).

- **Long-axis – Aortic Valve (Figure 6.19)**
  The view is particularly useful for evaluation of the LVOT, aortic valve, and ascending aorta.
- **Long-axis – Tricuspid Valve (Figure 6.20)**
  Relative to the initial LV outflow tract position, ventral and slightly cranial angulation causes the scan plane to transect the right atrium, right atrial appendage, tricuspid valve, and RV inflow. This is often the best view to measure the tricuspid regurgitation velocity, if present. The right atrium appendage can be closely inspected from this vantage point for evidence of neoplasia.
- **Long-axis – Pulmonic Valve (Figure 6.21)**
  Relative to the initial LV outflow tract position, dorsal and slightly caudal angulation of the transducer, the scan plane encounters the left atrium and ventricle, RVOT, and pulmonary trunk; the pulmonary bifurcation and PDA (if present) may be visualized.

Vet-ebooks.com

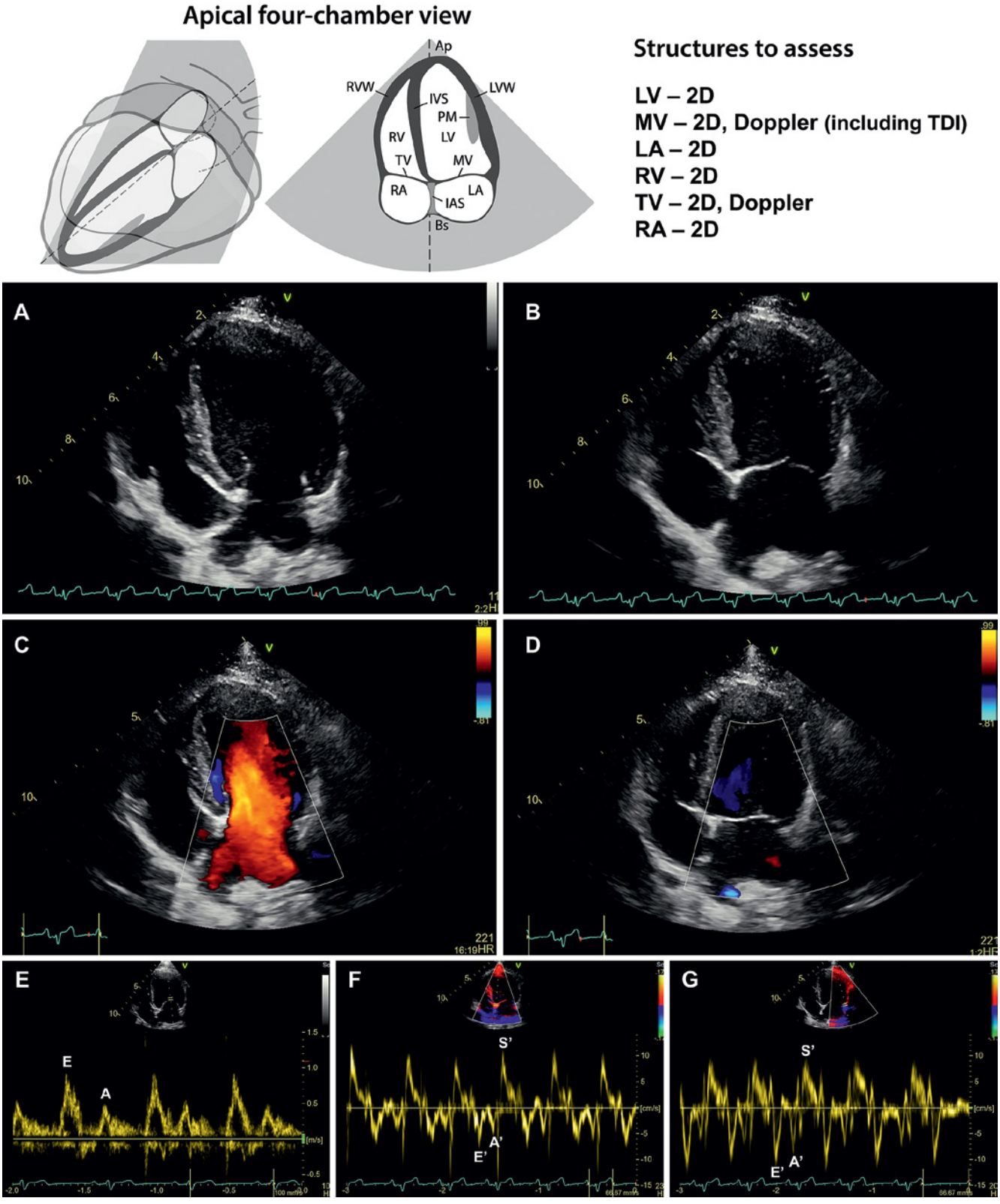


Figure 6.14. **Apical four-chamber view. (A, B)** 2D image in diastole **(A)** and systole **(B)**. **(C, D)** CDI of the mitral valve in diastole **(C)** and systole **(D)**. There is laminar transmitral flow in diastole. No mitral regurgitation is noted in systole. **(E)** Normal mitral inflow PWD recording showing two distinct phases, early left ventricular filling (E wave) associated with left ventricular relaxation and late left ventricular filling (A wave) due to left atrial contraction. **(F, G)** TDI recording of mitral annular velocity. Septal **(F)** and lateral **(G)** mitral annulus velocities are recorded. Diastolic annular velocity measurements mirror the mitral inflow pattern with two distinct phases of filling. The LV expands longitudinally in both early and late diastole, resulting in annular velocity away from the transducer and generation of the E′ and A′ waves, respectively. LV contraction entails a longitudinal component that is directed toward the transducer and generation of the systolic wave S′.

Vet-ebooks.com

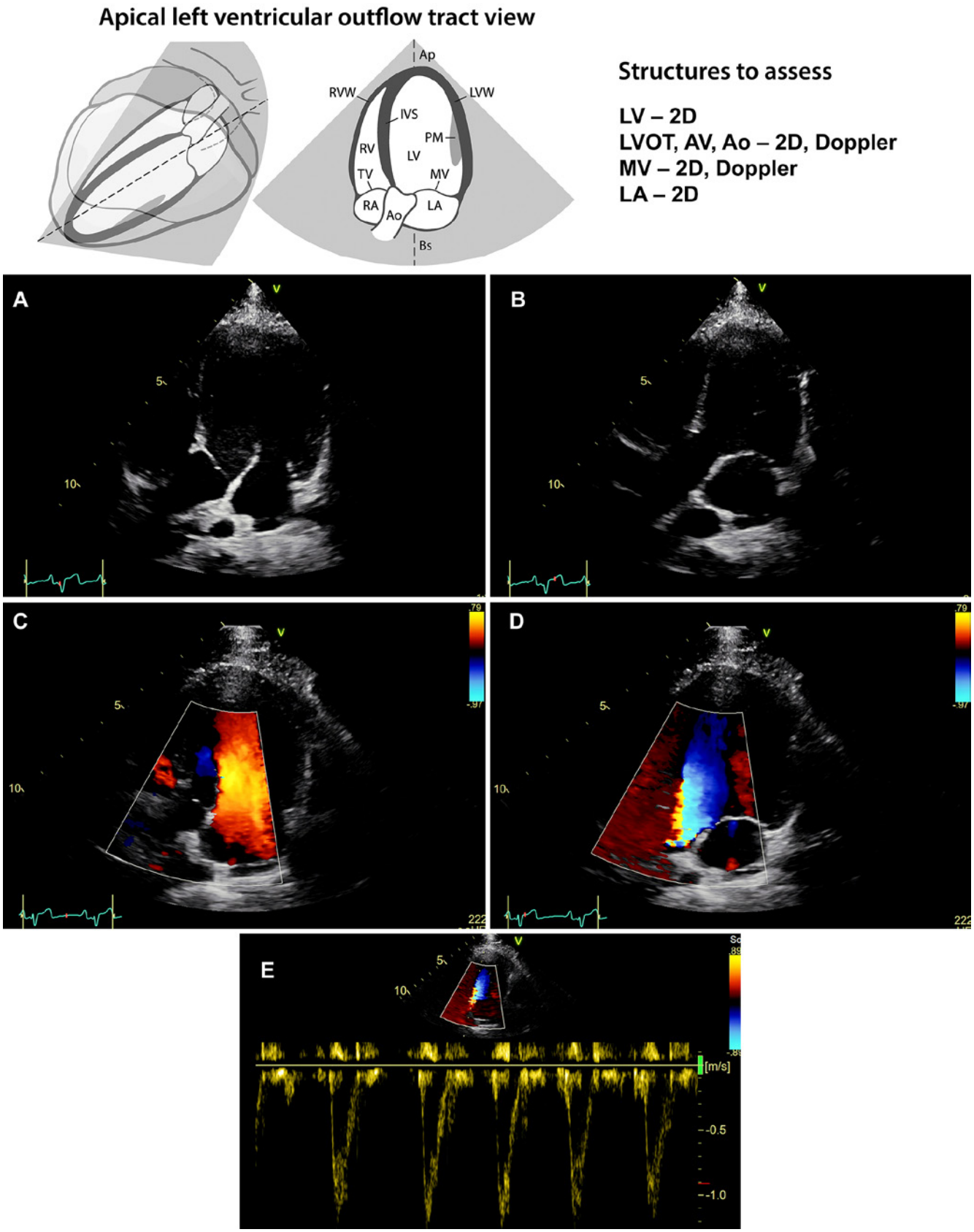


Figure 6.15. **Apical left ventricular outflow tract view. (A, B)** 2D images in diastole **(A)** and systole **(B)**. The aortic valve is closed during diastole and open during systole. **(C, D)** CDI of the LVOT, aortic valve, and proximal aorta in diastole **(C)** and systole **(D)**. There is no visible aortic insufficiency during diastole. During diastole, LV inflow is visualized. Aliasing is seen at the aortic valve level in systole (although the flow is laminar as confirmed by using PWD). **(E)** PWD shows laminar blood flow across the aortic valve in systole.

Vet-ebooks.com

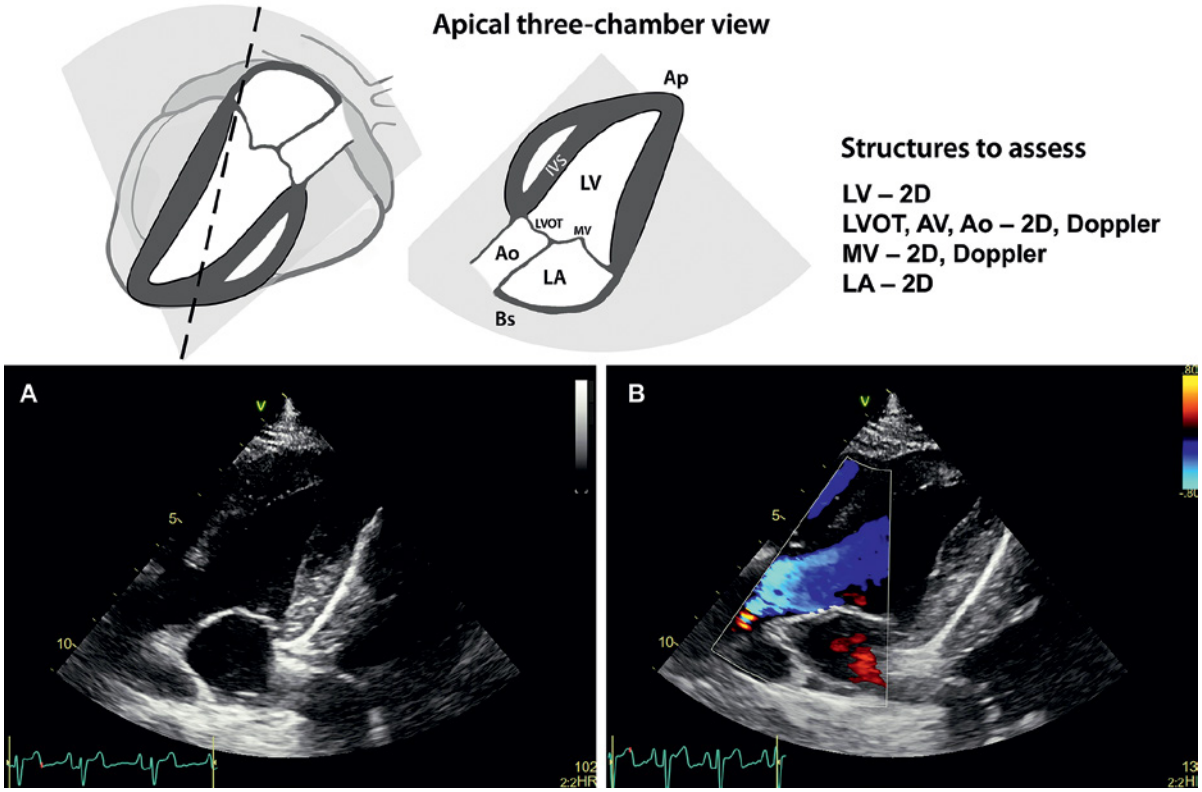


Figure 6.16. **Apical three-chamber view. (A)** 2D image in systole showing the LVOT, aortic valve, and proximal aorta. This view usually provides good beam alignment with the aortic flow. **(B)** CDI shows mild aliasing (although the flow is normal).

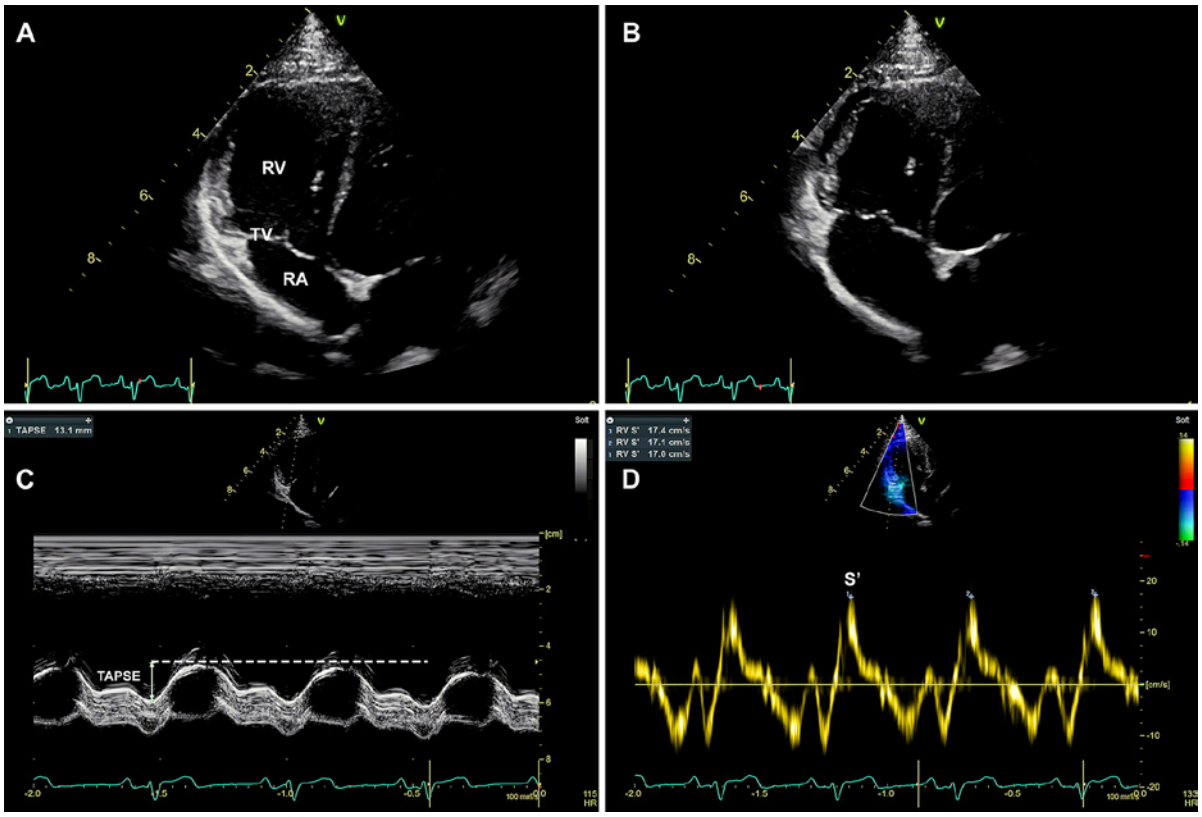


Figure 6.17. **Modified four-chamber view optimized for the right cardiac chambers. (A, B)** 2D image in diastole **(A)** and systole **(B)** showing the right atrium, tricuspid valve, and entire right ventricle. **(C)** Example of tricuspid annular plane systolic excursion (TAPSE) measurement. The M-mode cursor is aligned from the right ventricular apex through the hyperechoic fibrous region of the lateral tricuspid annulus. **(D)** Example of pulsed-wave TDI-derived peak systolic longitudinal myocardial velocity of the lateral tricuspid annulus (S′).

Vet-ebooks.com

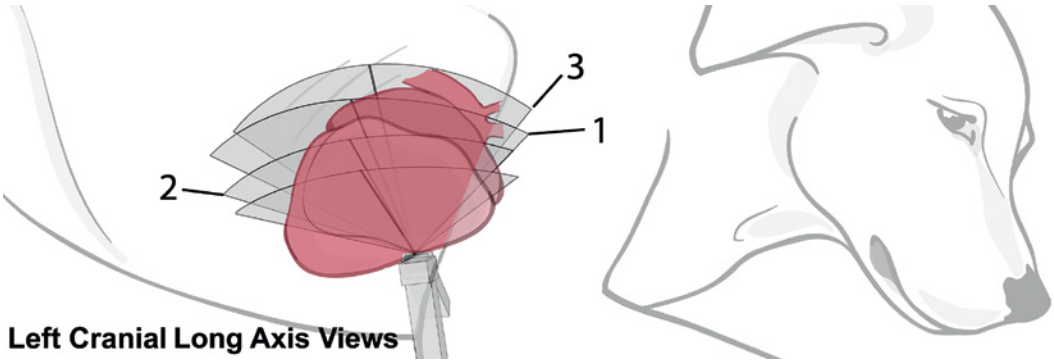


Figure 6.18. **Left cranial long-axis scanning technique.** The transducer is positioned near the left cranial border of the heart. Dorsal-ventral angulation of the transducer yields a series of LAx images. The authors' preference is to first obtain the LAx view at the aortic valve level (1). From this position, the long-axis view at the tricuspid valve level (2) is obtained by tilting the transducer down toward the sternum, and the LAx view at the pulmonic valve level (3) is obtained by tilting the transducer dorsally.

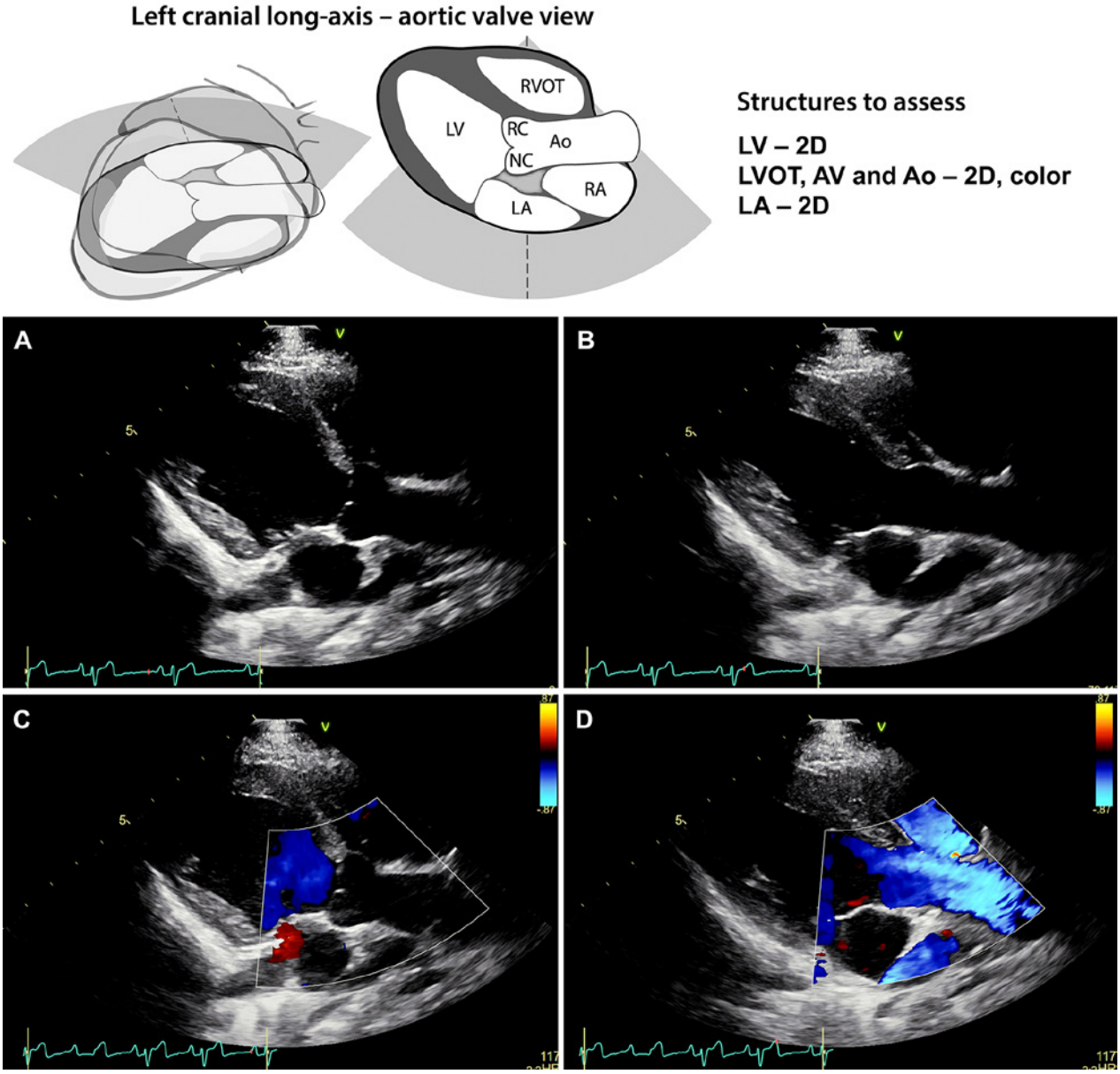


Figure 6.19. **Left cranial long-axis – aortic valve view. (A, B)** 2D image in diastole **(A)** and systole **(B)**. **(C, D)** CDI of the LVOT and aortic valve in diastole **(C)** and systole **(D)**. There is laminar transaortic flow in systole. No aortic insufficiency is noted in diastole.

Vet-ebooks.com

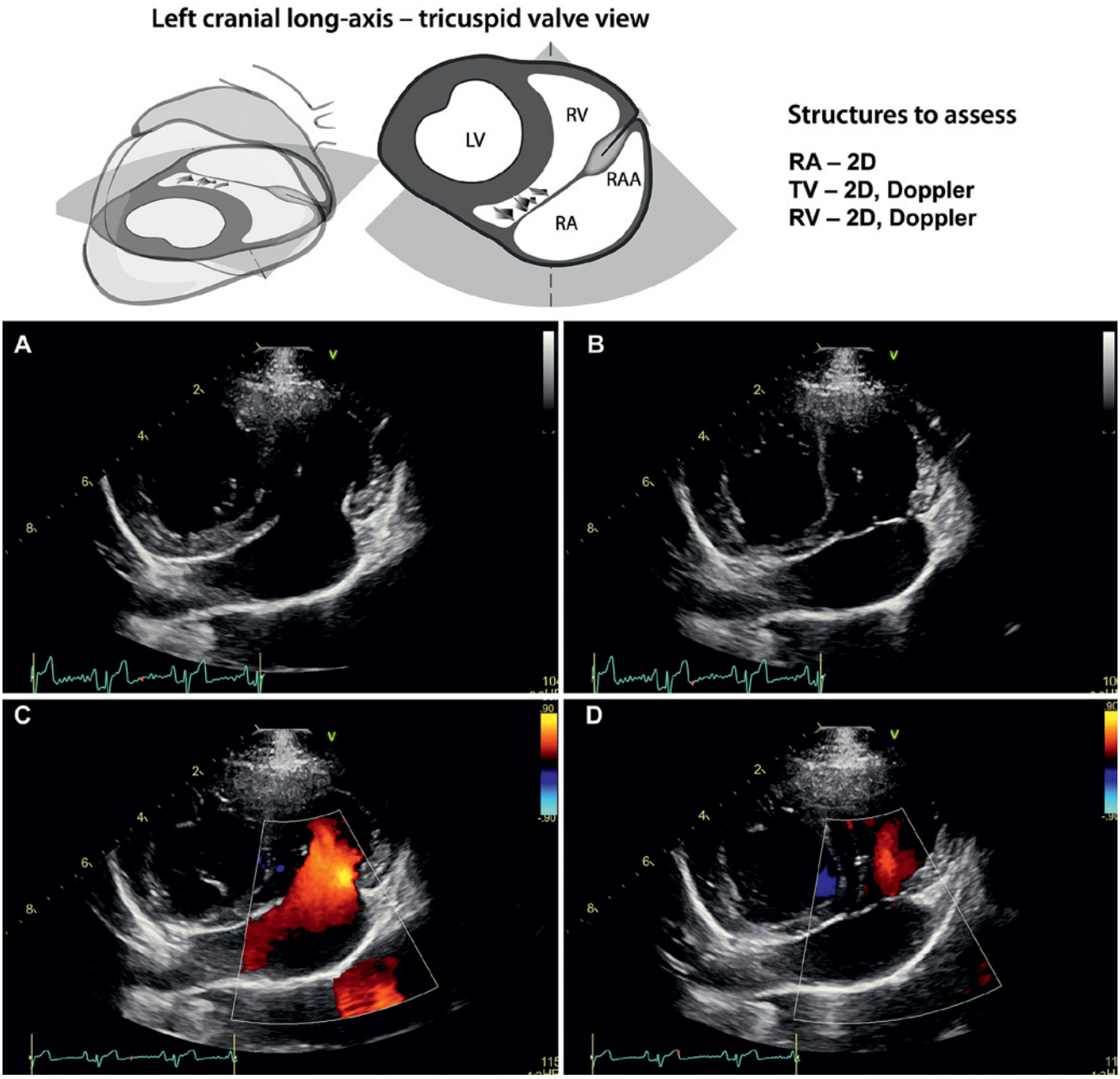


Figure 6.20. **Left cranial long-axis – tricuspid valve view. (A, B)** 2D image in diastole **(A)** and systole **(B)**. **(C, D)** CDI of the tricuspid valve in diastole **(C)** and systole **(D)**. There is laminar transtricuspid flow in diastole. No tricuspid regurgitation is noted in systole.

- **Short-axis – Right Ventricular Outflow Tract and Pulmonic Valve (Figure 6.22)**
  From the initial left cranial view of the LVOT, a clockwise twist results in a scan plane that slices the aortic root transversely. Fanning the transducer in a cranial-dorsal direction produces a range of images for optimal viewing of the right atrium, RV inflow and outflow tracts, and pulmonary trunk and proximal portion of the pulmonary branches.

Other Views

Subxiphoid Left Ventricular Outflow Tract View (Figure 6.23)

The subxiphoid view is obtained, with the patient in lateral recumbency, by positioning the transducer just caudal to the xiphoid process and pressing into the abdomen while pointing the transducer almost directly cranially. For Doppler aortic velocity

Vet-ebooks.com

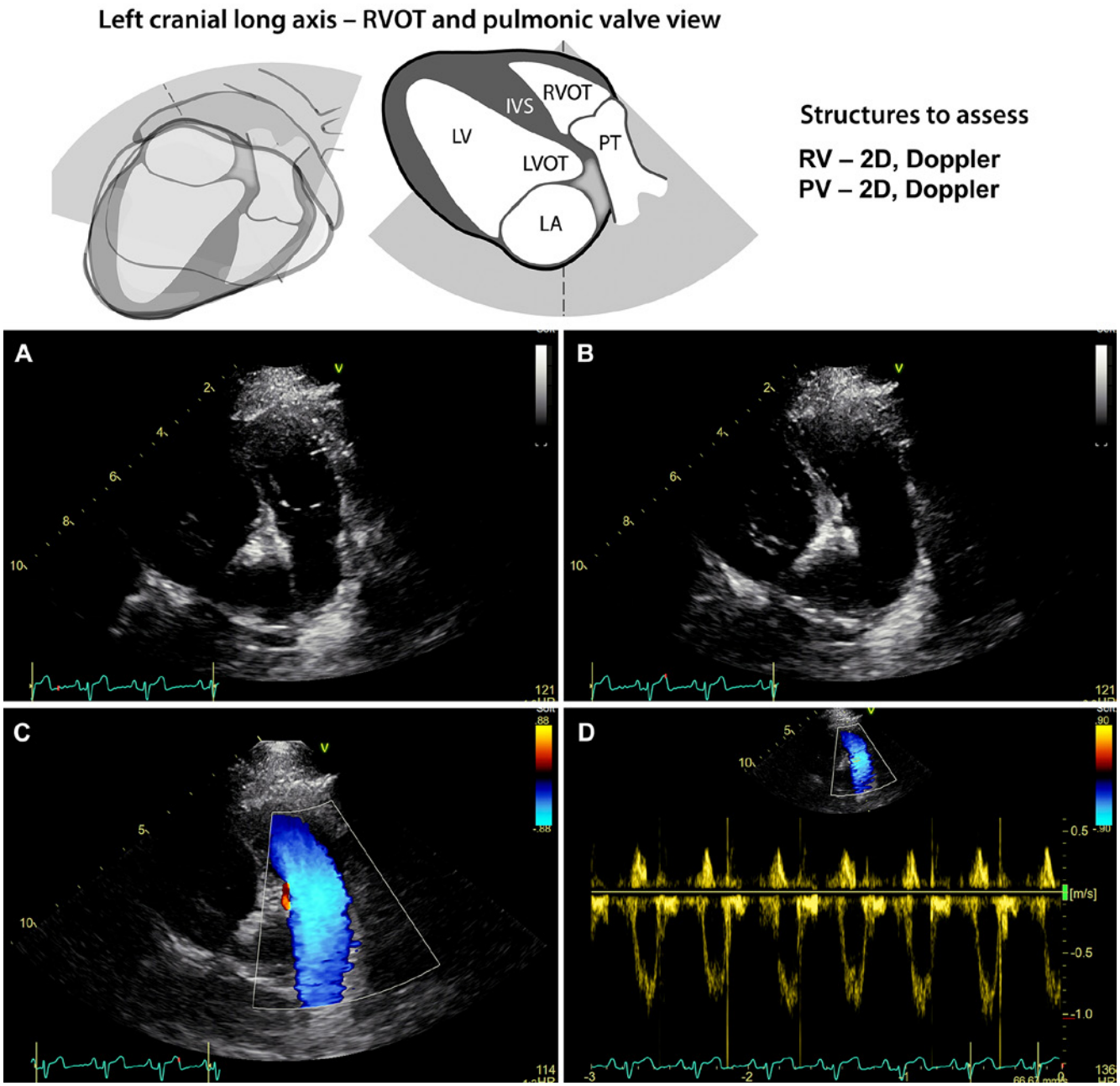


Figure 6.21. **Left cranial long-axis – pulmonic valve view. (A, B)** 2D image in diastole **(A)** and systole **(B)**. **(C)** CDI of the pulmonic valve in systole. **(D)** PWD recording of the transvalvular pulmonic flow. There is laminar transpulmonic flow in systole based on CDI and PWD recordings.

recordings, the transducer is fanned to include the aortic root.

Feline Left Cranial Left Auricular Appendage View (Figure 6.24)

This is an important view in cats, especially if LA enlargement has been previously identified. This view is obtained with the transducer placed between the apical and cranial positions on the left side of the thorax. It is used to identify left auricular thrombus or spontaneous echo contrast ("smoke").

Image Analysis

Besides direct visual observation, structural and functional evaluation of the heart may entail echocardiographic measurements of linear dimensions,

Vet-ebooks.com

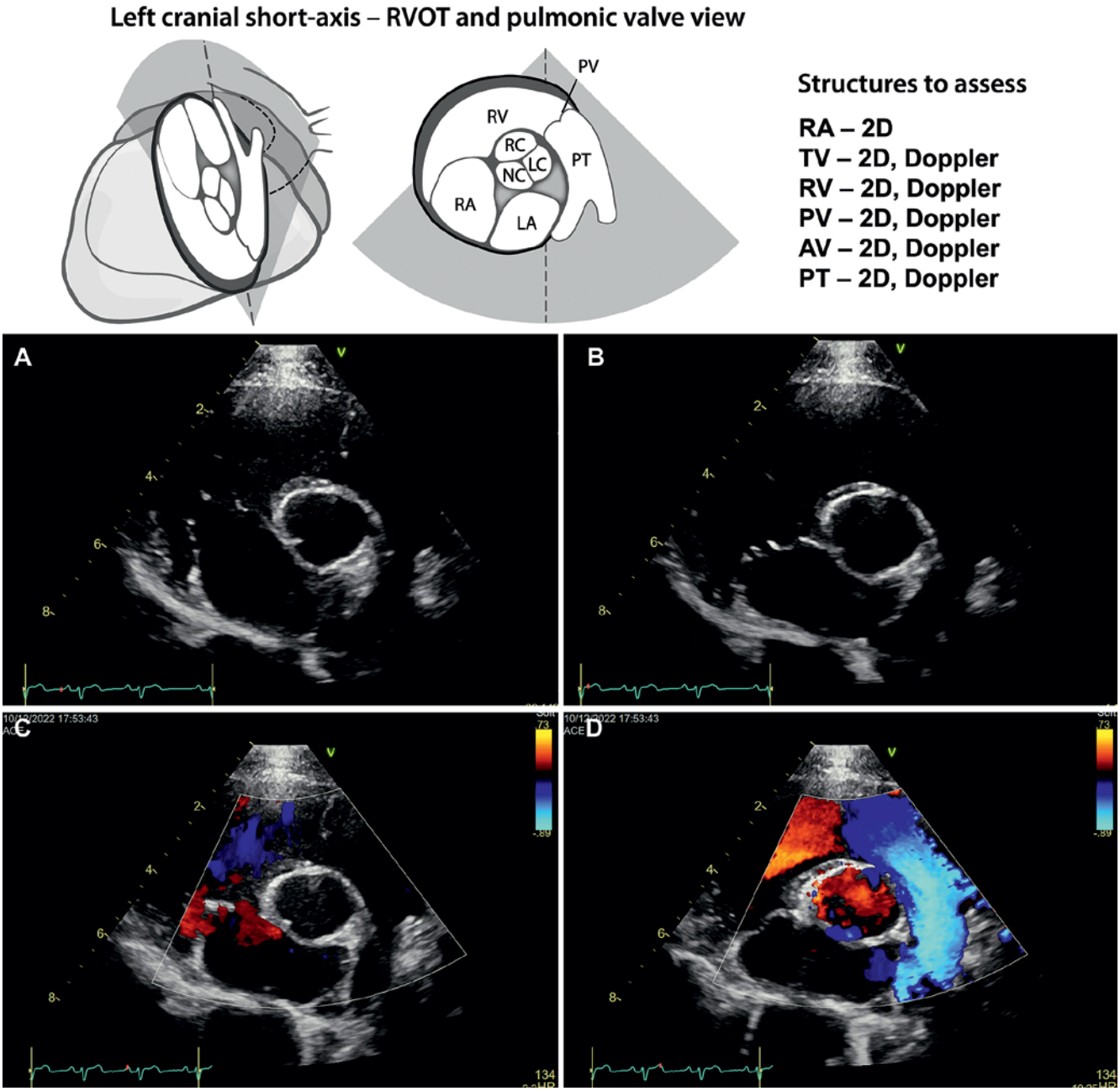


Figure 6.22. Left cranial short-axis – RVOT and pulmonic valve view. (A, B) 2D image in diastole **(A)** and systole **(B)**. **(C, D)** CDI of the RVOT, pulmonic valve, pulmonary trunk, and pulmonary bifurcation in diastole **(C)** and systole **(D)**. There is laminar pulmonic flow in systole. No pulmonic insufficiency is noted in diastole.

areas, volumes, time intervals, or velocities, and calculation of performance indices from these raw data. To characterize and quantify the heart echocardiographically, the echocardiographer must possess a detailed understanding of cardiovascular physiology, pathophysiology, and the sources of variation for observations (Table 6.5). This section will focus on the analysis of the left side of the heart. Historically, evaluation of right heart size and function has been limited to subjective assessment. More attention is recently being paid to the right heart, with more objective analyses being investigated in veterinary species (Figure 6.17). Only basic echocardiographic parameters used in routine evaluations are presented in this chapter.

Vet-ebooks.com

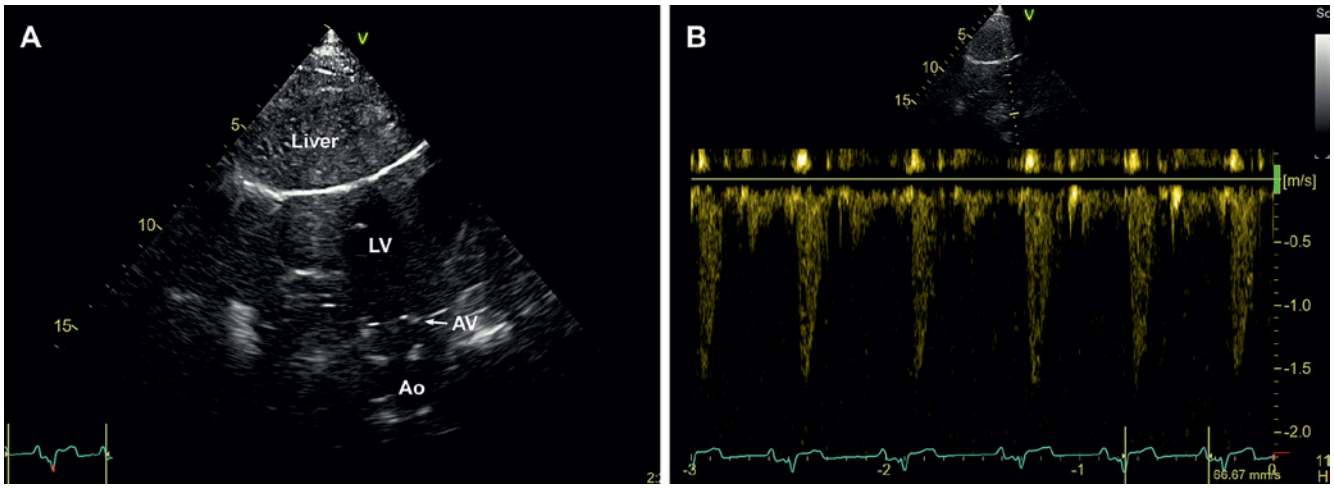


Figure 6.23. Subxiphoid view. This transducer position is used principally for Doppler recordings of aortic ejection and typically yields the best alignment with flow in dogs. The liver is interposed between the transducer and the heart. **(A)** 2D image showing the aortic valve and proximal aorta. **(B)** CWD recording the aortic flow used to measure maximal velocity.

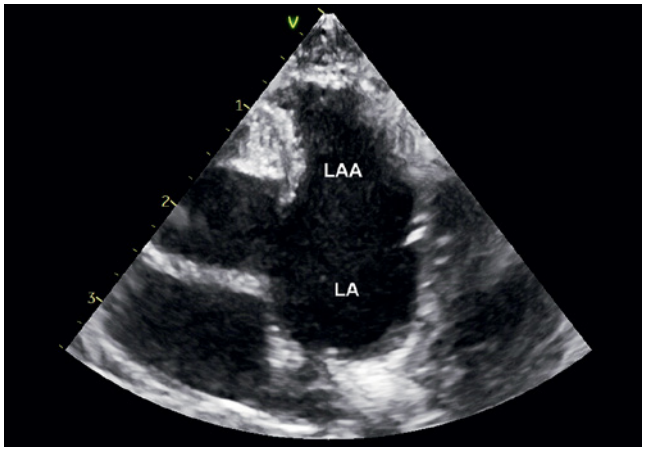


Figure 6.24. Feline left cranial left auricular appendage view. Image optimized for the left atrium and left auricle in a cat. There is no evidence of thrombus or spontaneous echo contrast on this image.

Table 6.5
Sources of echocardiographic variation

Image acquisition	**Genetic variation**
Observer technique	Body size
Instrument settings	Species variation
Measurement from images	Breed variation
Observer technique	Individual variation
Hemodynamic variation (short term)	**Pathophysiology**
Autonomic balance	Disease consequences
Preload	Cardiovascular remodeling
Afterload	**Interpretive methods**
Contractility	Observer experience
Heart rate	Statistical methods
Drugs	Spectrum of normal
Environmental variation (long term)	Data availability
Nutrition	
Athletic training level	
Drugs	

Expertise as an echocardiographer necessitates an extensive understanding of these factors and interrelationships.

Assessment of Cardiac Size

A basic, but troublesome, aspect of veterinary cardiology has been to interpret raw measurements for the range of body size and breed variations encountered, particularly for dogs. Although no entirely satisfactory approach has been determined, a common feature of many well-normalized indices is that they derive from a ratio of two measurements with the same physical units. Echocardiographic ratio indices have long been used in cardiology, with examples dating from the beginning of the technique. LA size, for example, may be expressed in terms of aortic (Ao) dimension (LA/Ao). It is often preferable, to index cardiac linear dimensions in terms of the body weight (BW, in kg) raised to approximately the one-third power (Cornell et al. 2004; Visser et al. 2019a). Cardiac volumes are often indexed to BW (in kg) or body surface area (in m^2) (Visser et al. 2019a; Wess et al. 2010).

Normal values for raw echocardiographic measurements and ratio indices are available throughout the veterinary literature.

Vet-ebooks.com

- **Assessment of Left Ventricular Size**
  M-mode recordings suitable for accurate and reproducible linear measurements require 2D guidance, for both transducer placement and cursor alignment. For LV measurements, the RPS SAx papillary muscle level is typically used, with the M-mode scan line placed between the two papillary muscles, transecting the LV central axis near the tips of the open mitral leaflets. M-mode linear measurements are made vertically along the *y*-axis of the strip chart, i.e., at a specific instant in time (Figure 6.25). A simultaneous electrocardiogram facilitates timing of the cardiac cycle where the QRS complex signals the end of diastole. It is typical for the maximal diastolic LV internal dimension (LVIDd) to occur during the QRS complex, and it is often possible to observe a slight presystolic distension induced by atrial contraction. End-systole occurs near the end of the electrocardiographic T wave, but the timing of the systolic measurement is determined from the echocardiogram itself at the occurrence of the minimum LV internal dimension (LVIDs).

  Although the majority of published LV dimensional data are from M-mode recordings, and therefore they are still frequently obtained in veterinary cardiology, measurements from 2D images (Figure 6.26) are recommended in human guidelines to avoid oblique sections of the LV (Lang et al. 2015). LVIDd and LVIDs may be obtained from LAx or SAx echocardiographic images, using 2D images or M-mode; however, results are not interchangeable between the measurement methods (Kruckman et al. 2022). Therefore, care should be taken to utilize the same method when performing serial measurements on individual patients, and when comparing patients to published reference values.

  When LVIDd is indexed to BW raised to the power of approximately 1/3 (e.g., LVIDd/($BW^{0.294}$, Cornell et al. 2004), a value greater than 1.7 is likely to represent diastolic LV dilation in most dogs (Table 6.6). When LVIDs is indexed to BW raised to the power of approximately 1/3 (e.g., LVIDs/($BW^{0.315}$, Cornell et al. 2004), a value greater than 1.14 is likely to represent an increased systolic LV chamber size for most dogs (Cornell et al. 2004; Esser et al. 2020; Visser et al. 2019a). For some individuals, additional linear parameters may be useful in identifying LV dilation, such as sphericity index (SI) and EPSS in Doberman Pinschers (Table 6.6; Figure 6.27).

  Measurements of the LV wall and IVS thickness may similarly be obtained from M-mode or 2D LAx and/or SAx views. Obtaining LV wall measurements are particularly important in cats when evaluating for hypertrophic cardiomyopathy (HCM). The authors prefer to measure feline LV walls from both

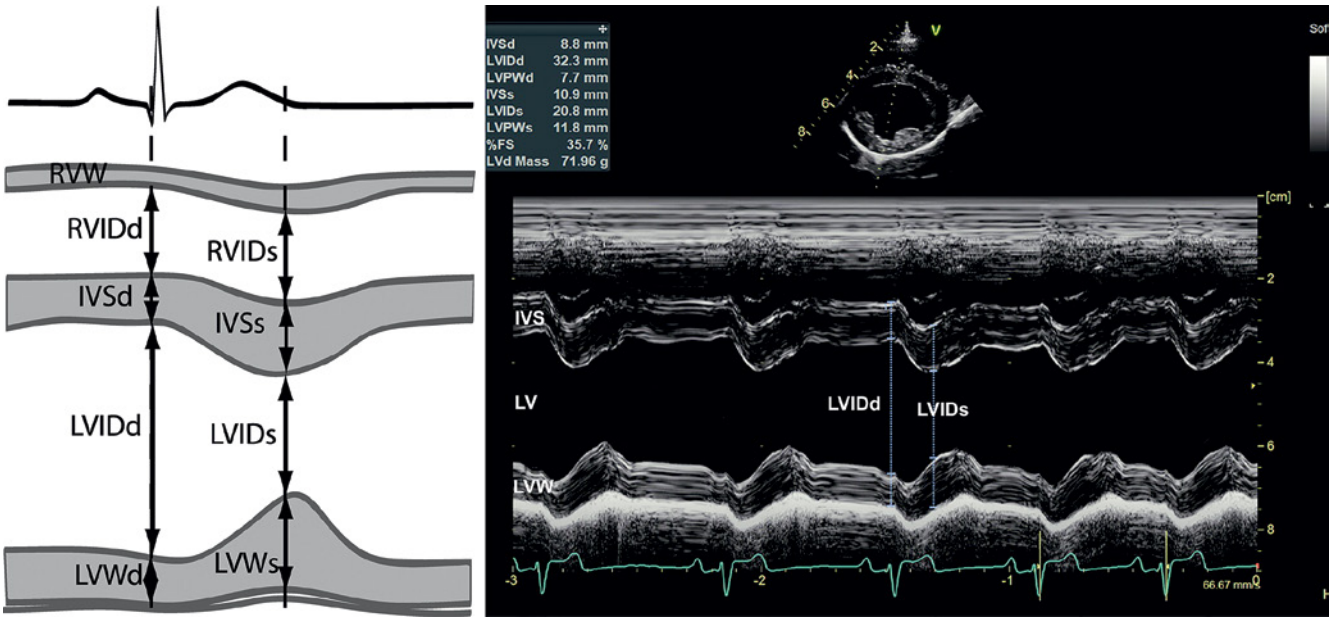


Figure 6.25. Linear ventricular measurements from M-mode echocardiography. 2D guidance for transducer placement and M-mode scan-line selection is paramount for accurate and reproducible results. Subscripts "d" and "s" refer to diastolic and systolic determinations, respectively, where end diastole coincides with the greatest LVIDd, typically shortly after the onset of the QRS complex, and systole coincides with the smallest LVID (LVIDs). Linear measurements are made vertically across the strip chart.

Vet-ebooks.com

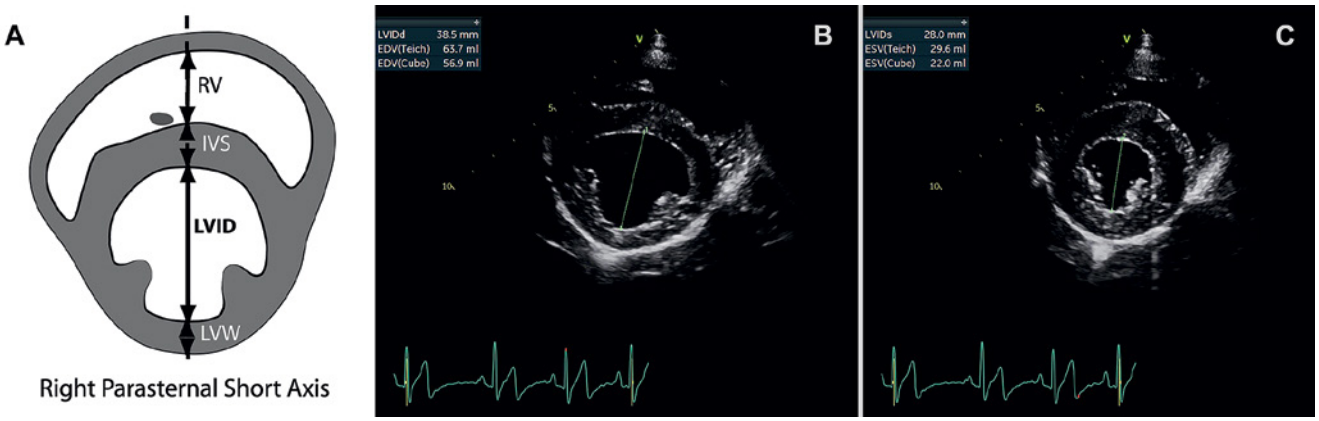


Figure 6.26. Linear left ventricular measurements from 2D images. (A) The short-axis left ventricular internal diameter (LVID) corresponds to the LVID from M-mode, although cannot necessarily be used interchangeably with M-mode measurements. **(B, C)** LVID measurements in diastole and systole, respectively, with a calculated FS of 27.3%.

Table 6.6
Common assessments of LV size in dogs

Measurement	Description	Normal values	Reference
LVIDdN (cm/BW$^{0.294}$)	LVIDd normalized to BW	<1.7	Cornell et al. (2004)
LVIDsN (cm/BW$^{0.315}$)	LVIDs normalized to BW	<1.14	Cornell et al. (2004)
LVEDV (mL/kg)	Left ventricular end-diastolic volume-indexed to body weight	1.3–3.2 (non-sighthound) 1.9–4.1 (sighthound)	Wess et al. (2021)
LVESV (mL/kg)	Left ventricular end-systolic volume-indexed to body weight	0.3–1.5 (non-sighthound) 0.7–2.1 (sighthound)	Wess et al. (2021)
LVEDV (mL/m^2)	Left ventricular end-diastolic volume-indexed to body surface area	<95 (Doberman)	Wess et al. (2010)
LVESV (mL/m^2)	Left ventricular end-systolic volume-indexed to body surface area	<55 (Doberman)	Wess et al. (2010)
SI	Sphericity index (LV length/LVIDd)	>1.65 (Doberman)	Holler and Wess (2014)
EPSS (mm)	E-point to septal separation	<6.5 (Doberman)	Holler and Wess (2014)

LAx and SAx 2D views (Figure 6.28), as wall measurements from M-mode imaging may be more likely to erroneously include structures such as papillary muscles or false tendons. Although there is no consensus surrounding how feline LV wall measurements should be taken (i.e., whether to include or exclude endocardial borders), it is important to utilize a standard technique, particularly when performing serial exams on individuals. It is important to exclude chordae tendineae, false tendons, papillary muscles, or other structures. It is generally accepted that a cut off of 6.0 mm is used to identify hypertrophy of both the feline IVS and LV free wall in diastole (Luis Fuentes et al. 2020).

Ventricular volume measurements may be preferable to linear chamber assessments as they may account for more regional/segmental variations in size and cardiac function. The most commonly used method to evaluate LV volume is the method of discs (modified Simpson's rule), which is recommended in human and canine echocardiography for volume assessment (Table 6.6; Figure 6.29) (Bonagura and Visser 2022; Lang et al. 2015). While it is ideal to use two imaging planes to perform the method of discs, in veterinary medicine it is common to use a single-plane approach (Visser et al. 2019a; Wess et al. 2021). The RPS LAx four-chamber view and/or the left apical

Vet-ebooks.com

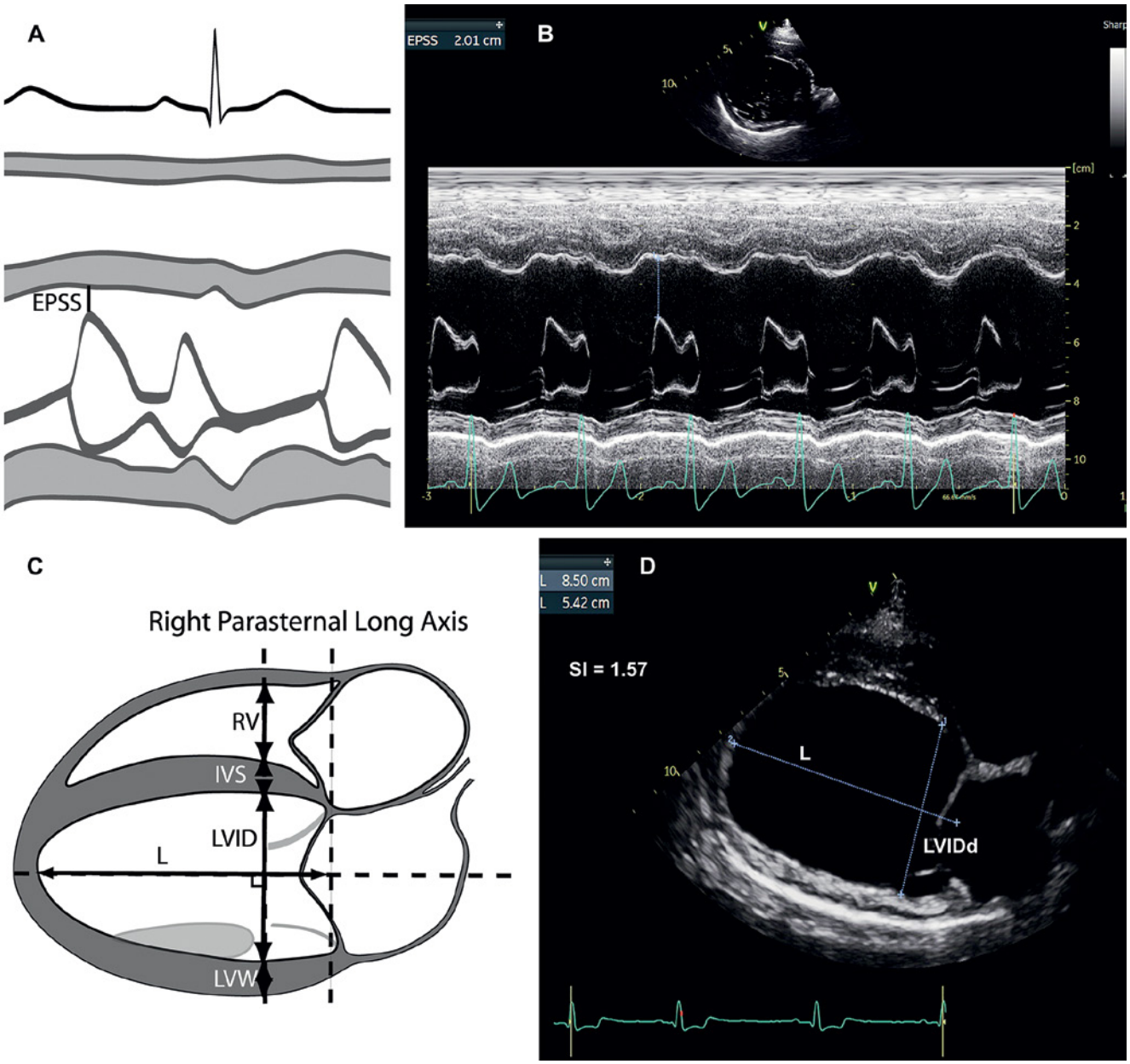


Figure 6.27. Additional left ventricular size parameters in dogs. (A) E-point to septal separation (EPSS) is usually obtained via M-mode through the mitral valve, measured from the IVS to the tip of the AML leaflet during early diastole (E-point). **(B)** In this M-mode through the RPS SAx view at the level of the mitral valve in a Doberman Pinscher, the EPSS is markedly increased (EPSS >6.5 mm) consistent with DCM in Doberman Pinschers (Holler and Wess 2014). **(C)** LV length (L) is measured from the plane of the mitral annulus to the LV apex along the central LV axis. LV sphericity index (SI) is calculated as LV length/LVIDd; therefore, smaller numbers indicate a more dilated (spherical) LV. **(D)** In this example of an RPS LAx four-chamber view from a Doberman Pinscher, the SI is mildly low (SI < 1.65) that is consistent with LV dilation in Doberman Pinschers. Holler and Wess (2014).

four-chamber view may be used to trace the LV endocardial border, excluding the papillary muscles, from the anterior (septal) to posterior (lateral) aspect of the MV annulus. The LV end-diastolic volume (LVEDV) is obtained from the first frame after closure of the mitral valve, and the LV end-systolic volume (LVESV) when the LV chamber is at its smallest, typically the last frame before MV opening.

- **Assessment of Left Atrial Size**

LA size embodies relevant diagnostic and prognostic information, but quantification is problematic because of the irregular three-dimensional shape

Vet-ebooks.com

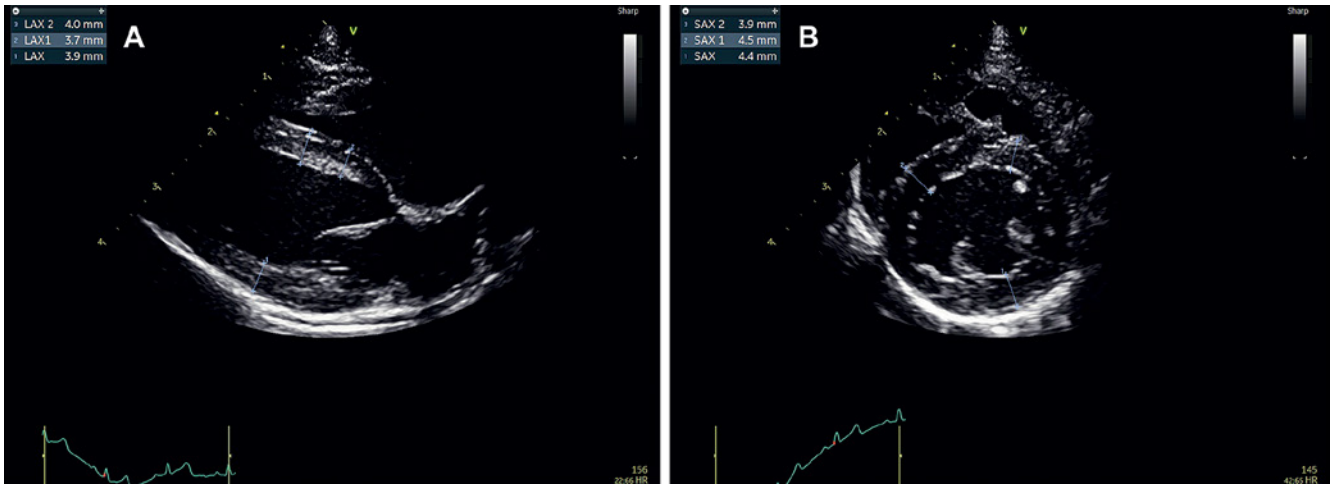


Figure 6.28. Wall measurements of the feline left ventricle. The authors recommend obtaining feline LV wall measurements from both the LAx and SAx 2D images. Some echocardiographers use a systematic approach to measure the walls as seen in **(A)** and **(B).** Wagner et al. 2010.

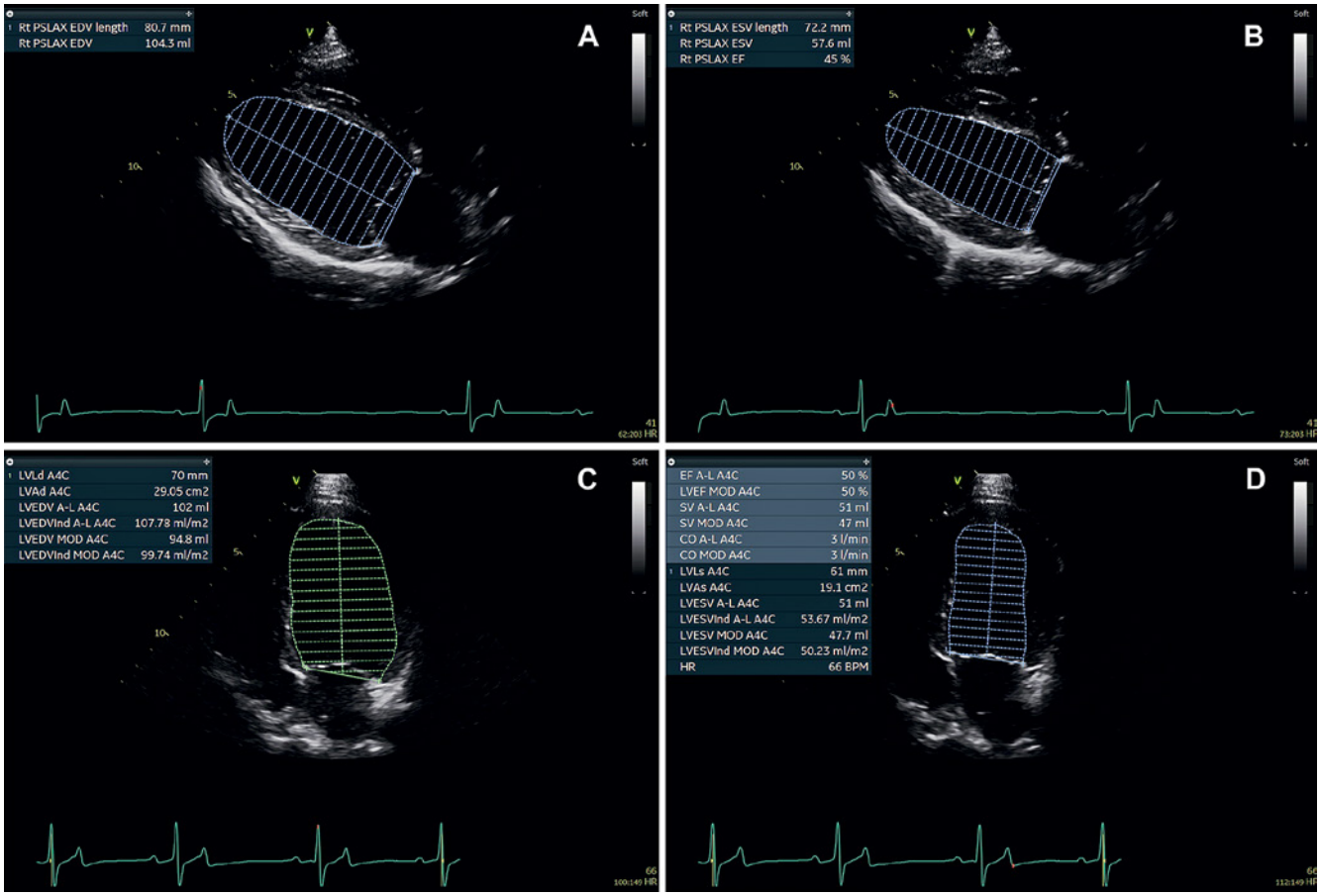


Figure 6.29. Left ventricular volume measurements. Method of discs (Simpson's rule) to obtain LV volume estimates from the RPS LAx four-chamber view **(A, B)** and the left apical four-chamber view **(C, D)**. The endocardial border of the LV is traced in end-diastole **(A, C)**, and end-systole **(B, D)**, LV apical to basilar length is obtained, and the echocardiographic software fills the chamber with a series of "discs," the volume of which are summated to estimate the LV volume. Care should be taken to not foreshorten the LV, which would lead to underestimation of volumes.

Vet-ebooks.com

(Hansson et al. 2002; Rishniw and Erb 2000). The original measurement derived from M-mode recordings exemplifies this issue because it includes only a small portion of the structure – the atrial appendage – plus a variable thickness of adipose tissue that lies between the aorta and appendage (Figure 6.30). Body-size normalization of the M-mode measurement in dogs has been accomplished through division by the measured aortic dimension (M-Mode LA/Ao). Mean values of this ratio are near 1.0 across the entire body-size spectrum but with normal maximum values up to 1.4, depending on the breed (Cornell et al. 2004; Hansson et al. 2002). Linear 2D LA measurements from SAx and LAx images afford advantages in sensitivity over M-mode determinations (Figure 6.30). Like their M-mode counterparts, maximal 2D LA size determinations are made at end systole, in the first frame after aortic valve closure (for SAx images) or just prior to the mitral valve opening (for LAx images). The ratio of 2D SAx LA diameter to SAx Ao diameter (2D LA/Ao) should be less than 1.6 in most normal dogs (Rishniw and Erb 2000) and cats (Abbott and MacLean 2003). Care should be taken to avoid extending the SAx LA measurement into the pulmonary venous ostia. Measurement of the maximal LA diameter (LAx LAD) in the RPS LAx four-chamber view is taken parallel to the mitral valve annulus, midway between the mitral annulus and roof of the LA. This LA measurement is particularly useful in cats, for which it should be <16 mm in normal individuals (Märtz et al. 2006).

Assessment of Blood Flow

Doppler echocardiography uses the Doppler principle to determine the velocity of moving blood (or tissue) and can assist in identifying laminar, turbulent, or

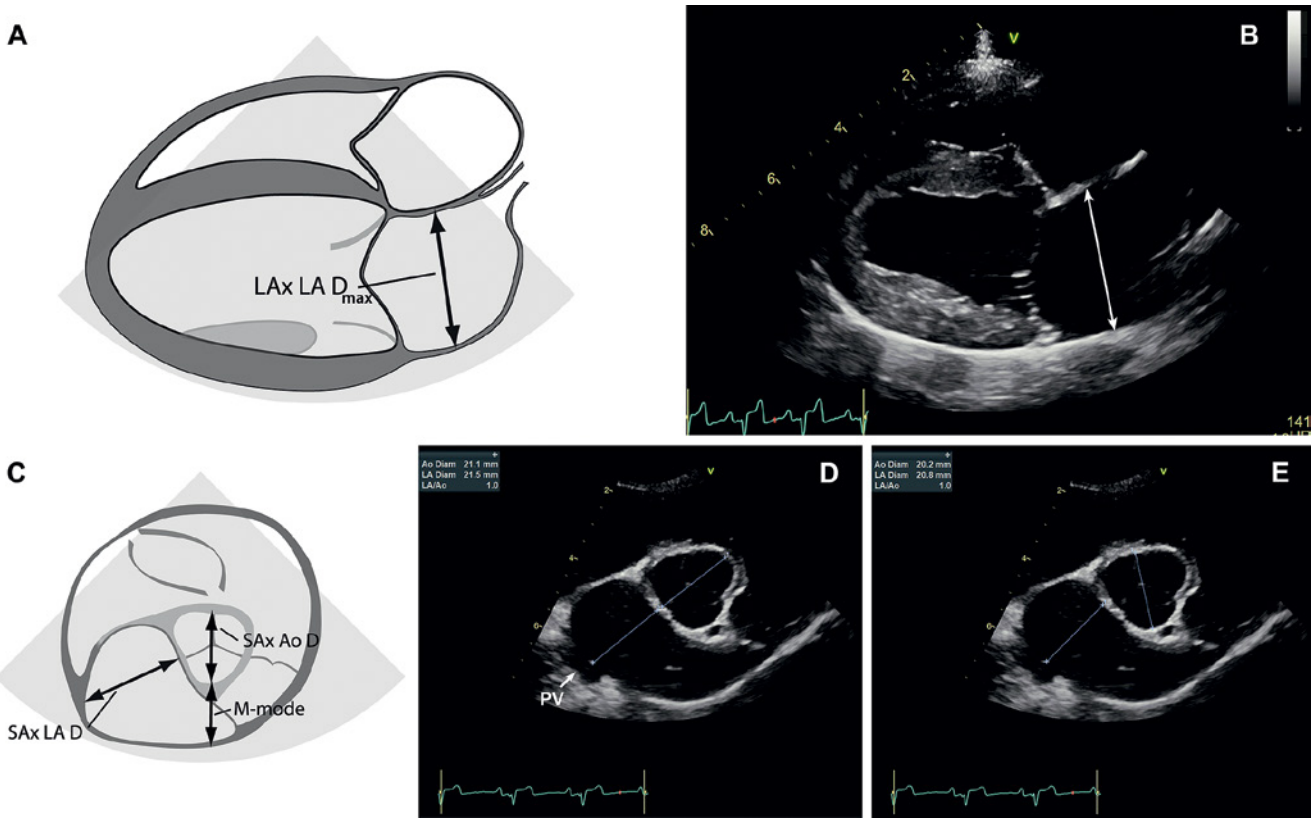


Figure 6.30. Left atrial size determination. LA size determination is problematic because of the irregular three-dimensional shape. In dogs, the SAx M-mode measurement includes only a small portion of the LA, i.e., the LAA. Linear measurements made from the 2D RPS SAx and LAx are more representative of atrial size but still suffer from angular dependence. **(A, B)** LA maximal diameter measured on the LAx view is obtained parallel to the MV annulus, midway between the annulus and LA roof**. (C, D, E)** The LA/Ao measured from the RPS SAx image is a frequently utilized ratio to assess LA size, with the Ao diameter measured either along the commissure between the noncoronary and left coronary aortic valve cusps **(D)** or along the commissure between the noncoronary and right coronary aortic valve cusps **(E).** In either instance, a normal LA/Ao is up to 1.6 in most dogs and cats. The pulmonary venous ostia (PV) should be excluded from the LA measurement.

Vet-ebooks.com

regurgitant blood flow (Figures 6.31, 6.32). With PWD, the round-trip time of the ultrasound pulse is used to determine the tissue depth at which the velocity occurs; the maximum depth dictates a specific pulse-repetition frequency. In turn, repetitive pulsation of the ultrasound is directly responsible for the aliasing phenomenon whereby measured velocity is observed to occur at an alias velocity. The alias velocity may be a gross misrepresentation of actual velocity (Figure 6.33). In contrast to PWD, ultrasound is emitted continuously in the CWD modality, which does not suffer from the velocity ambiguity of PWD. There is no practical limit to the velocity magnitude that can be measured with CWD. However, this mode does not enable the determination of the tissue depth from which the measured velocities arise, so the anatomical location of velocities must be inferred or determined using other means (e.g., 2D images and PWD).

CDI is a pulsed-wave modality in which velocity characteristics are encoded to a color display, via a user-selected mapping, and overlaid onto the real-time 2D echocardiography image. This enables the echocardiographer to visualize directly the source of velocities within the heart and great vessels within the anatomical framework of the image. Being a pulsed-wave modality, CDI is subject to velocity measurement ambiguity caused by aliasing. PWD and CDI are better

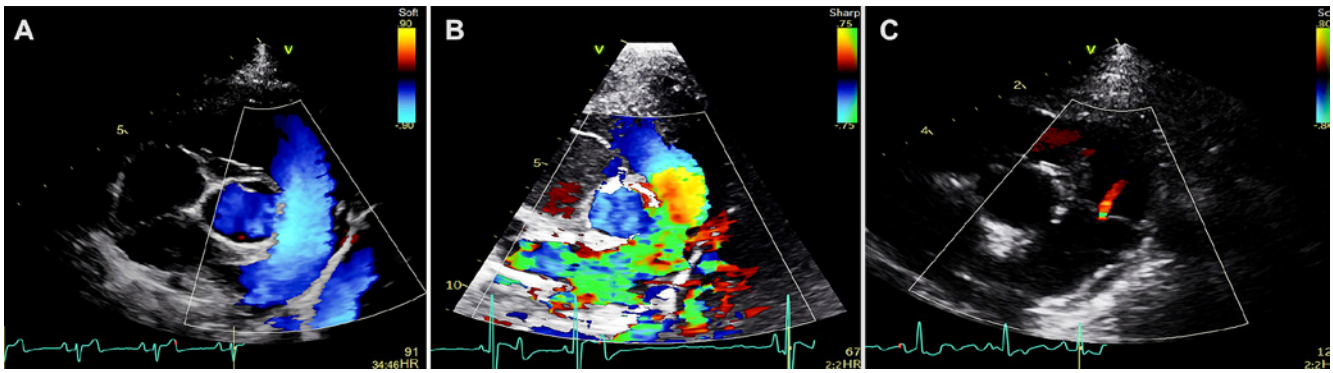


Figure 6.31. Color Doppler imaging. (A) RPS SAx view at the pulmonic valve level showing laminar flow across the pulmonic valve in systole. By convention, shades of blue demonstrate blood flow moving away from the transducer, as seen in the color scale in the top-right corner of the image. **(B)** The same view in a patient with valvular pulmonic stenosis, showing systolic turbulent blood flow across the valve. **(C)** A canine patient with mild pulmonic insufficiency (regurgitation) in diastole, a common finding in normal dogs. By convention, shades of red demonstrate blood flow moving toward the transducer, as seen in the color scale in the top right corner of the image.

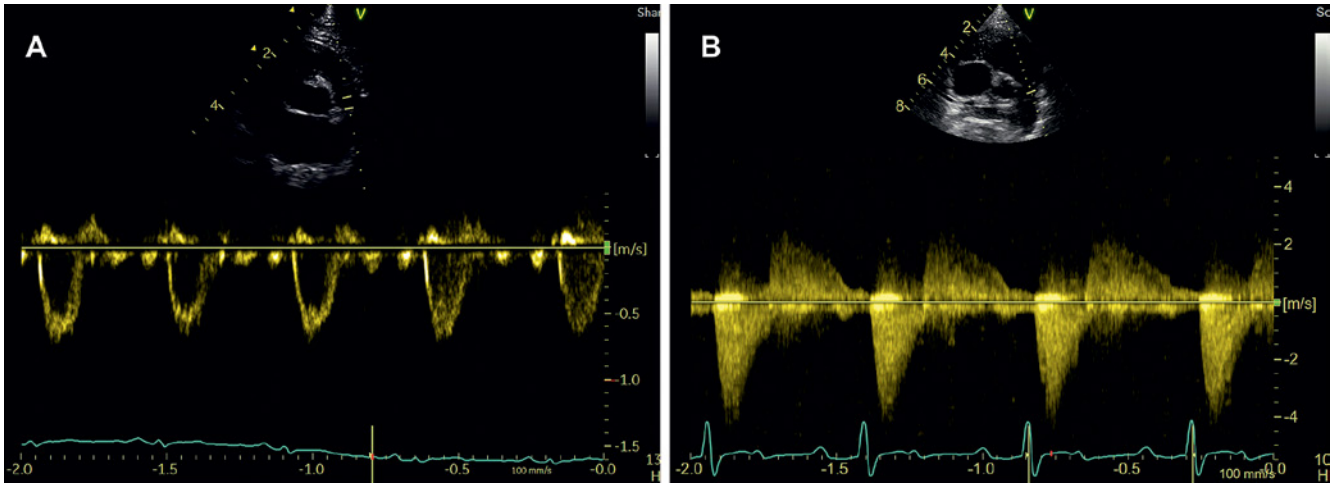


Figure 6.32. Laminar versus turbulent flow. (A) The PWD pulmonic ejection signal, recorded from RPS SAx view at the level of the pulmonic valve in a cat, demonstrates a laminar flow signal. **(B)** In contrast, a CWD recording of a turbulent pattern from a dog with pulmonic stenosis and pulmonic insufficiency. This results in a wide range of Doppler frequencies (i.e., velocities) at each moment during the ejection and spectral broadening of the signal; the velocity envelope is filled in (yellow) throughout ejection.

Vet-ebooks.com

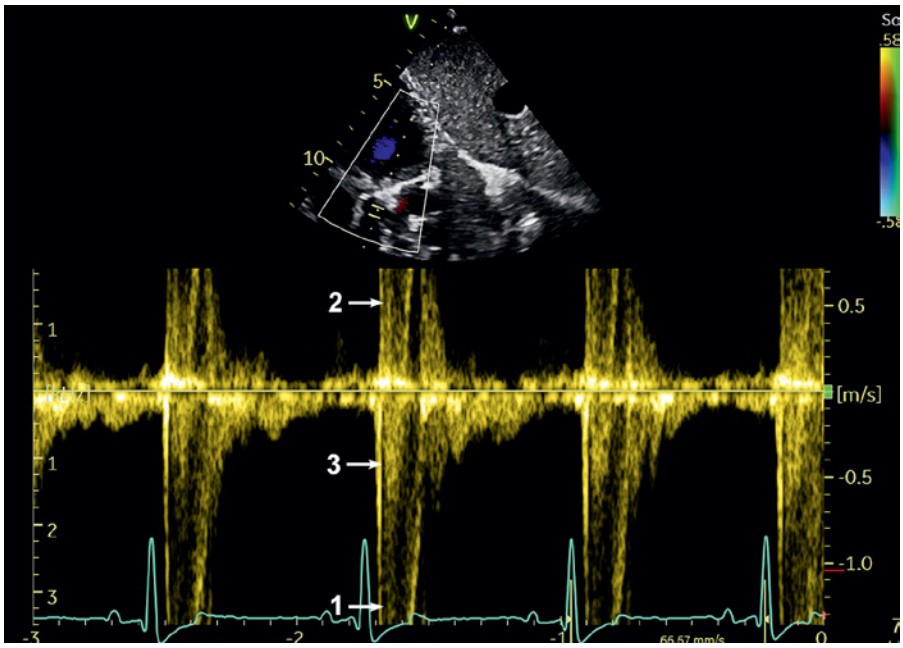


Figure 6.33. Spectral pulsed-wave Doppler aliasing. Spectral PWD recordings represent velocity along the *y*-axis, corresponding to Doppler shift frequency, and time along the *x*-axis. In this example of aortic ejection, flow is directed away from the transducer, and velocity in this direction is depicted below the baseline. The velocity reaches the alias velocity (Nyquist limit) at position 1 and further increases, causing the signal to wrap around to the positive side of the velocity scale (position 2). Velocity continues to increase, passing the zero baseline to the peak velocity indicated at position 3.

suited than CWD for differentiation between laminar and turbulent flow patterns.

Much of the quantitative value of Doppler studies stems from the application of fluid dynamic principles to the interpretation of measured velocities through the modified Bernoulli equation. The modified Bernoulli equation is expressed as $\Delta P = 4V^2$, where velocity (V) is in meters per second (m/s) and the calculated pressure gradient is in millimeters of mercury (mmHg). Optimized velocity recordings are accomplished at the time of the recording by diligent positioning of the transducer at the appropriate body wall location, aided by cues from the CDI image and both visual and auditory feedback from the spectral Doppler display. Transducer position varies with the specific lesion to be evaluated as well as nuances specific to the individual.

Assessment of Systolic Function

Although myocardial contractility cannot be directly measured, there are several echocardiographic parameters that may be employed to estimate systolic function of the LV (Table 6.7; Figure 6.34). The most commonly employed parameters are those that measure the difference in LV size from diastole to systole, namely, FS, fractional area change (FAC), and ejection fraction (EF). All are highly influenced by loading conditions.

Table 6.7
Indices of left ventricular systolic function

Index	Calculation	Normal values
FS	(LVIDd – LVIDs)/LVIDd	>25%
FAC	(LV diastolic area – LV systolic area)/ LV diastolic area	>40%
EF	(LVEDV – LVESV)/LVEDV	>45%

For each of these indices, it is common practice to multiply the result by 100 and express the value as a percentage.

Fractional shortening is calculated as (LVIDd-LVIDs)/LVIDd, typically multiplied by 100 to obtain a percent value. As FS assesses the change in chamber size in a single dimension of the LV, it will not reliably assess global systolic function, particularly in situations of regional hypokinesis and will underestimate systolic function when there is LV dyssynchrony. However, FS is commonly used as it is relatively simple and rapid to obtain. Most normal dogs will have an FS of >25% (Cornell et al. 2004; Visser et al. 2019a).

Vet-ebooks.com

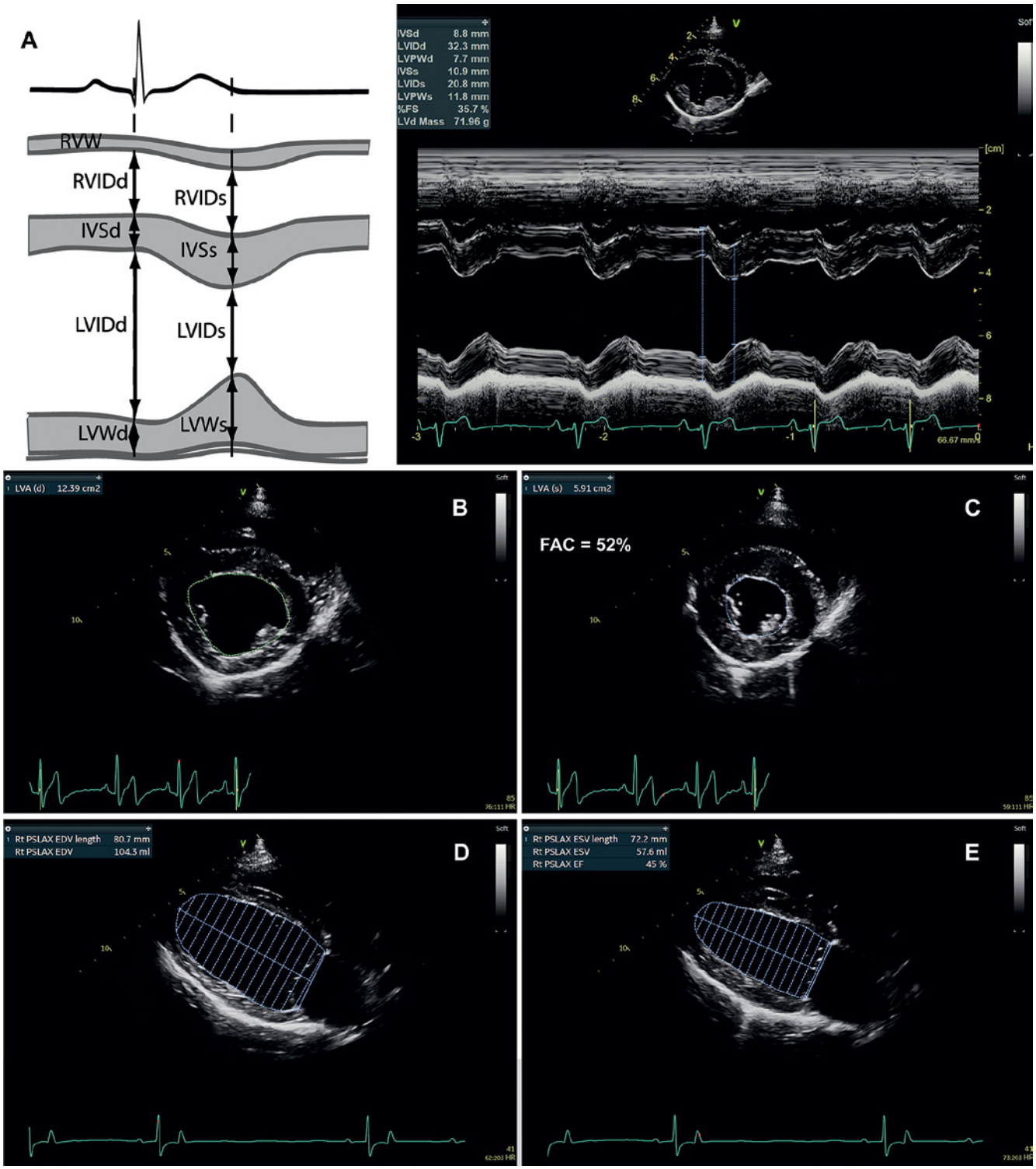


Figure 6.34. **Common indices of left ventricular systolic function. (A)** M-mode of the LV from a RPS SAx view at the papillary muscle, showing a normal FS of 35.7%. **(B, C)** RPS SAx view at the papillary muscle level in diastole **(B)** and systole **(C)**, with the LV endocardial borders traced to calculate a normal FAC of 52%. **(D, E)** RPS LAx four-chamber view in diastole to obtain LVEDV **(D)** and systole to obtain LVESV **(E)**, and a calculated normal EF of 45%.

Vet-ebooks.com

Fractional area change is the change in the 2D area of the LV measured from the RPS SAx view at the papillary muscle level. The LV endocardial border is traced, excluding the papillary muscles, in both diastole and systole, and FAC is calculated as (diastolic LV area - systolic LV area)/diastolic LV area. As with FS, the value obtained is multiplied by 100 to obtain a percent value. Most normal dogs will have an FAC of >40% (Visser et al. 2019a).

Ejection fraction is calculated as (LVEDV-LVESV)/LVEDV x 100 and may be considered the "gold-standard" echocardiographic assessment of systolic function, particularly when the bi-plane method or 3D echocardiography is used. The calculation of EF from LV volumes obtained by 2D echocardiography still requires some geometric assumptions of the LV shape. Most normal dogs will have an EF of >45% (Visser et al. 2019a; Wess et al. 2021).

Assessment of Diastolic Function

Evaluation of diastolic function is complex and beyond the scope of this chapter. Left ventricular diastolic dysfunction is a hallmark of feline cardiomyopathies (Schober and Chetboul 2015). Frequently obtained measurements include mitral inflow velocity signals including the velocity magnitude of the E (early filling) and A (atrial contraction) (Figure 6.35). Factors affecting the form of inflow velocities are complex and pertain to diastolic ventricular function and ventricular filling pressures. The different Doppler mitral inflow patterns and their meaning are presented in Figure 6.36. The mitral inflow pattern can only be interpreted in the absence of summation of the E and A waves, which occur in tachycardic animals.

TDI is employed to quantify the velocity of motion of cardiac tissue directly. The most common use of TDI in cardiology is to record the longitudinal (base-apex) velocity of the mitral annulus from the apical four-chamber position (Figure 6.37). Pulsed-wave TDI velocity recordings may be obtained from either the septal or lateral mitral annulus, adjusting the transducer position so that the annular motion of the chosen site is directed along the Doppler scan line to the extent possible. This is especially useful in cats with cardiomyopathies to distinguish normal from pseudonormal transmitral flow.

The isovolumic relaxation time (IVRT) refers to the time between completion of systole (aortic valve closure) and the onset of transmitral flow. IVRT represents a phase of diastole with no change in ventricular volume and tends to be prolonged in cats with HCM (Figure 6.38) (Bright et al. 1999; Schober and Chetboul 2015). The ratio between peak velocity of early mitral inflow (E) and peak early TDI annular velocity (E:E′) has received considerable attention as a predictor of LV filling pressure in the human literature; however, this ratio has been less robust in predicting congestive heart failure (CHF) in dogs (Schober et al. 2010). In dogs with left-sided CHF due to chronic valvular disease or dilated cardiomyopathy (DCM) measurement of the IVRT, the ratio of mitral E wave to IVRT (E:IVRT), or a composite measure of diastolic functional class based on mitral inflow and TDI parameters are better predictors of CHF. The E:IVRT has also been identified as the best Doppler predictor of reduced filling pressures in response to treatment of dogs with both pacing-induced and naturally occurring CHF (Schober et al. 2008, 2011).

Congenital Heart Disease

Congenital Valvular Diseases

Aortic Stenosis

Aortic stenosis (AS) signifies an obstruction to LV outflow. It may be valvular, subvalvular (subaortic stenosis, SAS), or supravalvular. SAS is the most common congenital cardiac disease of large-breed dogs. Moderate to severe SAS causes characteristic, but variable, 2D abnormalities, including discrete or diffuse narrowing of the LVOT, poststenotic aortic dilation, and thickening of the aortic and anterior mitral valve leaflets (Figure 6.39). On the RPS LAx image, a subvalvular obstruction may appear as an echogenic ridge on the septum, mitral apparatus, or both, corresponding to a complete or incomplete hyperechoic ring of fibrocartilaginous tissue encircling the outflow tract. SAS is often associated with a steeper aorto-septal angle (Belanger et al. 2014; Quintavalla et al. 2010). Concurrent aortic insufficiency is also often present.

AS causes LV pressure overload and secondary LV concentric hypertrophy. The extent of hypertrophy is variably correlated with the severity of obstruction. Severe obstruction also may be accompanied by increased echogenicity of the papillary muscles and/or subendocardial myocardium, possibly secondary to ischemia of these regions and subsequent fibrosis or calcification.

CDI of the LVOT in systole reveals a region of flow acceleration proximal to the obstructive lesion, and turbulent or disturbed flow with increased velocity distally (Figure 6.39). Arbitrary prognostic categories

Vet-ebooks.com

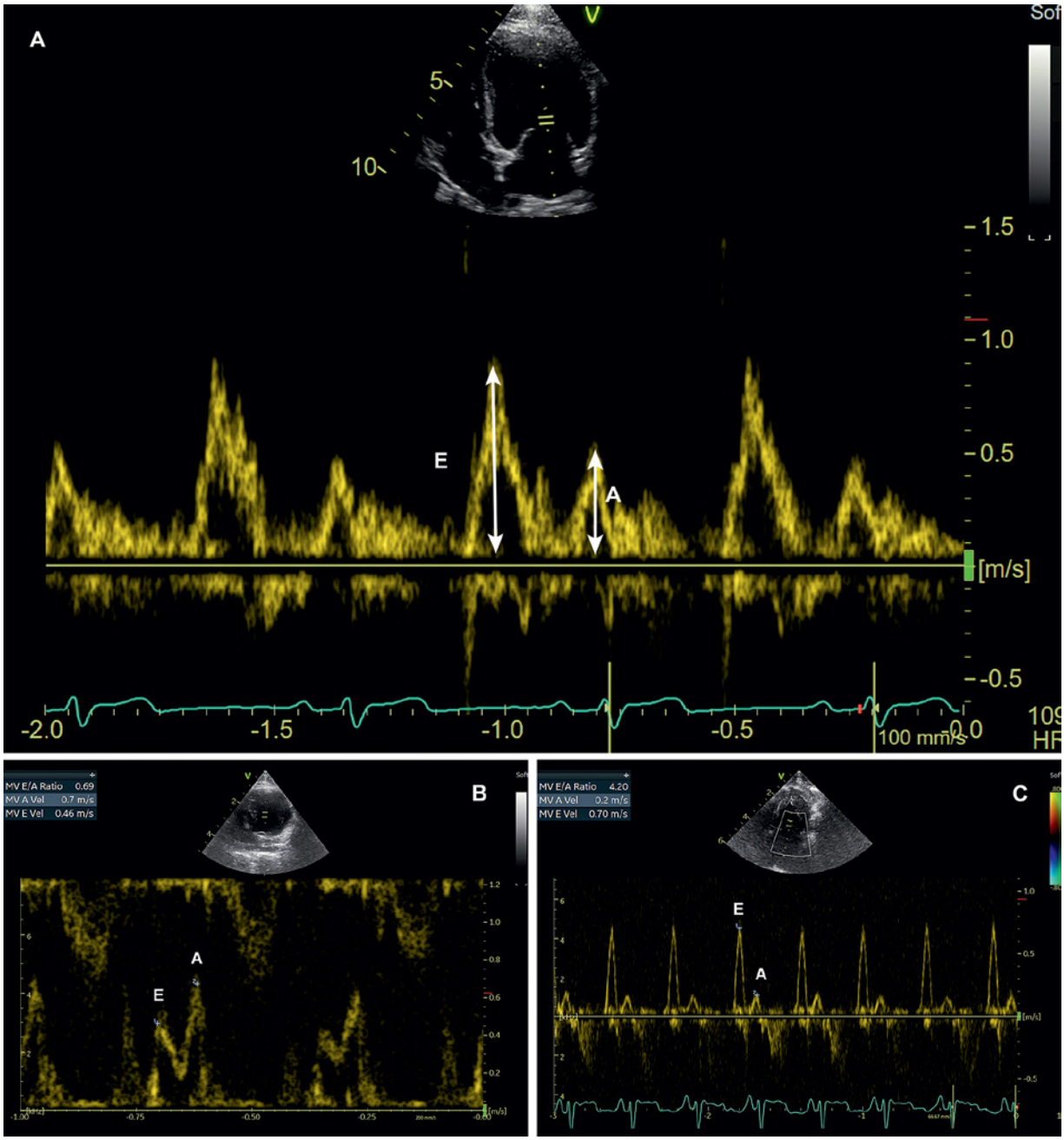


Figure 6.35. **Transmitral flow patterns.** Measurements include peak velocities for the E and A waves. The E:A peak velocity ratio, normally between 1.0 and 2.0, may be used to quantify the relative contributions of each to ventricular filling. Peak velocities are related to the peak atrial-ventricular pressure gradient through the Bernoulli equation and so elevated velocities may suggest valvular stenosis or increased LA pressure. **(A)** A normal transmitral flow pattern with an E:A > 1. **(B)** A delayed relaxation pattern with an E:A of <1. **(C)** A restrictive filling pattern with an E:A of ≥2.

based on the pressure gradient are mild (<50 mmHg), moderate (50–80 mmHg), severe (80–130 mmHg), and very severe (>130 mmHg). A recent study showed that the survival time of dogs with very severe SAS was significantly decreased compared to all other categories (Eason et al. 2021). The pressure gradient and peak velocity are flow-dependent indices of severity. This means that the severity of obstruction may be overestimated in dogs that are stressed, excited, or affected by a concurrent PDA (due to increased cardiac output). It may also be underestimated, in the presence of myocardial failure, or under anesthesia, for example. It can be especially challenging to differentiate dogs with very mild SAS from normal dogs. Breeds

Vet-ebooks.com

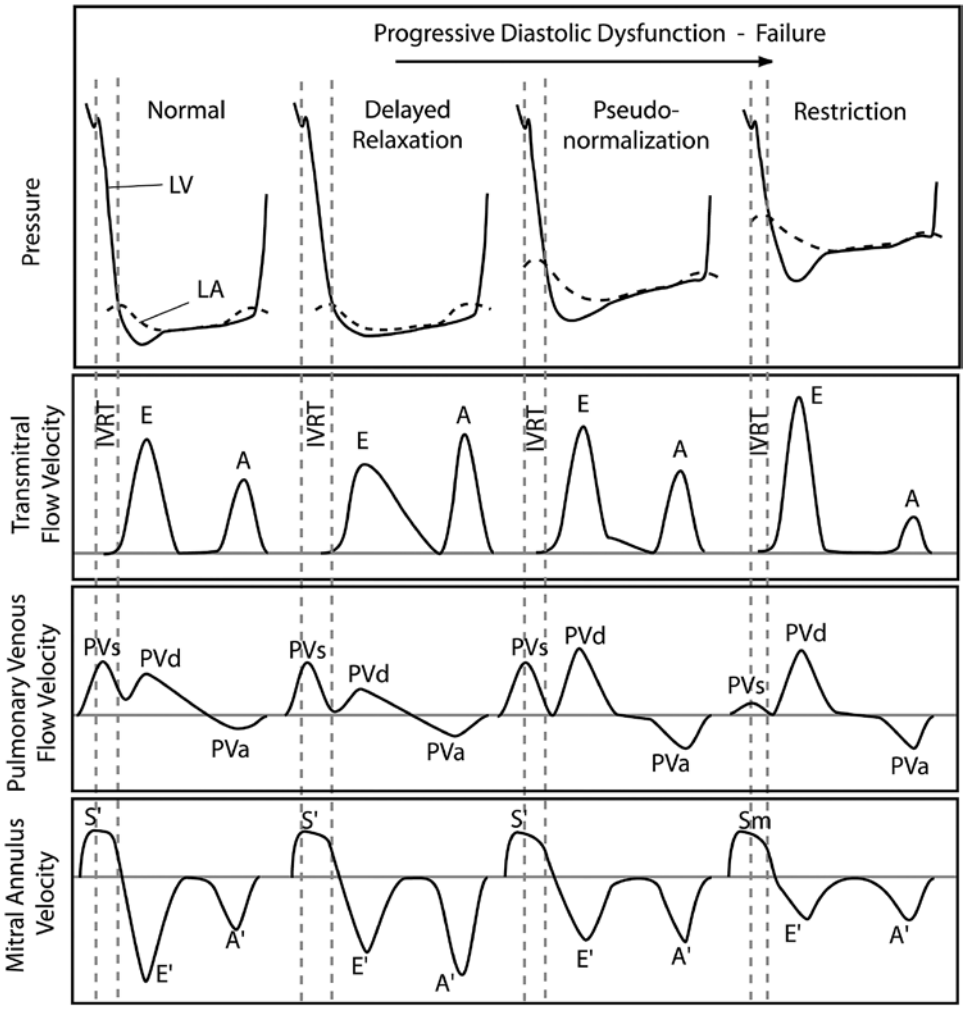


Figure 6.36. **Diastolic dysfunction.** A schematic overview of diastology can be encapsulated in terms of left ventricular (LV) and left atrial (LA) pressures (top tier), mitral blood inflow velocity patterns, and longitudinal mitral annular velocity. In the early stages of diastolic dysfunction, delayed relaxation of the LV increases the IVRT and there are decreases in both the early diastolic transmitral pressure gradient and the size of the Doppler E wave relative to A, and E wave deceleration time may be increased. The early relaxation phase of mitral velocity (E′) is diminished relative to motion associated with atrial systole (A′). With progressive diastolic dysfunction, IVRT and mitral inflow patterns are returned toward normal (pseudonormalization) in association with the compensatory increase in LA and venous pressure, which act to restore the early filling phase. This condition is difficult to differentiate from normal by mitral flow pattern alone but is distinguished by further decreases in E′ and equalization of E′ and A′. Left atrial dilation is also expected at this time. End-stage restrictive physiology characteristically includes an increased transmitral pressure gradient early in diastole, associated with an increased Doppler E wave magnitude, but inflow is terminated abruptly as the incompliant ventricle reaches its elastic limit and atrial-ventricular pressure equalization occurs. A shortened E wave deceleration time is characteristic. The incompliant ventricle can accept little additional volume with atrial systole and the A wave is small or diminutive. Further decreases in mitral annular velocity coincide with impaired relaxation. Features of the classic description may depend dramatically on hemodynamic circumstances (e.g., preload) and heart rate.

such as Boxers or Pit bulls tend to have slightly smaller outflow tract diameters and maximal velocity measurements up to 2.3 or 2.4 m/s can be seen in healthy individuals.

Cases of pure valvular AS are less common. The aortic cusps may be thickened and/or fused. Rarely, the number of aortic cusps may be abnormal (Figure 6.40).

Pulmonic Stenosis

Pulmonic stenosis (PS) is one of the most common congenital cardiac diseases in dogs but is uncommon in cats. PS signifies an obstruction to RV outflow and may occur at subvalvular, supravalvular, or valvular locations, the latter being the most common site in

Vet-ebooks.com

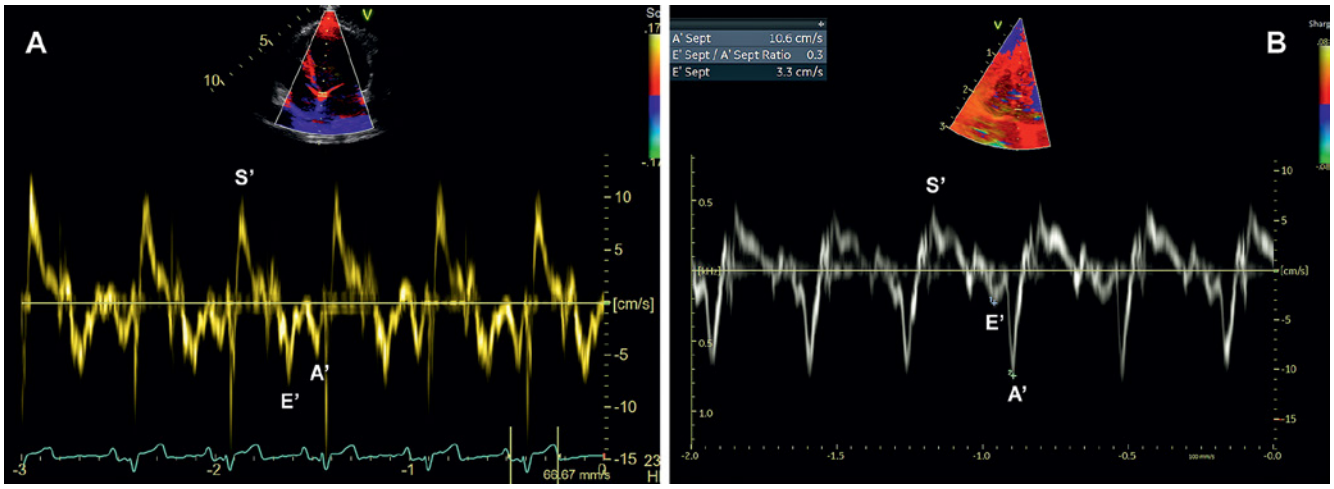


Figure 6.37. Tissue Doppler recording of mitral annular velocity. Velocity sampling placed to record the septal mitral annulus velocity in both **(A, B)**. Diastolic annular velocity measurements mirror the mitral inflow pattern with two distinct phases of filling. The LV expands longitudinally in both early and late diastole, resulting in annular velocity away from the transducer and generation of the E′ and A′ waves, respectively. LV contraction entails a longitudinal component that is directed toward the transducer and generation of the systolic wave S′. In **(A)**, the TDI pattern is normal, whereas in **(B)** the E′:A′ is reversed (E′:A′ <1) showing delayed relaxation.

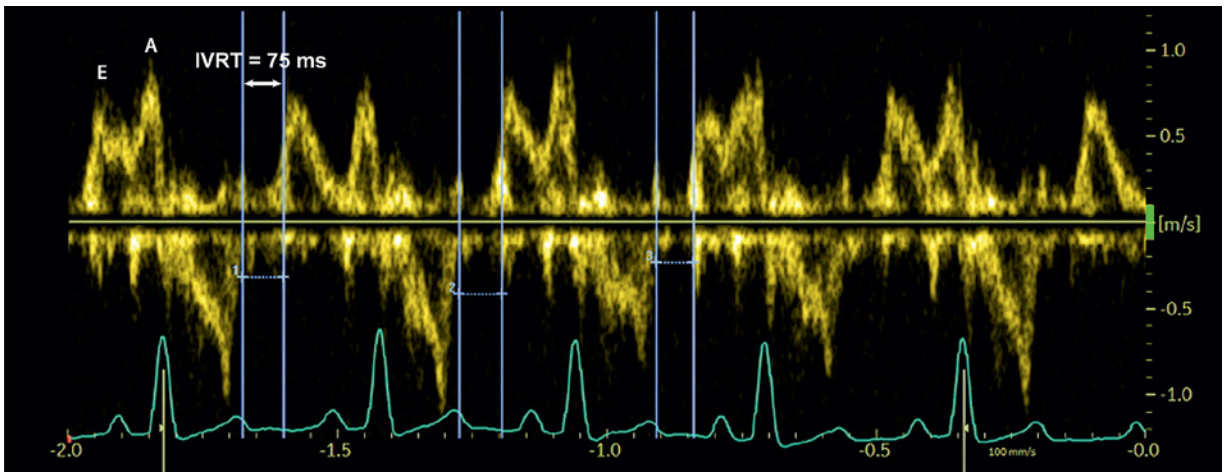


Figure 6.38. Pulsed-wave Doppler recording of isovolumic relaxation time (IVRT) of the left ventricle in a cat with hypertrophic cardiomyopathy. From the apical five-chamber view, a 5–10 mm sample volume is positioned into the LV in an intermediate position between the LV outflow tract (LVOT) and the mitral inflow profiles. The IVRT of the LV is measured as the time interval between the end of the aortic systolic ejection flow wave recorded from the LVOT to the onset of the early diastolic mitral flow wave. In this cat, the IVRT is prolonged at 75 ms (normal usually between 40 and 60 ms) and the mitral inflow profile is consistent with delayed relaxation (E:A <1).

dogs. Potential echocardiographic features in common with all forms of PS include right atrial enlargement, poststenotic dilation of the pulmonary trunk, and concentric hypertrophy of the RV with increased thickness of the septum and RV wall (Figure 6.41) (Visser et al. 2019b). Increased echogenicity of the RV myocardium may be associated with severe obstruction and presumed ischemic myocardial damage. Severe RV pressure overload causes flattening of the IVS. LV volume underload in this circumstance may erroneously suggest concentric LV hypertrophy (pseudohypertrophy) with increased LV wall thickness and decreased LV and LA internal dimensions (Figure 6.41).

In valvular PS, cusps may be thickened and/or fused at the commissures such that cusp separation is impaired; the fused cusps may form a valvular dome as they bulge into the pulmonary trunk during systole.

Vet-ebooks.com

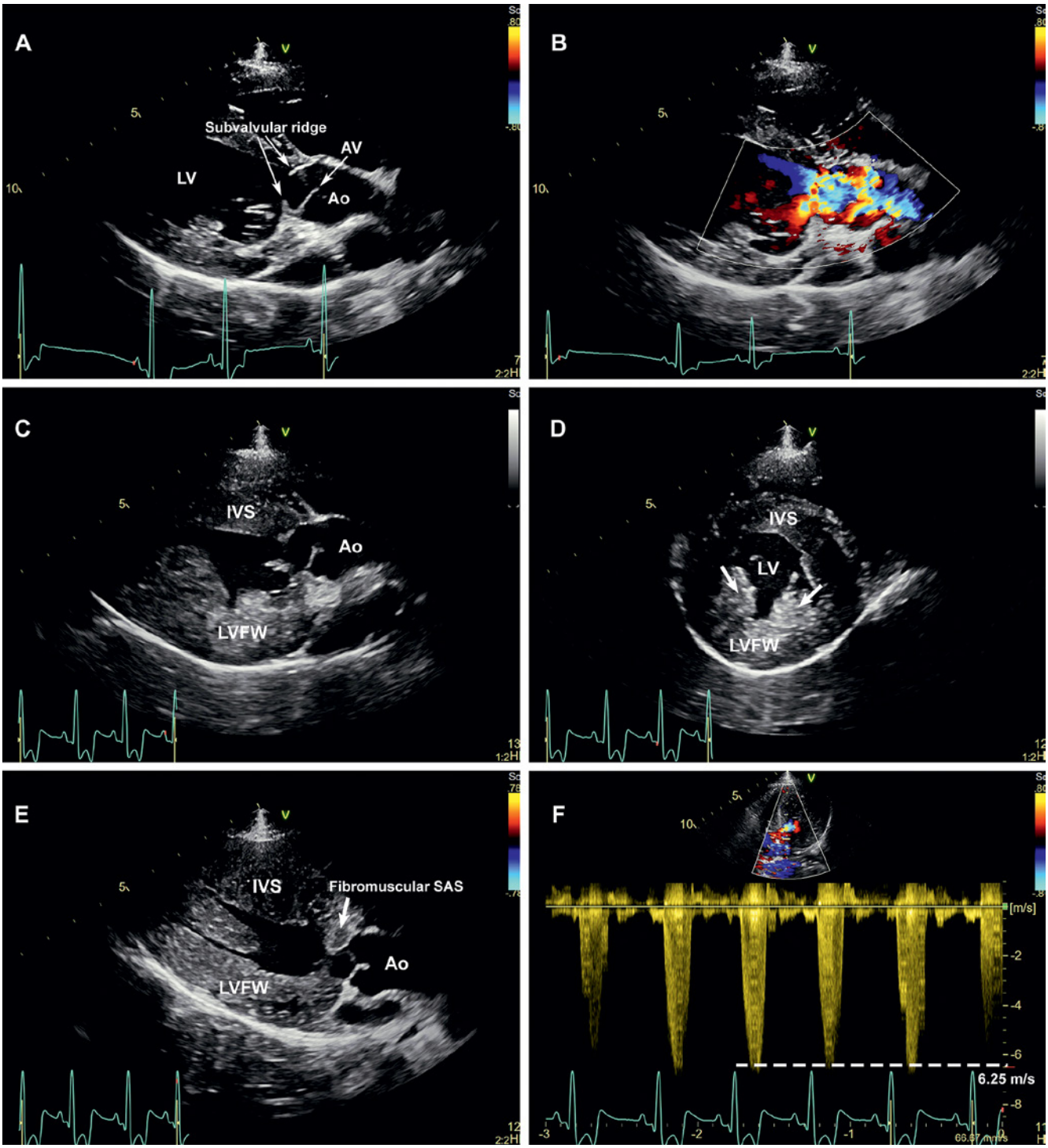


Figure 6.39. **2D and Doppler images from dogs with subaortic stenosis (SAS). (A)** RPS LAx LVOT view in a dog with moderate SAS. The aortic cusps are evident and appear morphologically normal. The obstruction in SAS is most typically at the immediate subvalvular location. The example shown here includes both septal and mitral aspects of the encircling obstructive lesion. **(B)** CDI image (same view). During systole, color aliasing occurs proximal to the obstruction and a turbulent mosaic pattern is apparent distally in the Ao. **(C)** RPS LAx LVOT view in a dog with severe SAS. In this case, thickened LVW and IVS, caused by concentric hypertrophy, are evident. **(D)** RPS SAx view at the level of the papillary muscles in the same dog with severe SAS. Concentric left ventricular hypertrophy is again evident. There is a subendocardial echogenicity (arrows), which is thought to represent fibrosis, secondary to ischemia. **(E)** Left cranial LAx view in the same dog with severe SAS. A fibromuscular subvalvular obstructive lesion is seen. **(F)** Spectral Doppler recording obtained from the apical LVOT view. A temporal peak velocity of 6.25 m/s for the stenosis corresponds to a maximum pressure gradient of $4 \times 6.25^2 = 156$ mmHg and a very severe stenosis.

Vet-ebooks.com

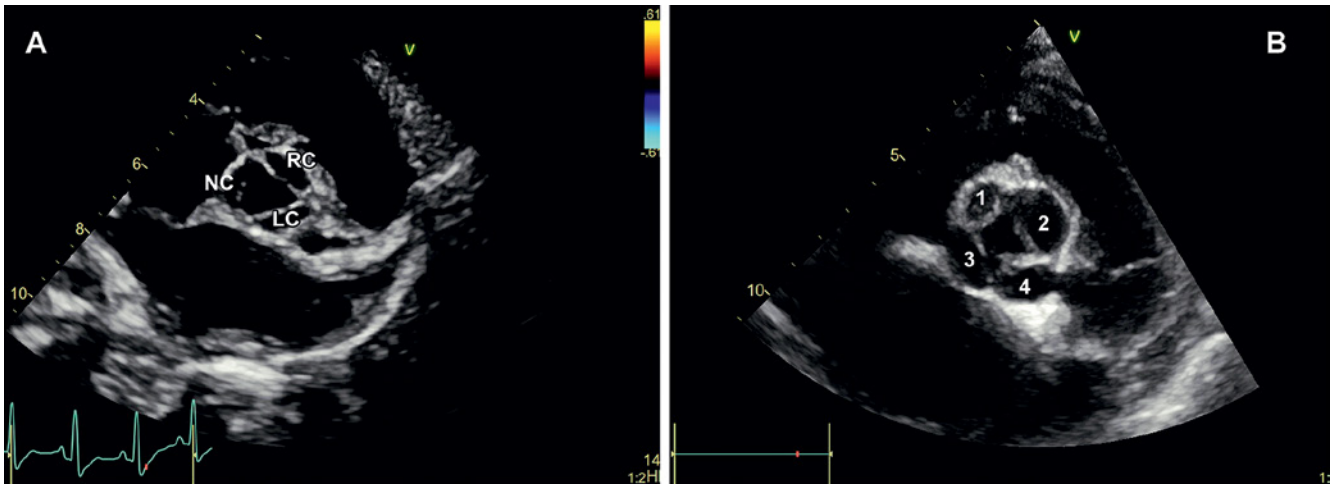


Figure 6.40. Valvular aortic stenosis in two dogs. (A) RPS SAx view at the aortic valve level in a dog with moderate AS. Three cusps are evident (normal) but there is incomplete excursion of the aortic cusps in systole. LC: left coronary cusp; NC: noncoronary cusp; RC: right coronary cusp. **(B)** RPS SAx view at the aortic valve level in a dog with a quadricuspid aortic valve with both severe AS and severe aortic insufficiency.

The RVOT itself may be hypoplastic and echogenic in conjunction with valvular lesions. Some dogs with PS, particularly brachiocephalic breeds such as English or French Bulldogs and Boxers, may have an anomalous prepulmonic (cranial) coronary artery originating from a single left or right coronary ostium, encircling the pulmonary trunk and contributing to the obstructive lesion (Figure 6.42) (Buchanan 2001; Visser et al. 2013). The coronary anatomy must be closely scrutinized in any dog anticipated to undergo balloon valvuloplasty (Fonfara et al. 2010), as an aggressive dilation procedure in a dog with aberrant coronary anatomy may result in avulsion of the coronary and immediate death of the dog. Optimal visualization of the coronary arteries may be difficult to achieve echocardiographically in some dogs, particularly English Bulldogs. CT angiography, aortic root angiography, or selective coronary angiography should then be considered in such patients prior to balloon valvuloplasty. In Bulldogs, PS is often complex, characterized by a combination of valvular and supravalvular stenosis, for example, and associated with pulmonary trunk hypoplasia (Chetboul and Taton 2018).

Combined Doppler examination of the RVOT enables peak gradient quantification (CWD) and confirms the location of the obstruction, indicated by the velocity step up (PWD) or flow convergence zone (CDI) just proximal to the lesion. Suggested prognostic categories based on the pressure gradient are mild (<50 mmHg), moderate (50–80 mmHg), and severe (>80 mmHg). Specificity and sensitivity of these categories for specific outcomes have not been determined; however, dogs with severe PS are likely to benefit from balloon valvuloplasty. Mild to moderate tricuspid regurgitation and patent foramen ovale (PFO) with right-to-left shunt commonly coexist with significant pressure overload of the right heart (Fujii et al. 2012).

Other types of obstructive lesions with similar hemodynamic consequences include cases of stenosis in the mid-right ventricle due to anomalous muscle bundles (this is named double-chambered right ventricle, Figure 6.43) and more localized fibrosis in the proximal RVOT (this is named pulmonic infundibular stenosis).

Tricuspid Valve Dysplasia

Dysplasia of the tricuspid valve may entail a wide range of structural abnormalities (Figure 6.44). The condition is transmitted genetically in Labrador Retrievers, the most frequently affected canine breed. Echocardiographic findings may include abnormal numbers or arrangement of papillary muscles; chordae tendineae may be foreshortened or papillary muscles may attach directly to a valve leaflet. Tricuspid leaflets may be elongated or shortened and abnormally tethered to the septum or RV wall, thereby restricting motion and function; leaflet fusion may cause stenosis. The entire tricuspid apparatus may be displaced toward the cardiac apex, similar to Ebstein's malformation in human patients. Tricuspid dysplasia may cause valvular regurgitation and variable degrees of RV volume overload with dilation of the RV and right atrium. Increased tricuspid regurgitation jet velocity (e.g., >3.0 m/s) should prompt consideration of concurrent pulmonary hypertension or PS and atrial

Vet-ebooks.com

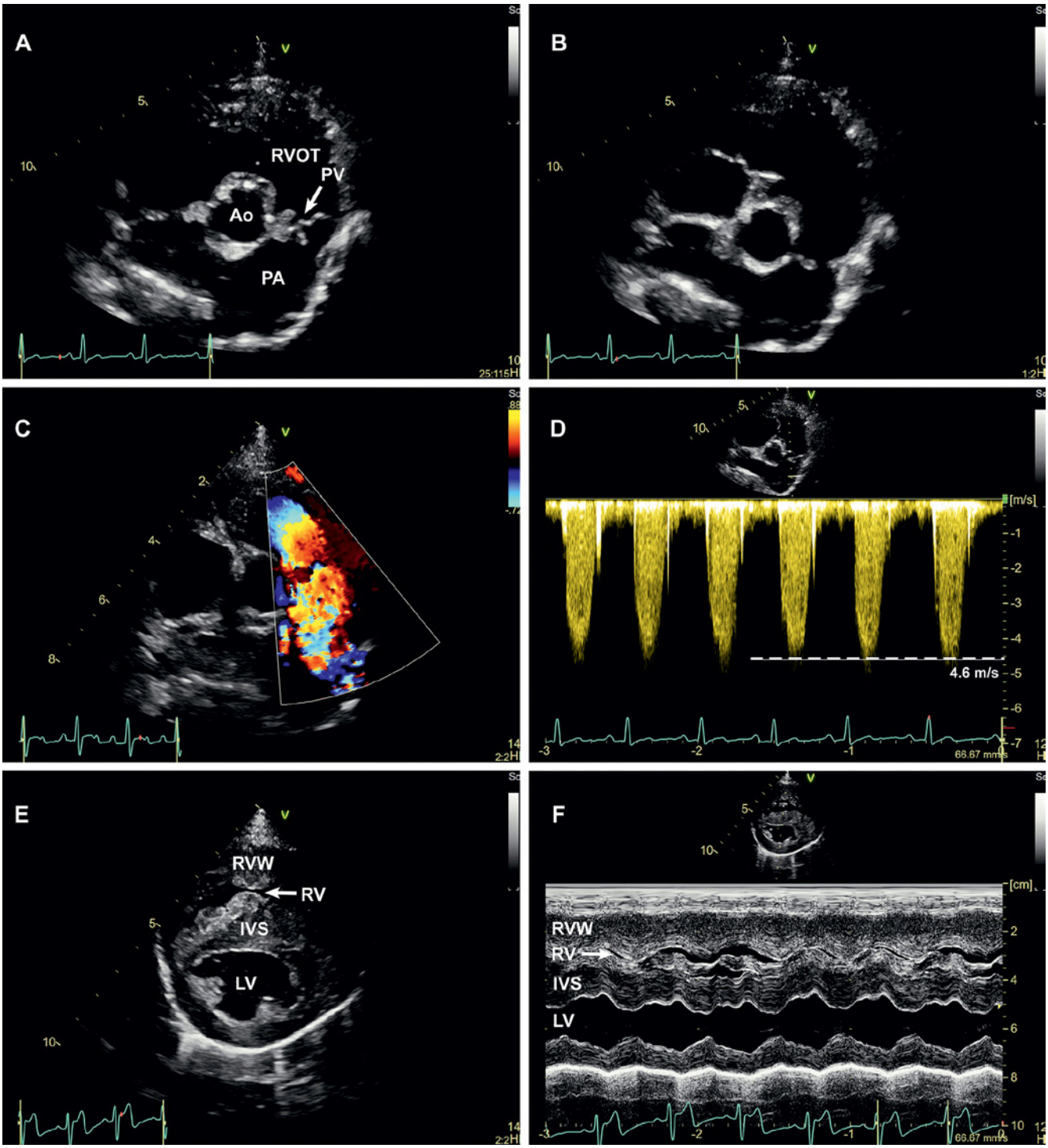


Figure 6.41. **Valvular pulmonic stenosis in a dog. (A)** RPS SAx 2D image at the level of the pulmonic valve from a dog with moderate PS. The pulmonic cusps are seen in diastole and appear thickened. Poststenotic dilation of the pulmonary trunk can be appreciated. **(B)** Same view in systole. The fused pulmonic cusps are forming a dome as they bulge into the pulmonary trunk. **(C)** RPS CDI at the PV which confirms the location of the obstruction at the valve. **(D)** CWD of the pulmonic flow jet from a dog with severe valvular pulmonic stenosis. A velocity of 4.6 m/s corresponds to a peak pressure gradient of $4 \times 4.6^2 = 85$ mmHg and severe obstruction. **(E, F)** RPS SAx transventricular 2D image and M-Mode showing concentric hypertrophy of the right ventricle. The increased echogenicity of the right myocardium is thought to be caused by ischemia and fibrosis. The septum is displaced toward the LV, thus causing an ovoid LV cross section because of the flattened septum.

Vet-ebooks.com

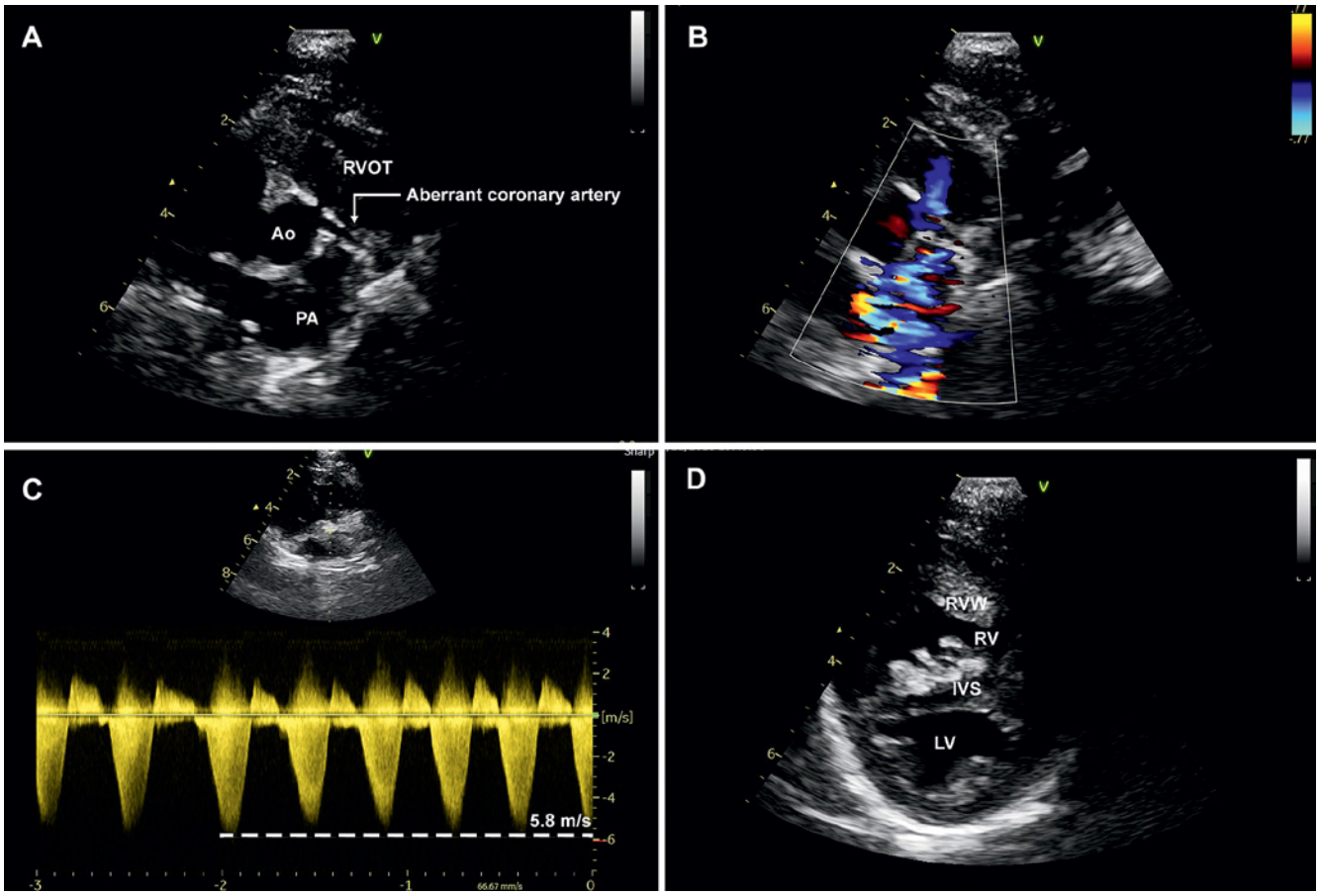


Figure 6.42. Aberrant coronary artery in a French Bulldog puppy with pulmonic stenosis. **(A)** RPS SAx 2D image at the level of the pulmonic valve in a dog with an aberrant coronary artery (likely a single right coronary artery). The aberrant coronary artery is arising from the aorta and is encircling the RVOT. **(B)** CDI indicates turbulent blood flow arising from the aberrant coronary artery region. **(C)** CWD of the pulmonic flow jet showing severe PS as well as pulmonic insufficiency. A velocity of 5.8 m/s corresponds to a peak pressure gradient of $4 \times 5.8^2 = 135$ mmHg and severe obstruction. **(D)** RPS SAx transventricular 2D image showing concentric hypertrophy of the RV, prominent RV papillary muscles, flattening of the interventricular septum, and hyperechogenicity of the myocardium.

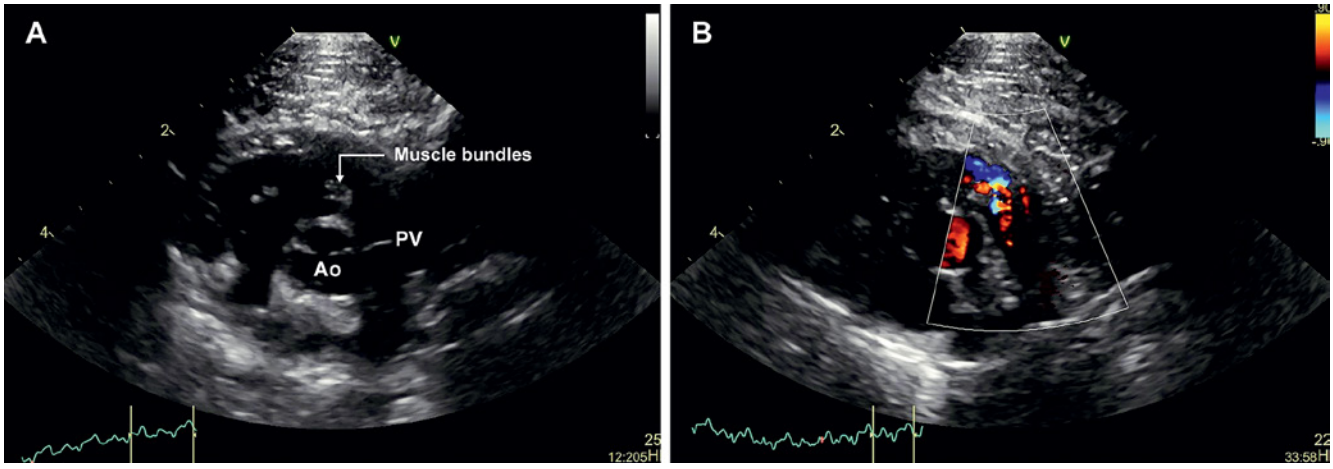


Figure 6.43. Double-chambered right ventricle in a cat. RPS SAx 2D **(A)** and CDI **(B)** images at the level of the pulmonic valve showing anomalous muscle bundles separating the RV into a proximal hypertrophied chamber and a distal, low-pressure chamber.

Vet-ebooks.com

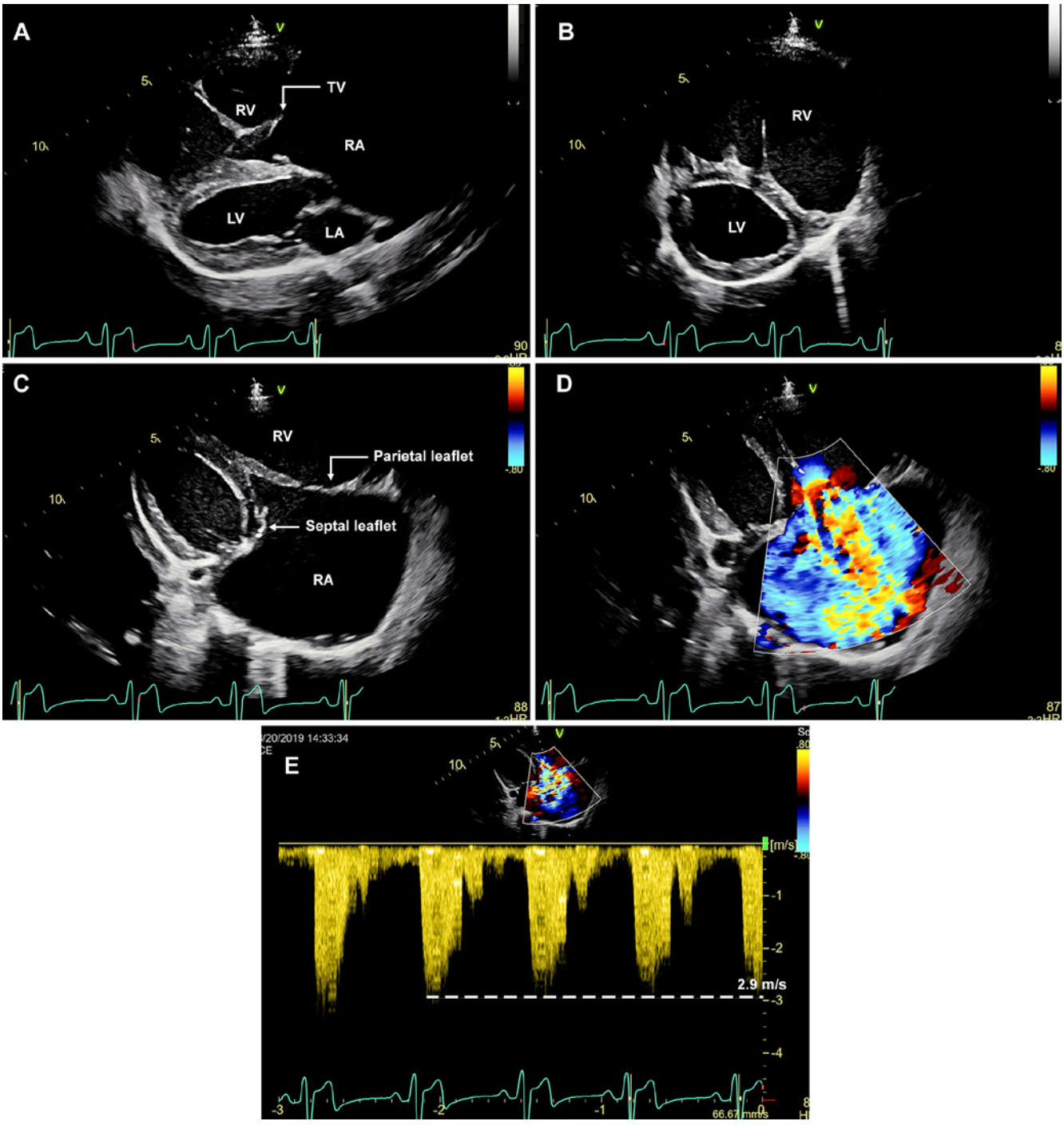


Figure 6.44. **Tricuspid dysplasia in an English Springer Spaniel with right-sided congestive heart failure. (A)** The RPS LAx four-chamber view demonstrates extreme RA and RV dilation and a dysplastic tricuspid valve apparatus. **(B)** The RPS SAx transventricular view demonstrates extreme RV dilation. **(C)** A left cranial view demonstrating a short tricuspid septal leaflet tethered to the IVS. The parietal leaflet appears elongated and directly attached to a papillary muscle. **(D)** CDI image demonstrating marked TR. **(E)** A TR jet velocity of 2.9 m/s is consistent with a normal or near-normal systolic RV pressure.

septal defect (ASD) may also accompany the condition. Tricuspid stenosis may also be caused by dysplasia of this valve leading to a diastolic flow of increased velocity (e.g., >2.0 m/s) into the RV.

Mitral Valve Dysplasia

Mitral valve dysplasia (MD) may entail a wide range of structural and functional abnormalities, including abnormal numbers or origins of papillary muscles;

Vet-ebooks.com

excessively shortened, lengthened, or thickened chordae tendineae, abnormal chordal attachments to nonvalvular structures, and abnormal leaflet morphology (Figure 6.45). Clinically relevant forms of MD cause hemodynamically significant mitral valve regurgitation (MR) (most commonly), mitral stenosis, or LVOT obstruction.

Congenital Shunts

Patent Ductus Arteriosus

Left-to-right PDA is another common congenital heart defect in dogs. A PDA is best visualized from the RPS short-axis view at the pulmonic valve level or from a left cranial view (Figure 6.46). The PDA is usually funnel-shaped and tapers on the pulmonic side, but different morphologies have been described (Miller et al. 2006). Associated echocardiographic features of this condition include LA dilation and LV eccentric hypertrophy (dilation) due to volume overload. Both the aorta and pulmonary trunk may be dilated in conjunction with increased blood flow. CDI of the pulmonary trunk reveals continuous turbulent flow and is useful in establishing the site of the ductus itself. CWD velocity quantification reveals continuous flow into the pulmonary trunk and a peak velocity during systole of roughly 4.5–5.5 m/s, corresponding to the normal systolic aortic–pulmonic gradient of 80–120 mmHg. Velocities significantly lower than this value may suggest pulmonary hypertension or a more complex lesion. It is valuable to image the ductus directly and to determine carefully its suitability for interventional closure (Figure 6.47). When the PDA is closed early in life, cardiac dimensions often return to normal or near-normal after closure. Systolic dysfunction is often evident after PDA closure but does not tend to affect long-term outcomes (Hamabe et al. 2015; Saunders et al. 2014).

Right-to-left shunting PDA (**reverse PDA**) is uncommon but most typically occurs in dogs with a large ductus and persistent fetal circulation. In most cases of reverse PDA, the flow is actually bidirectional (Figure 6.48). Failure of the normal reduction of pulmonary vascular resistance at birth produces pulmonary pressures that approach or exceed aortic values and consequent reversal of the shunt flow direction and arterial desaturation, which may persist from birth. This scenario is consistent with echocardiographic findings of a thickened RV wall and septum typical of a RV pressure overload (Figure 6.48). The alternate reverse PDA scenario, i.e., left-to-right PDA producing progressive pulmonary hypertension and eventual shunt reversal (Eisenmenger physiology), occurs less commonly. The latter would be expected to include LV dilation secondary to LV stroke volume overload.

Reverse PDA is suspected when there is clinical and echocardiographic evidence of RV pressure overload in the absence of an obstructive pulmonary lesion. The diagnosis may be confirmed by an echocontrast study (bubble study; not covered in this chapter), if necessary (Goodwin and Holland 1995).

Abnormalities of Cardiac Septation

Failure of cardiac septation during embryogenesis results in a defect between the right and left sides of the heart, including ASD, VSD, or a combination of the two. Septation abnormalities may cause a wide spectrum of functional diseases. Because of the normal distributions of intracardiac pressure and chamber compliance, both ASD and VSD most typically cause left-to-right shunting of blood and pulmonary overcirculation.

- **Atrial Septal Defect**
  An ostium secundum ASD is a defect near the normal position of the fossa ovalis in the mid-interatrial wall (Figure 6.49). In distinction, an ostium primum ASD is a defect in the ventral atrioventricular septum just above the atrioventricular valves (Figure 6.50). The ostium primum ASD is recognized as a form of atrioventricular septal defect (formally called endocardial cushion defect, or atrioventricular canal defect) that may cause ASD, VSD, or both. Sinus venosus ASD, which is rare in small animals, occurs near the junction of the cranial vena cava (Figure 6.49). PFO is not an anatomical defect, but results when functional closure of the foramen ovale at birth is not permanent. Echo drop out is often present on 2D images in the region of the fossa ovalis and should not be overinterpreted as an ASD. ASD flow is typically generated by a small pressure gradient and the degree of shunting depends on the size of the defect. Large ASDs are usually associated with right atrial and ventricular enlargement as well as pulmonary overcirculation. Blood flow velocity in the main pulmonary artery is elevated due to the increased blood volume flowing in the pulmonary artery (Figure 6.50).
- **Ventricular Septal Defect**
  VSDs also occur in a range of anatomical and functional types. One aspect of classification relates to whether the VSD is small and restrictive, where the pressure gradient between the right and left ventricles is maintained and jet velocity is close to 5 m/s, in contrast to nonrestrictive, where the large

Vet-ebooks.com

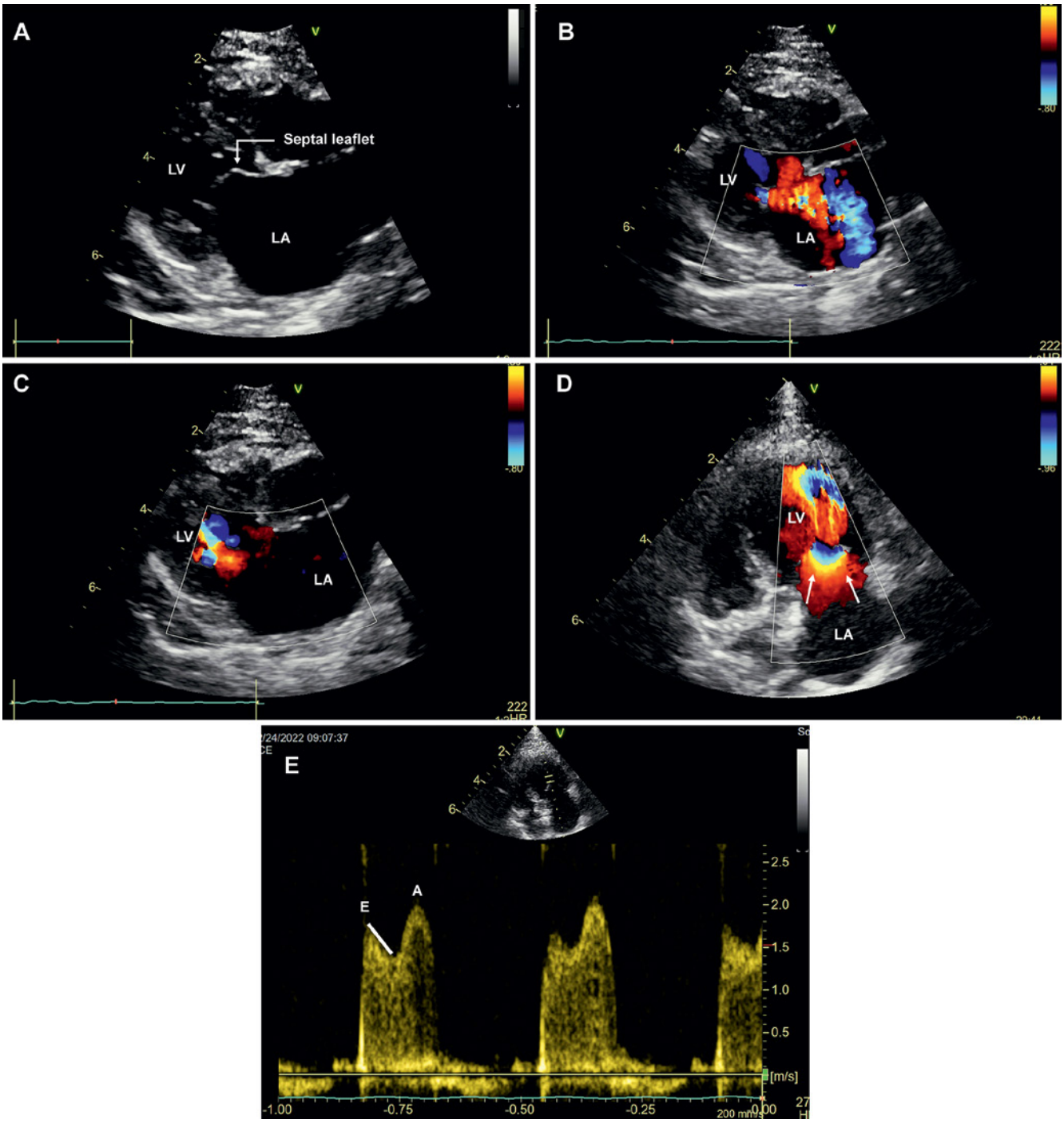


Figure 6.45. **Mitral dysplasia with valvular stenosis and regurgitation in a cat. (A)** RPS LAx four-chamber view obtained during maximal diastolic separation of the MV leaflets. The tip of the septal leaflet is tethered, so that the valve cannot open normally. The septal leaflet has a characteristic "hockey stick" appearance. The left atrium is dilated. **(B)** CDI of the mitral valve in systole showing moderate MR. **(C)** CDI of the mitral valve in diastole showing turbulent flow into the LV due to mitral valve stenosis. **(D)** CDI obtained during diastole demonstrating a flow convergence zone at the atrial side (arrows) of the MV and a high-velocity aliased inflow jet within the LV. **(E)** The PWD recording (left apical transducer position) demonstrates a turbulent diastolic inflow signal (spectral broadening). The E wave approaches 1.7 m/s and the A wave 2 m/s, corresponding to a 16 mmHg peak pressure gradient across the MV (modified Bernoulli equation). There is a prolonged pressure-half time (white line) of the E wave due to the stenosis. Note that the A wave velocity is higher than the E wave velocity.

Vet-ebooks.com

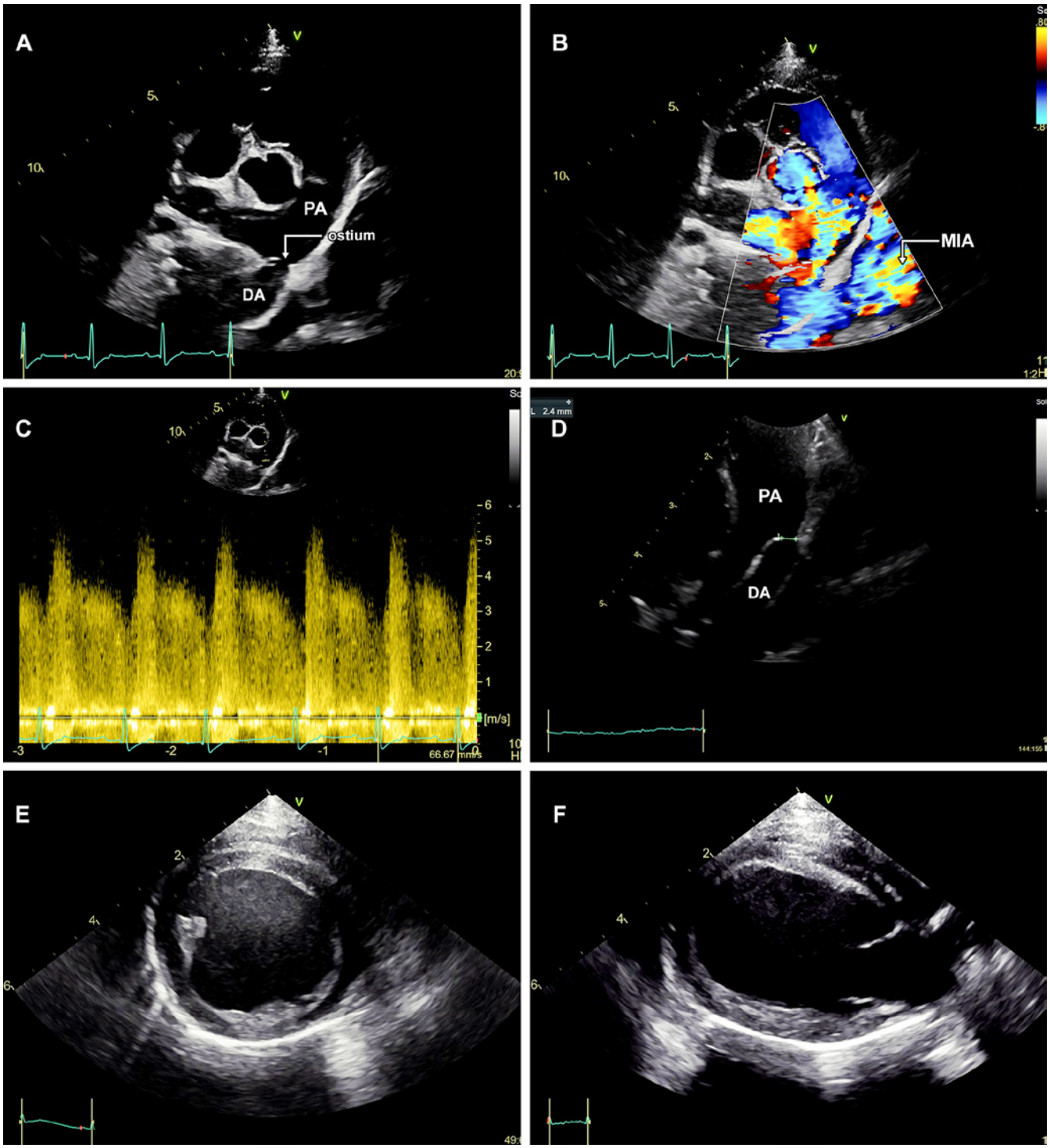


Figure 6.46. **Left-to-right shunting patent ductus arteriosus (PDA) in a Labradoodle. (A)** RPS SAx image at the pulmonic valve level showing a funnel-shaped ductus arteriosus that narrows at its entry into the pulmonary circulation (ostium). **(B)** CDI is used to demonstrate the presence of continuous flow from the PDA causing turbulence in the pulmonary trunk during the entire cardiac cycle (i.e., during systole and diastole). Note the prominent CDI mirror image artifact (MIA). **(C)** CWD is used to confirm the orientation of the PDA and to measure the pressure gradient between the PDA and the main pulmonary artery. The maximal PDA shunting velocity is close to 5 m/s, which is consistent with a normal aortic-to-pulmonic gradient of 100 mmHg. **(D)** The left cranial view is often the best view to measure the PDA ostium, which is especially important when planning minimally invasive closure of the PDA. **(E, F)** PDA causes LV dilation due to volume overload.

Vet-ebooks.com

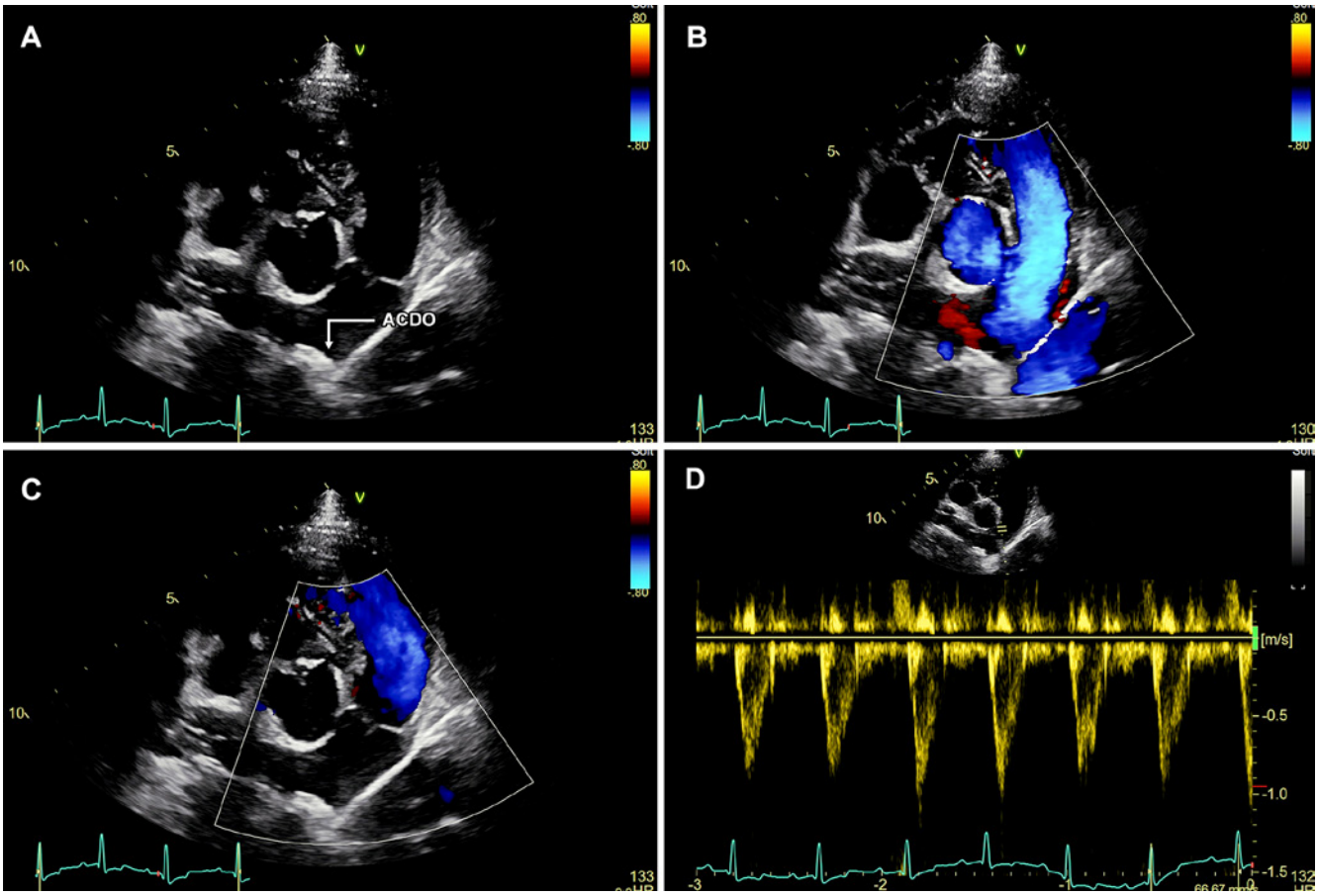


Figure 6.47. Left-to-right shunting patent ductus arteriosus (PDA) closed with an Amplatz Canine Duct Occluder (ACDO). (A) The ACDO is seen at the location of the PDA ostium. The two short parallel hyperechoic lines correspond to the two discs of the ACDO. **(B, C)** There is no visible residual flow through the ductus arteriosus in systole **(B)** and diastole **(C)**. **(D)** Systolic pulmonic flow is laminar with a normal velocity.

size of the defect approximates a single ventricle with pressure equilibration between the right and left sides (e.g., <3 m/s).

The most common form of VSD, named perimembranous VSD, is caused by a defect in the membranous septum located at the cranial aspect of the tricuspid valve and separating aortic from tricuspid valve (Figure 6.51). Perimembranous VSDs result in fibrous continuity of the aortic and tricuspid valve. Muscular VSDs are completely surrounded by muscular septum. Juxtaarterial VSDs (also named outlet VSDs or doubly committed VSDs) are located in the outlet septum immediately below the pulmonic and aortic valves resulting in fibrous continuity of the two valves. The term "malalignment VSD" indicates that the aorta is mispositioned over the plane of the IVS, as seen with tetralogy of Fallot (TOF) (Figure 6.52).

Miscellaneous and Complex Congenital Disease

A wide range of cardiac congenital defects and combination defects is possible, with varying severity and clinical importance of each. Echocardiographic principles are applied in each case to determine the presence of connections between vessels and chambers and pressure gradients between the connections. Diagnosis of complex congenital heart disease is one of the most challenging applications of echocardiography and is largely beyond the scope of this chapter.

Tetralogy of Fallot (TOF)

TOF is the most common cyanotic congenital cardiac disease in small animals but is part of a wide spectrum of conditions called conotruncal defects. TOF is named

Vet-ebooks.com

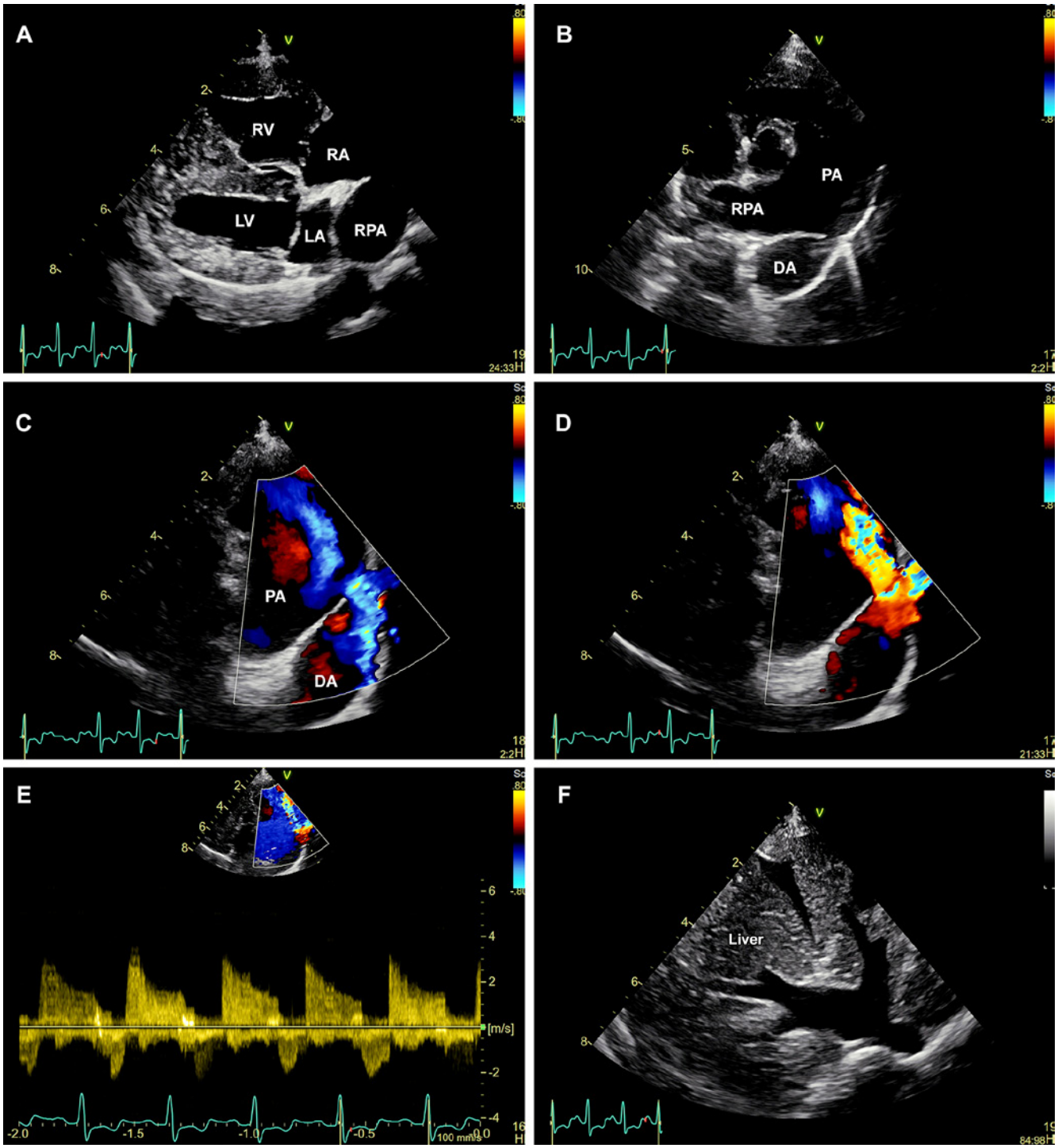


Figure 6.48. **Reverse patent ductus arteriosus (reverse or right-to-left PDA). (A)** The RPS LAx image depicts marked RV hypertrophy and moderate right atrial dilation. The LV appears somewhat small and thick-walled (pseudohypertrophy) because of volume underload and compression by the RV. A cross section of the right pulmonary artery (RPA) is seen. The RPA is severely dilated. **(B)** The RPS SAx image at the PV level shows marked dilation of the pulmonary trunk and RPA. A large PDA is seen. **(C, D)** CDI shows right-to-left shunting during systole **(C)** and left-to-right shunting during diastole **(D)**. Reverse PDA is usually characterized by bidirectional blood flow through the PDA. **(E)** CWD confirms the presence of bidirectional flow through the PDA. Note that the velocity of blood shunting left-to-right is lower than normally expected due to pulmonary arterial hypertension. **(F)** This image shows hepatic congestion and ascites secondary to increased right-sided pressures.

Vet-ebooks.com

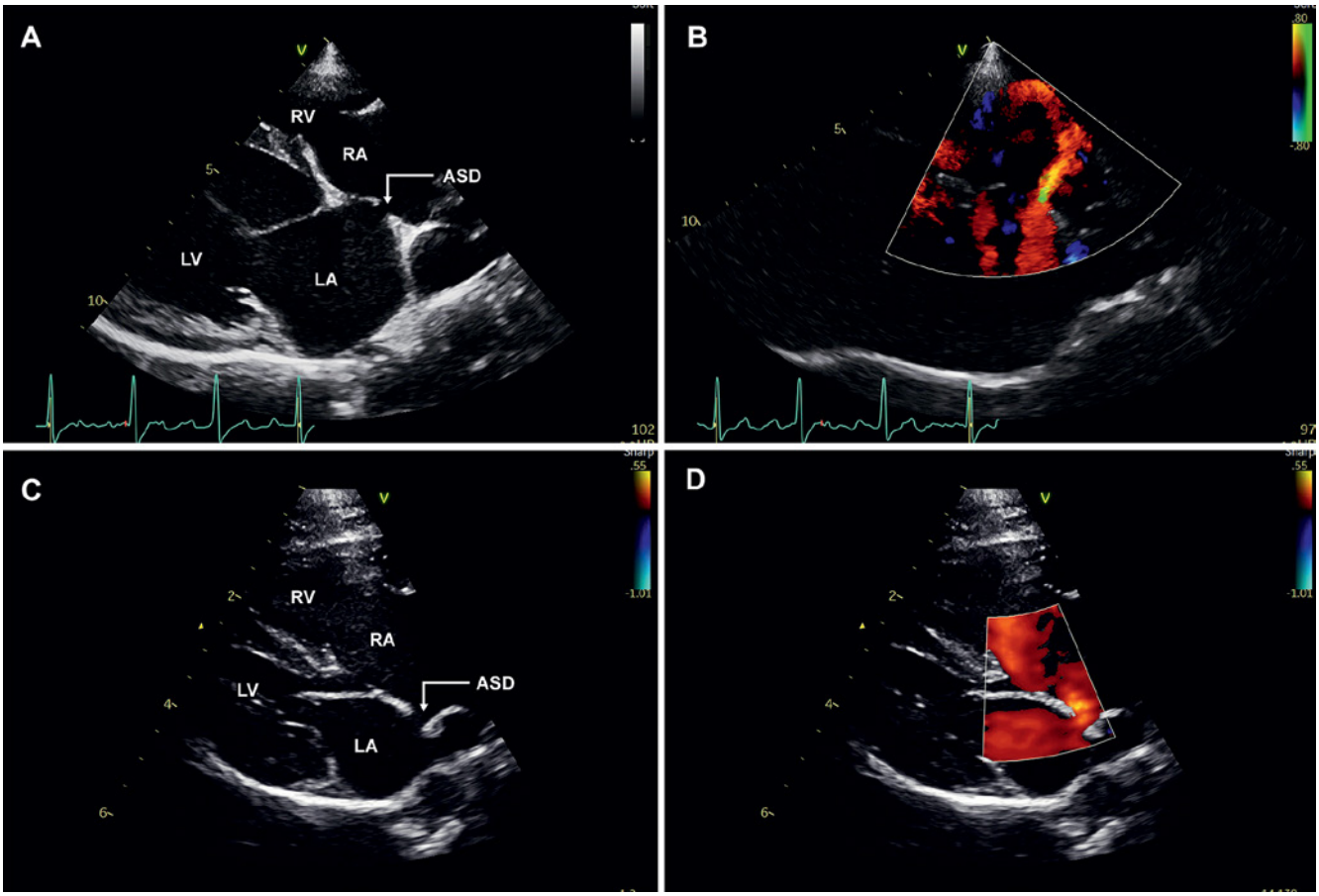


Figure 6.49. **Ostium secundum atrial septal defect (ASD) in a dog and sinus venosus ASD in a cat. (A)** RPS LAx 2D image from a dog with a small ostium secundum located in the mid-interatrial septum. **(B)** CDI shows that blood is shunting from the left atrium into the right atrium. **(C)** RPS LAx 2D image from a cat with a small sinus venosus ASD located in the dorsal interatrial septum. This cat also had a ventricular septal defect and enlargement of the right atrium and ventricle is present. **(D)** CDI shows that blood is shunting from the left atrium into the right atrium.

after the French pathologist who described the four components of this condition: 1. A large malalignment VSD, 2. Overriding (malalignment) of the aortic root, 3. PS, 4. Secondary RV hypertrophy (Figure 6.52).

Cor Triatriatum

Cor triatriatum is an unusual condition characterized by the presence of an accessory atrial chamber, separated from the atrium proper by a perforated membrane partition (Figure 6.53). Blood received by the accessory chamber must flow through the perforation, which may be restrictive. A significant pressure gradient across the membrane implies congestion of tissues and organs with venous drainage to the accessory chamber. Cor triatriatum may occur in the right atrium (cor triatriatum dexter) or the left (cor triatriatum sinister).

Peritoneal-pericardial Diaphragmatic Hernia

Peritoneal-pericardial diaphragmatic hernia, which implies a communication between the pericardial space and the abdominal cavity, is probably related to abnormal fetal development of the septum transversum or pleuroperitoneal folds. The condition is most common in cats and may be diagnosed subsequent to the incidental discovery of an enlarged cardiac silhouette on thoracic radiography. Echocardiography reveals a range of abdominal organs within the pericardial space. Often, cardiac function is little affected, and determining whether clinical signs are related to the hernia may be difficult (Figure 5.58 in Chapter 5).

Acquired Heart Disease

Acquired Valvular Heart Disease

Degenerative Valve Disease

Degenerative valve disease, also called myxomatous valve disease or endocardiosis, is the most common acquired heart disease of dogs and is particularly

Vet-ebooks.com

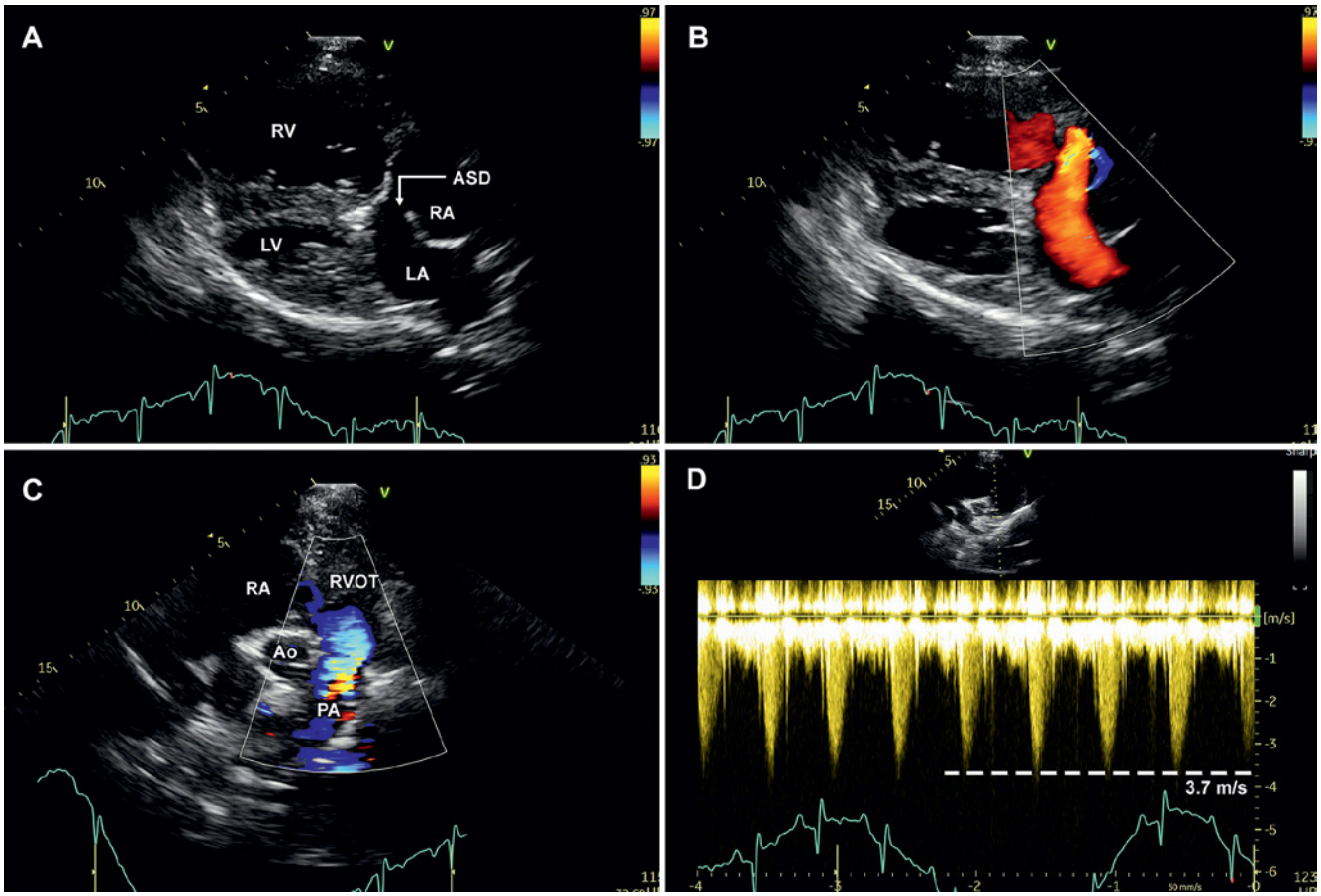


Figure 6.50. **Large ostium primum atrial septal defect (ASD) in a dog. (A, B)** RPS LAx 2D and CDI images from a dog with a large left-to-right shunting ostium primum ASD. The defect is located just above the atrioventricular valves. The mitral valve annulus and tricuspid valve annulus are located along the same anatomical plane which is a feature of atrioventricular septal defects (the tricuspid valve annulus is normally slightly more apical than the mitral valve annulus). The right atrium and ventricle are severely dilated. The dorsal portion of the interatrial septum is deviated toward the left atrium likely due to volume overload and dilation of the right atrium. The left ventricle appears small due to the large volume of blood shunting to the right instead of flowing into the left ventricle. **(C, D)** There is increased blood flow velocity in the pulmonary artery due to pulmonary overcirculation ("relative pulmonic stenosis"). The pulmonic valve is morphologically normal.

prevalent among smaller breeds. The mitral valve is most often affected (degenerative mitral valve disease, DMVD), but the tricuspid valve may be affected concurrently and/or preferentially in some individuals. Exemplary 2D echocardiographic findings of DMVD include thickening, increased echogenicity, and prolapse of the valvular leaflets resulting in valvular regurgitation (MR) seen using CDI. Characteristic remodeling changes secondary to MR include progressively increasing LA and diastolic LV internal dimensions (Figure 6.54), with preserved end-systolic LV internal dimension in many cases, which coincides with a normal to increased FS. Some dogs, however, particularly larger breeds, may have concurrent systolic dysfunction secondary to DMVD (Borgarelli et al. 2004). Although advanced Doppler techniques can be utilized to evaluate ventricular diastolic function and filling pressures (Bonagura and Schober 2009), interpretation of these methods may be rendered ambiguous by age-related changes in diastolic function and the influence of increased preload on most of the Doppler parameters. Diastolic functional class, IVRT, and E:IVRT are the best echocardiographic predictors of left-sided CHF in dogs with DMVD (Schober et al. 2010, 2011).

Echocardiographic techniques for the evaluation of MR range from qualitative measures to semiquantitative. One of the simplest, albeit subjective, methods is to evaluate the MR jet size by visual inspection on a color Doppler image. Alternatively, a ratio can be calculated (i.e., estimated jet area divided by LA area) to provide a semiquantitative estimate of MR severity. Unfortunately, the extent of the MR jet is highly dependent on color Doppler control settings, jet

Vet-ebooks.com

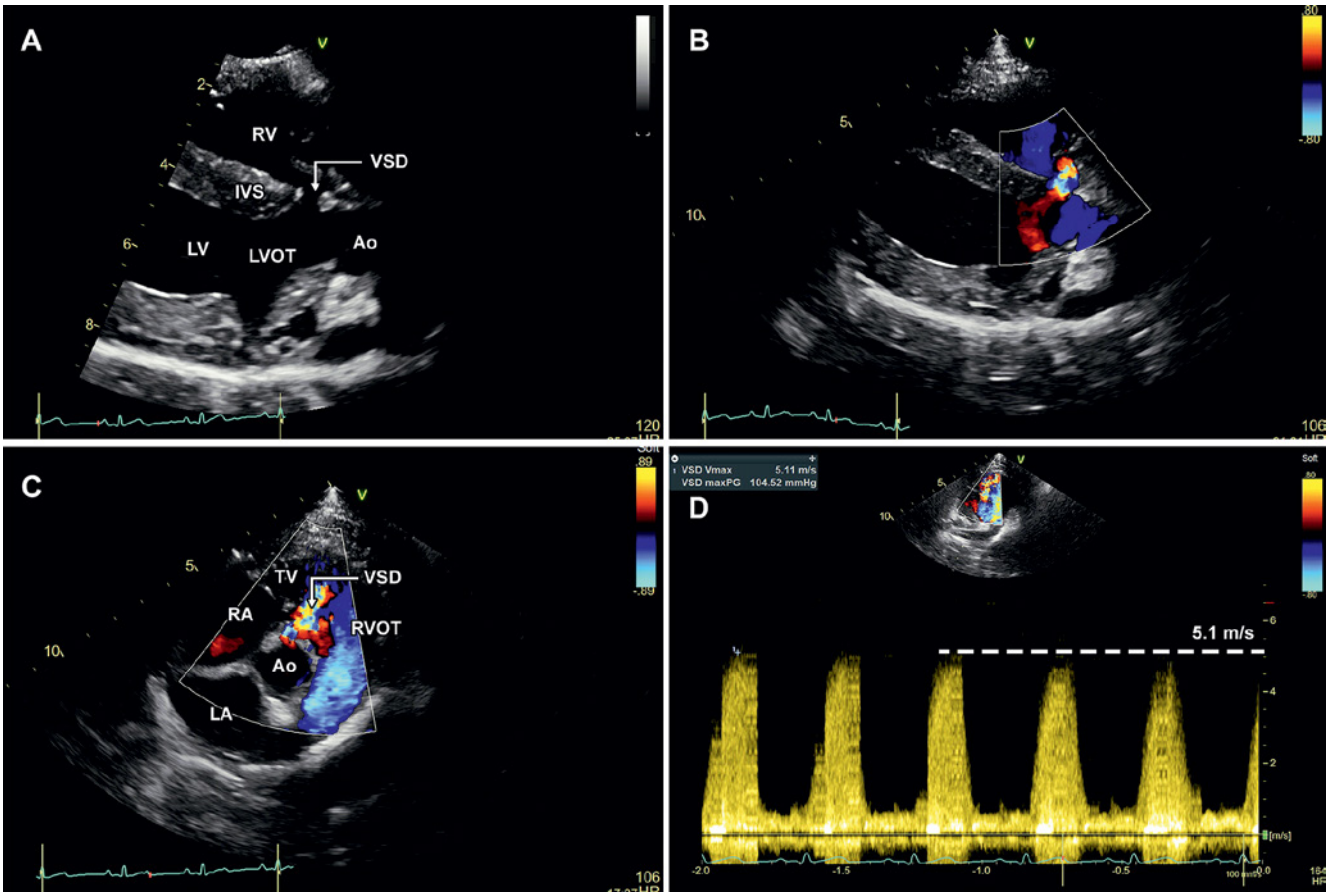


Figure 6.51. Perimembranous ventricular septal defect (VSD) in a dog. RPS LAx 2D **(A)** and CDI **(B)** images from a dog with a perimembranous VSD. An echo dropout is seen immediately proximal to the aortic valve, adjacent to the septal leaflet of the tricuspid valve. A turbulent mosaic color flow pattern is visible in the RV. **(C)** RPS SAx CDI image showing the same defect with left-to-right shunting. **(D)** Blood flow velocity across the VSD is high at 5.1 m/s due to the expected high-pressure gradient of approximately 100 mmHg between the two ventricles. This VSD is named restrictive.

and chamber geometry, and ambient hemodynamic conditions. Additionally, the regurgitation jet that exists in three dimensions is often poorly assessed by 2D imaging. For practical purposes, the degree of LA and LV dilation gives a good assessment of MR severity (in most cases), while also reflecting chronicity. Note that dogs with DMVD and a sudden increase in MR volume due to a ruptured chordae tendineae may have smaller LA and LV dimensions than expected since those chambers did not have time to stretch.

The American College of Veterinary Internal Medicine (ACVIM) consensus guidelines separate DMVD into four stages (Keene et al. 2019). Echocardiography plays an important role in differentiating stage B1 (asymptomatic DMVD dogs without evidence of cardiac remodeling/enlargement) and stage B2 (asymptomatic DMVD dogs with sufficiently severe MR to have caused left atrial and left ventricular enlargement) (Figure 6.54). Practically, the cutoff values for identifying stage B2 dogs include those likely to benefit from pimobendan therapy (Boswood et al. 2016). The criteria used in the aforementioned study are presented in Table 6.8.

Infective Endocarditis

Infective endocarditis is an unusual, but potentially devastating, consequence of bacteremia and/or sepsis most commonly affecting medium-sized and large dogs. Lesions most typically involve the aortic and/or mitral valves but can also extend to surrounding myocardial tissue, with possible periannular abscessation (Figure 6.55).

Nonspecific echocardiographic signs include thickened hyperechoic aortic and mitral valve leaflets, chordal rupture, and regurgitation across the affected valve(s). Thrombosis of the damaged valve can lead to the presence of a thrombus that might oscillate when

Vet-ebooks.com

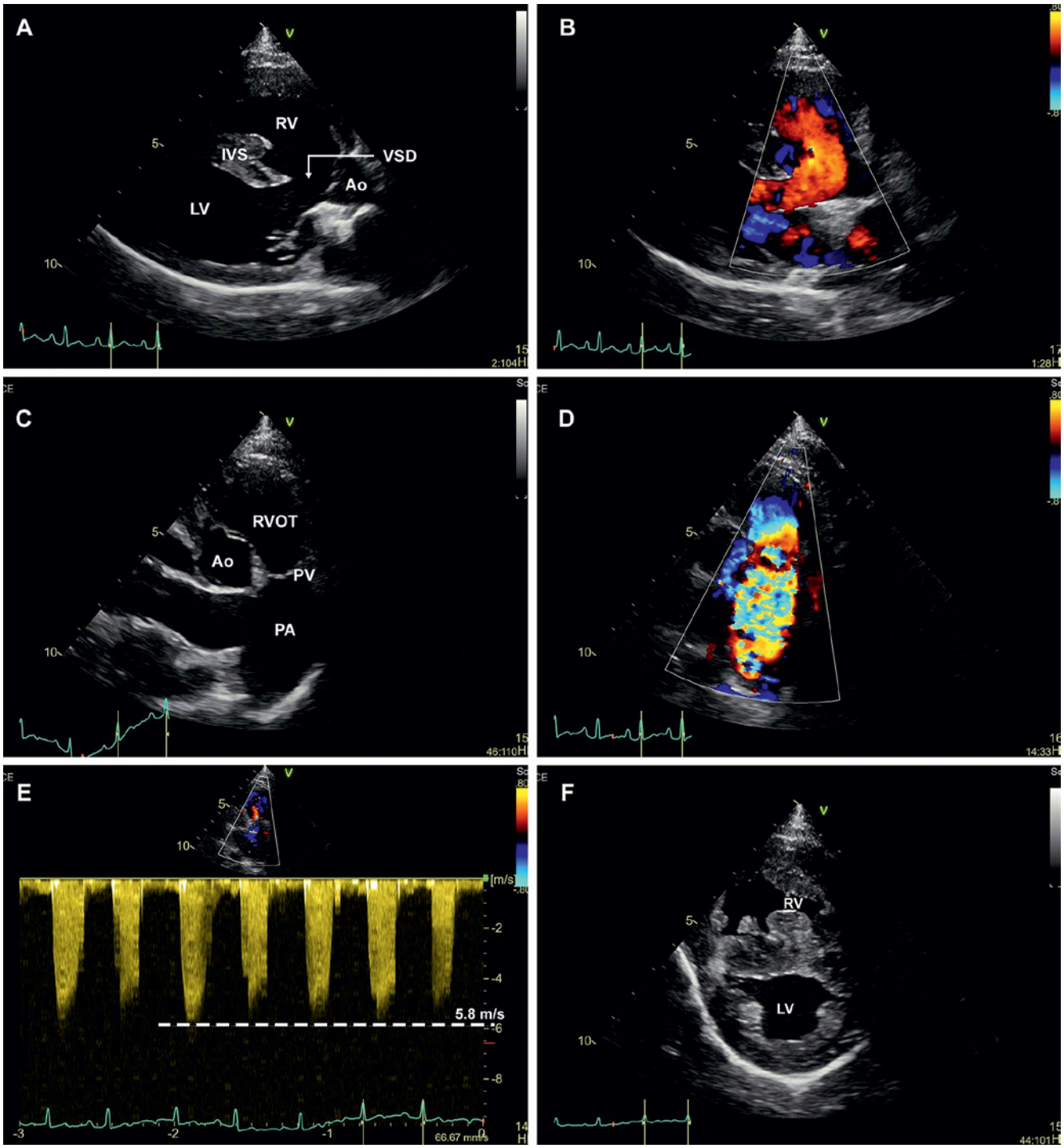


Figure 6.52. **Tetralogy of Fallot (TF) in a French Bulldog. (A, B)** RPS 2D and CDI LAx images showing a large VSD and an overriding aortic root that appears to straddle the interventricular septum. **(C–E)** RPS SAx images at the level of the pulmonic valve. PS is present. In this case, the PS is severe and mostly valvular due to fused pulmonic cusps. TOF is often associated with infundibular narrowing (not present in this case). **(F)** RPS 2D SAx transventricular image showing marked RV concentric hypertrophy due to severe PS.

Vet-ebooks.com

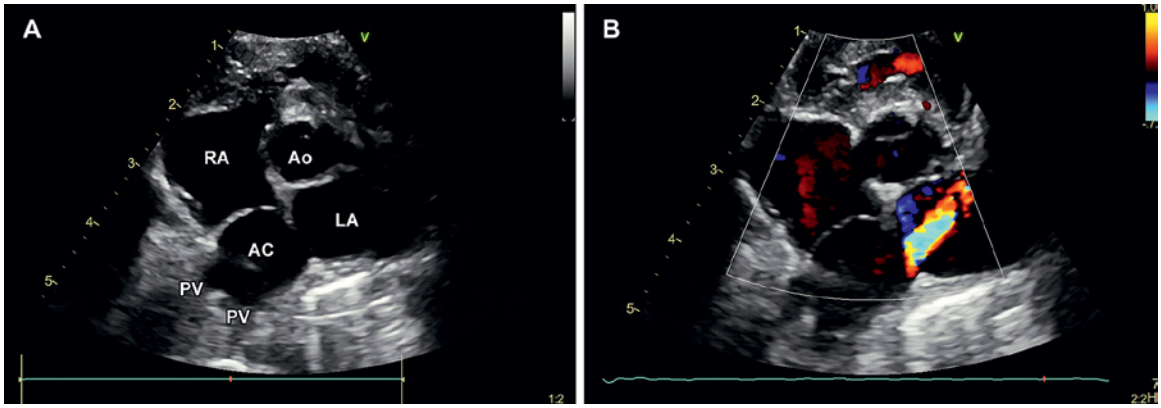


Figure 6.53. **Cor triatriatum sinister in a cat. (A)** RPS SAx 2D image of cor triatriatum sinister in a young cat. An accessory chamber (AC) is separated from the left atrium by a restrictive membrane. The AC receives the pulmonary veins. **(B)** CDI shows turbulent flow from the AC into the left atrium through the restrictive membrane.

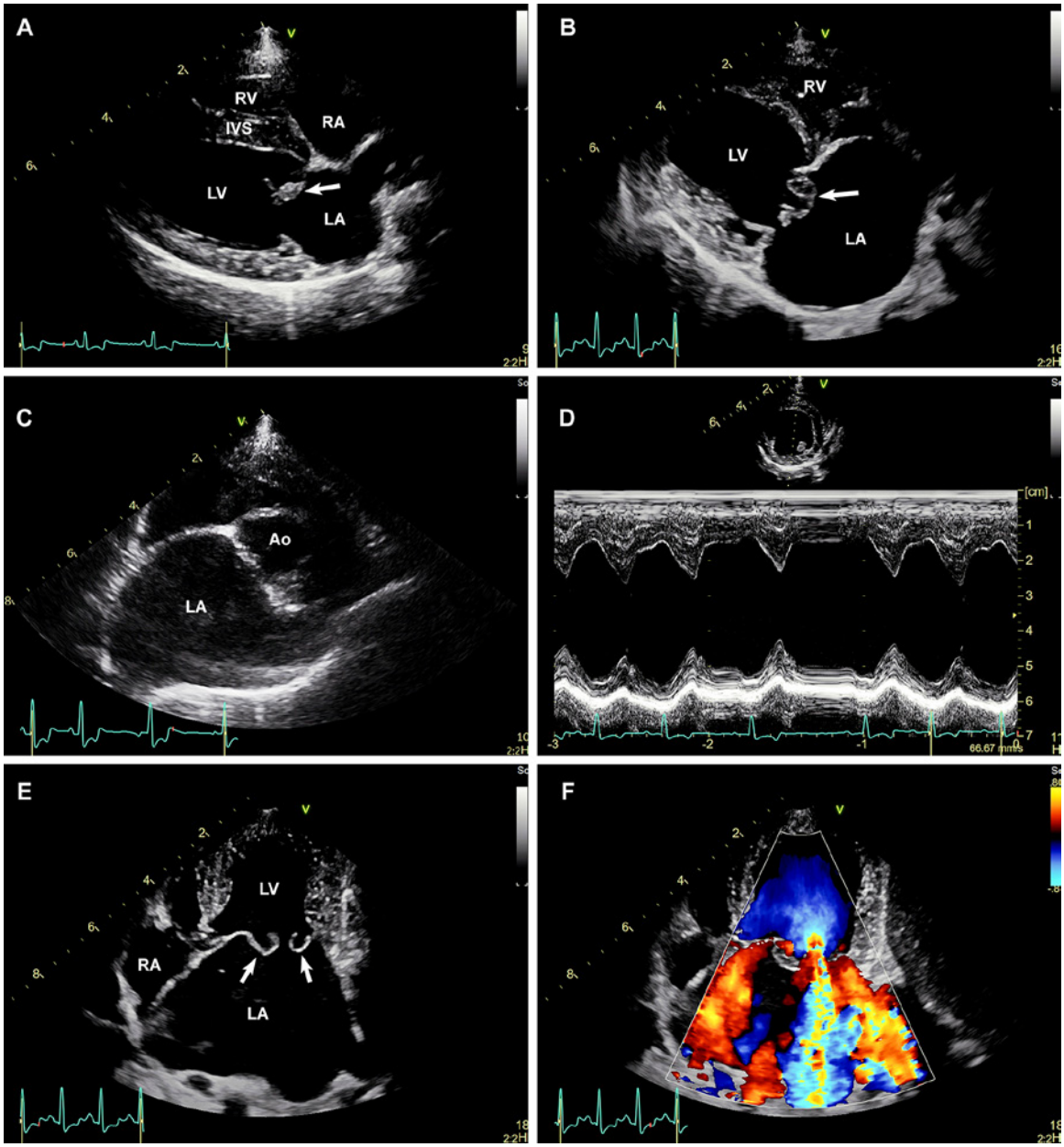


Figure 6.54. **Degenerative mitral valve disease (DMVD).** (for full caption, see facing page)

Vet-ebooks.com

Table 6.8
Inclusion criteria for enrolment in the EPIC study

Age	≥6 years
Weight	4.1–15 kg
Murmur	Systolic mitral murmur ≥ grade 3/6
Vertebral heart score	>10.5
LA/Ao	≥1.6
LVIDdN	≥1.7

LVIDdN, left ventricular internal diameter in diastole, indexed to body weight (see Assessment of cardiac size). Adapted from Boswood et al. (2016).

the valve is open. The diagnosis of endocarditis might be difficult if lesions are small or involve only the mitral valve of dogs predisposed to DMVD. The use of the zoom function may be helpful in identifying small or subtle vegetative lesions that can be visualized as focal elevations located on the atrial surface of the valve. Endocarditis echocardiographic follow-up may be useful in these cases by revealing rapid valvular changes.

Large vegetative lesions may cause valvular stenosis or insufficiency, or both. Endocarditis is the most likely cause of substantial acquired aortic insufficiency in dogs. The volume overload (due to insufficiency or regurgitation of either the mitral valve or aortic valve) or pressure overload (AS) is often acute. Hence, cardiac remodeling may not be apparent even though marked functional compromise is present. Doppler echocardiography enables confirmation and quantification of the valvular dysfunction.

Myocardial Disease

Dilated Cardiomyopathy Phenotype

Cardinal echocardiographic features of a DCM phenotype include chronically increased ventricular internal dimensions and depressed systolic function, commonly identified as reduced FS and EF (Figure 6.56), with the LV more severely affected than the RV in many cases. Other findings include increased EPSS and decreased SI (SI < 1.65) (Holler and Wess 2014). As the disease progresses, with further impairment of systolic and diastolic function, atrial dilation occurs.

Doppler studies most commonly demonstrate functional atrioventricular valve regurgitation due to dilation of the mitral and/or tricuspid annuli (Figure 6.56). Typically, MR in DCM is not as voluminous as in DMVD, but both diseases may occur concomitantly in some individuals and produce a mixed echocardiographic pattern.

Genetic or familial DCM is often suspected when the above findings are identified in a breed known to have a high prevalence of disease, including the Doberman Pinscher, Great Dane, and Irish Wolfhound, among others (Wess 2022). Differential diagnoses of primary DCM include tachycardia-induced cardiomyopathy or nutritional causes (such as in dogs eating a grain-free legume-based diet or with taurine deficiency, Figure 6.57), both of which may be reversible, as well as end-stage DMVD, myocarditis, or toxic cardiomyopathy (such as doxorubicin toxicity). Systemic conditions such as severe hypothyroidism can also lead to a DCM phenotype.

Arrhythmogenic Right Ventricular Cardiomyopathy

As the name implies, the pathology of arrhythmogenic RV cardiomyopathy (ARVC) is initiated in the right heart but may cause global cardiac disease (Baumwart et al. 2005). ARVC is common in Boxers as a familial disease (previously termed Boxer cardiomyopathy). The majority of affected dogs demonstrate ventricular arrhythmias without demonstrating echocardiographic changes (Figure 6.58). A small percentage of affected dogs will have a DCM morphology on echocardiogram and can experience right-sided, left-sided, or biventricular CHF (Meurs 2017). ARVC may also be seen in cats with otherwise unexplained RV enlargement (Harvey et al. 2005) (Figure 6.59).

Figure 6.54. Degenerative mitral valve disease (DMVD). (A) This RPS LAx view in mid-diastole demonstrates characteristic thickening of the AML (arrow) but with normal LA and LV size (ACVIM stage B1). **(B)** This RPS LAx view in early systole demonstrates dilation of the LV and LA along with thickening and prolapse of the AML, which appears as a displacement into the LA (arrow). DMVD stage B2 is characterized by dilation of the LA and LV, as seen in **(C)** (SAx view at the level of the Ao root demonstrates dramatic LA dilation) and **D** (M-mode through the LV shows LV chamber dilation). **(E)** This apical four-chamber view demonstrates dramatic LA dilation and marked prolapse of both anterior and posterior mitral leaflets (arrows) in a dog with advanced DMVD and CHF (ACVIM stage D). **(F)** This apical four-chamber view CDI image taken in systole demonstrates marked MR.

Vet-ebooks.com

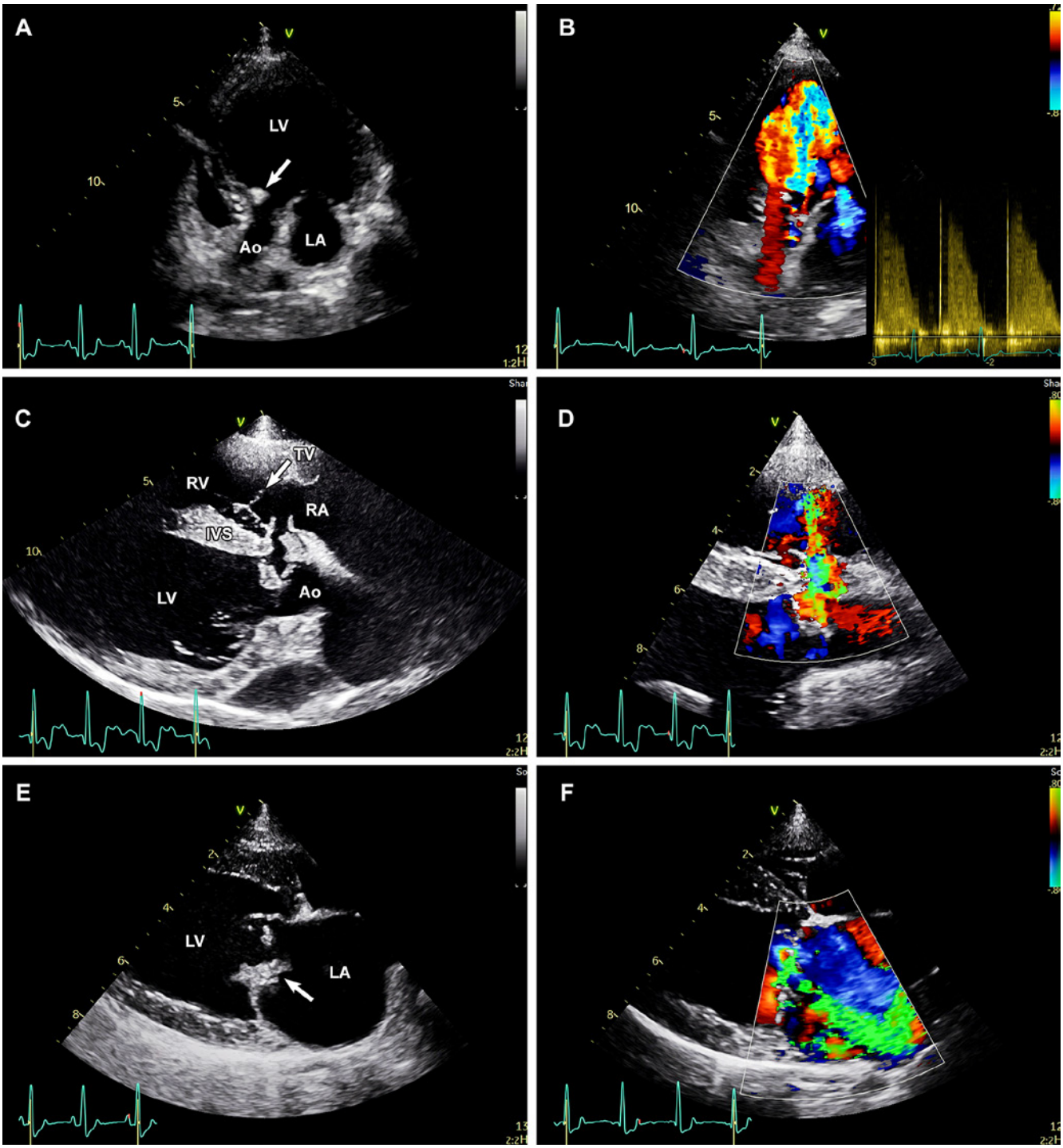


Figure 6.55. Endocarditis of the aortic valve (A–D) and mitral valve (E–F). Apical LVOT view **(A, B)** and RPS LAx view **(D–G)** images from dogs with aortic endocarditis. **(A, B)** A hyperechoic vegetative lesion on the right coronary cusp of the aortic valve (arrow) and marked aortic insufficiency are seen. There is also LV dilation. In severe cases, abscessation or even rupture of adjacent cardiovascular structures may occur, as in **(C, D)** there is a rupture of the right sinus of Valsalva resulting in an acquired fistula from the aorta to the right atrium secondary to aortic endocarditis. Continuous (systolic and diastolic) left-to-right flow occurred across this defect because of the persistent pressure gradient between the aorta and right atrium. **(E, F)** A large vegetative lesion is seen on the posterior mitral valve leaflet (arrow), resulting in moderate eccentric MR.

Vet-ebooks.com

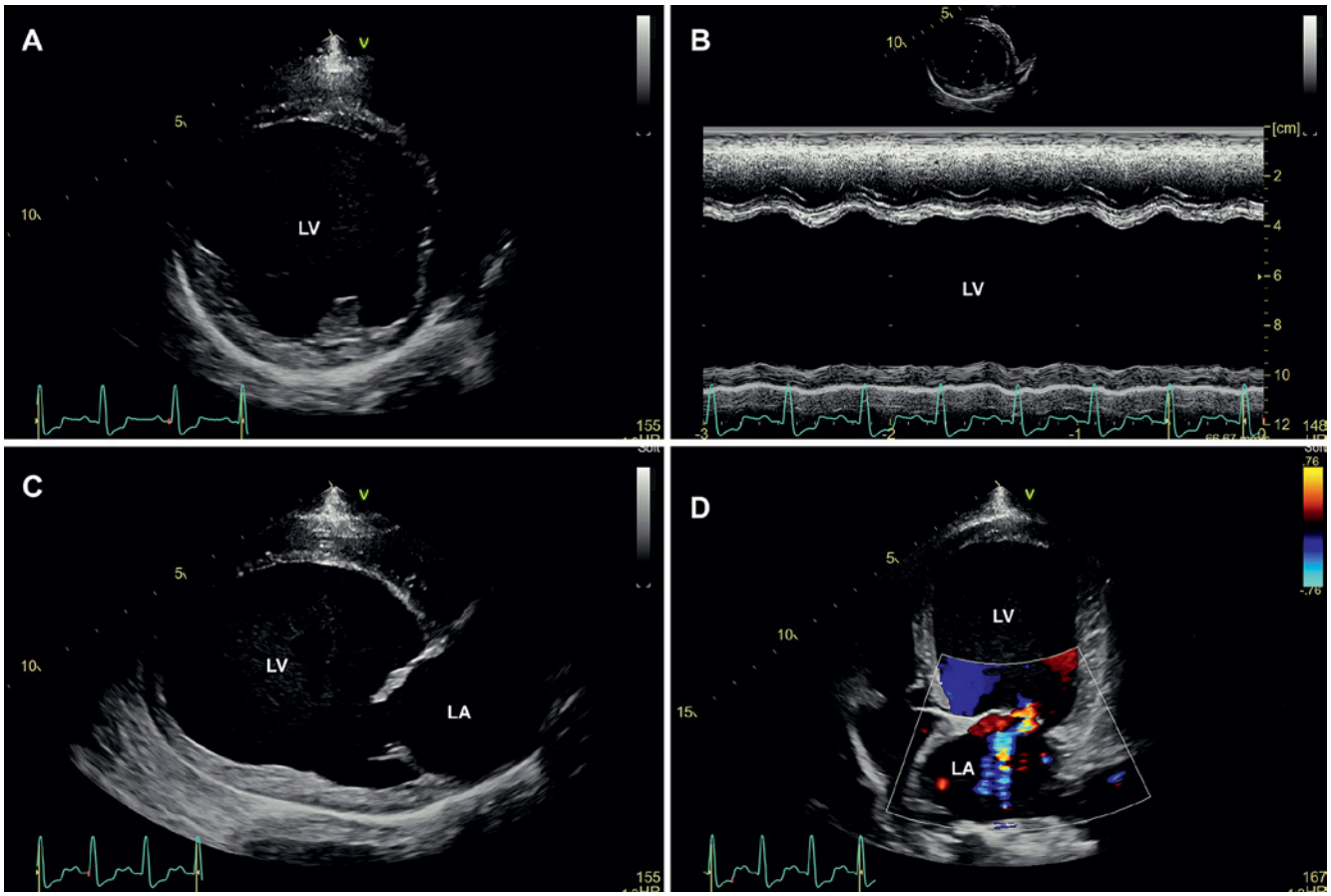


Figure 6.56. **Dilated cardiomyopathy (DCM) in a dog. (A)** RPS SAx view of the LV at the papillary muscle level in late diastole showing a dilated LV. At the same level, an M-mode recording (**B**) demonstrates a markedly reduced fractional shortening. **(C)** RPS LAx four-chamber view demonstrating marked LV dilation. **(D)** Functional AV valve regurgitation is often centrally directed, secondary to annular dilation, as seen in this apical four-chamber view CDI image showing MR.

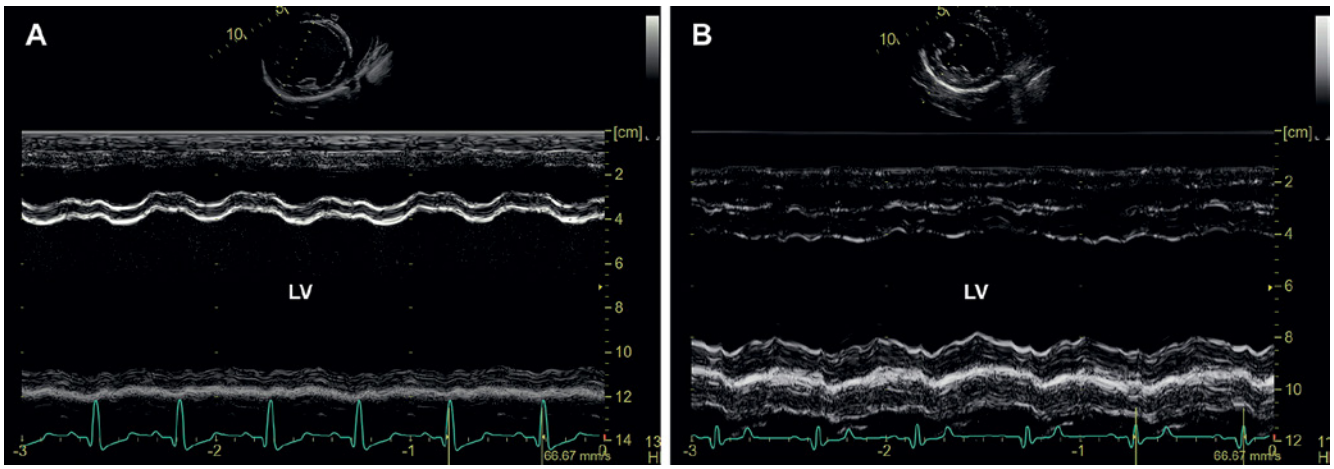


Figure 6.57. **Suspected nutritional DCM in a young German Shorthaired Pointer fed a grain-free legume-based diet. (A)** M-mode demonstrating marked LV dilation and reduced systolic function. **(B)** The same dog 32 months later, following standard treatment for CHF and a diet change. The dramatic improvement in LV size and systolic function is beyond what would be expected from medications alone.

Vet-ebooks.com

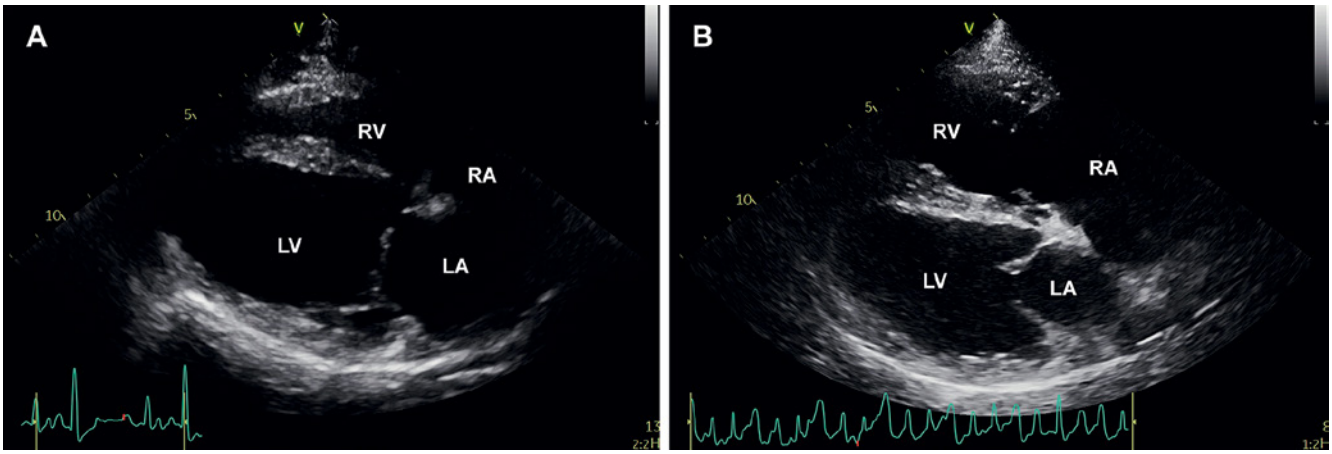


Figure 6.58. **Arrhythmogenic cardiomyopathy (ARVC) in a Boxer. (A)** RPS LAx four-chamber view in end-diastole showing normal chamber dimensions and function. There are isolated premature ventricular complexes on the simultaneous ECG (*). **(B)** The same dog 7 months later demonstrating dilation of the RA and RV. Note the simultaneous ECG showing a sinus tachycardia with motion artifact (panting).

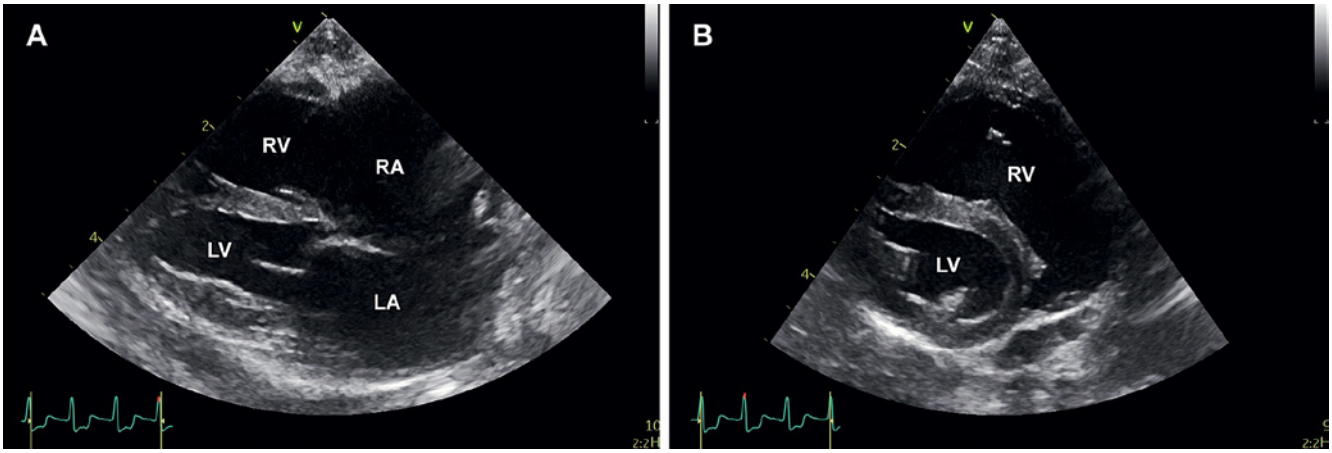


Figure 6.59. **Arrhythmogenic right ventricular cardiomyopathy (ARVC) in a cat.** RPS LAx **(A)** and SAx **(B)** views demonstrate marked dilation of the RA and RV chambers. The LA is mildly dilated as well.

Hypertrophic Cardiomyopathy Phenotype

HCM, a primary myocardial disorder, is the most common acquired heart disease in cats and is reported as a rare condition in dogs. Echocardiographic abnormalities caused by feline HCM relate principally to myocardial hypertrophy including increased wall thickness and diastolic dysfunction (Figure 6.60). Progressive diastolic dysfunction is commonly accompanied by progressive LA dilation. Although systolic function is typically normal to hyperdynamic in the early stages of the disease, cats with end-stage HCM may exhibit progressive systolic dysfunction and thinning of LV wall probably secondary to myocardial ischemia and fibrosis (Cesta et al. 2005).

M-mode echocardiography has traditionally been used to measure wall thickness; however, 2D imaging may be preferable as it allows measurement of the LV wall in multiple locations and prevents inadvertent measurement of papillary muscles. For the majority of cats, an end-diastolic LV wall or IVS thickness of ≥6.0 mm is consistent with hypertrophy, although body size, hydration status, and heart rate will influence wall thickness (Luis Fuentes et al. 2020).

SAM of the mitral valve may be seen on M-mode and/or 2D imaging, resulting in dynamic LVOT obstruction. HCM with dynamic LVOT obstruction is termed hypertrophic obstructive cardiomyopathy (HOCM) (Figure 6.61). While SAM is a common source of outflow obstruction, hypertrophy of papillary muscles or muscular trabeculae may cause intraventricular obstruction, observed as a turbulent systolic jet emanating from within the ventricular

Vet-ebooks.com

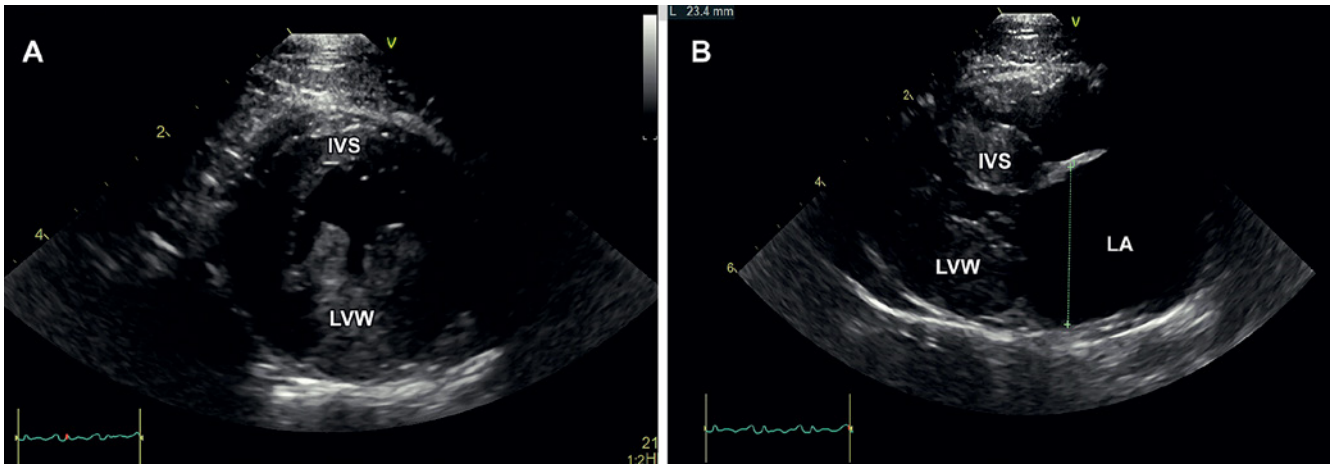


Figure 6.60. **Hypertrophic cardiomyopathy (HCM) in a cat. (A)** RPS SAx view at the papillary muscle level demonstrating hypertrophy of the LV free wall (LVW) and thickened papillary muscles. **(B)** RPS LAx four-chamber view demonstrating hypertrophy of the interventricular septum (IVS) and left ventricular free wall (LVW) along with marked LA dilation.

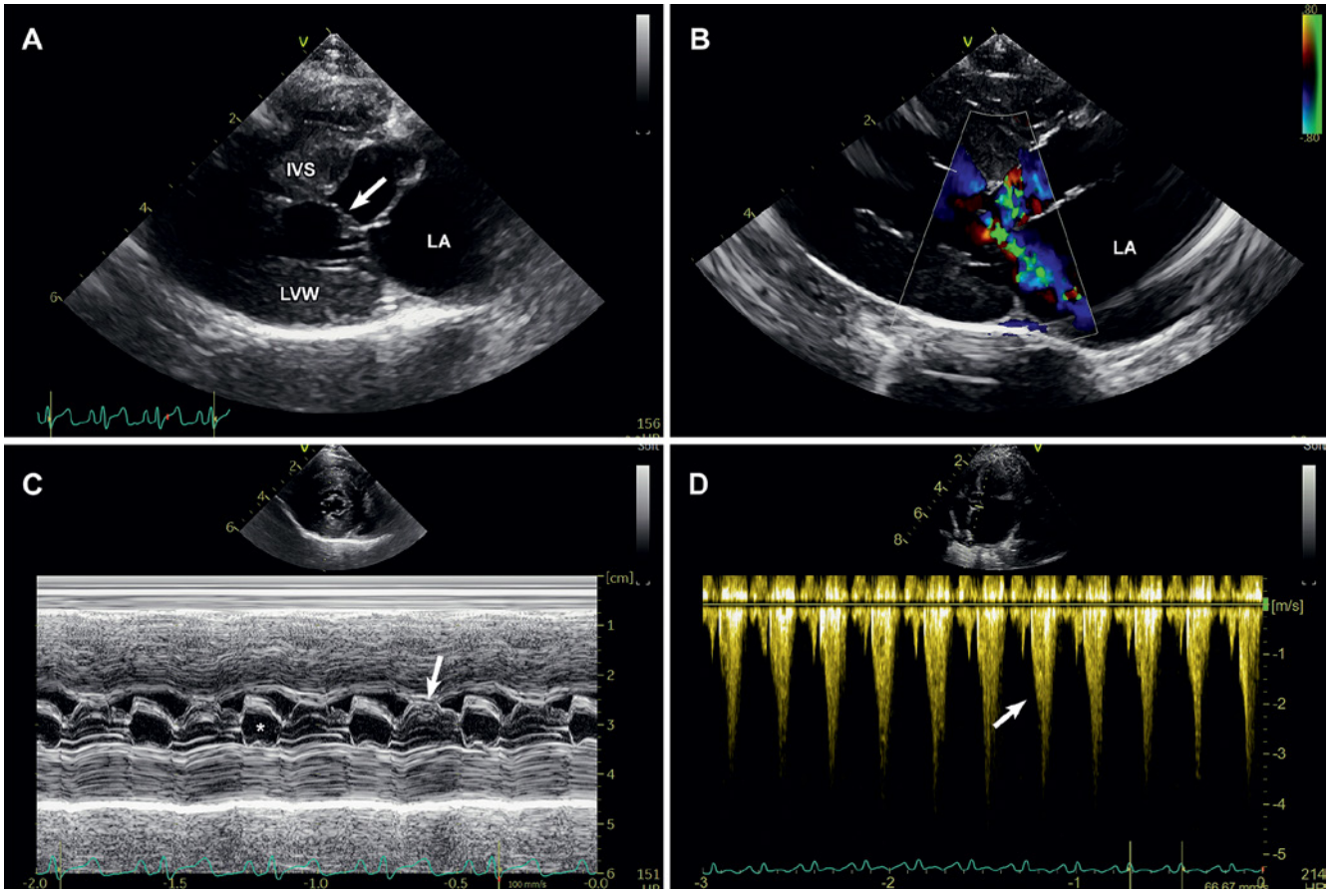


Figure 6.61. **Dynamic LVOT obstruction with HCM. (A)** RPS LAx view of the LVOT demonstrating systolic anterior motion (SAM) of the MV (arrow); the MV is displaced into the LVOT and obstructs systolic LV outflow. There is also thickening of the IVS and LVW. **(B)** This RPS LAx color Doppler image displays the functional result of SAM, including both intra-aortic turbulence, caused by dynamic obstruction, and MR due to or accentuated by the SAM of the AML leaflet. There is marked LA dilation. **(C)** M-mode has high temporal resolution, demonstrating SAM of the AML in systole (arrow). The (*) shows normal opening of the MV leaflets in diastole. **(D)** This apical LVOT CWD recording depicts increased peak velocity and a dagger-shaped velocity envelope. Increasing proximity of the MV to the interventricular septum, beginning at the arrow, causes an abrupt change in the envelope as the degree of obstruction increases.

Vet-ebooks.com

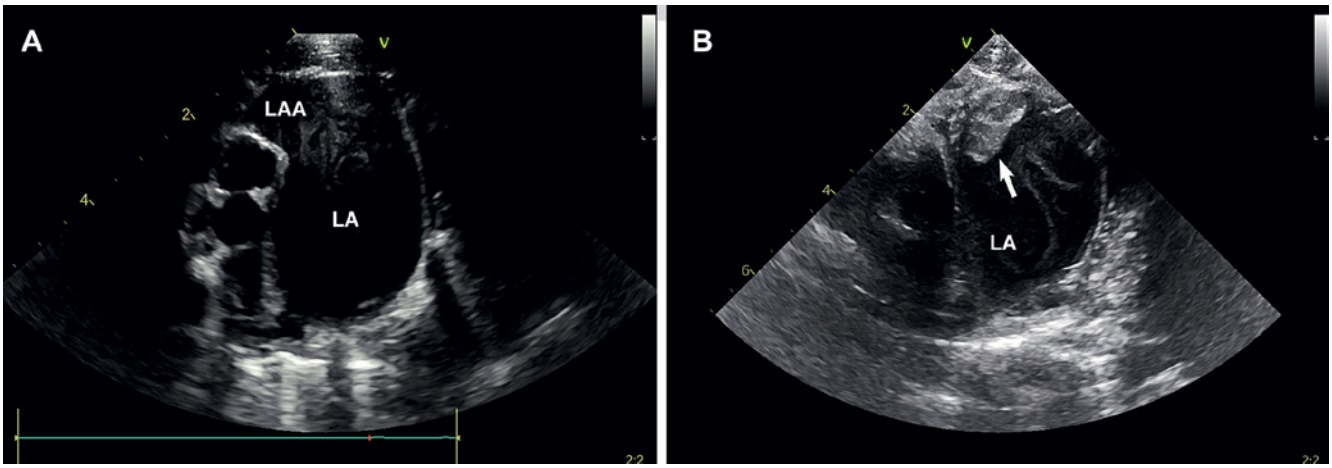


Figure 6.62. Left cranial left auricular appendage (LAA) view showing **(A) spontaneous echo-contrast** ("**smoke**") and **(B)** spontaneous echo-contrast and a **thrombus** in the LAA (arrow).

chamber. Spectral Doppler imaging establishes the outflow tract blood flow velocity associated with an obstruction. The study of mitral inflow velocities may suggest impaired diastolic function and/or elevated filling pressures (see Assessment of diastolic function).

The development of intracardiac thrombi can sometimes be observed echocardiographically, particularly within the LA appendage (Figure 6.62). Stagnant blood flow can manifest echocardiographically as spontaneous echo contrast, the so-called smoke within the dilated left atrium, suggesting a high propensity for thrombus formation.

Important differential diagnoses for the HCM phenotype include hyperthyroidism, systemic hypertension, reduced preload (causing pseudohypertrophy), transient myocardial thickening (Novo Matos et al. 2018), and neoplastic infiltration (Luis Fuentes et al. 2020).

Systemic hypertension (SHT), which may be identified in both dogs and cats, may cause increased LV wall thickness because of left-sided pressure overload. Alterations can resemble mild to moderate HCM in cats and thus require blood pressure determination for differentiation. The aortic root and proximal aorta may be dilated with mild to moderate aortic insufficiency.

Hyperthyroidism is the most common endocrinopathy in cats, and concurrent, nonspecific echocardiographic abnormalities are often observed. LV wall thickening and hypertrophy may occur, resembling HCM of mild to moderate severity (Moise et al. 1986). Tachycardia and increased indices of stroke volume may result, with variable dilation of all cardiac chambers. Atrioventricular valvular regurgitation may accompany the condition if there is sufficient remodeling of the heart to impair valve function, and CHF with pulmonary edema and/or pleural effusion may occur in severe cases. Hyperthyroid cats are occasionally seen with cardiac changes resembling DCM, including marked chamber dilation and depressed FS.

Restrictive Cardiomyopathy and Nonspecific Phenotype

Restrictive cardiomyopathy (RCM) includes a diverse array of diseases that can cause loss of ventricular compliance, restrictive physiology and, ultimately, severe signs of CHF (Fox 2004). The source of restriction in RCM may reside within the myocardium (myocardial form of RCM) or be localized to the endocardium (endomyocardial form of RCM).

Feline myocardial RCM is associated with a restrictive mitral inflow pattern characterized in severe cases by increased velocity of the mitral E wave followed by an abrupt termination of inflow with a shortened deceleration time and increased E:A (Figure 6.63). This pattern may occur in the presence of normal FS and EF and normal wall thicknesses and LV dimensions. Left atrial or biatrial dilation is often dramatic in RCM and predisposes patients to thromboembolic events. The LV endomyocardial form, also known as endomyocardial fibrosis, may include increased endocardial thickness and echogenicity, distortion and dysfunction of the mitral apparatus, or strands of echogenic tissue that bridge the ventricular chamber walls (Figure 6.63). Echocardiographic findings may entail a wide range of features, and a notable fraction of feline cardiomyopathies is not readily classified morphologically (nonspecific phenotype, commonly referred to as unclassified cardiomyopathy).

Vet-ebooks.com

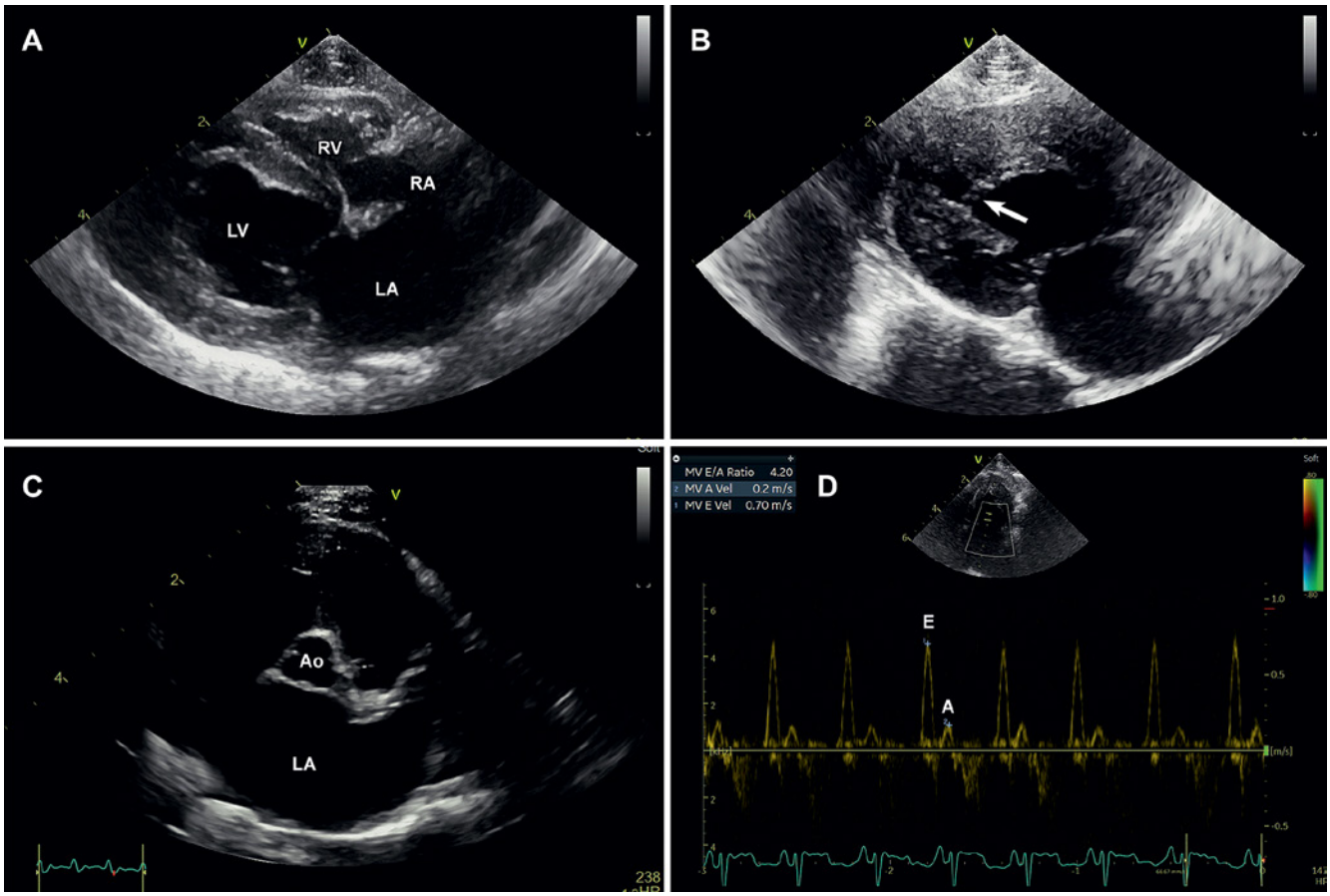


Figure 6.63. Restrictive cardiomyopathy (RCM) in cats. 2D LAx **(A, B)** and SAx **(C)** images and PWD mitral inflow **(D)** recordings from two cats with RCM. There is a dramatic atrial enlargement on the 2D images, particularly of the left atrium **(A–C)**. Nevertheless, wall thicknesses and chamber dimensions of the LV are normal. The cat in **(B)** demonstrates an endocardial bridging scar (arrow), which can be seen in the endomyocardial form of RCM. The PW mitral inflow recording **(D)** demonstrates a restrictive flow pattern. In this example, the E wave of mitral inflow is prominent and the A wave velocity is reduced; atrial contraction causes little additional ventricular filling because of loss of compliance (i.e., restriction).

Pulmonary Hypertension and Heartworm Disease (Dirofilariasis)

Pulmonary hypertension (PHT) refers to elevated pulmonary arterial pressure. In humans, it is defined as an increase in mean PA pressure ≥25 mmHg at rest as assessed by right heart catheterization. Although some specific conditions associated with PHT in animals differ from those encountered in humans, a similar classification has been proposed and updated in a consensus statement of the ACVIM (Reinero et al. 2020). This classification includes six groups, based on the underlying pathological process: (i) PH due to intrinsic pulmonary arterial disease (including idiopathic PHT and congenital systemic-to-pulmonary shunts), (ii) PHT with left-sided heart disease, (iii) PHT associated with lung disease and/or hypoxemia (Figure 6.64), (iv) PHT caused by thrombotic or embolic disease (Figure 6.65), (v) PHT caused by parasitic disease (*Dirofilaria* or *Angiostrongylus*) (Figure 6.66), and (vi) Miscellaneous (due to a mass compressing pulmonary vessels, for example). In groups 1, 3, 4, 5, and 6, PHT usually results from conditions affecting the arterial side of the pulmonary vascular system and is referred to as precapillary PHT. In group 2, PHT originates in the venous side of the pulmonary vascular system and the increase in hydrostatic pressure is then transmitted to the arterial side via the capillaries; this type of PHT is termed postcapillary hypertension.

Doppler echocardiography is essential to identify and quantify PHT (Figure 6.64). However, echocardiographic findings should always be interpreted within the context of other clinical findings including clinical signs suggestive of PHT. Echocardiography is used to estimate pulmonary

Vet-ebooks.com

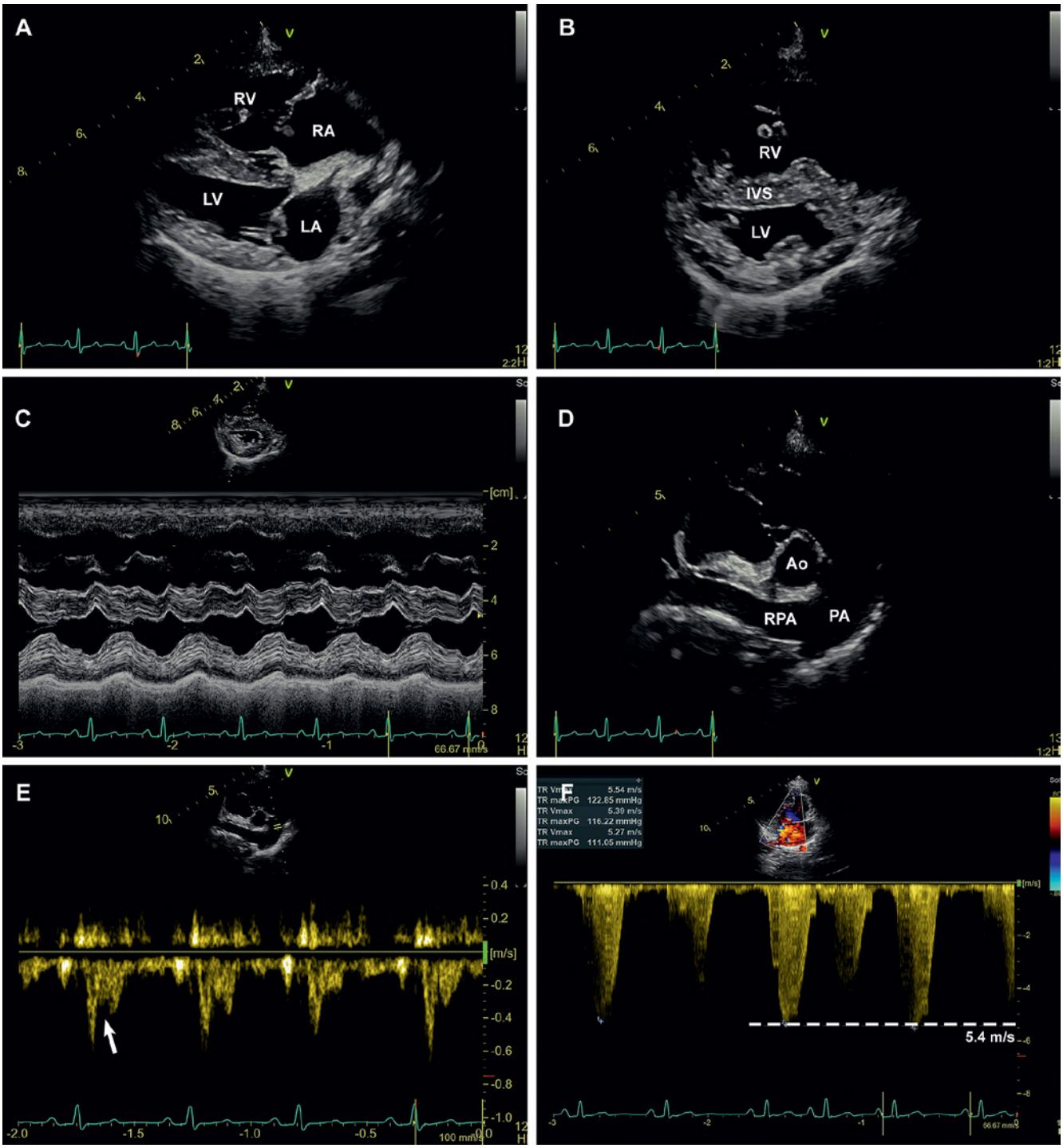


Figure 6.64. **Pulmonary arterial hypertension in a dog with chronic respiratory disease. (A)** This RPS LAx 2D image depicts RV dilation, RA dilation, deviation of the IVS toward the LV, and a small LV chamber. The RV PM is prominent because of hypertrophy, but RV wall thickening is not dramatic. Note that this dog is affected by concurrent degenerative mitral and tricuspid valve disease, but PHT is likely not secondary to left-sided heart disease in the absence of LA dilation. **(B, C)** The RPS SAx 2D image and M-Mode depict RV dilation, flattening of the IVS, and a small LV chamber. **(D)** This RPS SAx 2D image at the level of the pulmonic valve demonstrates dilation of the main PA and RPA; the PA diameter is larger than the Ao diameter. **(E)** PWD pulmonary flow tracing showing a sharp peak with a short acceleration time, followed by a notch (arrow) in the deceleration phase due to flow reversal. **(F)** The TRV is greater than 5.4 m/s, which corresponds to a systolic driving pressure of greater than 115 mmHg. This is consistent with severe PHT. Note that the TR envelope should be fully visible to accurately measure the TRV. Smaller poor quality signals are unreliable and should not be measured.

Vet-ebooks.com

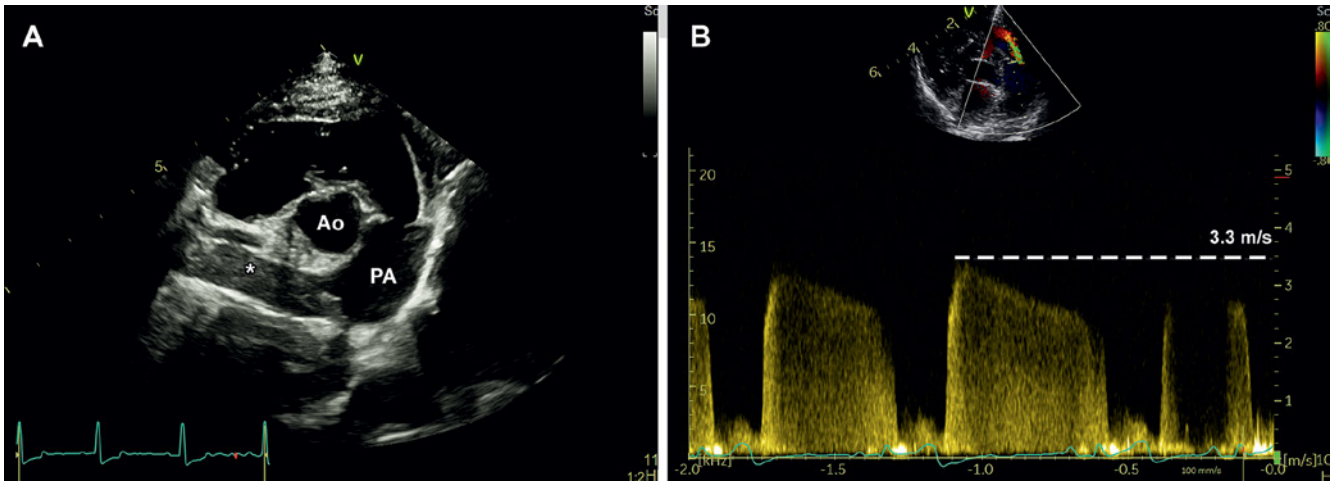


Figure 6.65. Pulmonary thromboembolism in a dog. (A) This 2D RPS SAx at the pulmonic valve level 2D image shows a large homogeneous and moderately echoic thrombus (*), which is seen occluding the RPA lumen. Notice the RPA and PA dilation. (B) The peak pulmonic insufficiency velocity is measured at 3.3 m/s, consistent with diastolic pulmonary arterial hypertension (diastolic driving pressure of about 44 mmHg).

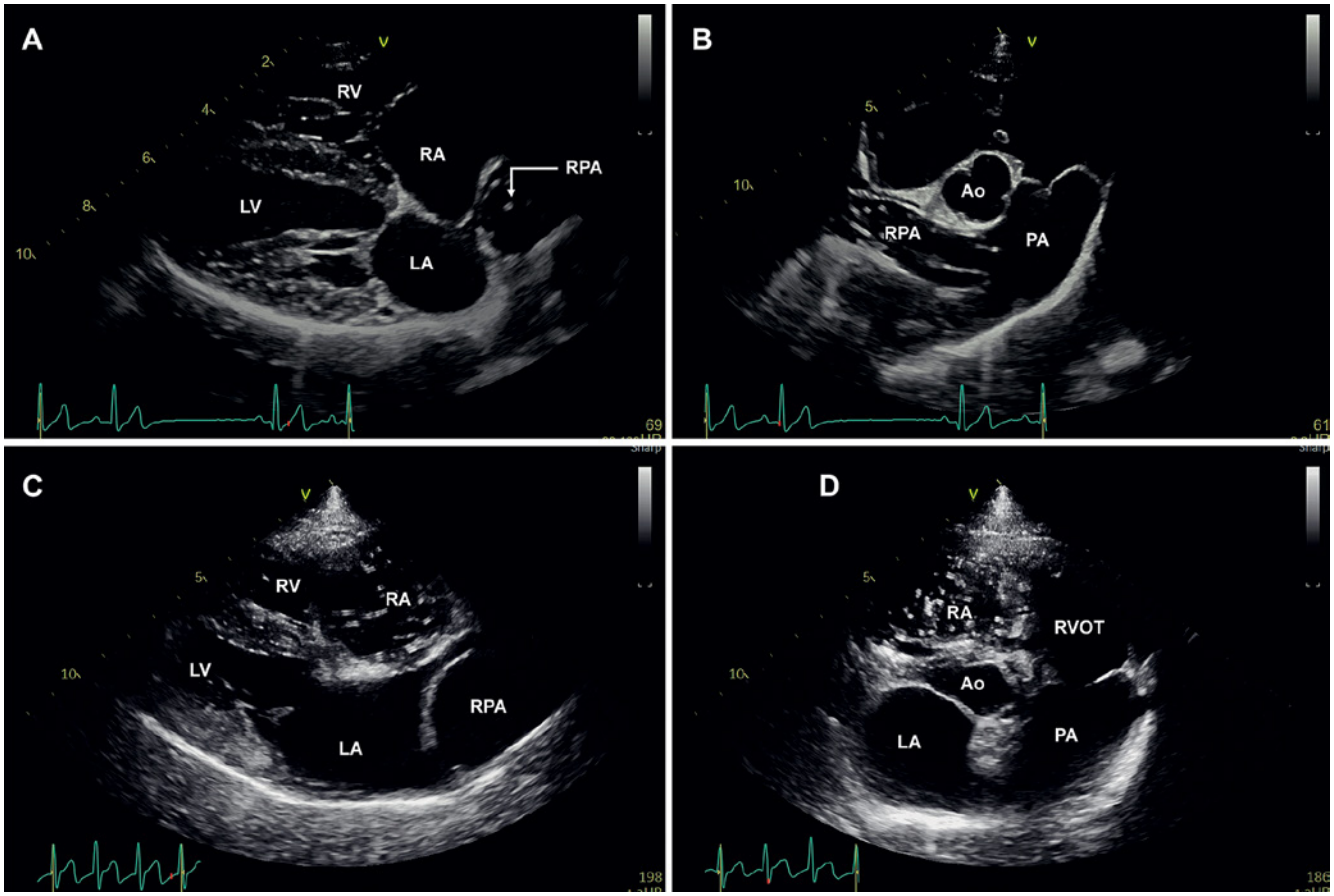


Figure 6.66. Heartworm disease (dirofilariasis). (A) This RPS LAx four-chamber 2D image from a dog with HWD depicts RV and RA dilation. A cross section of the RPA is seen and contains hyperechoic dots, which are cross sections of adult heartworms. **(B)** This 2D RPS SAx at the pulmonic valve level image shows several adult heartworms (hyperechoic linear structures) located in the RPA. The main PA and RPA are dilated. **(C, D)** RPS LAx and SAx views in a dog with caval syndrome caused by HWD. A high number of adult heartworms are present in the RA. There is moderate enlargement of the RA and RV as well as dilation of the PT and RPA.

Vet-ebooks.com

arterial pressure and to identify secondary changes consistent with PHT. CWD is used to indirectly estimate systolic pulmonary arterial pressure by measuring the tricuspid regurgitation peak velocity (TRV) and calculating the peak pressure gradient between the right ventricle and the right atrium using the simplified Bernoulli equation. This is only possible in the absence of RV outflow tract obstruction (e.g., PS). An estimate of right atrial pressure can be added to the calculated pressure gradient to obtain estimated systolic pulmonary arterial pressure. However, there is currently no validated method to estimate right atrial pressure, and the current recommendation is to simply use the TRV to determine the probability of PHT, as long as clinicians are aware that systolic pulmonary arterial pressure may be underestimated when severe right atrial hypertension is present.

Structural cardiac changes caused by PHT should also be evaluated to accurately diagnose PHT. Evidence from 2D echocardiography of PHT may include concentric and/or eccentric RV hypertrophy, RA dilation, as well as dilation of the pulmonary trunk and main branches. The left ventricle may appear ovoid in cross section in the RPS SAx image, with septal flattening because of compression and distortion imposed by the right heart; pseudohypertrophy of the left ventricle may occur from left-sided volume underload and septal hypertrophy (Figure 6.64). A consensus statement about PHT was recently published by the ACVIM (Reinero et al. 2020). The consensus document proposes a list of echocardiographic criteria used to determine the probability of PHT.

Heartworm disease (HWD or dirofilariasis) is an important cause of PHT in dogs. In addition to the echocardiographic abnormalities already noted, adult parasites may be visualized directly within the pulmonary arteries (most commonly), RV or right atrium, or vena cavae (Figure 6.66). Adult heartworms have a distinctive echocardiographic appearance because of the echogenicity of the parasite's cuticle relative to the gut. Echocardiography is an insensitive test for HWD in dogs because parasites may reside entirely within lobar and distal pulmonary arteries, which are inaccessible to 2D echocardiography. Nevertheless, when adults may be visualized in more proximal locations of the pulmonary circulation, 2D echocardiography facilitates qualitative evaluation of a parasite burden that becomes moderate to marked. **Caval syndrome** is characterized by a dramatic parasite burden within the RV, right atrium, and vena cava.

Pericardial Diseases and Cardiac Neoplasia

Pericardial Effusion and Cardiac Tamponade

Pericardial effusion (PE), which is the most common disorder involving the pericardium, is readily recognized echocardiographically (Figure 6.67). Effusions may be idiopathic, neoplastic, cardiogenic (CHF), inflammatory, infectious, or hemorrhagic in origin. PE typically appears as an anechoic or variably echogenic space between the epicardial surface of the heart and the echogenic parietal pericardium. Any significant fluid accumulation within the pericardium should prompt the ultrasonographer to search for a cause (advanced heart disease, neoplasia, or potential cardiac rupture) before completing the study. Cardiac tamponade results when PE accumulation is sufficient to elevate the intrapericardial pressure at the level of or above the right heart filling pressure. **Tamponade** is characterized echocardiographically by decreased ventricular size and early diastolic collapse of the RA, RV, or both. With large effusions, the heart may exhibit a swinging motion within the pericardial space.

Cardiac rupture in dogs is usually characterized by LA rupture secondary to severe MR and severe secondary LA dilation. Left atrial rupture should be suspected in dogs with known severe DMVD presenting with signs of PE and cardiogenic shock. Echocardiography often reveals the presence clotting blood within the pericardial sac (Figure 6.68).

Cardiac Neoplasia

Echocardiography is well suited for the diagnosis of cardiac neoplasia, which is common in dogs and a frequent cause of PE.

- **Hemangiosarcoma**
  Hemangiosarcoma is the most common cardiac malignancy, with a strong site predilection for the RA appendage, RA, and RV wall (Figure 6.69). Small tumors on the RA appendage may often be visualized from either the left cranial or RPS transducer positions, and visualization may be improved by placing the transducer at the most cranial aspect of the imaging window. Nonetheless, neoplasia cannot be ruled out by echocardiography and multiple transducer positions should be attempted if a tumor is suspected. PE may improve tumor visualization, providing an echo-free zone for contrast. Hemangiosarcoma may appear mottled or cavitated because of hypoechoic collections of blood within

Vet-ebooks.com

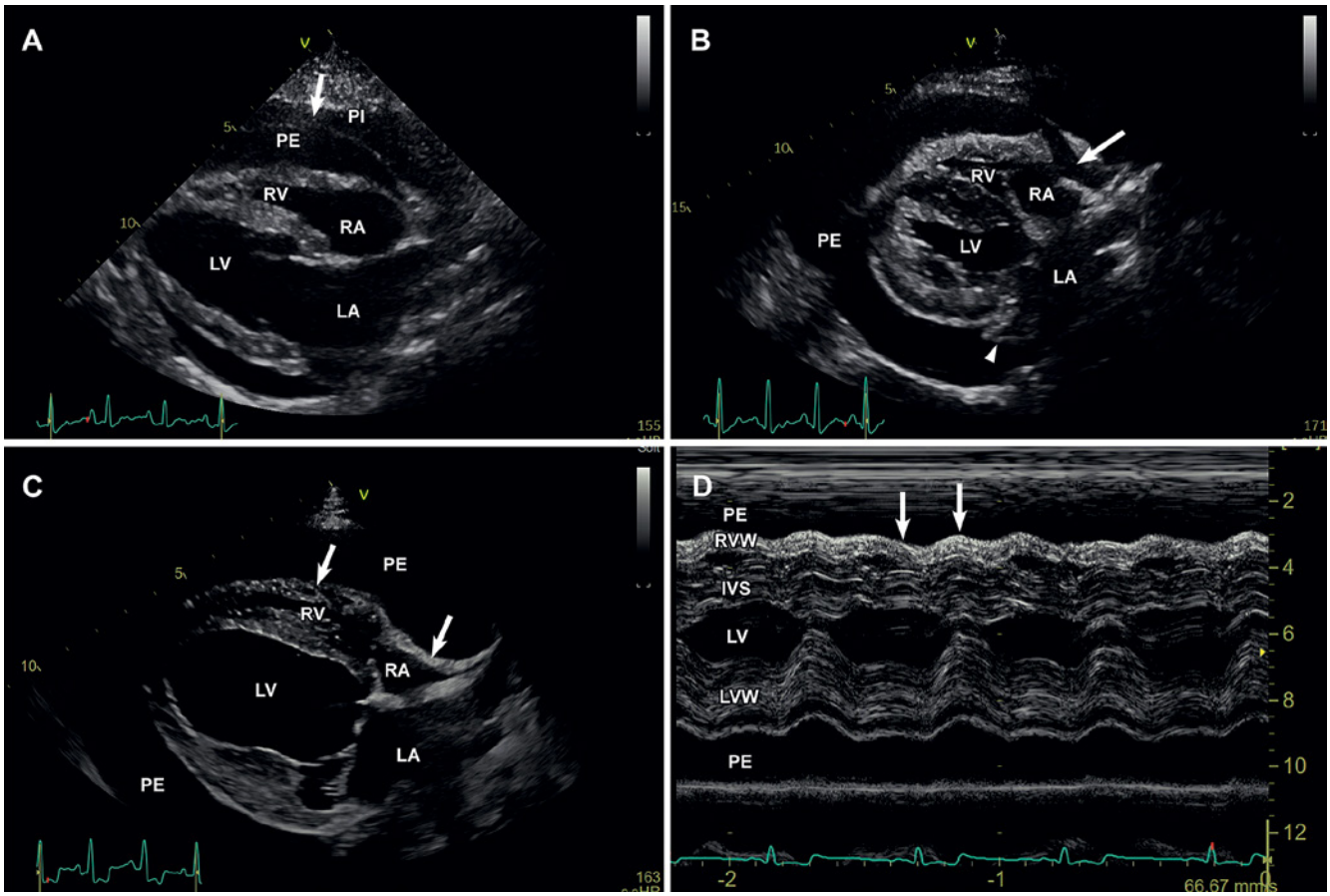


Figure 6.67. Pericardial effusion (PE) and tamponade. RPS LAx **(A, B)** and SAx **(C)** images from dogs with PE. The dog in **(A)** has concurrent PE and pleural effusion (Pl), with the pericardium identified as a thin rim between the effusions (arrow). In **(B, C),** there is cardiac tamponade. **(B)** diastolic collapse of the RA (arrow). **(C)** RPS SAx image at the pulmonic valve level demonstrating diastolic collapse of the RV (arrow). Pleural effusion can sometimes be confused for PE, and identifying the left and/or right auricle outlined in anechoic effusion can confirm PE, as seen in **(B**, arrowhead point to left auricle**)**.

the tumor; however, echocardiographic appearance and/or mass location cannot definitively identify tumor type (Rajagopalan et al. 2013)

- **Heart Base Tumors**

  Chemodectoma (aortic body tumor), which is a common tumor of brachiocephalic breeds, arises from aortic chemoreceptor cells that are often situated near the base of the heart (heart base tumor). Chemodectomas range in appearance from a small nodule, seemingly adherent to the ascending aorta, to a large mass that partially or completely surrounds the great vessels. Tumors are most often biologically benign and may be incidentally detected. However, they can cause clinical signs from PE or compression of the trachea, heart, or great vessels. Echocardiographic examination of a heart base tumor may necessitate imaging the ascending aorta far dorsal to the heart (Figure 6.70).

- **Other Cardiac Tumors**

  Thyroid carcinoma may arise from ectopic thyroid tissue, typically located at the heart base or within the RV outflow tract. Tumors may cause PE or obstruction of the RV outflow tract.

  Mesothelioma involving the pericardium may be difficult to diagnose echocardiographically because it does not typically produce a discrete, echogenic mass. Pericardial and/or pleural effusion of unexplained origin must include this cell type as a differential.

  Cardiac neoplasia in **cats** is uncommon. **Lymphoma** may occur within the heart, as one or more discrete masses or as a diffuse, infiltrative lesion causing altered and irregular myocardial echogenicity and/or PE.

Vet-ebooks.com

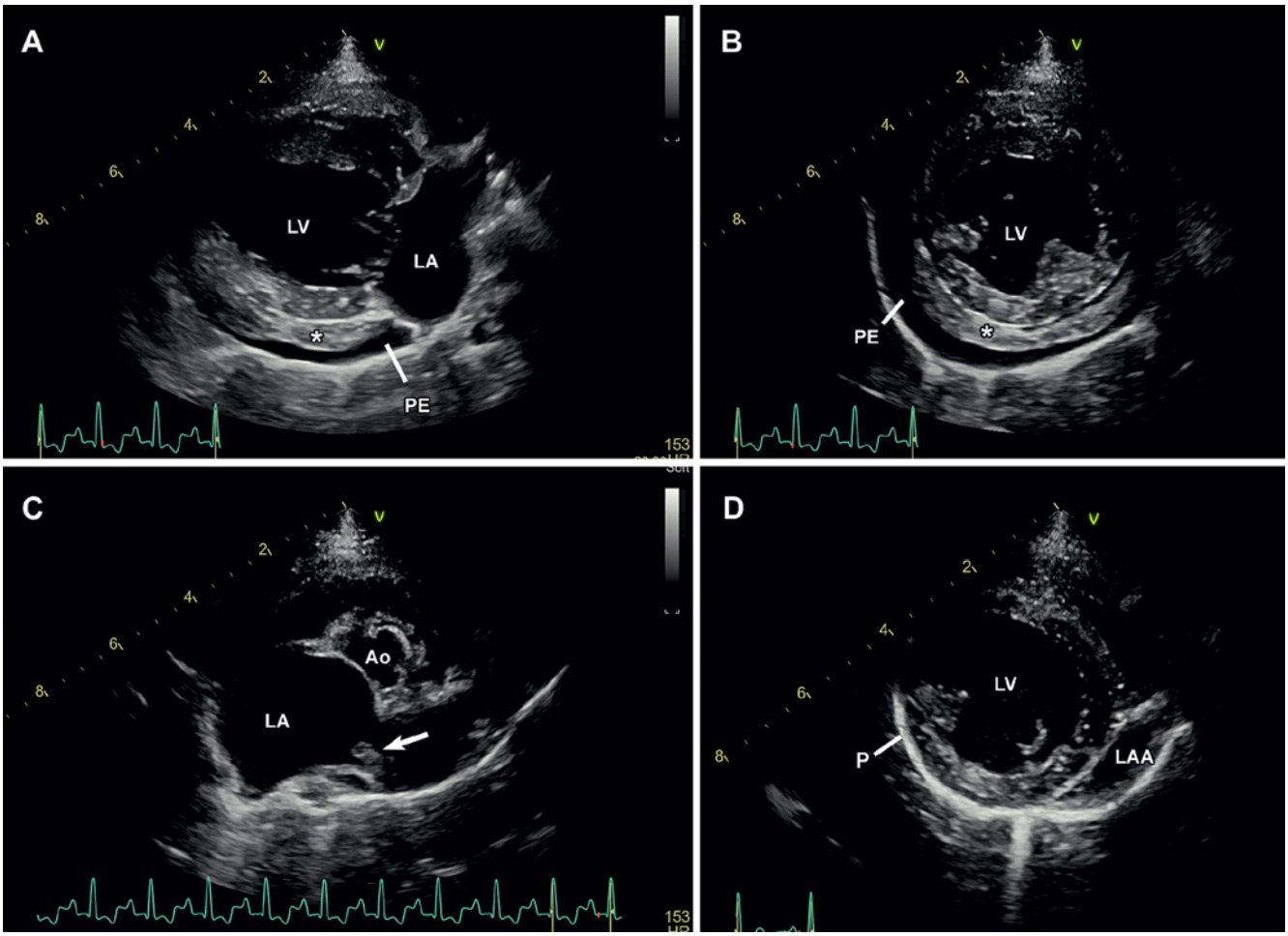


Figure 6.68. **Left atrial rupture in a dog with severe DMVD. (A, B)** RPS LAx four-chamber view (A) and SAx at the papillary muscle level view (B) from a dog with PE and LA rupture due to DMVD. A thrombus (*) is seen within the pericardial sac. Degenerative changes of the MV can be seen. **(C)** the LA is dilated and a thrombus (arrow) can also be seen within the LA (possibly at the site of LA tear). **(D)** RPS SAx image at the papillary muscle level showing a dilated left auricular appendage (LAA) in a dog with DMVD. The dilated LAA should not be confused for PE (note that the pericardium is in direct contact with the heart otherwise).

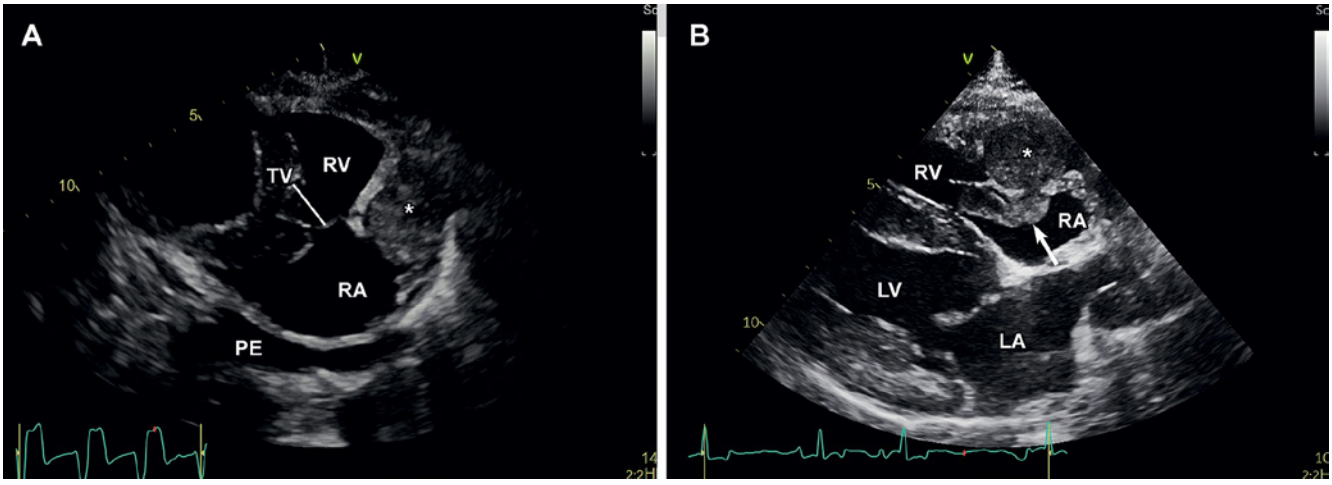


Figure 6.69. **Hemangiosarcoma (HSA). (A)** Left cranial LAx–tricuspid valve view demonstrating a mass in the RA auricle (*). **(B)** A large mass (*) involving the RA wall, with an extension of the mass into the RA chamber (arrow). Both **(A)** and **(B)** show typical locations for HSA in the dog.

Vet-ebooks.com

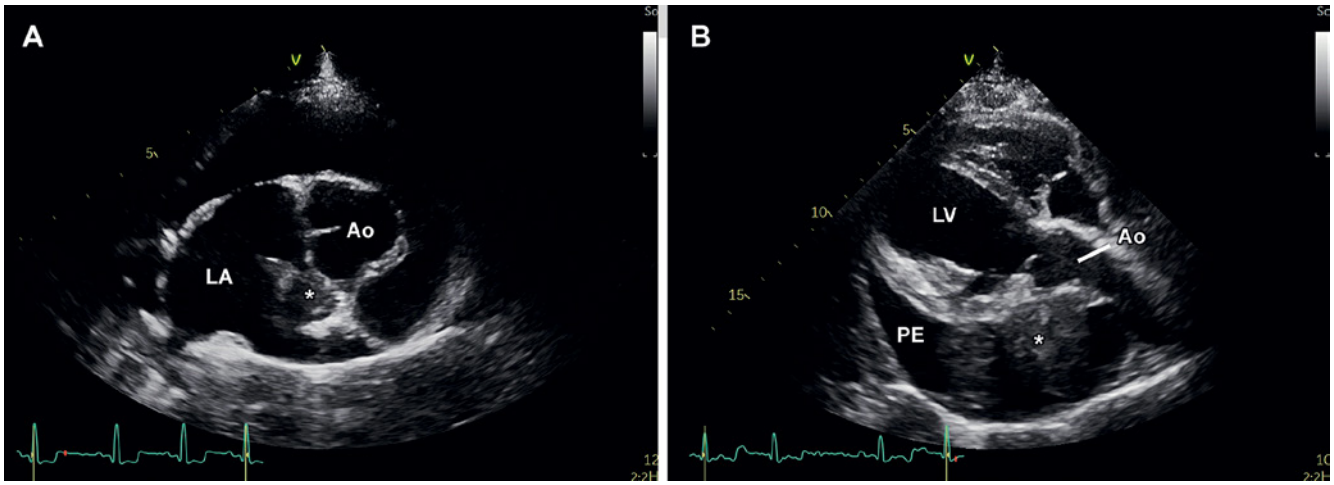


Figure 6.70. **Heart base tumor (HBT). (A)** RPS SAx view at the aortic valve level demonstrates a small HBT (*) adjacent to the aortic root (Ao). **(B)** Modified RPS LAx LVOT view showing a very large HBT (*) adjacent to the aorta (Ao), which has resulted in pericardial effusion (PE).

Visit our website at **www.SmallAnimalUltrasonography.com** for complementary video clips with annotations and text on:

- Normal short and long axes of the heart (dog)
- Normal short and long axes of the heart (cat)
- Chronic degenerative valvular disease
- Hypertrophic cardiomyopathy in a cat
- Dilated cardiomyopathy in a dog
- Pulmonary hypertension/cor pulmonale in a dog
- Idiopathic pericardial effusion and tamponade in a dog
- Cardiac tumor
- Patent ductus arteriosus in a dog
- Pulmonic stenosis in a dog
- Subaortic stenosis in a dog
- Ventricular septal defect in a cat

References

Abbott JA, MacLean HN (2003) Comparison of Doppler-derived peak aortic velocities obtained from subcostal and apical transducer sites in healthy dogs. Vet Radiol Ultrasound 44:695–698.

Anderson B (2016) Chapter 8 – technical quality. In Lang RM, Goldstein SA, Kronzon I et al., eds. ASE's Comprehensive Echocardiography, 2th edition. Elsevier, pp. 19–45. doi: 10.1016/B978-0-323-26011-4.09960-5

Baumwart RD, Meurs KM, Atkins CE, Bonagura JD, et al. (2005) Clinical, echocardiographic, and electrocardiographic abnormalities in Boxers with cardiomyopathy and left ventricular systolic dysfunction: 48 cases (1985–2003). J Am Vet Med Assoc 226:1102–1104.

Belanger MC, Côté E, Beauchamp G (2014) Association between aortoseptal angle in Golden Retriever puppies and subaortic stenosis in adulthood. J Vet Intern Med 28(5):1498–1503.

Bonagura JD, Luis Fuentes V (2015) Chapter 8 – echocardiography. In Mattoon JS, Nyland TG, ed. Small Animal Diagnostic Ultrasound, 3rd edition. W.B. Saunders, pp. 217–331. doi: 10.1016/B978-1-4160-4867-1.00008-8

Bonagura JD, Schober KE (2009) Can ventricular function be assessed by echocardiography in chronic canine mitral valve disease? J Small Anim Pract 50(Suppl. 1):12–24.

Bonagura JD, Visser LC (2022) Echocardiographic assessment of dilated cardiomyopathy in dogs. J Vet Cardiol 40:15–50.

Borgarelli M, Zini E, D'Agnolo G, Tarducci A, et al. (2004) Comparison of primary mitral valve disease in German Shepherd dogs and in small breeds. J Vet Cardiol 6:27–34.

Boswood A, Häggström J, Gordon SG, Wess G, et al. (2016) Effect of Pimobendan in dogs with preclinical myxomatous mitral valve disease and cardiomegaly: the EPIC study – a randomized clinical trial. J Vet Intern Med 30:1765–1779.

Bright JM, Herrtage ME, Schneider JF (1999) Pulsed Doppler assessment of left ventricular diastolic function in normal and cardiomyopathic cats. J Am Anim Hosp Assoc 35(4):285–291.

Buchanan JW (2001) Pathogenesis of single right coronary artery and pulmonic stenosis in English Bulldogs. J Vet Intern Med 15:101–104.

Cesta MF, Baty CJ, Keene BW, Smoak IW, et al. (2005) Pathology of end stage remodeling in a family of cats with hypertrophic cardiomyopathy. Vet Pathol 42:458–67.

Chetboul V, Taton C (2018) Chapitre 3 – Examen Doppler cardiaque conventionnel: principes, réglages, aspect normal. In Chetboul V, Taton C, eds. Encyclopédie animée d'imagerie cardiovasculaire ultrasonore du chien et du chat. Elsevier Masson, pp. 95–143. doi: 10.1016/B978-2-294-74873-8.00003-5

Chetboul V, Tidholm A, Nicolle A, Sampedrano CC, et al. (2005) Effects of animal position and number of repeated measurements on selected two-dimensional and M-mode

Vet-ebooks.com

echocardiographic variables in healthy dogs. J Am Vet Med Assoc 227(5):743–747.
Cornell CC, Kittleson MD, Della Torre P, Häggström, J, et al. (2004) Allometric scaling of M-mode variables in normal adult dogs. J Vet Intern Med 18:311–321.
Eason BD, Fine-Ferreira DM, Leeder D, Stauthammer C, et al. (2021) Natural history of subaortic stenosis in 166 dogs (1999-2011). J Vet Cardiol 37:71–80.
Esser LC, Borkovec M, Bauer A, Häggström J, et al. (2020) Left ventricular M-mode prediction intervals in 7651 dogs: Population-wide and selected breed-specific values. J Vet Intern Med 34(6):2242–2252.
Fonfara S, Martinez Pereira Y, Swift S, Copeland H, et al. (2010) Balloon valvuloplasty for treatment of pulmonic stenosis in English Bulldogs with an aberrant coronary artery. J Vet Intern Med 24:354–359.
Fox PR. Endomyocardial fibrosis and restrictive cardiomyopathy: pathologic and clinical features (2004). J Vet Cardiol 6(1):25–31.
Fujii Y, Nishimoto Y, Sunahara H, Takano H, et al. (2012) Prevalence of patent foramen ovale with right-to-left shunting in dogs with pulmonic stenosis. J Vet Intern Med 26:183–185.
Goodwin JK, Holland M (1995) Contrast echoartography as an aid in the diagnosis of right-to-left shunting patent ductus arteriosus. Vet Radiol Ultrasound 36:157–159.
Hamabe L, Kim S, Yoshiyuki R, Fukayama T, et al. (2015) Echocardiographic evaluation of myocardial changes observed after closure of patent ductus arteriosus in dogs. J Vet Intern Med 29(1):126–131.
Hansson K, Haggstrom J, Kvart C, Lord P (2002) Left atrial to aortic root indices using two-dimensional and M-mode echocardiography in cavalier King Charles spaniels with and without left atrial enlargement. Vet Radiol Ultrasound 43:568–575.
Harvey AM, Battersby IA, Faena M, Fews D, et al. (2005) Arrhythmogenic right ventricular cardiomyopathy in two cats. J Small Anim Pract 46(3):151–156.
Holler PJ, Wess G (2014) Sphericity index and E-point-to-septal-separation (EPSS) to diagnose dilated cardiomyopathy in Doberman Pinschers. J Vet Intern Med 28(1):123–129.
Keene BW, Atkins CE, Bonagura JD, Fox PR, et al. (2019) ACVIM consensus guidelines for the diagnosis and treatment of myxomatous mitral valve disease in dogs. J Vet Intern Med 33:1127–1140.
Kellihan HB, Stepien RL, Hassen KM, Smith LJ (2015) Sedative and echocardiographic effects of dexmedetomidine combined with butorphanol in healthy dogs. J Vet Cardiol 17(4):282–292.
Kruckman L, Fries RC, Kadotani S, Stack JP, et al. (2022) Comparison of three two-dimensional echocardiographic methods of assessing left ventricular size in Doberman Pinschers. J Vet Cardiol 40:110–118.
Lai WW, Geva T, Shirali GS, Frommelt PC, et al. (2006) Pediatric council of the American society of echocardiography. Guidelines and standards for performance of a pediatric echocardiogram: a report from the task force of the pediatric council of the American society of echocardiography. J Am Soc Echocardiogr 19(12):1413–1430.
Lang RM, Badano LP, Mor-Avi VM, Afilalo J, et al. (2015) Recommendations for cardiac chamber quantification by echocardiography in adults: an update from the American society of echocardiography and the European association of cardiovascular imaging. J Am Soc Echocardiogr 28:1–39.
Luis Fuentes V, Abbott J, Chetboul V, Côté E, et al. (2020) ACVIM consensus statement guidelines for the classification, diagnosis, and management of cardiomyopathies in cats. J Vet Intern Med 34(3):1062–1077.
März I, Schober K, Oechtering G (2006) Echocardiographic measurement of left atrial dimension in healthy cats and cats with left ventricular hypertrophy. Tieraerztl Prax 34(5):331–340.
Meurs KM (2017) Arrhythmogenic right ventricular cardiomyopathy in the boxer dog: an update. Vet Clin North Am Small Anim Pract 47(5):1103–1111.
Miller MW, Gordon SG, Saunders AB, Arsenault WG, et al. (2006) Angiographic classification of patent ductus arteriosus morphology in the dog. J Vet Cardiol 8(2):109–114.
Mitchell C, Rahko PS, Blauwet LA, Canaday B, et al. (2019) Guidelines for performing a comprehensive transthoracic echocardiographic examination in adults: recommendations from the American Society of Echocardiography. J Am Soc Echocardiogr 32(1):1–64.
Moise NS, Dietze AE, Mezza LE, Strickland D, et al. (1986) Echocardiography, electrocardiography, and radiography of cats with dilatation cardiomyopathy, hypertrophic cardiomyopathy, and hyperthyroidism. Am J Vet Res 47:1476–1486.
Novo Matos J, Pereira N, Glaus T, Wilkie L, et al. (2018) Transient myocardial thickening in cats associated with heart failure. J Vet Intern Med 32(1):48–56.
Quintavalla C, Guazzetti S, Mavropoulou A, Bussadori C (2010) Aorto-septal angle in Boxer dogs with subaortic stenosis: an echocardiographic study. Vet J 185(3):332–337.
Rajagopalan V, Jesty SA, Craig LE, Gompf R (2013) Comparison of presumptive echocardiographic and definitive diagnoses of cardiac tumors in dogs. J Vet Intern Med 27(5):1092–1096.
Reinero C, Visser LC, Kellihan HB, Masseau I, et al. (2020) ACVIM consensus statement guidelines for the diagnosis, classification, treatment, and monitoring of pulmonary hypertension in dogs. J Vet Intern Med 34(2):549–573.
Rishniw M, Erb HN (2000) Evaluation of four 2-dimensional echocardiographic methods of assessing left atrial size in dogs. J Vet Intern Med 14:429–435.
Saunders AB, Gordon SG, Boggess MM, Miller MW (2014) Long-term outcome in dogs with patent ductus arteriosus: 520 cases (1994-2009). J Vet Intern Med 28(2):401–410.
Schober KE, Chetboul V (2015) Echocardiographic evaluation of left ventricular diastolic function in cats: hemodynamic determinants and pattern recognition. J Vet Cardiol 17 Suppl 1:S102–S133.

Vet-ebooks.com

Schober KE, Stern JA, DaCunha DN, Pedraza-Toscano AM, et al. (2008) Estimation of left ventricular filling pressure by Doppler echocardiography in dogs with pacing-induced heart failure. J Vet Intern Med 22:578–585.

Schober KE, Hart TM, Stern JA, Li X, et al. (2010) Detection of congestive heart failure in dogs by Doppler echocardiography. J Vet Intern Med 24:1358–1368.

Schober KE, Hart TM, Stern JA, Li X, et al. (2011) Effects of treatment on respiratory rate, serum natriuretic peptide concentration, and Doppler echocardiographic indices of left ventricular filling pressure in dogs with congestive heart failure secondary to degenerative mitral valve disease and dilated cardiomyopathy. J Am Vet Med Assoc 239:468–479.

Visser LC (2017) Right ventricular function: imaging techniques. Vet Clin North Am Small Anim Pract 47(5):989–1003.

Visser LC, Scanse BA, Schober KE (2013) Single left coronary ostium and an anomalous prepulmonic right coronary artery in 2 dogs with congenital pulmonary valve stenosis. J Vet Cardiol 15:161–169.

Visser LC, Ciccozzi MM, Sintov DJ, Sharpe AN (2019a) Echocardiographic quantitation of left heart size and function in 122 healthy dogs: a prospective study proposing reference intervals and assessing repeatability. J Vet Intern Med 5:1909–1920.

Visser LC, Nishimura S, Oldach MS, Bélanger C, et al. (2019b) Echocardiographic assessment of right heart size and function in dogs with pulmonary valve stenosis. J Vet Cardiol 26:19–28.

Wagner T, Fuentes VL, Payne JR, McDermott N, et al. (2010) Comparison of auscultatory and echocardiographic findings in healthy adult cats. J Vet Cardiol 12(3):171–182.

Wess, G (2022) Screening for dilated cardiomyopathy in dogs. J Vet Cardiol 40:51–56.

Wess G, Mäurer J, Simak J, Hartmann K (2010) Use of Simpson's method of disc to detect early echocardiographic changes in Doberman pinschers with dilated cardiomyopathy. J Vet Intern Med 24:1069–1076.

Wess G, Bauer A, Kopp A (2021) Echocardiographic reference intervals for volumetric measurements of the left ventricle using the Simpson's method of discs in 1331 dogs. J Vet Intern Med 35:724–738.

Vet-ebooks.com

Vet-ebooks.com

CHAPTER SEVEN

Hepatobiliary System

Marc-André d'Anjou[1], Dominique Penninck[2], and Heather Spain[3]

[1]Animages, Brossard, Québec, Canada
[2]Department of Clinical Sciences, Cummings School of Veterinary Medicine, Tufts University, North Grafton, MA, USA
[3]Veritas Veterinary Partners, San Rafael, CA, USA

Preparation and Scanning Technique

Hair clipping of animals should cover the entire cranial abdomen and ideally the last one or two intercostal spaces, particularly in deep-chested dogs or if microhepatia is suspected. Animals can be scanned in dorsal, left, or right recumbency after acoustic gel application. The ability to visualize the liver in small animals is related to body conformation, liver size, and overlying gastrointestinal content. In small dogs and cats, the liver can usually be entirely scanned in transverse and longitudinal planes by means of a subcostal approach (Figure 7.1), if the stomach is not overly distended with ingesta or gas. The transverse colon can also limit hepatic visibility, particularly if filled with gas or feces, or if the liver is small. In these instances, an intercostal approach can provide a useful alternative. In large, deep-chested dogs, the liver is completely hidden by the rib cage, routinely requiring the use of an intercostal approach to reach all parts of the liver. In these dogs, and especially if the liver is atrophied, several other structures, such as the spleen, can move under the costal arch and should not be confused for a portion of the liver. In obese animals, the presence of a large amount of falciform fat can also reduce hepatic visibility by increasing the distance between the probe and the organ and by degrading image quality because of beam scattering.

The **appropriate probe** must be chosen based on the size and depth of the liver. In small or medium-sized dogs and cats, a medium- to high-frequency probe (5–8 MHz and higher) can be used, whereas a probe with more penetration (lower than 5 MHz) is often required in larger dogs. Sectorial or convex probes are preferred over linear probes because of the triangular-shaped scanned field of view that enables larger portions of the liver to be imaged. A smaller footprint also enables most parts of the liver to be reached through limited acoustic windows such as intercostal spaces. Gain settings and focal zones must be constantly adjusted during the exam to optimize ultrasonographic penetration and image quality (see Figure 1.8).

Ultrasonographic Anatomy of the Normal Liver

Parenchyma and Size

In dogs and cats, the liver is composed of four lobes, and two processes – left lobe (lateral and medial), quadrate lobe, right lobe (lateral and medial), and caudate lobe (caudate and papillary processes) (Evans 1993a, 1993b; Hudson and Hamilton 1993) – which cannot be easily distinguished unless separated by peritoneal effusion (Figure 7.2).

The left lobe forms a third to nearly half of the entire liver. The quadrate lobe is relatively central. The gallbladder (GB) lies between the quadrate and right medial lobe in dogs, while the GB is lodged on the right medial lobe in cats. The caudate process of the caudate lobe is the most caudal extension of the liver, on the right side, and extends to the level of the right kidney. The hepatic and portal veins (PVs) of each of

Atlas of Small Animal Ultrasonography, Third Edition. Edited by Dominique Penninck and Marc-André d'Anjou.
© 2025 John Wiley & Sons, Inc. Published 2025 by John Wiley & Sons, Inc.
Companion website: www.SmallAnimalUltrasonography.com

Vet-ebooks.com

these hepatic lobe divisions are relatively constant in dogs and can represent useful ultrasonographic landmarks (Carlisle et al. 1995).

A large part of the liver is beneath the costal arch, just cranial to the stomach, in dogs and cats. Its cranial margin lies against the diaphragm and lung interface. The diaphragm appears as a curved hyperechoic line, often associated with artifacts such as a mirror-image artifact (Figure 1.19).

Caudally, the liver is often in contact with the spleen on the left side and with the right kidney at the level of the renal fossa of the caudate lobe. The hepatic volume is difficult to evaluate objectively in cats and dogs, mainly because of the variability in body conformation. As with radiography, the costal arch and location of the stomach can help in subjectively evaluating liver size, considering body conformation. The caudal extension of the hepatic lobes can be compared with the location of the last pair of ribs (Figure 7.3A). In deep-chested dogs, the liver does not usually reach the costal arch, and the stomach often interferes with its evaluation. Conversely, in small dog breeds and in

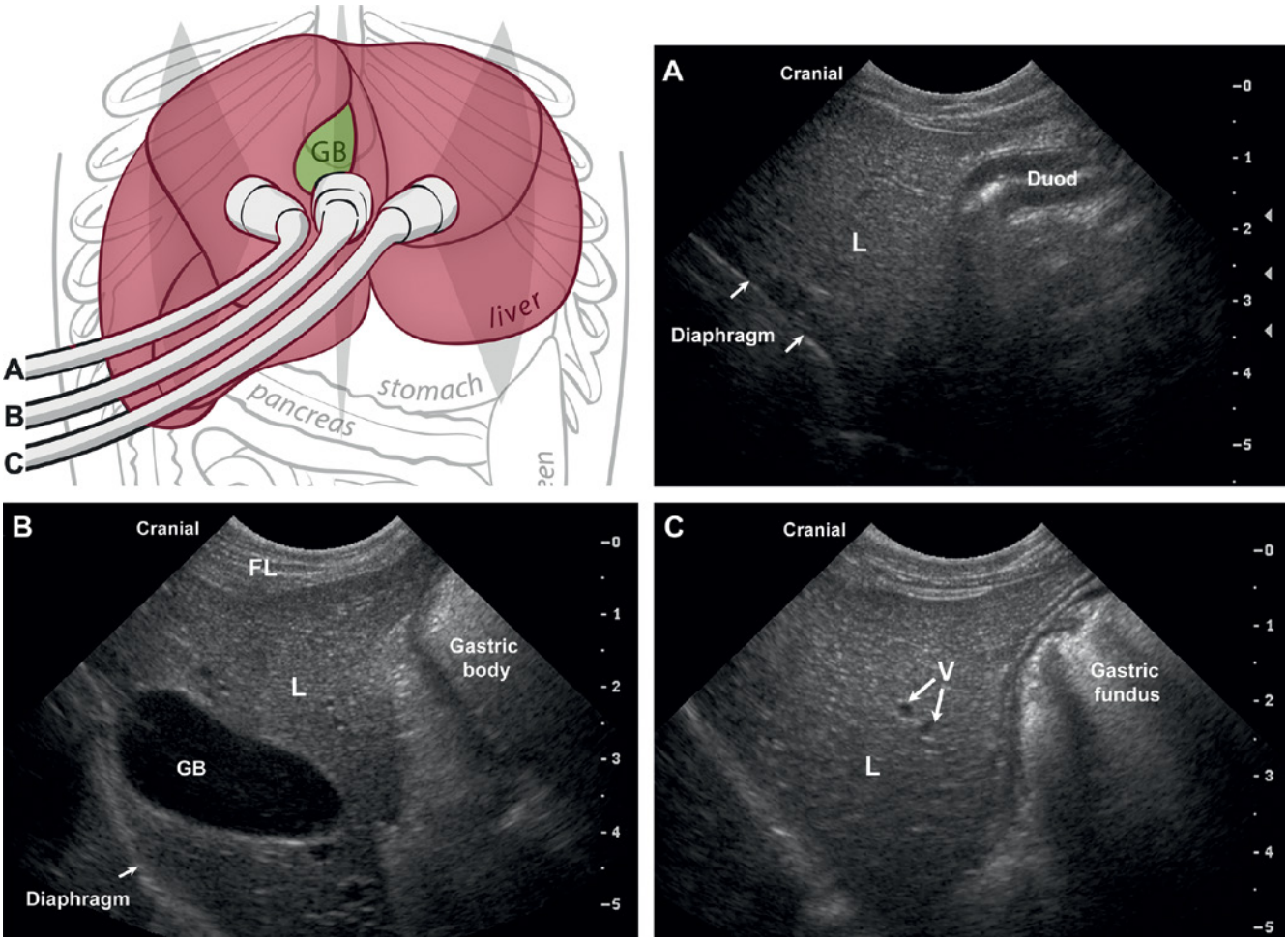


Figure 7.1. Ultrasonographic approach and anatomy of the normal liver. Illustration of the scanning technique using a subcostal approach with a dog or a cat in dorsal recumbency. The ultrasound probe must be moved in order to cover the entire liver, sequentially in the sagittal **(A–C)** and transverse **(D–F)** planes. The additional use of oblique planes, as well as an intercostal approach, is necessary in some patients. **(A–C)** Using a longitudinal plane in a dog, the probe is sequentially moved from the right **(A)** to the left **(C)** of the liver (L). The intimate relationship between the duodenum (Duod), stomach and the liver is visualized. The falciform ligament (FL), which can vary in size because of fat deposition, is in the near field. Hepatic vessels (V) appear as round, anechoic structures on cross section. The gallbladder (GB), located to the right of the midline, is a useful landmark. **(D–F)** By using a transverse plane, the liver is also entirely scanned, from its cranioventral portion **(D)** to its caudodorsal portion **(F)**. The GB is seen on the right in the mid-portion of the liver **(E)**. Branching portal veins (PV) with hyperechoic boundaries are also recognized.

Vet-ebooks.com

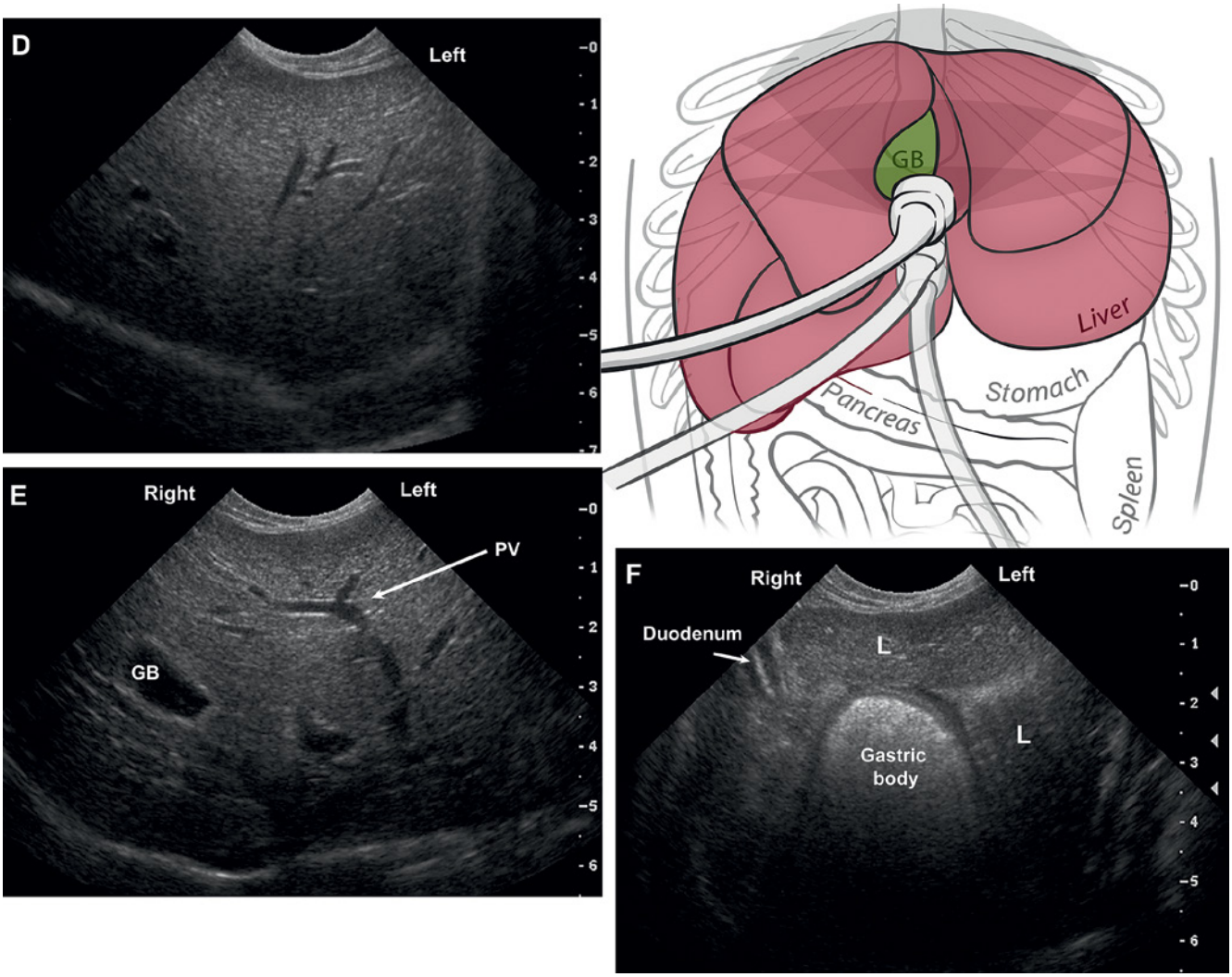


Figure 7.1. (Continued)

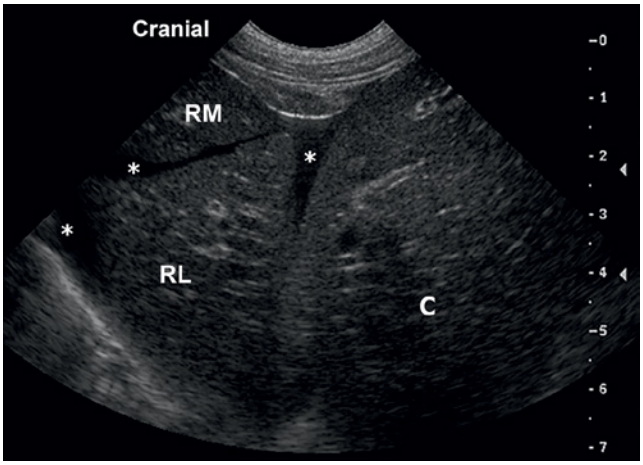


Figure 7.2. Effusion separating hepatic lobes. Longitudinal oblique image of the right portion of the liver with three distinct separate lobes well outlined by peritoneal effusion (*). C, caudate lobe; RL, right lateral; RM, right medial.

Vet-ebooks.com



Figure 7.3. Evaluation of liver size. (A) Normal liver. Left parasagittal image of the cranial abdomen in a normal small-breed dog with the caudal tip of the liver (arrowheads) extending to the level of the last rib (at the costochondral junction). Acoustic shadowing (*) is noted deep to this hyperattenuating structure. The tip of the liver appears smooth and pointy. **(B) Hepatomegaly**. In this dog with Cushing's disease, the left lateral liver lobe (arrowheads) extends beyond the gastric fundus and has a rounded tip. **(C) Microhepatia**. Longitudinal image of the central portion of the liver of a dog with a congenital extrahepatic portosystemic shunt. Because of the significant reduction in hepatic volume, the spleen is displaced cranially and the portal vein cannot be easily followed to the liver.

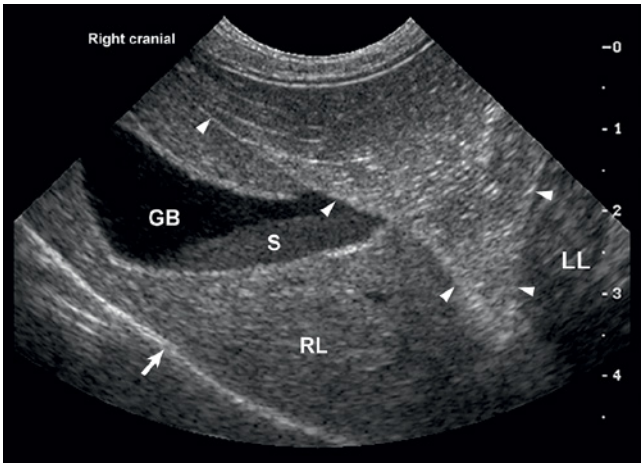


Figure 7.4. Falciform fat. On this sagittal oblique ultrasonographic image of the liver, the falciform fat (arrowheads) appears as a triangular hyperechoic structure with a coarse echotexture protruding between the right and left portions of the liver. The gallbladder (GB) contains a small amount of biliary sludge (S) in its dependent portion (dorsal recumbency). The arrow points to the lung–diaphragm interface. LL, left liver; RL, right liver.

cats, the liver normally extends to the costal arch. It may also extend beyond that point in some small breeds of dogs, particularly in puppies. The caudal tips of the hepatic lobes are normally pointed. With hepatomegaly, these tips become rounded and can extend beyond the right kidney and/or reach the left kidney, depending on the symmetry of the enlargement (Figure 7.3B). With microhepatia, the liver is more difficult to reach by a subcostal approach and its assessment may be limited by the stomach located under the costal arch (Figure 7.3C).

The **falciform ligament**, filled with a variable amount of fat, is ventral to the liver and protrudes between the right and left portions, dorsal to the xiphoid process (Figure 7.4). This poorly defined structure is usually isoechoic or slightly hyperechoic to the liver and presents a coarse echotexture relative to the liver parenchyma. However, obese cats may have a liver that is hyperechoic to the falciform fat (Nicoll et al. 1998). The normal hepatic parenchyma is uniformly hypoechoic, with a coarser echotexture, when compared with the spleen. Its echogenicity relative to the renal cortices is variable, although usually hyperechoic to isoechoic (Figure 7.5).

Biliary System

The biliary system is relatively similar in dogs and cats with intrahepatic and extrahepatic components. The intrahepatic biliary tree, composed of **biliary canaliculi** and **biliary ducts**, is not seen in normal patients.

The **GB** is the bile reservoir and is generally a teardrop-shaped structure with a rounded apex and tapering neck; a conical to tubular extension, the cystic duct, connects the GB to the remainder of the extrahepatic biliary system. The GB can show a different morphology in 12–24% of cats (Griffin 2019; Spain et al. 2022), predominantly with a bilobed appearance (Figure 7.6). The clinical relevance of bilobed GB is unclear; they are generally presumed to be an incidental finding, though few investigations have posited a potential predisposition to inflammation (Spain et al. 2017). The **wall** of the normal GB appears as a

Vet-ebooks.com

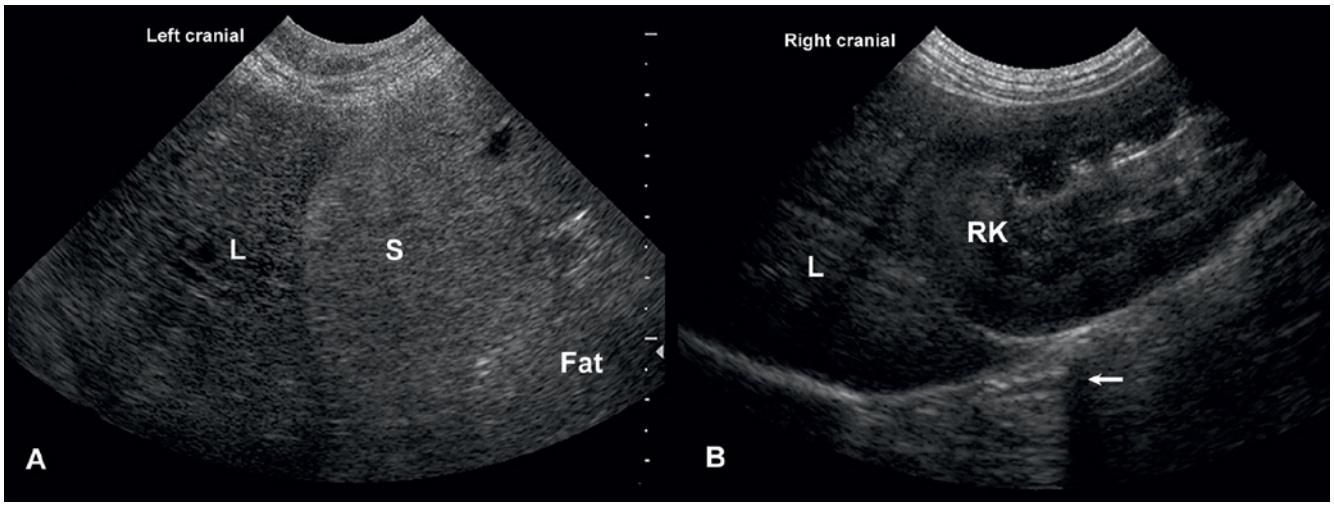


Figure 7.5. **Liver, spleen, and kidney relative echogenicities and echotextures. (A)** Sagittal image obtained in the left cranial abdomen of a normal dog. The liver (L) is in contact with the spleen (S) and is relatively hypoechoic and more granular in echotexture. **(B)** Sagittal image obtained in the right cranial abdomen of a normal dog. The liver (L) appears relatively isoechoic to the cortex of the right kidney (RK). Acoustic shadowing (arrow) is caused by one of the last ribs.

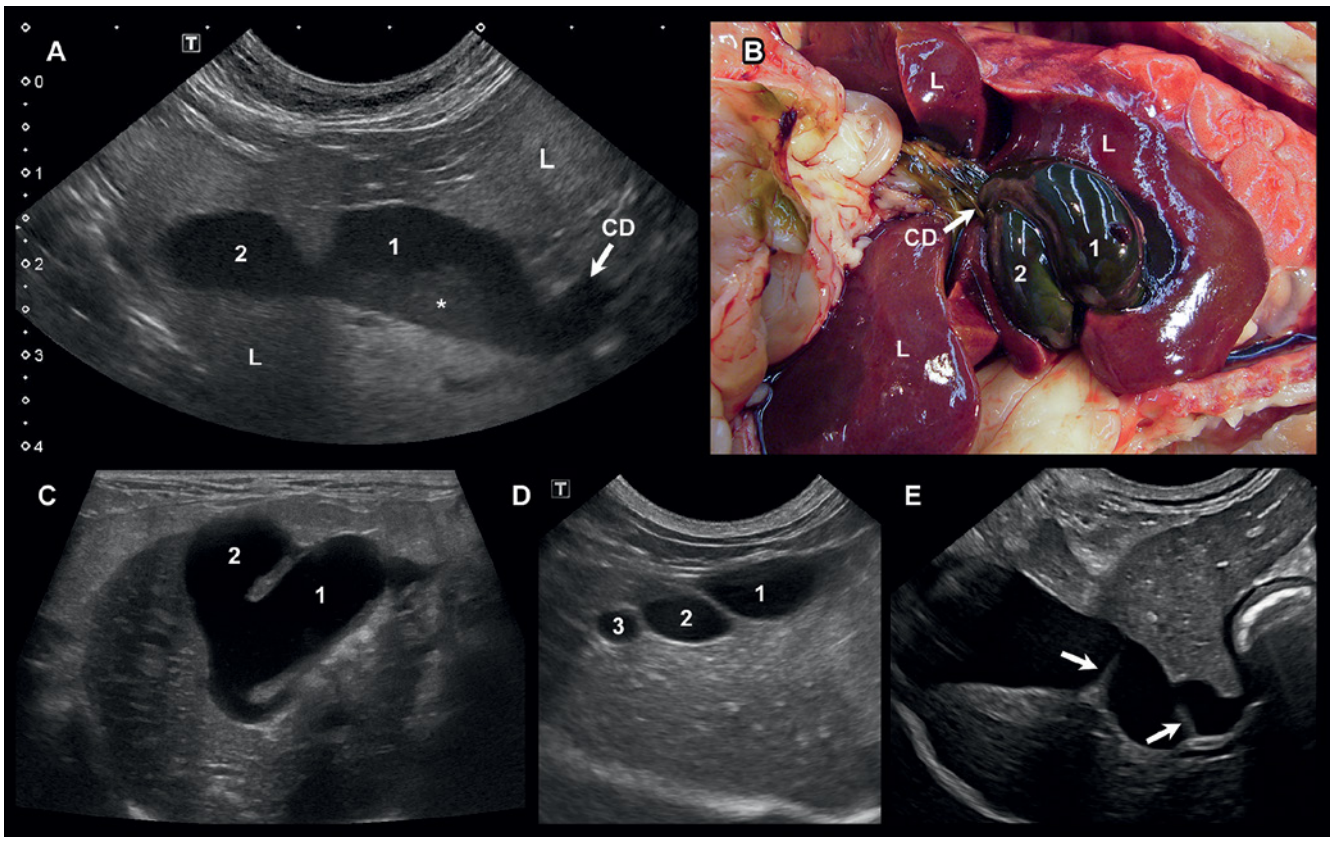


Figure 7.6. **Bilobed gallbladder in cats.** Sonographic **(A)** and gross anatomical **(B)** images of the gallbladder (GB) of a cat that is partially divided into two compartments (1 and 2), sharing the same cystic duct (CD). **(C)** In this other cat, the GB has a valentine shape, with two symmetrical compartments. **(D, E)** The GB can also present a different morphology. For instance, it can present three asymmetrical compartments (1–3 in **D**) or transverse echogenic septations at multiple locations (**E**). L, liver.

Vet-ebooks.com

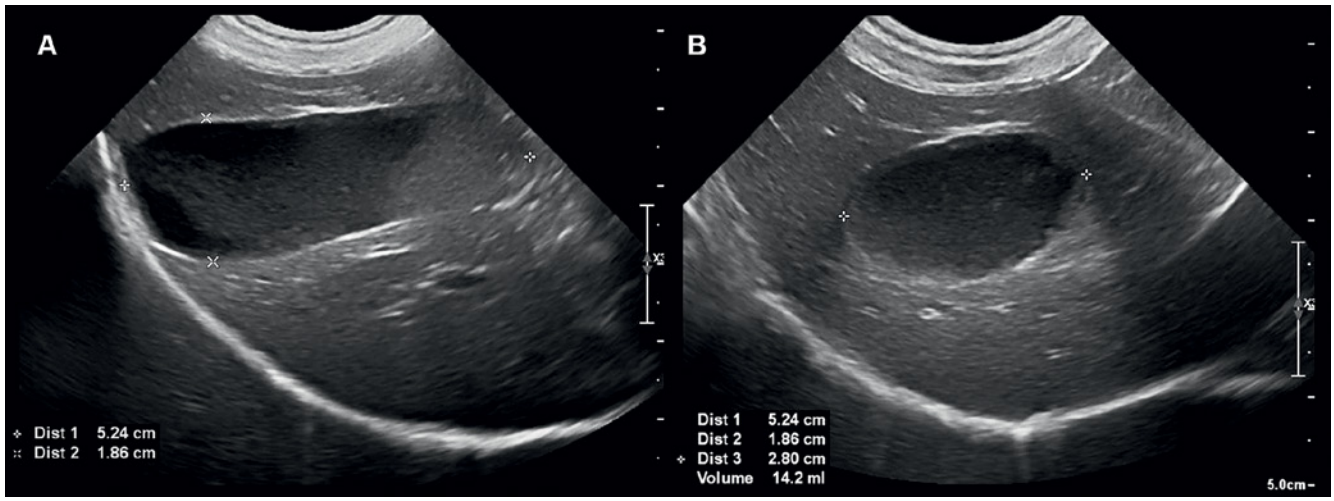


Figure 7.7. Gallbladder volume estimation using the ellipsoid method. Longitudinal **(A)** and transverse **(B)** sonograms of a gallbladder with three sets of measurements (length, height, and width) contribute to obtaining the estimated volume of the gallbladder of 14 mL in this 15-year-old dog.

thin, smooth hyperechoic line, reported to measure up to 1 mm in thickness in cats (Hittmair et al. 2001) and up to 1.3 mm in dogs (Martinez et al. 2023).

GB volume can be estimated using the ellipsoid method (Figure 7.7) (Penninck et al. 2010). It can vary markedly in size and become quite large in anorexic patients so that GB volume alone cannot be used as a reliable sign of biliary obstruction. Yet, monitoring its reduction in volume postprandially may help to exclude outflow obstruction. In cats, GB width can be used to assess its postprandial change in volume (Diana et al. 2012).

Normal bile is anechoic and commonly associated with acoustic enhancement (see Chapter 1 – artifacts), which can alter the appearance of the distal GB wall and deep hepatic parenchyma. **Biliary sludge** – which sonographically appears as echogenic, mobile/gravity dependent, nonshadowing amorphous material – is composed of precipitated cholesterol or calcium crystals, glycoproteins, cellular debris, and mucins. It is often seen in the GB of healthy dogs, with a reported prevalence ranging from 35 to 67% (Bromel et al. 1998; Butler et al. 2022; Cook et al. 2016; DeMonaco et al. 2016) (Figure 7.8). Sludge is mobile but may sometimes give the impression of an aggregate, mimicking a wall thickening or mass. GB wall thickening can be encountered with mucosal hyperplasia, and the concurrent presence of sludge can be challenging to distinguish form the thickening. Doppler can assist in assessing the presence of vascularity. The distribution of the sludge should respond to gravity after the animal is repositioned, although this may take time in some dogs.

The clinical significance of GB sludge in dogs remains unclear. There is growing evidence in the literature that the presence of biliary sludge may indicate altered GB function and dysmotility (Butler et al. 2022; DeMonaco et al. 2016; Tsukagoshi et al. 2012). In one investigation, dogs that had >25% of the GB lumen occupied by sludge also had increased GB volume (Cook et al. 2016), suggesting reduced ejection fraction/cholestasis. However, when GB sludge was assessed within a healthy canine population and monitored over a 12-month period, it persisted in 88% of dogs who remained asymptomatic with normal biochemical parameters throughout the study (DeMonaco et al. 2016), suggesting that sludge can also be incidental. Distinguishing nondependent GB sludge from mobile sludge may be clinically relevant as this could be a potential risk factor for development of GB mucocele (Butler et al. 2022).

GB sludge in cats can be predictive of increased liver enzymes and total bilirubin (Harran et al. 2011) (Figure 7.8), but it may also be encountered without evidence of biliary disease (Villim et al. 2022).

The **common bile duct (CBD)**, which represents the continuation of the connecting GB **cystic duct** and biliary ducts, can be seen more easily in normal cats than in normal dogs. The CBD can be traced ventral to the PV, nearly parallel to it over a few cm, before entering the duodenum through the major duodenal (Figure 7.9). Its lumen can measure up to 4 mm wide in normal cats (Léveillé et al. 1996) and is considered normal by the authors when up to 3 mm (luminal diameter) in dogs. The wall of the CBD, as for the GB, is often barely visualized and should not exceed 1 mm.

Vet-ebooks.com

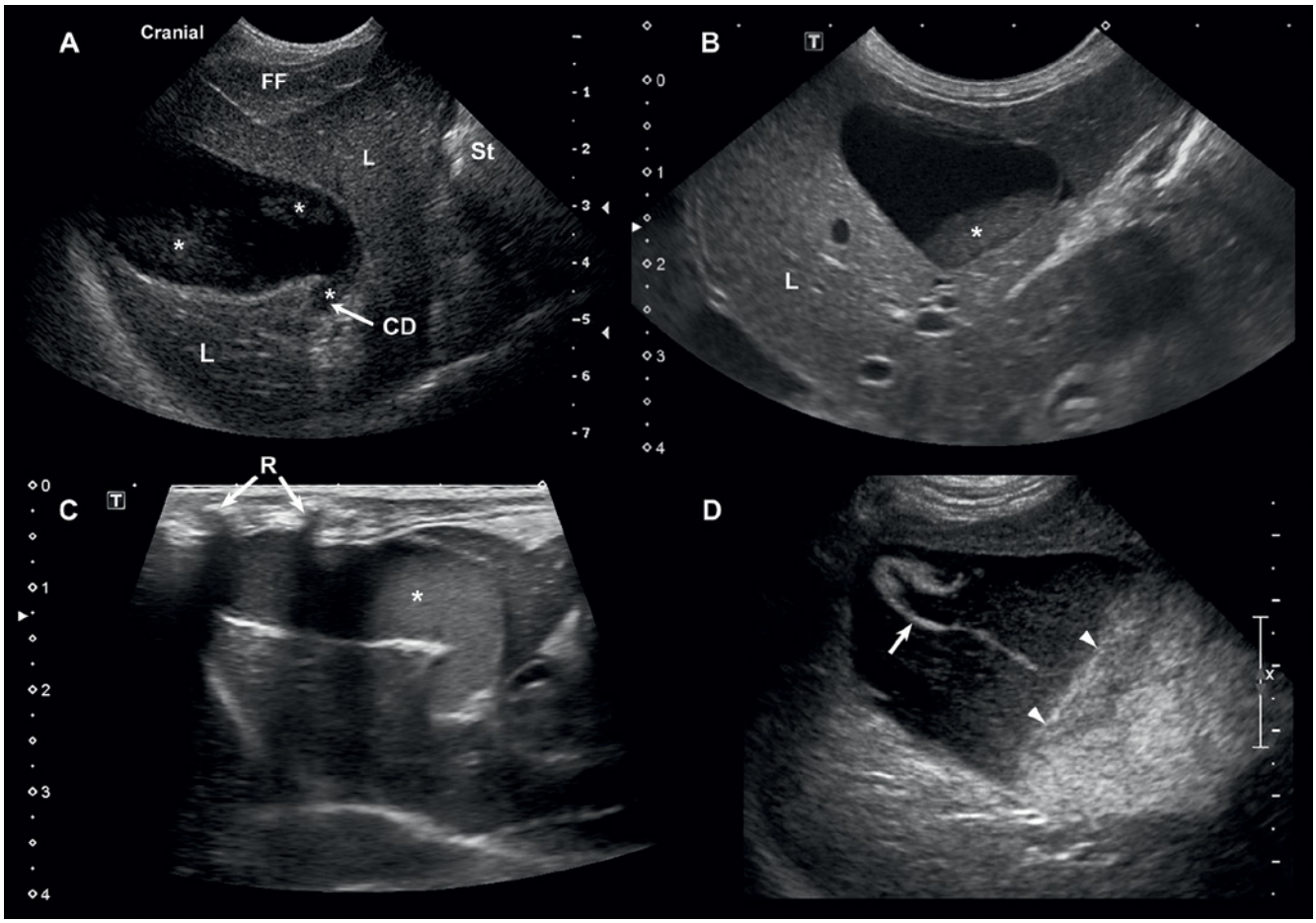


Figure 7.8. **Biliary sludge in dogs and cats. (A)** Longitudinal image of the right-central portion of the liver of a normal dog with the gallbladder and cystic duct (CD) containing poorly defined echogenic material (*) consistent with biliary sludge. The mobility of this sludge was confirmed by repositioning the animal during the exam. FF, falciform fat; L, liver; St, stomach. **(B)** In this cat with normal liver enzymes, the biliary sludge (*) accumulates in the dependent portion of the gallbladder. **(C)** In another cat with cholangiohepatitis, the gallbladder is filled with sludge (*). R, ribs. **(D)** In this 12-year-old Golden Retriever, hyperechoic sludge is collecting in the dependent portion of the gallbladder. The orientation of the sediment (arrowheads) is oblique because of the orientation of the probe. Sludge can also form floating layers (arrow).

Hepatic and Extrahepatic Vasculature

Refer to Chapter 16 for a complete description of the normal vascular anatomy of the liver.

Ultrasonographic Features of Hepatic Disorders

Several hepatic disorders are found in dogs and cats and cause focal, multifocal, or diffuse parenchymal alterations. The evaluation of the liver must include several parameters: liver **size** and **contour**, **parenchymal echogenicity**, **ultrasound-beam attenuation**, and the **distribution of abnormalities**. Although some of these disorders have characteristic ultrasonographic features, most changes are not pathognomonic of one process. A more definite diagnosis is usually based on the combination of clinical presentation, blood test results, ultrasonographic findings, and cytological or histopathologic results.

Diffuse Hepatic Parenchymal Disorders

Diffuse hepatic disorders can be difficult to differentiate from poorly defined multifocal diseases. Typically, these disorders affect all lobes, although not always

Vet-ebooks.com

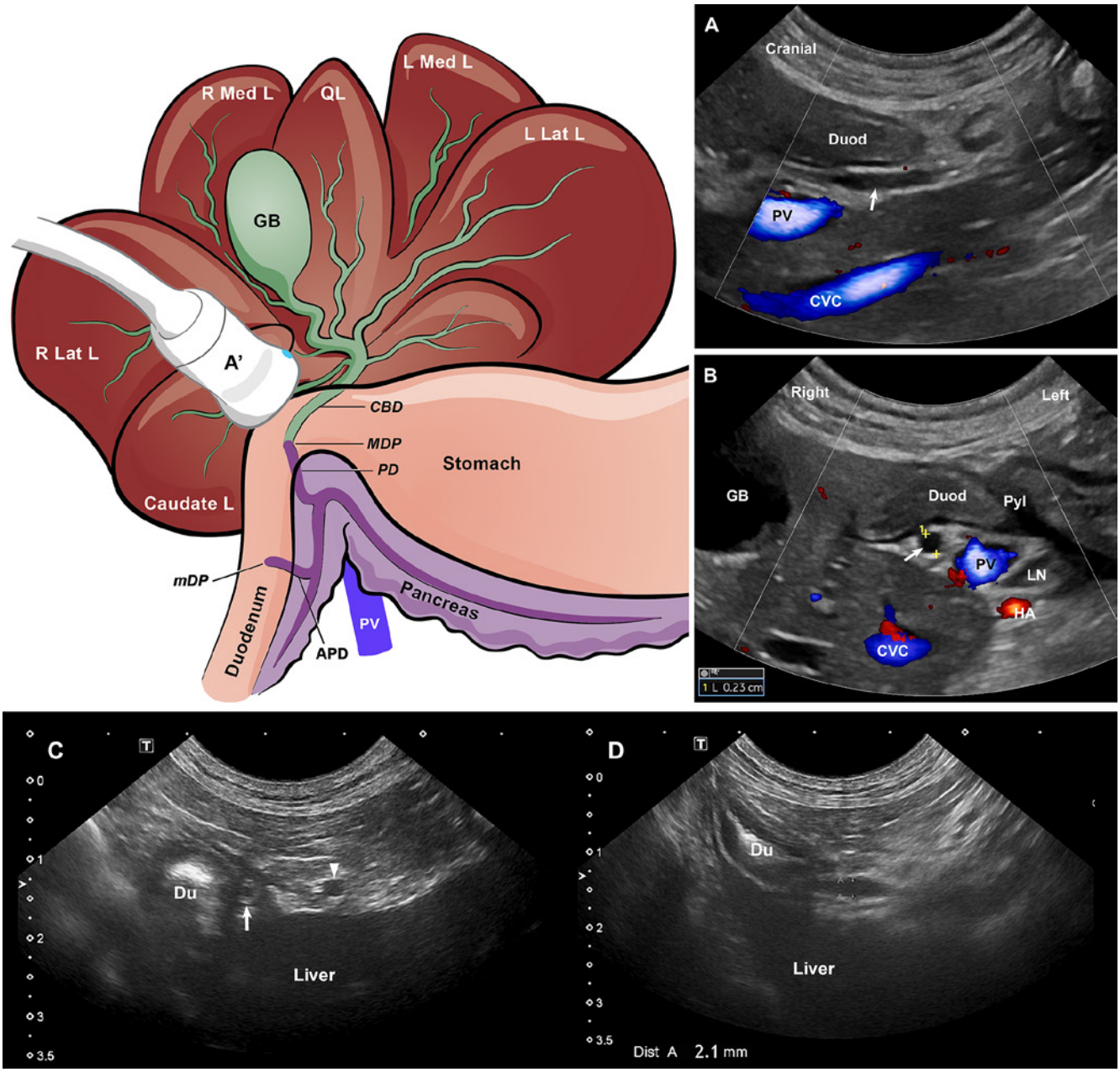


Figure 7.9. Normal common bile duct in a cat and a dog. (A-B) Scanning technique for the common bile duct in a cat. Schematic representation of the regional anatomy and landmarks of the biliary tract in the cat, with the ultrasound probe (A′) placed to obtain a longitudinal view **(A)** of the common bile duct (CBD). The probe is then rotated to obtain a transverse plane **(B)**. The common bile duct (2.3 mm wide, arrow) is found just ventral to the portal vein (PV) and dorsal to the proximal duodenum (Duod). This duct can sometimes be followed to the level of the major duodenal papilla (MDP), at the same level as the pancreatic duct (PD) termination. APD, accessory pancreatic duct; CVC, caudal vena cava; Duod, duodenum; GB, gallbladder; HA, hepatic artery; L Lat L, left lateral lobe; L Med L, left medial lobe; LN, hepatic lymph node; mDP, minor duodenal papilla; PV, portal vein; Pyl, pylorus; QL, quadrate lobe; R Lat L, right lateral lobe; R Med L, right medial lobe. **(C, D) Normal common bile duct in a Lhasa Apso dog**. The common bile duct (CBD) can sometimes be recognized in dogs as it enters the duodenal (Du) papilla (arrow in **C**). In this dog, the lumen of the CBD measures 2.1 mm **(D)**. Color Doppler may serve in distinguishing the duct from the nearby pancreaticoduodenal vein (arrowhead in **C**). Image **C** was obtained with a transverse plane in relation to the duodenum, whereas the probe was oriented obliquely to highlight the CBD in a longitudinal plane **(D)**.

Vet-ebooks.com

uniformly. The parenchymal echogenicity can be increased, reduced, or unaffected. These disorders can also affect the parenchymal uniformity and distort the hepatic margin. The evaluation of the liver contour is facilitated by the presence of peritoneal effusion (Figure 7.2). With the exception of congenital portal vascular anomalies such as portosystemic shunting, chronic hepatitis, and cirrhosis, most disorders tend to be associated with symmetrical or asymmetrical hepatomegaly. Two or more hepatic disorders, such as hepatitis, vacuolar hepatopathy, or nodular hyperplasia, can be found in the same patient, complicating the ultrasonographic diagnosis. The correlation between ultrasound findings and cytological and histopathological results is relatively poor for diffuse parenchymal diseases, justifying fine-needle aspiration cytology, or ideally biopsy, in most cases (Feeney et al. 2008; Guillot et al. 2009; Kemp et al. 2013; Warren-Smith et al. 2012). Table 7.1 lists the typical diagnostic differential for diffuse changes in hepatic parenchymal echogenicity, and Table 7.2 lists the causes of diffuse or focal/asymmetrical hepatomegaly.

Vacuolar Hepatopathies and Nodular Hyperplasia

Hepatic lipidosis and **steroid-induced** and other **vacuolar hepatopathies** are among the most common diffuse parenchymal disorders in cats and dogs, respectively. Degenerative vacuolar hepatopathy is often present with other primary disorders in dogs (Wang et al. 2004). These hepatopathies are usually associated with a diffuse increase in parenchymal

Table 7.1
Diagnostic differentials for diffuse alterations in hepatic parenchymal echogenicity

Diffuse hyperechogenicity	Diffuse hypoechogenicity	Mixed echogenicity
Steroid hepatopathy	Passive congestion	Steroid hepatopathy associated with benign hyperplasia, or other combinations of processes
Lipidosis	Acute hepatitis or cholangiohepatitis	Hepatitis
Other vacuolar hepatopathies	Lymphoma	Round cell neoplasia
Chronic hepatitis	Leukemia	Hepatocellular carcinoma
Fibrosis	Histiocytic sarcoma	Metastases
Cirrhosis		Necrosis
Lymphoma		
Mast cell tumor		

Table 7.2
Diagnostic differentials for alterations in hepatic volume

Diffuse hepatomegaly	Focal or asymmetrical hepatomegaly	Small liver
Steroid hepatopathy	Primary or metastatic neoplasia	Congenital portosystemic shunting
Lipidosis	Abscess	Microvascular dysplasia or primary portal vein hypoplasia
Hepatitis or cholangiohepatitis	Cyst(s)	Cirrhosis
Passive congestion	Granuloma	Fibrosis
Round-cell neoplasia: lymphoma, malignant histiocytosis, mast cells	Thrombosis	Severe hypovolemia
Massive hepatocellular carcinoma or metastases	Lobar torsion	Hypoadrenocorticism
Amyloidosis	Necrosis	
	Hematoma	

Vet-ebooks.com

echogenicity and hepatomegaly (Figures 7.10-7.12). The parenchyma can also appear hyperattenuating, i.e., result in excessive sound-beam attenuation. Consequently, the far gain must be increased (or bottom time gain compensation cursors moved to the right) in many of these patients in order to evaluate the deepest portions of the liver. Additionally, the parenchyma can appear heterogeneous or contain hypoechoic or hyperechoic nodular foci that may represent **nodular hyperplasia** or **regenerative nodules** (7.12).

Hepatitis, Cholangitis/cholangiohepatitis, and Cirrhosis

Diffuse hepatic inflammatory processes can show variable ultrasonographic features, especially as concurrent copper storage disease and vacuolar changes can be present (Rodriguez et al. 2020). In cats, **cholangitis/cholangiohepatitis** was reported to be commonly associated with a decrease in parenchymal echogenicity and an increase in visibility of the portal

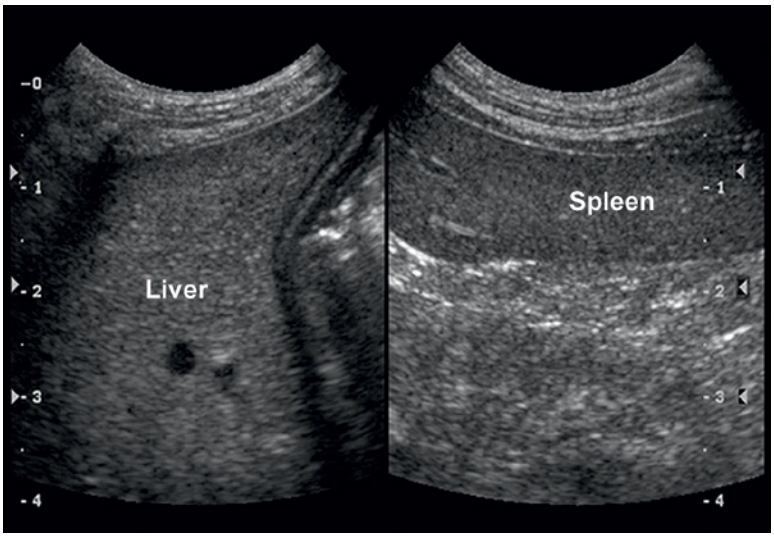


Figure 7.10. Hyperechoic liver. Dual images of the liver and spleen of a dog that was obtained with identical settings (depth, gain, and focus), allowing hepatic and splenic parenchymal echogenicities to be compared. Hepatic lipidosis that caused a diffusely hyperechoic liver, isoechoic to the spleen, was diagnosed.

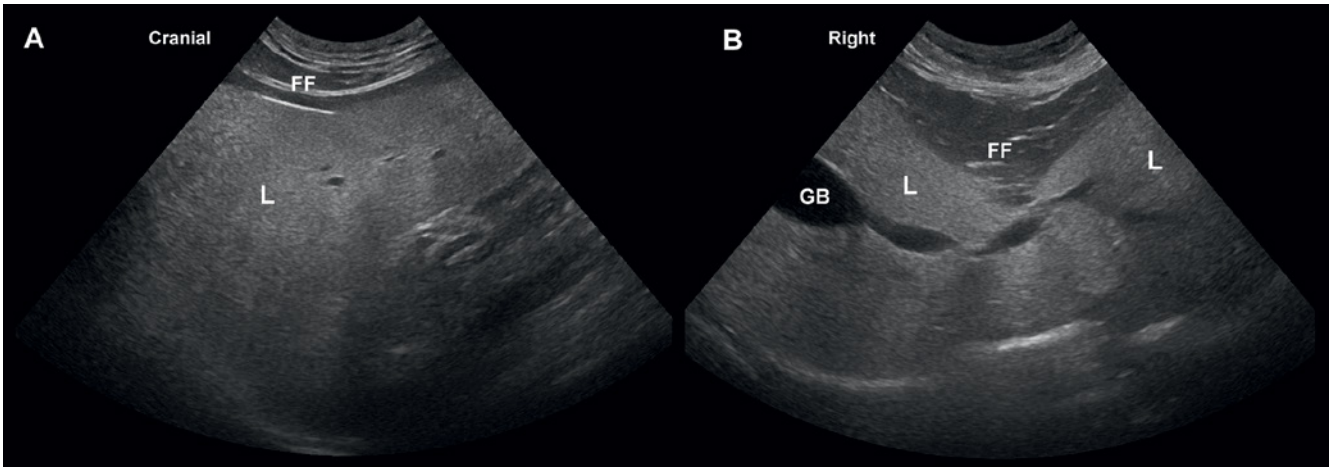


Figure 7.11. Feline hepatic lipidosis. Sagittal **(A)** and transverse **(B)** images of the liver in a cat with diffuse hyperechogenicity and ultrasound beam hyperattenuation. The liver (L) is markedly enlarged and hyperechoic to the falciform fat (FF), at least superficially. The echoes coming from the deepest portions of the liver were reduced and could only be partially compensated for by increasing far gain. GB, gallbladder.

Vet-ebooks.com

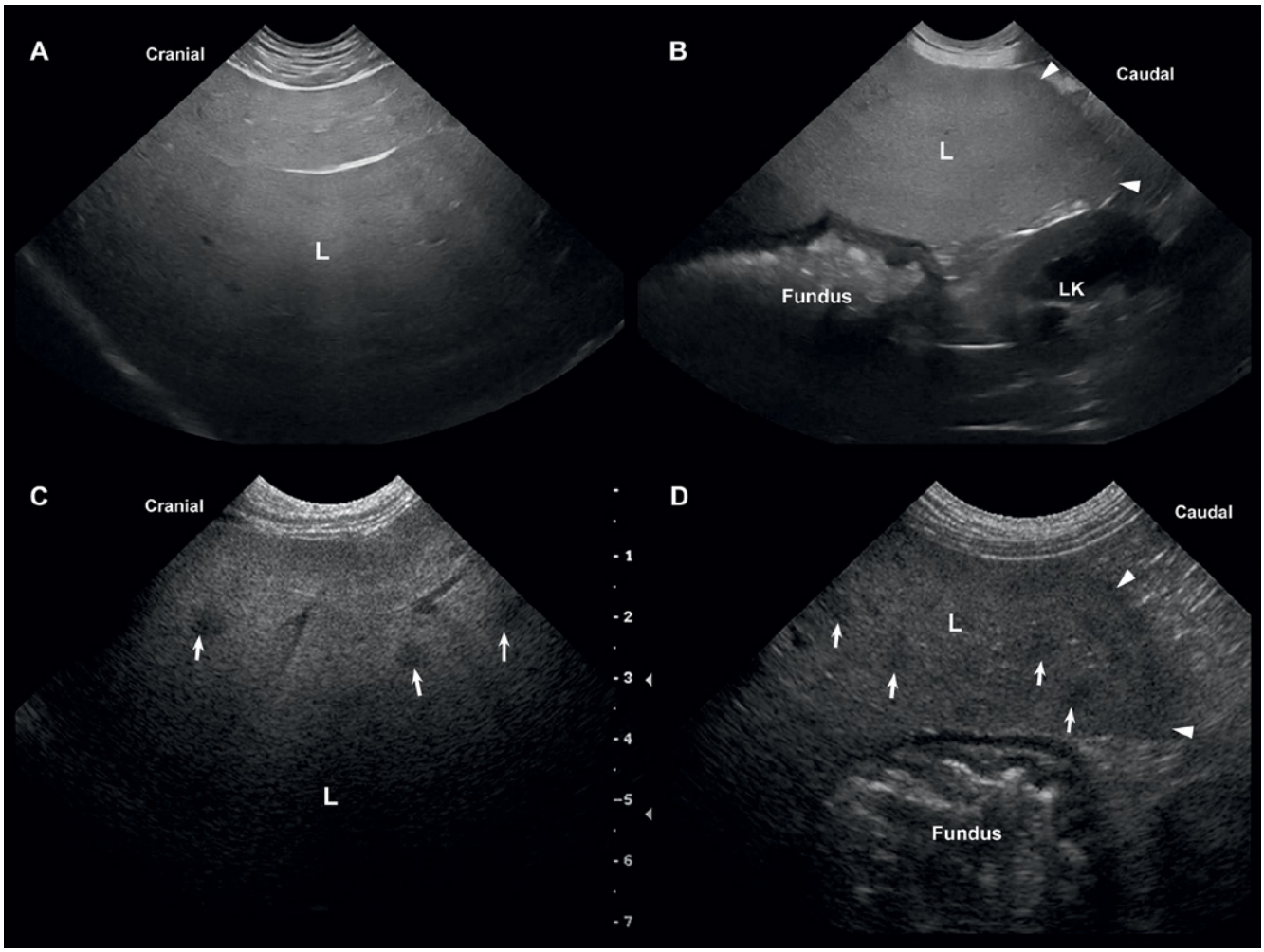


Figure 7.12. Steroid hepatopathy in two dogs. Longitudinal images (**A–D**) of the left portion of the liver in two dogs with pituitary-dependent hyperadrenocorticism. In both cases, the liver (L) is markedly enlarged and the caudal margin of the left lateral lobe is rounded (arrowheads). In the first dog (**A, B**), the liver parenchyma is uniformly, markedly hyperechoic. In the second dog (**C, D**), the parenchyma is more heterogeneous and multiple hypoechoic nodular foci, less than 1 cm wide, are noted **(A)** (arrows). In both dogs, the deep portion of the liver is difficult to assess because of increased ultrasound-beam attenuation. In the second dog, ultrasound-guided biopsy indicated vacuolar hepatopathy and benign nodular hyperplasia.

vasculature (Newell et al. 1998), although the liver may appear normal, hyperechoic, or heterogeneous (Marolf et al. 2012; Penninck and Berry 1997) (Figure 7.13). Additionally, this process is often associated with biliary anomalies, such as biliary sludge, **cholelithiasis,** or wall thickening, and with pancreatitis. In dogs, **acute hepatitis** also tends to cause diffuse liver hypoechogenicity, as seen with leptospirosis (Figure 7.14).

Chronic liver inflammatory processes, on the other hand, tend to be associated with **fibrosis**, which typically results in increased echogenicity (Figures 7.15 and 7.16). The presence of chronic active inflammation, consisting of a mixture of inflammatory cells, edema, fibrosis, necrosis, as well as regenerative nodules (hyperplasia) can cause a markedly heterogeneous liver with variable echogenicity. Although **cirrhosis** classically causes the liver to appear small, hyperechoic, and irregular in contour, its appearance can vary and sometimes mimic hepatocutaneous syndrome or neoplasia (Figure 7.17). However, chronic hepatitis and its ultimate outcome, cirrhosis, usually do not cause hepatic enlargement, as opposed to massive neoplastic infiltration.

Vet-ebooks.com

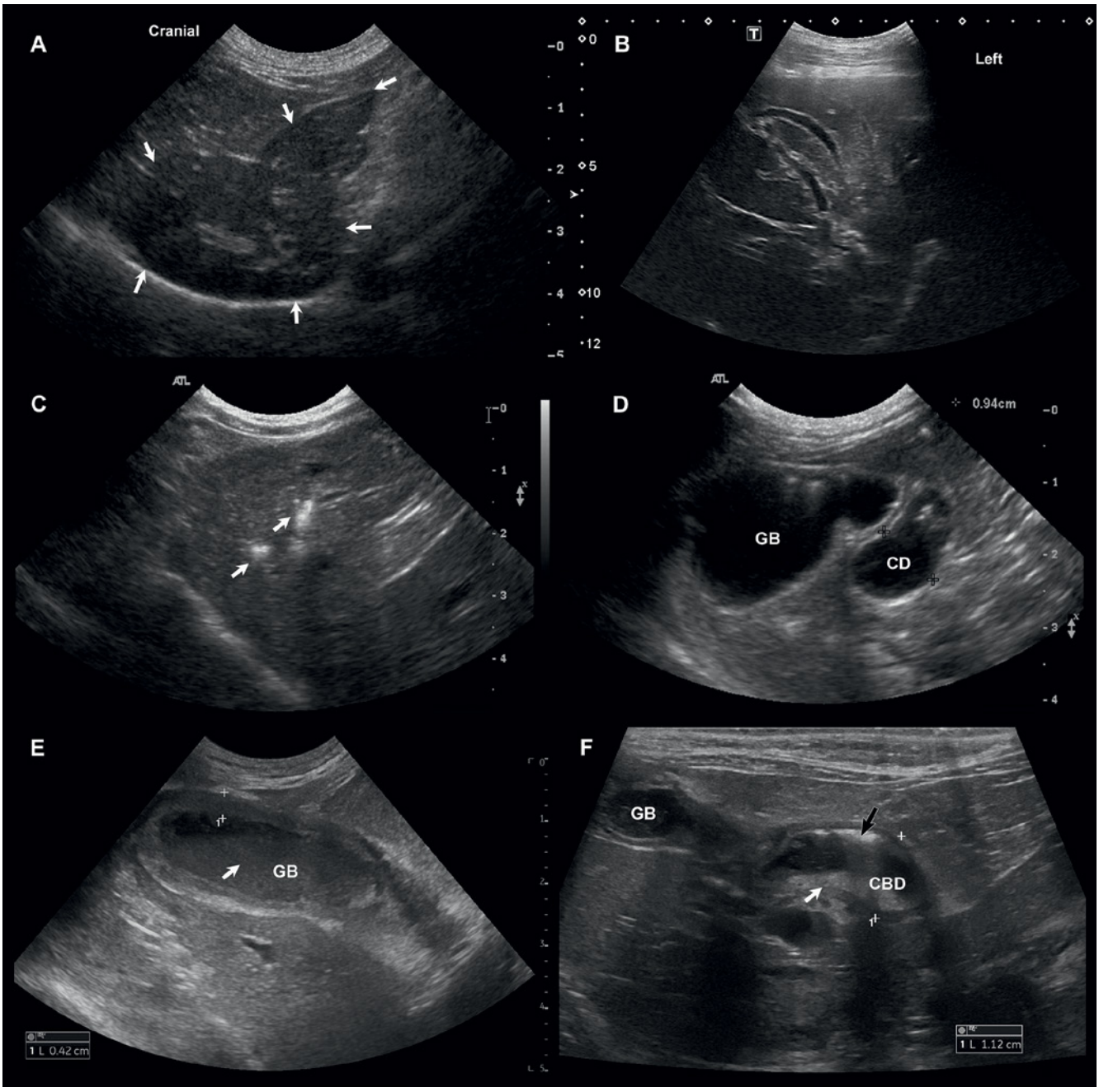


Figure 7.13. **Cholangiohepatitis in four cats. (A)** Longitudinal image of the left portion of the liver (arrows) of a cat with fever and icterus. The liver parenchyma is diffusely hypoechoic, and the portal vein margins appear prominent. These features are suggestive of cholangiohepatitis or cholangitis in cats. **(B)** Dorsal oblique image of the left portion of the liver in another cat with cholangiohepatitis. Similar features are observed. The liver is enlarged and hypoechoic. **(C, D)** Chronic, severe suppurative cholangiohepatitis and cholelithiasis (arrows) in an 8-year-old cat. The liver parenchyma in this case is hyperechoic. The cystic duct (CD) is also dilated and tortuous. GB, gallbladder. **(E, F)** In this 9-year-old female spayed diabetic cat presented for acute vomiting and dysorexia, the gallbladder (GB) is filled with echogenic sludge (arrow) and its wall is severely thickened (4.2 mm). The common bile duct (CBD) is distended (11 mm) and contains sludge (white arrow) as well as gas (black arrow). Fine-needle aspiration of the GB content and liver parenchyma revealed suppurative inflammation. Culture was negative but the cat improved with antibiotics.

Vet-ebooks.com

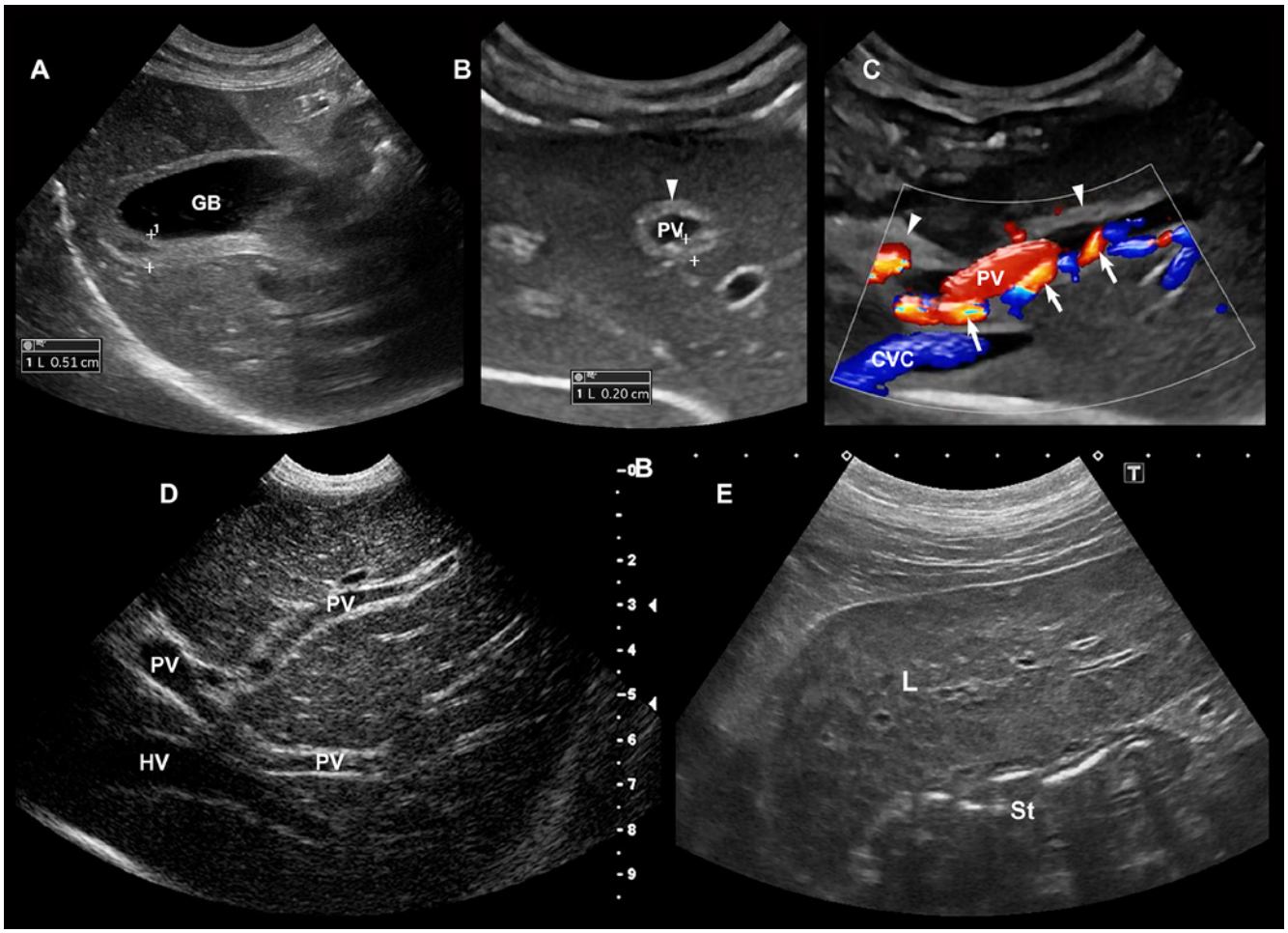


Figure 7.14. Suppurative hepatitis/cholangiohepatitis in four dogs. (A–C) In this 3-year-old Chihuahua with acute suppurative cholangiohepatitis, note the thickened gallbladder (GB) wall (**A**) and periportal tissue (arrowheads in **B, C**), and the enlarged and tortuous hepatic arteries (arrows in **C**) indicating hypertension. **(D)** Transverse oblique image of the left side of the liver in a dog with leptospirosis. The portal veins (PV) are prominent because of diffuse parenchymal hypoechogenicity. The main left hepatic vein (HV) is also observed, but its wall is less apparent. The prominence of the PV boundaries may have also been related to the inflammatory process. **(E)** Chronic suppurative hepatitis. In this 6-year-old Labrador, the liver (L) is heterogeneously hyperechoic. St, stomach.

Hepatic Neoplasia

Although several primary and secondary neoplastic processes can affect the liver in dogs and cats, diffuse hepatic involvement is less common and is usually caused by diffuse round-cell infiltration. Hepatomegaly is expected in most types of diffuse neoplasia, although its magnitude can vary with the level of infiltration.

Lymphoma can involve the liver without detectable ultrasonographic changes or cause diffuse parenchymal hypoechogenicity, hyperechogenicity, or mixed echogenicity, with or without hypoechoic nodules (Lamb et al. 1991; Whiteley et al. 1989) (Figure 7.18) **Histiocytic sarcomas** are more commonly associated with hypoechoic nodules and masses, although diffuse hepatic hypoechogenicity has been reported (Cruz-Arambulo et al. 2004) (Figure 7.19). Conversely, **mast cell infiltration** of the liver tends to cause diffuse hyperechogenicity (Sato and Solano 2004), although, as for other round-cell infiltrations, several manifestations are possible (Figure 7.20). **Hepatic carcinomas** can also be diffuse, or involve one or multiple lobes, with a variable ultrasonographic appearance that depends on the presence of necrosis, inflammation, hemorrhage, or cavitation. A mixed pattern of echogenicity is common with these malignant tumors (Figure 7.21).

Miscellaneous Diffuse Hepatic Disorders

Other types of hepatopathies can be encountered in small animals, although less commonly. **Amyloidosis**, primarily affecting Shar-peis and Abyssinian and

Vet-ebooks.com

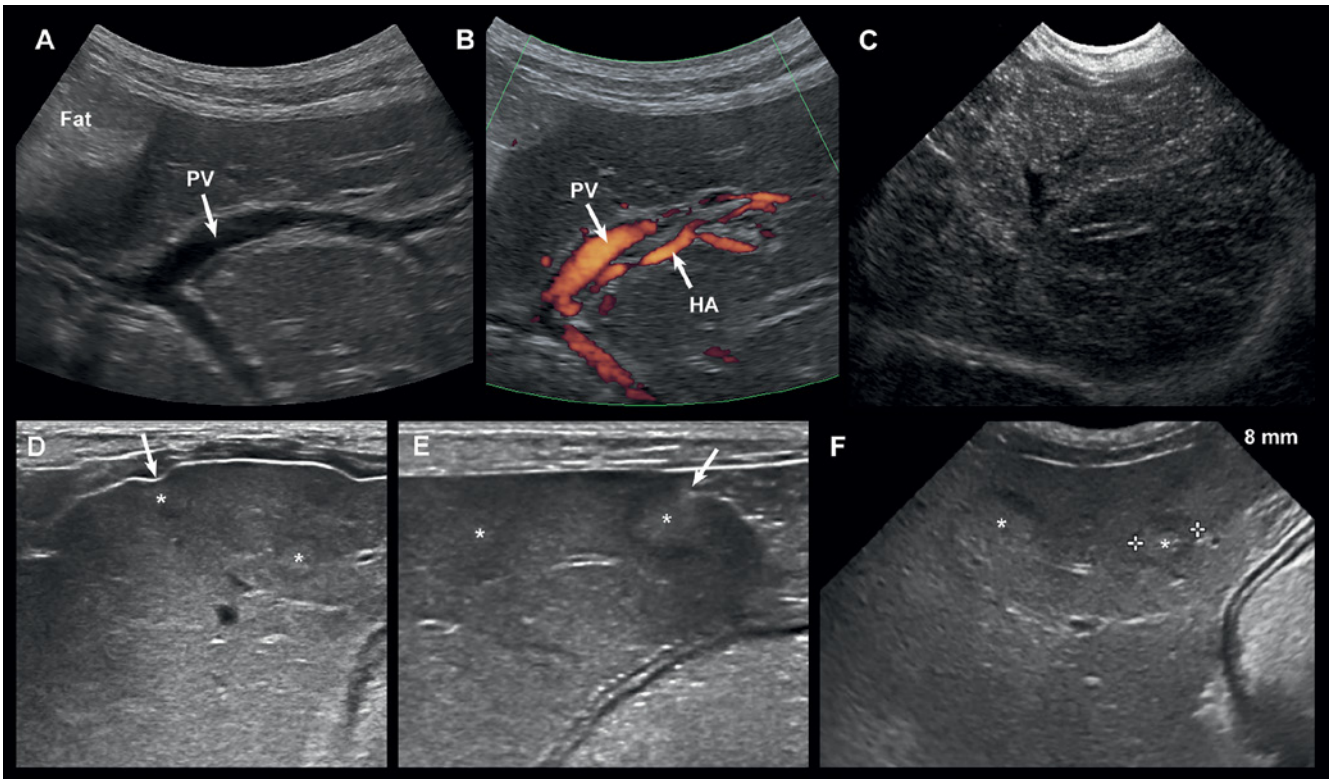


Figure 7.15. **Granulomatous cholangiohepatitis in dogs. (A, B)** In these longitudinal B-mode **(A)** and Power Doppler **(B)** images of a dog with mildly elevated alanine aminotransferase (ALT), the periportal spaces are thickened and irregular and the hepatic arterial (HA) flow is prominent. The falciform fat is hyperechoic. Surgical biopsies revealed severe inflammation primarily involving the portal triads and periportal tissues of unknown etiology (normal cultures and copper level). PV, portal vein. **(C) Parasitic infestation** (***Heterobilharzia americana***) in a 6-year-old Dachshund with increased liver enzyme elevation detected on a lab work screening before an elective dental procedure. The liver is very coarse and core biopsies revealed multifocal granulomatous cholangitis and moderate hepatocellular hypertrophy. In the center of many of the granulomas were foci of mineral and/or degenerate parasites. See Figure 9.32 for intestinal changes in the same dog. **(D–F)** In this 6-year-old with severe, coalescing granulomatous hepatitis, numerous faint, target-like lesions (*) were noted in the enlarged and mostly hyperechoic liver. The most superficial nodules displayed concave depression (arrows), along the surface of the liver. The nodule marked by calipers measures 8 mm in diameter.

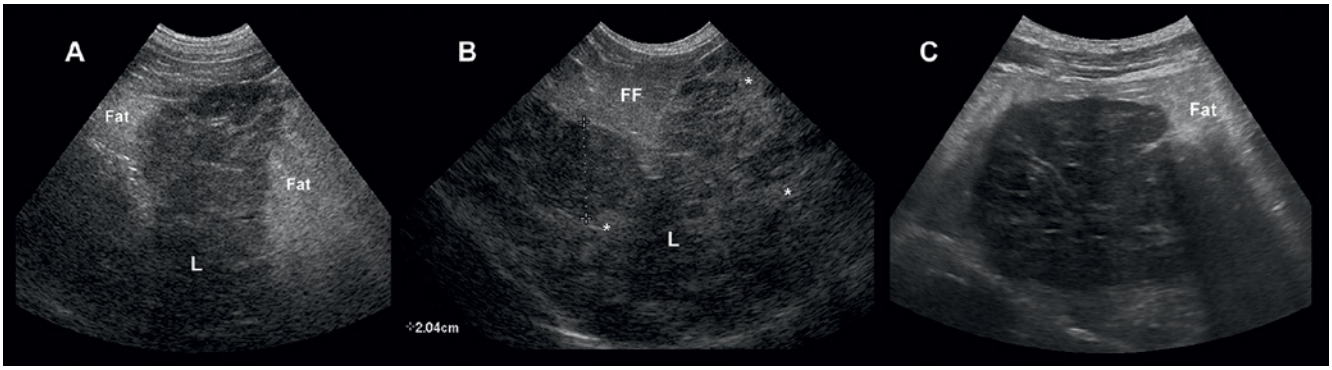


Figure 7.16. **Chronic active hepatitis and nodular hyperplasia. (A)** Longitudinal image of the left portion of the liver (L), which appears diffusely hypoechoic, and with irregular and ill-defined contours. The adjacent fat is hyperechoic. Chronic active hepatitis was diagnosed on fine-needle aspiration and ultrasound-guided biopsy. **(B)** Transverse image of the left portion of the liver (L) in another dog with diffuse parenchymal heterogeneity. Several hypoechoic coalescing nodules are found that reach up to 2 cm as well as hyperechoic patches (*). Ultrasound-guided biopsy-confirmed chronic hepatitis with fibrosis and nodular hyperplasia. FF, falciform fat. **(C)** In this 5-year-old, male Doberman pinscher with copper-storage chronic hepatitis, the liver is hypoechoic and mildly inhomogeneous, surrounded with hyperechoic fat.

Vet-ebooks.com

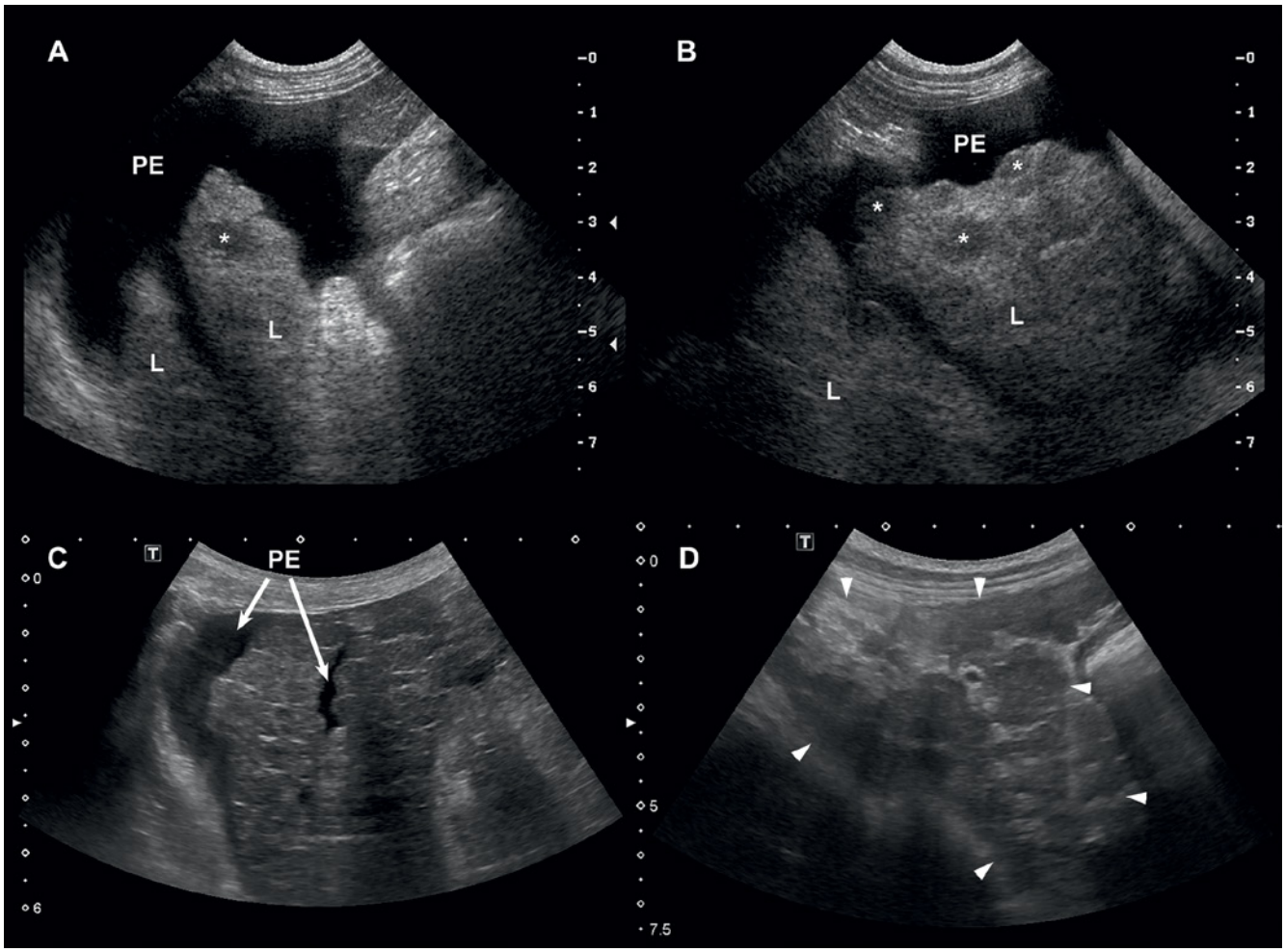


Figure 7.17. Hepatic cirrhosis in three dogs. Transverse oblique images of the right **(A)** and left **(B)** portions of the liver (L) in a dog with chronic hepatic insufficiency. All lobes are small and hyperechoic. Hypoechoic nodules (*) are found throughout the parenchyma, irregularly deforming its contours. These contours are visualized because of the presence of a large volume of anechoic peritoneal effusion (PE). These findings are common in end-stage cirrhosis in dogs. **(C)** In this Cocker Spaniel, the liver is more uniformly echogenic, with nodular contours that are made evident by the presence of PE. **(D)** The liver (arrowheads) of this other small-breed dog is more heterogeneous with hyperechoic areas. A small volume of effusion was present but not seen in this image.

Siamese cats, can cause hepatic enlargement and parenchymal ultrasonographic changes. In cats, the liver tends to become diffusely heterogeneous with mixed hyperechoic and hypoechoic foci (Beatty et al. 2002). Spontaneous hepatic rupture and hemoabdomen can also be caused by massive hepatic amyloidosis or also reported in peliosis hepatis in cats (Brown et al. 1994). In dogs with **hepatocutaneous syndrome** (superficial necrolytic dermatitis), the liver can become highly hyperechoic with diffusely distributed 0.5–1.5 cm-wide hypoechoic regions, producing a honeycomb pattern (Nyland et al. 1996, Burn-DeMArle et al. 2021) (Figure 7.22).

Focal Hepatic Parenchymal Disorders

The improvement in ultrasound equipment technology has increased the sensitivity of ultrasonography in detecting focal hepatic lesions. It has been suggested that well-differentiated carcinomas (also called hepatomas) exceeding 5 mm can be detected in ideal imaging conditions in people (Nyman et al. 2004). The conspicuity of a focal lesion is also greatly influenced by its imaging characteristics. Hence, for a given size, an anechoic cyst is more likely to be detected than a soft-tissue nodule of echogenicity similar to one of adjacent normal parenchyma. Although various types of focal lesions can be detected with ultrasonography, the

Vet-ebooks.com

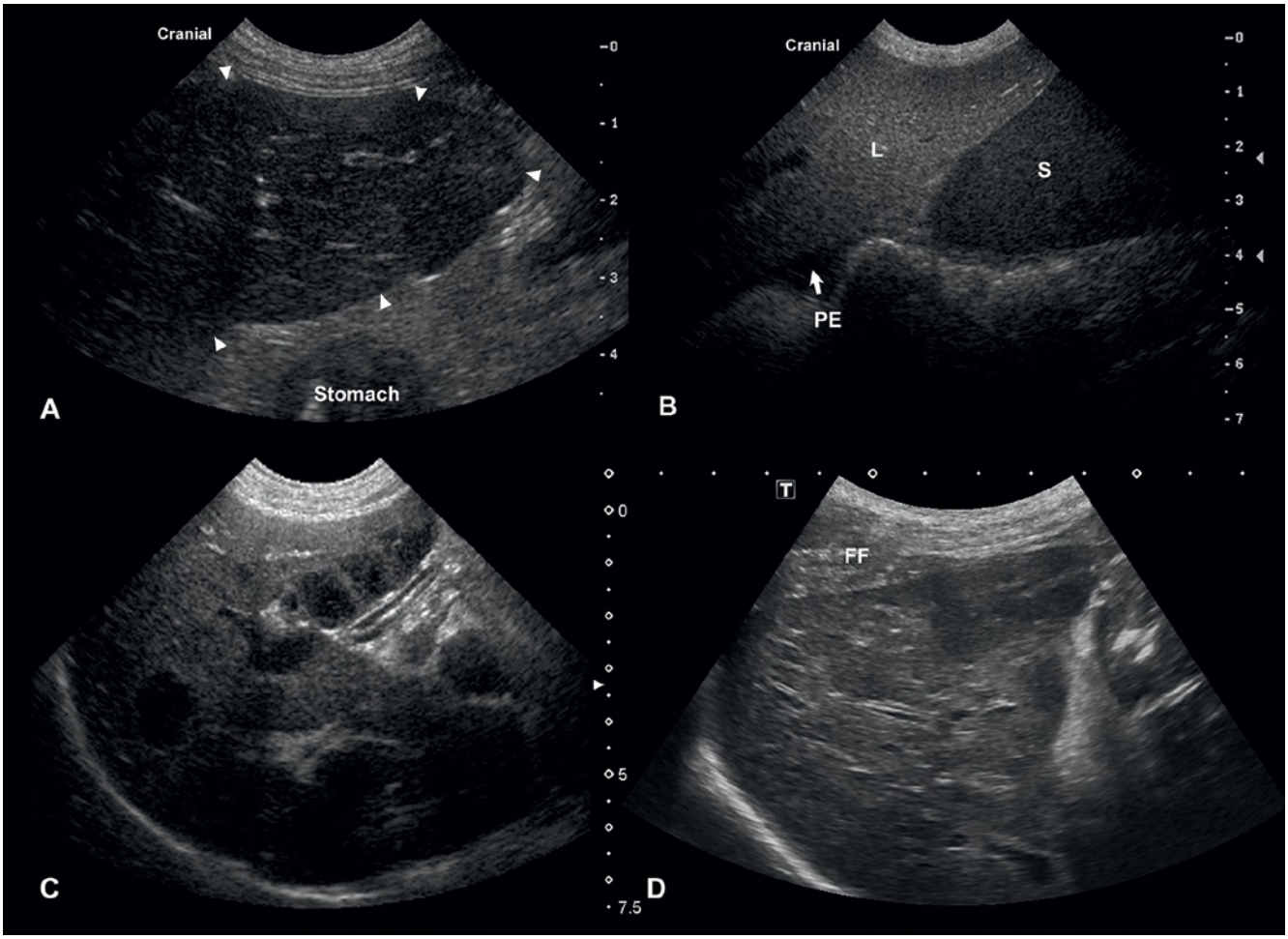


Figure 7.18. **Lymphoma in four dogs. (A)** Transverse oblique image of the left portion of the liver in a dog with multicentric lymphoma. The portal vein walls are prominent because of diffuse parenchymal hypoechogenicity. The left lateral hepatic lobe is enlarged (arrowheads), extending several centimeters caudal to the stomach, and its caudal tip is rounded. **(B)** Lymphoma can also cause diffuse hepatic hyperechogenicity (L), as seen in another dog. The spleen (S) is relatively hypoechoic. Both organs are enlarged and their borders are rounded. Peritoneal effusion is also present (PE). **(C)** In another dog with lymphoma, multiple, well-defined, hypoechoic nodules (*) are noted throughout the liver. **(D)** The liver of this other dog is heterogeneous. FF, falciform fat.

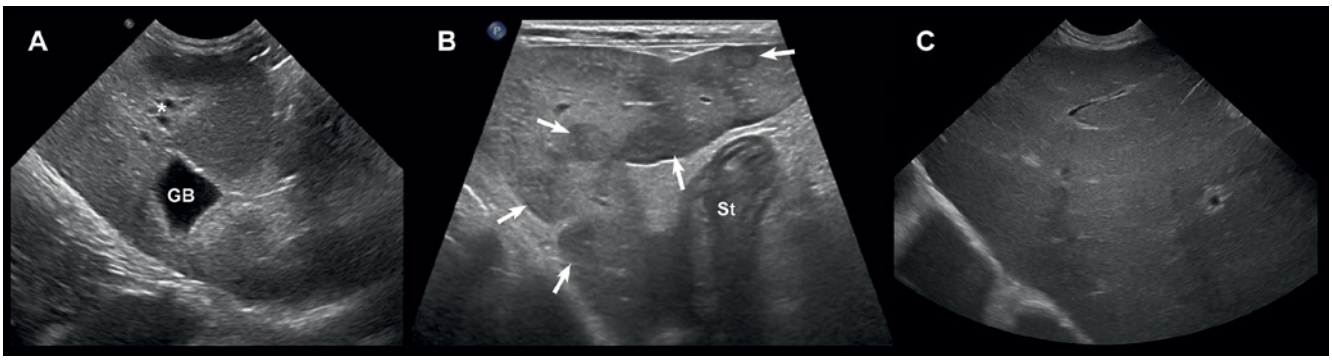


Figure 7.19. **Diffuse hepatic histiocytic sarcoma in two dogs. (A, B)** 9-year-old Beagle with hepatomegaly and increased liver enzymes. The dog is otherwise doing well. The liver is moderately enlarged and hyperechoic with hyperechoic and partially lacy foci (arrow). The liver lobes are irregularly shaped and deform the contour of the gallbladder (GB). Using a high-resolution linear probe (in **B**), faint and deforming hypoechoic to target-like nodules are also noted (arrows). At times, these lesions can mimic granulomatous hepatitis and inversely, histopathologically. St, stomach. **(C)** In this 7-year-old male Husky, the liver is markedly enlarged, but remains normal in echogenicity and uniformity. The spleen and several abdominal lymph nodes were also enlarged.

Vet-ebooks.com

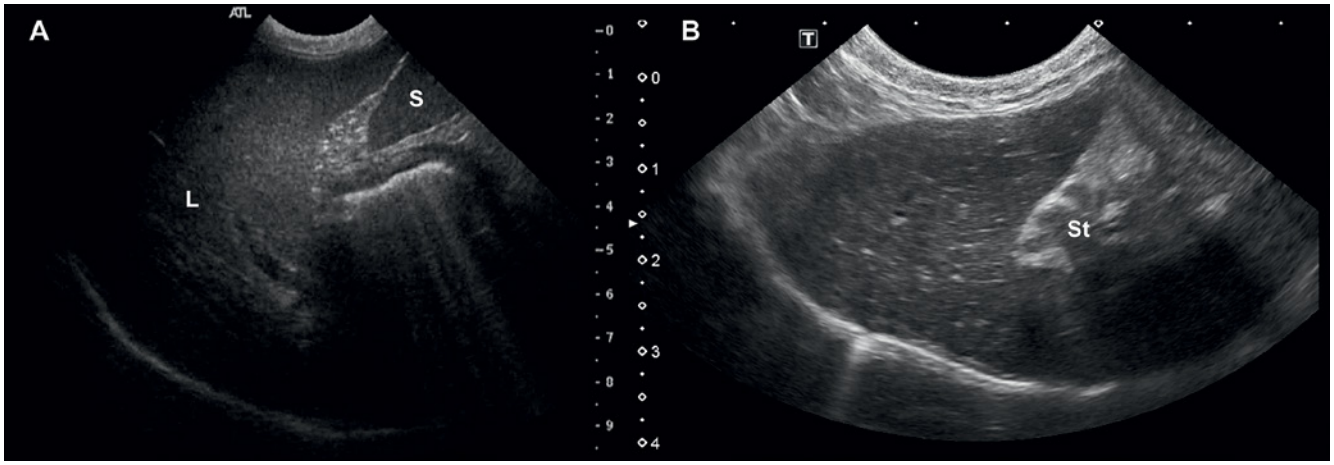


Figure 7.20. **Mast cell infiltration in a dog and a cat. (A)** In this dog, the liver (L) is uniformly hyperechoic. S, spleen. **(B)** In this cat, by contrast, the liver was hypoechoic, confirming that round-cell infiltrations can manifest variable echogenic patterns.

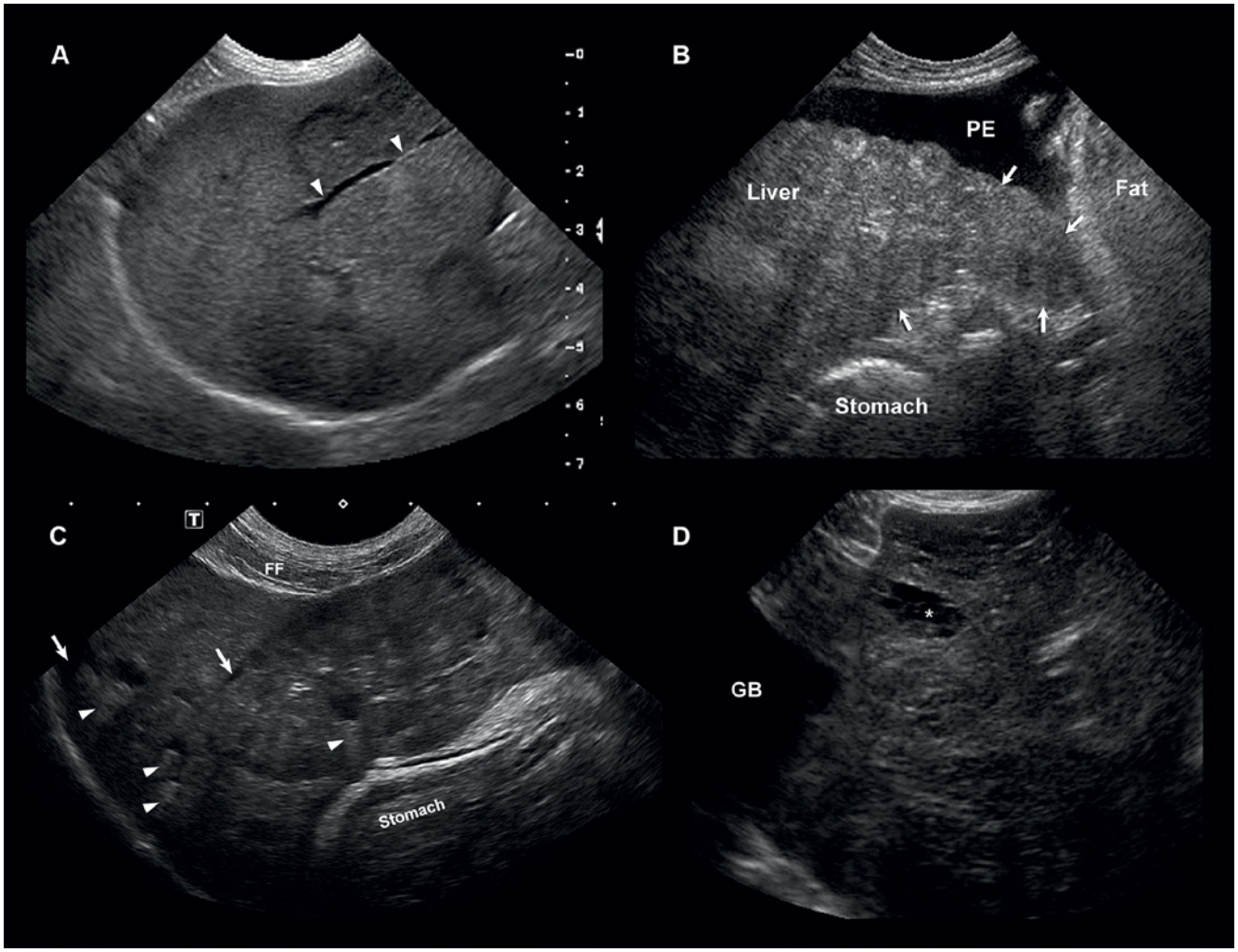


Figure 7.21. **Diffuse hepatic carcinoma and hemangiosarcoma. (A) Hepatic adenocarcinoma in a cat**. The liver is moderately enlarged and mildly inhomogeneous, with several ill-defined hypoechoic areas. The neoplastic infiltration deforms the vasculature (arrowheads). **(B) Hepatocellular carcinoma in a dog**. Longitudinal image of the left lateral hepatic lobe in a dog with diffuse hepatocellular carcinoma. This lobe extending caudal to the stomach (arrows) is hyperechoic and presents a nodular border. Marked peritoneal effusion is also evident ventrally (PE). **(C) Hepatic carcinoma in a cat**. In this 11-year-old cat with weight loss and increased liver enzymes, the liver is heterogeneous and presents several anechoic cavitary areas, some of which are associated with acoustic enhancement (arrowheads). Peritoneal effusion (arrows) is also present between liver lobes and along the diaphragm. FF, falciform fat. **(D) Diffuse hemangiosarcoma in a dog**. The infiltrative process mimicked benign vacuolar hepatopathy with biliary cystic (*) changes. GB, gallbladder.

Vet-ebooks.com

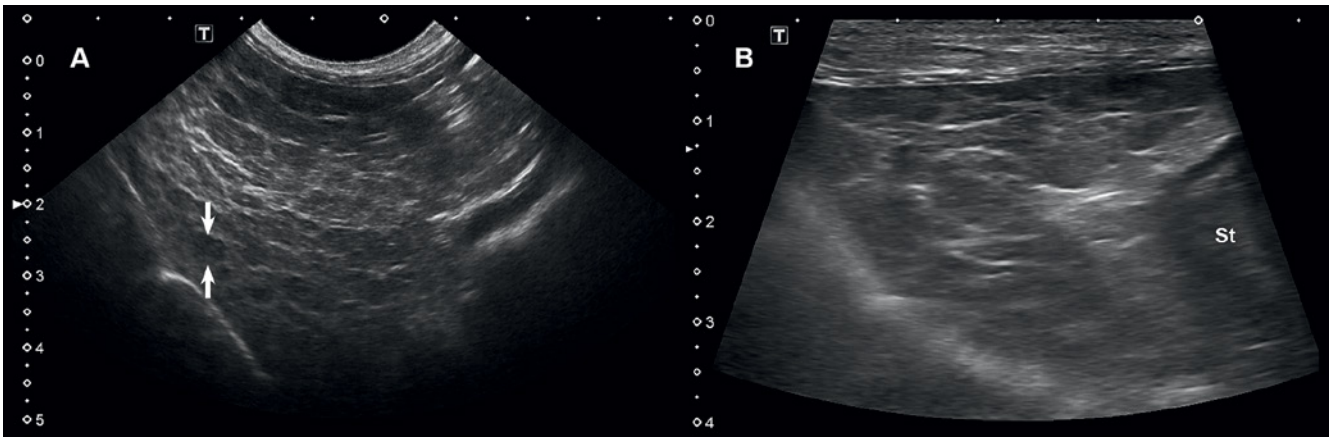


Figure 7.22. **Hepatocutaneous syndrome in two dogs. (A)** Sagittal image of the left central portion of the liver of a dog with superficial necrolytic dermatitis. Diffusely distributed hypoechoic irregular foci (arrows) are surrounded by hyperechoic parenchyma, giving a honeycomb pattern. **(B)** Similar changes are present in this 9-year-old spayed female Bichon with the same condition. St, stomach.

Table 7.3
Diagnostic differentials for focal hepatic lesions with ultrasonography

Anechoic	Hypoechoic	Hyperechoic	Mixed echogenicity
Cyst	Nodular hyperplasia	Nodular hyperplasia	Nodular hyperplasia
Cystic tumor	Metastasis	Primary neoplasia	Primary neoplasia
Necrosis	Lymphoma	Metastasis	Metastasis
Hematoma	Histiocytic sarcoma	Mineralization or cholelithiasis	Abscess
Abscess	Primary hepatic neoplasia	Abscess	Hematoma
	Abscess	Fat or myelolipoma	Granuloma
	Necrosis	Granuloma	
	Hematoma	Gas	
	Complex cyst	Metallic clip	

appearance of several of these processes is quite variable, resulting in limited diagnostic specificity. The advances in contrast harmonic ultrasonography have helped to increase the overall diagnostic accuracy and may prove to be useful in clinical settings (Nyman et al. 2004; O'Brien et al. 2004).

Table 7.3 lists the diagnostic differential for focal hepatic lesions, based on their typical appearance. Although some trends in ultrasonographic appearance have been reported for some of these processes, a definitive diagnosis usually requires fine-needle aspiration or biopsy.

Benign Hyperplasia and Neoplasia

Nodular hyperplasia is common, particularly in dogs, and accounts for many focal hepatic lesions identified with ultrasonography. Although these regenerative nodules can vary in echogenicity and size, they tend to appear as hypoechoic nodules measuring less than 5–15 mm wide (O'Brien et al. 2004; Stonewater et al. 1990) (Figure 7.23). As for most other types of focal lesions, their margin can be well or poorly defined. Hepatic **adenomas** cannot be differentiated from **carcinomas** or **hepatomas**; they appear as masses of variable size and are usually isoechoic to hyperechoic, although they may also present cavities (O'Brien et al. 2004) (Figure 7.24).

Malignant Neoplasia

The liver is a common target for **metastases**, mainly through the portal system, which drains most abdominal structures. Primary hepatic neoplasms such as **hepatocellular carcinomas** can also be seen as focal or multifocal masses, although less frequently than metastasis. The variable tissue characteristics of primary and metastatic neoplastic processes, including tissue density,

Vet-ebooks.com

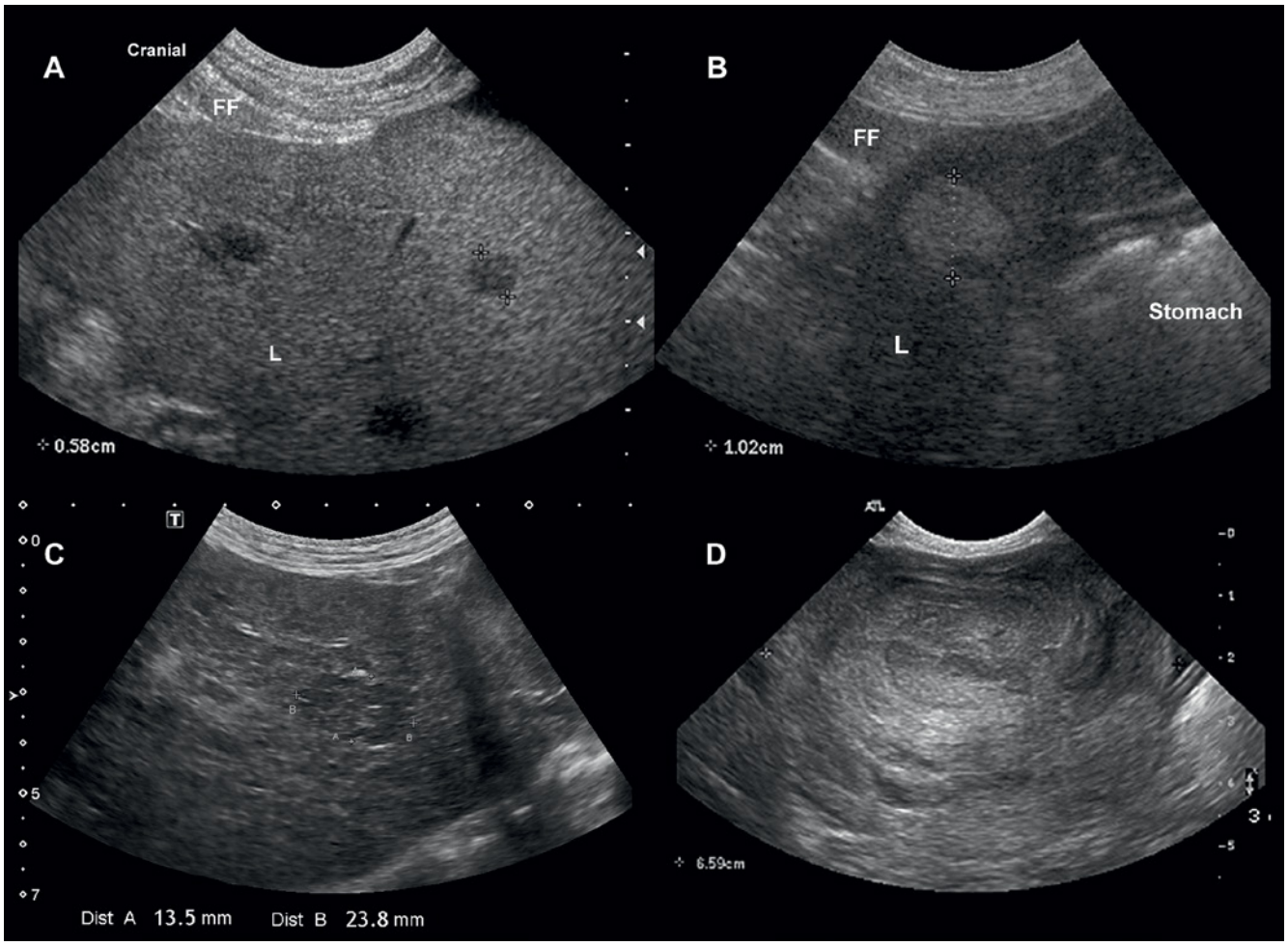


Figure 7.23. **Nodular hyperplasia in four dogs. (A)** Several poorly defined hypoechoic foci measuring less than 1 cm wide are noted in a liver (L) that is otherwise hyperechoic. FF, falciform fat. **(B)** The regenerative nodule in this other dog is hyperechoic and well defined. **(C)** Nodular hyperplasia (between cursors) can also appear more heterogeneous. **(D)** Nodular hyperplasia with acute and chronic hemorrhage and necrosis forming a 6.6 cm heterogeneous mass in this 11-year-old Pomeranian dog.

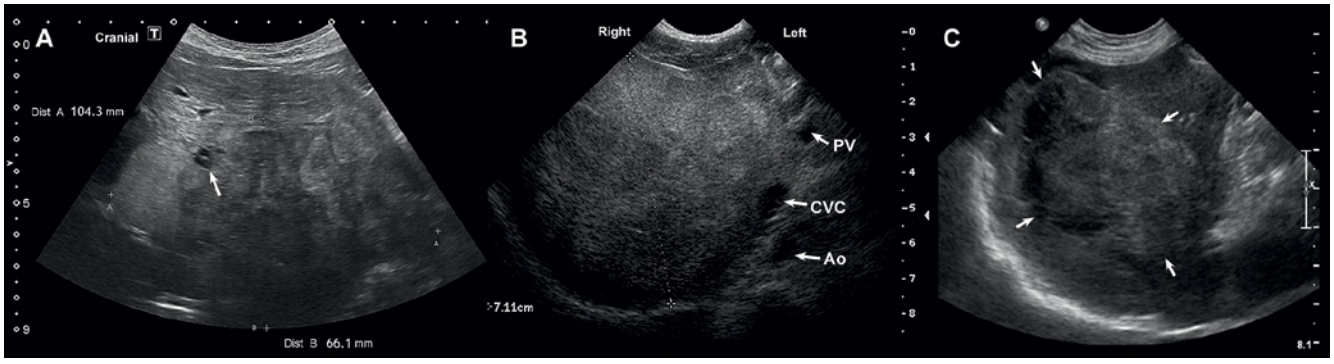


Figure 7.24. **Well-differentiated hepatic carcinoma in three dogs. (A)** Irregular and poorly defined mass in the left portion of the liver of this 12-year-old small breed dog. The mass (between cursors) is moderately echogenic and mildly heterogeneous, with a few small cavities (arrow indicates one present in this image). **(B)** Transverse image of the right portion of the liver of another dog with increased liver enzymes. A large, mildly hyperechoic and mildly heterogeneous mass measuring at least 7 cm wide is in the right portion of the liver and in contact with the portal vein (PV) and caudal vena cava (CVC), and close to the aorta (Ao). The extent of this mass and the lack of vascular invasion could not be confirmed on ultrasound and required computed tomography. **(C)** A large (over 4.5 cm) inhomogeneous hyperechoic mass with an irregular hypoechoic center is present in this 13-year-old cocker spaniel cross. The mass was surgically removed and diagnosed as a well-differentiated hepatic carcinoma with a necrotic center

Vet-ebooks.com

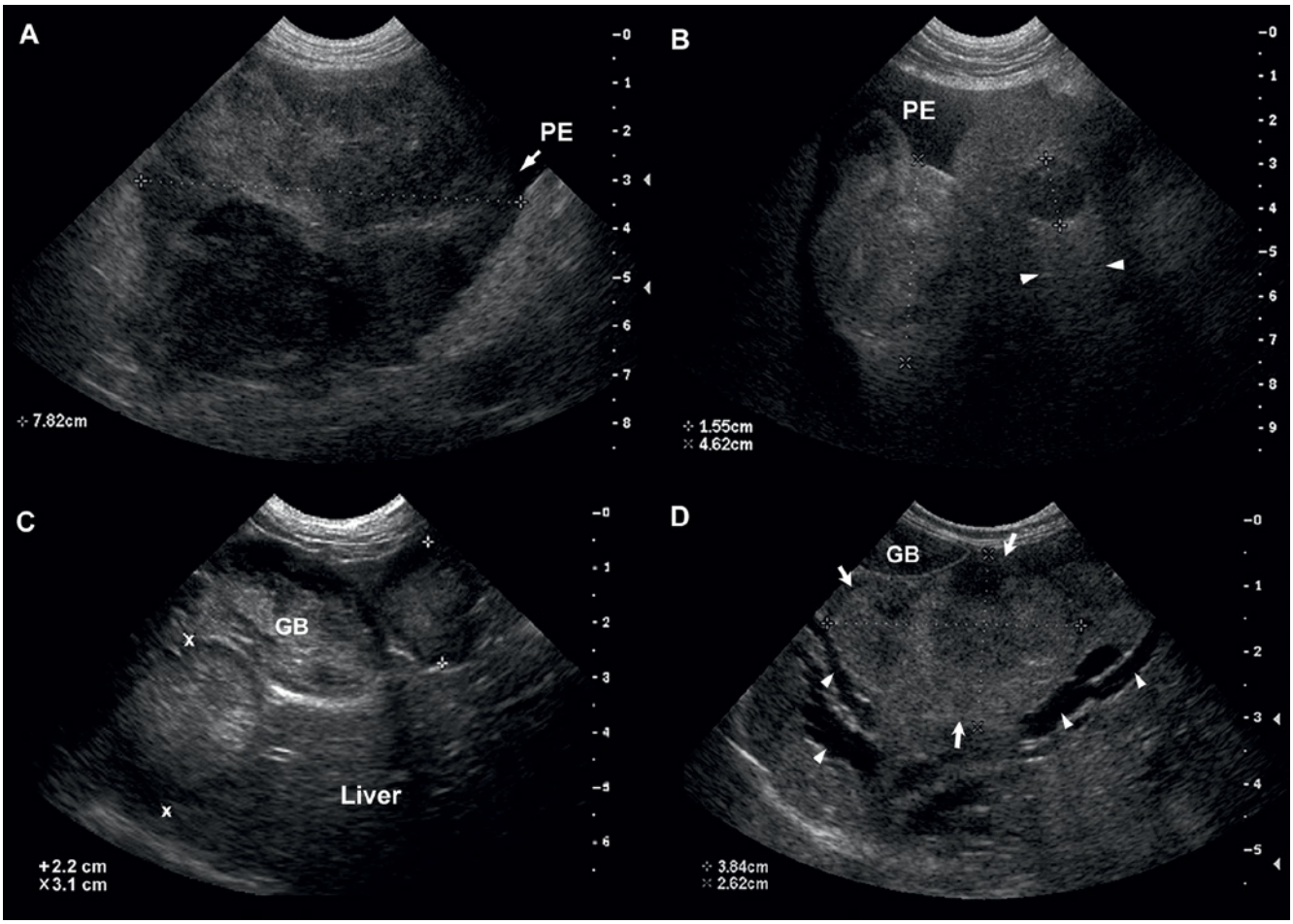


Figure 7.25. **Liver carcinomas. (A) Hepatocellular carcinoma in a dog**. Transverse image obtained in the right cranial abdomen of a dog with a hemoabdomen. An irregular, inhomogeneous and poorly defined mass (7.8 cm wide) is deforming the architecture of a liver lobe. A small amount of peritoneal effusion (PE) is noted around the mass. **(B) Hepatic adenocarcinoma and metastasis in a dog**. A spherical, hyperechoic mass (4.6 cm) is deforming the contour of a liver lobe and surrounded by mildly echogenic PE. Another small, hypoechoic nodule (1.6 cm) in the same lobe is associated with acoustic enhancement in the far field (arrowheads). **(C) Neuroendocrine carcinoma in a dog**. Multiple mildly hyperechoic masses (2.2–3.1 cm) demonstrating a hypoechoic halo were found in the liver of this dog, with a histological diagnosis of neuroendocrine carcinoma. GB, gallbladder. **(D) Biliary carcinoma in a cat**. Transverse image of the liver in a cat with icterus. A lobulated, mildly hyperechoic, inhomogeneous mass (arrows and cursors) is displacing the gallbladder (GB) ventrally. Irregular, anechoic, tubular structures (arrowheads) are also noted throughout the liver, consistent with dilated intrahepatic biliary ducts.

vascular pattern, necrosis, liquefaction, and calcification, cause variable ultrasonographic appearances (O'Brien et al. 2004; Whiteley et al. 1989) (Figures 7.24-7.31). Focal hypoechoic lesions with a hyperechoic center, also termed **target lesions**, are usually predictive of metastases (Figures 7.26 and 7.29), although benign processes such as nodular hyperplasia or granulomas can cause a similar pattern (Cuccovillo and Lamb 2002; O'Brien et al. 2004, Prentice et al. 2023) (Figure 7.15 D-F). It has been reported that the finding of at least one target lesion in the liver or spleen had a positive predictive value of 74% for malignancy in small animals (Cuccovillo and Lamb 2002). Other features supportive of malignancy include lesion size (>3 cm) and the presence of peritoneal effusion (Guillot et al. 2009; Murakami et al. 2012). Additional features distinguishing malignant from benign hepatic masses may be found with triple-phase computed tomography (CT) (Kutura et al. 2013).

Histiocytic sarcoma and **lymphoma** can demonstrate similar imaging characteristics. Although findings do vary, particularly with lymphoma, multifocal nodules or masses, hypoechoic or mixed in echogenicity, are commonly found with these processes (Cruz-Arambulo et al. 2004; Ramirez et al. 2002) (Figures 7.18, 7.19, and 7.31). Significant hepatic lymphadenopathy is also common with these neoplasms of round-cell origin and their presence often helps in diagnosing these processes.

Vet-ebooks.com

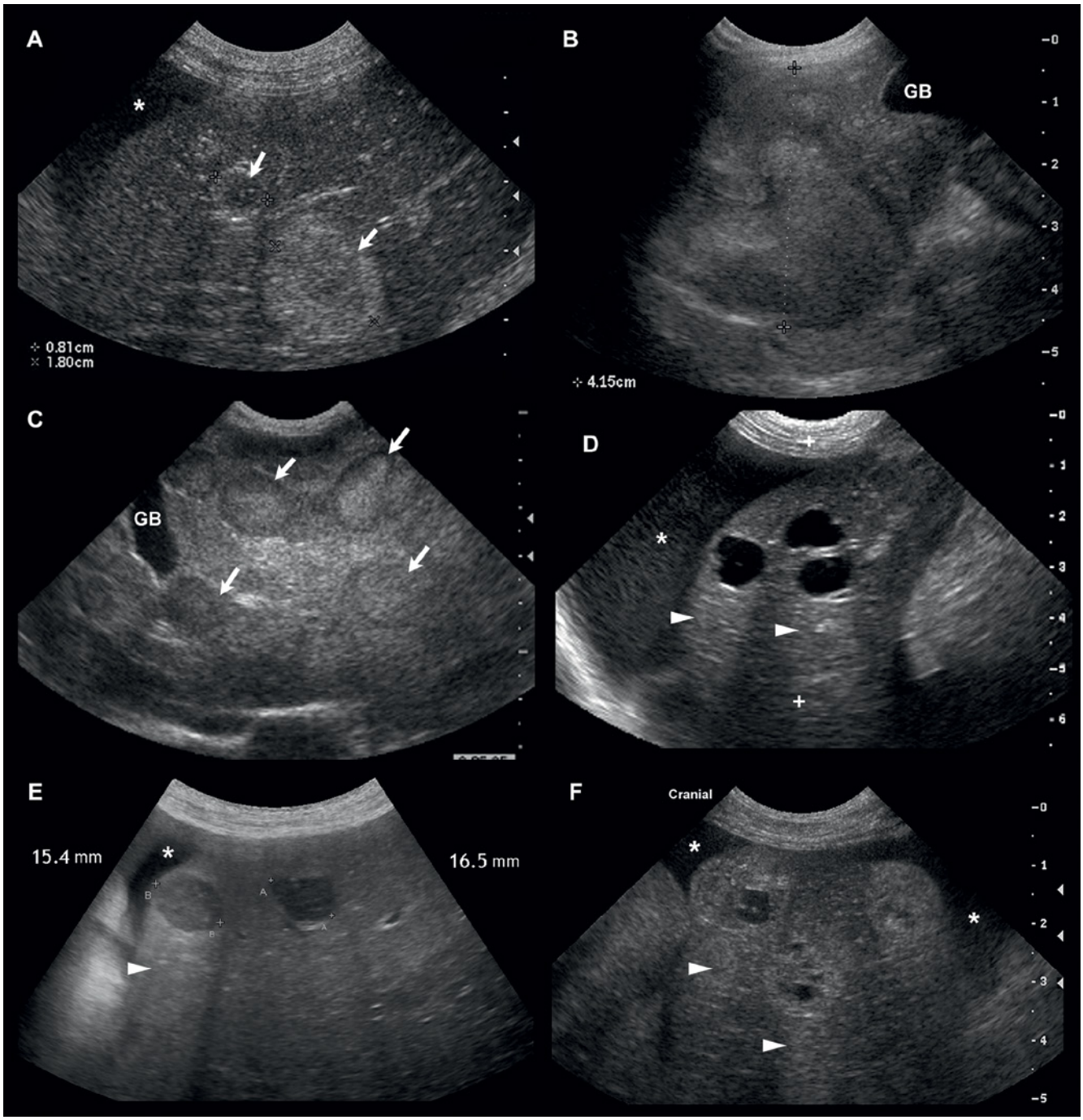


Figure 7.26. **Hepatic metastases. (A, B)** From **pancreatic adenocarcinoma in two dogs**. **(A)** Oblique image of the left hepatic lobe with two distinct metastatic nodules (arrows). A smaller hypoechoic nodule with a thin hyperechoic rim and a larger hyperechoic nodule are present, measuring 0.8 and 1.8 cm wide, respectively. Mildly echogenic peritoneal effusion (*) is present. **(B)** A 4-cm inhomogeneous mass is in the liver of this other dog with malignant pancreatic neoplasia. The findings on fine-needle aspiration supported a diagnosis of pancreatic metastasis. GB, gallbladder. **(C)** From **thyroid carcinoma in a dog**. Multiple "target" lesions (arrows) are seen throughout the liver. The hypoechoic halo seen at the periphery of these rather hyperechoic nodules is a feature that is most commonly observed with metastases. GB, gallbladder. **(D–F)** From **splenic hemangiosarcomas in three dogs**. Nodules of variable echogenicity are seen, many associated with acoustic enhancement (arrowheads), which is consistent with a cavitary component that is commonly seen with these metastases. Hemoabdomen was present in all three (*).

Vet-ebooks.com

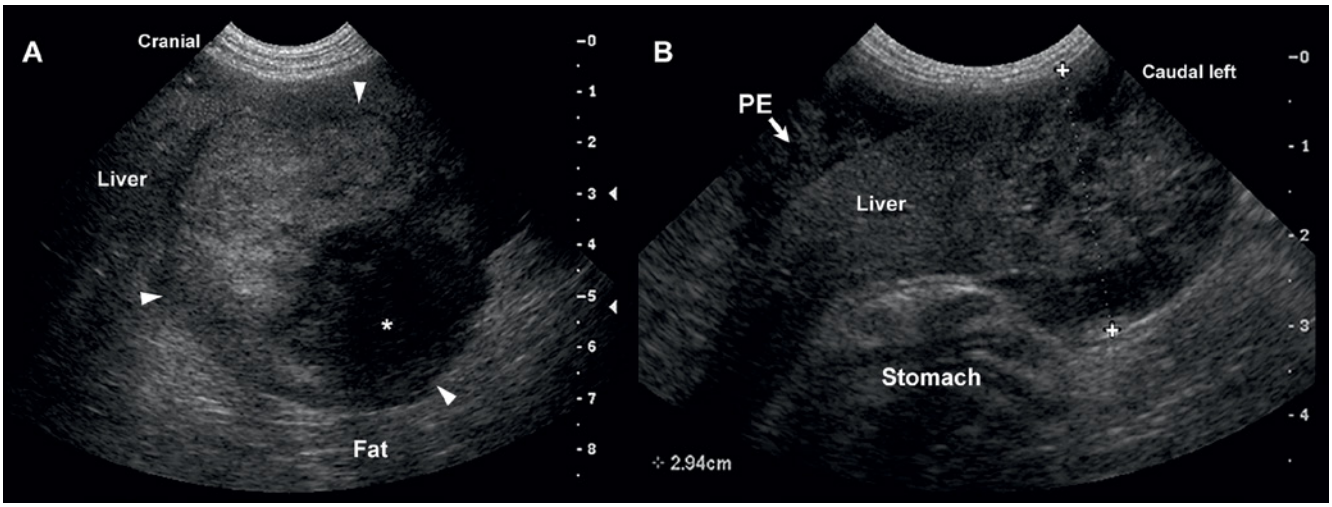


Figure 7.27. **Hepatic hemangiosarcoma in a dog and a cat. (A)** Longitudinal image obtained of the left portion of the liver in a dog with acute hemoabdomen. A large hyperechoic mass (arrowheads) with a hypoechoic necrotic area (*) involves the margin of a hepatic lobe. These features are common with malignant tumors. **(B)** Oblique image of the left portion of the liver in a cat with hemoabdomen. A 3-cm-wide inhomogeneous mass with small anechoic cavitary portions is at the caudal tip of the left lateral liver lobe. Peritoneal effusion (PE) with echogenic floating structures is identified in the cranioventral abdomen, consistent with hemorrhage.

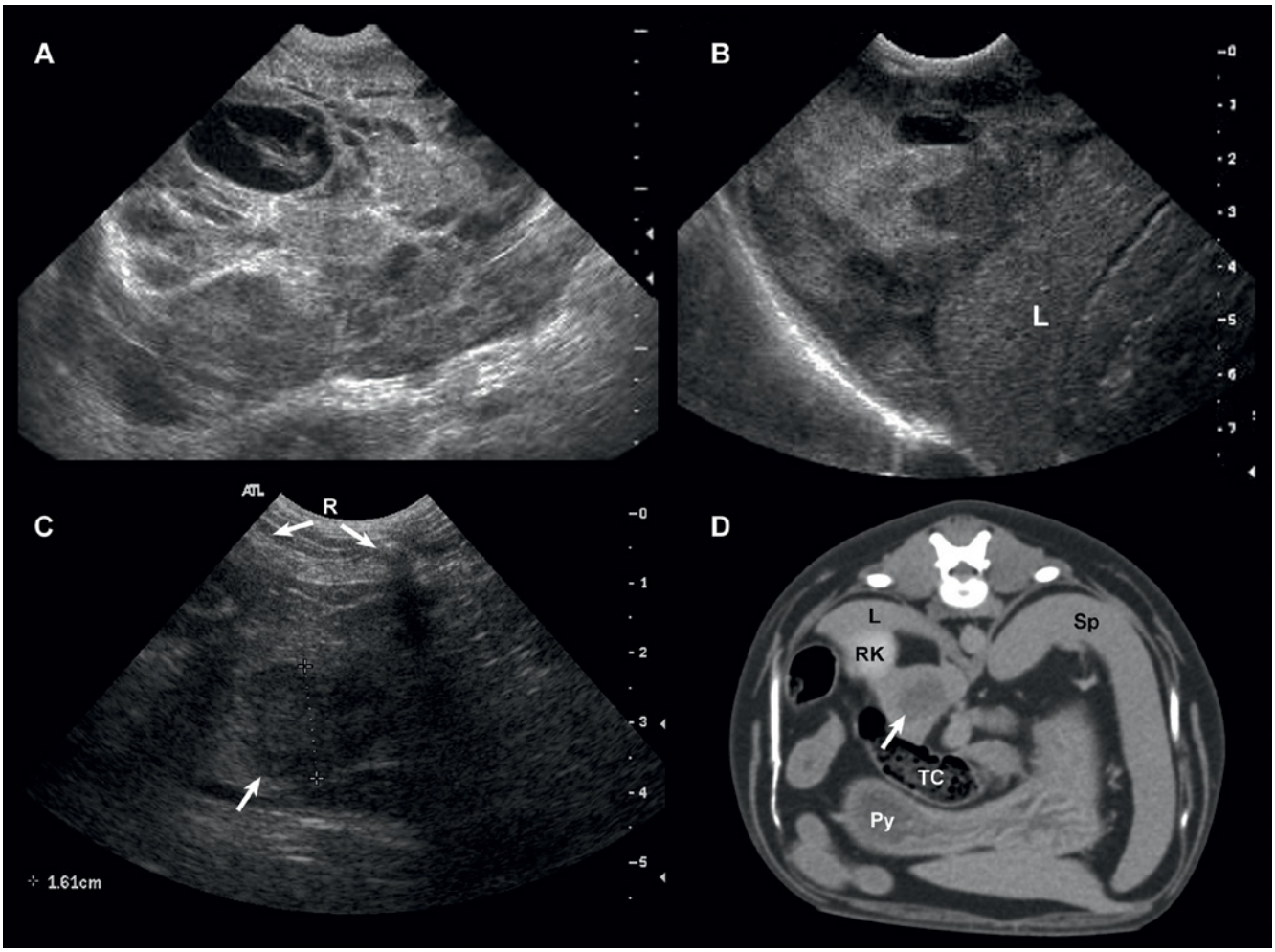


Figure 7.28. **Unusual liver tumors in two dogs. (A, B) Myxosarcoma**. A large, markedly heterogeneous, cavitated mass in the liver of this dog **(A)** is disturbing most of the hepatic architecture. The same tumor was reimaged 3 months later **(B)**. In this image, a clear distinction is made between the heterogeneous mass and the normal liver (L). **(C, D)** In another dog with hypoglycemia, a small **insulinoma-like tumor** was identified in the caudate liver lobe (arrows). A longitudinal sonographic image **(C)** was obtained from a right intercostal approach. R, ribs. Computed tomography **(D)** was used to confirm the location of this mass. L, liver; Py, pyloric antrum; RK, right kidney; Sp, spleen; TC, transverse colon.

Vet-ebooks.com

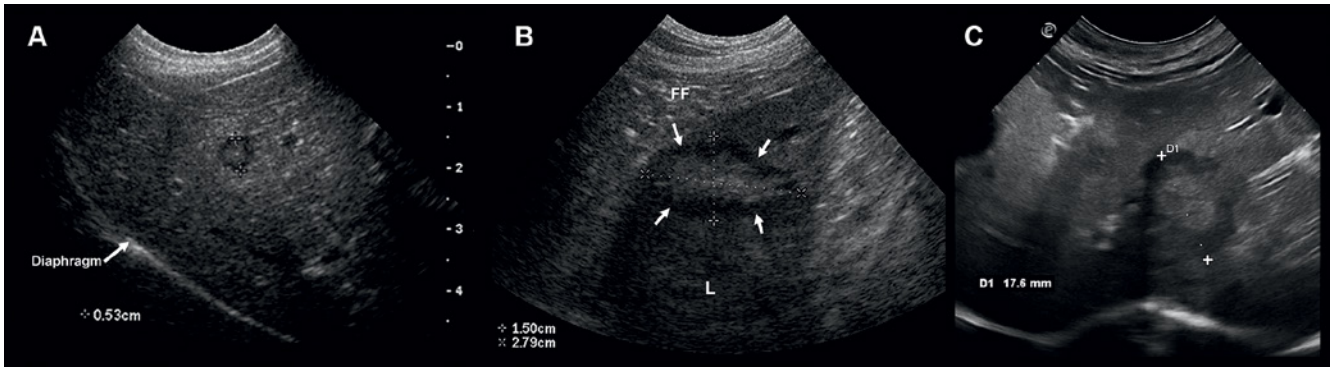


Figure 7.29. **Target lesions. (A)** Longitudinal image of the mid-portion of the liver in a dog with **intestinal carcinoma**, on which a small nodule outlined by a peripheral hypoechoic halo is seen. The central portion of this lesion is more echogenic, giving the impression of a target. **(B)** Longitudinal oblique image of the left portion of the liver of a dog with a primary **hepatocellular carcinoma** identified in the right lateral lobe. An ovoid nodule with a peripheral hypoechoic halo and a more echogenic center (arrows), consistent with metastasis, is in the liver (L). Smaller but similar target lesions were found in the rest of the liver. FF, falciform fat. **(C)** Transverse image of the liver of an 8-year-old cat with **pancreatic adenocarcinoma**.

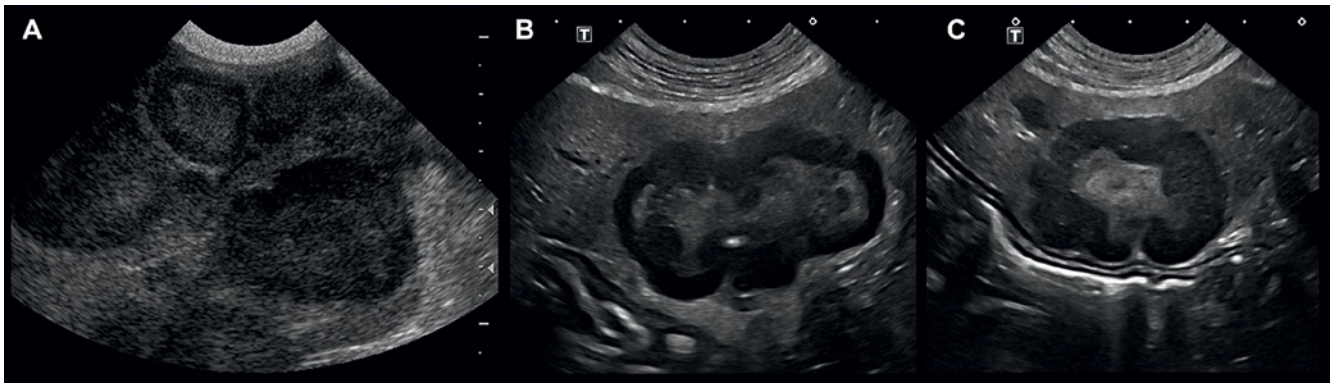


Figure 7.30. **Disseminated histiocytic sarcoma in two dogs. (A)** Multiple hypoechoic nodules and masses (more than 3 cm wide) are in the liver of this Bernese Mountain dog. These lesions are relatively well circumscribed and have a mildly echogenic center. The liver was also enlarged. **(B, C)** Long (B) and short (C) axis views of an irregularly shaped, heterogeneous, mixed hypo- and hyperechoic, almost targetoid, mass identified within the liver of a Pembroke Welsh Corgi. Additional similar nodules/masses were detected elsewhere in the liver, the spleen, the kidneys, and throughout the mesentery.

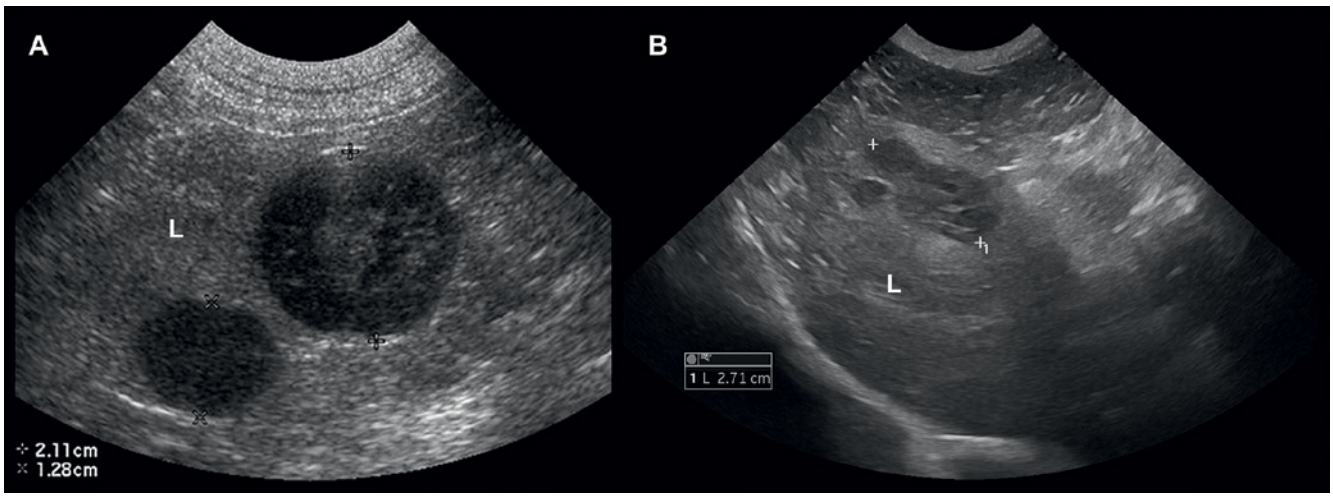


Figure 7.31. **Lymphoma in two dogs. (A)** Close-up longitudinal image of the left portion of the liver (L) of a dog with multicentric lymphoma. Two well-defined hypoechoic nodules, reaching 2.1 cm wide, are present, and the central portion of the largest nodule is more echogenic. **(B)** Several lobulated hypoechoic nodules surrounded with hyperechoic parenchyma were seen in this other dog. These features are commonly recognized with lymphoma and histiocytic sarcoma (see Figure 7.30) in dogs. Round-cell neoplasms can however result in variable features (see Figures 7.18–7.20).

Vet-ebooks.com

Cavitary Lesions

Hepatic and biliary **cysts** are sometimes identified in dogs and cats and appear as well-circumscribed, regular or irregular, anechoic foci, typically associated with far-enhancement artifacts (Figure 7.32). In these benign cysts, the adjacent parenchyma is usually normal. These cavitary lesions must be differentiated from cystic tumors, such as biliary cystadenomas and cystadenocarcinomas, commonly demonstrating a multilocular pattern and a change in tissue appearance around the anechoic cavitations (Nyland et al. 1999) (Figure 7.33). Although more common in cats, cystic or cavitary tumors are also seen in dogs (Figure 7.34).

Hepatic **abscesses**, which are uncommon in dogs and cats, tend to appear as poorly marginated, round to oval, regular or irregular, hypoechoic lesions, which are often cavitated (Schwarz et al. 1998) (Figure 7.35). Enhancement artifacts, abdominal effusion, regional lymphadenopathy, and hyperechoic perihepatic fat are commonly seen in affected animals. Abscesses can also show pus sedimentation in the central cavitations or appear as complex or more echogenic masses. Hyperechoic foci with reverberation consistent with gas can also be observed. Cellular debris or hemorrhage

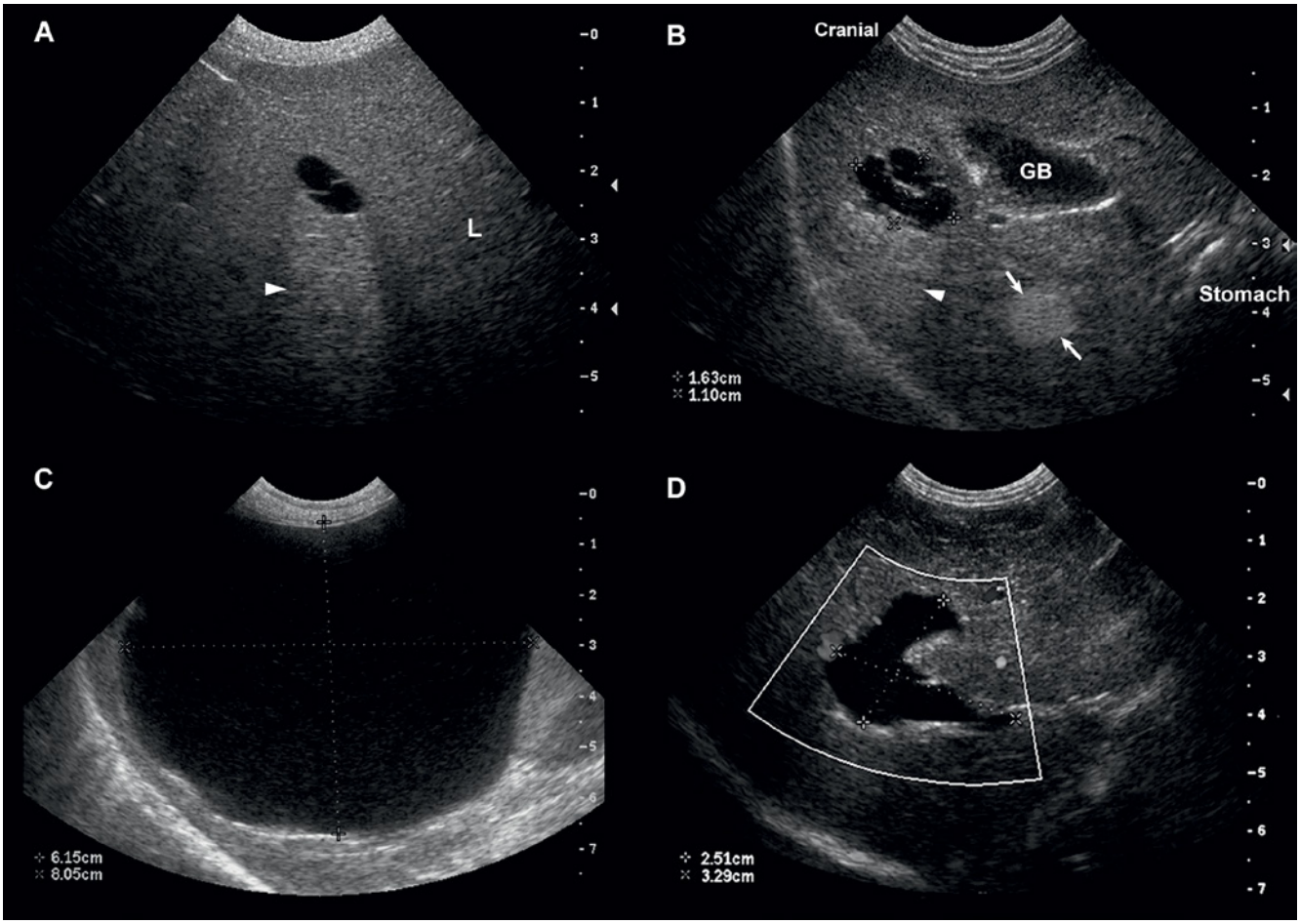


Figure 7.32. **Benign hepatic cyst-like lesions in dogs. (A)** Transverse image of the liver (L) of a dog with a discrete anechoic structure (approximately 1 cm wide) that is septated and associated with far acoustic enhancement (arrows), consistent with hypoattenuating content. A clear fluid was aspirated with ultrasound guidance. The peripheral hepatic parenchyma is homogeneous. **(B)** Longitudinal image of the liver of a dog with a well-circumscribed, loculated, anechoic structure. Irregular contours and far enhancement (arrowheads) are present. Bile was aspirated. The clinical significance of this finding was not determined in this patient. A hyperechoic regenerative nodule (arrows) is also present. The gallbladder (GB) wall is thickened and irregular, presumably because of cholecystitis. **(C, D)** Ultrasound images of a large liver cyst in a dog with abdominal pain that were obtained before **(C)** and after **(D)** ultrasound-guided drainage. The peripheral liver parenchyma is normal.

Vet-ebooks.com

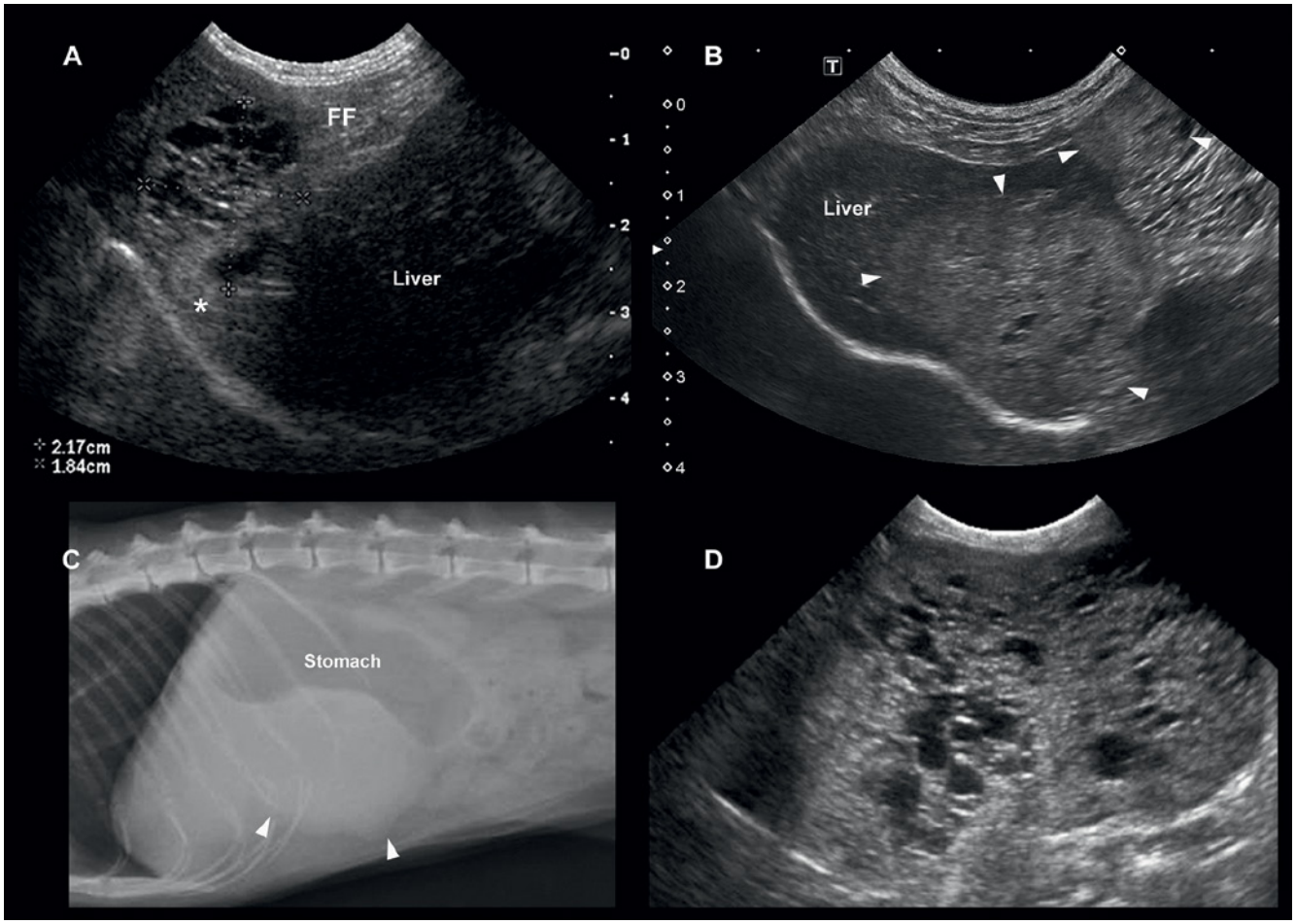


Figure 7.33. **Biliary cystadenomas and cystadenocarcinomas in cats. (A)** Transverse ultrasonographic image of the liver of a cat with increased hepatic enzymes. A multiloculated mass (cursors) is identified in the right portion of the liver. Far acoustic enhancement is noted (*) because of the presence of hypoattenuating fluid-filled cavities. Biliary cystadenocarcinoma was confirmed through ultrasound-guided biopsy. FF, falciform fat. **(B)** In this other 13-year-old domestic shorthair cat, several hyperechoic masses (arrowheads) filled with small anechoic cavities are detected in the liver, with a presumptive diagnosis of malignant epithelial tumor on fine-needle aspirations. **(C, D)** In this cat, a large hepatic soft-tissue mass (arrowheads) displaces the gas-distended stomach on the radiograph. The cystadenoma appears as a moderately echogenic mass filled with numerous anechoic cavities.

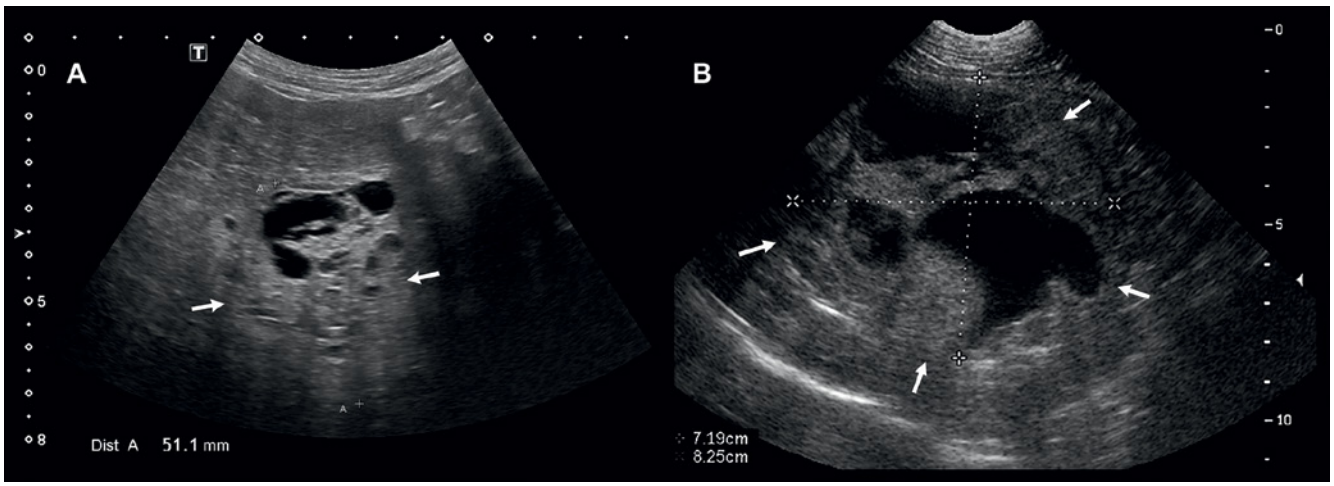


Figure 7.34. **Biliary carcinomas in two dogs. (A)** A poorly defined, 5-cm hyperechoic mass (between cursors and arrows) with irregular anechoic cavities is identified in this 9-year-old dog. Histology revealed biliary cystadenocarcinoma. **(B)** Longitudinal image of the right portion of the liver in an icteric dog with a large cavitated mass. This poorly defined mass (arrows) contains irregular hypoechoic and anechoic cavitations. The findings on ultrasound-guided fine-needle aspiration of the more solid portions of the mass were suggestive of biliary carcinoma.

Vet-ebooks.com

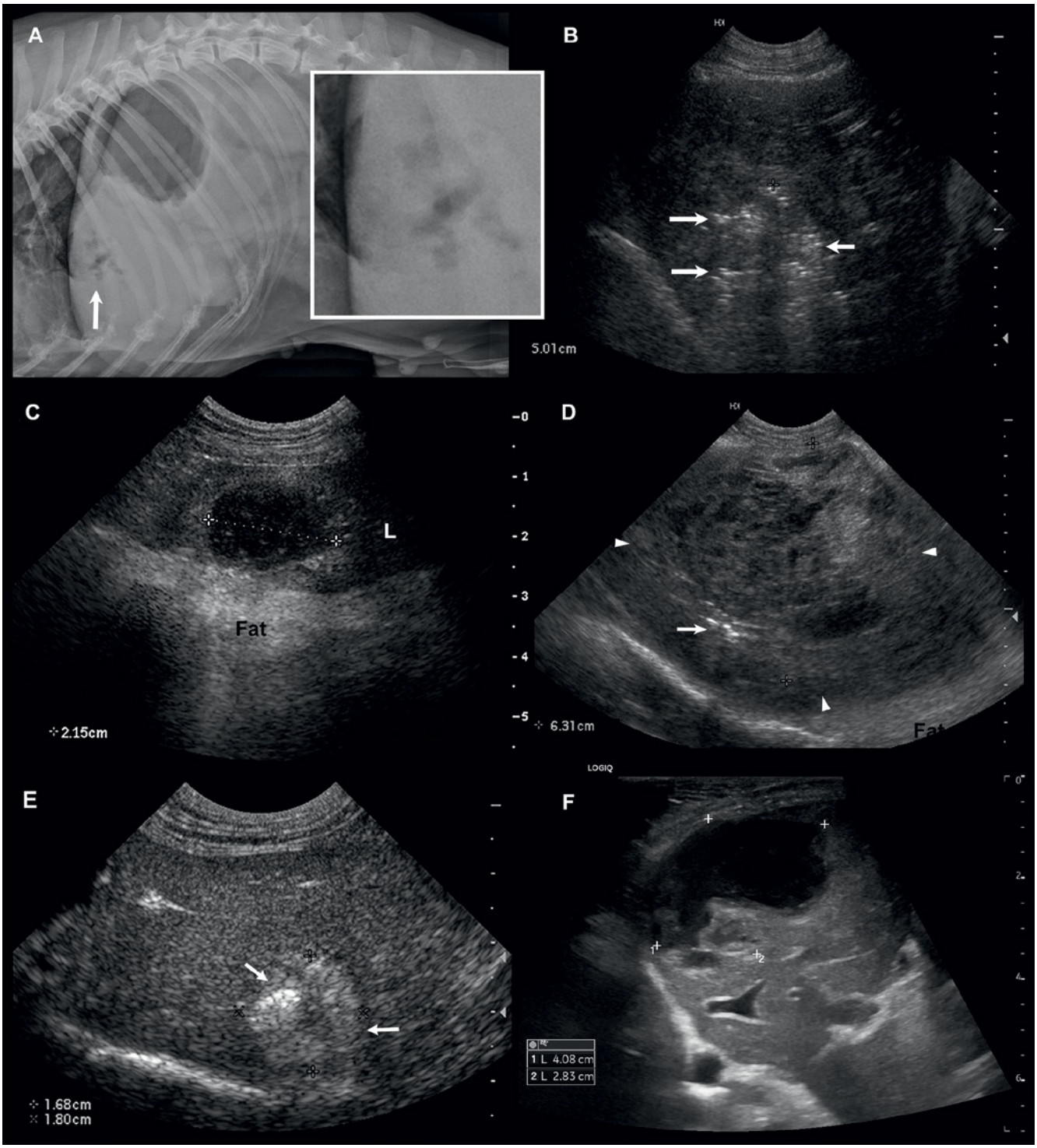


Figure 7.35. Hepatic abscesses in dogs. Lateral radiograph (**A**) and longitudinal sonographic image (**B**) of the liver of a medium-sized dog in which a hepatic abscess was identified. The abscessed region (arrows), deep in the liver, is poorly marginated and contains several reverberating, hyperechoic foci consistent with gas, which are evident on the radiograph. **(C)** Longitudinal image of the left portion of the liver in a febrile dog with abdominal pain. An irregular hypoechoic lesion (arrowheads) can be seen. The abdominal fat adjacent to the liver (L) border is hyperechoic and hyperattenuating, suggesting steatitis. Ultrasound-guided fine-needle aspiration confirmed the presence of an abscess. **(D)** In this other dog with abdominal pain and fever, there is a complex mass (arrowheads). Intraparenchymal reverberating hyperechoic foci consistent with gas are noted dorsally (arrow). **(E)** Longitudinal oblique image of the left portion of the liver in a febrile dog. A poorly defined hyperechoic nodule (arrows) with a hypoechoic center is found at the dorsal margin of this lobe, which was supportive of a septic abscess. **(F)** Voluminous cavitary lesion in the right portion of the liver of a 15-year-old Dachshund presented with anorexia and fever. A large benign mass had been removed 3 years prior to this abscess.

Vet-ebooks.com

accumulating in benign hepatic cysts can mimic abscesses, although these lesions typically show a thinner, more well-defined rim. **Parasitic cysts** occurring with liver flukes or hydatid disease can look similar to abscesses with the addition of mineralization (Nyland et al. 1999). Fine-needle aspiration can be useful in confirming the nature of the fluid contained in cavitary lesions and enabling drainage of abscesses.

Granulomas, Hematomas, and Mineralization

Hepatic **granulomas** or **pyogranulomas** can sometimes occur in dogs and cats, particularly with fungal diseases, with feline infectious peritonitis or with feline eosinophilic fibroplasia (Weissman et al. 2012) (Figure 7.36). Granulomatous lesions tend to be hyperechoic and inhomogeneous, as is the case in humans (Mills et al. 1990). Granulomatous hepatitis in dogs is often associated with hepatomegaly and can have diffuse or multifocal changes, including target-like lesions (Figure 7.15) and/or hyperechoic parenchymal periportal bands (Prentice et al. 2023).

Hepatic **hemorrhage** is rare in dogs and is usually related to hemangiosarcoma or trauma (Whiteley et al. 1989). Hepatic hematomas can also develop following ultrasound-guided procedures such as biopsies and demonstrate variable ultrasonographic changes related to clot organization and resorption (Figure 7.37). With time, hematomas tend to develop a cystic component following clot lysis. This feature, as well as the progressive reduction in size on follow-up exams, should help in differentiating spontaneous hematomas from neoplastic processes. Hepatic **mineralization** other than cholelithiasis can accompany benign processes (such as hematoma or granuloma) or malignant processes. Mineralization typically appears as strongly hyperechoic foci associated with acoustic shadowing (Figure 7.38).

Hepatic Lobe Torsion, Infarction, and Gas

Liver lobe torsion, which leads to lobar congestion, hemorrhage, and necrosis, can show variable signs that can mimic neoplasia or abscess formation. In a reported series, the affected lobe was commonly hypoechoic or mixed in echogenicity, and Doppler assessment of the lobe revealed reduced vascularity in many dogs (Hinkle Schwartz et al. 2006) (Figure 7.39). **Spontaneous infarction** is less common in the liver when compared with the spleen but can show a similar pattern of an irregular and poorly echogenic area with reduced flow on color Doppler or power Doppler (Figure 7.40). Hyperechoic foci associated with reverberating artifact, consistent with **gas**, can be seen in the liver, most often in the biliary tract, following surgery. Gas can also form because of bacterial infection (Figure 7.41). Metallic clips used with surgical biopsies appear as short, strongly hyperechoic lines with reverberation, mimicking gas. A radiograph can be used, if needed, to differentiate gas from metal.

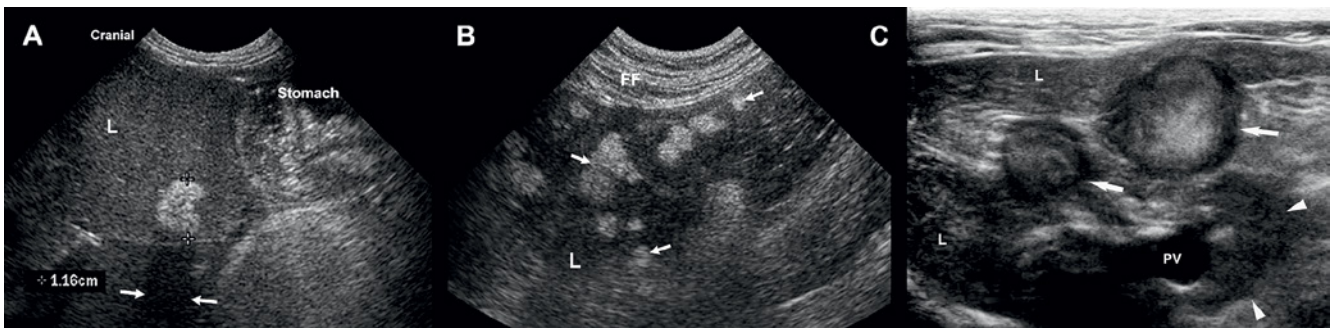


Figure 7.36. **Hepatic granulomas in a dog and two cats. (A)** Longitudinal image of the left portion of the liver (L) in a dog with a relatively well-defined hyperechoic focus associated with acoustic shadowing (arrows). A granuloma was diagnosed, although no underlying etiology could be identified. This granuloma was thought to be an incidental finding. **(B)** Longitudinal image of the right portion of the liver in an icteric cat with irregular hyperechoic nodules (arrows) dispersed within a hypoechoic liver (L). The diagnosis was pyogranulomatous cholangiohepatitis in relation to feline infectious peritonitis. FF, falciform fat. **(C)** Longitudinal sonogram of the liver of an 8-year-old cat, showing three inhomogeneous nodules diagnosed as eosinophilic sclerosing hyperplasia. Two of them (arrows) were clearly originating from the liver (L) during the real-time evaluation, while the third nodule (arrowheads) was located near the porta hepatis and was suspected to originate from either the hepatic lymph node or liver. PV, portal vein.

Vet-ebooks.com

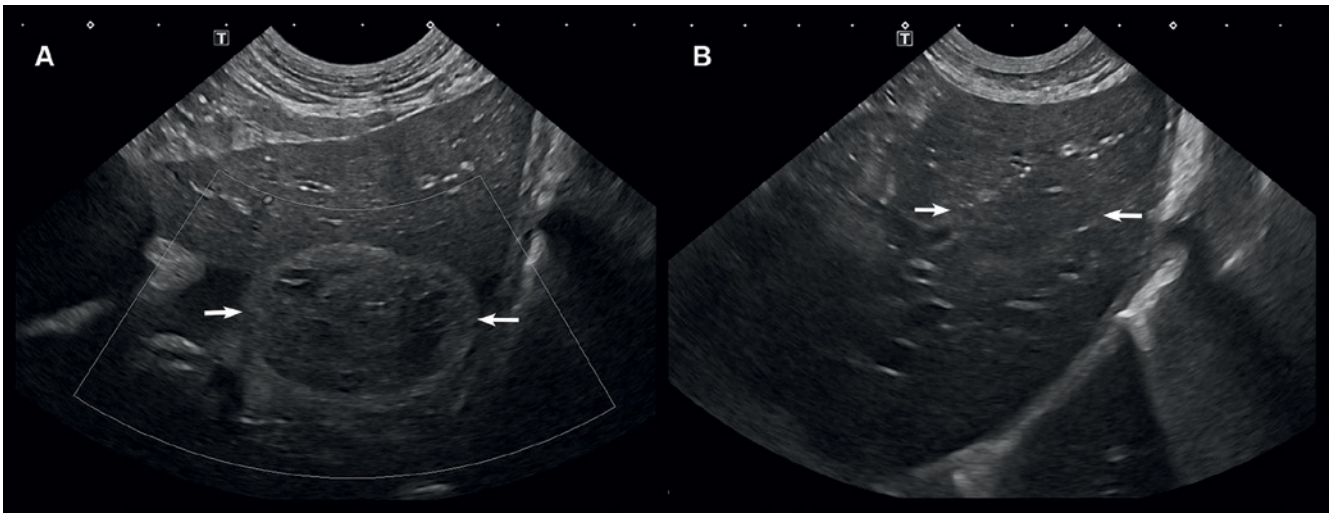


Figure 7.37. Presumed hepatic hematoma in a dog with follow-up. Two-year-old German Shepherd mix presented for evaluation following blunt trauma with marked ALT elevation noted on screening bloodwork. **(A)** Within the left lateral aspect of the liver, there is a 2.3 cm × 3.1 cm lesion that is centrally heterogeneously hypoechoic and has a hyperechoic peripheral rim (arrows). When interrogated with color Doppler, there is no flow within this lesion. The surrounding parenchyma is normal, and there is scant concurrent effusion. **(B)** Recheck evaluation 1 month later. The previous focal hepatic lesion is resolved (arrows). No effusion is documented.

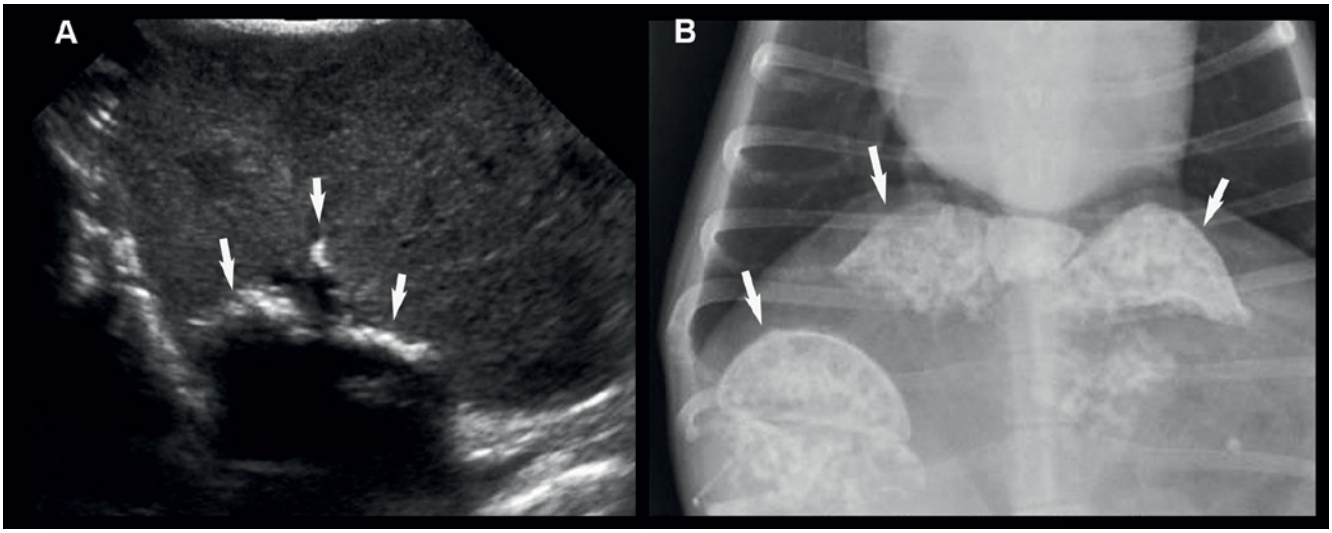


Figure 7.38. Parenchymal mineralization in a 14-year-old Shih Tzu with chronic hepatopathy with lithiasis. (A) Numerous irregular hyperechoic interfaces (arrows) associated with strong shadowing are noted throughout the liver. The visible liver parenchyma is coarse with several small, ill-defined hypoechoic nodules. **(B)** On this ventrodorsal radiograph, the extent of the hepatic mineralization (arrows) is more obvious.

Disorders of the Biliary System

Congenital Anomalies of the Biliary Tree

Congenital cystic changes of the biliary system can affect any portion of the biliary tree, including the intra- and extrahepatic biliary ducts. They originate from malformations of the embryologic biliary primordium referred to as the ductal plate; a spectrum of disorders result from **ductal plate malformation** (DPM) with the location and morphology of the anomalies reflecting the developmental stage at which the derangement occurs (Santiago et al. 2012). A macroscopic, segmental, nonobstructive dilatation of large intrahepatic bile ducts is categorized as Caroli's

Vet-ebooks.com

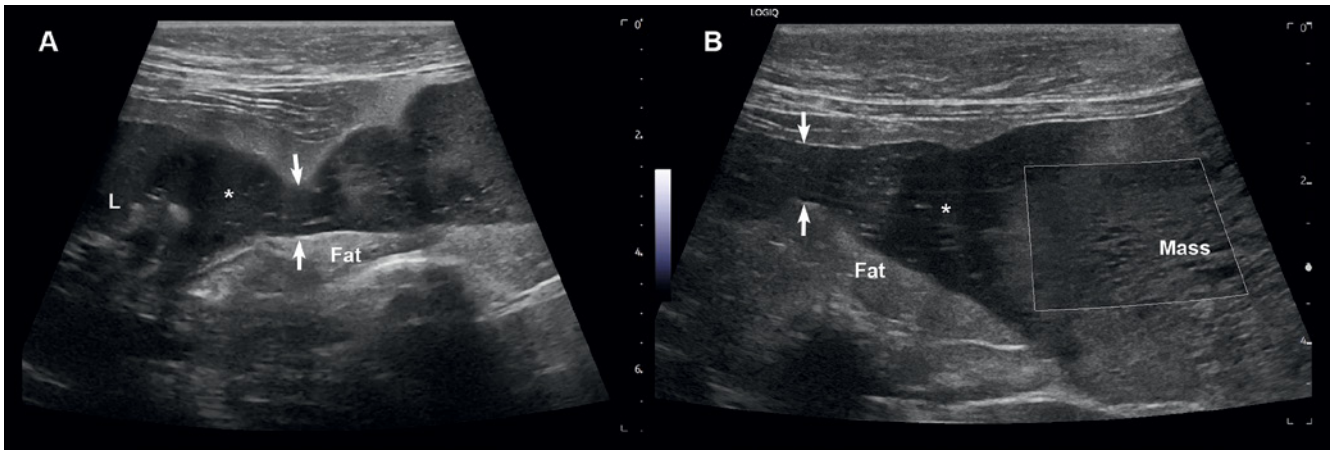


Figure 7.39. Hepatic lobe torsion in a 14-year-old cat with underlying cystadenoma. The left lateral lobe is focally narrowed (arrows) at the site of torsion and surrounded with hyperechoic fat. Its parenchyma is hypoechoic (*) except for its extremity that presents a large, oval hyperechoic polycystic mass. A characteristic vascular *swirl sign* was noted at the site of torsion upon dynamic examination. There was no color Doppler signal detected distal to the site of torsion. Minimal peritoneal effusion was present (not seen here).

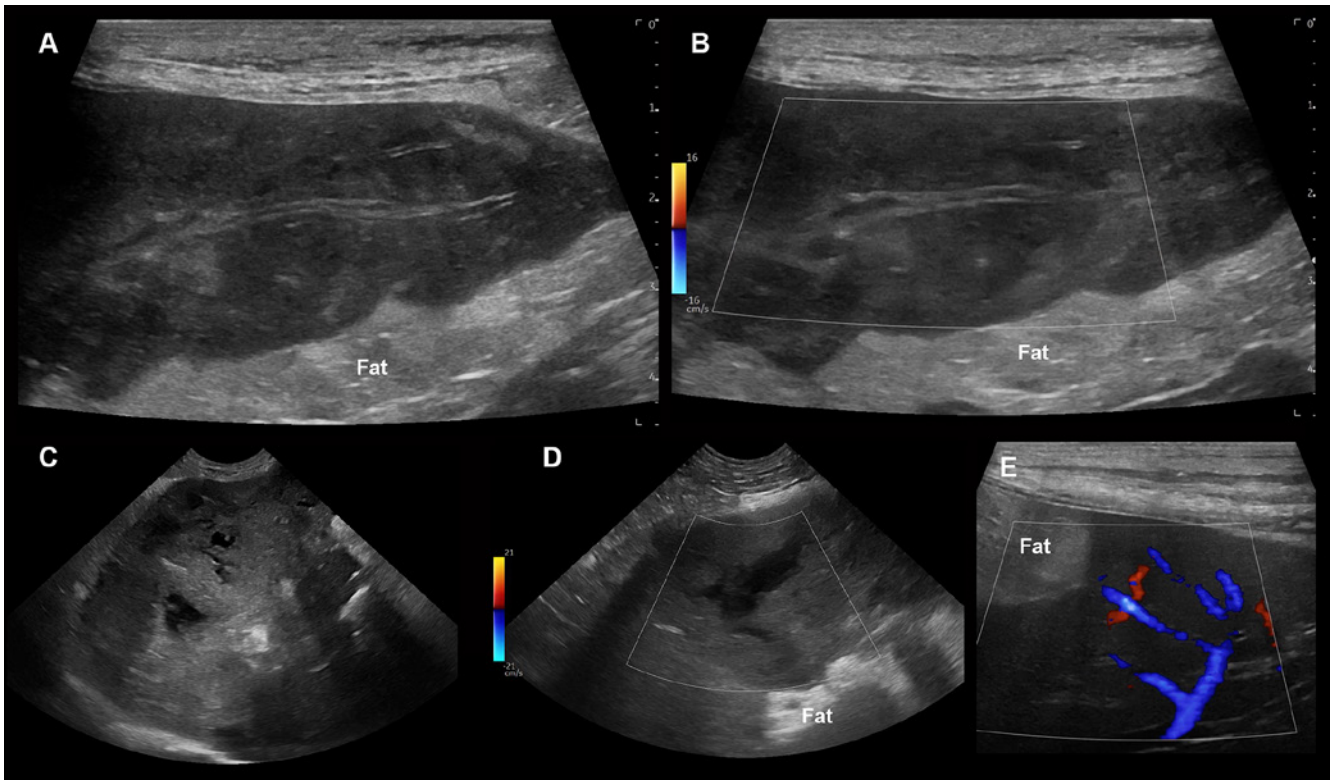


Figure 7.40. Hepatic infarction following cholecystectomy. This 11-year-old female Siberian Husky had a cholecystectomy for a gallbladder mucocele 3 days earlier. Follow-up ultrasound was performed given the anorexia, abdominal pain, and fever, as well as markedly elevated ALT, which progressed after surgery. **(A, B)** The caudal extremity of the right lateral lobe extends beyond the costal arch with a lobulated contour. Its parenchyma is heterogeneous and surrounded with hyperechoic fat. No flow is detected using Power Doppler (in **B**). **(C, D)** The base of the lobe is also enlarged and markedly heterogeneous with fluid-filled cavities. There is no vascular flow (in **D**) when compared to the rest of the liver parenchyma (in **E**) using the same Doppler parameters. Lobar torsion was initially suspected, but spontaneous infarction was rather identified in surgery.

Vet-ebooks.com

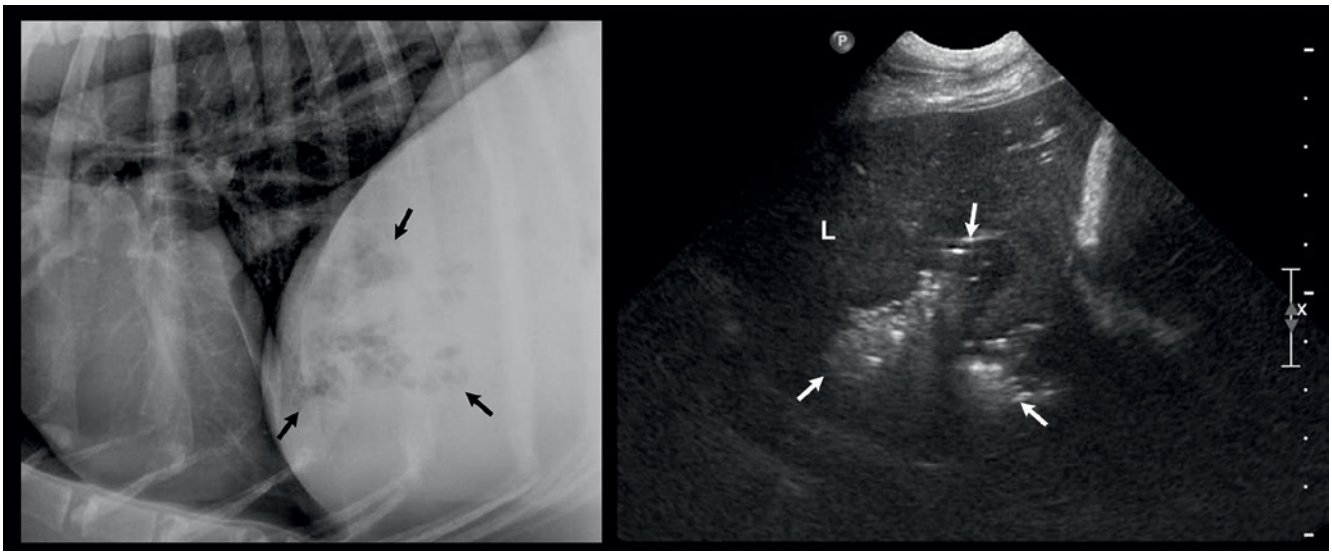


Figure 7.41. Emphysematous hepatitis. Corresponding lateral abdominal radiograph and sonogram of a dog with emphysematous hepatitis. Gas foci (arrows) are radiotransparent on the radiograph and hyperechoic with reverberation artifacts on the ultrasound image. L, liver.

disease and has been described in both dogs and cats (Center et al. 2022; Glavan 2022; Gorlinger et al. 2003; Last et al. 2006; Pillai et al. 2016; Roberts et al. 2018). **Choledochal cysts** (CCs) are defined as segmental dilatations of the CBD, which are further classified based on location, extent, and shape; these anomalies have been previously reported in cats (Best et al. 2010; Spain et al. 2017) (Figure 7.42). The anatomical complexity of these malformations makes it difficult to differentiate them from obstructive biliary disease, but in the absence of icterus and hepatic biochemical changes, they should not be misinterpreted as signs of mechanical obstruction. Identification of a GB and the connection of the extrahepatic bile ducts to the CBD are paramount in diagnosing these anomalies. Commonly, these segmental dilations are associated with inflammation or infection. Thickening of the biliary duct walls and echogenic bile are then noted (Figure 7.43).

Congenital polycystic disease involving the kidneys, liver, and pancreas is well reported in cats (Bosje et al. 1998). The concurrent presence of multiple cysts in the kidneys assists in the diagnosis of this condition.

Congenital agenesis or atresia of the GB has been rarely reported in dogs (Austin et al. 2006; Ciammaichella et al. 2023; Kamishina et al. 2010; Kelly et al. 2019; Mestrinho et al. 2022; Pillai et al. 2016; Sato et al. 2018; Vitullo et al. 2023). CT, CT cholangiography, or MRI may be used to differentiate collapse, fibrosis, rupture, or ectopia when sonography fails to identify the GB (Kamishina et al. 2010; Kelly et al. 2019; Vitullo et al. 2023). Dilation of the CBD +/− extra/intrahepatic biliary tree is frequently identified in these patients, which may reflect a compensatory storage mechanism for bile in the absence of a GB or be the result of cholestasis versus biliary dyskinesia (Figure 7.44). Liver biopsy in dogs with GB agenesis commonly demonstrates diffuse changes compatible with DPM (Ciammaichella et al. 2023; Pillai et al. 2016; Sato et al. 2018; Vitullo et al. 2023).

Few reports of GB agenesis in the cat are present in the literature (Center et al. 2022; Noguchi et al. 2023); concurrent DPM was also documented in patients included in the study by Center et al.

Umbilicobiliary fistula is a rare congenital disorder and has been recently reported in a dog with concurrent GB agenesis (Mestrinho et al. 2022) (Figure 7.45).

Biliary Obstruction and Other Causes of Biliary Ectasia

Ultrasonography is an essential investigative tool in assessing icteric dogs and cats with biliary obstruction. After complete obstruction of the CBD, retrograde dilatation is expected that initially affects the CBD and GB, followed by the extra- and intrahepatic ducts (Nyland and Gillett 1982). With extrahepatic biliary obstruction, the cystic duct and CBD dilate and often become tortuous proximal to the site of obstruction

Vet-ebooks.com

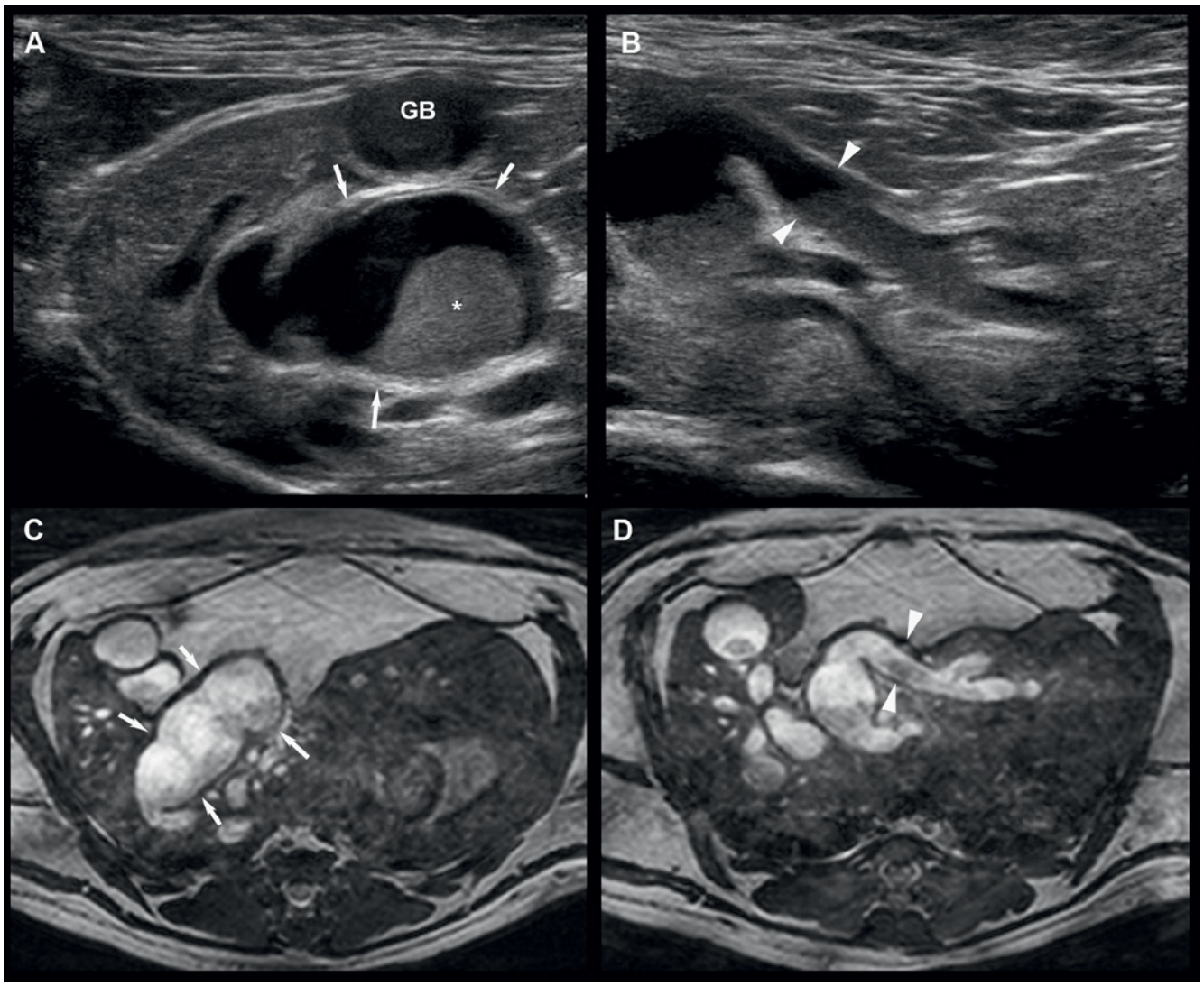


Figure 7.42. Choledochal cyst in a 7-year-old cat with chronic cholangiohepatitis and inflammatory bowel disease. (A, B) Sonograms of the markedly dilated common bile duct segment – choledochal cyst (arrows) – containing a large amount of echogenic material (*). Several dilated extrahepatic ducts (arrowheads) are connecting the choledochal cyst **(B)**. **(C, D)** Transverse T2 HASTE magnetic resonance images of the choledochal cyst (arrows) and dilated extrahepatic ducts (arrowheads). GB, gallbladder.

(Figures 7.46–7.50). A CBD of more than 4–5 mm wide is usually predictive of obstruction in cats (Gaillot et al. 2007; Léveillé et al. 1996). This is probably also true in dogs, although it has not been described. Within 5–7 days, irregular and tortuous anechoic tubes with hyperechoic walls can be found in the liver, paralleling the PVs but without color flow signal, indicating dilated intrahepatic ducts. This sign, also referred to as the "too many tubes" sign, is usually indicative of complete obstruction (Figure 7.46 and 7.47). Additionally, these anechoic tubes can be associated with acoustic far enhancement, which is not expected with vessels that contain a more attenuating cellular fluid (Nyland and Gillett 1982). Although the GB can be dilated with biliary obstruction (Figure 7.48), wall contraction or inflammation possibly associated with fibrosis can limit its capacity to distend. Furthermore, reduced compliance of the peripheral liver parenchyma may limit GB dilatation. GB dilatation was in fact seen in <50% of cats with extrahepatic biliary obstruction (Gaillot et al. 2007). Thus, the absence of GB distension should not be used to rule out biliary obstruction.

Extrahepatic biliary obstruction (EHBO) more commonly involves the CBD, mainly in its distal segment, in

Vet-ebooks.com

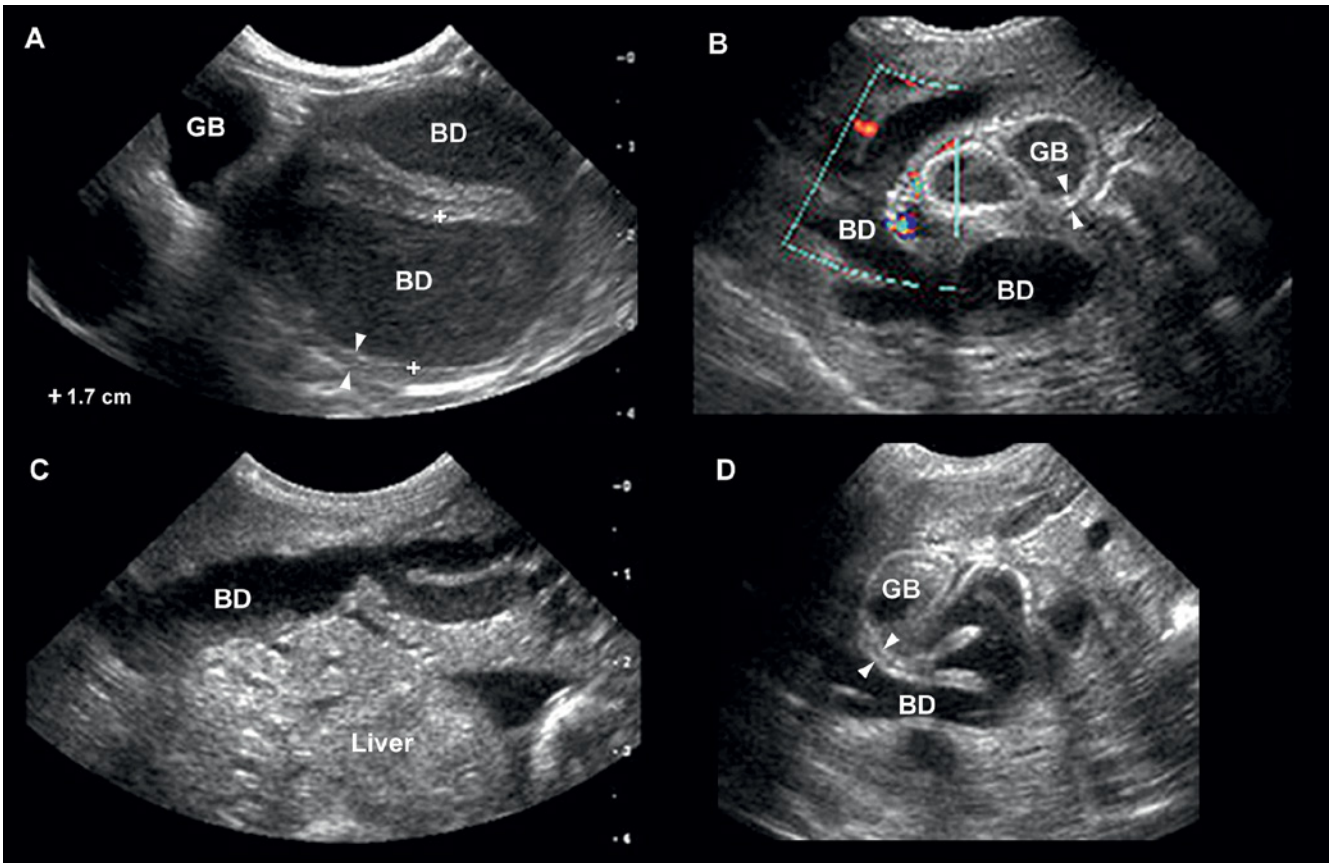


Figure 7.43. Congenital malformation with biliary ectasia in two cats. (A) Sagittal image at the porta hepatis in a 2-year-old cat with biliary obstruction. Numerous bile ducts (BD), including the common bile duct, are markedly dilated (lumen between the cursors) and show a thickened wall (arrowheads). The bile content is also more echogenic than normal. Extensive biliary tree fibrosis and stenosis were identified, and an underlying congenital defect was suspected. GB, gallbladder. **(B–D)** Similar changes observed in an 8-month-old cat. The BD are distended and irregular. The GB contains echogenic sludge and shows a thickened, hyperechoic wall (arrowheads). Color Doppler **(B)** was used to confirm the absence of flow in these BD, distinguishing those from hepatic vessels. A congenital defect such as hypoplasia or atresia of the common bile duct was suspected at necropsy.

proximity to the major duodenal papilla. Obstructions may be extraluminal, mural, or intraluminal. Pancreatitis is often responsible for CBD obstruction, particularly in dogs, because of edema, inflammation, and fibrosis involving the duodenal wall and major papilla and/or the CBD (Fahie and Martin 1995; Léveillé et al. 1996; Mayhew et al. 2002; Wilkinson et al. 2020) (Figure 7.48). Chronic duodenitis (IBD) or cholecystitis can also be associated with fibrous tissue proliferation and subsequent stenosis of the distal CBD or duodenal papilla. Inflammatory processes involving the biliary tract can be associated with amorphous plugs and cholelithiasis, although it is often difficult to determine what came first (Mayhew et al. 2002). The CBD must be evaluated thoroughly for the presence of echogenic amorphous plugs and choleliths, which may or may not cause acoustic shadowing (7.49). Choleliths and amorphous mucus plugs were found to be responsible for the obstruction in 7 out of 30 cats in a study by Gaillot et al. (2007).

Several types of neoplasia (predominantly carcinomas) involving the biliary tract, the duodenum, or the pancreas can cause biliary obstruction (Center et al. 2022; Fahie and Martin 1995). Nodules or masses of variable echogenicity, sometimes with a cystic component, can be observed (Figure 7.50). Evaluation of the rest of the abdomen, especially the liver parenchyma and lymph nodes, can help in differentiating benign from malignant processes, although tumor and inflammation often share similar sonographic features (Gaillot et al. 2007). Fine-needle aspiration or biopsy is recommended if the abnormal tissue can be safely reached. Regional tissues (liver, lymph nodes) should also be targeted if abnormal.

Other uncommon causes of EHBO include duodenal or CB foreign bodies, luminal parasites, diaphragmatic hernias, and pyloroduodenal polyps (Center et al. 2022; Griffin 2019; Venier et al. 2021).

Vet-ebooks.com

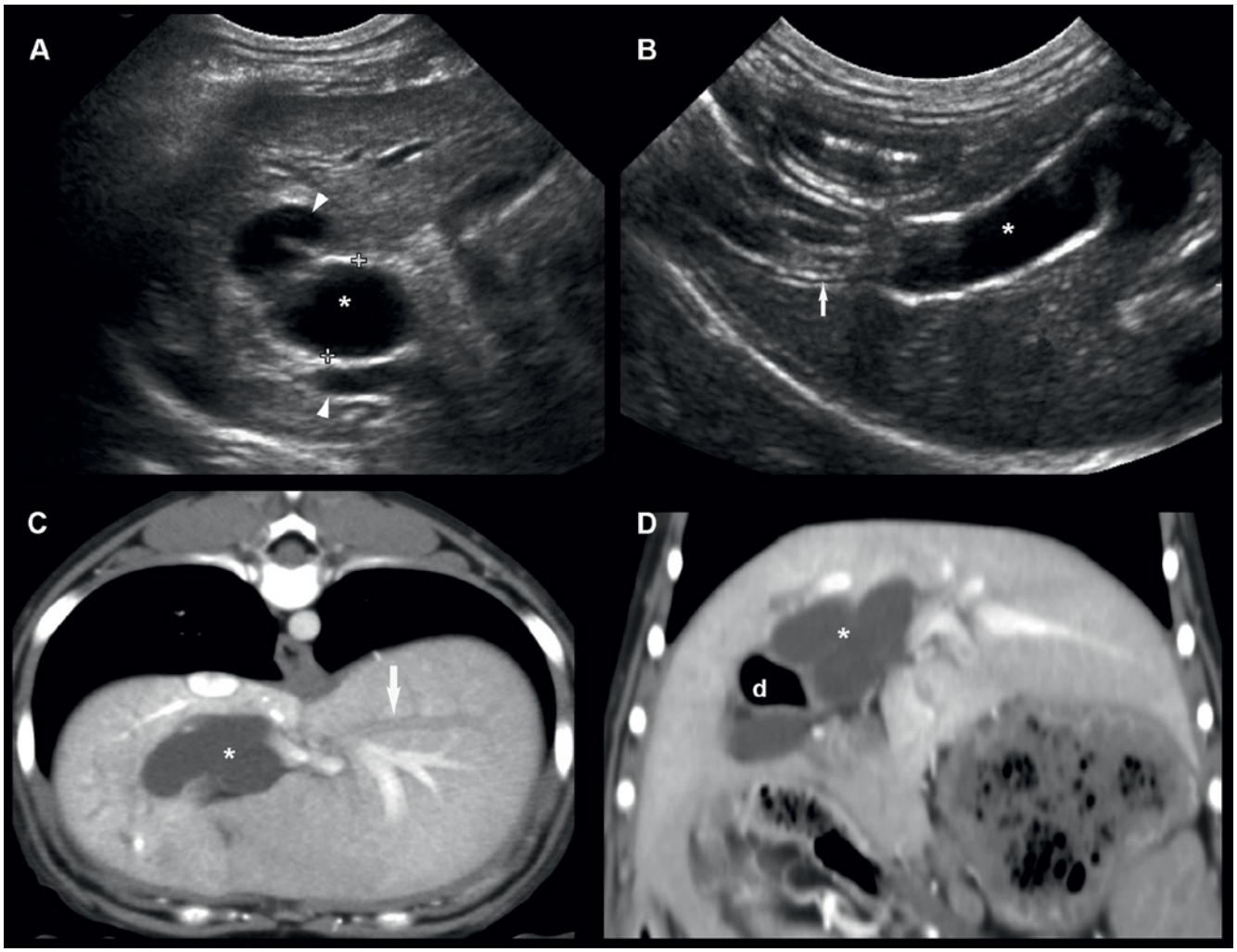


Figure 7.44. Gallbladder agenesis in a 4-month-old Australian sheepdog presented with increased liver enzymes and bile acids. (A) Sonogram of the slightly hyperechoic liver and the dilated common bile duct (CBD, *), to which the extrahepatic ducts (arrowhead) are connected. **(B)** Sonogram of the distal portion of the CBD, near the duodenal papilla (arrow). **(C)** Transverse CT showing the dilated CBD (*) and one of the dilated hepatic ducts (arrow). Note the adjacent vessels filled with contrast. **(D)** Dorsal CT of the lobulated and dilated CBD (*), near the duodenum (d).

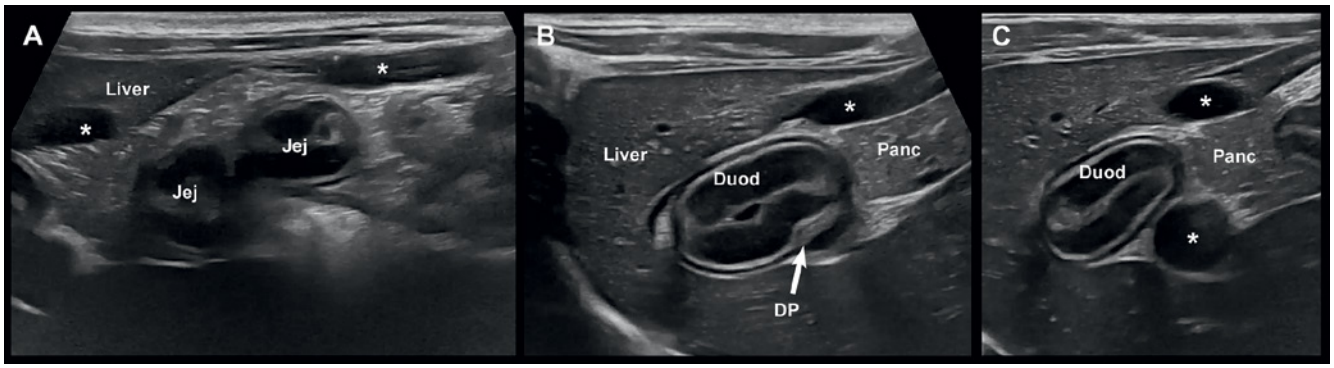


Figure 7.45 Umbilico-biliary fistula in a puppy leaking yellow fluid (bile) from the umbilicus. **(A–C)** A fluid-filled, tubular structure (*) extends from the umbilical remnant, along the ventral abdominal wall, dives dorsally along the liver margins, before entering the duodenal papilla (DP). Jej, jejunum; Panc, pancreas. Courtesy Ulrich Zegen, Centro Veterinario Specialisito, Rome, Italy.

Vet-ebooks.com

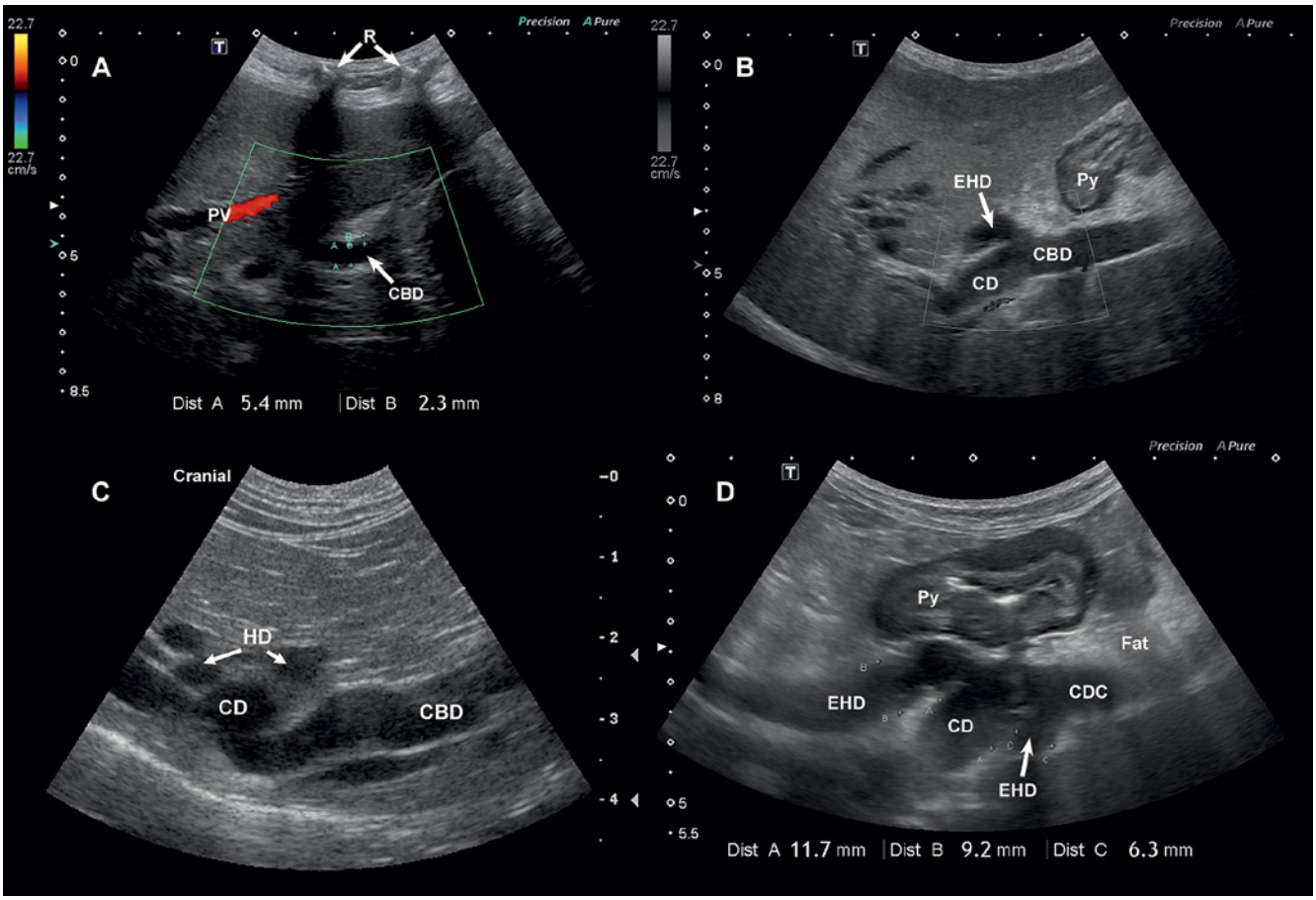


Figure 7.46. **Extrahepatic biliary obstruction in three dogs and a cat. (A)** Longitudinal image obtained through the last intercostal spaces on the right to identify the common bile duct (CBD) in a dog with gallbladder mucocele. The CBD wall is thickened (2.3 mm) and the lumen is dilated (5.4 mm). PV, intrahepatic portal vein. R, 12th and 13th ribs. **(B)** Longitudinal subcostal image in another dog with duodenal carcinoma causing biliary obstruction. The CBD is dilated as well as well as the cystic duct (CD) and one of the extrahepatic biliary ducts (EHD) that terminates into the CDC. The pylorus (Py) is nearby. **(C)** Longitudinal image obtained in the central perihilar region of the liver of an icteric cat. Tortuous hypoechoic to anechoic tubular structures representing the dilated hepatic duct (HD), the CD, and the CBD indicate extrahepatic biliary obstruction. **(D)** Longitudinal image of a 6-year-old Miniature Schnauzer with severe pancreatitis. The CBD is dilated up to an area of inflamed hyperechoic fat. Proximally, the cystic duct (CD) and two EHDs are also distended. Py, pylorus.

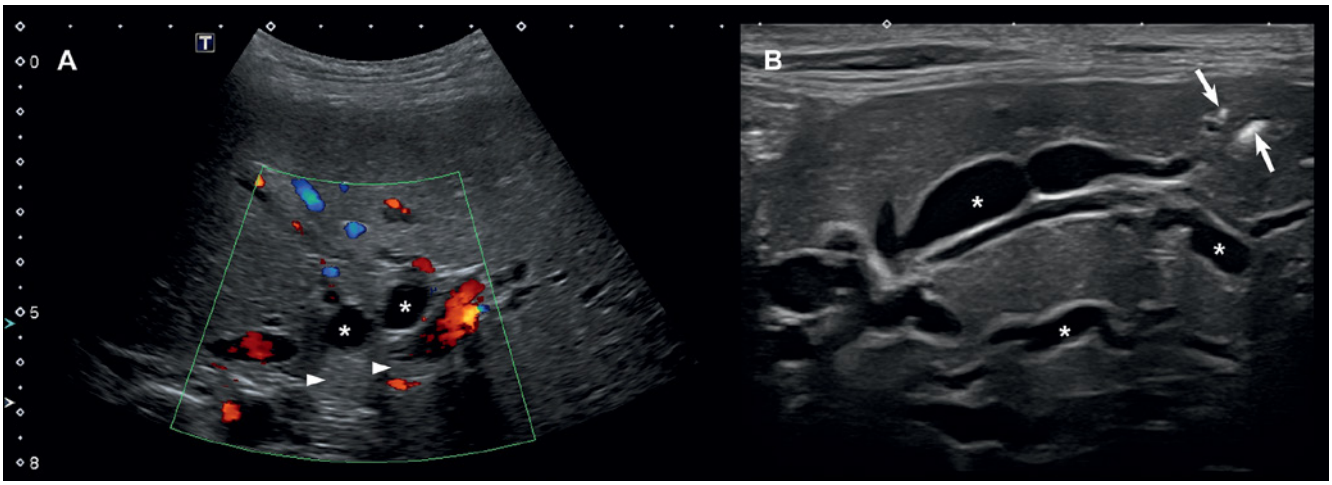


Figure 7.47. **Chronic extrahepatic biliary obstruction in a dog and a cat. (A)** Sonographic images of the liver in a dog in which intrahepatic biliary ducts (arrows) are dilated and tortuous, and lack Color Doppler signal compared with nearby hepatic vessels. Another distinctive feature is that acoustic enhancement artifacts (*) are present in the far field. This is not expected with vessels. **(B)** In this 14-year-old cat with an obstructive cholelith in the distal common bile duct, the intrahepatic bile ducts are markedly dilated and tortuous (*). Multifocal hyperechoic, shadowing choleliths were seen in the intrahepatic ducts (arrow). There was concurrent severe diffuse dilation of the pancreatic ducts with hyperechoic sedimented debris.

Vet-ebooks.com

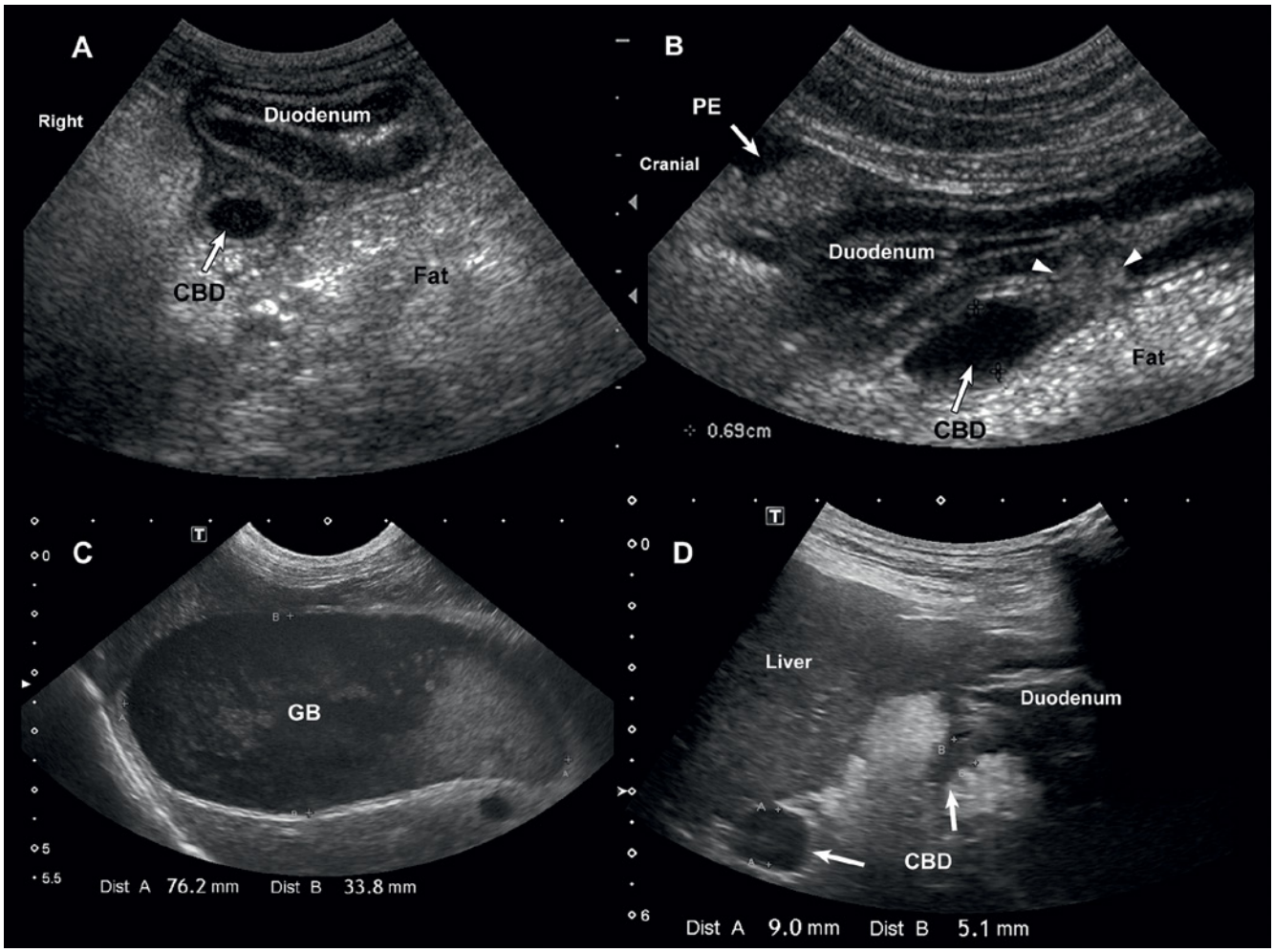


Figure 7.48. Pancreatitis and biliary obstruction in two dogs. Transverse **(A)** and longitudinal **(B)** images of the proximal duodenum of a dog with pancreatitis. The distal portion of the common bile duct (CBD) is dilated. The peripheral fat is markedly hyperechoic, and a small amount of peritoneal effusion (PE) is noted. The duodenal papilla (arrowheads) is hyperechoic and subjectively enlarged, and the wall of the common bile duct appears thickened. These changes suggest an extension of the inflammatory process to these structures, which causes biliary obstruction. **(C, D)** In another dog with chronic severe pancreatitis, the gallbladder (GB) is distended, contains sludge and its wall is mildly thickened. The CBD is inflamed and thickened (up to 5 mm) distally in proximity to the duodenal papilla and severely dilated more proximally (9 mm).

Gallbladder and Common Bile Duct Wall Anomalies

GB **wall thickening** (>1 mm in cats, >1.3 mm in dogs) can be caused by inflammation (cholecystitis/cholangitis/cholangiohepatitis), edema (portal hypertension, hypoalbuminemia, biliary obstruction, or inflammation) (Lisciandro et al. 2021), cystic mucosal hyperplasia, or, rarely, neoplasia (Hittmair et al. 2001; Spaulding 1993) (Figure 7.51,7.52). In cases of GB inflammation, the chronicity and severity of the process influences the appearance of the wall. The thickened wall may have a double-rim pattern (particularly in acute cases) or diffuse wall hyperechogenicity, sometimes associated with dystrophic mineralization (Figure 7.51).

GB **mural edema** commonly appears as a hypoechoic band of variable thickness surrounded by inner and outer hyperechoic lines, described as a "double-rim" or a "gallbladder halo" (Figure 7.52). Mural edema is a nonspecific finding that can be associated with various etiologies including cholecystitis, pancreatitis, hepatobiliary neoplasia or other primary liver disease, biliary obstruction, portal hypertension, right-sided heart failure, pericardial effusion, hypoproteinemia, chemotherapeutic drugs, renal failure, anaphylaxis, blood transfusion, IMHA, sepsis, SIRS, DIC, and transiently

Vet-ebooks.com

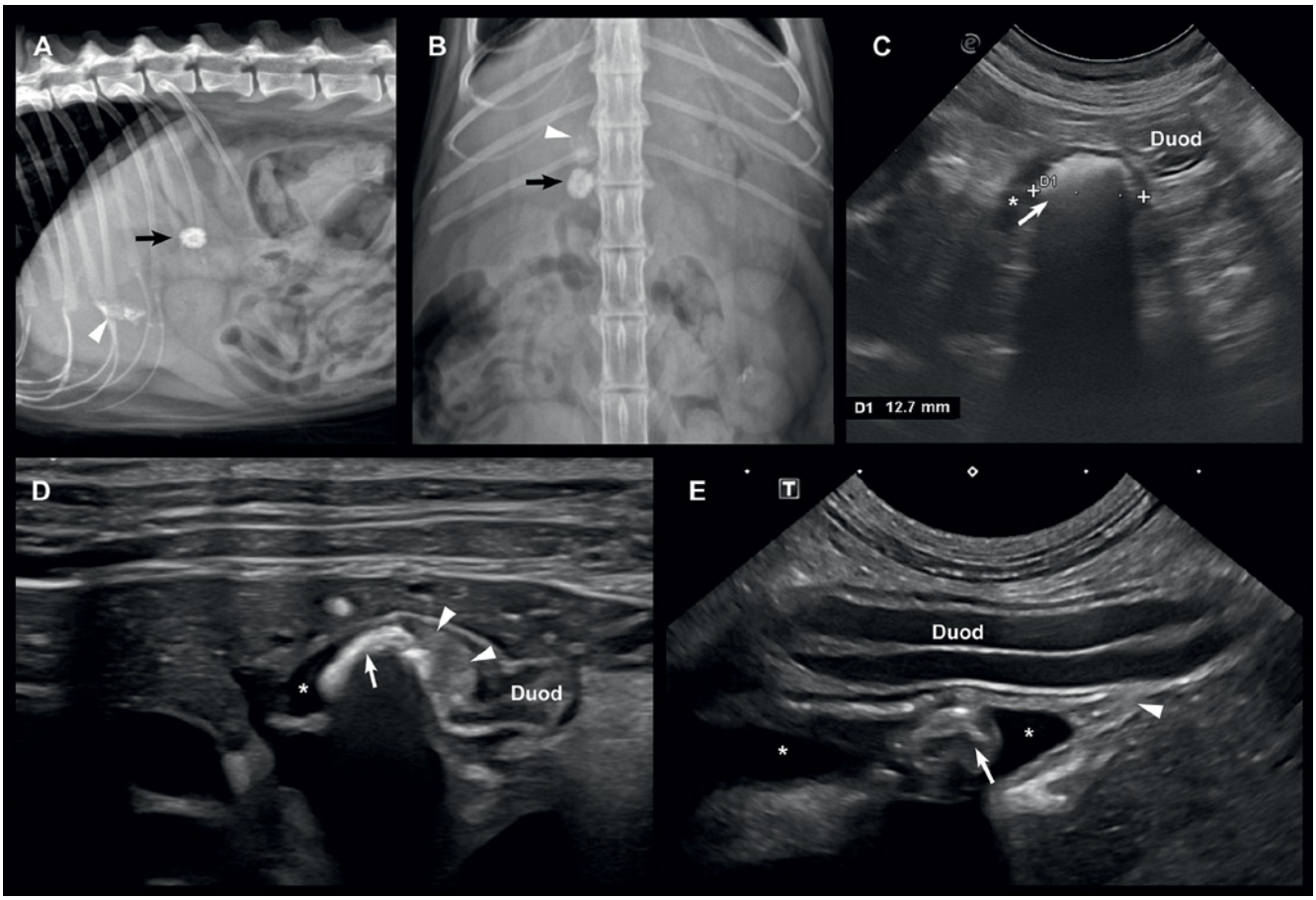


Figure 7.49. Biliary obstruction by a cholelith in two cats and one dog. (A, B) Lateral and ventrodorsal radiographs of an 8-year-old cat presented for acute vomiting. A round, irregular mineral opacity (9 mm) is seen in the cranial abdomen (arrows), initially suspected to represent a gastric foreign body. This opacity is however located on the right side of the midline on the ventrodorsal radiograph, which in a cat is closer to the location of the proximal duodenum. Other more amorphous mineral foci are noted in the area of the liver or gallbladder (arrowheads). **(C)** Ultrasound confirmed a cholelith in the distal extremity of the common bile duct (CBD). Duod, duodenum. **(D)** A 14-year-old cat with lethargy; biochemical panel showed elevated ALT and hyperbilirubinemia. Within the distal CBD, at the level of the duodenal papilla, there is a discrete, angular, hyperechoic, strongly shadowing choledocholith (arrow) measuring up to 6.5 mm in diameter. The CBD is dilated (up to 8.4 mm diameter) (*). There is distortion of the duodenal wall at the level of the papilla (arrowheads). **(E)** A 16-year-old male castrated Cocker Spaniel presented for lethargy, inappetence, and vomiting. A discrete, irregularly marginated, hyperechoic, strongly shadowing choledocholith is seen in the distal aspect of the CBD measuring ~10 mm in diameter (arrow); the duct is dilated proximally with diameter ~9.1 mm and tapers distally (*). The duodenal papilla was normal (arrowhead).

in some patients administered Dexmedetomidine prior to imaging (Lisciandro et al. 2021; Seitz et al. 2021; Sparago et al. 2021).

GB **neoplasia** is rare. Sonographically, GB neoplasia can manifest as a discrete, predominantly sessile, soft tissue mass of variable echogenicity or as irregular wall thickening. Neuroendocrine carcinoma is the most commonly reported GB neoplasm in dogs and cats; other reported tumor types include leiomyoma, lymphoma, cholangiocellular carcinoma, adenoma, and metastatic GIST (Broadbridge et al. 2021; Griffin 2019; McLeod et al. 2023).

Thickening of the CBD wall and luminal dilatation are common with cholecystitis/cholangitis/cholangiohepatitis (Figure 7.50). In cats, CBD dilation (>4 mm) appears to be a more reliable indicator of extrahepatic biliary obstruction than the GB distension (Gaillot et al. 2007). However, at times it can be difficult to differentiate obstructive dilation of the CBD from dilatation associated with stasis secondary to chronic inflammation of the biliary system (Léveillé et al. 1996). In these cases, regular ultrasound rechecks along with biochemical follow-up are useful. In chronic outflow obstruction, the CBD can remain dilated even after the

Vet-ebooks.com

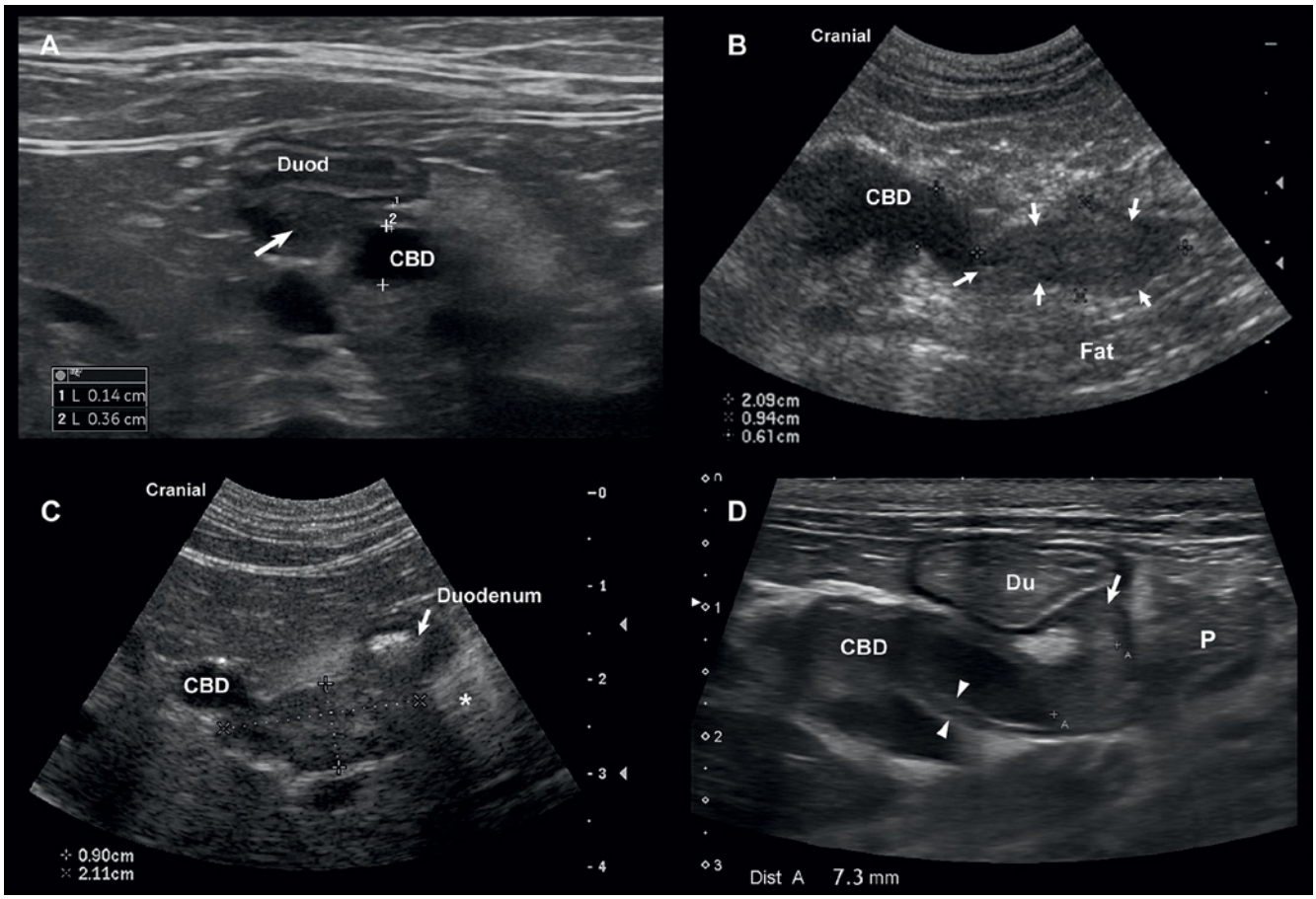


Figure 7.50. **Biliary obstruction caused by fibrous stricture or neoplasia in four cats. (A)** A small nodule (arrow) is present at the distal extremity of the common bile duct (CBD) in this cat with **chronic cholangitis**. The duct is dilated and its wall is thickened (1.4 mm). Fibrous tissue forming a **stricture** was found in surgery. **(B)** Longitudinal image of the CBD with a uniform, mildly echogenic mass (arrows and cursors) obliterating its lumen. These features can indicate chronic cholecystitis with fibrosis, or a neoplastic process. **Biliary carcinoma** was identified at surgery. **(C)** Longitudinal image of the CBD in a cat with **chronic suppurative cholangiohepatitis and cholecystitis**. Within the distal CBD is a mass (cursors) that suggests a neoplastic process. However, this mass was confirmed to represent pyogranulomatous inflammation associated with fibrous tissue. Adjacent hyperechoic fat (*) is consistent with steatitis. **(D) Chronic cholangitis and pancreatitis in a cat**. The CBD is dilated and its wall is thickened (arrowheads). A small, moderately echogenic mass is present in the distal CBD, just proximal to the duodenal (Du) papilla (arrow). Surgical exploration confirmed the presence of fibrous tissue causing the stenosis, associated with adjacent chronic pancreatitis (P).

cause of obstruction has been alleviated. In dogs with EHBO, the GB distension is seen more often than in cats, and at times, the CBD, although dilated, may be difficult to trace.

GB **mucoceles** typically affect older dogs of small and medium-sized breeds and represent an important cause of biliary (Besso et al. 2000; Choi et al. 2013). The specific etiopathogenesis of GB mucocele formation is still unclear, but is likely multifactorial with genetic predisposition (commonly affected breeds include: Shetland Sheepdog, Cocker Spaniel, Miniature Schnauzer, Pomeranian, and Chihuahua), metabolic abnormalities (high incidence in patients with endocrinopathies such as hyperadrenocorticism and hypothyroidism or dyslipidemia), and potentially environmental contributors (exogenous steroids or other drugs) (Butler et al. 2022; Jaffey 2022). This complex pathology is characterized by cholestasis and mucus progressively leading to overdistension and possibly mural pressure necrosis and rupture. In affected GBs, a characteristic peripheral accumulation of anechoic mucus is seen along the inner margin of the wall, centrally displacing the echogenic biliary sludge, which becomes immobile; in early stages of mucocele formation, the mucus cast can be relatively thin with most of the GB lumen containing echogenic nondependent sludge (Choi et al. 2013) (Figure 7.53). As the mucocele is progressively formed, the peripheral

Vet-ebooks.com

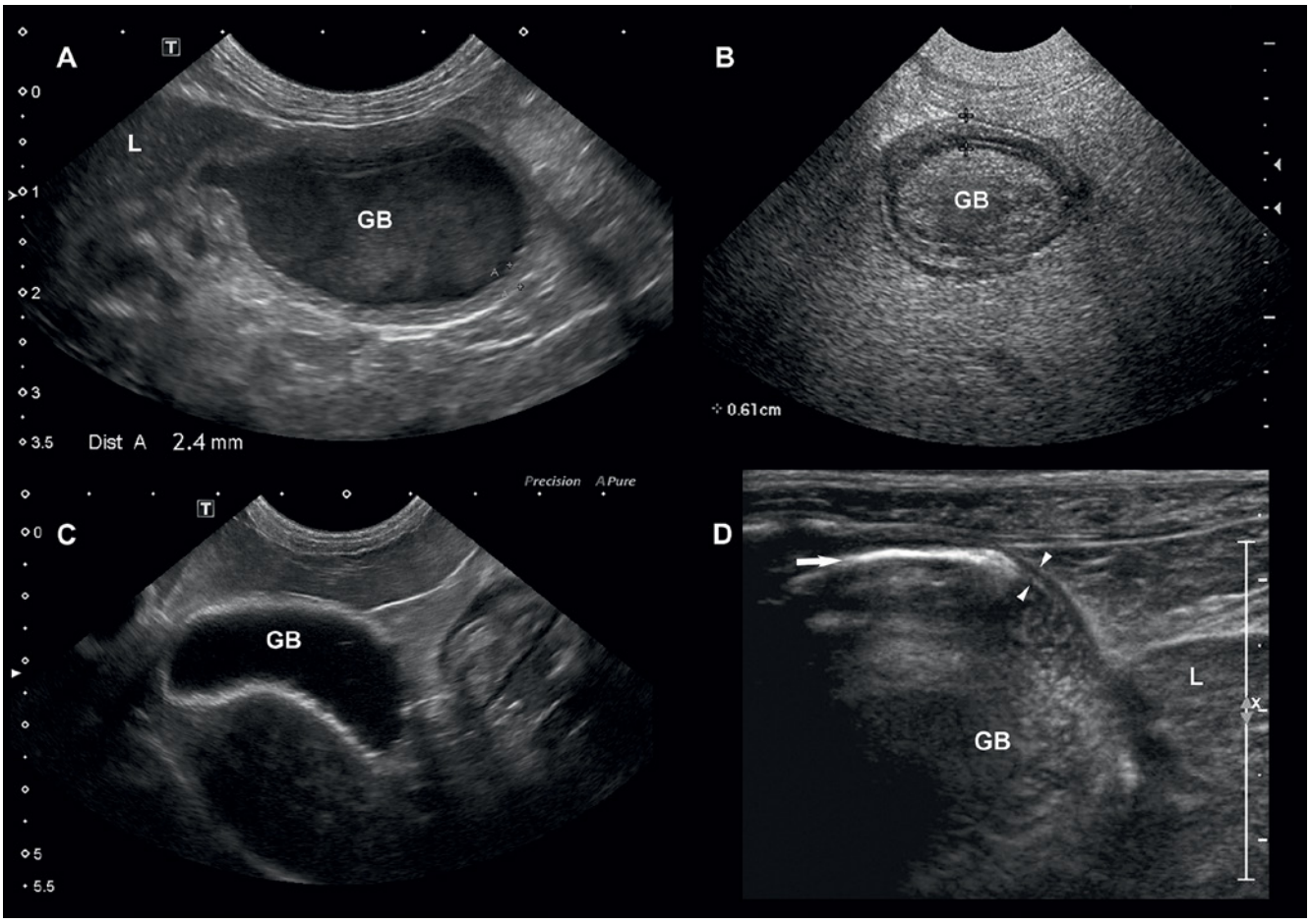


Figure 7.51. Cholecystitis in two cats and two dogs. (A) Longitudinal image of the gallbladder (GB) of a febrile cat. The GB wall is thickened (2.4 mm) and its lumen is filled with echogenic sludge. L, liver. Ultrasound-guided cholecystocenthesis yielded a positive bacterial culture. **(B)** Transverse image of the GB of a dog with a clinical history of fever and increased liver enzymes. The GB wall is thickened and associated with a multilayered pattern because of severe wall inflammation, edema, and necrosis. **(C)** Longitudinal image of the right-central portion of the liver of a febrile cat. The GB is thickened and has a hyperechoic, irregular wall with ill-defined margins (arrows). **(D)** Emphysematous cholecystitis in an 8-year-old Rat Terrier with immune-mediated thrombocytopenia, anemia, and increased liver enzymes. Gas (arrow) is dissecting the GB wall (arrowheads). The GB is moderately filled with echogenic sludge, and the liver (L) is enlarged and inhomogeneously decreased in echogenicity.

mucus casts become thicker, often with triangular shape, and more significant extension into the GB lumen with persistent centralized echogenic material dissecting between the casts to create a **stellate pattern** (Figure 7.53A); this is reported to be the most commonly identified pattern of GB mucocele identified in dogs regardless of the presence of clinical signs (Choi et al. 2013). As the mucocele continues to organize, the mucus fills most of the GB lumen and there is the appearance of immobile, thin, hyperechoic, radiating striations that lead to a **kiwi fruit-like pattern** (Figures 7.54–7.56) (Besso et al. 2000; Choi et al. 2013). Mucus fragments may detach from the wall and appear as anechoic to hypoechoic structures floating in centralized hyperechoic biliary sludge at any stage of mucocele formation (Figures 7.53B-D, 7.55B); intraluminal mucinous plugs can also extend or migrate into the CBD and cause distal obstruction (Jaffey 2022). The GB wall may appear thickened, hyperechoic or double layered, and irregular because of edema, inflammation (concomitant sterile or septic cholecystitis), mucosal hyperplasia, and/or necrosis. Assessment of GB wall integrity in these patients is of utmost importance as presence of GB rupture (most often identified in the fundic region) is an indication for emergency exploratory laparotomy. Indirect sonographic signs of potential rupture include the presence of pericholecystic hyperechoic fat and effusion (Figure 7.54). A discontinuity in the GB wall ("hole sign") is an important sign of rupture, but this can be difficult to identify if the

Vet-ebooks.com

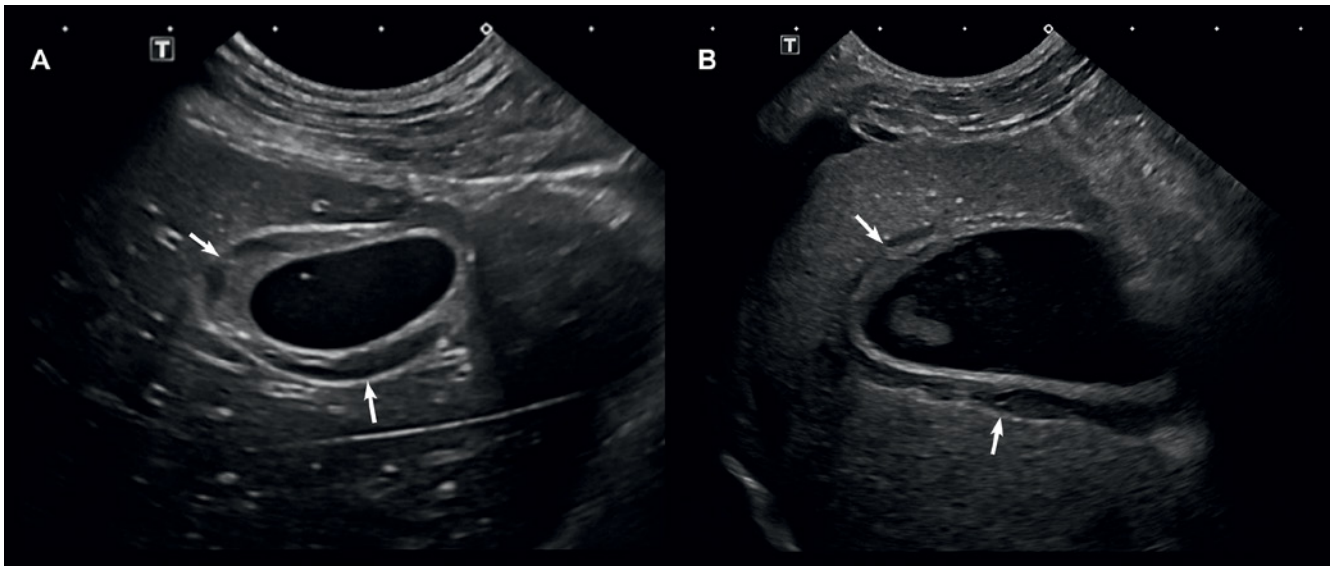


Figure 7.52. Gallbladder wall edema in two dogs. (A) Transverse image of the gallbladder in a 3-year-old male castrated Aussie-doodle presented for acute vomiting and hematemesis; immediately prior to development of gastrointestinal signs the patient was on a walk and became acutely pruritic; the patient had a history of an anaphylactic reaction to a bee sting 1 year prior. On this transverse image, the gallbladder wall (arrows) is circumferentially, diffusely thickened (up to 2.9 mm) with a "double walled" or "halo" appearance. Mural edema was presumed secondary to **anaphylaxis** in this case. **(B)** Longitudinal sonogram of the gallbladder in a 9-year-old male castrated Labrador Retriever mix presented for lethargy, anorexia, and acute vomiting with clinical and laboratory findings suggestive of emerging sepsis. There is asymmetric mural thickening predominantly affecting the dorsal wall of the gallbladder (arrows). In this case, it was unclear whether mural edema was a result of an initial anaphylactic type reaction, cholecystitis, or potentially severe systemic inflammation and hepatic venous congestion secondary to sepsis.

area is directly abutting the liver parenchyma or due to beam attenuation from regional steatitis. The reported sensitivity of ultrasound for detection of GB wall rupture is variable ranging from 50 to 93% across multiple investigations (Asakawa et al. 2022; Bargellini et al. 2016; Besso et al. 2000; Choi et al. 2013; Jaffey et al. 2018; Pike et al. 2004). Contrast-enhanced ultrasound (CEUS) has been reported to have higher sensitivity and specificity for detecting mural necrosis and rupture when compared to conventional ultrasonography (Bargellini et al. 2016); however, CEUS is currently not widely utilized in private practice. One recent publication demonstrated that conventional ultrasound results paired with elevated serum C-reactive protein (concentrations >6.3 mg/dL) increased accuracy for preoperative identification of GB rupture (Asakawa et al. 2022). Following GB wall rupture, a mucocele can potentially migrate into the peritoneal cavity and be identified as a free-floating mass or fragments with typical echo-characteristics of a GBM (Besso et al. 2000; Burchell et al. 2019) (Figure 7.56). Most affected dogs have concurrent clinical evidence of hepatobiliary disease, but GB mucoceles can also be found incidentally on ultrasound with one study reporting up to 23% of dogs being asymptomatic (Choi et al. 2013). Although surgery is generally recommended (Choi et al. 2013), GB mucoceles (without mural necrosis/rupture) may respond to medical management (Walter et al. 2008). GB mucoceles have been very rarely reported in cats with only three cases in the literature to date (Bennett et al. 2007; Gaillot et al. 2007; Woods et al. 2012). The sonographic features of mucocele in these cats were inconsistent and did not correspond to the classic appearance reported in dogs (Griffin 2019).

GB **wall polyps** and malignant neoplastic processes, although rarely seen in dogs and cats, can be associated with biliary obstruction. Although it can be difficult to differentiate these processes, pedunculated echogenic masses protruding into the GB lumen are more typical of polyps (Figure 7.57A).

Spontaneous GB mural hematomas are rare; one report described an eccentric, noncircumferential, heterogeneous, nonvascularized mass interposed between the serosal and mucosal layers of the GB wall with secondary distortion of GB shape (Jerrems et al. 2020). Underlying etiologies for GB mural hematoma include cholecystitis, cholelithiasis, tumors, vascular anomalies, coagulopathy, or trauma.

Vet-ebooks.com

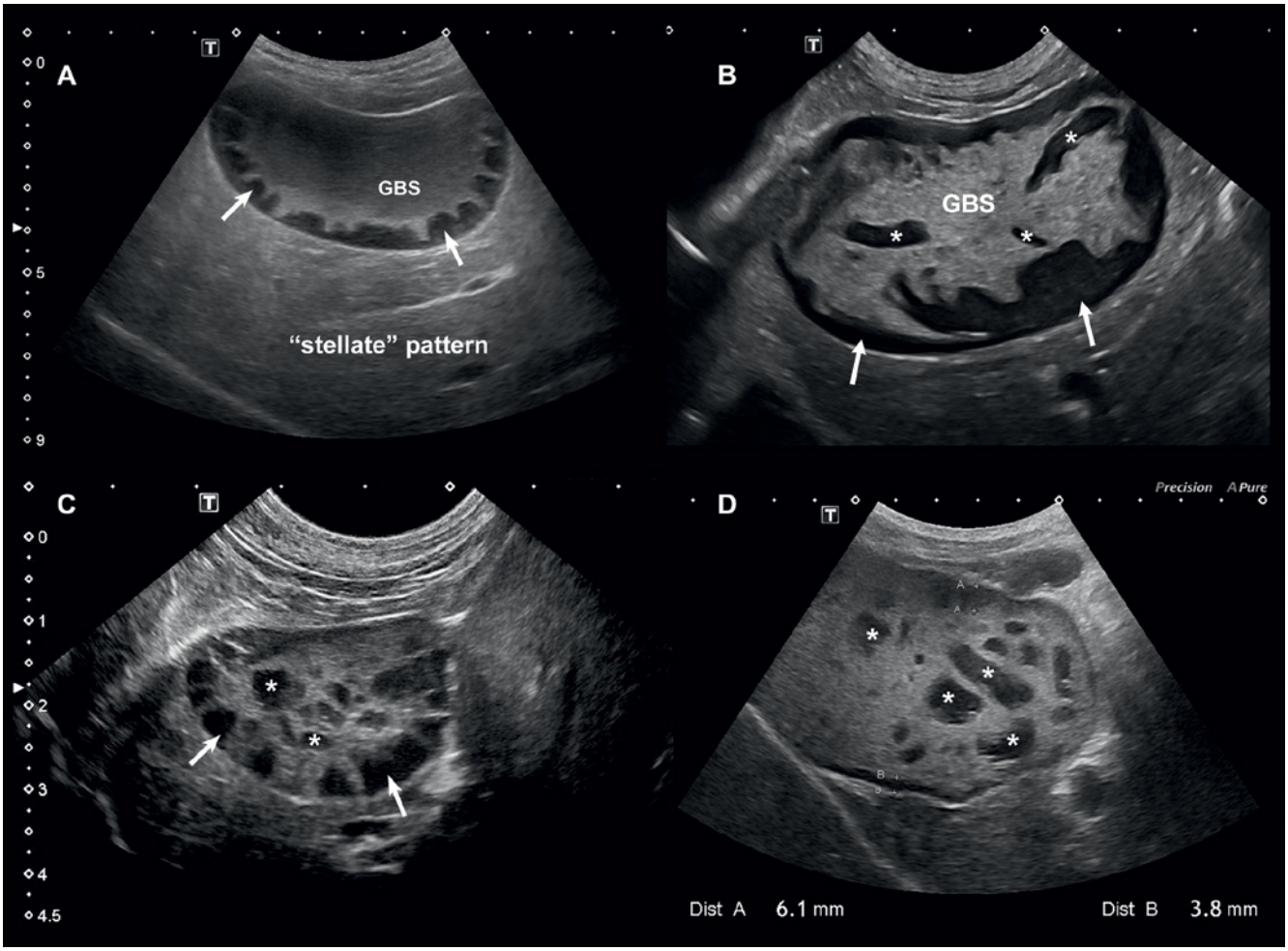


Figure 7.53. Partial or immature gallbladder mucocele in dogs. Transverse **(A)** and longitudinal **(B)** images of the gallbladder of two dogs with normal total bilirubin. The gallbladder is distended with echogenic biliary sludge (GBS) filling most of the lumen. An interrupted and irregular, hypoechoic to anechoic rim is visible at the inner periphery of the gallbladder, consistent with mucus (arrows). The triangular shape of these hypoechoic foci (arrows in dog **A**) has been referred to as the ***stellate pattern***. Mucus fragments may detach from the wall and appear as hypoechoic floating structures (*) – often geometrical in shape – surrounded with hyperechoic sludge. A stellate pattern is also present in dog **(C)** (arrows), whereas the mucus rim (between cursors) is smoother in **(D)**.

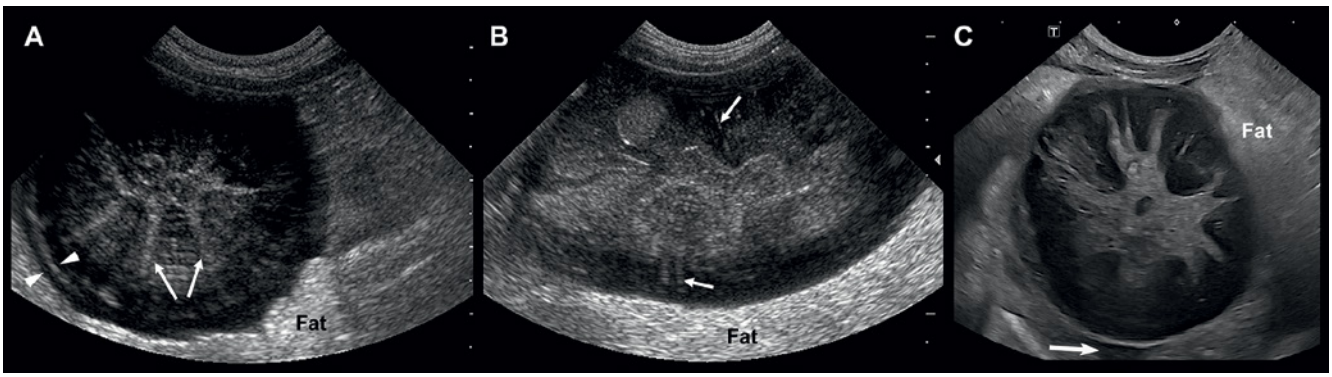


Figure 7.54. Complete or mature gallbladder (GB) in two dogs with mucocele. Transverse **(A)** and longitudinal **(B)** images of the GB of a dog with icterus and acute abdominal pain. The GB is distended and shows a pattern of hyperechoic striations (arrows) radiating toward its center. The central hyperechoic area is heterogeneous and completely immobile. These features are described as a ***kiwi fruit-like pattern***, which is a pathognomonic sign of gallbladder mucocele. The gallbladder wall is also thickened (arrowheads) and the adjacent fat is hyperechoic, suggesting imminent or recent wall rupture. **(C)** A similar pattern is seen in the GB of this 7-year-old Terrier-crossed dog in which a rupture was confirmed at laparotomy. Note the peripheral hyperechoic fat (*) and peritoneal effusion (arrow) that were suggestive of perforation.

Vet-ebooks.com

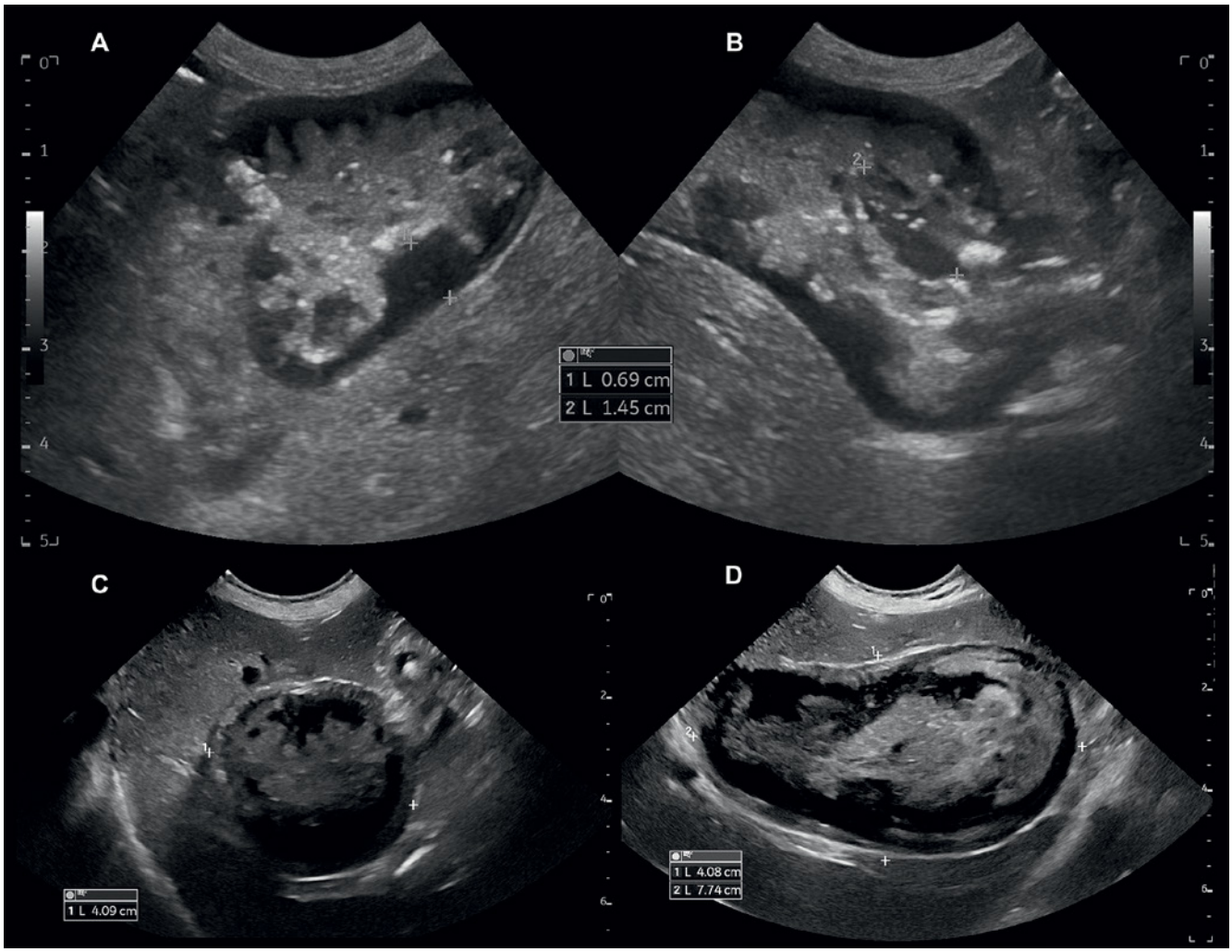


Figure 7.55. Maturation of a mucocele in a dog. Transverse (**A** and **C**) and longitudinal (**B** and **D**) images of the gallbladder (GB) of an 8-year-old male Shetland dog obtained before and after 2 years of Ursodiol therapy. Despite treatment, the volume of the mucocele progressed to occupy now more than 2/3 of the GB lumen.

Cholelithiasis

Choleliths can be found within any portion of the biliary tract in dogs and cats. Cholelithiasis is a reportedly uncommon condition in veterinary patients; the prevalence of cholelithiasis is low in both dogs (1–13%) and cats (~1%) (Allan et al. 2021; Brunet et al. 2023; Jaffey 2022; Ward et al. 2020). In both species, choleliths are predominantly categorized as "pigment stones" and are composed of variable proportions of bilirubin, calcium salts, and some cholesterol (Allan et al. 2021; Brunet et al. 2023; Jaffey 2022). On ultrasound, these calculi typically appear as well-defined, hyperechoic, shadowing foci with a tendency to form linear tracts when located in the intrahepatic ducts or a sediment in the GB lumen and cystic duct (Figure 7.57B-D). Choleliths can be identified on survey radiographs; however, a significant proportion (up to 40%) are of soft tissue opacity because of low calcium content; stones may also be radiographically inapparent due to very small size and/or superimposition of gastrointestinal structures (Ward et al. 2020). In the authors' experience, some radiographically apparent mineralized stones may not demonstrate the typical hyperechoic shadowing appearance on ultrasound. Subsequent intrahepatic or extrahepatic biliary obstruction can be observed, although choleliths may also form secondary to an obstruction (Mayhew et al. 2002).

In dogs, most patients with cholelithiasis (53–87%) are reportedly asymptomatic (Allan et al. 2021; Kanemoto et al. 2017; Ward et al. 2020). In contrast, one recent study documented that most cats within their population (59%) were symptomatic (Brunet et al. 2023); the presence of underlying concurrent inflammatory

Vet-ebooks.com

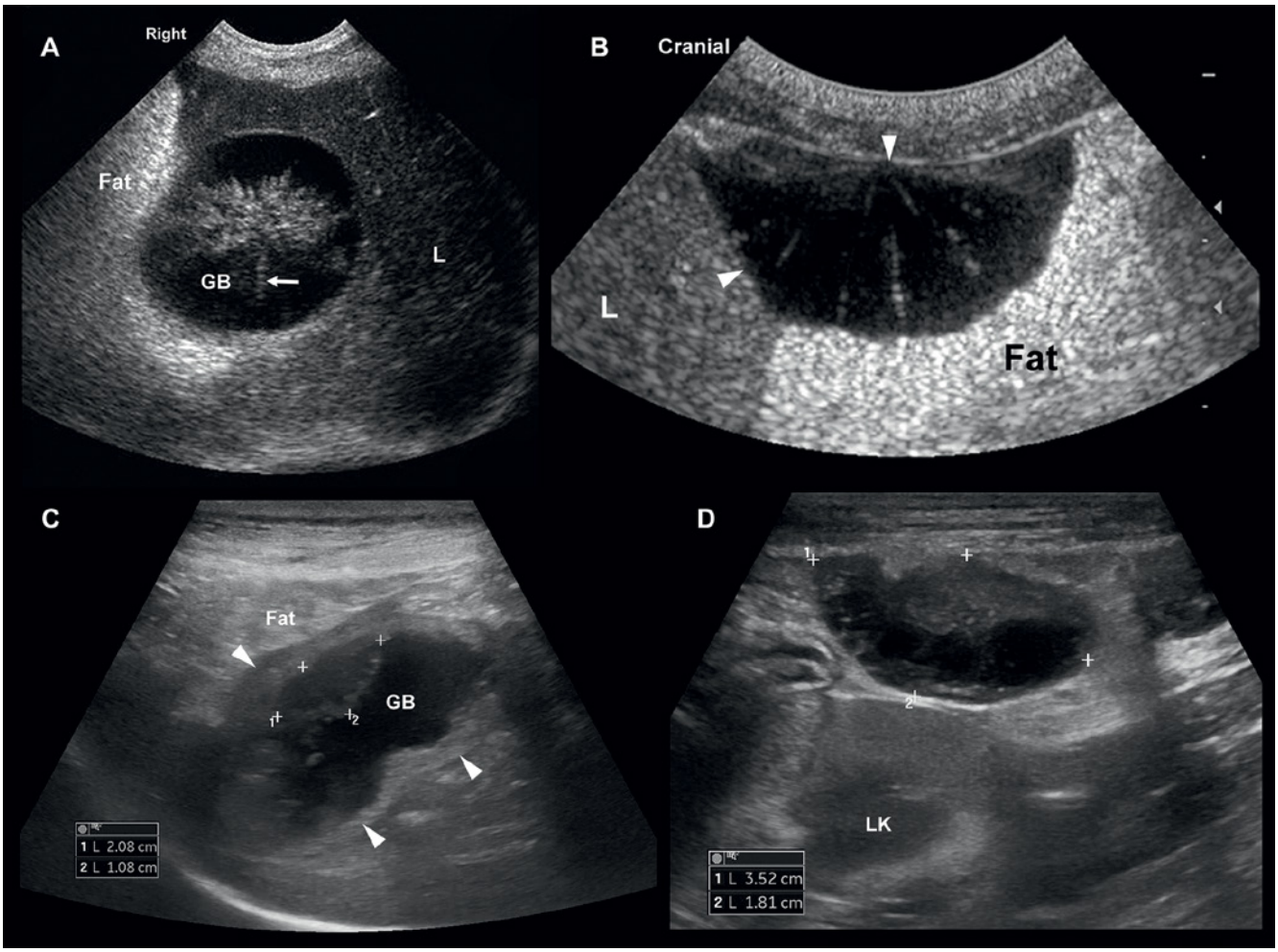


Figure 7.56. Gallbladder rupture and fragments migration in dogs. (A) Transverse image of the gallbladder in a dog with signs of acute abdominal pain. A ***kiwifruit-like pattern*** of striations, consistent with mucocele, is noted (arrow) in the gallbladder (GB). The fat at the right and ventral aspects of the GB is markedly hyperechoic and hyperattenuating, highly suggestive of wall perforation and was confirmed with surgical exploration. L, liver. **(B) Migrating mucocele**. Longitudinal image of the region just caudoventral to the liver (L) in a dog with GB mucocele. A crescent-shaped anechoic structure with fine radiating striations (arrowheads) is found at the caudal margin of the liver. This structure represents a fragment of mucocele that migrated after GB rupture. Consecutive bile peritonitis was present, associated with hyperechoic fat. **(C, D)** Ruptured mucocele in a 5-year-old Bernese mountain dog with several fragments found near the spleen and left kidney (LK in **D**). A fragment remains attached to the GB wall (in **C**) but most of the mucocele was expelled. The GB volume is reduced and its wall is thickened (arrowheads). There is hyperechoic fat around the GB and mucocele fragments, but only minimal effusion was present.

disease (e.g., cholangitis/cholangiohepatitis, cholecystitis, chronic enteropathy, and pancreatitis) was common in these cats (>75% of cases), consistent with prior literature (Eich and Ludwig 2002). In both species, patients with stones located in the CBD were more likely to be symptomatic. In general, the presence and severity of clinical signs are largely associated with secondary complications of cholelithiasis, which include EHBDO, GB rupture, hepatobiliary inflammation, cholecystocutaneous fistula formation, and potentially pain/biliary colic as the CBD is well innervated (Allan et al. 2021; Fabbi et al. 2014; Jaffey 2022). The specific pathogenesis of cholelith formation is unclear, but a complex interaction of biliary stasis, altered bile composition/hypersaturation, mucus hypersecretion, and infection causing chronic inflammation is a commonly encountered hypothesis (Brunet et al. 2023; Jaffey 2022; Kanemoto et al. 2017; Ward et al. 2020).

Vet-ebooks.com

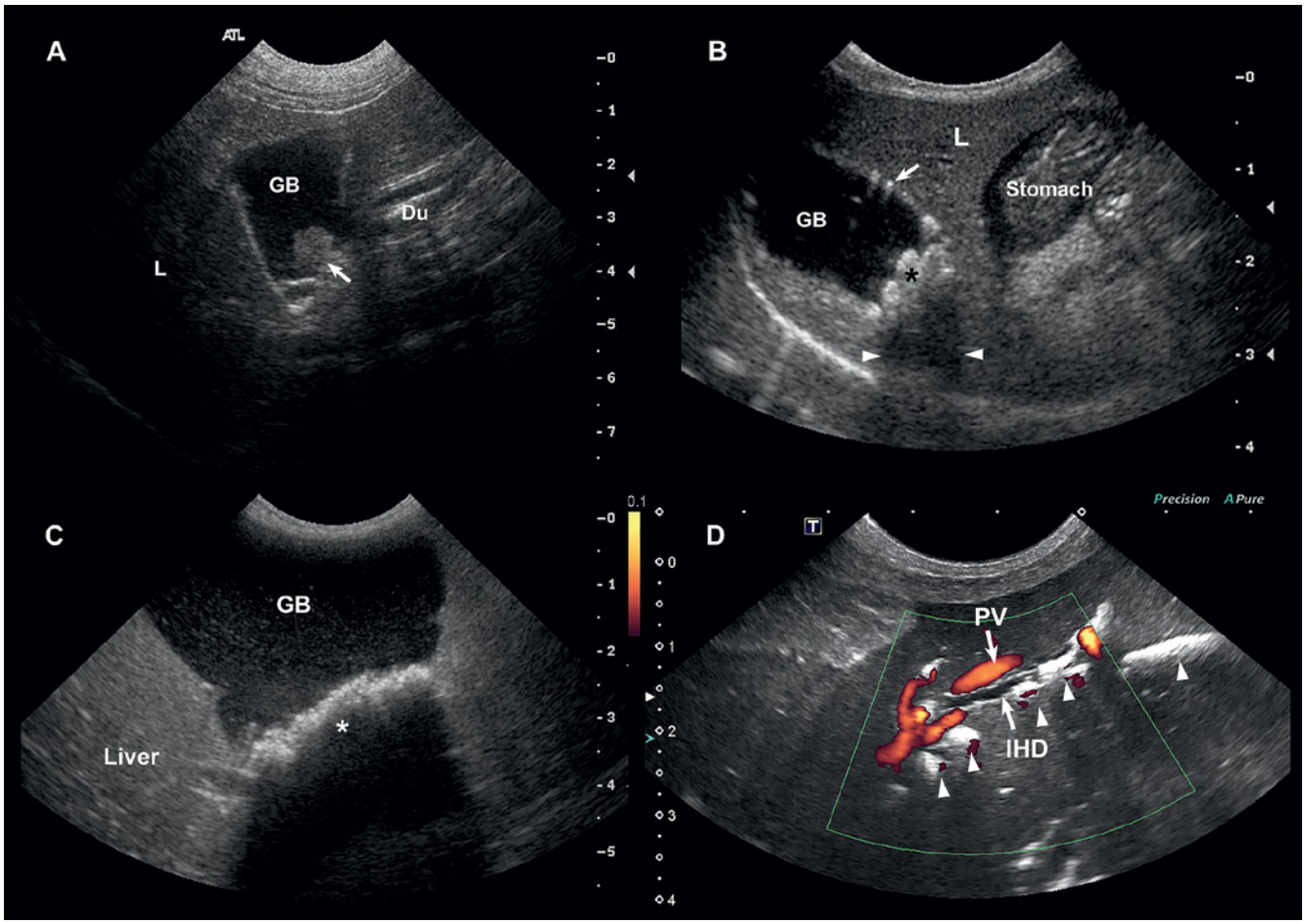


Figure 7.57. Biliary polyp and cholelithiasis in four dogs. (A) In this medium-sized mixed-breed dog, a 1-cm irregular structure of moderate echogenicity is attached to the wall of the gallbladder (GB). Its structure remained fixed in position regardless of patient positioning and followed over serial examination, presumed to represent a polyp. **(B)** Longitudinal image of the central portion of the liver (L) in a small dog with acute pancreatitis. Several rounded hyperechoic structures (*) associated with acoustic shadowing (arrowheads), consistent with choleliths, are in the GB neck. Small hyperechoic foci, associated with some reverberation (arrow), are in the nondependent ventral region of the GB. These foci could indicate small choleliths adhered to the wall or indicate gas. There was no increase in liver enzymes in this dog. The gallstones were not considered clinically significant. **(C)** A larger volume of cholelithiasis (*) is in the dependent portion of the GB of this other larger dog with Cushing's disease. Similar ultrasound features are observed. **(D)** Transverse oblique power Doppler image of the left portion of the liver of a dog with increased liver enzymes. Several linear hyperechoic tracts and mineral fragments (arrowheads), causing partial acoustic shadowing, are present in the intrahepatic biliary ducts (IHDs) in proximity to the portal veins (PVs).

Interventional Procedures

Ultrasound-guided **fine-needle aspiration and biopsy** have become routine procedures complementing hepatic ultrasonography (Penninck and Finn-Bodner 1998). The choice of needle size (gauge) and length depends on the size, the vascularity, and the depth of the targeted tissue. Various needle gauge can be used for aspiration; it appears that little difference in sampling quality is noted between the 22-, 23-, and 25-gauge needles (Llanos et al. 2023). Fourteen- to eighteen-gauge needles are commonly used for automated core biopsy. Fine-needle aspiration can usually be performed with patients under minimal sedation, whereas biopsy usually requires general anesthesia. Aspiration can be performed with a customized biopsy-needle guide placed on the probe or by using a freehand technique. The latter, which is more commonly used especially on superficial lesions, can usually be performed more quickly and limits possible lacerations (Figure 7.58). Although freehand aspiration is relatively safe and easy to

Vet-ebooks.com

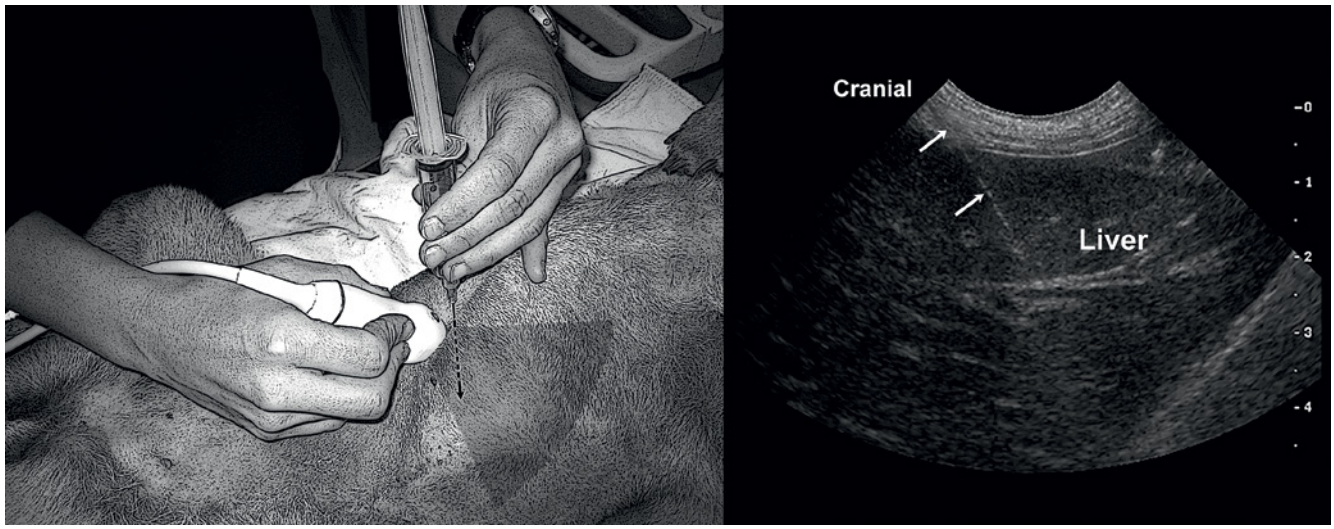


Figure 7.58. Ultrasound-guided fine-needle aspiration. In the photograph, a freehand, ultrasound-guided, fine-needle aspiration is performed. The needle is inserted through the skin just caudal to the xiphoid process and costal arch, and through the left portion of the liver. This technique is preferred when diffuse processes are suspected, because it prevents inadvertent gallbladder puncture. The corresponding ultrasound image is also shown. The hyperechoic fine needle can be seen obliquely into the parenchyma (arrows).

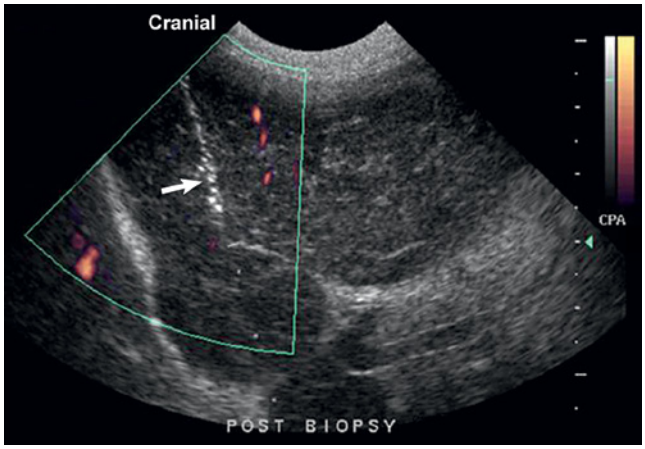


Figure 7.59. Ultrasound-guided percutaneous biopsy. Longitudinal image obtained using power Doppler after biopsy of the left portion of the liver of a dog with suspected hepatitis. A hyperechoic needle tract can be seen along the biopsy guide path (small aligned dots at the arrow) without evidence of hemorrhage. The left portion of the liver was chosen to avoid the gallbladder.

perform in cases of diffuse hepatic disorders, it can be more challenging if small, deep lesions are targeted. With the assisted technique, the needle is placed through the biopsy guide tunnel and introduced along a precise path, which, however, cannot be modified (Figure 7.59).

Vacuolar hepatopathies, such as lipidosis and hyperadrenocorticism, are reliably diagnosed through cytological specimens obtained with fine-needle aspiration (Wang et al. 2004). Some neoplastic processes, such as lymphoma, and inflammatory processes can also be diagnosed through cytological examination, although a more confident diagnosis may require biopsy. **Fine-needle drainage** of cavitary lesions, such as cysts or abscesses, can also be performed as a diagnostic and/or therapeutic procedure.

Hemorrhage represents the most common complication observed with ultrasound-guided aspiration and biopsy, particularly if the liver is friable and/or if a coagulopathy is present. Preinterventional coagulation profiles are recommended in most cases. Additionally, postinterventional ultrasonographic examination should be performed to monitor the presence of hemorrhage (Figure 7.60).

Needle tract implantation of neoplastic or infectious processes, although not well investigated in small animals, can represent a limiting factor, particularly if surgical excision is planned.

Ultrasound-guided **cholecystocentesis** can be used to obtain a sample of bile for culture or for GB decompression in animals with extrahepatic biliary obstruction secondary to an inflammatory process, such as pancreatitis (Herman et al. 2005) (Figure 7.61). Although infrequent, bile leakage and subsequent peritonitis, as well as peritoneal hemorrhage, are potential complications. Risks of complications are increased if the GB is distended or if its wall is diseased. A transhepatic approach has been suggested to be the

Vet-ebooks.com

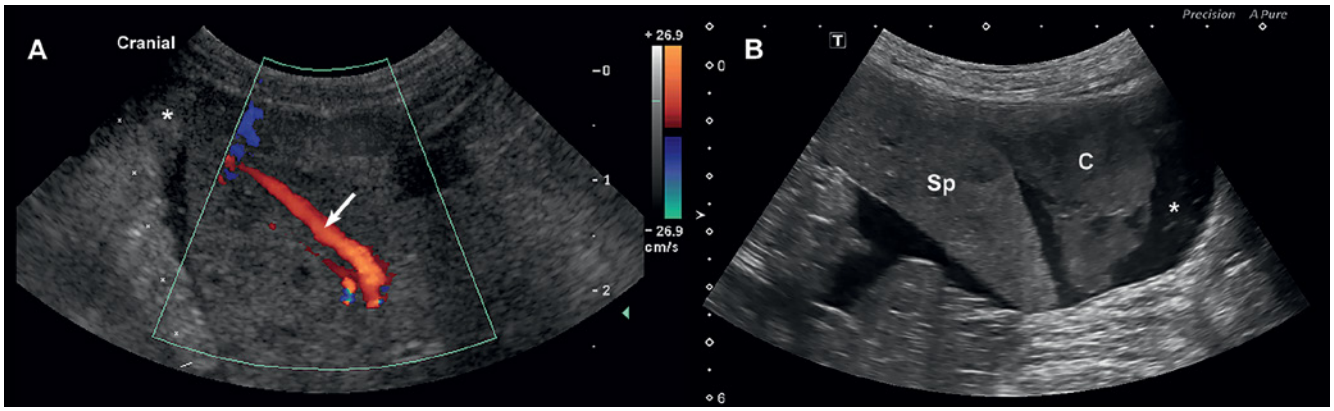


Figure 7.60. **Postbiopsy hemorrhage. (A)** Longitudinal image obtained after ultrasound-guided biopsy of the left portion of the liver of a dog with chronic active hepatitis. A red-signal linear tract (arrow), consistent with retrograde hemorrhage, is observed along the biopsy tract. Echogenic peritoneal effusion is at the cranial aspect of the biopsy site (*), consistent with peritoneal hemorrhage. **(B)** In this other dog with a severe degenerative hepatopathy, biopsies resulted in prolonged hemorrhage (*). A blood clot (C) is eventually formed next to the spleen (Sp).

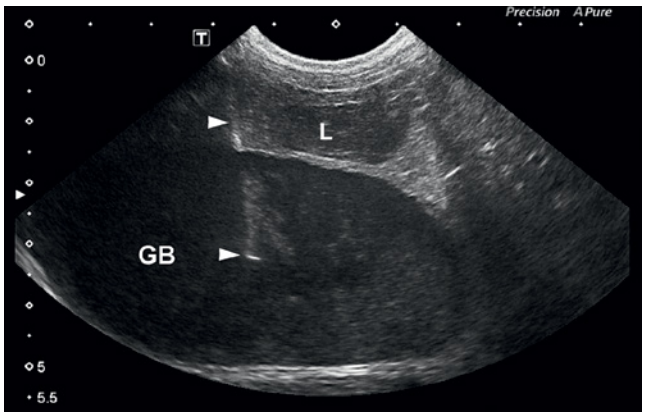


Figure 7.61. **Ultrasound-guided cholecystocenthesis.** In this dog with extrabiliary obstruction due to severe pancreatitis, gallbladder (GB) pressure was reduced by removing nearly 50 mL of bile. This resulted in short-term clinical improvement. Arrowheads point to the needle traversing the liver (L) parenchyma before entering the distended GB.

safest percutaneous method of bile aspiration, enabling the liver parenchyma to seal the area of GB puncture (Center 1996).

Visit our website at **www.SmallAnimalUltrasonography.com** for complementary video clips with annotations and text on:

- Normal liver and biliary system
- Lipidosis
- Steroid-induced and other vacuolar hepatopathies
- Nodular hyperplasia
- Chronic active hepatitis
- Cholangitis/cholangiohepatitis in cats
- Cirrhosis
- Hepatocellular carcinoma
- Hepatic metastases
- Hepatic lymphoma
- Cystadenoma
- Gallbladder mucocele
- Extrahepatic biliary obstruction
- Gallbladder sludge
- Cholelithiasis

References

Allan F, Watson PJ, McCallum KE.(2021) Clinical features and outcomes in 38 dogs with cholelithiasis receiving conservative or surgical management. J Vet Intern Med.35(6):2730–2742. https://doi.org/10.1111/jvim.16284. Epub 2021 Oct 29.

Asakawa M, Fukuzawa M, Asawaka MG, Flanders JA (2022) Preoperative serum C-reactive protein concentration can be used to detect gallbladder rupture in dogs with gallbladder mucocele. Am J Vet Res 83: 23–32.

Austin B, Tillson DM, Kuhnt LA (2006) Gallbladder agenesis in a Maltese dog. J Am Anim Hosp Assoc 42:308–311.

Bargellini P, Orlandi R, Paloni C, Rubini G, et al. (2016) Evaluation of contrast-enhanced ultrasonography as a method for detecting gallbladder necrosis or rupture in dogs. Vet Radiol Ultrasound 57:611–620.

Beatty JA, Barrs VR, Martin PA, Nicoll RG, et al. (2002) Spontaneous hepatic rupture in six cats with systemic amyloidosis. J Small Anim Pract 43:355–363.

Bennett SL, Milne M, Slocombe RF, Landon BP (2007) Gallbladder mucocoele and concurrent hepatic lipidosis in a cat. Aust Vet J 85:397–400.

Besso JG, Wrigley RH, Gliatto JM, Webster CRL (2000) Ultrasonographic appearance and clinical findings in 14 dogs with gallbladder mucocele. Vet Radiol Ultrasound 41:261–271.

Vet-ebooks.com

Best EJ, Bush DJ, Dye C (2010) Suspected choledochal cyst in a domestic shorthair cat. J Feline Med Surg 12:814–817.

Bosje JT, van den Ingh TS, van der Linde-Sipman JS (1998) Polycystic kidney and liver disease in cats. Vet Q 20:136–139.

Broadbridge C, Taylor SS, Renfrew H, Gemignani F, et al. (2021) Gallbladder adenoma in a domestic shorthair cat. JFMS Open Rep 7(1):2055116921997665. doi: 10.1177/2055116921997665

Bromel C, Barthez PY, Léveillé R, Scrivani PV (1998) Prevalence of gallbladder sludge in dogs as assessed by ultrasonography. Vet Radiol Ultrasound 9:206–210.

Brown PJ, Henderson JP, Galloway P, O'Dair H, et al. (1994) Peliosis hepatis and telangiectasis in 18 cats. J Small Anim Pract 35:73–77.

Brunet A, Duperrier-Simond C, Amoyal S, Benchekroun G, et al. (2023) Prevalence and clinical relevance of cholelithiasis in cats: a multicenter retrospective study of 98 cases. J Vet Intern Med 37:2157–2170.

Burchell RK, Thornton L, Lim CK, Murakami M, et al. (2019) Presumptive migrating gall bladder mucocoele in two dogs with gall bladder rupture. J Small Anim Pract 60:58–61.

Burn-DeMArle K, Webster CR, Penninck D, Ferrer L. Approach to the diagnosis of hepatocutaneous syndrome in dogs: a retrospective study and literature review. J Am Anim Hosp Assoc 2021; 57:15–25. https://doi.org/10.5326/JAAHA-MS-7072.

Butler T, Bexfield N, Dor C, Fantaconi N, et al. (2022) A multicenter retrospective study assessing progression of biliary sludge in dogs using ultrasonography. J Vet Intern Med 36:976–985.

Carlisle CH, Wu JX, Heath TJ (1995) Anatomy of the portal and hepatic veins of the dog: a basis for systematic evaluation of the liver by ultrasonography. Vet Radiol Ultrasound 36:227–233.

Center SA (1996) Diseases of the gallbladder and biliary tree. In: Guilford WG, Center SA, Strombeck DR et al., eds. Strombeck's Small Animal Gastroenterology, 3rd edition. WB Saunders: Philadelphia, pp. 860–882.

Center SA, Randolph JF, Warner KL, Flanders JA, et al. (2022) Clinical features, concurrent disorders, and survival time in cats with suppurative cholangitis-cholangiohepatitis syndrome. J Am Vet Med Assoc 260:212–227.

Choi J, Kim A, Keh S, Oh J, et al. (2013) Comparison between ultrasonographic and clinical findings in 43 dogs with gallbladder mucoceles. Vet Radiol Ultrasound 55:202–207.

Ciammaichella L, Foglia A, Del Magno S, Cola V, et al. (2023) Perforated duodenal ulcer in a dog with gallbladder agenesis. Open Vet J 13:376–381.

Cook AK, Jambhekar AV, Dylewski AM. (2016) Gallbladder sludge in dogs: ultrasonographic and clinical findings in 200 patients. J Am Anim Hosp Assoc 52:125–131.

Cruz-Arambulo R, Wrigley R, Powers B (2004) Sonographic features of histiocytic neoplasms in the canine abdomen. Vet Radiol Ultrasound 45:554–558.

Cuccovillo A, Lamb CR (2002) Cellular features of sonographic target lesions of the liver and spleen in 21 dogs. Vet Radiol Ultrasound 43:275–278.

DeMonaco SM, Grant DC, Larson MM, Panciera DL, et al. (2016) Spontaneous course of biliary sludge over 12 months in dogs with ultrasonographically identified biliary sludge. J Vet Intern Med 30:771–778.

Diana A, Guglielmini C, Specchi S, Di Tommaso M, et al. (2012) Ultrasonographic evaluation of preprandial and postprandial gallbladder volume in healty cats. Am J Vet Res 73:1583–1588.

Eich CS, Ludwig LL (2002) The surgical treatment of cholelithiasis in cats: a study of nine cases. J Am Anim Hosp Assoc 38:290–296.

Evans HE (1993a) Chapter 7: the digestive apparatus and abdomen. In: Evans HE, Christensen GC, eds. Miller's Anatomy of the Dog, 3rd edition. WB Saunders: Philadelphia, pp 385–462.

Evans HE (1993b) Veins. In: Evans HE, Christensen GC, eds. Miller's Anatomy of the Dog, 3rd edition. WB Saunders: Philadelphia, pp 682–716.

Fabbi M, Volta A, Quintavalla F, Zubin E, et al. (2014) Cholecystocutaneous fistula containing multiple gallstones in a dog. Can Vet J 55:1163–1166.

Fahie MA, Martin RA (1995) Extrahepatic biliary tract obstruction: a retrospective study of 45 cases (1983–1993). J Am Anim Hosp Assoc 31:478–482.

Feeney DA, Anderson KL, Ziegler LE, Jessen CR, et al. (2008) Statistical relevance of ultrasonographic criteria in the asessment of diffuse liver disease in dogs and cats. Am J Vet Res 69:212–221.

Gaillot HA, Penninck DG, Webster CR, Crawford S (2007) Ultrasonographic features of extrahepatic biliary obstruction in 30 cats. Vet Radiol Ultrasound 48:439–447.

Glavan C (2022) Imaging findings and monitoring of a rare case of congenital intrahepatic bile duct ectasia (Caroli-like disease) and a pancreatic cyst in a 2-month-old cat. Vet Rec Case Rep 10:e450.

Gorlinger S, Rothuizen J, Bunch S, van den Ingh TSGAM (2003) Congenital dilatation of the bile ducts (caroli's disease) in young dogs. J Vet Intern Med 17:28–32.

Griffin S (2019) Feline abdominal ultrasonography: what's normal? What's abnormal? The biliary tree. J Fel Med Surg 21:429–441.

Guillot M, d'Anjou MA, Alexander K, Bédard C, et al. (2009) Can sonographic findings predict the results of liver aspirates in dogs with suspected liver disease? Vet Radiol Ultrasound 50:513–518.

Harran N, d'Anjou MA, Dunn M, Beauchamp G (2011) Gallbladder sludge on ultrasound is predictive of increased liver enzymes and total bilirubin in cats. Can Vet J 52:999–1003.

Herman BA, Brawer RS, Murtaugh RJ, Hackner SG (2005) Therapeutic percutaneous ultrasound-guided cholecystocentesis in three dogs with extrahepatic biliary obstruction and pancreatitis. J Am Vet Med Assoc 227: 1782–1786.

Hinkle Schwartz SG, Mitchell SL, Keating JH, Chan DL (2006) Liver lobe torsion in dogs: 13 cases (1995–2004). J Am Vet Med Assoc 228:242–247.

Vet-ebooks.com

Hittmair KM, Vielgrader HD, Loupal G (2001) Ultrasonographic evaluation of gallbladder wall thickness in cats. Vet Radiol Ultrasound 42:149–155.

Hudson LC, Hamilton WP, eds. (1993) Atlas of Feline Anatomy for Veterinarians, 1st edition. WB Saunders, Philadelphia, p. 287.

Jaffey JA (2022) Canine extrahepatic biliary disease. J Small Anim Pract 63:247–264.

Jaffey JA, Graham A, VenEerde E, Hostnik E, et al. (2018) Gallbladder mucocele: variables associated with outcome and the utility of ultrasonography to identify gallbladder rupture in 219 dogs (2007–2016). J Vet Intern Med 32:195–200.

Jerrems O, de Mello Souza CH, Wavreille V, Davids BI (2020) Spontaneous mural gallbladder hematoma in a dog. Can Vet J 61:35–38.

Kamishina H, Katayama M, Okamura Y, Sasaki J, et al. (2010) Gallbladder agenesis in a Chihuahua. J Vet Med Sci 72:959–962.

Kanemoto H, Fukushima K, Ohno K (2017) Intrahepatic cholelithiasis in dogs and cats: a case series. Can Vet J 58:971–973.

Kelly D, Moreno-Aguado B, Lamb V (2019) Gallbladder agenesis in a dog: clinicopathological, histopathology, and computed tomography findings. J Am Anim Hosp Assoc 55:556–602.

Kemp SD, Panciera DL, Larson MM, Werre SR (2013) A comparison of hepatic sonographic features and histopathologic diagnosis in canine liver disease: 138 cases. J Vet Intern Med 27:806–813.

Kutura K, Seki M, Ishikawa C, Sakai M, et al. (2013) Triple-phase helical computed tomography in dogs with hepatic masses. Vet Radiol Ultrasound 55:7–15.

Lamb CR, Hartzband LE, Tidwell AT, Pearson SH (1991) Ultrasonographic findings in hepatic and splenic lymphosarcoma in dogs and cats. Vet Radiol Ultrasound 32:117–120.

Last RD, Hill JM, Roach M, Kaldenberg T (2006) Congenital dilatation of the large and segmental intrahepatic bile ducts (Caroli's disease) in two Golden retriever littermates. J S Afr Vet Assoc 77(4):210–214.

Léveillé R, Biller DS, Shiroma JT (1996) Sonographic evaluation of the common bile ducts in cats. J Vet Intern Med 10:296–299.

Lisciandro GR, Gambino JM, Lisciandro SC (2021) Thirteen dogs and one cat with ultrasonographically detected gallbladder wall edema associated with cardiac disease. J Vet Intern Med. 35:1342–1346.

Llanos C, Holmes E, White C, Jasensky AK, et al. (2023) Diagnostic quality of ultrasound-guided fine-needle aspirate samples from the canine liver and spleen is not significantly affected by using 22-,23-, and 25-gauge needles. Vet Radiol Ultrasound 64:966–972.

MacLeod AN, Reichle JK, Szabo D, Cohen EB, et al. (2023) Ultrasonographic appearance of gallbladder neoplasia in 14 dogs and 1 cat. Vet Radiol Ultrasound 64:537–545.

Marolf AJ, Leach L, Gibbons DS, Bachand A, et al. (2012) Ultrasonographic findings of feline cholangitis. J Am Anim Hosp Assoc 48:36–42.

Martinez C, Davies D, Hoey S, Shiel RE, et al. (2023) Ultrasonographic measurement of gallbladder wall thickness in fasted dogs without signs of hepatobiliary disease. J Vet Intern Med 1–6.doi: 10.1111/jvim.16810

Mayhew PD, Holt DE, McLear RC, Washabau RJ (2002) Pathogenesis and outcome of extrahepatic biliary obstruction in cat. J Small Anim Pract 43:247–253.

Mestrinho LA, Monteiro C, Sobral C, Travancinha J, et al. (2022) A case of a congenital umbilicobiliary fistula associated with gallbladder agenesis in a dog. Braz J Vet Med 44:e002821. doi: 1029374/2527-2179.bjvm 002821

Mills P, Saverymuttu S, Fallowfield M, Nussey S, et al. (1990) Ultrasound in the diagnosis of granulomatous liver disease. Clin Radiol 41:113–115.

Murakami T, Feeney DA, Bahr KL (2012) Analysis of clinical and ultrasonographic data by use of logistic regression models for prediction of malignant versus benign causes of ultrasonographically detected focal liver lesions in dogs. Am J Vet Res 73:821–829.

Newell SM, Selcer BA, Girard E, Roberts GD, et al. (1998) Correlations between ultrasonographic findings and specific hepatic diseases in cats: 72 cases (1985–1997). J Am Vet Med Assoc 213:94–98.

Nicoll RG, O'Brien R, Jackson MW (1998) Quantitative ultrasonography of the liver in obese cats. Vet Radiol Ultrasound 39:47–50.

Noguchi A, Iwanaga T, Miura N, Sogawa T, et al. (2023) Common bile duct perforation due to choledocholithiasis in a cat with gallbladder agenesis. J Fel Med Surg Open Rep 1–7. doi: 10.1177/20551169221146513

Nyland TG, Gillett NA (1982) Sonographic evaluation of experimental bile duct ligation in the dog. Vet Radiol Ultrasound 23:252–260.

Nyland TG, Barthez PY, Ortega TM, Davis CR (1996) Hepatic ultrasonographic and pathologic findings in dogs with canine superficial necrolytic dermatitis. Vet Radiol Ultrasound 37:200–205.

Nyland TG, Koblik PD, Tellyer SE (1999) Ultrasonographic evaluation of biliary cystadenomas in cats. Vet Radiol Ultrasound 40:300–306.

Nyman HT, Kristensen AT, Flagstad A, McEvoy FJ (2004) A review of the sonographic assessment of tumor metastases in liver and superficial lymph nodes. Vet Radiol Ultrasound 45:438–448.

O'Brien RT, Iani M, Delaney F, Young K (2004) Contrast harmonic ultrasound of spontaneous liver nodules in 32 dogs. Vet Radiol Ultrasound 45:547–553.

Penninck DG, Berry C (1997) Diagnostic imaging of the feline liver. Semin Vet Med Surg (Small Animals): Feline Liver Disease 12:10–21.

Penninck D, Finn-Bodner ST (1998) Updates in interventional ultrasonography. Vet Clin North Am Small Anim Pract 28:1017–1040.

Penninck D, Brisson JO, Webster CR (2010) Sonographic assessment of gallbladder volume in cats. Vet Radiol Ultrasound 51:665–666.

Vet-ebooks.com

Pike FS, Berg J, King NW, Penninck DG, et al. (2004) Gallbladder mucocele in dogs: 30 cases (2000–2002). J Am Vet Med Assoc 10:1615–1622.

Pillai S, Center SA, McDonough SP, Demarco J, et al. (2016) Ductal plate malformation in the liver of boxer dogs: clinical and histological features. Vet Pathol 53:602–613.

Prentice KD, Callahan-Clark JE, Parry NM, Schwarz LA, et al. (2023) Characterization of clinical presentation, histological features, ultrasonographic findings and survival in 29 dogs with granulomatous hepatitis. J Vet Intern Med 1–9. doi: 10.1111/jvim.16937

Ramirez S, Douglass JP, Robertson ID (2002) Ultrasonographic features of canine abdominal malignant histiocytosis. Vet Radiol Ultrasound 43:167–170.

Roberts ML, Rine S, Lam A (2018) Caroli's-type ductal plate malformation and a portosystemic shunt in a 4-month-old kitten. JFMS Open Rep 4(2):2055116918812329. doi: 10.1177/2055116918812329

Rodriguez A, Leal LO, Girod M, Dally C, et al. (2020) Canine copper-associated hepatitis: a retrospective study of 17 clinical cases. Open Vet J 10(2):128–134.

Santiago I, Loureiro R, Curvo-Semedo L, Marques C, et al. (2012) Congenital cystic lesions of the biliary tree. AJR 198:825–835.

Sato A, Solano M (2004) Ultrasonographic findings in abdominal mast cell disease: a retrospective study of 19 patients. Vet Radiol Ultrasound 45:51–57.

Sato K, Sakai M, Hayakawa S, Sakamoto Y, et al. (2018) Gallbladder agenesis in 17 dogs: 2006–2016. J Vet Intern Med 32:188–194.

Schwarz LA, Penninck DG, Leveille-Webster C (1998) Hepatic abscesses in 13 dogs: a review of the ultrasonographic findings, clinical data and therapeutic options. Vet Radiol Ultrasound 39:357–365.

Seitz MA, Lee AM, Woodruff KA, Thompson AC (2021) Sedation with dexmedetomidine is associated with transient gallbladder wall thickening and peritoneal effusion in some dogs undergoing abdominal ultrasonography. J Vet Intern Med 35:2743–2751.

Spain HN, Penninck DG, Webster CRL, Daure E, et al. (2017) Ultrasonographic and clinicopathologic features of segmental dilatations of the common bile duct in four cats. JFMS Open Rep 3(1):2055116917716881. doi: 10.1177/2055116917716881

Spain HN, Penninck DG, Thelan M (2022) Ultrasonographic prevalence and proposed morphologic classification of bilobed gallbladder in cats. J Fel Med Surg 10:986–993.

Sparago J, Rademacher N, Dehghanpir S, Post J, et al. (2021) Investigation of the association between gall bladder wall thickness and hypoalbuminaemia in dogs. J Sm Anim Pract 62:973–978.

Spaulding KA (1993) Ultrasound corner gallbladder wall thickness. Vet Radiol Ultrasound 34:270–272.

Stonewater JL, Lamb C, Shelling SH (1990) Ultrasonographic features of canine hepatic nodular hyperplasia. Vet Radiol Ultrasound 31:268–272.

Tsukagoshi T, Ohno K, Tsukamoto A, Fukushima K, et al. (2012) Decreased gallbladder emptying in dogs with biliary sludge or gallbladder mucocele. Vet Radiol Ultrasound 53:84–91.

Venier F, Compagnone K, Kerinsand A, Rosa C (2021) Common bile duct obstruction caused by a helminth in a cat in the UK: ultrasonographic findings, histopathology and outcome. JFMS Open Rep 7(1):2055116920984391. doi: 10.1177/2055116920984391

Villm J, DeMonaco S, Larson M (2022) Prevalence of gallbladder sludge and associated abnormalities in cats undergoing abdominal ultrasound. Vet Radiol Ultrasound 63:601–608.

Vitullo I, Bobis-Villagrá D, Veiga-Parga T, Carla Vilaseca V, et al. (2023) Gall bladder agenesis in a crossbreed. Vet Rec Case Rep 11:e728.

Walter R, Dunn ME, d'Anjou MA, Lécuyer M (2008) Nonsurgical resolution of gallbladder mucocele in two J Am Vet Med Assoc 11:1688–1693.

Wang KW, Panceria DL, Al-Rukibat RK, Radi AZ (2004) Accuracy of ultrasound-guided fine-needle aspiration of the liver and cytologic findings in dogs and cats: 97 cases (1990–2000). J Am Vet Med Assoc 224:75–78.

Ward PM, Brown K, Hammond G, Parkin T et al. (2020). Cholelithiasis in the dog: prevalence, clinical presentation, and outcome. J Am Anim Hosp Assoc May/Jun;56 (3):152. https://doi.org/10.5326/JAAHA-MS-7000. Epub 2020 Mar 17.

Warren-Smith CMR, Andrew S, Mantis P, Lamb CR (2012) Lack of associations between ultrasonographic appearance of parenchymal lesions of the canine liver and histological diagnosis. J Small Anim Pract 53:168–173.

Weissman A, Penninck D, Wester C, Hecht S, et al. (2012) Ultrasonographic and clinicopathological features of feline gastrointestinal eosinophilic sclerosing fibroplasia in 4 cats. J Feline Med Surg 15:148–154.

Whiteley MB, Feeney DA, Whiteley LO, Hardy RM (1989) Ultrasonographic appearance of primary and metastatic canine hepatic tumors: a review of 48 cases. Ultrasound Med 8:621–630.

Wilkinson AR, DeMonaco SM, Panciera DL, Otoni CC, et al. (2020) Bile duct obstruction associated with pancreatitis in 46 dogs. J Vet Intern Med 34:1794–1800.

Woods, K, Brisson BA, Defarges AMN, Oblak Ml (2012) Congenital dupplex gallbladder and biliary mucocele associated with partial hepatic cholestasis and cholelithiasis in a cat. Can Vet J 53:269–273.

Vet-ebooks.com

CHAPTER EIGHT

Spleen

Mathieu Harel[1] and Wilfried Mai[2]

[1]*SONHAR, Veterinary Diagnostic Imaging, Ecully, France*
[2]*School of Veterinary Medicine, Section of Radiology, University of Pennsylvania, Philadelphia, PA, USA*

Preparation and Scanning Technique

Ultrasonographic examination of the spleen is usually performed with the animal in dorsal recumbency. For evaluation of the craniodorsal extremity of the spleen in large and deep-chested dogs, it may be beneficial to position the dog in right lateral recumbency and use a left intercostal approach. The abdomen and, if necessary, the left caudal thoracic wall are clipped, and acoustic coupling gel is applied. Depending on the size of the animal, a 5–11-MHz curvilinear transducer is routinely used. Because of the superficial location of the spleen, a linear transducer should be used when feasible, particularly in small dogs and cats.

The craniodorsal extremity of the spleen is located in the left craniodorsal abdomen immediately caudal to the stomach and adjacent to the body wall. Its position varies with gastric filling. This part is sonographically evaluated through an abdominal retrocostal or left intercostal approach. From this point, the remainder of the spleen is followed caudally and ventrally until the caudoventral extremity is reached. In dogs, the caudoventral extent of the spleen and hence the location of the caudal extremity is highly variable necessitating modification of the ultrasonographic approach in individual patients (Figure 8.1). In cats, the entire spleen is fairly consistently positioned along the left abdominal wall, lateral to the left kidney (Hanson et al. 2001).

Tracing the spleen to the hilus and caudal extremity can be done by positioning the transducer in a plane transverse to the splenic long axis. However, as the spleen extends beyond the transducer's field of view in most dogs, a thorough examination of the abdomen with meandering probe movement is usually necessary to facilitate examination of the entire organ. In cats, the spleen is smaller and thus easier to follow.

If the spleen is not found, previous splenectomy should be first excluded with the patient's medical history. Abnormal position of the spleen ("wandering spleen") due to laxity of the splenic supporting ligaments has also been described (Yuki and Narita 2021) in a cat. Otherwise, failure of in-utero development may be considered and is called asplenia.

Sonographic Anatomy of the Normal Spleen

The spleen is elongated and tongue-shaped in the long axis, and triangular or lenticular in cross section. The dorsal extremity is in a very dorsal location and is commonly seen to form a "hook" between the gastric fundus and left kidney (Figure 8.2). The splenic **parenchyma** is homogeneous and has a fine echotexture. However, in puppies younger than 60 weeks, the spleen can be heterogeneous, particularly between 28 and 36 weeks of age (Hwang et al. 2020). The spleen is covered by a thin and very hyperechoic capsule (Figure 8.3). However, the visibility and echogenicity of the splenic capsule depends on its position relative to the ultrasound beam, and while scanning, some portions of the capsule may appear discontinuous. In comparison with liver and renal cortices, the canine spleen is most often hyperechoic (Nyland et al. 1995) (Figure 8.4); in cats, it is only mildly hyperechoic to the renal cortex and is in fact commonly isoechoic to the kidney, particularly in castrated male cats (Reese et al. 2013). Normal

Atlas of Small Animal Ultrasonography, Third Edition. Edited by Dominique Penninck and Marc-André d'Anjou.
© 2025 John Wiley & Sons, Inc. Published 2025 by John Wiley & Sons, Inc.
Companion website: www.SmallAnimalUltrasonography.com

Vet-ebooks.com

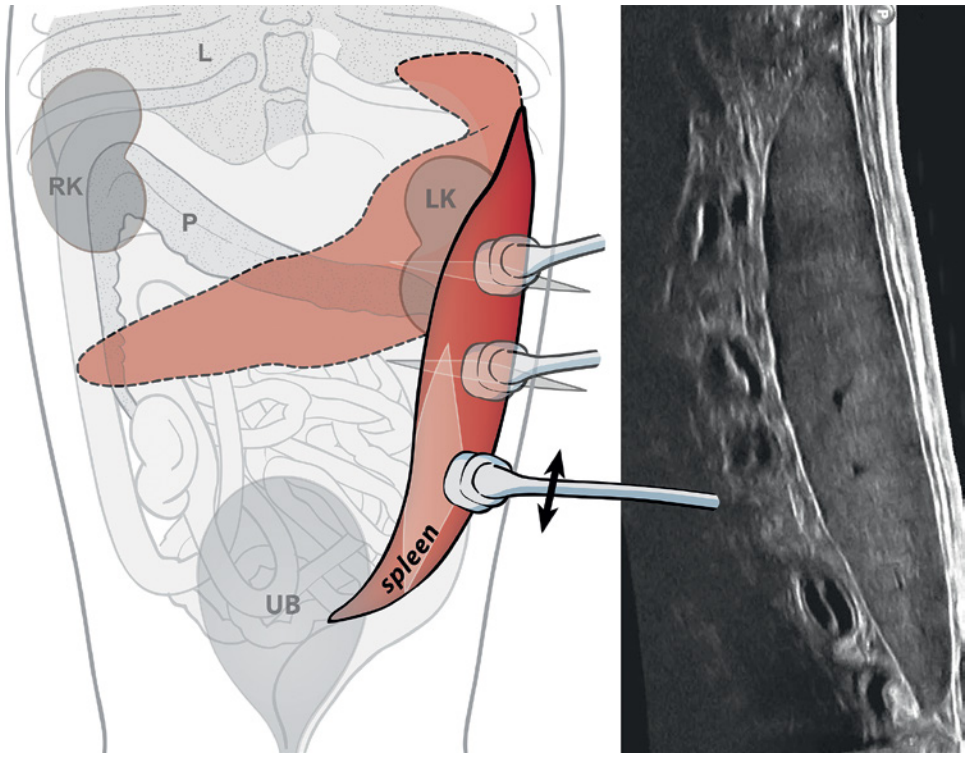


Figure 8.1. **Normal anatomy and scanning technique in a dog. Left:** A schematic representation of the spleen and its variable position in the abdomen. Ultrasound-probe positioning has to accommodate individual patients. **Right:** A panoramic ultrasonographic view of the spleen performed parallel to the left abdominal wall. L, liver; LK, left kidney; P, pancreas; RK, right kidney; UB, urinary bladder.

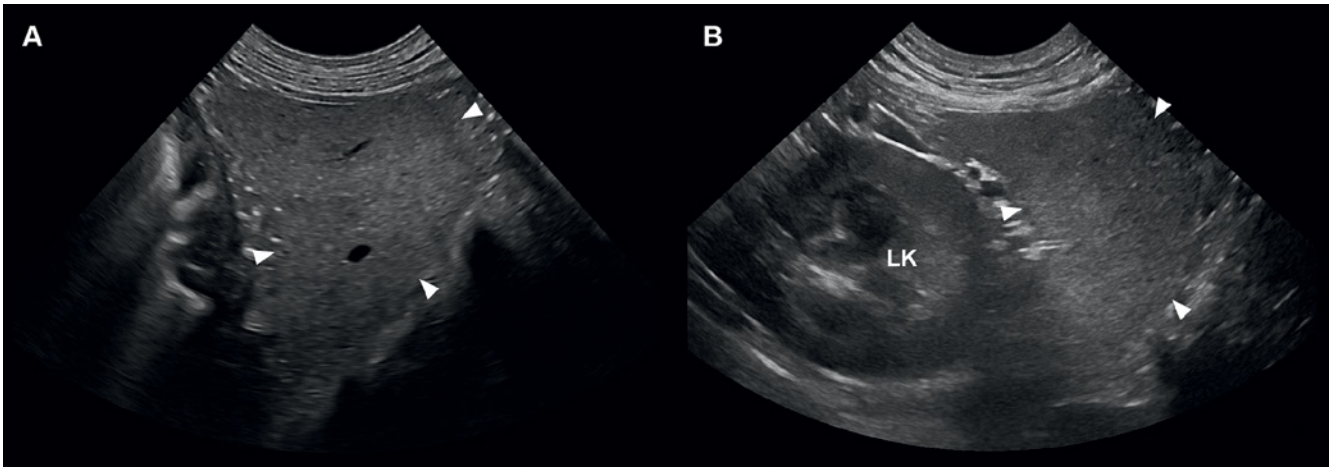


Figure 8.2. **Normal ultrasonographic appearance of the craniodorsal extremity of the spleen in two dogs. (A)** Image obtained with sagittal lateral oblique transducer orientation. The cranial portion of the spleen courses dorsally between the rib cage and the stomach. **(B)** Image obtained with transverse transducer orientation. The cranial extremity of the spleen (arrowheads) courses along the left abdominal wall laterally to the left kidney (LK), whose cranial part is visible on cross section.

accumulation of lipids in the tubules of the feline renal cortex can cause renal hyperechogenicity and can make the spleen appear iso- to hypoechoic relative to the renal cortex (Yeager and Anderson 1989).

Branches of the **splenic vein** are seen as tubular anechoic structures within the splenic parenchyma and exit the spleen at the hilus (Figure 8.5). Splenic vein tributaries exiting the spleen may cause mild

Vet-ebooks.com

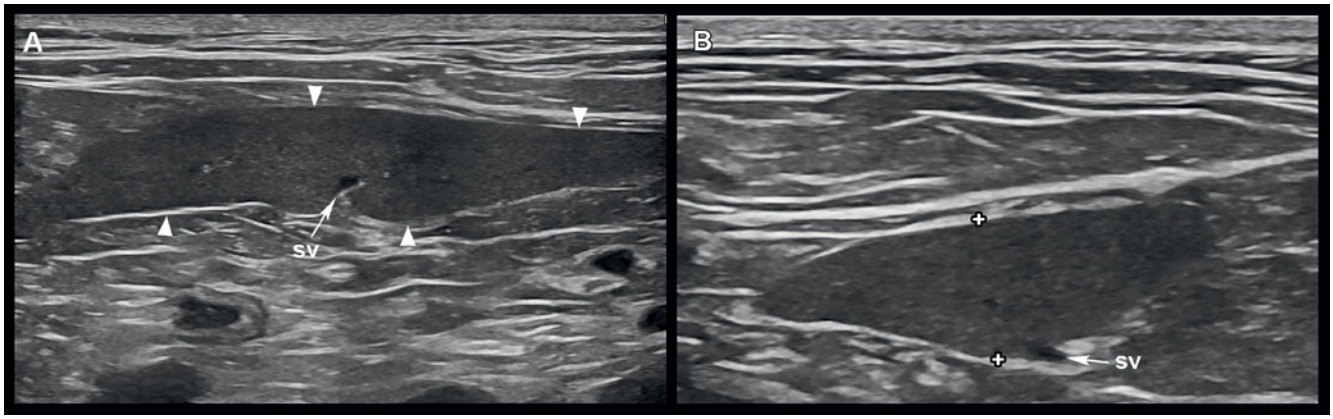


Figure 8.3. **Normal feline spleen. (A)** Sagittal sonogram of a normal spleen. The spleen is visible in the near field as a homogeneous tongue-shaped organ. The cranial extremity of the spleen is to the left of the image and the hyperechoic capsule is well visible along the cranial ventral border. The mild undulation of the visceral surface of the spleen is a normal finding. **(B)** Transverse sonogram of a normal spleen. The spleen appears as a sharply marginated triangular structure of homogeneous echotexture. Its capsule becomes prominent when perpendicular to the orientation of the ultrasound beam due to specular reflection. Calipers show the correct way to measure the splenic height. Sv, splenic vein.

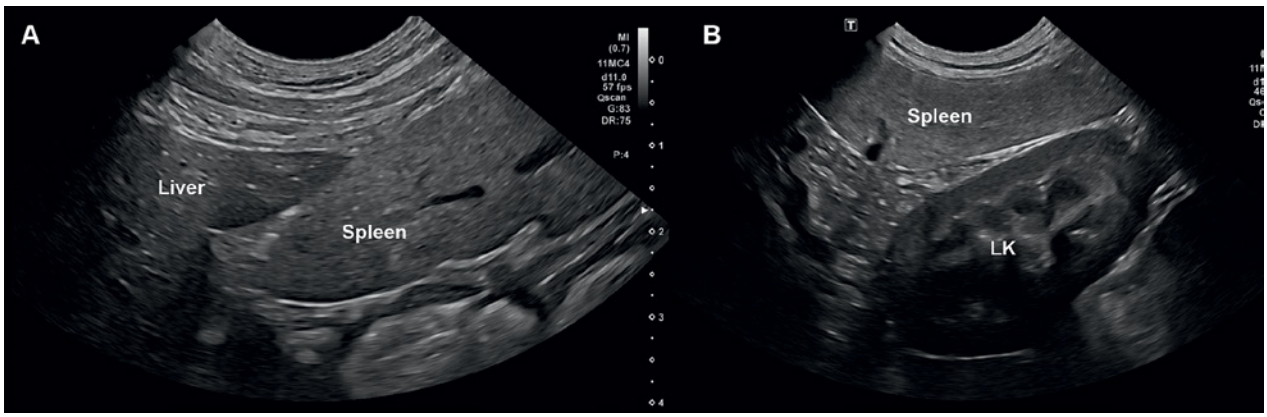


Figure 8.4. **Normal splenic echogenicity in a 2-year-old medium-breed dog (A) and in a 6-month-old Golden Retriever (B). (A)** Comparison between normal splenic and hepatic parenchyma. The cranial extremity of the spleen curves dorsally along the liver and is hyperechoic to this organ. Its echotexture is also finer than the one of the liver. **(B)** Comparison between normal splenic and renal echogenicity. The spleen in the near field is hyperechoic to the cortex of the left kidney (LK).

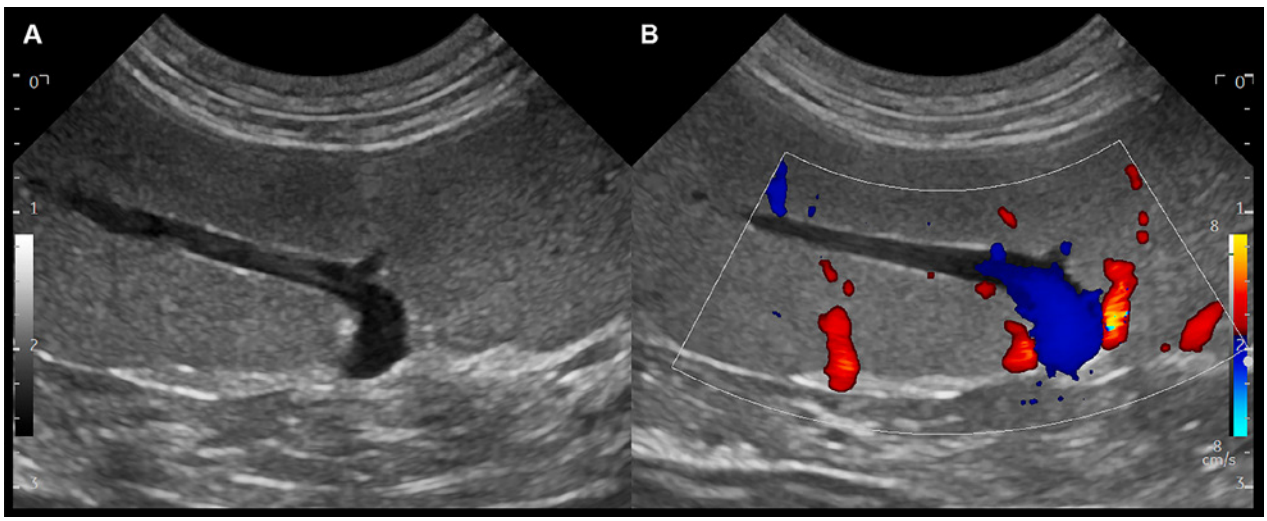


Figure 8.5. **Normal splenic vascularization in a dog. (A)** Longitudinal sonogram of a normal spleen showing a branch of the splenic vein leaving the spleen at the splenic hilus. The splenic arteries are not visible. **(B)** Color Doppler at the same level. There is normal low-velocity flow without evidence of turbulence or thrombosis in the splenic vein. As it moves away from the transducer, this flow appears blue on the color map. Splenic arterial blood flow is also visible, appearing red on the color map.

Vet-ebooks.com

undulations along the visceral surface (Figure 8.3). Splenic arteries are usually not seen unless color-Doppler imaging is used (Figure 8.5).

Splenic **size** is often evaluated subjectively in dogs, as it is quite variable due to the blood storage function of this organ and breed-related variations. In cats, the splenic volume is more consistent, and objective measurements can be done. The height of the dorsal third of the spleen (dorsal extremity) in a transverse plane when a splenic vessel is visible at the visceral surface has been shown to be the least variable (Sayre and Spaulding 2014) (Figure 8.3). The mean height was reported to be 7.1 mm, ranging from 5.1 to 9.1 mm.

The size and even echogenicity of the spleen can be affected by some drugs used for tranquilization or anesthesia (Auger et al. 2019; Finck et al. 2021; Reese et al. 2013; Sutil et al. 2017; O'Brien et al. 2004).

Sonographic Findings in Splenic Disorders

Diagnostic differentials for diffuse alterations in splenic parenchymal echogenicity or focal and multifocal lesions of the spleen are found in Tables 8.1 and 8.2.

Splenomegaly with Normal Echogenicity

Ultrasonographic assessment of splenic size is subjective. In dogs with splenomegaly, the margins of the spleen appear rounded, and the organ extends further

Table 8.1
Diagnostic differentials for diffuse alterations in splenic parenchymal echogenicity

Normoechoic splenomegaly	Heterogeneous splenomegaly	Hypoechoic splenomegaly
Sedation	Sedation	Torsion (often lacy pattern)
Extramedullary hematopoiesis	Extramedullary hematopoiesis	Massive infarction (often lacy pattern)
Benign lymphoid hyperplasia	Benign lymphoid hyperplasia	Lymphoma (or other round cell)
Splenic torsion (acute)	Neoplastic infiltration (round-cell tumor)	Histoplasmosis (cat)
Diffuse malignant infiltration (round cell tumor)	Splenic torsion (subacute)	
	Splenitis	

Table 8.2
Diagnostic differentials for focal and multifocal lesions of the spleen

Hyperechoic nodule or mass[a]	Hypoechoic nodule or mass	Mixed echogenicity[b] solid lesions, with or without cavitary components	"Target-like" lesions	Cyst-like lesions
Myelolipoma (more common)	Nodular lymphoid hyperplasia	Nodular lymphoid Hyperplasia	Metastasis (more common)	Pseudocyst (post hematoma)
Granuloma	Extramedullary hematopoiesis	Extramedullary hematopoiesis	Extramedullary hematopoiesis	Cyst
Nodular lymphoid hyperplasia	Round cell tumor	Primary neoplasia (hemangiosarcoma, round cell, other)	Nodular lymphoid Hyperplasia	Abscess
Hematoma	Other primary or metastatic neoplasia.	Metastatic neoplasia	**Focal hypoechoic, territorial, wedge-shaped, lacy pattern:**	
Neoplasia (primary or metastatic)	Pyogranuloma	Hematoma	Infarct	
Extramedullary hematopoiesis	Abscess	Infection (splenitis, abscess)		
Infection (splenitis, abscess)		Necrosis		

[a] *The term mass is used by many when a nodular lesion measures more than 3 cm but the distinction between nodule and mass remains widely arbitrary.*

[b] *Several processes can coexist (ex. necrosis, hemorrhage, inflammation, neoplasia, etc.) and explain tissue heterogeneity.*

Vet-ebooks.com

caudally and to the right side of the abdomen. In cats, folding of the spleen upon itself may indicate splenic enlargement (Hanson et al. 2001). In cats, splenic thickness of more than 9 mm may suggest splenomegaly (Sayre and Spaulding 2014), but a threshold of 1 cm is more commonly used. Splenomegaly with homogeneous echotexture is a frequent finding in dogs sedated with acepromazine, thiopental (Sutil et al. 2017; O'Brien et al. 2004), ketamine, and diazepam (Wilson et al. 2004). Acepromazine may in addition cause increased echogenicity in dogs (O'Brien et al. 2004). Increased splenic volume has also been shown in cats sedated with acepromazine (Auger et al. 2019) as well as alfaxalone combined with butorphanol (Finck et al. 2021) (Figure 8.6). Butorphanol alone (Auger et al. 2019) or coupled with dexmedetomidine (Finck et al. 2021) is not associated with significant splenic enlargement. These changes, when present in cats, are often mild compared to dogs because the feline spleen is not an important blood reservoir.

Splenomegaly without echogenicity changes may also be encountered secondary to extramedullary hematopoiesis, infectious diseases (Figure 8.7), splenic torsion, splenic vein thrombosis, or malignant infiltration, which occurs in lymphoma and mast cell tumors (Hanson et al. 2001; Nyland et al. 1995; Sato and Solano 2004; Saunders et al. 1998) (Figures 8.8, 8.9).

Diffuse Changes of the Splenic Parenchyma

Generalized splenomegaly with parenchymal heterogeneity or hypoechogenicity can be observed in various splenic disorders, including extramedullary hematopoiesis, lymphoid hyperplasia, neoplastic infiltration (e.g., round-cell tumors) (Figures 8.10, 8.11), bacterial/viral infection (Figures 8.12, 8.13), and vascular compromise (Figures 8.14, 8.15). Hypoechoic splenomegaly has also been reported in cats with histoplasmosis (Atiee et al. 2014).

A diffuse, lacy, hypoechoic echotexture of the spleen is commonly encountered in dogs with splenic torsion



Figure 8.7. Splenomegaly in a 7-year-old mixed-breed dog with splenic leishmaniasis. The spleen is diffusely enlarged with an undulating visceral surface. It is slightly inhomogeneous but retains normal echogenicity.

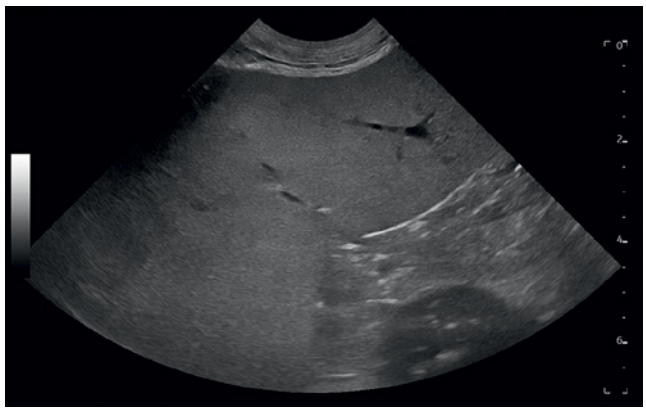


Figure 8.8. Splenomegaly in a 9-year-old mixed breed dog. The spleen is enlarged with rounded edges but a homogeneous parenchyma of normal echogenicity.

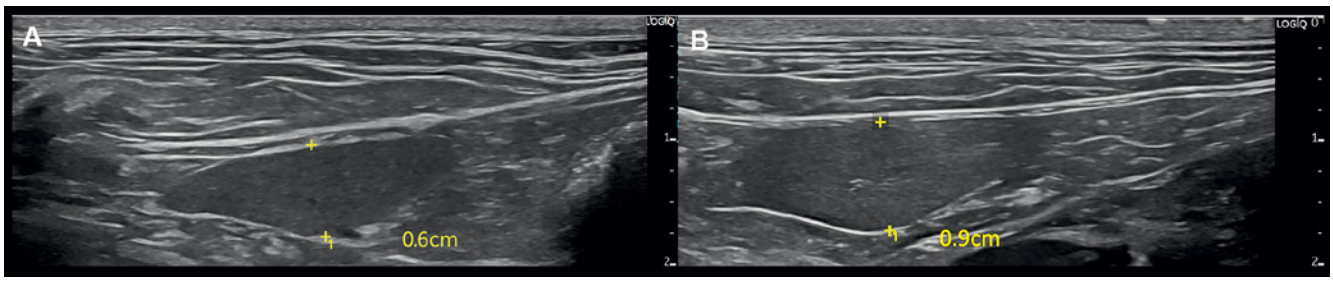


Figure 8.6. Splenomegaly following sedation in a 7-year-old cat. (A) Image of the spleen prior to sedation. The maximum thickness of the spleen is 6 mm. **(B)** Splenic enlargement is seen approximately 15 min after administration of butorphanol and alfaxalone. The maximum thickness of the spleen is 9 mm.

Vet-ebooks.com



Figure 8.9. Splenomegaly in a 9-year-old domestic shorthair cat with mast cell tumor. The spleen is enlarged, measuring 17 mm in height, of normal echogenicity, echotexture, and margination.

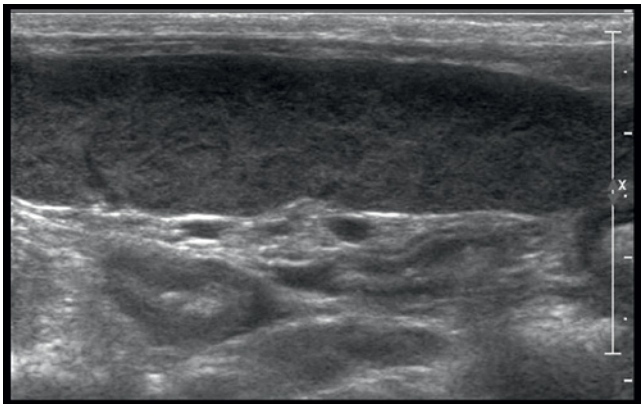


Figure 8.10. Lymphoma in a 12-year-old domestic shorthair cat. The spleen is enlarged (13 mm in height) and has an inhomogeneous echotexture.



Figure 8.11. Splenic lymphoma in a 14-year-old mixed-breed dog. The spleen is enlarged, inhomogeneous with numerous small hypoechoic nodules. This honeycomb pattern is often seen with lymphoma, but also with benign conditions.

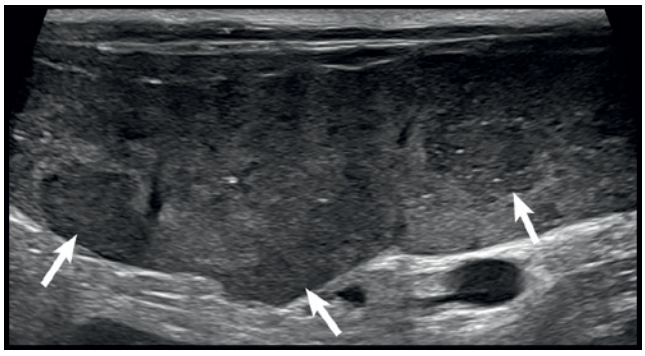


Figure 8.12. Granulomatous splenitis in a 6-year-old cat secondary to feline infectious peritonitis. The spleen is enlarged and markedly heterogeneous with several ill-defined nodules (arrows) and irregular margins.

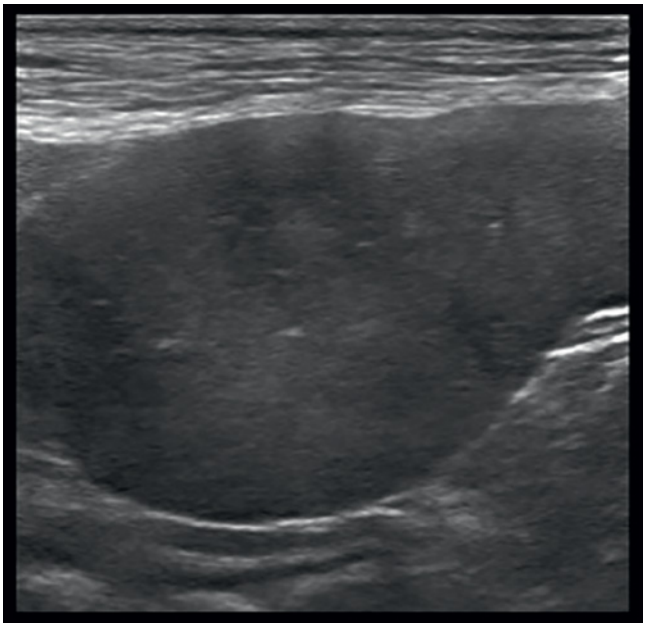


Figure 8.13. Bacterial splenitis (*Staphylococcus aureus*) in a 13-year-old Labrador Retriever. There is an uneven enlargement of the spleen with heterogeneous parenchyma.



Figure 8.14. Multifocal splenic infarctions and necrosis in an 11-year-old German Shepherd. On this panoramic sonogram, the spleen is enlarged and inhomogeneous with numerous poorly echogenic nodular areas. The numerous infarctions associated with thrombi were of undetermined etiology.

Vet-ebooks.com

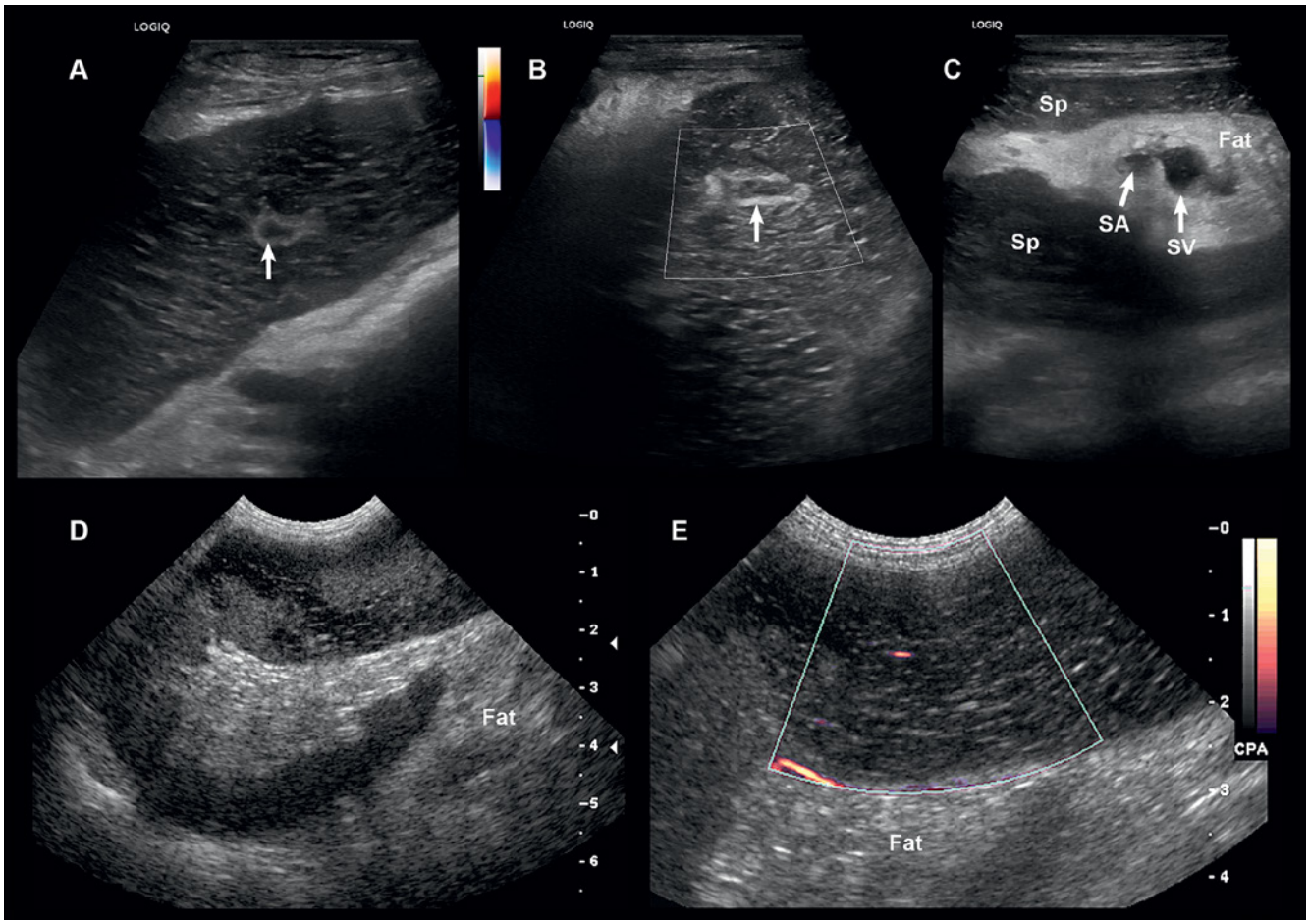


Figure 8.15. **Splenic torsion in two dogs. (A, B, C)** In this 12-year-old German Shepherd, the spleen is enlarged and diffusely hypo- to anechoic with a lacy pattern characteristic of torsion, consistent with infarction and necrosis. The central splenic vein (arrows) has a thickened wall **(A)** and shows a thrombus on color Doppler **(B)**. **(C)** The spleen (Sp) is folded around its hilus, which shows hyperechoic fat and venous congestion. SA, splenic artery; SV, splenic vein. **(D, E)** 10-year-old Labrador Retriever with acute abdominal pain. B-mode **(D)** and power Doppler **(E)** images of the torsed spleen. Several regions show a hypo- echoic to anechoic, lacy echotexture. Power Doppler revealed reduced blood flow.

(Saunders et al. 1998) (Figure 8.15). However, the appearance of the spleen may vary with the degree and duration of torsion.

Focal and Multifocal Abnormalities of the Splenic Parenchyma

Splenic **nodules** of variable echogenicity and size are common and nonspecific findings. Differential diagnoses include nodular hyperplasia, fibrous histiocytic nodule, extramedullary hematopoiesis (Figures 8.16, 8.17), hematoma (Figure 8.18), infection (Figures 8.19, 8.20), infiltrative neoplasia such as lymphoma, mast cell disease, and histiocytic or poorly differentiated sarcoma (Figures 8.21, 8.22), and metastatic disease (Figure 8.23) (Book et al. 2011; Crabtree et al. 2010; Crevier and Wrigley 2000; Hanson et al. 2001; Lamb et al. 1991; Ramirez et al. 2002; Sato and Solano 2004; Wrigley et al. 1988). Differentiating malignant and nonmalignant splenic nodular lesions based on ultrasound appearance is not possible, though a study suggested that multiple similarly appearing nodules are more commonly associated with malignancy, whereas single lesions tend to be more often benign (Ballegeer et al. 2007).

A spotted (also referred to as "honeycomb-like," "Swiss-cheese," "moth-eaten," or "leopard-spotted") echotexture of the spleen with multiple small hypoechoic nodules is highly suggestive of lymphoma (Figure 8.21) in dogs (Crabtree et al. 2010; Sumping et al. 2022). However, this pattern can also be seen in other malignant conditions (Figure 8.22) and in benign changes such as nodular hyperplasia. Even though a honeycomb appearance of the spleen may also be seen with lymphoma in cats (Figure 8.24), this finding is

Vet-ebooks.com

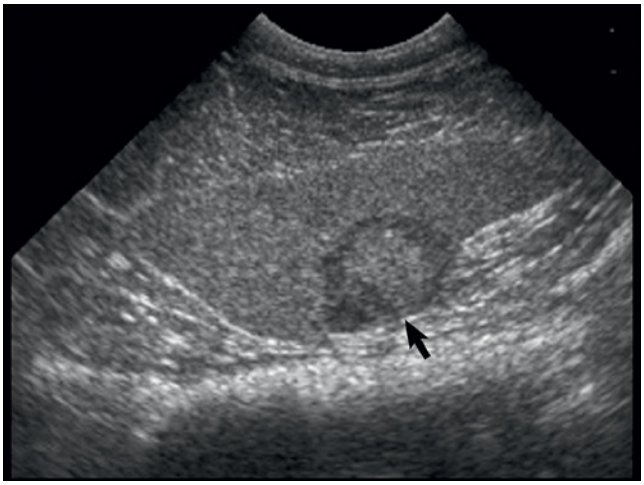


Figure 8.16. Extramedullary hematopoiesis in a 12-year-old Rottweiler. Ultrasonographic image of the spleen obtained during abdominal staging for mast cell tumor. Several nodular lesions were noted in the spleen. One of the nodules (arrow) has a smooth, well-defined, mildly hypoechoic border displacing the splenic capsule, consistent with a target-lesion pattern. Fine-needle aspiration revealed the presence of extramedullary hematopoiesis involving all the nodules.

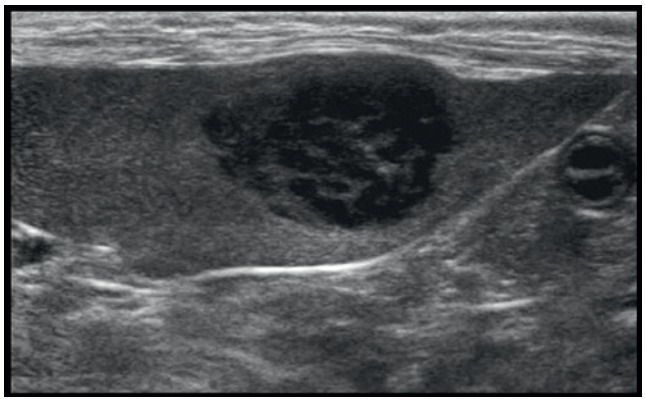


Figure 8.17. Fibrous histiocytic nodule in a cat. On this longitudinal sonographic image, there is a well-defined, hypoechoic nodule of approximately 1 cm in diameter in the splenic parenchyma and deforming its contour.

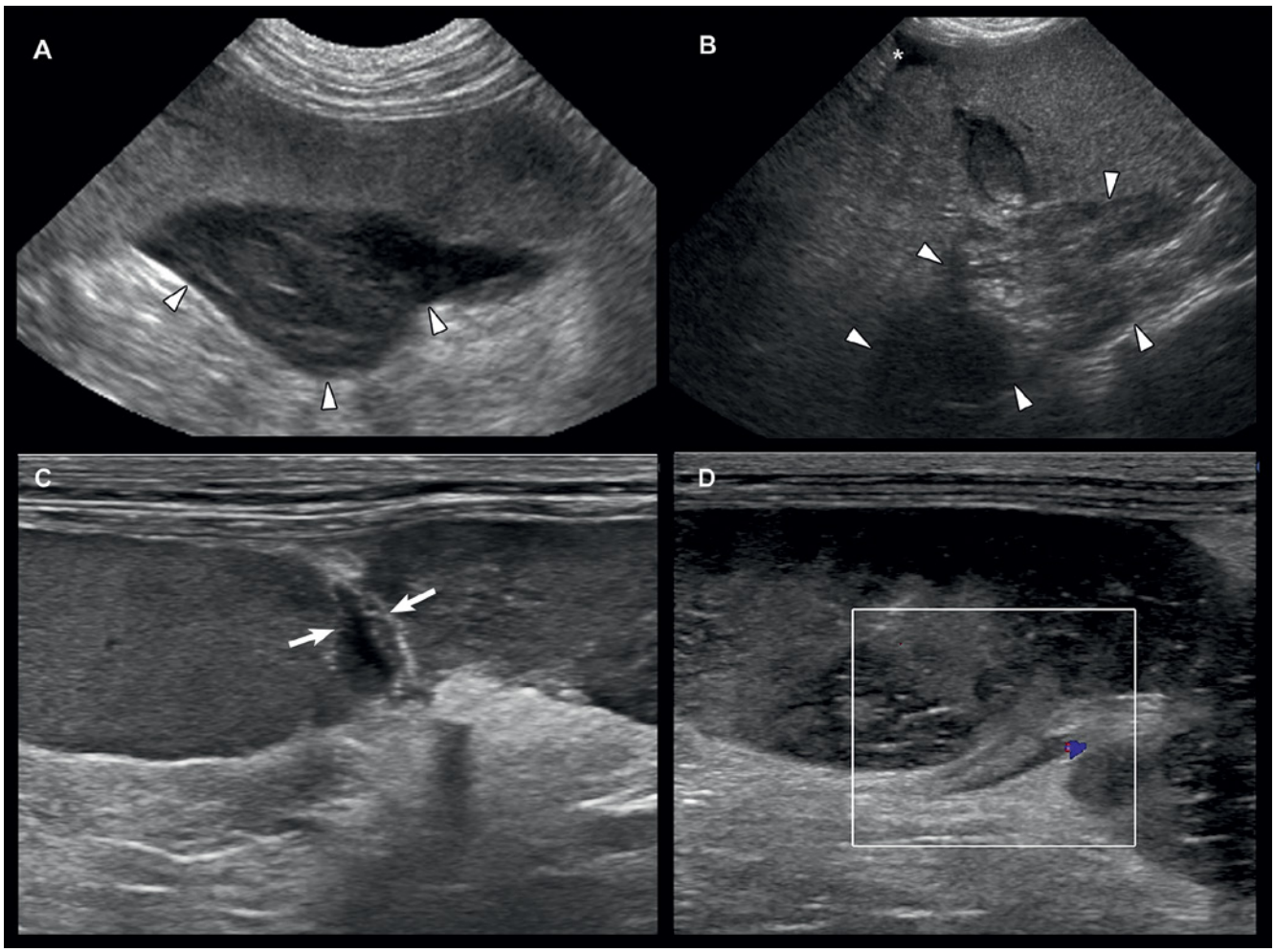


Figure 8.18. Splenic trauma in three dogs. (for full caption, see facing page)

Vet-ebooks.com

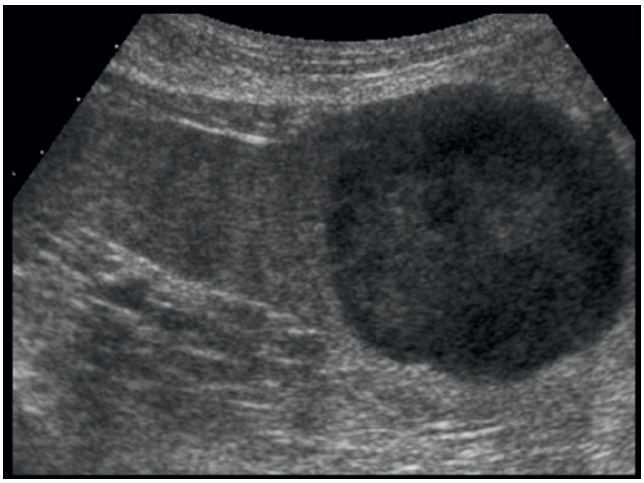


Figure 8.19. Pyogranulomatous splenitis in a 9-year-old Weimaraner. A single homogeneous hypoechoic mass is associated with the splenic parenchyma. Fine-needle aspiration yielded a diagnosis of pyogranulomatous inflammation with necrosis and hemorrhage. Fungal or bacterial etiology was considered most likely; however, an underlying infectious agent was not identified on routine and special stains.

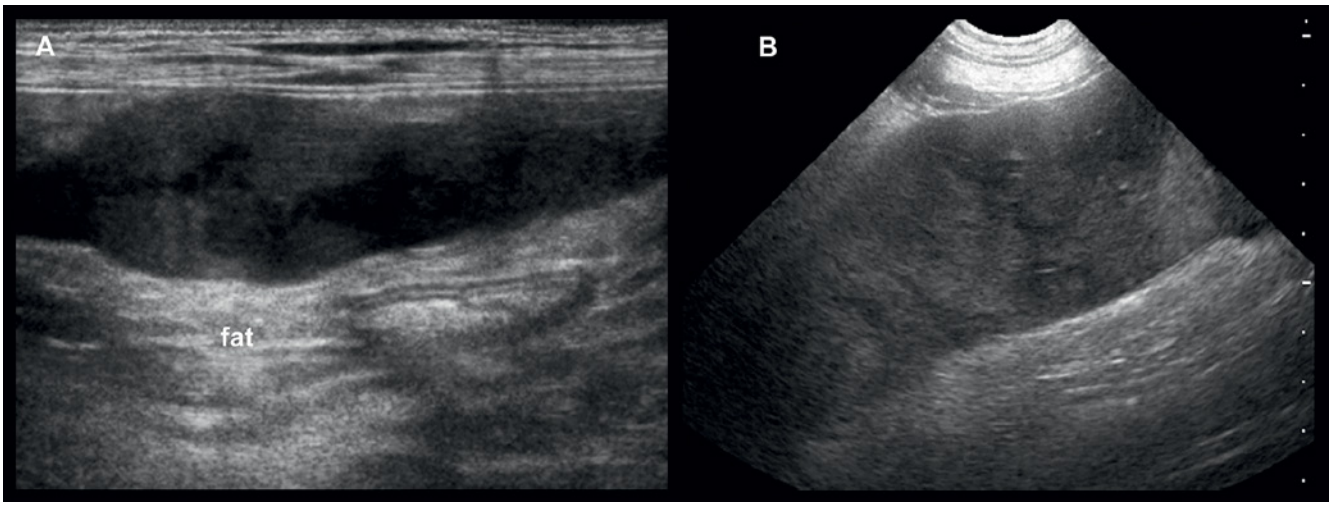


Figure 8.20. Splenitis in two dogs. (A) Bacterial splenitis in a 13-year-old Bichon Frise with a history of *Escherichia coli* septicemia. On the sagittal image, the spleen is irregular in contour, with multiple hypoechoic to anechoic areas and nodules. The adjacent mesenteric fat is hyperechoic. **(B)** The spleen of an 8-year-old Rhodesian Ridgeback is enlarged and very inhomogeneous with irregular contour and is surrounded by hyperechoic fat. A splenectomy was performed and necro-suppurative splenitis with lymphoid hyperplasia was diagnosed. An infectious etiology was considered likely in this dog presented for fever of unknown origin.

Figure 8.18. Splenic trauma in three dogs. (A) Longitudinal sonogram of the tip of the spleen, outlined on its visceral surface by an irregularly hypoechoic region (arrowheads). This lesion represents a subcapsular hematoma in this dog recently hit by a car. **(B)** Splenic hematoma in a Bernese Mountain dog with recent blunt trauma to the abdomen. A large, amorphous echogenic structure (arrowheads) representing a blood clot is bordering the spleen. The faint linear hypoechoic area in the spleen and the inhomogeneous oval region near the hilus likely correspond to the fractured spleen. Mild peritoneal effusion is present (*). **(C, D)** Splenic fracture and massive infarction secondary to splenic venous thrombosis in a 6-year-old female spayed mixed-breed dog that was hit by a car 8 days ago. **(C)** Note the irregular mixed echogenicity fracture line (arrows) between the dorsal extremity of the spleen (left) and the remainder of the organ (right). The latter is mottled. **(D)** Image obtained of the body and ventral extremity of the spleen, ventral to the fracture line shown in (**C**). That portion of the spleen is enlarged with a heterogeneous hypoechoic parenchyma with a lacy pattern suggestive of massive infarction. There is an occlusive echogenic thrombus in the splenic vein with absent flow on color-Doppler examination.

Vet-ebooks.com

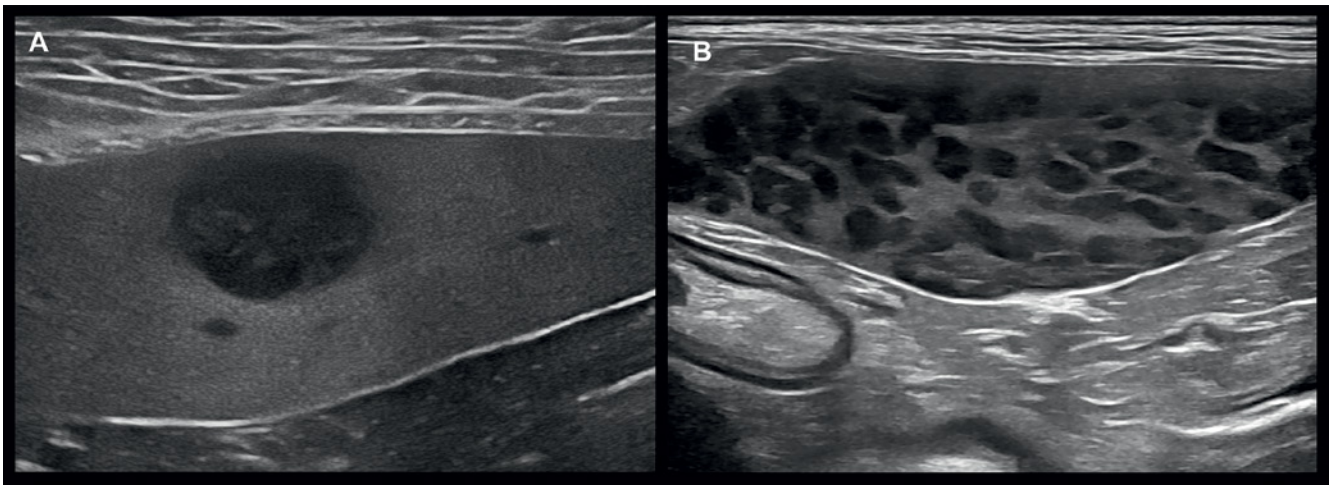


Figure 8.21. **(A) Lymphoma in a 7-year-old mixed breed dog.** There is a hypoechoic nodule associated with the spleen. **(B)** B-cell lymphoma in a 10-year-old Dachshund. Note the markedly spotted appearance of the spleen with a distinct honeycomb pattern.

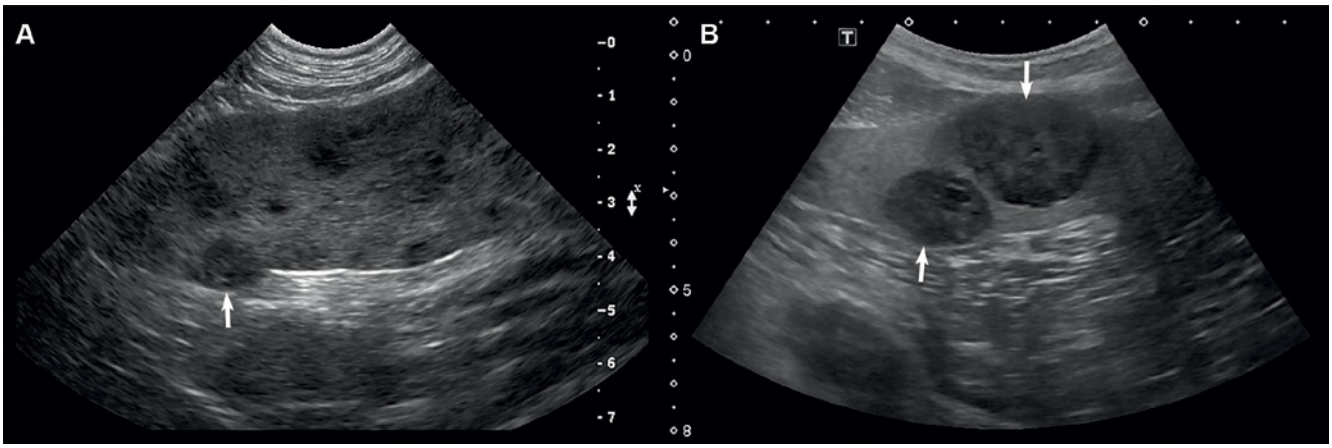


Figure 8.22. **Disseminated histiocytic sarcoma in a 7-year-old (A)** and a 6-year-old **(B)** Bernese Mountain Dogs. There are multiple hypoechoic nodules throughout the spleen in both dogs, some of which deform the splenic border (arrows).

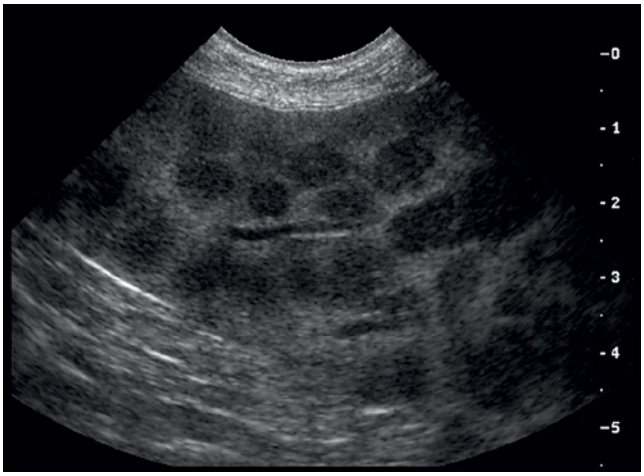


Figure 8.23. **Metastatic anal sac adenocarcinoma in a dog.** The spleen is enlarged and has extensively distributed hypoechoic nodules. Fine-needle aspiration revealed epithelial metastatic disease throughout the spleen, liver, and abdominal lymph nodes, although lymphoma was initially expected based on the ultrasonographic features.

Vet-ebooks.com

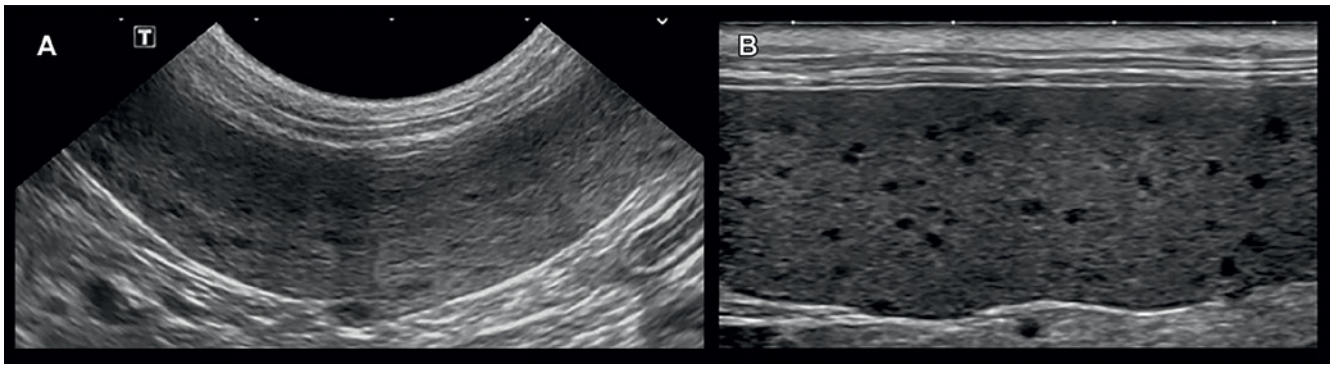


Figure 8.24. Lymphomatous infiltration of the spleen in a 10-year-old cat. The honeycomb pattern is slightly visible with the microconvex probe (**A**), while it is more clearly depicted with the linear probe (**B**). The spleen is moderately enlarged (14 mm in height).

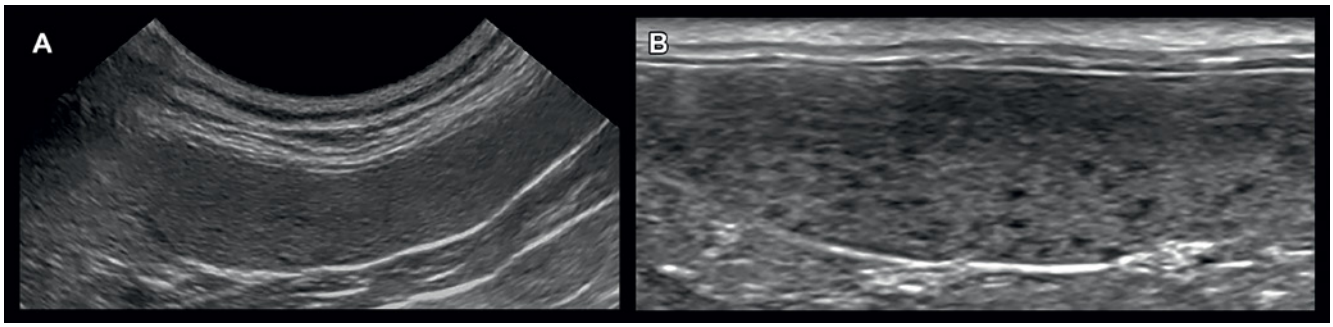


Figure 8.25. Extramedullary hematopoiesis in a 5-year-old cat. (A) A microconvex 8 MHz probe is used and the honeycomb pattern is not clearly visible. **(B)** With a linear 18 MHz probe, multiple small hypoechoic nodules are clearly depicted. The spleen is of normal size, measuring 9.1 mm in height.

reported with benign pathology (Figure 8.25) such as lymphoid hyperplasia (Bertal et al. 2018; Harel et al. 2020; Quinci et al. 2020). Detectability of such splenic patterns in cats is significantly higher with high-frequency linear transducers than with microconvex ones (Bertal et al. 2018; Harel et al. 2020).

Strongly hyperechoic nodules along the visceral surface of the spleen, with or without distal acoustic shadowing, are a common incidental finding, especially in older dogs and cats. These lesions represent **myelolipomas** (Cleveland and Casale 2016; Schwarz et al. 2001) (Figure 8.26). These benign lesions can also appear deeper in the splenic parenchyma, commonly along vessels. Their size and number vary greatly. In rare instances, these lesions can reach considerable size (Figure 8.26C, D).

Splenic **masses** (> 3cm in dogs) can deform the splenic border. They are of variable size, shape, margination, and echogenicity and may be cavitated (Saunders 1998). As in the case of splenic nodules, splenic masses may be benign or malignant and cannot be differentiated only based on their ultrasonographic appearance. The presence of cavitations within the mass is not predictive of hemangiosarcoma, not even of malignancy, in dogs with nontraumatic hemoabdomen (Millar and Zersen 2021). Differential diagnoses of splenic masses include benign lesions (Figure 8.27) such as nodular hyperplasia (which can reach sizes up to more than 15 cm in diameter (Day et al. 1995)), hematomas (Figures 8.18, 8.28, and 8.29), malignancies such as hemangiosarcoma (Figures 8.32–8.33), other sarcomas (Figure 8.36), round-cell neoplasms (Figure 8.31, 8.34, 8.35, 8.37), and metastases, and rarely splenic abscesses (Abdellatif et al. 2014). Benign splenic mass lesions are more common than malignant mass lesions in dogs (Fife et al. 2004). It was reported that canine splenic benign lesions have a higher mass-to-splenic volume ratio than malignant masses (Mallinckrodt and Gottfried 2011), although a more recent study found larger masses to be more commonly malignant (Lee et al. 2018). In cats, it was recently reported that nodules larger than 1 cm are suggestive of malignancy (Bertal et al. 2018). Although rupture of a malignant splenic mass, particularly hemangiosarcoma, is a common cause of nontraumatic hemoabdomen in dogs (Figures 8.32, 8.33), rupture of a benign splenic lesion is seen in more than 10% of dogs

Vet-ebooks.com

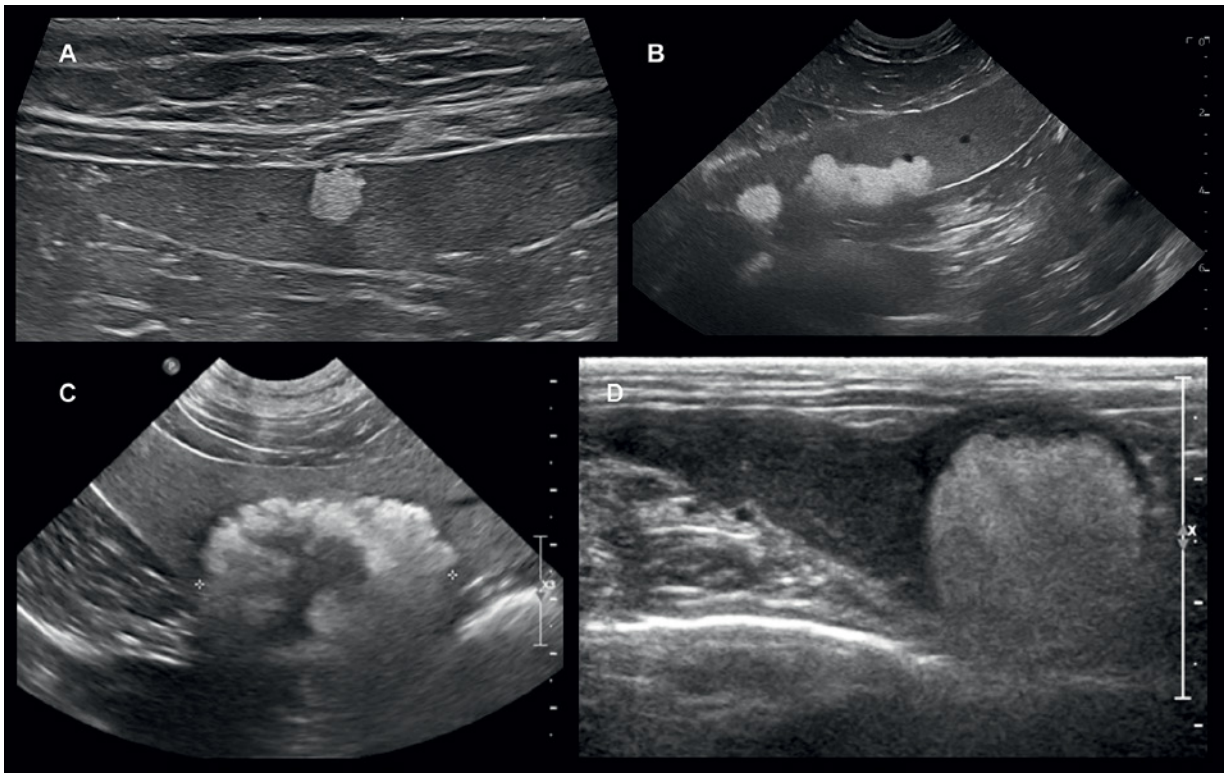


Figure 8.26. **Examples of splenic myelolipomas. (A)** A strongly hyperechoic nodule associated with acoustic shadowing is seen within the spleen of a 6-year-old cat. **(B)** Siberian husky with a cluster of strongly hyperechoic nodules seen along the dorsal border of the spleen. **(C)** A large hyperechoic mass with an irregular hypoechoic necrotic center deforms the dorsal margin of the spleen of this 11-year-old Labrador cross. **(D)** A large uniformly hyperechoic mass is deforming the spleen in this 12-year-old cat.

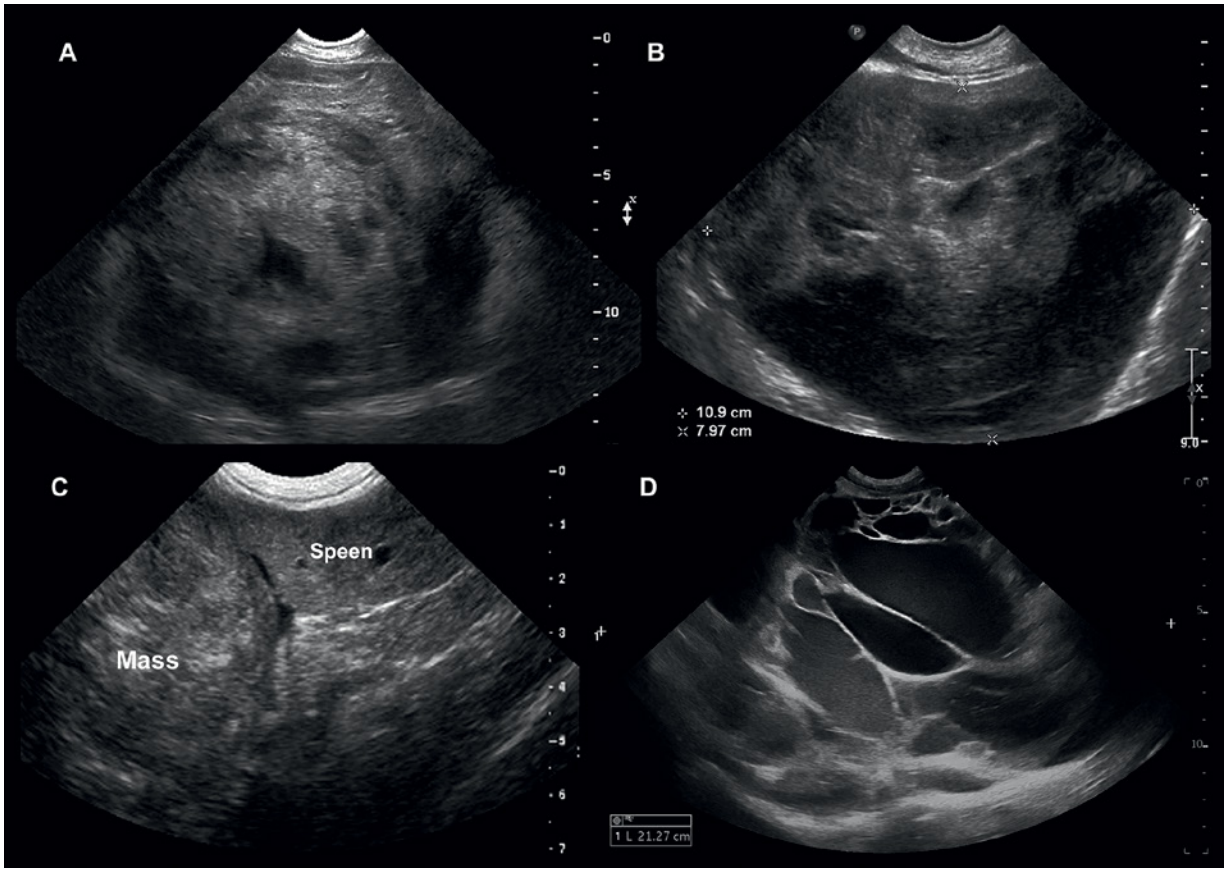


Figure 8.27. **Large benign splenic masses in four dogs.** (for full caption, see facing page)

Vet-ebooks.com

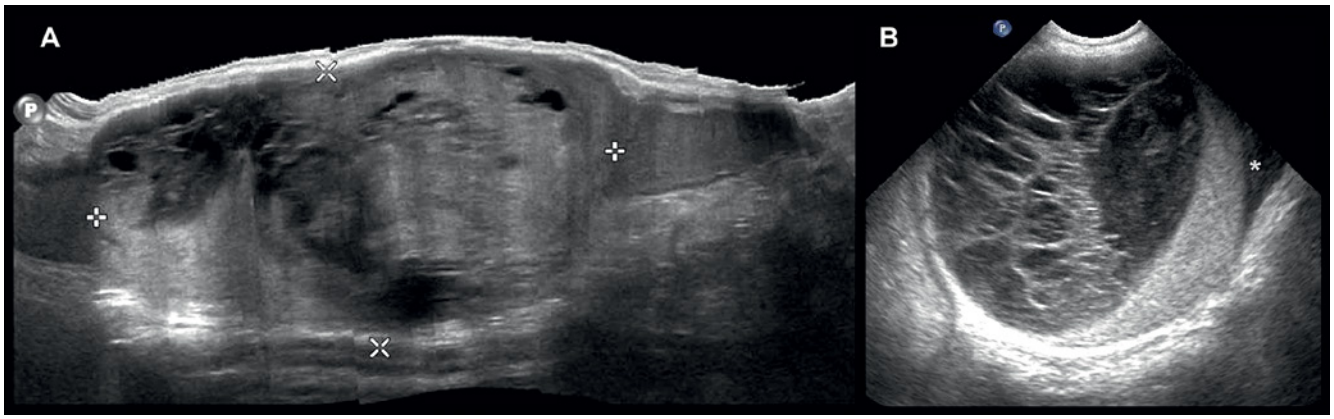


Figure 8.28. Splenic nodular hyperplasia, chronic hematoma, hemorrhage, and extramedullary hematopoiesis in a 13-year-old cross dog. (A) On this panoramic image, a 15 by 8 cm, mixed echogenic and partially cavitated mass is originating from the spleen. **(B)** On this transverse image, mildly echogenic effusion is noted in the abdomen (*).

with hemoabdomen (Fleming et al. 2018) (Figure 8.28). Splenic cysts and abscesses are rare and manifest as fluid-filled cavities of variable echogenicity within the splenic parenchyma, similar to hepatic cysts and abscesses (Abdellatif et al. 2014). When complex in appearance, these cannot be differentiated from hematomas or cavitated tumors based on their ultrasonographic appearance (Figure 8.28).

In case of diffuse and/or focal splenic lesions associated with anemia and possibly thrombocytopenia, **hemophagocytic histiocytic sarcoma** must be considered. This neoplastic process is part of histiocytic diseases causing severe anemia secondary to the marked erythrophagocytosis by neoplastic macrophages. On ultrasound, the spleen is reported to be enlarged with ill-defined masses of variable echogenicity (Figure 8.38). Immunohistochemistry is required for diagnosis as this neoplastic infiltration may be missed with routine cytology and staining (Huber and Leleonnec. 2020; Kerboeuf et al. 2021; Moore et al. 2006).

Nodules or masses with a hypoechoic rim and a hyperechoic to isoechoic center, often referred to as **target lesions**, are commonly associated with malignant processes such as metastasis (Cuccovillo and Lamb 2002) (Figure 8.32). However, they may also be seen with benign processes such as extramedullary hematopoiesis and nodular hyperplasia (Figure 8.16).

Malignant neoplasms and less commonly benign lesions such as nodular hyperplasia may occasionally disrupt the splenic capsule and invade the adjacent mesentery (Day et al. 1995).

Color and power Doppler ultrasound cannot reliably differentiate between malignant and benign splenic lesions (Sharpley et al. 2012). Contrast-enhanced ultrasound has shown variable results with some studies reporting differences in a perfusion pattern between malignant and benign lesions, while more recent studies reported a perfusion pattern of nodular lymphoid hyperplasia similar to that previously reported in malignant lesions (Mangano et al. 2019; Rossi et al. 2008; Ohlerth et al. 2008).

Vascular Disorders

Thrombosis of the splenic vein and splenic vein branches may indicate various concurrent disease processes and conditions, including neoplasia, exogenous

Figure 8.27. Large benign splenic masses in four dogs. (A) Splenic nodular hyperplasia in an 11-year-old Labrador Retriever. An approximately 15-cm mixed echogenic mass is associated with the cranial extremity of the spleen. Histopathologic examination indicated no evidence of malignancy. **(B)** Splenic nodular hyperplasia intermixed with extramedullary hematopoiesis and associated with a large hematoma and active hemorrhage in an 11-year-old Rottweiler dog. A more than 12-cm-diameter (between cursors) mixed echogenic and cavitary mass is associated with the spleen. A small amount of effusion was also noted (not shown). **(C)** Large benign splenic mass in a dog. The histopathologic diagnosis was nodular hyperplasia and extramedullary hematopoiesis. **(D)** Splenic lymphoid hyperplasia, hemorrhage, and necrosis in a 13-year-old mixed-breed dog. An ill-defined, over 21 cm, mixed echogenic and cavitated mass occupied a large portion of the abdomen. There was no evidence of malignancy on histopathologic examination.

Vet-ebooks.com

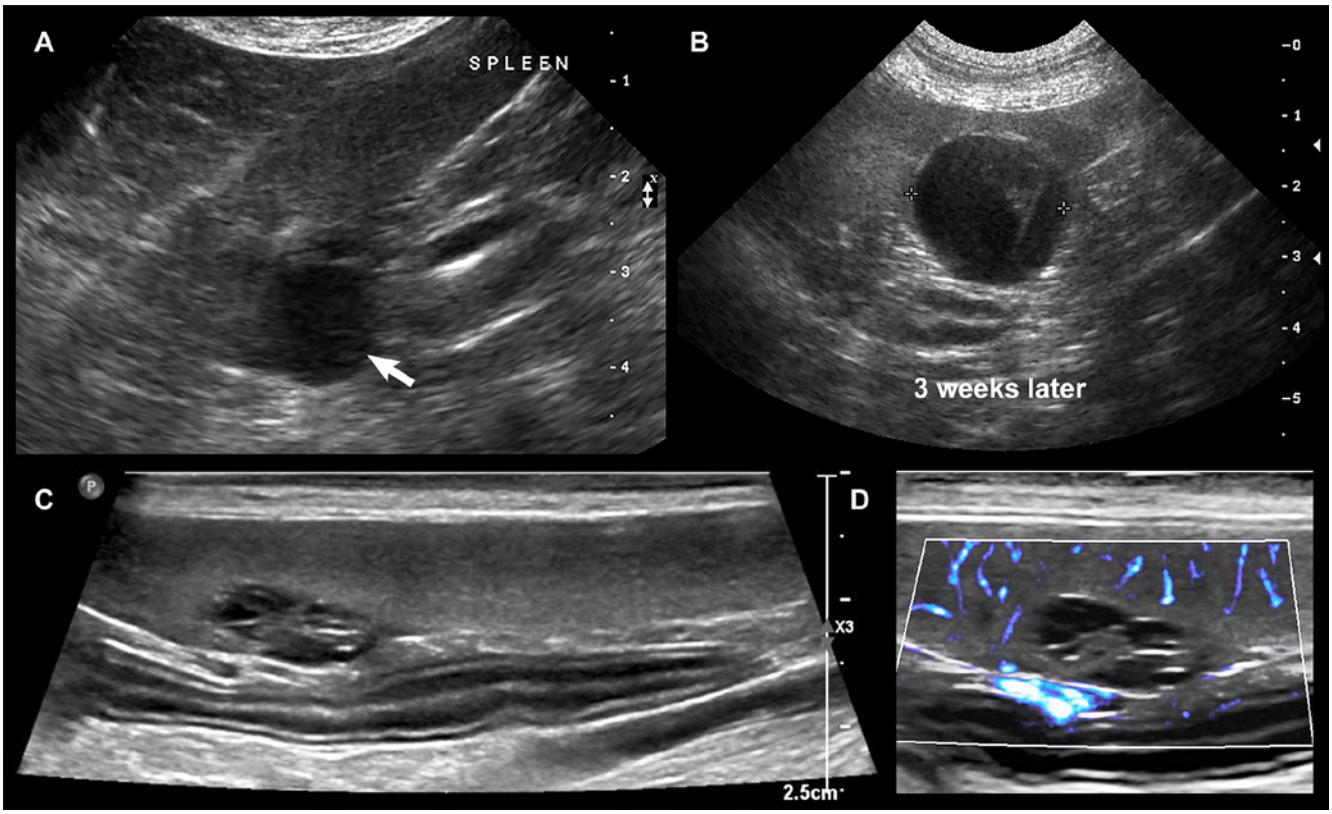


Figure 8.29. Splenic nodular hyperplasia and hemorrhage in a 13-year-old Labrador Retriever previously diagnosed with hemangiosarcoma of the thoracic wall. (A) The initial examination shows a well-circumscribed hypoechoic nodule of approximately 1 cm diameter associated with the spleen (arrow). **(B)** Examination 3 weeks later shows that the nodule (between the cursors) has doubled in size (2.2 cm diameter) and is almost anechoic, indicating cavitation. There was no evidence of malignancy on histopathologic examination. **(C, D)** Hematoma in a 14-year-old poodle with chronic GI signs. A small (1.5 cm long) loculated, cystic lesion is bordering the mid-spleen (**C**), and no vascularization is outlined on Doppler assessment (**D**). The spleen was removed at the time of GI surgical biopsies and was confirmed to be a benign hematoma.

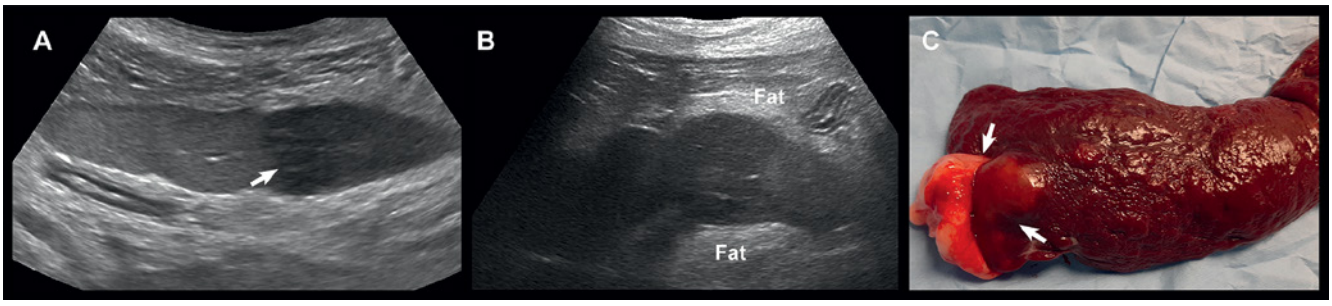


Figure 8.30. Segmental splenic infarction and abscessation in a 13-year-old Labrador Retriever with inappetence, lethargy, and fever. (A) Part of the spleen was hypoechoic and had a lacy echotexture (arrows) and no blood flow on Doppler assessment (not shown). **(B)** A focal portion of the affected segment was enlarged with rounded margins and its contour was highlighted by hyperechoic fat consistent with steatitis. **(C)** This corresponded to the abscessation (arrows) noted on the surgical specimen. The dog had vegetative thickening of the mitral valve supportive of endocarditis and urinary tract infection (*E. coli*). Streptococcus was cultured in the spleen.

Vet-ebooks.com

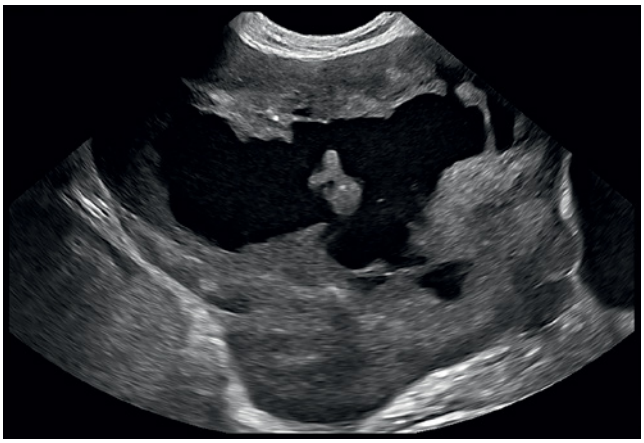


Figure 8.31. Large splenic mass in an 11-year-old Siamese cat. The mass is cavitary and distorts the spleen margins. Cytological examination revealed splenic lymphoma.

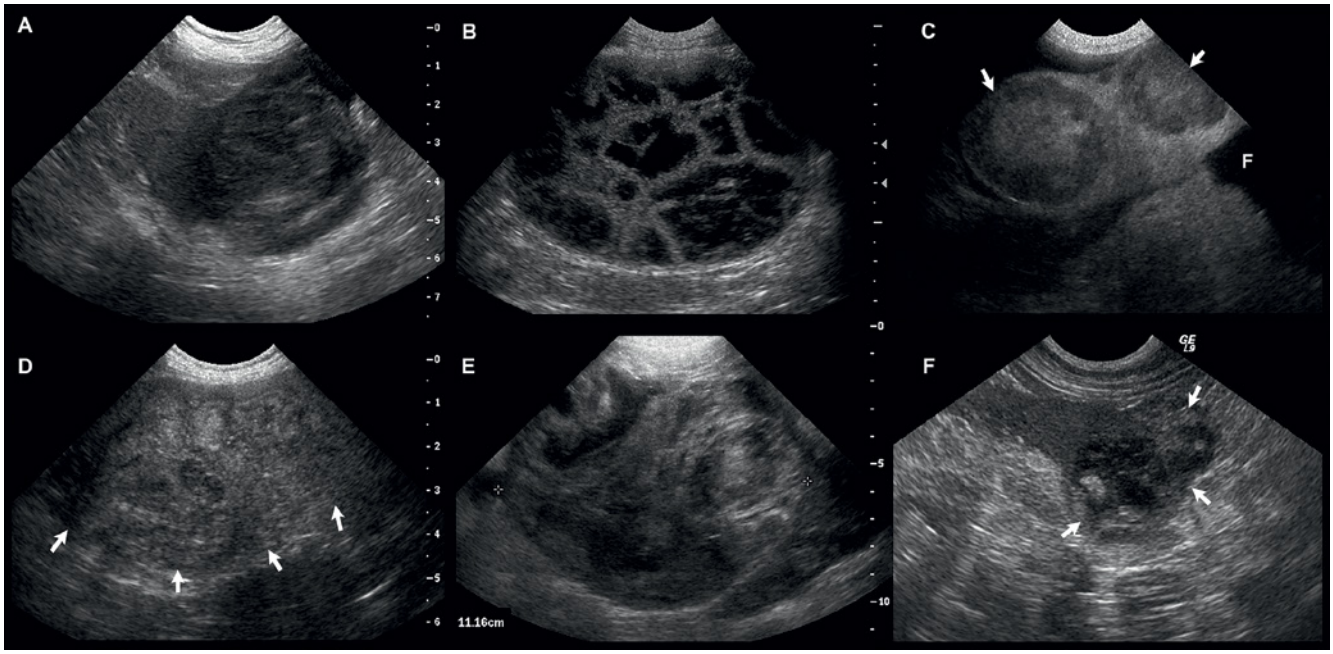


Figure 8.32. Variable appearances of splenic hemangiosarcoma in five dogs and in a cat. (A) Approximately 6-cm-diameter, mixed echogenic and mainly hypoechoic mass in a 12-year-old Border Collie. **(B)** A round, well-circumscribed, mixed echogenic, and cavitated mass of 8 cm diameter in a 4-year-old Golden Retriever. **(C)** Splenic hemangiosarcoma and hemoabdomen in an 8-year-old Labrador Retriever. There are two masses (arrows), which are characterized by a hypoechoic rim and a hyperechoic center (target lesions). A large volume of echogenic abdominal effusion **(F)** is noted. **(D)** Ill-defined, mixed echogenic mass (arrows) associated with the spleen of a 9-year-old Golden Retriever, replacing most of the normal parenchyma. **(E)** Mixed echogenic mass of more than 11 cm diameter associated with the spleen (between the cursors) in an 8-year-old German Shepherd dog. **(F)** Splenic hemangiosarcoma in a 12-year-old cat. A heterogeneous mostly solid and mildly cavitated mass (arrows) causes distortion of the splenic margins.

corticosteroid administration, systemic inflammatory response syndrome, disseminated intravascular coagulation, pancreatitis, and immune-mediated disease (Hardie et al. 1995; Laurenson et al. 2010). It manifests as variably echogenic material within the otherwise anechoic lumen of the vessel. Thrombi may remain inconsequential if occlusion of the vessel is incomplete or collateral vessels provide venous drainage of the affected areas (Figures 8.39, 8.40). Occasionally, malignant splenic tumors invade splenic vessels and cause splenic vein thrombosis and splenic infarction.

Vet-ebooks.com

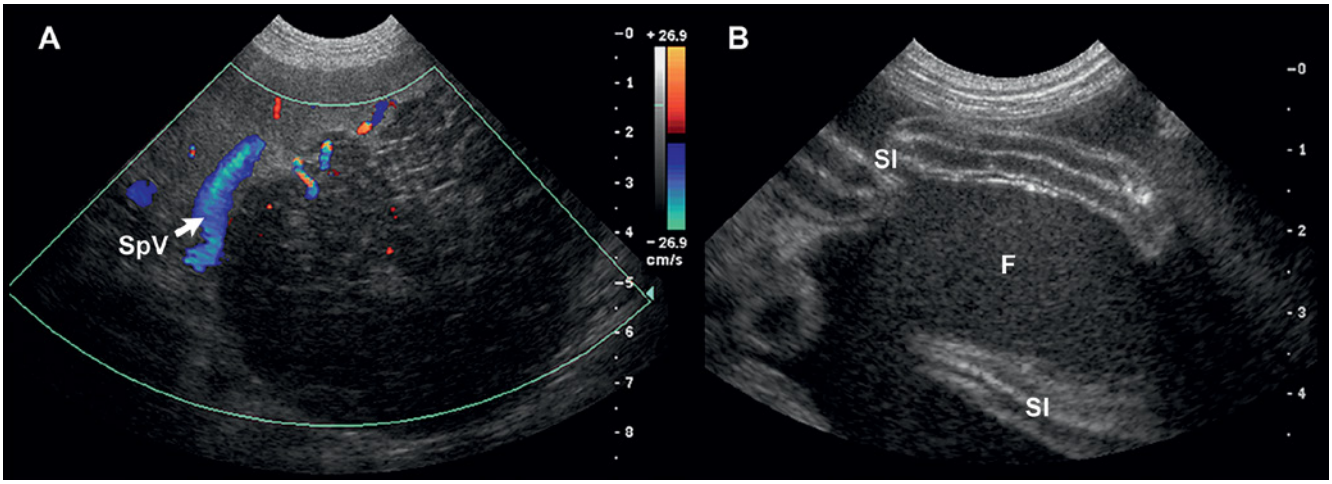


Figure 8.33. Splenic hemangiosarcoma and hemoabdomen in a large-breed dog in which an abdominal mass was palpated. **(A)** Ultrasound image of the spleen in which an irregular, well-defined, hypoechoic mass of approximately 8 cm diameter is attached to spleen. Using color Doppler, numerous short vessels connecting the mass with the spleen are seen in the near field, which confirms the origin of this mass. The main splenic vein (SpV) is displaced. **(B)** Severe, echogenic, peritoneal effusion (F) is present, consistent with hemorrhage. SI, small intestine.

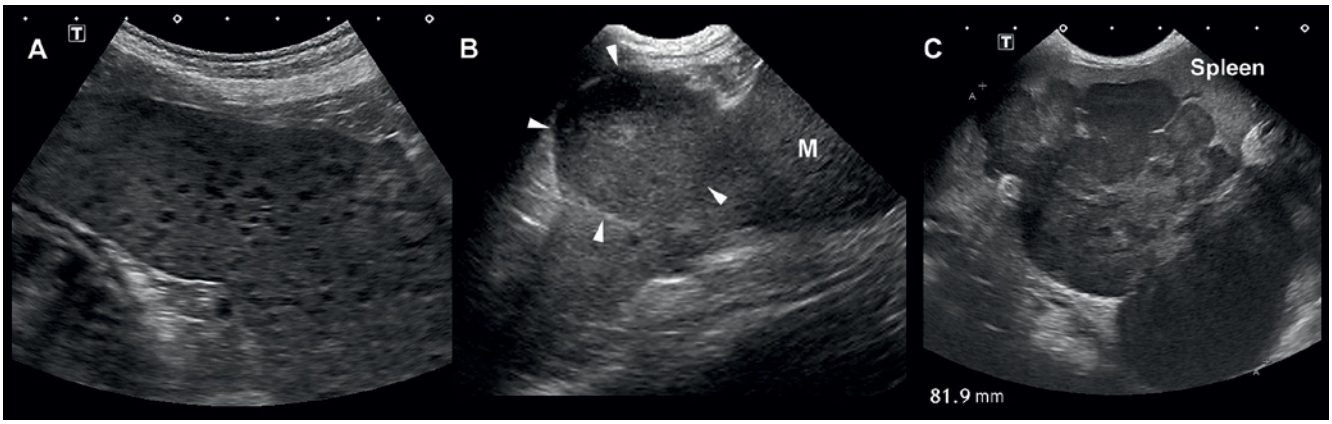


Figure 8.34. Histiocytic sarcoma in three dogs. **(A)** Histiocytic sarcoma in a Bernese Mountain Dog. On this sonogram, numerous hypoechoic nodules are disseminated throughout the splenic parenchyma, giving a honeycomb pattern. **(B)** Histiocytic sarcoma in a 9-year-old Golden Retriever. A large, nearly isoechoic splenic mass (M) and a similar echogenic nodule (arrowheads) deform the splenic contour. (**C**) In this other large breed dog, there is a large, lobulated hypoechoic mass deforming the splenic parenchyma and capsule.

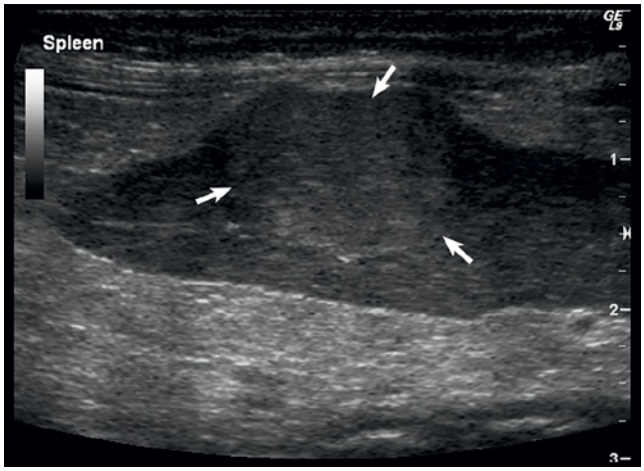


Figure 8.35. Plasma cell tumor in a 12-year-old domestic shorthair cat. An iso- to slightly hyperechoic mass is noted, causing deformation of the ventral splenic border.

Vet-ebooks.com

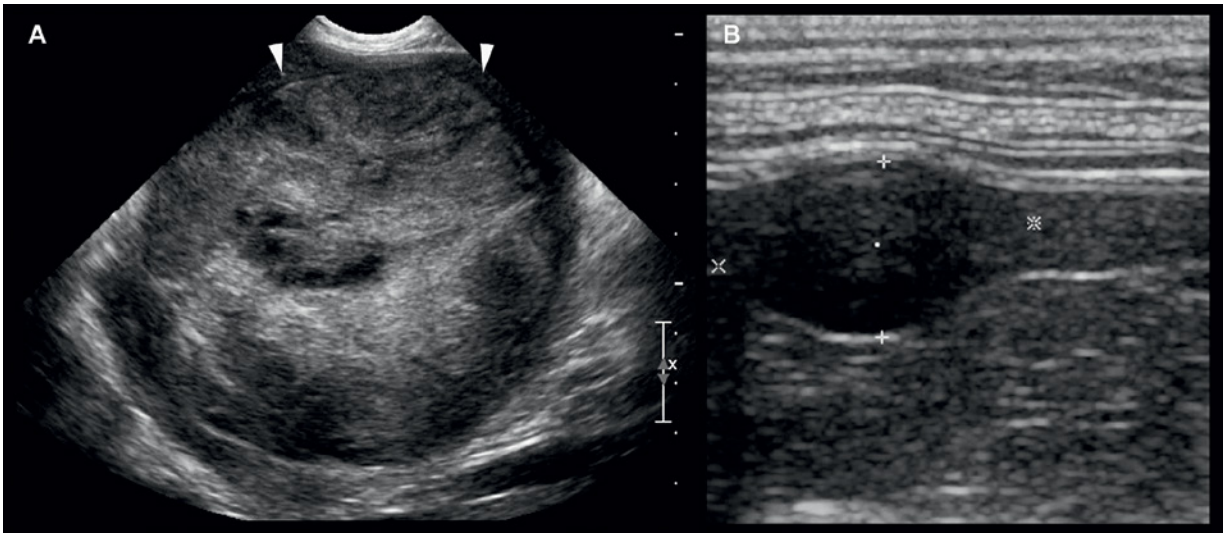


Figure 8.36. **Soft tissue sarcoma in a dog and a cat. (A)** In a dog with high-grade soft-tissue sarcoma, there is an approximately 8cm mainly inhomogeneous mass associated with the spleen. Normal spleen is present in the near field (arrowheads). **(B)** In a 10-year-old cat with splenic sarcoma, a homogeneous hypoechoic nodule (between the cursors) is deforming the splenic border.

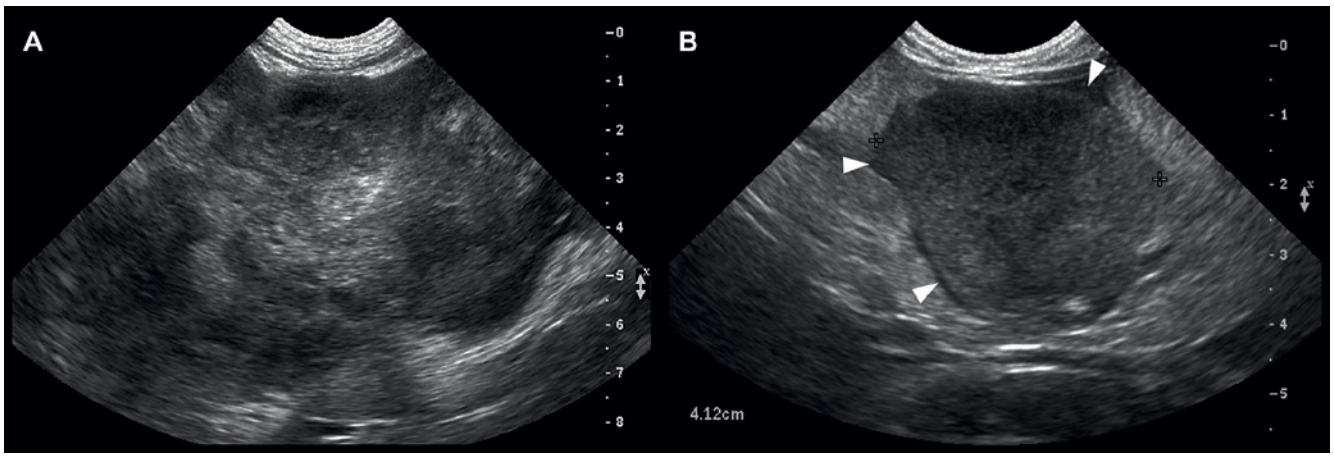


Figure 8.37. **Splenic round-cell neoplasia in two cats. (A)** Round-cell tumor of the spleen in a 10-year-old coonhound. There is severe generalized splenomegaly, and the normal parenchyma is replaced by numerous ill-defined mass lesions of variable echogenicity. **(B)** Splenic mast cell tumor in a cat. A more than 4cm homogeneous mass of medium echogenicity is associated with the spleen (between the cursors). A small volume of abdominal effusion is noted in the periphery of this mass (arrowheads).

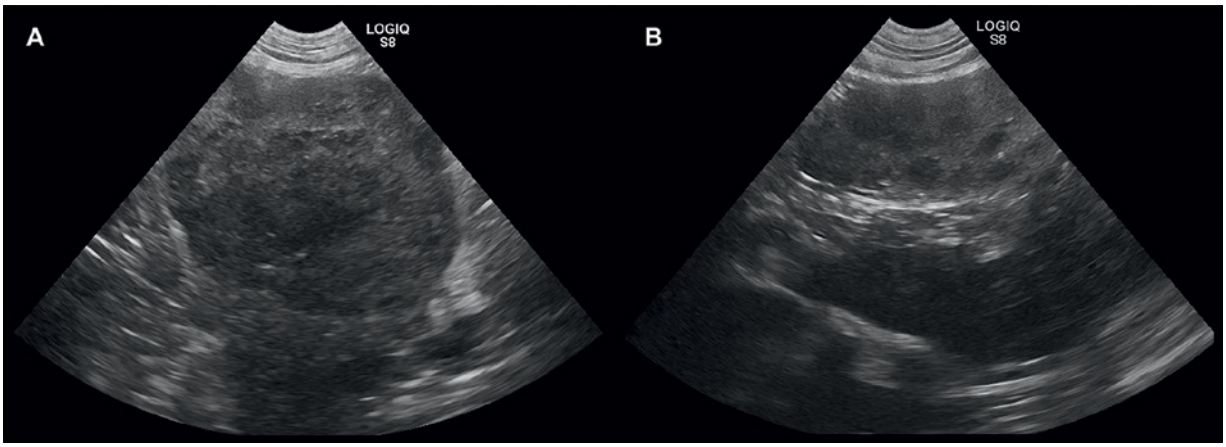


Figure 8.38. **Hematophagocytic histiocytic sarcoma in an 8-year-old Labrador Retriever. (A)** A large heterogeneous mass lesion deforms the splenic margins. **(B)** Multiple ill-defined rounded hypoechoic nodules are present in the remainder of the splenic parenchyma.

Vet-ebooks.com

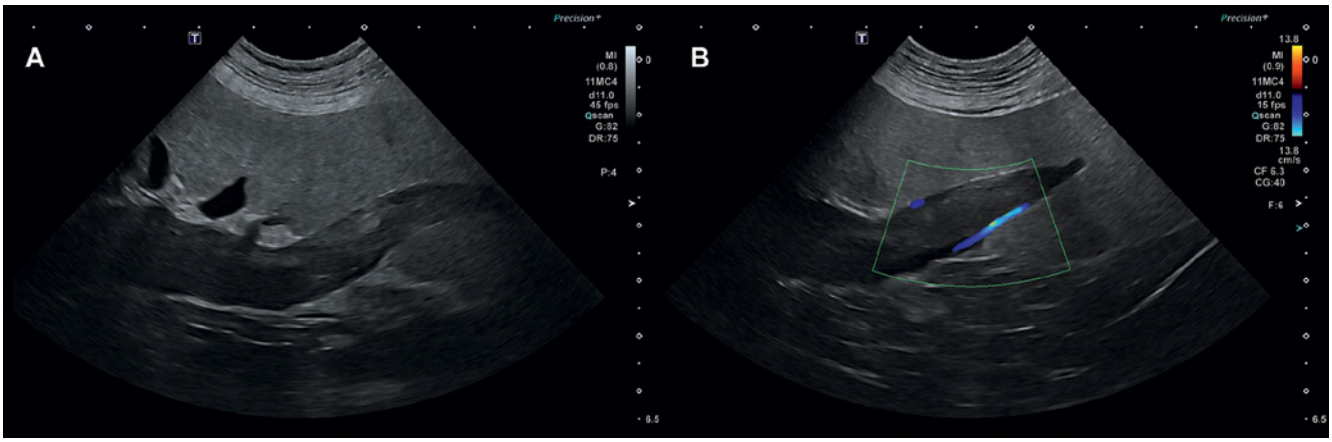


Figure 8.39. Splenic vein thrombus without evidence of splenic infarction in a 10-year-old malamute. (A) Echogenic heterogeneous material is associated with one of the branches of the splenic vein. The splenic parenchyma is within normal limits. **(B)** On color-Doppler examination, blood flow is noted around the thrombus, indicating incomplete vascular occlusion.

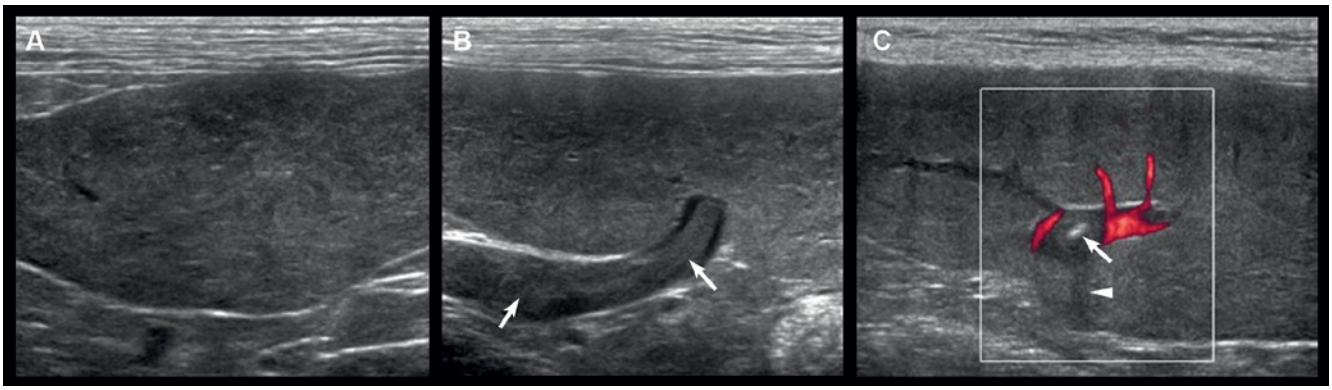


Figure 8.40. Splenic vein thrombosis in a 4-year-old Australian Shepherd (A) In this longitudinal image, the spleen is enlarged and inhomogeneous, which was revealed to represent extra-medullary hematopoiesis on cytology. **(B)** A long echogenic material occupies the lumen of the splenic vein (arrows). **(C)** Power Doppler shows persistent flow around the thrombus, which shows a hyperechoic focus (arrow) with distal acoustic shadowing (arrowhead), indicating mineralization of the clot.

When splenic **infarction** occurs, the affected areas appear hypoechoic to anechoic, at times with a lacy pattern, sharply demarcated from the adjacent parenchyma, and show decreased or absent blood flow on color or power Doppler examination (Figure 8.30). In contrast to splenic masses, infarcts do not tend to distort the normal organ contour, although this can occasionally be seen (Figures 8.41).

Splenic **torsion** is a rare disorder in dogs. Usually, there is progressive enlargement of the spleen, with decreased to absent blood flow. The parenchymal echogenicity and echotexture vary as the congestion, hemorrhage, or infarction progresses. The parenchyma is typically mottled, and lacy anechoic to hypoechoic areas are observed, focally or diffusely, throughout the spleen (Mai 2006; Saunders et al. 1998) (Figures 8.15, 8.42, 8.43). Static, echogenic thrombi can sometimes be seen in the lumen of splenic vessels. Additionally, the bordering fat can become hyperechoic, and a hilar, perivenous, hyperechoic triangle has been described as a supportive sign of acute splenic torsion in dogs (Mai 2006) (Figure 8.43). However, these changes can also be found with extensive venous thrombosis and/or diffuse neoplastic infiltration (e.g., lymphoma).

Other Abnormalities

In some animals, accessory spleens called **splenunculi** can be found in the immediate vicinity of the spleen; these represent areas of normal ectopic splenic tissue, supplied by branches of the splenic artery, and can be congenital or secondary to autoimplantation of splenic

Vet-ebooks.com

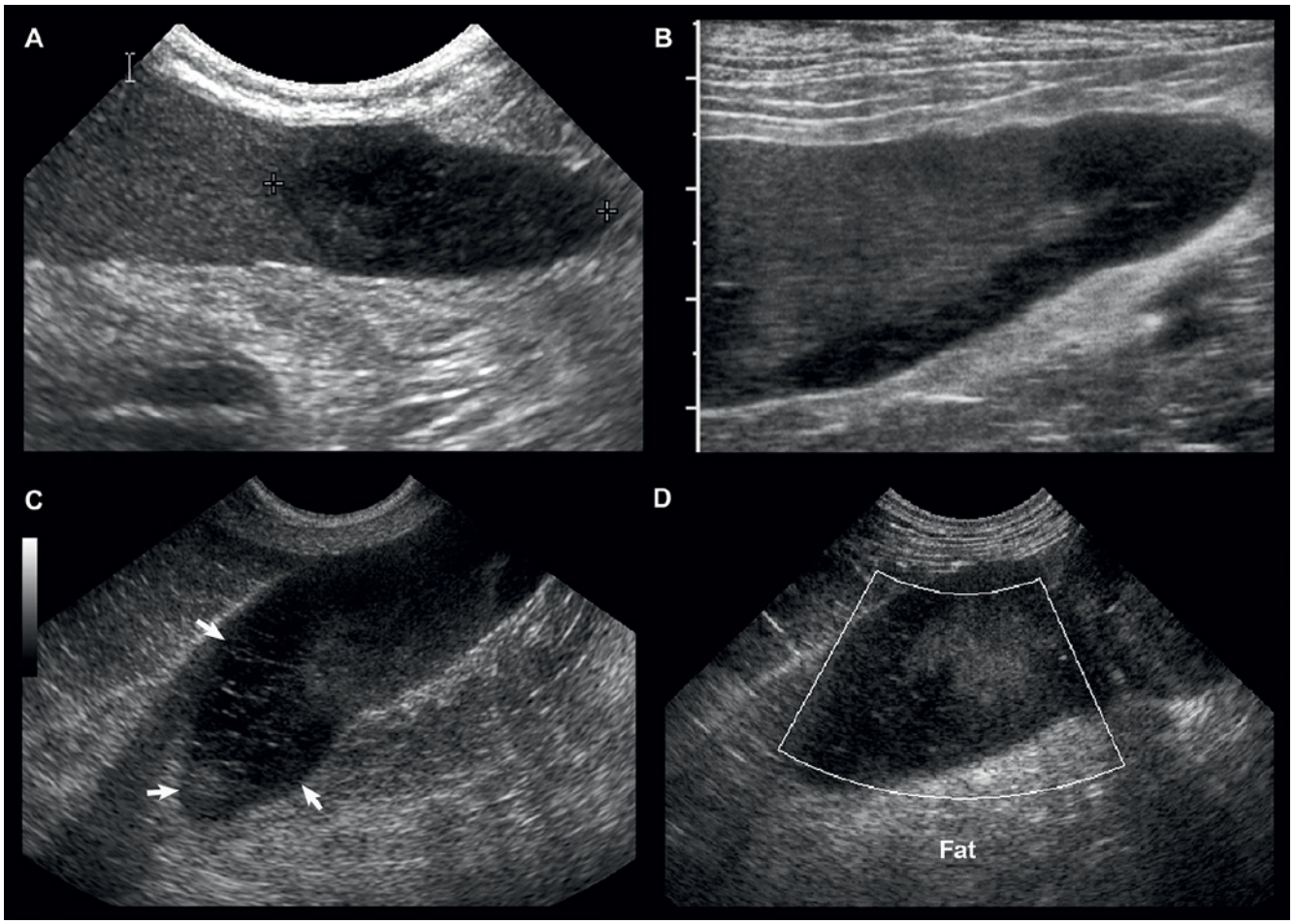


Figure 8.41. **(A, B) Splenic infarcts in four dogs. (A)** In a 10-year-old Australian Shepherd, a sharply demarcated, lacy hypoechoic area is observed at the caudal extremity of the spleen (between the cursors), which is confined to the normal splenic border without evidence of a mass effect. **(B)** In a 9-year-old mixed-breed dog, the infarcted area follows the margins of the caudal extremity of the spleen while sparing the center. **(C)** Splenic infarct in a 12-year-old male mixed-breed dog. A sharply demarcated hypoechoic area with a lacy pattern is associated with the cranial aspect of the spleen (arrows). On color flow Doppler (not shown), there is no evidence of blood flow in this triangular infarcted region. **(D)** Splenic infarct in a 15-year-old Golden Retriever. An inhomogeneous lacy hypoechoic area within the spleen does not show blood flow on color-Doppler examination. The fat at the dorsal margin of the spleen is hyperechoic.

tissue following surgery or trauma (Figure 8.44). They are usually located between the spleen, stomach, pancreas, and left lobe of the liver and should not be confused with focal perisplenic lesions such as enlarged splenic lymph nodes, pancreatic nodules, or mesenteric abscess or granuloma. Accessory spleens are round to triangular in shape, 1–3 cm in size, isoechoic to the normal spleen, and often surrounded by hyperechoic fat (Rossi et al. 2010) (Figure 8.44). They can be affected by the same diseases as the nonectopic spleen. Torsion of an accessory spleen has been reported and can be mistaken for a liver lobe torsion in the face of a normal spleen in normal location (Mergle et al. 2002). More rarely, accessory ectopic splenic tissue may be found within the pancreatic parenchyma and may mimic pancreatic neoplasia (Tomura et al. 2022), see Chapter 10, Figure 10.25.

Normal splenic lymph nodes are usually not seen ultrasonographically. Enlarged lymph nodes may be visualized in cases of metastatic or infiltrative neoplasia as isoechoic to hypoechoic, rounded, soft-tissue nodules along the splenic vessels close to the hilus (Figure 8.45).

Strongly hyperechoic areas with strong distal acoustic shadowing are indicative of dystrophic mineralization or a mineralized neoplasm such as extraskeletal osteosarcoma (Figure 8.46).

Gas inclusions in the spleen, though rarely seen, are indicative of infection with gas-producing bacteria, particularly Clostridium spp. This has been reported

Vet-ebooks.com

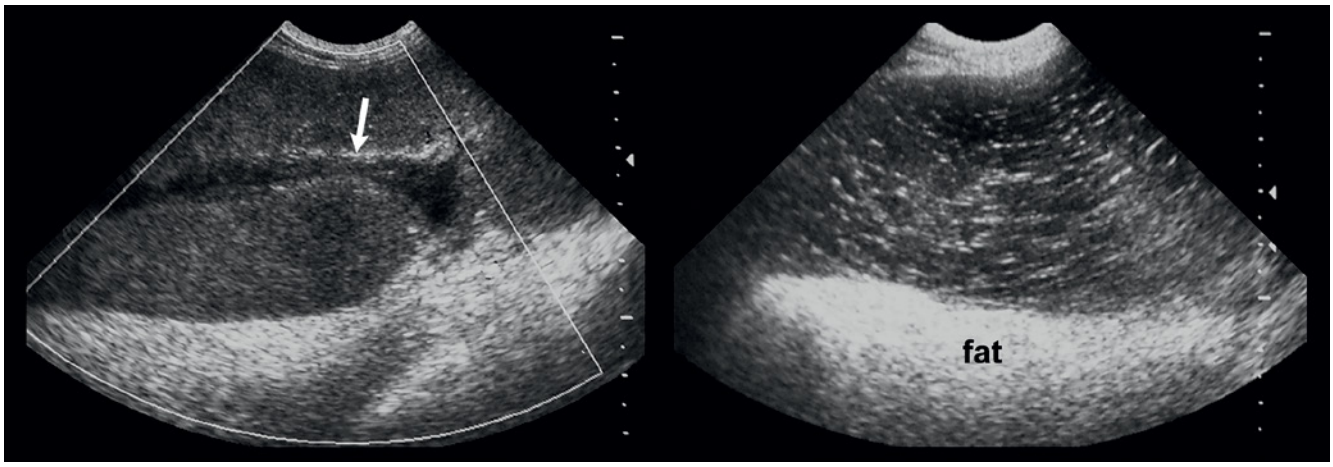


Figure 8.42. **Splenic torsion in a 6-year-old standard Poodle. Left:** Sonographic image of the spleen at the time of presentation. The spleen is homogeneously hypoechoic and within normal limits for size. Upon Doppler examination, no flow was detected in the splenic veins, and a hyperechoic thrombus is seen (arrow). **Right:** Sonographic image of the splenic parenchyma 2 days later. The spleen is enlarged and has a diffuse, lacy hypoechoic echotexture. The adjacent fat is hyperechoic.

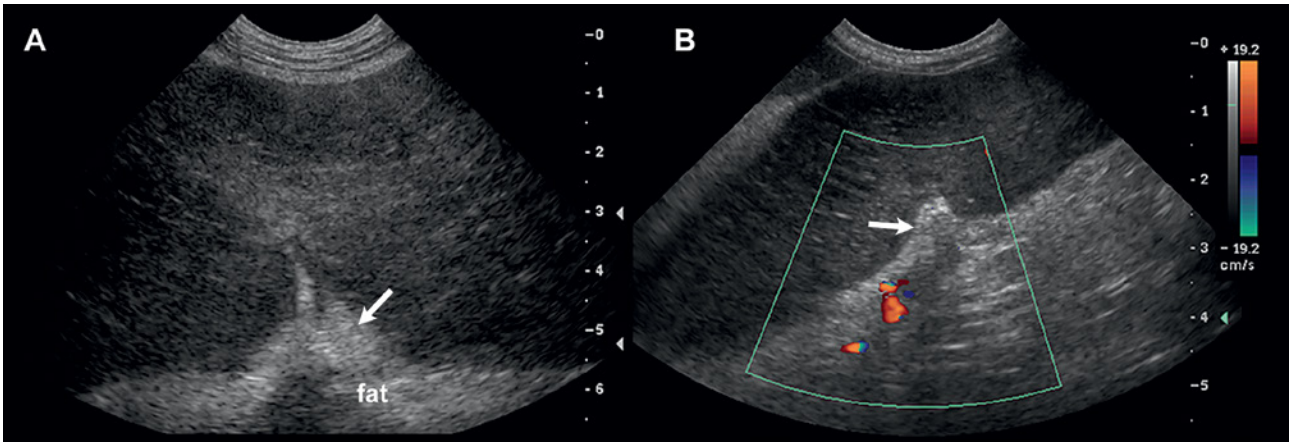


Figure 8.43. **Perivenous hyperechoic triangle at the level of the splenic hilus in two dogs. (A)** A hyperechoic triangle (arrows) is a common feature observed with splenic torsion. **(B)** This feature can also be observed with massive splenic infarction. The second dog (**B**) was suffering from severe necrotic pancreatitis and progressively developed splenic infarction. At surgery, the spleen was not twisted, but was removed because of the complete venous thrombosis. In each case, the adjacent fat was hyperechoic.

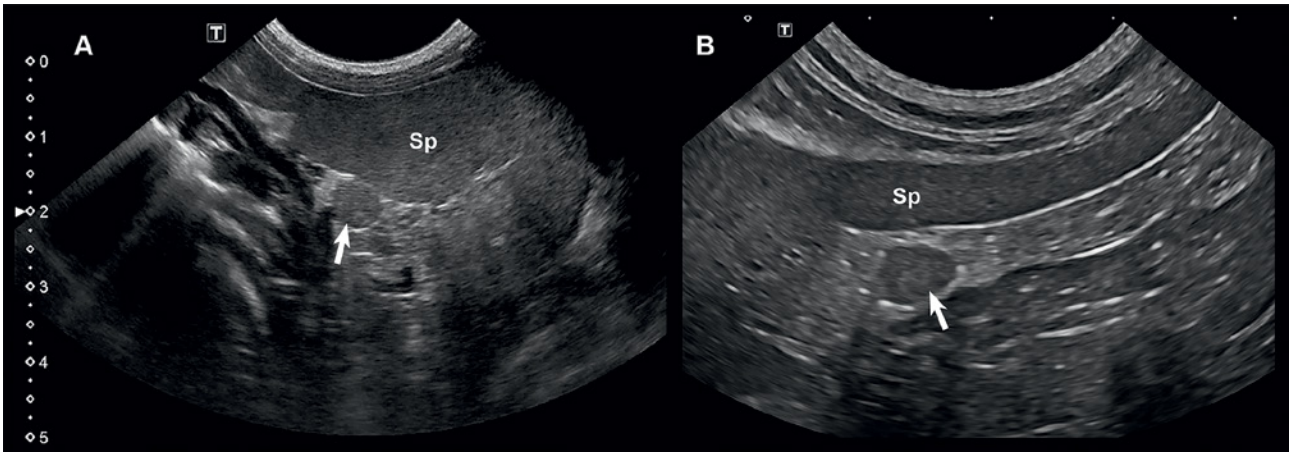


Figure 8.44. Accessory spleen (**splenunculus)** in a dog and in a cat. **(A)**. A small, rounded structure (arrow) is present along the mesenteric side of the spleen of this dog, near the hilus. It has similar echogenicity as the spleen (Sp). **(B)** in this cat, a small, rounded structure is visible along the visceral surface of the spleen, surrounded by slightly hyperechoic fat.

Vet-ebooks.com

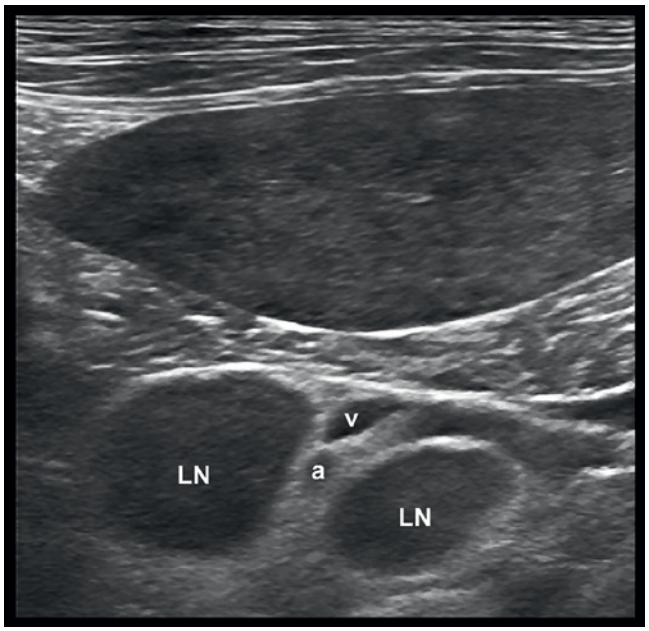


Figure 8.45. Lymphoma in a 7-year-old mixed breed dog. Note the ill-defined honeycomb pattern in the splenic parenchyma in the near field. In the far field, there are two enlarged lymph nodes adjacent to a branch of the splenic vein (v) and artery (a). The nodes are rounded, hypoechoic and there is hyperechogenicity of the perinodal fat.

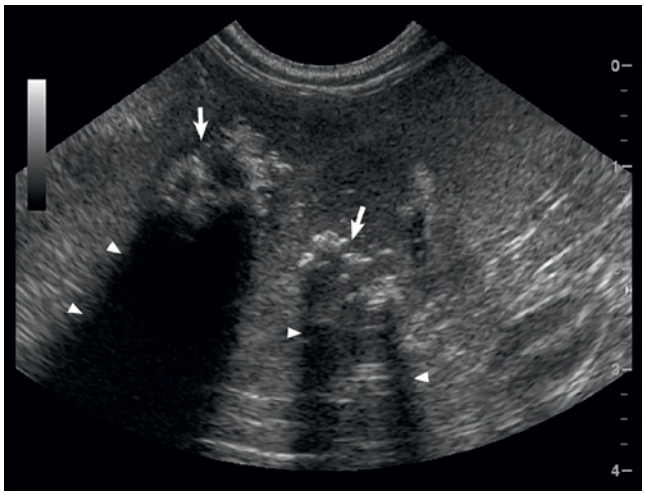


Figure 8.46. Extraskeletal osteosarcoma in a 10-year-old female mixed-breed dog. Irregularly marginated hyperechoic lesions (arrows) associated with the splenic parenchyma show strong distal acoustic shadowing (arrowheads).

in dogs with (Gaschen et al. 2003) and without splenic torsion (Battiato et al. 2021). Gas typically appears as hyperechoic foci with reverberation or dirty shadowing artifacts (Figure 8.47).

At times, a spleen of normal size may appear speckled with numerous small and nonshadowing

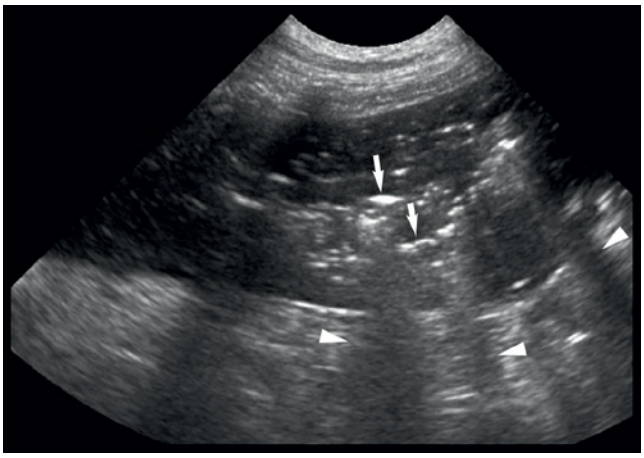


Figure 8.47. Infection with gas-producing bacteria secondary to torsion and necrosis in a 3-year-old Labrador. The enlarged, poorly echogenic and lacy spleen has several hyperechoic foci (arrows) associated with reverberation and shadowing artifacts (arrowheads). A moderate amount of echogenic effusion, and free gas was noted in the abdomen (not shown).

hyperechoic speckles or stripes (Figure 8.48). These findings are most commonly associated with Cushing's disease, diabetes mellitus, or chronic corticosteroid use (Schlax et al. 2017).

Interventional Procedures

Fine-needle aspiration of the spleen is routinely performed with ultrasound guidance and is particularly useful in the diagnosis of diffuse infiltrative disorders such as lymphoma or mast cell tumor in which the spleen may appear sonographically normal (Book et al. 2011; Crabtree et al. 2010; Mesquita et al. 2022). This is particularly important for staging of high-risk mast cell tumors, in which ultrasound was shown to have very poor sensitivity to detect splenic metastatic infiltration (Book et al. 2011; Pecceu et al. 2020). In most cases, freehand aspiration is possible because of the organ's superficial location and the capillarization technique yields higher cellularity and less blood contamination of the sample (LeBlanc et al. 2009). Aspiration of cavitated splenic mass lesions such as hemangiosarcomas or hematomas frequently remains inconclusive because of blood dilution and correlation with histology is poor (Ballegeer et al. 2007). In addition, fine-needle aspiration of cavitary splenic lesion may cause hemorrhage. When compared to histopathology, cytology of splenic lesions has only moderate accuracy (61–73%) (Ballegeer et al. 2007; Tecilla et al. 2019). Regarding neoplastic lesions, cytology has a low sensitivity and

Vet-ebooks.com

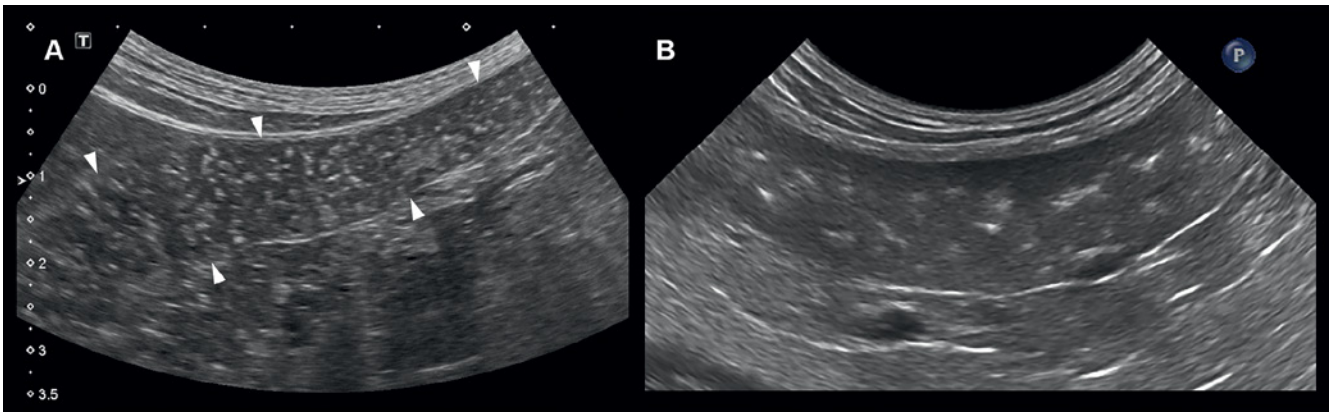


Figure 8.48. **Speckled spleen with Cushing's disease. (A)**. In this 12-year-old Lhasa Apso, numerous small hyperechoic foci are seen throughout the spleen (arrowheads). **(B)** In this 13-year-old Chihuahua with diabetes mellitus, note the multifocal pinpoint to linear hyperechoic foci scattered throughout the parenchyma.

negative predictive value but very high specificity and positive predictive value (Tecilla et al. 2019). The decision to perform ultrasound-guided sampling of splenic lesions depends on the clinical context; in addition, some ultrasound findings such as larger nodular lesions, a large number of target-like lesions, and concurrent peritoneal effusion increase the likelihood that clinically significant splenic pathology may be detected at cytology (Yankin et al. 2020). In the face of a negative cytological diagnosis but strong clinical or imaging suspicion for neoplasia, further sampling should be considered. Splenic tissue **core biopsy** is considered safe (Watson et al. 2011), although rarely performed because splenectomy is preferred, particularly in case of a cavitary mass for which biopsy should be avoided due to the risk of hemorrhage.



Visit our website at **www.SmallAnimalUltrasonography.com** for complementary video clips with annotations and text on:

- Normal spleen anatomy and scanning
- Myelolipomas
- Splenic lymphoma
- Nodular hyperplasia and extramedullary hematopoiesis
- Hemangiosarcoma and peritoneal effusion
- Splenic torsion
- Splenic venous thrombus and infarcts

References

Abdellatif A, Günther C, Peppler C, Kramer M (2014) A rare case of splenic abscess with septic peritonitis in a German shepherd dog. BMC Vet Res 10:201.

Atiee G, Kvitko-White H, Spaulding K, Johnson M (2014) Ultrasonographic appearance of histoplasmosis identified in the spleen in 15 cats. Vet Radiol Ultrasound 55:310–4.

Auger M, Fazio C, de Swarte M, Bussières G, et al. (2019) Administration of certain sedative drugs is associated with variation in sonographic and radiographic splenic size in healthy cats. Vet Radiol Ultrasound 60:717–728.

Ballegeer EA, Forrest LJ, Dickinson RM, Schutten MM, et al. (2007) Correlation of ultrasonographic appearance of lesions and cytologic and histologic diagnoses in splenic aspirates from dogs and cats: 32 cases (2002-2005). J Am Vet Med Assoc 230:690–696.

Battiato P, Fernandez Y, Salgüero R, Novellas R, et al. (2021) Spontaneous emphysematous splenitis: radiographic and ultrasonographic findings in three Golden Retriever dogs. Vet Radiol Ultrasound 62:309–315.

Bertal M, Norman Carmel E, Diana A, Desquilbet L, et al. (2018) Association between ultrasonographic appearance of splenic parenchyma and cytology in cats. J Feline Med Surg 20:23–29.

Book AP, Fidel J, Wills T, Bryan J, et al. (2011) Correlation of ultrasound findings, liver and spleen cytology, and prognosis in the clinical staging of high metastatic risk canine mast cell tumors. Vet Radiol Ultrasound 52:548–554.

Cleveland MJ, Casale S (2016) Incidence of malignancy and outcomes for dogs undergoing splenectomy for incidentally detected nonruptured splenic nodules or masses: 105 cases (2009-2013). J Am Vet Med Assoc 248:1267–73.

Crabtree AC, Spangler E, Beard D, Smith A (2010) Diagnostic accuracy of gray-scale ultrasonography for the detection of hepatic and splenic lymphoma in dogs. Vet Radiol Ultrasound 51:661–664.

Crevier FR, Wrigley RH (2000) The sonographic features of splenic lymphoid hyperplasia in 31 dogs: a retrospective study (1980–2000) [abstract]. Vet Radiol Ultrasound 41:566.

Cuccovillo A, Lamb CR (2002) Cellular features of sonographic target lesions of the liver and spleen in 21 dogs and a cat. Vet Radiol Ultrasound 43:275–278.

Vet-ebooks.com

Day MJ, Lucke VM, Pearson H (1995) A review of pathological diagnoses made from 87 canine splenic biopsies. J Sm Anim Pract 36:426–433.

Fife WD, Samii VF, Drost WT, Mattoon JS, et al. (2004) Comparison between malignant and nonmalignant splenic masses in dogs using contrast-enhanced computed tomography. Vet Radiol Ultrasound 45:289–297.

Finck C, Steagall P, Beauchamp G (2021) Effects of butorphanol with alfaxalone or dexmedetomidine on feline splenic size and appearance on ultrasound and computed tomography. Front Vet Sci 2(8):572146. doi: 10.3389/fvets.2021.572146.

Fleming J, Giuffrida MA, Runge JJ, Balsa IM, et al. (2018) Anatomic site and etiology of hemorrhage in small versus large dogs with spontaneous hemoperitoneum. Vet Surg 47:1031–1038.

Gaschen L, Kircher P, Venzin C, Hurter K, et al. (2003) Imaging diagnosis: the abdominal air-vasculogram in a dog with splenic torsion and clostridial infection. Vet Radiol Ultrasound 44:553–555.

Hanson JA, Papageorges M, Girard E, Menard M, et al. (2001) Ultrasonographic appearance of splenic disease in 101 cats. Vet Radiol Ultrasound 42:441–445.

Hardie EM, Vaden SL, Spaulding K, Malarkey DE (1995) Splenic infarction in 16 dogs: a retrospective study. J Vet Intern Med 9:141–148.

Harel M, Touzet C, Barthélemy A, Ségard-Weisse EM (2020) Prevalence and diagnostic value of the ultrasonographic honeycomb appearance of the spleen in cats. J Feline Med Surg 22:186–192.

Huber B, Leleonnec M (2020) Diagnosis and treatment of hemophagocytic histiocytic sarcoma in a cat. JFMS Open Rep 6:2055116920957196.

Hwang Y, Noh D, Choi S, Choi H, et al. (2020) Changes of ultrasonographic pattern of the spleen examined with a high-frequency linear transducer during growth in puppies. Vet Radiol Ultrasound 61:577–582.

Kerboeuf M, Brun-Hansen H, Oscarson M, Sjetne Lund H (2021) Case report: haemophagocytic histiocytic sarcoma in an english setter. Vet Med Sci 7:1154–1158.

Lamb CR, Hartzband LE, Tidwell AS, Pearson SH (1991) Ultrasonographic findings in hepatic and splenic lymphosarcoma in dogs and cats. Vet Radiol Ultrasound 32:117–120.

Laurenson MP, Hopper K, Herrera MA, Johnson EG (2010) Concurrent diseases and conditions in dogs with splenic vein thrombosis. J Vet Intern Med 24:1298–1304.

Leblanc CJ, Head LL, Fry MM (2009) Comparison of aspiration and nonaspiration techniques for obtaining cytologic samples from the canine and feline spleen. Vet Clin Pathol 38:242–6.

Lee M, Park J, Choi H, Lee H, et al. (2018) Presurgical assessment of splenic tumors in dogs: a retrospective study of 57 cases (2012-2017). J Vet Sci 19:827–834.

Mai W (2006) The hilar perivenous hyperechoic triangle as a sign of acute splenic torsion in dogs. Vet Radiol Ultrasound 47:487–491.

Mallinckrodt MJ, Gottfried SD (2011) Mass-to-splenic volume ratio and splenic weight as a percentage of body weight in dogs with malignant and benign splenic masses: 65 cases (2007-2008). J Am Vet Med Assoc 239:1325–7.

Mangano C, Macrì F, Di Pietro S, Pugliese M, et al. (2019) Use of contrast-enhanced ultrasound for assessment of nodular lymphoid hyperplasia (NLH) in canine spleen. BMC Vet Res 15:196.

Mergl JC, Hanselman B, Kirsch M (2002) Chronic splenic torsion in a dog with an accessory spleen. Can Vet J 63:147–151.

Mesquita L, Finotello R, Ferreira A, Maddox T (2022) Comparison between computed tomographic and ultrasonographic findings of the liver and spleen in dogs with confirmed hepatic or splenic lymphoma involvement. Vet Rec 190:e780.

Millar SL, Zersen KM (2021) Diagnostic value of the ultrasonographic description of a splenic mass or nodule as cavitated in 106 dogs with nontraumatic hemoabdomen. Am J Vet Res 82:970–974

Moore PF, Affolter VK, Vernau W (2006) Canine hemophagocytic histiocytic sarcoma: a proliferative disorder of CD11d+ macrophages. Vet Pathol 43:632–45.

Nyland TG, Mattoon JS, Herrgesell ER, Wisner ER (1995) Spleen. In Nyland TG, Mattoon JS, eds. Small Animal Diagnostic Ultrasound. Philadelphia: WB Saunders, pp. 128–143.

O'Brien RT, Waller KR, Osgood TL (2004) Sonographic features of drug-induced splenic congestion. Vet Radiol Ultrasound 45:225–227.

Ohlerth S, Dennler M, Rüefli E, Hauser B, et al. (2008) Contrast harmonic imaging characterization of canine splenic lesions. J Vet Intern Med 22:1095–1102.

Pecceu E, Serra Varela JC, Handel I, Piccinelli C, et al. (2020). Ultrasound is a poor predictor of early or overt liver or spleen metastasis in dogs with high-risk mast cell tumours. Vet Comp Oncol 18:389–401.

Quinci M, Sabattini S, Agnoli C, Bettini G, et al. (2020) Ultrasonographic honeycomb pattern of the spleen in cats: correlation with pathological diagnosis in 33 cases. J Feline Med Surg 22:800–804.

Ramirez S, Douglass JP, Robertson ID (2002) Ultrasonographic features of canine abdominal malignant histiocytosis. Vet Radiol Ultrasound 43:167–170.

Reese SL, Zekas LJ, Iasbik MC, Lehman A, et al. (2013) Effect of sevoflurane anesthesia and blood donation on the ultrasonographic appearance of the spleen in 60 healthy cats. Vet Radiol Ultrasound 54:168–175.

Rossi F, Leone VF, Vignoli M, Laddaga E, et al. (2008) Use of contrast-enhanced ultrasound for characterization of focal splenic lesions. Vet Radiol Ultrasound 49:154–64.

Rossi F, Rabra S, Vignoli M, Haers H, et al. (2010) B-mode and contrast-enhanced sonographic assessment of accessory spleen in the dog. Vet Radiol Ultrasound 51:173–177.

Sato AF, Solano M (2004) Ultrasonographic findings in abdominal mast cell disease: a retrospective study of 19 patients. Vet Radiol Ultrasound 45:51–57.

Vet-ebooks.com

Saunders HM (1998) Ultrasonography of abdominal cavitary parenchymal lesions. Vet Clin North Am Small Anim Pract 28:755–775.

Saunders HM, Neath PJ, Brockman DJ (1998) B-mode and Doppler ultrasound imaging of the spleen with canine splenic torsion: a retrospective evaluation. Vet Radiol Ultrasound 39:349–353.

Sayre RS, Spaulding KA (2014) Formulation of a standardized protocol and determination of the size and appearance of the spleen in healthy cats. J Feline Med Surg 16:326–332.

Schlax AJ, Suran JN, Cáceres AV (2017) Associated between hyperechoic splenic speckling on ultrasound and several medical conditions in 69 dogs [abstract] Vet Radiol Ultrasound 59:225.

Schwarz LA, Penninck DG, Gliatto J (2001) Canine splenic myelolipomas. Vet Radiol Ultrasound 42:347–348.

Sharpley JL, Marolf AJ, Reichle JK, Bachand AM, et al. (2012) Color and Doppler ultrasonography for characterization of splenic masses in dogs. Vet Radiol Ultrasound 53:586–590.

Sumping JC, Maddox TW, Killick D, Mortier JR. (2022) Diagnostic accuracy of ultrasonography to detect hepatic and splenic lymphomatous infiltration in dogs and cats. J Small Anim Pract 63:113–119.

Sutil DV, Mattoso CRS, Volpato J, Weinert NC, et al. (2017) Hematological and splenic Doppler ultrasonographic changes in dogs sedated with acepromazine or xylazine. Vet Anaesth Analg 44(4):746–754.

Tecilla M, Gambini M, Forlani A, Caniatti M, et al. (2019) Evaluation of cytological diagnostic accuracy for canine splenic neoplasms: an investigation in 78 cases using STARD guidelines. PLoS One 14:e0224945.

Tomura S, Toshima A, Nomura A, Hirata M, et al. (2022) Intrapancreatic accessory spleen mimicking pancreatic insulinoma with intrapancreatic metastasis in a cat. J Vet Med Sci 84:439–444.

Watson AT, Penninck D, Knoll JS, Keating JH, et al. (2011) Safety and correlation of test results of combined ultrasound-guided fine-needle aspiration and needle core biopsy of the canine spleen. Vet Radiol Ultrasound 52:317–322.

Wilson DV, Evans AT, Carpenter RA, Mullineaux DR (2004) The effect of four anaesthetic protocols on splenic size in dogs, Vet Anaesth Analg 31:102–108.

Wrigley RH, Konde LJ, Park RD, Lebel JL (1988) Ultrasonographic features of splenic lymphosarcoma in dogs: 12 cases (1980–1986). J Am Vet Med Assoc 193:1565–1568.

Yankin I, Nemanic S, Funes S, de Morais H, et al. (2020) Clinical relevance of splenic nodules or heterogeneous splenic parenchyma assessed by cytologic evaluation of fine-needle samples in 125 dogs (2011-2015). J Vet Intern Med 34:125–131.

Yeager AE, Anderson WI (1989) Study of association between histologic features and echogenicity of architecturally normal cat kidneys. Am J Vet Res 50:860–863.

Yuki M, Narita M (2021) Subclinical wandering spleen in a cat with gastrointestinal lymphoma. Clin Case Reports 9:e04891.

Vet-ebooks.com

CHAPTER NINE

Gastrointestinal Tract

Dominique Penninck[1], Marc-André d'Anjou[2], and Heather Spain[3]

[1]*Cummings School of Veterinary Medicine, Tufts University, North Grafton, MA, USA*
[2]*Animages, Brossard, Québec, Canada*
[3]*Veritas Veterinary Partners, San Rafael, CA, USA*

Preparation and Scanning Procedure

Animals can be scanned while they are in dorsal recumbency, right or left recumbency, or standing position, if needed, to optimize an acoustic window by displacing the intraluminal fluid to the region of interest. Left lateral recumbency helps with the evaluation of the fundus, whereas right lateral recumbency improves the evaluation of the pylorus and duodenum. The standing position can be helpful for evaluating the ventral aspect of the pylorus and body of the stomach. However, the results of these positional studies also depend on a dog's conformation, the degree of stomach dilation, the nature of gastric contents, and patient cooperation.

A high-frequency (7 MHz and higher) microconvex or linear transducer is recommended to best evaluate the gastrointestinal (GI) wall layering. Microconvex probes with a small footprint are useful because they can more easily be placed below the rib cage or between ribs for the assessment of the stomach and proximal duodenum. Transverse and longitudinal/sagittal views of the GI segments are required to fully assess the thickness and the extent of a suspected lesion (Figure 9.1).

Little preparation is needed; a fast of 12 hours can reduce interference with gastric contents and gas, but the results are inconsistent. Gas in the GI tract is the most common cause of artifacts (Figure 9.2A–C and see Chapter 1).

Ultrasonographic Anatomy of the Normal Gastrointestinal Tract

The wall thickness, layering, and relative motility of different segments of the GI tract can be evaluated. The thickness of the GI tract can be measured by placing calipers on the outer aspect of the serosa and on the mucosal inner border.

Table 9.1 lists the range of normal thickness of the GI wall in dogs and cats. Also, graphs 9.1 and 9.2 displayed the proportion of the relative layer thickness for dogs and cats. This data is inspired by several publications and based on the authors' experience (Delaney et al. 2003; Di Donati et al. 2014; Gladwin et al. 2014; Goggin et al. 2000; Gory et al. 2014; Haln et al. 2015; Leroux et al. 2016; Newell et al. 1999; Penninck et al. 1989; Winter et al. 2014). It is important to remember that assessing the thickness of the GI tract is only one contributing factor to diagnose a GI disorder.

The distal/intra-abdominal **esophagus** and gastroesophageal junction can at times be visualized ultrasonographically in dogs (Gory et al. 2014) (Figure 9.3A) and cats. The esophagus cranial to the diaphragm cannot be imaged transabdominally because of interposition of gas in the surrounding lungs. Due to its deep location, significant pressure is required to obtain an adequate sagittal image of the terminal esophagus. In contrast to the remainder of the GI tract, the mucosal layer of the terminal esophagus appears echogenic rather than hypoechoic, presumed to be due to its squamous nature histopathologically (Gory et al. 2014). The gastric cardia is demarcated

Atlas of Small Animal Ultrasonography, Third Edition. Edited by Dominique Penninck and Marc-André d'Anjou.
© 2025 John Wiley & Sons, Inc. Published 2025 by John Wiley & Sons, Inc.
Companion website: www.SmallAnimalUltrasonography.com

Vet-ebooks.com

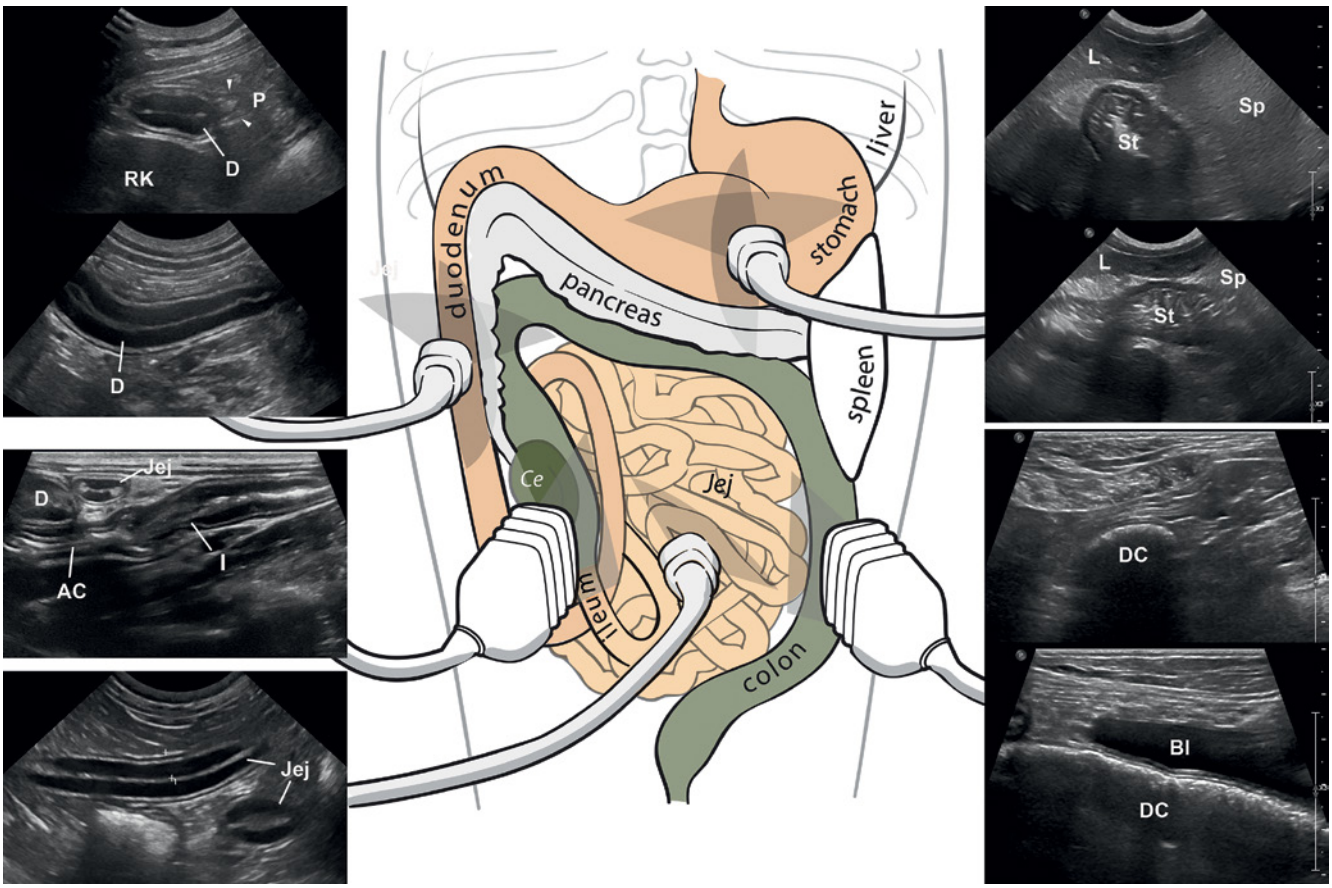


Figure 9.1. Ultrasonographic anatomy of the normal canine gastrointestinal tract in dorsal recumbency. Illustration of the gastrointestinal segments, with placements of the probe. The examination starts with a complete evaluation of the stomach, from fundus to the pylorus, then, tracing the duodenum, jejunum, ileum, ileocecocolic junction, cecum, and colon, using longitudinal and transverse planes. Documenting these segments of the GI tract allows assessment of the thickness and layering of the wall. AC, ascending colon; Bl, bladder; Ce, cecum; D, duodenum; DC, descending colon; I, ileum; Jej, jejunum; L, liver; P, pancreas; RK, right kidney; St, stomach; Sp, spleen. **Plane A** shows the position of the probe on the stomach. Both transverse (top sonographic image) and longitudinal images (bottom sonographic image) are obtained by sliding the probe along the long axis of the stomach. **Plane B** shows the position of the probe on the descending duodenum. Both transverse (top image) and longitudinal images (bottom image) are displayed. **Plane C** shows the position of the probe on the jejunum. Transverse and longitudinal sections are displayed on the same image. **Plane D** shows the position of the probe on the ileocolic junction. The corresponding longitudinal image is displayed. **Plane E** shows the position of the probe on the descending colon. Both transverse (top image) and longitudinal images (bottom image) of the colon are displayed.

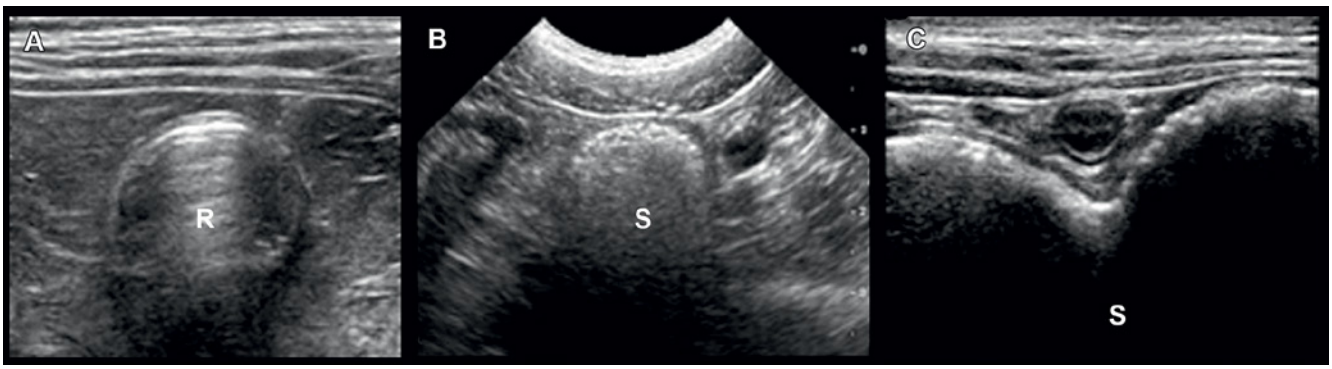


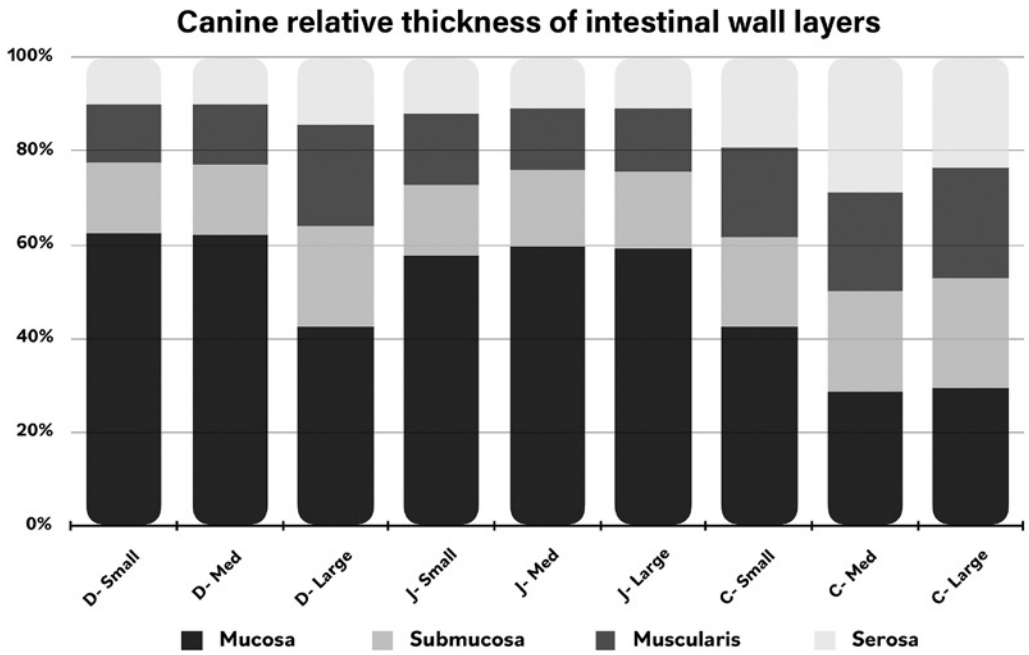
Figure 9.2. Artifacts commonly seen associated with the gastrointestinal tract. (A) Gas in the colon of this dog creates a reverberation artifact (R) masking most of the far wall. The sound is entirely reflected by the gas and then bounces back and forth between the probe and the gas, creating multiple echoes from one ultrasound pulse. **(B, C)** The mixture of gas and fecal material in the colon often creates acoustic shadowing (S) appearing as an area of low-amplitude echoes created by highly attenuating structures. The shadowing can be dirty **(B)** or clean **(C)**, depending on its homogeneity.

Vet-ebooks.com

Table 9.1
Mean and/or (range) reference values for gastrointestinal wall thickness based on the authors' experience and litterature (in mm).

	Stomach*	Duodenum	Jejunum	Ileum	Cecum	Colon
Dog						
<15 kg	2–5	3.8 (3–5)	3.0 (3–4)	3.0 (3–4)	As colon	Up to 1.5
15–30 kg	2–5	4.6 (3–6)	3.5 (3–5)	3.5 (3–4)	As colon	Up to 1.5
>30 kg	2–5	4.4 (4–6)	3.8 (3–5)	3.8 (3–5)	As colon	Up to 1.5
Cat	2–4	2.2 (2–2.5)	2.2 (2–2.7)	2.8 (2.5–3.5)	2–3	Up to 1.3

These values are only useful when used in combination with other sonographic features, such as wall layering and distribution of changes, and placed in the context of the clinical presentation.
*Stomach: These values depend on the degree of gastric distention.
Ileum values include fold. Publications included are Di Donato et al. (2014), Gladwin et al. (2014), Goggin et al. (2000).



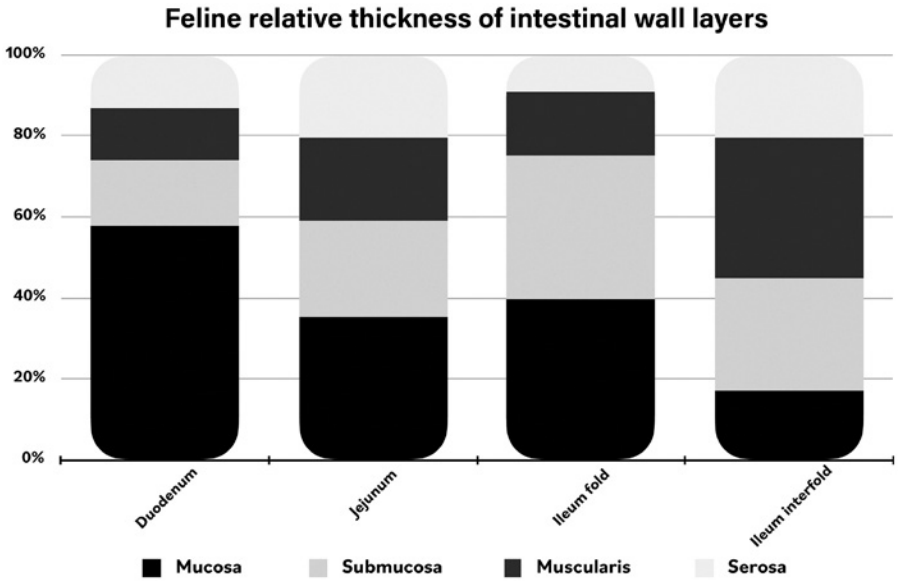
Graph 9.1. Relative thickness of individual wall layers in the duodenum, jejunum, and colon of small, medium, and large breed dogs. Adapted from Gladwin et al. (2014).

from the esophagus by an abrupt transition to hypoechoic mucosa with discrete rugal folds and with gradual thickening of the muscularis layer, most notable along the ventral wall (Gory et al. 2014, Couturier et al. 2012).

The **stomach** is the largest portion of the GI tract and can be identified easily by its rugal folds (Figures 9.1A, 9.3, and 9.5A). Regions of the stomach include the fundus, body, and the pylorus. The gastric wall is challenging to measure when the stomach is collapsed. There is a significant difference between the wall thickness at the rugal folds compared to the interrugal location. The thickness of the wall varies depending on the degree of gastric distension and the size of the patient. Following meals, active postprandial peristalsis can be observed at a rate of up to four to five contractions per minute in normal dogs. The pyloroduodenal junction (PDJ) can be identified, especially in small dogs and cats (Figure 9.3D), but it tends to be more challenging in deep-chested dogs. The PDJ is a zone of transition often appearing more echogenic than the proximal duodenum and the rugal folds, as the result of various amount of fibrous connective tissue and glandular distribution (Balducci et al. 2024).

Interestingly in cats, an increase in echogenicity of the gastric wall (centered on the submucosa) is

Vet-ebooks.com



Graph 9.2. Relative thickness of individual wall layers in the duodenum, jejunum, and ileum of cats. Adapted from Di Donato et al. (2014).

commonly seen, corresponding to fat deposits as seen radiographically (Figure 9.3E, F).

The descending **duodenum** (Figures 9.1B, 9.4) is the thickest segment of small bowel in dogs and has a superficial and rectilinear course along the right lateral abdominal wall. Definitive identification of the duodenum is made by first locating the pyloric outflow tract and tracing the loop caudally; if the PDJ cannot be clearly visualized, the duodenum is generally the most laterally located small bowel segment, lateral and ventral to the right kidney. At times, Peyer's patches can be seen as small, irregularly spaced mucosal depressions that should not be mistaken for ulcers (Figure 9.6). They can be seen in dogs with no clinical signs of active current GI disease, but as they are not seen in most dogs, it is unclear if they are seen only when they are reactive. The duodenum in cats has a thickness similar to the jejunum.

The major **duodenal papilla** (MDP) (Figures 9.4, 9.5) is easily identified in both the dog and the cat; it is located within the dorsal wall of the proximal portion of the descending duodenum along the medial/mesenteric aspect of the bowel loop. The MDP represents the insertion point of the common bile duct and pancreatic duct in both species. In a transverse imaging plane, it appears as a round or ring-like structure while in the longitudinal plane it appears ovoid or short and tubular. Normal mean dimensions of the MDP in the transverse plane (most common plane of assessment) are 6.3 mm (±1.6 mm) wide and 4.3 mm (±1 mm) high in dogs and 3.1 mm (±0.7 mm) wide and 2.5 mm (±0.6 mm) high in cats (Coeuriot et al. 2022; Mortier et al. 2016); in dogs, there is a positive correlation between patient body weight and dimensions of the MDP (Mortier et al. 2016). The normal MDP is most often homogeneous and nearly isoechoic to surrounding fat in the cat (Coeuriot et al. 2022) and has a layered appearance in the dog (Mortier et al. 2016). The minor duodenal papilla, which is smaller and less conspicuous, can sometimes be identified in the dog a few centimeters distal to the MDP (Figure 9.4) The minor duodenal papilla is inconsistent in cats, present in only 20–25% of individuals.

A multisegmental asymmetrical hypoechoic extra layer bisecting the submucosa can be identified in the ileum and distal jejunum of young cats while using high-frequency transducers (Nielsen et al. 2016) (Figure 9.6). In immature animals they are thought to represent reactive lymphoid tissue (Peyer's patches). In immature animals, they are thought to likely represent reactive tissue.

The **jejunum** is the longest intestinal portion and is made of numerous loops of similar diameter and wall layering, dispersed in the central abdomen (Figure 9.4)

On a transverse plane of any small intestinal loop, one can see an extended hyperechoic stripe on each side of the lumen, likely representing the altered alignment of villi in collapsed bowel segments (Rault et al. 2004) (Figure 9.4).

Vet-ebooks.com

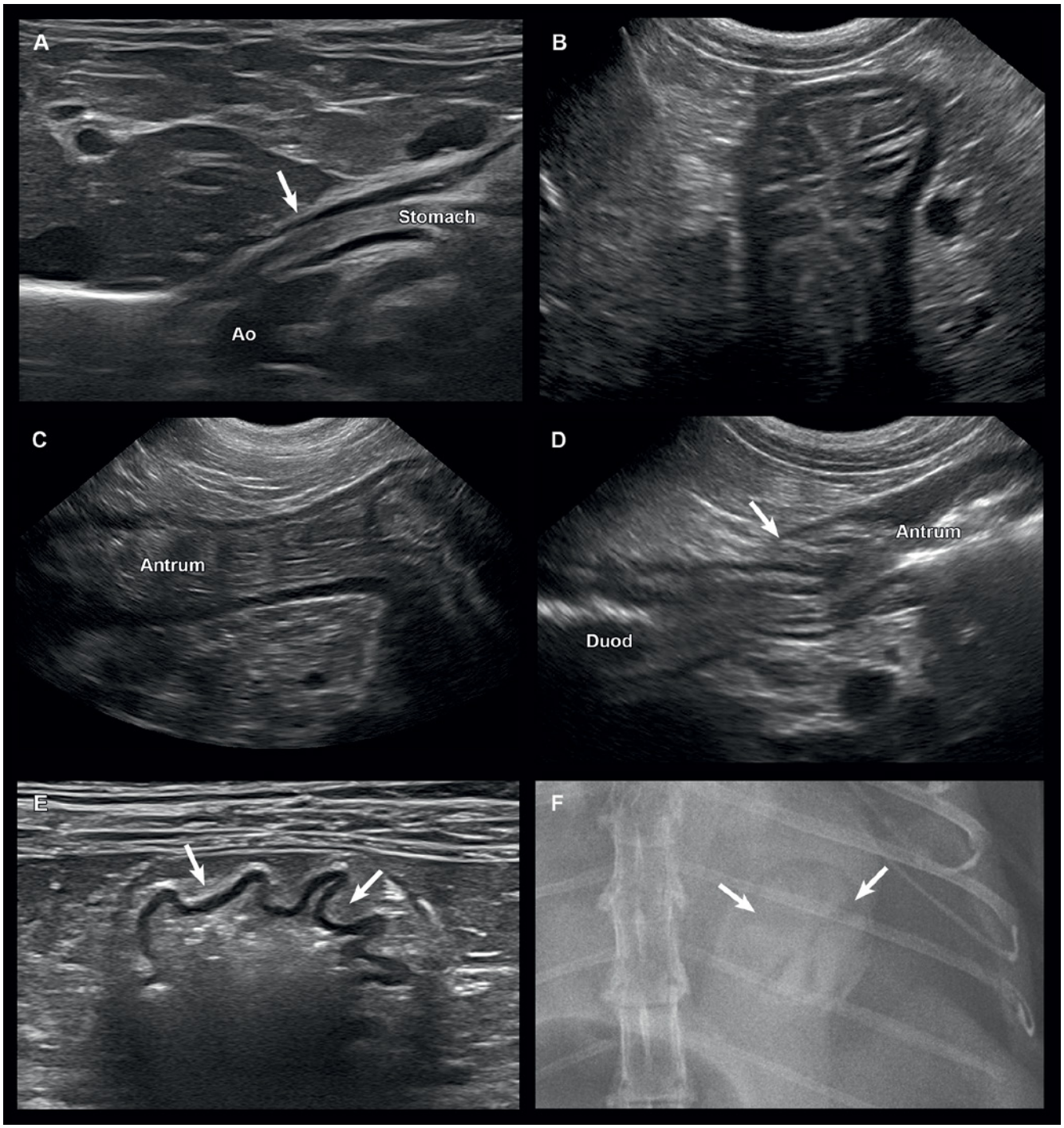


Figure 9.3. **Sonograms of normal esophagus and stomach in normal dogs and cats. (A)** On transabdominal approach, the esophagus is rarely seen. In this 8-year-old cat, the most distal portion of the esophagus (arrow) is visible. In the same image is a transverse view of the aorta (Ao) and the fundus of the stomach. **(B)** The fundus of the stomach is easily recognized by its location and the presence of rugal folds. When the stomach is collapsed like in this dog, it is difficult to assess the wall thickness accurately. **(C)** The gastric antrum of a normal dog, in the longitudinal plane. The stomach is collapsed. **(D)** Longitudinal view of the pyloroduodenal junction in a dog. Notice the bulge (arrow) at the point of transition. Duod, duodenum. **(E)** On this transverse sonogram of the stomach, the mucosal lining contrasts with the rest of the wall that is moderately echogenic; corresponding to the more radiolucent fat deposit (arrow) as commonly seen radiographically **(F)**.

Vet-ebooks.com

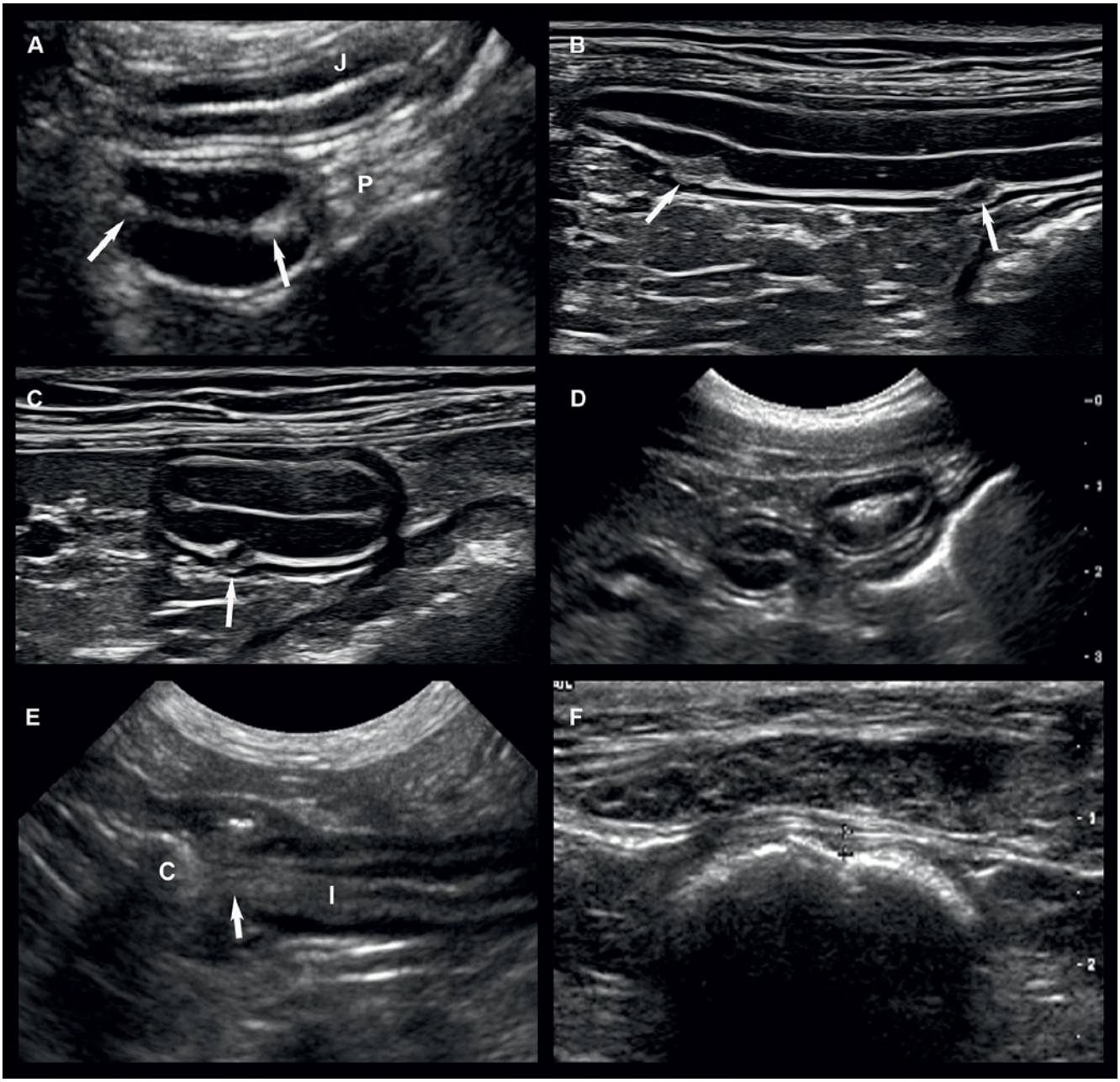


Figure 9.4. **Sonograms of normal small intestines and colon in dogs. (A)** The proximal duodenum has a thicker wall than the adjacent jejunal loops (J). On this transverse plane, notice the extended stripe on each side of the lumen (arrows), this is a normal finding. P, pancreas**. (B)** On this longitudinal plane of the duodenum, the major and the minor papillae (arrows) are visible. **(C)** In the proximal portion of the descending duodenum, the major duodenal papilla, seen on the transverse plane on this image (arrow) can easily be identified. **(D)** Jejunal segments are freely looping in the midabdomen. The wall layering is visible. **(E)** The ileocecocolic junction (arrow) can be difficult to identify because gas collected at that location. In this dog, the ileum (I) is seen entering the ascending colon (C) on a longitudinal plane. **(F)** The colon, often gas or feces filled, has a thinner wall than the small bowel. In this dog, the finely layered colonic wall is 1.5 mm thick (between calipers).

Figure 9.6. **Sonograms of lymphoid tissue in dogs and cats. (A)** Longitudinal image of the descending duodenum in a dog without gastrointestinal signs. Regularly spaced mucosal wall indents (arrows) are noted along the antimesenteric margin, they represent Peyer's patches. **(B)** An oblong anechoic structure is present at the mucosal/submucosal interface (arrows) and results in an asymmetric appearance of this jejunal segment of a young cat. **(C)** Small, hypoechoic to anechoic nodules (arrows) can be seen in the cecal wall of cats and give it a follicular pattern. These represent lymphoid aggregates and may be seen in the absence of GI signs. **(D)** Similarly, small hypoechoic nodules (arrows) can be present along the colonic wall in cats. In this cat with diarrhea, the nodules resolved after medical management.

Vet-ebooks.com

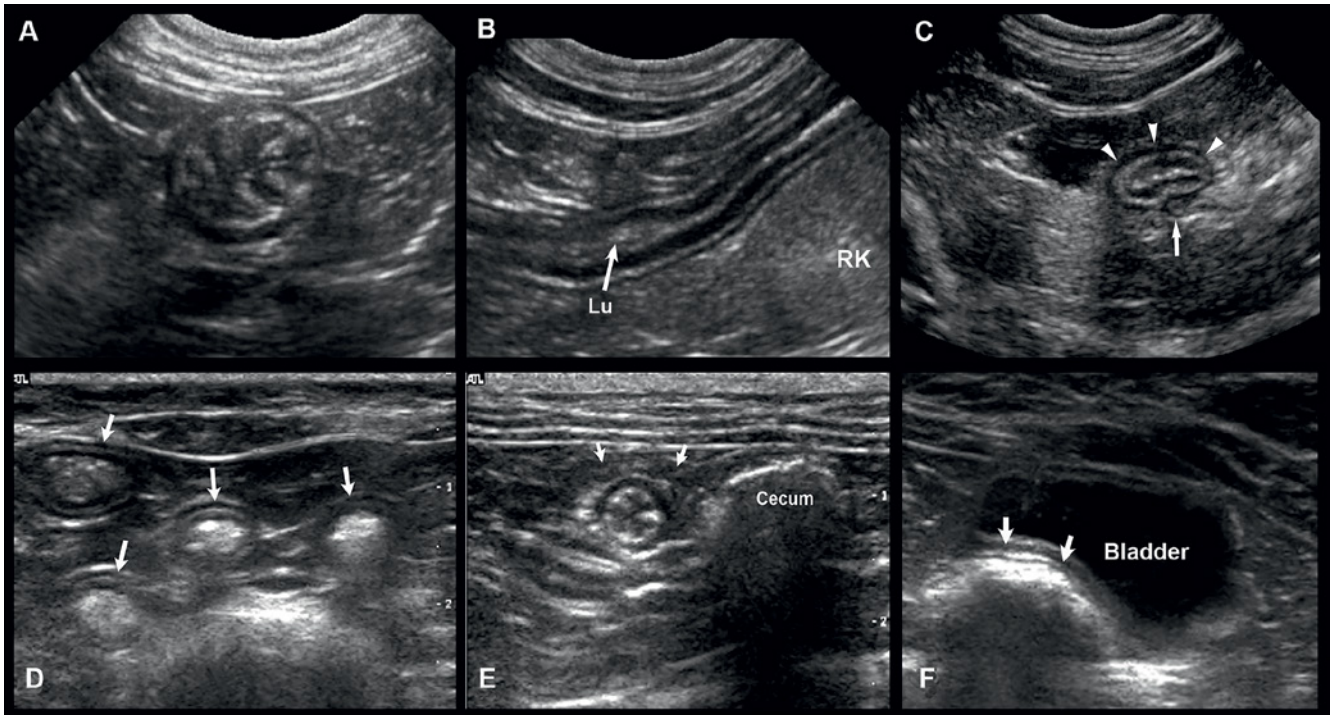


Figure 9.5. **Sonograms of normal gastrointestinal segments in cats. (A)** Transverse sonogram of the collapsed gastric fundus in an adult cat. Rugal folds are well seen. **(B)** Longitudinal sonogram of the duodenum. The wall layering is visible. **(C)** Transverse sonogram of the descending duodenum (arrowheads). The duodenal papilla is well delineated (arrow). **(D)** Several loops of jejunum, containing fluid and gas, are present (arrows). There is no significant difference between the thickness of duodenum and jejunum in cats. **(E)** Transverse sonogram of the ileum. The gas-filled cecum is on the right of the ileum, and the ileum is entering the echogenic fluid-filled ascending colon (arrows). This short segment of bowel has more prominent submucosa and muscularis than the remaining bowel segments in cats. **(F)** Transverse sonogram of the feces-filled descending colon in a normal cat. The thin wall and its layering are barely visible (arrows), just ventral to the hyperechoic interface created by the presence of feces and its associated shadow in the far field. Lu, lumen; RK, right kidney.

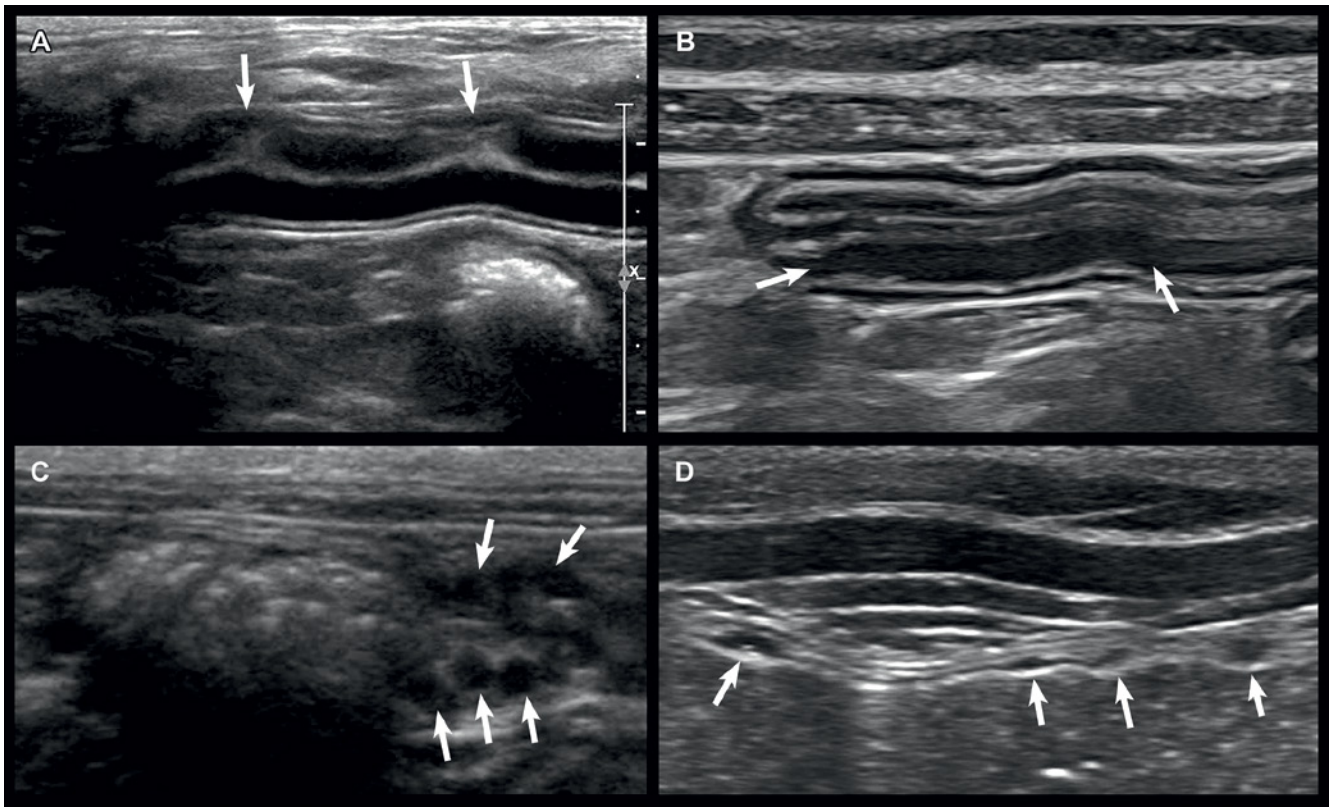


Figure 9.6. **Sonograms of lymphoid tissue in dogs and cats.** (for full caption, see facing page)

Vet-ebooks.com

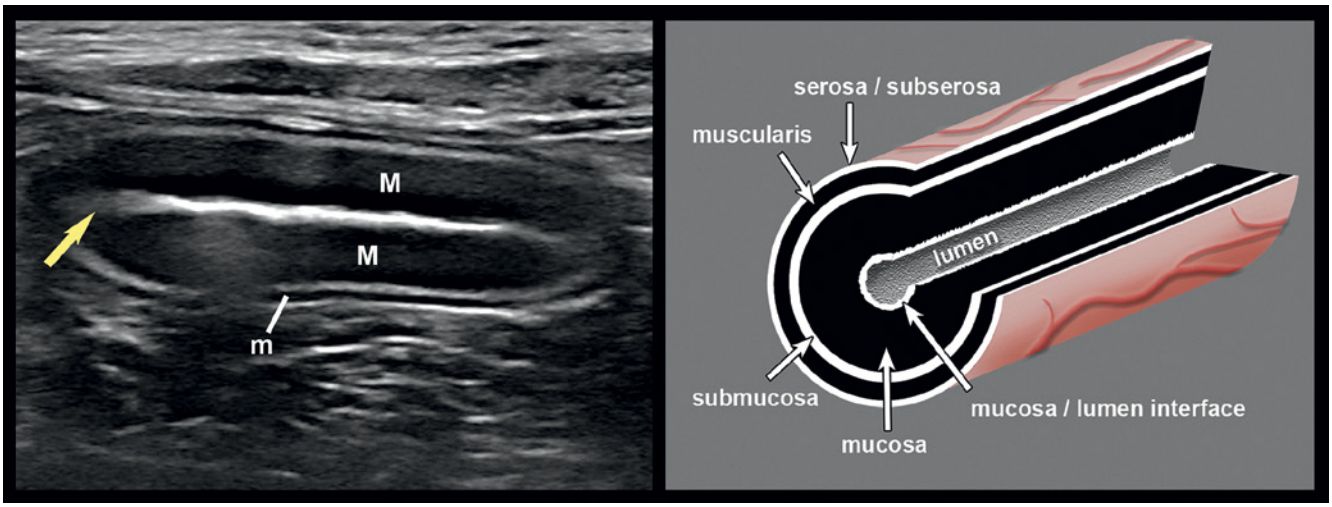


Figure 9.7. Normal intestinal layers. Sonogram of one sagittal intestinal segment. The yellow arrow points to the lumen. On the right, the five ultrasonographic interfaces are illustrated. The lumen varies in echogenicity according to its content. It is bordered by a hyperechoic interface that delineates the thick nearly anechoic mucosal layer. Then, the thin hyperechoic submucosa, thin nearly anechoic muscularis, and thin hyperechoic subserosa/serosa can be visualized. M, mucosa; m, muscular layer.

The **ileum** in cats (Figure 9.5) is a short intestinal segment with a prominent hyperechoic submucosa and muscularis, resulting in an intestinal segment thicker than the rest of the intestinal tract. The ileocecocolic junction (ICJ) is normally identified in the right cranial abdominal quadrant. The ICJ (Figure 9.4E) can be challenging to identify in dogs because the **cecum** is most commonly gas filled. In cats, the ileocecocolic junction (Figure 9.5) can be more easily recognized. The cecum is a flattened conical or comma-shaped structure in cats and is a spiral-shaped structure in dogs.

The wall of the normal **feline cecum** can display numerous small, round and coalescing hypoechoic lymphoid follicles that originate in the submucosal layer and expand into the mucosal layer; it is called the follicular layer. Normal mean thicknesses of the feline cecum at the proximal and distal aspects of the wall are 2.5 and 3.1 mm, respectively (Hahn et al. 2017). The ultrasonographic appearance of the normal ileocecocolic junction in dogs has been recently published (Azoulay et al. 2024).

The **colon** is made of three parts: the ascending colon along the right mid to cranial abdomen, the transverse colon along the greater curvature of the stomach, and the descending colon along the left abdominal wall. It has a thin, layered wall and often contains gas and feces (Figures 9.1C, 9.2, 9.4, and 9.5).

Four ultrasonographic layers can be identified throughout the GI tract. From the lumen to the serosal surface, one can identify the hyperechoic mucosal interface in contact with the lumen, the hypoechoic mucosa layer, the hyperechoic submucosa, the anechoic to hypoechoic muscular layer, and the combined hyperechoic subserosa and serosa (Figure 9.7). Several publications (Di Donati et al. 2014; Gladwin et al. 2014; Winter et al. 2014) report the **relative proportion of each wall layer** to the overall thickness of the wall (Graphs 9.2, 9.3).

In the canine small intestine (duodenum and jejunum), the mucosa is the thickest layer (~60–63%); the submucosa (~14–16%) and muscularis (~13–15%) layers are relatively similar in thickness; and the serosal layer is the thinnest (~9–11%). In the colon, all layers have a similar contribution to overall wall thickness (Gladwin et al. 2014).

In cats, the mucosa represents about 58% of the total wall thickness of the duodenum and about 55% of the total wall thickness of the jejunum; while the muscular layer represents about 13% (duodenum) and 14% (for the jejunum) of the total wall thickness. For the ileum in cats, the total thickness and relative layer thickness vary depending on the location where the measurements are taken (including folds versus between folds). In the feline ileum, the submucosa and muscular layers are more prominent than in the rest of the small intestines (Di Donato et al. 2014). These reference values are useful in evaluating disorders of some of the layers of the GI wall.

Wall layering is described as *normal* when all wall layers can be identified and have normal echogenicity,

Vet-ebooks.com

altered when all wall layers can be identified but there are changes in echogenicity and/or relative thickness, or *lost* when layers are no longer discernable (Penninck et al. 2003).

The normal luminal contents can vary and may consist of food, mucus, fluid, or gas (Figure 9.8). Some foods may have an unusual appearance and mimic foreign material (Figure 9.9).

The hepatic, gastric, pancreatico-duodenal, jejunal, and colic lymph nodes are involved in the lymphatic drainage of the GI tract (see Chapter 15) and should be evaluated when a GI disorder is suspected.

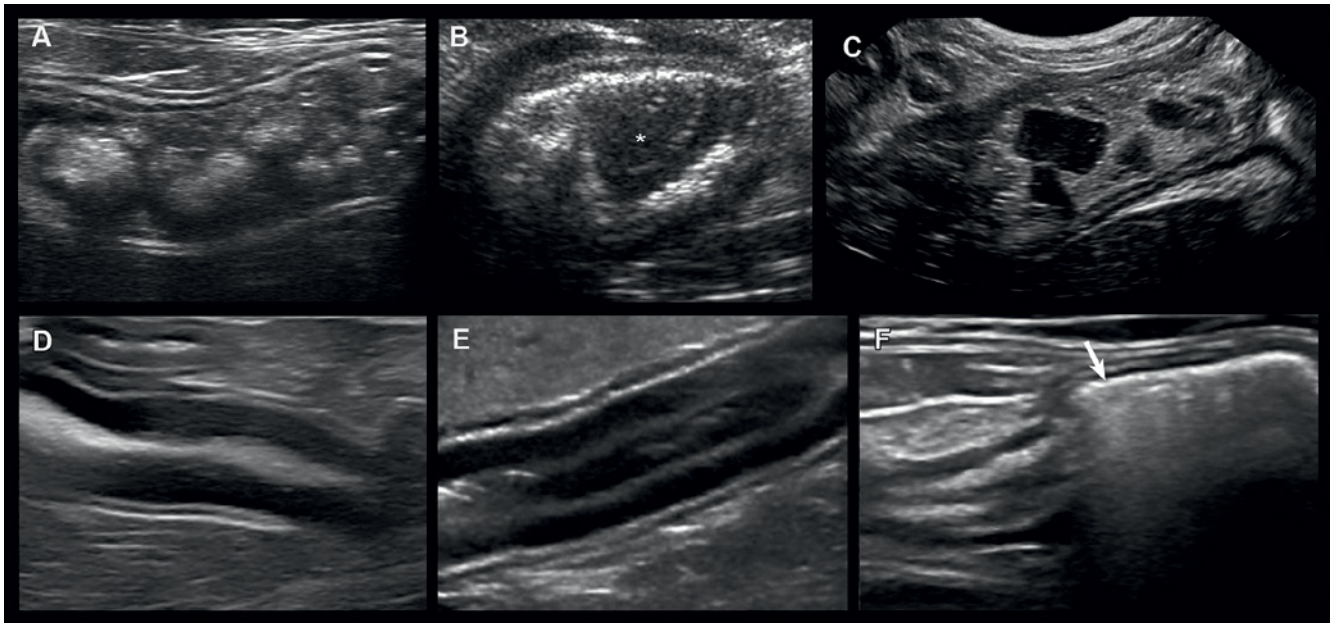


Figure 9.8. Normal luminal contents. (A–C) The alimentary pattern consists of food particles of variable size and shape in the gastric lumen. It may or may not be associated with imaging artifacts. **(A)** In this dog, small, rounded, echogenic balls of food can be identified in the gastric lumen. **(B)** A large amount of food or large pieces of food like in this dog (*) can occasionally mimic a mass or a foreign body in the stomach. **(C)** Numerous variable shape and size structures are seen in the stomach of a dog after a homemade meal. **(D)** The mucous pattern appears as a bright interface in the lumen of this jejunal segment. Note the absence of artifacts with this pattern. The gastrointestinal wall can be fully evaluated. **(E)** The fluid pattern is characterized by anechoic to uniformly echogenic luminal contents. This pattern optimizes the visualization of the wall layers on each side of the lumen. **(F)** The gas pattern appears as an intraluminal, hyperechoic, reflective surface. At the ileocolic junction in this cat, a small amount of gas (arrow) is seen in the ascending colon. The gas is associated with faint reverberation artifact.

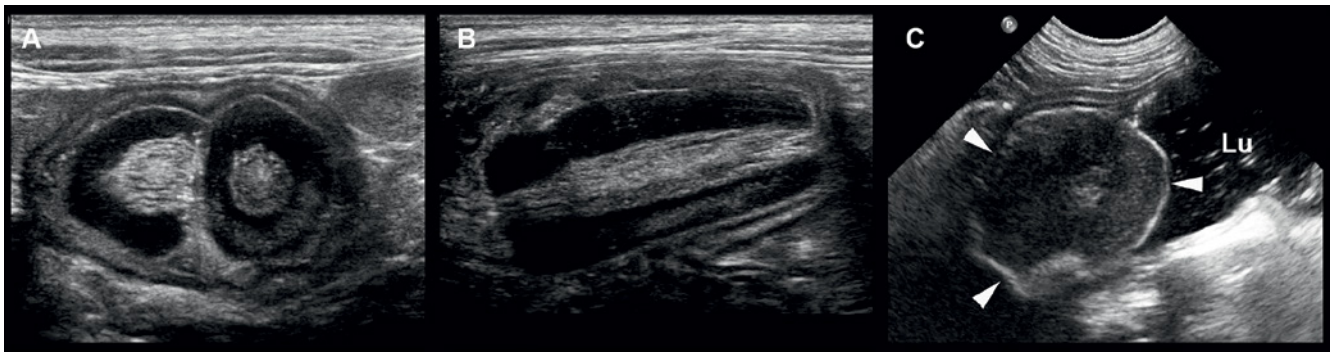


Figure 9.9. Unusual luminal contents. (A, B) Baby carrots. Transverse **(A)** sonogram of two-layered structures present in the gastric lumen of a 7-month-old Pug. The baby carrot has a distinct appearance in the longitudinal plane **(B). (C)** An irregularly rounded and echogenic structure (arrowheads) is noted in this 2-year-old Collie presented for acute vomiting, likely resulting from ingestion of **raw potatoes** which are toxic in dogs. Lu, fluid-filled lumen of the stomach.

Vet-ebooks.com

Sonographic Features of Gastrointestinal Disorders

Intussusception

The main ultrasonographic feature of an intussusception is the multilayered appearance of the wall (also called *concentric rings* or *ring sign*) representing the superimposed wall layers of the intussusceptum (i.e., the part prolapsing into the other) and intussuscipiens (part receiving it) (Figure 9.10).

In dogs and cats (Lamb and Mantis 1998; Patsikas et al. 2003), the appearance of intussusception varies somewhat with the location and length of the GI segment involved, the duration of the process, and the orientation of the scan plane relative to the axis of the intussusception. The intussuscipiens (outer bowel segment) is often thickened, edematous, and hypoechoic, whereas the thickness and layering of the intussusceptum may appear normal. The invaginated portion can involve different segments of the GI tract, such as the stomach (Figure 9.11), small bowel (Figure 9.12), or colon (Figures 9.13, 9.14).

Gastric intussusception is rare, but when encountered can be challenging to diagnose ultrasonographically (Graham et al. 2020; Hoffman 2003; Lee et al. 2005). It may involve part of the esophagus, segments of stomach, or proximal duodenum. Frequently, in jejuno-jejunal or jejuno-ileo-ceco-colic invaginations, mesenteric fat and vessels invaginate within the intussuscipiens. On occasion, inflammatory pseudocysts, enlarged lymph nodes (Figure 9.12), foreign bodies (Figure 9.12), or a tumoral mass (Figure 9.14) in older patients can be seen within or near the intussusception site.

At times, lesions affecting the GI tract, such as plication associated with linear foreign bodies (Figure 9.15), sacculation, or hyperplastic gastric mucosa protruding into the lumen, can simulate the

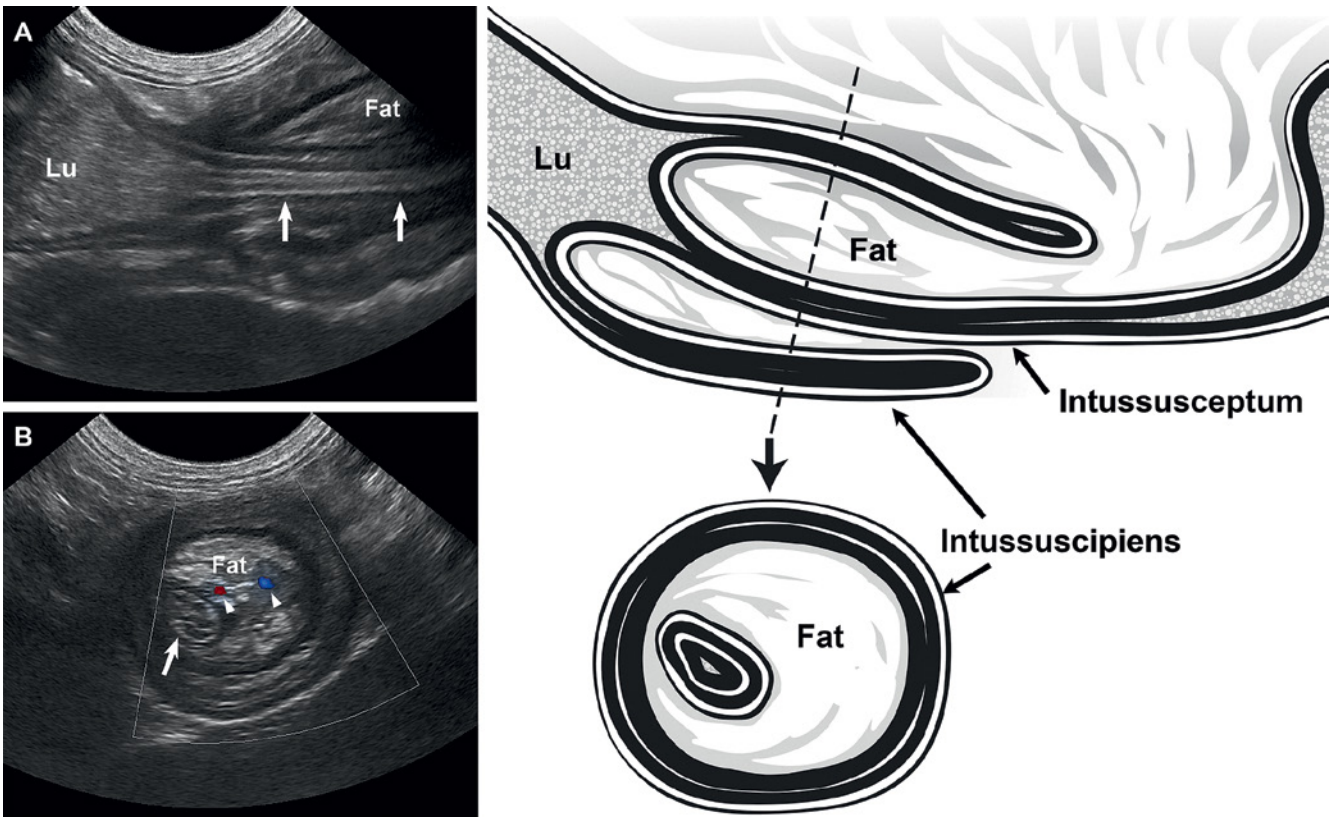


Figure 9.10. Intussusception in a dog. Illustrations of the relationship of the intussuscipiens, intussusceptum, and surrounding structures. On the top **(A)** is the longitudinal sonogram of a jejunoileal intussusception and its corresponding schematic illustration. On the bottom **(B)** is the transverse sonogram of a jejunoileal intussusception and its corresponding schematic illustration. The intestinal lumen (Lu) is dilated with fluid because of mechanical obstruction, and hyperechoic mesenteric fat is invaginated with the intussusceptum within the intussuscipiens. Mesenteric vessels (arrowheads) often follow the mesenteric fat within the intussuscipiens.

Vet-ebooks.com

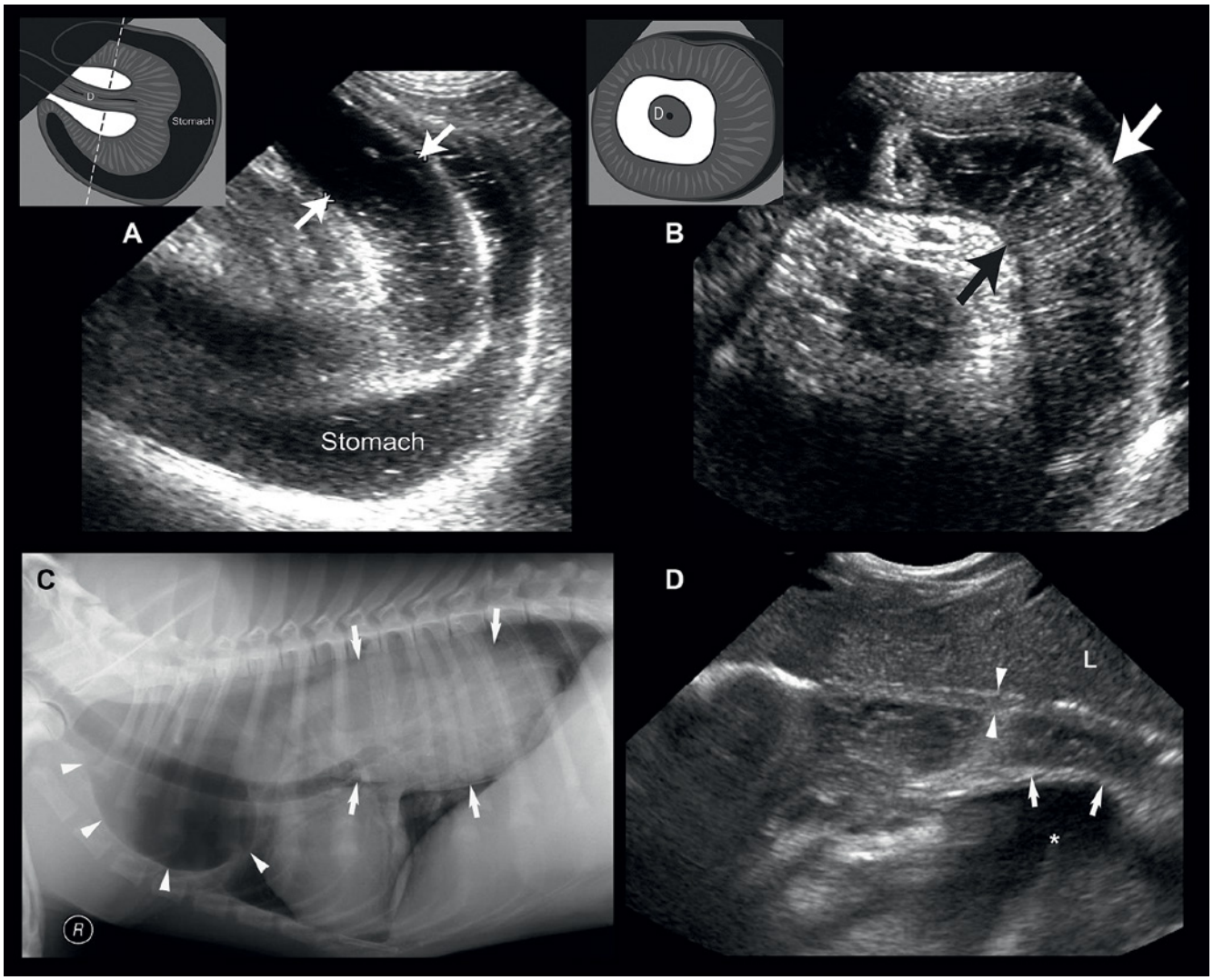


Figure 9.11. **Gastric intussusception in two dogs. (A, B)** A **duodenogastric** intussusception in a 6-year-old male Labrador retriever with glomerulonephritis and presented because of severe, acute vomiting. The most proximal portion of the duodenum is invaginated within the pylorus, which protrudes within the fluid-filled gastric body (stomach). The gastric wall was markedly thickened and hypoechoic because of severe edema (arrows). This change mimics a mass. **(C, D)** Lateral radiograph of the thorax of a **gastroesophageal** intussusception in a 6-month-old German shepherd. The esophagus is gas distended (arrowheads) cranially, and an elongated soft tissue mass (arrows) is present in its caudal aspect; this represents part of the invaginated stomach. **(B)** The sagittal sonogram shows a partially fluid-filled gastric lumen (*). The thickened and edematous gastric wall (arrows) is located cranial to the diaphragm (arrowheads). D, duodenum; L, liver located in the cranial abdomen.

pattern of intussusception. By evaluating the lesion in several planes, one can avoid such pitfalls.

Foreign Bodies

GI foreign bodies greatly vary in size, shape, and echogenicity. Segmental fluid or gas accumulation within the stomach or part of the intestinal tract is an indicator of mechanical ileus (obstruction). When present, abnormal fluid distension facilitates the detection of foreign material (Figure 9.16).

Balls are easily identified because of their characteristic curved interface. They may vary in echogenicity, depending on the composition of their material (Figure 9.17). At times, gastric foreign material (such as balls) may be incidental findings; therefore, it is important to consider the clinical history to appropriately manage the patient's presenting signs.

Independently from the type of foreign body, the presence of bright interface associated with strong shadowing is highly suggestive of a foreign material (Tidwell and Penninck 1992). However, fluid or gas

Vet-ebooks.com

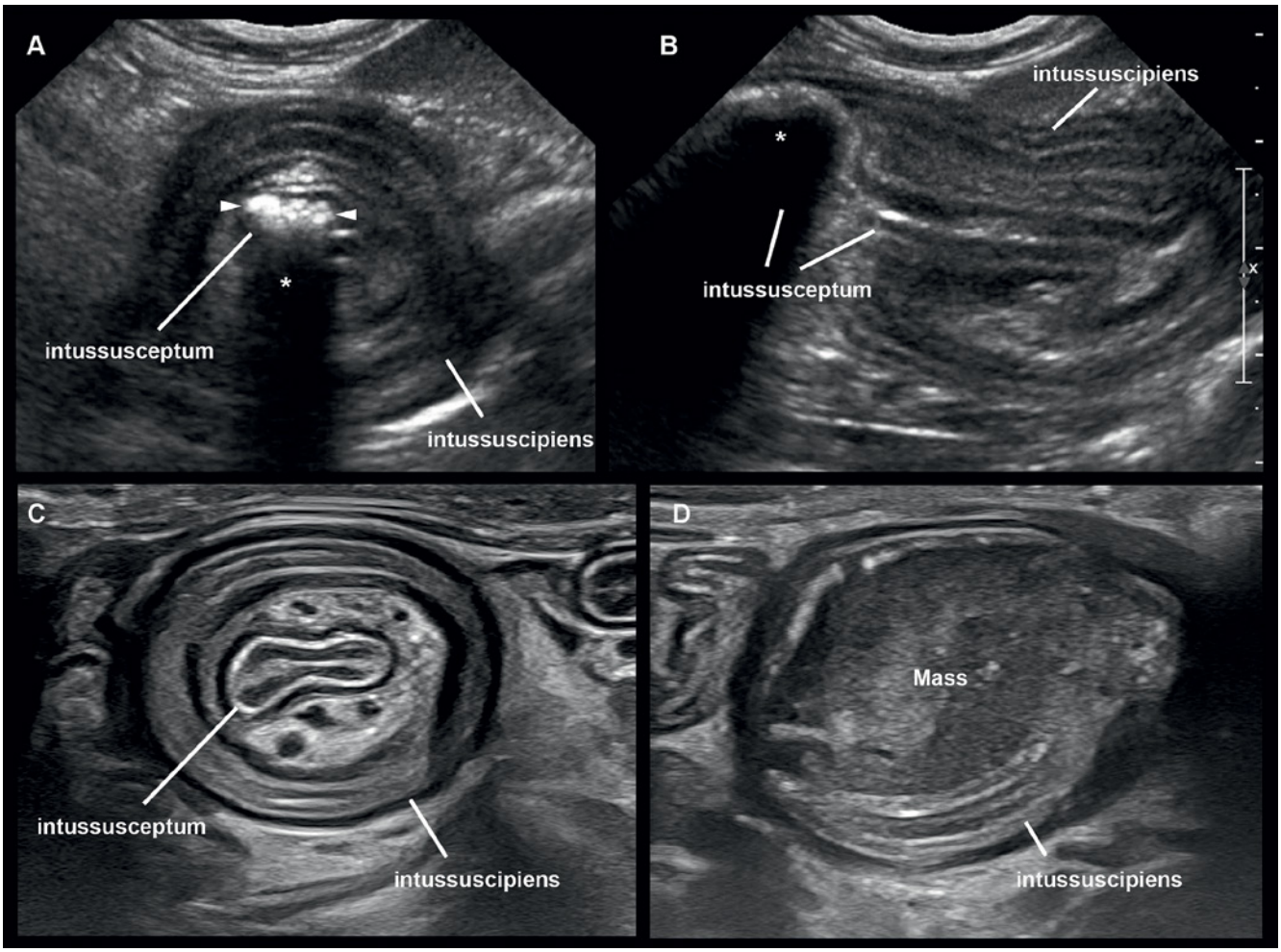


Figure 9.12. **Jejunal intussusception in a dog and a cat.** Transverse **(A)** and longitudinal **(B)** sonograms of a jejunojejunal intussusception identified in a young Labradoodle. The intussuscepted segment contains a linear foreign body (arrowheads) associated with acoustic shadowing (*). Note the numerous wall layers of the intussusceptum and intussuscipiens segments on both views. **(C, D)** Sonograms of a jejunojejunal intussusception in a 1-year-old domestic shorthair cat. The cat was presented for chronic vomiting and poor body condition. A heterogeneous, medium echogenic, mass-like lesion was identified at the aborad end of the intussusception extending into the lumen of the intussuscipiens. Histopathologic evaluation was compatible with a chronic intussusception with multifocal mucosal ulceration and marked granulation tissue formation.

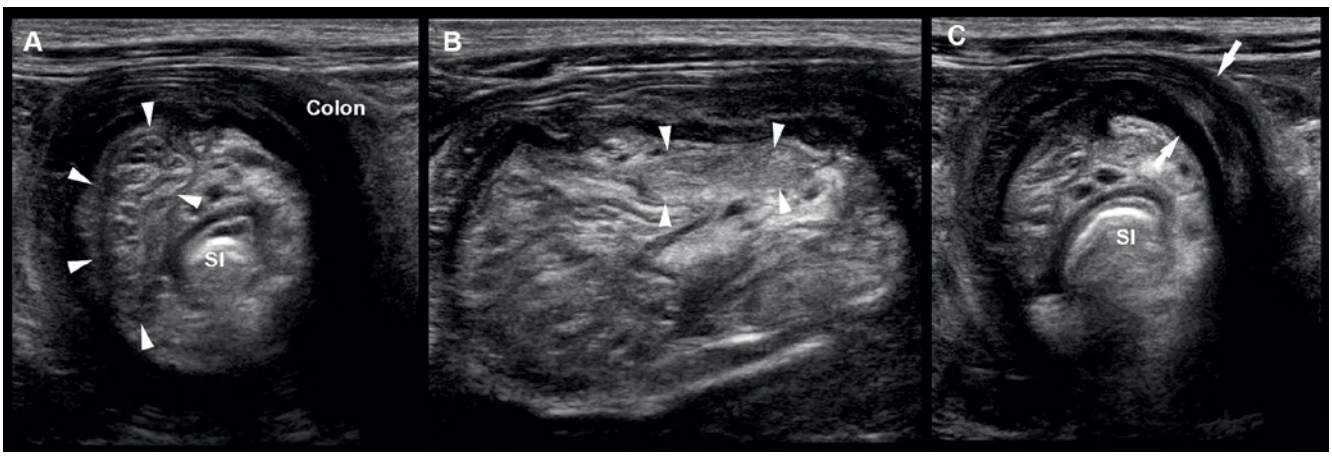


Figure 9.13. **Jejunocolonic intussusception.** Transverse **(A, C)** and longitudinal **(B)** sonograms of a distal jejunocolonic intussusception detected in a 4-month-old Golden Retriever. In **(A)**, the colon is moderately thickened and edematous. The arrowheads outline the invaginated cecum located next to a small intestinal segment (SI). In **(B)**, the arrowheads point to one of the invaginated jejunal lymph nodes. In **(C)**, the colonic wall (arrows) is thickened and layers are barely seen.

Vet-ebooks.com

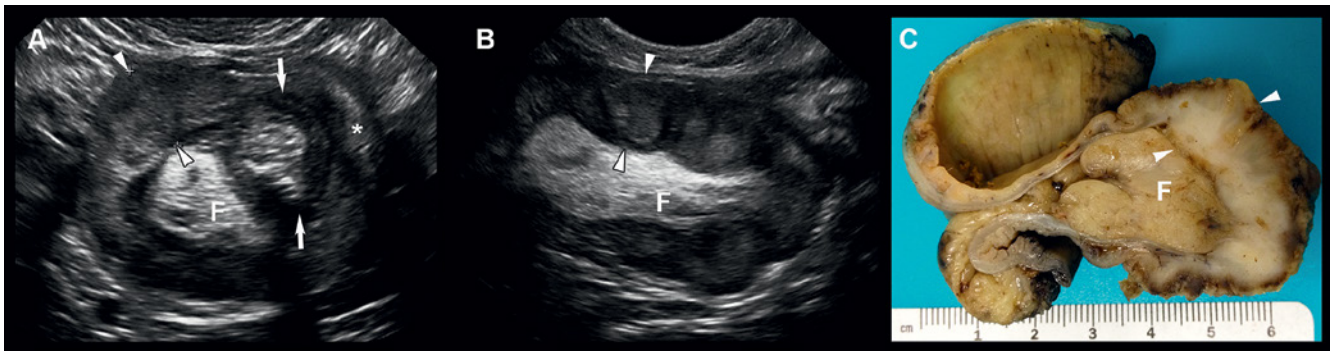


Figure 9.14. Colonic intussusception and adenocarcinoma. Transverse sonographic **(A)** and sagittal **(B)** sonograms of a large nodular echogenic colonic thickening/mass (arrowheads) associated with an intussusception in a 15-year-old cat. The mass was diagnosed as a colonic adenocarcinoma. The arrows point to the invaginated segment of colon with a small amount of echogenic fluid in its lumen. F, invaginated fat; and an asterisk is placed on the lumen of intussusceptum in **(A)**. **(C)** Gross specimen of the intussusception associated with an asymmetric transmural adenocarcinoma. F, fat.

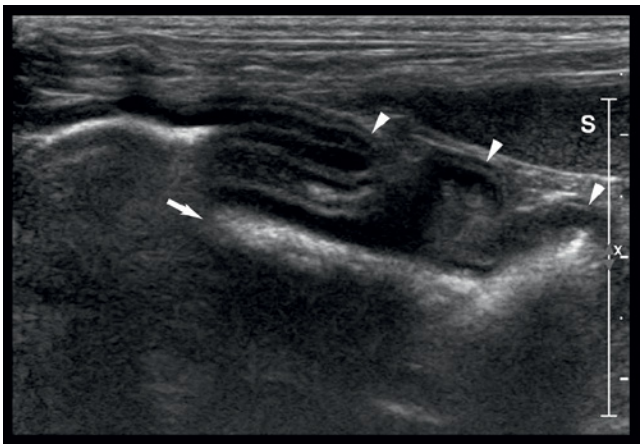


Figure 9.15. Plication mimicking intussusception. Longitudinal sonogram of a long plicated intestinal segment with a linear foreign body (arrow) in the lumen of this 2-year-old Dashund presented with 4 days of anorexia. The exuberant folds of the plication (arrowheads) can mimic an intussusception.

accumulation orad to the foreign material is necessary to confirm the obstructive nature of the obstruction. Feces in the colon can simulate foreign material, and compact fecal material is similarly associated with strong shadowing. It is thus critical to identify accurately the segment of the intestinal tract, especially differentiating small bowel from colon (Figure 9.2). Occasionally, the contour of the interface can enable the identification of the type of foreign body such as a regularly lobulated surface of a peach pit.

Gastric trichobezoars, also called *hairballs*, are commonly seen in cats. These compact foreign bodies are typically fusiform and appear as smooth to irregular hyperechoic interfaces with a strong, uniform, clean acoustic shadow (Figure 9.18A). In dogs and cats, several types of foreign bodies can be encountered that have variable size, shape, echogenicity, and acoustic shadowing (Figure 9.18).

Perforating foreign bodies, such as ingested teriyaki sticks, are usually anchored within the stomach and may affect the surrounding soft tissue within and outside the cranial abdominal cavity (Penninck and Mitchell 2003) (Figure 9.19). The perforated wall is locally thickened, and focal loss of layering is common. The adjacent fat often is hyperechoic as a result of regional steatitis.

Linear foreign bodies often present as hyperechoic linear interfaces, commonly associated with shadowing, and the affected bowel segment often appears plicated (Figure 9.20). The degree of plication varies with duration and severity. Intestinal distension often is less pronounced than with larger obstructive foreign bodies. Linear foreign bodies vary in diameter, contour, and length and part of the foreign material may be anchored in the pyloric antrum or any place along the intestinal tract. Thin or sharp foreign bodies can penetrate the wall and cause perforation.

The presence of GI **parasites** can mimic the appearance of linear foreign bodies. Roundworms (*Ascaris*) appear as smooth, tubular hyperechoic structures (Figure 9.21). Shadowing is usually not observed with these adult parasites.

At times, foreign material accumulates at a pathologically narrowed intestinal site. The narrowing can be caused by intussusception, post-traumatic or surgical stricture, or focal neoplastic infiltrate (Figure 9.22).

Hernia and Volvulus

In some instances, the intestines may be displaced and/or trapped in abnormal location; this can lead to vascular compromise of the incarcerated intestinal

Vet-ebooks.com

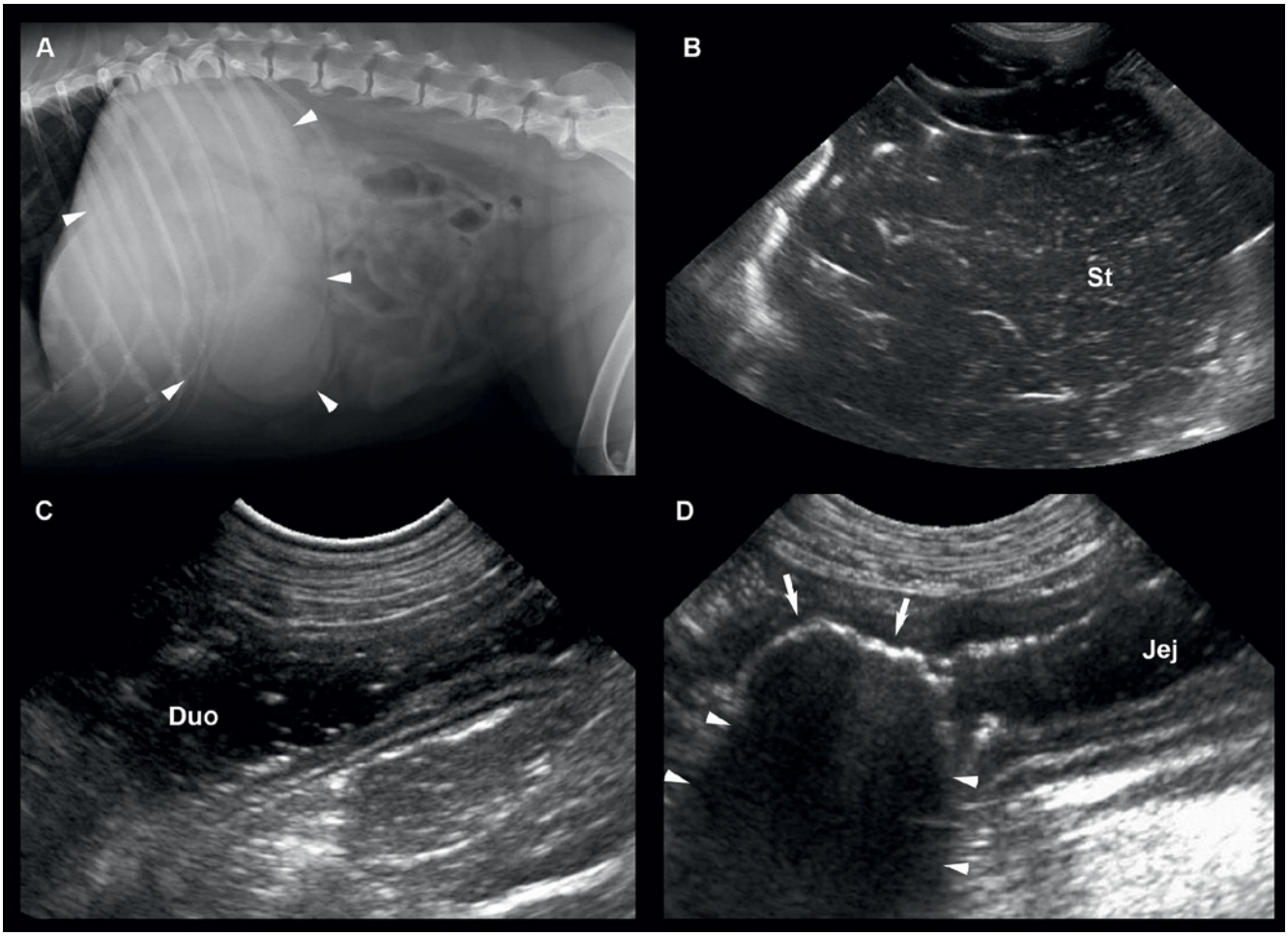


Figure 9.16. **Proximal jejunal obstructive foreign body. (A)** Lateral radiograph of a 13-year-old Cocker with 3 days of vomiting and anorexia showing a moderately fluid and gas-distended stomach (arrowheads). **(B)** Transverse sonogram of the fluid-distended stomach. Decreased gastric motility is noted during the examination. **(C)** The descending duodenum (Duo) is fluid distended. **(D)** The proximal jejunum (Jej) is also fluid distended up to the obstructive foreign body (arrows) associated with strong shadowing (arrowheads).

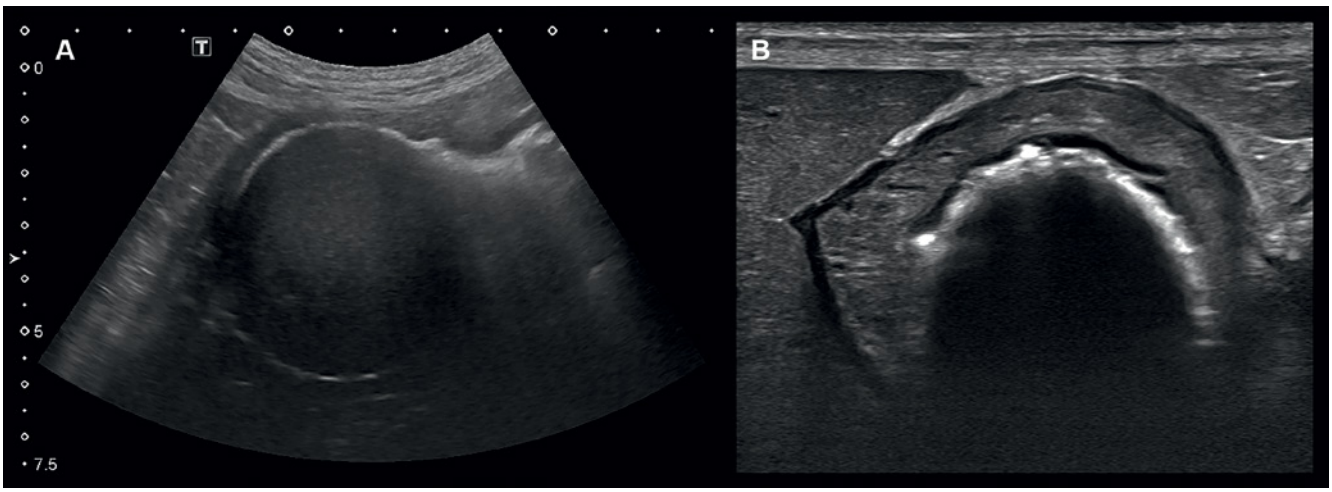


Figure 9.17. **Gastric foreign bodies in two dogs. (A)** A **rubber ball** was present in the stomach of this dog over several examinations, without causing clinical signs. The foreign object is spherical and of mild, uniform echogenicity with only partial acoustic shadowing. **(B)** In this 12-year-old Dachshund dog presented for vomiting, a **plastic foreign object mixed with hair** appears as a bright curvilinear interface associated with strong distal acoustic shadowing. The gastric wall is thickened and edematous with submucosal thickening and reduced definition of wall layers; the luminal surface of the mucosa also appears irregular, suggestive of mucosal erosion/ulceration.

Vet-ebooks.com

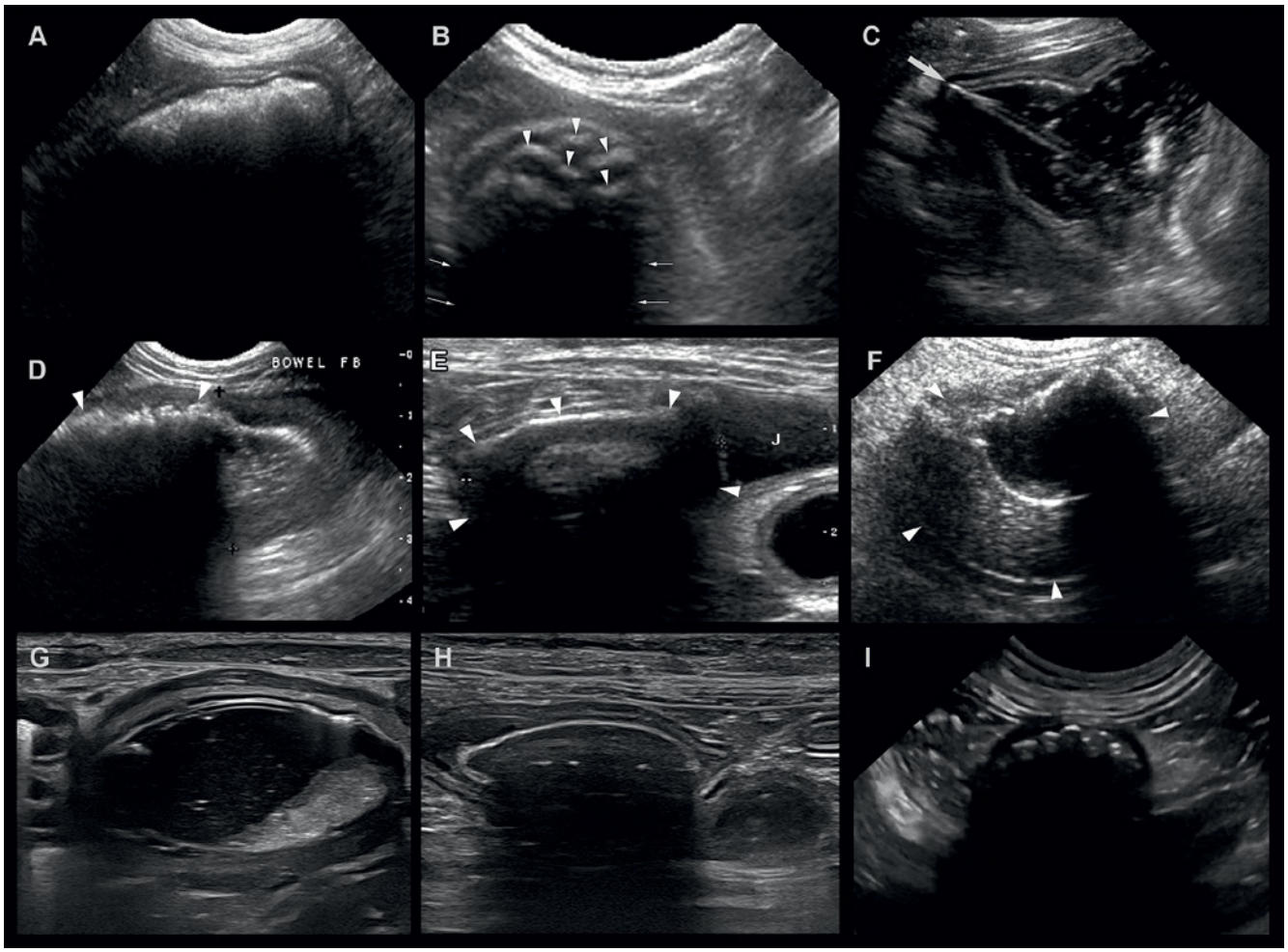


Figure 9.18. **Intestinal foreign bodies.** A wide range of foreign materials can be found in the gastrointestinal tract. Most of them are associated with strong acoustic shadowing. **(A) Trichobezoars** are compact foreign bodies with a bright interface and a uniform and clean acoustic shadow, as seen in the stomach of this long-hair domestic cat. **(B) Elastic bands** in the stomach of a young cat mimic prominent rugal folds (arrowheads). The spacing and the uniform shadowing (arrows) supported the presence of foreign material. **(C)** Several sharp **pine needles** were present in the stomach of a dog. One of them (arrow) penetrates the wall. **(D)** A large piece of **corncob** (arrowheads) is in this dilated and thickened jejunal segment. **(E)** A poorly echogenic object with an echogenic center (arrowheads) is noted in the fluid-dilated jejunum (J) of a cat. A piece of a **plastic toy** was removed surgically. **(F)** A rounded and nearly layered structure (arrowheads) is in a dilated segment of small intestine. At first, this appearance was confused for a thickened bowel segment. At surgery, a large fragment of a **"Kong" toy** was removed. **(G)** A squeaker toy is identified in the stomach; the squeaker is filled with anechoic fluid, making the foreign body predominantly sonolucent except for the thin, smooth, peripheral, hyperechoic plastic wall. **(H)** A discrete, smoothly marginated, hard shadowing foreign body is identified in the jejunum of a cat; a thin, interrupted, linear hyperechogenicity with subtle reverberation is seen bisecting the foreign body. An **almond** was removed at laparotomy. **(I) Peach pit** inside the jejunum of a 6-year-old male Pug, showing a characteristic lobulated contour.

segment. This usually happens following a traumatic event, or previous surgeries. Displaced intestinal segments can then be seen in the thorax, through the diaphragm or abdominal wall, inguinal ring (Figure 9.23), or perineal region. It is useful to evaluate the affected bowel segments for altered layering, integrity of the wall, and vascular deficit using Doppler mode. Mesenteric volvulus refers to an abnormal rotation of the mesenteric root resulting in vascular compression and ischemia of the entrapped intestinal segments. It is important to make the diagnosis quickly as this represents a surgical emergency. On ultrasound, one or several intestinal loops may appear moderately distended with gas and fluid and have thickened walls with altered layering. The extent, severity, and length of time of the volvulus can

Vet-ebooks.com

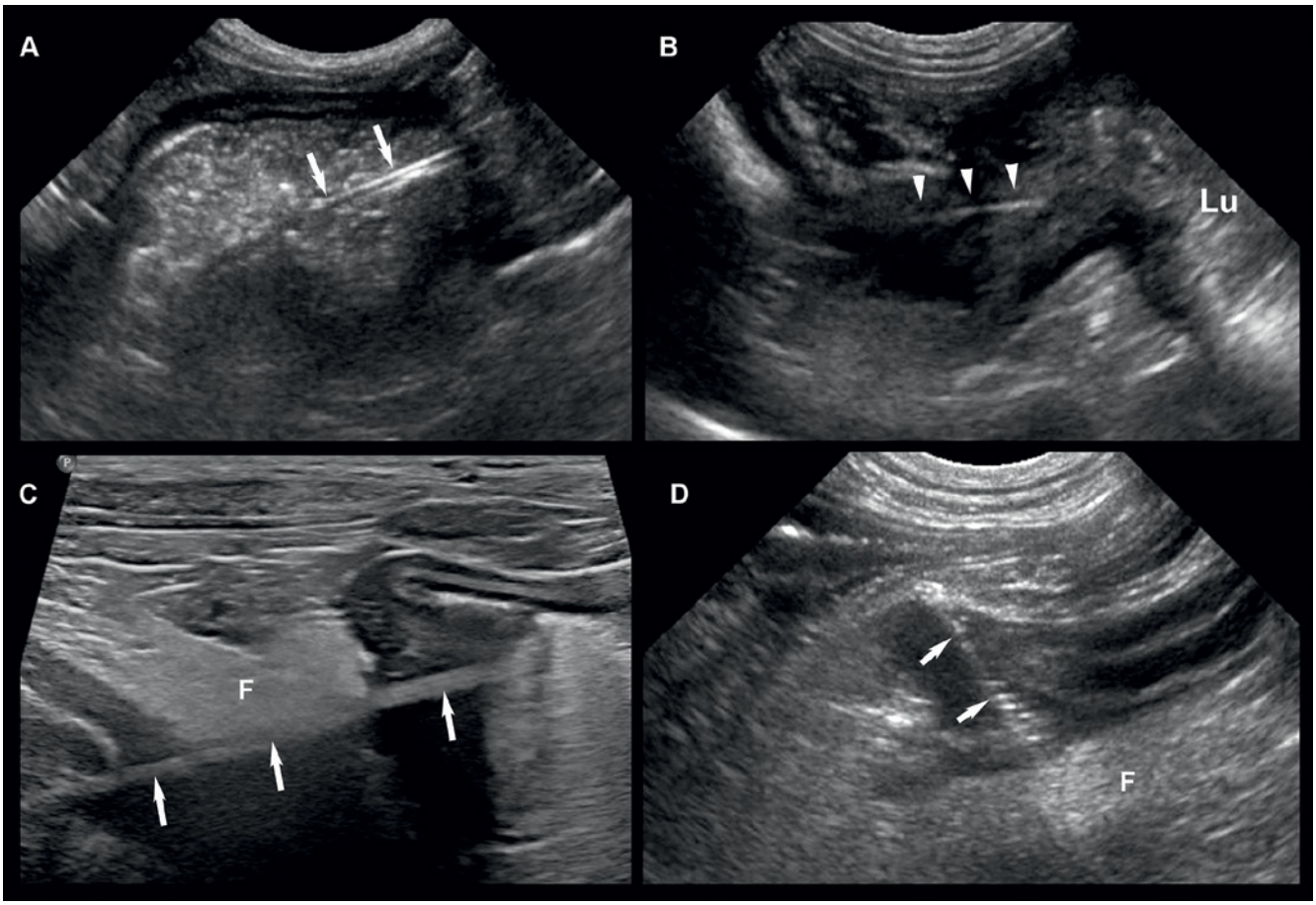


Figure 9.19. **Perforating foreign bodies. (A, B)** Part of a **hard plastic foreign body** (arrows in A) appears as long, linear, bright interfaces anchored within the pylorus (arrowheads in B) of this 4-year-old Boston terrier. In this dog, there was also hypertrophy of the pyloric canal (not well seen on this image). These findings were confirmed at surgery. Lu, gastric lumen. **(C)** A **wooden stick** (arrows) is crossing the gastric wall in an 8-year-old dog. The adjacent fat (F) is hyperechoic, supportive of steatitis. **(D)** A **toothpick** (arrows) is crossing a jejunal segment in this dog without GI signs. Gas bubbles were tracking near the distal point of perforation. The local fat (F) is hyperechoic.

vary but identifying a mechanical obstruction by observing two populations of bowel diameter is key to expedite the surgical correction. With time, compromised intestinal segments are necrotic and sloughing of the mucosa may lead to a thinner intestinal wall and amorphous echogenic contents (Figure 9.24).

Inflammatory Diseases

Wall thickening is a common finding in inflammatory diseases, but this finding is not specific. Symmetry, extent of the wall thickening, and layer identification are useful parameters in distinguishing inflammation from neoplasia (Gaschen 2011; Penninck et al. 2003). Inflammation is usually characterized by extensive and symmetrical wall thickening with preserved layering. However, depending on the severity of the inflammation and the presence of wall edema or hemorrhage, layering can be altered as seen by a change in echogenicity or relative thickness of one or more layers.

In **gastritis**, diffuse or localized wall thickening with decreased motility can be identified. Commonly, the stomach is collapsed during the ultrasound evaluation, limiting accurate assessment of the wall thickness. In severe gastritis, the wall thickening can be associated with increased echogenicity or decreased visualization of the wall layers (Figure 9.25).

Gastric **ulcers** may be identified as discrete, mucosal defects outlined by hyperechoic gas bubbles accumulated at the crater site (Figure 9.26). Hyperechoic speckles representing gas can also be observed in the affected wall. Fluid accumulation and decreased gastric motility are common findings in ulcerative disease (Penninck et al. 1997). Ulcers can be seen in both inflammatory and neoplastic diseases. As there is

Vet-ebooks.com

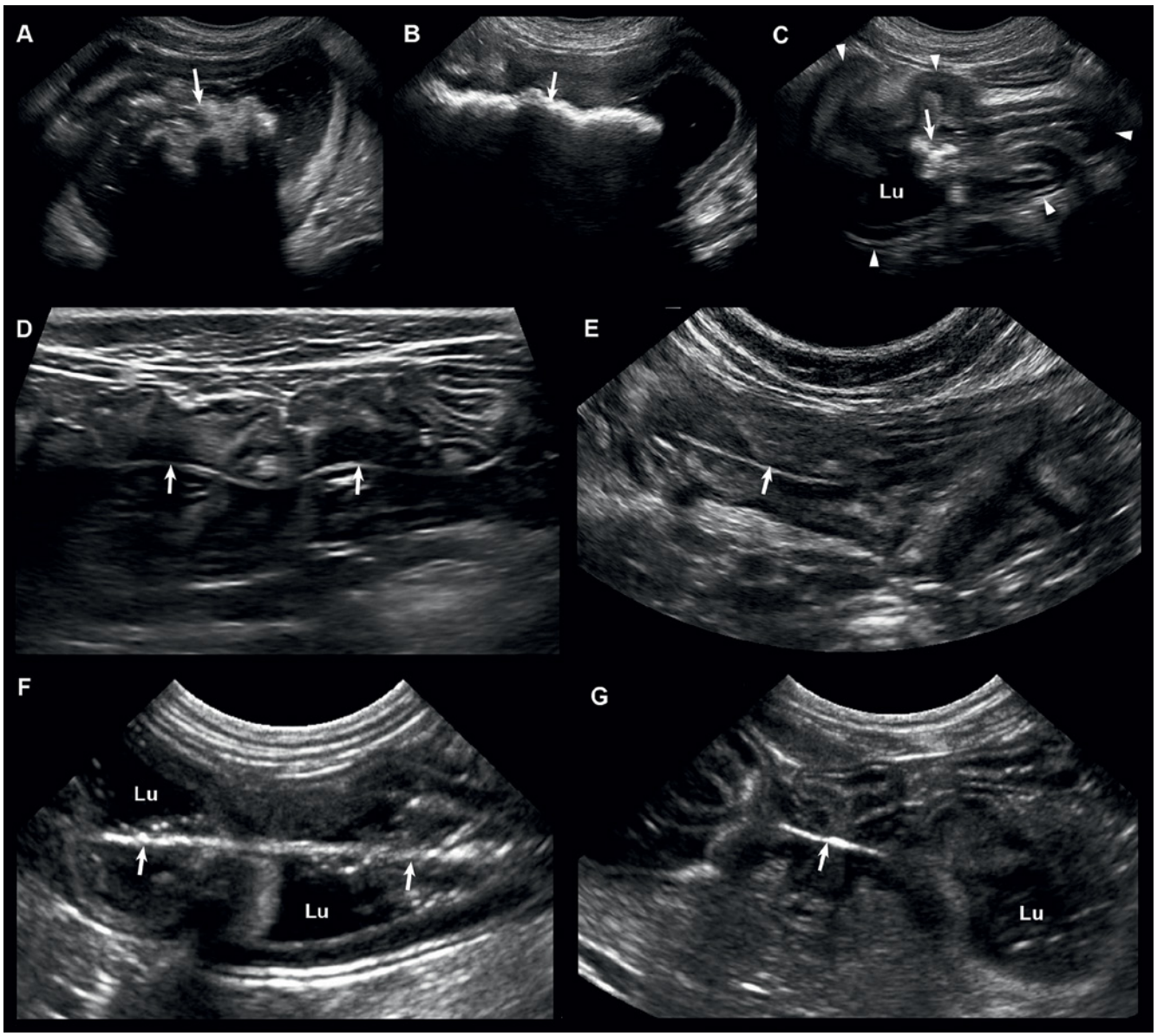


Figure 9.20. **Linear foreign bodies in two dogs and one cat. (A)** Foreign material (arrows) associated with strong shadowing is present in the stomach of this 3-year-old English Bulldog. **(B)** The content extends into the descending duodenum. **(C)** Numerous plicated jejunal loops (arrowheads) are seen on each side of the lumen (Lu). **(D, E)** In a cat with a thin linear foreign body (arrows) extending into the small intestine, severely plicated bowel pattern is seen. **(F, G)** In an 11-year-old Irish setter, extensive duodenal and jejunal plication was noted due to a string (arrows). Lu, intestinal lumen.

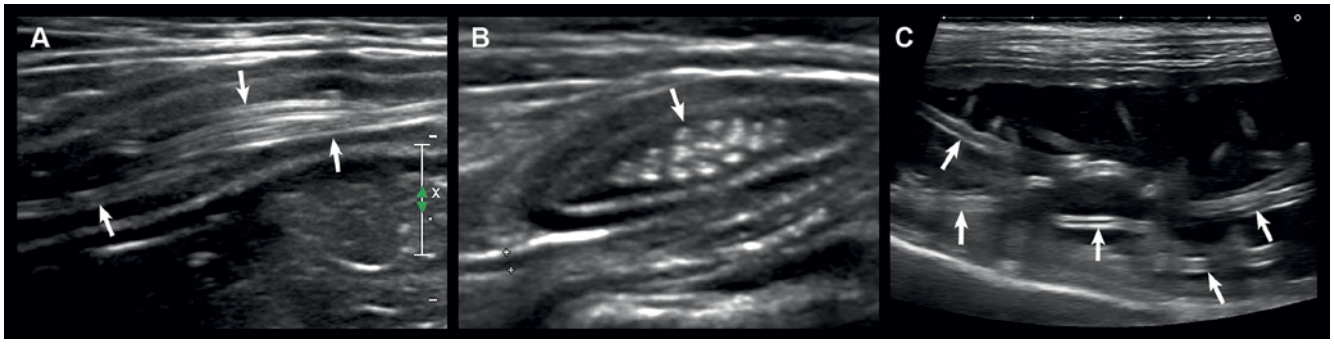


Figure 9.21. **Intestinal worms.** Numerous tubular structures were present in the lumen of the intestinal tract of this 5-month-old kitten. **(A)** Longitudinal view of the descending duodenum with altered layering (thickened muscular layer) and several (arrows) worms in its lumen. **(B)** Oblique view of an intestinal segment showing several worms in the transverse plane. **(C)** Distended jejunal segment filled with fluid and numerous roundworms (arrows) in this 10-year-old Beagle with chronic IBD.

Vet-ebooks.com

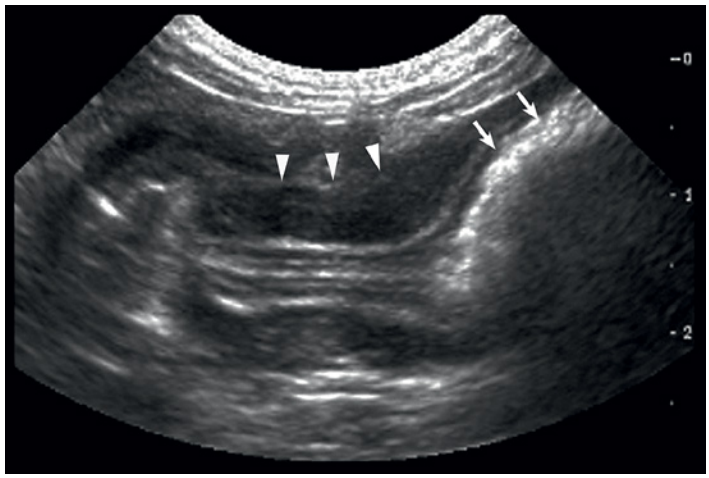


Figure 9.22. Partially obstructive intestinal adenocarcinoma. Foreign material (arrows) accumulated proximal to the focally thickened (arrowheads) jejunal segment. Surgical resection was performed, and the histopathological diagnosis was adenocarcinoma.

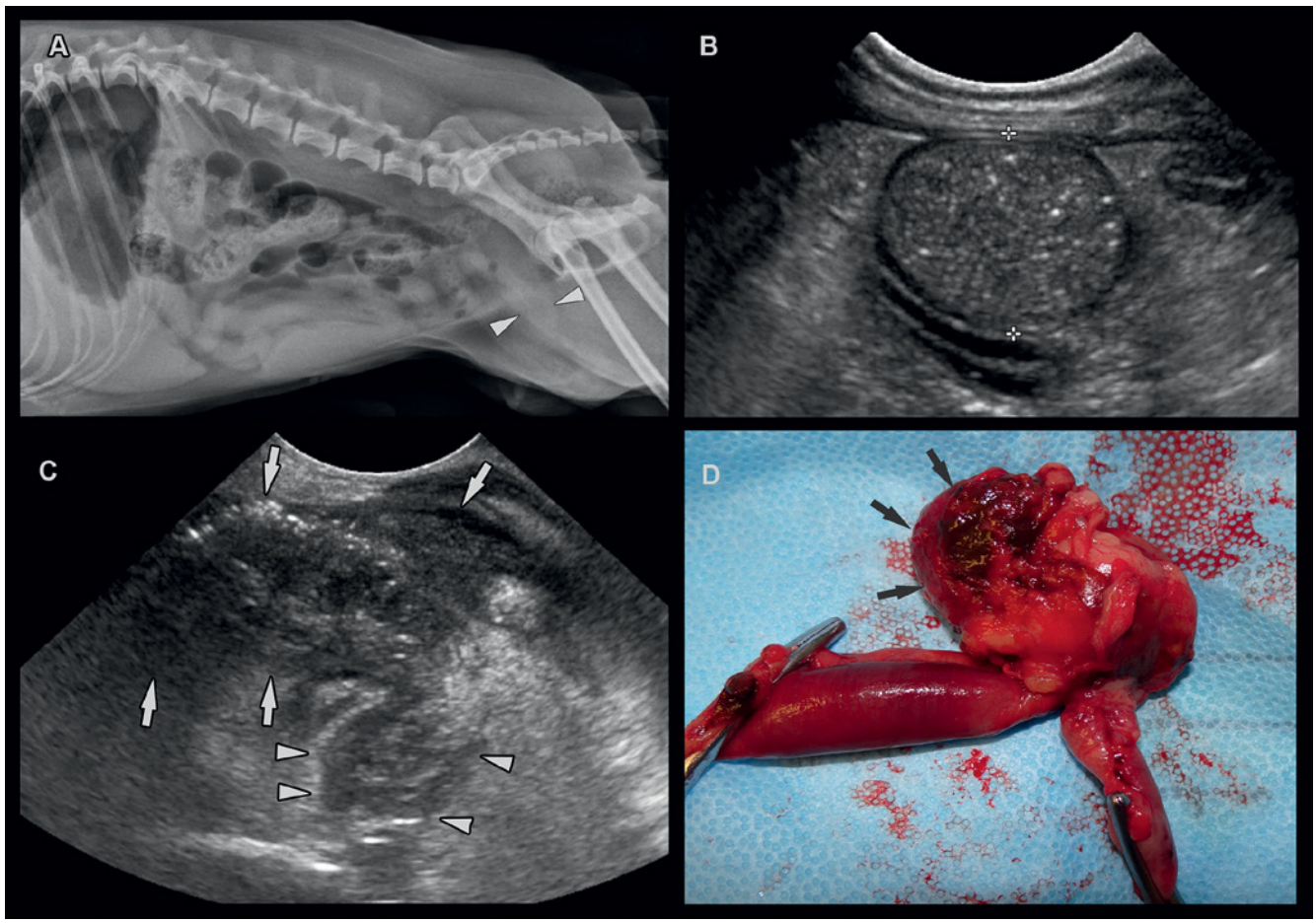


Figure 9.23. Jejunal segment herniation in an 11-year-old Pomeranian dog with an inguinal swelling. **(A)** Lateral radiograph showed subtle increased opacity in the caudo-ventral abdomen, with a tubular structure superimposed to the inguinal region (arrowheads). **(B)** A dilated jejunal segment (between cursors) compared to an adjacent segment located dorsally to it. **(C)** In the inguinal swelling, the dilated jejunal segment (arrowheads) appears in continuity with an enlarged structure suspected to represent a necrotic intestinal segment (arrows). The peripheral fat is hyperechoic. **(D)** Surgical specimen of the resected jejunal segment found in the inguinal hernia. The wall was confirmed to be necrotic and friable. Intestinal contents leaked into the hernia.

Vet-ebooks.com

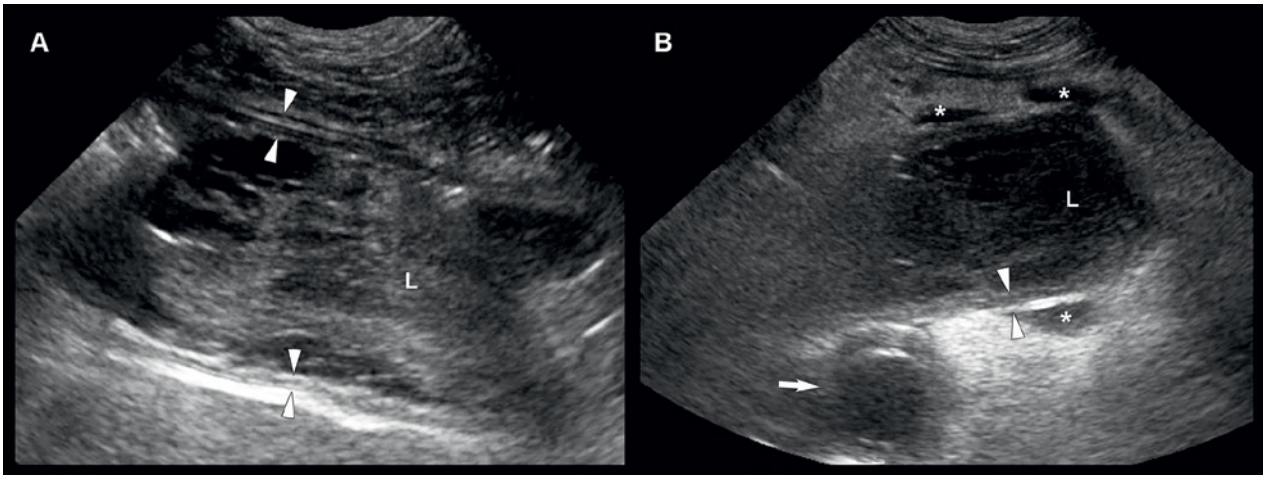


Figure 9.24. **Mesenteric rent and volvulus in a 5-year-old Labrador dog presented for acute vomiting and abdominal pain.** **(A)** Sagittal sonogram of one of several distended jejunal loops. It contains amorphous echogenic fluid in the lumen (L) and the wall (arrowheads) is thin (less than 2 mm at some locations). **(B)** The fat surrounding the bowel loops is hyperechoic, limiting the visualization of the affected intestines. Moderate echogenic effusion (*) is present in the abdomen. A mesenteric volvulus due to a mesenteric rent was diagnosed at surgery and the resected jejunal loops were confirmed to be necrotic and hemorrhagic on histopathological evaluation.

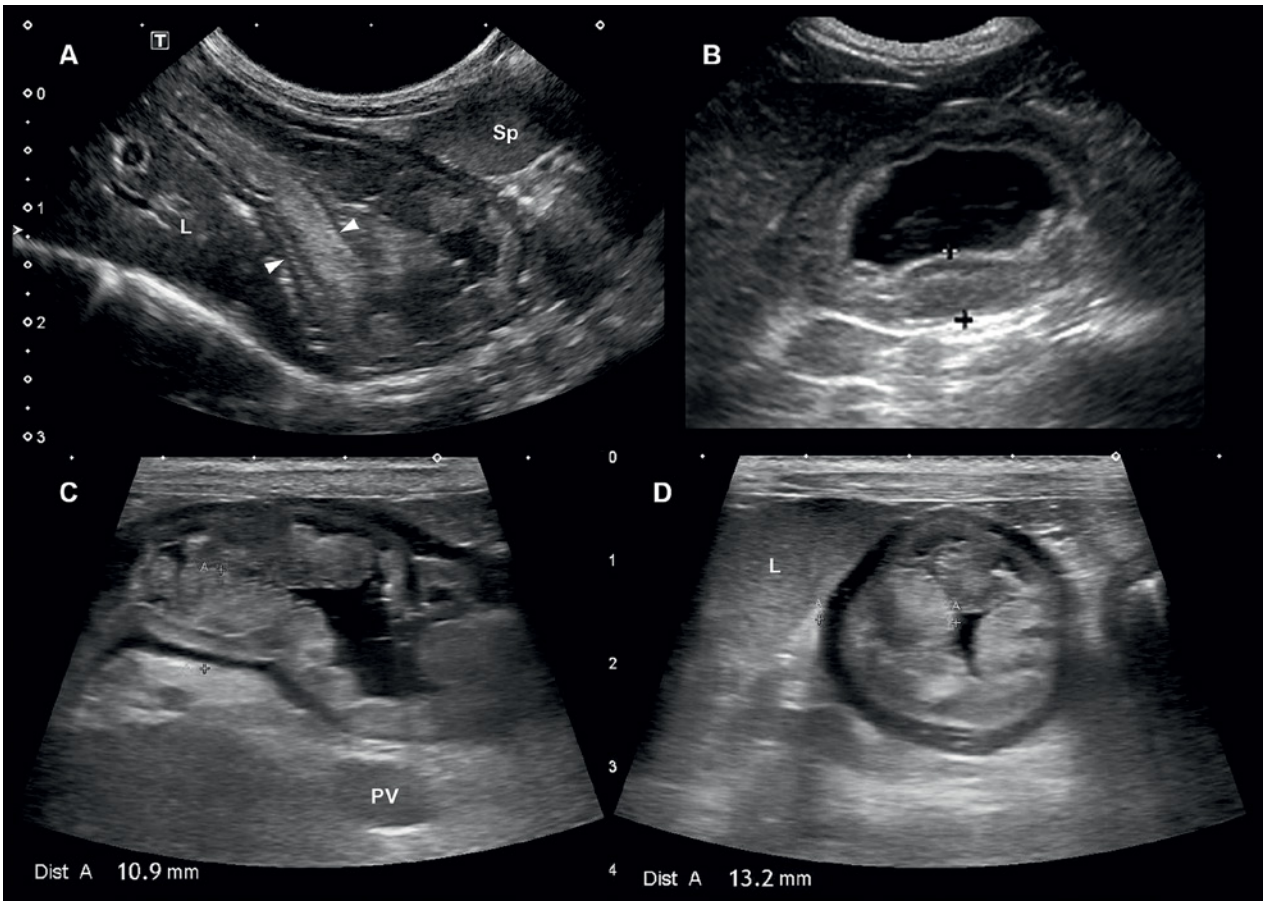


Figure 9.25. **Gastritis.** **(A)** In this 4-year-old Lhasa Apso with acute vomiting, the stomach is mildly dilated with fluid and shows a thickened wall (arrowheads) and a hyperechoic mucosa. These signs resolved on follow-up examination 1 week later. **(B)** A moderately thickened (8 mm, between cursors) and hyperechoic wall is noted in this 1-year-old cat with severe chronic ulcerative gastritis. **(C, D)** Longitudinal **(C)** and transverse **(D)** images of the gastric body of a 5-year-old, small mixed-breed dog with chronic vomiting. The wall (between cursors) and more specifically the gastric mucosa are markedly thickened and hyperechoic, forming almost polypoid projections into the gastric lumen. Endoscopic biopsies confirmed severe lymphocytic gastritis with mucosal hyperplasia. L, liver; PV, portal vein; Sp, spleen.

Vet-ebooks.com

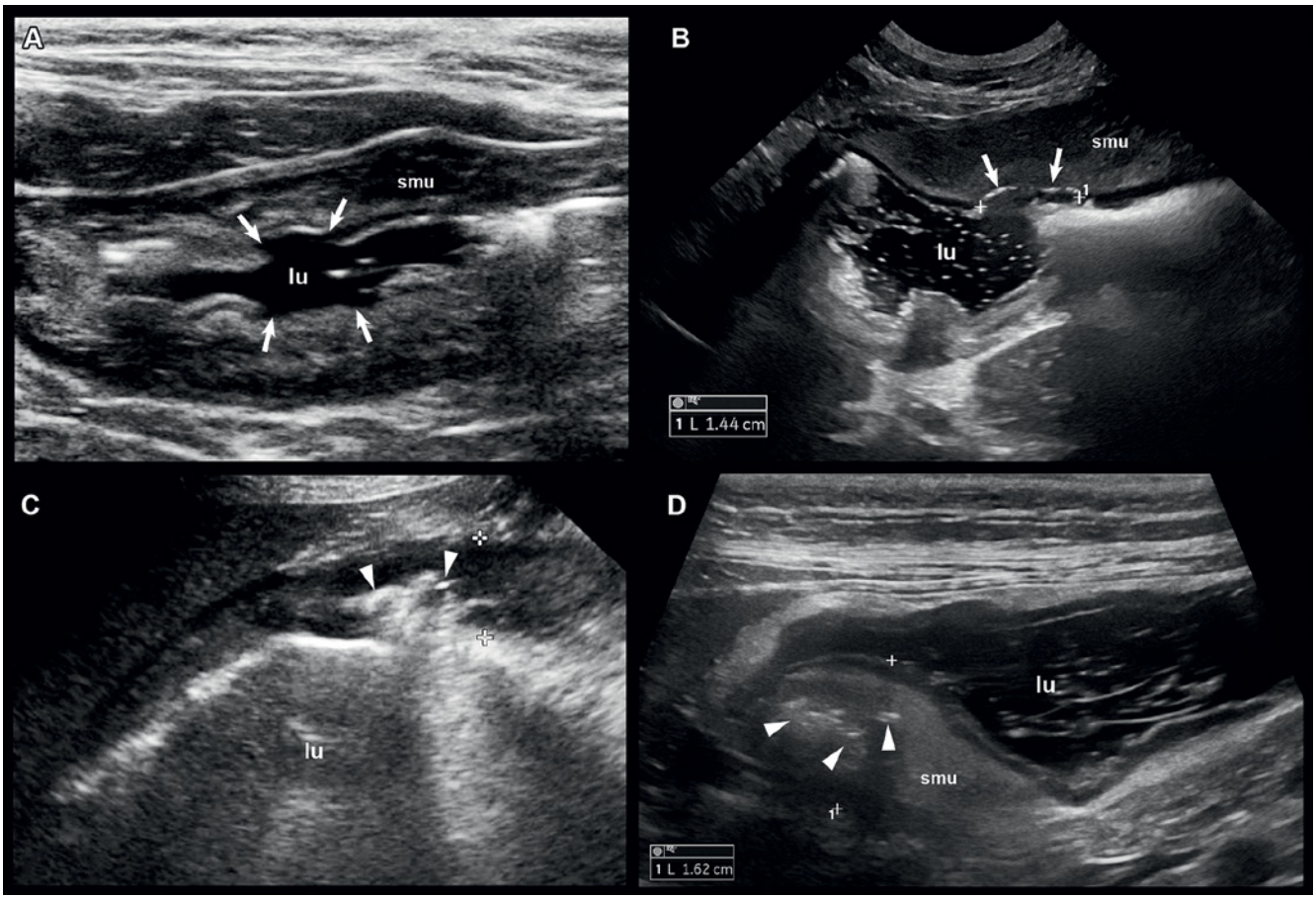


Figure 9.26. **Gastric ulcers. (A)** Sagittal sonogram of the stomach of a Siamese cross with an extensive gastric ulcer and submucosal (smu) edema. A small amount of echogenic fluid is seen in the gastric lumen (lu). The wall is thickened and there are well-demarcated interruptions of the mucosal layer, on its side of the lumen, consistent with ulcers (arrow). **(B)** In this 2-year-old Labrador retriever, the stomach is mildly dilated with gas and fluid, delineating an irregular mucosa that is eroded in multiple areas, with a larger crater-like lesion (arrows) that reaches the submucosa (smu) and is consistent with an ulcer. Lu, lumen. **(C)** Hyperechoic speckles (arrowheads), consistent with gas, are found in the thickened wall of this dog with uremic gastritis and ulcerations. The layers are ill-defined. The edematous wall opposite to the ulceration reaches 1.6 cm in thickness (between the cursors). **(D)** In this 12-year-old domestic shorthair cat presented for acute vomiting, the gastric wall is markedly thickened (1.6 cm), mainly affecting the submucosa (smu) that also presents several hyperechoic speckles (arrowheads) consistent with gas. Several mucosal ulcers (not seen on this image) were present in nearby areas of the wall. Lu, lumen.

often marked focal thickening with loss of layering, the underlying disorder cannot be characterized reliably.

Gastric edema, which is commonly associated with underlying inflammation and ulceration, appears as extensive and moderate thickening with altered layering. The thin inner mucosal hypoechoic to anechoic layer borders the remaining loosely striated wall (Figure 9.27). Because of the degree of thickening and the disrupted layering, this condition can easily be mistaken for a tumor. Gastric edema is also encountered in the presence of pancreatitis (Figure 9.27); when secondary to pancreatitis, gastric edema is often regional/segmental and adjacent to the affected pancreatic parenchyma; the submucosal layer is most affected, and sometimes multifocal small anechoic fluid pockets can be identified, creating a lacey appearance; the muscularis layer may also be thickened (Murakami et al. 2019). Gastric edema was detected in approximately 21% of dogs with hypoalbuminemia in one study (Murakami et al. 2020). Gastric edema can also result from local or more diffuse vascular impairment such as hypotension (Figure 9.27C) or cardiac failure.

Uremic gastropathy can be seen in patients with chronic uremia. The ultrasonographic features are a moderately thickened gastric wall with prominent rugal folds and a thin hyperechoic line at the mucosal–luminal interface secondary to mineralization of the mucosa (Grooters et al. 1994) (Figure 9.28).

Vet-ebooks.com

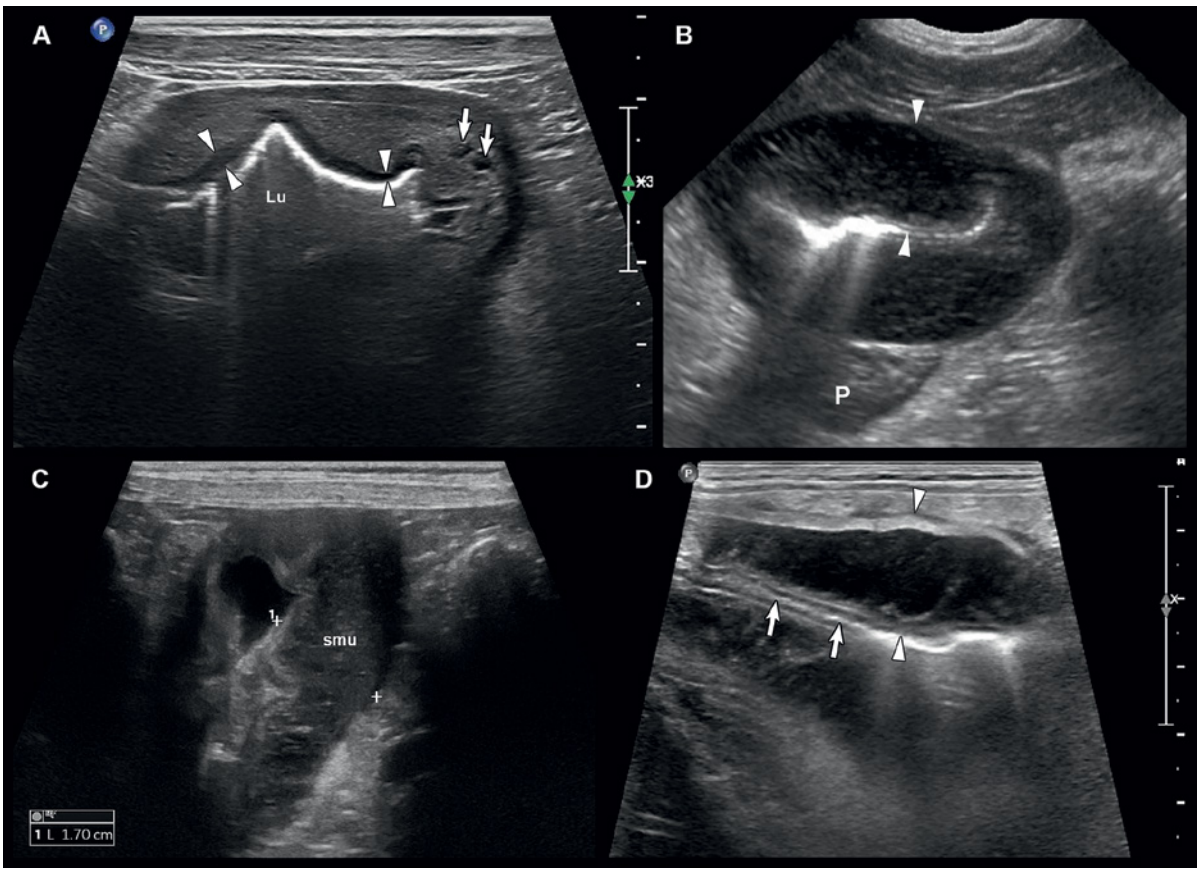


Figure 9.27. **Gastric edema in four dogs. (A)** Transverse sonogram of the pylorus of an 8-year-old Beagle cross with gastritis with erosions that resolved over time. The gastric wall is moderately thickened, and the wall layering is altered, but a hypoechoic band representing the mucosa can be seen (arrowheads). Small anechoic cyst-like (arrows) changes are noted in the submucosa. Gas and a small amount of fluid are in the gastric lumen (Lu). **(B)** Transverse sonogram of the moderately thickened and edematous gastric wall (arrowheads) of a 5-year-old Cocker with anuric renal failure. Hyperechoic foci associated with a mixture of shadowing and reverberation are present in the lumen. P, pancreas. **(C)** This 8-year-old spayed female Dachshund had a recent surgery for disc extrusion and was severely hypotensive and vomiting intensely, including mucosal fragments. On ultrasound, the gastric wall is severely thickened (up to 1.7 cm), with altered layers. The submucosa (smu) is variably thickened and hypoechoic with a granular appearance in some areas. **(D)** In this 6-year-old Jack Russell terrier cross with leptospirosis, the gastric wall is markedly thickened (arrows) and nearly anechoic with faint striations. The thin mucosa is seen on each side of the collapsed lumen (arrowhead) containing a small amount of gas.

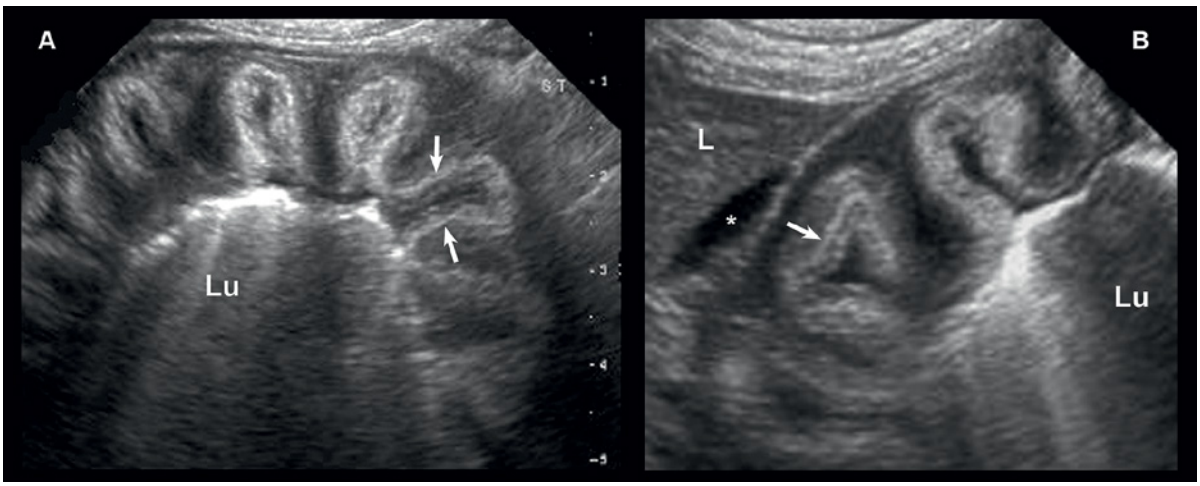


Figure 9.28. **Uremic gastropathy. (A)** Uremic gastropathy is seen in dogs or cats suffering from chronic uremia. Thickening of the wall with a hyperechoic line (arrows) along the gastric mucosa and mineralization at the mucosal–luminal interface are common findings. **(B)** An enlarged view of the gastric wall changes. A scant amount of effusion (*) is present between the liver and stomach. L, liver; Lu, lumen.

Vet-ebooks.com

Common **intestinal inflammatory diseases** (IBDs) are associated with mild to moderate wall thickening that most commonly affects several or all intestinal segments with a variable degree of severity (Rudorf et al. 2005). Other intestinal disorders to keep in mind include eosinophilic enteritis, granulomatous enteritis, lymphangiectasia, and food allergies. In these disorders, mild to moderate wall thickening can affect primarily the mucosa, the submucosa, and/or the muscular layer. In the mucosa, the changes can be diffuse increased echogenicity of the mucosa, echogenic mucosal speckles, hyperechoic striations, or a hyperechoic line paralleling the lumen. Increased mucosal echogenicity and mucosal speckles have been described in lymphocytic–plasmacytic enteritis (Baez et al. 1999; Penninck et al. 2003; Gashen et al. 2008, 2016). However, mucosal speckles can also be encountered in dogs recently fed; in these cases, the speckles disappear at the end of digestion (Figure 9.29) and postprandial changes of the mucosal layer can vary (Gaschen et al. 2016). In some cases, a discrete hyperechoic border is noted on the luminal margin of the mucosa; this finding has been described as likely representing the intestinal villi portion of the mucosa and at times has anecdotally resolved in dogs initially presented for acute GI signs (Figure 9.30B) (Leroux et al. 2016). Also, Peyer's patches in the descending duodenum may become prominent in dogs with transient GI signs (Figure 9.6). A hyperechoic line of variable thickness present within the mucosa can often be encountered with the newer high-resolution transducers; this line has been reported to represent

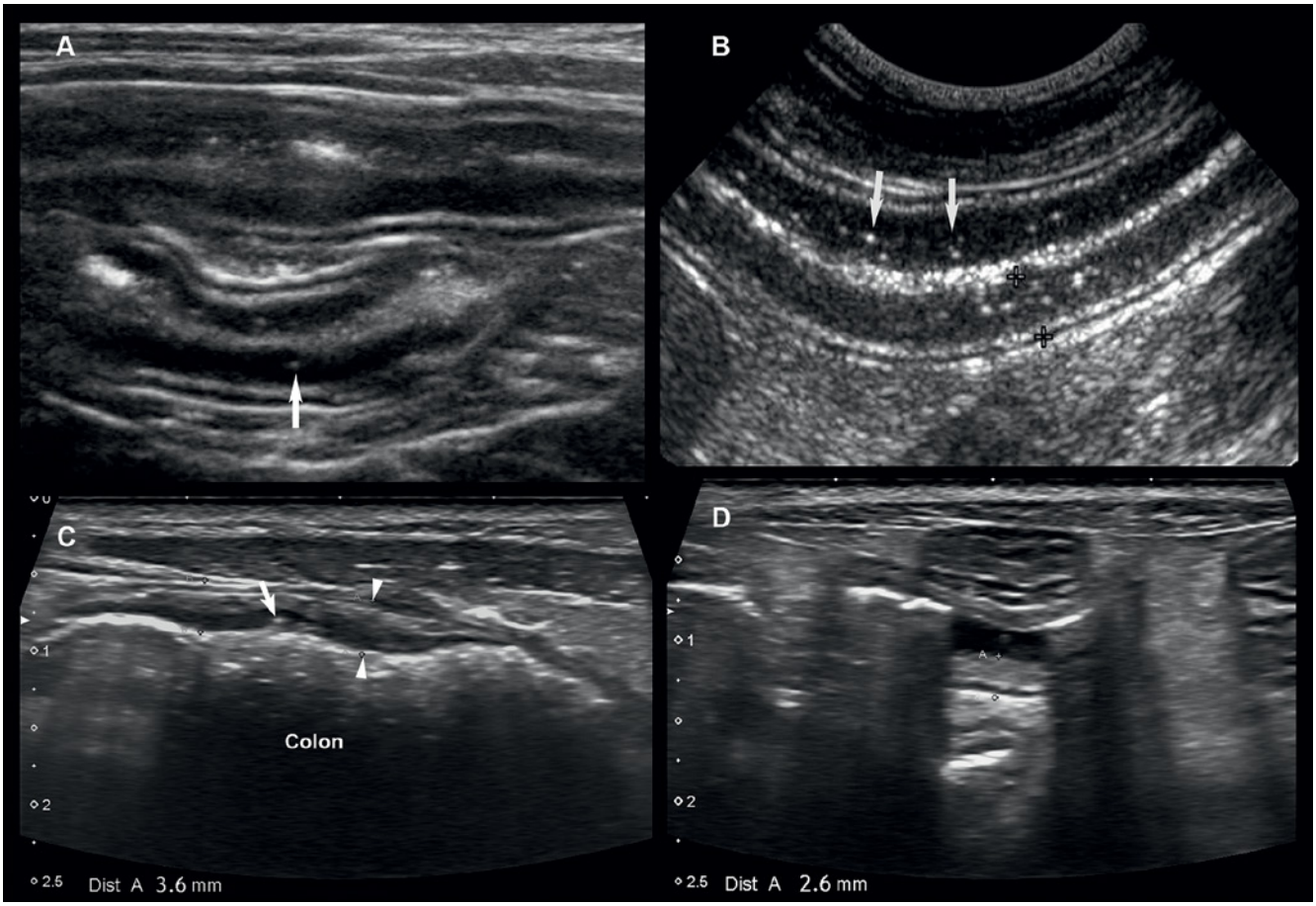


Figure 9.29. **Mucosal changes. (A)** Hyperechoic speckles (arrow) are seen along the luminal side of the intestinal mucosa and represent post-prandial changes in this dog that ate 2 hours prior the evaluation. **(B)** A couple of hours later, mucosal speckles are present in several small intestines while they were absent on the preprandial evaluation. **(C)** Longitudinal sonogram of the descending colon of a small mixed-breed dog with ulcerative colitis. The wall is variably thickened (arrowheads) and several erosions and ulcers were detected. The arrow points to a speckle inside the eroded mucosa consistent with gas or mucus. **(D)** In a cat with acute enteritis, several intestinal segments were thickened, hypermotile, and partially fluid filled. The wall layers were visible, but the mucosa appeared hyperechoic.

Vet-ebooks.com

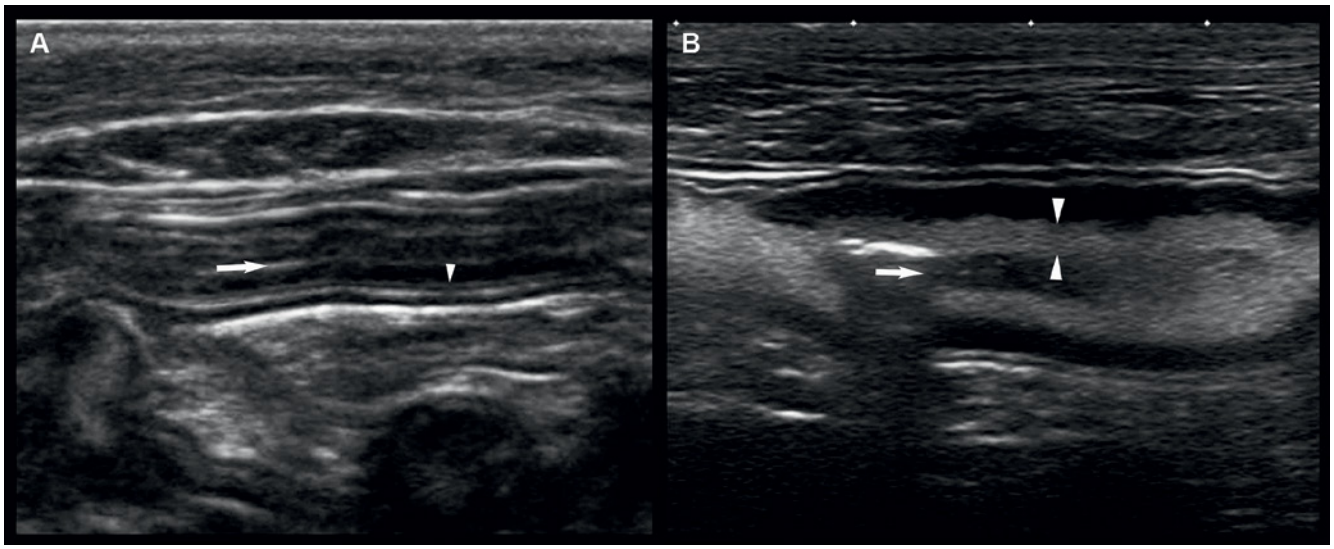


Figure 9.30. **Mucosal line parallel to the lumen. (A)** A fine hyperechoic line (arrowhead) near the submucosa is paralleling the lumen (arrow) of this jejunal segment in a cat without gastrointestinal signs. This line likely represents fibrosis. **(B)** A thick hyperechoic band (arrowheads) is noted on the luminal side of the mucosa of several jejunal segments in this dog presented for acute vomiting and diarrhea. On the ultrasound recheck performed several weeks later, the band was no longer visible. The arrow points to the lumen.

fibrosis, which may or may not be associated with concurrent inflammatory condition (Penninck et al. 2010) (Figure 9.30A). The possibility of this line to represent visible lymphatic vessels has also been presented (Pollard et al. 2013).

Hyperechoic striations within the mucosa and aligned perpendicularly to the lumen axis most likely represent dilated lacteals (Figure 9.31). This finding is commonly associated with **protein-losing enteropathy** and **lymphangiectasia**, and occasionally this pattern was reported in dogs with diffusely infiltrative tumors such as histiocytic sarcoma (Sutherland-Smith et al. 2007).

Primary submucosal thickening can be seen in various inflammatory disorders but can be especially pronounced in parasitic infections (Kvitko-White et al. 2011). Parasites such as *Heterobilharzia americana* can affect dogs but the infestation may be subclinical (Figure 9.32).

Smooth muscle thickening is reported in **eosinophilic enteritis**, particularly in cats (Tucker et al. 2014), but this finding is not specific and can be present in other disorders, such as mechanical obstruction secondary to foreign material, IBD, or tumoral infiltration such as round cell neoplasia (Diana et al. 2003; Penninck 2002; Zwingenberger et al. 2010) (Figure 9.33).

Common GI findings in puppies with canine **parvoviral enteritis** include a fluid luminal pattern, hypomotility to atony, duodenal and jejunal mucosal layer thinning and hyperechogenicity (Figure 9.34A, B) with variable speckling and striation, normal to increased overall small intestinal mural thickness and segmental corrugation (Stander et al. 2010).

The most frequent intestinal changes appreciated in cats with **feline panleukopenia enteritis** include diffuse thinning and hyperechogenicity of the small intestinal mucosal layer, irregularity of the mucosal margins, and thickening of the muscularis layer (Isaya et al. 2021) (Figure 9.34C–D).

In **hemorrhagic enterocolitis**, unlike most of the inflammatory disorders we just described, there is thinning of the wall, as the combined result of atonic, fluid-filled intestinal segments, and sloughing of the mucosa (Figure 9.35).

Corrugation of the small bowel appears as regular and symmetrical undulations of the wall, but the serosa remains relatively linear (Figure 9.36). This nonspecific finding can be associated with regional inflammation such as enteritis, pancreatitis, peritonitis, abdominal neoplasia, or bowel ischemia (Moon et al. 2003). This should not be mistaken for intestinal plication that causes asymmetrical undulation of bowel walls (see Figure 9.20).

In cases of severe inflammatory changes encountered with lymphoplasmacytic, eosinophilic, or granulomatous enteritis (fungal, parasitic, or post-traumatic), edema, hemorrhage, and fibrosis can severely disrupt the wall layering and be associated with mass lesions suggestive of a tumoral process (see Section on Non-tumoral Mass).

Vet-ebooks.com

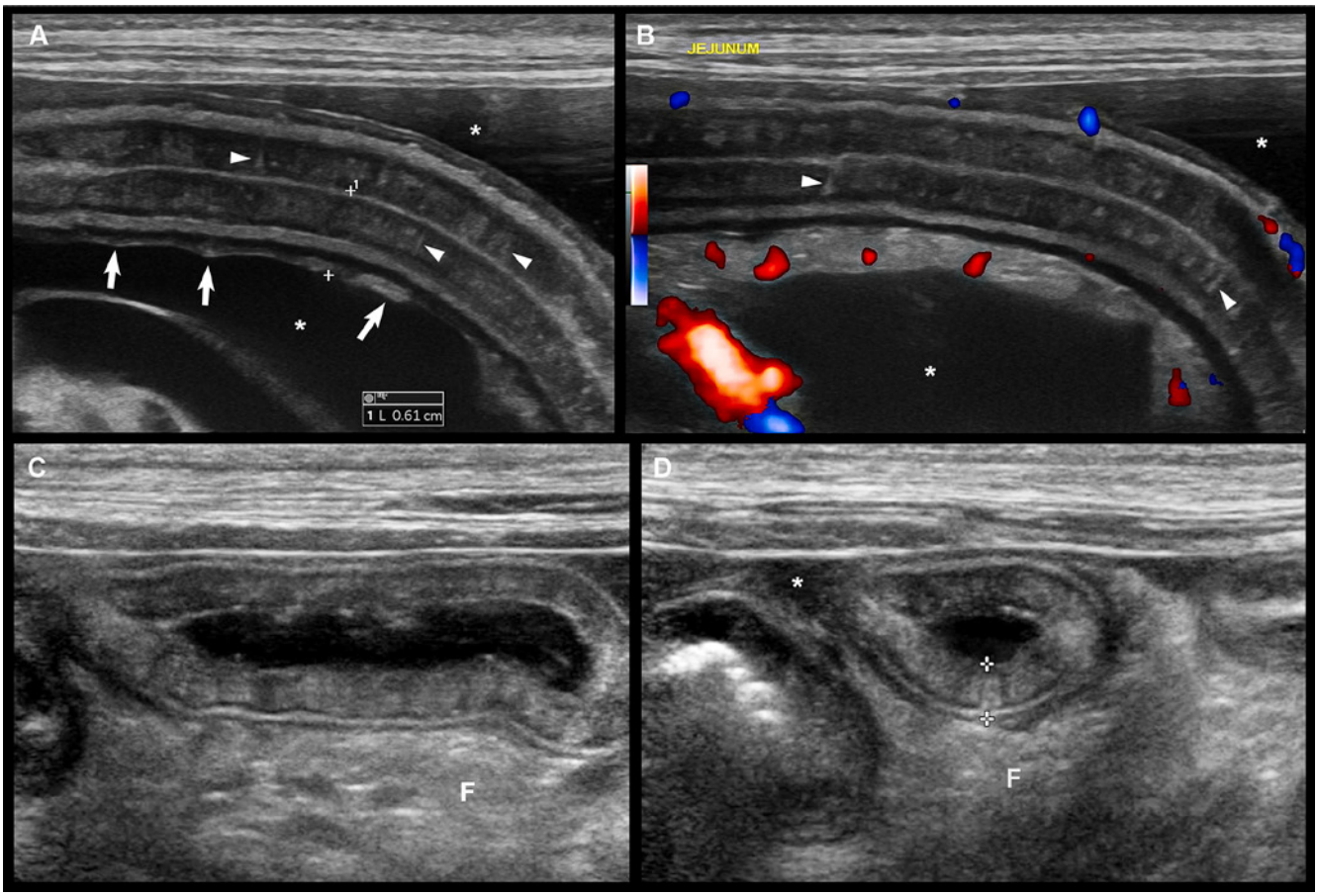


Figure 9.31. **Mucosal hyperechoic striations.** Longitudinal B-mode **(A)** and color-Doppler **(B)** sonograms of a thickened jejunal segment with ill-defined hyperechoic foci and linear striations (arrowheads) within the mucosal layer of a 10-year-old American Bulldog with **lymphangiectasia** and **IBD**. Note the irregular thickening of the muscularis and serosal layers (arrows in **A**) and the increased perfusion of the periphery of the bowel (in **B**). Severe peritoneal effusion is present (*). **(C, D)** The mucosal changes are more diffuse in this 9-year-old Jack Russell terrier presented with **protein-losing enteropathy**. Note the thickened and hyperechoic adjacent fat (F), often present in these cases.

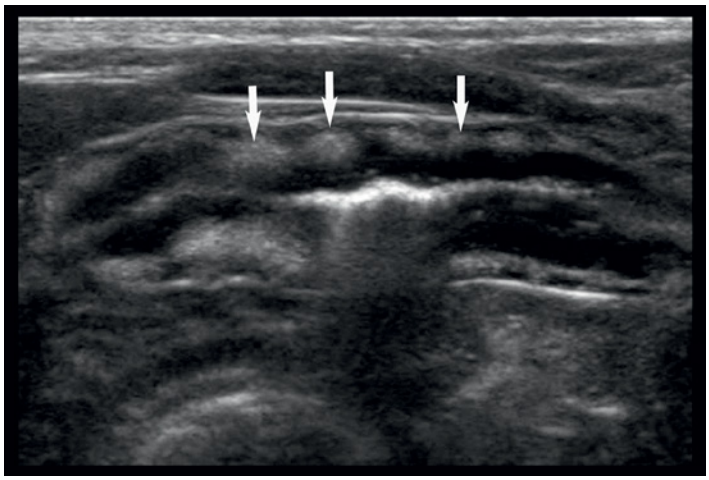


Figure 9.32. **Submucosal change.** There is nodular thickening of the submucosa (arrows) of most intestinal loops in this Dachshund with **parasitic infestation** (*Heterobilharzia Americana*). The dog had no clinical signs.

Vet-ebooks.com

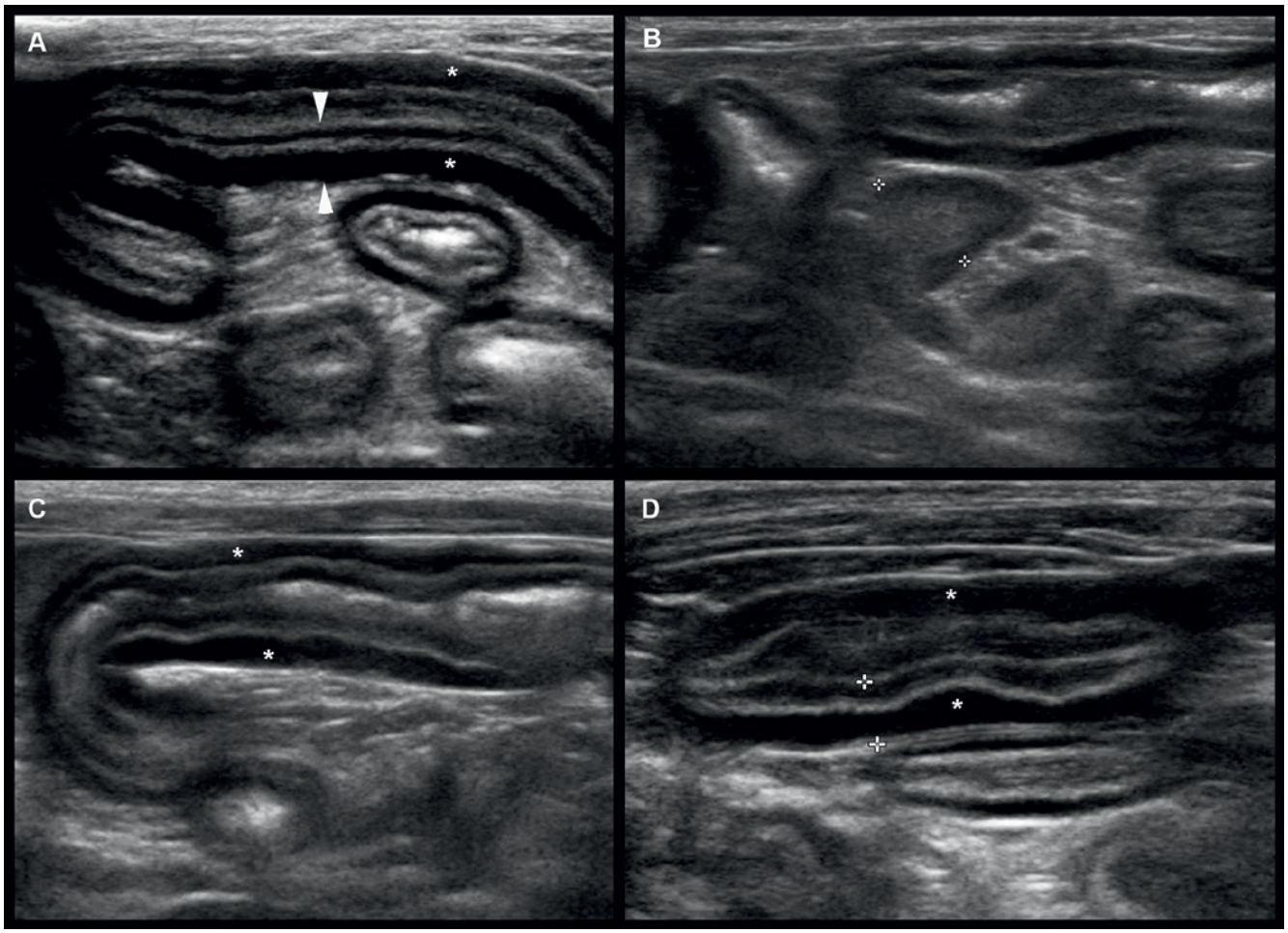


Figure 9.33. **Intestinal wall muscular thickening. (A, B)** 5-year-old cat with **marked lymphoplasmacytic enteritis**. The intestinal wall is thickened (3.5 mm, arrowheads), especially the muscular layer (*). The jejunal lymph nodes are mildly enlarged (7 mm, between cursors). **(C, D)** An 8-year-old cat with a jejunal mass confirmed to represent **feline eosinophilic sclerosing fibroplasia** (see Figure 8.68B). Numerous thickened (arrowheads) intestinal segments have hypertrophic muscular layers (*) of variable thickness. Notice the slight variation in the appearance of the mucosa and submucosa in jejunal loops seen in **(C, D)**.

Inflammation, such as pancreatitis and duodenitis, can also be caused by regional extension of affected adjacent tissue (Figure 9.37).

Cecal inflammation called **typhlitis** appears as poorly echogenic or nodular thickening of the cecal wall (Taeymans et al. 2011) (Figure 9.38). Ultrasound recheck is helpful in assessing response to treatment, especially as these changes may be similar in round cell infiltrates.

Colonic inflammatory changes may be subtle such as mild thickening of the wall with the presence of discrete small submucosal hypoechoic nodules that are speculated to represent intraparietal reactive lymphoid follicles (Citi et al. 2013) (Figure 9.6). Redundancy of the folds resulting in wall thickening but still visible wall layering may represent wall edema (Figure 9.39). In **ulcerative colitis**, the luminal mucosal border is irregular because of the numerous small superficial ulcers affecting the mucosa (Figure 9.39E, F).

Gas dissection within the wall, or **pneumatosis**, can be seen at any segment of the GI tract. This finding is of unclear clinical significance, and in the presence of GI clinical signs, the authors recommend following up on the changes that usually resolve within 1 month (Figure 9.40).

Parasitic infestations such as peritoneal cestodiasis are rare. Cystic subserosal lesions have been described

Vet-ebooks.com

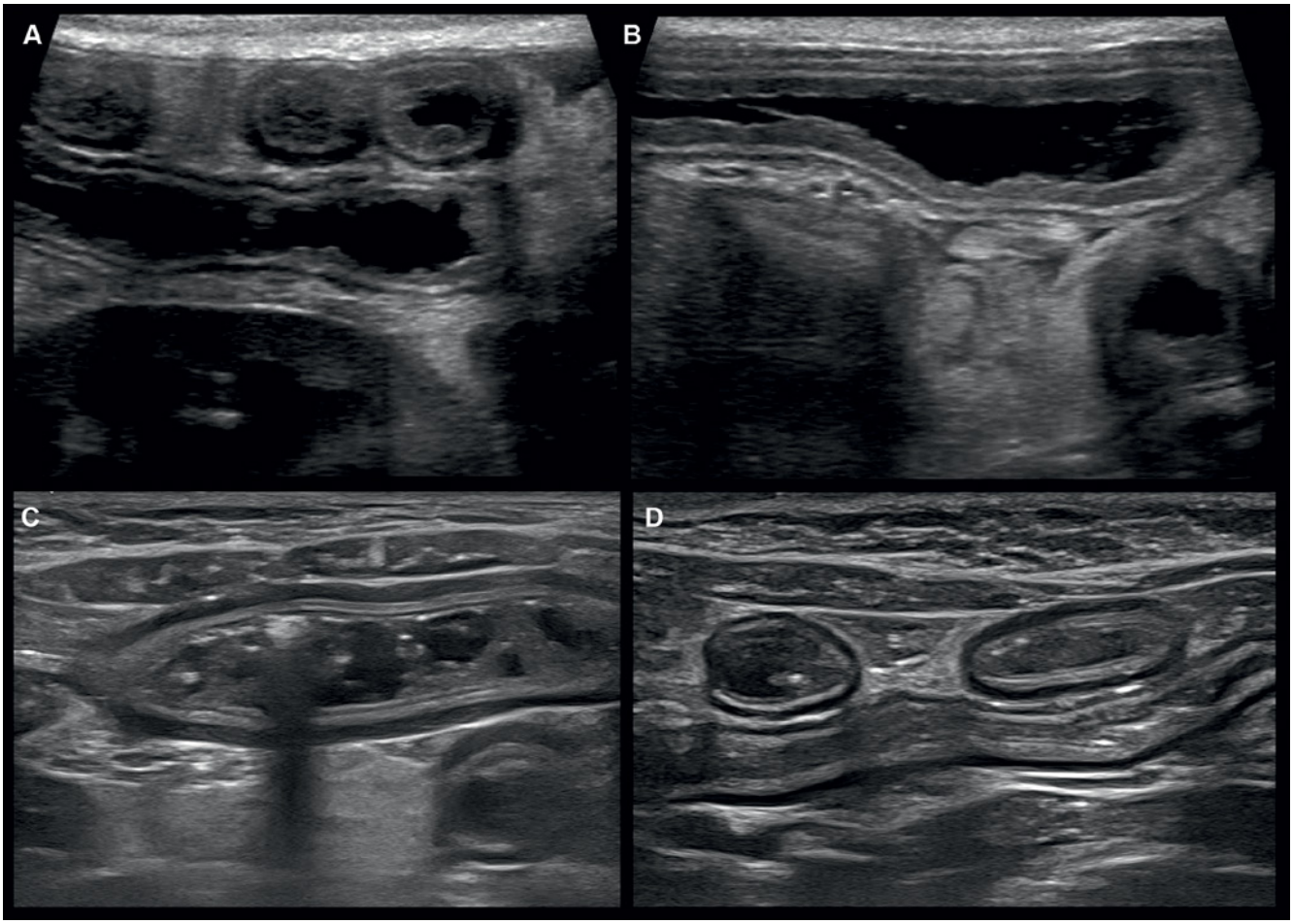


Figure 9.34. **Viral enteritis in a dog and a cat. (A, B)** Sonograms of a 3-month-old Chow cross presented with lethargy, vomiting, and diarrhea. Most intestinal segments were fluid-filled **(A)** with thin walls, while some of them had a hyperechoic mucosa **(B)**. **(C, D)** Sonograms of a 3-month-old domestic shorthair presented with lethargy and vomiting associated with panleukopenia. There is diffuse intestinal fluid accumulation with functional ileus and altered wall layering characterized by mucosal hyperechogenicity, mucosal thinning, and thickening of the muscularis layer.

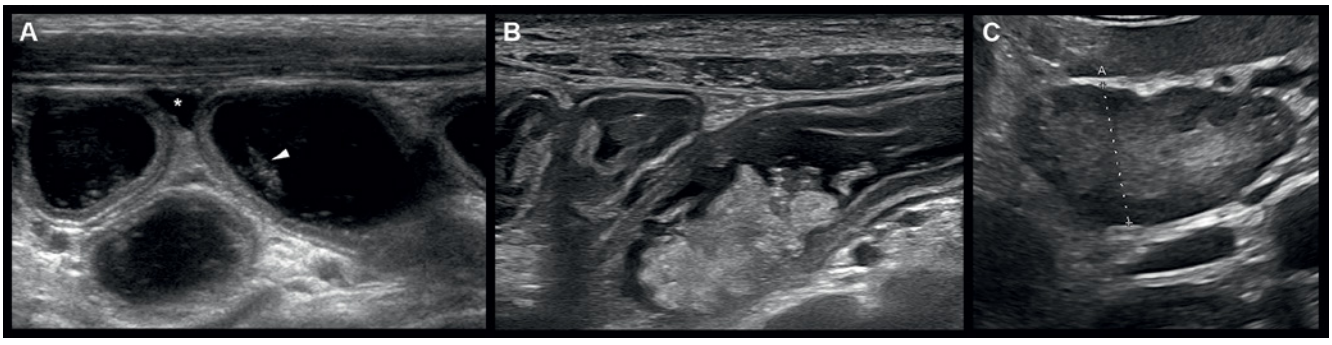


Figure 9.35. **(A) Hemorrhagic enterocolitis in an 8-month-old English Pointer with acute abdominal pain.** The jejunal segments are fluid filled, atonic and the wall thickness is 1.3 mm. Amorphous echogenic material (arrowhead) representing either sloughed mucosa or blood clot is present in the lumen. A small amount of effusion (*) is present. **(B, C) Images from a 1-year-old Pit Bull presented for lethargy, inappetence, bloody diarrhea, and waxing/waning fever.** The small intestines are diffusely fluid filled with multiple loops containing suspended, echogenic luminal material. The intestinal mucosa (both small and large intestine) is mildly hyperechoic; there is also variable mural thinning with the jejunal wall measuring 2.3 mm in some areas **(B)**. There is concurrent moderate multifocal lymphadenopathy with jejunal nodes reaching 1.5 cm in thickness **(C)**. Scant anechoic effusion and mild splenomegaly with mottled parenchymal echogenicity were also identified. **Salmon poisoning** disease was confirmed via the identification of *Nanophyetus salminocola* intestinal flukes on fecal OPG testing.

Vet-ebooks.com

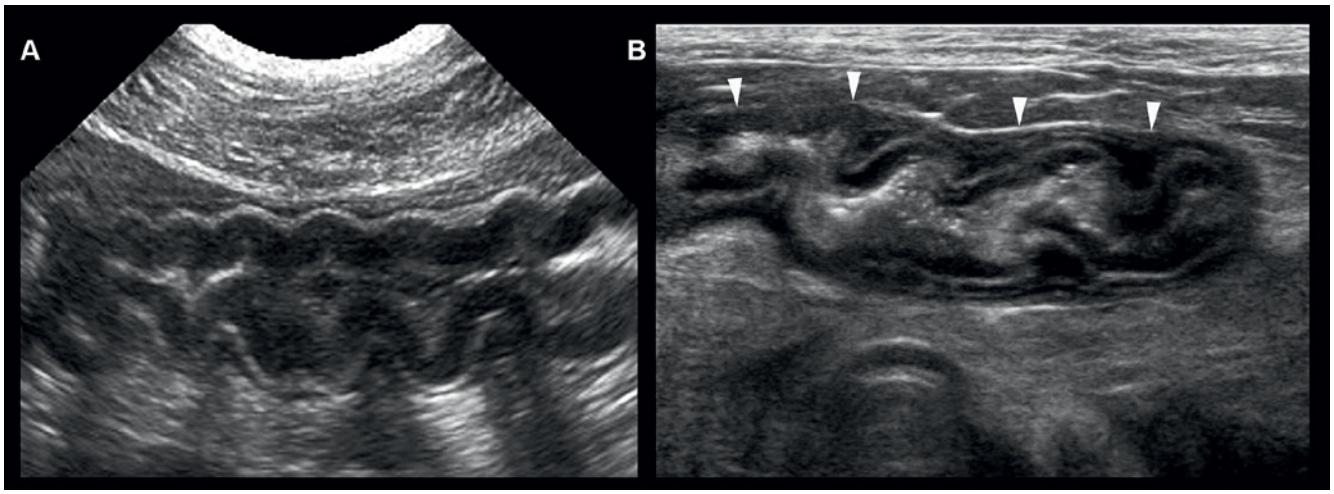


Figure 9.36. **Bowel corrugation. (A)** Several corrugated bowel segments are present in this 5-year-old Weimaraner. Chronic peritonitis secondary to multifocal perforation of the jejunum was present at surgery. **(B)** Similar corrugation is seen in this jejunal segment of a 10-year-old Yorkie with protein-losing enteropathy. Note that the serosal contour (arrowheads) is straight relative to the other layers.

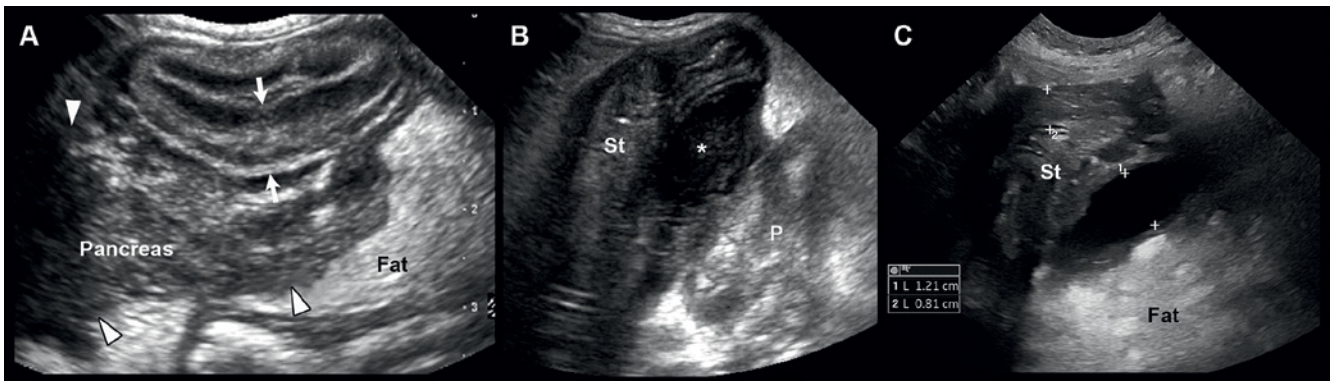


Figure 9.37. **Gastroduodenitis and pancreatitis in three dogs. (A)** The duodenum is thickened, and the wall layering appears affected but still visible (arrows). The adjacent right limb of the pancreas is enlarged and hypoechoic (arrowheads). Hyperechoic mesenteric fat outlines the margins of the inflamed pancreas. **(B)** In this other dog, the stomach (St) is collapsed, and its poorly defined wall is deformed by a nearly anechoic space confined against the enlarged hypoechoic pancreas that is outlined also by hyperechoic fat. The space (*) likely represents edema and fluid collection; this should not be confused for a mass as it resolved after adequate medical treatment. **(C)** In this third dog with severe acute pancreatitis, the wall of the stomach (St) is thickened and associated with a well-demarcated fluid collection (between calipers) along the greater curvature at the pyloric antrum, surrounded with hyperechoic fat but distinct from the pancreas. This pseudocyst resolved after treatment for the pancreatitis.

on the GI tract of affected dogs or cats (Venco et al. 2005) (Figure 9.41).

Postoperative Changes, Perforation, Dehiscence, and Adhesions

In normal postoperative enterotomy or enterectomy, the surgical site can be identified by the regular alignment of sutures, which appear as small bright interfaces along or around the bowel, depending on the choice of surgical procedure (Matthews et al. 2008) (Figure 9.42). Focal thickening of the bowel with loss of layering is commonly seen but can partially resolve over time (Mareschal and Penninck 2010).

In large dogs, preventive gastropexy is performed to reduce the risk of gastric torsion/volvulus. The surgical site appears as several hyperechoic foci that represent the sutures between the craniolateral

Vet-ebooks.com

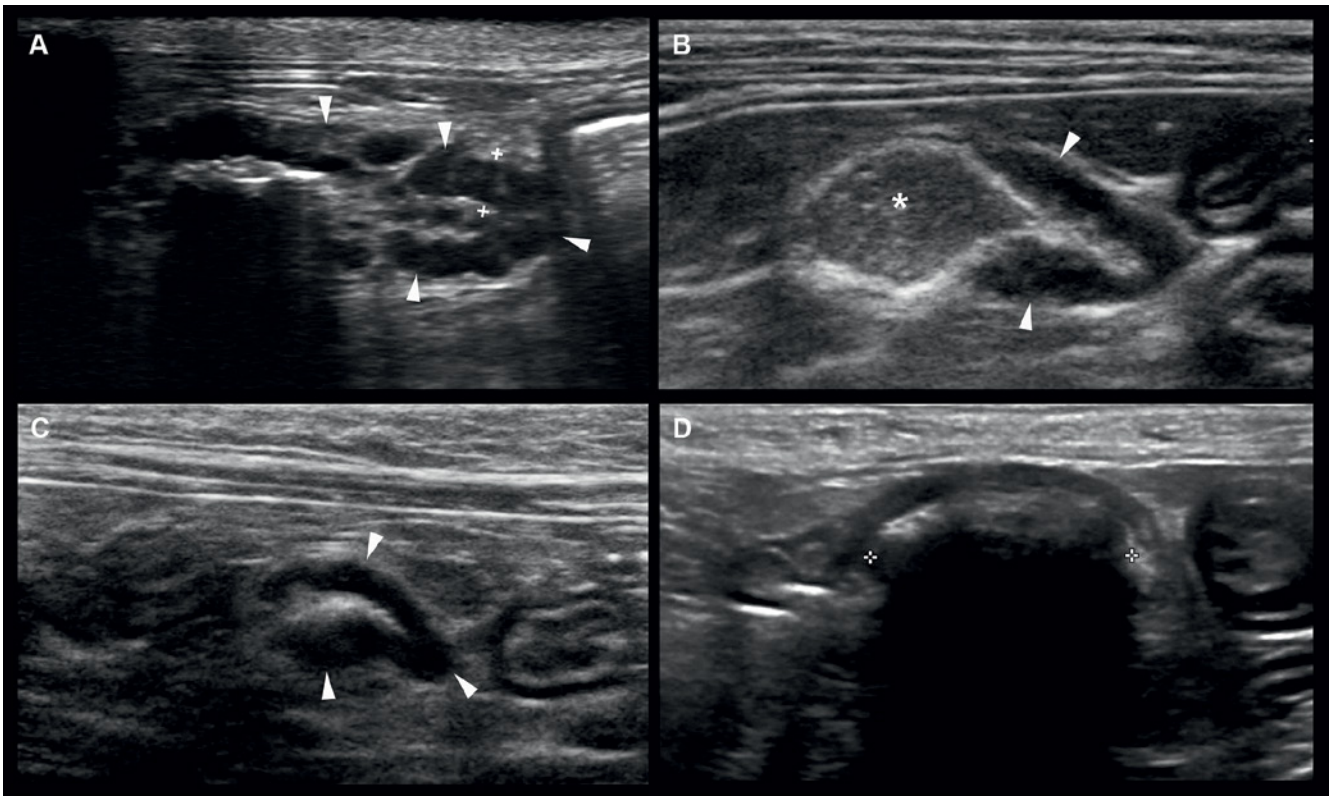


Figure 9.38. **Typhlitis in cats. (A)** In this cat presented for diarrhea, the cecal wall (arrowheads) is thickened (4.5 mm) and has a pronounced follicular appearance. The ascending colonic wall was also thickened. **(B)** In this 1-year-old Siamese cross, the cecal wall (arrowheads) is thickened (3 mm) and hypoechoic. Worms were noted in the small intestines. Echogenic fluid is noted in the adjacent colon (*). This change was resolved over time. **(C)** A 12-year-old cat with 3 days of vomiting has a thickened and hypoechoic cecal wall (arrowheads delineating the cecum). The adjacent (not shown) colic lymph nodes were hypoechoic and rounded. In the absence of any other GI changes, these features support typhlitis and a recheck ultrasound is recommended. Notice that in these three cases of cecal inflammation, the cecum maintains its overall shape. **(D)** In this lethargic 10-year-old cat, the cecum is distended with hyperechoic, shadowing concretions measuring 1.7 cm in length (radiopaque on radiographs), the adjacent ascending colon and the ileum (not shown) were thickened. The cecum was removed, and the diagnosis was moderate neutrophilic and lymphoplasmacytic typhlitis.

abdominal wall and the antrum of the stomach (Figure 9.43).

Postoperative **dehiscence** can be challenging to diagnose ultrasonographically as free fluid and gas are expected to be present up to 1 week after surgery, and these features are hallmarks of perforation as well. The presence of a moderate amount of fluid free in the abdomen and/or trapped near the enterectomy site as well as possible hyperechoic track or disruption of the wall at the site support dehiscence (Figure 9.44A, B) (Costanzo et al. 2023). Sampling the free fluid and the entrapped fluid collection is recommended.

In **perforation** secondary to foreign-body migration (Figure 9.44C, D), deep ulceration, or postoperative dehiscence, the affected wall is thickened and can be hypoechoic, with focal loss of layering (Boysen et al. 2003). At times, a hyperechoic track can be seen crossing the wall, and the adjacent mesentery is significantly increased in echogenicity because of focal steatitis, vasculitis, or peritonitis (Figures 9.44, 9.45). Fluid accumulation can often be seen near the perforation or dehiscence site, and free peritoneal gas can sometimes be detected as short, bright, linear interfaces in the most upper portion of the abdomen and be associated with comet-tail artifacts (Figures 9.44B and 15.10). In septic peritonitis, the free abdominal fluid is often echogenic (Figures 9.46, 15.6 and 15.9). Perforation has been reported secondary to NSAID therapy, steroid administration, underlying neoplasia, penetrating trauma (including foreign bodies), hepatic disease, intussusception, and parvoviral enteritis (Oh et al. 2022).

At times, a **stricture** can be seen at a previous enterotomy or enterectomy site. Abnormal fluid, gas, or food accumulation is then noted proximal to the

Vet-ebooks.com

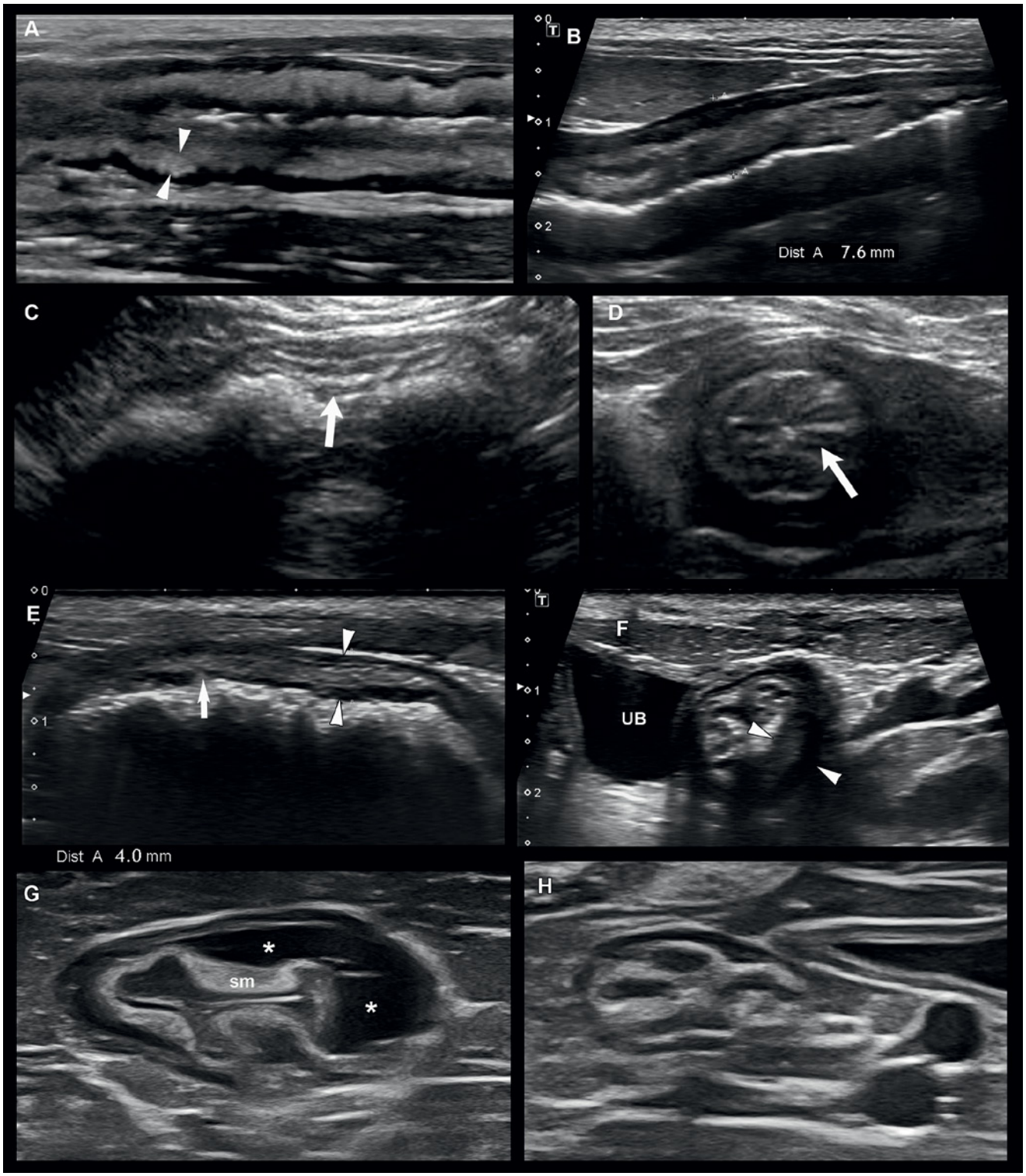


Figure 9.39. Colonic wall thickening. (A) Sagittal image of the thickened colonic wall of an 8-year-old cat with **lymphoplasmacytic colitis**. Notice the prominent irregular and submucosa (between arrowheads). **(B)** In this other cat with **severe eosinophilic colitis**, the wall of the descending colon is markedly thickened. The layering pattern is altered in this sagittal image in part because of the wall redundancy. **(C, D) Colonic wall redundancy** is also seen in this other cat presented for obstipation. Numerous folds can be identified (arrows) on the longitudinal **(C)** and transverse **(D)** planes. **(E, F)** Sagittal **(E)** and transverse **(F)** sonograms of the descending colon in a puppy with **parasitic (hookworm) colitis**. The wall is moderately thickened (arrowheads) and associated with mucosal ulcers (arrow). *UB, urinary bladder*. **(G, H)** Transverse images of the descending colon in a 1-year-old domestic shorthair cat presented for rectal prolapse. There is **severe mural edema** immediately following the reduction of the prolapse with thickening of the submucosal layer (sm) and anechoic fluid (*) dissecting between the submucosal and muscular layers (G). There is complete resolution of mural edema with normal wall thickness and layering on recheck 5 days later (H).

Vet-ebooks.com

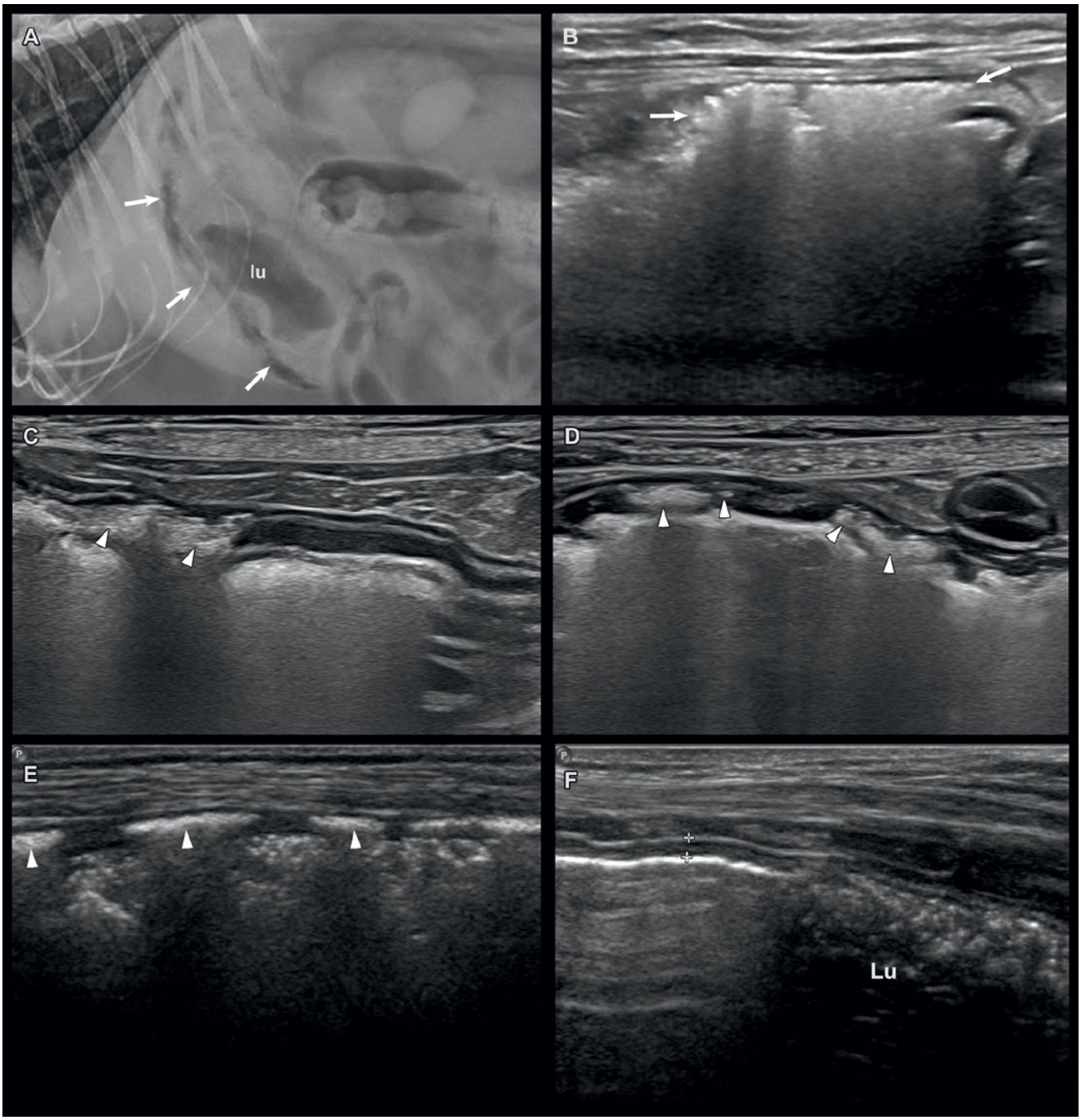


Figure 9.40. **Gastrointestinal pneumatosis. (A)** On this lateral radiograph of a 3-year-old cat, there is gas dissecting the gastric wall (arrows), not to be confused with the luminal gas (Lu). **(B)** On ultrasound, the gastric wall contains gas (arrows) that resolved within 2 weeks, supporting the suspicion of emphysematous gastritis. **(C, D)** Longitudinal sonograms of the jejunum in a 5-year-old Schnauzer presented for lethargy, hyporexia, and vomiting with a history of underlying diabetes mellitus and hyperadrenocorticism. There are segmental regions of intramural gas accumulation (arrowheads) within the jejunal wall seen as patchy, irregularly marginated, reverberating hyperechogenicities within the mucosal layer, and in some regions extending to or beyond the submucosal layer; in addition to pneumatosis intestinalis, scant portal gas was also identified (not shown) in this patient. **(E)** Pneumatosis coli is noted in the colon of this 6-year-old Pomeranian dog with diarrhea. **(F)** The recheck ultrasound of the colon in this dog showed a normal colonic wall, 3 weeks after the initial pneumatosis coli was detected. Lu, lumen.

Vet-ebooks.com

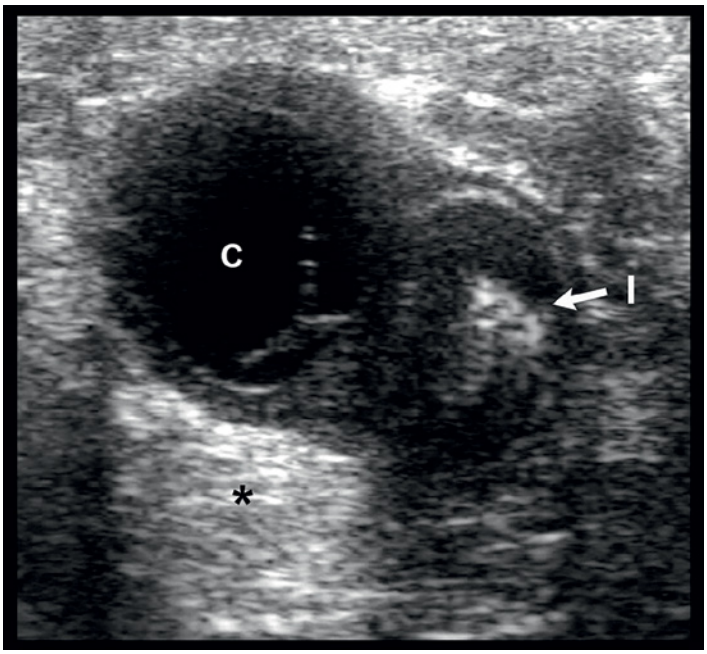


Figure 9.41. Peritoneal cestodiasis. Peritoneal cestodiasis in this 6-year-old mixed-breed dog is associated with a round, anechoic cystic lesion (C) associated with the serosal surface of an intestinal segment (I). Far enhancement is noted beyond the hypoattenuating fluid as a hyperechoic band (*). This sonographic image was obtained with a transverse plane. Reproduced with permission from Venco et al. (2005)/John Wiley & Sons.

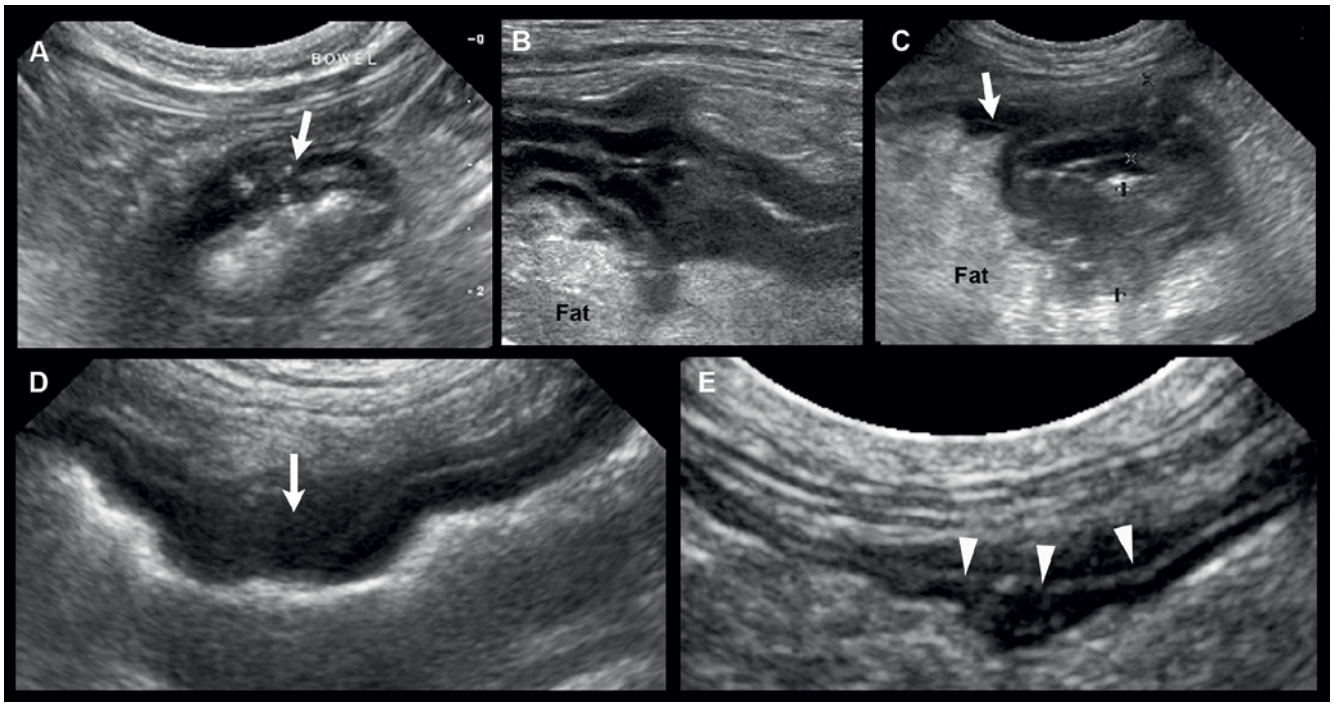


Figure 9.42. Postoperative enterotomy. (A) Normal immediate postoperative sonogram of an enterotomy site in a dog. The sutures appear as discrete, small, hyperechoic interfaces (arrow). **(B, C)** Longitudinal **(B)** and transverse **(C)** planes obtained at the site of anastomosis. The wall layering is disrupted, and the wall margins are deformed (between the cursors). Free gas and free fluid (arrow) are commonly encountered. The surrounding fat is hyperechoic. **(D)** Several days later, the wall layering remains disrupted (arrow) in this longitudinal sonogram. **(E)** Several weeks after surgery, despite a persistent focal thickening, the submucosa layer can be seen crossing the previous surgical site (arrowheads) in this dog with no gastrointestinal signs.

Vet-ebooks.com

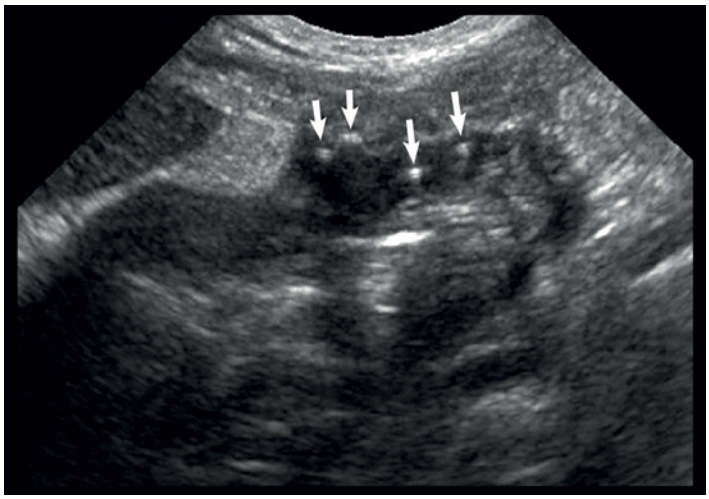


Figure 9.43. Four days postoperative gastropexy. In this 6-month-old German Shepard, several hyperechoic foci (arrows) are seen on the margins of the antrum sutured to the body wall. During real-time evaluation, reduced sliding motion is noted while the animal is breathing.

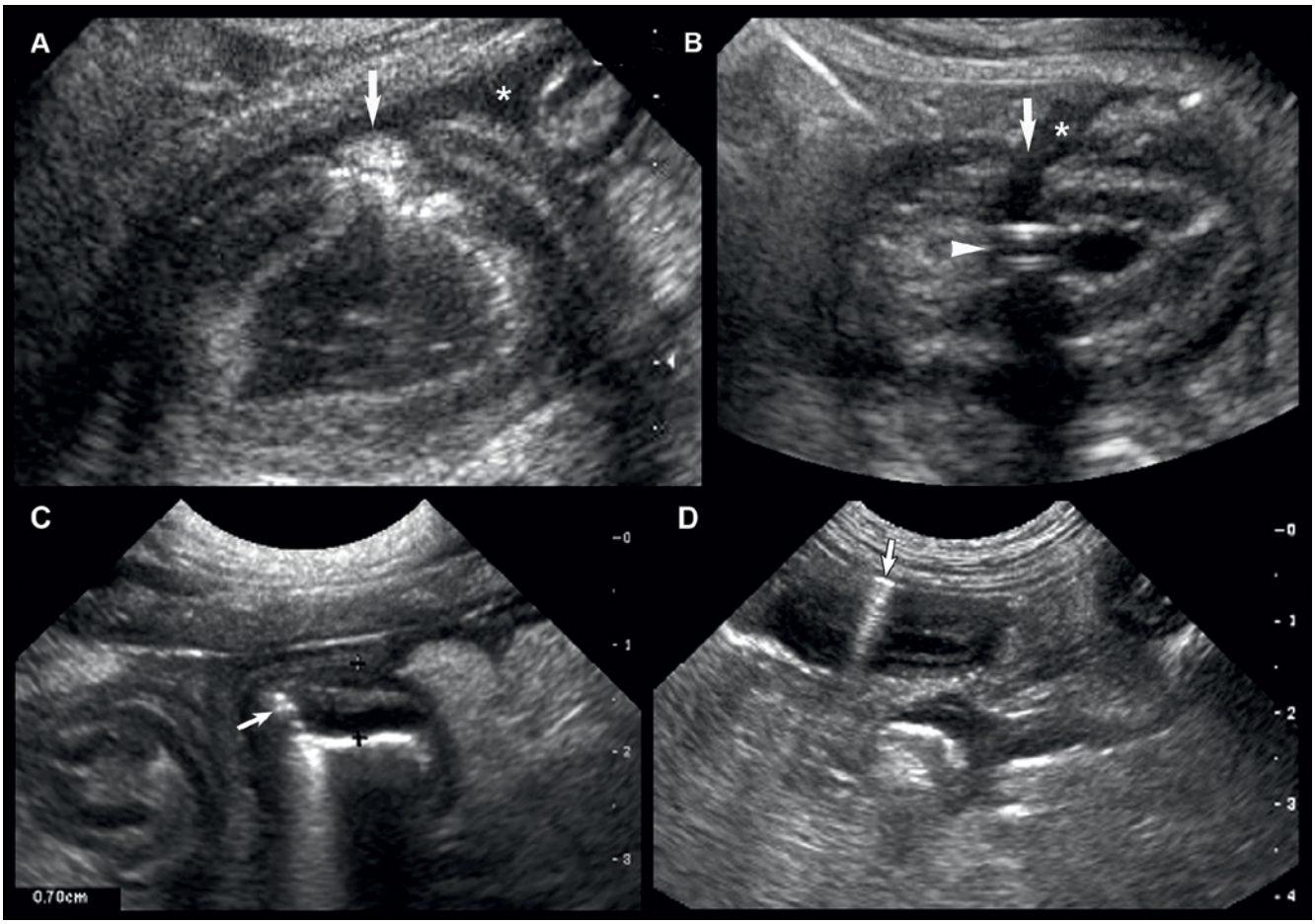


Figure 9.44. Intestinal dehiscence (A, B) and perforation (C, D). (A) There is dehiscence at the duodenal suture site in this 4-year-old Jack Russell terrier. Fluid accumulation (*) and hyperechoic fat are centered at the dehiscence site. Discontinuity of the duodenal wall is identified (arrow). **(B)** Transverse sonogram of the proximal descending duodenum of a 9-year-old Poodle with dehiscence as evidenced by the disruption of the wall (arrow). An arrowhead points to a stent (recently placed in the duodenal papilla because of extrahepatic biliary obstruction). Abdominal effusion (*) is also present. **(C)** A jejunal perforation secondary to foreign bodies (hairpins) was surgically confirmed in this 5-year-old Weimaraner. A hyperechoic gas tract (arrow) dissects the focally thickened jejunal segment (between the cursors). **(D)** Free gas (arrow) with reverberation artifact, and a moderate amount of echogenic fluid (not seen on this image) in the abdomen indicate perforation.

Vet-ebooks.com

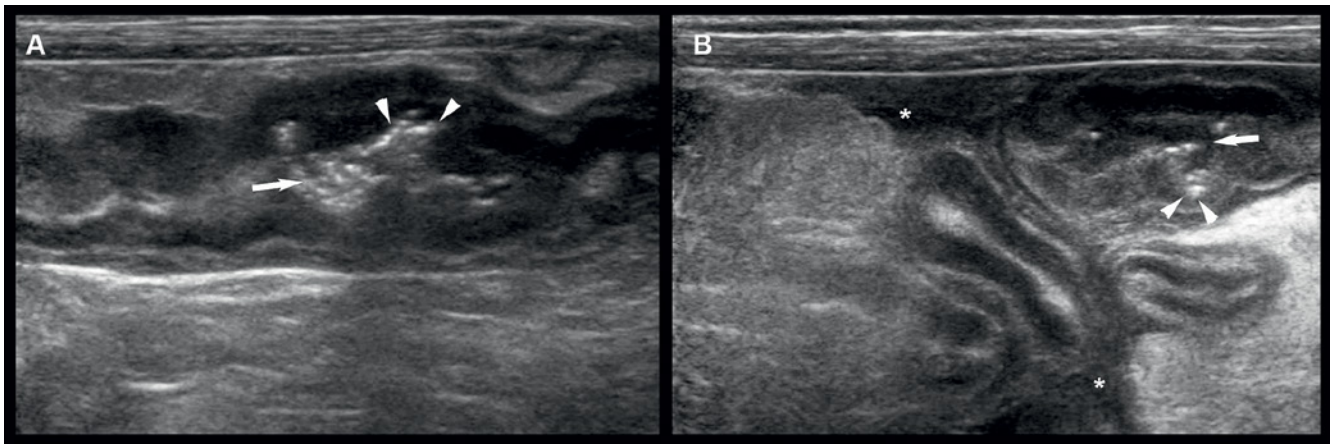


Figure 9.45. **Perforating ulcers.** Numerous enteric ulcerations are present in this 15-year-old miniature Pinscher. (**A**) The arrow points to the lumen. The arrowheads point to the irregular mucosal surface (ulcers). (**B**) The fat adjacent to the perforation site is hyperechoic, indicative of focal steatitis or peritonitis. Echogenic fluid is present in the abdomen (*).On histopathology, there was diffuse ulcerated histiocytic sarcoma in the small intestines (see also Figure 9.66).

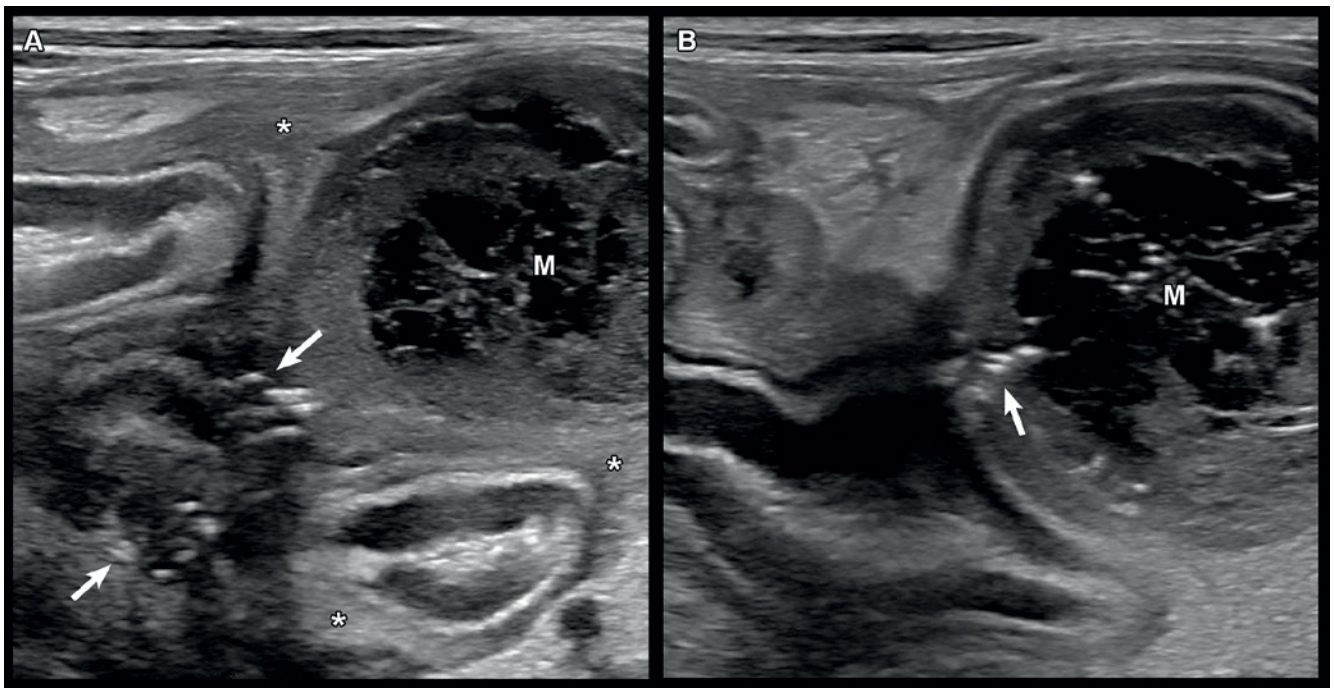


Figure 9.46. **Intestinal dehiscence and peritoneal abscess.** A 1-year-old dog had an enterectomy performed 1 week ago. **(A)** The enterectomy site (arrows) is visible. Hyperechoic peritoneal fluid (*) is noted and the mesenteric fat is hyperechoic. A large cavitary mass (M) is present adjacent to the surgical site. **(B)** The tract between the jejunal segment and localized fluid pocket representing an abscess cavity (M) is visible (arrow). Surgical dehiscence with local abscessation and peritonitis were confirmed.

stricture site, which can vary in length and is often associated with loss of wall layering and hyperechoic peri-intestinal mesentery (Figure 9.47) (Halloway et al. 2019). The fibrotic wall may be thickened enough to mimic neoplasia.

Intestinal **adhesions** are common postoperative sequelae. Changes can be subtle on ultrasound and challenging to recognize. Tracking poorly to moderately echogenic tissue can be seen between bowel segments and possibly other organs (Figure 9.48). On real-time

Vet-ebooks.com

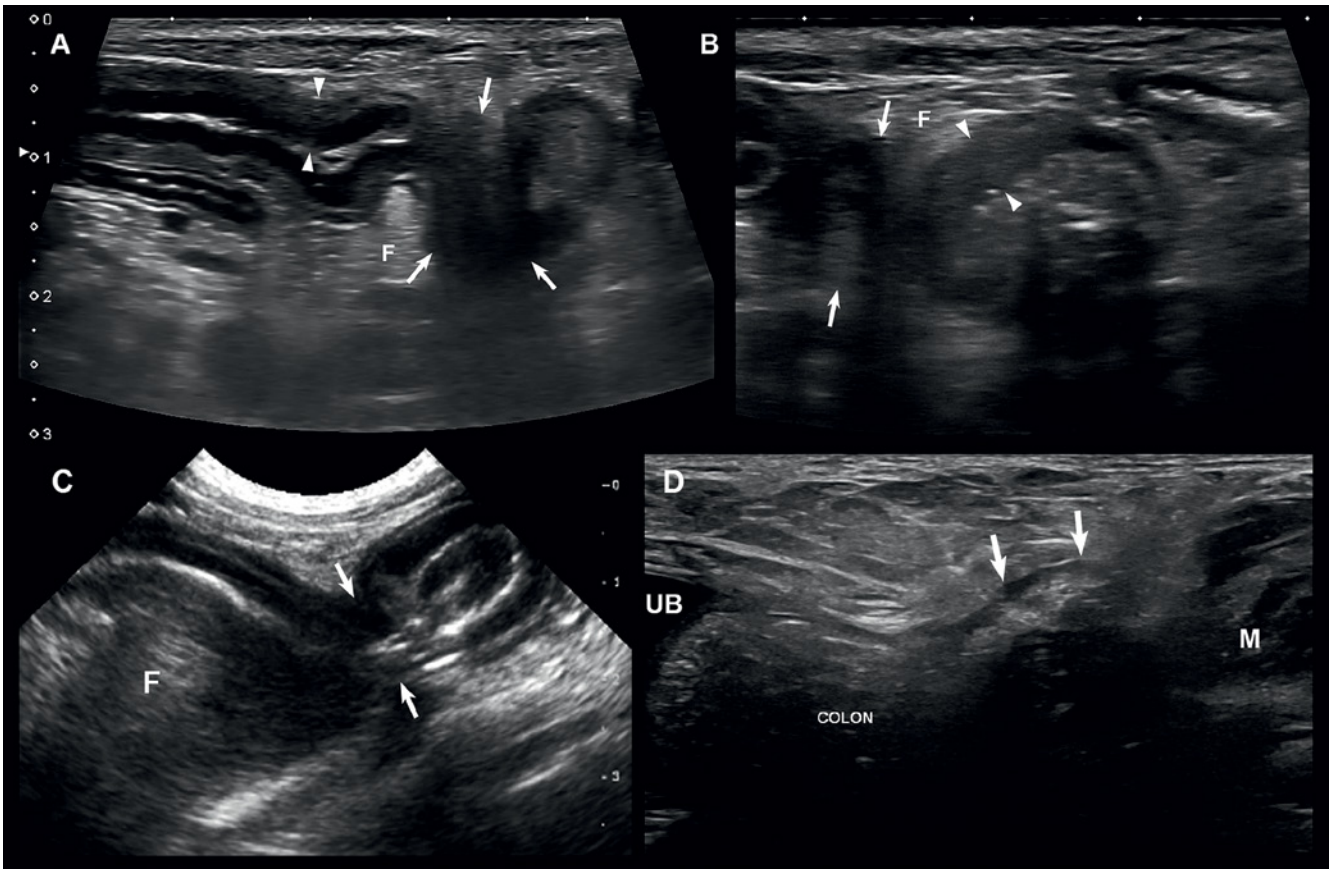


Figure 9.47. **Intestinal strictures in three dogs. (A, B) Intestinal strangulation in a dog with spontaneous mesenteric hernia. (A)** A segment of jejunum is focally deviated, poorly defined, and associated with loss of wall layers (arrows). The adjacent fat (F) is hyperechoic. Aborally, the wall is mildly thickened, and its layers are partly affected (arrowheads). **(B)** Orally, the segment is dilated and associated with moderate wall thickening with loss of layering (arrowheads). Incarceration of a segment of jejunum through a defect in the mesentery was identified in surgery. The wall of the strangulated portion was necrotic and required resection. **(C) Stricture at previous surgical site in another dog.** Severe fluid distension (F) is noted proximal to the stricture site (arrows) in this dog with previous enterectomies for intestinal foreign bodies. Suboptimal peristaltic activity was noted throughout the intestinal tract. Stricture at the surgical site was diagnosed surgically. **(D) Inguinal herniation of the descending colon** (arrows) in a 6-year-old Chihuahua presented for pain and constipation. M, pelvic limb musculature; UB, urinary bladder.

evaluation, limited movement between bowels can sometimes be observed.

A fluid pocket representing a sterile seroma may accumulate near or at a recent surgical or ultrasound-guided biopsy site (Figure 9.49). This is a rare and transient complication of surgical intestinal biopsies.

Gastrointestinal Tumors

GI neoplasia is often associated with motility disturbances resulting in luminal fluid or gas accumulation near the affected site; this may optimize the visualization of the lesion (Penninck 1998).

In dogs and cats, the most common ultrasonographic findings in **GI lymphoma** are transmural thickening associated with loss of normal wall layering, reduced wall echogenicity, decreased localized motility, and regional lymphadenopathy (Penninck et al. 1994). These features are similar in the stomach and along the intestinal tract. Gastric masses can have variable sizes, from extensive infiltration to segmental involvement (Figure 9.50). The thickening of the GI wall can range widely, from 5 mm to over 25 mm and is often associated with lost wall layering (Figures 9.50–9.56). Mesenteric lymphadenopathy is a common finding in intestinal lymphoma and in some instances can be responsible for most of the

Vet-ebooks.com

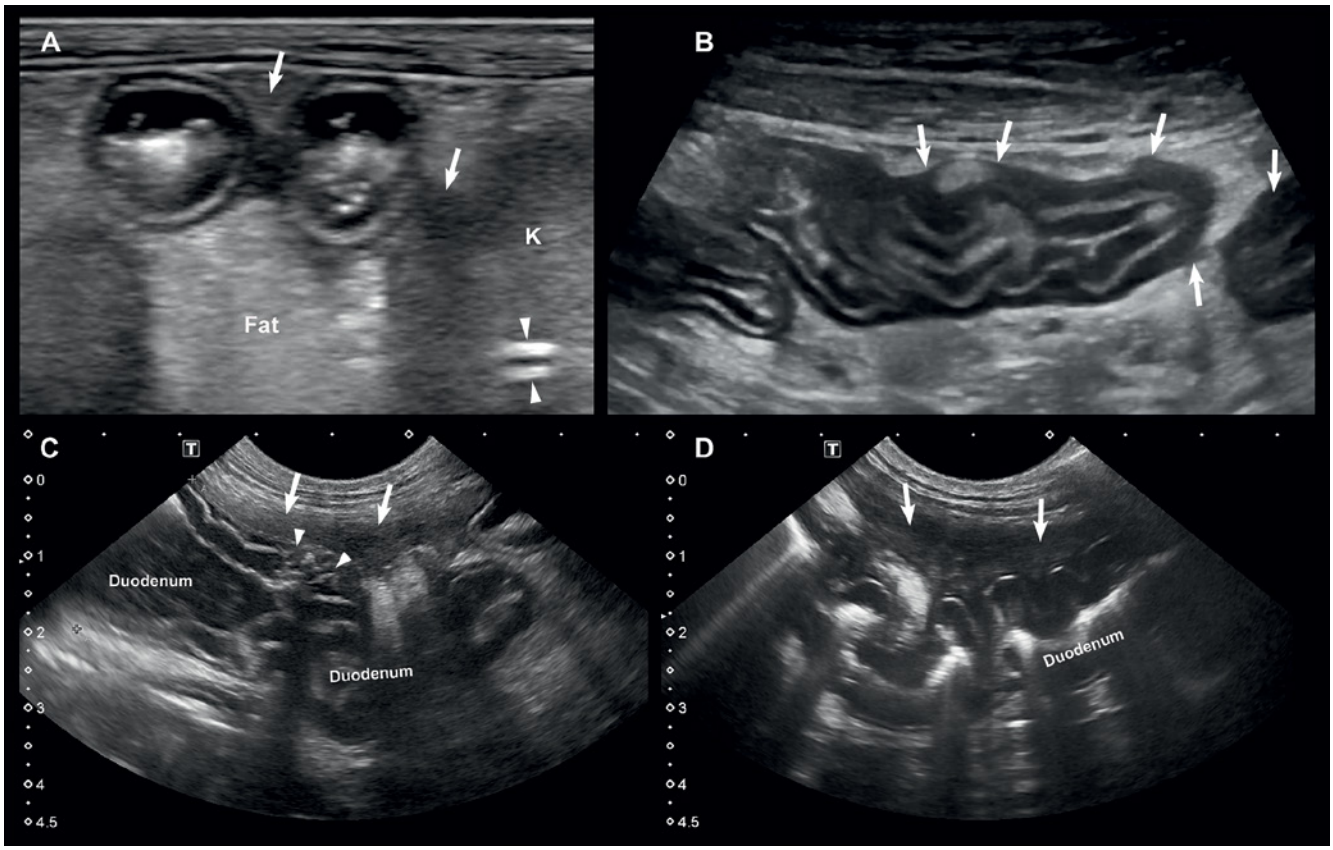


Figure 9.48. Postoperative intestinal adhesions. (A) In this 11-year-old miniature Schnauzer that previously had surgery for ureteral stent placement, thin hypoechoic bands (arrows) are seen between two bowel segments and the kidney (K). The adjacent fat is hyperechoic. Part of the stent is visible on this image (arrowhead). **(B)** In this 2-year-old Doberman that had two previous laparotomies for foreign-bodies removal, there is evidence of irregular hypoechoic tissue at the serosal margins of several jejunal loops (arrows), some with a triangular shape, consistent with fibrous adhesions. Note the irregularity of the affected bowel loop that remained static during the sonographic exam. **(C, D)** Follow-up ultrasound of another dog that a duodenal enterotomy for foreign-body removal that shows moderate dilatation of the descending duodenum just proximal to the enterotomy site (arrowheads). Note the adjacent hypoechoic fibrous adhesions (arrows) and the corrugation of the distal duodenum.

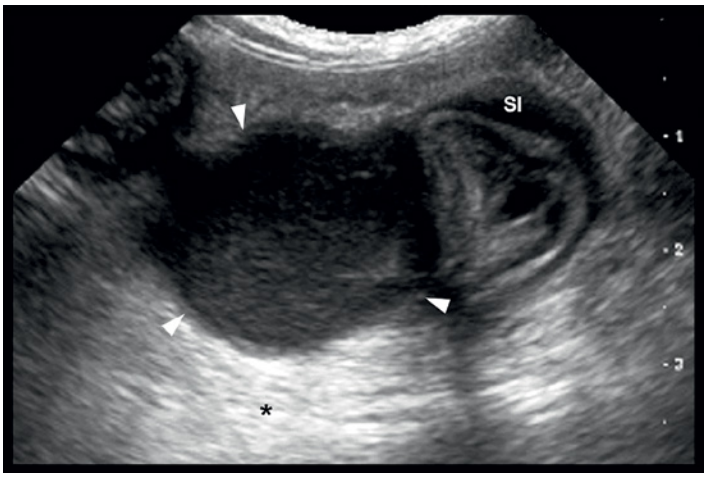


Figure 9.49. Subserosal seroma following surgical biopsy. A discrete, rounded, and hypoechoic fluid cavity (arrowheads) associated with acoustic enhancement (*) is deforming the adjacent intestinal (SI) wall and lumen. This represents a cystic seroma secondary to a recent surgical intestinal biopsy. The dog had no clinical signs related to this finding.

Vet-ebooks.com

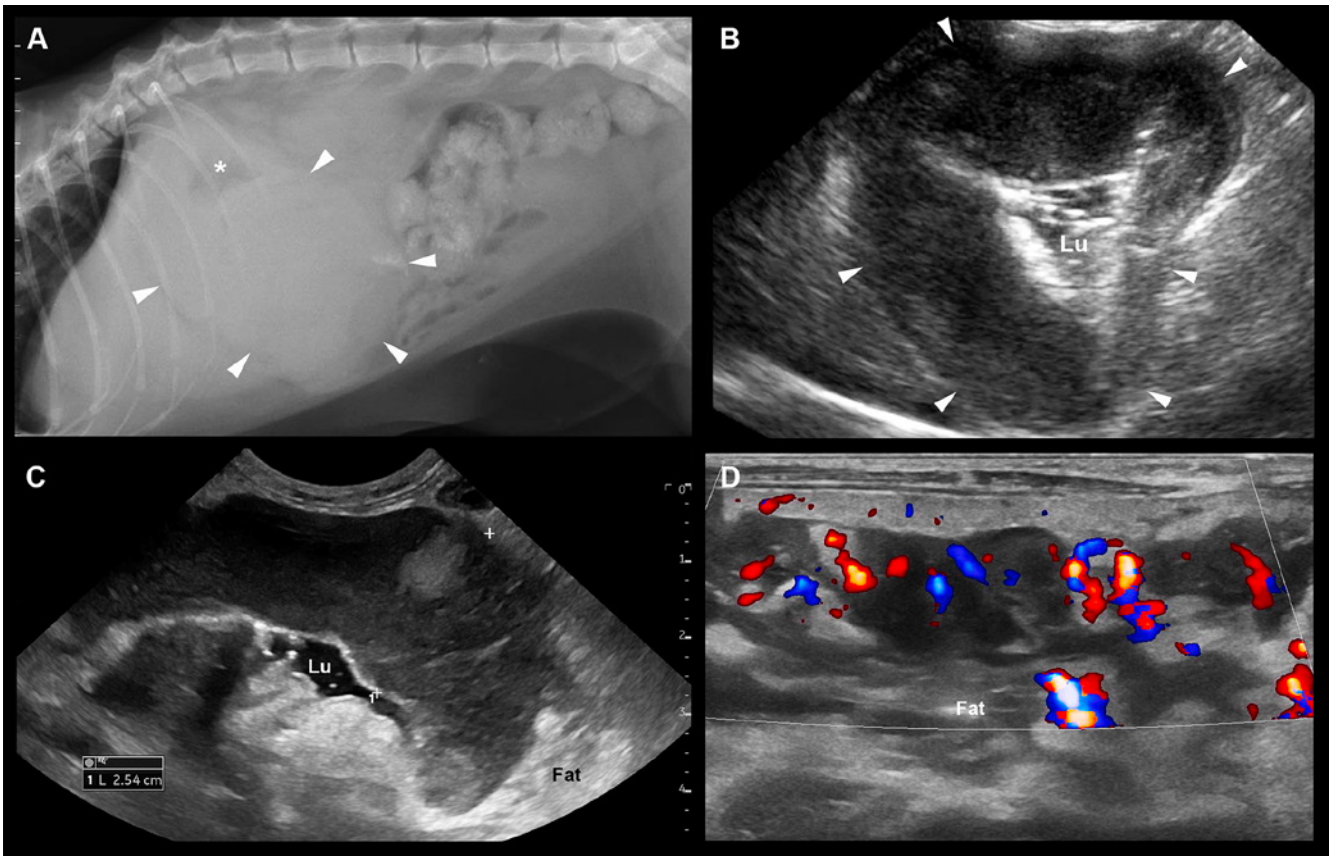


Figure 9.50. Gastric lymphoma in two cats. (A) Lateral radiograph of an 11-year-old cat with vomiting. A large soft-tissue mass (arrowheads) replaces the stomach containing a small amount of gas (*) in its lumen. **(B)** Transverse sonogram of the stomach seen in **(A)**, showing transmural, circumferential but asymmetric thickening of its wall with loss of layering. Lymphoma was diagnosed on fine-needle aspirates. **(C, D)** In this 16-year-old cat, there is severe thickening of the gastric wall with lost layering (between calipers). The regional fat is hyperechoic and infiltrated with an irregular and poorly defined vascularized hypoechoic tissue that was confirmed to represent lymphomatosis on fine-needle aspirations. Lu, lumen.

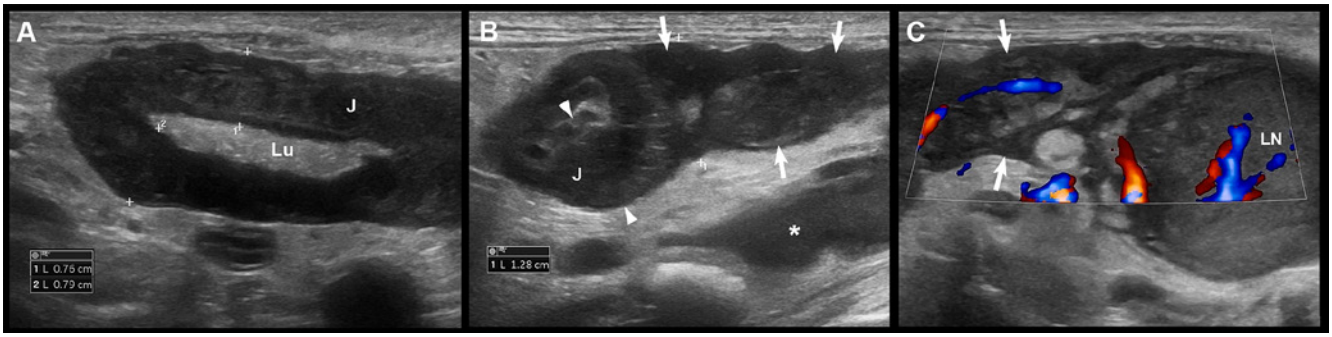


Figure 9.51. Intestinal lymphoma in a 15-year-old cat with anorexia and weight loss. **(A)** Longitudinal sonogram of segment of jejunal (J) with transmural thickening (up to 8 mm) and loss of wall layering. A small amount of echogenic material is noted in the lumen (Lu). **(B)** Transverse sonogram of this jejunal (J) segment that shows asymmetrical thickening of its wall (between arrowheads), with altered layering and associated with an extension of the hypoechoic tissue into the adjacent mesentery (arrows). Peritoneal effusion is present (*). **(C)** Color Doppler of this layer of hypoechoic and heterogeneous tissue (arrows) invading the mesentery and that reaches and partly englobes a markedly enlarged jejunal lymph node (LN).

Vet-ebooks.com

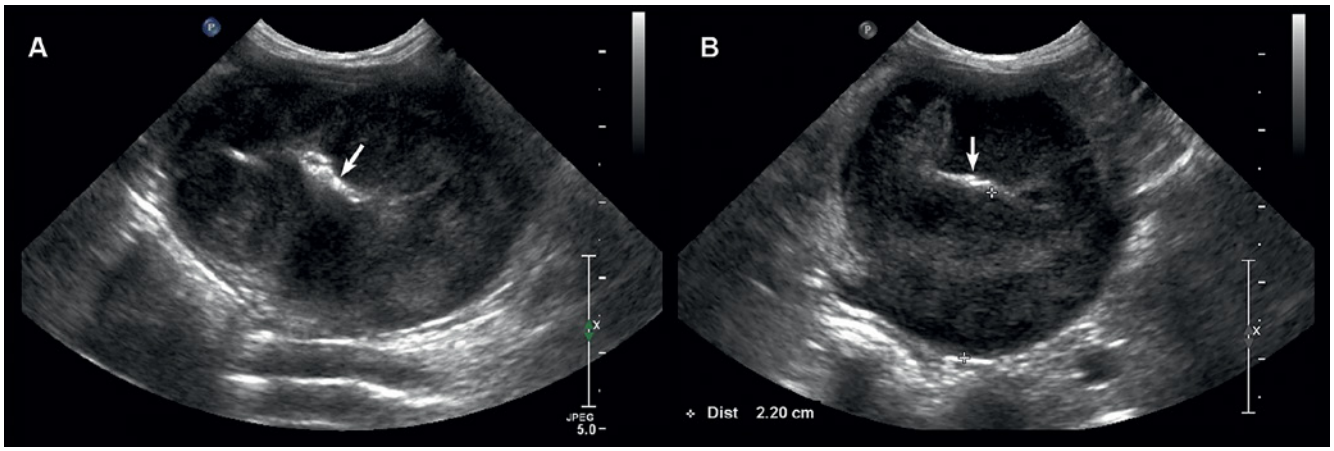


Figure 9.52. Intestinal lymphoma in an 11-year-old Greyhound. Oblique **(A)** and transverse **(B)** sonograms of the thickened jejunum. There is circumferential, irregular thickening (between the cursors: 2.2 cm) with complete loss of wall layering. The lumen (arrows) is collapsed.

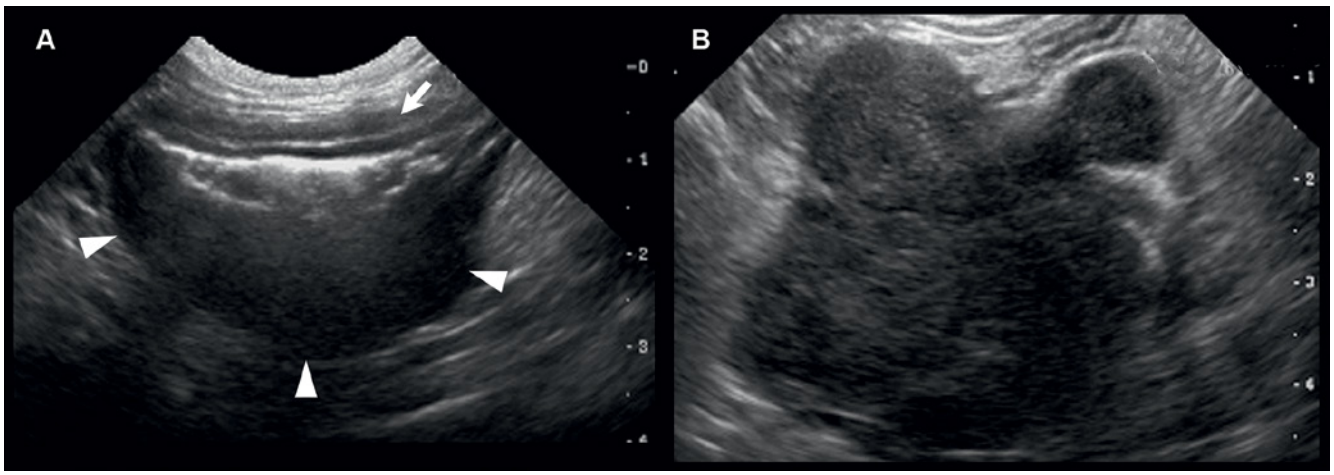


Figure 9.53. Intestinal lymphoma. (A) Longitudinal sonogram of an asymmetrically thickened (1.5 cm) bowel segment in an 11-year-old cat diagnosed with alimentary lymphoma. The loss of layering involved mostly one side of the wall (arrowheads). The muscular layer appears particularly thickened in the opposite wall (arrow). **(B)** The jejunal lymph nodes were markedly enlarged (4.5 cm thick), lobulated, and hypoechoic.

midabdominal mass effect (Figure 9.53B). Occasionally, the omentum and mesentery may be diffusely infiltrated and are responsible for the large mass effect, detected on palpation or seen radiographically (Figure 9.54). Ulcerated lymphoma can be encountered as an irregular mucosal surface or as a large defect centered on the affected portion of the GI tract (Figure 9.55). GI lymphoma can display several lesions along the GI tract, and they uncommonly create partial or complete obstruction. In cats, alimentary (small cell) lymphoma is sometimes affecting the intestinal tract without fully disrupting the wall layering, and in some of these cats, the muscular layer of the intestinal wall is thickened (Figure 9.56), making the distinction between inflammatory and neoplastic changes more challenging (Tucker et al. 2014; Zwingenberger et al. 2010, Daniaux et al. 2014). Serosal infiltration is rare, but if it occurs, it may restrict the lumen (Figure 9.56). Lymphoma is the most common type of GI neoplasia in the cat, reported to account for 47% of all intestinal neoplasia (Rissetto et al. 2011).

The most common ultrasonographic finding in **gastric carcinoma** is wall transmural thickening that is associated with altered wall layering that correlates with the unevenly layered tumor distribution noted

Vet-ebooks.com

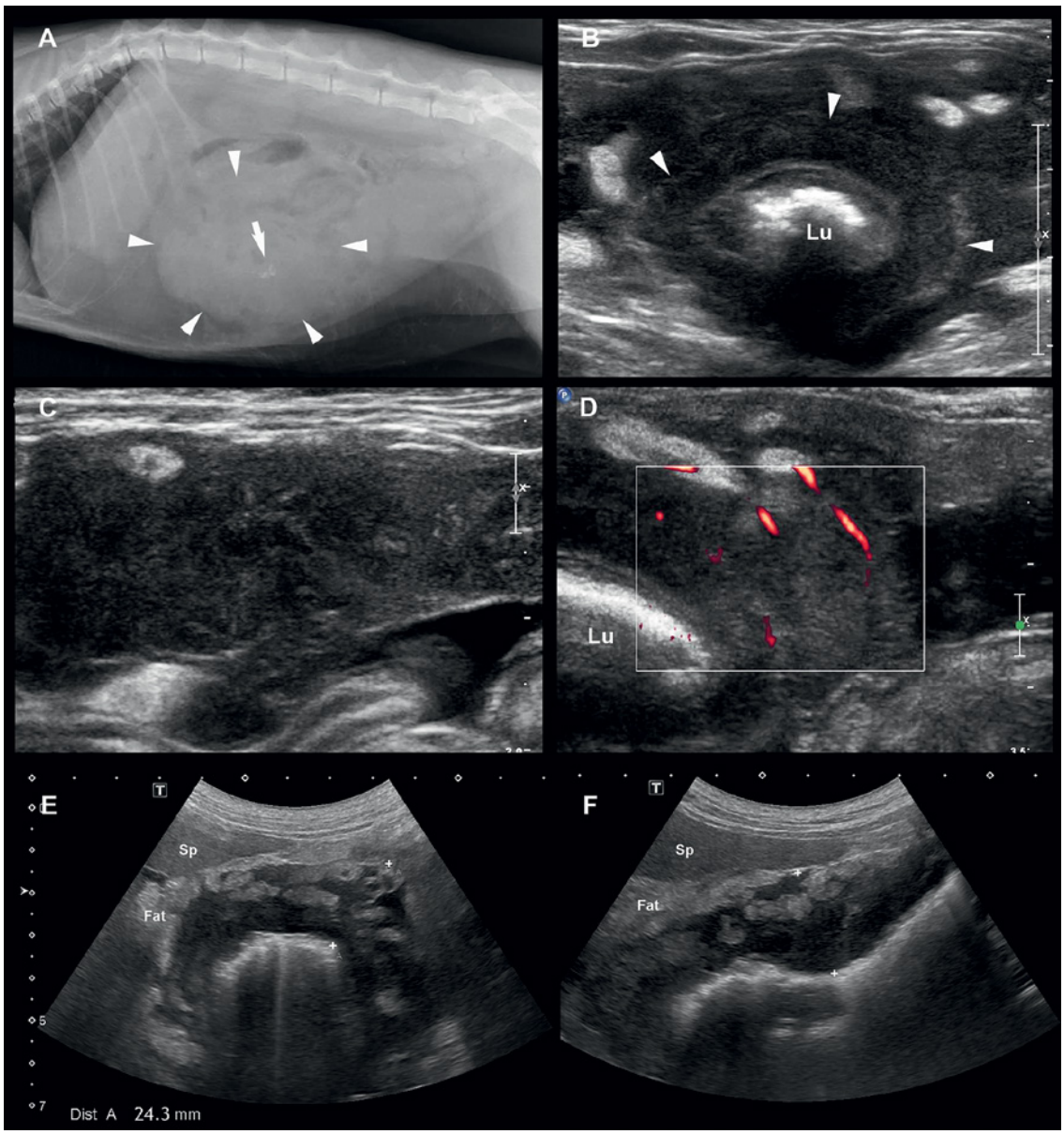


Figure 9.54. **Jejunal and omental lymphoma in a cat and in a dog. (A–D)** In a 2-year-old cat, **(A)** the lateral radiograph showing regional decreased serosal detail of the abdomen (arrowheads) that supports a mass effect with suspected abdominal effusion or infiltration. A small amount of radiopaque debris (arrow) is located in this region, and presumed to be within the GI tract. Notice the wet hair artifacts along the ventral abdominal wall. **(B)** Transverse sonogram of a jejunal segment with marked thickening of the wall (outlined by arrowheads) and extensive omental invasion, as also noted in **(C, D)** Peritoneal effusion is present. The omental thickening, even poorly echogenic can be distinguished from fluid because of the detection of blood vessels **(D)**. **(E, F)** In this 4-year-old Labrador retriever with weight loss and abdominal distension and pain, a segment of jejunum is markedly thickened (24.3 mm) and heterogeneous with indistinct layering. The lymphoma infiltrates the peripheral fat, making it difficult to differentiate wall from fat. Lu, lumen; Sp, spleen.

Figure 9.56. **Feline lymphoma with altered layering. (A)** A 12-year-old domestic shorthair cat presented for evaluation of chronic intermittent diarrhea and acute hyporexia and vomiting. There is diffuse intestinal mural thickening (up to 4.3 mm) with the increased relative thickness of the muscularis layer. Alimentary small cell lymphoma (T cell) was confirmed on endoscopic biopsy. **(B)** The jejunal lymph nodes are rounded and enlarged (8 mm) (arrows). **(C, D)** A 11-year-old cat presented for constipation, dehydration, and anorexia. There is diffuse relative thickening of the muscularis layer with discrete, round to ovoid, hypoechoic nodules arising from the muscularis layer and causing bulging of the serosal margin seen in the longitudinal **(C)** and transverse **(D)** planes. Lymphoma was confirmed via FNA of one of the mural nodules. **(E, F)** A 9-year-old cat with progressive weight loss**. (E)** In the near field, several intestines are fluid dilated and hyperperistaltic. At the junction of maximally dilated jejunum and normal jejunum (arrow), a segment of jejunum folded on itself (arrowheads) is noted. **(F)** After surgical resection, the specimen was scanned in a water bath. There is again evidence of a tightly folded segment of jejunum (arrowheads) with visible layers. The histopathological diagnosis was lymphoma primarily confined to the serosa.

Vet-ebooks.com

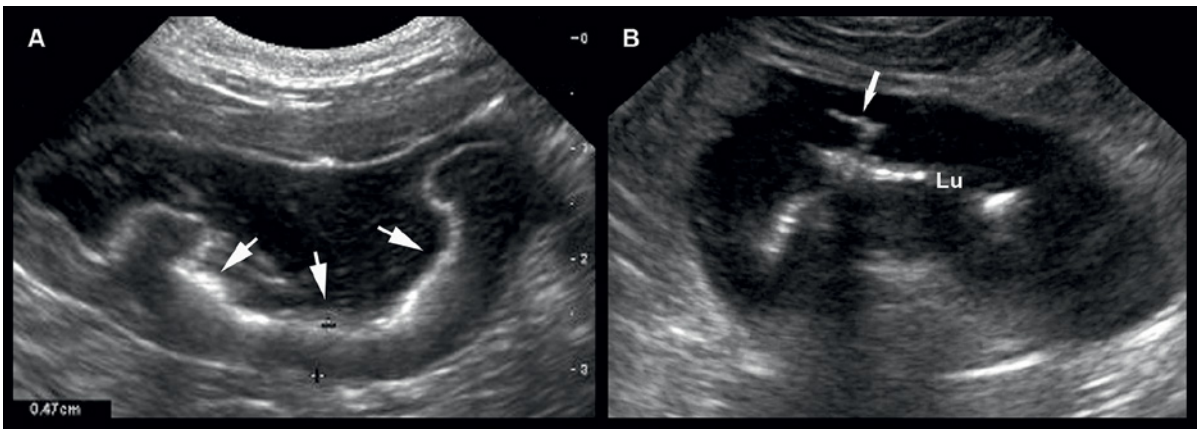


Figure 9.55. **Ulcerated lymphoma. (A)** Longitudinal sonogram of an ulcerated lymphoma in a 15-year-old cat with vomiting and depression. Part of the gastric wall is moderately thickened (4.7 mm), with complete loss of layering. The mucosal surface appears irregular, and a layer of hyperechoic microbubbles has accumulated at the site of the extensive ulceration (arrows). The stomach is filled with fluid and was hypomotile during the exam. **(B)** Sagittal sonogram of an ulcerated jejunal lymphoma in an 11-year-old cat with decreased appetite. An irregular hyperechoic tract (arrow) is crossing the thickened and poorly echogenic wall. Lu, lumen.

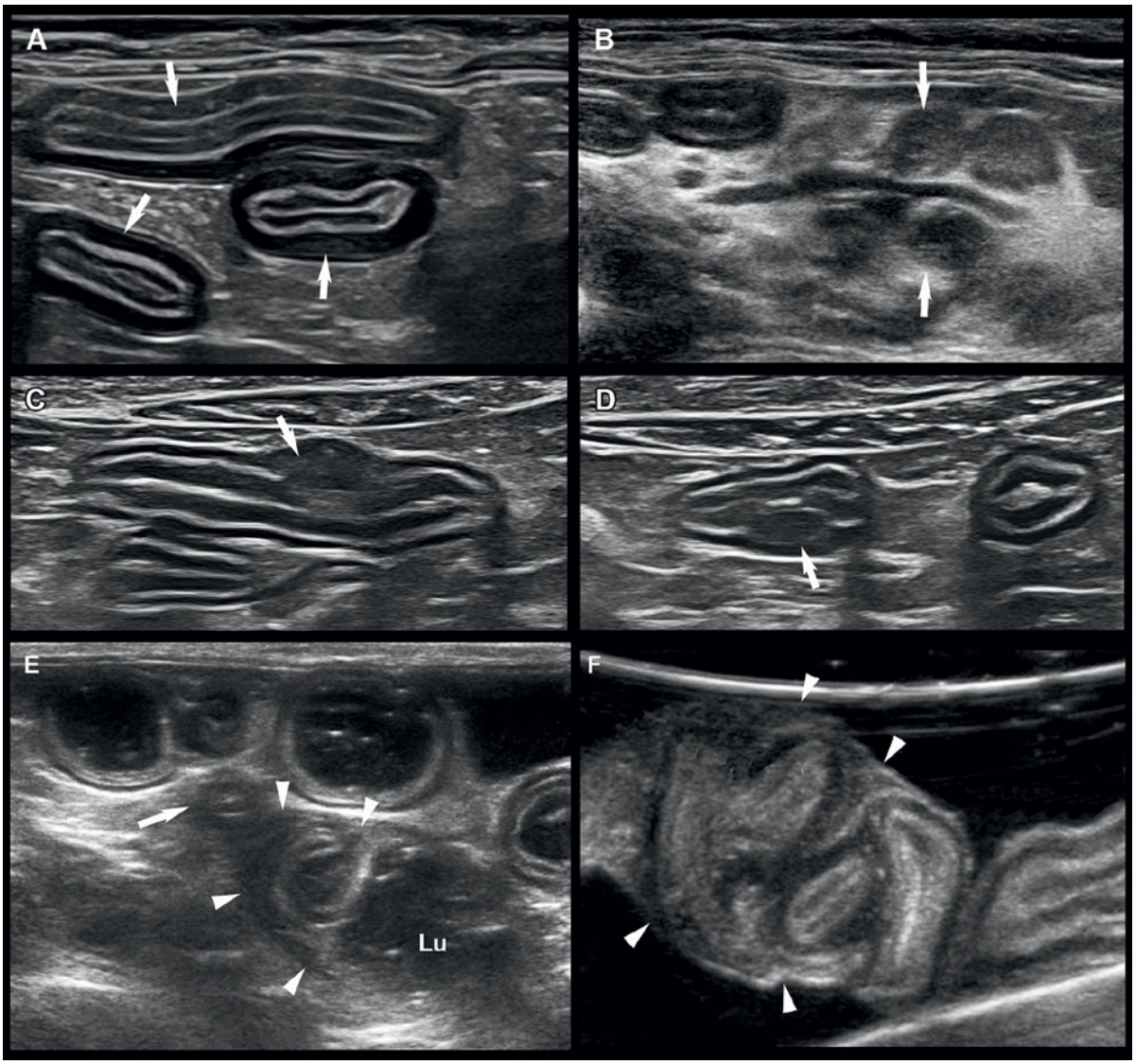


Figure 9.56. **Feline lymphoma with altered layering.** (for full caption, see facing page)

Vet-ebooks.com

histopathologically (Penninck et al. 1998). This altered layering, also called pseudo-layering, appears as a moderately echogenic zone surrounded by outer and inner, poorly echogenic lines and is present in many dogs. When present, this particular ultrasonographic feature is strongly suggestive of gastric carcinoma. However, other associated mural changes, such as edema, inflammation, fibrosis, or hemorrhage, can mask this hallmark feature (Figure 9.57).

Intestinal carcinomas have been documented in dogs and cats, although it is encountered less frequently in cats. The most common ultrasonographic findings are transmural thickening with a complete loss of layering, which is often associated with lymphadenopathy (Paoloni et al. 2002) (Figure 9.58). In the majority of these cases, fluid/gas accumulation proximal to the focal intestinal thickening indicates a mechanical ileus. A **gravel sign** is a typical finding on radiographs because of chronic partial obstruction (Figure 9.58A, B). Intestinal carcinoma shares some of the ultrasonographic features seen in intestinal lymphoma, but the length of the lesion tends to be shorter in carcinoma than in lymphoma, and mechanical ileus is more common in carcinoma than in lymphoma (Figures 9.58, 9.59). The behavior of intestinal carcinoma may vary according to the histopathological type. Hyperplastic and adenomatous changes may evolve into malignant tumors and therefore the ultrasonographic features may be confusing (Figure 9.60).

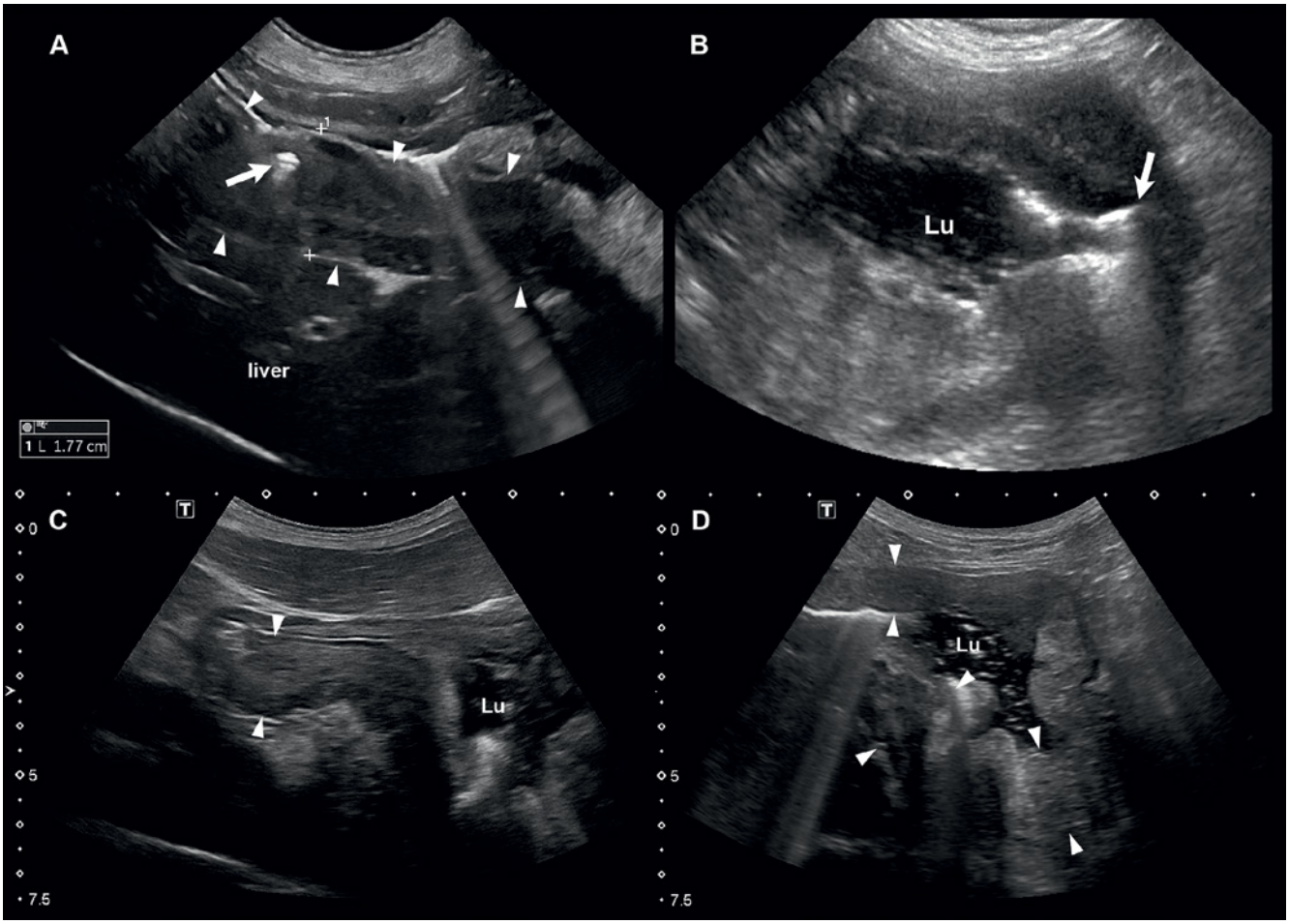


Figure 9.57. Gastric altered layering with adenocarcinoma in three dogs. (A) Longitudinal sonographic image of the pyloric antrum of a 12-year-old Belgian shepherd with gastric adenocarcinoma. The gastric wall (arrowheads) is markedly thickened (up to 1.8 cm) and shows reduced layer demarcation as well as hyperechoic focus (arrow) that generates reverberation artifact consistent with intramural gas resulting from ulceration. **(B)** In this 9-year-old, Old English Sheepdog with vomiting and weight loss, the wall of the gastric body is up to 1.8 cm thick and a defect (arrow) outlined by a small amount of gas represents a deep ulcer. **(C, D)** In this 12-year-old Chow, the pseudolayering is more evident at the gastric body (arrowheads in **C**), whereas the wall is more heterogeneous at the fundus **(D)** presumably due to necrosis, edema, or hemorrhage. The stomach is also fluid filled (Lu, lumen), which can be present because of increased wall rigidity.

Vet-ebooks.com

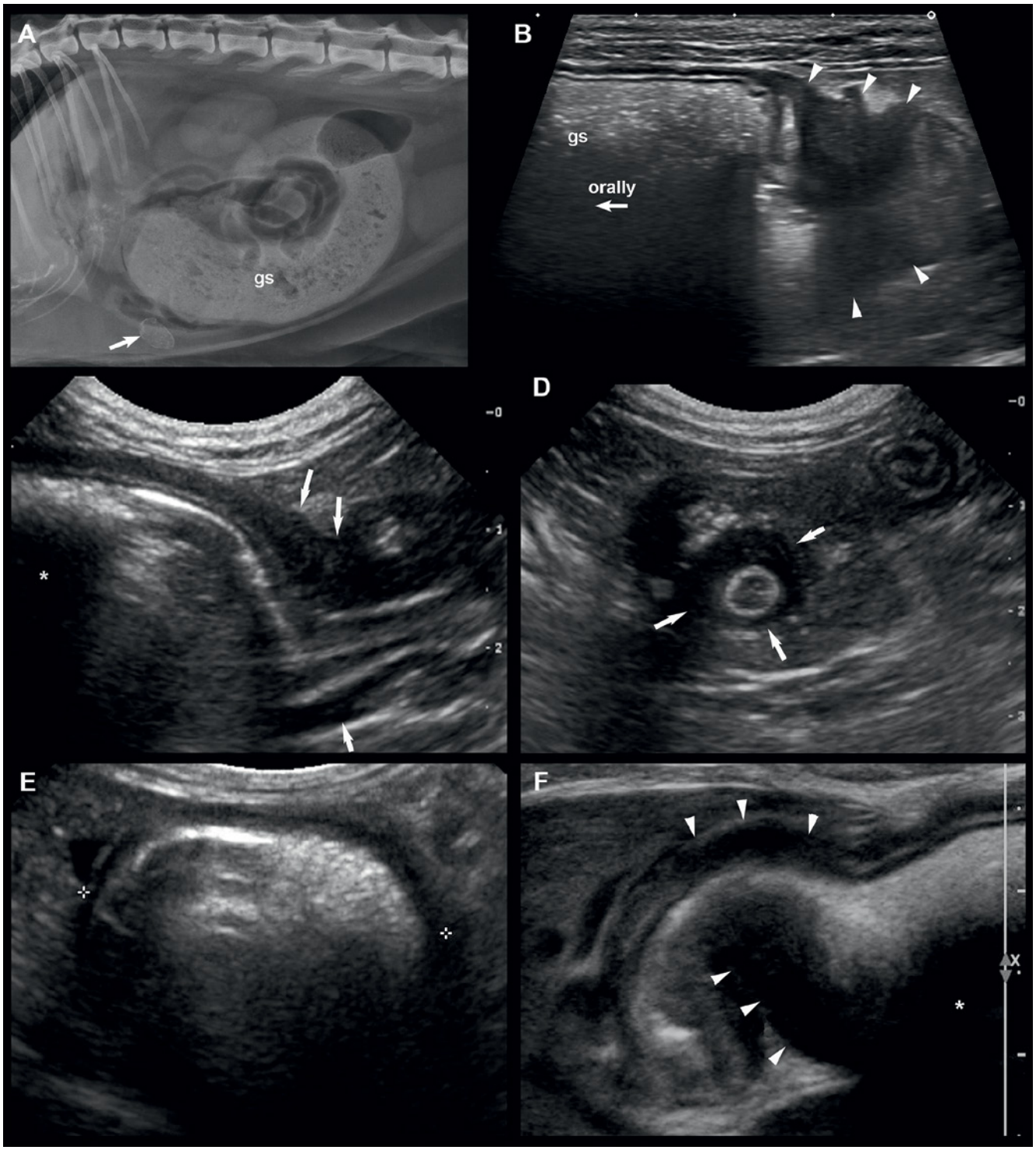


Figure 9.58. Intestinal adenocarcinomas with obstruction in 3 cats. Lateral abdominal radiograph **(A)** of an old cat presented for weight loss showing an intestinal segment distended with a radio-opaque granular content consistent with a gravel sign (gs). An incidental focus of nodular fat necrosis is seen (arrow). Ultrasound **(B)** revealed severe circumferential thickening of the wall of the ascending colon, forming a hypoechoic mass with irregular contour (arrowheads), responsible for chronic subocclusion that led to the accumulation of indigestive ingesta orally, correlating with the gravel sign (*). **(C)** Longitudinal sonogram of an intestinal adenocarcinoma in a cat with weight loss and anorexia. Proximal to the obstruction site, there is intestinal distension and foreign-material accumulation (*). The arrows point to the narrowed and affected bowel segment. **(D)** Transverse sonogram of the same lesion. The arrow points to the thickened ileum. **(E)** In this 9-year-old cat, there is marked jejunal distention (between cursors, up to 2.5 cm wide), proximal to the obstruction site. **(F)** At the tumoral site, there is a short and narrowed segment of jejunum (arrowheads) with loss of layering. The affected portion of intestine is curved on itself. Note the strongly shadowing material (*) accumulated proximal to the obstruction site.

Vet-ebooks.com

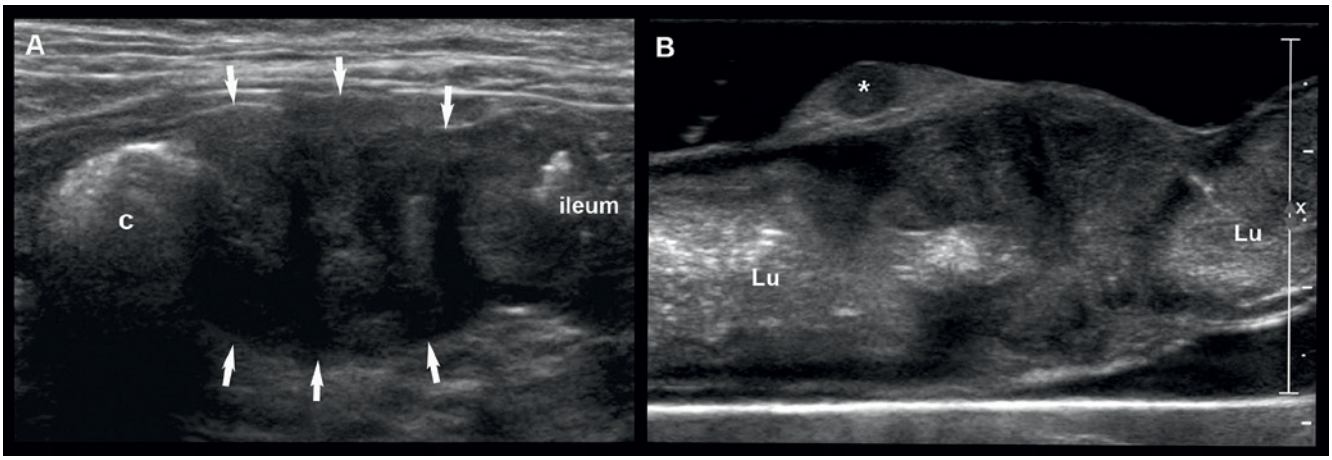


Figure 9.59. **Adenocarcinoma of the ileocecocolic junction of a 12-year-old cat. (A)** Longitudinal sonogram of a focally invasive and unevenly circumferential adenocarcinoma invading the ileocecocolic junction of this cat (arrows). **(B)** After surgical removal, the specimen was placed in a water bath. The extent and echogenicity of the mass can clearly be seen. A small nodule (*) is present in the adjacent mesentery. C, colon; Lu, lumen.

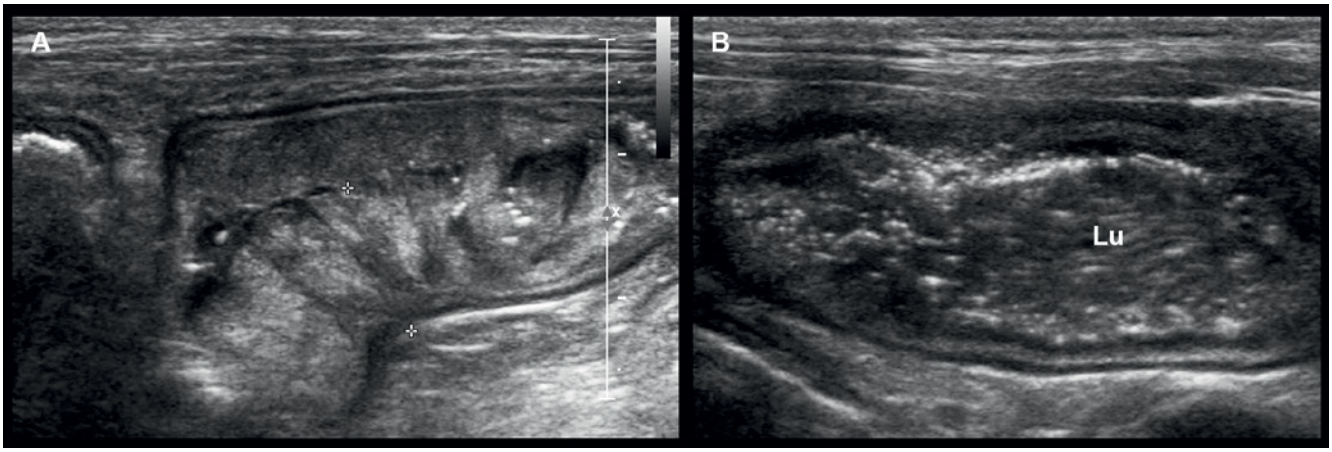


Figure 9.60. **Jejunal carcinoma in a 7-year-old Pug with chronic watery diarrhea. (A)** Longitudinal sonogram of the affected intestine. **(A)** 1-cm-thick polypoid-like thickening primarily affecting the mucosa is noted. **(B)** A jejunal segment orad to the lesion is moderately fluid filled. The mass was resected, and the final diagnosis was colonic intramucosal papillary adenocarcinoma. Considering the chronic clinical signs and the marked dysplastic changes, it was speculated that the papillary carcinoma might be a malignant transformation of long-standing adenomatous polyp. Over 2 years later, the dog has no evidence of recurrence of intestinal mass or GI signs. Lu, lumen.

Smooth muscle tumors (leiomyoma, leiomyosarcoma) have been described as the most common mesenchymal tumors of the GI tract; however, with the advance in histoimmunochemistry, **gastrointestinal stromal tumors (GISTs)** are being more reliably diagnosed and their prevalence is still unknown. Several ultrasonographic features of GI mesenchymal tumors are helpful in differentiating them from other types of GI neoplasia. Smooth muscle tumors tend to be large (over 3 cm) intramural lesions growing out of the serosa as large eccentric or extraluminal masses (Myers and Penninck 1994) (Figures 9.61, 9.62). Because of their common exophytic distribution and their large size, it is difficult to assess the anatomical origin of the mass and even more so to determine the precise layer of tumor origin. During real-time evaluation, it is important to identify within the mass any gas and/or the small amount of fluid located in the distorted lumen. The presence of a reverberation artifact indicates the presence of gas and attempts to connect this artifact to an adjacent bowel segment should be made to confirm the GI

Vet-ebooks.com

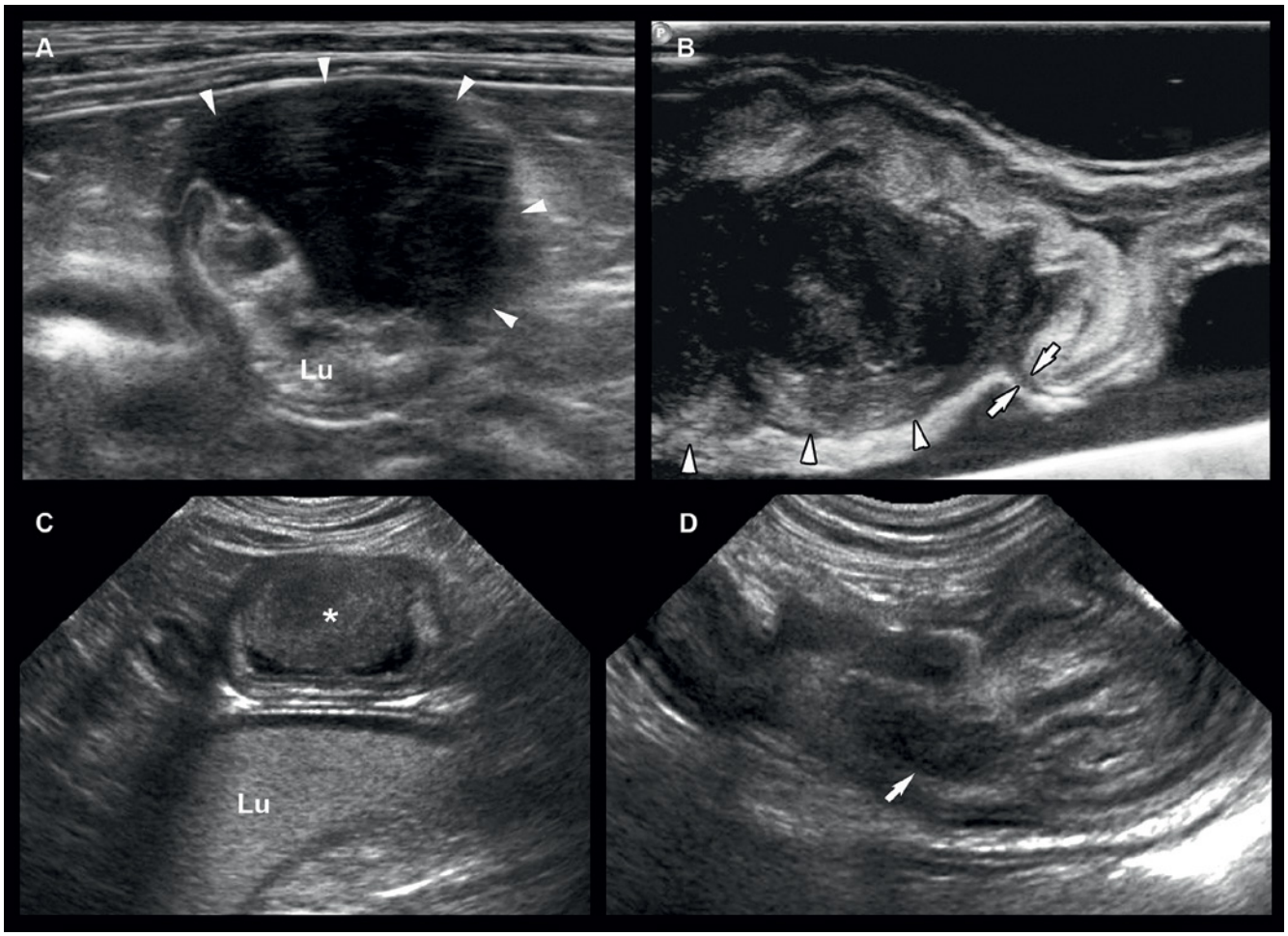


Figure 9.61. **Leiomyoma in two dogs. (A)** Transverse sonogram of the tumor in a 7-year-old Cairn terrier without any GI signs. **(B)** Longitudinal sonogram of the surgical specimen placed in a water bath. **(A)** The mass is nearly anechoic and homogeneous (arrowheads), deforming the outer contour of the jejunum. The layers are focally indistinct. **(B)** In the water bath specimen, the connection of the mass (arrowheads) to the muscular layer (arrows) is more obvious. **(C)** A sagittal sonogram of a fluid-distended jejunal segment is seen orad to a jejunojejunal intussusception that was associated with a discrete echogenic nodule (*). **(D)** Sagittal view of part of the leiomyoma (arrow) next to the beginning of the invagination. Lu, lumen.

origin. Large GI mesenchymal tumors tend to be heterogeneous with a mixed echogenic pattern. The presence of anechoic and hypoechoic foci within the mass may correlate with the areas of central degeneration and necrosis frequently found in these large lesions. There is no ultrasonographic feature reliably distinguishing smooth muscle tumors from GIST (Figures 9.62, 9.63). GIST might have a higher incidence in cecal location (Hobbs et al. 2015). When gastric in origin, these tumors tend to project into the GI lumen (Figure 9.64).

Intestinal **leiomyosarcoma** is the most common intestinal sarcoma recognized in dogs; in cats, GI leiomyosarcoma is much less commonly reported (~1.2% of intestinal neoplasms in a large study) with tumors affecting the small and large bowel with equal frequency; there is only one case report of gastric leiomyosarcoma in a cat (Hart et al. 2018).

Though much less frequently encountered, **malignant peripheral nerve sheath tumor** (MPNST) can also affect the GI tract and may appear like leiomyosarcoma and GIST, both ultrasonographically and histopathologically; therefore, MPNST could be considered an additional differential diagnosis (Ahn et al. 2022; Boland et al. 2019; Ribas et al. 2017).

Other less commonly reported tumors include mast cell tumor (Figure 9.65), histiocytic sarcoma (Figure 9.66), carcinoid/neuroendocrine tumor, neurilemoma, nerve-sheath tumor, hemangiosarcoma (Figure 9.67), plasmocytoma, extraskeletal osteosarcoma, and metastases (Culp et al. 2008, Stimson et al. 2000, Dominguez et al. 2014). **Mast cell tumors** have been

Vet-ebooks.com

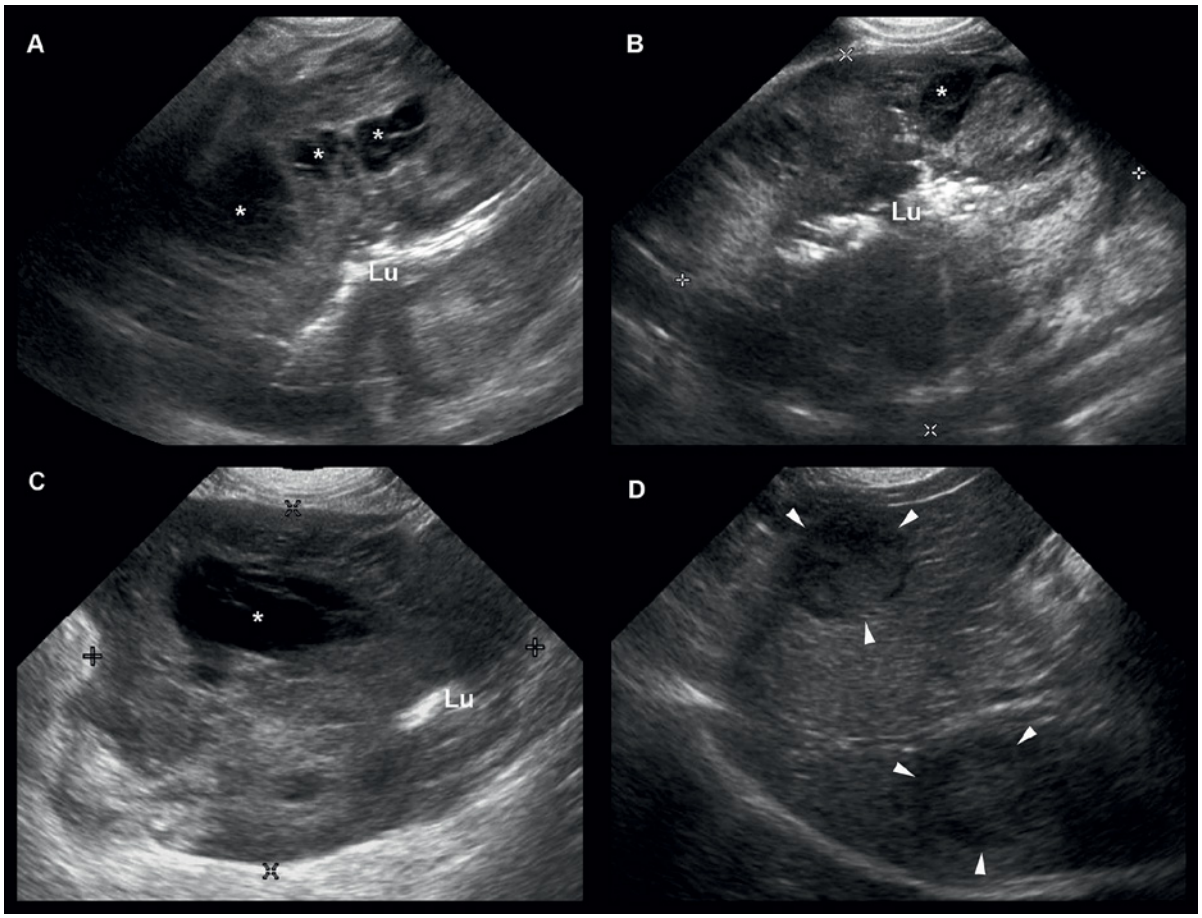


Figure 9.62. Intestinal leiomyosarcoma in two dogs. (A) Sonogram of a jejunal leiomyosarcoma in a 9-year-old Pittbull. The mass is large, inhomogeneous with several cavitary areas (*) that most likely are areas of degeneration and necrosis. **(B)** Transverse sonogram of the same mass, displaying similar features, but at the edge of the lesion, the lumen is more centrally located. **(C)** In this 8-year-old Golden Retriever, there is also evidence of a large, eccentric, and inhomogeneous mass with cavitations (*). **(D)** Additionally, two hypoechoic masses (arrowheads) were present in the liver. They are hepatic metastases from the colonic leiomyosarcoma. Lu, lumen.

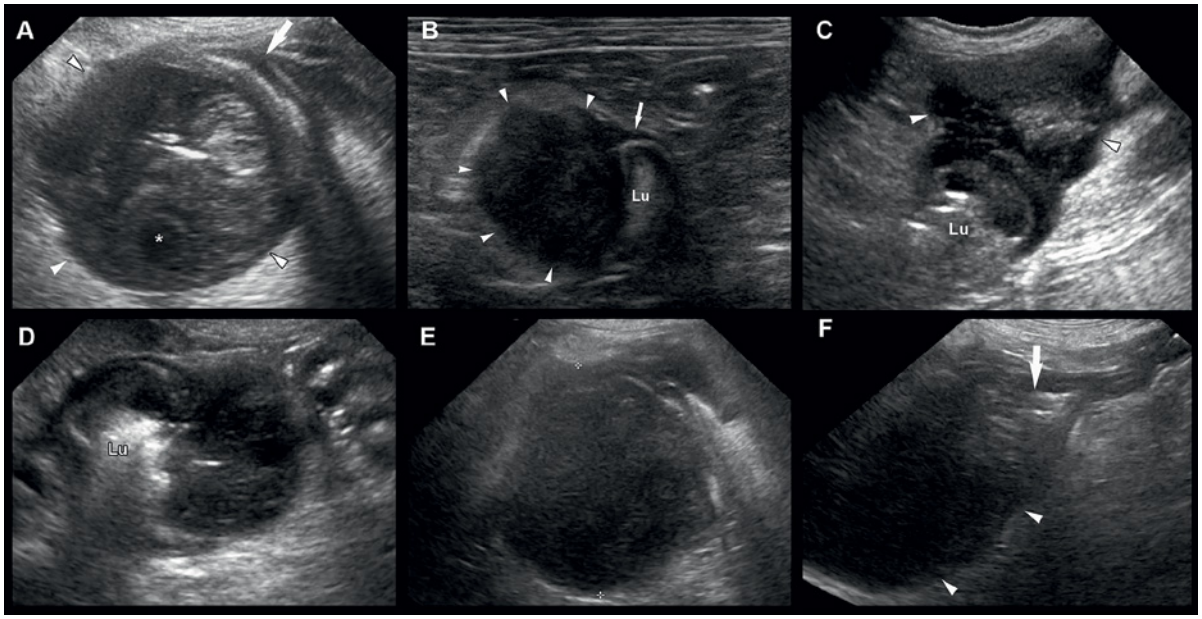


Figure 9.63. Gastrointestinal stromal tumors (GISTs) in five dogs. (for full caption, see facing page)

Vet-ebooks.com

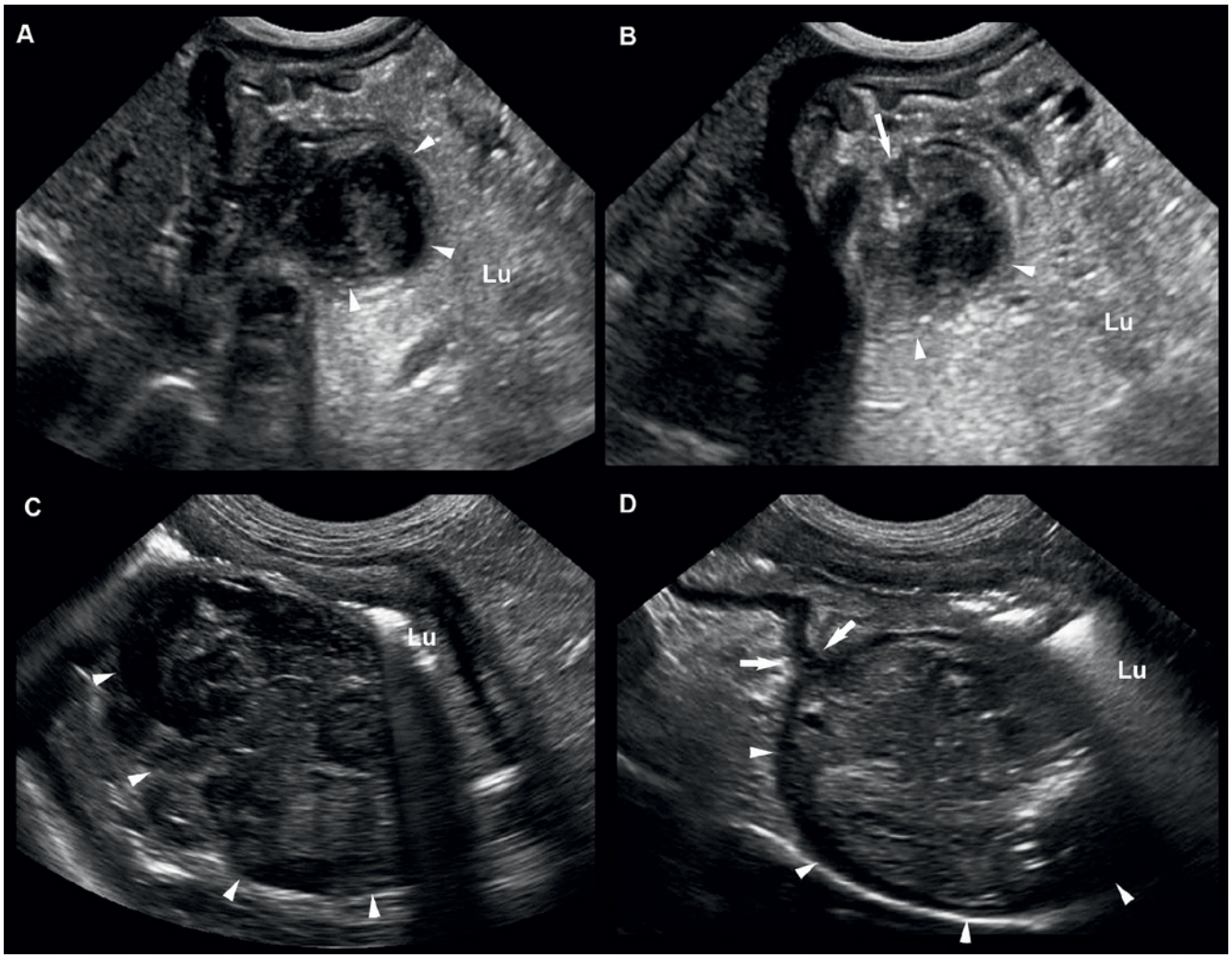


Figure 9.64. **Leiomyoma of the stomach in two dogs. (A, B)** Sonograms of the small (2.2 cm) poorly echogenic nodule projecting into the lumen of the greatly fluid-distended stomach of a 10-year-old Xolo dog presented for vomiting and collapse. The arrowheads outline the lesion. In **(B)**, the arrow points to the ulcerated portion of the nodule, responsible for the severe bleeding. The lesion was close to the cardia but was completely and successfully resected. **(C, D)** Sonograms of a large (over 4 cm) and inhomogeneous gastric mass (arrowheads), near the cardia, in a 13-year-old West Highland White Terrier. In **(D)**, the arrows point to the visible connection with the muscular layer. Lu, lumen.

Figure 9.63. **Gastrointestinal stromal tumors (GISTs) in five dogs. (A)** Transverse sonogram of an inhomogeneous mass in an 8-year-old Labrador Retriever. The connection to the intestine in the near field (arrow) was confirmed during the evaluation. A small hypoechoic area (*) is noted in the mass, and it may represent necrosis. **(B)** A small poorly echogenic eccentric mass (arrowheads) is asymmetrically disrupting the jejunal wall layering in a 10-year-old Labrador. At the junction with the wall, it appears that the mass arises from the muscular layer of the wall (arrow). Hyperechoic fat is noted around the lesion. **(C)** A similar finding of eccentric distribution (arrowheads) is noted in the lesion found in a 14-year-old mix dog In a 5-year-old Boxer **(D)**, the lesion is similarly eccentric in distribution. **(E-F)** A large (about 10 cm long) poorly echogenic mass (arrowheads) was noted in this 8-year-old Labrador. The intestinal origin is confirmed as the gas on the edge of the mass extends into the intestinal segment in the near field (arrow).

Vet-ebooks.com

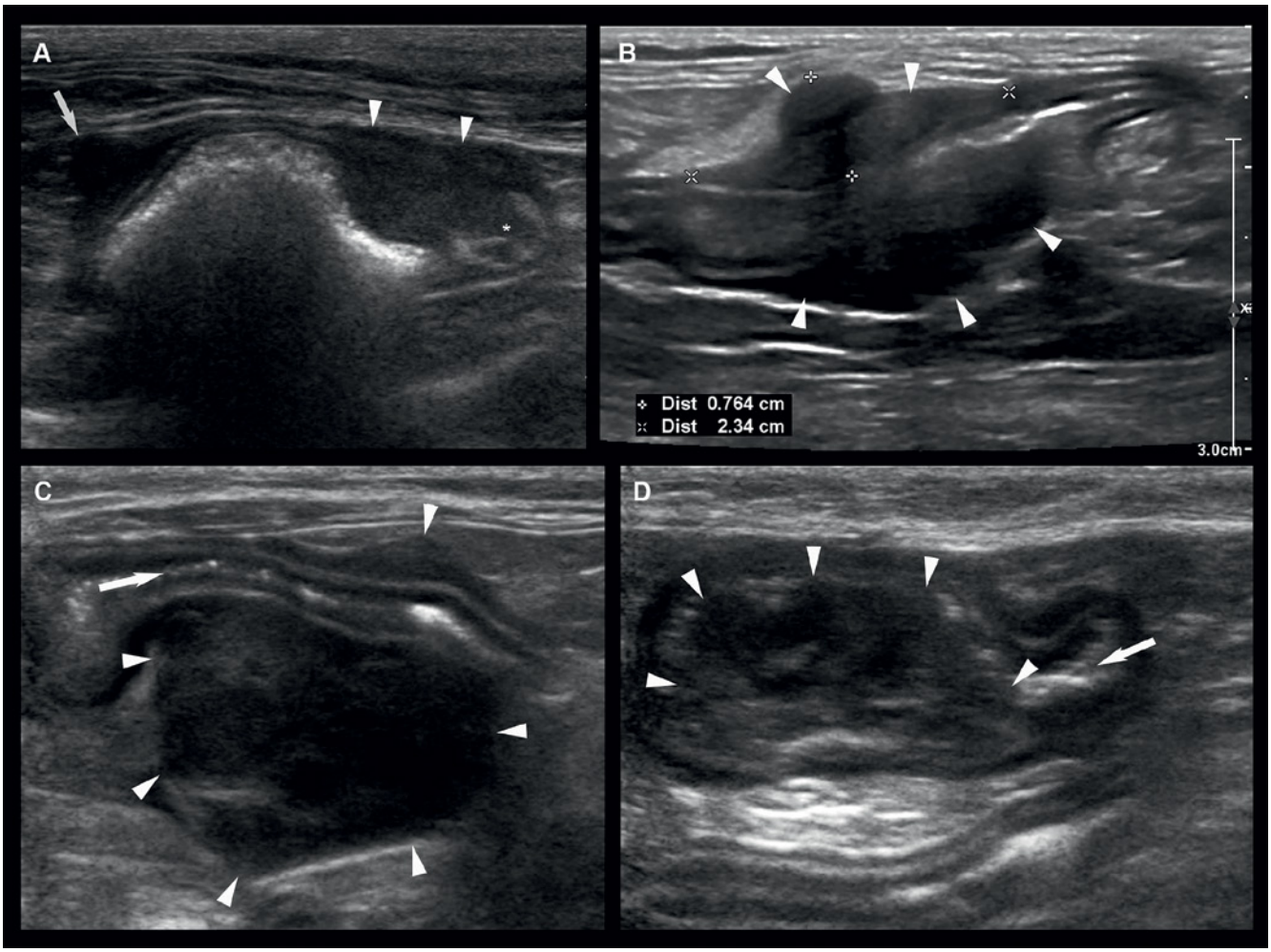


Figure 9.65. **Mast cell tumors in cats. (A)** On this transverse sonogram, lesions are seen in the ileocecocolic junction of a 14-year-old cat. Transmural thickening with loss of layering is noted in the cecum (arrowheads). Altered layering and asymmetric thickening of the proximal ascending colonic wall are also present, creating a bulge on the serosal surface (arrow). An asterisk is placed on the ileum. Mast cell tumor was diagnosed on ultrasound-guided fine-needle aspirates. **(B)** Longitudinal sonogram of a segment of jejunum in another 14-year-old cat with marked, asymmetrically circumferential thickening of the wall (arrowheads). The adjacent fat is mildly hyperechoic. **(C, D)** In this 12-year-old cat with chronic weight loss, there are several hypoechoic jejunal masses. **(C)** One mass is primarily eccentric (arrowheads) and is not projecting into the intestinal lumen (arrow). **(D)** Another large mass is projecting into the lumen (arrow) of the affected jejunal loop (arrowheads). There was no evidence of mechanical ileus.

described in cats as often focal hypoechoic, eccentric, and asymmetric nodules/masses (Laurenson et al. 2011). Metastases from a mammary carcinoma have been described as discrete small hypoechoic nodules in the jejunal muscular layer (Dominguez et al. 2014).

Gastrointestinal Non-tumoral Nodule or Mass

At times, the hypertrophic mucosal or hyperplastic glandular changes of the gastric wall may appear as a discrete nodule or mass. Exuberant hyperplastic or hypertrophic mucosal or muscular changes cannot be differentiated from benign polyps based on their imaging or gross appearance; however, their overall echogenicity is usually increased in comparison to malignant lesions. **Gastric polyps** can appear as large, moderately echogenic nodules or masses projecting into the gastric lumen (Diana et al. 2009) (Figure 9.68). They often are asymptomatic unless located in the pylorus, thus creating a gastric outflow disturbance. In small-breed dogs and especially brachycephalic breeds, **chronic hypertrophic pyloric stenosis** can be encountered (Figure 9.69). The hypertrophic and/or

Vet-ebooks.com

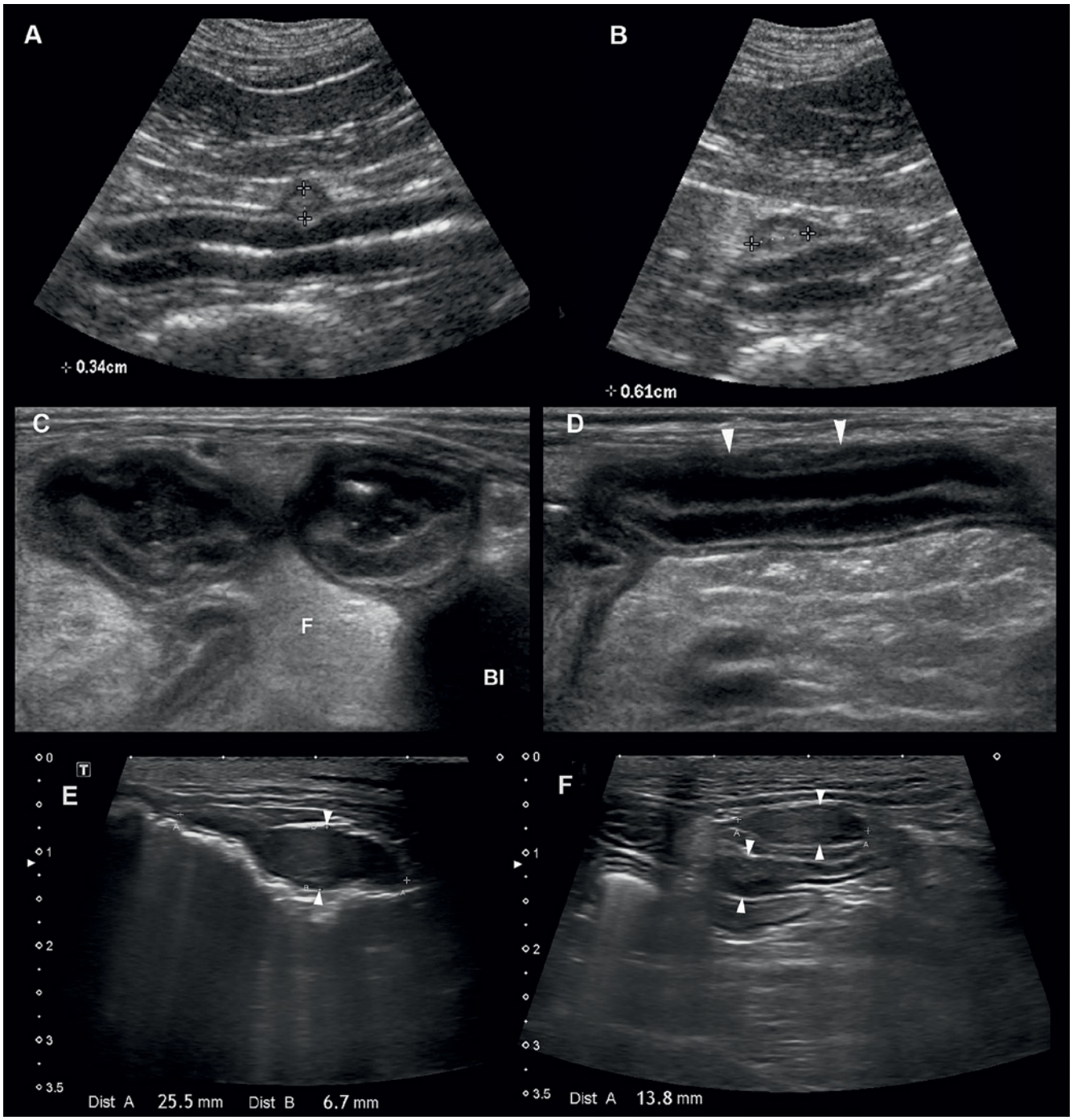


Figure 9.66. **Histiocytic sarcoma. (A)** Longitudinal **(A)** and transverse **(B)** sonograms of a segment of jejunum in a Bernese Mountain dog with disseminated histiocytic sarcoma. A small, well-defined, hyperechoic nodule is present within the muscularis, deforming the contour of the submucosa. Similar lesions were observed in other intestinal segments. All nodules, including those in the liver, were hyperechoic. **(C, D)** A 15-year-old miniature Pinscher with disseminated histiocytic sarcoma throughout the GI tract, liver, and bone marrow. **(C)** Most intestinal segments had altered layering (hyperechoic mucosa, mucosal ulceration), hyperechoic fat (F), and echogenic effusion (same case as Figure 9.45). Bl, bladder. **(D)** Note the thickened serosa on this jejunal segment (arrowheads). Tumoral infiltrates were reported histopathologically more severe on the serosa. **(E, F)** In this 6-year-old Bernese Mountain dog, lesions were identified in the tibia, the kidneys, and several intestinal segments. Focal areas of wall thickening primarily affecting the muscular layer are present (arrowheads) in these sonograms. The infiltration is uniform and slightly more echogenic than the normal muscular layer. F, fat.

Vet-ebooks.com

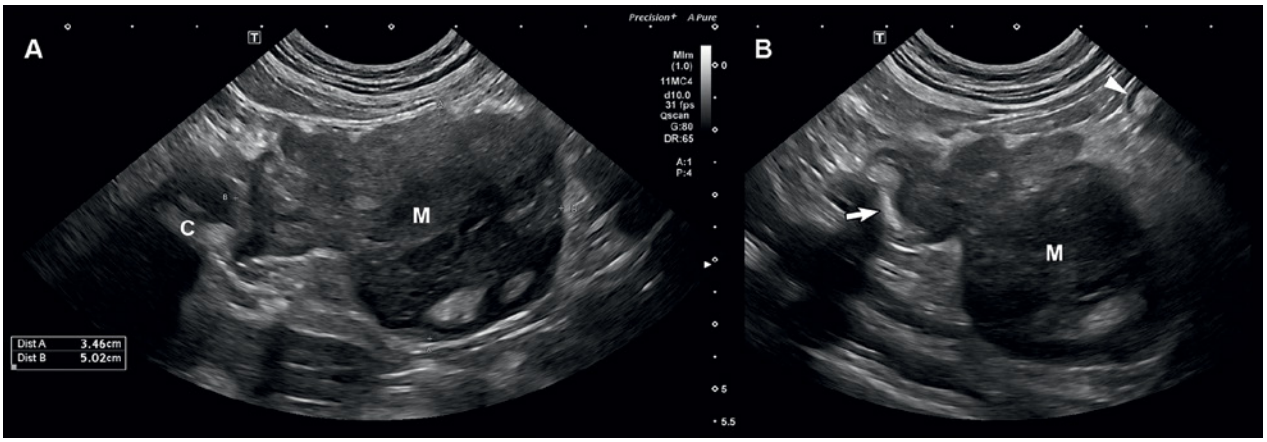


Figure 9.67. Cecal hemangiosarcoma in a 9-year-old domestic shorthair cat presented for evaluation of anemia and melena. (A) A large, lobular, heterogeneously hypoechoic, poorly vascularized mass measuring approximately 3.5 × 5.0 cm is arising from the cecum. **(B)** The mass (M) is bulging into the lumen of the ascending colon (arrows); the distal ileum can also be seen in this image (arrowhead). The adjacent mesentery is moderately hyperechoic.

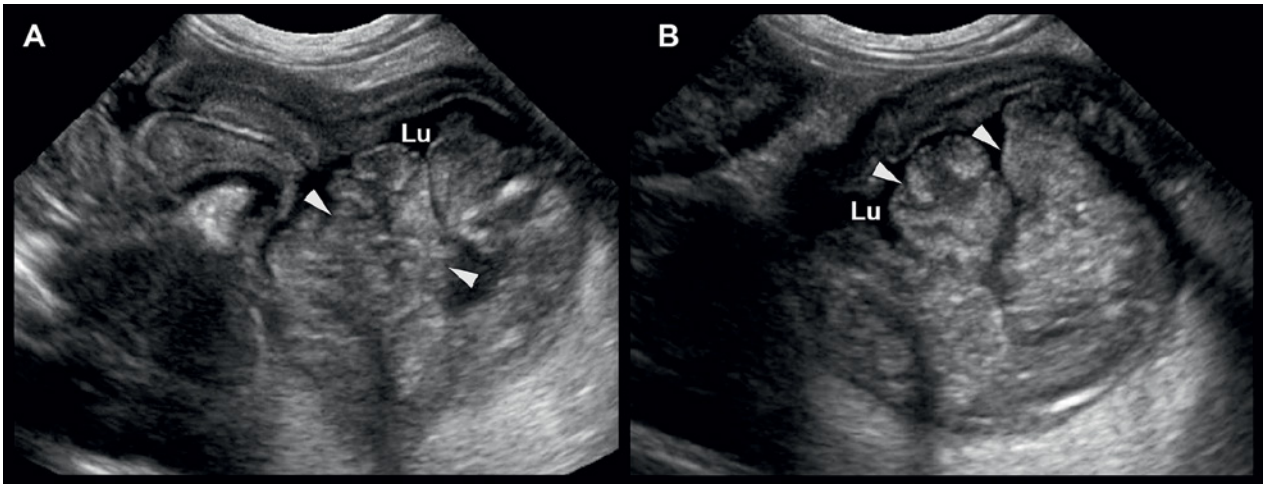


Figure 9.68. Adenomatous polyps in the stomach in an 11-year-old Jack Russell terrier. Longitudinal **(A)** and transverse **(B)** sonograms show extensive polypoid projections (arrowheads) filling a large portion of the gastric lumen (Lu).

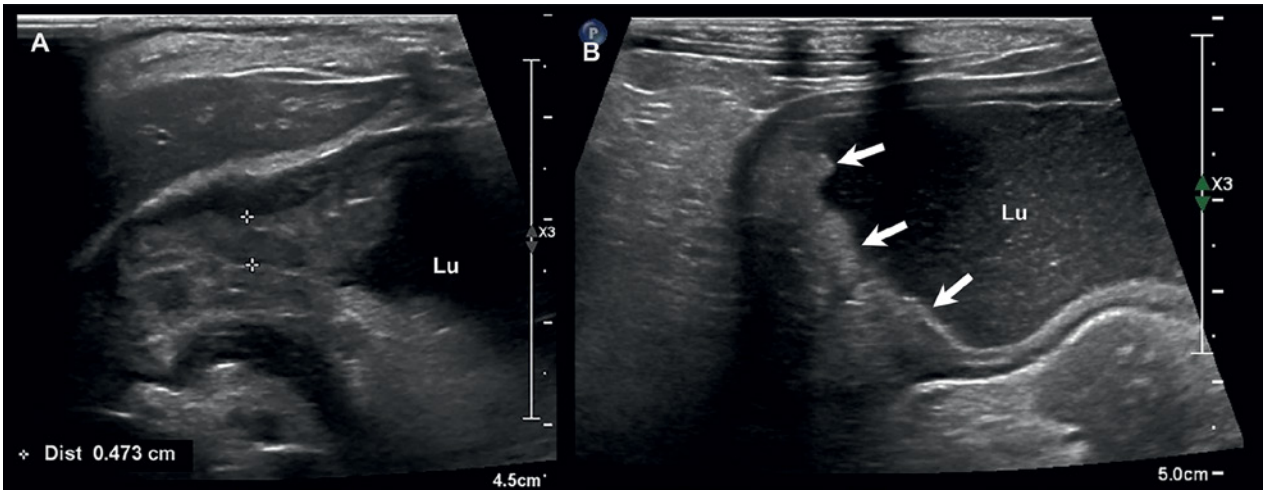


Figure 9.69. Chronic hypertrophic pyloric stenosis in one dog. (A, B) There is moderate wall thickening at the pyloroduodenal junction in this 13-year-old Coton de Tulear presented for increased frequency of vomiting. Notice the thickened pyloric wall, including both the mucosa (between calipers) and the muscular layer. In **(B)**, a large amount of fluid is present in the gastric lumen (Lu) and the hyperplastic mucosa appears as irregular projections (arrows) into the lumen.

Vet-ebooks.com

hyperplastic changes primarily affect the smooth muscle layer of the pylorus (Biller et al. 1994; Rhim et al. 2018), but it is common to see concurrent mucosal changes. Because of this chronic condition, the stomach tends to be flaccid, and a moderate amount of fluid or food accumulates in it. **Mucosal hyperplasia** most commonly is seen at the antrum of the stomach. It may appear as repeated hyperechoic short lines, running perpendicular to the luminal mucosal surface ("palisade pattern"). At the PDJ, mucosal hyperplasia may be seen wrapping over polyps. This change should not be confused with a variable degree of hyperechogenicity at the PDJ (Figure 9.70).

Extensive hyperplastic changes can be found at other locations along the GI tract. If located within the proximal portion of the descending duodenum, these changes may induce outflow obstruction or compromise the bile flow (Figure 9.71).

Duodenal adenomatous polyps have been reported in cats (Daure et al. 2017; MacDonald et al. 1993); they can be associated with bleeding ulcers. They can easily be missed on ultrasound as they often are

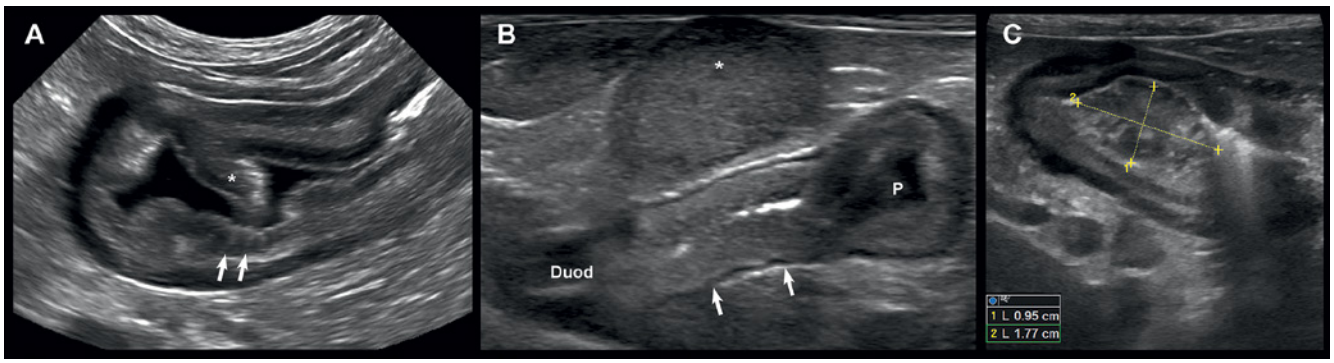


Figure 9.70. Gastric polyps in 2 Yorkshire terriers. In this 16-year-old Yorkie without GI signs **(A, B)**, there is a gastric polyp (*). Notice the picket-fence appearance of the luminal mucosal surface, likely representing mucosal hyperplasia (arrows). **(B)** At the pyloroduodenal junction, there is a hyperechoic zone (arrows) including the submucosa and mucosa, presumed to represent an anatomical transition with possibly increased connective fibrous tissue and submucosal glands. The pancreaticoduodenal lymph node (*) is enlarged and homogeneously echogenic. In this 12-year-old Yorkie with chronic vomiting **(C)**, a Small, polypoid mass with heterogeneous echogenicity is present in the pyloric antrum. There was evidence of multifocal hyperplasia of the gastric mucosal layer.

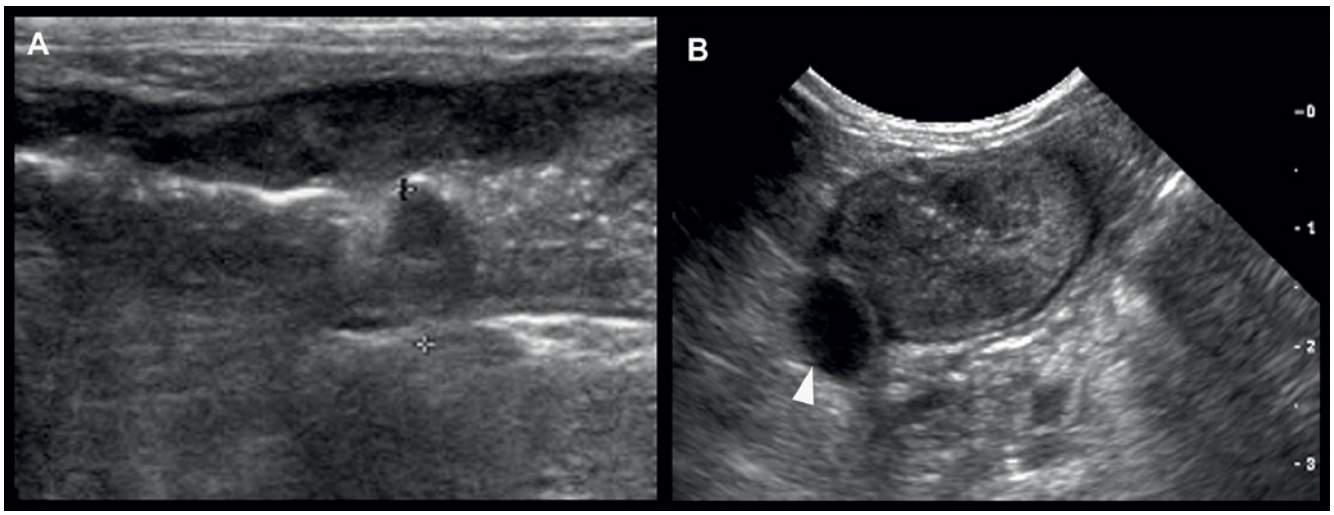


Figure 9.71. Duodenal mucosal hyperplasia evolving into adenocarcinoma. (A, B) Longitudinal **(A)** and transverse **(B)** images of marked diffuse duodenal thickening (between the cursors) in a 13-year-old cat. The distal CBD is fluid dilated (arrowhead). Initial surgical biopsies were diagnostic of extensive tubulovillous, adenomatous, mucosal hyperplasia. Drastic surgical resection was performed 7 months later, and the final histopathologic diagnosis was duodenal adenocarcinoma. The sonographic features had not progressed during this long period.

Vet-ebooks.com

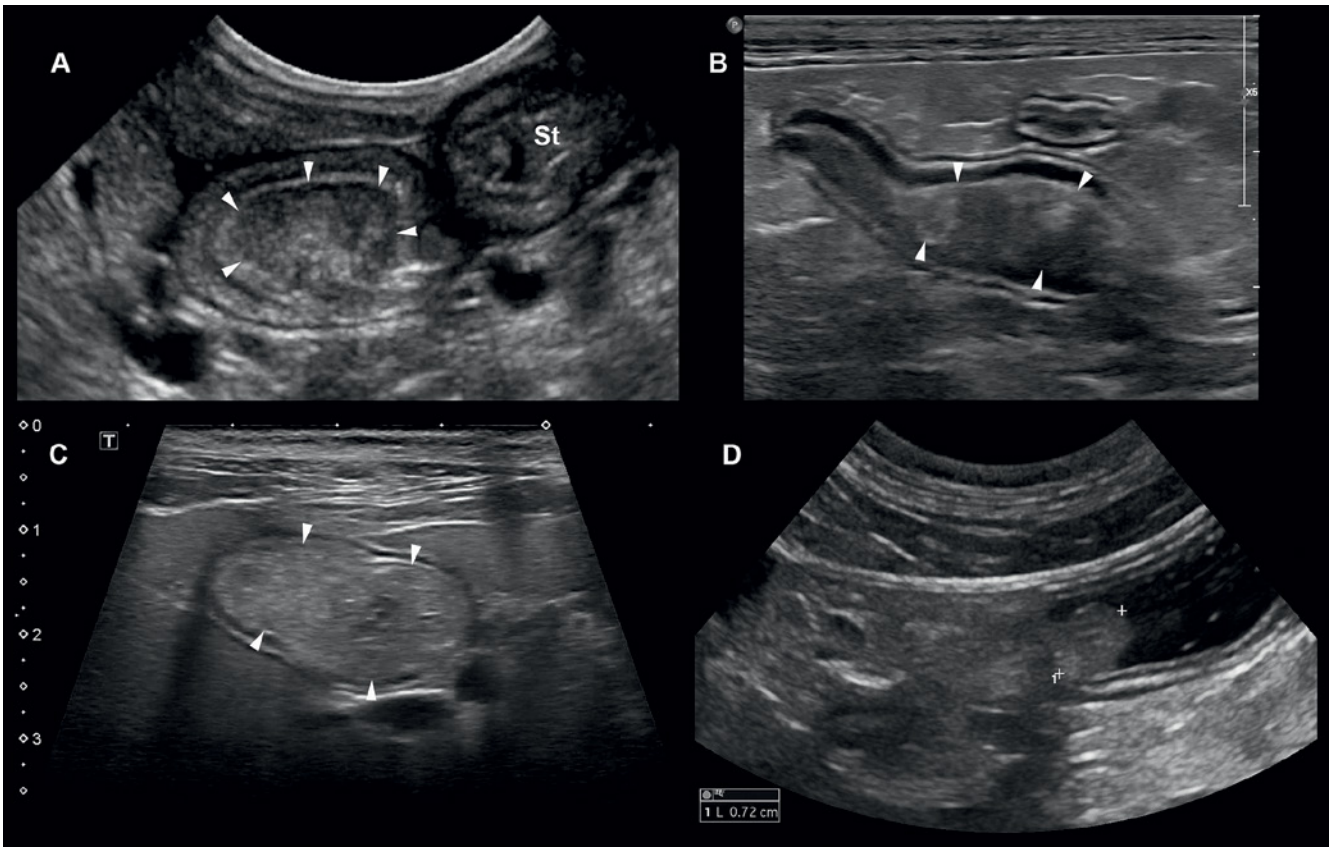


Figure 9.72. **Duodenal polyp in four cats. (A)** In an 11-year-old cat, an echogenic nodular lesion (arrowheads) is filling the lumen of the antral/proximal duodenal lumen. St, stomach. **(B)** In this other cat, adenomatous hyperplasia was extensive (arrows) but was not obstructive; it was resected surgically and confirmed histologically. **(C)** Large hyperechoic mass (arrowheads) distending the proximal duodenum of a 19-year-old diabetic cat. This mass was unchanged from previous exam (2 months prior) and consistent with an adenomatous polyp. **(D)** Incidental adenomatous polyp protruding into the pyloric antrum of another 7-year-old cat presented for renal disease.

uniformly echogenic and can blend with the surrounding GI contents (Figure 9.72).

Large single or multiple masses of mixed echogenicity, described as **feline eosinophilic sclerosing fibroplasia** (Weissman et al. 2012), have features similar to neoplasia (e.g., loss of layering and deformity of the wall), but they tend to be associated with hyperechoic areas within the mass, likely corresponding to the fibrosis (Figure 9.73).

Similarly, any **granulomatous lesions** affecting any segment of the GI tract may have features suggestive of neoplasia. Granulomatous masses may be associated with trauma (healed foreign-body perforation), parasitic, viral such as feline infectious peritonitis (Müller et al. 2023), fungal such as pythiosis (Graham et al. 2000), histoplasmosis (Berle et al. 2021), or bacterial infections (Figure 9.74).

Lipogranulomatous lymphadenitis is a granulomatous inflammation targeting the lymph vessels, the mesentery and intestinal wall of intestinal segments affected with chronic enteropathy (De Magistris et al. 2023) (Figure 9.74E, F).

Performing aspirates or biopsies of these lesions is essential not to misdiagnose them as neoplastic and to choose the optimal treatment modality.

Congenital or Hereditary Disorders

Congenital GI disorders are rare in small animals. **Intestinal duplication** has been reported in the literature (Spaulding et al. 1990, Parry-Smith et al. 2008). They can be encountered in any segment of the GI tract, and even though they represent a benign process that may be incidentally detected later in life, they are

Vet-ebooks.com

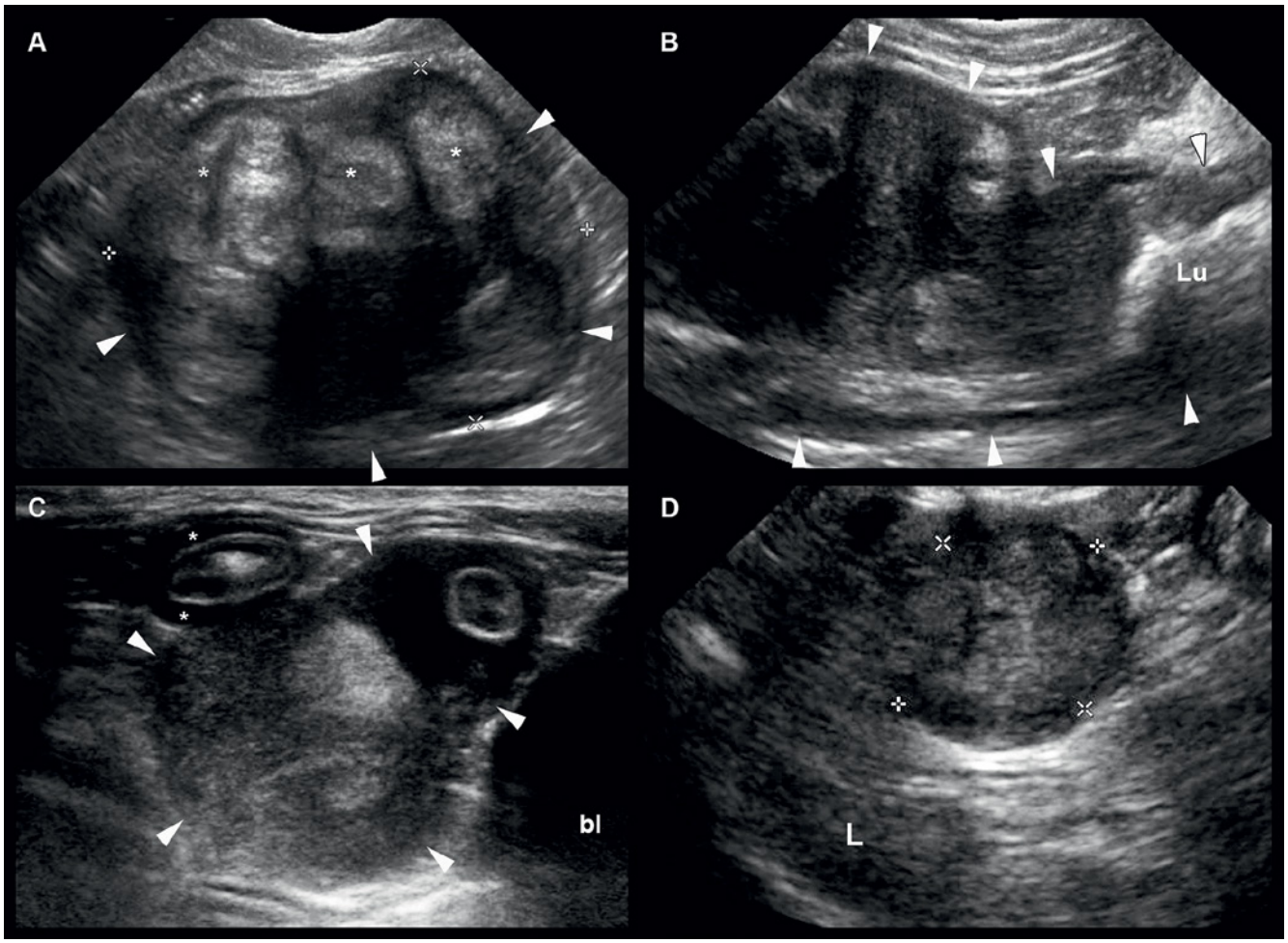


Figure 9.73. Feline eosinophilic sclerosing fibroplasia in two cats. Transverse **(A)** and longitudinal **(B)** sonograms of a large asymmetric and inhomogeneous mass (arrowheads) deforming the contour of the colon in a 10-year-old Ragdoll cat. Notice the large hyperechoic areas (*) within the mass, corresponding to the abundant fibrosis. **(C, D)** An eccentric jejunal mass (arrowheads) with hyperechoic area is present in an 8-year-old cat. **(D)** An inhomogeneous mixed echogenicity nodule (between cursors) is also seen in the liver (L) and was also confirmed as eosinophilic sclerosing fibroplasia. Concurrent muscular hypertrophy (*) is noted in adjacent intestines, as seen in the near field on **(C)**. Lu, lumen.

sometimes associated with pancreatitis (if duodenal in origin), or neoplasia (Figure 9.75).

Short colon syndrome has been reported in cats and dogs (Fluke et al. 1989, King et al. 2024). In these cases, the ileocecocolic junction is then located in the mid to left side of the abdomen and the descending colon appears short (Figure 9.76). It can be encountered in cats with or without diarrhea or other GI signs.

Congenital pyloric stenosis mostly reported in brachycephalic dogs results in concentric, symmetric hypertrophy of the circular smooth muscle layer. **Gastric hyperplastic polyp** associated with outflow obstruction is described in French Bulldog (Kuan et al. 2009) and the pedunculated growths are often asymmetric (Figure 9.77).

GI Vascular Disorders

Infarction, ischemia, and angiodysplasia are uncommon and very challenging to diagnose (Fan et al. 1999; Wallack et al. 2003). **Bowel infarction** possibly associated with **mesenteric volvulus** may be difficult to identify with ultrasound initially (Junius et al. 2004). The affected segment(s) may become dilated with variable wall thickening with normal layering. Subsequently (72 hours after presentation), wall thickening becomes more obvious, and layers become indistinct. The adjacent fat becomes hyperechoic and peritoneal effusion develops (Figure 9.78). Mesenteric vessels should be assessed for the presence of thrombosis, although

Vet-ebooks.com

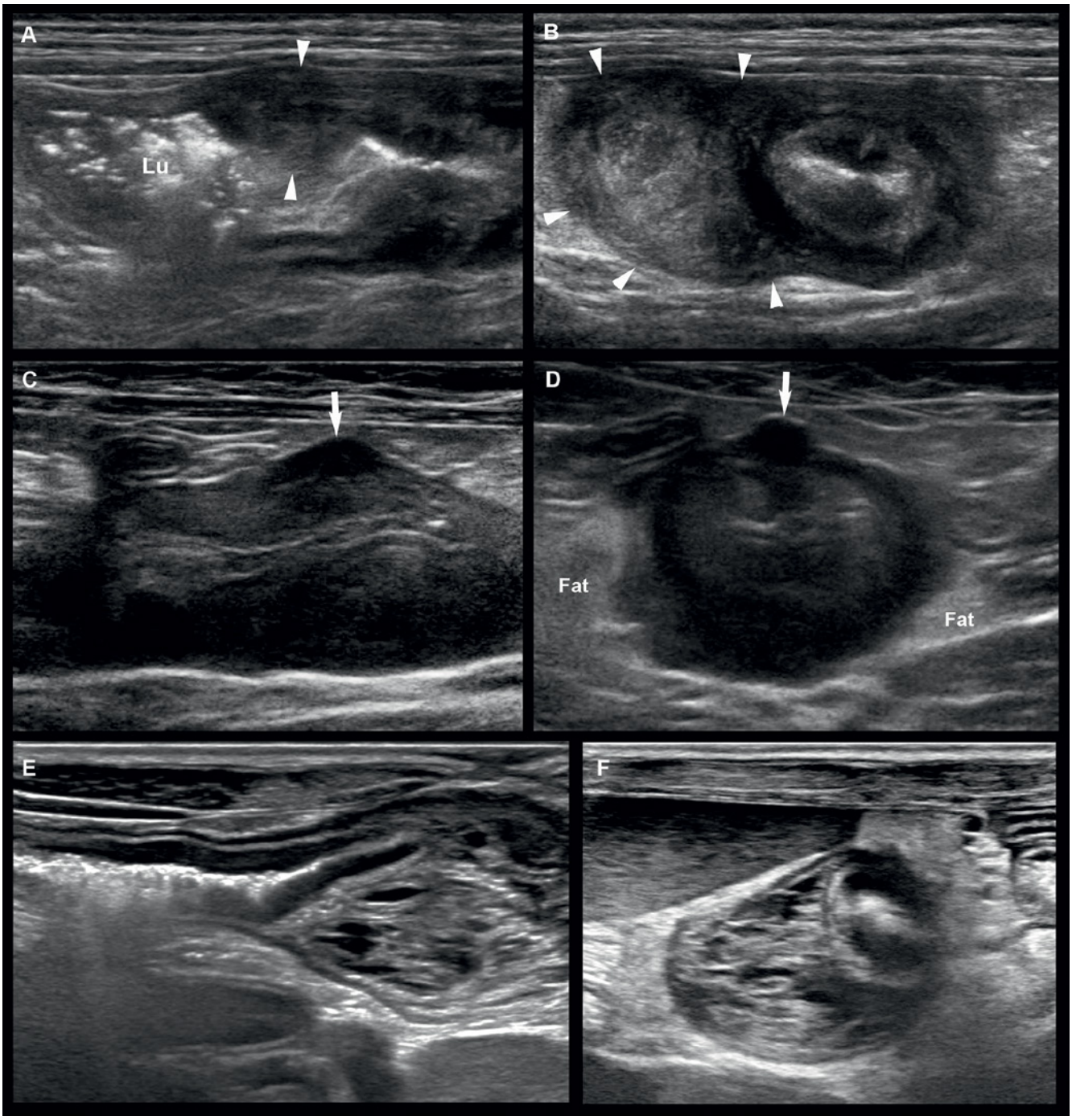


Figure 9.74. **Granulomatous enteritis.** Sagittal **(A)** and transverse **(B)** sonograms of a segment of jejunum in a Portuguese water dog. The wall (arrowheads) of this jejunal segment is thickened and associated with loss of layering, and its lumen (Lu) has irregular contours. In transverse view **(B)**, the asymmetric and eccentric distribution is more obvious (arrowheads). Longitudinal **(C)** and transverse **(D)** sonograms of the thickened descending colon in a 1-year-old cat with suspected FIP. The serosal contour is irregular (arrow). Marked disruption of the wall layering is noted. The regional fat is also hyperechoic. **(E, F)** Lipogranulomatous lymphangitis in a 3-year-old French Bulldog with acute vomiting, anorexia, and painful abdomen. A lacy and multicystic eccentric mass is wrapping along a segment of jejunum, as seen on these sagittal **(E)** and transverse **(F)** imaging planes, without affecting normal wall layering. The surrounding mesentery is hyperechoic.

Vet-ebooks.com

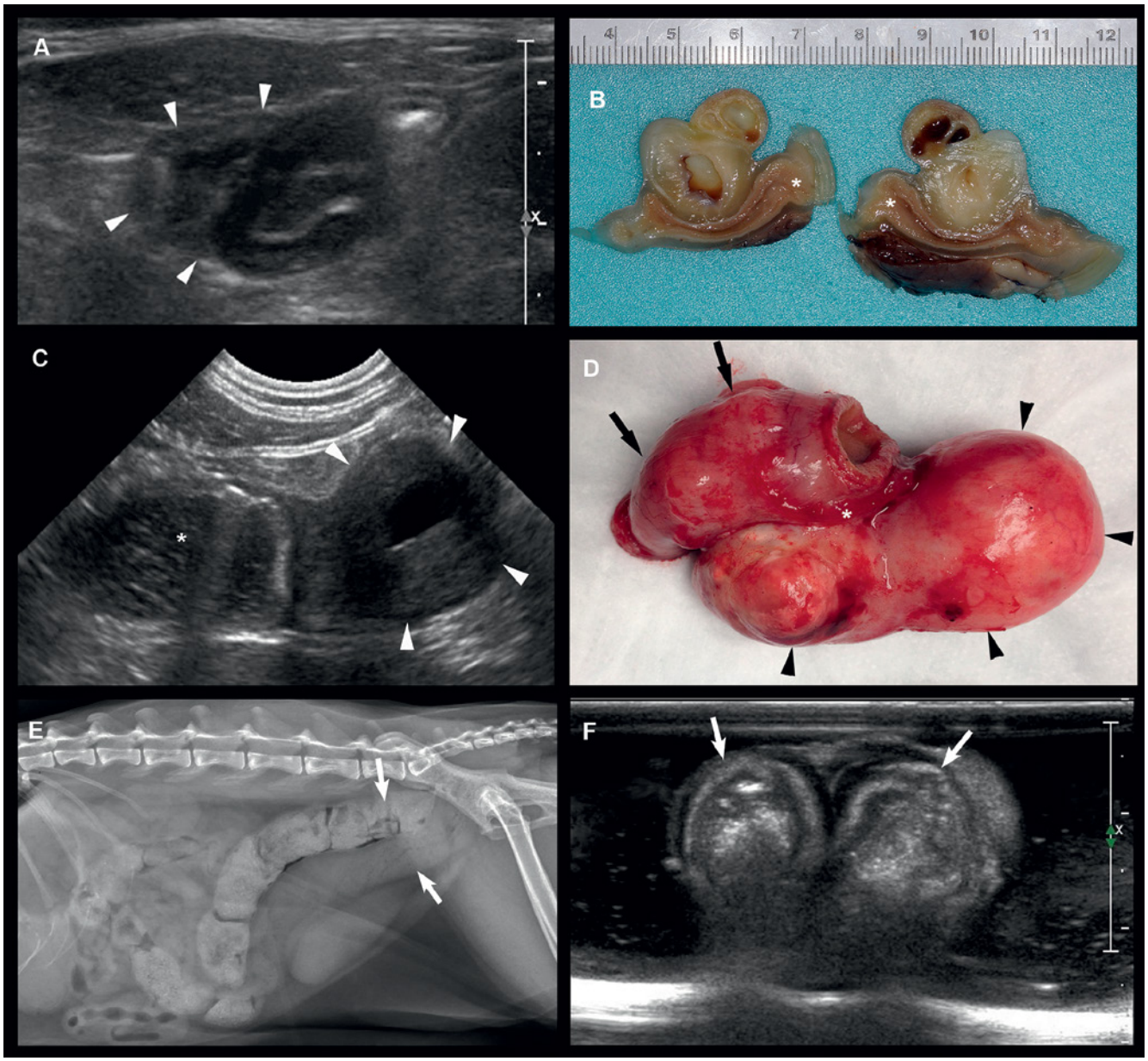


Figure 9.75. **Intestinal duplication in three cats. (A, B)** An 8-year-old cat with decreased appetite. **(A)** The mesenteric border of the duodenum (arrowheads) is deformed by a thick-walled cavitated structure. **(B)** Corresponding gross sections of the resected duodenum (*) and the duplication (arrowheads), confirmed histopathologically**. (C, D)** A 15-year-old cat presented for vomiting. **(C)** The fluid distended duodenum (*) is obstructed by the adjacent thick walled, cystic mass protruding in the duodenal lumen. **(D)** Corresponding gross sections of the resected duodenum (*) and the duplication (arrowheads). The final histopathological diagnosis was duodenal duplication with adenocarcinoma (arrows). **(E, F)** Colonic duplication of an 11-year-old cat. On the lateral radiograph, two discrete feces-filled descending colons are seen (arrows). An ultrasound was performed to best evaluate the extent of the duplication and the wall demarcation of each segment. Notice the two well-defined colons (arrows).

this evaluation may be limited by hyperattenuating fat and require contrast-enhanced CT for accurate diagnosis.

In severe congenital or acquired vascular disorders, numerous anomalous vessels (arteriovenous fistulae or varices) may develop as the result of portal hypertension and also affect the GI tract (Figure 9.79). In these cases, it is recommended to perform a CT angiogram to assess the abdominal vasculature more completely.

Vet-ebooks.com

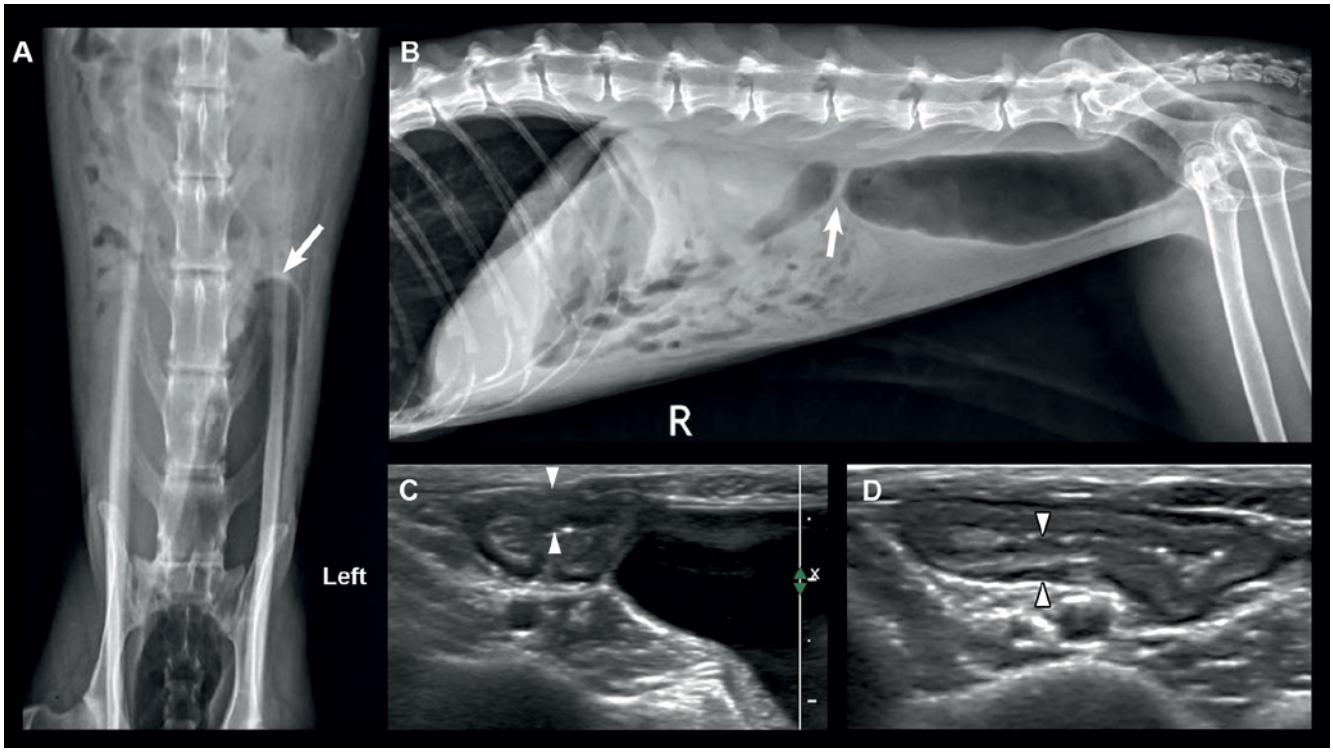


Figure 9.76. **Short colon in a 16-year-old cat. (A, B)** The lateral and VD abdominal radiographs showed the short colon that abruptly terminates ventral to the L4–5 junction (arrows). On ultrasound, the ileocolic junction **(C)** was well identified on the left side of the abdomen. The wall of the descending colon **(D)** is thickened (3 mm) but still layered.

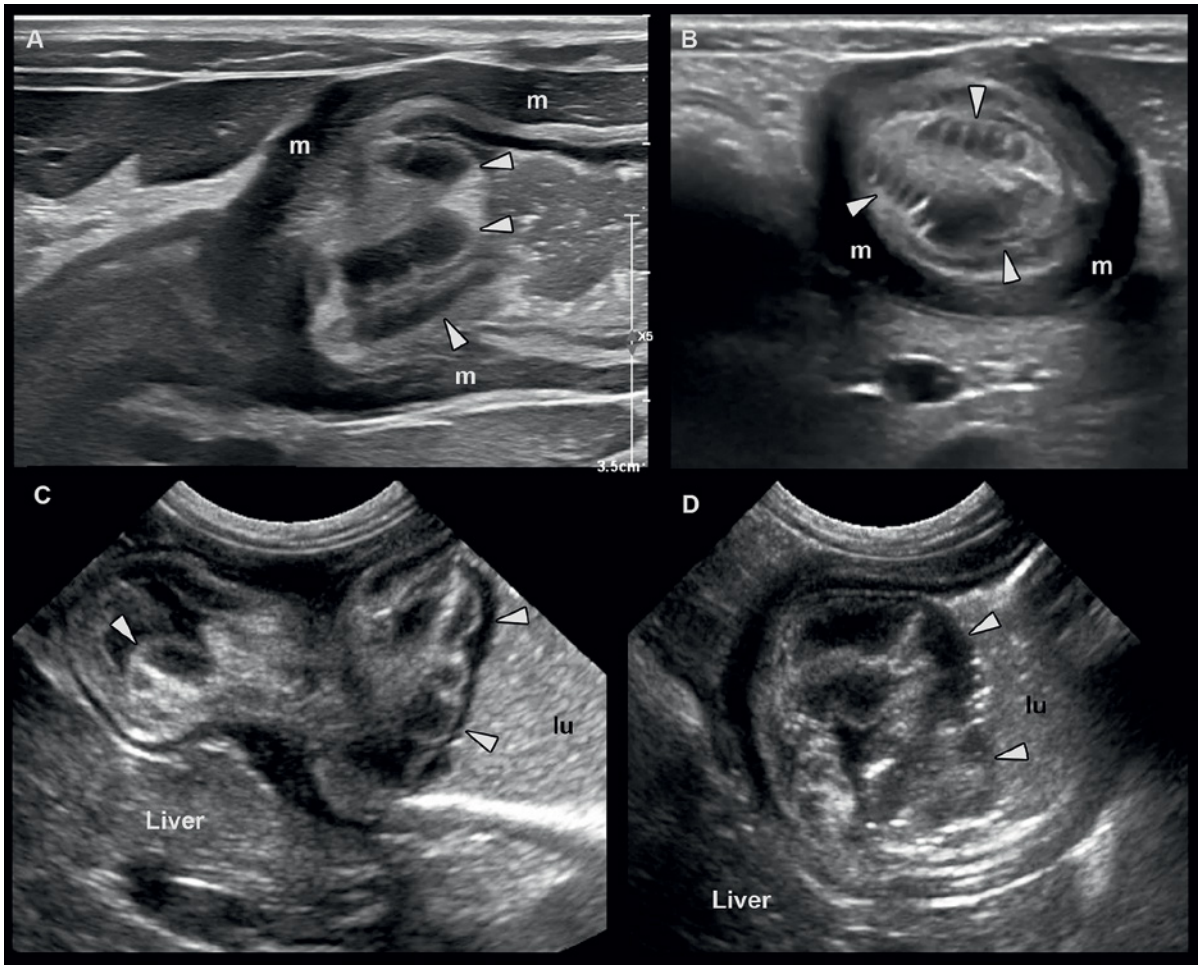


Figure 9.77. **Gastric hyperplastic polyp in two young French Bulldogs.** (for full caption, see facing page)

Vet-ebooks.com

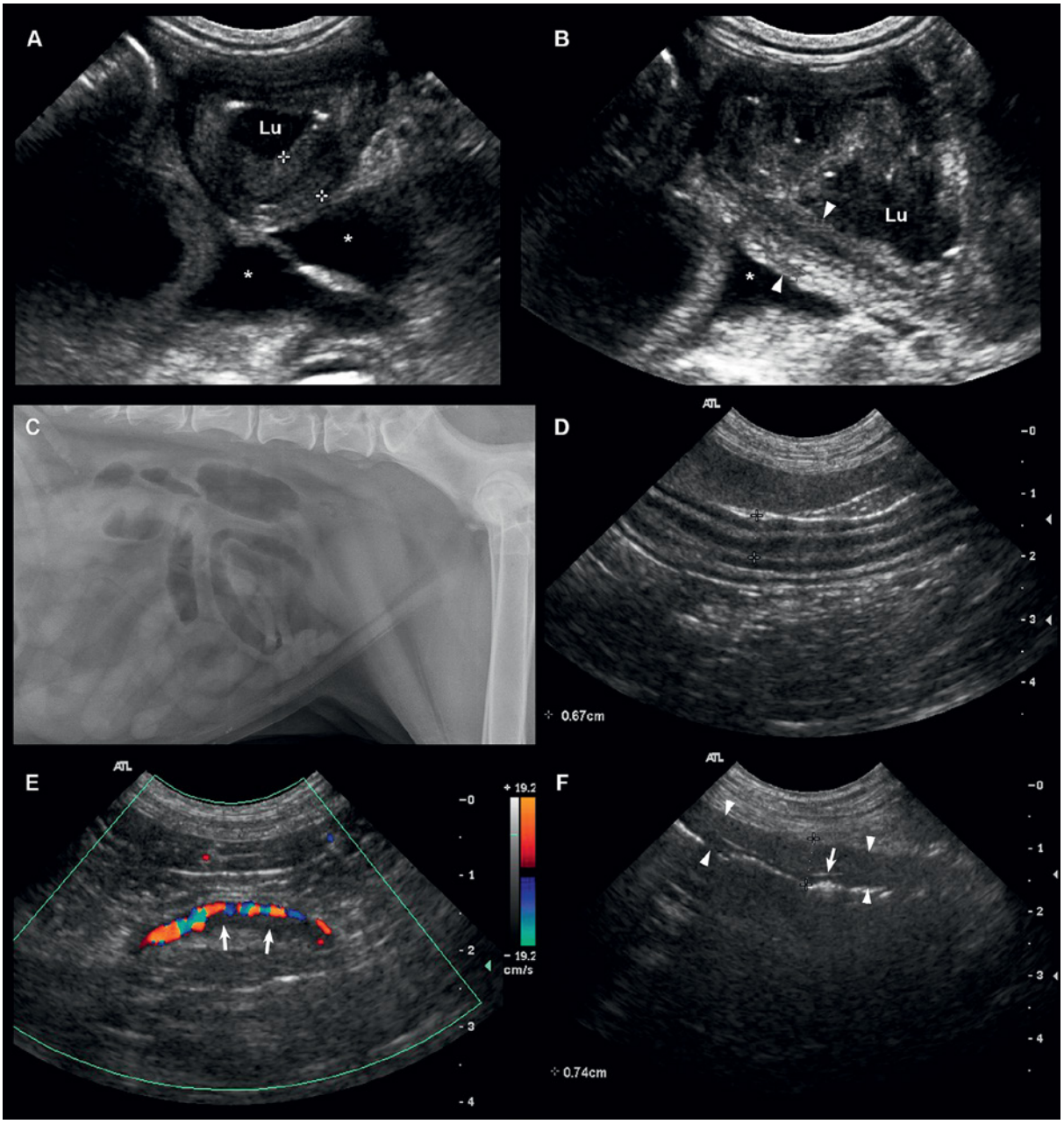


Figure 9.78. **(A, B) Vascular compromise due to intestinal volvulus in a 3-year-old Poodle presented for acute abdominal pain and vomiting.** In **(A)**, most intestinal loops are thickened (6–7 mm) with loss of layering (arrowheads) and hypomotile. Peritoneal effusion (*) is present. In **(B)**, amorphous echogenic structures floating within the lumen were shown to be blood clots and mucosal sloughing on autopsy. Lu, intestinal lumen. **(C–F)** Mesenteric thromboembolism and infarction in a Golden Retriever with glomerulonephritis and hypercoagulability. **(C)** Lateral abdominal radiograph obtained at the time of presentation in which several intestinal loops are mildly dilated with gas and fluid. **(D, E)** Subsequent ultrasound examination showed moderate thickening of a few segments of jejunum (0.67 mm, cursors in **A**) and partial thrombosis (arrows) of a branch of the cranial mesenteric artery. **(F)** On follow-up examination after the beginning of thrombolytic therapy (2 days later), jejunal wall thickening progressed (between arrowheads and cursors) and layers became indistinct. Additionally, pneumatosis (arrow) dissecting the wall was present. The abdominal fat was also markedly hyperechoic and hyperattenuating, preventing identification of vessels.

Figure 9.77. **Gastric hyperplastic polyp in two young French Bulldogs.** Sagittal **(A)** and transverse **(B)** sonograms of an exuberant polypoid lesion at the pylorus of this 4-month-old French Bulldog with a history of lethargy and regurgitation. The multilayered pattern of the lesion can mimic an intussusception. The arrowheads on **A** outline the asymmetrical but circumferential lesion protruding into the gastric lumen. Notice the marked thickening of the muscular (m) layer of the gastric wall. The superficial striations along the mucosal surface, outlined by arrowheads on **B** represent mucosal hyperplasia. **(C, D)** Similar lesions are also present in this 2-year-old French Bulldog. In these two dogs, the final diagnosis after surgical resection was chronic mucosal hyperplasia/hyperplastic polyp. Lu, lumen of pyloric antrum.

Vet-ebooks.com

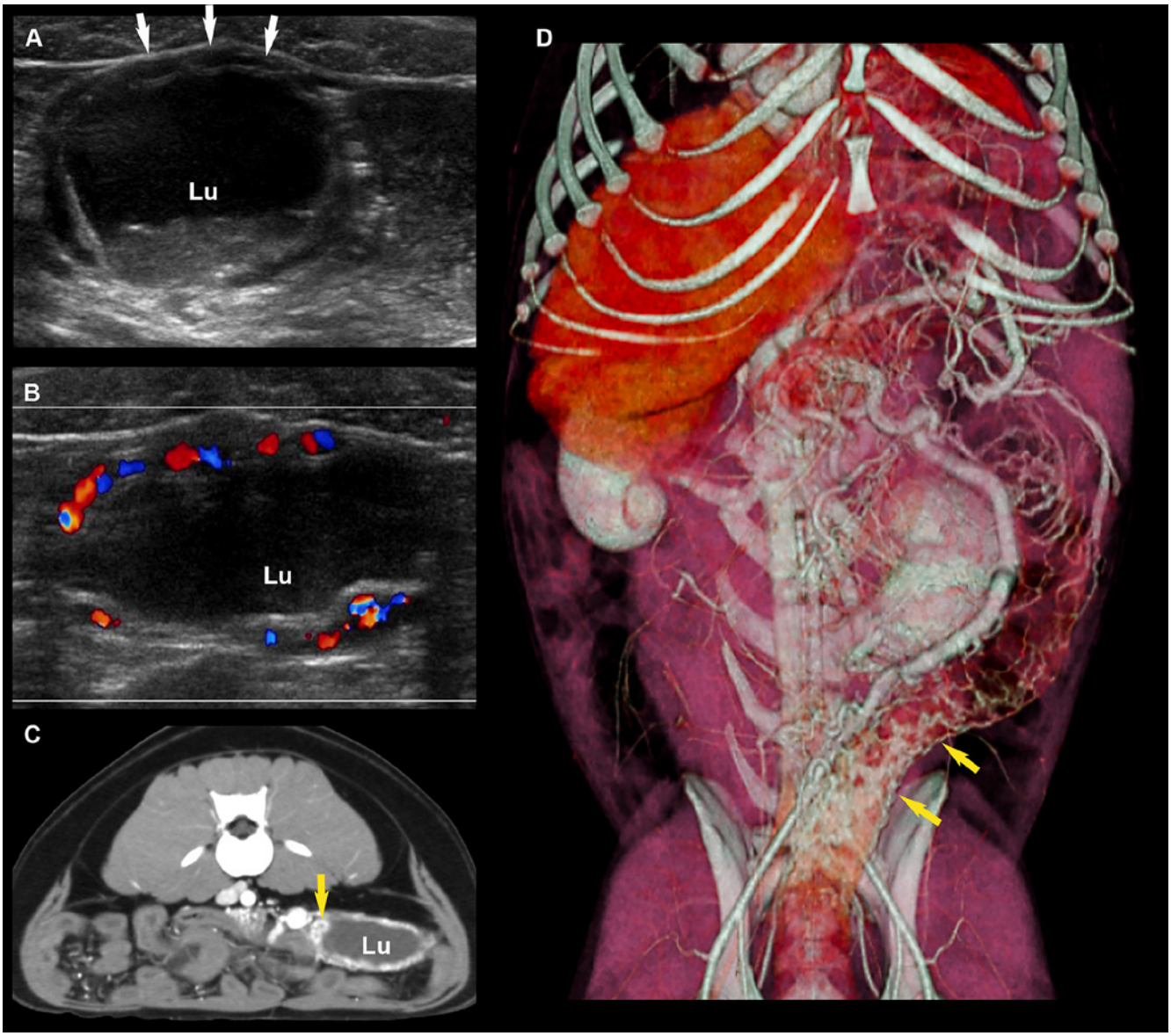


Figure 9.79. **Intestinal vascular anomaly in a 9-month-old Labrador dog with vomiting and diarrhea. (A, B)** Transverse sonograms of one fluid-filled colonic segment with a thickened, nodular-like wall made of intramural enlarged varices (arrows in **A**), as confirmed using color flow Doppler (in **B**). A large network of numerous anomalous small vessels was seen throughout the abdomen, especially in the mesentery and near the main portal vein. **(C)** Transverse postcontrast CT image of the caudal abdomen showing the intramural colonic vessels (arrow). **(D)** Reconstructed CT dorsal image illustrating the numerous anomalous enlarged and tortuous vessels supportive of portal hypertension and acquired portosystemic shunts (arrows). The left side of the liver is nearly absent. Because of the guarded prognosis, the dog was euthanatized, and the final diagnosis is arteriovenous malformation with marked arteriolar proliferation and hypertrophy, venous ectasia, lobular atrophy, and fibrosis.

Interventional Procedures

Percutaneous ultrasound-guided fine-needle aspiration and automated microcore biopsy of GI lesions are safe alternative procedures to use instead of endoscopic or surgical biopsy. The guided techniques of fine-needle aspiration can be performed with a 25-, 23-, 22-, or 20-gauge hypodermic needle. The gauge and length of the needle depends on the location and type of lesion, and the patient's compliance. Microcore automated biopsy using an 18-gauge Tru-Cut needle, assisted by an automated

Vet-ebooks.com

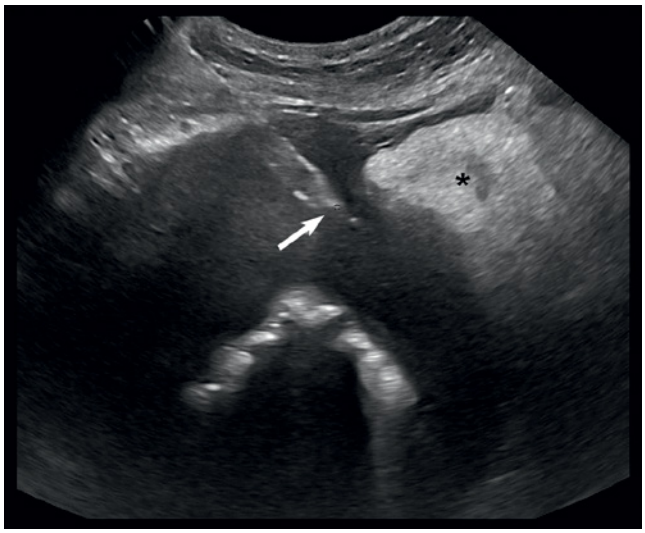


Figure 9.80. Ultrasound-guided biopsy and fine-needle aspiration. An ultrasound-guided sampling was performed on this markedly thickened intestinal wall of a 12-year-old Labrador diagnosed with lymphoma. This procedure can be performed safely. Notice the needle tip (arrow) inserted in the mass, away from the lumen. The adjacent fat (*) is hyperechoic.

biopsy gun, is an efficient and safe method of obtaining a diagnostic sample in larger lesions (Penninck et al. 1993) (Figure 9.80).

They are especially useful when lesions are not accessible endoscopically – because of their location in the GI tract or when involving a deep portion of the wall – and when surgical resection is not a safe option for a compromised patient. One paramount safety rule is to carefully locate and avoid the lumen.

In the presence of a GI lesion associated with regional lymphadenopathy, it is recommended to target both structures to increase the chance of obtaining one or more diagnostic samples.

Complications such as local hemorrhage or seroma collection (Figure 9.49) are uncommon. Intestinal content leakage, which can be a serious complication, can be avoided by careful selection of the biopsy site.



Visit our website at **www.SmallAnimalUltrasonography.com** for complementary video clips with annotations and text on:

- Normal GI anatomy and scanning
- Intussusception
- Foreign bodies
- Enteritis
- Lymphangiectasia
- Ulceration
- Lymphoma
- Carcinoma
- Mesenchymal tumor

References

Ahn H, Song W, Choi S, Kim J, et al. (2022) A rare case of cecal malignant peripheral nerve sheath tumor in a dog. J Vet Med Sci 84:1051–1055.

Azoulay F, Fritz J, Rault D, Cauvin E et al. (2024) Ultrasonographic assessment of the normal ileocecocolic junction in dogs. Vet Radiol Ultrasound https://doi.org/10.1111/vru.13452

Baez JB, Hendrick MJ, Walker LM, Washabau RJ (1999) Radiographic, ultrasonographic, and endoscopic findings in cats with inflammatory bowel disease of the stomach and small intestine: 33 cases (1990–1997). J Am Vet Med Assoc 215:349–354.

Balducci J, Piedra-Mora C, Jennings S, Anson A, et al. (2024) Hyperechogenicity of the pyloroduodenal junction in small dogs: population prevalence in 175 dogs and histological correlation in 14 specimens. Vet Radiol Ultrasound 000:1–8. doi: 10.1111/vru.13348

Berle ECP, KuKanich K, Biller D (2021) Ultrasonographic findings of gastrointestinal histoplasmosis in dogs. Vet Radiol Ultrasound 62:108–115.

Biller DS, Partington BP, Miyabayashi T, Leveille R (1994) Ultrasonographic appearance of chronic hypertrophic pyloric gastropathy in the dog. Vet Radiol Ultrasound 35:30–33

Boland L, Setyo L, Sangster C, Brunel L, et al. (2019) Colonic malignant peripheral nerve sheath tumor in a cat. JFMS Open Reports, 5(1), doi: 10.1177/2055116919849979

Boysen SR, Tidwell AS, Penninck DG (2003) Sonographic findings in dogs and cats with intestinal perforation: a retrospective study (1995–2001). Vet Radiol Ultrasound 44:556–564.

Citi S, Chimenti T, Marchetti V, Millanta F, et al. (2013) Micronodular lesions in the colonic submucosa in 42 dogs and 14 cats. Vet Radiol Ultrasound 54:646–651.

Coeuriot C, Pontarrasse J, Bouhsina N, Lazard M, et al. (2022) Ultrasound appearance of the duodenal papilla in clinically healthy cats. J Feline Med Surg 24:1267–1273.

Costanzo G, Linta N, Auriemma E, Perfetti S, et al. (2023) Ultrasonographic assessment of early leakage in intestinal sutures in dogs. Front Vet Sci 10:1094287. doi: 10.3389/fvets.2023.1094287

Couturier L, Rault D, Gatel L, Belli P (2012) Ultrasonographic characterization of the feline cardia and pylorus in 34 healthy cats and three abnormal cats. Vet Radiol Ultrasound 53:342–347.

Culp WT, Drobatz KJ, Glassman MM, Baez JL, et al. (2008) Feline visceral hemangiosarcoma. J Vet Intern Med 22:148–52.

Daniaux LA, Laurenson MP, Marks SL, Moore PF, et al. (2014) Ultrasonographic thickening of the muscularis propria in feline small intestinal small cell T-cell lymphoma and inflammatory bowel disease. J Feline Med Surg 16:89–98.

Daure E, Jania R, Jeninngs S, D'Anjou MA, et al. (2017) Ultrasonographic and clinicopathological features of pyloroduodenal adenomatous polyps in cats. J Feline Med Surg 19:141–145.

Vet-ebooks.com

De Magistris AV, Linta N, Specchi S, Procoli F et al. (2023) Ultrasonographic features of lymphadematous lymphangitis in 10 dogs. Vet Radiol Ultrasound 1–9, doi: 10.1111/vru.13269

Delaney F, O'Brien RT, Waller K (2003) Ultrasound evaluation of small bowel thickness compared to weight in normal dogs. Vet Radiol Ultrasound 44:577–580.

Di Donato P, Penninck DG, Pietra M, Cipone M, et al. (2014) Ultrasonographic measurement of the relative thickness of intestinal wall layers in clinically healthy cats. J Feline Med Surg 16:333–339.

Diana A, Pietra M, Guglielmini C, Boari A, et al. (2003) Ultrasonographic and pathologic features of intestinal smooth muscle hypertrophy in four cats. Vet Radiol Ultrasound 44:566–569.

Diana A, Penninck DG, Keating JH (2009) Sonographic findings of gastric polyps in 7 dogs. Vet Radiol Ultrasound 50:201–204.

Dominguez E, Anadon E, Espada Y, Grau-Roma L, et al. (2014) Imaging diagnosis – ultrasonographic appearance of small bowel metastasis from canine mammary carcinoma. Vet Radiol Ultrasound 55:208–212.

Fan TM, Simpson KW, Polack E, Dykes N, et al. (1999) Intestinal haemorrhage associated with colonic vascular ectasia (angiodysplasia) in a dog. J Small Anim Pract 40:25–30.

Fluke MH, Hawkins EC, Elliott GS, Blevins WE. Short colon in two cats and a dog. J Am Vet Med Assoc. 1989;195(1):87–90.

Gaschen L (2011). Ultrasonography of small intestinal inflammatory and neoplastic diseases in dogs and cats. Vet Clin Small Anim 41:329–344.

Gaschen L, Kircher P, Stüssi A, Allenspach K, et al. (2008) Comparison of ultrasonographic findings with clinical activity index (CIBDAI) and diagnosis in dogs with chronic enteropathies. Vet Radiol Ultrasound 49:56–64.

Gashen L, Granger A, Oubre O, Shannon D, et al. (2016). The effects of food intake and its fat composition on intestinal echogenicity in healthy dogs. Vet Radiol Ultrasound 57(5):546–550. doi: 10.1111/vru.12384

Gladwin NE, Penninck D, Webster CRL (2014) Ultrasonographic evaluation of the thickness of wall layers in the intestinal tract of dogs. Am J Vet Res 75:349–353.

Goggin JM, Biller DS, Debey BM, Pickar JG, et al. (2000) Ultrasonographic measurement of gastrointestinal wall thickness and the ultrasonographic appearance of the ileocolic region in healthy cats. J Am Anim Hosp Assoc 36:224–228.

Gory G, Rault DN, Gatel L, Dally C, et al. (2014) Ultrasonographic characteristics of the abdominal esophagus and cardia in dogs. Vet Radiol Ultrasound 55:552–560.

Graham JP, Newell SM, Gregore GB, Lester NV (2000) Ultrasonographic features of canine intestinal pythiosis. Vet Radiol Ultrasound 41:273–277.

Graham LT, Auger M, Watson AM, et al. (2020) Imaging and clinical features of a true gastrogastric intussusception in a dog. Can Vet J 61:715–718.

Grooters AM, Miyabayashi T, Biller DS, Merryman J (1994) Sonographic appearance of uremic gastropathy in four dogs. Vet Radiol Ultrasound 35:35–40.

Hahn H, Freiche V, Baril A, Charpentier J, Desquilbet L, et al. (2015) Ultrasonographic, endoscopic and histologic appearance of the caecum in clinically healthy cats. J Feline Med Surgery 19:85–93.

Hahn H, Pey P, Baril A, Charpentier A, Desquilbet L, et al. (2017) Ultrasonographic, endoscopic and histologic appearance of the caecum in cats presenting with chronic clinical signs of caecocolic disease. J Feline Med Surgery 19:94–104.

Hart K, Brownlie HB, Ogden D, Atencia S (2018) A case of gastric leiomyosarcoma in a domestic shorthair cat. JFMS Open Reports 4(2), doi: 10.1177/2055116918818912.

Hobbs J, Sutherland-Smith J, Penninck D, Jennings S, et al. (2015) Ultrasonographic features of canine gastrointestinal tumors compared to other gastrointestinal spindle cell tumors. Vet Radiol Ultrasound 56:432–438.

Hoffman KL (2003) Sonographic signs of gastroduodenal linear foreign body in 3 dogs. Vet Radiol Ultrasound 44:466–469.

Holloway A, Pivetta M, Rasotto R. (2019) Ultrasonographic and histopathological features in 8 cats with fibrotic small intestinal stricture. Vet Radiol Ultrasound 60:423–431.

Isaya R, Ciccarelli S, Enache D, Specchi S, Pesaresi M, et al. (2021) Gastrointestinal ultrasonographic findings in cats with feline panleukopenia: a case series. BMC Vet Res 17(143), doi: 10.1186/s12917-021-02856-3.

Junius G, Appeldoorn AM, Schrauwen E (2004) Mesenteric volvulus in the dog: a retrospective study of 12 cases. J Small Anim Pract 45:104–107.

King A, Donovan TA, Cohen E, Marin J, LeRoux AB. (2024) Short colon syndrome in cats. J Vet Intern Med 38:2138–2150.

Kuan S, Hoffman K, Tisdall P (2009) Ultrasonographic and surgical findings of a gastric hyperplastic polyp resulting in pyloric obstruction in an 11-week-old French bulldog. Aust Vet J 87:253–255.

Kvitko-White HL, Sayre RS, Corapi WV, Spaulding KA (2011). Imaging diagnosis – Heterobhilharzia Americana infection in a dog. Vet Radiol Ultrasound 52:538–541.

Lamb CR, Mantis P (1998) Ultrasonographic features of intestinal intussusception in 10 dogs. J Small Anim Pract 39:437–441.

Laurenson MP, Skorupski KA, Moore PF, Zwingenberger AL (2011) Ultrasonography of intestinal mast cell tumors in the cat. Vet Radiol Ultrasound 52:330–334.

Le Roux AB, Granger A, Wakamatsu N, Kearney MT, et al. (2016) Ex-vivo correlation of ultrasonographic small intestinal wall layering with histology in dogs. Vet Radiol Ultrasound 57:534–545.

Lee H, Yeon S, Lee H, Chang D, et al. (2005) Ultrasonographic diagnosis: pylorogastric intussusception in a dog. Vet Radiol Ultrasound 46:317–318.

MacDonald JM, Mullen HS, Moroff SD (1993) Adenomatous polyps of the duodenum in cats: 18 cases (1985-1990). J Am Vet Med Assoc 202:647–651.

Vet-ebooks.com

Mareschal A, Penninck D (2010) Long term ultrasonographic follow-up of intestinal surgical sites in dogs. Vet Radiol Ultrasound 51:652–655.

Matthews AR, Penninck DG, Webster CRL (2008) Assessment of post-operative ultrasonographic appearance of uncomplicated enterotomy or enterectomy sites in dogs. Vet Radiol Ultrasound 49:477–483.

Moon ML, Biller DS, Armbrust LJ (2003) Ultrasonographic appearance and etiology of corrugated small intestine. Vet Radiol Ultrasound 44:199–203.

Mortier JR, Maddox TW, White GM, Blundell RJ, et al. (2016) Ultrasonographic appearance of the major duodenal papilla in dogs without evidence of hepatobiliary, pancreatic or gastrointestinal tract disease. Am J Vet Res 77:597–603.

Müller T, Penninck D, Webster CRL, Conrado FO.(2023) The abdominal ultrasonographic findings of cats with feline infectious peritonitis:an update. J Feline Med Surg, doi: 10.1177/1098612X231216000

Murakami M, Heng HG, Lim CK, Parnell NK, et al. (2019) Ultrasonographic features of presumed gastric wall edema in 14 dogs with pancreatitis. J Vet Intern Med 33:1260–1265.

Murakami M, Heng HG, Lim CK, Parnell NK, et al. (2020) Ultrasonographic features and prevalence of presumed gastric wall edema in dogs with hypoalbuminemia. J Vet Intern Med 34:1867–1871.

Myers NC, Penninck DG (1994) Ultrasonographic diagnosis of gastrointestinal smooth muscle tumors in the dog. Vet Radiol Ultrasound 35:391–397.

Newell SM, Graham JP, Roberts GD, Ginn PE, et al. (1999) Sonography of the normal feline gastrointestinal tract. Vet Radiol Ultrasound 40:40–43.

Nielsen T, Lindstrom L, Ingman J, Uhlhorn M, et al. (2016) High-frequency ultrasound of Peyer's patches in the small intestine of young cats. J Feline Med Surgery 18:303–309.

Oh D, Kim K, Yoon J (2022) Duodenal perforation in a puppy with canine parvovirus infection. Can Vet J 63:23–26.

Paoloni MC, Penninck DG, Moore AS (2002) Ultrasonographic and clinicopathologic findings in 21 cases of canine intestinal adenocarcinoma. Vet Radiol Ultrasound 43:562–567.

Parry-Smith P, Czerwinska M, Krudewig C (2008) Duodenal duplication cyst in a young cat. Vet Rec 162:826–827.

Patsikas MN, Papazoglou LG, Papaioannou NG, Savvas I, et al. (2003) Ultrasonographic findings of intestinal intussusception in seven cats. J Feline Med Surg 5:335–343.

Penninck DG (1998) Ultrasonographic characterization of gastrointestinal tumors. Vet Clin North Am 28:777–797.

Penninck DG (2002) Gastrointestinal tract. In Nyland T, Mattoon J, eds. Small Animal Diagnostic Ultrasound, 2nd edition. Philadelphia: WB Saunders, pp. 207–230.

Penninck D, Mitchell SL (2003) Ultrasonographic detection of ingested and perforating wooden foreign bodies in four dogs. J Am Vet Med Assoc 223:206–209.

Penninck DG, Nyland TG, Fisher PE, Kerr LY (1989) Normal ultrasonography of the canine gastrointestinal tract. Vet Radiol Ultrasound 30:272–276.

Penninck DG, Crystal MA, Matz ME, Pearson SH (1993) The technique of percutaneous ultrasound guided fine-needle aspiration biopsy and automated microcore biopsy in small animal gastrointestinal diseases. Vet Radiol Ultrasound 34:433–436.

Penninck DG, Moore AS, Tidwell AS, Matz ME, et al. (1994) Ultrasonography of alimentary lymphosarcoma in the cat. Vet Radiol Ultrasound 35:299–304.

Penninck DG, Matz M, Tidwell AS (1997) Ultrasonographic detection of gastric ulceration. Vet Radiol Ultrasound 38:308–312.

Penninck DG, Moore AS, Gliatto J (1998) Ultrasonography of canine gastric epithelial neoplasia. Vet Radiol Ultrasound 39:342–348.

Penninck DG, Smyers B, Webster CRL, Rand W, et al. (2003) Diagnostic value of ultrasonography in differentiating canine enteritis from intestinal neoplasia. Vet Radiol Ultrasound 44:570–575.

Penninck D, Webster CRL, Keating JH (2010) The sonographic appearance of intestinal mucosal fibrosis in cats. Vet Radiol Ultrasound 51:458–461.

Pollard R, Johnson EG, Pesavento PA, Baker TW, et al. (2013) Effect of corn oil administered orally on conspicuity of ultrasonographic small intestinal lesions in dogs with lymphangiectasia. Vet Radiol Ultrasound 54:390–397.

Rault DN, Besso JG, Boulouha L, Begon D (2004) Significance of a common extended mucosal interface observed in transverse small intestine sonograms. Vet Radiol Ultrasound 45:177–179.

Ribas A, Miller R, Rasotto R (2017) Small intestinal peripheral nerve sheath tumor in a cat. JFMS Open Reports 3(1), https://doi.org/10.1177/2055116917710394

Rissetto K, Villamil JA, Selting KA, Henry CJ (2011) Recent trends in feline intestinal neoplasia: an epidemiologic study of 1,129 cases in the veterinary medical database from 1964 to 2004. JAAHA 7:28–36. https://doi.org/10.5326/JAAHA-MS-5554.

Rudorf H, van Schaik G, O'Brien RT, Brown PJ, et al. (2005) Ultrasonographic evaluation of the thickness of the small intestinal wall in dogs with inflammatory bowel disease. J Small Anim Pract 46:322–326.

Rhim H, Moon S, Lee G, Park S, et al. (2018) Unusual ultrasonographic features of chronic hypertrophic pyloric gastropathy in two dogs. J Vet Clin 35:302–307.

Spaulding KA, Cohn LA, Miller RT, Hardie EM (1990) Enteric duplication in two dogs. Vet Radiol Ultrasound 31:83–88.

Stander N, Wagner W, Goddard A, Kirberger RM (2010) Ultrasonographic appearance of canine parvoviral enteritis. Vet Radiol Ultrasound 51:69–74.

Stimson EL, Cook WT, Smith MM, Forrester SD, et al. (2000) Extraskeletal osteosarcoma in the duodenum of a cat. J Am Anim Hosp Assoc 36:332–336.

Sutherland-Smith J, Penninck DJ, Keating JH, Webster CRL (2007) The morphological significance of ultrasonographic intestinal hyperechoic striations in dogs. Vet Radiol Ultrasound 48:51–57.

Vet-ebooks.com

Taeymans O, Holt N, Penninck D, Webster CR (2011) Ultrasonographic characterization of feline ileocecocolic abnormalities. Vet Radiol Ultrasound 52:335–339.

Tucker S, Penninck DG, Keating JH, Webster CRL (2014) The histopathologic and ultrasonographic features of eosinophilic enteritis in cats: 27 cases (2002-2011). J Feline Med Surg 16:950–956.

Tidwell AS, Penninck DG (1992) Ultrasonography of gastrointestinal foreign bodies. Vet Radiol Ultrasound 33:160–169.

Venco L, Kramer L, Pagliaro L, Genchi C (2005) Ultrasonographic features of peritoneal cestodiasis caused by Mesocestoides sp. in a dog and in a cat. Vet Radiol Ultrasound 46:417–422.

Wallack ST, Hornof WJ, Herrgesell EJ (2003) Ultrasonographic diagnosis: small bowel infarction in a cat. Vet Radiol Ultrasound 44:81–85.

Weissman A, Penninck D, Wester C, Hecht S, et al. (2012) Ultrasonographic and clinicopathological features of feline gastrointestinal eosinophilic sclerosing fibroplasia in 4 cats. J Feline Med Surg 15:148–154.

Winter MD, Londono L, Berry CR, Hernandez JA (2014) Ultrasonographic evaluation of relative gastrointestinal layer thickness in cats without clinical evidence of gastrointestinal tract disease. J Feline Med Surg 16:118–24.

Zwingenberger AL, Marks SL, Baker TW, Moore PF (2010) Ultrasonographic evaluation of the muscularis propria in cats with diffuse small intestinal lymphoma or inflammatory bowel disease. J Vet Intern Med 24:289–292.

Vet-ebooks.com

CHAPTER TEN

Pancreas

Dominique Penninck[1], Marc-André d'Anjou[2], and Mylène Auger[2]

[1]*Cummings School of Veterinary Medicine, Tufts University, North Grafton, MA, USA*
[2]*Animages, Brossard, Québec, Canada*

Preparation and Scanning Procedure

The pancreas is a thin, elongated organ located along the greater curvature of the stomach and the mesenteric border of the descending duodenum. Gas in the gastrointestinal tract often hampers complete evaluation. A 12-hour fast may reduce gas interference.

The anatomical landmarks used to locate the **right pancreatic lobe** are the right kidney, the descending duodenum with its straight course along the right ventral abdominal wall, and the pancreaticoduodenal vein paralleling the descending duodenum (Figure 10.1). The right pancreatic lobe can be imaged from a ventral or lateral approach, with a longitudinal scan-plane orientation used to find the descending duodenum and right kidney. Using the ventral approach, the transducer is placed under the last rib of the animal and angled dorsally to image the right kidney. The scan plane is then moved medially until the descending duodenum is imaged medial to the right kidney. Alternatively, the ventral approach can start caudal to the xiphoid process. In a longitudinal scan plane, the stomach is identified, and the scan plane is moved laterally toward the right following the pyloric antrum into the descending duodenum. This latter approach is often limited to cats and small dogs.

The lateral approach is preferred to locate the descending duodenum in deep-chested dogs. Once the descending duodenum is located by using the ventral or lateral approach, the right pancreatic lobe and the pancreaticoduodenal vein can be identified. In large and deep-chested dogs, it is often necessary to use an intercostal window to access the most cranial portion of the descending duodenum and the corresponding portion of the pancreas. On occasion, the right pancreatic lobe is best scanned from the right side, with the animal in a right lateral recumbency as gastric fluid moves in the dependent pyloric antrum.

The **pancreatic body** can be imaged from ventrally or from the right side, with the animal in a dorsal, left, or right lateral recumbent position, by moving the scan plane craniomedially to the proximal descending duodenum and caudally to the pyloric antrum. The portal vein is a useful landmark located just dorsal and to the left of the body of the pancreas (Figure 10.1). A transverse scan just caudal to the porta hepatis and pylorus may be used to locate this vein and the body of the pancreas. The **left pancreatic lobe** is more difficult to image in dogs because of gas interference in the adjacent stomach and transverse colon. However, in cats, the left limb can usually be more easily identified than the right limb.

High-frequency transducers (8 MHz and above) are recommended to evaluate the pancreas, especially in cats and small to medium-sized dogs. The small contact area of sectorial, narrow curvilinear, or microconvex transducers facilitates access to the right cranial abdominal quadrant for imaging under or between the right ribs.

Atlas of Small Animal Ultrasonography, Third Edition. Edited by Dominique Penninck and Marc-André d'Anjou.
© 2025 John Wiley & Sons, Inc. Published 2025 by John Wiley & Sons, Inc.
Companion website: www.SmallAnimalUltrasonography.com

Vet-ebooks.com

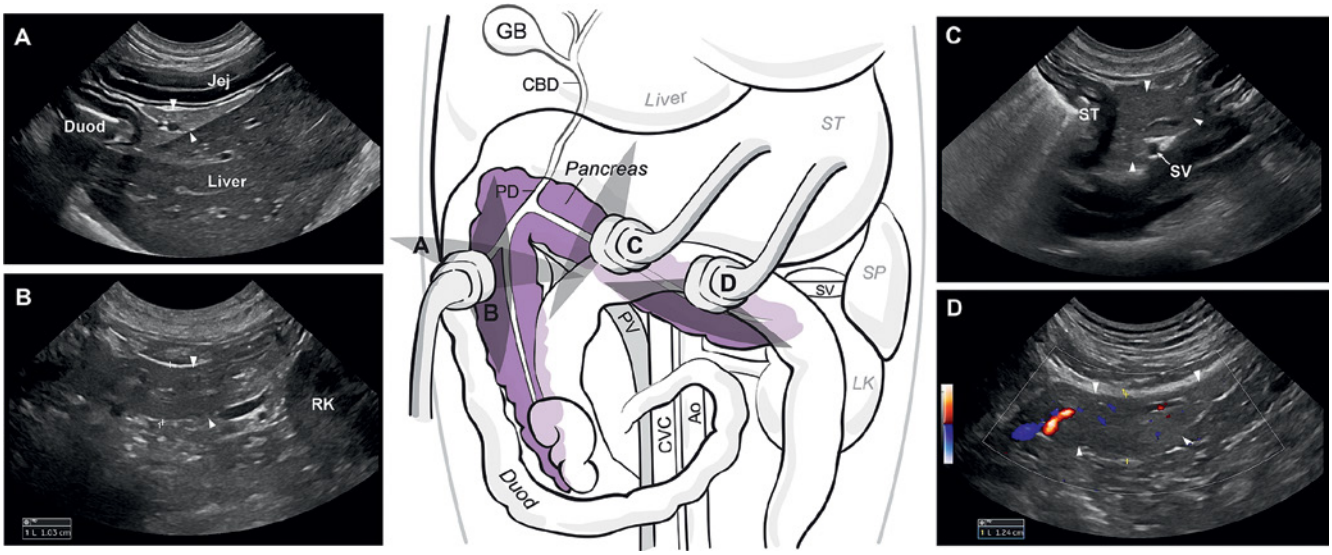


Figure 10.1. Approach to the normal canine pancreas. Illustration of the pancreas within the abdominal cavity, with the probe positioned along the right and left lobes of this organ at locations **(A–D)**. **(A, B)** Transverse and longitudinal sonograms of the right lobe of the pancreas (arrowheads). This lobe is immediately adjacent to the layered descending duodenum, a segment of jejunum, and the liver. The right kidney is also nearby. The pancreaticoduodenal vein and arteries appear as an anechoic rounded structure within the lobe. The pancreatic duct is not visualized. **(C, D)** Transverse and longitudinal sonograms of the left lobe (arrowheads) seen adjacent to the stomach (St) and the splenic vein (SV). Ao, aorta; CBD, common bile duct; CVC, caudal vena cava; Duod, duodenum; GB, gallbladder; Jej, Jejunum; L, liver; LK, left kidney; RK, right kidney; PD, pancreatic duct; PV, portal vein; SP, spleen; ST, stomach; SV, splenic vein.

Ultrasonography of the Normal Pancreas

In Dogs

The pancreas is thin, amorphous, and poorly distinct from the adjacent mesenteric fat (Saunders 1991; Hecht and Henry 2007). The pancreas is divided into three portions: right lobe, left lobe, and body (Figure 10.1). The **right lobe** lies in the mesoduodenum, dorsomedial to the descending duodenum, ventral to the right kidney, and ventrolateral to the portal vein. Most of the time, the veins draining the right lobe are seen ultrasonographically. The **body** lies caudal to the pyloric region in the right cranial abdomen, craniomedial to the right kidney and ventral to the portal vein. The **left lobe** originates at the pancreatic body, lies dorsocaudal to the gastric antrum, and continues across midline between the stomach and the transverse colon. The normal left lobe occasionally is seen in the triangular region defined by the spleen, stomach, and left kidney. The normal pancreas is homogeneous and is isoechoic or slightly hyperechoic to the liver. In some healthy dogs, the pancreas can be heterogeneous, possibly due to the highly echogenic pancreatic duct and periductal connective tissues, creating the sonographic appearance of hyperechoic foci dispersed throughout the pancreatic parenchyma (Granger et al. 2015). The pancreaticoduodenal vein is seen clearly in the right lobe and can be followed into the gastroduodenal vein and portal vein.

Seldom, a normal pancreas can be diffusely hyperechoic but within the normal range for size (Figure 10.2). The underlying cause for diffuse pancreatic

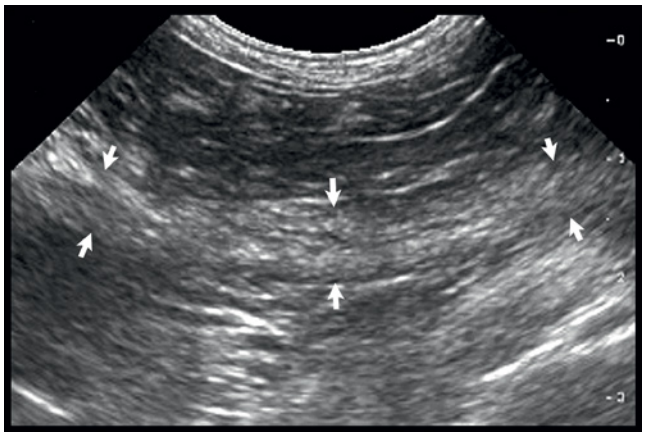


Figure 10.2. Normal pancreas in an old dog. Longitudinal sonogram of the left lobe of the pancreas in this 12-year-old Yorkie. The pancreas (arrows) is diffusely increased in echogenicity but maintains a normal size. The histopathology of the pancreas was unremarkable.

Vet-ebooks.com

Table 10.1
Mean pancreatic measurements in dogs and cats

	Left lobe thickness	Body thickness	Right lobe thickness	Pancreatic duct diameter
Dogs[a]	6.5 mm	6.3 mm	8.1 mm	0.6 mm
Cats[b]	5.8 mm	6.2 mm	4.4 mm	1–2.5 mm

[a]In dogs without clinical signs of gastrointestinal disease (Penninck et al. 2013). The authors also found that pancreatic thickness in all lobes and diameter of the pancreatic duct significantly increased with body weight.
[b]The means presented in the table are compiled means obtained from three references (Etue et al. 2001; Hecht et al. 2006; Moon et al. 2005).

hyperechogenicity is not currently known, but possible causes include fat deposition and/or fibrosis. A diffusely hyperechoic pancreas has also been reported to occur more commonly in dogs with hyperadrenocorticism than in healthy dogs, but its origin remains undetermined (Granger et al. 2015).

The mean **measurements** of the normal canine pancreas and pancreatic duct are summarized in Table 10.1. A useful reference value for the thickness of a normal pancreas in a medium-sized dog (15–30 kg) is about 1 cm (Penninck et al. 2013). Unlike previously reported, the pancreatic duct can be seen in normal dogs, especially in the right lobe.

Penninck et al. (2013) also reported that pancreatic thickness and pancreatic duct diameter correlate with body weight, but not with age.

In Cats

In contrast to dogs, the caudal third of the feline right limb curves cranially, giving it a hook-like appearance (Etue et al. 2001). The pyloroduodenal angle and the pancreatic body are more centrally located, and the angle formed by the left and right lobes with the pancreatic body is narrower. The normal sonographic appearance of the feline pancreas is isoechoic to slightly hyperechoic to the adjacent liver lobes and nearly isoechoic to the surrounding mesenteric fat (Figure 10.3).

The mean thickness **measurements** for each part of the pancreas and the pancreatic duct in cats are summarized in Table 10.1. The left lobe of the pancreas is often more easily identified than the right lobe. It is also important to know that in older cats (over 10 years), the pancreatic duct diameter can be dilated up to 2.5 mm without concurrent pancreatic disorders (Hecht et al. 2006, 2007).

On contrast-enhanced ultrasonography, the normal pancreas has a very intense, uniform, but brief perfusion pattern in cats and dogs. Contrast enhancement in the right pancreatic limb is seen initially in the pancreaticoduodenal artery, followed by uniform parenchymal enhancement. Contrast medium is then recognized in the pancreaticoduodenal vein. The parenchymal enhancement occurs coincidental to duodenal wall perfusion in dogs (Johnson-Neitman et al. 2012) and cats (Leinonen et al. 2010, Diana et al. 2015).

Ultrasonographic Features of Pancreatic Disorders

Pancreatitis

Pancreatitis has various ultrasonographic appearances, depending on the severity, duration, and extent of pancreatic and peripancreatic tissue inflammation.

In **acute pancreatitis**, the pancreas is enlarged and diffusely hypoechoic while the surrounding fat appears moderately hyperechoic and often hyperattenuating as the result of fat saponification (Figure 10.4). In dogs, the right limb of the pancreas tends to be most affected, whereas in cats, the changes tend to be more severe in the body and left limb.

In cats, similar changes can be seen in acute pancreatitis, but pancreatic enlargement and diffuse changes in pancreatic and surrounding fat echogenicity may be less obvious (Figure 10.5). A combination of tests such as feline pancreatic lipase immunoreactivity (fPLI) and abdominal ultrasound can optimize the noninvasive diagnosis of feline pancreatitis (Forman et al. 2004, Cridge et al. 2020).

Pancreatitis in cats has been reported to be associated with hepatic lipidosis, inflammatory bowel disease, and cholangiohepatitis (Akol et al. 1993). Furthermore, in cats, diabetes and pancreatitis often coexist (Xenoulis and Fracassi 2022). Acute kidney injury has been reported as a potential comorbidity in dogs with acute pancreatitis and is associated with a higher mortality rate in these dogs (Gori et al. 2019). Recheck ultrasound exams can be valuable in assessing progress (Figures 10.5F).

Thickened gastric and/or duodenal wall and regional peritoneal effusion can be seen in association with pancreatitis (Murakami et al. 2019; Saunders et al. 2002) (Figure 10.6). In most cases, the thickening of the gastric and duodenal wall is not associated with

Vet-ebooks.com

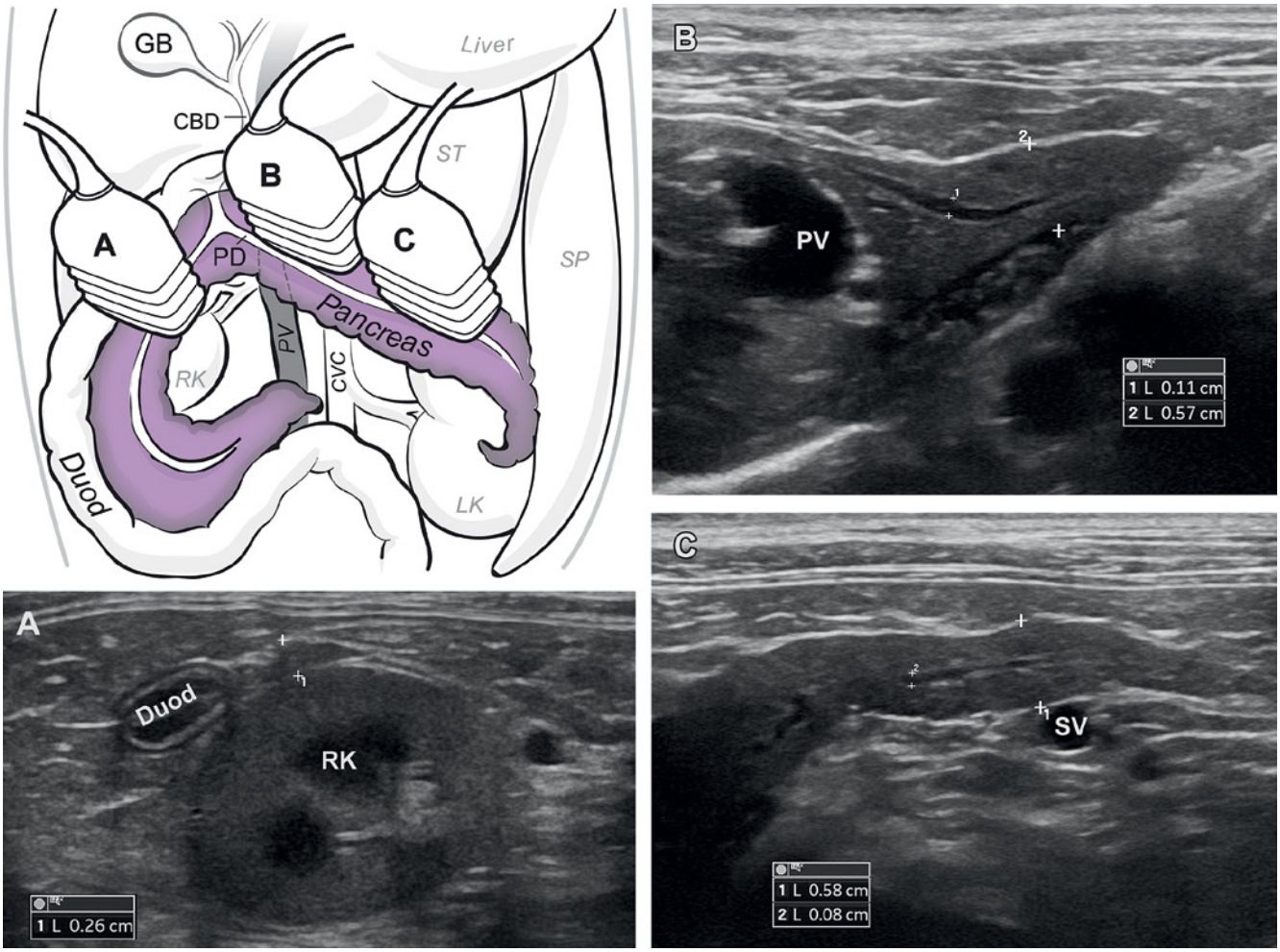


Figure 10.3. Approach to the normal feline pancreas. Illustration of the pancreas within the abdominal cavity with the probe positioned along the right **(A)** and left **(B, C)** lobes of this organ. **(A)** Transverse sonogram of the right lobe, which is next to the duodenum and right kidney. **(B, C)** Longitudinal sonograms of the body (B) and left lobe. Notice the portal vein (PV) dorsal to the medial extremity of the lobe and the pancreatic duct (measuring between 0.8 and 1.1 mm in this cat) in the center of the pancreas. The splenic vein (SV) is dorsal to the extremity of the lobe that lies medial to the spleen (not seen). CBD, common bile duct; CVC, caudal vena cava; Duod, duodenum; GB, gallbladder; L, liver; LK, left kidney; PD, pancreatic duct; PV, portal vein; RK, right kidney; SP, spleen; and ST, stomach.

complete loss of layering, although the wall layers can be altered, and gastric wall edema may be present (Murakami et al. 2019) (Figure 10.6). Occasionally, the adjacent transverse colon can also be affected (Figure 10.4).

In severe **hemorrhagic, necrotizing pancreatitis**, irregular hypo- to anechoic area(s) represent necrosis and hemorrhage of part of the pancreas and peripancreatic tissue (Figure 10.7). The pancreatic margins can be ill-defined, and the margins of the pancreas are not well demarcated. The adjacent mesentery is hyperechoic and hyperattenuating because of regional inflammation and edema.

Pancreatic edema appears as numerous hypoechoic stripes demarcating pancreatic lobulation and dissecting the enlarged pancreas (Figure 10.8). Pancreatic edema may be associated with pancreatitis (Figure 10.8A, B), although it can also be caused by hypoalbuminemia or portal hypertension (Lamb 1999) (Figure 10.8C).

Focal pancreatic lesions caused by acute pancreatitis contain combined areas of pancreatic necrosis, hemorrhage, and surrounding inflamed mesentery (Edwards et al. 1990), these lesions can be further outlined with Contrast CT (Jaeger et al. 2003). The hypoechoic and anechoic areas corresponding to collections

Vet-ebooks.com

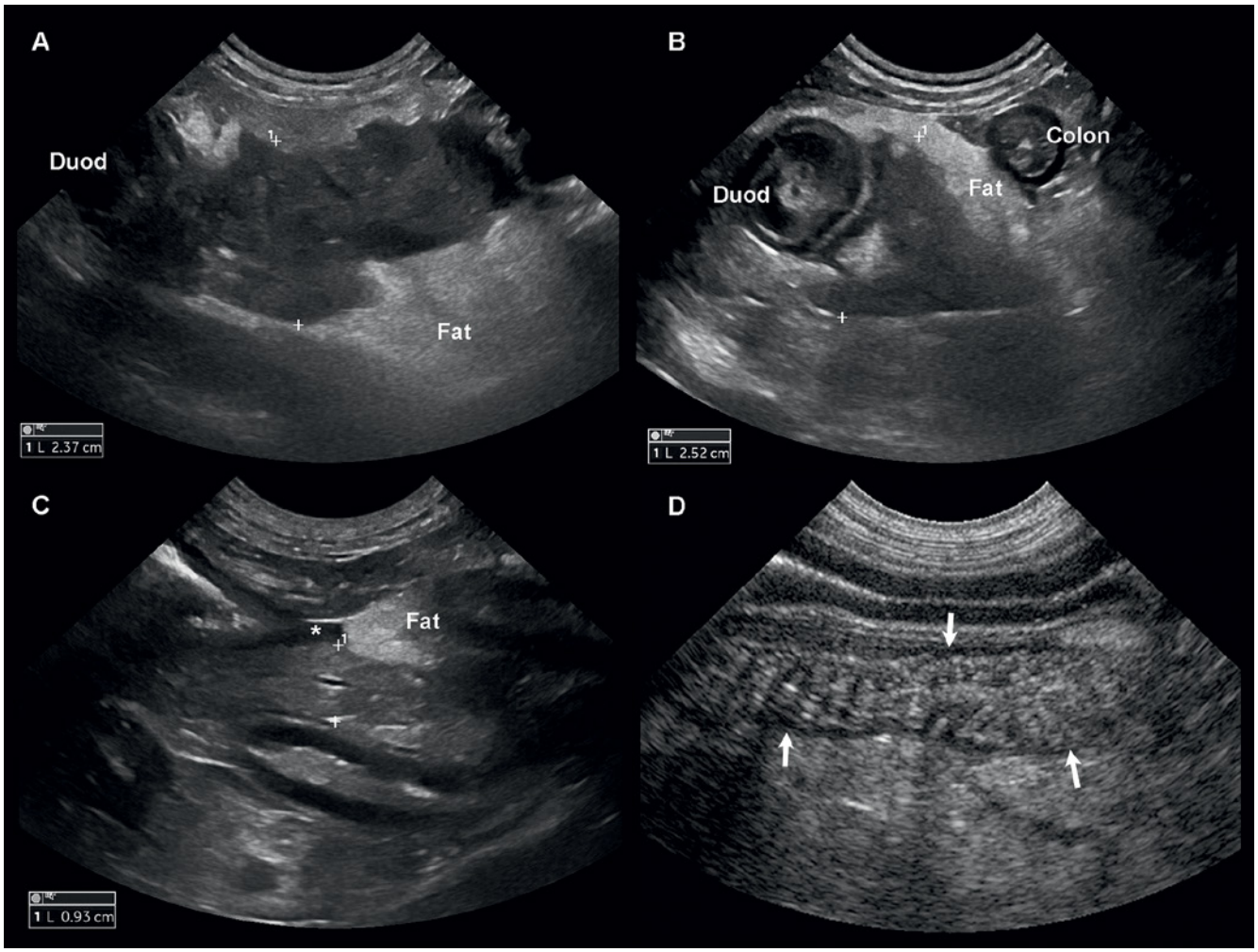


Figure 10.4. **Acute pancreatitis in two dogs. (A–C)** In this 9-year-old male Pug presented for acute vomiting, the right pancreatic lobe is markedly thickened (up to 2.5 cm, between cursors), irregular and hypoechoic in longitudinal **(A)** and transverse **(B)** images. The surrounding mesenteric fat is hyperechoic and the adjacent descending duodenum (Duod) and colon are thickened. In comparison, the left lobe is of normal size (9.3 mm), shape, and echogenicity. Notice the small amount of anechoic effusion (*) between the bowel loops. **(D)** In another dog, the colon (arrows) is corrugated, along the inflamed left lobe of the pancreas (not shown). A normal bowel is in the near field.

of hemorrhage and necrotic tissue may vary with chronicity, become more organized, and develop into pseudocyst or abscess. **Pseudocysts** are fluid-filled lesions that are surrounded by a capsule of fibrous tissue. The fluid is composed of pancreatic secretions originating from a ruptured duct. Pancreatic pseudocysts are anechoic to poorly echogenic rounded lesions, occasionally associated with acoustic enhancement in the far field. They are reported in both dogs and cats (Hines et al. 1996; Rutgers et al. 1985; VanEnkevort et al. 1999) (Figure 10.9). Sometimes, large pseudocysts may cause extrahepatic biliary obstruction (Marchevsky et al. 2000).

Retention cysts are caused by pancreatic duct blockage and cannot be differentiated from congenital cysts or pseudocysts (Figure 10.10).

Pancreatic **abscesses** are a circumscribed collection of pus, usually located within the pancreas or close to it, containing little or no pancreatic necrosis (Salisbury et al. 1988). They are more common in dogs (Figure 10.11) than in cats (Figure 10.12). Ultrasonographic differentiation among these different fluid-filled pancreatic lesions is impossible. Abscesses with echogenic fluid may also mimic masses.

In addition to color Doppler, contrast-enhanced ultrasound can be used to evaluate and quantify

Vet-ebooks.com

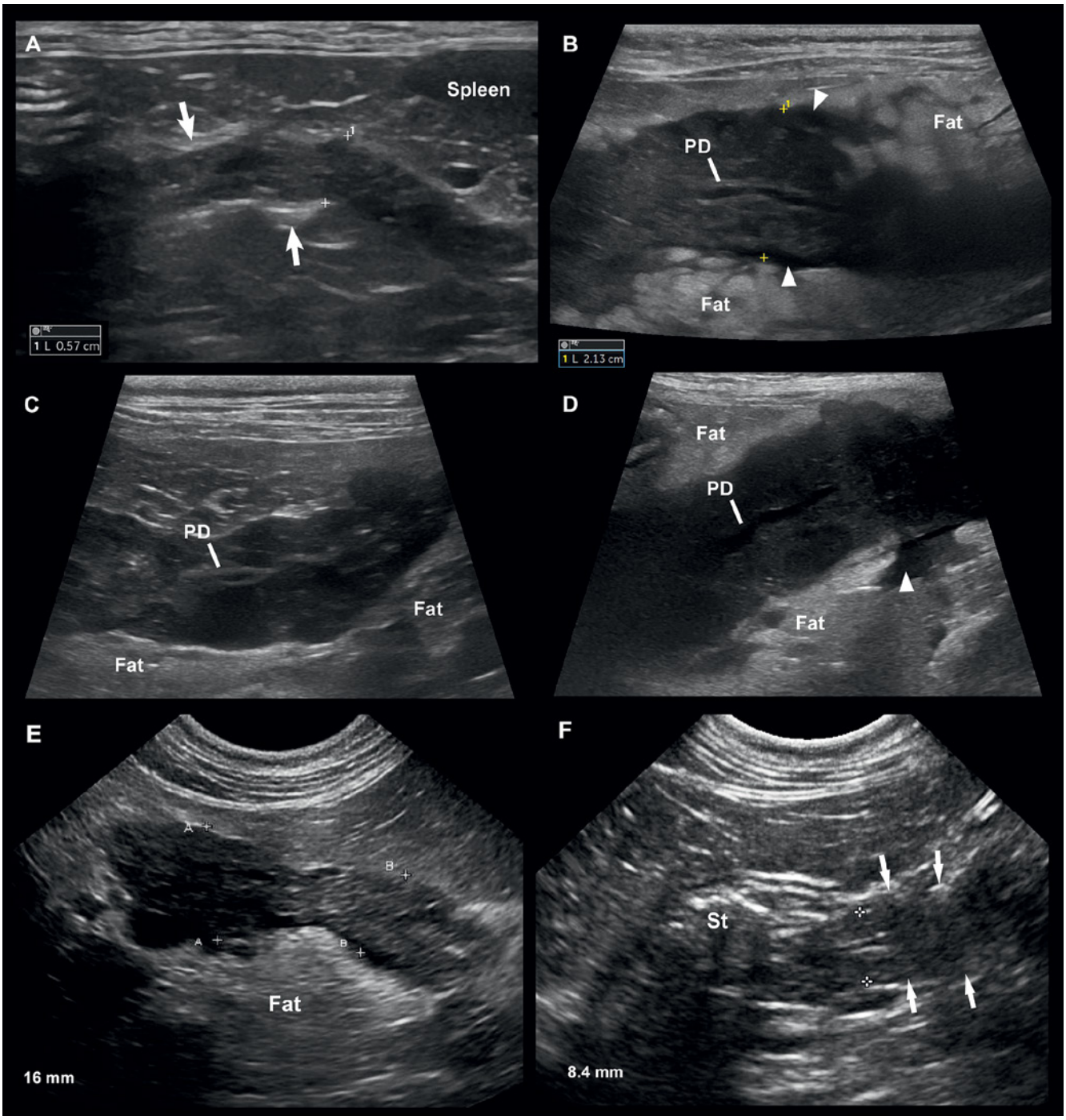


Figure 10.5. **Acute pancreatitis in six cats. (A)** Longitudinal sonographic image of the left lobe of a 13-year-old female Tonkinese cat with mild, acute pancreatitis. The pancreas is mildly hypoechoic and heterogeneous, but of normal size. The peripheral fat is mildly hyperechoic in a few areas (arrows). **(B)** Longitudinal sonogram of a 10-year-old domestic shorthair cat showing a severely enlarged and hypoechoic pancreas surrounded by mild anechoic effusion (arrowheads) and hyperechoic and heterogeneous fat. The pancreatic duct (PD) is tortuous and shows a thickened wall. **(C)** In this 12-year-old domestic shorthair cat, the pancreas is moderately thickened with irregular margins and is diffusely mildly hypoechoic and heterogeneous. The PD is displaced and deformed, likely due to asymmetric parenchymal swelling, and shows a thickened wall. The surrounding fat is mildly hyperechoic. Ultrasound-guided fine needle aspiration of the left pancreatic limb revealed mild neutrophilic pancreatitis. **(D)** Longitudinal sonogram of the left lobe of the pancreas in a 16-year-old domestic shorthair cat. The lobe is markedly thickened, hypoechoic, and surrounded by hyperechoic local fat and there is a small amount of peritoneal effusion (*). The PD is mildly tortuous. Ultrasound-guided pancreatic fine-needle aspiration revealed pyogranulomatous inflammation as well as numerous tachyzoites consistent with *Toxoplasma gondii*. Toxoplasmosis infection is an uncommon cause of pancreatitis in cats. **(E, F)** Diffuse and severe acute pancreatitis with follow-up in a 6-year-old cat. The pancreas is markedly thickened (16 mm), hypoechoic, surrounded by hyperechoic fat on initial examination (E). On the 8 days recheck (F), the pancreas (between arrows and calipers) is reduced in size (8.4 mm) and has normal echogenicity.

Vet-ebooks.com

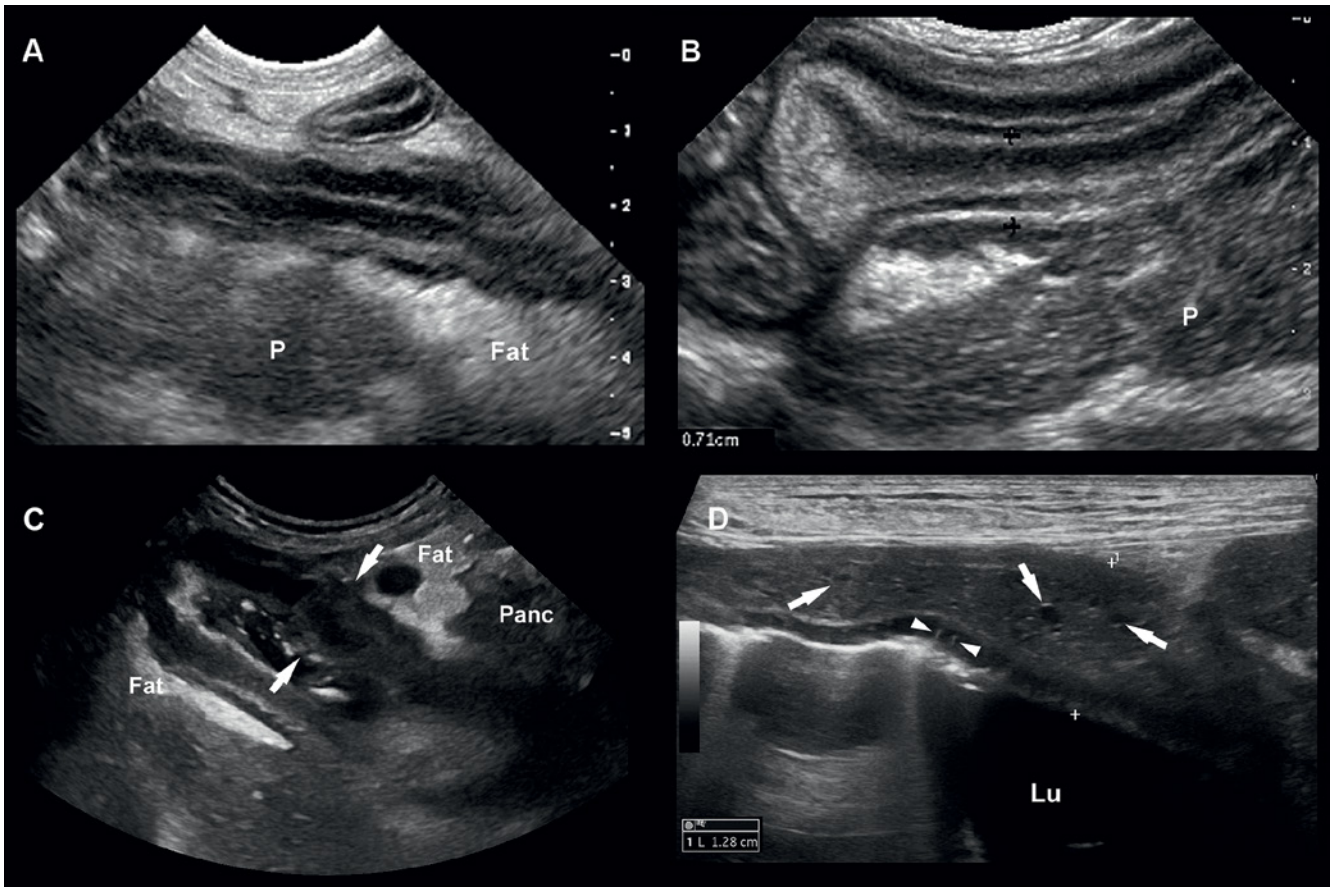


Figure 10.6. Duodenal and gastric changes associated with pancreatitis in three dogs. (A, B) Longitudinal sonograms of two dogs diagnosed with severe acute pancreatitis. In both, the duodenum is thickened and atonic, and the wall layering is altered. The right pancreatic (P) limb is hypoechoic, and the surrounding fat is hyperechoic. **(C)** In this 6-year-old Pomeranian male dog with severe necrotizing pancreatitis, the duodenal wall is moderately thickened with disrupted layering on the mesenteric side (arrows). **(D)** In this other dog with severe pancreatitis, the gastric wall is thickened (between calipers) with mucosal striations (arrowheads). The submucosal layer is particularly thickened with a granular echotexture consistent with edema and several cysts (arrows). Lu, gastric lumen.

pancreatic perfusion, and when available, can aid in the diagnosis of pancreatitis and pancreatic necrosis, and can be helpful for monitoring disease progression (Lim et al. 2015; Rademacher et al. 2016).

Ultrasound-guided fine-needle aspiration is recommended to determine the nature of the collection. Peritoneal effusion secondary to pancreatitis is more common with the severe, hemorrhagic, necrotizing form of pancreatitis. The effusion tends to accumulate in small pockets between the pancreas and adjacent mesentery.

Bile duct obstruction secondary to pancreatic inflammation and subsequent fibrosis can cause gallbladder and bile duct distension (Wilkinson et al. 2020). In these cases, the common bile duct (CBD) is dilated and tortuous (Figure 10.13). In normal dogs, the CBD is not always visible and can be up to 3–4 mm wide. Whereas in cats, the CBD can be more systematically visualized and considered normal up to 4 mm in diameter. A CBD exceeding 4 mm in diameter is suggestive of biliary obstruction in cats (Léveillé et al. 1996) but the clinical context is important as CBD may become quite distended without mechanical obstruction (i.e., choledochal cyst). Serial ultrasonographic examinations of the biliary tract can be necessary to document progressive mechanical obstruction. Progressive dilation of the biliary tract from the CBD to the peripheral intrahepatic ducts occurred 1 week after experimental bile duct ligation (Nyland and Gillette 1982). Dilation of the extrahepatic bile ducts and gallbladder might persist despite reestablishment of normal bile flow after obstruction.

Vet-ebooks.com

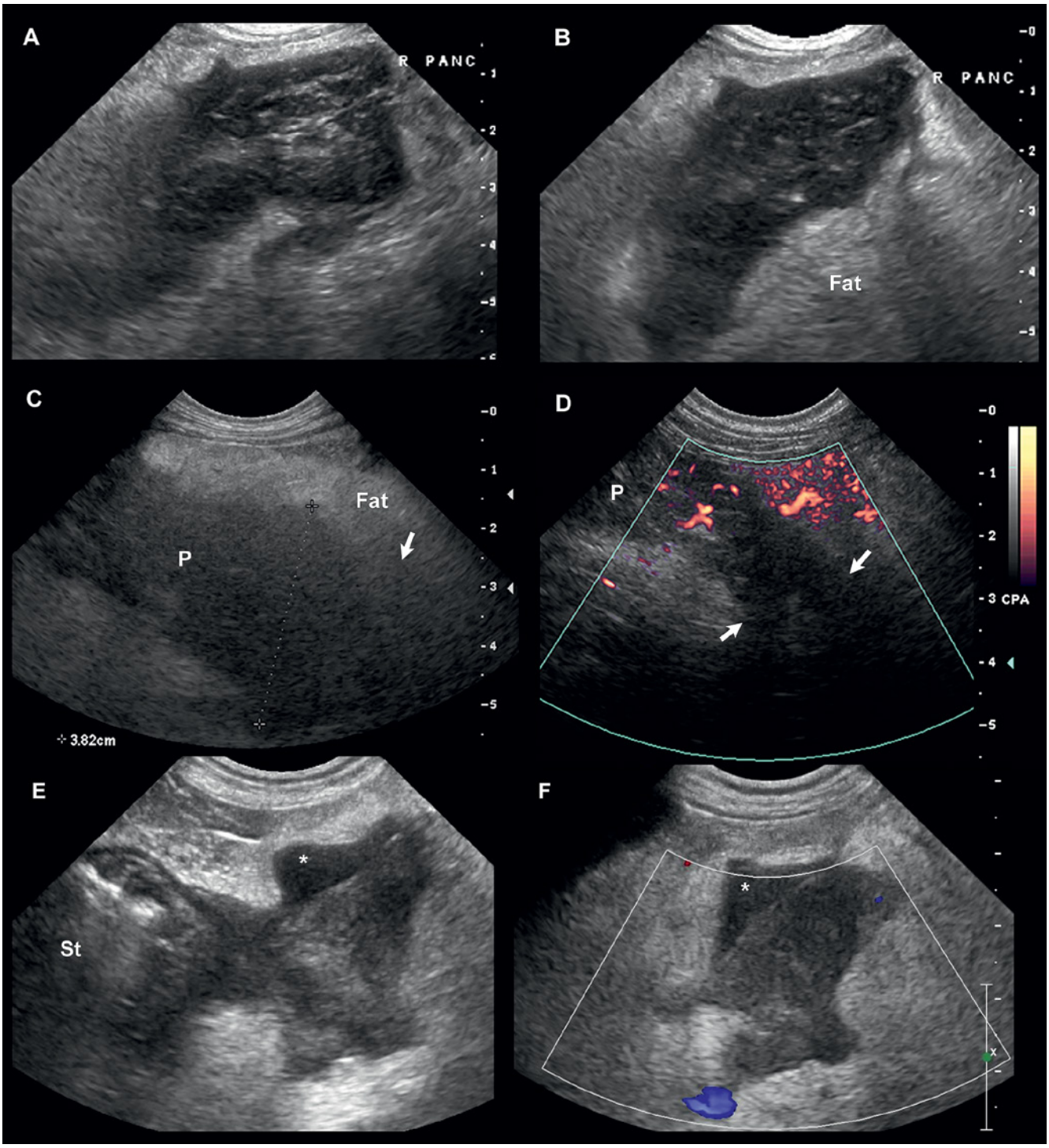


Figure 10.7. Necrotizing hemorrhagic pancreatitis in two dogs. Transverse **(A)** and longitudinal **(B)** sonograms of the thickened pancreas of an 8-year-old Labrador retriever with active suppurative pancreatitis with areas of hemorrhage and necrosis. The inhomogeneous and hypoechoic pancreas has irregular margins outlined by bright fat. **(C, D)** Longitudinal sonograms of the right pancreatic limb in a 10-year-old golden retriever with severe necrotic, hemorrhagic pancreatitis. The pancreatic limb (P) is markedly enlarged, hypoechoic, and ill-defined, particularly in its distal extremity (arrows). Using Power Doppler **(D)** in this same region, there is no evidence of vascular flow motion, in comparison with the proximal portion of the limb. The superficial fat shows increased vascularity. **(E)** Transverse sonogram of the left limb of the pancreas of a 7-year-old miniature Schnauzer. The pancreas is enlarged, poorly echogenic bordered by an anechoic region (*) likely representing a developing pseudocyst. **(F)** With color Doppler, no vascularization is present in this segment of the affected pancreas. St, stomach.

Vet-ebooks.com

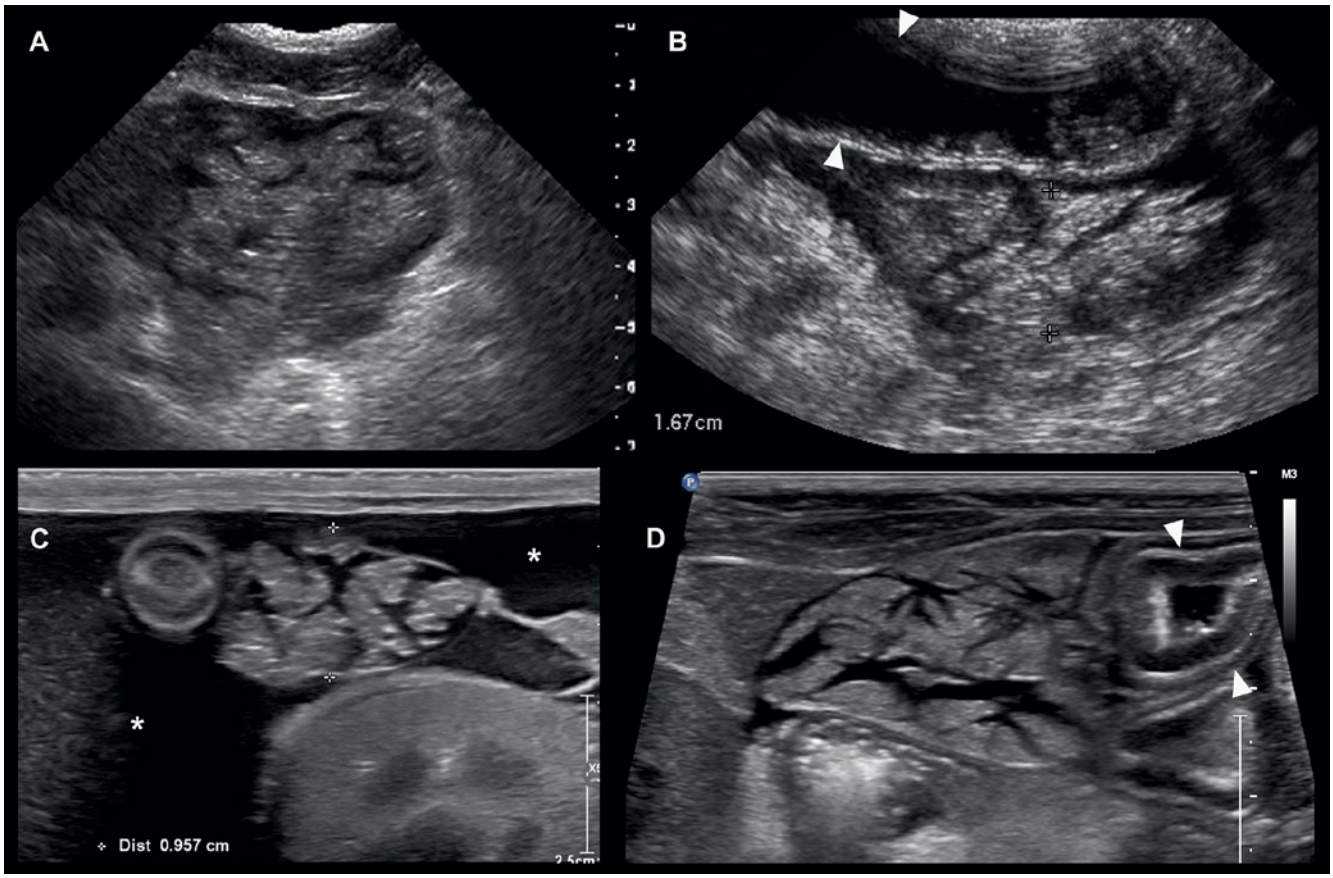


Figure 10.8. **Pancreatic edema in three dogs and one cat. (A)** Transverse sonogram of the edematous thickened pancreas (the same dog as in Figure 9.7A, B). The pancreas is enlarged and has anechoic stripes. The surrounding fat is hyperechoic. **(B)** Longitudinal sonogram of the right pancreatic lobe of a 3-year-old Welsh corgi with pancreatitis. Hypoechoic striations are crossing the pancreas, and the contours of the pancreas are outlined by fluid. A dilated, fluid-filled segment of bowel is noted in the near field (arrowheads). **(C)** Transverse sonogram of the right pancreatic lobe in an 8-year-old cat with liver failure. The lobe is thickened (about 1 cm thick between calipers) and numerous anechoic stripes are crossing the parenchyma. A large amount of anechoic peritoneal effusion is present (asterisk). **(D)** Transverse sonogram of the right pancreatic limb in an 11-year-old Jack Russel Terrier with pancreatitis. The pancreas is thickened, and multiple anechoic linear striations are crossing the pancreas. There is a small amount of anechoic peritoneal fluid (asterisk). The descending duodenum (arrowheads) is mildly fluid-distended, and the duodenal wall is thickened, consistent with duodenitis.

The mass effect created by an inflamed hypoechoic pancreas and hyperechoic peripancreatic tissue can displace the descending duodenum. Because the right pancreatic lobe is located dorsomedial to the descending duodenum, this loop of bowel is at times displaced ventrolaterally. In **subacute to chronic active pancreatitis,** the pancreas remains a distinct, well-defined hypoechoic structure that contrasts with the slightly hyperechoic peripancreatic mesentery (Figure 10.14A). At times, irregular margins of the pancreas and foci of mineralization can be seen (Figure 10.14B). **Chronic pancreatitis** characterized by interstitial fibrosis with acinar atrophy and lymphocytic infiltrates is rarely suspected clinically. Most cases encountered have vague clinical signs and nonspecific laboratory values. In these cases, the pancreas can be within the normal range for size, and the parenchyma often is inhomogeneous with hyperechoic nonshadowing foci or lines (Figure 10.14C, D). In cats, chronic pancreatitis is twice more frequent than acute pancreatitis. As this condition is often subclinical, it is very difficult to confirm the pancreatic changes histopathologically. On ultrasound, the changes can be similar to those described in dogs or subtle to inexistent (Figure 10.15). Acute necrotizing pancreatitis cannot reliably be differentiated from chronic nonsuppurative pancreatitis based on clinicopathologic testing and/or sonographic abnormalities

Vet-ebooks.com

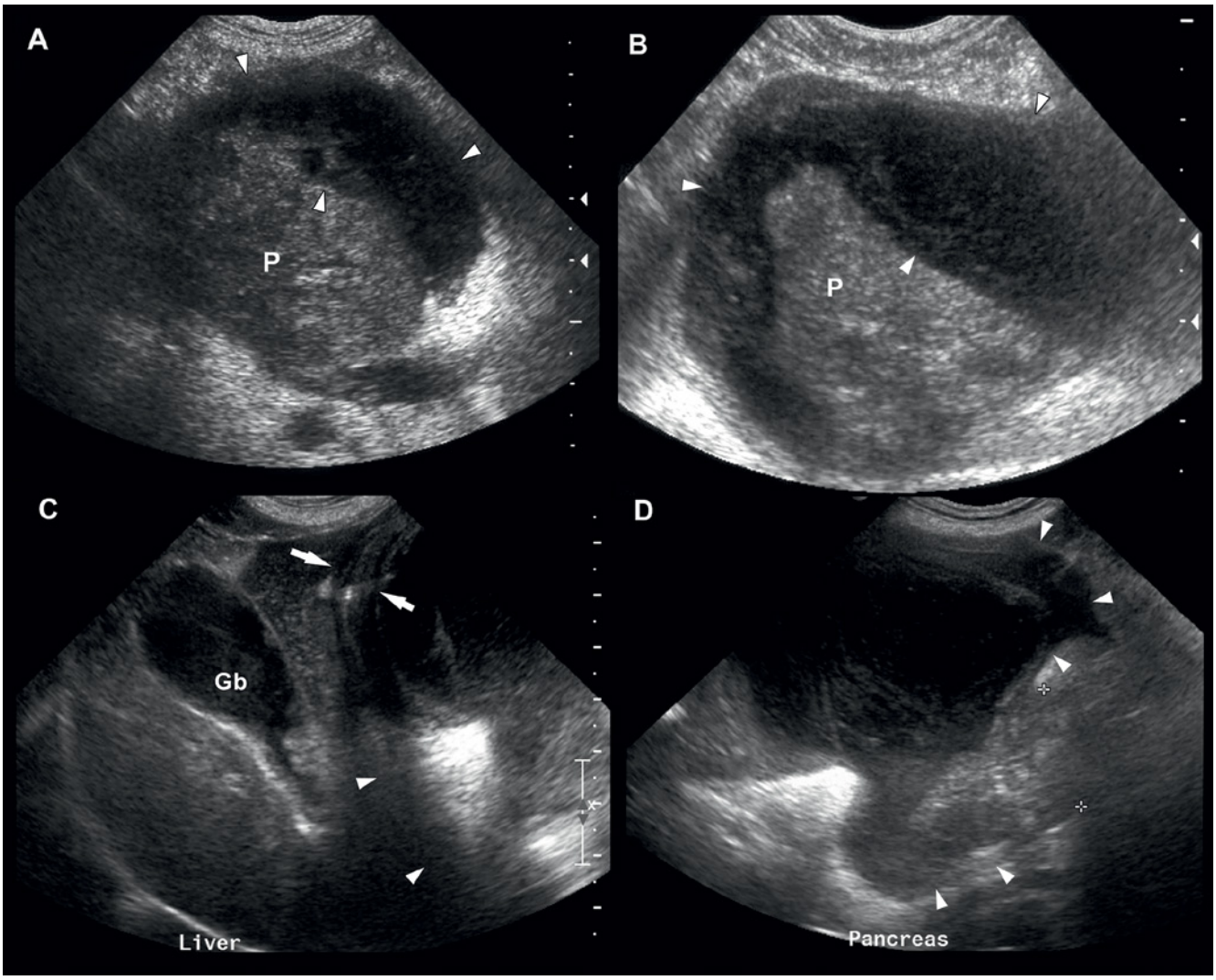


Figure 10.9. Pancreatic pseudocyst in two dogs. Transverse **(A)** and longitudinal **(B)** sonograms of a large pancreatic pseudocyst associated with severe acute pancreatitis. Part of the thickened and hypoechoic pancreas (P) is in the center of the hypoechoic to nearly anechoic lesion representing the pseudocyst (arrowheads). Ultrasound-guided fine-needle aspiration confirmed the diagnosis. **(C, D)** 6-year-old Beagle with a very large fluid cavity (arrowheads) containing settling echogenic sediments and associated with the left lobe of the pancreas. The lesion is drastically displacing the stomach cranially (arrows) to the point that the mass was initially thought to originate from the stomach.

(Ferreri et al. 2003). A tissue core biopsy (ultrasound guided, laparoscopic, or surgical) can be obtained to confirm the diagnosis.

In cats, the pancreatic duct can appear dilated (up to 2.5 mm) especially in older cats with no clinical evidence of active or chronic pancreatic disease. It can be at times also associated with acute pancreatitis (Wall et al. 2001) or chronic pancreatitis. A recent study evaluating the feline pancreatic duct on CT reported that cats with an elevated fPLI were more likely to have dilation of the pancreatic duct in the region of the pancreatic body compared to normal cats (Park et al. 2020).

Exocrine Pancreatic Insufficiency

Exocrine pancreatic insufficiency (EPI) in dogs usually results from pancreatic acinar atrophy and is commonly diagnosed in breeds such as German shepherds. In cats, it is usually caused by chronic/end-stage pancreatitis, but is less commonly in dogs (Watson 2003). Only a few publications have reported the sonographic appearance of EPI. Often, minimal to no sonographic pancreatic changes are seen, however when present, reported pancreatic abnormalities in cats with EPI include a thinned pancreatic

Vet-ebooks.com

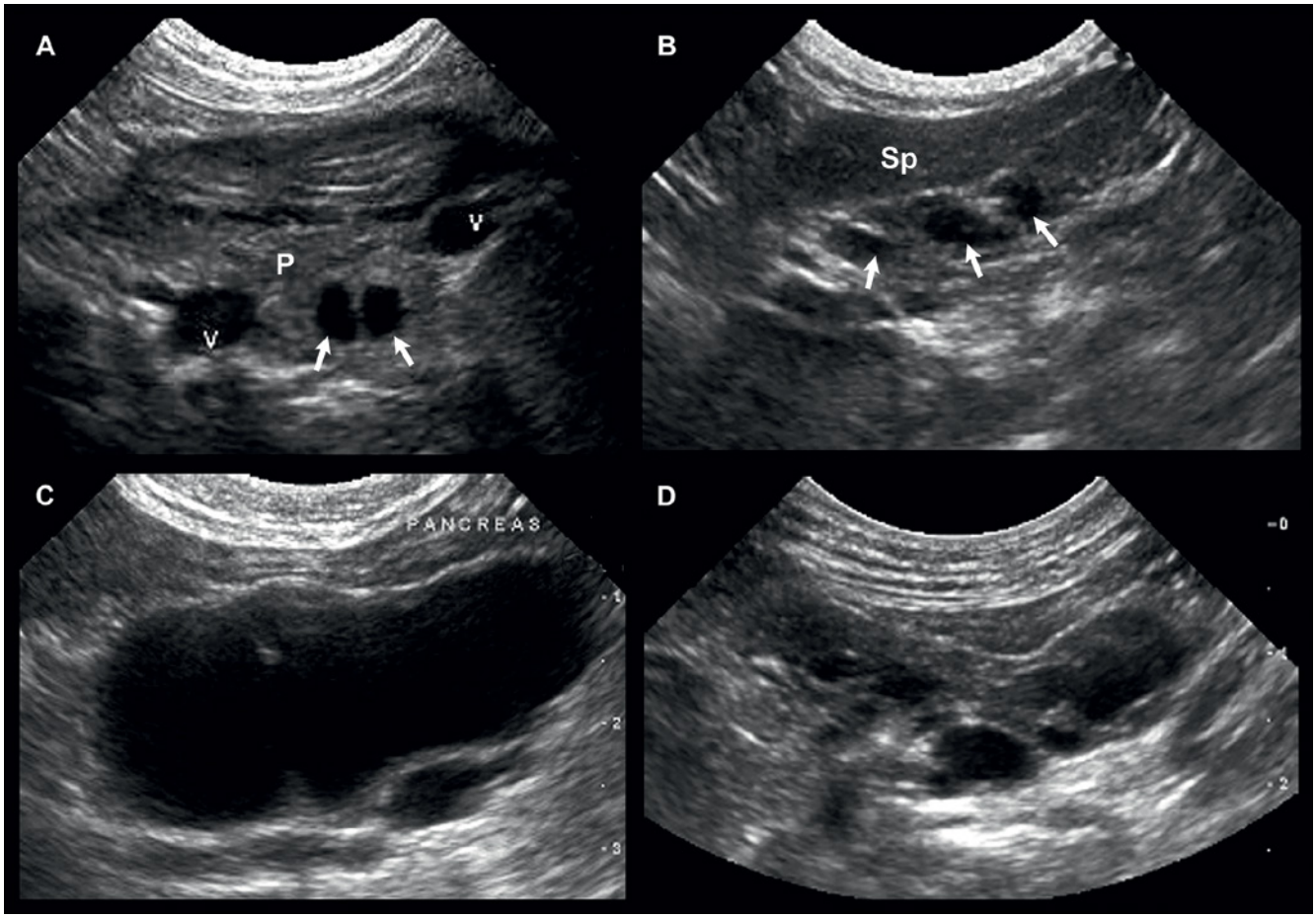


Figure 10.10. **Pancreatic cysts in dogs and cats. (A)** Oblique sonogram of two small cystic lesions (arrows) in the left pancreatic lobe (P) of an 11-year-old miniature schnauzer. **(B)** Longitudinal sonogram of the distal extremity of the left pancreatic lobe of an 18-year-old cat with several cyst-like changes (arrows). This cat had no clinical history of previous pancreatitis. **(C)** Large pancreatic cyst on the left lobe and body of the pancreas in a 16-year-old cat. **(D)** The same region after ultrasound-guided drainage of the cyst presented in Figure 10.10C. Sp, spleen; V, adjacent vessels.

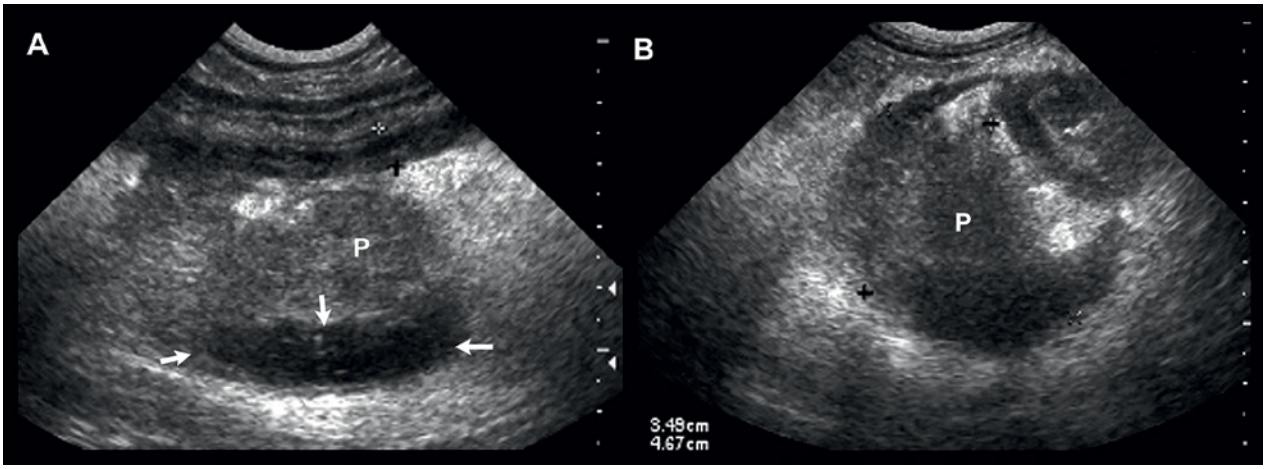


Figure 10.11. **Pancreatic abscess in two dogs. (A)** Longitudinal sonogram of an ovoid discrete hypoechoic cavity (arrows) in the right pancreatic lobe (P) of a 6-year-old cocker spaniel. Notice the thickened and atonic (fluid filled) duodenum in the near field (cursors). The muscularis layer of the duodenal wall is especially prominent. Hyperechoic fat is seen around the pancreas. The cavity was confirmed by ultrasound-guided aspiration to be an abscess. **(B)** Transverse sonogram of an abscess (arrows) in the right pancreatic lobe (P) of a 10-year-old Labrador crossed. The peripheral fat is hyperechoic, indicating steatitis.

Vet-ebooks.com

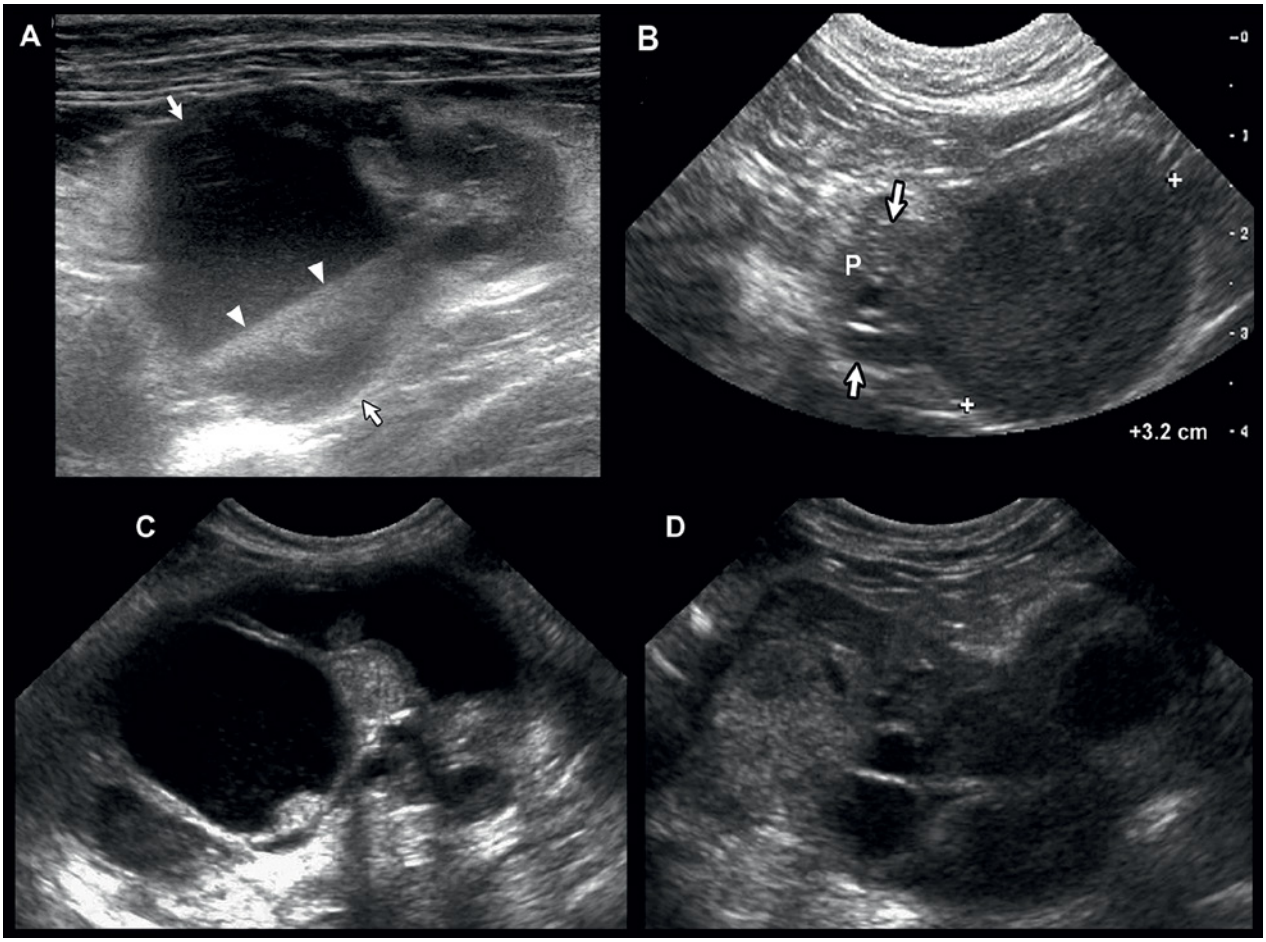


Figure 10.12. **Pancreatic abscess in three cats. (A)** Sonogram of a 5-year-old cat with pancreatitis with a large cavity in the pancreatic body (between the arrows). The lesion deforms the contour of the pancreas and is outlined by focally bright fat. Note the echogenic line (arrowheads) representing settled echogenic content (pus, confirmed by sampling). **(B)** In another cat, a large cavity containing a mildly echogenic fluid (between the cursors) severely deforming the right lobe of the pancreas (P, between the arrows) is seen. With gentle pressure, the echogenic fluid moved on real-time examination**. (C, D)** Complex cystic changes on the pancreas in a 6-year-old Norwegian forest cat. Several cavities of variable size and echogenicity are present. FNAs confirmed abscessation.

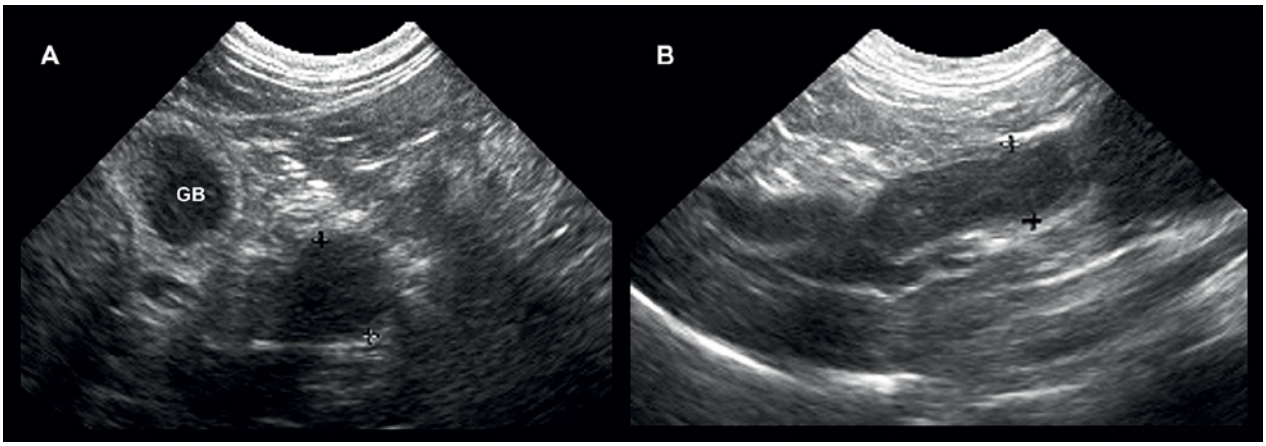


Figure 10.13. **Dilated common bile duct in a cat with pancreatitis.** Transverse **(A)** and longitudinal **(B)** sonograms of the common bile duct (between the cursors) in a cat with pancreatitis and pancreatic abscess (the same cat as in Figure 10.12B). The CBD is greatly distended, reaching 1.4 cm in diameter proximally **(A)** and 1.2 cm distally **(B)**. Notice that the CBD and gallbladder (GB) walls are thickened.

Vet-ebooks.com

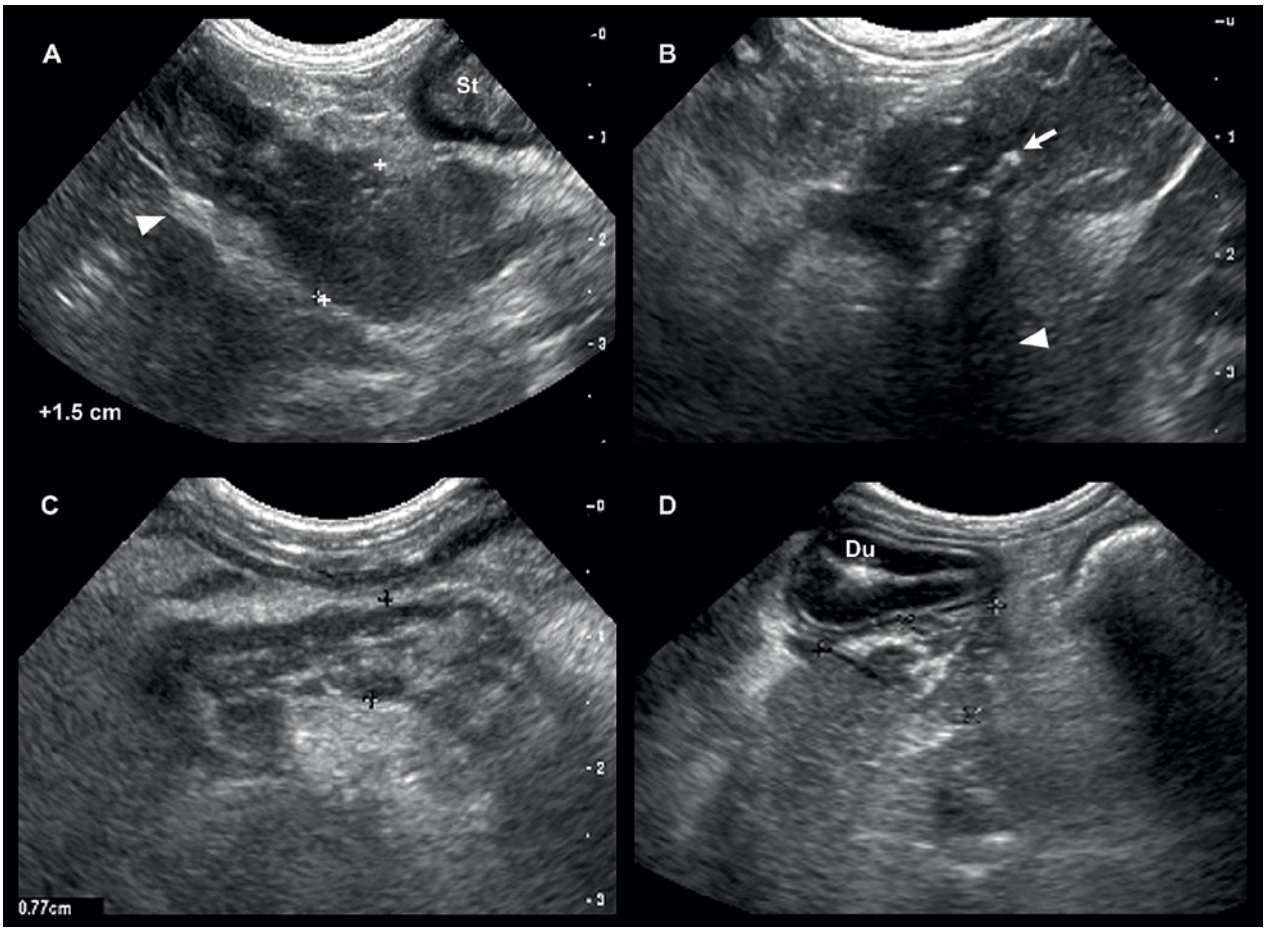


Figure 10.14. **Chronic pancreatitis in three dogs. (A)** Diffuse chronic active necrotizing pancreatitis with fibrosis and regeneration in a 14-year-old Shih Tzu. The pancreas (cursors) is markedly irregular and mostly hypoechoic, with a few inhomogeneous areas. It is 1.5 cm thick. **(B)** Chronic pancreatitis in an 11-year-old mixed-breed dog. Numerous hyperechoic foci are seen in the pancreas (arrow). Some of these foci are associated with shadowing (arrowhead), suggesting mineralization. The pancreas is hypoechoic, but the surrounding fat is normal. The longitudinal **(C)** and transverse **(D)** sonograms of the right pancreatic lobe (between the cursors) in an 8-year-old Australian shepherd, showing a pancreas that is within normal range for size but very inhomogeneous, globally hypoechoic with hyperechoic foci. Du, duodenum, St, stomach.

parenchyma and pancreatic duct dilatation, which can be tortuous and/or have a variable diameter (Auger et al. 2021). In dogs, decreased pancreatic thickness compared to the normal reference range is the most reported feature (Pelligra et al. 2022). Hyperechogenic and inhomogeneous parenchyma have also been reported in cats and dogs (Hecht et al. 2006; Watson 2003). In confirmed cases of EPI, the authors have also encountered a hyperechoic parenchyma and dilated pancreatic duct with or without calculi (Figures 10.16, 10.17). An additional reported feature of EPI includes a hypermotile intestinal tract, which is distended with echogenic contents (Auger et al. 2021; Pelligra et al. 2022), possibly related to the malabsorption encountered with EPI (Figure 10.17).

Pancreatolithiasis and Abnormal Pancreatic Duct

Pancreatolithiasis refers to the presence of calculi in the pancreatic ductal system or parenchyma. This uncommon occurrence can be diagnosed radiographically or sonographically (Figures 10.17, 10.18). The size and number of calculi can widely vary. Calculi are associated with shadowing. It can be associated with a variable degree of ductal dilation or anomalies such as pseudobladder and underlying chronic pancreatitis (Bailiff et al. 2004). Pseudobladder is described as a dilated segment of the pancreatic duct of unknown etiology; this fluid-filled focal dilation can be confused with a pseudocyst or abscess.

After surgical ligation of pancreatic duct in four dogs, a study showed endoscopic evidence of progressive

Vet-ebooks.com

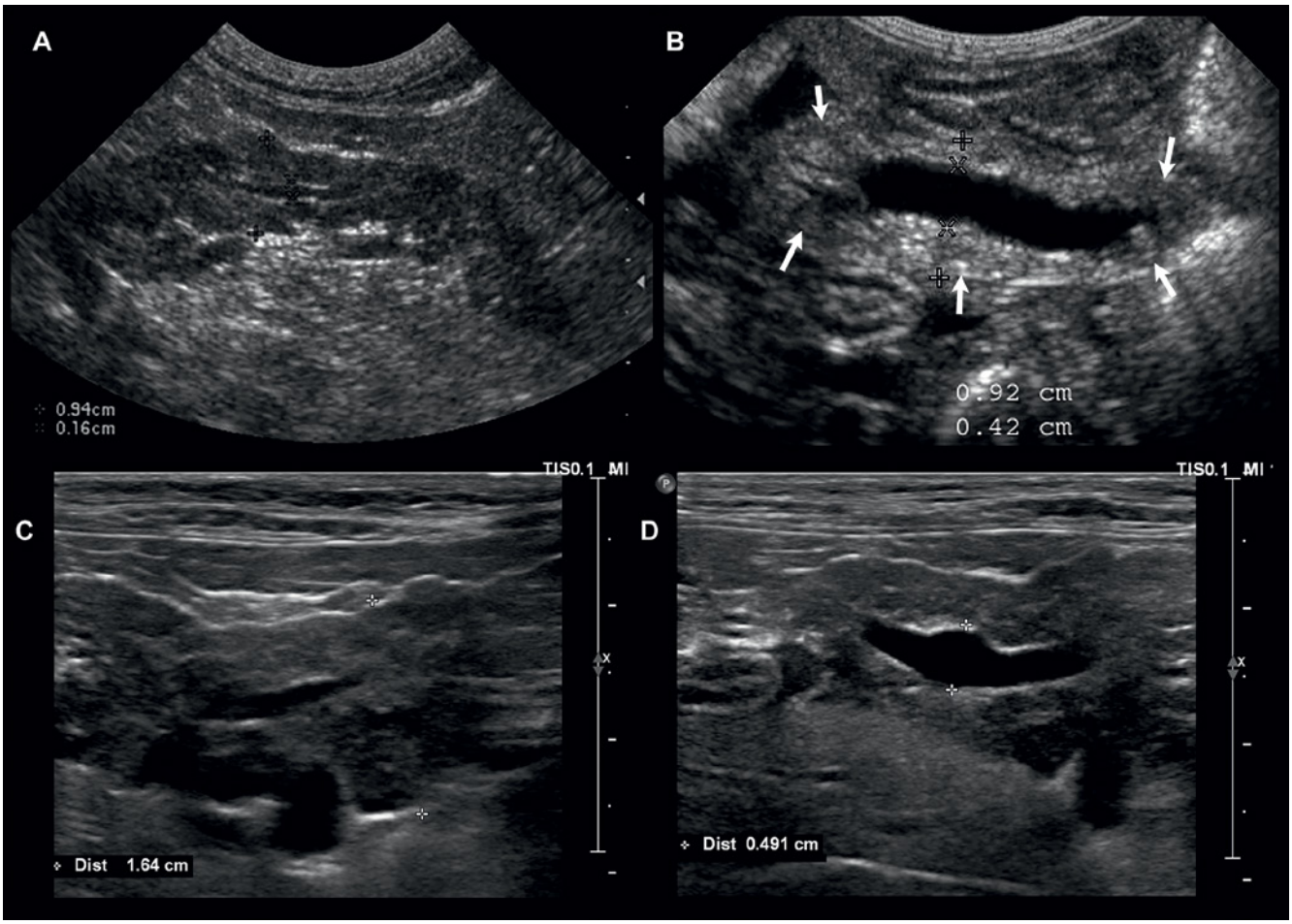


Figure 10.15. **Chronic pancreatitis in three cats. (A)** Longitudinal sonographic image of the left pancreatic limb of a cat with diffuse lymphoplasmocytic pancreatitis. The pancreas is irregular and mildly hypoechoic. The central pancreatic duct appears normal. **(B)** Chronic pancreatitis with pancreatic atrophy and Islet cell fibrosis in another cat. The pancreas (arrows) appears thickened (9.2 mm) and hyperechoic, but the pancreatic duct (D) is dilated (4.2 mm), counting for nearly half of the overall pancreatic lobe thickness. **(C, D)** A 16-year-old Bengal cat with lymphocytic and neutrophilic chronic pancreatitis. **(C)** Longitudinal sonographic image of the left pancreatic limb (between cursors). The pancreas is diffusely thickened with irregular, nodular margins and is moderately heterogeneous. **(D)** There is also diffuse, irregular dilatation of the pancreatic duct (between cursors).

dilation of the pancreatic ductal system and atrophy of the acinar tissue replaced by fibrosis and fat, resulting in increased echogenicity of the parenchyma (Morita et al. 1998).

In cats, the authors also encountered marked saccular dilation of the pancreatic duct without evidence of obstruction (Figure 10.18F). In these uncommon cases, the pancreatic duct wall is mildly thickened and mixed anechoic to echogenic fluid is noted in the lumen. The exact etiology of this severe distention is unknown.

Pancreatic Nodules and Masses

Pancreatic **nodular hyperplasia** is occasionally seen in the pancreas of older dogs and cats. Well-defined hypoechoic to nearly isoechoic nodules that can vary in size are recognized (Hecht et al. 2007) (Figure 10.19). These nodules can be confused for neoplastic disorders, such as insulinomas or carcinomas. They may also look similar to cysts, although far acoustic enhancement is not usually associated with soft-tissue nodules.

Pancreatic **exocrine tumors** such as adenocarcinomas (Figure 10.20) arise from acinar cells or ductal epithelium. Even though these tumors are rare, they are the most common type of pancreatic neoplasia in small animals. They tend to develop in the central portion of the gland. As they grow, they may compress the CBD, invade the adjacent gastric and duodenal segments, and frequently metastasize to the liver (Figure 10.21) (Lamb et al. 1995). They often are poorly echogenic nodules or masses that can be associated with mineralized foci. Carcinomatosis may

Vet-ebooks.com

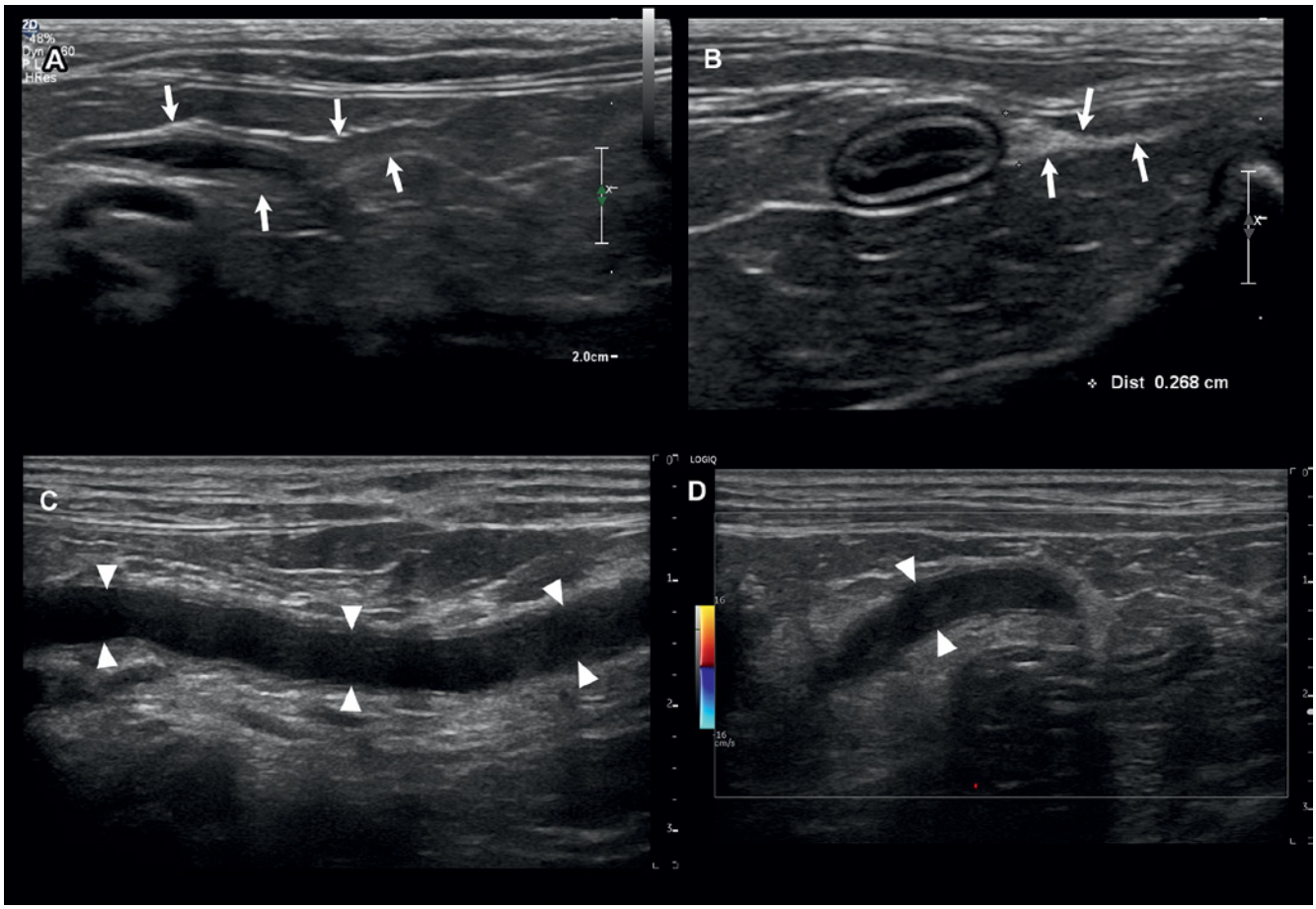


Figure 10.16. Exocrine pancreatic insufficiency in two cats. (A, B) Longitudinal sonographic image of the left pancreatic limb (between arrows) of a 4-year-old Norwegian Forest cat. The pancreatic duct is mildly diffusely dilated, and the pancreatic parenchyma is markedly thinned to nearly absent**. (B)** Transverse sonographic image of the right pancreatic limb (between arrows), which is markedly thinned and moderately hyperechoic. **(C, D)** Longitudinal sonographic images of the left pancreatic limb (between arrowheads) in a 6-year-old Egyptian Mau. There is moderate diffuse dilation of the pancreatic duct with markedly thinned to nearly absent pancreatic parenchyma. The peripancreatic fat is diffusely mildly hyperechoic, suggesting underlying chronic active pancreatitis. In D, the absence of blood flow upon color Doppler interrogation confirms that the tubular anechoic structure is indeed the pancreatic duct.

appear as a mass centered on the pancreas with numerous poorly echogenic nodules disseminated throughout the abdominal cavity and possibly affecting the abdominal wall; abdominal effusion is a common finding in this neoplasm (Figure 10.21 and see Figure 15.17).

Other tumors have occasionally been encountered in the pancreas of dogs and cats: cystadenoma, adenoma (Figure 10.22), metastatic carcinoma, hemangiosarcoma, fibrosarcoma, pleiomorphic sarcoma, and lymphoma (Figure 10.23) (Törner et al. 2020).

Pancreatic **endocrine tumors** such as glucagonomas, insulinomas, and gastrinomas are uncommon. From that group, insulinomas are the most commonly encountered in dogs. The ultrasound detection rate varies depending on the size and distribution of the lesions, the equipment quality, and the operator's experience. The visibility of these lesions may also be affected by the presence of overlying gastrointestinal content and by body conformation (e.g., deep-chested or obese dogs). Insulinomas can present as a solitary nodule, multiple nodules, or an ill-defined area of abnormal echogenicity (Figure 10.24). The size of the pancreatic lesions varies greatly, but a majority of the lesions tend to be small and poorly echogenic (Lamb et al. 1995). Contrast-enhanced ultrasound when available can be used to further characterize pancreatic nodules and masses (Vanderperren et al. 2014). Contrast-enhanced ultrasound may help increase conspicuity of pancreatic insulinomas and may allow detection of small insulinomas not detected with conventional ultrasound (Cervone et al. 2019; Nakamura et al. 2014). Cross-sectional imaging modalities such as CT and MRI can be very useful in identifying

Vet-ebooks.com

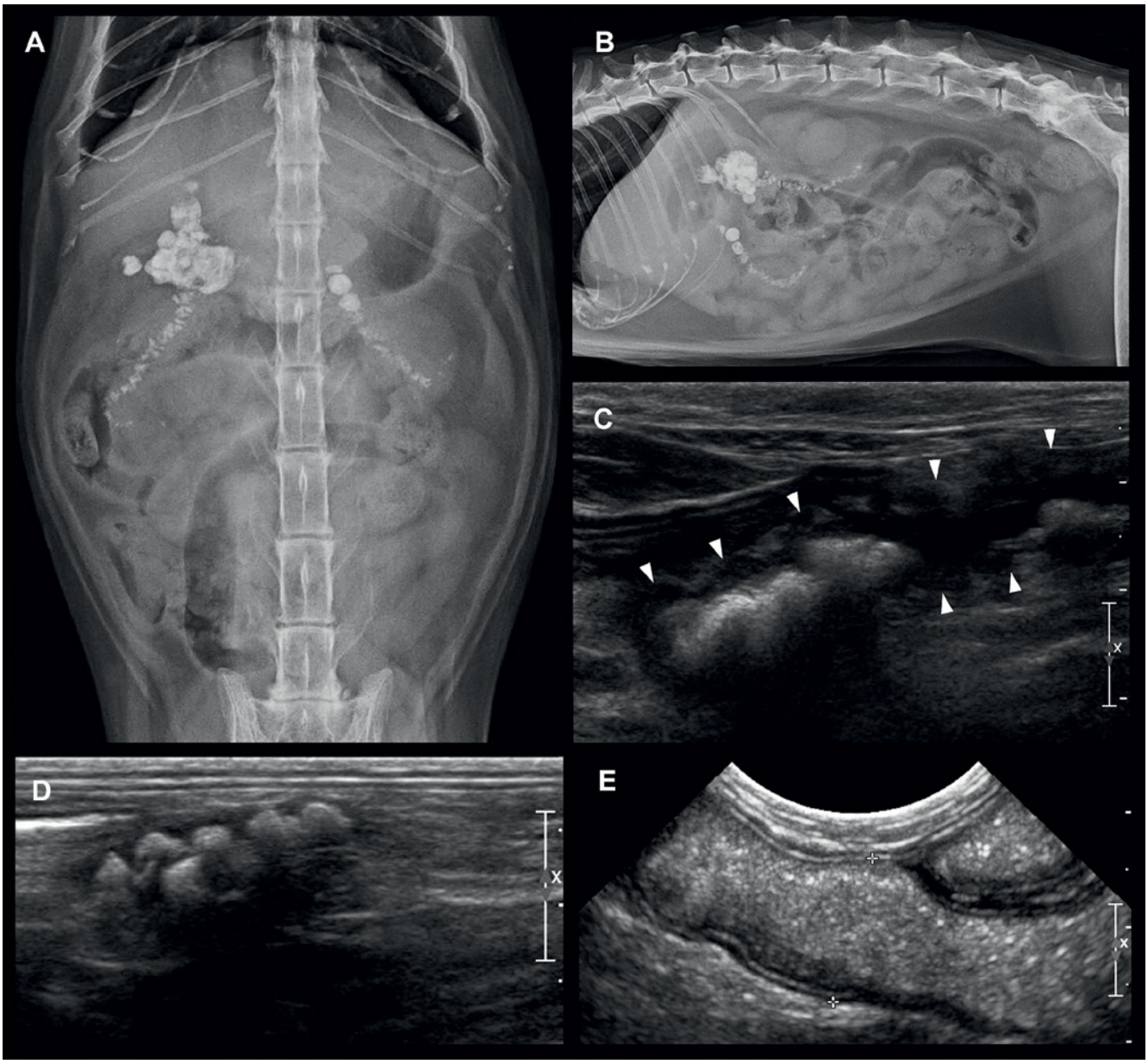


Figure 10.17. Exocrine pancreatic insufficiency in a 17-year-old DSH cat with chronic pancreatitis. The ventrodorsal **(A)** and the right lateral **(B)** radiographs showed a long string of calculi along the trajectory of the entire pancreatic duct and were suspected to be also a part of the biliary system. On ultrasound, there are numerous irregular calculi **(C, D)** associated with shadowing. The pancreatic tissue is barely seen in this cat (arrowheads). **(E)** The intestines of this cat are hyperperistaltic and dilated (1.3 cm) with echogenic contents; this may support the malabsorption seen in EPI.

insulinomas (Figure 10.24) in cases where ultrasound failed to detect a lesion despite strong clinical suspicion (Robben et al. 2005, Mai and Careres 2008).

Most endocrine tumors are malignant and tend to spread to the regional lymph nodes and liver. Therefore, sonographic screening of the hepatic parenchyma and regional lymph nodes is recommended to detect possible hepatic metastasis (Figure 10.21). Metastatic lymph nodes tend to be enlarged and hypoechoic. The close anatomical relationship between the hepatic lymph nodes and the body of the pancreas can complicate the distinction

Vet-ebooks.com

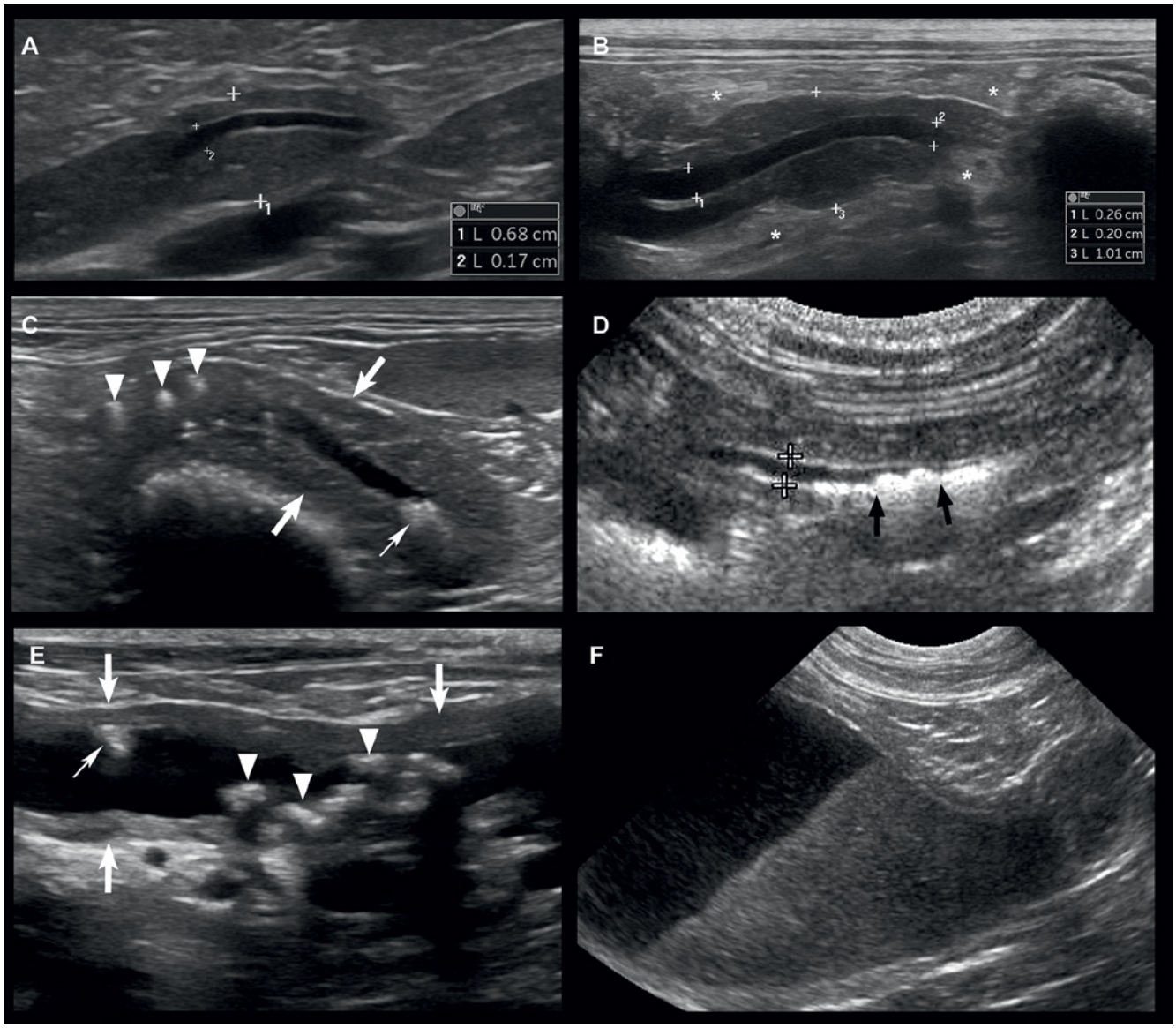


Figure 10.18. **Dilated pancreatic duct (PD) in cats. (A)** Mildly dilated, 1.7-mm-wide PD in an 8-year-old cat with renal disease. The pancreas is normal. **(B)** Moderately dilated (up to 2.6 mm wide) PD in a 10-year-old cat with mild chronic pancreatitis. The peripancreatic fat is mildly hyperechoic (*). **(C)** Longitudinal ultrasound image of the left pancreatic limb (between white arrows) in a 13-year-old domestic shorthair cat with well-controlled diabetes mellitus. The pancreatic duct is diffusely moderately dilated (up to 5 mm) and there is an accumulation of intraluminal partially shadowing calculi (arrowheads), with some mineralized debris also adhered to the ventral wall (thin white arrow). **(D)** Dilated PD with thickened walls and small intraluminal calculi and mineralized sediments. **(E)** Dilated PD with several intraluminal punctate to linear calculi (arrowheads), one of them appears adherent to the wall (thin arrow). The margins of the pancreas are between the white arrows. **(F)** Hugely dilated pancreatic duct in a 15-year-old cat presented for progressive inappetence. The markedly dilated pancreatic duct contains partially settling cellular fluid. No calculi were seen. The pancreas was barely visible in some segments.

between pancreatic nodules from hepatic lymphadenomegaly. Whereas pancreatic tumors usually present as a focal nodule or mass, neoplasia cannot reliably be differentiated from pancreatitis or nodular hyperplasia.

Rarely, **ectopic splenic tissue** can be found within the pancreas (Figure 10.25) of cats and dogs, which can present as one or more pancreatic nodules that are hypoechoic to the pancreas and of similar echogenicity and echotexture to the spleen (Ramirez et al. 2013).

Vet-ebooks.com

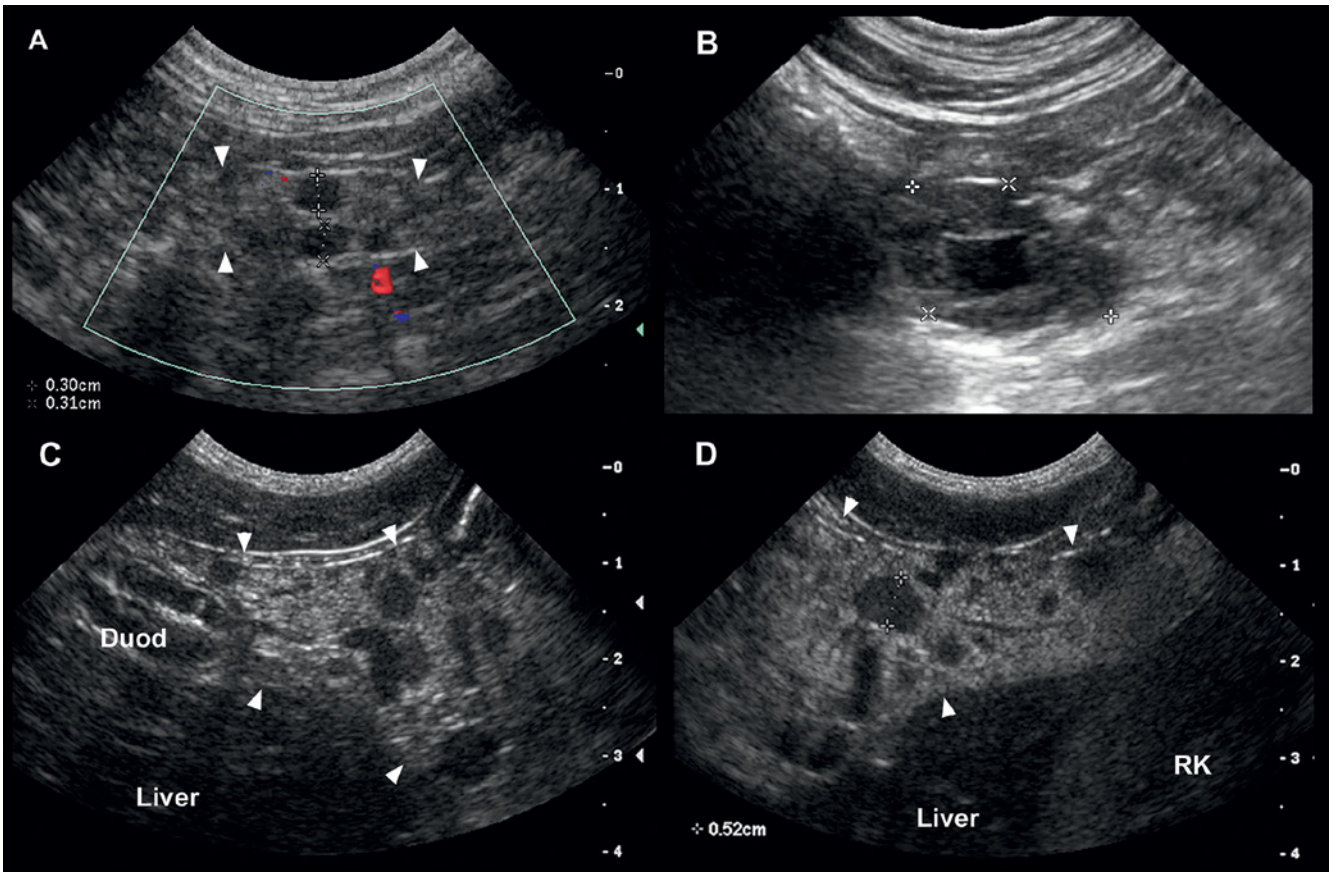


Figure 10.19. **Nodular hyperplasia in a cat and a dog. (A)** Longitudinal sonographic image with color Doppler of the pancreas of a cat with chronic inflammatory bowel disease. Two well-defined 3-mm hypoechoic nodules (between the cursors) are identified in the left pancreatic limb (arrowheads). The rest of the pancreas is mildly heterogeneous. **(B)** A 15-year-old cat with heart murmur had a cavitated nodule in the pancreas that was aspirated under ultrasound guidance. It was interpreted as likely nodular hyperplasia and did not change in the appearance on recheck ultrasound performed 3 months later. **(C, D)** Transverse **(B)** and longitudinal **(C)** sonographic images of the right pancreatic limb of a small-breed dog with diabetes mellitus. Several well-defined, hypoechoic nodules of variable size and shape are seen throughout the hyperechoic pancreatic tissue (arrowheads). There was no evidence of changes to the peripheral fat. Fine-needle aspiration of the pancreas revealed the presence of mild, chronic pancreatitis with nodular hyperplasia. Duod, duodenum; RK, right kidney.

This can represent a diagnostic challenge, as intrapancreatic ectopic splenic tissue can mimic hypervascular pancreatic neoplasms, such as insulinoma (Tomura et al. 2022; Ramirez et al. 2013). In rare instances, neoplastic infiltration of intrapancreatic splenic tissue can also occur, with a mast cell tumor within intrapancreatic splenic tissue reported in one cat (Törner et al. 2020).

Special Procedures

Fine-needle aspirations or core biopsies of diffuse or focal pancreatic lesions can be performed safely if adequate precautions are taken to avoid laceration of large vessels or pancreatic parenchyma. An experimental study in dogs, evaluating the effects of ultrasound-guided aspirations and surgical pancreatic biopsies, showed no serum lipase elevation during the time frame (Cordner et al. 2010). Additional retrospective studies in dogs (Cordner et al. 2015) and cats (Crain et al. 2015) having undergone ultrasound-guided pancreatic fine-needle aspiration reported low rates of clinical complications and good diagnostic yield.

Fluid-filled lesions, such as pseudocysts and abscesses, can also be sampled and drained safely under ultrasound guidance (Figure 10.26). The presence of anechoic fluid in cavitary lesions can be misleading to the type of fluid to be aspirated. Even

Vet-ebooks.com

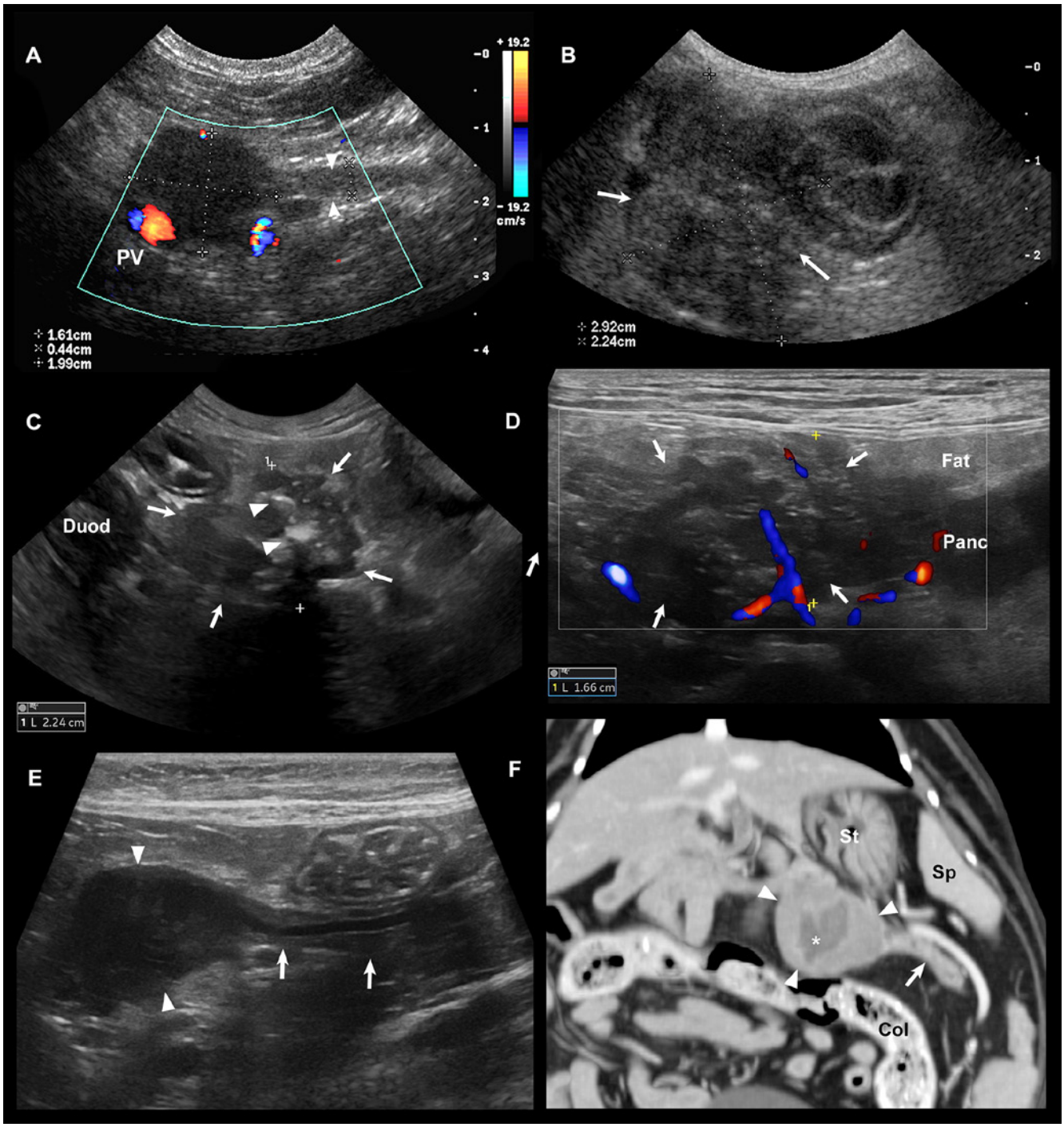


Figure 10.20. **Pancreatic carcinomas in dogs and cats. (A)** A hypoechoic mass found in the proximal portion of the left pancreatic limb of this cat. This mass is adjacent to the portal vein (PV). The rest of the left limb (arrowheads) is normal. Pancreatic adenocarcinoma was confirmed histologically. **(B)** Transverse sonographic view of a pancreatic mass (arrows) invading the wall of the duodenum in a dog. A poorly differentiated carcinoma was diagnosed with cytology after fine-needle aspiration. **(C, D)** In this 14-year-old Jack Russel terrier, an irregular and poorly-defined mass (arrows) was found in the right limb of the pancreas while the rest of the pancreas was hypoechoic, mildly enlarged, and surrounded by hyperechoic fat, supporting concurrent pancreatitis. Note the shadowing hyperechoic foci in the mass (arrowheads in C), which is common with pancreatic adenocarcinoma. **(E, F)** Pancreatic carcinoma in a 14-year-old domestic shorthair cat. **(E)** There is a well-defined large ovoid hypoechoic mass (between arrowheads) arising from the proximal portion of the left pancreatic limb at its junction with the pancreatic body. The pancreatic lobe is otherwise normal (white arrows) with a mildly dilated pancreatic duct. The surrounding fat is mildly hyperechoic, suggesting concurrent pancreatitis. St, stomach. **(E)** Note the large (between cursors) hypoechoic and mildly heterogeneous pancreatic mass adjacent to the stomach. **(F)** Postcontrast dorsal multiplanar reconstructed CT image displaying the ovoid pancreatic mass at the proximal portion of the left pancreatic limb (between arrowheads), caudal to the stomach, and cranial to the colon. There is a hypoenhancing center (white asterisk), most consistent with necrosis. The remainder of the left pancreatic limb (white arrow) is normal in thickness with mild dilation of the hypoattenuating pancreatic duct. Histopathology following left pancreatectomy was consistent with pancreatic carcinoma. Col, colon; Sp, spleen; St, stomach.

Vet-ebooks.com

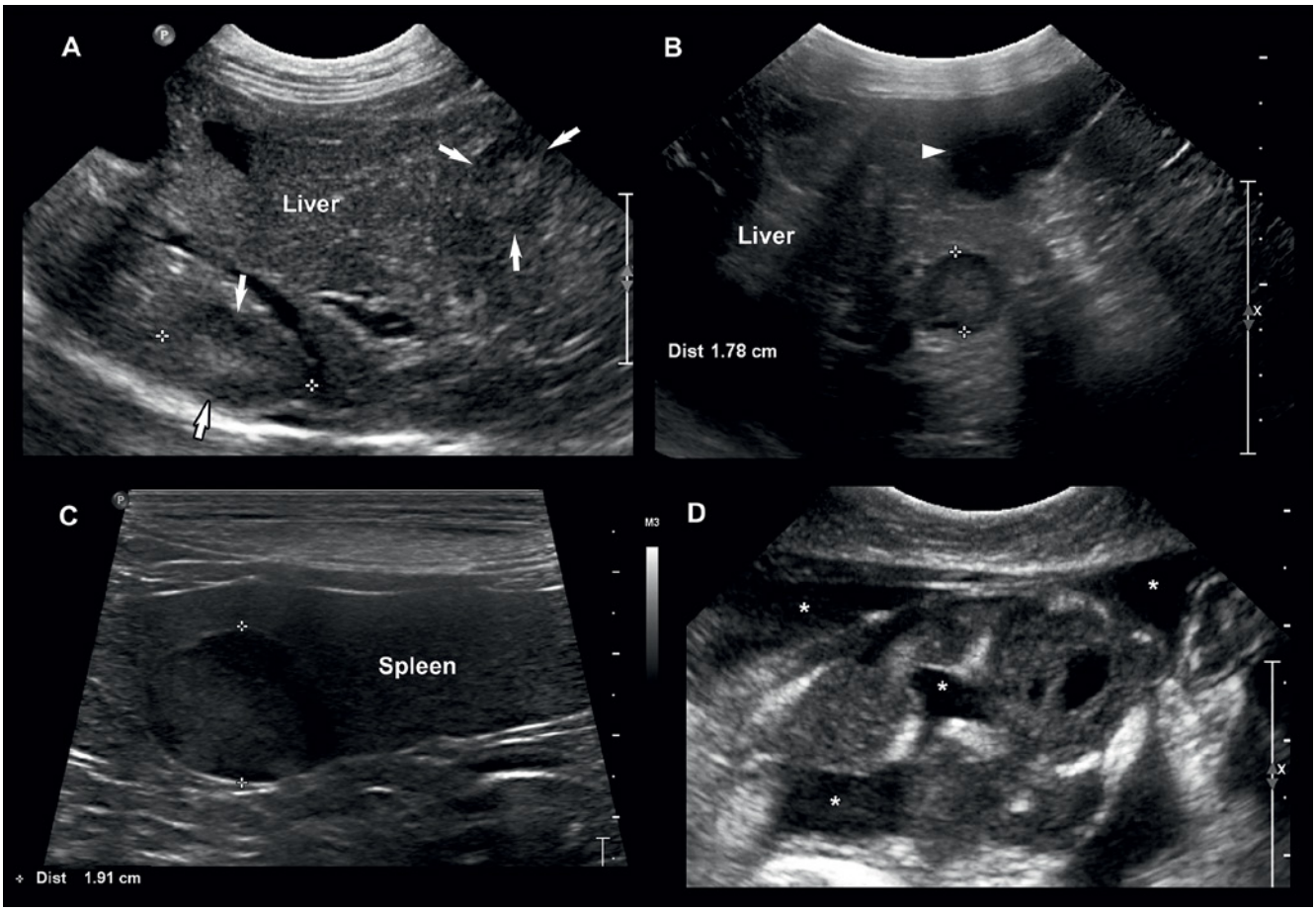


Figure 10.21. **Metastases from pancreatic carcinomas in two cats and one dog**. **(A)** Several target-like hepatic nodules (arrows and cursors) are present in the liver of this 11-year-old cat with pancreatic carcinoma. **(B-C)** A "target-like" nodule is noted in the hepatic parenchyma (between cursors) of this 7-year-old Golden Retriever as well as a more uniformly hypoechoic nodule (arrows). A larger mixed-echogenicity nodule (between cursors on) is also found in the spleen, focally bulging splenic margins. Ultrasound-guided fine-needle aspirations were performed, and cytology results were consistent with pancreatic carcinoma with hepatic and splenic metastases. **(D)** In this 11-year-old cat with a large pancreatic mass, the mesentery was thickened and nodular, "floating" in the effusion (*), consistent with carcinomatosis.

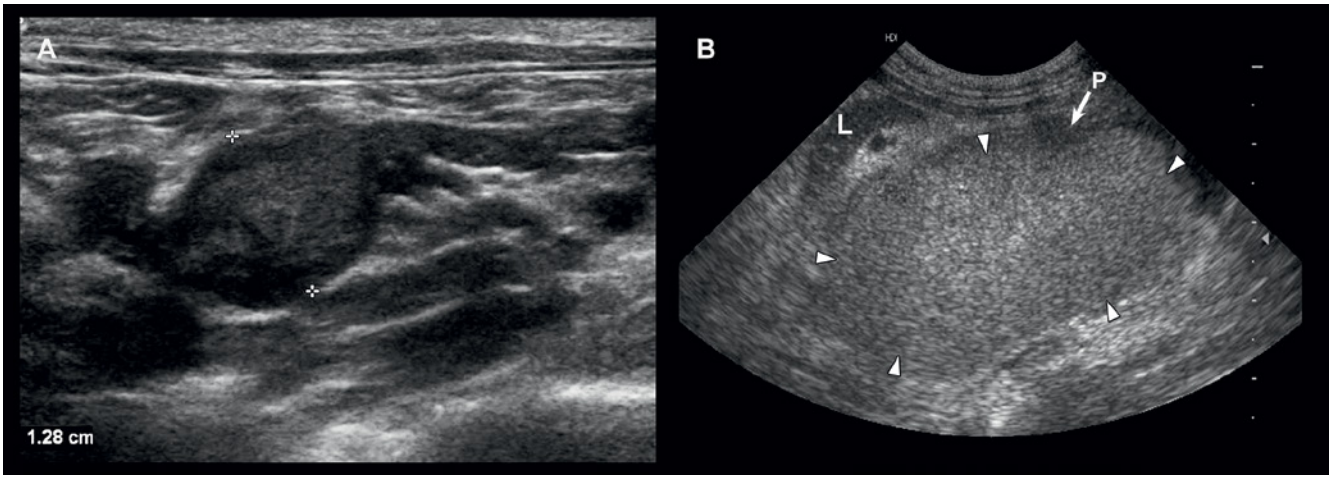


Figure 10.22. **Pancreatic adenoma in two cats. (A)** An incidental 1.3 cm nearly isoechoic nodule is deforming the contour of the right limb of the pancreas. An ultrasound-guided fine-needle aspirate diagnosed an adenoma. The nodule is regularly monitored to assess any change in size or echogenicity. **(B)** In this other 12-year-old cat presented for inappetence and vomiting, a smooth, uniformly echogenic mass was identified in proximity to the pancreas (P) and the regional fat was hyperechoic. Exploratory surgery and histopathology revealed a pancreatic adenoma with pancreatitis.

Vet-ebooks.com

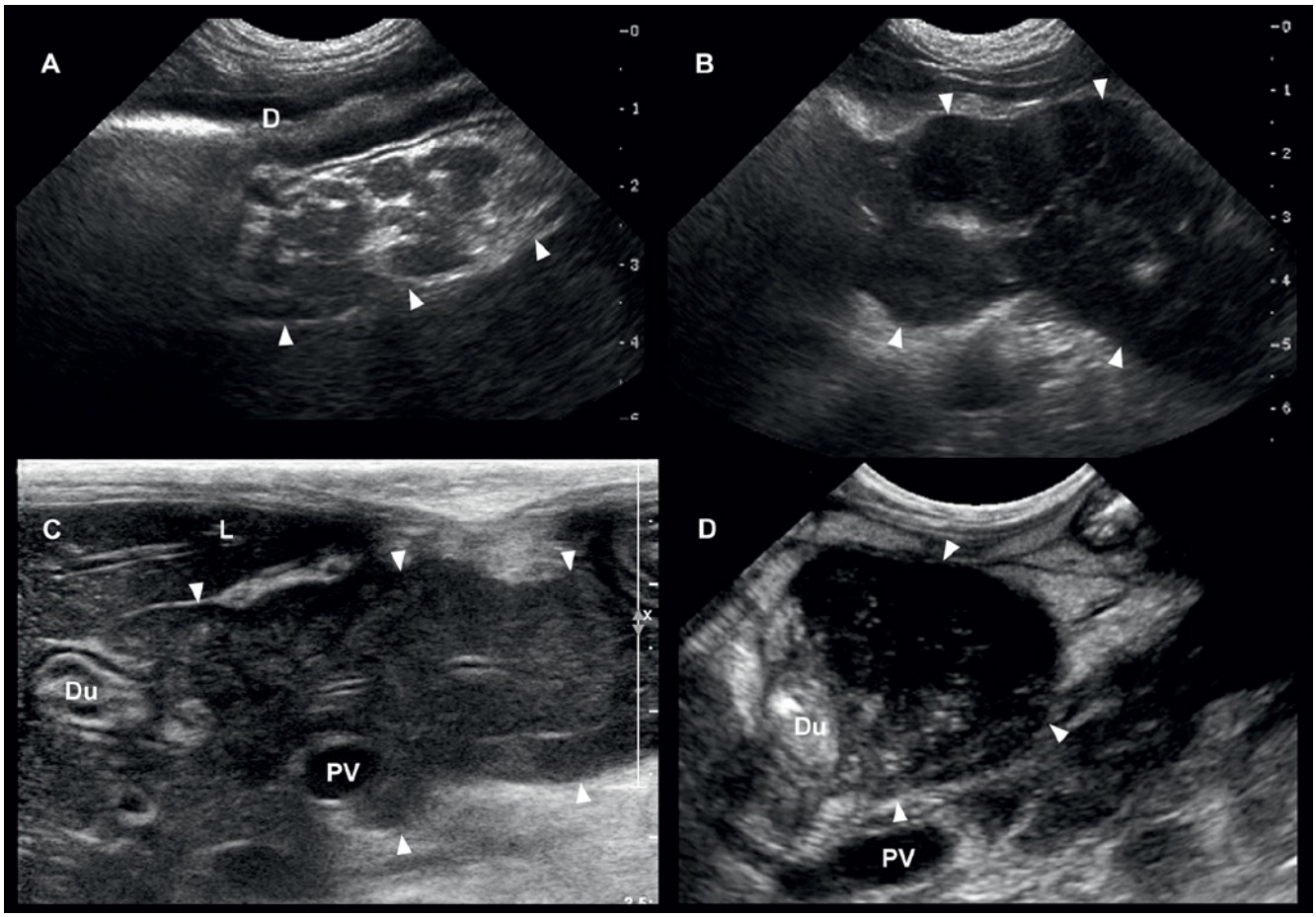


Figure 10.23. **Pancreatic lymphoma in two dogs and one cat. (A)** Numerous variably sized hypoechoic nodules replace the normal echotexture of the pancreas (arrowheads) in this 4-year-old mixed-breed dog. The duodenum (D) is seen in the near field. **(B)** Diffuse pancreatic enlargement (arrowheads) associated with diffuse hypoechogenicity in this 7-year-old Labrador retriever. **(C, D)** In this cat, lymphoma was diagnosed in the pancreas, mesentery, and gastrointestinal tract. The pancreas is markedly and diffusely thickened and hypoechoic with irregular margins (arrowheads). The surrounding fat is hyperechoic, and several anechoic stripes are noted in the near field **(D)**. Du, duodenum; PV, portal vein.

though the fluid may be poorly cellular, its consistency cannot be predicted by its echogenicity. Anechoic fluid might be very viscous and therefore difficult to drain.

Patients with extrahepatic biliary obstruction secondary to severe pancreatitis often have a prolonged disease course. These patients can improve clinically with medical management alone, however in some cases, will benefit from ultrasound-guided cholecystocentesis to alleviate the clinical signs due to extrahepatic biliary obstruction, as these patients are often poor candidates for surgery (Herman et al. 2005; Wilkinson et al. 2020). The procedure can be repeated if clinically indicated.

Serial ultrasound examinations are useful in monitoring resolution or progression of fluid-filled lesions or response to treatment (Figure 10.26).



Visit our website at **www.SmallAnimalUltrasonography.com** for complementary video clips with annotations and text on:

- Normal pancreas
- Pancreatitis in dogs
- Pancreatitis in cats
- Pseudocyst
- Necrotizing pancreatitis in dogs
- Pancreatic carcinoma
- Insulinoma

Vet-ebooks.com

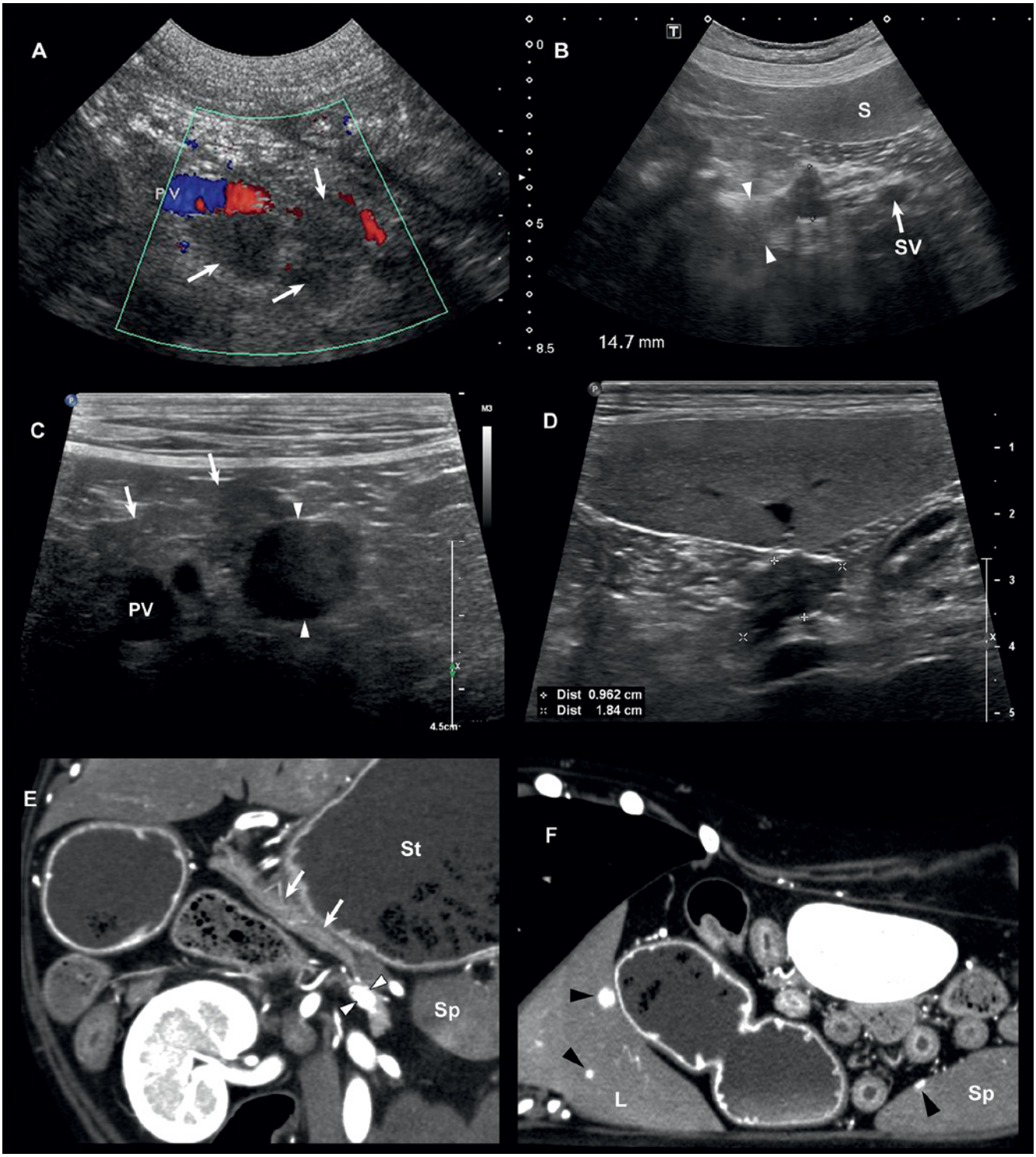


Figure 10.24. **Pancreatic insulinoma in four dogs.** Insulinomas can appear as single or multiple hypoechoic nodules **(A–C)**. **(A)** Color-Doppler assessment of the pancreatic region with several small hypoechoic nodules (arrows). The portal vein (PV) is ventral to the body of the pancreas. **(B)** In this other dog, a 15-mm hypoechoic nodule (cursors) was identified in the left pancreatic limb, in proximity to the splenic vein (SV) and spleen (S). **(C)** A well-defined hypoechoic nodule (between arrowheads) is noted in the left pancreatic limb (arrows) of this 7-year-old Golden Retriever with persistent hypoglycemia, confirmed to be an islet cell carcinoma on histopathology. **(D–F)** Ultrasound and CT images in a 5-year-old mixed breed dog with insulinoma. **(D)** An ill-defined hypoechoic nodule is noted in the distal extremity of the left pancreatic limb (between cursors). **(E)** Arterial phase postcontrast CT angiogram outlining the same left pancreatic nodule as seen on ultrasound (arrowheads), which is strongly contrast-enhancing in the arterial phase, highly suggestive of insulinoma. The remainder of the left pancreatic limb is outlined with white arrows. **(F)** A few strongly contrast-enhancing hepatic and splenic nodules (black arrowheads) are noted in arterial phase postcontrast CT images, highly suggestive of insulinoma metastases. Histopathology was consistent with a malignant islet cell tumor with splenic and hepatic metastases. CT can be complimentary to ultrasound in characterizing pancreatic nodules and evaluating for metastatic spread. PV, portal vein; Sp, spleen; St, stomach.

Vet-ebooks.com

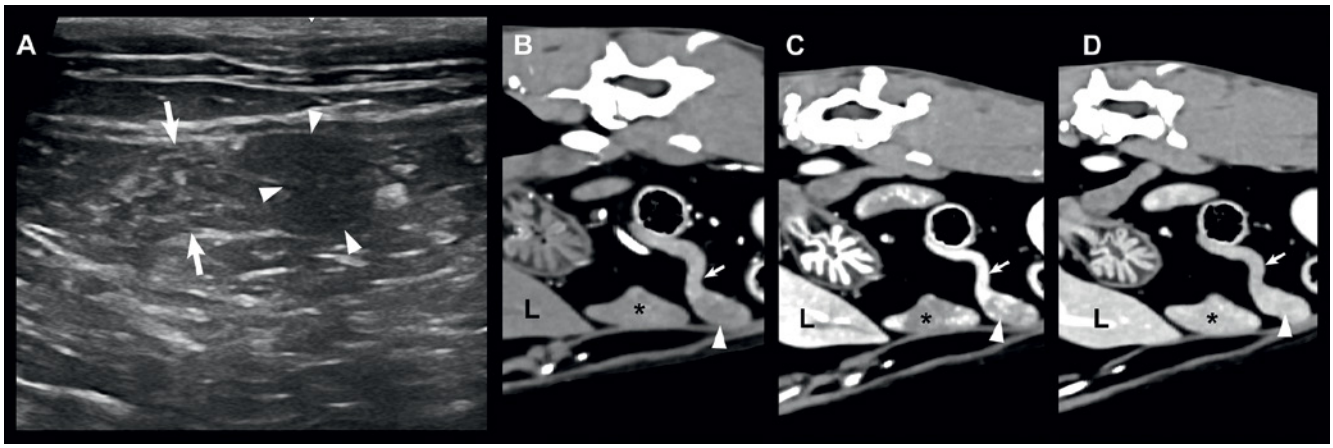


Figure 10.25. **Ectopic intrapancreatic splenic tissue in an 8-year-old male neutered Maine Coon cat. (A)** An ill-defined, ovoid, hypoechoic nodule (between arrowheads) is noted in the extremity of the left pancreatic limb (arrows). **(B–D)** Sagittal multiplanar reconstructed computed tomography (CT) images of the abdomen in arterial **(B)**, portal venous **(C),** and delayed **(D)** postcontrast phases. The left pancreatic nodule (arrowheads) seen on ultrasound is hypoattenuating to the adjacent pancreas in the arterial and portal venous postcontrast phases and displays similar contrast enhancement features to the spleen (asterisk). In the delayed postcontrast phase, the splenic nodule is isoattenuating to the spleen and adjacent pancreatic parenchyma. Ultrasound-guided fine-needle aspiration of this nodule was consistent with normal splenic tissue. Multiphase contrast-enhanced CT can be complimentary to ultrasound in characterizing pancreatic nodules. L, liver.

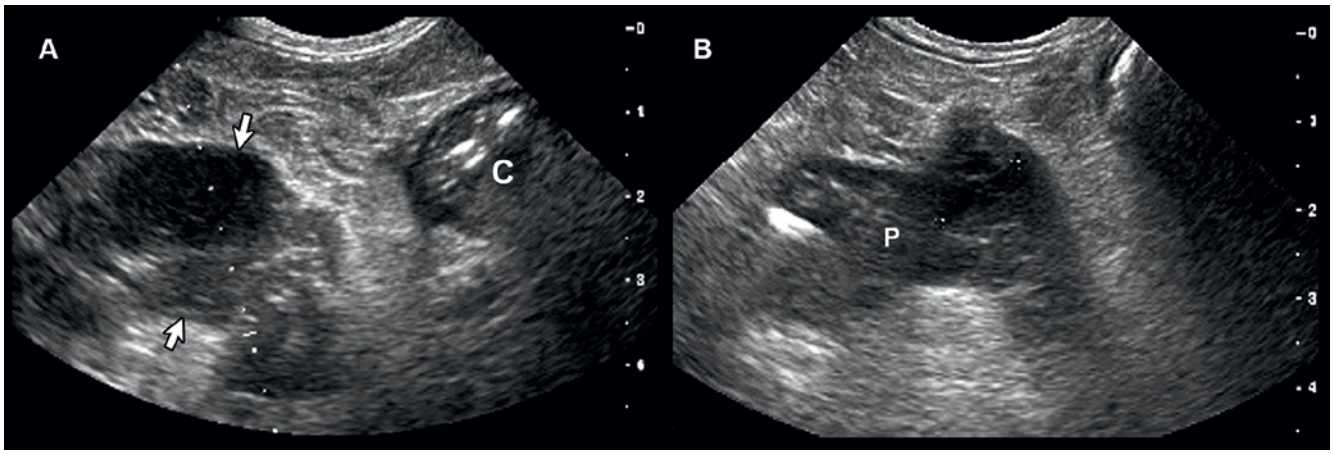


Figure 10.26. **Drainage of cavitary lesion in 9-year-old Australian shepherd. (A)** A hypoechoic cavity (arrows) is present in the inflamed pancreas of this dog. The needle track guide is centered on the cavity. The cavity was drained, and about 10 mL of bloody purulent fluid was withdrawn. The final diagnosis was a sterile abscess. **(B)** A recheck 1 week later shows a smaller and poorly defined cavity (between the cursors) in the same portion of the pancreas (P), and the dog's condition improved clinically. The peripheral fat remained hyperechoic. C, colon.

References

Akol KG, Washabau RJ, Saunders HM, Hendrick MJ (1993) Acute pancreatitis in cats with hepatic lipidosis. J Vet Intern Med 7:205–209.

Auger M, Fazio C, Steiner JM, Penninck DG, et al. (2021) Abdominal ultrasound and clinicopathologic findings in 22 cats with exocrine pancreatic insufficiency. J Vet Intern Med 35:2652–2661.

Bailiff NL, Norris CR, Seguin B, Griffey SM, et al. (2004) Pancreatolithiasis and pancreatic pseudobladder associated with pancreatitis in a cat. J Am Anim Hosp Assoc 40(1):69–74.

Cervone M, Harel M, Ségard-Weisse E, Krafft E. (2019) Use of contrast-enhanced ultrasonography for the detection of a feline insulinoma. J Feline Medicine Surg Open Reports 5:1–7.

Cordner AP, Armstrong PJ, Newman SJ, Novo R, et al. (2010) Effect of pancreatic tissue sampling on serum pancreatic enzyme levels in clinically healthy dogs. J Vet Diagn Invest 22:702–707.

Cordner AP, Sharkey LC, Armstrong PJ, McAteer KD (2015) Cytologic findings and diagnostic yield in 92 dogs

Vet-ebooks.com

undergoing fine-needle aspiration of the pancreas. J Vet Diagn Invest 27:236–240.
Crain SK, Sharkey LC, Cordner AP, Knudson C, et al. (2015) Safety of ultrasound-guided fine-needle aspiration of the feline pancreas: a case-control study. J Feline Med Surg, 17:858–863.
Cridge H, Sullivan AM, Wills RW, Lee AM, et al. (2020) Association between abdominal ultrasound findings, the specific canine pancreatic lipase assay, clinical severity indices, and clinical diagnosis in dogs with pancreatitis. J Vet Intern Med 34(2):636–643.
Diana A, Linta N, Cipone M, Fedone V, et al. (2015) Contrast-enhanced ultrasonography of the pancreas in healthy cats. Vet Res 11:64–70.
Edwards DF, Bauer MS, Walker MA, Pardo AD, et al. (1990) Pancreatic masses in seven dogs following acute pancreatitis. J Am Anim Hosp Assoc 26:189–198.
Etue SM, Penninck DG, Labato MA, Pearson S, et al. (2001) Ultrasonography of the normal feline pancreas and associated anatomical landmarks: a prospective study of 20 cats. Vet Radiol Ultrasound 42:330–336.
Ferreri JA, Hardam E, Kimmel SA, Saunders HM, et al. (2003) Clinical differentiation of acute necrotizing from chronic nonsuppurative pancreatitis in cats: 63 cases (1996–2001). J Am Vet Med Assoc 223:469–474.
Forman MA, Marks SL, De Cock HEV, Hergesell EJ et al (2004) Evaluation of serum feline pancreatic lipase immunoreactivity and helical tomography versus conventional testing for the diagnosis of feline pancreatitis. J Vet Intern Med 18:807–815.
Gori E, Lippi I, Guidi G, Perondi F, et al. (2019) Acute pancreatitis and acute kidney injury in dogs. Vet J 245:77–81.
Granger LA, Hilferty M, Francis T, Steiner JM, et al. (2015) Variability in the ultrasonographic appearance of the pancreas in healthy dogs compared to dogs with hyperadrenocorticism. Vet Radiol Ultrasound, 56:540–548.
Hecht S, Henry G (2007) Sonographic evaluation of the normal and abnormal pancreas. Clin Tech Small Anim Pract 22:115–121.
Hecht S, Penninck DG, Mahony OM, King R, et al. (2006) Relationship of pancreatic duct dilation to age and clinical findings in cats. Vet Radiol Ultrasound 47:287–294.
Hecht S, Penninck DG, Keating JH (2007) Imaging findings in pancreatic neoplasia and nodular hyperplasia in 19 cats. Vet Radiol Ultrasound 48:45–50.
Herman BA, Brawer RS, Murtaugh RJ, Hackner SG (2005) Therapeutic percutaneous ultrasound guided cholecystocentesis in three dogs with extrahepatic biliary obstruction and pancreatitis. JAVMA 227:1782–1786.
Hines BL, Salisbury SK, Jakovljevic S, De Nicola DB (1996) Pancreatic pseudocyst associated with chronic-active necrotizing pancreatitis in a cat. J Am Anim Hosp Assoc 32:147–152.
Jaeger JQ, Mattoon JS, Bateman SW, Morandi F (2003) Combined use of ultrasonography and contrast enhanced computed tomography to evaluate acute necrotizing pancreatitis in two dogs. Vet Radiol Ultrasound 44:72–79
Johnson-Neitman JL, O'Brien RT, Wallace JD (2012) Quantitative perfusion analysis of the pancreas and duodenum in healthy dogs by use of contrast-enhanced ultrasonography. Am J Vet Res 73:385–392.
Lamb CR (1999) Pancreatic edema in dogs with hypoalbuminemia and portal hypertension. J Vet Intern Med 13:498–500.
Lamb CR, Simpson KW, Boswood A, Matthewman LA (1995) Ultrasonography of pancreatic neoplasia in the dog: a retrospective review of 16 cases. Vet Rec 37:65–68.
Leinonen MR, Raekallio MR, Vainio OM, Ruohoniemi MO, et al. (2010) Quantitative contrast-enhanced ultrasonographic analysis of perfusion in the kidneys, liver, pancreas, small intestine, and mesenteric lymph nodes in healthy cats. Am J Vet Res 71:1305–1311.
Léveillé R, Biller DS, Shiroma JT (1996) Sonographic evaluation of the common bile duct in cats. J Vet Intern Med 10:296–299.
Lim SY, Nakamura K, Morishita K, Sasaki N et al. (2015) Quantitative contrast-enhanced Ultrasonographic assessment of naturally occurring pancreatitis in dogs. J Vet Intern Med 29:71–78.
Mai W, Caceres AV (2008) Dual phase computed tomographic angiography in three dogs with pancreatic insulinoma. Vet Radiol Ultrasound 49:141–148.
Marchevsky A, Yovich JC, Wyatt KM (2000) Pancreatic pseudocyst causing extrahepatic biliary obstruction in a dog. Asu Vet 78:99–101.
Moon ML, Panciera DL, Ward DL, Steiner JM, Williams DA (2005) Age-related changes in the ultrasound appearance of the normal feline pancreas. Vet Radiol Ultrasound 46:138–142.
Morita Y, Takiguchi M, Yasuda J, Eom KD et al (1998) Endoscopic ultrasonographic findings of the pancreas after pancreatic duct ligation in the dog. Vet Radiol Ultrasound 39:557–562.
Murakami M, Heng HG, Lim CK, Parnell NK et al (2019) Ultrasonographic features of presumed gastric wall edema in 14 dogs with pancreatitis. J Vet Intern Med, 33:1260–1265.
Nakamura K, Lim SY, Ochiai K, Yamasaki M' et al. (2014) Contrast-enhanced ultrasonographic findings in three dogs with pancreatic insulinoma. Vet Radiol Ultrasound 56:55–62.
Nyland TG, Gillette NA (1982) Sonographic evaluation of experimental bile duct ligation in the dog. Vet Radiol Ultrasound 23:252–260.
Park JY, Bugbee A, Sharma A, Secrest S (2020) Feline pancreatic ducts are consistently identified on CT and more likely to be dilated in the body of pancreas in cats with elevated feline pancreatic lipase immunoreactivity. Vet Radiol Ultrasound, 61:255–260.
Pelligra T, Puccinelli C, Marchetti V, Citi S (2022) Ultrasonographic findings of exocrine pancreatic insufficiency in dogs. Vet Sci 9:407.
Penninck DG, Zeyen U. Tayemans O, Webster CR. (2013) Ultrasonographic measurement of the pancreas and

Vet-ebooks.com

pancreatic duct in clinically normal dogs. Am J Vet Res 74(3):433–437.
Rademacher N, Schur D, Gaschen F, Kearney M, et al. (2016) Contrast-enhanced ultrasonography of the pancreas in healthy dogs and in dogs with acute pancreatitis. Vet Radiol Ultrasound 57:58–64.
Ramírez GA, Altimira J, García-González B, Vilafranca M (2013) Intrapancreatic ectopic splenic tissue in dogs and cats. J Comp Pathol 148:361–364.
Robben JH, Pollack WE, Kirpensteijn J, Boroffka SA, et al. (2005) Comparison of ultrasonography, computed tomography and single-photon emission tomography for the detection and localization of canine insulinoma. J Vet Intern Med 19:15–22.
Rutgers C, Herring DS, Orton EC (1985) Pancreatic pseudocyst associated with acute pancreatitis in a dog: ultrasonographic diagnosis. J Am Anim Hosp Assoc 21:411–416.
Salisbury SK, Lantz GC, Nelson RW, Kazacos EA (1988) Pancreatic abscess in dogs: six cases (1978–1986). J Am Vet Med Assoc 193:1104–1108.
Saunders HM (1991) Ultrasonography of the pancreas. Probl Vet Med 3:583–603.
Saunders HM, VanWinkle TJ, Drobatz K, Kimmel SE, et al. (2002) Ultrasonographic findings in cats with clinical, gross pathologic, and histologic evidence of acute pancreatic necrosis: 20 cases (1994–2001) J Am Vet Med Assoc 221:1724–1730.
Tomura S, Toshima A, Nomura A, Hirata M, et al. (2022) Intrapancreatic accessory spleen mimicking pancreatic insulinoma with intrapancreatic metastasis in a cat. J Vet Med Sci 84:439–444.
Törner K, Staudacher M, Steiger K, Aupperle-Lellbach H (2020) Clinical and pathological data of 17 non-epithelial pancreatic tumors in cats. Vet Sci 7:55.
Vanderperren K, Haers H, Van der Vekens E, Stock E et al. (2014) Description of the use of contrast-enhanced ultrasonography in four dogs with pancreatic tumours. J Small Anim Pract 55:164–169.
VanEnkevort BA, O'Brien RT, Young KM (1999) Pancreatic pseudocysts in 4 dogs and 2 cats: ultrasonographic and clinicopathologic findings. J Vet Intern Med 13:309–313.
Wall M, Biller DS, Schoning P, Olsen D, et al. (2001) Pancreatitis in a cat demonstrating pancreatic duct dilatation ultrasonographically. J Am Anim Hosp Assoc 37:49–53.
Watson PJ (2003) Exocrine pancreatic insufficiency as an end stage pancreatitis in four dogs. J Small Anim Pract 44:306–312.
Wilkinson AR, DeMonaco SM, Panciera DL, Otoni CC et al. (2020) Bile duct obstruction associated with pancreatitis in 46 dogs. J Vet Intern Med 34:1794–1800.
Xenoulis PG, Fracassi F (2022) Feline comorbidities: clinical perspective on diabetes mellitus and pancreatitis. J Feline Med Surg 24:651–661.

Vet-ebooks.com

Vet-ebooks.com

CHAPTER ELEVEN

Urinary Tract

Dominique Penninck[1], Marc-André d'Anjou[2], James Sutherland-Smith[3], Emmanuelle Butty[1], and Marilyn Dunn[4]

[1]*Department of Clinical Sciences, Cummings School of Veterinary Medicine, Tufts University, North Grafton, MA, USA*
[2]*Animages, Brossard, Québec, Canada*
[3]*VetCT, Newton, MA, USA*
[4]*Interventional Medicine, Faculté de médecine vétérinaire, Université de Montréal, Saint-Hyacinthe, Québec, Canada*

Preparation and Scanning Technique

Prior to the ultrasonographic examination of the urinary tract, the animal's hair should preferably be clipped, and ultrasonic gel applied to the skin to optimize image quality. Animals can be scanned in dorsal, left, or right recumbency.

Kidneys

The left kidney can usually be well visualized with a ventrolateral approach, although the presence of gas or feces in the descending colon can sometimes limit its evaluation. The right kidney is typically more difficult to image, especially in deep-chested dogs, because of its dorsal localization in the cranial abdomen. A right ventrolateral subcostal approach is usually sufficient. However, in certain dogs, a lateral approach through the 11th or 12th intercostal space might be necessary. The visualization of the right kidney can also be affected by the presence of intestinal content, especially in the descending duodenum, ascending colon, or cecum.

Kidneys vary in depth according to the animal's body conformation. In small dogs and cats, a high-frequency sonographic probe (7.5 MHz and higher) is recommended, whereas kidneys of larger dogs may require a probe with more penetration (5 MHz and lower). Convex probes are generally more useful because they enable the entire kidney to be imaged. Microconvex probes have a smaller footprint and can more easily be used intercostally. Linear probes provide higher spatial resolution and are favorably used in animals with superficial kidneys. Spatial compounding allows a wider field of view so that the entire kidney can be included in the image.

Kidneys should be scanned from cranial to caudal and lateral to medial, in several transverse and longitudinal planes, to fully assess all portions, including the cortex, medulla, and collecting system (Figure 11.1).

Bladder

A transabdominal approach with the animal in dorsal recumbency is preferred to evaluate the bladder but left or right lateral recumbency or a standing position may be used in confirming the presence of intraluminal sediment or calculi, which will fall toward the gravity-dependent wall. If the penile urethra is to be imaged, then hair may need to be clipped from the perineum and the region cranial to the scrotum.

A medium- to high-frequency (5–8 MHz or higher) convex, linear, or sector transducer is recommended. A microconvex transducer with a small contact area has the advantage of being easier to point toward the intrapelvic structures but a linear probe with higher resolution (10Hz and higher) can provide better detail, especially for assessing the more superficial portion of the bladder. Two complementary transverse and longitudinal planes are used to fully assess the bladder and urethra (Figure 11.2).

The best ultrasound images of the bladder are obtained when it is moderately distended. If the bladder is empty and pathology is suspected, it is advisable to rescan the bladder after waiting for it to refill naturally or to catheterize it and fill it with sterile isotonic (0.9%) saline, or to administer intravenous furosemide.

Atlas of Small Animal Ultrasonography, Third Edition. Edited by Dominique Penninck and Marc-André d'Anjou.
© 2025 John Wiley & Sons, Inc. Published 2025 by John Wiley & Sons, Inc.
Companion website: www.SmallAnimalUltrasonography.com

Vet-ebooks.com

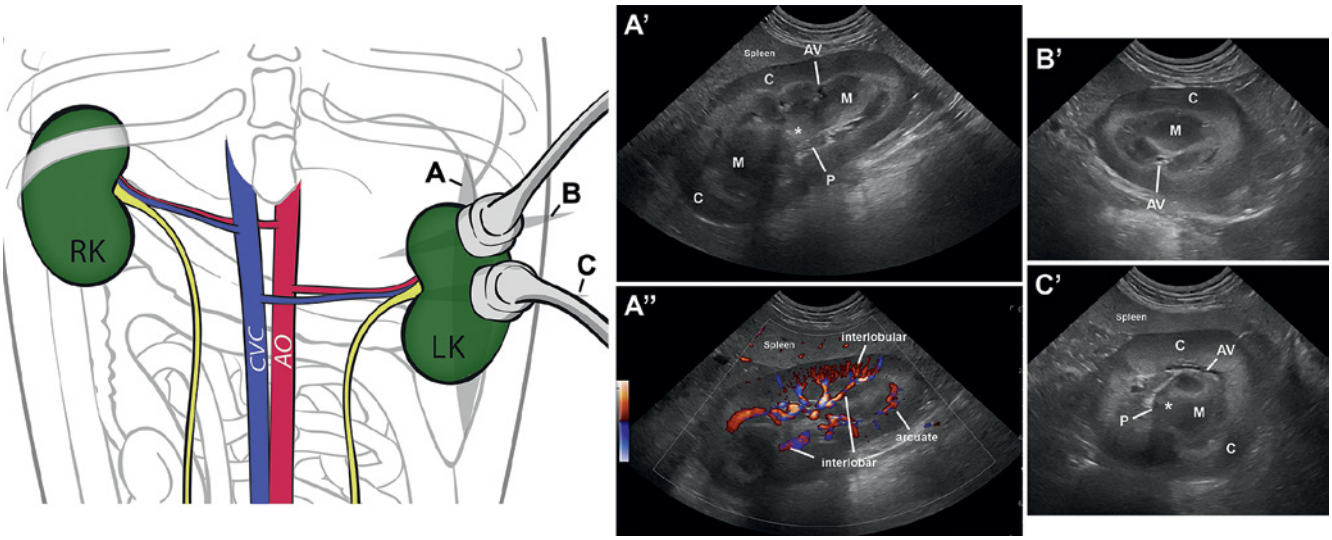


Figure 11.1. Illustration and sonographic approach and normal anatomy in the dog. In dorsal recumbency, a ventrolateral approach to the left kidney is used. The probe is moved through the kidney, in longitudinal **(A)** and transverse **(B, C)** planes. **(A′–C′)** Corresponding longitudinal and transverse B-mode sonograms of the left kidney. C, cortex; M, medulla; P, pelvis; renal crest (*); and arcuate vessels (AV). **(A″)** Longitudinal Angio Doppler sonogram of the left kidney, highlighting the vasculature. AO, aorta; CVC, caudal vena cava; LK, left kidney; RK, right kidney.

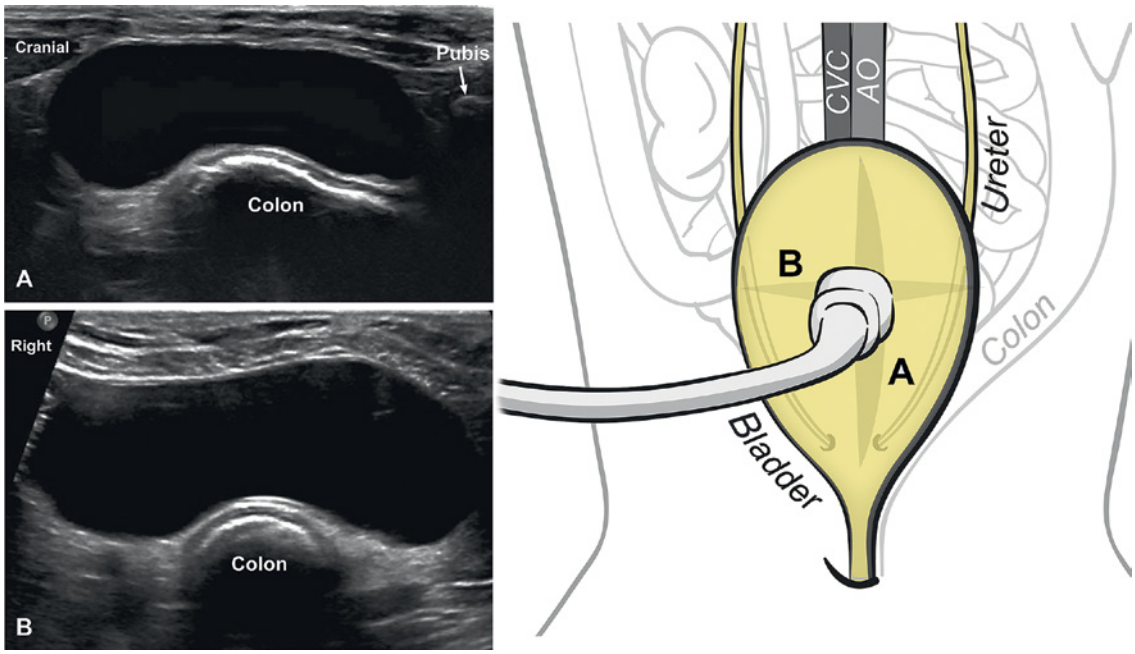


Figure 11.2. Composite image of the urinary bladder and adjacent anatomical structures in a dog. The schematic diagram on the right shows the position of the urinary bladder, the dorsally located colon, aorta (Ao), and caudal vena cava (CVC) as well as transducer positions for the standard longitudinal and transverse imaging planes. **(A)** A longitudinal sonogram of the urinary bladder filled with normal anechoic urine. **(B)** A transverse sonogram of the urinary bladder. The colon is located dorsally in the far field and is causing mild indentation of the dorsal bladder wall. AO, aorta; CVC, caudal vena cava.

Vet-ebooks.com

Normal Ultrasonographic Anatomy

Kidneys

In many dogs, the left kidney can be evaluated through the spleen, which provides a good acoustic window and allows comparing their echogenicity. The right kidney is more cranial and dorsal, particularly in large dogs, and usually is in contact or proximity with the hepatic parenchyma at the level of the caudate lobe. Both kidneys are symmetrical in size and shape in cats and dogs. Kidneys can be oval, particularly in cats, or bean shaped, which is more common in dogs.

Kidneys can be measured on all planes, and volumes can be estimated. The renal length in normal cats usually varies between 3.0 and 4.5 cm and is influenced by breed and sexual status. For instance, Ragdoll, British Shorthair, and Sphinx cats were reported to have length values (in cm) of 3.87 ± 0.41, 3.77 ± 0.43, and 4.09 ± 0.33, respectively. Kidneys are also typically larger in intact cats and often become smaller with advancing age. The right kidney may also be longer than the left (Debruyn et al. 2013).

In dogs, absolute measurements must also consider total body weight and conformation, because great variations exist (Barr et al. 1990). The renal length can also be compared to the aorta diameter or to the length of L5 or L6 in dogs (Barella et al. 2012; Mareschal et al. 2007) (Figure 11.3), although the range of normal remains relatively large with these ratios, limiting their usefulness in practice.

Renal cortex, medulla, and the collecting system can be visualized with ultrasonography in dogs and cats (Figures 11.1, 11.4). The renal medulla is hypoechoic when compared with the cortex, which is usually

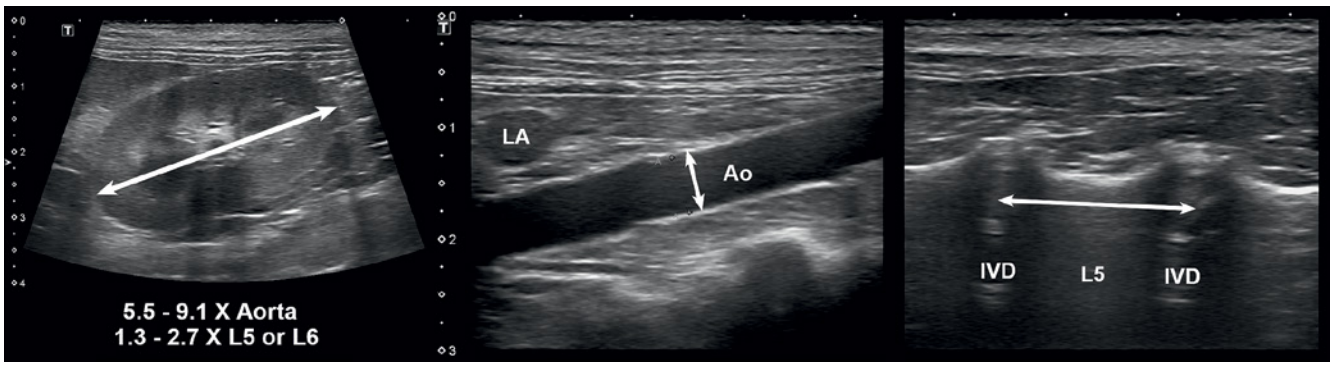


Figure 11.3. Normal ranges for renal-to-aorta and renal-to-L5 (or L6) ratios in dogs. The maximal renal length is compared to the maximal luminal diameter of the aorta or to the length of L5 or L6.

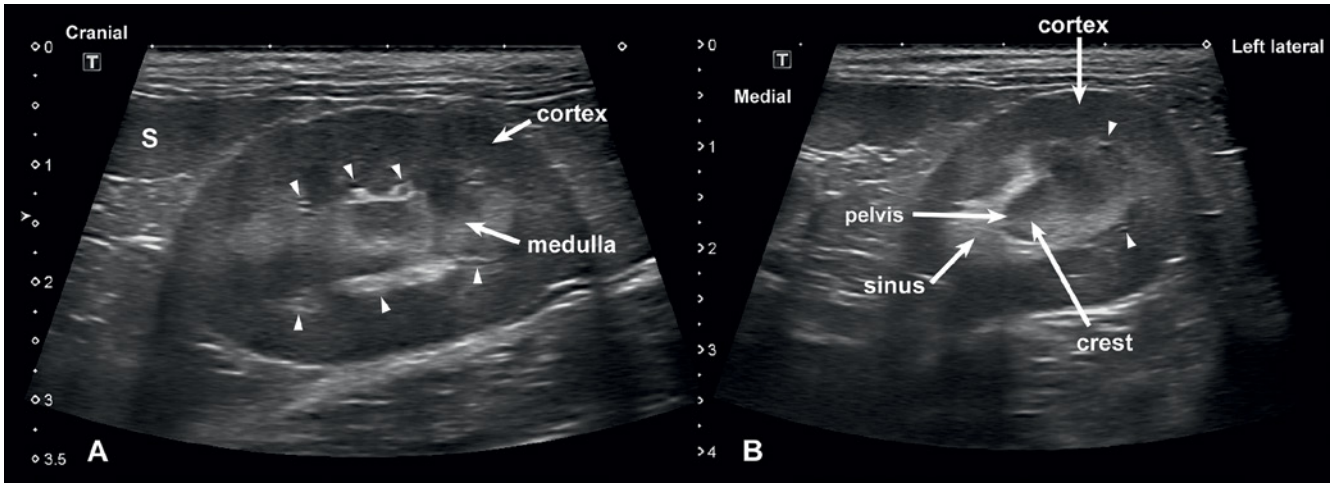


Figure 11.4. Normal feline kidney. Longitudinal **(A)** and transverse **(B)** images of the left kidney in a normal cat. The renal cortex hyperechoic to the medulla, but isoechoic when compared to the superficial spleen (S). The renal crest may be more echoic as in this cat. The renal pelvic is surrounded by the hyperechoic sinus. Arcuate vessels (arrowheads) appear as short parallel hyperechoic lines at the corticomedullary junction.

Vet-ebooks.com

hypoechoic or isoechoic to the liver and typically hypoechoic to the spleen. However, in dogs and cats without evidence of renal dysfunction, renal cortices can be slightly hyperechoic to the liver (Ivancic and Mai 2008). In cats, the accumulation of fatty vacuoles in the renal cortex appears to contribute to its hyperechogenicity (Yeager and Anderson 1989) (Figure 11.5). The angle of insonation may also influence the echogenicity of the cortex. Renal extremities may be more echogenic because of the difference in tubule angulation (i.e., anisotropy), with conventional or spatial compounding imaging (Ruth et al. 2013) (Figure 11.5). Sonographers should be careful when using this area as landmark for comparing renal cortex and nearby structures' echogenicity.

The medulla appears separated into several lobulated segments by the presence of echogenic lines representing borders of the interlobar vessels and diverticuli. The medulla appears nearly anechoic in some animals and should not be confused with dilatation of the renal pelvis. The outer medulla, which parallels the cortex below the arcuate arteries, may also be isoechoic to the cortex, giving the impression of cortical thickening, or even hyperechoic to it, forming a hyperechoic band near the arcuate arteries (Figure 11.5C,D). This is more frequent in small breeds and in young dogs (Hart et al. 2013). The renal crest is the prolongation of the renal medulla and is in contact with the pelvis.

The walls of the arcuate arteries can be observed as paired, short, hyperechoic lines at the corticomedullary junction, which can sometimes generate a faint acoustic shadow and must be differentiated from mineralization (Figures 11.4, 11.5). These vessels, as well as the larger renal and interlobar vessels, can also be evaluated with color Doppler or power Doppler

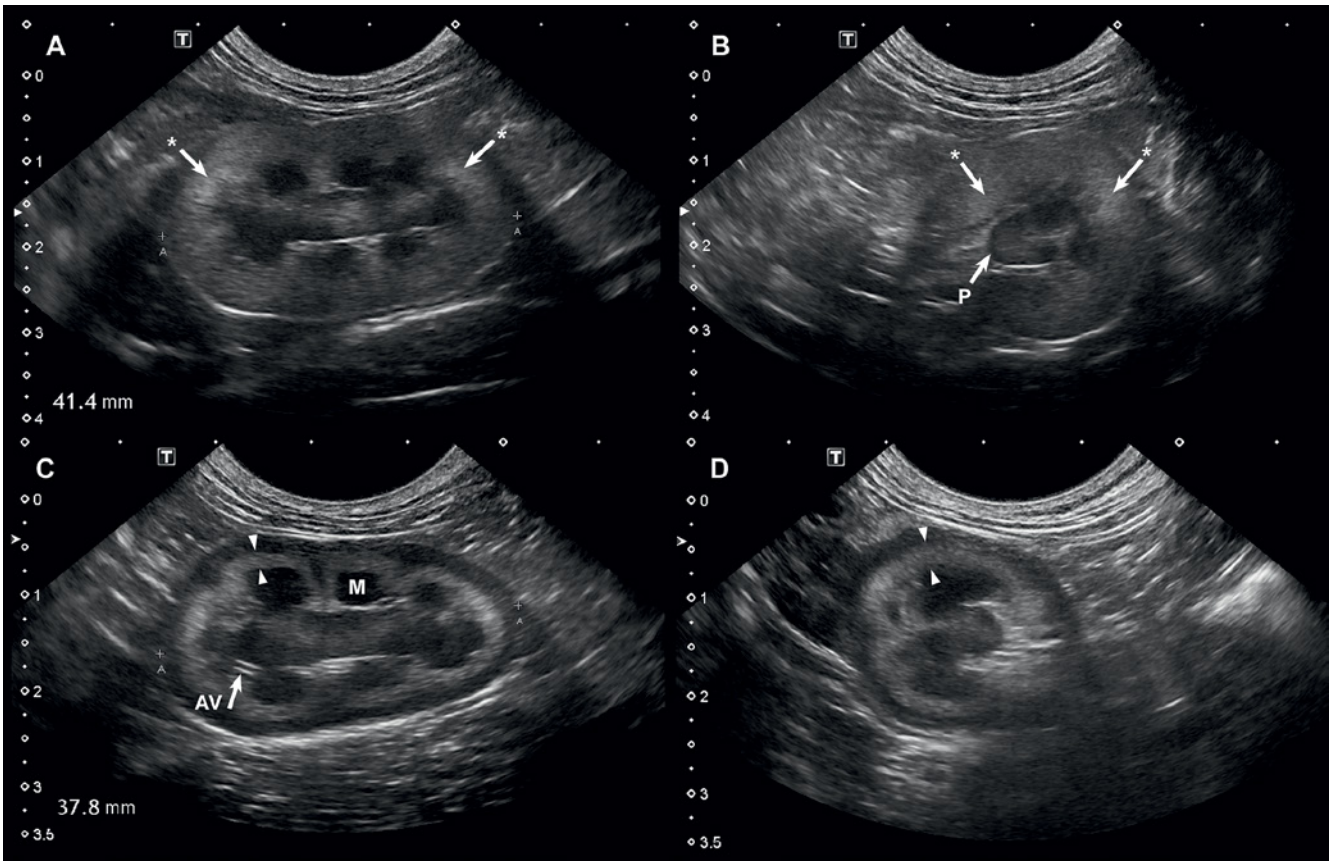


Figure 11.5. **Normal variants in cats and dogs. (A, B)** The renal cortex is hyperechoic in this cat with normal renal values, presumably due to the accumulation of lipids. Note that some areas of the cortex are more echogenic (*) because of the difference in tubule angulation (i.e., anisotropy). The pelvis is minimally dilated, which is considered normal. **(C, D)** These longitudinal **(C)** and transverse **(D)** sonographic images of the right kidney were obtained in a clinically normal 1-year old Lhasa Apso. The outer medulla is hyperechoic, forming a band (between arrowheads) at the periphery of the inner medulla (M). AV, arcuate vessels.

Vet-ebooks.com

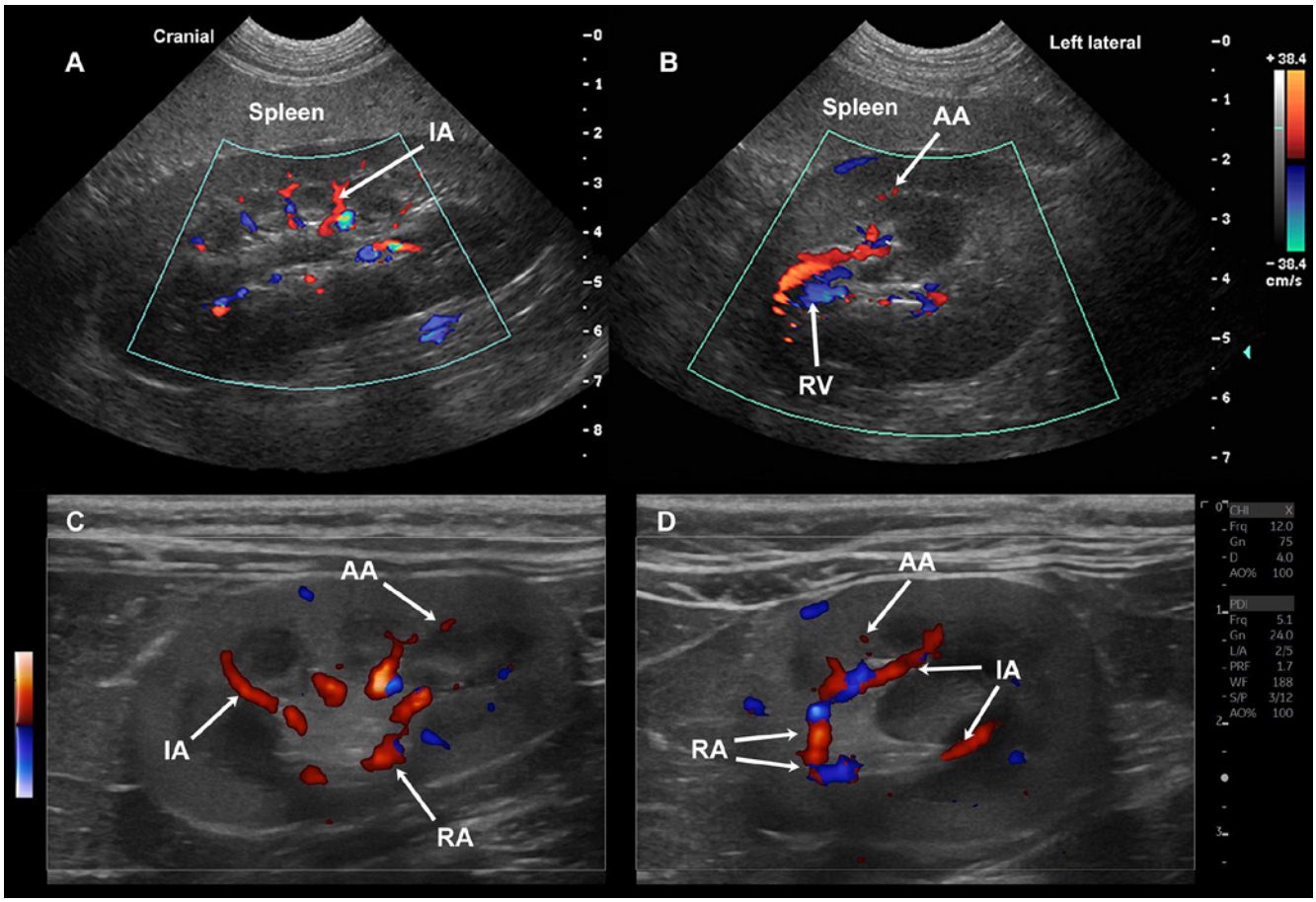


Figure 11.6. Renal vasculature in dogs and cats. Longitudinal **(A)** and transverse **(B)** color Doppler images of the left kidney of a 4-year-old male Golden retriever. The vascular flow can be observed with color Doppler through the renal, interlobar, and arcuate vessels. Longitudinal **(C)** and **(D)** transverse images of the left kidney of a 3-year-old domestic short hair female spayed cat with power-Doppler imaging, outlining well the smaller vascular branches. AA, arcuate artery; IA, interlobar artery; RA, renal artery and RV, renal vein.

(Figure 11.6). The renal arteries and veins, usually single on each side, can be followed from the hilus to the aorta and caudal vena cava, respectively. These vessels must be differentiated from dilated ureters.

Pelvis and Ureters

The renal pelvis is often visualized in dogs and cats without evidence of renal dysfunction and particularly when diuresis is triggered by intravenous fluids or diuretics (d'Anjou et al. 2011). The pelvic height in dogs and cats usually measures less than 2 mm when using a transverse plane (Figure 11.4). It is important to place the value of these measurements in the context of clinical presentation. The renal diverticuli and ureters are normally collapsed and therefore not seen. The pelvis is surrounded by the sinus, which contains fat and appears hyperechoic and is particularly prominent in obese cats.

Bladder

The bladder is within the caudoventral abdomen, and the urethra extends into the pelvic canal. The descending colon, aorta, and caudal vena cava are dorsal to the urinary bladder (UB). These vessels can be identified by their location and by using color Doppler (See Chapter 16). In intact females, the uterine body is between the UB and the colon.

The four histological bladder wall layers are the mucosa (hypoechoic), submucosa (hyperechoic), muscularis (hypoechoic), and serosa (hyperechoic). However, these layers are difficult to define sonographically compared with the gastrointestinal tract. The bladder wall thickness decreases as the UB volume increases (Figure 11.7).

The trigone of the bladder is not clearly delineated from the remainder of the bladder wall. **Ureteral papillae** (or ureterovesical junctions) in dogs may be seen

Vet-ebooks.com

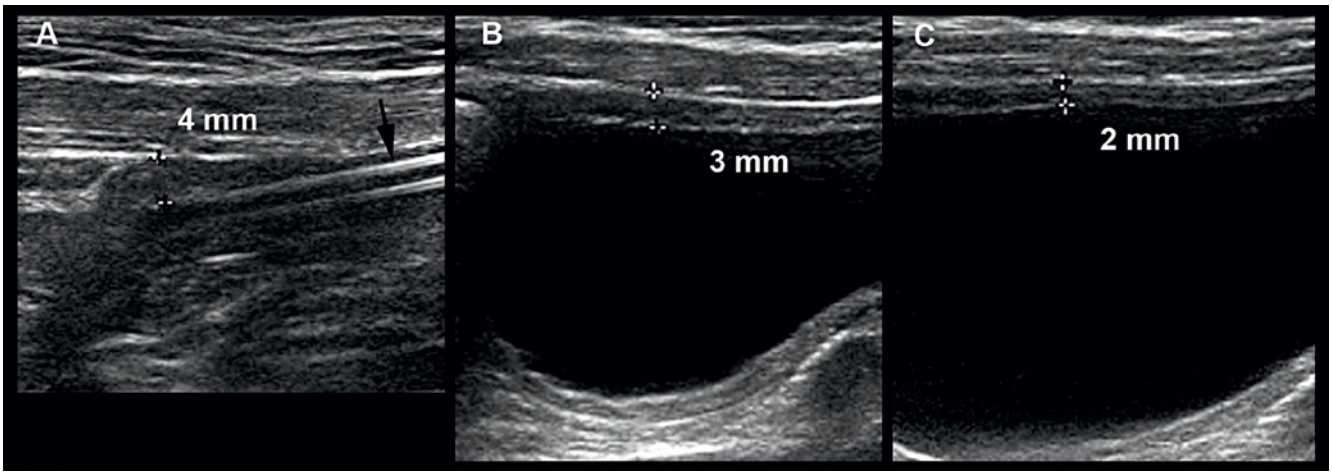


Figure 11.7. Normal bladder thickness and distension in a 30-kg dog. A series of longitudinal ultrasound images of the urinary bladder with different volumes of sterile saline infused into the bladder lumen. **(A)** Longitudinal sonogram of an empty urinary bladder with an indwelling red-rubber urinary catheter (arrow). The urinary bladder wall thickness is 4 mm. **(B)** A total of 60 mL (2 mL/kg) of saline is infused, and the bladder wall thickness now is 3 mm. **(C)** With a total volume of 120 mL (4 mL/kg), the bladder wall thickness is 2 mm.

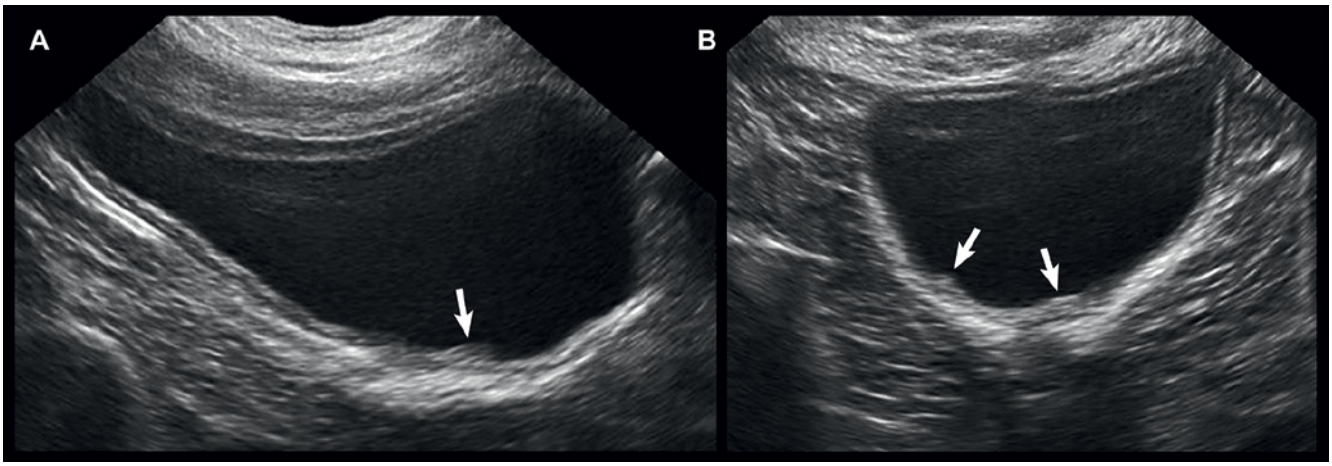


Figure 11.8. Normal ureterovesical junctions in a dog. (A) Longitudinal sonogram of the trigone of the urinary bladder. There is a smooth, broad-based echogenic protuberance at (arrow) the dorsocaudal aspect of the urinary bladder. **(B)** Transverse sonogram showing the bilateral protuberances that represent ureteral papillae (arrows).

extending from the mucosal surface of the dorsal wall and should not be confused with other causes of focal wall thickening (Figure 11.8). The ureteral papillae in cats are located near or at the proximal urethra and therefore are not seen on ultrasound.

Ureteral jets of urine may be seen emerging from the dorsal bladder wall at the trigone. These ureteral jets appear as a burst of hyperechoic speckles on B-mode ultrasound or a pulse of positive (red) signal on color flow Doppler (Figure 11.9). The visualization of ureteral jets is variable because it requires a difference in the specific gravity between the urine in the bladder and the urine exiting the ureter. Intravenous furosemide (0.5 mg/kg) can be utilized to enhance the visualization of ureteral jets within the UB (Gremillion et al. 2021).

The normal urine within the UB is usually anechoic. However, echogenic urine is not necessarily indicative of urinary tract disease. For example, the presence of **lipid droplets** is commonly seen in clinically normal cats therefore, a urinalysis can assist in determining its significance (Sislak et al. 2014) (Figure 11.10). In addition, images of the UB are prone to side-lobe and grating-lobe artifacts that can create the appearance of

Vet-ebooks.com

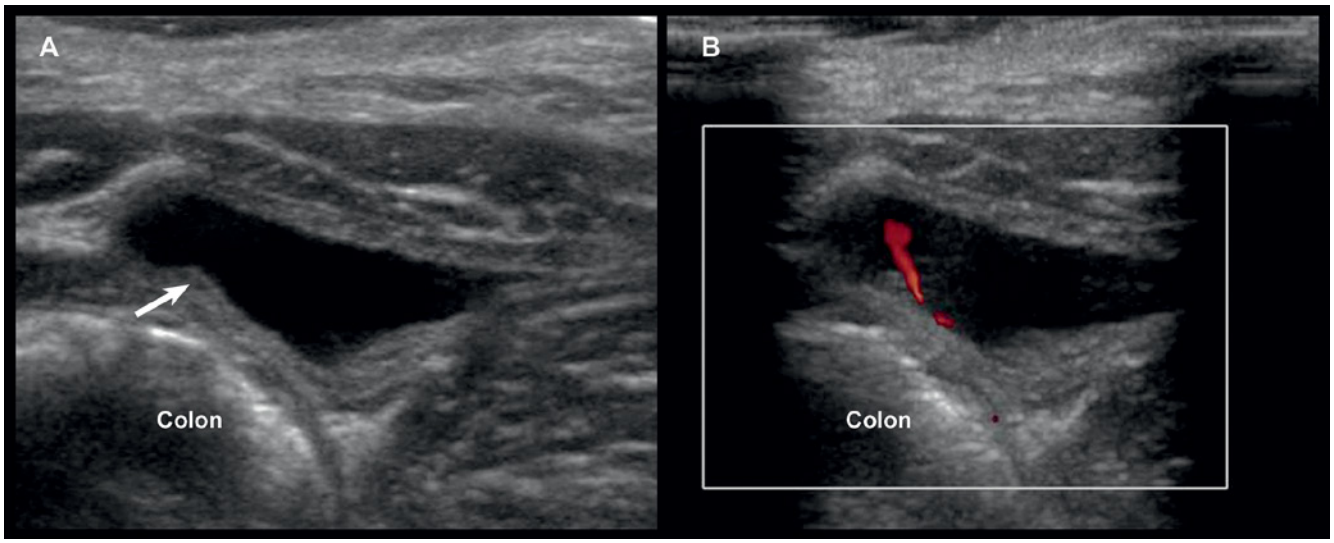


Figure 11.9. **Ureteral jet in a dog. (A)** transverse sonogram of a bladder in the trigone region using B-mode ultrasound. No ureteral jets are visible in proximity to the right ureterovesicular junction (arrow). **(B)** Transverse color flow Doppler sonogram of a ureteral jet. The use of color flow Doppler can aid the detection of ureteral jets. The red indicates flow toward the transducer.

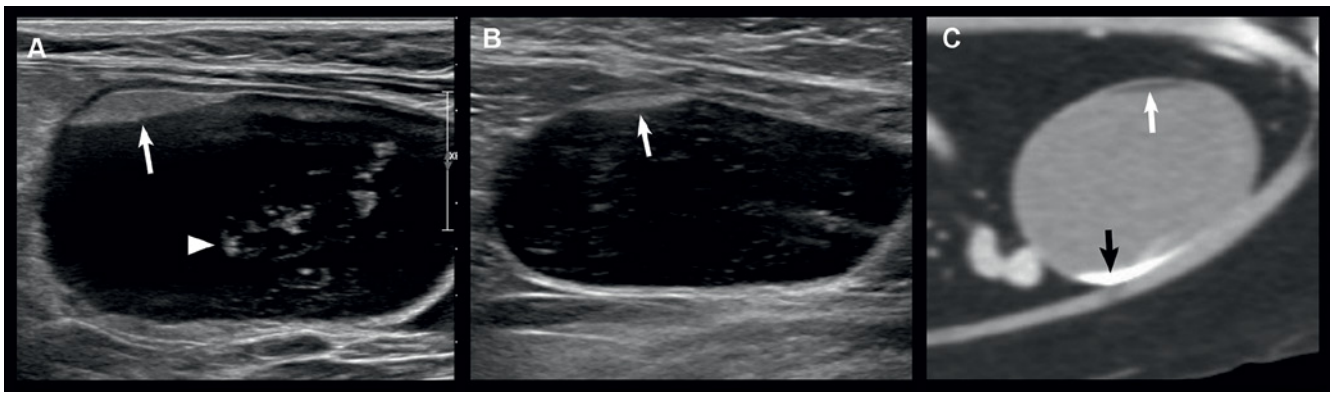


Figure 11.10. **Lipid droplets in the bladder of two cats. (A)** Floating echogenic droplets (arrowheads) in this cat's bladder with a hyperechoic layer of lipid (arrow) along the nondependent, cranioventral wall. **(B)** Floating droplets and superficial linear aggregation (arrow) along the cranioventral wall of the bladder of another cat. **(C)** The corresponding CT image confirmed that the coalescent, linear material represents fatty droplets (hypoattenuating to the bladder urine) (white arrow). Note the hyperattenuating iodinated contrast medium in the dependent portion of the bladder (black arrow).

pseudo-sludge (Figure 1.21). Adjustment of the gain and use of spatial compounding and harmonic ultrasound (Figure 1.10) help reduce the formation of these confusing echoes.

Urethra

Retrograde positive contrast urethrography remains the preferred modality for assessing the entire urethra. Ultrasound is a useful and complementary modality for part of the accessible urethra. The urethra extends caudally from the bladder into the pelvic canal (Figure 11.11).

In male dogs, the prostate surrounds the proximal urethra. Shadowing from the pubis obscures the caudal intrapelvic portion of the urethra. The proximal penile urethra is located within the corpus spongiosum between the corpus cavernosum dorsally and the bulbospongiosus and retractor penis muscles ventrally. The distal penile urethra is located within the urethral groove of the os penis dorsally and the bulbus glandis ventrally (Figure 11.12). The urethral lumen is not normally seen unless there is UB distension, in which case urethral obstruction should be considered. The urethral wall is composed of the same histological layers as the UB but are not readily resolved when normal.

Vet-ebooks.com

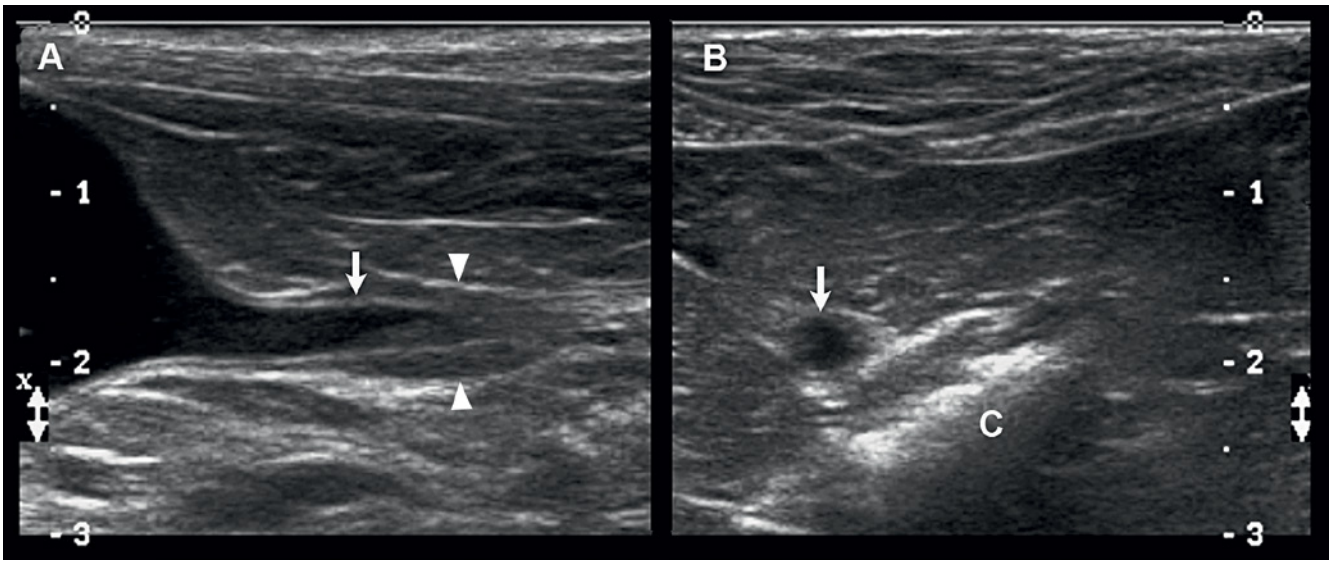


Figure 11.11. **Normal urethra in a male dog.** Duplex sonogram of the proximal urethra (arrow) in longitudinal **(A)** and transverse **(B)** planes. Distal to the prostate (arrowheads) the urethral lumen is not visible. The descending colon (C) is seen in the far field in **(B)**.

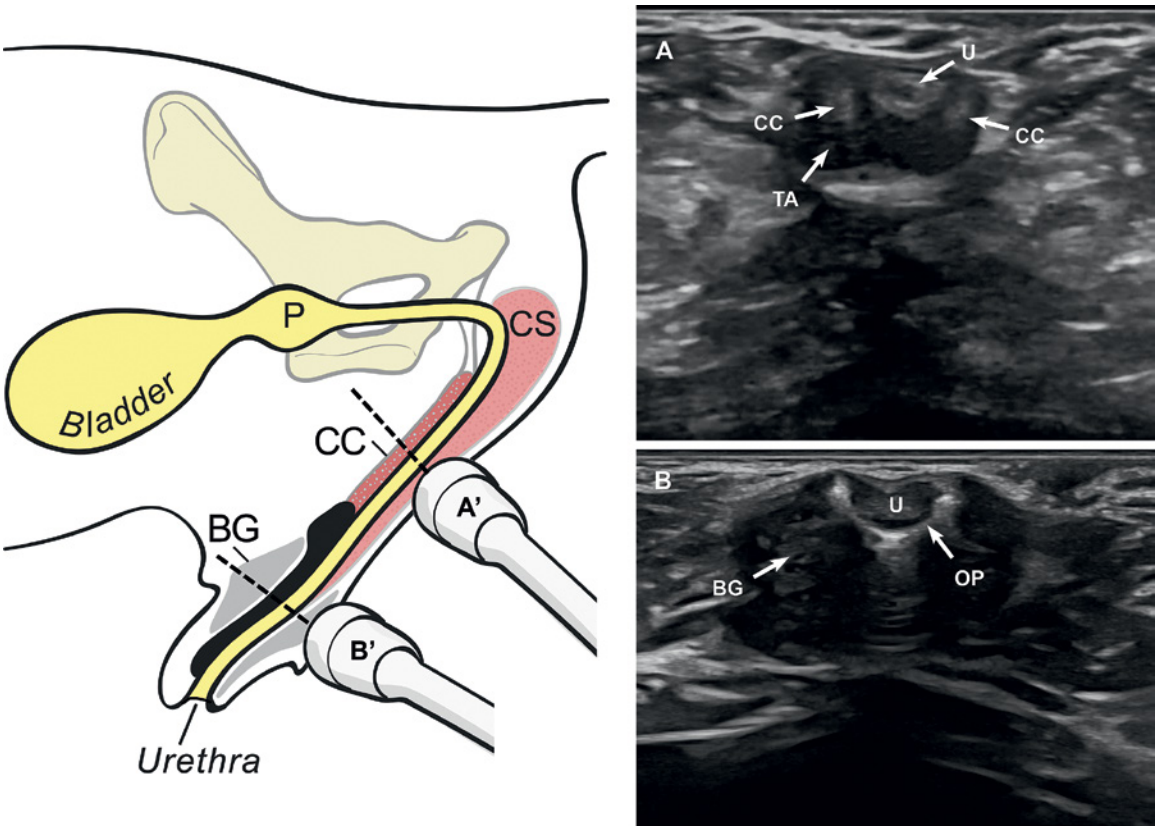


Figure 11.12. **Normal penile urethra in a dog.** On the left, an illustration of the anatomical structures near the urethra are presented. The dotted lines (A′, B′) correspond to the transverse planes seen on the sonograms on the right. P, prostate**. (A)** Transverse sonogram of the mid-penile urethra at a level just cranial to the scrotum. The urethra (U) is located within the ventral portion of the corpus spongiosum (CS). **(B)** Transverse sonogram of the distal penile urethra (U) at the level of the os penis (OP), which is seen as a hyperechoic U-shaped structure with distal shadow. The urethra is located within the anastomosing tissue of the corpus spongiosum and bulbus glandis. The bulbus glandis (BG) forms the bulk of the tissue surrounding the os penis. CC, corpus cavernosum; TA, tunica albuginea.

Vet-ebooks.com

Ultrasonographic Features of Urinary Disorders

Congenital and Inherited Urinary Malformations

Kidneys

Except for polycystic kidney disease (PKD) and ectopic ureters, congenital malformations of the upper urinary tract are rare in dogs and cats. Crossed fused renal ectopia, fusion, and duplication have been seldomly reported (Allworth and Hoffman 1999; Esterline et al. 2005; Hecht et al. 2005) (Figure 11.13).

Crossed fused renal ectopia can appear as variable degree of parenchymal fusion (Figure 11.14) and involvement of the collecting system (Seo et al. 2021, Slinkard et al. 2023).

Renal agenesis (complete absence) or hypoplasia/dysplasia is often associated with compensatory enlargement of the contralateral kidney (Figure 11.15). **Renal dysplasia**, also called renal maldevelopment, is defined as disorganized development of renal parenchyma, focally or globally, because of anomalous differentiation such as a persistence of immature glomeruli. It may affect several breeds of dogs, with or without having a familial basis. The sonographic changes vary according to the severity of the disease. Subclinical renal maldevelopment may show a hyperechoic or speckled medulla with loss of corticomedullary distinction (Seiler et al. 2010). Severely affected kidneys tend to become small, irregular, and diffusely hyperechoic, similarly to kidneys with chronic inflammatory disease (Abraham et al. 2003) (Figure 11.16). These young dogs may be predisposed to ascending pyelonephritis, which contributes to the morphological modifications observed on ultrasound (Abraham et al. 2003). **Juvenile nephropathy** is another form of renal disease affecting young dogs. Boxers are particularly affected and often present concurrent urethral sphincter mechanism (Cavalera et al. 2021; Chandler et al. 2007) (Figure 11.17).

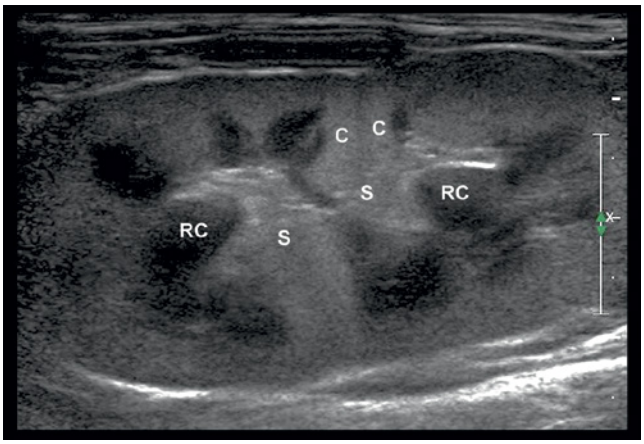


Figure 11.14. Congenital renal fusion. Sagittal ultrasound image of a 6-year-old male cat with normal renal function. Notice the fused renal cortices (C) and medullae with both renal crests (RS) and pelvises facing each other. S, sinus.

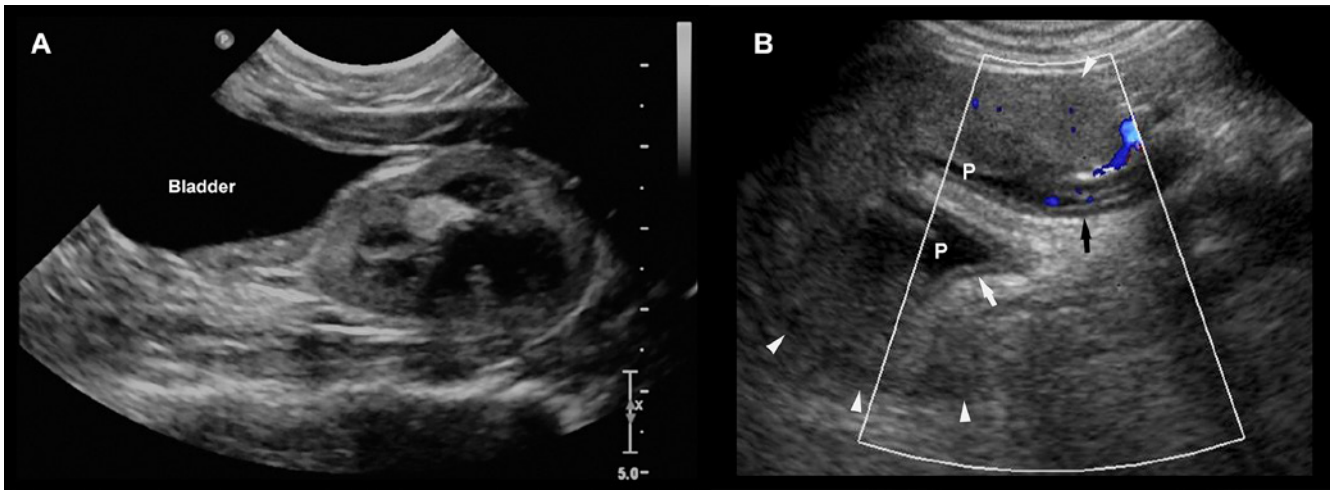


Figure 11.13. Congenital malformations of kidneys and ureters. (A) Ectopic kidney in an 8-year-old cat presented for acute vestibular signs. The right kidney is located caudo-dorsally to the urinary bladder. The kidney is 3.3 cm long and deformed. The hyperechoic area near the center represents the renal sinus. **(B) Renal pelvis duplication in an English Bulldog** presented for azotemia. The right kidney (arrowheads) of this 3-year-old spayed female dog was associated with two ureters (white and black arrows) connected to two pelvises (P). Both ureters were hyperperistaltic.

Vet-ebooks.com

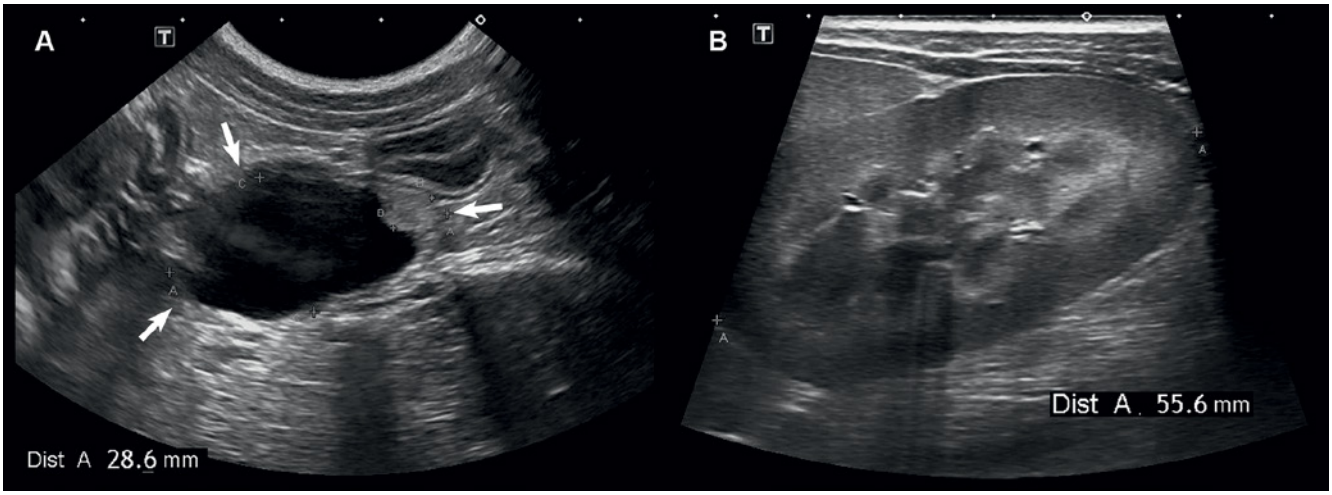


Figure 11.15. **Unilateral renal dysgenesis in a 7-month-old intact Dachshund. (A)** The right renal parenchyma is markedly hypoplastic (arrows) and associated with severe hydronephrosis. **(B)** The left kidney is mildly enlarged and shows a mildly hyperechoic medulla, presumably due to compensatory hypertrophy. The right ureter was ectopic (see Figure 11.22).

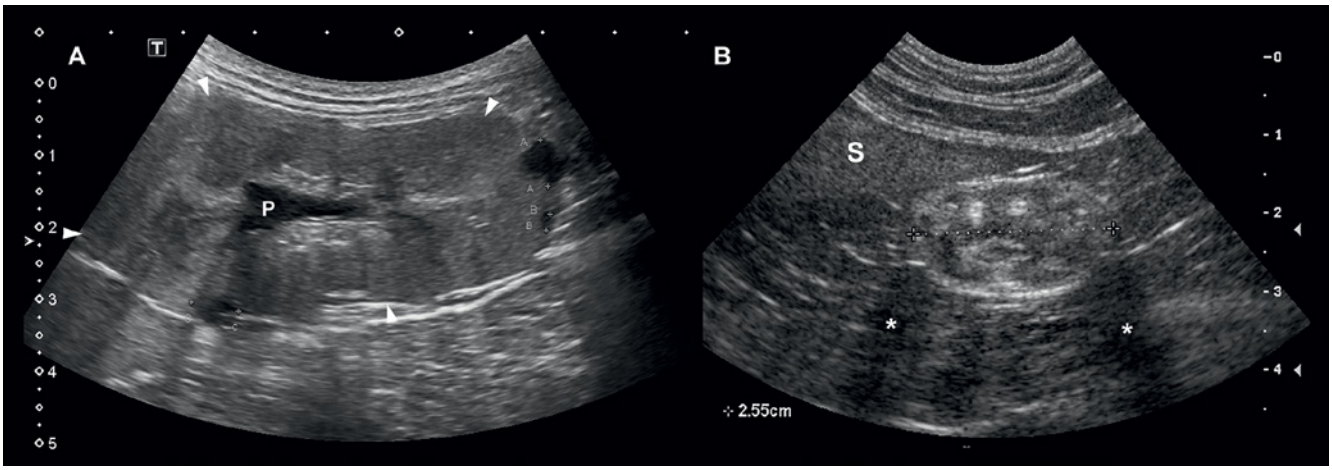


Figure 11.16. **Renal dysplasia in two dogs. (A)** Longitudinal image of the left kidney (arrowheads) of a 10-month-old Labrador retriever with bilateral renal dysplasia. Each kidney is deformed, smaller than normal and the corticomedullary distinction is greatly reduced. Also, several spherical anechoic cysts are present (between calipers) and the pelvis (P) is mildly dilated and distorted. **(B)** In this other adult mixed-breed dog, the left kidney is small and hyperechoic to the spleen. Edge shadowing is also observed (*). The right kidney is normal (not shown).

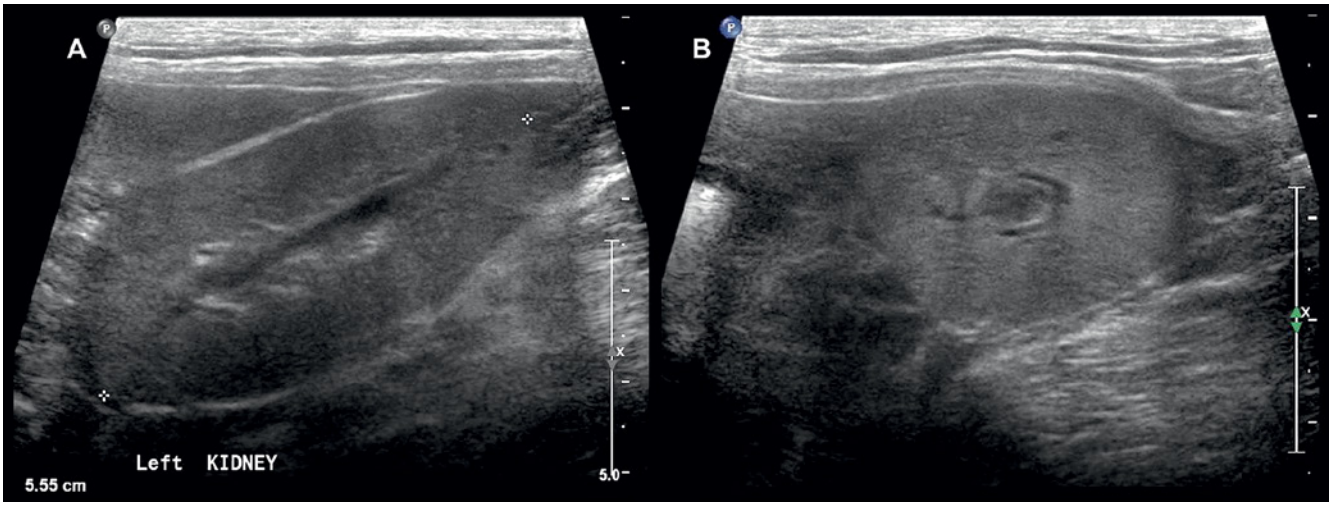


Figure 11.17. **Bilateral renal dysplasia**. In this 1-year-old Eurasier dog, both kidneys have poor cortico-medullary demarcation, as shown on the longitudinal **(A)** and transverse **(B)** images of the left kidney. Tiny cysts are present in the renal parenchyma.

Vet-ebooks.com

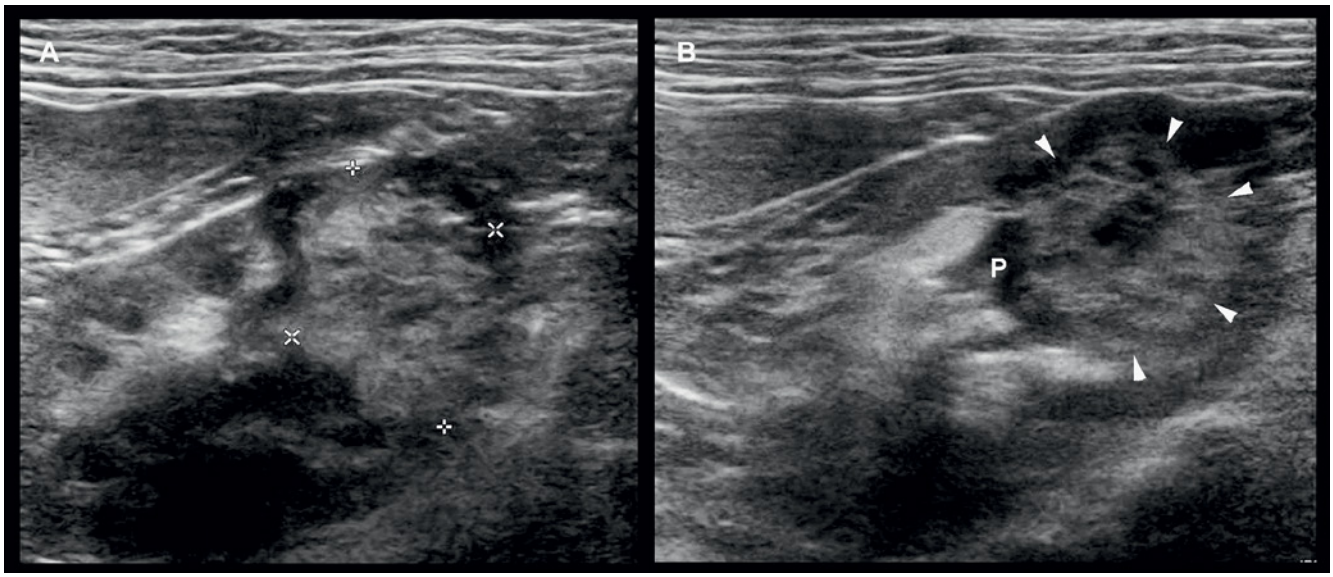


Figure 11.18. Telangiectasia in a 11-year-old Welsch Corgie presented for hematuria. (**A-B**) An ill-defined primarily hyperechoic nodule (2.1 × 1.8 cm, cursors) with numerous cystic changes is present in the mid-to caudal region of the left kidney. The kidney was removed, and the diagnosis was multifocal, coalescing telangiectasia. P, pelvis.

Although these renal anomalies can be confirmed only with histological analysis, renal maldevelopment (dysplasia) or juvenile nephropathy should be suspected in a young dog with deformed kidneys and clinical evidence of chronic renal disease.

Renal telangiectasia has been reported in Welsh Corgi dogs and consists of cavernous lesions filled with blood (Moore and Thornton 1983) than can mimic neoplasia. (Figure 11.18) (Logwood et al. 2021).

Ureters

Unilateral or bilateral congenital **ectopic ureters**, which are more common in female dogs, can sometimes be identified and followed to their termination site (the urethra, most commonly, but at times the vagina, the prostate, or the colon) (Figures 11.19–11.22). Ectopic ureters may be identified ultrasonographically by either dilated ureters coursing beyond the dorsal bladder neck caudally and/or by an absence of ureteral jets in the trigone region. Absence of ureteral jets may also be found in case of imperforated ureter. Cystoscopy and fluoroscopic ureterography are often required to differentiate extra- and intramural ureters in dogs and cats, however, ultrasound evaluation in the hands of an experienced sonographer has been shown to be an effective diagnostic method (Taylor et al. 2022).

Ectopic ureters are often distended because of partial obstruction at the site of termination or intramural tunneling, ileus, and/or ascending infection

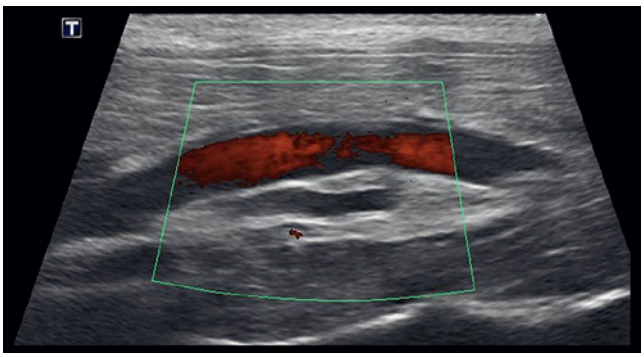


Figure 11.19. Hydroureter. Longitudinal image obtained with Power Doppler in the left midabdomen of a 5-year-old female cat with hydronephrosis due to obstructive ureteral calculi. A 3-mm-wide anechoic tubular structure can be seen coursing from the renal pelvis to the caudal abdomen, consistent with a dilated ureter, proximal to the calculus (not shown). No flow is present within that structure, unlike the vessel seen ventral to it.

(Figures 11.19–11.22). Hydronephrosis can also be present, especially when there is marked hydroureter. With B-mode or with color or power Doppler ultrasonography, an intravesical urine jet can sometimes be observed adjacent to the ureterovesical junction (Lamb and Gregory 1998). The visualization of the ureteral jet can be facilitated by administering a diuretic. A jet of diluted urine can be more easily observed within a

Vet-ebooks.com

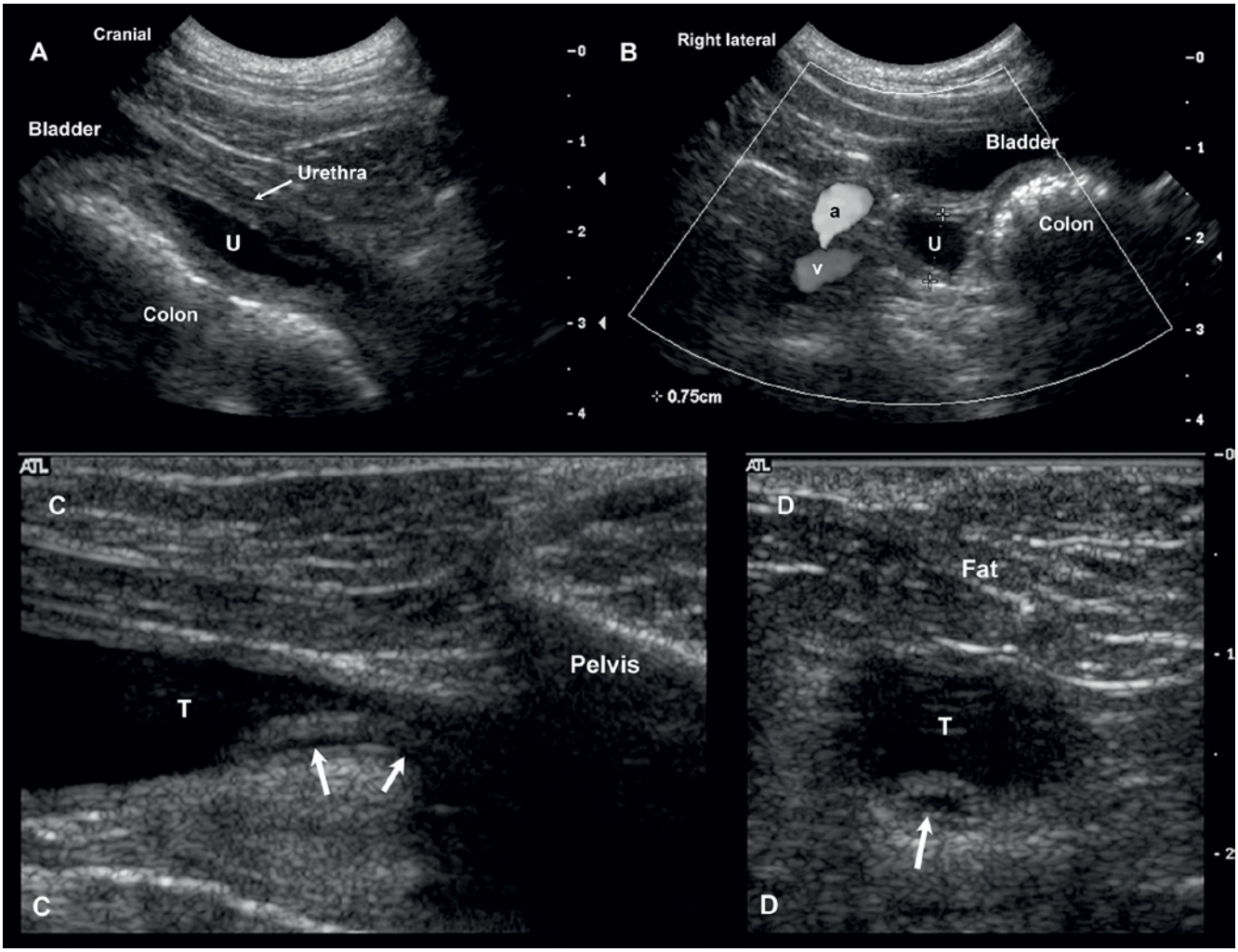


Figure 11.20. **Ectopic ureters. (A, B)** Longitudinal **(A)** and transverse **(B)** images obtained in the region of the bladder trigone, in which a tubular structure filled with an anechoic fluid (U) extends beyond the ureterovesicular junction, along the distal colon. There is no flow on color Doppler, as opposed to the external iliac artery (a) and vein (v), which supports a diagnosis of ureteral ectopia. Excretory urography confirmed a termination into the distal portion of the urethra. **(C, D)** Longitudinal **(C)** and transverse **(D)** images of the bladder trigone (T) in a young female dog with urinary incontinence. A fluid-filled tubular structure (arrows) consistent with a distal ureter extends through the wall of the bladder, on the dorsal midline, beyond the ureteral papilla. Because of the shadow created by the pelvis, the termination of this ureter could not be determined with ultrasonography. An intramural (tunneling) ectopic ureter terminating into the urethra was confirmed at surgery.

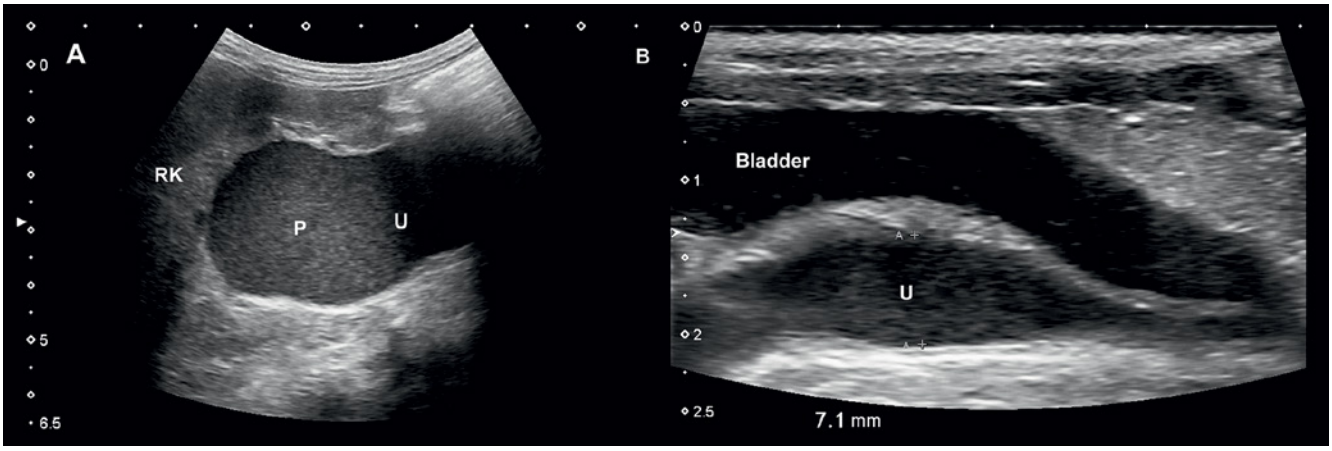


Figure 11.21. **Ectopic ureter with ascending infection.** Longitudinal sonographic images of the proximal **(A)** and distal **(B)** portions of the right ectopic ureter in a young dog with chronic incontinence and recent onset of lethargy. The right renal pelvis (P) and ureter (U) are severely distended with echogenic urine, consistent with pus. The ureter (7.1 mm in diameter in **B**) extends beyond the bladder to terminate into the pelvic urethra. RK, right kidney.

Vet-ebooks.com

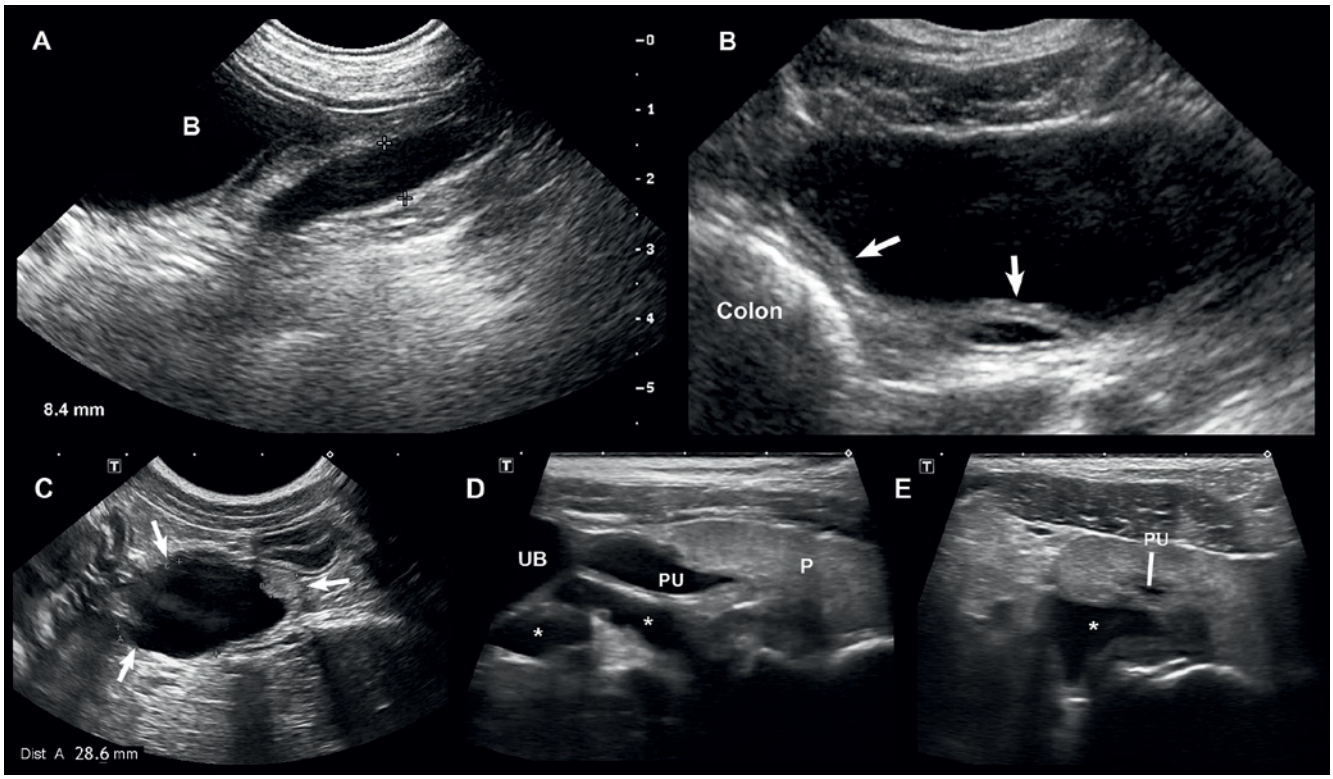


Figure 11.22. **Ectopic ureter in two dogs. (A)** Longitudinal sonogram of a dilated ureter (8.4 mm cursors), which was followed from the left kidney and courses caudal to bladder neck (B), consistent with an ectopic ureter**. (B)** Transverse sonogram of the bladder, showing the intramural trajectory of both mildly dilated ureters (arrows) in this 1-year-old Labrador with long standing incontinence. The bilateral intramural ectopia was confirmed on cystoscopy. **(C–E)** In this 7-month-old intact Dachshund with an hypoplastic right kidney (see Figure 11.15), the right ureter is enlarged and tortuous and extends distally (* in **D–E**) dorsal to the neck of the urinary bladder (UB) and prostatic ureter (PU), before penetrating the right lobe of the prostate (P), dorsal to the prostatic ureter (PU).

bladder filled with more concentrated urine. However, the visualization of a urine jet into the bladder lumen cannot exclude the possibility of tunneling ectopic ureters with or without several fenestrations.

Ureterocele is another congenital ureteral malformation, which can sometimes be associated with ectopia (Stiffler et al. 2002). Ureteroceles are cystic dilations of the terminal ureter within the UB. They can be subdivided as orthotopic or ectopic, depending on whether the ureters enter the bladder at a normal location. Ureteroceles are thin-walled, smooth, spherical, and cyst like structures that protrude into the bladder lumen and are filled with anechoic fluid (Figure 11.23).

Circumcaval ureters are uncommon and are the result of embryologic anomaly of the venous system. The abnormal course of the ureter around the CVC can be associated with ureteral compression and obstruction and therefore should be considered in cats, especially when a proximal right-sided ureteral obstruction is suspected and no calculus is seen (Pey et al. 2015; Steinhaus et al. 2015).

Bladder

Although uncommon, various congenital UB abnormalities may be identified sonographically. They may predispose patients to incontinence or urinary tract infections or may be incidental findings. Anomalous conditions include urachal diverticulum, patent urachus, urachal cysts, vesicovaginal, vesicouterine or vesicorectal fistulas, bladder or urethral duplication (Coffman et al. 2019)

A **vesicourachal diverticulum** is a fluid-filled structure that extends as a convex out-pouching of the bladder lumen, usually with a thin wall, although it can become thick and irregular in cases of chronic cystitis. These diverticuli can vary in size and are typically in the cranioventral aspect of the UB wall (Figure 11.24). Diverticulum may also occur at other locations because of trauma or cystitis.

Pelvic bladder can at times be suspected on ultrasound when the bladder apex is rounded rather than pointed, and the bladder neck region extends within the pelvis despite a moderate distention (Figure 11.25).

Vet-ebooks.com

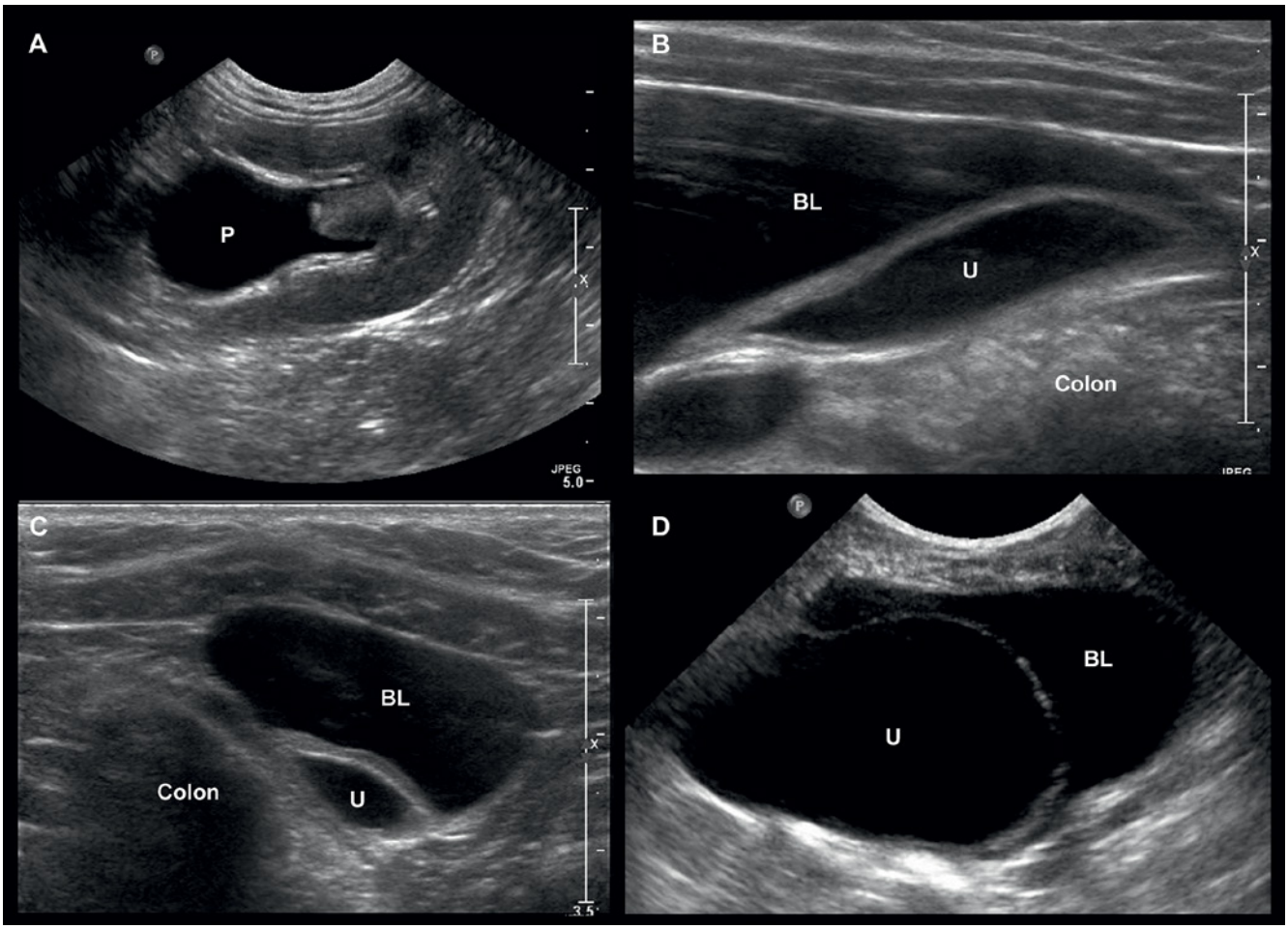


Figure 11.23. **Ureterocele in two dogs. (A–C)** In this 4-month-old Labrador spayed female, there is marked dilatation of the left renal pelvis (P, in transverse sonogram **A**) and protrusion of a dilated ureter (U) into the bladder (BL) neck, seen in longitudinal **(B)** and transverse **(C)** sonograms, consistent with ureterocele. **(D)** Transverse sonogram of the bladder (BL) of a 2-year-old Dashund with the markedly dilated ureterocele (U) protruding into the bladder lumen (BL), on the right side. Notice the thin wall of the ureterocele. Severe ipsilateral hydroureter and hydronephrosis are also present (not shown) in this dog.

Diffuse Parenchymal Renal Diseases

Changes in size and echogenicity are important features to combine while diagnosing renal diseases. For example, renomegaly can be encountered in several disorders such as obstructive nephropathy, metabolic disorders such as diabetes (Figure. 11.26), acute nephritis, infiltrative neoplasia; but beyond the size, the echogenicity and changes in renal architecture are essential in prioritizing the differential diagnosis.

Increased renal echogenicity is one of the most common findings in dogs and cats with chronic kidney disease. Several renal diseases can be associated with increased cortical and/or medullary echogenicity in the acute or chronic phases of the process. Other than renal dysplasia or juvenile nephropathy, interstitial and glomerular nephritis, acute tubular necrosis (caused by ethylene glycol, grapes in dogs, and lily in cats), end-stage renal disease, and nephrocalcinosis can all cause renal hyperechogenicity (Adams et al. 1991; Barr et al. 1989; Eubig et al. 2005; Forrest et al. 1998). In some of these disease processes, the cortical echogenicity can be more specifically increased, enhancing the corticomedullary distinction. This can be dramatic in cases of acute tubular necrosis and calcium oxalate deposition caused by ethylene glycol toxicity (Eberlé et al. 2022) (Figure 11.27). In other cases, both medulla and cortex can become hyperechoic, causing reduced corticomedullary border distinction, with at times presence of fine striations (Bentley et al. 2022) (Figure 11.28). This is particularly evident in dogs and cats with chronic renal disease

Vet-ebooks.com

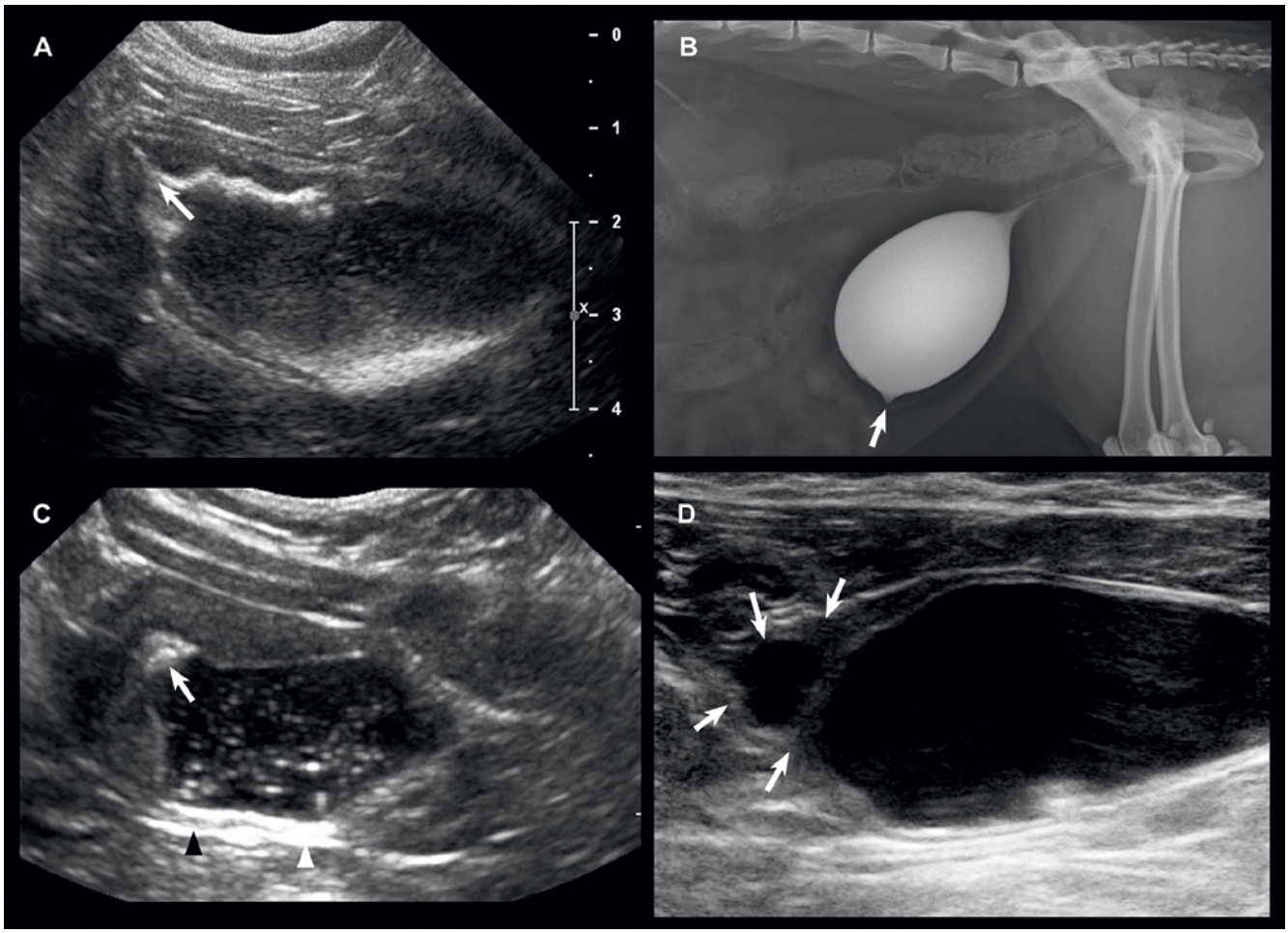


Figure 11.24. **Vesicourachal diverticulum in two cats. (A)** Longitudinal sonogram of the bladder in a 6-year-old castrated male cat presented for pollakiuria and recurrent episodes of urethral obstruction. A focal depression/track (arrow) is present in the cranioventral aspect of the bladder, which is thickened and irregular. A moderate amount of echogenic sediment is present in the lumen. **(B)** The lateral radiograph with positive contrast cystogram displays the urachal diverticulum (arrow). **(C)** Longitudinal sonogram of the bladder of a 5-year-old cat with chronic cystitis. A similar depression is noted in the cranioventral aspect of the bladder (arrow), and a small amount of hyperechoic sediment is collected at this level (arrowheads). **(D)** Three months later, a well-defined sacculation (arrows) is visible in the cranioventral bladder wall. On sequential exams, calculi were seen lodged in the diverticulum. Courtesy of C. Warman, Veterinary Specialist Group, Auckland, New Zealand.

(Figures 11.29, 11.30). The medulla may be more specifically hyperechoic with leptospirosis, diffusely or forming a band as the result of congestion, edema, hemorrhage, and necrosis (Figures 11.31, 11.32) (Forrest et al. 1998). A hyperechoic medullary band parallel to the corticomedullary border – also known as the ***medullary rim sign*** – has also been observed in several other disease processes, such as acute tubular necrosis (ethylene glycol toxicity), nephrocalcinosis, and pyogranulomatous vasculitis caused by feline infectious peritonitis as well as in normal cats and dogs (Barr et al. 1989; Biller et al. 1992; Forrest et al. 1998; Mantis and Lamb 2000) (Figures 11.33). This hyperechoic band has been attributed to an insult to the renal tubules in the deepest portion of the medulla, which is most metabolically active and therefore more susceptible to ischemia (Biller et al. 1992). Due to their relatively high prevalence in dogs and cats, renal hyperechogenicity and medullary rim signs should not be considered accurate indicators of active renal disease; however, the possibility remains that these findings could represent sentinel signs of early renal disease or past renal insult (Cordella et al. 2020; Mantis and Lamb 2000). A thick hyperechoic ill-defined rim sign was more frequently associated with kidney disease in cats compared to a thin hyperechoic well-defined rim sign (Cordella et al. 2020).

Kidneys of nonazotemic dogs and cats can present several alterations without clinical evidence of renal disease (Figure 11.17). Apart from parenchymal

Vet-ebooks.com

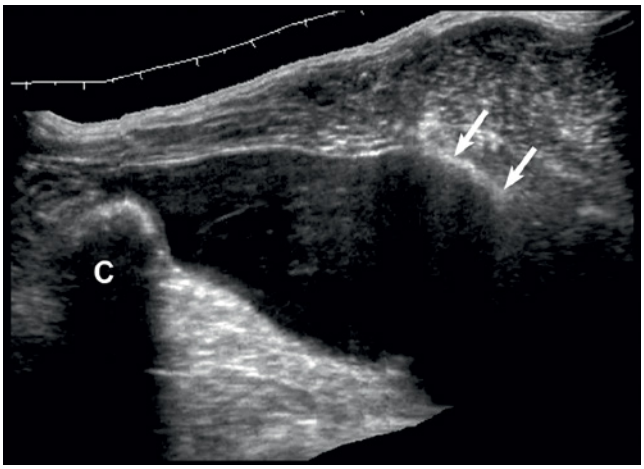


Figure 11.25. Pelvic bladder in a 1.5-year-old male Doberman presented for incontinence. A panoramic image of the bladder shows a pointed apex and wide bladder trigone/neck region, resulting in a reversed pear-like shape. The bladder neck is partially covered by the pubis (arrows). C, colon.



Figure 11.27. Increased renal echogenicity with ethylene glycol toxicity in a 9-year-old Yorkie. On this longitudinal image of the right kidney, the cortex and medulla are moderately hyperechoic because of oxalate crystal deposition and tubular necrosis. A hyperchoic rim sign is present in the medulla (arrowheads).

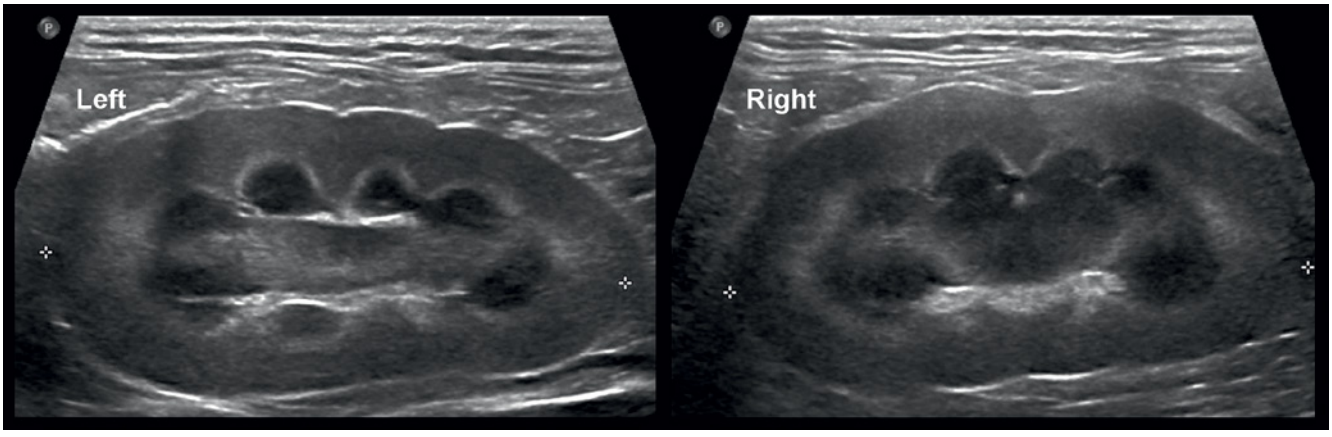


Figure 11.26. Bilateral renomegaly and diabetes. Both kidneys are moderately enlarged (Left: 5.6 cm long; Right: 5.8 cm long) in this 5-year-old male cat with DKA. Both kidneys have slightly irregular contours but normal cortico-medullary distinction.

echogenicity, interpretation must also take into consideration parameters such as size, shape, contour, and internal architecture. Small, irregular, and diffusely hyperechoic kidneys are generally indicative of chronic interstitial nephritis (Figures 11.28, 11.29). The remodeling process affecting these kidneys, which involves fibrosis, causes architectural distortions. Degenerative cysts may appear in the cortex (Figure 11.34). Linear or patchy dystrophic mineralization can also be observed in these kidneys, especially in the region of the collecting system, where the mineralization appears as poor or well-defined hyperechoic foci that cause acoustic shadowing (Figure 11.30). These mineral foci are usually difficult to differentiate from true nephroliths, which can also accompany chronic renal diseases. Kidneys affected with acute processes, such as **infectious pyelonephritis**, **interstitial nephritis** (e.g., caused by leptospirosis), or **acute tubular necrosis** (e.g., caused by ethylene glycol), can become enlarged and hyperechoic, with a contour that usually remains smooth (Figures 11.31, 11.32). Perinephric effusion can also be observed in patients with acute kidney injury (Forrest et al. 1998; Holloway and O'Brien 2007).

Immune-mediated or nonimmune mediated glomerular disease, such as **glomerulonephritis** and **renal amyloidosis**, cannot be distinguished from other types of diffuse renal disorders. Affected kidneys are

Vet-ebooks.com

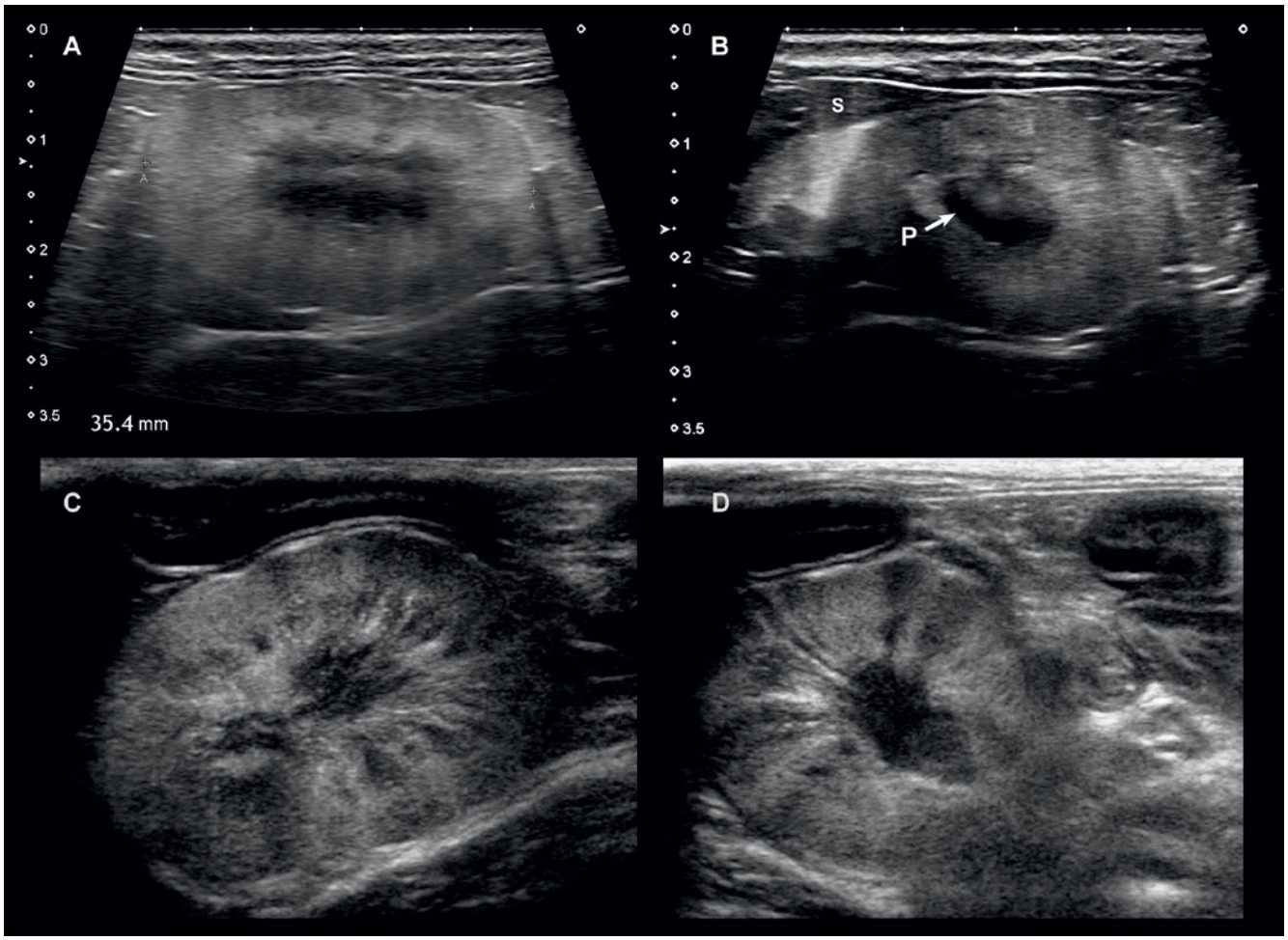


Figure 11.28. **Chronic interstitial nephritis in two cats.** On these longitudinal **(A)** and transverse **(B)** images of the left kidney of 12-year-old domestic short hair cat, both the cortex and medulla appear hyperechoic and poorly demarcated. The changes are more pronounced in the outer portion of the medulla. The renal contour is irregular, but the kidney remains normal in size. The renal pelvis is mildly dilated due to increased diuresis. S, spleen. **(C, D)** Renal tubular lipidosis and moderate multifocal lymphocytic plasmacytic interstitial nephritis in a 6-year-old Oriental short hair cat presented for a 6-month history of azotemia. **(C)** (longitudinal) and **(D)** (transverse) sonograms show small, rounded kidneys with irregular margins. Radiating hyperechoic striations are noted through the cortex and medulla; they likely represent the marked tubular vacuolation (lipid) with multifocal tubular necrosis.

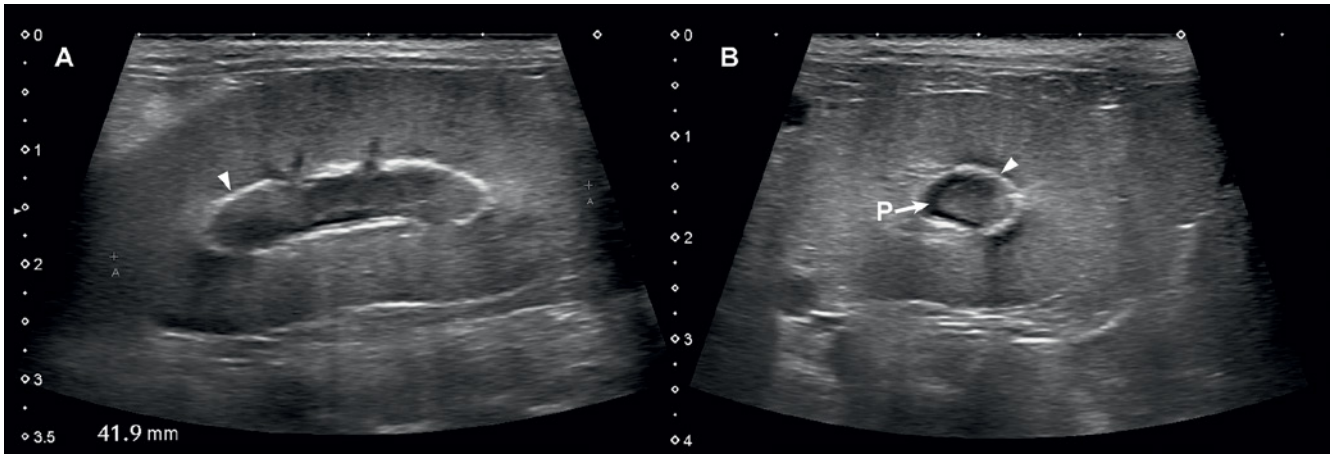


Figure 11.29. **Chronic renal disease in a 11-year-old small breed dog with creatininemia and proteinuria.** On these longitudinal **(A)** and transverse **(B)** images of the left kidney, the cortex is hyperechoic and thickened. A thin hyperechoic rim sign is present in the outer medulla (arrowheads). The pelvis (P) is mildly dilated. Glomerulonephritis and amyloidosis are first considered based on the clinical and sonographic findings.

Vet-ebooks.com

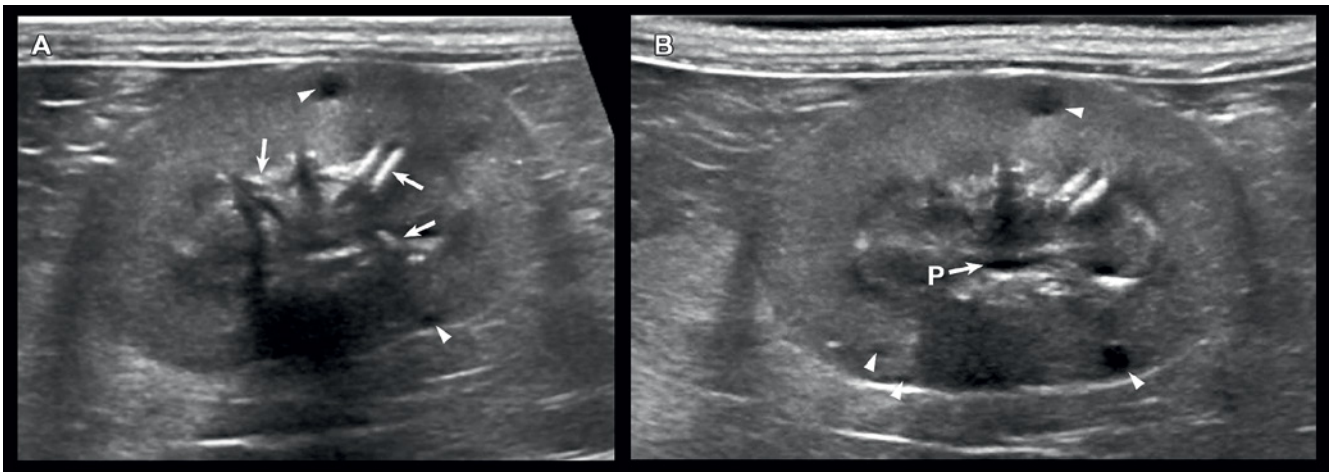


Figure 11.30. **Chronic renal changes with dystrophic mineralization. (A)** Longitudinal image of the left kidney in a 11-year-old Shih-Tzu cross with chronic renal insufficiency. This kidney is slightly irregular and hyperechoic. The corticomedullary distinction is reduced, and several linear and irregular hyperechoic lines are noted along the diverticuli (short arrows), and are associated with acoustic shadowing. Small cysts (arrowheads) are noted in the periphery of the cortex. **(B)** On this longitudinal plane crossing the pelvis (P), additional small peripheral cortical cysts are noted (arrowheads), and the pelvis is mildly dilated.

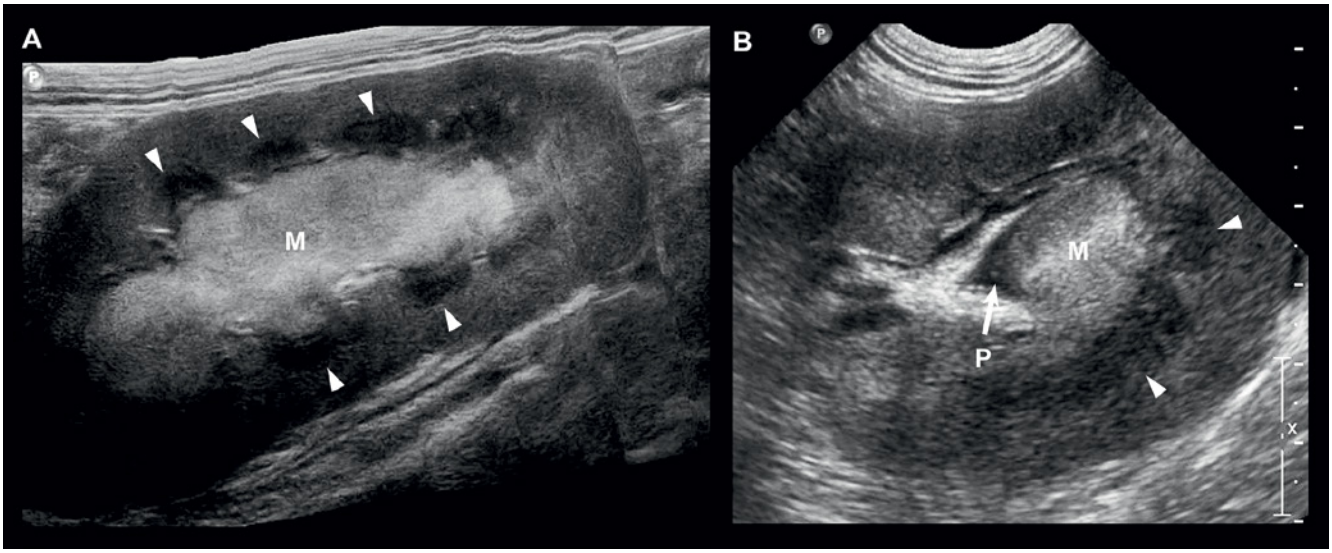


Figure 11.31. **Leptospirosis in a 2-year-old German shepherd with acute kidney insufficiency.** Longitudinal **(A)** and transverse **(B)** images of the right kidney on which the inner medulla (M) is markedly hyperechoic, while the outer medulla (arrowheads) and cortex appear normal. Moderate pyelectasia (P) is also present.

commonly hyperechoic and can vary in size according to the chronicity of the disease (Figure 11.35).

Renal parenchymal mineralization (**nephrocalcinosis**) in dogs and cats with or without hypercalcemia can cause renal diffuse cortical and/or medullary hyperechogenicity, a medullary rim sign, and/or dispersed hyperechoic foci (Figure 11.36).

Neoplastic processes vary in appearance from focal or multifocal renal changes to diffuse infiltration. With **lymphoma** in cats, the kidneys typically become enlarged, irregular, and variably echogenic with often a hypoechoic subcapsular thickening (Valdès-Martinez et al. 2007) (Figure 11.37). Other findings can include hyperechoic foci or striations throughout the medulla, pyelectasia, and hypoechoic medullary or cortical nodules or masses. **Other tumors**, such as squamous cell carcinoma, papillary carcinoma, and nephroblastoma, may extensively infiltrate the kidney and markedly distort the renal architecture (Figure 11.38).

Vet-ebooks.com

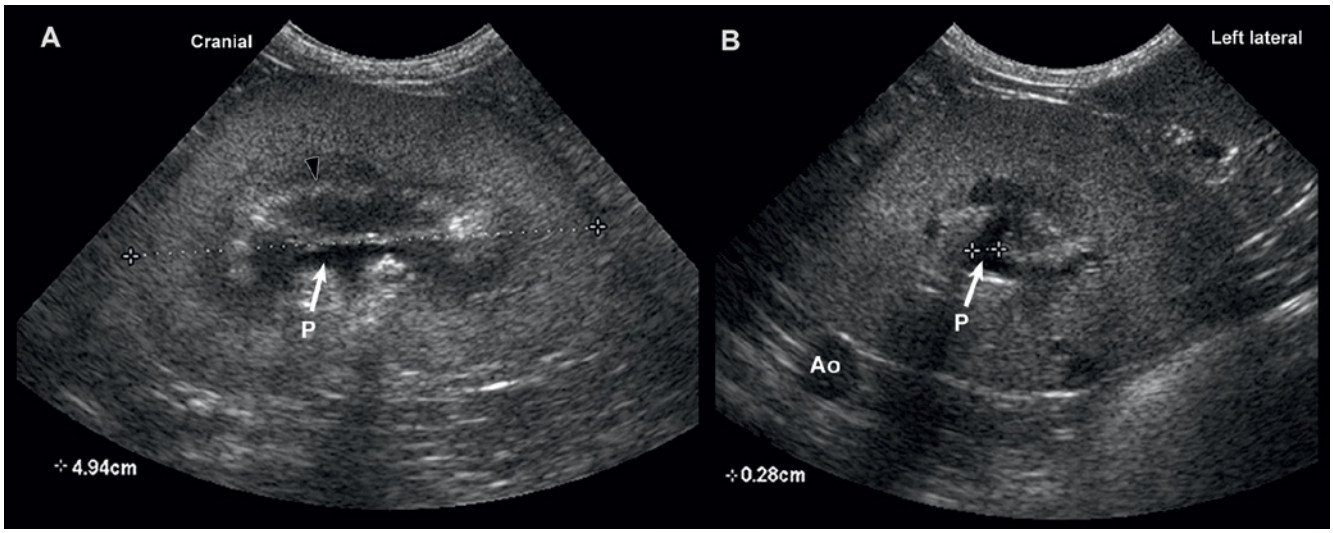


Figure 11.32. **Acute leptospirosis.** Longitudinal **(A)** and transverse **(B)** image of the left kidney (arrowheads) in a small-breed dog diagnosed with leptospirosis. The kidney is smoothly enlarged and hyperechoic, and the corticomedullary distinction is reduced. The renal pelvis (P) is also dilated. Additionally, a medullary rim sign is present (arrowhead). Ao, aorta.

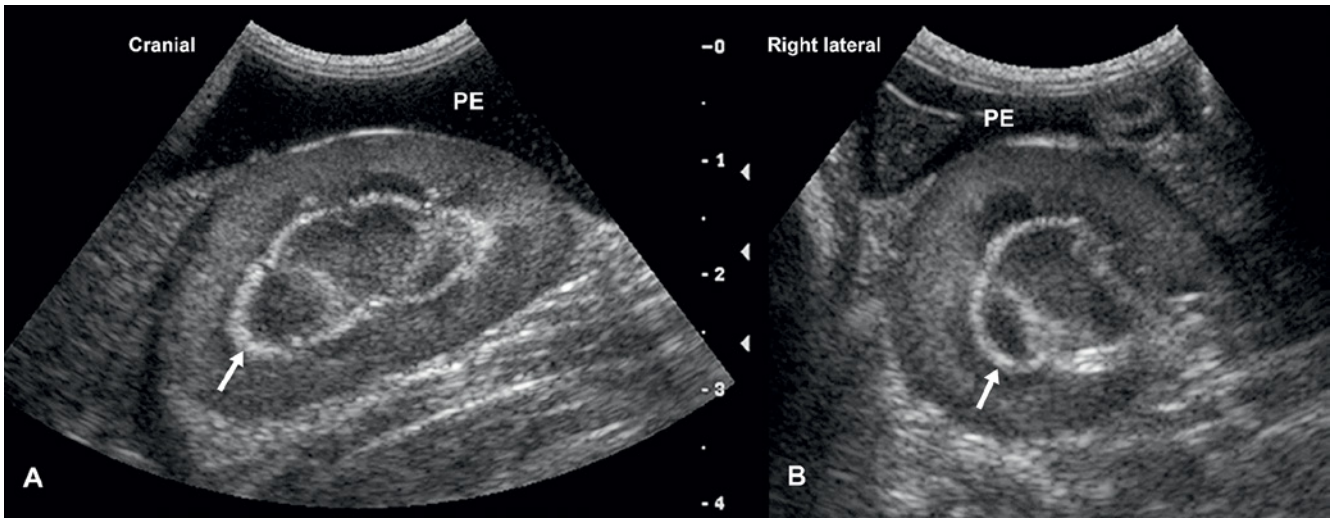


Figure 11.33. **Pyogranulomatous vasculitis.** Longitudinal **(A)** and transverse **(B)** images of the right kidney in a cat diagnosed with feline infectious peritonitis. A prominent hyperechoic band is in the medulla (arrow), parallel to the cortical margin, consistent with a medullary rim sign. Pronounced peritoneal effusion (PE) is also present.

Focal Parenchymal Renal Disorders

In comparison to diffuse parenchymal lesions for which ultrasound lacks sensitivity and specificity, several types of focal lesions can be identified with superior accuracy. Renal cysts, nephroliths or dystrophic mineralization, and cortical infarcts are more common than primary or metastatic neoplasia, granulomas, and abscesses.

Renal Cavitary Lesions

Benign **renal cysts** typically appear as round to oval, anechoic structures with a thin, well demarcated, echogenic rim and often show distal acoustic enhancement (Reichle et al. 2002) (Figure 11.39A, B). Cysts can be solitary or multifocal and vary in size. In some patients, internal echoes or septations can be observed in association with hemorrhage or necrotic debris.

Vet-ebooks.com

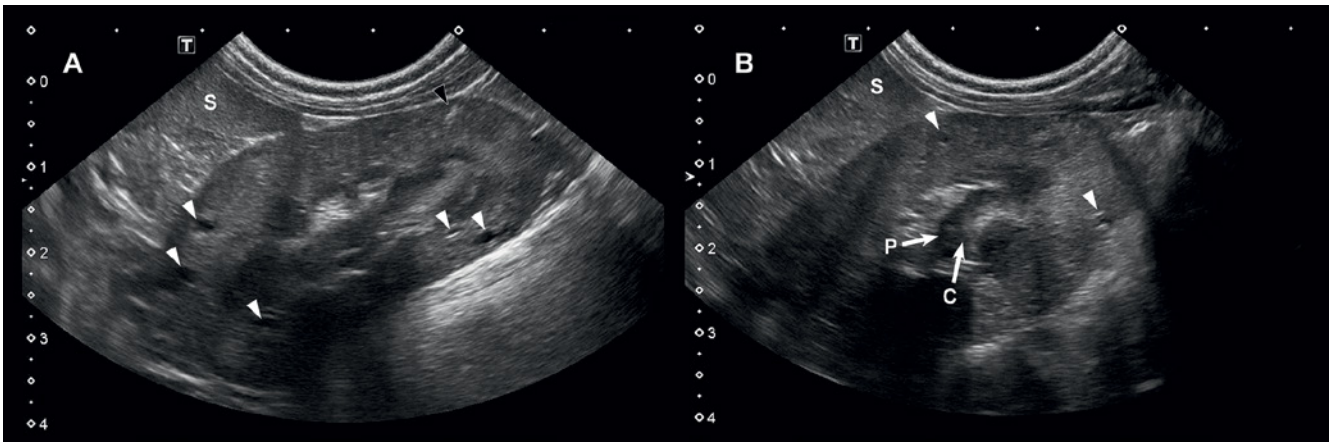


Figure 11.34. Renal degeneration in a 12-year-old mixed-breed dog with normal creatinine serum concentration. In these longitudinal **(A)** and transverse **(B)** images of the left kidney, the renal cortex is isoechoic to the adjacent spleen (S) and filled with small anechoic cysts (white arrowheads) and hyperechoic lines (black arrowhead). The renal crest (C) is hyperechoic, and the pelvis is mildly dilated.

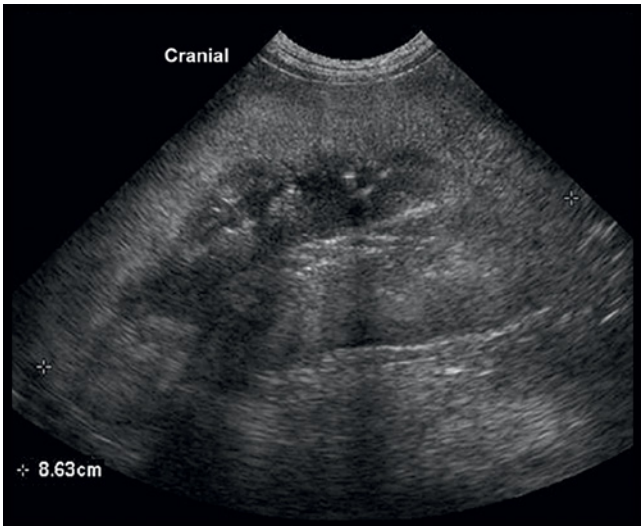


Figure 11.35. Glomerulonephritis. Longitudinal image of the left kidney of a German shepherd diagnosed with bilateral glomerulonephritis. The kidney appears smoothly enlarged and hyperechoic, particularly at the level of the cortex, which also appears subjectively thickened

Autosomal-dominant polycystic kidney disease (PKD) mainly affects Cairn terriers and Persian and Persian-related cats. PKD can be variable in severity, can be sometimes associated with chronic interstitial nephritis, and may cause significant renal distortion (Figure 11.39C, D). Most of these cysts are in the cortex or at the corticomedullary junction (Reichle et al. 2002). Ultrasound scanning by an experienced sonographer at 10 months of age appears reliable for PKD diagnosis (Wills et al. 2009). With improved equipment and higher frequency (10–14 MHz) probes, PKD may even be diagnosed with 96% sensitivity and 91% specificity as early as 3 months of age (Bonazzi et al. 2009).

Degenerative cysts can also be secondary to chronic renal diseases in dogs and cats (Figure 11.34).

Solitary cysts, which can sometimes become relatively large and present a complex architecture with debris or septa (Figure 11.39D), may mimic solitary solid or cavitary masses, abscesses, and hematomas (Figure 11.40). Renal **abscesses** can usually be differentiated from true cysts by the presence of echoes and sedimentation within the cavitary lesion and especially by a poorly demarcated and irregular contour. Distal enhancement may still be present if the cellular count remains relatively small. Infected renal cysts may resemble cysts with cellular debris or hemorrhage, requiring fine-needle aspiration for diagnosis (Figures 11.40A, 11.41).

Solid masses or nodules are typically associated with static internal echoes that can be affected by gain settings and that are usually not associated with distal acoustic enhancement. Large solid masses can also be cavitated because of necrosis. Renal cystadenomas and cystadenocarcinomas often have a cystic component of variable size (Figure 11.42). Renal cystadenocarcinomas have been also reported in German shepherds and are usually associated with dermatofibrosis (Moe and Lium 1997). The fluid-filled cavity (or cavities) varies in size and if large, may distort the renal margin. Similar features can be encountered with renal cystadenoma, which was reported in a domestic shorthair cat as a large complex cystic structure occupying most of the renal parenchyma (Mosenco et al. 2008).

Vet-ebooks.com

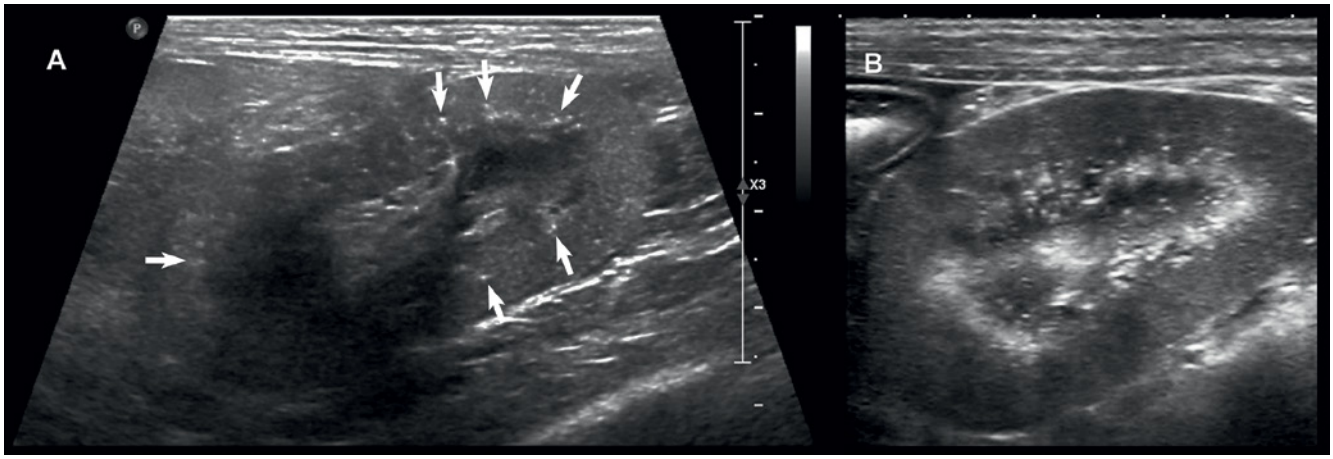


Figure 11.36. **Nephrocalcinosis in two dogs with hypercalcemia. (A)** On this longitudinal image of the left kidney of a 2-year-old dog, small hyperechoic foci (arrows) are seen, predominantly involving the cortex, consistent with extensive renal calcification. This dog was previously diagnosed with leptospirosis. The changes were bilateral. **(B)** In this other dog, hyperechoic dots are seen in the medulla, while the cortex is less affected.

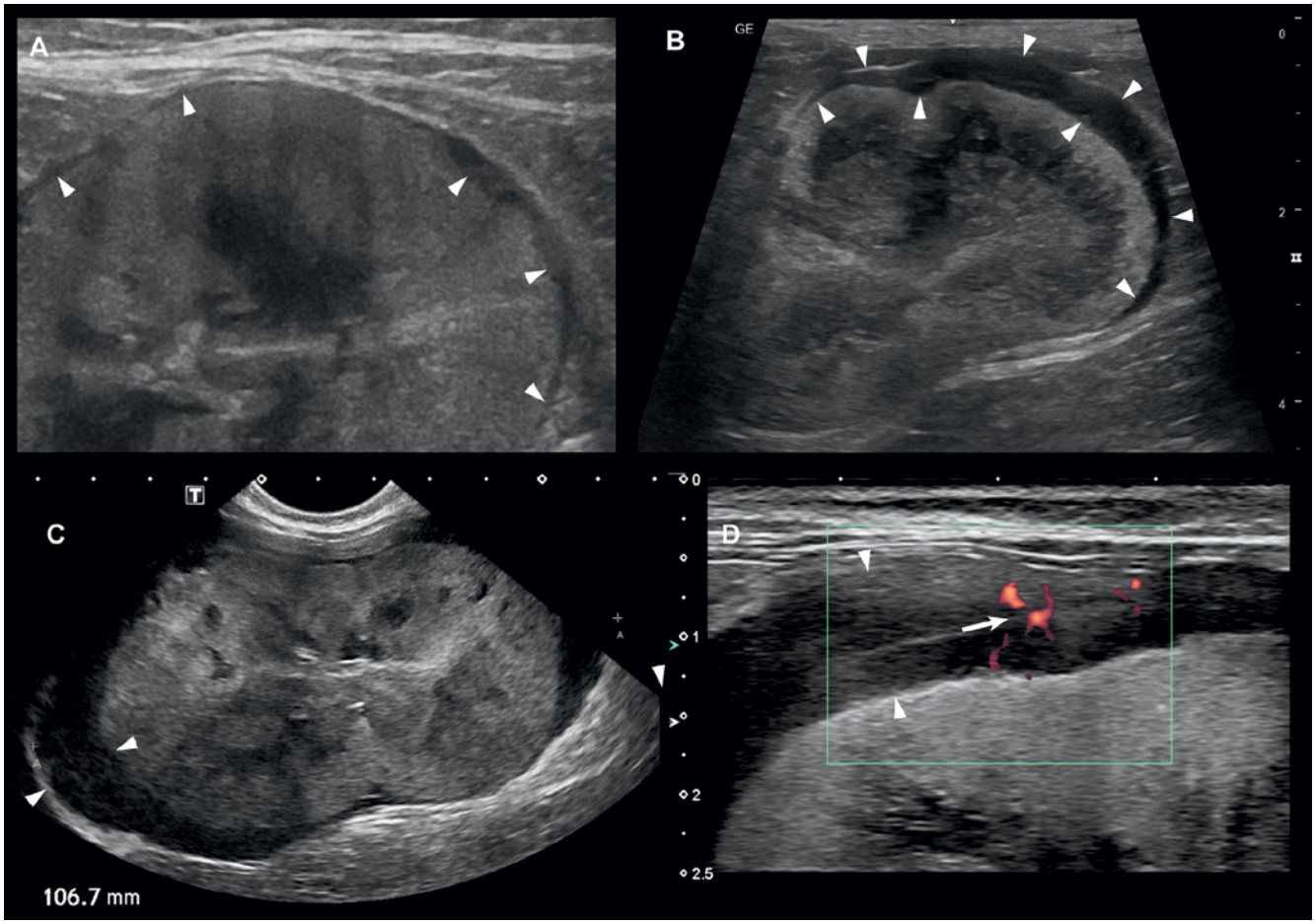


Figure 11.37. **Renal lymphoma in three cats. (A)** Transverse image of the left kidney of 10-year-old domestic spayed female cat with an irregular hypoechoic layer of tissue (1–3 mm in thickness) at the periphery of the renal cortex (arrowheads), consistent with a halo sign. The kidney is enlarged and mildly hyperechoic with loss of corticomedullary distinction. **(B)** Longitudinal image of an enlarged and heterogeneous left kidney (6 cm in length) of another cat. The medulla is distorted and appears enlarged. There is a more pronounced halo sign at the periphery of the cortex (arrowheads). **(C, D)** In this third cat, the peripheral subcapsular hypoechoic layer (between arrowheads) is more pronounced and traversed by vessels (arrow in D). The renal parenchyma is deformed, heterogeneous and associated with poor corticomedullary distinction.

Vet-ebooks.com

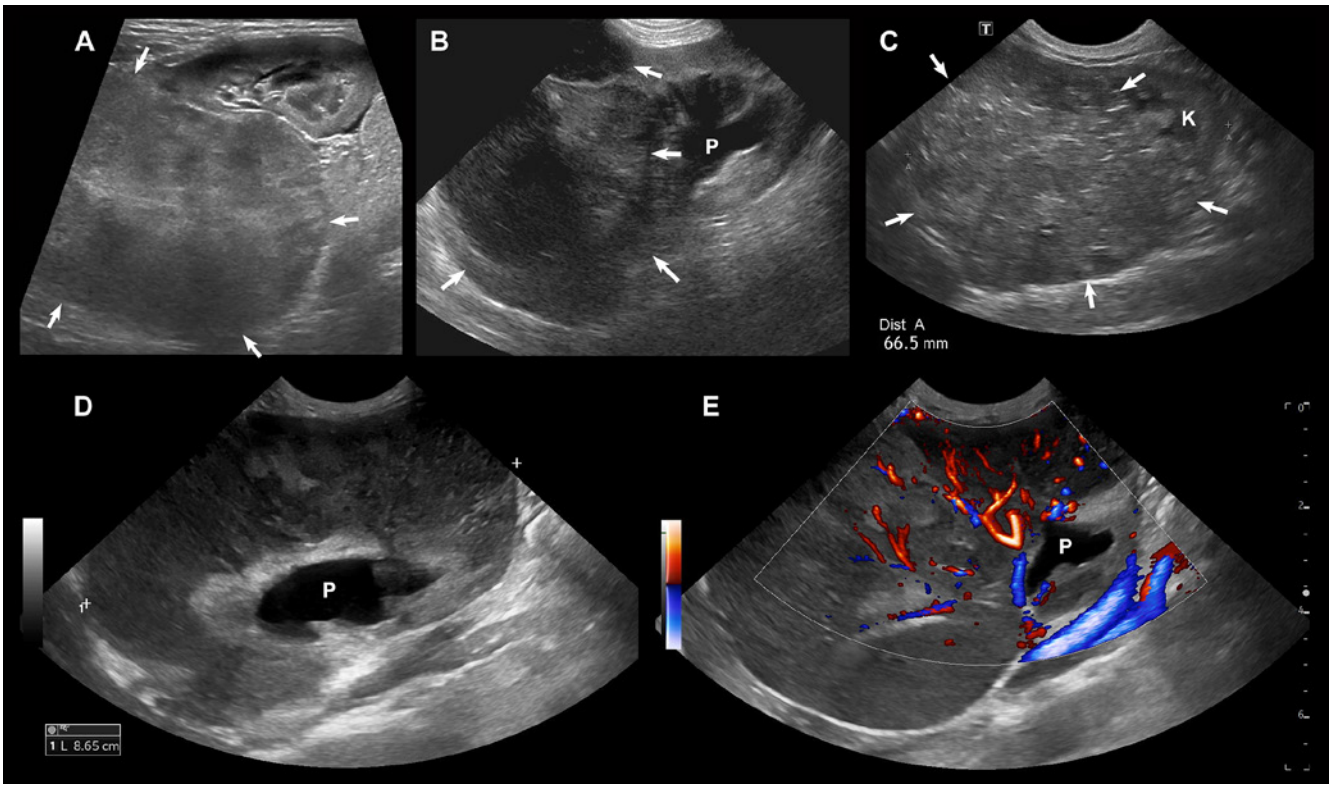


Figure 11.38. **Extensive renal neoplasia of two dogs and two cats. (A)** Longitudinal sonogram of the right kidney of a 4-year-old Golden Retriever cross dog. The kidney is replaced by a large mostly hyperchoic mass (arrows). The histopathological diagnosis was **renal cell carcinoma (B**) A large and partially **cystic papillary carcinoma** deforms the contours of the kidney of this 2-year-old Hound. The mass was compressing the collecting system and moderate pyelectasia is present (P). In both dogs, part of the caudal pole of kidney can still be identified. **(C) Undifferentiated sarcoma** in a 12-year-old castrated male domestic short hair cat presented for dysorexia. A 6.6 cm-wide, moderately echogenic mass with a coarse echotexture and a few small cysts invades the cranial portion of the right kidney (K). **(D, E) Large-cell lymphoma** in a 5-year-old castrated male miniature Poodle. The left kidney is diffusely infiltrated by a heterogeneous, mostly hypoechoic and hypervascular (in E) tissue distorting the renal pelvis (P).

Renal Solid Nodule or Mass Lesions

Solid-tissue proliferative diseases can appear as homogeneous or heterogeneous, hypoechoic, isoechoic or hyperechoic, regular or irregular lesions, with variably well-defined margins (Figures 11.43–11.49). This variable ultrasonographic appearance depends on the cell type as well as the variable presence and distribution of vessels, tissue necrosis, fibrosis, mineralization, and hemorrhage. The renal internal architecture is variably altered depending on the size and invasiveness of the process. Nearby vascular invasion or thrombosis may also be present (Figure 11.47). Renal primary or metastatic neoplastic processes have variable and overlapping characteristics, anf therefore they cannot be easily distinguished with ultrasonography only. However, lymphoma and malignant histiocytosis (histiocytic sarcoma) tend to appear as hypoechoic nodules or masses (Figures 11.44, 11.45).

Other types of neoplastic masses include adenocarcinomas, hemangiomas, nephroblastomas, and several types of sarcomas, including hemangiosarcoma as well as metastases (Gasser et al. 2003). These neoplastic processes can be well defined or ill-defined and can be associated with retroperitoneal hemorrhage or completely replace normal parenchymal architecture (Figures 11.46, 11.47A). The absence of an identifiable kidney in the region lateral to the origin of the renal vessels might be the only sign that can help in confidently suspecting a renal mass. Other imaging tests (excretory urography, computed tomography, or magnetic resonance) can be required to confirm the origin of the mass and determine its extent for surgical planning.

Other less common nodular lesions, such as granulomas (fungal diseases), pyogranulomas (feline infectious peritonitis), hematomas or solid abscesses tend to

Vet-ebooks.com

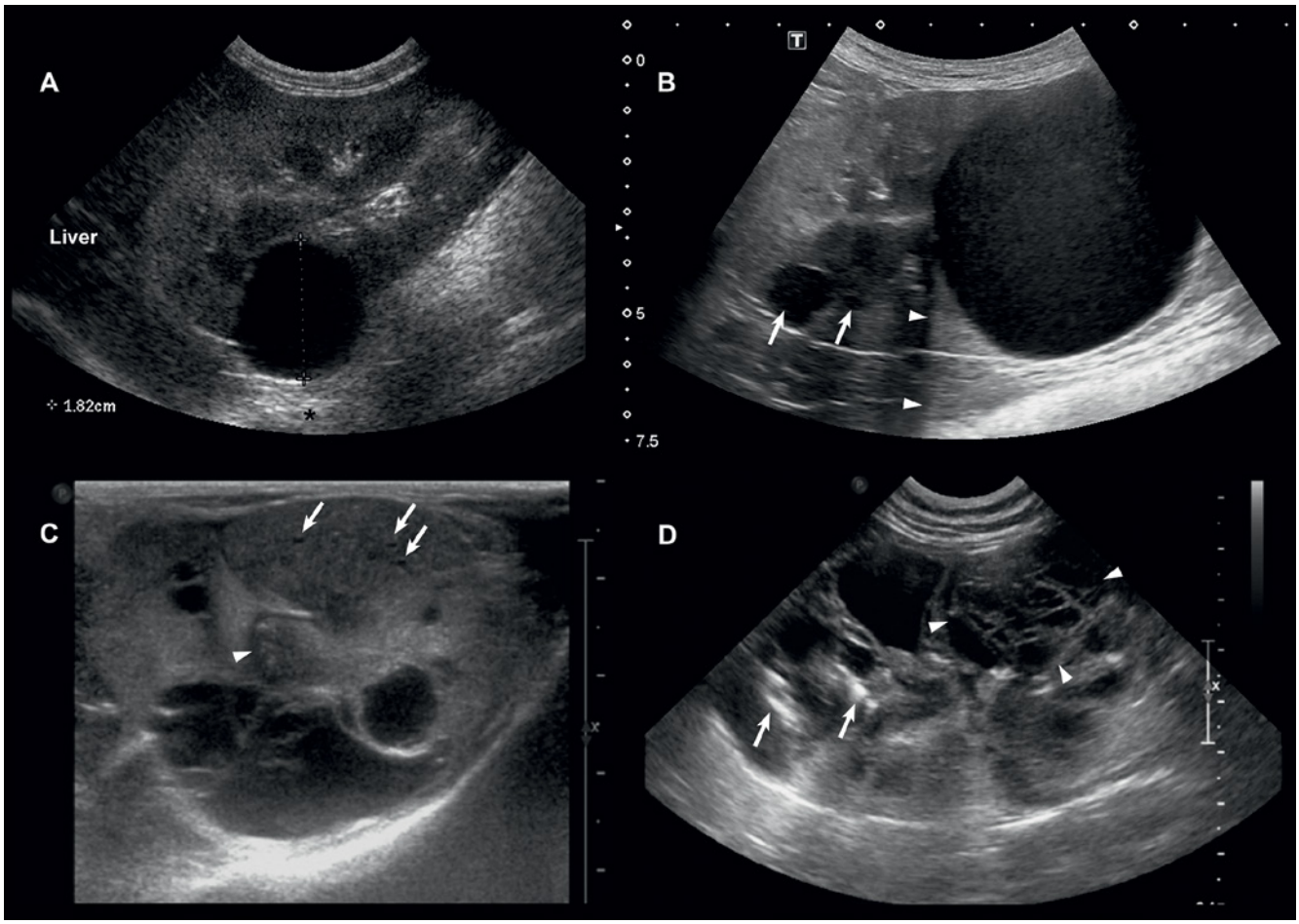


Figure 11.39. **Renal cysts and polycystic kidney disease (PKD) in dogs and cats. (A)** Longitudinal image of the right kidney in a dog with an incidental cortical cyst, which appears as a 1.8 cm, round, well-defined, anechoic structure, associated with distal acoustic enhancement (*). The renal cortex is hyperechoic to the adjacent liver, although there was no clinical evidence of renal failure. **(B)** In this other dog, a 6 cm-wide cyst with smooth borders deforms the caudal pole of the left kidney, while small cysts (arrows) are also present cranially. Note the far acoustic enhancement artifact dorsal to the larger cyst (arrowheads). Transverse **(C)** and longitudinal **(D)** images of kidneys in two different cats with PKD. In **(C)**, a large cyst deforms the dorsal portion of the left kidney, while smaller cysts are present more ventrally (arrows). The arrowhead points to the pelvis. In **(D)**, the renal parenchyma is completely replaced by cysts of variable size and shape. Some of the cysts show a complex architecture (between arrowheads). Calcifications are also present (arrows).

be hyperechoic but can mimic neoplastic processes (Figure 11.48A–D). Hence, fine-needle aspiration or biopsy is required in most cases to achieve a final diagnosis.

Other Focal Lesions

Mineral foci are commonly identified in kidneys of older dogs and cats because of soft-tissue mineralization or urolithiasis (Figures 11.30, 11.49). The appearance of these hyperechoic foci and associated acoustic shadows depends on their size and differs between conventional and spatial compound imaging (Heng et al. 2022). With spatial compounding, the mineral foci are typically more echogenic and thus more conspicuous. However, the multiangle compound image reduces the strength of acoustic shadowing, which may even disappear.

Renal **infarcts** are commonly detected, especially in cats and may be associated with an underlying cardiomyopathy (Hickey et al. 2014). They can be identified as linear or wedged-shaped, well-defined hyperechoic lesions in the cortex, perpendicular to the capsule. Although their appearance can vary, chronic infarcts are typically hyperechoic and cause focal cortical depression or atrophy (Figure 11.50). These chronic infarcts may also be hyperattenuating, generating an acoustic shadow. Benign renal infarcts can also

Vet-ebooks.com

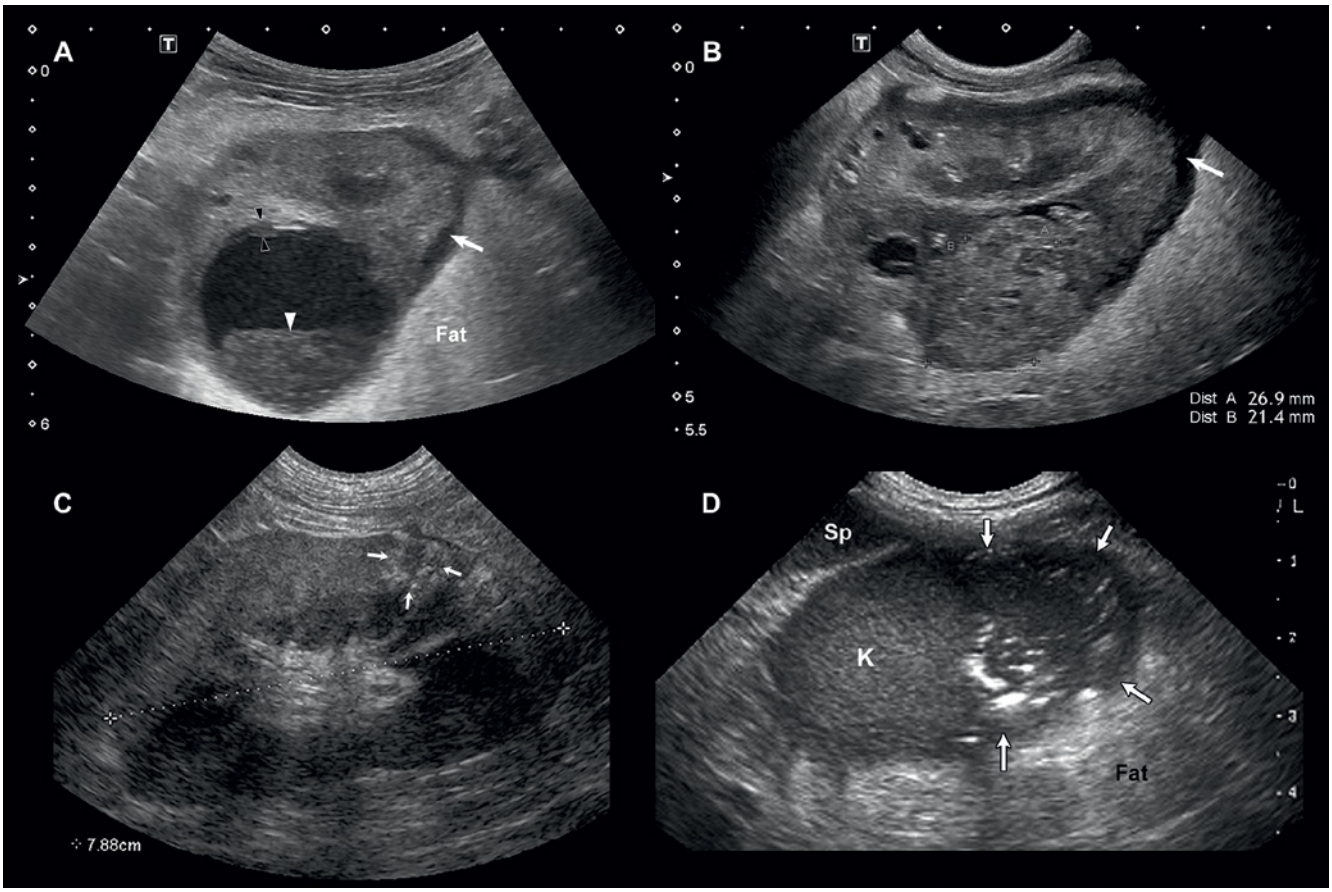


Figure 11.40. **Renal abscesses in three dogs. (A, B) Abscess associated with chronic nephropathy. (A)** On initial examination, a cavitary lesion with a hypoechoic wall (between black arrowheads) was identified in the craniodorsal portion of the left kidney. The lesion contained nearly anechoic fluid on top and cellular sediment on the bottom (white arrowhead). The retroperitoneal fat was hyperechoic, and subcapsular and perirenal effusion (arrow) was present. **(B)** Following fine-needle aspiration under ultrasound guidance, the abscess was drained, but hemorrhage developed, forming a clot that filled the cavity. Subcapsular and perirenal effusion was again present (arrow), and the kidney showed numerous cysts and reduced corticomedulary distinction. Presumably, one of the cysts became infected. Culture revealed *E. Coli*. **(C) Septic embolus and abscess formation.** Longitudinal image of the left kidney in a golden retriever diagnosed with bacterial septicemia. An ill-defined hyperechoic rim-like focus (arrows), with a hypoechoic center, is at the level of the renal cortex. A septic exudate was aspirated with ultrasound guidance. **(D) Renal abscess caused by a wooden foreign-body perforation.** A poorly echogenic cavity (arrows) with a few bright echoes (mixture of debris and gas) involves the caudal pole of the left kidney (K). The retroperitoneal fat is hyperechoic, and a small amount of fluid is noted in the near field, adjacent to the abscess, which was confirmed at surgery. Sp, spleen.

resemble septic emboli, although these tend to be more heterogeneous in appearance (Figures 11.40C, 11.50D). Although extremely rare, **gas foci** can also be present within kidneys because of hematogenous/ascending infection (Figure 11.40D) or following iatrogenic intervention.

Disorders of the Collecting System

The renal pelvis and diverticuli are not distended in normal dogs and cats. Dilatation of the pelvis, also termed **pyelectasia**, is more easily recognized and more reliably measured on a transverse plane at the level of the renal hilus (Figure 11.51). It appears as an anechoic crescent at the medial margin of the renal crest (the deep portion of the medulla) (Figures 11.4B, 11.5B, 11.53B and 11.54B). Mild dilatation of the pelvic diverticuli can sometimes be difficult to differentiate from adjacent interlobar vessels without the use of color or power Doppler (Figure 11.52).

Mild pyelectasia can be observed in normal animals and those with increased diuresis (e.g., diuretic therapy or chronic kidney disease), congenital malformation (e.g., ureteral ectopia), pyelonephritis, upper and

Vet-ebooks.com

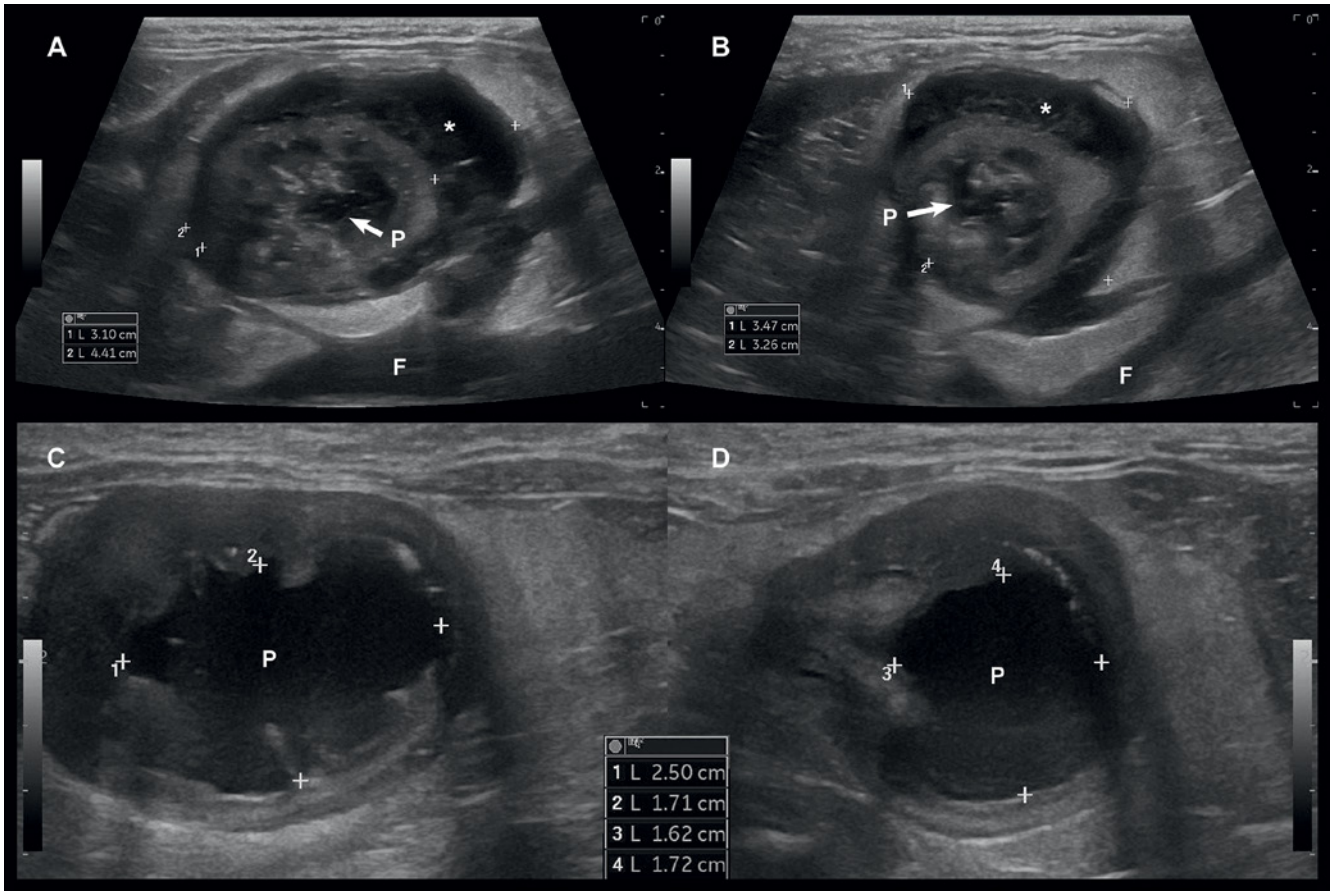


Figure 11.41. **Subcapsular septic empyema with unilateral pyelonephritis in a 14-year-old spayed female cat** presented for severe lethargy, uremia and leucocytosis. Longitudinal **(A)** and transverse **(B)** sonographic images of left kidney at presentation. There is a wide, asymmetric subcapsular hypoechoic halo (*) that is surrounded with hyperechoic fat and retroperitoneal fluid (F). The kidney is at the lower range of normal in length, irregular and diffusely hyperechoic with mild to moderate pyelectasia (P). Renal lymphoma was initially considered, but a neutrophilic exudate with rod-shaped bacteria was confirmed with fine-needle aspiration. **(C, D)** 1 month after antibiotics, the subcapsular empyema was resolved, but the renal pelvis (P) was now severely dilated with a mildly echogenic content. Mild perirenal steatitis remained.

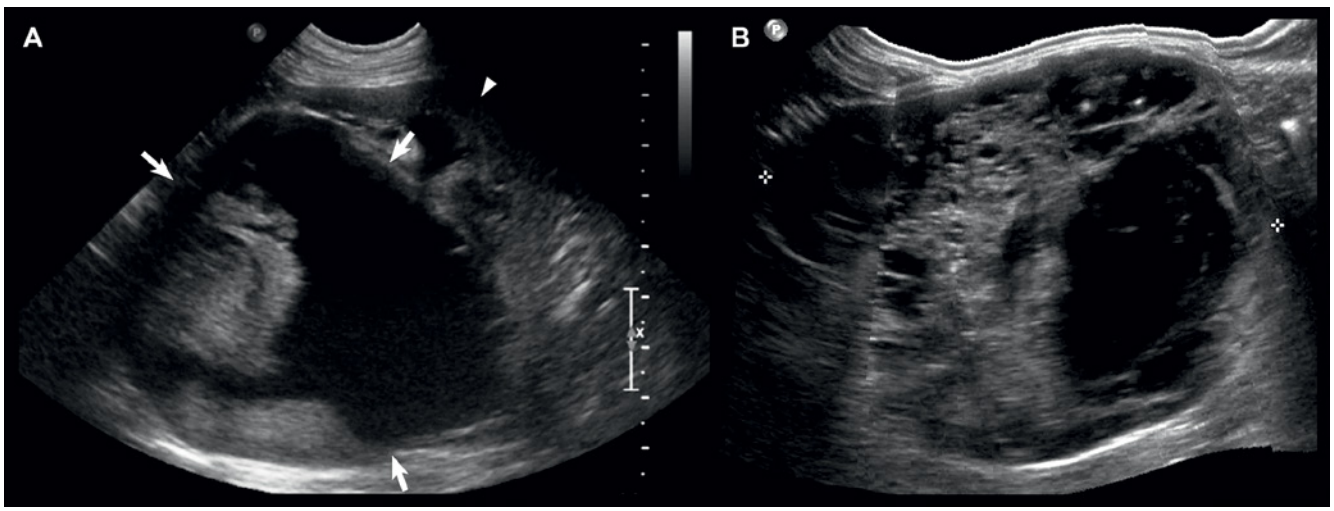


Figure 11.42. **Large cystic renal masses in a dog and a cat. (A)** A very large, primarily cystic mass (arrows) is deforming most of the cranial and central portions of the left kidney of this 11-year-old golden retriever without abdominal clinical signs. A nephrectomy was performed, and **cystadenoma** was confirmed histologically. **(B)** A very large, inhomogeneous and partially cavitated, irregular mass is disrupting the renal architecture in this 13-year-old cat without clinical signs. This mass was discovered by palpation during his annual physical exam. The diagnosis was **cystadenocarcinoma**.

Vet-ebooks.com

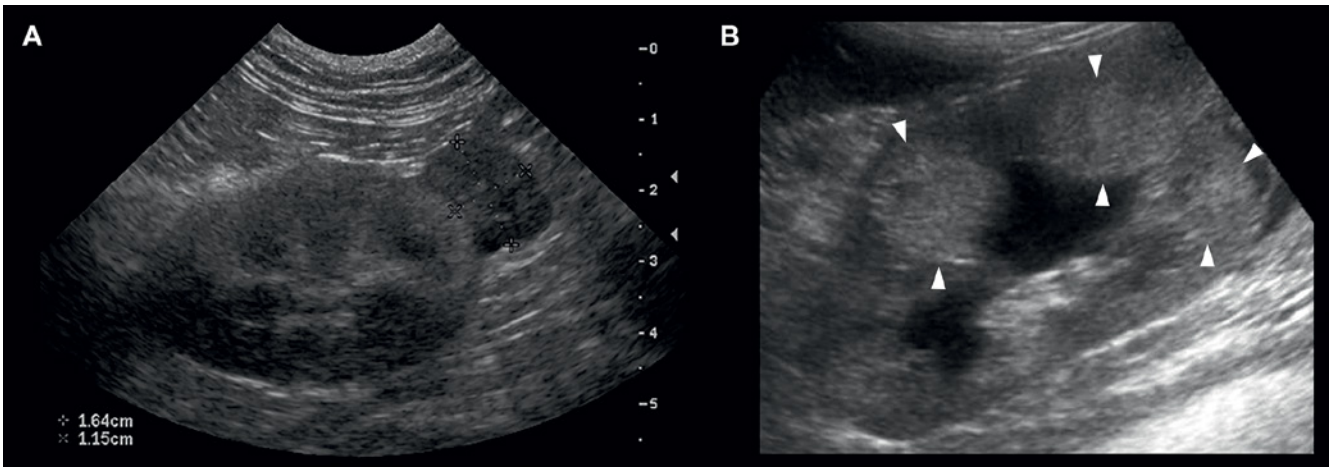


Figure 11.43. **Renal metastases. (A)** Longitudinal image of the left kidney of a cat in which a pulmonary mass was identified on radiographs. Tumor staging revealed a paracortical hypoechoic nodule at the caudal renal pole. A metastatic focus of **bronchoalveolar carcinoma** was suspected on cytological examination**. (B)** Longitudinal sonogram of the left kidney in a 6-year-old Labrador cross with **splenic hemangiosarcoma** that was removed several months ago. The several hyperechoic nodules disrupting the normal renal architecture are metastases.

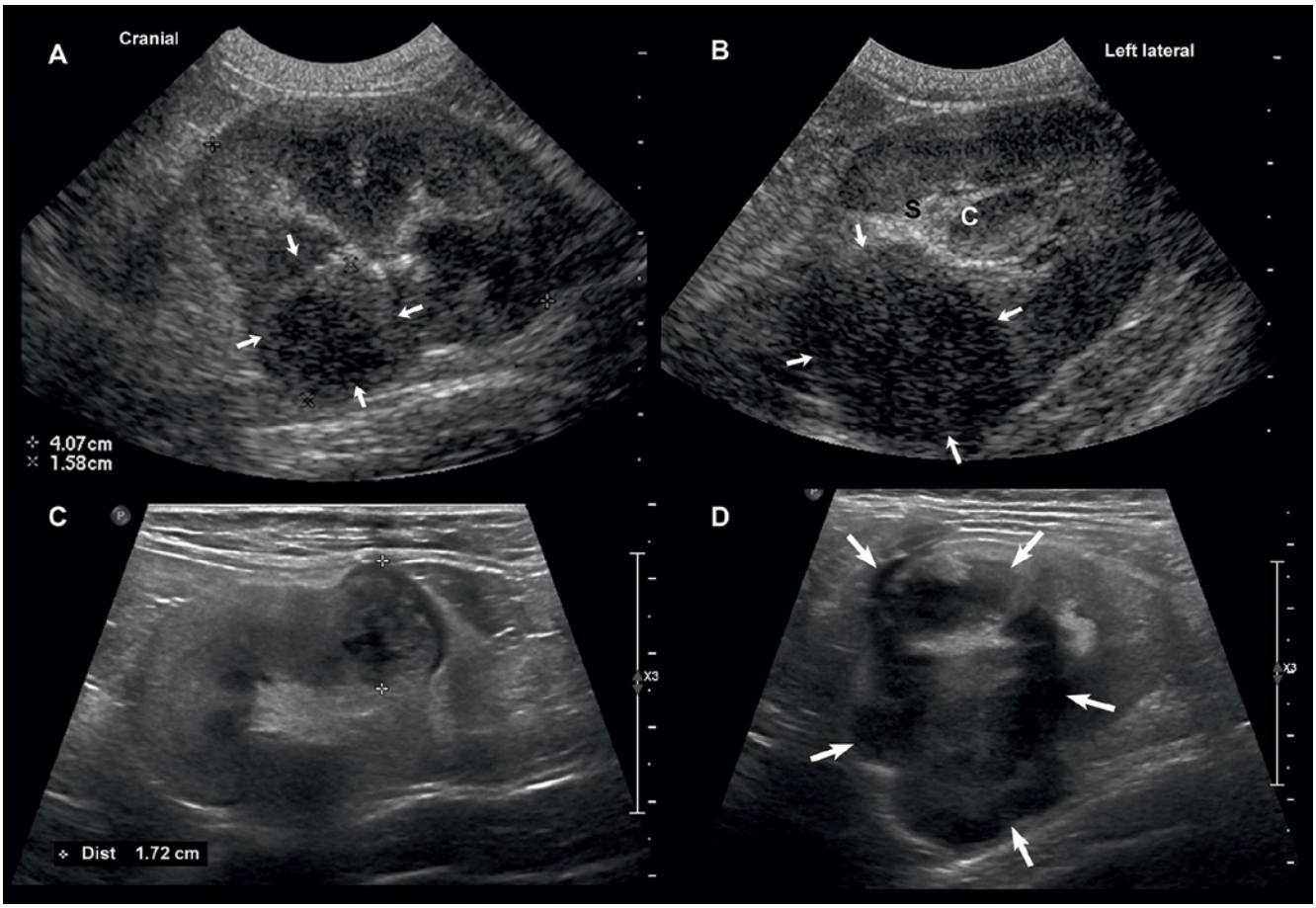


Figure 11.44. **Renal nodules in a dog and a cat with lymphoma.** Longitudinal **(A)** and transverse **(B)** images of the left kidney in a Lhasa apso with multicentric lymphoma. A hypoechoic nodule (arrows) is in the renal cortex, adjacent to the renal sinus (S) and crest (C). **(C, D)** In this 10-year-old cat, both kidneys are enlarged, deformed and there is poor corticomedullary distinction and an incomplete peripheral halo (arrowhead). The left kidney **(C)** is deformed by cortical nodules (between calipers); the right kidney **(D)** is more distorted by a multilobulated and poorly echogenic mass (arrows). This pattern is another manifestation of lymphoma in cats.

Vet-ebooks.com

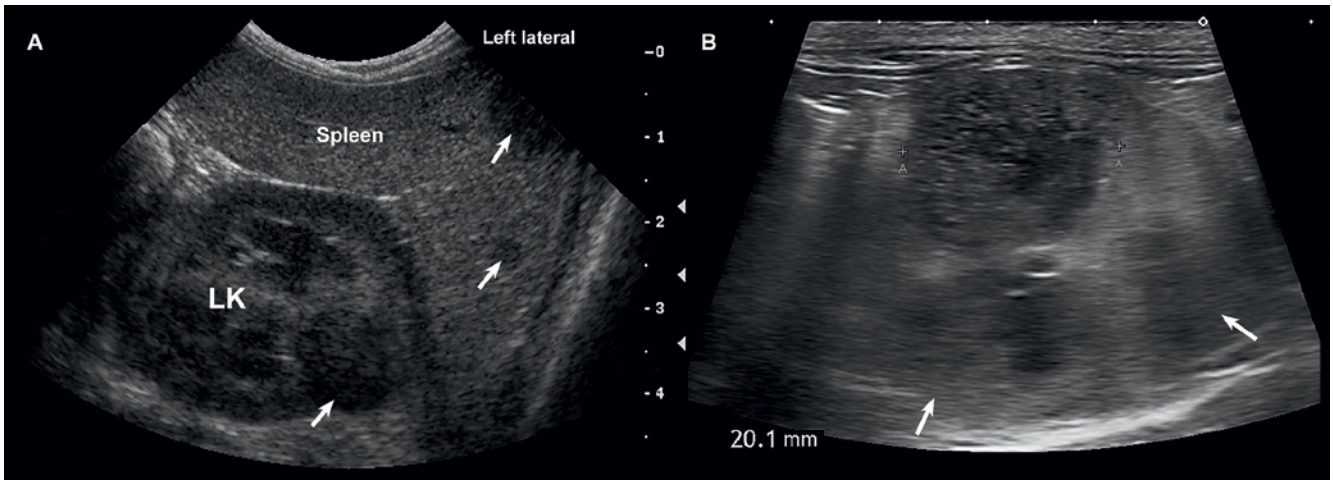


Figure 11.45. Disseminated histiocytic sarcoma in two dogs. (A) Transverse image of the left kidney (LK) in a medium-sized dog. A hypoechoic nodule (arrow) involves the renal cortex, deforming its contour. This nodule is not associated with far acoustic enhancement. Similar nodules of variable size were also detected in the liver and spleen (other arrows). **(B)** In this Bermese moutain dog, both kidneys were filled with hypoechocic nodules of variable size. This image of the left kidney shows a 2 cm well-defined hypoechoic nodule with small hyperechoic dots (between corsors) and ill-defined hypoechoic foci (arrows). Tumors of round-cell origin should be considered when these lesions are found.

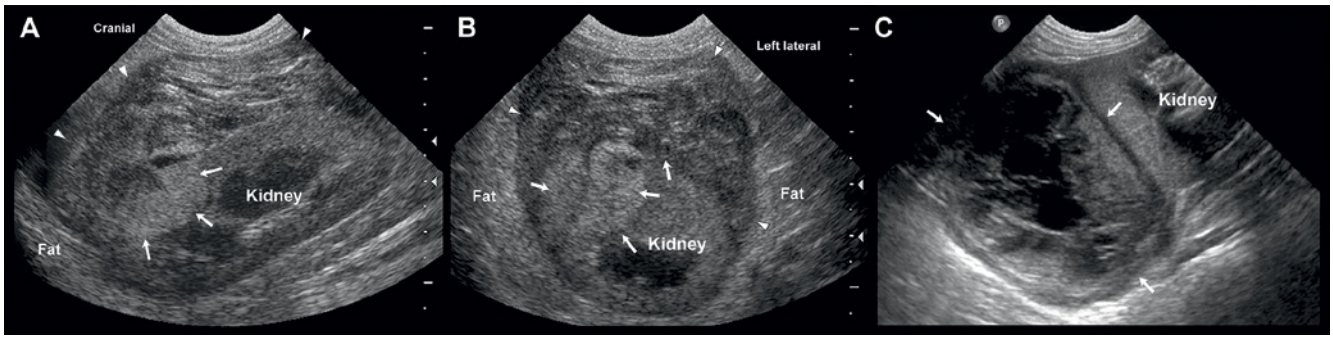


Figure 11.46. Renal hemangiosarcoma in two dogs. Longitudinal **(A)** and transverse **(B)** ultrasonographic images of the left kidney in a large dog with suspected intra-abdominal hemorrhage. A large, ill-defined and heterogeneous mass encircles the ventral aspect of the left kidney (arrowheads). The most ventral component of this mass appears lamellate, consistent with hemorrhage. A smaller portion of this retroperitoneal mass appears more solid, uniform and hyperechoic (arrows), and appears to invade the renal cortex, consistent with a primary renal hemangiosarcoma. **(C)** Longitudinal sonogram of a large partially cavitated mass (arrows) deforming the cranial pole of right kidney of this 13-year-old German Shepherd.

lower urinary obstruction, and neoplasia (d'Anjou et al. 2011; Lemieux et al. 2021) (Figures 11.30, 11.31, 11.32, 11.34, and 11.52–11.56). The ureter can also be seen in some of these patients and be most easily identified on transverse planes at the level of the hilus, central to the renal vessels. Table 11.1 lists common causes of pyelectasia and hydronephrosis in dogs and cats.

When pyelectasia is more pronounced or if hydronephrosis develops because of urinary flow obstruction, renal diverticuli appear as rounded, anechoic finger-like projections that connect with the renal pelvis (Figures 11.52, 11.53, 11.55, 11.57, and 11.59–11.61). Markedly dilated diverticuli and pelvis must be differentiated from renal cysts or sections of the medulla. The presence of protein or cells (pus or hemorrhage) may increase the urine echogenicity and even be associated with sedimentation, such as sometimes seen in cases of pyelonephritis (Figure 11.53–11.56).

Pyelonephritis is generally associated with pyelectasia (Figures 11.53–11.56), although the renal pelvis may remain normal in mild or early pyelonephritis (Neuwirth et al. 1993). With chronic pyelonephritis, in addition to parenchymal changes, the pelvis and diverticuli can become distorted and show a hyperechoic rim because of fibrous tissue remodeling (Figures 11.55, 11.56).

Vet-ebooks.com

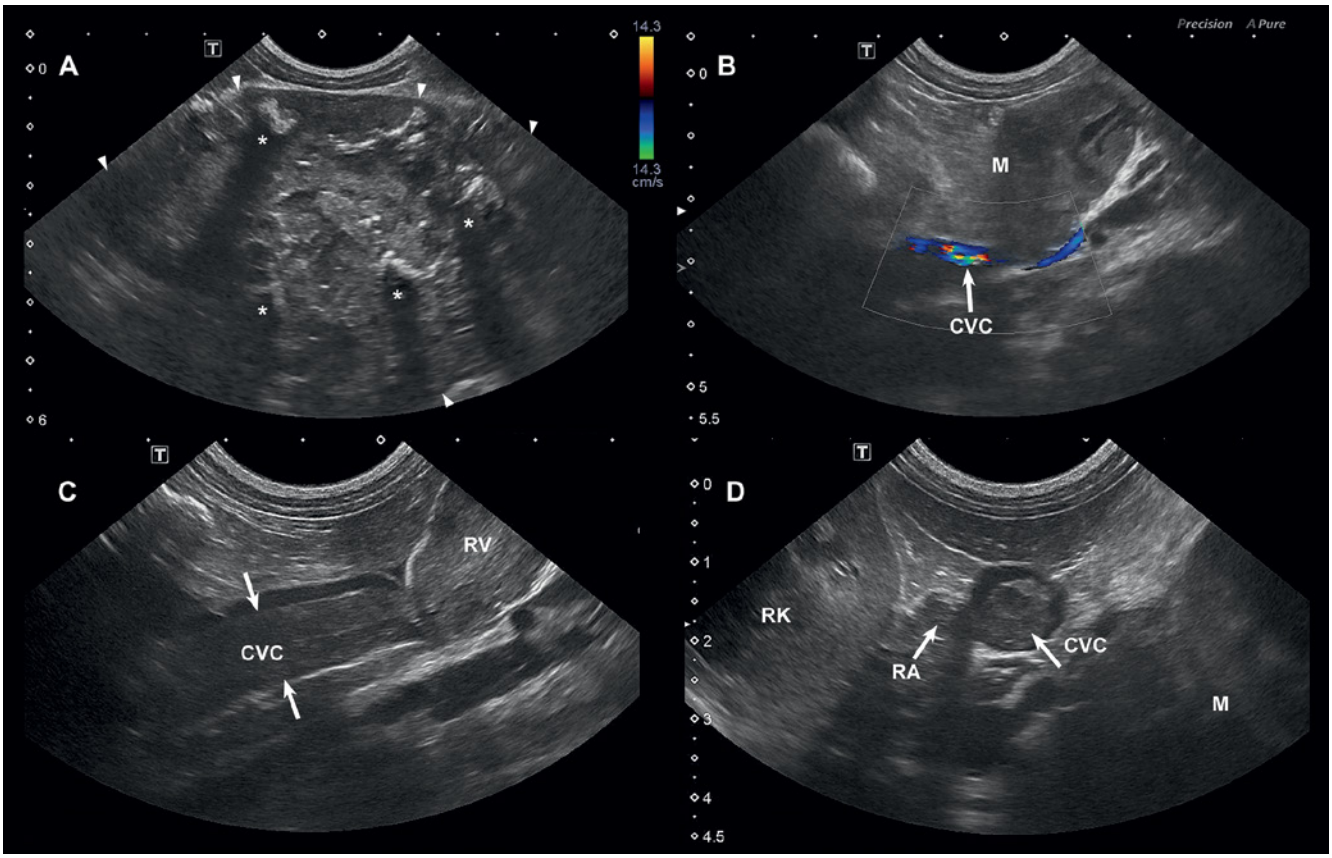


Figure 11.47. Undifferentiated sarcoma invading the left kidney with venous thrombosis in a dog. (A) The large mass (arrowheads) is moderately echogenic and heterogeneous and shows several mineral foci casting shadows (*). It compresses the caudal vena cava (CVC in **B**) and is associated with massive thrombosis that begins in the left renal vein (RV) to extend into the CVC cranially (in **C**). The thrombus fills more than 75% of the CVC lumen (in **D**). Mild peritoneal and retroperitoneal effusions were also present. M, mass; RA, right adrenal gland; RK, right kidney.

The term **hydronephrosis** is used when obstruction is present, such as that caused by the migration of a nephrolith or caused by an infiltrating or compressing process involving the pelvis, the ureter, or possibly the ureterovesicular junction (Meler et al. 2018). A pelvic height of ≥13 mm measured on a transverse image is predictive of outflow obstruction caused by one of these conditions (d'Anjou et al. 2011). However, pelvic dilatation is not a sensitive sign of obstruction, as pelvic height can remain ≤2 mm with partial obstruction (Figure 11.58) (Lemieux et al. 2021) and overlap exists in both pelvic and ureteral measurements in cats with pyelonephritis, ureteral obstruction, and chronic disease (Quimby et al. 2017). In cases of chronic obstruction, progressive distension of the renal pelvis and diverticuli can cause marked parenchymal atrophy (Figures 11.59–11.61).

The presence of moderately echogenic content dispersed or filling the pelvis or generating a fluid-debris level responding to gravity, should be considered strong indicator of pyonephrosis (Choi et al. 2010). **Pyonephrosis** represents a consequence of obstructive pyelonephritis, or outflow obstruction with secondary ascending infection (Figure 11.62).

Ureteral distension, also termed **hydroureter**, is usually observed in combination with hydronephrosis in cases of urine outflow obstruction. Distended ureters, which can become markedly enlarged and tortuous with long-standing obstructions, can usually be followed caudally to the level of the obstruction. Color or Power Doppler can be useful in differentiating an abdominal vessel from a distended ureter (Figure 11.19). **Uroliths** appear as hyperechoic structures that are usually associated with acoustic shadowing (Figures 11.57, 11.58, 11.63–11.66). With complete obstruction, the ureter appears dilated cranially and abruptly blunted caudally at the level of the urolith. Several migrating uroliths may be present, justifying a detailed examination of the entire region of each

Vet-ebooks.com

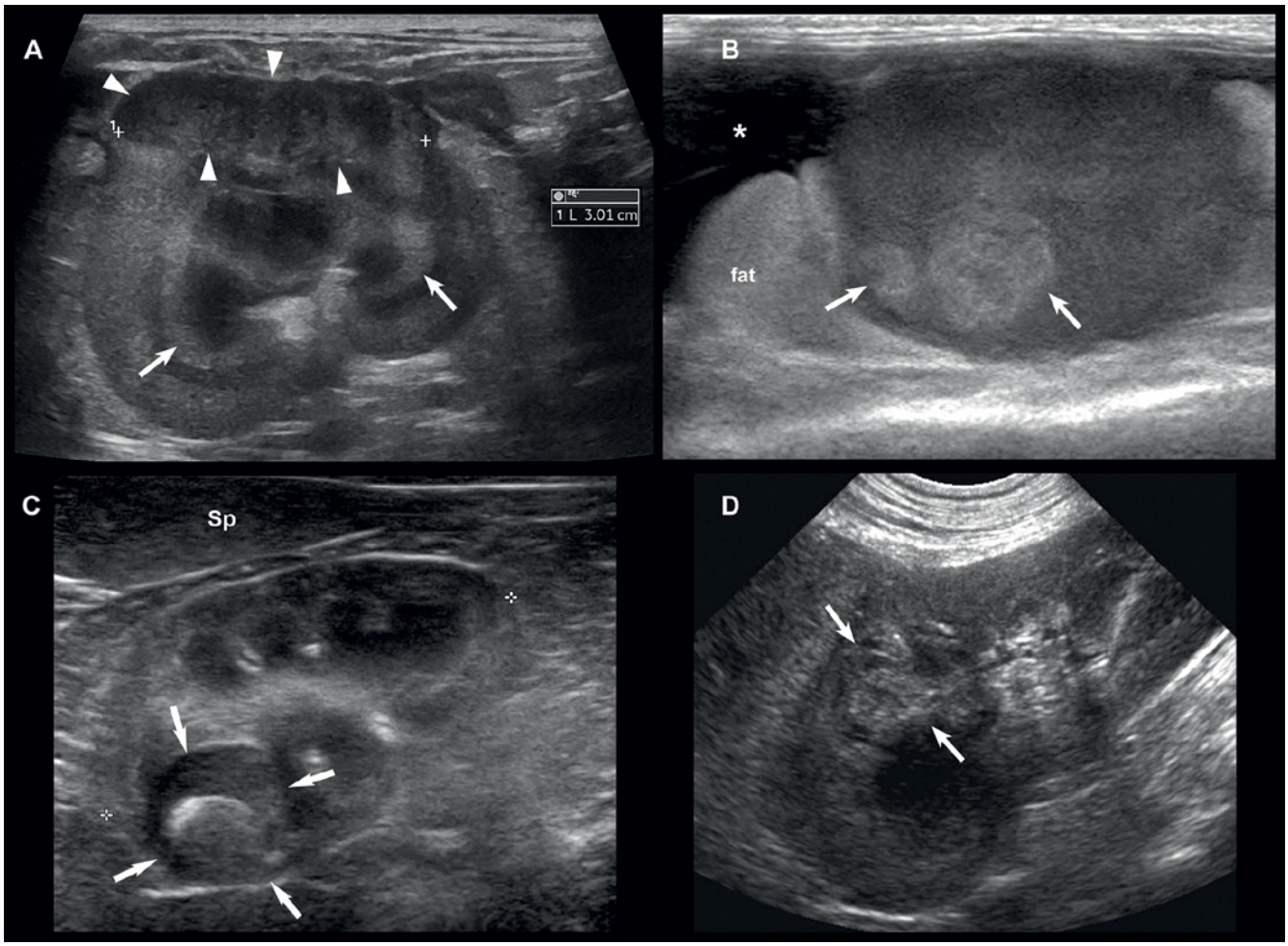


Figure 11.48. **Non-neoplastic nodules in two cats and two dogs. (A)** Longitudinal image of the left kidney of a 6-month-old Siamese kitten with infectious peritonitis (FIP). A 3-cm heterogeneous nodule (cursors) deforms the ventral portion of the kidney. Note the hyperechoic rim sign (arrows) in the medulla. **Pyogranulomatous nephritis** was diagnosed by fine-needle aspiration of the nodule. **(B)** Parasagittal image of the kidney of a 1-year-old cat with confirmed **FIP**. Several hyperechoic nodules are present in the cranial pole of the kidney. These lesions were only seen on the periphery of the kidney and did not disrupt most of the renal architecture. The cat had moderate abdominal effusion (*), hyperchoic fat and several enlarged abdominal lymph nodes. **(C)** Longitudinal sonogram of the left kidney of a 9-year-old Pekinese cross presented for vomiting and heart murmur. A 1.35-cm inhomogeneous nonvascularized nodular lesion is present in the cranial pole of the kidney. Fine-needle aspiration was performed, and only necrotic tissue was seen. Follow-up examinations (more than 6 months) showed partial regression of the lesion and a remodeled echogenicity (not shown). It was assumed that this lesion represented an **old hematoma or granuloma. (D)** An inhomogeneously hyperechoic, ill-defined nodule is present in the left kidney of a 10-year-old Australian Shepherd presented for chronic hematuria. The lesion was sampled (see dotted line for guidance) and was diagnosed as a **chronic hematoma**. It progressively regressed over time.

ureter, up to the level of the bladder. The identification of small uroliths can be limited by the presence of overlying gastrointestinal structures, such as the descending colon or by the lack of significant ureteral distension (Kyles et al. 2005) (Figures 11.58, 11.64). When combining radiography and ultrasonography, the sensitivity to detect urolithiasis in cats has been reported to reach 90% (Kyles et al. 2005).

Although transitional cell carcinomas infiltrating the bladder trigone and/or ureter are more commonly responsible for ureteral obstruction (Figure 11.82), especially in dogs, other processes such as lymphoma, retroperitoneal soft tissue sarcomas, abscesses, or granulomas, can also compress and/or infiltrate the ureter (Figure 11.66). **Ureteral fibroepithelial** polyps have also been reported in

Vet-ebooks.com

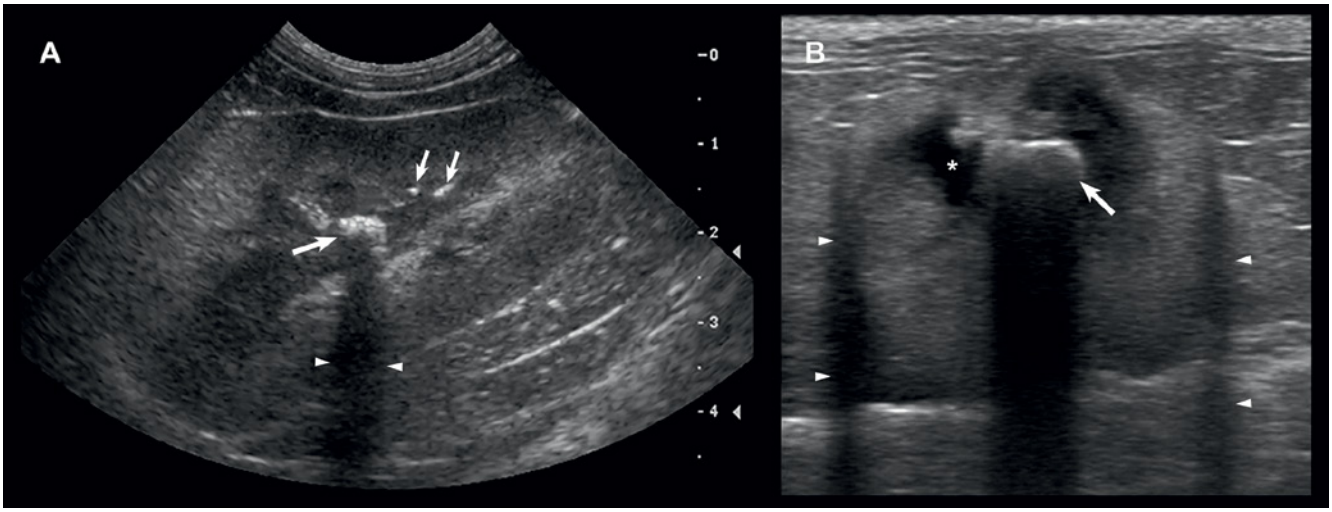


Figure 11.49. **Renal mineralization and nephroliths in one dog and one cat. (A)** Longitudinal image of the left kidney of a clinically normal dog. Several foci of mineralization (arrows) are in the region of the collecting system, the largest being associated with acoustic shadowing (arrowheads). These mineral foci may represent nephroliths and/or dystrophic mineralization. **(B)** In this 12-year-old azotemic cat, organized mineralization (arrow) associated with shadowing is present in the pelvis that is also mildly dilated (*). The small kidney has irregular contours and nearly lost cortico-medullary distinction. Notice the edge shadowing bordering the kidney (arrowheads). The cat had also ureteroliths and cystoliths (not shown).

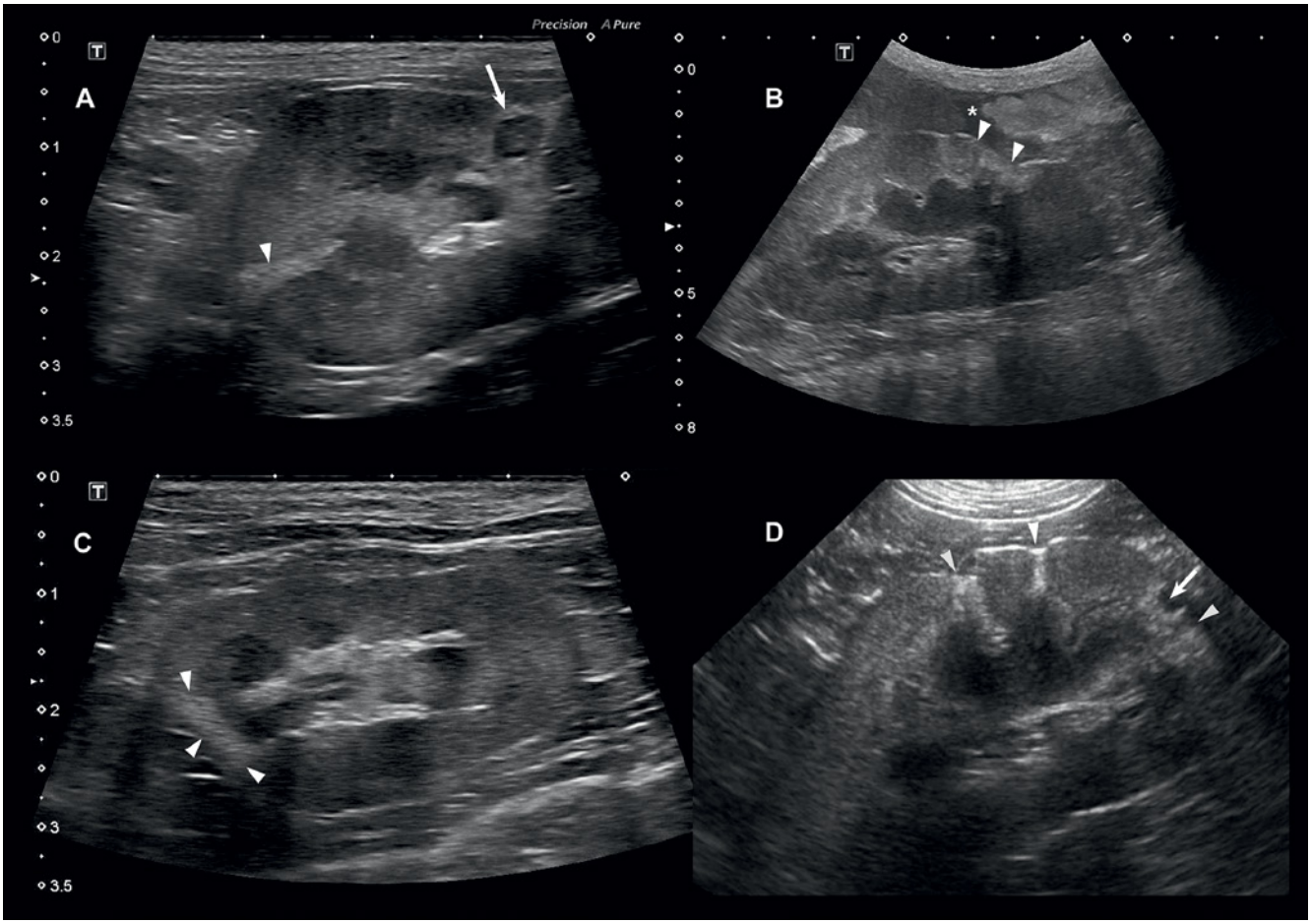


Figure 11.50. **Cortical infarction in two cats and two dogs. (A)** In this longitudinal sonographic image centered on the cranial pole of the left kidney of a cat with renal insufficiency, there is evidence of a triangular shaped hyperechoic focus in the cortex of the cranial pole (arrowhead), consistent with an infarct. A small cavitary focus was also present in the central portion of another infarct (arrow), for which fine-needle aspiration revealed necrotic tissue without inflammation. **(B)** In this dog with hemoabdomen(*), hyperechoc depressions (arrowheads) indicating chronic infraction are present at the caudal margin of the left renal cortex. **(C)** In this 8-year-old cat with normal renal function, the hyperechoic region representing an infarction results in flattening (arrowheads) of the cranial pole of the kidney. **(D)** Extensive embolic infarction in a 11-year-old Labrador presented for lethargy and thrombocytopenia. Hyperechoic, triangular areas associated with cortical indentation are present (arrowheads) some of which with a hypoechoic focus (arrow) consistent with septic embolism.

Vet-ebooks.com

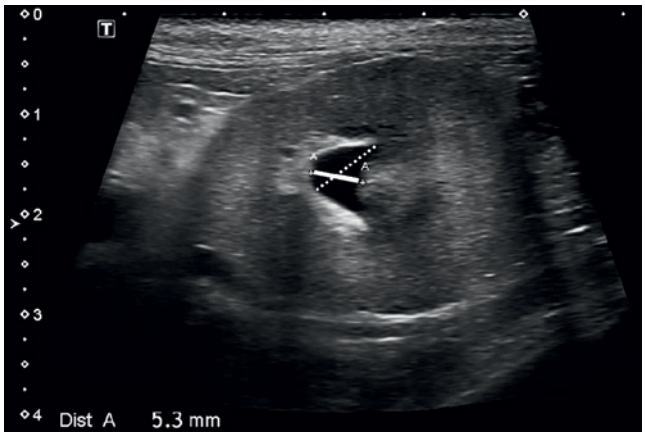


Figure 11.51. Renal pelvis measurement. The renal pelvis can be more accurately detected and measured in transverse plane, ensuring that the height of the pelvis is measured perpendicularly (along full line). Measurements obtained in longitudinal plane may overestimate its size, depending on the angle of the transducer relative to the kidney (as illustrated with the white dotted line).

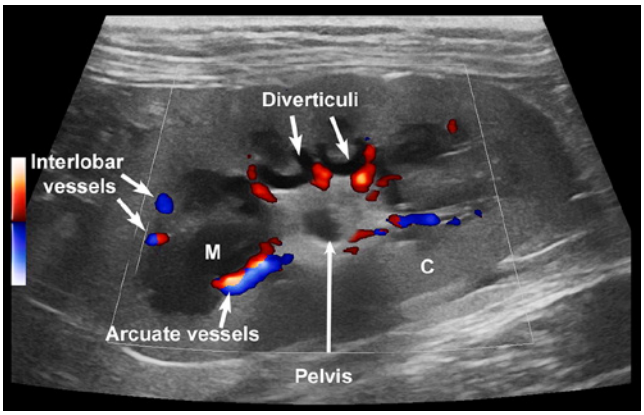


Figure 11.52. Dilated diverticuli and pelvis in a dog with ureteral obstruction. Longitudinal sonographic image of the left kidney on which the pelvis is mildly dilated, as well as the diverticuli that appear distinct from the arcuate and interlobar vessels on power Doppler.

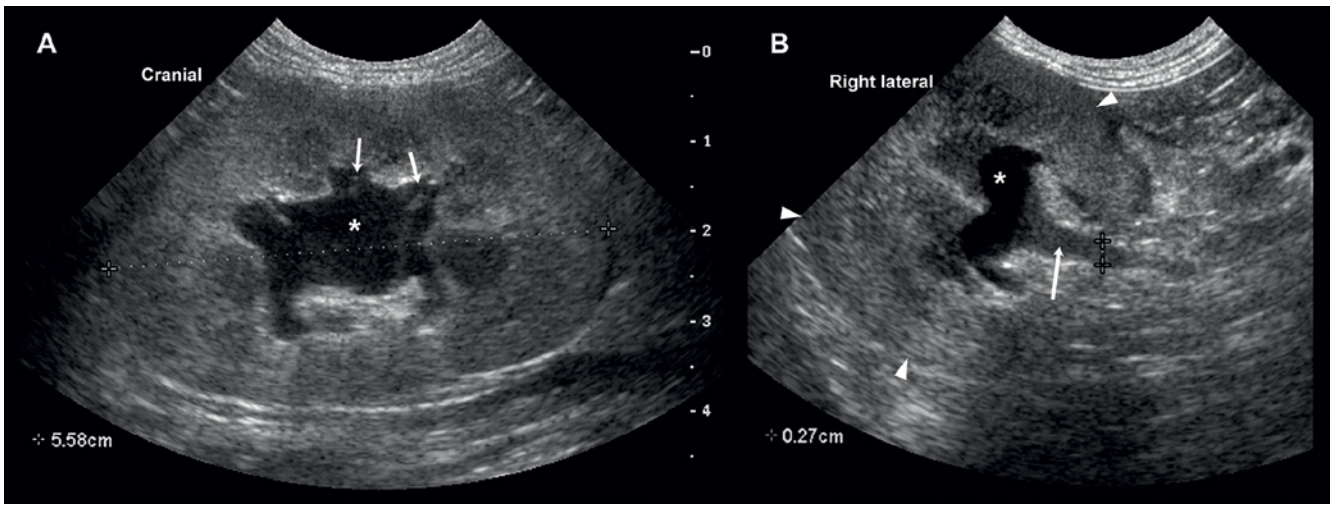


Figure 11.53. Dilated pelvis and ureter in a dog with pyelonephritis. Longitudinal **(A)** and transverse **(B)** ultrasonographic images of the right kidney of a small-breed dog with acute renal failure and abdominal pain. The kidney (arrowheads) is enlarged (between calipers) and hyperechoic, and the corticomedullary distinction is attenuated. The renal pelvis (*) and diverticuli (short arrows) are moderately dilated. The proximal ureter is also mildly dilated and contains highly echogenic urine (long arrow), consistent with pus. These signs were caused by ascending urinary infection that probably resulted in some level of obstruction sign the size of the pelvis. Note the sharp, oblique line of cellular sediment in the pelvis on the transverse view, which was parallel to the exam table.

dogs as intraluminal, pedunculated masses causing ureteral obstruction and hydronephrosis (Reichle et al. 2003) (Figure 11.67).

Ureteral obstruction can also be caused by a blood clot or an inflammatory stricture (responsible for 25–30% of benign feline ureteral obstructions), which can be more challenging to diagnose and differentiate. On rare occasions, the obstruction is associated with ureteral tear/rupture that is associated with retroperitoneal effusion. In such cases, other imaging tests, such as excretory urography, ultrasound-guided pyelography (Etadali et al. 2018) which can be combined with computed tomography, might be required in patients in which a definitive diagnosis and location of the leak cannot be made by using ultrasonography alone (Figure 11.68).

Vet-ebooks.com

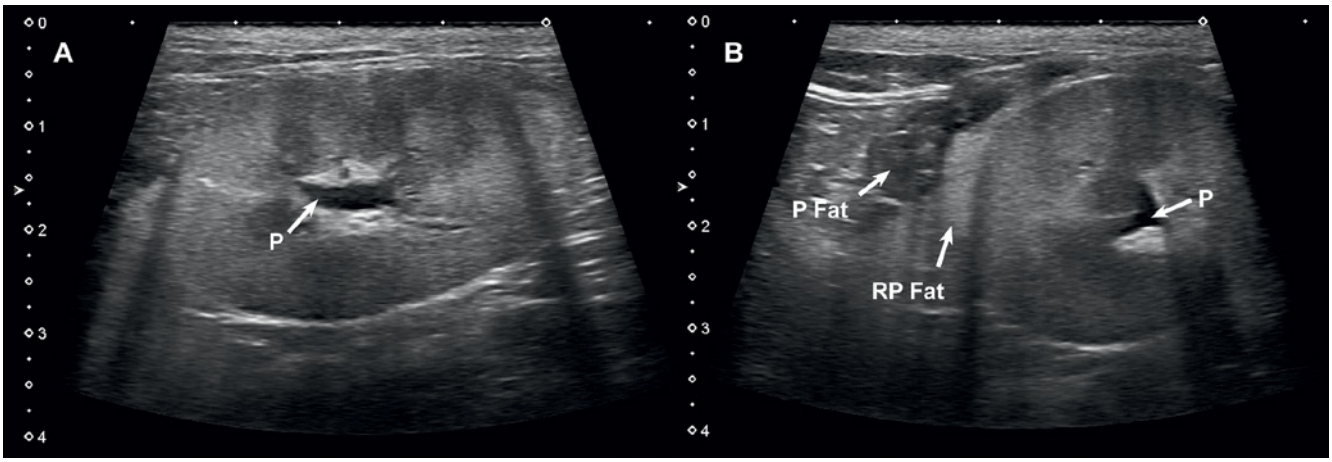


Figure 11.54. **Acute pyelonephritis in a cat.** Longitudinal **(A)** and transverse **(B)** sonographic images of the right kidney of a domestic short hair cat with acute renal failure and abdominal pain. The renal pelvis (P) is mildly dilated (2 mm in height) and the retroperitoneal (RP) fat is hyperechoic when compared to the adjacent peritoneal (P) fat.

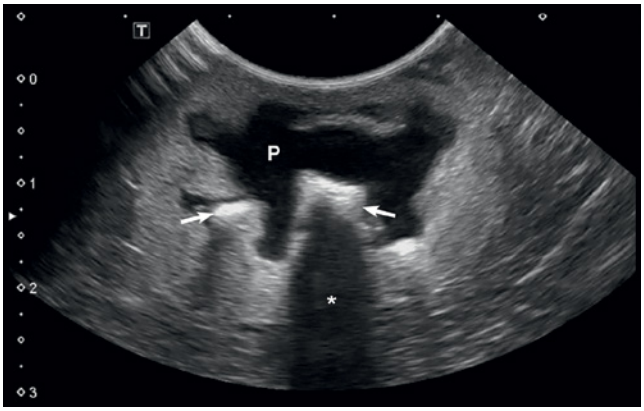


Figure 11.55. **Chronic pyelonephritis and nephroliths in a cat.** Longitudinal image of the left kidney of a cat with renal failure and abdominal pain. The kidney is hyperechoic and irregular, and its pelvis (P) and diverticuli are distended. Irregular hyperechoic and hyperattenuating foci (arrow), associated with acoustic shadowing (*) are in the center of the pelvis, consistent with small nephroliths. The corticomedullary junction is indistinct. These signs are caused by chronic pyelonephritis in association with urolithiasis.

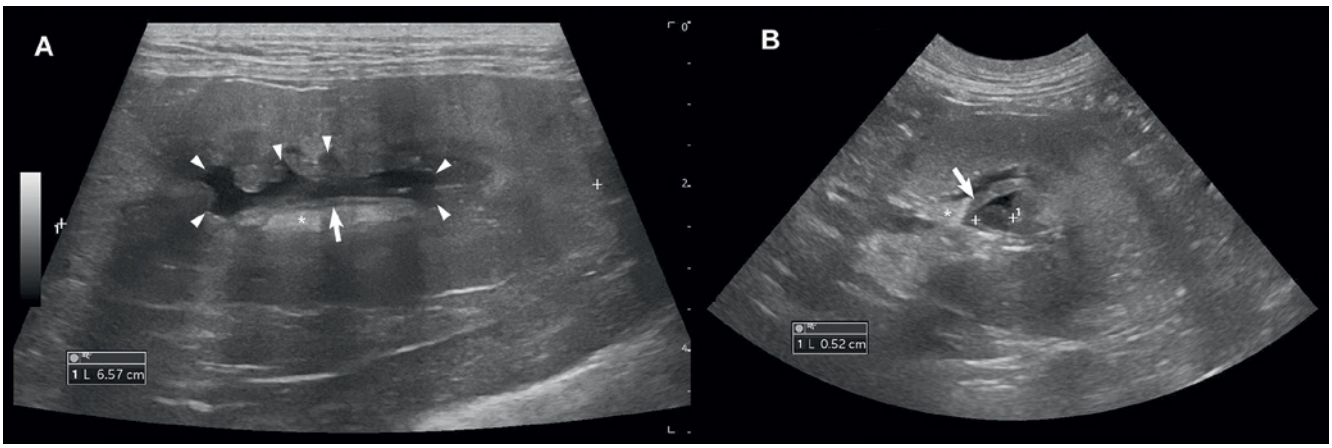


Figure 11.56. **Chronic pyelonephritis in a 12-year-old English springer.** Longitudinal **(A)** and transverse **(B)** image of the left kidney that is irregular, heterogeneous and mildly hyperechoic, with poor corticomedullary distinction. The renal pelvis is irregularly dilated (arrowheads in **A** and between calipers in **B**) and contains echogenic material consistent with inflammatory debris. Its wall is also thickened (arrow). The renal fat sinus is hyperechoic (*).

Vet-ebooks.com

Table 11.1
Differential diagnosis of pyelectasia and hydronephrosis in small animals

Pyelectasia
Intravenous fluid therapy
Diuretic therapy
Increased diuresis caused by chronic renal disease or other condition
Pyelonephritis and ureteritis
Distended bladder
Ectopic ureter or another congenital malformation
Hydronephrosis
Pelvic or ureteral obstruction caused by calculus, infiltrative mass at bladder trigone, ureter or renal pelvis, stricture, cellular debris (e.g., blood clot), or retroperitoneal mass
Lower urinary-tract obstruction
Congenital malformation

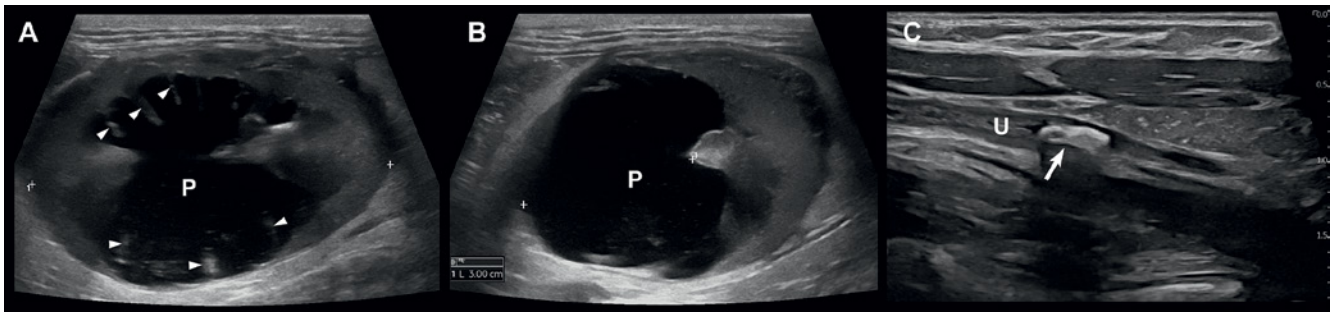


Figure 11.57. **Obstructive hydronephrosis in a cat.** Longitudinal **(A)** and transverse **(B)** images of the left kidney in a cat with ureteral obstruction caused by a ureterolith (arrow, in **C**). The distended pelvis (P, and between calipers) and diverticuli are rounded and partially separated by septa (arrowheads) that contain interlobar arteries and veins. The ureteral (U) walls are thickened but there is no dilatation cranial to the urolith.

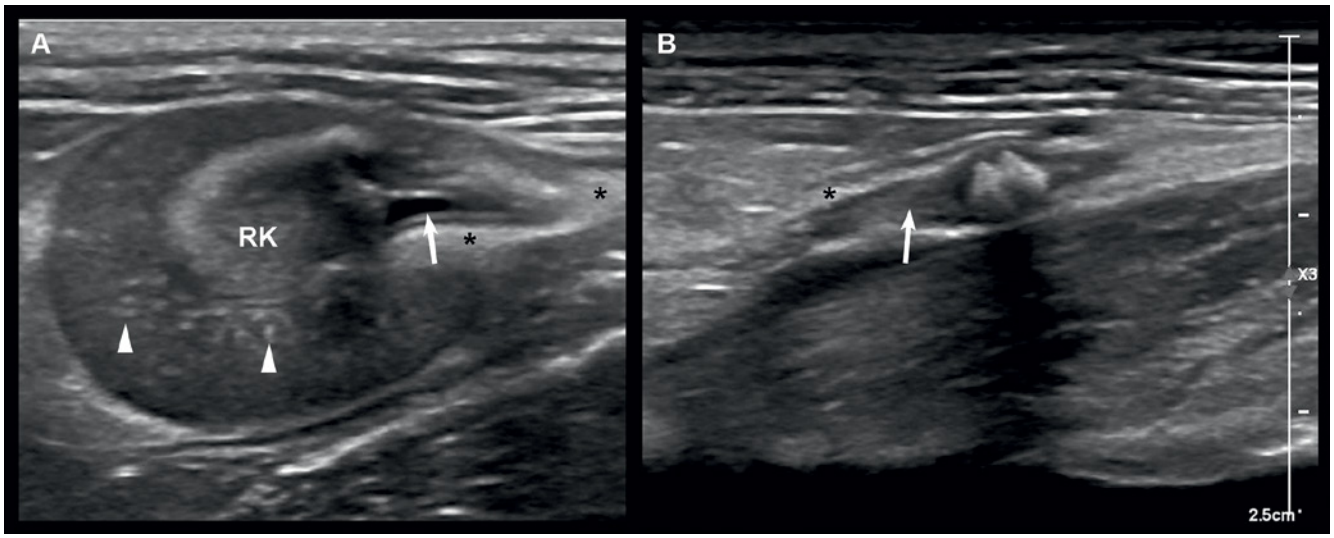


Figure 11.58. **Uroliths with scant pyelectasia in a cat. (A)** Transverse image obtained at the level of the right renal hilus of a cat with discomfort. Notice the numerous hyperechoic foci (arrowhead) dispersed in the cortex and medulla, nephrocalcinosis was noted bilaterally. **(B)** A spiculated hyperechoic focus is present in the thickened right ureter (arrow). The peripheral fat is hyperechoic (*), suggesting ureteritis. There is no evidence of complete ureteral outflow obstruction.

Vet-ebooks.com

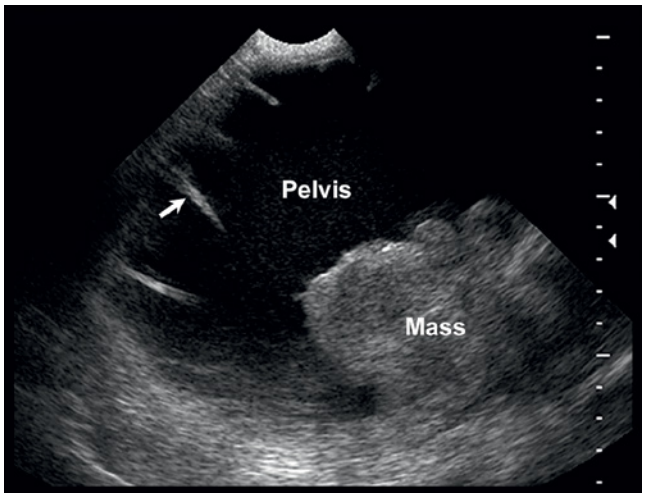


Figure 11.59. Severe hydronephrosis. Longitudinal image of the left kidney in a dog with severe renomegaly detected on radiographs. The kidney appears as a fluid-filled cavity with peripheral hyperechoic bands consistent with interdiverticular septa (arrow). A large, irregular, hyperechoic mass at the level of the renal hilus is invading the renal pelvis and ureter and causing the hydronephrosis. Surgical resection confirmed the presence of a **soft-tissue sarcoma**.

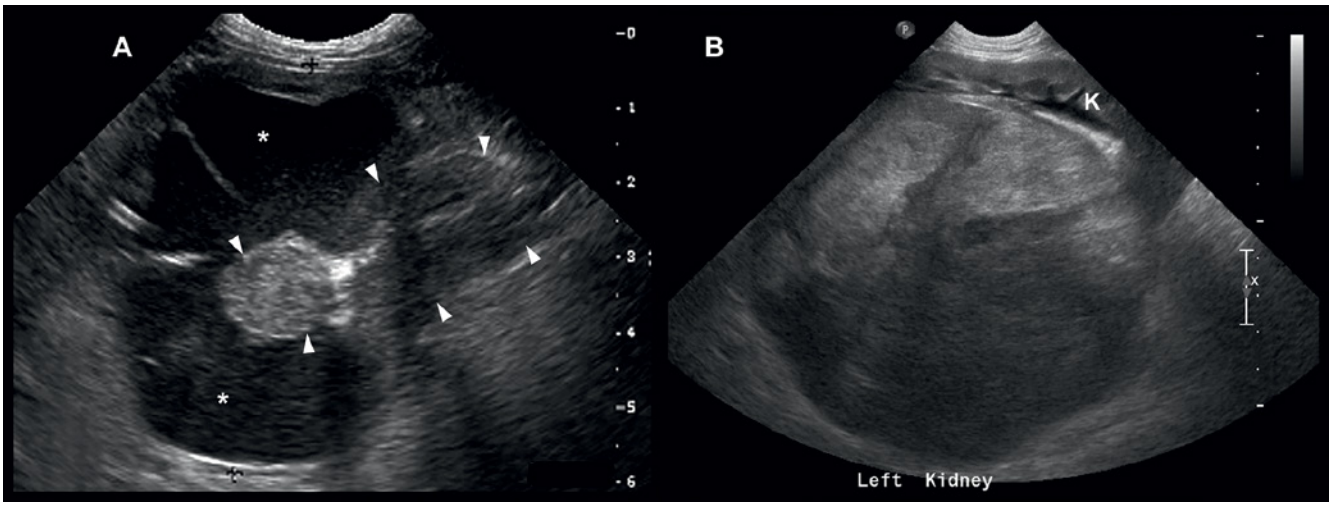


Figure 11.60. Renal hemangiosarcoma in two dogs. (A) The mass (arrowheads) is centered on the pelvis and is responsible for the severe hydronephrosis affecting the right kidney of an elderly dog. The renal diverticula are markedly dilated (*) and contain echogenic fluid, particularly in the dependent portion, consistent with hemorrhage. **(B)** In contrast, this large, inhomogeneously echogenic mass that is distorting the renal architecture of the left kidney (K) of a 13-year-old Hound cross appears solid.

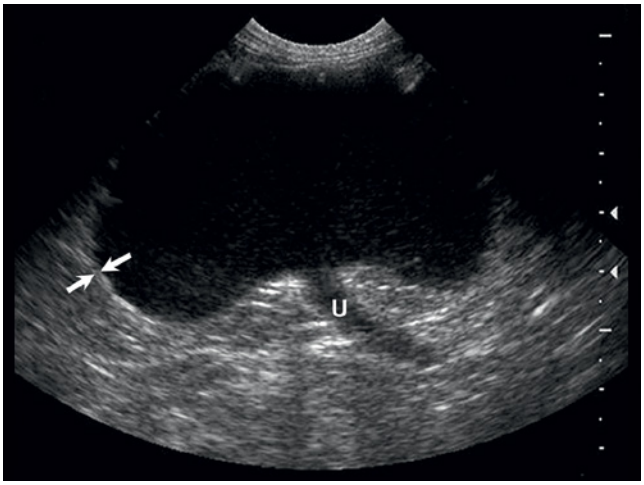


Figure 11.61. Severe hydronephrosis. Longitudinal image of the left kidney in a cat with severe renomegaly. The kidney is completely replaced by nearly anechoic fluid, with a rim of parenchyma remaining that is only a few millimeters thick (arrows). Hydroureter is also identified (U). Inadvertent ligation of the distal ureter, secondary to a recent ovariohysterectomy, was identified during exploratory surgery.

Vet-ebooks.com

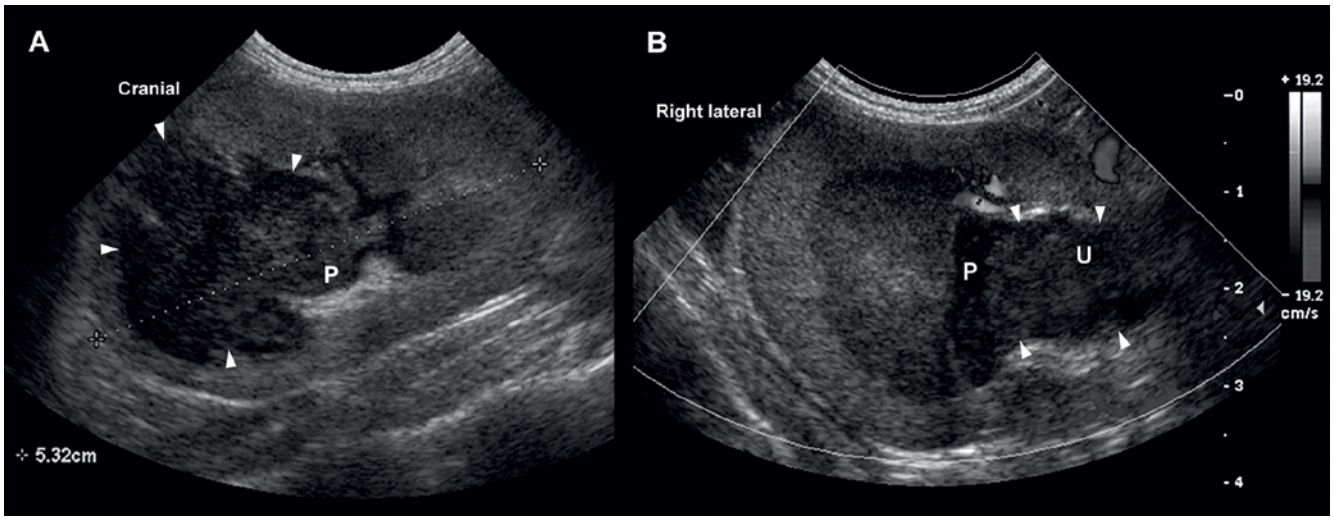


Figure 11.62. **Pyonephrosis and ureteral abscess.** Longitudinal **(A)** and transverse **(B)** images of the right kidney of a dog with fever and abdominal pain. The renal pelvis (P) and diverticuli are asymmetrically dilated in the cranial pole of the kidney (arrows). The proximal portion of the ureter (U) is also distended. These portions of the collecting system contain echogenic material diagnosed as pus by means of ultrasound-guided pyelocentesis.

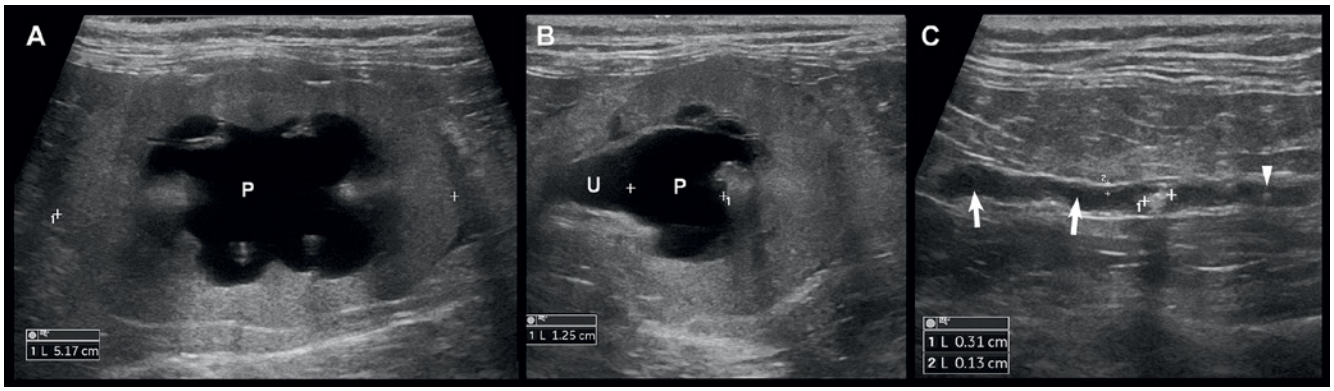


Figure 11.63. **Obstructive ureterolith in a cat with hydronephrosis.** Longitudinal **(A)** and transverse **(B)** images of the left kidney of a 7-year-old domestic short hair cat with acute vomiting and anorexia. The kidney is enlarged (5.1 cm in length) and mildly hyperechoic and heterogeneous with reduced corticomedullary distinction. The renal pelvis (P) is markedly dilated, measuring nearly 1.3 cm in height in transverse plane, excluding the proximal ureter (U) that is also dilated. (**C**). An irregular 3.1-mm hyperechoic structure is found in the mid ureter that is moderately dilated (arrows, up to 3.1 mm) and a thickened and irregular wall (1.3 mm). An acoustic shadow is seen deep to the obstructive urolith. A smaller hyperechoic focus is seen more distally (arrowhead).

Disorders of the Perinephric Retroperitoneal Space

Several types of fluid can accumulate in the retroperitoneal space at the periphery of one or both kidneys. Acute kidney injury caused by nephrotoxicity, leptospirosis, or interstitial nephritis predisposes to bilateral perirenal effusion, whereas unilateral effusion may be more indicative of pelvic or ureteral obstruction or rupture (Holloway and O'Brien 2007). Retroperitoneal transudate appears as linear or triangular to oval-shaped, anechoic to hypoechoic foci at the periphery of the renal cortex. It may also present a "marble-like" pattern due to alternating bands of retroperitoneal fat and fluid pockets (Figures 11.69, 11.70).

Vet-ebooks.com

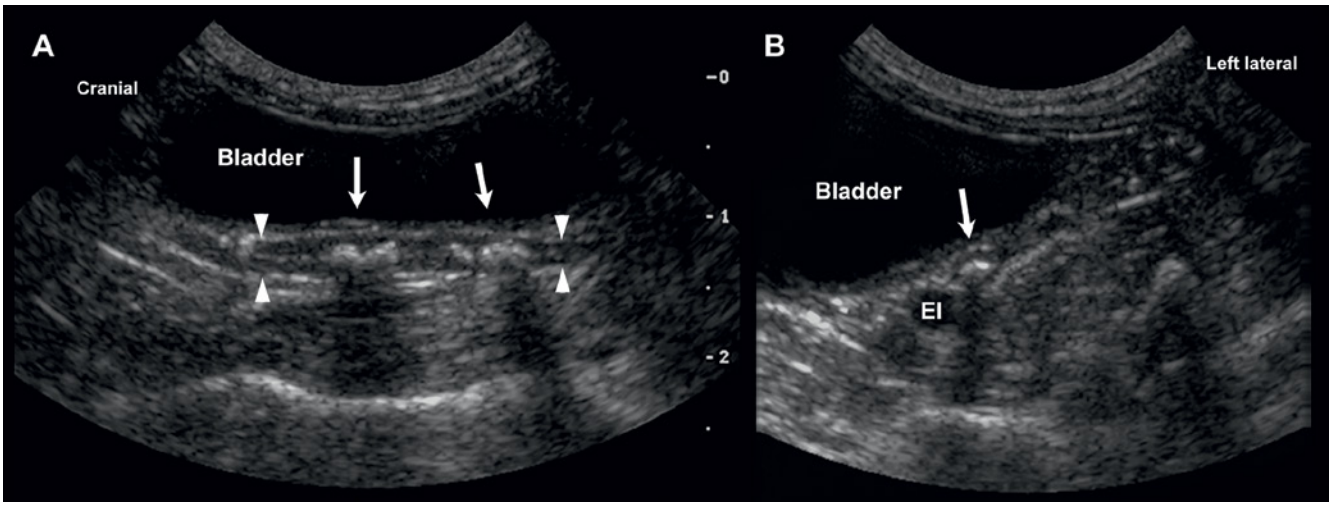


Figure 11.64. **Nonobstructive uroliths in a cat.** Longitudinal **(A)** and transverse **(B)** images of the distal right ureter of a cat with a chronic history of urolithiasis. Several hyperechoic foci (arrows) are found in the ureter (arrowheads) of this cat without evidence of hydroureter or hydronephrosis. Acoustic shadows are noted in the far field. Some of these calculi were eventually found in the bladder. The ureteral wall is mildly thickened due to edema and/or inflammation. EI, external iliac vessel.

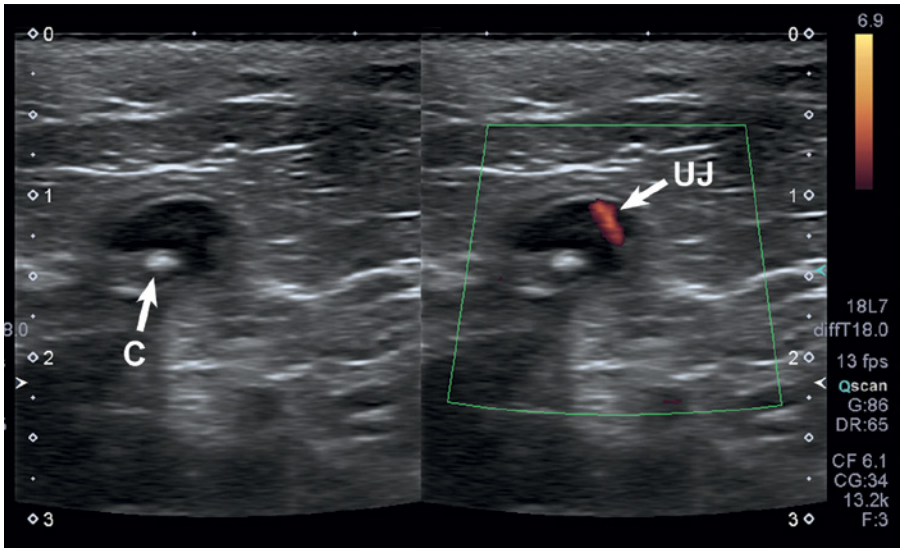


Figure 11.65. **Urolith in distal ureter.** Transverse B-Mode **(left)** and power Doppler **(right)** sonographic images obtained at the bladder trigone of a cat with right-sided hydronephrosis. A hyperechoic structure consistent with a calculus (C) is lodged in the distal portion of the right ureter. Urine jet (UJ) is only visible from the left ureter.

These changes can also be found with the accumulation of urine or blood, usually following trauma to the kidney and/or ureter, or from spontaneous ureteral rupture due to severe infection of the collecting system (Figures 11.70, 11.71). Although the effusion can be confirmed and characterized with ultrasonography and fine-needle aspiration, the rupture cannot be easily localized and usually requires other imaging tools, such as excretory urography or ultrasound-guided pyelography (Specchi et al. 2012).

Retroperitoneal inflammatory processes result in hyperechoic and hyperattenuating fat. These changes are common with acute pyelonephritis and ureteritis, and renal abscess (Figures 11.41, 11.54). Exudates and acute hemorrhage tend to be more echogenic because of their higher cell count.

Perinephric pseudocysts, which have been more commonly reported in cats, appear as an accumulation of fluid, usually anechoic, around one or both kidneys, and most commonly between the capsule and the renal

Vet-ebooks.com

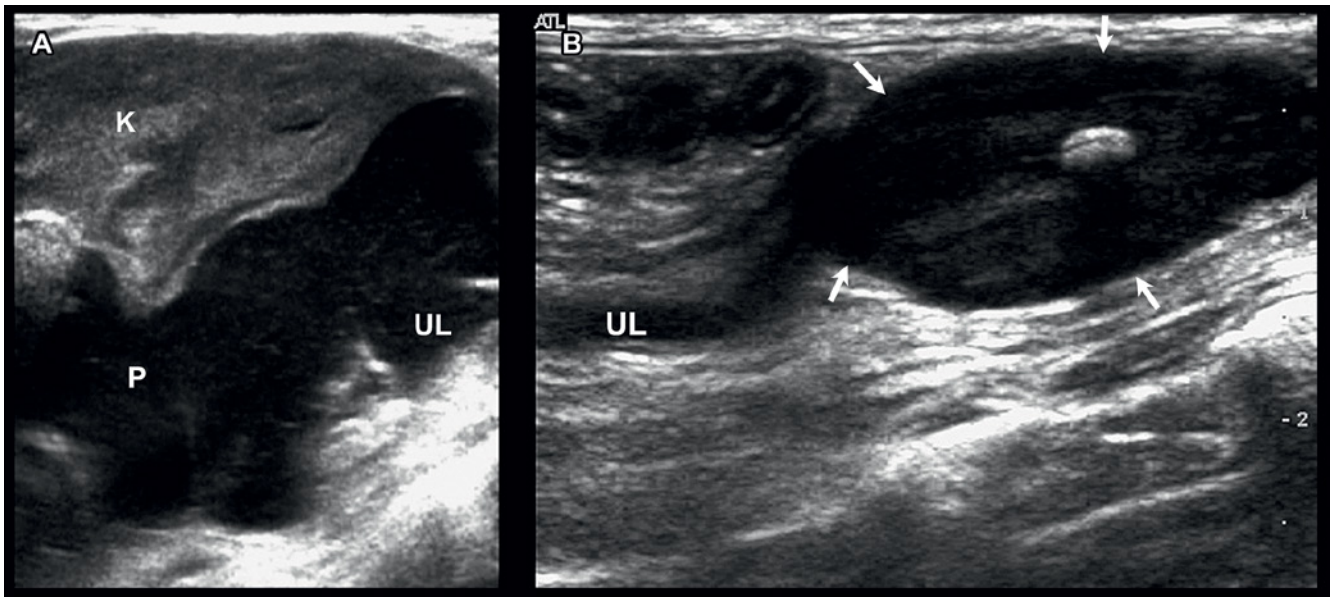


Figure 11.66. Infiltrative ureteral lymphoma in a cat. Longitudinal images obtained at the level of the right kidney **(A)** and mid-right ureter **(B)** in a cat. The kidney (K) is deformed, and the corticomedullary distinction is significantly reduced. The renal pelvis (P) and proximal ureter (UL) are dilated. An oval, hypoechoic, uniform mass (arrows) is found at the level of the right ureter. The ureteral lumen (UL) is dilated cranially. A 3-mm hyperechoic structure in the center of this mass is associated with partial acoustic shadowing and consistent with a concurrent urolith, obstructed at the level of by the infiltrative mass. Histopathology revealed the presence of an unusual lymphoma infiltrating the kidney and ureter.

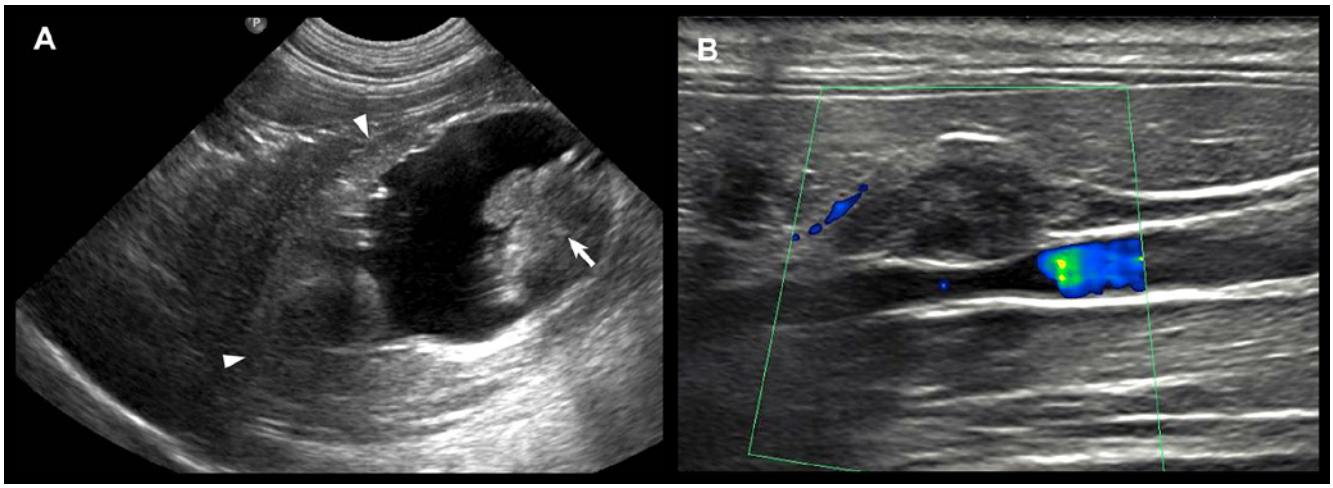


Figure 11.67. Fibroepithelial polyp in a dog and in a cat. (A) Longitudinal image of the right kidney of a 10-year-old Scottish terrier presented for vomiting (jejunal obstruction). The right kidney (arrowheads) is deformed by a lobulated mass (arrow) associated with marked pelvic dilation. The right kidney was surgically removed and diagnosed as fibroepithelial polyp with hydronephrosis. **(B)** In an 1.5-year-old castrated male Ragdoll cat presented for chronic hematuria (10 months duration), a non-obstructive inhomogeneous hypoechoic nodule is present along the left ureter, which is mildly distorted. The histopathological diagnosis was focal intramural nodularity with fibrosis, reduplication/hyperplasia/dilation of transitional mucosal epithelium.

cortex (Beck et al. 2000; Ochoa et al. 1999) (Figure 11.72). These pseudocysts typically encircle the kidneys, although they can be focal (Miles and Jergens 1992). According to a report on 26 cats, subcapsular perirenal pseudocysts are formed by accumulation of a transudate between the capsule and parenchyma of the kidney, because of underlying parenchymal disease, and may contribute to abdominal discomfort (Beck et al. 2000). Urine may also be contained in these pseudocysts (Ochoa et al. 1999).

Vet-ebooks.com

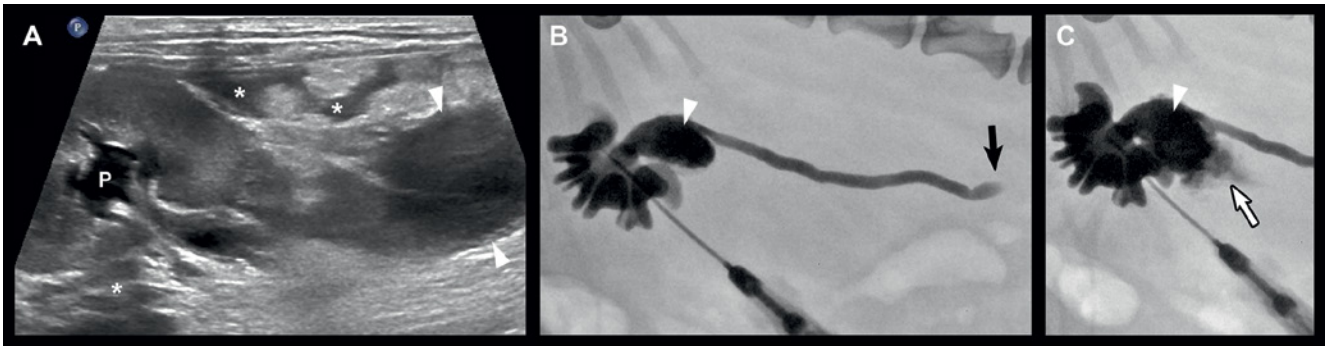


Figure 11.68. **Ureteral rupture in a 5-year-old Shih Tsu. (A)** There is evidence of pyelectasia (P), and a focal, ampullar dilation (arrowheads) of the proximal ureter is also noted. Moderate retroperitoneal effusion is present (*), and the retroperitoneal fat is hyperechoic. (**B-C**) A radiographic contrast study was performed by placing the catheter directly into the renal pelvis, confirming the focal proximal diverticulum (arrowhead) and progressive leakage (white arrow) as best seen in (**C).** Note: A distal ureteral stricture (black arrow) was seen on contrast study and was not detected on ultrasound.

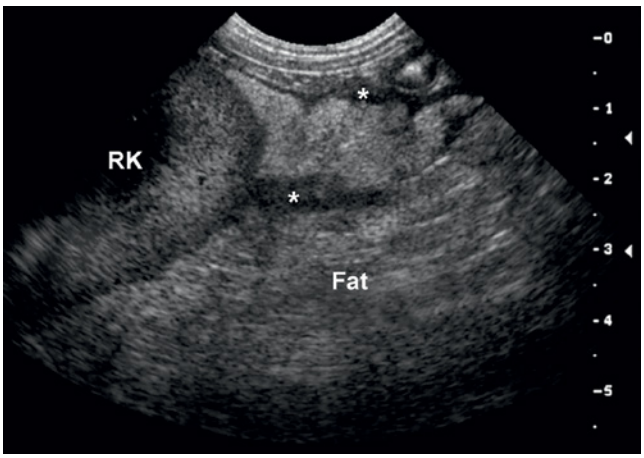


Figure 11.69. **Retroperitoneal effusion.** Longitudinal image obtained in the region just caudal to the right kidney (RK) of a dog with acute renal insufficiency caused by leptospirosis. Irregular linear hypoechoic regions (*) are within the retroperitoneal space, caudal to the renal cortex, consistent with transudation. The fat appears hyperechoic, which was attributed to edema and/or steatitis.

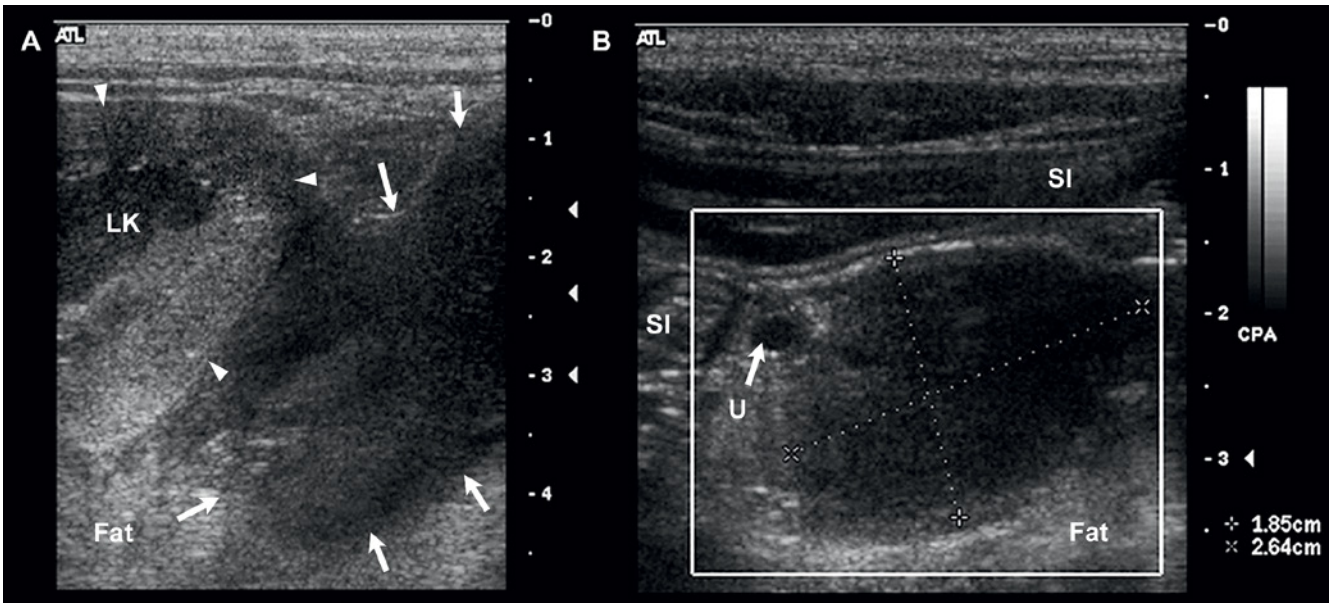


Figure 11.70. **Ureteral rupture, retroperitoneal urinoma, and abscess.** Longitudinal **(A)** and transverse **(B)** ultrasound images obtained with a linear transducer at the caudal aspect of the left kidney (LK, arrowheads). A poorly defined accumulation of hypoechoic fluid (arrows) is in the retroperitoneal space, caudal to the kidney **(A)** and lateral to the left ureter (U) **(B)**. The retroperitoneal fat is hyperechoic. In **(B)**, power Doppler is used to differentiate the mildly dilated ureter from an abdominal vessel. The peri-ureteral fluid collection was sampled with ultrasound guidance, and urine and pus were identified. SI, small intestine.

Vet-ebooks.com

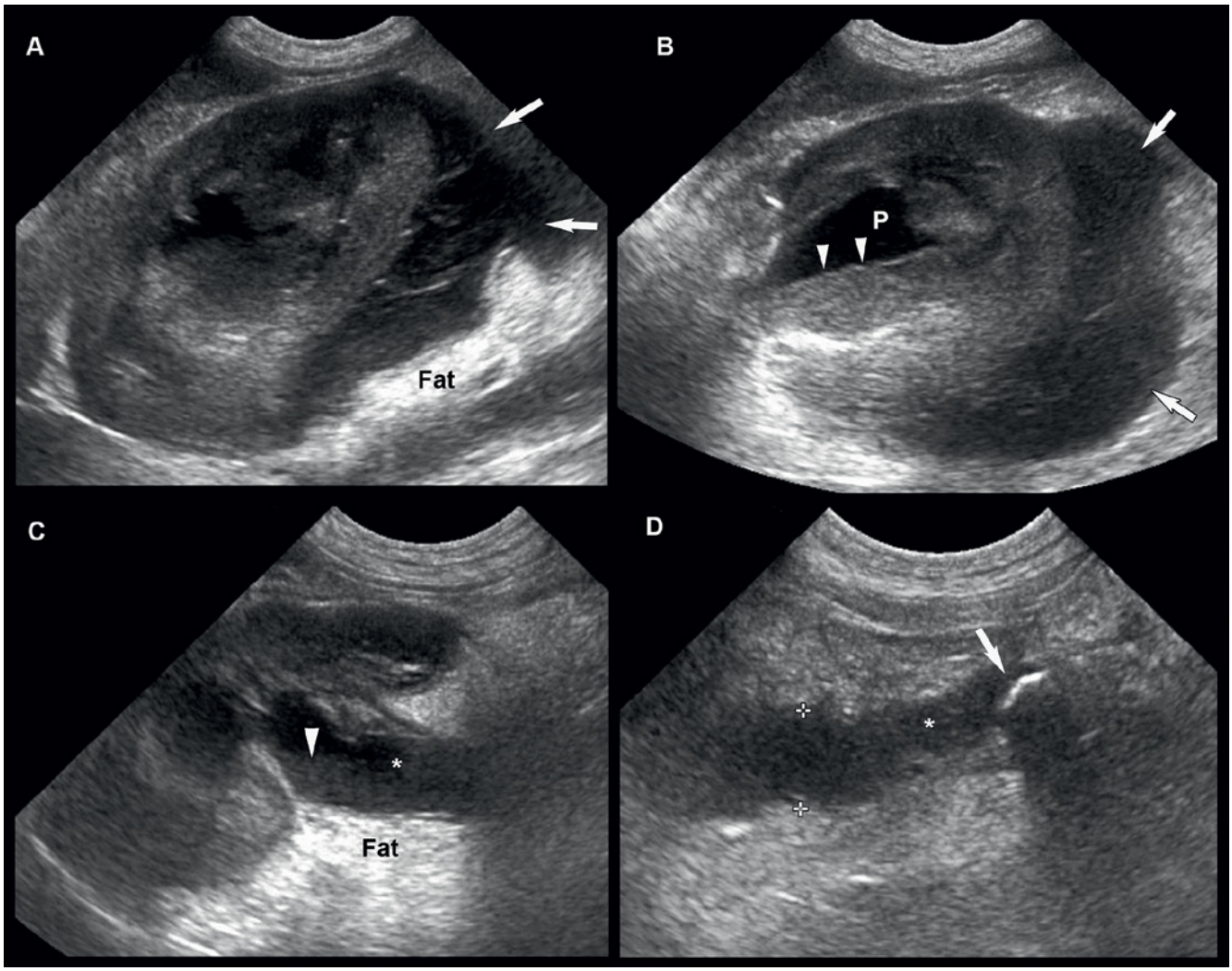


Figure 11.71. **Ureteral calculi and rupture in a 11-year-old Lhapso/poodle mix. (A)** Faintly striated fluid is noted in the subcapsular space of the left kidney (arrows), which was confirmed to be a subcapsular hematoma at surgery. The adjacent fat is hyperechoic. **(B)**, the kidney presents a distended pelvis (P) with settled echogenic sediment (arrowheads). Subcapsular and retroperitoneal fluid (arrows) is present and the fat is hyperechoic. **(C)** At the hilus of the kidney, the dilated pelvis and proximal ureter (*) contain echogenic urine (pus-arrowhead). Image **(D)** was obtained along the proximal dilated ureter (between cursors, and *) and one of the two obstructing calculi (arrows) is seen associated with acoustic shadowing.

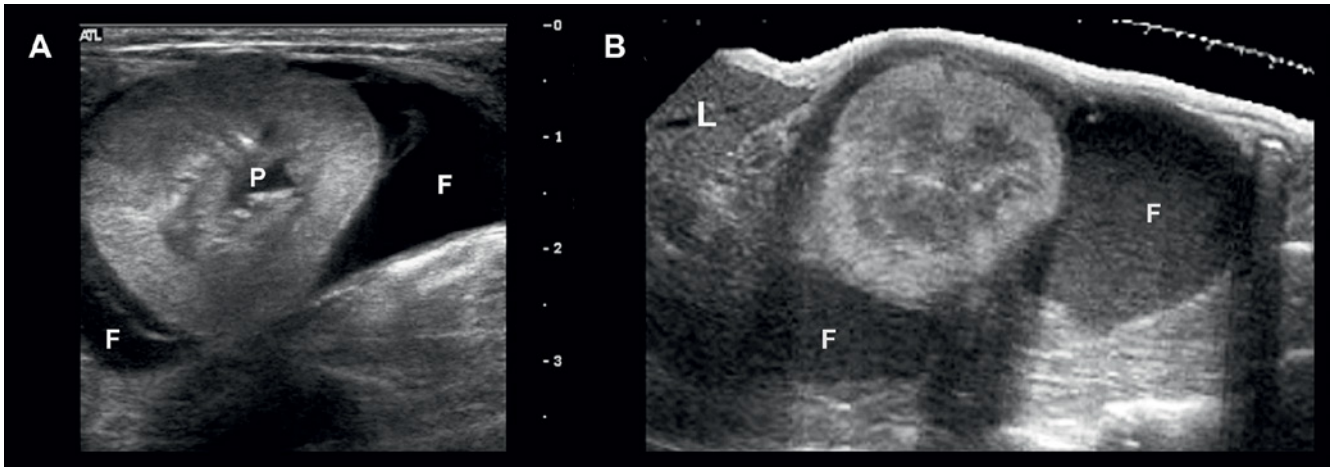


Figure 11.72. **Perinephric pseudocyst associated with different types of renal disease in two cats. (A) Chronic interstitial nephritis**. Longitudinal image of the left kidney (LK) of a cat with chronic renal insufficiency. The kidney is small (2.54 cm), deformed, irregular, and diffusely hyperechoic because of chronic interstitial nephritis. The kidney is contained in a large anechoic fluid-filled cavity (F), consistent with a perinephric pseudocyst. **(B) Diffuse squamous cell carcinoma in another cat.** Panoramic longitudinal view of the right kidney showing the subcapsular echogenic fluid distention (F). The kidney was distorted and hyperechoic.

Vet-ebooks.com

Urinomas, described as an encapsulated accumulation of urine caused by traumatic extravasation (Figure 11.70), can mimic the appearance of pseudocysts. Fine-needle aspiration can be helpful in confirming the nature of the perirenal fluid and temporarily decreasing the volume. However, this procedure often is palliative and subtotal capsulectomy might be necessary (McCord et al. 2008).

Ultrasonographic Features of Bladder and Urethral Disorders

Cystitis

Cystitis most commonly causes extensive irregular thickening of the UB wall. This thickening is usually greatest at the cranioventral aspect of the UB (Figure 11.73). Etiologies are typically inflammatory or bacterial. The thickened hypoechoic/hyperechoic or layered bladder wall can be associated with other findings, such as pus, calculi, necrotic debris, mucus, and/or blood clots. Less common infectious causes of cystitis with similar or worsened ultrasound features include parasite infestation and fungal infection. **Granulomatous fungal cystitis** (*Histoplasma capsulatum)* has been reported in one cat to cause marked diffuse uniformly hyperechoic UB wall thickening (Taylor et al. 2012). Fungal pyogranulomatous cystitis and ureteritis (*Scedosporium apiospermum*) has been reported in dogs in combination with a regional peritonitis (Kockenburger et al. 2019; Tsoi et al. 2021). Other fungal agents such as candida and Aspergillus can also be encountered, especially in immune compromised animals. Multiple small hyperechoic, nonshadowing fungal balls have been reported as the consequence of a *Candida albicans* cystitis (Choo et al. 2021).

Pseudomembranous cystitis in dogs and cats is associated with severe diffuse ulceration, necrosis, and hemorrhage of the bladder wall as well as intraluminal necrotic, fibrinous, and hemorrhagic tags and debris. These detached tags and debris can predispose to UB outflow obstruction. The ultrasound features include UB wall thickening as well as multiple hyperechoic luminal septations, they have been described in both cats and dogs (Le Bodec et al. 2011; Puccinelli et al. 2021) (Figure 11.74). At times, mineralization is present along the wall and/or the pseudomembranes (Labelle. et al. 2023)

Encrusting cystitis is characterized by deposits of mineralized precipitates on or within the bladder mucosa, often resulting from a chronic infection by urease-producing bacteria. (Briscoe et al. 2010) (Figure 11.75).

Emphysematous cystitis is characterized by gas-forming bacteria such as *Escherichia coli*, *Aerobacter aerogenes*, *Proteus mirabilis*, and *Clostridium* sp. within the bladder wall and is seen commonly in diabetic animals with glucosuria. The sonographic appearance is multifocal irregular hyperechoic interfaces with distal reverberation artifact (Petite et al. 2006) (Figure 11.76). The main features reported are either diffuse or focal wall thickening, polyps with the presence of gas within the wall and/or the lumen (Lippi et al. 2019). By using alternative patient positions, free luminal gas (often seen in catheterized patients) can be distinguished from emphysematous cystitis. The free luminal gas will move with patient position, whereas the bladder wall gas will remain in the same location.

Polypoid cystitis is an uncommon form of cystitis reported in dogs. It can present as a hyperechoic polypoid to pedunculated mass or masses projecting into the lumen as well as diffuse bladder wall thickening in some cases (Martinez et al. 2003) (Figure 11.77). These masses occur most commonly in the cranioventral aspect of the UB (Martinez et al. 2003). Polypoid cystitis with mass-like mucosal proliferations and severe diffuse bladder wall thickening from severe suppurative or granulomatous cystitis can overlap the ultrasound features associated with neoplasia, and suction or cystoscopic biopsies are recommended in these cases. Malignant transformation of polypoid cystitis to transitional cell carcinoma has also been reported further supporting careful monitoring of these lesions (Butty et al. 2021)

Follicular cystitis is uncommon and has been reported in dogs with recurrent lower urinary tract disorders. There is limited report of its sonographic appearance (Sul et al. 2014; Viitanen et al. 2023). We encountered some cases with several tiny blisters seen along the mucosal surface of the bladder wall; these blisters were confirmed on cystoscopy (Figure 11.78).

Bladder wall inversion is a rare condition that is speculated to be associated with cystitis in dogs and cats. It has ultrasound features of an apical mass-like tissue thickening with the folded bladder wall protruding into the lumen. The inversion results in an indented apical serosal margin of the bladder. The thickened and inverted bladder wall has preserved wall layering resulting in characteristic multiple hyperechoic and hypoechoic interfaces (Adin et al. 2011) (Figure 11.79). This condition may also be encountered as a temporary event after long-term catheter placement.

Vet-ebooks.com

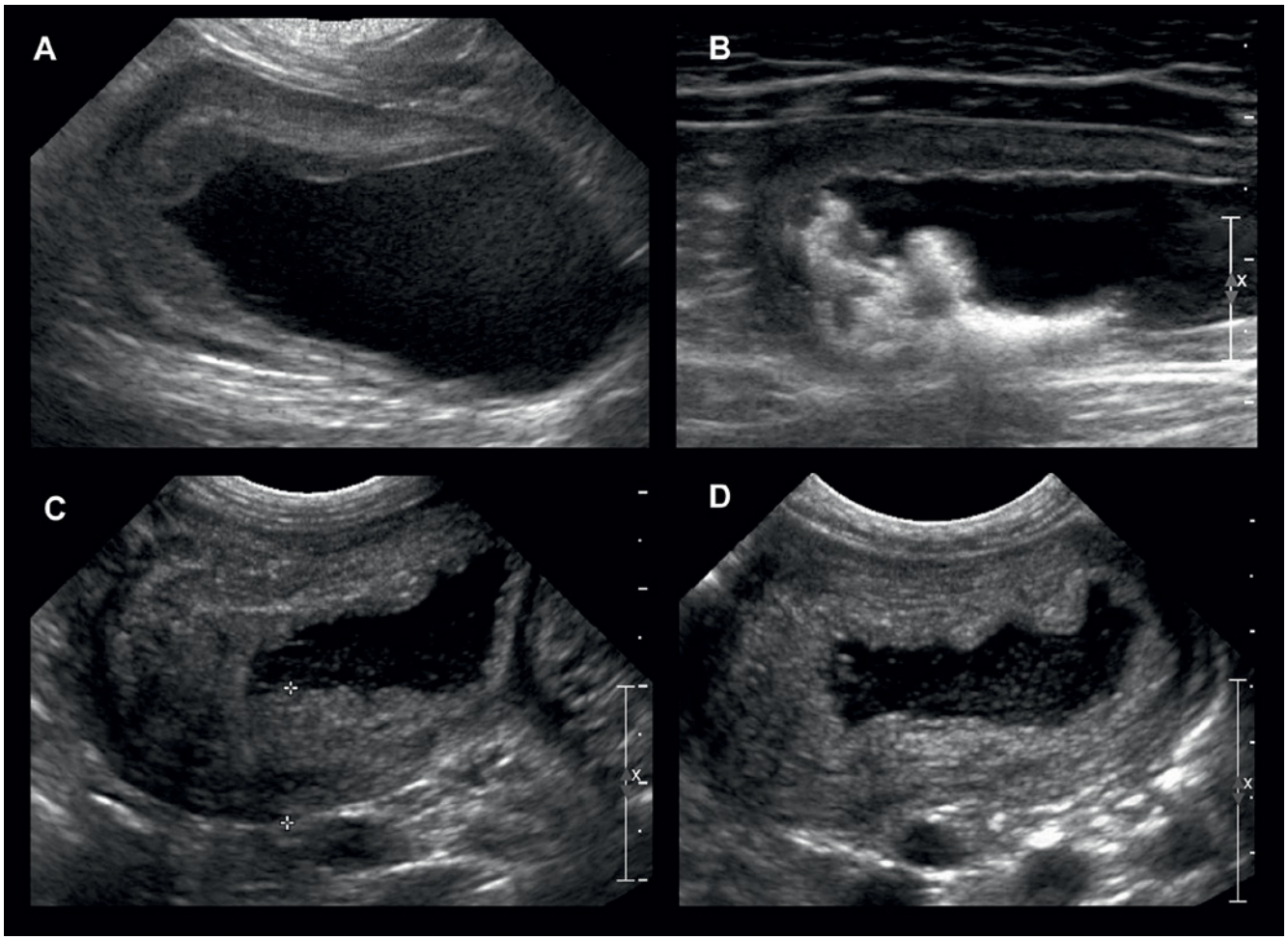


Figure 11.73. **Cystitis in two dogs and one cat. (A)** Longitudinal sonogram of the urinary bladder showing moderate cranioventral thickening of the bladder wall. The urine from the dog cultured positive for *Escherichia coli* on multiple occasions. **(B)** Longitudinal sonogram of the urinary bladder showing moderate, diffuse, hypoechoic, thickening of the bladder wall in this cat. Notice the presence of a large amount of sediment and calculi in the dependent portion of the bladder. **(C)** Longitudinal sonogram of a severe cystitis in a Chow dog with concurrent prostatitis. Notice the marked thickening (1.3 cm) affecting most of the bladder wall. **(D)** Transverse sonogram of the same dog in **C**.

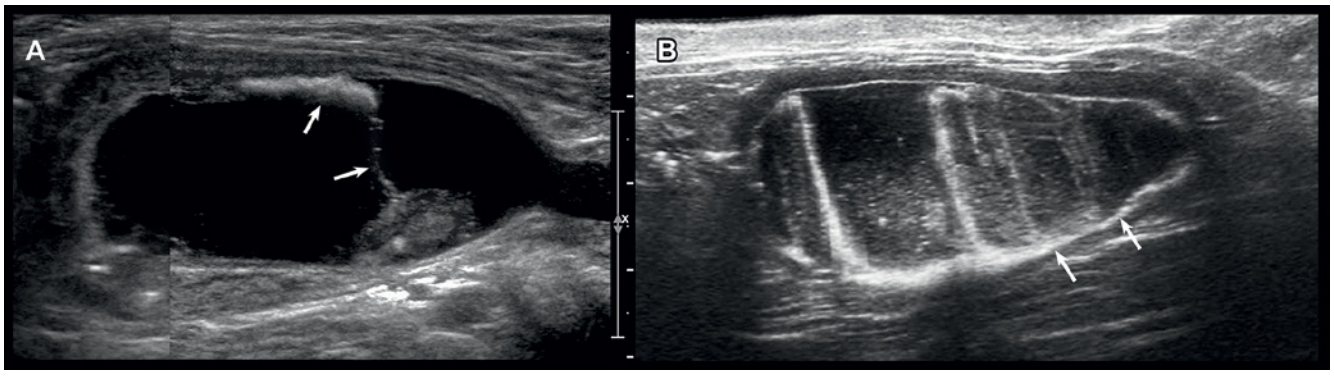


Figure 11.74. **Pseudomembranous cystitis in one dog and one cat. (A)** Composite of two longitudinal sonograms of the bladder of a 2-year-old Chihuahua with hematuria and urinary obstruction. Moderate thickening of the wall with uneven mucosal surface is noted. In addition, the ventral wall displays a hyperechoic band (arrows) that represents the sloughing mucosa with fibrin strands extending dorsally (as the dog is in dorsal recumbency). Mycoplasma and other bacteria were confirmed in this patient**. (B)** In this 5-year-old female spayed cat, numerous complete and hyperechoic septations are crossing the lumen. A thin circumferential hyperechoic lining (arrows) is seen along the bladder mucosa.

Vet-ebooks.com

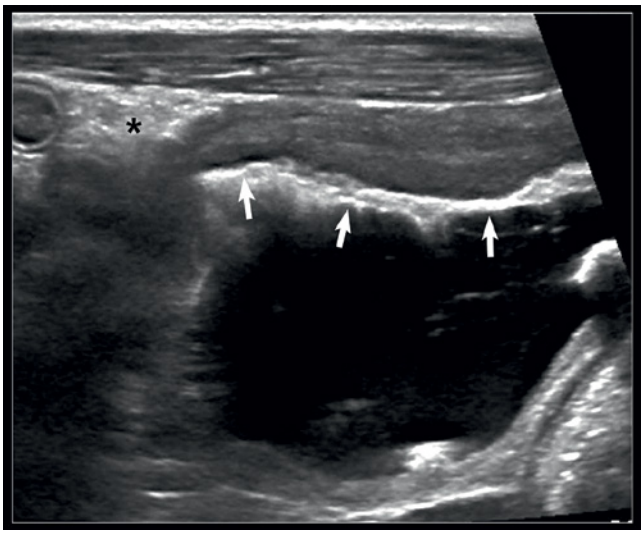


Figure 11.75. Encrusting cystitis. In this 3-year-old male German shorthair Springer presented for stranguria and recurrent cystitis, the ventral bladder wall is markedly thickened (8 mm) and has an irregular luminal surface lined up with hyperechoic material (arrows) associated with dirty shadowing, likely representing mineralization. Two calculi were also present in the lumen. The fat near the bladder apex is hyperechoic (*). Urine culture revealed *Staphylococcus Pseudintermedius* (urease-producing bacteria).

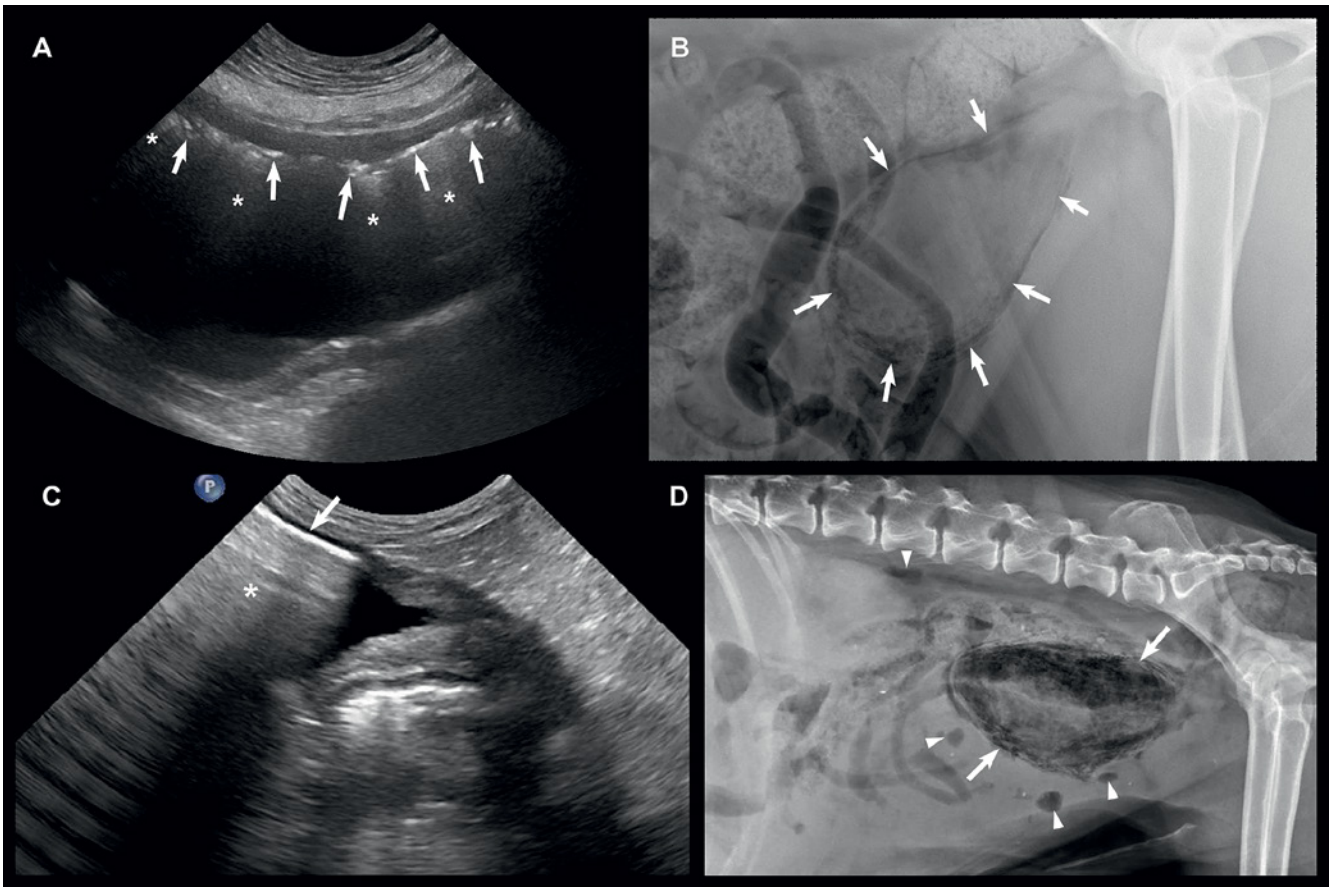


Figure 11.76. Emphysematous cystitis in two diabetic dogs. (A) In this 11-year-old Pitbull with diabetic ketoacidosis (DKA), hyperechoic foci are seen along the ventral wall of the bladder (arrows), several of which are associated with reverberation artifacts (*). **(B)** A lateral radiograph confirmed the presence of gas inside the wall and lumen of the bladder. **(C, D)** In this 11-year-old miniature Schnauzer with diabetes, a large amount of gas (with reverberation artifact) in the bladder wall can be challenging to confidently locate, but the lateral radiograph confirms the presence of both the intramural gas (arrows) and the pneumoperitoneum (arrowheads).

Vet-ebooks.com

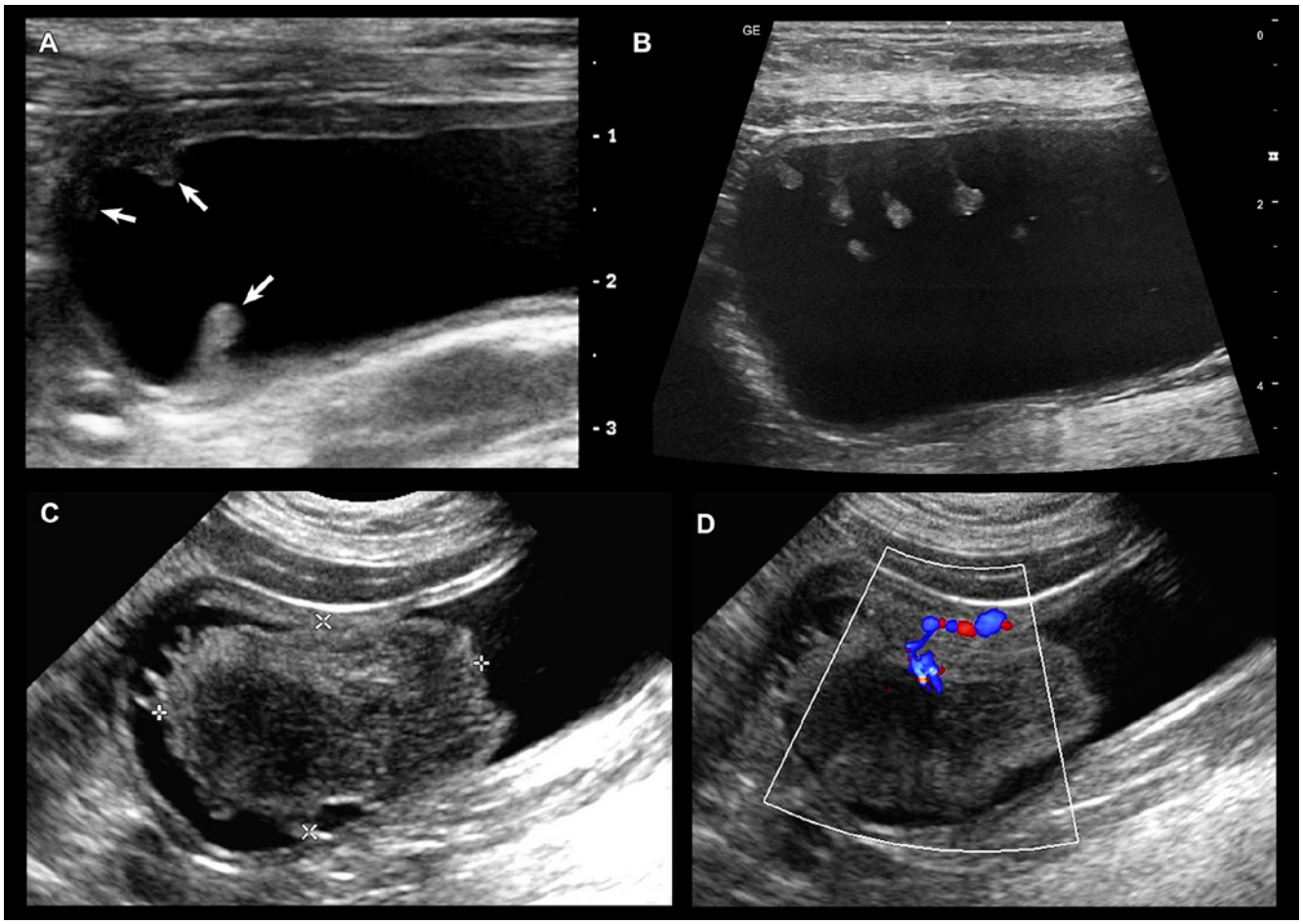


Figure 11.77. **Polypoid cystitis in three dogs. (A)** Longitudinal sonogram of the urinary bladder of an 8-year-old Fox Terrier with three small pedunculated lesions (arrows) extending from the right bladder wall into the bladder lumen, confirmed to be polypoid cystitis. The bladder wall thickness is otherwise within normal limits. **(B)** In this 7-year-old female spayed Shetland sheepdog with chronic pollakiuria, multiple polyps protrude into the lumen from the ventral bladder mucosa. **(C, D)** Large, irregular and slightly inhomogeneous mass filling a large part of the bladder lumen of this 12-year-old female Jack Russell terrier cross presented with chronic urinary tract infection, The color Doppler assessment pointed to vessels likely indicating the origin of the mass along the ventral wall. Histopathology revealed a polypoid cystitis.

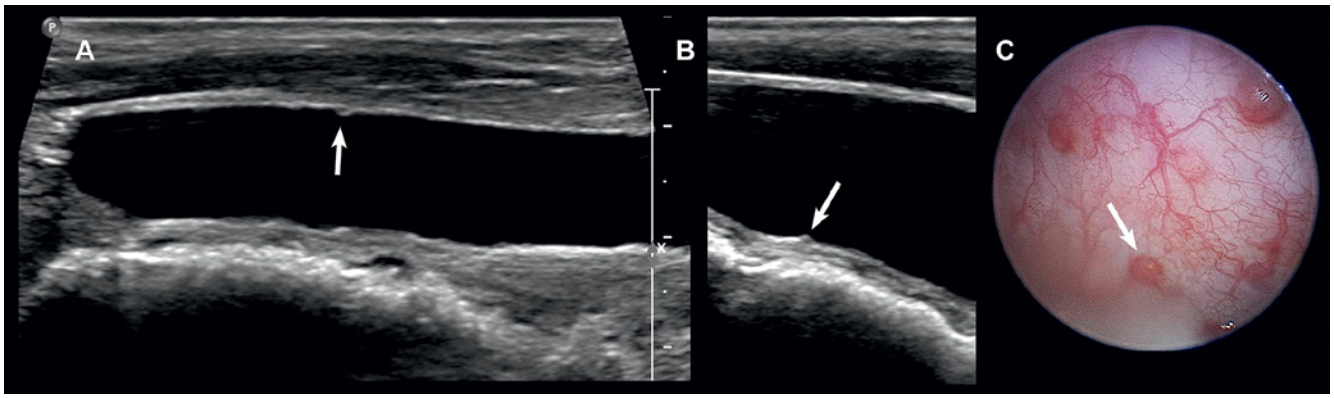


Figure 11.78. **Follicular cystitis in a 7-month-old Golden Retriever cross**. **(A, B)** On these sagittal sonograms, several tiny blisters (arrows) are noted along the mucosal surface of the bladder and were confirmed with cystoscopy (**C**).

Vet-ebooks.com

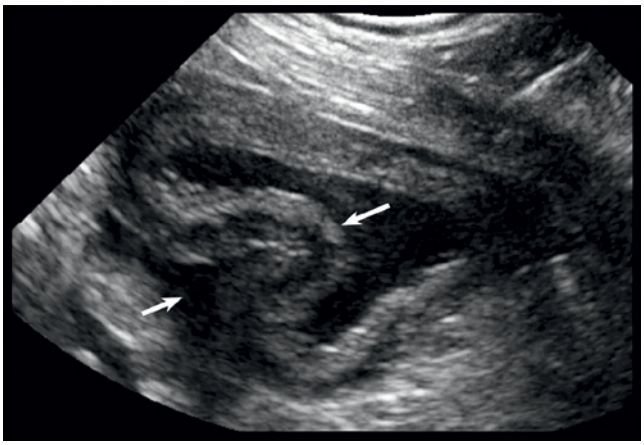


Figure 11.79. Bladder wall inversion in a 13-year-old Labrador cross. The unusual apical "mass" (arrows) represents a fold of the wall projecting into the lumen. This dog had chronic cystitis with numerous successive catheter placements. The fold disappeared over time.

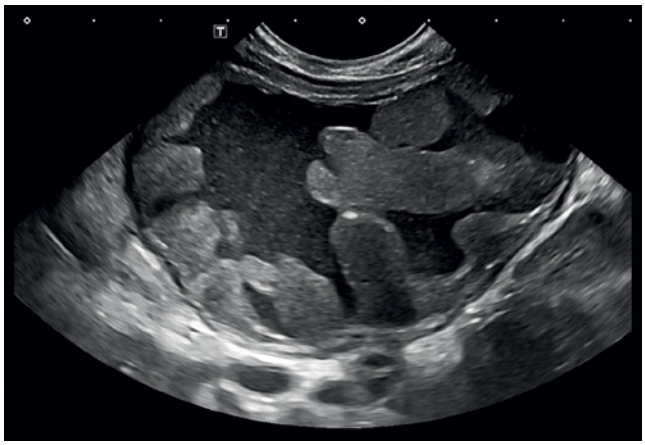


Figure 11.80. Malakoplakia of the Bladder of a 4-month-old female English Bulldog presented for long-standing incontinence and previous cystitis. Numerous finger-like echogenic projections are filling a large part of the bladder lumen. There was no evidence of calculi. These findings are highly supportive of malakoplakia. Courtesy of Dr. Chee Kin Lim, VetCT.

The combination of chronic cystitis, immunodepression and defective lysosomal function can lead to a rare condition called **malakoplakia** (Benzimra et al. 2019). It mostly affects young animals (dog and cat) and appears as numerous finger-like projections filling the UB lumen (Figure 11.80).

Neoplasia

Transitional cell carcinoma (also called **urothelial carcinoma**) is the most common neoplasm of the UB in dogs and cats (Hamlin et al. 2019). Transitional cell carcinoma is typically an irregular bladder wall mass with a broad-based attachment projecting into the UB lumen. The echogenicity is often mixed and has an overall appearance that can be poorly to moderately echogenic. It may also be partly mineralized, which can be confused for calculi. The masses are described commonly in the bladder neck (trigone) region and dorsal bladder wall (Leveille et al. 1992), however, they can be seen at any location in the bladder (Figure 11.81). Because of the location of the ureteral papilla in the trigone region, unilateral or bilateral hydroureter may be encountered (Figure 11.82). It is common for the mass to extend into the proximal urethra. Dogs with transitional cell carcinoma may have concurrent cystitis, urethritis, calculi, and/or blood clots. Ultrasound features associated with reduced survival times include a trigonal location, lesion extension within the UB wall, and a heterogeneous echogenicity (Hanazono et al. 2014).

A wide variety of **other bladder tumor types** are possible, including epithelial (squamous cell carcinoma) and mesenchymal tumors (botryoid rhabdomyosarcoma, chemodectoma, peripheral nerve sheath tumor, leiomyosarcoma, leiomyoma (Biedak et al. 2023), fibroma, fibrosarcoma, ganglioneuroma, osteosarcoma hemangioma, hemangiosarcoma, lymphangiosarcoma, histiocytic sarcoma (Amores-Fuster et al. 2011), hemangioma, hemangiosarcoma, lymphoma (Benigni et al. 2006), and mast cell tumor) (Figures 11.83–11.87).

Ultrasonographic differentiation of tumor type and differentiation from non-neoplastic disease is often impossible without a biopsy. However, a mass with a smooth luminal surface and serosal extension is more likely to have a mesenchymal origin. Uncommonly, bladder tumors can diffusely invade the bladder wall (Figures 11.86, 11.87B-D).

The most common urethral neoplasms in dogs include transitional cell carcinoma, squamous cell carcinoma, and adenocarcinoma. Proximal urethral neoplasms are often caused by local spread of bladder or prostatic neoplasms. Urethral transitional cell carcinoma has a markedly hyperechoic nonshadowing mucosal line and may be associated with hypoechoic thickening of the urethral wall (Figure 11.82) (Hanson and Tidwell 1996, Nevins et al. 2015). Squamous cell carcinoma is commonly associated with the distal urethra. Other types of neoplastic processes can compress or invade the urethra along its path (Figure 11.88).

Enlargement of the medial iliac, external iliac, sacral, or superficial inguinal lymph nodes is not specific to bladder or urethral disease, and they should be located

Vet-ebooks.com

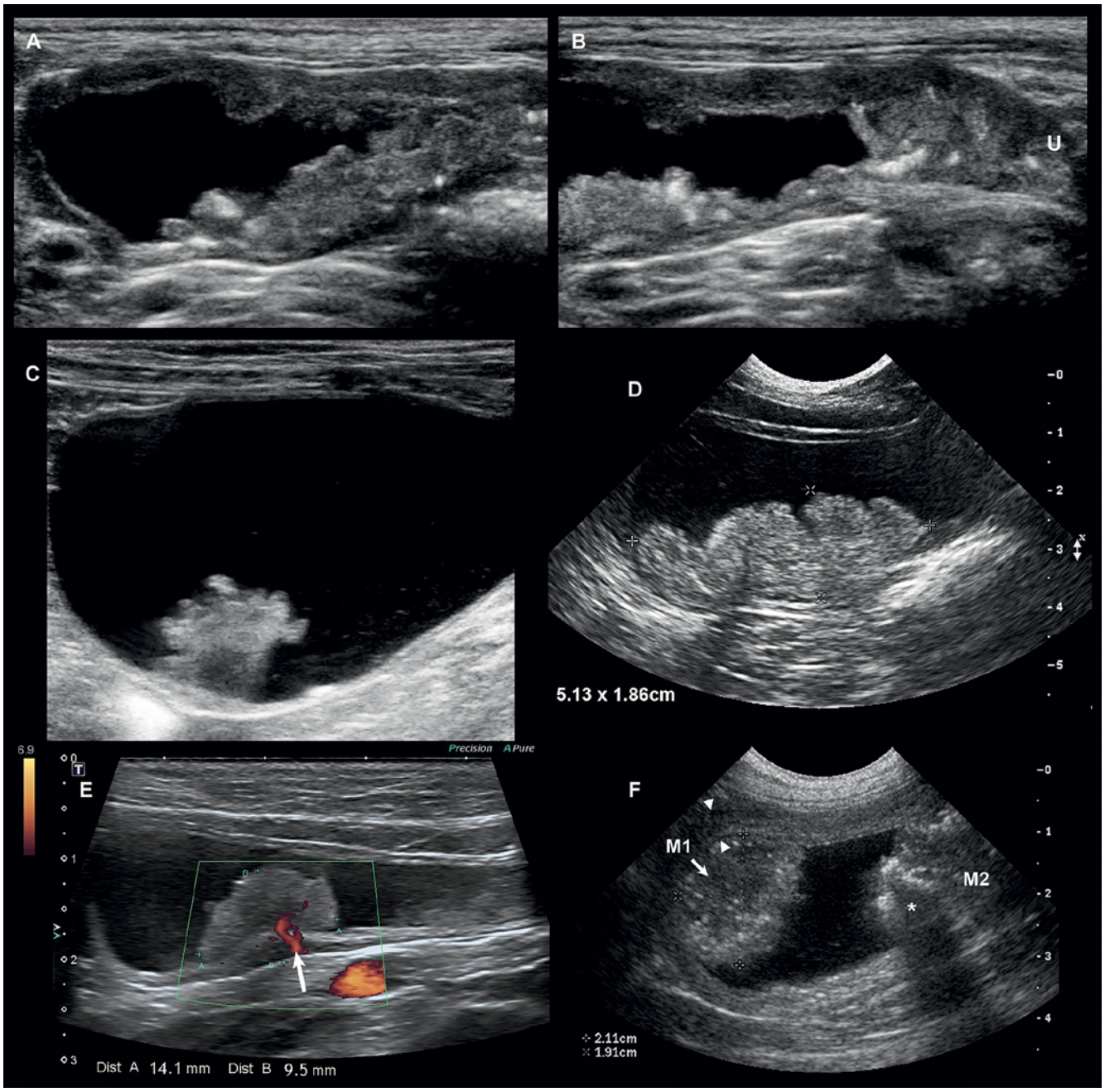


Figure 11.81. **Transitional cell carcinoma (TCC) in four dogs and one cat. (A)** Longitudinal sonogram of an extensive TCC affecting the ventral and dorsal bladder wall, in a 10-year-old Lhapsa Apso. **(B)** In the same dog as **(A),** the TCC extends caudally into the bladder neck and urethra (U). **(C)** A cauliflower shaped nodule arising from the craniodorsal wall was found incidentally in another dog presented for urinary obstruction secondary to a urethral calculus. It was confirmed as papillary noninfiltrating TCC after surgical removal. **(D)** Longitudinal sonogram of a broad-based hyperechoic mass associated with the craniodorsal bladder wall, consistent with transitional cell carcinoma. **(E)** Longitudinal sonogram in 12-year-old cat with chronic hematuria. Power Doppler signal (arrow) confirms that this lesion was attached to the bladder wall, as opposed to a blood clot. **(F)** Two separate transitional cell carcinoma masses (M1 and M2) in another dog with mineralization causing acoustic shadowing (*). The arrowheads delineate the apical bladder wall.

Vet-ebooks.com

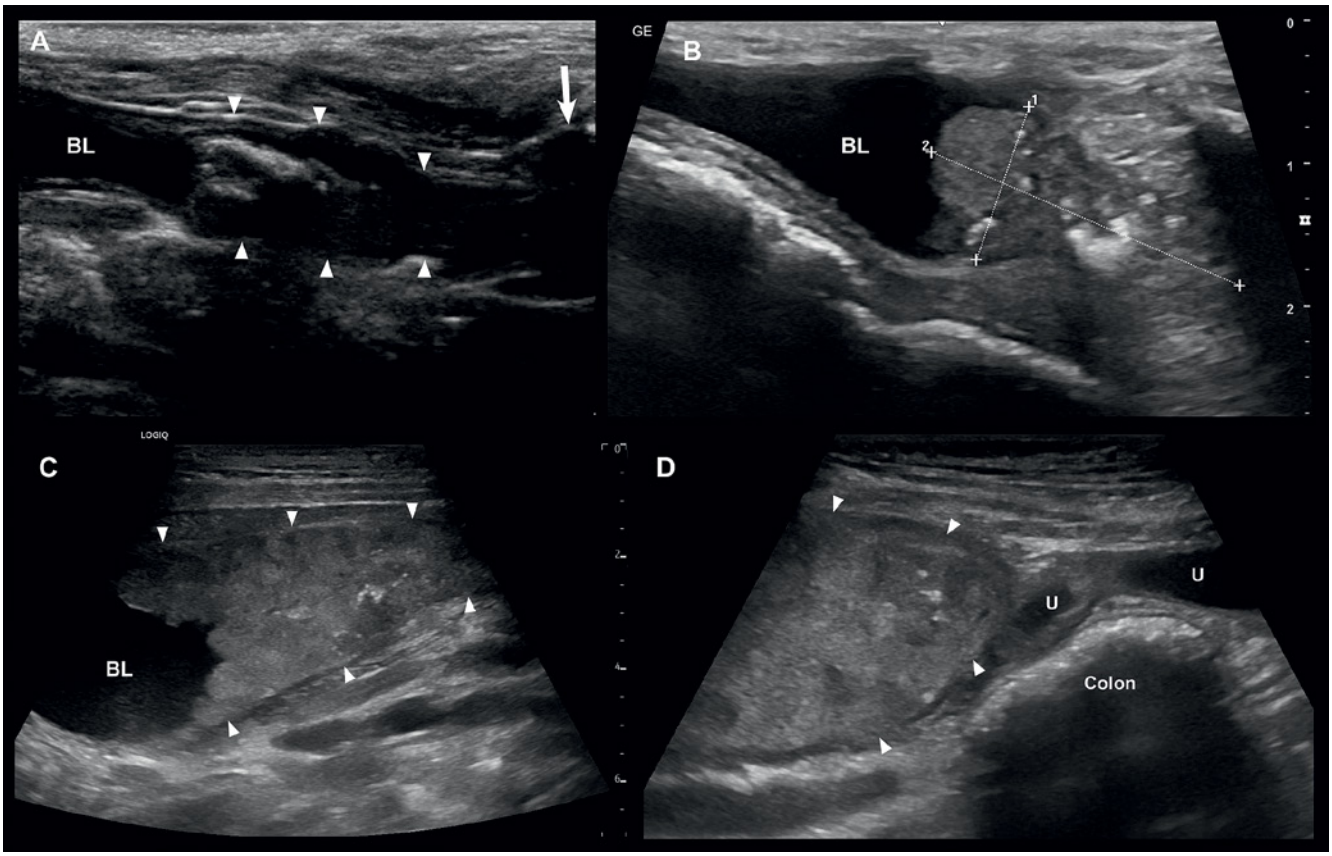


Figure 11.82. **Urethral transitional cell carcinoma in three dogs. (A)** In this 14-year-old female Cairn terrier, the proximal urethra is thickened (arrowheads) and mineralized areas are present. The pubic bone (arrow) and its associated shadowing prevented a complete assessment of the lesion. A suction biopsy confirmed transitional cell carcinoma. **(B)** An irregular proliferative tissue with hyperechoic foci consistent with mineralization invades the proximal urethra of this 8-year-old Yorkshire terrier, protruding into the bladder (BL) neck. The arrow points to the pubic bone that creates an acoustic shadow preventing visualization of the intrapelvic portion of the urethra. **(C, D)** In this 7-year-old castrated male Labrador, there is a moderately echogenic mass discrete mineral foci infiltrating the prostatic urethra and bladder (BL) neck, involving the left ureterovesicular junction and causing hydronephrosis. Note the dilatation of the adjacent distal ureter (U).

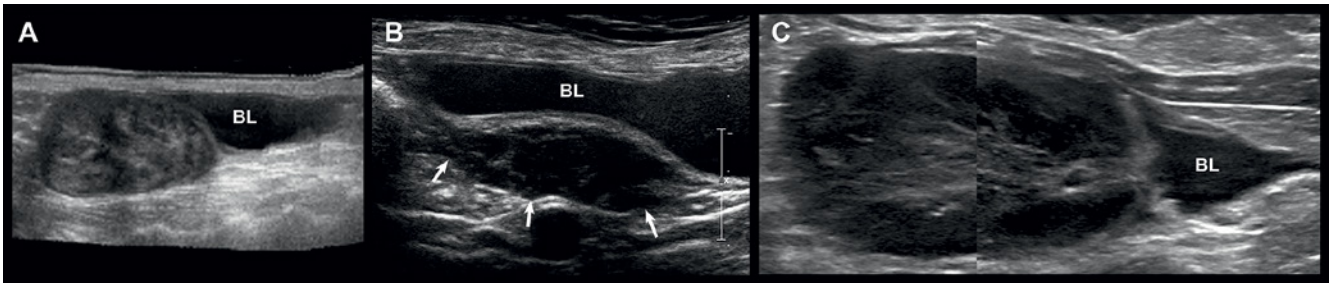


Figure 11.83. **Bladder smooth muscle tumors in two dogs (A, B), and one cat (C). (A)** Longitudinal panoramic sonogram of a large eccentric, echogenic mass deforming the cranial contour of the bladder (BL), but not affecting the lumen. The mass was diagnosed as low-grade leiomyosarcoma**. (B)** Longitudinal sonogram of the bladder of a large fusiform mass (arrows) deforming the craniodorsal wall of the bladder (BL). The mass was diagnosed as a leiomyoma. **(C)** Composite longitudinal sonogram of a 9-year-old female cat with intermittent hematuria for 6 months. A large, irregularly striated mass occupies most of the bladder lumen. This mass originating from the cranioventral aspect of the bladder was a leiomyoma.

Vet-ebooks.com

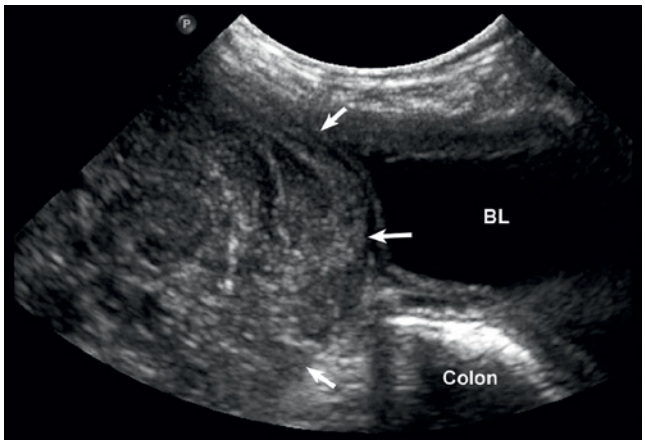


Figure 11.84. Bladder hemangiosarcoma in a dog. Longitudinal sonogram of a large (over 7 cm long) inhomogeneous mass (arrows) associated with the cranial bladder (BL) wall. The mass was removed surgically, and the histopathologic diagnosis was hemangiosarcoma.

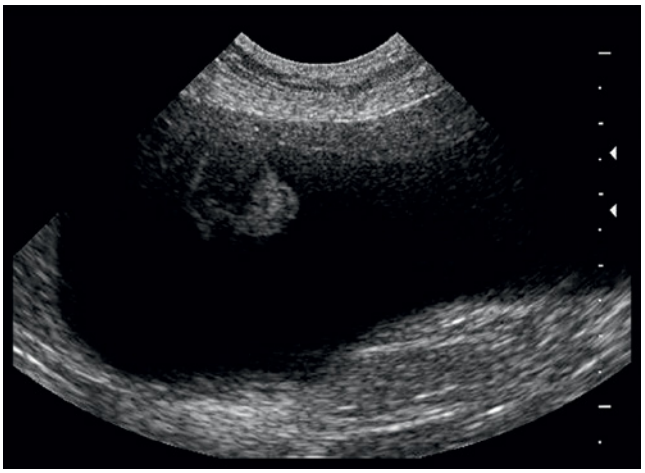


Figure 11.85. Bladder mast cell tumor in a dog. Longitudinal sonogram of a urinary bladder with a highly vascular, pedunculated, mixed-echogenicity mass originating from the cranioventral bladder wall. Cytology of the mass with special stains was consistent with a mast cell neoplasm.

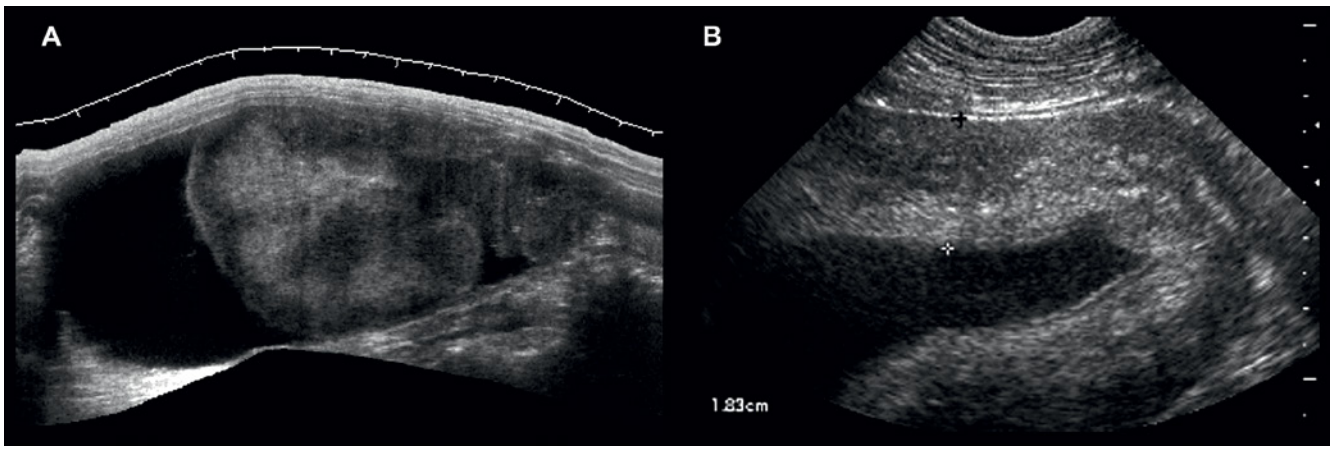


Figure 11.86. Extensive bladder carcinomas in two dogs. (A) Panoramic longitudinal sonogram of a large caudal bladder mass involving the trigone of a dog. The histopathology obtained at necropsy revealed a poorly differentiated carcinoma. **(B)** Longitudinal sonogram of the bladder of a 6-year-old Labrador retriever with diffuse carcinomatous infiltration of the wall.

and measured to aid the staging of a suspected neoplastic disease. Due to dynamic changes within the UB wall with different volumes of urine and the variation between operators, the response of bladder wall to therapy can be difficult to accurately assess with ultrasound (Hume et al. 2010).

Calculi

High-frequency bladder ultrasound may have a similar accuracy as radiographic contrast procedures in calculi detection (Weichselbaum et al. 1999). However, ultrasound tends to overestimate true cystolith size by several millimeters compared to other imaging modalities (Byl et al. 2010). Cystic or urethral calculi are usually mobile and collect in the dependent portion of the lumen. They are usually spherical, with a hyperechoic curvilinear interface. However, they can vary in number, size, and shape. A distal shadow is only variably present and is more likely seen with a higher transducer frequency and with calculi of a greater thickness and width and/or with an irregular surface (Figure 11.89). A reverberation artifact may also occur distal to cystic calculi. The presence or absence of these

Vet-ebooks.com

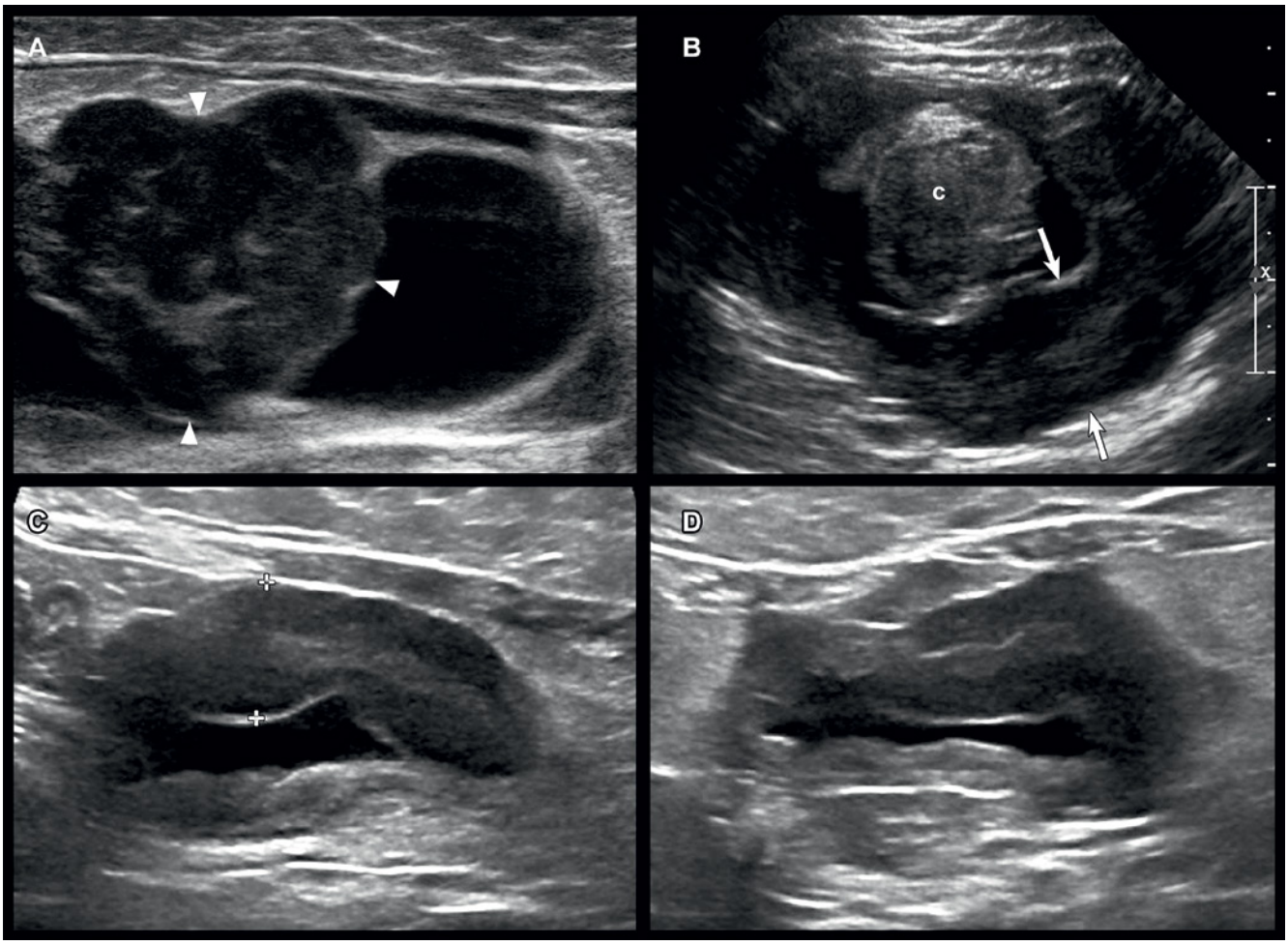


Figure 11.87. **Lymphoma in three cats. (A)** A multilobulated, poorly echogenic mass (arrowheads) is deforming the cranial aspect of the bladder in this 11-year-old cat with multicentric lymphoma. **(B)** In this 3-year-old cat with hematuria and straining to urinate, the bladder is unevenly but diffusely thickened (arrows) and an echogenic amorphous structure is filling most of the lumen, this represents a blood clot (c). **(C, D)** On this longitudinal (C) and transverse (D) sonograms of the bladder wall of this 10-year-old cat, there is smooth and uneven thickening (1.2 cm between calipers). The confirmed lymphoma affected both kidneys and the bladder; the lesions regressed in 1 month after chemotherapy was initiated.

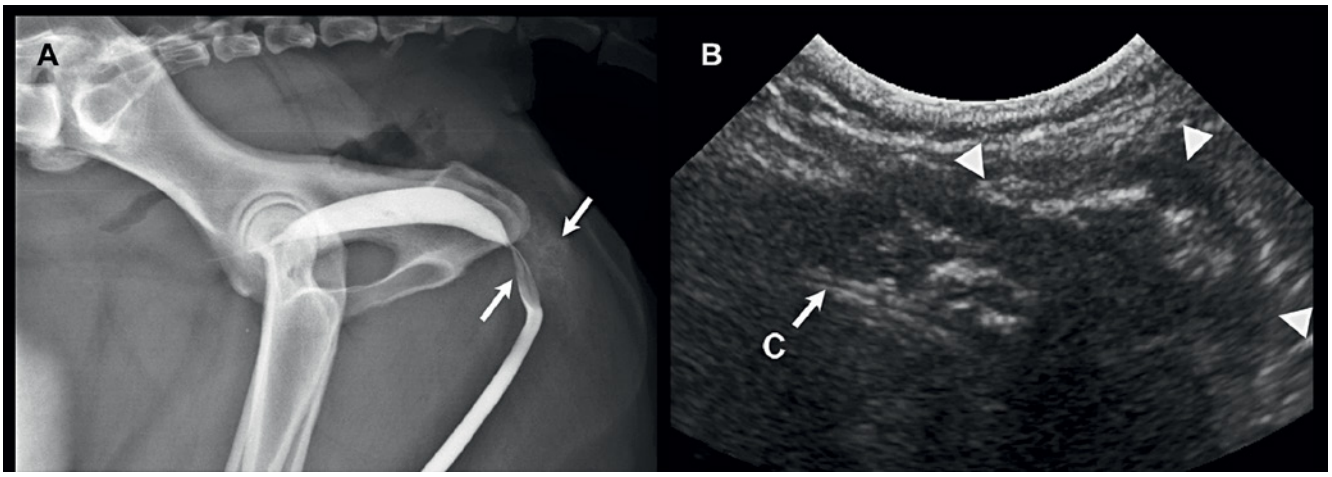


Figure 11.88. **Urethral osteosarcoma in a dog. (A)** Positive-contrast retrograde urethrogram showing a mineral opacity mass (arrows) causing marked attenuation of the urethral contrast. **(B)** Longitudinal sonogram of the caudal membranous urethra, which contains an indwelling catheter (**C**). A hyperechoic shadowing mass (arrowheads) is caudodorsal to the urethra. The histopathologic diagnosis from an ultrasound-guided microcore biopsy was osteosarcoma.

Vet-ebooks.com

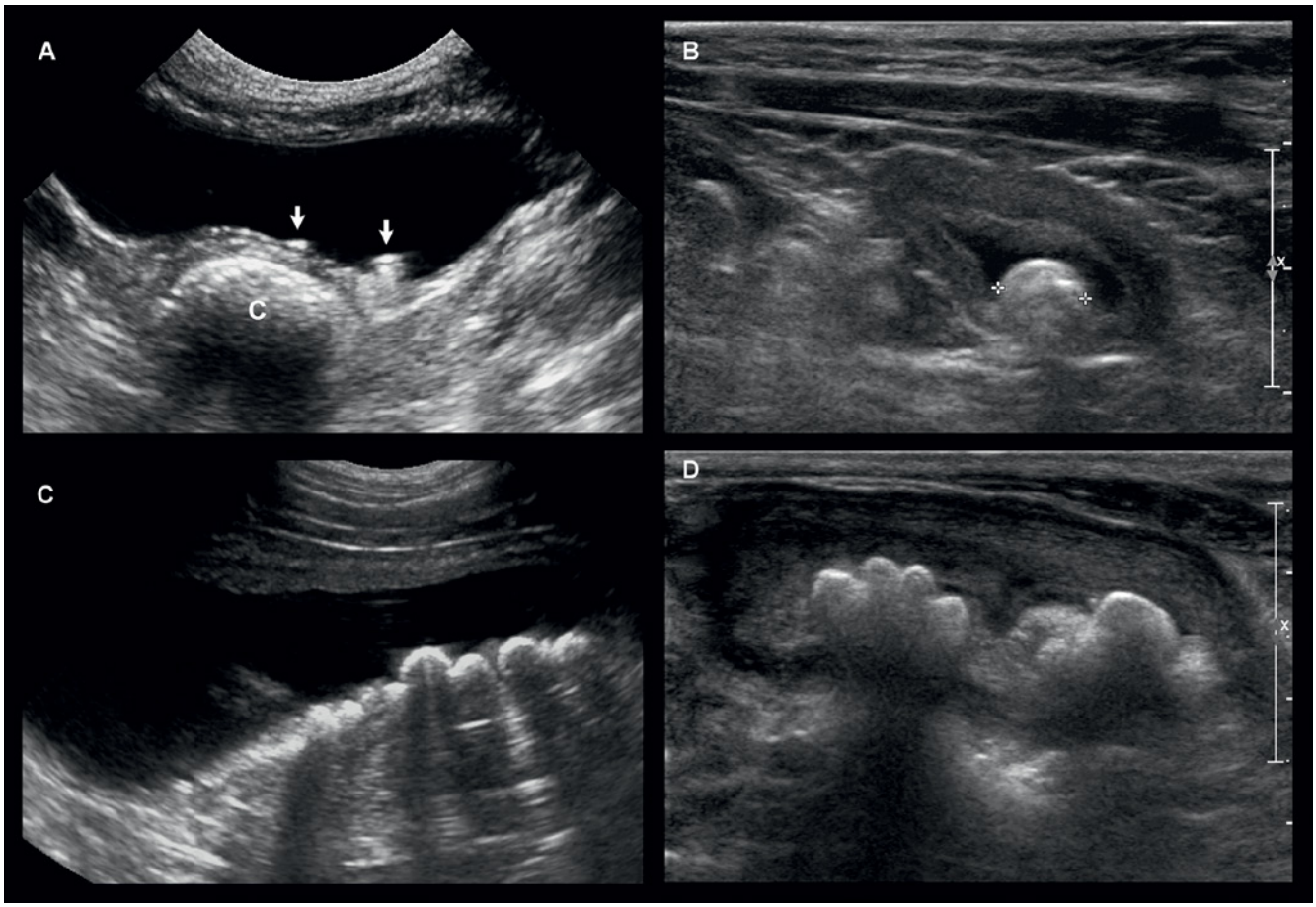


Figure 11.89. **Cystic calculi in dogs and cats. (A)** Transverse sonogram of the urinary bladder showing two small hyperechoic structures associated with the dependent bladder wall (arrows) that are thought to represent small cystic calculi, even if acoustic shadowing is not present. Urinalysis revealed calcium oxalate crystalluria. The colon (C) is associated with acoustic shadowing. **(B)** Longitudinal sonogram in a 3-year-old Ragdoll cat with a nearly collapsed and thickened bladder containing a spherical calculus (between calipers) associated with faint shadowing. **(C)** Numerous, variable size calculi are present in the bladder of a 3-year-old Australian Shepherd cross. **(D)** Longitudinal sonogram of a collapsed and thickened bladder filled with numerous rounded calculi associated with shadowing.

artifacts does not correlate with the composition of the calculus (Weichselbaum et al. 2000). Although the appearance is nonspecific, crystalluria may be seen as a collection of swirling moderate-intensity intraluminal echoes. A collection of small calculi or mineralized sediment may generate a linear interface (Figure 11.90). This sediment usually suspends with gentle agitation of the UB or with a change in position of the animal. Although generally less echogenic, pyuria may share similar features appearing as an echogenic collection settling on the dependent portion of the bladder (Figure 11.91).

When color flow Doppler is used, a twinkle artifact can be observed (Andrulli et al. 2010). This useful artifact appears as a zone of rapidly flashing red and blue color signals (mimicking vascular turbulence), distal to a highly reflective structure helps support the etiology as mineral calculi or sediment (Figure 11.92).

Although the urethra cannot be evaluated completely with ultrasound, urethral calculi may be identified, particularly in the penile portion of the urethra in male dogs (Figure 11.93). Enlargement of the UB with dilation of the urethral lumen can support urethral obstruction (Figure 11.94) but can also be seen in patients with distended bladder with no obstruction.

The descending colon can indent and appear confluent with the dorsal wall of the UB. The hyperechoic interface and shadowing artifact generated by the colon can mimic a large cystic calculus (Figure 11.89A). Rotation of the transducer into the longitudinal plane will reveal the colon as a linear interface running the length of the image, whereas the calculi should remain

Vet-ebooks.com

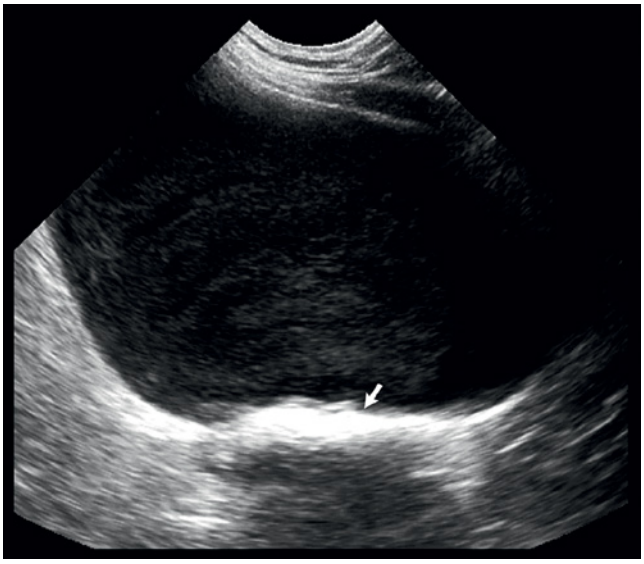


Figure 11.90. Bladder mineral sediment in a dog. Transverse sonogram of diffusely echogenic urine and a collection of hyperechoic material (arrow) on the dependent bladder wall with distal shadowing. The urinalysis showed 3+ amorphous crystalluria.

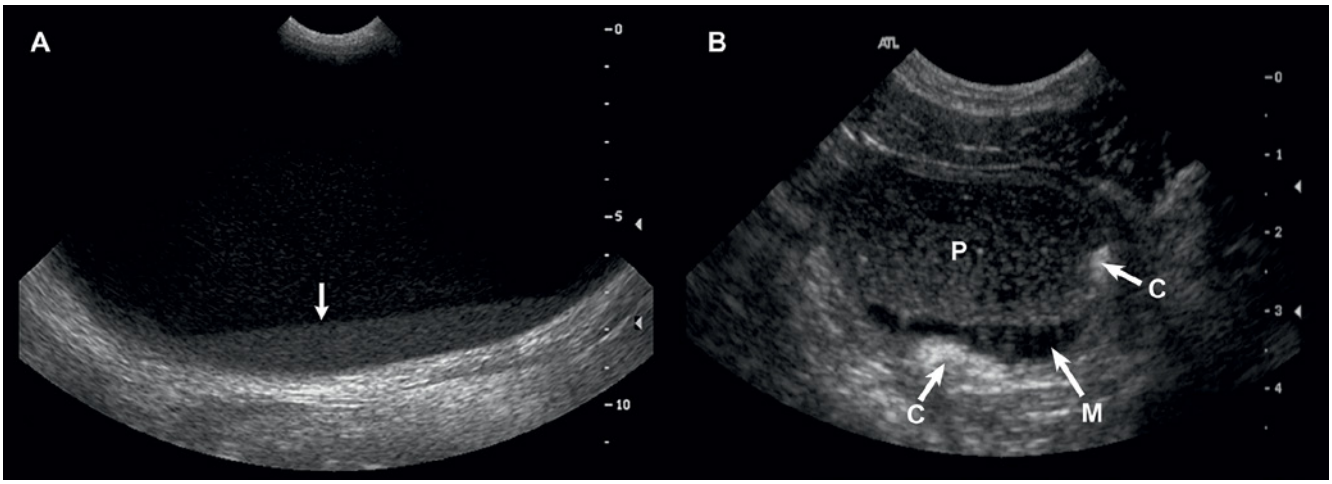


Figure 11.91. Pyuria in two dogs. (A) Pyuria appears as nonshadowing, moderately echogenic sludge that progressively sediments during the exam. A straight horizontal border is seen (arrow). It should not be confused with a side-lobe artifact. **(B)** In this other dog with pyuria, a layer of hypoechoic mucus (M) with hyperechoic striations is found between the pus in suspension (P) and calculi (C) and the dorsal bladder wall.

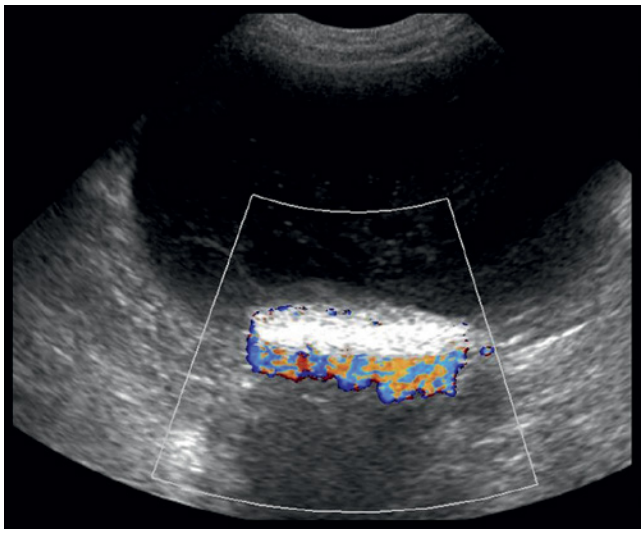


Figure 11.92. Twinkle artifact with calculi. Using color flow Doppler, an area of rapidly flashing colored signals is displayed when encountering mineralized structures. In this 5-year-old Beagle cross, the twinkle artifact is present distal to the small calculi and mineralized sediment seen in the bladder. This may be useful is detecting small calculi or mineralized sediments, especially in the absence of shadowing artifact.

Vet-ebooks.com

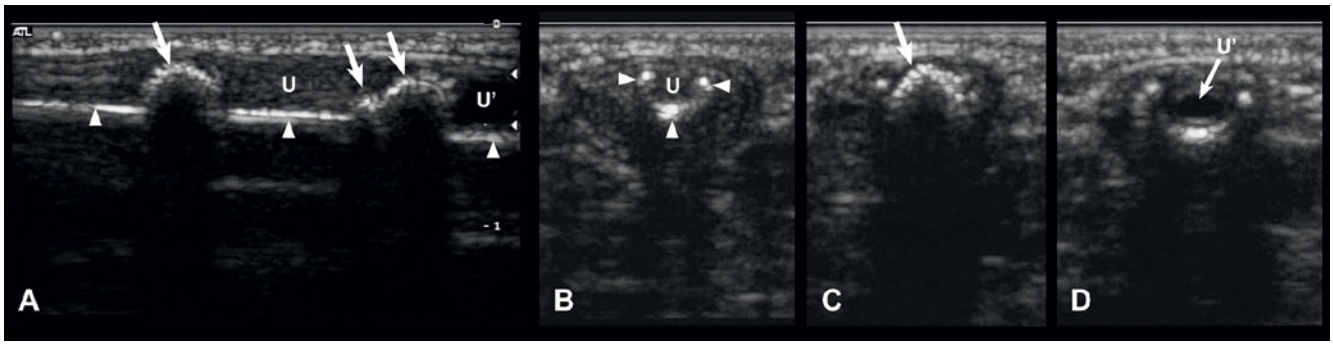


Figure 11.93. Urethral calculi in a dog. Longitudinal **(A)** and contiguous transverse **(B–D)** sonograms of the distal penile urethra in dog presented for urinary obstruction. Two larger, mildly irregular, hyperechoic calculi (arrows) with distal shadowing are lodged in the urethra (U), which is distended proximally (U'). Transverse image B was obtained distal to the most proximal (or caudal) calculus (C), whereas image **(D)** was obtained just proximal (or caudal). The ventral portion of the os penis appears as a linear hyperechoic interface in longitudinal plane (**A**, arrowheads) and U-shaped in transverse plane (**B**, arrowheads). On analysis, the calculi are made of calcium oxalates.

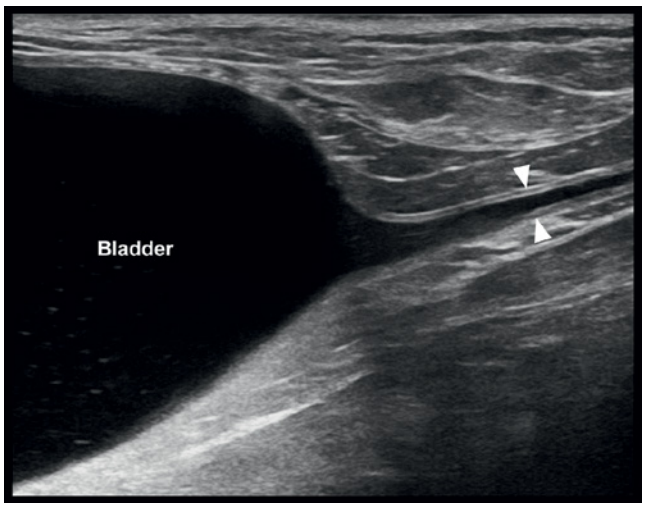


Figure 11.94. Urethral distension in a blocked cat. Longitudinal sonogram of the dilated urethra. The lumen (not normally visualized) contains nearly anechoic urine (U). Mildly thickened urethral wall can be visualized (arrowheads).

approximately spherical. In addition, repositioning the animal into a standing or lateral position should cause any calculi to fall to the dependent wall, whereas the colon remains in a dorsal location.

Intraluminal Blood Clots and Mural Hemorrhage

Blood clots and mural hemorrhage may be caused by bladder trauma, cystitis, a generalized bleeding disorder, upper urinary tract bleeding (Idiopathic renal hematuria), or neoplasia. Blood within the UB lumen or wall can have a variable appearance and can mimic exuberant inflammatory disease or neoplasia. Intraluminal clots vary in echogenicity and range from thin linear structures to large round masses (Figure 11.95).

Mural hemorrhage may cause diffuse uniform wall thickening. Recheck examinations will help differentiate neoplastic or inflammatory mural disease as bladder wall thickening secondary to systemic bleeding disorders resolves rapidly at the approximate rate of 1 mm/day once the underlying abnormalities are corrected (O'Brien and Wood 1998). Intraluminal blood clots can be differentiated from a neoplastic mass by their absence of color flow Doppler signal. In addition, the mobility of these intraluminal structures may also be demonstrated with repositioning of the patient.

Trauma and Foreign Bodies

A positive-contrast retrograde cystourethrogram is the preferred method of diagnosing rupture of the urethra or UB. On ultrasound, the ruptured UB wall is thickened (Figure 11.96), and there is abdominal effusion of echogenicity that depends on urine cellularity. Calculi or other debris can also accumulate in the peritoneal cavity. A hypoechoic bladder wall defect or tract may be seen occasionally.

This should be distinguished from a refraction artifact associated with the cranial aspect of the UB when abdominal effusion is present. The interpretation of the artifact is aided by a concurrent edge shadow and absence of bladder wall thickening (Figure 11.97).

Vet-ebooks.com

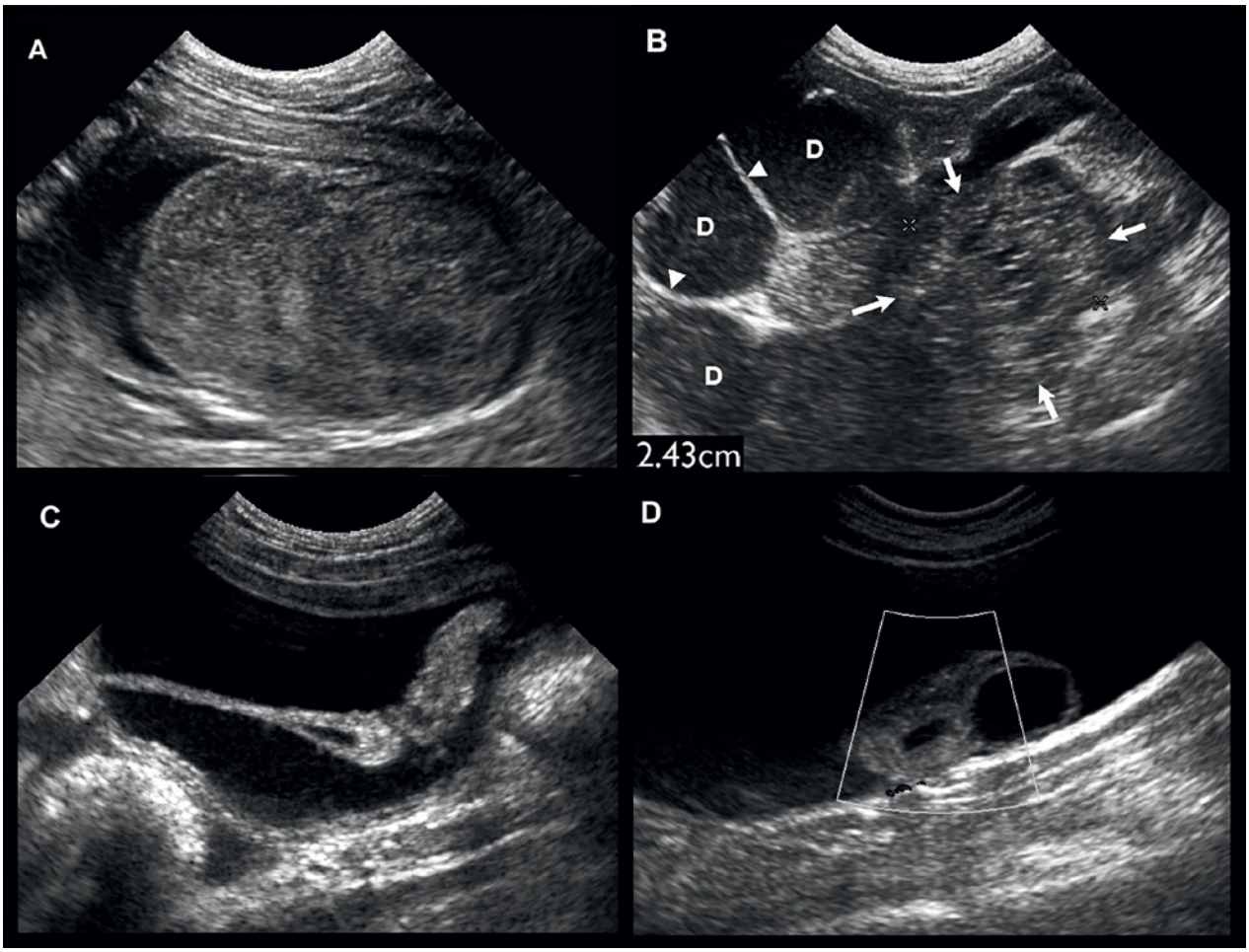


Figure 11.95. **Bladder blood clots dogs. (A)** Longitudinal sonogram of the urinary bladder, which contains a smooth, ovoid, inhomogeneous, echogenicity mass. Differential diagnoses included a bladder neoplasm or a hematoma. **(B)** A transverse sonogram of the right kidney of the same dog as **(A)** with a 2.43-cm-diameter right hilar renal mass (arrows). The hyperechoic bands of tissue (arrowheads) radiating from the hilus to the periphery are characteristic of hydronephrosis. Echogenic urine is found in the dilated diverticuli (D), consistent with hemorrhage. At necropsy, the urinary bladder mass was a hematoma secondary to renal hemangiosarcoma**. (C)** Longitudinal sonogram of the urinary bladder, which contains a floating linear hyperechoic structure of variable thickness. A urinalysis revealed numerous red blood cells highly suggestive of a suspended blood clot**. (D)** A longitudinal sonogram of the bladder containing an amorphous structure with an echogenic periphery and an anechoic center. The mass had no identifiable color flow Doppler signal.

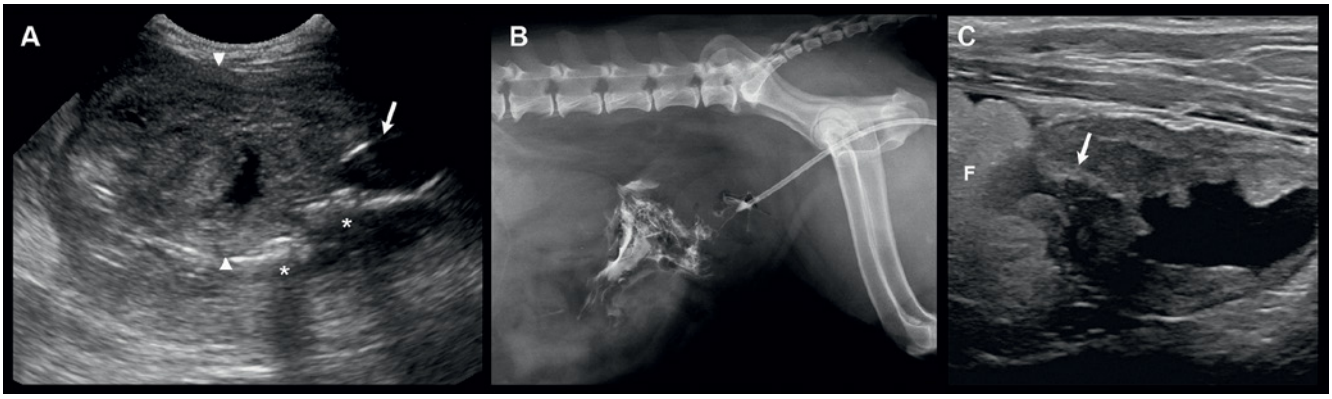


Figure 11.96. **Ruptured urinary bladder in a dog and in a cat. (A)** Longitudinal sonogram of the bladder in a dog with car-related trauma. The indwelling, saline-filled Foley catheter can be seen caudally (arrow). There is marked thickening of the bladder wall (arrowheads) and a loss of visualization of the bladder lumen. Abdominal effusion is also noted. Hyperechoic foci are noted in the dorsally displaced bladder lumen, associated with acoustic shadowing (*), consistent with calculi. **(B)** Lateral radiograph of the caudal abdomen following a retrograde positive contrast cystogram. Contrast is free within the peritoneal space. At surgery, the bladder rupture and hematoma were identified. **(C)** Longitudinal sonogram of the ruptured bladder of a 13-year-old Siamese cat that was stepped on, by the owner. Notice the marked, irregular thickening of the bladder wall and the hyperechoic line (arrow) crossing the wall. The adjacent fat (F) is hyperechoic and a small amount of fluid (urine) was present in the abdomen.

Vet-ebooks.com

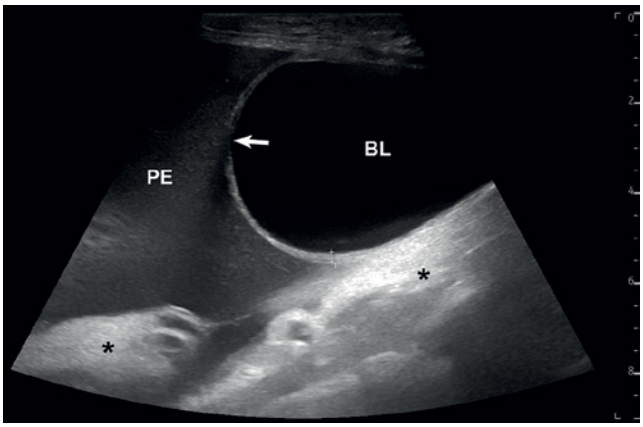


Figure 11.97. Refraction artifact versus bladder rupture in a dog. Longitudinal sonogram of the bladder containing anechoic urine surrounded by echogenic abdominal effusion (PE). The refraction artifact at the cranial aspect of the bladder mimics bladder wall rupture (arrow), but no bladder wall rupture is present. Note the hyperechogenicity of the fat (*) deep to the peritoneal fluid and bladder due to with acoustic enhancement.

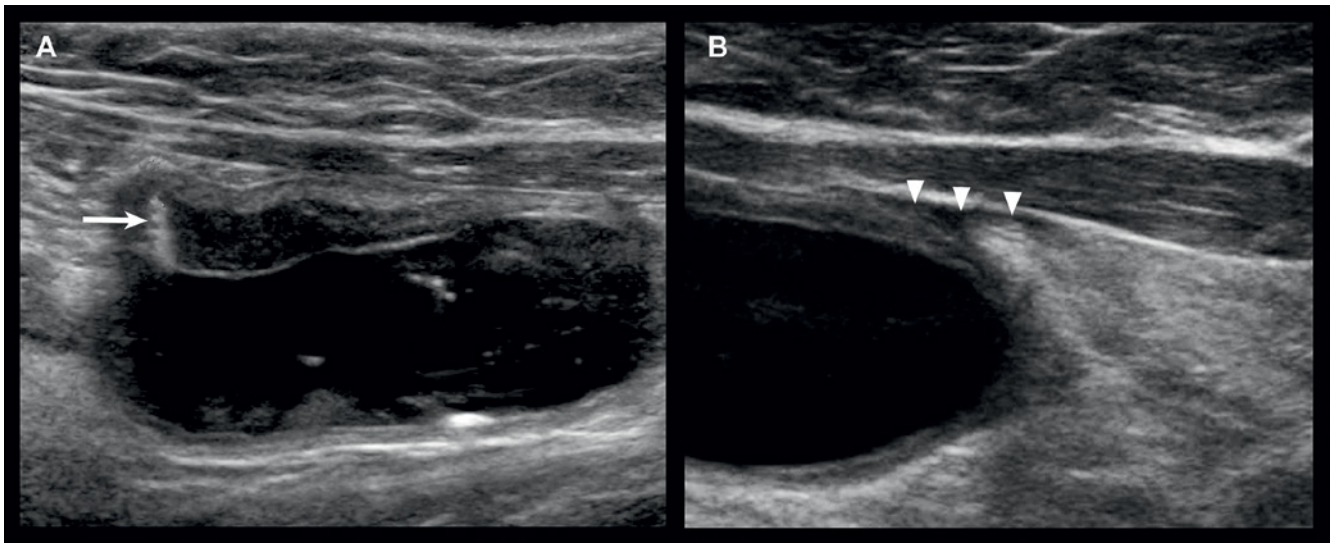


Figure 11.98. Traumatic cystocentesis. A blind cystocentesis was performed in this 11-year-old cat. **(A)** On this longitudinal sonogram, there is thickening of the cranioventral bladder wall, supportive of cystitis, and small calculi were seen on the dependent portion of the bladder. In addition, a hyperechoic line (arrow) is crossing the wall, representing the tract of the recent cystocentesis. **(B)** A small amount of fluid (arrowheads) is present near the bladder neck and the regional fat is hyperechoic. 2 weeks later, these changes had resolved.

Iatrogenic wall trauma during cystocentesis is very uncommon, but may be encountered, especially it the wall is abnormal (Figure 11.98).

At times, surgical sites may appear abnormally thickened as the result of suture reaction, in these instances, the wall remains excessively thickened and a suture pattern can be seen. (Figure 11.99)

On rare occasions, **foreign bodies** can be found in the bladder lumen, they can include grass awn (Cherbinsky et al. 2010; Lomez 2021), hair (Pinto et al. 2021), parts of catheters (Figure 11.100A, B), or even parasites such as Dioctophyme renale (Sombrio et al. 2022).

Ultrasound Guidance in Interventional Nephro-Urology

Kidneys

Ultrasound-Guided Fine-Needle Aspiration (FNA)

The choice of needle size (gauge) and length depends on the size, vascularity, and depth of the targeted tissue. Usually, a 20-, 22-, 23-, or 25-gauge needle is used. FNA can be performed with the animal under mild

Vet-ebooks.com

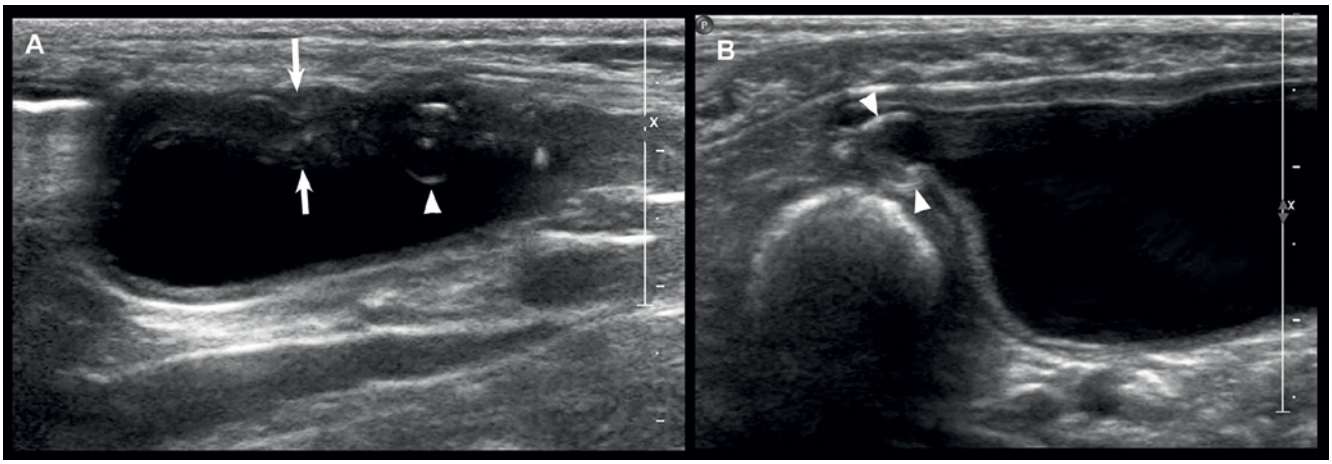


Figure 11.99. **Postsurgical incision follow-up. (A)** An 11-year-old Corgie had a cystotomy performed 11 weeks ago for ureteral calculi. The bladder wall is thickened, irregular (arrows), and a curvilinear structure (arrowhead) can be seen within the wall, likely representing suture material. This reactive incision was removed and was diagnosed as marked submucosal edema with neutrophilic and lymphocytic inflammation. **(B)** On this longitudinal sonogram of a dog with surgery performed 3 months ago, there is a focal thickening of the cystotomy site, and a curvilinear structure (arrowheads) is noted within the incision, likely representing suture material. The cranioventral wall is also mildly thickened (not shown) and a small amount of mineralized sediment is seen (not shown) in the dependent portion of the bladder. This likely represents cystitis, but the presence of suture visible in the lumen may contribute to a focal inflammation.

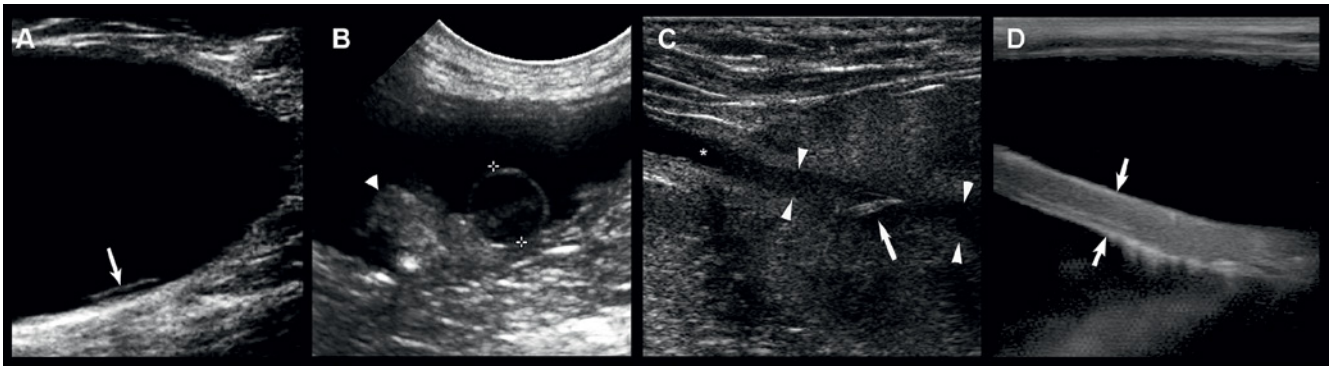


Figure 11.100. **Luminal foreign bodies and parasites. (A)** Longitudinal sonogram of the bladder of a 13-year-old cat recently catheterized. At removal, the tip of the catheter was missing. A small, linear structure (arrow) with faint double line was seen on the dependent portion of the bladder. The **catheter tip** was then removed via cystoscopy. **(B)** Longitudinal sonogram of the bladder of a 6-year-old Corgie with severe cystitis, mucosal hyperplasia (not shown), mineralized sediment (not shown), and fibrin strands (arrowhead). A rounded anechoic structure (between cursors) with a central double line was seen floating in the bladder. This is presumed to represent a broken off **Foley catheter balloon**. **(C)** Longitudinal sonogram of the prostatic urethra (arrowheads) in a dog with a **grass awn** (arrow) lodged in the lumen. Courtesy of Dr Ulrich Zeyen, Centro Veterinario Specialisito, Rome, Italy. **(D)** Longitudinal sonogram of the bladder of a 5-year-old hunting dog with dysuria. The central tubular structure in the bladder lumen represents a worm (***Dioctophyme renale***). Courtesy of Dr Thiago Muller, Uniradio Telerradiologia, Florianópolis, Brazil.

Vet-ebooks.com

sedation, especially if a smaller needle is used (e.g., 23 or 25 gauge). Neoplastic disease, such as lymphoma or carcinoma can be readily identified on cytologic specimens, although biopsy may be required to confirm the diagnosis.

Ultrasound-Guided Renal Biopsy

Ultrasound guided renal biopsies can be performed percutaneously or laparoscopically, to further investigate a focal lesion or when glomerular disease is suspected (Rawlings et al. 2003). Renal biopsy can be essential to obtain a definitive diagnosis thus allowing appropriate therapeutic recommendations. A patient's blood pressure and coagulation status should be evaluated and normalized as much as possible prior to biopsy. Renal biopsy is performed under deep sedation with a sterile preparation and 16- or 18-gauge automated core biopsy device (Figure 11.101). In dogs, an 18-gauge needle was reported to be inferior to a 16-gauge needle to obtain a core of sufficient diagnostic quality (Crivellenti et al. 2018). Complications have been reported in 3.4% of dogs and 15% of cats (Crivellenti et al. 2018; Vaden et al. 2005). The most common complication reported in 522 dogs was hematuria (3.4%) and the most common complications reported in 26 cats was hemorrhage (Vaden et al. 2005).

Ultrasound-Guided Fine-Needle Drainage

Drainage of cavitary lesions, such as renal cysts or abscesses, can be performed as a diagnostic and/or therapeutic procedure (Figure 11.102). Fluid cytology can fail to differentiate between benign and neoplastic renal lesions in dogs (Vagias et al. 2022). Some dogs and cats can benefit from palliative drainage of large renal cysts or pseudocysts (Ochoa et al. 1999). Therapeutic drainage and lavage of the renal pelvis can also help remove obstructive pus in dogs with pyonephrosis (Szatmari et al. 2001). A larger needle (e.g., 20-gauge) may help in removing dense fluid.

Ultrasound-Guided Antegrade Pyelography

Fine-needle aspiration of a distended pelvis (pyelocentesis) can be performed and followed by intrapelvic injection of an iodine-based contrast medium (Rivers et al. 1997) (Figure 11.103). Following sedation or anesthesia and a sterile preparation, a 22-gauge spinal needle with a 45° angle is inserted through the lateral margin of the kidney, a volume of contrast equal to one-half of the aspirated volume of urine is injected with ultrasound guidance prior to radiographs. Antegrade pyelography can be a useful alternative in the diagnosis and localization of ureteral obstruction in azotemic cats (Adin et al. 2003;

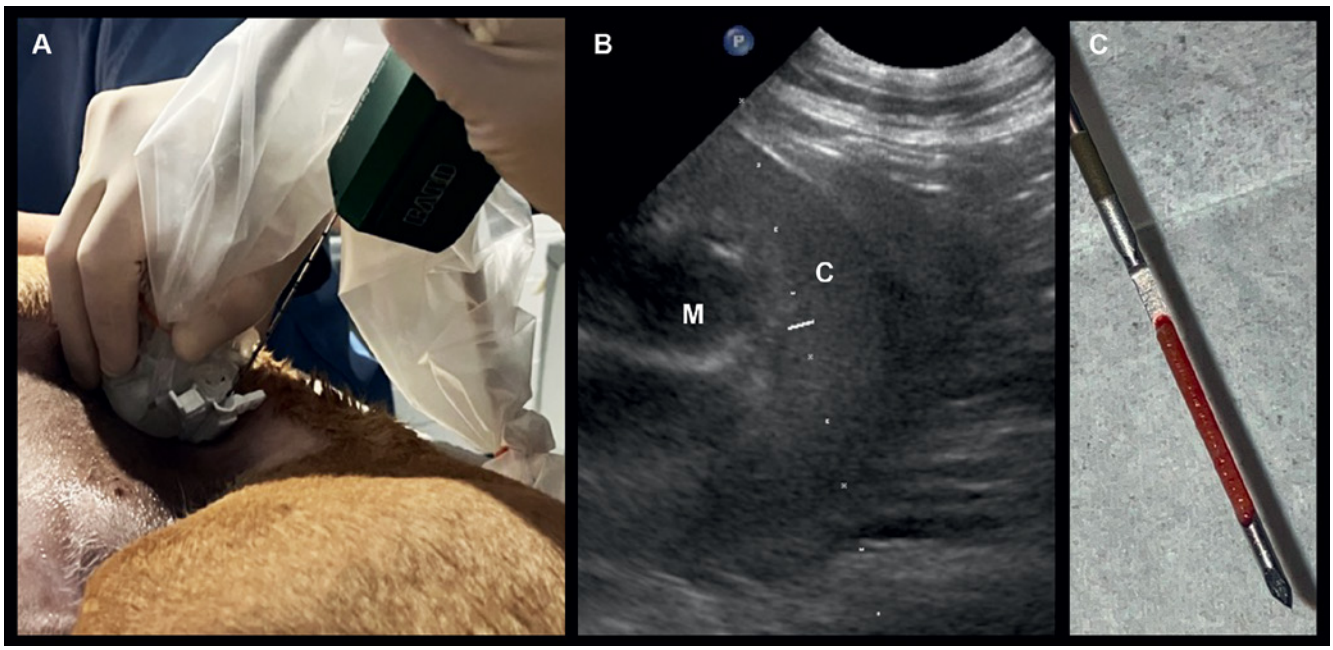


Figure 11.101. Ultrasound-guided renal biopsy. (A) The tru-cut biopsy needle is engaged in the guide clipped on the probe. **(B)** A biopsy is performed through the lateral cortex (C) of the kidney. The dotted line representing the tract for the needle is placed into the cortex, avoiding the medulla (M). **(C)** The tissue core is lying in the opened tru-cut needle.

Vet-ebooks.com

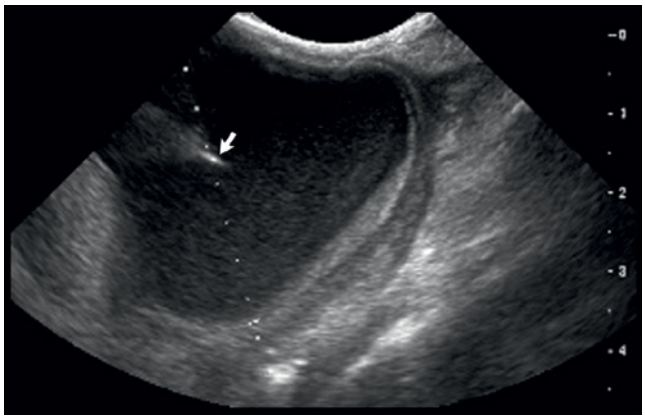


Figure 11.102. Ultrasound-guided aspiration-drainage. A fine-needle aspiration is performed on a perirenal pseudocyst in a cat. The needle tip (arrow) is in the fluid-filled cavity.

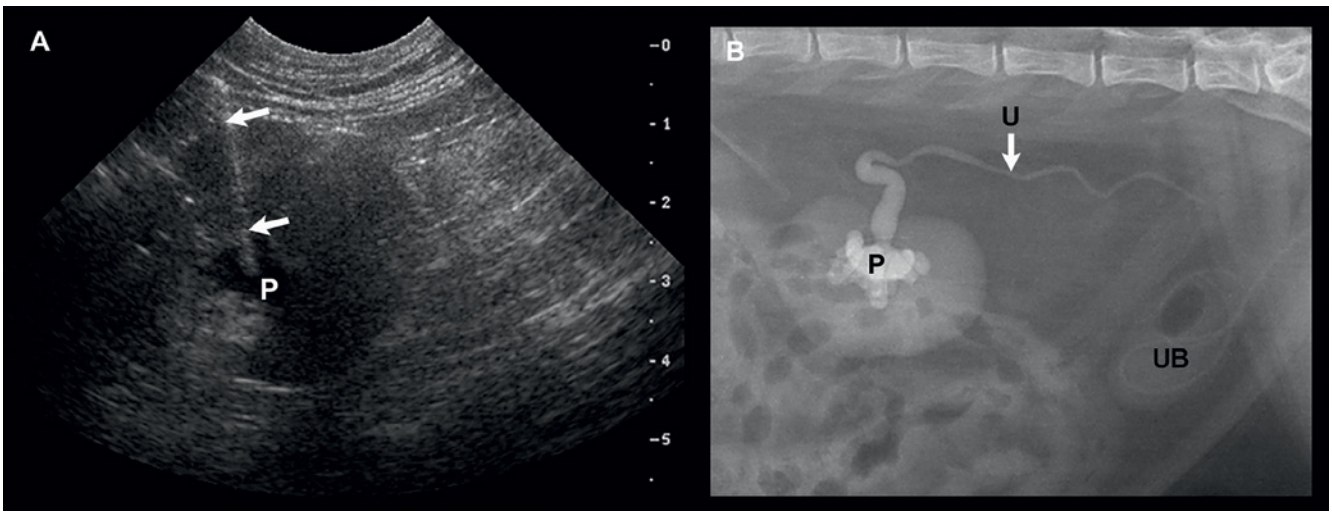


Figure 11.103. Ultrasound-guided pyelocentesis and pyelography. (A) Transverse ultrasound image of the left kidney in cat with anuric acute kidney injury. The right kidney was previously removed for a suspected tumor. A 21-gauge 1.5-in.-long needle (arrows) was inserted into the renal pelvis (P) for urine collection. This was followed by the injection of 5 mL of iopamidol (300 mg iodine/mL). **(B)** On a lateral radiograph of the caudal abdomen obtained 10 min later, opacification of the pelvis and ureter (U) is observed. A urinary catheter and an oval gas bubble are visible in the bladder. Ureteral obstruction is indicated by the lack of contrast medium reaching the distal ureter and urinary bladder (UB). At surgery, an obstructive clot was identified in the distal ureter.

Etedali et al. 2018; Lemieux et al. 2021). Complications are rare and as with renal fine needle aspiration, hematuria can occur.

Ultrasound-Guided Ethanol Sclerotherapy

Renal cysts in dogs and cats are often asymptomatic and do not require treatment as long as no malignant nor infectious disease is suspected. Intervention may be needed if clinical signs such as outflow obstruction, infection or pain occur. The aim of sclerotherapy is the destruction of the secretory epithelium, but recurrence can happen (Vagias et al. 2022). With the animal under anesthesia, a 22-gauge spinal needle is inserted into the cyst under ultrasound-guidance and connected to an extension set with a three-way valve. The fluid volume should be measured, and a sterile portion collected for cytology and culture. Sclerotherapy is performed with an injection of 95% ethanol solution, using 50% of the volume drained. The 95% ethanol solution should be slowly injected, left in place for 3 minutes and slowly drained. The procedure should be performed twice. Complications reported are minor (Agut et al. 2008; Vagias et al. 2022; Zatelli et al. 2007).

Vet-ebooks.com

Nephro-Ureteral Procedures/Implants

Subcutaneous Ureteral Bypass (SUB)

SUBs are currently standard of care for the treatment of feline ureteral obstruction. Ureteral stenting is generally preferred in dogs. SUBs are placed through an open celiotomy under fluoroscopic-or ultrasound guidance (Figure 11.104) (Norfolk Manual; Butty & Labato 2021). A nephrostomy catheter is placed through the caudal pole of the kidney, a cystostomy catheter is placed at the apex of the bladder and both catheters are connected to a subcutaneous port. When evaluating a SUB, it is important to know the version of the SUB (1.0 versus 2.0 versus 3.0) used to best evaluate them. SUBs can be placed in patients with variable degree of hydronephrosis. If renal pelvic dilation is minimal (>1–4 mm), the catheter can be placed through the renal pelvis and into the proximal ureter without looping in the renal pelvis as a small pelvis cannot accommodate the loop of the nephrostomy catheter. Following SUB placement, a significant decrease in renal pelvic width in the short (2.4 mm, range 0–7 mm) and long term (>3 months following placement (1.7 mm, range 0–3.5 mm) was reported (Fages et al. 2018).

Ultrasound Monitoring of SUB Flushing

SUBs allow direct sampling of urine via puncture of the subcutaneous port. A SUB flush should be performed every 3–6 months and ultrasound is the

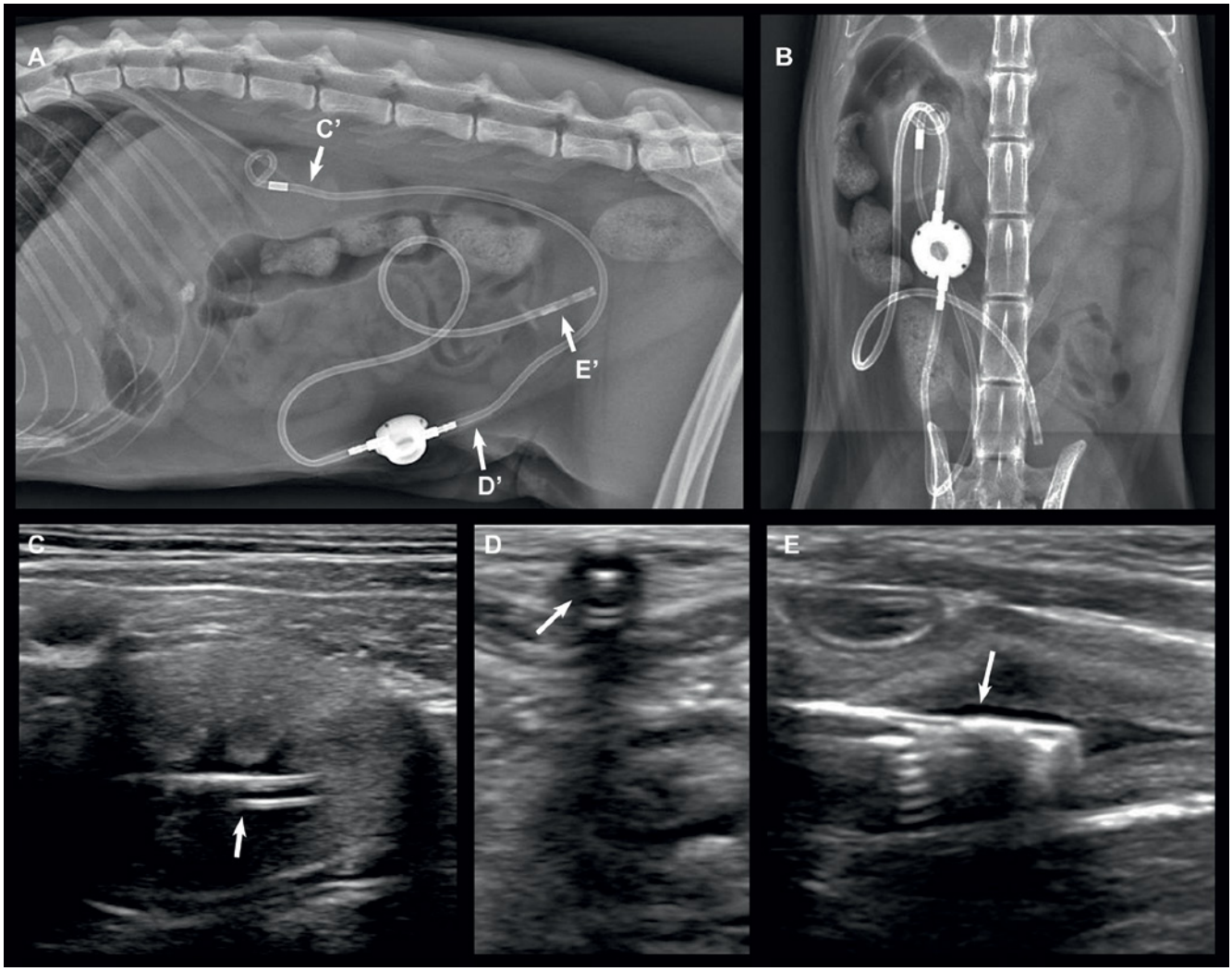


Figure 11.104. SUB assessment in a 10-year-old cat. The SUB apparatus is easily identified on the lateral **(A)** and ventrodorsal radiographs **(B)**. **C′, D′** and **E′** correspond to the different segments assessed on ultrasound. **(C)** The curled renal component is seen in the collapsed pelvis (arrow). **(D)** The tubing (arrow) can also be traced in the abdomen and subcutaneous fat **(D)**. **(E)** The distal component (arrow) is located in the bladder lumen.

Vet-ebooks.com

optimal method of monitoring. Agitated saline is injected quickly in 1 mL increments (ensuring to withdraw the 1 ml prior to each injection) while observing the renal pelvis on ultrasound. Saline bubbles seen within the renal pelvis and proximal ureter confirm patency of the nephrostomy catheter. Once patency is confirmed, the flush is repeated while observing the bladder on ultrasound. Appearance of bubbles in the trigone before exiting the cystostomy catheter may indicate that the native ureter has regained patency. The infusion of TetraEDTA (tEDTA) following SUB flushing may decrease the rate of mineralization and infection (Milligan abstract ACVIM 2021; Mas abstract VIRIES 2021).

Complications reported following SUB placement include luminal mineralization (Figure 11.105), kinking or break of a catheter implant (Figure 11.106), migration and fistulation of the subcutaneous port. Encrustation can be relieved with the use of tEDTA infusions into the SUB once or twice a day for 3–5 days or until the obstruction is relieved (Chik et al. 2019; Anders et al. 2012; Duval et al. 2022). tEDTA is infused directly into the port under ultrasound-guidance.

Ureteral Stenting

Ureteral stents can also be used for the treatment of ureteral obstruction, preferably in dogs. Ureteral stents are composed of polyurethane and have two pigtails at each end. One pigtail is placed in the renal pelvis, the other in the bladder and the shaft of the stent passes through the ureteral lumen (Figure 11.107). Ureteral stents are generally radio opaque. Contrary to SUBs, stents can be easily removed once the cause

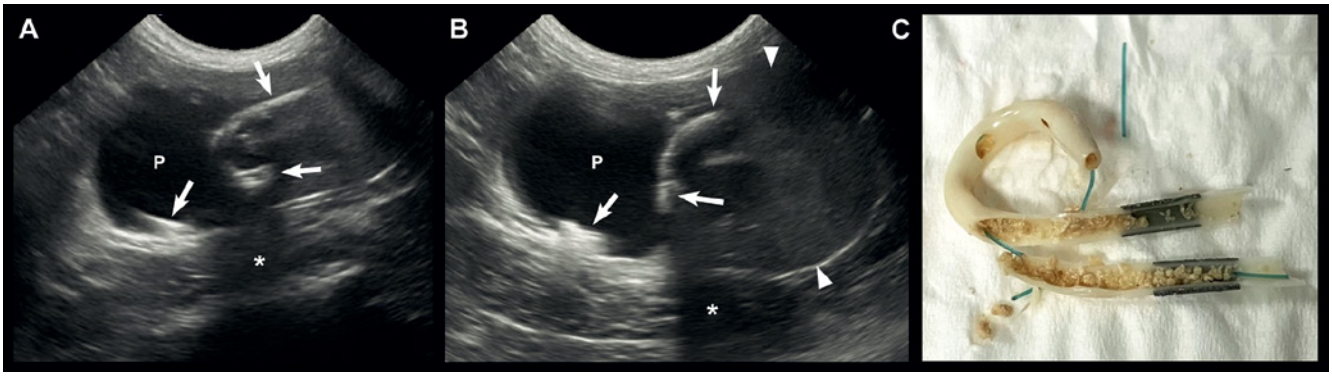


Figure 11.105. SUB complication. During the SUB flush of a 5-year-old cat DSH, the nephrostomy tube appeared nonpatent during the flush. Note the marked hydronephrosis (P) and the wide acoustic shadowing (*) caused by the SUB device (arrows) mineralization. in these ultrasound images **(A, B)**. Arrowheads delineate the renal parenchyma. Patency could not be restored with a frequent flushing protocol. The old nephrostomy device filled with mineral debris **(C)** was replaced with a new one.

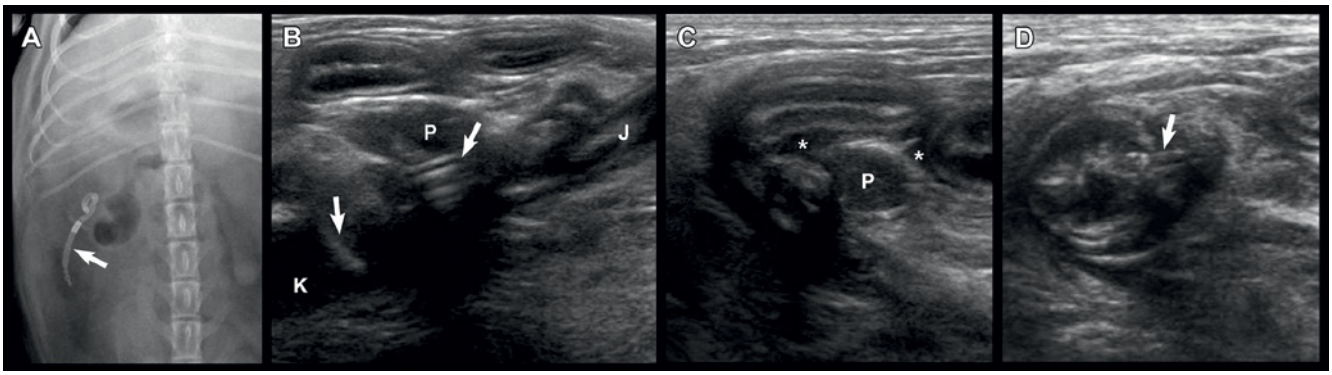


Figure 11.106. SUB complication. At an evaluation of an 8-year-old Shih Tzu with a SUB that broke 3 year ago **(A)** and presented for a persistent right cranial wound, the broken renal part of the device (arrows) was seen still engaged in the right kidney **(B)** and lying along a jejunal segment. **(C)** The broken piece is associated with shadowing and there is local adhesion (*) to the bowel segments and part of the pancreas. **(D)** On transverse view of the affected jejunum, the tip of the tube is anchored in the wall (arrow). This appears chronic as there is minimal bright fat at the site. J, jejunum; K, kidney; P, pancreas.

Vet-ebooks.com

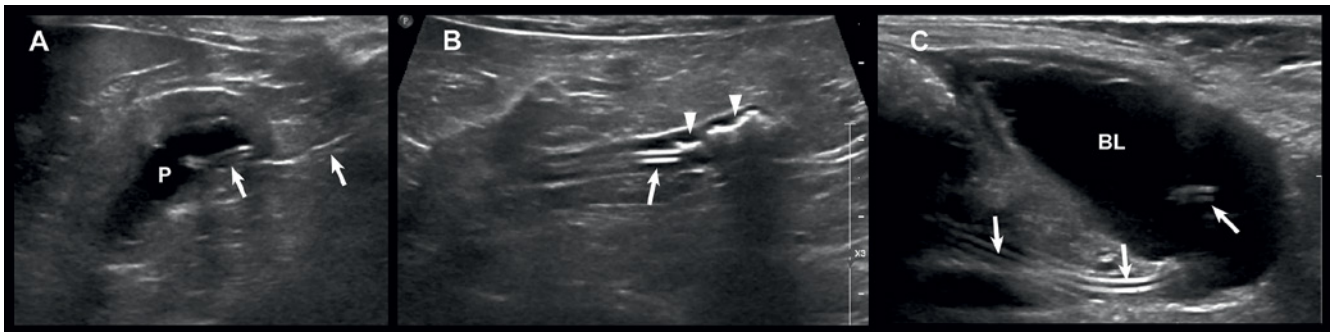


Figure 11.107. Ultrasound monitoring of renal stenting in a 12-year-old Yorkie with chronic obstruction. Ultrasound is useful to confirm the placement and location of stent extremities and follow ureteral patency. (**A-C**) The stent appears as a hyperechoic tubular structure (arrows), extending from the moderately distended pelvis (P), through the ureter, along ureteral calculi (arrowheads) and into the bladder (BL).

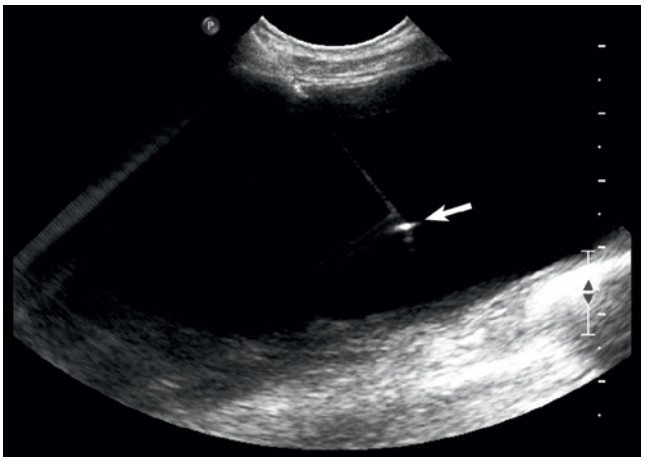


Figure 11.108. Cystocentesis in a dog. Longitudinal sonogram of the urinary bladder during cystocentesis. The fine hyperechoic line created by the needle and the hyperechoic needle tip (arrow) within the lumen are visualized.

of obstruction has resolved or left in place long term. Radiographs and ultrasound are used to assess possible complications such as stent migration, mineralization, fistula formation, and infection.

Bladder and Urethra

Ultrasound-Guided Cystocentesis

It can be safely performed on a sufficiently distended bladder. A 22- or 23-gauge, 1- or 1.5-in needle attached to a 5-mL syringe is typically used. Starting with a longitudinal image of the UB, the needle is placed just cranial to the transducer while trying to keep the needle aligned with the plane of the ultrasound beam. The needle appears as a fine linear hyperechoic interface that often causes distal reverberation or shadowing artifacts (Figure 11.108). Cystocentesis and percutaneous fine-needle aspiration of a mass is not recommended when a **urothelial carcinoma** in suspected because the technique can lead to regional spread of the tumor along the needle tract, as seen on rare occasion postsurgically (Figure 11.109).

Ultrasound-Guided Bladder Biopsy

For a suction assisted procedure, an appropriately sized red-rubber catheter with side holes is connected to a 20-mL syringe and aseptically inserted retrograde into the UB. The rubber catheter tip is visualized within the UB (Figure 11.110). Manual compression of the caudal abdominal wall may assist in directing the catheter toward the mass. The syringe plunger is pulled back. Once negative pressure can be maintained, the pressure is applied and released 3–4 times, collecting tissue from the adjacent mucosa. The urinary catheter is abruptly withdrawn 4–6 cm from the bladder while the suction

Vet-ebooks.com

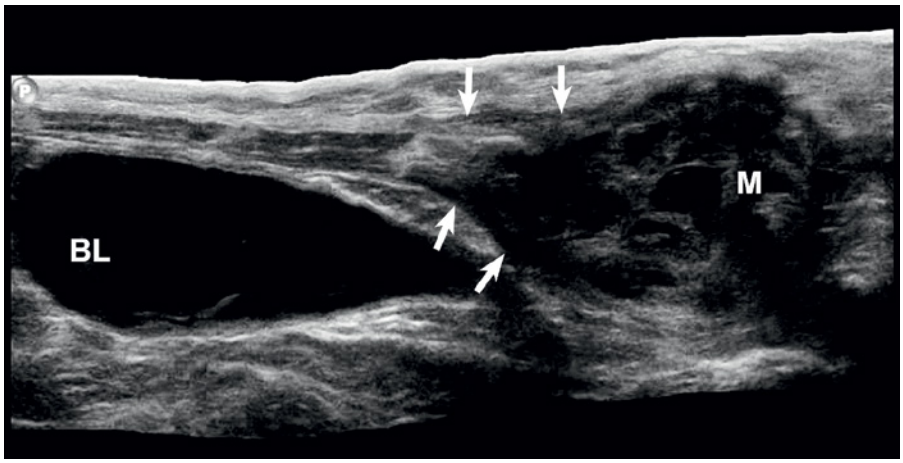


Figure 11.109. TCC seeded in the rectus abdominis of a 10-year-old Maine Coon cat. Longitudinal panoramic sonogram of the caudal abdomen, including the bladder (BL) and the irregular mass (M) invading part of the rectus abdominis (arrowheads). This cat has a TCC mass previously removed surgically. There is no evidence of tumor recurrence at the bladder site.

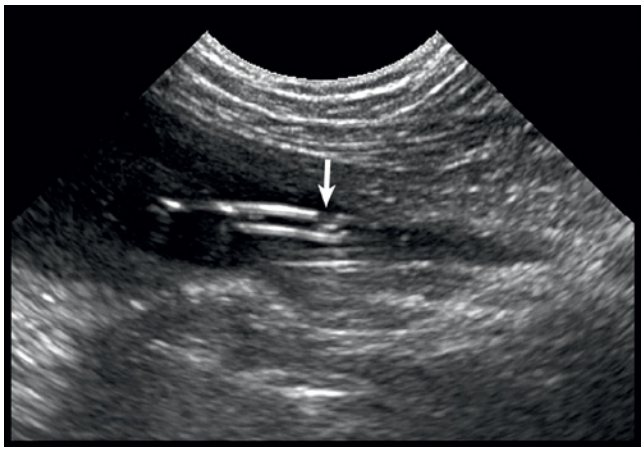


Figure 11.110. Suction biopsy in a dog. Longitudinal sonogram of the urinary bladder and an indwelling red-rubber catheter during a suction biopsy. The catheter walls are hyperechoic and the lumen hypoechoic. A small defect in the catheter wall (arrow) corresponds to one of the side holes in the catheter, which can be guided into the desired location of the biopsy.

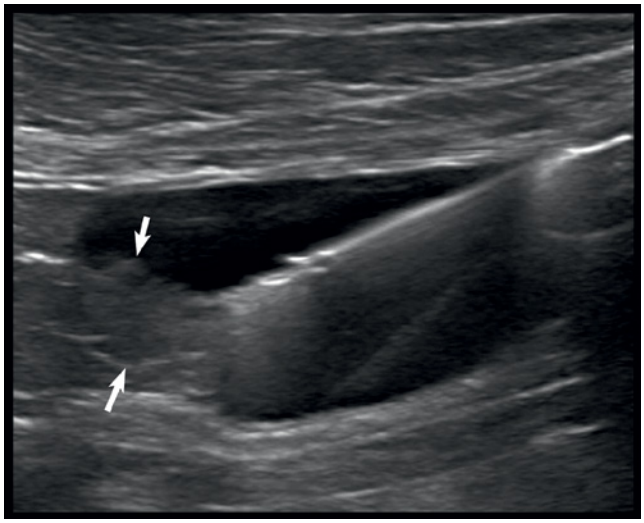


Figure 11.111. US monitoring of transurethral biopsy of a bladder mass in a 16-year-old cat, using endoscopic forceps. The mass (arrows) is located along the cranial bladder wall and the diagnosis was urothelial cell carcinoma.

is held, with the aim of pulling a large fragment of tissue from the mass. Bladder wall hemorrhage can be seen during this procedure (Lamb et al. 1996).

Endoscopic biopsy forceps can also be used to obtain biopsies of bladder lesions. Careful measurement of the distance from the distal urethra to the bladder apex is essential to prevent inadvertent bladder perforation from advancing the biopsy forceps too cranially; this can be safely done under ultrasound guidance (Figure 11.111) (Shimizu et al. 2021).

Laser Ablation Monitoring

Over 95% of ectopic ureters in dogs are identified as intramural (Anders et al. 2012; Berent et al. 2012; Hoey et al. 2020; Holt and Moore 1995; McLoughlin and Chew 2000). Once intramural course is confirmed, the medial wall of the intramural ectopic ureter is transected until the ureteral orifice inserts cranial to the urethral sphincter well within the trigone. This procedure can be monitored under ultrasound guidance (Figure 11.112). Perforation of the lower urinary tract, stricture at the UV

Vet-ebooks.com

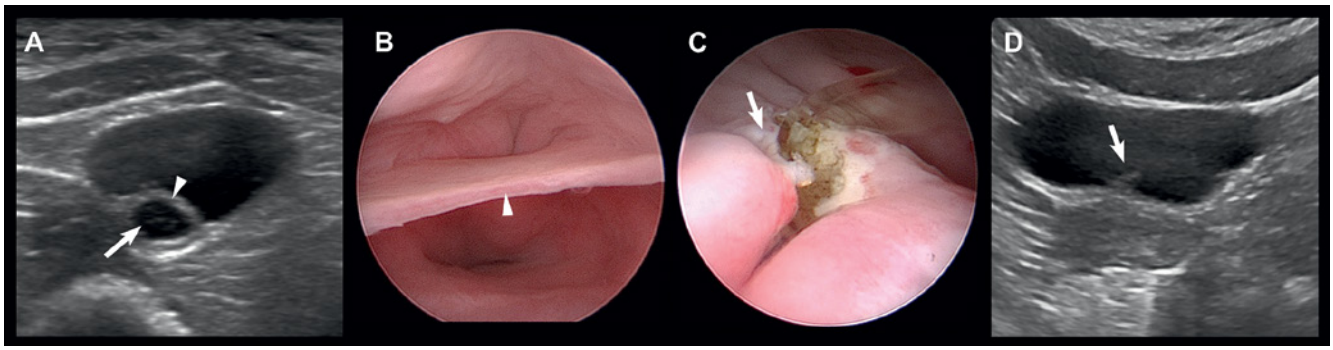


Figure 11.112. **US assistance of laser ablation of ectopic ureter** in a 5-month-old female intact Labrador Retriever with persistent incontinence since adoption. **(A)** A left intramural ectopic ureter is suspected on ultrasound: the medial wall of the intramural ectopic ureter (arrowhead) separates the bladder from the ureter. **(B)** The ectopic ureter is confirmed on cystoscopy: the opening of the ureter is located in the urethra and the medial wall of the ectopic ureter (arrowhead) separates the urethra and ureter. **(C)** The medial wall of the intramural ectopic ureter is transected until the new ureteral orifice (arrow) opens cranial to the trigone and urine is jetting within the bladder. **(D)** An ultrasound is performed 6 weeks after laser ablation to rule out laser reaction with proliferative tissue at the new UVJ that could result in worsening hydroureter/nephrosis. The new UVJ is healed (arrow), and urine was jetting in the bladder (not shown).

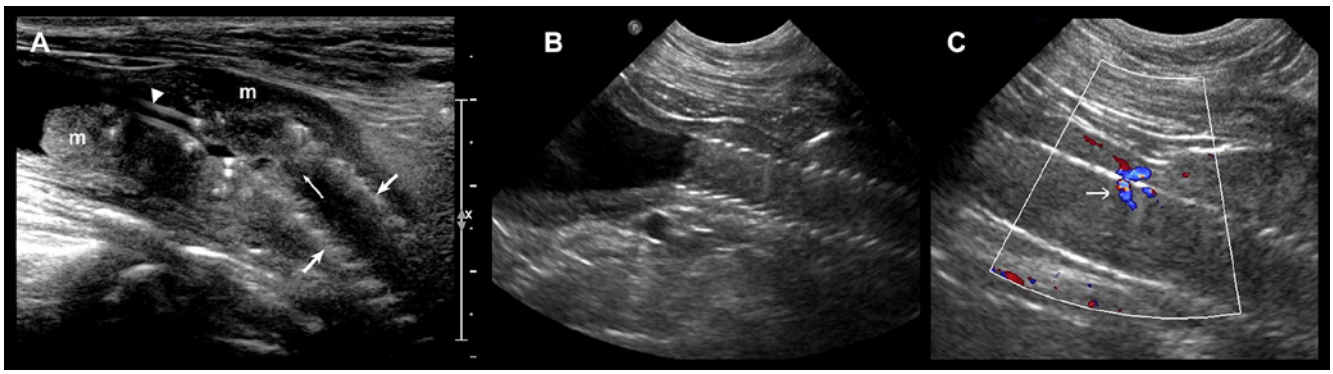


Figure 11.113. **Urethral stent in two dogs. (A)** Longitudinal sonogram of a dog with progressive TCC mass (m) at the bladder neck and urethra. After a few months of placement of a urethral stent (large arrows), the stent patency is compromised (thin arrow) by echogenic structure obliterating its lumen. Part of a ureteral catheter is seen (arrowhead). **(B, C)** In this other dog with TCC also extending into the stent. The entire visible stent has an echogenic luminal filling, and the color flow Doppler **(C)** confirms that there is vascularity in the tissue.

or recanalization are rare complications that can be diagnosed with ultrasound or cysto-urethrogram (Berent et al. 2008, 2012; Hoey et al. 2020; Smith et al. 2010). Other laser procedure such as correction of orthotopic ureterocele secondary to ureterovesicular stenosis can be monitored with ultrasound (Auger et al. 2018).

Urethral Stent

Urethral stenting is performed in patients with partial or complete urinary tract obstruction due to a malignant (urethral, trigonal, prostatic neoplasia) or benign (urethral stricture, proliferative urethritis) process. After measurement of the length and width of the obstruction, an appropriately sized stent is deployed under fluoroscopic guidance to restore patency. Ultrasound is useful in monitoring treatment response and stent patency (Figure 11.113).

Ultrasound has also been advocated to guide and monitor palliative cystoscopic laser ablation of transitional cell tumors (Cerf and Lindquist 2012) or can assist flushing procedure to distinguish amorphous mucus accumulation from soft-tissue mass (Figure 11.114).

Vet-ebooks.com

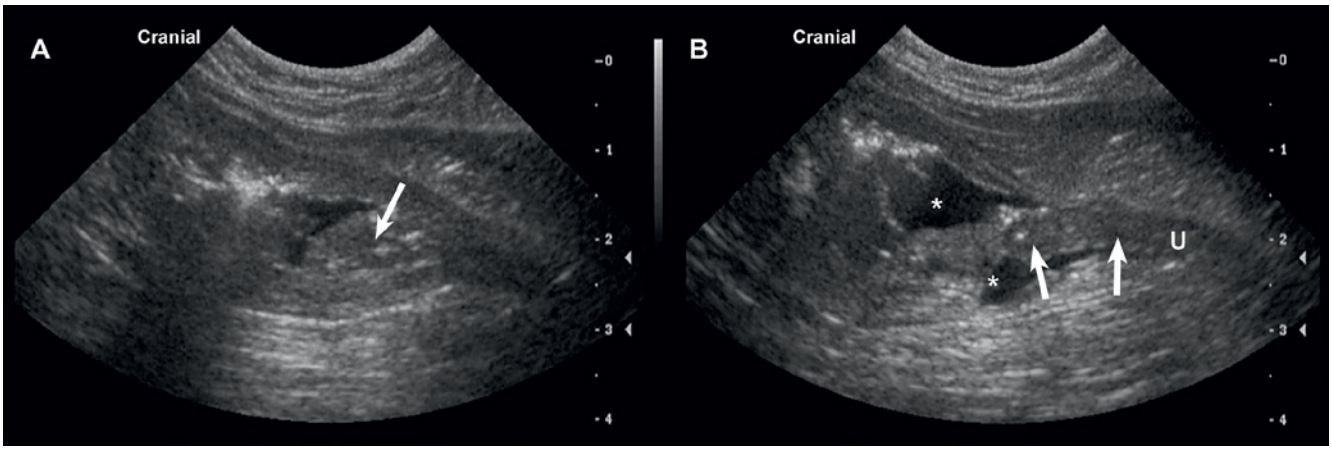


Figure 11.114. Mucus plug in an obstructed cat. Initial longitudinal sonographic images **(A)** showed a hyperechoic structure (arrow) silhouetting with the dorsal bladder wall at the trigone. **(B)** Once saline was injected through a urinary catheter, the "mass"detached from the wall, forming a tubular structure delineated by anechoic urine mixed with saline (*). This plug extended into the urethra (U). It was removed surgically and confirmed to represent mucus mixed with cellular debris and crystals.

Visit our website at **www.SmallAnimalUltrasonography.com** for complementary video clips with annotations and text on:

- Normal kidneys
- Chronic interstitial nephritis
- Acute nephritis
- Pyelonephritis
- Renal lymphoma
- Renal primary neoplasia
- Polycystic renal disease
- Perinephric pseudocyst
- Obstructive nephrolithiasis and hydronephrosis
- Ectopic ureters
- Normal bladder and urethra
- Cystitis
- Polypoid cystitis
- Calculi
- Blood clot
- Ureteral jet
- Bladder tumors

References

Abraham LA, Beck C, Slocombe RF (2003) Renal dysplasia and urinary tract infection in a bull mastiff puppy. Aust Vet J 81:336–339.

Adams WH, Toal RL, Breider MA (1991) Ultrasonographic findings in dogs and cats with oxalate nephrosis attributable to ethylene glycol intoxication: 15 cases (1984–1988). J Am Vet Med Assoc 199:492–496.

Adin CA, Herrgesell EJ, Nyland TG, Hughes JM, et al. (2003) Antegrade pyelography for suspected ureteral obstruction in cats: 11 cats (1995–2001). J Am Vet Med Assoc 222: 1576–1581.

Adin CA, Chew DJ, Heng HG, Townsend KL, et al. (2011) Bladder inversion and secondary hematuria in a 6-month-old domestic shorthair cat. J Am Vet Med Assoc 239(3):370–373.

Agut A, Soler M, Laredo FG, Pallares FJ, et al. (2008) Imaging diagnosis—ultrasound-guided ethanol sclerotherapy for a simple renal cyst. Vet Radiol Ultrasound 49(1):65–67.

Allworth MS, Hoffman KL (1999) Crossed renal ectopia with fusion in a cat. Vet Radiol Ultrasound 40:357–360.

Anders KJ, McLoughlin MA, Samii VF, Chew DJ, et al. (2012) Ectopic ureters in male dogs: review of 16 clinical cases (1999–2007). J Am Anim Hosp Assoc 48(6):390–8. https://doi.org/10.5326/JAAHA-MS-5302

Andrulli S, Turin A, Bigi MC, Ravani P, et al. (2010) Colour Doppler twinkling in kidney stones: artifact or sign? NDT Plus 3:151–154.

Auger M, Bua AS, Carmel EN, Dunn M (2018) Use of cystoscopic-guided laser ablation for treatment of unilateral ureterovesicular stenosis and secondary orthotopic ureterocele in a female dog J Am Vet Med Assoc 253:463–469.

Barella G, Lodi M, Sabbadin LA, Faverzani S (2012) A new method for ultrasonographic measurement of kidney size in healthy dogs J Ultrasound 15:186–191.

Barr FJ, Petteson MW, Lucke VM, Gibbs C (1989) Hypercalcemic nephropathy in three dogs: sonographic appearance. Vet Radiology Ultrasound 30:169–173.

Barr FJ, Holt PE, Gibbs C (1990) Ultrasonographic measurements of normal renal parameters. J Small Anim Pract 31:180–184.

Vet-ebooks.com

Beck JA, Bellenger CR, Lamb WA, Churcher RK, et al. (2000) Perirenal pseudocysts in 26 cats. Aust Vet J 78:166–171.

Benigni L, Lamb CR, Corzo-Menendez N, Holloway A, et al. (2006) Lymphoma affecting the urinary bladder in three dogs and a cat. Vet Radiol Ultrasound 47:592–596.

Bentley C, Williams TL, Constantino-Casas F, Genain MA (2022) The ultrasonographic appearance of renal striations and their association with renal disease and renal histopathology in domestic cats. Vet Radiology Ultrasound 30:169–173.1–8.

Benzima C, Job C, Pascal Q, Bureau S, et al. (2019) Malakoplakia of the bladder in a 4-month-old puppy. J Am Anim Hosp Assoc 55:261–265.

Berent AC, Mayhew PD, Porat-Mosenco Y. (2008) Use of cystoscopicguided laser ablation for treatment of intramural ureteral ectopia in male dogs: four cases (2006–2007). J Am Vet Med Assoc 232:1026–1034.

Berent AC, Weisse C, Mayhew PD, Todd K, et al. (2012) Evaluation of cystoscopic-guided laser ablation of intramural ectopic ureters in female dogs. J Am Vet Med Assoc 240(6):716–25. https://doi.org/10.2460/javma.240.6.716.

Biedak NR, Penninck D, Biswell E (2023) Ultrasonographic features of a urinary bladder leiomyoma in a cat. J Feline Med Surg Open Rep 9(1):20551169231165247.

Biller DS, Bradley GA, Partington BP (1992) Renal medullary rim sign: ultrasonographic evidence of renal disease. Vet Radiol Ultrasound 33:286–290.

Bonazzi M, Volta A, Gnudi G, Cozzi MC, et al. (2009) Comparison between ultrasound and genetic testing for the early diagnosis of polycystic kidney disease in Persian and exotic shorthair cats. J Feline Med Surg 11:430–434.

Briscoe KA, Barrs VR, Lindsay S, Hoffman KL et al. (2010) Encrusting cystitis in a cat secondary to *Corynebacterium urealyticum* infection. J Fel Med Surg 12:974–977.

Butty EM, Labato MA (2021) Subcutaneous ureteral bypass device placement with intraoperative ultrasound guidance, with or without microsurgical ureterotomy, in 24 cats. J Feline Med Surg 23(12:1183–1191. doi: 10.1177/1098612X211002014.Epub. PMID: 33754880.

Butty EM, Hahn S, Labato MA. (2021) Presumptive malignant transformation of chronic polypoid cystitis into an apical transitional cell carcinoma without BRAF mutation in a young female dog. J Vet Intern Med. 35(3):1551–1557. doi: 10.1111/jvim.16107. Epub 2021 Mar 19. PMID: 33739477; PMCID: PMC8163141.

Byl KM, Kruger JM, Kinns J, Nelson NC, et al. (2010). In vitro comparison of plain radiography, double-contrast cystography, ultrasonography, and computed tomography for estimation of cystolith size. Am J Vet Res 71(3): 374–380.

Cavalera MA, Germone F, Uva A, D'Ippolito P, et al (2021) Clinical and histopathological features of renal maldevelopment in boxer dogs: a retrospective case series (1999–2018). Animals 11(3), 810; https://doi.org/10.3390/ani11030810

Cerf DJ and Lindquist EC (2012) Palliative ultrasound-guided endoscopic diode laser ablation of transitional cell carcinomas of the lower urinary tract in dogs. J Am Vet Med Assoc 240(1):51–60.

Chandler ML, Elwood C, Murphy KF, Gajanayake I, et al. (2007) Juvenile nephropathy in 37 boxer dogs. J Sm Anim Pract 48:690–694.

Cherbinsky O, Westropp J, Tinga S, Jones B, et al. (2010) Ultrasonographic features of grass awns in the urinary bladder. Vet Radiol Ultrasound 51:462–465.

Chik C, Berent A, Weisse C, et al. (2019) Therapeutic use of tetrasodium ethylenediaminetetraacetic acid solution for treatment of subcutaneous ureteral bypass device mineralization in cats. J Vet Intern Med 33:2124–2132.

Choi J, Jang J, Choi H, Kim H, et al. (2010) Ultrasonographic features of pyonephrosis in dogs. Vet Radiol Ultrasound 51:548–553.

Choo D, Lee K, Yoon H (2021) Fungal balls detected using ultrasonography in the urinary bladder of a dog. Vet Radiol Ultrasound 1–4, doi: 10.1111/vru.13034.

Coffman JM, McConkey M, Ellison G, Huynh E et al. (2019) Complete urogenital and anorectal duplication in a dog. Case reports. Vet Med, doi:10.1155/2019/3696978.

Cordella A, Pey P, Dondi F, Dunn M, et al. (2020) The ultrasonographic 'rim sign' versus medullary band sign in cats and their association with renal disease. J Vet intern Med 34:1932–1939.

Crivellenti LZ, Cianciolo R, Wittum T. et al. (2018) Associations of patient characteristics, disease stage, and biopsy technique with the diagnostic quality of core needle renal biopsy specimens from dogs with suspected kidney disease. J Am Vet Med Assoc 252(1):67–74. https://doi.org/10.2460/javma.252.1.67.

D'Anjou MA, Bédard A, Dunn ME (2011) Clinical significance of renal pelvic dilatation on ultrasound in dogs and cats. Vet Radiol Ultrasound 52(1):88–94.

Debruyn K, Paepe D, Daminet S, Combes A, et al. (2013) Comparison of renal ultrasonographic measurements between healthy cats and three cat breeds: ragdoll, British Shorthair and Sphinx. J Feline Med Surg, doi: 10.1177/1098612X12471057

Duval V, Dunn M, Vachon C. (2022) Use of tetrasodium EDTA acid for the treatment of intraluminal obstruction of subcutaneous ureteral bypass devices. J Feline Med Surg.; 24(10): e330–e337. https://doi.org/10.1177/1098612X221107795

Eberlé O, Pouzot-Nevoret C, Barthélemy A, Drumond B, et al. (2022). Ultrasonographic and radiographic findings of the kidneys in six dogs and one cat with ethylene glycol intoxication. Vlaams Diergeneeskundig Tijdschrift 2022(91):113–121.

Esterline ML, Biller DS, Sicard GK (2005) Ureteral duplication in a dog. Vet Radiol Ultrasound 46:485–489.

Etadali N, Reetz J, Foster J (2018) Complications and clinical utilityof ultrasonographically-guided pyelocenthesis and antegrade pyelography in cats and dogs 49 cases (2007-2015). J Am Vet Med Assoc 254(7):826–834.

Eubig PA, Brady MS, Gwaltney-Brant SM, Khan SA, et al. (2005) Acute renal failure in dogs after the ingestion of

Vet-ebooks.com

grapes or raisins: a retrospective evaluation of 43 dogs (1992–2002). J Vet Intern Med 19:663–674.

Fages J, Dunn M, Specchi S, Pey P (2018) Ultrasound evaluation of the renal pelvis in cats with ureteral obstruction treated with a subcutaneous ureteral bypass: a retrospective study of 27 cases (2010-2015). J Fel Med & Surg 20(10):875–883.

Forrest LJ, O'Brien RT, Tremelling MS, Steinberg H, et al. (1998) Sonographic renal findings in 20 dogs with leptospirosis. Vet Radiol Ultrasound 39:337–340.

Gasser AM, Bush WW, Smith SS, Walton R (2003) Extradural spinal, bone marrow, and renal nephroblastoma. J Am Anim Hosp Assoc 39:80–85.

Gremillion C, Cohen, E.B., Vaden, S. et al (2021) Optimization of ultrasonographic ureteral jet detection and normal ureteral jet morphology in dogs. Vet Radiol Ultrasound 62(5) https://doi.org/10.1111/vru.13000

Hamlin AN, Chadwick LE, Fox-Alvarez SA, Hostnik ET (2019) Ultrasound characteristics of feline urinary bladder transitional cell carcinoma are similar to canine urinary bladder transitional cell carcinoma.Vet Radiol Ultrasound 60(5):552–559.

Hanazono K, Fukomoto S, Endo Y, Ueno H, et al. (2014). Ultrasonographic findings related to prognosis of canine transitional cell carcinoma. Vet Radiol Ultrasound 55(1): 79–84.

Hanson JA, Tidwell AS (1996) Ultrasonographic appearance of urethral transitional cell carcinoma in ten dogs. Vet Radiol Ultrasound 37:293–299.

Hart DV, Winter MD, Conway J, Berry CR (2013) Ultrasound appearance of the outer medulla in dogs without renal dysfunction. Vet Radiol Ultrasound 54:653–658.

Hecht S, McCarthy RJ, Tidwell AS (2005) What is your diagnosis? Ectopic kidney. J Am Vet Med Assoc 227: 223–224.

Heng HG, Ramos-Vara JA, Fulkerson CM, Fourez LM, et al (2022). Ultrasonographic detection of apex nodules in the urinary bladder of Scottish terriers. Vet Radiol Ultrasound 63(2):234–239.

Hickey MC, Jandrey K, Farrell KS, Carlson-Bremer D (2014) Concurrent diseases and conditions in cats with renal infarcts. J Vet Intern Med 4(28):319–323.

Hoey CSFK, Friend E, Meakin MA, Chanoit G (2020) Long-term outcome of female dogs treated for intramural ectopic ureters with cystoscopic-guided laser ablation. Vet Surg 2021;50:1449–1462.

Holloway A, O'Brien R (2007) Perirenal effusion in dogs and cats with acute renal failure. Vet Radiol Ultrasound 48: 574–579.

Holt PE, Moore AH.(1995) Canine ureteral ectopia: an analysis of 175 cases and comparison of surgical treatments. Vet Rec 136:345–349.

Hume C, Seiler G, Porat-Mosenco Y, Caceres A, et al. (2010) Cystosonographic measurements of canine bladder tumours. Veterinary and Comparative Oncology 8(2):122–126.

Ivancic M, Mai W (2008) Qualitative and quantitative comparison of renal vs. hepatic ultrasonographic intensity in healthy dogs. Vet Radiol Ultrasound 49:368–373.

Kochenburger J, Eriksson C, Green-berg M, Hoyt L. (2019) Ultrasonography of a ureteral and bladder fungal granuloma caused by Scedosporium apiospermumin a basset hound. Vet Radiol Ultrasound 60:E6–E9. doi:10.1111/vru.12518

Kyles AE, Hardie EM, Wooden BG, Adin CA, et al. (2005) Clinical, clinicopathologic, radiographic, and ultrasonographic abnormalities in cats with ureteral calculi: 163 cases (1984–2002). J Am Vet Med Assoc 226:932–936.

Labelle O, Penninck D, Butty EM, Haln S, et al. (2023) Pseudomembranous cystitis in cats with presumed or confirmed mineralization: a retrospective study of 26 cases (2016-2021). J Vet Intern Med 2023; 1–9. doi:10.1111/jvim.16819

Lamb CR, Gregory SP (1998) Ultrasonographic findings in 14 dogs with ectopic ureter. Vet Radiol Ultrasound 39:218–223.

Lamb CR, Trower ND, Gregory SP (1996) Ultrasound-guided catheter biopsy of the lower urinary tract: technique and results in 12 dogs. J Small Anim Pract 37:413–416.

Le Boedec K, Pastor ML, Lavoué R, Reynolds BS (2011) Pseudomembranous cystitis, an unusual condition associated with feline urine outflow obstruction: four cases. J Feline Med Surg 13(8):588–593.

Lemieux C, Vachon C, Beauchamp G, Dunn M (2021) Minimal renal pelvis dilation in cats diagnosed with benign ureteral obstruction by antegrade pyelography: a retrospective study of 82 cases (2012-2018). J Fel Med & Surg 23(10):892–899.

Leveille R, Biller DS, Partington BP, Miyabayashi T (1992) Sonographic investigation of transitional cell carcinoma of the urinary bladder in small animals. Vet Radiol Ultrasound 33:103–107.

Lippi I, Mannucci T, Della Santa D, Barella G, et al. (2019) Emphysematous cystitis: retrospective evaluation of predisposing factors and ultrasound features in 36 dogs and 2 cats. Can Vet J 60:514–518.

Logwood K, Penninck D, Priest K, Marie Butty E (2021) Ultrasonographic features of presumed renal telangiectasia in three Pembroke welsh corgis. J Am Anim Hosp Assoc 57:301–305.

Mantis P, Lamb CR (2000) Most dogs with medullary rim sign on ultrasonography have no demonstrable renal dysfunction. Vet Radiol Ultrasound 41:164–166.

Mareschal A, d'Anjou MA, Moreau M, Alexander K, et al. (2007) Utrasonographic measurement of kidney-to-aorta ratio as a method os estimating renal size in dogs. Vet Radiol Ultrasound 48(5):434–438.

Martinez I, Mattoon JS, Eaton KA, Chew DJ, et al. (2003) Polypoid cystitis in 17 dogs (1978–2001). J Vet Intern Med 17:499–509.

McCord K, Steyn PF, Lunn KF (2008) Unilateral improvement in glomerular filtration rate after permanent drainage of a perinephric pseudocyst in a cat. J Feline Med Surg 10(3):280–3.

McLoughlin MA, Chew DJ (2000) Diagnosis and surgical management of ectopic ureters. Clin Tech Small Anim Pract 15(1):17–24.

Meler E, Berent A, Weisse C, Dunn M (2018) Treatment of congenital ureterovesicular junction stenosis by

Vet-ebooks.com

endoscopic laser ablation in dogs: 10 cases 2009-2013. J Am Vet Med Assoc 253(4):452–462.
Miles KG, Jergens AE (1992) Unilateral perinephric pseudocyst of undetermined origin in a dog. Vet Radiol Ultrasound 33:277–281.
Moe L, Lium B (1997) Hereditary multifocal renal cystadenocarcinomas and nodular dermatofibrosis in 51 German shepherd dogs. J Small Anim Pract 38:498–505.
Moore FM, Thornton GW (1983) Telangiectasia of Pembroke Welsh corgi dogs. Vet Pathol 20:203–208.
Mosenco AS, Culp WTN, Johnson V, French A, et al. (2008) Renal cystadenoma in a domestic shorthair. J Feline Med Surg 10:102–105.
Neuwirth L, Mahaffey M, Crowell W, Selcer B, et al. (1993) Comparison of excretory urography and ultrasonography for detection of experimentally induced pyelonephritis in dogs. Am J Vet Res 54:660–669.
Nevins JR, Mai W, Thomas E (2015) Associations between ultrasound and clinical findings in cats with urethral obstruction. Vet Radiol Ultrasound 56(4):439–447.
O'Brien RT, Wood EF (1998) Urinary bladder mural hemorrhage associated with systemic bleeding disorders in three dogs. Vet Radiol Ultrasound 39:354–356.
Ochoa VB, DiBartola SP, Chew DJ, Westropp J, et al. (1999) Perinephric pseudocysts in the cat: a retrospective study and review of the literature. J Vet Intern Med 13:47–55.
Petite A, Busoni V, Heinen MP, Billen F, et al. (2006) Radiographic and ultrasonographic findings of emphysematous cystitis in four nondiabetic female dogs. Vet Radiol Ultrasound 47:90–93.
Pey P, Marcon O, Drigo M Specchi S, et al. (2015). Multidetector-row computed tomographic characteristics of presumed preureteral vena cava in cats. Vet Radiol Ultrasound 56:359–366.
Puccinelli C, Lippi I, Pelligra T, Mannucci T, et al. (2021) Pseudomembranous cystitis: an uncommon ultrasound appearance of cystitis in cats and dogs. Vet Sci 8: 125–134.
Quimby J, Dowers K, Herndon A, Randall E (2017) Renal pelvic and ureteral ultrasonographic characteristics of cars with chronic kidney disease in comparison with normal cats, and cats with pyelonephritis or ureteral obstruction. J Fel Med & Surg 10(8):784–790.
Rawlings CA, Diamond H, Howerth EW, Neuwirth L, et al. (2003) Diagnostic quality of percutaneous kidney biopsy specimens obtained with laparoscopy versus ultrasound guidance in dogs. J Am Vet Med Assoc 223:317–321.
Reichle JK, DiBartola SP, Léveillé R (2002) Renal ultrasonographic and computed tomographic appearance, volume, and function of cats with autosomal dominant polycystic kidney disease. Vet Radiol Ultrasound 43:368–373.
Reichle JK, Peterson II RA, Mahaffey MB, Schelling CG, et al. (2003) Ureteral fibroepithelial polyps in four dogs. Vet Radiol Ultrasound 44:433–437.
Rivers BJ, Walter PA, Polzin DJ (1997) Ultrasonographic-guided, percutaneous antegrade pyelography: technique and clinical application in the dog and cat. J Am Anim Hosp Assoc 33:61–68.
Ruth JD, Heng HG, Miller MA (2013) Effect of anisotropy and spatial compound imaging on renal echogenicity in dogs. Vet Radiol Ultrasound 54:659–665.
Seiler GS, Rhodes J, Cianciolo R, Casal ML (2010) Ultrasonographic fingings in cairn terriers with preclinical renal dysplasia. Vet Radiol Ultrasound 51:453–457.
Seo S-H, Lee H-A, Suh S-I Choi R, et al. (2021) Crossed fused renal ectopia in a Persian cat. J Feline Med Surg Open Rep 3: 2055116917695875.
Shimizu N, Hamaide A, Soliveres E, Heimann M et al (2021) Ultrasound-guided transurethral urinary bladder biopsy using an endoscopic biopsy forceps in dogs: 27 cases (2016-2019). J Small Anim Pract 62:788–794.
Sislak MD, Spaulding KA, Zoran DL, Bauer JE, et al. (2014) Ultrasonographic characteristics of lipiduria in clinically normal cats Vet Radiol Ultrasound 55:195–201.
Slinkard S, Anson A, D. Penninck, Specchi S et al (2023). Renal ectopia and fusion in 13 cats. J Feline Med Surg 25 (10):1098612X231196810
Smith AL, Radlinsky MG, Rawlings CA (2010). Cystoscopic diagnosis and treatment of ectopic ureters in female dogs: 16 cases (2005–2008). J Am Vet Med Assoc 2010; 237:191–195.
Sombrio MS, Grotti GC, Brizola PB, Müller T (2022). What is your diagnosis? JAVMA 259(S1):1–3.
Specchi S, Lacava G, d'Anjou MA, Zini E, et al. (2012) Ultrasound-guided percutaneous antegrade pyelography with computed tomography for the diagnosis of spontaneous partial ureteral rupture in a dog. Can Vet J 53:1187–1190.
Steinhaus J, Berent AC, Weiss C, Eatroff A, et al. (2015) Clinical presentation and outcome of cats with circumcaval ureters associated with a ureteral obstruction. J Vet Intern Med 29:63–70.
Stiffler KS, Stevenson MAM, Mahaffey MB, Howerth EW, et al. (2002) Intravesical ureterocele with concurrent renal dysfunction in a dog: a case report and proposed classification system. J Am Anim Hosp Assoc 38:33–39.
Sul RM, Hammond G, Pratschke K (2014) Follicular cystitis in a dog. Vet Rec Case Rep 2(1):1–4.
Szatmari V, Osi Z, Manczur F (2001) Ultrasound-guided percutaneous drainage for treatment of pyonephrosis in two dogs. J Am Vet Med Assoc 218:1796–1799.
Taylor AR, Barr JW, Hokamp JA, Johnson MC, et al. (2012) Cytologic diagnosis of disseminated histoplasmosis in the wall of the urinary bladder of a cat. J Am Anim Hosp Assoc 48(3):203–208.
Taylor O., Knight R, Genain MA, Owen L (2022) Ultrasonography as a sensitive and specific diagnostic modality for the detection of ectopic ureters in urinary incontinent dogs. Vet Radiol Ultrasound 63:328–336.
Tsoi MF, Kline MA, Conkling A, Mani R, et al. (2021) Scedosporium apiospermum infection presenting as a mural urinary bladder mass and focal peritonitis in a Border Collie. Med Mycol Case Rep 33: 9–13. https://doi.org/10.1016/j.mmcr.2021.05.003
Vaden SL, Levine JF, Lees GE, Groman RP, et al. (2005) Renal biopsy: a retrospective study of methods and complications in 283 dogs and 65 cats. J Vet Intern Med 19:794–801.

Vet-ebooks.com

Vagias M, Chanoit G, Bubernik-Angapen LJ, Gibson EA et al. (2022) Perioperative characteristics, histologic diagnosis, complications, and outcomes of dogs undergoing percutaneous drainage, sclerotherapy or surgical management of intrarenal cystic lesions: 18 dogs (2004-2021). BMC Vet Res 18:233–254.

Valdès-Martinez A, Cianciolo R, Mai W (2007) Association between renal hyopechoic subcapsular thickening and lymphosarcoma in cats. Vet Radiol Ultrasound 48:357–360.

Viitanen SJ, Tuomisto L, Salonen N, Eskola K et al. (2023) Escherichia coli-associated follicular cystitis in dogs: clinical and pathologic characterization. J Vet Intern Med 37:1059–1066.

Weichselbaum RC, Feeney DA, Jessen CR, Osborne CA, et al. (1999) Urocystolith detection: comparison of survey, contrast radiographic and ultrasonographic techniques in an in vitro bladder phantom. Vet Radiol Ultrasound 40:386–400.

Weichselbaum RC, Feeney DA, Jessen CR, Osborne CA, et al. (2000) Relevance of sonographic artifacts observed during in vitro characterization of urocystolith mineral composition. Vet Radiol Ultrasound 41:438–446.

Wills SJ, Barrett EL, Barr FJ, Bradley KJ, et al. (2009) Evaluation of repeatability of ultrasound scanning for detection of feline polycystic kidney disease. J Feline Med Surg 11:993–996.

Yeager AE, Anderson WI (1989) Study of association between histologic features and echogenicity of architecturally normal cat kidneys. Am J Vet Res 50:860–863.

Zatelli A, D'Ippolito P, Bonfanti U, Zini E.(2007) Ultrasound-assisted drainage and alcoholization of hepatic and renal cysts: 22 cases. J Am Anim Hosp Assoc 43(2):112–116. https://doi.org/10.5326/0430112

Vet-ebooks.com

CHAPTER TWELVE

Adrenal Glands

Marc-André d'Anjou[1], Dominique Penninck[2], and Pascaline Pey[3,4]

[1]*Animages, Brossard, Québec, Canada*
[2]*Department of Clinical Sciences, Cummings School of Veterinary Medicine, Tufts University, North Grafton, MA, USA*
[3]*IMPCOM-MEDICAL, Bologna, Italy*
[4]*Antech Imaging Services, Irvine, CA, USA*

Preparation and Scanning Technique

The adrenals are small, paired glands located in the craniodorsal abdomen, medial and often cranial to the ipsilateral kidney, and adjacent to the aorta (left) and caudal vena cava (CVC) (right) (Figure 12.1) in the retroperitoneal space. The cells of the adrenal cortex produce cortisol and other corticoids, aldosterone, androgens, estrogens, and progestins, whereas the chromaffin cells of the medulla produce catecholamines (Feldman and Nelson 2004). The adrenal glands are a key component of the endocrine system, and their deranged function can produce a wide range of clinical signs, which may be vague or nonspecific. The ultrasonographic evaluation of the adrenal glands may be technically challenging, particularly in large dogs, but their assessment is considered part of a complete abdominal scan in both dogs and cats. Although the glands are small, a competent sonographer using good-quality equipment can identify both glands in most patients. For a ventral or lateral approach, the mid-abdominal hair coat should be clipped caudal to the costal arch and extend laterally to the level of the lumbar musculature and over the last few intercostal spaces on the right. Evaluation of the adrenal glands requires a sound knowledge of the regional anatomy and is facilitated using convex probes with small footprints, as these can be more easily manipulated. In small patients, high-frequency linear probes are recommended for both adrenals as they produce images of higher spatial resolution and diagnostic quality. Due to its location, the right adrenal (RA) gland may be more difficult to assess with these probes, because of their larger footprint and narrow field of view. Sedation may be necessary in evaluating agitated, aggressive, or painful patients, and in obese patients, because it relaxes the abdomen and allows the operator to apply pressure with less patient discomfort.

Sonography of the Normal Adrenal Glands

In Dogs

Normal ultrasound features are illustrated in Figure 12.1. The normal adrenal glands are hypoechoic to the surrounding fat and well defined. They may also exhibit a thin hyperechoic rim running parallel to the capsule, representing the junction between cortex and medulla, or a more uniformly hyperechoic medulla. The presence of well-demarcated cortex and medulla is considered by the authors to be supportive of normality. The left gland has an elongated bilobed shape, frequently described as resembling a peanut. The RA gland has a more complex shape. Its cranial pole is often folded, boomerang- or V-shaped, and is therefore more difficult to clearly visualize in the same plane than the caudal pole. Its caudal pole is elongated and more consistently identified.

The adrenal glands are accessible from a ventral or lateral approach, in dorsal or lateral recumbency, respectively. Gas, ingesta, and feces in the gastrointestinal tract can limit their access. When scanning

Atlas of Small Animal Ultrasonography, Third Edition. Edited by Dominique Penninck and Marc-André d'Anjou.
© 2025 John Wiley & Sons, Inc. Published 2025 by John Wiley & Sons, Inc.
Companion website: www.SmallAnimalUltrasonography.com

Vet-ebooks.com

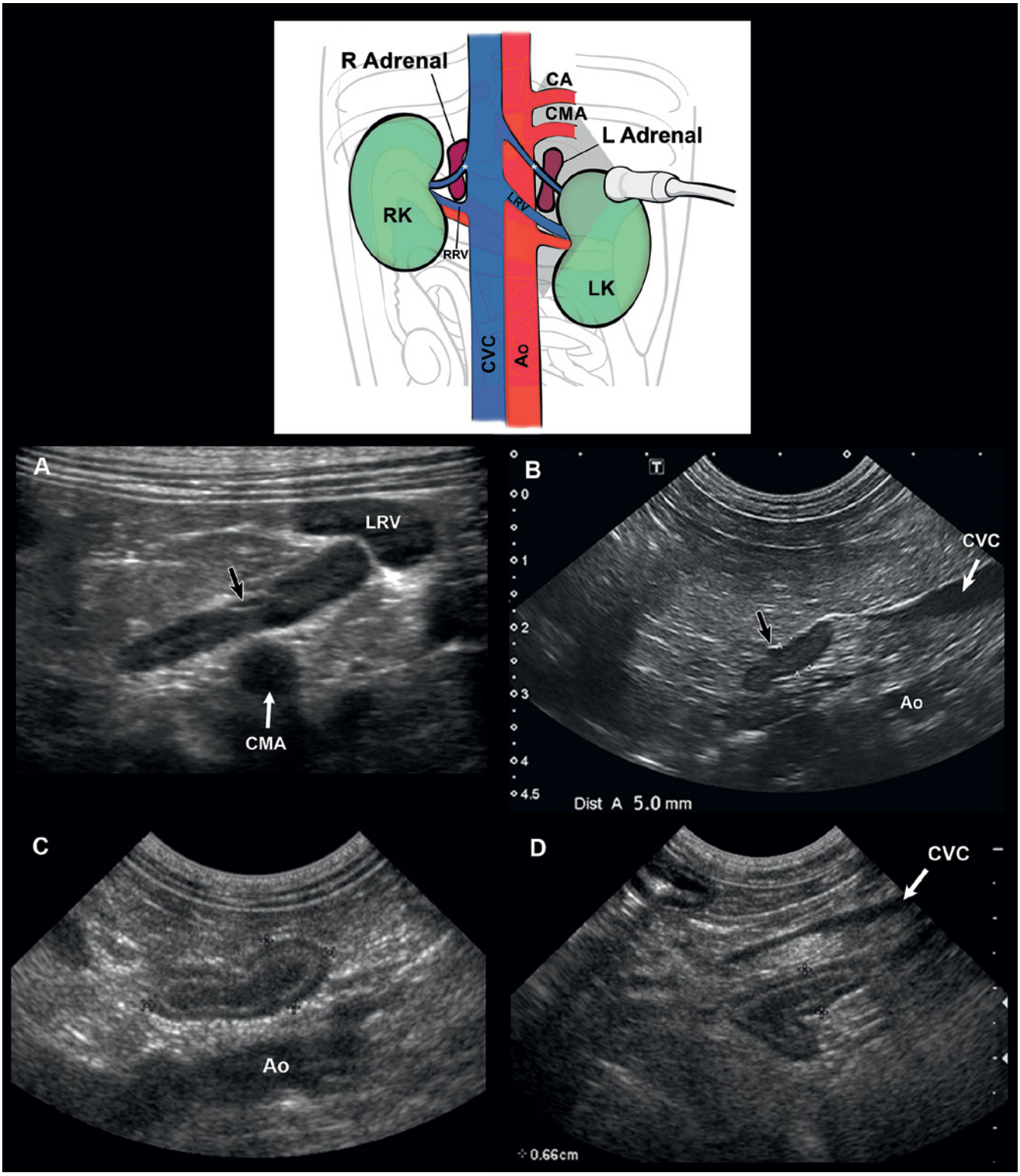


Figure 12.1. **Normal adrenal glands in dogs.** The schematic drawing illustrates the localization of the adrenal glands in a dog in dorsal recumbency (ventral approach). Note the phrenicoabdominal veins (*) extending ventral to mid-portion of each adrenal gland. **(A)** Sagittal oblique plane image of a normal canine left adrenal gland. Note the elongated bilobed shape with a portion of the left phrenicoabdominal vein in cross-section within the ventral groove (black arrow). The anechoic structure caudal and lateral to the gland is the left renal vein (LRV), whereas the cranial mesenteric artery (CMA) lies deep to the mid-body of the adrenal gland. **(B)** Sagittal oblique plane image of a normal right adrenal gland in a Golden Retriever. The gland is fusiform and is parallel to the aorta (Ao) in the far field. It is also lying close to the caudal vena cava (CVC), which is compressed by the transducer. Hyperechoic borders of the phrenicoabdominal vein are noted at the mid-ventromedial aspect of the gland (black arrow) **(C, D)** Sagittal plane images of normal left **(C)** and right **(D)** adrenal glands in a clinically normal toy Poodle. A well-defined hyperechoic rim is at the corticomedullary junction. The left gland is slightly oblique in regard to the aorta (Ao), located dorsally, and has a characteristic peanut shape, and the right gland appears as an arrowhead cranially. The CVC is compressed in the near field. CA, celiac artery; LK, left kidney; RK, right kidney.

Vet-ebooks.com

patients in dorsal recumbency, it may be helpful to tilt them to enable placement of the probe further dorsally. Gentle pressure may be necessary to move an overlying segment of bowel. When scanning patients in lateral recumbency, the probe is placed on the upper side of the abdomen as far dorsal as possible, just ventral to the lumbar transverse processes, to minimize interference from interposed gas in the small intestine and colon.

To identify the **left adrenal (LA) gland**, the probe is placed on the left abdominal wall, slightly caudal to the last rib, more ventrally if the patient is placed in dorsal recumbency, or laterally if in right lateral recumbency. The probe is smoothly fanned using a sagittal to dorsal plane depending on the conformation of the patient, the presence of overlying intestinal content and patient recumbency. The left kidney is initially imaged in the longitudinal plane before the probe is moved medially to find the aorta. The probe is then rotated until a longitudinal image of the aorta is obtained. The gland is located at the left ventral aspect of the aorta, just cranial to the origin of the left renal artery (LRA), and ventral or caudal to the origin of the cranial mesenteric and celiac arteries (Figures 12.1, 12.2). Alternatively, the probe can follow the left renal vein (LRV) in its transverse plane from a longitudinal view of the kidney to identify the adrenal gland just cranial as the vein crosses the aorta. In thin animals, the gland is close to the aorta. As the body fat increases, it is laid down around the adrenal gland, increasing separation from the aorta but also providing contrast and making the gland more prominent. The long axis of the LA gland may be slightly tilted in comparison with the long axis of the aorta, and the probe may need to be rotated until the length of the LA gland is maximized. The phrenicoabdominal vein may be seen ventrally to the hilus of the adrenal gland (Figure 12.1A), whereas the phrenicoabdominal artery always runs dorsal. The phrenicoabdominal vessels may be quite small and not seen on B-mode images, but blood flow can usually be seen with color Doppler examination (Figure 12.2B). The connection with the adrenal veins originating directly from the medullary sinus may be sometimes appreciated with color Doppler interrogation. The arterial supply of the adrenal gland (cranial, middle, caudal adrenal arterioles, branches from the renal arteries, and adrenal aortic artery), but the phrenicoabdominal artery, is generally not identified on B-mode or Doppler ultrasound. All these small arteries approach the glands and penetrate the capsule from the entire surface. The largest artery is the penetrating medullary artery that provides oxygenated blood directly to the medulla, explaining the early medullary wash-in and centrifugal direction of the contrast medium on contrast-enhanced ultrasonography (Pey et al. 2012), and the early visualization of contrast medium on post-contrast computed tomographic study The venous drainage generally is through the adrenal veins that are not visible on ultrasound and the phrenicoabdominal vein, which is visible ventrally to the hilus of the gland and results from the fusion of the caudal phrenic vein (cranial, dorsal, and lateral to the adrenal gland) and the cranial

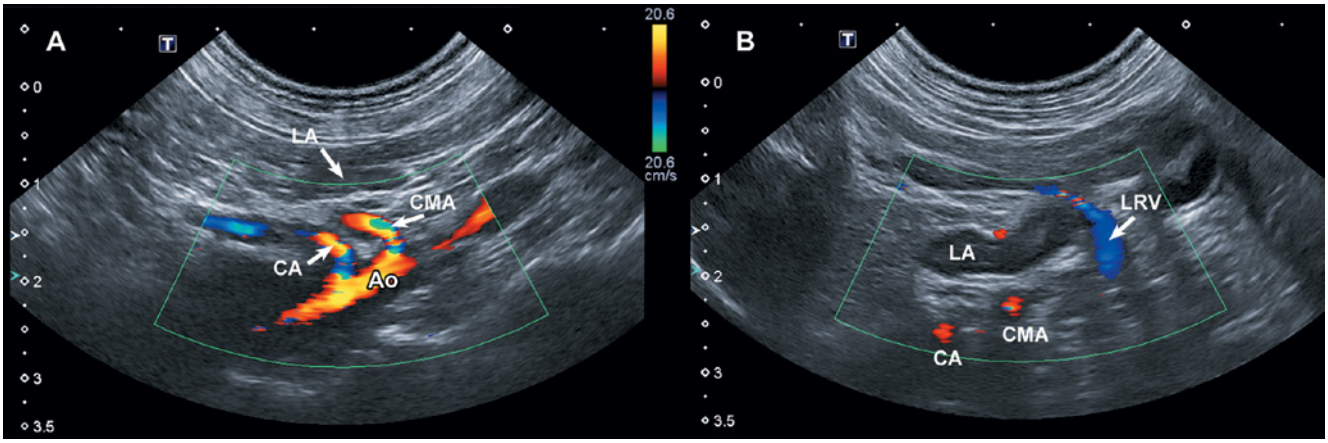


Figure 12.2. **Vascular landmarks for the left adrenal gland in dogs. (A, B)** Sagittal sonographic images of a normal left adrenal gland and nearby vascular landmarks in a small-breed dog in dorsal recumbency. The left adrenal (LA) lies ventrolateral and somewhat caudal to the celiac artery (CA) and cranial mesenteric artery (CMA), as they exit the aorta (Ao). The gland is also located just cranial to the left renal vein (LRV) that crosses the ventral border of the aorta to reach the caudal vena cava. Note the color pattern of these vessels on color Doppler that depends on the direction of blood flow. Color flow aliasing is recognized as a layered pattern of colors in the central portion of the celiac and cranial mesenteric arteries due to high velocity (see Chapter 1 for more information on this artifact).

Vet-ebooks.com

abdominal vein (caudal, dorsal, and lateral to the adrenal gland). On the left side, the left phrenicoabdominal vein anastomoses to the LRV or directly into the CVC, and very close to the point of anastomosis of the LRV, in most of the dogs (Pey et al. 2012), whereas the right phrenicoabdominal vein directly anastomoses into CVC on the right side and away from the right renal vein (RRV). This is important information for surgical planning in case of vascular invasion (Knight et al. 2019).

To identify the **RA gland**, the probe is placed on the ventrolateral aspect of the right abdominal wall, just caudal to the last rib and oriented craniodorsally. Using an oblique longitudinal plane, the probe is fanned dorsal and ventral from the right kidney (RK) until CVC is identified. A common error is to apply too much pressure to the abdomen, which collapses CVC and prevents its identification. The CVC may appear to pulse because of referred motion from the adjacent aorta but may be distinguished from the aorta by applying mild or moderate pressure, which will cause the vessel to collapse (Figures 12.1D, 12.3). Alternatively, Doppler interrogation reveals low-velocity venous flow within the CVC that appears blue in standard color flow Doppler, whereas the aorta shows a pulsatile, high-velocity red color signal. The CVC and aorta are close together in the mid-abdomen, and in some dogs, both vessels can be seen in the same scan plane and become separate more cranially. Once the CVC is imaged in longitudinal plane, the probe is gently moved laterally to identify the RA gland that often partly impinges on the lumen of that vein. Its caudal pole is flatter and more easily identified, whereas its cranial pole is often folded. It may be necessary to place the probe in one of the last two or three intercostal spaces if the gland cannot be imaged by angling the probe cranially from a position caudal to the last rib (Brinkman et al. 2007).

The adrenals have been reported to vary between 3 and 16 mm in maximum thickness and between 10 and 50 mm in length in normal dogs (Barthez et al. 1995; Douglass et al. 1997; Grooters et al. 1995). This broad range of reported sizes reflects the patient selection; they were described as normal, young, old, healthy, or not showing signs of any endocrine disease but these studies may have included dogs with subclinical or nonfunctional adrenal lesions. The maximum thickness of the adrenal gland at the caudal pole is most representative of adrenal size and is generally used for discriminating normal dogs from those with adrenal hyperplasia or neoplasia. It is also proven to be less variable between ultrasonographers. Adrenal measurements vary in dogs of different sizes and may vary from left to right (Choi et al. 2011; de Chalus et al. De Chalus et al. 2013). It must, however, be pointed out that patient positioning and probe angulation may affect this measurement, which is also limited by the spatial resolution of the system used. Given the potential for measuring errors, particularly for deep glands in large dogs, this reference number should be combined with other features, such as the shape and echogenicity of the gland. Thickness cutoffs used by the authors to help distinguishing physiological from pathological adrenal enlargement are **6 mm for small**

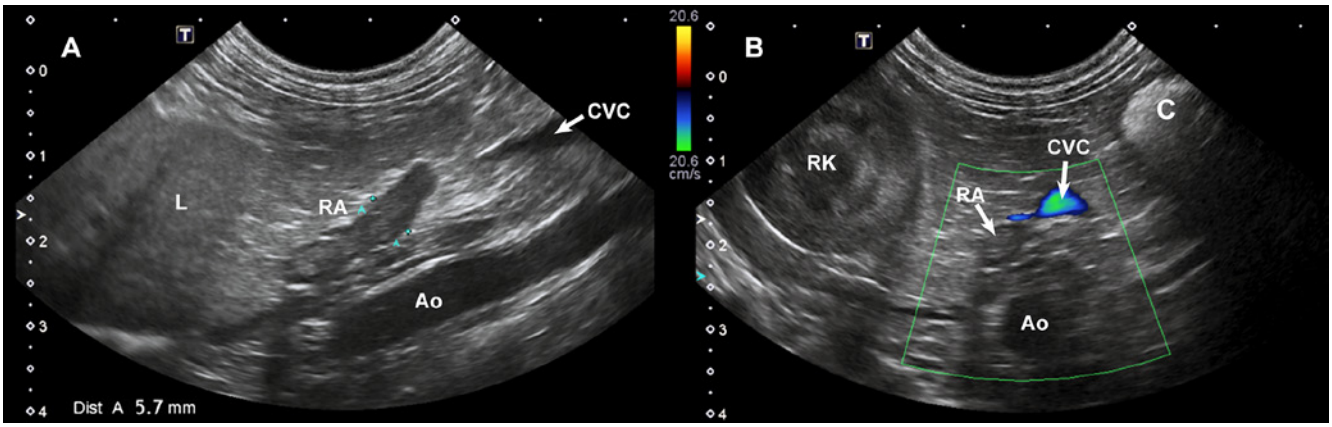


Figure 12.3. Normal right adrenal gland in a Labrador Retriever. Sagittal **(A)** and transverse **(B)** sonographic images in which the right adrenal (RA) gland is seen in proximity to important vascular landmarks. It lies between the caudal vena cava (CVC) and the aorta (Ao), caudal to the liver (L) and dorsomedial to the right kidney (RK). The CVC is collapsed as pressure is applied by the sonographer to get closer to the gland in this large dog. Note the distinction between the hyperechoic medulla and hypoechoic cortex, which is used by the authors as a sign of normality. C, colon.

Vet-ebooks.com

breed dogs, 7.5 mm for medium breed dogs, and **9 mm for large breed dogs** (Barthez et al. 1995; Bento et al. 2016; Choi et al. 2011; de Chalus et al. De Chalus et al. 2013; Melian 2021). See Table 12.1 for reference.

Table 12.1
Range of measurements in the longitudinal plane for normal adrenal glands in dogs and cats used by the authors

	Thickness or width (mm)[a]
Small dogs (<15 kg)	3–6
Medium dogs (15–30 kg)	4.5–7.5
Large dogs (>30 kg)	6–9
Cats	3.5–4.5 (up to 5 if large cats)

[a] Normal range assuming the shape of the gland is normal.

In Cats

The adrenal glands in cats are located by using a similar approach to that described in dogs. In most cats, scanning the area medial to the kidney and adjacent to the aorta or CVC is sufficient to identify the adrenal glands. The same vascular landmarks as used in dogs can also be used to find the feline adrenal glands. The adrenals glands are most of the time ovoid and uniformly hypoechoic, but variable shapes are possible (Figure 12.4). With high-frequency transducers, one can sometimes distinguish between cortex and medulla. In normal cats, both adrenal glands are typically 10–11 mm long and 3.5–4.5 mm in maximum thickness (Cartee et al. 1993; Combes et al. 2012; Zatelli et al. 2007; Zimmer et al. 2000). Small hyperechoic foci may be found in otherwise normal adrenal glands of older cats (Combes et al. 2012) (Figure 12.5). These are believed to indicate microscopic calcification and may

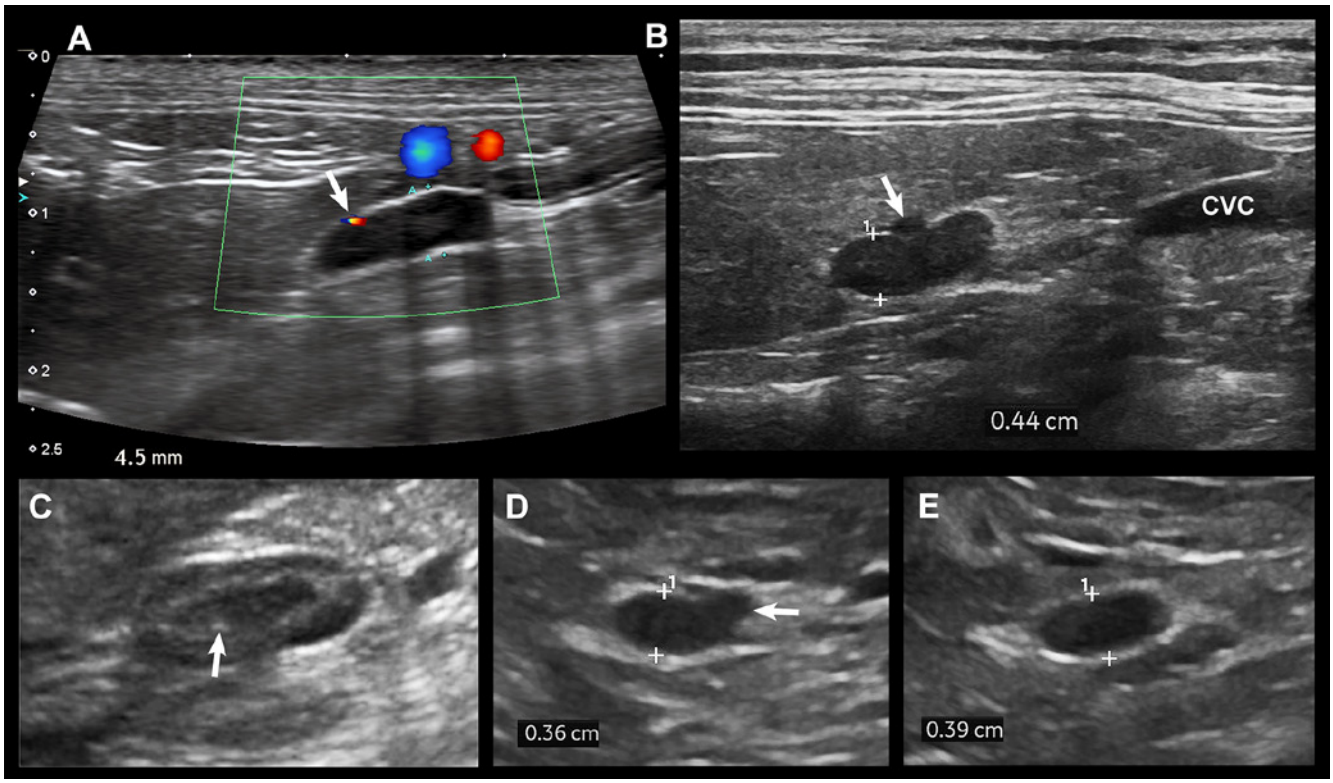


Figure 12.4. **Normal adrenal glands in cats. (A)** Sagittal sonographic image of a normal feline left adrenal gland. The gland is ovoid (between the cursors, 4.5 mm in thickness), lying dorsal to the left renal vein and artery, with blue and red color Doppler signals, respectively. The left kidney being more mobile in cats, these vessels change in position in regard to the gland. Note the small phrenicoabdominal vein (arrow) at its ventral border. **(B)** Sagittal image of a normal right adrenal gland in another cat. The gland appears as peanut-shape hypoechoic structure (between the cursors). The caudal vena cava (CVC) is compressed due to probe pressure. Note the phrenicoabdominal vein located ventral to the adrenal (arrow). **(C)** In this other cat, a hyperechoic band is seen at the corticomedullary junction and a few discrete hyperechoic foci suggesting incidental mineralization are present (arrow). **(D, E)** Left **(D)** and right **(E)** normal adrenals in another cat. These adrenals are shorter and more oval than the adrenals in **(A)** and **(B)**. The caudal pole of the left adrenal is somewhat fusiform in shape (arrow).

Vet-ebooks.com

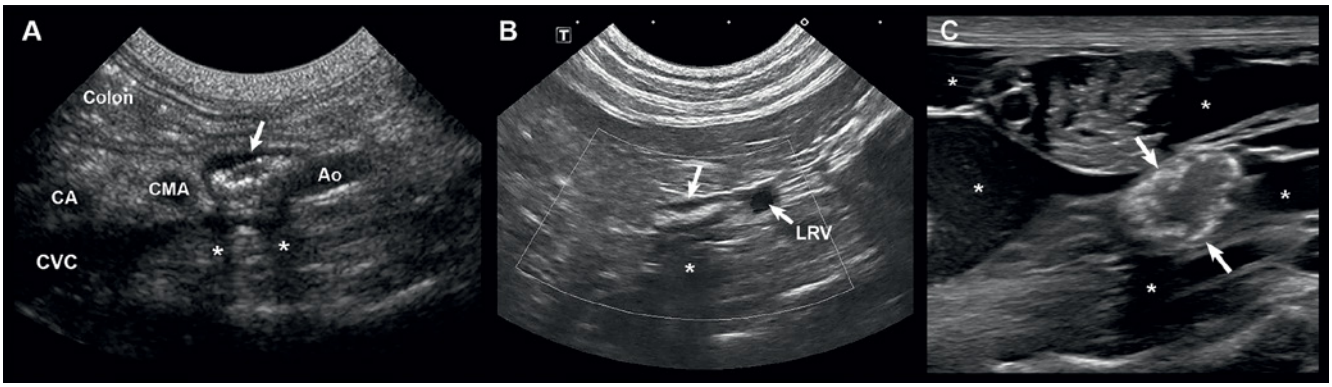


Figure 12.5. **Incidental adrenal mineralization in three old cats. (A, B)** Sagittal oblique sonographic images of variably mineralized left adrenal glands (arrows) in two cats. The mineralization results in acoustic shadowing (*) in each case, but without evidence of adrenomegaly. Similar changes were apparent on the right side. Vascular landmarks are noted. Ao, aorta; CA, celiac artery; CMA, cranial mesenteric artery; CVC, caudal vena cava; LRV, left renal vein. **(C)** Peripheral mineralization of the left adrenal gland of a 8 year old cat with liver failure. Note the multifocal accumulation of free fluid (*) due to hypoalbuminemia.

be associated with acoustic shadowing depending on their size and the type of transducer used.

Sonographic Findings in Adrenal Disorders

Cushing's Syndrome

Cushing's syndrome or hyperadrenocorticism is one of the most common endocrinopathies in dogs. Ultrasound is frequently used as part of the medical database in these dogs (Behrend et al. 2002). However, ultrasound cannot be used alone in diagnosing hyperadrenocorticism. **Pituitary-dependent hyperadrenocorticism (PDH)** accounts for approximately 80% of dogs with hyperadrenocorticism. If a patient's history, clinical signs, and laboratory test results support a diagnosis of hyperadrenocorticism, PDH should be suspected if both adrenal glands appear symmetrically enlarged (Barthez et al. 1998; Feldman and Nelson 2004) (Figure 12.6).

Unfortunately, the adrenal glands may measure within the normal range in some cases of PDH or may demonstrate unilateral or asymmetrical enlargement (Barthez et al. 1995; Benchekroun et al. 2010). As already mentioned, some healthy dogs have adrenal glands that exceed 8 mm in maximal thickness. Some dogs with chronic nonendocrine disease may also exhibit mild symmetrical adrenal enlargement (Figure 12.7). **Macronodular hyperplasia** leading to asymmetrical enlargement of a gland is often seen in aged dogs without clinical significance (***incidentaloma***).

Adrenal tumor hyperadrenocorticism (ATH) caused by functional adrenocortical tumors accounts for approximately 20% of dogs with naturally occurring hyperadrenocorticism. In dogs with compatible clinical signs and clinicopathologic findings, ATH should be considered if one adrenal gland is enlarged, contains a nodule, or has been effaced by a mass, while the contralateral gland is small (≤5.0 mm) or not seen, suggesting that it has been suppressed (Benchekroun et al. 2010) (Figure 12.8). The contralateral gland may remain of normal size. Further confounding the diagnosis, there are reports of dogs with tumors of both the pituitary gland and the adrenal cortex (van Bokhorst et al. 2019) as well as bilateral primary adrenal neoplasia (Greco et al. 1999).

In dogs with hyperadrenocorticism caused by exogenous steroid administration, the adrenal glands may appear small or may not be seen. These changes are reversible within 1 month after the end of therapy (Pey et al. 2012).

Cushing's syndrome is uncommon in **cats**, but ultrasonography may be helpful in determining whether the disease is pituitary dependent or caused by a functional adrenocortical tumor. The criteria are like those in dogs (Feldman and Nelson 2004; Watson and Herrtage 1998).

Addison's Disease

A diagnosis of Addison's disease cannot be made based on ultrasonographic findings alone. However, in a dog with consistent clinical and laboratory findings, the detection of adrenal glands measuring 3.4 mm or less, or

Vet-ebooks.com

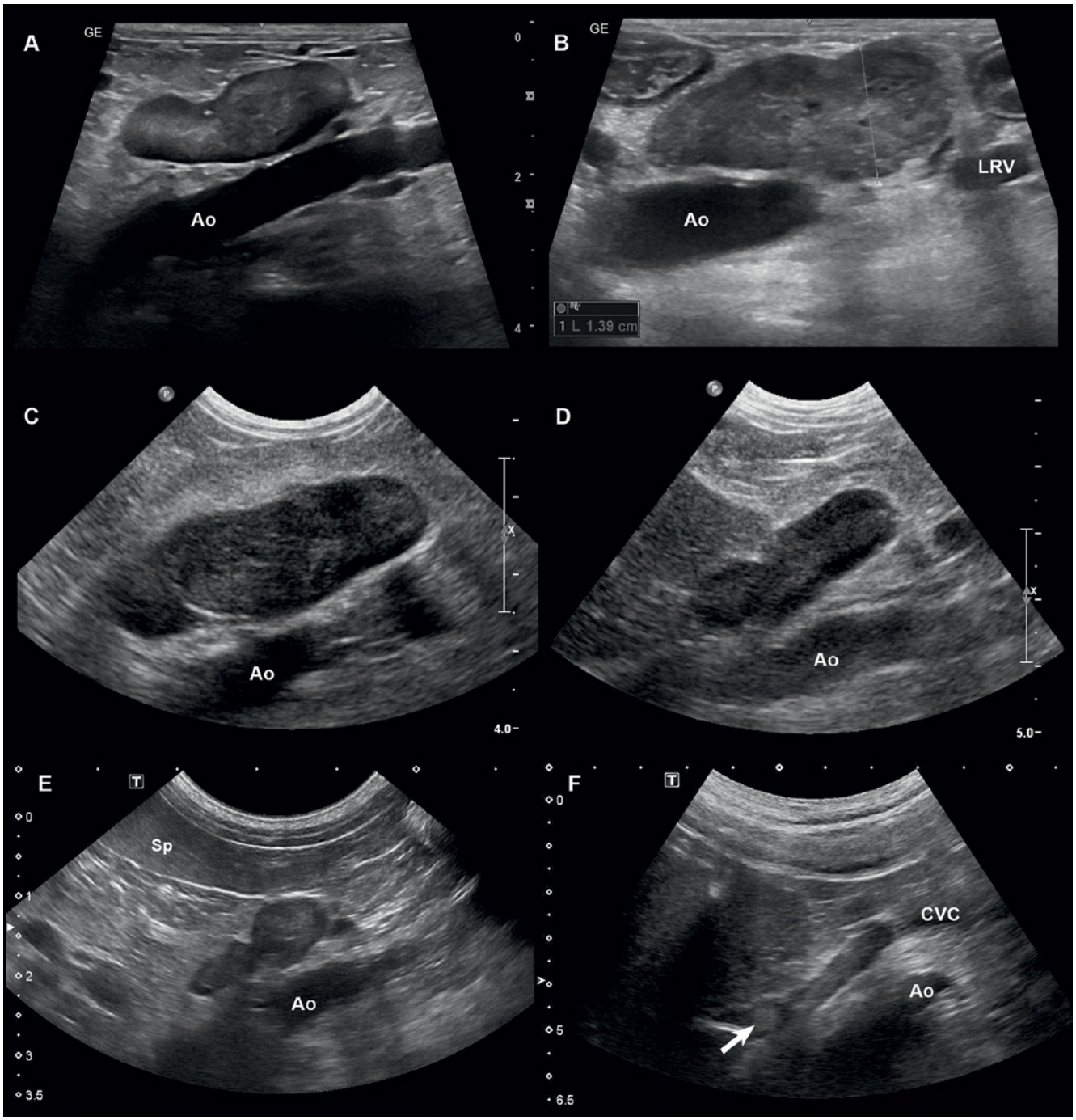


Figure 12.6. **Pituitary-dependent adrenal hyperplasia (PDH) in dogs. (A, B)** In this medium-sized dog, the left adrenal gland **(A)** is asymmetrically enlarged, with its caudal pole reaching 11 mm in thickness, while the right gland **(B)** is more uniformly enlarged (caudal pole reaching 13.9 mm in thickness). **(C, D)** In this 20 kg dog with PDH, the left adrenal **(C)** is moderately enlarged (15 mm in thickness) and mildly irregular and heterogeneous. The right adrenal **(D)** is mildly thickened (11 mm). Ao, aorta. **(E, F)** In another dog with PDH, hyperechoic nodules are present in both glands, the largest in the caudal pole on the left and cranial pole on the right (arrows). Ao, aorta; CVC, caudal vena cava; Sp, spleen.

Vet-ebooks.com

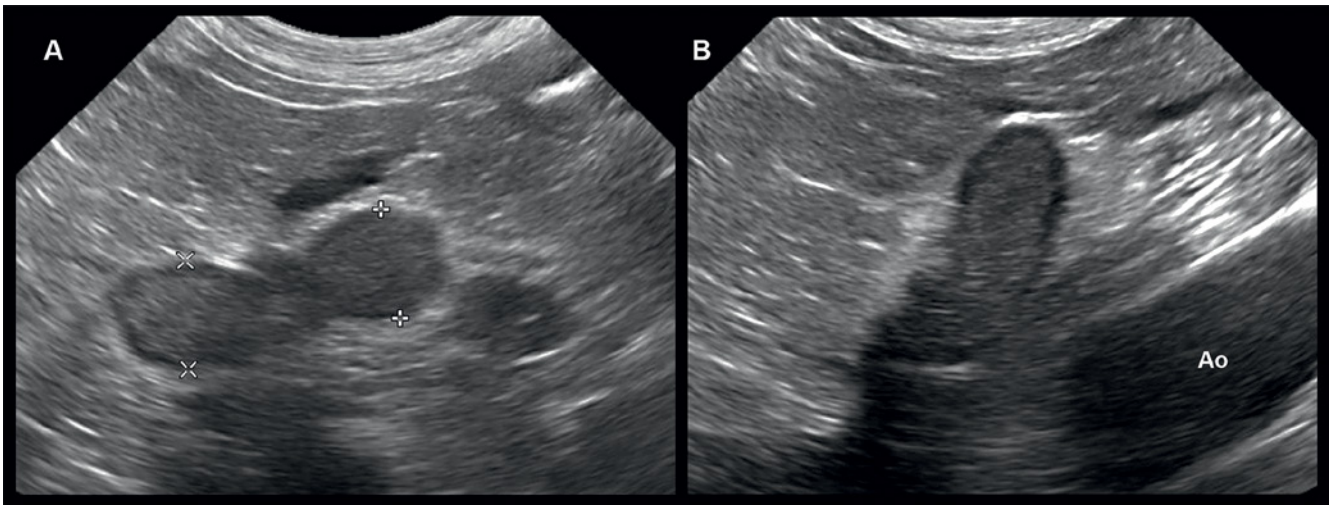


Figure 12.7. Rounded poles of adrenal glands in a dog with a chronic, non-endocrine disorder. Bilateral adrenomegaly in a 14-year-old English Setter with mast cell tumor and no endocrine disease. Both adrenal glands are symmetrically mildly enlarged but the shape and dual echogenicity are preserved.

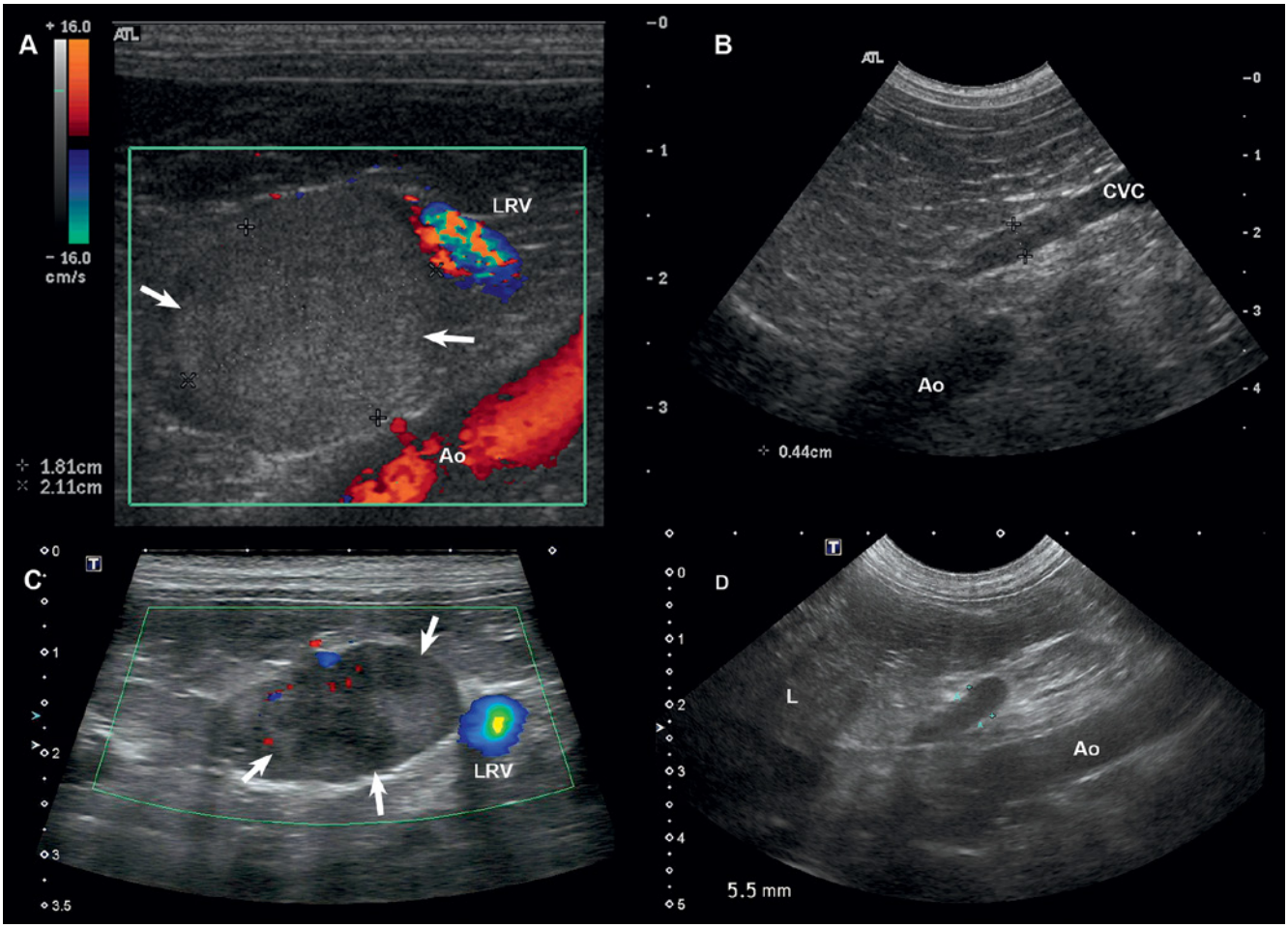


Figure 12.8. Adrenal-dependent hyperadrenocorticism in two dogs. Sagittal oblique sonographic images of the left **(A)** and right **(B)** adrenal glands in a large dog with Cushing's disease. A 2-cm, uniform, and moderately echogenic adrenocortical adenoma (arrows) invades the left adrenal gland, in contact with the left renal vein (LRV). The contralateral gland is at the lower range of normal in thickness, probably due to suppression. **(C, D)** In this other dog, the left adrenal gland is deformed by a 13 × 17 mm mass (arrows) that is more inhomogeneous, consistent with a carcinoma. The right adrenal is normal in thickness (5.5 mm). Ao, aorta; L, liver; LRV, left renal vein.

Vet-ebooks.com

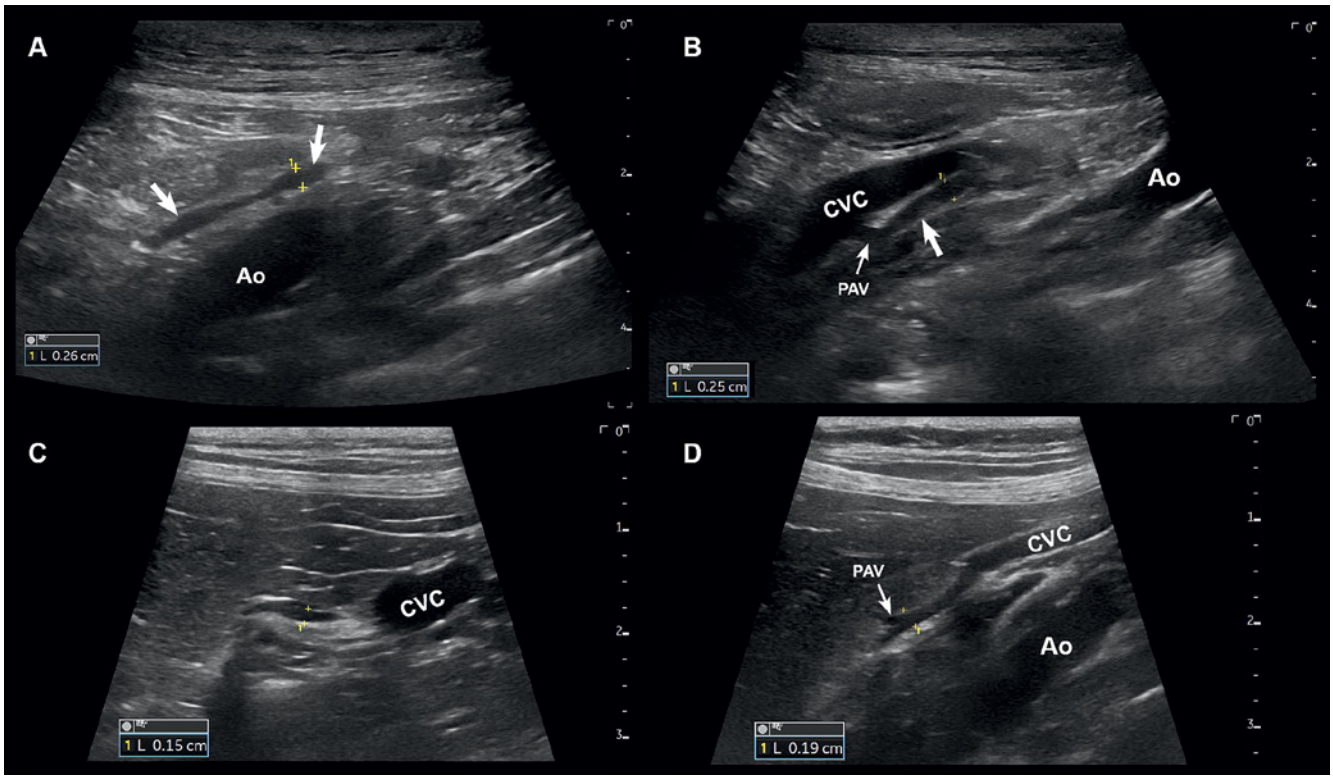


Figure 12.9. **(A, B) Addison's disease in a dog.** Sagittal ultrasound images of the left **(A)** and right **(B)** adrenal glands in a 6-year-old Labrador dog with spontaneous hypoadrenocorticism. Both glands are significantly reduced in thickness (arrows). **(C, D) Bilateral adrenal atrophy in a cat receiving corticosteroids**. Both adrenals measure less than 2 mm in maximal thickness. Ao, aorta; CVC, caudal vena cava; PAV, phrenicoabdominal vein.

failure to detect the glands, despite a technically adequate study, can be considered circumstantial evidence supporting a diagnosis of hypoadrenocorticism (Hoerauf and Reusch 1999; Wenger et al. 2010) (Figure 12.9A, B). Adrenal atrophy can also be seen in dogs and cats receiving corticosteroids (Figure 12.9C, D).

Adrenal Nodules and Masses

The sonographic appearance of adrenal nodules and masses is nonspecific (Figures 12.10–12.13). The differential diagnosis for solid lesions includes adrenocortical adenoma, adrenocortical carcinoma, pheochromocytoma, metastasis, lymphoma, and macronodular hyperplasia. Adrenocortical tumors may or may not be functional. Seldom cases of hemangioma, cysts, granuloma, hematoma, and myelolipomas have also been reported.

Adrenal tumors can produce excessive cortisol, causing clinical signs of hyperadrenocorticism, excessive aldosterone, or rarely several types of sex hormones (Briscoe et al. 2009; Hill et al. 2005; Millard et al. 2009). **Pheochromocytomas** commonly result in hypertension but may also produce vague, nonspecific, or intermittent clinical signs (Galac 2017). Their sonographic features are also nonspecific (Figures 12.10B, 12.11, and 12.13).

Adrenal nodules and masses vary in size and echogenicity. Solid lesions exceeding 2 cm generally predict benign or malignant neoplasia rather than hyperplasia (Besso et al. 1997). Recent publications tend to confirm that masses larger than 2 cm are more likely to be malignant (Barrera et al. 2013; Gregori et al. 2015; Pey et al. 2012; Yoshida et al. 2016). The most reliable sign of malignancy is evidence of invasion of local tissues and vessels, which can occur with adrenocortical carcinomas and pheochromocytomas (Platt et al. 1998). These tumors may invade the adjacent kidney or musculature, or be associated with metastases, affecting surgical resectability and affecting prognosis (Figures 12.11 and 12.13). In some cases, the adrenal origin of a mass may be difficult to establish with ultrasound when extensive and poorly marginated. Nonadrenal retroperitoneal malignancies, such as hemangiosarcomas (see Figure 15.24), retroperitoneal extra-adrenal paragangliomas (Figure 12.14), and renal carcinomas, may be confused for adrenal tumors, requiring computed tomography (CT) or magnetic resonance imaging (MRI) for better distinction.

Vet-ebooks.com

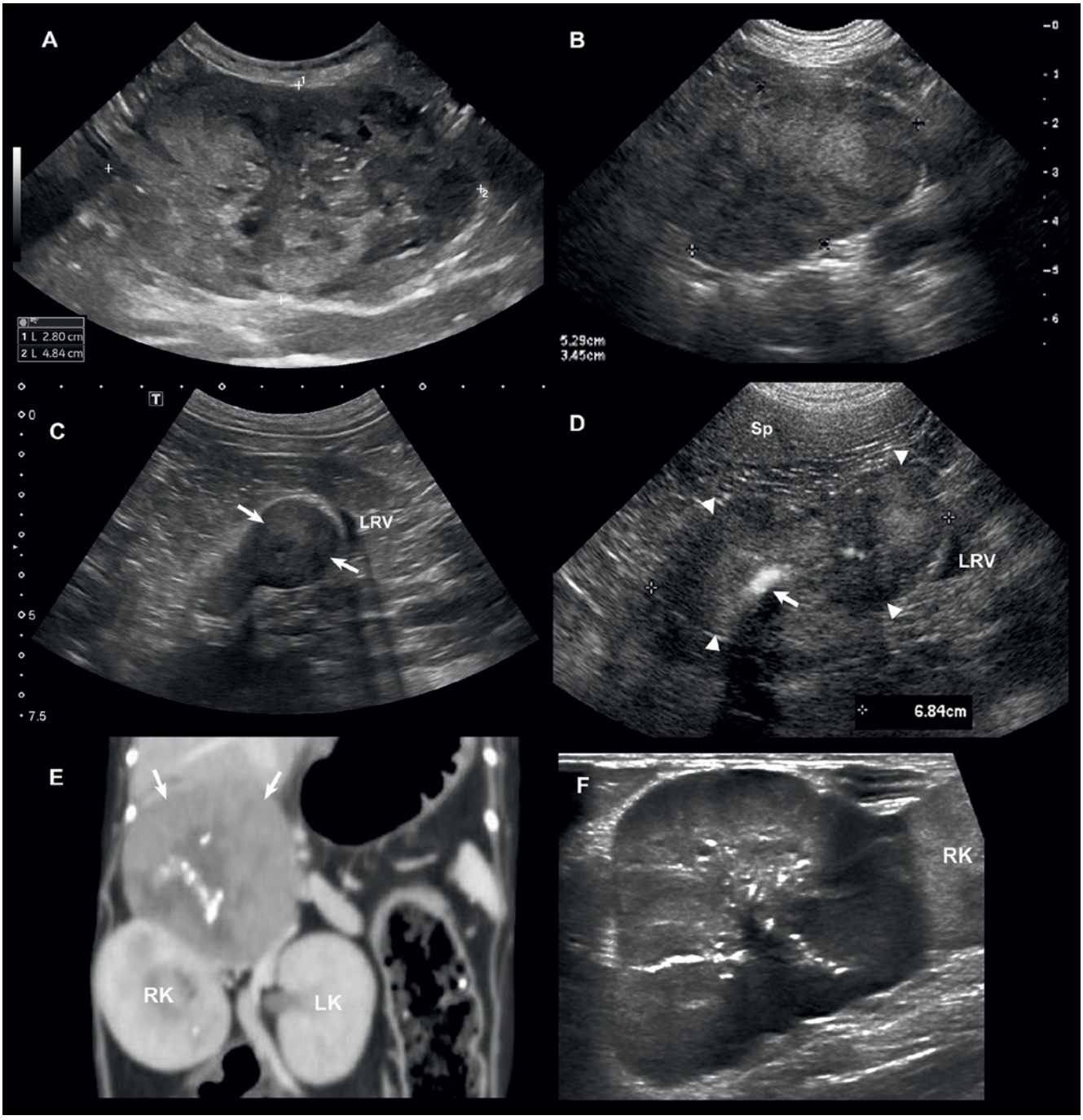


Figure 12.10. **Adrenal nodules and masses in four dogs and one cat. (A)** Longitudinal sonogram of the left adrenal gland of a 10-year-old Pug with a well-defined, large, heterogeneous mass that was confirmed to represent an **adenoma**. Note the small hypoechoic cavities and discrete hyperechoic foci. (**B)** Longitudinal sonogram of a **pheochromocytoma** in an 8-year-old Boxer crossed. A large inhomogeneous mass is identified medial to the left kidney, but not invading the adjacent vessels. (**C)** Longitudinal sonogram of the left adrenal gland of a Bernese Mountain dog with **histiocytic sarcoma**. A 2-cm nodule is identified in the caudal pole of the adrenal gland, deforming the adjacent left renal vein (LRV). Fine-needle aspiration of the nodule confirmed metastasis. **(D)** Transverse sonogram of a **carcinoma** of the left adrenal gland in an 11-year-old large-breed dog. A large, irregular, inhomogeneous mass (arrowheads) has replaced the left adrenal gland. This mass contains amorphous mineralization, as shown as shadowing hyperechoic foci (arrow). There was no sonographic evidence of vascular invasion, although caudal displacement and compression of the left renal vein (LRV) are seen. Sp, spleen. Dorsal plane CT **(E)** and longitudinal sonogram **(F)** of a large (4 cm × 3.7 cm), partially mineralized mass (arrows) invading the right adrenal gland in a 13-year-old cat. The mass compresses and displaces the CVC but does not invade it. The mass was removed and diagnosed as adrenal **adenocarcinoma**. LK, left kidney; LRV, left renal vein; RK, right kidney.

Vet-ebooks.com

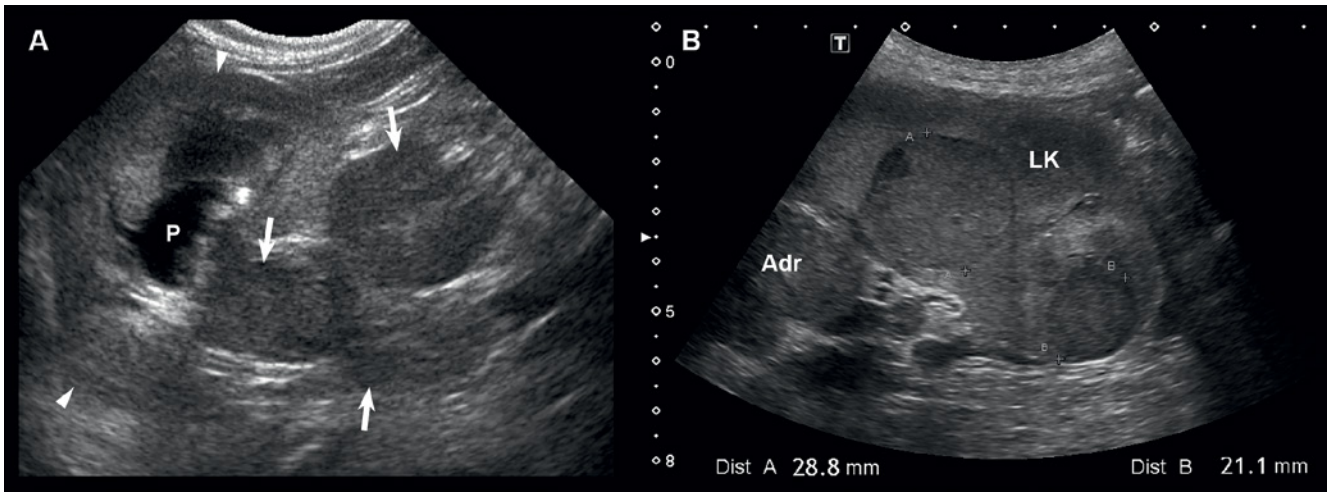


Figure 12.11. **Adrenal pheochromocytomas in two dogs. (A)** Dorsal plane image obtained in the right craniodorsal abdomen of a dog with invasive pheochromocytoma. The right kidney is in the near field (arrowheads), and the renal pelvis (P) is moderately dilated. A lobulated, hypoechoic mass (arrows) extends into the hilus of the kidney. The pelvic dilation suggests partial obstruction of the ureter by invasion or encasement by the mass. **(B)** In this 7-year-old Rottweiler with adrenal pheochromocytoma, several nodules were found in the adjacent left kidney (LK), confirmed to represent metastases. A mildly hyperechoic nodule is seen in the caudal pole of the adjacent adrenal (Adr).

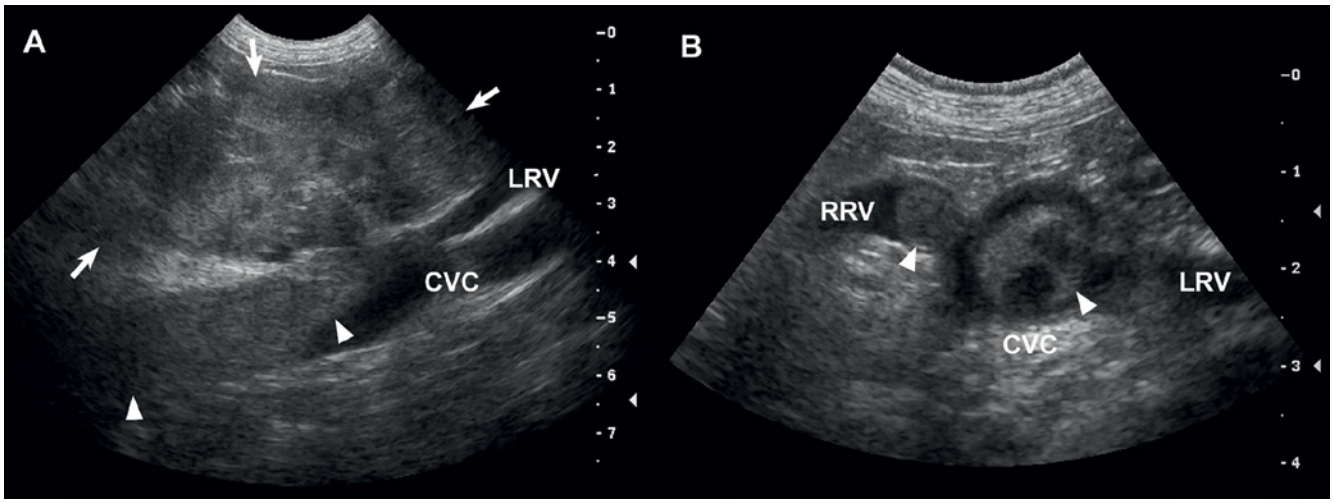


Figure 12.12. **Adrenocortical carcinoma and venous thrombosis in a dog.** Sagittal **(A)** and transverse **(B)** plane images obtained in the left mid-abdomen of a dog with peritoneal effusion and pelvic limb swelling. A large, irregular, inhomogeneous mass (arrows) is ventral to the caudal vena cava (CVC), displacing the left renal vein caudally (LRV). A moderately echogenic structure, with hypoechoic portions **(B)**, is found in the lumen of the CVC, protruding into the right renal vein (RRV), consistent with thrombosis (arrowheads). At surgery, there was no evidence of vascular invasion by the mass, although this was initially suspected.

At times, adrenal tumors may be associated with contained or localized hemorrhage (Figure 12.15).

Ultrasound represents a good screening tool for identifying **invasion of the CVC** and **thrombus formation** that may occur with adrenal malignancies (Davis et al. 2012) (Figures 12.12, 12.13 and 16.26). Other local vessels may also be invaded, such as the renal and phrenicoabdominal veins. The presence of a venous thrombus adjacent to an adrenal mass is highly suggestive of malignancy. Tumor thrombi are generally growing cranially into the CVC and in some rare instances, may reach the right atrium of the heart, or extend into intrahepatic veins, which will complicate surgery. The prognosis of surgical removal of an adrenal tumor and tumor thrombus highly depends on the length of the former (Barrera et al. 2013; Mayhew

Vet-ebooks.com

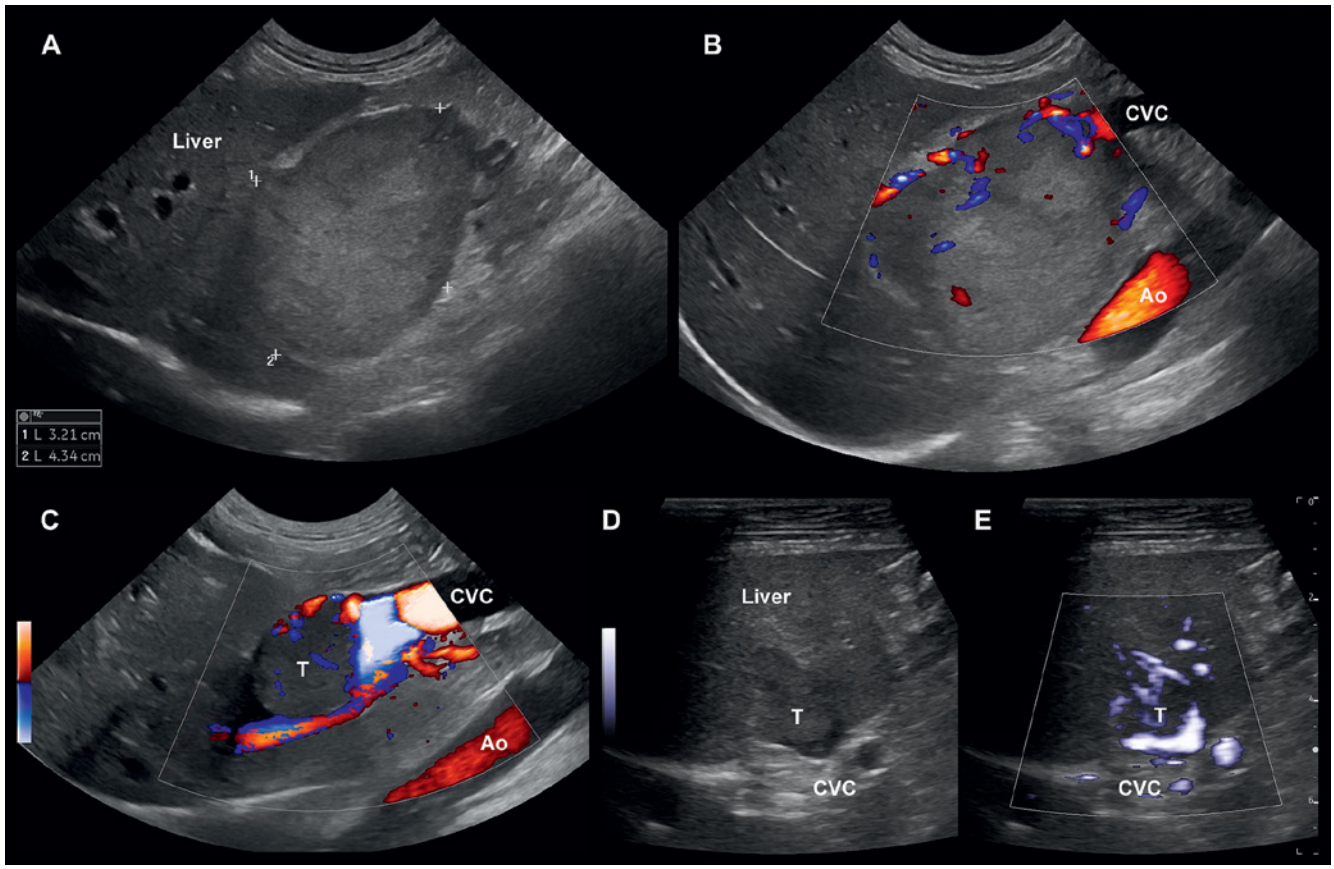


Figure 12.13. Pheochromocytoma and malignant CVC thrombosis in a 9-year-old mixed terrier dog presented for intermittent anorexia. **(A)** Sagittal sonographic image of a large pheochromocytoma (between cursors) of the right adrenal gland. The mass is mildly to moderately hyperechoic and mildly heterogeneous. (**B)** With Color Doppler, the mass shows peripheral vascularization. (**C)** A component of the mass invades the caudal vena cava (CVC), showing vascularization, consistent with malignant thrombosis (T). Note the distortion and turbulence of the CVC flow. **(D, E)** Simultaneous B-mode **(D)** and Power Doppler mode **(E)** of the malignant thrombus (T) invading the CVC in transverse plane. Ao, aorta.

et al. 2019). Invasion of the CVC, particularly tumor thrombus extension beyond the hepatic hilus or the long axis of the thrombus >5 cm are generally associated with a higher postoperative mortality rate but does not affect long-term prognosis in dogs undergoing adrenalectomy. Hyperadrenocorticism may cause a hypercoagulable state, and, in this condition, aortic thrombus can also be detected.

Hyperechoic foci with distal acoustic shadowing, representing **mineralization**, are not specific to malignancy. Both benign and malignant lesions can become mineralized (Figures 12.10, 12.16, and 12.17). The presence of calcification in the adrenal parenchyma is rarely encountered in pheochromocytoma (Gregori et al. 2015; Pey et al. Pey et al. 2012; Yoshida et al. 2016). Smooth contours are generally more associated with benign processes, as it may be a sign of capsule integrity. Carcinomas are more likely to spontaneously bleed and rupture compared to adenoma and pheochromocytoma. Pheochromocytomas tend to present with longer tumor thrombus in the CVC, compared to carcinomas. They are also more frequently associated with vascular invasion, compared to carcinomas, although the latter is also commonly seen with carcinomas (Pey et al. 2012).

Adrenal tumors are rare in **cats** and can result in variable clinical signs due to mass effect, hemorrhage, vascular invasion or compression, or hormonal secretion such as acromegaly, hyperadrenocorticism or hyperaldosteronism (Figures 12.17, 12.18). An adrenal gland tumor should be considered in neutered cats with newly developed physical and sex-related behavioral changes (Millard et al. 2009).

Adrenal nodules and small masses have become more common incidental findings as operator experience has increased and machine performance has improved. These are sometimes referred to as "**incidentalomas**" (Figure 12.19) and leave clinicians with the dilemma of how far the diagnosis should be

Vet-ebooks.com

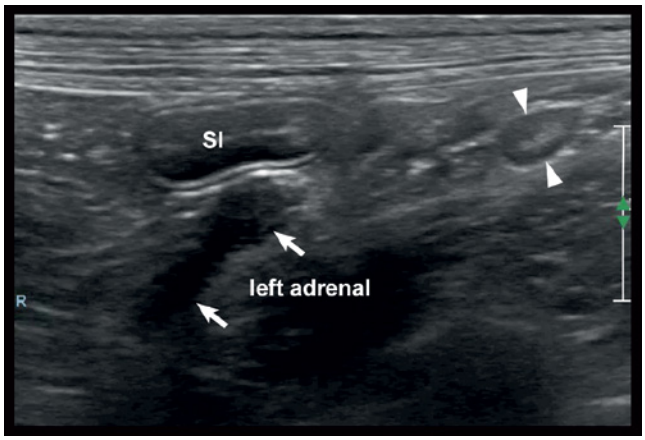


Figure 12.14. Paraganglioma in a dog. B-mode sagittal sonographic image of an extra-adrenal retroperitoneal paraganglioma in a 13-year-old male mixed breed dog, presented for hypertensive crises and screening for pheochromocytoma. The left adrenal gland is visible cranial and demonstrates a normal appearance, whereas a small ovoid homogeneous smoothly outlined tissue is visible caudal to it (arrowheads), caudal to the left renal artery and ventral to the aorta. This tissue was initially interpreted as a left renal or aortic lymph node. Fine-needle aspiration cytology suggested a tumor of neuroendocrine. A paraganglioma was confirmed on histopathology after surgical resection. SI, small intestine.

pursued. Their prevalence on ultrasound has been reported to be 4% (Cook et al. 2014). Many of these lesions cause no clinical signs, and a diagnosis is rarely confirmed. Reported diagnoses include normal tissue, nonfunctional adrenocortical tumors, granulomas, adrenal cysts, myelolipoma, hemorrhage, metastatic tumor, and pheochromocytoma (Feldman and Nelson 2004; Morandi et al. 2007). The medical history and clinical signs should be reviewed for evidence of endocrine disease. Clinicopathologic tests are indicated if any such signs are identified. Larger masses or nodules (>2 cm) are more likely to be neoplastic, so surgical removal should be considered. However, many of these patients are old and may have serious concurrent illnesses, so such invasive approach may not be indicated or acceptable to the owner. If there is no evidence of endocrine disease or sonographic evidence of invasiveness, serial ultrasound examinations at 1- to 3-month intervals can be used to monitor for enlargement or progression of the lesion. Finally, metastases to the adrenals are under-reported and often under-diagnosed. Necropsy studies report a frequency of 20–25% of adrenal nodules or masses (Labelle and De Cock 2005). They may present with similar sonographic characteristics than the primary tumor. Any adrenal nodule or mass associated with the presence of a primary tumor should raise the suspicion of metastasis and should be investigated with further testing, such as ultrasound-guided fine needle aspiration (FNA) for cytological analysis, as this would have an impact on therapeutic planning and prognosis.

Other Adrenal changes

Chronic illness and stress influence the pituitary–adrenals axis and may alter adrenal size in dogs and cats. Adrenals may be normal (Ramspott et al. 2012) or enlarged in cats with **hyperthyroidism**, and hyperechoic foci may be more prevalent (Combes et al. 2012). Adrenomegaly may also be associated with **hyperaldosteronism** (Figure 12.17), **acromegaly** (Figure 12.20), and **hyperprogesteronism** in cats (Brisco et al. 2009).

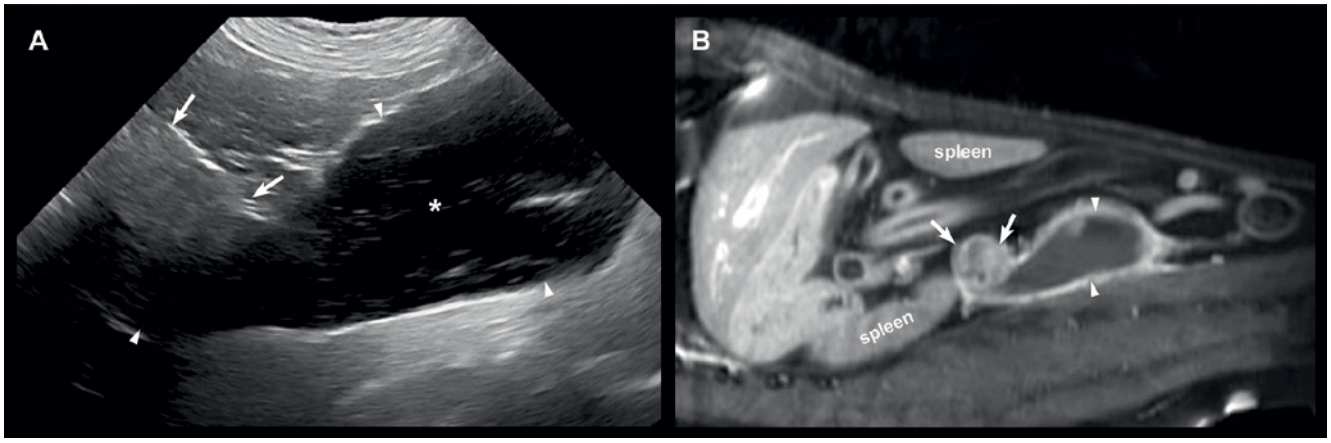


Figure 12.15. Hemorrhagic adrenocortical carcinoma in a dog. Longitudinal sonogram **(A)** and referral MRI T1 postcontrast image **(B)** of a large left adrenal gland (arrows) deformed by an expansile nearly anechoic region (*) that represents hemorrhage surrounded with a capsule (arrowheads) and that extends caudal to the gland. The final diagnosis was adrenocortical carcinoma.

Vet-ebooks.com

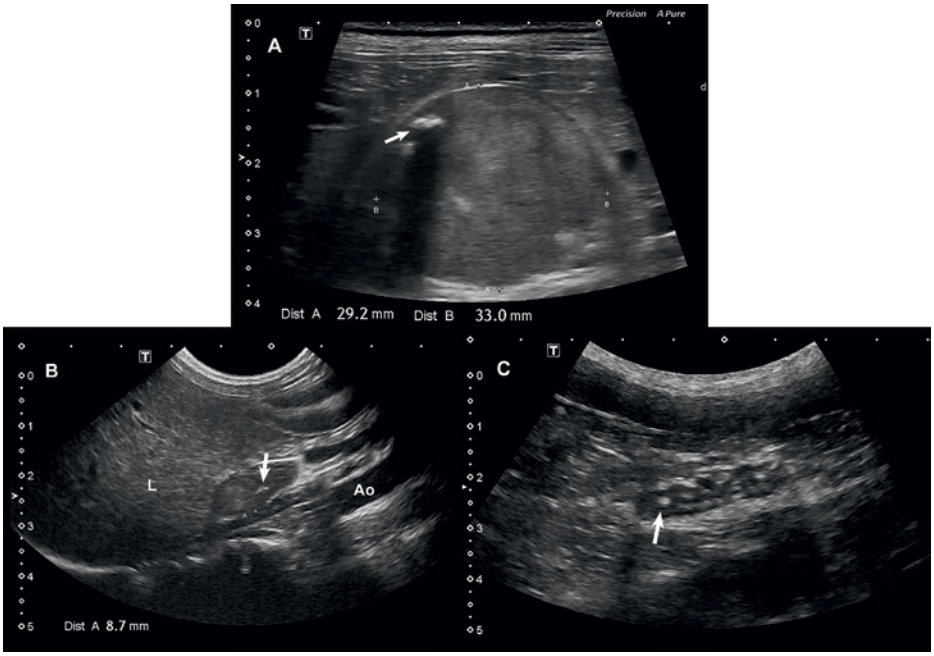


Figure 12.16. **Mineralization of benign adrenal lesions in dogs. (A)** Adrenal adenoma with mineralization (arrow) casting a shadow in a medium-sized dog with primary hyperadrenocorticism. **(B)** Hyperechoic focus (arrow) suggesting mineralization in the right adrenal gland of a Lhasa Apso with biochemical evidence of pituitary-dependent hyperadrenocorticism (PDH). The cranial pole is deformed by a mildly hyperechoic nodule. Ao, aorta; L, liver. **(C)** Sagittal sonographic image of the left adrenal gland of another dog treated over 2 years for PDH. Note the contour irregularity of the gland and the numerous hyperechoic foci (arrow), most of which are near the corticomedullary junction. These foci may represent fibrosis that can mimic mineralization on ultrasound.

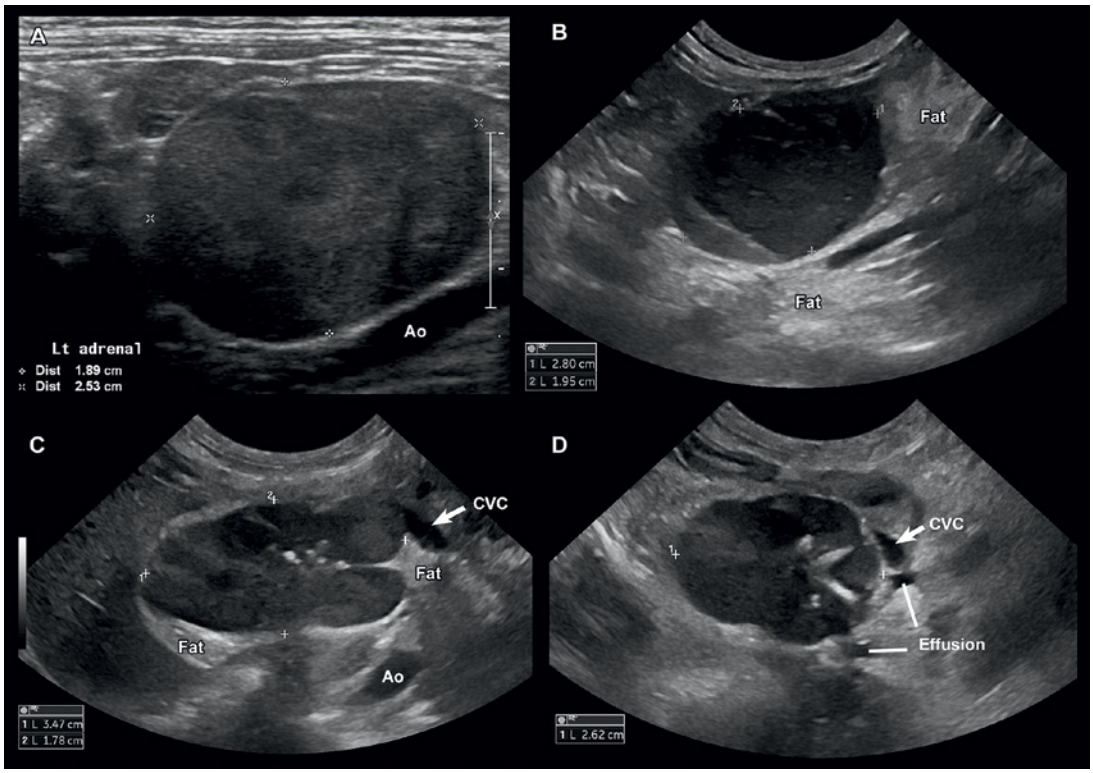


Figure 12.17. **Adrenal masses in cats with hyperadrenocorticism.** In **(A)**, an **adenoma** of the left gland was confirmed after surgery. In this other cat **(B)**, the right adrenal mass increased in size over time, but the hypokalemia was controlled medically. **(C, D) Adrenocortical carcinoma in a 14-year-old short hair cat.** Longitudinal **(C)** and transverse **(D)** sonographic images of an irregular, hypoechoic mass with hyperechoic foci consistent with mineralization in the region of the right adrenal gland in a cat with chronic hypokalemia now presented with lethargy and abnormal behavior. The caudal vena cava (CVC) is deviated and compressed, and minimal retroperitoneal effusion is present. The peripheral fat is hyperechoic. Ao, aorta.

Vet-ebooks.com

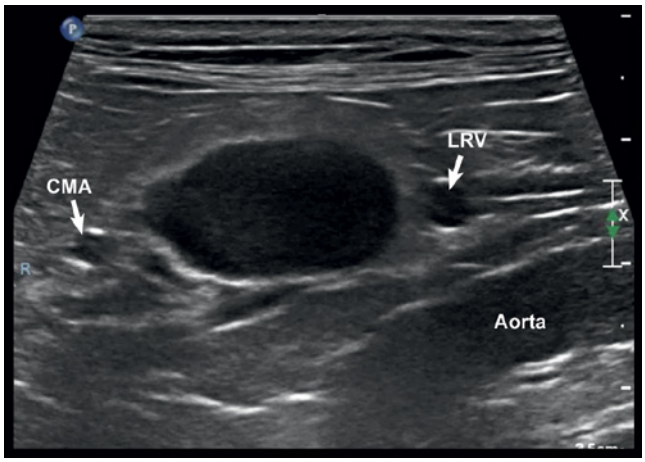


Figure 12.18. **Adrenal lymphoma in a cat.** Both adrenal glands were enlarged and uniformly nearly anechoic. The left gland (in this image) measured 1 cm in thickness and was surrounded with mildly hyperechoic fat. CMA, cranial mesenteric artery; LRV, left renal vein.

Trilostane therapy, in patients with Cushing's syndrome, has been suspected to induce **adrenal parenchyma necrosis** (Figure 12.21). Repeated administration of ACTH in the Trilostane treatment monitoring is another consideration for the cause of these cases of necrosis. The ultrasonographic appearance of presumed necrosis induced by Trilostane has been reported (Leroux Leroux 2016). Enlargement of the adrenal glands, with adjacent retroperitonitis, decreased echogenicity, and heterogeneity of the adrenal parenchyma are ultrasonographic signs suggesting adrenalitis, necrosis, and hemorrhage. Concomitant thrombosis of the CVC or phrenicoabdominal vein, or signs of phlebitis, are additional abnormalities that may be observed. Using ultrasound as a monitoring tool in these cases of Trilostane treatment has been suggested (Masnov et al. 2022).

Other cases of presumed drug-induced adrenalitis or necrosis of the adrenal parenchyma have been

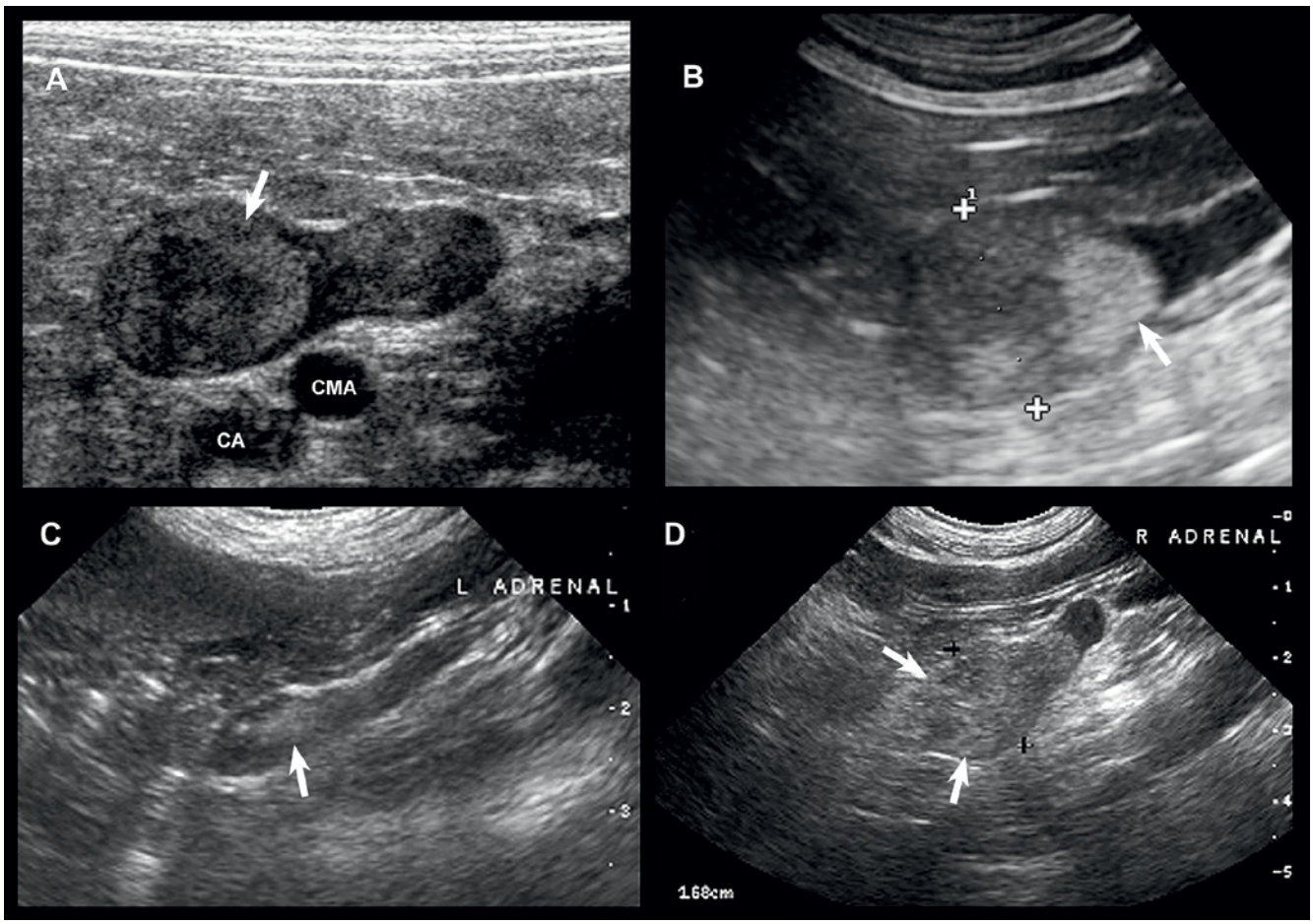


Figure 12.19. **Incidental adrenal lesions in dogs. (A)** Dorsal plane image of a left adrenal gland. A well-defined, inhomogeneous, hyperechoic nodule is in the cranial pole of the adrenal gland (arrows). The nodule was an incidental finding and remained unchanged on serial examinations. Anechoic cross-sections of the celiac (CA) and cranial mesenteric (CMA) arteries are seen dorsally. **(B)** Primarily hyperechoic but slightly inhomogeneous nodule (arrow) in the left adrenal gland of a dog confirmed to represent a myelolipoma in the center of an adenoma. **(C, D)** Sagittal sonogram of both adrenal glands of a 15-year-old Siberian Husky with incidental bilateral changes in echogenicity and shape (arrows). These changes remained unchanged on serial examinations.

Vet-ebooks.com

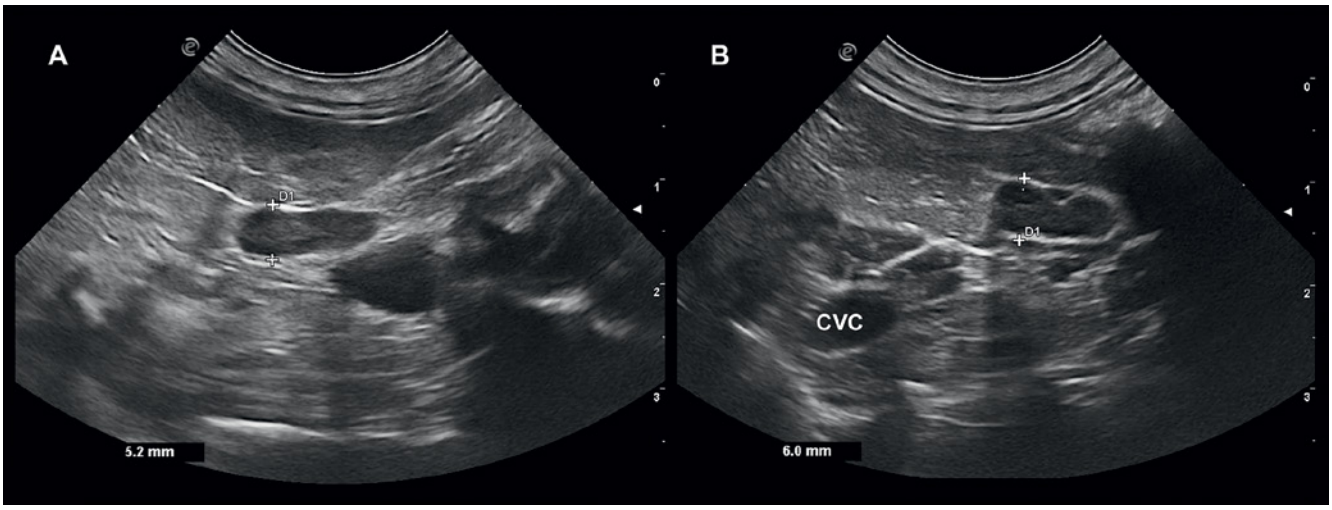


Figure 12.20. **Acromegaly in a male castrated cat.** Both left **(A)** and right **(B)** adrenal glands were mildly enlarged in this cat that also presented bilateral renomegaly and hepatomegaly without cytological abnormalities on fine-needle aspiration. CVC, caudal vena cava.

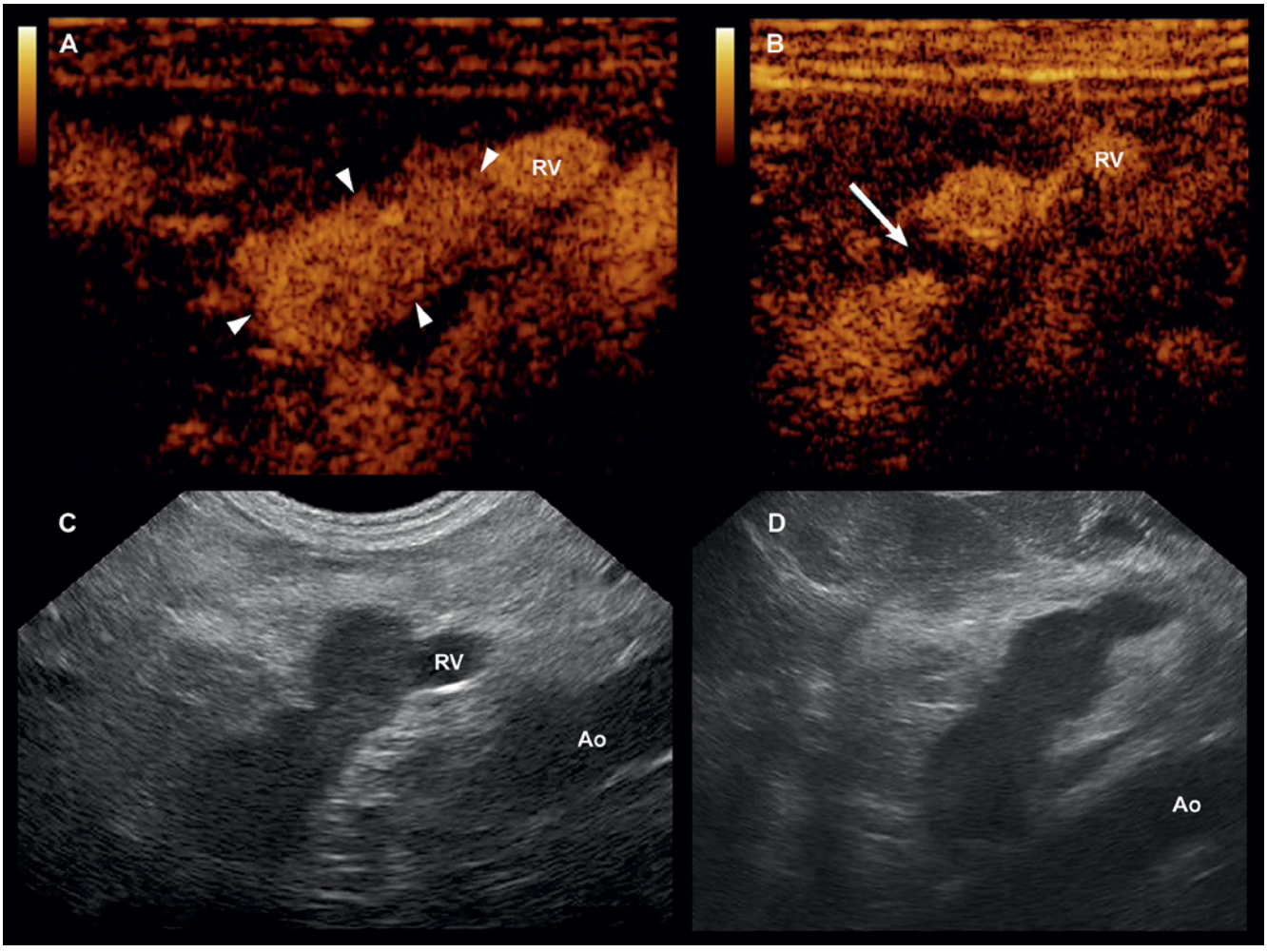


Figure 12.21. **Trilostane toxicity in two dogs**. **(A, B)** Contrast-enhanced ultrasonography (harmonic mode, displayed in orange hue) of the left adrenal gland of a patient with ACTH-dependent hyperadrenocorticism performed at the time of diagnosis **(A)** and after 1 year of Trilostane treatment **(B)**. At the time of diagnosis **(A)**, the adrenal gland and ipsilateral renal vein (RV) show homogeneous contrast enhancement, whereas a focal area located close to the hilus of the gland (arrow) does not show any contrast uptake, after 1 year of Trilostane treatment **(B)**. On blood work, the patient presents a relapse and failure to respond to Trilostane treatment. The absence of contrast enhancement is strongly suggestive of necrosis (no histopathological analysis). **(C D)** Longitudinal sonograms of the right **(C)** and left **(D)** enlarged and poorly echogenic adrenal glands in a 15-year-old dog with Cushing's and treated with Trilostane. Notice the hyperechoic retroperitoneal fat bordering the glands. Ao, aorta.

Vet-ebooks.com

encountered by the authors. Clinically, patients may present with Addison's crisis due to adrenal insufficiency. The adrenal changes usually resolve over time.

Extra-adrenal or Retroperitoneal Paragangliomas

Retroperitoneal paragangliomas can be identified adjacent to the anatomical location of the adrenal gland or along the abdominal aorta (Gombert et al. 2022). Like the adrenal medulla, paraganglias are derived from the neural crest and are associated with the autonomous system. Paragangliomas of the retroperitoneal space present with relatively characteristic sonographic features and characteristic topography compared to the adrenal gland and adjacent vasculature (Figure 12.14). These tumors are most likely underdiagnosed and misdiagnosed, as they can be silent, of small size or confused with lymph nodes.

Ectopic adrenal tissue has also been reported to occur surrounding the adrenal gland, from the outer portion of the adrenal capsule to adjacent adipose tissue (Evans 2013). From an imaging point-of-view, it is difficult to differentiate an extra-adrenal paraganglioma from an ectopic adrenal tumor or from an aortic lymph node. Only histopathological analysis can assist for differentiation.

Interventional Procedures

Percutaneous ultrasound-guided FNA of adrenal gland lesions has been controversial in veterinary medicine. However, based on the recollection of 200 FNA of adrenal lesions (performed by 65 radiologists), a mortality rate of only 1% was estimated (Pey et al. 2020). Adrenal cytology can discriminate the origin (cortical or medullary) of an adrenal neoplasm with a high diagnostic accuracy (90–100%). The evaluation of an adrenal cytological sample can therefore be beneficial in the diagnostic approach of adrenal lesions, although its accuracy for distinguishing benign from malignant lesions remains low (Figure 12.22).

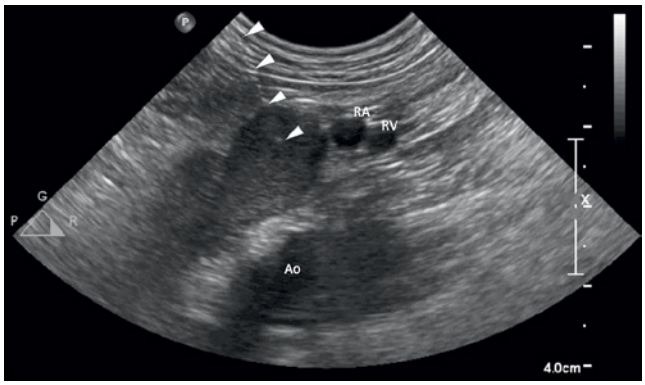


Figure 12.22. Fine-needle aspiration of an adrenal mass in a dog. The adrenal mass deforming the caudal pole of the left adrenal gland is displayed in sagittal plane, with the aorta (Ao) located dorsal, renal artery (RA), and renal vein (RV) visible caudally. Color Doppler interrogation was not used during the procedure as these vessels were nicely identified on B mode. A 22-gauge spinal needle (arrowheads) was used. No complication was encountered during the procedure. The final diagnosis was **adrenocortical adenocarcinoma**.



Visit our website at **www.SmallAnimalUltrasonography.com** for complementary video clips with annotations and text on:

- Normal adrenal glands in a dog
- Normal adrenal glands in a cat
- Adrenal hyperplasia with PDH in dogs
- Adrenal adenoma and adenocarcinoma in dogs
- Adrenal pheochromocytoma in a dog

References

Barrera JS, Bernard F, Ehrhart EJ, Withrow SJ, Monnet E (2013) Evaluation of risk factors for outcome associated with adrenal gland tumors with or without invasion of the caudal vena cava and treated via adrenalectomy in dogs: 86 cases (1993–2009). J Am Vet Med Assoc 242(12):1715–1721.

Barthez PY, Nyland TG, Feldman EC (1995) Ultrasonographic evaluation of adrenal glands in dogs. J Am Vet Med Assoc 207:1180–1183.

Barthez PY, Nyland TG, Feldman EC (1998) Ultrasonography of the adrenal glands in the dog, cat, and ferret. Vet Clin North Am Small Anim Pract 28:869–885.

Behrend EN, Kemppainen RJ, Clark TP, Salman MD, et al. (2002) Diagnosis of hyperadrenocorticism in dogs: a survey of internists and dermatologists. J Am Vet Med Assoc 220:1643–1649.

Benchekroun G, de Fornel-Thibaud P, Rodríguez Piñeiro MI, Rault D, et al. (2010) Ultrasonography criteria for differentiating ACTH dependency from ACTH independency in 47 dogs with hyperadrenocorticism and equivocal adrenal asymmetry. J Vet Intern Med 24:1077–1085.

Bento PL, Center SA, Randolph JF Yeager AE, et al. (2016) Association between sex, body weight, age and ultrasonographically determined adrenal thickness in dogs with non-adrenal illness J Am Vet Med Assoc 248:652–660.

Besso JG, Penninck DG, Gliatto JM (1997) Retrospective ultrasonographic evaluation of adrenal lesions in 26 dogs. Vet Radiol Ultrasound 38:448–455.

van Bokhorst, K.L., Kooistra, H.S., Boroffka, S.A. and Galac, S., 2019. Concurrent pituitary and adrenocortical lesions on computed tomography imaging in dogs with spontaneous hypercortisolism. J Vet Intern Med *33*(1):72–78.

Brinkman EL, Biller DS, Armbrust LJ, O'Brien RT (2007) The clinical utility of the right lateral intercostal ultrasound scan technique in dogs. J Am Anim Hosp Assoc 43:179–186.

Vet-ebooks.com

Briscoe K, Barrs VR, Foster DF, Beatty JA (2009) Hyperaldosteronism and hyperprogesteronism in a cat. J Feline Med Surg 11:758–762.

Cartee RE, Finn-Bodner ST, Gray BW (1993) Ultrasound examination of the feline adrenal gland. J Diagn Med Sonogr 9:327–330.

Choi J, Kim H, Yoon J (2011) Ultrasonographic adrenal gland measurements in clinically normal small breed dogs and comparison with pituitary-dependent hyperadrenocorticism. J Vet Med Sci 73:985–989.

Combes A, Vandermeulen E, Duchateau L, Peremans K, et al. (2012) Ultrasonographic measurements of adrenal glands in cats with hyperthyroidism. Vet Radiol Ultrasound 53:210–216.

Cook AK, Spaulding KA, Edwards JF (2014) Clinical findings in dogs with incidental adrenal gland lesions determined by ultrasonography: 151 cases (2007–2010). J Am Vet Med Assoc 244(10):1181–1185.

Davis MK, Schochet RA, Wrigley R (2012) Ultrasonographic identification of vascular invasion by adrenal tumors in dogs. Vet Radiol Ultrasound 53:442–445.

De Chalus T, Combes A, Bedu A, Pey P, et al. (2013) Ultrasonographic adrenal gland measurements in healthy Yorshire terriers and Labrador retrievers. Anat Histol Embryol 42:57–64.

Douglass JP, Berry CR, James S (1997) Ultrasonographic adrenal gland measurements in dogs without evidence of adrenal disease. Vet Radiol Ultrasound 38:124–130.

Howard E. Evans (2013) Miller's Anatomy of the Dog - E-Book. https://books.google.ca/books/about/Miller_s_Anatomy_of_the_Dog_E_Book.html?id=6eBOAQAAQBAJ&redir_esc=y

Feldman EC, Nelson RW (2004) The adrenal gland. In Feldman EC, Nelson RW, eds. Canine and Feline Endocrinology and Reproduction, 3rd edition. St Louis: WB Saunders, pp. 394–439.

Galac S (2017). Pheochromocytoma. In S. Ettinger, E. Feldman, & E. Cote (Eds.), Textbook of Veterinary Internal Medicine (8 ed., Vol. 2, pp. 1838–1843). Elsevier.

Gombert A, Diana A, Hecht S, Nicoli S, Fracassi F, Mortier J, Reyes-Gomez E, Pey P (2022) Imaging features of retroperitoneal extra-adrenal paragangliomas in 10 dogs. Vet Radiol Ultrasound 63(4):393–402.

Greco DS, Peterson ME, Davidson AP, Feldman EC, et al. (1999) Concurrent pituitary and adrenal tumors in dogs with hyperadrenocorticism: 17 cases (1978–1995). J Am Vet Med Assoc 214:1349–1353.

Gregori T, Mantis P, Benigni L, Priestnall SL, Lamb CR (2015) Comparison of computed tomographic and pathologic findings in 17 dogs with primary adrenal neoplasia. Vet Radiol Ultrasound 56(2):153–159.

Grooters AM, Biller DS, Merryman J (1995) Ultrasonographic parameters of normal canine adrenal glands: comparison to necropsy findings. Vet Radiol Ultrasound 36:126–130.

Hill KE, Scott-Moncrieff JC, Koshko MA, Glickman LT, et al. (2005) Secretion of sex hormones in dogs with adrenal dysfunction. J Am Vet Med Assoc 226:556–61.

Hoerauf A, Reusch C (1999) Ultrasonographic evaluation of the adrenal glands in six dogs with hypoadrenocorticism. J Am Anim Hosp Assoc 35:214–218.

Knight RC, Lamb CR, Brockman DJ, Lipscomb VJ (2019) Variations in surgical technique for adrenalectomy with caudal vena cava venotomy in 19 dogs. Vet Surg 48(5):751–759.

Labelle P, De Cock HEV (2005) Metastatic tumors to the adrenal glands in domestic animals. Vet Pathol 42(1):52–58.

Leroux A (2016) What is your diagnosis? J Am Vet Med Assoc 249(12):1353–1355.

Masnov B, Tiemessen I, Stosic A (2022) Ultrasonographic changes of adrenal glands size under Trilostane therapy, their correlation with clinical signsand endocrine tests and possibility of introducing ultrasound as additional monitoring modality of Cushing's syndrome. Open J Vet Med 12:57–70.

Mayhew PD, Boston SE, Zwingenberger AL, Giuffrida MA, Runge JJ, Holt DE, Raleigh JS, Singh A, Culp WT, Case JB, Steffey MA (2019) Perioperative morbidity and mortality in dogs with invasive adrenal neoplasms treated by adrenalectomy and cavotomy. Vet Surg 48(5):742–750.

Melian C, Perez-Lopez L, Saavedra P Ravelo-García AG, et al. (2021) Ultrasound evaluation of adrenal size in clinically healthy dogs and in dogs with hyperadrenocorticism. Vet Rec 1888, doi: 10.1002/vetr.80

Millard RP, Pickens EH, Wells KL (2009) Excessive production of sex hormones in a cat with an adrenocortical tumor. J Am Vet Med Assoc 234:505–508.

Morandi F, Mays JL, Newman SJ, Adams WH (2007) Imaging diagnosis – bilateral adrenal adenomas and myelolipomas in a dog. Vet Radiol Ultrasound 48(3):246–249.

Pey P, Daminet S, Smets PM, Duchateau L, et al. (2012) Effect of glucorticoid administration on adrenal gland size and sonographic appearance in beagle dogs. Vet Radiol Ultrasound 53:204–209.

Pey P, Diana A, Rossi F, Mortier J, Kafka U, Veraa S, Groth A, MacLellan M, Marin C, Fracassi F (2020) Safety of percutaneous ultrasound-guided fine-needle aspiration of adrenal lesions in dogs: perception of the procedure by radiologists and presentation of 50 cases. J Vet Intern Med 34(2):626–635.

Platt SR, Sheppard BJ, Graham J, Uhl EW, et al. (1998) Pheochromocytoma in the vertebral canal of two dogs. J Am Anim Hosp Assoc 34:365–371.

Ramspott S, Hartmann K, Sauter-Louis C, Weber K, et al. (2012) Adrenal function in cats with hyperthyroidism. J Feline Med Surg 14:262–266.

Watson PJ, Herrtage ME (1998) Hyperadrenocorticism in six cats. J Small Anim Pract 39:175–184.

Wenger M, Mueller C, Kook PH, Reusch CE (2010) Ultrasonographic evaluation of adrenal glands in dogs with primary hypoadrenocorticism or mimicking diseases. Vet Rec 167:207–210.

Yoshida O, Kutara K, Seki M, Ishigaki K, Teshima K, Ishikawa C, Iida G, Edamura K, Kagawa Y, Asano K (2016) Preoperative differential diagnosis of canine adrenal tumors using triple-phase helical computed tomography. Vet Surg 45(4):427–435.

Zatelli A, D'Ippolito, FI, Zini E (2007) Ultrasonographic evaluation of the size of the adrenal glands in 24 diseased cats without endocrinopathies. Vet Rec 160: 658–660.

Zimmer C, Horauf A, Reusch C (2000) Ultrasonographic examination of the adrenal gland and evaluation of the hypophyseal-adrenal axis in 20 cats. J Small Anim Pract 41:156–160.

Vet-ebooks.com

CHAPTER THIRTEEN

Female Reproductive Tract

Delphine Rault[1] and Silke Hecht[2]

[1]*Azurvet Referral Center, Saint Laurent du Var, France*
[2]*Department of Small Animal Clinical Sciences, College of Veterinary Medicine, University of Tennessee, Knoxville, TN, USA*

Examination Technique

The ovaries, uterus, and abdominal part of the vagina are the female reproductive organs routinely visualized ultrasonography. The vulva and clitoris, and mammary glands, are usually not evaluated unless a mass or other abnormality is suspected.

Indications for sonographic examination of the female reproductive tract include pregnancy detection, assessment of normal fetal development and viability, vaginal discharge, clinical signs compatible with hormonal imbalances suggesting ovarian dysfunction, and abdominal mass lesions in intact cats and dogs. Indications for ultrasonographic examination of the mammary glands include abnormal findings on palpation (swelling, pain, and heat) and a need to assess the extent of mammary gland neoplasia.

The examination is performed with the animal in dorsal recumbency (Figure 13.1). Lateral recumbency may prove useful for examining the ovaries. A 5–8-MHz transducer is usually sufficient to visualize an enlarged, fluid-filled uterus, fetal structures, or abdominal mass lesions; however, a 10 MHz or higher frequency transducer provides better detail in the examination of smaller, superficial structures. A high-resolution linear probe is recommended for cats and for the examination of the mammary glands.

Ovaries

Normal Sonographic Anatomy

The ovaries are oval structures located caudal, and often lateral, to the caudal pole of the kidneys, which are used as landmarks for their identification. Depending on pubertal versus prepubertal status and phase of the cycle, ovaries measure approximately 1–2 cm long in dogs and 0.8–1.2 cm long in pubertal cats (Gatel et al. 2020; Levy and Fontbonne 2007; Malandain et al. 2011; Vercellini et al. 2022). As reported earlier, the appearance and size of the ovary vary during the estrus cycle due to the number and size of the follicles (Gatel et al. 2020; Reynaud et al. 2012; Yeager and Concannon 1995) (Figures 13.2–13.7). In prepubertal dogs, the first antral follicles could be identified in 5–6-month-old dogs and measure 0.15–0.3 mm (Reynaud et al. 2012), and antral follicles <1 mm are visualized in prepubertal 3-month-old cats (Vercellini et al. 2018) (Figure 13.2). During anestrus, the ovary is small, oval, and uniform in echogenicity or has a mixed appearance with hyperechoic rete ovary surrounded by hypoechoic cortex. Tiny primary follicles may be visualized in dogs and cats. In dogs, antral follicles measure 0.2–0.6 mm at the start of anestrus and may reach 1 mm at the end of anestrus (Reynaud et al. 2012) (Figure 13.3A, B). During proestrus, the ovary enlarges and becomes more spherical, and the follicles increase in size. After the final stages of follicular growth, they will reach 6–9 mm at the time of ovulation in dogs and 3–4 mm in cats (Figure 13.3C, D). The diameter of growing follicles is positively correlated with the body size of the dogs. In cats, because ovulation is considered induced without preovulatory luteinization, hormone assessment is not valuable to determine the optimal day of ovulation. Ultrasonographic follow-up of heat is an interesting tool to optimize the ovulation induction in this species. The follicular growth is 0.2 mm/day until the largest follicle diameter reaches

Atlas of Small Animal Ultrasonography, Third Edition. Edited by Dominique Penninck and Marc-André d'Anjou.
© 2025 John Wiley & Sons, Inc. Published 2025 by John Wiley & Sons, Inc.
Companion website: www.SmallAnimalUltrasonography.com

Vet-ebooks.com

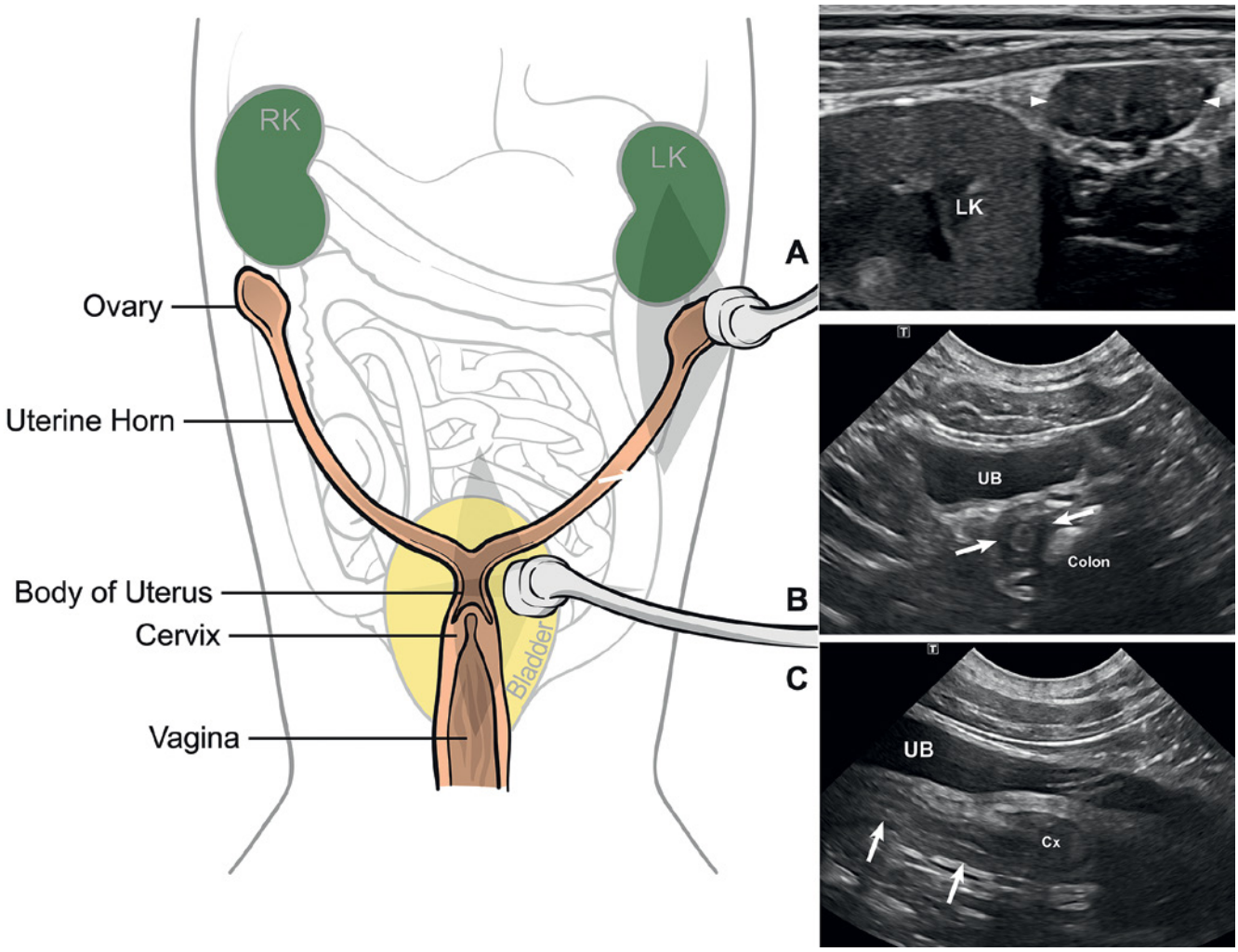


Figure 13.1. **Normal female dog reproductive tract.** On the left is a schematic representation of the anatomy of the female reproductive tract. The ovaries are located caudal and often lateral to the kidneys. The cervix and body of the uterus are located dorsal to the urinary bladder. The uterine horns extend craniolaterally from the uterine body and are infrequently visible during anestrus. **(A)** Sagittal image of a normal **left ovary** (arrowheads). The left kidney (LK) is used as a landmark, and the ovary is identified as an ovoid soft-tissue structure of medium echogenicity caudolateral to the caudal pole of the kidney. **(B)** Transverse and sagittal **(C)** images of the normal canine **uterus during anestrus**. On the transverse image, the uterus (arrows) is identified as a circular structure between the urinary bladder (UB) and colon, which are used as landmarks. On the sagittal image, the uterus (arrows) is seen as a tubular structure of medium echogenicity dorsal to the urinary bladder cranial to the cervix (Cx) of the uterus.

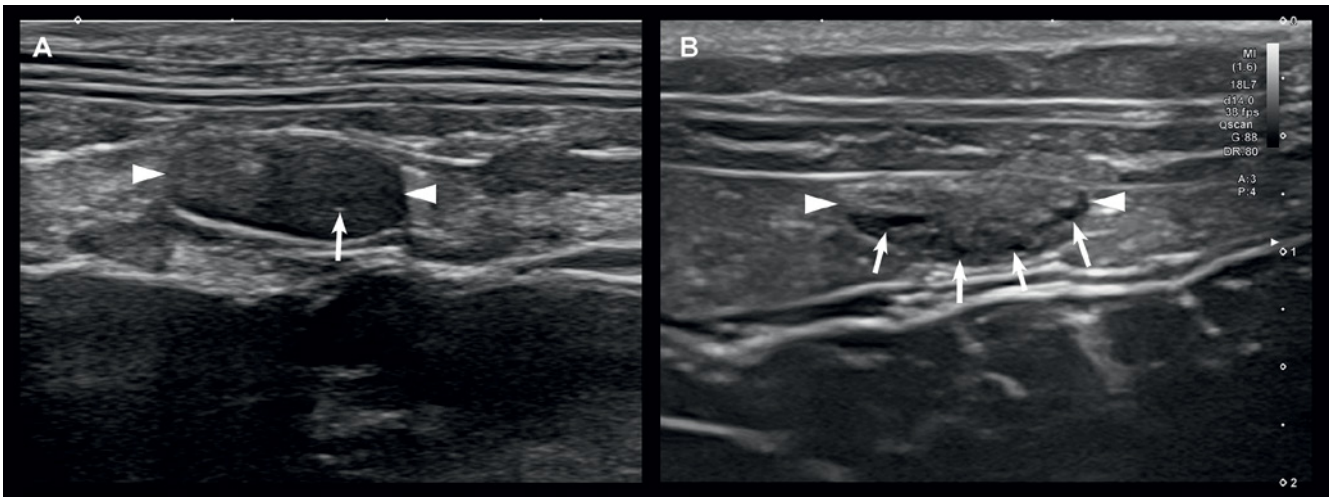


Figure 13.2. **Normal ovaries in prepuberal animals. (A)** Sagittal image of the left ovary (arrowheads) in a 5.5-month-old German Shepherd **bitch**. The ovary is relatively homogeneous and hypoechoic. A small anechoic cystic focus is visible compatible with a small antral follicle (arrow). **(B)** Sagittal image of an ovary (arrowheads) in a 3-month-old Bengal **queen**. Tiny anechoic foci (arrows) are identified, consistent with primary follicles.

Vet-ebooks.com

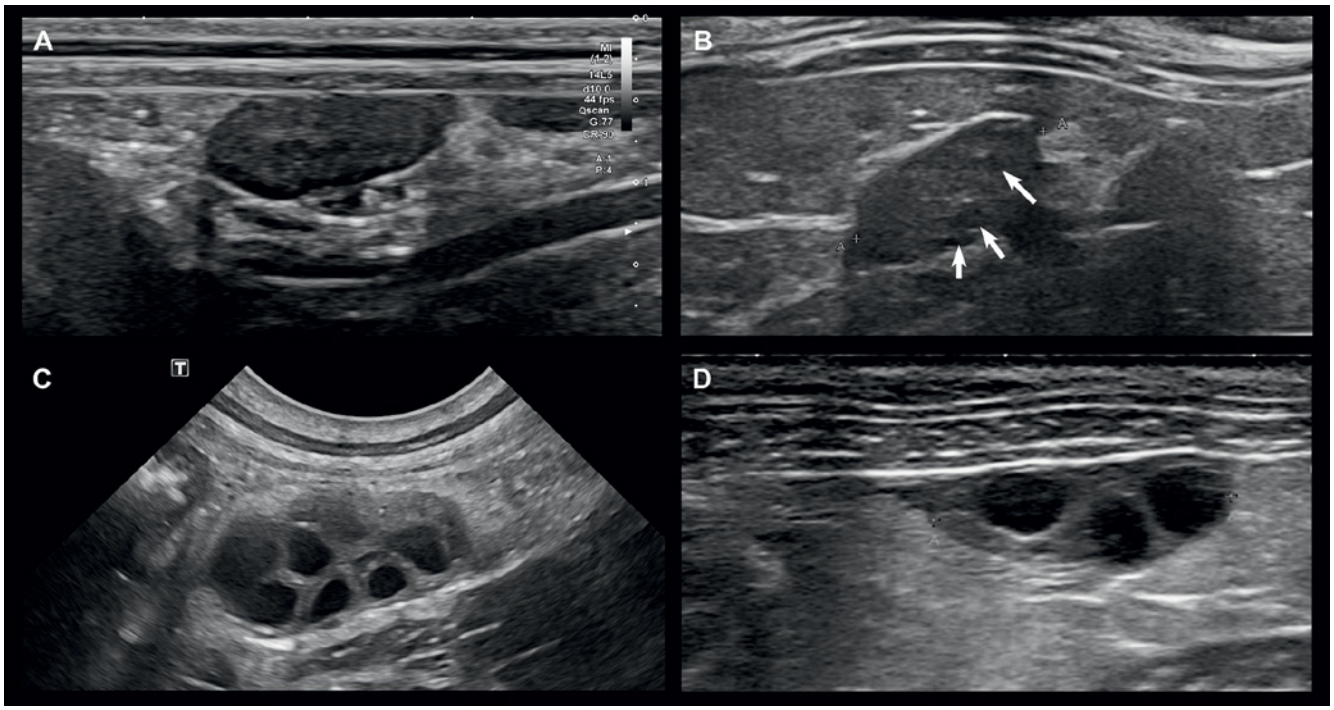


Figure 13.3. **Normal ovaries in a dog and a cat**, during **anestrus (A, B)** and **proestrus/estrus (C, D). (A)** Sagittal image of the ovary in anestrus of a 3-year-old Pointer and in a 1.5-year-old Maine Coon cat. **(B)** Tiny anechoic foci corresponding to small antral follicles are identified (arrows). **(C)** Sagittal image of the right ovary in a 1-year-old Bullterrier. Multiple anechoic follicles (3–4.6 mm in diameter) are visible corresponding to a mid-proestrus period. **(D)** In an adult cat, three anechoic cavitary structures of 2.6–3.1 mm diameter are visible, consistent with follicles. Courtesy of Dr. Laure Gatel, Sudvetia, France.

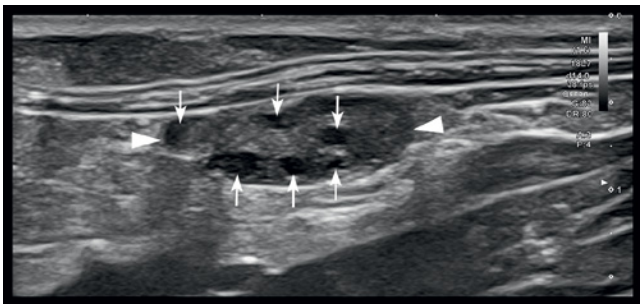


Figure 13.4. **Anovulatory cycle in a 3-year-old Bengal cat, 2 weeks after heat (interestrus phase).** Sagittal image of the ovary (arrowheads) showing multiple anechoic follicles (1–1.7 mm diameter) (arrows), corresponding to follicular atresia.



Figure 13.5. **Normal ovary during estrus and metestrus in a 1.5-year-old Chihuahua. (A)** Sagittal images of the left ovary at the **end of folliculogenesis**. Two preovulatory follicles have anechoic content with a thick wall (arrowheads), presumably because of preovulatory luteinization. **(B) Two days after, at ovulation**. Fluid-filled follicles are replaced by corpora lutea. One corpus luteum appears isoechoic and solid (*), and the other is thick-walled with a small internal anechoic center (arrow). **(C) One month after ovulation**, the ovary is reduced in size. Corpora lutea are difficult to identify.

Vet-ebooks.com

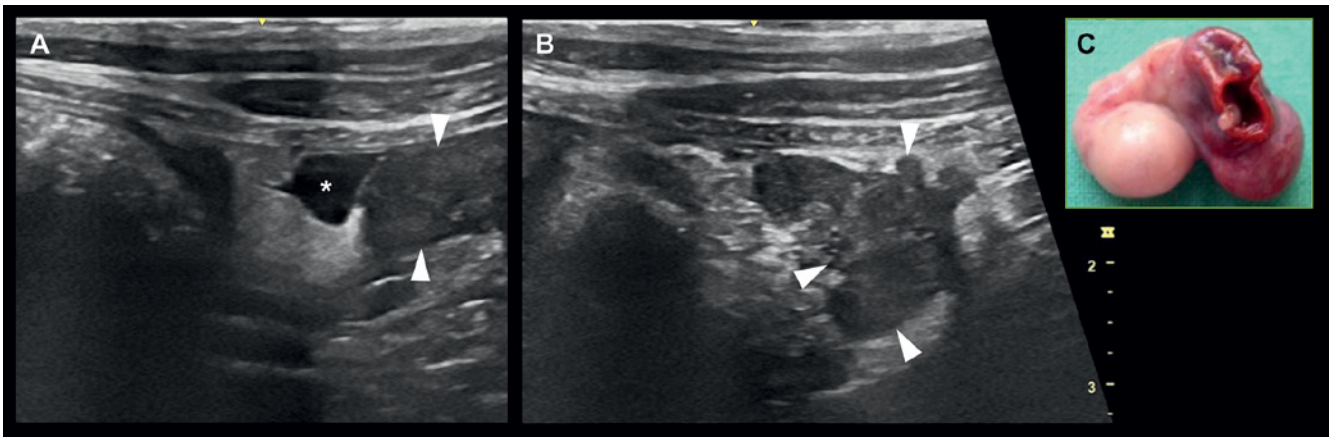


Figure 13.6. Normal ovaries during ovulation in a 3.5-year-old Czechoslovakian wolfhound (progesterone [Minividas, Biomérieux] = 11,60 corresponding to the end of ovulation). **(A)** Sagittal image of the **left ovary** (arrowheads). A small amount of free fluid is visible in the ovary bursa (*). **(B)** Sagittal image of the **right ovary**. No follicle is visible. The irregularity of the ovarian contour (arrowheads) is compatible with the rupture of the follicle. **(C)** Postsurgical image after ovariectomy postovulation. Courtesy of Dr Xavier Levy, CRECS, France.

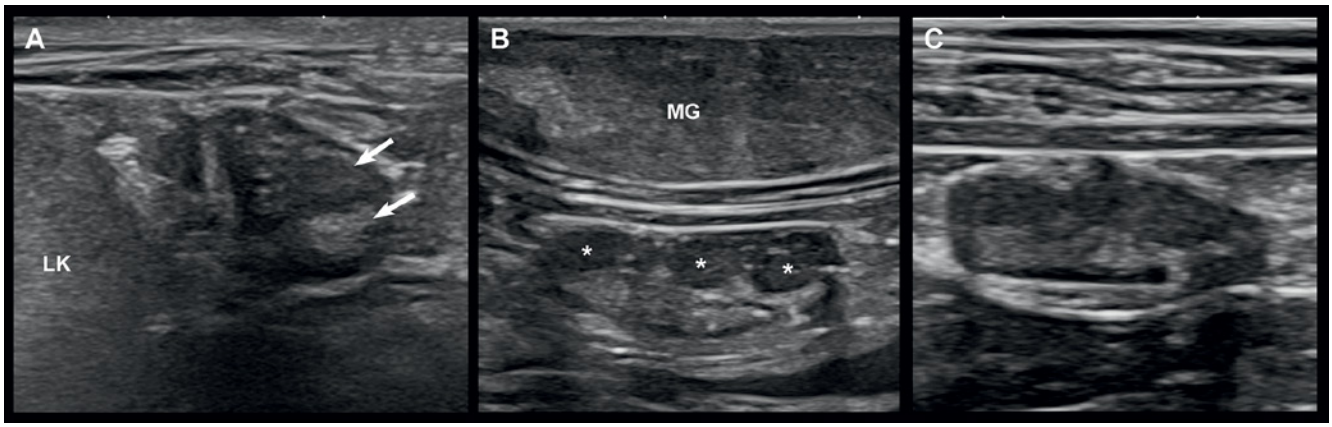


Figure 13.7. Normal left ovaries in two dogs during metestrus (A) and postpartum (B, C). A Sagittal image in metestrus of a Bedlington terrier. Corpora lutea are increased in echogenicity and appear as round hyperechoic nodules (arrows). **(B, C)** Sagittal image of left ovary in a Shetland Sheepdog bitch postpartum. **(B)** At 6-weeks postparturition, corpora lutea are still identified (*). The mammary glands (MG) are thickened. **(C)** At 14 weeks after parturition, the ovary is slightly inhomogeneous. Faint hypoechoic round structures are barely visible.

between 3 and 4.1 mm. Without stimulation, follicle atresia starts with decreased size of the follicle at the pace of 0.1 mm/day during interestrus (Malandain et al. 2011) (Figure 13.4). In dogs, at the LH peak, mucification of the cumulus-oocyte complex may be visible as an echogenic point in the center of some preovulatory thick-walled follicles in the dog (Figure 13.5). On the day of ovulation, the follicle number decreases and the remaining noncollapsed follicles reduce in size. The contour of the ovary may be bumpy, and a scant amount of fluid may be seen in the ovarian bursa in the dog (Figure 13.6). The anechoic antrum of the follicle disappears (Levy and Fontbonne 2007; Silva et al. 1996). Doppler evaluation shows a decreased perfusion of the uterine artery 2 days prior to ovulation and a gradual increase in uterine and ovarian perfusion after ovulation in dogs (Barbosa et al. 2013). These specific features (Doppler values and ovarian ultrasound images) may be useful to estimate the date of ovulation in dogs but need a daily assessment. In practice, it is commonly admitted that in dogs, the exact time of ovulation by ultrasonographic examination is difficult to predict because the ovarian follicles just before ovulation and young hemorrhagic corpora lutea just after ovulation look very similar (England et al. 2003; Silva et al. 1996; Yeager and Cncannon 1995). After ovulation, corpora lutea are 5–9 mm diameter in dogs and tend to be thicker-walled with internal anechoic

Vet-ebooks.com

structures and more variable in shape compared with preovulatory follicles (Silva et al. 1996). During metestrus, the ovarian contour remains bumpy and its size reduces. The corpora lutea gradually decrease in size while increasing in echogenicity (Figure 13.7). Around 10–14 days after ovulation, the corpora lutea appear solid and remain as such for the duration of metestrus. In cats, the echogenicity of the corpora lutea depends on the luteinization phase or luteal atresia and may be difficult to identify (Gatel et al. 2020).

Ovarian Changes

In many cases, a presumptive diagnosis of an ovarian abnormality is made based on clinical findings, and ultrasonography is used to confirm the suspicion rather than serving as the primary means of diagnosis (England et al. 2003).

Ovarian cysts appear as anechoic, well-circumscribed, and thin-walled structures with distal enhancement (Figure 13.8). Hormonally inactive cysts arising from the ovarian bursa and hormone-producing follicular and luteinizing cysts cannot be differentiated through ultrasonography. Cysts are more frequent in old cats, and para-ovarian and cystic rete-ovaries are relatively common in this species. Periovarian cysts are incidental gonadal disorders corresponding to retained abnormally dilated embryonic ducts. Follicular cysts are the most common cysts in older dogs. They are single or multiple unilocular thin-walled round anechoic structures. Luteal cysts are solitary with a thicker wall compared to follicle cysts, and frequently range from 1.5 to 3 cm in diameter (Sasidharan et al. 2021). Cysts of subsurface epithelium (or germinal cyst) are rarely larger than 5 mm. Large follicles and cavitary corpora lutea may be confused with ovarian cysts and can only be differentiated by serial ultrasound examinations. Follicles should not persist longer than 30 days and corpora lutea for more than 60 days. The finding of fluid-filled structures associated with the ovary must be interpreted considering the clinical presentation when serial examinations are not being performed. However, cysts are prioritized over normal follicles if their diameter exceeds 8 mm in dogs and 5 mm in cats (Fulton 2021; Malandain et al. 2011).

Ovarian tumors (epithelial tumors, sex-cord stromal tumors, and germ-cell tumors) are rare. Granulosa cell tumors are most frequently diagnosed. They appear as nodules or masses of variable size and echogenicity with metastases in the peritoneal cavity (Figure 13.9). Tumors may have a cystic or mineral component (Figures 13.10, 13.11). Tumor types cannot be differentiated ultrasonographically, although teratomas and teratocarcinomas have the tendency to become very large and partially mineralized. The origin of an ovarian mass can be difficult to determine when the enlarged organ changes position and moves ventrally from its original location (Diez-Bru et al. 1998). Common concurrent findings include ascites, pyometra, and cystic endometrial hyperplasia.

Ovarian remnant syndrome is usually a consequence of residual tissue left behind during ovariohysterectomy

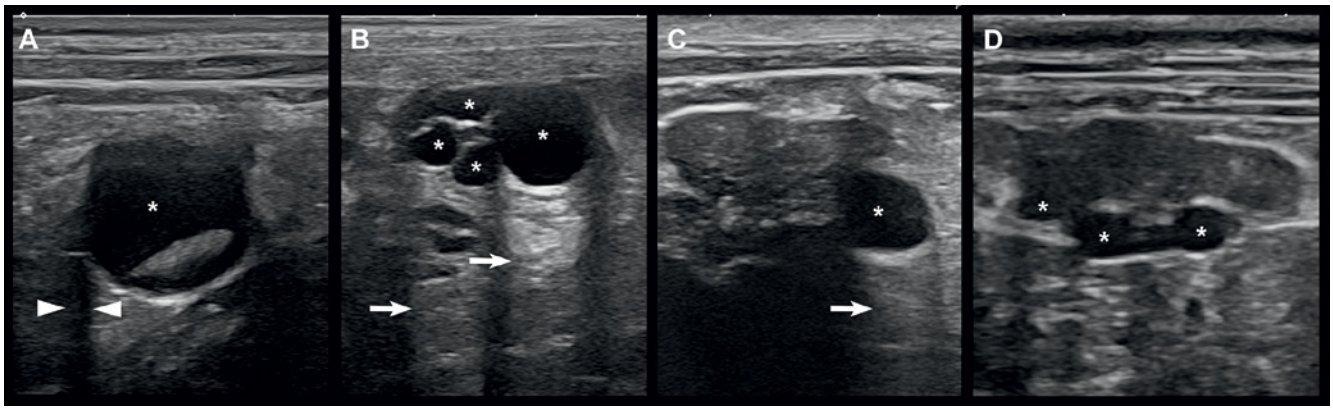


Figure 13.8. **Ovarian cysts in four dogs. (A)** Solitary cavitary structure, 16 mm in diameter, thin walled, with anechoic content (*), distal enhancement and edge shadow (arrowheads) in a large breed dog. A follicular cyst was confirmed by puncture and analysis of estrogen level of the cystic fluid. Image courtesy of Dr. Julien Fritz, Azurvet, France. **(B)** Multiple cavitary anechoic lesions (*), ranging from 3.6 to 10 mm in diameter, in a dog with abnormal heat. Acoustic enhancement bordered by edge shadowing is seen distal to these fluid-filled cysts (arrows). **(C)** The ovary is homogeneous (arrowheads), and an incidental paraovarian cyst (*) measuring 4.6 × 6 mm is visualized in a Bedlington terrier during anestrus, with acoustic enhancement (arrow). **(D)** Sagittal image of several cysts (*) at the periphery and hilus of the left ovary in a 11-year-old Chihuaha. Rete ovarii cysts (asymptomatic embryological malformation) were confirmed by histology.

Vet-ebooks.com

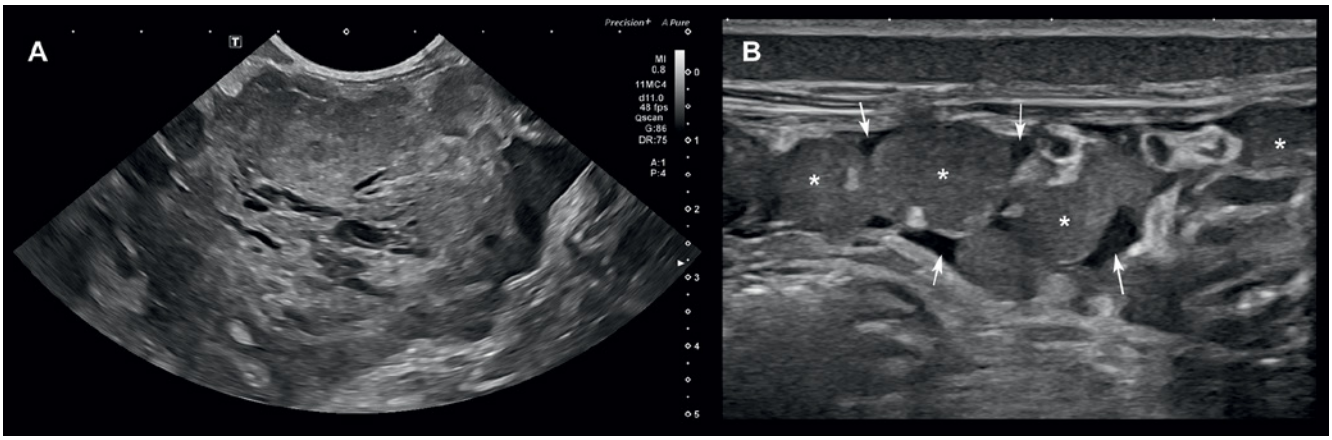


Figure 13.9. **Granular cell ovarian carcinoma arising from remnant tissue in a 6-year-old cat with carcinomatosis. (A)** A large heterogeneous mass is visualized at the extremity of the left uterine horn. **(B)** Free fluid (arrows) and peritoneal nodules (*) are observed. Fine needle aspirates of the mass and nodules confirmed the diagnosis.

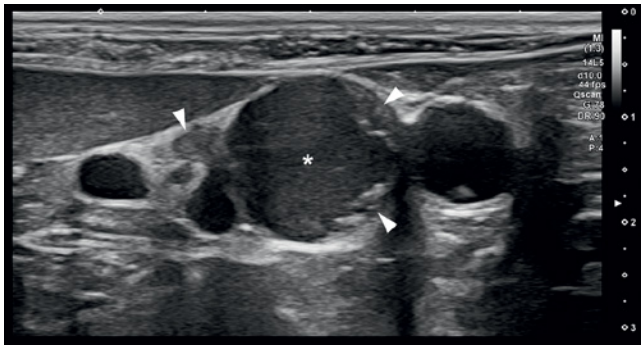


Figure 13.10. **Luteoma arising from residual ovarian tissue in a 9-year-old Cocker Spaniel** (8 years after ovariectomy). A large thick irregular cavitary structure with echoic fluid (*) and hyperechoic peripheral tissue (arrowheads) associated with 3 thin-walled cystic foci is located at the end of left uterine horn. Histologic analysis confirmed the presence of a luteoma in the remnant ovarian tissue located at the uterine horn ligation.

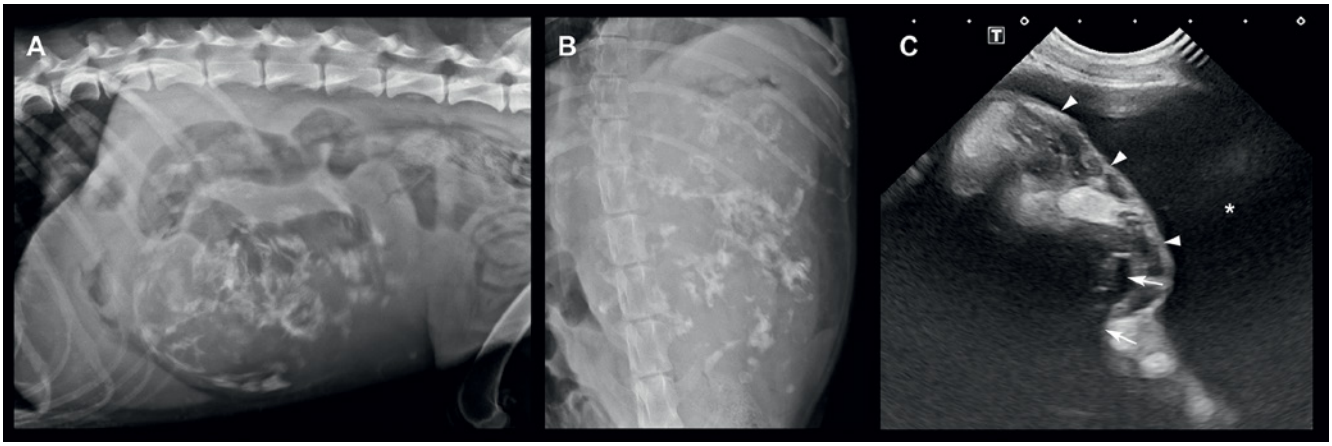


Figure 13.11. **Left ovarian teratoma in a 2-year-old Husky. (A, B)** A large radiopaque, soft tissue mass with several mineralized regions is visible in the mid and left lateral abdomen. **(C)** This large inhomogeneously echogenic mass (arrowheads) in the mid-abdomen has a mixed pattern (hypoechoic and hyperechoic foci with acoustic shadows; thin arrows). The mass is associated with peritoneal effusion (*). Ovarian tumor containing ossified material and hair was confirmed at surgery and histology.

or due to the presence of accessory ovarian tissue (Figure 13.12). Animals usually present with clinical signs of proestrus or estrus with variable occurrence after the ovariectomy. In most circumstances, ovarian remnant tissue is in the region of ovarian pedicles and may appear as a cyst-like lesion. However, the entire area from the caudal poles of the kidneys to the level of the bladder should be searched for abnormal tissue (Davidson and Baker 2009). It is recommended to perform the ultrasonographic examination while the animal is in estrus to best identify cyst-like structure in the remnant tissue. Animals with ovarian remnants may also develop stump pyometra, cystic endometrial hyperplasia, vaginal tumor, or ovarian tumor (Ball et al. 2010).

Vet-ebooks.com

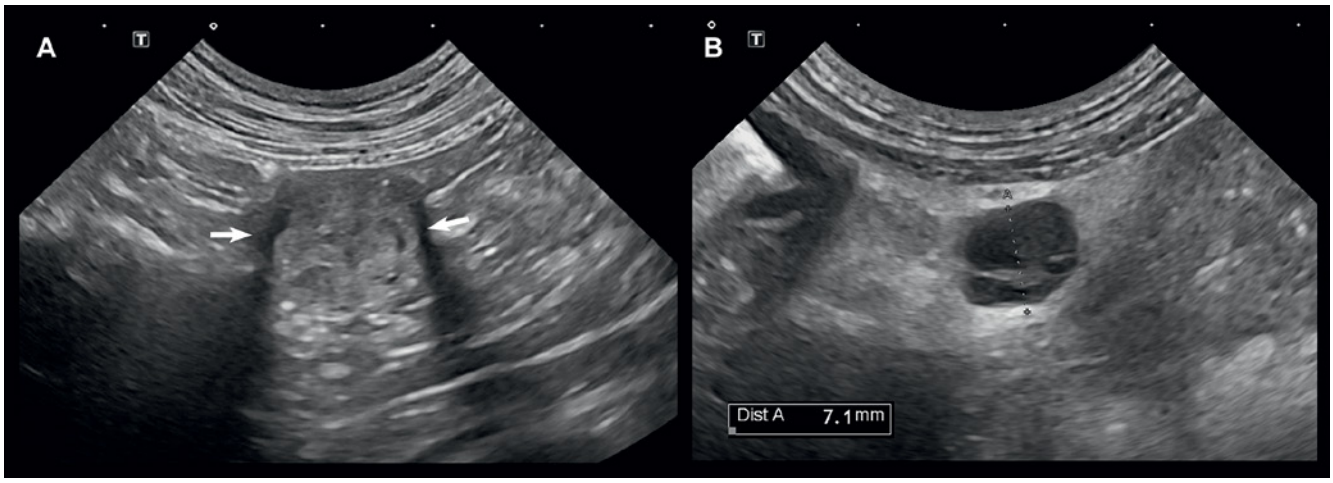


Figure 13.12. Ovarian remnants in the region of ovarian pedicles in two dogs. (A) A round slightly heterogeneous structure bordered by edge shadowing (arrows) is identified in a Beauceron dog presenting for vaginal discharge 7 years after spay surgery. **(B)** A round, partially cystic structure is visible in a 4-year-old Yorkshire terrier presenting for vaginal discharge since ovariectomy 2 years ago.

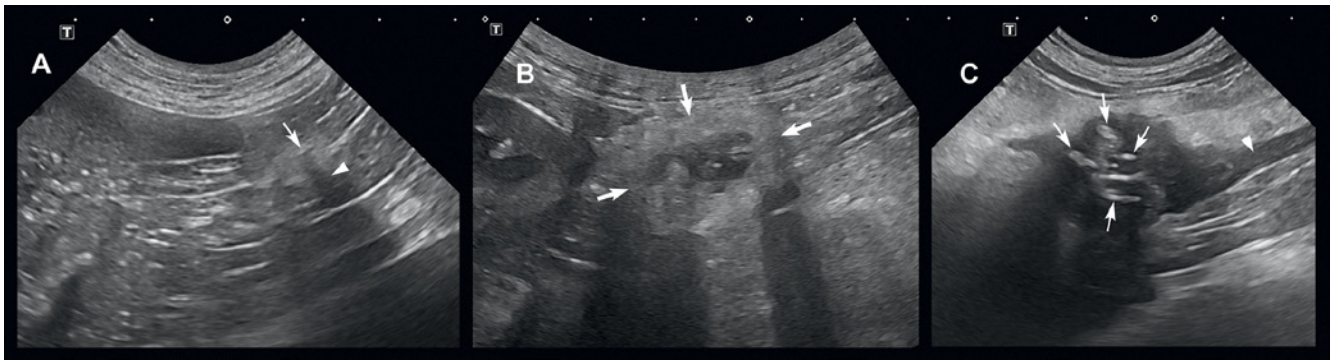


Figure 13.13. Sagittal images of postovariectomy sites. (A) Normal hyperechoic appearance of ovariectomy site, **1 week after surgery**. The mesovarian ligature is hyperechoic (arrow) with acoustic shadow (arrowhead). **(B)** The ovariectomy site has a heterogeneous appearance with a hypoechoic center and adjacent moderately hyperechoic fat **3 days after surgery**, supporting excessive hemorrhage as reported during surgery. **(C)** The ovariectomy site of a crossbreed hunting dog presented with a long-standing fistula (arrowhead) is hypoechoic with numerous central hyperechoic foci with acoustic shadowing; these correspond to nonabsorbable suture (fishing nylon) (arrows). The dog had an **ovariectomy 11 years ago**.

The normal appearance of ovarian ligation after surgery has been described (Costa et al. 2019; Nilsson et al. 2023). In a recent study assessing the normal postoperative abdominal findings after ovariohysterectomy, the mesovarian ligature was heterogeneous and hyperechoic with central shadowing in the first 15 days (Figure 13.13). Hyperechoic structures with faint acoustic shadow, outlined by local hyperechoic fat, were still visible 1 month after surgery using monofilament absorbable suture. The hyperechoic rim persists up to 2 and 3 months after surgery, and no more reaction is expected 4 months after surgery.

Other abnormalities of the mesovarian ligature site are hematoma or exuberant inflammation around suture material. In these instances, the ligature site appears hypoechoic surrounded with hyperechoic fat. Amorphous hypoechoic tracts may be identified corresponding to bleeding or fistula. The diagnosis depends on the clinical signs and the follow-up assessment (Figure 13.13C).

Uterus

Normal Sonographic Anatomy

The normal nongravid uterus is identified in the caudal abdomen and is made of two horns, the uterine body and the cervix. The uterine size and appearance depend on the size of the animal, previous pregnancies, pubertal versus prepubertal status, and stage of the estrus cycle (Figures 13.14–13.17). The **uterine horns** may be challenging to visualize because of their smaller size and surrounding intestinal segments. The **uterus** appears as a tubular structure in

Vet-ebooks.com

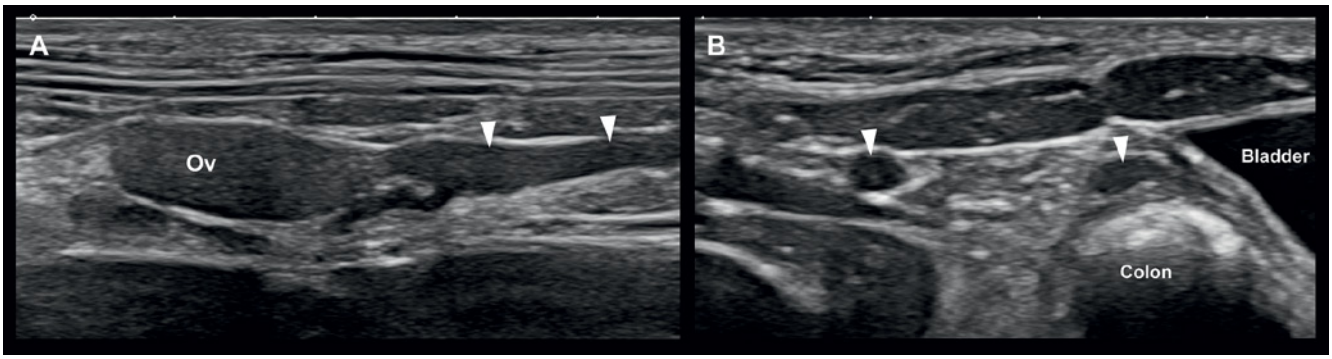


Figure 13.14. **Normal uterus in a prepubertal medium size dog. (A)** Longitudinal section of the uterus and vary. The ovary (Ov) is homogeneous and hypoechoic. The uterine horn is thin and hypoechoic, without visible layers (arrowheads). **(B)** Transverse section of the uterine horns, which appear as small, round, hypoechoic structures of 2–2.5 mm diameter (arrowheads).

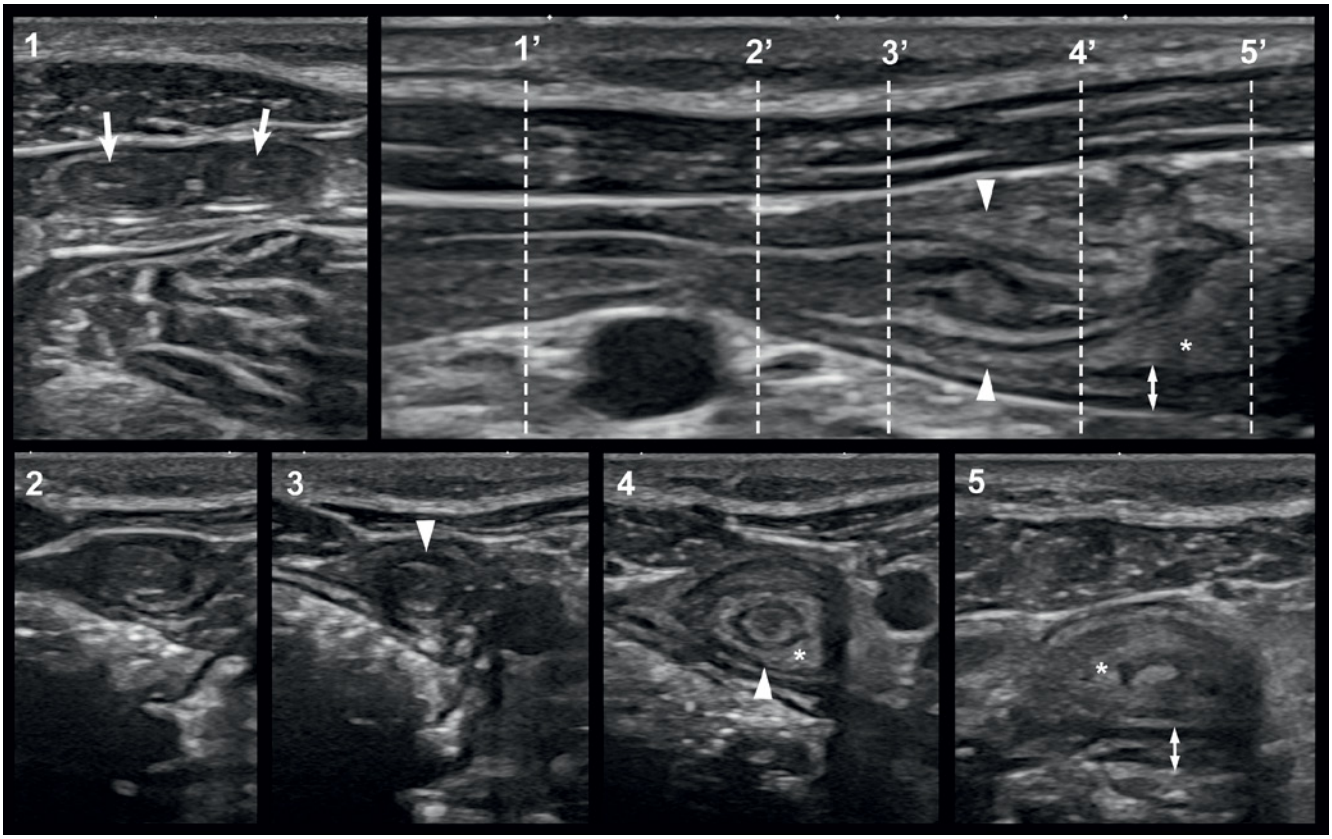


Figure 13.15. **Normal uterus in a 1.5-year-old Jack Russel Terrier during metestrus.** Transverse sonograms obtained at different levels of the uterus, as depicted on the dashed lines on the longitudinal image on top right. On this longitudinal sonogram, the uterine cervix is protruding into the vagina lumen (arrowheads). **(1)** Transverse sonogram of the **cranial uterine body** just before the bifurcation of the two horns. **(2)** Transverse sonogram of the **uterine body** with a single lumen. **(3)** Transverse sonogram of the **cranial cervix** (arrowhead) protruding into the vagina lumen. **(4)** Transverse sonogram of the **caudal cervix** (arrowhead) protruding into the vagina lumen, note hyperechoic endometrium of the vagina (*). **(5)** Transverse sonogram of the **vagina**; note the hyperechoic endometrium (*) and layered myometrium (Two hypoechoic layers separated by a thin hyperechoic line) (double headed arrow).

Vet-ebooks.com

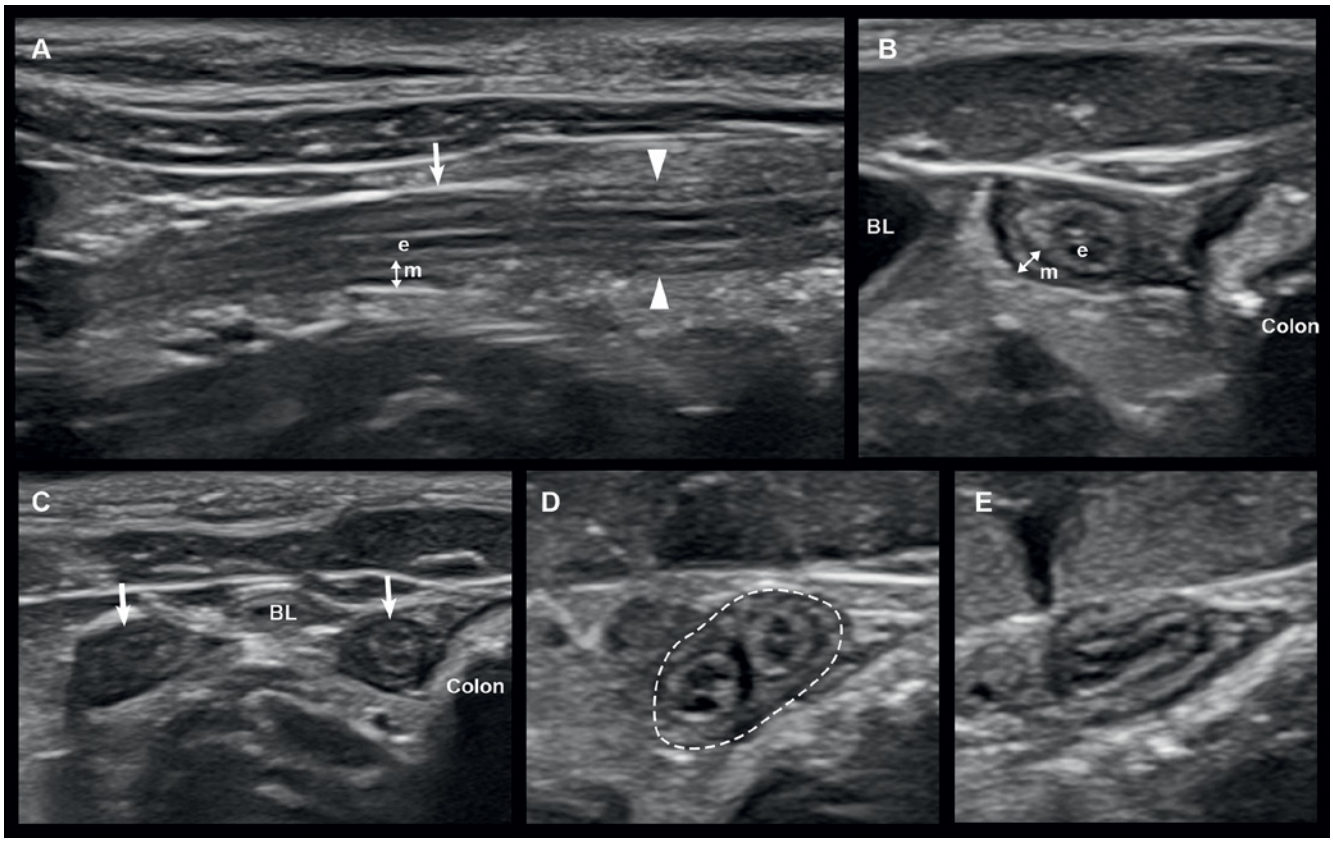


Figure 13.16. **Normal uterus of a cat.** Sagittal **(A)** and transverse **(B)** sonograms of the **uterus** (between arrowheads) with wall layering: hyperechoic serosa (arrow); hypoechoic endometrium (e); layering of the myometrium (m): Two hypoechoic layers separated by a thin hyperechoic line (double headed arrow). **(C)** Transverse sonogram of **uterine horns** (arrows) ventral to the urinary bladder (BL). **(D)** Transverse sonogram of the **uterine body** before the bifurcation of the horns. Two uterine lumens are visible in a single round structure (uterine body underlined by dotted circle). An internal septum (the uterine velum) is present between the two horns. **(E)** Transverse sonogram of the **cervix or cranial vagina**. The cervix is not clearly identified by ultrasound in queens. BL, urinary bladder.

longitudinal section and round structure in transverse section, between the urinary bladder (UB) (ventral) and the descending colon (dorsal) (Figure 13.14). Once the **cervix** or the **uterine body** is identified, the uterine horns may be traced cranially to the level of each ovary. An alternative approach is to identify the uterine horns close to their respective ovary; however, their small diameter at this location may hinder identification. The uterine body appears as a single round to ovoid structure. An internal partition (**uterine velum**) exists in the cranial body lumen, separating the two horns and making them distinctly visible before their divergence (Figures 13.15, 13.16D). The cervix is not identified by ultrasonography in cats. In dogs, it corresponds to a bulging of the uterine diameter, due to the protrusion of the caudal cervix into the vaginal lumen. In prepubertal or ovariectomized females, the uterus is small and hypoechoic. Concentric uterine layers may be identified in pubertal active females; an inner hypoechoic layer representing the **endometrium**, two outer hypoechoic layers corresponding to the circular and longitudinal **myometrium** separated by a thin hyperechoic vascular and collagen fiber tissue. The most outer hyperechoic interface corresponding to the **serosa** (England et al. 2003; Gatel et al. 2020). The body measures between 5 and 8 mm in diameter and is smaller in prepubertal dogs (England et al. 2003). During proestrus and estrus, the uterine diameter increases, and the wall appears hypoechoic due to edema. During the early luteal phase, the uterine diameter continues to increase and the edema decreases (England et al. 2003). In cats, the uterine body diameter measures 1.5–5.3 mm and the uterine horn diameter measures 1–5.8 mm. The thicker the uterine wall, the more visible the layers are (Gatel et al. 2020).

Vet-ebooks.com

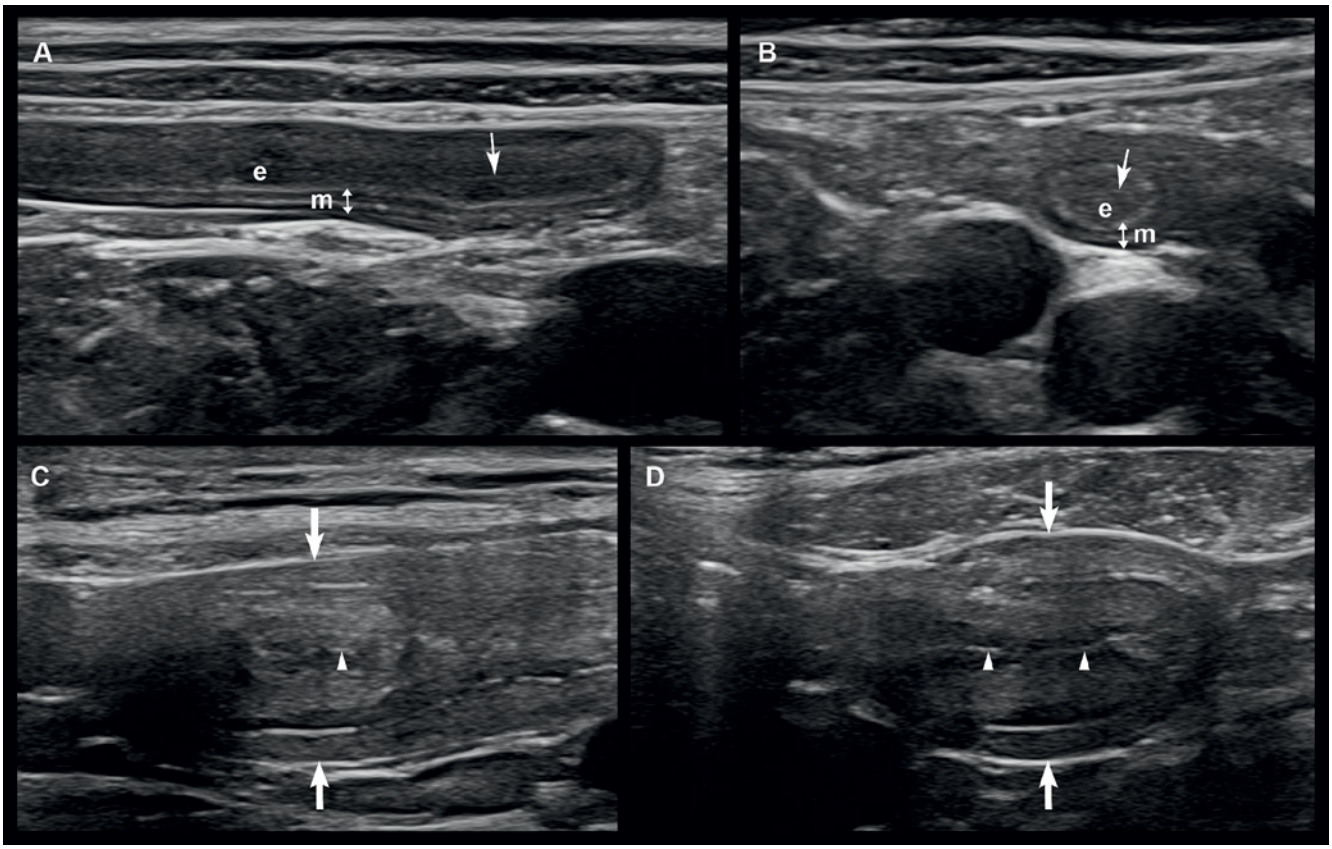


Figure 13.17. Normal uterus of a dog during estrus. (A, B) Longitudinal **(A)** and transverse **(B)** sonograms of the **uterine horn**. The uterine horn is tubular and hypoechoic on longitudinal section and rounded on transverse section. There is a faint concentric layering appearance of the uterine wall: the lumen is an inner thin hyperechoic line (arrow); the endometrium (e) a thick hypoechoic layer; the myometrium (m) (double headed arrow) two hypoechoic lines consistent with the two muscular layers separated by a thin hyperechoic vascular and collagen fiber tissue. **(C, D)** Longitudinal **(C)** and transverse **(D)** sonograms of the **uterine cervix**. The cervix appears as a conical or tubular bulging of the uterus protruding into the lumen of the vagina (between arrows). The os (ostium) cervix is a central hyperechoic stripe (arrowheads).

Ovariohysterectomy Sites

In spayed dogs, the uterine **stump** is usually inconspicuous and may be visible as a blind-ended tubular structure between UB and colon (Figure 13.18D). In a recent study assessing the normal postoperative abdominal findings after ovariohysterectomy, the cervical stump appeared heterogeneously hypoechoic with hyperechoic surrounding tissue in the first 15 days with an increased diameter at day 4–6 after surgery (Nilsson et al. 2023) (Figure 13.18).

Pregnancy

Normal Pregnancy

Ultrasonography is a reliable method for diagnosing pregnancy in dogs and cats. Inconsistency exists in the literature regarding the time of the earliest definitive diagnosis, partly because of the difficulty to determine the time of conception in dogs. The improved image detail provided by more recent ultrasound systems could contribute to earlier diagnosis.

The most used definition of **gestational age** is the number of days after luteinizing hormone (LH) peaks (ovulation occurs 2 days after LH surge) in dogs and the number of days after breeding in cats.

Ultrasonography is useful in monitoring normal embryonic and fetal development (Beccaglia et al. 2016; Beck et al. 1990; England et al. 1990; Lopate 2008, 2018 Yeager et al. 1992; Zambelli et al. 2002) (Figures 13.19–13.25). **Gestational timing** can be based on the assessment of embryonic and fetal structures and extra-embryonic or fetal membranes. The first reliable ultrasonographic indicator of pregnancy is the detection of **gestational chambers**, which appear as small, thin-walled, round, anechoic vesicles of 1–2 mm in

Vet-ebooks.com

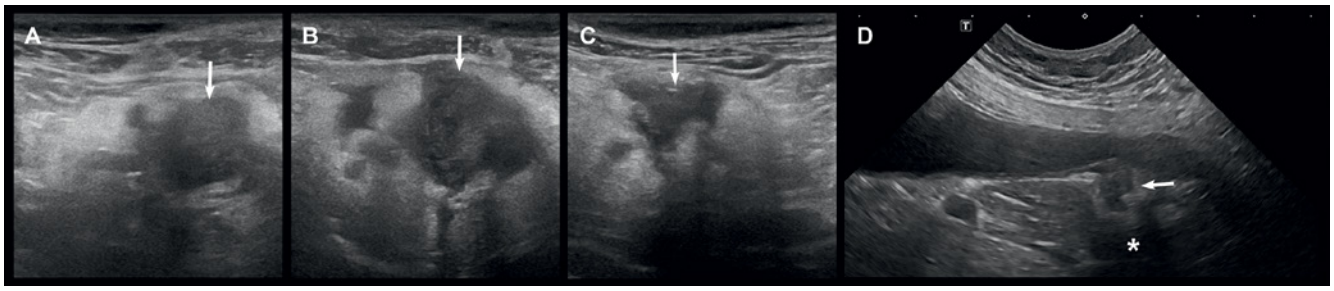


Figure 13.18. **Normal sonograms of cervical stump after ovariohysterectomy in a dog.** Transverse sonograms at 1 day **(A)**, **4–6 days (B)** and **10–15 days. (C)** The cervical stump appears heterogeneous, hypoechoic (arrows) with hyperechoic surrounding tissue in the first 15 days. There is an increased diameter of the stump 4–6 days after the surgery. **(D)** Sagittal sonogram at **day 20 after surgery**. The cervical stump appears heterogeneous and contains hyperechoic foci (arrow) with acoustic shadowing (arrow). Surrounding tissue is of mixed echogenicity. Courtesy of Mia Nilsson, Evidensia, Sweden.

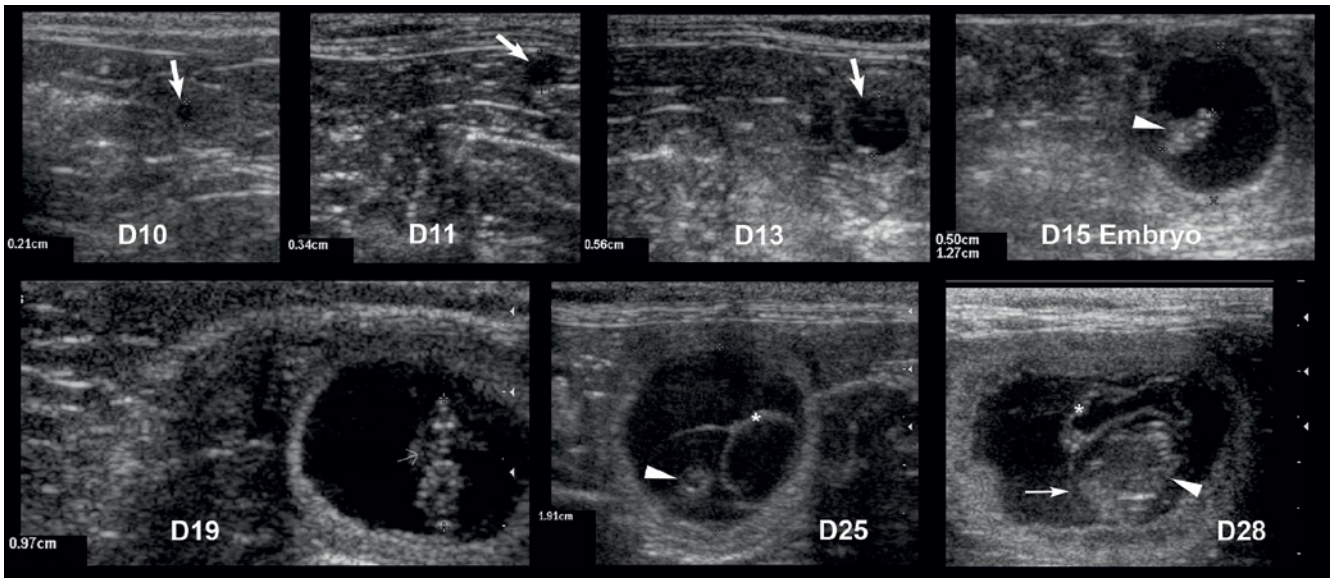


Figure 13.19. **Progression of normal first half of pregnancy in an Abyssinian cat. Day 10, 11, and 13 After Mating**: The gestational chamber is a round anechoic structure (arrows), measuring 2 mm, 3.4 mm, and 5.6 mm in diameter, respectively. **Day 15**: The embryo (arrowhead) measures 5 mm and is visible within the periphery of the gestational sac. Placenta is visible. **Day 19**: Embryonic heartbeats were detectable in real time, and surrounding placenta is visible. **Day 25**: Yolk sac membrane is visible (*) adjacent to a portion of the embryo (arrowhead). **Day 28**: Collapse of the yolk sac membrane (*) and faint identification of the allantoic membrane (thin arrow) that surrounds the embryo (arrowhead).

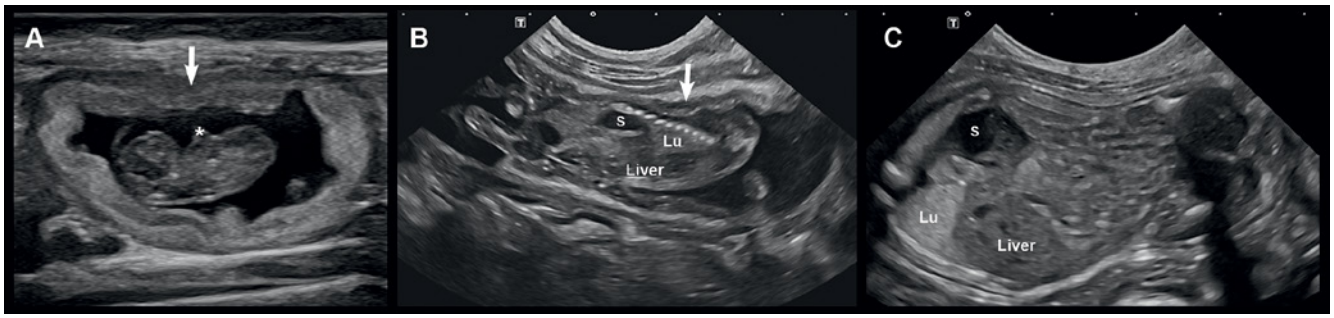


Figure 13.20. **Normal mid- to late-term pregnancy in three cats. (A) Day 26**: The embryo with limb buds (*) is visible. The placenta is in the near field (arrows). **(B) Day 37**: Sagittal image of the fetus with the head to the right. The lung (L) is hyperechoic to the liver, and the fluid-filled stomach (S) is visible. The aligned hyperechoic dots represent early mineralization of the skeleton. The placenta is in the near field (arrows). **(C) Day 57**: Sagittal image of the fetus. The fluid-filled stomach (S) and liver are easily visualized. The lung (Lu) is hyperechoic to the liver. The layered intestines are distinguishable.

Vet-ebooks.com

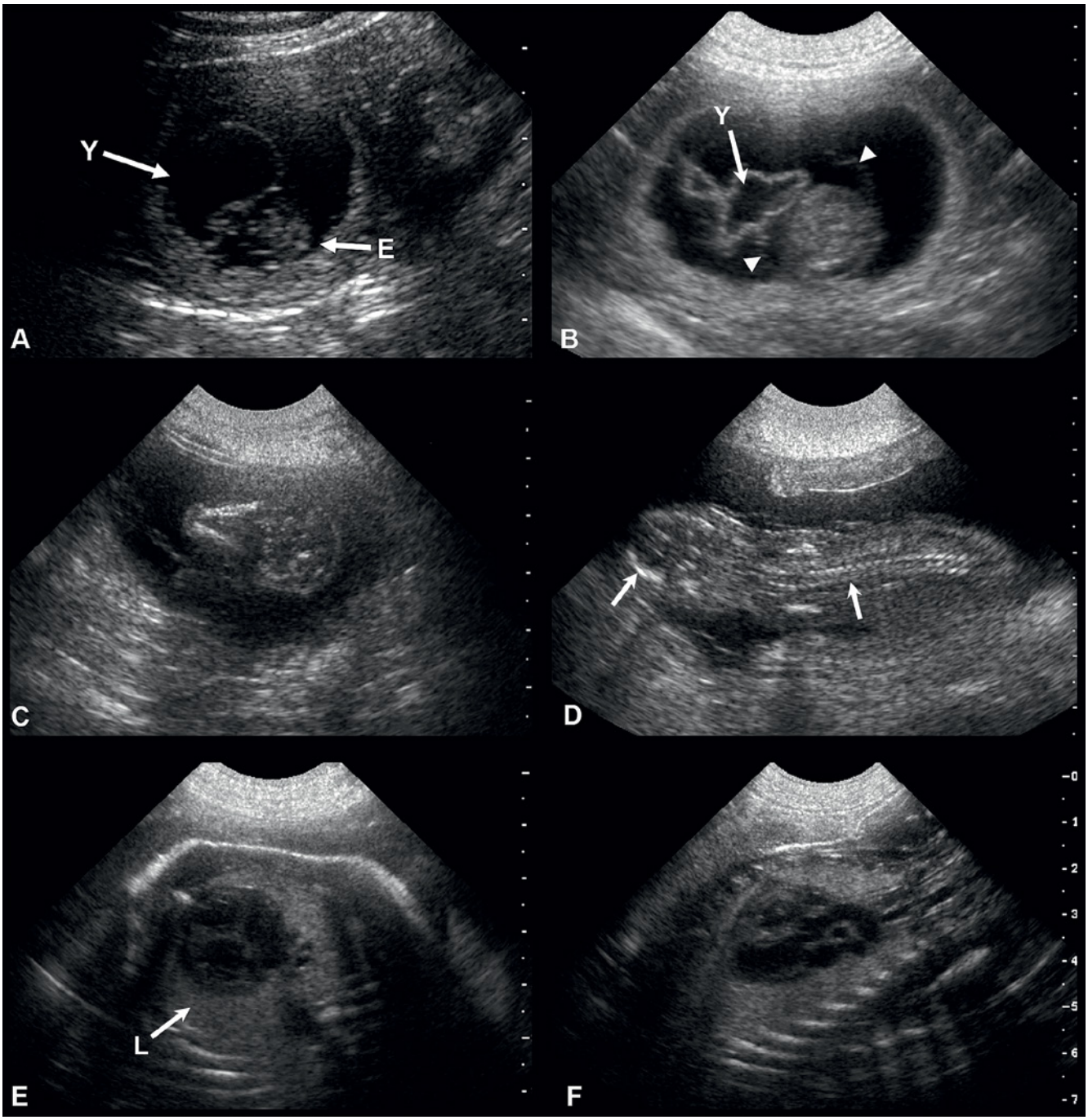


Figure 13.21. Progression of normal pregnancy in a 4-year-old Labrador Retriever. The dog was bred twice during the last estrus. **(A) Day 28 after last breeding.** An embryo (E) is visible in the fluid-filled gestational sac. A flickering heartbeat was observed on real-time examination. The yolk sac (Y) is the fluid-filled structure adjacent to the fetus. **(B) Day 35.** Transverse image of the fetus. The surrounding allantoic membrane is indicated by arrowheads. The yolk sac (Y) is the folded fluid-filled structure adjacent to the fetus. **(C) Day 42.** Dorsal plane image of the fetal head. The mandible is to the left on the image, and the cranium and brain are to the right. **(D) Day 42.** Dorsal plane image of the fetal body. Skull (to the left of the image) and vertebral column are clearly visible (arrows). **(E) Day 60.** Transverse image of the fetal thorax. The heart is clearly visible and is surrounded by hyperechoic lung (L). **(F) Day 60.** Sagittal image of the fetal thorax. Cardiac chambers and large vessels are clearly visible. The surrounding lung is hyperechoic.

Vet-ebooks.com

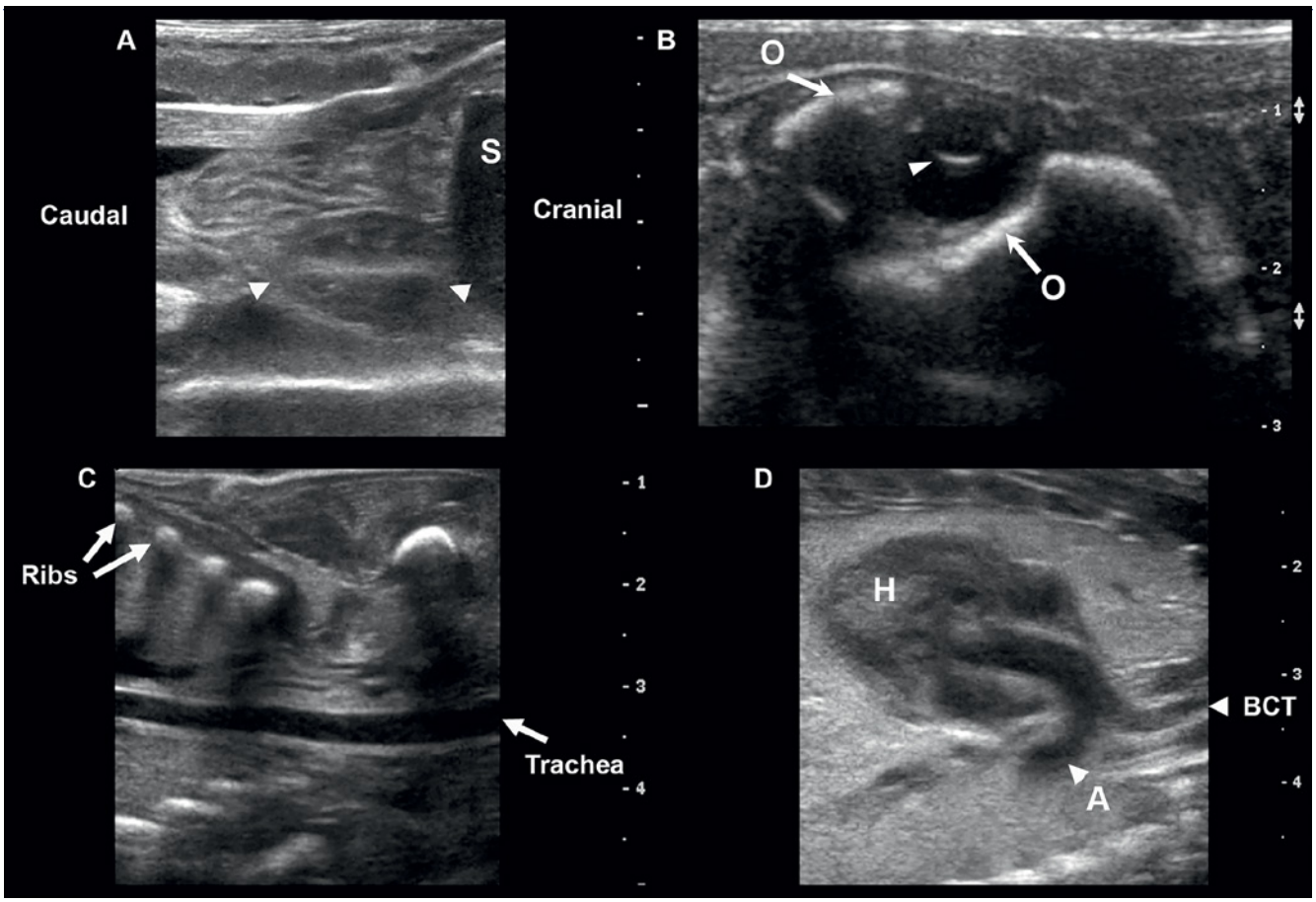


Figure 13.22. **Normal late-term pregnancy in a 4-year-old Pointer.** Ultrasonographic examination was performed **2 months after last breeding**. The dog had four healthy puppies delivered by Cesarean section 2 days after the ultrasonographic examination. **(A)** Sagittal image of the fetal abdomen. The left kidney (arrowheads), with distinct cortex and medulla, is caudal to the fluid-filled stomach (S). Tubular intestinal segments are in the near field. **(B)** Sagittal image of the fetal eye, which appears as a circular anechoic structure within a hyperechoic osseous orbit (O). The posterior capsule of the lens is clearly seen (arrowhead). **(C)** Dorsal image of fetal caudal neck and cranial thorax. The trachea is tubular and fluid-filled. The ribs are characterized by small curvilinear bright interfaces associated with strong shadows. **(D)** Sagittal image of the thorax. The aortic arch and proximal aorta (A) are well visualized, originating from the heart (H). The aortic arch gives rise to the brachiocephalic trunk (BCT).

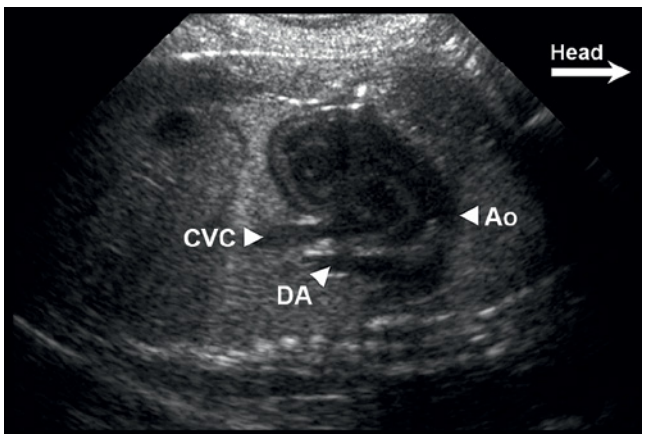


Figure 13.23. **Normal fetal circulation.** The head of the fetus is to the right of the image. The caudal vena cava (CVC) and the aorta (Ao) enter and leave the right and left heart, respectively. The aorta gives off the ductus arteriosus (DA).

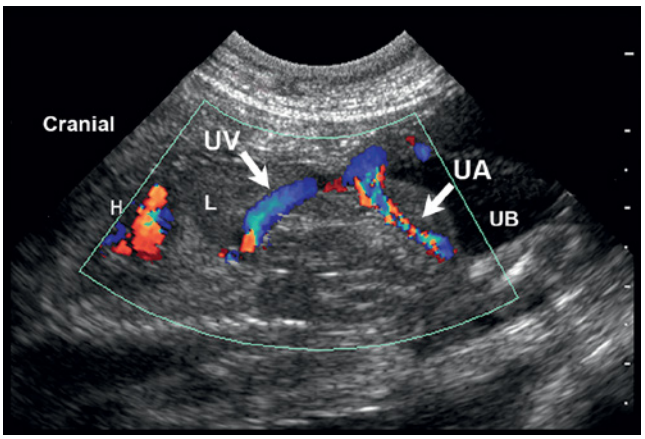


Figure 13.24. **Normal fetal circulation.** The head of the fetus is to the left of the image. The umbilical vein (UV) and umbilical artery (UA) extend cranially to the liver (L) and caudally to the cranial aspect of the fluid-filled urinary bladder (UB), respectively. The heart (H) is visible cranial to the diaphragm. The mosaic color pattern observed in the umbilical artery is caused by aliasing, a Doppler artifact related to high-velocity blood flow.

Vet-ebooks.com

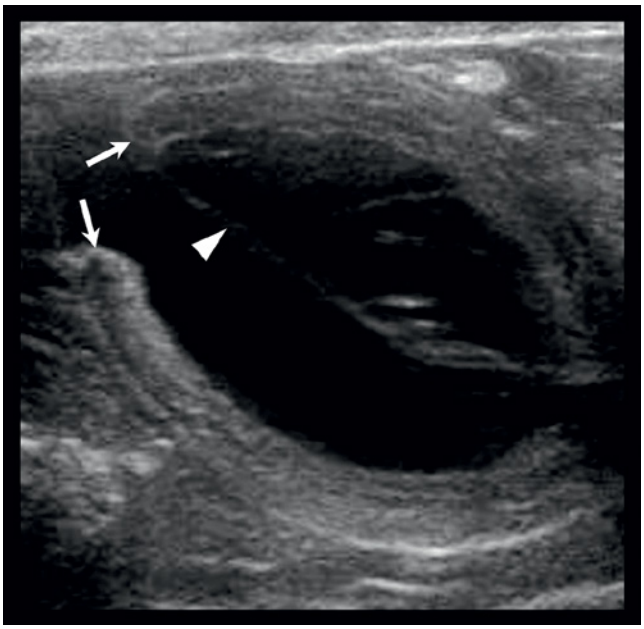


Figure 13.25. Sonogram of a 25-day-old canine fetus. The zonular placenta is distinctly identified (arrows). The arrowhead points to a thin membrane probably representing either part of the allantoic membrane or the yolk sac.

diameter within the uterus on day 20 after LH surge (18 days after ovulation) in dogs, and 10 days after mating in cats. **Embryos** can be discerned 22–24 days after LH surge in dogs, and 14 days post mating in cats, as a 1–2 mm echogenic structure at the periphery of a 6–8 mm elongated vesicle. On day 17 post mating, the embryo has a characteristic C shape in cats. Embryonic heartbeats are usually detectable 23–25 days after LH surge in dogs, and 16–18 days after mating in cats. A yolk membrane is visible between day 25 and 27 after LH surge in dogs and 10–11 days post-mating in cats (Figure 13.19). The embryo has a bipolar shape with limb buds on day 28 after LH surge in dogs and day 20 after mating in cats. **Litter size** is easily evaluated between days 25 and 30 but is not reliable in late gestation (Lenard et al. 2007; Toal et al. 1986). The **fetus** develops rapidly after day 30. The yolk membrane collapses (day 31–34 after LH surge in dogs, day 25–27 post mating in cats), and the abdomen/thorax and internal organs can be identified (Figures 13.20–13.22). The lung becomes hyperechoic to the liver between days 38 and 42 after LH surge in dogs and 29–32 days after mating in cats. The heart chambers can be identified after day 50 (Figure 13.23). Canine fetal sex determination is possible from day 55 to term and easier in the feline fetus between days 38 and 43 of pregnancy. The visualization of intestines is a good landmark of the end of organogenesis 57–63 days after the LH surge (Figures 13.20, 13.22). Regular intestinal peristalsis and collapsed renal pelvises corresponding to the end stage of maturation are observed approximately 4 days before parturition (Gil et al. 2015, 2018). In dogs, the assessment of fetal fluxes can also help predict imminent parturition or fetal distress (Figure 13.24). A summary of ultrasonographic findings at different stages of pregnancy is presented in Table 13.1.

Ultrasound measurement of extra-fetal and fetal structures is a common method for **parturition prediction** or **gestational age estimation** (Table 13.2). The measurement of gestational sac diameter [inner chorionic cavity (ICC)] can be used to predict gestational timing and days before parturition (DBP), while the

Table 13.1
New ultrasonographic diagnosis of pregnancy

Ultrasonographic findings	Dog (days after LH[a] surge)	Cat (days after breeding)
Gestational chamber	20	10
Placental layers of uterine wall	22–24	15–17
Embryo and heartbeat	23–25	16–18
Fetal movement	34–36	30–34
Skeleton	33–39	30–33
Bladder and stomach	35–39	29–32
Liver (hypoechoic) and lung (hyperechoic)	38–42	29–32
Intestinal layers	57–63	52–56

[a] LH, luteinizing hormone.
Data from Yeager et al. (1992) and Zambelli et al. (2002).

Table 13.2
Prediction of parturition using measurement of gestational sac diameter and biparietal diameter

	Diameter biparietal (DBP)
Small dogs (up to 10 kg)	DBP = (ICCmm – 68.68)/1,53
	DBP = (BPDmm-25,11)/0,61
Medium dogs (up to 10 kg)	DBP = (ICCmm – 82.13)/1,8
	DBP = (BPDmm – 29.18)/0,7
Large dogs (up to 10 kg)	DBP = (ICCmm – 105.1)/2,5
	DBP = (BPDmm – 30)/0.8
Giant dogs (>40 kg)	DBP = (ICCmm – 88.1)/1,9
	DBP = (BPDmm – 29)/0.7
Cats	DBP = (ICCmm – 62.03)/1.1
	DBP = (BPDmm – 23.39)/0.47

Data from Arlt S (2020).

Vet-ebooks.com

measurement of BPD (biparietal diameter) corresponding to the head diameter is preferred after 30 days of gestational age. Specific formulas for small and medium size breed dogs and cats are available to predict time of parturition (Beccaglia and Luvoni 2012; Beccaglia et al. 2016; Kutzler et al. 2003; Luvoni and Grioni, 2000). In cats, a threshold of 23 mm for BPD presents a good predictive value. If BPD > 23 mm, the likelihood of parturition is 50% within 24 hours, 83% within 48 hours, and 100% within 72 hours. If BPD < 22 mm, parturition should not occur within 3 days in 99% of cases (Topie et al. 2015). However, BPD is too variable within and among litters to be the only parameter to determine appropriate timing for a cesarean section.

Gestational length can be affected by breed and litter size in both dogs and cats and by age and body weight in cats (Gatel et al. 2015). In this study on queens, a larger litter size and older age were associated with shorter gestation, whereas higher body weight was associated with longer gestation.

The **placenta** can be identified at day 22–24 in dogs. Zonary placenta is identified at day 27–31 after LH surge in dogs and day 25 after mating in cats, giving the gestational sac a lemon shape (Yeager et al. 1992; Zambelli and Prati 2006) (Figure 13.25). The placenta appears as a hypoechoic band with homogeneous vascularization, wrapping around the central part of the conceptus. The surface of the placenta is hyperechoic and wavy. The edge of the placenta on longitudinal section may be curved and thickened, corresponding to normal marginal hematoma (England et al. 2003). The placenta increases in size throughout the gestation. The endometrium is thicker and more hyperechoic at placentation zones than in interplacentation zones (England et al. 2003; Gatel et al. 2020) (Figure 13.26).

Normal Postpartum Uterus

Ultrasonographic changes during normal involution of the postpartum uterus have been described (Ferretti et al. 2000; Pharr and Post 1992; Yeager and Concannon 1990). Dogs and cats have zonular placentation. In the early postpartum stage, the uterine diameter is irregular, and the placentation sites are thicker than interplacentation sites. Uterine wall thickness and volume of intraluminal fluid decrease, and the uterus becomes more regular and thinner over time. The luminal content is hypo- to anechoic and inconsistently visible until 11 weeks in dogs. Uterine wall layers may be identified. The myometrium may be stratified with two hypoechoic layers separated by a hyperechoic layer corresponding, respectively, to the two muscle bundles (circular and longitudinal) and vascular and collagen fiber tissue in between. The endometrium is a thin inner hyperechoic layer in the interplacentation zones and appears as a heterogeneous, less echoic, and thicker layer at the placentation sites (Figure 13.27A–F). The thickness of the endometrium decreases rapidly during the first 2 weeks and then gradually until 12 weeks after parturition in dogs. The exact date of uterine involution is unclear. Uterine involution is believed to take 12–15 weeks postpartum in dogs and 24 days in cats. The uterine diameter becomes regular and thin, the endometrium faintly hypoechoic (Figure 13.27G–H).

Sonography of Abnormal Pregnancy

The most common abnormalities of pregnancy in dogs and cats are resorption (embryonic death before 25 days) and abortion (fetal death after 35 days). **Embryonic resorption** manifests as loss of the normal

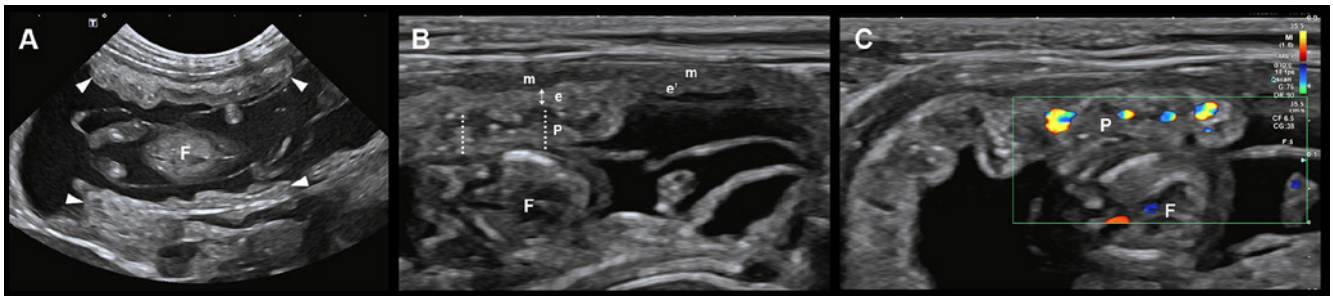


Figure 13.26. **Normal placenta in a pregnant Maine Coon cat, day 32 post mating. (A)** Sagittal image of the placenta that appears as ring-shaped echogenic structure (arrowheads) on each side of the fetus (F). **(B)** Transverse section including placentation zone and interplacentation zone. The placenta (P, dotted lines) is a multilayered structure with a wavy echoic surface wrapping around the fetus (F). The endometrium (e) at the placentation zone (double headed arrow) is thicker and hyperechoic compared to the endometrium at the interplacentation zone (e'). **(C)** Color Doppler shows strong and uniform vascularization within the placenta (P).

Vet-ebooks.com

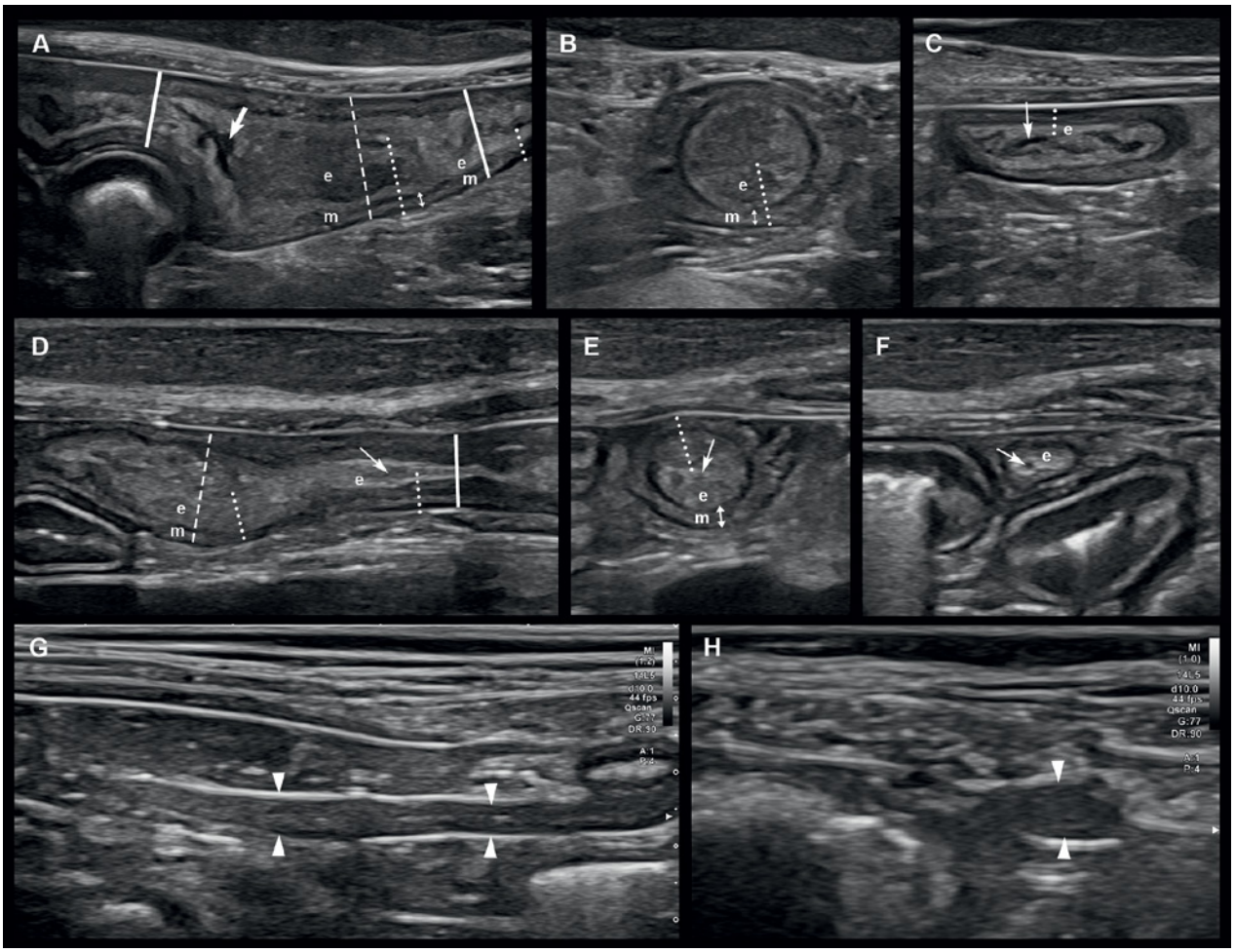


Figure 13.27. **Normal involution of a 4 days postpartum uterus in a 4-year-old Shetland sheepdog. (A–C).** **(A)** sagittal image of the uterine horn with placentation zone (dashed line) and interplacentation zones (full lines), **(B)** transverse image of the placentation site, **(C)** transverse image of the interplacentation site. **Placentation zone** uterine diameter (Ud: dashed line) 12–15 mm/uterine wall thickness (Uw: dotted line) 8 mm. **Interplacentation zone** Ud 9 mm (full line)/ Uw 3–4 mm (dotted line). In an early postpartum stage, the uterine wall (dotted lines) is thicker at the placentation site than at the interplacentation site. Endometrium (e) is echogenic and thick at the placentation site, hyperechoic and thin at the interplacentation site. Myometrium (m, double-arrows) is layered with two hypoechoic muscular layers and a hyperechoic vascular/ fibrous layer between. Serosa is a thin external layer. A small amount of fluid is identified in the uterine lumen (arrow). **(D–F) 6-weeks postpartum uterus**, **(D)** sagittal image of the uterin horn with placentation zone (dashed line) and interplacentation zones (full line), **(E)** transverse image of the placentation site, **(F)** transverse image of the interplacentation site. **Placentation zone** Ud 8 mm/ Uw 3–4 mm. **Interplacentation zone** Ud 5 mm/ Uw 2 mm. The thickness of the wall (dotted lines) decreases due to the decreased size of the endometrium (e). Minimal fluid content can be visualized (arrow). **(G, H) 14-weeks postpartum uterus**, **(G)** sagittal and **(H)** transverse images of the uterine horn. Ud 3.5–3 mm Uw 2–1.5 mm. The uterus is nearly normal in diameter (arrowheads), homogeneous, hypoechoic with collapsed lumen consistent with a complete uterine involution.

anechoic gestational chamber, with accumulation of echogenic material within the lumen, loss of embryonic heartbeat, embryonic disintegration, and ultimately collapse of the gestational chamber with thickening of the uterine wall (England 1998) (Figures 13.28, 13.29).

Signs of **fetal death** include absence of heartbeat and fetal movement, abnormal fetal posture, reduced volume and increased echogenicity of fluid in the gestational sack, accumulation of gas within fetus or uterus, and fetal disintegration (England et al. 2003) (Figure 13.30). Failure of implantation of the conceptus, small size or underdevelopment of the conceptus for true gestational age, and abnormal location of the conceptus within the uterus usually cannot be diagnosed (England 1998). Ultrasonography is especially useful in assessing fetal viability and distress. **Normal fetal heart rate** has been reported to be twice that of maternal heart rate and is usually above 220 beats/min in dogs and around 265 beats/min in cats. It is a reliable indicator of fetal viability. **Bradycardia**

Vet-ebooks.com

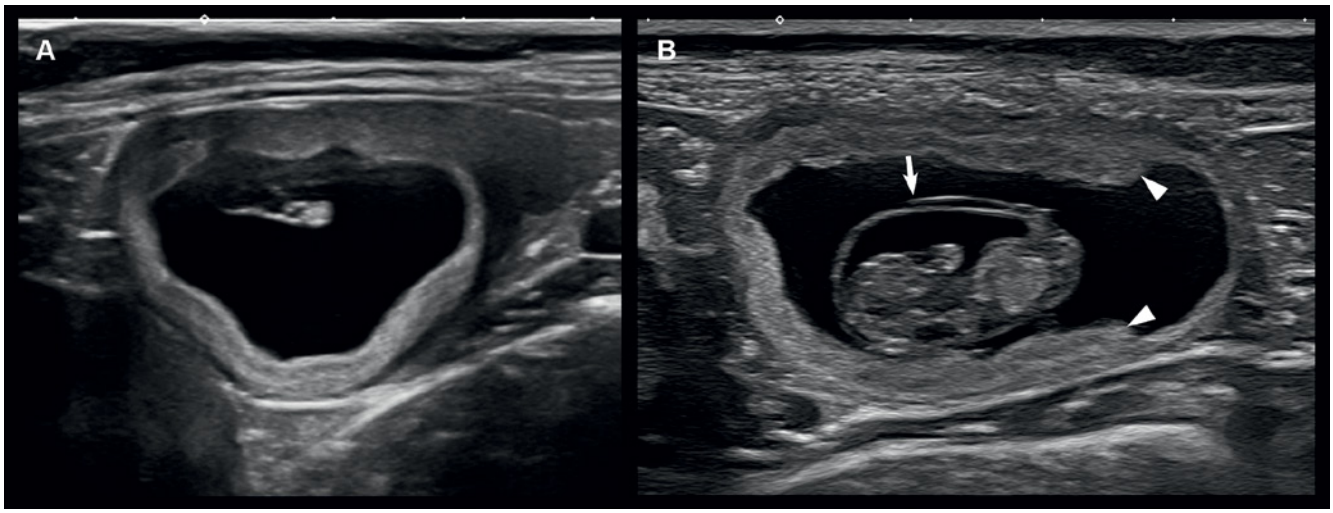


Figure 13.28. **Embryonic resorption in a cat, 26 days after last breeding. (A)** Transverse image of a collapsed thick-walled gestational chamber, which contains a small amount of anechoic fluid. The embryo is no longer identified. **(B)** Transverse image of a viable embryo with bipolar shape and limb buds in an anechoic ovoid cavity. Normal appearance of allantoic membrane (arrow) and zonary placenta (arrowheads).

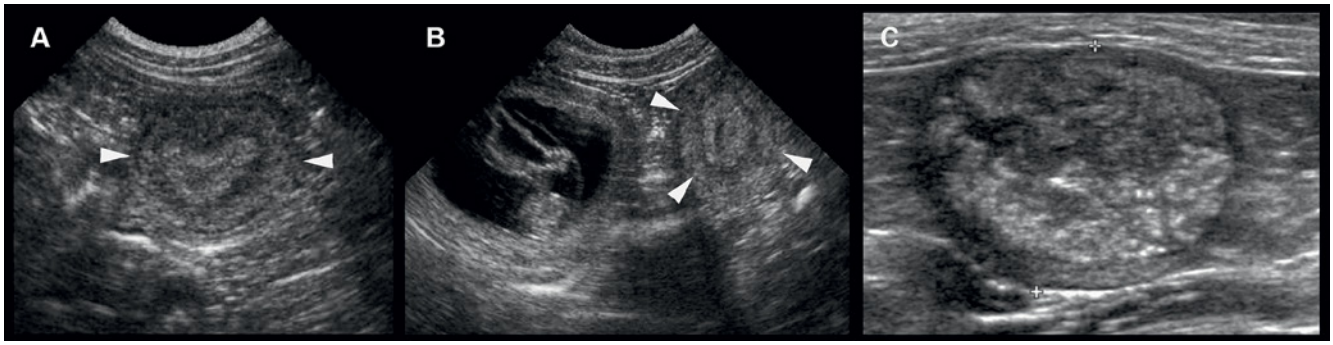


Figure 13.29. **Embryonic resorption in a dog and a cat. (A)** Ultrasonographic examination 35 days after the last breeding of a 7-year-old Vizsla. A thick-walled gestational chamber (arrowheads) is filled with echogenic material and fluid. Embryonic structures are not visible. **(B)** Transverse image of a viable fetus on the left and a collapsed gestational chamber (arrowheads). **(C)** Transverse image of uterine horn in a queen. A marked focal enlargement of the uterus is seen (1.4 cm) with a largely distended lumen. The luminal content is heterogeneous with a mixture of hyperechoic pinpoint foci, and hypoechoic to anechoic larger areas. Courtesy of Dr.Laure Gatel, Sudvetia, France.

is the normal response of a fetus to hypoxia and is an important parameter to identify in dystocia. It has been reported that fetal heart rates less than 150 beats/min or even less than 180 beats/min indicate severe distress and require immediate intervention (Fulton 2021).

Although many **congenital defects** can occur in dogs and cats, these defects are very rarely diagnosed in utero. Examples of fetal abnormalities that can be detected by means of ultrasonography include hydrocephalus, fetal pleural effusion, and hydrops fetalis or anasarca (Allen et al. 1989). Only a few other pregnancy disorders have been reported in small animals including uterine hernia (Figure 13.31) or torsion. **Uterine torsion** is a potentially life-threatening condition that is characterized by infarction of the affected uterine segment, with subsequent wall thickening and increased echogenicity of the uterine wall (Figure 13.32).

Abnormal Postpartum Uterus

Ultrasonographic evaluation may be useful to diagnose postpartum diseases such as hemorrhage, metritis with possible retained fetal membrane, and subinvolution. Vaginal discharge is common for 4–7 weeks after parturition in normal dogs. However, malodorous discharge or hyperthermia occurring usually within 1 week of whelping can be signs of **postpartum metritis**

Vet-ebooks.com

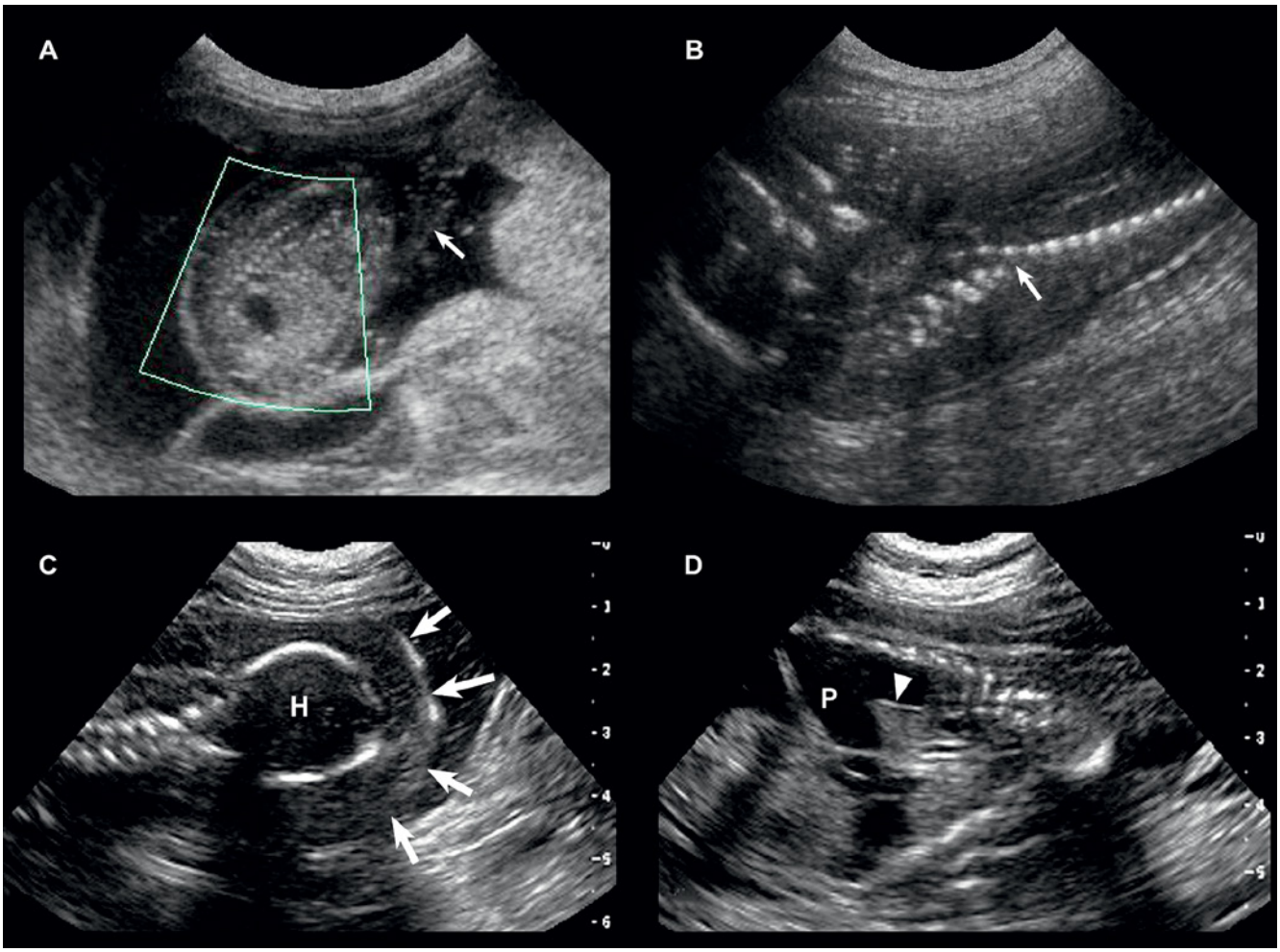


Figure 13.30. **Fetal abnormalities. (A)** 1-year-old Chihuahua bred 30 days before presenting for acute hemorrhagic vulvar discharge. Doppler interrogation confirms a lack of fetal circulation. Echogenic material in the uterus is concerning for hematoma formation (arrow). **(B)** This sagittal image taken of a fetus in a 5-year-old Chesapeake Bay Retriever 50 days after breeding shows malalignment of the axial skeleton (arrow) and disruption of the skull. **(C, D)** Anasarca in a Chinook dog. The affected fetus was surrounded by contained fluid (arrows in **C**), best seen here around the head (H) and neck. A moderate pleural effusion (P) associated with retracted echogenic lungs (arrowheads) is noted (in **D**).

associated with **retained placenta**. The endometrium appears thicker than expected with an inner hypoechoic and heterogenous layer (Figure 13.33). Persistent bloody discharge after 4–7 weeks is consistent with subinvolution of the placental site. The subinvolution is an abnormal repair of the endometrial placental site with a late involution, which on ultrasonographic follow-up assessment manifests as persistent heterogeneous content.

Uterine Diseases

Disorders of sexual development (DSD) are rare conditions in dogs and cats. The classification includes chromosomal sex, gonadal and phenotypic disorders causing abnormal sexual differentiation. **Periovarian cysts** are incidental gonadal disorders corresponding to retained abnormally dilated embryonic ducts. **Segmental aplasia or hypoplasia or atresia** of the uterus are rare but more frequent in cats (0.09%) than in dogs (0.05%) (Figure 13.34). It is due to failure in the development of the paramesonephric ducts. An ipsilateral ovary is usually present, and in 30% of cases, ipsilateral renal agenesis is noticed. Concomitant hypoplasia of the cervix or canalization failure between the cranial and the caudal vagina has been described.

Uterine cysts are common in dogs and cats. Cysts can arise from the serosa, the myometrium, and endometrium, or may be secondary to abnormal developmental lesions. **Cystic endometrial hyperplasia** is the most frequent uterine disease and causes thickening of the endometrium, with cystic lesions embedded in the uterine wall because of proliferation of endometrial glands (Voges and Neuwirth 1996) (Figures 13.35, 13.36). The hyperplasia is commonly associated with fluid accumulation within the uterine lumen and may

Vet-ebooks.com

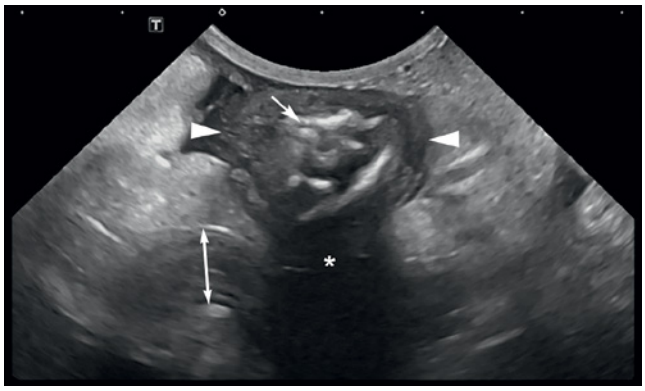


Figure 13.31. Right inguinal hernia with uterine horn and mummified fetus in a 6-year-old. Porcelaine dog (French scent hound). A round structure (arrowheads) with layered wall and hyperechoic content (arrow) associated with acoustic shadow (*) is visible within the hernia. The surrounding fat is hyperechoic and there is a small amount of free fluid. A part of the right uterine horn is identified deep to the mummified fetus (double headed arrow). Courtesy of Dr.Laure Gatel, Sudvetia, France.

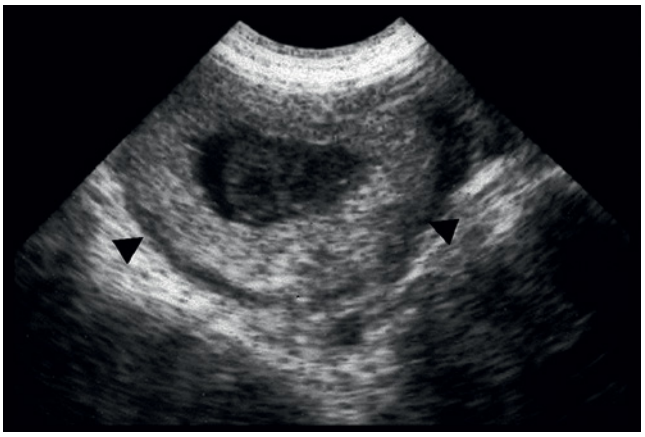


Figure 13.32. Uterine torsion in a pregnant cat. This transverse sonogram shows a uterine horn (arrowheads) that is thickened, hyperechoic, and contains echogenic material. A small volume of peritoneal fluid is noted around it.

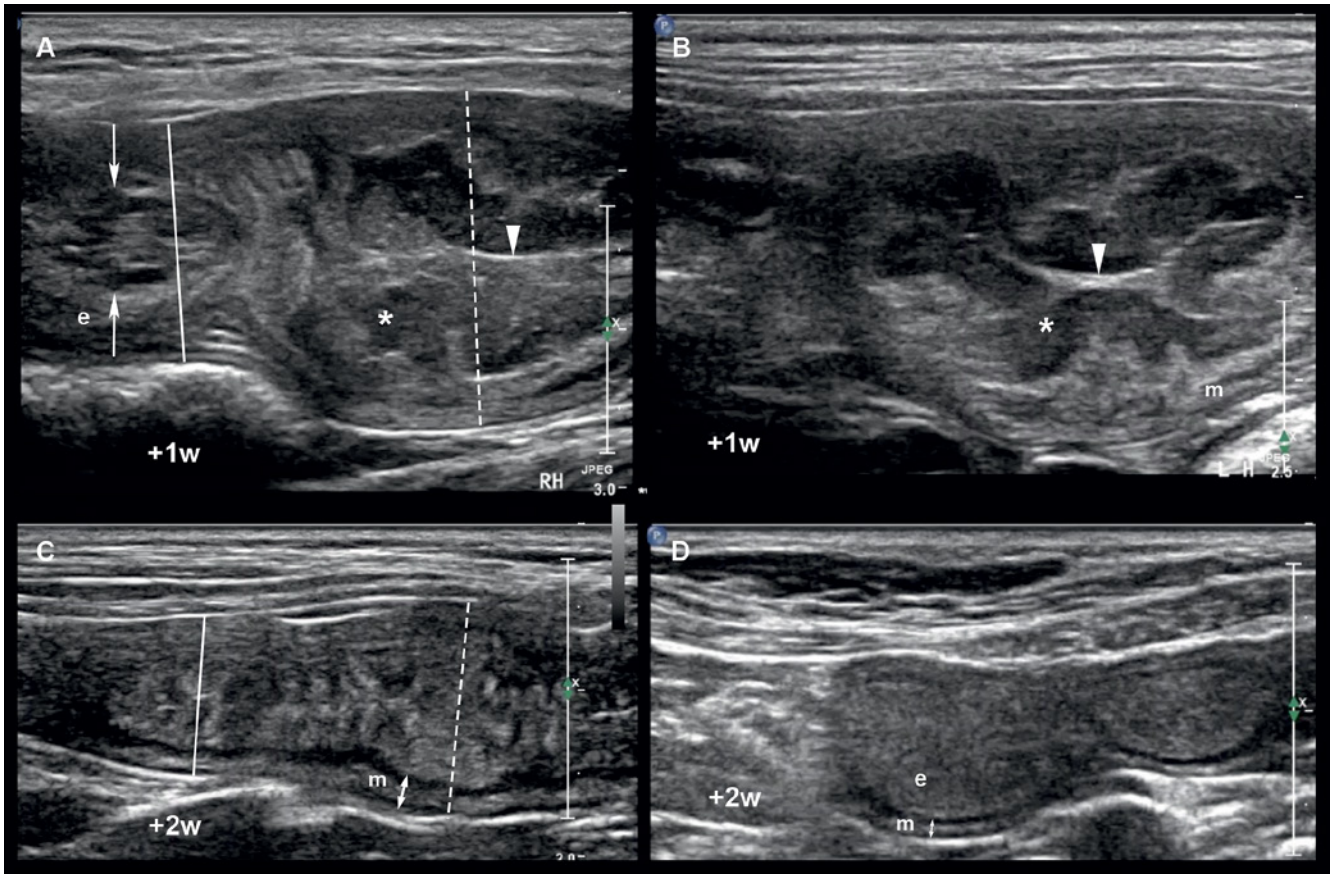


Figure 13.33. Postpartum metritis in a small breed bitch, presented with marked purulent. vaginal discharge. **(A, B)**, **1 week post-partum** (+1wk). Sagittal **(A)** image of the uterine horn and transverse **(B)** image of the placentation site. At the interplacentation site, the uterus (full line) is dilated by a heterogeneous content (arrows) suspected to represent retained placenta. The endometrium (e) is hyperechoic. At the placentation site, the uterus is enlarged (dashed line), the lumen is collapsed (arrowhead), the myometrium (m) is visible, and the endometrium is thick and irregular with an inner hypoechoic band (*).**(C, D) 2-weeks postpartum** (+2wk). Sagittal image of the uterine horn (arrow in **C**) and transverse image of the placentation site **(D)**, after symptomatic treatment of the postpartum metritis. A dramatic improvement of the size of the uterus is observed. At the placentation site (dashed line), the endometrium is still moderately thickened and echoic (e). The inner hypoechoic rim is no longer visible. At the interplacentation site (full line), the lumen is collapsed, and the endometrium is still thick with a striated appearance. Courtesy of Dr.Laure Gatel, Sudvetia, France.

Vet-ebooks.com

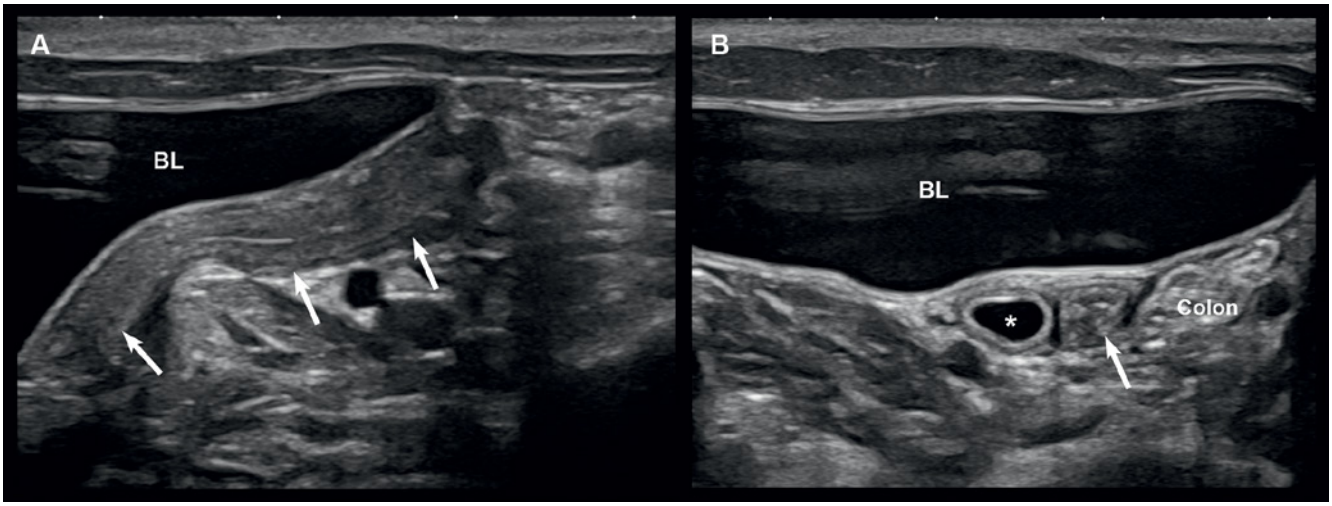


Figure 13.34. Uterine unicornis in a young cat. During ovariectomy, absence of the left uterine horn was noted, and the left ovary was not found. After surgery, the queen was presented for persistent signs of estrus. Ultrasonographic examination revealed the presence of a left isolated ovary without left horn. The left kidney was identified. The right uterine horn has normal appearance with faint layering. **(A)** Sagittal image of the right uterine horn (arrows) with a normal layering appearance, dorsal to the urinary bladder (BL). **(B)** Transverse image of the body or caudal part of the uterus. A blind-ended cavitary structure was visible adjacent to the identified uterine horn (*), with layers similar to the myometrium and serosa of the adjacent horn (arrow). The surgery confirmed the absence of the left uterine horn, the left ovary was removed. A hysterectomy of the right horn and uterine body was performed during the second surgery. The histologic exam revealed two uterine horn lumina in the cranial part of the uterine body: one collapsed and the other one dilated with fluid. The cervix and cranial vagina were normal. Uterine hypoplasia was diagnosed.

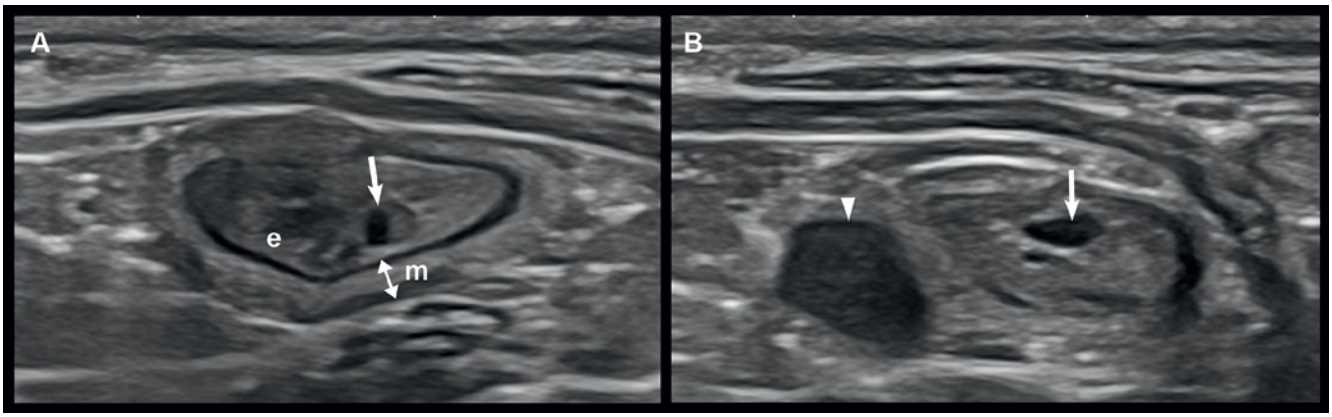


Figure 13.35. Moderate endometrial hyperplasia in a 6-year-old Chihuahua. (A, B). On these transverse images of the uterine horn, the endometrium (e) is thickened and contains several cysts (arrow). A larger peripheral cyst (arrowhead) is located within the myometrium (m). The diagnosis was confirmed histologically.

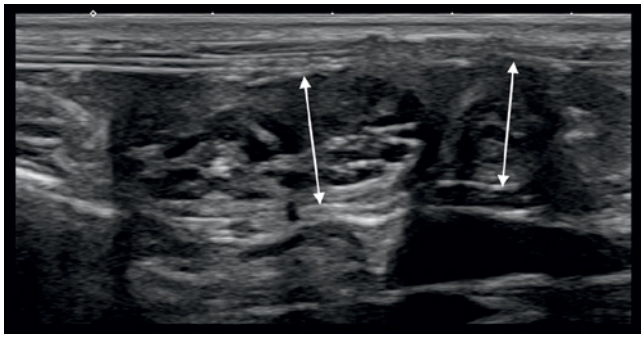


Figure 13.36. Severe cystic endometrial hyperplasia in a Cocker Spaniel. Sagittal image of one uterine horn that is thickened (double headed arrows) with numerous small anechoic cysts.

Vet-ebooks.com

precede the development of mucometra or pyometra (Figures 13.37, 13.41, 13.42) or be associated with endometritis. A second endometrial hyperplasia form is described in dogs, termed "**pseudo-placentation endometrial hyperplasia.**" This form occurs from the metestrus to the early anestrus and is characterized by a segmentally organized endometrial hyperplasia mimicking the maternal placenta in dogs. The endometrium is thick and hypoechoic with striations (Figure 13.38). The etiology is not clearly understood but seems to be an expression of the reactive uterus to foreign bodies, embryos or infectious organisms. **Papillary endometrial hyperplasia** is another rare type; the uterus is thick and homogeneously echogenic (Figure 13.39).

Fluid within the uterus is easily visualized, and the echogenicity of the luminal contents is variable. Although **hydrometra** and **mucometra** are usually characterized by anechoic luminal fluid (Figure 13.40), and **hemometra** and **pyometra** tend to show echogenic luminal contents (Figures 13.37, 13.41, 13.42), ultrasonographic differentiation of these entities is often not possible. Pyometra usually involves the entire uterus

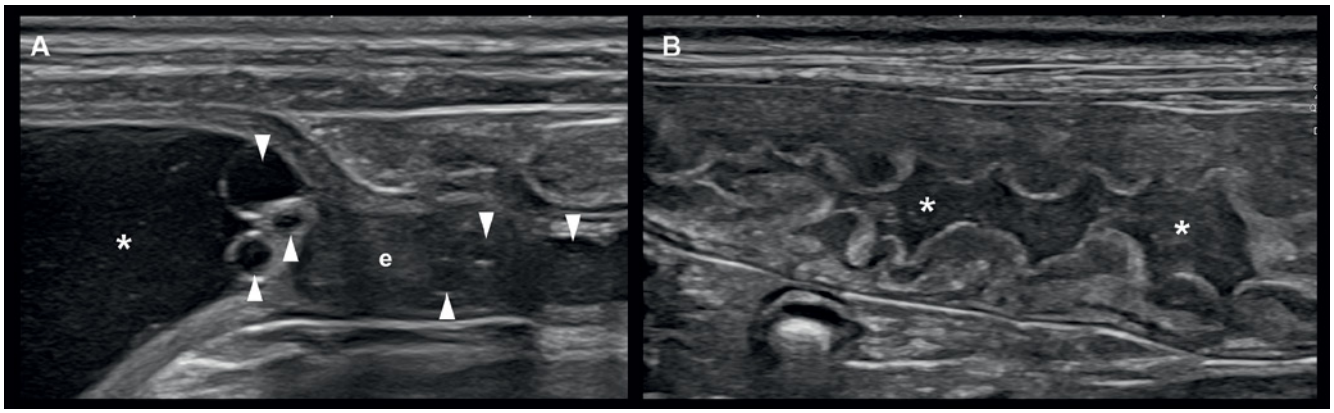


Figure 13.37. Endometrial uterine hyperplasia in two Chihuahua dogs. (A) On the sagittal image of the left uterine horn of a 6-year-old Chihuahua, severe segmental fluid-dilatation (*) of the cranial part of the left uterine horn is noted. Thickening of the endometrium (e) with cysts (arrowheads) is present caudally. Endometrial uterine hyperplasia with mucometra, focal endometrial hemorrhage, and adenomyosis was confirmed by histology. **(B)** In this 11-year-old Chihuahua, the endometrium is markedly thick (without cyst) and layered. The horn is dilated by a slight to moderate amount of echoic intraluminal fluid (*). Endometrial uterine hyperplasia with marked suppurative endometritis and pyometra were confirmed histologically.

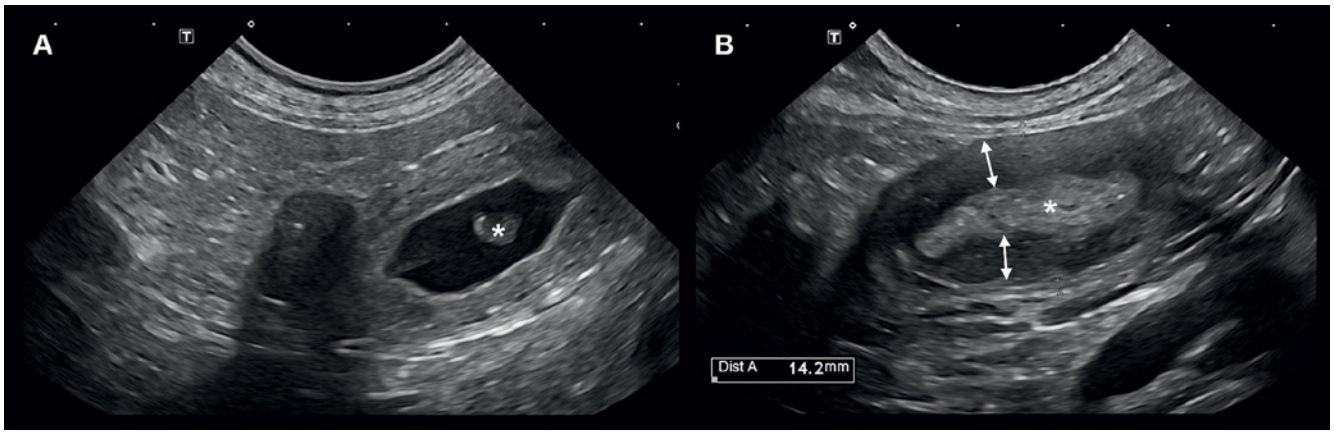


Figure 13.38. Suppurative pseudoplacentation in a 4-year-old Norwich Terrier dog. The dog was presented for dysorexia and was in heat 2 months ago (mating was excluded). **(A)** A segmental «lemon shape» enlargement of the left horn was noticed with echogenic, homogeneous, and moderately thickened uterine wall. The lumen is anechoic and has an echogenic focus in the center (*). This image mimics a placentation zone with resorption. **(B)** On follow-up study performed **1 week later,** a thick inner primarily hypoechoic uterine wall was noticed. The lumen was collapsed with echogenic content. Segmental ovoid endometrial hyperplasia can mimic placenta with thick wall (double arrows) and an echogenic center (*) due to suppurative content confirmed by surgery. No embryo was found. The rest of the uterine horn appeared normal.

Vet-ebooks.com

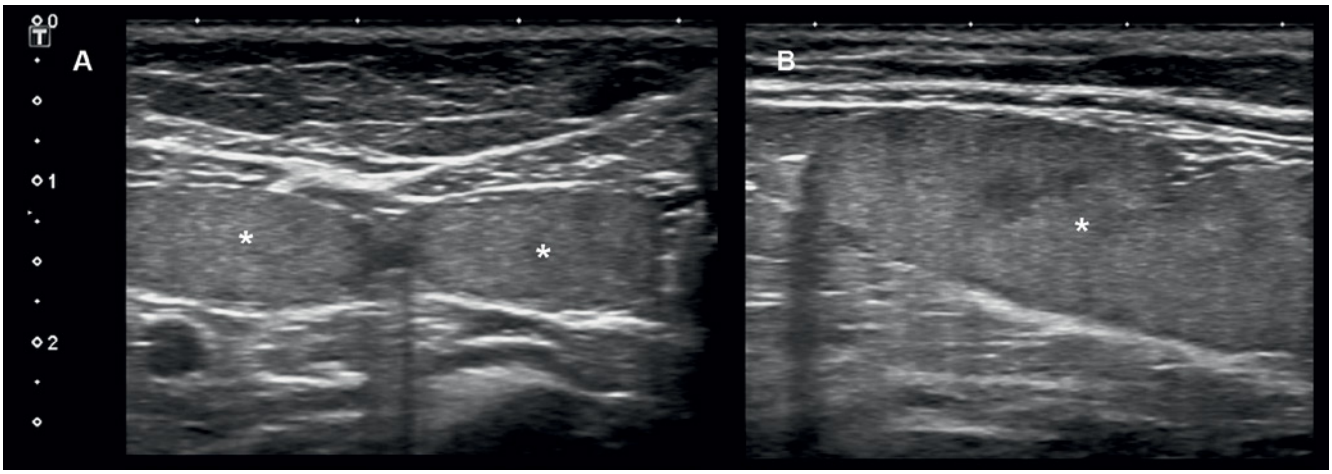


Figure 13.39. Papillary endometrial hyperplasia in a 4-year-old Maine Coon cat. Transverse image of the two horns **(A)** and longitudinal image of one uterine horn **(B)**. The uterine horns (*) are thickened, echogenic with loss of layering. Courtesy of Dr. Laure Gatel, Sudvetia, France.

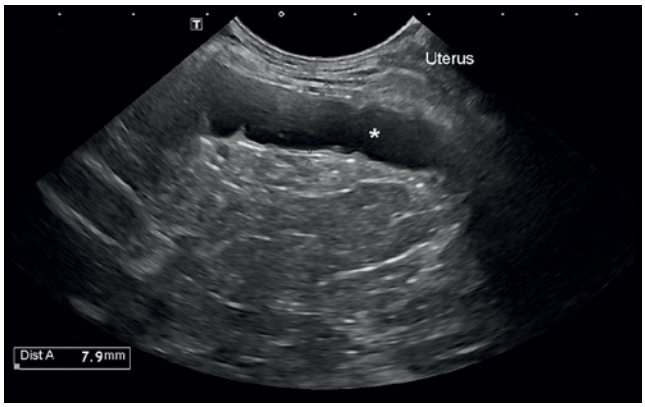


Figure 13.40. Mucometra in an asymptomatic 10-year-old Yorkshire Terrier. On this sagittal image of the left uterine horn, there is moderate dilation (7.9 mm in diameter) with anechoic fluid content (*).

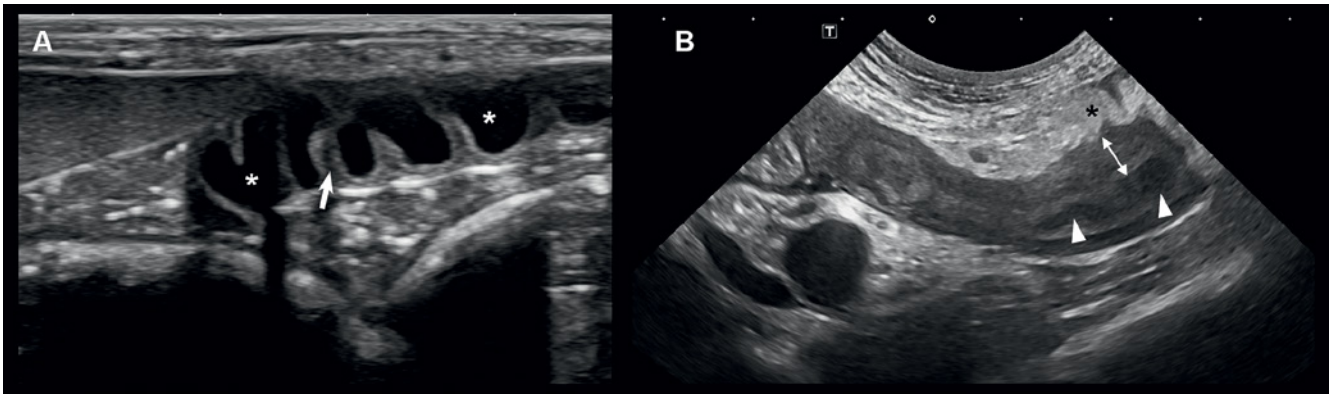


Figure 13.41. Endometritis and pyometra in two dogs. (A) Longitudinal image of the uterine horn of a young Chihuahua. The uterine wall is irregular and corrugated (arrow). The lumen is moderately dilated by anechoic fluid (*). **(B)** Sagittal image of the left uterine horn of a 10-year-old cross breed dog. The horn has a thick wall (double headed arrow) and a small amount of echogenic fluid content (arrowheads). There is hyperechoic peripheral fat (*) with a small volume of peritoneal effusion due to peritonitis secondary to ruptured pyometra.

Vet-ebooks.com



Figure 13.42. Marked cystic endometrial hyperplasia and pyometra in an 8-year-old Jack Russel Terrier. On this longitudinal image, the uterus is filled with mildly echogenic fluid (*) and is thick walled with anechoic cysts embedded in the uterine wall.

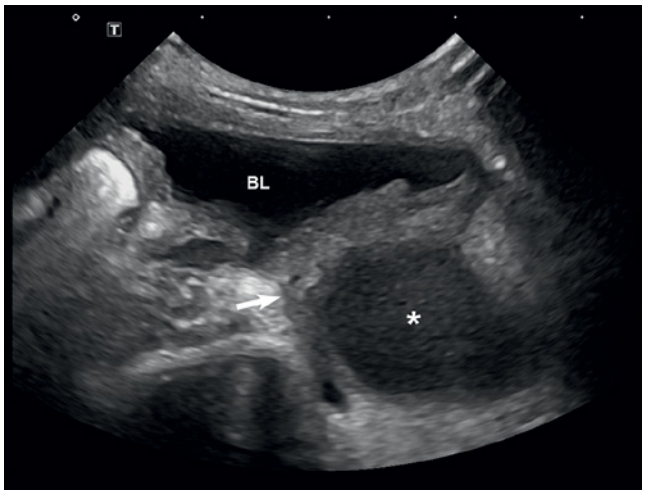


Figure 13.43. Stump pyometra in a 13-year-old spayed Maltese dog. Dorsally to the urinary bladder (BL), the uterine stump is pouch-shaped stump, abnormally dilated with echogenic fluid (*) with an abrupt end (arrow). The peripheral fat is hyperechoic. Stump pyometra was confirmed at surgery without evidence of foreign body. Courtesy of Dr. Julien Fritz, Azurvet, France.

but may also be segmental. Rupture and **peritonitis** may be potential complications (Figure 13.41). **Uterine stump pyometra** manifests as a fluid-filled, blind-ended pouch between the UB and descending colon (Figure 13.43).

Stump granuloma secondary to suture material reaction, nosocomial infection, or foreign body, may resemble stump pyometra or may form a hypo to mixed

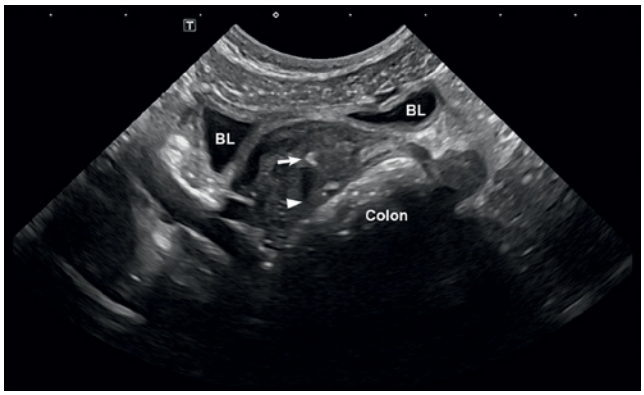


Figure 13.44. Stump granuloma due to vegetal foreign body confirmed by surgery in a 4-year-old cross breed dog. On this transverse image, the uterine stump appears as a hypoechoic mass with central hyperechoic foci (arrow) associated with acoustic shadow (arrowhead). This can mimic a tumor with mineralization. BL, bladder. Courtesy of Dr Caroline Benzimra, Micen Vet, France.

pattern echogenicity mass surrounded by hyperechoic fat between the UB and colon (Figure 13.44). Differential diagnoses may be challenging to exclude based on ultrasound findings and include hematoma, normal healing of the uterine stump within the first 2 weeks, or neoplasia. Foreign bodies in the vagina and uterus are sporadically reported. Complications secondary to migrating vegetal **foreign bodies** such as uterine fistulas or granulomas are rarely described, as uterine or cranial vaginal grass awn foreign bodies seem to be well tolerated (Agut et al. 2016; Benzimra et al. 2021) (Figure 13.45).

Neoplasms of the uterus and vagina such as polyps, leiomyomas, leiomyosarcomas, or adenocarcinomas, are rare (Klein 1996). They appear as nodules or masses of variable shape, size, and echogenicity and may be associated with fluid accumulation within the uterine lumen (Figures 13.46, 13.48–13.50). Uterine torsion may be a complication and appears as an inhomogeneous mass surrounded by echoic fat and peritoneal effusion. The organ of origin may be difficult to identify (Figure 13.47). Vaginal masses can be visualized when they become large enough to extend from the pelvic canal into the abdomen (Figures 13.48–13.50).

Mammary Glands

Sonography of Normal Mammary Glands

The appearance of mammary glands changes under hormonal influences (late-term pregnancy and lactation). Normal mammary tissue in nonlactating dogs is coarse and hypoechoic (Chandra et al. 2010) (Figure 13.51). In

Vet-ebooks.com

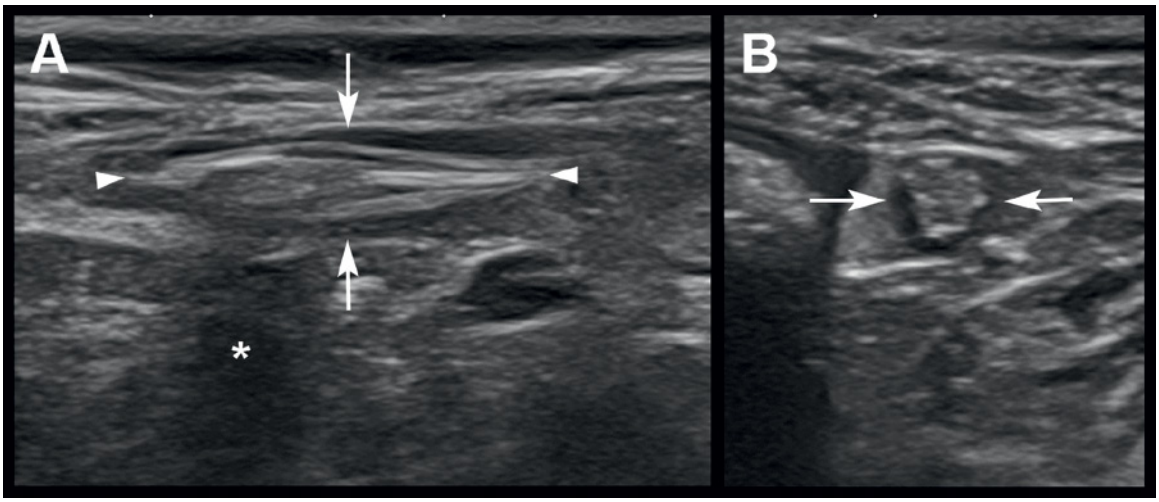


Figure 13.45. Grass awn in a uterine horn of a 3-year-old neutered Spitz dog. Longitudinal (**A**) and transverse images (**B**) of the left uterine horn. There is no significant widening of the uterine diameter (arrows) or thickening of the uterine wall. A spindle shaped hyperechoic structure (arrowheads) with faint acoustic shadow (*) is visible within the uterine lumen.

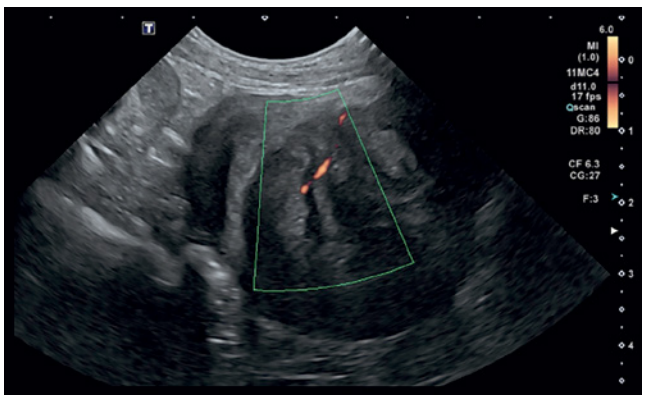


Figure 13.46. Uterine leiomyoma in a 12-year-old Jack Russel Terrier bitch. A large heterogenous mass is visualized in the mid-abdomen. Courtesy of Dr.Laure Gatel, Sudvetia, France.

lactating dogs, mammary tissue is more prominent, large vessels enter the glands, and milk-filled ducts are encountered (Figures 13.52, 13.53). There is little information regarding the appearance of mammary glands during pregnancy and lactation in cats.

Sonography of Abnormal Mammary Glands

Abnormalities of the mammary glands include neoplasia, cysts, inflammation, hyperplasia, and fibroadenomatous hyperplasia. **Fibroadenomatous hyperplasia** is a benign proliferation of mammary ducts and connective tissue. This disease occurs in young cats at time of puberty, during pregnancy and pseudopregnancy, or under progestin treatment in males or females (Hayden et al. 1981). Ultrasonographic abnormalities include a slightly hyperechoic well-delineated mammary mass with parenchymal and peripheral anechoic areas (Figure 13.54). **Cysts** may be associated with mastitis, tumor or primary duct ectasia. **Primary duct ectasia** may be induced by administration of progestogens but has also been reported in spayed or untreated dogs (Miller et al. 2001).

Mammary tumors appear as irregular, mixed echogenic mass lesions of variable size (Figures 13.55, 13.56). Benign and malignant mammary tumors cannot be differentiated based on their appearance using conventional or color-flow Doppler ultrasound; however, malignant tumors are characterized by a

Vet-ebooks.com

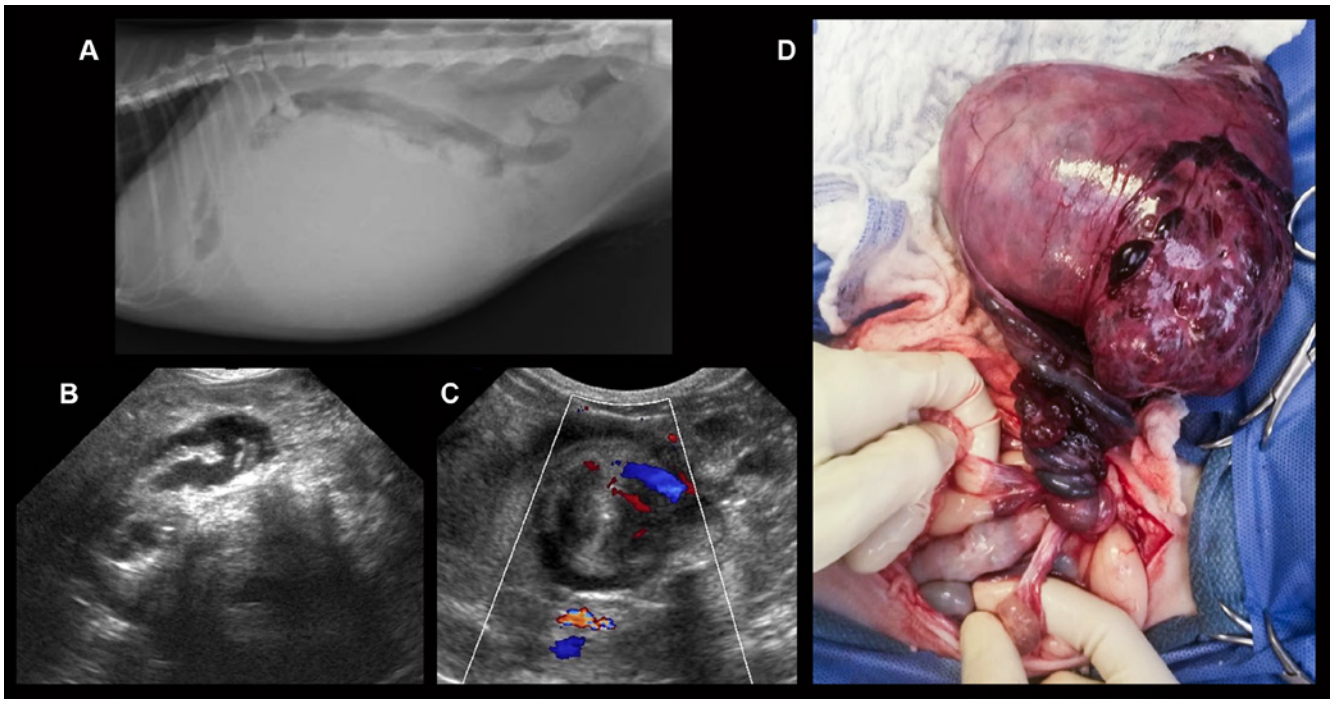


Figure 13.47. Uterine torsion associated with a uterine leiomyoma in a 10-year-old cat. (A) A very large soft-tissue mass is present in the cranial to central abdomen on this lateral radiograph. **(B)** On ultrasonographic examination, the mass is inhomogeneous and partially cavitated. It was challenging to identify the organ of origin. **(C)** Near the bladder, a swirling pattern was noted and included twisted vessels, indicating the site of torsion. **(D)** At surgery, the origin of the mass and the torsion were confirmed.

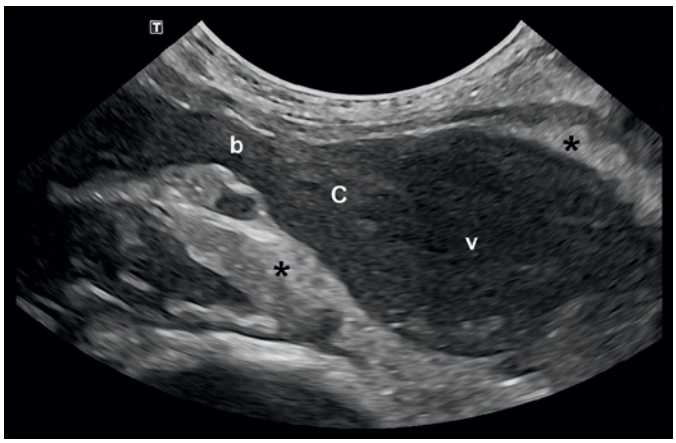


Figure 13.48. Vaginal and uterine lymphoma in a 12-year-old spayed cat. Sagittal image of prepubic vagina (v), uterine cervix (c), and body (b) showing a large hypoechoic, homogeneous mass that infiltrates the vagina, the cervix, and the uterine body. The surrounding fat tissue is hyperechoic (*). FNA favored high grade lymphoma. Courtesy of Dr Laurent Couturier, AzurVet France.

significantly higher blood flow velocity compared to benign tumors when using Triplex Doppler ultrasound (Feliciano et al. 2012). As metastases are common in malignant tumors, the axillary and/or inguinal lymph nodes should be examined for enlargement and abnormal echotexture. **Mastitis** manifests as swelling and hypoechogenicity of the mammary tissue, with abscessation in severe cases (Figure 13.57).

Vet-ebooks.com

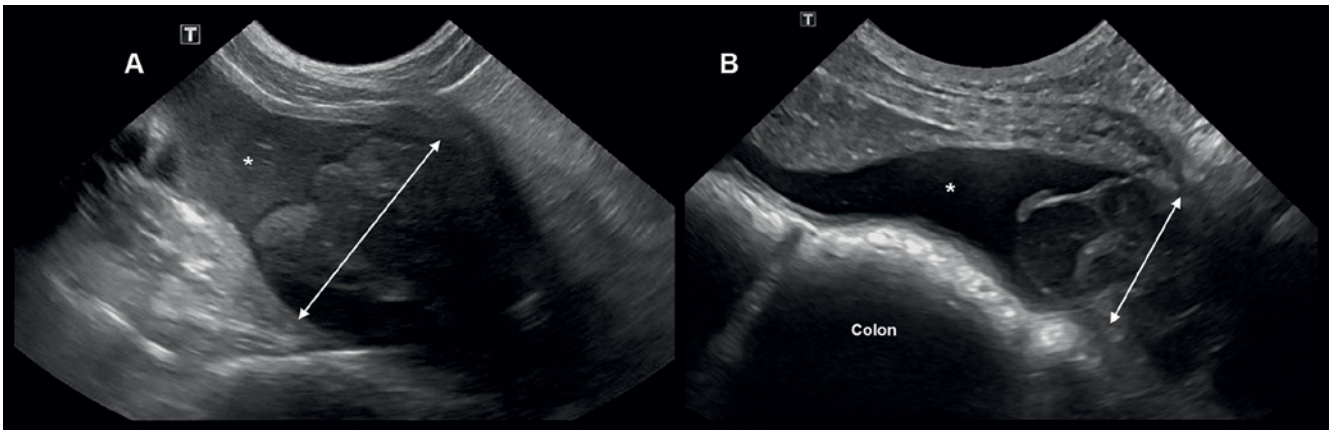


Figure 13.49. **Vaginal smooth muscle tumors in two dogs. (A)** Sagittal image of the prepubic vagina in a 14-year-old spayed Poodle. A large homogeneous echogenic mass with lobulated contour is identified in the pelvic part of the vagina (double headed arrow). This is associated with echogenic fluid filling the vagina cranially (*), consistent with hemorrhage. It was a **leiomyoma**. **(B)** Sagittal image of the prepubic vagina in a 9-year-old ovariectomized Jack Russel Terrier. A lobulated heterogenous mass infiltrates the pelvic part of the vagina (double headed arrow). The abdominal vagina cranially to the mass and the uterus are dilated with anechoic mucoid fluid (*). This was a **leiomyosarcoma**.

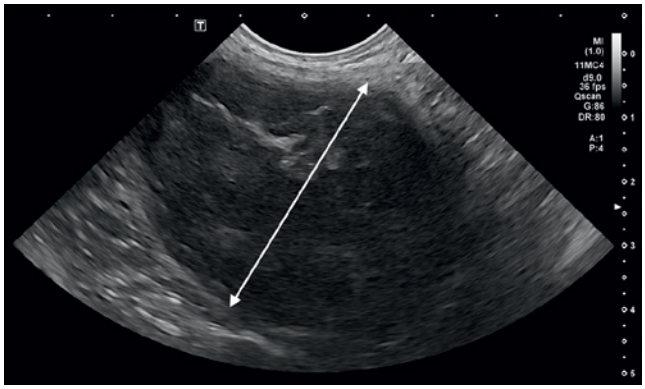


Figure 13.50. **Vaginal schwannoma in a 10-year-old Cocker Spaniel.** Longitudinal image of the vestibular part of the vagina. A large, well-delineated, heterogeneously hypoechoic mass (double headed arrow) is visible within the pelvic canal using a perineal approach.

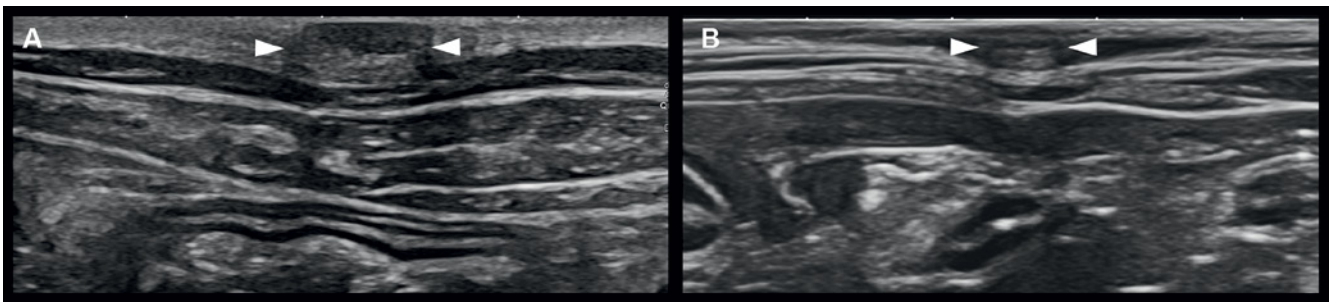


Figure 13.51. **Inactive mammary tissue.** Ultrasonographic images of teat and mammary tissue (arrowheads) of a 2-year-old neutered crossbreed dog (**A**) and in an intact 2-year-old Shetland Sheepdog during heat **(B)** appearing as inconspicuous, small, hypoechoic nodules.

Vet-ebooks.com

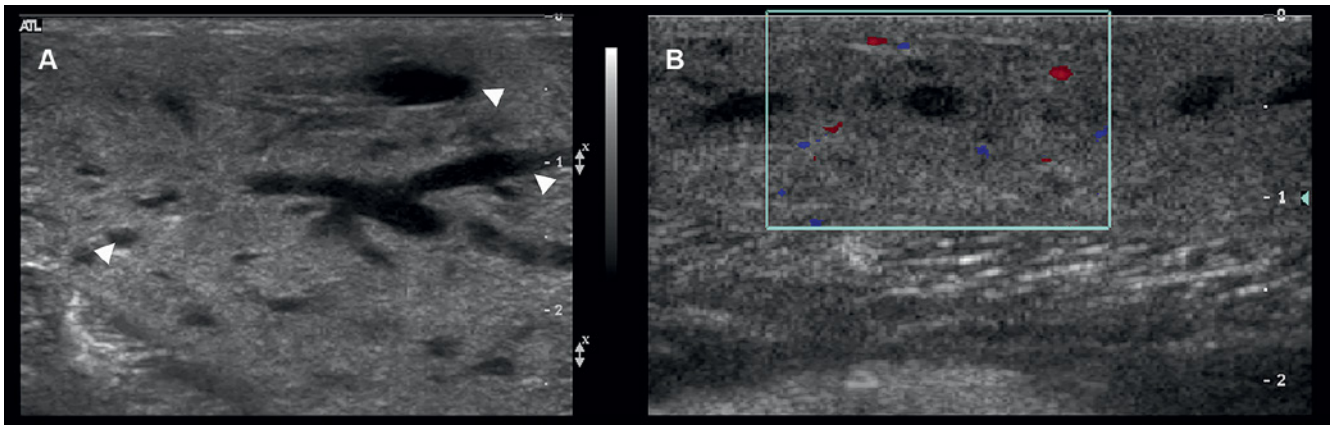


Figure 13.52. Active mammary tissue in 4-year-old dog 2 days prior to parturition. (A) The mammary tissue measures up to 3 cm in thickness, is of medium echogenicity, and contains numerous tubular milk-filled ducts (arrowheads). **(B)** On color Doppler examination, there is no color signal detected in the ducts.

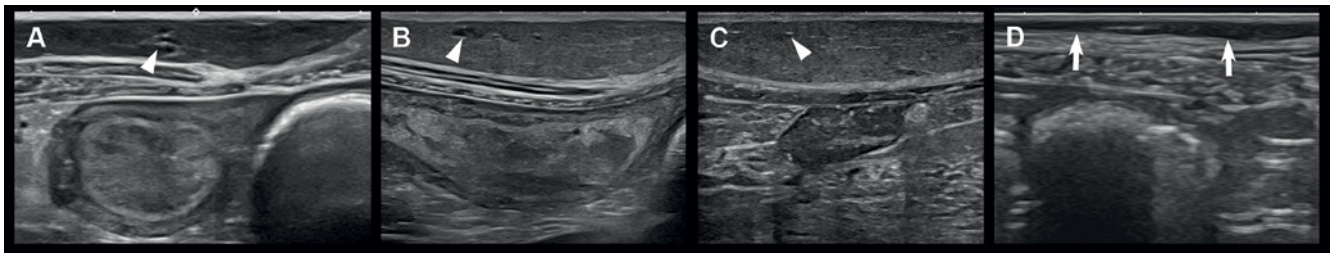


Figure 13.53. Normal active mammary tissue during lactation in a 4-year-old Shetland Sheepdog. (A–C) Through lactation period: **4 days (A)**, **8 days (B)**, and **weeks (C)** postpartum. The mammary tissue increases in size in the first days and has a stable appearance during lactation. It is of medium echogenicity and contains small milk-filled ducts. Adjacent subcutaneous fat has medium echogenicity. **(D) 14-weeks postpartum without lactation.** The mammary tissue is decreased in thickness and is hypoechoic to the surrounding subcutaneous fat (arrows).

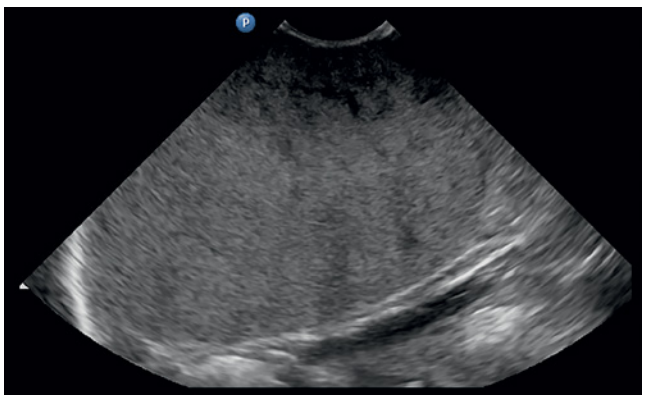


Figure 13.54. Fibroadenomatous hyperplasia of the mammary gland in 2-year-old primiparturient cat during early pregnancy. The mammary gland is enlarged and appears as a solid echogenic mass with ill-defined hypoechoic areas in the parenchyma. The age of the cat, the history of rapid and marked mammary swelling in the first weeks of pregnancy are consistent with this diagnosis.

Interventional Procedures

Depending on size and location, fine-needle aspiration or biopsy of mass lesions associated with the ovary or the uterus can be performed under ultrasound guidance following the same principles and precautions as in other organ systems. Ultrasound-guided aspiration of ovarian cysts may be an option for treatment, with 56% whelping described in dogs with follicular cysts (Bassu et al. 2004). Because of the risk of leakage into the peritoneal cavity, uterine fluid is usually not aspirated. Amniocentesis is not a routine procedure in the assessment of pregnant dogs or cats.



Visit our website at **www.SmallAnimalUltrasonography.com** for complementary video clips with annotations and text on:

- Normal ovaries and uterus
- Normal pregnancy: different stages
- Pyometra
- Cystic endometrial hyperplasia

Vet-ebooks.com

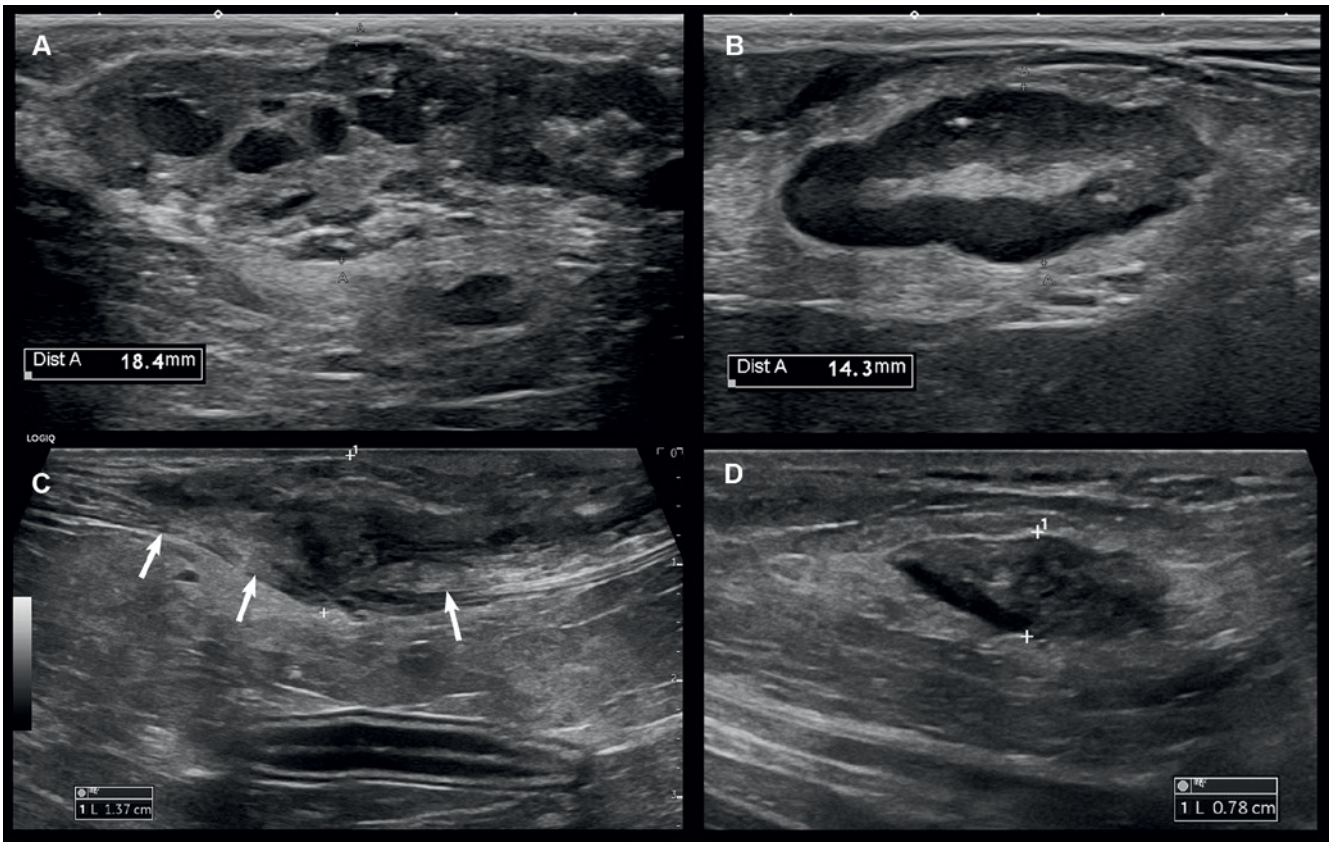


Figure 13.55. **Mammary tumors in two dogs. (A, B) Mixed mammary tumor** in an 11-year-old Golden Retriever. An approximately 4 × 1.8 cm heterogeneous multicystic mass is associated with a mammary gland. Note the hyperechoic appearance of the surrounding fat. The inguinal lymph node (in **B**) is enlarged, irregular, hypoechoic, and surrounded by hyperechoic fat consistent with lymph node metastasis. Image courtesy of Dr. Eddy Cauvin, Azurvet, France) **(C, D) Sclerosing mammary adenocarcinoma** invading the abdominal muscular wall (arrows in **C**) in a 10-year-old intact female Stafford terrier dog with confirmed metastases to the regional superficial inguinal lymph node (in **D**).

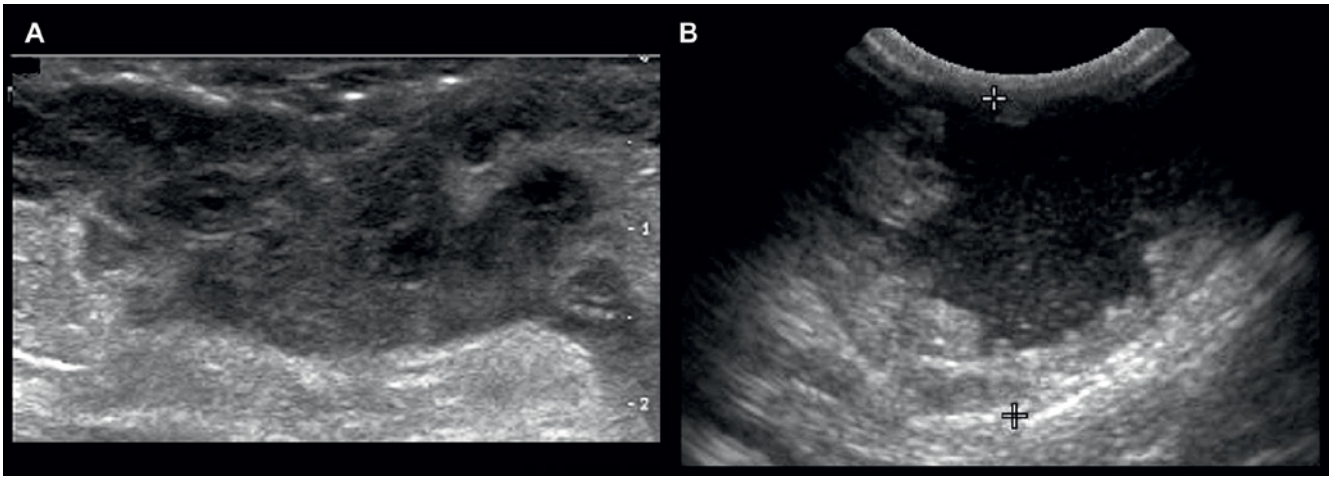


Figure 13.56. **Complicated mammary carcinomas in a cat and in a dog. (A)** The ulcerated and extensive mass invades most of the right middle to caudal mammary chain in a 14-year-old cat. The mass is poorly echogenic, highly vascularized on color flow Doppler (not shown) and has irregular margins. **(B)** This is an abscessed mammary carcinoma in a 12-year-old long-haired Dachshund. A thick-walled mass is shown (cursors) with an accumulation of echogenic fluid centrally. The mass arose from the right caudal mammary gland.

Vet-ebooks.com

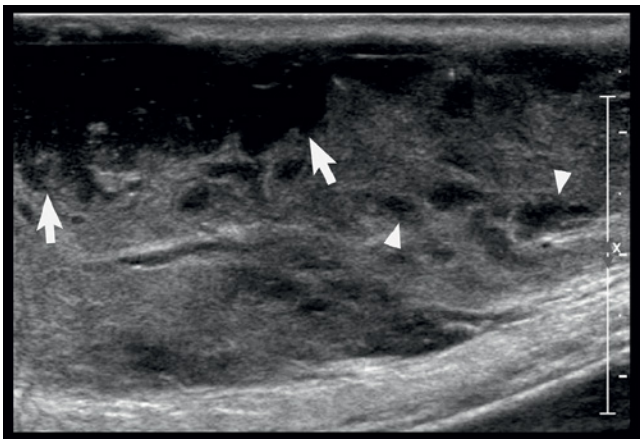


Figure 13.57. Mastitis and abscess in an 11-year-old intact Afghan dog with recurrent pseudo-gestation. The mammary gland is diffusely enlarged and inhomogeneous with several small echogenic cavities (arrowheads). A larger superficial collection of fluid (arrows) is present, and pus was sampled.

References

Agut A., Carrillo J.D., Anson A., Belda E., et al. (2016) Imaging diagnosis-urethrovaginal fistula caused by a migrating grass awn in the vagina. Vet Radiol Ultrasound 57(3):E30.

Allen WE, England GCW, White KB (1989) Hydrops foetalis diagnosed by real time ultrasonography in a bichon frisé bitch. J Small Anim Pract 30:465–467.

Arlt S. (2020) The bitch around parturition. Theriogenology 150:452–457.

Ball RL, Birchard SJ, May LR, Threlfall WR, et al. (2010) Ovarian remnant syndrome in dogs and cats: 21 cases (2000-2007) J Am Vet Med Assoc; 236(5):548–53

Barbosa C, Souza MB, Freitas LA, Silva TFP, et al. (2013) Assessment of uterine involution in bitches using B mode and Doppler ultrasonography. Anim Reprod Sci 139(1–4):121–126.

Bassu G, Rault D, Besso J, Marseloo N, et al. (2004) Ultrasound-guided aspiration in management of ovarian follicular cysts in the bitch. In: Proceedings of the 4th Congress of the European Veterinary Society for Small Animal Reproduction: 20–28.

Beccaglia M, Luvoni GC (2012) Prediction of parturition in dogs and cats: accuracy at different gestational ages. Reprod Domest Anim 47(Suppl 6):194–196.

Beccaglia M, Alonge S, Trovo C, Luvoni GC (2016) Determination of gestational time and prediction of parturition in dogs and cats: an update. Reprod Domest Anim 51(1):12–17

Beck KA, Baldwin CJ, Bosu WTK (1990) Ultrasound prediction of parturition in the queen. Vet Radiol Ultrasound 31:32–35.

Benzimra C, Couturier L, Gatel L, Cauvin E, et al. (2021) Ultrasonographic findings associated with uterine migrating grass seeds in eleven dogs. Vlaams Diergeneeskundig Tijdschrift 90:5–10.

Chandra SA, Cline JM, Adler RR. (2010) Cyclic morphological changes in the Beagle mammary gland. Toxicologic Pathology 38:969–983.

Costa MR, Oliveira AL, Vidal LW, Ramos RM, et al. (2019) Comparison of macroscopic resorption time for a self-locking device and suture material in ovarian pedicle ligation in dogs. Vet Rec 184(15):478.

Davidson AP, Baker TW (2009) Reproductive ultrasound of the bitch and queen. Topics Companion Anim Med 24(2):55–63.

Diez-Bru N, Garcia-Real I, Martinez EM, Rollan E, et al. (1998) Ultrasonographic appearance of ovarian tumors in 10 dogs. Vet Radiol Ultrasound 39:226–233.

England GCW (1998) Ultrasonographic assessment of abnormal pregnancy. Vet Clin North Am Small Anim Pract 28:849–868.

England GCW, Allen WE, Porter DJ (1990) Studies on canine pregnancy using B-mode ultrasound: development of the conceptus and determination of gestational age. J Small Anim Pract 31:324–329.

England GCW, Yeager AE, Concannon PW (2003) Ultrasound imaging of the reproductive tract of the bitch. In Concannon PW, England GCW, Verstegen JP, Linde-Forsberg C, eds. Recent Advances in Small Animal Reproduction. Ithaca, NY: International Veterinary Information Service, Available at: https://www.ivis.org/library/recent-advances-small-animal-reproduction/ultrasound-imaging-of-reproductive-tract-of-bitch (accessed 22 October 2024).

Feliciano MAR, Vicente WRR, Silva MAM (2012) Conventional and Doppler ultrasound for the differentiation of benign and malignant canine mammary tumours. J Small Anim Pract 53:332–337.

Ferretti LM, Newell SM, Graham JP, Roberts GD (2000) Radiographic and ultrasonographic evaluation of the normal feline postpartum uterus. Vet Radiol Ultrasound 41:287–291.

Fulton RM (2021) Focused ultrasound of the Fetus, female and male reproductive tracts, pregnancy, and dystocia in dogs and cats. Clin North Am Small Anim Pract 51(6):1249–1265.

Gatel L, Rault DN, Chalvet-Monfray K, Saunders J, et al. (2015) Prediction of parturition time in queens using radiography and ultrasonography. Anat Histol Embryol 44:241–246.

Gatel L, Rault DN, Chalvet-Monfray K, De Rooster H, et al. (2020) Ultrasonography of the normal reproductive tract of the female domestic cat. Theriogenology 142:328–337.

Gil E, Garcia D, Froes T (2015) In utero development of the fetal intestine: sonographic evaluation and correlation with gestational age and fetal maturity in dogs. Theriogenology 84:681–6.

Vet-ebooks.com

Gil E, Garcia D, Giannico A, Froes TR (2018) Early results on canine fetal kidney development ultrasonographic evaluation and value in prediction of delivery time. Theriogenology 107:180–7.

Hayden DW, Johnston SD, Kiang DT, Johnson KH, et al. (1981) Feline mammary hypertrophy/fibroadenoma complex: clinical and hormonal aspects. Am J Vet Res 42:1699–1703.

Klein MK (1996) Tumors of the female reproductive system. In Withrow SJ, MacEwen EG, eds. Small Animal Clinical Oncology. Philadelphia: WB Saunders, pp. 347–355.

Kutzler MA, Yeager AE, Mohammed HO, Meyers-Wallen VN (2003) Accuracy of canine parturition date prediction using fetal measurements obtained by ultrasonography. Theriogenology 60:1309–1317

Lenard ZM, Hopper BJ, Lester NV, Richardson JL, et al. (2007) Accuracy of prediction of canine litter size and gestational age with ultrasound. Aust Vet J 85:222–225.

Levy X, Fontbonne A (2007) Determining the optimal time of mating in bitches: particularities. Rev Bras Reprod Anim, Belo Horizonte 31(1):128–134

Lopate C (2008) Estimation of gestational age and assessment of canine fetal maturation using radiology and ultrasonography: a review. Theriogenology 70:397–402.

Lopate C (2018) Gestational aging and determination of parturition date in the bitch and queen using ultrasonography and radiography. Vet Clin Small Anim 48:617–38.

Luvoni GC, Grioni A (2000) Determination of gestational age in medium and small size bitches using ultrasonographic fetal measurements. J Small Anim Pract 41:292–294.

Malandain E, Rault D, Froment E, Baudon S, et al. (2011) Follicular growth monitoring in the female cat during estrus. Theriogenology 76(7):1337–1346.

Miller MA, Kottler SJ, Cohn LA, Johnson GC, et al. (2001) Mammary duct ectasia in dogs: 51 cases (1992-1999). J Am Vet Med Assoc 218(8):1303–1307.

Nilsson M, Toresson L, Ljungvall I, Nyman Lee H, et al. (2023) Ultrasonographic features of the uncomplicated postoperative abdomen in dogs treated for pyometra by ovariohysterectomy. Vet Radiol Ultrasound 2023;1–9. doi:10.1111/vru.13310

Pharr JW, Post K (1992) Ultrasonography and radiography of the canine postpartum uterus. Vet Radiol Ultrasound 33:35–40.

Reynaud K, Fontbonne A, Saint-Dizier M, Thoumire S, et al. (2012) Folliculogenesis, ovulation and endocrine control of oocytes and embryos in the dog. Reprod Domest Anim 47(6):66–69.

Sasidharan JK, Patra MK, Singh LK, Saxena AC, et al. (2021) Ovarian cysts in the bitch: an update. Top Companion Anim Med 43:100511.

Silva LDM, Onclin K, Verstegen JP (1996) Assessment of ovarian changes around ovulation in bitches by ultrasonography, laparoscopy and hormonal assays. Vet Radiol Ultrasound 37:313–320.

Toal RL, Walker MA, Henry GA (1986) A comparison of real-time ultrasound, palpation and radiography in pregnancy detection and litter size determination in the bitch. Vet Radiol Ultrasound 27:102–108.

Topie E, Bencharif D, Briand L, Tainturier D (2015) Monitoring the foetal phase of gestation in the queen with a 12.5-MHz ultrasound probe and prediction of the parturition by combining the measurements of head and abdominal diameters. Reprod Domest Anim 50(4):560–566

Vercellini R, Blanco PG, Arizmendi A, Diez M, et al. (2018) Ovarian and uterine two-dimensional and Doppler ultrasonographic changes in the feline peri-estrus period. J Feline Med Surg 24(10):1053–1059.

Vercellini, R., Blanco, P.G., Arizmendi, A., Diez, M., Rodríguez, R. and Gobello, C., 2022. Ovarian and uterine two-dimensional and Doppler ultrasonographic changes in the feline peri-estrus period. *J Feline Med Surg*, *24*(10), pp.1053–1059. https://doi.org/10.1177/1098612X211067016.

Voges AK, Neuwirth L (1996) Ultrasound diagnosis: cystic uterine hyperplasia. Vet Radiol Ultrasound 37:131–132.

Yeager AE, Concannon PW (1990) Serial ultrasonographic appearance of postpartum uterine involution in beagle dogs. Theriogenology 34:523–533.

Yeager AE, Concannon PW (1995) Ultrasonography of the reproductive tract of the female dog and cat. In Bonagura JD, ed. Kirk's Current Veterinary Therapy XII. Philadelphia: WB Saunders, pp. 1040–1052.

Yeager AE, Mohammed HO, Meyers-Wallen V, Vannerson L, et al. (1992) Ultrasonographic appearance of the uterus, placenta, fetus, and fetal membranes throughout accurately timed pregnancy in beagles. Am J Vet Res 53:342–351.

Zambelli D, Prati F (2006) Ultrasonography for pregnancy diagnosis and evaluation in queens. Theriogenology 66:135–144.

Zambelli D, Caneppele B, Bassi S, Paladini C (2002) Ultrasound aspects of fetal and extrafetal structures in pregnant cats. J Feline Med Surg 4:95–106.

Vet-ebooks.com

CHAPTER FOURTEEN

Male Reproductive Tract

Silke Hecht[1] and Julie De Lasalle[2]

[1]*Department of Small Animal Clinical Sciences, College of Veterinary Medicine, University of Tennessee, Knoxville, TN, USA*
[2]*Animages, Brossard, Québec, Canada*

Preparation and Scanning Procedure

An ultrasonographic examination of male reproductive organs is commonly performed in dogs but rarely in cats. Examination technique, normal findings, and disorders of the male reproductive tract described in this chapter pertain to dogs unless indicated otherwise.

Indications for examination of the male reproductive tract include andrological evaluation of breeding dogs; identification of retained testicles; difficulties or abnormalities in urination or defecation; abdominal, scrotal, and penile pain or discomfort; caudal abdominal mass lesions; perineal hernia; clinical signs compatible with hormonal imbalances (hyperestrogenism); scrotal or penile trauma; abnormalities noted on rectal examination; and palpable scrotal abnormalities.

The prostate is usually examined transabdominally after routine clipping and application of acoustic gel. The dog is usually positioned in dorsal recumbency. A transrectal approach is the standard in human medicine for ultrasonographic evaluation of the prostatic gland and has been described in dogs (Culp et al. 2019; Zohil and Castellano 1995) but is not used routinely. A 5.0-MHz transducer may be sufficient to identify gross prostatic abnormalities such as paraprostatic cysts or prostatic abscesses; however, a higher frequency (7.5–24 MHz) transducer provides better resolution and is recommended for most indications. The prostate is located in the caudal abdomen or pelvic canal. It is identified caudal to the urinary bladder and ventral to the distal descending colon and rectum. Examination is performed in transverse and sagittal planes (Figure 14.1). Instillation of saline into the urinary bladder may improve the acoustic window (Feeney et al. 1989; Johnston et al. 1991b). In some dogs, especially in neutered dogs with an empty or intrapelvic bladder, ultrasonographic identification of the prostate may be challenging. In these cases, a concurrent digital rectal examination can be performed to identify the prostate and push it toward the ultrasound transducer. Color or power Doppler ultrasound may be used to evaluate vascularity of the prostate and of prostatic lesions (Newell et al. 1998). Contrast-enhanced ultrasound for evaluation of the prostate has been described in intact (Bigliardi and Ferrari 2011; Russo et al. 2009, 2012; Troisi et al. 2015; Vignoli et al. 2011) and castrated male dogs (Spada et al. 2021) but is at this point not widely used. One study mentions that it might help differentiate between malignant and benign lesions, but that larger studies are needed (Vignoli et al. 2011).

The testicles should be examined with a high-frequency transducer (7.5–24 MHz). A linear transducer with broad contact area and good resolution in the near field is preferable over a sector or curvilinear transducer. Use of a standoff pad is recommended by some examiners. Clipping of the scrotum is usually not performed to avoid possible irritation and secondary self-trauma. Ultrasound gel is preferred as a contact medium over alcohol because of the risk of scrotal irritation. The testicles are scanned in at least two planes (sagittal and transverse) (Figure 14.2). Color or power Doppler ultrasound and B-flow may be helpful in the assessment of the vascularity of testicular and other scrotal lesions (Orlandi et al. 2022) and allow evaluation of the epididymis. Contrast-enhanced ultrasound

Atlas of Small Animal Ultrasonography, Third Edition. Edited by Dominique Penninck and Marc-André d'Anjou.
© 2025 John Wiley & Sons, Inc. Published 2025 by John Wiley & Sons, Inc.
Companion website: www.SmallAnimalUltrasonography.com

Vet-ebooks.com

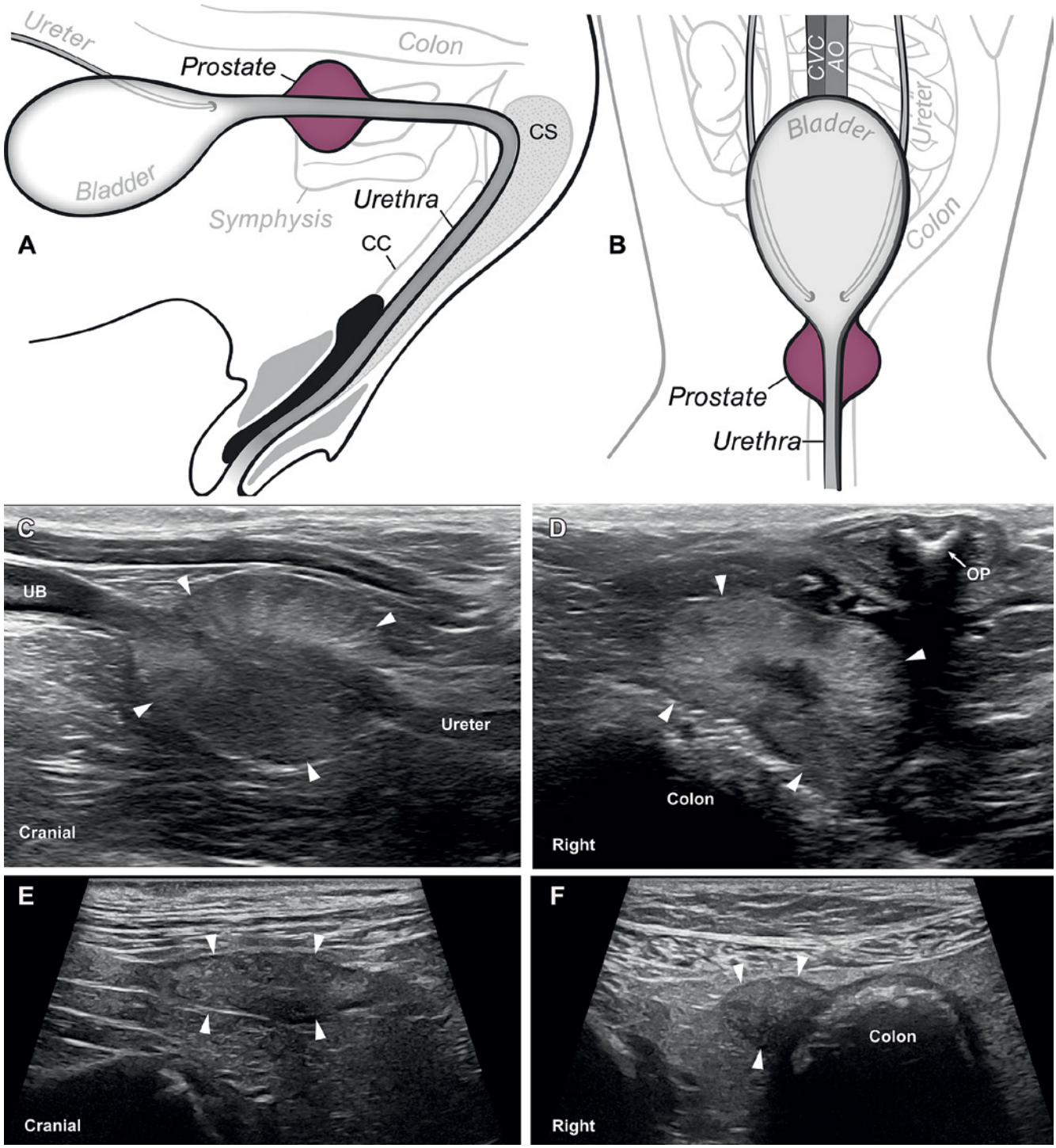


Figure 14.1. Normal anatomy of the canine prostate. Sagittal **(A)** and ventral **(B)** illustrations of the prostate and the surrounding structures in an intact adult male dog. **Sonograms of normal prostates** (arrowheads) in a 6-month-old intact Bernese Mountain cross dog **(C, D)** and a 7-year-old castrated Chihuahua **(E, F)**. Ao, aorta; BG, bulbus glandis; CC, corpus cavernosum; CS, corpus spongiosum; CVC, caudal vena cava; OP, os penis; UB, urinary bladder.

for evaluation of testicular lesions (Cicirelli et al. 2022; Tenuta et al. 2021) and pulse-wave Doppler pulsatility and resistive indexes of the testicular artery (Gloria et al. 2020) have been described in dogs, but more studies are required, and these techniques are at this point not widely used.

The penis is occasionally examined to evaluate regional swelling or mass lesions or to assess the integrity

Vet-ebooks.com

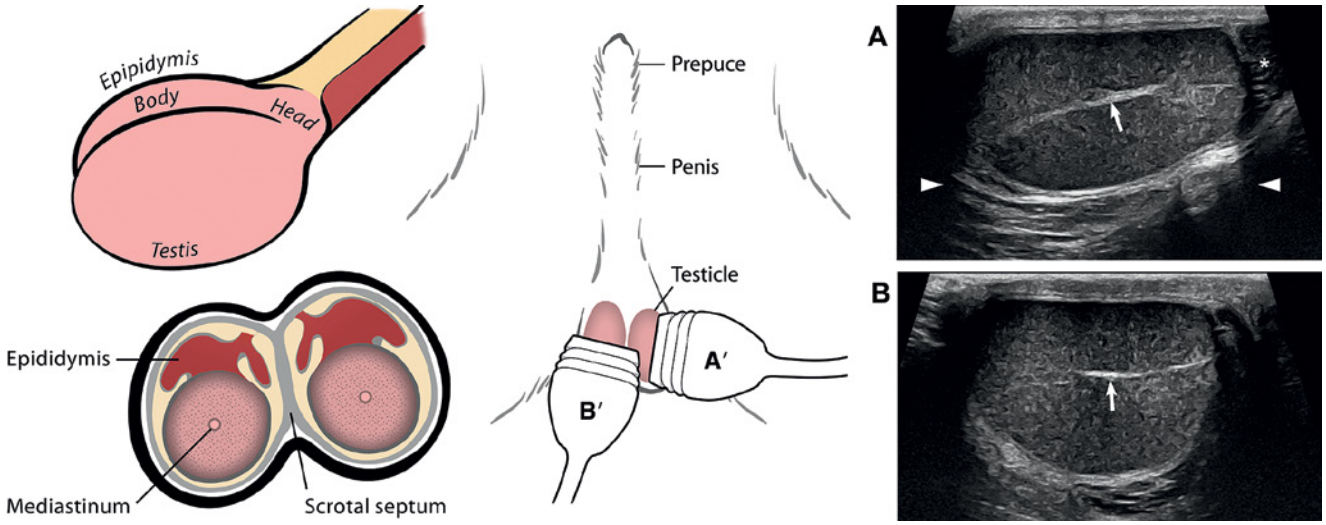


Figure 14.2. Scanning technique and normal sonographic anatomy of the testicle in an 11-month-old intact Yorkshire Terrier. The left of the figure shows a schematic representation of the anatomy and position of the probe on the testicles (**A**′ and **B**′ correspond to the sonograms on the right). **(A) Longitudinal sonographic image of the testicle**. The testicle is oval, of medium echogenicity, and of fine and homogeneous echotexture. The tunica albuginea is smooth, thin, and hyperechoic. The mediastinum testis is seen as a central linear hyperechoic band (arrow). The epididymis is seen on the caudal aspect of the testis (*). Edge shadowing occurs at the cranial and caudal pole of the testicle (arrowheads). **(B) Transverse sonographic image of the testicle**. The testicle is round and of medium echogenicity. The mediastinum testis is seen as a central or slightly eccentric hyperechoic focus.

of the os penis. The **penile urethra** is more commonly evaluated by means of ultrasound to identify urethral abnormalities and/or urethral calculi. Dependent on the examiner's preference, a linear or curvilinear high-frequency transducer (7.5MHz or higher) may be used. The examination is started at the level of the prepuce and is continued proximally to the level of the ischium. Evaluation of the penile urethra may be enhanced by instillation of saline using a balloon-type catheter inserted into the distal penile urethra.

Prostate

Normal Sonographic Anatomy of the Prostate

The location, size, and appearance of the prostate varies with age, previous disease, and status (intact versus neutered) (Feeney et al. 1989; Johnston et al. 1991b). In intact dogs, the prostate is of medium echogenicity and homogeneous, with a fine to medium coarse echotexture and smooth margins (Mattoon and Nyland 2021). On sagittal images, the shape is rounded to ovoid. On transverse images, the two prostatic lobes are symmetrical. The **vertical raphe** and **prostatic urethra** with surrounding urethralis muscle are generally visible as a hypoechoic area between both lobes, in the centro-dorsal portion of the prostate (Figures 14.1, 14.3). The urethral structures may be associated with edge shadowing on transverse images, which should not be misinterpreted as a lesion. Occasionally, the paired **vas (ductus) deferens** can be visualized from the prostatic urethra (at the colliculus seminalis) to the craniodorsal aspect of the prostate and followed to the inguinal canal (Figure 14.4). In intact males, age-related changes in ultrasonographic appearance of the prostate include an increase in size and echogenicity (Figures 14.1, 14.5). Prostatic cysts are a common incidental finding in older dogs (Mattoon and Nyland 2021; Ruel et al. 1998). Prostatic size in intact dogs is significantly correlated with age and body weight (Atalan et al. 1999; Haverkamp et al. 2019; Ruel et al. 1998) (Table 14.1). In neutered dogs, the prostate is small, inconspicuous, hypoechoic, and homogeneous. The two lobes usually cannot be distinguished (Figure 14.6). A correlation between prostatic size and body weight was demonstrated in castrated dogs and can be described as r^2 of 0.69 and 0.53 for prostatic length and depth, respectively (Bosma et al. 2022). Incidental parenchymal inhomogeneities may be observed during prostatic involution after castration or in the prostate of dogs neutered at a higher age (Figure 14.7).

Vet-ebooks.com

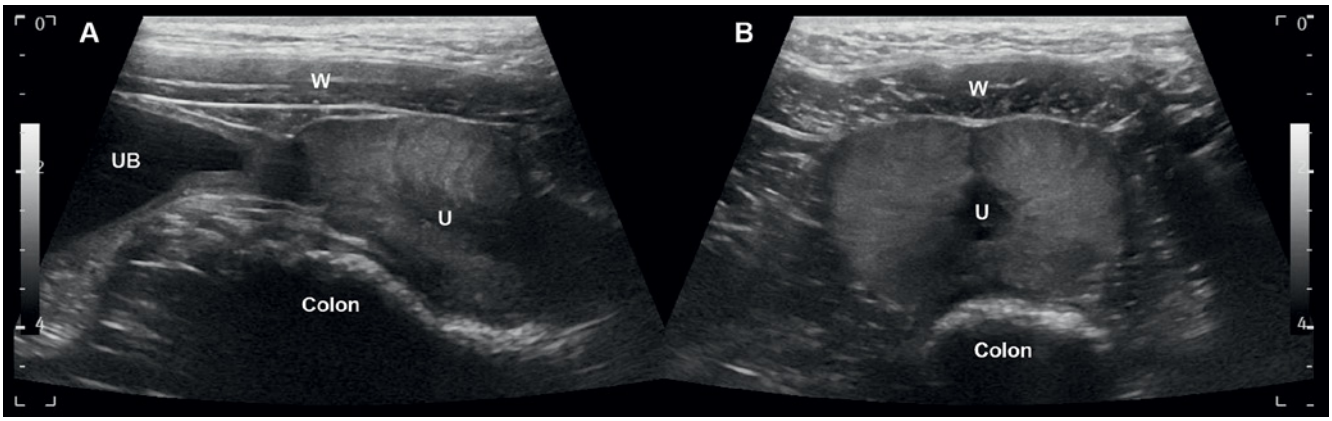


Figure 14.3. Normal prostate in a 1-year-old intact Labrador Retriever. (A) Sagittal image. The prostate appears as an ovoid, homogeneous structure of medium echogenicity dorsal to the abdominal wall (W), ventral to the colon, and caudal to the urinary bladder (UB). The irregular, hyperechoic interface that casts a strong shadow in the colon is caused by the presence of feces. U, central prostatic urethra and urethralis muscle. **(B) Transverse image.** The prostate is bilobed. The lobes are symmetrical and homogeneous. The central prostatic urethra and urethralis muscle (U) are hypoechoic. The colon is dorsal to the prostate. W, abdominal wall.

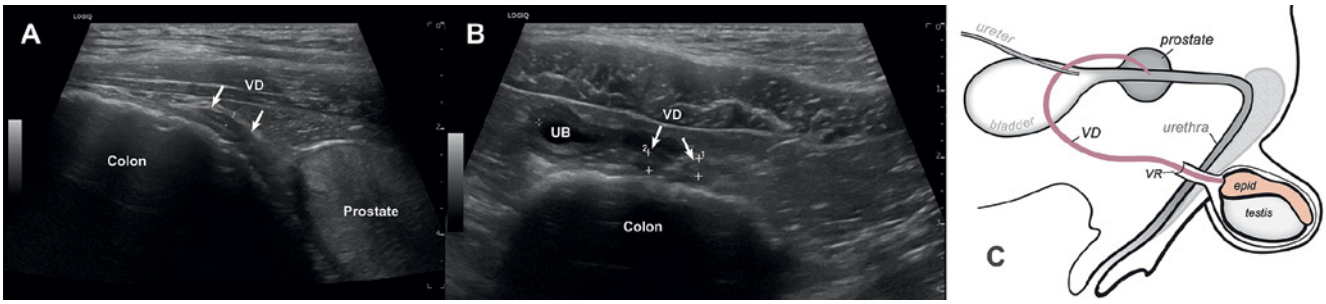


Figure 14.4. Anatomic reference and normal vas (ductus) deferens in a 6-year-old intact Beauceron. (A) Sagittal sonographic image of the left vas deferens (VD), extending from the craniodorsal aspect of the prostate, ventral to the colon. **(B)** Transverse image, at the level of the urinary bladder trigone. Paired vasa deferentia (VD) are visible in transverse plane as two small ovoid structures, ventral to the colon and dorsal to the urinary bladder trigone. **(C)** Illustration of the regional anatomy. Each vas deferens (VD) extends from the epididymis (epid) and traverses the vaginal ring (VR), circling around the ipsilateral ureter before penetrating the prostatic urethra.

Sonographic Findings in Prostatic Abnormalities

Benign prostatic hyperplasia (BPH), bacterial prostatitis, paraprostatic cysts, and prostatic neoplasia are the most common prostatic disorders in dogs. Prostatic cysts are a common incidental finding or may be seen in association with BPH and other prostatic diseases. Prostatic abscesses may develop as a complication of bacterial prostatitis and/or infected cysts.

Prostatic hyperplasia, traditionally called **BPH**, is an enlargement of the prostate associated with hormone production and is a common incidental finding in older intact dogs. The prostate is enlarged, of normal to increased echogenicity, and of homogeneous or inhomogeneous echotexture (Figure 14.8). On transverse images, the two lobes are usually symmetrical, although asymmetrical enlargement may occur. Intraprostatic cysts are common and manifest as circular to irregularly shaped anechoic areas of variable size (Figure 14.9).

Acute and chronic infections occur in the canine prostate, usually secondary to ascent of urethral bacteria into a gland with BPH (**bacterial prostatitis**) (Johnston et al. 2000). The prostate may be of normal size or enlarged. Echogenicity and echotexture of the prostatic parenchyma are variable, ranging from normal to heterogeneous. Although changes in echogenicity and echotexture tend to be more severe than those seen with BPH, ultrasonographic differentiation of

Vet-ebooks.com

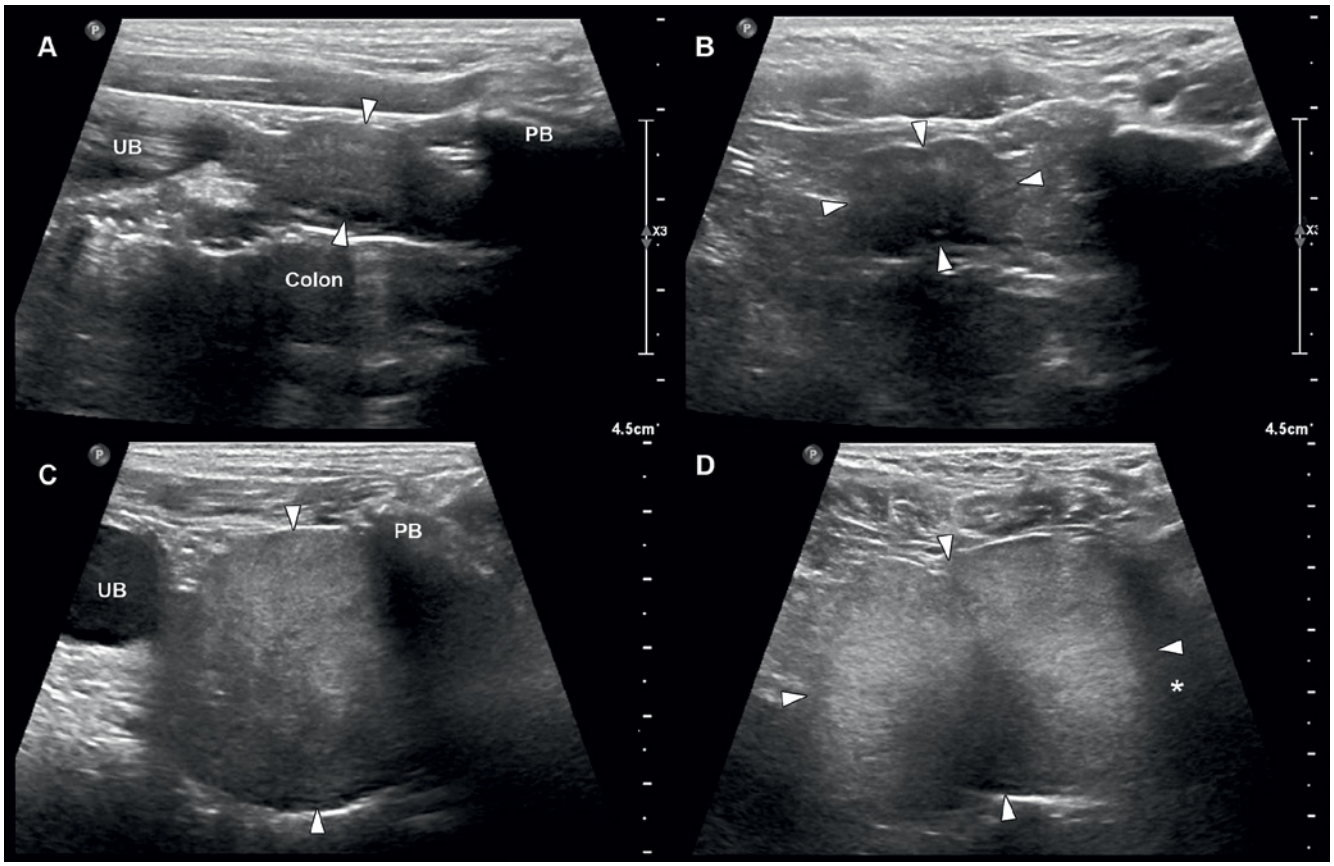


Figure 14.5. Comparison of the appearance of the normal prostate in a juvenile and a 6-year-old intact large breed dog. **(A, B)** Sagittal **(A)** and transverse **(B)** images of the prostate in a 6-month-old Golden retriever. The prostate (arrowheads) is ovoid, hypoechoic, and small (12 mm in dorsoventral dimension). The urinary bladder (UB) is noted cranial to the prostate. The acoustic shadow caused by the pubic bone (PB) limits the full assessment of the prostate. **(C, D)** Sagittal **(C)** and transverse **(D)** images of the prostate in a 6-year-old German Shepherd. The prostate (arrowheads) is rounded, of medium echogenicity, and measures 4 cm in dorsoventral dimension. Edge shadowing (*) limits the conspicuity of the lateral margins of the prostate in transverse plane. PB, pubic bone; UB, urinary bladder.

Table 14.1
Prostatic dimensions in healthy intact dogs and correlation to age and body weight

	Ruel et al. (1998)	Atalan et al. (1999)
Length (cm)	1.7–6.9	1.8–5.0
Height (on transverse image) (cm)	1.3–4.7	1.4–3.6
Width (cm)	1.8–6.9	1.4–4.3
Volume (cm^3)	2.3–80.0	8.1–28.2
Correlation between prostatic length (L [cm]), age (A [years]), and body weight (BW [kg])	$L = (0.055 \times BW) + (0.143 \times A) + 3.31$	
Correlation between prostatic height (H [cm]), age (A [years]), and body weight (BW [kg])	$H = (0.044 \times BW) + (0.083 \times A) + 2.25$	
Correlation between prostatic width (W [cm]), age (A [years]), and body weight (BW [kg])	$W = (0.047 \times BW) + (0.089 \times A) + 3.45$	
Correlation between prostatic volume (V [cm^3]), age (A [years]), and body weight (BW [kg])	$V = (0.867 \times BW) + (1.885 \times A) + 15.88$	$V = 8.48 + (0.238 \times BW)$ $V = 9.79 + (0.871 \times A$

Source: Adapted from Ruel et al. (1998) and Atalan et al. (1999).

Vet-ebooks.com

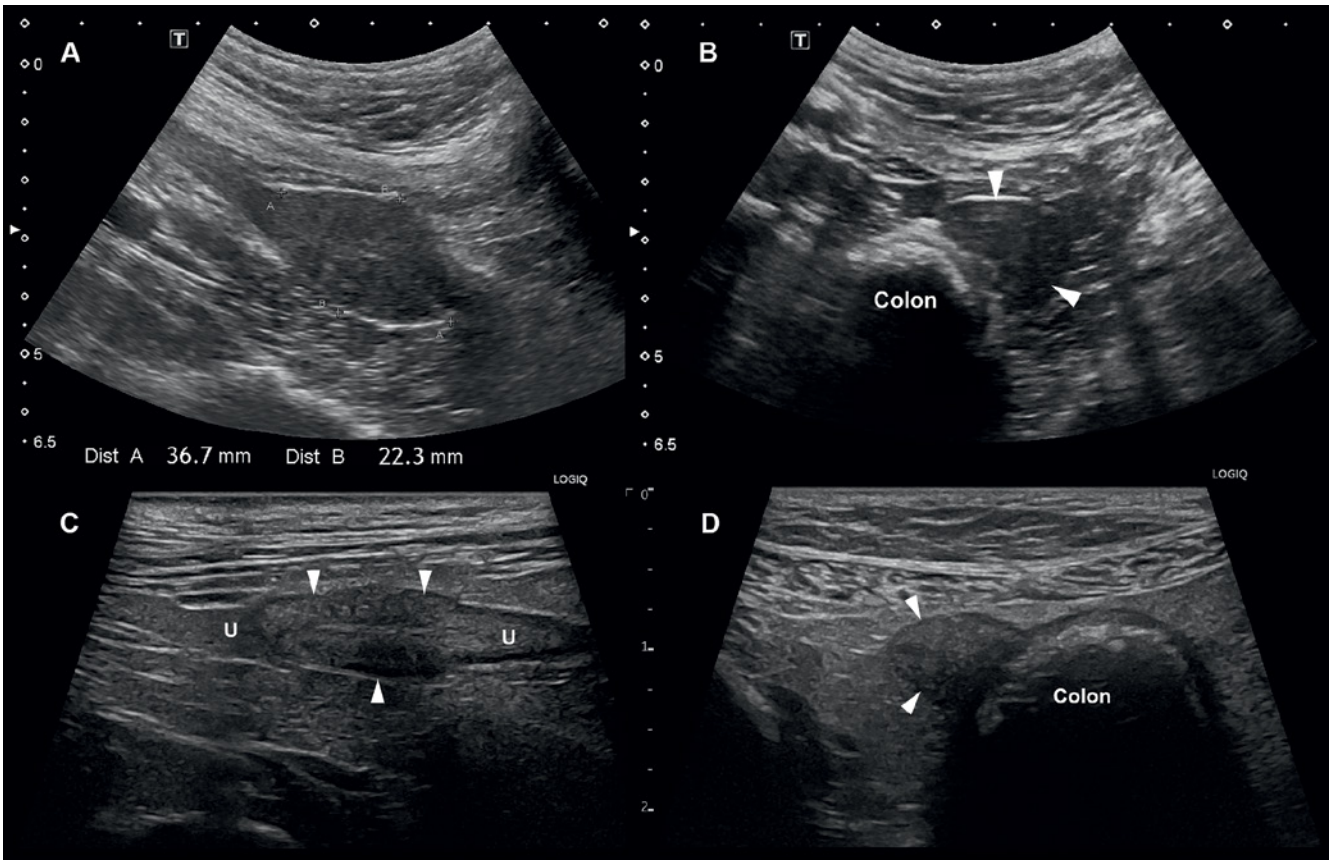


Figure 14.6. **Normal prostate in two neutered dogs. (A, B)** Sagittal **(A)** and transverse **(B)** images in a 5-year-old Dalmatian that was neutered at the age of 2 years. The prostate (between the cursors and arrowheads) is ovoid and ventral and to the left of the colon. Its two lobes, which are well seen in the transverse view, are homogeneously hypoechoic. **(C, D)** Sagittal **(C)** and transverse **(D)** images in an 8-year-old neutered mixed Chihuahua. The prostate (arrowheads) is small (6mm in thickeness), elongated in the sagittal view, oval in the transverse view, and of medium echogenicity with a coarse echotexture that is more obvious using this high-resolution (22MHz) linear transducer. U, urethra.

these conditions is often not possible, and prostatitis in many cases complicates pre-existing BPH (Figure 14.10). In some cases of acute prostatitis, hyperechoic fat or a scant volume of effusion may be detected adjacent to the prostate (Figures 14.10, 14.11). **Prostatic abscesses** can develop subsequent to prostatitis and may appear similar to prostatic cysts (Figures 14.12, 14.13). Similar as with prostatitis, hyperechogenicity of periprostatic fat and abdominal effusion may be noted (Figure 14.13). Other ultrasonographic findings in prostatic abscessation include development of a thick wall around the abscess cavity, intracavitary accumulation of echogenic fluid, gas inclusions in case of infection with gas-producing bacteria, and septation (Figure 14.14). Dystrophic mineralization may be encountered in chronic prostatitis (Bradbury et al. 2009) (Figure 14.12). **Fungal prostatitis** (e.g., secondary to blastomycosis or cryptococcosis) is rare, causes variable ultrasonographic changes, and may mimic prostatic neoplasia (Totten et al. 2011) (Figure 14.15). **Chronic noninfectious lymphoplasmacytic prostatitis** has also rarely been reported (Newell et al. 1998; Palmieri et al. 2014) and in one case was associated with urethral obstruction (Kalogianni et al. 2022). Medial and internal iliac lymphadenomegaly may be seen in association with prostatitis and/or prostatic abscesses.

Prostatic cysts, as previously mentioned, can be associated with BPH, prostatitis, and/or neoplasia. They contain anechoic fluid, may be surrounded by a thin hyperechoic wall, and may communicate with the prostatic urethra.

Paraprostatic cysts are fluid-filled structures that extend along the margin or outside the prostate, into the abdomen or into the pelvic canal (Palmieri et al. 2022; Renfrew et al. 2008). Unlike true intraprostatic cysts, paraprostatic cysts are in the vicinity of the prostate but may communicate with intraprostatic cavitations and/or the urethra. They occur predominantly in older

Vet-ebooks.com

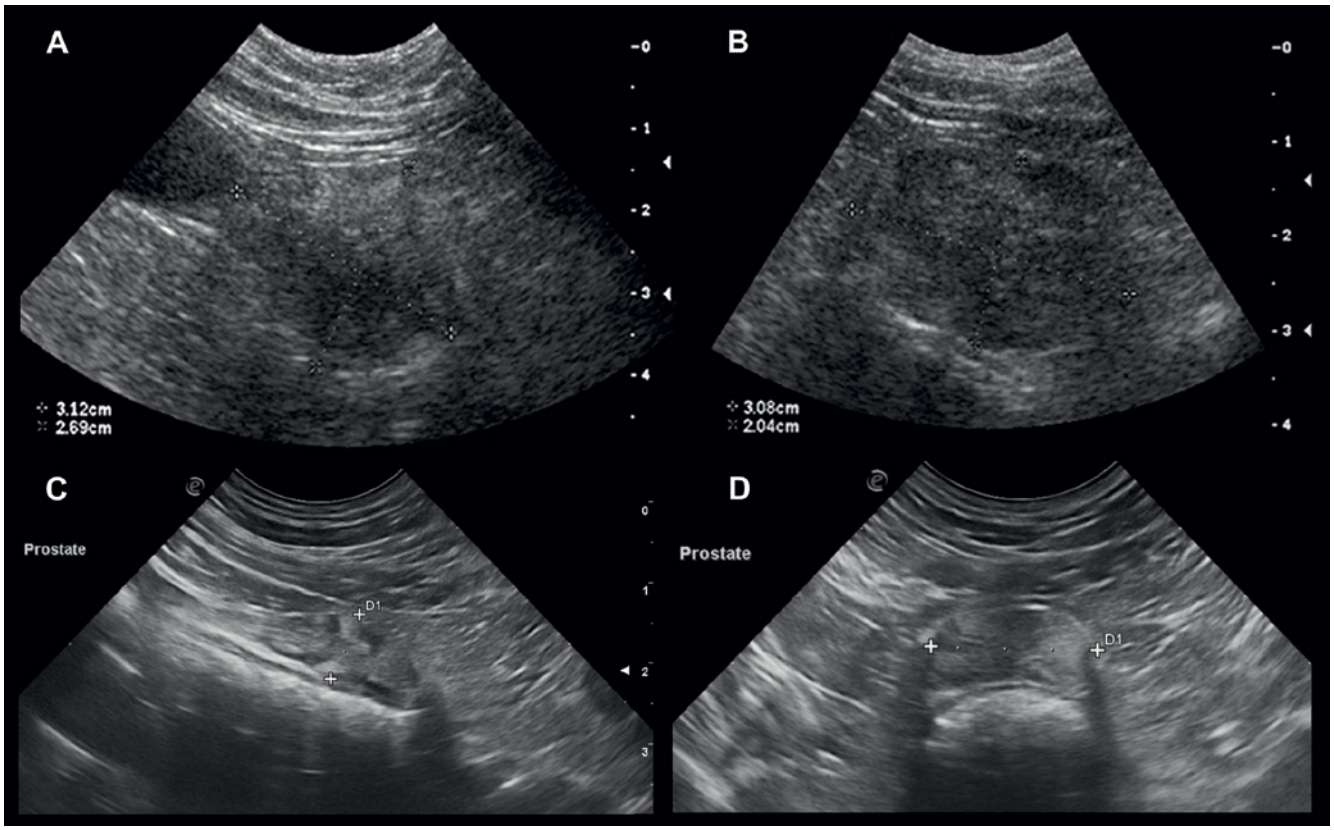


Figure 14.7. Prostatic remodeling in two dogs. Sagittal **(A)** and transverse **(B)** images of the prostate in a 10-year-old dog neutered at the age of 8 years. The prostate (between the cursors) is larger than seen in dogs neutered at a younger age and appears heterogeneous. Biopsies revealed the presence of normal prostatic tissue with fibrosis and small residual cysts. Some of these changes may be attributed to previous prostatitis. The appearance of the prostate did not significantly change on follow-up examinations. Sagittal **(C)** and transverse **(D)** images of the prostate in a 4-year-old Kerry Blue Terrier neutered at the age of 1 year and 7 months. The prostate (between the cursors) is atrophied but the prostatic parenchyma appears heterogeneous.

medium- to large-breed dogs (Renfrew et al. 2008; Stowater and Lamb 1989). They may originate from vestigial embryological remnants of the paramesonephric (Müllerian) duct system (uterus masculinus) and manifest as single or double (bi-horned) fluid-filled structures extending from the craniodorsal aspect of the prostate (Lim et al. 2014; Palmieri et al. 2022) (see also below under "Disorders of sexual development"). This cystic enlargement might be stimulated by hyperoestrogenism in dogs with Sertoli cell tumors (Atilola and Pennock 1986). One case of a paraprostatic cyst has been reported in a cat (Newell et al. 1992). Paraprostatic cysts contain anechoic to echogenic fluid, can become very large, may contain internal septa, have variable wall thickness, and may be mineralized (Renfrew et al. 2008; Zekas et al. 2004) (Figures 14.16–14.18). In case of difficulty distinguishing paraprostatic cysts from the urinary bladder, catheterization of the urinary bladder with evacuation of urine or infusion of saline may be helpful.

In contrast to other prostatic disorders, neutered dogs seem commonly affected by **prostatic neoplasia**. Although some studies reported that castrated dogs may be predisposed to prostatic neoplasia (Teske et al. 2002), according to a recent review, carcinoma of the prostate occurs with the same prevalence in intact and neutered dogs (Palmieri et al. 2022). Carcinoma is considered the most common prostatic tumor type and can be classified into prostatic adenocarcinoma and prostatic urothelial carcinoma. Other tumor types include undifferentiated carcinoma, squamous cell carcinoma, transitional cell carcinoma, lymphoma, and hemangiosarcoma. Rare cases of prostatic lymphoma (Winter et al. 2006), leiomyoma (Holdsworth et al. 2015), and leiomyosarcoma (Bacci et al. 2010; Hayden et al. 1999; Trovatelli et al. 2021) have also been reported. Bladder or urethral transitional cell carcinoma can extend into the prostatic parenchyma. Ultrasonographic findings in prostatic neoplasia are variable. Typically, the prostate is enlarged and irregular, with a hypoechoic to heterogeneous echotexture (Figures 14.19, 14.20). On transverse images, the prostatic lobes are usually asymmetrical (Figures 14.19, 14.21). Cavitation/necrosis within

Vet-ebooks.com

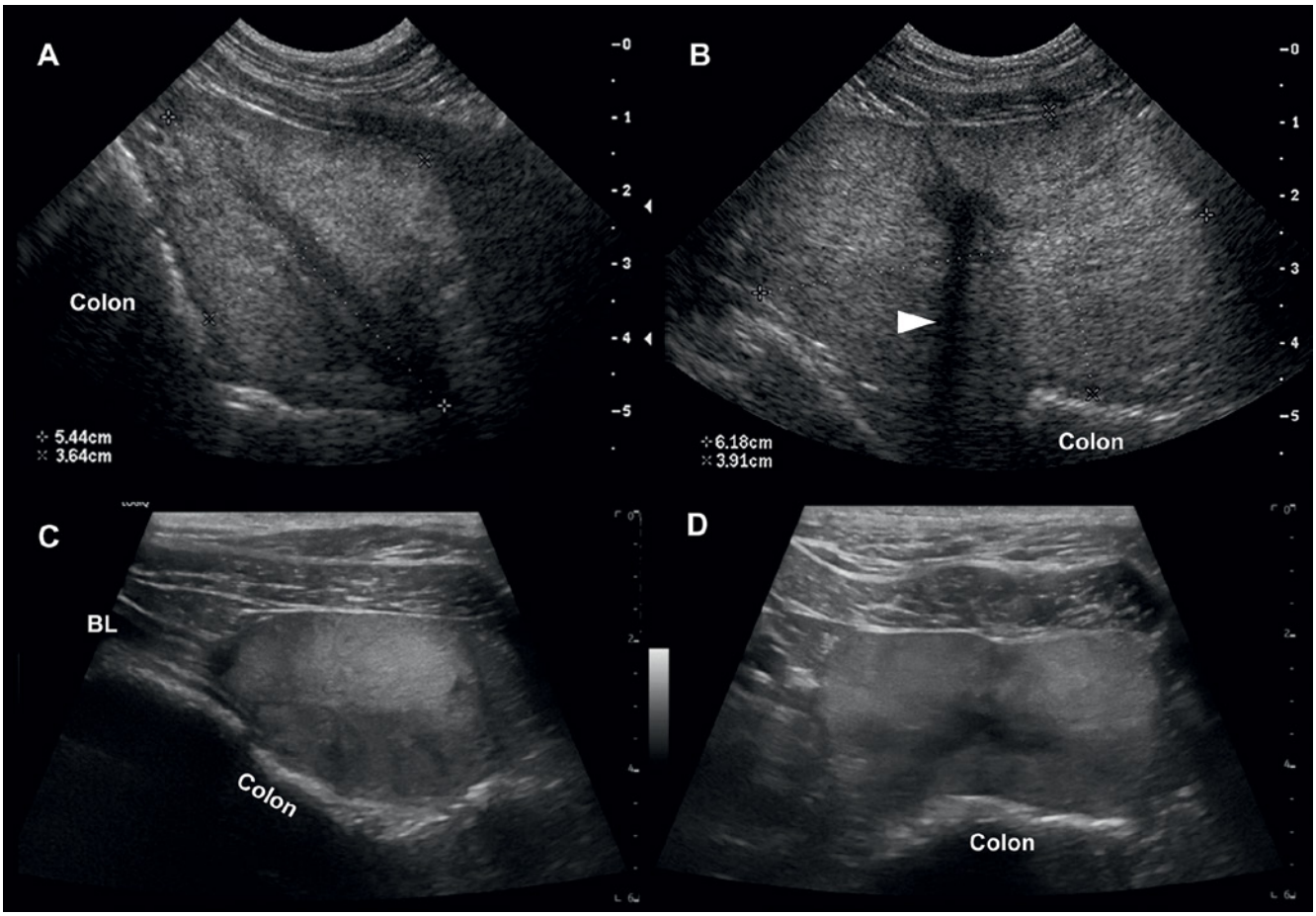


Figure 14.8. **Benign prostatic hyperplasia in two intact dogs. (A, B)** Sagittal **(A)** and transverse **(B)** images of the prostate of a 6-year-old Rottweiler. The prostatic parenchyma is mostly hyperechoic and slightly inhomogeneous. An edge shadow (arrowhead) noted on the transverse image is caused by the presence of the round, central urethra. **(C, D)** Sagittal **(C)** and transverse **(D)** images of the prostate of a 6-year-old Beauceron in which similar signs are observed. The difference in prostatic tissue echotexture in these two dogs is probably due to differences in ultrasound technology and image filtering.

the abnormal prostatic parenchyma is possible (Figure 14.19), and mineralization of the prostatic parenchyma is often present (Bradbury et al. 2009). The tumor may extend into the trigone of the urethra, the urinary bladder, and, eventually, invade the ureterovesicular junction. Urethral and/or ureteral obstruction, with secondary hydroureter and hydronephrosis, is possible. Metastases to the medial iliac +/− internal iliac and sacral lymph nodes are common (Figure 14.20). The lymph nodes may be enlarged, hypoechoic or heterogeneous, and the perinodal fat may be hyperechoic. Irregular bony proliferation of the ventral margin of the vertebral bodies of the caudal lumbar vertebrae may be seen, consistent with bone metastases. Other metastatic sites reported are the pelvic musculature, lung, liver, urethra and urinary bladder, colon and rectum, spleen, heart, kidney, distant lymph nodes, and adrenal glands (Sun et al. 2017).

Prostatic calculi are rare. They can be exogenous (migration from the urinary bladder into the prostatic urethra) or endogenous (formation within the prostate, usually within a cyst) (Palmieri et al. 2022).

Prostatic atrophy is seen secondary to castration (Figure 14.22), hormonal therapy, or can be associated with chronic inflammation (Palmieri et al. 2022).

TESTICLES

Normal Sonographic Anatomy of the Testicles

Normal testicles are of medium echogenicity and have a fine, homogeneous echotexture (Pugh et al. 1990). The testicular border is characterized by a thin, smooth, and hyperechoic **tunica albuginea**. On sagittal images, a central hyperechoic line is visible that represents the

Vet-ebooks.com

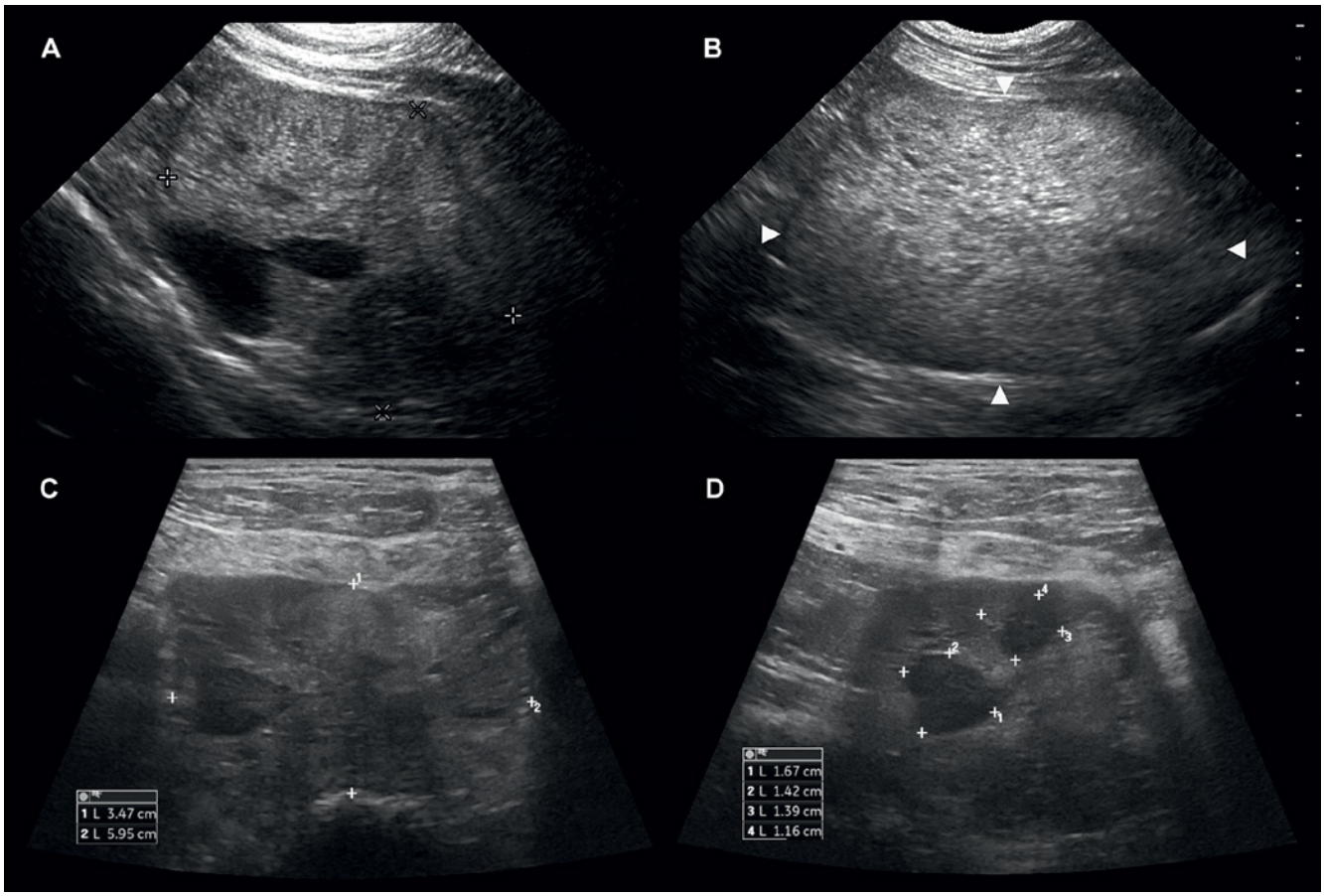


Figure 14.9. **Benign prostatic hyperplasia in three intact dogs. (A)** A sagittal image of the prostate in a 10-year-old Husky shows prostatic enlargement (5.3 × 4.4 cm), inhomogeneity of the parenchyma, and multiple anechoic areas consistent with prostatic cysts. **(B)** This parasagittal image of the prostate in a 10-year-old Golden Retriever shows prostatic enlargement (between arrowheads; 7.2 × 4.2 cm) and generalized hyperechogenicity of the parenchyma, with numerous interspersed hypoechoic foci consistent with small cysts. **(C, D)** Transverse images of the prostate in a 9-year-old intact Husky show prostatic enlargement and inhomogeneity of the parenchyma. The hypochoic areas might represent prostatic cysts in formation or areas of parenchymal hemorrhage. There was no evidence of prostatitis or neoplasia on cytology.

mediastinum testis (Figure 14.2A). On transverse images, the mediastinum testis appears as a centrally located hyperechoic focus (Figure 14.2B). In very young dogs, the testicles are small but homogeneous, and the mediastinum can be identified (Figure 14.23). In older dogs, small hyperechoic foci representing testicular septa are occasionally visible. Testicular size is directly related to body weight (Hecht 2001; Hecht et al. 2003) (Table 14.2).

The head and tail of the **epididymis** are located at the cranial and caudal poles of the testicle, respectively, and the body is found along its dorsal aspect. In comparison with testicular parenchyma, epididymal parts are hypoechoic and have a coarse echotexture (Figure 14.24). Examination of the entire epididymis in one plane is usually not possible because of its location and course and requires repositioning of the ultrasound probe with examination in at least two planes. The **spermatic cord** can be followed from the head of the epididymis to the inguinal ring. It contains the vas deferens and surrounding nerves, lymph and blood vessels including the large tortuous anechoic venous structures of the **pampiniform plexus**. This plexus presents a prominent and complex flow pattern on color or power Doppler (Figure 14.24). The paired **vas deferens** or ductus deferens arises from the tail of the epididymis, passes through the inguinal canal, penetrates the prostate gland craniodorsally, and courses caudoventrally to join the prostatic urethra at the colliculus seminalis (Figure 14.4).

Vet-ebooks.com

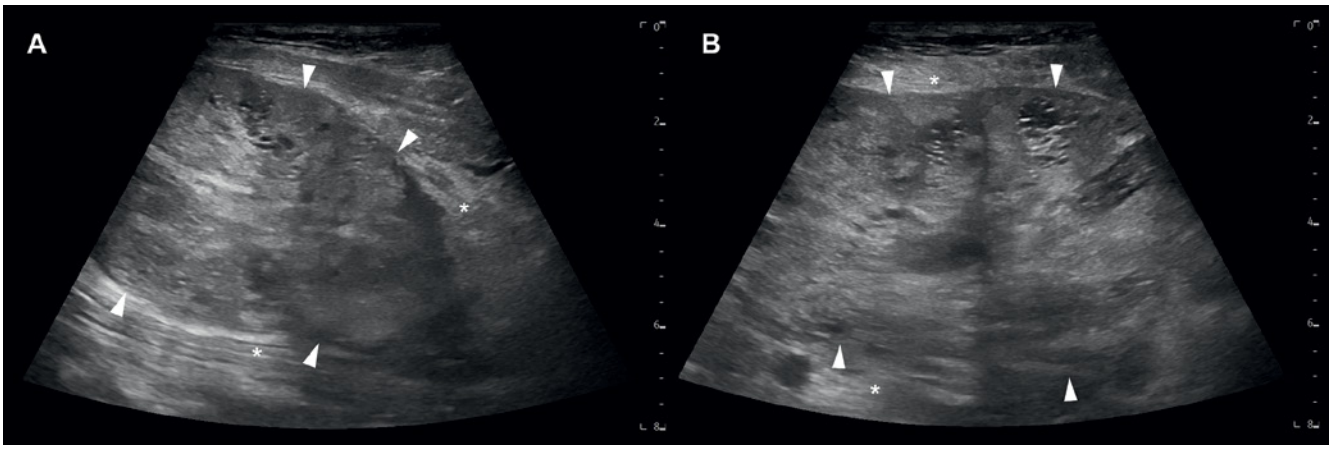


Figure 14.10. Prostatitis and benign prostatic hyperplasia. Sagittal **(A)** and transverse **(B)** images of the prostate in a 7-year-old intact Husky with benign prostatic hyperplasia and acute concomitant bacterial prostatitis. The prostate is enlarged (arrowheads) and heterogeneous with multiple hypoechoic/anechoic foci and has an irregular contour. The fat surrounding the prostate is hyperechoic (*), consistent with steatitis, and there is mild periprostatic effusion. There was also mild secondary medial iliac lymphadenomegaly (not shown here).

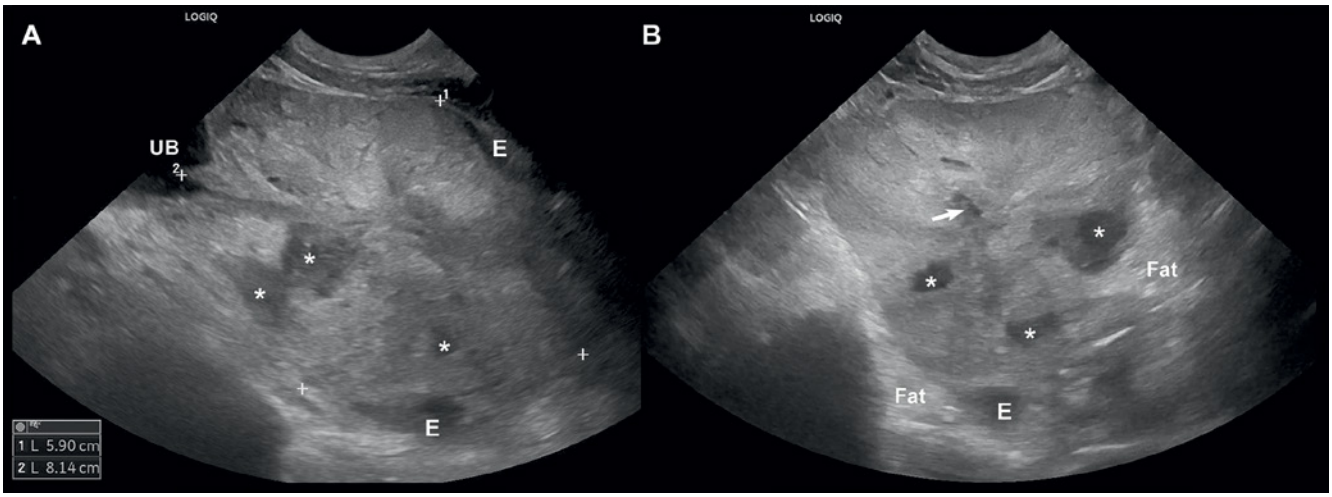


Figure 14.11. Acute prostatitis, benign prostatic hyperplasia, and intraprostatic cysts in a 5-year-old intact Husky Dog. The diagnosis of prostatitis was based on clinical and ultrasonographic findings as well as on the presence of suppurative inflammation on fine-needle aspiration although there was no bacterial growth. Concurrent pyelonephritis was also suspected. On sagittal **(A)** and transverse **(B)** sonographic images, the prostate (between the cursors in **(A)** is enlarged (8.1 cm long X 5.9 cm thick), heterogeneously hyperechoic, and has multiple hypoechoic cavitations (*) of up to 1 cm diameter, some with an echogenic content. A small volume of abdominal effusion (E) and hyperechoic fat is adjacent to the prostate, consistent with secondary steatitis. The arrow in B points to the urethra. UB, urinary bladder.

Sonographic Findings in Testicular Abnormalities

Testicular disorders include developmental disorders (cryptorchidism), testicular neoplasia, inflammatory disorders (orchitis and epididymitis), testicular or epididymal cysts, duct ectasia of the epididymis, torsion, infarction, atrophy, mineralization (microlithiasis), and trauma. Other disease processes that affect the scrotum include accumulation of fluid (hydrocele or hematocele), nontesticular mass lesions, and scrotal hernia.

While **cryptorchidism** is relatively common, other disorders of sexual development are poorly documented in dogs and cats. Cryptorchid testicles are usually small and hypoechoic but have normal architecture with a central hyperechoic mediastinum (Figures 14.25–14.27). They can be found anywhere between the caudal pole of the kidneys to the inguinal area. If the mediastinum testis is not developed, identification of

Vet-ebooks.com

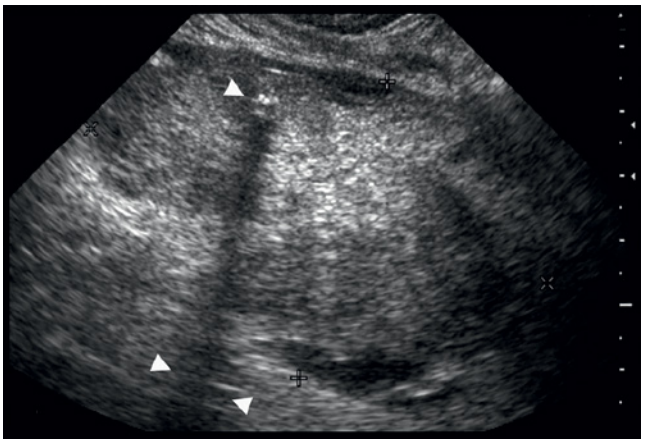


Figure 14.12. Severe, diffuse, chronic-active, suppurative prostatitis with multifocal necrosis, abscessation, and interstitial hemorrhage in a 9-year-old mixed-breed dog. Sagittal sonogram of the prostate (between cursors) shows that it is enlarged (7.5 × 4.8 cm), irregular in contour, and mixed in echogenicity, with multiple irregularly marginated anechoic areas consistent with abscesses. Parenchymal mineralization is seen as a strongly hyperechoic focus with distal shadowing (arrowheads).

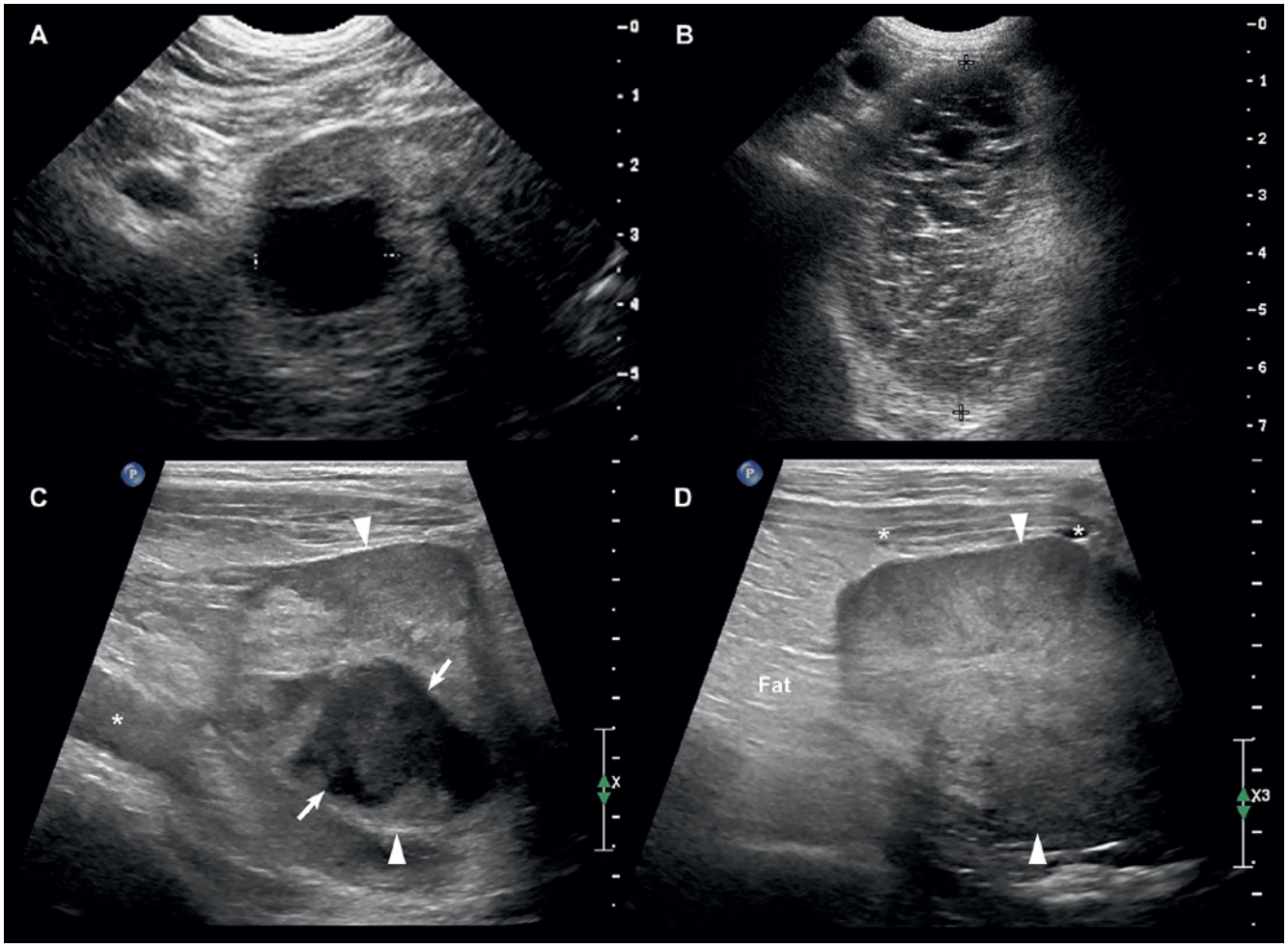


Figure 14.13. Prostatic abscesses in three dogs. (A) Septic abscess in a 3-year-old Border Collie. This transverse sonogram centered on the right lobe of the prostate shows a well-defined anechoic cavity (between the cursors). The volume of the lesion is estimated at 3.9 mL. **(B)** Sterile prostatic abscess in an 8-year-old Boxer. This transverse image shows a lacy hypoechoic to anechoic septated lesion of more than 6 cm maximum diameter associated with the right lobe (between the cursors). **(C, D)** Ruptured prostatic abscess (arrows) and secondary septic abdomen in a 4-year-old Belgian Malinois. The prostatic gland (arrowheads) is heterogenous and irregularly marginated. The periprostatic fat is markedly diffusely hyperechoic, and there are multifocal variably echogenic fluid pockets (*) in the vicinity of the prostate.

Vet-ebooks.com

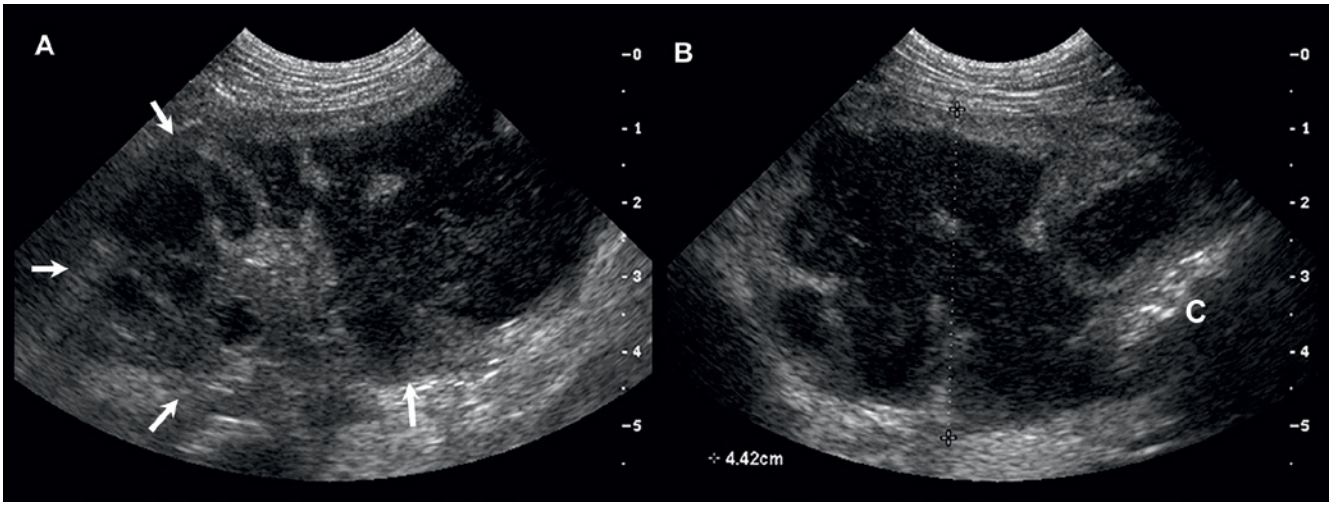


Figure 14.14. Septic prostatitis in a dog. Sagittal **(A)** and transverse **(B)** images of the prostate of an intact male dog with signs of abdominal pain and fever. The prostate is markedly enlarged and deformed (arrows) because of multiple hypoechoic cavitary lesions, the largest reaching 4.4 cm in diameter. Ultrasound-guided aspiration of these cavitations revealed the presence of neutrophils with bacteria. C, descending colon.

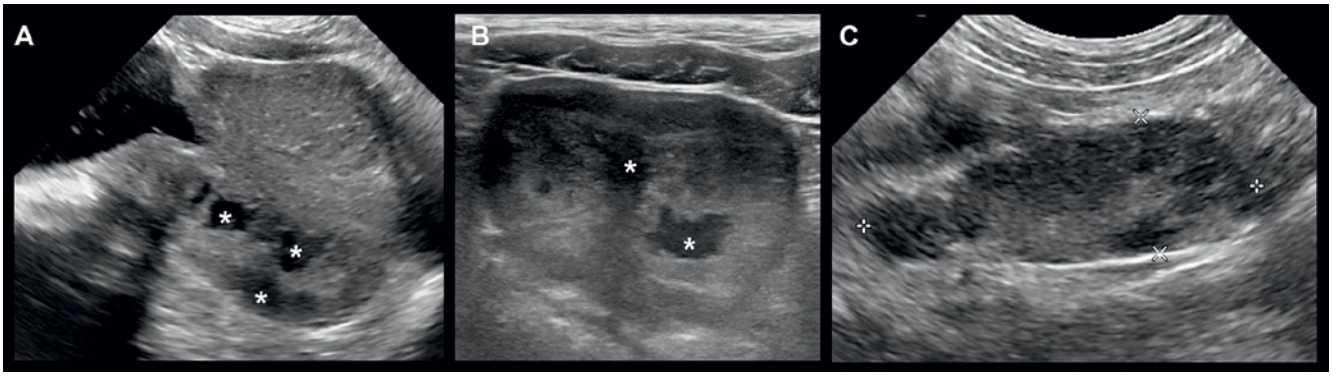


Figure 14.15. Fungal prostatitis (blastomycosis) in a 1.5-year-old recently castrated Labrador. The sagittal **(A)** and transverse **(B)** images show an enlarged, mildly irregularly marginated, inhomogeneous, and partially cavitated prostate (asterisk) with surrounding hyperechoic fat. Enlarged and inhomogeneous medial iliac lymph nodes were also noted, the right **(C)** measuring 3.75 cm in length and 1.3 cm in thickness. The scrotum (not shown) was swollen.

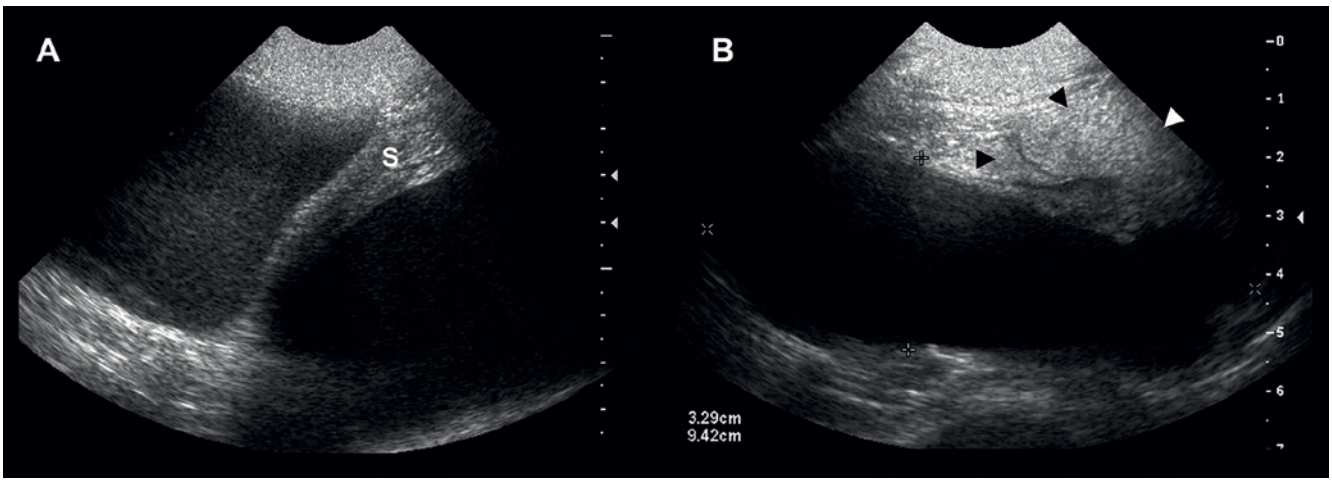


Figure 14.16. Paraprostatic cysts in a 4-year-old cryptorchid Labrador Retriever (A) and a middle-aged dog (B). (A) The transverse image was acquired at the level of the mid-abdomen. The fluid-filled structures were separate from the urinary bladder (not shown). A thick echogenic septum (S) separates a compartment filled with highly echogenic fluid (left) from one with less echogenic fluid (right). **(B)** The cyst (between the cursors) is seen as a tubular anechoic structure without a discernible wall extending cranially from the dorsal aspect of the hyperechoic prostate (arrowheads).

Vet-ebooks.com

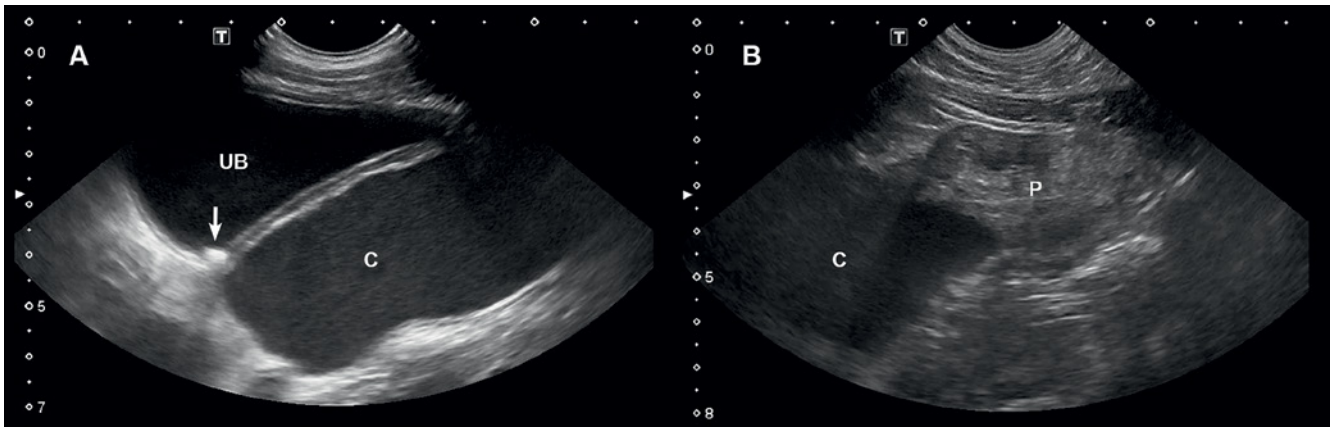


Figure 14.17. Paraprostatic cysts and acute prostatitis in an 7-year-old Bullmastiff. (A) A large cyst (C) is dorsal to the bladder (UB), which contains a small urolith in its dependent portion (arrow). The fluid inside the cyst is mildly echogenic due its proteinaceous content. **(B)** This cyst connects with the prostate (P), whichis moderately enlarged and heterogeneous.

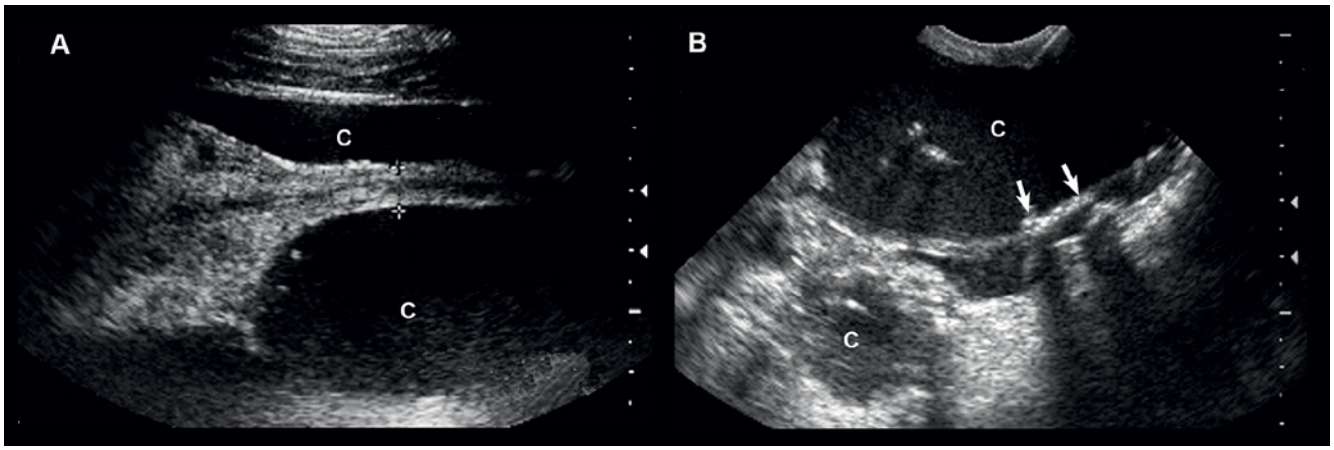


Figure 14.18. Complex paraprostatic cysts and suppurative prostatitis in a German Shepherd Dog. Numerous cysts (C) are in the mid- and caudal abdomen. **(A)** The cyst walls measure up to 6 mm thick (between the cursors). The echogenicity of cystic fluid ranges from anechoic to echogenic. **(B)** Mineralized foci are associated with the wall (arrows) and lumen of some of the cysts.

an undescended testicle may be difficult. The sensitivity of ultrasound for the identification of inguinal or abdominal cryptorchid testicles in dogs and cats is high (Felumlee et al. 2012; Hecht 2001). Occasionally, the gubernaculum testis is visualized. It appears as a tubular structure extending from the caudal pole of the retained testicle to the inguinal ring (Figure 14.28). Testicles located in the abdomen or inguinal region are predisposed to neoplastic transformation and can reach considerable size.

Testicular tumors are common in dogs. Leydig (interstitial) cell tumors are frequent incidental findings in descended testicles in older animals and may occur bilaterally. They are usually benign, although malignant form with cutaneous and muscles metastasis has been reported (Canadas et al. 2016; de Lima Nascimento et al. 2019; Kudo et al. 2019; Togni et al. 2015). Seminomas and Sertoli cell tumors can affect cryptorchid and descended testicles. Other tumor types are rare. All testicular tumors have the potential for hormone production and metastases. Testicular tumors in cryptorchid testicles tend to exhibit more malignant behavior than in descended testicles and occur in younger animals (Hecht 2001). Also, testicular atrophy may represent a risk factor for tumor development in dogs, as reported in man (Giudice et al. 2014). Ultrasonographic findings in testicular tumors range from circumscribed small nodules to large complex masses with disruption of normal testicular anatomy (Johnston et al. 1991a) (Figures 14.29–14.32). Contrast-enhanced ultrasound for evaluation of the testicles has been described

Vet-ebooks.com

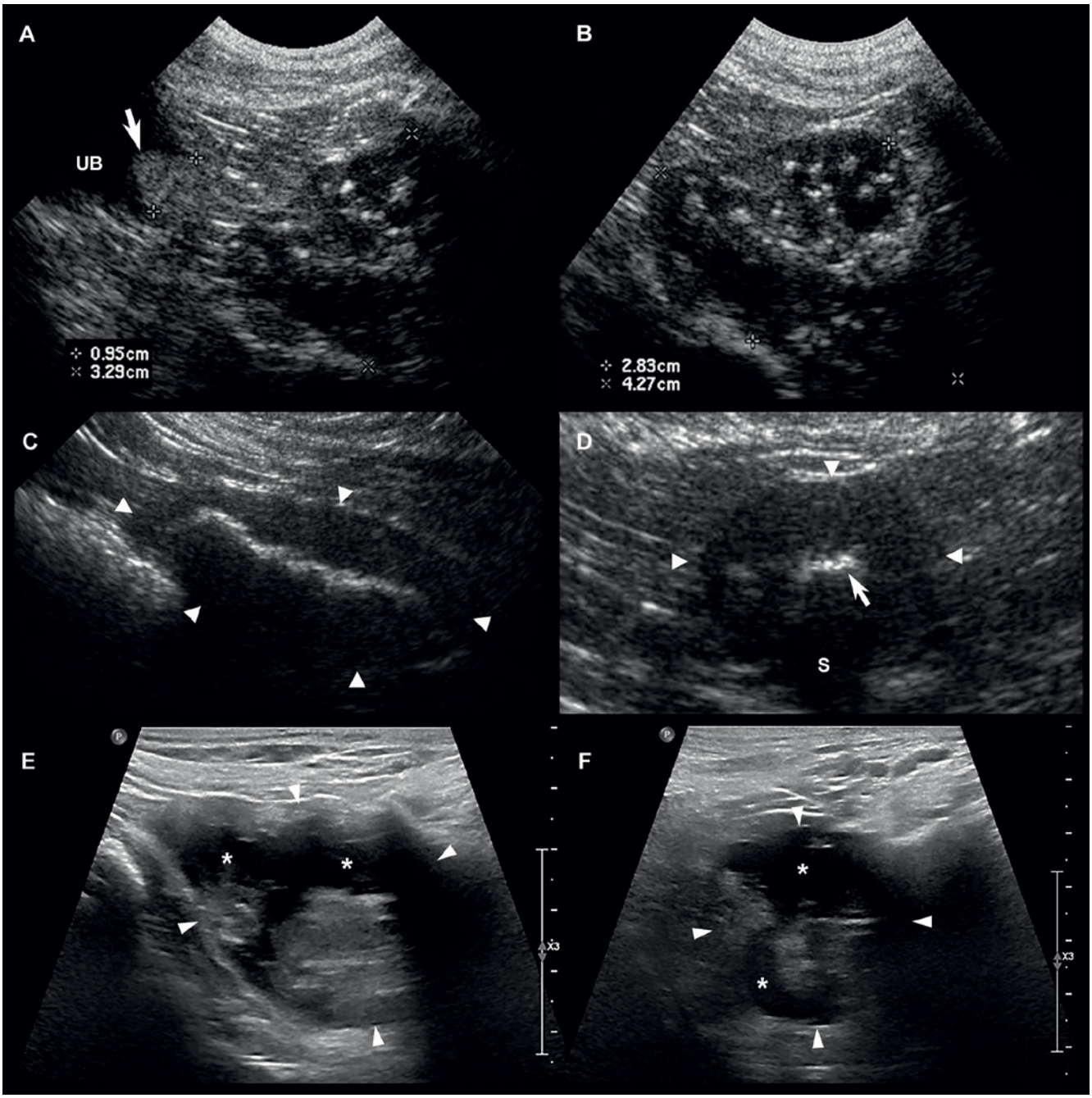


Figure 14.19. **Prostatic urothelial carcinomas in four dogs. (A, B)** Sagittal **(A)** and transverse **(B)** images of a prostatic adenocarcinoma in an older, neutered, large-breed dog. The prostate is enlarged, irregular, and relatively hypoechoic, with several small hyperechoic foci. A protuberance (arrow) is also seen projecting into the urinary bladder (UB) secondary to tumor invasion. **(C, D)** Sagittal **(C)** and transverse **(D)** images of transitional cell carcinoma, probably originating from the prostatic urethra, in a 12-year-old, neutered Labrador Retriever. The prostate (arrowheads) has retained a relatively normal shape but is large for a neutered dog. Prostatic parenchyma is hypoechoic. The centrally located, strongly hyperechoic line with distal acoustic shadowing (arrow, **S**) is consistent with urethral mineralization. **(E, F)** Sagittal **(E)** and transverse **(F)** images of a prostatic carcinoma with necrosis in a 14-year-old mixed breed dog. The patient was cryptorchid and presented with a markedly swollen prepuce, which was also diagnosed as a carcinoma (see Figure 14.57C, D). The prostatic gland (arrowheads) is enlarged and heterogeneous, with numerous hypoechoic to anechoic regions (*).

Vet-ebooks.com

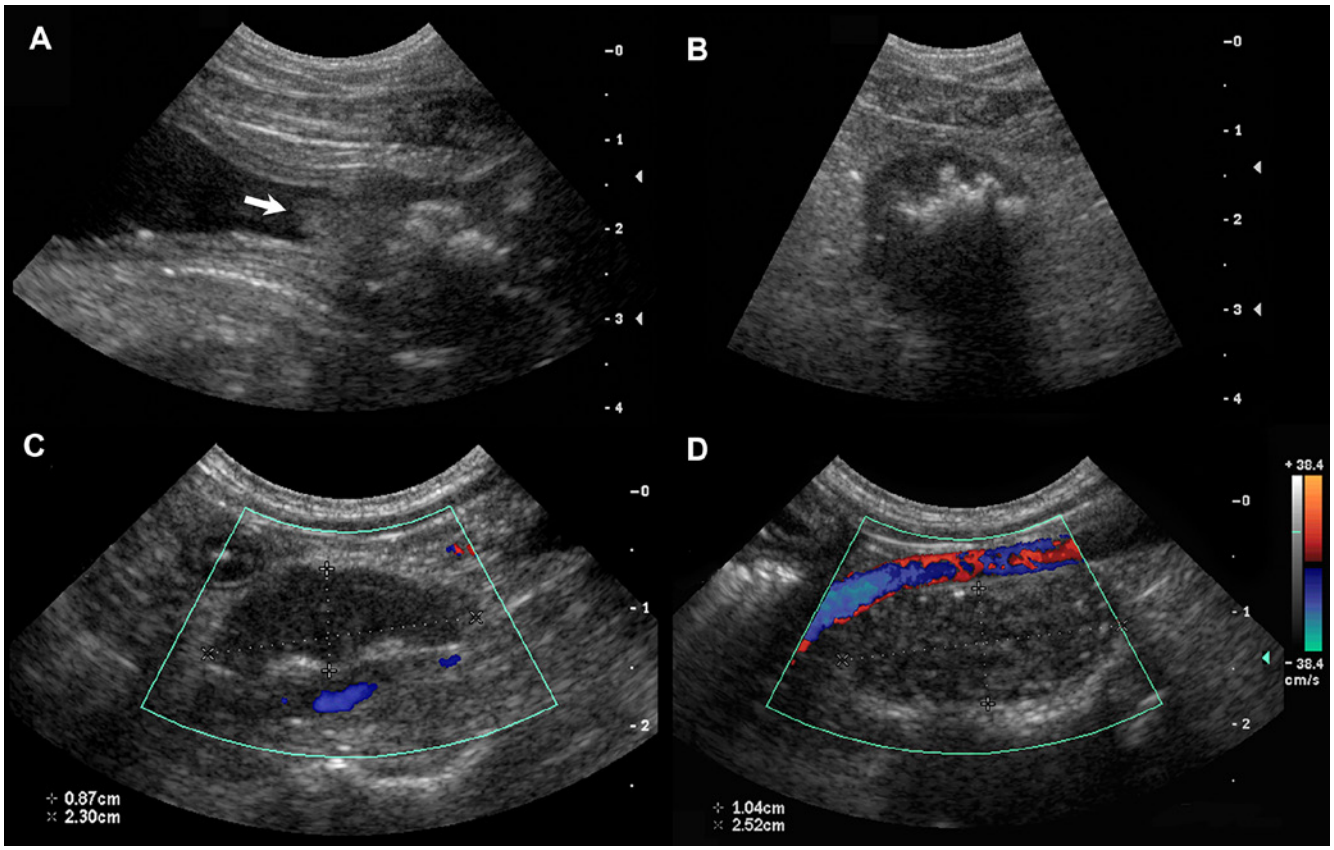


Figure 14.20. Transitional cell carcinoma and regional lymphadenopathy in an old, neutered dog with hematuria and dysuria. Sagittal **(A)** and transverse **(B)** images of the bladder neck and prostate. Strongly shadowing hyperechoic foci are noted in the prostate, and a soft-tissue projection extends into the bladder lumen (arrow). Sagittal images of right medial iliac **(C)** and internal iliac **(D)** lymph nodes, which appear enlarged and irregular. The medial iliac node **(C)** is relatively uniform and nearly anechoic in comparison with the internal iliac **(D)** node that is heterogeneous and coarse in echotexture. These lymph nodes are adjacent to the external and internal iliac vessels, respectively.

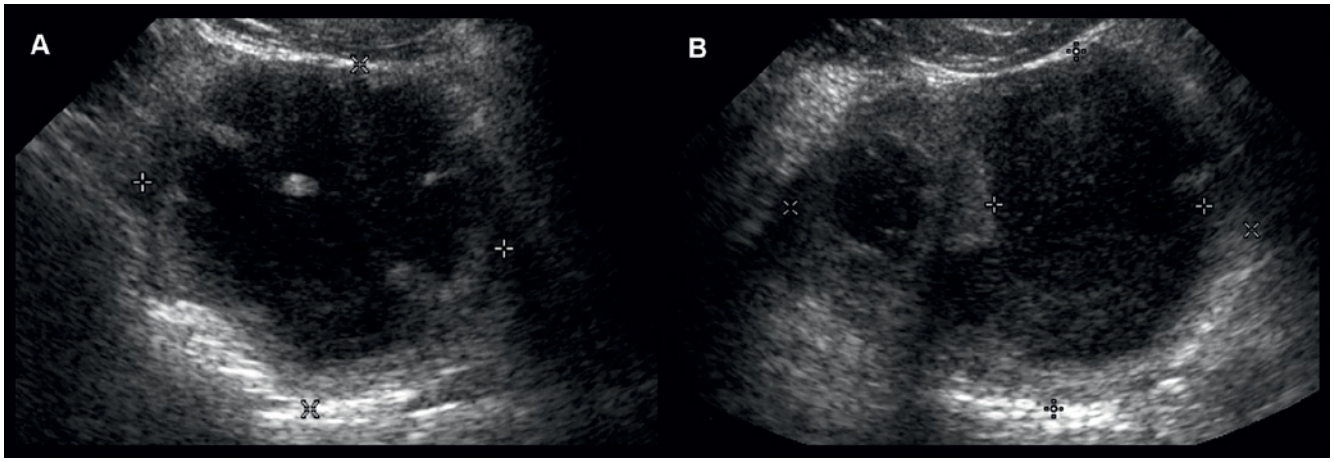


Figure 14.21. Prostatic hemangiosarcoma in a 10-year-old, neutered Greyhound. (A) Sagittal image. The prostate (between the cursors) is enlarged with echogenic margins and a central hypoechoic to anechoic area. **(B)** Transverse image. There is asymmetry and inhomogeneity of the prostatic lobes. The prostate (between the cursors) is of mixed echogenicity, with hypoechoic to anechoic cavitary areas.

Vet-ebooks.com

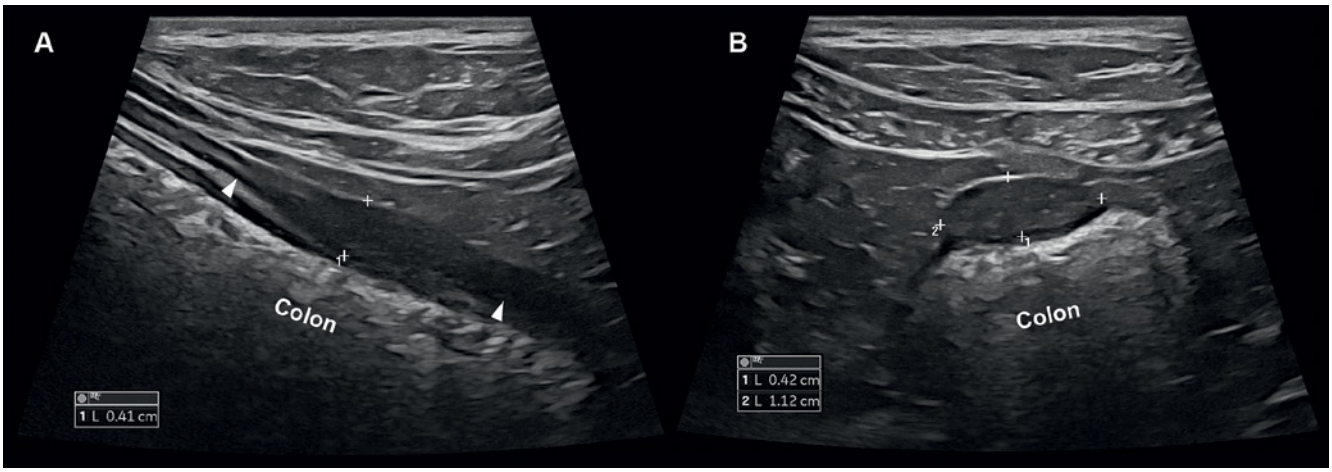


Figure 14.22. Atrophied prostate in a neutered 5-year-old Pomeranian. The prostate (between cursors) is hypoechoic and reduced in size in sagittal **(A)** and transverse **(B)** planes. The arrowheads point the urethra cranial and caudal to the prostate.

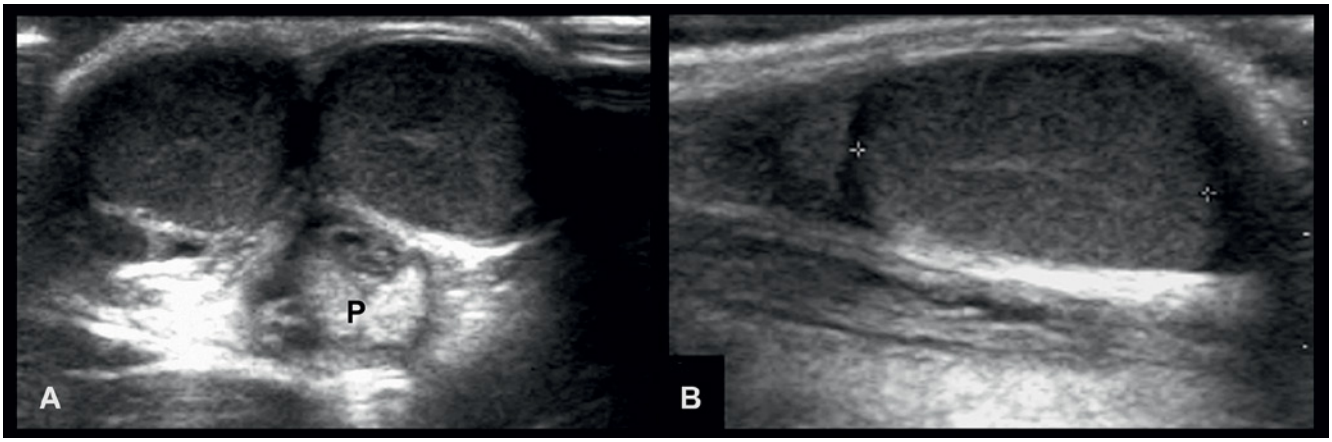


Figure 14.23. Normal testicles in a 3-month-old Pointer. The testicles (between the cursors) are small (less than 2 cm long), ovoid, and homogeneous. **(A)** Transverse sonogram of both testicles. Part of the penis (P) is visible in the far field. **(B)** Sagittal sonogram of the left testis (between the cursors). The mediastinum testis is seen. The head of the epididymis is visible on the left of the image.

Table 14.2
Testicular dimensions in healthy intact dogs and correlation to body weight

Body weight (kg)	Length (cm)	Width (cm)	Height (cm)	Mediastinal width (cm)
1–10	1.5–3.3	1.0–2.2	0.8–1.6	0.1–0.2
11–20	2.0–3.9	1.4–3.2	1.3–2.2	0.1–0.2
21–30	3.0–4.0	1.5–3.6	1.5–2.4	0.1–0.3
31–40	2.6 to >4.0[a]	1.7–3.7	1.6–3.2	0.1–0.3
>40	3.4 to >4.0[a]	2.6–3.8	1.6–3.0	0.1–0.3

[a]The transducer field of view was limited to 4 cm, and accurate measurements were not possible beyond that point. Source: Adapted from Hecht (2001).

Vet-ebooks.com

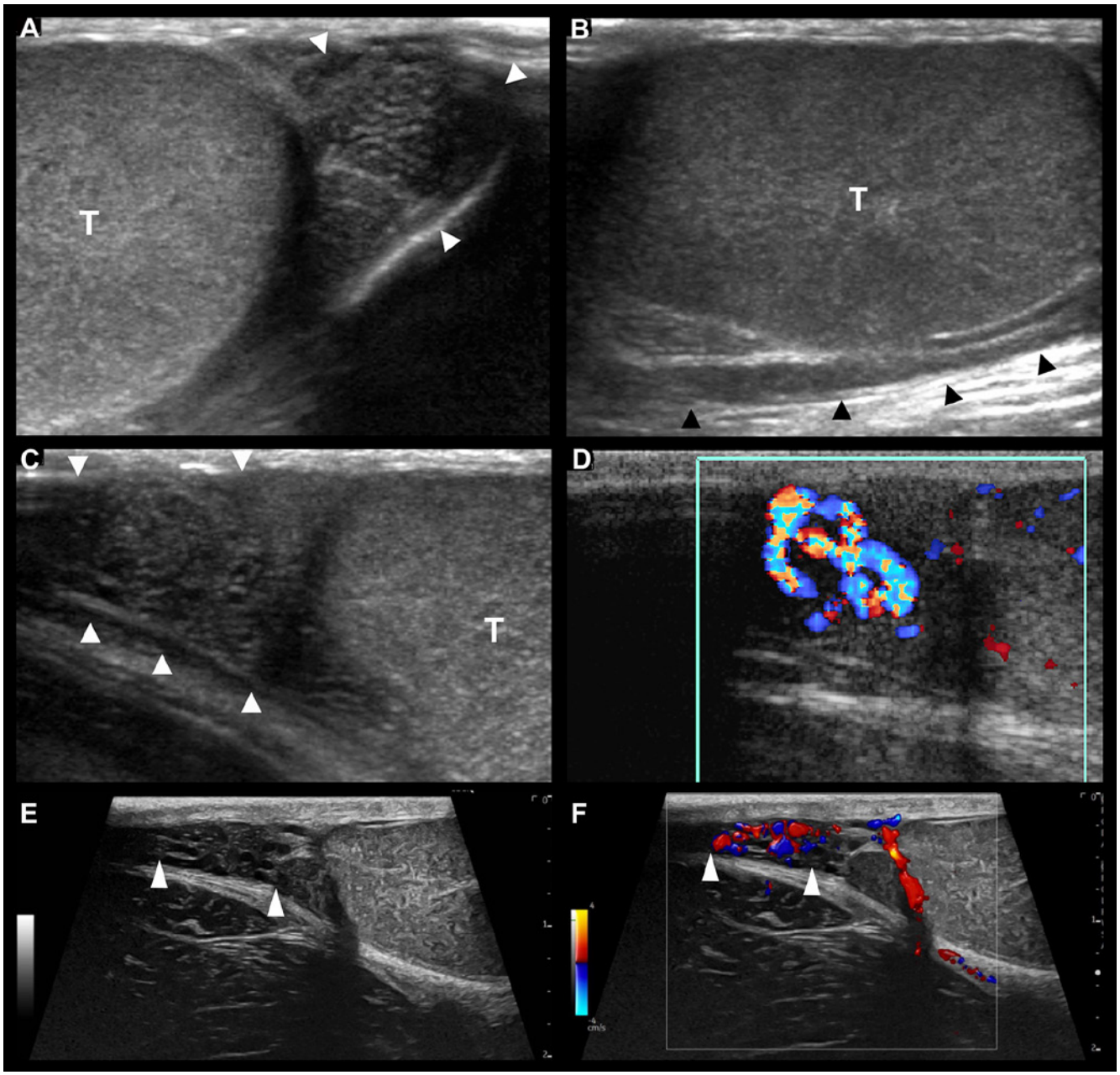


Figure 14.24. Normal epididymis and pampiniform plexus in two dogs. (A–D) 9-year-old mixed-breed dog. (A) Sagittal image of the epididymal tail (arrowheads). It is caudal to the testicle (T), hypoechoic, and has a coarse echotexture. **(B)** Parasagittal image of the testicle demonstrating the tubular body of the epididymis (arrowheads) dorsolateral to the testicle (T). **(C)** Sagittal image of the epididymal head and adjacent part of the spermatic cord (arrowheads), which appear hypoechoic and coarse in comparison with the cranial pole of the testicle (T). **(D)** Sagittal color Doppler image of part of the spermatic cord. Tortuous vessels of the pampiniform plexus are recognized by the color flow signal. **(E, F)** Sagittal B-Mode **(E)** and Color Doppler **(F)** images of the head of the epididymis and pampiniform plexus (arrowheads) in an 11-month-old Yorkshire Terrier show numerous tubular vascular structures cranial to the cranial pole of the testicle.

(Volta et al. 2014) and may help distinguish neoplastic and non-neoplastic lesions but is not widely used at this point.

Different tumor types cannot be distinguished ultrasonographically (Hecht et al. 2003; Pugh and Konde 1991). However, recent studies in dogs concluded that vascular pattern subtly differed between testicular tumor types (Orlandi et al. 2022) and showed an increased color Doppler flow in neoplastic testicular lesions compared to non-neoplastic lesions (Bigliardi

Vet-ebooks.com

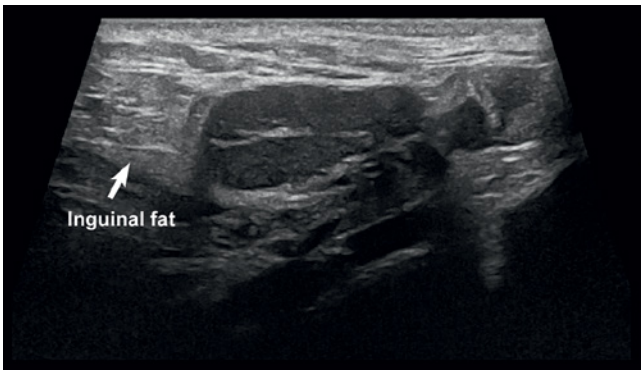


Figure 14.25. Inguinal cryptorchidism in a 5-month-old dog. The retained testicle is visible as an oval hypoechoic structure with a central hyperechoic line (mediastinum testis) in the inguinal region and is bordered by mildly hyperechoic fat.

et al. 2019). Concurrent prostatic changes such as BPH or squamous metaplasia are common, especially in hormone-producing tumors. Hyperestrogenism can also lead to contralateral testicular atrophy (Mattoon and Nyland 2021) and bone marrow suppression (Salyer et al. 2022; Sanpera et al. 2002; Withers et al. 2016). In case of metastatic neoplasia, enlarged medial iliac lymph nodes may be seen.

Tumors of the epididymis are rare and may result in generalized epididymal enlargement or focal mass lesions. Papillary carcinoma, fibroma/fibrosarcoma, and leiomyoma/leiomyosarcoma have been reported (Balao da Silvia et al. 2019; McCormack 1975). Other types of tumors are possible such as lymphoma and mast cell tumor (Figure 14.33).

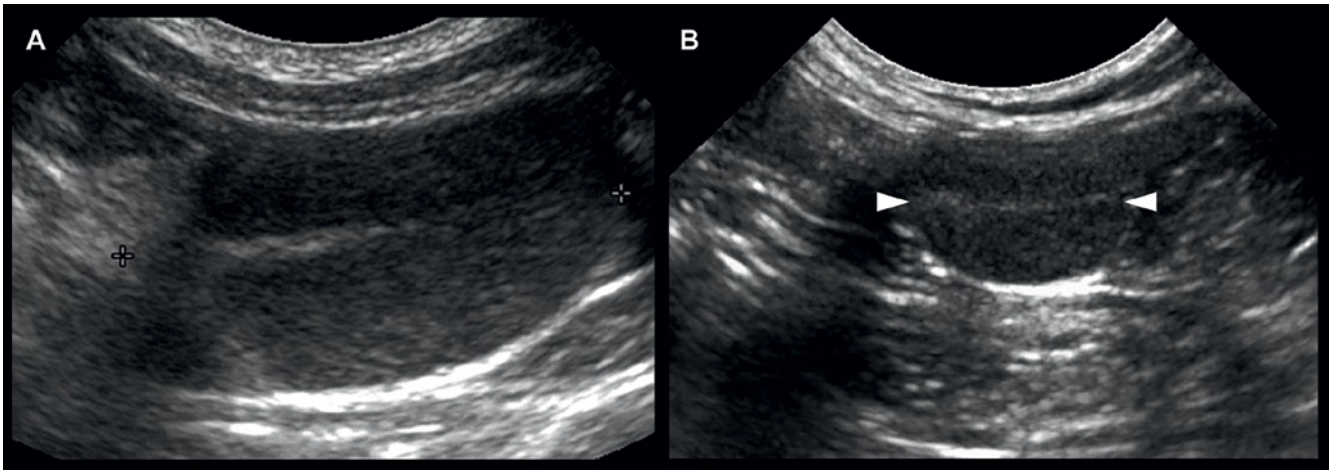


Figure 14.26. Abdominal cryptorchidism in two dogs. (A) The left testicle (between the cursors) in a 1-year-old Golden Retriever is intra-abdominal, small (3.1 cm long), hypoechoic, and of normal architecture. **(B)** The left testicle (between the cursors) in a 9-year-old Dachshund is intra-abdominal, small (1.4 cm long), and of normal architecture.

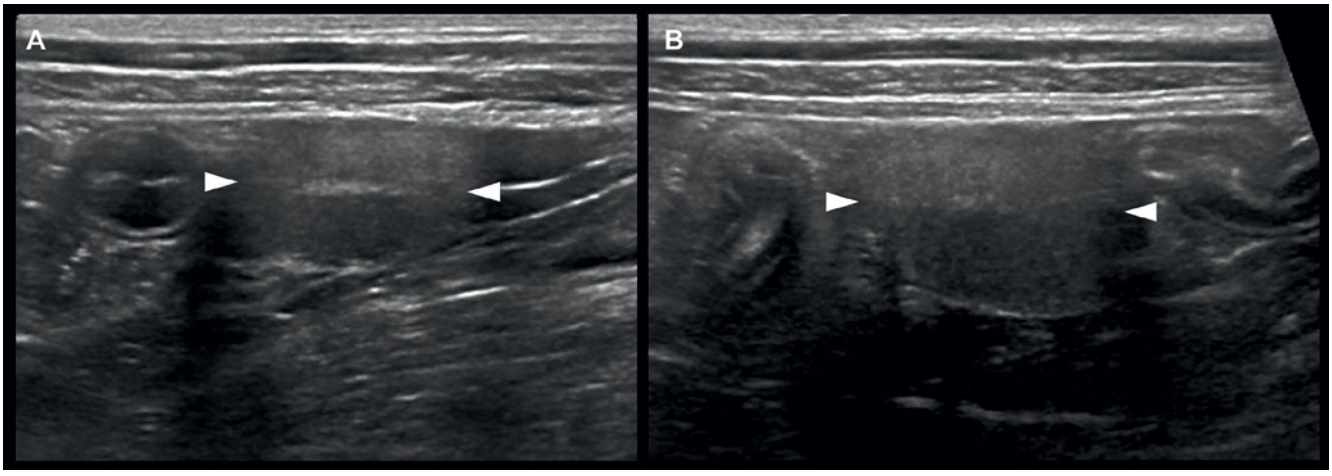


Figure 14.27. Abdominal bilateral cryptorchidism in a 3-year-old Weimaraner dog recently adopted with unknown history of castration. The left **(A)** and right **(B)** testicles were found on each side of the caudoventral abdomen. The mediastinum testis can be identified. Adjacent intestinal segments are visible.

Vet-ebooks.com

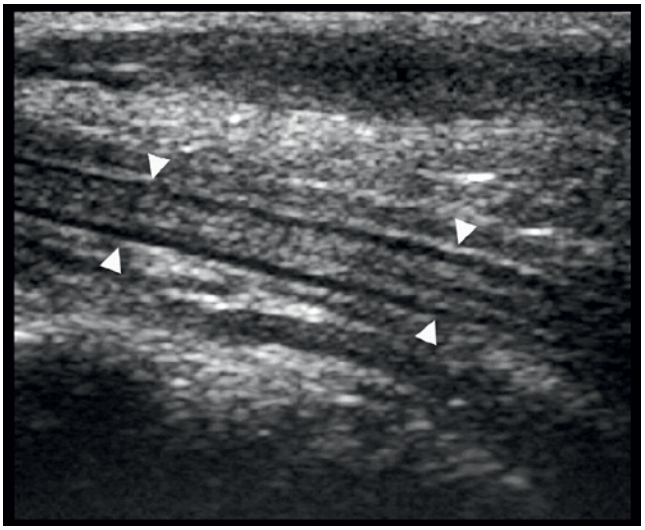


Figure 14.28. Prominent gubernaculum testis in a cryptorchid 5-month-old Mastiff. The gubernaculum (arrowheads) appears as tubular structure of 3 mm diameter and was seen extending from the caudal pole of the intra-abdominal right testicle to the inguinal ring.

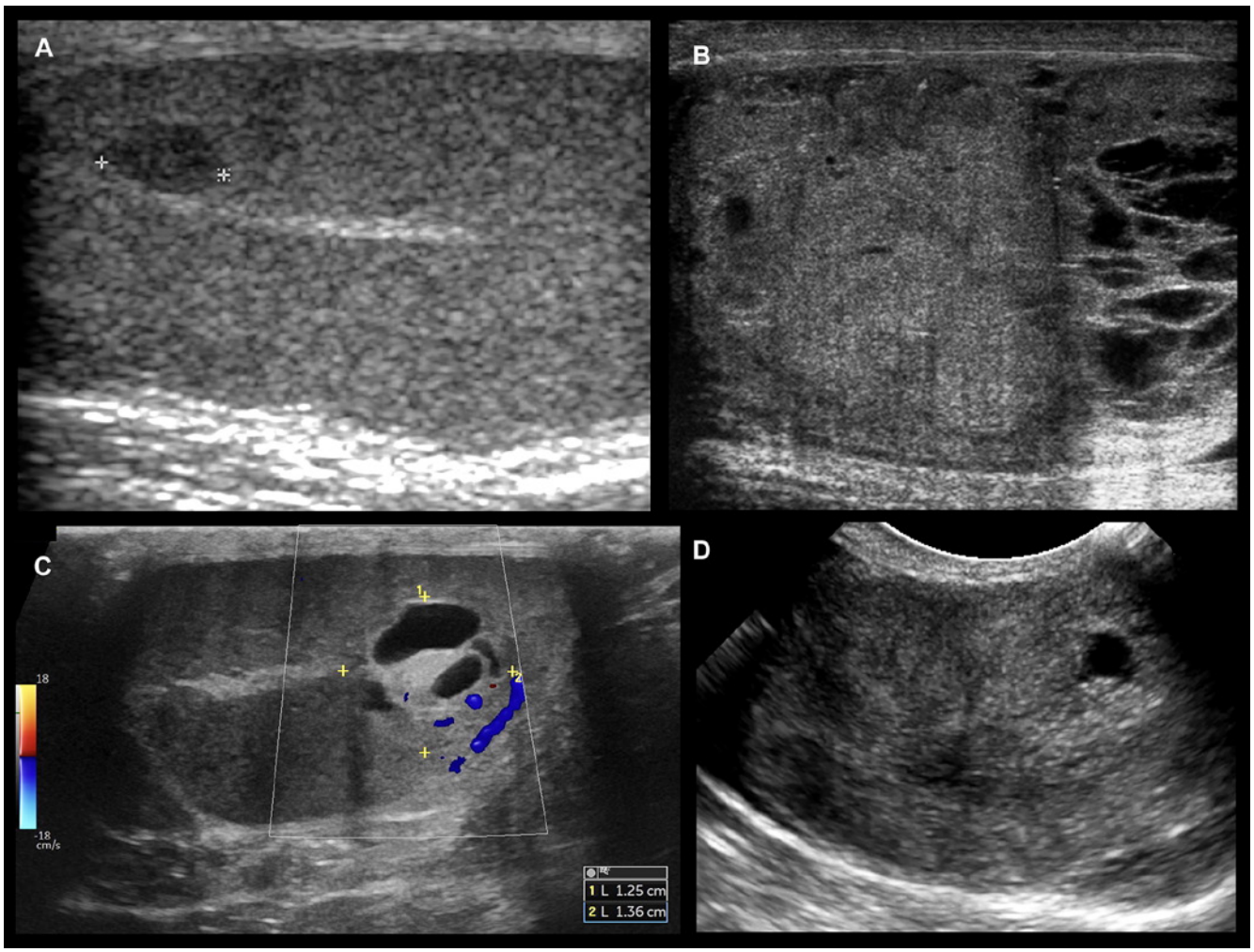


Figure 14.29. Leydig cell tumors in four dogs. (A) Sagittal image of the left testicle in a 15-year-old Labrador Retriever. A hypoechoic nodule of 5 mm diameter (between the cursors) is associated with the testicular parenchyma adjacent to the linear hyperechoic mediastinum testis. **(B)** Sagittal image of the left testicle in a 10-year-old Boxer. The testicle is enlarged and of heterogeneous echotexture with complete obliteration of normal testicular parenchyma and large cavitations in the caudal part. **(C)** Sagittal image of the left testicle in a 9-year-old Husky. A large mixed echogenic and cavitary nodule of approximately 1.5 cm diameter is visible at the caudolateral pole of the testicle. **(D)** Sagittal image of the left testicle in a 13-year-old sheltie. The testicular parenchyma is of mixed echogenicity, the testicle has an irregular margin, and the mediastinum testis is not visible.

Vet-ebooks.com

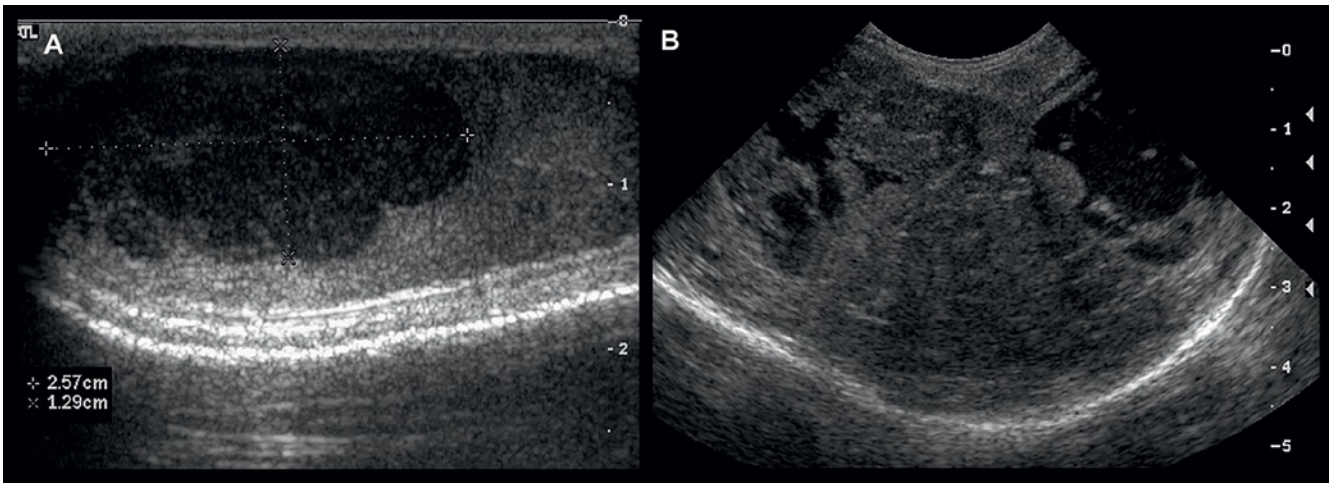


Figure 14.30. **Seminomas in two dogs. (A)** Sagittal image of the left testicle in an 8-year-old large-breed dog. An irregular, but well-defined, hypoechoic nodule measuring 2.6 × 1.3 cm is noted within the testicle (between the cursors). **(B)** Sagittal image of the left testicle in a 10-year-old Labrador Retriever with an enlarged, firm scrotum. The testicular parenchyma is completely replaced by an inhomogeneous mass with several irregular cavitations containing anechoic to echogenic fluid.

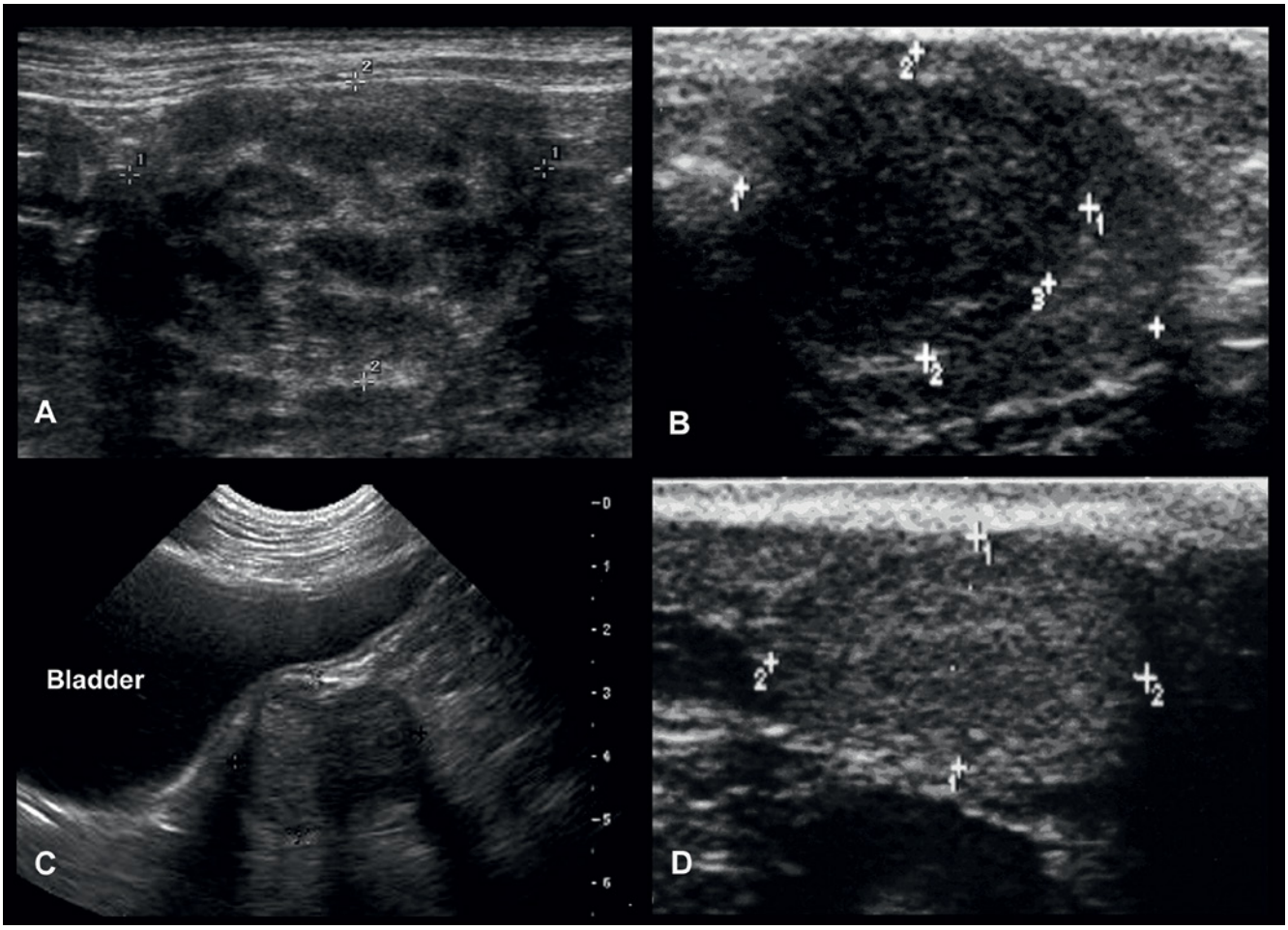


Figure 14.31. **Sertoli cell tumors in four dogs. (A)** Sagittal image of a left abdominal cryptorchid testicle (between the cursors) in a 6-year-old Jack Russell Terrier. The testicle is enlarged (3.4 × 2.6 cm) and heterogeneous. **(B)** Transverse image of a right inguinal cryptorchid testicle in an 8-year-old mixed-breed dog. A 1.9 × 1.8 cm hypoechoic nodule (between the cursors) is associated with the testicle. **(C)** Sertoli cell tumor of a retained right testicle in an 8-year-old Boxer. An echogenic mass of approximately 2.5 cm diameter dorsal to the bladder is associated with strong edge shadows. **(D)** Sagittal image of the left testicle in a 12-year-old West Highland White Terrier. The testicle is within the scrotum and of normal size and shape. The testicular parenchyma is of mixed echogenicity, and the mediastinum testis is not visible.

Vet-ebooks.com

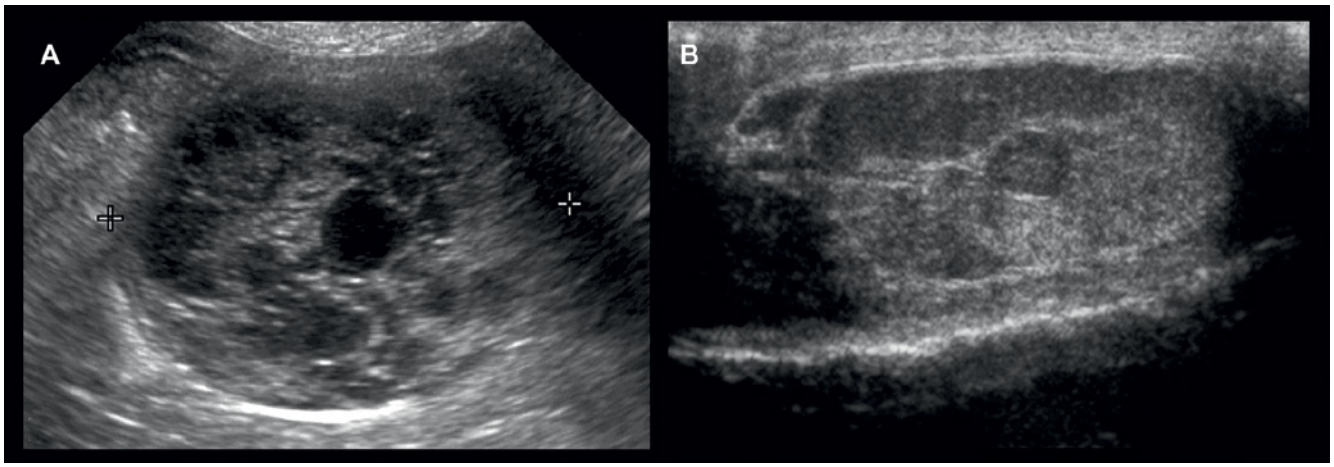


Figure 14.32. **Mixed testicular tumors in two dogs. (A)** Mixed tumor (seminoma and Sertoli cell tumor) of an abdominal cryptorchid testicle in a 13-year-old Shetland. The enlarged (4.5 cm), mixed echogenic testicle (between the cursors) has multiple anechoic areas. **(B)** Mixed tumor (Leydig cell tumor and seminoma) of a scrotal testicle in an 8-year-old Golden Retriever. The testicle is relatively small, heterogenous, and a mediastinum testis is not identified.

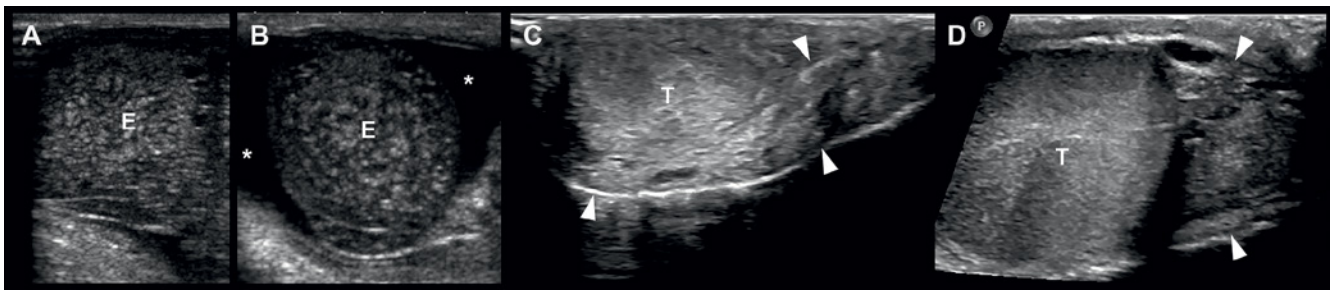


Figure 14.33. **Tumors of the epididymis in two dogs. (A, B)** Lymphoma in a 5-year-old Rottweiler. Sagittal **(A)** and transverse **(B)** images of the head of the right epididymis **(E)** show marked diffuse enlargement and a coarse echotexture. A small volume of fluid (*) is present adjacent to the epididymis, consistent with a mild hydrocele. **(C, D)** Mast cell tumor in a 15-year-old mixed breed dog. Sagittal **(C)** and transverse **(D)** images show diffuse enlargement and heterogeneity of the entire epididymis (arrowheads). T, testicle.

Orchitis and **epididymitis** may occur after hematogenous spread of infectious organisms, may result from urinary tract or prostatic inflammation/infection, or may be caused by scrotal trauma. Autoimmune orchitis has also been reported (Davidson et al. 2015; Donnelly et al. 2016). Inflammatory scrotal disorders exhibit variable ultrasonographic characteristics, ranging from diffuse echogenicity changes of the testicle and/or epididymis to complex masses and anechoic areas subsequent to abscess formation (Hecht et al. 2003; Ober et al. 2004; Pugh and Konde 1991) (Figures 14.34–14.37). Secondary fluid accumulation within the scrotum (Figures 14.37, 14.38) or scrotal thickening may be present. Whereas testicular and epididymal size increases in acute inflammation, it decreases with chronicity.

Testicular or epididymal cysts are occasional incidental findings. They appear as anechoic, well-circumscribed, rounded areas, often with distal acoustic enhancement (Figures 14.39, 14.40). Abnormal focal or generalized enlargement (**ectasia**) **of epididymal ducts** is occasionally noted and is of uncertain etiology and significance (Figure 14.41). **Vas deferens enlargement** and vasitis secondary to chronic exogenous estrogen exposure have been reported in a dog (Harris et al. 2022).

Testicular torsion most commonly affects retained neoplastic testicles (Pearson and Kelly 1975). In this instance, the ultrasonographic examination shows an abdominal mass of variable size and echogenicity, with decreased or absent blood flow on color Doppler examination (Hecht 2001; Miyabashi et al. 1990) (Figure 14.42). Intra-abdominal and intrascrotal torsion of non-neoplastic testicles and vascular compromise of other etiology (infarction or space-occupying lesions within the inguinal ring) are rare (Hecht et al. 2004; Slaughter et al. 2022) (Figures 14.43, 14.44).

Vet-ebooks.com

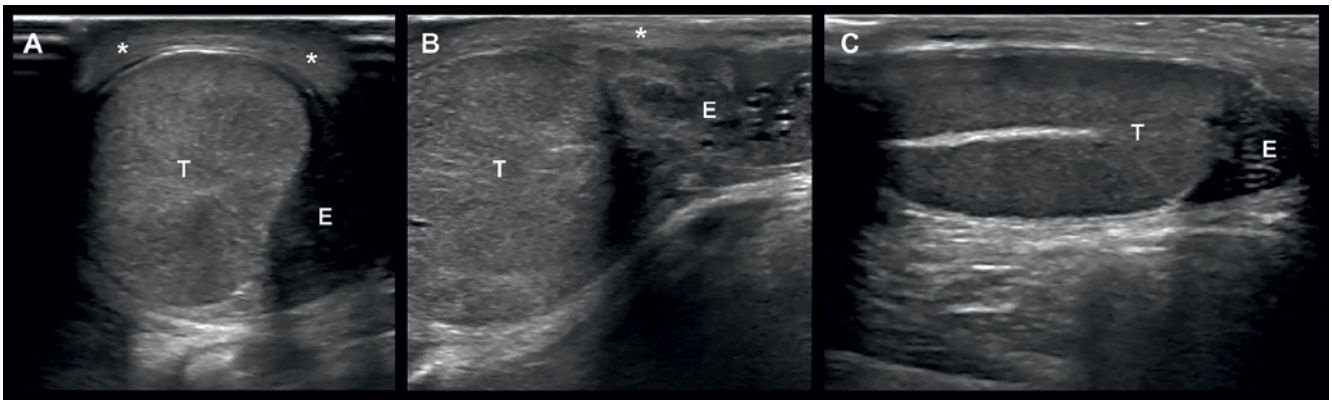


Figure 14.34. Severe, necrosuppurative and edematous orchitis, epididymitis, and vasitis/funiculitis in a 7-year-old Springer Spaniel with left testicular swelling. Sagittal **(A)** and transverse **(B)** images of the left testicle and epididymis. The testicle (T) is enlarged and mildly heterogeneous, with disruption of normal architecture, compared to the right testicle. The epididymis (E) is also enlarged and appeared hypervascular on color Doppler (not shown). The vas deferens was swollen as it entered the abdominal cavity. Notice the thickened scrotum (*). **(C)** The right testicle (T) and epididymis (E) are normal.

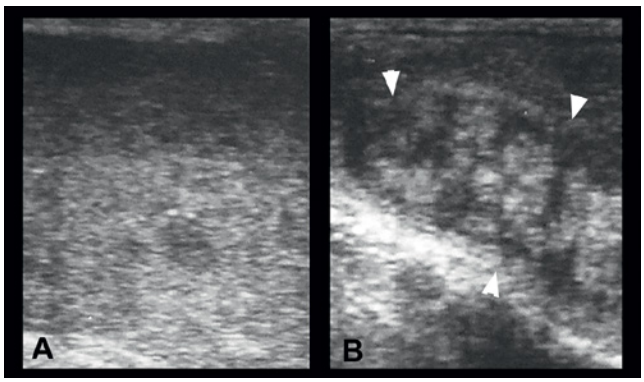


Figure 14.35. Fungal orchitis and epididymitis (blastomycosis) in a 3-year-old Walker hound. Sagittal images of the right testicle **(A)** and head of the epididymis **(B)** show testicular and epididymal (arrowheads) enlargement and inhomogeneity.

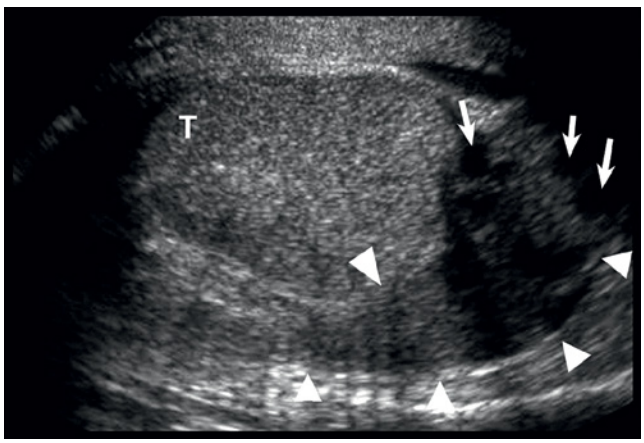


Figure 14.36. Epididymitis in a 9-year-old Labrador Retriever. On the parasagittal image of the left testicle, the epididymis (arrowheads) is larger than usual and of mixed echogenicity. Several anechoic areas are noted in the tail of the epididymis (arrows), which may represent cysts, small abscesses, or dilated ducts. The testicle (T) is within normal limits for size and echotexture.

Depending on the degree and duration of vascular occlusion, the affected testicle may appear hyperechoic or hypoechoic, increased, normal or decreased in size, with initially normal architecture. Concurrent abdominal or scrotal effusion is common, especially in acute cases.

Testicular atrophy may have several causes, such as thermal insult (e.g., in cryptorchid testicles), previous orchitis, hormonal influences, degenerative (age-related) changes, or vascular compromise (Donnelly et al. 2016). Atrophic testicles are small and hypoechoic but generally maintain their

Vet-ebooks.com

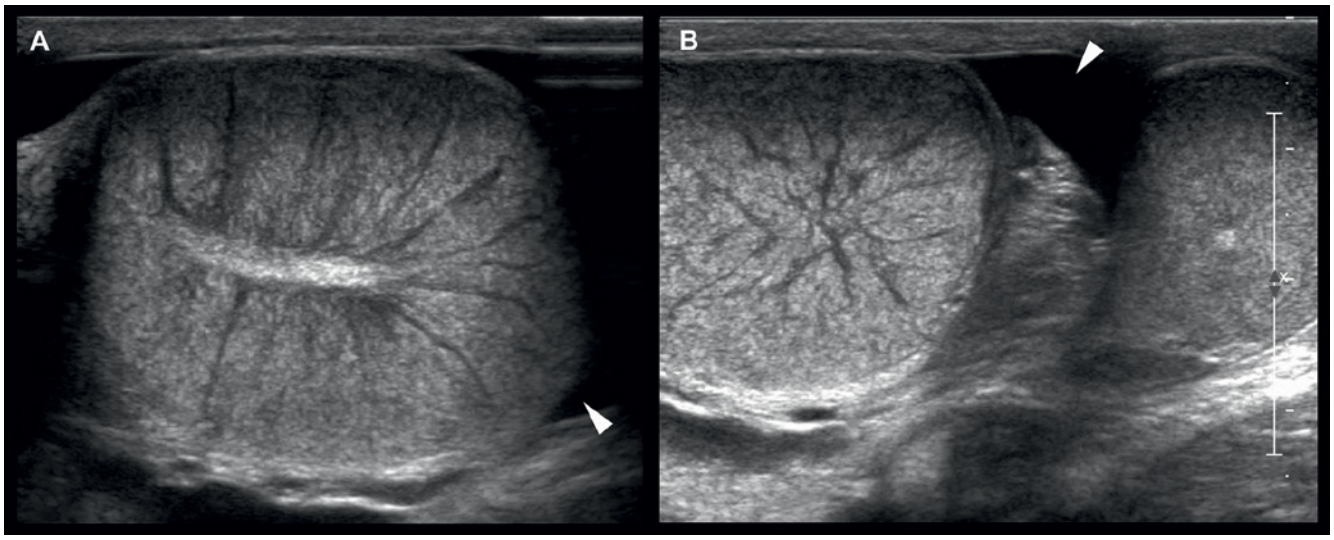


Figure 14.37. Severe orchitis in a 9-year-old Glen of Imaal Terrier. (A) The sagittal image shows an enlarged and hyperechoic right testis with a stellar pattern, corresponding to the severe parenchymal edema histologically reported. **(B)** The transverse image of both testicles shows the size and echogenicity discrepancy. A moderate amount of fluid (arrowhead) is present around the affected testis and epididymis. No infectious organisms were found.

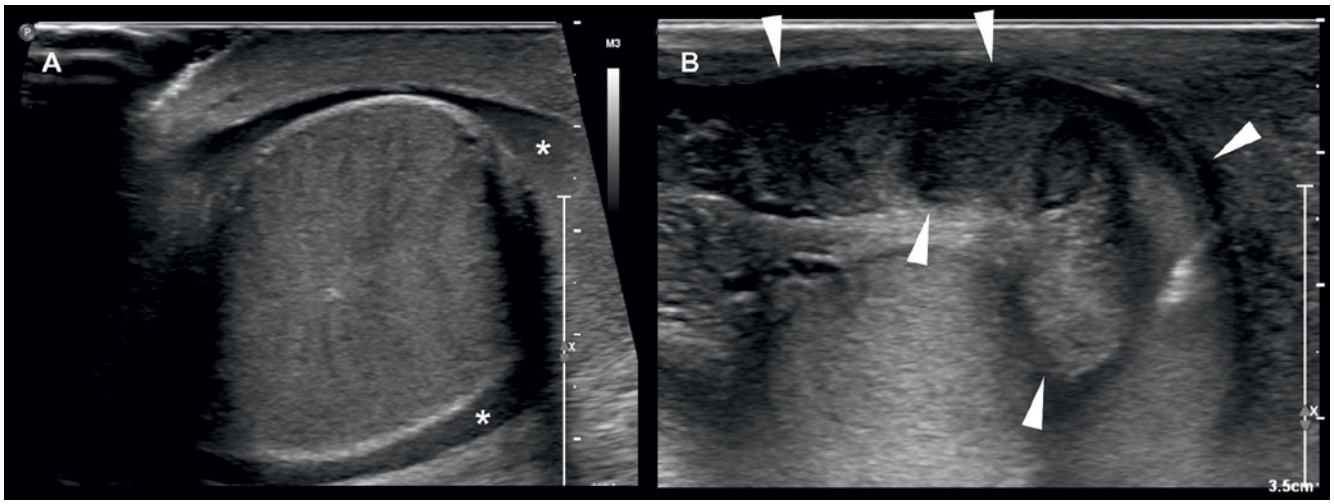


Figure 14.38. Severe bacterial orchitis and epididymitis in an 8-year-old Labrador Retriever. (A) The oblique image of the scrotum shows a swollen testis with a stellate echopattern, which is surrounded by markedly echogenic scrotal effusion (*). **(B)** On the oblique/dorsal plane image of the scrotum marked diffuse thickening of the epididymis is noted (arrowheads).

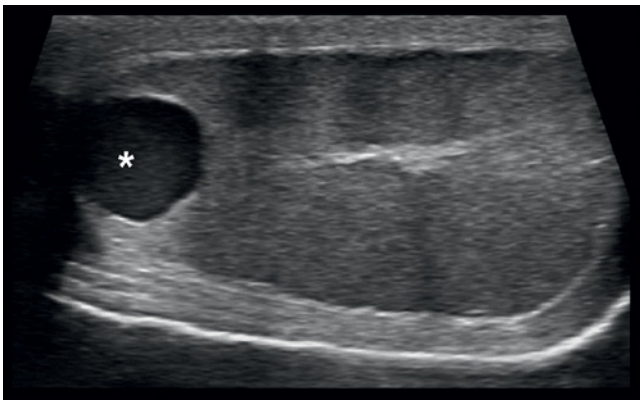


Figure 14.39. Cyst associated with the cranial pole of the right testicle in a dog. A round structure of 5 mm diameter containing a mildly echogenic fluid delineated by a thin wall is present in the testicular parenchyma.

Vet-ebooks.com

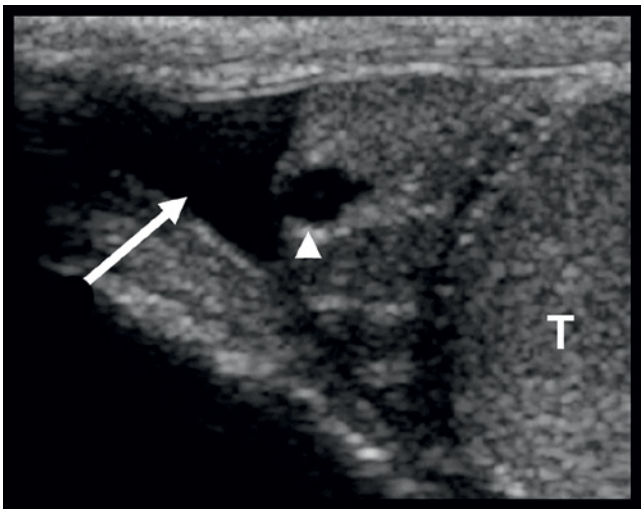


Figure 14.40. Epididymal cyst and mild hydrocele in a 7-year-old mixed-breed dog. An anechoic structure of approximately 3 mm diameter is associated with the head of the epididymis (arrowhead), just cranial to the testicle (T). The triangular anechoic area cranial to the head of the epididymis is consistent with a small volume of intrascrotal fluid (arrow).

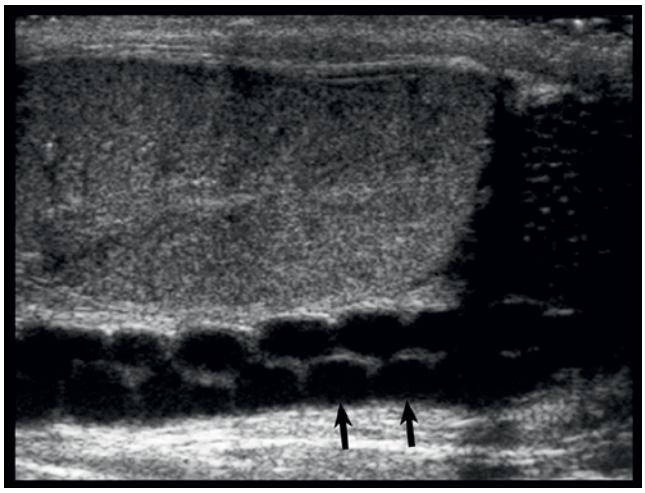


Figure 14.41. Marked diffuse duct ectasia of the epididymis in a 9-year-old Weimaraner. The sagittal image of the right testicle shows distinct tubular structures (arrows) filled with anechoic fluid throughout the tail and body of the epididymis.

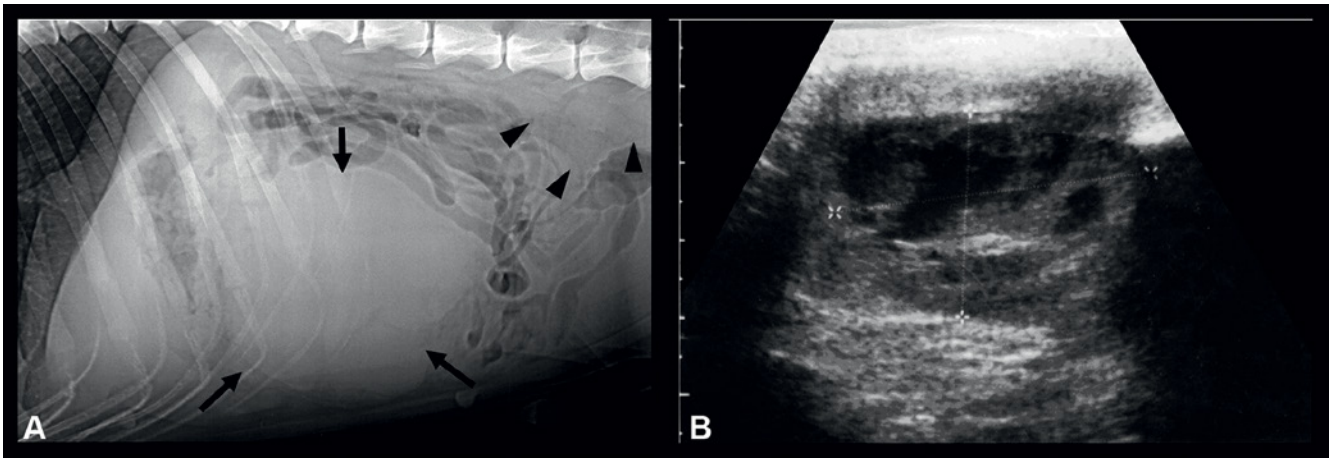


Figure 14.42. Intra-abdominal torsion of a retained neoplastic testicle (Sertoli cell tumor) in a 9-year-old German Shepherd Dog. (A) The lateral abdominal radiograph shows a lobulated soft-tissue mass of >20 cm diameter associated with the cranial ventral abdomen (arrows). Enlarged sublumbar lymph nodes (arrowheads) are consistent with metastatic disease. Prominent mammillae are noted, consistent with feminization caused by the hormone-producing tumor. **(B)** The ultrasonographic image shows a mixed echogenic mass (only shown in part).

normal architecture (Figures 14.45, 14.46; see also Figures 14.25–14.27).

Testicular microlithiasis is rare and mostly reported in human medicine. It represents microcalcification deposits in the lumen of the seminiferous tubules and typically affects both testicles. It is generally an incidental finding but considered a marker of tubular degeneration. On ultrasound it is seen as multiple strongly hyperechoic foci within the testicular parenchyma (Figure 14.47).

Whereas ultrasonography plays a major role in assessing human patients with **scrotal trauma**, it is rarely performed for this indication in dogs. Possible findings include scrotal hematoma, hematocele, contusion, intratesticular hematoma, and testicular rupture. **Scrotal hematomas** with accumulation of

Vet-ebooks.com

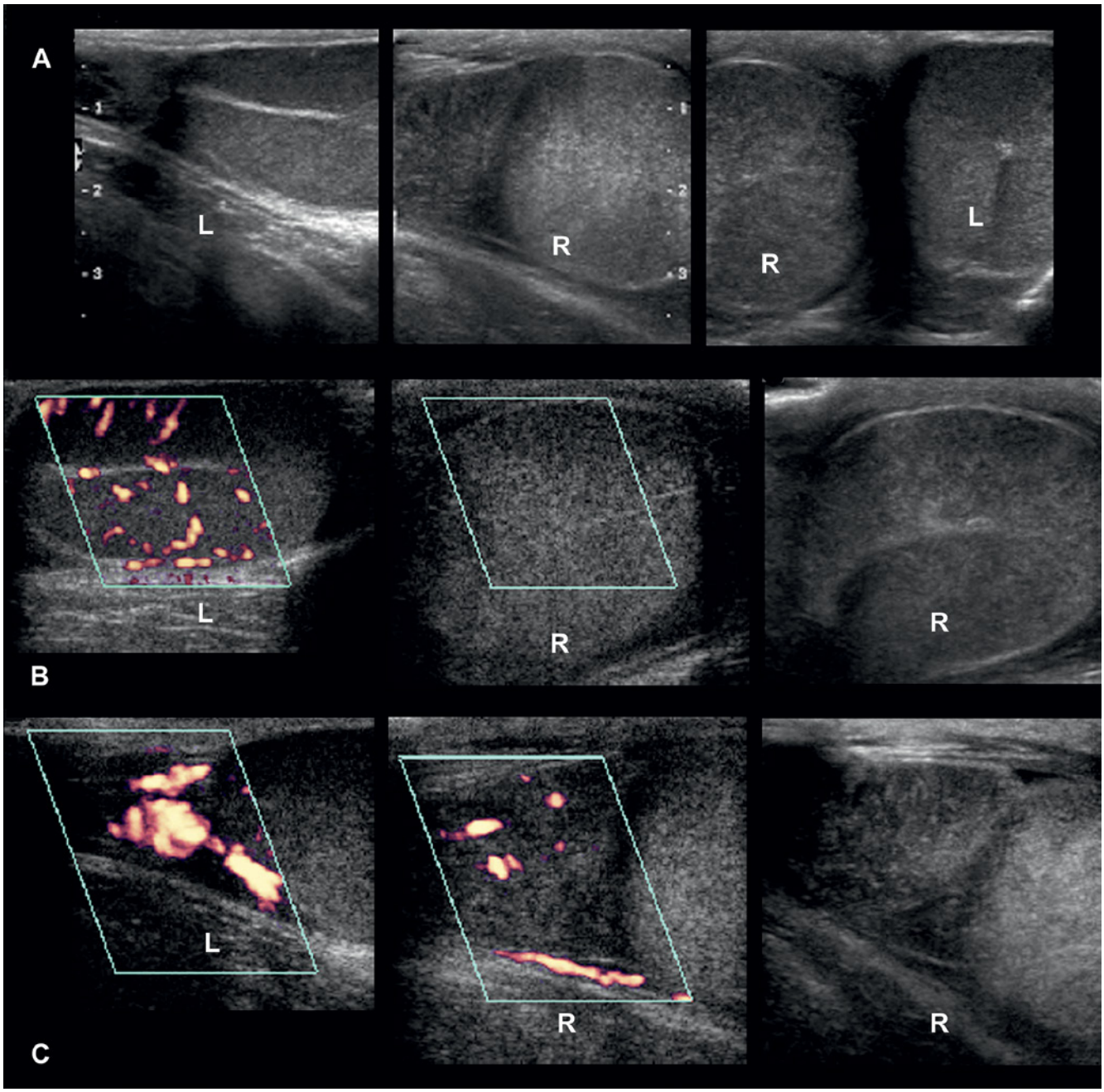


Figure 14.43. **Scrotal testicular torsion in a 1-year-old Border Collie.** The left testis (L) is normal, whereas the right testicle (R) has hemorrhage and numerous thrombi, compatible with torsion and underlying orchitis and epididymitis. **(A)** The left and right testicles are imaged side by side. The right testicle and epididymis are notably larger than the left. **(B)** Comparative color Doppler signal between the left (normal) and the right testis (no flow). **(C)** Comparative color Doppler signal between the left (normal) and the right epididymis (poor flow).

blood within the scrotal soft tissues manifest as space-occupying lesions of variable echogenicity that displace the testicle and epididymis (Figures 14.48, 14.49). With **hematocele** formation, there is intrascrotal fluid accumulation of variable echogenicity. **Testicular contusions** and **hematomas** appear as diffuse echogenicity changes to the testicular parenchyma or mass lesions of variable echogenicity. Differentiation from testicular lesions of inflammatory or neoplastic etiology is mainly based on medical history rather than ultrasonographic characteristics. Inhomogeneous echotexture of the testicular parenchyma with loss of contour definition indicates testicular rupture.

Vet-ebooks.com

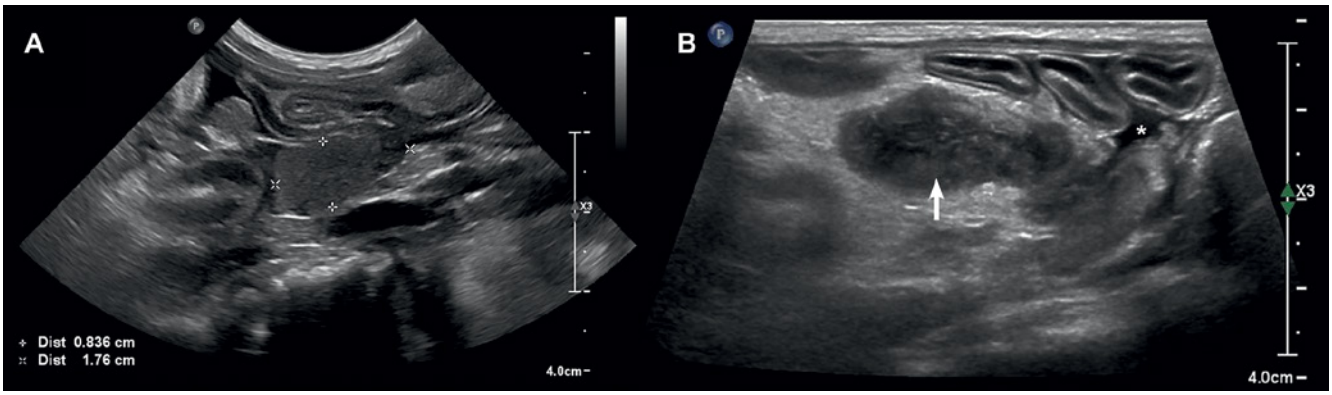


Figure 14.44. Intra-abdominal torsion of an immature testicle in a 3-month-old, bilaterally cryptorchid Boxer. (A) Sagittal sonogram of the right intra-abdominal immature testicle. **(B)** Sagittal sonogram of the left intra-abdominal and torsed testicle (arrow). The testicle is deformed and inhomogeneously hypoechoic. It is surrounded by hyperechoic fat and a scant amount of effusion (*) is noted in the abdomen.

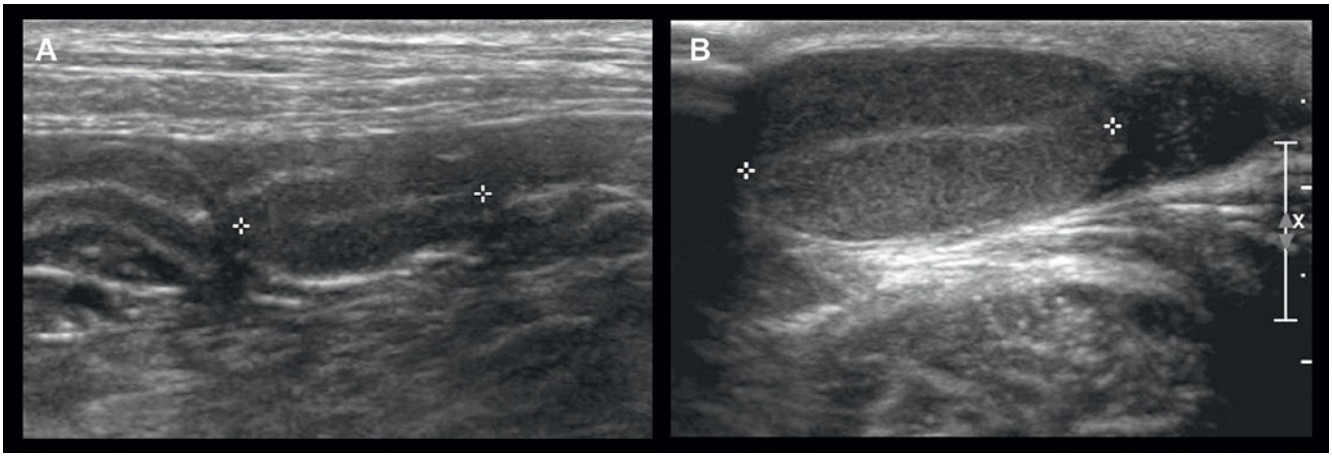


Figure 14.45. Testicular atrophy in a 1.5-year-old, right-sided cryptorchid Shi Tzu. On the sagittal image, the right testicle (**A,** between cursors) is small (1.4 cm long) while the left scrotal testicle (**B**, between cursors) is normal in size (2.2 cm long).

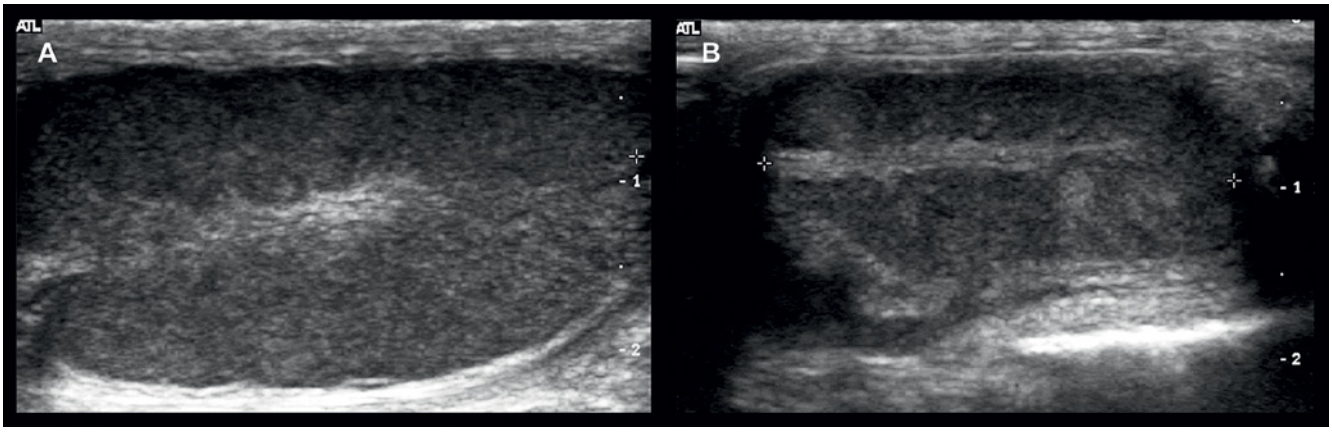


Figure 14.46. Testicular atrophy of unknown etiology in a 12-year-old Doberman. (A) Sagittal image of normal right testicle. The testicle measures 3.8 cm long (between the cursors), is of normal medium echogenicity, homogeneous, and with centrally located linear hyperechoic mediastinum testis. **(B)** Sagittal image of the atrophic left testicle. The testicle is smaller than the right (2.7 cm long [between the cursors]), hypoechoic, and slightly inhomogeneous. The centrally located mediastinum testis is visible.

Vet-ebooks.com

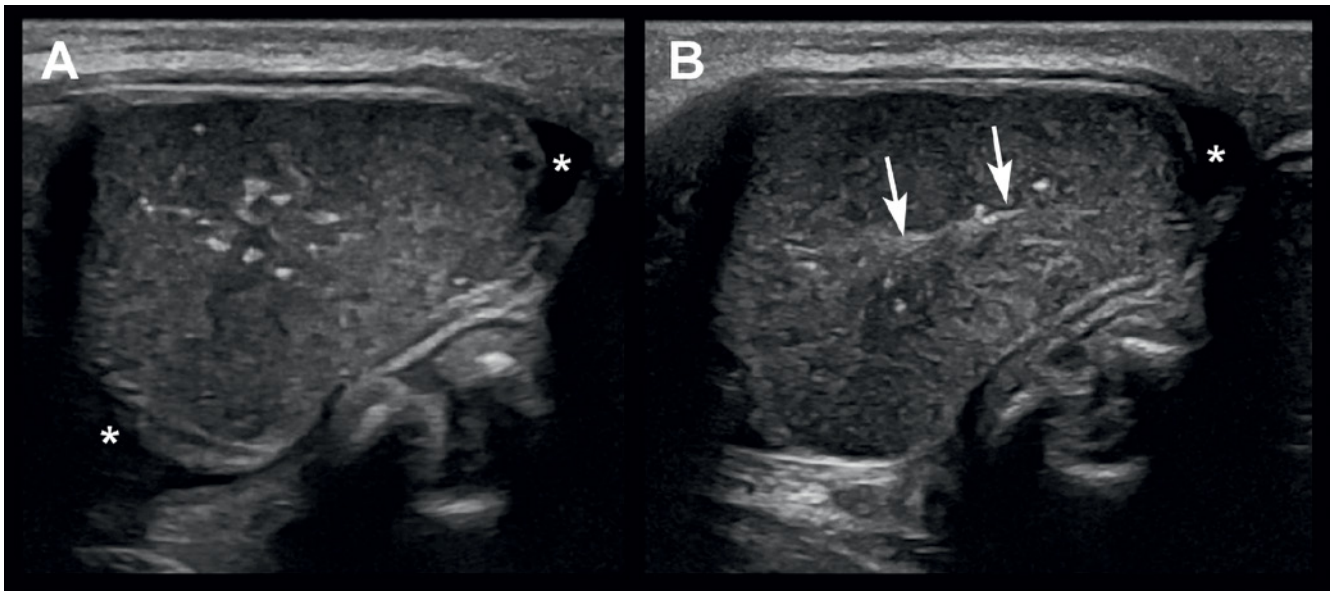


Figure 14.47. Microcalcification/microlithiasis of the testicles in a 9-year-old Bichon Frise. (A) Sagittal image. **(B)** Transverse image. Multiple punctate hyperechoic foci are visible in both testicles, some distributed in a linear/branching pattern (arrows) consistent with microlithiasis (microcalcification deposits in the lumen of the seminiferous tubules).

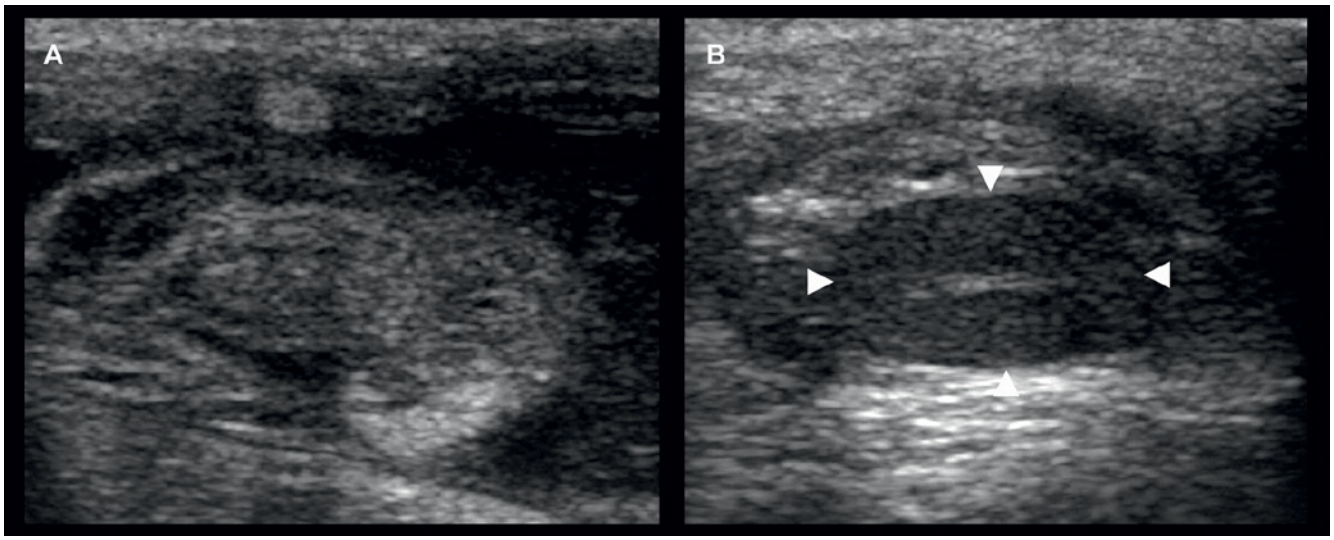


Figure 14.48. Blunt scrotal trauma in a 5-month-old dog. (A) The scrotum is enlarged and filled with material of mixed echogenicity, representing a hematoma at varying stages of organization. **(B)** The left testicle (arrowheads) is displaced and surrounded by material of mixed echogenicity.

Hydrocele manifests as anechoic to echogenic material adjacent to the testicles. This condition is rare in dogs. It may be an occasional incidental finding but is more commonly found secondary to scrotal disorders (e.g., orchitis and testicular torsion, see Figure 14.38). It may also occur secondary to ascites when abdominal fluid descends through the inguinal ring (Figure 14.50).

With **inguinal or scrotal hernia**, abnormal contents (e.g., bowel loops or mesenteric fat) may be found within the inguinal ring or scrotum (Figure 14.51). Concurrent findings include hydrocele, testicular congestion, or infarction. A case of inguinal herniation of a mineralized paraprostatic cyst has been reported in a dog (Vititoe et al. 2017).

Vet-ebooks.com

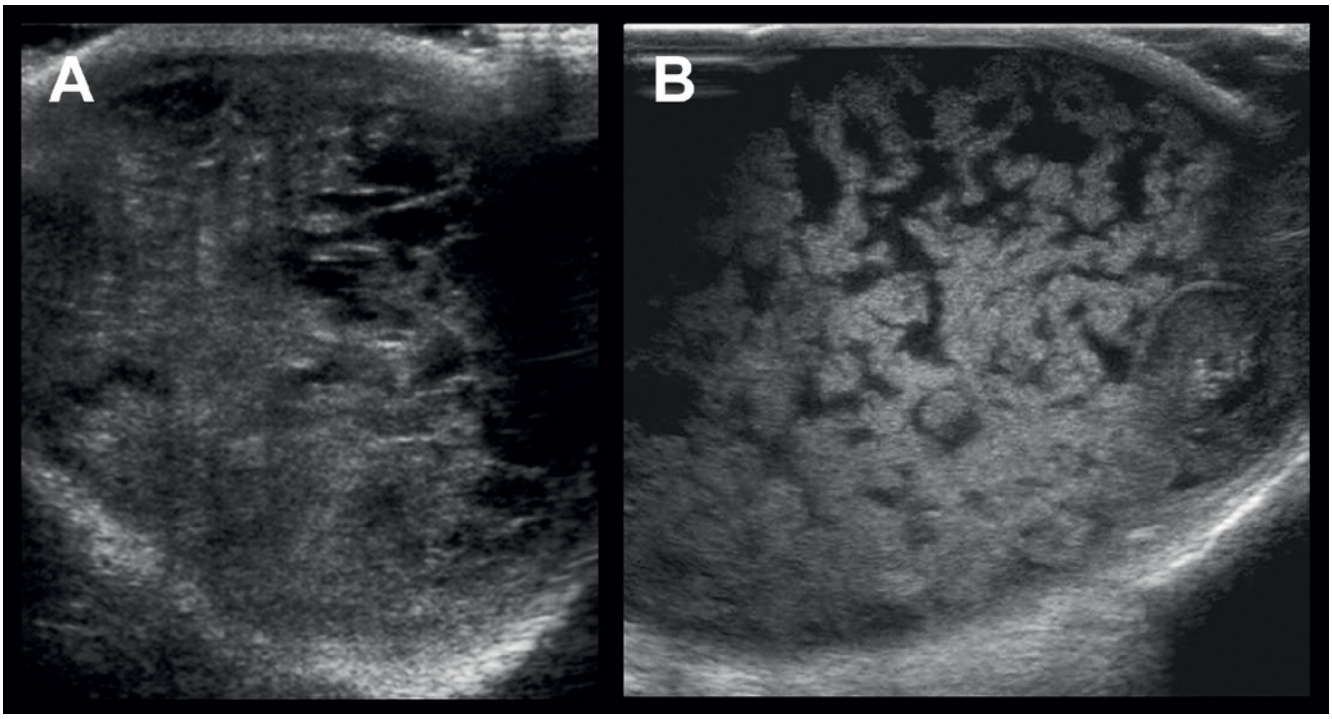


Figure 14.49. Scrotal hematomas following surgical castration in two dogs. (A) In a 1-year-old Weimaraner, the scrotum contains a large (>6 cm diameter) mixed echogenic mass. **(B)** An old, organized hematoma is noted in the scrotum of this 2-year-old Golden Retriever, castrated several months ago. It was confirmed at surgery.

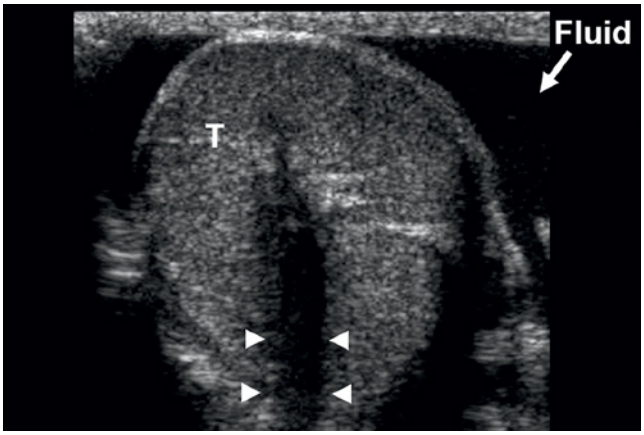


Figure 14.50. Transverse image of the right hemiscrotum in a 9-year-old dog with ascites and subsequent hydrocele. The testicle (T) is surrounded by anechoic fluid. Acoustic shadowing (arrowheads) is observed distal to the centrally located mediastinum testis.

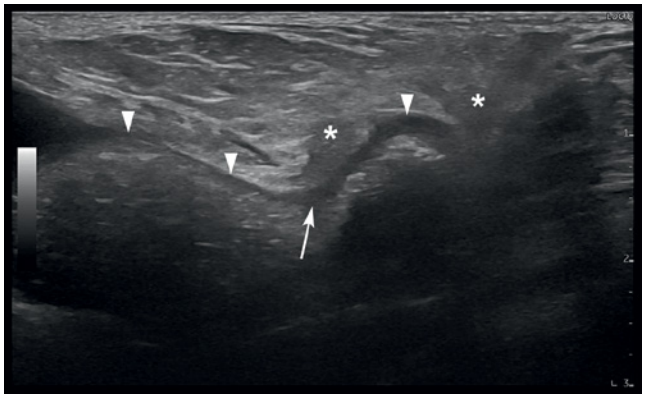


Figure 14.51. Inguinal hernia in an 8-year-old male neutered Chihuahua. The colon (arrowheads) extends from the abdomen through the inguinal ring (indicated by arrow) into the subcutaneous region. The adjacent inguinal fat is hyperechoic (*).

Penis and Prepuce

Normal Sonographic Anatomy of the Penis

The penis in **male dogs** extends from the perineal region (caudal aspect of the pelvis) to the tip of the prepuce at the mid-caudal ventral abdomen (Goericke-Pesch et al. 2013). At the level of the distal penis, the smooth, hyperechoic interface of the os penis is surrounded by penile soft tissues (glans penis, pars longa glandis, and tunica albuginea) and the prepuce. The urethra is located within a V-shaped ventral groove in the os penis (Figure 14.52). Proximal to the os penis, the penile soft tissues (corpus cavernosum, corpus spongiosum, and muscles of the penis)

Vet-ebooks.com

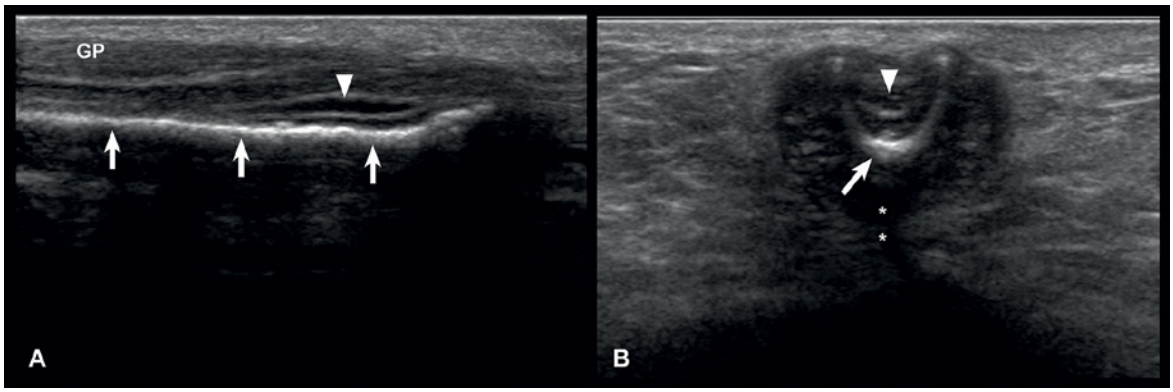


Figure 14.52. **Normal canine penis.** Sagittal **(A)** and transverse **(B)** sonographic images of the penis in an adult intact dog. On sagittal image **(A)**, the prepuce and part of the glans penis (GP) are in the near field ventral to the linear strongly hyperechoic interface of the os penis (indicated by arrows). A dilated portion of the penile urethra is visible (arrowhead). On transverse image **(B)**, the hyperechoic groove of the os penis (arrow) is characterized by distal shadowing (*). The urethra is visible (arrowhead). The surrounding penile soft tissues are symmetrical.

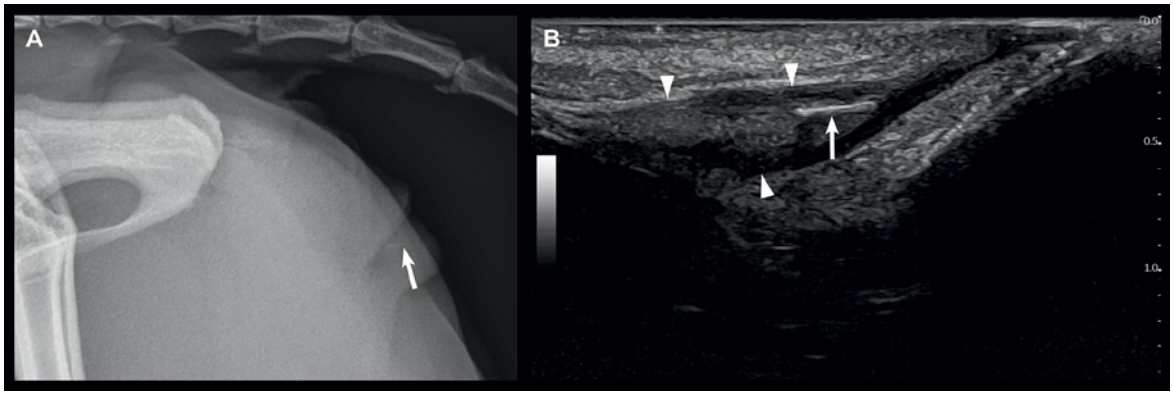


Figure 14.53. **Normal feline os penis.** Lateral radiographic projection **(A)** and sagittal ultrasonographic image **(B)** of a feline os penis. The os penis (arrows) may be visualized as a mineral opaque **(A)** or hyperechoic **(B)** linear structure in the perineal area of male cats. This should not be confused with urethral calculus. Arrowheads delineate penile tissue.

are of medium echogenicity and inconspicuous (see Figure 11.12, Chapter 11; Urinary). In contrast to dogs, the penis in **male cats** is short. An os penis may be visualized on radiographic (Piola et al. 2011; Figure 14.53A) and ultrasonographic examination (Figure 14.53B) and should not be confused with a urethral calculus.

Sonographic Findings in Penile and Preputial Abnormalities

Abnormalities of the penis that warrant ultrasonographic examination include urethral **calculi** (Figure 14.54) and other urethral lesions, **fracture, or neoplasia of the os penis**, and **regional swelling or mass lesions.** Lesions of the os penis cause **discontinuity of its osseous contour** (Figure 14.55). Concurrent soft tissue changes such as **hematoma** and **edema** may be encountered, particularly in acute trauma (Figure 14.56). **Penile tumors** are rare and are unlikely to have a specific pattern (Figure 14.57). Urethrography remains the imaging modality of choice for assessing urethral patency, stricture, integrity, and to exclude pelvic urethral calculi.

Other Findings

Disorders of Sexual Development

These can be subdivided into three categories: chromosomal abnormalities, gonadal abnormalities, and phenotypic abnormalities (Christensen 2012; Meyers-Wallen 2008). A diagnosis is typically achieved by means other than ultrasonography. Testicular hypoplasia or testicular tumors may be found in animals affected with **XXY trisomy**. **XX male hermaphrodites** are typically bilaterally cryptorchid. **Male pseudohermaphrodites**

Vet-ebooks.com

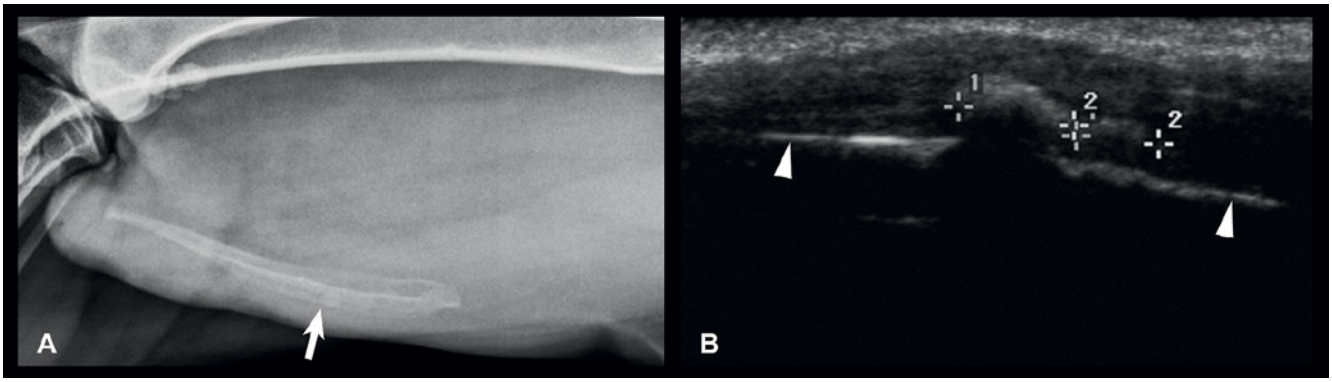


Figure 14.54. Urethral calculi (urate stones) in a 1-year-old Dalmatian. A lateral radiograph of the caudoventral abdomen with the legs flexed forward **(A)** shows a faint round mineral opacity superimposed over the ventral aspect of the os penis (arrow). On the sagittal ultrasonographic image of the penis **(B)** two hyperechoic urethral calculi (between cursors), measuring 5 and 7 mm in diameter, respectively, are clearly recognized in the near field immediately ventral to the linear hyperechoic os penis (arrowheads).

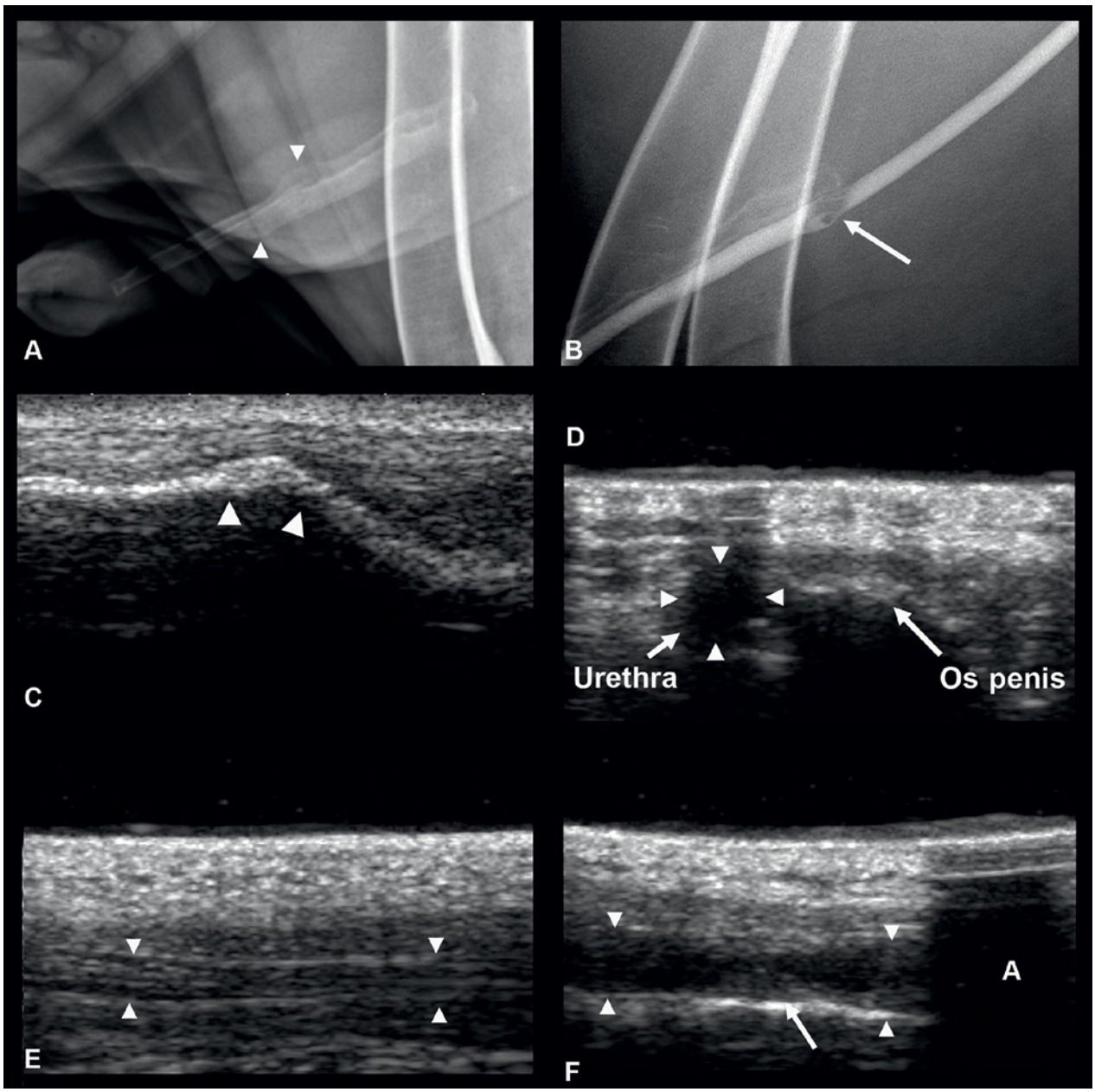


Figure 14.55. Healed fracture of the os penis and mural urethral lesion (urethritis) in a 6-year-old Mastiff with dysuria. (for full caption, see facing page)

Vet-ebooks.com

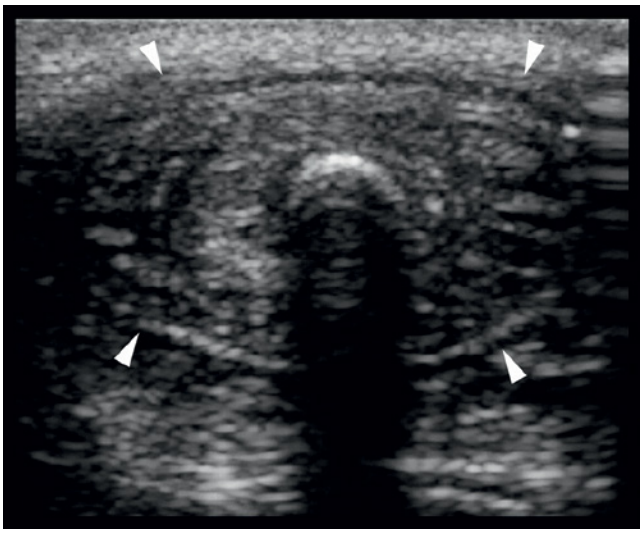


Figure 14.56. Penile trauma in a 4-year-old Belgian Malinois. The transverse image at the level of the os penis (recognized as the central hyperechoic structure with distal acoustic shadowing) shows diffuse edematous swelling of the prepucial and penile soft tissues (arrowheads) without evidence of an underlying bone lesion.

with persistent Müllerian duct syndrome have Müllerian duct derivatives (oviducts, uterus, and cervix) along with bilateral testes (commonly cryptorchid) and normal internal male genitalia.

Persistent paramesonephric ducts in males give rise to the development of Mullerian ducts into horns and body. Internal testes may develop at the extremities of the two ducts, mimicking an internal female apparatus it is called ***uterus masculinus*** (Figure 14.58). Pyometra or hydrometra may be associated with these abnormalities.

Animals with failure of androgen-dependent masculinization possess two testicles, but internal and external male genitalia fail to develop, and the external phenotype may be female.

Perineal Hernia

Perineal hernias are caused by separation of perineal muscles and occur mainly in older intact male dogs (Åhlberg et al. 2022). The hernial sac is accessible for direct ultrasonographic examination via a perineal approach and may contain pelvic and retroperitoneal fat, serous fluid, rectum, prostate, urinary bladder or small intestine (Hedlund and Welch Fossum 2007; Figure 14.59).

Neuticles

Testicular prostheses may be implanted in neutered dogs and appear as well circumscribed structures within the scrotum. Their echogenicity is variable, and concurrent artifacts (distal shadowing, edge shadowing, or reverberation) may be noted (Figure 14.60).

Interventional Procedures

Percutaneous fine-needle aspiration or biopsy of the prostate is easily performed. The same principles and precautions used in other interventional procedures apply. To avoid urethral injury during the procedure, a urinary catheter may be placed to facilitate identification of the prostatic urethra. In cases of suspected **prostatic neoplasia**, sampling by means of traumatic catheterization or prostatic massage may be given preference because of

Figure 14.55. Healed fracture of the os penis and mural urethral lesion (urethritis) in a 6-year-old Mastiff with dysuria. **(A)** The lateral radiograph shows irregularity of the penile contour at the mid-body of the os penis (arrowheads), consistent with previous fracture. **(B)** The urethrogram demonstrates a filling defect associated with the penile urethra at the most caudal level of the os penis (arrow). **(C)** Sagittal ultrasonographic image of the mid-body of the os penis. There is an irregular contour to the hyperechoic interface of the os penis at the previous fracture site (arrowheads). **(D)** Transverse image of the penis during instillation of saline to facilitate urethral identification. The os penis is characterized by its irregular hyperechoic surface and distal shadowing. The fluid-distended urethra is visible as an anechoic circular structure (arrowheads) lateral to the os penis. The unusual urethral position was attributed to previous trauma. **(E)** Sagittal image of the urethra, which appears as an inconspicuous tubular structure (arrowheads). **(F)** Sagittal image of the urethra during instillation of saline. The urethra (arrowheads) is fluid-filled. The filling defect identified during the urethrogram manifests as urethral wall thickening and irregularity (arrow). The hypoechoic area around the letter A is artifactual because of poor transducer-to-skin contact. **(D–F)** The anechoic area in the near field represents part of the standoff pad.

Vet-ebooks.com

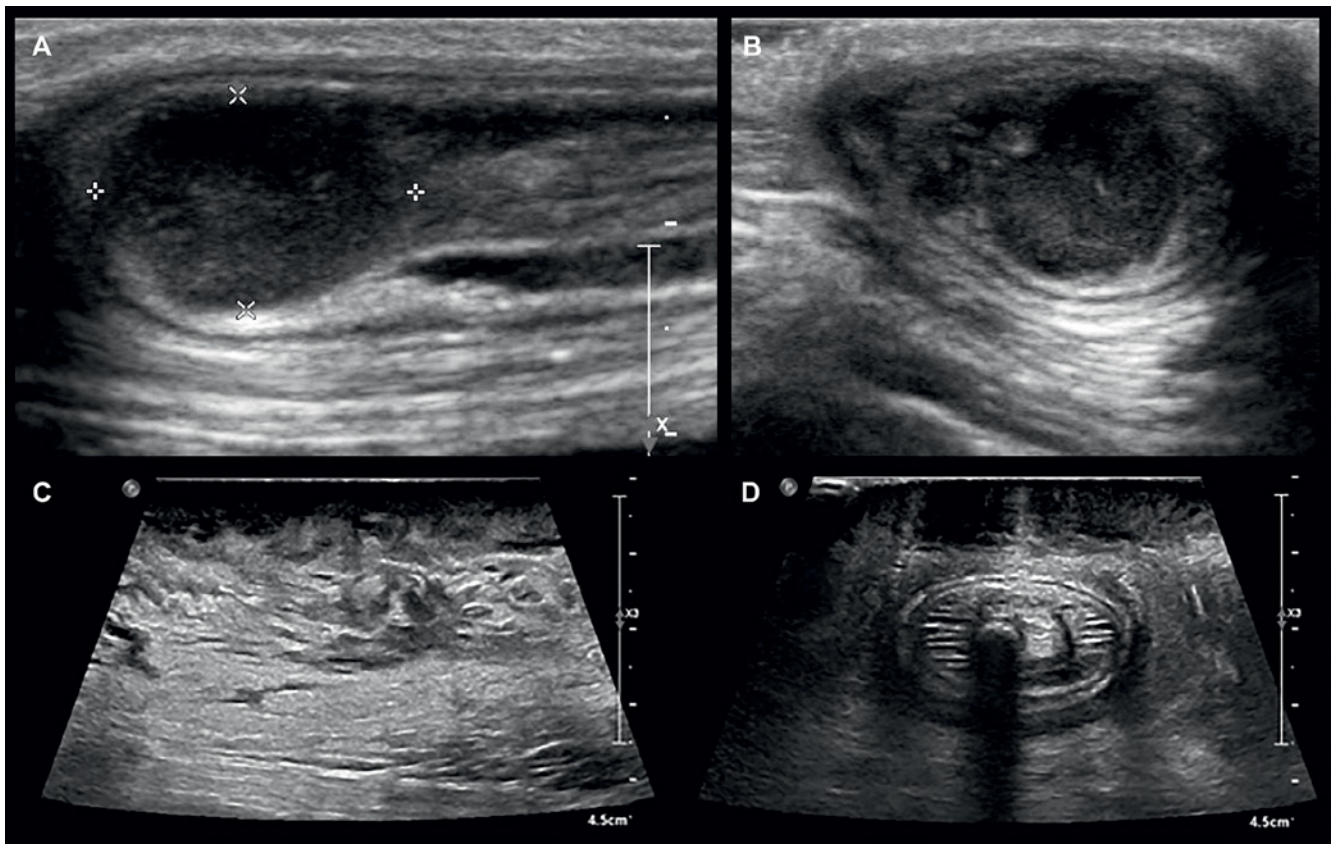


Figure 14.57. Penile/preputial tumors in two dogs. (A, B) Soft tissue sarcoma (suspected hemangiosarcoma) in a 7-year-old Beagle. The sagittal **(A)** and transverse **(B)** images show a discrete, poorly echogenic nodule associated with the tip of the penis. **(C, D)** Prepucial carcinoma in a 14-year-old mixed breed dog (same patient as shown in Figure 14.19E, F). Sagittal **(C)** and transverse **(D)** images show a severely diffusely swollen and markedly heterogeneous prepuce. The prepucial tumor was believed to be most likely secondary (metastatic) to the prostatic carcinoma diagnosed in this dog.

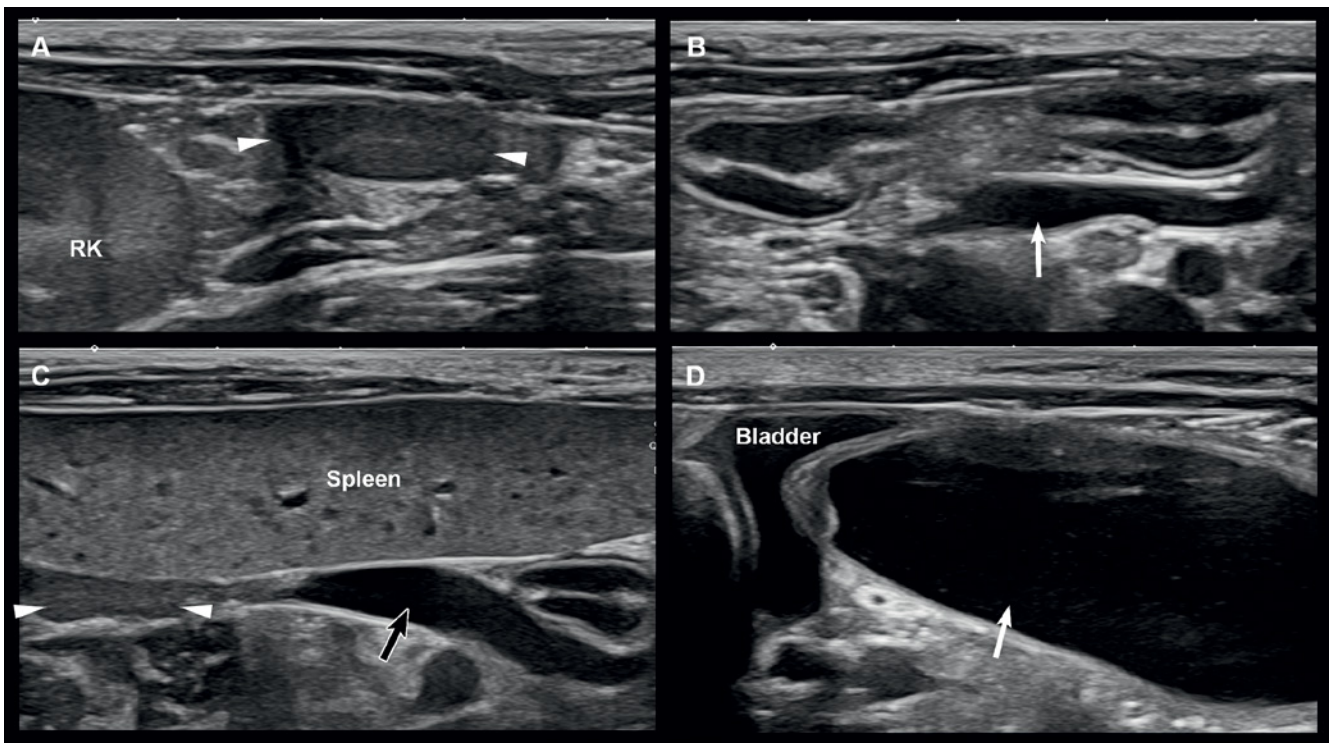


Figure 14.58. Uterus masculinus in a 2.5-month-old Picard Shepherd dog. (for full caption, see facing page)

Vet-ebooks.com

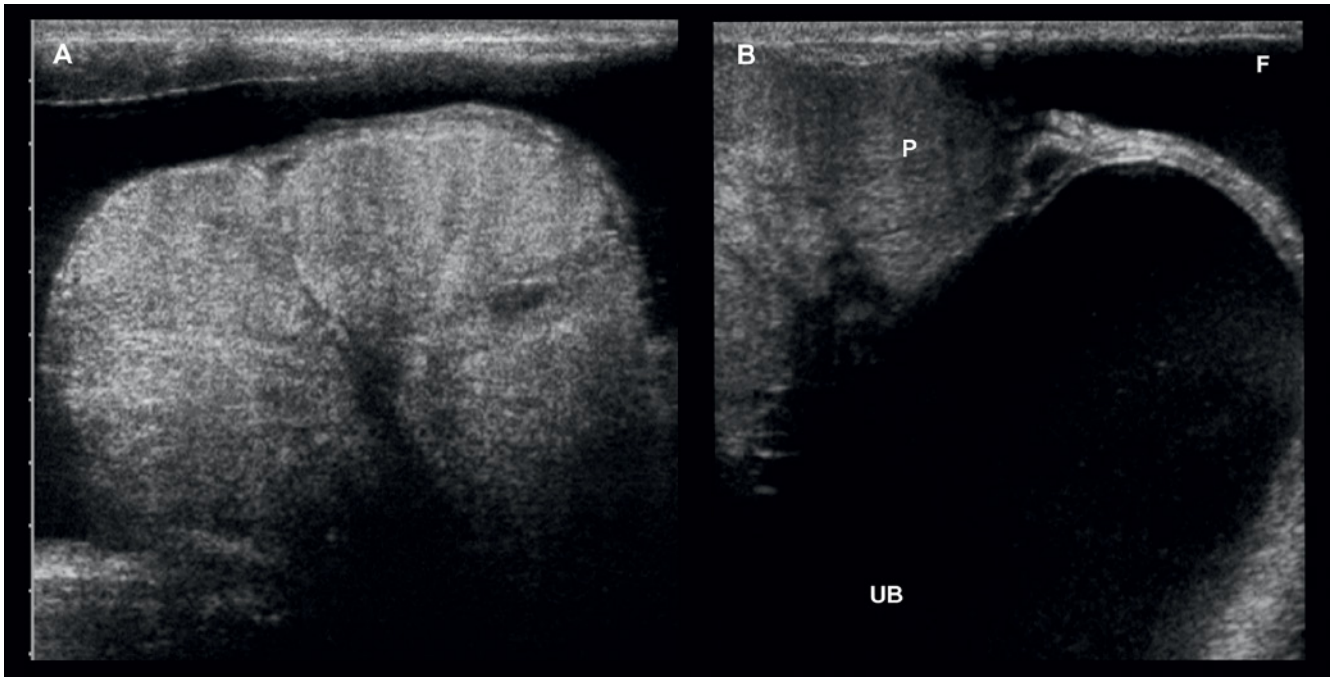


Figure 14.59. **Perineal hernia in a 9-year-old mixed-breed dog. (A)** The transverse image shows the entire prostate being located within the hernia sac. The prostate is diffusely hyperechoic and contains a small hypoechoic lesion in the left lobe, consistent with benign prostatic hyperplasia and a small prostatic cyst. **(B)** The sagittal image demonstrates herniation of the urinary bladder (UB) along with the prostate (P). Fluid (F) surrounds the prostate and bladder on both images.

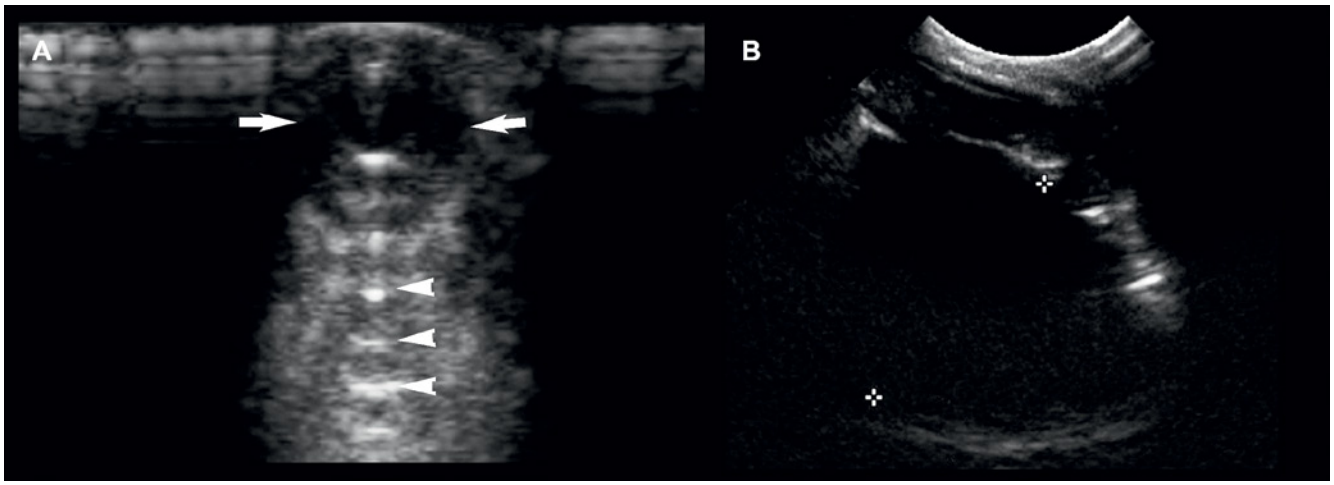


Figure 14.60. **Neuticles in two dogs. (A)** The sagittal image of the scrotum in this 10-year-old mixed-breed dog demonstrates a round and mostly hypoechoic, approximately 8-mm-diameter structure with distal reverberation artifacts. **(B)** In this Great Dane, the neuticle (between cursors) is about 3 cm long and anechoic.

Figure 14.58. **Uterus masculinus in a 2.5-month-old Picard Shepherd dog.** This dog was presented with ambiguous external genitalia (vulva and os clitoris). Abnormalities on ultrasonographic examination of the abdomen mimicked hydrometra or pyometra. Two fluid-filled anechoic horns (arrows) **(B, C)** are visible in the mid-abdomen running cranio-laterally on each side of the abdomen. They contact cranially to two ovoid homogenous hypoechoic structures (arrowheads) located caudolaterally to the right kidney **(A)** and left kidney **(C),** respectively, and caudally to a large cystic anechoic structure (black arrow) located dorsocaudally to the urinary bladder **(D).** The ovoid structures correspond to intra-abdominal testis, the two horns are abnormal dilated remnants of Müllerian duct, and the large cystic structure is a prostatic utricle (Müllerian duct remnant), which communicates with the urethra. The diagnosis of *uterus masculinus* was confirmed by histology and genetic testing.

Vet-ebooks.com

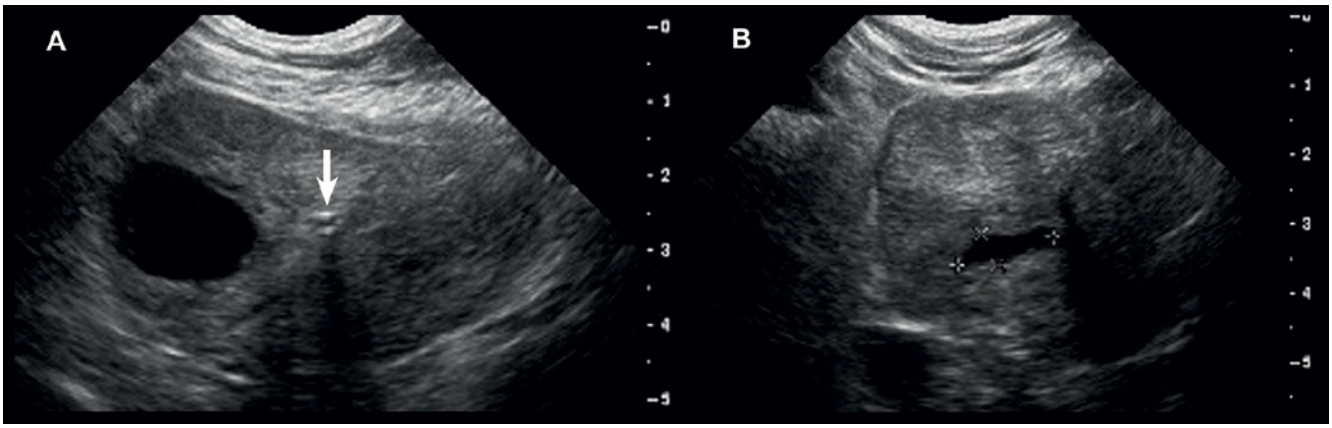


Figure 14.61. Drainage of a prostatic abscess in a 3-year-old Border Collie. (A) Transverse sonogram of the prostate with a right lobe hypoechoic abscess. The arrow points to the urethral catheter that has been placed to better identify and avoid the urethra during the procedure. **(B)** Transverse sonogram of the prostate after drainage. The abscess cavity is nearly collapsed (between cursors).

the risk of implantation of tumor cells along the needle tract after percutaneous aspiration (Nyland et al. 2002). This been said, the risk for needle-tract implantation of neoplastic or inflammatory cells appears to be very low in veterinary (Nyland et al. 2002; Rodak et al. 2018) as well as in human patients with an incidence of less than 1% according to one review series (Volanis et al. 2015).

Percutaneous drainage of **prostatic abscesses** and in situ injection of antibiotics is a valid alternative method to surgical intervention, especially in immunocompromised patients (Boland et al. 2003) (Figure 14.61). Percutaneous drainage of **paraprostatic cysts** can be performed to temporarily relieve patient discomfort. However, recurrent filling usually warrants surgery at a later stage.

Fine-needle aspiration or biopsy of **intra-abdominal testicular tumors** can be performed, following the same principles and precautions as in biopsies of other abdominal organs. Fine-needle aspiration of **intrascrotal testicles** is infrequently performed in veterinary medicine. However, the procedure has a high accuracy in the diagnosis of testicular neoplasms, with a low risk of adverse effects (Dorsch et al. 2006; Gouletsou et al. 2011).



Visit our website at
www.SmallAnimalUltrasonography.com
for complementary video clips with annotations and text on:

- Scanning of the normal male reproductive tract in a dog
- Benign prostatic hyperplasia
- Prostatic tumor
- Prostatic abscess
- Testicular tumor

REFERENCES

Åhlberg TM, Jokinen TS, Salonen HM, Laitinen-Vapaavuori OM, et al. (2022) Exploring the association between canine perineal hernia and neurological, orthopedic, and gastrointestinal diseases. Acta Vet Scand 64:39.

Atalan G, Holt PE, Barr FJ (1999) Ultrasonographic estimation of prostate size in normal dogs and relationship to bodyweight and age. J Small Anim Pract 40:119–122.

Atilola MAO, Pennock PW (1986) Cystic uterus masculinus in the dog, six case history reports. Vet Radiol Ultrasound 27:8–14.

Bacci B, Vignoli M, Rossi F, Gallorini F, et al. (2010) Primary prostatic leiomyosarcoma with pulmonary metastases in a dog. J Am Anim Hosp Assoc 46:103–106.

Balao da Silvia C, Gomez Gordo L, Cuesta Gernevo JM, Ortega-Ferrusola C, et al. (2019) A rare case of a primary unilateral low-grade paratesticular leiomyosarcoma in a 2 years old dog. Front Vet Sci 6:83.

Bigliardi E, Ferrari L (2011) Contrast-enhanced ultrasound of the normal canine prostate gland. Vet Radiol Ultrasound 52:107–110.

Bigliardi E, Denti L, De Cesaris V, Bertocchi M, et al. (2019) Colour Doppler ultrasound imaging of blood flows variations in neoplastic and non-neoplastic testicular lesions in dogs. Reprod Domest Anim 54:63–71.

Boland LE, Hardie RJ, Gregory SP, Lamb CR (2003) Ultrasound-guided percutaneous drainage as the primary treatment for prostatic abscesses and cysts in dogs. J Am Anim Hosp Assoc 39:151–159.

Bosma F, Wijsman S, Huygens S, Passon-Vastenburg M (2022) Ultrasonographic measurements of the prostate gland in castrated adult dogs. Acta Vet Scand 64:15.

Bradbury CA, Westropp JL, Pollard RE (2009) Relationship between prostatomegaly, prostatic mineralization, and cytologic diagnosis. Vet Radiol Ultrasound 50:167–171.

Vet-ebooks.com

Canadas A, Romao P, Gartner F (2016) Multiple cutaneous metastasis of a malignant Leydig cell tumour in a dog. J Comp Pathol 155:181–184.

Christensen BW (2012) Disorders of sexual development in dogs and cats. Vet Clin North Am Small Anim Pract 42:515–526.

Cicirelli V, Macrì F, Di Pietro S, Leoci R, et al. (2022) Use of contrast-enhanced ultrasound of the testes after non-surgical sterilization of male dogs with $CaCl_2$ in alcohol. Animals (Basel) 12:577.

Culp W, Johnson E, Giuffrida MA, Palm CA, et al. (2019) Use of transrectal ultrasonography for assessment of the size and location of prostatic carcinoma in dogs. Am J Vet Res 80: 1012–1019.

Davidson AP, von Dehn BJ, Schlafer DH (2015) Adult-onset lymphoplasmacytic orchitis in a Labrador Retriever stud dog. Top Comp Anim Med 30: 31–34.

Donnelly CG, Cheong SH, Gilbert RO (2016) Unilateral autoimmune orchitis with concurrent contralateral testicular atrophy in a 2-year-old Newfoundland dog. Vet Rec Case Rep 4:e000277. doi: 10.1136/vetreccr-2015-000277.

Dorsch R, Majzoub M, Hecht S, Hartmann K, et al. (2006) Diagnostische Wertigkeit der Hodenzytologie beim Hund. Tieraerztl Prax 34:91–98.

Feeney DA, Johnston GR, Klausner JS, Bell FJ (1989) Canine prostatic ultrasonography: 1989. Semin Vet Med Surg 4:44–57.

Felumlee AE, Reichle JK, Hecht S, Penninck D, et al. (2012) Use of ultrasound to locate retained testes in dogs and cats. Vet Radiol Ultrasound 53: 581–5.

Giudice C, Banco B, Veronesi MC, Ferrari A, et al. (2014) Immunohistochemical expression of markers of immaturity in Sertoli and Seminal cells in canine testicular atrophy. J Comp Pathol 150:208–215.

Gloria A, Di Francesco L, Marruchella G, Robbe D, et al. (2020) Pulse-wave doppler pulsatility and resistive indexes of the testicular artery increase in canine testis with abnormal spermatogenesis. Theriogenology 158:454–460.

Goericke-Pesch S, Hölscher C, Failing K, Wehrend A 2013 Functional anatomy and ultrasound examination of the canine penis. Theriogenology 80:24–33.

Gouletsou PG, Galatos AD, Leontides LS, Sideri AI (2011) Impact of fine- or large-needle aspiration on canine testes: clinical, in vivo ultrasonographic and seminological assessment. Reprod Domest Anim 46:712–719.

Harris OS, Eitzer AD, Saver A, Sample SJ, et al. (2022) Ultrasonography and CT of the vas deferens in a neutered male dog with chronic exogenous estrogen exposure. Vet Radiol Ultrasound 63(4):E1–E6.

Haverkamp K, Harder LK, Kuhnt NSM, Lüpke M, et al. (2019) Validation of canine prostate volumetric measurements in computed tomography determined by the slice addition technique using the Amira program. BMC Vet Res 15:49

Hayden DW, Klausner JS, Waters DJ (1999) Prostatic leiomyosarcoma in a dog. J Vet Diagn Invest 11:283–286.

Hecht S (2001) Sonographische Diagnostik des Skrotalinhaltes beim Hund unter besonderer Beruecksichtigung testikulaerer Neoplasien. Doctoral Thesis, Munich: Chirurgische Tierklinik, Ludwig-Maximilians University.

Hecht S, Matiasek K, Koestlin R (2003) Die sonographische Untersuchung des Skrotalinhaltes beim Hund unter besonderer Beruecksichtigung testikulaerer Neoplasien. Tieraerztl Prax 31:199–210.

Hecht S, King R, Tidwell AS, Gorman SC (2004) Ultrasound diagnosis: intra-abdominal torsion of a non-neoplastic testicle in a cryptorchid dog. Vet Radiol Ultrasound 45:58–61.

Hedlund CS, Welch Fossum T (2007) Surgery of the digestive system. In Welch Fossum T, ed. Small Animal Surgery, 3rd edition. St Louis: Mosby Elsevier, pp. 339–530.

Holdsworth A, Bléhaut T, Reeve L, Warren-Smith C, et al. (2015) An incidental prostatic leiomyoma in a dog. Vet Rec Case Rep 3:1–5.

Johnston GR, Feeney DA, Johnston SD, O'Brien TD (1991a) Ultrasonographic features of testicular neoplasia in dogs: cases (1980–1988). J Am Vet Med Assoc 198:1779–1784.

Johnston GR, Feeney DA, Rivers B, Walter PA (1991b) Diagnostic imaging of the male canine reproductive organs: methods and limitations. Vet Clin North Am Small Anim Pract 21:553–589.

Johnston SD, Kamolpatana K, Root-Kustritz MV, Johnston GR (2000) Prostatic disorders in the dog. Anim Reprod Sci 60–61:405–415.

Kalogianni L, Pardali D, Garcia-Gonzalez B, Konstantinidis OA, et al. (2022) Lymphoplasmacytic prostatitis associated with urethral obstruction in a dog; a case report. Top Companion Anim Med;46:100593. doi:10.1016/j.tcam.2021.100593.

Kudo T, Kamiie J, Aihara N, Doi M, Sumi A, et al. (2019) Malignant Leydig cell tumor in dogs: two cases and a review of the literature. J Vet Diagn Invest 31:557–561.

Lim CK, Heng HG, Hui TY, Thompson CA, et al. (2014) Ultrasonographic features of uterus masculinus in six dogs. Vet Radiol Ultrasound, 56:77–83.

de Lima Nascimento HH, Tochetto C, Lucena RB, Kommers GD (2019) Testicular interstitial cell tumor with disseminated cutaneous metastasis in a dog. Acta Sci Vet, 47, doi:10.22456/1679-9216.96391 Case report (supplement).

Mattoon JS, Nyland TG (2021) Prostate and testes. In Nyland TG, Mattoon JS, eds. Small Animal Diagnostic Ultrasound, Philadelphia: WB Saunders, pp. 635–664.

MCCormack M (1975) Bilateral fibrosarcoma of the epididymis. J Clin Pathol 28:576–9.

Meyers-Wallen VN (2008) Inherited disorders of the reproductive tract in dogs and cats. In Bonagura J, ed. Kirk's Current Veterinary Therapy. Philadelphia: WB Saunders, pp. 1034–1039.

Miyabashi T, Biller DS, Cooley AJ (1990) Ultrasonographic appearance of torsion of a testicular seminoma in a cryptorchid dog. J Small Anim Pract 31:401–403.

Newell SM, Mahaffey MB, Binhazim A, Greene CE (1992) Paraprostatic cyst in a cat. J Small Anim Pract 33:399–401.

Newell SM, Neuwirth L, Ginn PE, Roberts GD, et al. (1998) Doppler Ultrasound of the prostate in normal dogs and in dogs with chronic lymphocytic-lymphoplasmocytic prostatitis, Vet Radiol Ultrasound 39:332–336.

Vet-ebooks.com

Nyland TG, Wallack ST, Wisner ER (2002) Needle-tract implantation following US-guided fine-needle aspiration biopsy of transitional cell carcinoma of the bladder, urethra, and prostate. Vet Radiol Ultrasound 43:50–53.

Ober CP, Spaulding K, Breitschwerdt EB, Malarkey DE, et al. (2004) Orchitis in two dogs with rocky mountain spotted fever. Vet Radiol Ultrasound 45: 458–465.

Orlandi R, Vallesi E, Boiti C, Polisca A, et al. (2022) Characterization of testicular tumor lesions in dogs by different ultrasound techniques. Animals (Basel) 12:210.

Palmieri C, Lean FZ, Akter SH, Romussi S, et al. (2014) A retrospective analysis of 111 canine prostatic samples: histopathological findings and classification. Res Vet Sci 97:568–73.

Palmieri C, Fonseca-Alves CE, Laufer-Amorim R (2022) A Review on canine and feline prostate pathology. Front Vet Sci 26:881232.

Pearson H, Kelly DF (1975) Testicular torsion in the dog: a review of 13 cases. Vet Rec 97:200–204.

Piola V, Posch B, Aghte P, Caine A, et al. (2011) Radiographic characterization of the os penis in the cat. Vet Radiol Ultrasound 52:270–272.

Pugh CR, Konde LJ (1991) Sonographic evaluation of canine testicular and scrotal abnormalities: a review of 26 case histories. Vet Radiol Ultrasound 32:243–250.

Pugh CR, Konde LJ, Park RD (1990) Testicular ultrasound in the normal dog. Vet Radiol Ultrasound 31:195–199.

Renfrew H, Barrett EL, Bradley KJ, Barr FJ (2008) Radiographic and ultrasonographic features of canine paraprostatic cysts. Vet Radiol Ultrasound 49:444–448.

Rodak O, Dzimira S, Podolak A, Płóciennik M, et al. (2018) Accuracy of ultrasonography and fine-needle aspiration cytology in the diagnosis of prostate diseases in dogs. Reprod Domest Anim 53(Suppl. 3):79–84.

Ruel Y, Barthez PY, Mailles A, Begon D (1998) Ultrasonographic evaluation of the prostate in healthy intact dogs. Vet Radiol Ultrasound 39:212–216.

Russo M, Vignoli M, Catone G, Rossi F, et al. (2009) Prostatic perfusion in the dog using contrast-enhanced doppler ultrasound. Reprod Domest Anim 44(Suppl 2):334–335.

Russo M, Vignoli M, England GC (2012) B-mode and contrast-enhanced ultrasonographic findings in canine prostatic disorders. Reprod Domest Anim 47(Suppl 6):238–42.

Salyer SA, Lapsley JM, Palm CA, Culp WTN, et al. (2022) Outcome of dogs with bone marrow suppression secondary to Sertoli cell tumour. Vet Comp Oncol 20:484–490.

Sanpera N, Masot N, Janer M, Romeo C, et al. (2002) Oestrogen-induced bone marrow aplasia in a dog with a Sertoli cell tumour. J Small Anim Pract 43(8):365–9.

Slaughter SA, England GCW, Vignoli M, Carluccio A, et al. (2022) Computed tomography of testicular torsion in a juvenile dog with unilateral cryptorchidism. Can Vet J 63:515–520.

Spada S, England GCW, Vignoli M, Carluccio A, et al. (2021) Contrast-enhanced ultrasound imaging of prostate gland in neutered dogs. Animals (Basel) 11:559.

Stowater JL, Lamb CR (1989) Ultrasonographic features of paraprostatic cysts in nine dogs. Vet Radiol Ultrasound 30:232–239.

Sun F, Baez-Diaz C, Sanchez-Margallo FM (2017) Canine prostate models in preclinical studies of minimally invasive interventions: part II, benign prostatic hyperplasia models. Transl Androl Urol 6(3):547–555.

Tenuta M, Sesti F, Bonaventura I, Mazzotta P, et al. (2021) Use of contrast enhanced ultrasound in testicular diseases: a comprehensive review. Andrology 9:1369–1382.

Teske E, Naan EC, van Dijk EM, Van Garderen E, et al. (2002) Canine prostate carcinoma: epidemiological evidence of an increased risk in castrated dogs. Mol Cell Endocrinol 29:251–5.

Togni A, Rütten M, Bley CR, Hurter K (2015) Metastasized Leydig cell tumor in a dog. Schweiz Arch Tierheilkd 157:111–115.

Totten AK, Ridgway MD, Sauberli DS (2011) Blastomyces dermatitidis prostatic and testicular infection in eight dogs (1992–2005). J Am Anim Hosp Assoc 47:413–8.

Troisi A, Orlandi R, Bargellini P, Menchetti L, et al. Contrast-enhanced ultrasonographic characteristics of the diseased canine prostate gland (2015) Theriogenology 84:1423–30.

Trovatelli M, Bassi J, Giudice C, Ferrari R, et al. (2021) Prostatic leiomyosarcoma in a dog treated using a multimodal approach. J Vet Intern Med 35:1105–1110.

Vignoli M, Russo M, Catone G Rossi F, et al. (2011). Assessment of vascular perfusion kinetics using contrast-enhanced ultrasound for the diagnosis of prostatic disease in dogs. Reprod Domest Anim 46:209–213.

Vititoe KP, Grosso FV, Thomovsky S, Lim CK, et al. (2017) Inguinal herniation of a mineralized paraprostatic cyst in a dog. Can Vet J 58:1309–1312.

Volanis, D, Neal, DE, Warren, AY, Gnanapragasam, VJ (2015) Incidence of needle-tract seeding following prostate biopsy for suspected cancer: a review of the literature. BJU Int115:698–704.

Volta A, Manfredi S, Vignoli M, Russo M, et al. (2014) Use of contrast-enhanced ultrasonography in chronic pathologic canine testes. Reprod Domest Anim 49:202–209.

Winter MD, Locke JE, Penninck DG (2006) Imaging diagnosis: urinary obstruction secondary to prostatic lymphoma in a young dog. Vet Radiol Ultrasound 47:597–601.

Withers SS, Lawson CM, Burton AG, Rebhun RB, et al. (2016) Management of an invasive and metastatic Sertoli cell tumor with associated myelotoxicosis in a dog. Can Vet J 57:299–304.

Zekas LJ, Forrest LJ, Swainson S, Phillips LA (2004) Radiographic diagnosis: mineralized paraprostatic cyst in a dog. Vet Radiol Ultrasound 45:310–11.

Zohil AM, Castellano C (1995) Prepubic and transrectal ultrasonography of the canine prostate: a comparative study. Vet Radiol Ultrasound 36:393–396.

Vet-ebooks.com

CHAPTER FIFTEEN

Abdominal Cavity and Lymph Nodes

Marc-André d'Anjou and Éric Norman Carmel

Animages, Brossard, Québec, Canada

Preparation and Scanning Technique

To have access to all portions of the abdominal cavity of dogs and cats, hair must be clipped ventrally and laterally between the costal arch and caudal margin of the abdomen. Clipping may be extended more cranially in deep-chested dogs to better visualize the subcostal region. After the application of acoustic gel, the animal can be scanned in dorsal, left, or right recumbency. Some disorders of the peritoneal space, such as effusion or free air, respond to gravity and may require repositioning the animal to reach a diagnosis (see Chapter 2).

Ultrasonographic probes must be selected according to the size of the animal and the depth of the evaluated region(s). A high-frequency probe (7.5 MHz and higher) is recommended in cats and small dogs or if superficial structures are examined, whereas probes with more penetration (5.0–7.5 MHz and lower) are useful when assessing deep portions of larger dogs. Convex probes are preferred because they can reach all portions of the abdomen, including the subcostal region, as opposed to linear probes, which have a larger footprint. Linear probes may however help in detecting small volumes of fluid or gas located closer to the probe.

Ultrasonographic Anatomy of the Normal Peritoneal and Retroperitoneal Cavity, Fat, and Lymph Nodes

The **peritoneum** is composed of a thin serous membrane that is divided into parietal and visceral components. The **peritoneal cavity** is a potential space located between these two layers that contains only a scant volume of fluid that serves as a lubricant. With more recent ultrasound systems, a minute amount of physiological peritoneal fluid is frequently identified in very young patients (Stander et al. 2010) and can also be found incidentally in healthy young adults (Lisciandro et al. 2020). The peritoneum appears as a smooth hyperechoic interface that is better appreciated when a moderate volume of ascites is present. A variable amount of **fat** is present, mainly in the falciform ligament, omentum, mesentery, and retroperitoneum. The fat appears coarse in echotexture and of low to moderate echogenicity with hyperechoic speckles. The mesentery and omentum cannot be easily distinguished, although the mesentery may be recognized as it contains larger vessels and lymph nodes that can be visualized in most patients.

Atlas of Small Animal Ultrasonography, Third Edition. Edited by Dominique Penninck and Marc-André d'Anjou.
© 2025 John Wiley & Sons, Inc. Published 2025 by John Wiley & Sons, Inc.
Companion website: www.SmallAnimalUltrasonography.com

Vet-ebooks.com

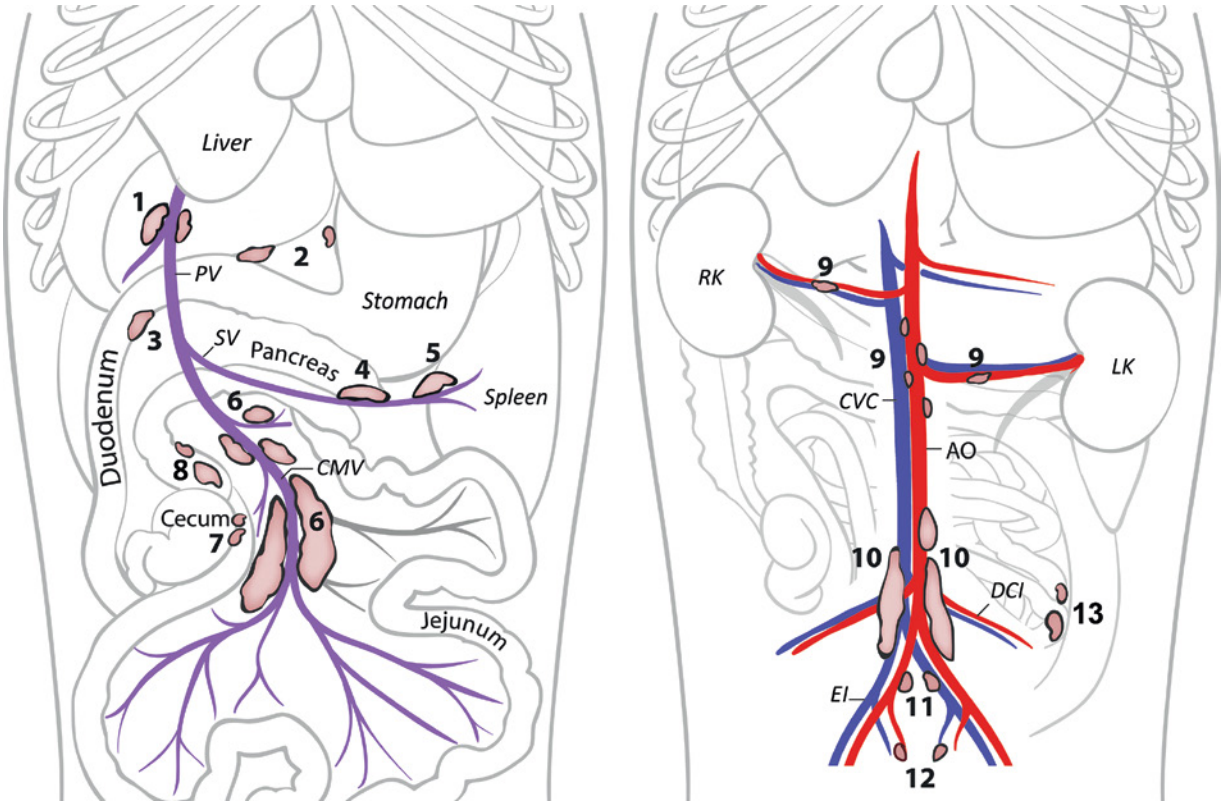


Figure 15.1. Schematic illustration of abdominal lymph nodes. Note the intimate anatomical relationship between lymph nodes and vessels. **Lymph nodes**: 1, hepatic; 2, gastric; 3, pancreaticoduodenal; 4 and 5, splenic; 6, jejunal; 7, right colic; 8, middle colic; 9, renal and lumbar aortic; 10, medial iliac; 11, internal iliac; 12, sacral, and 13, left colic. **Vessels**: AO, aorta; CMV, cranial mesenteric vein; CVC, caudal vena cava; DCI, deep circumflex iliac vessels; EI, external iliac vessels; PV, portal vein; SV, splenic vein**. Other landmarks**: LK, left kidney; RK, right kidney.

Abdominal lymph nodes are routinely evaluated in dogs and cats. These nodes drain several organs and structures and can therefore be affected by several benign and neoplastic conditions. Several of these nodes are easily identified, especially for more superficial nodes, in young and smaller patients, and when using recent ultrasound units (Figure 15.1). Their location tends to be constant, but lymph nodes can vary in number and size between individuals.

Table 15.1 lists the location and drainage of the abdominal lymph nodes in dogs and cats (Bezuidenhout 2020; Pugh 1994; Schreurs et al. 2008; Tobón et al. 2022). It must be underlined that there is considerable inconsistency in the nomenclature of some of these nodes in the literature, particularly for the colic and internal iliac nodes, which can make comparison between cited references difficult. The nomenclature used throughout this chapter is consistent with that of Miller and Evans' Anatomy of the Dog (Bezuidenhout 2020).

Lymph nodes are generally uniformly isoechoic to slightly hypoechoic to the adjacent fatty tissues, with fine echotexture, smooth in contour, and fusiform to oval (Llabrés-Diaz 2004; Mayer et al. 2010; Nyman and O'Brien 2007) (Figure 15.2). A thin hyperechoic capsule is often identified, and occasionally normal hyperechoic central lines corresponding to vascular walls and fat can be seen crossing these nodes in the region of the nodal hilus. Blood flow may, however, not be apparent with color Doppler examination. For jejunal nodes, such flow can be detected in only 33% of dogs, particularly when younger than 2 years of age (Agthe et al. 2009).

Reference values for lymph node dimensions have been reported, but not for all groups of nodes. As for the adrenals, measuring maximal thickness (i.e., smallest axial dimension) or width (i.e., largest axial dimension) is more reliable than length when estimating lymph node size in dogs and cats. Reference ranges reported in dogs and cats are summarized in Table 15.2. Lymphoid tissue reaches its greatest development at sexual maturity (Bezuidenhout 2020) and jejunal lymph nodes tend to be relatively larger in young healthy puppies (mean diameter of 6–7 mm), often irregular, and hypoechoic or with a hypoechoic rim

Vet-ebooks.com

Table 15.1
Location and drainage of abdominal lymph nodes in dogs and cats

Lymph nodes	Location	Drainage areas
Celiac lymphocenter		
Hepatic	Along the portal vein, caudal to the *porta hepatis*	Liver, stomach, duodenum, and pancreas
Splenic	Along the splenic veins and the left pancreatic lobe	Liver, spleen, esophagus, stomach, pancreas, and omentum
Gastric	Between the liver and lesser curvature, near the pyloric antrum	Diaphragm, liver, esophagus, stomach, duodenum, pancreas, and peritoneum
Pancreaticoduodenal	Near the cranial duodenal flexure, between the pylorus and the right pancreatic limb	Duodenum, pancreas, and omentum
Cranial mesenteric lymphocenter		
Jejunal	Along the mesenteric vascular tree (cranial mesenteric artery and vein)	Jejunum, ileum, and pancreas
Colic	Near the ileocolic junction (right colic[a]), mesocolon (middle colic[b]), and the caudal descending colon (left colic[c])	Ileum, cecum, and colon
Lumbar aortic and renal	Along aorta and near the kidneys	Spinal structures, ribs, peritoneum, kidneys, adrenals, bladder, uterus, prostate, and gonads
Iliosacral lymphocenter		
Medial iliac, internal iliac,[d] and sacral	At the caudal aortic trifurcation, between the deep circumflex and the external iliac arteries (medial iliac), medial to the internal iliac arteries (internal iliac) and along the median sacral artery (sacral)	Ureters, bladder, uterus, prostate, gonads, peripelvic and pubic areas, abdominal skin, caudal vertebrae, pelvis, hindlimb muscles, and bones
Superficial inguinal	In the subcutaneous fat between the abdominal wall and inguinal mammary gland (female) or dorsolateral edge of the penis (male dog).	Abdominal wall, abdominal and inguinal mammary glands (variable), penis/scrotum, and pelvic limb

Alternative lymph node appellations:
[a] Ileocolic [b] Colic [c] Caudal mesenteric [d] Hypogastric

(Krol and O'Brien 2012; Stander et al. 2010). This enlargement and reduced cortical echogenicity are probably explained by the fact that the intestinal tract of young animals is continuously exposed to new antigens (Agthe et al. 2009).

Due to the great variation in lymph node dimensions among dogs and cats, the shape of these nodes may represent a more useful feature than absolute measurements. A ratio comparing the short and long axes measuring less than 0.5 is generally considered normal (Llabrés-Diaz 2004; Nyman et al. 2004). This has been validated for medial iliac and superficial inguinal nodes in dogs (Mayer et al. 2010). However, this ratio has limited usefulness for other lymph nodes, such as jejunal nodes, that tend to be much longer and may exceed the field of view or present a curved shape (Agthe et al. 2009). A ratio comparing the height of the lymph node to the diameter of the aorta in longitudinal plane has also been proposed for medial iliac lymph nodes to take into account the relative size of the patient, with a ratio of less than 0.58 being considered normal (Citi et al. 2020).

Lymph nodes routinely identified include the jejunal (or mesenteric) and medial iliac lymph nodes. Jejunal nodes appear as a group of fusiform nodes aligned with the cranial mesenteric artery and vein and their branches within the omentum. Some of these nodes can be relatively long. The iliosacral lymphocenter is the group formed by the sublumbar lymph nodes, which are located along the caudal aortic trifurcation. In some instances, medial iliac lymph nodes may be more easily identified from a lateral flank approach

Vet-ebooks.com

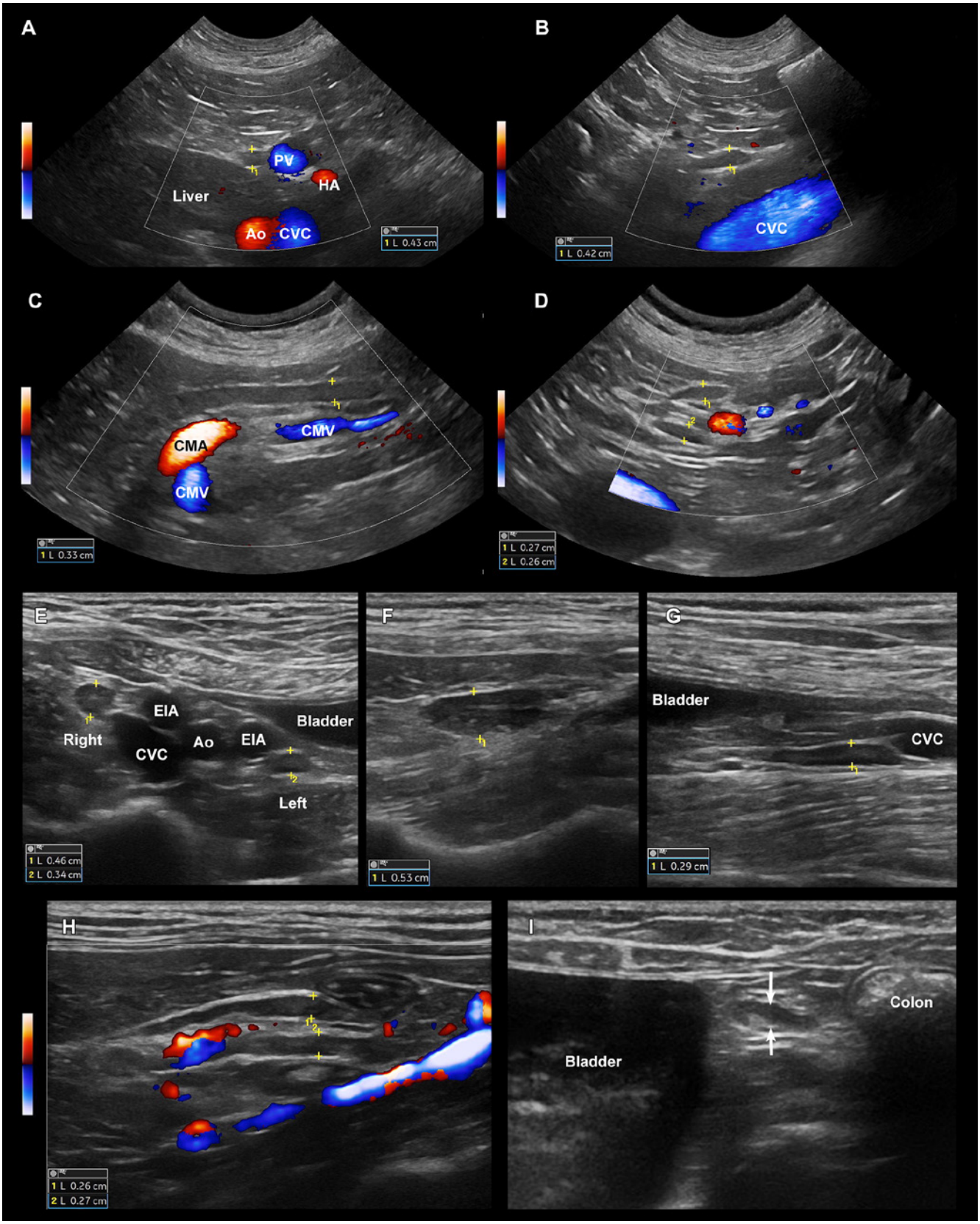


Figure 15.2. **Normal lymph nodes. (A–D)** Sonographic images of normal hepatic (**A**: transverse, **B**: longitudinal) and jejunal (**C**: longitudinal, **D**: transverse) lymph nodes in a 9-year-old Golden retriever dog. Ao, aorta; CMA, cranial mesenteric artery; CMV, cranial mesenteric vein; CVC, caudal vena cava; HA, hepatic artery; PV, portal vein. **(E–G)** Transverse (**E**) image of the medial iliac lymph nodes in the same dog, with longitudinal views of the right (**F**) and left (**G**) nodes, which are asymmetrical in thickness. EIA, external iliac arteries. **(H)** Longitudinal sonogram of normal jejunal lymph nodes in a cat. **(I)** Transverse image of a normal left colic node in another cat.

Vet-ebooks.com

Table 15.2
Lymph node dimensions in normal dogs and cats

	Maximal thickness or height (mm)	Maximal thickness used by the authors
Adult dog		
Jejunal	3.9 (1.6 – 8.2)[a]	4–8 mm[g]
Medial iliac	4.6–4.8 (±0.18 – 0.20)[b]	4–8 mm[g]
Superficial inguinal	3.1 (±0.12)[b]	2–3 mm[g]
Pediatric dog (4- to -12 week old)		
Jejunal	7.1 ± 2.2 (1.5 – 12.5)[c]	5–10 mm[g]
Medial iliac	3.6 (±1.3)[d]	5–10 mm[g]
Cat		
Gastric	2.5–3.1 (±0.72 – 0.28)[e]	3–4 mm
Pancreaticoduodenal	4.6 (3.6 – 6.2)[f]	4–5 mm
Hepatic	2.9 (2.5 – 3.6)[e,f]	3–4 mm
Jejunal	5 (2.8 – 7.2)[f]	4–6 mm
Right colic (ileocecal)	4.1 (2.7 – 4.8)[f]	5 mm
Left colic (caudal mesenteric)	3.5 (±0.98)[e]	5 mm
Medial iliac	4.5 (1.3–14)[f]	5–6 mm

Results are displayed as median (range) or mean (standard deviation).
[a] In dogs without clinical signs of GI disease (Agthe et al. 2009). Authors suspected that some of these nodes might have been reactive, especially in dogs less than 2 years of age.
[b] In clinically healthy adult dogs (Mayer et al. 2010). Right and left medial lymph nodes were not different in size.
[c] In 7- to 12-week-old healthy Beagle puppies (Stander et al. 2010).
[d] In 7 clinically normal 10-week-old small breed puppies (Pugliese et al. 2016).
[e] In 6 cadavers of clinically healthy cats older than 1 year (Tobon et al. 2022).
[f] In 10 adult cats without clinical evidence of abdominal disease (Schreurs et al. 2008). These nodes were identified in more than 50% of the cats.
[g] Depending on dog size.

rather than from the ventral abdomen (Llabrés-Diaz 2004). These nodes can vary in number, but, commonly, a node reaching 7–8 mm in thickness in large dogs is often recognized on the left and right sides of the aorta and caudal vena cava (CVC), respectively, and usually just cranial to the circumflex iliac arteries and veins. Smaller internal iliac nodes are sometimes recognized more caudally, medial to the internal iliac arteries and veins, although these nodes may be inaccessible with ultrasound.

Except for pathological dilatation, abdominal lymphatic vessels and trunks are not readily visible. They join to form the **cysterna chyli**, which can be found in the mid-dorsal retroperitoneal space in dogs and cats as a small oval to semicircular tubular anechoic structure partly encircling the abdominal aorta in the area of the cranial mesenteric artery (Etienne et al. 2013). When visible, the cisterna is usually less than 7 mm thick in dogs and 3 mm in cats without chylous effusion (Figure 15.3).

Peritoneal and Retroperitoneal Effusion

Peritoneal fluid distribution depends on its nature and on gravity. Free fluid moves with gravity, between abdominal organs, and locates itself according to the position of the animal. Free fluid is more likely to be detected when scanning the dependent portion of a dog that is in lateral recumbency (Boysen et al. 2004; see Chapter 2). Small volumes of free fluid often appear as triangular collections that are anechoic or hypoechoic to the surrounding tissues and are better identified at the left lateral margin of the spleen, between hepatic lobes or intestinal loops, or cranial to the apex of the bladder (Spaulding 1993). However, trapped or loculated fluids can remain in the nondependent portion of the abdomen. Trapped fluids are more commonly associated with chronic exudates. Figure 15.4 illustrates the variable appearance of peritoneal effusion depending

Vet-ebooks.com

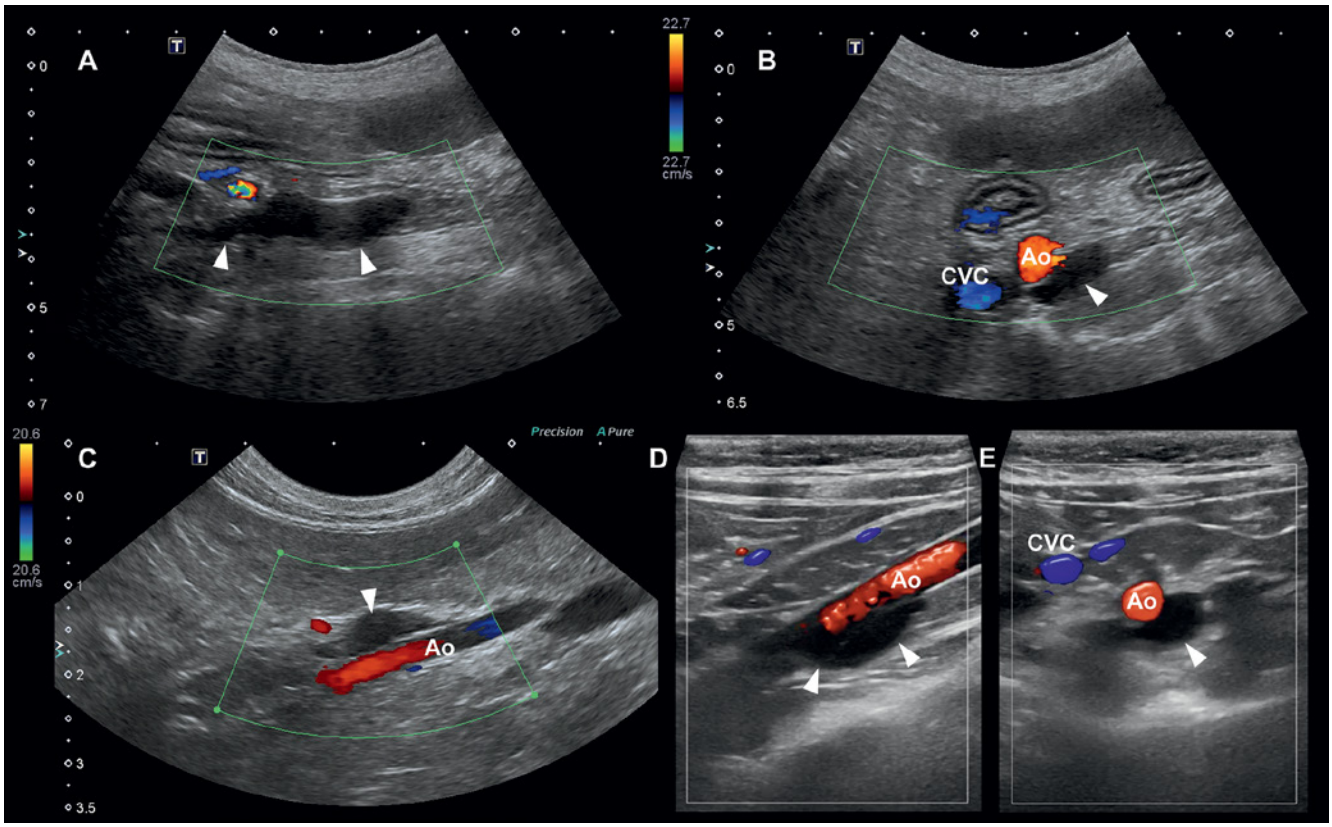


Figure 15.3. **Cysterna chyli with variable location in a dog and two cats.** (for full caption, see facing page)

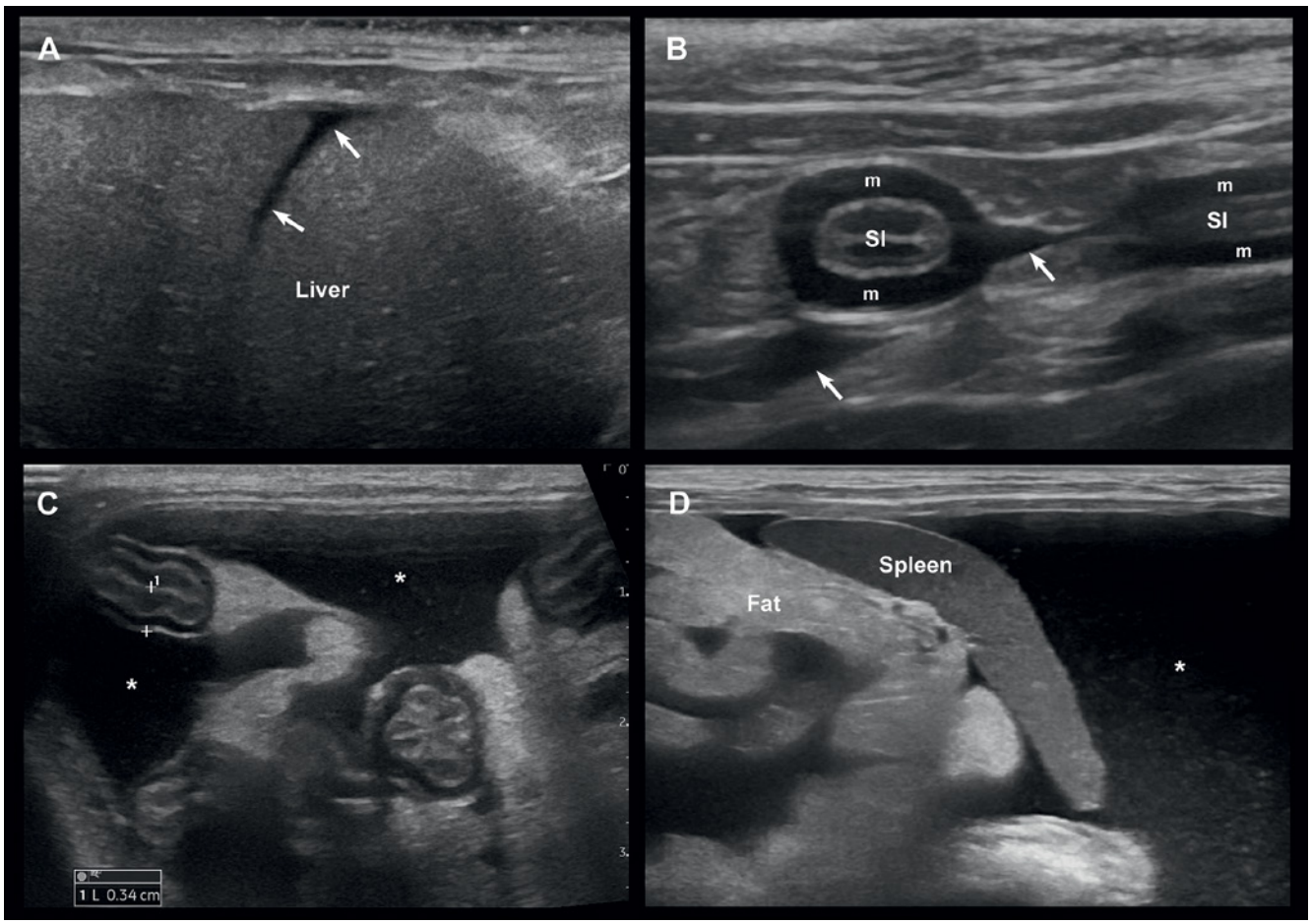


Figure 15.4. **Pure or modified transudates in cats.** (for full caption, see facing page)

Vet-ebooks.com

Figure 15.3. **Cysterna chyli with variable location in a dog and two cats. (A, B)** In this 10-year-old Labrador dog, the cysterna (arrowheads) appears as a well-defined collection of anechoic fluid partly encircling the mid-abdominal aorta on its dorsal left border. It appears fusiform in the longitudinal plane (**A**) and oval to semicircular in the transverse plane (**B**). There was no peritoneal effusion or other signs of lymphatic congestion. **(C)** In this 13-year-old domestic short-hair female spayed cat with acute pyelonephritis and mild peritoneal effusion, the cysterna (arrowheads) is seen ventral to the aorta. **(D, E)** The cysterna chyli (arrowheads) can vary in location. It is seen dorsal and to the left of the aorta in this other cat. Ao, aorta; CVC, caudal vena cava.

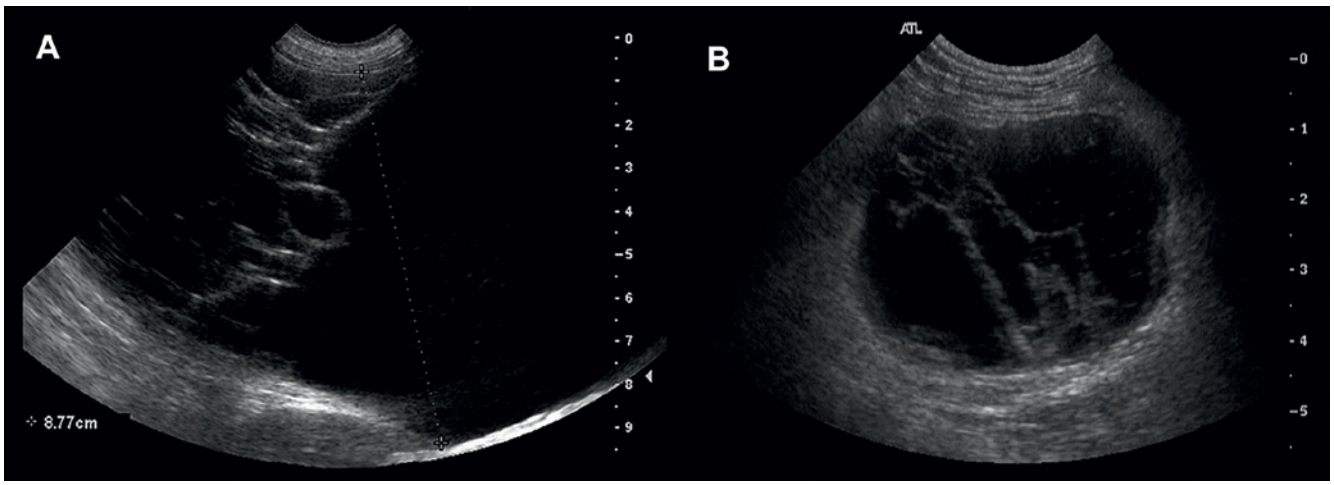


Figure 15.5. **Loculated fluid. (A)** Longitudinal image obtained in the right abdominal quadrant of a cat with a chronically distended abdomen. A large fluid-filled multiloculated cyst is identified, displacing all surrounding structures. Several septae are seen throughout this benign cavitary structure that originated from the omentum. **(B)** Omental seroma in a dog following intestinal surgery. The cavitary area is filled with anechoic fluid and septae. This cystic mass was confirmed not to be an abscess, via fine-needle aspiration.

on its localization and magnitude. Care must be taken not to confuse free or trapped peritoneal fluid with fluid-filled structures, such as severe hydronephrosis, hydroureter, dilated bowel loops, or cysts (Figure 15.5). Structures such as bowel loops or mesenteric folds are usually observed moving within the fluid, particularly if a large volume of peritoneal fluid is present (Figure 15.4C, D).

Retroperitoneal effusion is often seen around the kidneys, such as with acute nephropathies (Figures 11.40, 11.68), but can also accumulate more cranially or caudally with several conditions. The distinction between retroperitoneal and peritoneal effusions may be challenging in some cases and may require repositioning the animal to assess its movement. Effusion in both spaces can coexist with systemic diseases such as vasculitis or hypoalbuminemia.

The echogenicity of the fluid is usually proportional to its content in cells and other debris, which act as ultrasound reflectors. Low cellular fluids, such as transudates, are typically anechoic to hypoechoic (Figure 15.4), in comparison with exudates, which are typically moderately echogenic (Figure 15.6). Highly cellular and homogeneous purulent exudates can appear isoechoic to soft-tissue organs, such as the spleen, and sometimes be recognized only because of their visible motion and lack of vascularity. Exudates can also be septated because of fibrin strands that commonly develop with this type of effusion, particularly with purulent peritonitis (Spaulding 1993).

Figure 15.4. **Pure or modified transudates in cats. (A)** Minimal anechoic peritoneal effusion (arrows) between the liver lobes of a cat with lipidosis. **(B)** Minimal anechoic peritoneal effusion (arrows) in a cat with small intestinal (SI) lymphoma. Note the thickened muscularis wall layer (m). **(C)** Transverse sonographic image of another cat with inflammatory bowel disease and chronic liver disease in which a large volume of mildly echogenic effusion (*) is seen, consistent with a modified transudate. The small intestinal walls (between cursors) were mildly thickened. **(D)** Severe modified transudate in another cat with peritoneal carcinomatosis. The effusion (*) is mildly echogenic and the abdominal fat is thickened and hyperechoic.

Vet-ebooks.com

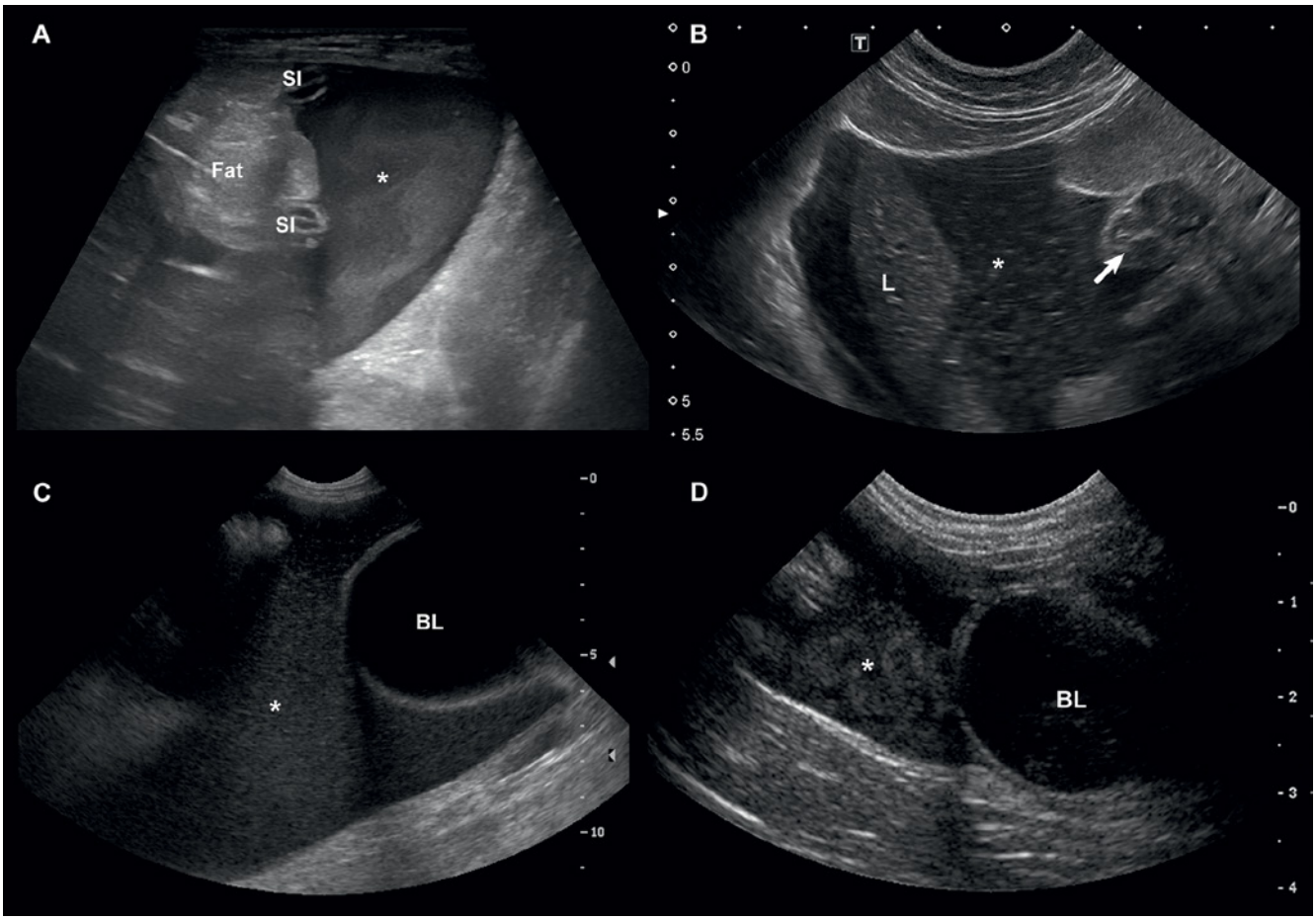


Figure 15.6. Echogenic peritoneal effusions in dogs and cats. (A) Sonographic image of an 8-year-old Labrador with an infiltrated liver with cavitary masses. A large volume of echogenic peritoneal effusion (*) is seen around the mesenteric fat and small intestine (SI). These features are compatible with cellular effusion, such as acute hemorrhage. **(B)** In this cat with pancreatic adenocarcinoma and carcinomatosis, there is marked peritoneal effusion (*), which presents hyperechoic speckles. A hypoechoic nodule (arrow) is detected in the omentum. **(C)** Chylous effusion (*) is typically of moderate to high echogenicity, as in this dog. BL, bladder. **(D)** Longitudinal image of the caudal abdomen of a cat diagnosed with multifocal biliary carcinomas. Floating, echogenic structures (*), not attached to any structure and consistent with blood clots, were identified cranial to the bladder (BL).

Carcinomatosis may also be associated with hyperechoic fluid (Figure 15.6B). Chylous effusion tends to be associated with echogenic effusion (Figure 15.6C).

Peritoneal and retroperitoneal hemorrhage varies in appearance according to the interval between the onset of bleeding and the time of the ultrasonographic examination. Fresh peritoneal blood may appear anechoic or echogenic, with swirling of particles within the fluid (Pintar et al. 2003) (Figures 15.6, 15.7A–C). Hematomas can develop and initially appear as amorphous masses of homogeneous echogenicity (Figure 15.8C). Lysis of the hematoma produces a more heterogeneous appearance, with the formation of cystic areas and septa (Figure 15.8B). In a previous study of 39 dogs with nontraumatic hemoabdomen, a malignancy was identified in 80% of cases and hemangiosarcoma in 70% (Pintar et al. 2003).

However, it must be pointed out that some overlap exists regarding the echogenic appearance of different types of fluids. Hence, modified transudates may look similar to exudates. Other ultrasonographic findings, such as the presence of nodules on the surface of the peritoneum in cases of carcinomatosis, or in the presence of a large splenic mass, should be used to orient the diagnosis.

Table 15.3 describes the typical appearance of variable types of peritoneal and retroperitoneal effusion in dogs and cats.

Vet-ebooks.com

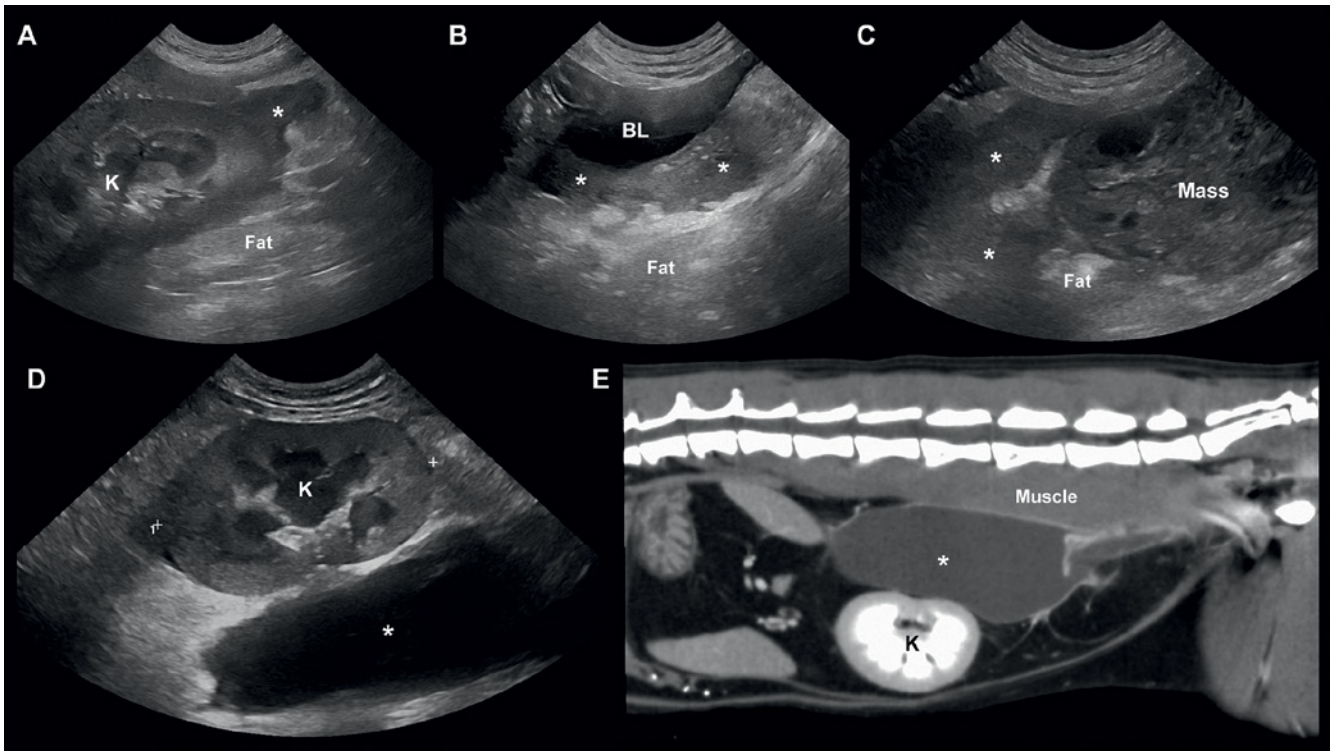


Figure 15.7. Retroperitoneal effusion. (A–C) In this 8-year-old Boxer presented for lethargy and abdominal pain, a moderate volume of echogenic effusion (*) is found in retroperitoneal space, surrounding both kidney (K) and the bladder (BL), consistent with spontaneous hemorrhage. A 5-cm cavitary mass of mixed echogenicity was found more caudally at the origin of this spontaneous hemorrhage (C). **(D, E)** In this cat with traumatic iatrogenic urethral rupture following repeated catheterizations, there is a well-circumscribed accumulation of fluid (*) in the left retroperitoneal space between the left kidney (K) and the bladder, which appears anechoic on ultrasound (D). Urine content (*) was found after ultrasound-guided centesis and confirmed to directly communicate with an urethral leakage site on CT, indicating an urinoma. As the retroperitoneal space encompasses the bladder and communicates with the pelvic canal caudally, urethral tears in cats can cause retrograde urine accumulation into the retroperitoneal space.

Peritonitis, Steatitis, and Pneumoperitoneum

A variable amount of effusion is observed with peritonitis in dogs and cats, usually with moderate to high echogenicity because of the high cellular content (Boysen et al. 2003) (Figure 15.9C). The peritoneum, omentum, and mesentery may also appear thickened, hyperechoic, and hyperattenuating, focally or diffusely (Figure 15.9A–C). These features can significantly limit the penetration of the ultrasound beam and consequently the ability to visualize and assess deep organs. In these instances, the abdominal structures appear ill-defined, and their inner architecture cannot be well recognized. An area of mesenteric fat hyperechogenicity is suggestive of inflammation (steatitis/vasculitis) in dogs and cats and should be thoroughly investigated for a possible nearby source of inflammation, such as intestinal perforation or pancreatitis (Boysen et al. 2003). A ruptured biliary tract with secondary bile peritonitis must also be considered when focal effusion associated with hyperechoic fat is present in the cranial abdomen at the liver hilus or around the gallbladder (see Chapter 7). Bladder rupture is also typically associated with a variable amount of effusion and hyperechoic fat in the caudal abdomen (Figure 15.7C–D, see also Chapters 6 and 11). Hyperechoic fat is often seen at the ileocecocolic junction in cats and may not be clinically significant (Hahn et al. 2017).

Leakage or rupture of the gastrointestinal (GI) tract is one of the most common causes of septic peritonitis in dogs and cats. GI leakage may be caused by postsurgical intestinal dehiscence, GI perforation caused by a penetrating foreign body, GI ulcer (benign or malignant), gastric dilatation and volvulus, intestinal intussusception, intestinal infarction, penetrating abdominal trauma, or iatrogenic cause (Figures 15.8A, 15.9C–F) (Boysen et al. 2003). Inflamed perienteric fat often

Vet-ebooks.com

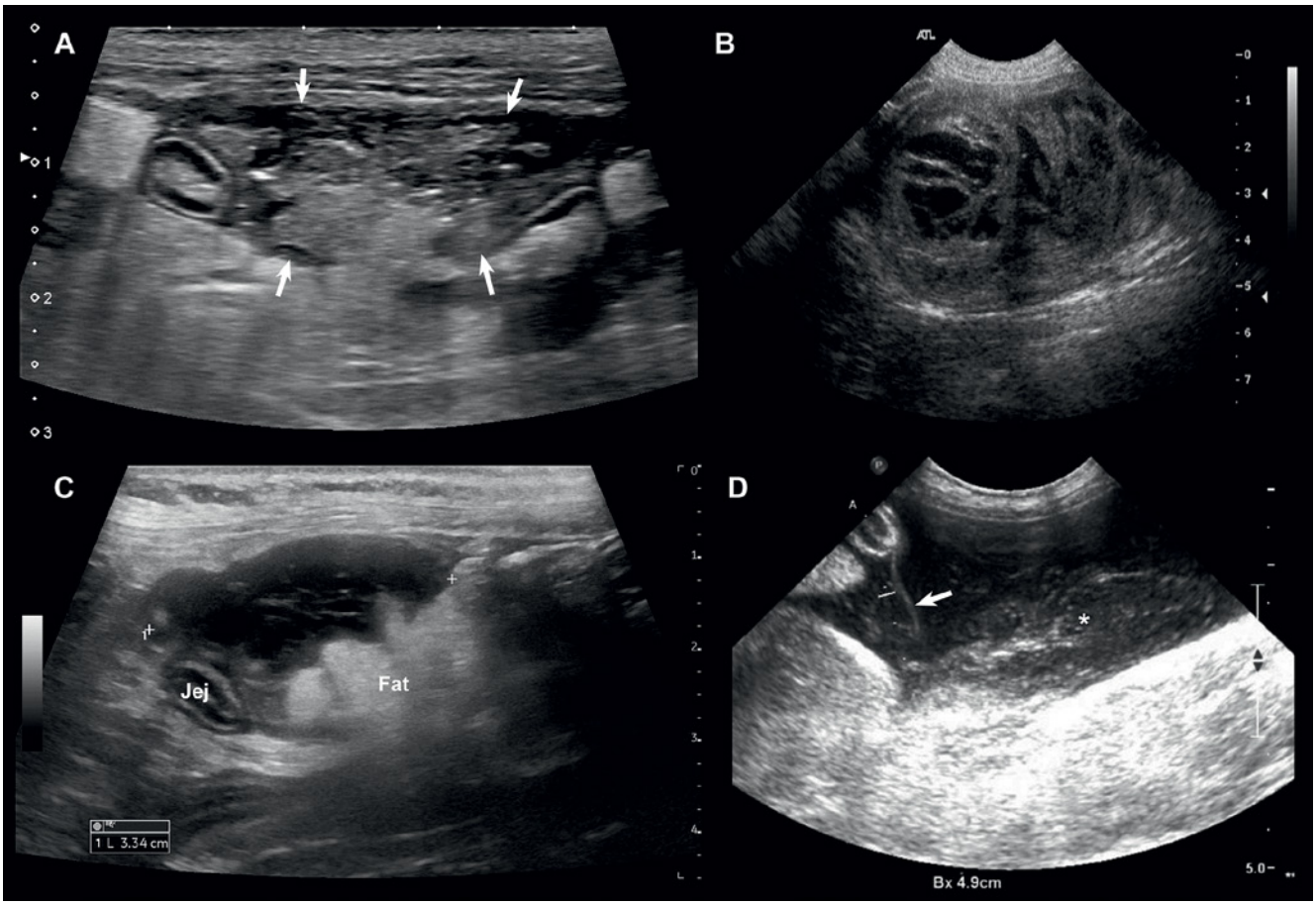


Figure 15.8. **Peritoneal hematomas.** (for full caption, see facing page)

Table 15.3
Typical ultrasonographic appearance of peritoneal and retroperitoneal effusions

Ultrasonographic appearance	Diagnostic differential
Anechoic or hypoechoic fluid	Pure or modified transudate Serohemorrhagic fluid Urine leak Chylous effusion
Echogenic with mobile particles	Fresh hemorrhage Modified transudate Feline infectious peritonitis Purulent exudate or loculated abscess Serosanguinous exudate Carcinomatosis Chylous effusion
Highly echogenic with fibrous strands	Purulent exudate
Mobile echogenic masses	Blood clots Masses or nodules attached to the mesentery, omentum, or visceral serosa (carcinomatosis, lymphomatosis, sarcomatosis)

appears as a mass, displacing adjacent structures such as intestinal loops. In addition to the other ultrasonographic changes, GI ileus with fluid accumulation is commonly observed. Primary bacterial peritonitis with no identifiable intra-abdominal source of infection or penetrating injury is also described in dogs and cats, generally producing an exudative effusion and similar inflammatory changes (Culp et al. 2009). GI contents such as foreign material or free gas can sometimes be recognized in the peritoneal space. Free gas appears as echogenic foci or lines that are associated with reverberation artifacts, such as comet tails. These lines collect between the nondependent abdominal wall and intra-abdominal structures, such as the liver, omentum, stomach, or intestine, but they may also be contained in tissues surrounding the GI tract, such as the mesentery (Figure 15.10). When peritoneal effusion is present, gas bubbles can appear as floating echogenic foci. Free gas tends to shift in position with bowel or patient movement.

Pneumoperitoneum can also be caused by laparotomy, abdominal wall trauma, bladder rupture, an extension of pneumothorax, splenic necrosis, and clostridial peritonitis, or it can be idiopathic (Saunders

Vet-ebooks.com

Figure 15.8. Peritoneal hematomas. (A) Longitudinal image of the mid-ventral abdomen of a dog that had previous intestinal surgery for removing a foreign body. Postoperative dehiscence resulted in peritonitis and a large hematoma formed between intestinal loops. This hematoma appears as a large mass (between arrows) of heterogeneous echogenicity, with a few hyperechoic speckles presumably indicating trapped air bubbles. **(B)** This mass of mixed echogenicity was found in the peritoneal cavity of another dog with splenic hemangiosarcoma. While the appearance of this mass suggested metastasis, it was confirmed to represent a large hematoma. **(C)** This 5-year-old mixed Pittbull was presented for abdominal pain after jumping off a balcony. There is an irregular 3.3 cm hypoechoic mass partly confluent with the wall of a jejunal segment (Jej), surrounded by hyperechoic fat. This presumed hematoma resolved on a follow-up ultrasound exam. **(D)** Postrenal biopsy bleeding in a 1-year-old Cocker Spaniel. Amorphous clot formation is seen (*). Swirling hyperechoic lines were also present (arrow) during the examination, indicating active bleeding.

and Tobias 2003). If a large volume of free air is in the peritoneal cavity, ultrasonographic visualization of deep structures may be significantly hampered by reverberation artifacts or shadowing. Free air resulting from celiotomy usually resolved 7–10 days after the procedure, but the significance of free air found in dogs or cats after surgery must be interpreted with caution, particularly if other signs of intestinal dehiscence are not present, as it can sometimes persist longer. Similarly, in these postsurgical cases, a small amount of effusion of low echogenicity and mildly hyperechoic fat are often recognized, usually resolving between 3 and 10 days (Matthews et al. 2008). Small linear hyperechoic foci associated with comet-tail artifacts crossing the intestinal wall near the suture and free-flowing in the peritoneal cavity or reaching fluid pocket may be features of dehiscence of the intestinal suture (Costanzo et al. 2023). Abdominal centesis and follow-up examinations may be required to rule out dehiscence.

Peritoneal adhesions may develop following peritonitis, laparotomy, or other conditions, causing pain or affect the function of abdominal structures such as GI motility and patency (Figure 15.11).

Omental and mesenteric sterile steatitis has also been recognized in dogs and cats (Adamama-Moraitou et al. 2008; Komori et al. 2002; Zini et al. 2007). Although the etiology of this condition is unknown, predisposing factors could include recent surgery, retained surgical material, prior abdominal trauma, ulcerative disease, autoimmune disease, hypocalcemia, or drugs. Sonographic features include a well-defined hyperechoic mass in the root of the mesentery, displacing intestinal loops (Figure 15.12).

Infectious or noninfectious sclerosing encapsulating peritonitis is a rare condition mainly characterized by centrally located bowel loops surrounded by a large amount of echogenic effusion. Rounding of liver and spleen margins, fluid loculations, and adherences between organs and thickened peritoneal lining may also be observed (Gremillet et al. 2022; Veiga-Parga et al. 2015) (Figure 15.13).

Peritoneal and Retroperitoneal Abscesses, Granulomas, and Pyogranulomas

Abscess formation can precede or follow the onset of peritonitis. Ultrasonographically, peritoneal abscesses often present as fluid pockets with particles, surrounded by an ill-defined hyperechoic wall and sometimes internal septa or gas foci (Campbell 2009; Marvel and MacPhail 2013) (Figures 15.14, 15.15). The cavitary portion of the abscess is often hypoechoic and far acoustic enhancement may be recognized unless the cell count is high, or there is gas with reverberating artifact when gas is present. Conversely, caseous abscesses may be associated with some acoustic shadowing (Figure 15.14D).

Peritoneal and retroperitoneal granulomas or pyogranulomas are rare in small animals. They can be found with feline infectious peritonitis (FIP), mycobacterial or fungal diseases, or caused by foreign bodies, such as retained surgical sponges (Merlo and Lamb 2000; Share and Utroska 2002). FIP presents with a wide range and distribution of sonographic lesions, usually multifocal, with effusion and abdominal lymphadenopathy being the most prevalent findings, affecting more than 80% of cats (Müller et al. 2023) (Figure 15.16).

Foreign bodies can produce a suppurative granulomatous or pyogranulomatous response of variable size (Figure 15.17). Some foreign bodies, such as wooden sticks or grass awns, can migrate through the abdominal wall or GI and create a sinus tract that can be recognized by their tubular, often tortuous shape and their marked hypoechogenicity in comparison with the surrounding tissues, which appear hyperechoic because of the inflammatory reaction and/or scar tissue (Penninck and Mitchell 2003; Stander and Kirberger 2011). The foreign body itself is not always

Vet-ebooks.com

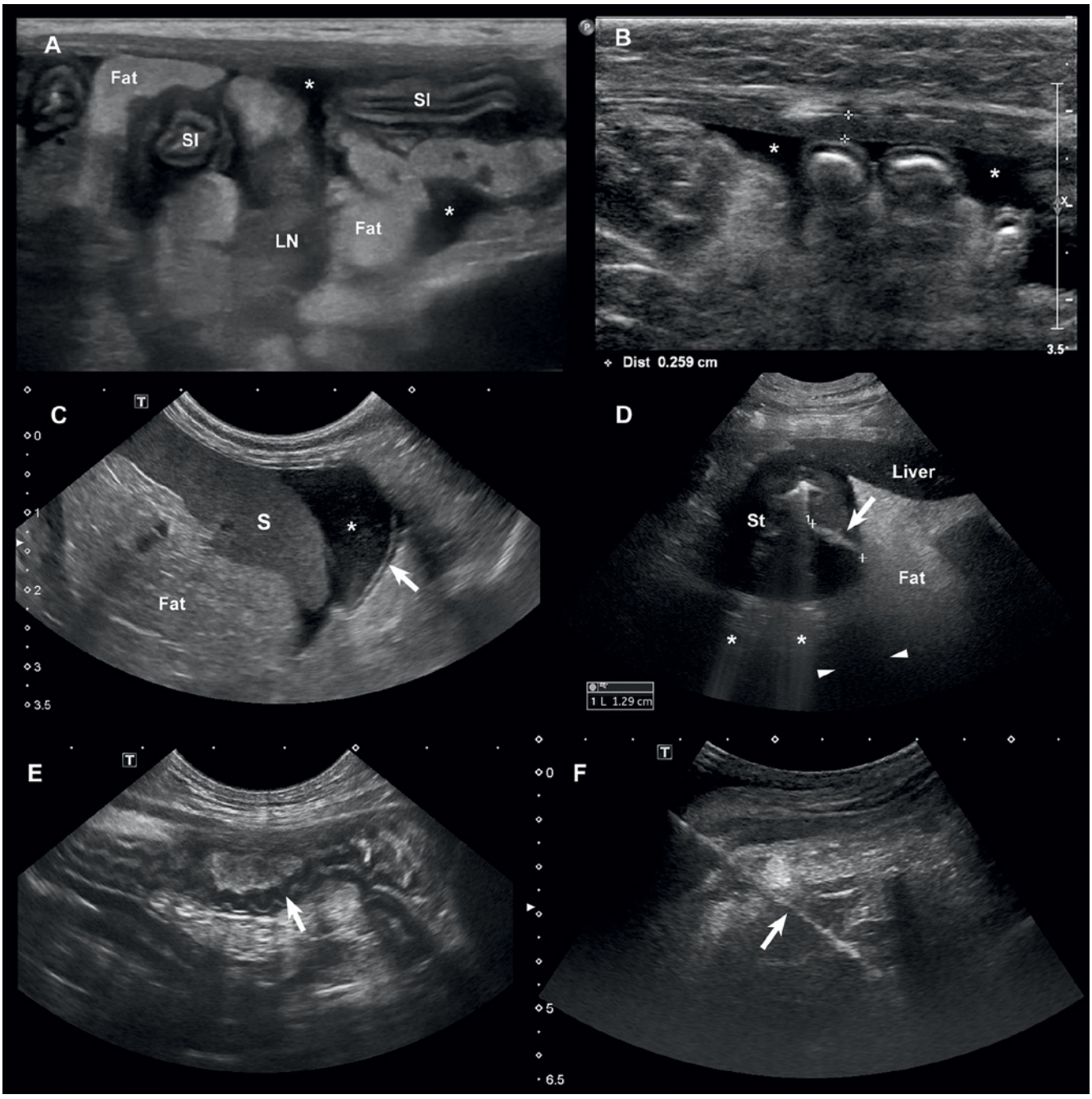


Figure 15.9. **Peritonitis and steatitis. (A) Feline infectious peritonitis (FIP)**. A large volume of hypoechoic peritoneal effusion (*) is seen around a markedly thickened, irregular, hyperechoic mesentery (fat). The changes to the mesentery were caused by pyogranulomatous vasculitis and steatitis. **(B)** In another 13-year-old cat with **FIP**, the parietal peritoneum is thickened (2.6 mm), delineated with anechoic peritoneal fluid (*). **(C) Surgical dehiscence following cystotomy in a small dog**. Echogenic peritoneal effusion (*) is detected between the spleen (S) and the thickened peritoneum (arrow). **(D) Gastric wall perforating foreign body**. Oblique image obtained in the left cranial abdomen of a dog with a history of acute vomiting and severe abdominal pain. A 12.9 mm hyperechoic interface (arrow) is penetrating the wall of the stomach (St), associated with partial acoustic shadowing (arrowheads), consistent with a foreign body. The peripheral fat is markedly hyperechoic and hyperattenuating. Reverberating artifacts (*) are seen deep to gas bubbles present in the stomach. **(E)** Intestinal corrugation (arrow) secondary to **septic peritonitis** in a dog with gastric ulcer perforation. The corrugated bowel is surrounded by hyperechoic fat. **(F) Migrating wooden stick in a dog**. In this dog that presented for recurrent craniolateral abdominal pain and swelling, a hyperechoic linear foreign body (arrow) casting partial acoustic shadowing was detected originating from the stomach and reaching the subcutaneous tissues.

Vet-ebooks.com

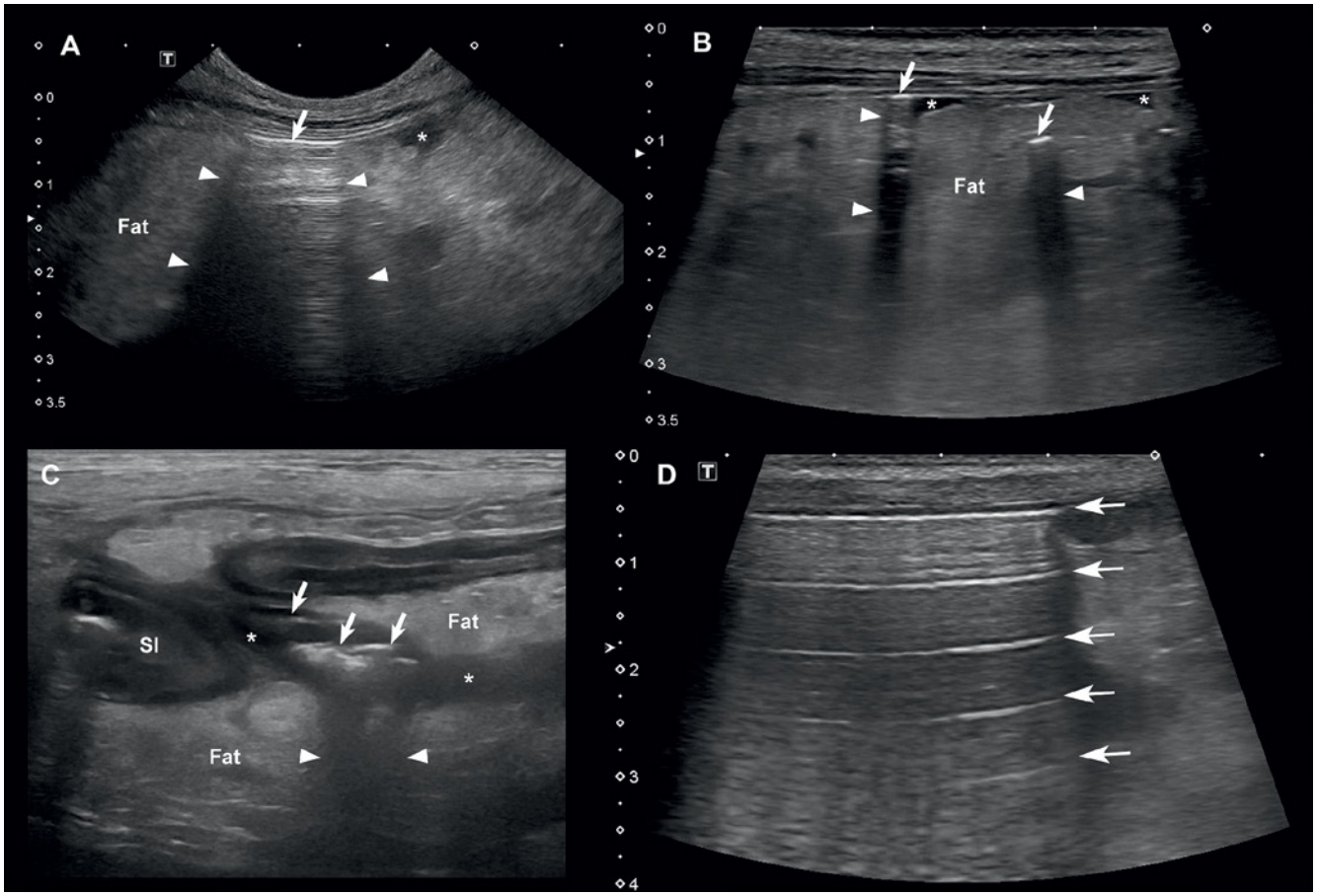


Figure 15.10. **Free air in the peritoneal space and mesentery in dogs with intestinal perforation**. **(A)** In the cranioventral abdomen, hyperechoic lines are detected between the abdominal wall and omental fat, which correspond with the upper side abdomen of this dog in dorsal recumbency. A combination of distal shadowing and reverberation artifacts, including "comet tails," is present (between arrowheads). These artifacts move during the exam along the inner surface of the abdominal wall, indicating free air. **(B)** In the same dog, more caudally, shorter hyperechoic lines consistent with air bubbles (arrows) are seen between the abdominal wall and the mesenteric fat as well as within the mesentery. A combination of distal shadowing and reverberation artifacts is also present (arrowheads). A small volume of peritoneal effusion (*) is also detected. **(C)** In this second dog, there is a collection of hypoechoic inflammatory tissue (*) in the central abdominal fat, which is heterogeneously hyperechoic. Several hyperechoic gas interfaces (arrows) are entrapped in this collection of tissue, casting a dirty shadow (between arrowheads). The adjacent small intestinal (SI) wall is thickened with altered layers at the site of perforation. **(D)** When a large volume of gas is present, a reverberation artifact that appears as a series of parallel and equally spaced hyperechoic lines (arrows) can be seen (also see Figure 1.18).

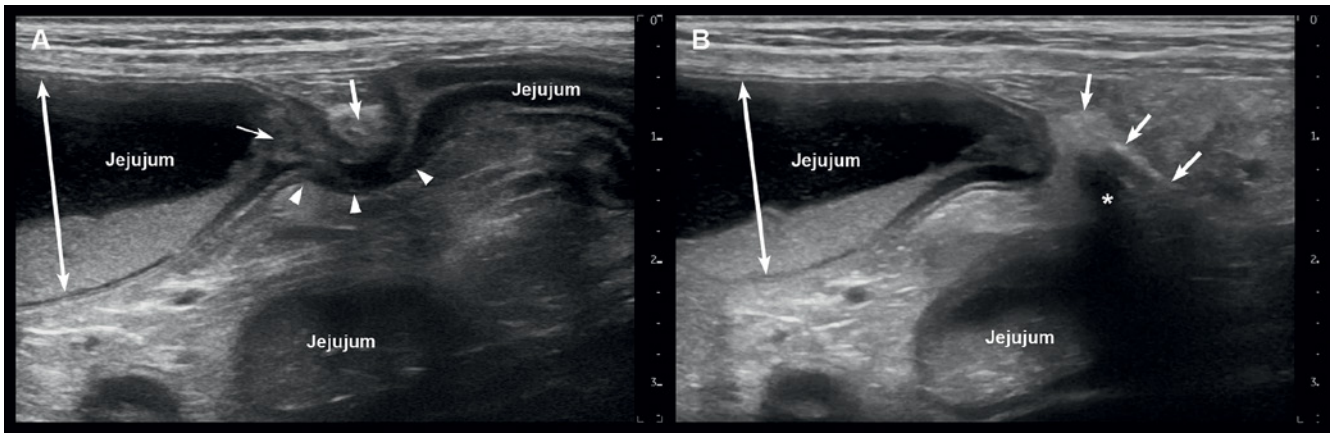


Figure 15.11. **Adhesions causing small intestinal obstruction. (A, B)** In this 2-year-old Chihuahua presented for chronic vomiting, a hyperchoic and hyperattenuating band of tissue (larges arrows) is partly encircling a segment of jejunum, causing mechanical obstruction. The oral portion of the bowel lumen is severely dilated (double-arrow) and abruptly interrupted (thin arrow) at the site of the external stenosis. Note the focal dorsal deviation of the intestinal wall in **(A)** (arrowheads). In **(B)**, the band of fibrous tissue (adhesion) extends dorsally and is associated with relatively acoustic shadowing (*). Note the well-demarcated horizontal border of echogenic debris inside the distended bowel that is consistent with chronic ileus.

Vet-ebooks.com

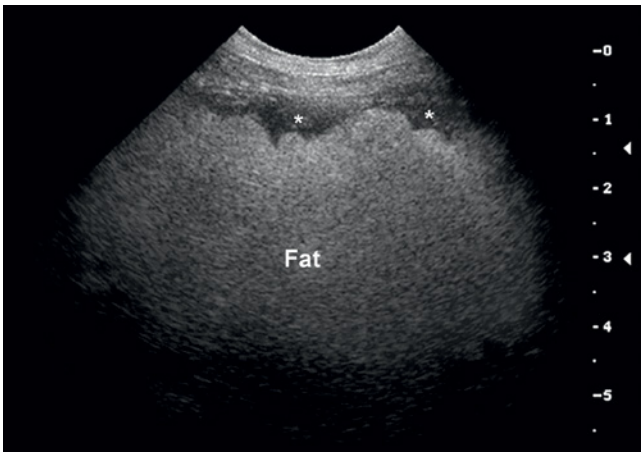


Figure 15.12. Omental or mesenteric steatitis. Longitudinal image of the right abdomen of a dog that had a recent surgery for splenic torsion. An irregular, hyperechoic, hyperattenuating mass occupies a large portion of the right abdomen and is surrounded by hypoechoic peritoneal effusion (*). These changes were attributed to omental or mesenteric steatitis, possibly secondary to surgical manipulation. They eventually resolved. The ultrasonographic changes to the fat prevented any visualization of deep abdominal structures.

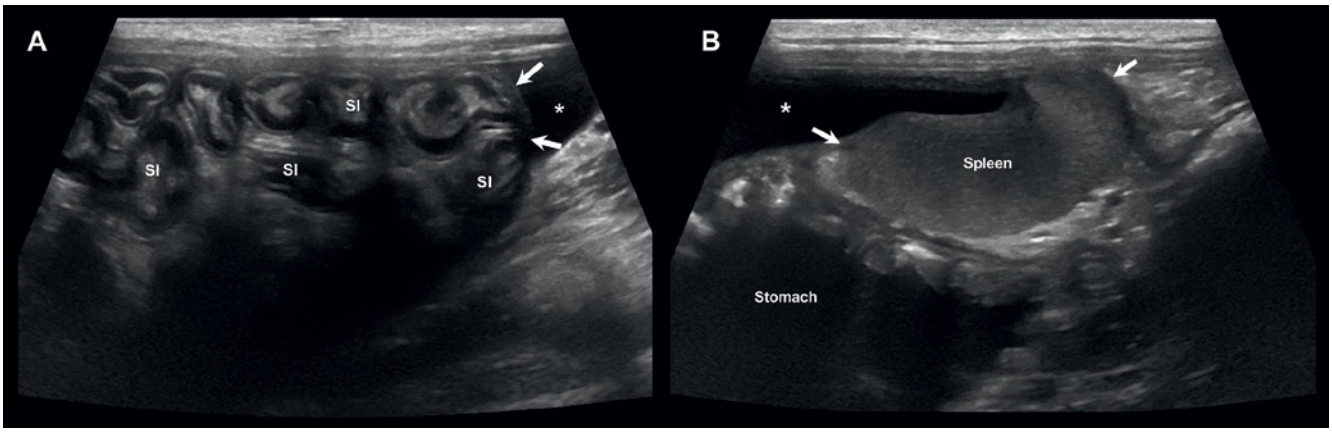


Figure 15.13. Sclerosing encapsulating peritonitis in a 5-month-old puppy. **(A)** Small bowel loops (SI) are gathered in the central abdomen, surrounded by a thick hypoechoic capsule (arrows) and mildly echogenic fluid (*). **(B)** Fluid was also present in the rest of the abdomen (*), and both liver and spleen were small with rounded margins (arrows).

ultrasonographically visible or associated with signs of peritonitis. Wooden sticks usually appear as linear hyperechoic interfaces, with acoustic shadowing in most cases (Figure 15.9F). However, plant materials chronically embedded in tissues can undergo a degradation that can render these objects less attenuating and therefore less likely to be associated with acoustic shadowing (Staudte et al. 2004). Grass awns appear as spindle-shaped, linear, hyperechoic interfaces measuring 3–4 cm long, with acoustic shadowing less commonly observed than with wood (Gnudi et al. 2005; Staudte et al. 2004) (Figure 15.17A, B). However, identification of grass awns in the abdominal cavity is often difficult on ultrasound, the changes being more generally limited to nonspecific signs of peritonitis (Griffeuille et al. 2023). Retained surgical sponges typically appear as a hypoechoic mass with central hyperechoic foci or bands and are associated with other variable signs of peritonitis (Merlo and Lamb 2000) (Figure 15.18), although the sonographic appearance may vary depending on the type of sponge or the presence of a concurrent abscess (Mai et al. 2001).

Nodular Fat Necrosis

Nodular fat necrosis, also referred to as **Bates body**, is a benign and incidental finding in dogs and cats, appearing as partially mineralized circular to oval soft-tissue masses in the abdominal fat. With ultrasound, these foci can be recognized as well-defined hyperechoic and hyperattenuating (acoustic shadow) nodules or masses in the abdominal fat, which can be multiple in the same patient (Schwarz et al. 2000) (Figure 15.19). A hypoechoic center may also be observed.

Vet-ebooks.com

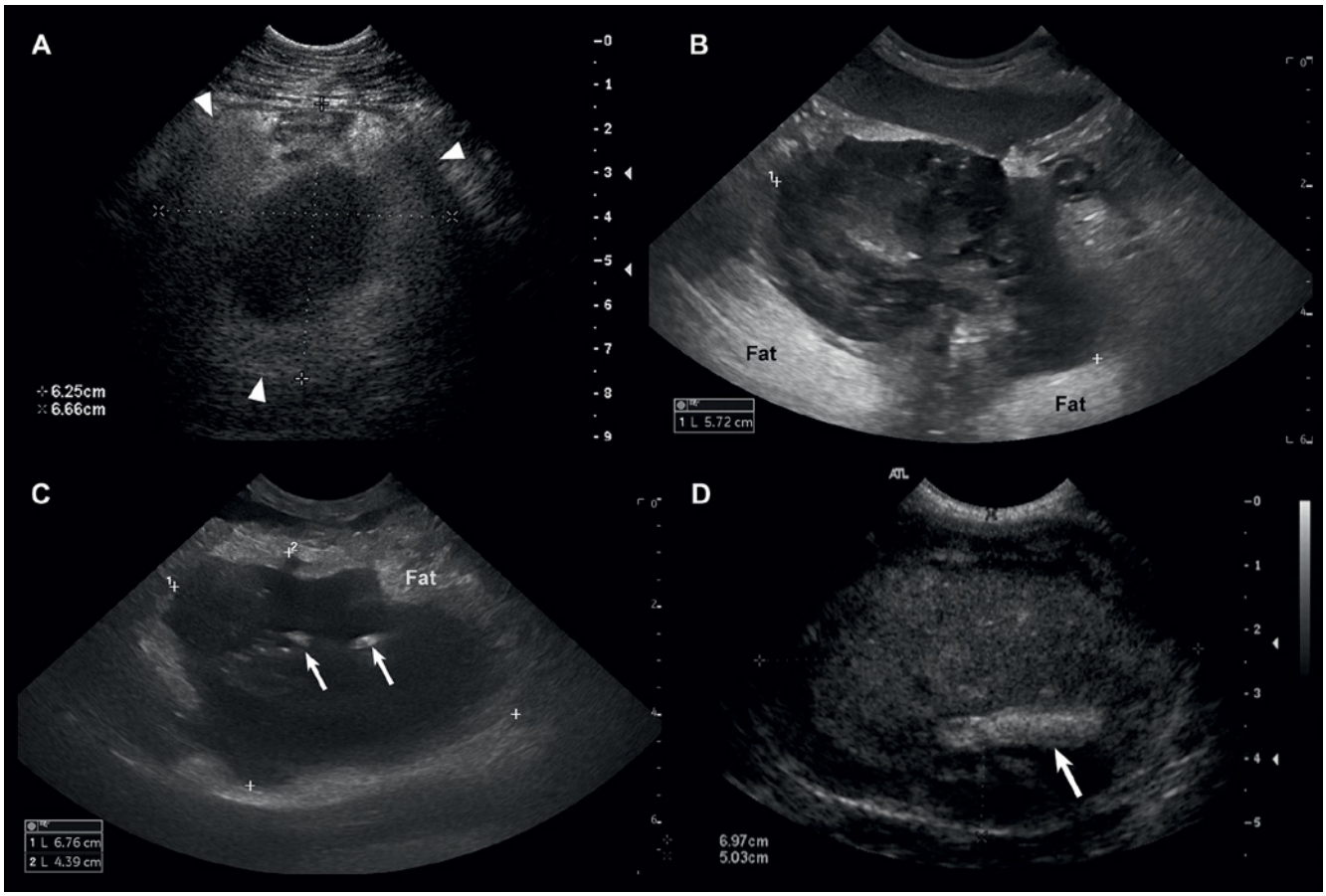


Figure 15.14. **Peritoneal abscesses in four dogs. (A)** Transverse image of the left caudal abdomen of a dog with abdominal pain. An ill-defined hypoechoic area, surrounded by an ill-defined hyperechoic rim of steatitis (arrowheads), is present without evidence of organ involvement. A sterile abscess, attached to the omentum and mesentery, was confirmed at surgery. **(B)** In this 15-year-old Dachshund with a 2-week history of abdominal pain, a 5.7 cm heterogeneous hypoechoic mass with small hyperechoic foci was found in the central abdomen, surrounded by hyperechoic fat. This mass was adjacent to the cecum that showed a thickened wall with a loss of layers. This was consistent with a chronic abscess due to cecal perforation. **(C)** Subacute abscess in a third dog with a perforating intestinal foreign body. A 6.8 cm hypoechoic mass with gas foci (arrows) and surrounded by hyperechoic fat was found in the mesentery. **(D)** In a fourth dog with a history of chronic abdominal pain, a 7-cm-long oval mass of mixed echogenicity was detected and confirmed to represent a caseous abscess with vegetal fragments. The abscess presents a hypoechoic wall containing pus and debris of moderate echogenicity, and a hyperechoic structure (arrow) presumably consistent with the caseous portion, casting mild acoustic shadowing.

Peritoneal and Retroperitoneal Neoplasia

Peritoneal soft-tissue masses seen with ultrasonography are most often related to abdominal organs, such as the spleen, liver, pancreas, or intestine. **Lipomas**, infiltrative or not, may also be found within the omentum, mesentery, or other portions of the abdomen (Figure 15.20). These fatty masses are typically hyperechoic and can be hyperattenuating, some with a necrotic center mimicking an abscess (Mayhew and Brockman 2002).

Mesothelioma is a rare primary neoplastic process of the peritoneum that may infiltrate the omentum or mesentery. Extensive abdominal effusion is the most common change in both dogs and cats, with variable omental and mesenteric nodular infiltration (Geninet et al. 2003; Heerkens et al. 2011).

Widespread dissemination of neoplasia throughout the peritoneum, a condition referred to as **carcinomatosis**, is more common than primary peritoneal tumors. The term carcinomatosis is used in veterinary medicine to include peritoneal invasion by epithelial, mesenchymal, or hematopoietic tumors (Monteiro and O'Brien 2004), although sarcomatosis

Vet-ebooks.com

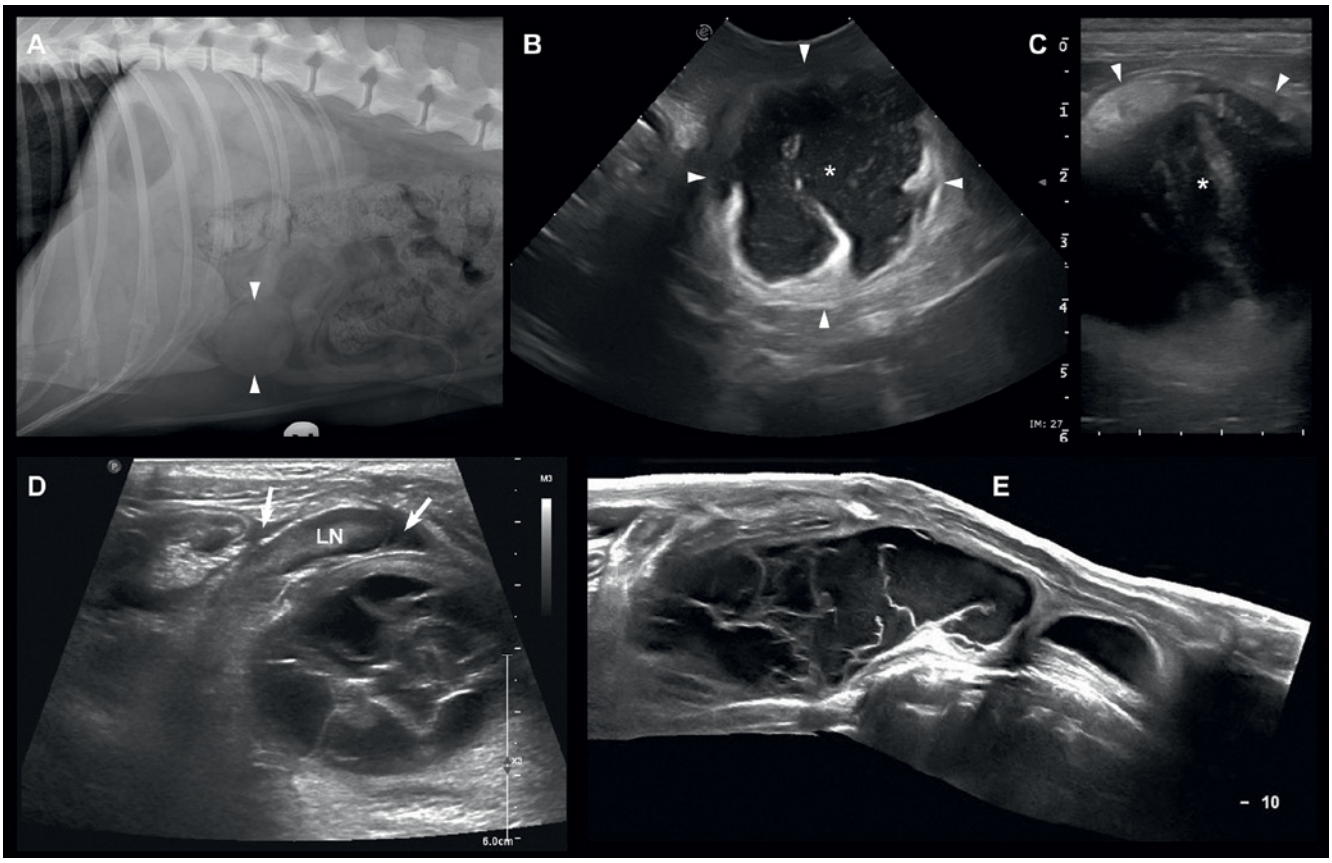


Figure 15.15. **Peritoneal abscesses in two other dogs.** (for full caption, see facing page)

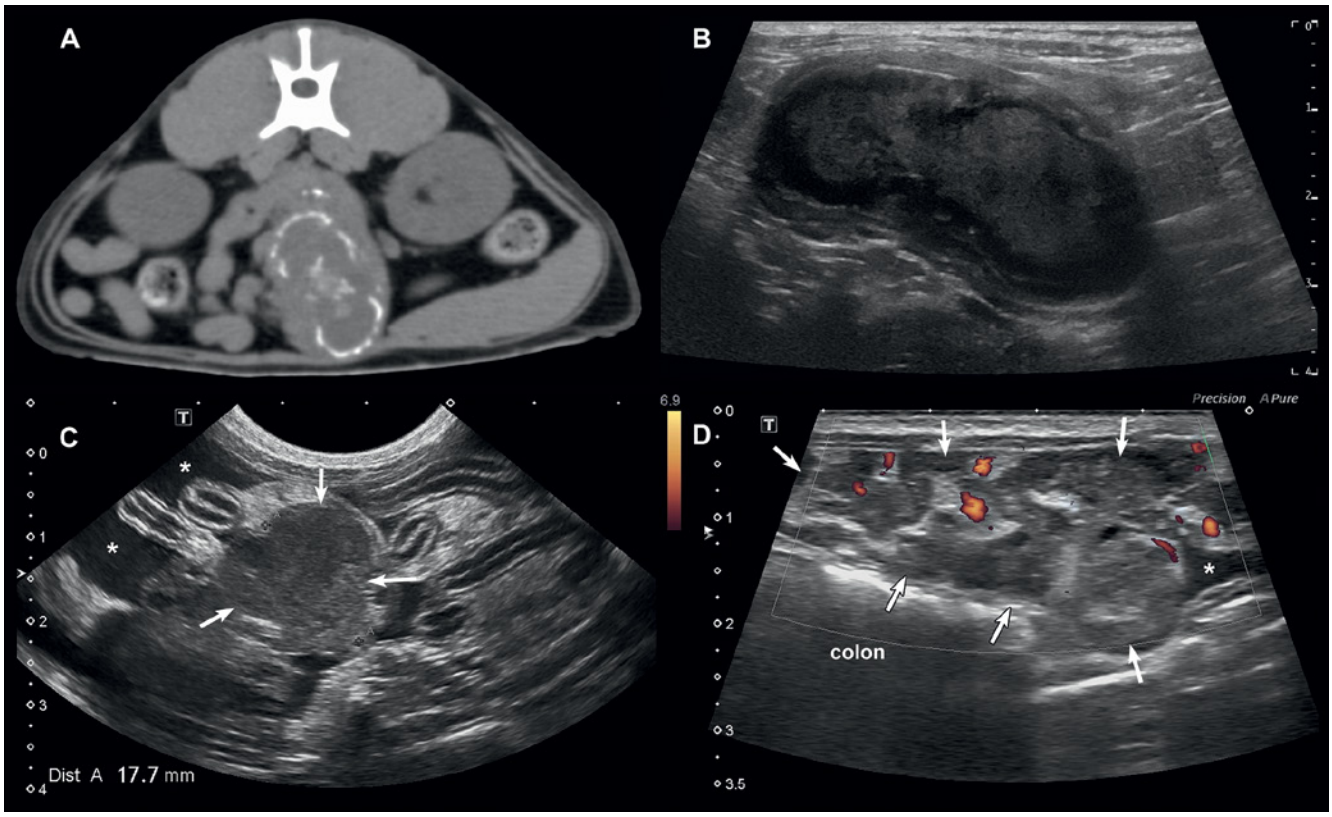


Figure 15.16. **Pyogranulomas in three cats.** (for full caption, see facing page)

Vet-ebooks.com

Figure 15.15. Peritoneal abscesses in two other dogs. **(A)** Initial right-lateral radiograph of the cranial abdomen of an 11-year-old dog presented in shock with a 2-week history of abdominal pain, on which a well-defined, round soft-tissue mass is seen caudal and ventral to the body of the stomach (arrowheads). **(B, C)** Sonographically, this mass presents a large central fluid cavity with echogenic contents (*) and surrounded by a capsule (arrowheads), which is more conspicuous using a higher-frequency probe (in C). The abscess was embedded in fat adjacent to the stomach, without evidence of other organ involvement. Caseous content was confirmed by fine needle aspiration. **(D, E)** In this 3-month-old dog presented 3 weeks post-ovariohysterectomy with fever, mild abdominal effusion (arrows) and a large, multicystic mass occupying a large part of the abdomen, was seen. The effusion was taped and revealed a septic suppurative inflammation with cocci. The extensive peritonitis with multifocal fibrosis surrounding the abscess. The panoramic sonogram (**E**) represents well the extent of the lesion. Surgical debridement and peritoneal lavage were curative.

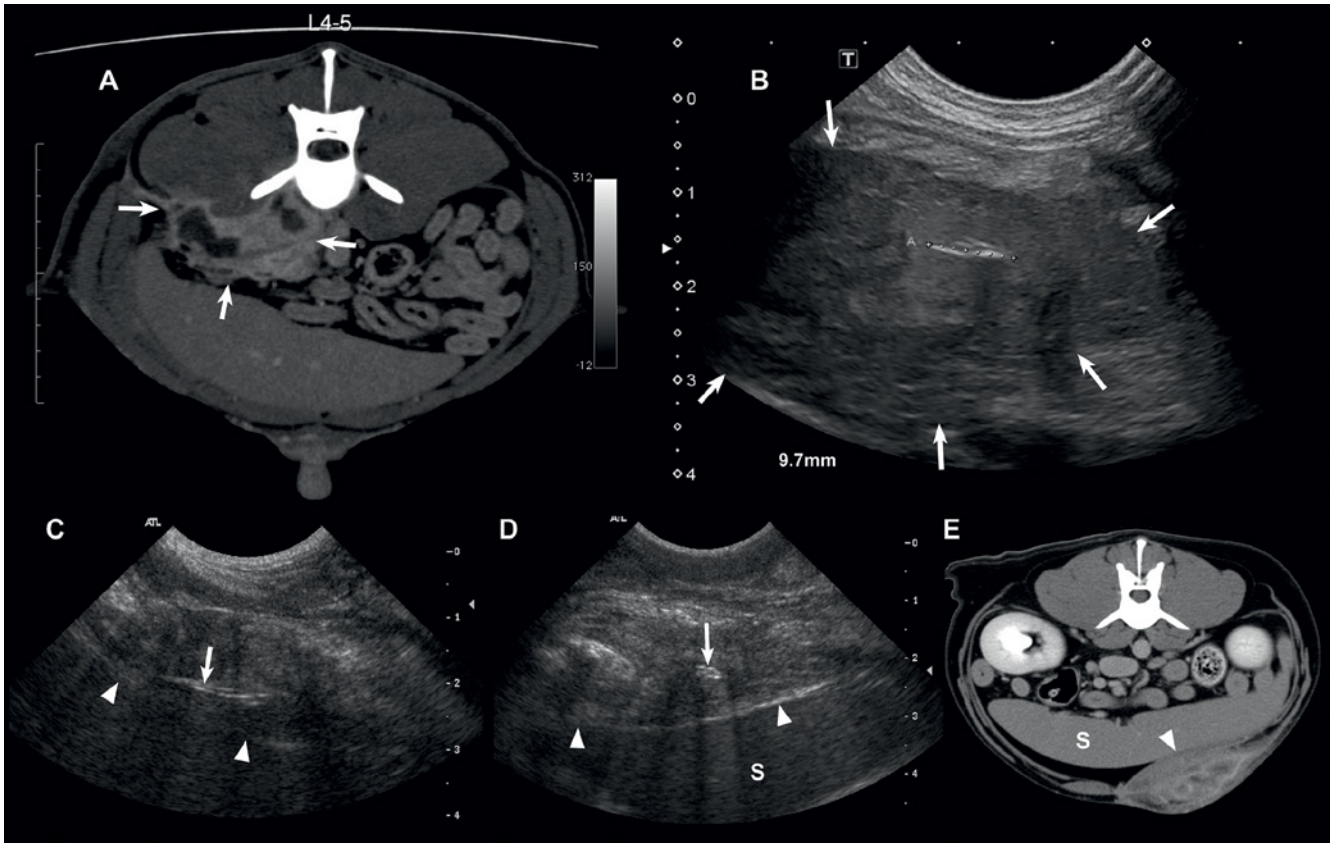


Figure 15.17. Grass awn migration in two dogs. (A, B) Chronic sublumbar abscess in a dog. **(A)** Computed tomographic (CT) transverse image at the level of L4 on which a 4 cm × 5 cm mass with heterogeneous contrast enhancement is present in the right ventral sublumbar muscles (arrows). Using ultrasound with a ventrolateral approach **(B)**, a nearly 1-cm-long fusiform hyperechoic structure consistent with a grass awn (between cursors) is detected within a soft-tissue mass of moderate echogenicity (arrows). This type of foreign body is typically not detected with CT. Courtesy of Laurent Couturier, Azurvet, France. **(C–E)** Sagittal (**C**) and transverse (**D**) sonographic images of a dog presented for recurrent ventral abdominal swelling. Hypoechoic heterogeneous tissue thickening is seen ventral to the peritoneal surface (arrowheads). In the sagittal plane (**C**), a 3-cm-long, fusiform structure composed of nearly parallel, sharply demarcated hyperechoic lines is detected (arrow). This structure is tubular in the transverse plane (**D**). **(E)** This mass of tissue delineated by the peritoneum (arrowhead) was initially interpreted as probable neoplasia with contrast-enhanced computed tomography. Retrospective assessment did not help in identifying the grass awn. Ultrasound was also used to locate the foreign object during surgery.

Figure 15.16. Pyogranulomas in three cats. **(A, B)** Large necrotic pyogranuloma in the mid-abdomen of this in this 1-year-old Lycoi cat presented with persistent fever. On ultrasound (B), the heterogeneous echogenic center corresponding to necrotic debris is surrounded by a thick capsule with a thin hyperechoic line confirmed as mineralization on computed tomography images (A). A chronic abscess was suspected following histopathological analysis but all cultures were negative. **(C, D)** Feline infectious peritonitis in two cats in which several hypoechoic nodules and heterogeneous masses (arrows) were found in the mesentery (**C**) and add adhered to several serosal surfaces (**D**), consistent with pyogranulomas. Peritoneal effusion was also present (*).

Vet-ebooks.com

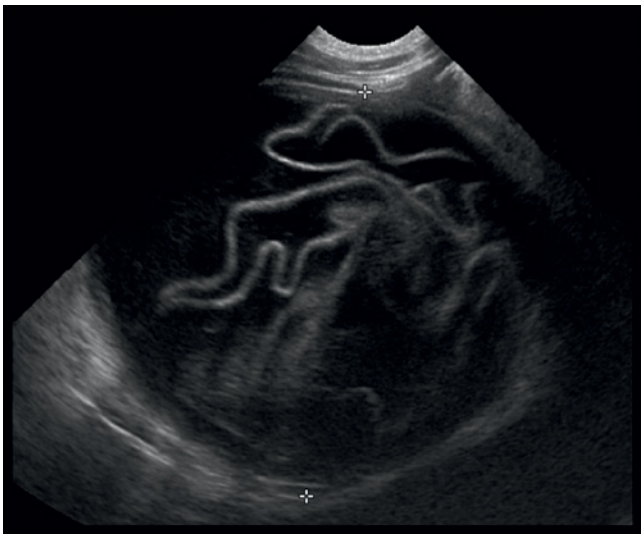


Figure 15.18. Retained surgical sponge in a 7-month-old Mastiff. A rounded mass with an unusual internal pattern made of well-demarcated, folded layers is noted. At surgery, this was confirmed to be a gossypiboma.

and lymphomatosis are often used for peritoneal dissemination sarcomas and lymphomas, respectively. In cats, the most common sites of primary carcinomas associated with carcinomatosis are the liver, pancreas, and intestine (Monteiro and O'Brien 2004). In dogs, peritoneal spread by ruptured hemangiosarcoma probably represents the most common type of carcinomatosis or sarcomatosis (Monteiro and O'Brien 2004). Free peritoneal effusion is expected in most cases of carcinomatosis. The volume and echogenicity of the fluid can vary and may be influenced by a high protein content, concurrent presence of sterile or septic peritonitis, or hemorrhage. Peritoneal effusion contributes to the visibility of nodules attached to the peritoneal surfaces or within the floating omentum or mesentery. Metastatic nodules tend to appear isoechoic to the abdominal wall or hypoechoic to adjacent fat (Monteiro and O'Brien 2004), although their echogenicity, as well as their size and shape, can vary (Figures 15.21, 15.22). Infiltrated omentum or mesentery can appear focally or diffusely thickened, sometimes described as "omental or mesenteric cakes," or show large masses (Figure 15.22B). Additionally, mineral foci may be observed as hyperechoic foci casting an acoustic shadow. Sensitivity of ultrasound to detect omental nodular metastases in abdominal staging remains however limited in certain conditions, particularly in deep-chested dogs or with spontaneous hemoabdomen due to reactive steatitis and blood clots; ultrasound findings may not always correlate with gross observation in surgery (Cudney et al. 2021).

Peritoneal **lymphomatosis** appears to be associated with alimentary B-cell lymphoma in cats (Morgan et al. 2018; Oetelaar et al. 2020). In addition to a mural mass with loss of wall layering, characteristic sonographic changes of lymphomatosis are discrete-to-coalescing plaques of thickened hypoechoic tissue throughout the mesentery or omentum with a variable amount of free fluid and nodules on the parietal and/or visceral peritoneal surfaces (Morgan et al. 2018) (Figure 15.23).

Soft-tissue sarcomas, especially hemangiosarcoma, can be found in the retroperitoneal space, particularly in dogs (Liptak et al. 2004) (Figure 15.24). Ultrasonography can be useful in differentiating a retroperitoneal mass from retroperitoneal effusion, renomegaly, or renal mass suspected on radiographs. Retroperitoneal soft-tissue masses are often heterogeneous and ill-defined and may invade major vessels such as the CVC, aorta, or renal vessels. However, it can be difficult to differentiate true large retroperitoneal masses from masses originating from the adrenal glands or urinary system. Alternate imaging such as computed tomography and magnetic resonance imaging may also help in better defining the origin and extent of retroperitoneal masses.

Lymphadenopathy

Changes in **size**, **shape**, **contour**, and **internal echogenicity**, and **echotexture** are important criteria that help detect lymphadenopathies and differentiate benign from malignant processes.

Enlarged lymph nodes typically become more rounded. Ratios comparing their short (S) and long (L) axes increase more significantly with neoplastic infiltration (Llabrés-Diaz 2004; Nyman et al. 2004). S/L axis ratios >0.7 are usually predictive of neoplasia

Vet-ebooks.com

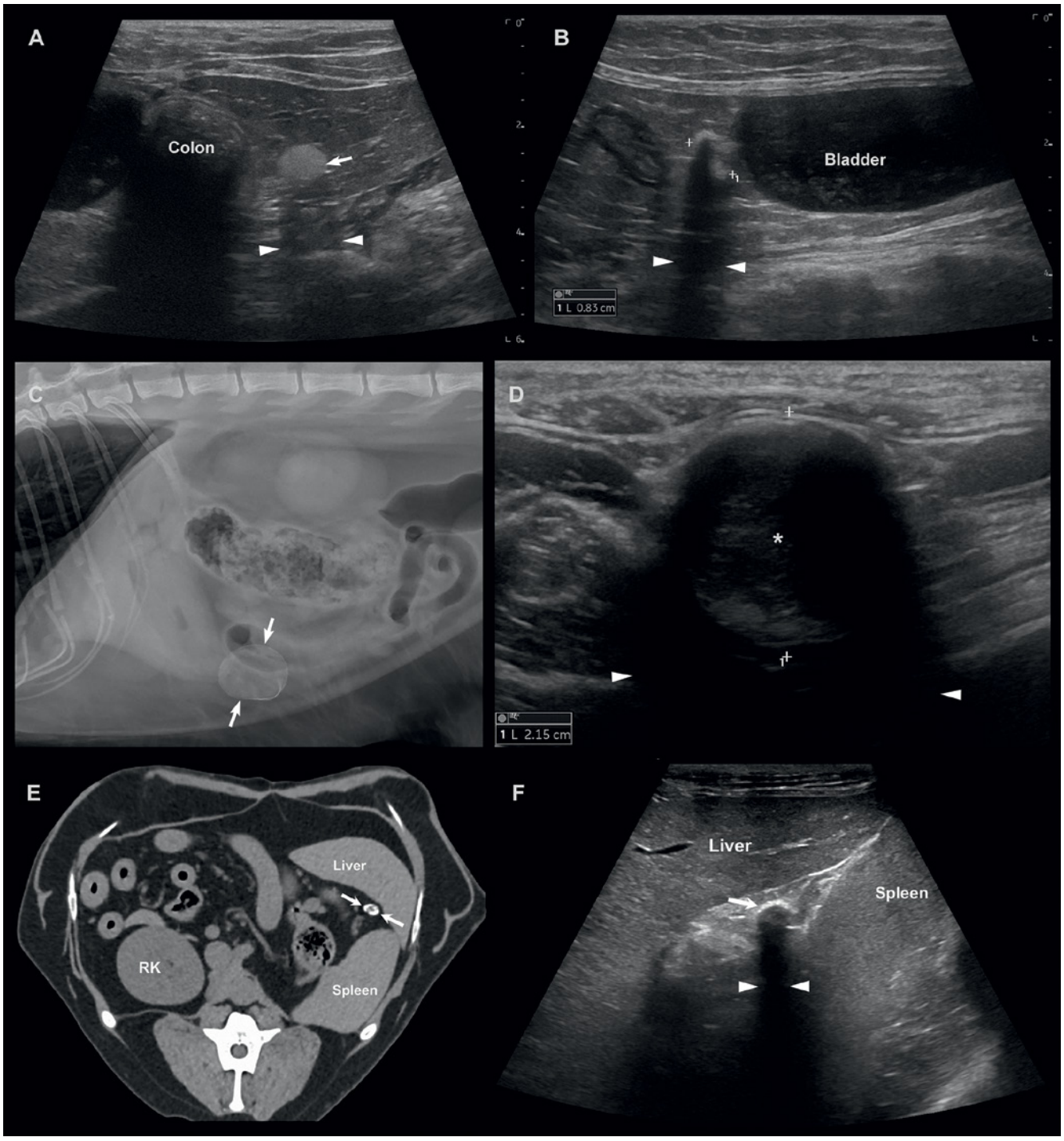


Figure 15.19. **Fat nodular necrosis (Bate's bodies). (A, B)** Sonographic images in the same cat with numerous Bate's bodies at different stages. In the early stage, nodular fat necrosis appears as a hyperechoic nodule (arrow) that may cause mild acoustic shadowing (arrowheads). With time, the nodule mineralizes and becomes more hyperechoic with stronger acoustic shadowing. **(C, D)** Chronic fat nodular necrosis in another cat, which appears as a well-defined, oval, shell-like mineral body on radiographs (arrows) (**C**) Sonographically, it appears as a smooth, well-defined oval structure with a thin hyperechoic rim and casting strong acoustic shadowing, which limits the visualization of the central portion of the nodule (*). **(E, F)** Sonographic and CT images of incidental chronic fat nodular necrosis between the liver and spleen in an old dog, with similar sonographic features, i.e., well-defined, convex hyperechoic structure (arrow) casting strong acoustic shadowing (arrowheads). It appears as a ring-like mineral focus on CT (arrows in **E**). RK, right kidney.

Vet-ebooks.com

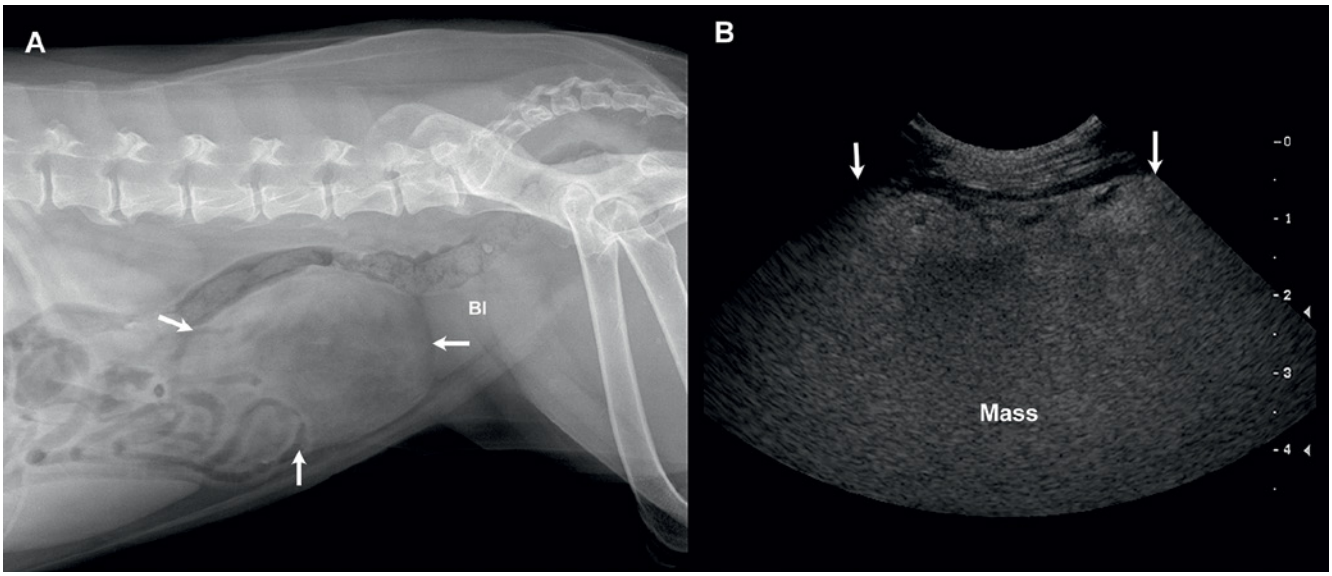


Figure 15.20. **Mesenteric lipoma. (A)** Lateral abdominal radiograph of the abdomen of a large-breed dog with a palpable abdominal mass. A mildly inhomogeneous mass (arrows) in the caudal abdomen is deforming the descending colon and bladder (Bl). The mass is of intermediate opacity between fat and soft tissue. **(B)** Longitudinal sonographic image of a portion of this mass that contacts the ventral abdominal wall (arrows) and extends beyond the limits of the scanned field of view. This mass is hyperechoic, hyperattenuating, and relatively uniform. A mesenteric lipoma was surgically confirmed.

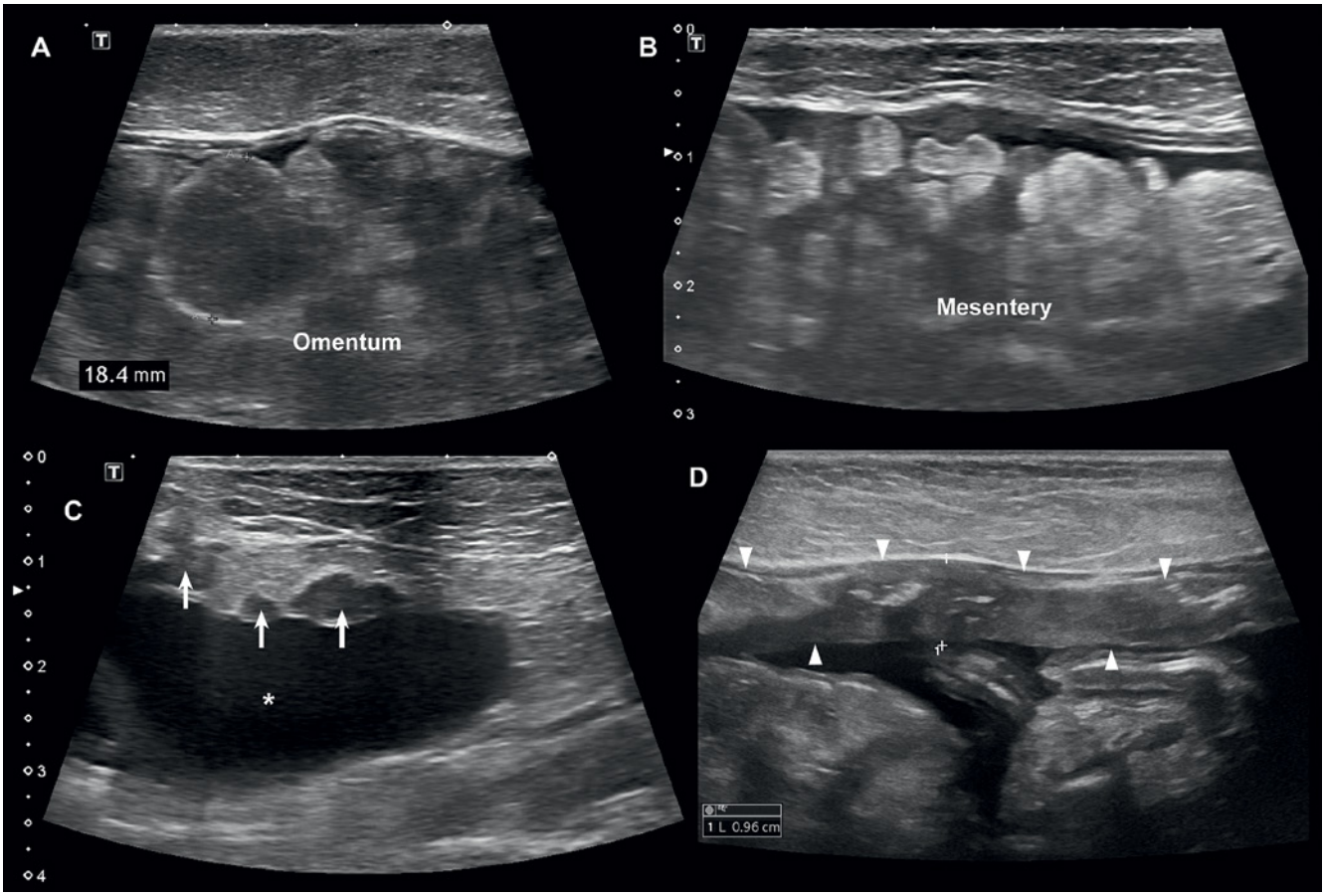


Figure 15.21. **Carcinomatosis in three cats. (A, B)** In these three cats with pancreatic adenocarcinoma, nodules of variable echogenicity are disseminated in the omentum and mesentery as well as on serosal linings. **(C)** In one of these cats (the same one as in **A**), hypoechoic nodules also invade the peritoneal lining and adjacent abdominal wall, delineated dorsally by the peritoneal fluid (*). **(D)** In the third cat, there is more diffuse, severe thickening (nearly 1 cm) of the peritoneal lining (arrowheads) with dystrophic mineralization.

Vet-ebooks.com

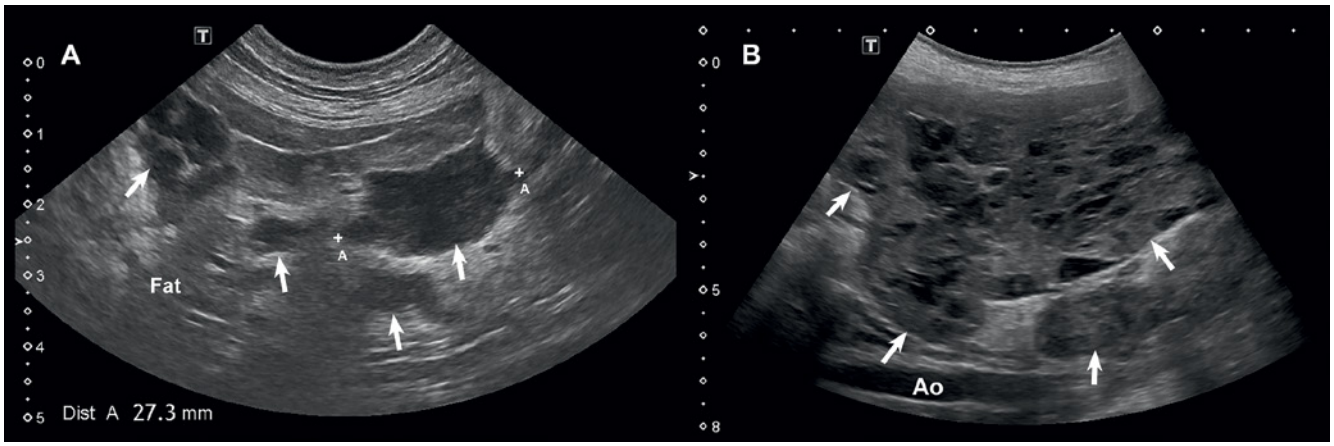


Figure 15.22. **Carcinomatosis and sarcomatosis in two dogs. (A)** In this 9-year-old Basset hound with pancreatic carcinoma, numerous nodules of variable echogenicity were found in the abdominal fat and on organ serosal surfaces. **(B)** In this dog with undifferentiated soft-tissue sarcoma, masses (arrows) were found throughout the abdominal cavity, consistent with sarcomatosis. Ao, aorta.

(Figures 15.25, 15.26), as opposed to ratios <0.7, which more consistently indicate normal or reactive lymph nodes (Figure 15.27) (Nyman and O'Brien 2007). However, this ratio must be used with caution for certain nodes, such as jejunal nodes, which are much longer and therefore associated with a lower S/L axis ratio, even when malignant.

Internal nodal architecture tends to be more affected by neoplastic infiltration (Llabrés-Diaz 2004; Nyman et al. 2004). Reactive lymph nodes tend to present a normal hyperechoic hilus unlike with neoplastic infiltrations (Figure 15.27D). Primary or metastatic neoplastic lymph nodes are commonly hypoechoic (Figures 15.25, 15.26), facilitating their identification, although areas of hyperechogenicity may be present if coagulative necrosis, hemorrhage, or mineralization is also present (Figures 15.25I, 15.26C, D). Lymph node heterogeneity has also been significantly associated with malignancy in dogs, but not in cats (Kinns and Mai 2007).

Massively infiltrated lymph nodes can become markedly enlarged and distorted (Figures 15.25, 15.28). Hypoechoic or anechoic areas may also be seen as a result of liquefaction necrosis or cyst formation (Llabrés-Diaz 2004) (Figure 15.29A, B). Malignant nodes may also be inflamed or abscessed and can therefore become markedly heterogeneous (Figure 15.29C). However, the majority of cyst-like lesions in abdominal lymph nodes are associated with various chronic non-neoplastic pathologies and are more likely to be secondary to sinusoid hemorrhage and ectasia (Liota et al. 2017), or loss of lymphoid tissue in aging, and atrophied lymph nodes (Elmore 2006) (Figure 15.29D–G). Based on the authors' experience, **cyst-like lesions** appear to be particularly prevalent in hepatic lymph nodes, frequently without other concomitant changes.

Inflammatory and metastatic lymph nodes also tend to be ill-defined and associated with perinodal hyperechoic fat, whereas hyperplastic lymph nodes are more likely to have normal perinodal fat (Davé et al. 2017).

Purulent lymphadenitis or **nodal abscesses** limited to the intra-abdominal (mesenteric) lymph nodes are sometimes seen in dogs and cats, usually young (Figure 15.30). The cause is often uncertain, but bacterial translocation from the digestive tract is the most cited cause and can lead to septic peritonitis or sepsis (Salavati Schmitz 2016).

However, some overlap exists in the ultrasonographic appearance of benign and malignant lymph node pathologies. For example, **granulomatous diseases**, such as pythiosis, histoplasmosis, or FIP, can mimic neoplasia by producing severe abdominal lymphadenomegaly or even masses (Graham et al. 2000; Lewis and O'Brien 2010) (Figures 15.31, 15.32).

Lymph node **mineralization** is seen with certain granulomatous and neoplastic diseases.

Pinpoint mineralization has also been reported in the mesenteric lymph nodes of dogs with schistosomiasis (Graham et al. 2021).

In aging dogs, some lymph nodes become diffusely hyperechoic due to **adipose infiltration**, making them more difficult to distinguish from adjacent fat (Figure 15.33).

Color or spectral Doppler, power Doppler, or contrast ultrasonography may increase the accuracy in differentiating benign from malignant nodes (Nyman

Vet-ebooks.com

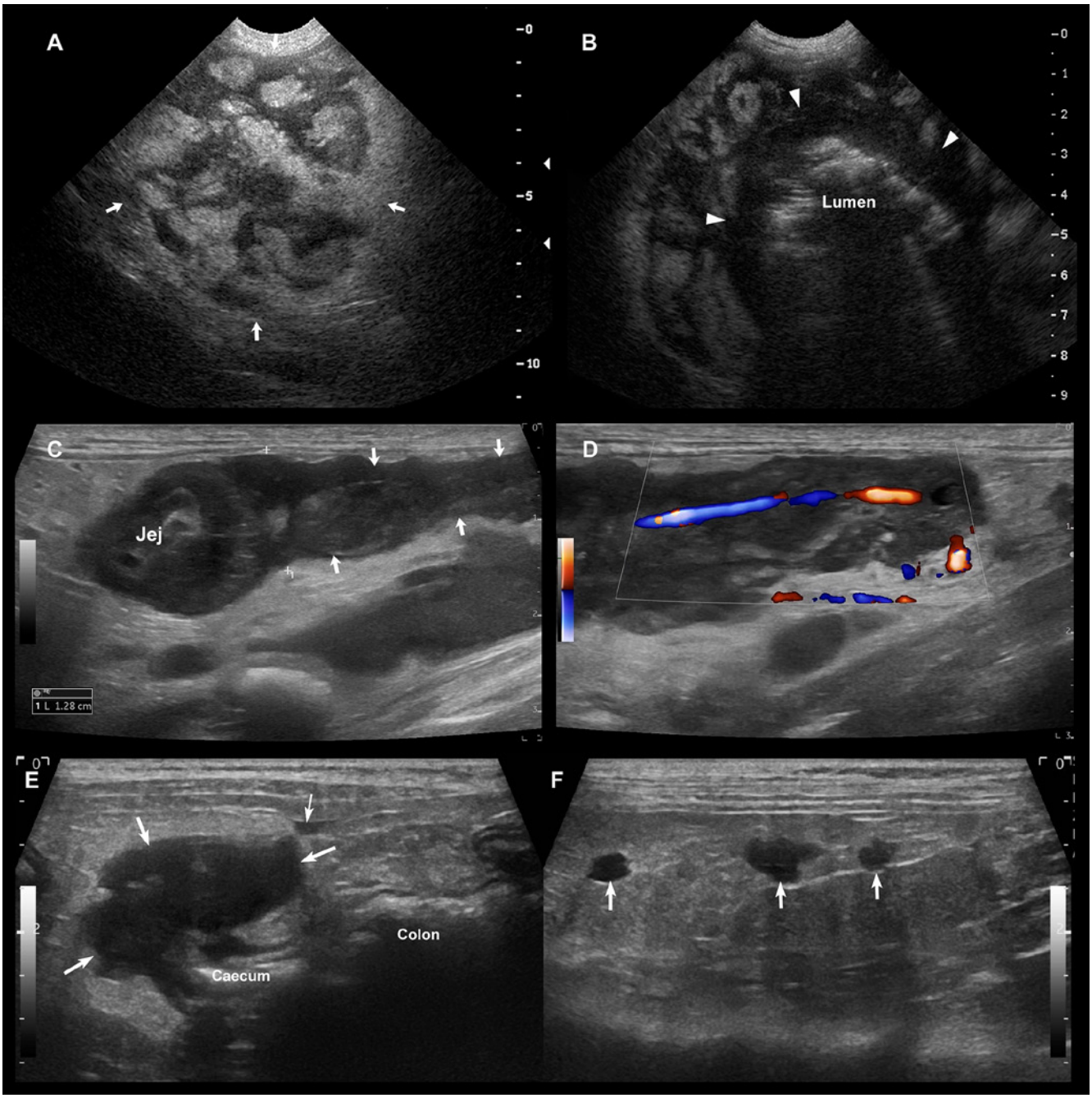


Figure 15.23. **Mesenteric infiltration by lymphoma in a dog and two cats. (A, B)** Transverse images obtained in the right caudal abdomen of a dog with intestinal lymphoma. **(A)** A large ill-defined mass with mixed echogenicity is observed (arrows), surrounded by hyperechoic fat. **(B)** In the central portion of this mass, a segment of small intestine is found with thickened and irregular hypoechoic walls (arrowheads). Mesenteric infiltration by the intestinal lymphoma was confirmed. **(C, D)** In this cat, a cake-like, hypoechoic tissue infiltrates the mesentery, surrounding a jejunal vein (in D), next to a jejunal (Jej in C) segment that has a thickened wall with loss of wall layering. **(E)** Cecal lymphoma in another cat with a large hypoechoic mass (arrows) at the tip of the cecum that shows focal loss of wall and surrounded by hyperechoic fat and a trace of effusion (thin arrow). **(F)** Multiple hypoechoic and irregular nodules were found in the mesenteric fat of this cat. Disseminated lymphomatosis was confirmed with ultrasound-guided aspirations.

Vet-ebooks.com

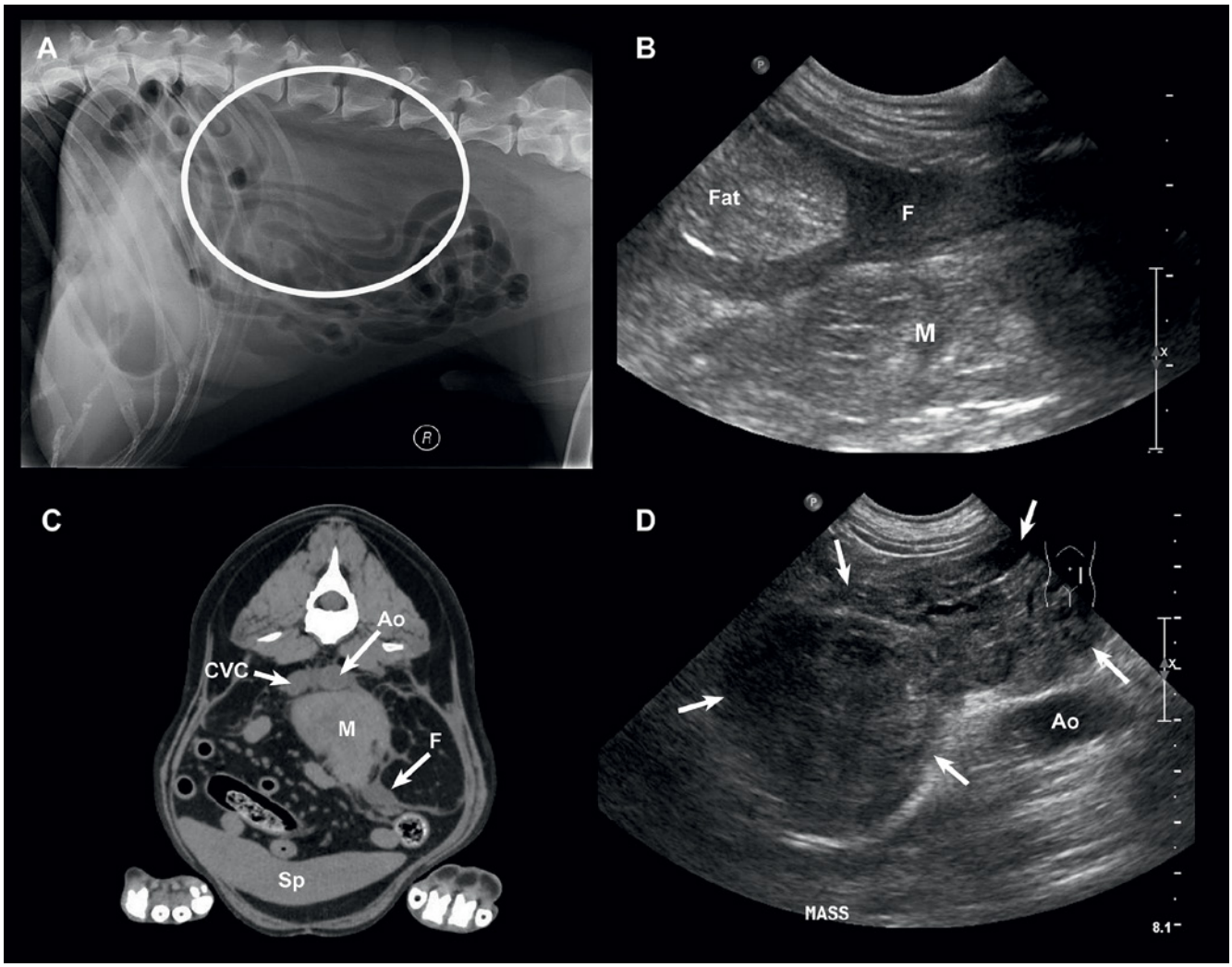


Figure 15.24. Retroperitoneal hemangiosarcoma in an 11-year-old Labrador cross. (A) On the lateral abdominal radiograph, there is an increased opacity in the retroperitoneal space, and the kidneys are not clearly identified. **(B)** A mild amount of echogenic fluid (F) is present in the retroperitoneal space and represents hemorrhage. M, mass. **(C)** On this transverse computed tomography image, the retroperitoneal mass (M) and the adjacent retroperitoneal fluid (F) are seen. Ao, aorta; CVC, caudal vena cava; Sp, spleen. **(D)** Longitudinal sonogram of part of the inhomogeneous mass (arrows) invading most of the retroperitoneal space, ventral to the aorta (Ao).

and O'Brien 2007; Nyman et al. 2004; Nyman et al. 2005; Prieto et al. 2009), although Doppler evaluation may be difficult to achieve in some deep lymph nodes (de Swarte et al. 2011). In benign nodes, the blood flow distribution is primarily hilar, whereas it tends to be more peripheral or mixed with malignancies (Figure 15.25E).

Because of the overlap of results for each ultrasound criterion, these parameters should be considered conjointly for increased accuracy in the differentiation of malignant and benign lymph nodes. For instance, the combination of irregular contour and perinodal hyperechoic fat is predictive of malignancy in dogs (de Swarte et al. 2011). These studies also highlight the fact that malignant nodes cannot be reliably differentiated from benign nodes with ultrasound, justifying cytologic or histopathologic sampling.

While ultrasound remains an excellent screening tool for neoplastic staging, abnormal lymph nodes may be undetected due to lack of visualization or accessibility (e.g., GI content overlying bone). Tomographic modalities such as CT can allow more abnormal lymph nodes to be detected, such as with apocrine gland adenocarcinoma of the anal sac metastasizing to the iliosacral lymphocenter in dogs (Palladino et al. 2016, Pollard et al. 2017). On the other hand, lymph node echotexture may allow earlier detection of lymph node metastases when lymphadenomegaly is not present on CT (Pollard et al. 2017).

Vet-ebooks.com

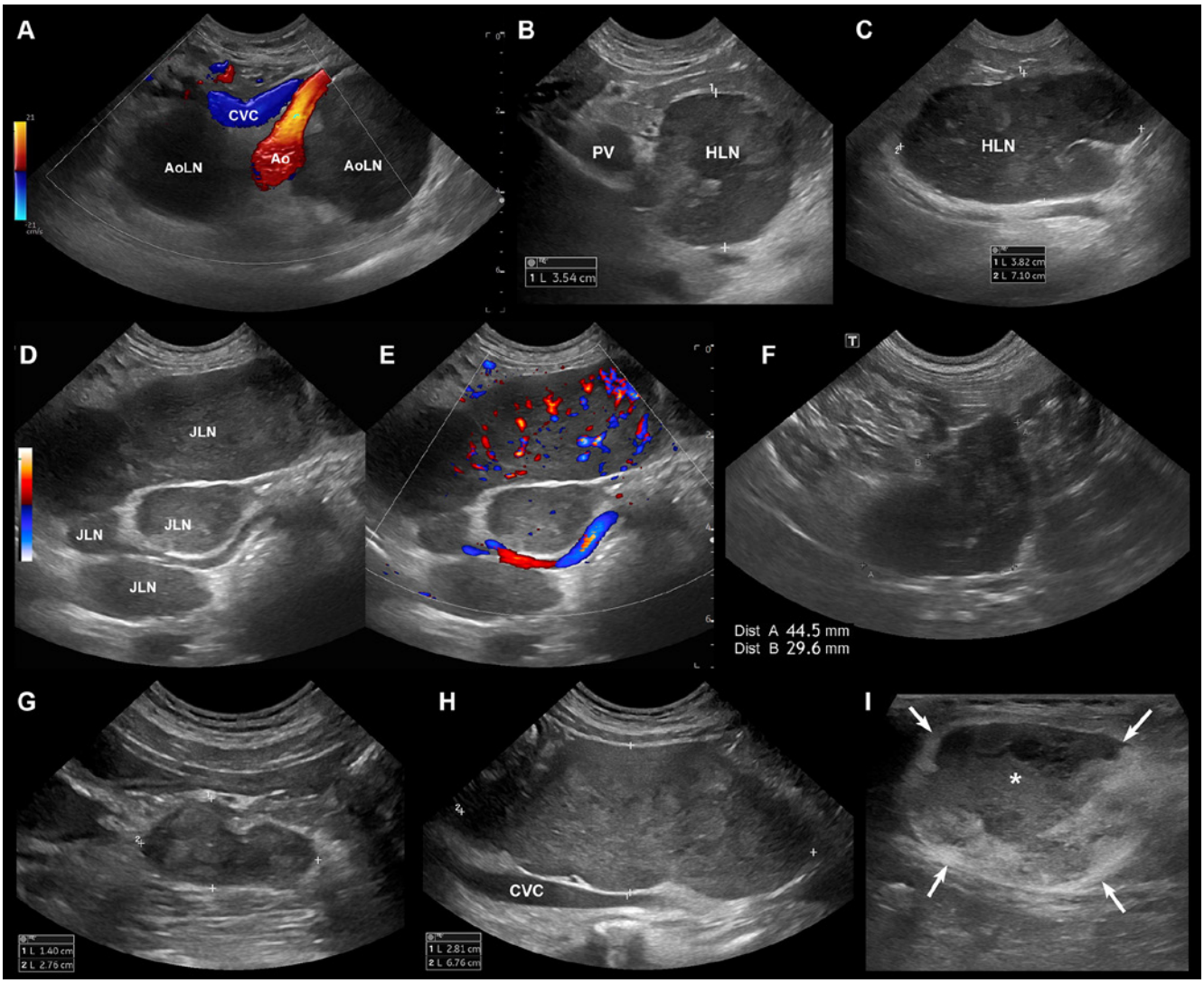


Figure 15.25. **Neoplastic lymph nodes in dogs. (A–C) Multicentric B-cell lymphoma** in a 2-year-old golden retriever. Transverse (A) sonographic image of severely enlarged and hypoechoic aortic lymph nodes (AoLN). Transverse (B) and longitudinal (C) images of the left hepatic lymph nodes (HLN) with similar features. The surrounding fat is hyperechoic. Ao, aorta; CVC, caudal vena cava; PV, portal vein. **(D, E) Metastatic mast cell tumor** to the jejunal lymph nodes (JLN) of another dog. Note the hypervascularity of the most enlarged node located ventrally as evidenced by color Doppler (in **E**). **(F)** In this third dog with **disseminated histiocytic sarcoma**, one of the jejunal lymph nodes is severely enlarged, hypoechoic, irregular, and in part ill-defined. **(G, H) Metastatic apocrine gland anal sac adenocarcinoma (AGASACA)** to the left (G) and right (H) medial iliac lymph node of a 6-year-old Boxer. The caudal vena cava (CVC) is compressed by the massive right retroperitoneal lymph node. **(I)** Another **metastatic AGASACA** in a dog. This inguinal lymph node is severely enlarged and highly heterogeneous (*) with superficial cavitary areas and an irregular peripheral hyperechoic rim (arrows).

Abdominal Wall Abnormalities

Hernias of the abdominal wall may be congenital or traumatic in origin. Congenital hernias are typically located on the midline, with variable amounts of fat herniating through the defect (Figure 15.34A, B). Larger defects can be associated with herniation of visceral structures such as intestines, spleen, or bladder (Figure 15.34C–E).

Abdominal organs can also herniate through the inguinal canal. Widening of the inguinal canal or the presence of an abdominal wall defect and abnormal separation of the wall layers are the main ultrasound signs of a hernia, and ultrasound is especially useful in determining the nature of the herniated tissues (Figure 15.35).

Vet-ebooks.com

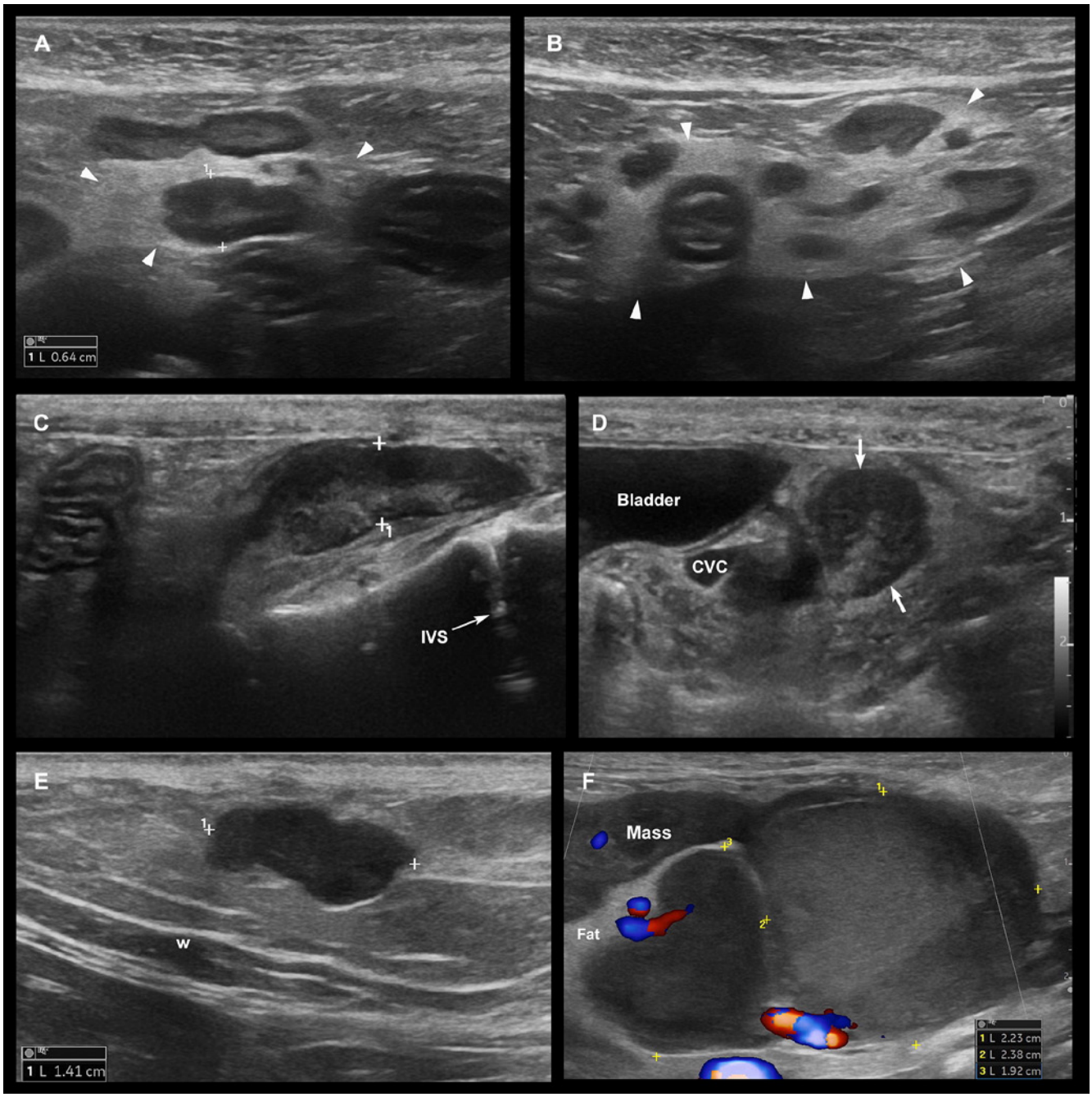


Figure 15.26. **Neoplastic lymph nodes in cats**. **(A, B)** In this 10-year-old cat with diffuse mild to moderate thickening of the small intestine and colon, several jejunal (A) and right colic (B) lymph nodes are mildly to moderately thickened, hypoechoic, and irregular. The surrounding mesenteric fat is hyperechoic (arrowheads). **Small-cell lymphoma** was diagnosed. **(C, D)** Longitudinal (C) and transverse (D) sonograms of an enlarged and heterogeneous colic lymph node (between cursors and arrows) in a 13-year-old cat with **multinodal abdominal mastocytosis**. Perinodal fat is hyperechoic with poorly defined hypoechoic striations. CVC, caudal vena cava; IVS, intervertebral disc space. **(E)** In this 7-year-old cat with left-sided **mammary gland adenocarcinoma**, the ipsilateral superficial inguinal lymph node is moderately enlarged, hypoechoic, and irregular. W, ventral abdominal wall. **(F)** In this other cat with intestinal lymphoma infiltrating the mesentery (mass), the jejunal lymph nodes are markedly enlarged (up to 2.2 cm in thickness). The largest of the two is mildly heterogeneous but relatively normal in echogenicity, whereas the other one is diffusely hypoechoic. The surrounding fat is hyperechoic.

Vet-ebooks.com

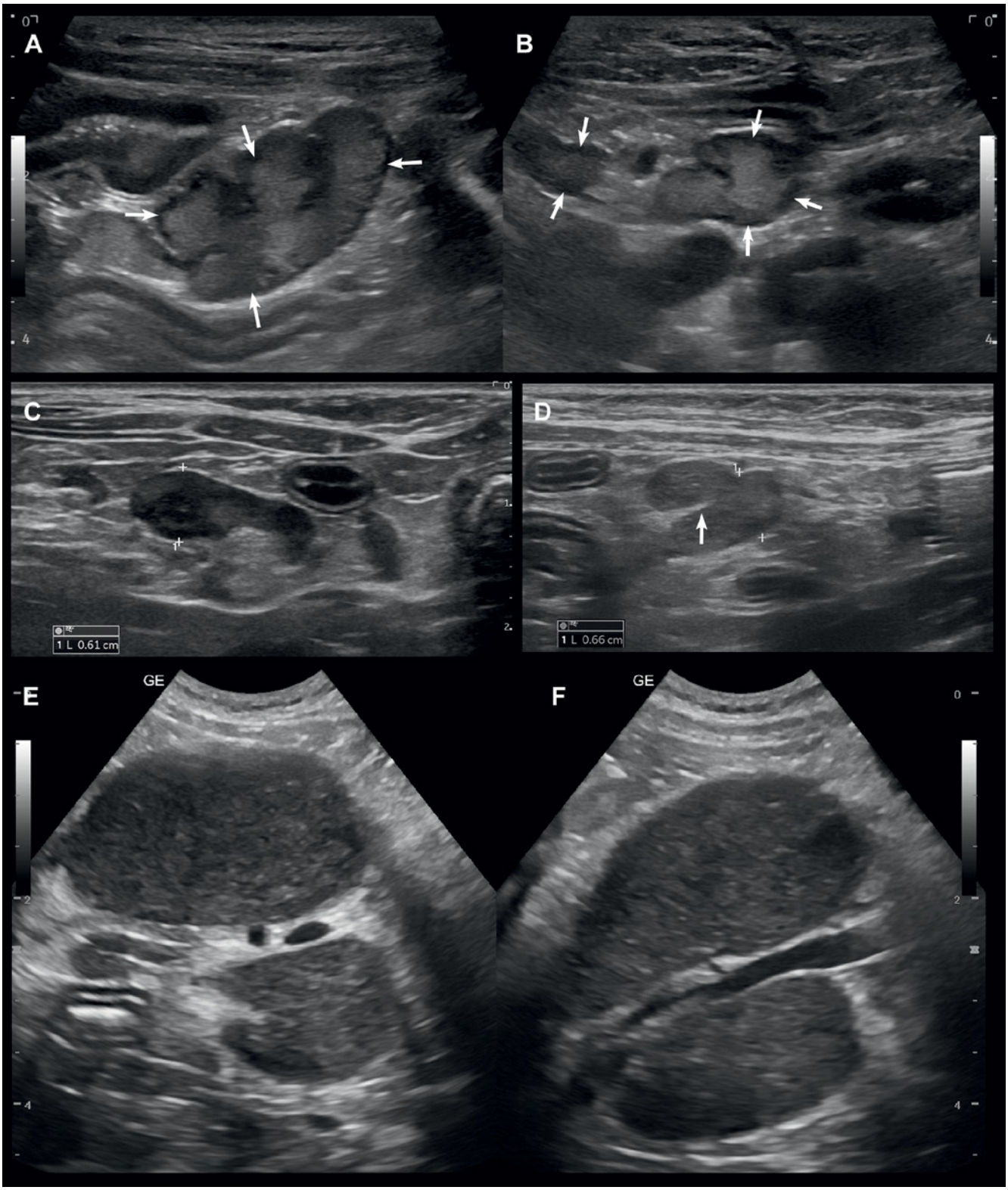


Figure 15.27. **Hyperplastic lymphadenopathy. (A, B)** Hyperplastic jejunal lymph nodes in a 5-month-old puppy presented for a urinary problem. Lymph nodes of pediatric patients are proportionally larger and rounder, with this characteristic peripheral hypoechoic band (arrows). **(C)** Mildly enlarged, hypoechoic, and heterogeneous jejunal lymph node in a cat with inflammatory bowel disease. **(D)** Enlarged jejunal lymph node in another cat with colonic carcinoma that was free of metastases on histopathology. Note the intact hyperechoic hilus (arrow) that is more often preserved with hyperplasia versus neoplasia. **(E, F)** Severely enlarged jejunal lymph nodes with granular echotexture in this cat with eosinophilic lymphadenitis. Eosinophilic lymphadenitis may be associated with gastrointestinal eosinophilic sclerosing fibroplasia (see Chapter 9).

Vet-ebooks.com

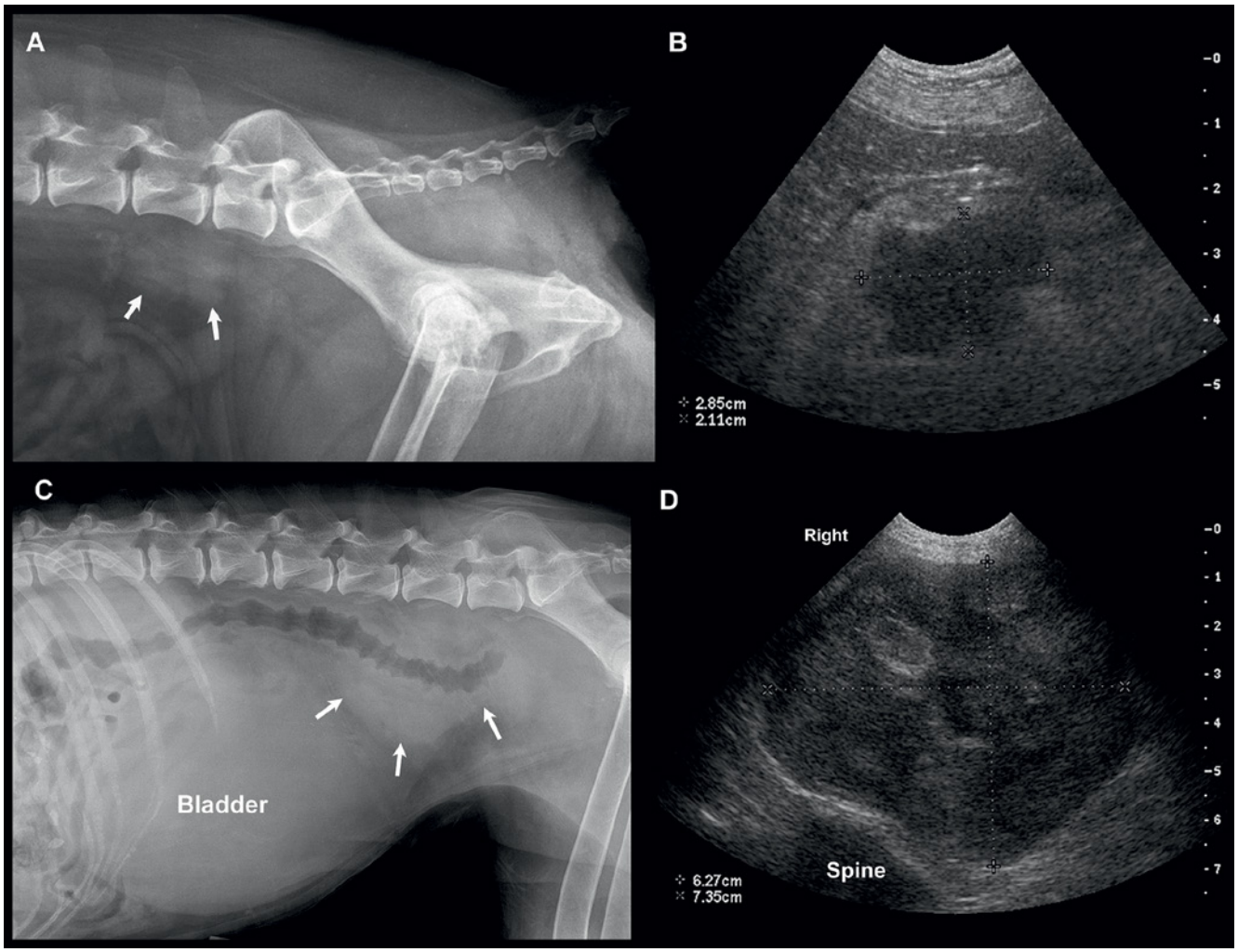


Figure 15.28. **Sublumbar lymphadenopathy caused by metastases in two dogs. (A)** Lateral abdominal radiograph of a medium-sized breed dog with metastatic carcinoma. An ill-defined, lobulated, soft-tissue opacity (arrows) is ventral to the sixth and seventh lumbar vertebrae. **(B)** Longitudinal sonographic image obtained in the same region, lateral to the right iliac artery and vein (not shown). An irregular, hypoechoic mass with surrounding mildly hyperechoic fat, consistent with metastatic disease, is at the location of a medial iliac lymph node. **(C)** Lateral abdominal radiograph of another large-breed dog with partial urinary obstruction and signs suggestive of colitis. A somewhat lobulated soft-tissue opacity is in the caudodorsal abdomen and displacing the descending colon ventrally and associated with marked bladder distension. The colon is corrugated. **(D)** Transverse sonographic image obtained in the caudal abdomen. The mass suspected on radiographs is large and heterogeneous (between the cursors). Metastatic soft-tissue sarcoma to lymph nodes was highly suspected based on fine-needle aspiration. These two cases illustrate the benefit of radiographs for identifying the retroperitoneal location of the masses, which can be challenging to confirm on ultrasound, particularly with large masses.

Several types of **neoplastic processes** can infiltrate the skin, the subcutaneous fat, mammary glands, inguinal lymph nodes, and abdominal muscles (Figure 15.36).

Inflammatory processes can also affect the abdominal wall tissues, such as due to puncture wounds or foreign bodies and as postoperative complications (e.g., infection and exuberant suture material) (Figure 15.37).

Interventional Procedures

Fine-needle aspiration (FNA) of peritoneal fluids is used routinely with ultrasonography in dogs and cats. With minimal practice, even small amounts of fluids can be securely aspirated. Abdominal masses and lymph nodes can also be aspirated or biopsied. Cavitated

Vet-ebooks.com

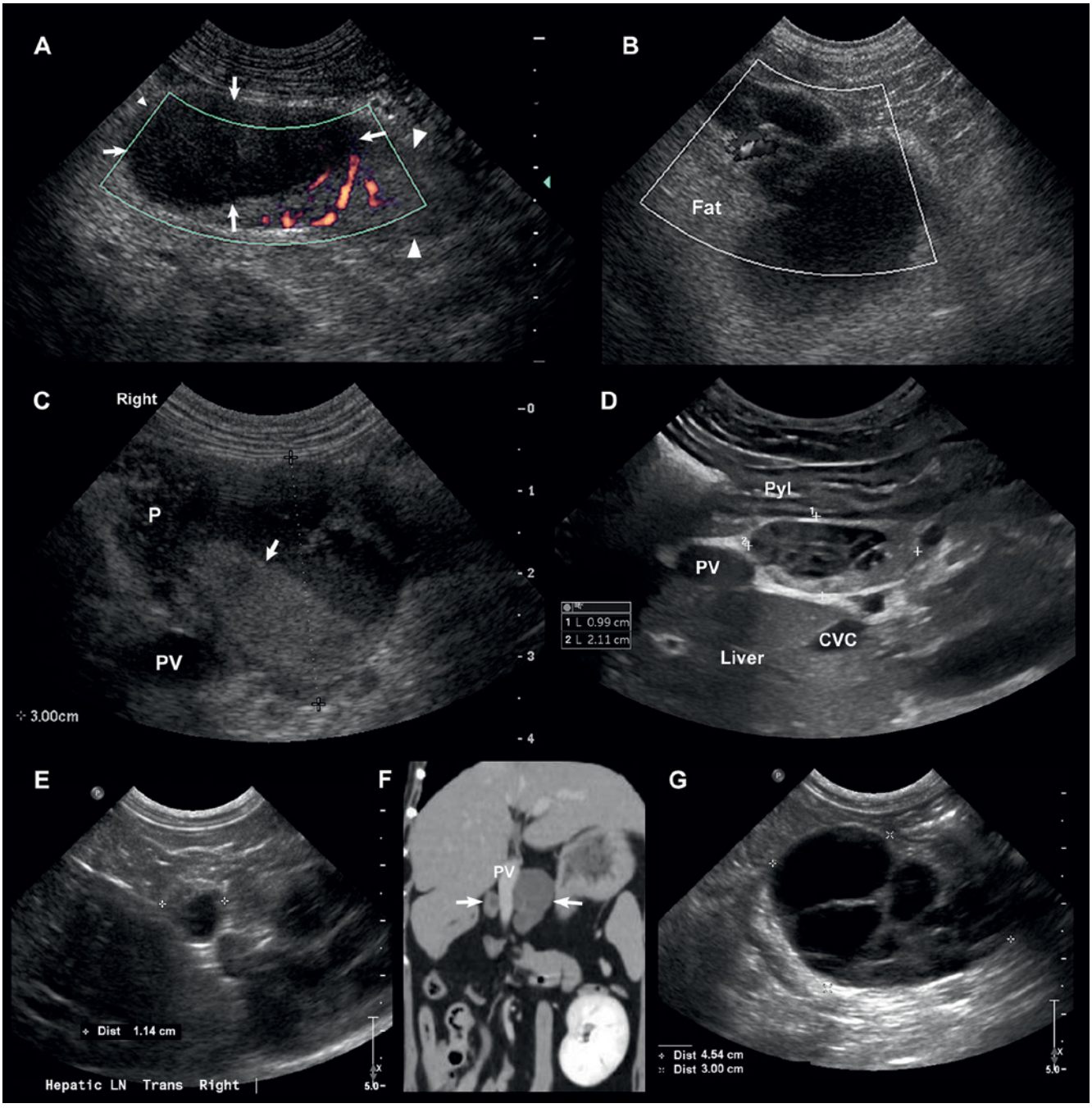


Figure 15.29. **Cavitary lymph nodes. (A) Cystic node with lymphoma**. Longitudinal image of a jejunal lymph node in a dog with multicentric lymphoma. A large, oval, anechoic, avascular area (arrows) is in the cranial region of the enlarged lymph node (arrowheads). Fine-needle aspiration confirmed the presence of a fluid-filled cavity or cyst within this portion of the node, and lymphoma was confirmed in the caudal solid portion. **(B) Necrosis**. On this ultrasound image, two adjacent jejunal lymph nodes are severely enlarged, nearly anechoic, and ill-defined. The surrounding fat is markedly hyperechoic. Fine-needle aspiration revealed the presence of metastatic carcinoma associated with necrosis and inflammation. **(C) Abscessed malignant node**. Transverse image of a severely enlarged hepatic lymph node in a dog with multicentric lymphoma and suspected pancreatitis. Echogenic fluid is in the affected node, with a cellular sediment forming a line (arrow) parallel to the horizontal plane (probe placed obliquely). The adjacent pancreas (P) is hypoechoic and the peripheral fat is mildly hyperechoic. **(D) Benign cystic node**. Multiple, irregular, well-defined anechoic cysts are incidentally found in the left hepatic node of this dog with urinary calculi. CVC, caudal vena cava; PV, portal vein; Pyl, pyloric antrum. **(E–G) Cystic hepatic lymph nodes** in an 11-year-old mixed breed dog with previous cutaneous hemangiosarcoma. The right hepatic lymph node (in **E**) is mildly enlarged and mostly cystic, as seen also on the dorsal CT reconstruction (**F**). The left hepatic node (in **G**) is markedly enlarged and deformed by numerous cysts. On necropsy, the node changes were thought to represent sinus ectasia.

Vet-ebooks.com

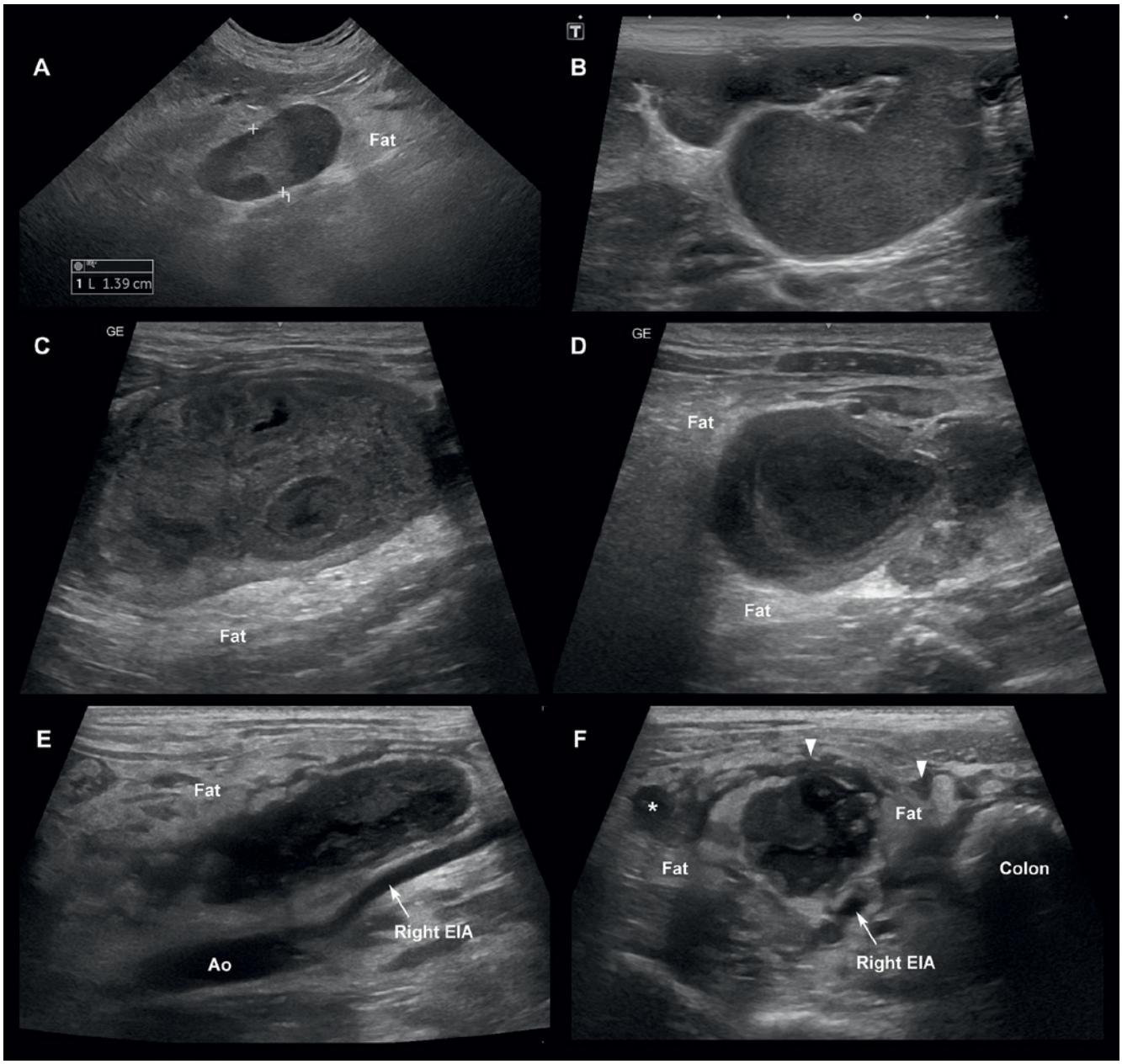


Figure 15.30. **Infectious lymphadenitis**. **(A)** Longitudinal sonographic image of the left superficial inguinal lymph node of a 6-year-old intact male Rottweiler with bacterial prostatitis. The inflamed lymph node is thickened, hypoechoic, and heterogeneous, surrounded by hyperechoic fat. **(B)** *Salmonella* lymphadenitis in a 5-month-old puppy. This jejunal lymph node is enlarged with rounded margins. Node parenchyma remains fairly homogeneous and perinodal fats are mildly hyperechoic. Salmonellosis is often associated with a raw diet in young dogs. **(C, D)** Severe septic suppurative lymphadenitis in a 5-year-old cat. This severely enlarged jejunal lymph node (**C**) is very heterogeneous with several small cavitary lesions corresponding to abscesses. A larger cavitary lesion is noted in this other jejunal lymph node (**D**), with echogenic contents and a thick capsule. Perinodal steatitis is noted in both cases. **(E, F)** Septic peritonitis secondary to abscessation of the right medial iliac lymph node. This right medial iliac lymph node is hypoechoic and heterogeneous with irregular margins. The surrounding fat is diffusely hyperechoic and thickened with numerous hypoechoic striations (arrowheads). A small pocket of echogenic fluid (*) is present in the reactive fat. Ao, aorta; EIA, external iliac artery.

Vet-ebooks.com

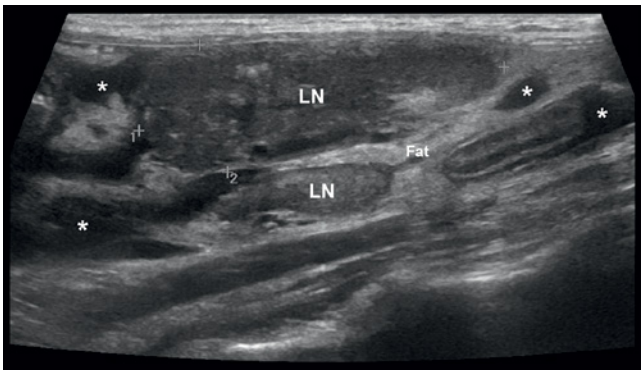


Figure 15.31. Granulomatous lymphadenopathy in a cat with feline infectious peritonitis. The right colic nodes (LNs) are asymmetrically enlarged with hyperechoic foci, which are more obvious in the largest of these nodes. The regional fat is hyperechoic and mild peritoneal effusion is present (*).

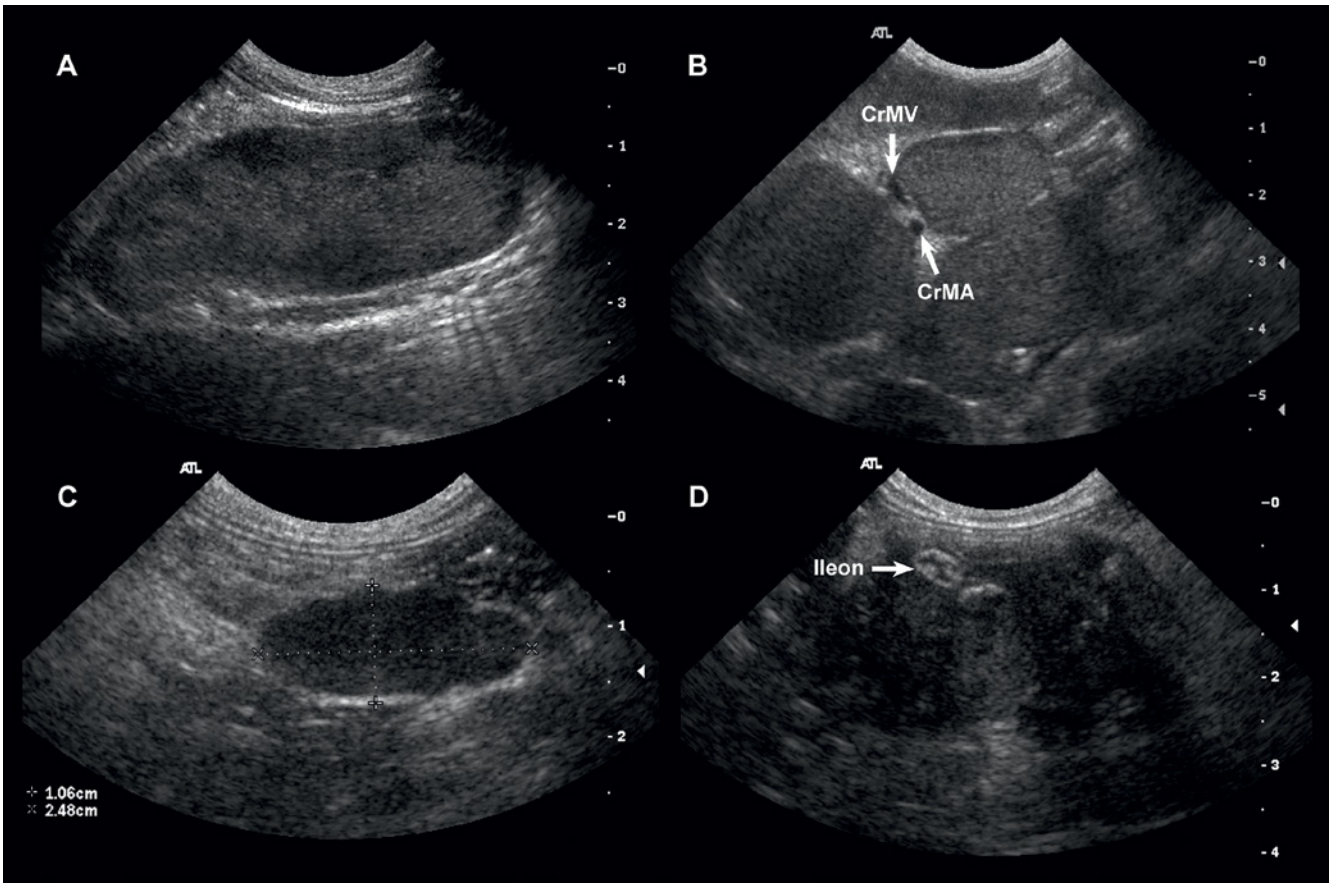


Figure 15.32. Granulomatous lymphadenopathy. (A) Longitudinal image obtained in a dog diagnosed with an intestinal mass and a jejunal lymph node that appears moderately enlarged (2 cm thick × 6 cm long). This lymph node is not as hypoechoic as typically seen with lymphoma. Surgery confirmed the presence of severe granulomatous enteritis caused by pythiosis. **(B)** Transverse image of the mid-abdomen of another dog with mycobacteriosis. The jejunal lymph nodes are markedly enlarged and uniformly hyperechoic, surrounding the cranial mesenteric vein (CrMV) and artery (CrMA). **(C, D)** In this cat, one of the jejunal lymph nodes is enlarged and hypoechoic (between cursors in **C**). An irregular and ill-defined hypoechoic mass is seen surrounding the ileocecal junction, infiltrating the intestinal walls and adjacent lymph nodes. These features were initially suspected to indicate neoplasia, but a granulomatous infiltration due to histoplasmosis was confirmed.

Vet-ebooks.com

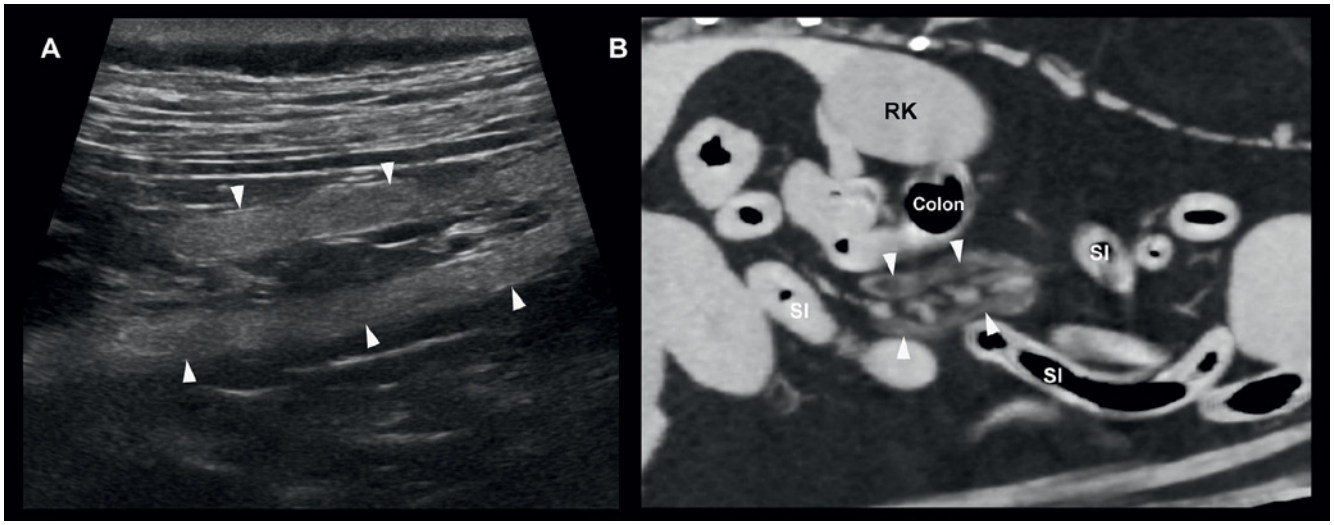


Figure 15.33. **Hyperechoic lymph nodes**. **(A)** The jejunal lymph nodes (arrowheads) in this dog are diffusely hyperechoic, but normal in size. Contrast between these hyperechoic nodes and the adjacent mesenteric fat is often reduced and can make their identification more challenging. **(B)** CT longitudinal reformatted image showing hypoattenuating fatty replacement in these two lymph nodes (arrowheads), which explains their sonographic hyperechogenicity. RK, right kidney; SI, small intestine.

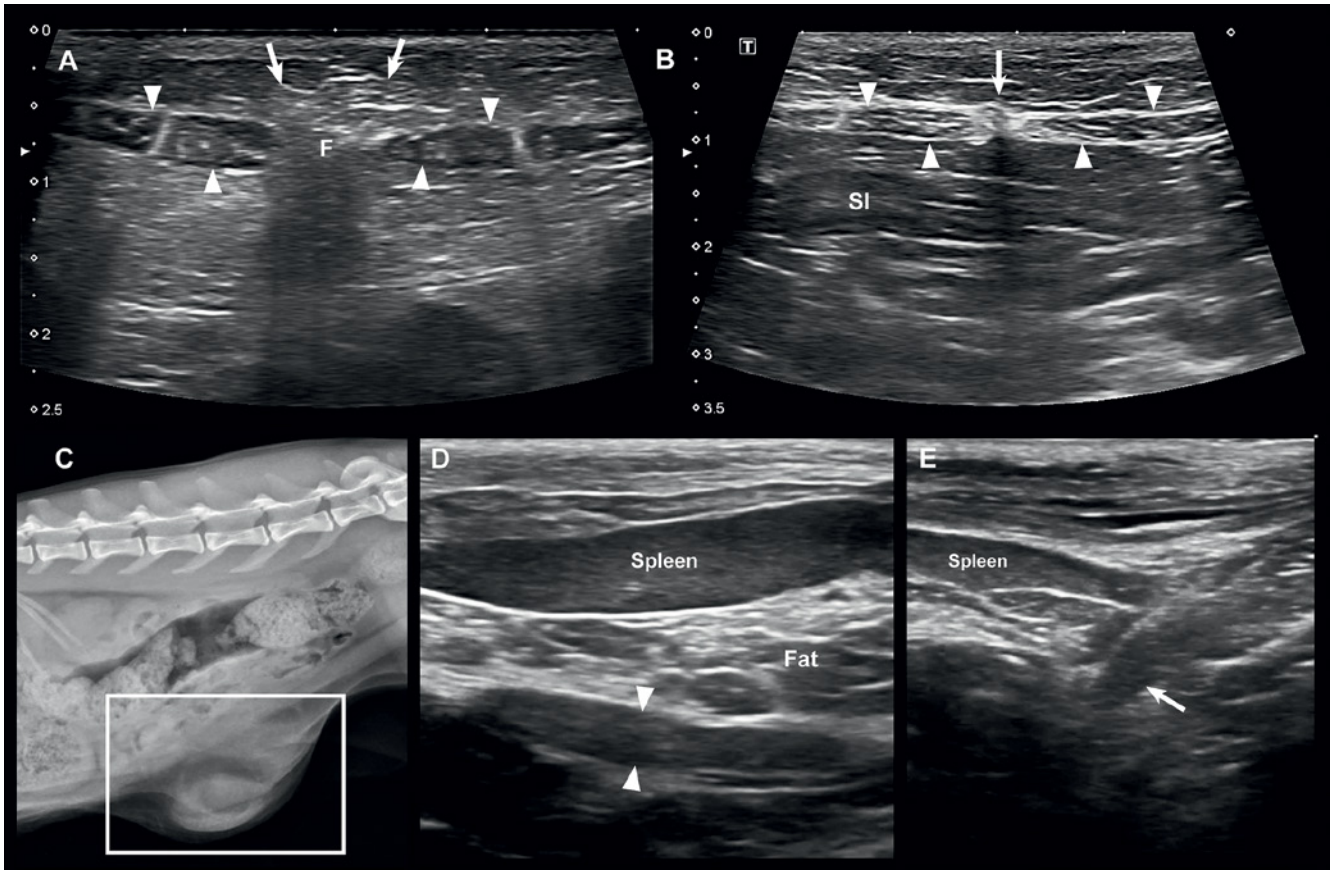


Figure 15.34. **Abdominal wall hernia in three cats. (A)** In this cat with palpable and reducible mid-abdominal hernia, there is a wall defect on the midline filled with an amorphous tissue of mild echogenicity consistent with fat (F). There is no evidence of bowel loops or other organs in the subcutaneous tissues. The muscular wall on each side (arrowheads) is thicker than normally seen, because of reduced tension. **(B)** The normal linea alba (white line, arrow) in another cat is associated with distal shadowing. Note the appearance of the normal abdominal wall musculature (between arrowheads). SI, small intestine. **(C–E)** Cat attacked by a dog. The lateral radiograph (**C**) shows an inhomogeneous soft-tissue opacity lying along the mid-ventral abdominal wall. On the sonograms (**D, E**), the spleen is displaced in the subcutaneous tissues. The arrowheads (**D**) outline the intact portion of the ventral abdominal wall and the arrow (**E**) points to the site of wall disruption.

Vet-ebooks.com

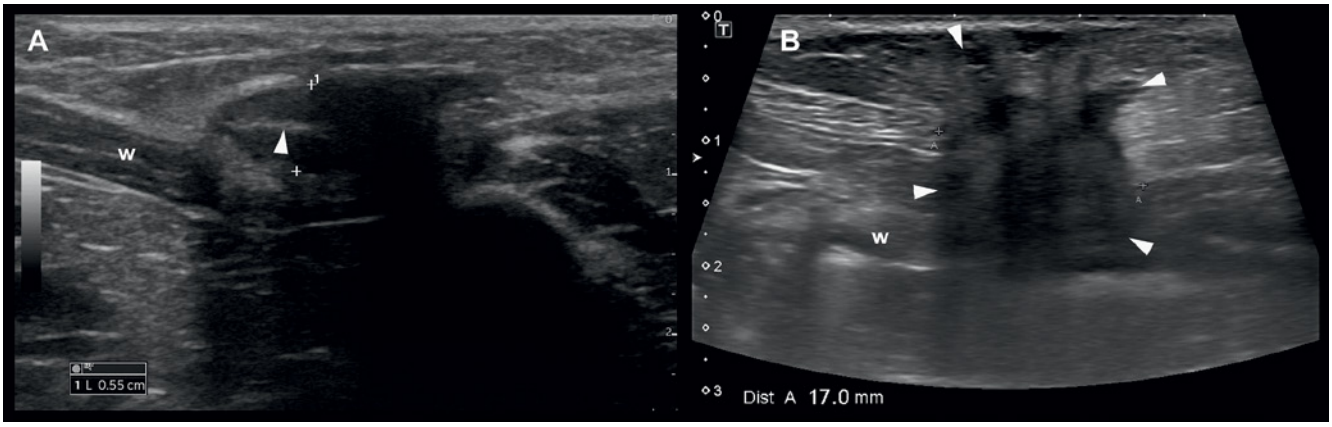


Figure 15.35. **Inguinal hernia in a cat and a dog. (A) Inguinal cryptorchidy** in a young cat. One of the testicles is recognized ventral to the abdominal wall (w) in the inguinal area. The arrowhead points to the characteristic median testis. **(B)** In this small-breed dog presented for acute swelling in the right inguinal area, an irregular and ill-defined hypoechoic nodule (arrowheads) is seen ventral to the abdominal wall (w) that cannot be fully visualized due to partial acoustic shadowing caused by this tissue, which was consistent with **herniated fat** entrapped by the inguinal ring.

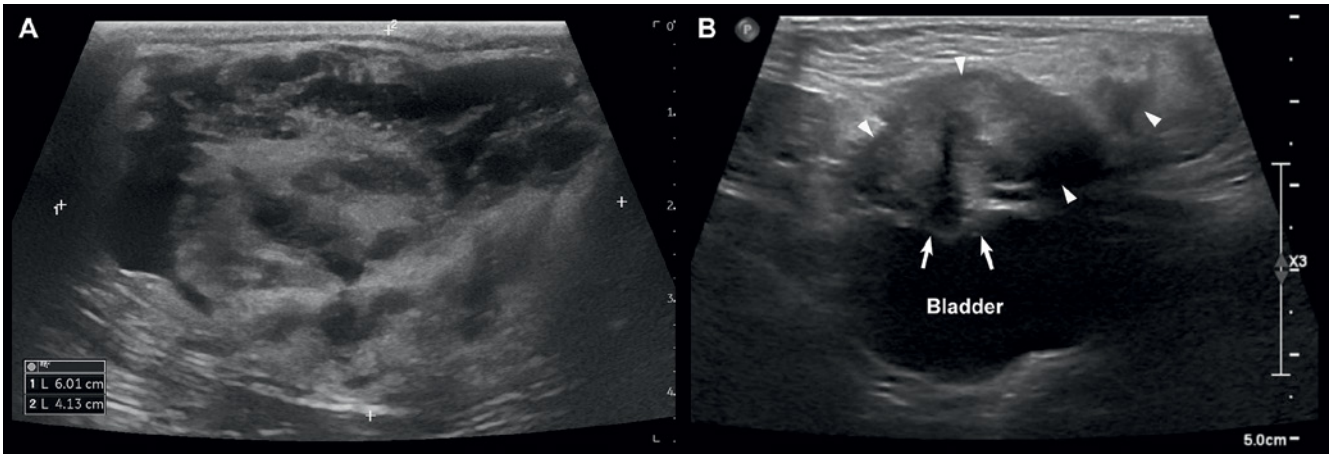


Figure 15.36. **Abdominal wall neoplasia. (A)** Large heterogeneous subcutaneous mass infiltrating the abdominal wall of a 12-year-old Cocker spaniel confirmed to represent a hemangiosarcoma. **(B)** A 15-year-old cat diagnosed with urothelial carcinoma of the bladder wall 1 year ago was rechecked because of lethargy and weight loss. An irregularly shaped mass (arrowheads) is extending from the bladder wall previous cystotomy site through the caudal ventral abdominal wall. The ventral bladder wall (arrows) is deformed by the mass.

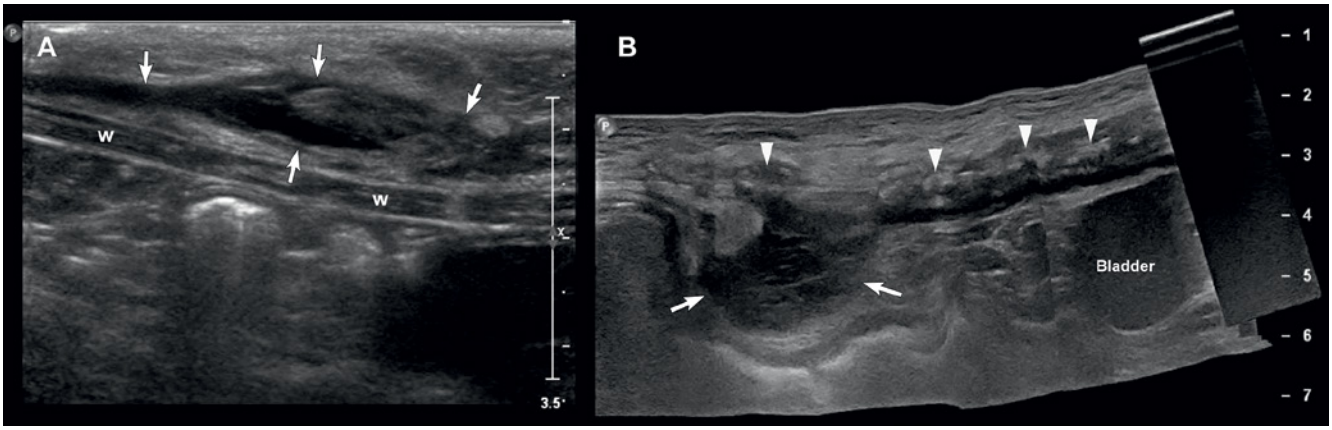


Figure 15.37. **Postoperative complications. (A)** In this 6-month-old cat with a recent (3 weeks ago) cystotomy, an elongated, hypoechoic to anechoic (arrows) space is noted along the ventral abdominal wall (w). This represents a postsurgical seroma. **(B)** In this 3-year-old Golden retriever who had surgery 3 weeks ago for an abdominal abscess, the cranial aspect of the ventral abdominal wall incision shows a large, rounded hypoechoic and faintly striated structure deforming internally the wall (arrows). This is an exuberant postoperative reaction and, in this dog, it represents a seroma. Sampling is at times recommended to rule out abscessation, if clinically suspected. It contrasts with the rest of the abdominal wall (arrowheads) that appears still thickened with hyperechoic foci (suture scars), but this is expected for a recent celiotomy.

Vet-ebooks.com

masses, abscesses, or cysts can also be drained with ultrasound guidance.

FNA of peritoneal fluid, omental and mesenteric lesions, and abdominal lymph nodes is of value as a first-line diagnostic approach with a diagnostic yield greater than 70% to classify general disease processes between inflammatory and neoplastic (Feeney et al. 2013). However, abdominal lymph nodes have a higher proportion of nondiagnostic samples (30–56%) compared to other tissues (Feeney et al. 2013; Liffman and Courtman 2017). An adequate technique including a minimum of three FNAs without aspiration (to minimize hemodilution) for each lymph node and extra care when making smears to avoid rupture of the cells are therefore recommended to maximize the quality of samples (Liffman and Courtman 2017).

Needle gauge is a contributing factor to FNA sample quality, but the ideal size remains controversial. Smaller gauges (25G) produce less pain and less hemodilution compared to larger gauges (22G), which results in higher cellularity and less cellular damage. Using a 22G needle with 3 mL of negative pressure could increase the probability of obtaining a diagnostic sample for abdominal lymph nodes (Whitlock et al. 2021).



Visit our website at **www.SmallAnimalUltrasonography.com** for complementary video clips with annotations and text on:

- Normal abdominal wall, cavity, fat, and lymph nodes
- Peritoneal effusions
- Mesenteric mass
- Peritonitis
- Carcinomatosis
- Lymphadenopathy
- Abdominal wall and umbilical hernia

References

Adamama-Moraitou KK, Prassinos NN, Galatos AD, Tontis DK, et al. (2008) Isolated abdominal fat tissue inflammation and necrosis in a cat. J Feline Med Surg 10:192–197.

Agthe P, Caine AR, Posch B, Herrtage ME (2009) Ultrasonographic appearance of jejunal lymph nodes in dogs without clinical signs of gastrointestinal disease. Vet Radiol Ultrasound 50:195–200.

Bezuidenhout AJ (2020) The lymphatic system. In: Hermanson JW, de Lahunta A, Evans H, eds. Miller and Evans' Anatomy of the Dog, 5th edition. WB Saunders: Philadelphia, pp. 616–649.

Boysen SR, Tidwell AS, Penninck D (2003) Ultrasonographic findings in dogs and cats with gastrointestinal perforation. Vet Radiol Ultrasound 44:556–564.

Boysen SR, Rozanski EA, Tidwell AS, Holm JL, et al. (2004) Evaluation of a focused assessment with sonography for trauma protocol to detect free abdominal fluid in dogs involved in motor vehicle accidents. J Am Vet Med Assoc 225:1198–1204.

Campbell BG (2009) Primary omental abscessation or omental infarction in four dogs. J Am Anim Hosp Assoc 45:168–175.

Citi S, Oranges M, Arrighi E, Meucci V, et al. (2020) Sonographic evaluation of medial iliac lymph nodes-to-aorta ratio in dogs. Vet Sci 7(1):22.

Costanzo G, Linta N, Auriemma E, Perfetti S, et al. (2023) Ultrasonographic assessment of early leakage in intestinal sutures in dogs. Front Vet Sci 10:1094287.

Cudney, SE, Wayne, AS, Rozanski, EA (2021) Diagnostic utility of abdominal ultrasonography for evaluation of dogs with nontraumatic hemoabdomen: 94 cases (2014–2017). J Am Vet Med Assoc 258:290–294.

Culp WTN, Zeldis TE, Reese MS, Drobatz KJ (2009). Primary bacterial peritonitis in dogs and cats: 24 cases (1990–2006). J Am Vet Med Assoc 234:906–913.

Dave AC, Zekas LJ, Auld DM (2017) Correlation of cytologic and histopathologic findings with perinodal echogenicity of abdominal lymph nodes in dogs and cats. Vet Radiol Ultrasound 58:463–470.

De Swarte M, Alexander K, Rannou B, d'Anjou MA, et al. (2011) Comparison of sonographic features of benign and neoplastic deep lymph nodes in dogs. Vet Radiol Ultrasound 52:451–456.

Elmore SA (2006) Histopathology of the lymph nodes. Toxicol Pathol 34:425–454.

Etienne AL, Cavrenne R, Gomeren K, Bolen G, et al. (2013) Ultrasonographic characteristics of the cisterna chyli in eight dogs and four cats. Vet Radiol Ultrasound 54(4):398–402.

Feeney DA, Ober CP, Snyder LA, Hill SA, et al. (2013) ultrasound criteria and guided fine-needle aspiration diagnostic yields in small animal peritoneal, mesenteric and omental disease. Vet Radiol Ultrasound 54:638–645.

Geninet C, Bernex F, Rakotovao F, Crespeau FL, et al. (2003) Sclerosing peritoneal mesothelioma in a dog – a case report. J Veterinary Med Ser A 50:402–405.

Gnudi G, Volta A, Bonazzi M, Gazzola M, et al. (2005) Ultrasonographic features of grass awn migration in the dog. Vet Radiol Ultrasound 46:423–426.

Graham JP, Newell SM, Roberts GM, Lester NV (2000) Ultrasonographic features of canine gastrointestinal pythiosis, Vet Radiol Ultrasound 41:273–277.

Graham AM, Davenport A, Moshnikova VS, Gilmour LJ, et al. (2021) Heterobilharzia americana infection in dogs: a retrospective study of 60 cases (2010-2019). J Vet Intern Med 35(3):1361–1367.

Gremillet BCH, Porsmoguer C, Bolen G, Billen F, et al. (2022) Imaging findings in dogs and cats with presumptive sclerosing encapsulating peritonitis. Front. Vet. Sci. 9:891492.

Griffeuille E, Lebaut M, Lecourtois C, Baudin-Tréhiou C, et al. (2023) Septic peritonitis secondary to intraperitoneal grass awn migration: 7 cases (2014-2021). Can Vet J 64:217–224.

Vet-ebooks.com

Hahn H, Freiche V, Baril A, Charpentier J, et al. (2017) Ultrasonographic, endoscopic and histological appearance of the caecum in clinically healthy cats. J Feline Med Surg 19:85–93.

Heerkens TM-J, Smith JD, Fox L, Hostetter JM (2011). Peritoneal fibrosarcomatous mesothelioma in a cat. J Vet Diagn Invest 23:593–597.

Kinns J, Mai W (2007) Association between malignancy and sonographic heterogeneity in canine and feline abdominal lymph nodes. Vet Radiol Ultrasound 48:565–569.

Komori S, Nakagaki K, Koyama H, Yamagami T (2002) Idiopathic mesenteric and omental steatitis in a dog. J Am Vet Med Assoc 221:1591–1593.

Krol L, O'Brien R (2012) Ultrasonographic assessment of abdominal lymph nodes in puppies. Vet Radiol Ultrasound 53:455–458.

Lewis KM, O'Brien RT (2010) Abdominal ultrasonographic findings associated with feline infectious peritonitis: a retrospective review of 16 cases. J Am Anim Hosp Assoc 46:152–160.

Liffman R, Courtman N (2017) Fine needle aspiration of abdominal organs: a review of current recommendations for achieving a diagnostic sample. J Small Anim Pract 58:599–609.

Liotta, A, Billen, F, Heimann, M, Hamaide, A, et al. (2017) Prevalence, location and concurrent diseases of ultrasonographic cyst-like lesions of abdominal lymph nodes in dogs. Vet Rec 180:326–326.

Liptak JM, Dernell WS, Ehrhart EJ, Rizzo SA, et al. (2004) Retroperitoneal sarcomas in dogs: 14 cases (1992-2002). J Am Vet Med Assoc 224(9):1471–1477.

Lisciandro GR, Fosgate GT, Romero LA, Hauke SM, et al. (2020) The expected frequency and amount of free peritoneal fluid estimated using the abdominal FAST-applied abdominal fluid scores in healthy adult and juvenile dogs. J Vet Emerg Crit Care 31:43–51.

Llabrés-Diaz FJ (2004) Ultrasonography of the medial lymph nodes in the dog. Vet Radiol Ultrasound 45:156–165.

Mai W, Ledieu D, Venturini L, Fournel C, et al. (2001) Ultrasonographic appearance of intra-abdominal granuloma secondary to retained surgical sponge. Vet Radiol Ultrasound 42:157–160.

Marvel SJ, MacPhail CM (2013) Retroperitoneal abscesses in seven dogs. J Am Anim Hosp Assoc 49:378–384.

Matthews AR, Penninck DG, Webster CR (2008) Postoperative ultrasonographic appearance of uncomplicated enterotomy or enterectomy sites in dogs. Vet Radiol Ultrasound 49:477–83.

Mayer MN, Lawson JA, Silver TI (2010) Sonographic characteristics of presumptively normal canine medial iliac and superficial inguinal lymph nodes. Vet Radiol Ultrasound 51:638–641.

Mayhew PD, Brockman DJ (2002) Body cavity lipomas in six dogs. J Small Anim Pract 43:177–181.

Merlo M, Lamb CR (2000) Radiographic and ultrasonographic features of retained surgical sponge in eight dogs. Vet Radiol Ultrasound 41:279–283.

Monteiro CB, O'Brien RT (2004) A retrospective study on the sonographic findings of abdominal carcinomatosis in 14 cats. Vet Radiol Ultrasound 45:559–564.

Morgan KRS, North CE, Thompson DJ (2018) Sonographic features of peritoneal lymphomatosis in 4 cats. J Vet Intern Med 32:1178–1184.

Müller TR, Penninck DG, Webster CR, Conrado FO (2023) Abdominal ultrasonographic findings of cats with feline infectious peritonitis: an update. J Fel Med Surg 25(12): 1098612X231216000.

Nyman HT, O'Brien RT (2007) The sonographic evaluation of lymph nodes. Clin Tech Small Anim Pract 22:128–137.

Nyman HT, Kristensen AT, Flagstad A, McEvoy FJ (2004) A review of the sonographic assessment of tumor metastases in liver and superficial lymph nodes. Vet Radiol Ultrasound 45:438–448.

Nyman HT, Kristensen AT, Skovgaard IM, McEvoy FJ (2005) Characterization of normal and abnormal canine superficial lymph nodes using gray-scale B-mode, color flow mapping, power, and spectral Doppler ultrasonography: a multivariate study. Vet Radiol Ultrasound 46:404–410.

Oetelaar GS, Lim CK, Heng HG, Fulkerson CM, et al. (2020) Ultrasonographic features of colonic B-cell lymphoma with mesenteric lymphomatosis in a cat. Vet Radiol Ultrasound 61:E60–E63.

Palladino S, Keyerleber MA, King RG, Burgess KE (2016) Utility of computed tomography versus abdominal ultrasound examination to identify iliosacral lymphadenomegaly in dogs with apocrine gland adenocarcinoma of the anal sac, J Vet Intern Med 30(6):1858–1863.

Penninck D, Mitchell S (2003) Ultrasonographic detection of ingested and perforating wooden foreign bodies in four dogs. J Am Vet Med Assoc 223:206–209.

Pintar J, Breitschwerdt EB, Hardie EM, Spaulding KA (2003) Acute nontraumatic hemoabdomen in the dog: a retrospective anùalysis of 39 cases (1987–2001). J Am Anim Hosp Assoc 39:518–522.

Pollard RE, Fuller MC, Steffey MA (2017) Ultrasound and computed tomography of the iliosacral lymphatic centre in dogs with anal sac gland carcinoma. Vet Comp Oncol 15:299–306.

Prieto S, Gomez-Ochoa P, de Blas I, Gascon M, et al. (2009) Pathologic correlation of resistive and pulsatility indices in canine abdominal lymph nodes. Vet Radiol Ultrasound 50:525–529.

Pugh CR (1994) Ultrasonographic examination of abdominal lymph nodes in the dog. Vet Radiol Ultrasound 35:110–115.

Pugliese M, La Pietra A, Liotta L, Macri F, et al. (2016) Ultrasonographic measurements of abdominal lymph nodes in growing puppies. Vet Med – Czech 61:389–393.

Salavati Schmitz S (2016) Retrospective characterisation and outcome of canine idiopathic mesenteric purulent lymphadenitis and lymph node abscesses at a teaching hospital from 2005 to 2015. J Small Anim Pract 57(12):690–697.

Saunders WB, Tobias KM (2003) Pneumoperitoneum in dogs and cats: 39 cases (1983–2002). J Am Vet Med Assoc 223:462–468.

Vet-ebooks.com

Schreurs E, Vermote K, Barberet V, Daminet S, et al. (2008) Ultrasonographic anatomy of abdominal lymph nodes in the normal cat. Vet Radiol Ultrasound 39:68–72.

Schwarz T, Morandi F, Gnudi G, Wisner E, et al. (2000) Nodular fat necrosis in the feline and canine abdomen. Vet Radiol Ultrasound 41:335–339.

Share B, Utroska B (2002) Intra-abdominal botryomycosis in a dog. J Am Vet Med Assoc 220:1025–1027.

Spaulding KA (1993) Sonographic evaluation of peritoneal effusion in small animals. Vet Radiol Ultrasound 34:427–431.

Stander N, Kirberger RM (2011) Diagnostic imaging of migrating kebab (sosatie) sticks – a review of 8 cases. J S Afr Vet Assoc 82:160–165.

Stander N, Wagner WM, Goddard A, Kirberger RM (2010) Normal canine pediatric gastrointestinal ultrasonography. Vet Radiol Ultrasound 51:75–78.

Staudte KL, Hopper BJ, Gibson NR, Read RA (2004) Use of ultrasonography to facilitate surgical removal of non-enteric foreign bodies in 17 dogs. J Small Anim Pract 45:395–400.

Tobón Restrepo M, Novellas R, Aguilar A, Moll X, et al. (2022) Anatomic, computed tomographic, and ultrasonographic assessment of the lymph nodes in presumed healthy adult cats: the abdomen, pelvis, and hindlimb. Acta Vet Scand 64:18.

Veiga-Parga T, Hecht S, Craig L (2015) Imaging diagnosis – sclerosing encapsulating peritonitis in a dog. Vet Radiol Ultrasound 56:E65–E69.

Whitlock J, Taeymans O, Monti P. (2021) A comparison of cytological quality between fine-needle aspiration and non-aspiration techniques for obtaining ultrasound-guided samples from canine and feline lymph nodes. Vet Rec 188:1–6.

Zini E, Hauser B, Ossent P, Dennler R, et al. (2007) Pansteatitis and severe hypocalcaemia in a cat. J Feline Med Surg 9:168–171.

Vet-ebooks.com

Vet-ebooks.com

CHAPTER SIXTEEN

ABDOMINAL VESSELS

Marc-André d'Anjou[1], Swan Specchi[2,3], and Chick Weisse[4]

[1]*Animages, Brossard, Québec, Canada*
[2]*Antech Imaging Services, Fountain Valley, CA, USA*
[3]*AniCura Ospedale Veterinario I Portoni Rossi, Zola Predosa, Italy*
[4]*Animal Medical Center, New York City, NY, USA*

PREPARATION AND SCANNING TECHNIQUE

Hair clipping of animals should cover the entire abdomen and ideally including the last one or two intercostal spaces, particularly in deep-chested dogs or if microhepatia is suspected. Animals can be scanned in dorsal, left, or right recumbency after acoustic gel application. The ability to visualize the abdominal vasculature in small animals is related to body conformation, liver size, and overlying gastrointestinal content. In large, deep-chested dogs, or in dogs with microhepatica, the liver can be completely hidden by the rib cage and thus requiring the use of an intercostal approach to reach all parts of the cranial abdominal vessels. Probe selection (type and frequency) is based on the location of the vessels to assess and user preferences. Convex probes have a smaller footprint, often allowing vessels to be more easily followed, particularly when tortuous, or through an intercostal approach. Color and spectral Doppler modes are essential for accurate recognition of normal and abnormal vessels and for better assessing their flow profile. See Chapter 1 for a description of these modes.

ULTRASONOGRAPHIC ANATOMY OF THE NORMAL ABDOMINAL VASCULATURE

Portal Vein, Tributaries, and Branches

The afferent vascular flow to the liver is dual, with a larger proportion coming from the PV (80%) and the rest coming from the hepatic arteries (HAs) (Evans 1993) (Figure 16.1). The efferent flow follows the hepatic veins into the caudal vena cava (CVC). This vascular pattern is divided into all hepatic lobes and can aid in distinguishing these lobes. Only the hepatic and PVs (larger than the arteries) are usually seen as anechoic, branching, smoothly tapering tubular structures. The walls of the PVs appear hyperechoic, regardless of the orientation of the ultrasonographic beam, facilitating their identification (Figure 16.2). However, the walls of the hepatic veins can also appear hyperechoic when the ultrasonographic beam is directed perpendicularly. Note that the width of the portal branches should be similar to the one of the adjacent hepatic veins. The use of color Doppler facilitates the identification and distinction of these vessels. When using standard colormap settings, portal flow, which is directed from the center to the periphery, appears as a red signal, whereas hepatic venous flow appears as a blue signal (Figure 16.2). Arterial flow, also directed from the center to the periphery, can also demonstrate a red signal, depending on the size of the arteries and the Doppler settings, such as gain and filtration threshold. The intrahepatic arteries are, however, not consistently seen in normal dogs and cats.

The extrahepatic portion of the PV is relatively central in the abdomen, ventral to the CVC, and ventral and to the right of the aorta (Figure 16.3). The main PV is more tortuous than the CVC and aorta and curves slightly to the right side, along the ventral border of the pancreas, before entering the liver. In cats, the main PV can have a segmental distention and tortuous path prior to the liver entrance. On color Doppler, this tortuous path of the portal vein (PV) may give the impression of turbulent

Atlas of Small Animal Ultrasonography, Third Edition. Edited by Dominique Penninck and Marc-André d'Anjou.
© 2025 John Wiley & Sons, Inc. Published 2025 by John Wiley & Sons, Inc.
Companion website: www.SmallAnimalUltrasonography.com

Vet-ebooks.com

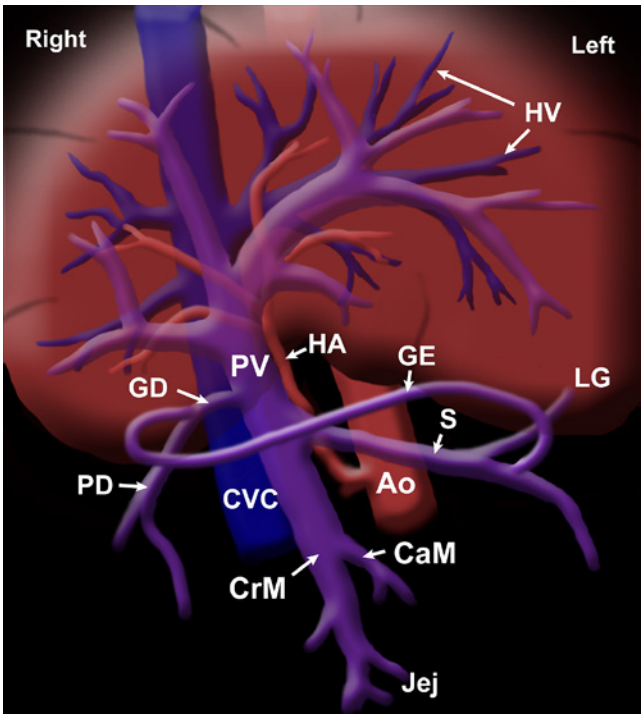


Figure 16.1. **Portal vascular system.** Schematic illustration of the hepatic vasculature and extrahepatic portal system of dogs and cats, as seen from a ventral approach. The liver receives its vascular supply through the portal vein (PV) and hepatic arteries (HAs). The PV receives several smaller veins draining most abdominal viscera. The relationship with the hepatic veins (HV), caudal vena cava (CVC) and aorta (Ao) is also illustrated. **Veins of the portal system**: CaM, caudal mesenteric; CrM, cranial mesenteric; GD, gastroduodenal; GE, gastroepiploic; Jej, jejunal; LG, left gastric, PD, pancreaticoduodenal; S, splenic.

flow that is, however, just related to the tortuous vascular anatomy.

When measured at the level of the porta hepatis, the PV luminal diameter varies between 3.4 and 5.0 mm in normal cats and between 3.3 and 10.5 mm in normal dogs (d'Anjou et al. 2004). When comparing the maximal luminal diameter of the PV and the aorta, **PV/aorta ratios** of 0.71–1.25 are normally expected in these two species.

The main PV is formed by the confluence of the cranial and caudal mesenteric veins and splenic vein (SV), and therefore drains most abdominal organs (Evans 1993) (Figure 16.1). It also receives a smaller tributary, the gastroduodenal vein, only a few centimeters caudal to the hepatic entrance. The gastroduodenal vein connects to the right-ventral aspect of the PV after receiving the pancreaticoduodenal and gastroepiploic veins. A few centimeters more caudally, the main PV receives the SV on the left side, which follows the left limb of the pancreas after receiving the left gastric vein. The cranial mesenteric vein receiving all jejunal branches represents the caudal extension of the main PV after the entry of the smaller caudal mesenteric vein another few centimeters caudal to the SV. These portal tributaries enlarge as they approach the main PV, and the flow of all is directed toward the liver (**hepatopetal flow**). The portal flow contained in these tributaries, as well as in the main PV, is normally parabolic and relatively constant, giving a characteristic spectral Doppler pattern (Figure 16.4). Portal flow mean velocity can be measured with spectral Doppler, after the use of an insonation angle correction of less

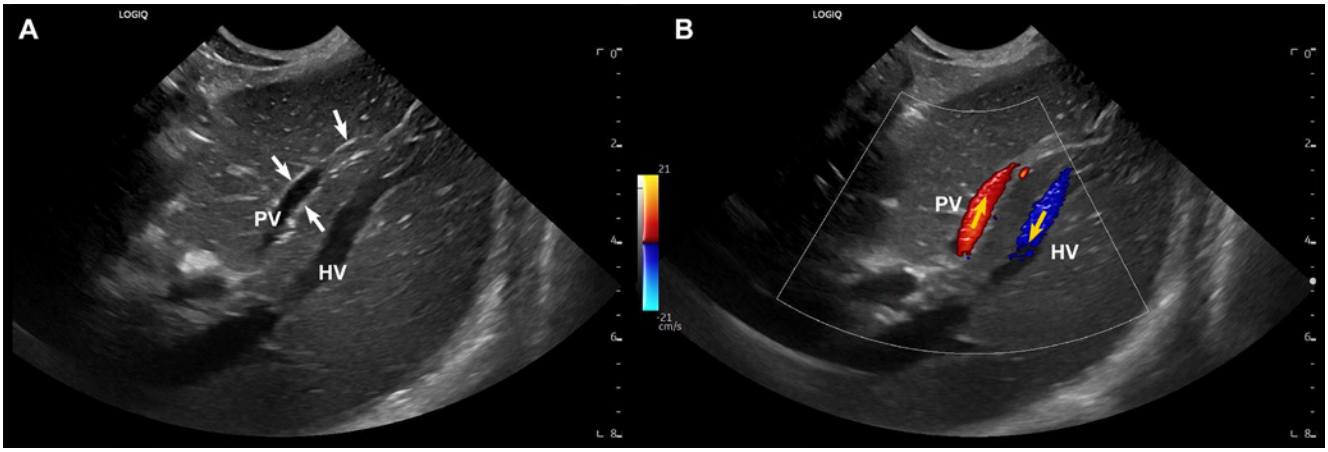


Figure 16.2. **Hepatic vasculature. (A)** Portal veins (PVs) can be differentiated from hepatic veins (HV) because of the consistent hyperechogenicity of their walls (arrows), regardless of the ultrasound beam orientation. **(B)** With conventional color Doppler, portal venous flow appears as a red signal directed toward the transducer, compared with a blue signal for the hepatic veins that drain in the caudal vena cava (i.e., away from the transducer).

Vet-ebooks.com

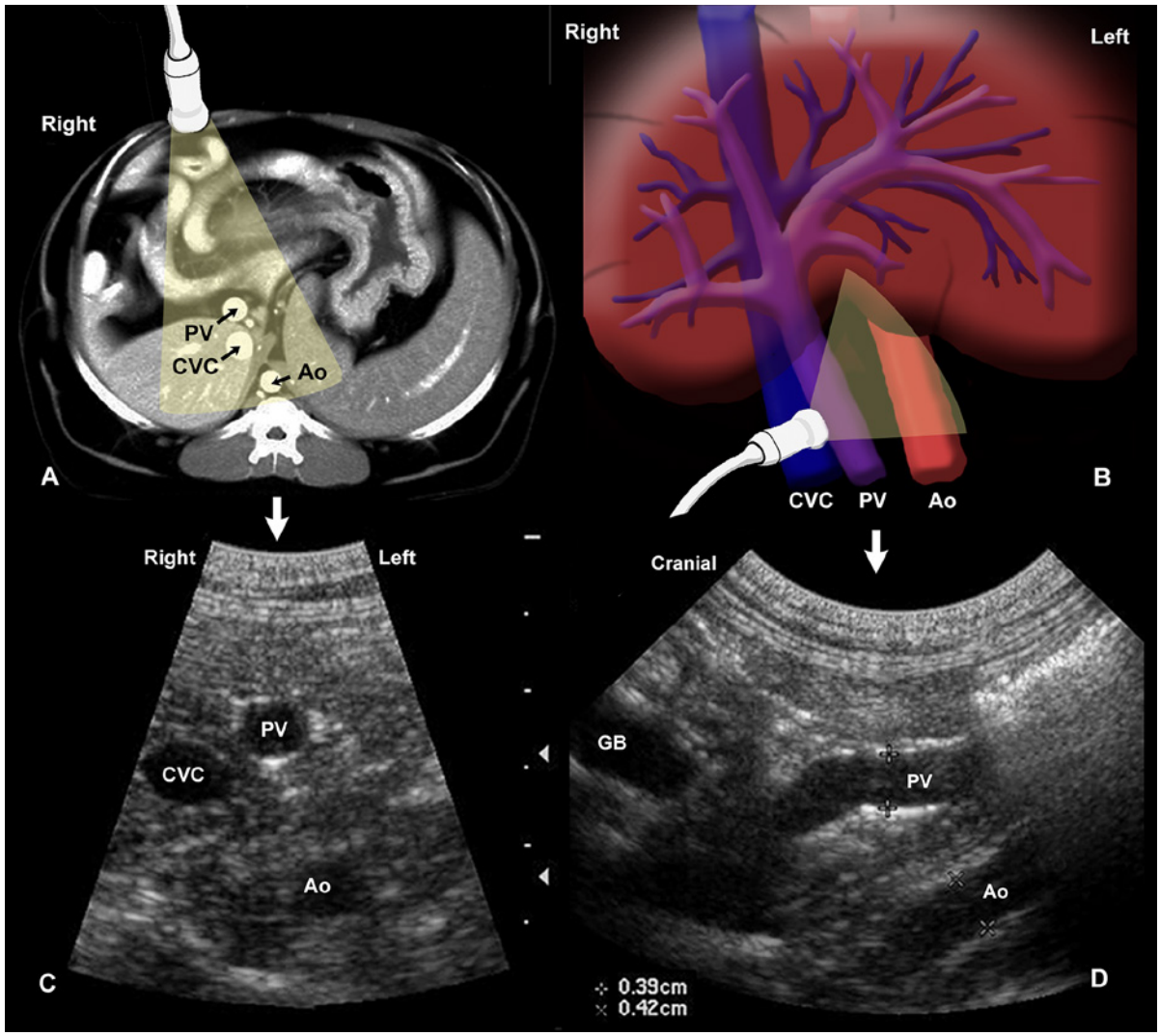


Figure 16.3. **Ultrasonographic approach to the hepatic vasculature.** Transverse computed tomographic image **(A)** and ventral schematic image **(B)** showing the relationship between the portal vein (PV), caudal vena cava (CVC), and aorta (Ao) caudal to the liver. On transverse **(C)** and longitudinal **(D)** ultrasonographic images obtained at the porta hepatis, these three vessels can usually be well visualized in normal dogs and cats and should be similar in size. When measured at the caudal margin of the liver, the portal vein should not be less than 65% of the diameter of the aorta. GB, gallbladder. Image **A** Courtesy of Matthew Winter, University of Florida.

than 60°. **Portal flow mean velocity** can be calculated by the ultrasound system by using the uniform insonation technique, which requires the application of a sample gate volume that fills the entire width of the main PV. Alternatively, a sample gate volume that fills approximately half of the vessel lumen placed in its center can be used to obtain maximal flow velocity. Because of the parabolic behavior of the portal flow, mean portal flow velocity can be estimated by multiplying this result by 0.57. Mean portal flow velocities have been reported to vary between 15 ± 3 and 18 ± 8 cm/s in normal dogs and 10–18 cm/s in normal cats (d'Anjou et al. 2004; Lamb 1998; Lamb and Mahoney 1994; Nyland and Fisher 1990). However, these measurements are susceptible to inaccurate estimations, especially with higher correction angles (more than 60°), and must therefore be used cautiously.

Portal flow in the right intrahepatic PV can also be measured as it can be more easily accessible in certain dogs (Belotta et al. 2018). While this flow may correlate with the global portal flow throughout the liver when uniformly distributed, this may not be the case when the flow is heterogeneous, such as with intrahepatic shunting or unevenly distributed liver disease.

Vet-ebooks.com

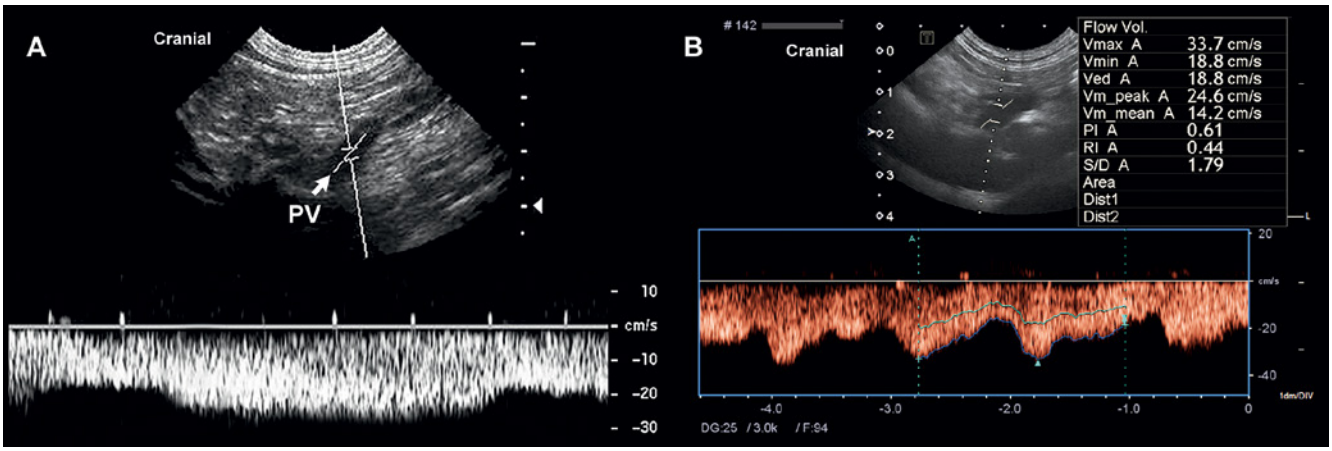


Figure 16.4. Spectral Doppler pattern of the portal flow in two dogs. With spectral Doppler, the flow within the portal vein (PV) can be assessed after placing the sample-volume gate in the center of the vascular lumen and correcting for the angle of flow direction. **(A)** The flow spectrum observed in this dog is broad and relatively linear, with some variations occurring because of movement of the sample volume during respiration in relation to the center of the vessel, where maximal velocity is reached. Assuming a parabolic flow profile, its mean velocity can be calculated by multiplying the maximal velocity (25 cm/s) by a factor of 0.57, which equals 14.3 cm/s. The angle of sample volume correction was 50°. **(B)** In this other dog, the flow is more irregular because of rapid respiration. Using the automated flow velocity measuring tool in this other ultrasound machine, the flow maximum (Vmax), minimum (Vmin), and mean (Vm) velocities can be measured in a segment of the spectral profile.

Abdominal Aorta, Caudal Vena Cava, and Tributaries

A thorough knowledge of vascular anatomy and hemodynamics is necessary to facilitate the identification and assessment of abdominal vessels. A schematic illustration of the principal vessels in the abdomen of dogs and cats is presented in Figure 16.5, along with typical waveforms on spectral Doppler. While the abdominal aorta supplies the arterial flow for all structures, the venous flow is separated between the portal system and the systemic circulation. In comparison with the portal system, a limited number of abdominal veins drain directly into the CVC. The CVC crosses the abdomen from caudal to cranial, remaining on the right of the midline. Visible veins with B-mode ultrasonography include, from caudal to cranial, the convergence of iliac veins (external, internal, common, and deep circumflex), renal veins (RVs), phrenicoabdominal veins, and hepatic veins. The aorta is more dorsal than the CVC in the cranial abdomen and remains on the left side, and then it lies next to it caudally. Major abdominal branches of the aorta that can be localized ultrasonographically include, from cranial to caudal, celiac artery (left gastric, hepatic, and splenic arteries), cranial mesenteric artery, renal arteries, and aortic trifurcation where external iliac arteries arise. These vessels are useful landmarks for identifying abdominal lymph nodes.

Anatomic variations in dogs and cats include different anatomy of the celiac tripod, multiple renal arteries, and fused origin of the celiac and cranial mesenteric arteries (Le Pommellet et al. 2017).

Duplication of the CVC (classified as caudal-partial split, partial duplication, and complete duplication) can sometimes be seen in dogs and cats (Chanyoung et al. 2019). While CVC duplication is not clinically significant, concurrent extrahepatic portosystemic shunts (PSS) are common in certain dogs, especially in Yorkshire Terrier, Poodle, West Highland White Terrier, and Maltese (Bertolini et al. 2014). Other rare anatomical variations of the CVC include left-sidedness, preureteral CVC, and transcaval ureter (ring-like segmental split of the CVC with a ureter passing through the ring) (Pey et al. 2015; Spediacci et al. 2022).

Blood Flow Velocities in the Major Abdominal Vessels

The mean aorta-CVC ratio in dogs with normal systemic pressure is around one while in dogs with systemic hypertension it reaches 1.5 (Holland et al. 2019). The median flow velocities are reported to be 63+/−18.6 cm/s for the CVC and 121+/−24 cm/s for the aorta (peak systolic) (Lee et al. 2004; Smith et al. 2018).

Vet-ebooks.com

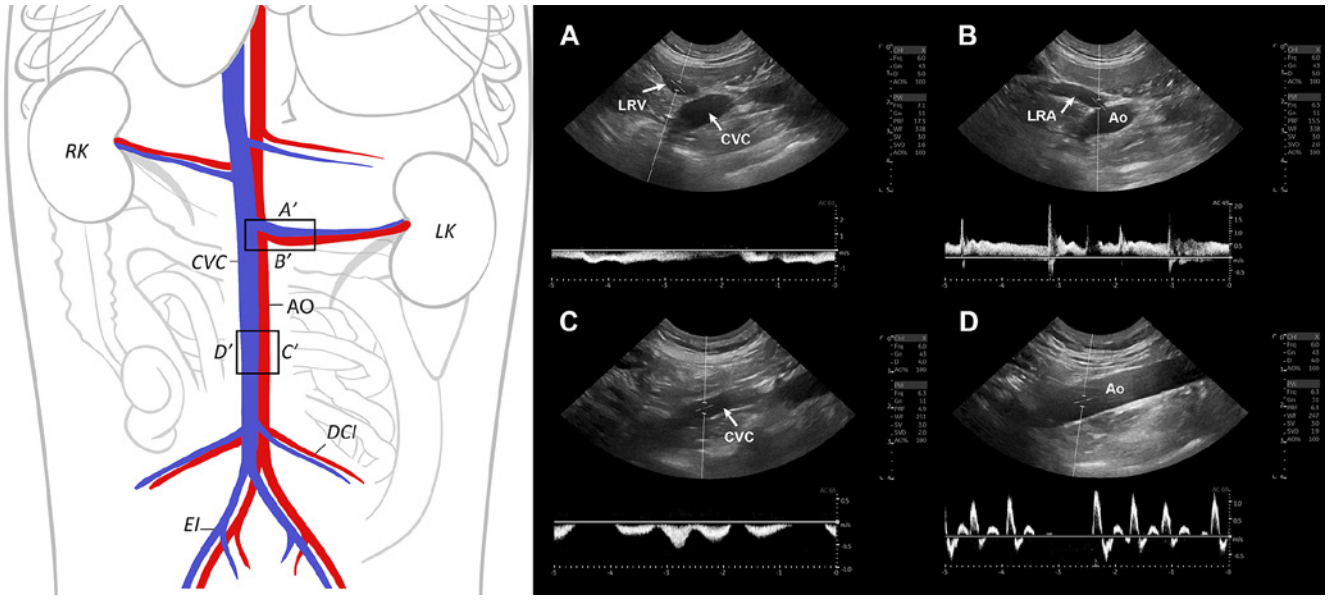


Figure 16.5. **Schematic illustration of the anatomy of the abdominal CVC and aorta, and their tributaries in dogs, with their typical normal flow pattern on spectral Doppler. (A)** The **left renal vein (LRV)** shows a flow of low velocity that is directed away from the probe and therefore placed below the horizontal line on the graph, with a sinuous to irregular pattern that is mildly affected by the cardiac cycle. **(B)** The **left renal artery (LRA) shows** a pulsatile flow of high velocity and mainly directed toward the probe (above the line). **(C)** The flow of the **caudal vena cava (CVC)** shows a characteristic sinuous flow that is affected by the cardiac cycle, reaching its highest velocity (50 cm/sec in this dog) during diastole and directed toward the heart, away from the probe (below the line). **(D)** The flow in the **aorta (Ao)** has a strongly pulsatile flow that is directed toward the probe during systole, but away from the probe during diastole, reaching a peak velocity of 150 cm/sec in this dog. Its graph shows a thin band because the sample box is small and collects only the central portion of the vessel, in which the blood flow has a uniform velocity during the cardiac cycle. EI, external iliac artery; DCI, deep circumflex iliac artery; LK, left kidney; RK, right kidney.

Congenital Disorders of the Portal Vasculature

Congenital Portosystemic Shunts

PSSs, which represent one of the most common vascular anomalies in dogs and cats, connect the portal system to the systemic circulation through the CVC or azygos vein. The use of ultrasonography in the detection and characterization of these anomalies has been well described (d'Anjou 2007; d'Anjou et al. 2004; Lamb 1996; Lamb et al. 1996a; Szatmari et al. 2004). Most PSS are congenital in dogs and cats, and more commonly detected in juvenile animals; however, a certain number of these shunts (in particular those joining the systemic venous circulation through the azygos vein) can remain undetected for several years in dogs and particularly in cats.

Because of the common reduction in hepatic volume in affected animals, a complete evaluation of the intrahepatic and extrahepatic portal vasculature can be challenging to achieve. A right-lateral approach through the 11th or 12th intercostal spaces may be required to visualize the liver and porta hepatis, as well as the region of the CVC, without overlying gastrointestinal content.

Congenital PSSs are most often single, but multiple distinct branches may be present, making the diagnosis sometimes challenging. Schematic morphological differences among congenital PSS are depicted in Figure 16.6.

Extrahepatic portosystemic shunts, arising from the main PV or a tributary (e.g., the splenic, right gastric, left gastric, or gastroepiploic vein), represent the most common type of PSS and are most prevalent in small breeds of dogs and in cats (d'Anjou et al. 2004; Lamb 1996; Lamb et al. 1996a; Szatmari et al. 2004). According to White and Parry (2013, 2015a,b, 2018), most of these shunts originate from the left gastric vein and join the systemic venous circulation with a direct short connection with the CVC, through the phrenic vein or azygos vein.

An anomalous tortuous vessel, containing hepatofugal flow and with a maximal diameter similar to the aorta, is typically seen originating from a branch of the portal system (Figure 16.7). A termination into the CVC

Vet-ebooks.com

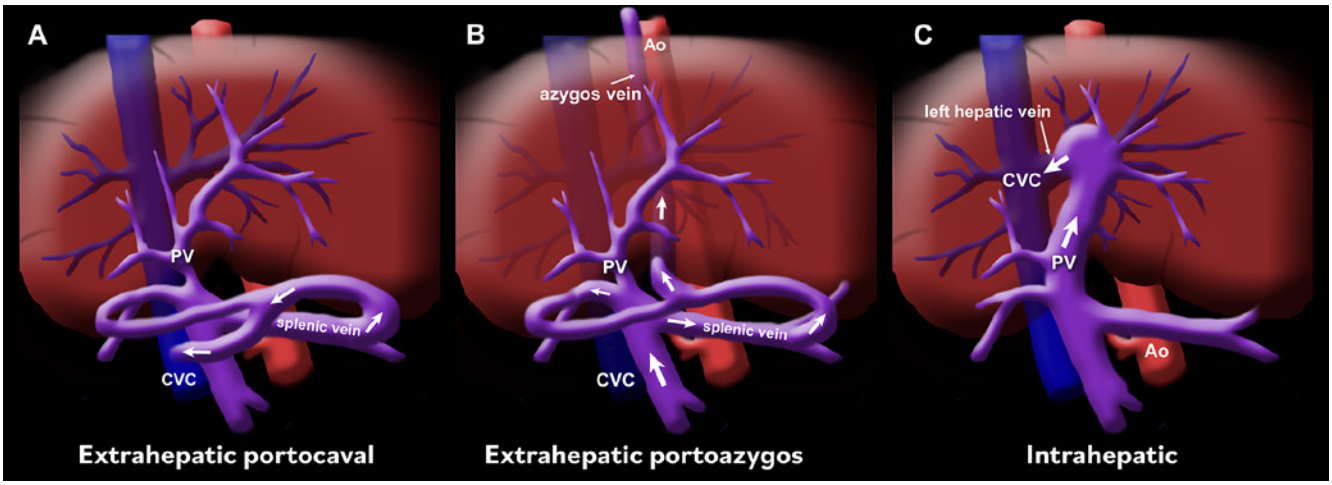


Figure 16.6. Main categories of congenital portosystemic shunts. Schematic illustrations of typical categories of congenital shunts showing the direction of shunting flow (arrows) in dogs and cats. Extrahepatic shunts can terminate into the caudal vena cava (**A**) or azygos vein (**B**). In either case, the diameter of the portal vein (PV) cranial to the origin of the shunt is significantly reduced because of flow diversion. A portoazygos shunt can be followed in the direction of the aortic hiatus, along the aorta (Ao), but its termination can be difficult to visualize. On the other hand, most portocaval shunt terminations can be seen with ultrasonography. **(C).** Intrahepatic shunts can have variable configurations. Left-sided intrahepatic shunts (*patent ductus venosus*) is one of the most common types of intrahepatic shunts. This shunt typically terminates into an "ampula" formed by the confluence of this shunt and a left hepatic vein, just before the caudal vena cava (CVC).

is often visualized in association with focal flow turbulence that appears as a mosaic pattern on color Doppler (d'Anjou et al. 2004; Lamb 1996) (Figure 16.7B).

Portocaval shunts typically terminate in the CVC cranial to the right RV (Figure 16.7C). The shunt termination can be more difficult to visualize when a shunt connects to the azygos vein. **Portoazygos shunts** typically dive craniodorsally, in the direction of the aortic hiatus, after originating from one of the portal branches (Figures 16.8, 16.9). The anomalous vessel can be followed dorsally and cranially to the transverse colon and stomach, unless this window is blocked by acoustic shadowing and/or reverberation caused by the presence of gas, ingesta, or feces. In some cases, a dilated vessel adjacent and parallel to the aorta can be seen that contains venous flow directed cranially (Figure 16.8B).

Intrahepatic PSSs are more prevalent in large-breed dogs and are defined as left-divisional, central divisional, or right-divisional. Recently, Plested et al. suggested a subclassification based on the hepatic veins with which the shunting vessels communicate (Plested et al. 2020). The subclassification may help surgeons in choosing the correct method for shunt attenuation.

Left-divisional shunts, sometimes caused by a **patent ductus venosus**, represent the most common form of intrahepatic shunt (Szatmari et al. 2004) (Figure 16.6C). With this type of PSS, a large tortuous vessel is seen originating from the intrahepatic PV and curving into the left portion of the liver before entering the CVC (Figures 16.10A, 16.11). Morphologically, these shunts typically connect to the left hepatic vein, which drains into the CVC. **Right-divisional shunts** often appear as a mirror image of patent ductus venosus PSS but instead curve into the right liver before connecting to a right hepatic vein or to the CVC (Figure 16.10B, C). **Central divisional shunts** may present as a window-type shunt between a closely aligned intrahepatic PV and the CVC. In such case, the PV is often dilated at the site of the foramen, and flow turbulence can be observed in the CVC (Figure 16.10D). A long tortuous intrahepatic vessel may also be seen, communicating with the CVC via the quadrate or dorsal right medial hepatic vein (Plested et al. 2020).

The **PV size** has a significant predictive value in shunt investigation. In fact, because of flow diversion, the size of the PV cranial to the shunt origin is significantly reduced (d'Anjou et al. 2004; Szatmari et al. 2004) (Figures 16.7A, 16.12). A congenital extrahepatic shunt is suspected if the main PV is smaller in diameter when compared with its tributaries. The search for the origin of the PSS is focused on the region where the PV, or a tributary, abruptly diminishes in size. A ratio comparing the luminal diameter of the PV, just before entering the liver, with the maximal luminal diameter of the cranial abdominal aorta can help predict the likelihood of an extrahepatic PSS in dogs and cats (d'Anjou

Vet-ebooks.com

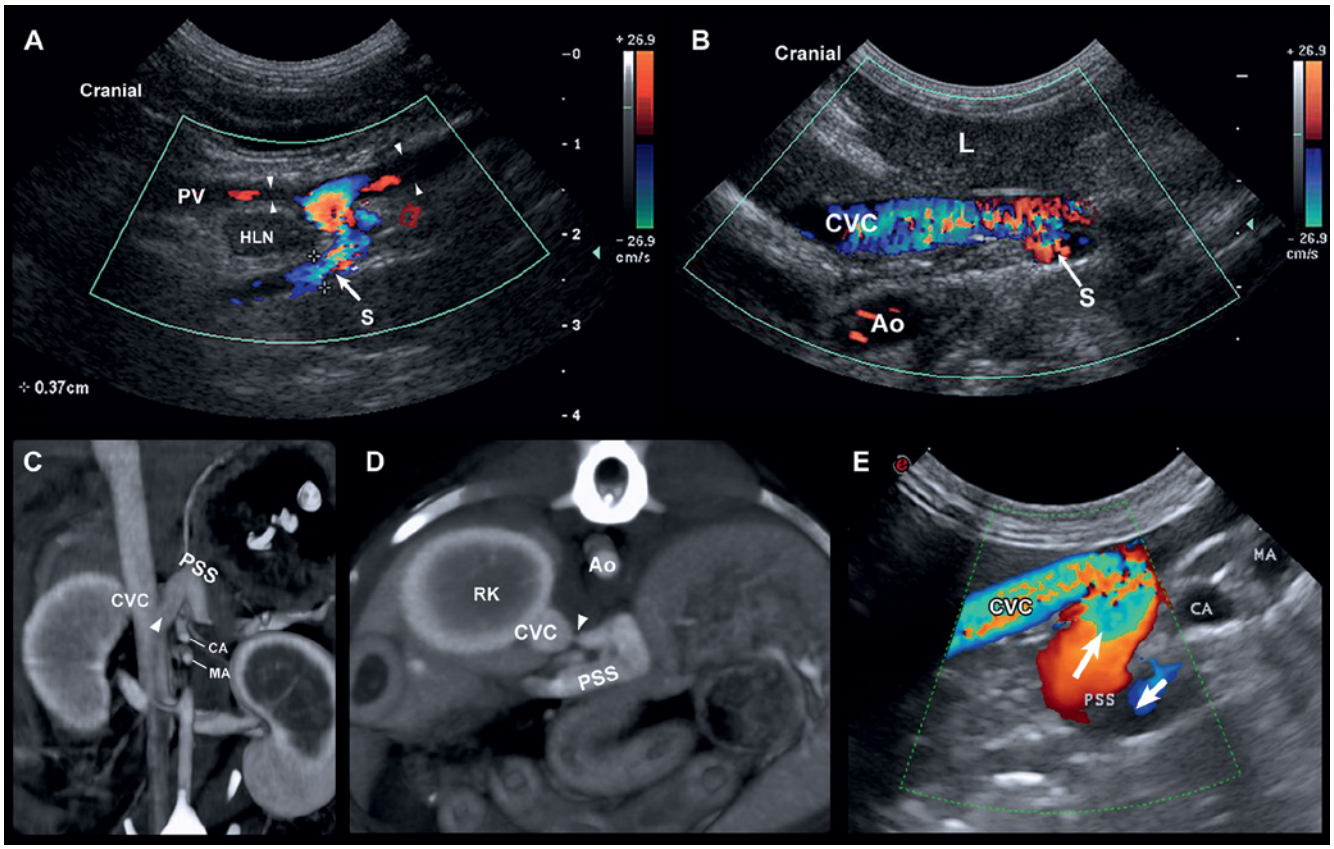


Figure 16.7. **Extrahepatic portocaval shunts in three dogs. (A)** Longitudinal color Doppler image of the abdomen of a Yorkshire Terrier. An anomalous shunting vein (S) just caudal to the stomach is seen originating from the main portal vein (PV), just caudal to the hepatic lymph nodes (HLN). This vessel contains hepatofugal flow and is directed craniodorsally. The PV diameter is significantly reduced cranial to the shunt origin (arrowheads). **(B)** Longitudinal color Doppler ultrasound image obtained in the craniodorsal abdomen of another dog with extrahepatic portocaval shunting. A mosaic pattern observed in the caudal vena cava (CVC) is consistent with flow turbulence at the site of shunt termination (S). **(C, D)** Dorsal **(C)** and transverse **(D)** postcontrast computed tomographic volume rendering images of a third dog with congenital extrahepatic splenocaval portosystemic shunt (PSS) visible as a short, large, and tortuous vessel with dorsal direction connecting the portal vein to the caudal vena cava (arrowhead). **(E)** Color Doppler US image of the same patient with a right-side abdominal window showing the shunting vessel (PSS) with red flow (from the splenic vein toward the caudal vena cava in the direction of the US probe). Note the flow turbulence in the CVC at shunt termination. Ao, aorta; CA, celiac artery; CVC, caudal vena cava; L, liver; MA, cranial mesenteric artery.

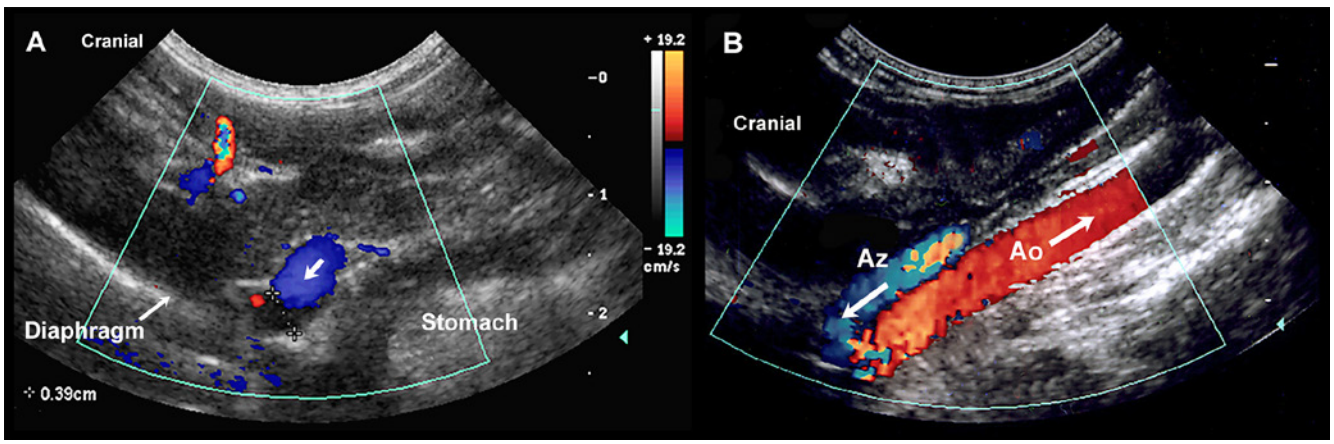


Figure 16.8. **Portoazygos shunts. (A)** Longitudinal oblique color Doppler image obtained in the craniodorsal abdomen of a young Yorkshire Terrier. An aberrant vein with hepatofugal flow (short arrow) is next to the gastric cardia and diaphragm. A portoazygos shunt was surgically confirmed. **(B)** Longitudinal color Doppler image obtained in the craniodorsal abdomen of a young cat with a right azygos vein (Az) abnormally apparent along the aorta (Ao). A shunt was detected connecting to this vein in the mid-abdomen.

Vet-ebooks.com

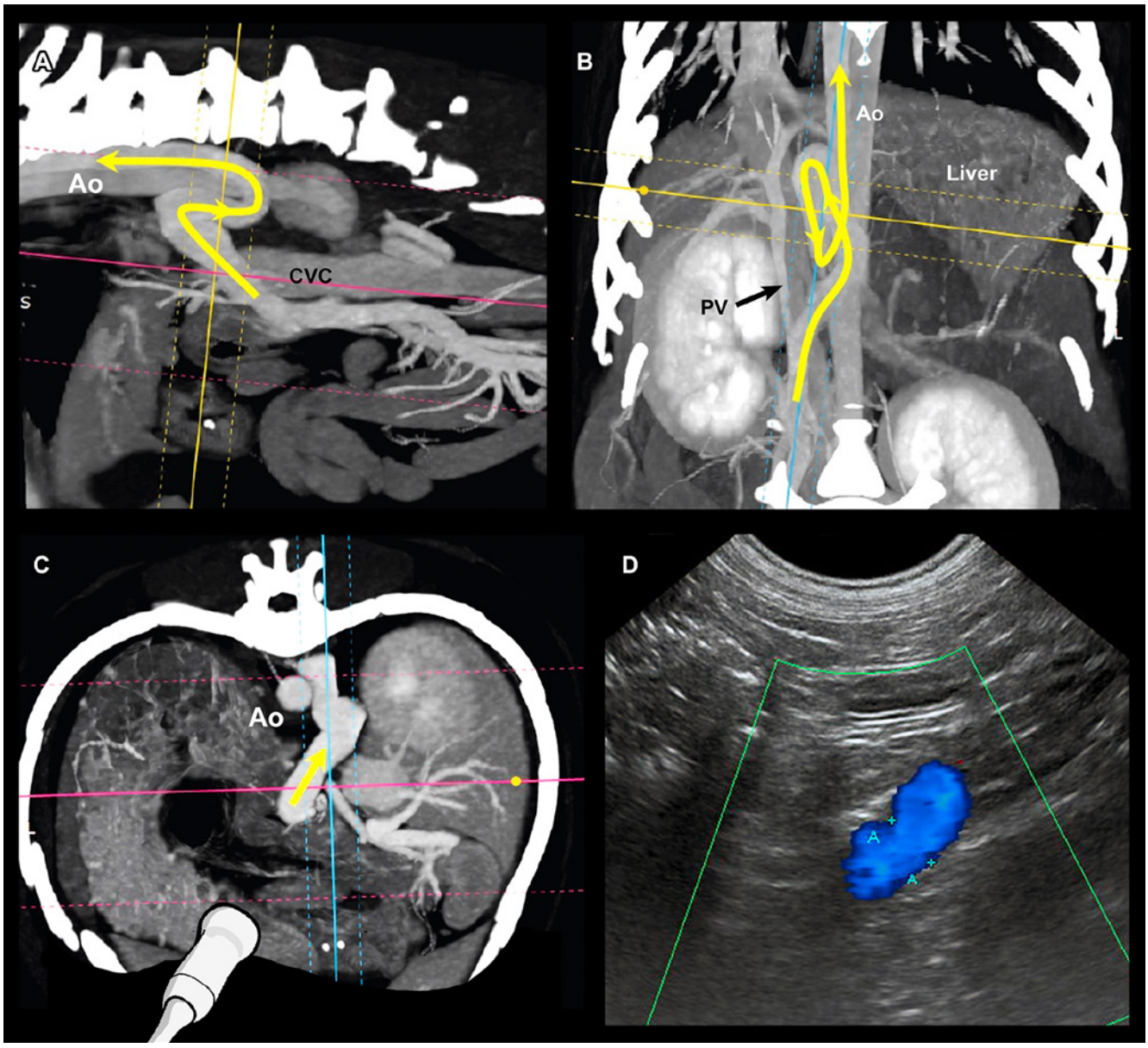


Figure 16.9. **Portoazygos shunt in a 3-year-old spayed female beagle with recent onset of hepatoencephalopathy. (A–C)** Reformatted CT images showing a long, tortuous extrahepatic shunt diving dorsally and curving backward before terminating into the azygos vein, dorsal to the aorta (Ao) (direction of flow depicted by yellow arrows). Note the reduction in diameter of the portal vein (PV) cranial to the origin of the shunt. **(D)** Oblique color Doppler image obtained with the probe placed as seen in C, showing only a portion of the shunting vessel. Inability to clearly visualize the termination of a porto-azygos shunt is common, especially in larger dogs, if the liver is small or if there is gastro-intestinal content.

et al. 2004). A **PV-aorta ratio** of ≤0.65 tends to predict the presence of an extrahepatic shunt (Figure 16.13), whereas a ratio ≥ 0.8 should exclude this type of PSS, if the PV is accurately identified and measured instead of the shunting vessel. However, a low PV/aorta ratio can also be found in dogs with **primary PV hypoplasia**, leading to multiple acquired PSS because of portal hypertension. PV/aorta ratios ≥0.8 should be seen only in animals with a normal portal system, microvascular dysplasia, intrahepatic PSS, or portal hypertension caused by chronic liver disease.

Multiple tortuous intrahepatic vessels depicting venous flow may be found in case of focal narrowing of the ostium of the intrahepatic shunt. These "multiple"

Vet-ebooks.com

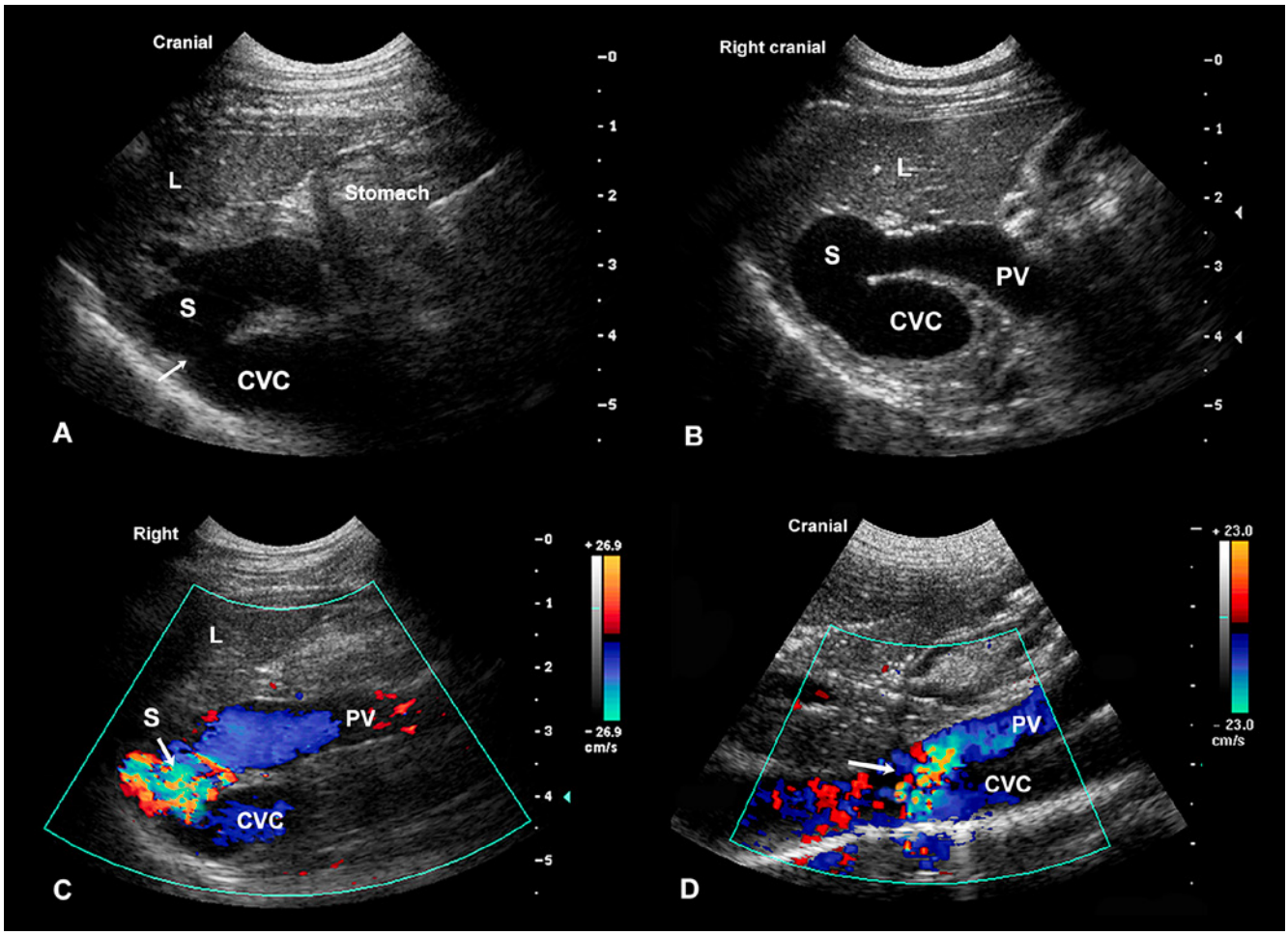


Figure 16.10. **Intrahepatic shunts in four dogs. (A) Patent ductus venosus**. Longitudinal oblique ultrasound image obtained in the left cranial abdomen of a young Golden Retriever. A large tortuous vein (S) apparent in the liver connects to the caudal vena cava (CVC and arrow). Hepatofugal flow observed on color Doppler was consistent with a left-divisional intrahepatic shunt (S). The liver (L) is reduced in volume. **(B) Right-divisional shunt**. Transverse ultrasound image of the liver (L) obtained through the right 12th intercostal space in a young Bernese Mountain Dog with suspected portosystemic shunting. A large, intrahepatic, tortuous vein (S) connects the portal vein (PV) to the CVC. **(C) Right-divisional shunt.** Longitudinal oblique ultrasound image obtained through the right 12th intercostal space in a young Akita with suspected portosystemic shunting. A large tortuous vein (S) is between the PV and the CVC in the liver (L). Turbulent flow is obvious, as manifested by a mosaic pattern on color mode at the site of communication of the shunt (arrow) with the caudal vena cava. **(D) Central divisional intrahepatic shunt**. Longitudinal color Doppler image obtained in the craniodorsal abdomen of a young large-breed dog with suspected portosystemic shunting. The intrahepatic PV dives dorsally and a "window" (arrow) containing turbulent flow (mosaic pattern) is seen connecting to the CVC.

IHPSS are intrahepatic collateral circulation secondary to focal hypertension due to the narrowing of the ostium (Seller et al. 2022).

Several other findings can be seen in dogs and cats affected with congenital PSS. Besides the microhepatia observed in most patients (particularly in dogs), the visibility of intrahepatic portal branches is often reduced because of hypoperfusion. When evaluated with spectral Doppler, the portal flow is commonly irregular because of cardiac cycle influence on the normally relatively constant portal flow (d'Anjou et al. 2004; Lamb 1996) (Figure 16.13). Comparing flow velocities in different sections of the PV and tributaries may also help identify an anomalous vessel with increased flow (Figure 16.14). The kidneys are commonly enlarged, especially in dogs, and uroliths are often recognized. The combination of **microhepatica**, **renomegaly**, and **urolithiasis** is highly predictive of PSS in young dogs with clinically suspected shunting (d'Anjou et al. 2004).

Vet-ebooks.com

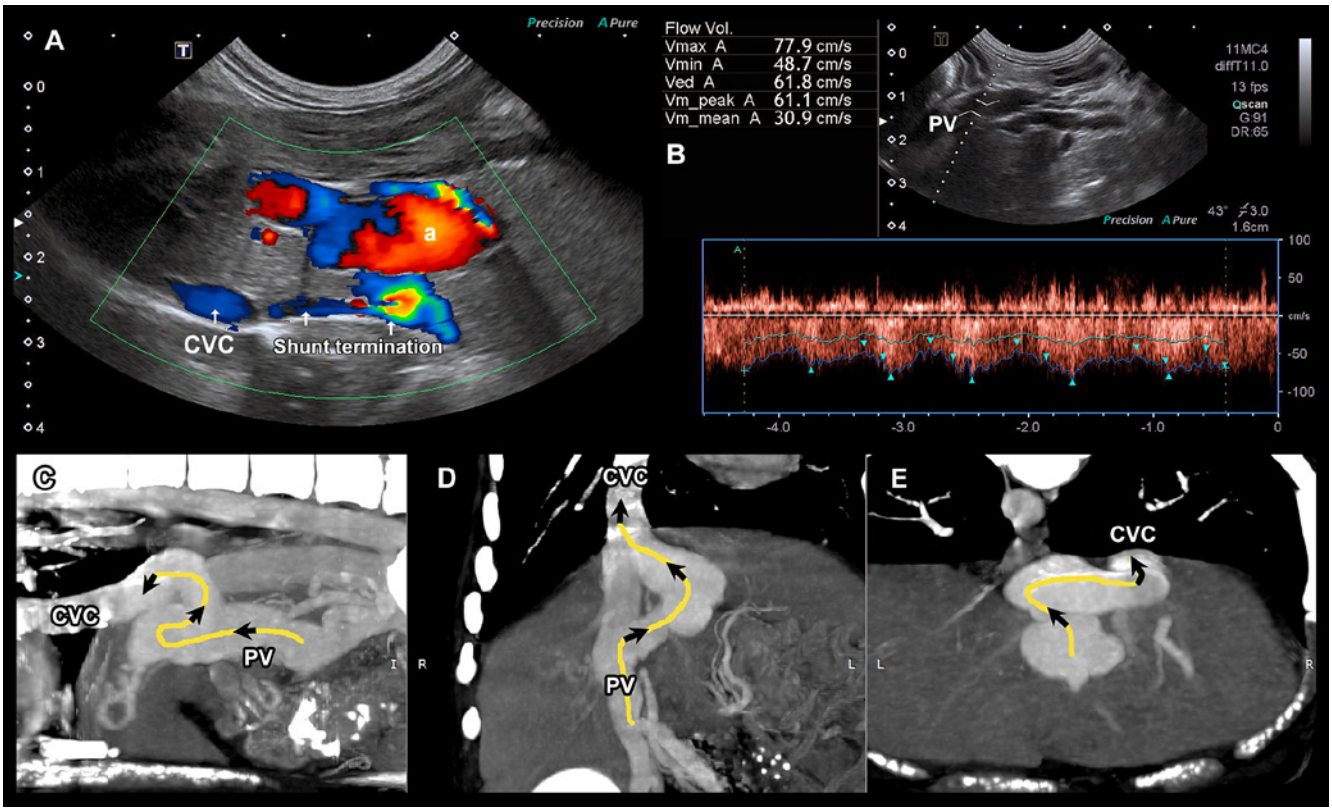


Figure 16.11. Left-divisional intrahepatic shunt in a 3-month-old male mixed Labrador. (A) Transverse oblique color Doppler image of the irregular shunting vessel that is focally dilated (ampula, a) before connecting to the caudal vena cava (CVC) through an enlarged left hepatic vein. **(B)** On spectral Doppler, the portal vein (PV) shows an irregular flow velocity that is increased because of the lower resistance. **(C–E)** Sagittal **(C)**, dorsal **(D)**, and transverse **(E)** reformatted postcontrast CT images of the shunt depicting the flow direction from the PV to the CVC.

A systematic approach is recommended in the detection of congenital and acquired PSS in animals (Figure 16.15).

Pre- and Postsurgical Assessment of Shunts

The evaluation of a patient in which a PSS is detected should target a maximum amount of pivotal information for surgical planning and prognosis. Computed tomography (CT) is an additional tool that can help the radiologist better understanding shunt anatomy and often facilitates communication with the surgeon, especially with 3D-rendering (Figures 16.9, 16.11).

Important information for the surgeon includes the shunting vessels actual anatomy, specifically the portal vessel of origin, the systemic vessel of insertion, and any contributing vessels that might be identified in surgery. Also important is the caliber of the PV entering the liver; specifically does the surgeon need to be concerned about the degree of portal perfusion present in this patient? Should a portogram be performed? Are portal pressures necessary? In cases of IHPSS, it is important to specify, if possible, through which intrahepatic vessel the shunt joins the CVC. The presence of additional findings in particular urolithiasis, nephromegaly, and peritoneal fluid should be mentioned.

Ultrasound is also a useful tool for monitoring the patency of PSS in dogs after surgical ligature of PSS or placement of occluding devices (Figures 16.16, 16.17).

Portal Vein Aplasia

Aplasia of the PV has been reported in association with CVC continuation into the azygos vein and PSS. In such cases, the PV cranial to the vascular anomaly is not visualized as well as the intrahepatic PV branches. Only the hepatic veins are visible in the liver. It must, however, be remembered that the PV can become very small with EHPSS and consequently not visualized with ultrasound. Sonographic diagnosis of PV aplasia can therefore be challenging.

Vet-ebooks.com

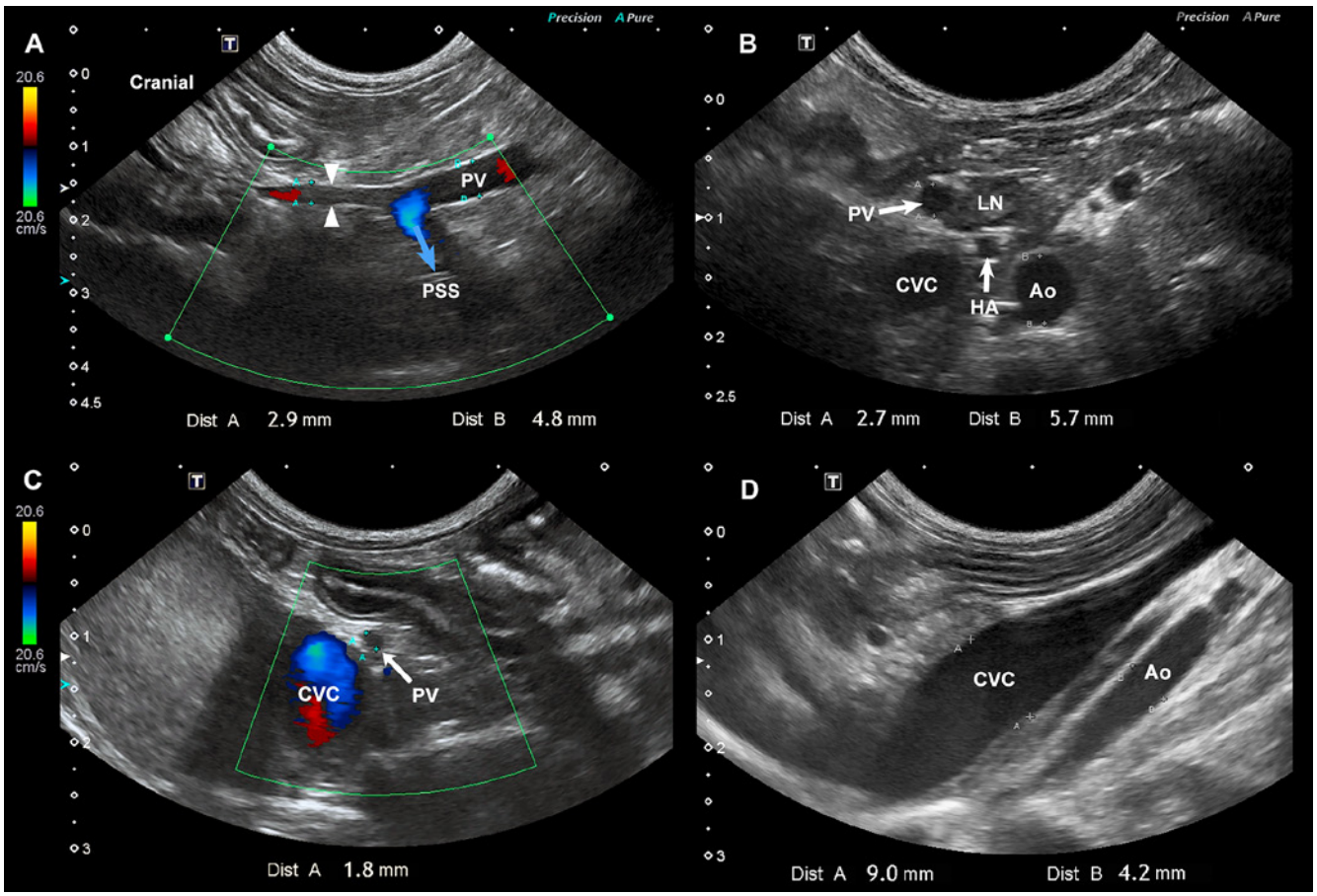


Figure 16.12. **Reduced portal vein/aorta ratio in two dogs with extrahepatic PSS. (A, B)** Longitudinal and transverse sonographic images obtained caudal to the liver in a 6-month-old Beagle dog with a congenital left gastric-azygos shunt (PSS). The portal vein (PV) is significantly reduced in diameter (between arrowheads) cranial to the splenic vein (leading to the shunt) and measures less than half of the diameter of the aorta (Ao), for a ratio of 0.47. The hepatic artery (HA) is well visualized (in B), which is also typical of PSS. Note the proximity of the left hepatic lymph node (LN) helping to recognize these vessels. **(C, D)** In this other dog with portocaval shunting, the portal vein (PV) is much smaller (luminal diameter of 1.8 mm) than the caudal vena cava (CVC, 9 mm) that receives the bypassing flow and its ratio with the aorta (4.2 mm) is reduced (0.52), which is consistent with the extrahepatic shunt. In **A and C**, note the absence of color Doppler signal in the PV due to the reduced flow velocity and/or their perpendicularity with the angle of insonation.

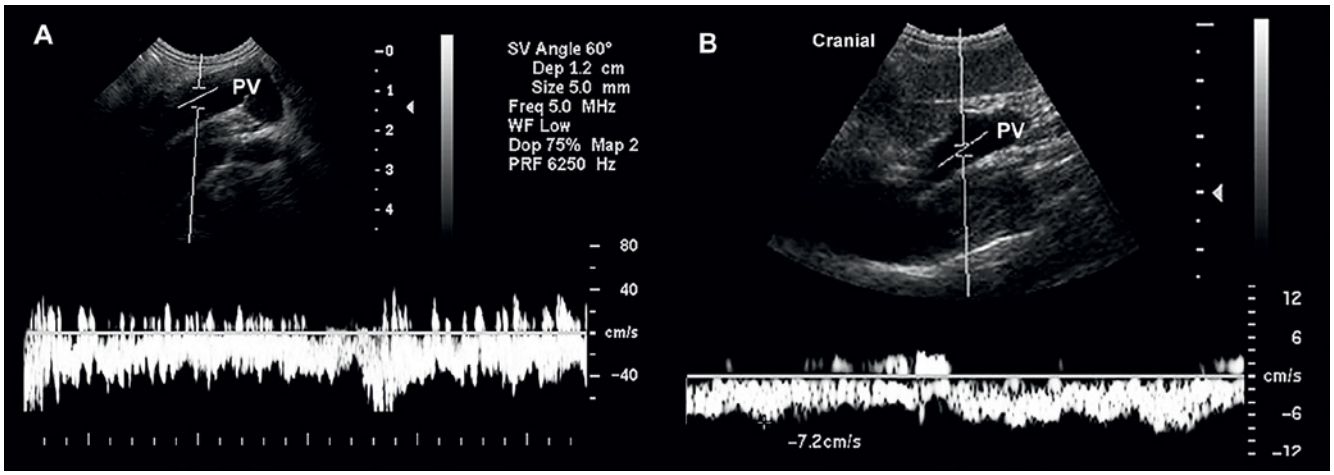


Figure 16.13. **Portal flow alterations. (A) Intrahepatic shunt**. Spectral Doppler evaluation of the portal flow characteristics in a dog with intrahepatic shunting. The flow velocity is markedly irregular in the main extrahepatic portal vein (PV) because of the retrograde influence of pressure variations in the caudal vena cava. **(B) Portal hypertension**. Spectral Doppler evaluation of the portal flow in a dog with chronic liver disease. The maximal flow velocity is reduced (7.2 cm/s) in the extrahepatic PV because of intrahepatic hypertension. Multiple acquired shunts were detected.

Vet-ebooks.com

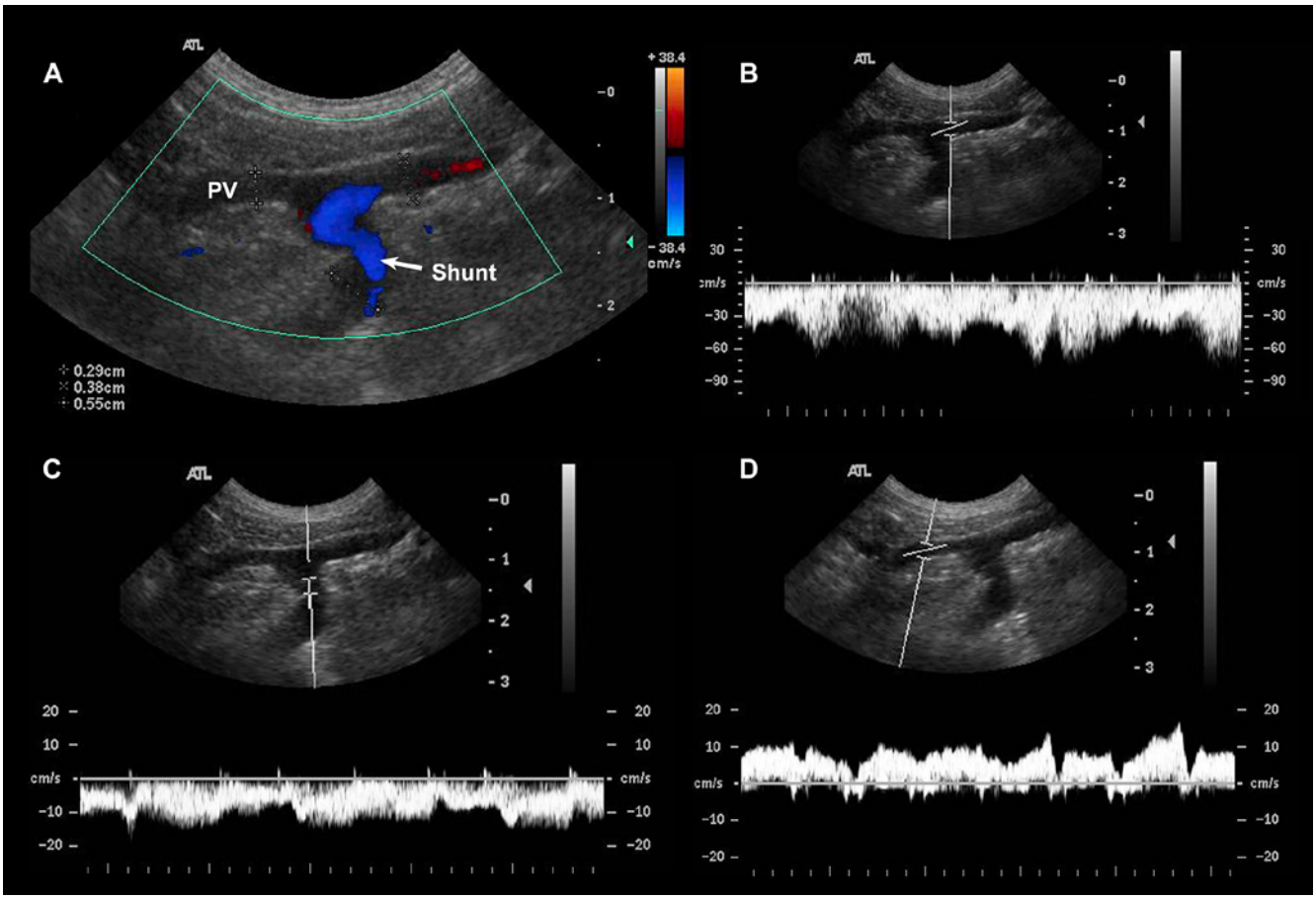


Figure 16.14. Portal flow velocities before and after shunt origin. (A) Color Doppler evaluation of the extrahepatic shunt originating from the proximal portal vein (PV). The blue color signal indicates hepatofugal flow in the anomalous vessel. No color flow is identified in the PV cranial to the shunt origin, mainly because of its perpendicular position regarding the insonation angle. **(B–D)** Spectral Doppler assessment of the flow velocities in the PV proximal to the shunt **(B)**, within the shunt **(C)**, and in the PV distal to the shunt **(D)**. The flow is irregular and becomes hepatofugal (i.e., reversed) in the PV distal to the origin of the shunt **(D)**.

Arterioportal Communications

Arterioportal communications (APC) are rare congenital anomalies subclassified as arterioportal fistulas and arterioportal malformations.

With **arterioportal fistula**, the afferent HA anastomoses with a single vessel of the portal system, whereas in **arterioportal malformations**, the communications between the hepatic arterial blood flow and the portal system happens through a network of multiple tortuous shunting vessels, called ***nidus***. These anomalies result in severe portal hypertension due to reversed portal blood flow, leading to secondary portal collateral circulation and variable degree of ascites.

APC may present with concomitant IHPSS. In this case, the resistance is lower in the systemic venous system compared to the portal system with blood flowing directly from the HA into the hepatic/posthepatic CVC preventing the development of portal hypertension (Specchi et al. 2018).

US features of APC include the presence of a single large (arterioportal fistula) or multiple small (nidus in arterioportal communication) tortuous anechoic tubular structure/s inside the liver consistent with anomalous blood vessels (Figures 16.18–16.20). In color Doppler, aliasing artifacts are usually observed due to flow turbulence provoked by the high-velocity arterial blood flow entering these vessels. On spectral Doppler, an arterial waveform is detected in the portal branches efferent of the APC along with reversed (**hepatofugal**) flow in the main PV. Aneurysmatic efferent portal vessels usually appear as dilated and tortuous anechoic tubular structures with a thickened hyperechoic wall.

Secondary findings in patients with APC include portosystemic collateral circulation (see later for US

Vet-ebooks.com

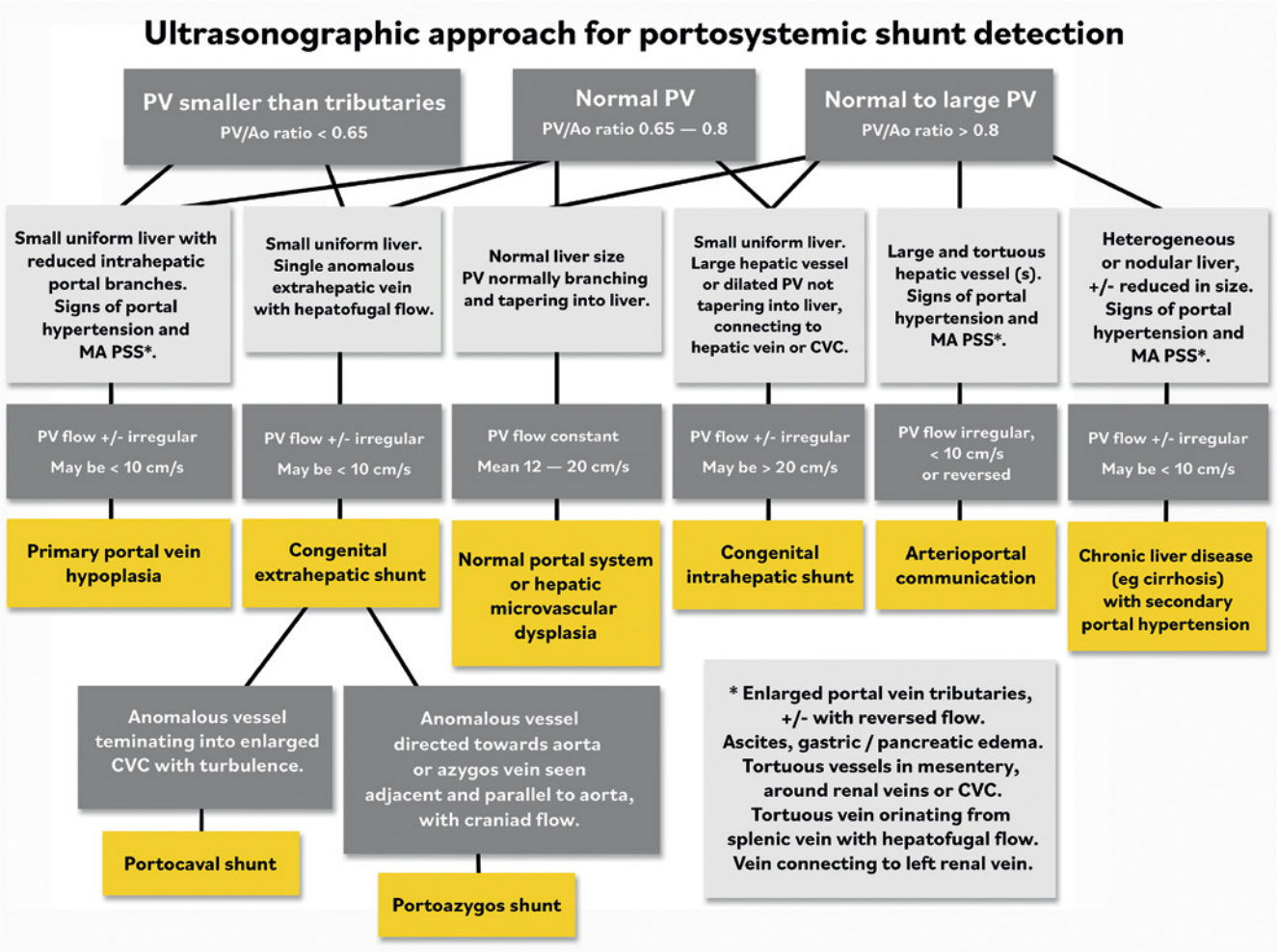


Figure 16.15. Portosystemic shunt search algorithm. Common findings observed with different categories of portosystemic shunts (PSS) are shown. The main portal vein (PV) is evaluated and its luminal diameter measured just caudal to its insertion into the liver. In that process, care must be taken not to confuse a portal tributary or an aberrant vein for the main portal vein. CVC, caudal vena cava; MA PSS, multiple acquired portosystemic shunts; and PV/Ao (aorta) ratio, ratio between the luminal diameter of the main portal vein and aorta (in systole).

description and localization), decreased aortic diameter caudal to the celiac artery (due to "blood-steal phenomenon"), and regional or generalized microhepatica.

Congenital Disorders of the Systemic Venous System

Azygos Continuation of the CVC with or Without PSS (Segmental Aplasia of the CVC)

Segmental aplasia of the CVC is caused by the absence of development of the prehepatic CVC, causing a redirection of the posthepatic CVC blood flow into the right azygos vein, or anomalous left azygos vein.

Azygos continuation of the CVC is typically not clinically significant and thus considered an incidental finding, however, the intermittent/dynamic dilation of the anomalous vascular connection between the azygos vein and CVC is thought to predispose these patients to thrombosis and thromboembolism in adult age (Bertolini and Caldin 2020).

Azygos continuation of the CVC with or without PSS appears on ultrasound as a large anomalous vein in the caudal to mid abdomen originating from the external iliac veins' anastomosis, showing laminar blood flow (i.e. smooth and linear) with caudo-cranial direction and absence of the renal/prehepatic CVC. The anatomy of the anomalous vessels is variable, but in the most frequent conformation, this vessel runs adjacent to one of the kidneys (Figure 16.21). A dorsal right intercostal

Vet-ebooks.com

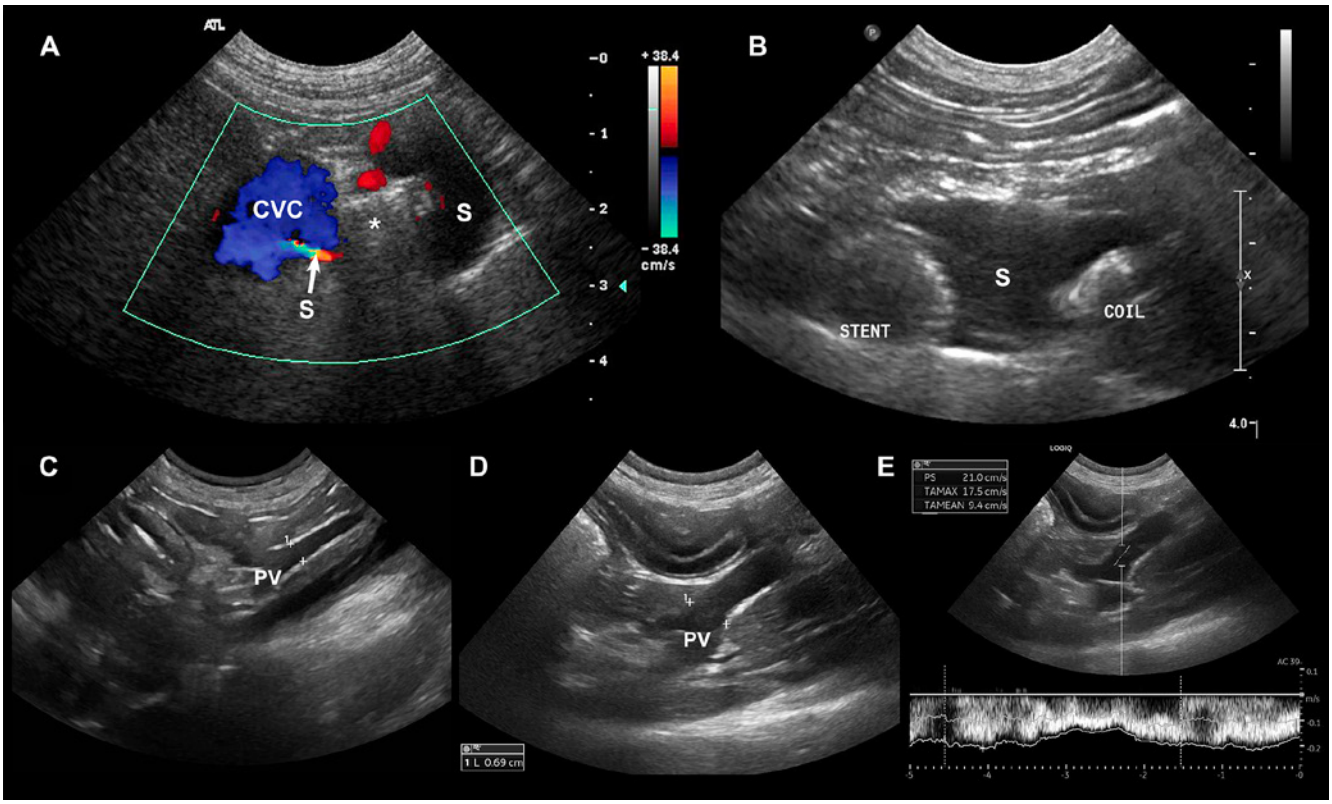


Figure 16.16. Follow-up of portosystemic shunt (PSS) after surgical occlusion in three dogs. (A) In this dog, an ameroid constrictor device (*) was placed next to the CVC at the site of termination of a congenital extrahepatic portocaval shunt. 1 week after the surgery, the shunt (S) remained patent, but it closed completely after 4 weeks. The ameroid causes acoustic shadowing and reverberation artifacts. **(B)** In this 9-month-old Beagle with an intrahepatic shunt (S), a stent was placed into the caudal vena cava, allowing coils to be safely expanded into the shunt. **(C–E)** A cellophane band was placed around the termination of a porto-azygos extrahepatic shunt in this 7-year-old castrated male Pug. The portal (PV) was small before surgery (PV/aorta ratio of 0.5) **(C)**, before expanding to a normal size 1 year later (PV/aorta ratio of 0.9) **(D)**. The flow velocity remained mildly reduced at that time **(E)** compared to normal ranges, but bile acids were back to normal.

window is useful to identify an enlarged azygos vein adjacent to the aorta. Using the same window, the PV diameter can be measured at the porta hepatis to help determine if concomitant PSS is present (clinical signs and signalment are usually very useful to help distinction). Significant reduction in PV diameter, or absence, greatly impacts prognosis (Fischetti and Kovak 2008; Martinez et al. 2017). CT and intraoperative portography are often required for more adequate assessment of the PV.

Acquired Disorders of the Abdominal Vascular System

Non-neoplastic Thrombosis

Vascular thrombosis is typically associated with at least one component of the **Virchow's triad**: hypercoagulability, blood flow disturbance, and/or endothelial injury. Accumulation of cholesterol or lipid material on the intima of arterial vessels is defined as atheromatous plaques. Sometimes the entire arterial wall thickness may be affected.

Arterial Thrombosis

Thrombosis may develop at the aortic trifurcation as a consequence of left atrial dilation favoring thromboembolism (e.g.,. cats with severe hypertrophic cardiomyopathy) or due to a hypercoagulability state. Ultrasound is a rapid and simple technique for confirming the presence and extent of aortic thrombosis (Figure 16.22). Aortic thrombosis may lead to ischemic myopathy or involve arterial branches (e.g., renal infarction and intestinal ischemia).

Venous Thrombosis

Thrombosis of the PV and/or of its tributaries (e.g., SV and mesenteric vein) may cause portal hypertension,

Vet-ebooks.com

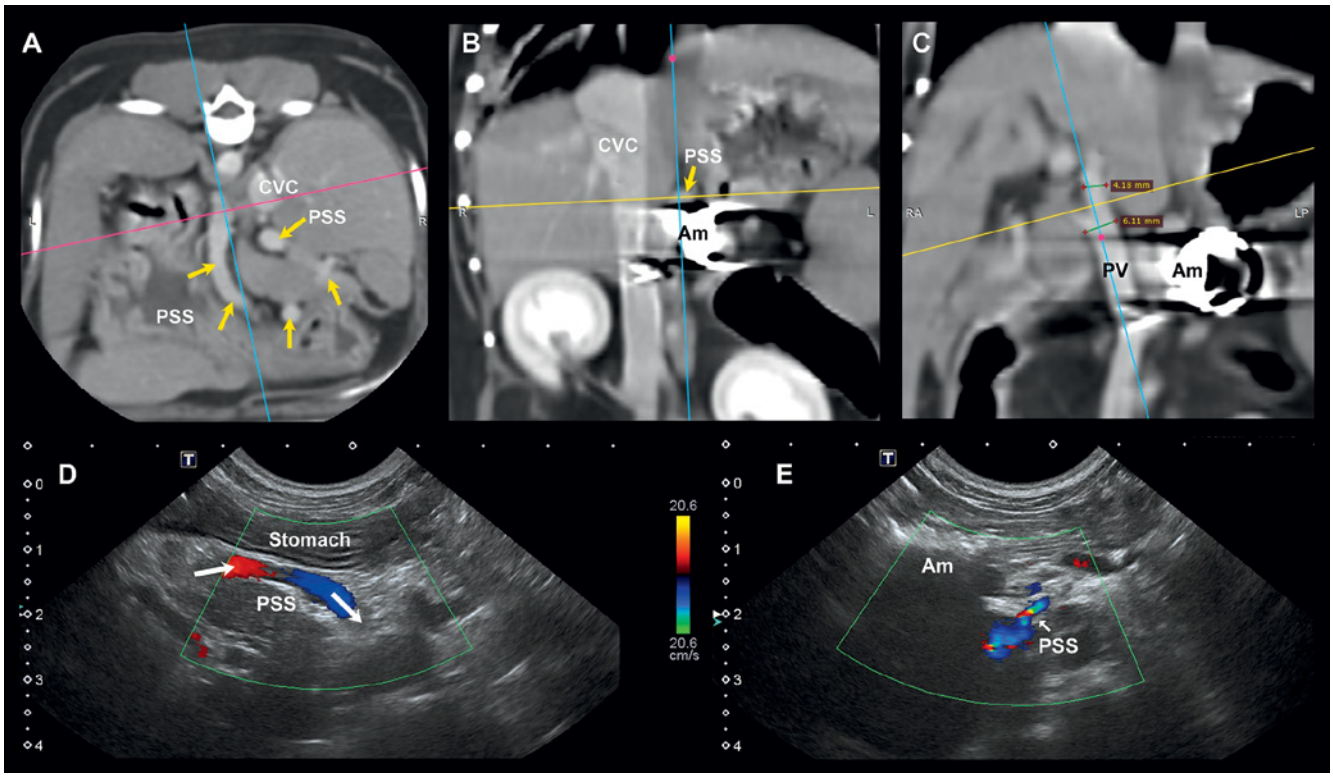


Figure 16.17. Two-year follow-up after ameroid placement in a Yorkshire dog with persistent bile acid elevation. (A–C) In these reformatted contrast-enhanced CT images, the extrahepatic shunt (PSS, yellow arrows) is smaller in diameter than on the presurgical scan but remains present. Its extent and termination cannot be well visualized due to the beam hardening artifacts caused by the metallic ameroid constrictor ring (Am) that was placed at the end of the shunt, adjacent to caudal vena cava (CVC). The portal vein (PV) remains small (**C**) but larger than before surgery. **(D, E)** Ultrasound was performed after CT to confirm residual flow through the PSS that cannot be seen beyond the ameroid constrictor ring (Am) due to acoustic shadowing. Note the change in hue of the color Doppler signal as the direction of flow changes in the tortuous shunt.

ascites, and collateral circulation (Figure 16.23). Coagulopathies (e.g., hypercoagulability in patients with Cushing's syndrome) and acute pancreatitis are the most frequent cause of PV thrombosis (Figure 16.24). Cavernous transformation of the PV may develop.

CVC thrombosis may develop with aneurysmatic dilatation (e.g., azygos continuation of the CVC) or with phlebitis (e.g.,. retroperitoneal infectious process). In case of thrombosis with complete obstruction of the CVC lumen, blood flow to the right atrium is guaranteed by collateral circulation through multiple pathways.

US findings in patients with non-neoplastic thrombosis include presence of an endovascular mildly echoic structure (hyperechoic to normal vessel lumen) that may partially or completely occlude blood flow (Figure 12.12). Amorphous hyperechoic areas/foci with variable degree of acoustic shadowing, representing dystrophic mineralization may develop in the thrombus over time (Figure 16.25).

Ultrasound allows to assess the extension of the thrombus, the percentage of vascular lumen occlusion, presence/absence of thrombus reperfusion (for follow up on patient treated with anticoagulant therapy), and possible underlying causes of thrombus formation (Specchi and d'Anjou 2019).

Neoplastic Thrombosis

Neoplastic vascular invasion with thrombus formation is most frequently observed in dogs with adrenal gland malignant neoplasia (carcinoma or pheochromocytoma) (Figure 12.13). Other tumors that may invade abdominal vessels include pancreatic carcinoma, insulinoma, and renal carcinoma (Figure 16.26). Other possible interactions between neoplastic tissue and vessels wall include adherence without invasion of the vascular wall or lumen, partial or complete incarceration of the vessel by neoplastic tissue, invasion of the wall of the adjacent vessel, and endoluminal invasion.

US findings with neoplastic thrombosis include an endoluminal vascular space occupying lesion, often

Vet-ebooks.com

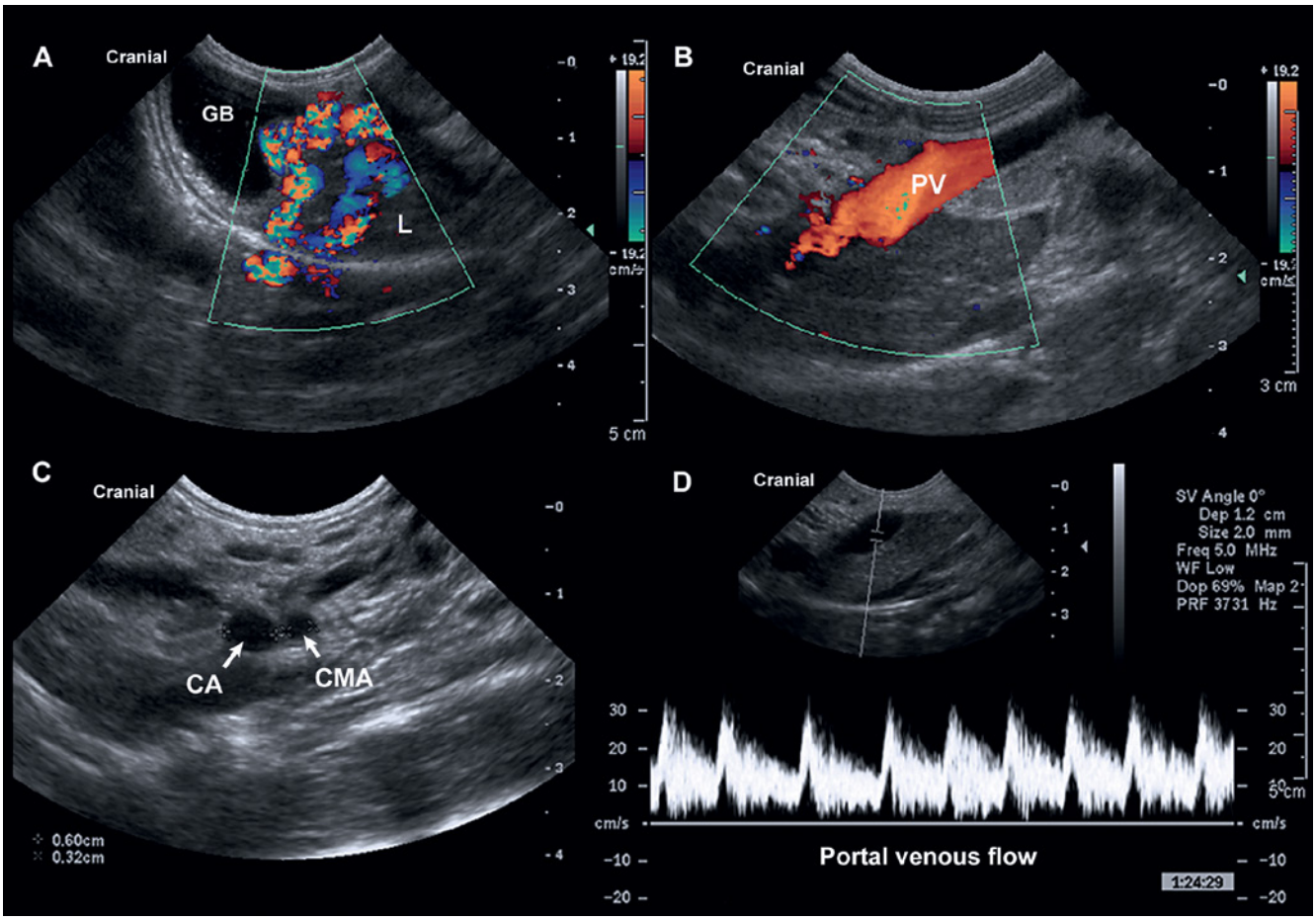


Figure 16.18. **Arterioportal communication in a young dog. (A)** On this longitudinal color Doppler image obtained in a young dog with suspected portosystemic shunting, a markedly tortuous vascular structure with turbulent flow is observed within the liver (L), just caudal to the gallbladder (GB). The portal vein (PV) is distended and associated with reversed flow (hepatofugal; red signal) on color Doppler **(B)** and abnormal pulsatility on spectral Doppler **(D)**. These signs indicate the presence of an arterioportal communication in the liver. **(C)** Additionally, the celiac artery (CA) is noted to be much larger than the cranial mesenteric artery (CMA). Multiple acquired shunts were detected during the exam (not shown).

focally dilating the vessel, with variable echogenicity that appears in continuity with the primary mass, with or without dystrophic mineralization. On color Doppler, the endoluminal mass may show multiple tortuous vessels indicating neoplastic neovascularization and should not be confused with normal blood flow in the vessel lumen or recanalization of the thrombus (Figures 12.13 and 16.26). Direct invasion of the wall by the neoplastic tissue (e.g., adrenal tumor) should also be assessed as this would guide the surgical technique (e.g., cavectomy versus cavotomy).

Alterations of the Vascular Wall

Phlebitis and Arteritis

Inflammation of the vascular wall veins (phlebitis) may result from acute pancreatitis (PV or SV) or migrating foreign bodies (e.g., grass awns in proximity of the CVC in the retroperitoneal space). Arterial wall inflammation (arteritis) may be observed as consequences of fungal infection (Morabito et al. 2020).

On ultrasound, the vascular wall will show increased thickness (that may be circumferential or asymmetrical) with heterogeneous echogenicity, often with peripheral fat hyperechogenicity (Morabito et al. 2020; Specchi and d'Anjou 2019) (Figure 16.27).

Aneurysm and Pseudoaneurysm

Segmental dilatation of a vessel lumen exceeding 50% with intact wall layering is called aneurysm. Pseudoaneurysm is instead defined as segmental vascular dilatation due to interruption in the *tunica intima* and possibly *tunica media* with secondary leakage of blood in the *tunica adventitia* and/or periadventitial tissues. Fungal arterial pseudoaneurysm

Vet-ebooks.com

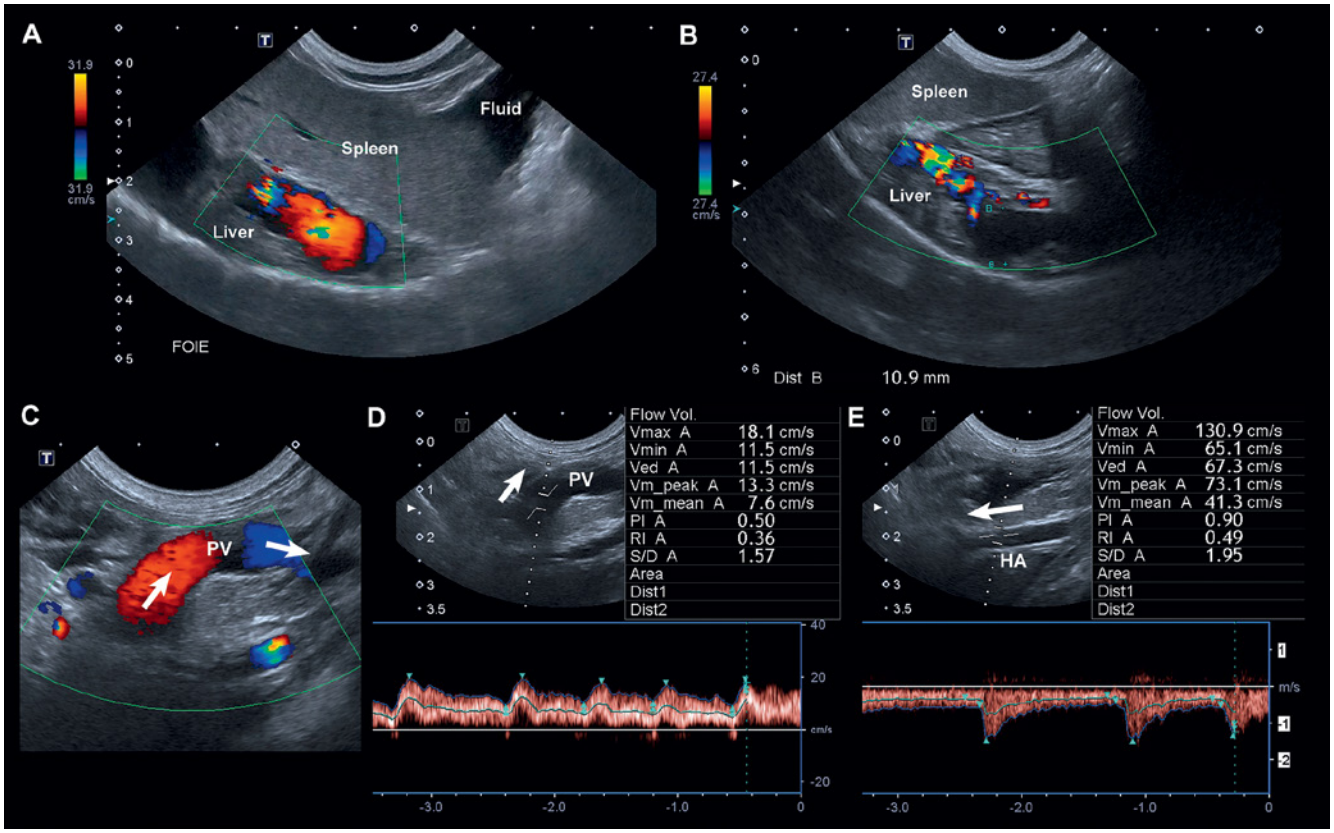


Figure 16.19. **Arterioportal communication in a 1-year-old female Miniature Schnauzer.** Longitudinal oblique color Doppler images **(A, B)** showing a looping, irregular vascular structure inside a small liver, with a turbulent flow mainly directed cranially in one portion **(A)** before becoming smaller, more tortuous and mainly directed caudally in the other portion **(B)**. This second portion is connected to the portal vein (PV) that is enlarged caudal to the liver, with hepatofugal flow seen on color **(C)** and spectral **(D)** Doppler. Note the pulsatility of the reversed portal flow on spectral Doppler, with a pulsatility index (PI) of 0.5. **(E)** The nearby hepatic artery (HA) is enlarged with a flow velocity reaching 131 cm/sec.

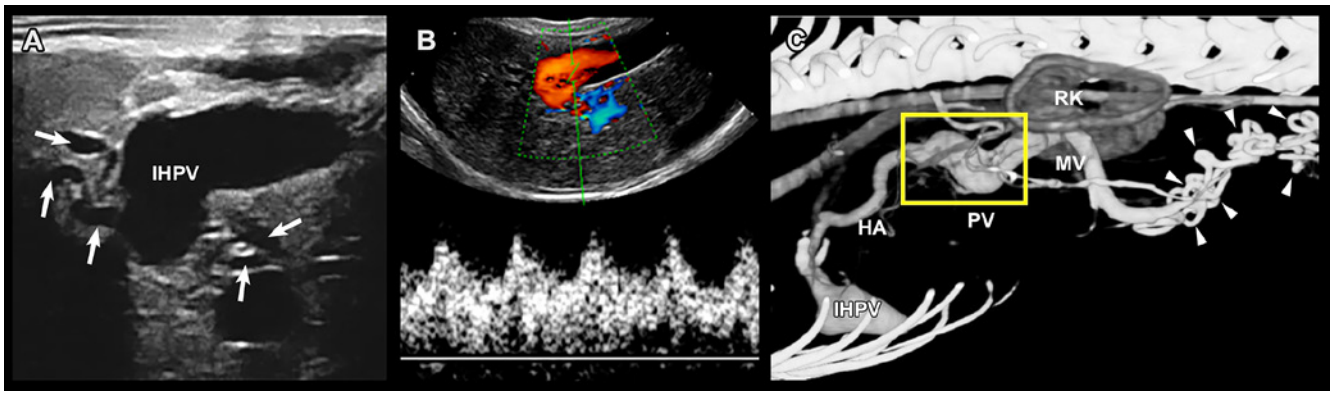


Figure 16.20. **Arterioportal communication in a cat. (A)** B-mode image of the arterioportal communication in the liver parenchyma with the presence of multiple tortuous abnormal vessels (arrows) communicating with one of the main intrahepatic portal branches (IHPV). **(B)** Color and pulsed Doppler evaluation (dynamic triplex evaluation) of the portal vein showing severe increased portal vein diameter and red flow (toward the probe) indicating hepatofugal flow. The pulsed Doppler evaluation indicates arterial flow waveform. **(C)** Postcontrast computed tomographic sagittal volume rendering image during the arterial phase in the same patient. Note the presence of contrast medium in the portal vein (PV) that is enlarged (in box), cranial and caudal mesenteric veins (MV), and left colic vein during the arterial phase (contrast medium should be only in the arteries) that indicates arterioportal communication. The dilated intrahepatic portal branch (IHPV) is also seen and there is a network of tortuous vessels in the caudal abdomen communicating with the left colic vein and representing enlarged rectal plexuses (acquired portosystemic communication)(arrowheads). HA, hepatic artery; RK, right kidney.

Vet-ebooks.com

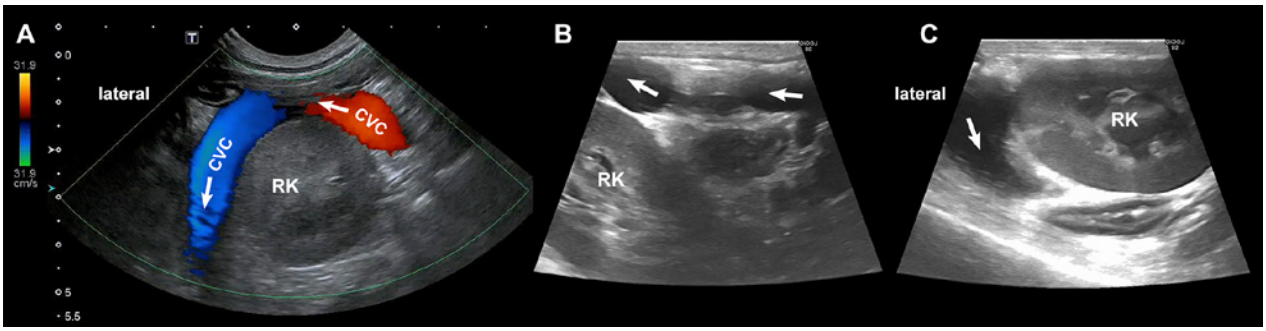


Figure 16.21. **Segmental aplasia of the caudal vena cava (CVC) in two dogs. (A)** Longitudinal oblique color Doppler image of the right kidney (RK) showing a large vein curving ventral and lateral to the kidney, diving into the azygos vein (not seen), consistent with segmental aplasia of the CVC, which was incidental in this 8-year-old castrated male mixed breed dog with chronic cystitis. The portal system was normal in this dog. **(B, C)** Caudal to the location of the renal veins, the CVC becomes a large tortuous vessel (arrows) with dorsal direction that passes lateral to the right kidney and joins the azygos vein. The prehepatic and hepatic tracts of the caudal vena cava are absent.

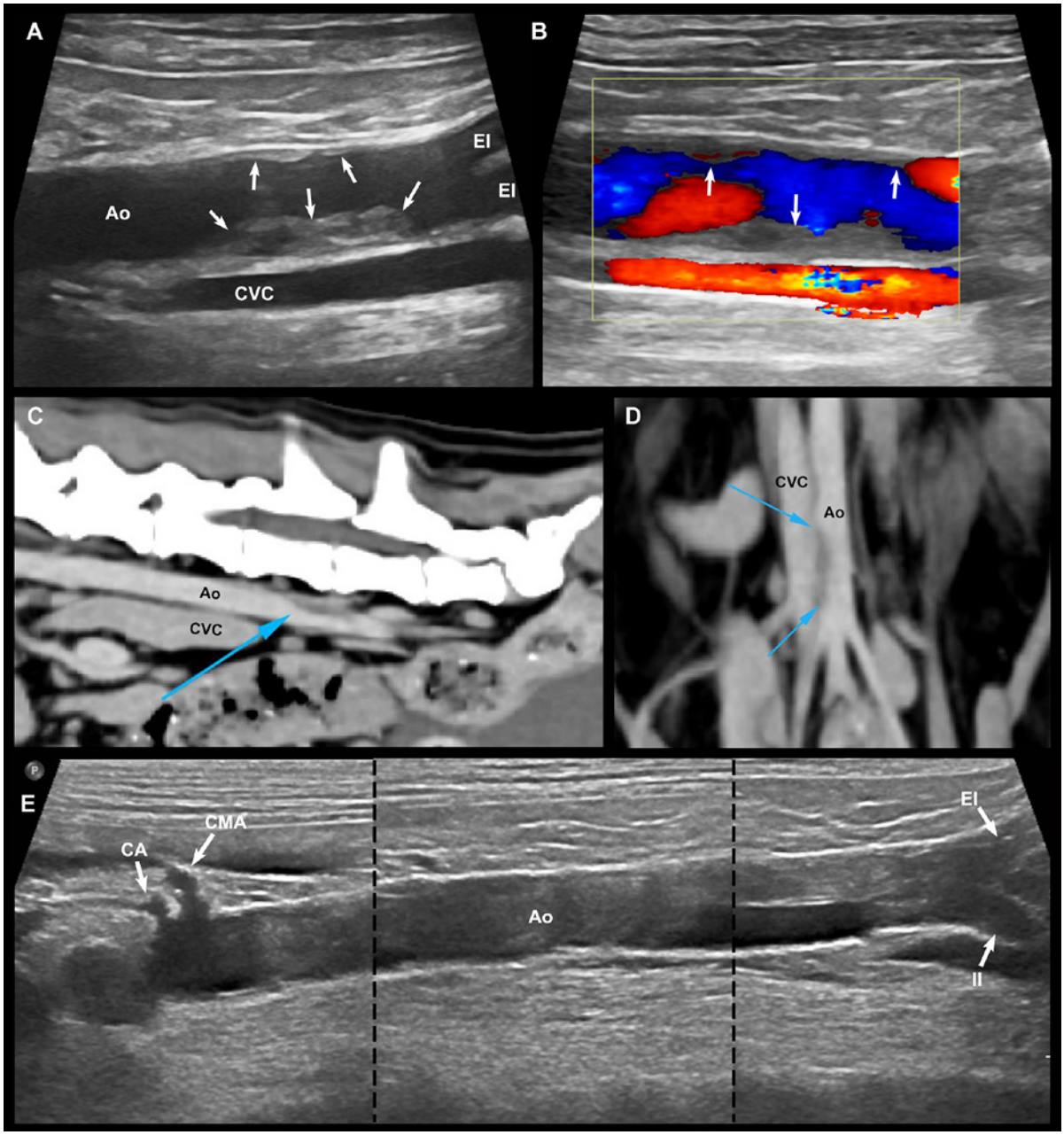


Figure 16.22. **Aortic thrombosis and/or atheromatous plaque in two dogs.** (for full caption, see facing page)

Vet-ebooks.com

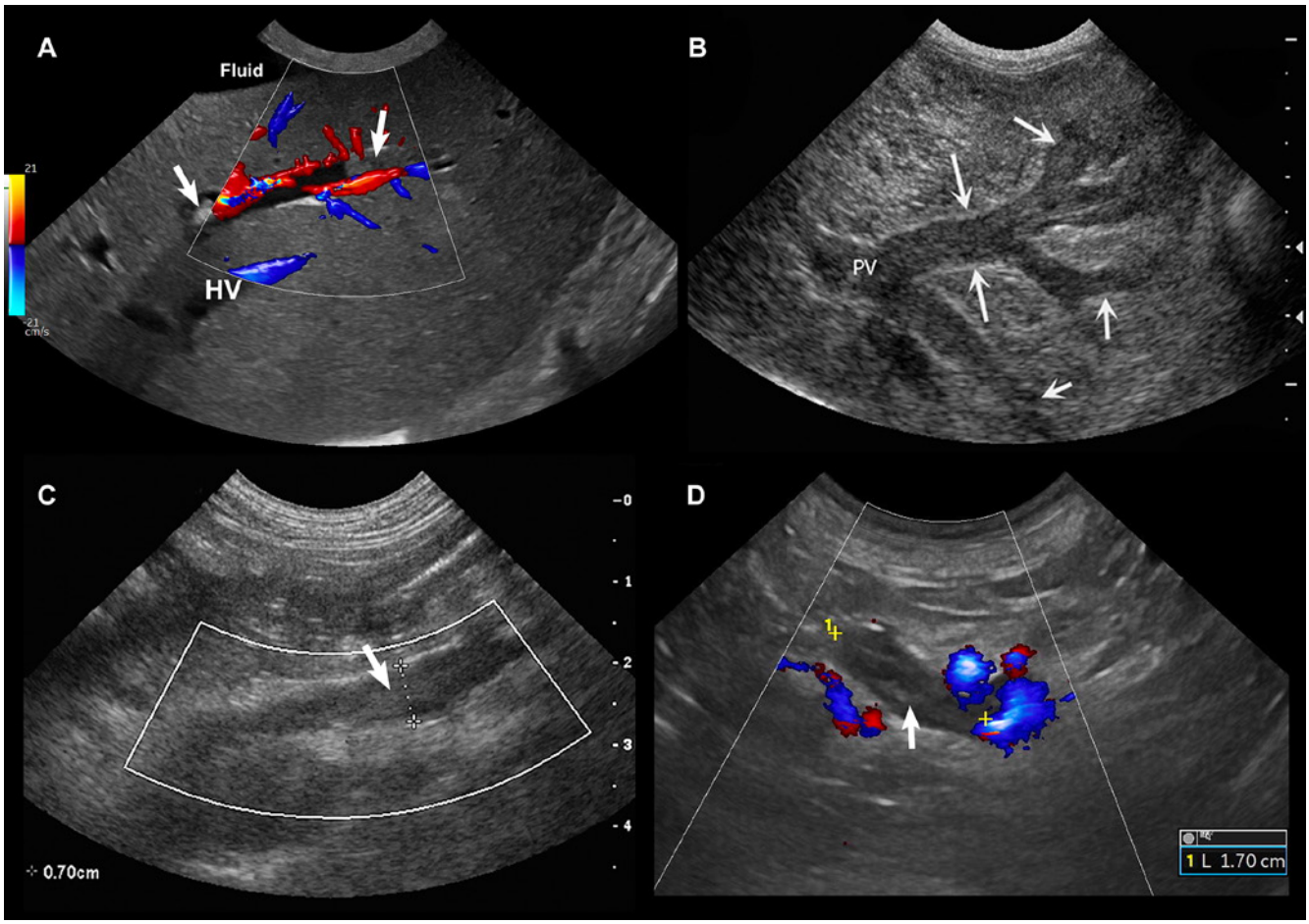


Figure 16.23. **Thrombosis of the portal vein and tributaries in four dogs. (A)** Transverse oblique image of the left lateral lobe of the liver in a cushingoid dog with a **hypercoagulable state**. Note the echogenic thrombi (arrows) inside the left intrahepatic portal vein, causing partial obstruction on color Doppler. HV, hepatic vein. **(B)** Transverse image of the left portion of the liver (L) in another dog with **severe chronic hepatitis**. The intrahepatic portal venous (PV) lumens (arrows) appear hyperechoic. Color Doppler confirmed the absence of flow and the presence of massive thrombosis. Secondary portal hypertension was also identified. **(C)** Longitudinal image of the portal vein in a small dog with **protein-losing nephropathy** and signs of portal hypertension. The portal vein is enlarged (cursors), irregular and presents a mildly hyperechoic luminal content (arrow) without evidence of flow on color Doppler, indicating thrombosis. The surrounding fat is mildly hyperechoic. Multiple acquired shunting vessels were also identified. **(D) Mesenteric venous thrombosis** (arrow) in another dog with portal vein thrombosis extending into multiple tributaries.

Figure 16.22. **Aortic thrombosis and/or atheromatous plaque in two dogs. (A)** US B-mode image of the aortic trifurcation (Ao, aorta; EI, external iliac arteries) and caudal vena cava (CVC) showing a plaque-like lesion lying on the aortic wall with heterogeneous echogenicity (arrows). **(B)** Color Doppler image of the same lesion showing absence of blood flow at the level of the plaque. The aortic flow is essentially blue, and the CVC flow is red due to the trapezoid US beam being completely perpendicular to the flow direction. **(C, D)** Sagittal and dorsal postcontrast computed tomographic maximum intensity projection image of the Ao and CVC in the same patient showing the filling defect in the aorta (arrows). **(E)** In this 14-year-old West Highland Terrier presented for progressive depression, weakness, anorexia, and vomiting, an extensive and partially occlusive echogenic, aortic thrombus was extending from the level of the right kidney vessel to the trifurcation. Only a small amount of vascular flow was detected. CA, celiac artery; CMA, cranial mesenteric artery. EI, external iliac artery; II, internal iliac artery.

Vet-ebooks.com

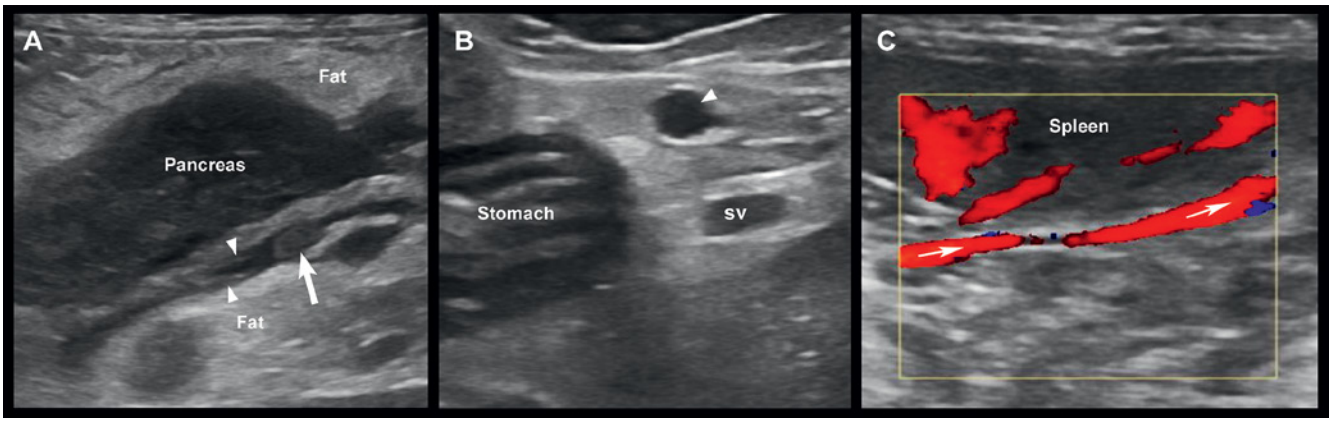


Figure 16.24. Splenic venous thrombosis associated with pancreatitis and splenic vein collateral circulation in a dog. (A) US B-mode image of the left pancreatic limb. The left pancreatic limb is enlarged with round margins and hypoechoic parenchyma. The peripancreatic fat is hyperechoic. Note the presence of an oval-shaped echogenic structure in the splenic vein lumen (arrow) consistent with thrombus formation. The splenic vein is decreased in diameter with diffuse thickening of the wall (arrowheads), consistent with phlebitis. **(B)** US B-mode image at the level of the gastric fundus showing an enlarged left gastroepiploic vein (arrowhead) representing collateral circulation of the splenic vein (SV). **(C)** Color Doppler image of the spleen. There is a vessel adjacent to the visceral aspect of the spleen with hepatofugal flow and originating from the splenic vein, consistent with splenogonadal communication (splenosystemic collateral circulation).

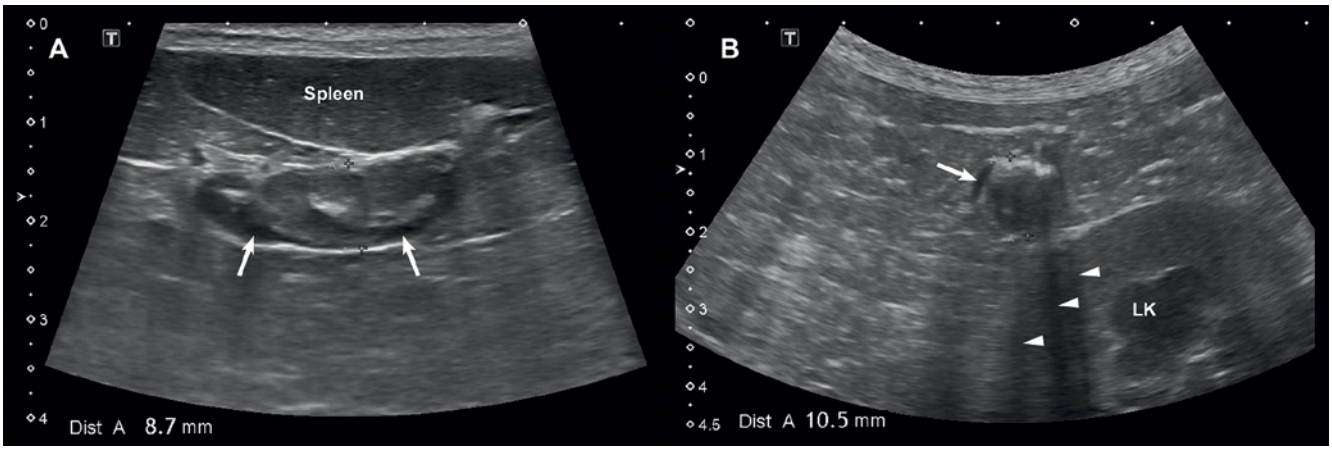


Figure 16.25. Chronic splenic venous thrombosis in a dog with suspected glomerulopathy. Longitudinal (**A**) and transverse (**B**) sonographic images showing an enlarged splenic vein filled with a heterogeneous, luminal structure consistent with a thrombus. Note the hyperechoic foci and partial acoustic shadow (arrowheads in **B**) consistent with calcification. Only a small area of the lumen remains patent (arrows). LK, left kidney.

has been reported in dogs at the level of the cranial mesenteric artery and aortic trifurcation (Morabito et al. 2020). Other causes of pseudoaneurysm include *Spirocerca lupi* infection and migrating grass awn.

On ultrasound, aneurysms are identified as segmental circumferential vascular dilation with normal walls (Figure 16.28). With pseudoaneurysm, the vessel is also segmentally dilated but with irregular walls of variable echogenicity, sometimes with regional fat hyperechogenicity (Morabito et al. 2020).

Atherosclerosis and Vascular Wall Mineralization

Atherosclerosis is characterized by atheromatous plaques in the intima of large- and medium-sized arteries. It is the most common form of arteriosclerosis and is often associated with mineralization. Ectopic calcification of the vascular walls may also be due to disturbance in the calcium/phosphorus metabolism (metastatic mineralization) or a consequence of necrotic/degenerated tissues (such as granulomas) in normocalcemic patients (dystrophic mineralization). Endocrinopathies such as hypothyroidism may be a

Vet-ebooks.com

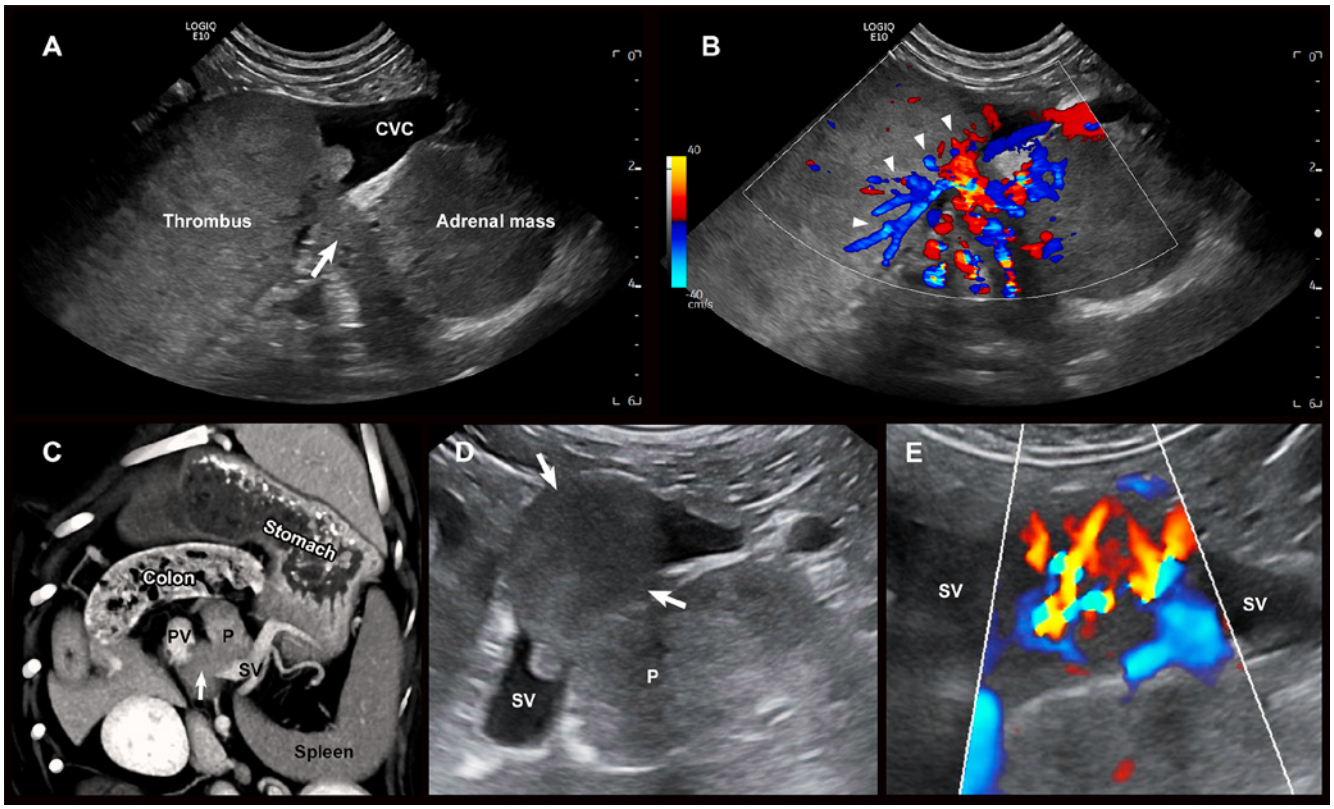


Figure 16.26. **Malignant thrombosis in two dogs. (A, B) Left adrenal tumor invading the caudal vena cava** (CVC) in a 6-year-old castrated male Beagle. Note the area of vascular invasion in **A** (arrow) that shows an intense vascular network (arrowheads in **B**) that propagates into the massive venous thrombus. **(C–E) Insulinoma invading the splenic vein in a dog. (C)** Dorsal oblique postcontrast computed tomographic volume rendering image showing a mass originating from the pancreas (P) and invading the splenic vein (SV) at the anastomosis with the portal vein (PV). **(D)** US B-mode image showing the same pancreatic (P) mass invading the lumen of the splenic vein (SV) at the level of the anastomosis with the portal vein. **(E)** Color Doppler of the pancreatic mass showing innumerable tortuous vessels with arterial flow that differ from the splenic vein blood flow.

cause of vascular wall mineralization in dogs. Systemic hypertension and renal failure have also been linked to aortic wall mineralization in cats (Keppie et al. 2006).

On ultrasound, mineralized vascular walls are hyperechoic with variable acoustic shadowing that may hide the vessel lumen making the recognition of the vascular structure difficult (Specchi and d'Anjou 2019) (Figure 16.29).

Abdominal Venous Collateral Circulation

When venous occlusion develops, collateral circulation of the venous system (PV, CVC, RV, and SV) allows blood to reach the right atrium through alternative pre-existing vascular routes. The blood flows through these alternative pathways and may have normal or reversed direction depending on the site and the degree of occlusion.

Portal Vein Obstruction and Hypertension

Portal hypertension is most often the result of chronic liver disease in dogs and cats, particularly involving fibrosis and diffuse nodular regeneration (cirrhosis), or infiltrative neoplasia, by reducing PV compliance and increased pressure. Portal hypertension can also be caused by congenital or developmental PV hypoplasia, arterioportal communication, portal thrombosis, or PV compression from an extraluminal mass.

Ultrasonographically, portal hypertension can be manifested by the presence of ascites and signs of edema involving several structures, such as the GB, gastric wall and pancreas (Figure 16.30, and see Figures in Chapters 9, 10, and 15). Portal hypertension is suspected when the portal flow is significantly reduced in velocity (mean < 10 cm/s) or reversed (hepatofugal), especially if the vein is normal in size or dilated

Vet-ebooks.com

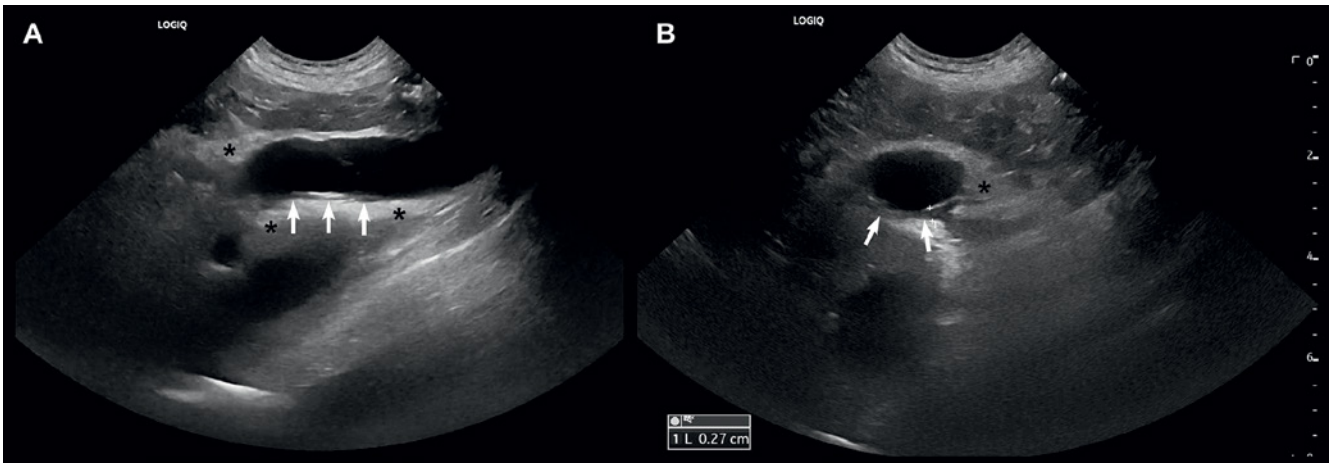


Figure 16.27. **Portal vasculitis**. This 7-year-old Golden doodle castrated male dog was presented for diffuse limb swelling, abdominal effusion and multiple ecchymosis. On these longitudinal **(A)** and transverse **(B)** ultrasonographic images, several vessels including the portal vein show a thickened and irregular wall (arrows) surrounded with hyperechoic fat (*).

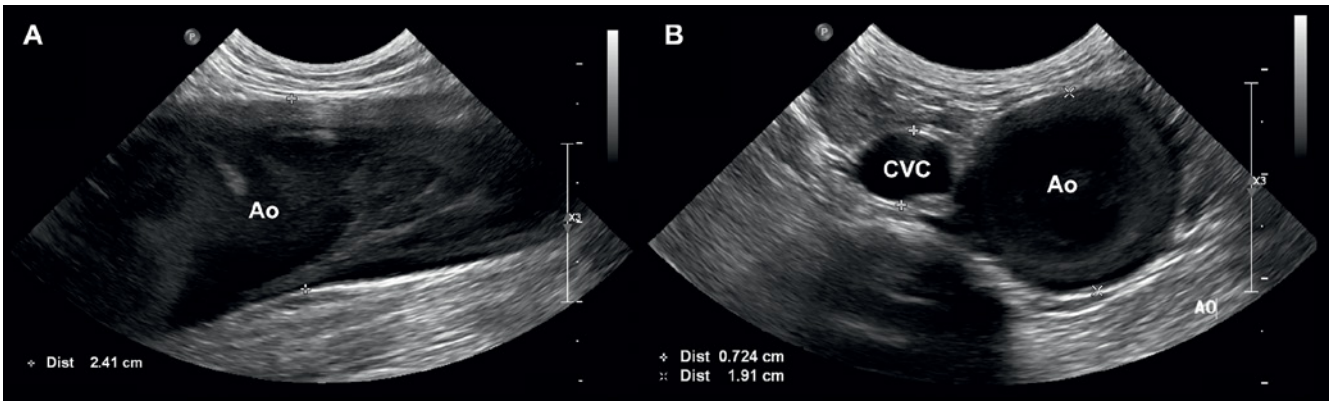


Figure 16.28. **Aortic aneurysm.** In this 13-year-old Australian Shepard with cardiomegaly and pericardial effusion, an extensive abdominal aortic (Ao) aneurysm was seen extending from the level of the liver, up to the caudal abdomen, as seen on these longitudinal **(A)** and transverse **(B)** images. Its diameter increased caudally (up to 2.4 cm) and on real time, several concentric echogenic layers are moving (spontaneous flow contrast). CVC, caudal vena cava.

(d'Anjou et al. 2004; Nyland and Fisher 1990) (Figure 16.13B). However, flow reduction or reversal may not be observed at the time of the exam.

Collateral circulation of the PV develops through pre-existing portosystemic communications (e.g., gastroesophageal, splenogonadal, and colic venous plexi). These vascular connections enlarge with sustained portal hypertension and become visible on ultrasound (Figure 16.31). The most frequent and easiest portosystemic communication that can be observed on ultrasound is the **splenogonadal communication**, visible as a network of tortuous vessels with hepatofugal flow originating from the SV caudal to the left kidney and joining the left gonadal vein before its termination in the CVC (Figure 16.32A, B) (Bertolini 2019; d'Anjou et al. 2004). The visualization of a vein connecting to the left renal vein (LRV), or to the CVC near the junction with the LRV, is consistent with a **dilated gonadal vein** indicating the termination of the splenogonadal anastomosis. It has been described as a specific sign of acquired PSS (Szatmari et al. 2004; Figure 16.32D). Small, tortuous, aberrant vessels can also be observed in the mesentery and surrounding the CVC, particularly when color or power Doppler is used (Figure 16.32C). Flow turbulence is typically seen in the CVC at the site of shunt entry (Figure 16.32B).

Sustained PV obstruction may also lead to cavernous transformation of the PV allowing blood flow through porto-portal communications (Specchi et al. 2015). On ultrasound, tortuous vessels can be seen at the hepatic hilus connecting the preobstructed PV with the

Vet-ebooks.com

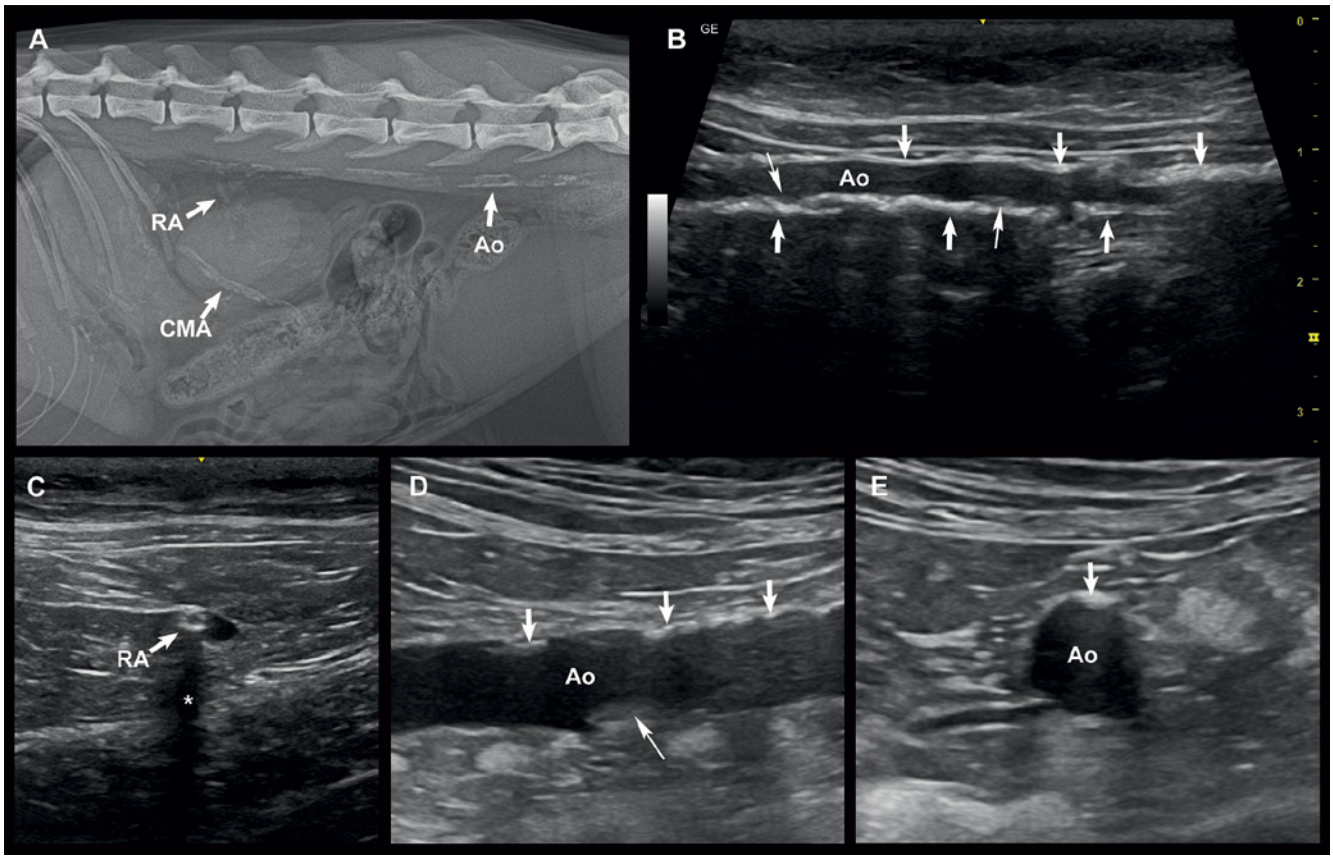


Figure 16.29. Atherosclerosis and vascular wall mineralization in a cat and a dog. (**A–C**) In this 10-year-old, castrated male domestic cat with **severe idiopathic hypercholesterolemia**, irregular, linear mineral opacities were initially noted on radiographs **(A)**, consistent with mineralization of the walls of the renal arteries (RA), cranial mesenteric artery (CMA), and aorta (Ao). On ultrasound **(B, C)**, interrupted hyperechoic plaques (wide arrows) were noted along the inner border of the aorta (Ao) and renal artery (RA), with variable acoustic shadowing (*). Plaques of less echogenicity in the Ao (thin arrows) are presumably consistent with lipid-rich deposits preceding calcification. **(D, E) Adult mixed large breed dog** with multiple hyperechoic plaques (wide arrows) on the intima of the abdominal aorta (Ao), some with acoustic shadowing, presumably consistent with **mineralized atheromatous plaques**. Thin arrows presumably point to lipid-rich deposits.

postobstructed tract. This allows hepatopetal flow to be seen on color Doppler.

Splenosystemic Communication in Spayed Female Cats

Splenosystemic shunts are occasionally detected in spayed female cats and believed to be related to the spaying surgery (Specchi et al. 2017). While these shunts are usually considered incidental, they may favor the development of hepatic encephalopathy if hepatic disease is present. Splenosystemic collateral circulation is visible on ultrasound as a long, sinuous vessel originating from the SV, with hepatofugal flow seen on color Doppler. The vessel extends caudally, becoming very tortuous at the caudal and lateral border of the left kidney before joining the left gonadal or external iliac vein (Figure 16.33).

CVC Obstruction

In case of obstruction of the hepatic/posthepatic CVC, postsinusoidal portal hypertension develops with secondary hepatic venous congestion, hepatomegaly and ascites, consistent with Budd–Chiari syndrome (Specchi et al. 2014). If the CVC obstruction occurs at the level of the prerenal to prehepatic CVC segments, CVC collateral circulation develops.

Collateral venous pathways are pre-existing vessels that increase in size due to augmented blood flow and become visible on ultrasound. Blood flow direction may be normal or reversed, depending on the site of obstruction (Figures 16.34, 16.35). CVC collateral pathways can be quite complex to comprehend on US, justifying the additional use of CT-angiography for optimal diagnosis (Specchi and d'Anjou 2019).

Vet-ebooks.com

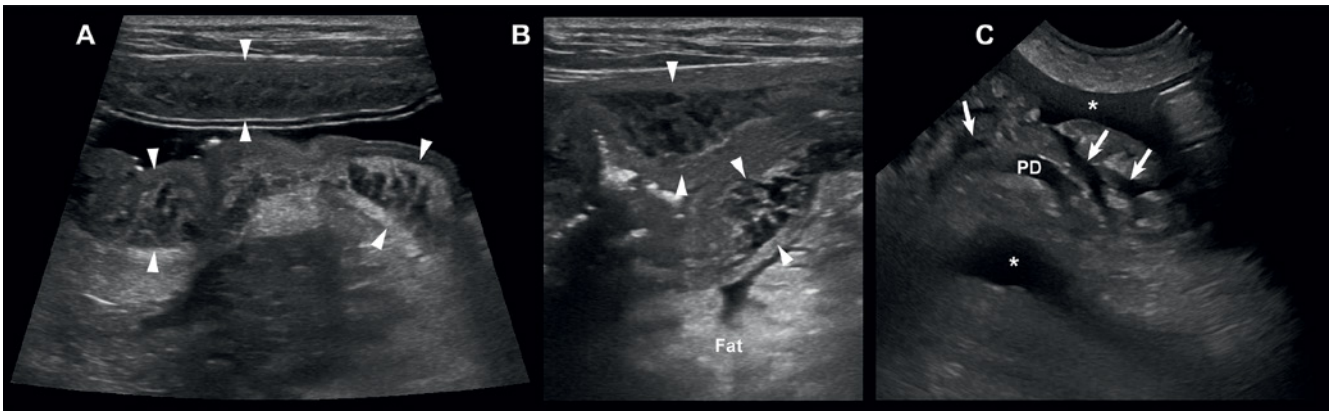


Figure 16.30. **Consequences of portal hypertension. (A, B) Severe gastric edema** in a 9-year-old castrated male cat with extensive thrombosis of the portal and mesenteric veins. The gastric wall is severely thickened, particularly at the submucosal layer (between arrowheads) that also shows a characteristic "spongy" pattern. The regional fat is hyperechoic and minimal anechoic effusion is seen. **(C) Pancreatic edema** in an 8-year-old castrated male Husky with suspected cirrhosis. Note the well-defined hypoechoic stripes (arrows) often referred to as the "tiger stripe" pattern inside the pancreas that is surrounded with peritoneal effusion (*).

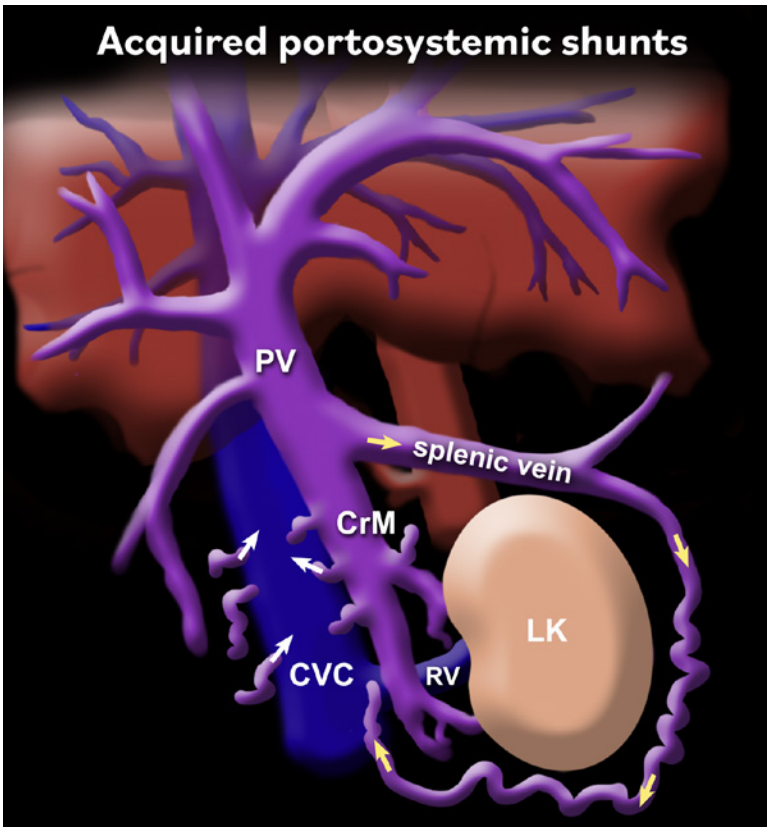


Figure 16.31. **Illustration of acquired portosystemic shunts most often detected on ultrasound in dogs.** A long, tortuous vein originating from the splenic vein with hepatofugal flow (yellow arrows) and terminating into the left renal vein (RV) is typical of an acquired shunt. Other shorter shunts may connect the mesenteric veins to the CVC (white arrows). CrM, cranial mesenteric vein; LK, left kidney; PV, portal vein.

Vet-ebooks.com

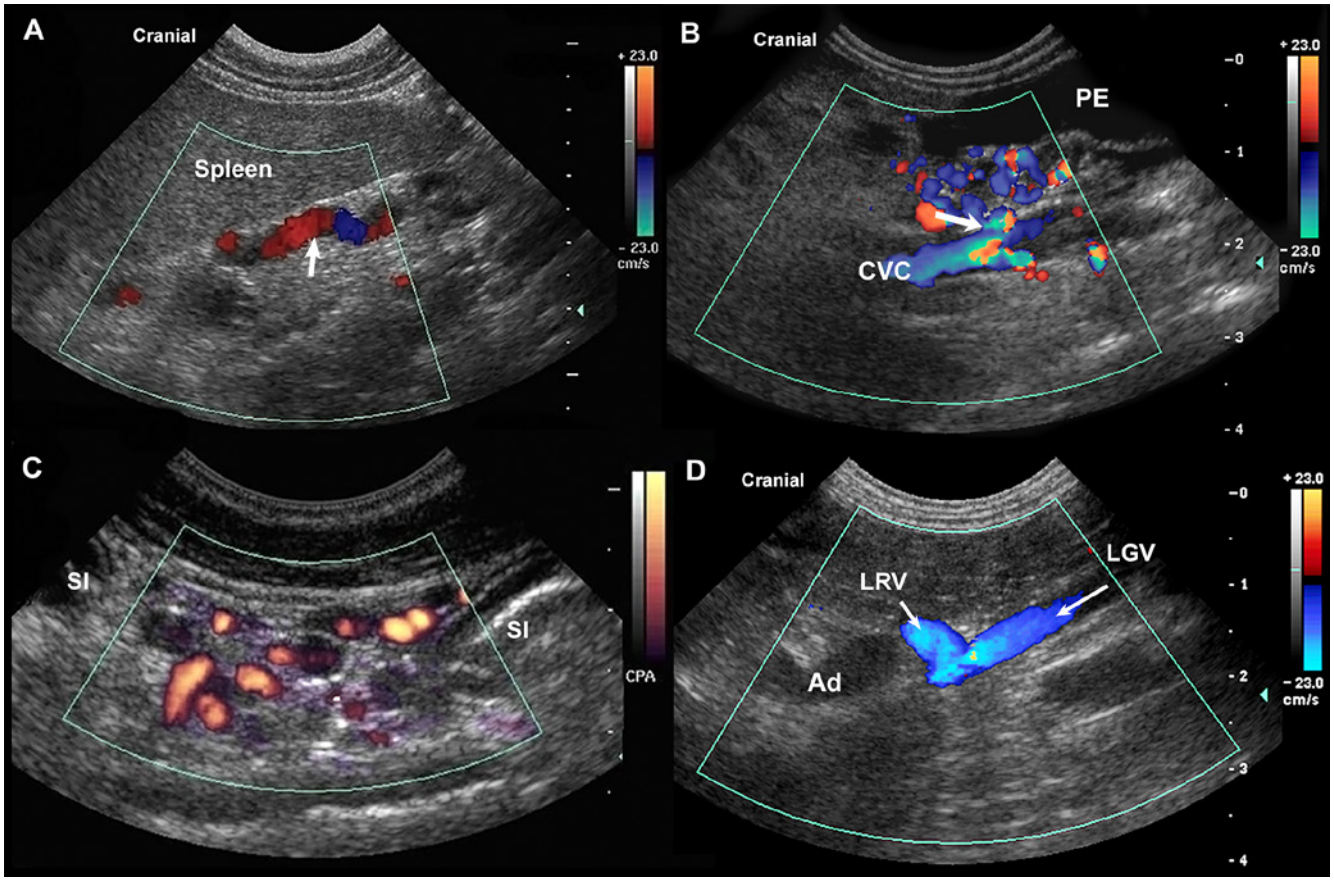


Figure 16.32. **Multiple acquired portosystemic shunts in four dogs. (A)** Longitudinal image obtained at the level of the spleen. A tortuous vein (arrow) containing flow directed caudally was connected to the splenic vein cranially and could be followed to the level of the right renal vein, caudally, consistent with an acquired **splenorenal anastomosis**. This dog had primary portal vein hypoplasia. **(B)** Longitudinal image of a dog with portal hypertension obtained in the mid-abdomen, at the level of the caudal vena cava (CVC). Multiple small tortuous vessels are seen in the mesentery, in proximity to the CVC, with a direct connection observed (arrow). Anechoic peritoneal effusion (PE) is also detected. **(C)** Longitudinal image obtained in the mid-abdomen, at the level of the omentum and small intestine (SI), of a dog with portal hypertension. Multiple small tortuous vessels are seen in the mesentery. **(D)** Longitudinal image obtained at the level of the left adrenal gland (Ad) in a dog with portal hypertension caused by portal venous thrombosis. An aberrant vein is seen connecting with the left renal vein (LRV), consistent with an enlarged **left gonadal vein** (LGV). This feature is specific to acquired portosystemic shunt in dogs.

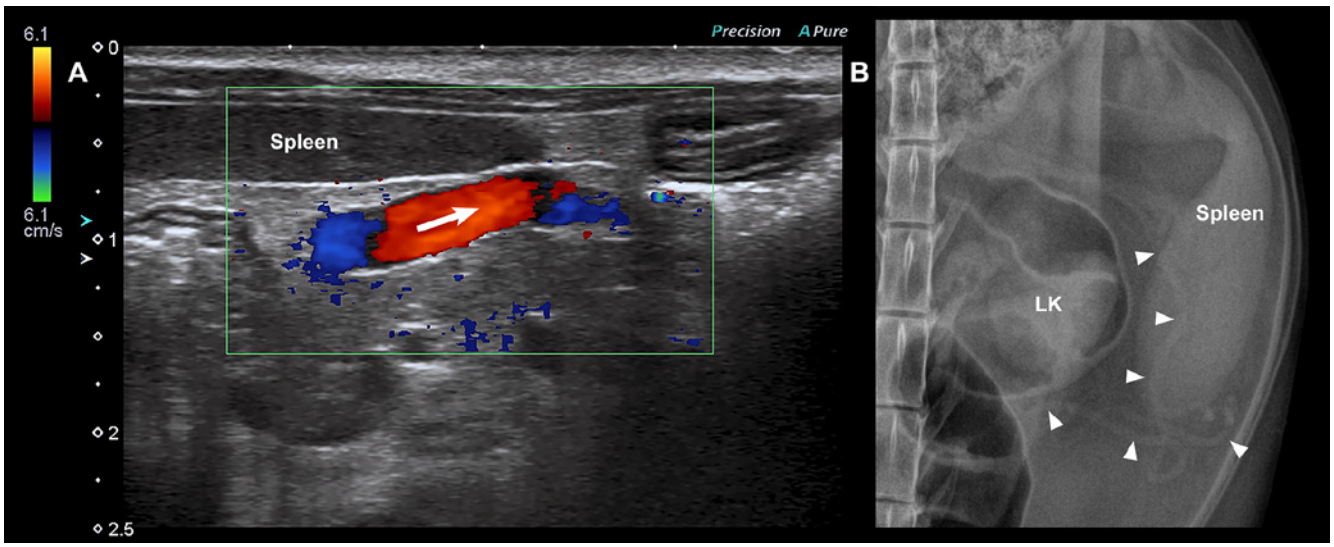


Figure 16.33. **Incidental splenosystemic communication in a cat. (A)** Longitudinal image obtained in the left lateral abdomen of a 12-year-old cat with chronic renal disease. A large anomalous vessel with hepatofugal flow (red color signal) extends caudally, along the dorsal border of the spleen. The liver was mildly inhomogeneous, but clinical signs of hepatic insufficiency were lacking to justify further investigation. **(B)** On ventrodorsal radiograph, the shunt appears as a long, tortuous opacity (arrowheads), consistent with the **"spaghetti sign."** LK, left kidney.

Vet-ebooks.com

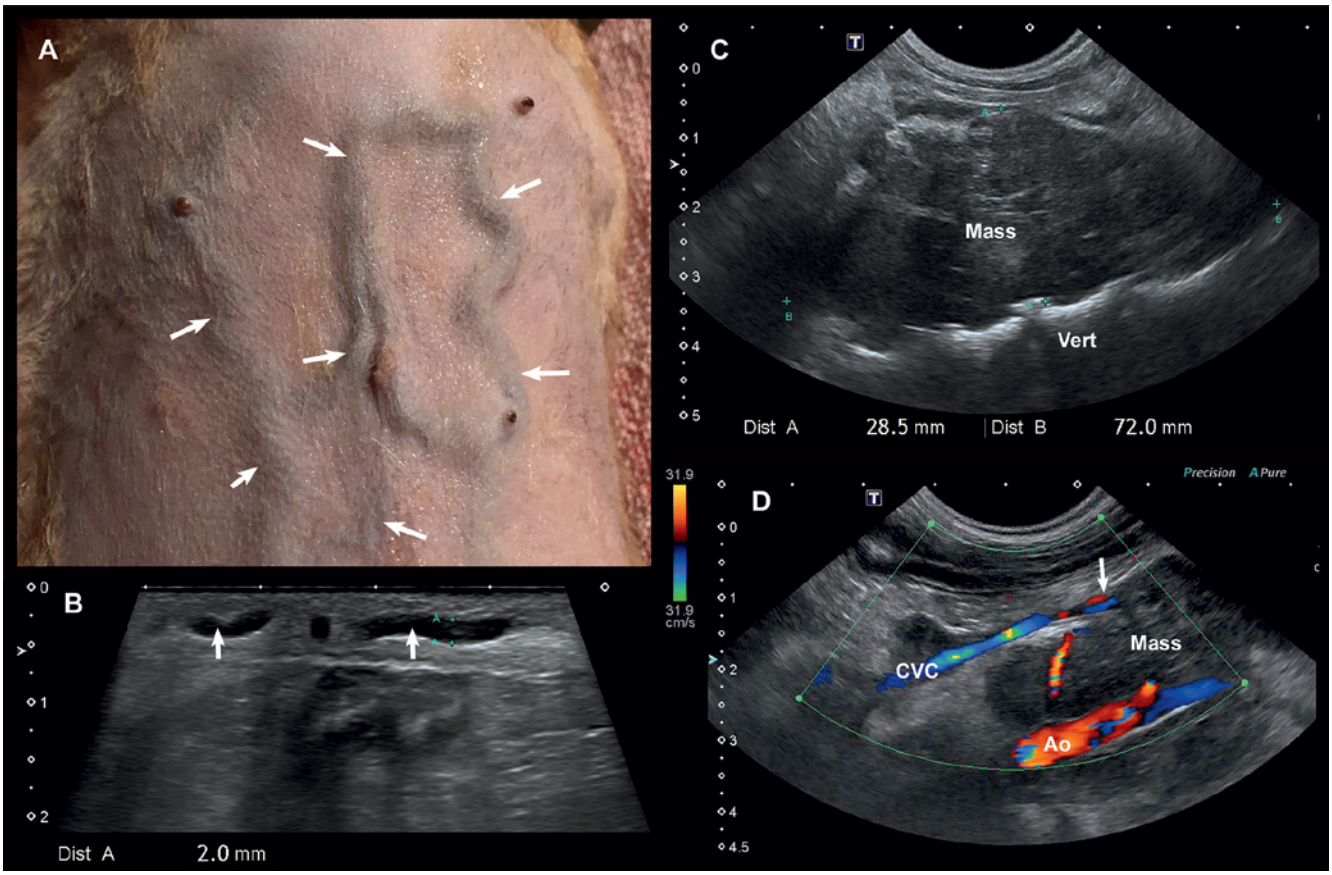


Figure 16.34. **Large retroperitoneal mast cell tumor causing CVC obstruction in a 8-year-old Chihuahua castrated male dog. (A)** Photograph of the abdomen of the dog before the ultrasound. Note the enlarged and tortuous subcutaneous veins (arrows), which are well seen on ultrasound (arrows in **B**). **(C)** A large, irregular, and poorly defined hypoechoic mass infiltrates the retroperitoneal space and sublumbar musculature, ventral to the vertberal column (Vert) measuring more than 7 cm in length. **(D)** This mass englobes the aorta (Ao) and displaces and compresses the caudal vena cava (CVC) that is abruptly attenuated (arrow), which lead to the development of a superficial collateral pathway.

Venous Obstruction (Other than CVC)

With RV obstruction, collateral pathways include ureteral vein, gonadal vein (on the left), and multiple subcapsular vessels that join the external circumflex iliac vein through a single retroperitoneal vessel. When the SV is occluded, collateral circulation can involve the left gastric vein, left gastroepiploic vein, or splenogonadal vein (Figure 16.24) (Specchi and Bertolini (2020) for schematic representations of these collateral pathways).

Visit our website at **www.SmallAnimalUltrasonography.com** for complementary video clips with annotations and text on:

- Normal portal system
- Normal abdominal major vasculature
- Portosystemic shunts
- Vascular thrombosis

References

Belotta AF, Teixeira CR, Padovani CR, Rahal SC, et al. (2018) Sonographic evaluation of liver hemodynamic indices in overweight and obese dogs. J Vet Intern Med 32:181–187.

Bertolini G (2019) Anomalies of the portal venous system in dogs and cats as seen on multidetector-row computed tomography: an overview and systematization proposal. Vet Sci, doi: 10.3390/vetsci6010010.

Bertolini G, Caldin M (2020) Percutaneous cava stenting in a dog with symptomatic azygos continuation of the caudal vena cava. Case Rep Vet Med 2020: 7523247.

Bertolini G, Diana A, Cipone M, Drigo M, et al. (2014) Multidetector row computed tomography and ultrasound characteristics of caudal vena cava duplication in dogs. Vet Radiol Ultrasound 55:521–530.

Chanyoung R, Sooyoung C, Hojung C, Youngwon L, et al. (2019) CT variants of the caudal vena cava in 212 small breed dogs. Vet Radiol Ultrasound 60:1–9.

Vet-ebooks.com

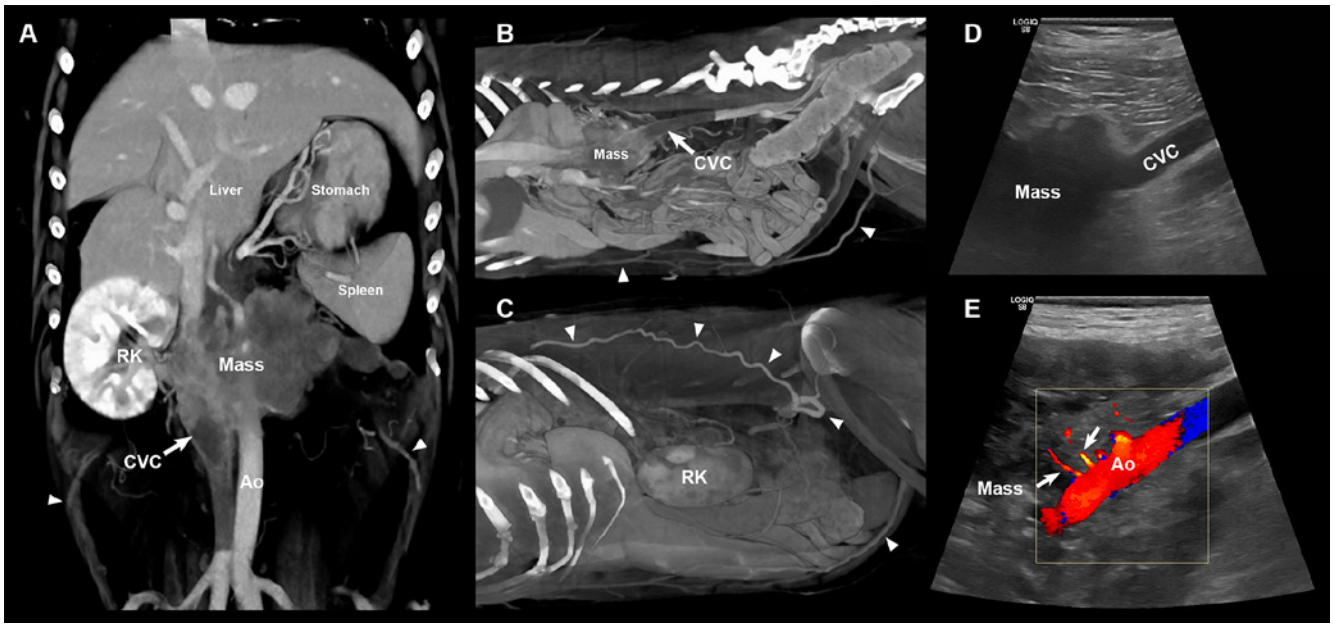


Figure 16.35. Right adrenal gland mass with invasion and obstruction of the caudal vena cava in a 11-year-old mixed breed neutered female dog. (A–C) Dorsal **(A)**, sagittal **(B)**, and sagittal oblique **(C)** volume rendered postcontrast CT images showing a right adrenal gland mass invading the renal tract of the caudal vena cava and a tubular filling defect in the prerenal tract of the caudal vena cava (CVC, arrow) consistent with a thrombus. Note the superficial venous collateral pathways (arrowheads) that allow the blood to bypass the site of CVC obstruction and reach the right atrium. The right kidney (RK) shows heterogeneous contrast enhancement consistent with infarcts. **(D)** B-mode ultrasound image of the same mass invading the lumen of the CVC. **(E)** Color Doppler ultrasound image of the aorta at the level of the right adrenal gland mass showing blood flow through the mass and the origin of the cranial mesenteric and celiac arteries (arrows) being completely incarcerated by the mass. Ao, aorta.

d'Anjou, MA (2007) The sonographic search for portosystemic shunts. Clin Tech Small Anim Pract 22:104–114.

d'Anjou MA, Penninck D, Cornejo L, Pibarot P (2004) Ultrasonographic diagnosis of portosystemic shunting in dogs and cat. Vet Radiol Ultrasound 45:424–437.

Evans HE (1993) Veins. In Evans HE, Christensen GC, eds. Miller's Anatomy of the Dog, 3rd edition. Philadelphia: WB Saunders, pp. 682–716.

Fischetti AJ, Kovak J (2008) Imaging diagnosis: azygos continuation of the caudal vena cava with and without portocaval shunting. Vet Radiol Ultrasound 49:573–576.

Holland M, Hudson J, Bao Y, Gaillard P (2019) Aortic to caudal vena cava ratio measurements using abdominal ultrasound are increased in dogs with confirmed systemic hypertension. Vet Radiol Ultrasound 1–9. doi: 10.1111/vru.12822

Keppie N, Nelson N, Rosenstein D (2006) Imaging diagnosis: mineralization of the aorta, celiac and cranial mesenteric arteries in a cat with chronic renal failure. Vet Radiol Ultrasound 47(1):69–71.

Lamb CR (1996) Ultrasonographic diagnosis of congenital portosystemic shunts in dogs: results of a prospective study. Vet Radiol Ultrasound 37:281–288.

Lamb CR (1998) Ultrasonography of portosystemic shunts in dogs and cats. Vet Clin North Am Small Anim Pract 28(4):725–753.

Lamb CR, Mahoney PN (1994) Comparison of three methods for calculating portal blood flow velocity in dogs using duplex-Doppler ultrasonography. Vet Radiol Ultrasound 35:190–194.

Lamb CR, Forster-van Hijfte MA, White RN, et al. (1996a) Ultrasonographic diagnosis of congenital portosystemic shunt in 14 cats. J Small Anim Pract 35:205–209.

Le Pommellet HM, Scansen BA, Mathys DA, Mollenkopf DF, et al. (2017) Arterial anomalies of the celiac trunk and medial arcuate ligament compression in dogs and cats assessed by computed tomography angiography. Vet Surg 47:252–260.

Lee K, Choi M, Yoon J, Jung J (2004) Spectral waveform analysis of major arteries in conscious dogs by Doppler ultrasonography. Vet Radiol Ultrasound 45(2): 166–171.

Martinez M, Carrillo J, Soler M, Skelly C et al. (2017) Imaging diagnosis: azygos continuation of a discontinuos caudal vena cava associated with portocaval shunting, incomplete situs inversus and polysplenia in a dog. Vet Rec Case Rep, doi: 10.1136/vetreccr-2017-000522.

Morabito S., Specchi S., Auriemma E., Ferro S., et al. (2020) Computed tomographic and ultrasonographic findings of abdominal arterial pseudoaneurysms caused by systemic mycosis in dogs. J Small Anim Pract 61:300–307.

Vet-ebooks.com

Nyland TG, Fisher PE (1990) Evaluation of experimentally induced canine hepatic cirrhosis using duplex Doppler ultrasound. Vet Radiol Ultrasound 31:189–194.

Pey P, Marcon O, Drigo M, Specchi S, et al. (2015) Multidetector-row computed tomographic characteristics of presumed preureteral vena cava in cats. Vet Radiol Ultrasound 56:359–366.

Plested MJ, Zwingenberger AL, Brockman DJ, Hecht S, et al. (2020) Canine intra-hepatic portosystemic shunt insertion into the systemic circulation is commonly through primary hepatic veins as assessed with CT angiography. Vet Radiol Ultrasound 61:519–530.

Seller S, Weisse C, Fischetti A (2022) Intrahepatic venous collaterals in dogs with congenital intrahepatic portosystemic shunts are associated with focal shunt or hepatic vein narrowing. Vet Radiol Ultrasound 63:64–72.

Smith RP, Koenigshof AM, Smith DJ, Strom PR, Nelson NC (2018) Influence of immune-mediated hemolytic anemia on flow velocities in the portal vein and caudal vena cava measured by use of pulsed-wave Doppler ultrasonography in dogs. Am J Vet Res 79(5):518–524.

Specchi S, Bertolini G (2020) CT angiography identifies collaterals in dogs with splenic vein obstruction and presumed regional splenic vein hypertension. Vet Radiol Ultrasound 61:636–640.

Specchi S, d'Anjou MA (2019) Diagnostic imaging for the assessment of acquired abdominal vascular diseases in small animals: a pictorial review. Vet Radiol Ultrasound 60:613–632.

Specchi S, D'Anjou MA, Carmel EN, Bertolini G (2014) Computed tomographic characteristics of collateral venous pathways in dogs with caudal vena cava obstruction. Vet Radiol Ultrasound 55:531–538.

Specchi S, Pey P, Ledda G, Lustgarten M, et al. (2015) Computed tomographic and ultrasonographic characteristics of cavernous transformation of the obstructed portal vein in small animals. Vet Radiol Ultrasound 56:511–519.

Specchi S, Panopoulos I, Adrian AM, Spattini G, et al. (2017) A "spaghetti sign" in feline abdominal radiographs predicts spleno-systemic collateral circulation. Vet Radiol Ultrasound 59:13–17.

Specchi S, Rossi F, Weisse C, Morabito S, et al. (2018) Canine and feline abdominal arterioportal communications can be classified based on branching patterns in computed Tomographic angiography. Vet Radiol Ultrasound 59:687–696.

Spediacci C, Longo M, Specchi S, Pey P, et al. (2022) Computed tomographic appearance of transcaval ureter in two dogs and three cats: a noval CVC congenital malformation. Front Vet Sci 9:965185. doi: 10.3389/fvets.2022.965185.

Szatmari V, Rothuizen J, van den Ingh GA, van Sluijs FJ, et al. (2004) Ultrasonographic findings in dogs with hyperammonemia: 90 cases (2000–2002). J Am Vet Med Assoc 224:717–727.

White RN, Parry AT (2013) Morphology of congenital portosystemic shunts emanating from the left gastric vein in dogs and cats. J Small Anim Pract 54:459.

White RN and Parry AT (2015a) Morphology of splenocaval congenital portosystemic shunts in dogs and cats. J Small Anim Pract 57:28.

White RN, Parry AT (2015b) Morphology of congenital portosystemic shunts involving the right gastric vein in dogs. J Small Anim Pract 56:430.

White RN, Parry AT (2018) Implications of shunt morphology for the surgical management of extrahepatic portosystemic shunts. Aust Vet J 96:433.

CHAPTER SEVENTEEN

Musculoskeletal System and Peripheral Nerves

Marc-André d'Anjou[1] and Laurent Blond[2]

[1] *Animages, Brossard, Québec, Canada*
[2] *Centre Hospitalier Vétérinaire Languedocia, Montpellier, France*

While magnetic resonance imaging (MRI) and computed tomography (CT) are optimal tools for thoroughly assessing the musculoskeletal system in dogs and cats, ultrasonography represents a complementary and cost-effective alternative, particularly for soft tissues when combined with radiography. It also enables dynamic assessment of joints, ligaments, and tendons, as well as guidance for fine-needle aspirations or biopsies, and even foreign body (FB) removals. Structures are typically scanned in both longitudinal and transverse planes, probe positioning being particularly critical to correctly assess fiber alignment in muscles or tendons. A high-frequency linear transducer is preferred but may not always be optimal due to the small and/or curved surface of some structures. Curvilinear probes may be useful for areas with curved surface or deeper portions that require lower transducer frequency.

Patient sedation is recommended for optimal examination, particularly in painful patients, and allows better dynamic assessment of joints, tendons and muscles. The size of some structures, particularly in smaller (<15 kg) dogs and cats, the system performance, and the complex anatomy represent limiting factors in ultrasonography for musculoskeletal disorders. Yet, numerous musculoskeletal conditions can be readily identified with this modality and their healing process can be monitored cost-effectively.

Shoulder

Scanning Technique

Ultrasonography of the shoulder joint and the surrounding tissues is best performed with a linear transducer using frequencies greater than 10 MHz (Figure 17.1A, B). Curvilinear probes may be used to facilitate the approach to deeper portions or areas with a curved surface, such as the axillary area (Figure 17.1C). The hair around the joint is clipped. All tendons and muscles are scanned longitudinally and transversely.

The sonogram of the shoulder joint starts by scanning the **supraspinatus** and **infraspinatus muscles** down to their attachment sites on the **greater tubercle** (Figures 17.1A, 17.2). Then, the **biceps tendon/muscle** is examined, after external rotation (supination) of the shoulder joint (Figure 17.1B). Abducting the limb may also allow better access to the region. The scan can begin at the muscle belly, along the craniomedial aspect of the humeral diaphysis. The probe is then gradually moved proximally along its proximal tendon, which lies within the **bicipital groove** and is at that level surrounded by its sheath, at the medial aspect of the shoulder joint and just medial to the greater tubercle. The biceps tendon is then followed proximally to its origin on the **supraglenoid tubercle** of the scapula. The tendon and its sheath are contained in the bicipital groove by a transverse ligament

Atlas of Small Animal Ultrasonography, Third Edition. Edited by Dominique Penninck and Marc-André d'Anjou.
© 2025 John Wiley & Sons, Inc. Published 2025 by John Wiley & Sons, Inc.
Companion website: www.SmallAnimalUltrasonography.com

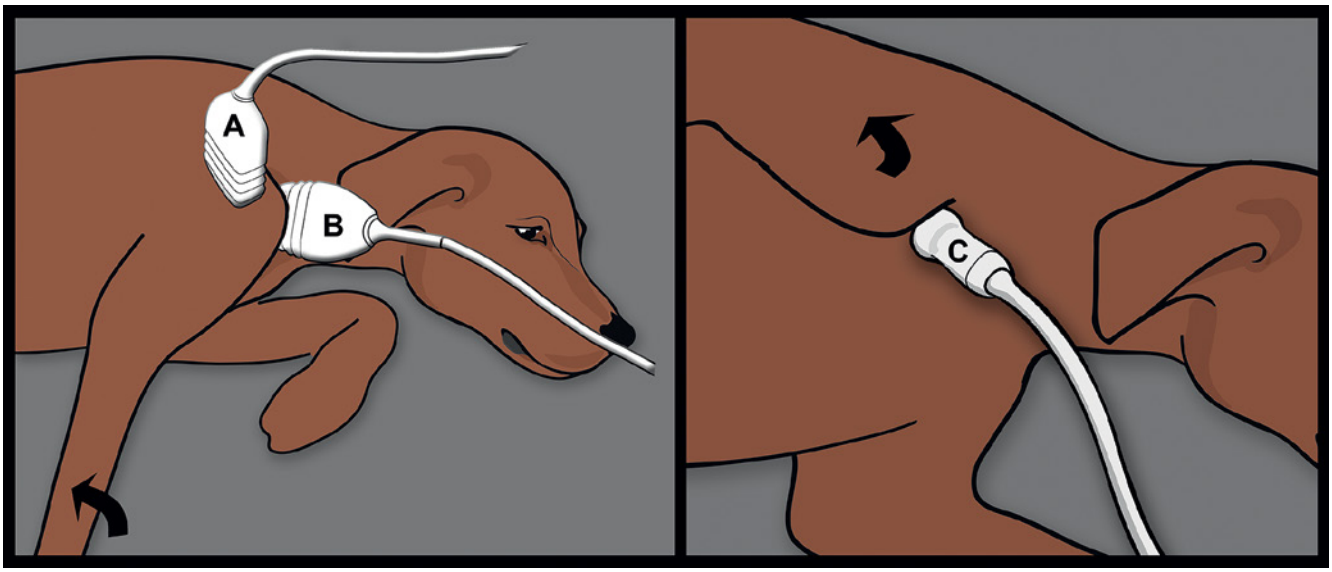


Figure 17.1. Scanning technique for the shoulder. Illustration showing the position of the dog and ultrasound probe for obtaining longitudinal images of the **supraspinatus** and **infraspinatus muscles (A)** and **biceps tendon (B)**. For the assessment of the biceps tendon, the leg must be pulled and supinated (curved arrow), facilitating the approach to the bicipital groove, which is located medial to the shoulder. **(C)** The medial aspect of the shoulder and axillary area can be more easily assessed with a convex probe. The leg must be abducted and the approach can be facilitated by pulling (as shown) or extending the leg. Sedation is essential for an optimal exam and dorsal decubitus may prove useful, especially when both shoulders are examined.

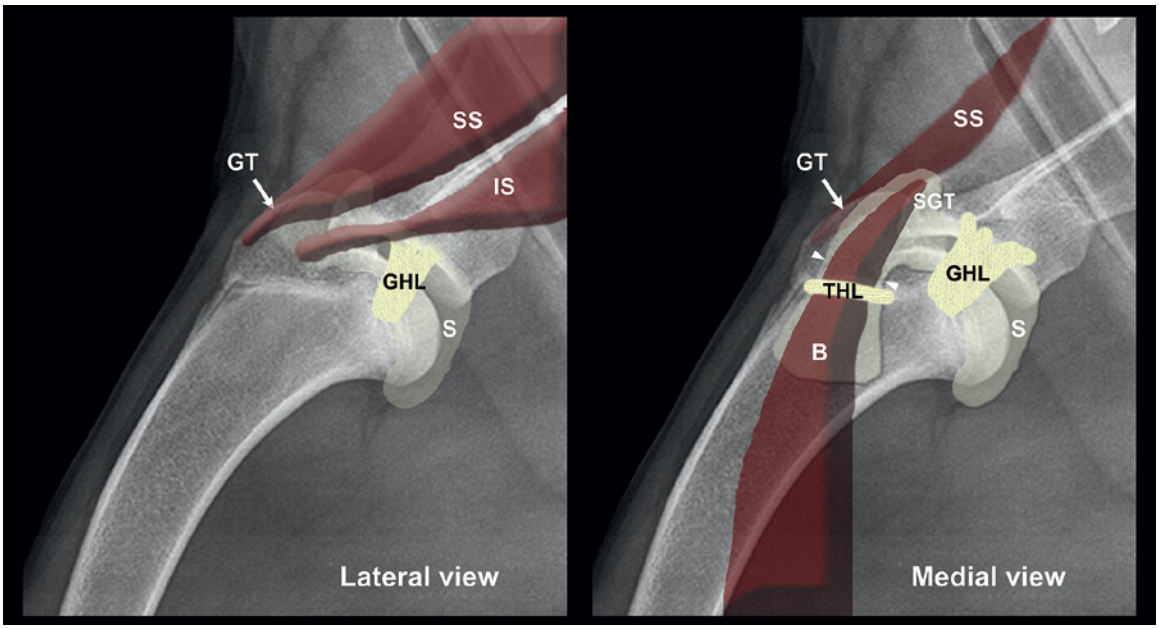


Figure 17.2. Schematic views of the normal shoulder anatomy in dogs. In the lateral view, the supraspinatus (SS) and infraspinatus (IS) muscles and tendons are cranial and caudal to the scapular spine, respectively. The SS tendon inserts on the greater tubercle (GT), just lateral to the bicipital groove. The IS inserts on the lateral aspect of the greater tubercle. The lateral glenohumeral ligament (GHL) is lateral to the joint capsule and synovial space (S). In the medial view, the biceps (B) muscle and tendon course along the medial aspect of the humerus. The tendon of origin is in the bicipital groove, just medial to the GT. It extends within a tendon sheath (arrowheads) that connects with the shoulder joint synovium (S) and is contained by the transverse humeral ligament (THL). The biceps tendon courses along the insertion site of the SS tendon, located craniolaterally, and originates on the supraglenoid tubercle (SGT). The medial GHL is fan-shaped proximally.

between the greater and lesser tubercles, but these are not clearly seen with ultrasound (Figure 17.2).

The intra-articular structures of the shoulder are imaged by positioning the transducer laterally in a caudocranial orientation immediately caudal to the acromion, which serves as a landmark. The transducer placed laterally, the joint is scanned by slowly adducting and simultaneously rotating the limb while the probe remains in the same position, in both longitudinal and transverse planes. Scanning the cranial aspect of the shoulder joint is difficult because of the presence of the greater tubercle, which allows only a small surface of probe contact. Imaging of the medial aspect of the shoulder joint may be facilitated by using a microconvex transducer, because of the intimate relationship between the thoracic limb and the thoracic wall.

Normal Sonographic Anatomy of the Shoulder

Supraspinatus and Infraspinatus Muscles and Tendons

The supraspinatus muscle originates on the supraspinatus fossa of the scapula and extends distally before spreading focally over the greater tubercle on which it inserts (Figures 17.2, 17.3). Proximally over the scapula, the muscle is hypoechoic, loosely striated, and smoothly marginated, before crossing over the craniomedial aspect of the shoulder joint. The greater tubercle appears as a convex, irregular, hyperechoic interface, with acoustic shadowing, on which the supraspinatus muscle inserts (Figure 17.3). Close to its insertion, the supraspinatus tendon displays a widened portion with a central hypoechoic area without a fibrillar pattern in comparison to the adjacent biceps tendon, as it is composed of poorly organized collagen bundles within a myxoid, mainly mucopolysaccharidic substance (Lassaigne et al. 2020).

The infraspinatus muscle is scanned in longitudinal and transverse planes from its origin on the infraspinatus fossa of the scapula to its short tendon at the caudolateral margin of the greater tubercle (Figure 17.4). The muscle belly is striated with thin hyperechoic bands that run obliquely, connecting a central line to the periphery, giving a characteristic fishbone pattern. The muscle belly becomes narrower distally, merging into a tendon beyond the joint. The tendinous tissue displays typical hyperechoic fibrils arranged in parallel lines, with a peripheral hyperechoic outline (peritendineum). The infraspinatus muscle is covered by the deltoid muscle, which displays typical muscle echotexture.

Biceps Brachii Muscle and Tendon

In the longitudinal plane, the biceps muscle appears hypoechoic, with a hyperechoic line in the center representing the border between the two fused muscle bellies. Hyperechoic lines extend from this central line and run at a slightly oblique angle to the longitudinal axis (fish-bone pattern). The transducer is then positioned proximal to the muscle–tendon interface, which is not well defined (Figure 17.5A, B). The proximal tendon runs within the bicipital groove, which lies medial to the greater tubercle, deep in the medial groove of the shoulder. The tendon is then followed across the joint

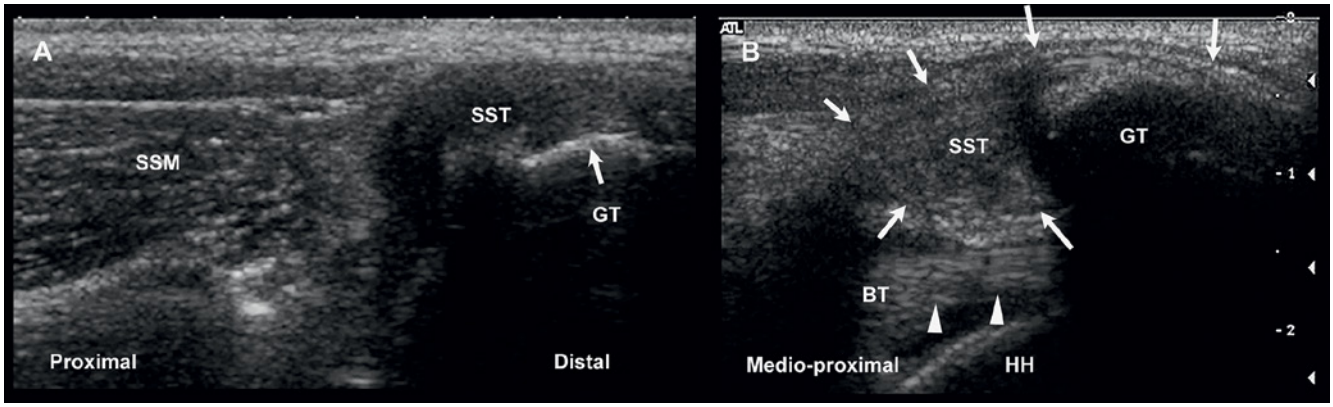


Figure 17.3. Normal sonographic anatomy of the supraspinatus muscle and tendon. Longitudinal **(A)** and transverse **(B)** sonographic and schematic images of the normal supraspinatus muscle (SSM) and supraspinatus tendon (SST) in a large-breed dog. The characteristic hypoechoic echotexture with small hyperechoic dots and lines of the supraspinatus muscle is seen. Because of the orientation and distribution of the tendon fibers, this portion also appears hypoechoic. It fans (arrows) around the humeral greater tubercle (GT) on which it inserts. The greater tubercle and the surface of the humeral head (HH) appear as thin, hyperechoic interfaces casting acoustic shadow. The biceps tendon (BT, arrowheads) and its sheath course caudally and medially, in proximity to the SST.

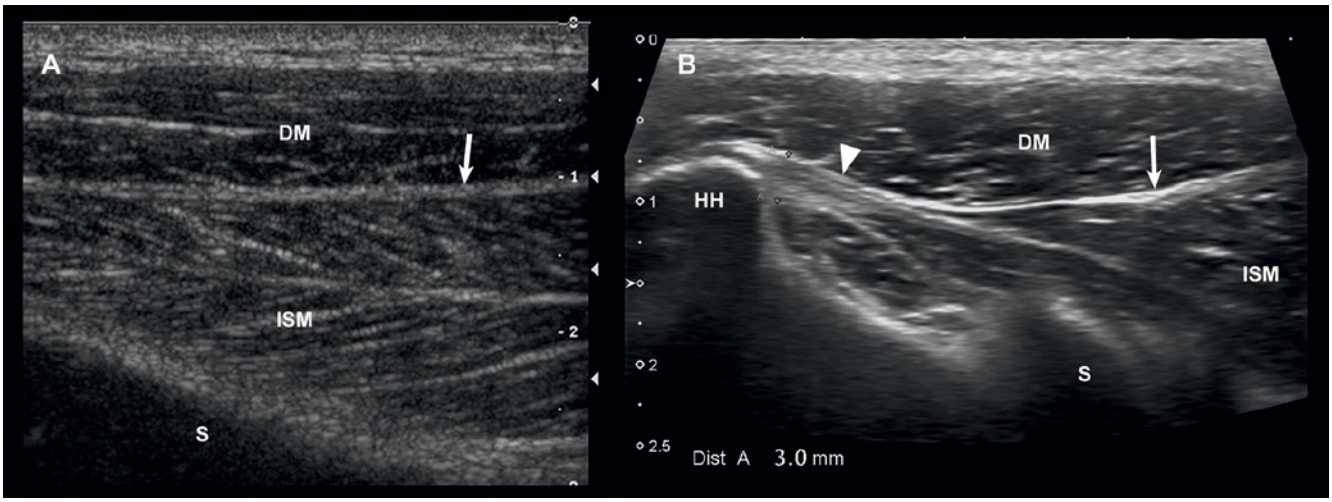


Figure 17.4. Normal sonographic anatomy of the infraspinatus muscle and tendon. (A, B) Longitudinal sonographic images of the normal infraspinatus muscle (ISM) and tendon obtained at two different levels. The characteristic fishbone echotexture of the muscle is present. The deltoid muscle (DM) is in the near field, separated by a thin hyperechoic interface (arrow) that represents the intermuscular fascia. The shadowing hyperechoic surface of the scapula (S) is seen in the far field in **(A)** and **(B)**. The infraspinatus tendon (arrowhead and between the cursors) inserts on the lateral surface of the humeral head (HH), just caudal to the greater tubercle and insertion site of the supraspinatus tendon.

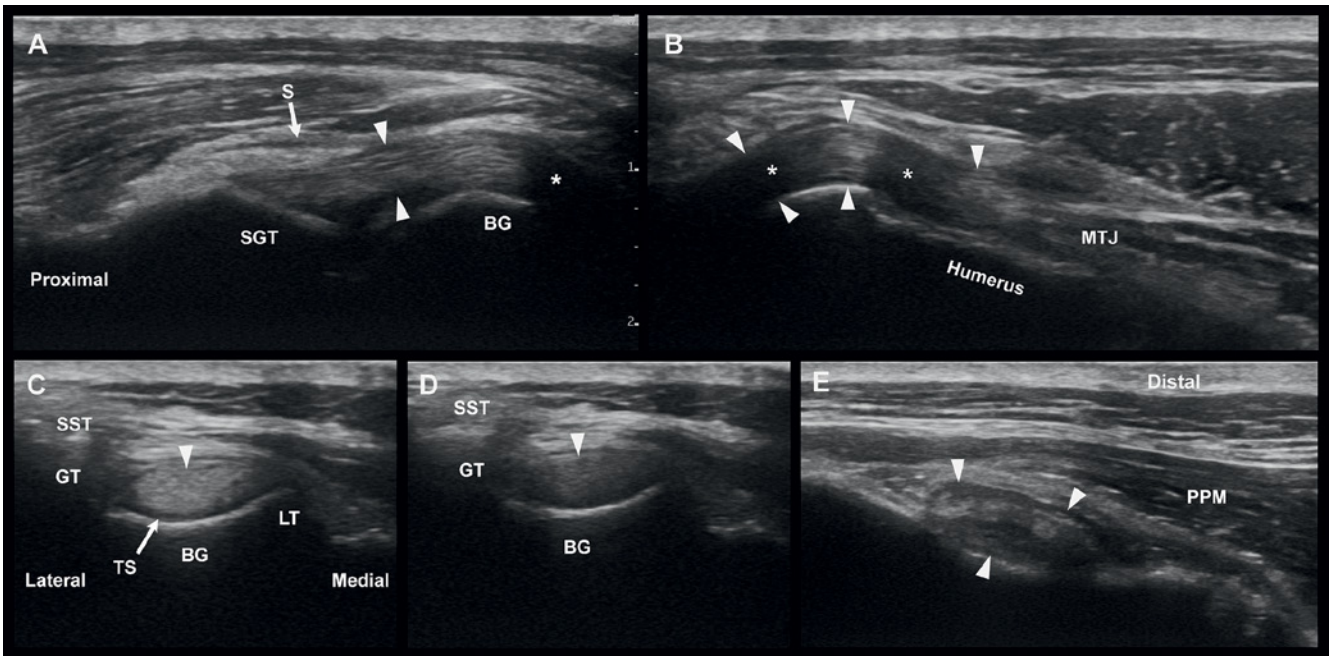


Figure 17.5. Normal sonographic anatomy of the biceps tendon in dogs. (A, B) In these longitudinal sonographic images of the normal biceps tendon, the most proximal **(A)** and distal **(B)** portions of this tendon are seen (between the arrowheads) (see probe B in Figure 17.1). Its origin on the supraglenoid tubercle (SGT) is visualized. The characteristic hyperechoic echotexture of the tendon is well visualized when imaged perpendicularly. The tendon becomes hypoechoic (*) when its fibers are no longer perpendicular to the probe, as in curved portions. Deep to the tendon, the bicipital groove (BG) appears as a curved, hyperechoic interface. The musculotendinous junction (MTJ) is seen distal to the humeral head and is ill-defined. **(C, D)** Transverse sonographic images obtained at the level of the BG. When the tendon is imaged perpendicularly (in C), it appears as a uniformly hyperechoic oval structure (arrowheads) surrounded by a thin hypoechoic rim representing the tendon sheath (TS), whereas it becomes hypoechoic (in D) when imaged obliquely due to anisotropy The biceps tendon slides along the lateral aspect of the lesser tubercle (LT), medial to the greater tubercle (GT), and supraspinatus tendon of insertion (SST). The musculotendinous junction (MTJ) is seen more distally. **(E)** Transverse image at the MTJ, which appears heterogeneously hypoechoic due to a mixture of tendon and muscular fibers. PPM, deep pectoral muscle.

to its origin on the supraglenoid tubercle of the scapula. More deeply, the hyperechoic convex line of the humeral head bony surface becomes visible. Proximal to this point of orientation, the hypoechoic to anechoic area of the joint space and, dorsally, the supraglenoid tubercle can be distinguished. The latter structure is visible as a slightly convex, hyperechoic interface associated with acoustic shadowing. Because of its curvature along the bicipital groove, the tendon hyperechoic echotexture can be evaluated only when perpendicular to the probe. At the level of the supraglenoid tubercle, the tendinous fibers curve and become hypoechoic as they reach the bone, mimicking a lesion. Finally, by flexing, extending, abducting, and adducting the shoulder joint, the tendon can be dynamically examined. This helps identifying potential adhesions and joint fragments. When the joint is flexed, the hypoechoic joint space enlarges to approximately twice its original size (Kramer et al. 2001b).

On a transverse plane (Figure 17.5C, D), the tendon appears as an oval, uniformly hyperechoic structure measuring approximately 3 mm thick in medium-sized to large dogs. The transducer must be placed carefully perpendicular to the tendon fiber to avoid a drop in tendon echogenicity (anisotropy) that could be confused for a lesion (Figure 17.5D). The tendon is surrounded by a thin hypoechoic halo, consistent with a minute amount of fluid within the tendon sheath, which is typically fusiform to oval on cross section. Thin, linear, hyperechoic interfaces can be seen at the superficial and deep margins of the sheath at the interface level of the tendon sheath wall and humeral surface, respectively. The greater tubercle appears as a hyperechoic convex line at the lateral aspect of the bicipital groove and tendon. It is more distinct than the lesser tubercle medially, which is seen only as a small elevation of the reflective line on the surface of the bone. The bicipital groove appears as a smoothly marginated concave hyperechoic line between these tubercles. The intertubercular ligament cannot be distinguished from the surrounding soft tissue. Distomedially, the distal outpouch of the synovial sheath can appear lobulated in some dogs.

Shoulder Joint Space and Medial Glenohumeral Ligament

Positioning of the transducer perpendicular to the joint space enables visualization of the surface of the humeral head as a semicircular, convex, hyperechoic line with distal acoustic shadowing (Figure 17.6). This hyperechoic subchondral interface should appear smooth and continuous and covered with a thin anechoic band that represents the articular cartilage.

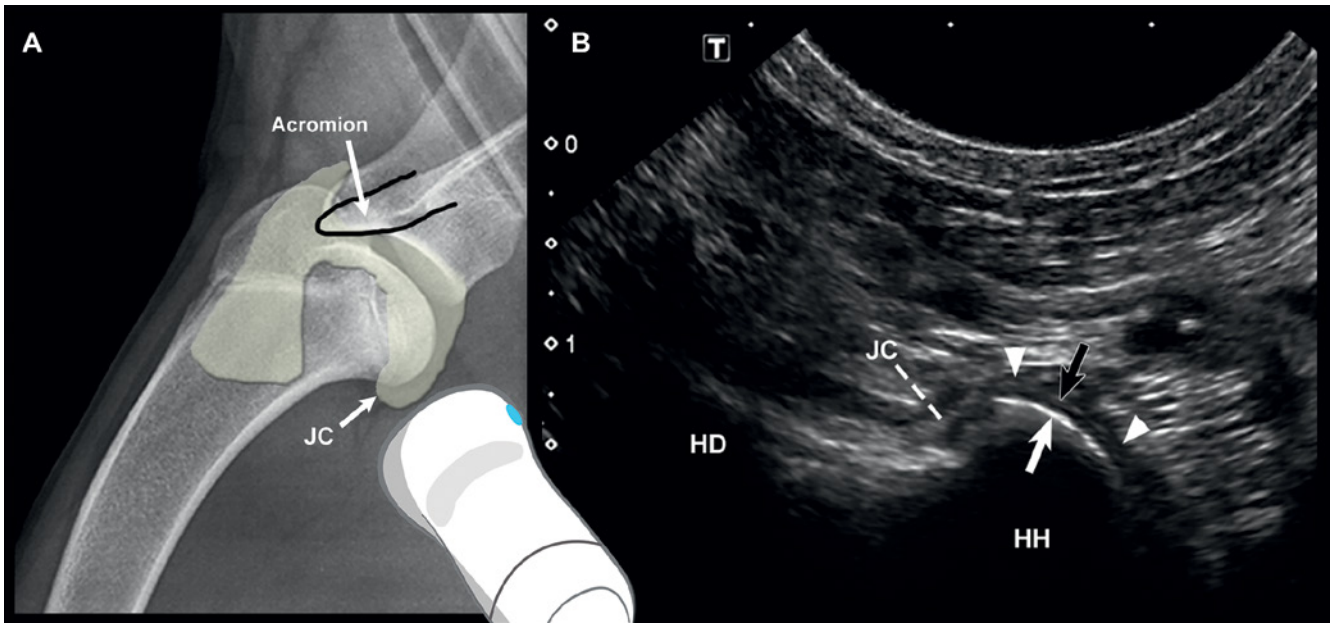


Figure 17.6. Normal sonographic approach and anatomy of the shoulder joint. (A) The caudolateral portion of the shoulder joint can be evaluated after placing the probe caudal to the acromion, which can be easily palpated. The caudal extent of the joint space and capsule (JC) can be assessed. **(B)** Longitudinal sonographic image obtained at the caudolateral aspect of the shoulder, showing a portion of the humeral diaphysis (HD) and head (HH). The subchondral bone plate appears as a shadowing, hyperechoic, convex interface (white arrow), covered with a thin anechoic layer representing the articular cartilage (black arrow), and a small volume of hypoechoic synovial fluid and hypoechoic synovium, which are often confluent (arrowheads). The joint capsule (JC) may be visualized, in part, as an outer hyperechoic layer, or confluent with the extra-articular tissues.

Because of the semicircular anatomy of the head, only a small section of the surface can be assessed at one time. The articular cartilage is covered by the hypoechoic synovium. The outer, curved line above the cartilage represents the joint capsule. This merges with the echotexture of the covering musculature. On the medial side of the joint, the medial glenohumeral ligament, although relatively thin, may sometimes be recognized (Cogar et al. 2008). Its sonographic assessment remains limited.

Sonographic Features of Shoulder Disorders

Supraspinatus Tendinopathy

Inflamed or degenerated supraspinatus tendons can be thickened and inhomogeneous because of fibrous disruption, hemorrhage, and/or fibrosis. Mineralization can also be found in the region of insertion on the greater tubercle in the distal part of the tendon. These mineral foci appear as small, hyperechoic, irregularly defined structures, with or without distal acoustic shadowing and with or without a surrounding hypoechoic to anechoic area (reaction tissue) (Long and Nyland 1999) (Figures 17.7, 17.8). While such mineralization may be associated with lameness in dogs and even impinge on the adjacent bicipital tendon and sheath, it may be found in clinically normal dogs, unilaterally or bilaterally (Lafluente et al. 2009).

Infraspinatus Contracture

Changes in both echogenicity and echotexture are seen in the affected muscle. The transition from muscle to tendon, and the tendon itself, is usually affected and the affected portions are inhomogeneous with hypoechoic and/or hyperechoic zones, with loss of the normal echotexture (Figure 17.9) (Franch et al. 2009; Siems et al. 1998).

Bicipital Tenosynovitis and Tendon Rupture

The bicipital tendon appears mildly to severely thickened, losing its normal flat to oval shape to become rounded (Figures 17.10–17.14). Its normal fibrillar pattern can also be affected and hypoechoic areas caused by partial tears and/or hemorrhage can be seen. The affected tendon may also appear significantly inhomogeneous. Tendon sheath effusion, which is often observed, appears as an enlarged hypoechoic to anechoic halo surrounding the affected tendon. The effusion can range from mild to severe and is well visualized on transverse images over the bicipital groove. In most cases, the thickened synovium cannot be easily distinguished from the synovial fluid, although irregular synovial thickening or flocculent synovial fluid can be observed in some dogs (Long and Nyland 1999). Fibrous adhesions with the tendon, particularly within the bicipital groove, can also be seen dynamically. In severe cases, the tendon sheath develops a bulge in the direction

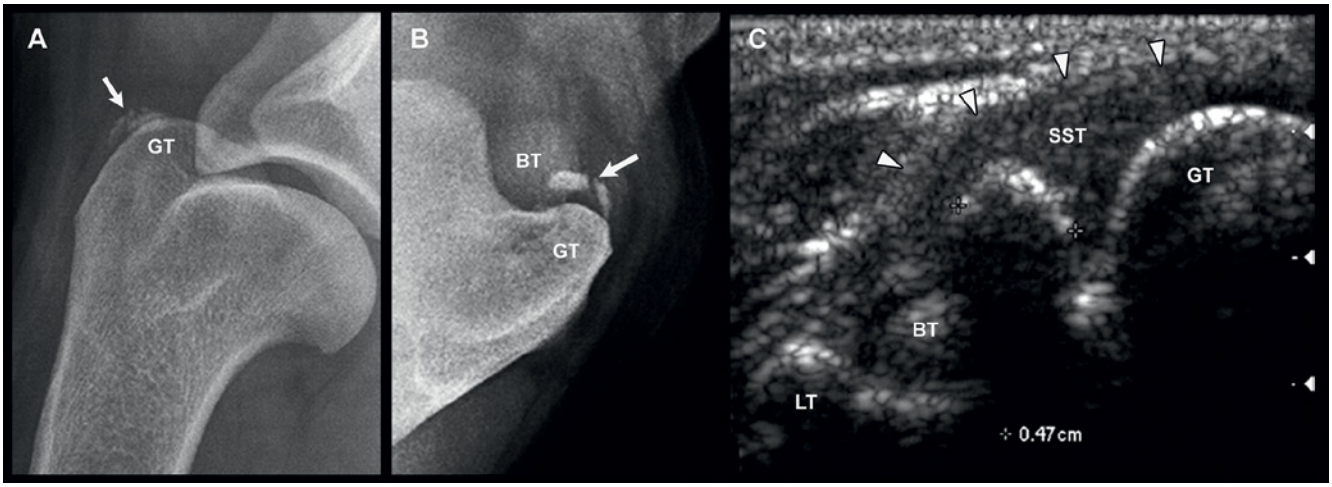


Figure 17.7. Calcifying supraspinatus tendinopathy. (A, B) Mediolateral and tangential radiographs of the bicipital groove in a large-breed dog with shoulder pain. Small mineral opacities (arrows) are observed in the region of insertion of the supraspinatus tendon on the greater tubercle (GT), located just lateral to the bicipital groove and biceps tendon (BT). **(C)** Transverse sonographic image of the bicipital groove in the same dog. An irregular, hyperechoic, shadowing focus is in the distal supraspinatus tendon (SST) that is also enlarged (arrowheads), consistent with mineralization. This mineralization, as seen in the tangential radiographic projection, is adjacent to the biceps tendon (BT). Moderate distension of the BT sheath is observed, as the result of tenosynovitis, which was suspected to be secondary to the supraspinatus tendon calcified body. GT, greater tubercle; LT, lesser tubercle.

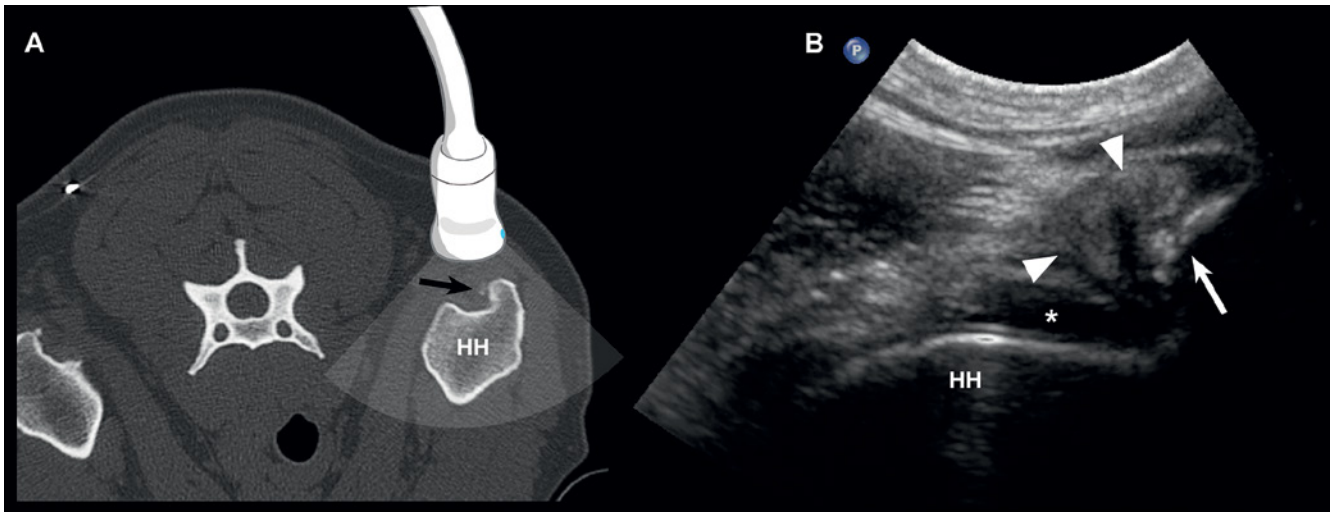


Figure 17.8. Chronic supraspinatus tendinopathy. Transverse computed tomographic **(A)** and sonographic **(B)** images of the insertion site of the supraspinatus tendon (arrowheads) in a large-breed dog with shoulder pain. The supraspinatus tendon is inhomogeneous and mostly hyperechoic, with small hyperechoic foci consistent with mineralization (arrows) next to the greater tubercle. The adjacent bicipital tendon sheath is distended (*). HH, humeral head.

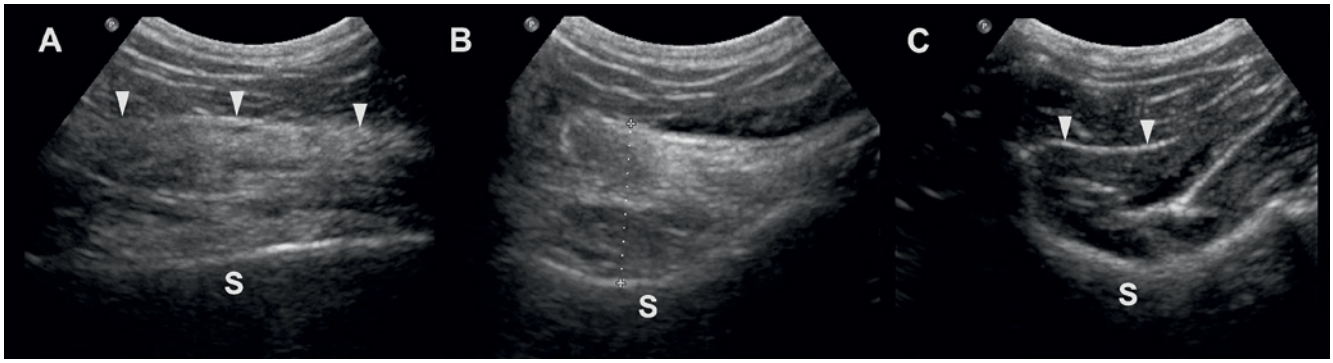


Figure 17.9. Contracture of the infraspinatus muscle in a dog with chronic lameness. Longitudinal **(A)** and transverse **(B)** sonographic images obtained with the probe placed over the caudal portion of the scapula (S) of a dog with chronic lameness. The infraspinatus muscle (between calipers, arrowheads) is enlarged and hyperechoic. **(C)** Transverse image of the contralateral muscle that is normal in size and echogenicity.

of the lesser tubercle (Esterline et al. 2005; Kramer et al. 2001b; Rivers et al. 1992).

Most **partial ruptures** occur in the area of the supraglenoid tubercle. The proximal part of the tendon tissue appears hypoechoic and mildly to moderately inhomogeneous. Small, hyperechoic bone fragments can be visible if fibers are avulsed, with or without acoustic shadowing (Figures 17.13A, 17.14). In contrast to a complete rupture, areas of tendon tissue displaying a normal fibrillar echotexture can be found in a transverse image. A hypoechoic to anechoic region can be found in the central portion of the affected tendon (core lesion), at the level of fibrillar disruption and hematoma formation, associated with tendon enlargement (Figures 17.10–17.13). A cleft can also be observed in some partially ruptured tendons. Tendon sheath effusion develops around the tendon.

With **complete rupture**, the fibrillar structure of the tendon is disrupted (Figure 17.14). The gap between retracted tendon stumps is usually anechoic or hypoechoic, and moderate to severe tendon sheath effusion can be observed as the result of hemorrhage. The distal stump, which is attached to the muscle, is typically more retracted and often of mixed echogenicity and echotexture.

Osteophytes and **enthesophytes** can form within the bicipital groove because of chronic degenerative joint disease (DJD) and/or bicipital tenosynovitis. They are attached to the tendon sheath and appear as irregular hyperechoic structures that cast shadows when larger

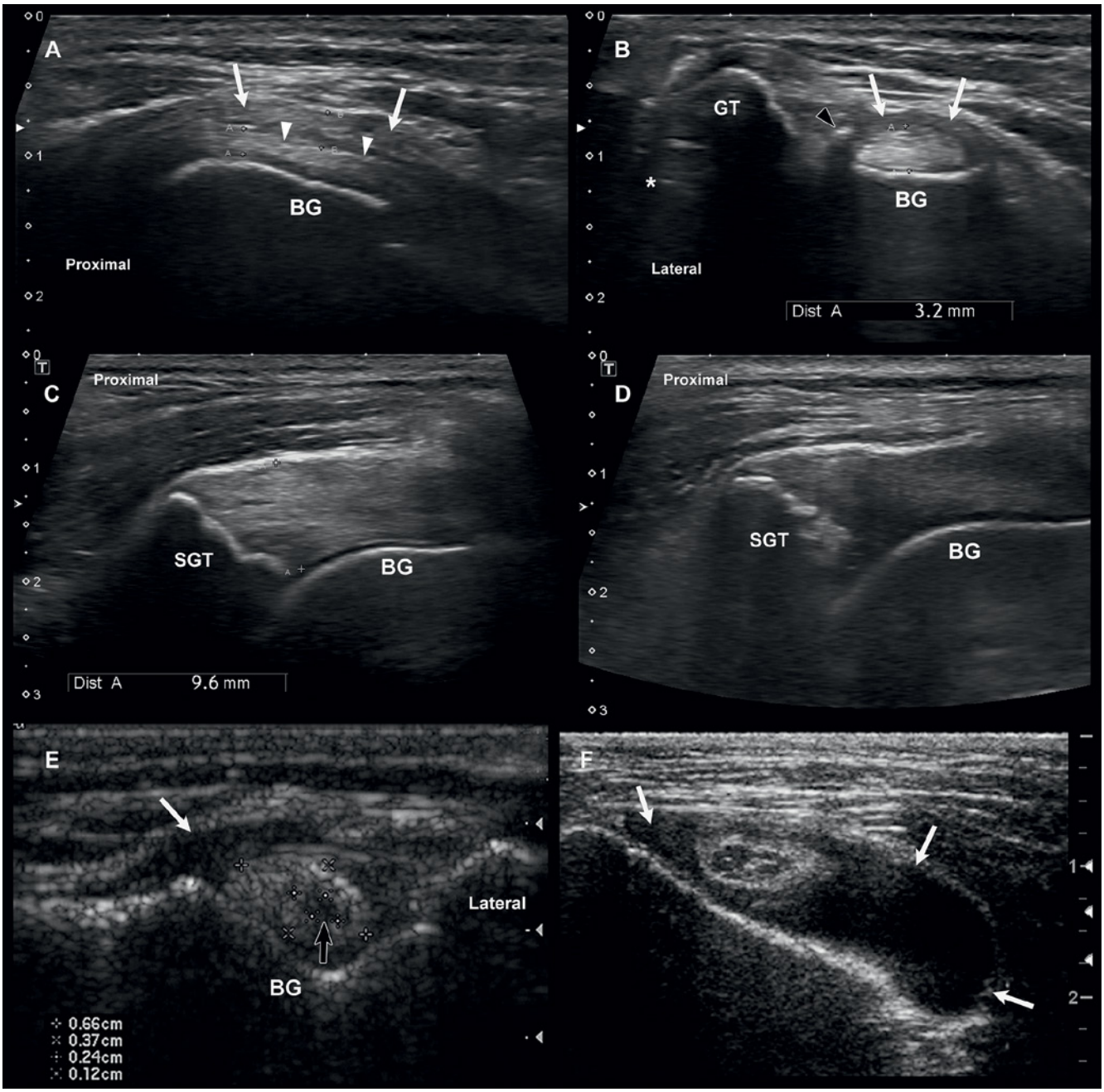


Figure 17.10. **Bicipital tenosynovitis in five dogs. (A, B)** Transverse **(A)** and longitudinal **(B)** sonograms of the biceps tendon (arrowheads) of a five-year-old Golden Retriever scanned at the level of the bicipital groove (BG). The tendon (white arrowheads) is surrounded with an echogenic tissue (arrows) consistent with synovial hyperplasia confirmed with arthroscopy. Dystrophic calcification is seen (black arrowhead) in the lateral portion of the tendon sheath, medial to the greater tubercle (GT). **(C)** In this other dog, the proximal portion of the biceps tendon is markedly thickened (9.6 mm) and inhomogeneous, with several areas of fiber pattern disruption. The supraglenoid tubercle (SGT) is irregular. **(D)** The supraglenoid tubercle shows a protuberant new bone formation at the origin of the biceps tendon in this other dog. **(E, F)** Tendon sheath distension (arrows) in two dogs with tenosynovitis. There is a 2.4 mm × 1.2 mm hypoechoic core lesion in the biceps tendon of the first dog (**E**, black arrow). In the other dog, the image shows the heterogeneous musculotendinous junction surrounded by marked distension of the tendon sheath. BG, bicipital groove.

than 1-2mm if a high-resolution probe is used (Figures 17.11, 17.12). In severe cases, this mineralization may form a semicircumferential cast around the tendon, significantly hampering its visualization. Calcified bodies found in the bicipital groove or in a joint recess may also represent migrating **osteochondral (OCD) fragments** (Figure 17.15) or **synovial osteochondromatosis**, another degenerative condition that may develop in dogs and cats.

Fractures of the Supraglenoid Tubercle

The fractured supraglenoid tubercle is visualized at the proximal extent of the biceps tendon as a hyperechoic, more or less convex structure with smooth margins and acoustic shadowing. The fragment can be seen moving with the tendon during dynamic flexion and extension of the shoulder, in association with moderate tendon sheath effusion. The surface of the tubercle appears irregular, and a bone defect is often

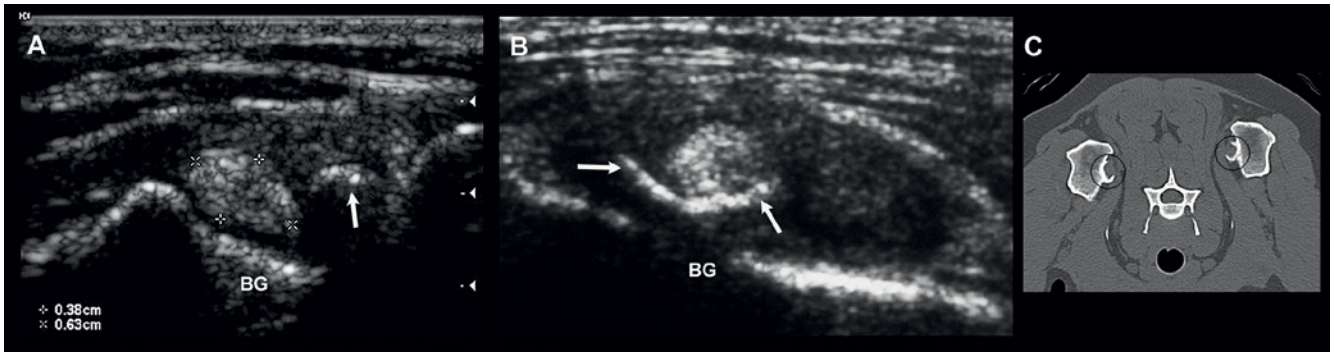


Figure 17.11. Chronic bicipital tenosynovitis with mineralization. Transverse sonographic **(A, B)** and computed tomographic (CT) **(C)** images obtained in three dogs at the level of the bicipital groove (BG). **(A)** A hyperechoic, shadowing mineral focus (arrow) is present at the lateral aspect of the bicipital tendon sheath. The adjacent tendon (between the cursors) is mildly thickened with an ill-defined core lesion. **(B)** Tendon sheath wall mineralization can appear as a hyperechoic semicircular groove (arrows) that may partially or completely encircle the biceps tendon**. (C)** The mineralization is well appreciated on this CT image as it partially encircles the biceps tendon.



Figure 17.12. Severe chronic bicipital tenosynovitis with mineralization. (A) Mediolateral radiographic view of the shoulder of a three-year-old Labrador retriever with chronic shoulder pain and lameness. Mineralization is found along the bicipital groove as well as in the region of the caudal articular recess (arrowheads). Periarticular new bone formation is also present at the caudal aspect of the shoulder, consistent with degenerative joint disease. Moreover, there is faint mineralization in the region of the supraspinatus tendon (black arrow). **(B, C)** Longitudinal (**B**) and transverse (**C**) sonographic images of the bicipital groove on which the bicipital tendon is enlarged and inhomogeneous with several hypoechoic defects in the fibrillar patter, consistent with cord lesions (arrows). The tendon sheath is markedly distended with fluid (*). An irregular and hyperechoic mineral cast partially encircles the biceps tendon (arrowheads). Mineral foci are also seen in the nearby supraspinatus tendon (SST) (black arrow).

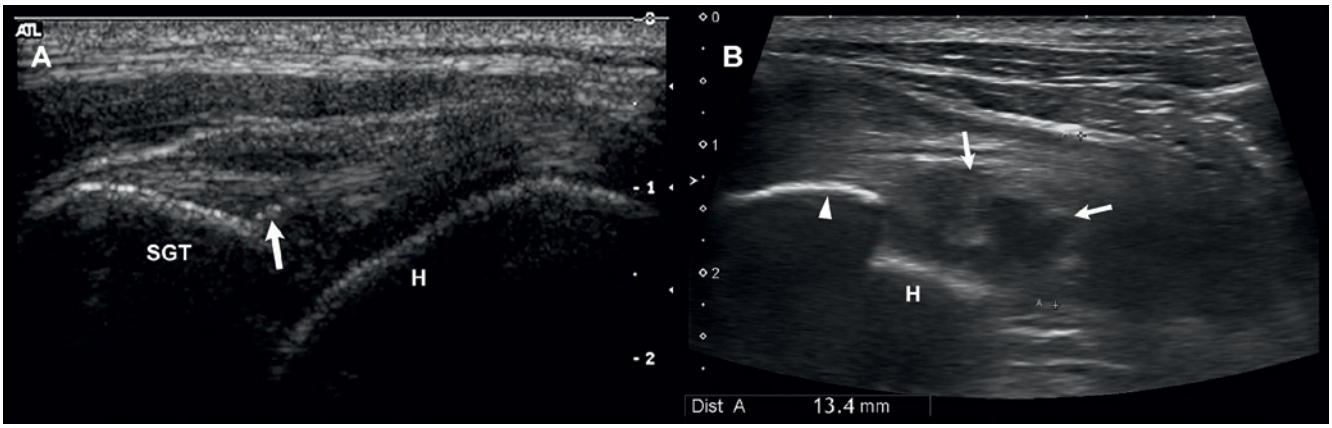


Figure 17.13. Partial bicipital tendon rupture in two dogs. (A) Longitudinal sonogram of the proximal portion of the biceps tendon in a dog with partial biceps tendon avulsion. An inhomogeneous, hypoechoic area (arrow) with small hyperechoic dots consistent with mineral fragments is just distal to the region of insertion on the supraglenoid tubercle (SGT). H, humerus. **(B)** Longitudinal sonogram in another dog with partial rupture at the musculotendinous junction. The proximal portion of the biceps muscle is enlarged (13 mm) and an irregular and heterogeneous hypoechoic lesion is seen at the tendinous junction (arrows). New bone formation is present in the bicipital groove (arrowhead). H, humerus.

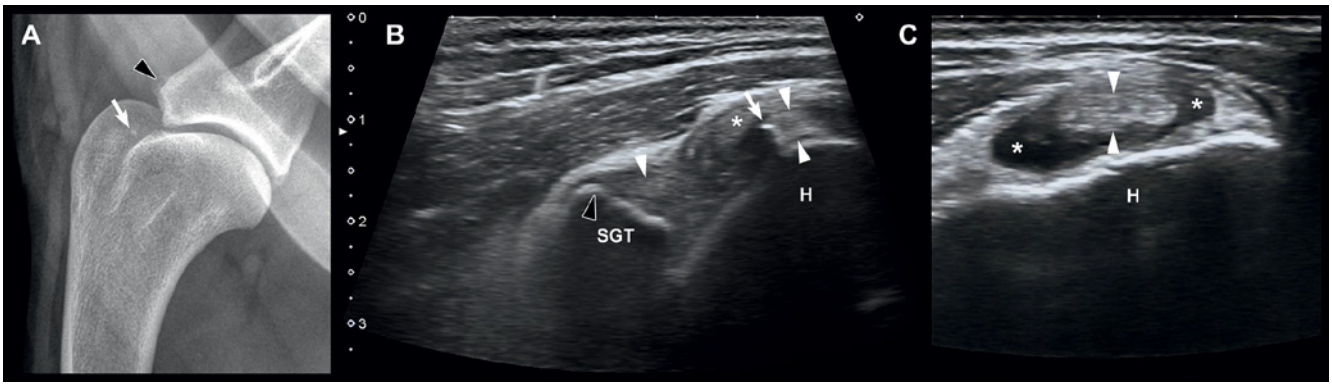


Figure 17.14. Complete bicipital tendon rupture in a dog with non-weight-bearing lameness. (A) Mediolateral radiograph showing mild irregular new bone formation on the supraglenoid tubercle (black arrowhead) and in the bicipital groove, with a small fragment (arrow). **(B, C)** Longitudinal **(B)** and transverse **(C)** sonographic images of the biceps tendon (white arrowheads). There is discontinuity of the fiber pattern in the proximal portion of the tendon and significant distension of the tendon sheath (*) is recognized, with echogenic content consistent with hemorrhage. The distal segment of the biceps tendon is retracted and appears thickened and inhomogeneous, with a hyperechoic mineral focus (arrow) correlating with the radiograph. The black arrowhead points to the mild new bone formation on the supraglenoid tubercle (SGT) correlating with the radiograph. Chronic bicipital tenosynovitis with rupture was diagnosed. H, humerus.

observed. In cases of partial avulsion fracture, small bone fragments can be identified as hyperchoic foci in the proximal tendon adjacent to the supraglenoid tubercle (Figure 17.13A, 17.14).

Tendon Luxation

Rupture of the transverse ligament causes medial luxation of the tendon over the lesser tubercle. This should be suspected when the tendon is not found in the bicipital groove but replaced with moderate effusion. The oval tendon with its typical fibrillar echotexture may be found in the region of the lesser tubercle (Figure 17.16). During dynamic examination, the tendon can slide back into the groove.

Instability

Shoulder joint instabilities represent an important source of thoracic limb lameness in dogs that remains difficult to diagnose. Abnormal gliding of the humeral head may be assessed dynamically, but this evaluation

is subjective and requires a comparison with the contralateral shoulder. The medial glenohumeral ligament may appear thickened and hyperechoic with surrounding effusion. However, the accuracy of this modality for detecting shoulder instability remains low (Cogar et al. 2008).

Osteochondritis Dissecans

The subchondral defect on the caudal part of the humeral head can be visualized as an irregularity in the hyperechoic convex bone surface. The defect appears hypoechoic, with or without hyperechoic dots or lines, because of disturbed endochondral

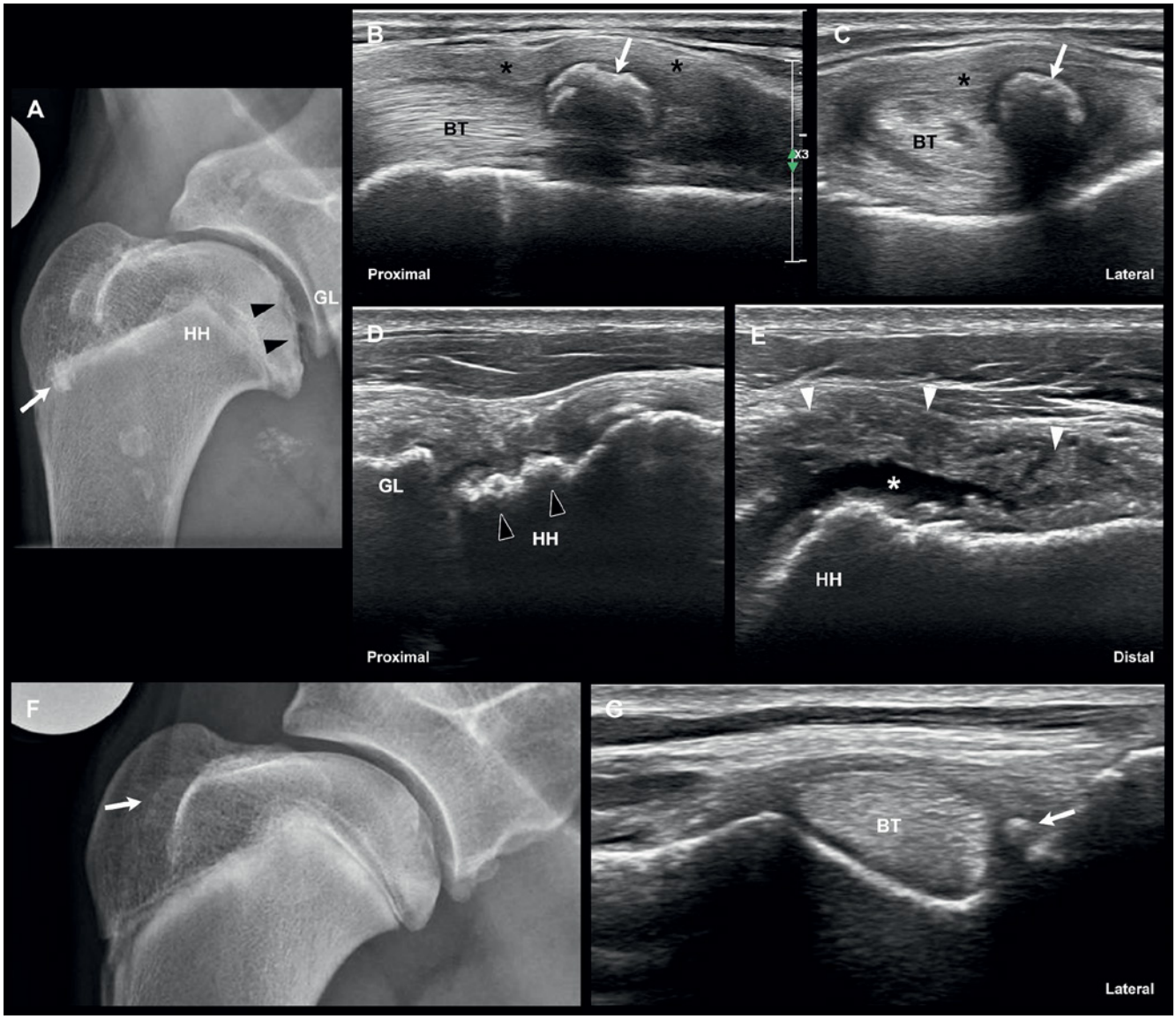


Figure 17.15. **Migrating OCD fragments. (A)** Mediolateral radiograph of the right shoulder of an 11-month-old Great Dane presented for shoulder pain and lameness. There is a wide, irregular subchondral defect at the caudal aspect (black arrowheads) of the humeral head (HH) consistent with osteochondritis dissecans (OCD). There is new bone formation in the bicipital groove and several calcified bodies in the distal area of the biceps tendon (arrow) and joint recesses. Longitudinal **(B)** and transverse **(C)** sonographic images of the bicipital tendon sheath confirming the migrated OCD fragment (arrow) and showing an inhomogeneous tendon (BT) with hypoechoic core lesions as well as synovial thickening (*). Moving the probe caudally shows the irregular osteochondral defect (black arrowheads) on the humeral head (HH) (**D**), opposite the glenoid rim (GL), then joint effusion (*) and marked synovial/joint capsule thickening (white arrowheads) at the caudal joint recess **(E)**. **(F)** The radiograph of the left shoulder also shows a wide subchondral defect on the humeral head and a few mineral discrete opacities in the bicipital groove that were confirmed to represent fragments (arrows) in the tendon sheath on transverse sonogram **(G)**. The bicipital tendon (BT) was normal and milder signs of tenosynovitis were present.

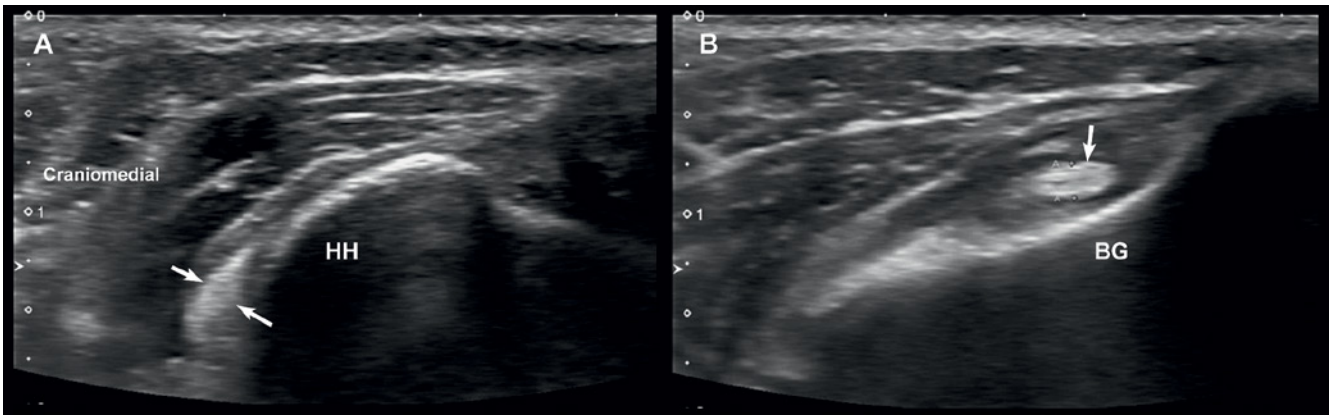


Figure 17.16. Biceps tendon dynamic luxation. On first examination (**A**), the biceps tendon (arrows) was medially displaced, whereas it moved back in its groove (BG) when extending the shoulder **(B)**. Note the mild tendon sheath effusion. HH, humeral head.

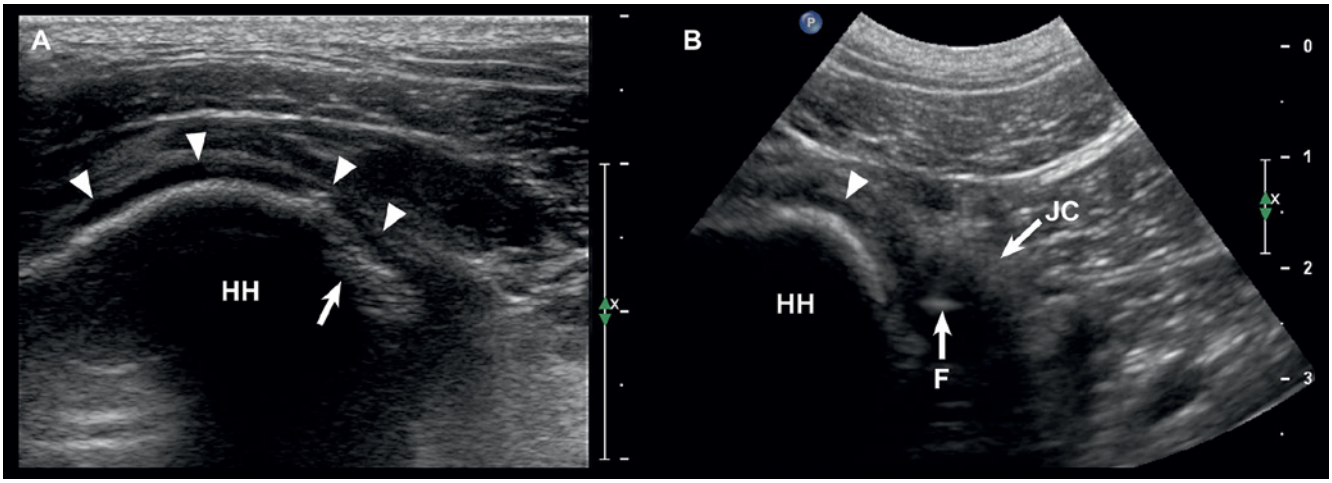


Figure 17.17. Humeral head OCD. Longitudinal sonographic images of the caudal portion of the humeral head (HH) **(A)** and the caudal joint recess **(B)** in a dog with osteochondritis dissecans (OCD). **(A)** The humeral cartilage (arrowheads) is irregular and hyperechoic in its centrocaudal portion, at the level of incomplete subchondral mineralization (arrow). **(B)** A mineralized osteochondral fragment (F) has migrated in the caudal joint recess. The joint capsule (JC) is thickened and hyperechoic. The arrowheads point to the intact humeral head (HH) cartilage.

ossification and osteochondral fissures or fragments (Figure 17.17A). "Joint mice" may be found in the caudal synovial recess of the joint, which is typically distended, or may migrate craniodistally into the bicipital tendon sheath (Vandevelde et al. 2006) (Figure 17.17B).

Elbow

Although radiography, CT, and MRI are most commonly used to image the elbow, ultrasonography represents a complementary tool in practice, particularly in the assessment of soft-tissue structures and identifying joint effusion and fragments. The approach to the normal canine elbow has been well described (Knox et al. 2003; Lamb and Wong 2005; Villamonte-Chevalier et al. 2015).

Scanning Technique and Normal Ultrasonographic Anatomy

A linear, high-frequency (>12 MHz) ultrasound transducer is preferred for assessing the small superficial portions of the elbow. The hair around the elbow is clipped, and the patient is initially placed in lateral recumbency with the elbow of interest up. After the lateral aspect of the joint has been evaluated, the patient is turned over to assess the medial structures more easily (Figure 17.18).

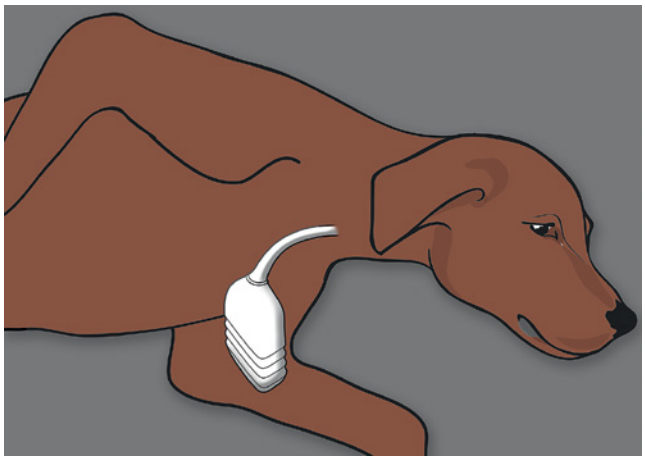


Figure 17.18. Scanning technique for the medial aspect of the elbow. Illustration showing the position of the dog and ultrasound probe when scanning the medial aspect of the elbow.

Medial Aspect: Medial Collateral Ligament, Medial Coronoid Process, and Flexor Tendons

In the proximal caudomedial region of the elbow, the two heads of the **triceps brachii muscle** can be differentiated. The **medial epicondyle** is initially assessed in a longitudinal plane and appears as a curved, slightly irregular, hyperechoic interface on the distomedial aspect of the humerus. The **medial collateral ligament**, which merges from the medial epicondyle, appears proximally as a thin, linear, hyperechoic structure that is densely packed with fine, parallel echoic lines (Figure 17.19). The ligament fibers spread caudally to the ulna and become slightly thicker near the radius. Because of the oblique course of the medial collateral ligament, it is often not possible to identify the fibrillar pattern in the distal portion (Lamb and Wong 2005). The **tendons of origin of the flexor muscles** can be assessed through the window used to evaluate the proximal part of the medial collateral ligament (Villamonte-Chevalier et al. 2015).

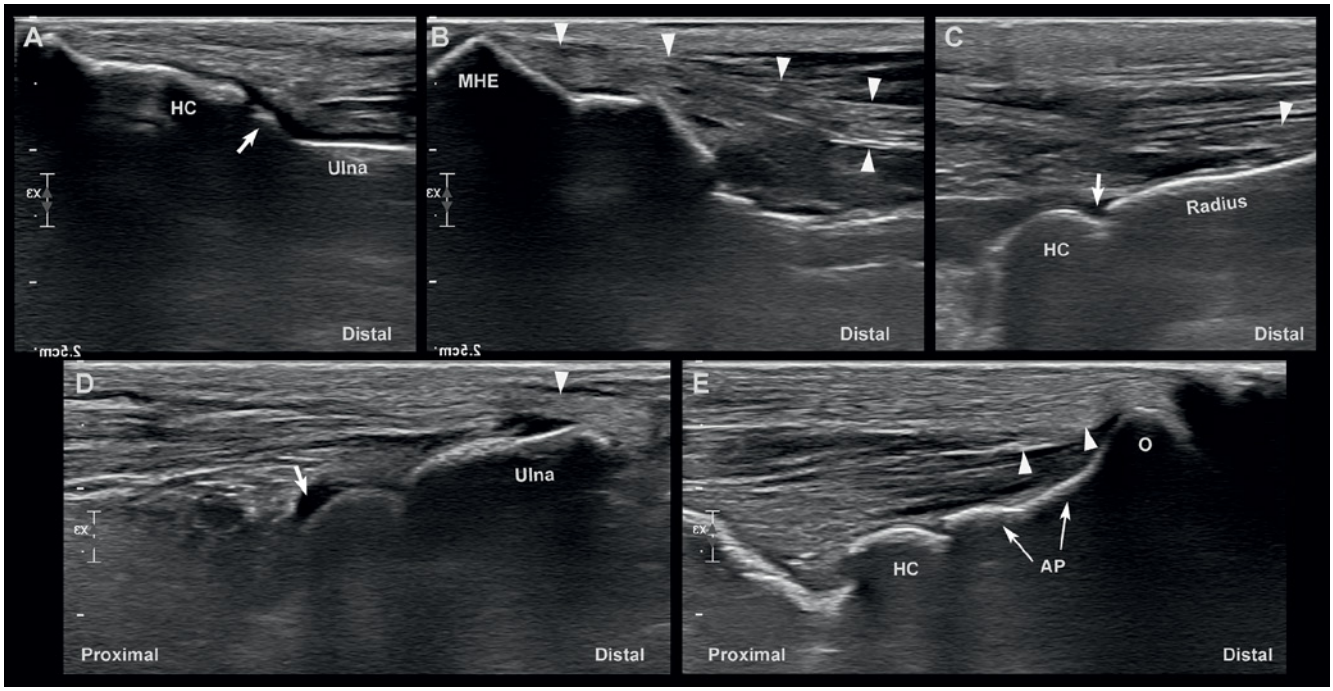


Figure 17.19. Normal sonographic anatomy of the canine elbow. (A) Longitudinal image of the medial aspect of the elbow showing the medial coronoid process of the ulna (arrow). HC, humeral condyle. **(B)** Longitudinal image of the caudomedial aspect of the elbow showing the tendon of the flexor carpi radialis muscle (arrowheads) originating on the medial humeral epicondyle (MHE). **(C)** Longitudinal image at the cranial aspect of the elbow showing one of the insertions of the tendon of the biceps brachii (arrowhead) on the proximomedial radius. There is minimal synovial joint fluid (arrow). **(D)** Longitudinal image at the dorsomedial aspect of the elbow showing the second insertion site of the bicipital tendon on the ulna (arrowhead). A small amount of synovial fluid is seen (arrow). **(E)** Longitudinal image with the elbow flexed of the distal tendon of the triceps muscle (arrowheads) inserting on the olecranon (O). The anconeal process (AP) is well visualized and appears unified. HC, humeral condyle.

The **biceps brachii tendon** can be visualized on the cranial aspect of the distal humerus and followed to its insertion sites on the ulnar and radial tuberosities, just adjacent to the medial coronoid process (MCP; Lamb and Wong 2005) (Figure 17.19). This tendon shows a typical echotexture with hyperechoic lines. The differentiation between the tendons of the biceps brachii and brachialis muscles at their insertion on the ulna can be achieved with a very high frequency probe (18 MHz) (Villamonte-Chevalier et al. 2015).

When the probe is moved proximally during a transverse scan, the surface of the **MCP** comes into view as an angular process on the medial aspect of the ulna (Figure 17.19A). The MCP is located deep to the medial collateral ligament and biceps tendon (Lamb and Wong 2005). A 90° flexion of the elbow and rotation of the forearm around its longitudinal axis may facilitate the identification of this structure.

Sonographic Features of Specific Elbow Disorders

Osteoarthritis

Even minor **effusion** can be visualized in a recess of the joint and is most commonly associated with elbow dysplasia. With chronic DJD, the joint capsule is visible as a hyperechoic, thick line between the synovium and synovial fluid, and the surrounding musculature. **Periarticular new bone formations**, caused by osteoarthritis, appear as irregularly circumscribed protuberances on the bony surfaces (Figure 17.20).

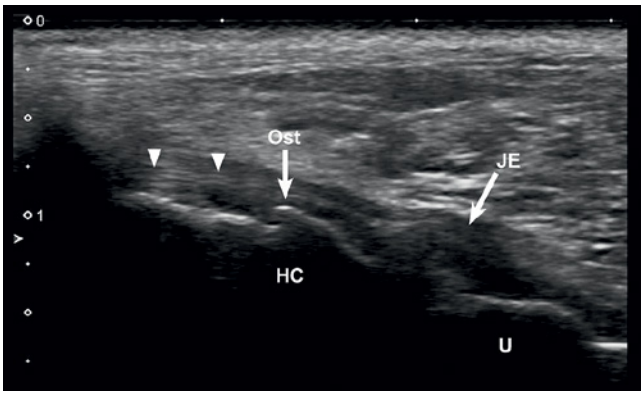


Figure 17.20. Elbow osteoarthritis. Longitudinal sonogram of the medial aspect of the elbow of a 16-month-old dog with elbow pain. Proximal is on the left, distal on the right. An osteophyte (Ost) projects on the medial aspect of the humeral condyle (HC) and moderate joint effusion (JE) is present. Fragmentation of the coronoid process was confirmed arthroscopically. U, ulna.

Fragmented Medial Coronoid Process (FMCP)

Sonographic detection of the FMCP in dogs is limited, for several reasons (Seyrek-Intas et al. 2009). Fissures and nondisplaced or deep fragments are difficult to visualize, and displaced fragments may be confused for an abnormally shaped MCP due to DJD. A completely detached coronoid bone fragment can sometimes be identified as an angular hyperechoic structure with acoustic shadowing, cranial or medial to its anatomically correct position (Figure 17.21). Performing a **dynamic examination** with mild flexion, extension, pronation and supination of the joint may help in identifying the fragment, which should move independently to the underlying bone (Seyrek-Intas et al. 2009).

Ununited Anconeal Process (UNAP)

Although UNAP is usually well recognized on a flexed lateral radiograph, it can be recognized on ultrasound as an interruption of the hyperechoic outline of the protuberance (Figure 17.22). In some cases, movement of the fragment can be demonstrated with a dynamic sonogram.

Osteochondritis Dissecans (OCD)

Osteochondrosis or OCD (its consequence), which typically affects the medial articular portion of the humeral condyle, is difficult to assess sonographically because of the localization of the defect, but displaced fragments may become visible.

Primary Flexor Enthesopathy

Calcification of the carpal and digital flexor muscles, which originate on the medial humeral epicondyle may relate to avulsion fracture or fragmentation, or to muscular degeneration and osseous metaplasia, a condition now referred to as primary flexor enthesopathy (Figures 17.23–17.25). This condition is commonly associated with different forms of **elbow dysplasia** (de Bakker et al. 2013; Van Ryssen et al. 2012). In affected dogs, there is irregular margination of the medial humeral epicondyle, sometimes with distinct calcified bodies inside the flexor tendons that are thickened, heterogeneous, and typically hypoechoic with loss of normal fibrillar pattern. Outward bowing of the flexor muscles is another common finding.

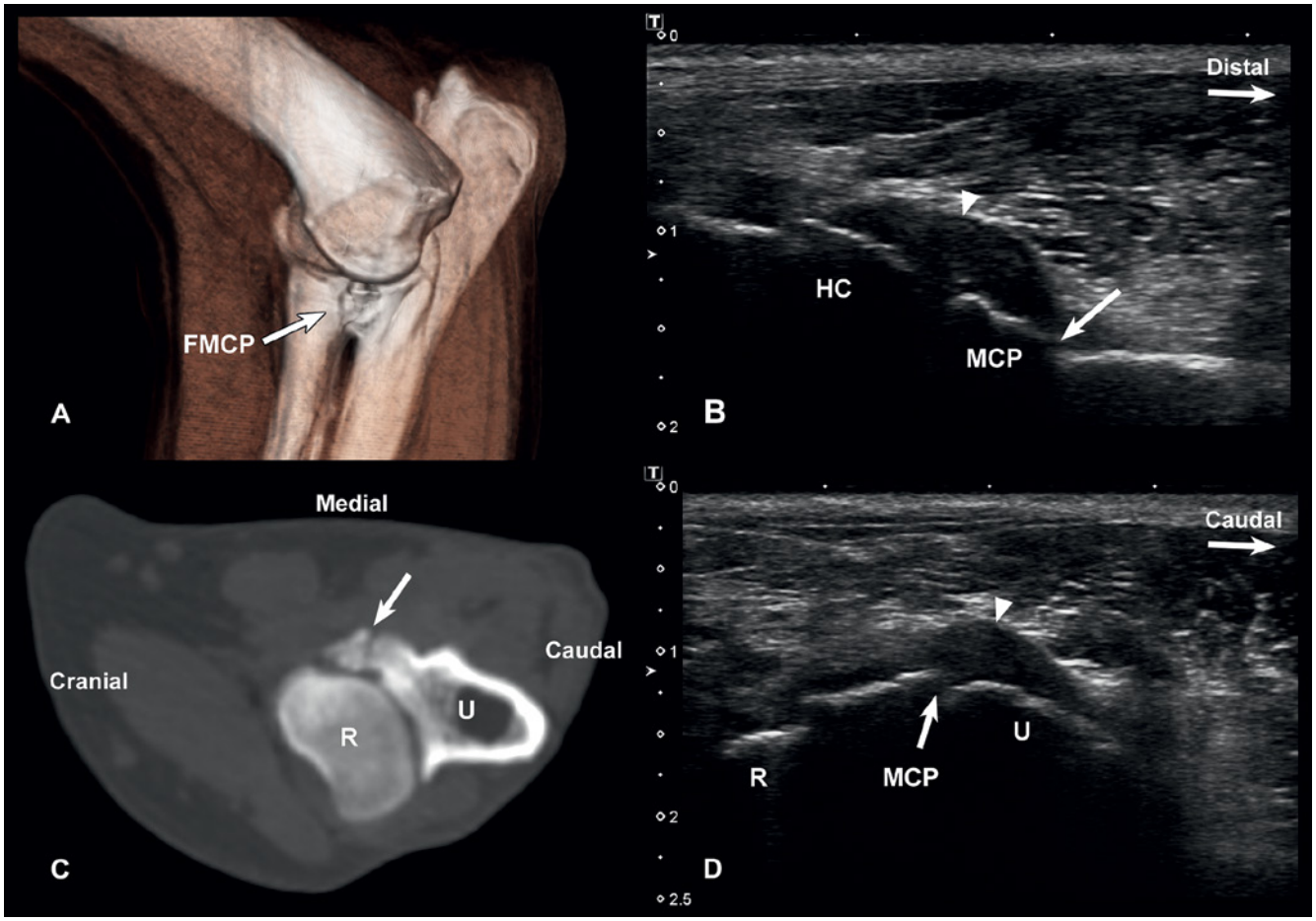


Figure 17.21. **Fragmentation of the medial coronoid process. (A)** Medial view of the elbow of a 12-month-old Labrador Retriever dog produced with computed tomographic (CT) volume-rendering, on which the fragmentation of the medial coronoid process (FMCP) is well visualized. **(B)** This longitudinal sonographic image was obtained with the probe placed medially on the joint, and the marker oriented proximally. The joint capsule is distended (arrowhead) and a gap (arrow) is present at the distal aspect of the medial coronoid process (MCP). The humeral condyle (HC) is mildly irregular. **(C, D)** Corresponding transverse CT **(C)** and sonographic **(D)** images in which a fissure (arrows) extends through the MCP. The joint capsule is distended (arrowhead). R, radial head; U, ulna.

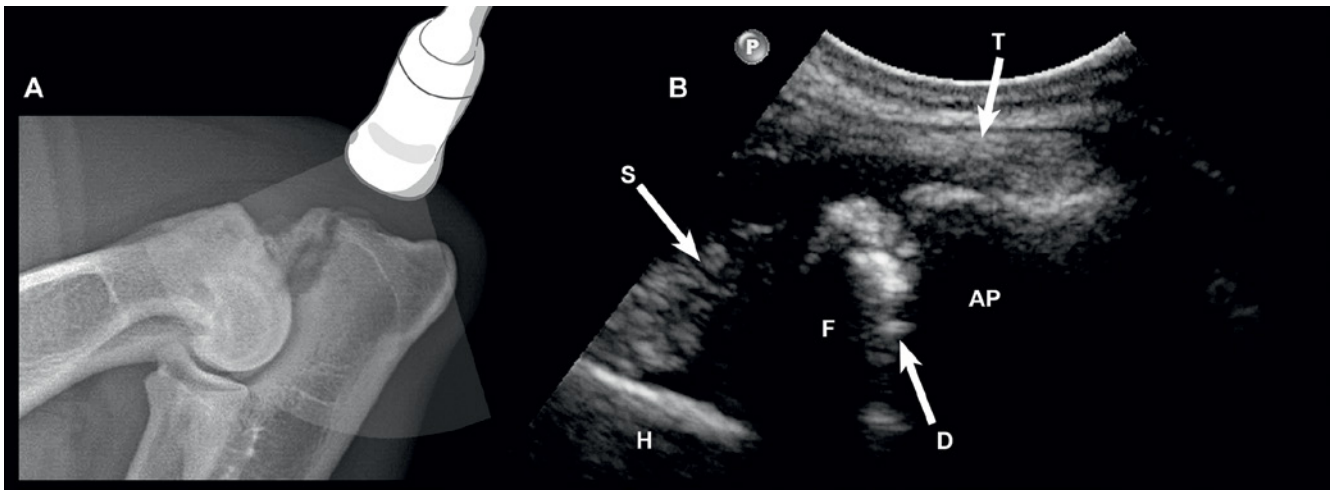


Figure 17.22. **Ununited anconeal process.** Lateral radiograph **(A)** and the corresponding sonographic image **(B)** that was obtained with the probe placed longitudinally on the triceps tendon (T). A defect (D) is present in the anconeal process (AP), leaving a fragment (F) that is displaced cranially. Synovial proliferation (S) consistent with synovitis is present cranially. H, humerus.

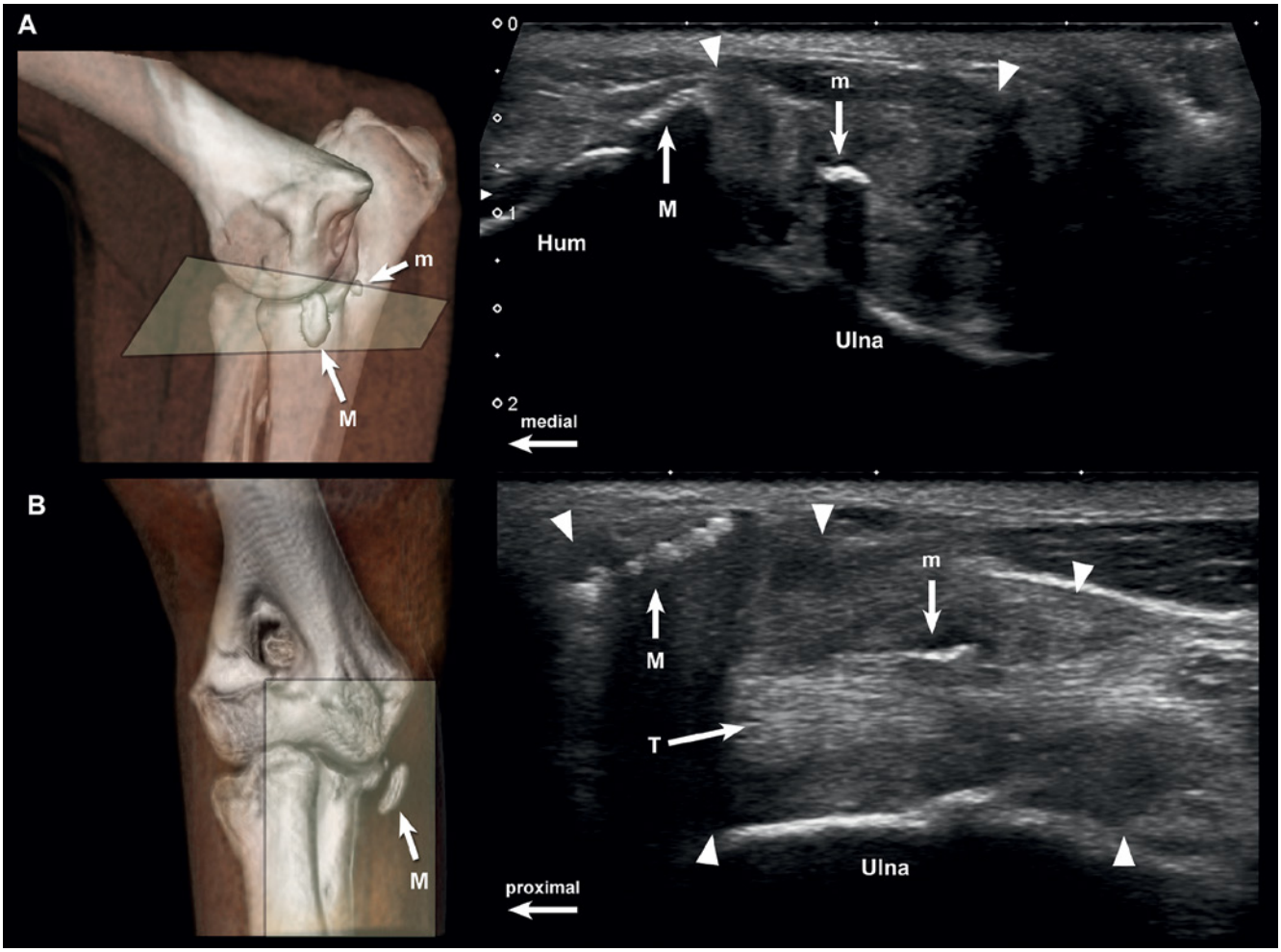


Figure 17.23. **Primary flexor enthesopathy in a dog.** (for full caption, see facing page)

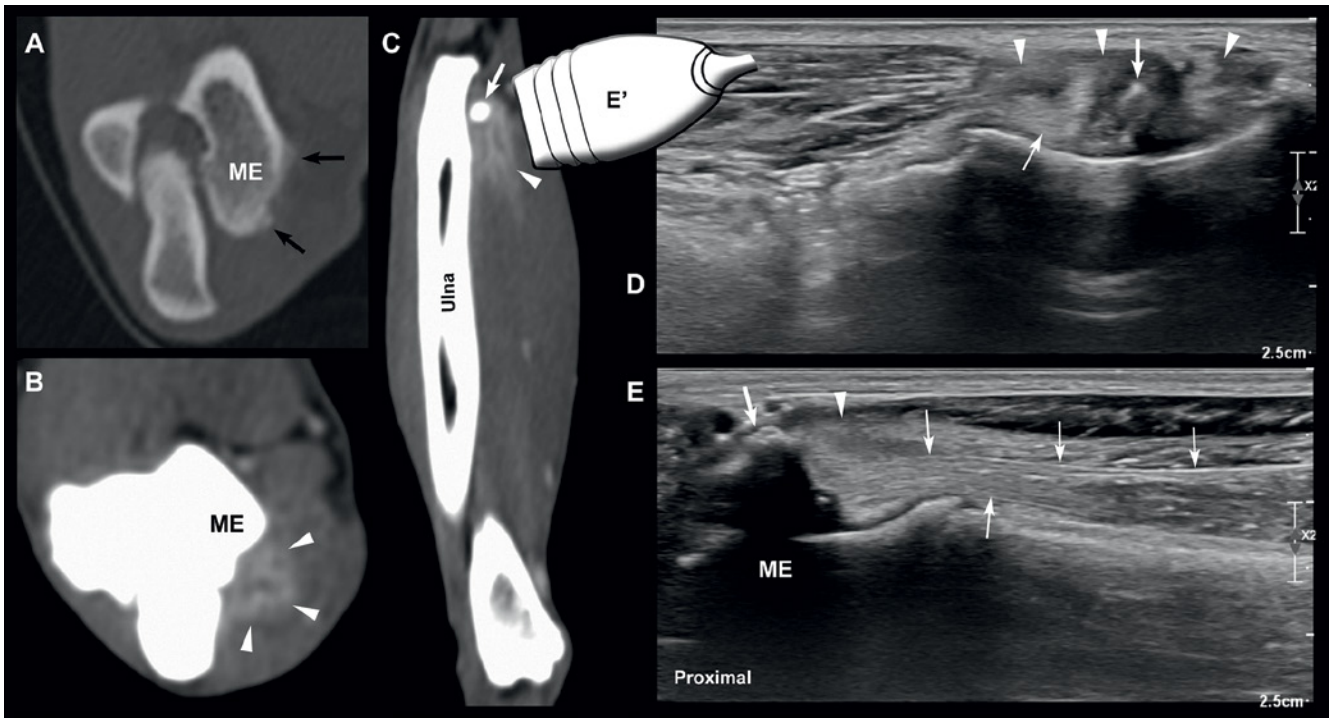


Figure 17.24. **Primary flexor enthesopathy in a second dog.** (for full caption, see facing page)

Figure 17.23. Primary flexor enthesopathy in a dog. Medial **(A)** and dorsal **(B)** views of the elbow of a 14-month-old Golden Retriever dog produced with computed tomographic (CT) volume rendering, with the overlying transverse and longitudinal planes used to produce the sonographic images on the right (respectively). Large (M) and small (m) mineral fragments are depicted in all images. These mineral bodies are embedded in a heterogeneous mass of moderate echogenicity (arrowheads), consistent with fibrous and metaplastic soft tissue, in part confluent with some of the flexor tendons (T). Note the stronger acoustic enhancement associated with the larger mineral bodies. Hum, humerus.

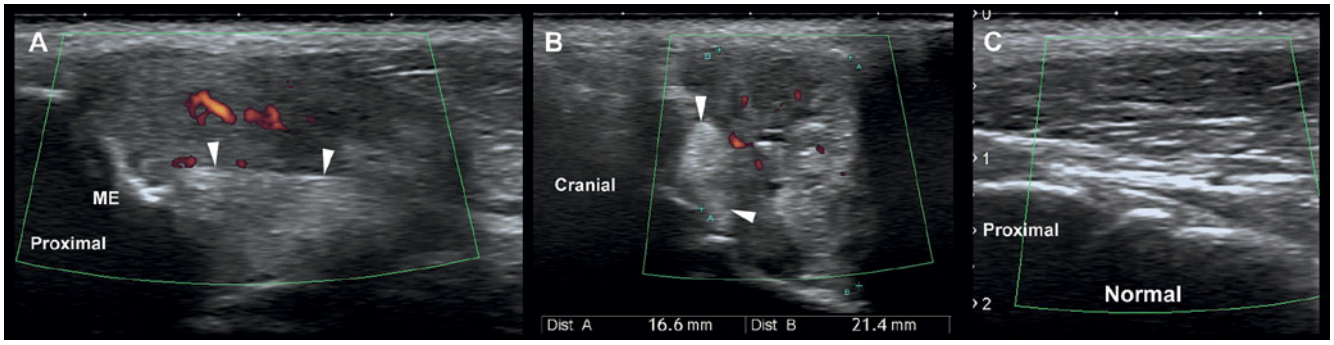


Figure 17.25. Primary flexor enthesopathy in a third dog. Longitudinal **(A)** and transverse **(B)** sonographic images obtained at the medial aspect of the left elbow, just distal to the humeral medial epicondyle (ME), on which a markedly heterogeneous, vascularized tissue surrounds one of the flexor tendons that is thickened (arrowheads). **(C)** By comparison, the flexor tendons had normal echotexture on the right side, which was clinically normal.

Hygroma

In large, heavy dogs, the olecranon bursa, which is located under the insertion of the triceps muscle, can become distended and/or inflamed. The bursa can be filled with variable fluid (blood, pus, or some other) of variable echogenicity. The capsule is hyperechoic and can be thickened (Figure 17.26).



Figure 17.26. Hemorrhagic hygroma. The olecranon bursa is markedly distended and filled with an anechoic fluid consistent with hygroma (Hy). Additionally, a large inhomogeneous structure is found in the distended bursa, which is indicative of a chronic hematoma (He).

Carpus

Scanning Technique and Normal Sonographic Anatomy

The normal ultrasonographic appearance of the dorsal superficially located and main palmar structures of the carpus was described in dogs of more than 20 kg with a high-frequency linear transducer (González-Rellán et al. 2021, 2023).

Figure 17.24. Primary flexor enthesopathy in a second dog. (A–C) CT images of the elbow of a five-year-old Staffforshire Bull terrier, in transverse bone **(A)**, and postcontrast in transverse **(B)** and dorsal **(C)** soft-tissue reconstructions. An irregular and ill-defined new bone formation is present on the medial humeral epicondyle (ME) (black arrows) and the adjacent soft tissues are thickened and associated with increased, heterogeneous enhancement (arrowheads), and dystrophic mineralization (white arrow). **(D, E)** Ultrasound using transverse **(D)** and longitudinal (**E**, at E′ probe placement) confirmed the presence of heterogeneous soft thickening (arrowheads) in the region of the flexor tendons (thin arrows), with several mineral bodies (wider arrows).

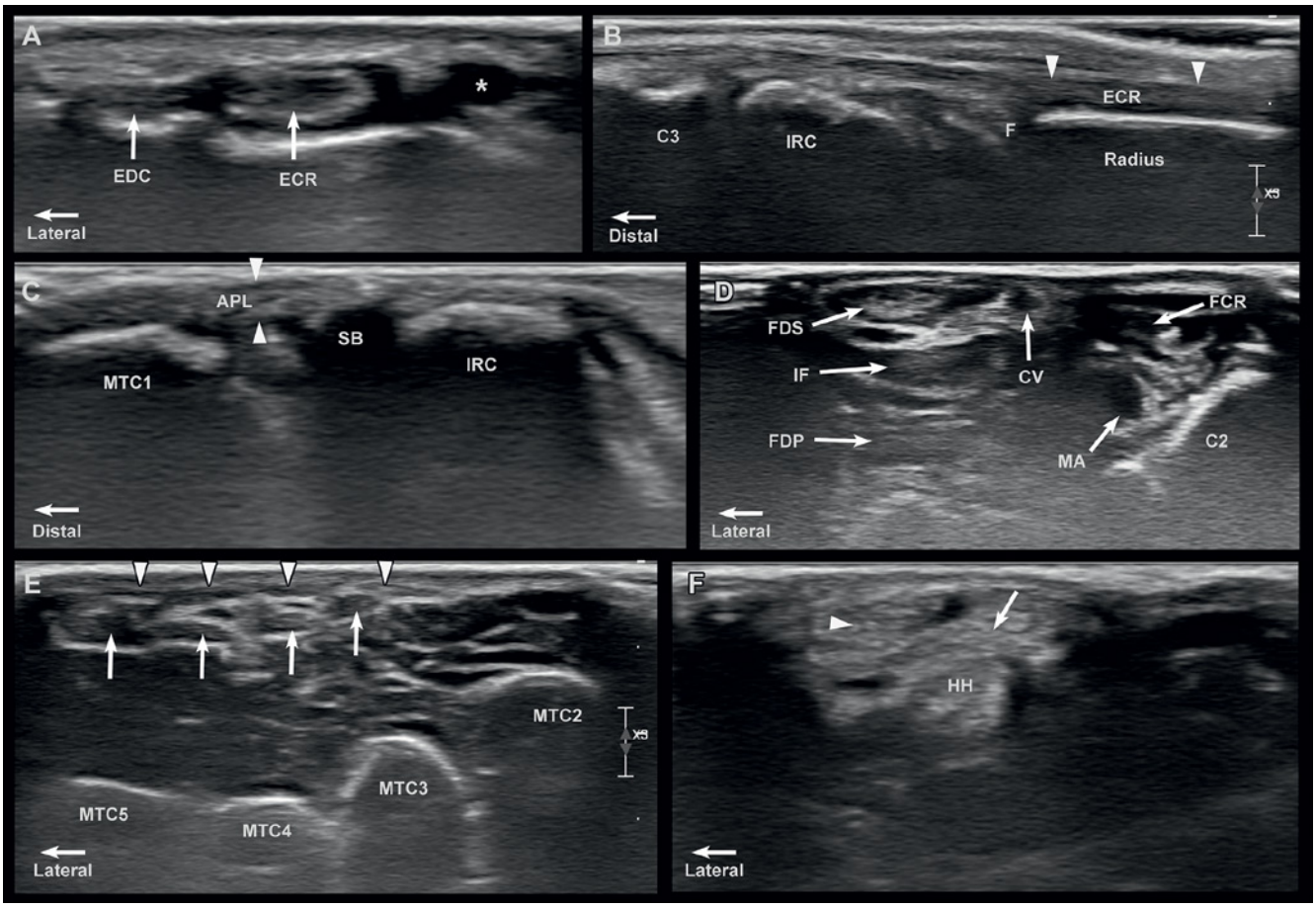


Figure 17.27. Normal carpus. (A) Transverse image at the dorsodistal aspect of the radius. EDC, extensor digitorum communis tendon; ECR, extensor carpi radialis tendon; radial artery (*). **(B)** Longitudinal image dorsal to the carpus. ECR, extensor carpi radialis tendon (arrowheads); F, intra-articular fat pad; IRC, intermedioradial carpal bone; C3, third carpal bone. **(C)** Longitudinal image dorsomedial to the carpus. APL, tendon of the abductor pollicis longus muscle; S, sesamoid bone; MTC1, first metacarpal bone. **(D)** Transverse image palmar to the carpus and distal to the accessory carpal bone, at the level of the intercarpal joint. C2, second carpal bone; CV, cephalic vein; FCR; tendon of the flexor carpi radialis muscle; FDP, tendon of the flexor digitorum profundus; FDS; tendon of the flexor digitorum superficialis muscle; IF, tendon of the interflexorius muscle; MA, median artery; RF, retinaculum flexorum. **(E)** Transverse image at the palmaroproximal metacarpal bones (MTC2 to MTC5), showing the divisions of the tendon of the flexor digitorum superficialis muscle (arrowheads) and of the flexor digitorum superficialis muscle (arrows). **(F)** Transverse image of the flexor carpi ulnaris tendon proximal to the accessory carpal bone, showing the ulnar head and its tendon (white arrowhead) and the humeral head (HH) and its tendon (arrow).

By positioning the probe in a transverse plane in the dorsomedial area of the carpus, over the distal aspect of the radius, the tendon of the ***abductor pollicis longus* (APL) muscle** is superimposed over the tendon of the ***extensor carpi radialis* (ECR) muscle** (Figure 17.27). The APL tendon can be followed distomedially through the medial sulcus of the radius that appears as a U-shaped hyperechogenic line and its sesamoid bone can be seen as a hyperechoic reflective line. The terminal part of this tendon presents a synovial sheath that appears as a thin hyperechoic layer separated from the tendon by a thin hypoechoic to anechoic band. The adjacent **medial carpal collateral ligament** is described as a hypoechoic fibrillar band demarcated by a thin hyperechogenic line between the radial styloid process and the medial part of the intermedioradial carpal bone. The two tendons composing the **ECR tendon** (***extensor carpi radialis longus***, medial, and ***extensor carpi radialis brevis***, lateral) can be differentiated and followed distally along the carpus to their insertion on the base of the second and third metacarpal bones, respectively. A fat pad is visible deep to these tendons. A slight carpal flexion may improve their examination. The tendon of the ***extensor digitorum communis*** is

examined laterally to the ECR tendon in the transverse plane. It begins to diverge over the fourth carpal bone and the tendons split completely at the carpometacarpal joint toward their respective digits (second to fifth). The dorsal **radiocarpal ligament** is examined by placing the transducer over the distal part of the lateral radial sulcus and maximal flexion of the carpus may improve its examination. It appears as a wide and slightly hypoechoic fibrillar structure, demarcated by a prominent hyperechoic line. The tendon of the ***extensor carpi ulnaris*** (ECU) **muscle** is visualized over the dorsolateral aspect of the ulna and carpus. Finally, the **lateral carpal collateral ligament** is seen as a thin hypo-echoic band in the longitudinal plane between the ulna and ulnocarpal bone.

The examination of the palmar region can be started with the evaluation of the tendon of the ***flexor carpi radialis*** **muscle**, located at the most medial aspect. The tendon of the ***flexor digitorum superficialis*** **(FDS) muscle** is seen deep to the ***retinaculum flexorum*** **(RF)** a thin subcutaneous hypoechoic band. The deep part of the RF limits palmarly the carpal canal that is limited dorsally by the common palmar ligament. The **carpal canal** contains the tendon of the *flexor digitorum profundus* muscle, the *interflexorius* muscle, and the median nerve, artery, and vein. The tendons of both flexor digitorum muscles flatten at the level of the metacarpal bones and split into five small tendons that follow their respective digits. The ***flexor carpi ulnaris*** is localized at the lateral aspect of the antebrachium laterally to the FDS tendon and can be followed to its insertion on the accessory carpal bone.

Tenosynovitis of the Abductor Pollicis Longus (APL) Tendon

Ultrasound may be considered if carpal disease is suspected showing tendinous, peritendinous, synovial, and bony changes. In cases of **stenosing tenosynovitis of the APL tendon** in dogs, the synovial sheath is thicker and hyperechoic with fluid accumulation (Hittmair et al. 2012) (Figure 17.28).

Hips and Iliopsoas Muscles

Scanning Technique and Normal Sonographic Anatomy

Animals are placed in lateral or dorsal recumbency depending on the region of interest. A high-resolution (>8–10 MHz) linear transducer is recommended.

The lateral and medial portions of the coxofemoral joint are assessed with the dog in lateral recumbency and its affected limb on top, and in dorsal recumbency with the affected hip placed in a frog position, respectively. The **femoral head** appears as a convex hyperechoic interface with acoustic shadowing. The shadowing caused by the femoral head represents a significant limiting factor in assessing the coxofemoral joint space and acetabulum (Greshake and Ackerman 1992). The **articular cartilage** appears as a smooth hypoechoic layer around the femoral head (Figure 17.29). The **joint capsule** appears as a hyperechoic line at the periphery of the head and is connected to the acetabular margins. Hips can be evaluated in puppies that are up to 7–8 weeks of age (Greshake and Ackerman 1992). The cartilage is thick at that time, and the subchondral bone is partially mineralized and irregular. In mature dogs, the shadowing bony structures hamper complete assessment of these joints.

Iliopsoas muscles and tendons are examined in dorsal recumbency using longitudinal and transverse planes (Cannon and Puchalski, 2008). The psoas major muscle originates from the transverse process of L3 and is visualized in longitudinal planes extending caudally as hypoechoic muscle interspersed with obliquely oriented hyperechoic, linear fibers (Figure 17.30A). The mid-body is then identified in longitudinal orientation using the vertebral bodies of **L4–L7** as landmarks, which lie dorsal to this large hypoechoic muscle that shows linear hyperechoic fibers oriented parallel to its long axis. Joining by the iliacus muscle, the formed iliopsoas tendon inserts on the **lesser trochanter**, which is recognized as a small, focal protrusion from the medial surface of the proximal femur (Figure 17.30B). The inserting tendon appears as a fusiform structure with concentric hyperechoic linear fibers.

Iliopsoas Myopathies

Iliopsoas myopathies may be underdiagnosed in practice. **Strain injuries** typically lead to muscle swelling associated with hypoechoic areas in the acute phase. **Fibrosing and calcifying iliopsoas myopathies**, which may or may not be traumatic in origin, are occasionally seen in lame or clinically normal dogs, also modifying the muscle and tendon normal size, echotexture, and echogenicity (Figure 17.30C, D). Mineralization appears as hyperechoic, irregular structures displaying acoustic shadowing.

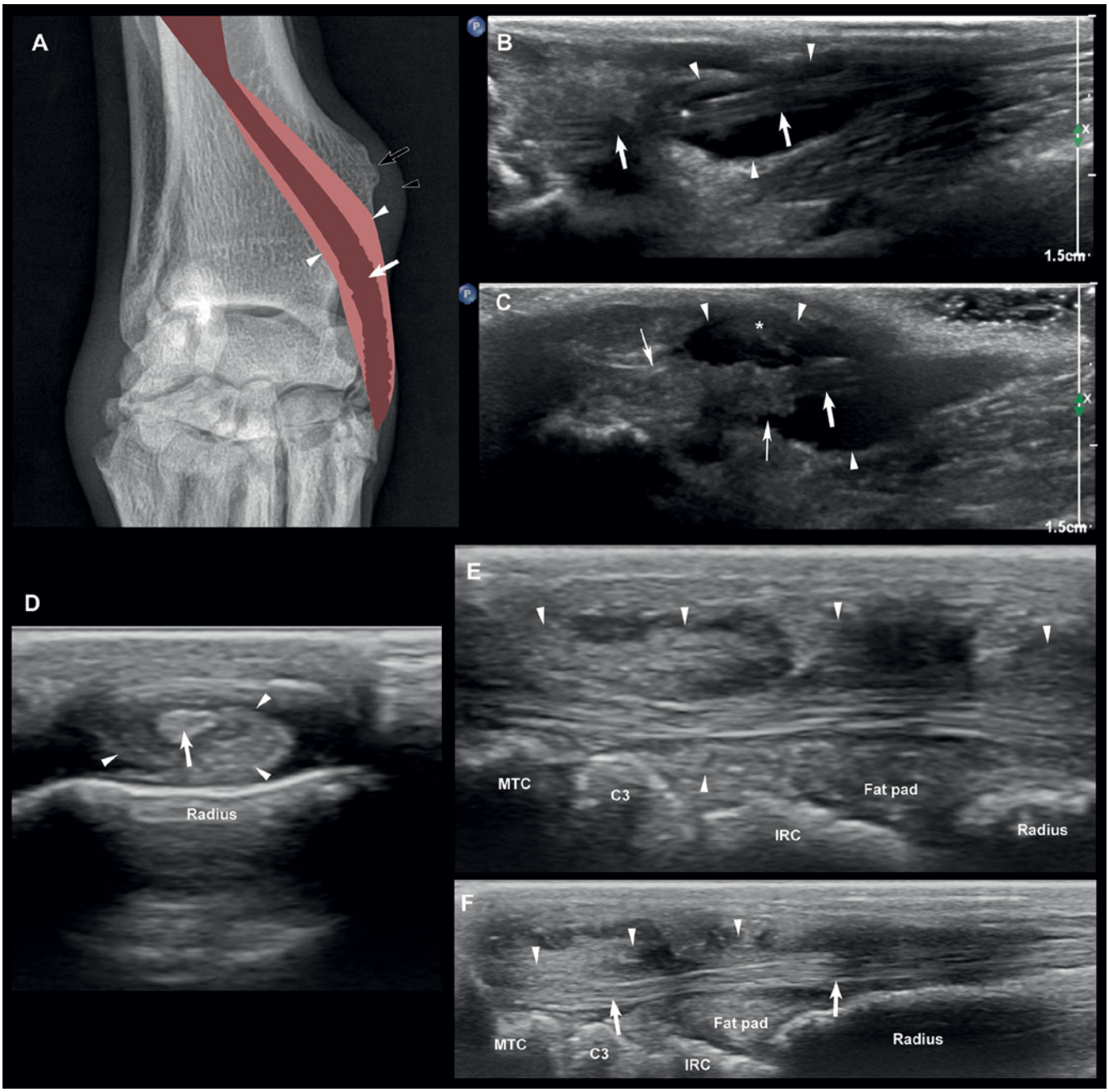


Figure 17.28. **Abductor pollicis longus stenosing tenosynovitis. (A)** Dorsopalmar radiograph of the left carpus of a nine-year-old Border Collie dog presented with chronic lameness. There is moderate new bone formation at the level of the radial groove (black arrow) with adjacent soft-tissue thickening (black arrowhead). The abductor pollicis longus (white arrow) and its sheath (white arrowheads) are illustrated. **(B, C)** Longitudinal sonographic images of the tendon (wide arrows) and sheath (arrowheads) acquired at the level of the radial groove (B) and medial carpus (C). There is marked distension of the tendon sheath (arrowheads) with synovial thickening (*). The distal portion of the tendon is moderately thickened with irregular margins (thin arrows) and loss of the normal fibrillar pattern. With ultrasound guidance, Triamcinolone and Mepivicaine were injected into the tendon sheath, resulting in marked clinical improvement. **(D–F) Granulomatous tenosynovitis of the extensor carpi radialis muscle**. On these transverse (**D**) and longitudinal (**E, F**) images obtained dorsal to the distal radius (**D**) and carpus (**E, F**), there is nodular thickening and heterogeneity of the synovial sheath (arrowheads) surrounding a mildly heterogeneous tendon (arrows). The periarticular osseous margins are irregular indicating arthrosis. C3, 3rd carpal bone; IRC, intermedioradial carpal bone; MTC, metacarpal bone.

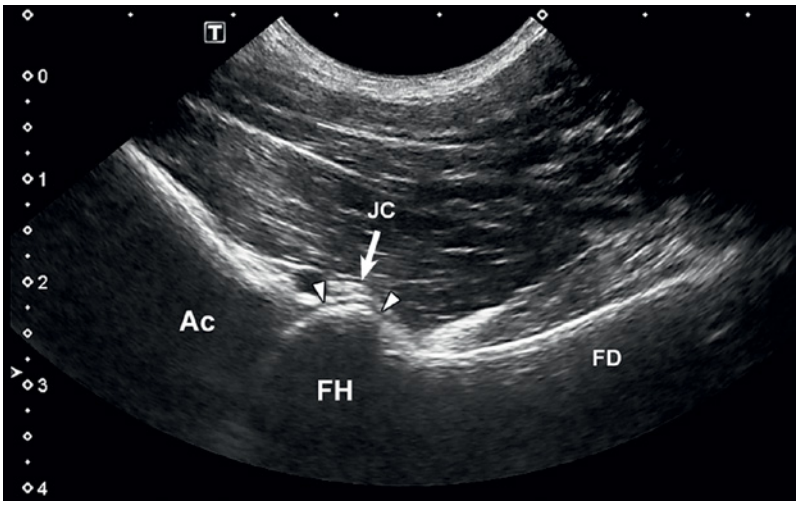


Figure 17.29. Normal hip. Ventral sonographic approach to the coxofemoral joint with the dog placed in dorsal recumbency. The joint capsule (JC) is hyperechoic and covers the synovial fluid and cartilage, which form a thin hypoechoic layer (arrowheads) covering the femoral head (FH) in this normal boxer. Ac, acetabulum; FD, femoral diaphysis.

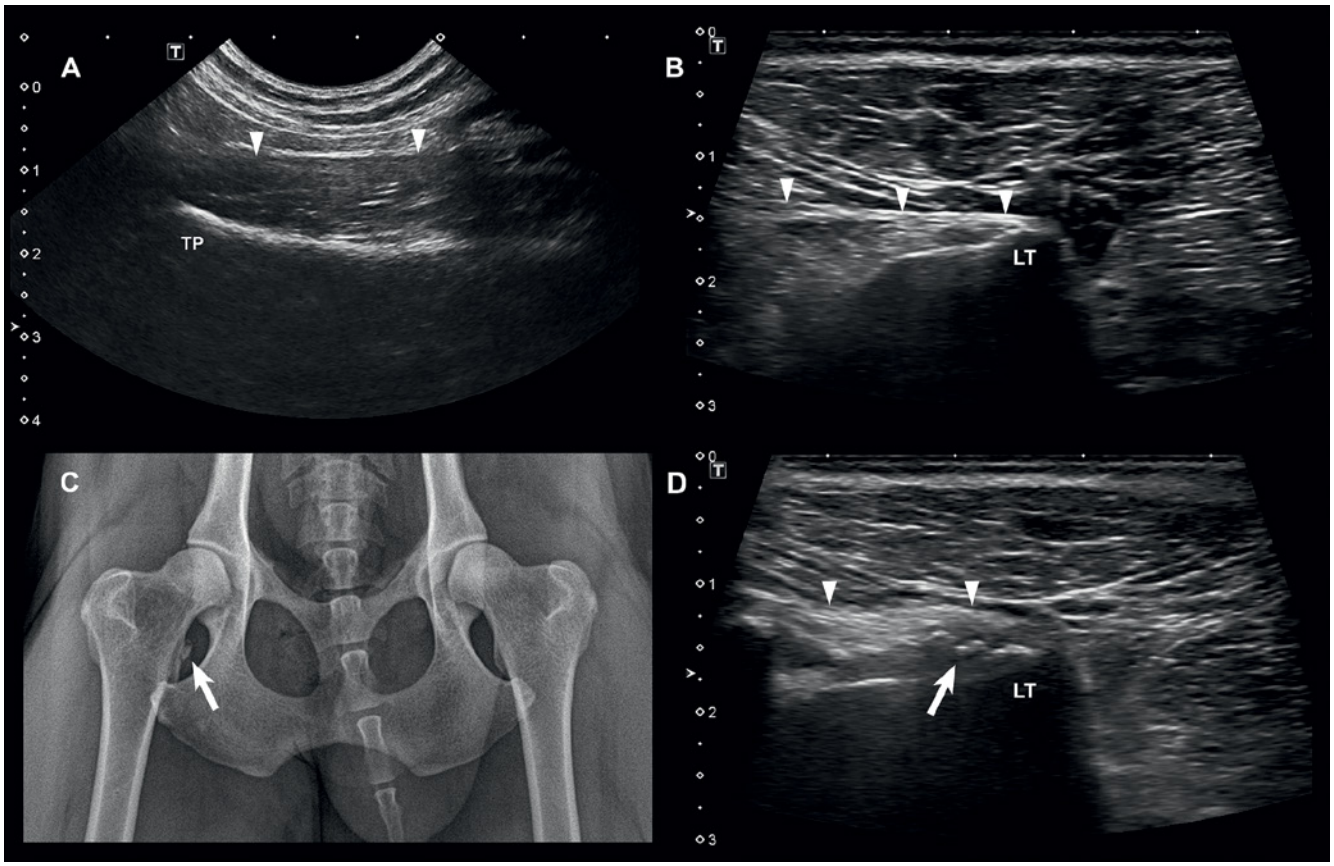


Figure 17.30. Normal and pathologic iliopsoas tendons. Longitudinal sonograms of the origin **(A)** and insertion **(B)** portions of the iliopsoas muscle and tendon in a normal Labrador Retriever dog. The muscular portion (arrowheads in **A**) is more hypoechoic, whereas the insertion tendon (arrowheads in B) has a characteristic hyperechoic fibrillar pattern as it inserts on the lesser trochanter (LT). **(C, D)** Ventrodorsal radiograph **(C)** and longitudinal sonogram **(D)** of another dog with partial avulsion of the iliopsoas tendon from the lesser trochanter (LT). Note the mineral fragments (arrows) and the change in shape and echotexture of the tendon (arrowheads) when compared to **(B)**.

Hip Dysplasia and Osteoarthritis

The use of ultrasound in the diagnosis of hip dysplasia has been investigated in young puppies. Although dynamic measurements may predict the onset of osteoarthritis in some dogs, such as Labrador Retriever–Golden Retriever mix puppies (Adams et al. 2000), it appears unreliable for early detection of hip dysplasia in puppies that are 16–49 days old (Fischer et al. 2010). Joint effusion and capsular thickening related to secondary osteoarthritis have the same sonographic appearance as described for other joints (Figure 17.31).

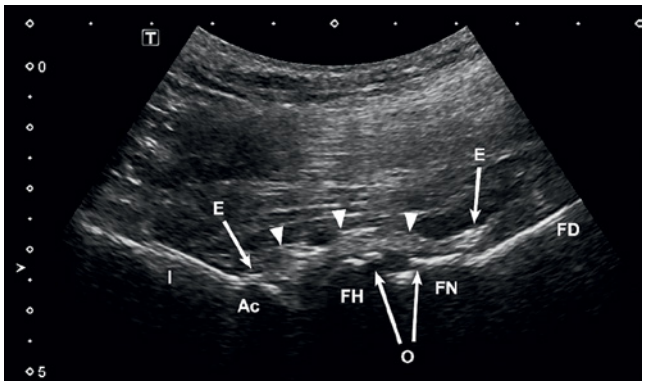


Figure 17.31. Hip joint osteoarthritis. In this sonographic image obtained from a ventral parasagittal approach, the coxofemoral joint capsule is thickened and hyperechoic (arrowheads) and associated with enthesophytes (E) at its insertion sites on the acetabular rim (Ac) and femoral neck (FN). The femoral head (FH) and neck are deformed by osteophytes (O). FD, femoral diaphysis; I, ilium.

Stifle

Scanning Technique and Normal Sonographic Anatomy

A high-frequency linear transducer (>12 MHz) is usually preferred for assessing all structures of the stifle. The hair must be clipped from the distal third of the femur to just below the tibial tuberosity. Initially, the dog is placed in lateral recumbency with the affected limb up (Figure 17.32A, B). The final dynamic examination requires flexion and extension of the joint as well as inward and outward rotation of the stifle in the area of the menisci (Kramer et al. 1999).

The stifle joint is examined from proximally to distally. After scanning the cranial, caudal, and lateral aspects of the joint, the dog is turned over so that the affected limb faces downward, allowing assessment of the medial region (Figure 17.32C). The stifle can be divided into five regions: suprapatellar, infrapatellar, lateral, caudal, and medial (Kramer et al. 1999). As opposed to human knees, the caudal approach provides low visibility of intra-articular structures in dogs and is therefore not used routinely.

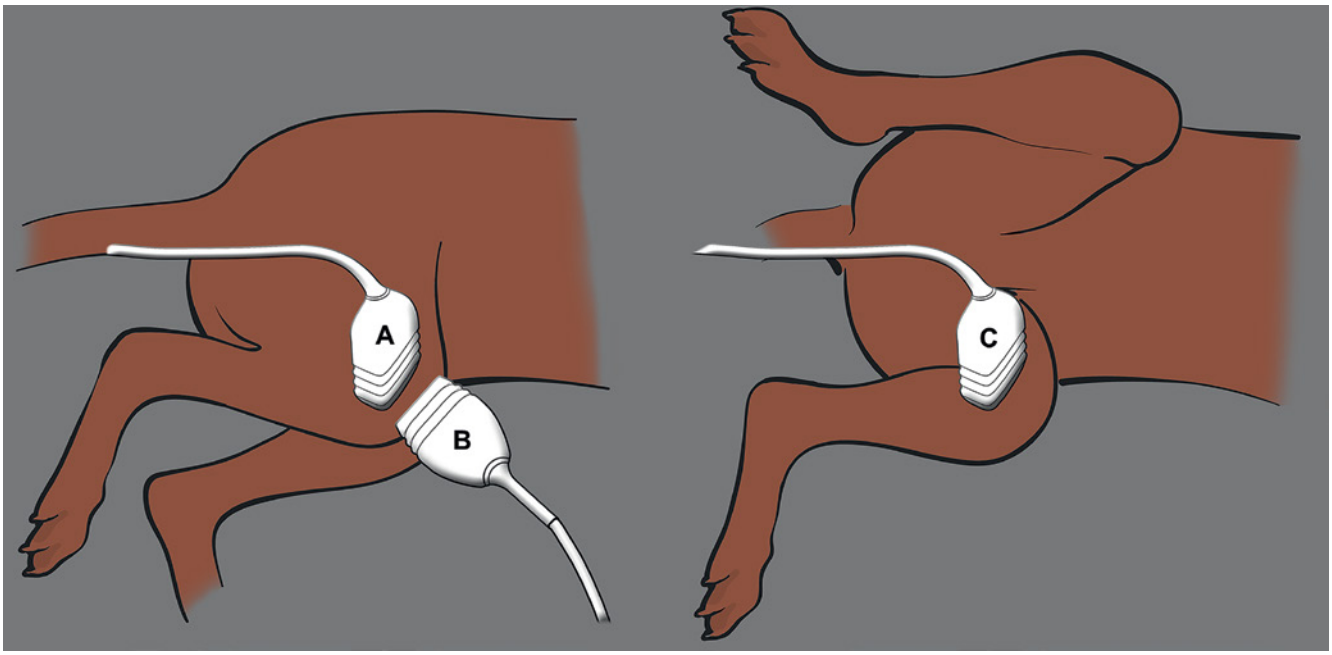


Figure 17.32. Scanning technique for the stifle. The positions of the dog and ultrasound probe when using longitudinal planes to scan the lateral **(A)**, cranial **(B)**, and medial **(C)** aspects of the stifle. Longitudinal and transverse planes must be used in all regions.

Suprapatellar Region: Quadriceps Tendon, Femoral Trochlea, and Proximal Joint Recess

The suprapatellar region, as its name indicates, includes the region proximal to the patella. The stifle flexed to 45°, longitudinal and transverse scans are used to focus on the distal femur, the **patella**, the **joint capsule**, the **suprapatellar recess**, and the **quadriceps femoris** muscle and tendon (Figure 17.32B). The hyperechoic convex surface of the patella can be used as a landmark. The suprapatellar indentation of the femoropatellar joint sac directly proximal to the patella is of particular interest. In a normal stifle, the **suprapatellar recess** is a 1- to 2-mm-thick (or smaller), anechoic, more or less inhomogeneous structure located on the cranial border of the hyperechoic distal femoral cortex (Figure 17.33A). The distal tendon of the quadriceps femoris muscle and

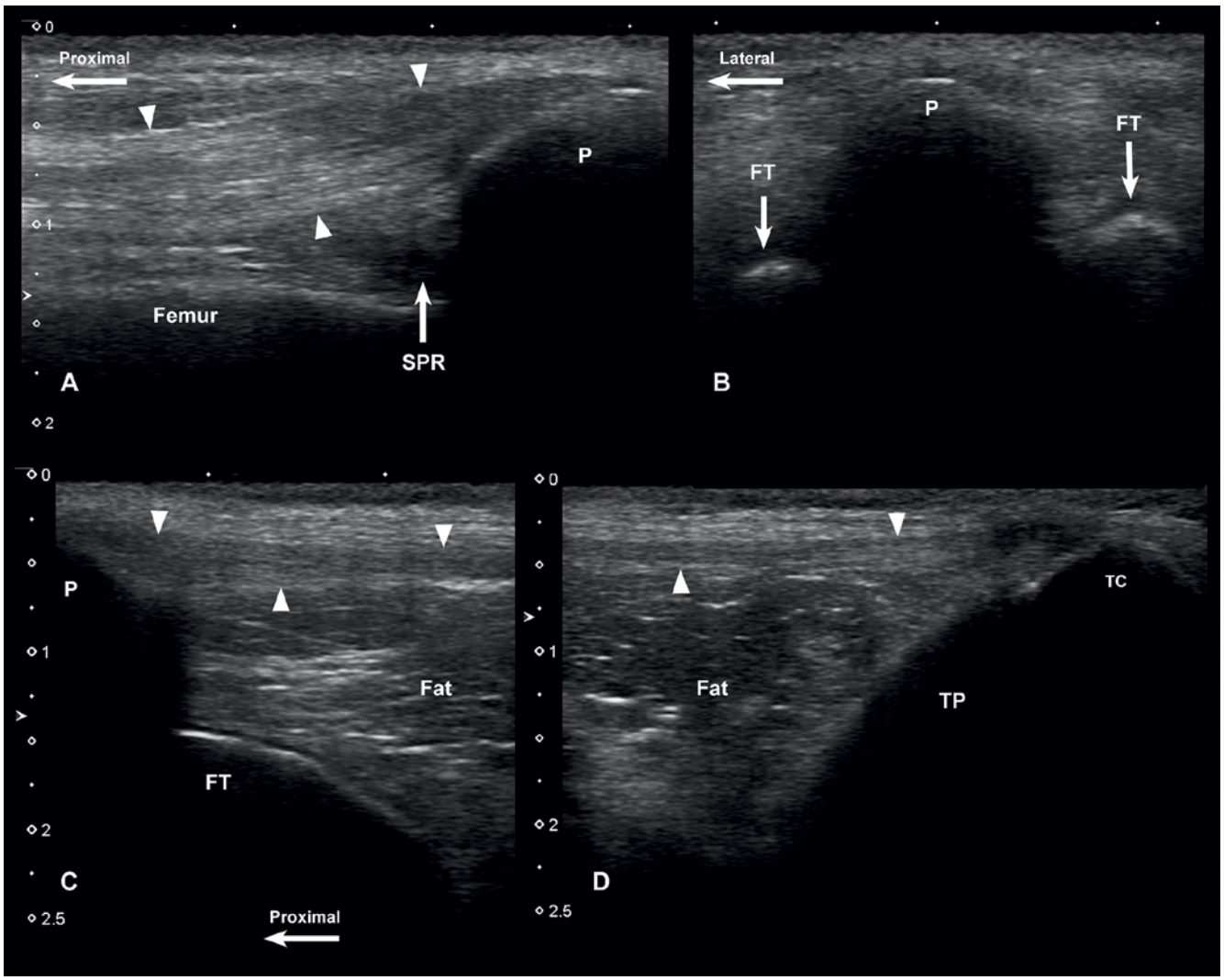


Figure 17.33. **Sonographic evaluation of the cranial aspect of the canine stifle (A) Normal suprapatellar region.** Longitudinal sonogram of the suprapatellar region. The suprapatellar recess (SPR) is seen as a small hypoechoic focus at the proximal aspect of the femoral trochlea, just proximal to the patella (P) and underneath the tendon of insertion of the quadriceps muscle (arrowheads). Only the convex, hyperechoic surface of the patella can be seen. This structure limits the visualization of the femoral trochlea. **(B) Normal patellar region**. Transverse sonogram of the patella (P) and of the medial and lateral ridges of femoral trochlea (FT) in a normal dog. The osseous portion of the ridge appears as a smooth, convex, hyperechoic line and is covered by a thin hypoechoic band that represents the cartilage and synovial fluid. These latter components cannot be distinguished. **(C, D) Normal infrapatellar region.** Longitudinal sonographic images obtained of the proximal **(C)** and distal **(D)** portions of the infrapatellar region of a normal dog. The patellar ligament (arrowheads) appears as a moderately echogenic, linear band connecting the patella (P) and the tibial crest (TC). The infrapatellar fat pad located caudal to the patellar ligament is relatively hypoechoic and granular in echotexture. Small vessels located within this fat body appear as hyperechoic dots and lines. A thin hypoechoic band (arrowheads) consistent with cartilage and synovial fluid is noted on the surface of the femoral trochlea (FT). It is too thin to be visualized on the tibial plateau (TP) of this dog.

the femoral trochlea, and covering cartilage, become clearly visible by means of a dynamic scan. The **articular cartilage** is a 1- to 2-mm-thick anechoic band located directly above the curvilinear, hyperechoic subchondral surface of the femoral trochlea. The depth and surface continuity of this cartilage can be partially examined (Figure 17.33B). The area above the patella can be easily evaluated in a transverse scan with the stifle maximally flexed. This position enables the assessment of the cartilage as well as the shape and depth of the **femoral trochlea**. At this point, a **dynamic examination** (flexion and extension) enables the assessment of the sliding movement of the patella into the trochlear groove.

Infrapatellar Region: Patella and Patellar Ligament, Femoral Condyles, Infrapatellar Fat Body, and Cruciate Ligaments

Because of the convexity of the **femoral condyles**, only a few areas of the joint surface can be assessed. Multiple imaging planes of each condyle are necessary. When the stifle is extended, the patella slides proximally on the trochlea, and the medial and lateral femoral condyles can be more fully examined. The joint cartilage is anechoic and smoothly marginated (Figure 17.33B, C), measuring 0.6–1.1 mm thick (Reed et al. 1995).

As the stifle is 90° flexed, the transducer is moved over the **patellar ligament** and **patella** (Figure 17.33B). The patella, which appears as a hyperechoic, convex line with strong acoustic shadowing, is partially embedded in the patellar ligament, which presents a characteristic hyperechoic band with a fibrillar echotexture (Figure 17.33C, D). A thin, echogenic, periligamentous sheath is also seen (Mattern et al. 2006). The distal margin of the patellar ligament appears slightly thicker and the insertion site is less echogenic than the rest of the structure. When viewed transversely, the curved margins of the ligament are not visible because of edge-shadowing artifacts.

Beneath the patellar ligament, the **infrapatellar fat body** is a triangular, poorly demarcated structure of moderate echogenicity and granular echotexture, located cranial to the joint space (Figure 17.33C, D). Within this infrapatellar fat body, vessels are often visible as hyperechoic thin, double-lined, tubular structures with an anechoic center. With the stifle still flexed, lateral rotation of the transducer by 20° enables visualization of the hypoechoic to anechoic cranial cruciate ligament, which extends from the cranial margin of the tibia to the region between the femoral condyles. The **caudal cruciate ligament** is difficult to visualize because of its orientation and limited space between the condyles (Arnault et al. 2009). It may be observed as a more or less ovoid hypoechoic structure when using a small footprint convex transducer on a maximally extended stifle. Differentiation between the infrapatellar fat body and the meniscus is usually not possible from a cranial approach (Kramer et al. 1999; Reed et al. 1995).

Lateral and Medial Aspects: Collateral Ligaments, Menisci, Joint Capsule, Synovium, and Other Structures

Each **fabella** appears as a convex hyperechoic structure caudoproximal to the stifle joint. When a longitudinal plane is used, the lateral and medial heads of the **gastrocnemius muscle** come into view next to the caudolateral and caudomedial outline of the condyle and the fabella, respectively. The muscle is identified by the presence of the fabella (or lateral sesamoid bone) within its tendon. The transverse parts of the biceps femoris muscle and the superficial digital extensor tendon run across the tibia on the lateral side.

By means of a longitudinal plane centered on the lateral joint space (Figure 17.34A), the **lateral femoral** and **tibial condyles** are visualized proximally and distally, respectively. Static and dynamic sonograms are obtained with stifle flexion and extension as well as internal and external rotations. The **joint capsule**, the **collateral ligament**, and the **lateral meniscus** can all be assessed on a longitudinal plane (Figure 17.34B). The same assessment is repeated on the medial side of the joint (Figure 17.34C).

Each **meniscus** appears as a triangle structure of uniform, medium echogenicity located between the femoral condyle and the tibial plateau. The abaxial surface of the meniscus should be linear and perfectly aligned with the surface of the adjacent femoral and tibial condyles. Additionally, a fine hypoechoic line may be seen on the femoral and tibial surfaces of the meniscus, consistent with articular cartilage and synovial fluid (Mahn et al. 2005) (Figure 17.34B). When the collateral ligament is used as a landmark, three different regions can be examined: the cranial horn, the middle portion, and the caudal horn (Mahn et al. 2005). Only the peripheral portion of the meniscus can be seen due to the convexity of the femoral condyle.

With the probe placed in the longitudinal plane on the lateral side of the joint, the **long digital extensor tendon** can be identified (Figure 17.34B). It demonstrates a typical fibrillar echotexture and runs between the lateral meniscus and the joint capsule, cranial to the collateral ligament. The origin of the tendon can be traced across the joint to the extensor fossa, a focal

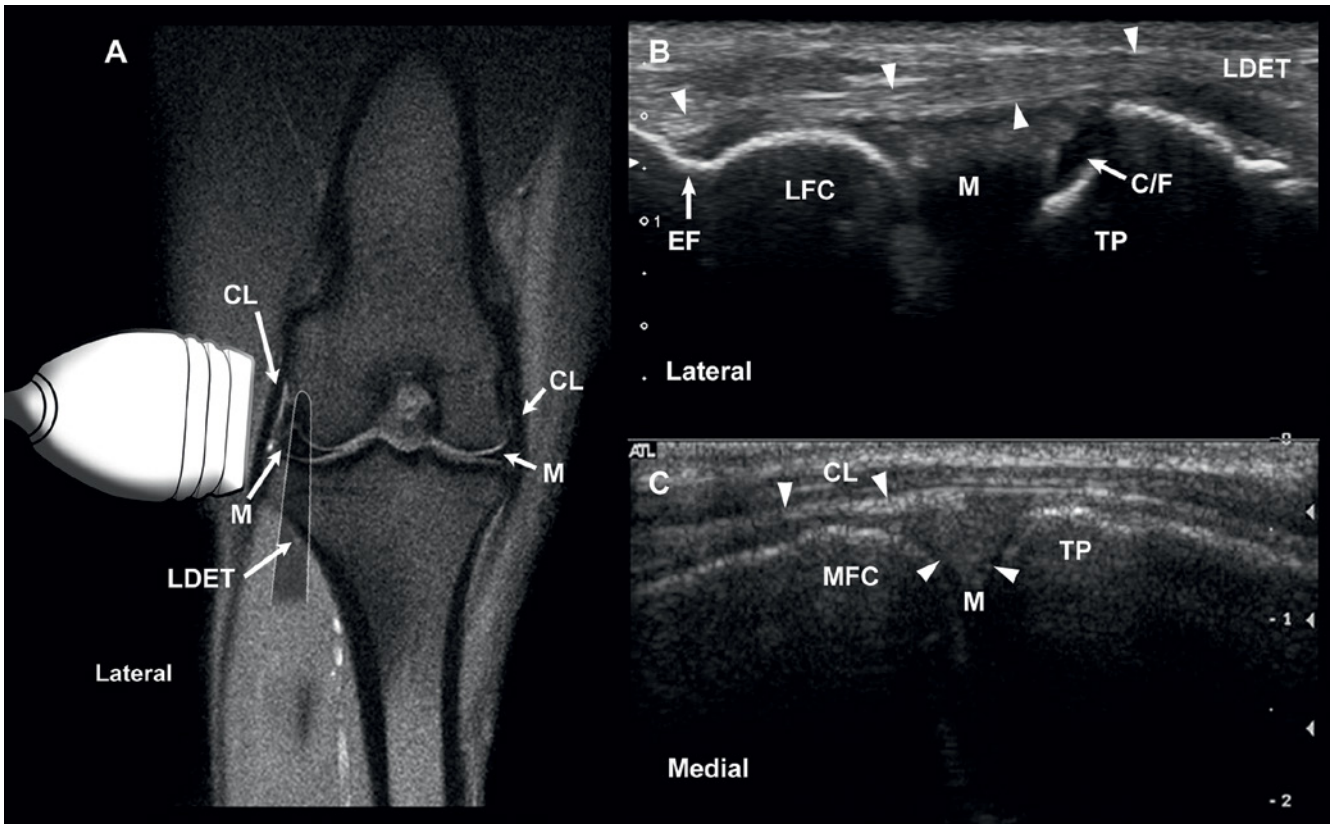


Figure 17.34. Lateral and medial aspects of the stifle: sonographic approach and normal anatomy. When scanned using a longitudinal plane **(A)**, the menisci appear as moderately echogenic, triangular structures (M) located between each femoral condyle and the opposite tibial plateau (TP). Thin hypoechoic layers consistent with articular cartilage and fluid (C/F) are observed on each side of the menisci. On the lateral side **(B)**, the long digital extensor tendon (LDET, arrowheads) can be identified just craniolateral to the lateral meniscus, as it inserts on its extensor fossa (EF). Collateral ligaments (CL) can also be seen crossing the medial and lateral aspects of the joint. The lateral CL is located just caudal to the LDET. Image **(B)** was obtained in a five-month-old Boxer and image **(C)** in an adult Labrador Retriever. LFC, lateral femoral condyle; MFC, medial femoral condyle.

depression in the craniolateral margin of the lateral femoral condyle. The tendon runs through the **tibialis cranialis muscle** and is surrounded by its sheath, formed by an indentation of the joint sac, but is not identified unless it is distended.

Sonographic Features of Stifle Disorders

Cranial Cruciate Ligament Rupture (CCLR)

The sensitivity of ultrasound to detect CCLR is limited, approaching 15% in a study on 13 dogs using a high-frequency linear probe (Arnault et al. 2009). While the ruptured ligament is difficult to recognize, especially in the acute phase, several signs may be present. First, joint effusion is typically observed and often extends proximally into the suprapatellar recess, forming an anechoic, tube-like structure surrounded by a hyperechoic line (joint capsule) (Figure 17.35A). Joint effusion also causes cranial displacement and compression of the infrapatellar fat body, which becomes outlined by the anechoic to hypoechoic fluid. This fat body often appears inhomogeneous and more echogenic (Figure 17.35B) and small cyst-like areas may be seen (Kramer et al. 1999). Distally, the distended synovial sheath that wraps around the tendon of the long digital extensor becomes clearly visible as an anechoic to hypoechoic tubular structure displacing the tibialis cranialis. CCLR is also typically associated with osteoarthritic periarticular new bone formations that develop at the contours of the patella, femoral trochlea ridges, condyles, and epicondyles as well as the tibial plateau (Arnault et al. 2009) (Figure 17.35C). In addition, the joint capsule appears as a thickened hyperechoic band, and redundant synovial thickening can be visualized, particularly if associated with significant joint effusion.

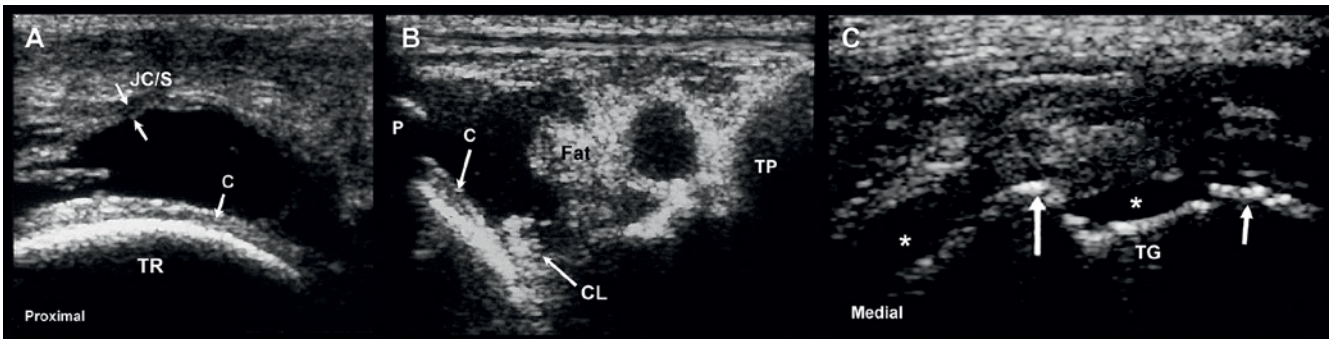


Figure 17.35. Stifle osteoarthritis in two dogs. (A, B) Longitudinal sonograms of the proximal joint recess (**A**) and infrapatellar region (**B**) in a dog with chronic stifle degenerative joint disease. Anechoic joint effusion is present, and the joint capsule and synovium (JC/S, arrows) are thickened. The cartilage (C) along the trochlea is hyperechoic and heterogeneous. The infrapatellar fat body is heterogeneous, and an irregular, hyperechoic structure is in the mid-portion of the joint, consistent with a degenerated and ruptured cranial cruciate ligament (CL). P, patella; TP, tibial plateau; TR, trochlear ridge. **(C)** Transverse sonographic image of the femoral trochlea in another dog with degenerative joint disease. The cranial surfaces of the trochlear ridges (arrows) are irregular because of osteophytosis. The proximal joint recesses at the medial aspect of the trochlea and over the trochlear groove (TG) are filled with anechoic fluid (*).

For direct assessment of the damaged cranial cruciate ligament, a cranial, longitudinal approach is used, and the stifle must be completely flexed, which may be difficult to accomplish in painful, unsedated dogs. In the region of the cranial cruciate ligament, an irregular, anechoic area (hematoma) can sometimes be identified (Gnudi and Bertoni 2001; Kramer et al. 1999). If the rupture has been present for a longer period (chronic rupture), the irregularly demarcated and hyperechoic stumps of the ligament may become evident, particularly at its insertion on the tibial plateau (Figure 17.36) (Kramer et al. 1999). The visibility of the cranial cruciate ligament is limited if a large volume of effusion is present, because this structure appears hypoechoic when scanned at an angle (Gnudi and Bertoni 2001; Kramer et al. 1999). Avulsion fragments may also be recognized as more or less shadowing hyperechoic foci in the central portion of the joint. Chronic ruptures are commonly associated with fibrous tissue proliferation in the region just cranial to the intercondylar groove, which appears as an irregular, hyperechoic structure (Gnudi and Bertoni 2001) (Figure 17.35B).

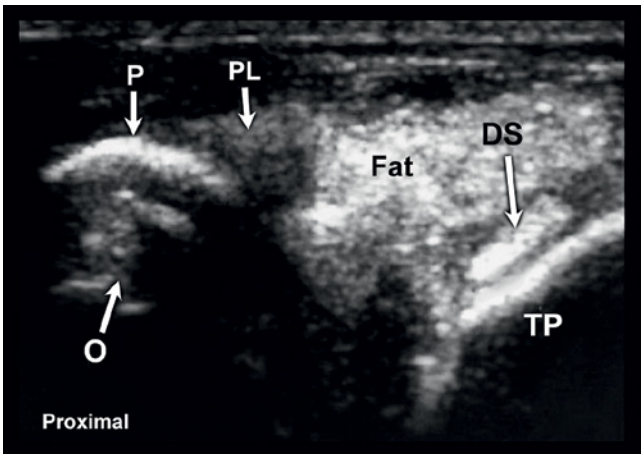


Figure 17.36. Cranial cruciate ligament rupture. Longitudinal sonographic image of the infrapatellar region in which the distal stump (DS) of the ruptured ligament appears as a hyperechoic band proximal to the tibial plateau (TP). O, osteophytosis over the femoral trochlea; P, patella; PL, patellar ligament.

Meniscal Tears and Degeneration

Meniscal tears and degenerative changes are more commonly observed medially and secondary to stifle instability caused by cranial cruciate rupture. The sensitivity and specificity of ultrasound for detecting meniscal lesions accompanying CCLR reach 82 and 93%, respectively (Arnault et al. 2009). Isolated meniscal damage is rare in dogs and may more commonly affect the lateral meniscus (Mahn et al. 2005). Most tears appear to present a bucket-handle configuration. However, because of the difficulty in visualizing the axial (internal) portion of the menisci, partial and complete tears can be difficult to visualize.

Affected menisci are typically inhomogeneous with hyperechoic and hypoechoic areas and show some abaxial displacement or bulging of their abaxial surface (Arnault et al. 2009) (Figure 17.37). A decrease in the visibility of a meniscus may indicate abnormal displacement due to rupture. A caudally or medially displaced medial meniscus is also usually indicative of rupture (Figure 17.38), although this phenomenon may be dynamic and not necessarily present during examination (Arnault et al. 2009). Joint effusion can be observed at the periphery of the affected meniscus. Ultrasonographic assessment of the

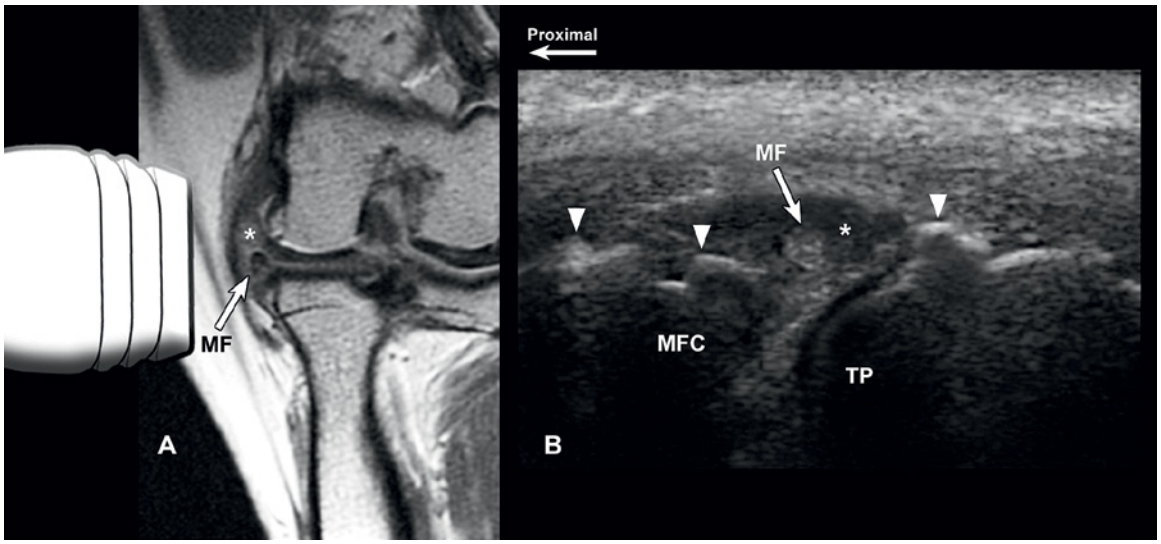


Figure 17.37. Meniscal tear and displacement. (A) In this dorsal magnetic resonance image of the stifle of a dog with cranial cruciate rupture, there is a meniscal fragment (MF) displaced medially and surrounded with synovial effusion and proliferation (*). **(B)** Placement of the ultrasound probe on the medial aspect of the joint (as in Figure 17.28C) allows good visualization of the meniscal fragment (MF), adjacent effusion and synovitis (*), and nearby osteophytosis (arrowheads). MFC, medial femoral condyle; TP, tibial plateau.

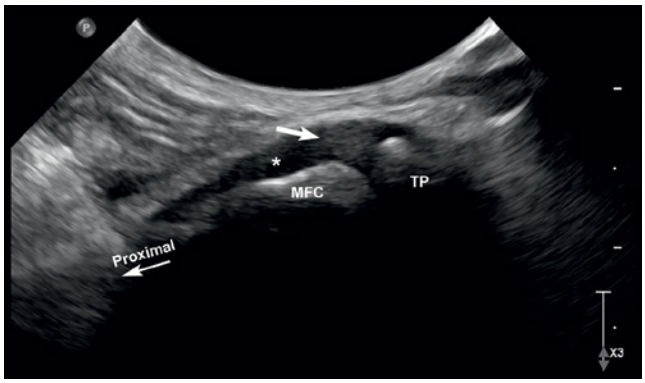


Figure 17.38. Meniscal luxation in a cat. There is medial displacement of the medial horn of the medial meniscus (arrow) with local synovial distension (*). MFC, medial femoral condyle; TP, tibial plateau.

menisci can be limited by several factors, including severe fibrosis of the soft tissues along the medial aspect of the joint, marked osteophytosis caused by severe DJD, and previous surgery (Mahn et al. 2005). The size of the dog may also represent a limiting factor because thinner menisci (small patients) or deeper menisci (very large or obese dogs) can be more difficult to visualize well.

Patellar Fractures and Desmopathies

A fracture of the patella is seen as an interruption of the outline of the smooth bone surface (Kramer et al. 1999) and is often associated with damage to the quadriceps tendon (proximally) or patellar ligament (distally).

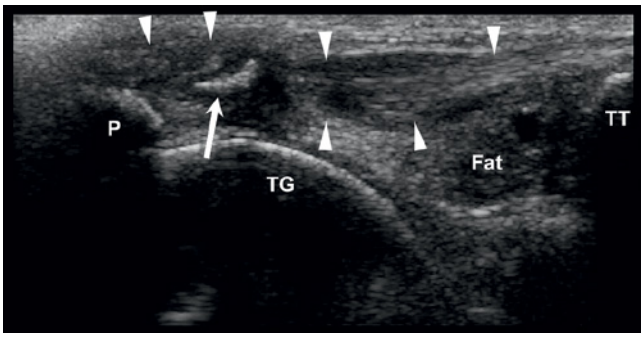


Figure 17.39. Avulsion fracture of the patella. Longitudinal sonographic image of the infrapatellar region in a dog with acute stifle pain and swelling. The patellar ligament (arrowheads) is irregularly thickened and heterogeneous. A hyperechoic, partially shadowing bony fragment (arrow) is just distal to the patella (P), consistent with fracture of the apex. The distal margin of the patella is abnormally flat, and the patella is displaced proximally. TG, trochlear groove; TT, tibial tuberosity.

Rupture of the patellar ligament can be partial or complete. In both cases, the ligament appears hypoechoic to hyperechoic, with irregular margins at the site of rupture. With **avulsion fracture**, small hyperechoic bone fragments are visible at the extremity of the ligament and are associated with acoustic shadowing if they are more than 2–3 mm wide (Figure 17.39). When a longitudinal plane is used, a separation of the ruptured ends can be observed as the stifle is flexed.

Patellar ligament thickening is also recognized following tibial plateau-leveling osteotomy (**TPLO**),

particularly in large dogs and particularly in its distal portion (Mattern et al. 2006). Postoperative changes noted at 1 month also include hypoechoic to anechoic central lesions with partially disrupted ligaments. These changes have been significantly linked to the degree of tibial plateau rotation during the procedure, supporting a role for increased stress in the development of patellar ligament desmitis (Mattern et al. 2006). Tibial tuberosity advancement (**TTA**) is also associated with ultrasonographically measurable thickening of the patellar ligament 6 weeks postoperatively (Kühn et al. 2011). However, these changes may be clinically insignificant in most dogs.

Avulsion fracture of the tibial tuberosity can also be visualized in the infrapatellar region. During a dynamic ultrasound exam, the acutely avulsed bony structure can move during flexion of the stifle, confirming the diagnosis. However, this motion can be limited, particularly if a fibrous callous is already present.

Collateral Ligament Rupture

In cases of severe and acute rupture of the medial or lateral collateral ligaments, a discontinuity of the affected ligament may be identified. Typically, hematomas are found at the level of the tear, seen as hypoechoic to anechoic, homogeneous to mildly inhomogeneous areas. When a longitudinal medial or lateral approach is used, a **dynamic examination** of the joint space while stressing its opening medially and laterally may confirm joint instability. Joint effusion rapidly develops and appears as bulging medial and/or lateral synovial recesses. Capsular tear may also be present, and fluid may have accumulated in the periarticular soft tissues.

Tendon Avulsion

In cases of avulsion fracture of the origin of the **long digital extensor tendon**, shadowing hyperechoic foci consistent with bone fragments can be found just distal to the level of the extensor fossa at the lateral femoral condyle (Kramer et al. 1999). **Popliteal tendon** avulsion can also be detected (Figure 17.40).

Osteochondritis Dissecans

Osteochondritis dissecans appears as an irregular defect on the contour of the subchondral bone, typically at the lateral condyle. The abnormal cartilage can vary in thickness and echogenicity but often appears hyperechoic and heterogeneous. Detached pieces of cartilage are seen as hyperechoic structures of variable size. Other free bodies may also be visible, and their location can be determined (Kramer et al. 1999) (Figure 17.41). Joint effusion is typically observed in association with OCD, and periarticular osteophytes develop in the chronic phase.

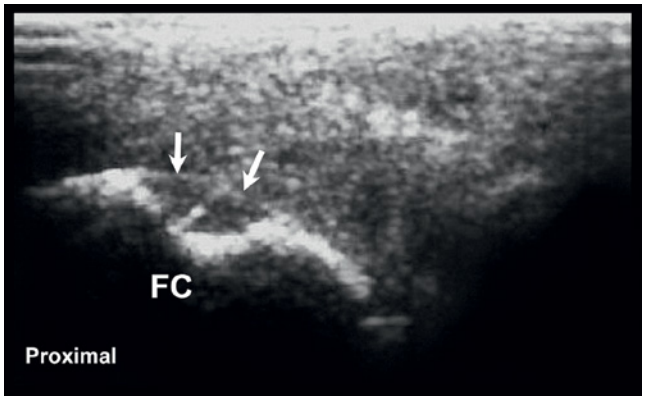


Figure 17.41. Osteochondritis dissecans. Longitudinal sonographic image of the lateral femoral condyle (FC) in a young dog. A concave defect (arrows) is filled with mildly echogenic and partially mineralized cartilage.

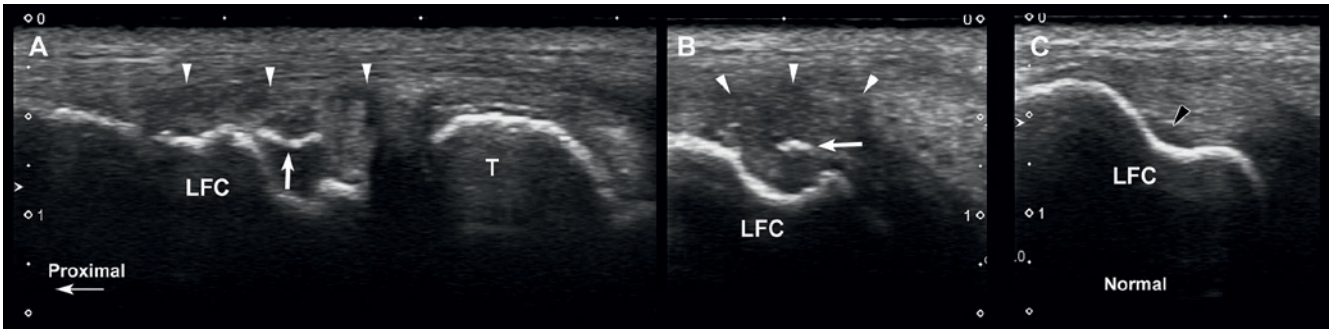


Figure 17.40. Popliteal tendon avulsion. Longitudinal oblique (**A**) and transverse (**B**) sonographic images of the caudolateral aspect of the stifle of a one-year-old Labrador retriever with a one-week history of acute lameness. There is irregular and heterogeneous soft-tissue thickening (arrowheads) at the caudolateral aspect of the lateral femoral condyle (LFC), which shows an irregular contour. A fragment (arrows) is also present. **(C)** The opposite tendon is well delineated at its origin (black arrowhead) on the lateral femoral condyle (LFC).

Tarsus

Scanning Technique and Normal Sonographic Anatomy

Several tarsal and periarticular soft-tissue structures can be assessed with ultrasound, especially in large dogs. Of these, the **calcaneal (Achilles) tendon**, **plantar** and **collateral ligaments**, and the **long and lateral digital extensor**, **tibialis cranialis**, and **deep digital flexor** muscles and tendons are of clinical interest.

The **calcaneal tendon** consists of all structures that attach to the calcaneal tuberosity. The **gastrocnemius** and the **superficial digital flexor (SDF) tendons** represent the two main components. Tendons of the **biceps femoris**, **semitendinosus**, and **gracilis** muscles form another **conjoined component**, also called the **common calcaneal (CC) tendon**. The medial and lateral gastrocnemius muscles fuse at their distal aspect, becoming one tendon that runs within the calcaneal tendon, lateral to the SDF tendon, and inserts on the calcaneal tuberosity. Distally, the SDF tendon becomes superficial to form a cap-like structure that contains the rest of the CC tendon and that inserts both laterally and medially on the tuberosity. This tendon is relatively thin at that level and may not be identified in small dogs (Caine et al. 2009). The CC tendon is the deepest portion of the calcaneal tendon and inserts on the dorsal aspect of the calcaneal tuberosity (Hermanson and Evans 1993).

Ultrasonography of the calcaneal tendon is performed in a standardized fashion: the tarsocrural joint is slightly flexed, stretching the tendon that can be more easily imaged (Figure 17.42). Initially, a longitudinal scan is performed by placing the probe over the calcaneal tuberosity at the tendon insertion. The transducer is then moved proximally to examine the whole structure as well as the musculotendinous junctions and muscles. Transverse views are then used to visualize individual portions of the tendon, from the level of their muscular origin to the level of the calcaneal tuberosity. Finally, a dynamic examination is performed (flexion and extension of the hock) (Kramer et al. 2001a; Lamb and Duvernois 2005). A longitudinal image directly above the tuber calcanei shows the surface of the calcaneus as a convex hyperechoic line with distal acoustic shadowing (Figure 17.42A). Immediately proximal to this bony protuberance, which serves as an important landmark, is a 5-mm × 5-mm, anechoic, ill-defined area representing the **calcaneal bursa** with its surrounding connective tissue (Figure 17.42A). The CC tendon is a moderately echogenic, homogeneous structure with parallel hyperechoic lines (fibrillar echotexture) inserting on the tuberosity (Figure 17.42A). The peritendineum is a smooth hyperechoic band at the periphery of the tendon. Further proximally, the muscles display their typical echotexture (see the section on musculature). On transverse images, the CC tendon is a moderately echogenic, round structure with multiple small hyperechoic dots, that inserts deeply on the dorsoproximal margin of the calcaneal tuberosity (Figure 17.42B, C). The peritendineum surrounding the tendon is visible as a hyperechoic line. However, the presence of edge shadowing prevents a clear visualization of its curved axial and abaxial borders (Kramer et al. 2001a; Lamb and Duvernois 2005; Rivers et al. 1997).

On the plantaromedial side of the tarsus, the **deep digital flexor (DDF) tendon** may also be recognized as it courses over the **sustentaculum tali**. It appears oval in transverse scan at the level of that bone, with typical fibrillar echotexture, before deviating centrally, on the medial aspect of the plantar ligament, which is larger and more echogenic than the DDF tendon, which becomes hypoechoic due to anisotropy artifact (Caine et al. 2009). Dorsal to the tarsus, the **long digital extensor tendon** can be found before it divides into four smaller tendons distally. It is closely associated with the **tibialis cranialis tendon**, which deviates medially at the distal tibia (Caine et al. 2009). Laterally, the closely associated lateral digital extensor tendon and peroneus longus tendons can be seen in large dogs, in part attached to the lateral tibial malleolus, and adjacent to the **lateral collateral ligaments**, which may not be distinctly visible (Caine et al. 2009). The **medial collateral ligament** may be identified in nearly half of large dogs (Caine et al. 2009).

Disorders of the Calcaneal Tendon

Partial and Complete Rupture and Healing Process

Injuries to the calcaneal tendon (Achilles tendon) are uncommon in small animals and are usually produced by direct trauma (Lamb and Duvernois 2005). In **complete rupture**, the echotexture of the CC tendon is completely interrupted, and a hypoechoic and inhomogeneous area (hematoma) is observed between the retracted ends of the tendon. The proximal and distal stumps of the tendon appear drumstick-like and inhomogeneous with a mixed echotexture. During **dynamic examination**, the movement of the ruptured ends is clearly visible.

With **partial tendon rupture**, the affected portion (deep or superficial) appears inhomogeneous and hypoechoic to anechoic with poorly demarcated areas (Figure 17.43). In contrast, the part of the tendon that is intact displays a normal fibrillar echotexture. Occasionally, a small anechoic fluid borderline is visible between the tendon and the peritendineum. In chronic

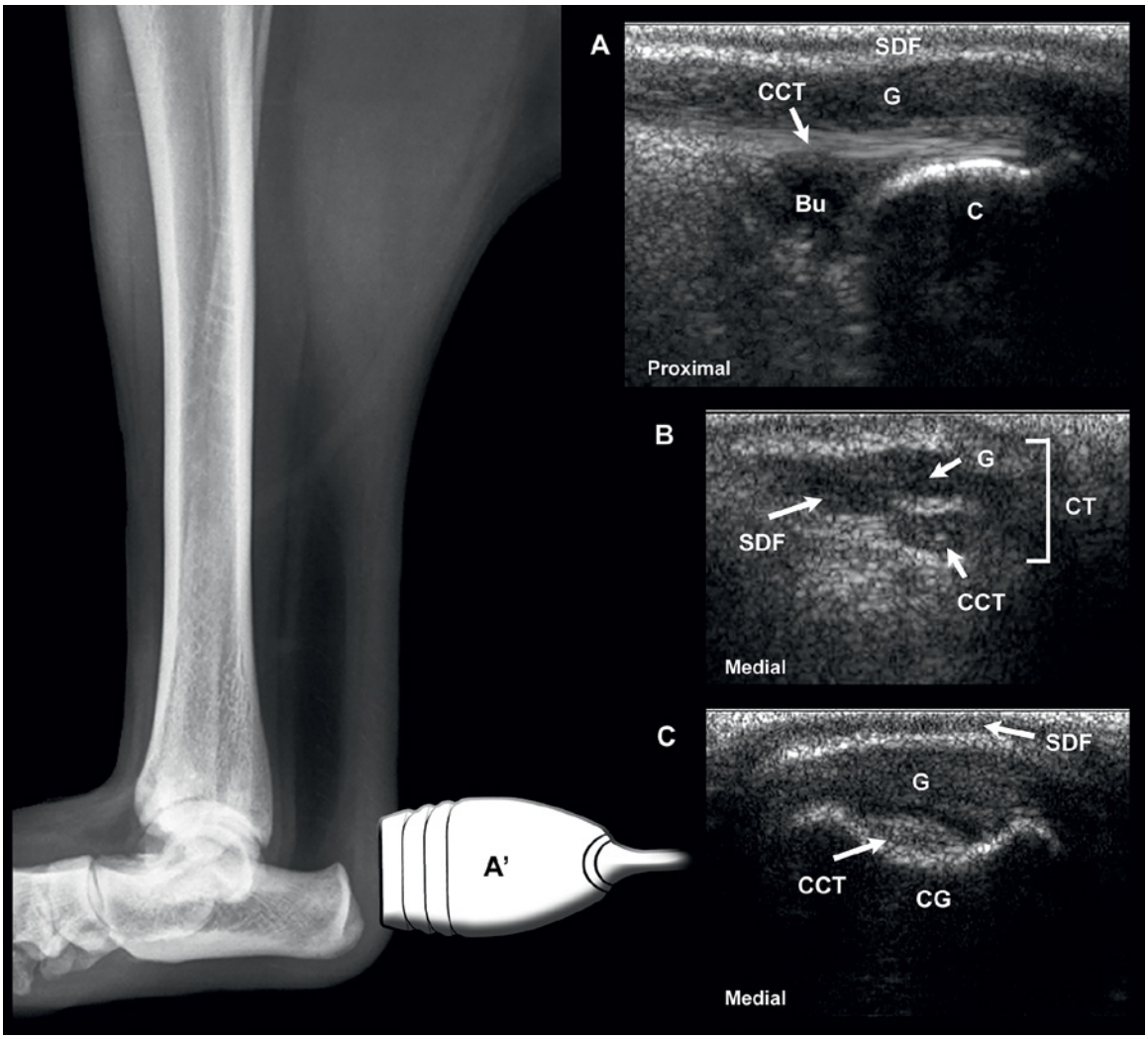


Figure 17.42. Normal sonographic anatomy of the calcaneal (Achilles) tendon. (for full caption, see facing page)

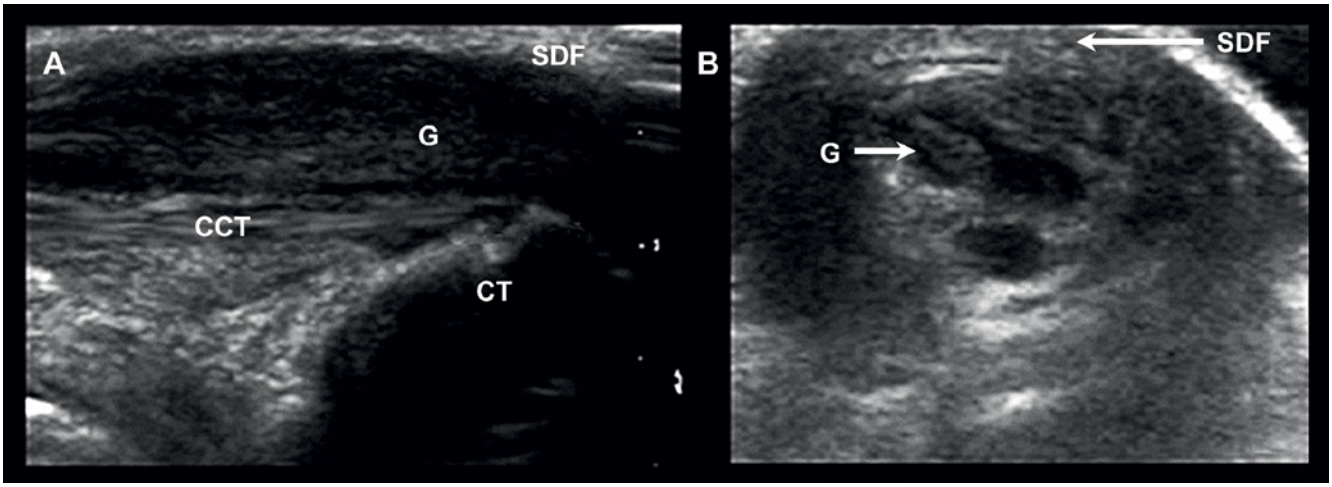


Figure 17.43. Partial rupture of the gastrocnemius tendon. Longitudinal **(A)** and transverse **(B)** sonograms of the calcaneal tendon in a dog with acute trauma. The gastrocnemius tendon (G) is markedly enlarged, and the superficial digital flexor tendon (SDF) is displaced caudally but appears intact. The common calcaneal tendon (CCT) is mildly inhomogeneous, which may also be because of partial rupture.

Figure 17.42. Normal sonographic anatomy of the calcaneal (Achilles) tendon. (A) Longitudinal sonogram corresponding to A' probe placement. The common calcaneal tendon (CCT), which is the deepest component of the calcaneal tendon, has a characteristic hyperechoic, linear echotexture when scanned perpendicularly. The other components of the calcaneal tendon, i.e., the gastrocnemius (G) and superficial digital flexor (SDF) tendons, are seen more superficially. The calcaneal bursa (Bu) appears as a small, triangular anechoic area just proximal to the calcaneal tuberosity. **(B, C)** Transverse sonogramsobtained at the mid-level **(B)** and distal level **(C)** of the calcaneal tendon (CT). The SDF lies medial to the gastrocnemius (G) through most of the calcaneal tendon, and caudal to the CCT. Distally, it becomes a cap-like structure around the calcaneal tuberosity and contains the G and CC tendons over the calcaneal groove (CG).

partial ruptures, images of the affected part of the tendon can vary from highly inhomogeneous to homogeneous and from hypoechoic to moderately hyperechoic (Figure 17.44). The surface of the calcaneal tuberosity may become irregular because of new bone formation. Avulsed fragments and/or dystrophic mineralization can be recognized within the affected tendon as dispersed hyperechoic foci, which can exhibit acoustic if large enough (Figure 17.44A) (Caine et al. 2009; Rivers et al. 1997; Swiderski et al. 2005).

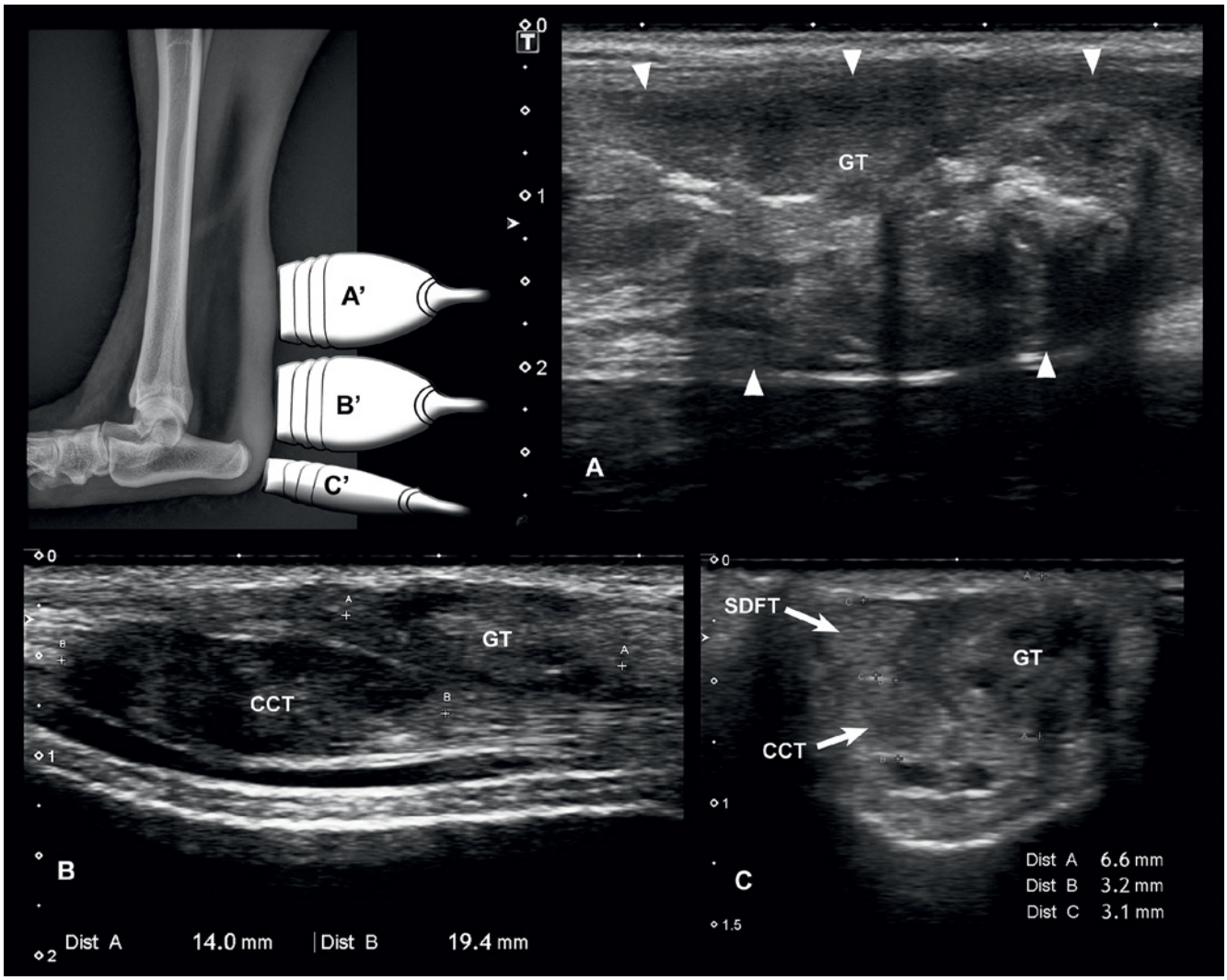


Figure 17.44. Chronic partial rupture of the calcaneal tendon. Longitudinal sonograms obtained at the mid- **(A)** and distal **(B)** calcaneal tendon on which the gastrocnemius tendon (GT) is markedly enlarged, irregular, and heterogeneous in echogenicity at two separate locations, consistent with chronic hemorrhage and fibrous tissue remodeling. Hyperechoic, shadowing foci consistent with dystrophic mineralization are also present proximally **(A)**. The common calcaneal tendon (CCT) is also enlarged and there is loss of its normal fibrillar pattern, also consistent with partial rupture. **(C)** In a transverse plane obtained just proximal to the calcaneus, the CCT and superficial digital flexor tendon (SDFT) are enlarged, but with a normal fibrillar pattern. Note the thickening of the calcaneal tendon on the radiograph.

A study on 43 dogs by Gamble et al. (2017) has proposed a classification of **calcaneal tendon strains**:

Grade I: Intact architecture, but thickening, with mild heterogeneity of the fibrillar structure.
Grade II: Partial disruption of the fiber alignment with hypoechoic fibers. Laxity may be seen during dynamic assessment.
Grade III: Complete disruption, characterized by the presence of a hypoechoic band bordered by the retracted hyperechoic tendon ends.

In this study, grade III strains were predominant, and damage occurred most commonly at the tendino-osseous insertion.

The healing process of the CC tendon with or without surgical intervention can be evaluated using ultrasonography (Kramer et al. 2001a). Within the first day after trauma, the hematoma between the ends of the tendon stumps appears hypoechoic to anechoic. Organization of the hematoma during the first and second week leads to a more inhomogeneous image with echogenic areas. From weeks 2–6, the diameter and the inhomogeneity of the injured area increase. After 8 weeks, replacement tissue begins to grow in a longitudinal direction, and both diameter and inhomogeneity decrease. The decrease in diameter is accompanied by the reappearance of the characteristic tendinous fibrillar echotexture. This healing process is completed by 10–12 weeks after trauma. However, the injured CC tendon remains much less homogeneous in comparison to the unaffected tendon for a long period (up to years). Nonresorbable suture material remains visible as hyperechoic dots.

Luxation of the SDF Tendon Medial or lateral luxation of the SDF tendon can be visualized by obtaining a transverse image above the calcaneal tuberosity. Adjacent to this convex, hyperechoic, shadowing structure, the medially or laterally displaced crescent-shaped to oval tendon comes into view. The luxated tendon can be enlarged and inhomogeneous, and a heterogeneous hematoma can also be observed at the level of fibrous avulsion on the medial or lateral aspect of the calcaneum (Figure 17.45).

Tarsal Joint Instability Damage to the medial or lateral collateral ligaments results in joint effusion that is typically more severe in the area of injury. While hematomas and fibrous tissue can be detected with ultrasound on the affected side(s), clear distinction of the collateral ligaments is limited by their size (Caine et al. 2009) and transducer resolution.

Tarsal OCD While the utility of ultrasound to detect tarsal osteochondral fragments in dogs has not been established, it was found that with this modality, 75% of the trochlear ridges of the talus can be seen, including the most commonly affected sites (Liuti et al. 2007).

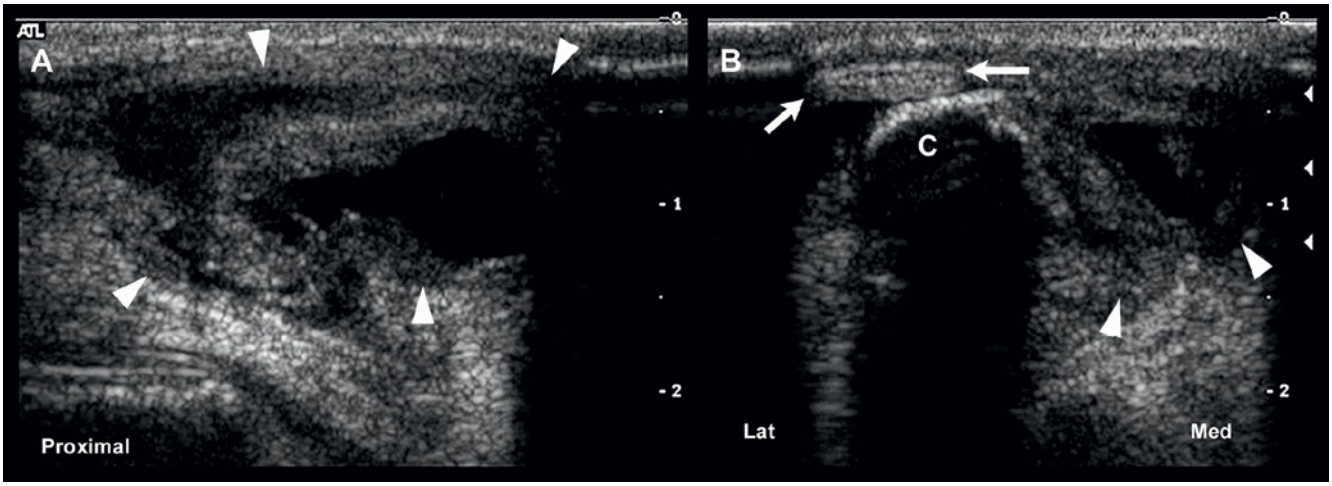


Figure 17.45. Chronic luxation of the superficial digital flexor tendon in a large dog. (A) In this longitudinal sonogram obtained medial to the calcaneum, an inhomogeneous mass (arrowheads) with anechoic fluid cavities is noted, which is consistent with chronic hematoma and fibrous tissue. **(B)** Transverse sonogram obtained at the plantaromedial aspect of the calcaneum (C), distal to the calcaneal tuberosity. The superficial digital flexor tendon (arrows) is displaced laterally. The changes caused by chronic hematoma and fibrous tissue thickening are noted medially (arrowheads) in the region of avulsion of tendon insertion. Lat, lateral; Med, medial.

Other Musculoskeletal Disorders

Musculature: Scanning Technique

Muscles that are located laterally, cranially, or caudally are examined by placing the patient in lateral recumbency with the limb of interest up. Medially located muscles are assessed with the affected limb facing down while abducting the upper limb. Individual muscles are scanned between their origin and insertion by using both longitudinal and transverse planes.

On longitudinal images, the **normal muscles** appear hypoechoic with fine, oblique, hyperechoic striations. The **fascias** appear as smooth, continuous, hyperechoic lines, particularly when scanned perpendicularly (Figures 17.4, 17.46). On transverse views, the background is hypoechoic, with echoic dots representing the muscle septa, giving a coarse echotexture to the muscle belly. Tangential muscle boundaries are more difficult to image because of edge shadowing (Kramer et al. 1997). Subcutaneous and intramuscular **fat planes** are usually slightly hyperechoic to muscle bellies, although their appearance can vary.

Muscle thickness can also be evaluated with ultrasound. A study evaluated that the measurement of thigh thickness from its lateral aspect at the proximal femoral location appears to be the most suitable measurement for detecting increases in muscle mass in dogs recovering from TPLO (Frank et al. 2019).

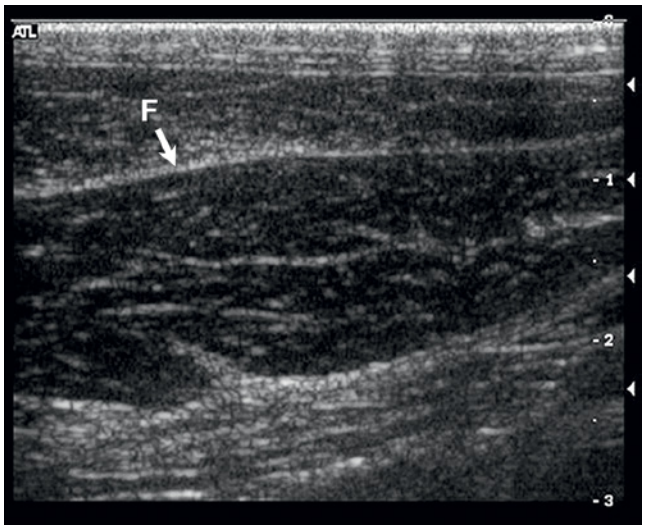


Figure 17.46. Normal muscle sonographic anatomy in a dog. Longitudinal sonographic image of a normal semimembranous muscle showing the characteristic hypoechoic echotexture with fine hyperechoic dots and lines. Intermuscular fascias (F) appear as thin, hyperechoic planes between muscle bellies.

Muscle and Tendon Trauma

The appearance of muscular trauma varies with the severity and onset of the injury. **Strain injuries**, which may or may not be secondary to a known traumatic event, probably represent an underestimated source of hind lameness in dogs (Breur and Blevins 1997; Nielsen and Pluhar 2004). Hip adductor, pectineus, and particularly iliopsoas muscles appear predisposed to strain injuries. In the **acute phase**, muscle swelling associated with hypoechoic areas is typically observed. If the muscle is partially ruptured, the normal muscular echotexture is partially lost, and the accompanying hematomas are visible as inhomogeneous, hypoechoic to anechoic, and poorly demarcated areas at the site of injury (Kramer et al. 1997; Swiderski et al. 2005). Following muscular trauma, the **healing process** can be evaluated sonographically. In the **chronic phase**, a hyperechoic and variably inhomogeneous area (with or without acoustic shadowing) at the level of the previous trauma is indicative of scar formation. The diameter of the muscle may be normal or smaller in the traumatized region.

A **fascial tear** appears as an interruption of the hyperechoic line enrobing the muscle belly, with protrusion of this muscle through the defect. In **complete muscle rupture**, the typical echotexture of the muscle structure at the site of trauma is no longer visible, but is replaced with an anechoic or hypoechoic area representing hemorrhage (Figure 17.47). In **chronic rupture**, the region appears highly inhomogeneous with mixed echotexture and echogenicity (organization of the hematoma). The muscle stump can be described as a cob-like, thickened, inhomogeneous structure that is more echogenic than the surrounding tissue. During a dynamic examination with flexion and extension of the limb, the separation of the muscle ends becomes evident (Kramer et al. 1997).

Traumatic avulsion of tendons can also be confirmed with ultrasound. Avulsed tendons are retracted according to the extent of the rupture and level of muscular contraction. **Fragments** are typically found at the extremity of the stump, appearing as hyperechoic foci with distal acoustic shadowing. In case of acute injury, these fragments are angular and well defined, whereas they tend to become rounded and ill-defined with chronicity. The site of avulsion is typically irregular and a bone defect consistent with the **fracture bed** can be observed (Figure 17.48). The retracted tendon is thickened and often heterogeneous with loss of normal echotexture.

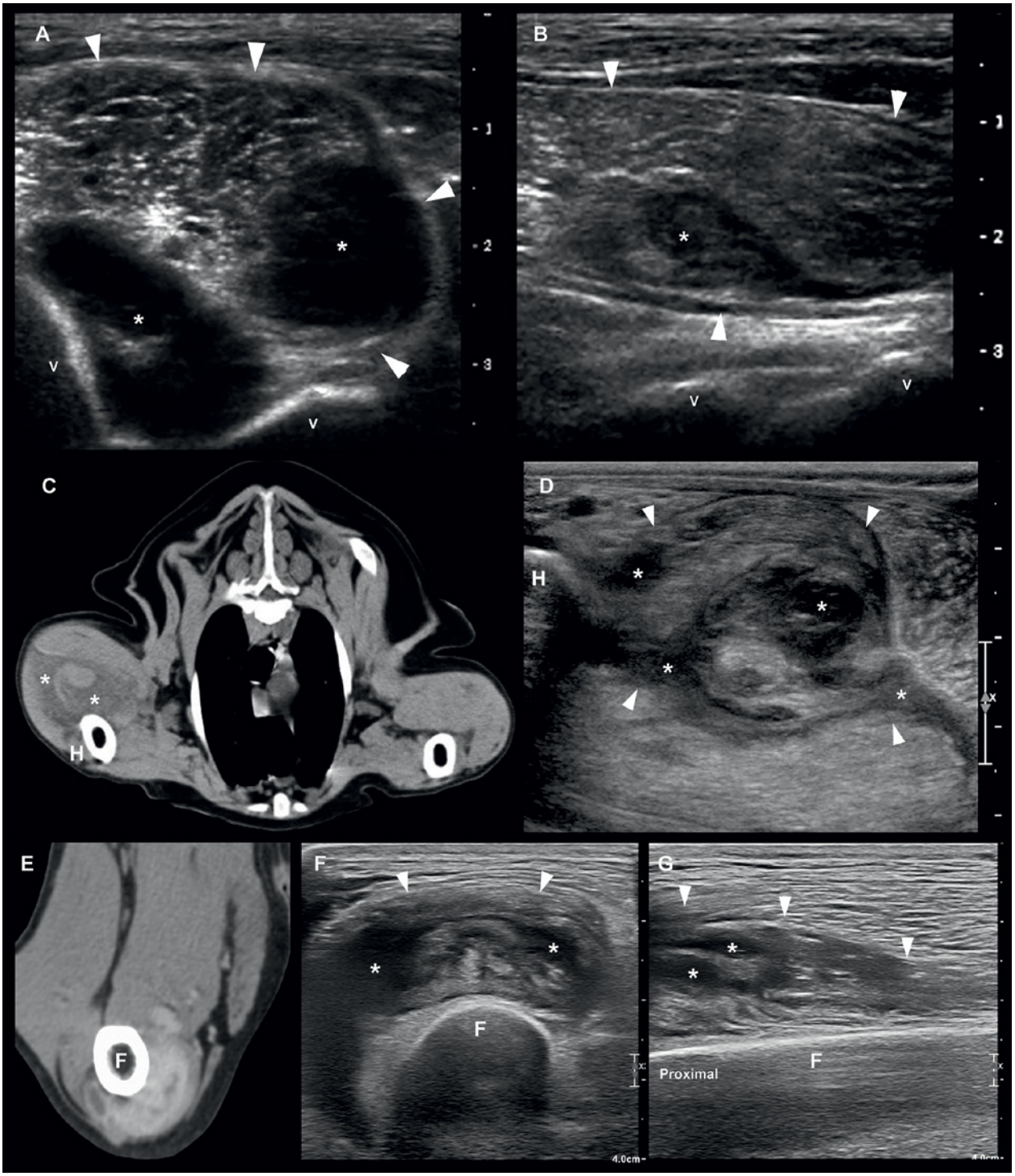


Figure 17.47. Acute muscle tear in three dogs. (A, B) Iliopsoas strain in an eight-year-old Boxer that became lame after a strenuous hike. Transverse (**A**) and longitudinal **(B)** sonograms of the right iliopsoas muscle obtained at the lateral aspect of the caudal lumbar spine. The muscle (arrowheads) is diffusely enlarged, and two large hypoechoic lesions (*) within the muscle are disrupting its architecture. These areas most likely represent tears associated with hemorrhage and edema. This process was bilateral. V, caudal lumbar vertebra. **(C)** Transverse CT image of an 11-year-old Golden retriever cross dog with acute lameness after strenuous exercise. The right triceps musculature is enlarged and associated with an irregular and ill-defined region of mixed attenuation with fluid to soft-tissue attenuating (30–40 HU) areas (*). The medial head of the triceps muscle was discontinuous on reformatted longitudinal plane. **(D)** Transverse ultrasound image of the muscular lesion (arrowheads), on which anechoic to hypoechoic areas (*) are seen consistent with acute hemorrhage and edema. H, humerus. **(E)** Postcontrast transverse CT image of the distal thigh of a mixed-breed dog with acute lameness. There is marked, heterogeneous contrast enhancement of the distal portion of the *vastus lateralis* muscle, which is also thickened adjacent to the femur (F). On transverse **(F)** and longitudinal **(G)** ultrasound, the muscle is enlarged (arrowheads) and markedly heterogeneous with hypo- to anechoic areas (*) consistent with acute muscle tear and hemorrhage. F, femur.

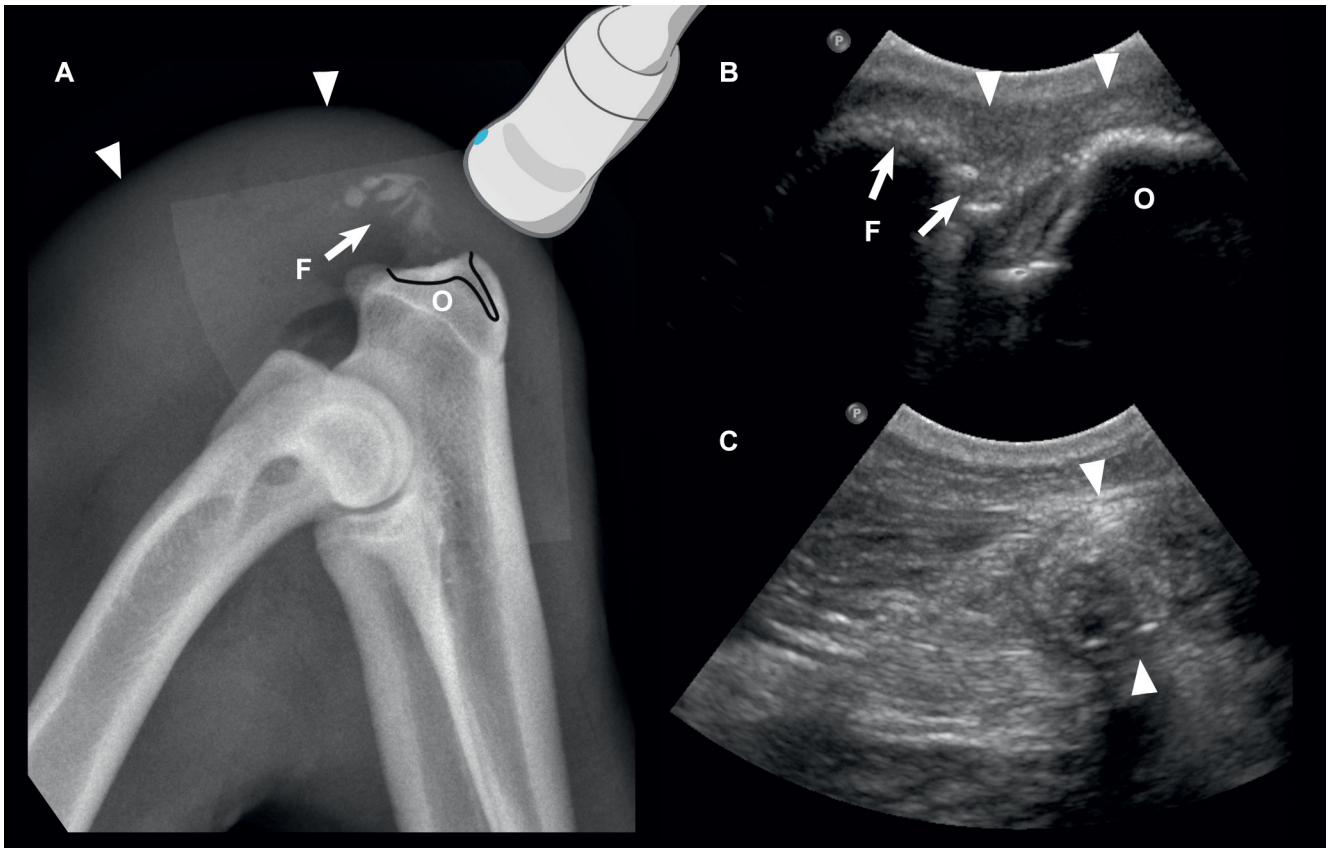


Figure 17.48. **Triceps tendon avulsion fracture. (A)** Flexed lateral radiograph of the elbow of a dog with severe thoracic lameness. Note the severe soft-tissue swelling (arrowheads) and the mineral fragments (F) proximal and dorsal to the olecranon (O). The insertion site (black curved line) of the triceps tendon on this bone is mildly irregular. **(B)** Sagittal sonographic image obtained at the level of the olecranon (O) showing the mineral fragments (F) casting complete acoustic shadow, distal to the tensor fasciae antebrachii (arrowheads). **(C)** Longitudinal sonographic image obtained proximal to the fragments. The triceps tendon (arrowheads) is focally enlarged and heterogeneous, with loss of the normal fiber pattern.

Fibrosing and Calcifying Myopathies and Tendinopathies

Fibrosing and calcifying myopathies and tendinopathies, which may or may not be traumatic in origin, are occasionally seen in lame or clinically normal dogs. The muscular and/or tendinous part of the **bicipital**, **supraspinatus**, **carpal/digital flexor**, **iliopsoas**, **gluteal**, and **calcaneal** are more commonly affected (Figures 17.7, 17.8, 17.23, 17.30, 17.44, 17.49, 17.50).

Gracilis and semitendinosus myopathy is a well-described entity in dogs resulting in characteristic clinical signs (Figure 17.51). The affected tendon or muscle may become enlarged, with an altered, inhomogeneous echotexture that varies in echogenicity. Mineral deposits may become visible as hyperechoic, irregular structures that display acoustic shadowing.

Ligaments: Scanning Technique, Sonographic Anatomy, and Desmopathies

The ligaments of dogs and cats are usually very small and frequently close to uneven bony surfaces, making sonographic assessment difficult. The use of high-frequency (ideally >12 MHz) linear transducers directed perfectly perpendicular to the ligament is essential.

In longitudinal scans, linear ligaments appear as hyperechoic structures with a fibrillar echotexture (Figure 17.34). Most ligaments are too small to be consistently identified, particularly in cross-sectional planes, and they cannot be distinguished from the surrounding structures (capsule and muscle fascia). Ligaments with fanning fibers are oriented obliquely (e.g., cruciate ligaments) and are usually hypoechoic.

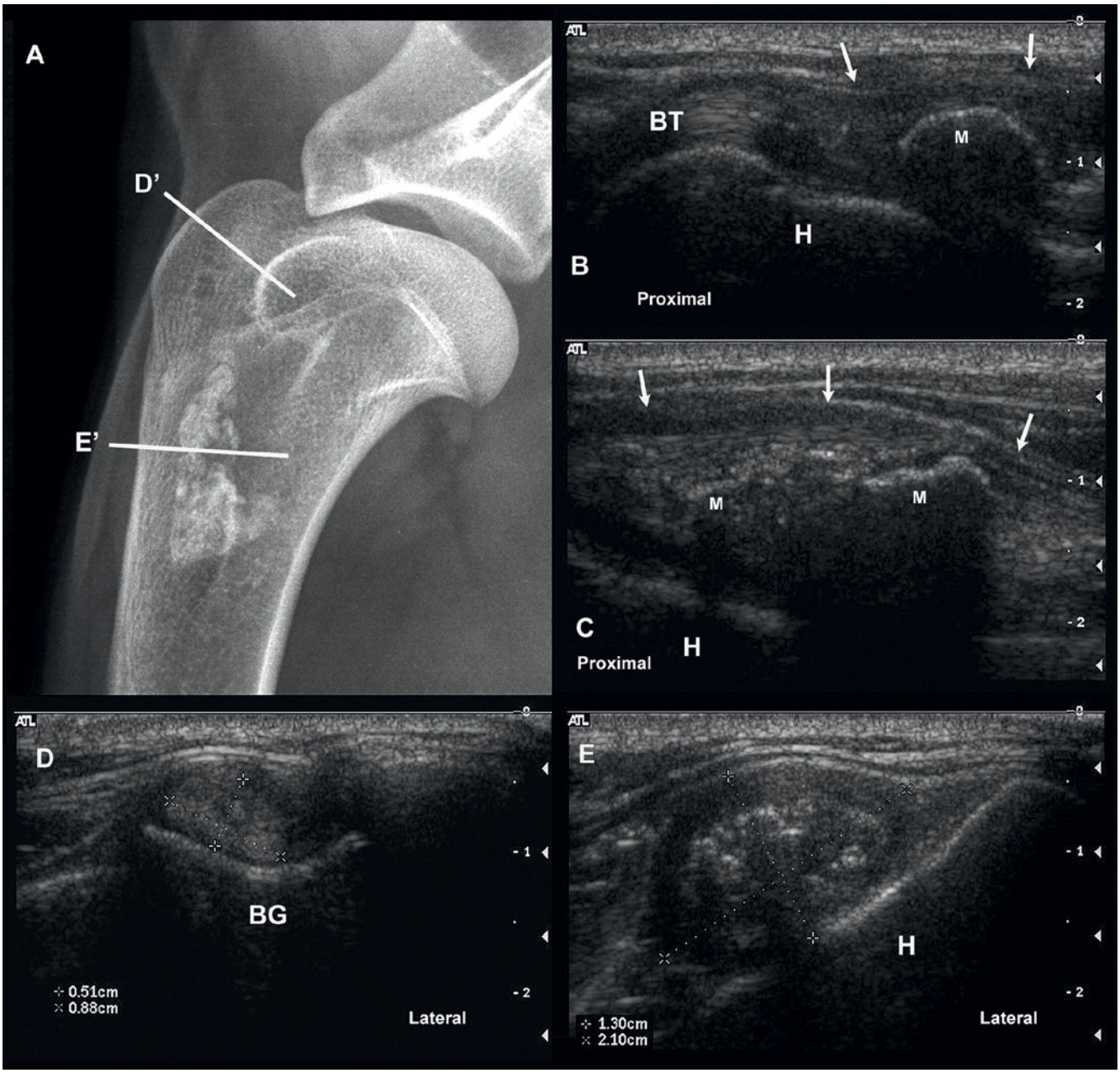


Figure 17.49. **Bicipital calcifying myopathy. (A)** Mediolateral radiograph of the shoulder region of a two-year-old large-breed dog with chronic front leg lameness. An irregular mineral opacity is noted superimposed over the proximal humeral metaphysis in the region of the biceps muscle. **(B, C)** Longitudinal sonograms obtained at the proximal aspect of the biceps muscle. This portion of the muscle is enlarged (arrows), heterogeneous, and contains irregular hyperechoic areas with acoustic shadowing, consistent with mineralization (M). BT, bicipital tendon. H, humerus. **(D, E)** Transverse sonograms. The biceps tendon (cursors) is also mildly enlarged on this transverse image **(D)** obtained at the level of the bicipital groove (BG) (plane D′ in **A**). Just distal to the bicipital groove (plane E′), the biceps muscle (between the cursors in **E**) is thickened and presents hyperechoic foci, some of which are associated with acoustic shadowing, consistent with mineralization and fibrosis. H, humerus.

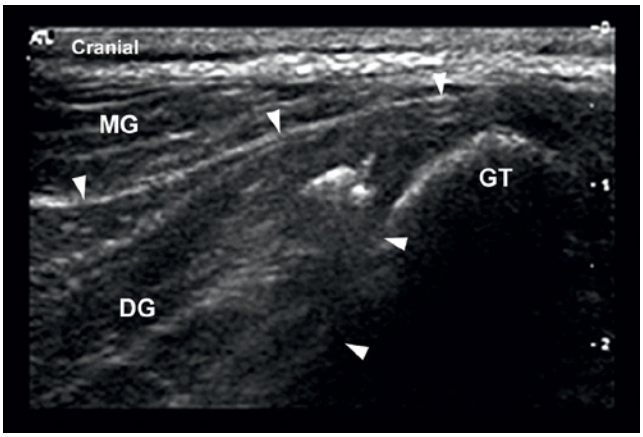


Figure 17.50. Gluteal calcifying myopathy. Longitudinal sonographic and enhanced images of the distal portion of the middle gluteal (MG) and deep gluteal (DG) muscles. The DG muscle (arrowheads) is heterogeneous and presents hyperechoic foci near its insertion site on the greater trochanter (GT), consistent with mineralization.

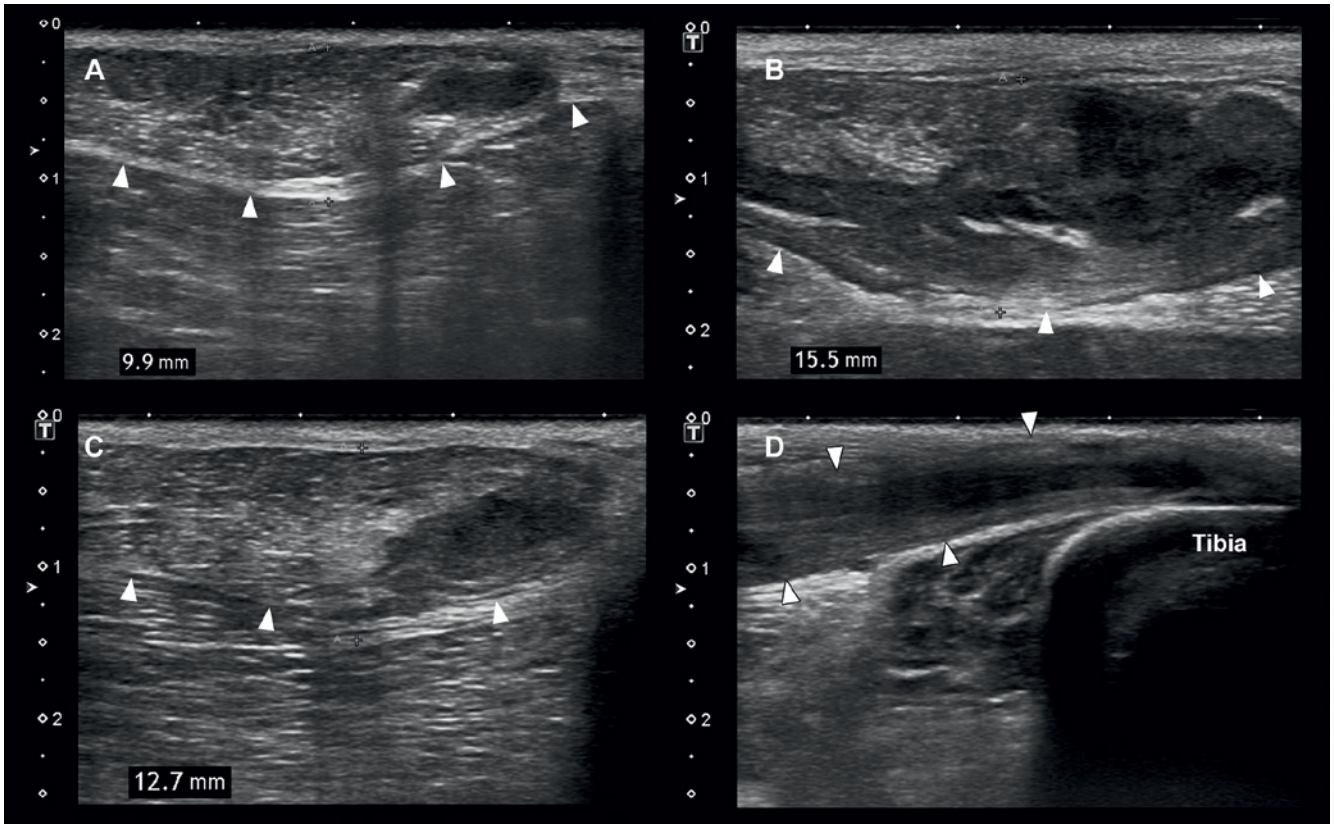


Figure 17.51. Gracilis fibrosing myopathy. (A–C) Transverse sonographic images obtained at the proximal, mid- and distal thirds of the thigh of a five-year-old German Shepherd dog with gradual onset of hind lameness, weakness, and pain. The gracilis muscle (arrowheads) is severely enlarged and mixed in echogenicity. Its echotexture is modified with several hyperechoic areas. Its tendinous portion (seen longitudinally in **D**) is also enlarged and hypoechoic, with its fibrillar pattern being partly lost.

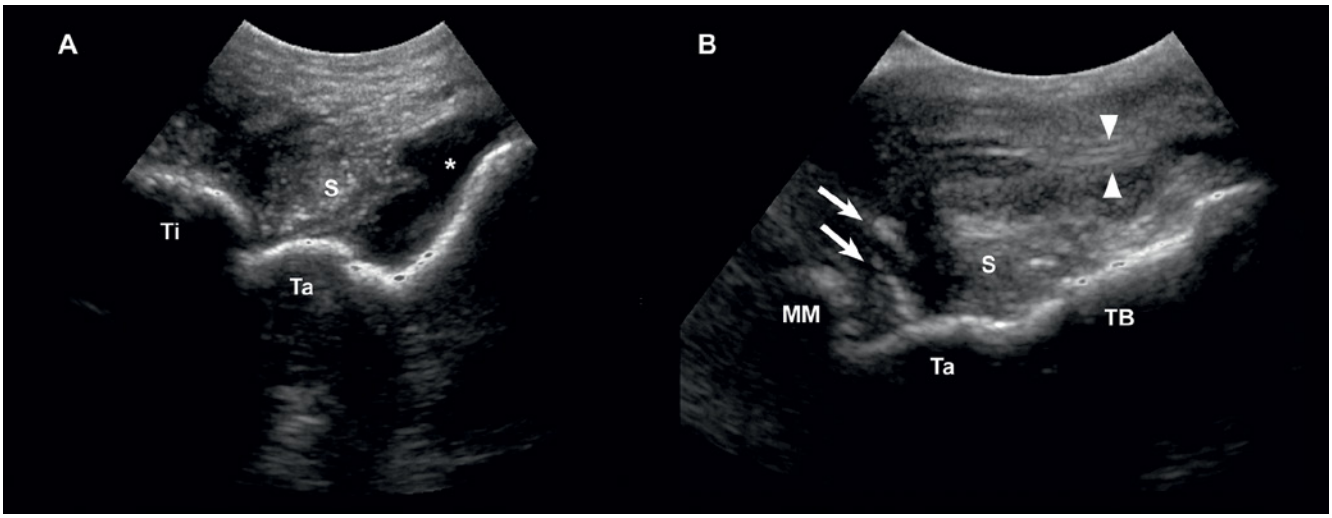


Figure 17.52. Talocrural medial collateral ligament rupture in a dog. Sagittal dorsal **(A)** and sagittal medial **(B)** sonographic images of the talocrural joint of a traumatized dog. The joint synovium (S) is thickened and associated with effusion (*) dorsal to the talus (Ta). Medially, several hyperechoic foci (arrows) are present distal to the tibial medial malleolus (MM), consistent with small bone and/or ligament fragments. The distal stump of the medial collateral ligament is visible more superficially and distally (arrowheads). TB, tarsal bone; Ti, tibia.

Because of their small size, acutely **ruptured ligaments** cannot be easily visualized with ultrasound. A small anechoic or hypoechoic hematoma in the area of rupture may be seen in the initial phase. If the injury is associated with a **bone avulsion fracture**, the fragment is visible as a hyperechoic structure with acoustic shadowing within the reactive tissue (Figure 17.52). The corresponding fragment bed may be recognized as a small concavity on the surface of the adjacent bone. Ruptured ligament stumps can become hyperechoic and thickened, particularly in the chronic phase. Ligament rupture may cause joint instability, which may be evidenced with a dynamic examination. Synovial and capsular thickening develop.

Joint Luxation

Ultrasound may help in identifying joint or ligament luxation when physical examination and radiographs are not sufficient. Coxofemoral joint luxation typically causes craniodorsal displacement of the femoral head. Ultrasound may help confirm the luxation from a lateral approach with the dog in lateral recumbency and the affected hip on top.

Cellulitis, Abscesses, and Foreign Bodies (FBs)

Cellulitis is an inflammatory process involving the connective tissue and typically appears as alternating anechoic and hyperechoic bands in the subcutaneous planes, often resulting in increased ultrasound-beam attenuation, which limits the assessment of deep structures (Figure 17.53). Inflamed tissue can become swollen. **Phlegmon** is a suppurative inflammation of the connective tissue that typically leads to accumulation of hypoechoic fluid pockets in the subcutaneous tissues (Figures 17.53, 17.54). **Necrotizing fasciitis**, which has been described in two puppies affected by *Streptococcus canis*, can also be associated with similar fluid pockets (Kulendra and Coor 2008). More confined **abscesses** may also develop and appear as cavitary lesions containing particulate fluid. A hyperechoic wall of variable thickness is often recognized in the chronic phase. Internal septa may also form. Thus, abscesses can be complex in ultrasonographic appearance and resemble neoplastic processes. An abscess can be identified as intramuscular or intermuscular, subfascial, or subcutaneous. Ultrasound-guided fine-needle aspiration or drainage may assist in the diagnosis and treatment of the suppurative process (Figure 17.54B).

Inflammatory processes may be secondary to the presence of **FBs**, such as wooden sticks (Figure 17.55), porcupine quills (Figures 17.56, 17.57), grass awns (Figure 17.58), glass, or plastic or metal objects. The accuracy of ultrasonography in detecting FBs, particularly if superficial, in people is high (Boyse et al. 2001; Brisson et al. 2004). Although most FBs are hyperechoic to normal soft tissues, their echogenicity can vary, depending on their physical and acoustic characteristics (Armbrust et al. 2003; Boyse et al. 2001). **Acoustic**

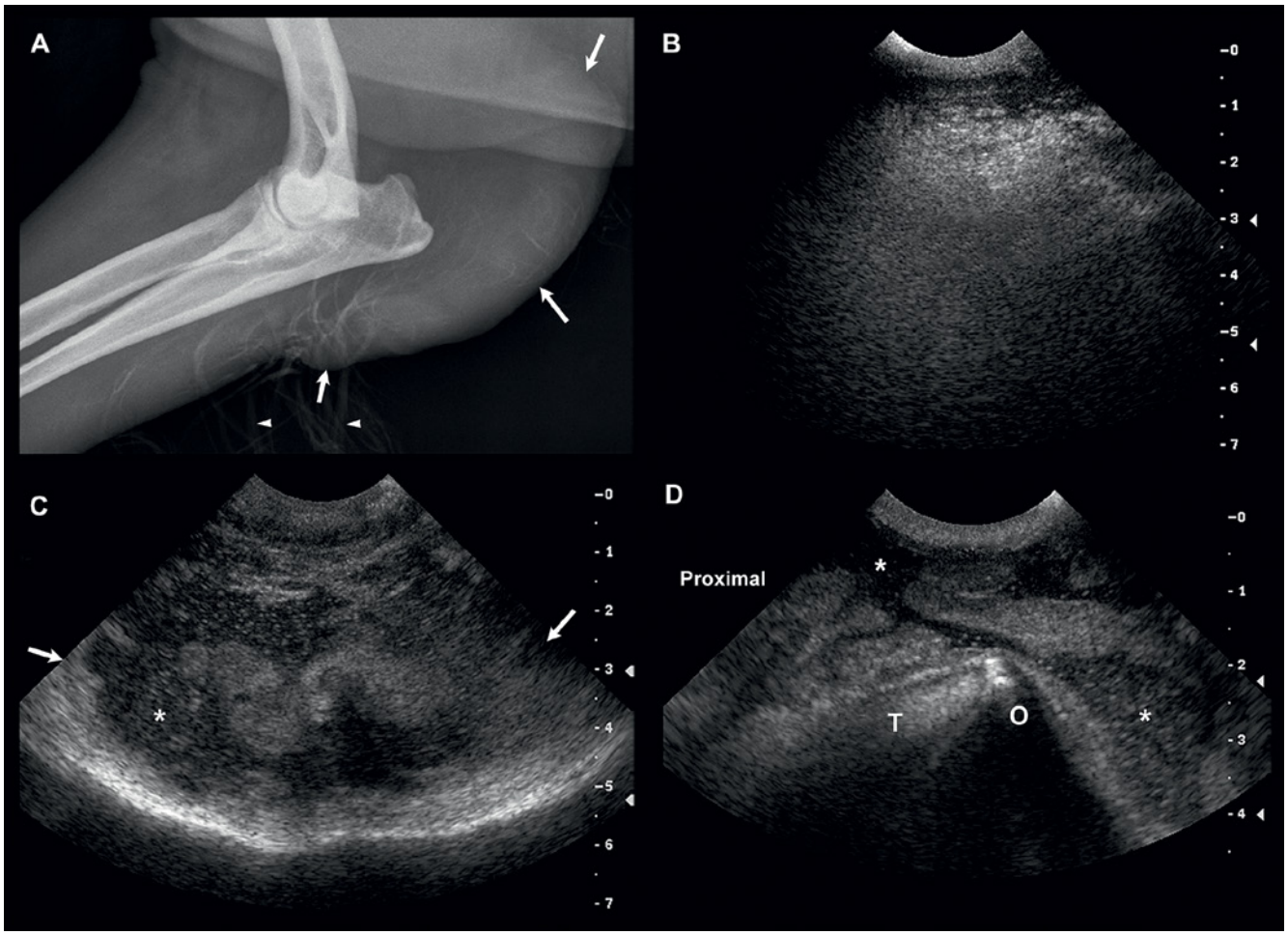


Figure 17.53. **Septic abscess in the elbow region of a dog. (A)** Mediolateral radiograph of the elbow region of a five-year-old large-breed dog with progressive, painful swelling caudal to the elbow. Soft-tissue swelling (arrows) is present without evidence of bone involvement or a radiopaque foreign body. This radiograph was obtained after the ultrasound exam, which explains the presence of artifacts caused by wet hair (arrowheads) caused by the presence of acoustic gel. **(B)** In the proximal region of the limb, the subcutaneous tissue appears hyperechoic and hyperattenuating as the result of cellulitis. **(C, D)** A large cavitary mass lesion (arrows) containing echogenic fluid (*) and mobile echogenic septa is caudal to the olecranon (O) and triceps tendon (T). An irregular, moderately echogenic capsule is noted proximally (arrow to the left in **C**).

shadowing is expected; however, it may only be partial, or it may be masked by the presence of a bony structure in the far field or by the ultrasonographic complexity of the associated soft-tissue reaction. **Wooden FBs** are hyperechoic and cast a shadow when inserted in cadaveric canine manus (Ober et al. 2008), but these may lose their echogenicity and become confounded by the surrounding tissue changes in chronically affected animals (Staudte et al. 2004). A hypoechoic rim, consistent with an **inflammatory cast or fistular tract**, commonly develops around an FB, helping its identification (Gnudi et al. 2005; Kramer et al. 1997; Shah et al. 1992) (Figure 17.55). A fistular tract that may contain **gas** may also be recognized (Figure 17.59). Also, in some instances, the artifacts associated with the FBs are more clearly visible than the FB itself. The characteristics of the artifacts present deeper to the objects appear to be related to the surface shape of the FBs rather than to its composition (Boyse et al. 2001). **Metal objects** such as BB pellets are typically associated with reverberation artifacts (comet tails), which may be confused with air bubbles. Metal objects of any size can easily be identifiable on standard radiographs. **Glass** is typically hyperechoic and may be recognized on radiographs. **Porcupine quills**, which are usually not visible on radiographs, appear as double-banded, fusiform, hyperechoic structures (Figures 17.56, 17.57). **Grass awns** typically appear as a double/triple spindle-shaped echogenic interface, often with acoustic shadowing (Gnudi et al. 2005) (Figure 17.58).

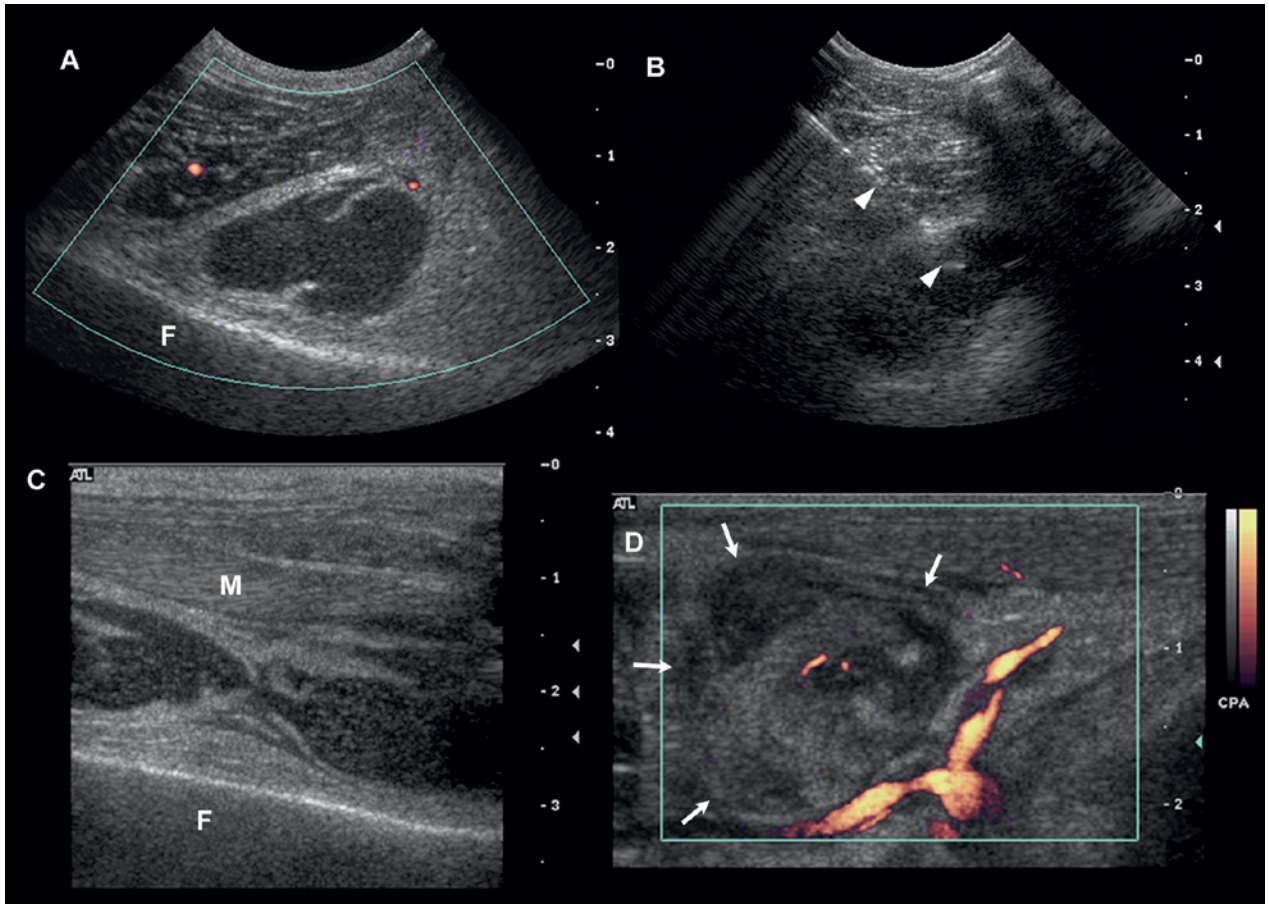


Figure 17.54. Paramuscular abscess and myositis in a cat. (for full caption, see facing page)

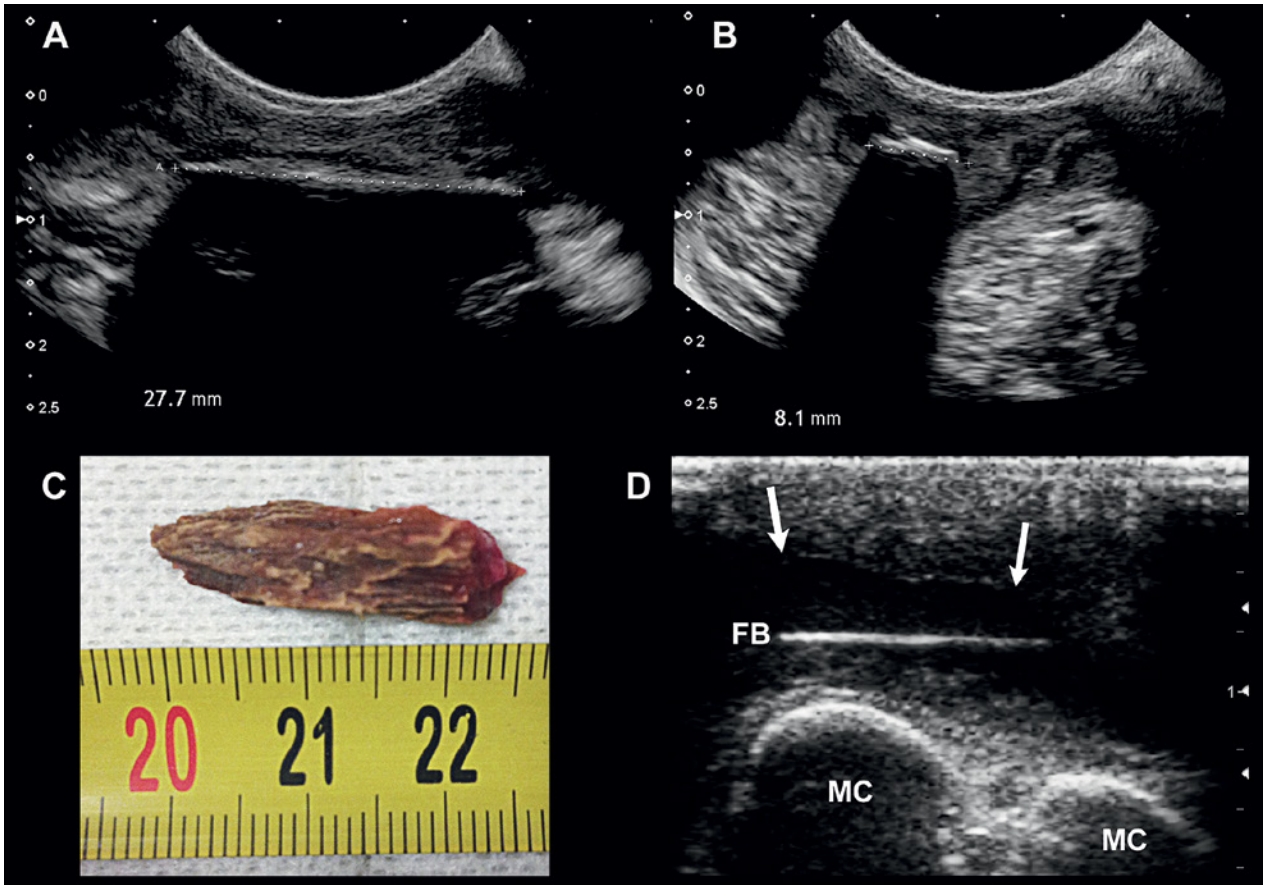


Figure 17.55. Wooden fragment foreign bodies in two dogs. (for full caption, see facing page)

Figure 17.54. **Paramuscular abscess and myositis in a cat.** Transverse **(A)** and longitudinal **(C)** sonographic images obtained at the caudal aspect of the femur (F) in a cat with pelvic limb swelling and fever. An irregular accumulation of echogenic fluid is found between one of the muscles (M) and the femur. **(B)** This cavitary lesion was aspirated using ultrasound guidance, which led to a diagnosis of a septic abscess. The arrowheads point to the needle. **(D)** A nearby inhomogeneous mass (arrows) was found adjacent to large vessels. Fine-needle aspiration confirmed the presence of septic and necrotic myositis.

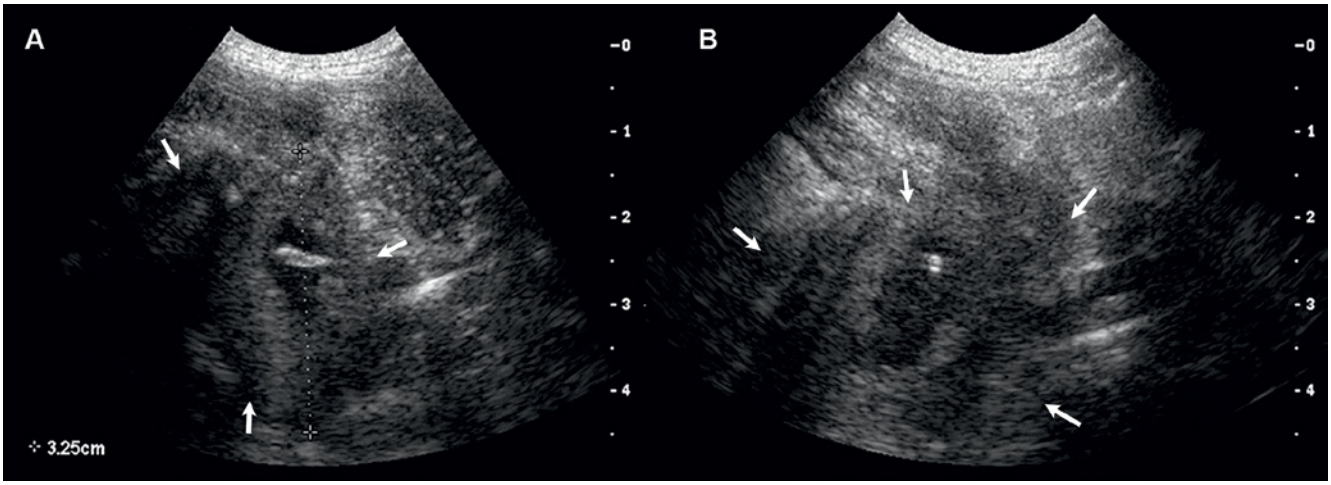


Figure 17.56. **Porcupine quill migration and abscess.** A 3.25-cm, moderately echogenic mass (arrows) is shown with a central fluid-filled cavity as well as a short, fusiform, double-lined hyperechoic structure when seen longitudinally **(A)** and circular when seen transversely **(B)**.

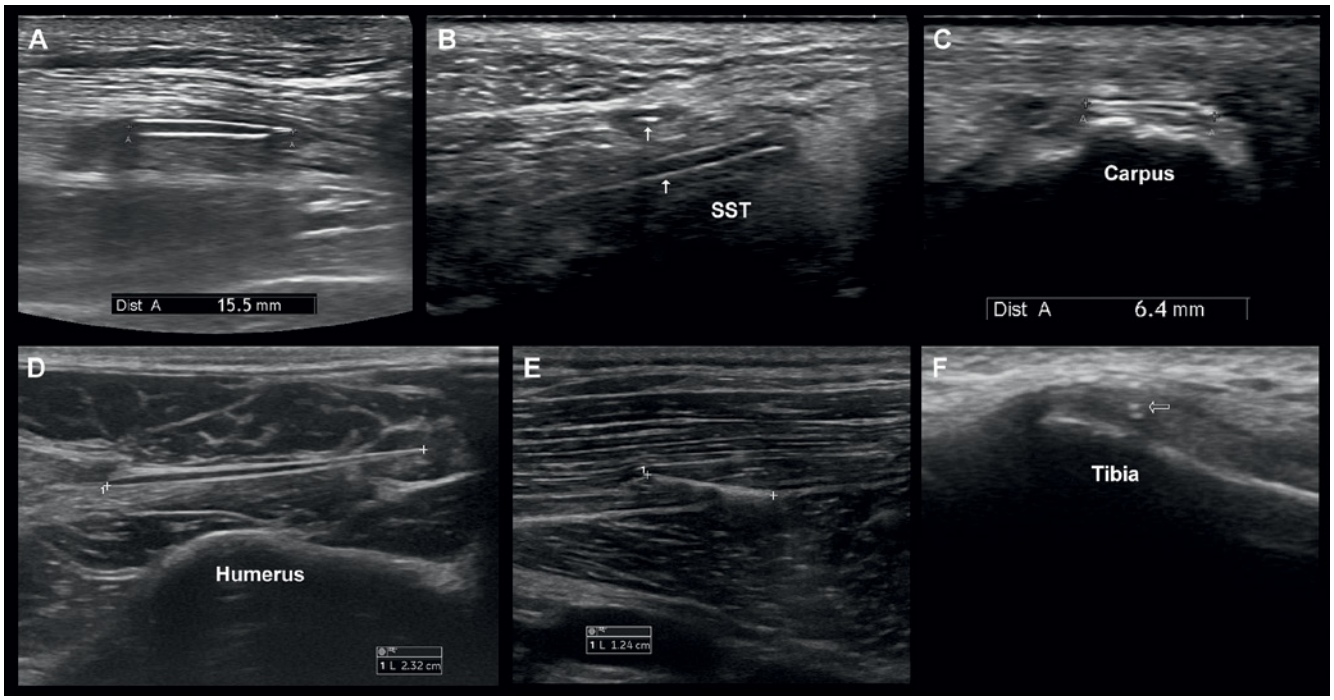


Figure 17.57. **Porcupine quills in two dogs with minimal soft-tissue reaction. (A–C)** At least 10 quill fragments (between calipers and arrows) were identified on ultrasound in several areas of the left thoracic limb of this five-year-old Airedale dog, most of which with none to minimal alteration of the nearby soft tissues. Some were very close to bony structures, making them challenging to identify. SST, supraspinatus tendon. **(D–F)** More than 20 quill fragments migrated in the soft tissues of this seven-year-old mixed Husky dog. Quills can be confused with other linear or tubular structures such as blood vessels, justifying the use of color Doppler for confirmation in some cases.

Figure 17.55. **Wooden fragment foreign bodies in two dogs. (A–C)** The wood fragment presents as a well-defined hyperechoic interface with strong acoustic shadowing, in longitudinal **(A)** and transverse **(B)** sonographic planes. **(D)** Transverse sonographic image obtained at the dorsal aspect of the metacarpal bones (MC) of another dog. A thin, straight, hyperechoic foreign body (FB) is surrounded by mildly echogenic inflammatory tissue (arrows). A wooden stick was identified at surgery. Courtesy of Laurent Couturier, Azurvet, France.

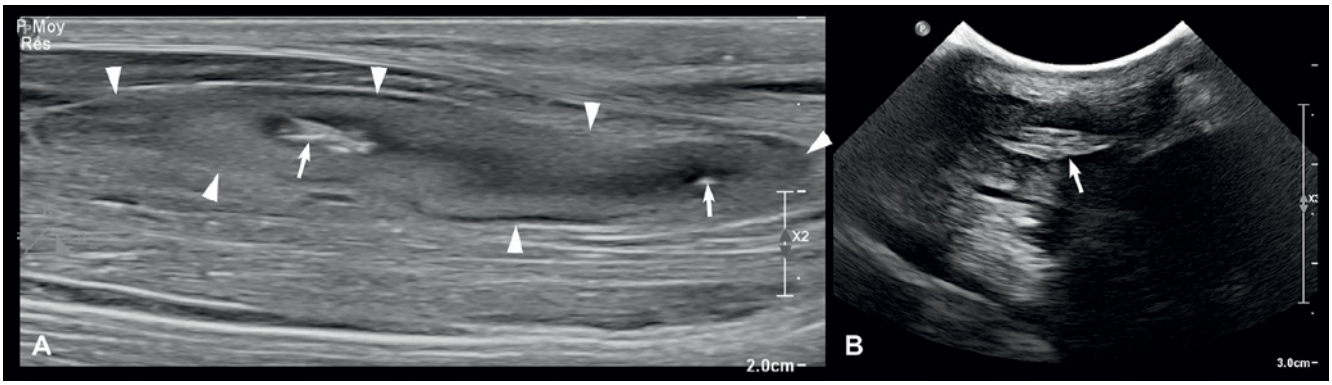


Figure 17.58. **Grass awn migration in two dogs**. **(A)** longitudinal sonographic image of an oblong abscess (arrowheads) with two grass awn fragments (arrows) surrounded by echogenic fluid, which was located deep to the ulnar flexor tendon. **(B)** Large fluid-filled abscess around the foreign body (arrow) near the carpus of another dog.

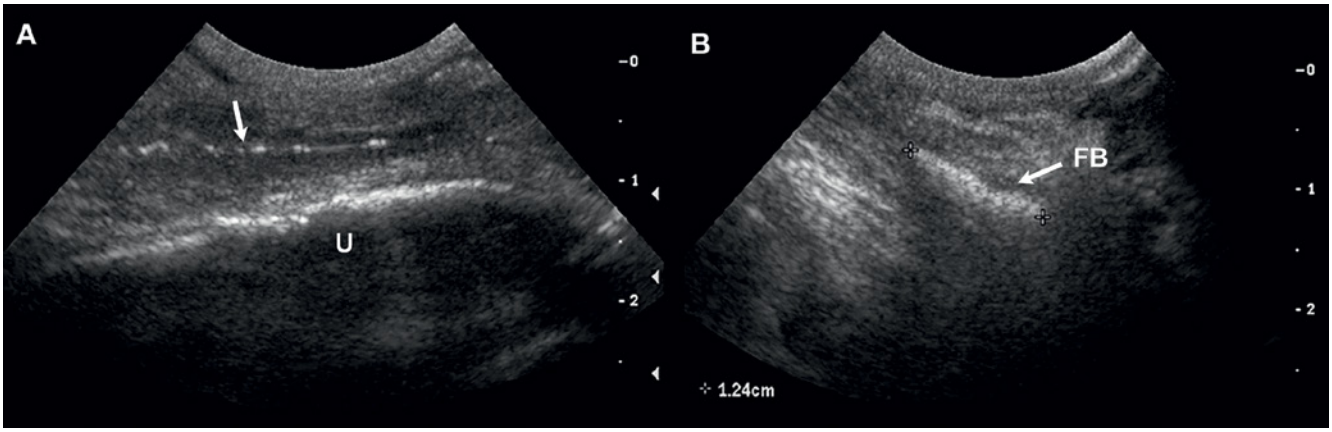


Figure 17.59. **Fistular tract and foreign body. (A)** Longitudinal image of the region caudal to the proximal ulna (U) in a dog with a chronic draining tract. An interrupted hyperechoic line (arrow), consistent with gas, is seen within a hypoechoic cast of fibrous tissue. The caudal surface of the ulna is irregular because of periostitis. **(B)** More distally, a 1.2-cm-long hyperechoic interface with dirty shadowing is found, which indicated a foreign body (FB).

Small FBs may remain undetected if smaller than 2–3 mm or if deeply embedded in tissues, depending on their location and the spatial resolution of the transducer. Furthermore, the presence of nearby mineral or aerated structures, such as in the region of the distal extremities (e.g., sesamoid bones) or the larynx and hyoid apparatus, may be confused for FBs or limit their identification.

Ultrasound may also be useful in the **surgical localization or removal** of the FB (see the section on interventional procedures).

Benign and Malignant Soft-Tissue Tumors

Tumors originating from muscles, subcutaneous fat, or other soft-tissue structures can usually be identified using ultrasonography, variably solid or cavitary in appearance. They may range from homogeneous to highly inhomogeneous in echotexture, and from anechoic to highly hyperechoic, sometimes with mineralization (Figures 17.60–17.64). The tumor margins may or may not be clearly visible. When **color Doppler** is used, malignant tumors can appear hypervascular with tortuous and randomly distributed vessels, or poorly perfused and/or necrotic (Figures 17.60, 17.61). Ultrasonography cannot accurately differentiate malignant and benign diseases such as spontaneous hemorrhage (Figure 17.65). Ultrasound-guided or surgical aspiration or biopsy is required in all cases.

Ultrasound may be useful to detect **metastases**. Hemangiosarcoma metastases, for example, appear as hypoechoic relatively homogeneous nodules (Fabbi et al. 2016).

Lipomas appear as mildly echogenic masses with diffuse hyperechoic dots and striations (Volta et al. 2006) (Figure 17.66). Lipomas can be located in

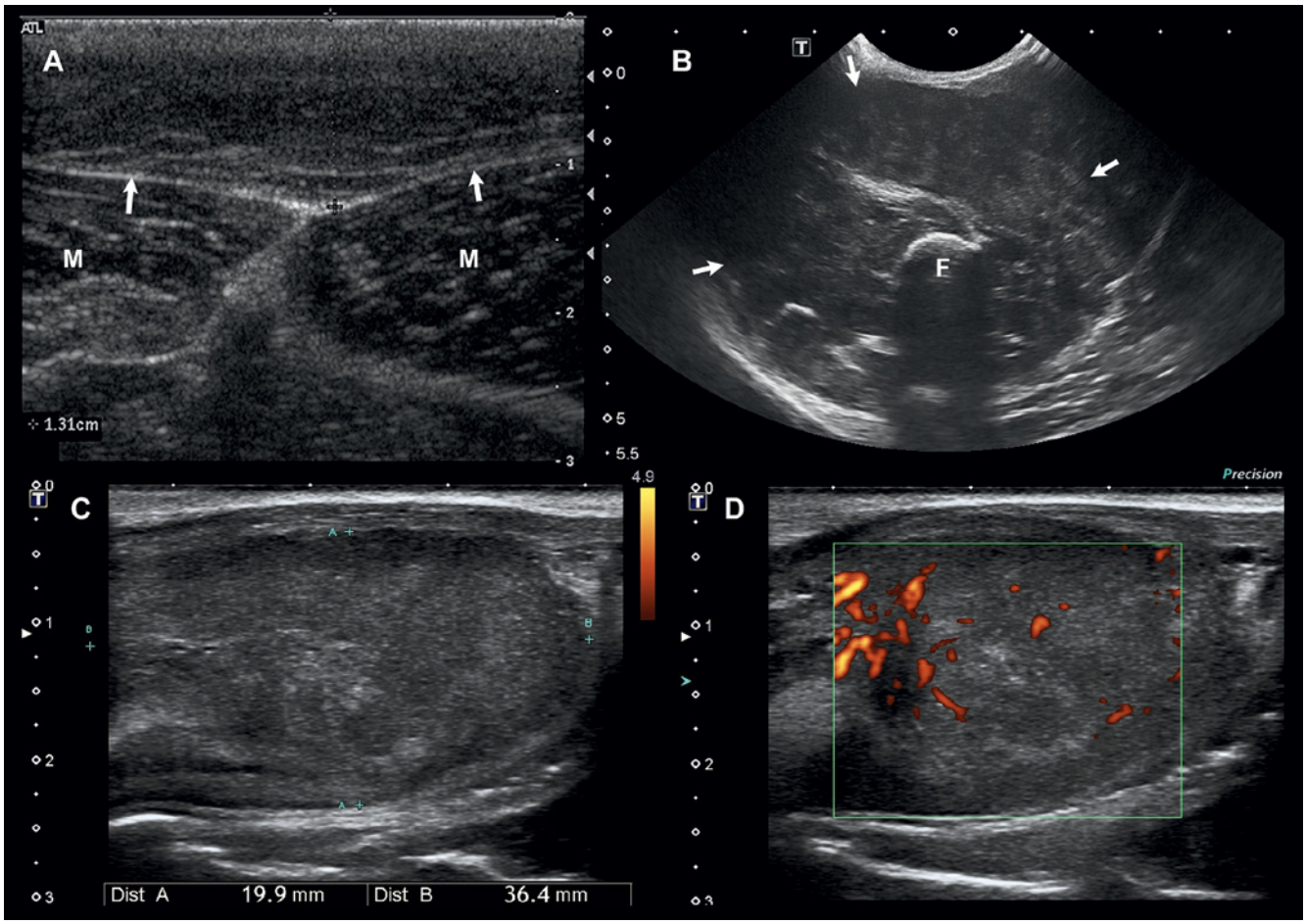


Figure 17.60. **Lymphoma in three cats. (A)** On this sonographic image obtained at the lateral aspect of the pelvic limb, a moderately echogenic band in the near field is silhouetting with the dermis. Muscle bellies (M) are displaced, but not invaded by the neoplastic process. The muscle fascias (arrows) remain well defined. **(B)** Transverse sonographic image obtained at mid-thigh in an 11-year-old cat presented for weight loss and pelvic limb swelling. The thigh musculature is infiltrated with mildly heterogeneous hypoechoic tissue (arrows) encircling the femur (F), with loss of distinction of the normal muscular echotexture. Several hypoechoic nodules were also detected in intestinal walls and kidneys. Fine-needle aspiration revealed lymphoblastic lymphoma. **(C, D)** Sonographic B-mode (**C**) and Power Doppler (**D**) sagittal images obtained on the midline in the intermandibular space showing a large hypoechoic and mildly heterogeneous mass showing a heterogeneous vascular supply. Mandibular lymphadenopathy was also present.

the subcutaneous or intermuscular planes or within muscles (intramuscular). They typically show a thin, well-defined hyperechoic capsule, although they can be ill-defined when invasive. Yet accurate distinction between invasive and noninvasive lipomas cannot be made by means of ultrasonography.

Ultrasound can also be very useful in the identification of **joint soft-tissue tumors**, such as synovial cell sarcoma or histiocytic sarcoma (Figures 17.61G–I, 17.64). These tumors can vary in echotexture and echogenicity but typically appear as an irregular soft-tissue thickening that crosses the joint space, invades the osteochondral junctions, and protrudes into the synovial space. The bone surface at the periphery of the joint becomes irregular, and soft-tissue nodules or masses can be seen to extend within the metaphyseal cortex and medulla. These changes may also resemble severe DJD or other arthropathies, which justifies fine-needle aspiration or biopsy that can be safely done under ultrasound guidance.

Joint Effusions

Joint effusion in OCD or osteoarthritis is typically anechoic. In comparison, septic effusions appear more echogenic, and floating particles are often observed (Figure 17.67). Hemorrhagic effusions can range in echogenicity, depending on their chronicity.

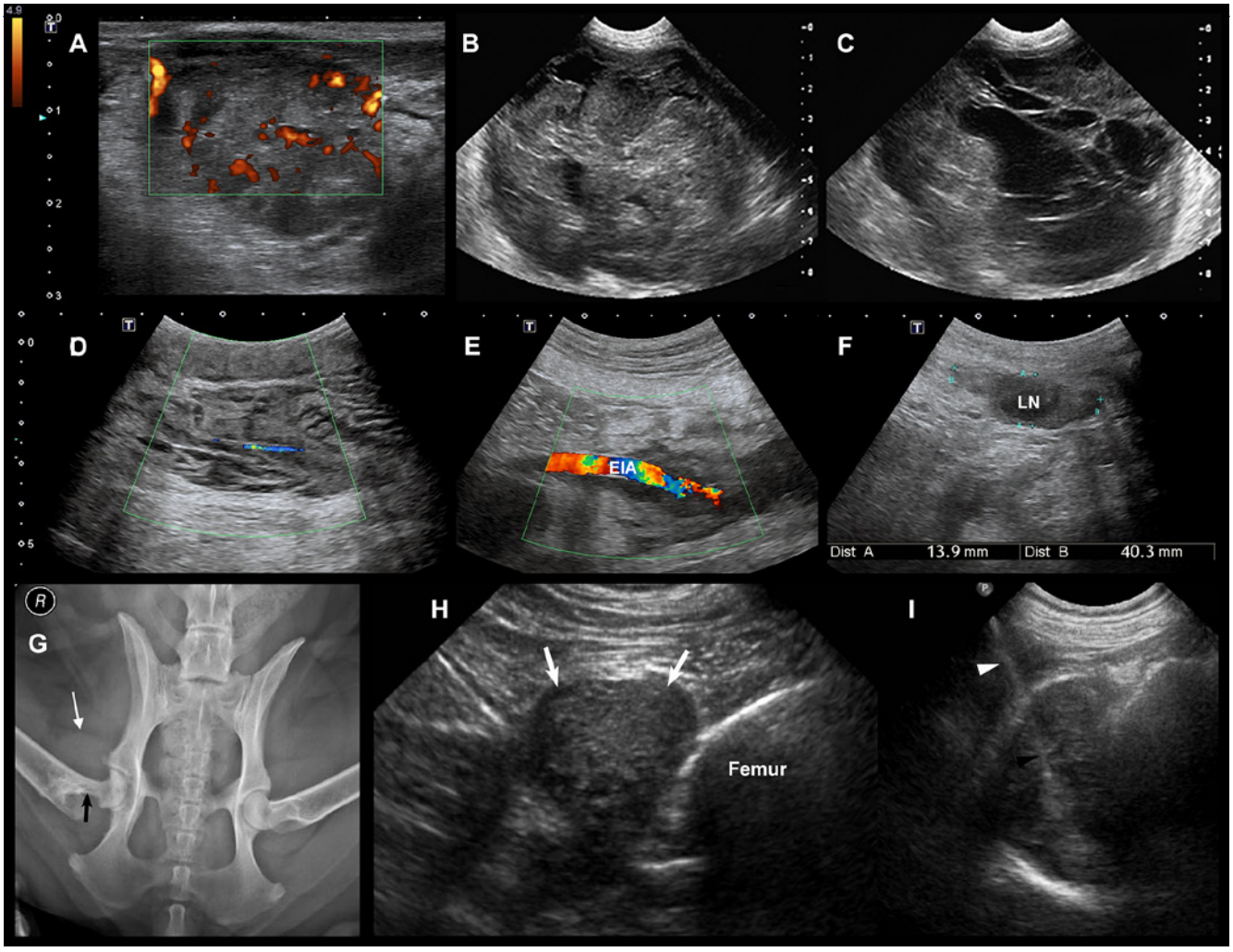


Figure 17.61. **Appendicular sarcomas in four dogs. (A)** Sonographic image of a 2.5-cm-wide **leiomyosarcoma** involving the gastrocnemius muscle of a dog. The mass is mildly echogenic and heterogeneous, and well vascularized, as evidenced by using color Doppler in the deep portion of the mass. **(B, C) Pelvic limb fibrosarcoma** in another dog. This mass is solid and moderately echogenic in most areas, but also presents anechoic, fluid-filled necrotic and hemorrhagic cavities. **(D–F) Undifferentiated sarcoma**. A markedly heterogeneous mass (in **D**) infiltrates the thigh musculature and extends proximally into the pelvic canal. A second mass was found in the region of the ipsilateral external iliac lymph node (in **E**), partly encircling the external iliac artery (EIA) and causing local edema. The superficial inguinal lymph node (LN in **F**) was also enlarged, hypoechoic, heterogeneous, and irregular. **(G)** Radiograph of the pelvis of a six-year-old Labrador retriever with right hind lameness showing a soft-tissue mass (white arrow) craniolateral to the right coxofemoral joint. The right femoral neck (black arrow) and head are atrophied and sclerotic, suggesting pressure atrophy and/or invasion by the mass. **(H, I)** Ultrasound confirmed the presence of a well-defined hypoechoic mass (arrows) and was used for fine-needle aspiration (arrowheads), which suggested a soft-tissue sarcoma. TruCut biopsies subsequently revealed a **histiocytic sarcoma**.

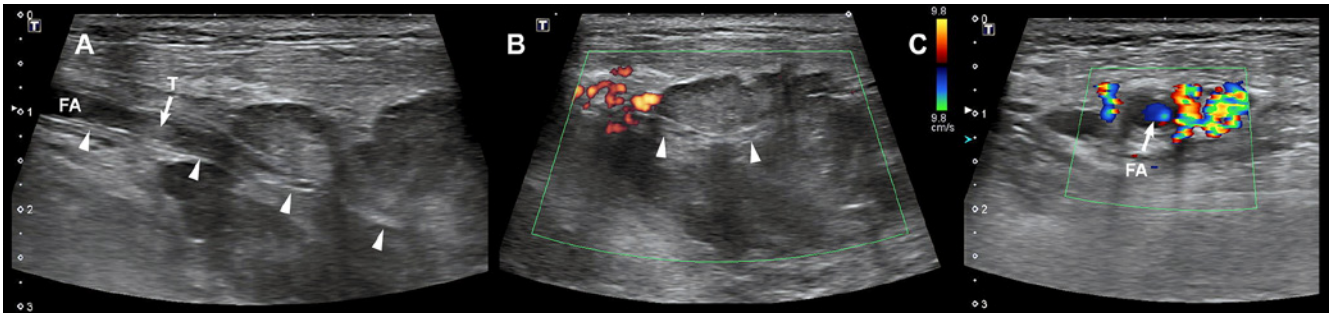


Figure 17.62. **High-grade soft-tissue sarcoma infiltrating the femoral artery.** This 10-year-old mixed breed dog was presented for severe pelvic limb swelling and lameness. Sonographic images in B-mode **(A)**, power Doppler **(B)**, and color Doppler **(C)** of the lobulated hypoechoic and heterogeneous mass infiltrating and distorting the femoral artery (FA, arrowheads), causing arterial hypertension that generated tortuous collaterals and local edema. A thrombus (T) is also present in the lumen of the femoral artery.

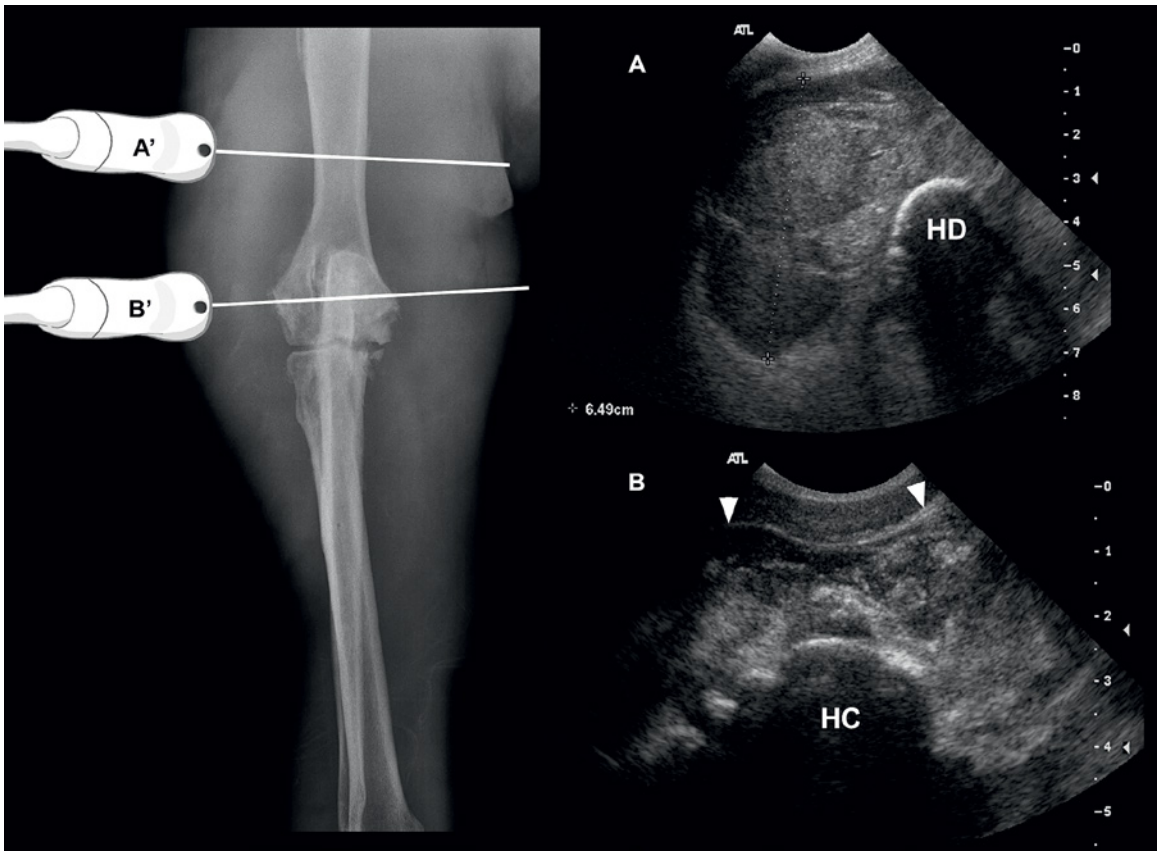


Figure 17.63. Large soft-tissue sarcoma in a 10-year-old mixed breed dog. The craniocaudal radiograph of the elbow of this dog shows severe soft-tissue swelling and an irregular new bone formation involving the humeral condyle and proximal radius and ulna. The convex sonographic probe was placed in transverse plane (A′ and B′) to obtain images **A** and **B**, at the level of the humeral diaphysis (HD) and humeral condyle (HC), respectively. Note the heterogeneous mass (arrowheads and between calipers) partly encircling the humerus of this dog.

Bones

Scanning Technique and Sonographic Anatomy

Although radiography remains the principal modality in the investigation of bone diseases, ultrasonography provides additional information, particularly with regard to the soft-tissue component of these processes. Linear transducers are preferred for superior resolution, although microconvex probes may be preferred when a smaller footprint is necessary. The exam is performed similarly as for muscles and tendons, with the patient in lateral recumbency.

The surface of a **long bone** is examined by slowly moving the probe along the long axis of the bone, usually in a longitudinal plane, which enables visualization of a larger portion of the bone surface (Risselada et al. 2003). This way, the area of interest can be compared with adjacent normal portions of the bone (e.g., tumor or fracture).

Because of the reflection and absorption of the sound waves, the bone surface appears as a smooth, hyperechoic, continuous line with strong acoustic shadowing. This surface is more irregular at the sites of origin and insertion of tendons and ligaments.

The **vertebrae** can also be assessed with ultrasound although its depts may limit its access in large dogs.

Sonographic Features of Bone Disorders

Bone Infection **Osteomyelitis** can vary in ultrasonographic appearance. An ill-defined, irregular hyperechoic interface can be seen superficial to the bone cortex when periosteal new bone formation develops. Peripheral inflamed soft tissues appear swollen, hypoechoic, and inhomogeneous (Figures 17.68, 17.69). The lytic cortical surface can be uneven, with multiple indentations (Kramer et al. 1997).

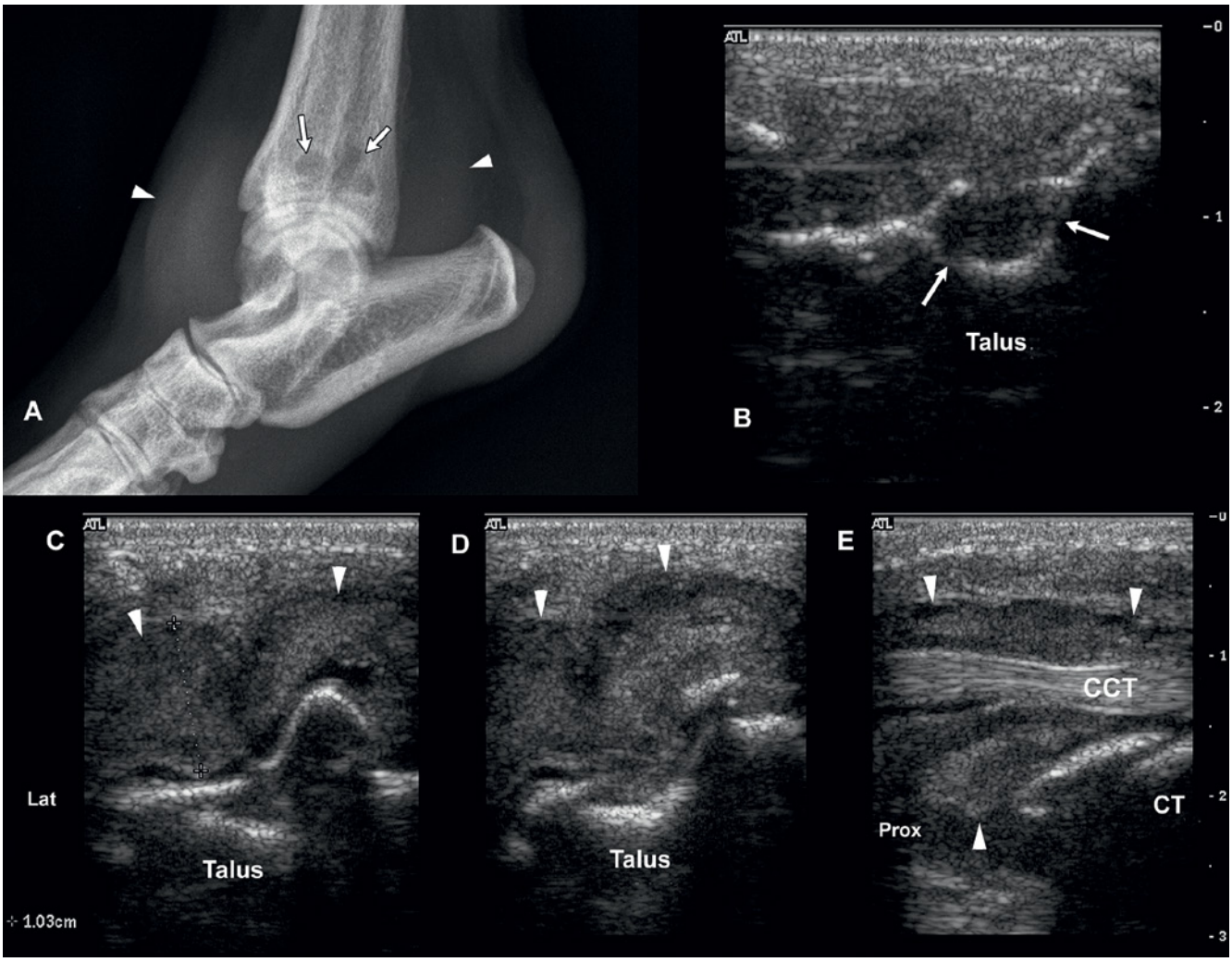


Figure 17.64. **Synovial cell sarcoma. (A)** Mediolateral radiograph of the tarsus of a six-year-old large-breed dog with chronic lameness. Soft-tissue swelling (arrowheads) is noted at the periphery of the tarsus as well as lytic foci in the distal tibial metaphysis (arrows) and an irregular periosteal reaction along the caudal aspect of the tibia. **(B–D)** Longitudinal **(B)** and transverse **(C, D)** sonograms of the dorsal aspect of the talus that show an irregular layer of echogenic tissue in the near field (arrowheads) as well as irregular bone defects (arrows). Lat, lateral. **(E)** Longitudinal sonogram obtained at the plantar aspect. The soft-tissue thickening (arrowheads) is noted at the periphery of the common calcaneal tendon (CCT), reaching the level of the calcaneal tuberosity (CT). These features are supportive of synovial cell sarcoma or synovial histiocytic sarcoma. Prox, proximal.

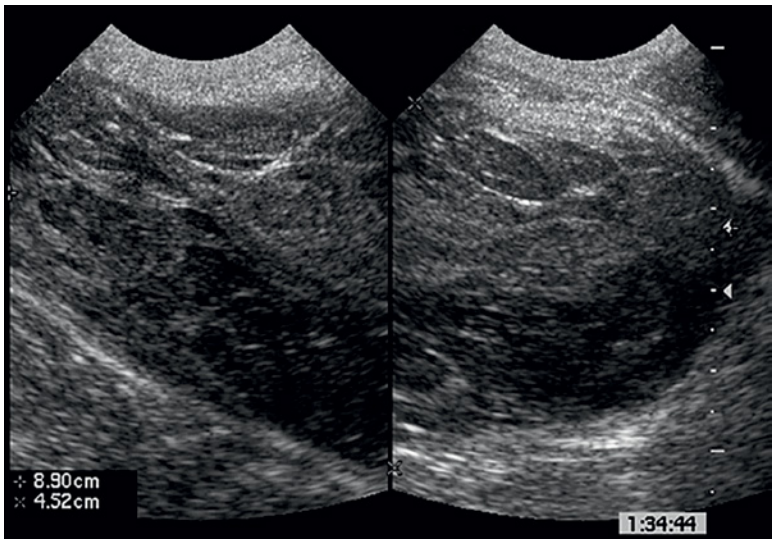


Figure 17.65. **Muscular hemorrhage.** Sonographic images of the pelvic limb of a dog with rapidly progressive swelling. A hypoechoic, inhomogeneous mass measuring more than 9 cm is noted involving the musculature. Hemorrhage was found on fine-needle aspiration. This mass resolved with time and was presumed to represent a benign spontaneous hematoma of uncertain origin.

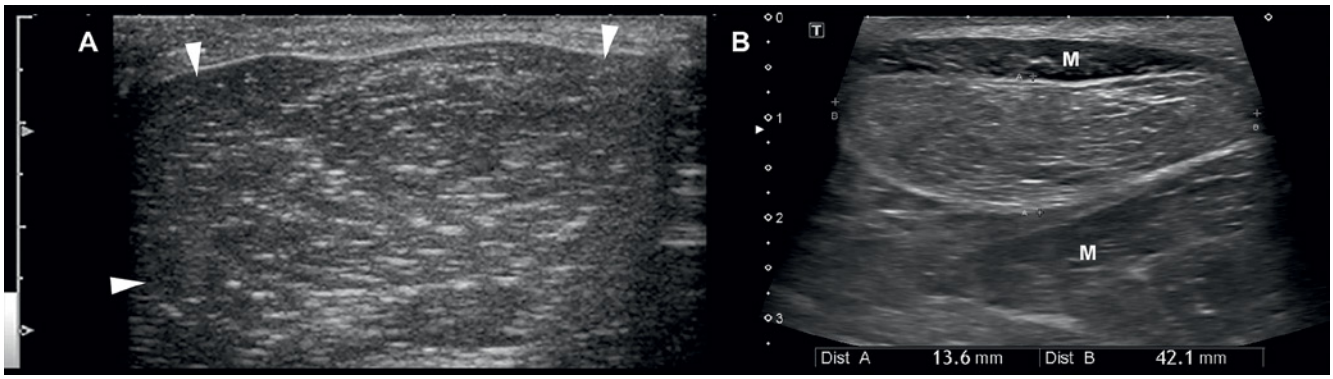


Figure 17.66. **Lipomas in two dogs. (A)** Sonographic image of a pelvic limb subcutaneous mass (arrowheads) with features characteristic of a lipoma. The mass is moderately echogenic and has uniformly distributed hyperechoic dots and short lines. **(B)** Intermuscular lipoma with well-defined margins in the pelvic limb of another dog. M, muscles.

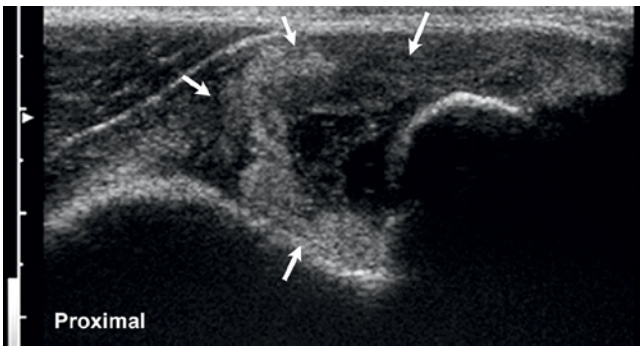


Figure 17.67. **Septic arthritis.** Longitudinal sonogram of the caudolateral aspect of the elbow of a dog with septic arthritis. A focal accumulation of inhomogeneous, echogenic fluid (arrows) is present, consistent with pus.

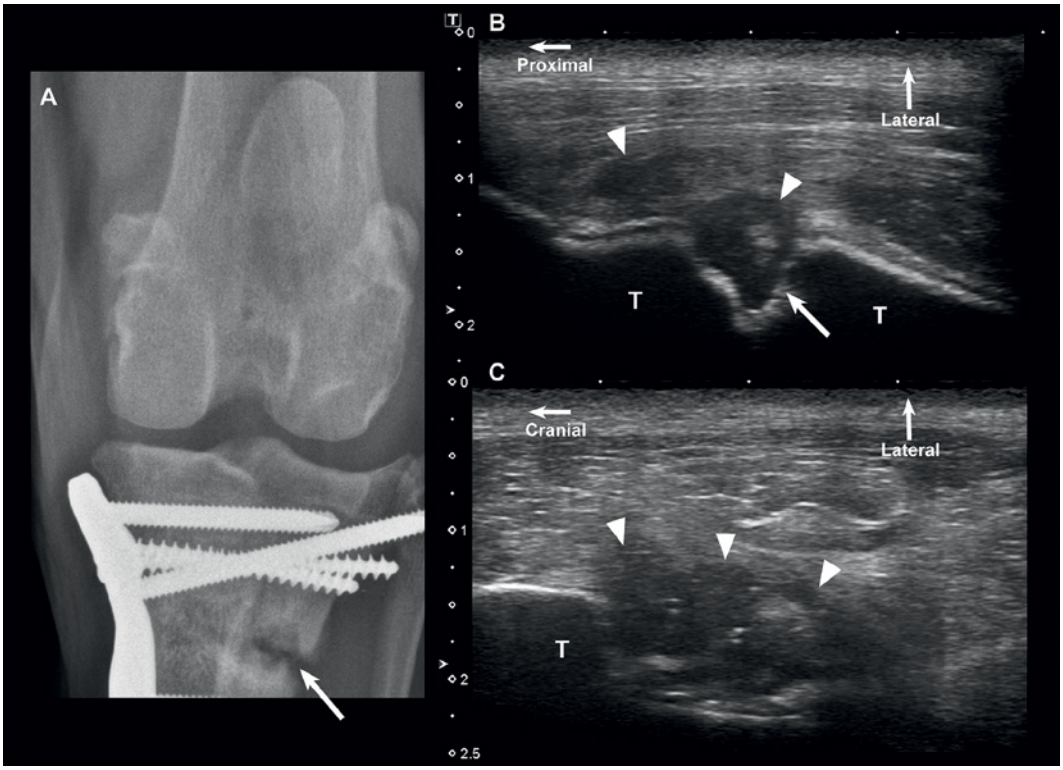


Figure 17.68. **Postsurgical osteomyelitis. (A)** Craniocaudal radiograph centered on the stifle of a dog 3 weeks following a tibial plateau-leveling osteotomy. The osteotomy line is enlarged, irregular, and ill-defined on the medial side, with surrounding sclerosis. Longitudinal **(B)** and transverse **(C)** sonograms were acquired at the site of the osteotomy (arrow in **B**). The hypoechoic area (arrowheads) was fine-needle-aspirated with ultrasound guidance, revealing a septic fluid. T, tibia.

Ultrasound may also be useful in confirming **discospondylitis**, especially at the lumbosacral junction that may be accessible for evaluation and even fine-needle aspiration (Figure 17.70).

Bone Tumors Primary and metastatic bone tumors associated with cortical lysis can be assessed sonographically, particularly if they extend into the surrounding soft tissue. They can vary in echogenicity

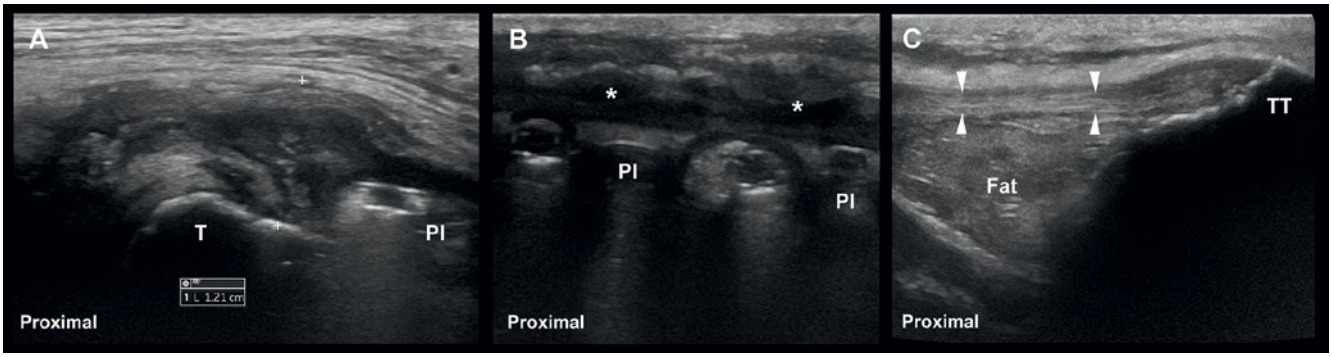


Figure 17.69. Spontaneous cellulitis and osteomyelitis. Two years after recuperating from a TPLO, this five-year-old Great Dane developed severe pelvic limb lameness. While radiographs were not diagnostic, parasagittal ultrasound images **(A, B)** obtained at the medial aspect of the proximal tibial (T) metaphysis revealed an irregular and poorly defined hypoechoic tissue at the proximal aspect of the orthopedic plate (Pl) and extending proximally, surrounded with thickened and heterogeneous subcutaneous fat containing fluid pockets (*) that were confirmed to represent pus. **(C)** There was no evidence of intra-articular involvement. The patellar ligament (arrowheads) and infrapatellar fat pad were normal. The bacterial culture from several fine-needle aspirates was negative, but the dog improved under antibiotics. TT, tibial tuberosity.

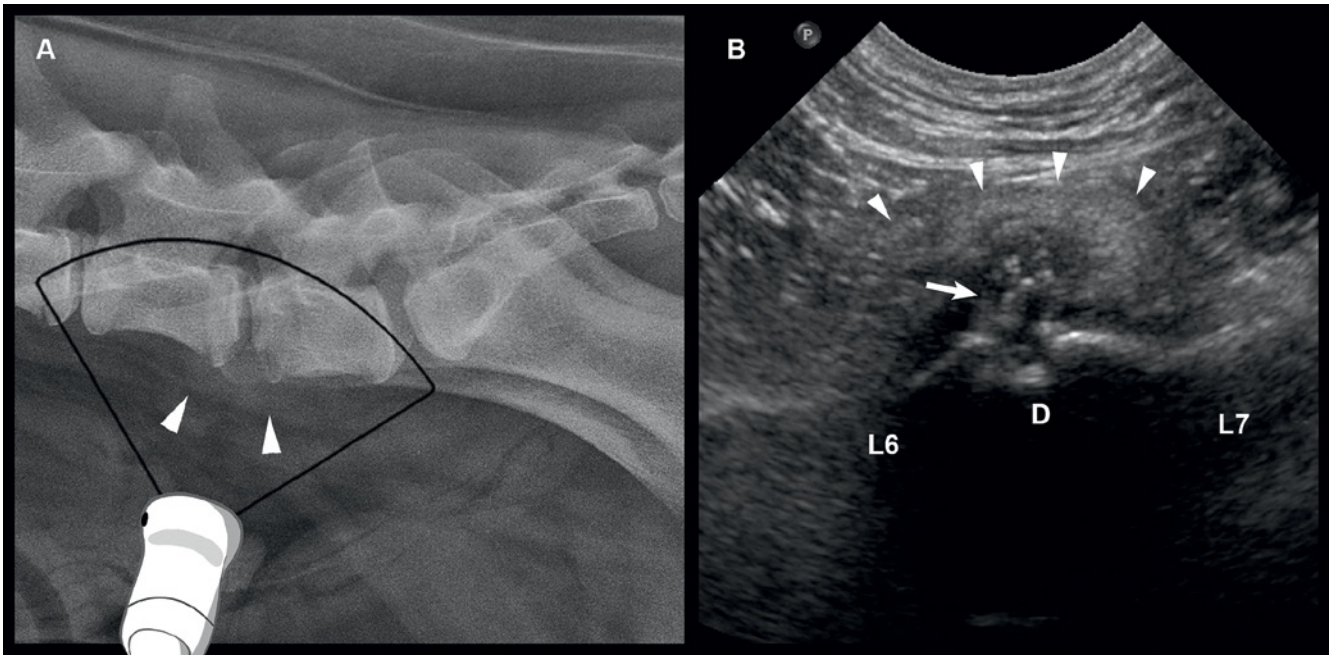


Figure 17.70. Discospondylitis in a puppy. **(A)** Lateral radiograph of the lumbosacral region showing lysis and osseous remodeling at the endplates of L6 and L7. Note the soft-tissue swelling ventral to the spine (arrowheads). **(B)** Longitudinal sonogram with the probe placed at the ventrolateral aspect of L6–L7 showing hyperechoic foci indicating mineralization (arrow) ventral to the intervertebral disc space (D), with ventral hyperechoic soft-tissue thickening (arrowheads) consistent with inflammatory tissue and fibrosis.

and uniformity (Figures 17.71–17.74). Occasionally, periosteal elevation (Codman's triangle) is seen. If sufficient cortical lysis is present, the deeper bone tissue can be visualized. Ultrasound is primarily performed in these instances to assist in **fine-needle aspiration or biopsy** of bone lesions, avoiding the need for surgical biopsy in some patients (Samii et al. 1999).

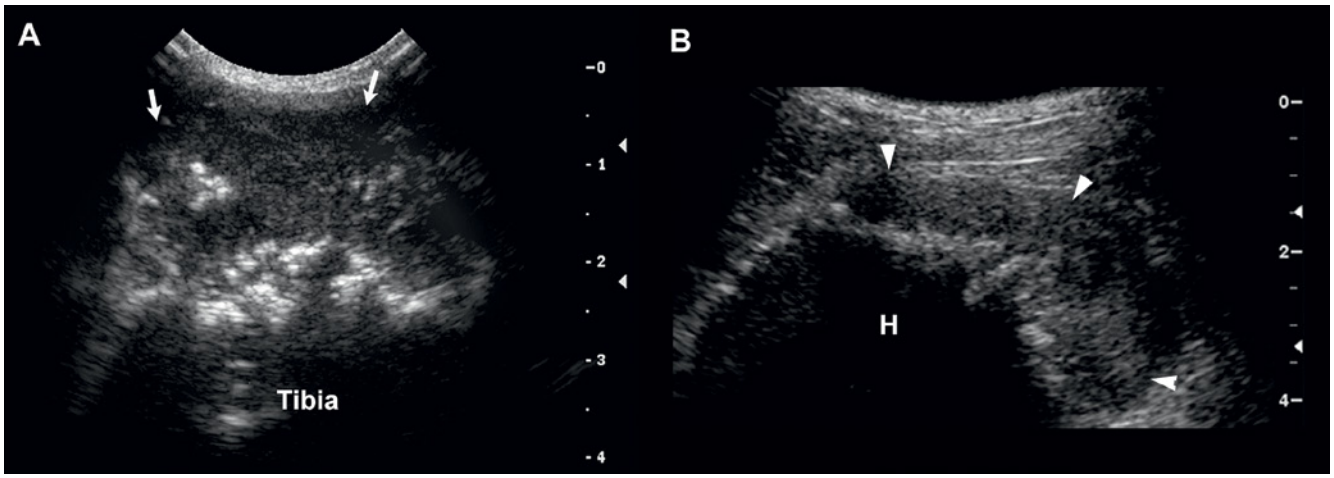


Figure 17.71. Osteosarcoma. Sonographic images of aggressive tibial **(A)** and humeral **(B)** mass lesions in two dogs. **(A)** An ill-defined, hypoechoic mass (arrows) has hyperechoic foci, some of which are associated with acoustic shadowing, consistent with mineralization. The underlying bone cortex is no longer visible because of the extensive lysis. **(B)** A well-defined, mildly echogenic mass (arrowheads) involves the humerus (H). The surface of the humerus is markedly irregular because of aggressive new bone formation and lysis.

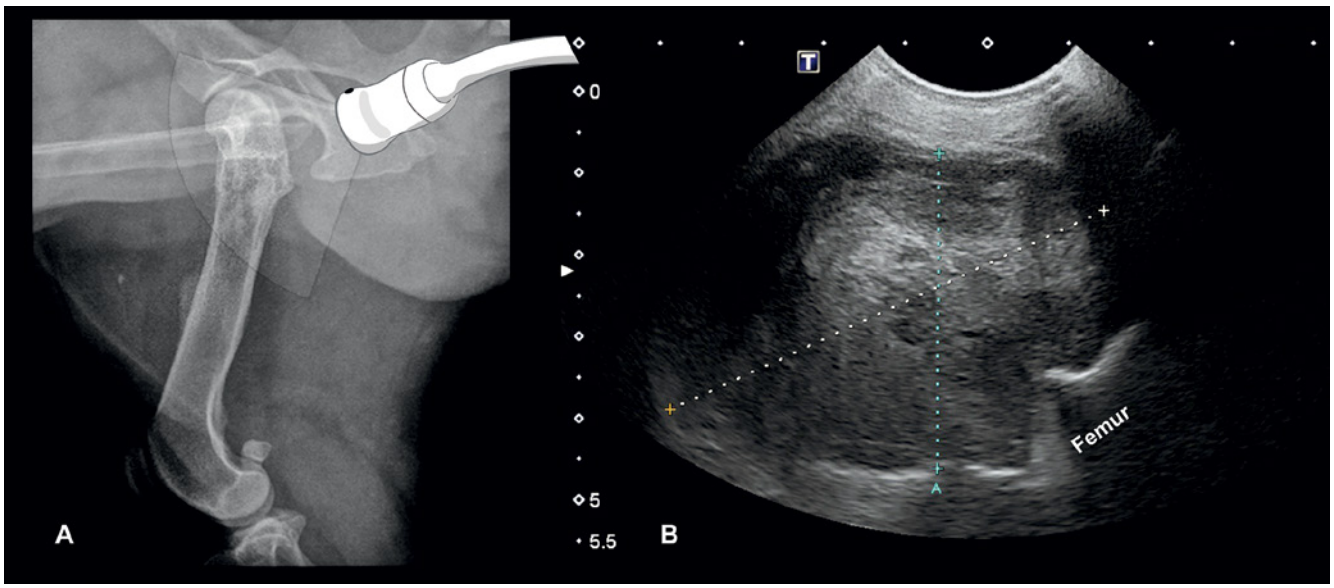


Figure 17.72. Femoral osteosarcoma in a 10-year-old Scottish Terrier. (A) Lateral radiograph of the femur on which moth-eaten lysis of the proximal diaphysis and metaphysis is detected, as well as a periosteal new bone formation on the cranial surface of the mid-femur. **(B)** The sonographic probe was placed laterally over the proximal thigh to obtain this image. The soft-tissue component of this primary bone tumor is exuberant. The mass is globally hypoechoic with hyperechoic ill-defined areas. Courtesy of Laurent Couturier, Azurvet, France.

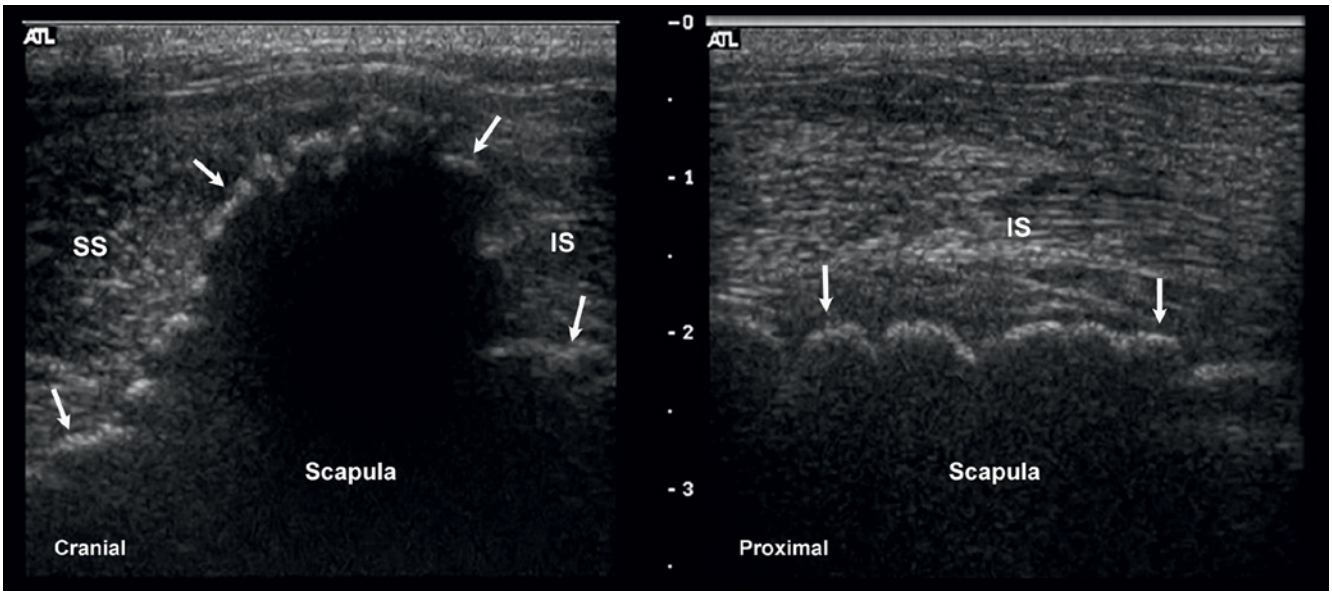


Figure 17.73. **Metastatic carcinoma to the scapula.** Transverse **(left)** and longitudinal **(right)** sonograms of the scapular spine in a dog with a transitional cell carcinoma and metastatic disease. Irregular new bone formation (arrows) is present at the level of the scapula. Adjacent supraspinatus (SS) and infraspinatus (IS) muscles are reduced in thickness and hyperechoic because of atrophy. Several similar lesions were identified in other bones, and metastatic carcinoma was confirmed histologically.

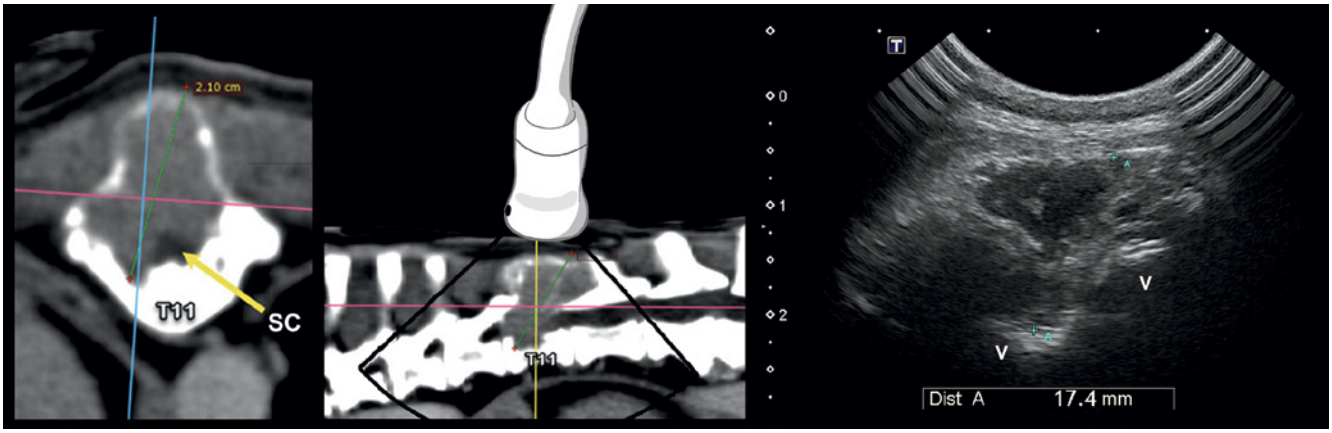
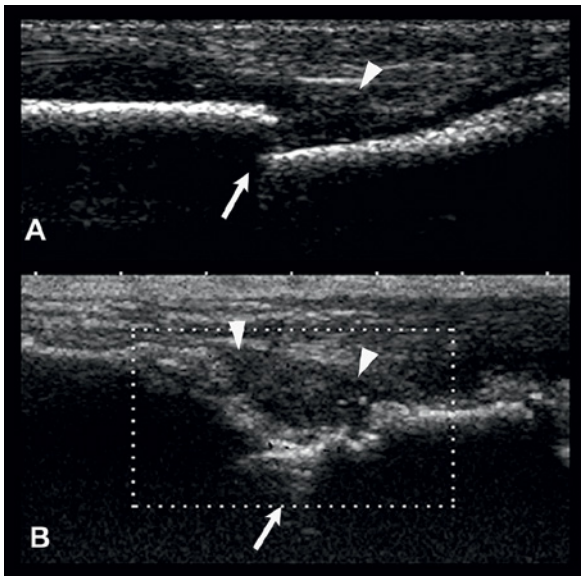


Figure 17.74. **Vertebral histiocytic sarcoma in a dog**. CT was initially performed in this dog presented for hind limb paresis. A contrast-enhancing, soft tissue-attenuating mass infiltrates the dorsal portion of T11, compressing the spinal cord (SC). Ultrasound was used to identify the hypoechoic and heterogeneous mass, allowing guidance for fine-needle aspirations. V, vertebral bony components.

Fractures Fractures of long bones and their **healing process**, as well as the associated soft-tissue damage (muscle rupture and hematoma), can be assessed ultrasonographically. Because there are no points of orientation, the exact relationship between the fractured ends is difficult to determine. To standardize the documentation of fracture healing of long bones, multiple and repeatable images must be obtained. The recommended transducer positions for the assessment of long bones are craniolateral (distal humerus, radius, ulna, and tibia) and caudolateral (proximal humerus cranial, femur medial, and fibula) (Risselada et al. 2003).

Ultrasonography can be used to evaluate **secondary fracture healing** in biologically treated fractures (Risselada et al. 2005). In comparison to radiography, the completion of fracture healing can be determined earlier. Secondary fracture healing can be divided into five stages (Figure 17.75).

During normal fracture healing, the newly developing tissues require more nutrients and have a higher metabolic rate. This requires the development of new



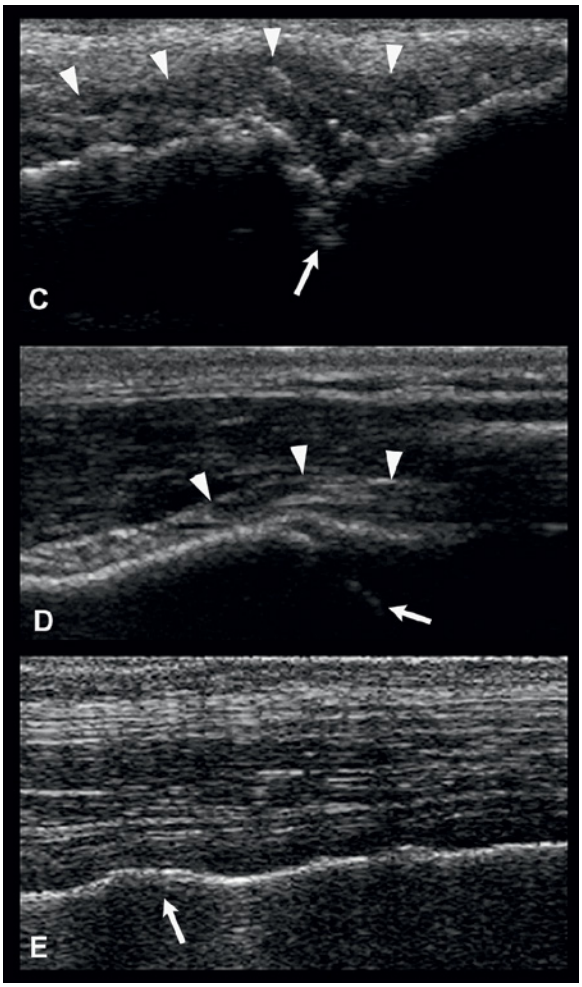


Figure 17.75. Bone fracture: healing process. Sequential sonograms showing progressive bone healing. **(A) Stage I (days 0–7)**. A discontinuity of the bone cortex is identified that is associated with sharp ends (arrow). Hypoechoic soft-tissue swelling is noted at the fracture site (arrowhead). **(B) Stages II–III (days 7–21)**. The bone defect (arrow) is progressively remodeled. A nonossified callus (arrowheads) is present. **(C) Stage IV (days 22–28)**. The nonossified callus is progressively more echogenic (arrowheads), and the fracture gap (arrow) is progressively narrower. **(D) Stage V (days 29–42)**. The fracture gap is nearly completely filled with new bone and poorly seen (arrow). The peripheral callus is reduced in volume (arrowheads). **(E) Stage VI (> 43 days)**. The fracture is healed. The surface of the bone remains mildly irregular (arrow).

vessels (neovascularization) at the fracture site and can be visualized using power Doppler ultrasound. A Doppler signal can be obtained as of day 10 after trauma, reaching a maximum between days 11 and 30, before gradually decreasing. Signals can be detected in and close to the callus (Risselada et al. 2006). Doppler assessment may thus help in investigating cases of **delayed bone union**.

Vascular Anomalies

Arteriovenous fistulas are rare, but when encountered, they typically result in limb soft-tissue swelling. A tortuous network of vessels is identified in proximity to a dilated vein showing a pulsatile flow pattern with color or pulsed-wave Doppler (Figure 17.76). The connection may sometimes be recognized.

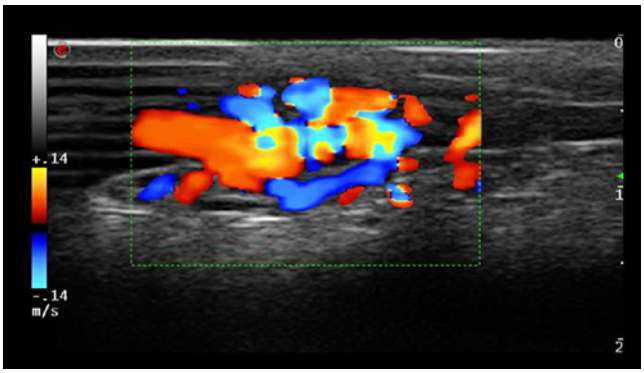


Figure 17.76. Arteriovenous fistula in the thoracic limb of a cat. A tortuous plexus of vessels with pulsatile flow was detected.

Scanning Technique and Normal Sonographic Anatomy of Spinal and Peripheral Nerves

Because of their small size and superficial location in extremities, **peripheral nerves** are preferably scanned with high-frequency (10 MHz and above) linear transducers. **Color flow Doppler** imaging is useful in differentiating adjacent vessels from nerves. In addition, nerves are not compliant to pressure, unlike vessels, and moving a limb can help in differentiating a tendon from a nerve. Sedation may be required in incompliant or painful patients, allowing limbs to be pulled or abducted more easily. Examination of controlateral nerves may help in confirming suspected abnormalities.

In longitudinal section, nerves of dogs and cats appear as 0.5–3-mm-wide, linear hypoechoic structures surrounded by a hyperechoic rim (Figures 17.77, 17.78) (Anson et al. 2013; Guilherme and Benigni 2008; Haro et al. 2011; Hudson et al. 1998). The walls of nerves are brighter and better defined than vessel walls; vascular walls are less distinct. In transverse section, nerves are circular or oval hypoechoic uniform structures or show individual components.

The scanning technique and sonographic anatomy of the **brachial plexus** have been described in both dogs (Guilherme and Benigni 2008; Hudson et al. 1998) and cats (Anson et al. 2013). Beginning with the dog placed in left lateral recumbency facilitates identification of the proximal portion of the right spinal nerves, using the C5–T1 transverse processes and intervertebral disc spaces as landmarks (Guilherme and Benigni 2008). Once the intervertebral disc space and foramen are located in the longitudinal plane, the probe is rotated approximately 90° to be transverse to the spine, with mild craniodorsal–caudoventral inclination to obtain longitudinal images of the origin of each spinal nerve (Figure 17.79). Each nerve appears dorsal to the corresponding **vertebral artery** and **vein**. The nerves are then imaged in the transverse plane and followed distally, as they gradually transform into clusters of 1–1.5-mm-wide round components. **Clustered nerve components** can

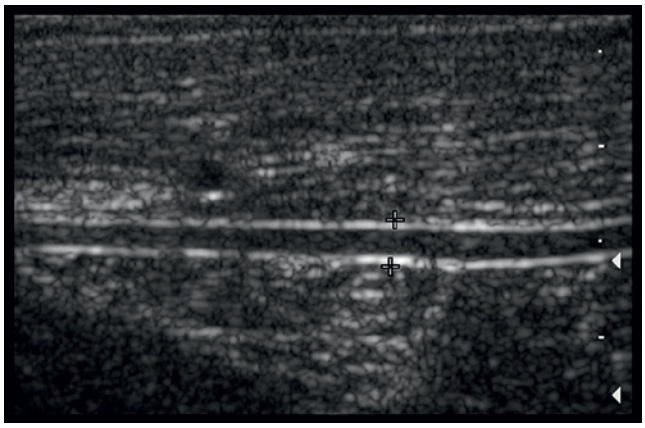


Figure 17.77. Sonographic appearance of a normal canine nerve. The central portion of the nerve is hypoechoic with speckles and surrounded with hyperechoic boundaries.

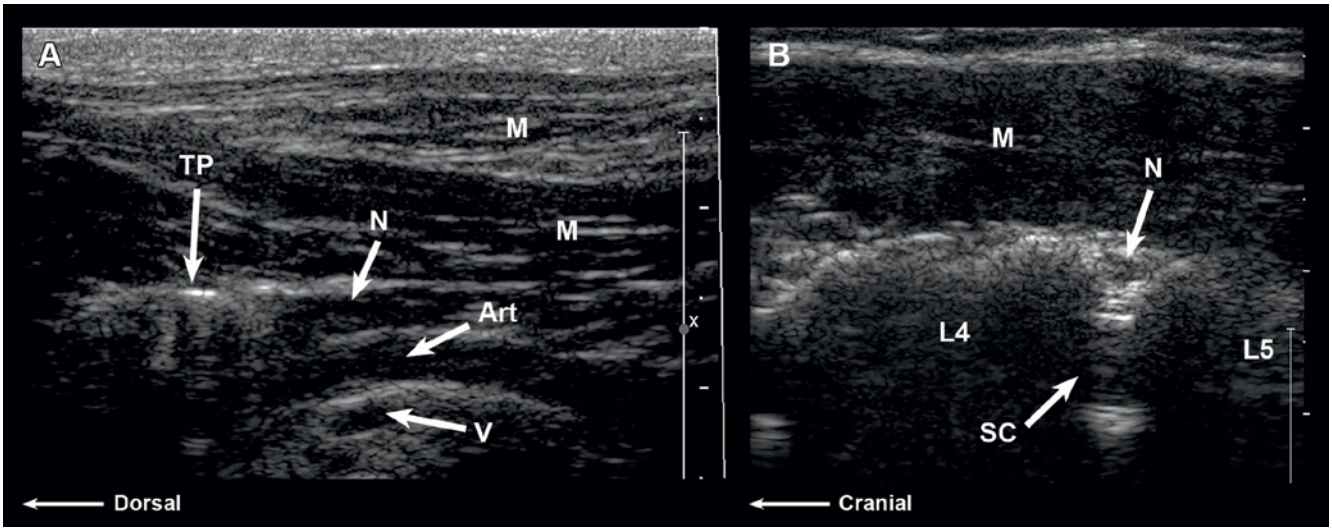


Figure 17.78. Spinal nerve as it exits its intervertebral foramen. (A) The spinal nerve (N) is identified in the longitudinal plane as it exits the intervertebral foramen, dorsal to the intervertebral artery (Art) and vein (V), ventral to the adjacent vertebral transverse process (TP). **(B)** This sonographic image was obtained with the probe held parallel to the lumbar vertebral column slightly lateral to the midline so that the beam passed through the intervertebral foramen in a dorsal oblique plane. The nerve (N) is seen in cross section as it exits the intervertebral foramen. The spinal cord (SC) can be seen deep to the foramen, between the shadowing fourth and fifth lumbar vertebrae (L4 and L5, respectively). M, paravertebral muscles.

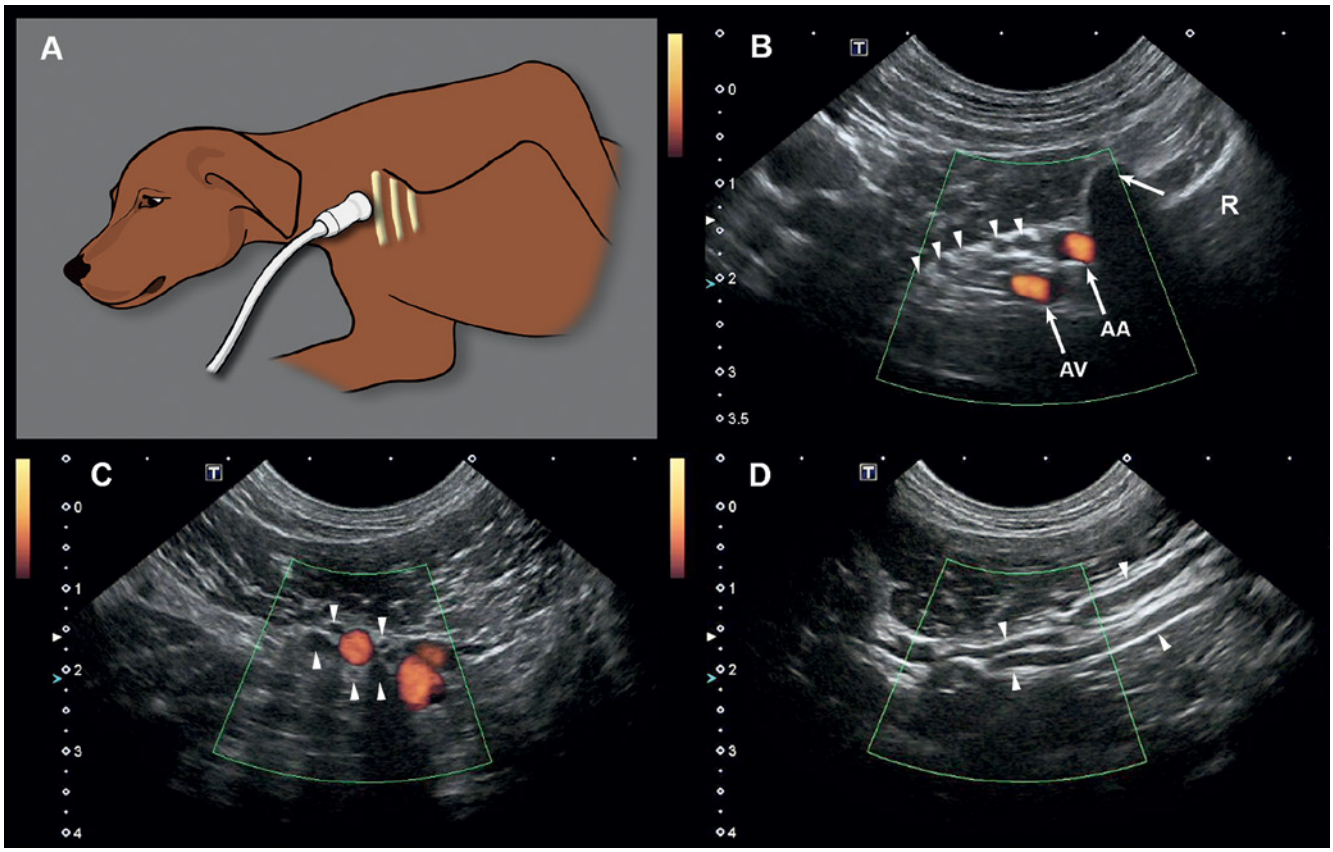


Figure 17.79. Approach to the left brachial plexus in a dog and normal sonographic appearance. (A) The dog is placed in right lateral recumbency and its left thoracic limb is pulled caudally. The probe is initially placed craniolateral to the first rib. The axilla is then examined, gently moving the probe in the transverse and parasagittal planes. **(B)** Components of the brachial plexus (arrowheads) are seen adjacent to the first rib (R) as round hypoechoic structures surrounded with hyperechoic tissue. The nerves measure between 0.5 and 2.5 mm. The axillary vein (AV) and artery (AA) are nearby with power Doppler orange signal. **(C, D)** Transverse (**C**) and longitudinal (**D**) sonographic images of the plexus nerves (arrowheads) obtained in the axilla. Note the prominence of their hyperechoic boundaries.

also be well visualized by placing the probe cranial to the first rib, pulling the limb caudally. Branches of the brachial plexus are further examined in the axilla, with the animal remaining in the same position but with the upper limb abducted, or in opposite lateral recumbency for a medial approach (Anson et al. 2013). The probe is placed in a parasagittal plane between the shoulder and sternum to identify the plexus in a transverse plane, close to the origin of the axillary artery and vein. These **vessels** are much larger than the nerves, particularly the vein that is easily compressible. Because of the sinusoidal orientation of these vessels, color Doppler signal may not be apparent. The median and ulnar nerves are caudal to the brachial artery, whereas the musculocutaneous nerve is located cranially. The probe can then be rotated to image the nerves in longitudinal section and can be slid distally to image the nerves in the midhumeral region (Figure 17.80). Transverse and longitudinal images of the musculocutaneous, median, and ulnar nerves are obtained from the medial aspect of the midhumeral regions by aligning the probe perpendicular or parallel to the limb, respectively. Similarly, the radial nerve can be evaluated at the caudomedial and distal lateral aspects of the antebrachium. This nerve appears at that level as a cluster of 0.5–1-mm components in both dogs and cats (Anson et al. 2013; Guilherme and Benigni 2008).

The **sciatic nerve** and its branches can also be examined in dogs and cats (Benigni et al. 2007; Haro et al. 2011). The caudal part of the lumbosacral trunk and the proximal portion of the sciatic nerves are recognized through the greater ischiatic foramen, using a parasagittal plane just medial to the shaft of the ilium. The sciatic nerve can be followed as it courses dorsolaterally over the acetabulum, bending toward the caudal aspect of the femur. Positioning the probe caudal to the greater trochanter enables a longitudinal image of the nerve that becomes parallel to the femoral neck (Figure 17.81).

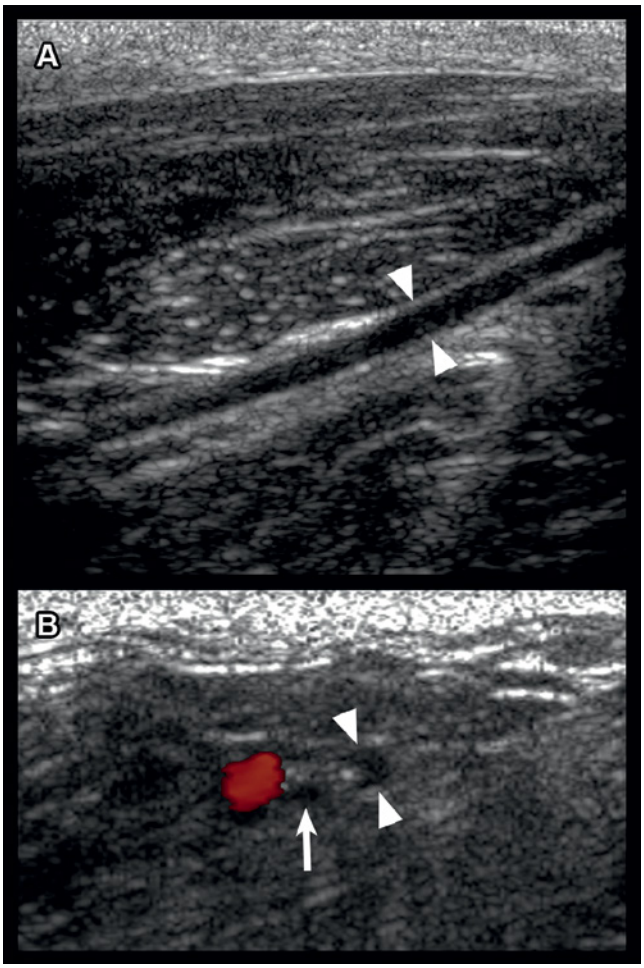


Figure 17.80. Normal ulnar nerve in a dog at the mid-humerus in longitudinal (A) and transverse (B) images. The ulnar nerve (arrowheads) is caudal to the brachial artery (red color Doppler signal in **B**) and median nerve (arrow).

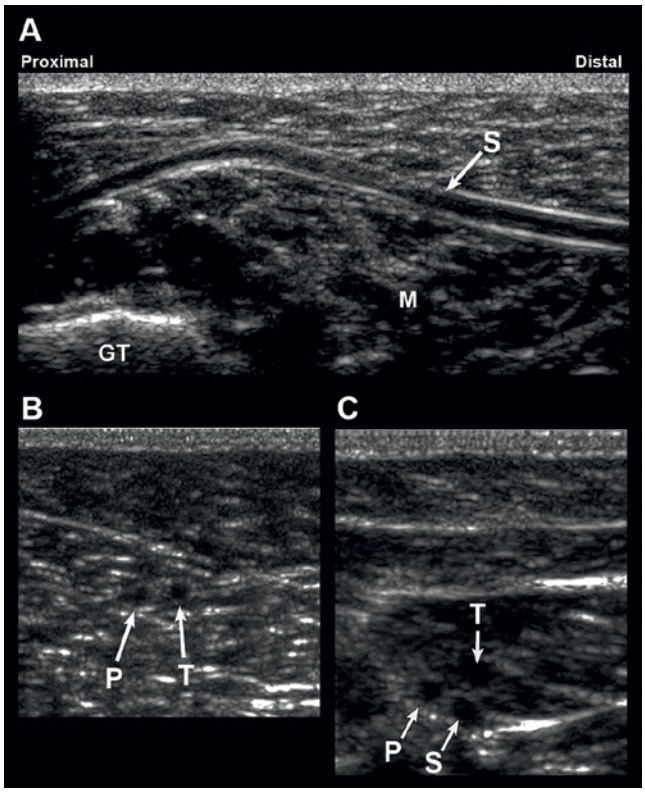


Figure 17.81. Normal sciatic nerve in a cat. The feline sciatic nerve is similar to that of the dog. **(A)** Proximal portion of the sciatic nerve (S) near the greater trochanter (GT). **(B)** Transverse image of the sciatic nerve in the mid-thigh showing the individual components representing the common peroneal nerve (P) and the larger tibial nerve (T). **(C)** Transverse image of the sciatic nerve obtained more distally. Three components are now apparent, representing the common peroneal nerve (P), the tibial nerve (T), and the caudal cutaneous sural nerve branch from the tibial nerve (S).

The nerve then becomes close to the caudal gluteal artery and vein, before extending distally, parallel and caudal to the femoral shaft, between the muscles of the thigh. In the transverse plane, two components of the sciatic nerve are distinguished, the common peroneal nerve, cranially, and the tibial nerve, just caudally.

Sonographic Features of Peripheral Nerve Disorders

Rupture and Demyelination

Rupture or transection of nerves can occur associated with fractures, sharp-object penetration, or other injuries. After injury, loss of visualization of the distal segment strongly suggests rupture.

In acute partial or complete **avulsions of the brachial plexus**, a hypoechoic to anechoic, inhomogeneous, and irregularly demarcated area is seen in the axillary region. This area represents the hematoma. Torn nerve tissue can usually not be seen sonographically.

Serial examination can be useful to determine if there is any evidence of repair after injury. In some animals, a **neuroma** may form at the site of transection, often appearing as a hypoechoic bulb. Regeneration has been described as irregular regrowth with or without neuroma formation.

Demyelination also can occur after trauma, compression by a mass, or inflammation that is not severe enough to cause transection. In such cases, the nerve is poorly visualized distal to the site of injury. Comparison with the nerve on the healthy contralateral side is helpful (Figure 17.82).

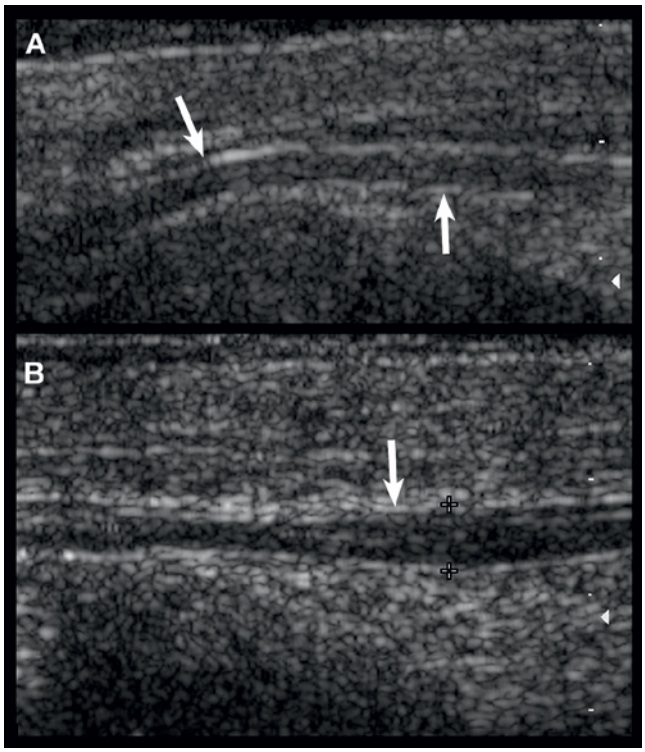


Figure 17.82. Longitudinal sonogram of the right sciatic nerve in a dog with neurological deficits. Compare these images with those of a normal sciatic nerve in Figure 17.81. **(A)** The sciatic nerve (arrows) near the greater trochanter. **(B)** The sciatic nerve near the mid-femoral region (arrows). The nerve has a variable diameter and irregular interrupted walls. The nerve is swollen in the mid-femoral region and measures 2.9 mm.

Neoplasia

While CT and MRI are generally considered more useful for detecting **peripheral nerve sheath tumors (PNSTs)**, ultrasound can be used as an initial diagnostic tool or to guide fine-needle aspiration or biopsy. Tumors of the spinal or peripheral nerves can usually be visualized by ultrasonography if they exceed 5 mm. PNSTs in dogs have been described as hypoechoic tubular structures or as fusiform to spherical masses exhibiting mixed echogenicity (Figures 17.83–17.85) (Platt et al. 1999; Rose et al. 2005). When tubular or fusiform in shape, color or power Doppler is useful for discriminating these from adjacent blood vessels (Figure 17.85). Peripheral nerve tumors can occur in unusual locations such as the thorax (Essman et al. 2002), urinary bladder wall (Pavia et al. 2012), and other organs.

Other Disorders of the Peripheral Nerves and Adjacent Tissues

Inflammatory neuropathies may be detected in some animals with ultrasound. Chronic lymphocytic – or hypertrophic – neuritis or ganglioneuritis is a rare condition that has been reported involving C2 spinal nerve in a dog (Rodenas et al. 2013). Affected nerves are thickened and hypoechoic, mimicking neoplasia.

In the case of **sciatic neuritis,** ultrasound may reveal thickening with hyperechoic and irregular borders of the sciatic nerve and concurrent deep gluteal muscle changes such as increased echogenicity and decreased volume, the piriformis muscle being most commonly involved (Toijala et al. 2021).

Metastases to the axillary lymph nodes near the brachial plexus can also be identified. Affected lymph nodes are typically rounded, moderately to severely enlarged, and mildly to moderately inhomogeneous. The hilar fat usually disappears. A definitive diagnosis can be obtained by ultrasound-guided needle biopsy.

Interventional Procedures

Ultrasound may not always replace CT or MRI for diagnostic purposes, but it allows interventional procedures to be performed in real time, often in awake or minimally sedated patients.

Ultrasound can be used to guide **biopsy** or **aspiration needles** into soft-tissue lesions that may not be detected or well characterized with radiography. Ultrasound may also serve to place needles into bone lesions through cortical defects, or into extraosseous soft-tissue extensions or fluid collections that may not be detected on radiographs. This may be particularly useful for suspected bone neoplastic lesions (Samii et al. 1999). Length and size of the needle (20–25-gauge) depends on the location and exfoliation of the targeted lesion. Spinal needle may be required if the lesion is deep. After removing the stylet, the needle is moved repeatedly back and forth within the mass (Da Costa et al. 2008). In the case of rigid masses that do not exfoliate well, aspiration may be necessary.

Ultrasound is useful for **intraoperative identification of FBs**, guiding surgeons in their surgical approach and confirming that all fragments have been successfully removed. This may be particularly valuable for **grass awns** migrating in the sublumbar muscles (Birettoni et al. 2017) or **porcupine quills**, which are often difficult to localize by palpation or surgical exploration (Figure 17.86). FBs may then be removed by a **surgical clamp** under ultrasound guidance, or using small, flexible **endoscopic forceps** through fistular tracts, or

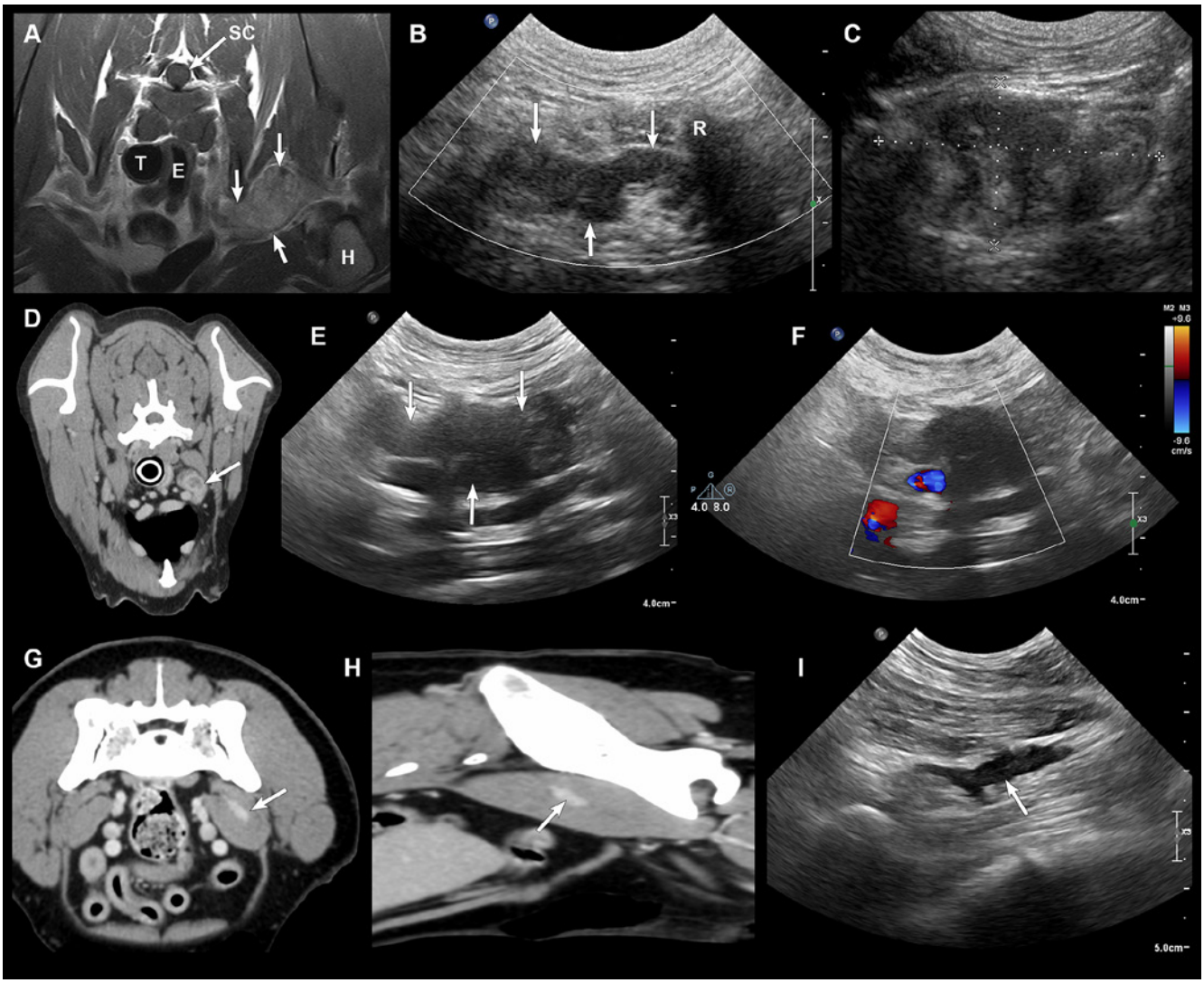


Figure 17.83. **Peripheral nerve sheath tumors in three dogs. (A–C)** Contrast T1-weighted transverse magnetic resonance image **(A)** showing an oblong, lobular mass (arrows) as it exits the spinal canal in this American Cocker Spaniel with moderate left thoracic limb lameness. Portions of the mass show contrast enhancement, although some areas remain hypointense. E, esophagus; H, humerus; SC, spinal cord; T, trachea. **(B)** On ultrasound, the radial nerve (arrows) is enlarged, irregular, and hypoechoic. R, rib. **(C)** The nerve becomes incorporated in a large heterogeneous mass (calipers) immediately cranial to the first rib. Histopathology following surgical biopsy revealed a peripheral nerve sheath tumor. **(D–F)** Deep axillary mass in another dog that is heterogeneous on contrast-enhanced CT (**D**) and hypoechoic and irregular in longitudinal (**E**) and transverse (**F**) sonograms. **(G–I)** In this third dog, the left femoral nerve (arrows) is irregularly enlarged and associated with intense contrast enhancement in transverse (**G**) and parasagittal (**H**) CT images, while being hypoechoic on ultrasound (**I**).

surgical incisions (Segalen and Durieux 2010; Staudte et al. 2004) (Figure 17.87). Injection of sterile saline solution into the fistular tract may facilitate identification of the FB fragment(s). Larger foreign objects or those embedded in fibrous tissue may require more extensive surgical exploration.

Ultrasound may also serve to **guide intra-articular or intra- or paratendinous injections**, for diagnostic or therapeutic purposes, or for **local anesthesia** (Figure 17.88). Lidocaine can be injected around the sciatic nerve at the lateral aspect of the canine thigh caudal to the femur and medial to the biceps femoris. The injected lidocaine can appear as a hypoechoic halo, which was termed a "donut sign" by the authors of one study (Echeverry et al. 2010). Injections can be made around the C6, C7, and C8 cervical spinal nerve roots with a 22-gauge spinal needle using the transverse processes and scalenus muscle as landmarks (Bagshaw

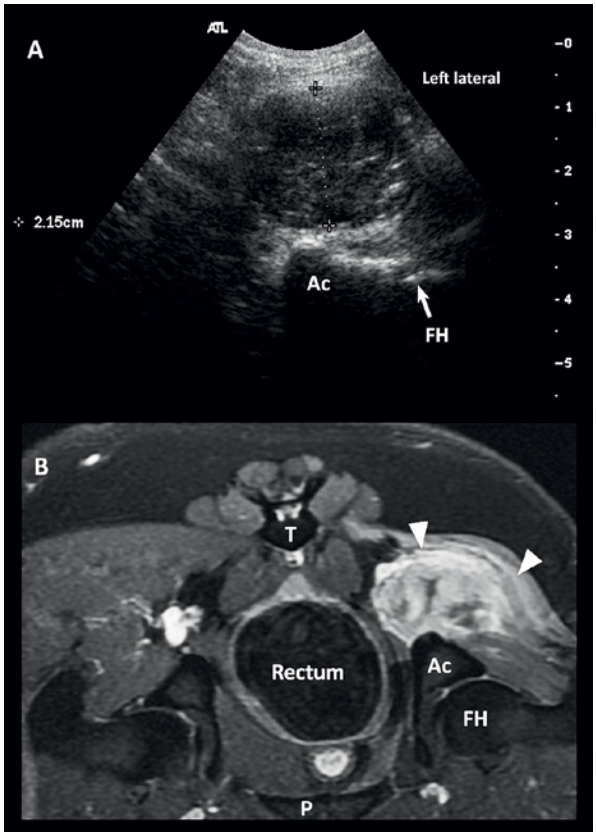


Figure 17.84. **Sciatic nerve sheath fibrosarcoma in a dog. (A)** Transverse sonographic image of a 2.15-cm-thick mildly echogenic mass located dorsal to the acetabular bone (Ac) and femoral head (FH). **(B)** Transverse postcontrast T1-weighted magnetic resonance sequence with fat saturation, highlighting the contrast-enhancing mass (arrowheads). The adjacent muscles are atrophied and hyperintense. P, pubis; T, tail.

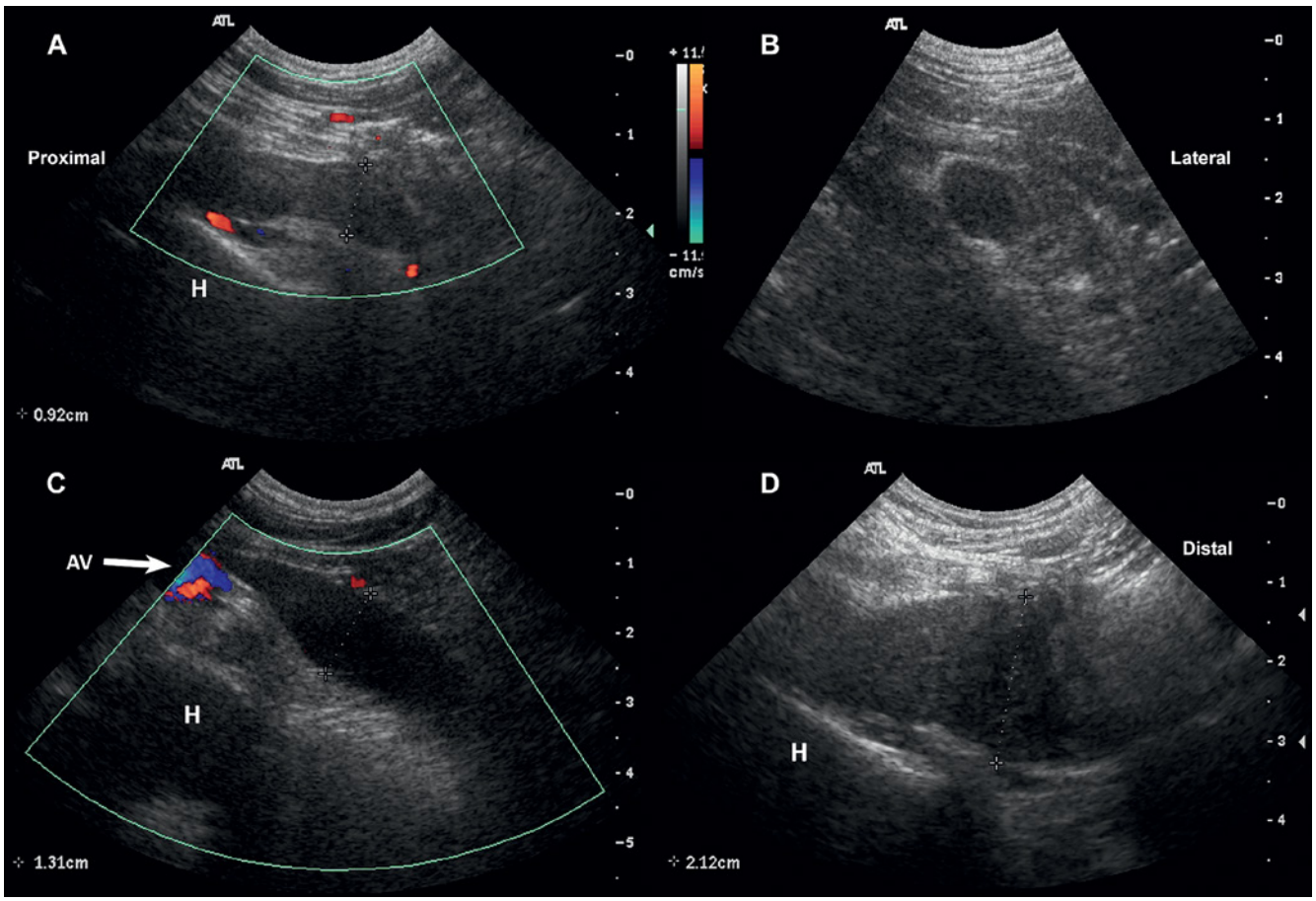


Figure 17.85. **Brachial plexus nerve sheath tumor in a dog.** Color Doppler can be useful in distinguishing enlarged nerves of the brachial plexus from nearby vessels. A well-defined hypoechogenic tubular structure without flow is identified next to the humerus (H) in this longitudinal color Doppler **(A)** and transverse B-mode **(B)** sonographic images. **(C)** This structure is followed distally, next to the axillary vein (AV) and (**D**) the humerus, becoming a larger mass approximating 2 cm in diameter.

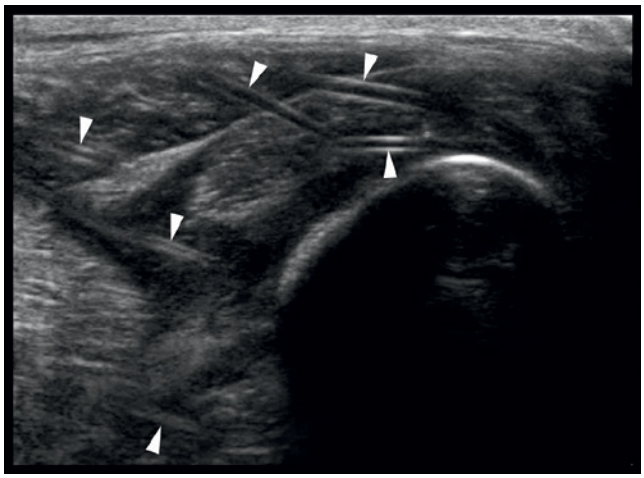


Figure 17.86. Intraoperative identification of residual porcupine quills in a dog. Ultrasound was used in this dog after four porcupine quills were surgically removed. While nothing was felt on palpation, several additional quills (arrowheads) were detected.

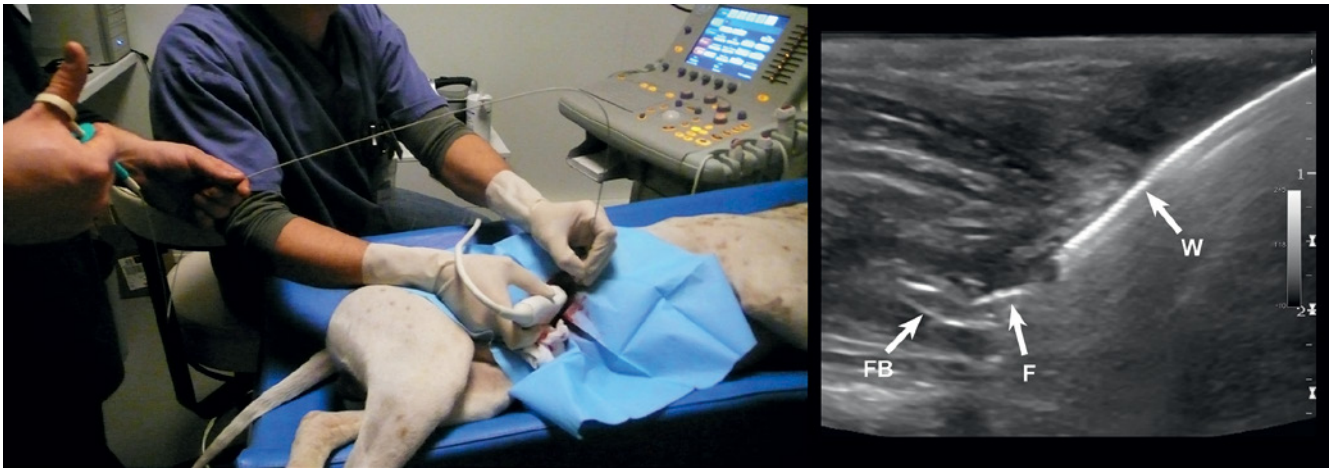


Figure 17.87. Use of small flexible endoscopic forceps for removal of a grass awn foreign body in a dog. The endoscopic forceps was inserted into the fistular tract and guided to the grass awn foreign body with ultrasound guidance. The endoscopic wire (W) and alligator forceps (F) appear as strongly echogenic interfaces with reverberation, while the grass awn foreign body (FB) is not shadowing. Courtesy of Franck Durieux, Aquivet, France.

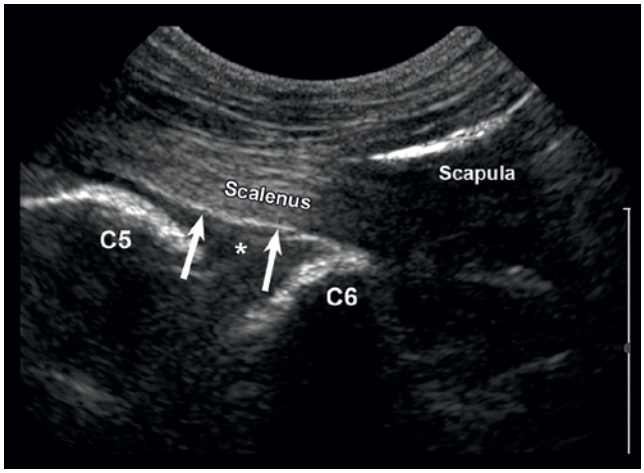


Figure 17.88. Landmarks for blocking the nerve roots of the brachial plexus in dogs. The probe is held in a dorsal plane parallel to the long axis of the neck, allowing identification of the C5 and C6 transverse processes. The cranial part of the spine is on the left side of the image. The scapula makes visualization of the C7 transverse process more difficult. Injections are made deep (*) to the fascial plane of the scalenus muscle (arrows), allowing the solution to be contained in the vicinity of the exiting spinal nerves (Bagshaw et al. 2009).

et al. 2009). Similarly, ultrasonography can be useful for guiding injections of local anesthetic agents to block the brachial plexus and origin of the femoral nerve in cats (Alvarez et al. 2011). For blocking the feline brachial plexus, the preferred approach included placement of the cat in dorsal recumbency and abduction of the limb to be blocked, while the opposite forelimb was pulled caudally (Anson et al. 2015). A dorsal approach was suggested for blocking the femoral nerve (Alvarez et al. 2011). Injection was made into the iliopsoas complex between the L6 and L7 transverse processes with the cats placed in lateral recumbency and the probe held perpendicular to the spine. The dorsal processes of the L6 and L7 lumbar vertebrae and the cranial margin of the proximal ilium can be useful landmarks for the procedure.

Additionally, ultrasonography can aid in locating transected nerve endings prior to surgical repair. Following anastomosis, ultrasonography can be used to monitor the nerves healing (Hudson et al. 1998).



Visit our website at **www.SmallAnimalUltrasonography.com** for complementary video clips with annotations and text on:

- Normal shoulder: Scanning technique and anatomy (dog)
- Normal common calcaneal tendon
- Bicipital tenosynovitis
- Supraspinatus tendinopathy
- Common calcaneal tendinopathy
- Gracilis myopathy in a dog
- Osteomyelitis
- Joint neoplasia
- Supraspinatous/infraspinatus abscess in a dog
- Peripheral nerve sheath tumor
- Vertebral mass invading the spinal canal

References

Adams WM, Dueland RT, Daniels R, Fialkowski JP, et al. (2000) Comparison of two palpation, four radiographic and three ultrasound methods for early detection of mild to moderate canine hip dysplasia. Vet Radiol Ultrasound 41:484–490.

Alvarez PH, Gil F, Laredo FG, Ayala MD, et al. (2011) Abstracts from the 2011 EVDI Annual Meeting (London, England). Ultrasound guidance for the femoral nerve block in cats: an imaging study. Vet Radiol Ultrasound 52:682.

Anson A, Gil F. Lardo F, Soler M, et al. (2013) Correlative ultrasound anatomy of the feline brachial plexus and major nerves of the thoracic limb. Vet Radiol Ultrasound 54:185–193.

Anson A, Gil F, Laredo FG, Soler M, et al. (2015) A comparison of two techniques for ultrasound-guided brachial plexus block in cats. J Feline Med Surg 17(6):476–485.

Armbrust LJ, Biller DS, Radlinsky MG, Hoskinsons JJ (2003) Ultrasonographic diagnosis of foreign bodies associated with chronic draining tracts and abscesses in dogs. Vet Radiol Ultrasound 44:66–70.

Arnault F, Caulvin E, Viguier E, Kraft E, et al. (2009) Diagnostic value of ultrasound to assess stifle lesions in dogs after CCL rupture:13 cases. Vet Comp Orthop Traumatol 22(6):479–485.

Bagshaw HS, Larenza MP, Seiler GS (2009) A technique for ultrasound-guided paravertebral brachial plexus injections in dogs. Vet Radiol Ultrasound 50:649–654.

Benigni L, Corr SA, Lamb CR (2007) Ultrasonographic assessment of the canine sciatic nerve. Vet Radiol Ultrasound 48:428–433.

Birettoni F, Caivano D, Rishniw M, Moretti G, et al. (2017) Preoperative and intraoperative ultrasound aids removal of migrating plant material causing iliopsoas myositis via ventral midline laparotomy: a study of 22 dogs. Acta Vet Scand 59:1–9.

Boyse TD, Fessell DP, Jacobson JA, Lin J, et al. (2001) US of soft-tissue foreign bodies and associated complications with surgical correlation. Radiographics 12:1251–1256.

Breur GJ, Blevins WE (1997) Traumatic injury of the iliopsoas muscle in three dogs. J Am Vet Med Assoc 210:1631–1634.

Brisson BA, Bersenas A, Etue SM (2004) Ultrasonographic diagnosis of septic arthritis secondary to porcupine quill migration in a dog. J Am Vet Med Assoc 9:1467–1470.

Caine, A., Agthe, P., Posch, B. and Herrtage, M., 2009. Sonography of the soft tissue structures of the canine tarsus. *Vet Radiol Ultrasound*, *50*(3), pp. 304–308.

Cannon, M.S. and Puchalski, S.M., 2008. Ultrasonographic evaluation of normal canine iliopsoas muscle. *Vet Radiol Ultrasound*, *49*(4), pp. 378–382.

Cogar S, Cook C, Curry S, Grandis A, et al. (2008) Prospective evaluation of Techniques for differentiating shoulder pathology as a source of forelimb lamenesss in medium and large breed dogs. Vet Surg 37:132–141.

Da Costa RC, Parent JM, Dobson H, Ruotsalo K, et al. (2008) Ultrasound-guided fine needle aspiration in the diagnosis of peripheral nerve sheath tumors in 4 dogs. Can Vet J 49:77–81.

De Bakker E, Gielen I, Saunders JH, Polis I, et al. (2013) Primary and concomitant flexor enthesopathy of the canine elbow. Vet Comp Orthop Traumatol 26(6):425–434.

Echeverry DF, Gil F, Laredo F, Ayala MD, et al. (2010) Ultrasound-guided block of the sciatic and femoral nerves in dogs: a descriptive study. The Vet J 186:210–215.

Essman SC, Hoover JP, Bahr RJ, Ritchey JW, et al. (2002) An intrathoracic malignant peripheral nerve sheath tumor in a dog. Vet Radiol Ultrasound 43:255–259.

Esterline ML, Armbrust L, Roush JK (2005) A comparison of palpation guided and ultrasound guided percutaneous biceps brachii tenotomy in dogs. Vet Comp Orthop Traumatol 18:135–139.

Fabbi M, Di Palma S, Manfredi S, Gnudi G, et al. (2016) Imaging diagnosis – ultrasonographic appearance of skeletal muscle metastases in a dog with hemangiosarcoma. Vet Radiol Ultrasound 58:E64–E67.

Fischer A, Flöck A, Tellhelm B, Failing K, et al. (2010) Static and dynamic ultrasonography for the early diagnosis of canine hip dysplasia. J Small Anim Pract 51:582–588.

Franch J, Bertran J, Remolins G, Fontecha P, et al. (2009) Simultaneous bilateral contracture of the infraspinatus muscle – clinical case in a five-year-old Berlgian shepherd dog. Vet Comp Orthop Traumatol 22:249–252.

Frank I, Duerr F, Zanghi B, Middleton R, et al. (2019) Diagnostic ultrasound detection of changes in femoral muscle mass recovery after tibial plateau levelling osteotomy in dogs. Vet Comp Orthop Traumatol 32:394–400.

Gamble LJ, Canapp D, Canapp S (2017) Evaluation of achilles tendon injuries with findings from diagnostic musculoskeletal ultrasound in canines – 43 cases. Vet Evid 2:1–23.

Gnudi G, Bertoni G (2001) Echographic examination of the stifle joint affected by cranial cruciate ligament rupture in the dog. Vet Radiol Ultrasound 42:266–270.

Gnudi G, Volta A, Bonazzi M, Gazzola M, et al. (2005) Ultrasonographic features of grass awn migration in the dog. Vet Radiol Ultrasound 46:423–426.

González-Rellán S, Fdz-de-Trocóniz P, Barreiro A (2021) Ultrasonographic anatomy of the dorsal region of the carpus of the dog. Vet Radiol Ultrasound 62:591–601.

González-Rellán S, Fdz-de-Trocóniz P, Barreiro A (2023) Ultrasonographic anatomy of the palmar region of the carpus of the dog. Vet Radiol Ultrasound 64:1–11.

Greshake RJ, Ackerman N (1992) Ultrasound of the coxofemoral joints of the canine neonate. Vet Radiol Ultrasound 33:99–104.

Guilherme S, Benigni I (2008) Ultrasonographic anatomy of the brachial plexus and major nerves of the canine thoracic limb. Vet Radiol Ultrasound 49(6):577–583.

Haro P, Gil F, Laredo F, Ayala MD, et al. (2011) Ultrasonographic study of the feline sciatic nerve. J Feline Med Surg 13(4):259–265.

Hermanson JW, Evans HE (1993) The muscoloskeletal system. In Evans HE, Christensen GC, eds. Miller's Anatomy of the Dog, 3rd edition. WB Saunders: Philadelphia, pp. 258–384.

Hittmair KM, Groessl V, Mayrhofer E (2012) Radiographic and ultrasonographic diagnosis of stenosing tenosynovitis of the abductor pollicis longus muscle in dogs. Vet Radiol Ultrasound53:135–141.

Hudson JA, Finn-Bodner ST, Steiss JE (1998) Neurosonography. Vet Clin North Am Small Anim Pract 28:943–971.

Knox VW IV, Sehgal CM, Wood AK (2003) Correlation of ultrasonographic observations with anatomic features and radiography of the elbow joint in dogs. Am J Vet Res 64:721–726.

Kramer M, Gerwing M, Hach V, Schimke E (1997) Sonography of the musculoskeletal system in dogs and cats. Vet Radiol Ultrasound 38:139–149.

Kramer M, Stengel H, Gerwing M, Schimke E, et al. (1999) Sonography of the canine stifle. Vet Radiol Ultrasound 40:282–293.

Kramer M, Gerwing M, Michele U, Schimke E, et al. (2001a) Ultrasonographic examination of injuries to the Achilles tendon in dogs and cats. J Small Anim Pract 42:531–535.

Kramer M, Gerwing M, Sheppard C, Schimke E (2001b) Ultrasonography for the diagnosis of diseases of the tendon and tendon sheath of the biceps brachii muscle. Vet Surg 30:64–71.

Kühn K, Ohlerth S, Makara M, Hassig M, et al. (2011) Radiographic and ultrasonographic evaluation of the patellar ligament following tibial tuberosity advancement. Vet Radiol Ultrasound 52:466–471.

Kulendra E, Coor S (2008) Necrotising fasciitis with subperiosteal Streptoccocus canis infection in two puppies. Vet Comp Orthop Traumatol 21:474–477.

Lafuente M, Fransson B, Lincoln J, Martinez S, et al. (2009) Surgical treatment of mineralized and nonmineralized supraspinatus tendinopathy in twenty-four dogs. Vet Surg 38:380–387.

Lamb C, Duvernois A (2005) Ultrasonographic anatomy of the normal canine calcaneal tendon. Vet Radiol Ultrasound 46:326–330.

Lamb C, Wong K (2005) Ultrasonographic anatomy of the canine elbow. Vet Radiol Ultrasound 46:319–325.

Lassaigne C, Boyer C, Sautier L, Taeymans O (2020) Ultrasound of the normal canine supraspinatus tendon: comparison with gross anatomy and histology. Vet Rec 186:e14.

Liuti T, Saunders J, Gielen I, Rycke L, et al. (2007) Ultrasound approach to the canine distal tibia and trochlear ridges of the talus. Vet Radiol Ultrasound 48:361–367.

Long C, Nyland TG (1999) Ultrasonographic evaluation of the canine shoulder. Vet Radiol Ultrasound 40:372–379.

Mahn MM, Cook JL, Cook CR, Balke MT (2005) Arthroscopic verification of ultrasonographic diagnosis of meniscal pathology in dogs. Vet Surg 34:318–323.

Mattern KL, Berry RB, Peck JN, de Haan JJ (2006) Radiographic and ultrasonographic evaluation of the patellar ligament following tibial plateau leveling osteotomy. Vet Radiol Ultrasound 47:185–191.

Nielsen C, Pluhar GE (2004) Diagnosis and treatment of hind limb muscle strain injuries in 22 dogs. Vet Comp Orthop Traumatol 18:247–253.

Ober C, Jones J, Larson M, Lanz O, et al. (2008) Comparison of ultrasound, computed tomography, and magnetic resonance imaging in detection of acute wooden foreign bodies in the canine manus. Vet Radiol Ultrasound 49:411–418.

Pavia PR, Havig ME, Donovan TA, Craft D (2012) Malignant peripheral nerve sheath tumour of the urinary bladder in a cat. J Small Anim Pract 53:245–248.

Platt, S.R., Graham, J., Chrisman, C.L., Collins, K., Chandra, S., Sirninger, J. and Newell, S.M., 1999. Magnetic resonance imaging and ultrasonography in the diagnosis of a malignant peripheral nerve sheath tumor in a dog. *Vet Radiol Ultrasound*, *40*(4), pp. 367–371.

Reed AL, Payne JT, Constaninescu GM (1995) Ultrasonographic anatomy of the normal canine stifle. Vet Radiol Ultrasound 36:315–321.

Risselada M, Kramer M, van Bree H (2003) Approaches for ultrasonographic evaluation of long bones in the dog. Vet Radiol Ultrasound 44:214–220.

Risselada M, Kramer M, de Rooster H, Taeymans O, et al. (2005) Ultrasonographic and radiographic assessment of uncomplicated secondary fracture healing of long bones in dogs and cats. Vet Surg 34:99–107.

Risselada M, Kramer M, van Bree H, Taeymans O, et al. (2006) Power Doppler assessment of the neovascularization during uncomplicated fracture healing of long bones in dogs and cats. Vet Radiol Ultrasound 47:301–306.

Rivers B, Wallace L, Johnston GR (1992) Biceps tenosynovitis in the dog: Radiographic and sonographic findings. Vet Comp Orthop Traumatol 5:51–57.

Rivers BJ, Walter PA, Kramek B, Wallace L (1997) Sonographic findings in canine common calcaneal tendon injury. Vet Comp Orthop Traumatol 10:45–53.

Ródenas S, Summers BA, Saveraid T, Denning A, et al. (2013) Chronic hypertrophic ganglioneuritis mimicking spinal nerve neoplasia: clinical, imaging, pathologic findings, and outcome after surgical treatment. Vet Surg 42(7):91–98.

Rose, S., Long, C., Knipe, M. and Hornof, B., 2005. Ultrasonographic evaluation of brachial plexus tumors in five dogs. *Vet Radiol Ultrasound*, *46*(6), pp. 514–517.

Samii VF, Nyland TG, Werner LL, Baker TW (1999) Ultrasound-guided fine-needle aspiration biopsy of bone lesions: a preliminary report. Vet Radiol Ultrasound 40:82–86.

Segalen M, Durieux F (2010) Superficial foreign body ultrasonography: diagnosis and mini-Invasive treatment [Échographie des corps étrangers superficiels: diagnostic et traitement mini-invasif] Pratique médicale et chirurgicale de l'animal de compagnie 45:127–134.

Seyrek-Intas D, Michele U, Tacke S, Kramer M, et al. (2009) Accuracy of ultrasonography in detecting fragmentation of the medial coronoid process in dogs. J Am Vet Med Assoc 234:480–485.

Shah ZR, Crass JR, Dubravka CO, Bellon EM (1992) Ultrasonographic detection of foreign bodies in soft tissues using turkey muscle as a model. Vet Radiol Ultrasound 33:94–100.

Siems JJ, Breur GJ, Blevins WE, Cornell KK (1998) Use of two-dimensional real-time ultrasonography for diagnosing contracture and strain of the infraspinatus muscle in a dog. J Am Vet Med Assoc 212:77–80.

Staudte KL, Hopper BJ, Gibson NR, Read RA (2004) Use of ultrasonography to facilitate surgical removal of non enteric foreign bodies in 17 dogs. J Small Anim Pract 45:395–400.

Swiderski J, Fitch RB, Staatz A, Lowery J (2005) Sonographic assisted diagnosis and treatment of bilateral gastrocnemius tendon rupture in a Labrador retriever repaired with fascia lata and polypropylene mesh. Vet Comp Orthop Traumatol 18:258–263.

Toijala TM, Canapp D, Canapp S (2021) Ultrasonography findings in the proximal sciatic nerve and deep gluteal muscles in 29 dogs with suspected sciatic neuritis. Front Vet Sci 8:704904.

Van Ryssen B, de Bakker E, Beaumlin Y, Samoy YCA, et al. (2012) Primary flexor enthesopathy of the canine elbow: imaging and arthroscopic findings in eight dogs with discrete radiographic changes. Vet Comp Orthop Traumatol 25:239–245.

Vandevelde B, Saunders JH, Kramer M, Van Ryssen B, et al. (2006) Comparison of the ultrasonographic appearance of osteochondrosis lesions in the canine shoulder with radiography, arthrography and arthroscopy. Vet Radiol Ultrasound 47:174–184.

Villamonte-Chevalier A, Soler M, Sarria R, Agut A, et al. (2015) Ultrasonographic and anatomic study of the canine elbow joint. Vet Surg 44(4):485–493.

Volta A, Bonazzi M, Gnudi G, Gazzola M, et al. (2006) Ultrasonographic features of canine lipomas. Vet Radiol Ultrasound 47:589–591.

Index

Note: Page numbers followed by 'f' indicate figures; and those followed by 't' indicate tables

A
Abdominal cavity and lymph nodes
  abdominal lymph nodes, 548f, 549t, 551t
  abdominal wall abnormalities, 570, 573
  abscesses formation, 557
  fat, 547
  foreign bodies, 557
  infectious or noninfectious sclerosing encapsulating peritonitis, 557
  interventional procedures, 573, 579
  nodular fat necrosis, 560
  normal lymph nodes, 550f
  omental and mesenteric sterile steatitis, 557
  peritoneal adhesions, 557
  peritoneal and retroperitoneal granulomas or pyogranulomas, 557
  peritoneal cavity, 547
  peritoneal fluid, 551, 552
  peritoneal hematomas, 556f
  peritoneum, 547
  peritonitis, 555
  pneumoperitoneum, 556–7
  preparation and scanning procedure, 547
  retroperitoneal effusion, 553, 555f
Abdominal cryptorchidism, 528f
Abdominal curtain sign (ACS), 31, 32f
Abdominal venous collateral circulation, 603–8
Abdominal vessels
  abdominal aorta, caudal vena cava, and tributaries, 586
  aorta ratios, 584
  arterioportal communications, 594–5
  blood flow velocities in, 586
  congenital portosystemic shunts, 587–8, 590–2
  portal flow mean velocity, 585
  portal vein aplasia, 592
  portal vein, tributaries, and branches, 583–5, 584f
  pre-and postsurgical assessment of shunts, 592
  preparation and scanning technique, 583
  PV size, 588
Abdominal wall abnormalities, 570, 577f
Abdominal wall neoplasia, 578f
Abductor pollicis longus (APL), 628, 630f
Abnormal pancreatic duct, 383–4
Abnormal postpartum uterus, 497–8
Abscess, 648
  cervical, 125–6f
  hepatic, 262, 264f
  pancreatic, 375, 381f, 382f
  peritoneal, 561f, 562f
  prostatic, 516, 521f, 544
  pulmonary, 162, 163f
  renal, 416, 420f
  retrobulbar, 101
  retroperitoneal, 434f
  subcutaneous, 648, 649–50f
  sublumbar, 563f
  thoracic wall, 142
Acoustic impedance, 1, 2t
Acoustic shadowing, 11, 12f, 648–9
Acquired heart disease
  acquired valvular heart disease
    degenerative valve disease, 218–20, 222–3f, 223t
    infective endocarditis, 220, 223, 224f
  cardiac neoplasia
    heart base tumors, 233, 235f
    hemangiosarcoma, 232–3, 234f
    mesothelioma, 233
    thyroid carcinoma, 233
  heartworm disease, 231f, 232
  myocardial disease
    ARVC, 223, 226f
    DCM, 223, 225f
    HCM, 226, 227f, 228, 228f
    RCM and nonspecific phenotype, 228, 229f
  pericardial effusion and cardiac tamponade, 232, 233f, 234f
  PHT, 229, 230f, 231f, 232
Acromegaly, 475, 478f
Acute and chronic infections, 514
Acute leptospirosis, 415f
Acute pancreatitis, 373, 375f, 376f
Acute prostatitis, 520f
Acute pyelonephritis, 428f
Acute retrobulbar cellulitis, 101, 102f, 103f
Addison's disease, 468, 471, 471f
Adenocarcinoma. *See also* Carcinoma; Tumor(s)
  adrenal, 471
  gastric, 347, 350f
  intestinal, 350, 351f, 352, 352f
  nasal, 101f
  pancreatic, 384, 389f, 390f
  renal, 418, 420f
  uterine, 503
Adenoma
  adrenal, 471, 473f
  lacrymal gland, 103f
  pancreatic, 390f
Adenomatous polyps, 356, 358f
Adipose infiltration, 567

Atlas of Small Animal Ultrasonography, Third Edition. Edited by Dominique Penninck and Marc-André d'Anjou.

© 2025 John Wiley & Sons, Inc. Published 2025 by John Wiley & Sons, Inc.

Companion website: www.SmallAnimalUltrasonography.com

Adrenal glands
adrenal nodules and masses, 471, 472f
appearance of the normal, 463–7, 464–8f, 467t
in cats, 467–8, 467f
Cushing's syndrome, 468
disorders of the, 468–79, 467–79f
in dogs, 463, 464f, 465–7
examination of the, 463–7, 464–8f, 467t
interventional procedures, 479
left adrenal (LA) gland, 465, 465f
preparation and scanning technique, 463
right adrenal (RA), 466, 466f
rounded poles of, 470f
tumor(s) of, 468–74, 472–8f
Adrenal parenchyma necrosis, 477
Adrenal pheochromocytomas, 473f
Adrenal tumor hyperadrenocorticism (ATH), 468
Agenesis
gallbladder, 268, 272f
renal, 405
Air bronchograms, 160
Aliasing, color Doppler, 18, 19f
Amyloidosis
hepatic, 247t, 251–3
renal, 413f, 415
Anisotropy, 16, 17f. *See also* Artifact
Anterior chamber, 72, 73f
Anovulatory cycle, 483f
Aorta
abdominal, 548, 548f
caudal trifurcation of the, 586, 548f
Aortic aneurysm, 604f
Aortic stenosis (AS), 204–6, 208f, 209f
Appendicular sarcomas, 654f
Arrhythmogenic right ventricular cardiomyopathy (ARVC), 223, 226f
Arterial thrombosis, 596, 600f
Arterioportal communications (APC), 594–5, 598f, 599f
Arterioportal fistula, 594
Arterioportal malformations, 594
Arteriovenous fistulas, 661, 661f
Artery(ies)
arcuate, 399f, 400
brachiocephalic, 141f, 209
celiac, 464f, 465, 465f, 586, 486f
common, carotid, 110f, 111f, 114
cranial mesenteric, 464f, 465, 465f, 548, 549f
external and internal maxillary, 116, 117f
external carotid, 110f, 111, 111f
hepatic, 486, 548f, 583, 593f
hyaloid, 72, 73f
internal carotid, 109, 110f, 116, 117f
main pulmonary, 175t, 181f
renal, 465
Arthritis, septic, 653, 657f
Artifact, 11–19
acoustic shadowing, 11, 12f
aliasing, color Doppler, 18, 19f
anisotropy, 16, 17f
comet tail, 12, 14f
electronic interference, 18, 18f
enhancement, 11, 13f
flash, Doppler, 18, 19f
mirror image, 14, 15f
partial volume averaging, 14, 16f
range ambiguity, 16
reverberation, 12, 14f
shadowing, clean, edge or dirty, 11, 12f
side-lobe and grating lobe, 16, 17f
speed error, 16, 17f
twinkling, 18, 18f
volume averaging, 14, 16, 16f
Ascites, portal hypertension and, 603
Aspiration. *See* Fine-needle aspiration
Asteroid hyalosis, 89, 90f
Atelectasis or lung collapse, 158, 159f
Atherosclerosis, 602–3
Atrial septal defect (ASD), 213, 218f, 219f
Avulsion fracture, 637–8, 637f

B

Bates body, 560
Benign and malignant soft-tissue tumors, 652
Benign prostatic hyperplasia (BPH), 514, 518–20f
Bicipital calcifying myopathy, 646f
Bicipital groove, 611
Bicipital tenosynovitis, 618f
Bilateral renal dysplasia, 406f
Bile duct obstruction, 377
Biliary ducts, dilatation of, 266–8
Biliary ectasia, 268–70, 270f
Biliary obstruction, 268–70, 270–5f
Biliary sludge, 242f, 244
Biliary system
disorders of the, 266–81
examination of the normal, 242–4, 243–6f
Biopsy, 169, 170f, 281, 308, 659, 665
bladder and urethral, suction, 456f
gastrointestinal tract, 363, 367, 367f
kidney, 432, 452f
liver, 282, 283f
neck lesion, 133, 135
pancreas, 385–8
prostate, 541, 544
spleen, 305, 307
thorax, 168, 169, 170f
thyroid, 122, 133
Bladder
blood clot in the, 332f, 447
disorders of the, 436–49
examination of the normal, 401–3
neoplasia of the, 440–3, 441f, 442f, 443f
rupture of the, 411f, 447
Bladder hemangiosarcoma, 443f
Bladder mast cell tumor, 443f
Bladder rupture, 449f
Bladder smooth muscle tumors, 442f
Bladder wall inversion, 436, 440f
Bones
avulsion fracture, 648
bone infection, 655
scanning technique and sonographic anatomy, 655
tumors, 658–9
Bowel. *See* Intestine
Bowel corrugation, 333, 337f
Brachial plexus, 662, 667f
Bronchiectasis, 166f
Bronchogram
air, 160
fluid, 160, 161f
Buphthalmos, 95, 96–7f
Bursa, calcaneal, 639, 641f

C

Calcaneal tendon, 639, 642
Calcification. *See* Mineralization
Calcified bodies, 619, 621f, 624
Calcifying supraspinatus tendinopathy, 616f
Calculus, or Calculi, 443, 445, 446f, 447
cystic, 445f
renal, 415
ureteral, 424, 431–2f, 452f
urethral, 440, 447f
Canine ocular gliovascular syndrome (COGS), 90, 93f
Carcinoma. *See also* Adenocarcinoma
adrenal, 471, 472–3f
biliary, 258f, 263f, 275f, 554f
hepatocellular, 255f, 256
laryngeal, 131
pancreatic, 384, 389f
pulmonary, 163f
renal, 418
thyroid, 118, 119f, 120f

transitional cell, 440, 441f
Carcinomatosis, 561, 566f, 567f
peritoneal, 561, 567f
pleural, 143
Cardiac linear dimensions, 193, 195t
Cardiac ratio indices, normal, 195, 202t
Cardiac point-of-care ultrasound (CPOCUS), 25, 27f
CPR, 59, 60f
echocardiography, 33, 35f
features, 33, 36t
left-atrial-aortic ratio, 54, 57f, 58f
left ventricular lumen size and function, 56, 58, 58f
pericardial effusion, 53, 55f, 56f
pericardial tamponade, 53, 57f
right sided heart changes, 58–9, 59f
Cardiac septation, 213, 218–21f
Cardiac tamponade, 232, 233f
Cardiac volume and mass estimation, 195
Cardiomyopathy
dilated, 223, 225f
hypertrophic, 226, 227f
restrictive, 228, 229f
Cardiopulmonary resuscitation (CPR), 59, 60f
Carotid-body tumors, 132, 132f
Cartilage, articular
abnormal, 622f, 636f, 638, 638f
normal, 616, 640f, 633, 633f, 635f, 631f
Cataracts, 82–3, 85f, 86f
Caudal lung regions, 25, 27f
Caudal vena cava (CVC), 9f, 25, 27f, 40, 605, 609f
caudal lung pathology, 40, 42f
gallbladder wall edema, 41, 42f
invasion of, 473
pericardial effusion, 40, 41f
pleural effusion, 40, 42f
segmental aplasia of, 595–6, 600f
size and index, 40, 41f
thrombosis, 597
urinary bladder volume estimation, 41, 43, 43f
Caval syndrome, 232
Cavitary lymph nodes, 574f
Cecal hemangiosarcoma, 353, 358f
Cellulitis, 648
Cervix, uterine, 482f, 489
Chemodectomas, 132, 132f
cardiac, 232
cervical, 132, 132f
Cholangitis/cholangiohepatitis, 248, 249, 250–3f
Cholecystitis, 273, 275–7f, 277
Choledochal cysts (CCs), 268, 269f
Cholelithiasis, 279–80, 281f
Cholecystocentesis, ultrasound-guided, 282, 283f
Cholelithiasis, 279–80, 281f
Chondrosarcoma, 143
Choroiditis, 45f, 93, 94f, 95f
Chronic bicipital tenosynovitis, 619f
Chronic hypertrophic pyloric stenosis, 356, 358f
Chronic interstitial nephritis, 413f
Chronic noninfectious lymphoplasmacytic prostatitis, 516
Chronic pancreatitis, 379, 383f, 384f
Chronic pyelonephritis, 428f
Chronic renal disease, 413f
Chronic rupture, 643
Chronic supraspinatus tendinopathy, 617f
Chylothorax, 147f, 151f
Circumcaval ureters, 409
Cirrhosis, 248, 249, 250–3f
Cirrhosis, hepatic, 248–51, 253f
Clean shadowing, 11, 12f
Clustered nerve components, 662
Collateral ligament rupture, 638
Colon. *See* Gastrointestinal
Colonic intussusception, 320, 323f
Colonic thickening, 323f, 335
Colonic wall, 312f, 313, 313t, 315f, 316f
Color Doppler imaging (CDI), 174, 176t, 652
Color flow Doppler, 662
Comet tail, 12, 14f
Common bile duct (CBD), 377, 382f
biliary sludge, 244, 245f
bilobed appearance, 242, 243f
dilation of the, 268, 269–71f
duodenum, 244, 246f
examination of the normal, 242, 246f
mucocele, 275–7, 278–80f
mural edema, 273–4, 277f
neoplasia, 274
volume, 244, 244f
wall polyps, 277, 281f
wall thickening, 273, 276f
Common calcaneal (CC) tendon, 639
Common carotid artery, 116, 117f
Complete rupture, 617, 639
Congenital heart disease
congenital shunts
cardiac septation, 213, 218–21f
PDA, 214f, 215–17f
congenital valvular diseases
aortic stenosis, 204–6, 208f, 209f
pulmonic stenosis, 206–7, 209, 210f, 211f
tricuspid valve dysplasia, 209, 212, 212f
cor triatriatum, 218, 222f
mitral valve dysplasia, 212–13, 214f
peritoneal-pericardial diaphragmatic hernia, 218
TOF, 216, 218, 221f
Congenital renal fusion, 405f
Congenital renal malformations, 399f, 405
Congestion, hepatic venous, 605
Congestive heart failure, 54
Consolidation, lung, 157, 159f, 160, 162f
Contrast media and software, 481–3, 493
Contrast ultrasonography, pancreas, 373
Contusion, lung, 160, 162f
Cortical infarction, 426f
Cor triatriatum, 218, 222f
Cranial cruciate ligament rupture (CCLR), 635–6, 636f
Cornea
disorders of the, 74, 75f, 80f
normal appearance of the, 67, 69, 69f, 70f, 71
Corpus cavernosum, 403, 404f, 512f, 538
Corpus spongiosum, 403, 404f, 512f, 538
Crossed fused renal ectopia, 405
Cryptococcosis, 155f, 516
Cryptorchidism, 520
Crystalluria, 445, 445f, 446f. *See also* Hyperadrenocorticism
Cushing's disease, 307, 308f
Cushing's syndrome, 468
Cyst (or) cyst-like lesion, 504, 567
cervical, 132
choledochal, 268, 269f
cranial mediastinal, 150, 150f
hepatic, 262f, 265, 299
laryngeal, 131
pancreatic, 375, 381f
prostatic cyst, 516, 519f, 543f
pulmonary, 162
renal, 13f
thyroid, 118, 118f
Cystadenoma and cystadenocarcinoma
biliary, 262, 263f
renal, 416
Cysterna chyli, 551, 552f
Cystic calculi, 445f
Cystic endometrial hyperplasia, 498

Cystic neoplasia
hepatic or biliary, 263f
renal, 419, 477f
thyroid, 118f
Cystitis, 436, 437f, 440
emphysematous, 436, 438f
polypoid, 438, 439f
Cystocentesis, 455

D
Deep digital flexor (DDF) tendon, 639
Degenerative mitral valve disease (DMVD), 218–20, 222–3f
Degenerative valve disease, 218–20, 222–3f, 223t
Dehiscence, gastrointestinal, 338, 342f, 343f, 555
Delayed bone union, 661
Demyelination, 664–5
Diaphragm
normal, 141, 141f
rupture of the, 163, 167f
Diaphragmatic disorders, 162–3, 167–70f, 168
Diastolic function, 204, 205–7f
Dilated cardiomyopathy (DCM), 223, 225f
Dilated gonadal vein, 604
Dilated pancreatic duct (PD), 387f
Dirofilariasis, 231f, 232
Dirty shadowing, 11, 12f
Discospondylitis, 658f
Disseminated histiocytic sarcoma, 293, 296f, 423f
Diverticulum, vesicourachal, 411f
Doppler aliasing, 18, 19f
Doppler effect, 8, 8f
Doppler flash artifact, 18, 19f
Doppler ultrasound, 8–10f, 19f
color, 8, 9f
power, 8, 9f
pulsed, or spectral, 8, 10f, 11
tissue, 185
Double-chamber right ventricle, 209, 211f
Drainage
pancreatic pseudocyst, 375, 380f
prostatic abscess, 544, 544f
ultrasound-guided, 262f, 451–6, 451f, 452f, 648
Duct(s)
biliary, 242, 244, 258f, 266, 272f, 281
common bile, 244, 246f, 250f, 273–9
cystic, 244, 245f, 250f, 268, 272f, 279
Ductal plate malformation (DPM), 266
Duodenal adenomatous polyps, 359, 360
Duodenal mucosal hyperplasia, 359, 359f, 360f
Duodenitis, 335, 379f
Dysplasia
hepatic, 247t, 590
hip, 632, 632f
microvascular, 247t, 590
mitral valve, 212–13, 214f
renal, 405, 406f
tricuspid, 209, 212f

E
Echocardiography, normal
color flow Doppler, 122
continuous-wave Doppler, 122
measurements and indices in, 124, 127
Echogenicity, 2f, 5f
relative, 3f
Ectasia, 531
Ectopic adrenal tissue, 479
Ectopic splenic tissue, 387
Ectopic ureters, 407, 408f, 409f
Edema, 539
gallbladder wall, 60f, 277f
gastric wall, 374
interfascial, 124
pancreatic, 374, 379f
subcutaneous, 132
tracheal wall, 157, 158f
Edge shadowing, 11, 13f
Effusion or fluid
joint, 622, 624f, 635, 636f, 636, 638, 653
pericardial, 232, 233f
peritoneal, 551–5, 554f, 556t
pleural, 48, 48f
retroperitoneal, 434f, 553, 555f, 556t
trapped or encapsulated, 146
Eisenmenger physiology, 213
Ejection fraction (EF), 204
Elbow dysplasia, 624
Elbow, examination of the, 622–7
Embryonic resorption, 495, 497f
Embryos, 494
Emphysematous cystitis, 436, 438f
Emphysematous hepatitis, 265, 268f
Encrusting cystitis, 436, 438f
Endocardial cushion defect, 213
Endocardiosis, 218
Endocarditis, infective, 220–3, 224f
Endometrial uterine hyperplasia, 501f
Enhanced peritoneal stripe sign (EPSS), 40
Enlarged sternal lymph nodes, 150, 151f
Enteritis. *See* Intestine
Eosinophilic enteritis, 333, 335f
Epididymal cysts, 531
Epididymis, normal, 513f, 519
Epididymitis, 531, 532f, 533f, 535f
Esophagus, 114, 115f, 127, 128f, 129f
examination of the normal, 111f, 114, 115f
inflammation of the, 127, 129f
neoplasia of the, 127
thickening or hypertrophy of the, 129f
Ethanol ablation of thyroid carcinoma, 135
Ethylene glycol toxicity, 410, 411
Exocrine pancreatic insufficiency (EPI), 380, 383, 385f, 386f
Extensive bladder tumors, 443f
Extensive renal neoplasia, 418f
Extensor carpi radialis (ECR) muscle, 628
Extensor carpi ulnaris (ECU) muscle, 629
Extensor digitorum communis, 628
External ear canal, 113f, 114, 116, 133
External jugular vein, 116, 117f
Extrahepatic portocaval shunts, 589f
Extrahepatic portosystemic shunts, 587
Extramedullary hematopoiesis, 293, 294f, 297, 297f
Extrapleural sign, 142, 144f
Extravascular lung water (EVLW), 49
Exudate
peritoneal, 420f, 421f, 551, 553, 554, 556
pleural, 146
retroperitoneal, 420f, 432
Eye
anatomy of the, 67–74
examination of the normal, 65–7
fetal, 73f
foreign body in the, 95–9, 98f, 99f, 100f
preparation and scanning technique
horizontal plane, 67, 69f
limbal and perilimbal approach, 65, 67f
probe placement, 65, 66f, 67f
probe position and orientation, 65, 66f
UBM, 67, 68f
ventral rotation, 66
visual axis, 65
zygomatic gland scanning, 67, 69f
trauma of the, 89, 96f
tumor of the, 95f, 100f, 101, 101f, 103f
ultrasonographic anatomy
anterior chamber, 71

ciliary body, 71
corneoscleral junction, 69
fetal eye, 72, 73f
globe wall, 67, 70f
iris, 71
lens, 69, 71
normal anterior segment, 67, 70f
perilimbal radial (meridional)/transverse, 71, 72f
posterior chamber, 71
retrobulbar space, 73, 74f
transcorneal axial plane, 71, 73f
vitreous body, 72

F

Fat
falciform, 240f, 242, 242f
mediastinal, 141, 148
necrosis, nodular, 560, 565f
retroperitoneal, 420f, 431, 434f, 478f, 541
Feline cecum, 318
Feline hepatic lipidosis, 248, 248f
Feline infectious peritonitis (FIP), 265, 265f, 292f, 360, 411, 415, 418, 557, 558f, 563f, 576f
Fetal abnormalities, 497, 498f
Female reproductive tract
abnormal postpartum uterus, 497–8
examination technique, 481
foreign bodies, 503
interventional procedures, 507
mammary glands, 503–7
sonography of abnormal mammary glands, 504–5
sonography of normal mammary glands, 503–4
normal postpartum uterus, 495
normal pregnancy, 490, 494–5
ovaries
normal sonographic anatomy, 481, 483f, 484–5
ovarian changes, 485–7
ovariohysterectomy sites
normal sonographic anatomy, 490
sonography of abnormal pregnancy, 495–7
uterine diseases, 498, 501, 503
uterus
neoplasms, 503
normal sonographic anatomy, 487, 488–90f, 489
Femoral osteosarcoma, 659f
Fetal abnormalities, 498f
Fetal death, 496
Fetus, 494
Fibroadenomatous hyperplasia, 504, 507f
Fibroepithelial polyp, 433f
Fibrosing and calcifying myopathies and tendinopathies, 645
Fibrosis
hepatic, 247t, 248, 248f
myocardial, 226, 228
Fibrous histiocytic nodule, 293, 294f
Fibrous strands, 556t
Fine-needle aspiration (FNA), 388, 573, 579, 659
adrenal, 475
gastrointestinal tract, 363, 637
kidney, 433, 451, 452f
liver, 282, 282f
musculoskeletal, 611, 648, 659
neck lesion, 123, 133
pancreas, 388, 391
peritoneal, 579
Fistular tract, 649, 652f
Flexor carpi radialis muscle, 629
Flexor digitorum superficialis (FDS) muscle, 629
Flow convergence zone, 209, 214f
Flow turbulence
cardiac, 215f
caudal vena cava, 588f, 589f, 604
Fluid bronchograms, 160
Fluid-filled lesions, 388
Focal parenchymal renal disorders, 415–20
Focal zone, 6, 14
Follicular cystitis, 436, 439f
Foreign bodies (FBs), 648
cervical, 123
gastrointestinal, 321–3
grass awn, 503, 668f
linear foreign body(ies), 322f, 323, 323f, 327f
musculoskeletal, 648–52, 649f, 650f, 651f, 652f, 668f
needle, 170f
ocular, 95–9
peritoneal, 561f
porcupine quill, 648, 649, 651f, 668f
surgical sponge, retained, 557, 560, 564f
teriyaki stick, 323
thoracic wall, 142f
wooden-stick, 558f, 557
Fractional area change (FAC), 204
Fractional shortening (FS), 202
Fractures, 660, 661f
assessment of long bone, 660, 661f
ligament or tendon avulsion, 645f
patellar, 637, 637f
supraglenoid tubercle avulsion, 619–20
Fragmented Medial Coronoid Process (FMCP), 624
Fungal disease
hepatic, 265
prostatic, 516
renal, 418
testicular, 532f
Fungal prostatitis, 516, 522f

G

Gain setting, 5, 6f
Gallbladder (GB)
biliary sludge, 244, 245f
bilobed appearance, 242, 243f
dilation of the, 269
duodenum, 244, 246f
examination of the normal, 240f, 273–8
herniation of the, 168f
mucoceles, 275–7, 278–80f
mural edema, 273–4, 277f
neoplasia, 274
rupture of the, 276, 280f
sludge, 242f
volume, 244, 244f
wall edema, 41, 42f
wall polyps, 277, 281f
wall thickening, 273, 276f
Gallstones. *See* Cholelithiasis
Gas
colonic *see* Pneumatosis
gastric *see* Pneumatosis
hepatic, 265, 265f
Gastric. *See* Stomach
Gastric distention, 313
Gastric foreign body, 156f, 274f, 324f
Gastric hyperplastic polyp, 361, 364–5f
Gastric polyp, 356, 359f
Gastric tumor(s), 344–56
Gastric ulcer, 326–30, 558f
Gastric wall
edema of the, 374
layering of, 344
normal appearance of, 312f, 318
thickness of, 313t
Gastritis, 326, 329f, 330f, 331f, 340f
Gastrointestinal stromal tumors (GISTs), 352, 353, 355f
Gastrointestinal (GI) tract
adhesions, 343, 345f
anatomy
artifacts, 311, 312f
colon, 318, 318f
dorsal recumbency, 311, 312f
duodenum, 314

Gastrointestinal (GI) tract (*continued*)
esophagus and gastroesophageal junction, 311, 315f
feline cecum, 318
ileum, 318
jejunum, 314
MDP, 314, 316f, 317f
stomach, 313–14, 315f
wall layering, 318–19
wall thickness, 311, 313t
carcinoma, 347, 350–2f
congenital/hereditary disorders, 360–1, 363f, 364f
dehiscence, 338, 342f, 343f
foreign bodies
balls, 321, 324f
linear, 323, 327f
parasites, 323, 328f
trichobezoars, 323, 325f, 326f
gastropexy, 337, 342f
hernia and volvulus, 323, 325–6, 328f, 329f
inflammatory diseases
bowel corrugation, 333, 337f
colonic wall thickening, 335, 339f
edema, 330, 331f
eosinophilic enteritis, 333, 335f
gastritis, 326, 329f
hemorrhagic enterocolitis, 333, 336f
IBDs, 332–3
parasitic infestations, 335, 337, 341f
pneumatosis, 335, 340f
typhlitis, 335, 338f
ulcers, 326, 330, 330f
uremic gastropathy, 330, 331f
viral enteritis, 333, 336f
intussusception, 320–1, 320–3f
lymphoma, 344, 346–9f, 347
nontumoral nodule/mass
adenomatous polyps, 356, 358f
chronic hypertrophicpyloric stenosis, 356, 358f
duodenal adenomatous hyperplasia, 359, 360f
feline eosinophilic sclerosing dysplasia, 360, 361f
granulomatous enteritis, 360, 362f
lipogranulomatous lymphadenitis, 360, 362f
mucosal hyperplasia, 359, 359f, 360f
perforation, 338, 343f
postoperative enterotomy, 337, 341f
smooth muscle tumors, 352–3, 353–6f, 356
stricture, 338, 343, 344f
surgical biopsy, 343, 345f
ultrasound-guided biopsy and fine-needle aspiration, 366–7
vascular disorders, 361, 363, 365f, 366f
Gestational age estimation, 494
Gestational chambers, 490
Gestational length, 495
Gestational timing, 490
Gliding sign, lung, 148
Glomerulonephritis, 416f
Gluteal calcifying myopathy, 647f
Gracilis and semitendinosus myopathy, 645
Gracilis fibrosing myopathy, 647f
Granuloma or pyogranuloma
hepatic, 265, 265f
peritoneal, 557
pulmonary, 162, 166f
renal, 410, 415, 418, 419f
Granulomatous diseases, 567
Granulomatous enteritis, 360, 362f
Granulomatous fungal cystitis, 436
Granulomatous lymphadenopathy, 576f
Granulomatous (or) pyogranulomatous process, 77f, 99f, 124f, 125f, 129f, 150, 155f, 162, 166f, 252f, 254f, 265, 265f, 275f, 292f, 295f, 332, 333, 360, 362f, 376f, 411, 415f, 425f, 436, 557, 558f, 567, 576, 630f
Grass awn migration, 563f, 649, 652f
Greater tubercle, 611

H
Halo sign, 41, 42f
Harmonic mode, 6, 7f
Healing process, 643
Heart, 25, 27f. *See also* Cardiac
acquired heart disease (*see* Acquired heart disease)
base tumor, 156f, 233
congenital heart disease (*see* Congenital heart disease)
conventional two-dimensional, M-mode and Doppler echocardiography
blood flow, 200–2
cardiac size, 195–200
diastolic function, 204, 205–7f
echocardiographic variation, 194, 195t
feline left cranial left auricular appendage view, 193, 195f
left-parasternal views, 185, 187–94
orientation and anatomy, 177f, 175t
right-parasternal views, 178–86
subxiphoid LVOT, 192–3, 195f
systolic function, 202–4
echocardiographic technique
instrumentation, 173
patient preparation and positioning, 173–4, 174f, 175–6t
examination of the, 173–204
neoplastic disorders of the, 232–5
Heart base tumors (HBT), 233, 235f
Heartworm disease (dirofilariasis), 229–32, 231f
Hemangiosarcoma (HSA), 232–3, 234f
bladder, 436
cardiac, 234f
hepatic, 259f
metastatic, 259f
renal, 423f
retroperitoneal, 561–4, 569f
splenic, 290t, 302f
Hematocele, 535
Hematomas, 535, 539
bladder, 448f
cervical, 123
hepatic, 265, 267f
ligament tear and, 636–7
muscular, 643, 656f
peritoneal, 283f, 553
pulmonary, 162, 167f
rib, 142
tendon tear and, 617, 618f, 639
Hemoabdomen
amyloidosis and, 253
hemangiosarcoma and, 255f
Hemometra, 501
Hemorrhage
bladder wall, 447, 448f
pleural, 143
postbiopsy, 281, 283f
pulmonary, 160
retroperitoneal, 418, 423f
Hemorrhagic adrenocortical carcinoma, 475f
Hemorrhagic enterocolitis, 333, 336f
Hemorrhagic hygroma, 627f
Hepatic granulomas, 265, 265f
Hepatic hemorrhage, 265, 266f

Hepatic mineralization, 265, 266f
Hepatic vasculature, 584f, 585f
Hepatitis, 248–50
  chronic active, 252f
  emphysematous, 268f
Hepatobiliary system
  cholelithiasis, 279–80, 281f
  congenital anomalies, 266, 268, 269–71f
  diffuse hepatic parenchymal disorders
    amyloidosis, 251
    diagnostic differentials, 247, 247t
    hepatitis, cholangitis/cholangiohepatitis, and cirrhosis, 248, 249, 250–3f
    hepatocutaneous syndrome, 253, 256f
    neoplasia, 251, 254f, 255f
    nodular hyperplasia, 247–8, 248f, 249f
    peritoneal effusion, 247
    vacuolar hepatopathies, 247–8, 248f, 249f
  focal hepatic parenchymal disorders
    benign hyperplasia and neoplasia, 256, 257f
    cavitary lesions, 262–4f, 265
    diagnostic differentials, 256, 256t
    granulomas, hematomas, and mineralization, 265, 265f, 266f
    lobe torsion, infarction, and gas, 265, 267f, 268f
    malignant neoplasia, 256, 258–61f
  hepatic and extrahepatic vasculature, 245
  obstruction and ectasia, 268–70, 272–5f, 273
  parenchyma and size, 239–40, 241–3f, 242
  preparation and scanning technique, 239, 240f
  ultrasound-guided fine-needle aspiration and biopsy, 281–3
Hepatocellular carcinomas, 256
Hepatocutaneous syndrome, 253, 256f
Hepatofugal flow, 587, 589f, 591f, 594, 594f, 599f, 602f, 604, 605, 606f, 607f
Hepatoma, 253, 256
Hepatomegaly, 242, 242f, 247, 247t, 248, 251, 254f, 265, 478f, 605
Hepatopathy
  steroid, 247t, 249f
  vacuolar, 247, 247t, 249f, 255f, 282
Hepatopetal flow, 584, 605
Hernia, 162–3, 167–70f, 168, 323, 325–6, 328f, 329f
  abdominal wall, 570–3, 577f
  diaphragmatic, 30t, 162, 163, 168f, 169f, 218
  peritoneo-pericardial, 169f, 218
High-grade soft-tissue sarcoma, 655f
Hip dysplasia, 632, 632f
Hip joint
  dysplasia of the, 632
  examination of the, 629, 632f
  luxation of the, 648
Histiocytic sarcomas, 251, 254f, 353, 357f
  disseminated, 151f, 163f, 261f, 296f, 357f, 423f, 570
  hepatic, 254
  renal, 418, 423f
Horner's syndrome, 132
Hyaloid artery, 72, 88
Hyaloid canal. *See* Hyaloid artery
Hydrocele, 537
Hydrometra, 501
Hydronephrosis, 407, 429t
Hydroureter, 407f, 424
Hygroma, 627
Hyoid apparatus, 114, 652
Hyperadrenocorticism
  adrenal changes with, 468–79
  liver changes with, 247–8, 249f
Hyperaldosteronism, 475, 476f
Hypercalcemiam, parathyroid glands and, 121–2
Hyperechoic liver, 248, 248f
Hyperechoic lymph nodes, 577f
Hyperparathyroidism, 121–2, 135
Hyperplasia, hepatic benign nodular, 256, 256t, 257f
Hyperplastic lymphadenopathy, 572f
Hyperplastic thyroid glands, 118, 118f
Hyperprogesteronism, 475
Hypertension
  portal, 273, 363, 366f, 374, 590, 593f, 594, 596f, 601f, 603–5, 606f, 607f
  pulmonary, 59f, 209, 213, 229–32
  systemic, 93, 228, 586, 603
Hyperthyroidism, 228, 475
Hypertrophic cardiomyopathy (HCM), 226, 227f, 228, 228f
Hypertrophy, concentric cardiac, 204, 207, 208f, 210f, 211f, 221f
Hypoadrenocorticism, 471f, 471
Hypothyroidism, 121, 121f, 135f, 223, 275, 602
Hypovolemia, 36t, 40, 54, 59
Hypoplasia, 498

I

Idiopathic esophageal hypertrophy, 127, 129f
Ileum, 318, *see also* Intestine
Iliopsoas myopathies, 629
Inactive mammary tissue, 506f
Incidentalomas, 474
Infarct (or) infarction
  hepatic, 267f
  intestinal, 555
  portal thrombosis and, 603
  renal cortical, 419, 596
Infectious lymphadenitis, 575f
Infective endocarditis, 220, 223, 224f
Infiltrative ureteral lymphoma, 433f
Inflammatory and metastatic lymph nodes, 567
Inflammatory cast or fistular tract, 649
Inflammatory diseases
  bowel corrugation, 333, 337f
  colonic wall thickening, 335, 339f
  edema, 330, 331f
  eosinophilic enteritis, 333, 335f
  gastritis, 326, 329f
  hemorrhagic enterocolitis, 333, 336f
  IBDs, 332–3
  parasitic infestations, 335, 337, 341f
  pneumatosis, 335, 340f
  typhlitis, 335, 338f
  ulcers, 326, 330, 330f
  uremic gastropathy, 330, 331f
  viral enteritis, 333, 336f
Inflammatory neuropathies, 665
Inflammatory processes, 573
Infraspinatus muscles, 611, 613
Inguinal or scrotal hernia, 537, 578f
Instability, joint, 638, 642, 648
Insufficiency
  aortic valve, 204
  pulmonary, 207
Insulinoma, 392f. *See also* Pancreatic tumor
Interactions between ultrasound waves and tissues, 2, 3f
Intestinal biopsy, 344, 345f
Intestinal carcinomas, 350, 351f, 352f
Intestinal dehiscence, 342f, 343f, 555, 557
Intestinal inflammatory diseases (IBDs), 332–3
Intestinal foreign body, 325f, 344f, 561f
Intestinal perforation, 555, 559f
Intestinal stricture, 344f
Intestinal tumor(s), 344–56
Intestinal wall, 335f
Intestine
  anatomy of the, 311–19, 312f

Intestine (*continued*)
biopsy of the, 366–7, 367f
contents, in the, 318, 319f
examination of the, 317f
Intussusception
appearance of, 320–1
colonic, 323f
duodenogastric, 321f
jejunal, 322f, 324f
Intra-abdominal testicular tumors, 544
Intrahepatic PSSs, 588
Intrahepatic shunts, 591f, 593f
Intraoperative identification of FBs, 665
Intrascrotal testicles, 544
Invagination. *See* Intussusception
Iridociliary cysts, 81, 83f
Iridocorneal angle (ICA), 76, 77f
Iris, normal appearance of the, 67f, 68f
Ischemia
bowel, 333, 334f
myocardial, 226
Isovolumic relaxation time (IVRT), 204

J
Jejunum, 314, *See also* Intestines
Joint effusion, 653
Joint luxation, 648
Joint mice, 621
Joint neoplasia, 535, 537f
Joint soft-tissue tumors, 653
Juvenile nephropathy, 405

K
Kidneys
congenital malformations, 405f
diffuse parenchymal disorders of the, 410–15
disorders of the collecting system of the, 420–31, 427–31f
examination of the normal, 399–401, 399–401f
focal disorders of the, 415–19, 419–26f
neoplasia of the, 415, 417–18f, 420–1f

L
Large soft-tissue sarcoma, 655f
Laryngeal cysts, 131
Laryngeal neoplasia, 127, 130f
Laryngeal paralysis, 131
Larynx, 114, 115f, 116, 127, 130f, 131–2, 131f
disorders of the, 127–32, 130f, 131f
examination of the normal, 109, 114–16, 115f
Laser ablation monitoring, 456–7
Lateral collateral ligaments, 639
Leakage or rupture of the gastrointestinal (GI) tract, 555
Left atrium, dilation of the, 228
Left pancreatic lobe, 371, 372
Left-parasternal views
apical views
four-chamber, 185, 187, 188f, 190f
LVOT, 187, 189f
scanning technique, 185, 187f
two-chamber/three-chamber, 187, 190f
cranial views
aortic valve, 187, 191f
pulmonic valve, 187, 192, 193f, 194f
RVOT, 192, 194f
scanning technique, 187, 191f
tricuspid valve, 187, 192f
Left ventricle
dilatation of the, 144
hypertrophy of the, 134, 144
Left ventricular outflow tract (LVOT), 178, 180f, 187, 189f
Leiomyoma, 352, 353f, 355f. *See also* Smooth muscle tumor(s)
gastric, 355f
intestinal, 352f
uterine, 504f, 505f
vaginal, 505f
Leiomyosarcoma. *See also* Smooth muscle tumor(s)
bladder, 440, 442f
intestinal, 353, 354
Lens
cataracts, 82–3, 85f, 86f
congenital anomalies, 81–2, 82f
displacement, 85–6, 87f
luxation of the, 86, 87f
normal appearance of the, 70f, 71
posterior lenticonus, 87–8, 88f
posterior rupture of the, 86f
vitreal herniation, 86, 87f
Leptospirosis, 414f
hepatic, 248, 251f
renal, 410, 413–15f
Leukemia, 247t
Leydig cell tumors, 529f
Ligament(s)
collateral, 634, 638
cranial cruciate, 635–6, 636f
disorders of, 645–8, 648f
examination of, 645
falciform, 240f, 242
patellar, 633f, 634, 636f, 637–8
Linear foreign body(ies), 323, 623f
Lipidosis, hepatic, 247–8, 248f
Lipogranulomatous lymphadenitis, 360, 362f
Lipomas, 561, 652, 657f
appendicular, 654
infiltrative, 143f
mesenteric, or abdominal, 564, 566f
Litter size, 494
Liver
diffuse parenchymal disorders of the, 245–7, 247t
examination of the normal, 239–45, 240–5f
focal parenchymal disorders of the, 253–6
neoplastic disorders of the, 251, 255–62, 255f, 259f, 261f
Local anesthesia, 666
Loculated fluid, 553f
Long digital extensor tendon, 639
Lung. *See also* Pulmonary
disorders of the, 157
examination of the, 140f
Lung point, 43
Lung pulse, 30
Lung sliding, 29, 30t
Lymphadenopathy, 564, 567, 569
abdominal, 564–70, 566–9f
cervical, 124, 124f
cranial mediastinal, 150, 150f
granulomatous or pyogranulomatous, 564, 576f
inflammatory, 567
necrotic, 574f
neoplastic or metastatic, 564, 574f
reactive, 567
sublumbar, 534f, 549, 573f
Lymph nodes (LN)
abscessed, 574f
anatomy, 112, 113f, 114, 115f
aortic, 548f, 549t
cavitary, or cystic, 574f
colic, 548f, 549t, 551t
cranial mediastinal, 141
examination of the normal, 547–51, 548f, 550f, 551t
gastric, 548f, 549t, 551t
hepatic, 548f, 549t, 551t
inguinal, 549
jejunal (or) mesenteric, 548f, 549t, 551t
mandibular, 111f, 113f, 653f
medial iliac, 520f, 522f, 528, 549, 550f, 570f, 573f, 575f, 549t, 551t
medial retropharyngeal, 110t, 112, 113f, 114, 120f, 121, 123, 123f, 125f
mineralization, 567

pancreaticoduodenal, 548f, 549t, 551t
sacral, 458f
and soft tissues, 123–4, 123–6f, 127
splenic, 458f
sternal, 141, 150, 151f
sublumbar, 534f, 573
Lymphofollicular laryngitis, 127, 131f
Lymphoma, 123, 131, 444f, 653f
bladder, 575f
cervical, 123, 132
cranial mediastinal mass, 150, 152f
gastrointestinal tract, 344, 346–9f, 347
hepatic neoplasia, 251, 254f
intestinal, 168, 344, 348f, 349f
laryngeal, 130f
malignant neoplasia, 258, 261f
mesenteric, 567
pancreatic, 391f
peritoneal, 564
renal, 417f, 421f
spleen, 293, 296f
ureteral, 433f
Lymphomatosis, 564
Lymphomatous infiltration, 293, 297f

M

Macronodular hyperplasia, 468
Major duodenal papilla (MDP), 314, 316f, 317f
Malakoplakia, 440, 440f
Male pseudohermaphrodites, 539
Male reproductive tract
penile urethra, 513
penis, 512, 538–9
preparation and scanning procedure, 511–13
prepuce, 538–9
prostate, 511, 513–18, 514f, 515f
testicles, 511, 513f, 518
Malignant thrombosis, 603f
Mammary glands
appearance of normal, 503–4, 506f
tumor of, 504–5, 508f
Mandible, 492f
Mandibular lymph nodes, 114
Mandibular salivary gland, 112
Massively infiltrated lymph nodes, 567
Mast cell tumors, 353, 354f, 356f
bladder, 436, 437f
cranial mediastinal, 141f
hepatic, 254f
Medial carpal collateral ligament, 628
Medial collateral ligament, 639
Medial coronoid process
fragmentation of the, 624, 625f
normal, 623–4, 623f
Medial humeral epicondyle, avulsion (or) fragmentation, 624, 625f
Mediastinum
abnormalities of the, 148–9
cranial mediastinal mass
cyst, 150, 150f
differential diagnoses, 149–50
domestic long-haired cat, 150, 155f
enlarged sternal lymph nodes, 150, 151f
gastric foreign body, 150, 156f
granulomatous, 150, 155f
lymphomas, 150, 152f
thymomas, 150, 153f
unusual, 150, 155f
vascular invasion, 150, 154f
mass in the, 149–54
mediastinal lesions
esophageal mass, 154, 157f, 158f
heart base tumors, 154, 156f
tracheal wall, 157, 158f
testis, 519
Medullary rim sign, 411
Medulloepitheliomas, 93
Megaesophagus, 127, 148
Melanoma, laryngeal, 130
Meniscal tears and degeneration, 636–7, 637f
Meniscus (or) menisci, femorotibial, 634–5, 635f, 637f
Mesenteric infiltration, 568f
Mesenteric lipoma, 566f
Mesentery
inflammatory processes of the, 555–7, 558–60f
neoplastic invasion of the, 561–4, 563f
normal, 547
Mesothelial remnant, 169f
Mesothelioma, 233, 561
Metallic clip, 256t, 265
Metal objects, 649
Metastases, 652
Metastasis (or) metastatic disease
bone, 518
cranial mediastinal, 151f
lymph node, 305
peritoneal, 561, 568f
pleural, 148
pulmonary, 162, 165f
renal, 256, 422f
Metastatic carcinoma, 660f
Microhepatica, 583, 591, 595
Microphthalmos, 95, 96f, 97f
Microvascular dysplasia, hepatic, 247t, 590
Mineralization, 474, 476f
adrenal, 468
hepatic, 265, 266f
neoplastic, 653
renal, 414f, 420, 427f
tendon or muscle, 611, 613, 617–19f, 624, 639, 641f
vascular wall, 602–3, 605f
Mirror image, 14, 15f. *See also* Artifact
Mitral valve dysplasia (MD), 212–13, 214f
Mosaic pattern, turbulent flow, 208f
Mucometra, 501
Mucocele, gallbladder, 275–7, 278–80f
Mucosal hyperplasia, 359
Muscle
biceps, 613–15, 613–14f
brachialis, 624
contracture, infraspinatus, 616, 617f
cricopharyngeal, 129f
deltoid, 613, 614f
digastricus, 112
examination technique of the, 643–55, 643f
extensor carpi radialis, 628, 628f
gastrocnemius, 634, 639, 654f
gluteal, 665
gracilis, 639, 647
iliopsoas, 629, 631f, 643, 644
infraspinatus, 611, 612f, 613, 614f, 617f, 660f
quadriceps femoris, 633
sternohyoid, 109, 116
sternothyroid, 109, 116
supraspinatus, 114, 613, 613f
thickness, 643
trauma, 643
triceps, 623f, 624, 644f
Musculature, examination of the, 643, 656f
Muscular hemorrhage, 656f
Musculoskeletal system
carpus
scanning technique, 627, 628f
stenosing tenosynovitis, 629
elbow
biceps brachii tendon, 624
flexor tendons, 623
medial collateral ligament, 623
medial coronoid process, 624, 625f
medial epicondyle, 623
osteoarthritis, 624, 624f
scanning technique, 622, 623f, 624
triceps brachii muscle, 623
hips and iliopsoas muscles, 629, 632
muscle and tendon trauma, 643
musculature, 643

Musculoskeletal system (*continued*)
preparation and scanning procedure, 611, 612f
shoulder, 611, 612f, 613
biceps brachii muscle, 613, 615
bicipital tenosynovitis and tendon rupture, 616–17
infraspinatus contracture, 616
instability, 620–1
joint space medial glenohumeral ligament, 615–16
supraspinatus and infraspinatus muscles, 613
supraspinatus tendinopathy, 616
tendon luxation, 620
stifle, 632, 632f
infrapatellar region, 634
lateral and medial aspects, 634–5
suprapatellar region, 633–4
tarsus, 639, 641–2
Myelolipoma
hepatic, 256t
splenic, 298f
Myocardial disease
ARVC, 223, 226f
DCM, 223, 225f
HCM, 226, 227f, 228, 228f
RCM and nonspecific phenotype, 228, 229f
Myopathy, or tendinopathy
fibrosing and calcifying, 645, 646–7f
iliopsoas, 629, 631f
Myositis, septic, 651f
Myxosarcoma, 260f

N
Neck
external ear canal and tympanic bullae, 116, 133, 134–5f
larynx and trachea, 114, 115f, 116, 127, 130f, 131–2, 131f
lymph nodes
anatomy, 112, 113f, 114, 115f
and soft tissues, 123–4, 123–6f, 127
nerves, 116, 117f
parathyroid glands
anatomy, 109, 111–12
nodules, 122, 122f
primary hyperparathyroidism, 121–2
secondary hyperparathyroidism, 122
procedures, 133, 135–6, 135f, 136f
salivary glands
anatomy, 112, 113f, 114, 115f
sialadenopathy, 127, 127f
sialocele, 127, 128f
scanning technique, 109, 110–11f
thyroid glands
anatomy, 109, 111–12
carcinoma, 118, 119–21f, 119f
cystadenocarcinoma, 118, 119f
cysts, 118
hyperplastic thyroid glands, 118, 118f
hypothyroidism, 121, 121f
tongue and esophagus, 114, 115f, 127, 128f, 129f
vessels
anatomy, 116, 117f
carotid-body tumors, 132, 132f
Necrosis
acute tubular, 410–12
hepatic, 247t, 251, 256t, 265
Necrotizing fasciitis, 648
Neoplasia, 440, 443, 665. *See also* Mass, Nodule, Tumor
appendicular, 654f
bladder, 440–3, 441f, 442f, 443f
bone, 655
cardiac, 232–3, 234f, 235f
carotid-body, 121, 132
gastrointestinal, 344–56
hepatobiliary, 251, 256–62, 259f
joint, 535, 537f
laryngeal, 127, 130f
mammary glands, 504, 508f
muscle, 653
nerve, 665
ocular, 77
pancreatic, 259f, 305, 384
parathyroid, 118
penis, 539, 541f
peritoneal, 561
prostatic, 440, 457, 514, 516, 517, 541
pulmonary, 160, 162
retroperitoneal, 561
renal, 418, 468, 479
retroperitoneal space, 431–6
splenic, 293–9
testicular, 523
thyroid, 119
urethral, 440–3
Neoplastic lymph node, 570f, 571f
Neoplastic processes, 573
Neoplastic thrombosis, 597–8
Nephritis, interstitial, 412, 413f, 416, 431, 435f
Nephroblastoma, 414, 418
Nephrocalcinosis, 417f
Nephrosis, acute tubular, 410
Nerve(s)
brachial plexus, 662, 663f
disorders of the, 665, 665f
examination of normal spinal and peripheral, 662–4, 662–4f
Nerve block (local anesthesia), 666
Neuroendocrine tumor, 132, 154f, 156f, 353
Neuroma, 664
Neuticles, 541, 543f
Nidus, 594
Nodal abscesses, 567
Nodular hyperplasia, 247–8, 248f, 249f, 256, 257f, 388f
adrenal, 472f
hepatic, 245–7, 247t
pancreatic, 383–4, 383f, 385
splenic, 290t, 293, 297, 299f, 300f
Non-neoplastic thrombosis, 596
Nonobstructive uroliths, 432f
Normal female reproductive tract, 483f
Normal fetal circulation, 493f
Normal lung surface, 32–3, 33f
Normal postpartum uterus, 495

O
Obstruction, ureteral, 409, 424, 425, 427, 427f, 429t, 429f, 431, 452f, 453, 454, 518
Obstructive hydronephrosis, 429f
Obstructive ureterolith, 431f
Omental or mesenteric steatitis, 560f
Omentum
inflammatory processes of the, 556, 561f
neoplastic invasion of the, 561, 563f, 564
normal, 547
Optic nerve
inflammation of the, 103
normal appearance of the, 73
Optic nerve sheath diameter (ONSD), 74
Orchitis, 520, 531–2, 532f, 533f, 535f, 537
Orbit. *See also* Eye
acute retrobulbar cellulitis, 101, 102f, 103f
cornea and anterior segment
anterior chamber abnormalities, 77, 80f
anterior uveal masses, 77, 79f
bullous keratopathy and corneal sequestra, 74, 75f
ciliary body adenoma, 77, 79–81f
diffuse corneal edema and buphthalmos, 76, 78f
ICA, 76, 77f
intumescent cataract, 77, 78f
iridociliary cysts, 81, 83f

limbal neoplasia, 76, 76f, 77f
Peters' anomaly, 74, 75f
technical artifacts, 77, 80–1f
tumors, 78
uveal melanocytic neoplasia, 77, 81f
uveitis, 81, 82f
interventional procedures, 105, 105f, 106f
intraocular and retrobulbar foreign bodies
computed tomography, 99, 100–1f
pellet gun, 95, 98f
plants parts, 96, 99f
porcupine quills, 96, 98f
lens
cataracts, 82–3, 85f, 86f
congenital anomalies, 81–2, 82f
displacement, 85–6, 87f
posterior lenticonus, 87–8, 88f
vitreal herniation, 86, 87f
optic nerve meningioma, 101, 104f
optic neuritis, 101, 103f
periocular tumors and secondary displacement, 99, 100f
polymyositis, 102, 104f
tumors, 101
vitreous and retina
acquired vitreal opacities, 89
asteroid hyalosis, 89, 90f
buphthalmos, 95, 96–7f
choroiditis, 93, 94f, 95f
detached vitreous, 89, 90f
hemorrhage, 89–90, 91f
microphthalmos, 95, 96f, 97f
persistent and hyperplastic primary vitreous, 88–9, 88f, 89f
primary tumors, 93
retinal detachment, 90, 91, 92–3f, 93, 94f
synchysis scintillans, 89
Orchitis, 531
Os penis, 539, 540f
Osseous metaplasia, deep digital flexor muscle, 624
Osteoarthritis (or) degenerative joint disease, 624, 624f, 632, 632f, 636f, 653
Osteochondral (OCD) fragments, 619, 621f
Osteochondritis dissecans, 621–2, 638, 638f
femoral condyle, 634–5, 635f
humeral condyle, 623–5f, 624, 655f
humeral head, 621–2f, 621
Osteochondroma (or) osteochondromatosis, 619
Osteochondrosis, 624
Osteomyelitis, 655, 658f
Osteophytes, 617
Osteosarcoma, 659f
appendicular, 659f
rib, 146f
splenic, 307
Otitis media, 133, 134f
Ovarian cysts, 485, 485f
Ovarian remnant syndrome, 485–6
Ovarian tumors, 485
Ovary
examination of, 481
normal appearance of, 481–7
Overcirculation, pulmonary, 213, 219f
Overload
pressure, 204, 207, 209, 213, 223, 228
volume, 41, 56, 58f, 209, 213, 215f, 219f, 223
Ovulation cycle, 483f

P

Pampiniform plexus, 519
Pancreas
approach to normal canine, 372f
approach to normal feline, 374f
drainage of cavitary lesion, 393f
ectopic intrapancreatic splenic tissue, 393f
ectopic splenic tissue, 387
examination of the, 374
measurements of normal canine, 373, 373t
nodules and masses, 384–8
normal appearance of the, 372–3
in old dog, 372f
preparation and scanning procedure, 371
ultrasonography of normal, 372–3
Pancreatic abscesses, 375, 381f, 382f
Pancreatic adenoma, 390f
Pancreatic body, 371
Pancreatic carcinomas, 389f, 390f
Pancreatic cyst, 381f
Pancreatic disorders, 373–80
Pancreatic duct, 372–3, 372f
Pancreatic edema, 374, 379f, 606f
Pancreatic endocrine tumors, 385
Pancreatic exocrine tumors, 384
Pancreatic insulinoma, 392f
Pancreatic lymphoma, 391f
Pancreatic nodular hyperplasia, 384
Pancreatic pseudocyst, 375, 380f
Pancreatic tumor(s), 387
Pancreatitis, 373–80
acute, 373, 375f
chronic, 379, 383f, 384f
duodenal and gastric changes, 377f
necrotizing hemorrhagic, 378f
subacute to chronic active, 379
Pancreatolithiasis, 383–4
Panoramic mode, 7, 8f
Papilla, duodenal major, 246f, 270, 314, 316f
Papillary endometrial hyperplasia, 53
Paraesophageal abscess, 127, 129f
Paraganglioma, 475f
Paramuscular abscess, 650f
Paraprostatic cysts, 516, 522f, 523f, 544
Parathyroid glands
abnormalities of the, 121–2, 122f
adenoma and carcinoma of the, 122f
anatomy, 109, 111–12
examination of the, 109–12, 110t, 111–12f
nodules, 122, 122f
primary hyperparathyroidism, 121–2
secondary hyperparathyroidism, 122
Partial ruptures, 617, 640f
Patellar fractures and desmopathies, 637
Patent ductus arteriosus (PDA), 214f, 215–17f
reversed, 603
Patent ductus venosus, 587, 588, 591f
Pelvic bladder, 412f
Penile tumors, 539
Penis
appearance of normal, 404, 511, 539f
examination of, 511
fracture of, 540f
Penrose drain, 136f
Percutaneous procedures. *See* Biopsy, Fine-needle aspiration
Perforation, gastrointestinal, 337f, 338, 340f
Pericardial effusion, 232, 233f
Pericardiocentesis, 22t
Perineal hernias, 541
Perinephric pseudocysts, 432–3, 435f
Periovarian cysts, 498
Peripheral nerve(s). *See* Nerve(s)
Peripheral nerve sheath tumors (PNSTs), 665, 666f
Peritoneal abscesses, 561f, 562f
Peritoneal cestodiasis, 335, 341f
Peritoneal lymphomatosis, 564
Peritoneocentesis, ultrasound-guided, 577
Peritoneo-pericardial diaphragmatic hernias (PPDHs), 162, 168, 218
Peritonitis
bile, 280f, 555–6
septic, 555–7, 556f, 556t

Pheochromocytoma, 474f
Phlegmon, 648
Piezoelectric crystals, 1–3
Pituitary-dependent hyperadrenocorticism (PDH), 468
Placenta, 495, 495f
Pleura
  abnormalities of the, 143, 146–8
  thickened, 147, 149f
Pleural neoplasia, 148, 148f, 149f
Pleural space, 25, 27f
Pleural space and lung ultrasound (PLUS)
  air/fluid bronchograms, 52, 54f, 55f
  A-lines, 31
  BAT sign, 29, 30f
  B-lines, 31, 49, 50f
  consolidation, 49, 50–2f, 51, 53t
  effusion, 48, 48f, 49f
  E-lines, 33
  lung pulse, 30
  lung sliding, 29, 30t
  pneumothorax, 43, 44–7f, 45, 48
  protocols, 28, 28f, 29f
Pleuritis, 147f, 148
Pneumatosis, 335, 340f
Pneumonia
  abscessing, 162
  aspiration, 160f
  pyogranulomatous, 166f
Pneumoperitoneum, 556f, 556–7
Pneumothorax, 148, 340f
Point of care ultrasound (POCUS)
  abdominal window, 25, 26f, 26t
    examination, 38, 39f, 39t
    peritoneal effusion, 38
    pneumoperitoneum, 38, 40, 40f
  ACS, 31, 32f
  caudal lung regions, 25, 27f
  clinical applications, 21, 22t
  CPOCUS, 25, 27f
    CPR, 59, 60f
    echocardiography, 33, 35f
    features, 33, 36t
    left-atrial-aortic ratio, 54, 57f, 58f
    left ventricular lumen size and function, 56, 58, 58f
    pericardial effusion, 53, 55f, 56f
    pericardial tamponade, 53, 57f
    right sided heart changes, 58–9, 59f
  CVC, 25, 27f
    caudal lung pathology, 40, 42f
    gallbladder wall edema, 41, 42f
    pericardial effusion, 40, 41f
    pleural effusion, 40, 42f
    size and index, 40, 41f
  urinary bladder volume estimation, 41, 43, 43f
  machine and probe selection, 23, 24f, 25f
  monitoring fluid therapy, 59, 60f
  normal lung surface, 32–3, 33f
  patient preparation, 21–3, 23f
  PLUS
    air/fluid bronchograms, 52, 54f, 55f
    A-lines, 31
    BAT sign, 29, 30f
    B-lines, 31, 49, 50f
    consolidation, 49, 50–2f, 51, 53t
    effusion, 48, 48f, 49f
    E-lines, 33
    lung pulse, 30
    lung sliding, 29, 30t
    pneumothorax, 43, 44–7f, 45, 48
    protocols, 28, 28f, 29f
  right parasternal long-axis views, 37–8, 38t
  right parasternal short-axis views, 33, 35f, 36t
  serial evaluations, 23, 25
  ventral pleural border, 33, 34f
  Z-lines and vertical line artifacts, 33, 34–5f
Polycystic kidney disease (PKD), 419f
Polyp
  bladder, 436
  gallbladder wall, 281f
  gastric wall, 359f
Polypoid cystitis, 436, 439f
Porcupine quills, 96, 98f, 649, 651f
Portal hypertension, 593f, 596f, 603–5, 606–7f
Portal system
  Doppler assessment of the, 586f, 589–91f
  normal, 583–4
  primary hypoplasia of the, 603
  thrombosis of the, 601f, 603
Portal vasculitis, 604f
Portal vein obstruction and hypertension, 603–5
Portoazygos shunts, 589f, 590f
Portosystemic shunt(s) or shunting
  acquired, 595–6f, 603–5, 606–7f
  congenital, 587–92, 591f
  extraheptic, 591f
  general ultrasound approach to, 596f
  intrahepatic, 591–2f
Postpartum metritis, 497
Postpartum uterus, 495
Postsurgical osteomyelitis, 657f
Power Doppler Imaging (PDI), 8, 9f
Pregnancy
  abnormal, 495–7
  gestational age in, 494t
  normal progression of, 490, 494–5, 492–3f
Prepuberal animals, 483f
Pressure gradient
  aortic stenosis and, 204–6
  atrial septal defect and, 219f
  mitral dysplasia and, 212–13
  patent ductus arteriosus and, 213
  pulmonic stenosis and, 219
  tricuspid dysplasia and, 209, 212
  ventricular septal defect and, 213, 218f
Primary duct ectasia, 504
Primary flexor enthesopathy, 624, 626f
Probe (or) transducer, 2–5, 5f
Prostate, 511, 512f
  appearance of the normal, 512f, 514f
  biopsy, 517
  examination of, 513
  measurement of, 515, 526
Prostatic abscesses, 516
Prostatic adenocarcinoma, 524f
Prostatic atrophy, 518
Prostatic calculi, 518
Prostatic cyst, 516, 520f
Prostatic hemangiosarcoma, 525f
Prostatic hyperplasia, 514
Prostatic neoplasia, 517, 541
Prostatic remodeling, 517f
Prostatic tumor, 518, 524f, 525f
Prostatic urethra, 513
Prostatitis, 520f
Pseudocyst, perinephric, 375
Pseudomembranous cystitis, 436, 437f
Pseudo-placentation endometrial hyperplasia, 501
Pseudosludge. *See* Artifact
Pulmonary disorders *See also* Lung
  atelectasis, 158–9
  consolidation, 159–61, 160–2f
  cysts, acute hematomas, pneumatoceles, abscesses, 162, 167f
  metastases, 162, 165–6f
  neoplasms and granulomas, 162, 163–5f
  ultrasonographic features, 157, 159f
Pulmonary hypertension (PHT), 229, 230f, 231f, 232
Pulmonic stenosis (PS), 206–7, 209, 210f, 211f
Purulent lymphadenitis, 567
Pupil, normal appearance of the, 68
Pyelectasia, renal, 420, 429t

Pyelocentensis, 452f, 451
Pyelography, 452f, 451
Pyelonephritis, 423
Pyloroduodenal junction (PDJ), 313, 314
Pyogranulomas, 562f *See also* Granuloma
Pyogranulomatous splenitis, 293, 295f
Pyogranulomatous vasculitis, 415f
Pyometra, 501
Pyonephrosis, 424, 431f
Pythiosis, 360, 576f
Pyuria, 446f

R
Ratio(s)
  kidney-aorta, 399, 399f
  portal vein-aorta, 584, 585f, 593f, 596f
Refraction artifact, 449f
Relative echogenicity, 3f
Renal. *See* Kidneys
Renal abscesses, 420f
Renal agenesis, 405
Renal-aortic ratio, 465
Renal calculus(i), 428f, 429t, 430f, 433f
Renal cavitary lesions, 415–16
Renal cyst(s), 415–16, 419f
Renal degeneration, 416f
Renal diseases
  chronic, 413f
  diffuse parenchymal, 410–14
  focal, 415–19, 419–22f
  polycystic, 416, 419f
Renal disorders, 415–20
Renal dysplasia, 405, 406f
Renal granuloma or pyogranuloma, 411, 415, 418, 425
Renal hemangiosarcoma, 423f, 430f
Renal infarcts, 419
Renal lymphoma, 417f
Renal maldevelopment, 405
Renal metastase, 422f
Renal mineralization, 426f
Renal nodules, 422f
Renal pelvis
  disorders of the, 420–1, 421f, 427f, 428f, 430f, 431f
  examination of the normal, 401
  measurement, 427f
Renal tumor(s) or neoplasia, 414, 418–19, 418f
Reproductive tract female. *See also* Ovary, Uterus, Pregnancy
  appearance of normal, 482f, 483f
  examination of, 481–5
Reproductive tract male. *See also* Prostate, Testis
  appearance of normal, 512f, 513f
  examination of, 511–13
Resolution
  contrast, 4–5, 5f
  spatial (axial, lateral, or elevational), 4, 4f, 5f
  temporal, 8
Restrictive cardiomyopathy (RCM), 228, 229f
Retinal detachment, 78, 81, 84f, 90f
Retained placenta, 498
Retention cysts, 375
Retinal detachment, 90, 91, 92–3f, 93, 94f
Retrobulbar space
  biopsy of the, 104f, 105, 105f
  mass of, 99, 105f
  normal appearance of, 73, 74f
Retroperitoneal effusion, 434f, 553
Retroperitoneal hemangiosarcoma, 569f
Retroperitoneal paragangliomas, 479
Reverberation, 12, 14f. *See also* Artifact
Rhabdomyosarcoma
  bladder, botryoid, 440
  diaphragmatic, 169f
Rib(s)
  aggressive lesion of the, 146f
  fractures, 142, 144f
  mass of the, 164f
  sarcoma, of, 170f
Rib osteosarcoma, 143, 146f
Right atrium, dilatation of the, 209, 219f
Right pancreatic lobe, 371, 372
Right-parasternal (RPS) views
  long-axis views
    four-chamber, 178, 179f
    LVOT, 178, 180f
    scanning technique, 178, 178f
  short-axis views
    aortic valve level, 183, 185f
    apex level, 178, 181f
    chordal level, 183, 183f
    mitral valve level, 183, 184f
    papillary muscle level, 181, 182f
    pulmonic valve level, 183, 186f
    scanning technique, 178, 181f
Right ventricle
  dilation of the, 209
  hypertrophy of the, 207
Roundworms, 323, 327f
Rupture, 664–5

S
Salivary duct cyst, 127, 128f
Salivary glands
  anatomy, 112–14, 113f, 127
  disorders of the, 112–14, 113f
  examination of the, 112–14, 113f
  sialadenopathy, 127, 127f
  sialocele, 127, 128f
Sarcoma
  disseminated histiocytic, 423f
  histiocytic (*see* Disseminated histiocytic sarcoma)
  soft-tissue, 145f, 303f, 564
  splenic, 303f
  undifferentiated, 424f
Sarcomatosis, 564, 567f
Sciatic nerve, 663
Sciatic neuritis, 665
Sclerosing encapsulating peritonitis, 560f
Scrotal hematomas, 534
Scrotal trauma, 534
Scrotum, 404f, 520
Secondary fracture healing, 660
Segmental aplasia, 498
Seminomas, 530f
Septal defect
  atrial, 213, 218f, 219f
  ventricular, 178, 213–16, 218f, 220f
Septic arthritis, 657f
Septic prostatitis, 522f
Seroma
  postoperative, 578f
  subserosal, 345f
Sertoli cell tumors, 530f
Severe hydronephrosis, 430f
Sexual development, 539–41
Shadowing, 11, 12f. *See also* Artifact
Shoulder
  disorders of the, 613–22f, 616–22
  examination of the normal, 613–22, 613–15f
Sialadenitis, 127, 127f
Sialadenopathy, 127, 127f
Sialocele, 127, 128f
Side-lobe and grating lobe, 16, 17f. *See also* Artifact
Sinus of Valsalva, 178, 224f
Smoke sign, left atrial, 36t
Smooth muscle tumors, 352–3, 353–6f, 356
Soft-tissue sarcomas, 564
Solitary cysts, 416
Sonography of abnormal pregnancy, 495–7
Spatial compound imaging, 6, 7f
Spectral Doppler imaging (CDI), 8, 10f, 11, 174, 176t
Spermatic cord, 519
Spleen
  anatomy, 287–90
  appearance of the normal, 288f, 289f

Spleen (*continued*)
Cushing's disease, 307, 308f
diagnostic differentials, 290, 290t
examination of the, 287
extramedullary hematopoiesis of, 290t, 291, 293, 294f, 297f, 299f
extraskeletal osteosarcoma, 305, 307f
fine-needle aspiration, 307–8
focal and multifocal abnormalities
benign splenic masses, 297, 298–9f
disseminated histiocytic sarcoma, 293, 296f
extramedullary hematopoiesis, 293, 294f, 297, 297f
fibrous histiocytic nodule, 293, 294f
hemangiosarcoma, 297, 301f, 302f
hematophagocytic histiocytic sarcoma, 299, 303f
histiocytic sarcoma, 297, 302f
infarction and abscessation, 297, 300f
lymphoma, 293, 296f
lymphomatous infiltration, 293, 297f
myelolipomas, 297, 298f
nodular hyperplasia, chronic hematoma, and hemorrhage, 297, 299f, 300f
plasma cell tumor, 297, 302f
pyogranulomatous splenitis, 293, 295f
round-cell neoplasia, 297, 303f
soft tissue sarcoma, 297, 303f
splenic mass, 297, 301f
trauma, 293, 294–5f
gas inclusions, 305, 307
hematoma of the, 290t, 295f, 300f
histoplasmosis of the, 290t
infarction of the, 292f, 300f, 301f, 304f, 306f
lymphoma, 305, 307f
myelolipoma of the, 290t, 298f
parenchyma, 291–3
preparation and scanning technique, 287, 288f
splenomegaly, echogenicity, 290–1, 291f, 292f
splenunculi, 304–5, 306f
thrombus of the, 295f, 304f, 306f
torsion of the, 290t, 291, 293f, 304, 306f, 307
tumor(s), of the, 301
vascular disorders, 299, 301, 304–6f
vessels of the, 290, 301, 304, 305
Splenic trauma, 293, 294–5f
Splenic venous thrombosis, 602f
Splenitis, 290t, 292f, 295f
Splenomegaly, 290–1, 291f, 292f
Splenosystemic shunts, 605
Spontaneous cellulitis, 658f
Squamous cell carcinoma, 131
Steatitis
abdominal, 557, 558f, 561f
neck, 124f
Stenosis
aortic or subaortic, 178, 204–6, 209f
mitral, 213
pulmonic, 201f, 206–9, 210f, 211f, 219f
tricuspid, 212
Steroid hepatopathy, 248, 249f
Stifle
disorders of the, 632–3f, 635–8, 635–8f
examination of the, 632–5, 632–3f
Stomach, 313–14, 315f. *See also* Gastric
contents of the, 319f
examination of the, 311, 312f, 313t, 315f
normal appearance of the, 312f, 313, 313t, 315f
Strain injuries, 629, 643
Stricture, intestinal, 323, 343f, 344f
Stroke length, 213, 228
Stump granuloma, 503, 503f
Subacute to chronic active pancreatitis, 379
Subcapsular septic empyema, 421f
Subcutaneous ureteral bypass (SUB), 453–4, 453f
Sublumbar lymphadenopathy, 573f
Superficial digital flexor (SDF) tendons, 639
Suppurative pseudoplacentation, 501f
Supraglenoid tubercle, 611, 619–20
Supraspinatus muscles, 611, 613
Surgical localization or removal, 652
Sustentaculum tali, 639
Synchysis scintillans, 89
Synovial cell sarcoma, 656f
Synovial osteochondromatosis, 619
Systemic hypertension (SHT), 228
Systolic anterior motion, 178, 227f
Systolic function, 202–4

T

Talocrural medial collateral ligament rupture, 648f
Target lesion(s)
hepatic, 253, 256, 256t
splenic, 39t, 298f, 299
Tarsal joint instability, 642
Tarsus, examination of the, 639, 642
Telangiectasia, renal, 407f
Tendon avulsion, 638, 638f
Tendon luxation, 620
biceps, 622f
superficial digital flexor, 642
Tendon, normal
biceps brachii, 623f, 624
calcaneal (Achilles), 639, 640–1f
gastrocnemius, 639, 640–1f
infraspinatus and supraspinatus, 613, 613–14f
long digital extensor, 634, 635f, 638, 639
superficial digital flexor, 639, 640–2f, 642
Tendon, rupture
bicipital, 616, 620f, 621
calcaneal (Achilles), 640f, 641f
infraspinatus, 611, 613, 614f
supraspinatus, 611, 613, 616f
Teriyaki stick, 323
Testicles, 511, 513f
Testicular contusions, 535
Testicular cysts, 531
Testicular microlithiasis, 534
Testis
appearance of, 513f
atrophy of, 531
examination of, 513, 513f
measurement of, 526t
torsion of, 531
tumor(s) of, 523
Tetralogy of Fallot (TOF), 216, 218, 221f
Thoracic wall. *See also* Lung, Thorax
abscessation, 142, 142f
benign/malignant neoplastic processes, 143, 145f
biopsy or fine-needle aspiration, 169
bony masses, 143, 146f
extrapleural sign, 142, 144f
foreign bodies, 142, 143f
rib fractures, 142, 144f
wall abscess, 143f
wall mass, 142
Thoracocentesis, ultrasound-guided, 148, 164f
Thorax
diaphragmatic disorders, 162–3, 167–70f, 168
inlet approach, 141
intercostal approach, 140–1, 140f, 141f
mediastinum (*see* Mediastinum)
pleural effusion, 143, 146, 147f
pleural lesions, 148, 148f, 149f
pneumothorax, 148
preparation and scanning technique, 139–40, 140f

pulmonary disorders
atelectasis, 158–9
consolidation, 159–61, 160–2f
cysts, acute hematomas, pneumatoceles, abscesses, 162, 167f
metastases, 162, 165–6f
neoplasms and granulomas, 162, 163–5f
ultrasonographic features, 157, 159f
thoracic wall
abscessation, 142, 142f
benign/malignant neoplastic processes, 143, 145f
bony masses, 143, 146f
extrapleural sign, 142, 144f
foreign bodies, 142, 143f
rib fractures, 142, 144f
transhepatic approach, 141, 141f
ultrasound, 168, 170f, 171
Thromboembolism
aortic (or) iliac, 22t, 39t
pulmonary, 52f, 53t, 59, 59f, 231f
Thrombosis, 132, 133f
Thrombus or thrombosis
aortic, 220
caudal vena cava, 477
formation, 473
left atrial, 220
malignant, 474, 603f
portal venous, 596, 601f
Thymoma, 144f, 150, 153f
Thymus, normal, 141
Thyroid carcinoma, 233
Thyroid glands
abnormalities of the, 118, 119f
adenoma of the, 118
anatomy, 109, 111–12
carcinoma and adenocarcinoma of the, 118, 119–21f, 119f
cystadenocarcinoma, 118, 119f
cysts, 118
examination of the, 109–12, 111f
hyperplastic thyroid glands, 118, 118f
hypothyroidism, 121, 121f
Tibialis cranialis tendon, 639
Time-gain compensation, 5, 6f
Tissue Doppler imaging (TDI), 185, 204
Tissue echogenicity, 1
Tongue, examination of the, 114, 115f, 127, 128f, 129f
Torsion
liver lobe, 265, 305
lung lobe, 161f
Toxicity
ethylene glycol, 410, 412f
grapes, 410
lily, 410
Trachea
abnormalities of the, 127, 130f, 131–2, 131f
examination of the, 114, 115f, 116
Tracheal collapse, 131–2
Transitional cell carcinoma (TCC), 440, 441f, 524f, 525f
Transudate, pleural, peritoneal or retroperitoneal, 431–2, 552f
Traumatic avulsion of tendons, 643
Traumatic cystocentesis, 449f
Trichobezoar, 323, 325f
Tricuspid valve dysplasia, 209, 212, 212f
Tricuspid valve regurgitation
endocardiosis and, 218
pulmonic stenosis and, 201f, 206–7, 210f, 211f
Trilostane therapy, 477
Trilostane toxicity, 478f
Tumor(s). *See* Neoplasia
Tumors of the epididymis, 528
Tunica albuginea, 518
Twinkling artifact, 18, 18f, 446f
Tympanic bullae (middle ear)
disorders of the, 133, 134–5f
examination of the, 116
Typhlitis, 335, 338f

U

Ulceration
duodenal, 326, 343f
gastric, 326, 330f
and tumor, 355f, 357f
Ultrabiomicroscopy (UBM), 67, 68f
Ultrasound-guided aspiration-drainage, 452f
Ultrasound-guided bladder biopsy, 455–6
Ultrasound-guided cystocentesis, 455
Ultrasound-guided ethanol sclerotherapy, 452
Ultrasound-guided pyelocentesis and pyelography, 452f
Ultrasound-guided renal biopsy, 451, 451f
Ultrasound probes, 1–5, 4f
Ultrasound transducers, 4f
Umbilicobiliary fistula, 268, 271f
Undifferentiated sarcoma, 424f
Unilateral renal dysgenesis, 405f
Ununited anconeal process (UNAP), 624, 625f
Uremic gastritis, 330, 331f
Ureteral abscess, 431f
Ureteral calculi, 435f
Ureteral distension, 424
Ureteral jet, 432f
Ureteral rupture, 434f
Ureteral stenting, 454–5
Ureteritis, 429f, 429t, 432, 436
Ureterocele, 409, 410f
Ureters
congenital malformations of, 405f
dilatation of the, 400, 410f, 420, 442f
ectopic, 407, 408f, 409f
Urethra
disorders of the, 444f, 447f, 539
examination of the normal, 404f
Urethral calculi, 447f, 539
Urethral distension, 447f
Urethral osteosarcoma, 444f
Urethral stent, 457, 457f
Urethral transitional cell carcinoma, 442f
Urinary tract
bladder and urethra, 455–8
calculi, 443, 445, 447
congenital and inherited urinary malformations
bladder, 409
kidneys, 405, 406f, 407
ureters, 407, 408f, 409
cystitis, 436, 437f, 440
diffuse parenchymal renal diseases, 410–14
disorders of the collecting system, 420, 423–5, 427
focal parenchymal renal disorders, 415–20
focal lesions, 419–20
renal cavitary lesions, 415–16
renal solid nodule or mass lesions, 418–19
intraluminal blood clots and mural hemorrhage, 447
neoplasia, 440, 443
nephro-ureteral procedures/implants, 453–5
normal ultrasonographic anatomy
bladder, 401–3, 402f
kidneys, 399–401, 399f–401f
pelvis and ureters, 401
ureteral jet, 403f
urethra, 403, 404f
preparation and scanning technique
bladder, 397
composite image of, 398f
kidneys, 397
retroperitoneal space, 431–6
trauma and foreign bodies, 447, 449
ultrasound-guided antegrade pyelography, 451–2
ultrasound-guided fine-needle aspiration, 449, 451

Urinary tract (*continued*)
ultrasound-guided fine-needle drainage, 451
ultrasound-guided renal biopsy, 451, 451f
Urinomas, 434f, 436
Uroliths (or) urolithiasis, 425, 429f
bladder, 424, 523f
renal, 428–9f
ureteral, 432–3f
urethral, 523f
Urothelial carcinoma, 440
Uterine diseases, 498, 499f, 500f, 501, 503
Uterine granuloma, 498, 500f
Uterine leiomyoma, 504f
Uterine involution, 495
Uterine stump pyometra, 503, 503f
Uterine torsion, 497
Uterus
cystic endometrial hyperplasia of, 485, 498, 500f, 503f
examination of, 481
fluid filled, 481
masculinus, 541, 542f
normal appearance of, 488–90f
tumors of, 503
Uveitis, 81, 82f

V
Vacuolar hepatopathies, 247–8, 248f, 249f
Vaginal schwannoma, 506f
Vagosympathetic trunk, 110t, 116, 132
Valvular disease, chronic degenerative, 174, 204, 205f
Vascular anomalies, 661
Vascular disorders, 299, 301, 304–6f
gastrointestinal tract, 361, 363, 365f, 366f
Vascular wall
aneurysm and pseudoaneurysm, 598
mineralization, 602–3
phlebitis and arteritis, 598
Vasculitis, pyogranulomatous, 411, 415f, 558
Vas deferens, 519
Vas (ductus) deferens, 513, 531
Vein(s)
agygos, 587, 588–90f, 592, 595, 596
caudal mesenteric, 584, 584f
cranial mesenteric, 584, 584f
deep circumflex, 548, 549t, 586, 587
external and internal maxillary, 117f
external jugular, 109, 111, 116, 117f, 132
gastroepiploic, 584f, 549t, 587, 602, 608
gonadal, left, 604, 605, 607f, 608
hepatic, 3f
iliac, 548f, 605, 608
jejunal, 568f, 584, 584f
left gastric, 584, 584f, 587, 608
linguofacial, 111f, 112, 114, 116
maxillary, 111f, 117f
pancreaticoduodenal, 371, 372, 372f
phrenicoabdominal, 464f, 465, 466, 467f, 471
portal, 3f
renal, 401, 424f, 464f, 465, 465f, 466, 467f, 468f, 472f, 477f, 479f, 586, 604
right gastric, 587
splenic, 3, 288, 289f, 293, 299, 301, 602f, 603, 607f
thyroid, 133f
Vena cava
caudal, 9f, 22t, 25, 27f, 41f, 175t, 586, 589f, 600f, 603f
cranial, 141, 141f
syndrome of the, 231f
Venous obstruction, 608
Venous thrombosis, 473f, 596–7
Ventricular septal defect (VSD), 213, 216, 220f, 221f
Vertebral histiocytic sarcoma, 660f
Vertical raphe, 513
Vesicourachal diverticulum, 409, 411f
Vessels
anatomy, 116, 117f
carotid-body tumors, 132, 132f
Virchow's triad, 596
Vitreal foci, 89
Vitreal retraction, 89
Vitreal body
anatomy of the, 67
degeneration of the. 85
hemorrhage in the, 91f, 96
Vocal folds
abnormal motion of the, 131
examination of the, 109
thickening of the, 131
Volvulus, gastric, 323, 325–6, 328f, 329f

W
Wall layering
bladder, 401, 402f
gastrointestinal tract, 311, 316–17f
Wooden FBs, 649, 650f

X
XX male hermaphrodites, 539
XXY trisomy, 539

Y
Yolk sac membrane, 491–2f

Z
Zygomatic salivary gland
inflammation of the, 111f
normal appearance, 67, 69f

WILEY END USER LICENSE AGREEMENT

Go to www.wiley.com/go/eula to access Wiley's ebook EULA.